Monday
6:30AM - 3:00PM
Long Beach Convention Center, Exhibit Hall B-(Lower Level) EdE

Education Exhibit Poster (EdE)-Adult Brain

EdE-09

6:30AM - 3:00PM

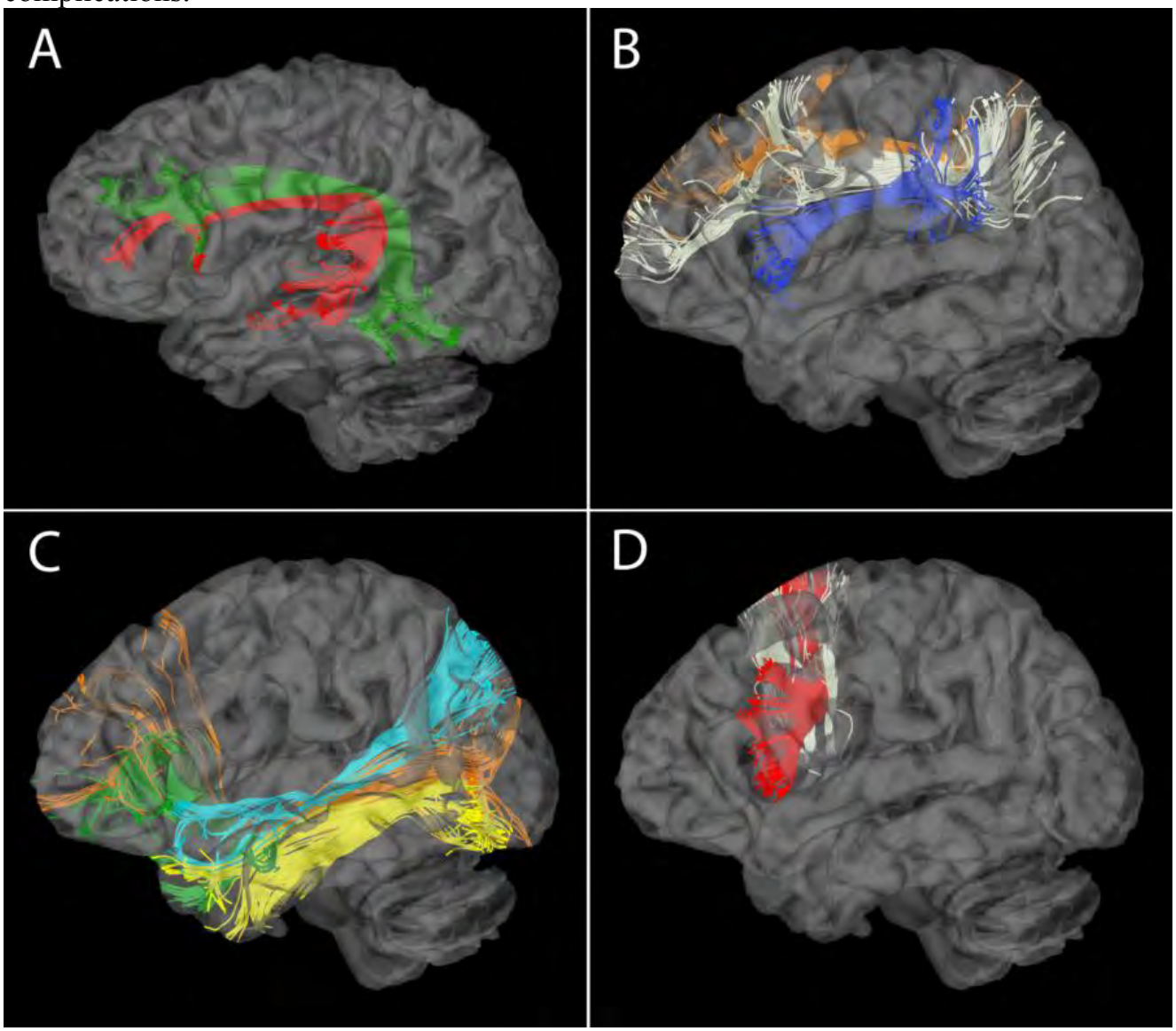
A Contemporary View of White Matter Tracts Subserving the Dorsal and Ventral Streams of Language

E Middlebrooks[1]
[1]*University of Alabama at Birmingham, Birmingham, AL*

Purpose
Modern research into human language function has shifted to field from a "localizationist" theory, based largely on the seminal works of Broca and Wernicke, to a hodotopical model in which language function is viewed as a wide-spread network process. Our purpose is the review of contemporary knowledge of the white matter tracts subserving these networks and their relevance to surgical planning.
Materials and Methods
A thorough literature review of both language theory and surgical science was conducted to highlight the most up-to-date knowledge of the function and anatomy of white matter tracts in the dorsal and ventral language streams and their significance for treatment planning.
Results
The white matter tracts of the dorsal stream include the arcuate fasciculus (AF) and the most lateral portion of the superior longitudinal fasciculus (SLF III). The AF consists of a ventral component (vAF), functioning in phonologic processing as predicted by the dorsal stream location, but also a dorsal component (dAF) believed to actually function in semantic processing. Damage to the dAF has a very high rate of phonologic paraphasias and repetition disorders which can mimic speech arrest. Damage to the vAF has a high association with transcortical motor aphasia. Injury to the SLF III results in a very high rate of severe dysarthria/anarthria. The ventral stream primarily consists of the inferior fronto-occipital fasciculus (IFOF), inferior longitudinal fasciculus (ILF), and uncinate fasciculus (UF). While the IFOF is associated with a high incidence of semantic speech deficit (>90%), the ILF appears to be redundant with no significant effects from damage. Recent evidence suggests impairments in famous face and object naming with damage to the UF. A 4th ventral tract, the middle longitudinal fasciculus, has an unclear role in language and appears to result in no significant language deficit. Additional frontal association tracts, the frontal aslant tract (FAT) and frontostriatal tract (FST) play a vital role in speech production, and their damage is likely to result in severe speech output impairments, such as nonfluent aphasia.

Conclusions

Literature has shown that damage to underlying white matter tracts often has more severe and irrecoverable effects than damage to corresponding cortical areas. A thorough knowledge of these tracts will provide more accurate risk/benefit analysis to patients undergoing surgical planning with the goal of improved outcomes and decreased complications.



(Filename: TCT_EdE-09_Fig.jpg)

EdE-03

6:30AM - 3:00PM

AARS-2 Leukoencephalopathy – Solving the Puzzle and Proposing a Pathway for Diagnosis of Adult Onset Leukodystrophy

G Mattar[1], S Michael[1], T Hayton[1], W Muhammad[1], V SAWLANI[1]

[1]*University Hospitals Birmingham, Birmingham, West Midlands*

Purpose

There are a greater number of leukodystrophies than a neuroradiologist is likely to encounter in a working lifetime. Leukodystrophies presenting in adulthood [Adult onset leukodystrophy (AOL)], can closely mimic acquired white matter diseases, both clinically and on imaging, therefore presenting a complex diagnostic challenge. We propose a diagnostic pathway which allows earlier diagnosis of this important group of conditions, while excluding more common treatable disease mimics earlier in the patient journey.

Materials and Methods

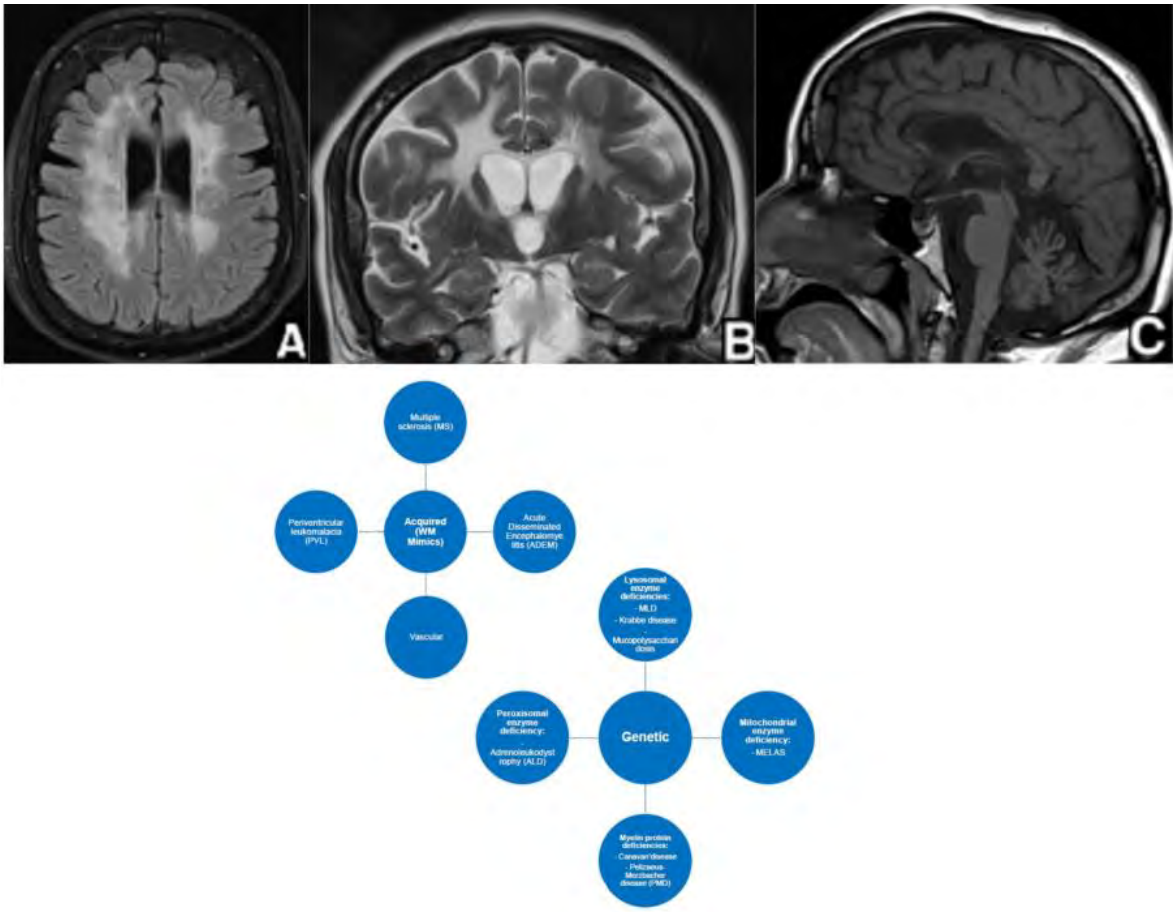
A series of biochemical, imaging and genetic investigations was developed through review of available literature. Following identification of white matter changes on MRI and clinical suspicion of AOL, the first step in our pathway is to exclude potentially treatable mimics such as multiple sclerosis, vasculitides, Wilson disease or HIV encephalopathy through inexpensive CSF/serum tests. Once excluded, we proceed to a series of focused serum and urinary biochemical tests including very long chain fatty acids, white cell enzymes and urinary organic acids. If the diagnosis is still not reached, we conduct a series of more specific genetic tests.

Results

We present the diagnostic pathway developed at our institution and show its application in clinical problem solving. We present the case of a 44-year-old patient with a mutation in the alanyl-transfer (t)RNA synthetase 2 (AARS2) gene (Figure A,B,C). Our pathway clearly predicted AOL. Having excluded treatable risk factors, we proceeded to a battery of investigations, eventually reaching the diagnosis via whole exome sequencing. We are currently building a regional AOL database, which currently holds 29 patients with diagnoses including vanishing white matter disease, x-linked adrenoleukodystrophy and cerebrotendinous xanthomatosis.

Conclusions

Our proposed diagnostic pathway has shown that definitive diagnosis can be achieved in difficult cases of suspected AOL through radiological and clinical pattern recognition, and selected investigations. These investigations can be carried out efficiently through a "day-case" admission for serum and CSF sampling.



(Filename: TCT_EdE-03_Image1.jpg)

EdE-18

6:30AM - 3:00PM

All That Glitters is Not Stroke: A Quiz on Diffusion-Weighted Imaging and Diseases of the Central Nervous System

B Mattson[1], J Hollingsworth[1], A Macrito[2], S Li[3]
[1]University of Massachusetts Medical School - Baystate Medical Center, Springfield, MA, [2]Baystate Medical Center, Springfield, MA, [3]University of Massachusetts Medical School, Longmeadow, MA

Purpose
Diffusion-weighted imaging (DWI) is most commonly applied to the diagnosis of acute cerebral infarction, but there are several other diseases of the brain and spinal cord that demonstrate restricted diffusion which radiologists must be familiar with that include vascular, neoplastic, infectious, traumatic, toxic/metabolic, and demyelinating processes. Radiologists often find interpretation of brain and spine MRIs challenging, and this exhibit will focus on how DWI and typical clinical presentation can be used to narrow the

differential in cases where there is low suspicion for acute cerebral infarction. The information will be provided in a quiz format followed by an answer/discussion section after each question. At the end of the exhibit the reviewer will become familiar with the characteristics of central nervous system diseases on T1, T2, FLAIR, DWI, and contrast-enhanced sequences, and most importantly understand how DWI can aid in the diagnostic challenge.

Materials and Methods

Diffusion-weighted imaging (DWI) is most commonly applied to the diagnosis of acute cerebral infarction, but there are several other diseases of the brain and spinal cord that demonstrate restricted diffusion which radiologists must be familiar with that include vascular, neoplastic, infectious, traumatic, toxic/metabolic, and demyelinating processes. Radiologists often find interpretation of brain and spine MRIs challenging, and this exhibit will focus on how DWI and typical clinical presentation can be used to narrow the differential in cases where there is low suspicion for acute cerebral infarction. The information will be provided in a quiz format followed by an answer/discussion section after each question. At the end of the exhibit the reviewer will become familiar with the characteristics of central nervous system diseases on T1, T2, FLAIR, DWI, and contrast-enhanced sequences, and most importantly understand how DWI can aid in the diagnostic challenge.

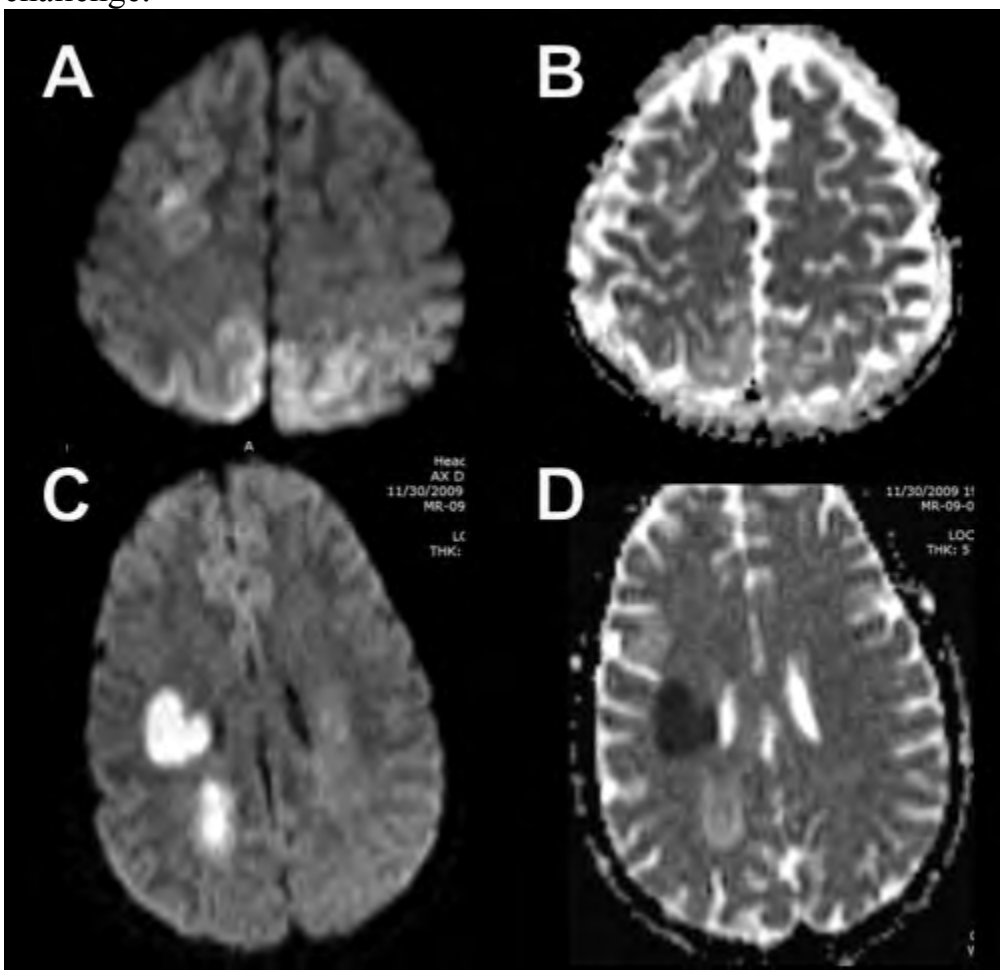
Results

Diffusion-weighted imaging (DWI) is most commonly applied to the diagnosis of acute cerebral infarction, but there are several other diseases of the brain and spinal cord that demonstrate restricted diffusion which radiologists must be familiar with that include vascular, neoplastic, infectious, traumatic, toxic/metabolic, and demyelinating processes. Radiologists often find interpretation of brain and spine MRIs challenging, and this exhibit will focus on how DWI and typical clinical presentation can be used to narrow the differential in cases where there is low suspicion for acute cerebral infarction. The information will be provided in a quiz format followed by an answer/discussion section after each question. At the end of the exhibit the reviewer will become familiar with the characteristics of central nervous system diseases on T1, T2, FLAIR, DWI, and contrast-enhanced sequences, and most importantly understand how DWI can aid in the diagnostic challenge.

Conclusions

Diffusion-weighted imaging (DWI) is most commonly applied to the diagnosis of acute cerebral infarction, but there are several other diseases of the brain and spinal cord that demonstrate restricted diffusion which radiologists must be familiar with that include vascular, neoplastic, infectious, traumatic, toxic/metabolic, and demyelinating processes. Radiologists often find interpretation of brain and spine MRIs challenging, and this exhibit will focus on how DWI and typical clinical presentation can be used to narrow the differential in cases where there is low suspicion for acute cerebral infarction. The information will be provided in a quiz format followed by an answer/discussion section after

each question. At the end of the exhibit the reviewer will become familiar with the characteristics of central nervous system diseases on T1, T2, FLAIR, DWI, and contrast-enhanced sequences, and most importantly understand how DWI can aid in the diagnostic challenge.



(Filename: TCT_EdE-18_DWI.jpg)

EdE-10

6:30AM - 3:00PM

An Overview of Functional DaT-SPECT Neuroimaging

B Chang[1], J Dubroff[2]
[1]University of Pennsylvania, Philadelphia, PA, [2]University of Pennsylvania, Philadephia, PA

Purpose
The evaluation of patients with suspected Parkinson's disease often poses a diagnostic dilemma for clinicians, and dopamine transporter imaging can play a critical role in narrowing the differential diagnosis. The goal of this educational exhibit is to give an

illustrative review of dopamine transporter SPECT (DaT-SPECT) imaging, from appropriate clinical indication to image interpretation.
Materials and Methods
Cases evaluated at the University of Pennsylvania Health System will be included in this interactive educational exhibit. Our experiences with clinical patient selection, patient preparation, image acquisition, and data postprocessing will be discussed.
Results
The exhibit will include a presentation of the following: - History of 123I-ioflupane development, - Appropriate clinical indications, - Patient preparation, - Image acquisition and postprocessing, - Representative image findings in a variety of pathologies.
Conclusions
The clinical diagnosis of Parkinson's disease often can be straightforward based on clinical signs/symptoms, the fulfillment of inclusion and exclusion criteria, and/or response to therapeutics such as levodopa. However, clinicians often are faced with equivocal clinical evidence which makes definitive diagnosis difficult. Although there are proposed MR-based protocols that have shown recent promise, routine cross-sectional imaging generally is nondiagnostic. The advent of dopamine transporter imaging has served to help clinicians distinguish Parkinsonian syndromes from other pathologic etiologies particularly when there is clinical ambiguity. DaT-SPECT neuroimaging is a critical modality in the neuroradiologist's evaluation of Parkinsonian syndromes.

EdE-11

6:30AM - 3:00PM

Anatomico-Functional Correlation of Intrinsic Brain Networks in Resting-State Functional MRI

A Tyan[1], F Mossa-Basha[1], J Wongsripuemtet[2], J Pillai[3], S Gujar[2], S Agarwal[4], H Sair[1]
[1]Johns Hopkins Medicine, Baltimore, MD, [2]Johns Hopkins Hospital, Baltimore, MD, [3]The Johns Hopkins Hospital, Baltimore, MD, [4]Johns Hopkins School of Medicine, Baltimore, MD

Purpose
Resting-state functional MRI (rs-fMRI) is a popular tool for analyzing brain function. Abnormal rs-fMRI connectivity has been demonstrated in numerous disorders, for example within the Default Mode Network (DMN) in Alzheimer Disease (1) or within the Salience Network (SN) in schizophrenia (2). Compared to these global patterns of intrinsic brain networks (IBNs), the specific anatomico-functional correlation of subsegments of the networks are less well known. We review the fundamentals of rs-fMRI, the general topology of the main IBNs, and then describe the functional relevance of the different components of the IBNs.

Materials and Methods

Three-dimensional coordinates of the subsegments of the common IBNs including the DMN, SN, Executive Control (EC), Attention (ATT), Sensorimotor (SM), Visual (VIZ), Language (LAN) are used to perform a literature review to determine convergent functional roles of specific brain regions.

Results

An abridged excerpt of the retrosplenial cortex (RSC), part of the DMN, is described here. Typically, the precuneus and the RSC demonstrate combined correlations in rs-fMRI (Figure 1, asterisk). The RSC (Figure 1, arrow) however demonstrates cytoarchitecturally transitional cortical lamination pattern comprised of four to five layers, compared to precuneus which has the more typical six-layered pattern. The RSC projects to the dorsolateral prefrontal cortex, parietal and occipital cortex, anterior thalamic nucleus, and hippocampus [3]. Task-fMRI studies demonstrate significant activation of the RSC during autobiographical memory retrieval, and in animal studies, the RSC is implicated in spatial memory and tasks requiring heterogeneous stimulus integration. The RSC is also classified as a network "hub" and is an early site of metabolic derangement in dementia.

Conclusions

This educational exhibit provides detailed descriptions of the subcomponents of the IBNs. Further insight into the organization and functional relevance of IBNs may aid in designing studies utilizing rs-fMRI.

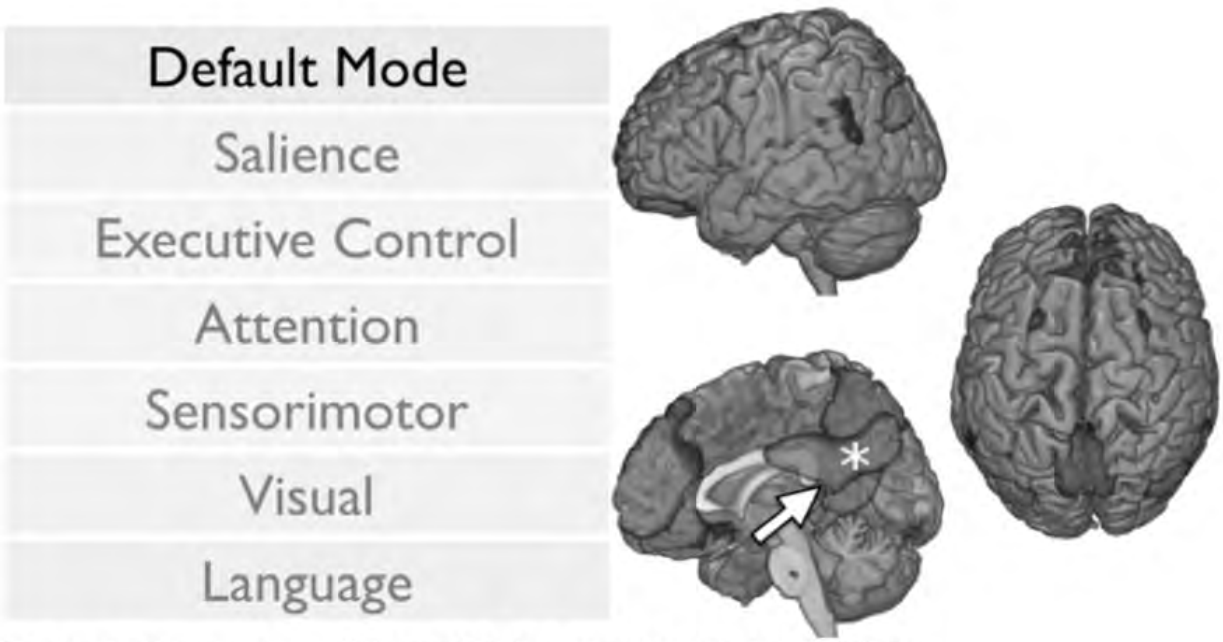


Figure 1. Components of the DMN; the arrow points to the RSC

(Filename: TCT_EdE-11_figure1.jpg)

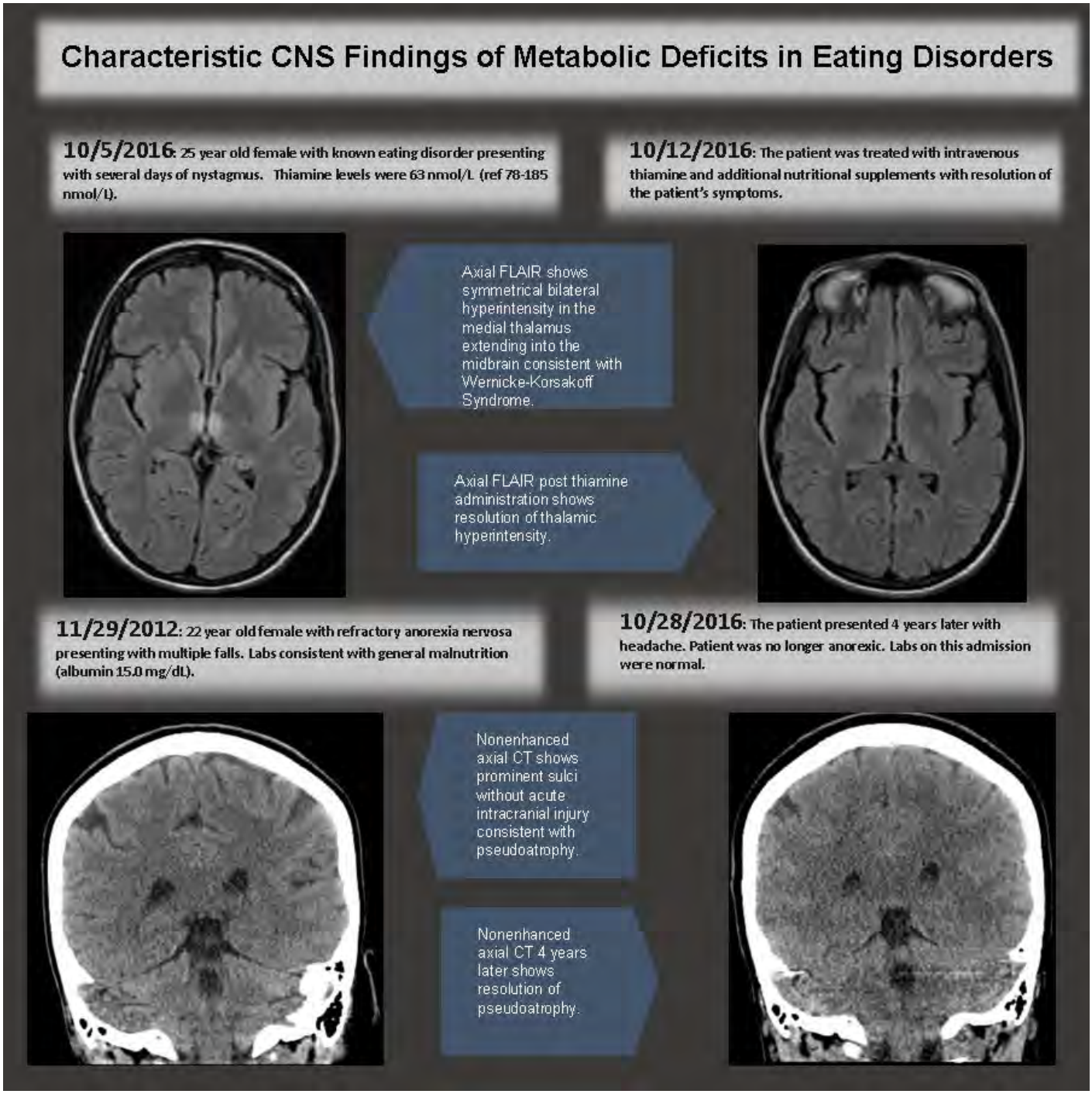
EdE-06

6:30AM - 3:00PM

Characteristic CNS Findings of Metabolic Derangements in Eating Disorders

D Rowcroft[1], P O'Halloran[1], N Martin[1], T Le[2], S Teoh[1], P Sasson[1]
[1]Mount Auburn Hospital, Cambridge, MA, [2]Mount Auburn Hospital, Cambridge , MA

Purpose
Approximately 30 million people in the United States suffer from eating disorders that may be overlooked in the emergency department. Clinical symptoms may be vague presenting as nonspecific dizziness, fatigue, syncope, and seizures. If not diagnosed in a timely manner, outcomes may be fatal. Radiologists can facilitate early eating disorder diagnosis by recognizing several imaging findings in the appropriate clinical setting. Thus, our exhibit discusses the manifestations of metabolic derangement from eating disorders on brain imaging.
Materials and Methods
A retrospective review of electronic medical records and radiographic studies in patients with known eating disorders and nutritional deficits will be performed with discussion of pertinent findings.
Results
Eating disorders are highly prevalent in patients who present to the ED. There are several characteristic imaging findings on brain imaging that can facilitate early detection of thiamine deficiencies, hypoglycemia, B12 deficiency, protein wasting, and other metabolic derangements.
Conclusions
Eating disorders in the United States are both highly prevalent, and possibly fatal when untreated. Radiologists should be cognizant of several characteristic CNS imaging findings to facilitate early diagnosis and intervention.



(Filename: TCT_EdE-06_Images.jpg)

EdE-23

6:30AM - 3:00PM

Deep and Superficial Venous Drainage of the Brain: A Review of Anatomy and Pathologic Conditions Affecting Intracranial Dynamics of Blood Flow

T Uribe[1], K Wang[1], N Nguyen[1], D Dunaway[2], S Chen[2], C Lincoln[2]
[1]Baylor College of Medicine, Houston, TX, [2]Baylor College of Medicine, Houston , TX

Purpose

Evaluation of the deep and superficial cerebral venous drainage system with neuroimaging can be challenging due to the complex anatomy (1). A review of normal variants and pathologic conditions involving the venous structures, including neoplastic, infectious, vascular, traumatic, and congenital etiologies, may increase familiarity and reinforce understanding in this subject. This presentation aims to provide a comprehensive review of the normal cerebral venous anatomy and different pathologies that can alter its normal dynamics.

Materials and Methods

An overview of the anatomy of dural venous sinuses and normal anatomic variants is performed initially and illustrated with MRI, MRV, and CTV. A summary of the multitude of cerebral venous pathology is highlighted with case-based illustrations comprised of clinical history and associated CT and MRI findings. Pathologies described and illustrated include infectious (tuberculosis, mastoiditis with thrombosis), trauma (carotid-cavernous fistula, lacerations), neoplasms (inverted papilloma, metastases, meningioma), idiopathic (idiopathic intracranial hypertension with dural sinus stenosis), congenital (arteriovenous malformations, arteriovenous fistulas), and vascular etiologies (venous sinus thrombosis).

Results

Having a strong familiarity with the complex anatomy of the venous drainage system of the brain can be challenging given the multiple normal variants and wide range of pathologies that can be encountered. Appreciating these anatomic nuances and familiarity with possible pathologies may allow radiologists to be more vigilant and keen of cerebral venous abnormalities, and ultimately help with refining and narrowing the differential diagnosis. The multimodality case-based illustrations in this educational exhibit will seek to provide an intuitive approach to cerebral venous findings.

Conclusions

Intracranial venous pathology and anatomical variants can make an accurate diagnosis challenging. This exhibit seeks to provide a comprehensive, cogent review of both anatomy and pathology to refine the diagnostic approach for radiologists encountering cerebral venous imaging findings.



(Filename: TCT_EdE-23_Tumoralsigmoissinusthrombosis.jpg)

EdE-12

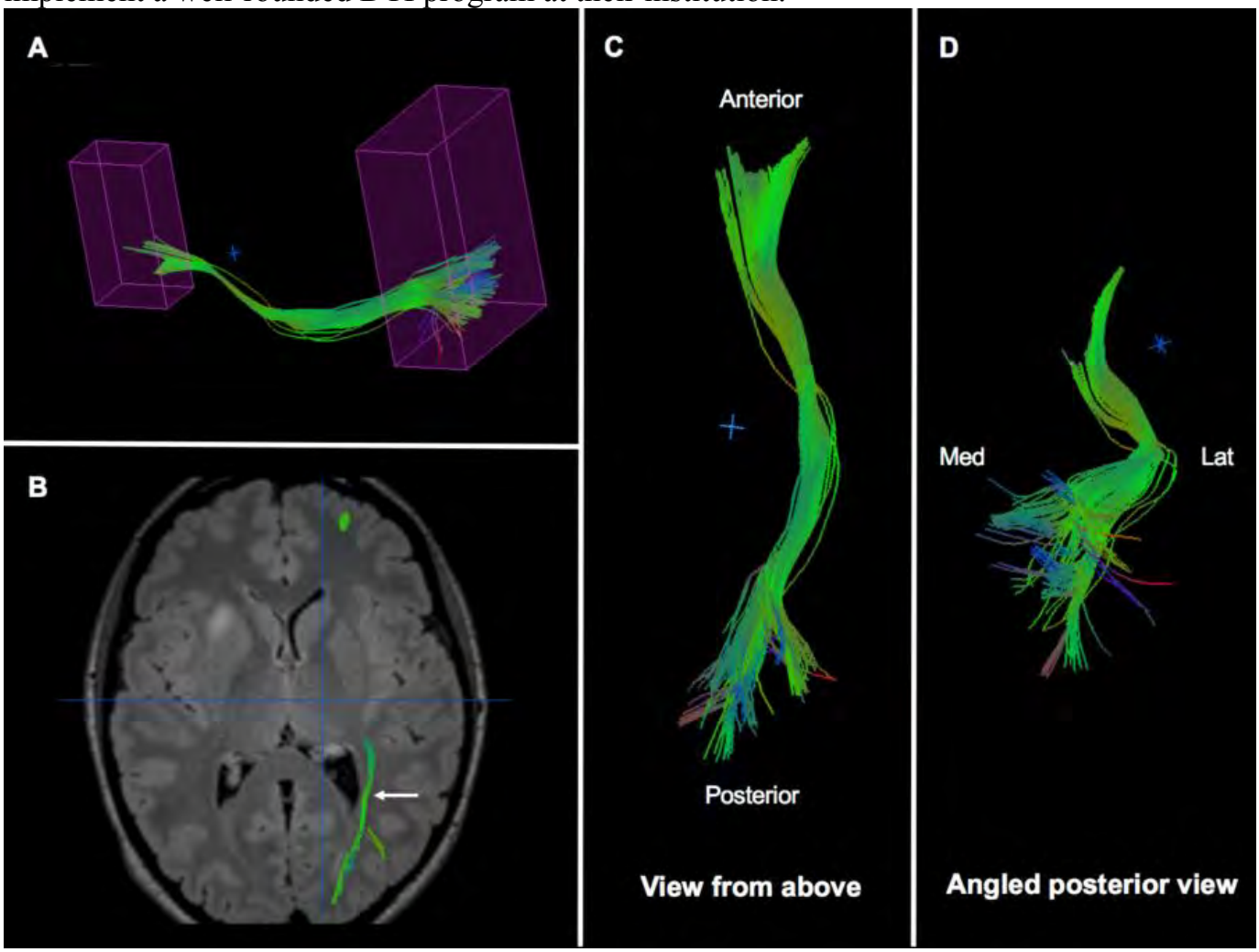
6:30AM - 3:00PM

Diffusion Tensor Imaging Tractography Tutorial and an Introduction to Major White Matter Tract Anatomy and Function

S Badhe[1], B Liu[2], A Korutz[3]
[1]Northwestern Unniversity, Chicago, IL, [2]Northwestern University Feinberg School of Medicine, Chicago, IL, [3]Northwestern University, Chicago, IL

Purpose
To describe efficient and accurate methods for performing diffusion tensor imaging (DTI) tractography in clinical practice as well elaborating on the anatomy and functions of the major white matter tracts.
Materials and Methods
We will discuss our methodology for performing ROI-based DTI tractography, including the preferred ROI sizes/location(s), choice of optimal fractional anisotropy values as well as expected spurious fibers which are often encountered and must be excluded manually. We also will include the general scan parameters used for performing DTI at our institution as well as basic DTI postprocessing tips and tricks.
Results
We will review the anatomy and function of the major white matter tracts which are encountered in clinical practice. These include the corticospinal/corticobulbar tracts, the arcuate fasciculus/superior longitudinal fasciculus, the inferior longitudinal fasciculus, the inferior fronto-occipital fasciculus, the optic radiations as well as the uncinate fasciculus.
Image 1 caption: Lateral oblique view (A) of the inferior fronto-occipital fasciculus (IFOF) which was generated with two ROIs, one in the anterior/inferior frontal lobe and the other in the occipital lobe. Figure B depicts the IFOF which has been overlaid on an axial FLAIR image. The white arrow depicts the tract's course within the sagittal stratum. Notably, the

IFOF also travels within the inferior aspect of the external/extreme capsules (not shown). Figures C and D depict superior and angled posterior views of the IFOF, respectively.
Conclusions
When using our DTI/tractography techniques combined with basic knowledge of the anatomy and function of the white matter tracts themselves, a radiologist can effectively implement a well-rounded DTI program at their institution.



(Filename: TCT_EdE-12_Image1.jpg)

EdE-38

6:30AM - 3:00PM

Dual Energy Computed Tomography of the Head

K Noguchi[1], N Naruto[1]
[1]*University of Toyama, Toyama, Japan*

Purpose

The major teaching point of this exhibit is to show the clinical usefulness of dual energy CT (DE-CT) of the head.

Materials and Methods

1. General statement of the DE-CT. 2. General application of the DE-CT in the head. 3. Sample cases. 4. Future directions.

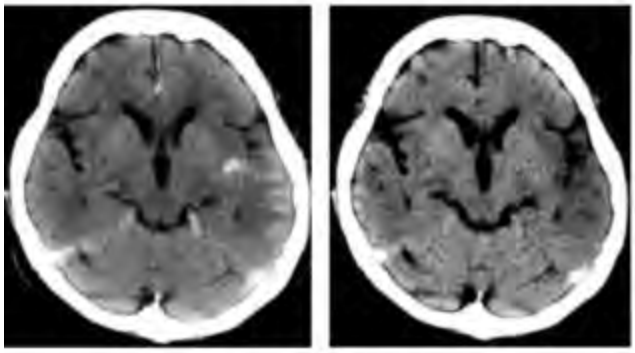
Results

1. General statement of the DE-CT. 2. General application of the DE-CT in the head: 1) Tissue differentiation with DE-CT. The advantage of DE-CT is the ability for material characterization and differentiation, based on high- and low- peak voltage acquisitions. Materials with equal Hounsfield densities at 120 kVp imaging can be differentiated by analyzing energy-dependent changes of the attenuation of materials (e.g., 80 vs Sn150 kVp). 1-1) Virtual noncontrast map, Iodine map differentiation of iodine and hemorrhage is used in high-density lesions, after intra-arterial recanalization in stroke patients or after administration of contrast media. In additon, detection of spot sign can be used in patients with acute intracerebral hemorrhage. 1-2) Automated bone removal CT - Automated bone removal CT is used in CTA and CTV of the intracranial vessels. 2) Monoenergetic CT - Monoenergetic reconstructions can be used in patients with or without metal implants in the brain and spine to reduce artifacts, improve CNR and SNR, or to improve iodine conspicuity. 3. Sample cases. 4. Future directions.

Conclusions

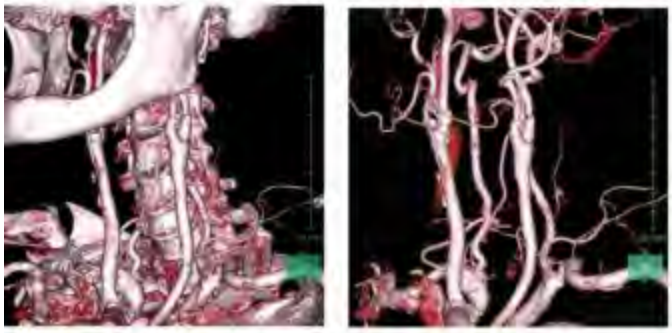
1. DE-CT can separate materials by two- and three-material decomposition, analyzing the difference in CT value in two different energies. 2. Brain hemorrhage application can distinguish contrast material from hemorrhage. 3. Bone removal application can remove bone and calcification without subtraction. 4. Monoenergetic Imaging application can choose the most suitable kV image in diagnosis. 5. DE-CT is a powerful tool to supplement simulated standard CT for characterizing intracranial lesions.

Figure1: Acute Cerebral infarction after mechanical thrombectomy



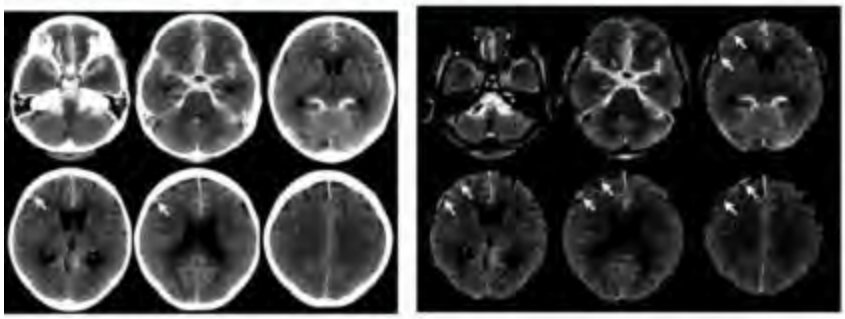
Simulated standard CT Virtual Non-contrast CT

Figure2: Dual Energy CT Angiography (DE-CTA)



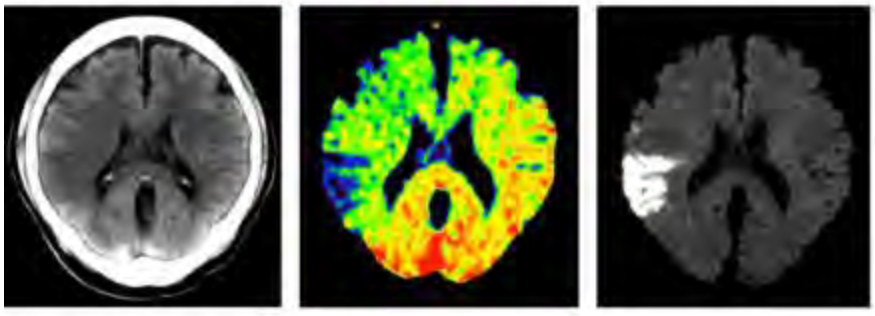
DE-CTA DE-CTA with bone removal

Figure3: Acute subarachnoid hemorrhage and small subdural hematoma



Simulated standard CT Bone-removal CT

Figure4: Acute Cerebral infarction



Simulated standard CT X-map of DECT Diffusion-weighted MRI

(Filename: TCT_EdE-38_1.jpg)

EdE-28

6:30AM - 3:00PM

Extracranial Metastasis of Glioblastoma: An Educational and Imaging Review of an Intriguing and Increasingly Recognized Entity

D Das[1], M Iv[2], T Massoud[3]
[1]Stanford Hospital and Clinics, Stanford, CA, [2]Stanford University Medical Center, Stanford, CA, [3]Stanford University School of Medicine, Stanford, CA

Purpose
Despite the locally aggressive malignant nature of glioblastoma (GBM), extracranial metastasis remains exceedingly rare. It is, however, an increasingly recognized feature of GBM natural history. In this educational exhibit we review our current knowledge of the nature of GBM metastasis, and present the imaging findings of local and distant dissemination.
Materials and Methods
We review a wide spectrum of imaging manifestations in local and systemic GBM metastases.
Results
The rate of GBM metastasis beyond the CNS is puzzlingly low at 0.2-2.0% (<250 reported cases). This rarity may be owing to: absent true CNS lymphatics, collapsibility of intracerebral veins, tough basal membranes around arteries, dura impermeable to tumor invasion, and possibly because of a selective disadvantage of GBM cells in their inability to invade connective tissue outside the brain. Moreover, aggressive GBMs may cause the patient's death before dissemination. When metastases occur, they may be local or distant, usually (but not always) after craniotomy or ventriculoperitoneal shunting. The presence of neoplastic cells in the circulation during GBM surgery has been documented previously, possibly explaining a potential hematogenous route for spread of genetically prone tumor cells. The imaging features of extracranial GBM metastases are nonspecific. We present examples of local skull base, masticator muscles, and scalp invasion; and of distant spread in lungs and pleura (60%), lymph nodes (51%), bone (30%), and liver (22%). Other locations include kidney, spleen, heart, and skin.
Conclusions
Neuroradiologists should be familiar with the manifestations of extracranial GBM metastasis. These can be both unexpected and challenging on imaging. Ongoing efforts to improve multimodal therapies and greater locoregional control of brain GBMs may prolong patients' lives to the extent that local and systemic dissemination of disease will be encountered more frequently. Although GBM metastases still carry very poor prognosis, their treatment may improve the quality and duration of survival.

EdE-25

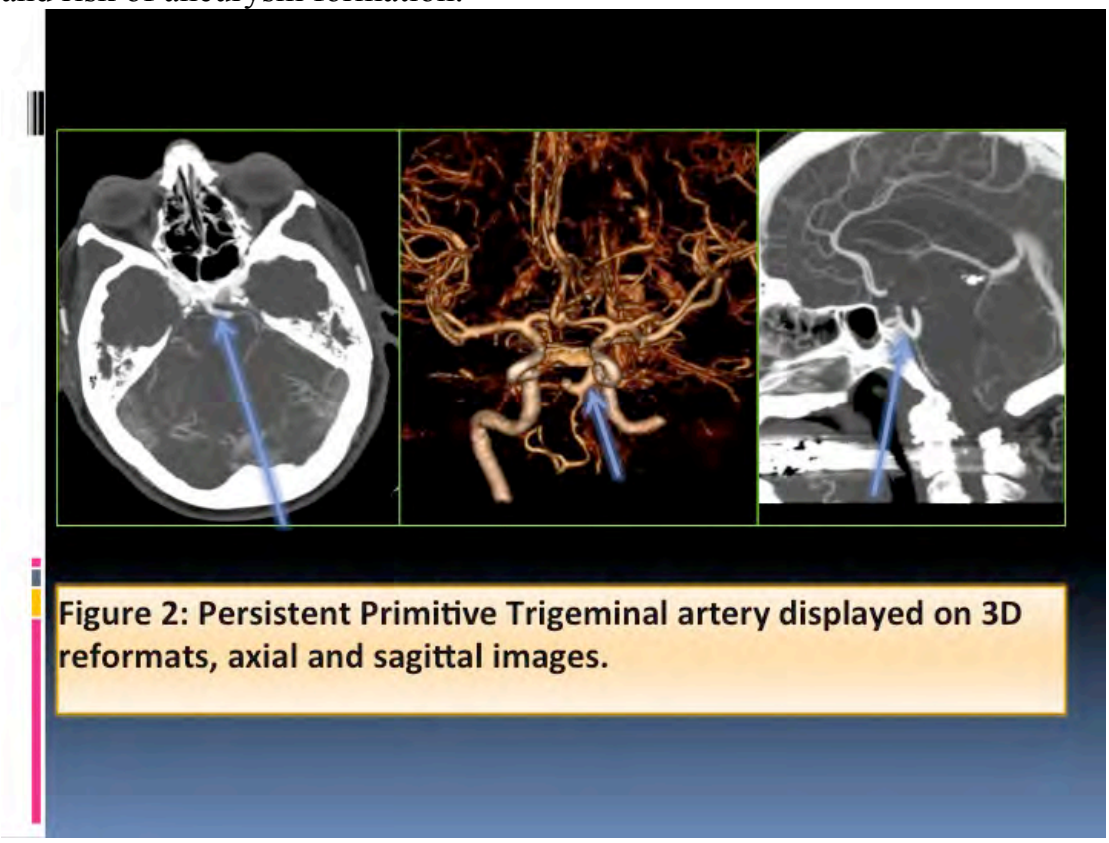
6:30AM - 3:00PM

Fundamental Anatomical Variations of Cerebral Circulation: A Pictorial Review with Emphasis on Clinical Relevance, Prevalence and Risk of Aneurysm Formation

S EZHAPILLI[1], Z Badar[2], A Mohamed[2], M Rachun[3]
[1]SUNY UPSTATE MEDICAL UNIVERSITY, SYRACUSE, NY, [2]SUNY Upstate Medical Center, syracuse, NY, [3]St. George's University of Medicine, great river, NY

Purpose
Multidetector CT angiography is the gold standard and first line modality for evaluation of cerebral circulation in the setting of subarachnoid hemorrhage and acute stroke. However, in these critical scenarios, it is vital to understand the anatomy of common variants with respect to their clinical relevance and risk of aneurysm formation. Prevalence and morbidity are other key factors to consider in understanding the significance of anatomical cerebral variants. Recent technological advances with 3D reformats of original CT angiography images has aided in optimal visualization of these variants.
Materials and Methods
A retrospective analysis of CT angiograms at our institution will demonstrate various anatomical variations in the cerebral circulation. 3D reformats will further aid in optimal visualization of these crucial variants. Our aim will focus on presenting a pictorial review illustrating clinical relevance and radiographic presentation of each variant. A detailed literature review will be conducted to obtain data with regards to the prevalence of variants and incidence of aneurysm formation. Cases of variants will include fenestrations involving the Circle of Willis and its branches, duplications involving the cerebral circulation, persistent trigeminal artery and other similar cases. Lastly, an algorithm will be provided within the pictorial review that will aid radiology residents in easily categorizing and identifying these cerebral variants on board examinations.
Results
Many challenges can be associated with being able to correctly identify anatomical variants in the setting of an acute stroke or subarachnoid hemorrhage. However, to avoid such pitfalls, anatomical cerebral variations can be assessed adequately on multidetector CT angiography with and without 3D reformats. A detailed discussion with regards to the prevalence, clinical relevance and incidence of aneurysm formation is critical for radiologists in being able to make the appropriate diagnosis based on characteristic imaging findings. Examples of such cases will include fenestrations within the posterior cerebral artery, fenestration of the basilar artery, duplications involving the cerebral circulation, persistent trigeminal artery, anterior communicating artery infundibulum, azygous anterior cerebral artery and other similar cases. Thus, correctly identifying these variants with respect to their anatomic relationships will improve neuroradiological evaluation.

Conclusions
Anatomical cerebral variants play a critical role in multidetector CT angiography and should be understood with their characteristic radiographic findings, prevalence, clinical relevance and risk of aneurysm formation.



(Filename: TCT_EdE-25_Slide2.jpg)

EdE-14

6:30AM - 3:00PM

Gadolinium-enhanced 3D-FLAIR MRI: Spectrum of Leptomeningeal Pathology and Imaging Pitfalls

D Titelbaum[1], R Engisch[2], E Schwartz[1], S Napoli[3]
[1]Shields Health Care, Brockton, MA, [2]Luzerner Kantonsspital, Lucerne, Switzerland, [3]Neurology Center of New England, Foxboro, MA

Purpose
Gadolinium-enhanced 3D-FLAIR MRI (Gd-3D-FLAIR) recently has been shown to identify pial lymphoid follicles in multiple sclerosis (MS) (1), and presumed leptomeningeal vasculopathy in Susac's Syndrome (SS) (2), neither visible on postcontrast T1-weighted (T1W) imaging. We demonstrate the spectrum of leptomeningeal findings of MS, SS, and some metastatic disease on Gd-3D-FLAIR, and demonstrate imaging pitfalls that can lead to

erroneous diagnosis. Awareness of these factors will be critical in future imaging assessment of pial disease.
Materials and Methods
The Gd-3D FLAIR appearance of pial disease in patients with MS, Susac's Syndrome, and metastatic disease is reported, and multiple examples of imaging pitfalls that can lead to erroneous diagnosis are illustrated. Imaging was performed at 1.5T except for one case of SS performed at both 1.5T and 3T.
Results
Gd-3D-FLAIR identified pial pathology in MS, SS, and some metastatic disease, not visible on postgadolinium T1W imaging. Pitfalls simulating or obscuring pathology in Gd-3D-FLAIR include pachymeningeal vascular enhancement, dural fat, arachnoid granulation, BLADE imaging artifact, and insufficient postinjection timing delay.
Conclusions
Gd-3D-FLAIR imaging is uniquely able to identify certain leptomeningeal pathologies that may ultimately prove to be imaging biomarkers of disease activity. Knowledge of pitfalls will facilitate accurate diagnosis. Future applications may include assessment of CD-20 inhibitor activity on modulating lymphoid follicles in MS, imaging correlate for SS disease activity, and more accurate assessment of occult metastatic disease.

EdE-34

6:30AM - 3:00PM

Glioblastoma Metastases: Extra-axial and Beyond

M Jurkiewicz[1], J Stein[1], N Cross[2], M Nasrallah[1], A Desai[1], S Brem[1], D O'Rourke[2], S Mohan[2]
[1]Hospital of the University of Pennsylvania, Philadelphia, PA, [2]University of Pennsylvania, Philadelphia, PA

Purpose
Glioblastoma (GBM) is the most common and deadly primary brain tumor in adults. It infiltrates widely in the brain, disseminates not uncommonly in the CSF, but spreads beyond the central nervous system very rarely, in less than 2% of patients (Ray et al., 2015). In this poster presentation, we explore unusual patterns and sites of spread of GBM extra-axially and beyond.
Materials and Methods
Eight patients with disseminated GBM (average age 60.4, range 45 to 87; five male), pathologically proven at both the primary and metastatic sites, were selected to demonstrate the imaging findings of intracranial and extracranial disease. Examples of intracranial spread include carcinomatous meningitis, dural-based metastatic deposits, distant subependymal lesions, and perineural spread of tumor. Cases of extracranial metastases include scalp deposits near and distant from the surgical site (Figure 1A). Examples of more distant

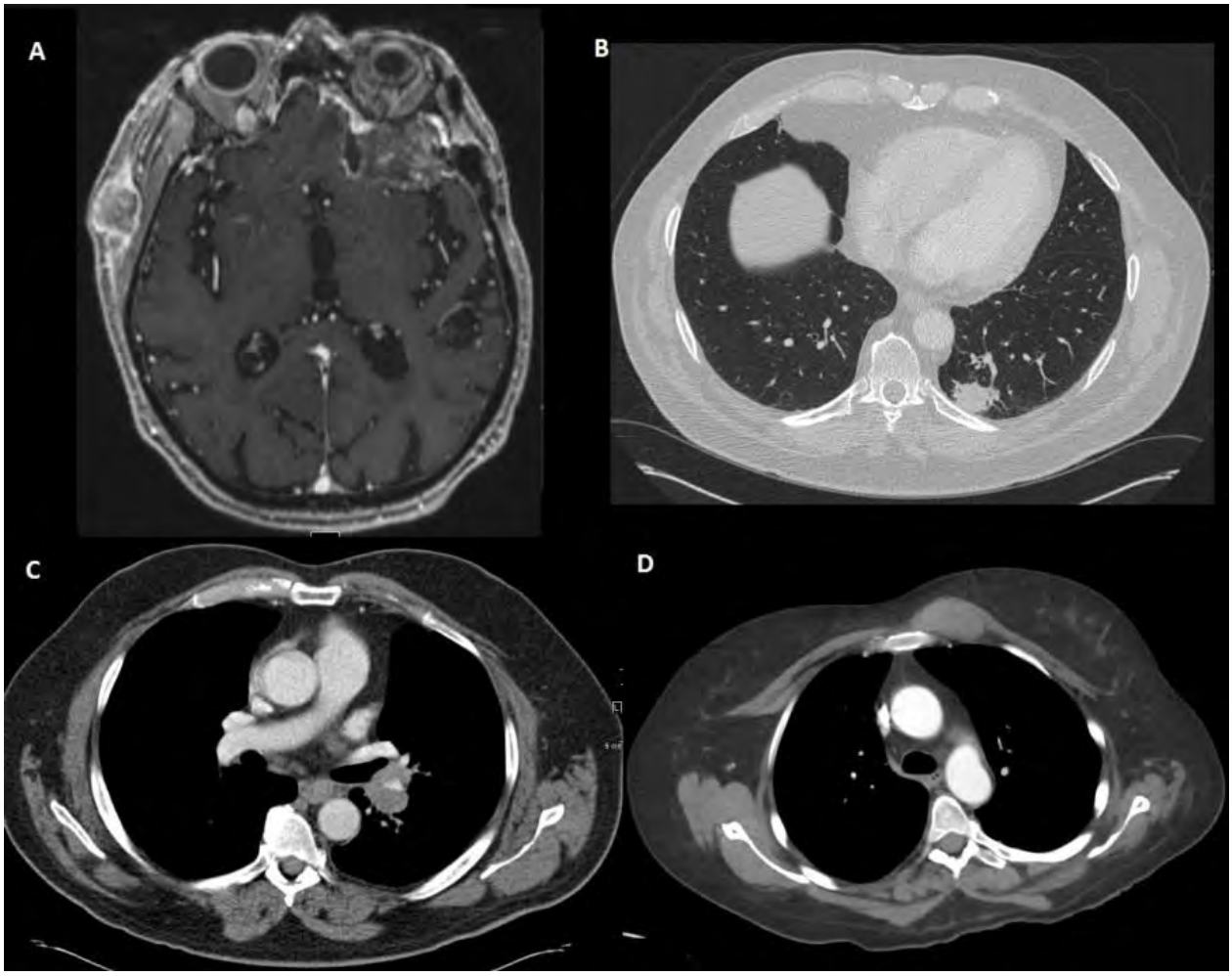
metastases consistent of deposits in the lung with associated mediastinal adenopathy (Figures 1B and C) and a metastasis to the chest wall (Figure 1D).

Results

One explanation for the rarity of metastases is the relatively short survival duration of GBM patients. The blood brain barrier and differences in venous and lymphatic drainage relative to other organ systems may limit systemic spread. Unfortunately, surgery can provide access beyond the neuraxis, via craniotomies or ventriculoperitoneal shunts. GBM can directly invade the skull and scalp or spread along cranial nerves. Depending on intracranial tumor burden, local or distant metastatic disease can alter management or require involvement of additional specialists. Tissue confirmation is important as second malignancies can certainly occur in GBM patients.

Conclusions

Glioblastoma dissemination within the neuraxis is not infrequent, but spread outside the skull or spinal canal is extremely rare. At presentation or follow-up, radiologists should be alert to the possibility of second primary malignancies in GBM patients as well as the rare extracranial GBM metastasis.



(Filename: TCT_EdE-34_Figure1.jpg)

EdE-33

6:30AM - 3:00PM

Glioblastoma: the Importance of MRI and Radiogenomics in Patient Management

A Gimeno[1], G Blasco[2], C Biarnes-Duran[3], M Puigdemont[4], P Daunis-i-Estadella[5], S Thio-Henestrosa[5], A Alberich-Bayarri[6], M Wintermark[7], K Nael[8], M Essig[9], S Pedraza[2], R Jain[10], J Puig[11]

[1]Department of Radiology (IDI), University Hospital Dr Josep Trueta, Girona, Girona, [2]Imaging Research Unit, IDI-IDIBGI, Hospital Dr Josep Trueta, Girona, None, [3]Research Unit of Diagnostic Imaging Institute (IDI), Girona Biomedical Research Institute (IDIBGI), Girona, Girona, [4]Catalan Institute of Oncology (ICO), Hospital Cancer Registry, University Hospital Dr Josep Trueta, Girona, Girona, [5]Department of Computer Science, Applied Mathematics and Statistics, University of Girona, Girona, Girona, [6]Hospital Universitario y Politecnico La Fe-QUIVIM, Valencia, None, [7]Stanford University, Stanford, CA, [8]Icahn School of Medicine at Mount Sinai, New York, NY, [9]Department of Radiology, University of Manitoba, Winnipeg, Manitoba, [10]NYU School of Medicine, New York, NY, [11]Research Unit of Diagnostic Imaging Institute (IDI), IDIBGI, University Hospital Dr Josep Trueta, Girona, Girona

Purpose

Glioblastoma is the most common primary malignant brain tumor in adults. Despite multimodality treatment comprising maximum safe resection, radiotherapy, and concomitant adjuvant chemotherapy, median survival is only 14 to 18 months.Glioblastoma usually is an expansive enhancing lesion with different patterns of contrast-enhancing lesion (CEL) and non-CEL. Different MRI modalities, such as DWI, DTI, PWI, and MR spectroscopy,are useful in the diagnostic work up and follow up. The Macdonald criteria define progression after treatment as ≥ 25% increase in the product of the perpendicular diameters of the largest area of CEL. However, transient treatment-related changes on imaging can mimick progressive disease;pseudoprogressionis seen in up to 20% of patients. Growing evidence suggests that glioblastoma exhibits profound intratumoral genetic heterogeneity: each tumor comprises multiple genetically distinct clonal populations with different therapeutic sensitivities. We outline the roles of pretreatment and follow-up MRI and of radiogenomics in patient management.

Materials and Methods

1. We illustrate the typical and atypical morphological MRI findings of glioblastoma. 2. We describe post-treatment imaging follow-up (intra-operative correlation) and the response criteria. 3. We review prognostic biomarkers for stratifying patients with glioblastoma. 4. We highlight the role of radiogenomics (combining data from MRI-phenotypes and microRNA expression) in patients' survival.

Results
This single-center study evaluated 125 patients with surgically managed glioblastoma, focusing on the Response Assessment in Neuro-Oncology Criteria by MRI. Apparent diffusion coefficient, relative cerebral blood volume, and vessels on MRI are reliable prognostic biomarkers for stratifying patients with glioblastoma. We explain the terms pseudoprogression and pseudoresponse and differentiate them from complications such as postsurgical infarct.
Conclusions
The accurate diagnosis and appropriate management of glioblastoma and its complications require an understanding of the MRI findings. Radiogenomics can help clarify the relationship between MRI findings and the response to treatment.

EdE-16

6:30AM - 3:00PM

Histiocytosis: The Spectrum of Neuroimaging Findings

S Aldhilan[1], F Alabdulkarim[2], M Alsuhaibani[3], M Nicolas Jilwan[1]
[1]King Faisal Specialist Hospital and Research Centre, Riyadh, Saudi Arabia, [2]king Faisal Specialist Hospital and Research Centre, Riyadh, Saudi Arabia, [3]KIng Faisal Specialist Hospital and Research Centre, Riyadh, Saudi Arabia

Purpose
The histiocytosis are rare systemic disorders frequently involving the central nervous system, craniofacial bones and spine. We highlight the characteristic imaging features of the most common Langerhans cell histiocytosis (LCH) as well as the non Langerhans cell histiocytosis including Erdheim-Chester disease, Rosai-Dorfman disease and hemophagocytic lymphohistiocytosis.
Materials and Methods
We selected the CT and MRI examinations of 16 patients aged 7 months to 55 years. Included are 9 patients with Langerhans cell histiocytosis aged 7 months to 34 years with disease manifestations encompassing the hypothalamic pituitary axis, brain parenchyma, dura, pineal gland, calvarium, facial bones, temporal bones and spine. Five hemophagocytic lymphohistiocytosis cases are presented, with an age range of 1 to 8 years and variable patterns of brain involvement. Our series also includes a 22-year-old patient with dural and pituitary axis involvement by Rosai-Dorfman disease as well as a 55-year-old male with Erdheim-Chester disease and extensive spinal epidural and tentorial infiltration.
Results
The cases we present illustrate the wide range of manifestations of Langerhans and non Langerhans histiocytosis. We highlight the characteristic features which suggest this frequently omitted diagnosis, including patient's age, distribution of the lesions, CT pattern of bony involvement and signal characteristics of the lesions.

Conclusions
We reviewed a wide spectrum of neuroimaging manifestations of histiocytosis, in an effort to emphasize that careful attention to the pattern of abnormality, along with patient's age and clinical presentation, frequently allow this rare diagnosis to be suggested at least.

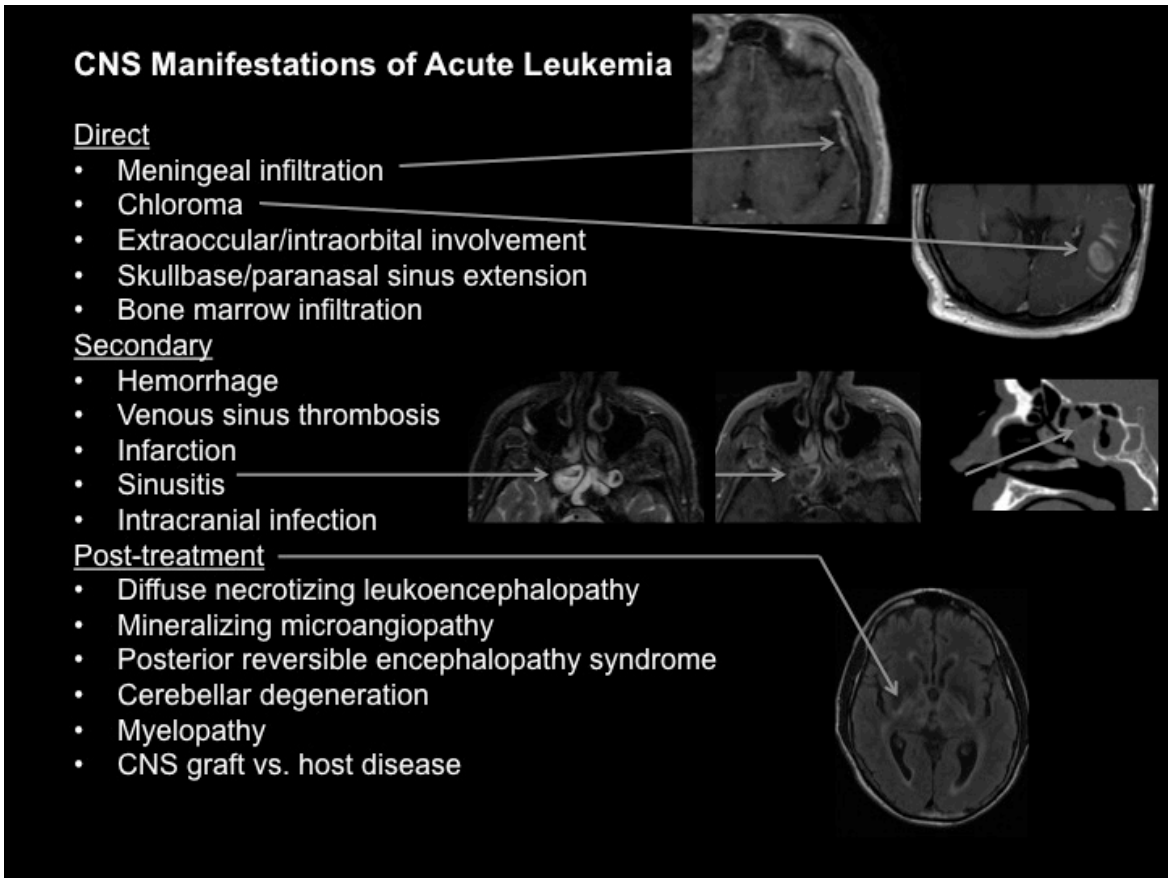
EdE-26

6:30AM - 3:00PM

Imaging Correlates of CNS Manifestations of Acute Leukemia

R Delfanti[1], J Bykowski[1]
[1]*University of California at San Diego, San Diego, CA*

Purpose
Acute leukemia in adults can directly involve the central nervous system (CNS), with additional CNS complications in the setting of the disease and treatment. Neuroradiologists should be familiar with these manifestations and vigilant about their identification, as many can be life threatening.
Materials and Methods
A review of the literature on CNS manifestations of acute leukemia in adults is highlighted. Cross-sectional imaging from a single institution experience is showcased to provide specific examples of these entities. Central nervous system sequelae following acute leukemia treatment also are presented as a comparison.
Results
Direct CNS manifestations of acute leukemia in adults include meningeal infiltration, chloroma, extraoccular or intraorbital involvement, extension into the skullbase and paranasal sinuses and bone marrow infiltration. Secondary findings related to malignancy include: hemorrhage, venous sinus thrombosis, infarction, sinusitis (including fungal), and intracranial infection. Post-treatment changes include: diffuse necrotizing leukoencephalopathy, mineralizing microangiopathy, posterior reversible encephalopathy syndrome (PRES), cerebellar degeneration, myelopathy and rarely CNS involvement of graft vs. host disease.
Conclusions
Understanding the CNS manifestations of acute leukemia in adults is essential for a neuroradiologist, as many of these can be life threatening requiring immediate intervention. Acknowledging the potential complications of treatment is equally important, and neuroradiologists should be familiar with the imaging findings.



(Filename: TCT_EdE-26_Slide1.jpg)

EdE-27

6:30AM - 3:00PM

Intracranial Complications of Radiotheraphy and Radiosurgery

S Bergamaschi[1], M Law[1], J Acharya[1], A Rajamohan[1], W Gibbs[1], P Kim[1], G Zada[1], E Chang[1]
[1]*University of Southern California, Keck School of Medicine, Los Angeles, CA*

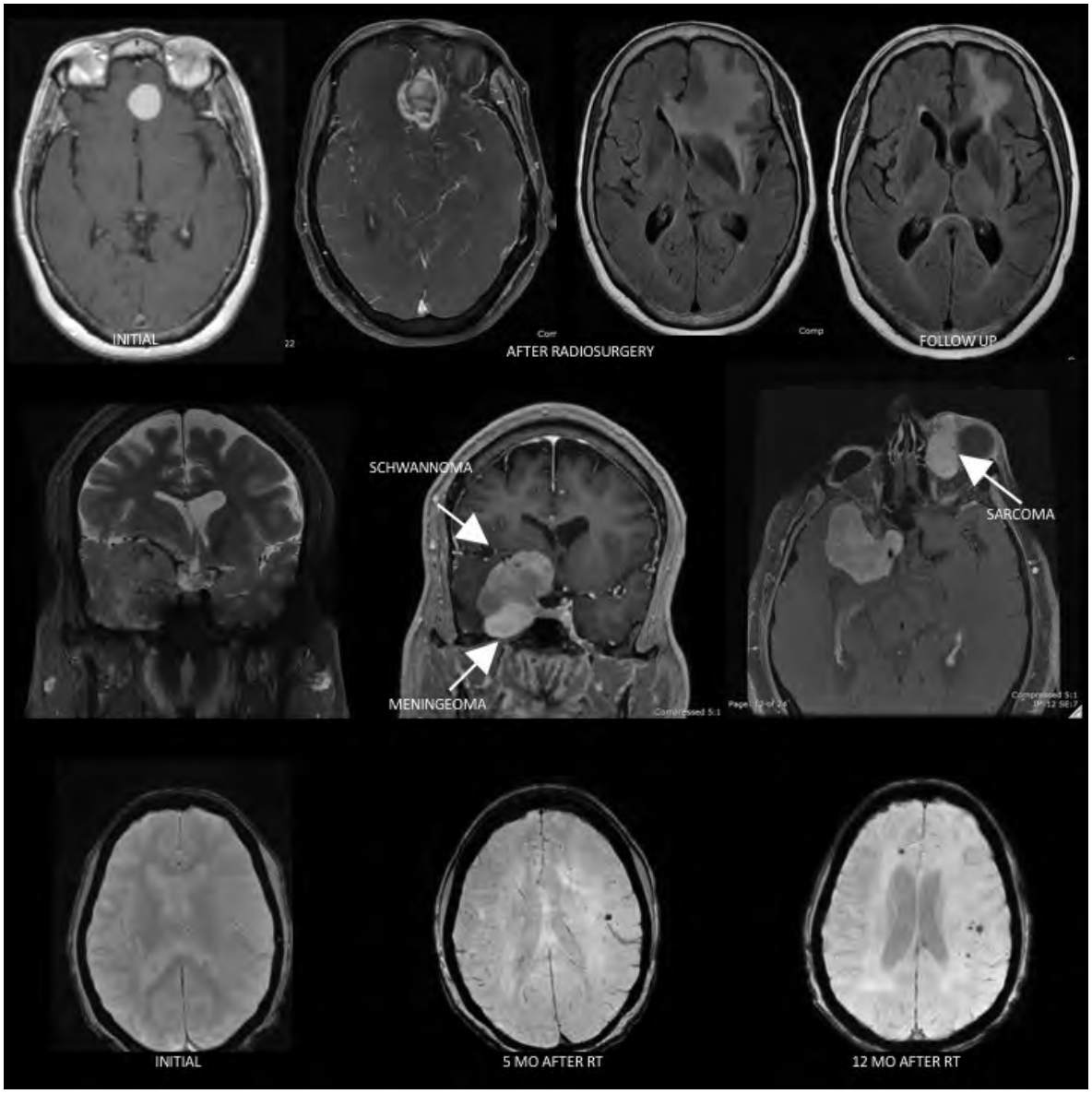
Purpose
Radiation therapy is part of the standard of care for many patients with brain tumors. Stereotactic radiosurgery (SRS) is used increasingly as an adjuvant therapy or primary treatment. However, despite newer, more focused techniques, radiation therapy can still cause significant neurotoxicity. Our purpose is to review the complications in patients receiving radiation therapy and SRS.
Materials and Methods
In this educational exhibit, we present case studies of patients who developed a variety of treatment-related complications related to conventional radiotherapy or radiosurgery for brain tumors.

Results

Radiation therapy can cause injury in 2 primary ways: by directly damaging the structures included in the radiation portal, or indirectly affecting the blood vessels, facilitate tumor development. We can categorize the lesions according to time of occurrence: 1) Acute (0-14 days), Early Delayed (4 weeks to months) and Late Delayed (months to years). Acute radiation encephalopathy is a rare complication, usually with a reasonably good prognosis. Pseudoprogression can occur in the first 3-6 months of glioma treatment, and can pose significant diagnostic difficulty. Delayed radiation necrosis usually occurs 1-2 years after radiation, but can be seen as early as 3 months. Patients submitted to radiation therapy also are at increased risk of developing leukoencephalopathy, dementia and normal pressure hydrocephalus. Radiation therapy also can predispose to delayed development of vascular malformations, including capillary telangiectasias and cavernous malformations. These patients also are at greater risk for large vessel atherosclerosis and small vessel disease. Tumors related to radiation therapy have a longer time to latency, the most common being meningiomas, followed by gliomas and sarcomas.

Conclusions

With the increasing application of radiotherapy for treatment of CNS tumors, it is important for the neuroradiologist to recognize the many possible radiation-related complications. Understanding the pathophysiology, typical time to onset, and imaging features allows for prompt diagnosis, appropriate treatment decisions, and increased probability of better patient outcomes.



(Filename: TCT_EdE-27_Exemplecomplicationsradiotherapy.jpg)

EdE-36

6:30AM - 3:00PM

Leptomeningeal Dissemination of Cancer: A Comprehensive Educational Review of Neuroimaging Findings and their Implications

M Ma[1], Y Kim[1], D Das[2], M Malhotra[1], R Paulmurugan[3], M Iv[4], T Massoud[1]
[1]Stanford University School of Medicine, Stanford, CA, [2]Stanford Hospital and Clinics, Stanford, CA, [3]Stanford University School of Medicine, Palo Alto, CA, [4]Stanford University Medical Center, Stanford, CA

Purpose
Entry of malignant cells into the subarachnoid space may result in multifocal or diffuse seeding of the leptomeninges along the surface of the neuraxis. If the primary is a solid tumor, this results in leptomeningeal carcinomatosis (LC). Leptomeningeal carcinomatosis is a serious complication of cancer, carrying significant morbidity and mortality, and usually is terminal. Recognition of LC is thus of the essence. In this educational exhibit we review the many neuroimaging manifestations of LC.
Materials and Methods
We comprehensively review and present a wide spectrum of neuroimaging findings in LC.
Results
First recognized by Eberth in 1870, LC remains a huge challenge in oncology. It occurs at presentation or as a late complication of cancer, most commonly by hematogenous metastases via leptomeningeal vessels, or direct extension from contiguous parenchymal tumors. Contrast-enhanced MRI is 77% sensitive and specific for LC, showing greatest infiltration at the basal cisterns, dorsal surface of the spinal cord, and the cauda equina. LC occurs with 1-5% of solid non-CNS tumors, and 1-2% of primary brain tumors. Adenocarcinomas most commonly produce LC, followed by small-cell lung cancers and melanomas. Breast cancers produce LC in 5% of cases, and because of its higher frequency, most patients with LC have breast cancer. Other LC is due to rhabdomyosarcoma, retinoblastoma, sarcomas, head and neck squamous cell carcinomas, and CNS tumors such as ependymomas, medulloblastomas, and germ-cell tumors. Importantly, the dismal prognosis of glioblastoma is especially true once it has spread to the leptomeninges (in 5-15%).
Conclusions
The diagnosis of LC is made with increasing frequency because of improved detection via routine use of MRI, and longer survival of patients by better systemic control. Neuroradiologists should be familiar with the imaging manifestations of LC which at times can be challenging. This presentation will aid in understanding the many imaging appearances of LC.

EdE-35

6:30AM - 3:00PM

Meningioma: Not Just Your Mother-in-Law's Tumor!

A Germana[1], J Gorman[1], J Whaley[1], A Cho[1], D Hawley[1], M Cathey[1]
[1]*Naval Medical Center San Diego, San Diego, CA*

Purpose
This electronic educational exhibit employs a case-based approach to provide an updated review of the wide spectrum of conventional and advanced imaging features associated with meningioma, emphasizing important considerations in atypical presentations.

Materials and Methods

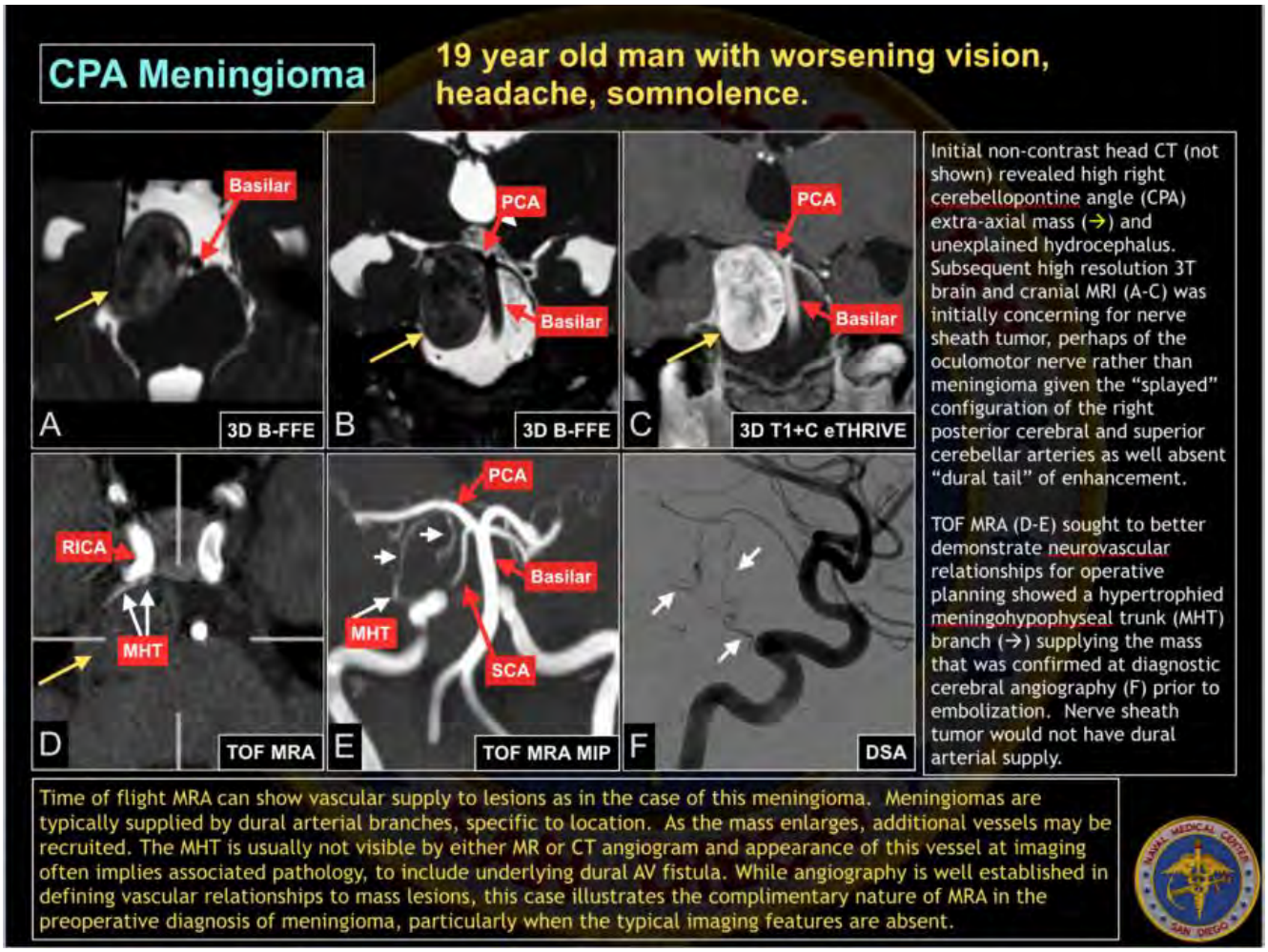
Case-based overview demonstrating the imaging abnormalities associated with meningioma, particularly those relating to unusual presentations of this otherwise common entity. We will review a variety of imaging characteristics that might lead one to propose meningioma as a lead diagnostic consideration, particularly in the absence of "classic" imaging signs. Key anatomic relationships most associated with meningioma will be highlighted and illustrated through the use of CT and high resolution 3T MR imaging, including MR angiography and spectroscopy.

Results

Meningioma accounts for up to a third of all reported primary central nervous system tumors in the United States. Accordingly, atypical presentations of this otherwise common entity should be expected to be encountered in general practice. Familiarity with both the classic and atypical imaging features of meningioma helps avoid false study interpretation that may otherwise increase patient morbidity at surgery. Advanced imaging techniques such as MR spectroscopy and MR angiography have been shown to increase specificity when the "classic" rules fail in providing diagnostic confidence. An understanding of the "many faces" of meningioma is a critical part of a neuroradiologist's practice.

Conclusions

Meningioma, while common, can present in a wide variety of fashions. If unrecognized, imaging features that might otherwise suggest meningioma as a lead diagnostic consideration can lead to misdiagnosis and unnecessary morbidity. The neuroradiologist plays a critical role in the diagnosis of meningioma and a comprehensive knowledge of this entity is paramount.



(Filename: TCT_EdE-35_CPAASNR2017.jpg)

EdE-29

6:30AM - 3:00PM

Metastatic SFT/HPC, an updated 2016 WHO reclassification and surveillance implication

T Le[1], D Kim[2], S Teoh[2], P Wen[3], P Sasson[2]
[1]Mount Auburn Hospital, Cambridge , MA, [2]Mount Auburn Hospital, Cambridge, MA, [3]Dana Farber Cancer Institute, Boston, MA

Purpose
"Intracranial hemangiopericytoma" accounts for 0.4% of CNS tumors and 2% of meningeal-based tumors is now re-classified under a single inclusive category of "solitary fibrous tumor/hemangiopericytoma" according to the updated 2016 World Health Organization (WHO) classification (1, 2). These mesenchymal tumors now are known to share a specific STAT6-NAB2 genomic fusion with higher grade subsets demonstrating the propensity for

local recurrence and delayed distant metastasis after a prolonged disease free interval (3). Our exhibit discusses a WHO grade II "solitary fibrous tumor/hemangiopericytoma" demonstrating delayed pancreatic metastasis after 7 years of dormancy. At the conclusion, we postulate a potential role for integrated radio-histo-genomic interpretation in future management of these tumors.

Materials and Methods

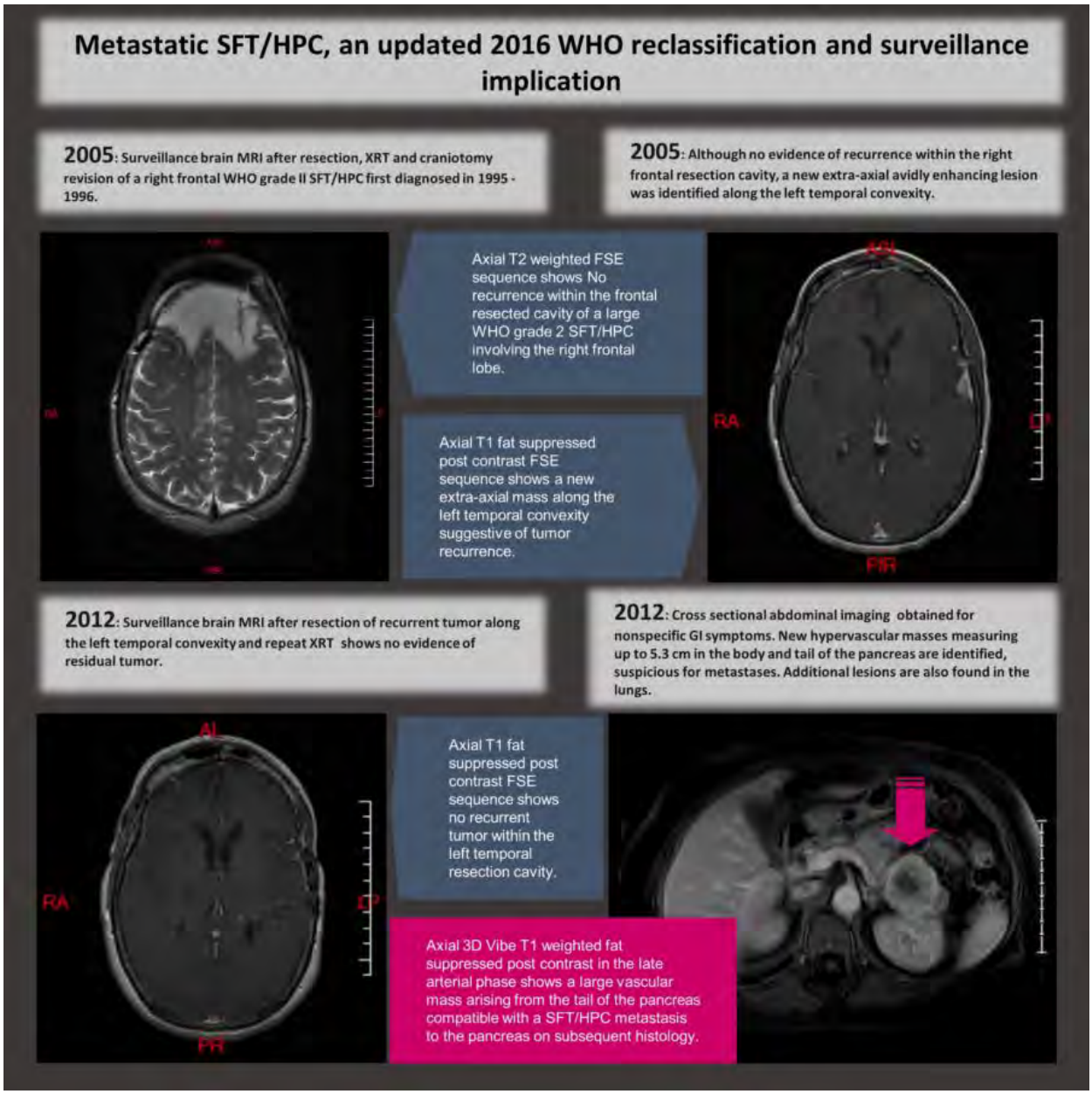
A retrospective review of electronic medical records and radiological imaging of a case of delayed metastatic WHO grade II "solitary fibrous tumor/hemangiopericytoma" initially diagnosed in 1995 with a disease-free interval from 2005 to 2012.

Results

"Intracranial hemangiopericytoma," now considered a WHO grade II neoplasm under the umbrella category of "solitary fibrous tumor/hemangiopericytoma," demonstrates a new paradigm shift in the understanding of neoplasms through the incorporation of both genetics and histology, potentially changing current treatment and surveillance. With future advancement in elucidating genomic biomarkers and radiological imaging, improvement in detection of aggressive tumors and their propensity for delayed extracranial metastases is possible (4). A broader surveillance strategy outside of the CNS should be advocated for higher grade tumors. In the context of the updated 2016 WHO classification for CNS tumor, there is a potential future utility of integrated radio-histo-genomic interpretation.

Conclusions

2016 WHO grade II "solitary fibrous tumor/hemangiopericytoma" has the propensity for local recurrence and delayed distant metastasis after a prolonged disease-free interval. There is a potential role for integrated radio-histo-genomic interpretation to guide treatment and surveillance.



(Filename: TCT_EdE-29_ASNRimagefile-TL-12062016.jpg)

EdE-05

6:30AM - 3:00PM

Neuroimaging Features in Deranged Glucose Metabolism

E Lee[1], Y Kang[2]
[1]Dongguk University Ilsan Hospital, Goyang-shi, Gyeonggi-do, [2]Dongguk University Ilsan Hospital, Goyang-si, Gyeonggi-do

Purpose

The brain is a glucose glutton, consuming more than half the body's total glucose. Blood glucose levels are tightly regulated and normally are maintained within a narrow physiologic range. Disorders of glucose metabolism (both hypoglycemia and hyperglycemia) can injure the CNS. The neurologic manifestions of deranged glucose metabolism range from mild, reversible focal deficits to status epilepticus, coma and death. In this educational exhibit, we depict characteristic neuroimaging features in acute and chronic hyperglycemia-associated disorders, as well as hypoglycemia-associated disorders.

Materials and Methods

The brain relies heavily on a continuous supply of glucose for optimal function. Significant variations in plasma glucose levels, be it hypoglycemia or hyperglycemia, can present with myriad clinical manifestations and may mimic stroke. Imaging can play a vital role by suggesting the correct diagnosis and ensuring early treatment. This is vital because delayed diagnosis affects morbidity and mortality. We present neuroimaging features on hyperglycemic and hypoglycemic conditions. Hyperglycemia-associated brain injury can be chronic or acute. In hypoglycemia-associated disorders, imaging findings in neonatal and adult hypoglycemia are separately depicted, because the clinical and imaging manifestations differ in neonates from those of older children and adults.

Results

The effects of chronic hyperglycemia on the brain are related to accelerated arteriolosclerosis and lipohyalinosis with silent infarcts, increased numbers of T2/FLAIR subcortical and periventricular hyperintensities and brain volume loss, leading to decreased cognitive functioning. Acute brain injury in hyperglycemia is less common than in hypoglycemia. Acute hyperglycemia-associated disorders include hyperglycemia-induced hemichorea-hemiballismus, hyperglycemia-induced seizures and acute bilateral basal ganglia lesions in diabetic uremic patients. In acute hyperglycemia-associated disorders, the clinical and imaging findings usually are reversible after correction of hyperglycemia or metabolic derangement. On MR imaging of adult hypoglycemia, the earliest changes are seen on DWI sequences. The involved regions show restricted diffusion. The extent of the abnormalities depends on severity and duration of hypoglycemia. Patients with focal involvement of the internal capsule, corona radiata, or splenium usually have a good prognosis. Involvement of the neostriatum and diffuse cortical lesions often portend dismal outcome. Transient hypoglycemia is relatively common in neonates as they transition from intrauterine to extrauterine environment. However, prolonged and/or severe hypoglycemia can result in devastating brain injury. Neuroimaging findings in neonatal hypoglycemia show a predilection for occipital and parietal lobe involvement.

Conclusions

Abnormal variations in plasma glucose levels are not uncommon and can show myriad imaging findings. Neuroimaging can suggest the diagnosis in unsuspected cases and can help in the assessment of the extent of neuronal damage in known cases. A timely and accurate

diagnosis would expedite correct treatment and limit neuronal injury in the early stage, when changes potentially are reversible.

EdE-01

6:30AM - 3:00PM

Neuroimaging of Primary Progressive Aphasia Variants

A Wasim[1], J McConathy[2], M Love[3], E Middlebrooks[2]
[1]University of Alabama at Birmingham, Birmingham , AL, [2]University of Alabama at Birmingham, Birmingham, AL, [3]UAB Neurology, Birmingham, AL

Purpose
Primary progressive aphasia (PPA) is a neurodegenerative syndrome with the common feature being aphasia in the absence of marked impairment in other cognitive and behavioral domains. Three clinical phenotypes are generally recognized: (1) nonfluent or agrammatic (navPPA); (2) semantic (svPPA); and (3) logopenic (lvPPA) variants(1). A fourth "mixed" phenotype also has been described; however, there is evidence that these patients show atrophy patterns identical to lvPPA. These diverse clinical phenotypes have considerable pathologic overlap with other neurodegenerative syndromes, such as Alzheimer disease and fronto-temporal dementia and clinical diagnosis can sometimes be challenging(1). Unfortunately, the unique imaging findings of the different phenotypes have highly variable sensitivity and specificity. The prevailing "dual-stream" model of language posts a dorsal and ventral stream of language processing. The dorsal components connect the posterior temporo-parietal region with the frontal operculum and are largely responsible for phonological encoding, fluency, and grammatical structure (2). The ventral components connect posterior peri-Sylvian language areas with the anterior temporal lobe and frontal operculum functioning primarily in lexicosemantic associations that link words to their meaning (2). Based on this knowledge, we can identify specific areas of atrophy or hypometabolism corresponding to clinical language deficits. Underlying white matter (WM) tract abnormalities also can be identified. These are important since evidence exists suggesting direct axonal injury, particularly in tau pathologies, rather than purely Wallerian degeneration. The aim of this exhibit is the portrayal of imaging features in PPA subtypes using MRI, PET, and diffusion MRI. Based on this information, the neuroradiologist potentially can add valuable information in correctly categorizing these patients and their potential underlying pathology.
Materials and Methods
A thorough literature review was performed with an emphasis on neuroimaging findings in primary progressive aphasia. In addition, other commonly used monikers, such as "semantic dementia" and "progressive nonfluent aphasia" also were searched. Lastly, AD and FTLD literature were reviewed to identify patients within select studies exhibiting features of any PPA subtype. Select example images also were collected from patients presenting to our

institutional memory disorders clinic with the confirmed diagnosis of PPA using the consensus diagnostic guidelines.

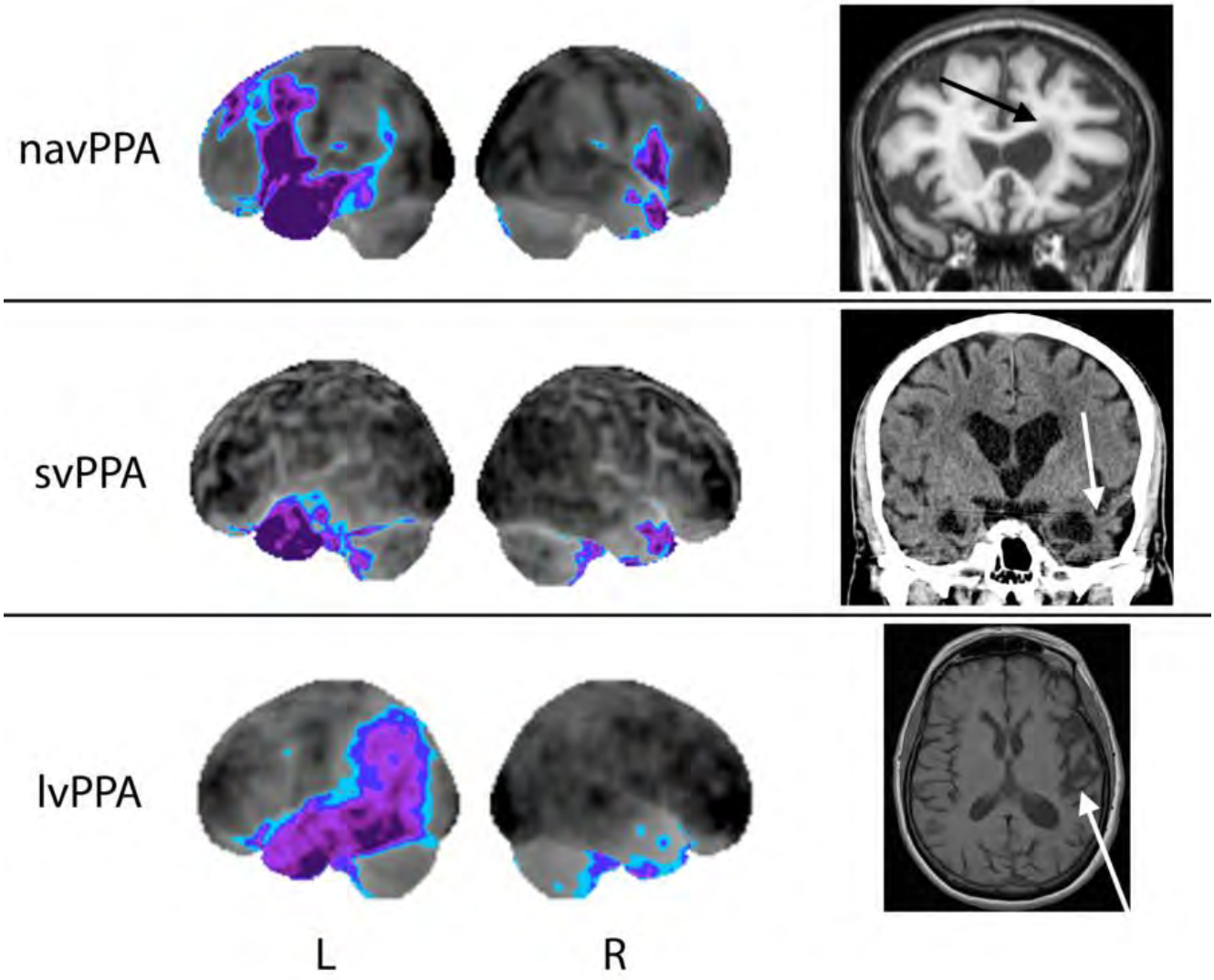
Results

navPPA: Agrammatism with relatively preserved single word comprehension, but abnormal sentence comprehension. Speech is effortful and nonfluent. Pathology is typically FTLD-tau(1). MRI: Predominant left posterior fronto-insular atrophy (Sens:67%;Spec:92%) (3). FDG-PET: Predominant left posterior fronto-insular hypometabolism. (Sens:91.6%;Spec:100%). DTI: Severe WM damage in dorsal tracts [frontal aslant tract and superior longitudinal fasciculus (SLF)] with relative sparing of ventral tracts. Severity suggests direct WM damage, typical of tauopathy, plus Wallerian degeneration(4). Other PET: Positive amyloid PET in 0-27%; Few tau PET studies - positive scans with left inferior fronto-parietal and insula uptake. svPPA: Abnormality of single word comprehension and confrontation naming with relatively preserved grammar, fluency, and repetition. Pathology is FTLD-TDP in 75-80%(1). MRI: Atrophy of the anterior temporal lobe (unilateral or bilateral) (Sens:100%;Spec:100%)(3). FDG-PET: Predominant an interior temporal hypometabolism.(Sens:60%;Spec:100%). DTI: Severe derangement in ventral stream [inferior fronto-occipital, uncinate, and inferior longitudinal fasciculi (ILF)] with relative sparing of dorsal tracts. Severity also suggests direct WM damage (4).Other PET: Amyloid PET positive 0-12.8%; Few tau PET studies - L>R anterior temporal uptake lvPPA: Slow speech with impaired repetition and comprehension. Relative sparing of grammar, motor control, and single word comprehension. Pathology is predominantly AD-type (1)MRI: Atrophy of the left posterior perisylvian region(Sens:57%;Spec:95%)3 FDG-PET: Predominant left posterior perisylvian hypometabolism (Sens:91.6%;Spec:94.4%) DTI: Milder, but widespread WM changes including dorsal tracts (arcuate fasciculus and SLF), as well as ventral tracts (ILF). Milder changes suggest primarily Wallerian degeneration, typical of amyloid pathology 4.Other PET: Amyloid positive in 84.9%; Few tau PET studies - L>R hemisphere uptake

Conclusions

Primary progressive aphasia encompasses a diverse group of neurodegenerative syndromes with a variety of underlying pathology. Although there are distinct clinical features as part of the diagnostic criteria, many patients fail to fit within these constrained clinical syndromes. The addition of neuroimaging may play a significant role in further characterizing these syndromic variants; therefore, it is essential to understand the spectrum of common imaging findings. Subjective structural MRI findings have a wide variability in predictive value with svPPA being relatively high, but navPPA and lvPPA being less sensitive. Quantitative neuroimaging to detect subtle cortical thickness change may be of some value, but currently there is no strong evidence supporting the role of such computer-based morphometrics in the clinical setting. The combination with functional neuroimaging, such as FDG-PET, can greatly increase the predictive value for diagnosing PPA; however, there is still substantial heterogeneity that likely has a basis in the heterogenous pathology of these clinical syndromes. The addition of novel PET radiotracers, such as tau and amyloid markers, may

help to better characterize the molecular pathology of these diseases in the future. In the current clinical setting, a knowledge of the typical distribution of atrophic change and hypometabolism can add value to the management of patients presenting with progressive language deficits.



(Filename: TCT_EdE-01_PPAFIG.jpg)

EdE-24

6:30AM - 3:00PM

Neuroimaging of Substance Abuse: A Pictorial Review

M Naveed[1], R Mehta[1], R Mangla[1], A Swarnkar[2], S Destain[1]
[1]SUNY Upstate Medical University, Syracuse, NY, [2]Upstate Medical University Hospital, Jamesville, NY

Purpose

Substance abuse is endemic in almost all age groups, races and socioeconomic backgrounds in United States. Use of drugs such as alcohol, marijuana, heroin, cocaine and amphetamines are associated with significant morbidity and mortality. Computed tomography and MRI imaging of brain are useful in diagnosing and assessing adverse effects due to this disease. This exhibit will review the neuroimaging features, complications and neuropathologic effects of substance abuse.

Materials and Methods

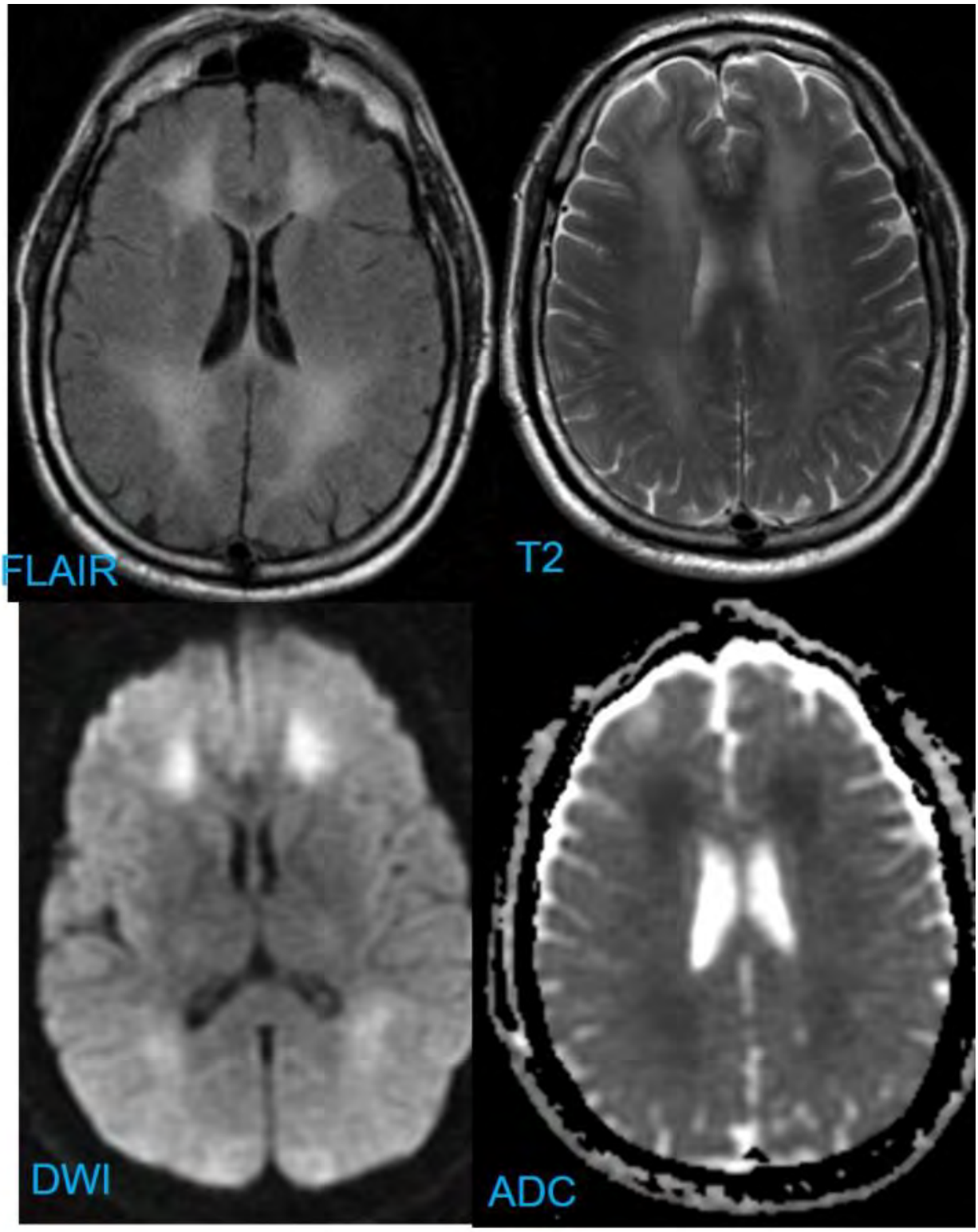
The goals of this exhibit are to describe the pathophysiology, and the acute and chronic changes related to various drugs, and will aid the radiologist in diagnosing, and the clinician in treating patients who suffer from this disease.

Results

This exhibit will include a pictorial review of the CT and MRI findings of commonly used drugs including alcohol, marijuana, heroin, methadone, cocaine, amphetamines and others. Classic imaging appearances that are useful to make the diagnosis will be reviewed. Secondary pathologic changes including vasculitis, thrombosis, vasospasm, white matter changes, cortical atrophy, edema, neuronal loss and gliosis will be depicted. As an example, the representative case shows periventricular white matter confluent and symmetric hyperintensities on the T2 and FLAIR images with sparing of subcortical U-fibers and same areas show diffusion restriction on DWI and ADC maps. These findings are suggestive of methadone toxicity.

Conclusions

Substance abuse may be challenging to diagnose, and it is important to correlate the clinical history with the neuroimaging findings. The pictorial review will allow the readers to gain familiarity with the myriad appearances of acute and chronic substance abuse and their associated complications in the brain. Readers should be familiar with the neuroimaging appearances, and able to differentiate substance abuse from other differential diagnostic possibilities such as ischemic, demyelinating, and infectious diseases. Early recognition of the findings and associated complications related to substance abuse are essential to proper management.



(Filename: TCT_EdE-24_Methadone.jpg)

Ede-07

6:30AM - 3:00PM

Neurologic Manifestations of Diabetes: A Pictorial Review

K Riley[1], J Tejada[1], J Kovoor[1], R Shastri[1]
[1]*Indiana University, Indianapolis, IN*

Purpose
Diabetes mellitus is a major cause of morbidity and mortality worldwide, affecting more than six percent of the adult population. Many of the primary comorbid conditions associated with diabetes including cardiovascular disease, retinopathy, nephropathy, and neuropathy are well understood by most healthcare providers. However, there are several intracranial and spinal manifestations associated with diabetes with distinct neuroimaging findings, some of which may have devastating consequences to the patient if not rapidly recognized and treated. The purpose of this exhibit is to review the typical neuroimaging findings of these conditions and help the interpreting radiologist to quickly recognize and communicate these findings.
Materials and Methods
This exhibit provides a comprehensive overview of the classic imaging findings on CT and MRI examinations of the maxillofacial bones, brain, and spine of several intracranial and spinal manifestations of diabetes, some of which portend an extremely poor prognosis if not quickly diagnosed and treated.
Results
Diabetes may manifest within the head, neck and spine in several different ways, including cerebral edema, invasive rhinosinusitis, cerebrovascular diseases, spinal epidural abscess, and also more rare conditions such as non-ketotic hyperglycemic hemichorea. Radiologists need to be familiar with the typical findings of these conditions, both in order to make a timely diagnosis but also to distinguish from other conditions that can appear similar, particularly in a scenario such as nonketotic hyperglycemic hemichorea where the basal ganglia are predominantly affected and may be confused for other toxic/metabolic etiologies.
Conclusions
This exhibit provides the reader with a greater understanding of the various intracranial and spinal manifestations of diabetes and their classic imaging findings. Knowledge of these conditions will allow the radiologist to make accurate and timely diagnoses and help to decrease patient morbidity and mortality.

EdE-20

6:30AM - 3:00PM

Neuroradiological Manifestations of IgG4 Related Disease

P Mehta[1], N Madan[2], Y Chang[3], J Gao[4]

[1]Beth Israel Deaconess Medical Center, Boston, MA, [2]Tufts Medical Center, Boston , MA, [3]Beth Israel Deaconess Medical Center, Newton, MA, [4]Tufts Medical Center, QUINCY, MA

Purpose

IgG4 - related disease (IgG4-RD) is an immune-mediated condition that comprises a group of disorders with common pathologic, serologic, and clinical features, usually precipitated by infiltration of IgG4-positive plasma cells and lymphocytes with fibrosis and tumor-like swelling of the involved organs. Most patients have an elevated serum IgG4-serum concentration, with the two most common presentations of this condition being type 1 autoimmune pancreatitis and salivary gland disease. Three major diagnostic criteria are commonly utilized: 1) elevated serum IgG4 concentrations, 2) characteristic swelling or masses in one or more organ groups and 3) histologic dense lymphoplasmacytic infiltrate rich in IgG4 plasma cells and storiform fibrosis. While many organ manifestations of IgG4-RD such as sclerosing pancreatitis, retroperitoneal fibrosis, and sclerosing cholangitis have been described, neurological manifestations of IgG4 disease are exceedingly rare. It is important for the radiologist to be familiar with head and neck manifestations of IgG4-RD as associated multi-organ involvement strongly supports the diagnosis of IgG4-RD. The purpose of this educational exhibit is to offer an instructional review of the imaging findings of neurological IgG4-RD.

Materials and Methods

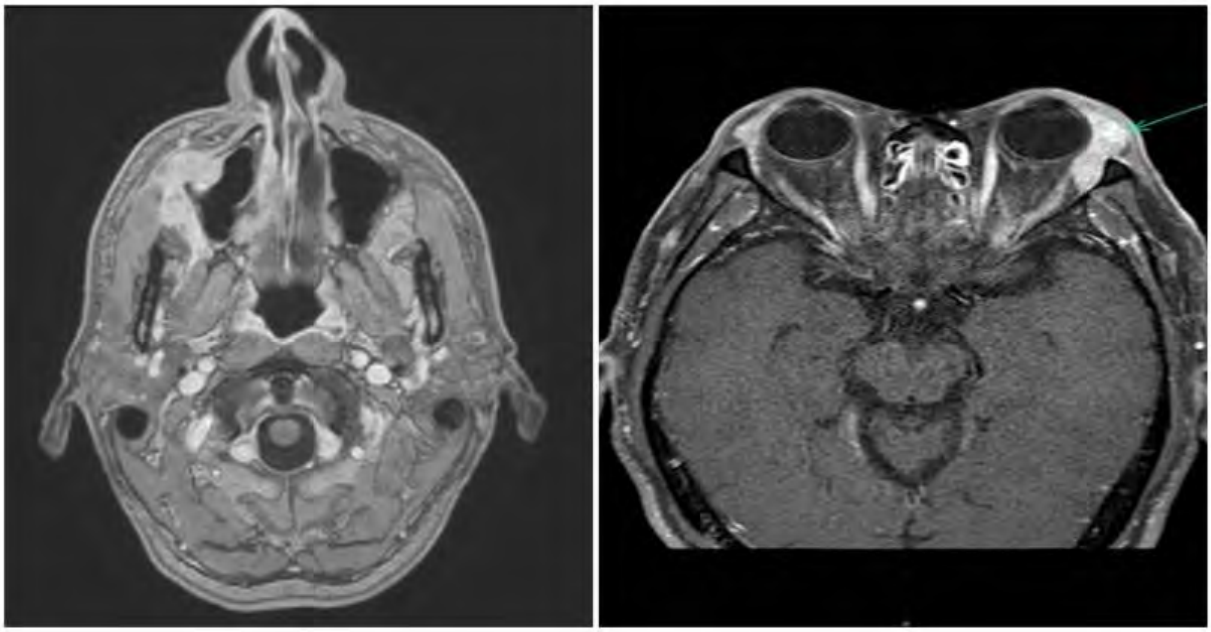
Imaging from Beth Israel Deaconess Medical Center and Tufts Medical Center in Boston, MA was obtained for 5 patients with serologically proven IgG4-RD and reviewed. In addition, a brief review of the existing literature will be presented.

Results

This educational exhibit will review many of the neurological manifestations of IgG4-RD including involvement of the lacrimal glands, bilateral trigeminal nerves, sialdenitis of the parotid and submandibular glands, retroantral fat and involvement of the cervical lymph nodes.

Conclusions

IgG4-related disease is a systemic disease with a wide variety of head and neck manifestations. Given that the disease responds well to corticosteroids, the neuroradiologist should be familiar with the neurological manifestations to avoid a delay in diagnosis, and more importantly, to avoid unnecessary invasive procedures.



(Filename: TCT_EdE-20_Presentation1.jpg)

EdE-39

6:30AM - 3:00PM

Neuroradiology, It's a Zoo Out There.

E Boomgarden[1], I Wu[2]
[1]Indiana University School of Medicine, Indianapolis, IN, [2]Indiana University, Carmel, IN

Purpose
Visual mnemonics are a powerful learning technique which make use of imagery as a tool for efficient memory retention. The more whimsical a visual mnemonic is, the greater the chance it will have to help a learner achieve memory retention. In radiology, such visual mnemonics, or "signs," are abundant and are often very useful for learning anatomical structures or pathologies. This electronic educational presentation will provide a subset of such visual mnemonics: specifically "animal signs" in neuroradiology. These signs include familiar ones such as "eye of the tiger" for pantothenate kinase-associated neurodegeneration

(PKAN) and "double eagle" sign for the hypoglossal canal. We also will provide our own novel signs. Multiple imaging examples of each sign will be provided to reinforce this whimsical, but valuable learning method in neuroradiology.
Materials and Methods
A retrospective review of images from a large tertiary referral center will be performed to obtain original CT and MR images of various animal signs, along with corresponding images of the animals and creatures. From these cases, a PowerPoint presentation is generated to provide a comprehensive list of these visual mnemonics.
Results
We have already come up with 15 animal signs in neuroanatomy, some of which are our own novel visual mnemonics. Examples of these new animal signs include "trail left by the snail" for the cochlear aqueduct and "click beetle" for Le Fort fractures.
Conclusions
Radiologists are by nature visual learners. Tapping into this inherent attribute aids in learning the complex anatomy found in the human brain. Whimsical visual aids, such as animal signs, can help turn one of the most laborious aspects of Radiology, learning complex anatomy, into a more fun and interesting endeavor.

EdE-15

6:30AM - 3:00PM

Post Cranial Surgical Complications: Review of Imaging Findings

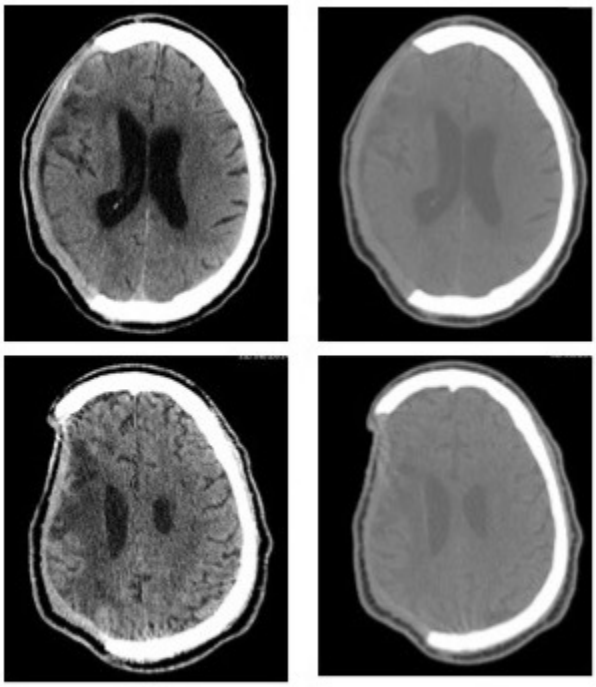
M Gharavi[1], M Markovic[2], s ganapathy[3]
[1]Northeastern Ohio Medical University/Aultman hospital, North canton, OH, [2]Aultman hospital, Caton, OH, [3]Akron Children Medical Center, Akron, OH

Purpose
The purposes of this study are: -To briefly review the normal cranial anatomy. -To review some of the standard neurosurgical techniques with their expected postoperative imaging appearances. -To review the common postneurosurgical complications that may occur and their imaging presentations.
Materials and Methods
The normal anatomy of scalp, skull vault and meninges will be reviewed.Then, some of the standard and commonly used neurosurgical techniques such as burr holes, cranioplasty, craniotomy and craniectomy along with their indications and expected postsurgical appearances on CT or MRI will be described. Subsequently, several cases of common postoperative complications such as brain abscess, extra-axial empyema, hemorrhage, tension pneumocephalus, CSF leakage, pseudomeningocele, sinking flap and paradoxical herniation will be presented and their imaging findings will be discussed.
Results
The details of the neurosurgical intervention often are not available for the reporting

radiologists.Therefore, knowing the expected postoperative appearance of the certain neurosurgical procedures as well as imaging presentations of postoperative complication will help the radiologists to determine what procedure has been performed and what complications may have occurred.

Conclusions

It is essential for the radiologists to be familiar with the normal CT and MR imaging appearances of the different types of neurosurgical intervention and complications that may occur with each of them to prevent a delay in treatment and diagnosis.



Sixty-five year old man post decompressive craniectomy (superior row) who developed sinking flap syndrome(inferior row).

(Filename: TCT_EdE-15_sinkingflap.jpg)

EdE-04

6:30AM - 3:00PM

Potent Potables: Examining Acute and Chronic CT and MRI Imaging Patterns Of Ethanol and Methanol Poisoning

V Yedavalli[1], S Chhadia[1], R Stimpson[1], A Patil[1]
[1]*Advocate Illinois Masonic Medical Center, Chicago, IL*

Purpose

In this review, we examine the characteristic CT and MRI imaging patterns of acute and chronic alcohol intoxication, focusing on ethanol and methanol, while correlating with the

pathophysiology of each subtypes to achieve a better understanding of the imaging manifestations. In doing so, we hope to achieve accurate diagnosis for timely patient care.
Materials and Methods
Alcohol intoxication can present in many forms leading to diagnostic dilemmas. We review both CT and MRI acute and chronic imaging patterns of ethanol and methanol toxicity. In acute ethanol intoxication, we delineate imagings findings of Wernicke's Encephalopathy, Marchiafava Bignami, Osmotic Demyelination Syndrome, and Acute Hepatic Encephalopathy with attention to characteristic CT and MRI imaging features of each entity. We similarly illustrate distinguishing imaging characteristics of acute methanol intoxication. We also delve into chronic ethanol poisoning by focusing on Chronic Acquired Hepatic Encephalopathy and Seizure Like Syndromes. Finally, we elucidate CT and MRI imaging features of chronic methanol poisoning as it can manifest as multiple sclerosis mimics. In addition to detailing the distinct imaging features, we also correlate these entities with their respective pathophysiology.
Results
Alcohol intoxication can be a life threatening condition in both acute and chronic forms. This review examines both ethanol and methanol toxicity and further stratifies into common acute and chronic subtypes of each entity. In doing so, we utilize a systematic approach to recognize differentiating CT and MRI imaging features of each subtype. Additionally, we further detail the pathophysiology behind each entity in order to gaining a deeper understanding how these imaging features occur.
Conclusions
With the varied presentations of alcohol intoxication, it is essential to have a systematic approach for both recognizing and understanding the distinguishing CT and MRI imaging patterns and underlying pathology of both acute and chronic subtypes of ethanol and methanol intoxication. In doing so, we hope to achieve accurate and timely diagnosis of these entities for improved clinical management.

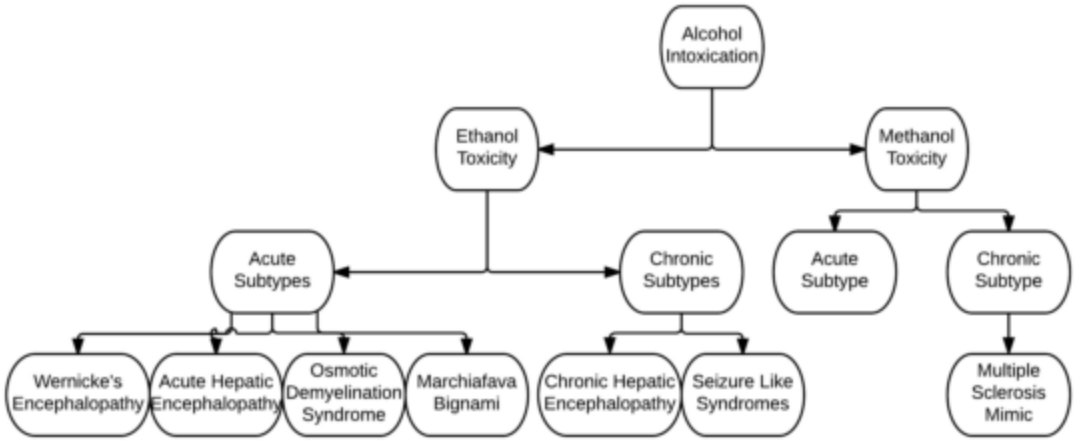


Figure 1: Flowchart of Differentiating Alcohol Intoxication, Stratifying Ethanol and Methanol into Acute and Chronic Subtypes.

(Filename: TCT_EdE-04_Alcohol_Intoxication_Diagram_-_Page_1_1_.gif)

EdE-08

6:30AM - 3:00PM

Preoperative Functional Assessment in Patients with Epilepsy

M Cekic[1], P Walshaw[2], N Salamon[3]
[1]Ronald Reagan UCLA Medical Center, Los Angeles, CA, [2]Ronald Reagan UCLA Medical center, Los Angeles, CA, [3]UCLA, Los Angeles, CA, David Geffen School of Medicine at UCLA, Los Angeles, CA, Los Angeles, CA

Purpose
Postoperative deficits in language and memory are a major risk following surgery for epilepsy, making accurate pre-operative functional mapping of hemispheric language and memory dominance of paramount importance in surgical planning. We propose to discuss current approaches to pre-operative functional evaluation in patients with epilepsy in terms of seizure focus determination, assessment of the operative risks, operative planning, and postoperative functional outcomes.
Materials and Methods
We will discuss the literature and our experience with approaches to pre-operative evaluation of a series of patients undergoing surgical intervention for epilepsy. We consider evaluation methods including neuropsychological testing, advanced imaging techniques (diffusion tensor imaging (DTI), functional MRI (fMRI), magnetoencephalography (MEG), positron emission tomography (PET) and more invasive procedures such as the intracarotid amobarbital (Wada) test and monitored and intra-operative electrocorticography (ECoG) and their scope, appropriateness, and benefit in pre-operative assessment. Consideration also is given to the validity of pre-operative assessment in comparison to postoperative evaluation and functional outcomes. Finally, we discuss emerging technologies and future directions.
Results
Pre-operative functional mapping has been shown to be beneficial in localizing epileptogenic foci, determining the proximity to and potential vulnerability of adjacent fiber tracts and/or eloquent cortex, and predicting the type and degree of functional (memory, language, motor) deficit expected after surgery. Pre-operative mapping also may be helpful in determining the optimal surgical approach. In a significant number of cases postoperative deficits may be reduced or at least anticipated; or it may be determined that surgery is not an option in cases where the lesion is in close proximity to eloquent cortex or key functional structures and alternative methods of treatment such as electrode implantation may be considered. Patients with atypical or unusual functional localization may additionally benefit from multimodal approaches prior to lesion resection.
Conclusions
Pre-operative functional brain mapping using advanced imaging techniques is of benefit in

terms of surgical planning and improved functional outcomes in patients undergoing neurosurgical intervention for epilepsy. We discuss the current approaches to pre-operative assessment and their application in a variety of clinical scenarios.

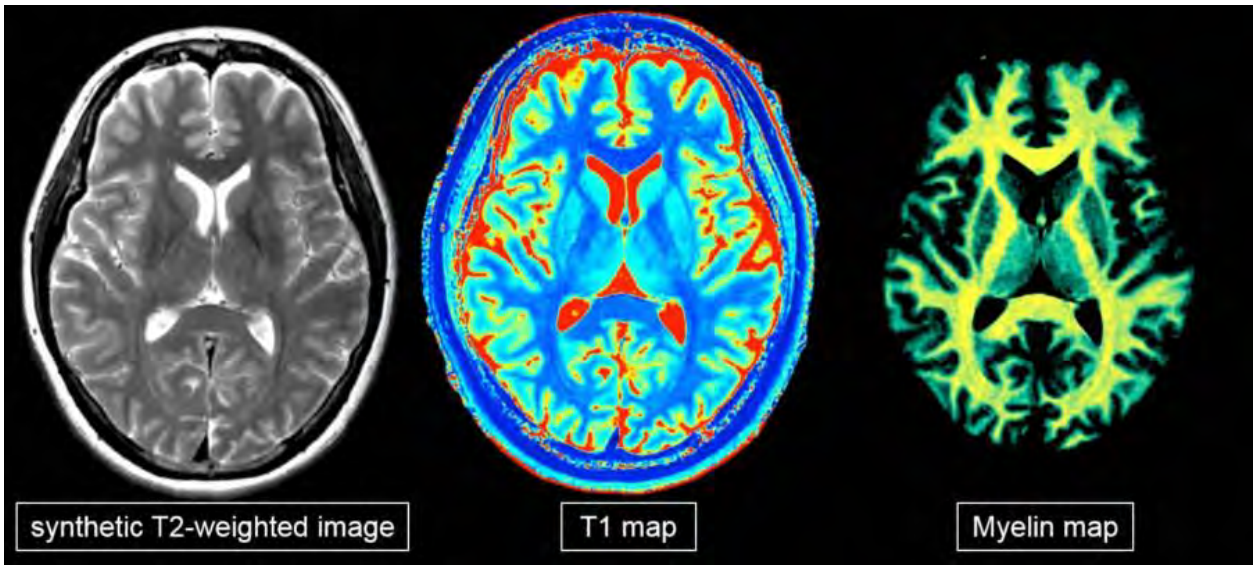
EdE-37

6:30AM - 3:00PM

Rapid Simultaneous Tissue Relaxometry and Synthetic MRI of the Brain

A Hagiwara[1], M Hori[1], C Andica[2], M Nakazawa[2], Y Takahashi[3], S Aoki[2]
[1]Juntendo University School of Medicine, Tokyo, Japan, [2]Juntendo University School of Medicine, Tokyo, Tokyo, [3]Juntendo University School of medicine, Bunkyoku, Tokyo

Purpose
Conventional MR images usually are evaluated using the image signal contrast between tissues and not on their absolute signal intensities. Quantification of tissue parameters, such as relaxation times and proton density, would provide absolute scales, which are independent of intrinsic scanner imperfections or pulse sequence variations. However, these methods have mainly been performed in a research setting. The development of rapid quantification, with scan times in the order of 6 minutes for full head coverage, provided the prerequisites for clinical use (1). This educational exhibit introduces a specific quantification method and synthesis of contrast-weighted images based on the acquired absolute values. We call these methods "SyMRI" as a whole. Furthermore, automatic segmentation of brain tissues (2) and myelin measurement (3), based on these quantitative values, and application of these techniques to various brain diseases also will be discussed.
Materials and Methods
The development of a new pulse sequence, which is called Quantification of Relaxation Times and Proton Density by Multiecho acquisition of a saturation-recovery using Turbo spin-Echo Readout (QRAPMASTER) realized simultaneous quantification of T1, T2 and PD in a scan time of around 6 minutes for full head coverage. The basic principles and applications of SyMRI and use of it for various diseases, e.g. multiple sclerosis, brain metastases, Sturge-Weber syndrome, and meningitis, are depicted in this exhibit.
Results
Quantitative analysis based on SyMRI enables objective description of brain diseases. SyMRI is useful for detecting brain lesions by adjusting contrast-weighting after quantification by virtually setting the TR, TE, and TI (4).
Conclusions
SyMRI is useful for evaluating brain disorders. The quantitative values can be used for automatic segmentation, volumetry and estimation of myelin volume. Any contrast-weighted image can be created based on these values.



(Filename: TCT_EdE-37_educational.jpg)

EdE-30

6:30AM - 3:00PM

Sagittal Midline T1W Image of the Brain: Give It the Attention It Deserve!!

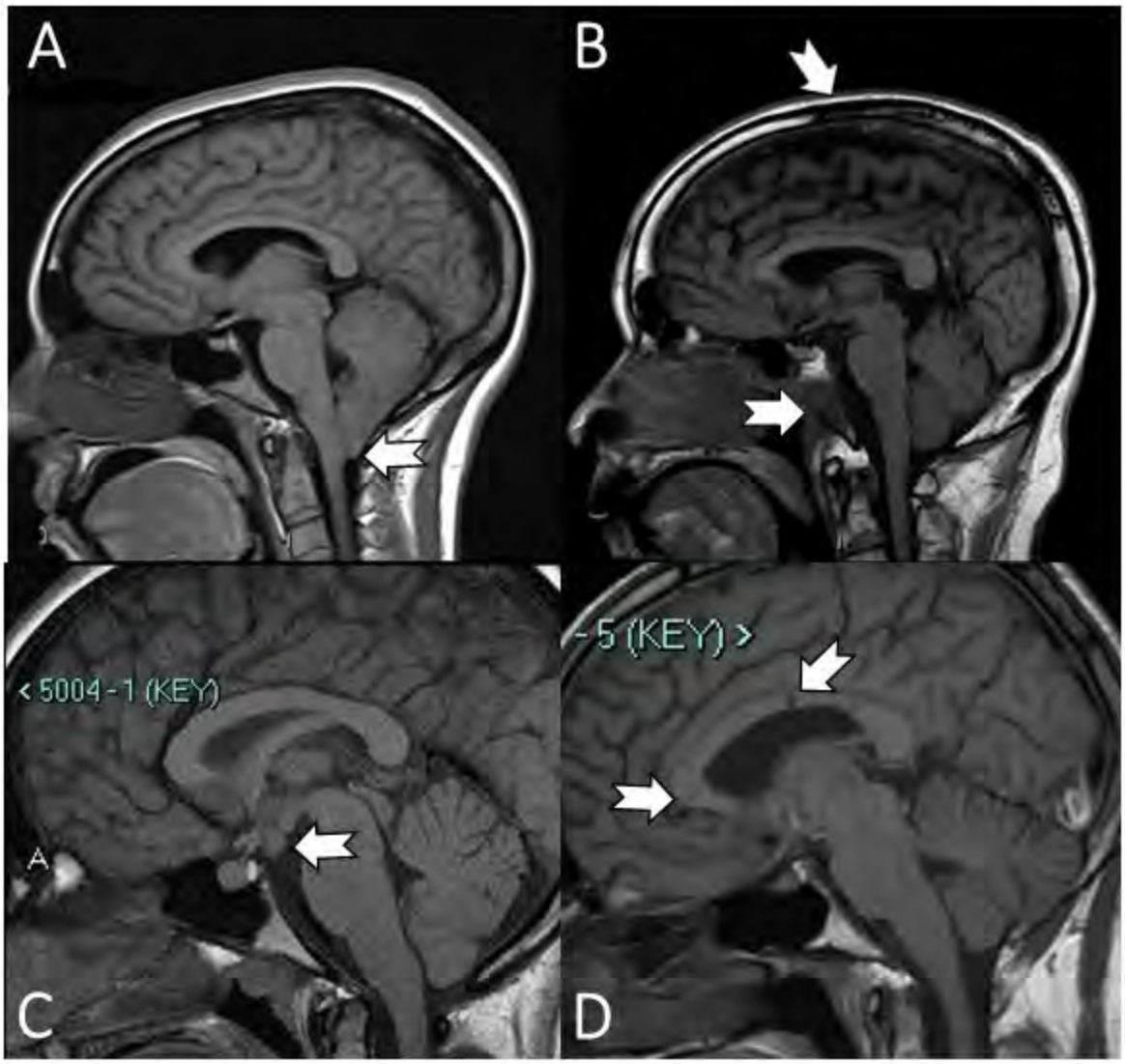
H El Khudari[1], P Prakash[2], R Rojas[3], Y Chang[4], R Bhadelia[3]
[1]St Vincent Hospital, Worcester, MA, [2]St Vincent Hospital, Worcester , MA, [3]Beth Israel Deaconess Medical Center, Boston, MA, [4]Beth Israel Deaconess Medical Center, Newton, MA

Purpose
A midline sagittal T1W image of the brain is a high yield image carrying immense information which might not be obvious on other sequences. It is however, often under-utilized. The purpose of our abstract is to discuss the anatomy and corresponding pathologies a radiologist should be looking for on a sagittal midline T1 image.
Materials and Methods
Specific examples will be used to enumerate and discuss the midline brain structures and associated disease processes. Examples include: 1. Pituitary gland and pituitary infundibulum. 2. Supra-sellar region and hypothalamus. 3. Corpus callosum. 4. Inferior frontal and occipital lobes. 5. Third ventricle, cerebral aqueduct and fourth ventricle. 6. Pineal gland. 7. Basilar artery. 8. Superior sagittal sinus, Vein of Galen, Straight sinus, Confluence of sinuses. 9. Foramen magnum and craniocervical junction. 10. Clivus and sphenoid sinus. 11. Nasopharynx and oropharynx. 12. Upper cervical spine.
Results
For a thorough evaluation, to minimize the misses while being efficient in the review, every radiologist relies on a search pattern. The sagittal T1W images of the brain demonstrate the midline brain anatomy better than any other sequences which are acquired as a part of the

routine brain MRI. It also allows for assessment of marrow signal in the clivus and skull. Hence, one can gather a lot of information including signal and thickness of corpus callosum; position of tonsils for Chiari malformation, marrow signal in clivus for osseous metastasis, sellar and suprasellar fossa masses, pineal gland masses, nasopharyngeal masses, etc. by spending a few minutes on one image slice in the data rich brain MRI. This detailed anatomy and possible associated pathology should be a part of every radiologist's "search pattern" to avoid subtle misses.

Conclusions

Understanding midline brain anatomy is very crucial for optimum utilization of Sagittal midline brain T1W MR imaging. Certain brain pathologies can be more easily and confidently diagnosed by properly reviewing the sagittal midline imaging. So radiologists and in particular neuroradiologists should have a detailed and comprehensive understanding of the anatomy and pathology of the midline brain structures in order to optimize the use of Sagittal midline T1W brain MR imaging.



A: Chiari 1 Malformation: Tonsills projecting more than 5 mm below foramen magnum. B: Clival Metastasis: T1 hypointense soft tissue lesion in the nasopharynx with T1 hypointense clival/ calvarial lesions. C: Hypothalamic hamartoma. D: Susac Syndrome: T1 Hypointense corpus callosal lesions.

(Filename: TCT_EdE-30_ASNR2017.jpg)

EdE-17

6:30AM - 3:00PM

Subcortical U-Fibers: Signposts to the Diagnosis of White Matter Disease

K Riley[1], D O'Neill[1], S Kralik[1]
[1]*Indiana University, Indianapolis, IN*

Purpose

Subcortical arcuate U-fibers are thin bundles of myelinated nerve fibers which travel in a tangential, rather than radial, fashion connecting cerebral cortex of adjacent gyri. U-fibers are among the slowest myelinating fibers, often incompletely myelinated until the third or fourth decade of life. A protective dual blood supply relatively spares these fibers from the effects of small vessel ischemic disease. This exhibit will review how recognizing the presence or absence of subcortical U-fiber involvement in white matter disease can help narrow what may otherwise be a very broad differential diagnosis.

Materials and Methods

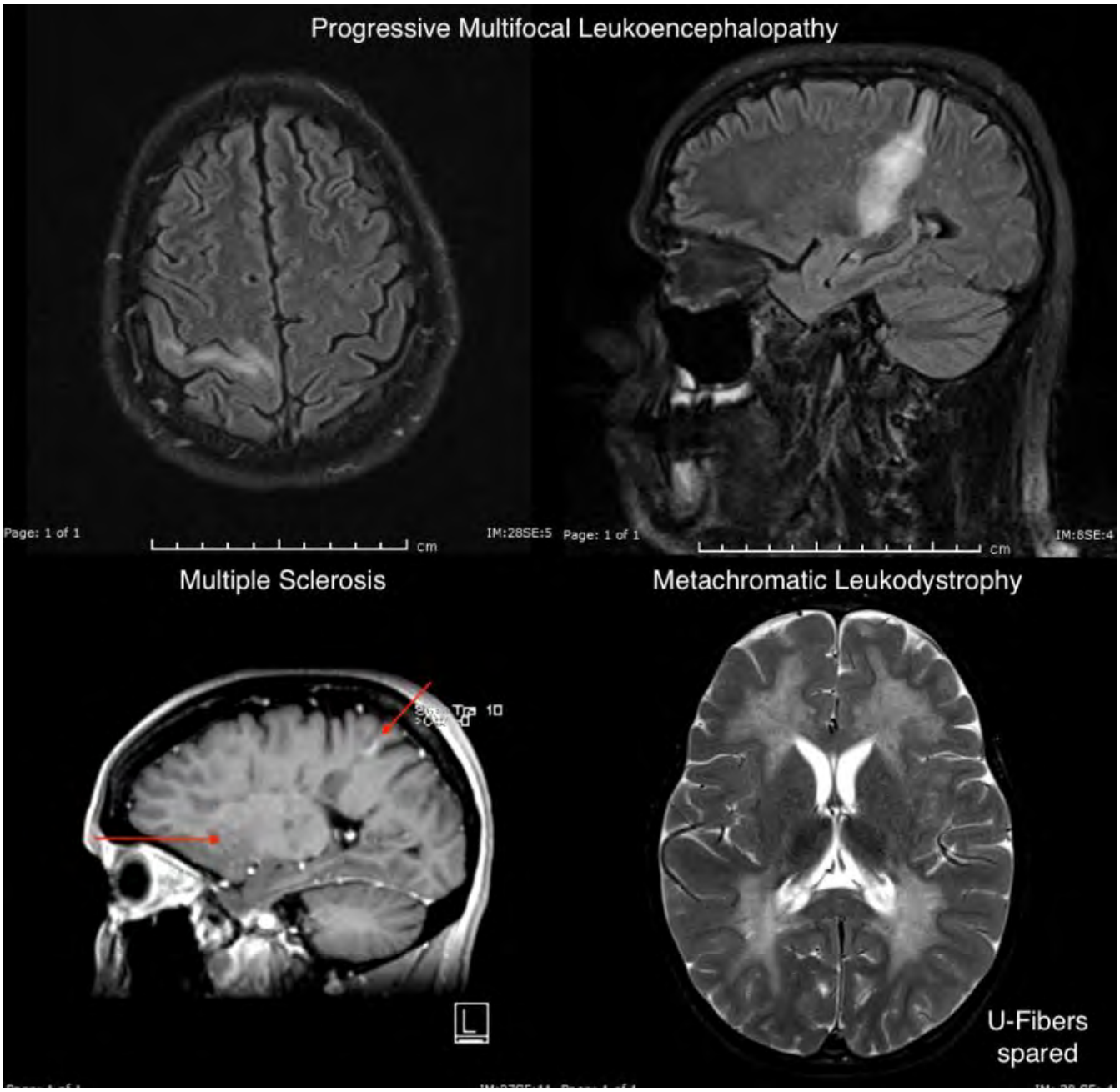
Pertinent background anatomy and development considerations regarding myelin, white matter organization, and subcortical U-fibers will be reviewed initially. Important neuroimaging manifestations associated with multiple white matter diseases then will be highlighted, including toxic/metabolic, infectious, genetic, autoimmune, and neoplastic etiologies, placing particular attention on how subcortical U-fibers may be spared or involved by the underlying disease.

Results

In general, white matter diseases can be broadly separated into three main categories; diseases that affect myelin metabolism, diseases that result in direct damage to myelin and/or oligodendrocytes, and vascular disease. Disorders of myelin metabolism (dysmyelinating disorders), including many inherited leukodystrophies, generally will spare the U-fibers with their relatively slower rate of myelin turnover. However, conditions in which direct damage to previously normal myelin and/or oligodendrocytes predominates (demyelinating disorders), including multiple sclerosis and progressive multifocal leukoencephalopathy, typically demonstrate early U-fiber involvement. Salient neuroimaging findings will be reviewed to increase confidence in assessing subcortical U-fiber involvement with white matter diseases.

Conclusions

White matter diseases can be very difficult to differentiate. However, recognizing the presence or absence of subcortical U-fiber involvement as a visible manifestation of the underlying pathophysiology can be extremely helpful in more confidently narrowing what may otherwise be a very broad differential diagnosis.



(Filename: TCT_EdE-17_ASNR2017UFiberGraphicFinalJPG.jpg)

EdE-40

6:30AM - 3:00PM

Susceptibility-weighted MR Imaging in Diagnosis of Ischemic Stroke

T Kinoshita[1], F Kinoshita[2]
[1]Research Instituite for Brain and Blood Vessels-Akita, Akita, Akita, [2]Research Institute for Brain and Blood Vessels-Akita, Akita, Akita

Purpose
The purpose of this exhibit is to demonstrate susceptibility-weighted MR imaging (SWI) findings of cerebral infarction during acute to subacute period.
Materials and Methods
The authors retrospectively reviewed SWI findings of acute cerebral infarction. The MR imaging protocol included SWI, diffusion-weighted imaging, T2-weighted imaging, and 3D time of flight MRA. We evaluated artery susceptibility sign and prominence of cerebral veins at SWI. Artery susceptibility sign was defined as the presence of hypointensity within the intracranial artery in which the diameter of hypointense signal within the vessel exceeded the diameter of adjacent vessel. Abnormal hypointensity of the cerebral veins at SWI was compared with change in oxygen extraction fraction (OEF) measured by 15O positron emission tomography (PET). Repeated MR imaging was performed in the subacute stage.
Results
Artery susceptibility sign was correlated with arterial occlusion at MRA, although it was difficult to detect internal carotid artery susceptibility sign due to the strong susceptibility artifact. Prominence of the deep medullary veins and superficial cerebral veins was ipsilaterally seen in extensive ischemia due to embolic occlusion. Corresponding to the decreased signal intensity areas at SWI, OEF was markedly increased at 15O PET. The increased OEF (misery perfusion) may lead to a decrease of oxyhemoglobin and a relative increase deoxyhemoglobin concentrations in cerebral capillaries and veins within the drainage territory. Follow-up SWI showed artery susceptibility sign alteration due to migration of acute emboli. Repeated SWI supplemented repeated MRA in evaluating arterial recanalization. Prominent middle cerebral artery representing early recanalization at MRA corresponded to diminished cerebral veins at SWI. Early reperfusion can result in relatively decreased deoxyhemoglobin concentrations in the draining veins due to excessive oxygen delivery. SWI allowed facile visualization of the hemorrhagic region.
Conclusions
Susceptibility-weighted imaging is a feasible method for identifying acute emboli as well as misery perfusion in acute ischemic stroke.

EdE-13

6:30AM - 3:00PM

The Clinical Impact of Functional MRI; Incorporating Functional MRI into Routine Clinical Practice to Aid in Neurosurgical Decision Making

V SAWLANI[1], G Mattar[1], K Kawsar[1], A Zisakis[1], N Davies[1], R Flintham[1], R Wesolowski[1], M Harley[1], R Chelvarajah[1]
[1]*University Hospitals Birmingham, Birmingham, West Midlands*

Purpose
The main aims in neuro-oncology and epilepsy surgery are to achieve maximal resection

with minimal patient impact. This requires identification of functionally eloquent regions in the brain prior to planning surgical resection margins. In cases where tumor distorts normal anatomy, it often is not possible to identify eloquent structures based on anatomical landmarks. Functional MRI (fMRI) is an essential tool in identification of these regions. We have introduced a clinical fMRI service aiming to aid in surgical planning, and have established a functional imaging multidisciplinary team (MDT) meeting for discussion of difficult cases.

Materials and Methods

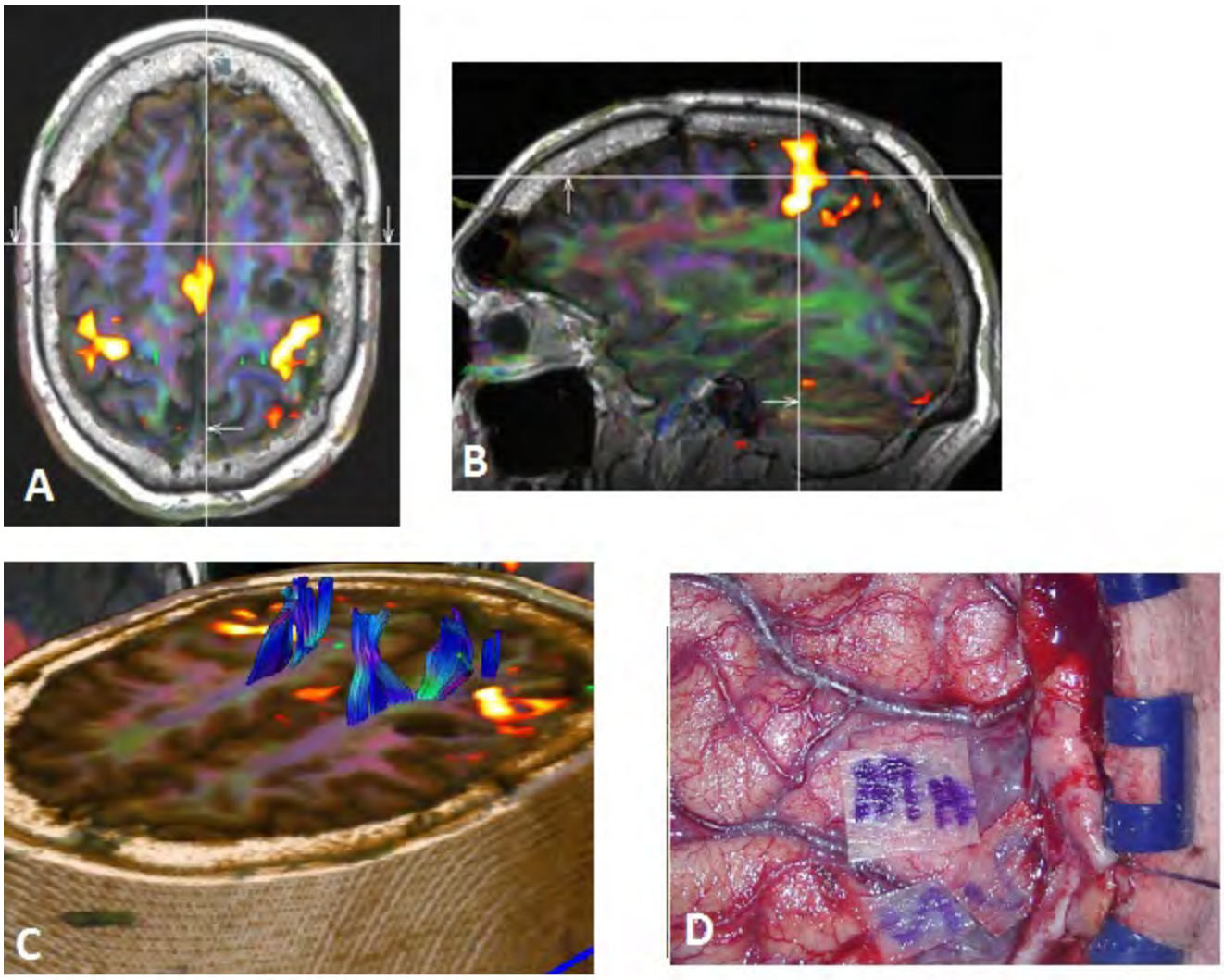
Since 2013, we have developed an in-house clinical fMRI service at our institution, a tertiary neurosurgical center. Patients are identified through the brain tumor and the epilepsy surgery MDTs. Driven by the requirements of local neurosurgeons, the service has expanded in the last 3 years to include motor fMRI with sensorimotor tractography, language fMRI with arcuate fasciculus DTI, optic pathway DTI and memory fMRI. Locally developed fMRI paradigms are undertaken on a 3T MRI scanner under the supervision of a consultant neuroradiologist.

Results

Since January 2013, 134 patients have been referred to the fMRI service with a total of 219 fMRI paradigms being acquired. In many patients, DTI also is performed in conjunction with fMRI. We have acquired 71 sensorimotor cortex fMRI, 45 corticospinal DTI, 58 language fMRI, 26 arcuate fasciculus DTI, and 19 memory fMRI. The service has thus far facilitated safe tumour resection in 97 patients and contraindicated resection in seven patients. There has been a diagnostic benefit (e.g., In lateralizing language, demonstrating lesional epileptogenesis) in 29 patients, and prognostic benefit (e.g., Predicting memory/speech deficit) in 23 patients.

Conclusions

Functional MRI has been incorporated successfully into our routine practice and has become indispensable in neuro-oncology and epilepsy surgical planning. It has shown clinical benefit in planning safe resection margin, prognostication and contraindication of surgical treatment. Within three years, the complex epilepsy surgery program has evolved with the backup of fully functional imaging support.



(Filename: TCT_EdE-13_Images.jpg)

EdE-02

6:30AM - 3:00PM

The Demonstrative Images Reflecting Vision Loss - A Case Based Review of Pathologies Affecting Vision Based on the Clinical Symptoms

H Nakamura[1], S Matsushita[2], Y Nakajima[2]
[1]St.Marianna University of medicine, Kawasaki, Japan, [2]St. Marianna University of Medicine, Kawasaki, Kanagawa

Purpose
1. To review the complex anatomy for normal vision. 2. To correlate clinical presentation in

order to optimize imaging and provide optimal image interpretation. 3. To demonstrate our role as radiologists in the diagnosis of disorders affecting vision.

Materials and Methods

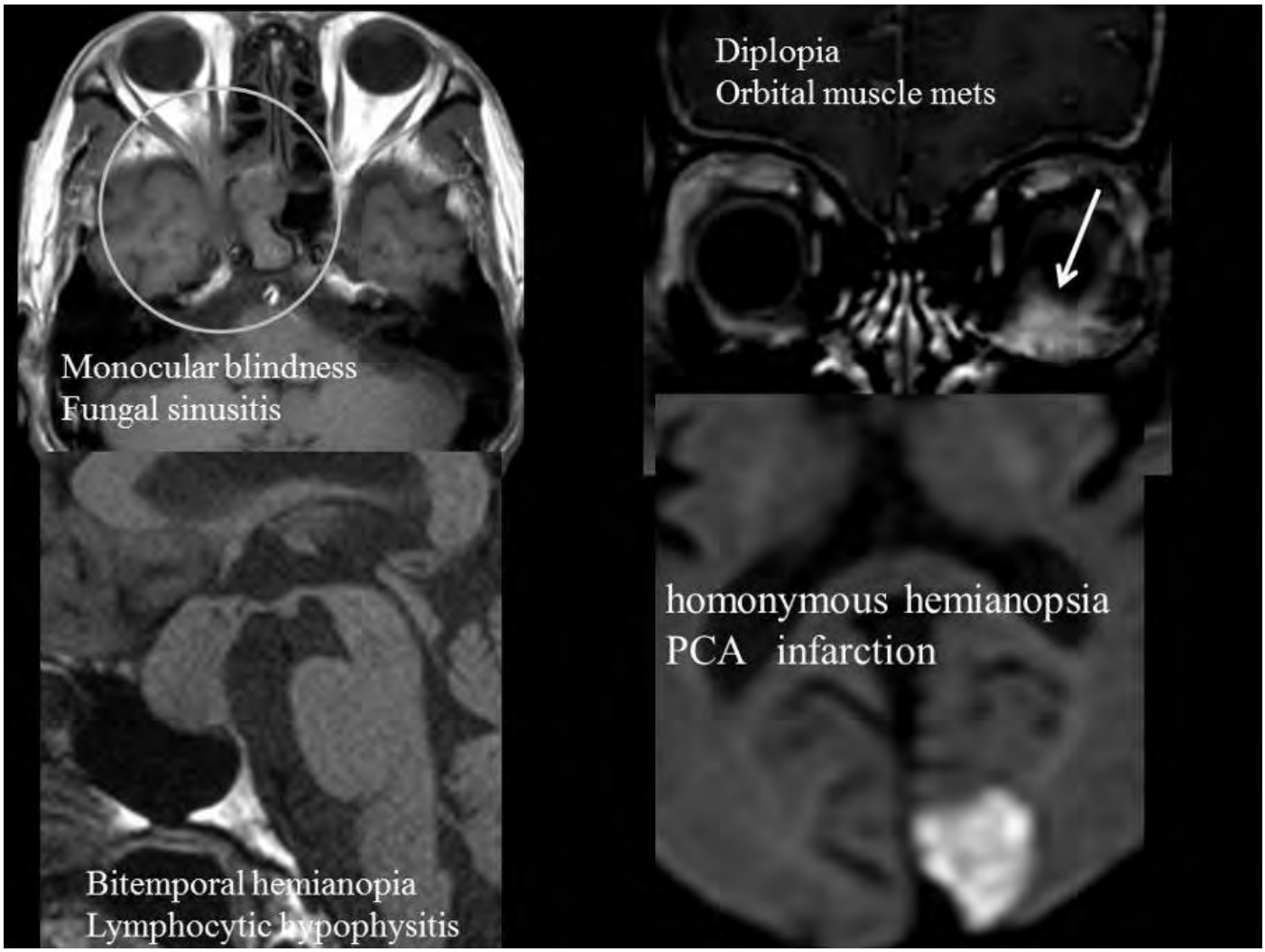
Visual anatomy is one of the most studied, and perhaps least understood systems in the human body. Because of its complexity and its intimate relationship with so much of our normal neurophysiology, disease states become clinically apparent readily and dramatically. Understanding this complex anatomy and physiology and the clinical manifestation is important to providing our patients and referring clinicians with the best imaging and image interpretation. Ophthalmologic symptoms are largely divided into three categories - loss of visual acuity, visual field disturbance and diplopia.

Results

Exhibit is presented as per the clinical presentation: (1) Monocular blindness (neuritis, ischemic neuropathy, neoplastic, sinusitis, and vascular lesions); (2) Bitemporal hemianopia (pituitary lesions, craniopharyngioma, ICA aneurysm,); (3) homonymous hemianopsianeoplasm (glioma), vascular (PCA infarcts, intra and subarachnoid hemorrhage, PRES) white matter lesions (MS, ADEM), (4) Diplopia : the cranial nerves (III, IV, and VI) disorders (IC-PC aneurysm, Tolosa Hunt syndrome), extra-ocular muscle disease (metastasis, thyroid ophthalmopathy). We especially included cases, which we overlooked due to the lack of the correlation with the anatomy.

Conclusions

We have provided a case-based review of the anatomy of vision and pathologies affecting vision. With enough knowledge of the normal anatomy, even the mildest of disease states or smallest of lesions affecting a single anatomic component can manifest clinically and can also allow for high clinical accuracy in pinpointing the anatomic site of pathology. It is important for radiologists to approach the evaluation of visual disturbances with the same level of scrutiny and detail as our referring clinicians expect and our patients deserve.



(Filename: TCT_EdE-02_20161209ASNR-presentation.jpg)

EdE-31

6:30AM - 3:00PM

The Intranasal Route for Administering Therapeutics and Imaging Agents to Target the Brain: What the Neuroradiologist Needs to Know

M Malhotra[1], R Paulmurugan[2], T Massoud[1]
[1]Stanford University School of Medicine, Stanford, CA, [2]Stanford University School of Medicine, Palo Alto, CA

Purpose

A particularly challenging aspect of targeting imaging and therapeutic agents to the brain is crossing the blood-brain barrier (BBB). Intranasal delivery offers an alternative anatomical route to bypass the BBB. Current preclinical research efforts are aimed at refining the intranasal delivery route toward clinical translation. This will allow future use of

nanoparticle-based agents for novel clinical MRI and molecular imaging applications in Neuroradiology.
Materials and Methods
We provide a pictorial and educational overview of intranasal delivery of molecules to the brain, and potential neuroimaging applications.
Results
We first illustrate the theory behind intranasal delivery. The nose-to-brain route exploits unique neuronal connections of the olfactory and trigeminal nerves between brain and the external environment. The olfactory mucosa is 'leaky', and mucus penetrating agents <20nm will gain paracellular access between epithelial cells and then spread perineurally along olfactory nerve projections to the brain within minutes. Larger molecules prefer transcellular epithelial transport and subsequent slow intraneural movement over hours to days. Various peptides, neuroprotective and chemotherapeutic drugs, therapeutic viruses, and neural stem cells have been delivered successfully intranasally. When compared to IV delivery, the intranasal route is effective in reducing rapid renal clearance, high enzymatic metabolism, and immunogenicity. However, large-volume intranasal delivery, and mucosal clearance are practical limitations. To enhance mucus penetration, we are developing nanoparticle-based formulations that are surface-modified with both MRI contrast and drug molecules. Tailoring novel nano-theranostic agents for intranasal delivery would be advantageous in allowing molecular imaging monitoring of neurotherapies that follow the nose-to-brain pathway.
Conclusions
Recent FDA approval for an intranasal drug delivery system will likely herald the advent of many neurological applications. The development of theranostic nanoformulations for intranasal delivery is a promising strategy to treat and image many brain diseases, e.g., glioblastoma. Neuroradiologists should be familiar with these translational research developments that will impact their future practice.

EdE-21

6:30AM - 3:00PM

The Optic Chiasm: A Comprehensive Pictorial and Educational Review of Common and Uncommon Abnormalities on Neuroimaging

F Zaccagna[1], T Matys[1], T Massoud[2]
[1]University of Cambridge, Cambridge, UK, [2]Stanford University School of Medicine, Stanford, CA

Purpose
The optic chiasm is a key anatomical structure along the visual pathway, situated at the crossroad between optic nerves and tracts. A wide range of diseases can affect the optic chiasm and its surrounding strategic region at the base of the brain. Scant attention has been

paid to date to comprehensive classification of neuroimaging manifestations of optic chiasm abnormalities. We review these and classify them according to etiology.
Materials and Methods
We comprehensively review and present the neuroimaging findings in a wide spectrum of pathologies originating from or involving the optic chiasm.
Results
We first describe the imaging anatomy of the optic chiasm and its surrounding structures. We then present a pictorial review of wide ranging abnormalities that include congenital lesions, e.g., ocular albinism and achiasmatism, iatrogenic pathologies such as radiation necrosis, and traumatic injuries consequent to skull base fractures. We review common and less commonly encountered neoplastic lesions, those arising from the optic chiasm itself and those invading it from nearby structures. Tumors include pituitary adenoma, craniopharyngioma, Rathke's cleft cyst, epidermoid and dermoid cysts, chordoma, teratoma, embryonal cell carcinoma, yolk sac tumors, choriocarcinoma, glioma, meningioma and metastatic lesions. Several inflammatory diseases also affect the optic chiasm, including sarcoidosis, ANCA-positive vasculitis, idiopathic optic chiasmitis, multiple sclerosis, lymphocytic hypophysitis, and xanthomatous hypophysitis. Infective diseases, such as tuberculosis, pituitary abscess and cryptococcus also may involve the optic chiasm. Considering the proximity to major vessels, vascular disorders may affect the optic chiasm, e.g., cavernomas, arteriovenous malformations, aneurysms, and ischemia.
Conclusions
Management strategies for optic chiasm abnormalities vary substantially depending on the abnormalities revealed on neuroimaging. We comprehensively review the imaging findings in a wide spectrum of pathologies encountered in this important CNS structure. This educational review will aid in differentiating the many neuroimaging appearances of lesions in this region.

EdE-19

6:30AM - 3:00PM

The Two Sides of Mucormycosis: Rhino-cerebral and Pulmonary Invasion

B Thomas[1], A Mammen[2], S Zhang[3], V Potigailo[3]
[1]Hahnemann university hospital/Drexel college of medicine, Glenolden, PA, [2]Hahnemann University Hospital/Drexel College of Medicine, Philadelphia, PA, [3]Hahnemann University Hospital, Philadelphia, PA

Purpose
Mucormycosis is an aggressive angioinvasive fungal infection with up to an 80% mortality rate. The paranasal sinuses are most commonly affected (39%), followed by pulmonary (24%) and dermal (19%) involvement. The most common underlying conditions are diabetes mellitus, solid organ/hematopoietic transplant, IV drug use, steroid or deferoxamine therapy,

or hematological malignancies. Mortality from rhino-cerebral infection ranges from 25-65% while mortality from pulmonary infection can be as high as 87%. The pathophysiology of Rhino-cerebral infection is based on the vasotropic behavior of the mucorales fungi, resulting in vasculitis, vascular occlusion, tissue necrosis and ischemia. The brain also may be seeded by direct organism extension from the paranasal sinuses. The symptoms begin with sinusitis and cellulitis, progressing to fever, facial pain, multiple cranial nerve palsies and infarcts. With pulmonary involvement, infection begins with inhalation of the spores through the nares followed by colonization in the alveoli. There is rapid progression often causing pneumonia, necrosis, hemoptysis, and disseminated spread. Due to high mortality, early diagnosis and initiation of aggressive antifungal therapy is paramount for improving clinical outcome.

Materials and Methods

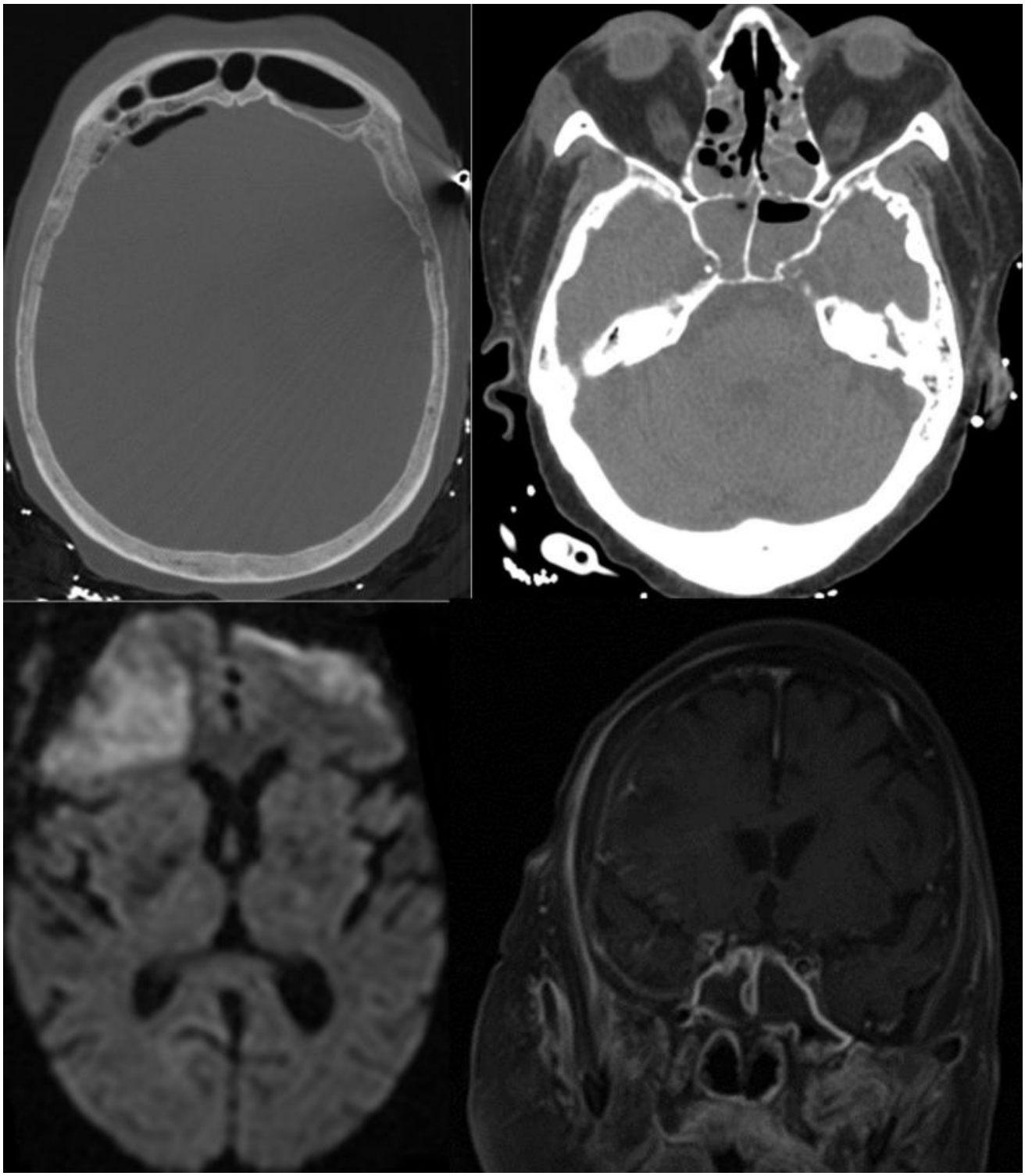
Images of cases encountered with biopsy proven mucormycosis infections were obtained and reviewed using a picture archiving and communication system (PACS). Select images demonstrating relevant pathology were incorporated into a poster presentation.

Results

We present the case of an immunosuppressed patient with multiple comorbidities including history of renal transplant who presented with lethargy and worsening mental status. Imaging revealed findings of acute bifrontal stroke, severe pansinusitis and erosion of the nasal septum. ENT endoscopy and biopsy of the hard palate revealed extensive mucormycosis infection. In addition, we present the case of a 64-year-old male with a history of renal transplant who presented with cough. Initial chest radiograph demonstrates a new large soft tissue mass arising from the right hilum. Subsequent chest CT showed a large cavitary mass with mediastinal invasion. Biopsy results confirmed pulmonary mucormycosis. The patient was followed with daily chest radiographs showing further progression and development of pneumopericardium.

Conclusions

These cases demonstrate the importance of a thorough exam (physical and radiological) in any immunocompromised patient with atypical neurological or pulmonary findings. Aggressive fungal rhino-cerebral mucormycosis is a rare but devastating infection, which mostly affects immunosuppressed patients. Intracranial extension of the fungus from the sinuses results from vascular invasion which can lead to vasculitis, cerebral infarctions, soft tissue necrosis and hemorrhage. A similar process can be seen with pulmonary involvement leading to cavitary abscesses which can invade nearby structures such as the mediastinum. Early diagnosis, antifungal therapy and surgical debridement are essential for an improved clinical prognosis.



(Filename: TCT_EdE-19_image.jpg)

EdE-32

6:30AM - 3:00PM

The World of Non-Coding RNAs: A Primer for the Neuroradiologist with Relevance to Theranostic Imaging of Glioblastoma

M Malhotra[1], Z Massoud[2], R Paulmurugan[3], T Massoud[1]
[1]Stanford University School of Medicine, Stanford, CA, [2]University of Bristol, Bristol, CA, [3]Stanford University School of Medicine, Palo Alto, CA

Purpose
Non-coding RNAs (ncRNAs) are diverse RNA molecules that are not translated into proteins following transcription. Many of these have important regulatory functions by controlling molecular interactions and pathways within cells. Dysregulated ncRNAs have been implicated in many neurological diseases. Thus, ncRNA-targeted strategies are emerging as a promising new generation of molecular therapies for cancer, including glioblastoma. In this exhibit, we review current translational research developments in use of ncRNAs, focusing on the potential of RNA-interference (RNAi). Therapeutic and diagnostic (theranostic) methods using nanoparticles are being developed and refined to target glioblastoma for RNAi, and to monitor therapy using molecular imaging techniques.
Materials and Methods
We provide a pictorial and educational overview of ncRNAs, and their potential and limitations as theranostics for glioblastoma.
Results
Recent research advances have shown that many ncRNAs play a prominent role in glioma molecular pathology. Theranostic possibilities are therefore emerging whereby ncRNA-based systems may be used to molecularly target and image glioblastoma in an effort to correct the underlying dysregulation. The most successful system in current developments is based on RNAi, e.g., an ongoing clinical trial to silence the tenascin-C gene, which therefore diminishs this protein's support of tumor cell proliferation and migration. However, a number of limitations exist in the clinical translation of ncRNA-based therapeutic systems, such as inefficient delivery mechanisms and cytotoxicity. Concerted preclinical translational research efforts are therefore underway to improve glioblastoma targeting and cell kill. MicroRNAs are ncRNAs that control gene expression. We currently are developing microRNA nanoparticle-based systems for theranostic applications in glioblastoma. Examples of these will be shown in this exhibit.
Conclusions
Nanoparticle-based theranostic applications using ncRNAs will likely impact the future practice of neuroradiologists once clinical translation is achieved. This presentation will aid in understanding the basic concepts and likely future relevance to neuroimaging of glioblastoma and other brain diseases.

EdE-41

6:30AM - 3:00PM

Uncommon Bones, Sutures, and Foramina of the Calvarium: A Pictorial and Educational Review of Potentially Confusing Fracture Mimics on Neuroimaging

M Ma[1], Y Kim[1], C Kim[1], H Dahmoush[2], T Massoud[1]
[1]Stanford University School of Medicine, Stanford, CA, [2]Stanford Hospital, Stanford, CA

Purpose
Diverse atypical patterns of calvarial ossification can result in accessory bones, ectopic sutures, and unusual foramina in the skull. Appreciation of these fracture mimics is important when interpreting trauma on head CT, and in children when imaging nonaccidental injury. In this educational exhibit we review the potentially confusing appearances of these unusual calvarial bony structures.
Materials and Methods
We present the anatomic basis and imaging manifestations of accessory bones, sutures, and foramina resulting from anomalous ossification of the calvarium.
Results
We describe the developmental and imaging anatomy of Wormian and accessory bones. Wormian bones (Olaus Worm, 1643) are small ossicles between two neighboring calvarial bones, surrounded by suture lines. These normal variants (that may also be present in certain congenital disorders) commonly are found near the lambdoid suture in 40% of skulls. At pterion they are called epipteric bones, or pterion ossicles, or Flower's bones. A third type is the preinterparietal or inca bone, at lambda. Conversely, accessory bones are larger and surrounded by more than two bones and sutures. They can either arise from independent ossification centers within sutures or fontanelles and may result in atypical craniosynostosis, or from unfused ossification centers within the occipital bone. There are 17 named sutures, i.e., synarthroses, unique to the skull. However, on account of complex embryology of the occipital bone, unfused sutural variants may persist, e.g., midline fissures, transverse occipital sutures (including Mendosal sutures), and superior median fissures. Unlike small (1-2 mm) parietal foramina that transmit emissary veins, enlarged parietal foramina (parietalia permagna or Catlin marks) are rare calvarial defects >5 mm in size that arise from ossification failures in both parietal bones.
Conclusions
Uncommon variants of calvarial ossification can be both unexpected and challenging on neuroimaging. This presentation will aid in differentiating true trauma from the many appearances of calvarial accessory bones, sutures, and foramina.

EdE-22

6:30AM - 3:00PM

Understanding Clinical Application of Blood Suppressed High Resolution Vessel Wall Imaging in The Vertebrobasilar System: Case Series and Systematic Review

S Niazi[1], K Patel[1], A Chukus[2], P Dubey[3]
[1]Mount Sinai Medical Center, Miami Beach, FL, [2]Stanford Hospital, Stanford, CA, [3]None, Scarsdale, NY

Purpose
To understand the acquisition protocol, patient selective optimization approaches, and specific technical considerations for intracranial high resolution vessel wall imaging (VWI) applied to posterior circulation. To understand the imaging characteristics of spectrum of normal, abnormal and artifactual findings on VWI with emphasis on the posterior circulation. To provide case-based review of clinical applications and update of recent literature.
Materials and Methods
Adult patients with a suspicion of vertebral or basilar artery dissection underwent high resolution T1-weighted pre and postcontrast imaging and black blood MRI (BBMRI) three dimensional (3D) acquisition techniques selectively optimized for posterior circulation. The MR imaging findings of arterial dissection including intramural hematoma, intimal flap, and arterial wall enhancement were evaluated.
Results
The posterior circulation optimized 3D high resolution VWI protocol allowed adequate field of view coverage in a single acquisition with an acceptable scan time (35 minutes), and isotropic resolution (0.9 x 0.9 x 0.9 mm) allowing multiplanar reconstruction with oblique orientations selective to specific vascular axis of interest. Evaluation of vessel wall characteristics allowed confident diagnosis of arterial dissection in the posterior circulation.
Conclusions
Conventional computed tomography, MR, and digital subtraction angiography rely on the presence of luminal narrowing for the identification of vascular pathology. However, the diagnosis of arterial dissection, especially in the posterior circulation, is not always apparent with luminal imaging techniques, as the dissection flap is commonly not visualized and arterial stenosis may not occur. Recent developments in neurovascular MR VWI has allowed improved evaluation of vessel wall characteristics while providing the same detail of the vessel lumen. Patient selective optimization approaches, and specific technical considerations for intracranial high resolution VWI applied to posterior circulation are important in order to achieve high yield in the diagnosis of arterial dissection, and keeping the scan times reasonable.

Monday
6:30AM - 3:00PM
Long Beach Convention Center, Exhibit Hall B-(Lower Level) EdE

Education Exhibit Poster (EdE)-Head & Neck

EdE-51

6:30AM - 3:00PM

CT and MR Imaging Evaluation of Tinnitus According to Auditory and Extra-auditory Causes

H Kim[1], Y Kim[2], J Cha[2]
[1]Samsung Medical Center, Sungkyunkwan University School of Medicine, Seoul, Korea, Republic of, [2]Samsung Medical Center, Seoul, WY

Purpose
Tinnitus is one of the most frequent symptoms of the auditory system, affecting approximately 17% of the general population. Theoretically it can arise from the diseases affecting anywhere within the auditory pathway. The purpose of this exhibition is to present the CT and MR imaging features in the evaluation of patients with tinnitus according to auditory and extra-auditory causes.
Materials and Methods
Tinnitus can simply be divided into two major categories, auditory and extra-auditory. Auditory tinnitus refers to tinnitus generated by the lesions located in either conductive (external and middle ear) or sensorineural [peripheral (inner ear and vestibulocochlear nerve) and central (brain stem nuclei to auditory cortex) vestibulocochlear neural pathway] auditory system. It is nonpulsatile in the majority of patients. In contrast, extra-auditory tinnitus is generated by para-auditory structures, usually from the vascular and muscular sources, and frequently Is pulsatile in nature. Distinction between auditory and extra-auditory forms of tinnitus is important because the evaluation and treatment of the two entities are substantially different. After addressing a brief review of the anatomy and physiology involved in tinnitus, CT and MR imaging features of various causes of tinnitus is presented in a systematic approach according to the lesion location, i.e., auditory and extra-auditory. The discussion on the roles of imaging evaluation in patients with tinnitus will be followed.
Results
The lesions of the cochlea, such as otosclerosis, Meniere's disease, and drug toxicity, are the most common causes of auditory tinnitus, although any conditions causing conductive and sensorineural hearing impairment, may attenuate external background noise, making somatosounds of normal intensity more audible. Though nonpulsatile in most cases, several conditions may produce pulsatile tinnitus, including middle ear cholesterol granuloma, vascular compression of the 8th nerve, and otosclerosis. Because the majority of patients with auditory tinnitus have a concomitant hearing loss or vertigo, radiological examinations for these patients generally are directed to search of the sources of hearing loss or vertigo. Although extra-auditory tinnitus is much less common than auditory tinnitus, its cause frequently can be identified, making the specific treatment possible. The abnormalities of the intracranial or extracranial arteries and veins are the most common causes of extra-auditory tinnitus. It also can be produced by various other diseases such as hypervascular tumors within/outside the middle ear and intracranial hypertension. Rarely, extra-auditory tinnitus

can occur in muscular disorders such as palatal myoclonus. The patients with extra-auditory tinnitus seldom present with other audiovestibular symptoms and so, the principal concern of radiological examination in these patients is directed to identify more or less curable intracranial or extracranial vascular lesions.
Conclusions
Although the exact pathophysiologic mechanism of tinnitus little is still unknown and the imaging studies would still demonstrate negative findings in a large group of patients with tinnitus, the radiologists, with the aid of technical development of CT and MR imaging, should be prepared for the effective involvement in management of the patients with tinnitus by a tailored imaging approach according to the lesion location.

EdE-53

6:30AM - 3:00PM

Disease Entities of the External Auditory Canal: A Pictorial Review

h Kim[1]
[1]*Hallym University Kangnam Sacred Heart Hospital, seoul*

Purpose
Our objective was to improve knowledge of these disease entities and to help for proper diagnosis.
Materials and Methods
In this article, we will review and describe the computed tomographic (CT) findings of various disease entities affecting the external auditory canal (EAC) and what we experienced from March 2013 to February 2015.
Results
The lesions were classified according to their diagnoses; osteoma, fibrous dysplasia, keratosis obturans, cholesteatoma, cholesterol granuloma, aural polyp, sebaceoma, squamous papilloma, candidiasis, tuberculous otitis, and squamous cell carcinoma.
Conclusions
In this article, we reviewed how the heterogeneous range of disease entities can affect the EAC. The imaging findings of disease entities at EAC have nonspecific or overlapping findings. Nonetheless, CT is a major tool for differential diagnosis and helpful for clinical decision-making such as performing surgery or not and the extent of resection. MR imaging also offers more detailed characterization of soft tissue and delineation of small lesion from other structures. Careful evaluation and being familiar with these imaging findings is needed for an accurate diagnosis.

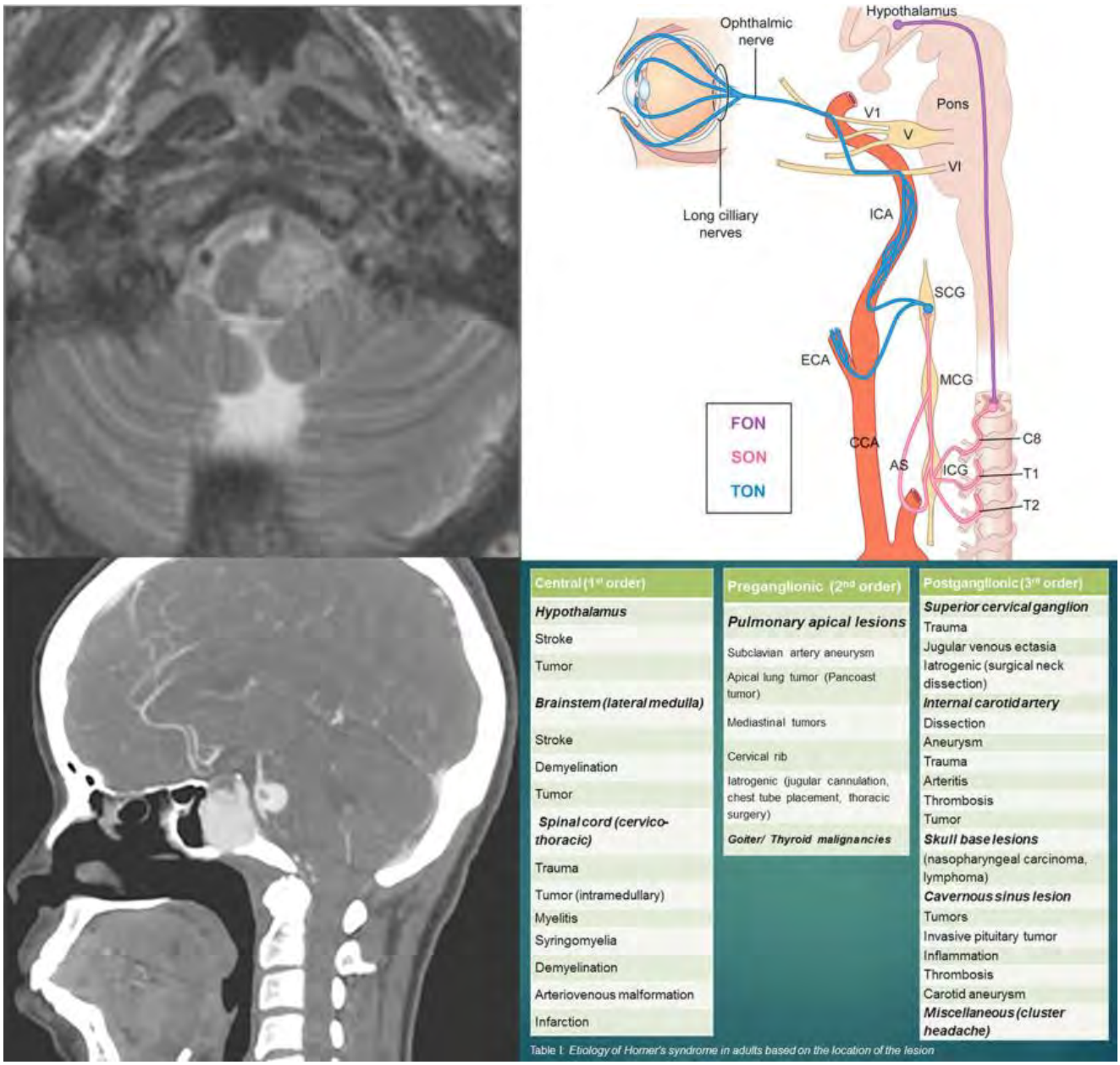
EdE-43

6:30AM - 3:00PM

Horner's Syndrome Revisited: A Review of the Oculosympathetic Pathway and Pathology

A Blanchard[1], J Gomez[1], E Palacios[2]
[1]*Tulane University School of Medicine, New Orleans, LA,* [2]*Tulane University, New Orleans, LA*

Purpose
The purpose of this exhibit is to provide an overview of Horner's syndrome by reviewing the anatomy of the oculosympathetic chain and the pathophysiology and various clinical and imaging manifestations of the condition.
Materials and Methods
Select cases of Horner's syndrome (HS) were reviewed from our institution. These cases were evaluated using chest radiographs, head and neck computed tomography (CT), 3D-CT reconstruction, magnetic resonance imaging (MRI) and magnetic resonance venography (MRV). Recent literature and guidelines were reviewed, and a search for HS was performed in PubMed. From the literature we were able to identify cases of HS and compare these to our case series. Localized anatomical landmarks were identified and pertinent findings are presented with each case.
Results
Horner's syndrome (HS), also known as oculosympathetic palsy, is a rare condition that manifests due to alteration of the sympathetic nervous pathway to the eye. The classic presentation of HS is ipsilateral ptosis, miosis, and anhidrosis. Horner's syndrome can be congenital, iatrogenic or secondary to benign or malignant processes. It is classified by where the sympathetic pathway is disrupted; first-order, second-order, or third-order neurons. First-order neuron fibers arise from the posterolateral hypothalamus and end in the intermediolateral column at spinal cord levels C8-T2. Second-order neuron fibers exit the spinal cord, ascend through the sympathetic chain and terminate at the superior cervical ganglion. Lastly, third-order neuron fibers travel with the carotid artery and reach the eye as the long and short ciliary nerves. Depending on the location of the lesion, patients can present with different symptoms.
Conclusions
A myriad of conditions can cause Horner's syndrome, and management is dependent on identifiying the underlying etiology. The radiologist plays a central role in the diagnosis and subsequent treatment of this condition. By understanding the clinical findings, anatomy, and imaging manifestations, the radiologist can provide the referring clinician with a prompt and accurate diagnosis.



(Filename: TCT_EdE-43_com42.jpg)

EdE-46

6:30AM - 3:00PM

Idiopathic Orbital Inflammatory Syndrome: Clinical Features and Imaging Correlation

D Shah[1], H Lee[1], L Yen[2]
[1]Rutgers New Jersey Medical School, Newark, NJ, [2]Rutgers- New Jersey Medical School, West Orange, NJ

Purpose
Idiopathic orbital inflammatory syndrome (IOIS) is the third most common acute orbital process following Graves disease and lymphoproliferative disease. The clinical presentation resembles that of orbital cellulitis, but treatment for IOIS is corticosteroids versus antibiotics for orbital cellulitis, making accurate diagnosis essential. The diagnosis commonly is made on clinical findings in combination with imaging studies.
Materials and Methods
A retrograde review of 20 cases of pathologically proven IOIS from 2004-2016. Thirteen patients had MRI, 6 had CT and one had both MRI and CT, all with IV administration of contrast.
Results
Age ranges from 8-89 years. Mean age of presentation is 51 years, 60% females and 40% males. Fifty-five percent of patients had orbital pain, 70% had orbital edema, 65% had restricted extraocular muscle movements, proptosis and decreased vision, and 15% had diplopia. Only 5% of patients demonstrated increased intraocular pressure. All IOIS lesions were iso to hyperdense on CT, and hypointense on T1 and T2WI MR, with homogenous contrast enhancement. There was associated orbital retrobulbar infiltration (35%), Dacryocystitis (25%), myositis (20%), dacryocystitis and myositis (15%), involvement of optic nerve sheath (30%), scleritis (10%), orbital apex (5%) and other(meninges, periorbital soft tissue involvement) (15%). None of these patients demonstrated involvement of cutaneous tissues or paranasal sinuses. Pathologically, 55% of cases showed lymphoid cell infiltration, 35% were sclerosing subtype and 10% showed granulomatous changes.
Conclusions
IOIS is a benign, noninfectious clinical syndrome characterized by features of nonspecific inflammatory conditions of the orbit without identifiable local or systemic etiology. Based on our analysis, it predominantly affects middle-aged females. The clinical presentation involves acute orbital pain, edema, proptosis, restricted eye movement and decreased vision. The MRI shows hypointensity on T2WI with homogenous contrast enhancement, with more common involvement of lacrimal glands, extraocular muscles and optic nerve sheath. More than half of the patients have lymphoid variant. One third of patients have sclerosing subtype, which is thought to be treatment resistant with a poorer prognosis.

EdE-47

6:30AM - 3:00PM

Imaging Diagnosis of Common Pediatric Solid Neck Masses: A Practical Approach

J Krauss[1], S Noujaim[1]
[1]*William Beaumont Hospital, Royal Oak, MI*

Purpose
This review aims to familiarize both radiologists and pediatricians with the typical imaging

features of common solid neck masses in children. After reviewing these cases, the reader will be able to better understand the common pathologies found in this region and their typical imaging presentation, improving their ability to help the clinician in developing a narrow differential, if not a definitive diagnosis.

Materials and Methods

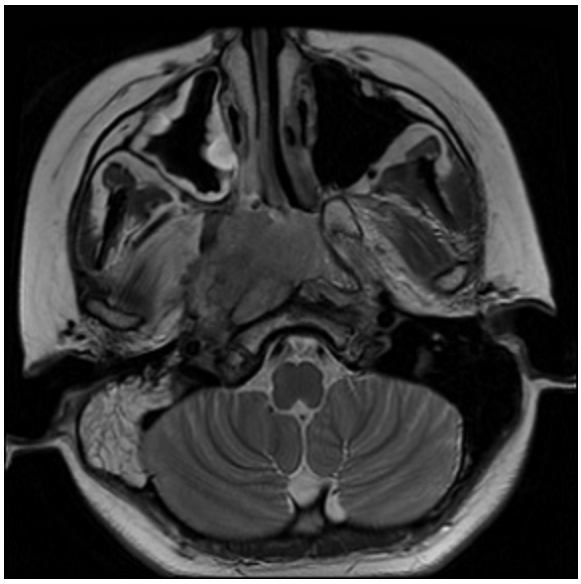
Original cases from a large tertiary medical center will be showcased and followed by a discussion of their clinical presentation, imaging findings, and appropriately narrowed differential diagnosis.

Results

Neck masses in the pediatric population are not uncommon. The majority of neck masses in the pediatric population are congenital or inflammatory in origin; however, malignancy must always be ruled out as they represent approximately 11%-15% of all neck masses in this population (1). Imaging plays an important role in their diagnosis and subsequent management. High-resolution ultrasound is generally the initial imaging modality of choice as it helps separate solid from cystic lesions. Often when dealing with solid lesions, cross-sectional imaging such as magnetic resonance imaging (MRI) and computed tomography (CT) are necessary for better assessment and more accurate diagnosis. This review describes imaging and clinical features of pediatric solid neck masses that are commonly seen in routine clinical practice. Benign and malignant conditions affecting infants, children, and adolescents will be presented, including, but not limited to: fibromatosis colli, infantile hemangioma, ectopic thymus, ectopic thyroid, neurofibroma, schwannoma, teratoma, neuroblastoma, rhabdomyosarcoma, nasopharyngeal carcinoma, lymphoma, and juvenile nasopharyngeal angiofibroma.

Conclusions

Solid neck masses are an entity not infrequently encountered in the pediatric age group. It is important that radiologists be aware of the breadth of pathologies that can occur in this region and their classic imaging characteristics so that they can provide the referring clinician with an appropriate differential to effectively and efficiently guide the next step in management and treatment.


(Filename: TCT_EdE-47_nasopharyngealcarcinoma.jpg)

EdE-50

6:30AM - 3:00PM

Imaging Findings in Acute Hearing Loss

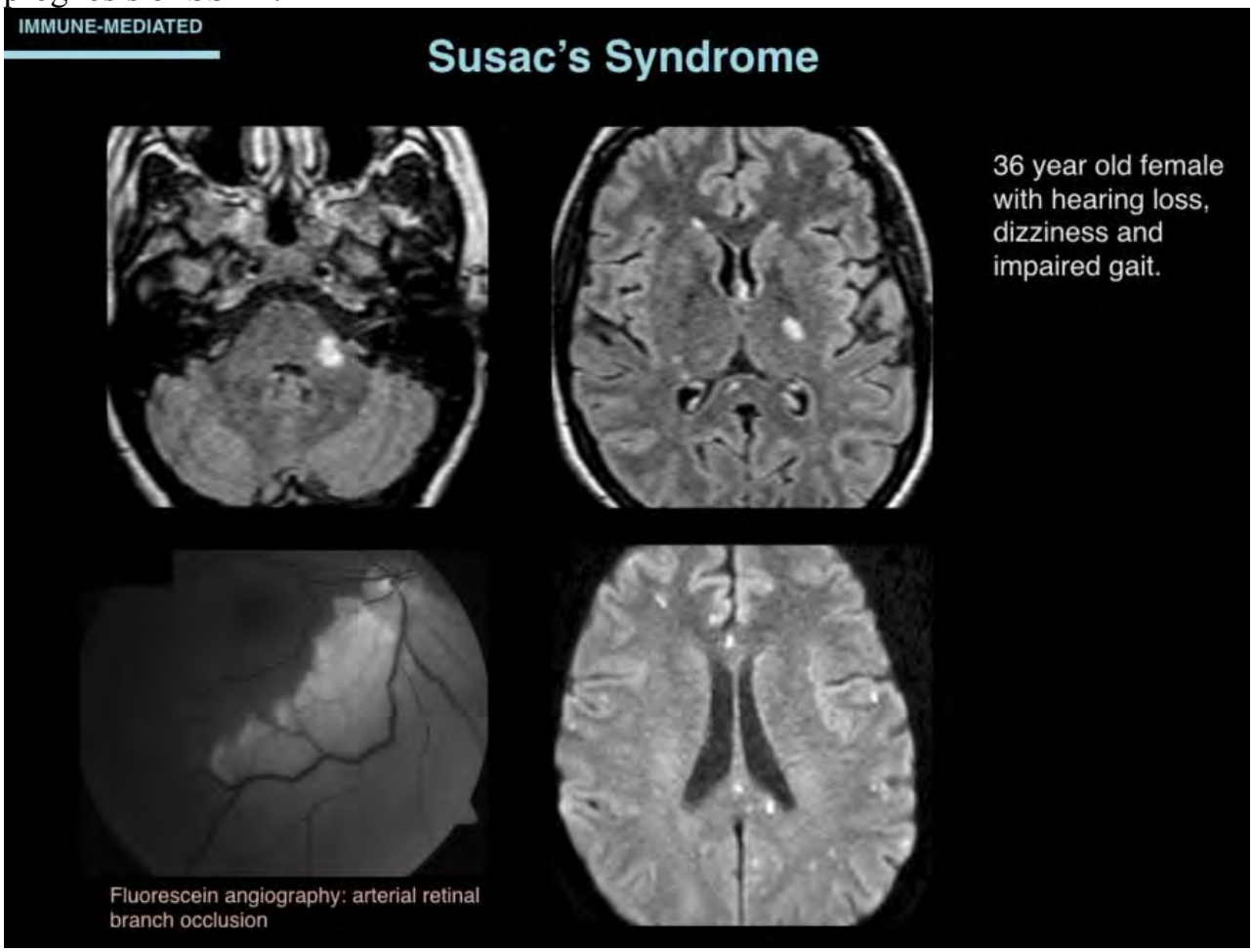
K Müller[1], S Bravo-Grau[2], R Zunino[1], S Waissbluth[1], I Huete[2], J Cruz[2]
[1]P. Universidad Católica de Chile, Santiago, RM, [2]P. Universidad Católica de Chile, Santiago, REGIÓN METROPOLITANA

Purpose
Review the imaging approach for patients presenting with acute hearing loss. Provide a pictographics review of diseases presenting with hearing loss. Show examples of the use of 3D-FLAIR for the detection of labyrinthine signal abnormalities in idiopathic sudden sensorineural hearing loss (SSHL).
Materials and Methods
Review of selected cases with demonstrated diseases that clinically present as acute hearing loss in patients with imaging studies performed at our health network. Emphasis will be given to those diseases where the imaging findings may aid in the differential diagnosis of hearing loss. Cases of idiopathic sudden sensorineural hearing loss for which 3D-FLAIR was used are discussed. An etiology-based classification of conditions presenting as sensorineural hearing loss is provided. Examples of cases will be given, with the ancillary findings and explanation of the signs observed in the different modalities.
Results
An etiology-based classification of acute hearing loss is shown: - Inflammatory/infectious: labyrinthitis, Ramsay-Hunt syndrome, - Neoplastic: schwannoma (vestibular - cochlear), leptomeningeal infiltration, - Vascular: cochlear hemorrhage, labyrinthine artery infarction, -

Trauma: temporal bone fracture, ossicular chain disruption, - Immune-mediated: multiple sclerosis, Susac syndrome, Cogan syndrome, - Others: cerumen impaction, postsurgical, ototoxic drugs (aminoglycosides, cisplatin), renal failure, hematological disorders. Causes of intralabyrinthine enhancement: labyrinthitis, Ramsay Hunt syndrome, Cogan syndrome, intralabyrinthine schwannoma. Spontaneous T1 signal hyperintensity in the cochlea: cochlear hemorrhage.

Conclusions

The majority of the diseases mentioned above have imaging findings in standard MRI protocols. Magnetic resonance imaging is considered the best imaging modality for the initial study of hearing loss. Contrast media is useful when inflammatory causes are suspected, specially on sudden onset hearing loss. On the other hand, CT is the imaging modality of choice in patients with a history of trauma. 3D-FLAIR is promising in the prognosis of SSHL.



(Filename: TCT_EdE-50_susac.jpg)

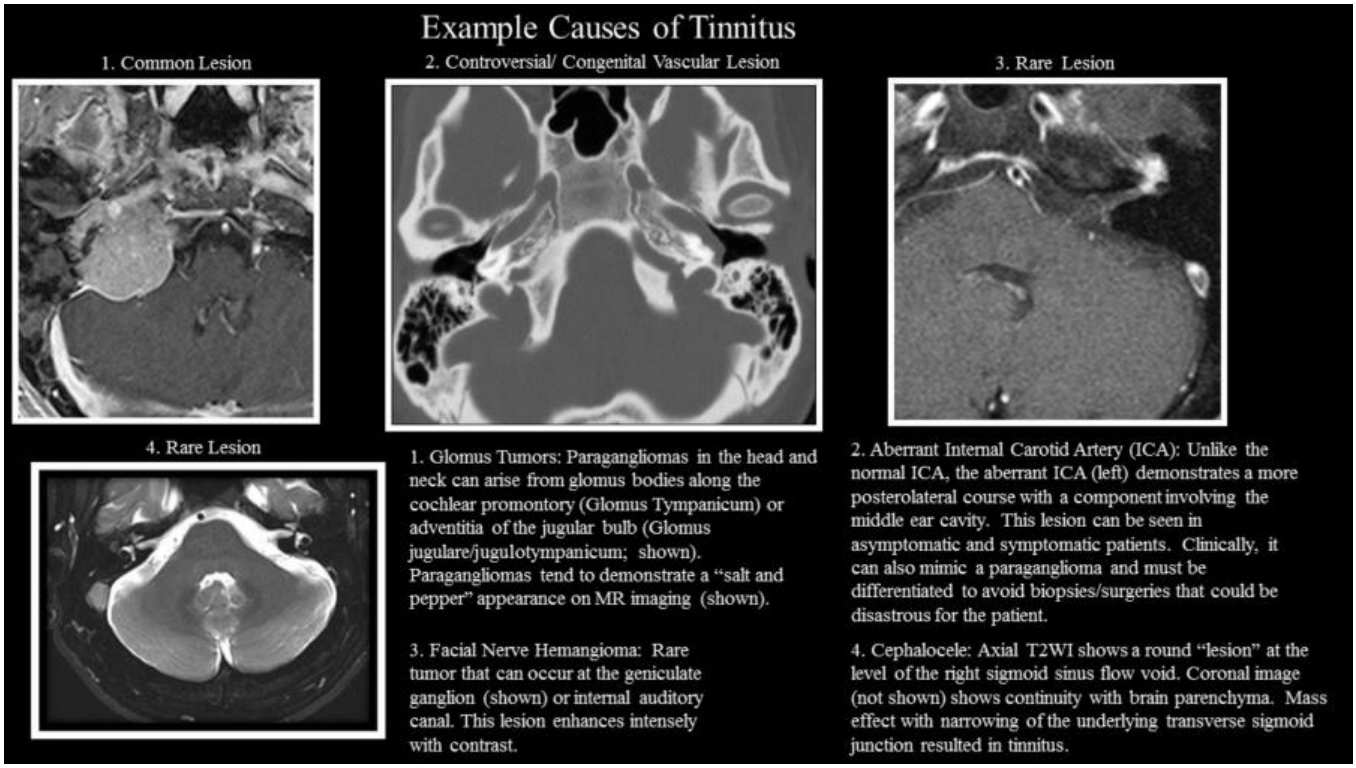
EdE-52

6:30AM - 3:00PM

Imaging of Tinnitus: Common, Controversial and Rare Causes

A Lal[1], G De La Vega Muns[2], R Medvid[3], N karamsadkar[4], R Mannava[3], R Bhatia[5], E SARAF LAVI[6], C Sidani[7]
[1]University of Miami Miller School of Medicine/Jackson Memorial Medical Center, Miami, FL, [2]Jackson Memorial hospital, miami, FL, [3]Jackson Memorial Hospital, Miami, FL, [4]University of Miami - Jackson Memorial Hospital, miami, FL, [5]University of Miami/Jackson Memorial Hospital, Miami, FL, [6]University of Miami, Miami, FL, [7]University of Miami miller School of Medicine, Miami, FL

Purpose
Tinnitus is a common and sometimes debilitating symptom affecting 10% of the US population. It has multiple causes and classifications. A subset of patients with tinnitus may have radiologically identifiable etiologies that are treatable. Thus, by adapting a systemic approach for finding these lesions, radiologists can have a significant impact on patient management and quality of life.
Materials and Methods
We reviewed our PACs system for all imaging performed on patients with the provided diagnosis of tinnitus. Examples of radiologically identifiable causes will be included in this exhibit. The aim is to create a framework that radiologists can use while reviewing the imaging studies for patients referred with tinnitus.
Results
We identified at least ten different entities that were suggested to be the cause of tinnitus. Etiologies include findings in or about the middle ear cavity such as vascular neoplasm, congenital vascular anomalies and acquired vascular abnormalities along with findings that are more central such as solid tumors and structural abnormalities with an intra-axial or extra-axial location. Discussion of tinnitus will consist of its definition and an introduction to its subtypes of pulsatile versus nonpulsatile, which can guide the imaging work-up and also organize the differential diagnosis for radiologists. Relevant anatomy will be presented, followed by examples of cases that represent the common, controversial and rare radiological findings of tinnitus. The cases will be divided into causes of either pulsatile or nonpulsatile tinnitus. Discussion of each case will include a brief description of the etiology and key imaging findings that help in diagnosing and differentiating the lesion from other entities on the differential diagnosis. Mention also will be made of "leave me alone" lesions that can mimic treatable causes and lead to disastrous outcomes when misdiagnosed.
Conclusions
In conclusion, despite an infrequent ability to explain the etiology of tinnitus on imaging studies, an imaging work-up is still important for the times a treatable cause can be discovered. Therefore, it is important for radiologists to both understand the different causes of tinnitus and develop a systematic approach for identifying them.



(Filename: TCT_EdE-52_GraphicsforANSR2017Abstract.jpg)

EdE-48

6:30AM - 3:00PM

Imaging Techniques and Pathology of the Vocal Cords: A Pictorial Essay

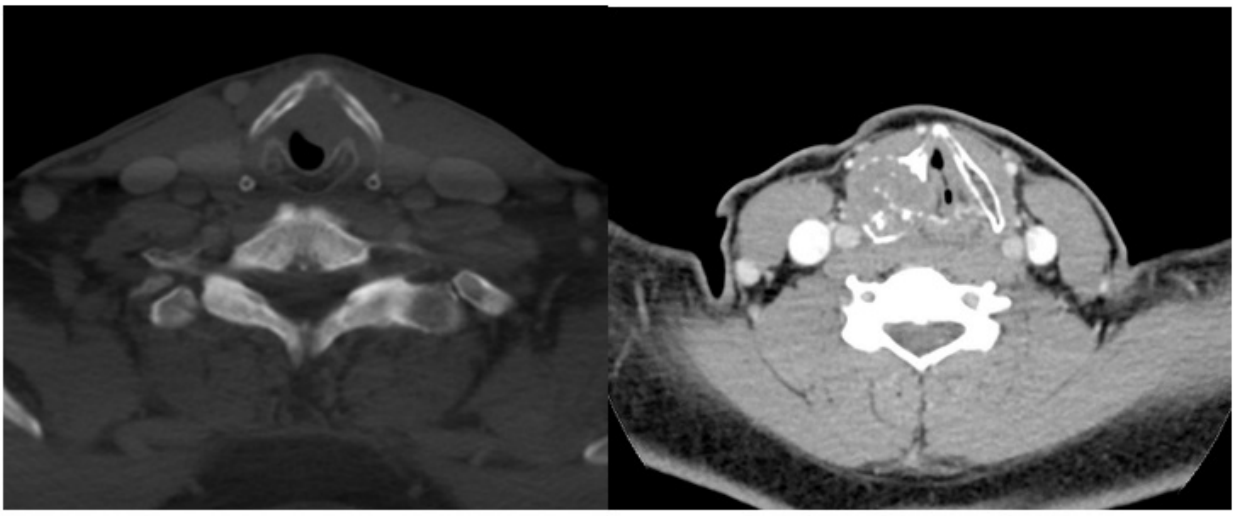
D Childers[1], A Singhal[1], S Gaddamanugu[1]
[1]*University of Alabama at Birmingham, Birmingham, AL*

Purpose
Vocal cord or glottis pathologies can present a diagnostic challenge to radiology residents and practicing radiologists at any training level. This exhibit is aimed at educating the audience on relevant anatomy, imaging techniques of the vocal cords, and illustration of both common and rare laryngeal pathologies.
Materials and Methods
Detailed anatomy of the vocal cords and larynx will be displayed on computed tomography (CT) and high resolution magnetic resonance imaging (MRI). Different CT protocols and MRI sequences for evaluation of the vocal cords will be illustrated and detailed. Common and less common vocal pathologies in our patient database will be illustrated. Imaging findings unique to rare vocal cord pathologies will be discussed. Imaging findings of vocal cord paralysis and its causes will be detailed.
Results
The vocal cords, or vocal folds, are mucosal and muscular folds which are attached to the

thyroid cartilage anteriorly and arytenoid posteriorly. Computed tomography is the most useful modality for identifying vocal cord pathology. Computed tomography in multiple phases such as in shallow breathing (causing vocal cords to open) and suspended respiration (vocal cords adduct and are in paramedian position) can illustrate vocal cord pathology and its extent better. Magnetic resonance imaging is more suitable for identifying paraglottic and cartilage invasion of tumor. While the most common pathology involving vocal cords is squamous cell cancer and vocal cord paralysis, other less common pathologies are cartilage-based tumors, neuro-endocrine tumors, salivary gland tumors, lymphoma, arthritis, trauma, and amyloidosis.

Conclusions

Knowledge of vocal cord pathology is important for accurate diagnosis and appropriate care of patients. With a better understanding of these pathologies and their pattern of growth, radiologists can avoid potential pitfalls and help clinicians with appropriate management.



Malignancy with cartilage erosion

Chondrosarcoma



Vocal cord paralysis

(Filename: TCT_EdE-48_ASNRImages.jpg)

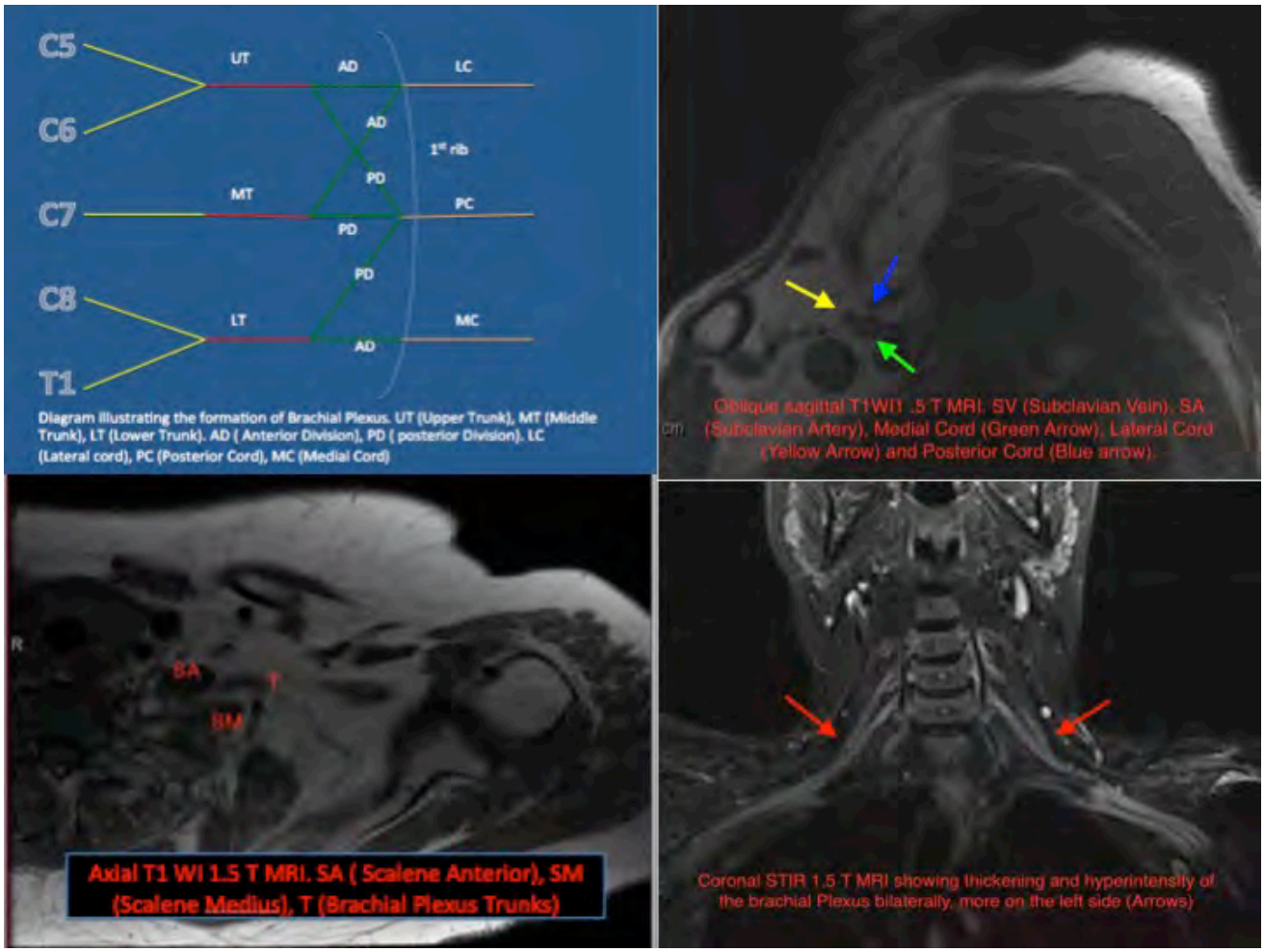
EdE-42

6:30AM - 3:00PM

MRI of Brachial Plexopathy: Radiological-clinical Correlation of Imaging, Electromyography, and Nerve Conduction Studies

H Al-Jadiry[1], o eissa[2], r eldaya[2], k Raj[3], K Raghuram[3]
[1]UTMB Galveston, Galveston, TX, [2]University of Texas Medical Branch, Galveston, TX, [3]UTMB, Galveston, TX

Purpose
Our purpose is to describe the MR imaging (MRI) technique and sequences used to evaluate the brachial plexus, review the anatomy of the brachial plexus and important landmarks, and review imaging findings and clinical signs/symptoms in several common and uncommon plexopathies. This study will help both trainees and practicing radiologists interpret challenging brachial plexus MRI.
Materials and Methods
We reviewed all brachial plexus MRIs performed in our department from January 2010 to November 2016. Two neuroradiologists with the context of patient history double read these studies, and findings were correlated with the results of EMG and nerve conduction studies.
Results
The brachial plexus is a complex network of nerves that originate from the cervicothoracic junction and supply sensory and motor innervation to the upper limb. Given the intricate anatomy, any degenerative, traumatic, infectious, inflammatory, neoplastic or radiation-induced processes related to the cervical or upper thoracic region or adjacent structures can result in upper limb neuropathy. The advances in and increased availability of MR imaging have had an evolving role in the evaluation of brachial plexus pathology. Imaging alone often is insufficient to establish a diagnosis and should be supported by clinical and electromyogram (EMG) data in order to achieve high quality patient care and the desired outcome. In our review, we found there is high correlation between the clinical presentation, the EMG/NCS results, and the MRI findings in localization of the involved part of the brachial plexus and the underlying pathological process.
Conclusions
MR imaging is the imaging modality of choice for evaluation of the brachial plexus and has a high sensitivity in establishing brachial plexus pathology and localization of disease processes as correlated clinically and with EMG.



(Filename: TCT_EdE-42_Slide1.jpg)

EdE-44

6:30AM - 3:00PM

Paragangliomas of Head and Neck: Spectrum of Imaging Findings

a abdel razek[1]
[1]*Mansoura faculty of medicine, mansoura, WY*

Purpose
1- To review basic background about paragangliomas of the head and neck. 2- To illustrate the common location of paragangliomas of the head and neck. 3- To present imaging appearance of paragangliomas of the head and neck.
Materials and Methods
1- Basic background about paragangliomas. 2- CT and MR imaging for assessment of paragangliomas. 3- MR angiography and CT angiography for assessment of paragangliomas. 4- Anatomical locations of paragangliomas in head and neck. 5- Role of CT and MR imaging in staging of glomus jugulare. 6- Imaging findings of glomus tympanicum. 7- CT

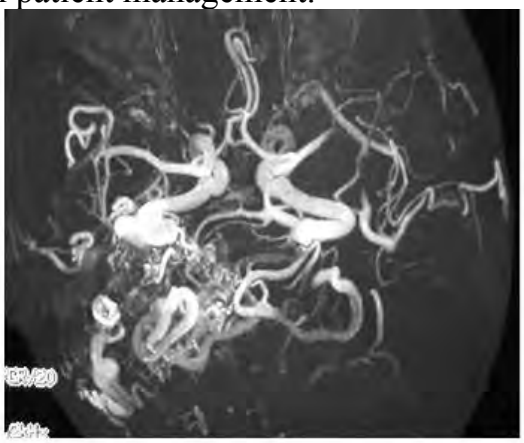
and MR imaging appearance of glomus caroticum. 8- Imaging appearance of glomus vagle. 9- Imaging of glomus in atypical sites such as nasal cavity and nasopharynx. 10- Diffusion MR in prediction of malignancy of paragangliomas. 11- Familial multiple paraganglioma syndromes in head and neck. 12- Conclusion and future directions.

Results

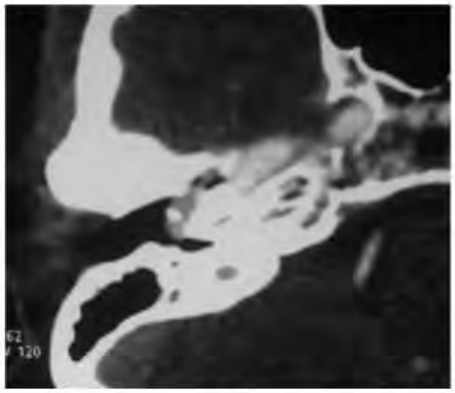
Cross-sectional imaging can helps in accurate localization and characterization of paragangliomas at different regions of head and neck. CT and MR angiography can detect vascularity of the lesions. Imaging can suspect malignancy and associated syndromes. This information is important for treatment planning and prognosis of the patients.

Conclusions

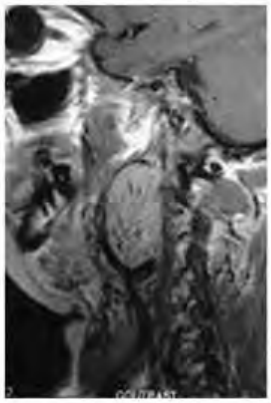
We concluded that imaging is important for accurate localization, characterization and extension of different subtypes of paragangliomas. It can predict malignancy and suspect familial form of the disease. This information is important for treatment planning and has impact on patient management.



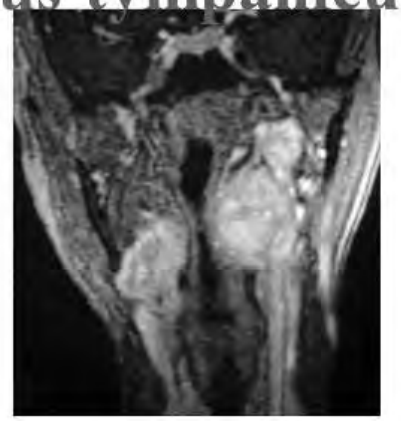
Glomus jugulare



Glomus tympanicum



Glomus caroticum



Familial glomus

(Filename: TCT_EdE-44_555.jpg)

EdE-55

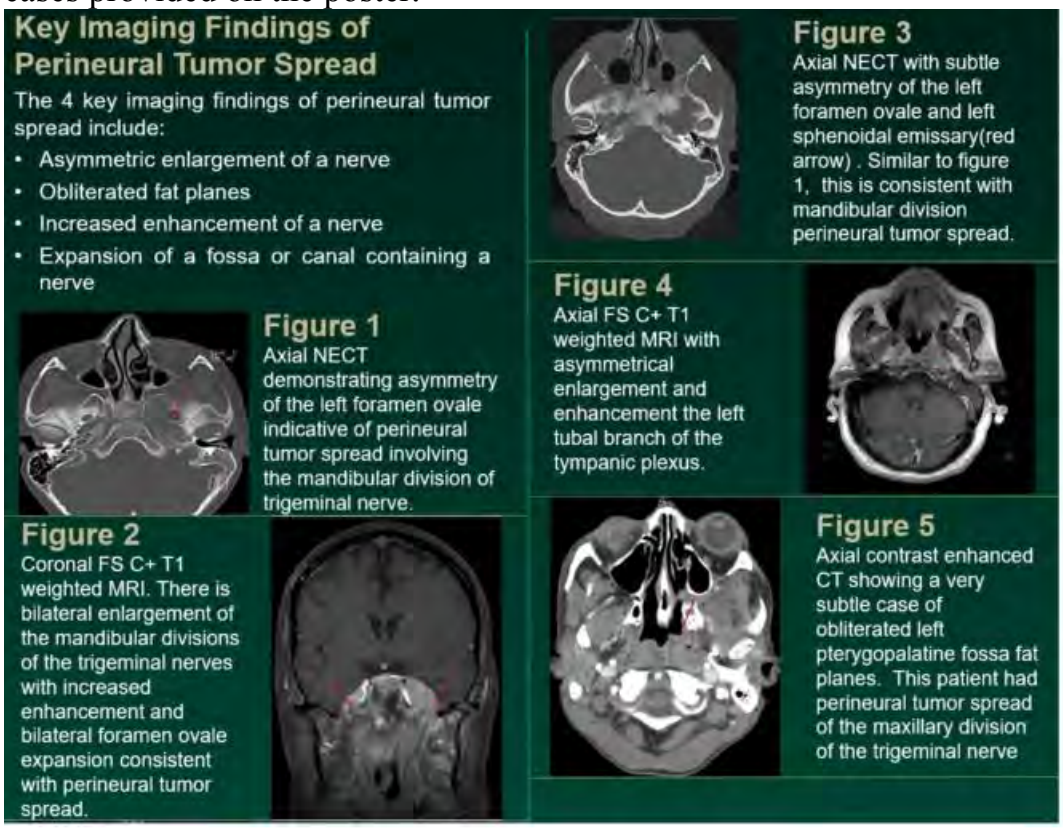
6:30AM - 3:00PM

Perineural Tumor Spread with 3D Print Correlation

C Cox[1], R Murtagh[2], R Shah[3], S Decker[4], J Ford[5]
[1]University of South Florida, Riverview, FL, [2]USF Morsani College of Medicine, Tampa, FL, [3]University of South Florida, Tampa, FL, [4]University of South Florida Morsani College of Medicine, Tampa, FL, [5]USF, Tampa, FL

Purpose
To provide a comprehensive review of perineural spread of head and neck malignancies. Additionally, a 3D print will be on display in front of my poster which was created from a computer generated model obtained from an MRI scan. The 3D print clearly demonstrates the anatomy of the cranial nerves that are commonly involved in perineural spread from head and neck malignancies. The 3D print will help reinforce the anatomy and the imaging findings of perineural tumor spread.
Materials and Methods
An MRI of the head was obtained on a normal patient and a 3D model was created of the skull and cranial nerves. Then a 3D printer was utilized to created a 3D print of the patients skull, cranial nerves, and brain stem. Next the brain stem and the trigeminal nerve were painted a different color than the clear skull so that you can visualize the trigeminal nerve origin, its course, and all of its branches. The trigeminal nerve was chosen to be emphasized since it is the most commonly involved nerve in perineural tumor spread. This 3D print will be on display in front of the hard copy poster. Additionally, a complete review of the most up to date information will be provided via a hard copy poster which will include presentation, common malignancies, prognosis, management, common imaging findings, and a review of 10 cases of perineural tumor spread with annotations of the imaging findings.
Results
Perineural spread of head and neck malignancies can be subtle especially in cases of remote history of prior head and neck cancer. With the prevalence of CT scans being obtained, this often can be overlooked. A comprehensive review will be provided along with the common pathways of perineural spread. This will establish the framework to allow detection of even the most subtle cases of tumor spread. The cranial nerves are the highways for perineural tumor spread, and thus the anatomy is very important to understand. To reinforce the cranial nerve anatomy a 3D printer will be utilized to build several models that will exemplify the cranial nerves, their individual courses, and provide correlation to the common imaging findings of perineural tumor spread. These 3D prints will be available in front of a a hard copy poster that will be a complete review of perineural spread along with 10 cases of

perineural tumor spread. The 3D prints will be available for all visitors to pick up and manipulate to help reinforce the imaging findings associated with perineural tumor spread.
Conclusions
The nerve courses are the highways for perineural tumor spread. By utilizing a 3D print that will be on display in front of the poster that all the visitors will be able to pick up and manipulate, the common "highways of perineural tumor spread" will be reinforced. Additionally, a hard copy poster with a comprehensive review of perineural tumor spread along with the pertinent imaging findings will be provided. This will help the audience visualize the anatomy and findings of perineural tumor spread with correlation with subtle cases provided on the poster.



(Filename: TCT_EdE-55_PNTS_abstract_ASNR.jpg)

EdE-49

6:30AM - 3:00PM

Something Smells Wrong - Imaging Findings in Patients with Hyposmia

S Bravo-Grau[1], K Müller[1], S Waissbluth[1], I Huete[1], J Cruz[1]
[1]*P. Universidad Católica de Chile, Santiago, RM*

Purpose

Review the spectrum of imaging findings in patients with hyposmia/anosmia and provide a practical approach for the main associated conditions.

Materials and Methods

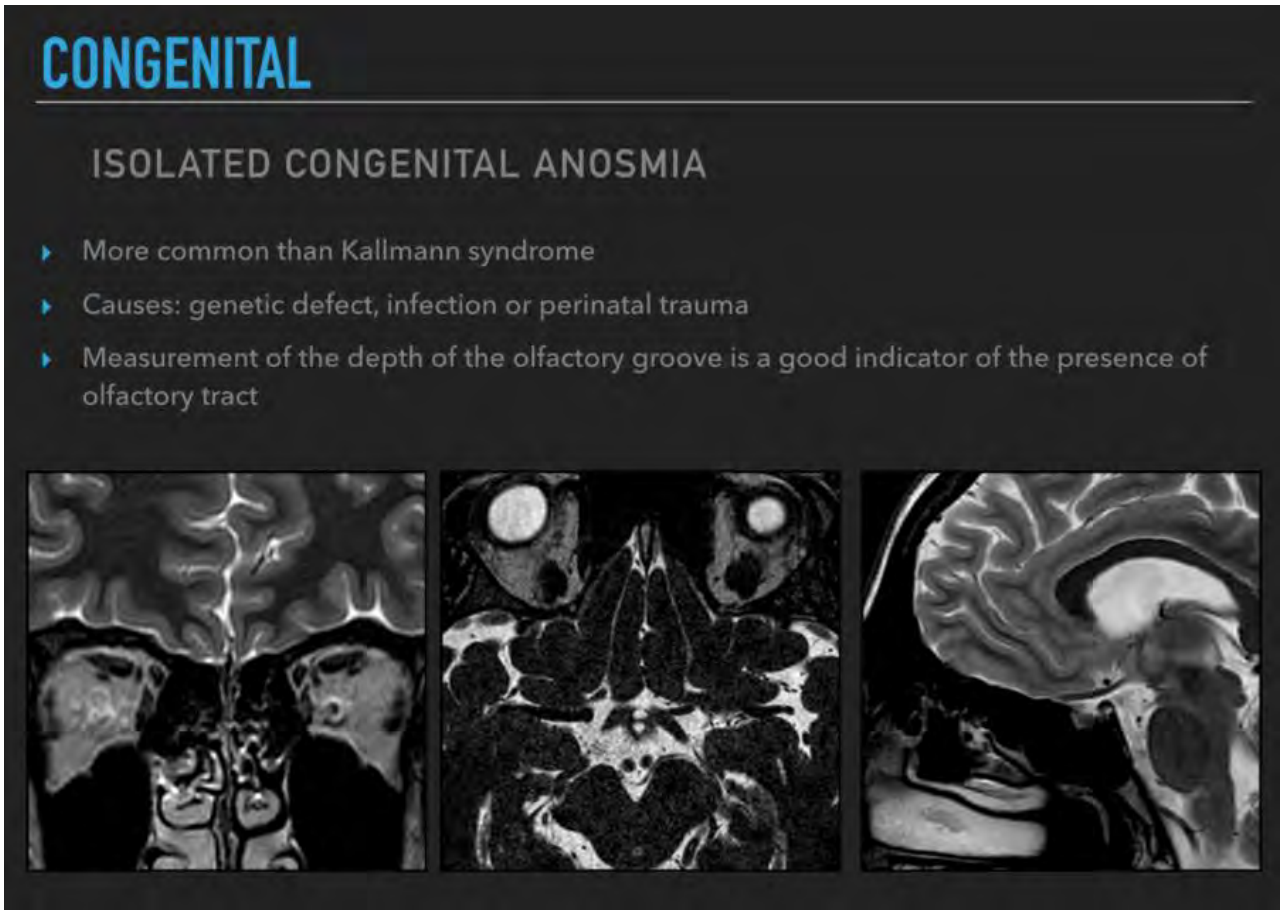
Review of selected cases with demonstrated diseases that clinically present as hyposmia in patients with imaging studies performed at our health network. Emphasis will be given to those diseases where the imaging findings may aid in the differential diagnosis of the spectrum of diseases that alter smell. The usefulness of the different MRI protocols are discussed according to medical history and clinical characteristics. Furthermore, key findings in other areas of the body are analyzed when evaluating a systemic disease. When necessary, other imaging modalities are described when useful for an early diagnosis in certain diseases (i.e., Parkinson's disease, metastasis).

Results

An imaging approach-based classification of the main diseases that may cause or present with hyposmia or anosmia is shown: - Congenital: olfactory bulb aplasia (isolated congenital anosmia), Kallmann syndrome, - Benign neoplasms: sinonasal polyposis, inverted papilloma, juvenile nasopharyngeal angiofibroma, osteofibrous lesions, meningioma, nerve sheath tumors, - Malignant neoplasms: squamous cell carcinoma, cystic adenoid carcinoma, esthesioneuroblastoma, rhabdomyosarcoma, metastasis, lymphoma, osteosarcoma, embryonal tumors (former PNET), - Inflammatory/infectious: upper respiratory tract infection, acute and chronic rhinosinusitis, mucormycosis, aspergillosis, cystic fibrosis, tuberculosis, - Neurodegenerative diseases: Alzheimer disease, Huntington's disease, Parkinson's disease (Hyposmia can be the initial manifestation of patients with Parkinson's disease), - Others: age, trauma, iatrogenic (postradiation, anterior fossa surgery or temporal lobectomy), metabolic, endocrine disorders, toxic: alcohol, solvents, cocaine, Down syndrome, Korsakoff's syndrome.

Conclusions

The main etiologies of hyposmia/anosmia are viral infections, chronic rhinosinusitis and traumatic brain injury. It is a prevalent symptom among the geriatric population. In pediatric patients it is important to be aware of isolated congenital anosmia and Kallman syndrome. Imaging studies are useful for a variety of etiologies, and they should be focused in nasal cavities, anterior cranial fossa and medial temporal lobe.



(Filename: TCT_EdE-49_congenitalanosmia.jpg)

EdE-54

6:30AM - 3:00PM

Update on 4D-parathyroid CT for Pre-operative Characterization of Parathyroid Adenoma as an Adjunct Modality to Sestamibi Scintigraphy: Case Studies and Systematic Review.

K Patel[1], P Dubey[2], S Niazi[1], J Jose[3], R Yeh[2], G Moonis[2], S Dundamadappa[3]
[1]Mount Sinai Medical Center, Miami Beach, FL, [2]Columbia University Medical Center, New York, NY, [3]University of Massachusetts, Worcester, MA

Purpose
1. To describe the imaging characteristics including attenuation profile, and enhancement patterns of parathyroid lesions on four-dimensional (4D) computed tomographic (CT) examinations with emphasis on anatomic characterization. 2. To discuss technical considerations for higher yield 4D-CT imaging protocol as an adjunct tool for parathyroid adenoma work up. 3. To emphasize the utility of 4D-CT examinations in identifying hyperfunctioning parathyroid glands and pre-operative planning.

Materials and Methods

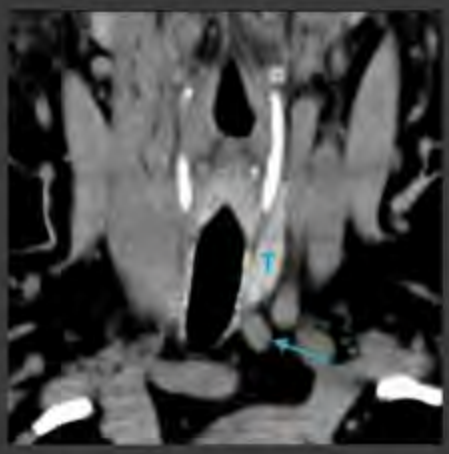
Adult patients with primary hyperparathyroidism with equivocal or negative findings on traditional imaging underwent 4D-CT examinations for localization of pre-operative planning at the author's institutions. Multiphase imaging was performed using standardized scanning protocol. With increasing experience with 4D-CT, its utility as a diagnostic tool in parathyroid adenoma work up has increased. It is unclear if this remains indicated in scenarios of failed localization on sestamibi scintigraphy or merits evaluation as a primary modality in parathyroid adenoma work up. We therefore also reviewed recent literature published in the past 5 years to assess the comparative effectiveness of 4DCT and sestamibi scintigraphy as independent tools of parathyroid adenoma work up.

Results

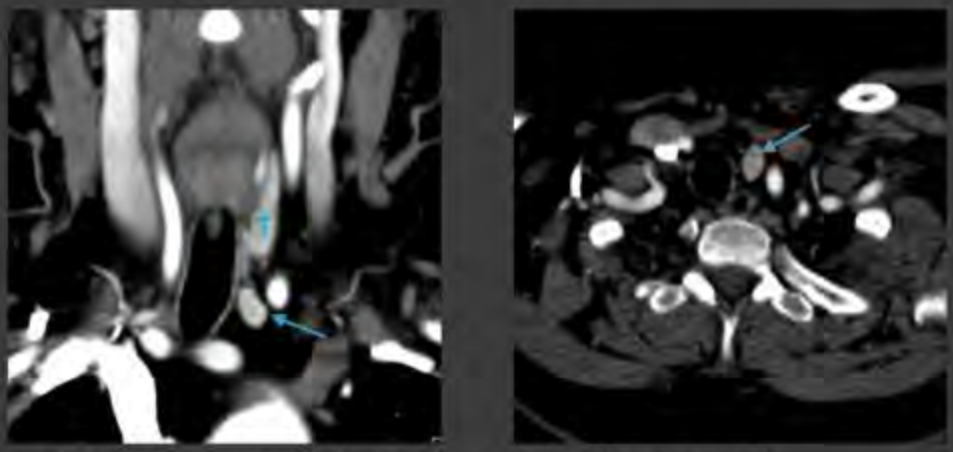
4D-CT is used to localize and characterize hyperfunctioning parathyroid glands. It usually is performed as a second line investigation to augment the findings on traditional imaging (ultrasound, scintigraphy). Non-contrast, arterial, and delayed/venous phase images are obtained from the sella to carina. The first three 'dimensions' are axial acquisition, and coronal and sagittal reformations. The fourth 'dimension' is the characteristic enhancement pattern of the parathyroid adenomas (low attenuation on non-contrast, peak enhancement on arterial phase, and early washout on delayed/venous phase). It is possible to accurately characterize the lesion, and guide the surgeon towards a minimally invasive parathyroidectomy and against an open neck dissection. Multiple studies have shown the significantly high diagnostic accuracy and precise localization of hyperfunctioning parathyroid glands. This has led to favorable surgical preference for minimally invasive parathyroidectomy with intraoperative parathyroid hormone monitoring, significantly decreasing hospital costs and patient morbidity.

Conclusions

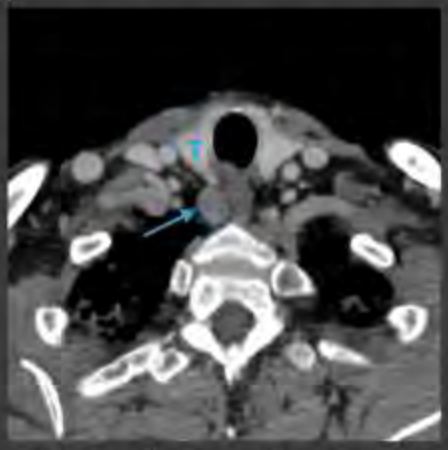
4D-CT provides high diagnostic accuracy for localization and anatomic characterization of hyperfunctioning parathyroid glands, with increasing diagnostic utility due to technical advancements. While traditionally used in the setting of failed localization on sestamibi scan, we also advocate its utility as an adjunct modality for precise anatomic characterization during pre-operative work up prior to parathyroidectomy in combination with intra-operative parathyroid hormone monitoring.



Noncontrast coronal image shows an oval hypoattenuating lesion (arrow) inferior to left thyroid lobe (T). Note the relative hyperattenuating appearance of the thyroid gland due to trapped iodine.



Arterial phase coronal and axial image in the same patient demonstrating early enhancement (arrows).



Delayed (venous) phase axial image in a different patient demonstrating washout of contrast material in the oval nodule (arrow) posterior to the right thyroid lobe (T).

(Filename: TCT_EdE-54_Images.jpg)

EdE-45

6:30AM - 3:00PM

Visual Review of Air within the Head, Neck and Spine: An Image Based Primer

F Janjua[1], J Shah[2], G Cruciata[2], E Greif[3], S Kantharia[2], N Cornish[4], E Stein[2]
[1]Maimonides medical center, Brooklyn , NY, [2]Maimonides Medical Center, Brooklyn, NY, [3]Maimonides Medical Center, Brooklyn , NY, [4]Maimonides Medical Center, Brooklyn,, NY

Purpose
1. Review the common and relevant anatomy of head, neck and spine structures across various modalities imaging. 2. Recognize the clinical characteristics of abnormalities (idiopathic, iatrogenic, infectious traumatic, etc.). 3. Describe these cases using diagrams and pictorial cases from our own institution. 4. Review pearls and pitfalls of these diagnoses.
Materials and Methods
Head, neck and spinal imaging are cornerstones of neuroimaging, and often provide urgently vital information necessary for patient care. As the amount of imaging increases across clinical contexts (emergency room, outpatient, etc.) and modalities (radiographs, CT scans, etc.) it is important to be familiar with a wide breadth of diagnoses. Unexpected air, a common foe of the radiologist, is however a rare entity in neuroradiology (unlike other divisions such as body and chest). As such it is important for the community radiologist to also understand the pathophysiology of air in neuroimaging in addition to being comfortable in detecting it across modalities. The careful delineation between benign and malignant causes of unexpected air is of the utmost importance.
Results
1. Head: a. Pneumocephalus, • extra-axial, • intra-axial, b. Abscess, c. Osteomyelitis, d. Mechanical Trauma, e. Postsurgical , f. Necrotic tumor. 2. Neck: a. Subcutaneous emphysema, b. Fistula, c. Perforated hollow viscous, d. Penetrating trauma, e. Post-surgical, f. Abscess, g. Necrotic Lymph node. 3. Spine: a. Pneumoracchis, b. Trauma, c. Abscess, d. Osteomyelitis, e. Vacuum Phenomenon, f. Pneumatic nerve root compression, g. Post Surgical. 4. Pearls and Pitfalls of detecting air on Imaging Modalities: a. x-ray, b. CT, c. MRI.
Conclusions
1. Air is a fairly common, but less considered imaging sign in neuroimaging, associated with morbidity and mortality. 2. Knowledge of the variations in the appearance of air within relevant spaces and anatomy are important tenets to keep in mind for the Neuroradiologist. 3. Determining the pathophysiology of the air, whether it is or benign or malignant, and the next steps are crucial to review for the community radiologist. 4. Complications of air can

cause pain, effect quality of life or result in death. Intervention can be offered by referring practitioners with proper recognition of pathology on imaging.

Monday
6:30AM - 3:00PM
Long Beach Convention Center, Exhibit Hall B-(Lower Level) EdE

Education Exhibit Poster (EdE)-Informatics

EdE-56

6:30AM - 3:00PM

Artificial Neural Networks and Machine Learning: An Introduction for the Neuroradiologist and Neurointerventionalist

S Arndt[1], D Goldman[1], J Milburn[1]
[1]*Ochsner Clinic Foundation, New Orleans, LA*

Purpose
The purpose of this educational exhibit is to review the basic principles and applications of machine learning models for predictive modeling, as well as the data requirements for model creation. Traditionally, logistic regression is used to analyze outcomes in major trials, but other modeling methods are underutilized for predictive analysis. This report will provide a framework for machine learning model creation and comparison of predictive models to assess various outcomes measures.
Materials and Methods
Data preprocessing including treatment of different variable categories, and the importance of standardization will be reviewed. Neural Network structure, and the importance of learning rate, momentum, and decay will be reviewed. Support vector machine kernel, C, epsilon, and loss function will be discussed. Naive Bayes classifier and LaPlace correction will be explained. Decision tree models will be reviewed, with respect to criterion for splits, pruning, depth, and prepruning. Model comparison techniques including bootstrap and K-fold cross validation will be explained and compared. All concepts reviewed will be geared toward the general radiologist.
Results
While logistic regression has been used in most major trials, much work still needs to be done to maximize predictive statistical analysis. The most important point to be drawn from data is the ability to understand the clinical course of our patients, and what can be done to affect it. Machine learning techniques are becoming more accessible, and provide better predictive power according to recent analysis. Understanding how these models are built, and the generalities of how these models work also is becoming more important.
Conclusions
Advanced modeling methods can provide a significant advantage when compared to

traditional logistic regression analysis. Implementation in free to use and code-free environments can be accomplished without significant difficulty. These methods can help improve predictive power of statistic analysis.

Monday
6:30AM - 3:00PM
Long Beach Convention Center, Exhibit Hall B-(Lower Level) EdE

Education Exhibit Poster (EdE)-Interventional

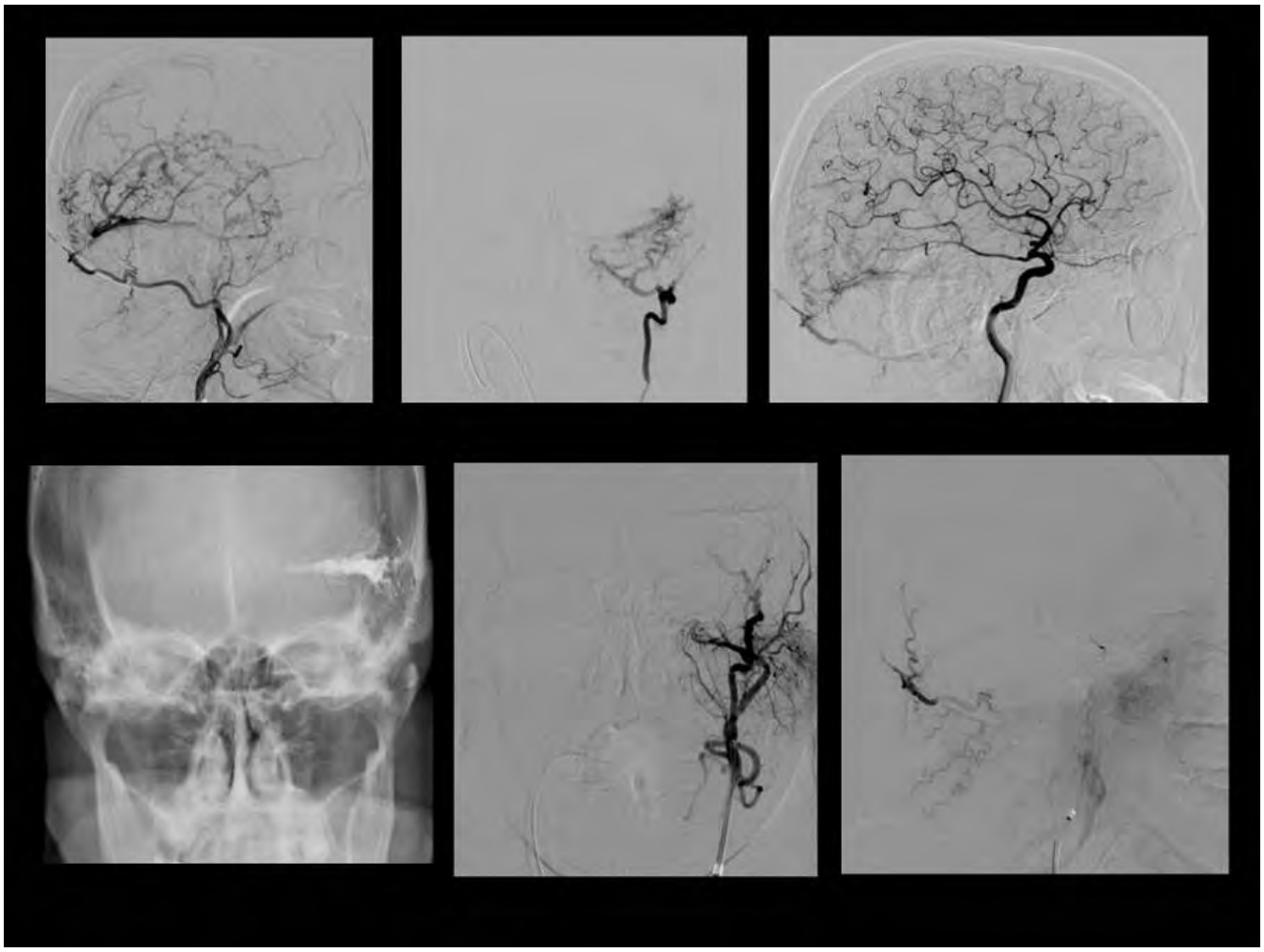
EdE-58

6:30AM - 3:00PM

Intracranial Dural Arteriovenous Fistula: The Spectrum Illustrated

H PENDHARKAR[1]
[1]*NATIONAL INSTITUTE OF MENTAL HEALTH & NEUROSCIENCES, BANGALORE, KARNATAKA*

Purpose
To illustrate on angiography the various types of intracranial arteriovenous fistulas and their endovascular management.
Materials and Methods
One case each of all five types of DAVFs is illustrated. The detailed angioanatomy is described. The technique of embolization is detailed followed by the check angiogram documenting the outcome of embolization. Clinical follow up of these patients is given.
Results
Newer liquid embolic Onyx is the agent of choice for obliteration of the fistula. The access route is presently transarterial, the middle meningeal artery being the most common artery used. Complete obliteration can be achieved in one sitting.
Conclusions
A complete six-vessel angiogram is mandatory to identify and map the dural arteriovenous fistula. Endovascular embolization with liquid embolics is the the treatment of choice.



(Filename: TCT_EdE-58_DAVF.jpg)

EdE-57

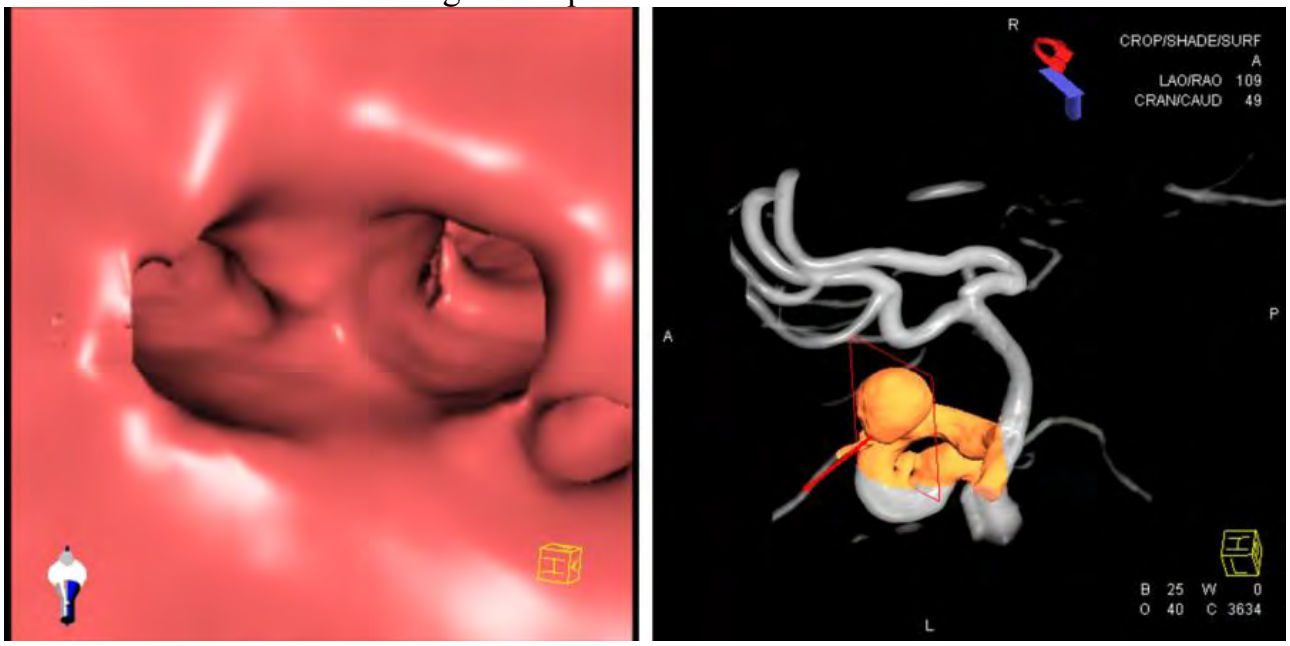
6:30AM - 3:00PM

Intraluminal Navigation to Assess Aneurysm Neck Geometry

K Raghuram[1]
[1]*University Of Texas Medical Branch, Galveston, TX*

Purpose
Use postprocessing techniques to assess the geometry at the neck of aneurysms to provide an endoluminal view. By generating images that allow virtual navigation through the lumen of the artery, the exact relationship between the neck of the aneurysm and the parent artery as well as the relationship to an adjacent branch can be accurately delineated. This would allow for more intricate planning of aneurysm coiling procedures, including whether or not to use adjunctive techniques such as balloons or stents.

Materials and Methods
Intracranial 3D digital subtraction angiographic images obtained on a Siemens Artis Zee angiography suite were reviewed on 15 patients with intracranial aneurysms. Postprocessing was performed on a dedicated Leonardo workstation. Vessel segmentation was performed. After applying thresholding, intraluminal navigation was performed using the platform to assess the geometry of the aneurysm neck. Neck width and length were measured. Relationship of the neck to adjacent arterial ostia also was assessed.
Results
Aneurysm neck dimensions (length and width) were very well visualized in the intraluminal navigation images. Relationship of vessel ostia to the neck also were well evaluated in this series.
Conclusions
Intraluminal navigation by postprocessing provides another tool to look at the neck of an intracranial aneurysm to allow better planning for endovascular embolization procedures. Particularly, neck width and length assessment would allow for selection of adjunctive balloon or stent-assisted coiling techniques if the neck is wide in two dimensions.



(Filename: TCT_EdE-57_Aneurysms8.jpg)

Monday
6:30AM - 3:00PM
Long Beach Convention Center, Exhibit Hall B-(Lower Level) EdE

Education Exhibit Poster (EdE)-Pediatrics

EdE-65

6:30AM - 3:00PM

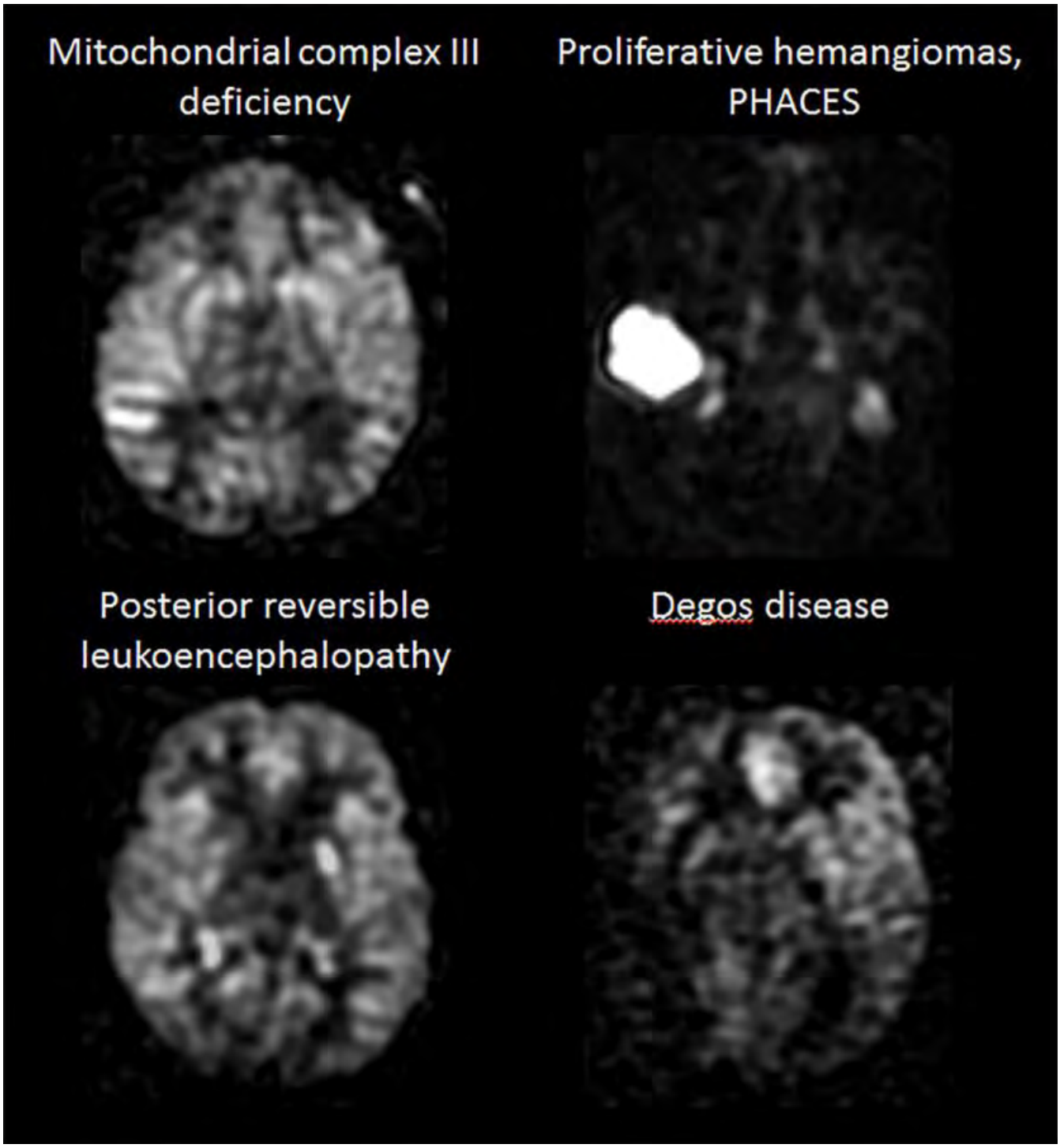
Arterial Spin Labeling: Pediatric Applications

M Ho[1], N Campeau[1], M Patterson[1]
[1]*Mayo Clinic, Rochester, MN*

Purpose
Arterial spin labeling (ASL) is a noncontrast MR perfusion technique that enables noninvasive and repeated measurements of absolute cerebral blood flow (CBF). Arterial spin labeling demonstrates special promise in the pediatric population, with clear safety advantages over nuclear medicine radioactive tracers and MR gadolinium-enhanced techniques. This pictorial review will discuss ASL physics, normal variants, and pathology in pediatric neuroimaging.
Materials and Methods
1. Review physics and technical considerations for ASL. 2. Illustrate spectrum of age-dependent variants and artifacts in pediatric ASL. 3. Demonstrate the added value of ASL for diagnosing diverse pathologies involving pediatric brain, head, and neck.
Results
TECHNICAL CONSIDERATIONS - Labeling pulse, - pCASL, VS-ASL, - Postlabel delays). NORMAL VARIANTS Age dependence: regional, global. Physiologic activity: - Frontal/visual cortex, limbic, DMN; - Nasal mucosa ARTIFACTS - Spin tag decay, - Selective/failed excitation, - Coil heterogeneity, - Motion, - Susceptibility, - Tissue masking, - Arterial transit artifact. IMAGING CASES ISCHEMIA/VASCULOPATHY Involved vessels, core infarct, ischemic penumbra, collateralization: - Arterial infarct, - Long tract signs, - CHD, - CVST, - Dysautoregulation: PRES, RCVS, - Hemiplegic migraine, - TGA; - TCA, - Moyamoya, - Vasculitis: lupus, lymphocytic, drugs, Degos; - HIE: preterm/term, child, adolescent, - Fat, septic emboli - Global hypoperfusion. VASCULAR MALFORMATIONS Vascular supply, shunting, extravasation, ischemic steal: - VGAM, DVA, - AVM, - DAVF, - CCF, - HHT, - Sturge-Weber, - Parry-Romberg, - Hemangioma, PHACES. EPILEPSY Ictal-interictal localization, propagation/lateralization, migrational, multifocal/systemic: - MTS, - FCD, Heterotopia, - PMG, - Schizencephaly, - HME, - TS, - Temporal intermittent rhythmic delta activity, - Febrile infection-related epilepsy syndrome, - Autoimmune epilepsy. GENETIC/METABOLIC Subclinical, disease distribution, - Serotonin syndrome, - Wernicke, - X-ALD, - Leigh disease, - Complex III deficiency, - Biotin-thiamine responsive basal ganglia disease, - Dynamin-1-like protein mutation, - Fatal familial insomnia. TUMORS Microvascular density, histologic grading, biopsy, follow-up: - JPA, AA, - GG, - PMA, - PXA, - DIA, - DIPG, - Optic glioma, - Medulloblastoma, - Ependymoma, - ATRT, - Schwannoma, - Lymphoma, - Metastasis, - Radiation necrosis. INFECTION/INFLAMMATION Vascularity, secondary ischemia, multifocal disease: - Mastoiditis with subdural empyema, - Pott puffy tumor, Invasive fungal sinusitis, - Multiple sclerosis, - ADEM, - Weston-Hurst, - Opsoclonus-myoclonus, - Rasmussen, - Hypertrophic pachymeningitis.

Conclusions

Arterial spin labeling (ASL) is a convenient and noninvasive technique for CBF assessment, with special considerations and applications in the pediatric population. Labeling parameters and postlabel delay should be tailored to the patient's age and disease category. Images should be interpreted in conjunction with anatomic sequences, and with knowledge of age-dependent variation and technical artifacts. Arterial spin labeling perfusion data provides added value for a variety of applications including ischemia/vasculopathy, vascular malformations, epilepsy, genetic/metabolic disorders, tumors, and infection/inflammation.



(Filename: TCT_EdE-65_Figure.jpg)

EdE-62

6:30AM - 3:00PM

Birds of Prey and Other Animal Signs: A Visual Primer for Neuroradiology Education

V Garg[1], H Marquez[1], E Sorra[1], R Suss[1], T Booth[2], D Veltkamp[2], K Koral[3], J Maldjian[4]
[1]University of Texas Southwestern Medical Center, Dallas, TX, [2]Children's Health System Texas, UT southwestern, Dallas, TX, [3]University of Texas Southwestern Medical Center and Children's Health, Dallas, TX, [4]University of Texas Southwestern, Dallas, TX

Purpose

To review neuroradiological disease entities associated with avian themes and other animal-inspired imaging findings.

Materials and Methods

A list of named signs pertinent to neuroradiology pathology was compiled as a starting point. We then reviewed cases from our department's adult and pediatric population over the past 5 years to find the best imaging correlate for the pathologic entity. Each sign was paired with an imaging example, along with a description of the imaging findings and underlying pathology. The avian-related names include: "Penguin/Hummingbird sign" secondary to Progressive Supranuclear Palsy; "Winking owl sign" secondary to an absent pedicle (and often seen with metastases); "Raptor beak sign" secondary to a Flexion-teardrop fracture; "Tectal beaking sign" secondary to a Chiari malformation; "absent Swallow tail sign" secondary to Parkinson's disease; "Klingon skull" secondary to craniosynostosis. A few more animal signs pertaining to neuroradiology include: "Bat wing sign" on CT secondary to Glutaric aciduria type 1 (GA-1); "Scotty dog sign" secondary to a fractured pars interarticularis;"Eye-of-the-Tiger sign" secondary to a PANK2 mutation; - "Tiger stripe sign" secondary to tonsillar inflammation; "Panda sign" secondary to Wilson's disease; "Rabbit sign" secondary to subclavian steal; "Codfish vertebrae sign" secondary to osteoporosis; - "Horseshoe crab sign" secondary to alobar holoprosencephaly; "Worm bag sign" secondary to an arteriovenous malformation.

Results

There are many named neuroradiology signs. Among these, there appears to be a predilection for associating neuro-imaging appearances with animals. This exhibit provides a compilation of many of these amusing associations. Associating characteristic imaging findings with domestic and exotic animals can provide an effective method of learning and recall.

Conclusions

This is a fun, engaging, and educational exhibit which reviews some of the neuroradiology imaging features and pathologies associated with avian themes and animals, spanning common entities to more esoteric pathology.



(Filename: TCT_EdE-62_BirdsofPrey.jpg)

EdE-63

6:30AM - 3:00PM

Brain Lesions in Twin To Twin Transfusion Syndrome (TTTS) treated with Fetoscopic Laser Coagulation (FLC): Prenatal and Postnatal Magnetic Resonance Imaging Findings

C Cinnante[1], E Scola[1], S Avignone[1], G Conte[2], i Fabietti[3], M Fumagalli[4], F Triulzi[5]
[1]Neuroradiology, Fondazione IRCCS Ca' Granda Ospedale Maggiore Policlinico, Milan, Italy, [2]Radiology, University of Milan, Milan, Italy, [3]Obstetrics and Ginecology, Fondazione IRCCS Ca' Granda Ospedale Maggiore Policlinico, Milan, Italy, [4]NICU, University of Milan, Fondazione IRCCS Ca' Granda Ospedale Maggiore Policlinico, Milan, Italy, [5]Neuroradiology, University of Milan,Fondazione IRCCS Ca' Granda Ospedale Maggiore Policlinico, Milan, Italy

Purpose
To discuss the pattern and pathophysiology of antenatal acquired brain lesions in fetuses and newborns from pregnancies complicated by twin-to-twin transfusion syndrome (TTTS)

treated with fetoscopic laser coagulation of placental anastomoses (FLC). Prenatal and postnatal brain MRI findings are presented.
Materials and Methods
Using a case-based format, the patterns of cerebral lesions in TTTS syndrome treated with FLC are illustrated with prenatal and postnatal MR images. Cases were selected from a database of 115 fetal MR studies of monochorionic biamniotic pregnancies complicated by TTTS and treated with FLC performed at our institution from 2012 to 2016. Twenty-three prenatal MR studies with postnatal MR confirmation of prenatal findings were chosen (43 newborns). Prenatal MR examinations were performed on a 1.5 T Philips Achieva scan after 15-21 days from FLC. Neonatal MR examinations were performed on a 3 T Philips Achieva scan at 40 weeks of gestational age (GA).
Results
Brain injury is depicted in donor and receiving twins; brain lesions are located in the cerebellum and in cerebral hemispheres. Ischemic and hemorrhagic lesions as well as cortical abnormalities are observed. Hemodynamic imbalance developing through a monochorionic placenta between a hypovolemic donor and a hypervolemic recipient can lead to cardiovascular decompensation in both twins as well as profound disturbance of brain perfusion. This may account for ischemic and hemorrhagic lesions observed. Moreover cortical abnormalities referred as polymicrogyria occur. The acquired polymicrogyria results from an external insult to a previously normally developing brain occurring whilst neuronal migration and/or cortical organization are still in progress (in the middle part of the second trimester).
Conclusions
TTTS complicates around 10% of all monochoronic multiple pregnancies. Although FLC has been shown to be associated with higher survival and lower neurological morbidity in the survivors than with alternative management strategies, brain lesions may be diagnosed in donor and receiving twins.

EdE-68

6:30AM - 3:00PM

Congenital Spine Anomalies: An Embryologic Approach

M Ho[1], N Wetjen[2]
[1]Mayo Clinic, Rochester, MN, [2]Mayo Clinic, Rochester , MN

Purpose
Utilize embryologic concepts to understand, describe, and classify congenital spine anomalies.
Materials and Methods
In this exhibit, we will highlight vital steps in prenatal/postnatal spine development that are key to understanding the pathogenesis of congenital spine anomalies. Important terminology

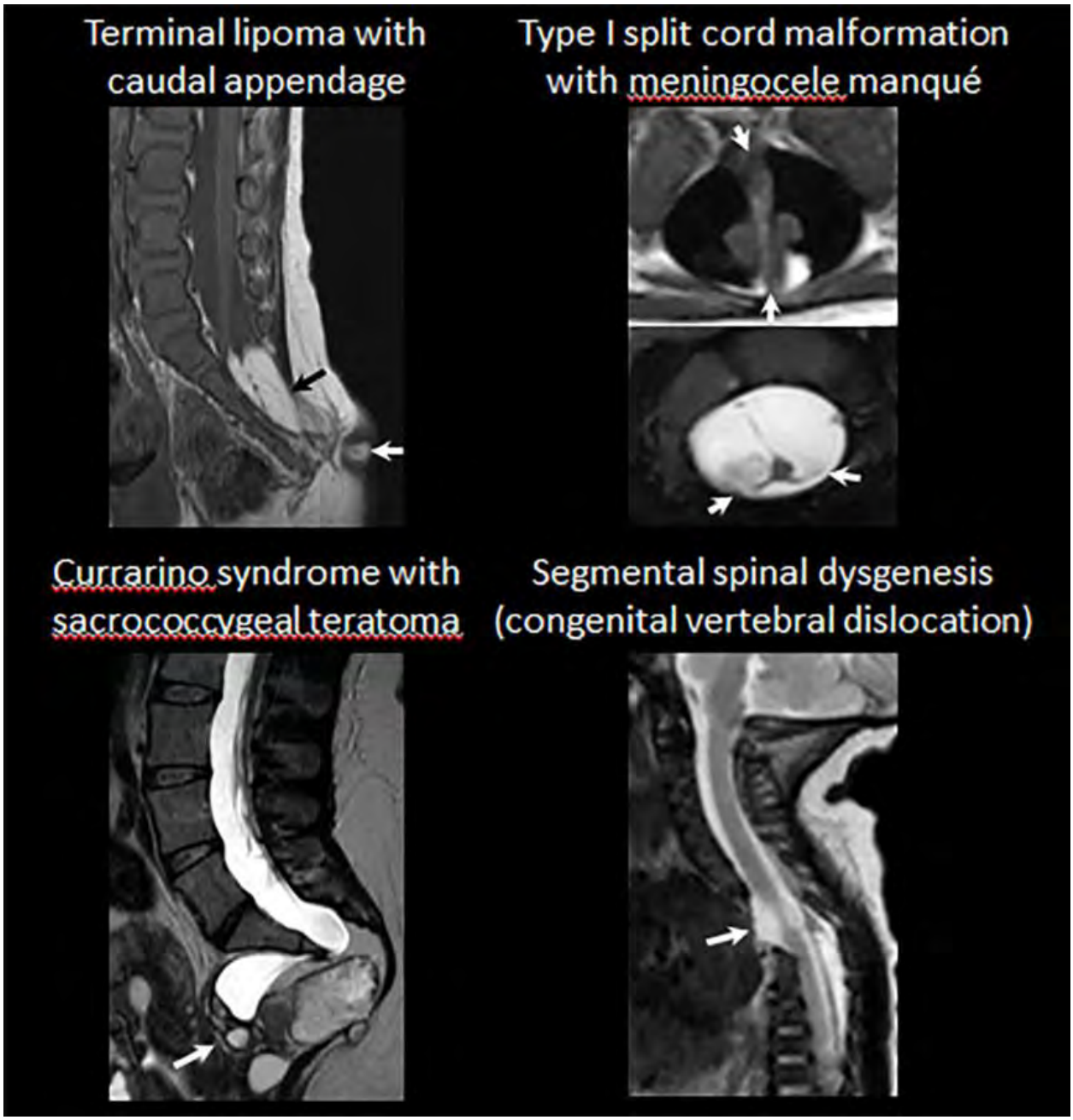
for describing spine/cord malformations will be introduced, with an emphasis on the interdependence of clinical and imaging features. Subsequently, we will present a rich case collection of developmental spine anomalies from basic to advanced, highlighting the key anatomic and pathophysiologic features in each process.

Results

SPINE EMBRYOLOGY - Gastrulation. - Primary neurulation: disjunction. - Secondary neurulation: canalization, retrogressive differentiation. - Vertebral segmentation. - Vertebral development: chondrification, primary ossification, secondary ossification. Terminology - Vertebral numbering and transitional anatomy. - Vertebral alignment: disorders of formation, segmentation. - Open vs. closed dysraphisms. - Neural placode: terminal, segmental. Clinical features - Low-risk vs. high-risk. IMAGING CASES - Tight filum terminale: retrogressive differentiation. Open spinal dysraphisms: segmental nondisjunction. - Myelocele, myelomeningocele, Closed spinal dysraphisms, - Meningocele, myelocystocele. Congenital spine masses: progenitor cells. - Lipoma, dermoid/epidermoid, sacrococcygeal teratoma, neurenteric remnant, hamartoma. Lipomatous malformations. - Lipomyelocele, lipomyelomeningocele: premature disjunction. - Terminal lipoma: caudal cell mass. - Transitional malformations, caudal appendage Split cord malformations: gastrulation. - Type I, II. - Hemi-OSD, meningocele manqué. Dorsal tracts: - Dermal sinus tract: disjunction. - Pseudo-dermal sinus tract: atretic fibrovascular stalk. Segmental spinal dysgenesis: notochordal encoding. - Klippel-Feil. - Congenital vertebral dislocation. - Caudal agenesis type I, II. Multisystem anomalies, - VACTERL, OEIS, Currarino. - Skeletal dysplasias

Conclusions

We illustrate an integrated approach to assessment of congenital spine malformations including application of embryologic concepts, utilization of accurate anatomic terminology, and synthesis with clinical information.



(Filename: TCT_EdE-68_Spine.jpg)

EdE-61

6:30AM - 3:00PM

Garre's Mandibular Osteomyelitis

W Gomez[1]
[1]*Bryn Mawr Hospital Main Line Health, Bryn Mawr, PA*

Purpose

To educate about Garre's mandibular osteomyelitis and present ultrasound and CT images from two companion cases.

Materials and Methods

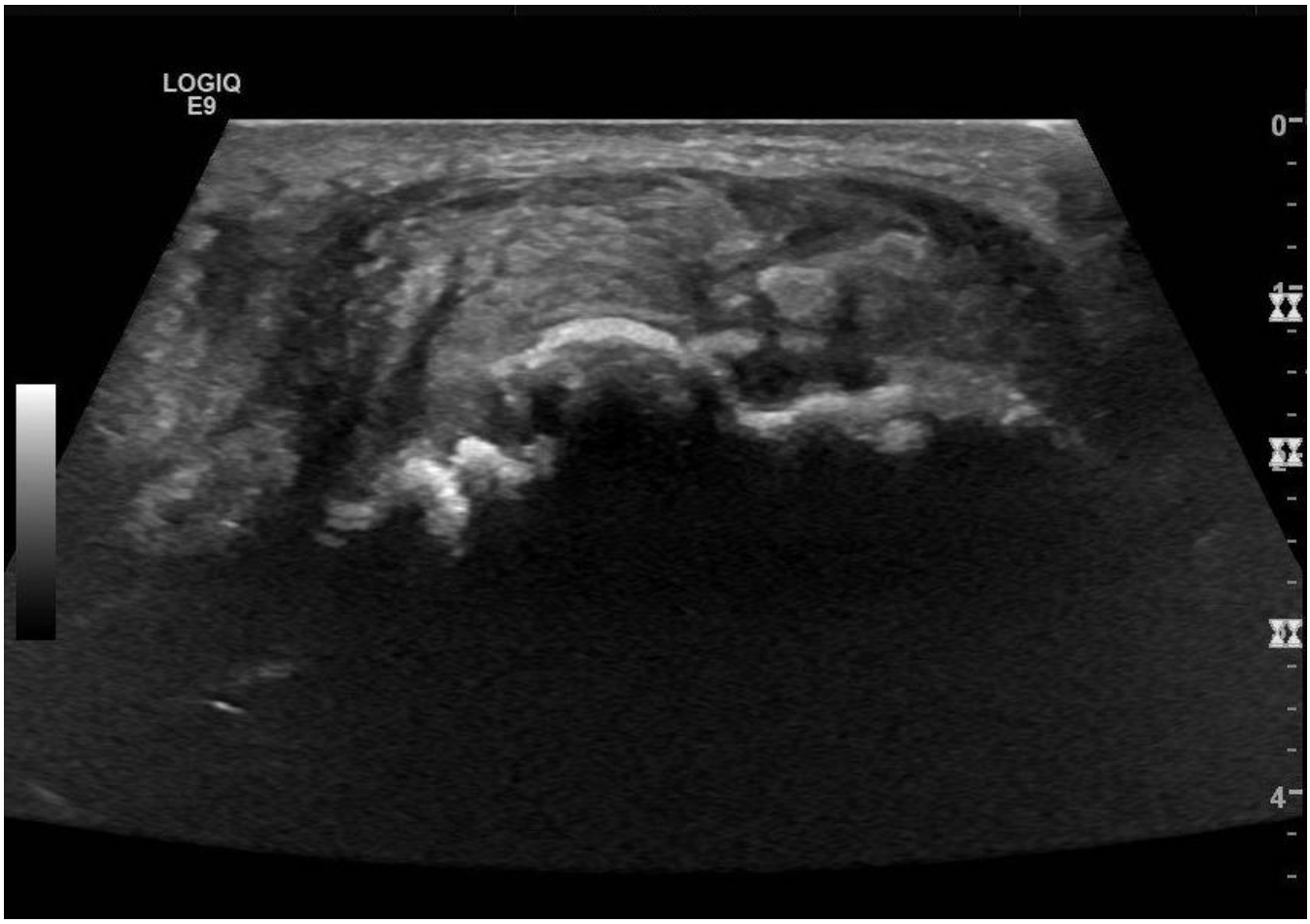
Sclerosing osteomyelitis of Garre is a specific type of chronic osteomyelitis, which was first described by Carl Garre in 1893. It generally affects children and adolescents. It also is known as chronic nonsuppurative sclerosing osteomyelitis and periostitis ossificans. It is considered an irritation-induced focal thickening of periosteum and cortex. It is a nonsuppurative inflammatory process, with subperiosteal bone deposition caused by mild irritation and infection. It typically involves the mandible (and less commonly, maxilla), and usually is due to an odontogenic source/infection, such as dental caries, mild periodontitis, dental eruption or previous dental extraction.

Results

Osteomyelitis of Garre is well-known in the dental literature. It is often a difficult diagnosis and classification of specific type of mandibular osteomyelitis have made it troublesome for clinicians to develop an improved understanding of this condition, which is indeed inflammatory, and has resulted in difficulties in planning treatment. The terms Garre's osteomyelitis and osteomyelitis with periostitis are used traditionally to describe lesions which demonstrate significant periosteal reaction. The differential diagnosis includes fibrous dysplasia, which may be clinically indistinguishable from Garre's osteomyelitis. The classic redundant cortical layering "onion-skin" appearance of the periosteal new bone formation of Garre's osteomyelitis distinguishes it from fibrous dysplasia. Other important differentials include Infantile cortical hyperostosis, syphilis, fracture callus and Ewing's sarcoma. When an obvious cause such as dental caries/periapical pathology are identified, along with pathonomonic imaging findings, a biopsy is not needed to confirm the diagnosis, and treatment may ensue based on imaging findings.

Conclusions

The main treatment for Garre's osteomyelitis is to treat odontogenic source, frequently with endodontic therapy or more aggressively with tooth extraction. The entity itself is rare as its occurrence depends on chronic infection in a young person, associated with a periosteum that is capable of significant osteoblastic activity, as occurs in pediatric patients and adolescents. More conservative endodontic therapy is the preferred treatment as this entity is mostly confined to the younger age group.



(Filename: TCT_EdE-61_1C.jpg)

EdE-67

6:30AM - 3:00PM

Gorlin's Syndrome: Genetic Manifestations, Imaging Appearance and Literature Review

A Blanchard[1], H Al Mrad[1], E Palacios[1]
[1]*Tulane University School of Medicine, New Orleans, LA*

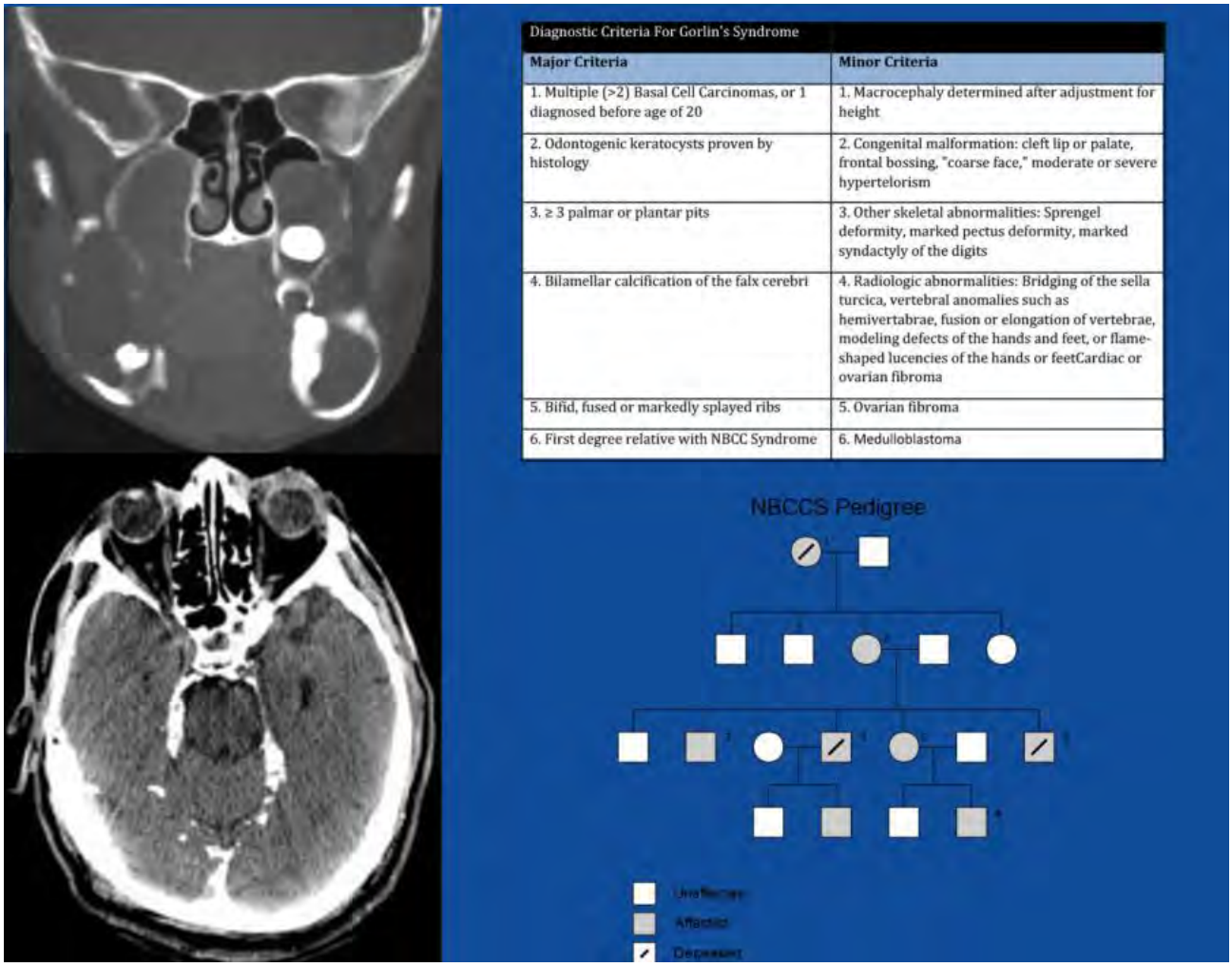
Purpose
The purpose of this presentation is to provide an educational overview of the genetics, clinical features, diagnostic criteria, imaging manifestations and management of Nevoid Basal-Cell Carcinoma Syndrome (NBCSS).
Materials and Methods
Select cases from our institution are taken from multiple generations of a family who exhibit various manifestations of the condition. Recent literature and guidelines were reviewed, and a search for Nevoid basal-cell carcinoma syndrome was performed in PubMed. Pertinent information was obtained from the literature and compared to our cases.

Results

Nevoid basal-cell carcinoma syndrome (NBCCS), also known as Gorlin-Goltz or simply Gorlin's syndrome, is a rare phakomatosis characterized by multiple basal cell carcinomas, craniofacial anomalies including odontogenic keratocysts (ODKs), and a predisposition for developing particular neoplasms including medulloblastoma and ovarian fibroma. The syndrome is inherited in an autosomal dominant pattern with complete penetrance although with variable expressivity. Kimonis et al. have devised criteria for the diagnosis of Gorlin syndrome, by which the diagnosis of NBCCS is made in the presence of two major criteria or one major and two minor criteria. Jaw cysts usually are the earliest manifestation of the disease and are the most common anomaly of the syndrome. Many of these features are not evident until adolescence; it is therefore important to be aware of the various clinical and radiologic findings to allow for the earliest possible diagnosis.

Conclusions

A comprehensive understanding of NBCSS will provide radiologists with the necessary tools for detecting this syndrome early in its course and subsequently participate in the care and optimal surveillance of affected patients. Our presentation highlights the variable expressivity of the syndrome, in which 8 affected patients in the same familial lineage demonstrated a wide spectrum of findings in NBCCS.



(Filename: TCT_EdE-67_Com43.jpg)

EdE-64

6:30AM - 3:00PM

Pediatric Scalp Masses: Spectrum of Pathology and Approach to Diagnosis

B Graner[1], N Supakul[1], S Kralik[2]
[1]Indiana University School of Medicine, Indianapolis, IN, [2]Indiana University, Indianapolis, IN

Purpose
To demonstrate a step-by-step approach of evaluating palpable masses of the pediatric scalp and skull using imaging modalities including ultrasound (US), computed tomography (CT), and magnetic resonance imaging (MRI).
Materials and Methods
A palpable mass in the pediatric head usually raises concern in parents and presents a diagnostic dilemma for the pediatricians. It is also a challenging situation for the radiologists

to provide an accurate diagnosis and adequate information to the clinician in order to guide clinical management. Pediatric scalp and skull masses may include congenital lesions (meningoencephalocele, dermoid/epidermoid cyst), benign neoplasms (neurofibroma, osteoma, fibrous dysplasia, osteoid osteoma, ossifying fibroma, giant cell tumor and aneurysm bone cyst), malignant lesions (neuroblastoma, lymphoma, Ewing's sarcoma and osteogenic sarcoma), post-traumatic processes (calcified cephalohematoma and leptomeningeal cyst), vascular lesions (hemangioma, sinus pericranii and arteriovenous fistula) and inflammatory processes (Langerhans cell histiocytosis, lymphadenopathy, myofibromatosis, cranial fasciitis and cranial osteomyelitis). Imaging plays an important role in the work up and differential diagnosis, as well as further management of a pediatric scalp mass.

Results

We will demonstrate plain radiography, US, CT and MRI of common and uncommon pediatric scalp masses. An imaging checklist and key imaging findings in each modality will be highlighted as a tool for interpretation. Radiography and US are usually the initial screening tools, followed by CT or MRI. Multi-detector CT and/or higher resolution MRI provide greater anatomic detail, which is critical for surgical planning. This presentation will demonstrate the imaging appearance of common and uncommon pediatric scalp masses from congenital lesions, benign neoplasms, malignant lesions, post-traumatic processes, vascular lesions, and inflammatory processes. This information will aid the radiologist in organizing a differential diagnosis, or obtaining a specific diagnosis.

Conclusions

Imaging plays an important role in the evaluation of pediatric scalp masses. Radiologists should be familiar with the differential diagnosis of pediatric scalp masses in order to improve accuracy in interpretation and appropriately assist clinicians in optimizing patient management and counseling.

EdE-59

6:30AM - 3:00PM

Pediatrics Vascular Disease of The Central Nervous System

E Bravo[1], F Montoya[1], F Torres[2], C Pinto[2]
[1]Instituto de Neurocirugía Dr. Asenjo, Santiago, Chile, [2]Instituto de Neurocirugía Dr. Asenjo, Santiago, Providencia

Purpose

Vascular diseases affecting the central nervous system (SNC) in children are under diagnosed and unsuspected. One of the few epidemiological articles studied a population in Dijon, France and reported an incidence of ischemic and hemorrhagic stroke of 7,9 and 5,11 per 100.000 inhabitant-year under 16 years old (1). Many conditions affecting adults also can be seen during the pediatric age but some of them are seen exclusively in the fetal or

pediatric age like vein of Galen aneurysmal malformation (VGAM). Neuroimaging plays a central role in the early diagnose of intracranial vascular lesions due to its sensitivity and specificity (2). Our purpose was to create a summary of the most frequent vascular pathologies affecting the SNC in our pediatric population.

Materials and Methods

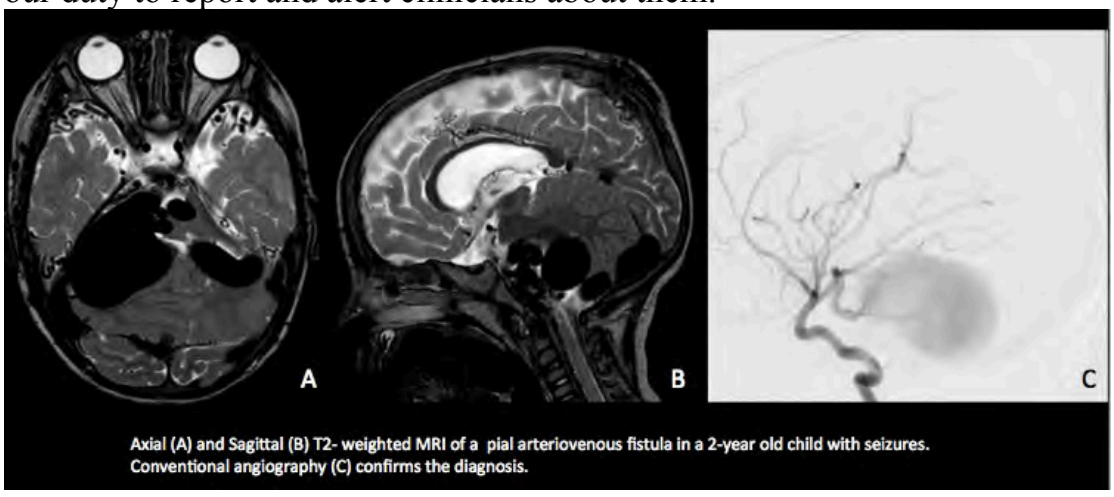
We reviewed our files from 1997 to 2016 of patients presenting with vascular pathologies affecting the SNC in pediatric population at the Instituto de Neurocirugía Dr. Asenjo, Santiago, Chile. We collected computed tomography (CT), magnetic resonance imaging (MRI) and conventional angiography records in order to find the most exemplifying images of pediatric vascular pathology.

Results

We collected a large amount of cases. Intracranial pathologies included arteriovenous malformations (AVM), arterial stroke, cerebral venous sinus thrombosis, aneuryism, dissecting aneuryism, oncotic aneuryism, vasculopathy, moya moya disease, pial and dural arteriovenous fistulas, venous sinus malformations, sinus pericranii, VGAM, traumatic cervical dissection and fistula and venous drainage anomaly, being the most frequently reported AVM. Spinal cord pathologies included spinal arteriovenous malformation and spinal intradural pial fistula. Superficial vascular pathology included capillary malformation, venous malformation and arteriovenous malformations.

Conclusions

Pediatric vascular disease is not a well-known illness. Computed tomography and MRI are excellent ways to make noninvasive diagnosis, and conventional angiography will confirm many of these diseases. We feel that radiologist must be aware of these pathologies for it is our duty to report and alert clinicians about them.



Axial (A) and Sagittal (B) T2- weighted MRI of a pial arteriovenous fistula in a 2-year old child with seizures. Conventional angiography (C) confirms the diagnosis.

(Filename: TCT_EdE-59_VascularPed.jpg)

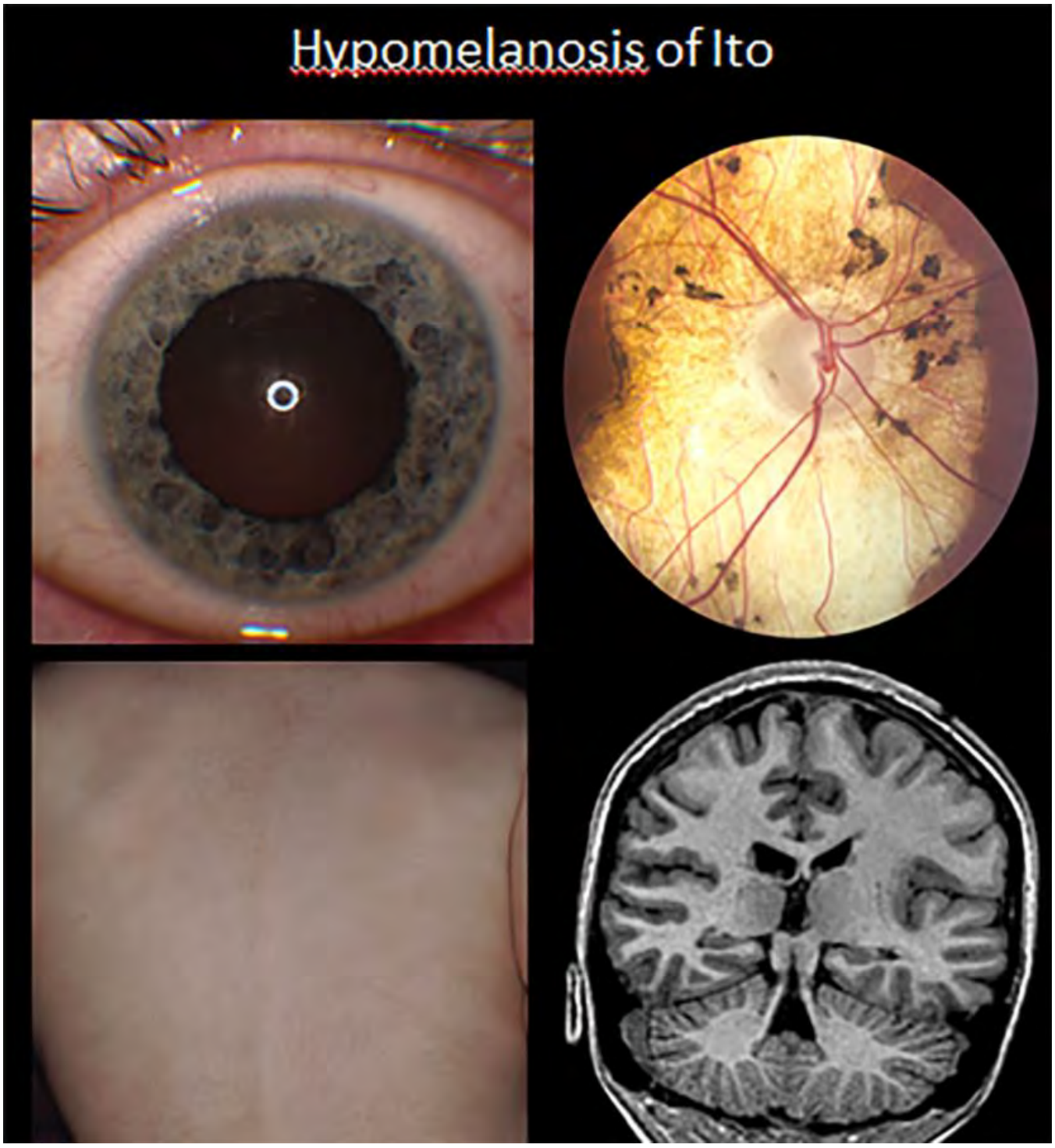
EdE-66

6:30AM - 3:00PM

Phakomatoses: Molecules to Morphology

M Ho[1], D Babovic-Vuksanovic[1], M Tollefson[1], J Chen[1], M Patterson[1]
[1]*Mayo Clinic, Rochester, MN*

Purpose
Utilize genetics as a framework for understanding multisystem manifestations of the phakomatoses. Demonstrate the value of multispecialty clinical/imaging expertise in evaluation of these patients.
Materials and Methods
The phakomatoses are complex multisystem ectodermal disorders, the diverse manifestations of which are best understood from a developmental/embryologic perspective. Multidisciplinary clinical and imaging assessment are key for patient diagnosis and follow-up. We present several illustrative examples of the common and rare neurocutaneous syndromes, with integrated interdisciplinary discussion including genetic etiology, dermatologic/ophthalmologic manifestations, central nervous system malformations, and other pertinent multisystem findings.
Results
Common syndromes: - Neurofibromatosis type 1: neurofibromin. - Neurofibromatosis type 2: schwannomin. - Tuberous sclerosis: hamartin + tuberin - Von Hippel-Lindau: cell cycle, VEGF. Vascular syndromes: - Sturge-Weber, - Parry-Romberg, - Wyburn-Mason, - Diffuse neonatal hemangiomatosis - PHACES. Rare syndromes: - Ataxia-telangiectasia: ATM: - Basal cell nevus: PTCH1, SUFU, - Neurocutaneous melanosis: NRAS - Mosaic hypopigmentation: incontinentia pigmenti, hypomelanosis of Ito, - Encephalocraniocutaneous lipomatosis: FGFR1. Overgrowth syndromes: PI3K-AKT, RAS/MAPK pathways: - Epidermal nevus, - PIK3CA: macrocephaly-capillary malformation, Klippel-Trenaunay-Weber, CLOVES: - PTEN: Cowden, Bannayan-Riley-Ruvalcaba, - AKT1-3: Proteus - RASA1: capillary malformation-arteriovenous malformation, Parkes-Weber
Conclusions
Phakomatoses are multisystem abnormalities that initially can be recognized by their cutaneous and ophthalmologic manifestations. Genotype-phenotype correlation plays a central role in diagnosis, prognosis, and treatment. Targeted imaging should include the neuraxis, and is important for initial patient assessment as well as surveillance.



(Filename: TCT_EdE-66_Figure.jpg)

EdE-69

6:30AM - 3:00PM

Put Your Back to It! - A Pictorial Essay of Congenital Malformations of the Spine and Spinal Cord

E Mtui[1], J Rozell[1], S Li[2]
[1]Baystate Medical Center, Springfield, MA, [2]Baystate Medical Center-Univ. of Mass Med Schl., Springfield, MA

Purpose

The aim of this exhibit is to review the many different congenital malformations of the spine and the spinal cord, including scoliosis, diastematomyelia, segmental spinal dysgenesis, tethered cord, and Lippel-Feil Spectrum, and to review the characteristic diagnostic imaging findings as well as associated secondary conditions.

Materials and Methods

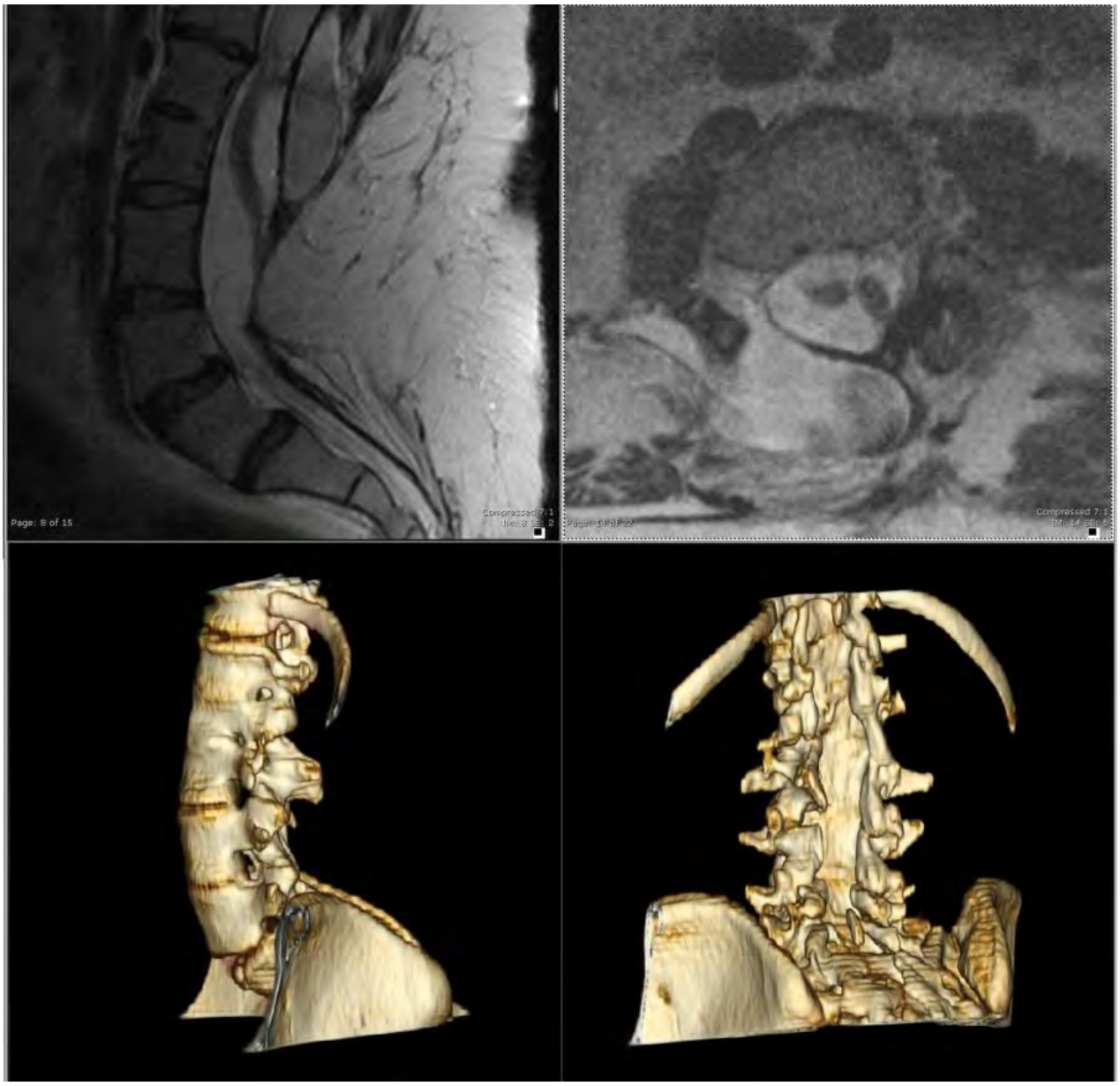
Related cases will be provided with initial presenting clinical signs and symptoms. Associated secondary conditions will be identified. Different imaging modalities from initial workup to advanced techniques including CT, MR, US, and 3D reconstructions then will be illustrated for each case. Post-treatment clinical course and imaging also will be included.

Results

1. Discuss embryology and/or environmental causes of spinal malformations. Pictorial examples of secondary conditions will be provided. 2. Case-based demonstration of characteristic imaging findings for diagnosis. Emphasis will be on advantages and disadvantages of various imaging modalities/techniques, which may include US, CT, or MRI. 3. Discuss identification of secondary underlying conditions such as cutaneous stigmata, lumbosacral hypogenesis, and VACTERL. 4. Discuss both short-term and long-term complications of spinal malformations. 5. Discuss differential diagnosis and pitfalls of misinterpretation. 6. Discuss importance of treatment, plans of intervention, and characteristic imaging findings during post-treatment phase.

Conclusions

There is a large spectrum of congenital malformations of the spine, some which are recognized easily early in life and others which often can be overlooked due to a lack of clinical signs and symptoms. Because early treatment can dramatically improve outcome and quality of life, an understanding of the many different spinal congenital pathologies, correlating conditions, and specific imaging characteristics are critical to physicians for both accurate and prompt diagnosis.



(Filename: TCT_EdE-69_SpineImages.jpg)

EdE-60

6:30AM - 3:00PM

Rare and Potentially Fatal Viral-Associated Encephalopathy in Children

A Achiriloaie[1], J Jacobson[1], B Holshouser[1]
[1]*Loma Linda University Medical Center, Loma Linda, CA*

Purpose
We report a series of children with viral-associated encephalopathy, including acute

necrotizing encephalopathy (ANE), malignant brain edema, hemorrhagic shock and reversible splenial lesion.

Materials and Methods

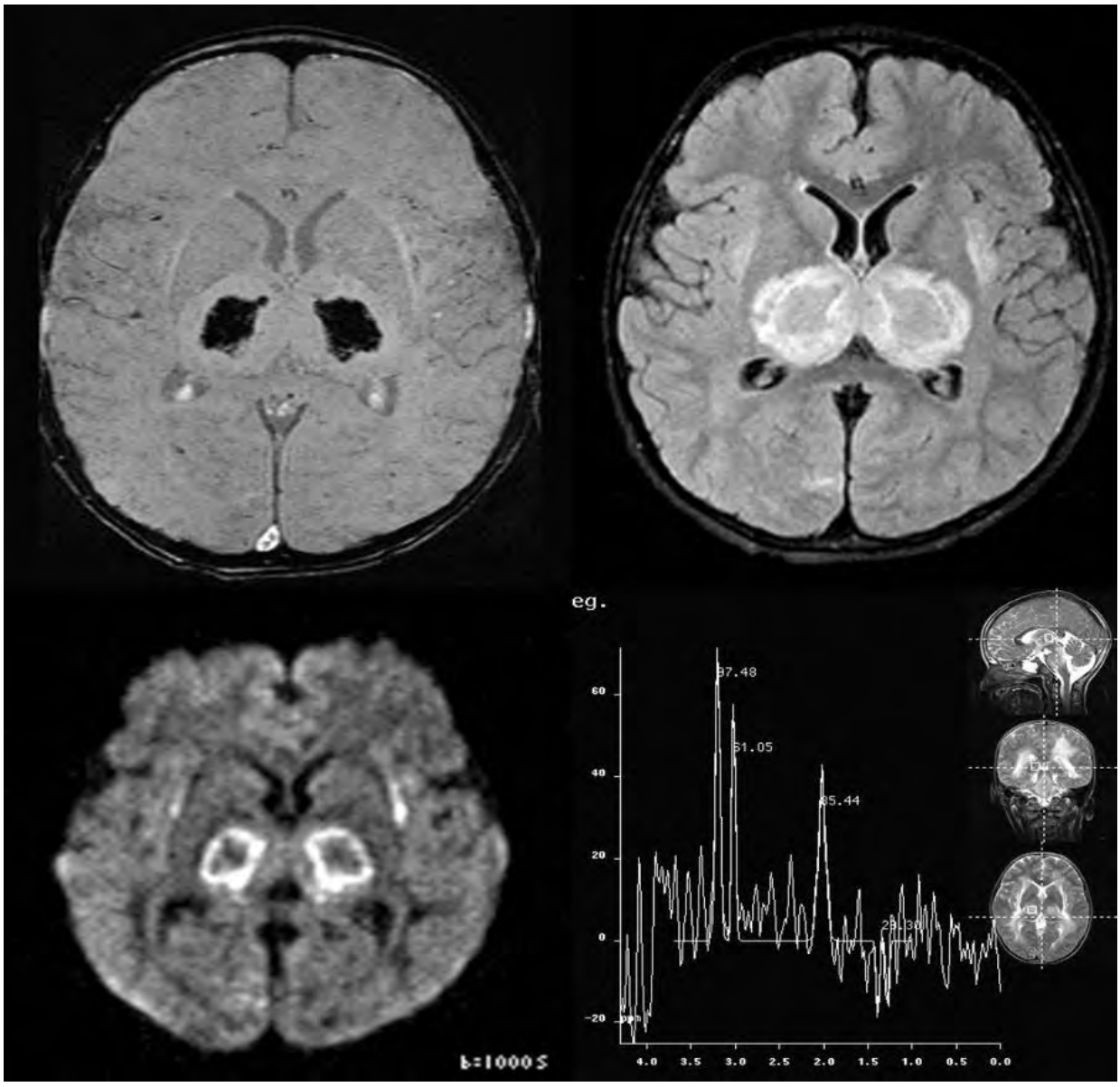
Five pediatric cases presented at our institution with recent viral illness and various clinical symptoms, including headache, weakness, seizure or respiratory failure. They all received brain imaging with CT and MRI. Their clinical data, hospital course and imaging studies were reviewed and revealed a constellation of findings compatible with more rare and, in some cases, fatal post-viral encephalopathy syndromes.

Results

Three non-fatal pediatric cases admitted for viral-induced encephalopathy had brain MRI/MRS with striking findings of ANE in both thalami, including marked hemorrhage on SWI and prominent lactate peaks on spectroscopy (Figure 1). Two of these three patients are siblings that tested negative for the RANBP2 gene mutation. A 5-year-old girl presented with bilateral leg weakness and initial brain MRI findings suggestive of acute disseminated encephalomyelitis (ADEM), however a head CT 2 days later showed diffuse brain edema and herniation leading to subsequent demise, compatible with malignant edema. Another fatal case of a 2-year-old boy presented with fever, respiratory failure and shock, had a normal initial head CT, with development of large bilateral hemorrhagic infarcts within 2 days, suggestive of hemorrhagic shock. A 10-year-old boy with headache, hallucinations and Influenza A showed abnormal findings in the splenium of corpus callosum, with near complete resolution of clinical symptoms before hospital discharge. The most common pediatric post-viral encephalopathy syndrome is ADEM, which has well-known imaging characteristics. The cases described constitute less common manifestations of post-viral encephalopathy that can have confusing initial imaging and clinical findings.

Conclusions

Post-viral encephalopathy syndromes that can be potentially fatal are relatively rare occurrences, therefore being aware of their early clinical and imaging characteristic can result in prompt diagnosis and improved prognosis.



(Filename: TCT_EdE-60_ANE1.jpg)

EdE-70

6:30AM - 3:00PM

Review of Subpial Hemorrhage in the Pediatric Population

B Cornwell[1], D Gunda[1], S Kuzminski[2], J Hughes[1]
[1]University of Oklahoma, Oklahoma City, OK, [2]Duke University Medical Center, Durham, NC

Purpose
The goal of this poster is to review the presumed pathophysiology and radiologic appearance

of subpial hemorrhage in infants/young children and to discuss the associations and incidence of bleeding within this compartment.

Materials and Methods

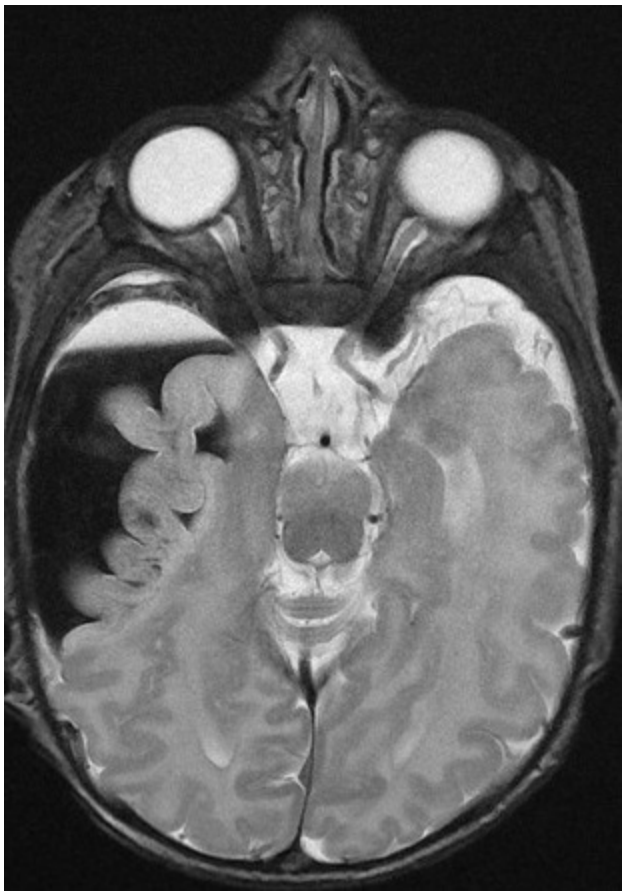
• Discuss the anatomy of the subpial region. • Describe the presumed pathophysiology of subpial hemorrhage. • Review the CT and MRI appearance of subpial hemorrhage. • Examine cases of subpial hemorrhage from our institution.

Results

Subpial hemorrhage is a distinct entity that remains poorly understood. While subpial hemorrhage has been described in adults, hemorrhage into this compartment most commonly occurs in infants and young children. Subpial hemorrhage may be related to head trauma in the region of calvarial sutures and possibly in association with venous compression/occlusion. The subpial region is located between the pia and outer cortical cell layer and is separate from the CSF containing subarachnoid space. Infants/young children may develop hemorrhage into this space. These subpial hemorrhages have characteristic anatomical locations, are commonly associated with overlying parenchymal restricted diffusion and often are in close proximity to calvarial sutures. These observations may implicate a specific mechanism of injury which results in subpial hemorrhage in this age group.

Conclusions

Subpial hemorrhage is a distinct entity in infants/young children which is poorly understood. The aim of this poster is to highlight the reproducible imaging appearance of subpial hemorrhage, describe the anatomy of this region and to discuss possible etiologies for this hemorrhage.


(Filename: TCT_EdE-70_Subpial_Hemorrhage.jpg)

Monday
6:30AM - 3:00PM
Long Beach Convention Center, Exhibit Hall B-(Lower Level) EdE

Education Exhibit Poster (EdE)-Socioeconomics

EdE-71

6:30AM - 3:00PM

3D Printing Knowledge: Transforming Medical Education with 3D Teaching Models

N Madhuripan[1], o atar[1], D Thut[1], A Macrito[1], G Gagnon[1], S Polansky[1]
[1]*UMMS-Baystate, Springfield, MA*

Purpose
Use of 3D models in classrooms offers a fundamentally new way of teaching with unprecedented potential. Learning complex anatomy and bringing the physical examination findings to the classroom in a personalized, reproducible and inexpensive way can enhance learning encouraging retention of educational material. We are describing our experience using 3D teaching models in education using craniosynostosis as an example.

Materials and Methods

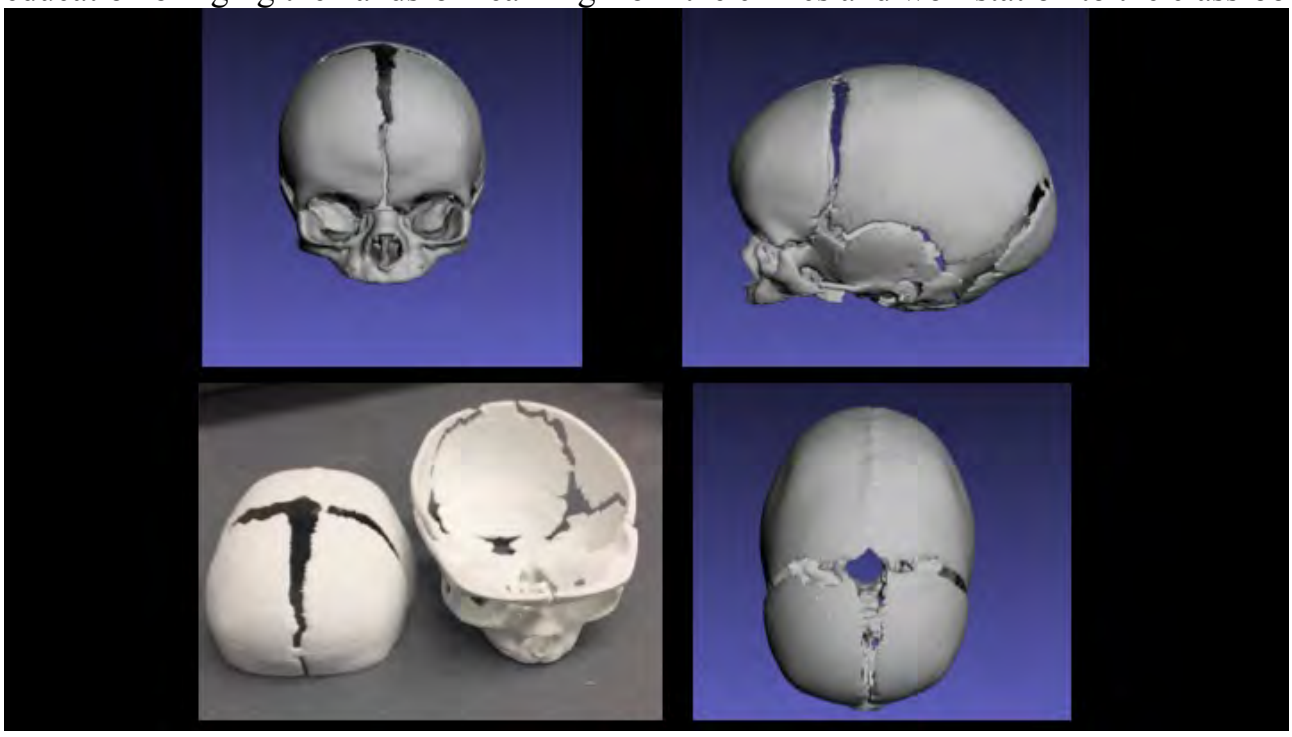
An augmented flipped classroom teaching session was organized for pediatrics residents, radiology residents, and medical students using the following general format. 1. Creation of a traditional teaching powerpoint. 2. Segmenting and printing the teaching models (Bone models-Sagittal synostosis, Unicoronal and Bicoronal synostosis, Lambdoid synostosis, Trigonocephaly; Surface models- Lambdoid synostosis, Positional plagiocephaly). 3. Using a flipped classroom hands on teaching approach with models. 4. Pre- and post-test for quantification.

Results

We will be discussing the basic methodology using open source software for 3D printing bone and surface models, which lend itself best to fast segmentation and inexpensive printing. We also will share our experience of using 3D models in education using craniosynostosis as an example. The options available for using 3D models include printing of STL files using inexpensive material and printers with print costs less than ten dollars per model on average. Alternatively the STL files can be shared among the learners who can use free online or freeware installed STL viewers with smartphones, tablets or laptops. The advantages of using 3D models include being able to demonstrate complex anatomy in a simple fashion, being able to demonstrate select clinical examination findings (such as the difference between positional plagiocephaly and lambdoid synostosis), and enhance learner retention.

Conclusions

Use of 3D models in education offers nearly endless opportunity in augmenting medical education bringing the hands-on learning from the clinics and workstation to the classroom.



(Filename: TCT_EdE-71_3Dprintingineducation.jpg)

EdE-72

6:30AM - 3:00PM

Errors in Neuroradiology—An Educational and Pictorial Overview: "The First Step Toward Change is Awareness"

Y Kim[1], M Ma[1], T Massoud[1]
[1]*Stanford University School of Medicine, Stanford, CA*

Purpose
All humans make errors, but understanding why can help limit their occurrence. An error is an unintentional deviation from accuracy, whereas a mistake is an error caused by a fault, usually misjudgment, carelessness, or forgetfulness. In this educational exhibit we review the types of errors encountered in Neuroradiology, their causes, mechanisms, and ways to reduce them.
Materials and Methods
We present the findings in a wide range of neuroimaging errors, classify them, and discuss their mechanisms.
Results
Errors are critical in Neuroradiology because CNS structures are vital, and neurological management heavily depends on neuroimaging. Clinically relevant discrepancies occur in <2% among attending neuroradiologists. We present examples of four main error categories in Neuroradiology: perceptual (misses); cognitive (misinterpretations); performance (not suggesting next appropriate test); and noncommunication in a timely and clinically appropriate manner. Causes of misses include scanning errors (failure to fix attention on the lesion), recognition errors (fixing on but not detecting the lesion), and decision-making errors (the most common, 45%) when pathology is incorrectly interpreted as normal, i.e., a false negative. Conversely, incorrect interpretations arise when misinterpreting a normal or variant structure as pathology (false positive), or giving a wrong differential. Errors occur on an individual level, e.g., insufficient index of suspicion, training, knowledge, reasoning, awareness, experience, high workload, and fatigue; or at a work system level. The 'Swiss cheese model' shows how latent errors become active errors when multiple such errors line up. Reducing errors should address both individual and system factors, and also more structured approaches, e.g., root cause analysis and QA/QI measures.
Conclusions
It is imperative that we understand medical errors. We should all learn from our mistakes, and if we are smart enough, we learn from the mistakes of others. This presentation will increase awareness of the causes and targets for reduction of errors in Neuroradiology.

Monday
6:30AM - 3:00PM

Long Beach Convention Center, Exhibit Hall B-(Lower Level) EdE

Education Exhibit Poster (EdE)-Spine

EdE-77

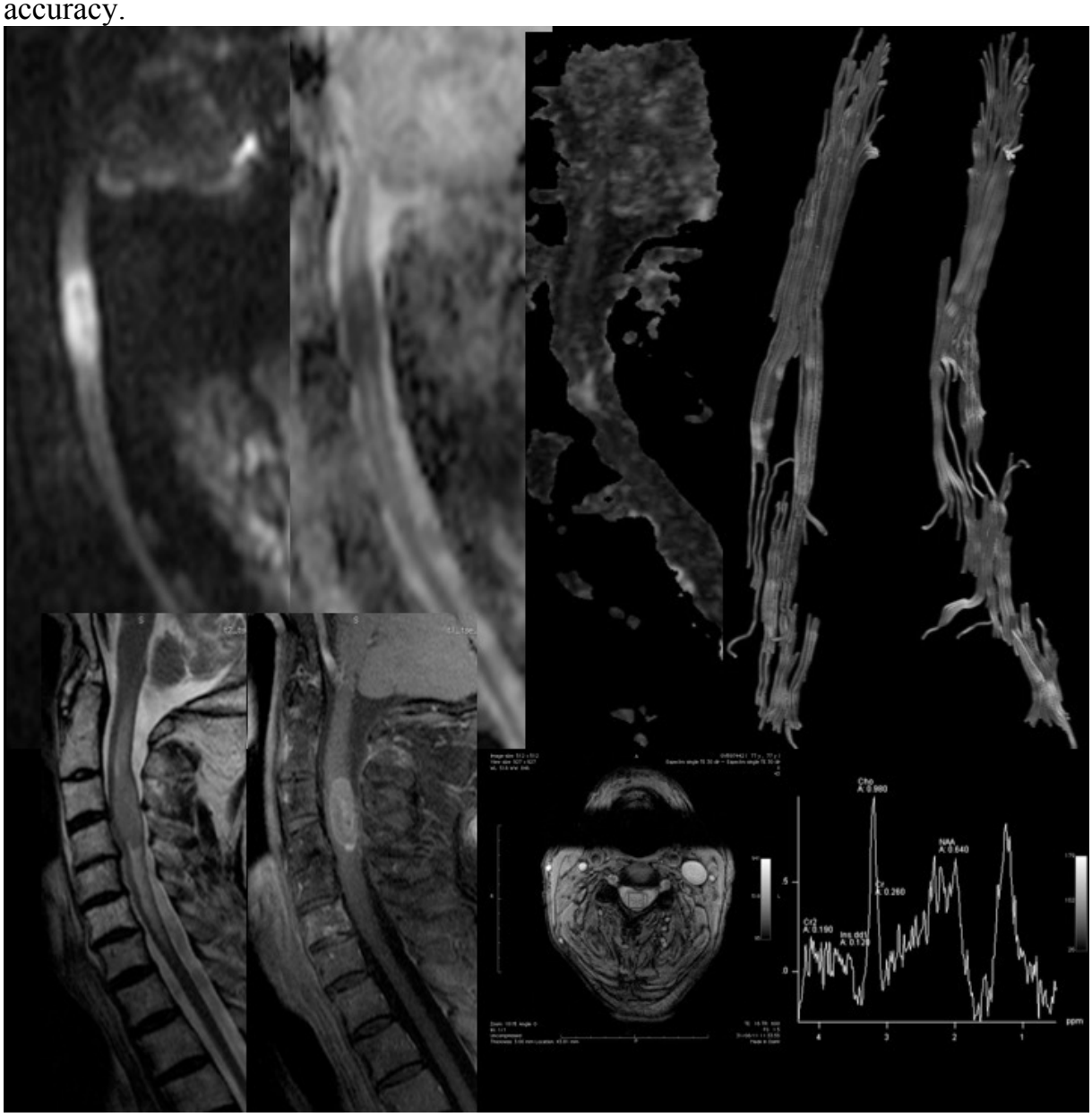
6:30AM - 3:00PM

Clinical Utility of Diffusion Weighted Imaging and Diffusion Tensor Imaging in the Spine

S Bergamaschi[1], M Law[1], L Hygino da Cruz[2], D Galheigo[3], E Gasparetto[4]
[1]University of Southern California, Keck Medical Center of USC, Los Angeles, CA, [2]CDPI-Clinica de Diagnostico por Imagem, Rio de Janeiro, RIO DE JANEIRO, [3]CDPI-Clinica de Diagnostico por Imagem, Rio de Janeiro, Rio de Janeiro, [4]DASA, São Paulo, São Paulo

Purpose
Diffusion-weighted imaging (DWI) and diffusion tensor imaging (DTI) are powerful techniques that exploit brownian motion of water molecules to provide tissue structural information. Because of some of the technical challenges, theses techniques still are not widely used clinically. The purpose of this exhibit is to describe the current clinical applications of DWI and DTI in the spine, discuss the technical requirements to optimize the image quality and how to avoid potential pitfalls.
Materials and Methods
In this educational exhibit, we present multiple clinical spine cases where the DWI and DTI provided helpful additional information, useful in the diagnosis. The data was obtained with a "zoomed EPI" diffusion-weighted or diffusion tensor sequence. We will review the imaging findings and the technical parameters used.
Results
Tumors in the spine, primary or metastasis, tend to be isointense with the normal cord, but diffusion restriction can be identified in tumors with high cellularity. Blood products or hemorrhage also can be identified. Hemangioblastomas, which happen frequently in patients with von Hippel Lindau syndrome, can show facilitated diffusion because of the considerable edmea. Diffusion tensor imaging tractography can provide additional information for differentiating intramedullary tumors. Diffusion imaging and fiber tractography usually demonstrates splaying of fibers in ependymoma, metastases, lymphoma versus infiltration in astrocytic tumors. Extra-axial lesion like metastatic disease and myeloma can show restricted diffusion. Diffusion-weighted imaging is very sensitive to ischemic changes, showing restricted diffusion earlier then T2 or fat suppressed sequences for cord infarct. Spinal cord diffusion restriction is an ominous sign in patients with traumatic or degenerative compressive lesion. Epidural collections can pose a significant diagnostic challenge, the presence of restriction diffusion helps leading to an infectious process, like an epidural abscess. Other infectious process, like myelitis related to mycobacterium tuberculosis, also can show restricted diffusion. Diffusion-weighted imaging

can show restricted diffusion in active demyelinating lesions in the spine. Similar to the brain active demyelinating plaques can affect the fiber tractography.
Conclusions
With optimization of technical parameters, DWI and DTI have the potential to provide diagnostic confidence in routine spine MRI and improve the radiologist's diagnosing accuracy.



(Filename: TCT_EdE-77_DWIspineexample.jpg)

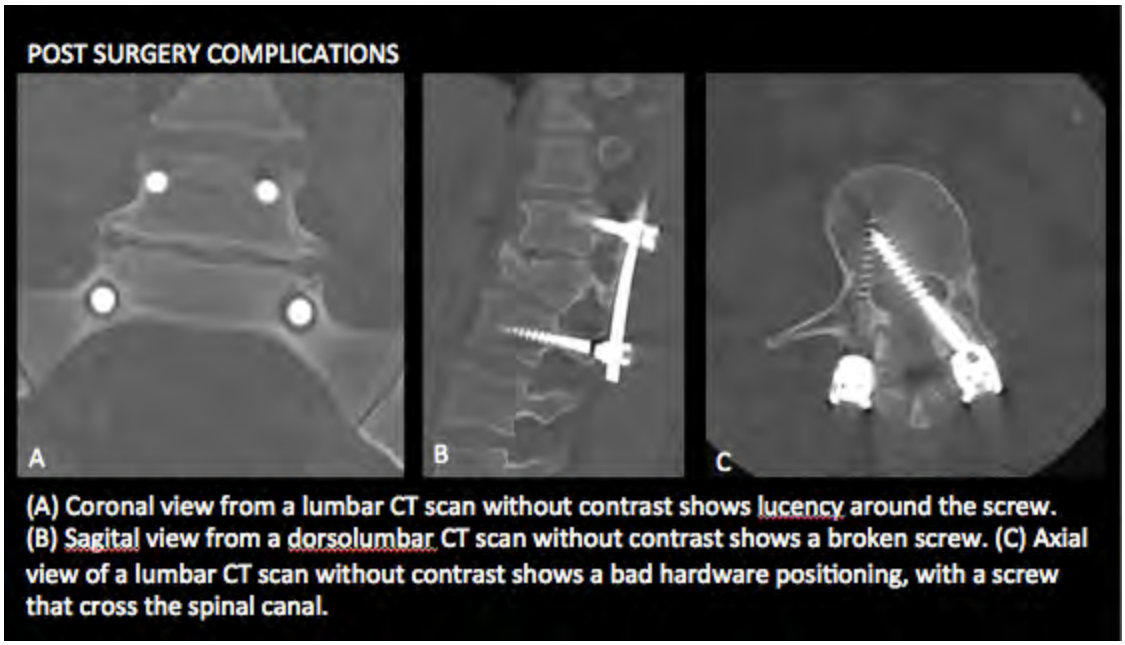
EdE-75

6:30AM - 3:00PM

Imaging of Spine Fusion: Post Surgery Complications

E Bravo[1], F Montoya[1], F De la Vega[2]
[1]Instituto de Neurocirugía Dr. Asenjo, Santiago, Chile, [2]instituto de Neurocirugía Dr. Asenjo, santiago, Providencia

Purpose
Lumbar spinal fusion has been performed since 1911 to prevent motion of a single or multiple spinal segments, to alleviate pain or to prevent neurologic compromise. A new neurologic deficit, worsening pain or signs of infection may draw attention to a possible postoperative complication. Our main objective is to describe some of the complication that may arise after lumbar spine fusion surgery.
Materials and Methods
We searched our files, computed tomography (CT) and magnetic resonance imaging (MRI) records in order to find the most exemplifying complication after spine surgery and we present the CT postprocessing and 3D images of the main complications in spinal fusion.
Results
There are many different techniques to achieve spinal fusion, each with different types of complications. We present hardware complications such as broken screws, broken bars, lucency changes surrounding the hardware, ejected cage, cage infections, pseudoarthrosis, root fibrosis, secondary spondylolysis or spinous process fracture, bad hardware positioning, and also a case of postoperative esophageal fistula.
Conclusions
Spinal surgery may produce various complications, which we need to be aware of. Timing of surgery, type of surgical procedure and presenting clinical details are fundamental. Computed tomography and MRI imaging are the main way to study these patients in order to identify the surgical complication. Magnetic resonance imaging is the imaging of choice for the evaluation of abnormal soft tissue or fluid collections. Computed tomography is the best imaging method for bone visualization and will give an accurate evaluation of all the metallic hardware used in spinal surgery. The radiologist must be aware of the different complications that may arise from the different hardware and techniques used to achieve spinal fusion.



(Filename: TCT_EdE-75_Columnas.jpg)

EdE-80

6:30AM - 3:00PM

Post-Traumatic Pseudomeningocele: Four Cases and a Review of the Literature

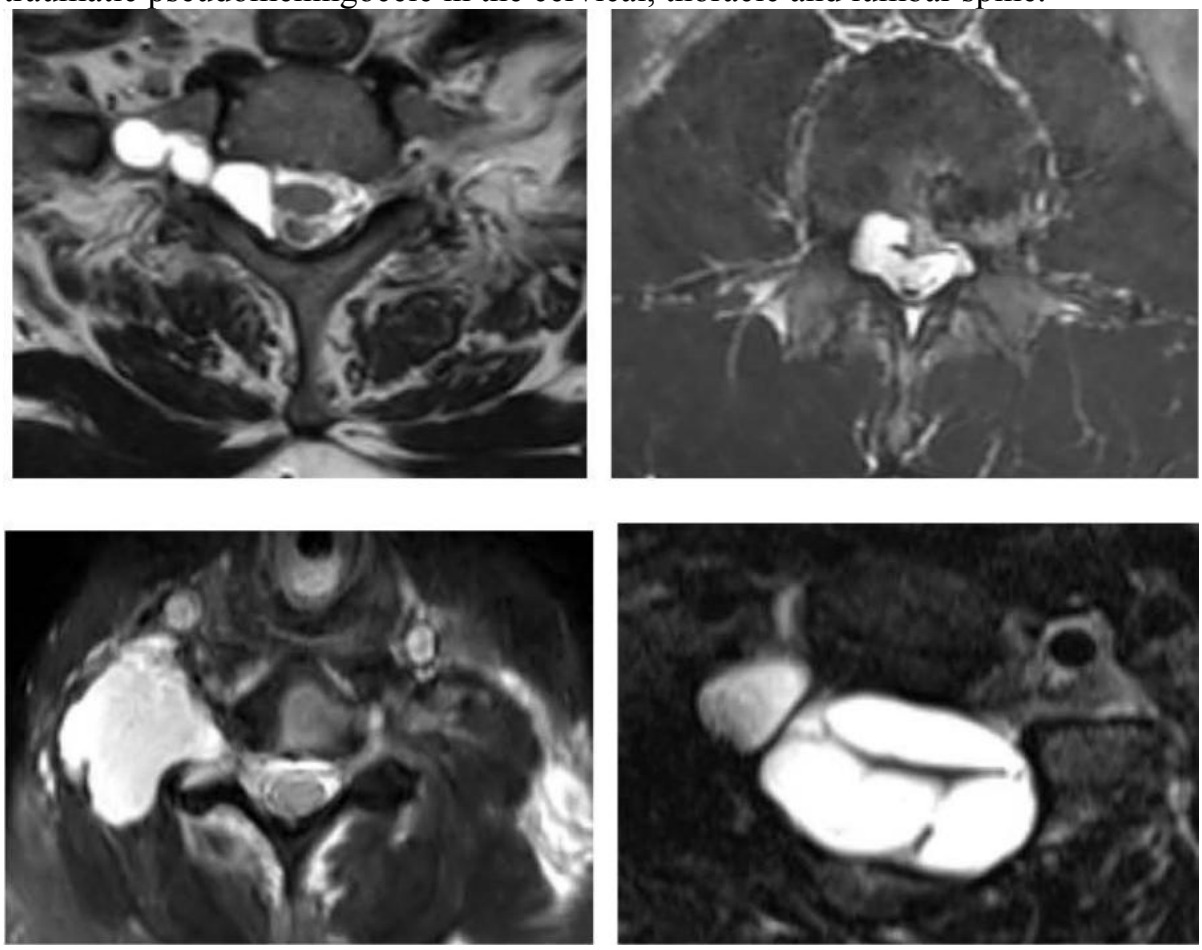
K Reddy[1], M Lammle[1]
[1]*University of South Alabama Medical Center, Mobile, AL*

Purpose
Here presented is a case series of four nonbirth-related post-traumatic pseudomeningoceles. While pseudomeningocele is a relatively common complication seen after lumbar laminectomy or diskectomy, post-traumatic pseudomeningocele is a rarely published entity as a review of the literature has revealed.
Materials and Methods
A retrospective search was performed of the University of South Alabama Medical Center database via the Montage search engine using the keywords pseudomeningocele, myelomeningocele and meningocele. Cases were selected to include only pseudomeningoceles that were post-traumatic. Birth trauma cases were excluded as they are more commonly reported in the literature.
Results
A total of four cases were identified demonstrating pseudomeningocele formation in the location of a known traumatic injury. Case 1: Rare presentation of pseudomeningocele extension into a lumbar vertebral body fracture in the context of a gun-shot wound in a 20-year-old female. Case 2: Delayed pseudomeningocele formation with cervical nerve root avulsion after motorcycle accident in a 48-year-old male. Case 3: 15-year-old with

pseudomeningocele and thoracic spinal cord injury due to flexion type injury from a motor vehicle collision. Case 4: 35-year-old male with traumatic pseudomeningocele and cervical nerve root avulsion from a motor vehicle collision.

Conclusions

Post-traumatic pseudomeningocele is a rare diagnosis with a variable appearance depending on the mechanism and location of injury. Correctly identifying pseudomeningocele can prove to be a challenge given its potential similarity in appearance to other traumatic, neoplastic, infectious or congenital entities. The diagnosis can further be complicated in the immediate postoperative period by the presence of edema, hematoma or associated injuries. The four cases presented here represent examples of the varying appearances of post-traumatic pseudomeningocele in the cervical, thoracic and lumbar spine.



(Filename: TCT_EdE-80_ptpm.jpg)

EdE-74

6:30AM - 3:00PM

Spectrum of Imaging Findings in Spinal Infections and Associated Complications: What the Radiologist Should Know

D Gandhi[1], M Adeb[2], Y Kumar[3], N Gupta[1]

[1]St. Vincent's Medical Center, Bridgeport, CT, [2]Bridgeport Hospital, Bridgeport, CT, [3]Yale New Haven Health at Bridgeport Hospital, Bridgeport, CT

Purpose

The purpose of the study is to discuss the role of CT and MRI in evaluation of spinal infections and associated complications. We also will describe spectrum of imaging findings in spinal infections and associated complications. Radiologist should know imaging findings, for an example, early infectious spondylitis or spondylodiskitis which may need to differentiate from noninfective or degenerative conditions in the spine and prevent diagnostic delay. If it is not diagnosed in early phase, the lesion may extend into the epidural space and the paravertebral soft tissues and create complications. MR imaging is helpful in such patients with spinal infection. We will describe important anatomic structures which need to be evaluated during imaging of a suspected spinal infection.

Materials and Methods

We randomly retrospectively identified patients with spinal infections and its associated complications such as bacterial or tuberculous spondylodiskitis, Septic facet arthritis, Epidural infection/abscess, Spinal meningitis and complications like ascending bacterial meningitis, ascending tuberculous meningitis, spinal cord abscess or cord compression. All patients underwent an MR study consisting of a sagittal T1-weighted localizer image, sagittal proton density-weighted studies, T2-weighted fast spin-echo studies, and sagittal and axial T1-weighted spin-echo studies before and after administration of gadolinium-based contrast. The characteristics of imaging findings in different spinal infection is described in axial and sagittal pre and postcontrast sequences. All MR examinations were performed at 1.5 T or 3T. Few patients also went for CT scan before the MRI study with the indication of back pain and further diagnosed in MRI.

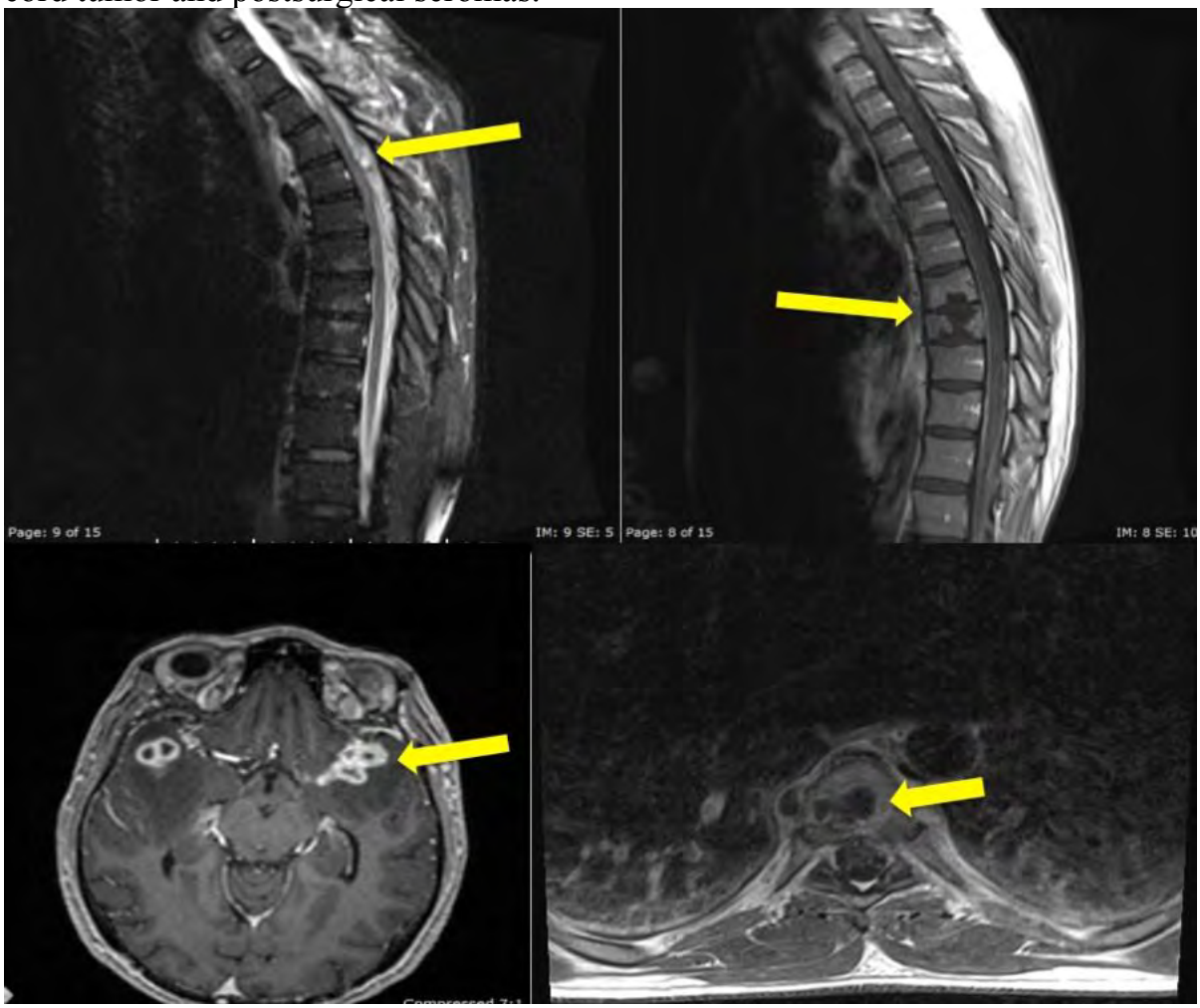
Results

Detailed descriptions of spinal infections: 1. Pathophysiology, 2. Epidemiology. Clinical presentation and diagnostic work up. Role of imaging: 1. CT, 2. MRI - Protocol and important sequences, 3. nuclear medicine - Importance of Galium scan and three phase bone scan, 4. Comparison of the different imaging modalities. • Types of spinal infections: with imaging examples: 1.Spondylodiskitis: 2. Bacterial spondylodiskitis; 3. Tuberculous spondylodiskitis; 4. Septic facet arthritis; 5. Fungal infections; 6. Epidural infection/abscess; 7. Subdural infection/abscess; 8. Spinal meningitis. • Complications: with different imaging examples: 1. Ascending infection to brain; 2. Ascending bacterial meningitis, ascending tuberculous meningitis; 3. Spinal cord abscess; 4. Cord compression; 5. Nerve root impingement; 6. Paraspinal abscesses; 7. Psoas abscess.

Conclusions

Infection in the spinal cord is important to diagnose in early phase to prevent complications and to be useful to differentiate from other noninfectious conditions like degenerative or neoplastic. Infection within the cord seen as increased signal intensity on T2-weighted images which may show enhancement on postcontrast T1-weighted images. The diagnosis of

septic myelitis needs to be considered in any patient with intramedullary high signal intensity and abnormal contrast enhancement on T2-weighted images. Diffusion-weighted imaging with ADC maps is helpful in accurate diagnosis of spinal and paraspinal infections and differentiate from epidural or subdural hemorrhage, disk herniation, synovial cyst, spinal cord tumor and postsurgical seromas.



(Filename: TCT_EdE-74_Figure1.jpg)

EdE-79

6:30AM - 3:00PM

The Spinal Canal: Demystifying Compartments and Extra-axial Hemorrhage

B Brown[1], D Wannemacher[1], R Hobohm[1]
[1]*University of Cincinnati, Cincinnati, OH*

Purpose
Although identifying the presence of spinal canal hemorrhage is not usually difficult on MRI, particularly when large and causing cord compression, there can be difficulty in

localizing hemorrhages within the appropriate compartment. This may be due to many reasons including the small imaged space of the spine, incomplete knowledge of the anatomic boundaries of the spinal canal, and not knowing that mixed patterns commonly occur. This is an important consideration for the surgeon and is a common question posed to the radiologist for pre-operative planning to determine whether the dura and/or arachnoid matter need to be violated to completely evacuate the hematoma. This presentation strives to take a detailed look at spinal canal compartment anatomy and use that information to evaluate MR images to differentiate epidural, subdural, subarachnoid, and commonly mixed spinal canal hemorrhages.

Materials and Methods

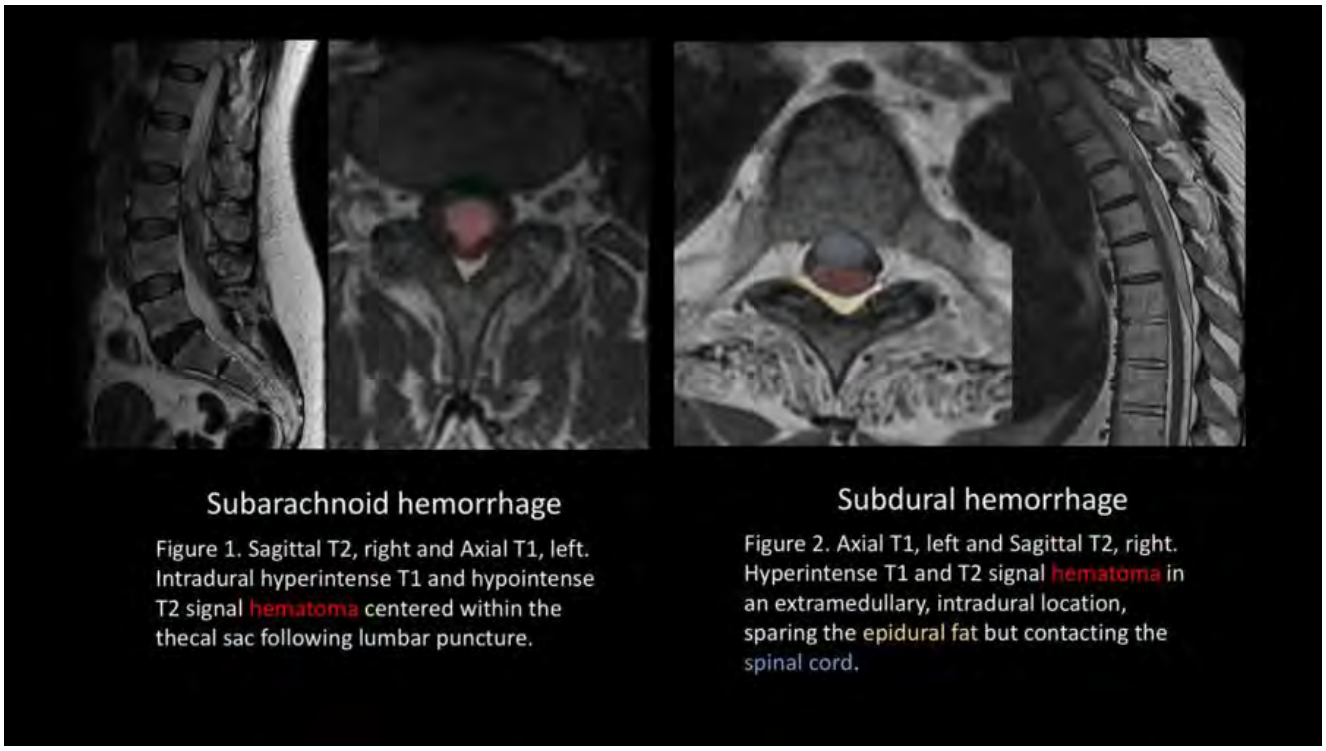
The anatomy of the spinal canal will be evaluated by using pictorial diagrams, as well as MR and Fluoroscopic/CT myelogram images. Three cases will be presented that demonstrate the fundamental approach to localize spinal canal hemorrhages into the subarachnoid, subdural, and epidural compartments. Finally, a challenging case will be presented to demonstrate the difficulties of compartmentalizing hemorrhage in the spinal canal and that many of these hemorrhages actually involve multiple compartments.

Results

Epidural hematomas are more common and have been well described in the literature. Epidural hematomas can be identified by their relationship to the dura, epidural fat, and adjacent osseous structures. Subdural hematomas are not as well described in the imaging literature. They appear as loculated, intradural collections that are clearly separated from epidural fat and adjacent osseous structures. They are located between the dura and arachnoid membrane and a split membrane can be seen on the caudal and cephalad margin. Subarachnoid hemorrhage usually freely disperses within the spinal canal and layers dependently within the thecal sac. However, if acute or if there is blockage of CSF flow, a more localized collection is possible that will be centrally located and associated with the spinal cord or cauda equina nerve roots. Mixed hemorrhages will have an unusual appearance but should be systematically evaluated for signs of involvement within each compartment.

Conclusions

Compartmentalizing spinal canal hemorrhages can be difficult because of the small imaged space of the canal, complex anatomy, and the possibility of mixed hemorrhages. However, with detailed knowledge of anatomy and the MRI appearance of intraspinal hemorrhages, accurate localization can be obtained for pre-operative planning and subsequent evacuation.



(Filename: TCT_EdE-79_Finalpicturespinalhem.jpg)

EdE-76

6:30AM - 3:00PM

Ultrasound Guided Injection of the Brachial Plexus Via Interscalene Triangle Approach

J Huang[1], E Zager[2], V Khoury[2]
[1]Pennsylvania Hospital, University of Pennsylvania, Philadelphia, PA, [2]Hospital of the University of Pennsylvania, Philadelphia, PA

Purpose
To demonstrate the steps involved in performing an ultrasound-guided brachial plexus injection via interscalene triangle approach for treatment of thoracic outlet syndrome.
Materials and Methods
Neurogenic thoracic outlet syndrome is a devastatingly painful disease with an obscure etiology, and a heterogeneous response to surgical decompression. The diagnosis is challenging both clinically and by imaging. In an attempt to both diagnose and treat the condition, various image-guided injections of the brachial plexus region have been described, though a standard-of-care approach is not well established. In order to test the efficacy of US-guided injections of medications in the interscalene triangle alone, the feasibility of this technique should be established. Procedure Details: Patient positioning: The patient is laid supine with the afflicted side closer to the interventionist, arms at the side

and head turned to the opposite side if possible. Technique: 1)The neck on the afflicted side is examined and the brachial plexus is identified. 2) The area over the brachial plexus then is marked with a marking pen and prepared with Chloraprep and draped in sterile fashion. 3) The marked area then is infiltrated with 2 mL of 1% lidocaine using a 25-gauge needle. 4) A 25-gauge needle is advanced into the interscalene triangle using a transverse approach, from posterior to anterior, under continuous sonographic guidance. 5) A medication solution consisting of 1.5 mL of 1% lidocaine and 0.5 mL of Kenalog and (20mg triamcinolone) is infused around the brachial plexus nerves, without injecting into scalene muscle. 6) Remove the needle and place bandage.
Results
A total of 61 patients underwent ultrasound-guided injection of the brachial plexus at a single institution from 11/25/2014 to 8/4/2016. All 61 patients were referred by a neurosurgeon who specializes in the condition. All procedures were technically successful and there were no immediate complications.
Conclusions
Real time ultrasound-guided injection of the brachial plexus via the interscalene triangle approach is a technically reproducible procedure. The safety and efficacy of this approach versus anterior scalene block is another subject of investigation by this group.

EdE-78

6:30AM - 3:00PM

Vascular Lesions of the Spine: A Case Based Review

R Gnesda[1], R Murtagh[1]
[1]*University of South Florida, Tampa, FL*

Purpose
Vascular lesions of the spine including spinal arteriovenous malformations (AVM)/arteriovenous fistulas (AVF), cord infarcts, cavernomas and hemangiomas represent a group of disorders which can result in progressive neurologic deterioration. Arteriovenous malformations and AVFs represent the most common vascular lesion and have been divided into four subtypes; spinal dural AVFs (Type 1), glomus AVMs (Type 2), juvenile AVMs (Type 3) and pial AVFs (Type 4). Spinal infarcts are rare representing approximately 5-8% of myelopathies. Cavernomas are a rare intramedullary lesion and hemangiomas are the most common benign vertebral neoplasm. The purpose of this exhibit is to demonstrate the imaging features which will allow radiologists to confidently diagnose these lesions.
Materials and Methods
The imaging findings associated with vascular lesions of the spine will be the focus of the presentation using a case-based approach. Additionally, there will be an image-based review of the normal spinal vascular anatomy. The presenting signs and symptoms, along with the pathophysiology, histologic findings, and treatment will be discussed.

Results
This educational exhibit will provide a case-based review of the specific imaging findings associated with vascular lesions of the spine using recent cases from our institution. These lesions will be illustrated on magnetic resonance imaging (MRI), conventional angiography, and computed tomography (CT).
Conclusions
Recognition of the imaging findings associated with vascular lesions of the spine is imperative to correctly diagnose this potentially reversible cause of myelopathy. Proper utilization of imaging allows radiologists to provide value added care in management of these patients. Our educational presentation provides a case-based review to highlight major concepts in radiographic evaluation of these lesions.

Monday
6:30AM - 3:00PM
Long Beach Convention Center, Exhibit Hall B-(Lower Level) eEdE

Electronic Education Exhibit (eEdE)-Adult Brain

eEdE-56

6:30AM - 3:00PM

2016 World Health Organization Classification of Brain Tumors: A Status Update

M Agarwal[1], J Rudie[2], M Nasrallah[3], I Agarwal[4], R Tondon[5], S Mohan[5]
[1]Medical College of Wisconsin, Milwaukee, WI, [2]Perelman School of Medicine at the University of Pennsylvannia, Philadelphia, PA, [3]Hospital of the University of Pennsylvania, Philadelphia, PA, [4]University of Chicago, Chicago, IL, [5]University of Pennsylvania, Philadelphia, PA

Purpose
In addition to histology, the recently updated WHO classification of central nervous system (CNS) tumors integrates molecular parameters to define many tumors, thus codifying developments over the past years in the genetic aspects of neuropathology in this era of personalized medicine. Our purpose is to review the latest 2016 WHO classification of brain tumors and discuss the changes most relevant to the neuroradiology community.
Materials and Methods
The 2016 WHO classification of brain tumors will be reviewed and multiple examples with neuropathological correlation will be presented. In particular, we will highlight key changes with relevant clinical examples highlighting the emerging role of radiogenomics.
Results
The 2016 WHO classification has taken a fresh look at brain tumors and has added various molecular parameters to histological criteria. This is a timely update given the explosion of molecular advancements in pathology. Gliomas now are formally subdivided by presence or

absence of mutation in the isocitrate dehydrogenase (IDH) gene, given the prognostic significance of this mutation. This mis-sense mutation results in the neomorphic reduction of isocitrate dehydrogenase resulting in an accumulation of the "oncometabolite" 2-hydroxyglutarate (2HG). Detection of 2HG can thus serve as a surrogate biomarker for these mutations, with significant translational implications. There has been restructuring of medulloblastomas and other embryonal tumors. New entities, variants and additional patterns also have been added, others removed, and some redefined. For example, diffuse intrinsic pontine glioma is now subsumed in the entity "diffuse midline glioma, H3K27M." "Epitheliod Glioblastoma" is added as a provisional variant. The CNS tumor diagnosis now consists of the histopathological name followed by genetic features such as diffuse astrocytoma, IDH-mutant; and Medulloblastoma, WNT-activated. The nomenclature reflects all genetic changes required for the diagnosis of each tumor; for example, the diagnosis of a grade II oligodendroglioma requires IDH mutational status and 1p/19q codeletion status, and hence is termed Oligodendroglioma, IDH-mutant and 1p/19q-codeleted. When genetic testing is not available, or the combined histological and genetic findings do not fit a WHO diagnosis, the tumor is designated as NOS (not otherwise specified). As an integral part of the neuro-oncology community, neuroradiologists need to keep abreast of these new WHO entities in order to better differentiate them on imaging.

Conclusions

There has been a major restructuring of brain tumors with the new 2016 WHO classification. Neuroradiologists must keep up to date with these changes for effective communication in neuro-oncology discussions, promoting relevant research, which might lead to improved decision making, and potentially result in improved patient outcomes.

eEdE-87

6:30AM - 3:00PM

A New Toy in the Town: Volumetric Assessment of Hippocampal Volume: Superior but not Perfect

M Agarwal[1], J Ulmer[2], C Squires[1], A Klein[2], L Mark[2], S Quinet[3], M Franczak[1]
[1]Medical College of Wisconsin, Milwaukee, WI, [2]Medical College of Wisconsin - Froedtert Hospital, Milwaukee, WI, [3]Medical College of Wisconsin, MILWAUKEE, WI

Purpose

To demonstrate the important role of hippocampal volumetric assessment in neurodegenerative, traumatic, epileptic and neuropsychiatric disorders.

Materials and Methods

The important supportive role of hippocampal volumetric assessment will be discussed. Relevant cases to emphasize the diagnostic role of volumetric assessment will be shown. Cases demonstrating the pitfalls of automated assessment and methods to minimize errors also will be shown. Multi-atlas based automated segmentation processing will be discussed

(Figs. A, B, C). Computation of z-scores to allow comparison with normative database will be shown (Fig. D).

Results

Loss of hippocampal volume in Alzheimer disease and mesial temporal sclerosis is well known. Research has shown that other brain disorders such as neuropsychiatric illnesses and traumatic brain injury also cause hippocampal volume loss. An inverse relationship of hippocampal volume to years of football played has been shown. Hippocampal volumetric assessment therefore can provide valuable diagnostic information and is increasingly becoming an integral part of work up in distinct patient groups such as dementia. Quantitative volumetric assessment can play an important supportive role to the qualitative T2 signal change in patients with mesial temporal sclerosis. Assessment of volume can be done by visual inspection, manual tracing or by use of automated computer software. Volumetric assessment by visual inspection is affected by neuroradiologist experience and inter-observer variability. Subtle volume changes are difficult for the human eye to detect. Automated volumetric assessment therefore proves to be an important tool in neuroradiology practice. However, there are potential pitfalls to automated assessment which may fail in cases of patient motion or severe hippocampal atrophy. Automated volumetric assessment should therefore be superimposed on anatomic images for accuracy (Figs. A, B and C).

Conclusions

The hippocampus is pivotal to memory and cognitive networks. Early detection of hippocampal volume loss can provide actionable information to neuroradiologists and clinicians. Automated computer software for volumetric assessment is a new and exciting tool in the neuroradiologist arsenal, although pitfalls for automated assessment should be borne in mind.

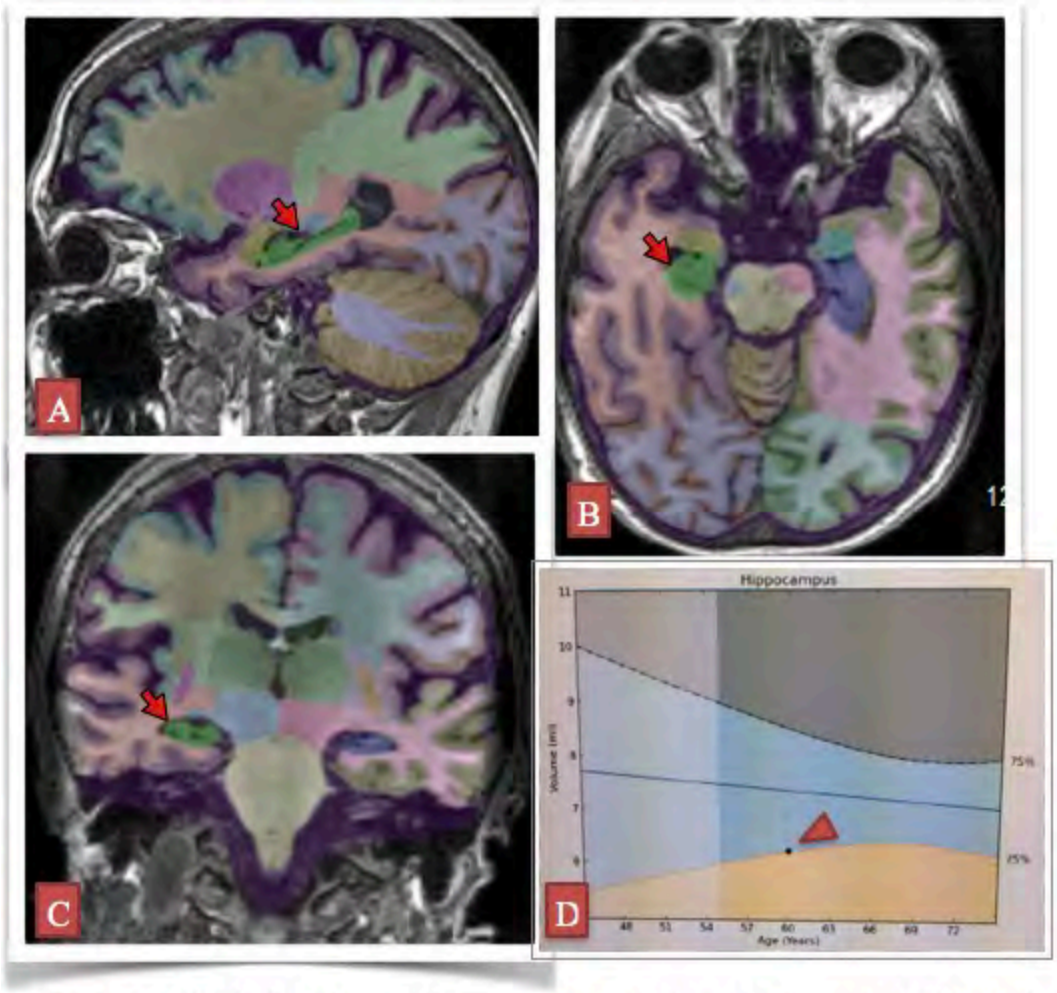


Fig. Sagittal (A), axial (B) and coronal (C) automated segmentation color map combined with anatomic images. The right hippocampus is shown in green color (red arrows). Fig. D shows the z-score of the right hippocampus at 25th percentile (red arrowhead) on the normative database.

(Filename: TCT_eEdE-87_Hippocampalvolumeimage.jpg)

eEdE-111

6:30AM - 3:00PM

Acute CT Brain Findings on Emergent CT Angiography in the Emergency Room in Patients with positive Neuro Trauma Findings on CT of the Brain

L Hahn[1], M Law[2], P Kim[3], M Shiroishi[4], W Gibbs[3], O Boyko[5]
[1]Keck School of Medicine of USC, Los Angeles, CA, [2]Keck Medical Center of USC, Los Angeles, CA, [3]University of Southern California, Keck School of Medicine, Los Angeles, CA, [4]Radiology Department, Los Angeles, CA, [5]University of Southern California, Los Angeles, CA

Purpose
Since the introduction and widespread adoption of multidetector spiral CT, there has been

increased use of spiral scanning technique for CT angiography of the head (CTAH) in the emergency room in the setting of positive trauma. The purpose of this exhibit is to define acute brain findings that are present within the 20 minutes that it requires to perform the CTAH after the noncontrast CT of the head (CTH). With the difference in radiation dose between the two studies, brain parenchymal traumatic findings/changes are less conspicuous on the CTAH than the CTH.
Materials and Methods
In the span of 6 months, retrospective review of CTAH performed immediately within a 20 minute time laps from a CTH was performed. Computed tomography angiography of the head were evaluated for progression of findings on the CTH and evolution of new parenchymal or extra-axial findings on the CTAH.
Results
A total of 37 CTAH scans were reviewed with a total of 5 positive findings including: 1. Increased intracranial pressure with venous compression and delay of outflow. 2. Acute extravasation of contrast/subarachnoid hemorrhage not present on the CTH. 3. Expanding subdural and epidural hematoma (2 cases). 4. Venous thrombosis/pseudoaneurysm/pontine enhancement.
Conclusions
With the increasing use of helical CTAH in the setting of acute positive head trauma, vigilant evaluation of brain parenchyma and extra-axial spaces for acute findings should be performed routinely in addition to the primary evaluation of arterial and venous integrity.

eEdE-11

6:30AM - 3:00PM

Advances in Alzheimer's Disease Imaging

K Hoque[1], W Gibbs[2], P Colletti[3]
[1]USC, Studio City, CA, [2]University of Southern California, Keck School of Medicine, Los Angeles, CA, [3]University of Southern California, Los Angeles, CA

Purpose
This educational exhibit will enable the viewer to gain an understanding of new and emerging concepts in imaging diagnosis of Alzheimer disease.
Materials and Methods
Using guided case-based presentation, this exhibit will guide the viewer initially through traditional qualitative structural assessment with magnetic resonance assessment (MRI). The exhibit then will detail more advanced quantitative techniques including analysis of cortical thickness and volumetric measurements. Attention then will be turned to techniques in nuclear radiology, detailing the role of 18F-Fluorodeoxyglucose-positron emission tomography computed tomography (FDG-PET CT) in physiological analysis, and ultimately explore novel disease specific radiotracers including amyloid plaque imaging agents. Both

qualitative and quantitative nuclear radiology techniques will be detailed. Basic pitfalls and artifacts of the novel PET radiotracers will be elucidated.
Results
This exhibit will build a basic understanding of the pathophysiology of Alzheimer disease. Discussion of natural progression of both anatomic and physiologic imaging findings will allow the reader to build an understanding for both the qualitative and quantitative imaging analysis techniques. Through exploration of emerging multimodal imaging techniques in neuroradiology and nuclear medicine, the reader will understand both the benefits and limitations of each technique. Basic pitfalls and artifacts of the novel PET radiotracers will be elucidated.
Conclusions
As Alzheimer disease continues to affect our rapidly growing population, detailed understanding of anatomic and physiologic multimodality appearance facilitates earlier and more accurate diagnosis.

eEdE-49

6:30AM - 3:00PM

Alphabet Soup: Making Sense of the New 2016 World Health Organization Central Nervous System Tumor Classification System and the Growing Importance of Molecular Markers

J Cagley[1], J Yu[1]
[1]*University of Wisconsin-Madison, Madison, WI*

Purpose
The newly released 2016 WHO CNS tumor classification reflects a paradigm shift where tumor molecular markers (including 1p19q codeletion status, ATRX loss, and p53 mutation) are now utilized for simplified classification of tumors into oligodendroglioma or astrocytoma lineages. Additionally, IDH mutation and MGMT methylation status are now important markers of dedifferentiated glioblastoma and predicative response to temozolomide therapy, respectively. This exhibit will examine the importance of implementing molecular marker status of primary glial neoplasms into everyday neuroradiology practice with a specific focus on response to therapy and differentiating progression from pseudoprogression.
Materials and Methods
A thorough discussion of the biologic function and mutation patterns of the aforementioned commonly tested molecular markers will be detailed. Additional minor molecular markers will be briefly discussed also. A local institutional PACS database search for case examples pertaining to each major molecular marker will be provided to aid in the discussion of why each marker has importance for everyday practice, namely as they apply to survival and prediction of progression.

Results
Molecular status has proven to be not only important for diagnosing tumor type, but also important radiologically by impacting the pretest probability and ultimately the diagnosis of progression versus pseudoprogression. Most importantly, on follow-up imaging, the radiologist must take into account the poor prognosis and early progression of IDH wild-type gliomas and the relative poor response of MGMT nonmethylated tumors to temozolomide therapy.
Conclusions
The new 2016 WHO CNS tumor classification system highlights the growing importance of tumor molecular markers in glioma diagnosis and prognosis prediction. As neuroradiologists, a working knowledge of these markers, their prognostic impact on tumor progression, and ability to differentiate progression from psuedoprogression, reflects a developing and important trend in neuroradiology.

eEdE-93

6:30AM - 3:00PM

An Automated, Open-Source System for Quantification of Stroke Effects Using Computed Tomography

E O'Connor[1], A Das[2], P Shah[3], T Zeffiro[4], T Zeffiro[5]
[1]University of Maryland Medical Center, Baltimore, MD, [2]Lewis Katz School of Medicine at Temple University, Philadelphia, PA, [3]Temple University, Philadelphia, PA, [4]Neurometrika, Potomac , MD, [5]Neurometrika, Potomac, MD

Purpose
Computed tomography (CT) is used widely to estimate ischemic damage prior to either thrombolysis or endovascular treatment. Nevertheless, many hospitals do not have continuous neuroradiology coverage for CT interpretation. While there have been efforts to develop computerized systems to score ischemic damage following stroke, none are based on open-source software, limiting their continued improvement and evolution. Research groups interested in applying recent advances in computational neuroanatomy and machine learning to the problem of acute stroke assessment might benefit from automated tools implementing the basic functions required to quantify the acute effects of stroke.
Materials and Methods
To assist physicians tasked with estimating stroke extent in acute contexts, we developed a prototype stroke assessment system using open-source software tools, mostly derived from SPM12 and its extensions, a MATLAB-based program widely used for analysis and display of structural and functional MRI data. The system incorporates functions to convert data from DICOM to NIFTI formats, spatially normalize images into standard anatomical space, apply atlas regions-of-interest to extract attenuation measures, export regional attenuation values for machine learning classification and visual display of ischemic regions. The system

features were tested on a set of 150 nonenhanced CT studies from patients with left hemisphere, right hemisphere and no abnormalities. Follow-up magnetic resonance imaging (MRI) examinations were used as the standard of comparison for lesion location and extent.
Results
The prototype system was able to process standard stroke protocol CT data, automatically yielding regional ischemia estimates. Comparison of these values with estimates derived from coregistered MRI studies provided a way to explore which CT image features might predict parenchymal damage.
Conclusions
Widely available open-source software tools can be configured into an automated system providing advisory information concerning ischemic damage in acute settings. Deployment of decision support systems in research settings could facilitate efforts to use CT data in acute treatment settings.

eEdE-48

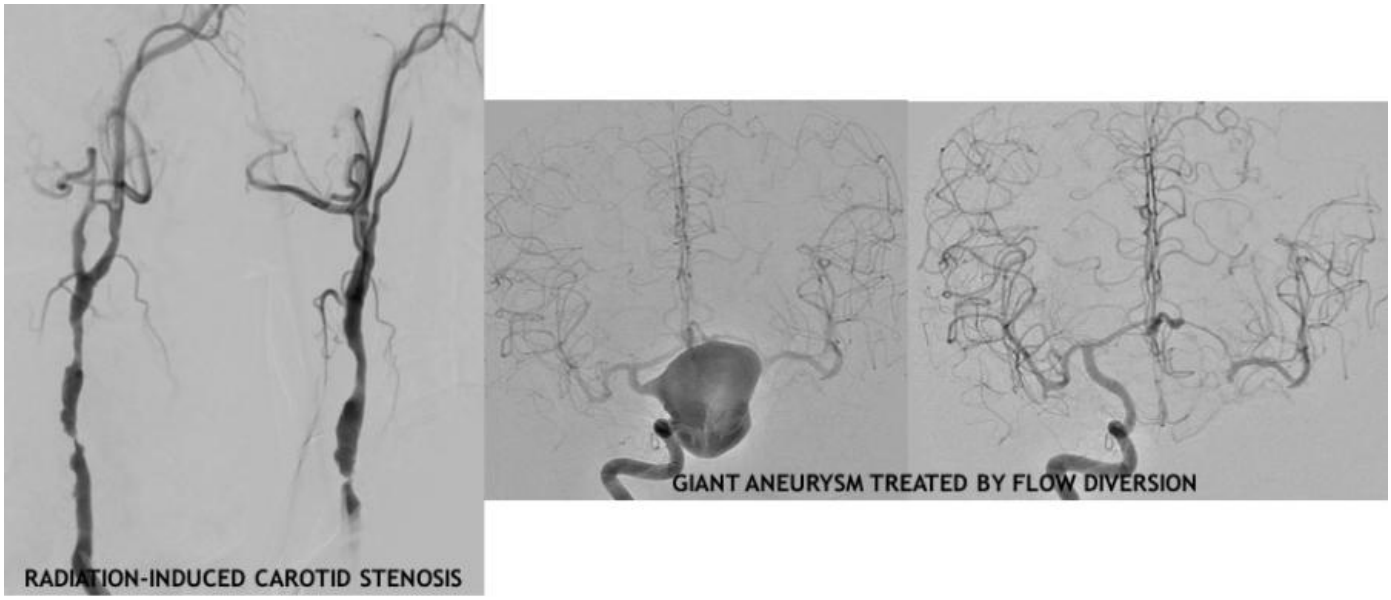
6:30AM - 3:00PM

Angiographic Patterns, Most Common Pathologies and Treatment Options for Cerebrovascular Diseases, a Pictorial Essay

J CHUDYK[1], C Bleise[1], P Diluca[1], R Salvatico[1], P Lylyk[1]
[1]*Instituto Médico ENERI - Clínica Sagrada Familia, BUENOS AIRES, Buenos Aires*

Purpose
To report the most frequent angiographic signs and patterns in vascular pathologies of the head and neck, as well as different treatment options and its evolution over time.
Materials and Methods
From January 2014 to December 2016, approximately 5500 endovascular procedures were analyzed including diagnostic and therapeutic procedures. The images were selected by a team of experienced neuroradiologists and divided into different groups as follows: carotid disease, ischemic stroke, brain aneurysms, flow diversion, hemorrhagic stroke, arteriovenous malformations and dural arteriovenous malformations, tumors, traumatic lesions and miscellaneous.
Results
From all the procedures analyzed, 110 patients were selected due to its significance and representativeness. Computed tomography angiography (CTA), magnetic resonance angiography (MRA) and digital subtraction angiography (DSA) images were collected and classified in groups of interest. Digital subtraction angiography was performed in all the patients. For therapeutic cases, the technique was described, as well as the follow up.
Conclusions
The knowledge of main features and angiographic patterns contributes to the early, accurate diagnosis and follow up of many vascular conditions. The relationship among different

modalities improve the understanding of pathologies and the evolution of the endovascular treatment of each case over time.



(Filename: TCT_eEdE-48_patrones.jpg)

eEdE-82

6:30AM - 3:00PM

Applications and Limitations of Dual Energy CT in Neuroradiology

O Khalilzadeh[1], A Khorsandi[2], R Gupta[3]
[1]Icahn School of Medicine at Mount Sinai, New York, NY, [2]Beth Israel Medical Center, New York, NY, [3]Massachusetts General Hospital, Boston, MA

Purpose
To review the application and limitations of Dual Energy CT (DECT) for material decomposition in neuroimaging.
Materials and Methods
The basic concept of Dual Energy CT is to characterize and quantify the composition of certain tissues and added contrast agents, based on differences in the attenuation when substances are imaged with two x-ray energies of known spectra. Dual Energy CT has several applications in neuroradiology including reconstruction of virtual nonenhanced images from contrast-enhanced acquisition, differentiation of iodine versus intracranial hemorrhage, and calcium/bone removal.
Results
In clinical applications, certain limitations on the technical capabilities of Dual Energy CT should be taken into account. These limitations include: presence of a fourth material; beam hardening/metallic spray artifact; spatial/temporal registration; cross scattering; and limited

field of view. In this exhibit, we will provide a pictorial example of clinical applications and limitations of Dual Energy CT in neuroimaging.
Conclusions
The applications of Dual Energy CT in material decomposition will be enhanced if certain limitations on the technical capabilities of Dual Energy CT are taken into account when interpreting the studies.

eEdE-18

6:30AM - 3:00PM

Arterial Spin Labeling (ASL) Perfusion: Problem-Solving and Clinical Cases Using a Non-Invasive, Non-Contrast Perfusion Technique

A Sung[1], J Bykowski[2], N Farid[1], J Chen[3]
[1]University of California, San Diego, San Diego, CA, [2]University of California at San Diego, San Diego, CA, [3]San Diego VA / UCSD Med. Center, La Jolla, CA

Purpose
To review the various types of arterial spin labeling (ASL) perfusion, including pulsed (PASL), pseudo-continuous (pCASL), and continuous (CASL) and highlight several clinical cases where ASL proved to be useful for problem-solving.
Materials and Methods
Our institution uses a rapid pseudo-continuous ASL (pCASL) with 3D fast spin-echo imaging. We present several cases which highlight the utility of perfusion imaging obtained with ASL.
Results
Examples will include clinical cases of: - Stroke – Rapidly evaluating the ischemic penumbra, degree of collaterals, and luxury perfusion without intravenous contrast. - Cerebrovascular reserve evaluation in moyamoya – Monitoring cerebral perfusion in a convenient single-session in patients requiring repeated surveillance. Short-tag life of ASL allows a single-session without need to wait for excretion or confounding recirculating contrast. - Tumors – Pseudo-continuous ASL using 3D fast spin-echo imaging also provides increased tumor conspicuity in regions of high susceptibility, such as the skull base, where T2* perfusion is challenging. Examples of cerebral blood flow for grading primary brain tumors and differentiating hyperperfused versus nonhyperperfused tumors (paraganglioma versus schwannomas). - Seizure – As with other functional imaging techniques, ASL demonstrates seizure activity as regions of hyperperfusion in the peri-ictal state, and hypoperfusion in the inter-ictal state.
Conclusions
Arterial spin labeling (ASL) perfusion imaging is a noncontrast, MR perfusion technique that provides useful information in a variety of clinical cases.

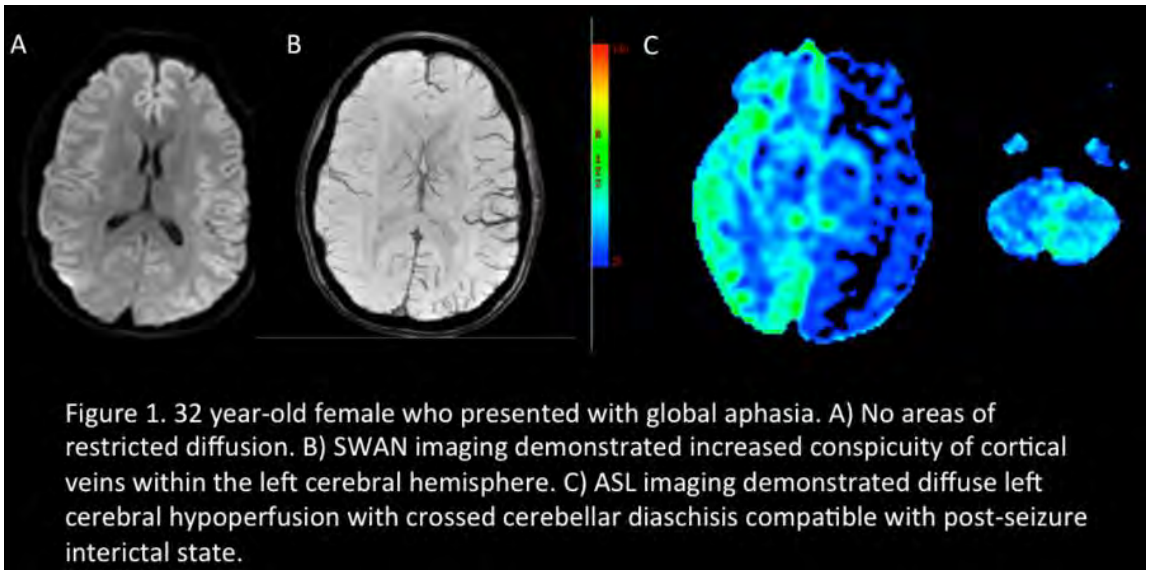


Figure 1. 32 year-old female who presented with global aphasia. A) No areas of restricted diffusion. B) SWAN imaging demonstrated increased conspicuity of cortical veins within the left cerebral hemisphere. C) ASL imaging demonstrated diffuse left cerebral hypoperfusion with crossed cerebellar diaschisis compatible with post-seizure interictal state.

(Filename: TCT_eEdE-18_Figure1-2.jpg)

eEdE-04

6:30AM - 3:00PM

Behavioral Variant Frontotemporal Dementia: The Importance of Integrating Both Clinical and Neuroimaging Correlates

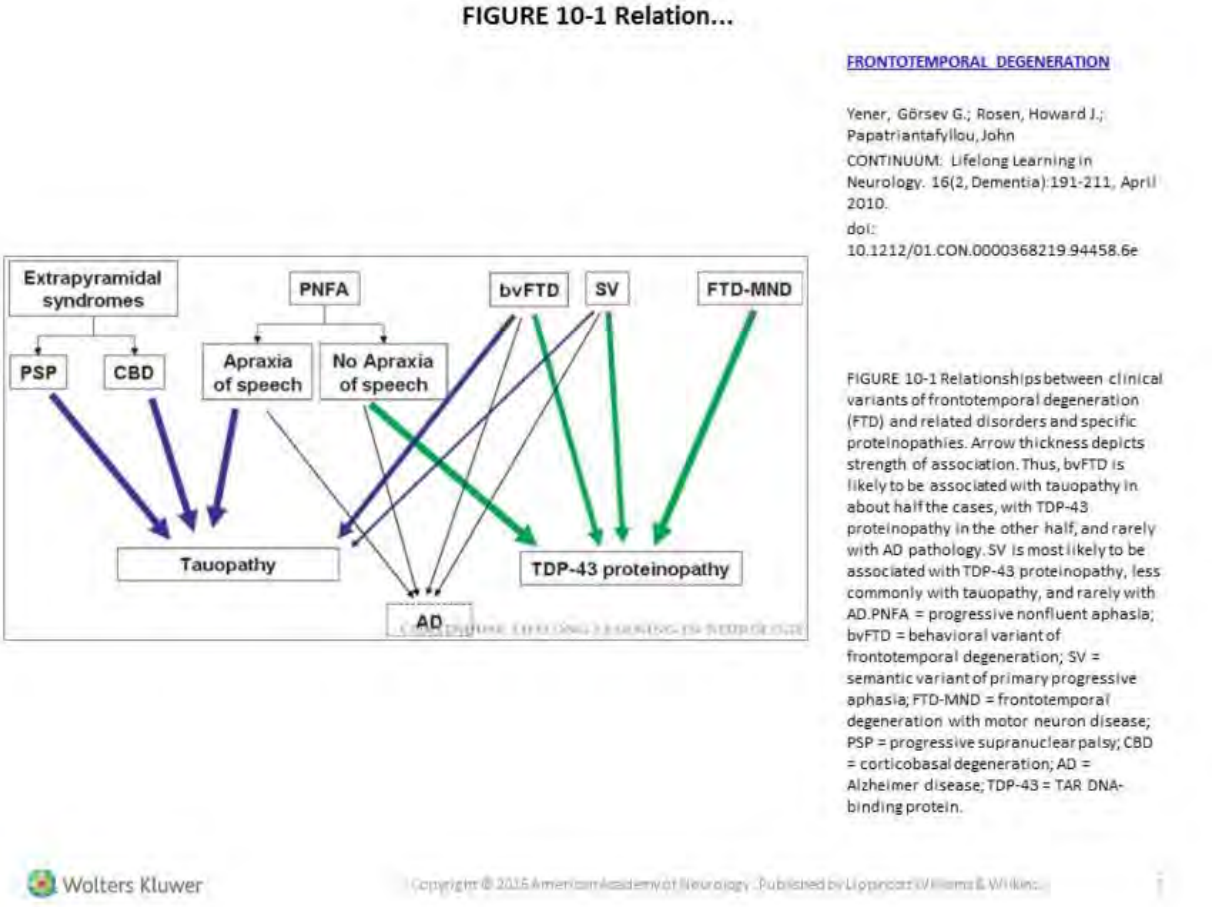
E Ulmer[1], S Franczak[2], D Sabsevitz[3], A Klein[4]
[1]University Lake School, Hartland, WI, [2]Divine Savior Holy Angels High School, Milwaukee, WI, [3]Medical College of Wisconsin, Milwaukee, WI, [4]Medical College of Wisconsin - Froedtert Hospital, Milwaukee, WI

Purpose
An understanding of clinical criteria for the diagnosis of behavioral variant frontotemporal dementia (bvFTD) is important in distinguishing the condition from otherwise seemingly nonspecific imaging features. The goal of the exhibit is to improve the accuracy of neuroimaging diagnosis through a knowledge-based approach.
Materials and Methods
The exhibit discusses the presentations, diagnosis, and therapeutic strategies for bvFTD. Clinical and imaging features for the neurological clinical algorithm are discussed. Neuropsychological evaluations that may demonstrate poor performance of executive functions, with relative sparing of visuospatial domains and episodic memory (hallmark of Alzheimer disease), are discussed. Neuropathology of bvFTD showing accumulation of tau or TDP-43 protein is illustrated. The importance of distinguishing imaging features and their integration with clinical criteria for this FTD subtype are discussed and illustrated with case series.
Results
Frontotemporal dementia (FTD) is the second most frequent form of neurodegenerative

early-onset dementia and is the clinical manifestation of progressive neuronal cell loss in the frontal and anterior temporal lobes. Frontotemporal dementia consists clinically and pathologically of a heterogeneous group of dementia disorders. Frontotemporal dementia as currently classified possesses several diagnostic challenges to clinicians because the disorder largely affects younger individuals, and symptoms in young age population often are mistaken for psychiatric or neurological disease causing a delay in correct diagnosis. Phenotypes of FTD generally are classified into either behavioral (bvFTD) variant or primary progressive aphasia language (PPA) syndromes. The bvFTD subtype, also known as the frontal variant, is the most common clinical syndrome accounting for more than 50% of FTD patients. Nearly 40% of cases are familial, and 10-15% are caused by an autosomal dominant inheritance. BvFTD usually presents between fourth and sixth decades and is expressed by progressive personality and behavioral changes and deterioration of social cognition and executive functions. The key to making an imaging diagnosis is an understanding of the clinical presentation in all its forms. In fact, bvFTD is the only FTD subtype in which characteristic imaging is required for diagnosis.

Conclusions

Understanding both the clinical and neuroimaging patterns associated with bvFTD is critical in separating its heterogeneous symptomatology from primary psychiatric disorders. Accurate, early diagnosis establishes prognosis as well as appropriate early treatment strategies and supportive care.



(Filename: TCT_eEdE-04_FTDimage_download.jpg)

eEdE-23

6:30AM - 3:00PM

Beyond Progressive Multifocal Leukoencephalopathy - Imaging Findings in Multiple Sclerosis Patients on Natalizumab

P Batchala[1], S Patel[1], D Ornan[1], D Abdullah[1], T Druzgal[1], S Mukherjee[1]
[1]*University of Virginia Health System, Charlottesville, VA*

Purpose
Early recognition of treatment-related complications especially progressive multifocal leukoencephalopathy (PML) from Natalizumab (NZB), a monoclonal antibody approved for the treatment of relapsing and remitting form of multiple sclerosis (RRMS), is crucial for patient survival. Other entities including PML immune reconstitution inflammatory syndrome (PML-IRIS), disease rebound and other CNS infections can confound and delay appropriate management. This exhibit describes how MRI imaging plays a crucial role in guiding management by distinguishing these complications.

Materials and Methods
We describe the clinical and typical imaging findings that help to differentiate PML from PML-IRIS and disease rebound in the background of NZB treatment.
Results
Appearance of a new peripheral, nonenhancing, T2/ FLAIR hyperintense subcortical white matter lesion involving U fibers with restricted diffusion and without mass effect is typical of PML in RRMS patients on NZB. Cerebrospinal fluid polymerase chain reaction test for JC virus DNA is confirmatory and warrants immediate discontinuation of NZB. Postdiagnosis of PML, discontinuation of the drug or treatment with plasma exchange can result in clinical worsening from PML-IRIS. Paradoxically, on imaging, the existing PML lesions show enlargement with enhancement. In nonPML patients, discontinuation of NZB can lead to disease progression or relapse termed as "rebound phenomenon", which is characterized by new enhancing or nonenhancing lesions typical of multiple sclerosis.
Conclusions
Knowledge of PML, PML-IRIS, rebound phenomenon and other entities in RRMS patients on NZB patients along with their imaging hallmarks is essential for early diagnosis and guiding further management.

eEdE-89

6:30AM - 3:00PM

Brain Connectivity Biomarkers and Functional Outcome After Stroke

J Puig[1], G Blasco[2], C Biarnes-Duran[3], P Daunis-i-Estadella[4], M Marti-Navas[1], M Rivero[5], J Gich[5], J Figueras[6], A Alberich-Bayarri[7], S Thio-Henestrosa[4], K Nael[8], M Wintermark[9], S Pedraza[2]
[1]Research Unit of Diagnostic Imaging Institute (IDI), IDIBGI, University Hospital Dr Josep Trueta, Girona, Girona, [2]Imaging Research Unit, IDI-IDIBGI, Hospital Dr Josep Trueta, Girona, None, [3]Research Unit of Diagnostic Imaging Institute (IDI), Girona Biomedical Research Institute (IDIBGI), Girona, Girona, [4]Department of Computer Science, Applied Mathematics and Statistics, University of Girona, Girona, Girona, [5]Department of Neurology-IDIBGI, University Hospital Dr JosepTrueta, GIRONA, GIRONA, [6]Department of Rehabilitation-IDIBGI, University Hospital DrJosepTrueta, GIRONA, GIRONA, [7]Hospital Universitario y Politecnico La Fe-QUIVIM, Valencia, None, [8]Icahn School of Medicine at Mount Sinai, New York, NY, [9]Stanford University, Stanford, CA

Purpose
Stroke results in various and variable deficits; depending on lesion size and location, stroke can affect motor function, sensory perception, cognition, emotion, and/or the ability to communicate. Approximately 33% of patients have persistent disability after stroke; the mechanisms involved in recovery are not well understood. Functional outcome from stroke has been linked to structural alterations in gray and white matter as well as to functional

changes in perilesional tissue. Diffusion tensor imaging provides information about the spatial relation between lesions and key tracts. Functional MRI techniques make it possible to study how the brain adapts to the ischemic lesion to compensate for deficits and relearn functions lost with stroke damage by focusing on changes in specific patterns of activation among different brain regions. Here we explain the roles of structural and functional brain connectivity (SF-BC) biomarkers in assessing brain integrity and its impact on functional outcome after stroke.
Materials and Methods
1. We use cases from our repository (BIOCONNECT Project) to present data (from acute, subacute, and chronic phases of stroke) about changes in spatial and temporal connectivityafter stroke. 2. We illustrate the clinical utility of SF-BC biomarkers in predicting long-term functional outcome in stroke patients.
Results
Growing evidence supports the idea that SF-BC biomarkers can be used as predictors of potential functional recovery and surrogate markers of chronic impairment. Incorporating imaging data at a much earlier stage may help clinicians set realistic rehabilitation goals and design customized rehabilitative strategies for individual patients.Incorporating SF-BC biomarkers into neurorehabilitation decision-making algorithms may help more patients benefit from rehabilitation because potential recovery through stimulating neuroplasticity may justify rehabilitation.
Conclusions
SF-BC biomarkers hold great promise for predicting functional outcome and for improving rehabilitation outcomes by allowing therapy to be tailored to individuals according to their capacity for neural reorganization and recovery.

eEdE-70

6:30AM - 3:00PM

Brain Lesions: Correlating MRI Findings with Histopathology

R Carmody[1], G Choudhary[2], J Becker[1], C Spicer[3], V Patel[1], C Harms[1], H Albasha[4], R Khan[1]
[1]University of Arizona Medical Center, Tucson, AZ, [2]Banner university medical center, Tucson, AZ, [3]University of Arizona Department of Medical Imaging, Tucson, AZ, [4]University of Arizona College of Medicine - Tucson, Tucson, AZ

Purpose
Most of the MR signal changes seen with brain lesions can be related directly to the histopathology of the abnormality. In many cases, the MR findings can be predicted by the underlying abnormalities at a cellular level. The purpose of this exhibit is to familiarize the reader with the microscopic appearance of a variety of brain lesions, and how they relate to the corresponding MR findings.

Materials and Methods
Electronic educational review.
Results
This educational exhibit will illustrate how MRI findings of brain lesions most often correlate with the microscopic findings. Specific examples are as follows: CNS lymphoma: Low ADC values, as a result of high cellular density and high nuclear-to-cytoplasmic ratio of tumor. Vestibular schwannoma: Low T2 signal intensity in the densely cellular Antoni A areas of the tumor, and higher T2 signal in the loosely-textured Antoni B regions. Pilocytic astrocytoma: High T2 values in the nodular portion of the tumor, as a result of the low cellularity. Chordoma: Very high T2 signal, resulting from high fluid content of the physaliphorous cells which make up the tumor. High-grade astrocytoma: High rCBV secondary to high vascularity of the tumor. Brain abscess: Markedly restricted diffusion secondary to protein-rich exudate, dead leukocytes, macrophages, and bacteria. Both the MR imaging and the microscopic sections will be displayed.
Conclusions
A basic knowledge of neuropathology is most helpful in understanding why certain brain lesions have characteristic MR signal changes. We find this to be a more meaningful learning tool than rote memorization.

eEdE-21

6:30AM - 3:00PM

Brain Parcellation from B to C: Brodmann to Connectome

W Fischer[1], R Shastri[2], J Tejada[3], J Kovoor[3]
[1]Indiana University School of Medicine, Indianapolis, IN, [2]University of Michigan Health System, Ann Arbor, MI, [3]Indiana University, Indianapolis, IN

Purpose
The purpose of this presentation is to discuss the historical context of Brodmann's areas, their development over the last century, and the current understanding of brain parcellation.
Materials and Methods
1. Literature review of neuroanatomical understanding beginning with Brodmann's foundational work on brain segmentation published in 1909. 2. Comparative evaluation of evolving literature of neuroanatomy understanding over the next century with the culmination of the recent developments related to the Human Connectome Project. 3. Comparison of Talairach atlas information with functional neurosurgical evaluations that led to parcellation of the brain by Glasser 2016.
Results
Korbinian Brodmann published his description of 43 brain areas in his 1909 text Localisation in the Cerebral Cortex. This established a baseline of neuroanatomical localization that dominated the field for the next century. As with early work in any field,

Brodmann's concepts were expanded upon leading to cortical maps of increasing convolution including von Economo and Koskinas in 1925 and Sarkisov in 1949. The development of noninvasive neuroimaging lead to further advances including Talairach and Tournoux's Coplanar Stereotaxic Atlas of the Human Brain (1988). Further technologic advances have allowed for increasingly accurate, applicable, and automatic brain parcellation exemplified by Glasser (2016) and the 180 areas per hemisphere his research found.
Conclusions
Korbinian Brodmann's work published in 1909 set the course of neuroanatomical understanding over the next century. Numerous increasingly complex brain mapping models were produced throughout the 20th century. Technological advances in imaging and computing have allowed for the most accurate brain parcellation to date. Continued advances will allow novel approaches to neuropathology and treatment of disease.

eEdE-74

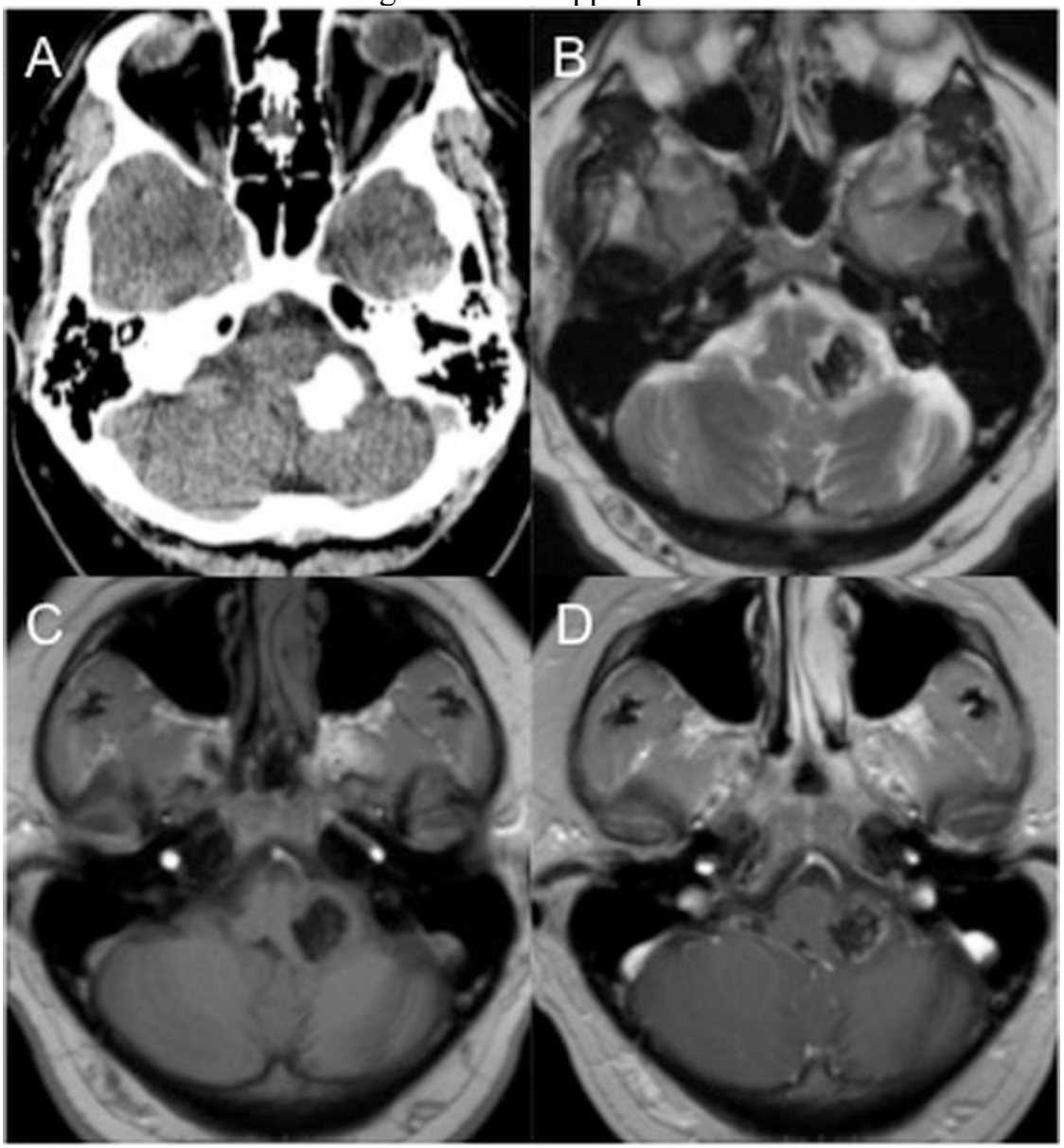
6:30AM - 3:00PM

Calcifying Pseudoneoplasm of the Neuraxis (CAPNON): Spectrum of Imaging Findings

M Kontzialis[1], M Alkaphoury[1], M Jhaveri[2], C Zamora[3], M Kocak[1]
[1]Rush University Medical Center, Chicago, IL, [2]Rush University Medical Center, chicago, IL, [3]University of North Carolina, Chapel Hill, NC

Purpose
Calcifying Pseudoneoplasm of the Neuraxis (CAPNON) is a rare and possibly reactive lesion that can occur anywhere along the neuraxis. The purpose of this review is to present the spectrum of imaging findings of CAPNON.
Materials and Methods
We searched our teaching file and electronic database for cases of CAPNON with histologic confirmation.
Results
CAPNON is an uncommon lesion that can be intra-axial or extra-axial, intradural or extradural. The lesion is benign and may gradually increase in size. The clinical presentation of patients with CAPNON is heterogeneous and generally depends on the location and size of the lesion. Typical imaging findings include solid calcifications on CT and hypointensity on T1- and T2-weighted images. The lesion may demonstrate no enhancement, rim enhancement or internal enhancement that may be homogeneous or heterogeneous. Differential considerations will be discussed based on anatomic location and imaging appearance. Surgical resection is the treatment of choice when feasible, and incidental lesions must be followed as they may grow and become symptomatic.
Conclusions
CAPNON is a rare benign lesion that may occur anywhere along the neuraxis. Familiarity

with the typical imaging findings may allow prospective diagnosis and/or inclusion of the lesion in the differential diagnosis when appropriate.



(Filename: TCT_eEdE-74_CAPNON_ASNR.jpg)

eEdE-34

6:30AM - 3:00PM

Case-Based Review of the Neuroimaging Findings of Intracranial Angioinvasive Fungal Infections

F Torres[1]
[1]*Kaiser Permanente, Los Angeles, CA*

Purpose

To describe characteristic and atypical brain MRI findings in patients presenting with angioinvasive fungal infections.

Materials and Methods

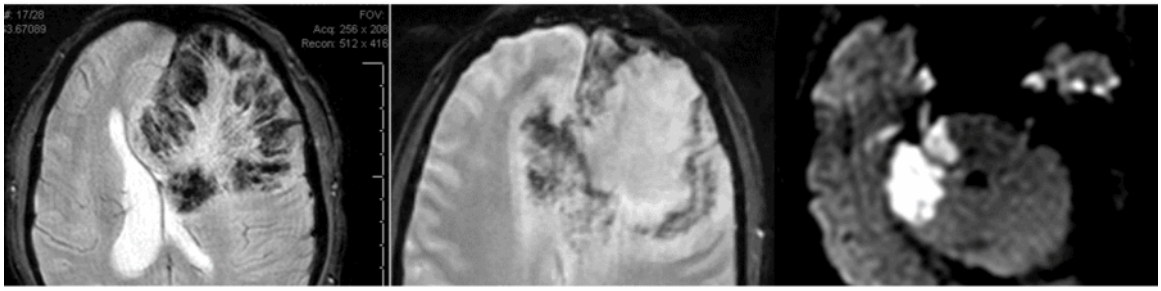
As a tertiary medical center for a healthcare organization that has experienced a very rapid growth over the past few years, we have noticed an associated increased number of patients that are immunosuppressed or on immunosuppresive medications. Subsequently, we have witnessed a recent number of neurological fungal infections that these patients are predisposed to acquiring compared to the general public. This case-based review identifies neuroimaging findings that help aid in the often challenging clinical and radiological diagnosis of angioinvasive fungal infections of the brain. We will specifically review the CT and MRI findings in 4 recent cases of patients that have suffered from fatal angioinvasive infections of the brain.

Results

Angioinvasive fungal infections of the brain can be neurologically devastating and commonly fatal. Early diagnosis is imperative as the patients are commonly immunosuppressed, allowing for rapid progression of the infection. Unfortunately, the early neurological symptoms also may be vague and nonspecific, with imaging findings that range from subtle abnormalities, to catastrophic appearing. We will present a spectrum of neuroimaging findings that will help diagnose angioinvasive infections of the brain by reviewing key imaging features that commonly are seen in fungal infections. In addition, we will discuss neuroimaging features of angioinvasive fungal infections that are not seen in other confounding etiologies. We will review the typical imaging findings in rhinocerebral and perineural spread of angioinvasive intracranial fungal infections, as well as an atypical fungal infection complicating an erosive mass of the skull base in a patient with post-transplant lymphoproliferative disorder.

Conclusions

Angioinvasive intracranial fungal infections can devastating, and early neuroimaging diagnosis often is challenging. We will present a spectrum of neuroimaging findings of 4 patients with fatal angioinvasive fungal infections of the brain, ranging from the subtle key early imaging features, to the often rapidly developing catastrophic findings. Our goal is to provide a diagnostic aid to the neuroradiologist to help early identification of this often fatal disease.



(Filename: TCT_eEdE-34_3separatecasesofMucor.gif)

eEdE-84

6:30AM - 3:00PM

CISS and SWI Sequences: Clues and Aids in Diagnosis

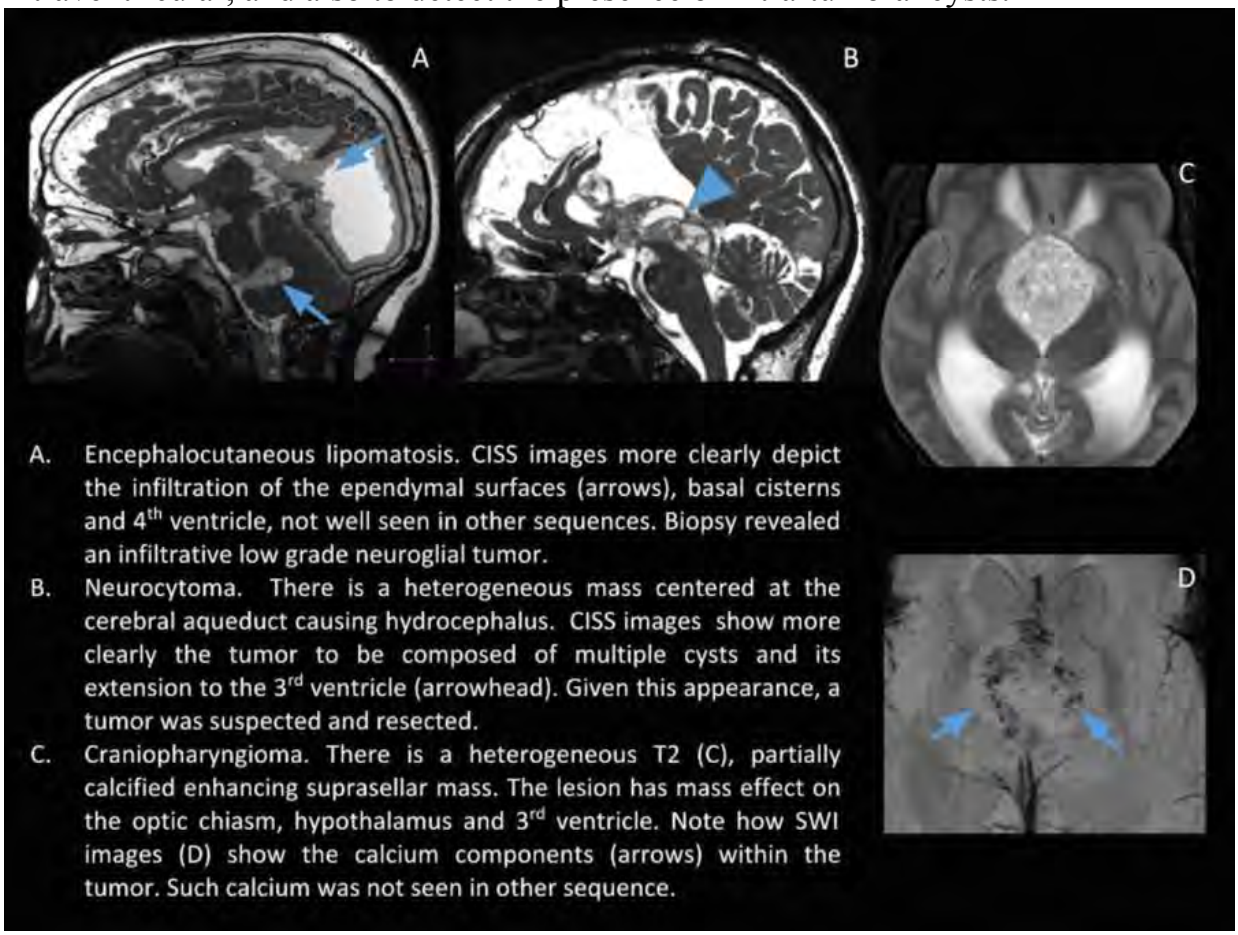
S Ferraciolli[1], P Puac[2], L Fajardo[3], M ARANHA[4], L Lucato[5], C Leite[6], M Castillo[7]
[1]InRad - HC- FMUSP, Sao Paulo, Brazil, [2]University of North Carolina at Chapel Hill, chapel hill, NC, [3]InRad - HCFMUSP, São Paulo , São Paulo, [4]SÃO PAULO UNIVERSITY, SÃO PAULO, Brazil, [5]Instituto de Radiologia do HC-FMUSP, Sao Paulo, Brazil, [6]University Of Sao Paulo, Sao Paolo, Brazil, [7]Univ. Of North Carolina School Of Medicine, Chapel Hill, NC

Purpose
We review several cases where CISS and SWI sequences were critical to give additional information and achieve a correct diagnosis, especially in tumor cases. Pertinent literature also is reviewed.
Materials and Methods
We searched the teaching files of two teaching institutions for representative cases in which CISS and SWI sequences were critical to the diagnosis and in which we believe a correct one would have been very difficult without them.
Results
The increased sensitivity of the 3D CISS sequence is an outcome of the accentuation of the T2 values between cerebrospinal fluid (CSF) and surrounding structures. It is very useful for evaluation of the cisternal spaces, cavernous sinuses, ventricular system and for detecting subtle CSF-intensity lesions that may be missed on routine spin-echo sequences.

Susceptibility-weighted imaging (SWI) is a technique that exploits the susceptibility difference between tissues to provide contrast for different regions of the brain. In essence it uses the deoxygenated hemoglobin and extravasated blood products as well as calcification as intrinsic contrast agents, allowing for better visualization of blood and vessels without administration of an external contrast agents.

Conclusions

Our purpose is to show cases where CISS and SWI were critical in the management of various neurologic disorders In tumor evaluation, Susceptibility-weighted imaging may show prominent blood vessels, hemorrhage, and/or calcifications not seen with any other technique and these findings may change the pre-operative diagnosis and surgical decisions. CISS is useful for detecting subtle CSF-intensity lesions that may be missed on routine spin-echo sequences, showing the exact location and extent of the tumor, especially when they are intraventricular, and also to detect the presence of intra-tumoral cysts.



(Filename: TCT_eEdE-84_ASNR2017SWI-CISSfigurepptx.jpg)

eEdE-36

6:30AM - 3:00PM

Clinical Application of Non-Invasive Dynamic 4D-CT Angiography

M Bazerbashi[1], M Buehler[1], A Alnemari[2], T Mansour[2], D Gaudin[2], J Schroeder[1], M Jumaa[3]
[1]University of Toledo, Toledo, OH, [2]university of toledo, Toledo, OH, [3]University of Toledo Medical Center, Toledo, OH

Purpose

To demonstrate the clinical usefulness of 4D-CTA in the evaluation of multiple neurovascular pathologies including stroke, moyamoya disease, and intracranial aneurysm.

Materials and Methods

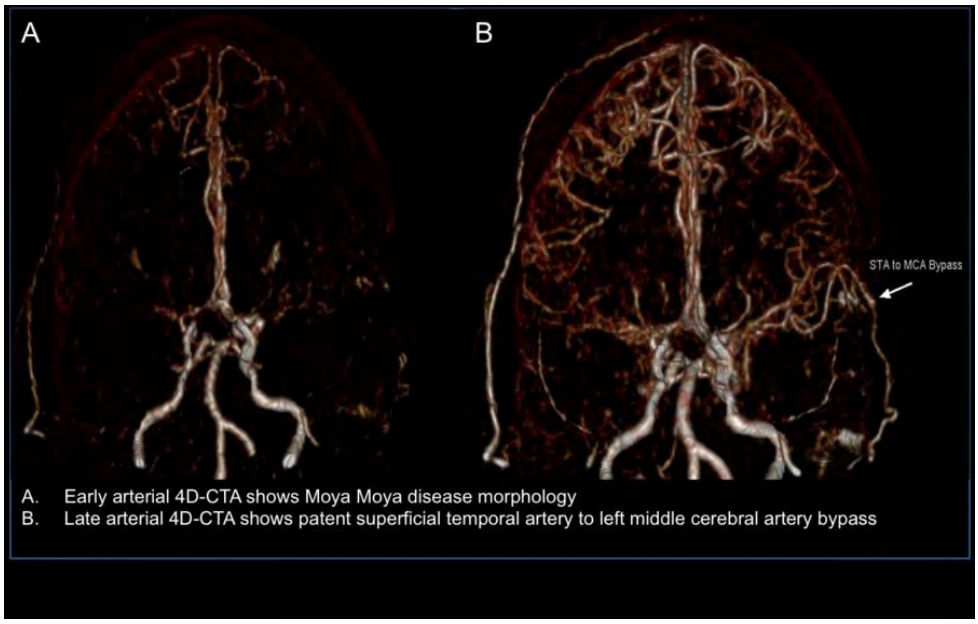
We highlight multiple cases showing the usefulness of dynamic 4D-CTA through case-based clinical presentations. Our presentation will feature annotated 3D images and 4D videos with emphasis on demonstrating the ability to characterize anatomy and flow dynamics in multiple neurovascular pathologies including ischemic stroke, superficial temporal artery to middle cerebral artery bypass in the setting of moyamoya disease, and intracranial aneurysm.

Results

Advances in noninvasive intracranial vascular imaging allows for a 4D-CTA acquisition which provides additional information on temporal lesion flow dynamics compared to CT angiography which provides information at one point in time. This technique combines the noninvasive nature of CTA with the dynamic capacity of digital subtraction angiography (DSA). The value of 4D-CTA in its ability to noninvasively characterize neurovascular diseases and expose flow dynamics through continuous volume CT acquisition. When compared to DSA, 4D-CTA has advantages in terms of time, cost, less neurological complications, and silent embolic events. Compared to conventional CTA, the cumulative radiation dose from 4D-CTA is higher, however the benefits of acquiring temporal vascular dynamics make 4D-CTA advantageous in characterizing certain vascular lesions as demonstrated by our presentation. We highlight the ability of 4D-CTA to characterize flow dynamics in the setting of ischemic stroke, to evaluate patency of superficial temporal artery to middle cerebral artery bypass in patients with moyamoya disease and to demonstrate dynamic pulsatile flow within intracranial aneurysm.

Conclusions

4D-CTA is an efficient noninvasive technique which allows for the dynamic evaluation and diagnosis of various neurovascular pathologies by providing information on vascular anatomy and flow dynamics.



(Filename: TCT_eEdE-36_4D-CTAMoyaMoyaDiseasewithpatentSTAtoMCABypass.JPG)

eEdE-52

6:30AM - 3:00PM

Cross Sectional Imaging of Intracranial Cystic Lesions

a abdel razek[1]
[1]*Mansoura faculty of medicine, mansoura, WY*

Purpose
1- To illustrate the causes of intracranial cystic lesions. 2- To review the typical and atypical cross-sectional imaging appearance of intracranial cystic lesions. 3- To describe the role of diffusion-weighted imaging in the differential diagnosis of intracranial cystic lesions.
Materials and Methods
1-Classification of intracranial cystic lesions. 2-Routine and advanced MR imaging such as diffusion MR imaging in assessment of intracranial cystic lesions. 3-Imaging of normal variant cysts such as cavum septum, choroid plexus cyst, dilated Virchow-robin spaces, sub ependymal cyst, pineal cyst, Rathke's pouch cyst and neuroglial cyst. 4-Imaging of developmental cyst such as epidermoid cyst, dermoid cyst, arachnoid cyst, neuroenetric cyst, colloid cyst and Rathke's cleft cyst. 5-Imaging appearance of acquired cysts as post-traumatic leptomeningeal cysts, infectious cysts such as neurocysticercosis and echinococcosis and neoplastic cysts such as cystic meningioma and hemangioblastoma. 6-Conclusion and future directions.
Results
There is spectrum of intracranial cystic lesions. Normal variant cysts include cavum septum, choroid plexus cyst, dilated Virchow-robin spaces, subependymal cyst, pineal cyst, Rathke's pouch cyst and neuroglial cyst. Developmental cyst include epidermoid cyst, dermoid cyst,

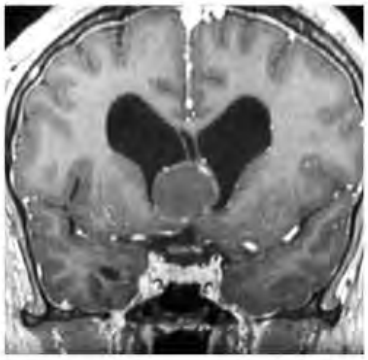
arachnoid cyst, neuroenetric cyst, colloid cyst and Rathke's cleft cyst. Acquired cysts are leptomeningeal cysts, neurocysticercosis, echinococcosis, cystic meningioma and hemangioblastoma.

Conclusions

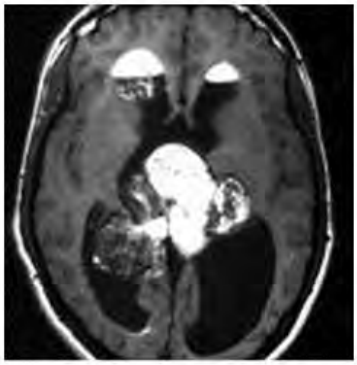
We concluded that cross-sectional imaging is important for accurate localization, characterization and extension of different subtypes of intracranial cystic lesions. The data are important for treatment planning of these patients.



Leptomeningeal cyst



Colloid cyst



Dermoid cyst



Epidermoid cyst

(Filename: TCT_eEdE-52_Picture2.jpg)

eEdE-88

6:30AM - 3:00PM

CT Angiography of the Head and Neck using Digital Subtraction: Pearls and Pitfalls

M Lammle[1], K Reddy[1], D Anand[1], S Cordina[2]

[1]University of South Alabama, Mobile, AL, [2]University of South Alabama Medical Center,, Mobile, AL

Purpose

CT angiography of the head and neck is a commonly used imaging protocol in the clinical evaluation of intracranial aneurysms, cerebral infarcts and carotid artery stenoses. While scan protocols for image acquisition generally are optimized for contrast timing and maximum image resolution with not much variation, currently there is no consensus on a standardized protocol for optimized postprocessing of the acquired data for routine clinical use. The aim of this presentation is to describe a successfully optimized protocol with standardized image acquisition and standardized combined multiplanar and 3D reconstructions using digital subtraction technique.

Materials and Methods

Protocol optimization was performed to minimize variations in image acquisition using a head holder device, wedge sponges and forehead tapes, and bolus tracking set at the aortic arch with fixed ROI size and triggering threshold, a standardized dual phase contrast and saline IV injection protocol and set helical image acquisition parameters for the CT scan protocol to provide a standardized 3D image data set for postprocessing. CT scanning of the head and neck was performed first without IV contrast and then with IV contrast in the arterial phase using identical CT imaging parameters. Postprocessing was performed on a dedicated workstation with multiplanar reformatting providing LAO and RAO views of the aortic arch and origins of supra-aortic vessels emulating standard conventional angiography views, and coronal and sagital reconstructions. Then 3D reconstructions were obtained following digital subtraction of the noncontrast and contrast-enhanced imaging data set and maximum intensity projections were obtained. 3D maximum intensity projections of the intracranial vasculature were set to spin around the horizontal and vertical axis to create scrollable standardized 3D views for interpretation. In addition, 3D maximum intensity projections of the aortic arch, supra-aortic and cervical vasculature were set to spin around the vertical axis using the entire field of view, and then dividing the field of view to provide separate reconstructions for the right and left side and create scrollable standardized 3D views of the carotid and vertebral arteries for interpretation.These reconstructions were set to provide the 3D views routinely used for MR angiography of the head and neck. Selected cases demonstrate a variety of vascular pathologies as visualized using this technique.

Results

The standardized CT scan protocol used for optimized image acquisition has proven a reliable base for postprocessing. The process of multiplanar reformatting and 3D reconstructions that was performed by CT technologists revealed itself as a time-consuming procedure taking up to 45 minutes after a several months period of practicing. The result however was rewarding with clinical useful 2D and 3D image sets demonstrating high image quality with high image contrast and resolution. While conventional postprocessing methods with dedicated workstations usually are limited in the evaluation of vascular segments located in proximity of osseous structures and the vertebral arteries usually cannot be evaluated, digital subtraction routinely provides accurate and unrestricted views of the cerebral and cervical vasculature with full evaluation of the posterior circulation.

Conventional angiography perspectives used for multiplanar and 3D reconstructions provide established clinical imaging views and are user friendly in the eyes of the interventionalist, neurologist or neurosurgeon. High image contrast and resolution allow for significant zooming of image findings for the purpose of close examination and characterization of pathologies and accurate measurements for stenoses and aneurysms as well as procedure planning. 3D views provided for interpretation are allowing for complete visualization of the intracranial and cervical vasculature. A variety of vascular pathologies have been found and are well visualized using this technique in clinical routine. However, several pitfalls were noted in the use of this method. Based on the automated nature of the digital subtraction method used, arterial segments including a metallic stent were subtracted out and lost for evaluation. The source images and multiplanar reformatted images obtained with our protocol however allowed for close examination of these segments to potentially find a stenosis within the stented arterial segment.

Conclusions

The standardized postprocessing protocol with multiplanar and 3D components in combination with a standardized CT scan protocol used for optimized image acquisition is a powerful tool of promising diagnostic value. While postprocessing is time consuming using the presented standard, our 2D and 3D image series demonstrate high image quality with high image contrast and resolution providing clinically relevant, accurate and unrestricted views of the cerebral and cervical vasculature with full evaluation of the posterior circulation. Conventional angiography and 3D MR angiography views are providing image perspectives that are familiar to the interpreting radiologist as well as to the interventionalist, neurologist or neurosurgeon.



(Filename: TCT_eEdE-88_CTA001demo.jpg)

eEdE-83

6:30AM - 3:00PM

CT Perfusion Troubleshooting – What's Wrong with That Image?

A Murphy[1], T Lee[2], C D'Esterre [3], M Lacasse[4], R Aviv[5]
[1]University of Toronto, Toronto, ON, [2]Robarts Research Institute, London, ON, [3]University of Calgary, Calgary, AB, [4]University of Toronto, Toronto, Ontario, [5]Sunnybrook Health Sciences Centre, Toronto, Ontario

Purpose
CT perfusion (CTP) is a diagnostic tool that has shown to be useful for understanding all stroke sub-types, including subarachnoid hemorrhage, and brain tumor hemodynamics. Regardless of the specific software used to process CTP maps, potential diagnostic benefits can be overshadowed by poor quality images secondary to technical shortcomings. The

purpose of this educational exhibit is to introduce these technical issues, and an approach to troubleshooting them, using several case examples.
Materials and Methods
Artifacts and technical shortcomings of CTP images are examined through several case examples. The technical issues accounting for poor quality CTP images are discussed and explained. An approach to troubleshooting images is described.
Results
The major technical issues underlying poor quality CTP images can be divided into two categories: issues at the scanner and issues at the workstation. While obtaining CTP images at the scanner, factors that may affect image quality include the volume and rate of contrast, scan duration, temporal resolution and dose. During processing of CTP maps, there is potential for variability in motion, arterial and venous inputs and image display parameters to impact the qualitative and quantitative CTP map output.
Conclusions
Knowledge of key technical factors important in obtaining and processing CTP maps may help to mitigate poor quality CTP images. Careful attention to these parameters at the scanner and workstation, with an approach to mitigate them could lead to improved quality CTP maps and useful diagnostic information.

eEdE-54

6:30AM - 3:00PM

Current Role of Imaging in the New Age of Glioma Genomics

I Littig[1], L Nunes[1], M Snuderl[2], S Patel[3], L Poisson[4], J Puig[5], P Chang[6], A Chi[7], R Jain[1]
[1]Department of Radiology, New York University School of Medicine, New York, NY, [2]Department of Pathology New York University Medical Center, New York, NY, [3]University of Virginia Health System, Charlottesville, VA, [4]Henry Ford Health System, Detroit, MI, [5]Research Unit of Diagnostic Imaging Institute (IDI), IDIBGI, University Hospital Dr Josep Trueta, Girona, Girona, [6]Columbia University Medical Center, New York, NY, [7]Division of Neuro-oncology, New York University School of Medicine, New York, NY

Purpose
Management of patients with gliomas has significantly changed with recent advances in tumor genomics and the World Health Organization (WHO) glioma classification update. The purpose of this educational exhibit is to describe the most important genomic markers and how to integrate them with imaging data, especially in order to generate better prognostic, predictive models and also how to use this information in routine clinical practice.
Materials and Methods
We will review the published literature on glioma genomics and radio-genomics. We also

will demonstrate clinical cases from our practice as well as from The Cancer Genome Atlas (TCGA)/The Cancer Imaging Archive (TCIA), to explain how major genomic markers correlate with imaging and patient prognosis. Detailed genomic data using next generation sequencing will be included for representative cases to demonstrate how it is affecting the clinical decision-making. We also will illustrate with follow-up imaging studies the expected natural history of different molecular subtypes of tumors and the most common changes that should be actively assessed by radiologists.
Results
It is well established that gliomas with IDH mutation show better prognosis than IDH wild type gliomas irrespective of the glioma grade. Similarly, there are some well-established imaging features which predict IDH mutation status pre-operatively, e.g. IDH mutated gliomas usually have larger size at presentation, lesser enhancing component, and much less necrosis/edema compared to IDH wild type gliomas. IDH wild type gliomas also have been known to have higher blood volume measurements, which correlate with their poor survival. We also will be discussing some specific imaging features which predict a specific molecular sub-group with high-degree of accuracy. We also will discuss role of deep learning tools in glioma and radio-genomics.
Conclusions
A better understanding of glioma molecular markers and its correlation with imaging is essential for radiologists to not just improve diagnosis and management of glioma patients, but also enhance their role as part of the multidisciplinary tumor boards. It also pushes boundaries of imaging research for better and noninvasive methods for detecting these molecular subgroups.

eEdE-95

6:30AM - 3:00PM

Current Role of Multiphase CTA in Acute Ischemic Stroke

G Watson[1], K Moulton[1]
[1]*University of Saskatchewan, Saskatoon, Saskatchewan*

Purpose
To review and summarize the rapidly evolving literature on multiphase CTA (mCTA) in the setting of acute ischemic stroke, including: current indications for mCTA; the acquisition and interpretation of mCTA; the advantages and disadvantages of mCTA; current evidence supporting mCTA in selecting patients for endovascular therapy, and; current evidence supporting mCTA in predicting clinical outcome.
Materials and Methods
A review of PubMed, MEDLINE, EMBASE, CINAHL and Cochrane Library database using the keyword 'multiphase computed tomography angiography in ischemic stroke' and related terms was performed. Returned abstracts were screened and relevant publications

reviewed in full. A summary of the literature with respect to the performance of mCTA in the setting of acute ischemic stroke then was synthesized, in accordance with our stated purpose. The approach to interpreting mCTA in the setting of acute ischemic stroke is incorporated into our presentation. Illustrative case examples from our local institution are included in an interactive, educational PowerPoint format.
Results
Multiphase CTA is a rapid, reliable, and powerful diagnostic tool in the setting of acute ischemic stroke. Multiphase CTA has been demonstrated to: improve detection of anterior circulation occlusion; improve the selection of patients who may benefit from endovascular therapy, and be helpful in predicting clinical outcome. As such, it is critical that neuroradiologists be familiar with the performance and interpretation of mCTA in order to help direct clinical management and provide patient prognostication.
Conclusions
Multiphase CTA is emerging rapidly as an indelible tool in the diagnosis, characterization, triage, and prognostication of patients presenting with acute ischemic stroke.

eEdE-47

6:30AM - 3:00PM

Deep Cerebral Brain Thrombosis: Imaging Findings and Differential Diagnosis

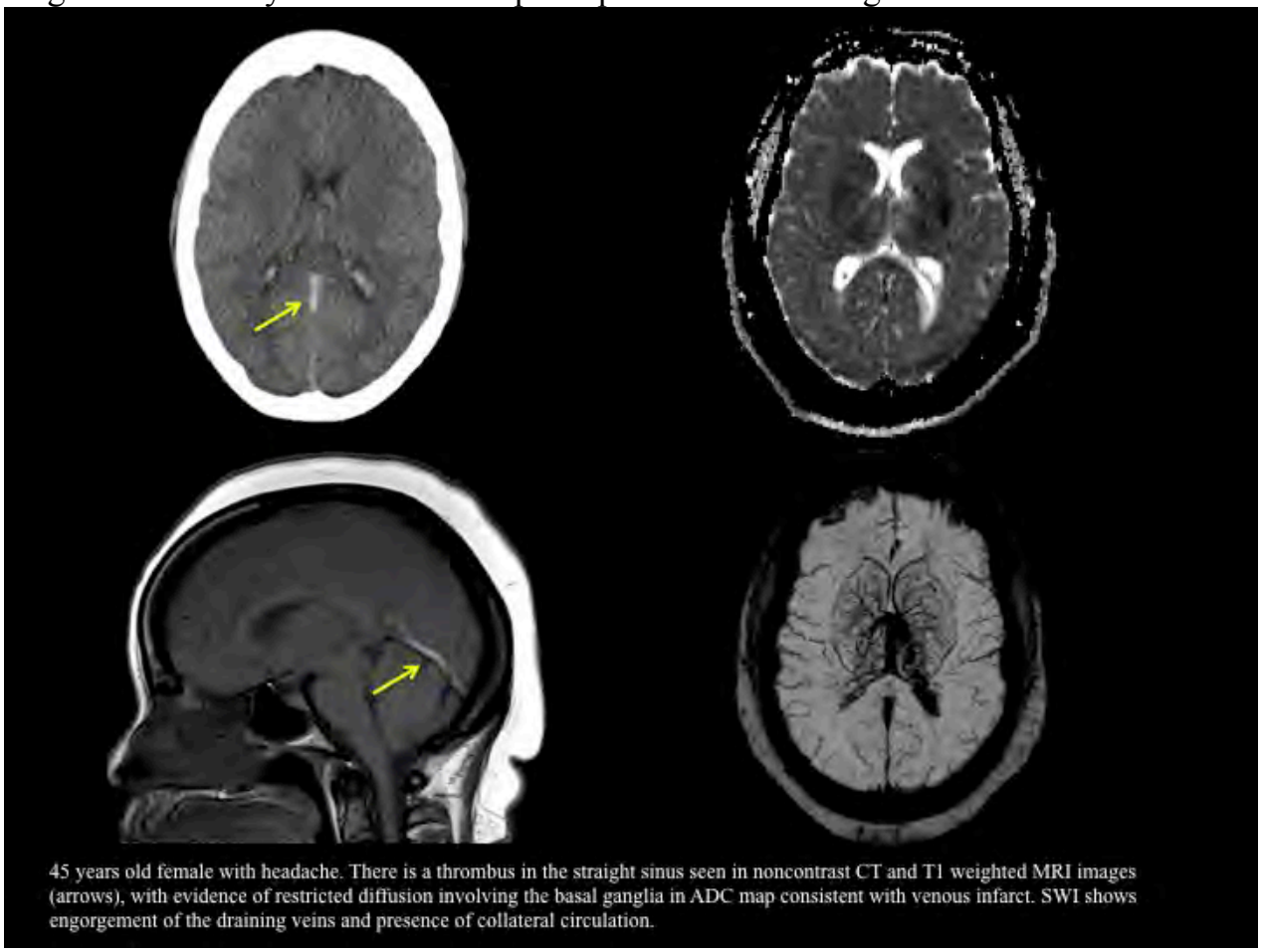
A Rodriguez[1], C Vallejo[1], R Camacaro[1], P Puac[1], M Castillo[1]
[1]*University of North Carolina at Chapel Hill, Chapel Hill, NC*

Purpose
Deep cerebral brain thrombosis is an entity in which there is involvement of the central cerebral veins, vein of Galen and/or straight sinus. This pattern is observed in approximately 16% of cases of cerebral venous thrombosis with multiple etiologies. Contrary to superficial sinus venous thrombosis, deep venous thrombosis can lead to major sequelae or death. Clinical presentations vary from headaches and nausea/vomiting to neurological symptoms and death. Neurologic deterioration can occur rapidly due to bilateral thalamic lesions and involvement of the corticospinal tracts. The purpose of this educational exhibit is to demonstrate the imaging findings in deep cerebral venous thrombosis as well as potential mimickers, providing the key findings for the diagnosis.
Materials and Methods
We reviewed the normal anatomy of deep cerebral venous system, discussed the clinical and imaging features of deep cerebral brain thrombosis and highlight the findings of its potential mimickers. To accomplish this we perform a search in our teaching files.
Results
Bilateral thalamic involvement is a hallmark of this condition and lesions usually extending to basal ganglia and periventricular white matter. Unilateral thalamic compromise occurs but is rare. Particular attention must be paid to hyperdense deep veins on CT or

absence/presence of filling defects on postcontrast MRI studies. Diffusion-weighted imaging (DWI) shows areas of restricted diffusion which may or may not correspond to the T2 abnormality and may show some contrast enhancement simulating true masses. Susceptibility-weighted imaging (SWI) shows hemorrhage and dilation of the central/deep venous system due to vasodilation of clot-filled veins. Key differential diagnoses include arterial infarcts, viral infection, ADEM, and masses especially when unilateral compromise is seen.

Conclusions

Deep venous brain thrombosis is a relatively uncommon condition with nonspecific symptoms that requires accurate diagnosis and treatment. Neuroimaging is the main test to diagnose this entity and rule out its principal differential diagnoses.



45 years old female with headache. There is a thrombus in the straight sinus seen in noncontrast CT and T1 weighted MRI images (arrows), with evidence of restricted diffusion involving the basal ganglia in ADC map consistent with venous infarct. SWI shows engorgement of the draining veins and presence of collateral circulation.

(Filename: TCT_eEdE-47_DCBT.jpg)

eEdE-80

6:30AM - 3:00PM

Deep Learning/Machine Learning: A Primer for Neuroradiologists

O Boyko[1], A Talebi[1], C Liu[2], P Cheng[1]

[1]University of Southern California, Los Angeles, CA, [2]University of Southern California Keck School of Medicine, Los Angeles, CA

Purpose
To provide a theoretical background and primer for neuroradiologists on Deep Learning/Machine Learning (DL/ML) and review use case scenarios and potential applications in neuroradiology.
Materials and Methods
1.To review recent research developments in "deep learning", particularly with respect to convolutional neural networks applied to image classification. 2. To illustrate fine-tuning of pretrained convolutional neural networks to recognize basic categories. 3. "Deep learning": a brief history of the renaissance of deep neural networks in machine learning. 4. Convolutional neural networks: how they work in image classification, and their increasingly accurate results outside of the medical domain. 5. Radiologic image classification summary of the literature as it relates to neuroimaging. 6. Define development and deployment workflows for building powerful deep learning solutions. 7. Introduce relevant toolkits and state-of-the-art deep learning computing platforms.
Results
Future cognitive assistance for neuroradiologists with vetted algorithms developed using Deep Learning/Machine Learning technology is evolving. Faster microprocessors are assisting in the evolution but development of curated large data sets to accelerate DL/ML is one rate-limiting step.
Conclusions
Deep Learning is rooted in machine learning and artificial neural networks, concepts which focus on teaching computers to learn to solve problems utilizing big data analytics. Faster microprocessors are assisting in the evolution but development of curated large data sets to accelerate DL/ML is one rate limiting step.

eEdE-101

6:30AM - 3:00PM

Diagnostic Features of Cerebral Venous Thrombosis in Trauma Patients

J Ortiz Jimenez[1], K Al-Ramadhani[2], C Torres[3]
[1]MCGILL UNIVERSITY - MONTREAL GENERAL HOSPITAL, MONTREAL, QC, [2]McGill University, Montreal, -- SELECT --, [3]McGill University, Montreal, Quebec

Purpose
Early diagnosis of cerebral venous thrombosis in trauma patients is important as it may lead to hemorrhagic infarction, increased intracranial pressure and other complications that can worsen the prognosis of the patient. We want to create an interactive presentation that will serve as a learning tool in the diagnosis of cerebral venous thrombosis in the setting of

trauma. We will use images extracted from the database of our institution, a major trauma referral center in Montreal (Canada).
Materials and Methods
An interactive electronic presentation will be created in order to explain the relevant anatomy, trauma mechanisms, imaging protocols, radiologic findings, possible diagnostic pitfalls and differential diagnosis.
Results
Venous sinus thrombosis is a challenging diagnosis in trauma patients. Previous studies have determined a high prevalence of dural sinus thrombosis in patients with fractures overlying the dural sinuses. However, in some patients venous thrombosis can develop in the absence of fracture, as a result of certain trauma mechanisms, due to the presence of compressive collections or associated comorbidities (prolonged hospital admission, surgical complications). A proper computed tomography (CT) or magnetic resonance imaging (MRI) venography and a precise knowledge of anatomy, particularly of anatomical variants, are key fundamentals in the correct diagnosis of this entity.
Conclusions
Our interactive presentation will allow the viewer to learn about the relevant anatomy, imaging protocols, radiologic findings, differential diagnosis and diagnostic pitfalls for the imaging diagnosis of cerebral venous thrombosis in the setting of trauma.

eEdE-107

6:30AM - 3:00PM

Differentiation of Diffuse Axonal Injury Versus Fat Embolism Syndrome Using MRI Imaging

K Naeini[1], N Akle[1]
[1]*Texas tech University, El Paso , TX*

Purpose
1. List the indications for imaging in the trauma setting. 2. Review relevant advanced magnetic resonance imaging (MRI) techniques. 3. Become familiar with clinical presentation and evolution of diffuse axonal injury (DAI) and fat embolism syndrome (FES) in the polytrauma setting. 4. Describe the characteristic imaging appearance of DAI and FES using advanced MRI techniques.
Materials and Methods
In diffuse axonal injury and cerebral fat emboli clinical histiry is the key: a) DAI: -Patient presents obtunded or with altered mental status (AMS) at time of presentation. -No lucent interval. -Unable to wean patient from ventilator despite lack of sedatives. b) FES: -Patient presents with a history of long bone fracture. -Lucent interval with AMS 12-72 hours after initial presentation. -May have co-current pulmonary embolus (PE). Trauma Imaging – a) Head CT without contrast. -Excellent sensitivity for detection of acute hemorrhage, mass

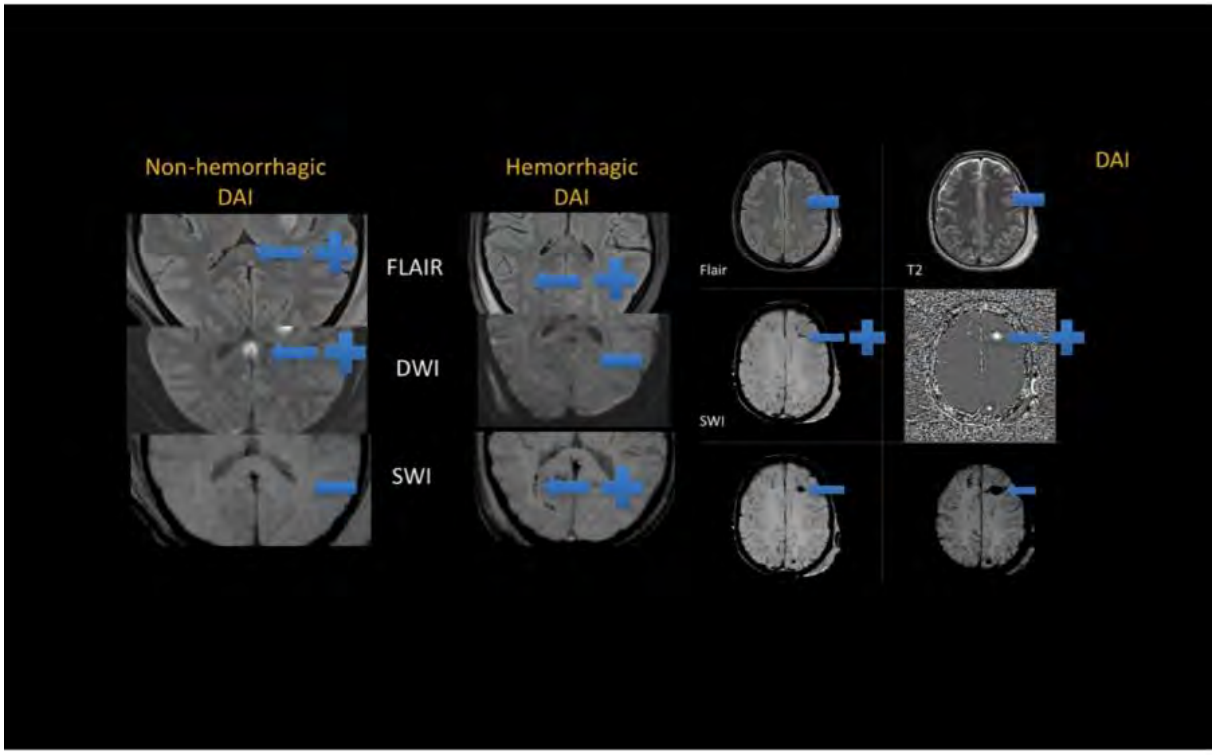
effect, ventricular size/configuration, bone injuries. -Widespread availability, rapid scanning, compatible with support devices. Limitations of head CT - Poor sensitivity for: -Small lesions adjacent to bony surfaces. -Non-hemorrhagic lesions. -DAI multiple small focal lesions. -Increased intracranial pressure (ICP). -Cerebral edema. -Hypoxic-ischemic injury (HIE). => MRI is used for the above. b) MRI head without contrast - limitations. -Limited availability in the acute trauma setting. -Long imaging times. -Sensitive to patient motion. -Incompatible with various life support devices. -Relatively insensitive to subarachnoid hemorrhage. -Risk of scanning with various indwelling devices – pacemakers, aneurysm clips, foreign bodies, etc.

Results

Imaging recommendations for DAI: -Best imaging tool is MR. -Protocol advice: a) Nonhemorrhagic: FLAIR + DWI ± DTI tractography. b) Hemorrhagic: SWI best (use T2* GRE if not available). Imaging Features: a) The image patterns of FES evolves with time and could be separated into 3 major types: -Type 1: Scattered cytotoxic edema in acute stage. -Type 2: subacute stage, confluent cytotoxic edema or vasogenic edema. -Type 3: late stage, chronic sequelae. b) MRI findings of DAI: A. FLAIR: a. Nonhemorrhagic DAI: Hyperintense foci. b. Hemorrhagic DAI: Hypointense foci. B. GRE: Most sensitive "routine" sequence. a. Microbleeds may be visible only on GRE. C. SWI: Depicts significantly more DAI foci than GRE. D. DWI: May show foci of restricted diffusion.

Conclusions

DAI: -Multiple lesions at gray white matter junctions. -Associated parenchymal contusions. -No lucent interval. FES: -Multiple lesions at deep and cortical watershed regions. -No cortical contusions. -Lucent interval. -Long bone fracture.



(Filename: TCT_eEdE-107_DWIandDAI.jpg)

eEdE-51

6:30AM - 3:00PM

Do You Smell That? The Olfactory System From Anosmia to Olfactory Hallucinations

T Uribe[1], K Wang[1], D Dunaway[2], C Lincoln[2], N Nguyen[1]
[1]Baylor College of Medicine, Houston, TX, [2]Baylor College of Medicine, Houston , TX

Purpose
The purpose of this exhibit is to provide a systematic review of olfactory anatomy and pathologies with pertinent MRI findings affecting odor reception, transmission, and processing.
Materials and Methods
A brief summary of the institutional brain MRI protocol is described. A targeted review then will be provided highlighting pertinent anterior cranial fossa anatomy with an emphasis on characteristic locations for olfactory function disruption (such as the nasal cavity, anterior crania fossa and the mesial temporal lobe). Moreover, the olfactory pathway is described in the context of the pertinent anatomy (from the olfactory epithelium to the respiratory

centers). Lastly, a systematic approach to interpreting brain MRI incorporating the spectrum of potential olfactory pathology and corresponding disease-specific imaging findings is proposed, and reinforced with case-based illustrative examples.

Results

The olfactory pathway involves the respiratory epithelium, olfactory nerves, olfactory bulbs, olfactory tract, accessory olfactory nuclei, olfactory tubercle, the pyriform and enterorhinal cortex, as well as portion of the amygdala. The respiratory epithelium comprises half of the upper nasal cavity mucosa, and possesses olfactory receptor neurons, composed of bipolar cells with unmyelinated axons, that transmit olfactory information centrally. Such cells have dendritic projections and cilia through the mucosa that are covered and protected by mucous. Axons extend through the cribriform plate to the bulb, tracts, and respiratory centers. Pyriform cortex identifies odor. The amygdala associates it with social contextualization, and the entorhinal cortex associates it with memory. Lesions affecting the upper nasal mucosa, cribiform plate, olfactory bulbs, tract, and primary olfactory cortex may result from anosmia to olfactory hallucinations. Olfactory dysfunction can be total (anosmia), incomplete (hyposmia), distorted (dysosmia), or unreal (phantosmia). Lesions affecting these locations can result from trauma (ethmoid fractures, traumatic brain injury), neoplasm (esthesioneuroblastoma, squamous cell carcinoma, melanoma, lymphoma, anterior cranial fossa meningioma, glioma, metastases of the olfactory cortex), infection (tuberculosis, cryptococcus), vascular insult, or neurodegenerative disease (Alzheimer or Parkinson).

Conclusions

An intimate understanding of the olfactory pathway and spectrum of pathology involved allows for a methodical evaluation of imaging in patients presenting with anosmia or hyposmia.



(Filename: TCT_eEdE-51_Esthesio.jpg)

eEdE-64

6:30AM - 3:00PM

Don't Miss Blind Spots! Avoiding Common Interpretive Errors in Brain Imaging

A Farkas[1], E Parker[1], M Khan[2]
[1]University of Mississippi Medical Center, Jackson, MS, [2]University of MS medical center, Madison, MS

Purpose
The "blind spots" in the brain are areas in which the radiologist is prone to make diagnostic errors during evaluation. This interactive electronic exhibit will highlight common interpretive errors related to these "blind spots."
Materials and Methods
Two main types of errors in imaging interpretation are perceptual errors and interpretive or cognitive errors. With perceptual error, the radiologist fails to see the abnormality, resulting in a false-negative interpretation. This can be related to many reasons including inexperience, motion, high study volume, incorrect protocol, tunnel vision, "satisfaction of search," edge artifacts, or an incomplete mental checklist. Interpretive error is when an abnormality is identified; however, the significance of the finding is not recognized and can result in false-positive interpretation. An example is when normal anatomic variance is reported incorrectly as a pathological finding.
Results
In particular, certain areas of brain imaging are more prone to interpretation pitfalls due to densely compact anatomy with overlap of vascular, neural, soft tissue and bony elements, which have many variants, making it harder to assess pathology. Hence, it is important that radiologists are cognizant of the pitfalls that can lead to false-positive and false-negative results. These blind spots are more likely to be misinterpreted by radiologists if a targeted search pattern of key areas is not employed while reviewing brain images. This educational exhibit will feature pathology related to blind spots in brain imaging, including cerebral sulci, dural sinuses, orbits, cavernous sinuses, clivus, Meckel's cave, brainstem, basilar artery, skull base, jugular fossa, and parapharyngeal soft tissues.
Conclusions
Radiologists will have greater success in identifying abnormalities in these locations when they are consciously sought as a part of a search pattern and may be incorporated into standard templates if used by the department, institution, or practice. This is especially important for trainees and general radiologists.

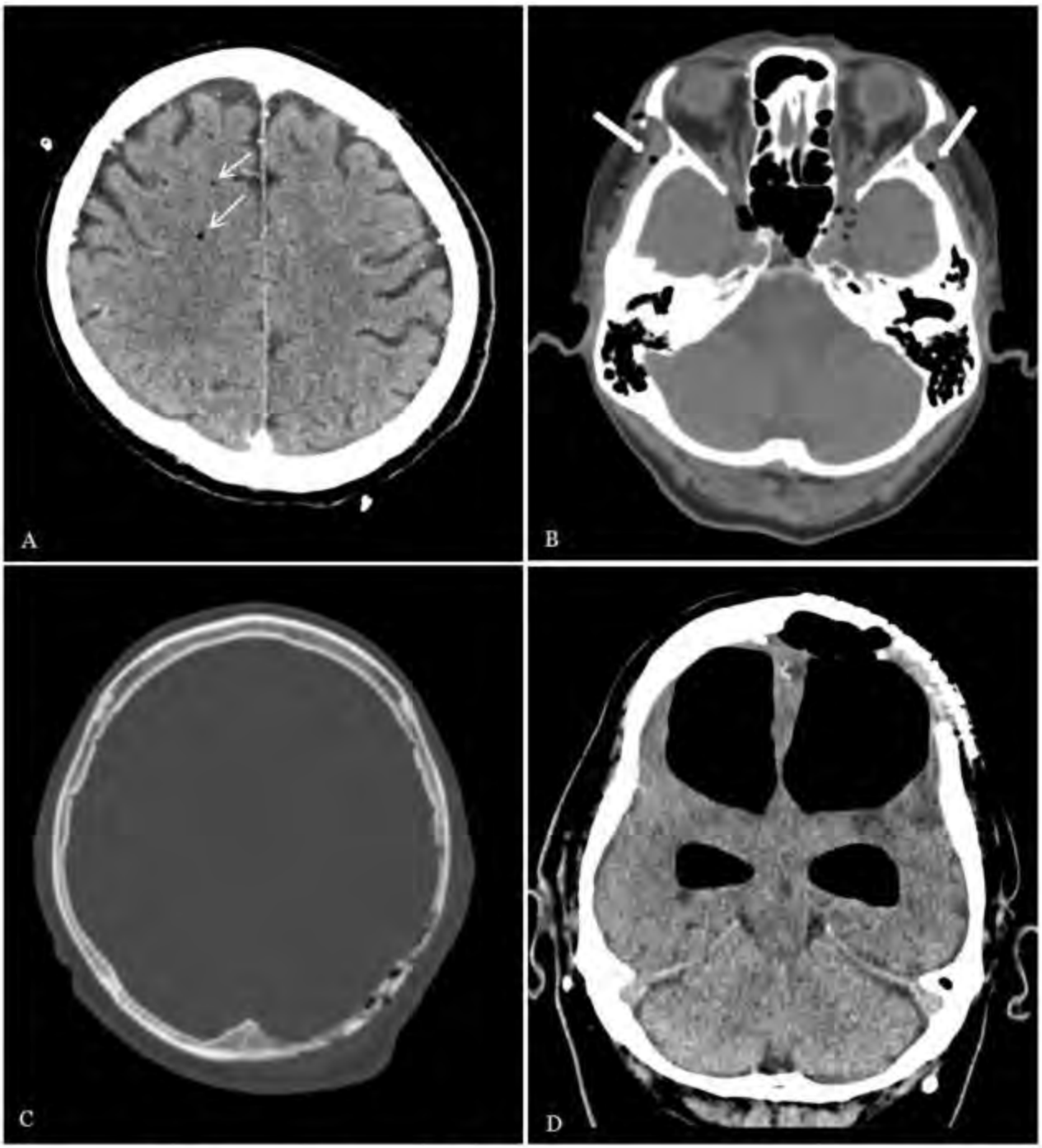
eEdE-28

6:30AM - 3:00PM

Don’t Be an Air-Head: Know the Various Causes of Gas on Head CT

S Swaminathan[1], L McAdory[2], R Chen[3]
[1]SingHealth, Singapore, Singapore, [2]Singapore General Hospital, Singapore, Singapore, [3]Singapore General Hospital, Singapore, Not Applicable

Purpose
Abnormal gas on a CT head is an infrequent but potentially challenging diagnosis for the neuroradiologist. In this pictorial review, we illustrate several interesting and less commonly seen causes of gas detected on a head CT.
Materials and Methods
Several less commonly seen cases of intracranial gas were collated from the authors' personal database, and organized according to anatomic location. For each case, we will attempt to elucidate the mechanism and underlying etiology of the air seen on head CT.
Results
Abnormal gas, from innocuous subcutaneous gas to life-threatening arterial gas embolism, may be encountered in routine head CT imaging. Detection and accurate localization of these abnormalities are critical as missed or delayed diagnosis may adversely impact the clinical outcome. Classifying abnormal gas based on its anatomical location can be helpful in determining its etiology. Arterial air embolism is a critical abnormality that appears as tiny, round or branching gas densities within the cortical sulci or peripheral brain parenchyma, localized in the small distal arterial branches. Venous gas is seen most frequently in the cavernous sinuses, presumably after iatrogenic IV injection or trauma. In determining the cause of intra-ventricular gas, one must be cognizant of its communication with the subarachnoid space and the cerebrospinal fluid space of the spinal cord. Air in the skull, extracranial soft tissues, and extra-axial spaces of the brain may be related to local gas-forming infection or underlying fistulas from the paranasal sinuses or mastoid air cells.
Conclusions
This article aims to illustrate some interesting cases of abnormal gas detected on head CT imaging, organized by anatomical location.



A few cases of abnormal gas on CT head: **Image A** demonstrates arterial gas embolism with a few tiny gas locules (short arrows) noted within the cortical and sub-cortical regions, possibly located in the small distal penetrating arterioles. A tiny gas locule was also seen within the pericallosal artery (not shown). Subsequent MRI (not shown) demonstrated acute cortical infarct affecting the right frontal lobe. **Image B** demonstrates small round gas densities within both cavernous sinus, small venules in the bilateral temporal fossae and bilateral pterygoid venous plexus (not shown), in keeping with venous gas embolism. **Image C** demonstrates left parieto-occipital intra-osseous gas from calvarial osteomyelitis. **Image D** demonstrates extensive recalcitrant intraventricular and subarachnoid gas from a post-surgical persistent fistula between the left frontal sinus and adjacent subarachnoid space. The patient had several failed revision surgeries.

(Filename: TCT_eEdE-28_Airhead.JPG)

eEdE-73

6:30AM - 3:00PM

DSC-MR Perfusion in Clinical Practice: A Primer for Residents & Fellows

A Gandhi[1], A Chan[2], P Moftakhar[3]
[1]Christiana Care Healthcare System, Newark, DE, [2]Christiana Care Health System, Wilmington, DE, [3]Christiana Healthcare system, Newark, DE

Purpose
The purpose of this electronic educational exhibit is to provide a step-by-step guide for residents and fellows on how to implement and problem solve with dynamic susceptibility contrast (DSC) MR technique in a variety of clinical scenarios which they will encounter in the reading room.
Materials and Methods
The authors will employ Microsoft Powerpoint and various other graphics software/applications to illustrate the fundamental concepts of DSC-MR, including medical physics and its clinical applicability.
Results
Bolus tracking MRI allows in vivo analysis of physiological information that complements morphological findings on conventional MRI which aids in the work-up and differentiation between CNS conditions including primary CNS tumors, metastases, tumefactive MS, infections, and vascular disease. This technique measures cerebral perfusion by extracting valuable hemodynamic parameters, including CBV, CBF, MTT, and leakage. Technique optimization parameters of interest include: TR, TE, flip angle, and leakage correction. Clinical concepts in perfusion imaging related to tumor biology that residents and fellows should be familiar with include: pseudoprogression, true-progression, pseudo-response, and peritumoral edema.
Conclusions
This electronic educational exhibit serves a primer for residents and fellows to understand the fundamental concepts of MR perfusion imaging. In addition, common pitfalls of DSC-MR will be discussed along with their associated remedies. Lastly, the clinical applications of this technique will be discussed.

eEdE-68

6:30AM - 3:00PM

Dural Based Lesions - A Pictorial Essay

R Glikstein[1], C Torres[1], V Tsehmaister-Abitbul[1], F Essbaiheen[1], J Davila[1]
[1]University of Ottawa, Ottawa, Ontario

Purpose
To present dural-based lesions, common and other less common but important pathologies to be included on the differential diagnosis.
Materials and Methods
Retrospective study from January 2008 to December 2016 including patients with neurosarcoidosis, chondroma, Wegener's, plasmacytoma, dural lymphoma, leptomeningeal ca mimicking subarachnoid hemorrhage, en-plaque meningioma, high grade meningioma, hemangiopericytoma, solitary fibrous tumor, pachymeningeal met of breast and prostate ca. 3T MRI of the brain with pre- and post-Gd sequences in three planes was performed.
Results
The most common pathology of the meninges is meningioma, which may be asymptomatic until reaching certain size or cause symptoms by compression of anatomical structures, presenting with headache, loss of vision, seizures or other neurological findings. They are followed in frequency by dural or leptomeningeal metastasis, generally related to breast ca or prostate ca, most of the time symptomatic. A series of other less frequent pathologies may be identified, such as hemangioperycitoma, multiple myeloma-plasmacytoma, even less common Wegener's, solitary fibrous tumor or chondroma. These entities also may express by compression symptoms of the adjacent brain parenchyma. Some pathologies may mimic dural lesions as observed on patient with intracranial hypotension.
Conclusions
The more common dural-based lesions are meningioma and metastasis. Other less frequent pathologies may be found as shown on this presentation.

eEdE-55

6:30AM - 3:00PM

Exhibit of the Major Changes in the 2016 World Health Organization Revised Central Nervous System Neoplasm Classification

Y Xie[1], S Imbesi[2], J Chen[3]
[1]University of California San Diego, San Dieog, CA, [2]University of California, San Diego, San Diego, CA, [3]San Diego VA / UCSD Med. Center, La Jolla, CA

Purpose
To discuss and review relevant major changes in the revised 2016 WHO Classification of neoplasms of the central nervous system (CNS) for practicing neuroradiologists.
Materials and Methods
Highlight the changes in the revised 2016 WHO Classification of neoplasms of the central nervous system including: tumor additions, deletions and revisions as well as the genetic markers. This will be accomplished with case-based examples of these changes.

Results
Revisions/Additions of the new classification will include: Diffuse astrocytic and oligodendroglial neoplasms: Astrocytoma (IDHwt/IDHmut), Diffuse astrocytoma (IDHwt/IDHmut), Anaplastic astrocytoma (IDHwt/IDHmut), Glioblastoma (IDHwt/IDHmut), Oligodendroglioma, (1p/19q-codeleted), and diffuse midline glioma (H3 K27M mutant). Meningioma: Brain invasion as criteria for atypical meningioma. Ependymal tumors: Ependymoma (RELA fusion positive). Neuronal and mixed neuronal-glial tumors: Diffuse leptomeningeal glioneuronal tumors. Mesenchymal, nonmeningothelial tumors: Solitary fibrous tumors/hemangiopericytoma combined into a single category. Deletions of new classification will include: Gliomatosis cerebri, protoplasmic and fibrillary astrocytoma variant, cellular ependymoma variant, and "primitive neuroectodermal tumor" terminology.
Conclusions
Central nervous system neoplasms are an extremely important component to the practices of neuroradiologists. The understanding of the changes in the revised 2016 WHO Classification is essential for clear communication and collaboration with treatment teams by using up to date, evidence-based classification terminology.

eEdE-29

6:30AM - 3:00PM

From the Womb to the Tomb: A Comprehensive Imaging Review of Neurological Manifestations of Herpesviridae in Humans

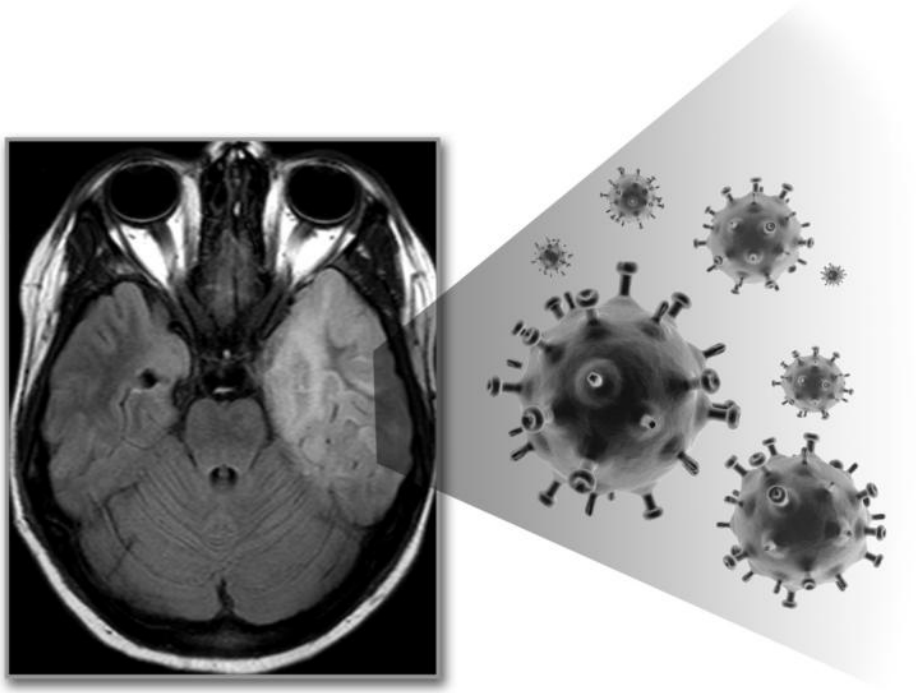
W Lindstrom[1], E Andrews[1], C Perez[1], M Pinho[1]
[1]*University of Texas Southwestern Medical Center, Dallas, TX*

Purpose
Herpesviridae is a complex family of eight DNA viruses that affects people of all ages, and in turn generates a vast spectrum of pathology. While herpes can infect multiple organ systems of both humans and animals, it has a particularly robust affinity for the central and peripheral nervous systems. This makes it imperative for the neuroradiologist to have a stout knowledge of the different pathological manifestations of this unique virus. We will provide a comprehensive neuro-imaging review of Herpesviridae infection in both adult and pediatric patients organized by the eight distinct viral types.
Materials and Methods
Representative applicable cases were obtained from multiple tertiary adult and pediatric academic medical centers. Cases will be organized into the eight applicable herpesviridae types affecting humans and further separated into both pediatric and adult patients.
Results
Simplexvirus (HSV1/HSV2) classically manifests neurologically as a temporal lobe encephalitis. HSV-2 causes neonatal encephalitis, with a peripartum onset of infection 2-4 weeks after delivery. It also can manifest in the brainstem and cerebellum, with early CT and

MR findings of edema and diffusion abnormalities, and later resulting in atrophy, cysts, and calcifications. HSV-1 causes both adult and pediatric encephalitis, predominantly affects the limbic system, and can become hemorrhagic. Varicellovirus (HHV-3) is classically acquired as a child or adult and manifested as "chicken pox", but can be transmitted vertically to the fetus during active infection, resulting in TORCH-like neurologic manifestations. The Zoster virus typically lies latent in peripheral or cranial nerves, but can become active resulting in Varicella Zoster Vasculitis, Ramsay Hunt Syndrome (CN7/CN8) or HSV Opthalmicus (V1). Epstein-Barr virus (HHV-4) causes Burkitt's and CNS Lymphoma, PTLD, nasopharyngeal carcinoma, and infectious mononucleosis. Cytomegalovirus (HHV-5) can cause encephalitis, meningitis, ventriculitis, etc., most commonly in the immunocompromised patient. Congenital CMV also is the most common intrauterine infection in the USA, with late manifestations including intracranial calcifications and microcephaly. Roseolovirus genus comprises both HHV-6A, HHV-6B and HHV-7. HHV-6 appears to much more commonly result in clinical symptomatology, most frequently a viral exanthem, but also can result in a limbic or insular pattern encephalitis and has been implicated in pediatric acute necrotizing encephalopathy. HHV-8 is most synonymous with Kaposi Sarcoma, which is seen most commonly in the immunosuppressed, and manifests as multiple avidly enhancing nodal, skin, and mucosal nodular lesions, with rare involvement of the CNS.

Conclusions

Herpesviridae, a ubiquitous family of DNA viruses in humans, has dynamic and far-reaching manifestations causing significant neurological morbidity across all age groups. Prompt recognition of the often typical associated imaging abnormalities by neuroradiologists is key to early institution of therapy and improved outcomes.



(Filename: TCT_eEdE-29_herpes.jpg)

eEdE-26

6:30AM - 3:00PM

Hemodynamics and Imaging of Intracranial Pressure--Hypertension, -Normotension and -Hypotension.

S Kanekar[1]
[1]*Penn State MiltonHershey Medical Center, Hershey, PA*

Purpose
1. To discuss the normal hemodynamics of the intracranial pressure. 2. To discuss with illustrations the imaging findings and causes of intracranial -Hypertension, -Normotension and -Hypotension.
Materials and Methods
Intracranial pressure (ICP) is defined as the pressure within the craniospinal compartment, a closed system that comprises a fixed volume of neural tissue, blood, and cerebrospinal fluid (CSF). Monro-Kellie doctrine states that an increase in the volume of one intracranial compartment will lead to a rise in ICP unless it is matched by an equal reduction in the volume of another compartment. We retrospectively reviewed the imaging studies from our PACS of 750 patients with neurological complications due to abnormal intracranial pressure, which form the basis of this exhibit. All patients had CT and MRI exam of brain. In addition, 73 patients had advanced imaging that includes perfusion imaging, and diffusion tensor imaging (DTI).
Results
For ease of understanding, this exhibit is reviewed under three broad categories of Intracranial pressure (ICP): -IC Hypertension, -IC Normotension and –IC Hypotension. Depending on the specific causes exhibit has been further categorized into: (A) Increased Intracranial Pressure: Space-Occupying Lesions: Intracerebral hemorrhage Epidural hemorrhage Subdural hemorrhage Tumor Abscess; Diffuse Cerebral Edema Meningitis Encephalitis Hepatic encephalopathy Reye's syndrome Acute liver failure Electrolyte shifts Dialysis Hypertensive encephalopathy Postanoxic brain injury Lead encephalopathy Uncompensated hypercarbia Head trauma Diffuse axonal injury Hydrocephalus Subarachnoid hemorrhage Meningitis Aqueductal stenosis Idiopathic Miscellaneous Pseudotumor cerebri Craniosynostosis Venous sinus thrombosis. (B) Normal-Pressure Hydrocephalus. (C) IC Hypotension: 1. True hypovolemic state 2. Traumatic CSF leaks a. Definite trauma (MVAs, sports injuries, etc) b. Thecal holes and rents from LPs and epidural catheterizations c. Spinal and cranial surgeries including skull base and some sinus surgeries d. Proximal brachial plexus avulsion injuries, nerve root avulsions 3. CSF shunt over drainage 4. Spontaneous CSF leaks a. Undetermined cause b. Pre-existing weakness of the dural sac, surgical anatomical observations i. Meningeal diverticula ii. Disorders of

connective tissue matrix 1. Marfan syndrome, c. Trivial trauma in the setting of preexisting dural weakness d. Spondylotic spurs, herniated disk.
Conclusions
1. For participants, this exhibit will be a core learning module to understand the hemodynamics of the intracranial pressure and pathophysiology of intracranial -hyper, -normo and –hypotension. 2. We illustrate the various imaging findings of the intracranial hypo and hypertension and imaging "pearls" to the underlying causes.

eEdE-42

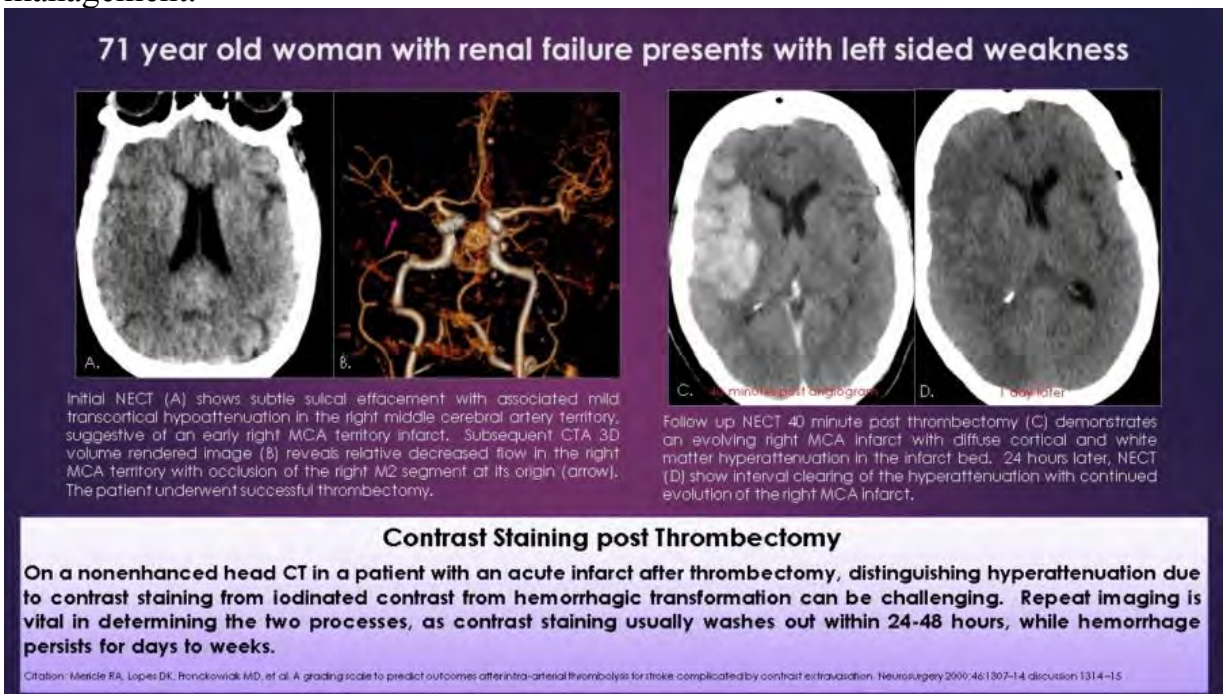
6:30AM - 3:00PM

Hemorrhage or No Hemorrhage, That is the Question: Pictorial Review of Non-Traumatic Causes of Hemorrhage and Mimics

C Chan[1], S Yoon[1], J Rodulfa[1], B Devenney-Cakir[1], J Li[1]
[1]*Einstein Medical Center, Philadelphia, PA*

Purpose
Nontraumatic causes of intracranial hemorrhage encompass a wide spectrum of pathology but have one underlying commonality: if the intracranial hemorrhage is misdiagnosed, it can be life threatening. Therefore, prompt and correct identification of intracranial hemorrhage as well as recognition of potential underlying pathology are essential for good patient care. Knowledge of mimics of intracranial hemorrhage is equally important, as patient management will vary significantly. We will discuss common and uncommon causes of intracranial hemorrhage as well as their mimics, focusing on imaging characteristics that may help differentiate between the two diagnoses.
Materials and Methods
We will present a wide range of causes of intracranial hemorrhage from our institution, including parenchymal, subarachnoid, interventricular, and subdural/epidural hemorrhages. Pathologic conditions that can mimic intracranial hemorrhage also will be presented. Cases will be organized by etiology, including vascular, coagulopathic, neoplastic, infectious, drug abuse, and systemic diseases. At the end of this activity, the radiologist will be able to accurately diagnose an intracranial hemorrhage, identify potential underlying causes, and discuss mimics of intracranial hemorrhage.
Results
Our exhibit includes a spectrum of intracranial hemorrhage caused by different disease entities, excluding trauma. Acute intracranial hemorrhage cases range from common entities including hemorrhagic conversion of an ischemic stroke, hypertensive hemorrhage, cavernous malformation, amyloid angiopathy, metastasis, and glioblastoma multiforme to less common pathologies such as venous sinus thrombosis, arteriovenous malformation, hemorrhagic variant of posterior reversible encephalopathy syndrome, herpes encephalitis, drug abuse, and hemorrhagic diathesis in the setting of leukemia.

Conclusions
Nontraumatic causes of intracranial hemorrhage vary considerably according to patient demographics, pertinent medical and surgical history, and clinical presentation. Prompt and accurate identification of potential underlying pathology on imaging can significantly improve patient outcome. Knowledge of possible mimics of intracranial hemorrhage is equally as important as investigation for those processes will help further guide patient management.



(Filename: TCT_eEdE-42_hemorrhageorno.jpg)

eEdE-19

6:30AM - 3:00PM

How We Do It: A Modular Approach to Planning Trans-Sulcal Parafascicular Subcortical Surgery Using 3D Tractography and an Integrated Planning Solution

M Fukui[1], J Jennings[1], S Chakravarthi[1], A Monroy Sosa[1], R Rovin[1], J Celix[2], S Walia[1], A Kassam[1]
[1]Aurora St. Luke's Medical Center, Milwaukee, WI, [2]Aurora St Luke's Medical Center, Milwaukee, WI

Purpose
To provide an overview of a modular approach to planning corridor-based parafascicular surgery taking into account key cortical, sulcal, and white matter anatomy. To review the concept of the white matter framework that underlies the main surgical trajectories. To report our experience in a multidisciplinary service line model in which preoperative planning is performed primarily by a neuroradiologist and reviewed and refined by a neurosurgeon.

Materials and Methods

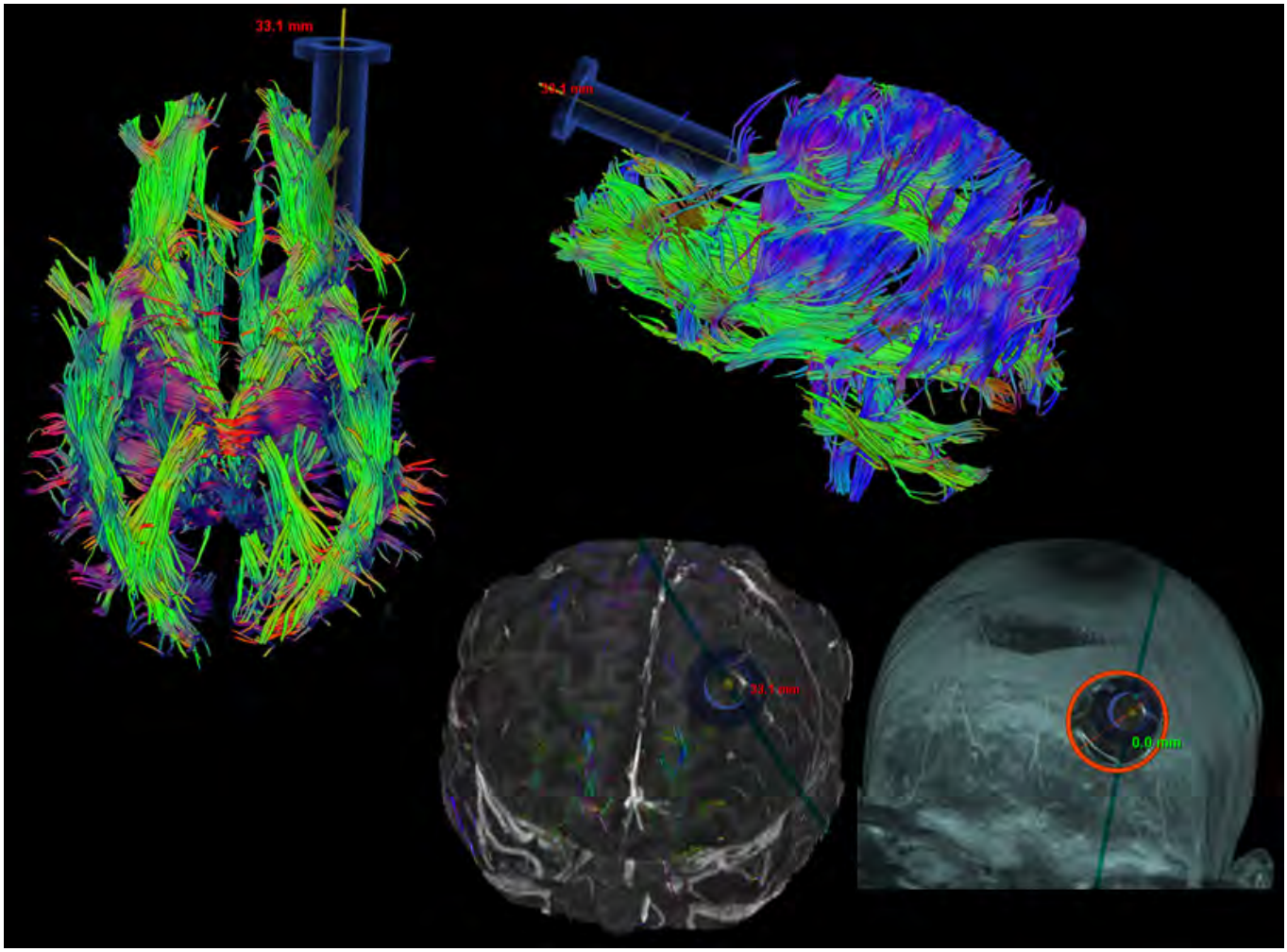
We identified several major, fundamental white matter and cortical structures that are reliably visible on clinically acquired structural diffusion tensor imaging (DTI) and that served as the primary constraints of parafascicular surgical corridors. The major white matter structures include: The superior longitudinal fasciculus (SLF); vertical rami of SLF (VR); corona radiata/corticospinal tracts (CR); cingulum (C); arcuate fasciculus (AF); inferior fronto-occipital fasciculus (IFOF); uncinated fasciculus (UF); optic radiations (OR); inferior longitudinal fasciculus (ILF). The primary cortical constraints include: dominant pars triangularis (Broca's); Wernicke's; precentral gyrus; superior parietal lobule; calcarine cortex; supplementary motor area (SMA).

Results

We established a scaffold of eloquent white matter and cortex that organized our surgical trajectories into the following preliminary modules, which continue to be refined: Anterior Superomedial; Anterior Superolateral; Anterior Inferomedial; Anterior Inferolateral; Posterior Superomedial; Posterior Superolateral; Posterior Inferomedial; Posterior Inferolateral. Peri-Rolandic and posterior fossa lesions were addressed separately.

Conclusions

In our experience, a modular approach to planning of corridor-based parafascicular surgery yielded surgical trajectories that were adopted by the operating surgeon, typically with only minor adjustments. Establishing a modular framework for surgical planning enhances understanding of complex functional anatomy in order to facilitate consideration of eloquent white matter anatomy that was previously inconspicuous.



(Filename: TCT_eEdE-19_2016-12-09_183829.jpg)

eEdE-85

6:30AM - 3:00PM

Hydrocephalus: The Radiologist's Handbook

L Lai[1], W Gibbs[1]
[1]*University of Southern California, Keck School of Medicine, Los Angeles, CA*

Purpose
Hydrocephalus is a common but important entity, as it may require neurosurgical intervention with shunting or endoscopic third ventriculostomy to relieve symptoms. It can be categorized into communicating/intraventricular and noncommunicating/extraventricular forms. Hydrocephalus varies in etiology across age groups and can be diagnosed by a variety of imaging methods. Our purpose is to evaluate the causes of hydrocephalus across age groups and to explore the utility of contemporary imaging modalities in diagnosis.

Materials and Methods

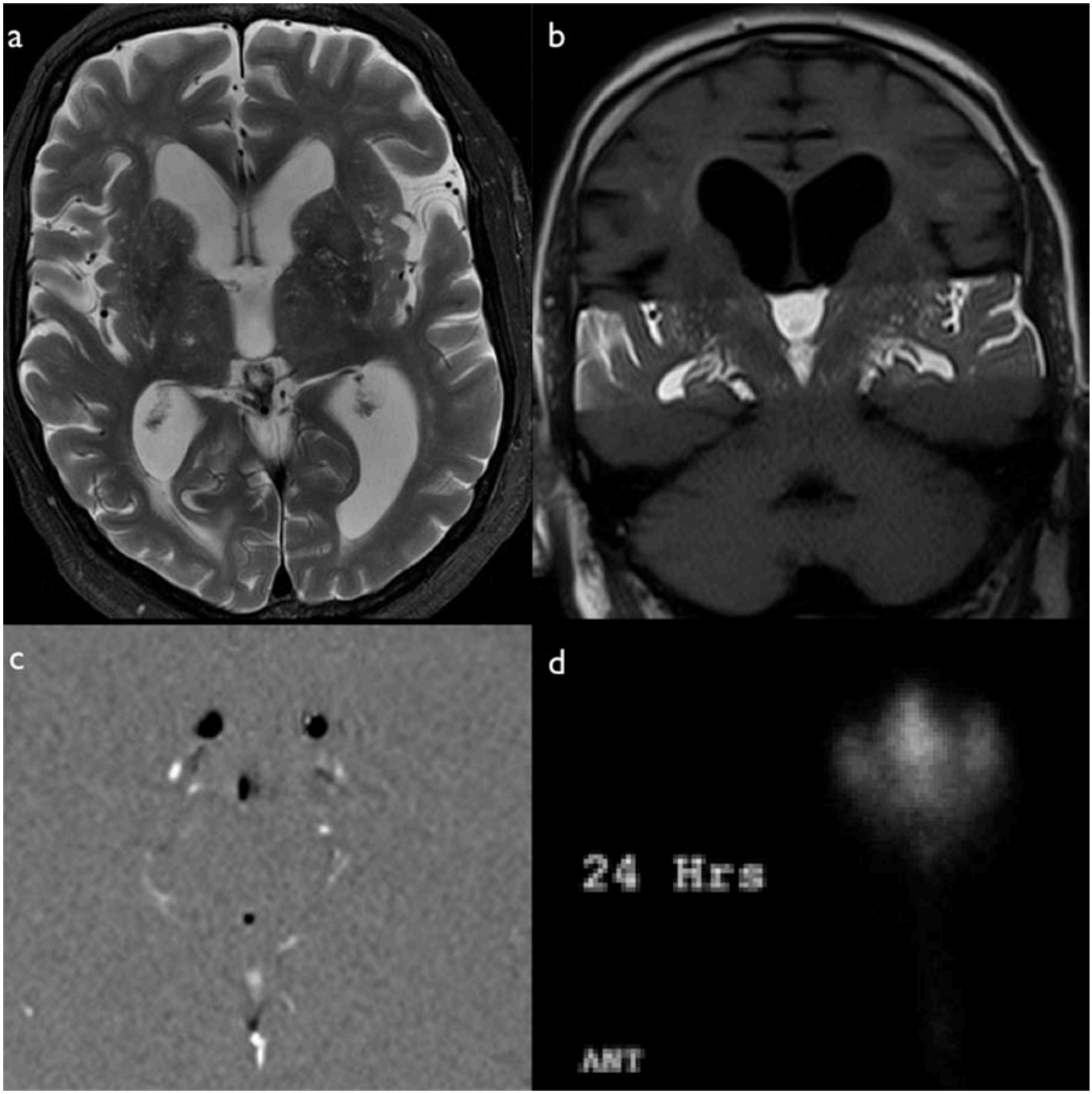
Based upon a thorough review of the literature and experience at our institution, we present a case-based approach to the common etiologies of pediatric and adult hydrocephalus. In addition, we describe the utility and efficacy of different imaging modalities and techniques used to diagnose hydrocephalus, including nuclear medicine, traditional CT and MRI (morphologic imaging), and dynamic MRI (phase-contrast and spin-tagging).

Results

Key etiologies of both communicating and noncommunicating hydrocephalus in pediatric patients include tumors, germinal matrix hemorrhage, aqueductal stenosis, Chiari malformations, and Dandy-Walker malformation. In adults, important etiologies include tumors, colloid cysts, normal pressure hydrocephalus, and sequela of subarachnoid hemorrhage or infectious or neoplastic meningitis. We highlight the current and emerging techniques for evaluating hydrocephalus and briefly discuss the etiology, clinical presentation, diagnosis, and management of hydrocephalus in these various settings. The example figure demonstrates a case of normal pressure hydrocephalus (NPH), which was corroborated by multiple imaging modalities. Normal pressure hydrocephalus was initially suspected on MRI due to findings of enlarged ventricles out of proportion to sulcal enlargement without an obstructing lesion (a). Time-SLIP, a recently described technique used to measure bulk CSF flow through spin-labeling, showed loss of normal reflux of CSF into the ventricles (b). Phase-contrast imaging revealed hyperdynamic flow (>20 ml/min) in the cerebral aqueduct (c). Finally, Indium-111 DTPA radionuclide cisternography showed prominent activity in the ventricles and lack of activity over the cerebral convexities at 24 hours (d).

Conclusions

Recognition of the various etiologies of hydrocephalus in both the pediatric and adult population is vital to determine the proper course of care. Likewise, knowledge of the utility of different imaging resources is important to select the most appropriate examination for effective diagnosis and follow up.



(Filename: TCT_eEdE-85_NPH.jpg)

eEdE-91

6:30AM - 3:00PM

Hypoxic-Ischemic Encephalopathy: A Systematic Review of Mechanisms of Injury and Patterns of Cerebral Involvement

A Hilario[1], E Salvador[1], P Martin[1], L Koren[2], G Ayala[3], F Ballenilla[1], J Millan[4], A Martínez de Aragón Calvo[5], A Ramos[6]

[1]Hospital 12 de Octubre, Madrid, Spain, [2]Hospital 12 de Octubre, madrid, spain, [3]Hospital 12 de octubre, Madrid, Madrid, [4]Hospital Puerta del Sur, Mostoles, Madrid, -- SELECT -- , [5]Hospital 12 de octubre, Madrid, Spain, [6]Hospital Madrid Puerta del Sur, Mostoles, Madrid, Spain

Purpose

Hypoxic-ischemic encephalopathy (HIE) is a significant cause of mortality and severe neurologic disability in both children and adults. Treatment of HIE consists largely of supportive care. Many of these treatment strategies, including hypothermia, have a limited window of effectiveness, making early detection of injury critically important. The objectives of this review are the following: 1) to describe the pathophysiological mechanisms involved in HIE, 2) to establish the differences between HIE in preterm and term population, older children and adults, and 3) to define the utility of conventional and functional MR imaging in the early diagnosis and predicting outcome of HIE.

Materials and Methods

Patterns of hypoxic-ischemic encephalopathy are reviewed using a selection of representative cases collected since 2010 through 2016 at high complexity tertiary university hospital for children and adults.

Results

Between 24 and 40 weeks of gestation, the human brain undergoes rapid changes that make the developing brain vulnerable to injury from hypoxia-ischemia. Key developmental processes during this time include the development of cerebral white matter, proliferation zones (dorsal cerebral subventricular zone and ventral germinative epithelium of the ganglionic eminence) and neuronal structures such as thalamus, cerebral cortex and basal ganglia. The classical imaging abnormalities in HIE involve three major types of lesions (periventricular leukomalacia, basal ganglia/thalami lesions and multicystic encephalopathy). Focal noncystic white matter injury is the most commonly recognized pattern of brain injury in the preterm population. In term babies with HIE, two major types of injury are involved: a watershed predominant pattern involving the white matter, particularly in the vascular watershed, extending to cortical gray matter following severe insult, and a basal ganglia predominant pattern involving the deep gray nuclei and perirolandic cortex, involving the cortex in severe injuryHIE in adults is more often a result of cardiac arrest and cerebrovascular disease, with secondary hypoxemia. Mild to moderate global ischemic insults to the brain usually result in watershed zone infarcts. Profound hypoxia-ischemia in this population affects the gray matter structures: the basal ganglia, thalami, cerebral cortex (in particular the sensorimotor and visual cortices), cerebellum and hippocampi. Diffusion-weighted imaging (DWI) is superior to conventional MRI because it detects abnormalities from day 1 after birth asphyxia and can be used as a predictor of clinical outcome. MR spectroscopy is perhaps more sensitive to injury in the first 24 hours after a hypoxic-ischemic episode, when conventional and DWI may yield false-negative findings or lead to underestimation of the extent of injury.

Conclusions
Imaging findings in HIE are highly variable and depend on a number of factors, including brain maturity, severity and duration of insult, and type and timing of imaging studies. MR spectroscopy and diffusion-weighted imaging are the most sensitive imaging modalities for detecting HIE in the acute period.

eEdE-05

6:30AM - 3:00PM

Imaging Algorithm of Adult-Onset Leukoencephalopathies.

G Romero-Sanchez[1], R La Piana[2], M Cortes[3], D Tampieri[4]
[1]Montreal Neurological Institute and Hospital, Montreal, Quebec, [2]Montreal Neurological Institute, Montreal, Quebec, [3]McGill University, montreal, Quebec, [4]Montreal Neurological Hospital and Institute, Montreal, Quebec

Purpose
Leukodystrophies commonly present in childhood; nevertheless, adults could be affected by genetic white matter disorders too. Our goal is to review the imaging characteristics of genetic versus acquired white matter disorders in adults.
Materials and Methods
a) We reviewed the imaging findings of the most common genetic adult-onset leukoencephalopathies (leukodystrophies and genetic vascular leukoencephalopathies) reported in the literature; b) We applied a radiological diagnostic algorithm to differentiate acquired versus genetic white matter disorders. The algorithm takes into account qualitative parameters (behavior on T1/T2-weighted images, morphology) and the spatial distribution of the imaging abnormalities.
Results
The presence of a multifocal, asymmetric pattern of involvement orients towards an acquired white matter disorder, while diffuse, homogeneous and symmetric signal abnormalities are suggestive of a genetic origin. The interpretation of MRI characteristics in genetic leukoencephalopathies is essential for the correct classification of each entity in the diagnostic algorithm and to differentiate them from acquired disorder. This process facilitates and accelerates the diagnostic process of white matter diseases in the adult population.
Conclusions
Adult-onset genetic leukoencephalopathies are clinically and radiologically heterogeneous and the radiological overlapping with acquired white matter diseases can lead to confusion in the diagnostic classification. The use of an imaging algorithm is helpful for radiologists that are presented with adult-onset white matter disorders.

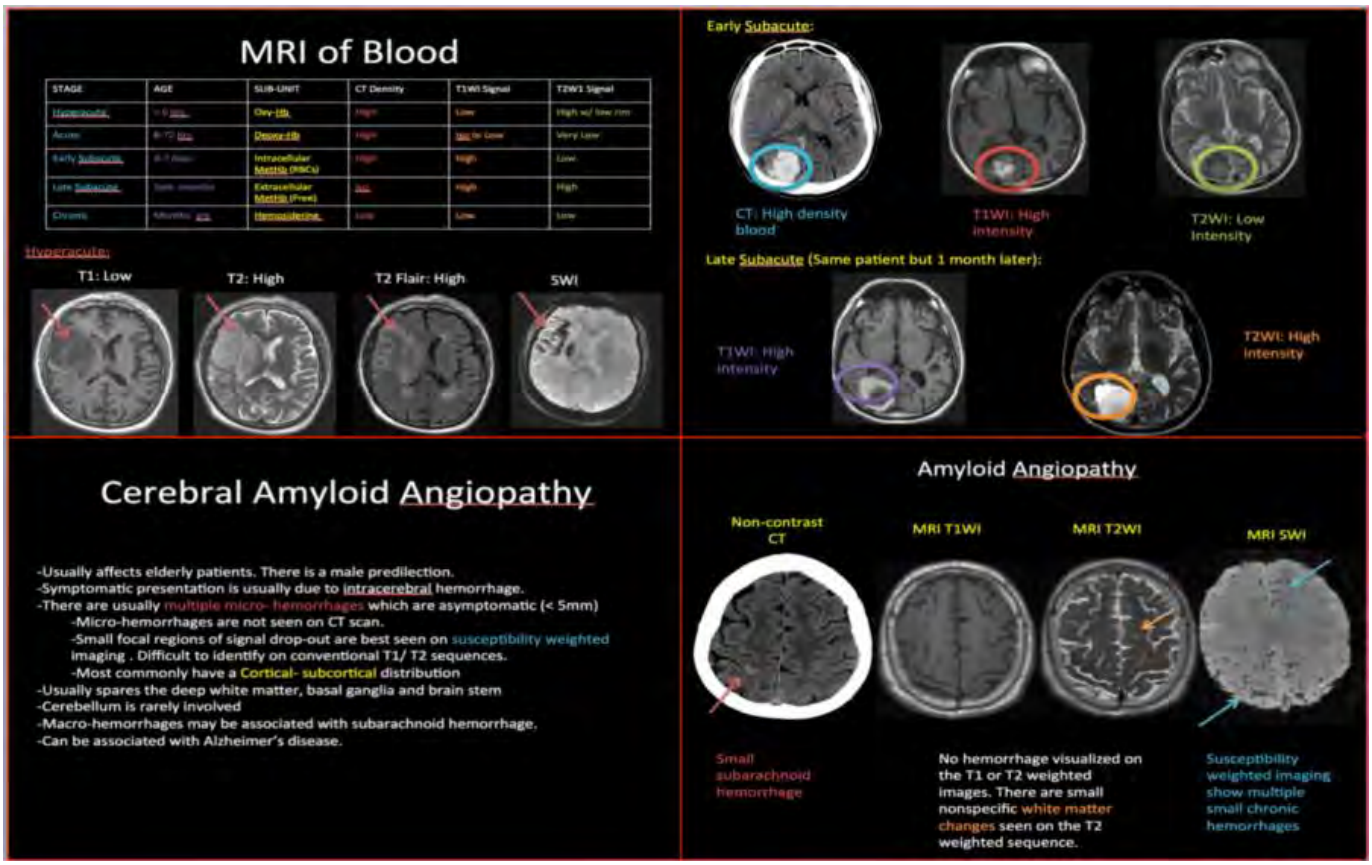
eEdE-108

6:30AM - 3:00PM

Imaging Characteristics of Intracranial Blood and Blood Products Depending on Chronicity and Imaging Modality

C Boyd[1], N Anand[2], A Salomon[3]
[1]Atlantic Health- Morristown Medical Center, MORRISTOWN, NJ, [2]morristown medical center, morristown , NJ, [3]Overlook Medical Center, Summit, NJ

Purpose
The purpose of this exhibit is to make radiologists and clinicians aware of the different imaging characteristics of intracranial blood and blood products depending on chronicity and imaging modality. Identifying intracranial blood is imperative for medical management. It is important to identify the different appearances of blood based on its chronicity and imaging modality. This presentation will review the many different appearances intracranial blood and blood products can have on MRI and CT scans.
Materials and Methods
Initially, a list of different etiologies of intracranial hemorrhage were made. These subsequently were entered into a search of all radiology reports at our institution from January 8, 2008 to January 1, 2016. This method yielded hundreds of different reports in which the searched terms were used. All applicable radiology reports were read and pertinent pathological cases were compiled for use in this exhibit. Special attention was given to the imaging characteristics of intracranial blood depending on chronicity and imaging modality.
Results
The topics for discussion and review of original images include, but are not limited to: - Intracranial hemorrhage intensity on MRI: T1 vs T2, and density on CT. - Hyperacute, Acute, Early subacute, Late subacute, Chronic. - Trauma: Intraparenchymal, Subarachnoid, Subdural, Epidural. - Hypertensive hemorrhage: Basal ganglia- thalamic, Lobar, Brain stem, Cerebellum. - Aneurysm. - Cerebral Cavernous malformation. - Hemorrhagic infarct: Venous, Arterial. - Venous thrombosis. - Coagulopathies. - Vasculitis. - Vascular dissection. - Intratumor hemorrhage. - Amyloid Angiopathy. - Hemosiderosis: Hemochromatosis, Sickle cell anemia, Superficial Siderosis. - Diffuse axional injury. - Drugs causing hemorrhage: Cocaine, Amphetamines, Ephedrine.
Conclusions
To conclude, we would like to make radiologists and clinicians aware of the MRI characteristics of intracranial hemorrhage depending on their chronicity. Additionally, we will discuss different causes of intracranial blood and their appearance on CT and MRI.



(Filename: TCT_eEdE-108_ShadesofRed.jpg)

eEdE-62

6:30AM - 3:00PM

Imaging Characteristics of Myeloid Sarcoma

A Chaudhry[1], A Chaudhry[2], M Gul[3]
[1]Johns Hopkins Medicine, Elkridge, MD, [2]Stony Brook University, Westbury, NY, [3]National Institute of Health, Elkridge, MD

Purpose
Myeloid (granulocytic) sarcoma can be the initial presentation of aleukemic leukemia that either resulted from myelodysplastic syndrome conversion into leukemia, de novo aleukemic leukemia or leukemia relapse. It can present weeks to months before the peripheral presence of the leukemia. Although myeloid sarcoma carries a broad differential diagnosis, it can be narrowed utilizing age, clinical features, and imaging characteristics of the lesion, such as location, enhancement pattern and presence of necrosis. By the conclusion of this presentation, the radiologist should have a better understanding of various clinical presentations of myeloid sarcoma and relevant imaging and pathologic findings.
Materials and Methods
We present a case-based review of the clinical features, imaging, pathophysiology, histologic

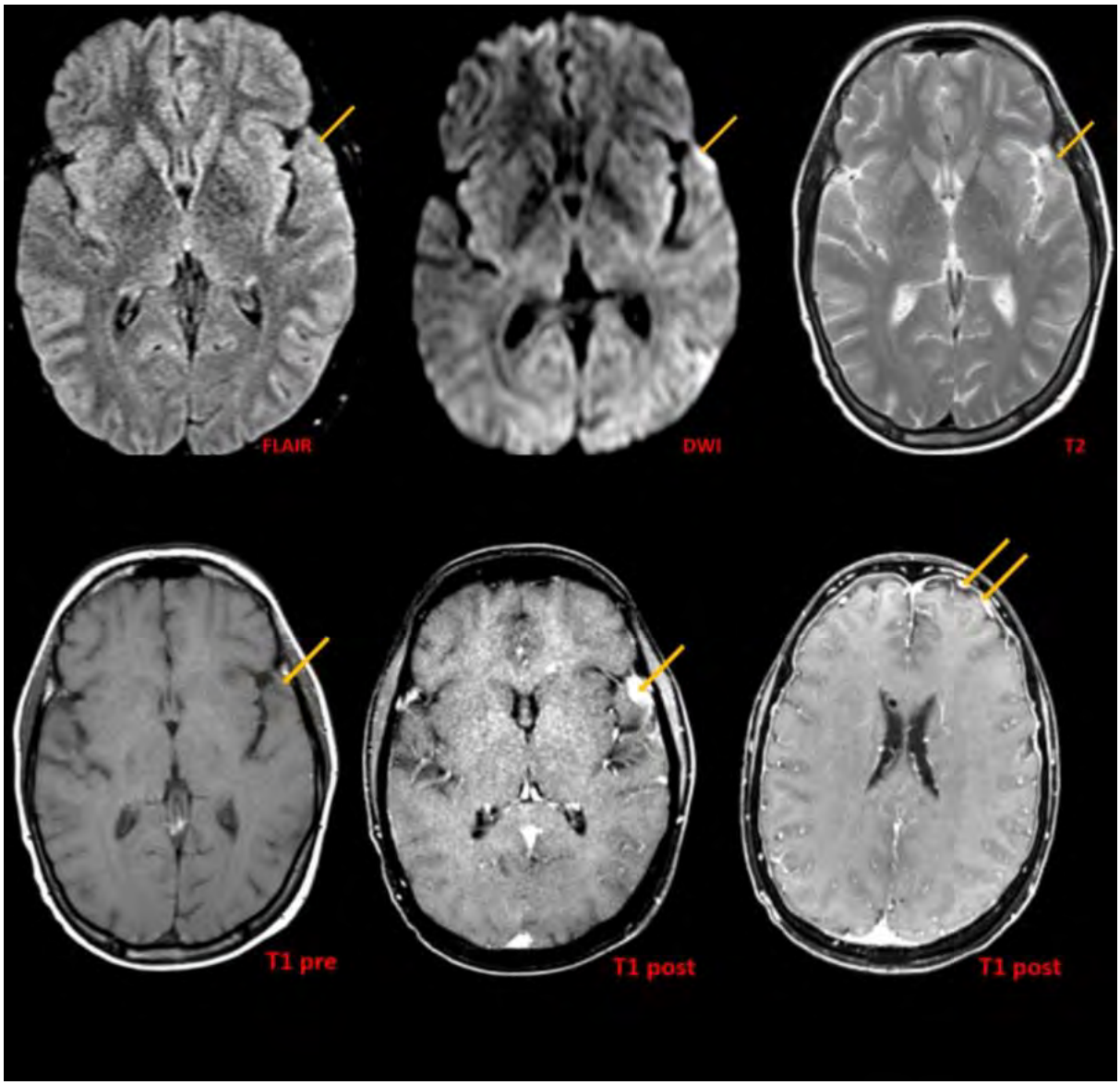
features, treatments and prognosis of myeloid sarcoma. We will describe the characteristic imaging (CT and MRI) features of myeloid sarcoma. Information will be presented on the various conditions associated with granulocytic sarcoma such as myelodysplastic syndrome and acute myelogenous leukemia; clinical presentation and histopathologic findings of each entity are discussed.

Results

Multiple different presentations of myeloid sarcoma will be shown, including brain parenchymal, ventricular, submandibular, orbital and spinal. We also will show cases of similar appearing entities such as lymphoma, metastases, infection, tuberculosis, astrocytoma, sarcoma, sarcoidosis, hemangiopericytoma and malignant fibrous histiocytoma, with an emphasis on differentiating these from granulocytic sarcoma. Additional processes resulting from infection, inflammation, injury and/or malignancy that may mask and/or mimic myeloid sarcoma will be discussed with emphasis on key points which help to narrow the differential diagnosis.

Conclusions

Myeloid sarcoma is a rare pathology that can be the initial manifestation of aleukemic leukemia. Knowledge of the imaging characteristics and differential considerations can play an important role and aid in the early diagnosis of this disease.



(Filename: TCT_eEdE-62_Myeloidsarcoma.jpg)

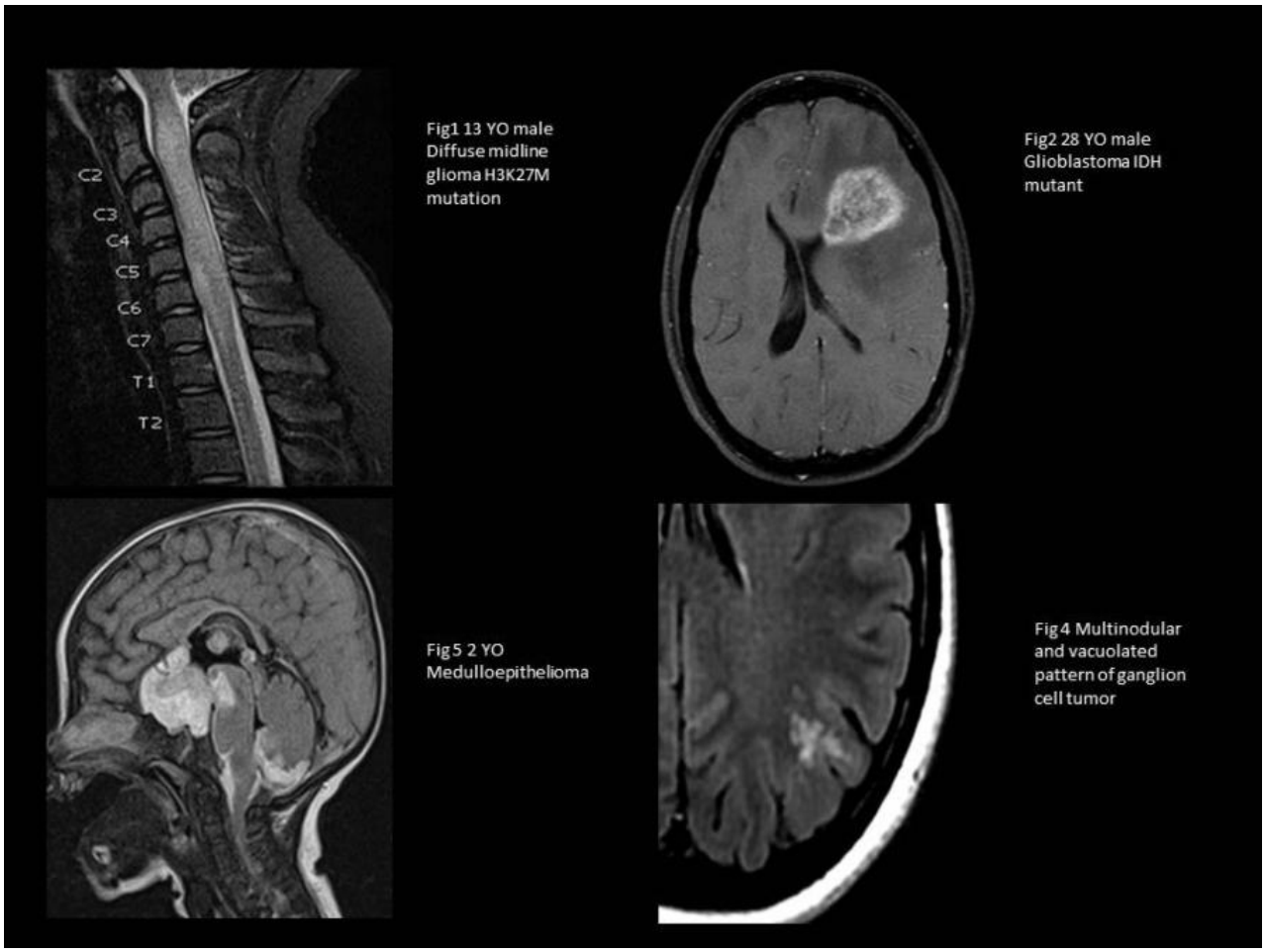
eEdE-60

6:30AM - 3:00PM

Imaging Findings of the New Entities, Variants, and Patterns in the 2016 Revised WHO Classification of CNS Tumors

R Camacaro[1], C Vallejo[1], P Puac[1], A Rodriguez[1], C Zamora[2], M Castillo[1]
[1]University of North Carolina at Chapel Hill, Chapel Hill, NC, [2]University of North Carolina, Chapel Hill, NC

Purpose
To present a review of magnetic resonance imaging (MRI) findings of the newly added and restructured central nervous system (CNS) tumor 2016 WHO classification.
Materials and Methods
We reviewed the changes in the WHO 2016 classification and compared them with same classification previously published in 2007. Specifically, we looked into newly identified entities and variants which allow more diagnostic precision, the use of molecular parameters in addition to histology, and MRI findings. We then search our electronic medical records, PACS, and teaching files for illustrative cases.
Results
The most notable changes in the new classification and the imaging findings related to them addressed in this exhibit will cover gliomas with IDH mutation status including: IDH wildtype, IDH mutant or not otherwise specified (NOS) if not is possible identify a specific molecular type. IDH mutant gliomas have better prognosis than wildtype ones and are more common in young patients. Oligodendrogliomas by definition have 1p19q co-deletion or are NOS. Diffuse midline glioma H3 K27M–mutant is another new entity with typical MRI findings. Ependymoma RELA fusion–positive are generally supratentorial ependymomas in childhood. Medulloblastoma classification is another important change which now incorportates 4 different groups with variable prognosis, location and imaging findings. Anaplastic pleomorphic xanthoastrocytoma, embryonal tumors with multilayered rosettes C19MC-altered, and diffuse leptomeningeal glioneuronal tumors are also new entities which will be discussed and shown. Multinodular and vacuolated pattern of ganglion cell tumor and brain invasion as a criterion for atypical meningioma, as well the elimination of gliomatosis cerebri will be addressed.
Conclusions
The 2016 WHO CNS tumor classification includes refinements which may be appreciated by the different MRI features that these tumors present.



(Filename: TCT_eEdE-60_Slide1.JPG)

eEdE-40

6:30AM - 3:00PM

Imaging Gallery of Computed Tomography Angiography(CTA) for Diffuse Subarachnoid Hemorrhage(SAH): Beyond Saccular Aneurysm

T Wu[1]
[1]*Chi-Mei medical center, Tainan, Taiwan*

Purpose
The purpose of this presentation is to investigate the CTA findings of diffuse subarachnoid hemorrhage and to discuss the possible differential diagnosis in different categories.
Materials and Methods
Given subarachnoid hemorrhage in the emergency department of our hospital, CTA has been the first-line image modality for etiology evaluation, management suggestion and prognosis prediction. Routine brain CTA protocol for diffuse SAH includes precontrast images, maximal intensity projection (MIP) and volume rendering (VR) reformation of arterial phase

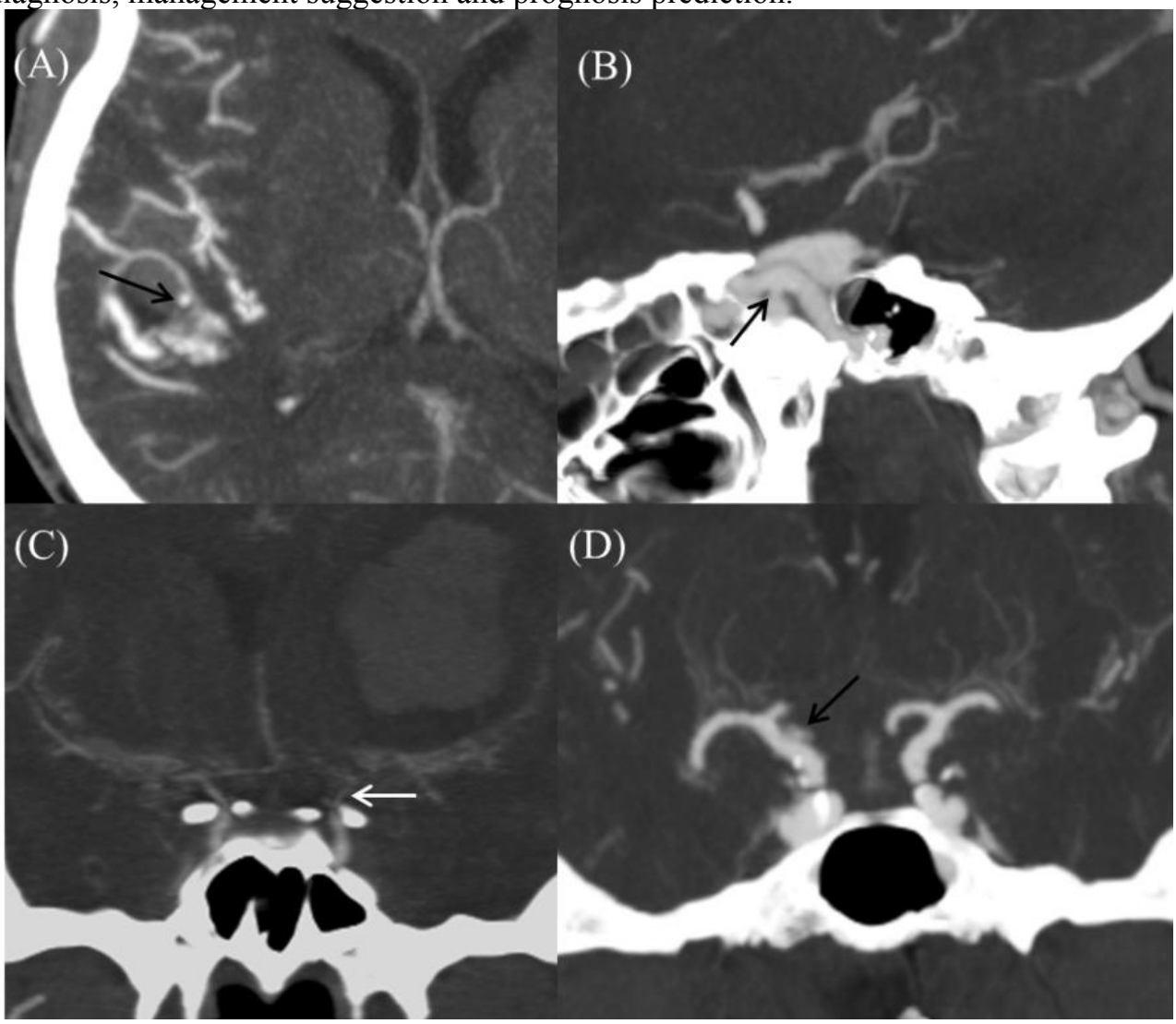
and postcontrast images in the delayed venous phases. In this presentation, we share our experience about the CTA evaluation of diffuse SAH and its clinical application.

Results

The indications of most cases are diffuse SAH and intraventricular hemorrhage (IVH). The possible differential diagnosis and its relevant findings including unusual presentation of cerebral aneurysms (active contrast extravasation, blood blister like aneurysm, dissecting aneurysm, traumatic pseudoaneurysm, partially thrombosed aneurysm and mycotic aneurysm), perimesencephalic hemorrhage, arteriovenous malformation (flow-related aneurysm, intranidal aneurysm and venous drainage pattern), cervical dural arteriovenous fistula, brainstem cavernous malformation, reversible cerebral vasoconstriction syndrome (RCVS), moyamoya disease, traumatic SAH, tumor bleeding and coagulopathy are reviewed.

Conclusions

Being familiar with CTA findings of diffuse SAH would be helpful in the differential diagnosis, management suggestion and prognosis prediction.



(Filename: TCT_eEdE-40_Imagecollection.jpg)

eEdE-63

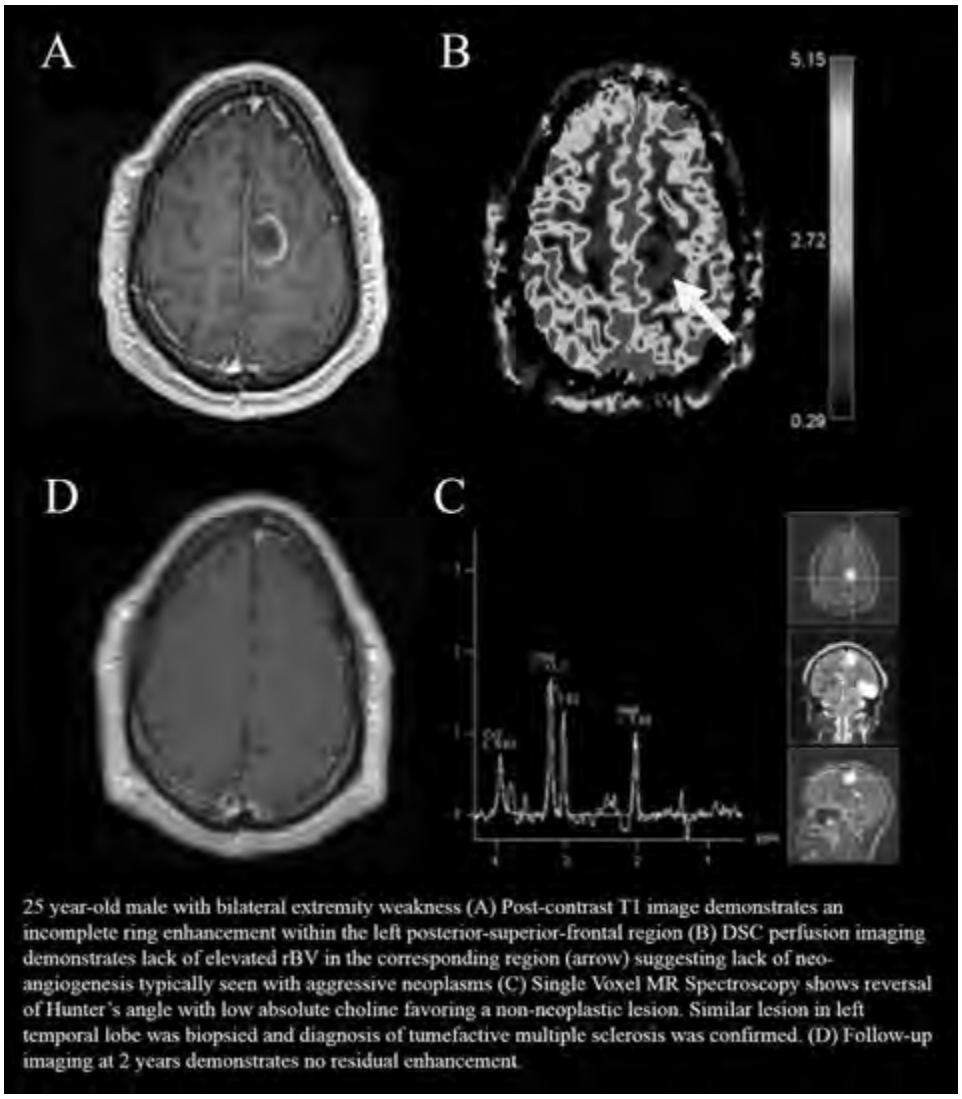
6:30AM - 3:00PM

Imaging Mimics of Brain Tumors: Radiologic-Histopathologic Correlation

O Kilinc[1], S Dastmalchian[1], M Coffey[2], M Cohen[3], L Rogers[4], J Sunshine[2], A Sloan[5], C Badve[2]
[1]Case Western Reserve University, Department of Radiology, Cleveland, OH, [2]University Hospitals Cleveland Medical Center, Department of Radiology, Cleveland, OH, [3]University Hospitals Cleveland Medical Center, Department of Pathology, Cleveland, OH, [4]University Hospitals Cleveland Medical Center, Department of Neurology, Cleveland, OH, [5]University Hospitals Cleveland Medical Center, Department of Neurological Surgery, Cleveland, OH

Purpose
1. To present an overview of different inflammatory, infectious, autoimmune, vascular, iatrogenic and developmental pathologies in brain that can present as tumor-like lesions on MR imaging and discuss their key radiological and pathological features. 2. To evaluate the role of advanced imaging techniques such as perfusion, spectroscopy and diffusion imaging in differentiating between neoplastic and non-neoplastic entities.
Materials and Methods
In this image-rich educational exhibit, a detailed imaging review of diseases that can mimic brain neoplasms is presented. The authors will discuss key histological features of these entities to enhance comprehension of underlying pathologies and thereby facilitate radiological-pathological correlation. Finally, a diagnostic approach for radiological evaluation of tumor mimics is outlined with emphasis on conventional and advanced imaging characteristics.
Results
A broad spectrum of non-neoplastic conditions such as amyloidosis, Behcet's disease, subacute stroke, tumefactive demyelination, radiation toxicity and heterotopia may present with radiological features that are similar to brain tumors. Detailed clinical evaluation and specific laboratory markers can help to differentiate non-neoplastic from neoplastic lesions. However, not uncommonly, these patients undergo aggressive interventions with significant side effects, only to receive a final diagnosis of a benign pathology. The knowledge of key differentiating features of such non-neoplastic entities is essential for the radiologist to facilitate accurate and timely diagnosis. Additionally, in such settings, judicious use of advanced imaging techniques such as perfusion imaging and spectroscopy can help the radiologist as problem-solving tools.
Conclusions
This exhibit focuses on detailed imaging review and radiological-pathological correlation of various tumor-like entities in brain and concludes with a practical diagnostic approach for

imaging assessment. This exhibit will serve as an engaging self-learning tool for the viewers. Residents and fellows will have an opportunity to familiarize themselves with this important clinical problem. Practicing radiologists will reinforce their confidence on this topic with this refresher module.



(Filename: TCT_eEdE-63_ASNR2017_TumorMimics_final_1129_501.jpg)

eEdE-90

6:30AM - 3:00PM

Imaging of Cerebral Venous Thrombosis

M KIMURA[1], L Hygino da Cruz[2], H Pinto[3], D Neves[4], G Andrade[3], E Gasparetto[5]
[1]CDPI-Clinica de Diagnostico por Imagem, RIO DE JANEIRO, Rio de Janeiro, [2]CDPI-Clinica de Diagnostico por Imagem, Rio de Janeiro, RIO DE JANEIRO, [3]CDPI-Clinica de Diagnostico por Imagem, Rio De Janeiro, RIO DE JANEIRO, [4]DASA/CDPI, Rio de Janeiro,

Rio de Janeiro, [5]CDPI-Clinica de Diagnostico por Imagem, UNIVERSIDADE FEDERAL DO RIO DE JANEIRO, RIO DE JANEIRO, RIO DE JANEIRO

Purpose

Show the direct signs of occlusion of the venous structures in conventional magnetic resonance imaging (MRI) and computed tomography (CT). Describe findings of thrombosis in venous MRA and CTA. Highlight the critical findings of venous thrombosis complications.

Materials and Methods

We reviewed our institution data of the last 6 years for the cases of venous thrombosis and searched our PACS for CT and MR imaging of these cases. Additional evaluation and 3D imaging reconstructions were performed for a didactic approach.

Results

Imaging findings in cerebral venous thrombosis plays an essencial role in the diagnosis and treatment of patients. Firstly, because main initial symptoms such as headache, nausea and vomiting are nonspecific for the disease. Secondly, the diagnosis requires some ability on imaging evaluation. The knowledge of normal appearance of dural sinus in conventional MRI is required since the first exam normally will be a standard brain scan. The specific radiologic findings of thrombus, and its several stages, are necessary too. Then, the hypointense signal on T2 of acute thrombus which simulates normal "flow void" or the isointense signal of longstanding thrombosed sinus must be known. Also, organized fibrous tissue may enhance and can be misinterpreted as recanalization. T2* GRE sequence is very important in the detection of cortical vein acute thrombus and petechial hemorrhages. Sometimes it is the only sequence capable of diagnosing thrombus in tiny cortical veins. Contrast-enhanced MRV is preferred to 2D TOF because of artifacts, and source images must be reviewed when flow gaps are found on MIP images. The "empty delta" sign is seen in just 25-30% of the cases. False positive diagnosis can be performed in conditions such as dural sinus hypoplasia-aplasia, high hematocrit, giant arachnoid granulations and acute subdural hematoma which mimic thrombosis. False negative diagnosis with normal density in unenhanced CT image can happen. Cortical/subcortical parenchyma areas of cytotoxic or vasogenic edema, hematomas, dural arteriovenous fistula are possible complications associated with the pathology. It is important to have in mind that parenchymal abnormalities may not be present and more importantly, they may be reversible with the correct treatment. All these aspects are illustrated in images and discussed along the educational exhibit.

Conclusions

Cerebral venous thrombosis is an emergency in view of the fact that it will progress to cerebral infarction, impaired consciousness, coma and early death in 13% of patients. Normally, the diagnosis involves a delay of 7 days between the onset of symptoms and the diagnosis, usually performed by the radiologist. Late deaths occur in approximately 9.4%. Importantly, 28% of patients are dependent at 12 months. Therefore, the increasing role of

neuroimaging in the diagnosis and management of cerebral venous thrombosis over the past 2 decades poses it as the first evaluation proposed in the algorithm for the management of the disease. The radiologist is a central figure in this scenario.

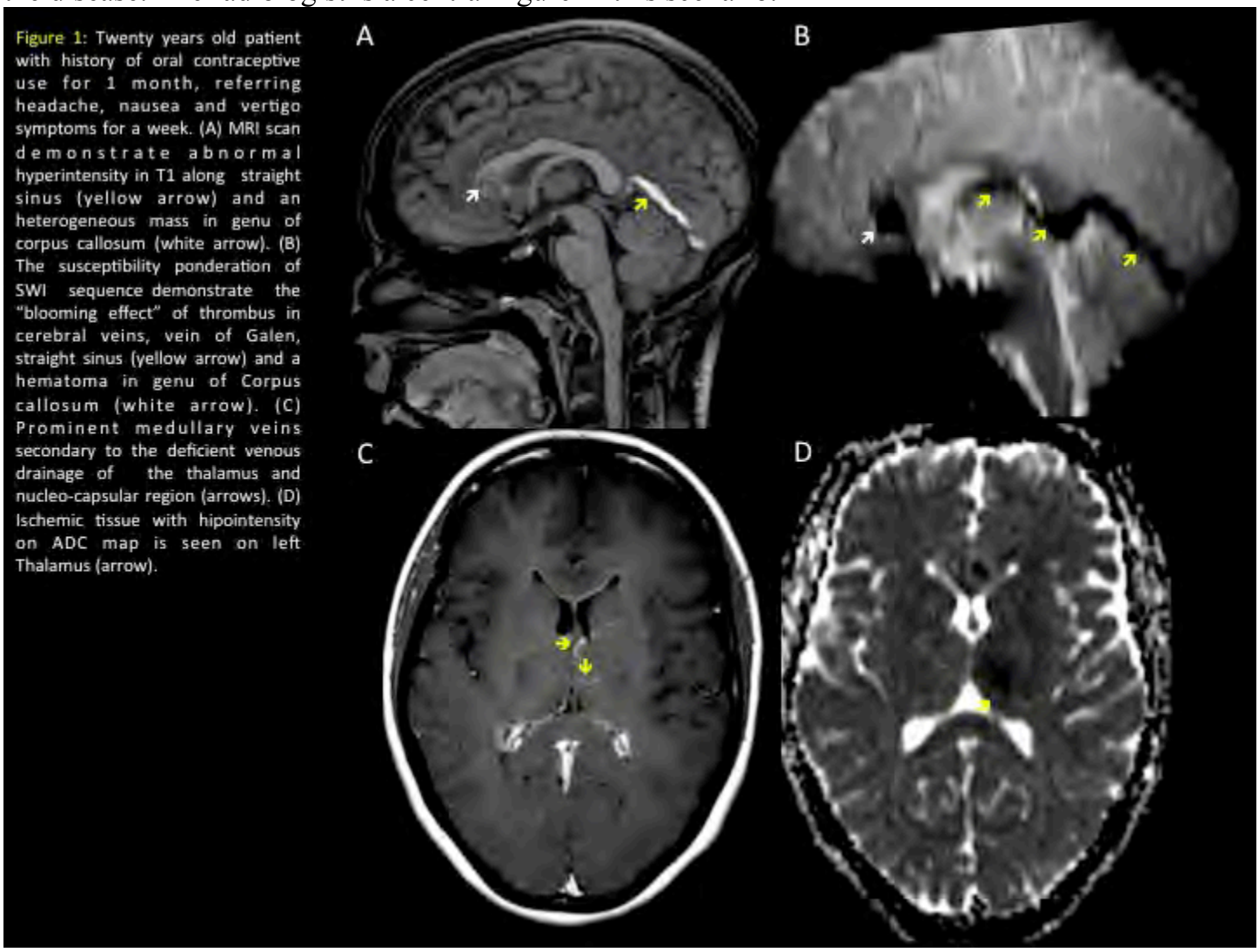


Figure 1: Twenty years old patient with history of oral contraceptive use for 1 month, referring headache, nausea and vertigo symptoms for a week. (A) MRI scan demonstrate abnormal hyperintensity in T1 along straight sinus (yellow arrow) and an heterogeneous mass in genu of corpus callosum (white arrow). (B) The susceptibility ponderation of SWI sequence demonstrate the "blooming effect" of thrombus in cerebral veins, vein of Galen, straight sinus (yellow arrow) and a hematoma in genu of Corpus callosum (white arrow). (C) Prominent medullary veins secondary to the deficient venous drainage of the thalamus and nucleo-capsular region (arrows). (D) Ischemic tissue with hipointensity on ADC map is seen on left Thalamus (arrow).

(Filename: TCT_eEdE-90_Slide2.jpg)

eEdE-38

6:30AM - 3:00PM

Imaging of the Cerebral Venous System (CVS): Size Doesn't Matter!

E Supsupin[1], J Choi[1], K Jobanputra[2], R Orata[3]
[1]University of Texas Health Science Center Houston, Houston, TX, [2]University of Texas, Health Science Center- Houston, Houston, TX, [3]Armed Forces of the Philippines Medical Center, Quezon City, WY

Purpose

The venous drainage of the brain is much more variable and less well known compared to their arterial counterparts [1]. A comprehensive review of cerebral venous anatomy and how this may be involved in a wide range of pathological processes is undertaken.

Materials and Methods

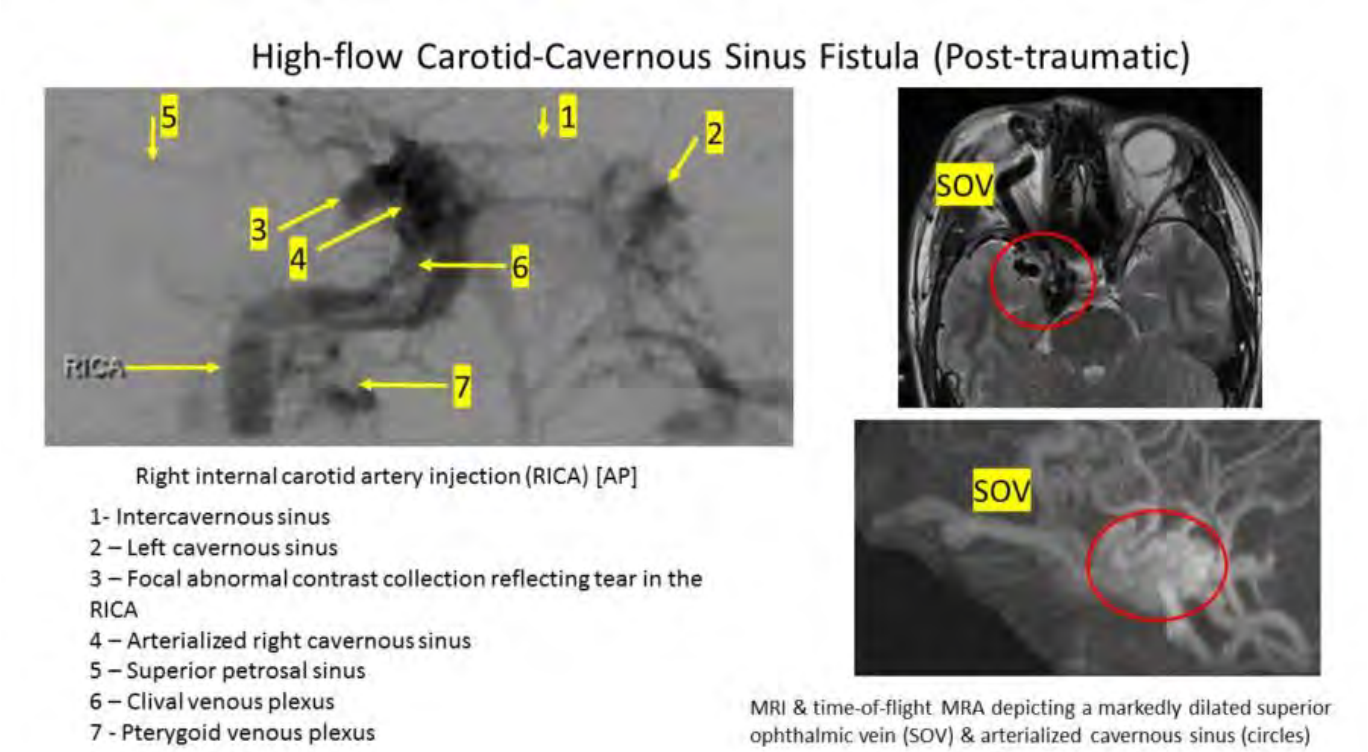
This presentation aims to accomplish the following: Review the angiographic anatomy of the cerebral venous system (CVS). Correlate angiography with gross anatomy and describe important anatomic and surgical landmarks. Briefly discuss the embryology and normal development of important venous channels. Illustrate how normal and variant anatomy may mimic disease states. Provide clinical scenarios that exemplify how the CVS may be directly or indirectly involved in various pathologic conditions.

Results

The CVS may be divided into 3 major groups namely: superficial, deep, and posterior fossa. Variability of venous drainage is common. Normal and variant anatomy may mimic disease states. For example, a prominent sphenoparietal sinus may be misinterpreted as subdural hemorrhage, particularly in the setting of trauma. A nondominant dural venous sinus must not be misconstrued as stenosed or thrombosed. Knowledge of venous anatomy and variants is imperative, and may help avoid misinterpretations. The CVS may be directly or indirectly involved in a wide range of pathologic processes, both congenital/connatal and acquired. Anomalous venous development is exemplified by vein of Galen malformation. Examples of acquired conditions include carotid cavernous sinus fistula (CCF), postseptal cellulitis extending to the cavernous sinus, and dural venous sinus thrombosis resulting from trauma, infection, or hypercoagulable states. Other common clinical scenarios exemplifying venous sinus pathology are presented.

Conclusions

Comprehensive review of anatomy, including how the CVS may participate in a broad range of pathologic conditions is undertaken. Knowledge of normal anatomy and variants may help avoid pitfalls in interpretation.



(Filename: TCT_eEdE-38_CSCollage.jpg)

eEdE-110

6:30AM - 3:00PM

Imaging of Traumatic and Nontraumatic Orbital Emergencies

Z Chaudhry[1], S Pulitzer[1], R Shinder[2], V Velayudhan[2]
[1]SUNY Downstate Medical Center, Brooklyn , NY, [2]SUNY Downstate Medical Center, Brooklyn, NY

Purpose
1. Review the anatomy of the orbits with an emphasis on features relevant to spread of disease and management, including surgery. 2. Learn the imaging features and clinical considerations of common and uncommon traumatic and nontraumatic orbital emergencies. 3. Establish an image-based algorithm to facilitate accurate detection and prompt management of orbital emergencies.
Materials and Methods
Material is presented in a quiz format to emphasize key points. Orbital anatomy is discussed and relevance to management and disease detection is highlighted. Relationships of the orbit to the adjacent intracranial compartment, vascular structures and skull base are discussed. After a review of anatomy, cases (including clinical history) are presented to demonstrate common as well as uncommon but important traumatic and nontraumatic orbital pathology. This is followed by a discussion of pathophysiology with an emphasis on discrete findings

and mechanisms associated with specific disease etiology as well as complications. An image-based algorithm is provided to facilitate detection and description of an emergent orbit.
Results
The compartmental anatomy of the orbit lends itself well to a systematic checklist approach, both in the presence and absence of trauma. Traumatic involvement of the bony orbit and its contents is very common. Penetrating and blunt injuries of the globe, including globe rupture, foreign bodies, lens dislocation, detachments of the layers of the globe (choroidal and retinal), herniation of orbital contents and muscle entrapment exemplify a compartment-based evaluation of orbital trauma in prompt detection of injuries requiring immediate treatment. The same approach can be used to identify nontraumatic conditions. This includes vascular lesions (e.g., cavernous sinus and ophthlamic vein thrombosis and ischemic infarction), primary infections (such as endophthlamitis and retinitis), orbital complications of sinus and facial infection, inflammatory diseases (such as idiopathic orbital inflammation) and demyelinating disease (multiple sclerosis and neuromelitis optica). The anatomic-based Chandler classification of orbital infections is discussed as well intracranial complications. Clinical and secondary imaging findings outside of the orbits that aid in the diagnosis of inflammatory and demyelinating diseases also are discussed. Normal and benign findings that can mimic disease also are reviewed.
Conclusions
Diseases involving the orbit have the potential to cause permanent vision loss and result in other serious and life-threatening complications. Prompt and accurate diagnosis by the radiologist is vital to expedite treatment and improve patient outcomes. Knowledge of pertinent anatomy, pathophysiology and common complications combined with a checklist approach improves diagnostic accuracy when evaluating the acute orbit.

eEdE-32

6:30AM - 3:00PM

Imaging Spectrum in ADEM: Don’t Let the Confused Brain Confuse You!

G BATHLA[1], p watal[2], G Riesberg[3], B Policeni[3], T Moritani[4]
[1]University of Iowa hospitals and Clinics, IOWA CITY, IA, [2]university of iowa hospital and clinics, iowa city, IA, [3]University of Iowa hospitals and Clinics, iowa city, IA, [4]University of Iowa Hospitals and Clinics, Iowa City, IA

Purpose
The authors aim to briefly review the pertinent epidemiology, natural history and existing imaging literature on acute disseminated encephalomyelitis [ADEM].
Materials and Methods
1. Educational exhibit based on retrospective review of imaging data. 2. This will include illustrative examples of imaging patterns of ADEM. Imaging of rare ADEM variants

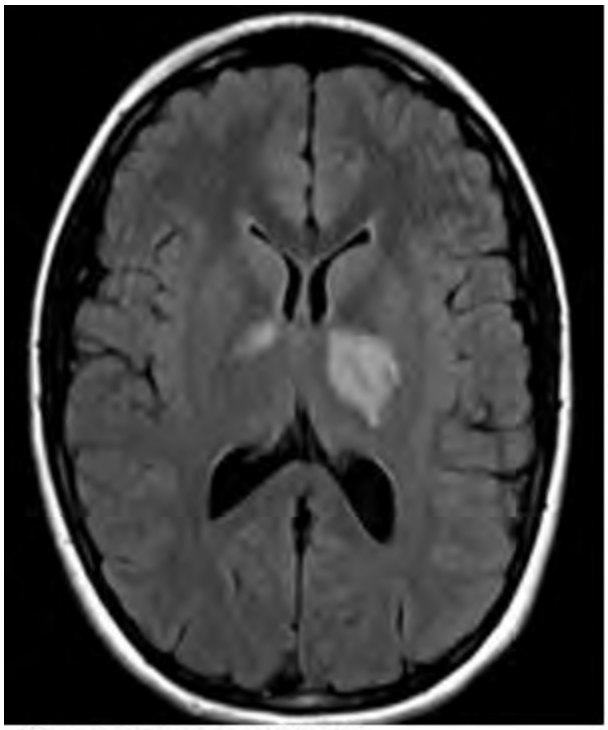
(Multiphasic, poststreptococcal, bithalamic, AHEM etc) also will be discussed with emphasis on key imaging findings. 3. Finally, imaging of common differential diagnosis with key distinguishing findings with regards to ADEM will be discussed briefly.

Results

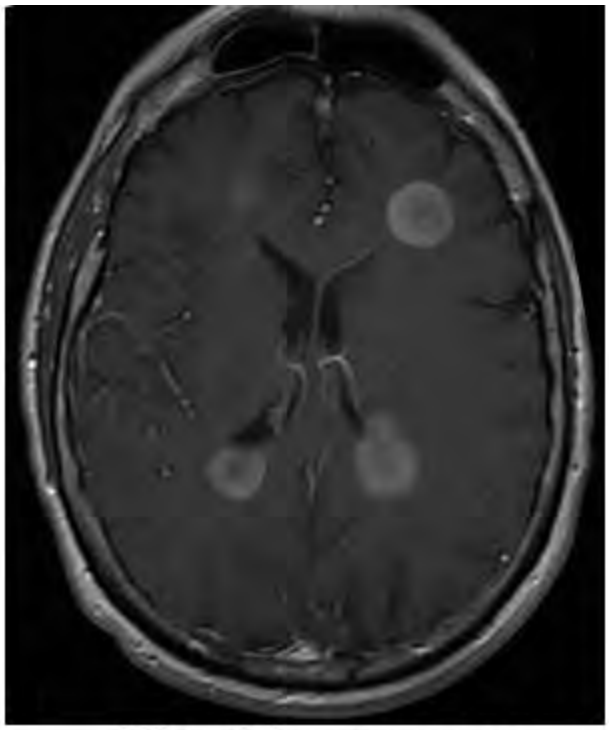
1. ADEM is a rare, usually monophasic, immunologically mediated inflammatory disease of the CNS. 2. It is seen most commonly in the pediatric population. A preceding history of infection may be elicited in about 67-93% of patients. 3. ADEM lesions predominantly involve the white matter, are large, asymmetric and have ill-defined margins. However, atypical variants may rarely occur and can be a source of considerable confusion, both clinically and on imaging. 4. Imaging plays an important role in not only diagnosing ADEM, but also excluding other causes of altered mental status. Imaging also is used to characterize, follow up and identify complications and relapse.

Conclusions

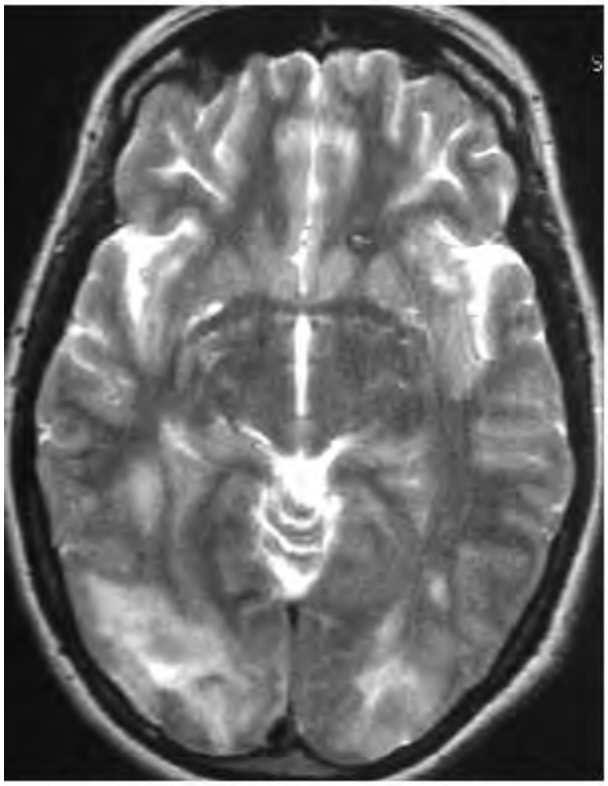
1. ADEM, though rare, is a great mimic, not just clinically but also on imaging. 2. A better understanding of the varied imaging manifestations and potentially avoid many diagnostic pitfalls and expedite the diagnosis.



Post streptococcal ADEM



ADEM with rim enhancement



Acute hemorrhagic encephalitis



Bilateral optic nerve involvement in ADEM

(Filename: TCT_eEdE-32_ASNRabsractADEM.jpg)

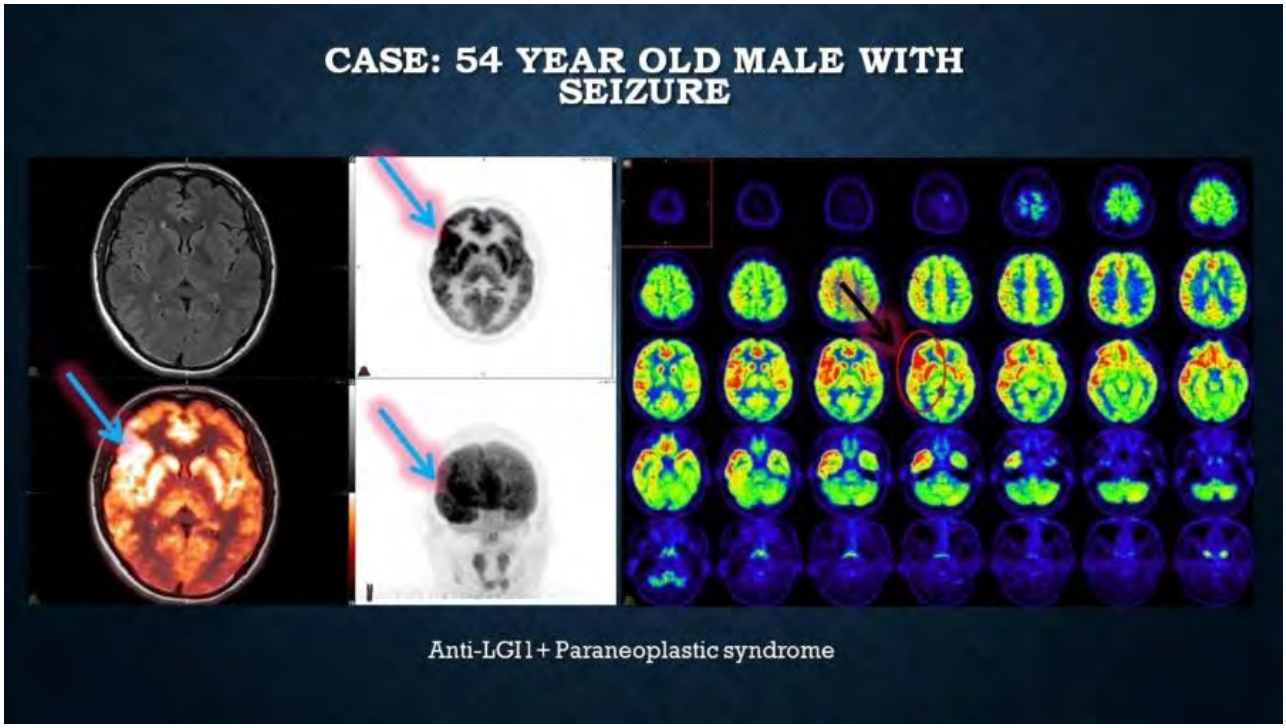
eEdE-24

6:30AM - 3:00PM

Imaging Spectrum of Paraneoplastic Syndrome and Mimics

A Chaudhry[1], A Chaudhry[2], M Gul[3], R Matthews[4]
[1]Johns Hopkins Medicine, Elkridge, MD, [2]Stony Brook University, Westbury, NY, [3]National Institute of Health, Elkridge, MD, [4]Stony Brook University Medical Center, Stony Brook , NY

Purpose
1. Pictorial review of central nervous system (CNS) anatomy highlight areas involved in paraneoplastic syndromes. 2. Case-based review highlighting common and uncommon causes of paraneoplastic syndrome. 3. Discuss differential diagnoses (physiologic process, congenital, infection, inflammation, trauma, vascular and/or malignancy) that can mimic imaging findings.
Materials and Methods
Common and uncommon presentations of paraneoplastic syndrome will be reviewed involving the brain and spine. Additionally, we will discuss mimics that may result from neoplasm (lymphoma, leukemia, etc.), infection (HSV, Lyme, etc.), inflammation (MS, ADEM, Lupus, etc.) with an emphasis on key findings (on CT, MRI, PET MRI) differentiating these entities.
Results
1. Discuss common clinical and laboratory findings seen in the various paraneoplastic syndromes. 2. Review characteristic imaging findings of various paraneoplastic syndromes. 3. Discuss diagnostic limitations of imaging findings and present an algorithmic approach that can assist in arriving at the correct diagnosis.
Conclusions
Paraneoplastic syndrome is not an uncommon cause of encephalitis. Knowledge of its clinical presentation, pathophysiology and immunology is essential in making the diagnosis. Although the differential diagnosis is broad, it can be narrowed utilizing age, clinical features, imaging characteristics (e.g., location, enhancement pattern, PET MRI findings, etc.) and pathology correlation. By the conclusion of this presentation, the viewer should have a better understanding of paraneoplastic syndrome and associated imaging findings, and should be able to aid in the work up, guide any potential biopsy/tissue sampling and imaging follow up.



(Filename: TCT_eEdE-24_paraneoplastic.jpg)

eEdE-08

6:30AM - 3:00PM

Imaging the Degenerative Brain: Patterns of Disease to Sort Through the Void

R Khan[1], J Chokr[2], C REYNOLDS[3], R Avery[4], V Patel[4], L MacKinnon[5], H Albasha[6], R Carmody[1]

[1]University of Arizona Medical Center, Tucson, AZ, [2]Banner University Medical Center, tucson, AZ, [3]UNIVERSITY OF ARIZONA, TUCSON, AZ, [4]University of Arizona, Tucson, AZ, [5]University of Arizona Department of Medical Imaging, Tucson, AZ, [6]The University of Arizona College of Medicine - Tucson, Oro Valley, AZ

Purpose

To familiarize the reader with the more common and some of the more rare degenerative brain conditions, using a case-based exhibit focused on MRI with CT, PET/CT, and SPECT/CT imaging correlates.

Materials and Methods

Electronic educational review.

Results

This educational exhibit will provide a practical review of the degenerative brain conditions on both 1.5T and 3T MRI with CT, PET/CT, and SPECT/CT imaging correlates. Brief, pertinent clinical background will be included discussing the etiology of the diseases which will include: Alzheimer disease, Dementia with Lewy Bodies, vascular dementia,

frontotemporal lobar degeneration, Creutzfeldt-Jakob disease, Parkinson disease, multi-system atrophy, supranuclear palsy, amyotrophic lateral sclerosis, Wallerian degeneration, crossed cerebellar diaschisis, and hypertrophic olivary degeneration. A brief discussion on the imaging of normal aging also will be presented.
Conclusions
After the reader has viewed the exhibit, they will be able to recognize the various patterns of degenerative brain disorders presented. They also will be more familiar with the pertinent clinical background of such diseases.

eEdE-39

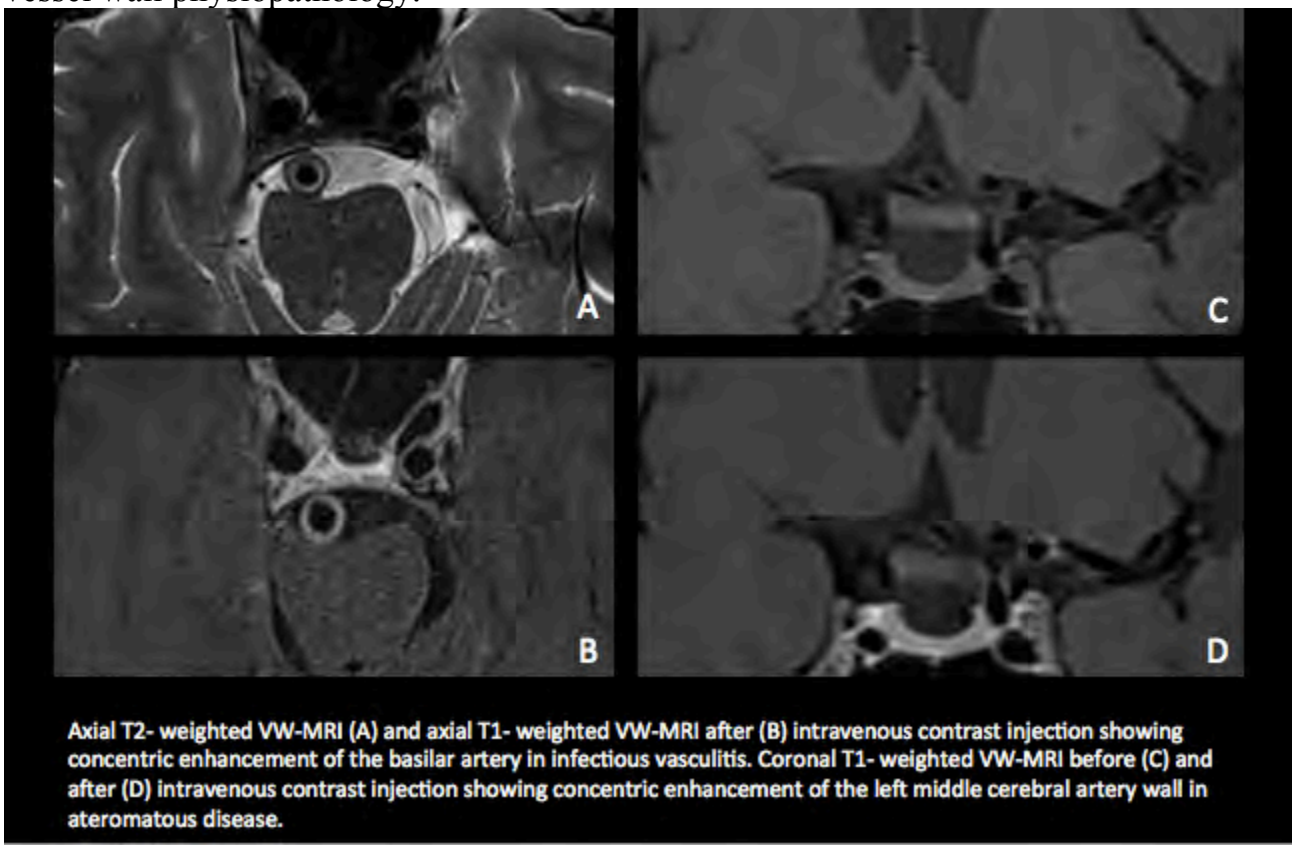
6:30AM - 3:00PM

Intracranial Vessel Wall Magnetic Resonance Imaging

E Bravo[1], F Montoya[1], J Caro[2], P Gallardo[2], F Torres[2]
[1]Instituto de Neurocirugía Dr. Asenjo, Santiago, Chile, [2]Instituto de Neurocirugía Dr. Asenjo, Santiago, Providencia

Purpose
Cerebral vascular pathology usually has been studied with cerebral computed angiotomography, cerebral magnetic resonance angiography (MRA) and conventional angiography. The American Society of Neuroradiology recently published a recommendation for the use of vessel wall magnetic resonance imaging (VW-MRI) for many different vascular pathologies (1). We adapted the VW-MRI protocol to our high-field MR imager (3.0 Tesla Magnetom Skyra, Siemens, Erlangen, Germany) with a 32-channel head coil.
Materials and Methods
We performed VW-MRI on different patients that came to our hospital (Instituto de Neurocirugía Dr. Asenjo) that showed an alteration on the 3D time of flight on the MRA in order to assess the wall vessel disease.
Results
An eccentric wall thickening with avid contrast enhancement has been seen on arteriosclerotic vasculopathy and actinic arteritis. Concentric wall thickening was seen in a patient with vasculitis secondary to HIV meningoencephalitis (Figures A and B), in vasculitis after primary varicella infection, in a dissecting aneurysm of a vertebral artery and also in another case of arteriosclerotic vasculopathy (Figures C and D). Concentric narrowing without enhancement was seen in moyamoya disease. We performed VW-MRI on a few aneurysms and found irregular wall enhancement in ruptured intracranial aneurysm and also on an edematous arterial venous malformation (AVM) and found irregular thickening with enhancement of some of the walls of the drainage veins adjacent to the edematous region.

Conclusions
We found that wall thickness and enhancement patterns differ in many causes of vascular narrowing. Our findings were similar to those published by Mandel, et all (1). We also performed VW-MRI on aneurysms and AVM and found this may be a good way to find the aneurysm responsible for a subarachnoid hemorrhage, or which vein may be inflamed in a AVM. We will continue performing this protocol in order to try to increase the knowledge of vessel wall physiopathology.



Axial T2- weighted VW-MRI (A) and axial T1- weighted VW-MRI after (B) intravenous contrast injection showing concentric enhancement of the basilar artery in infectious vasculitis. Coronal T1- weighted VW-MRI before (C) and after (D) intravenous contrast injection showing concentric enhancement of the left middle cerebral artery wall in ateromatous disease.

(Filename: TCT_eEdE-39_VW-MRI.jpg)

eEdE-27

6:30AM - 3:00PM

It Got into My Head: Opportunistic Infections of the Central Nervous System and Neuro-Immune Reconstitution Inflammatory Syndrome (Neuro-IRIS) in Patients with HIV and AIDS. A Case-based Tutorial.

S Sapozhnikova[1], B Marsh[1], A Grigorian[1], V Velayudhan[1]
[1]*SUNY Downstate Medical Center, Brooklyn, NY*

Purpose
To demonstrate distinguishing imaging characteristics of opportunistic infections affecting patients with HIV/AIDS. To illustrate the imaging and clinical features associated with

neuro-IRIS. To emphasize importance of integration of the clinical and laboratory findings with the imaging presentation of the disease in order to arrive at a diagnosis in a patient with HIV/AIDS.

Materials and Methods

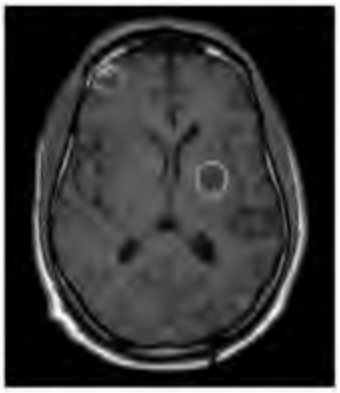
A series of unknown cases will be presented, accompanied by multiple choice questions. Pertinent imaging, clinical and laboratory findings will be highlighted in the discussion of the cases and the answer choices to help participants hone their diagnostic approach. Cases include: toxoplasmosis, lymphoma, progressive multifocal leukoencephalopathy, IRIS, cytomegalovirus ventriculitis, HIV encephalopathy, cryptococcal meningitis.

Results

Imaging plays an integral role in diagnosis and management of patients with HIV/AIDS, especially in evaluation of intracranial infections. Prompt diagnosis is critical as morbidity and mortality from untreated opportunistic infections is high. In some cases, the imaging findings are pathognomonic, but in many nonspecific. Correlation with the patient's clinical course and laboratory findings often portrays a characteristic picture allowing to derive at a specific entity or at least to narrow the differential diagnosis. With an advent of highly active retroviral therapy (HAART), the incidence of new AIDS cases and opportunistic infections have decreased dramatically. Treatment with HAART, however, can result in IRIS, an abnormal inflammatory response to a subclinical or previously treated infection. The condition manifests itself weeks to months post initiation of HAART and frequently alters imaging appearance of the underlying disease. Post-treatment clinical deterioration associated with atypical imaging findings and improving laboratory values is suspicious for IRIS.

Conclusions

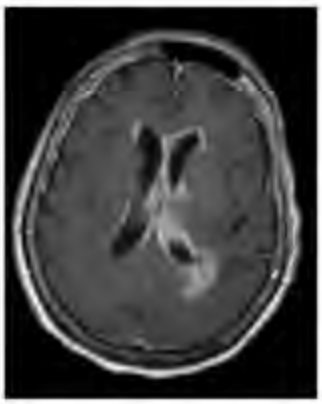
It is important to recognize imaging characteristics of common opportunistic infections. Coupled with clinical and laboratory findings, these will typically lead to making a correct diagnosis. Recognition of unusual imaging features post-treatment with HAART also can help in differentiating IRIS from the disease progression, reducing unnecessary hospitalizations and diagnostic interventions.



35 year old male with HIV, toxoplasmosis and known cryptococcal meningitis. Axial postcontrast T1WI demonstrates rim enhancing lesions in the right frontal lobe and left basal ganglia.



38 year old male with AIDS and toxoplasmosis. Axial postcontrast T1WI demonstrates a rim enhancing right thalamic lesion.



84 year old female with HIV and CMV ventriculitis. Axial postocontrast T1WI demonstrates diffuse, irregular enhancement along the lateral ventricles.



AIDS patient with progressive multifocal leukoencephalomalacia (PML) and lymphoma. Axial postcontrast T1WI demonstrates solidly enhancing lesion in the left frontal lobe (lymphoma) and incomplete rim enhancement in parietal white matter due to PML.

(Filename: TCT_eEdE-27_ASNR2017_final.jpg)

eEdE-71

6:30AM - 3:00PM

Large Sellar Masses: Atypical Pituitary Adenomas Versus Parasellar Masses

N Das[1], A Mahajan[1], A Malhotra[1], W Zucconi[1], R Bronen[1]
[1]*Yale School of Medicine, New Haven, CT*

Purpose
To demonstrate atypical imaging appearances of pituitary adenomas and contrast these imaging features to lesions invading the sella turcica from inferior, lateral or superior locations.
Materials and Methods
Pituitary adenomas with atypical MR imaging appearances will be presented - adenomas extending to suprasellar, cavernous sinus, bone invasion, sphenoid sinus, or clivus. These unusual pituitary macroadenomas will be contrasted with abnormalities arising adjacent to the sella. This review is based on an assessment of our database of 20,000 MRI reports with the terms ("pituitary" or "sella") and ("lesion", "mass" or "adenoma").
Results
Although large pituitary adenomas may have very unusual appearances, they usually are centered in the sella turcica. They should be differentiated from lesions originating from: (1) Below the sella - clival chordoma, esthesioneuroblastoma, lymphoma and squamous cell carcinoma, (2) Above the sella – craniopharyngioma, hypothalamic hamartoma, germinoma, arachnoid cysts, lymphoma, astrocytoma and radiation necrosis, (3) Lateral to the sella – meningioma, schwannoma, aneurysms. We will review the typical imaging features of these abnormalities and how they differ from unusual pituitary adenomas. A limited differential diagnosis can be obtained by (a) appropriately assessing the epicenter of the lesion, (b) understanding the typical imaging features of each particular entity, and (c) correlating clinical parameters, such as hormonal abnormalities characteristic of pituitary adenomas.
Conclusions
While it may not always be possible to definitely discern the etiology of a particular lesion, a reasonable limited differential diagnosis can be achieved.

Image 1: Imaging features: cystic rim-enhancing sellar/suprasellar lesion. Ddx: craniopharyngioma, pathology: adenoma

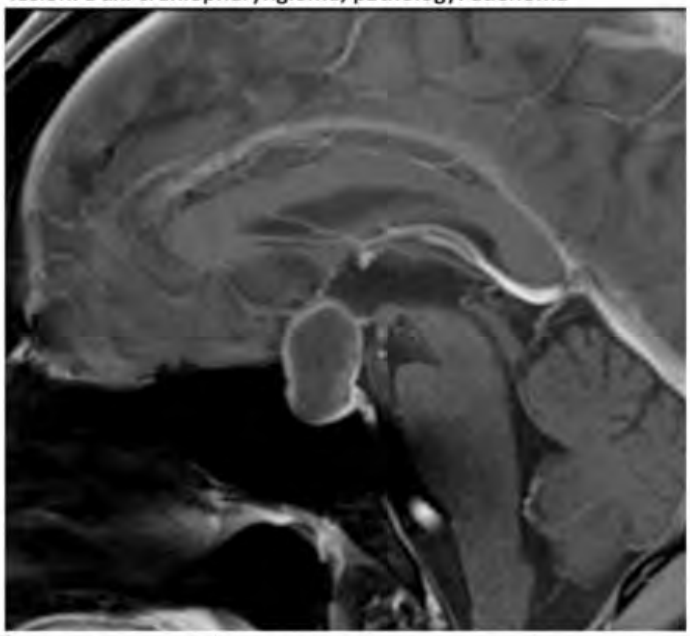


Image 2: Imaging features: enlarged, enhancing pituitary gland and stalk. Ddx: lymphocytic hypophysitis, diagnosis: metastasis

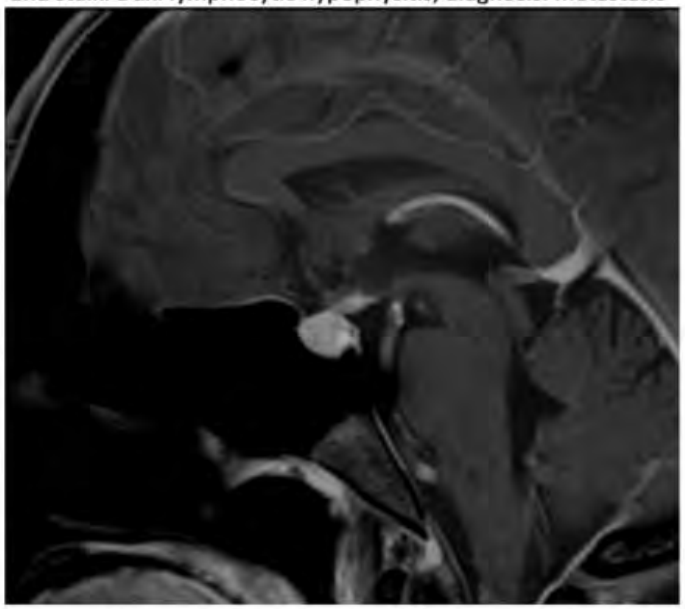


Image 3: Imaging features: large enhancing mass invading clivus, extending into the nasal cavity and pharynx. Diagnosis: adenoma

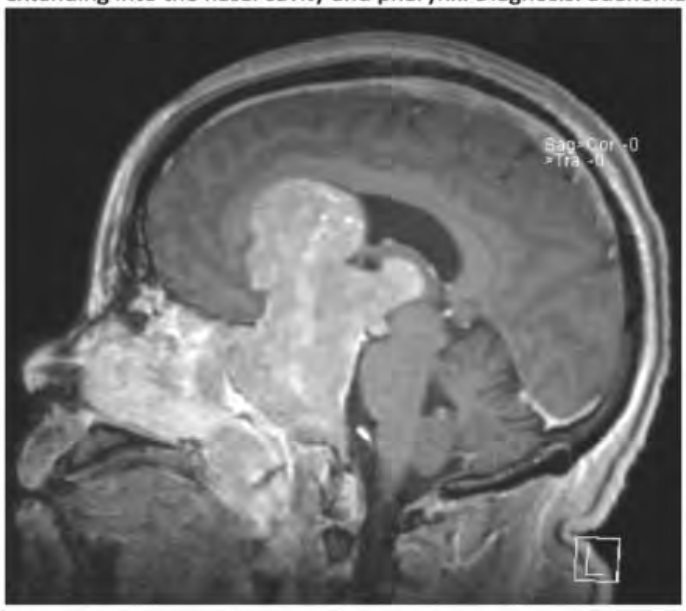
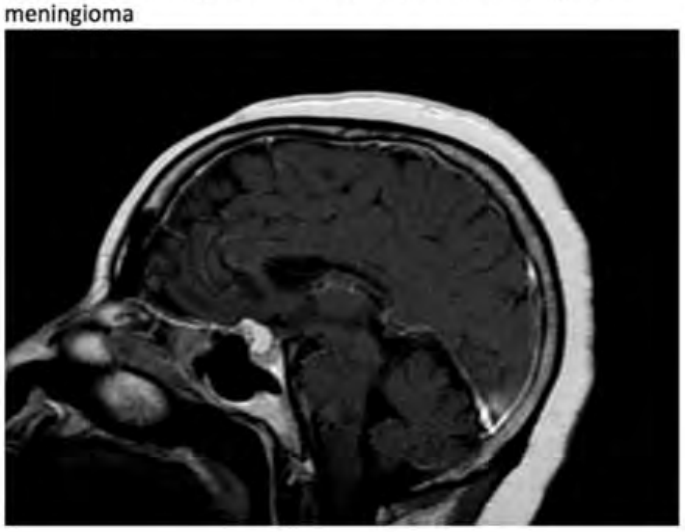


Image 4: Aid in diagnosis: pituitary displacement. Diagnosis: meningioma



(Filename: TCT_eEdE-71_Images.jpg)

eEdE-109

6:30AM - 3:00PM

MR Imaging of Neurological Emergencies: What On-Call Radiologists Need to Know

E Mtui[1], J Rozell[1], S Li[2]

[1]Baystate Medical Center, Springfield, MA, [2]Baystate Medical Center - UMass Medical School, Springfield, MA

Purpose

Although computed tomography (CT) is usually the first line of imaging method to evaluate emergent neurological situations in the emergency room, magnetic resonance (MR) has its special use and own validity to diagnose certain neurological disease entities in the ER. The aim of this educational exhibit is to review several common and uncommon neurological clinical scenarios such as headache, dizziness, weakness, back pain, altered mental status, numbness, and generalized trauma, that warrant the use of emergent brain and spine MRI in the emergency room setting when initial findings on CT were not diagnostic.

Materials and Methods

Noteworthy cases will be provided with discussion focusing on presenting clinical signs and symptoms, diagnostic planning, and initial CT imaging. Final diagnosis and MRI imaging characteristics for each associated pathology will be provided with follow-up discussions focused on the explanation for the use of emergent MRI and the consequences of missed diagnoses.

Results

1. Discuss presenting neurological clinical signs and symptoms for each case and initial CT imaging findings if available. 2. Discuss diagnostic planning and reasoning for use of emergent MRI for suspected pathologies of the brain and/or spine. 3. Discuss focused characteristic MR imaging findings for each provided final diagnosis. 4. Discuss differential diagnoses for the imaging characteristics and the consequences of either misinterpretation or failure to use emergent MRI.

Conclusions

Emergent neuroradiology has become key in the evaluation and appropriate triage of fairly common presenting chief complaints such as headache, dizziness, weakness, back pain, altered mental status, numbness, and generalized trauma. Though more often than not most of these subjective chief complaints result in negative radiologic findings, it is critical to both rapidly and accurately prioritize patients who require emergent neurological interventions from those who are clinically more stable.



(Filename: TCT_eEdE-109_Figure12-MRISpinalEpiduralAbscess.jpg)

eEdE-81

6:30AM - 3:00PM

MR Spectroscopy Physics for Residents & Fellows

A Chan[1], P Moftakhar[2]
[1]Christiana Care Healthcare System, Newark, DE, [2]Christiana Healthcare system, Newark, DE

Purpose
The purpose of this electronic educational exhibit is to introduce the basic physics and

concepts of magnetic resonance spectroscopy (MRS) to residents and fellows. In addition, the factors influencing spectral quality and their associated remedies along with common "behind the scene" postprocessing techniques will be explained.
Materials and Methods
An illustrative approach utilizing Microsoft Powerpoint and various other graphical software/applications will be employed to explain the basic physics of MRS and image acquisition/processing methods.
Results
The techniques of spectroscopy have been long employed by chemists elucidating the architecture of compounds well before the advent of nuclear magnetic resonance. Since that time, MRS has undergone exponential improvements and modifications, however, the complexities of which are unbeknownst to most residents and fellows. This presentation will emphasize conceptual understanding of the image acquisition/processing of MRS. The basic physics of commonly used single and multi-voxel sequences (such as PRESS, STEAM, and MVSI) will be explained followed by highlighting the TE value in clinical problem solving. Next, the presentation will discuss factors that affect spectral quality, such as nuclei sensitivity and signal contamination, which are alleviated by optimizing magnetic field strength and RF profiles, shimming field inhomogeneity, and methods of water/fat suppression. Furthermore, the orchestration of postprocessing techniques that result in the enhancement of the measured spectral signal, such as eddy current correction, noise reduction, resolution enhancement, apodization, zero filtering, phase correction, and baseline correction will be discussed. Throughout the presentation, a heavy reliance on illustrations will be utilized to enhance the understanding of MRS.
Conclusions
This electronic educational exhibit serves as a primer for residents and fellows to understand the foundations of MRS. Topics will include factors that affect spectral quality and their associated remedies, basics physics of image acquisition, and postprocessing methods will be discussed.

eEdE-43

6:30AM - 3:00PM

Multiple Cerebral Microhemorrhages- Common and Infrequent Etiologies and Mimics

V Tsehmaister-Abitbul[1], N Zakhari[2], C Torres[3]
[1]University of Ottawa, Ottawa, Ontario, [2]The Ottawa Hospital, Ottawa , Ontario, [3]The Ottawa Hospital, Ottawa, Ontario

Purpose
To review the differential diagnosis of cerebral microhemorrhages on MRI.

Materials and Methods
This pictorial essay will discuss the common, infrequent and rare etiologies of multiple cerebral microhemorrhages and their potential mimics.
Results
Cerebral microhemorrhages are defined as small, punctuate hypointense lesions of < 10 mm in diameter, seen in T2* gradient-recall echo (GRE) and susceptibility-weighted (SWI) magnetic resonance imaging (MRI) sequences, corresponding to areas of hemosiderin breakdown products from prior microscopic hemorrhages. With the recent advances in MRI technology, the increasing widespread use of higher magnetic field strength (3 Tesla) and the inclusion of susceptibility-weighted imaging (SWI) in the protocols to assess the brain, cerebral microhemorrhages have become an increasingly common neuroimaging finding. The SWI sequence augments the "blooming" effects thereby raising the sensitivity for detection of microbleeds. Although previously considered clinically silent, their important clinical relevance is now recognized, particularly, in the context of aging, cerebrovascular disease and dementia. Chronic systemic hypertension and cerebral amyloid angiopathy (CAA) are the most common causes of microhemorrhage. Less frequent causes include diffuse axonal injury (DAI), vasculitis, cerebral autosomal-dominant arteriopathy with subcortical infarcts and leukoencephalopathy (CADASIL) and hemorrhagic micrometastases. In this educational exhibit, we will show examples of these common and infrequent causes of microbleeds as well as other, rare etiologies such as familial cavernomatosis, fat emboli, septic emboli and disseminated intravascular coagulation (DIC). Possible mimics of cerebral microhemorrhages arise from the T2*-weighted MRI sensitivity to paramagnetic substances other than hemosiderin, including calcifications, iron deposits, deoxyhemoglobin, metastatic melanoma, flow voids in pial blood vessels and partial volume artifact from bone.
Conclusions
As neuroradiologists, we should be familiar with the many possible causes of multiple microhemorrhages in order to suggest the most appropriate diagnosis and guide patient management. In this pictorial essay, we address common, infrequent and rare causes of cerebral microbleeds based on the GRE or SWI sequences and we discuss the potential mimics.

eEdE-72

6:30AM - 3:00PM

Name That Tumor: Brain Tumor Challenge

J Fritz[1], A Ajam[2], D Boulter[2], W Slone[3]
[1]Wexner Medical Center at The Ohio State University, Columbus, OH, [2]The Ohio State University Wexner Medical Center, Columbus, OH, [3]The Ohio State University Wexner Medical, Columbus, OH

Purpose

There is a wide variation of appearances of brain tumors, and the imaging appearance provides key information for the diagnosis. The purpose of this exhibit is to provide an interactive review of common and uncommon brain tumors, with inclusion of common mimics in a quiz format.

Materials and Methods

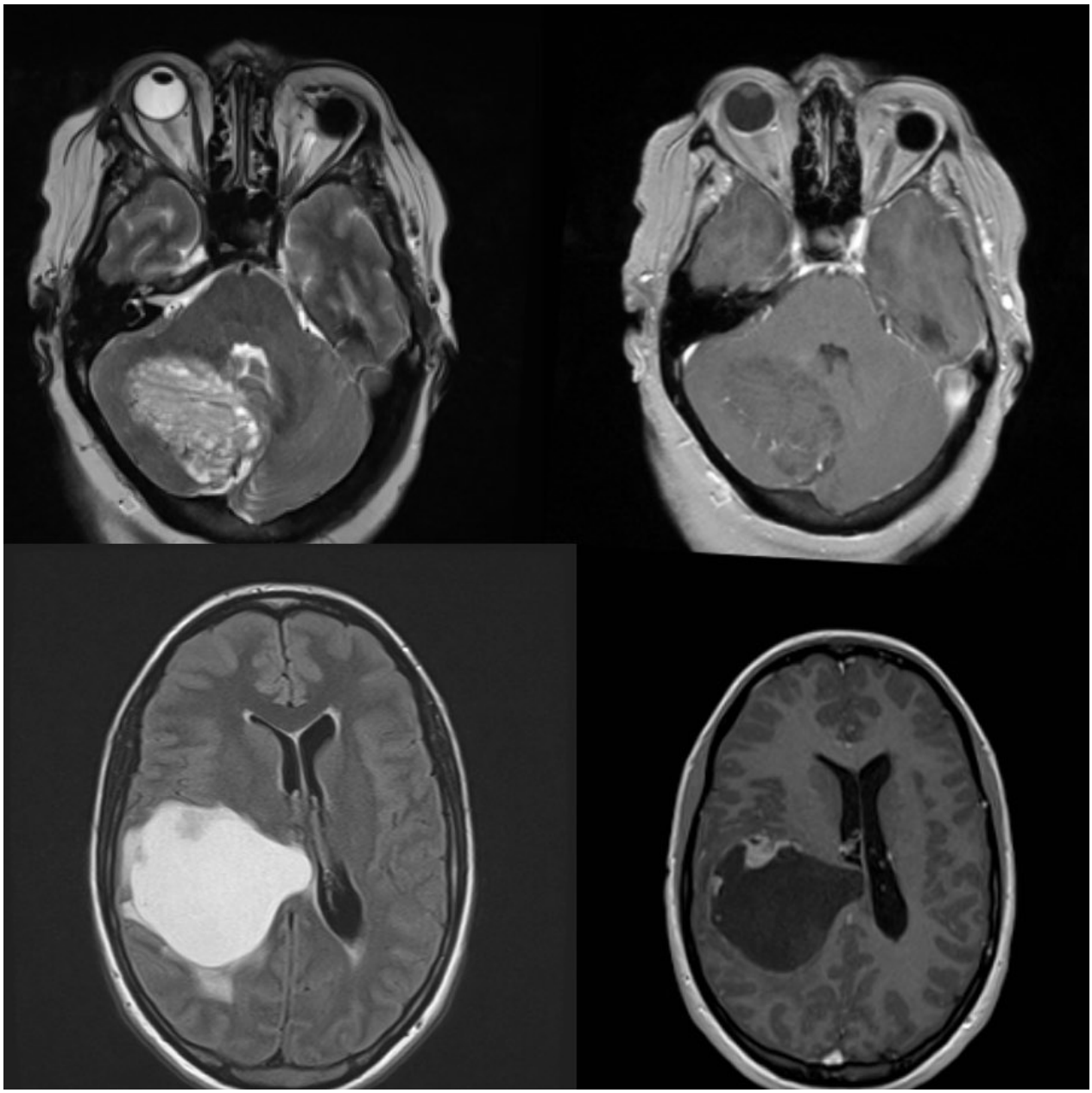
Imaging-based quiz with multiple choice questions of brain tumors. The images will be presented as unknowns, with 1-2 multiple choice questions regarding the diagnosis and key clinical features.

Results

Following each question, there is a brief discussion of the correct answer, including key imaging findings and treatment. A broad range of tumors will be included. This will range from common and classic tumors, such as oligodendrogliomas and dysplastic cerebellar gangliocytoma, to rare tumors, such as astroblastomas. A focused differential will be presented based on the imaging characteristics. Common mimics will be included in the quiz to better simulate routine reading and emphasize the imaging differences.

Conclusions

This exhibit will provide an interactive review of brain tumors and common mimics. This will allow the viewer to test their knowledge of brain tumors and to form a narrow differential. The viewer will become familiar with the imaging features which allows for better differentiation from tumors and common nonmalignant mimickers.



(Filename: TCT_eEdE-72_Braintumor.jpg)

eEdE-76

6:30AM - 3:00PM

Neuroanatomical Self-Assessment Educational Tool

D Saunders[1], H Cliffe[1], I Craven[1], D Warren[1], J Macmullen-Price[1], S Currie[1]
[1]*Leeds Teaching Hospitals Trust, Leeds, West Yorkshire*

Purpose
To provide a radiology-primed educational tool that provides the user with an accessible and

interactive review of neuroanatomy using pathology with some reference to the functional impact of individual pathologies.
Materials and Methods
A user-friendly electronic educational exhibit is presented that incorporates high quality radiological images and a range of pathologies to demonstrate important anatomical landmarks and associated functional deficits.
Results
Users are invited to an electronic educational radiological self-assessment tool covering surface, vascular, cisternal, cranial nerve and skull-base anatomy. The use of pathology to highlight the anatomical structure or region provides the learner with additional clinical relevance thus progressing the learner's path through the cognitive taxonomy. Succinct descriptions in a bulleted format empower rapid reading and review. Key learning points are emphasized and summarized.
Conclusions
This exhibit will serve as a valuable review for neuroradiologists and for other practicing neuroscience clinicians. It also will prove beneficial to students wishing to acquire an understanding of the anatomy in relation to function and pathology of the intracranial neuroaxis.

eEdE-02

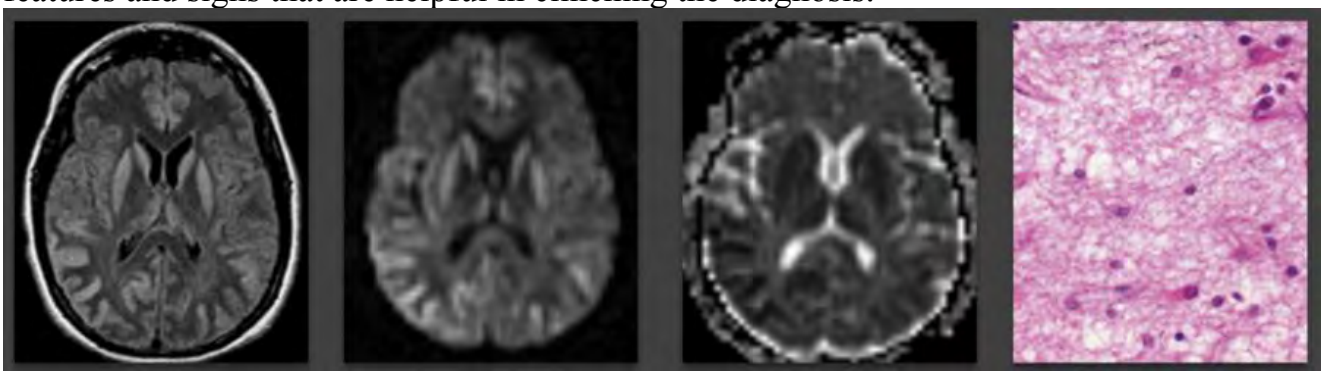
6:30AM - 3:00PM

Neurodegenerative Diseases from Accumulation of Substances in the Brain: What the Radiologist Needs to Know

J Kim[1], J Starkey[2], Y Numaguchi[3], T Moritani[4]
[1]University of Michigan, Ann Arbor, MI, [2]St. Luke's International Hospital, Tokyo, FM, [3]St. Luke's International Hospital, Tokyo, Tokyo, [4]University of Iowa Hospitals and Clinics, Iowa City, IA

Purpose
The purpose of this presentation is to illustrate various imaging manifestations of neurodegenerative diseases and to present a systematic approach for the radiologist.
Materials and Methods
Abnormal substances that can cause primary neurodegeneration are from Tau (Tauopathy), α-synuclein (Synucleinopathy), TDP-43, Polyglutamine, Prions, and iron accumulation (neurodegeneration with brain iron accumulation). We will show several cases with imaging and histopathologic correlation for each of these accumulating substances. We also will describe common imaging patterns and present a systematic approach to help the radiologist make the correct diagnosis.
Results
Aggregation and tangles of Tau (Tauopathy) are responsible for Alzheimer (β-amyloid),

frontotemporal dementia, progressive supranuclear palsy, corticobasal degeneration. Aggregation of α-synuclein (Synucleinopathy) include Parkinson's, multisystem atrophy, and dementia with Lewy bodies. Clumping of TDP-43 is found in Amyotrophic lateral sclerosis and frontotemporal lobar degeneration. Polyglutamine is responsible for Huntington's disease, dentatorubral-pallidoluysian atrophy, spinocerebellar ataxia. Prions are involved in Creutzfeldt-Jakob disease and Gerstmann-Straussler-Scheinker disease. High levels of iron in the brain are seen in a category of diseases called neurodegeneration with brain iron accumulation (NBIA), which include pantothenate kinase-associated neurodegeneration (PKAN) and static encephalopathy of childhood with degeneration in adulthood (SENDA).
Conclusions
Neurodegenerative diseases of the brain often have distinct and characteristic imaging features and signs that are helpful in clinching the diagnosis.



(Filename: TCT_eEdE-02_CJD.jpg)

eEdE-10

6:30AM - 3:00PM

Neuroimaging in Atypical Parkinsonian Disorders

M Ollivier[1], B Law-Ye[1], D Leclercq[1], D Dormont[1], N Pyatigorskaya[1]
[1]*AP-HP, Pitié-Salpétrière hospital, Paris, Ile de France*

Purpose
Atypical parkinsonian disorders (APD) are a heterogenous group of neurodegenerative diseases including progressive supranuclear palsy (PSP), multiple system atrophy (MSA) and cortico-basal degeneration (CBD). Distinguishing the different APD clinically carries a high rate of misdiagnosis because they share overlapping clinical features especially at the early stage of the disease. The purpose of this review is to illustrate the differentiating features of APD at MRI. The various MRI sequences helpful in the differentiation will be discussed, including newer methods, such as susceptibility-weighted images (SWI), diffusion tensor imaging (DTI), MR spectroscopy.
Materials and Methods
We reviewed the literature and selected interesting imaging findings of APD among patients

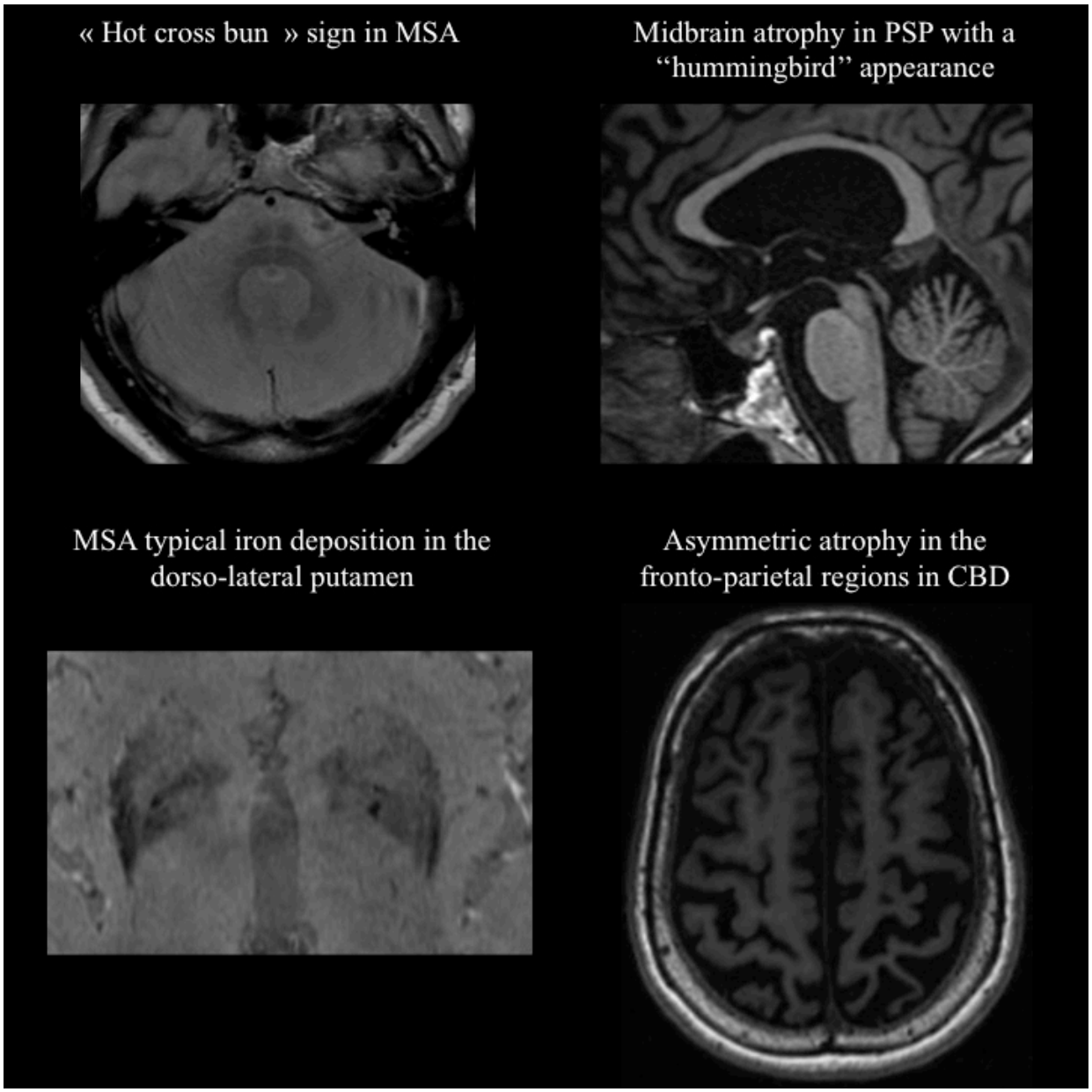
explored in our institution between 2014 and 2016. These cases are presented in order to highlight the useful elements for radiological diagnosis.

Results

- In PSP, MRI shows midbrain atrophy with a "hummingbird" appearance. The atrophy and signal changes in the superior cerebellar peduncle may be found (1). - In MSA, the volume of the cerebellum, thalamus, putamen, and brainstem are significantly reduced. Measurement of middle cerebellar peduncle (MCP) width may be useful (2). Putaminal hyperintense rim sign, "hot cross bun" sign in the pontine raphe and hyperintensity of the MCP on T2-weighted sequences are frequently observed. - In CBD, MRI usually shows asymmetric atrophy in the fronto-parietal regions (1). Different patterns of iron deposition in the brain are reported in APS. SWI detects the MSA typical iron deposition in the dorso-lateral putamen and the posterior thalamus (3). Microstructural region-specific changes can be identified by DTI in the different forms of APS (4). 1H-MRS is able to detect the presence of biochemical alterations, such as reduced NAA and increased mI, markers of neuronal degeneration and glial reaction, respectively, in the cerebellar hemispheres in APS (5).

Conclusions

Morphological and advanced MRI techniques are helpful tools to enhance the accuracy of clinical diagnosis in APS.



(Filename: TCT_eEdE-10_Diapositive1.jpg)

eEdE-01

6:30AM - 3:00PM

Neuroimaging in Liver Diseases

R Soliman[1], A Siddiqui[2], M Alsadiq[3], T Booth[4]
[1]Asyut University Hospitals/ King's College Hospital, Egypt-Asyut/ London,London, [2]King's College Hospital NHS Foundation Trust, London, London, [3]King's College Hospital, London, London, [4]Kings College Hospital, London, CA

Purpose
• To comprehensively review the neuroimaging findings associated with liver disorders in both adult and pediatric patients. • To understand the related pathogenesis and clinical findings.
Materials and Methods
We demonstrate the different neuroimaging findings associated with liver diseases and the related clinical findings using data obtained from a UK Academic Health Science Center where there are world-leading hepatology and neurosciences departments. We describe the pathophysiological mechanism related to each imaging finding, with a particular focus on MRI.
Results
Neurological clinical findings often are associated with patients with hepatic dysfunction. In adults, it is mainly caused by ammonia and manganese neurotoxicity. The most, well-recognized form is hepatic encephalopathy (HE). It reflects a wide spectrum of neurological manifestations, including neuropsychiatric, cognitive and motor disorders and may range from mild cognitive impairment to severe coma. HE is most commonly caused by acute liver failure as well as by chronic liver diseases such as liver cirrhosis. Acquired hepatocerebral degeneration (AHD) manifests predominantly as a motor disorder. It is due to manganese deposition in the basal nuclei with the formation of Alzheimer type II astrocytes. Therefore, both ADH and HE share some pathological similarity and may exhibit similar imaging findings. The most common MRI finding in liver disease is T1 hyperintensity in the basal ganglia. However, there are multiple other findings such as brain edema, white matter T2 hyperintensity and atrophy as well as cortical laminar necrosis which will be discussed in detail. In addition to the neurological and neuroimaging findings that occur as a consequence of hepatic dysfunction, we describe some conditions in which both the hepatic and central nervous system are simultaneously affected, e.g., alcohol-related changes and polycystic liver syndrome. In the neonate and pediatric age groups, central nervous system involvement in patients with liver disease is mainly caused by bilirubin toxicity, in addition to hyperammonemia. We describe the associated neuroimaging findings, as well as those associated with the rarer metabolic and genetic disorders.
Conclusions
A wide range of neurological findings are associated with patients with hepatic dysfunction. A combination of neuroimaging and clinical findings often helps to determine the underlying cause and therefore allows appropriate early treatment and the prevention of any subsequent complication.

eEdE-67

6:30AM - 3:00PM

Neuroimaging Manifestations of Hematologic Malignancies: A Compartmental Approach

K Buchanan[1], A Chan[1], R Fulbright[2], J Baehring[1], M Johnson[3]
[1]Yale University, New Haven, CT, [2]Yale University Medical Center, New Haven, CT, [3]Yale Univ. School Of Medicine, New Haven, CT

Purpose

Neurologic manifestations of hematologic malignancies (leukemias, lymphomas, myeloma) are common and multi-faceted. They can best be understood from a compartmental approach. Significant morbidity can result from hematogenous spread, leptomeningeal dissemination, infiltration along neurovascular structures, peripheral or cranial nerves. Direct tumor invasion can occur from adjacent bone or bone marrow. Indirect effects from leukostasis, coagulopathy or a resorptive hydrocephalus often are under-reported. Involvement can vary widely with the malignancy subtype; with frequent intraparenchymal involvement by aggressive non-Hodgkin lymphoma, leptomeningeal involvement in acute lymphoblastic leukemia (ALL), and more prominent dural infiltration in myelogenous leukemia. Systematic evaluation of these compartments is fundamental to ensure adequate evaluation for subtle lesions and early detection of asymptomatic involvement. This illustrated review will demonstrate the protean manifestations of hematologic malignancies with a compartmental approach to facilitate accurate diagnosis.

Materials and Methods

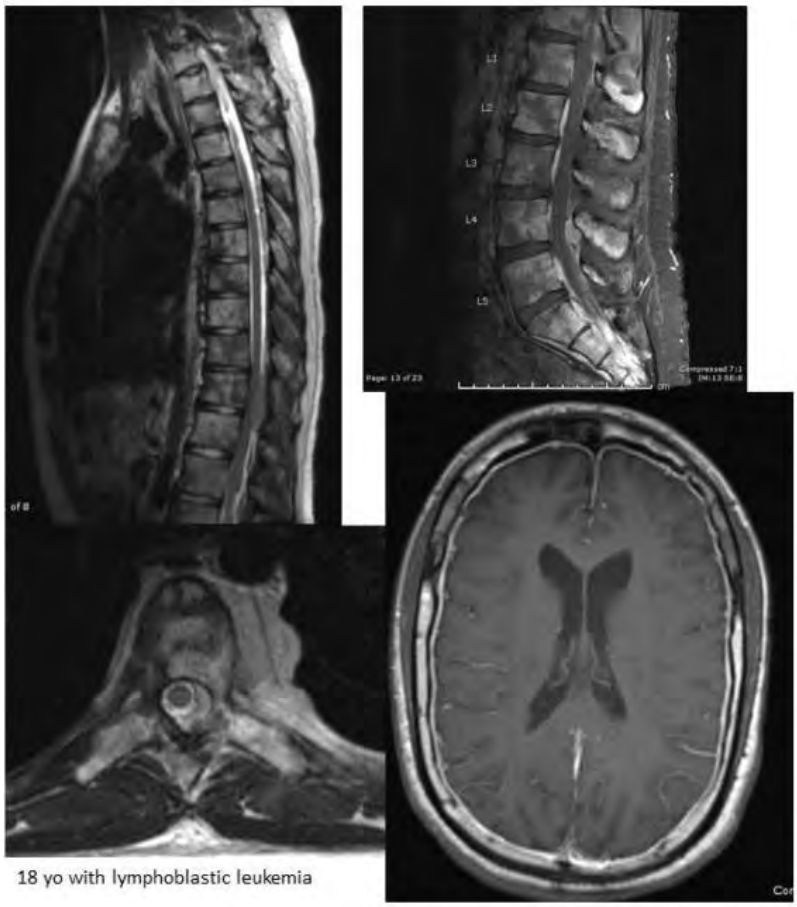
Exemplary cases of hematologic malignancies with neurologic involvement from our clinical archives will be utilized to demonstrate important compartments as follows: Osseous and bone marrow, extradural space, leptomeningeal, parenchymal, intravascular and neuro-lymphomatosis. Indirect effects of hematologic malignancy such as leukostasis, coagulopathy or a resorptive hydrocephalus also will be demonstrated. These imaging findings are correlated with the patient's disease type, prognosis and treatment.

Results

The compartmental approach to the analysis of neurologic findings in hematologic malignancies facilitates recognition and differential diagnosis in this complex group of patients. Detection of pathology is enhanced with a compartmental-based search pattern. Lesions are often in atypical locations as compared with solid neoplasms and may be subtle and possibly be overlooked without a structured approach.

Conclusions

Knowledge of the multiple presentations of hematologic malignancies in the central and peripheral nervous systems coupled with a pattern-based compartmental approach is crucial for accurate recognition and diagnosis. This approach is important and can increase sensitivity and specificity for the protean neurologic manifestations of hematologic malignancy.



(Filename: TCT_eEdE-67_thumbnail_hematologic_malignancies.jpg)

eEdE-58

6:30AM - 3:00PM

Neurologic Injury Following Oncologic Treatment

P Puac[1], S Ferraciolli[2], C Vallejo[1], A Rodriguez[1], F HIRATA[2], L Fajardo[2], M ARANHA[2], L Lucato[2], C Leite[2], M Castillo[1]
[1]University of North Carolina at Chapel Hill, Chapel Hill, NC, [2]Instituto de Radiologia do HC-FMUSP, Sao Paulo, Brazil

Purpose
The purpose of this exhibit is to review the imaging abnormalities found during and after chemotherapy, immunotherapy, and/or radiotherapy in the central nervous system (CNS).
Materials and Methods
Side effects of oncologic therapies are classified in a timeline fashion after initiation of therapy into acute, subacute and chronic stages. The most common drugs and radiotherapy regimens for oncologic treatment producing neurotoxicity are discussed and imaging

findings, behavior of changes (re/irreversibility), treatment dose, administration route and patient vulnerability also are addressed. Conventional and advanced MRI sequences which provide clues and key findings are emphasized.

Results

Classification of neurologic injuries: Chemotherapy: • Acute [posterior reversible encephalopathy syndrome (PRES), acute reversible encephalopathy, aseptic meningitis, ascending polyradiculoneuropathy, vascular events]. • Chronic [leukoencephalopathy, atrophy, mineralizing microangiopathy (Fig.1). Immunotherapy]: • Acute [progressive multifocal leukoencephalopathy (PML), hypophysitis (Fig. 2), pseudoresponse]. • Subacute (persistent diffusion-restricted lesions, abnormal signal in subarachnoid space). Radiotherapy: • Subacute (pseudoprogression, reversible leukoencephalopathy). • Chronic [radionecrosis, stroke-like migraine attacks after radiation therapy (SMART) syndrome (Fig. 3), irreversible leukoencephalopathy, induced vascular malformations/neoplasms].

Conclusions

Neurologic complications of cancer treatment are growing because of improved survival rates due to new/better therapies. Early and accurate diagnosis of these complications prevents irreversible neurological injuries and differentiates treatment-related effects from cancer progression.

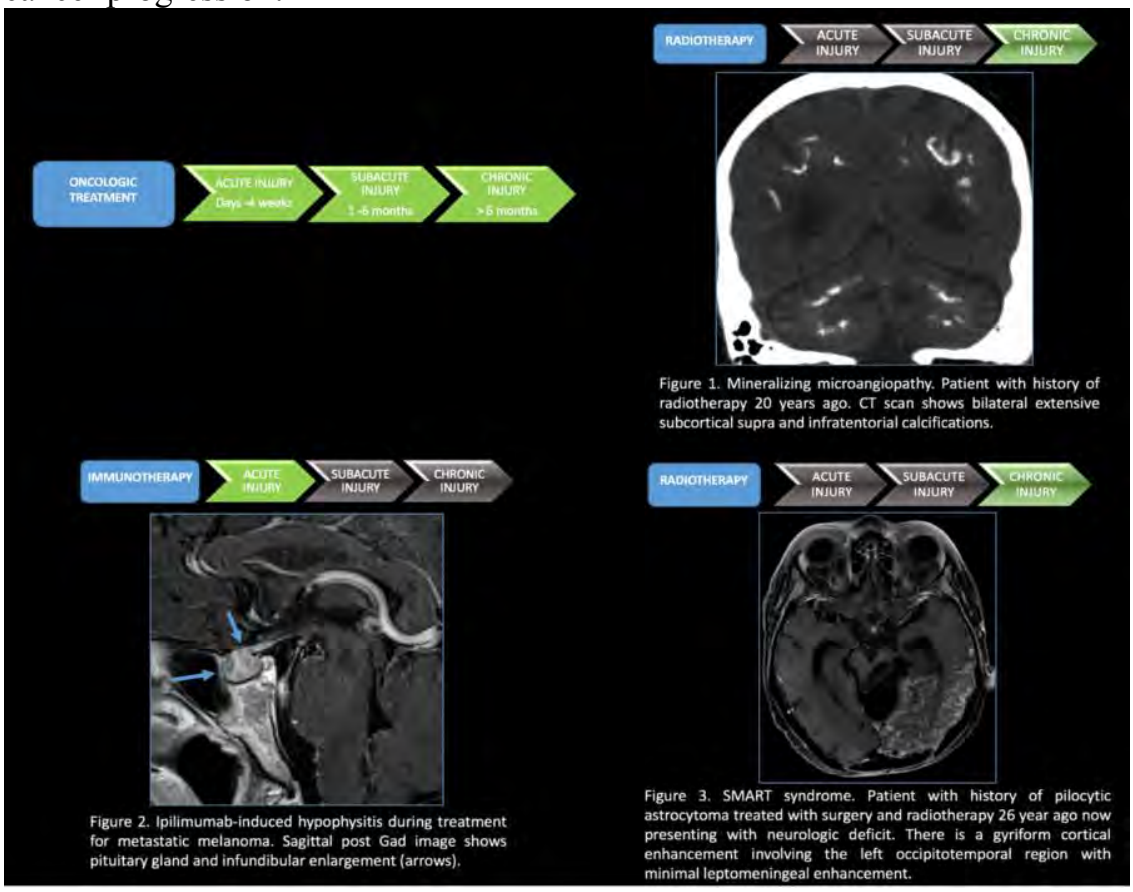


Figure 1. Mineralizing microangiopathy. Patient with history of radiotherapy 20 years ago. CT scan shows bilateral extensive subcortical supra and infratentorial calcifications.

Figure 2. Ipilimumab-induced hypophysitis during treatment for metastatic melanoma. Sagittal post Gad image shows pituitary gland and infundibular enlargement (arrows).

Figure 3. SMART syndrome. Patient with history of pilocytic astrocytoma treated with surgery and radiotherapy 26 year ago now presenting with neurologic deficit. There is a gyriform cortical enhancement involving the left occipitotemporal region with minimal leptomeningeal enhancement.

(Filename: TCT_eEdE-58_Graphicfile.jpg)

eEdE-75

6:30AM - 3:00PM

Neuroradiology Manifestations of Tumor Syndromes: An Imaging Review

W Fischer[1], A Capps[1], P Rajagopalan[1], R Seltman[1], A Kamer[1], N Koontz[1]
[1]*Indiana University School of Medicine, Indianapolis, IN*

Purpose
We provide a comprehensive guide to the imaging characteristics of tumor syndromes involving the brain, spine, and head & neck.
Materials and Methods
We performed a HIPAA-compliant retrospective review our institution's electronic medical record for illustrative cases of tumor syndromes involving the brain, spine, and head & neck, highlighting multimodality (CT, MRI, and nuclear medicine) imaging findings, as well as provide a review of the current medical literature.
Results
Several tumor syndromes have a propensity to involve the brain, spine, and head & neck. These can be subdivided into hereditary cancer syndromes, benign tumor syndromes, and the phakomatoses, although overlaps exist. Hereditary cancer syndromes confer an early onset of malignancy, sometimes manifesting as multiple independent primaries. Benign tumor syndromes may result in shortened life expectancies and significant disability. Phakomatoses present with characteristic CNS, skin, and sometimes ocular manifestations. We highlight clinicoradiololgic features and potential imaging pitfalls of several tumor syndromes, including multiple hamartoma (Cowden), Gardner, Turcot, Li-Fraumeni, Von Hippel-Lindau, multiple endocrine neoplasia, hereditary paraganglioma-pheochromocytoma, basal cell nevus (Gorlin), schwannomatosis, meningioangiomatosis, multiple cavernous malformations, Bannayan-Riley-Ruvalcaba, NF1, NF2, and tuberous sclerosis.
Conclusions
Neuroradiologists can add value through early recognition of tumor syndromes with propensity to involve the brain, spine, and head & neck. While some have a pathognomonic imaging appearance, many require review of the multi-organ system imaging findings, clinical history, and electronic medical record.

eEdE-78

6:30AM - 3:00PM

Neuroradiomics and Machine Learning: A Primer for Clinical Neuroradiologists

O Boyko[1], L Wolansky[2], A Madabhushi[3], P Tiwari[2], V Duddalwar[1]
[1]*University of Southern California, Los Angeles, CA,* [2]*Case Western Reserve University School of Medicine, Cleveland, OH,* [3]*Case Western Reserve University, CLEVELAND, OH*

Purpose
To review techniques of machine learning and faster microprocessors such as the NVIDIA DGX-1 that allows for high throughput extraction of mineable features in standard neuroimaging.
Materials and Methods
Neuroradiomics approaches include integrated approach of: 1. Image Signal (such as Density, Intensity, Echogenicity). 2. Physical Features (such as Size/Volume, Shape, Lobularity, Architecture). 3. Enhancement, Texture, Tumor-Organ Relation, Cluster Analysis. 4. Additional Layers (Genetics, Pathology, Epigenetics, Epidemiological). 5. One algorithm involves segmentation of lesion, radiomic texture features extraction, and feature selection with a support vector machine (SVM) and area under the receiver operating characteristic curve (AUC) and classification on a training cohort with statistical analysis.
Results
This exhibit highlights workflows and algorithms in order to extract hundreds of quantifiable features from standard of care medical images such as gadolinium deposition, feature extraction of FLAIR imaging of brain tumors.
Conclusions
Neuroradiomics has many approaches including those based on state of the art faster microprocessors such as NVIDIA DGX-1 platform that holds the promise to use machine learning/deep learning and artificial intelligence to improve individualized treatment selection, advance treatment monitoring, and provide decision support models of the brain at a local practice level.

eEdE-45

6:30AM - 3:00PM

Not So Posterior, Not Always Reversible: Atypical Imaging Manifestations of Posterior Reversible Encephalopathy Syndrome

S Mohajeri Moghaddam[1], M Potchen[2]
[1]University of Rochester Medical Center, Rochester, NY, [2]University of Rochester Medical Center, Rochester , NY

Purpose
Posterior reversible encephalopathy syndrome (PRES) was first described in association with eclampsia and those undergoing organ transplantation, though it also has since been linked to patients with sepsis with multi-organ failure, cytotoxic therapeutic agents, and those with autoimmune diseases. Classically, brain imaging in PRES demonstrates symmetric parieto-occipital vasogenic edema. However, atypical imaging abnormalities are being described more than previously perceived, expanding our understanding of the pathophysiological processes that underlie this syndrome.

Materials and Methods

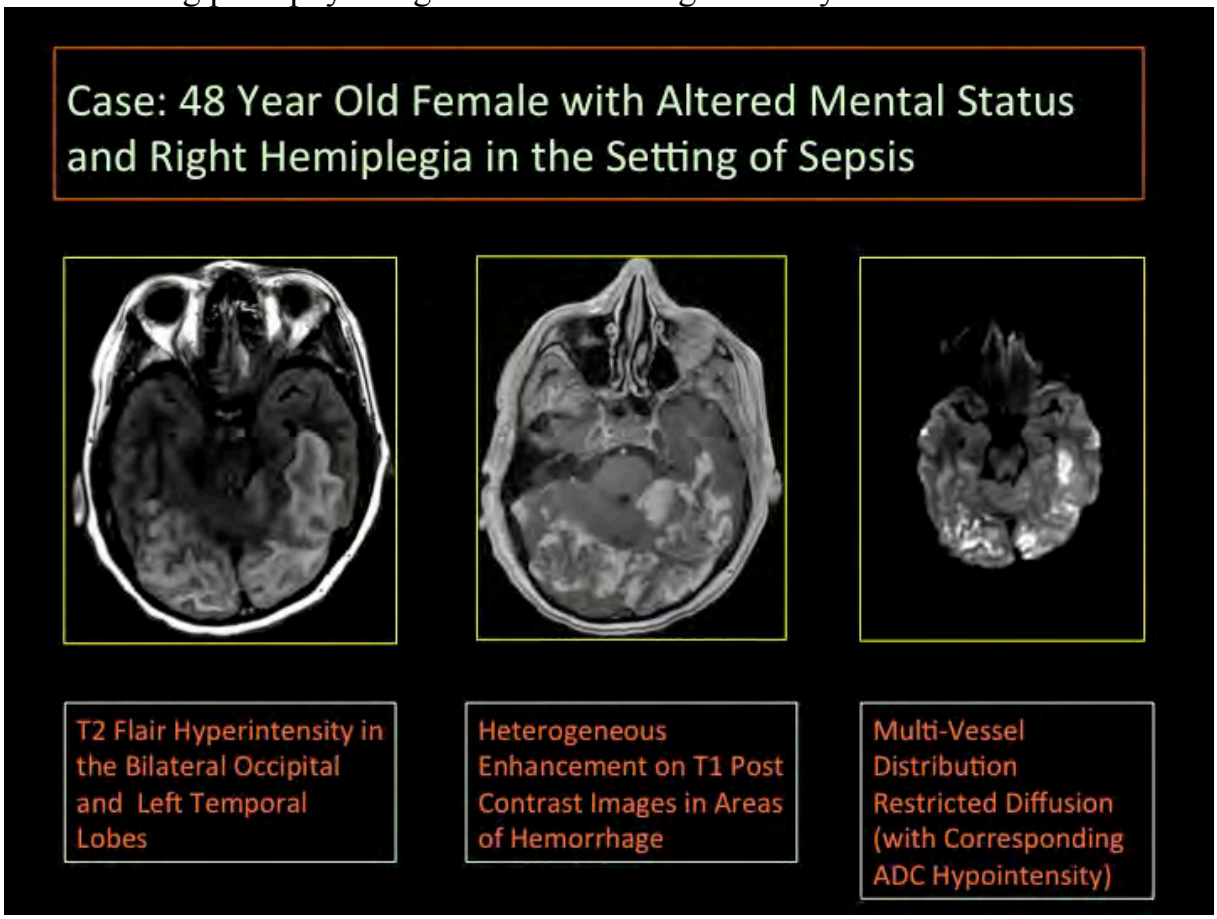
We will review the current pathophysiological understanding of PRES. Subsequently, we will describe classic imaging findings of patients with this syndrome. We then will present a series of atypical cases of PRES, focusing on the most widely reported atypical imaging features, and describe the clinical context in which these findings arise.

Results

We will describe the wide spectrum of typical and atypical imaging features of PRES via the following approach: Distribution of Findings: Parietooccipital, Basal Ganglia, Posterior Fossa, Frontal Regions; Symmetric versus Asymmetric Findings. Complications: Presence of Restricted Diffusion, Presence and Pattern of Hemorrhage, Presence of Contrast Enhancement, Reversibility.

Conclusions

Though PRES is classically described as a clinico-radiologic syndrome with symmetric parieto-occipital vasogenic edema, several atypical features are increasingly recognized within the context of various clinical settings. Awareness of the wide spectrum of findings in PRES will aid the neuroradiologist in making the correct diagnosis, and shed light on the ever evolving pathophysiological understanding of this syndrome.



(Filename: TCT_eEdE-45_Slide1.jpg)

eEdE-112

6:30AM - 3:00PM

Ocular Injuries and Cultural Influences in Afghanistan During 5 Months of Operation Enduring Freedom

D Paz[1]
[1]*Naval Medical Center San Diego, Coronado, CA*

Purpose
Addressing the cross-cultural dynamics affecting eye protection use among Afghan military could mitigate long-term adverse sequelae in Afghanistan. Objective: To understand the origin and determine the role cultural influence plays in proper adherence to eye protection among Afghan security forces.
Materials and Methods
Design: During a 5-month period, combat casualties received ophthalmologic and radiologic evaluation to determine the extent of injury incurred, most frequently from explosive injury. A review of literature and anecdotal evidence was obtained to better understand Afghan culture and the implications of eyewear. Setting: NATO Role 3 Multinational Medical Unit, Kandahar Afghanistan is one of the busiest combat hospitals, receiving NATO/Coalition and Afghan medical evacuation patients from the majority of Afghanistan. Participants: 276 combat casualties were evaluated from September 2012 through January 2013 at Kandahar. Forty-five of these patients had further evaluation by the ophthalmologist and radiologic imaging. Many of the patients undergoing eye exams were under anesthesia for other associated injuries from blast, such as amputation. Intervention(s): Computed tomography and ophthalmologic exam under anesthesia or surgery were performed, as indicated. Main Outcome Measure(s): Proper use of eye protection in a combat environment significantly decreases the risk of ocular injury secondary to blast or gunfire injury as evidenced on clinical and radiologic examination.
Results
Results: Forty-five patients sustained ocular injury. Twenty-four were wearing eye protection and only 1 patient (4%) sustained an open globe with small rocks embedded in the sclera, however ophthalmologic intervention preserved normal 20/20 vision. Twenty-one patients were not wearing eye protection and 9 (43%) had open globes with poor visual outcome; of these 3 patients ultimately required primary enucleation.
Conclusions
Conclusions and Relevance: Marked decrease in extent and severity of ocular injury was noted in those patients wearing eye protection. Literature review and anecdotal reports provided limited background into the use of eyewear among Afghans. Cultural implications were a central theme impacting the use of eye protection, which, if addressed during the development of an Afghan military by NATO forces, could mitigate the long-term sequela of vision impairment or loss among the local population.



(Filename: TCT_eEdE-112_asnr4.jpg)

eEdE-30

6:30AM - 3:00PM

On the Cutting Edge: Current Concepts in Gamma-Knife Treatment of Trigeminal Neuralgia

J Gao[1], L Watson[2], S Cohen[2], N Madan[3], H Bedi[4]
[1]Tufts Medical Center, QUINCY, MA, [2]Tufts Medical Center, Boston, MA, [3]Tufts Medical Center, Boston , MA, [4]Tufts Medical Center, Wellesley, MA

Purpose
Vascular compression is the most common cause of trigeminal neuralgia. In recent years, Gamma Knife stereotactic radiosurgery (GK-SRS) has become well-established as a viable noninvasive management option of trigeminal neuralgia. The purpose of this exhibit is to review the trigeminal nerve anatomy, important imaging findings in diagnosis and pre-

operative planning, as well as current concepts in postradiosurgical treatment imaging of trigeminal neuralgia.

Materials and Methods

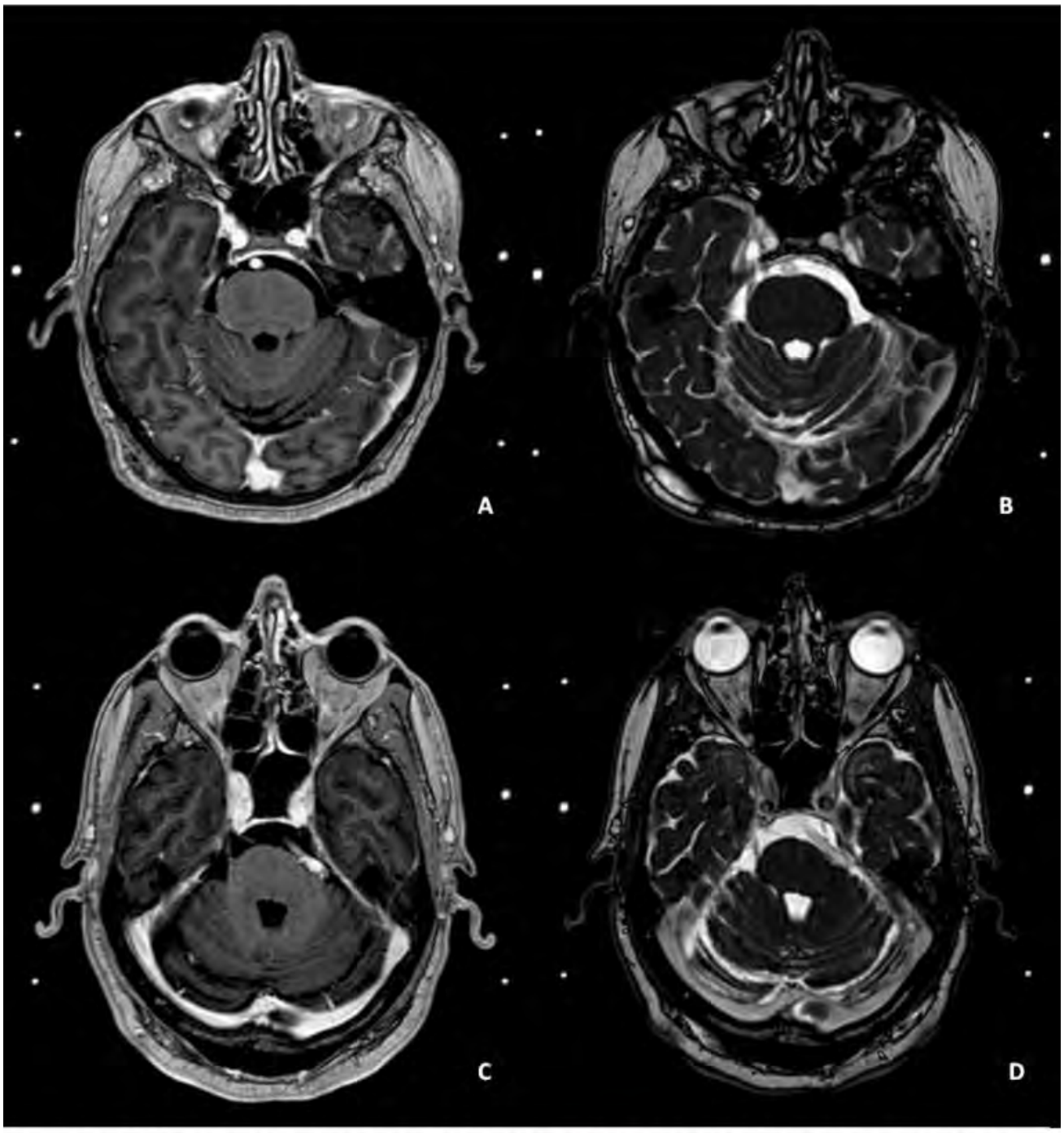
A literature review was conducted of relevant recent publications pertaining to the diagnostic imaging of trigeminal neuralgia with a focus on vascular compression, as well as most recent studies in post-treatment imaging in trigeminal neuralgia after GK-SRS. A case-based pictorial review illustrating these concepts was created.

Results

Particular attention should be paid to the dorsal root entry zone when evaluating compressive etiology of trigeminal neuralgia. Important MRI diagnostic sequences include FLAIR (either a volumetric sequence or traditional axial sequence), thin-section SSFP (BFFE, CISS, FIESTA) and postcontrast volumetric T1WI (T1 3D TFE, MPRAGE, SPGR). While MR angiography (and MR venography) are not needed routinely, it can be of benefit. Ideally, precise location of compression (including which half of the cisternal segment is being affected), type of compression (including arterial versus venous etiology), and degree of compression, should be described. Finally, recent studies have shown potential benefit to the use of diffusion tensor imaging and functional MRI as better predictor of efficacy of radiosurgery post-treatment.

Conclusions

Given that imaging frequently is obtained in both the diagnosis and treatment planning of trigeminal neuralgia, familiarity with the imaging approach is required of the radiologist. Moreover, given popularity of GK-SRS in its treatment, the radiologist also should understand the current concepts in pre and postradiosurgery imaging of trigeminal neuralgia. Such knowledge will aid the neurosurgeon and neurologist in the patient care, and ultimately improve the multidisciplinary treatment of trigeminal neuralgia.



A case of right SCA coursing adjacent to root entry zone / cisternal segment of the right trigeminal nerve, which is decreased in caliber and slightly angulated in course (A, B). A case of tortuous basilar artery swinging towards the left, immediately adjacent to the root entry zone of the left trigeminal nerve (C, D).

(Filename: TCT_eEdE-30_TN-JG.jpg)

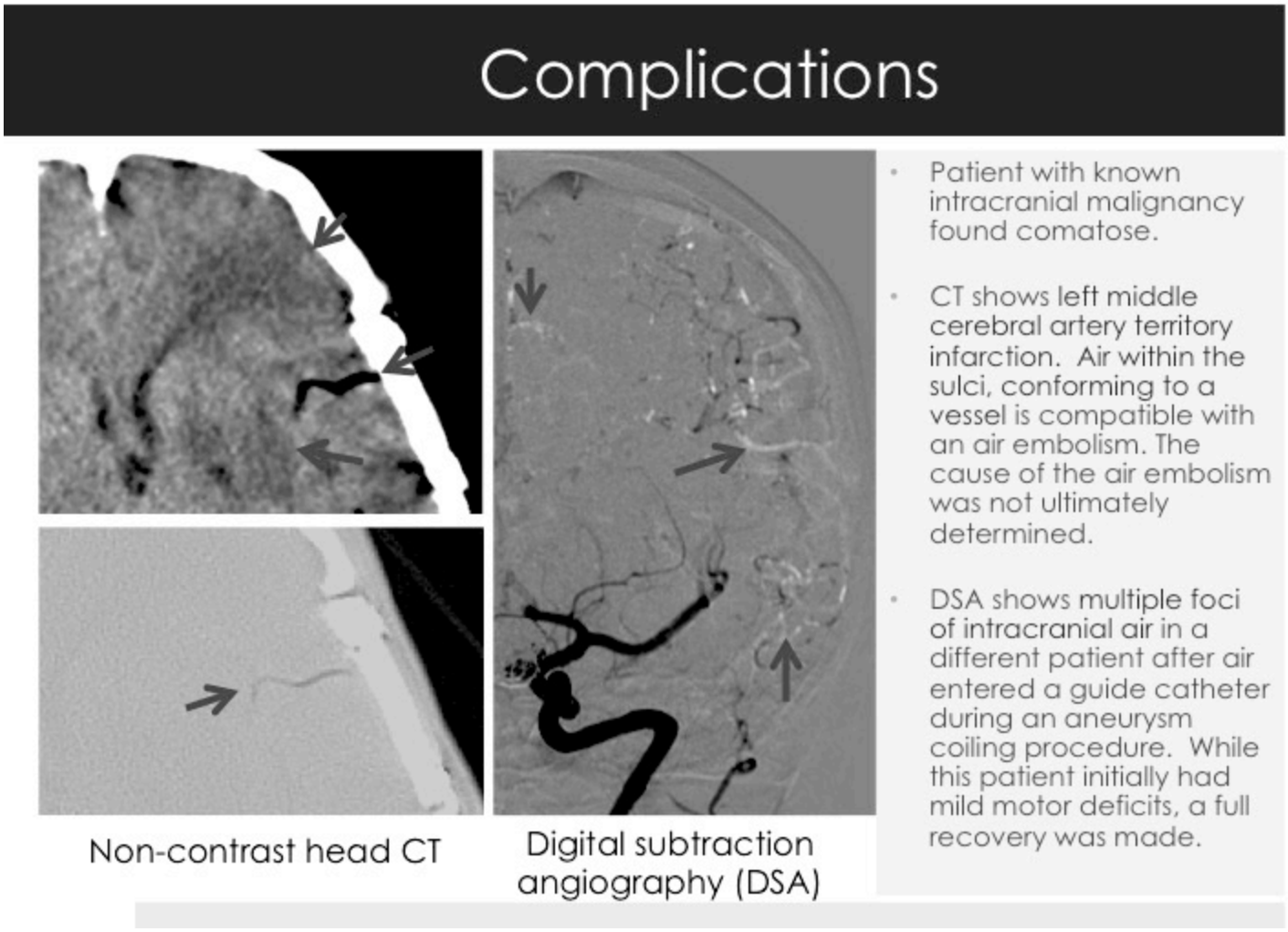
eEdE-100

6:30AM - 3:00PM

Out of Thin Air: A Review of Pneumocephalus, Its Imaging Appearance, and Why It's Always Abnormal

M Schecht[1], N Madan[2]
[1]*Tufts Medical Center, Boston, MA,* [2]*Tufts Medical Center, Boston , MA*

Purpose
The purpose of this educational exhibit is to provide an overview of the many ways in which pneumocephalus can be seen on imaging, and the differential diagnosis the radiologist should consider when pneumocephalus is identified.
Materials and Methods
This exhibit will review pneumocephalus through a series of cases collected from our institution, including the appearance on various modalities (US, CT and MRI), its anatomic locations, and various causes. Each case will provide a clinical history, a series of representative images, and a brief discussion. Cases will be organized by location (epidural, subdural, subarachnoid, intraparenchymal, intraventricular, intravascular) and by cause (traumatic, iatrogenic, postsurgical, infectious).
Results
Pneumocephalus can have multiple appearances on imaging and can be found in various locations intracranially. The finding of pneumocephalus on imaging is important and, in the absence of another apparent abnormality, should be a clue to more subtle pathology.
Conclusions
Pneumocephalus is the finding of intracranial air. It is a finding that has various causes, locations, and appearances on imaging. Pneumocephalus is always an abnormal finding and when encountered it must be explained.



(Filename: TCT_eEdE-100_pneumocephalus.jpg)

eEdE-50

6:30AM - 3:00PM

Overlapping MR Phenotypes of Diffuse Glioma with Distinct Molecular Profiles: Case Studies Elucidating Impact of Newly Adapted 2016 CNS WHO Classification in Everyday Clinical Practice

A Chukus[1], g moonis[2], A Malik[3], S El Hussein[3], P Dubey[4]
[1]Stanford Hospital, Stanford, CA, [2]Columbia University Medical Center, South Orange, NJ, [3]Mount Sinai Medical Center, Miami Beach, FL, [4]Columbia University Medical Center, Scarsdale, NY

Purpose

1. To recognize variable molecular profile of glial neoplasms that have profound impact on

progression and treatment response. For this reason, the recently updated 2016-CNS WHO classification has incorporated molecular markers as an additional layer to histopathology grading for more accurate prognostication, published June 2016 (1). 2. To understand morphologic distinctions and overlaps in the MR phenotype of glioblastoma and Grade II/III subtypes based on IDH1 mutation status (a key component in the new classification system). At the end of this exhibit, the reader will be able to understand the following: - Conventional MRI as used in standard clinical practice correlates strongly with histopathologic grading applied in 2007-CNS WHO. - Molecular profile is a key adjunct component of 2016-CNS WHO due to superior prognostic abilities not adequately characterized on histopathologic grading alone. - Conventional MRI in the currently applied form does not necessarily predict molecular profile, therefore in isolation has limited prognostic value. - This suggests that while we may continue the use of Grade II/III and IV or define as "anaplastic astrocytoma" or "glioblastoma", based on imaging morphology; the terms with strong prognostic implications such as "aggressive" or "low grade" or "indolent" should be avoided on conventional MRI reporting.

Materials and Methods

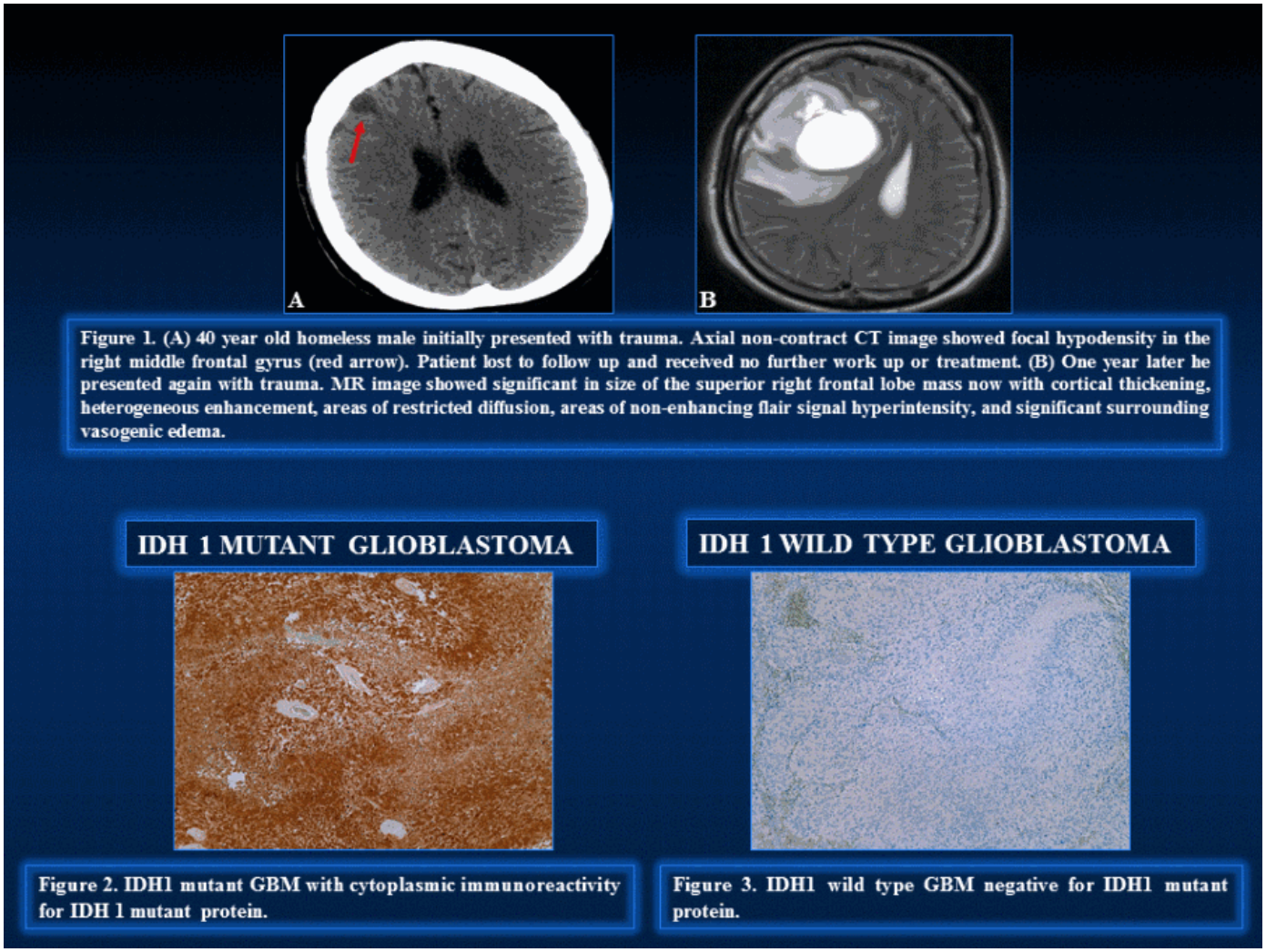
In this exhibit, we present pictorial review from our clinical practice to draw attention to the recently adapted changes using examples of primary/de-novo glioblastoma, secondary glioblastoma (WHO Grade IV), and low/intermediate grade gliomas (WHO Grade II/III). We summarize clinical and molecular profile with respect to IDH1 mutation status and describe lesion topology, enhancement, necrosis, extent of nonenhancing infiltrative neoplasm, ADC measurements and temporal evolution on imaging. These case series demonstrate that conventional imaging approaches correlate strongly with histopathologic grading but do not necessarily predict the molecular profile highlighting potential for misclassification of patient's prognostic category.

Results

Glioblastoma (GBM) is the most common primary CNS neoplasm, WHO grade IV, which based on histopathologic grading was considered to have worst prognosis and low survival. However, it is now known that GBM has a heterogenous prognosis which is better predicted in conjunction with the molecular profile. For example, the Isocitrate dehydrogenase 1 (IDH1) mutation status confers a relatively favorable survival and IDH mutant Grade II and Grade III tumors may not have markedly different clinical course or prognosis. Additionally, WHO Grade II/III that lack IDH1 mutation possess a high risk of progression to glioblastoma (secondary GBM).

Conclusions

Better understanding of advanced MR signatures of molecular subtypes of glioma synchronizing with the new molecular profile as shown in a recent study (2) will improve prediction of overall prognosis.



(Filename: TCT_eEdE-50_GBM-ASNRIMAGES-Final.gif)

eEdE-102

6:30AM - 3:00PM

Pattern-based Approaches to Emergency CT Imaging of the Brain

M Drabkin[1], S Lev[1]
[1]*Nassau University Medical Center, East Meadow, NY*

Purpose
To identify and elucidate patterns and constellations of emergent brain findings as a primer for the on-call neuroradiologist.
Materials and Methods
We present a variety of challenging computed tomography (CT) cases, both common and unusual, from our Level I trauma center in order to demonstrate the utility and importance of

understanding and recognizing patterns of both traumatic and nontraumatic neuroradiologic emergencies.
Results
Subtle clinically significant findings can be overlooked by the emergency radiologist on call. Conversely, over-scrutinization of minutia can lead to both inefficient workflow and inability to see a larger pattern. One key is the recognition of usual patterns and constellations of findings. Making an initial finding should prompt the interpreter's eyes to look for particular associated findings and in particular expected associated locations. Taking this one step further, certain CT findings also necessitate further imaging work ups. Through pattern recognition and anticipation, it becomes more readily clear what the next step in management should be. The cases we present challenge the viewer to recognize and anticipate patterns following the detection of an initial finding. A basic example would be seeing an area of cerebral contusion subjacent to a scalp hematoma and immediately searching for an associated contrecoup injury. Another example would be nontraumatic isolated convexal subarachnoid hemorrhage, which should prompt further imaging workup with MRI/MRA to evaluate for PRES, CVT, vasculitis and other vascular causes.
Conclusions
Through a series of challenging cases, this primer on expected patterns of findings on head CT, serves to increase the on-call radiologist's efficiency, accuracy and confidence.

eEdE-106

6:30AM - 3:00PM

Penetrating Neurotrauma: What the Radiologist Needs to Know

J Peacock[1], M Lanfranchi[2], A Betts[3], B Ritchie[4], V Timpone[3]
[1]San Antonio Unifomed Services Health Education Consortium, Fort Sam Houston, TX, [2]MGH, Boston , MA, [3]San Antonio Military Medical Center, San Antonio, TX, [4]San Antonio Military Medical Center, JBSA Fort Sam Houston, TX

Purpose
To describe and display various patterns of penetrating neurotrauma, with specific attention placed on role of neuroimaging in surgical decision making and prognostication.
Materials and Methods
The radiology databases at our institution were searched for cases of penetrating trauma to the brain, head/neck, and spine demonstrated on neuroimaging studies. Primary injury patterns, secondary injury patterns and complications, treatment considerations, prognostic markers and MR safety precautions are reviewed. Representative imaging examples are displayed.
Results
The following primary penetrating injury patterns are discussed: High velocity bullet ballistic trauma, low velocity bullet ballistic trauma, blast-related fragment injury, stab

wounds, and nonmetallic projectiles (wood, glass) (1, 2). Secondary injury complications reviewed include cerebral edema, hemorrhage, infection, cerebrospinal fluid (CSF) leak, vascular injury, foreign body migration and lead toxicity (3, 4).
Conclusions
It is important for the neuroradiologist to be familiar with the various imaging patterns of penetrating neurotrauma, and to relay clinically relevant information that can be utilized for surgical decision making and prognostication.

eEdE-96

6:30AM - 3:00PM

Perfusion CT-guided Management of Acute Stroke

M Alsadiq[1], T Booth[1]
[1]*King's College Hospital NHS Foundation Trust, London, London*

Purpose
To give insight into the increasingly important role of perfusion CT in the acute management of ischemic stroke.
Materials and Methods
Early evaluation of patients with suspected stroke is crucial to prevent irreversible damage to ischemic brain tissue, and it consists of a rapid neurological examination, and immediate brain imaging to confirm the diagnosis and to guide the treatment decision. A noncontrast CT scan is the most practical acute diagnostic imaging tool in the early management of suspected stroke because of its accessibility and rapid scanning time. However, a CT scan is insensitive to subtle early ischemic changes, and a therapeutic decision made on noncontrast CT findings is imperfect. Since the introduction of perfusion computed tomography (PCT), it has had a great impact on acute stroke management. Perfusion CT is proved to have many advantages over noncontrast CT in terms of detecting early ischemic changes as well as differentiating the irreversibly damaged tissue from viable hypoperfused tissue at risk of infarction. Furthermore, PCT parameters are independent predictors of early improvement and long-term clinical outcomes. Finally, PCT can identify the most suitable candidates for acute reperfusion therapy.
Results
This review is a systematic analysis of the latest evidence in the evolving role of PCT in the acute stroke work-up, including the diagnostic value of PCT in detecting the hypoperfused brain tissue, and the ability of PCT to guide treatment decisions for thrombolysis. In addition, we investigate the capability of PCT to predict the development of hemorrhagic transformation as well as early and long term functional outcomes.
Conclusions
Perfusion CT has a high diagnostic accuracy for detecting the infarct core and ischemic penumbra, providing important diagnostic and prognostic information that cannot be inferred

from clinical or other CT imaging modalities, in addition to improving patients' selection for acute reperfusion therapy.

eEdE-66

6:30AM - 3:00PM

Perivascular Spaces, Normal and Abnormal

Y Li[1], N Hatch[2], M Yazdani[3]
[1]MUSC, Charleston, SC, [2]Medical University of South Carolina, Charleston, SC, [3]Medical University of South Carolin, Charleston, SC

Purpose
The presence and physiologic importance of perivascular spaces in the brain is vague. Recent evidence shows a role in removal of interstitial solutes and proteins in a pathway termed the glymphatic system. Typically, normal perivascular spaces are barely seen; however, there is a positive correlation with age and small vessel disease. Prominent or enlarged perivascular spaces may be of no clinical significance. If the enlargement is pathologic, it is, unfortunately, usually nonspecific without appropriate clinical history. This presentation aims to illustrate the imaging features of normal perivascular spaces, benign variations of dilated perivascular spaces and pathologic conditions with enlarged perivascular spaces. We also will attempt to discuss the pathophysiology behind each condition.
Materials and Methods
Using a large series of illustrative brain MRI cases from our didactic imaging files we will show different conditions with dilated perivascular spaces. We will start by describing normal perivascular spaces and then discussing the recent glymphatic system. We will show prominent perivascular spaces in different parts of the brain. We then will show multiple cases including but not limited to: Mucopolysaccharidosis, Lowe syndrome, anterior temporal lobe perivascular space, tumefactive perivascular spaces, CADASIL, and cryptococcosis. Finally we will show a few neoplastic processes that mimic the appearance of dilated perivascular spaces.
Results
Our cases in conjunction with review of the current literature will enhance the pathophysiologic understanding normal and abnormal perivascular spaces.
Conclusions
The herein presentation expects to improve awareness, description, and identification of normal and abnormal perivascular spaces to all radiologists with an illustrative and instructive approach.

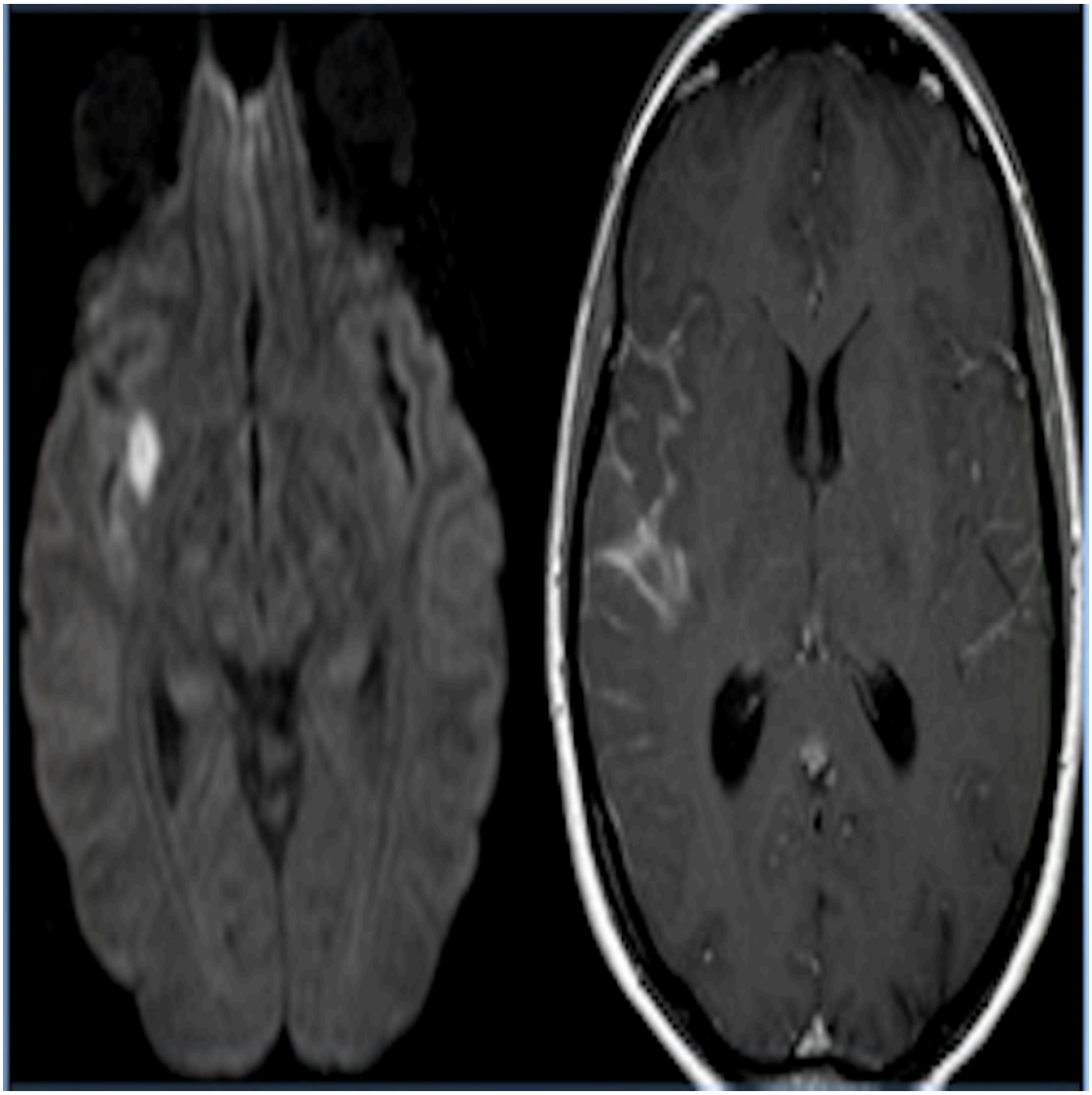
eEdE-97

6:30AM - 3:00PM

Pictorial Review of Infectious Causes of Cerebral Infarction

A Madhavan[1], I Djoukhadar[1], A Herwadkar[2], R Siripurapu[2]
[1]Salford Royal NHS Foundation Trust, Manchester, United Kingdom, [2]Salford Royal NHS Foundation Trust & Greater Manchester Neurosciences Centre, Manchester, United Kingdom

Purpose
The purpose of this electronic educational exhibit is to provide a detailed imaging review of infective causes of cerebral infarction.
Materials and Methods
We present a comprehensive review of various bacterial, viral and fungal central nervous system (CNS) infections that cause infarction. Both arterial and venous infarctions will be reviewed.
Results
Cerebral infarction is a relatively under-recognized complication of CNS infection and can be the only presenting feature. Infarction can occur due to thrombosis from local vessel involvement or secondary to para or post infectious CNS vasculitis. Infection can also cause thrombosis of cortical veins or dural venous sinuses which can result in venous infarction. Stroke is the most common neurological complication of infective endocarditis. Septic emboli causing infarction can progress to cerebritis and abscess formation. This exhibit discusses the imaging manifestations of various CNS infections such as infective endocarditis, bacterial meningitis, tuberculosis, syphilis, fungal, and viral infections including varicella zoster and HIV. This exhibit also highlights the importance of recognizing patients who may be at risk from developing infarction as patient management can be optimized to prevent this complication.
Conclusions
This exhibit illustrates the various infectious causes of stroke and highlights the importance of at risk patients and early recognition.



(Filename: TCT_eEdE-97_Infectiouscausesofcerebralinfarctionimage.jpg)

eEdE-46

6:30AM - 3:00PM

Posterior Inferior Cerebellar Artery Pathology: A Discussion of PICA Anatomy and the Challenges of Diagnosis and Treatment

I Akhtar[1], J Halpin[1], C Martin[1], W Holloway[1], B Chin[1], N Akhtar[1]
[1]*Saint Luke's Hospital of Kansas City, Kansas City, MO*

Purpose
To determine the complex anatomical variations of the posterior inferior cerebellar artery (PICA) by highlighting cross-sectional MRA/CTA and catheter cerebral angiogram findings, with the purpose of investigating various approaches to diagnosing and treating a wide array

of PICA pathology. PICA pathology that will be discussed include: ruptured and unruptured aneurysms, dissecting aneurysms, acute thrombotic occlusion (ischemic stroke), and arteriovenous malformations (AVM). Knowledge of the variations of the anatomy of the PICA will allow us to have a better understanding of PICA pathology and can assist in arriving at an effective treatment plan.

Materials and Methods

An institutional review board approved retrospective chart review of all cerebral catheter angiograms was conducted over a 4-year period at our facility. Any case with pathology of the PICA (aneurysms, dissecting aneurysm, acute occlusion, or AVM) discovered on cerebral angiography was considered for the study. Demographic data and history findings such as the symptoms at presentation will be discussed in this educational poster. Cases treated with conservative management and/or endovascular treatment will be detailed with rationale for the treatment modality chosen explained based on anatomical findings on cross-sectional CTA/MRA or cerebral angiography.

Results

1) We will illustrate anatomical variations, such as extradural origin of PICA, lumen diameter variations, and PICA arising from a duplicate trunk, as seen on CTA/MRA cross-sectional imaging and catheter cerebral angiography. 2) Clinical vignettes regarding diverse presentations of PICA pathology, such as lateral medullary syndrome, will be discussed. 3) An overview of treatment options: Discussion of conservative treatment (i.e.: anticoagulation) versus intervention (i.e.: stent-assisted coil embolization) in the treatment of PICA pathology with rationale in specific cases explained based on anatomical findings. 4) Discussion of the complications of treating PICA pathology with different treatment options, and how to treat challenges as they arise. Follow-up intervals and imaging recommendations will be emphasized.

Conclusions

PICA anatomy and its course is highly variable. Although PICA usually arises intracranially, a significant amount (5-20%) can arise extradurally (1). Furthermore, single or double PICA origin can occur, as well as variations in the lumen diameter. Knowledge of these anatomical variations, along with detailed imaging of the PICA prior to treatment, can greatly aid in developing an effective and appropriate treatment of the underlying PICA pathology.

eEdE-14

6:30AM - 3:00PM

Postoperative Complications of Carotid Endarterectomy: Recognize the Zebra and the Hippos!

J Schneider[1], J Whang[2], L Bagley[1], K Learned[3]

[1]Pennsylvania Hospital, Philadelphia, PA, [2]Hospital of the University of Pennsylvania, Philadelphia, PA, [3]Univ. Pennsylvania Health System, Philadelphia, PA

Purpose

Carotid endarterectomy (CEA) is a surgical procedure to reduce atherosclerotic plaque causing internal carotid artery stenosis in order to prevent ischemic stroke. The diagnostic value of imaging in the clinical paradigm of rare postsurgical complications will be presented.

Materials and Methods

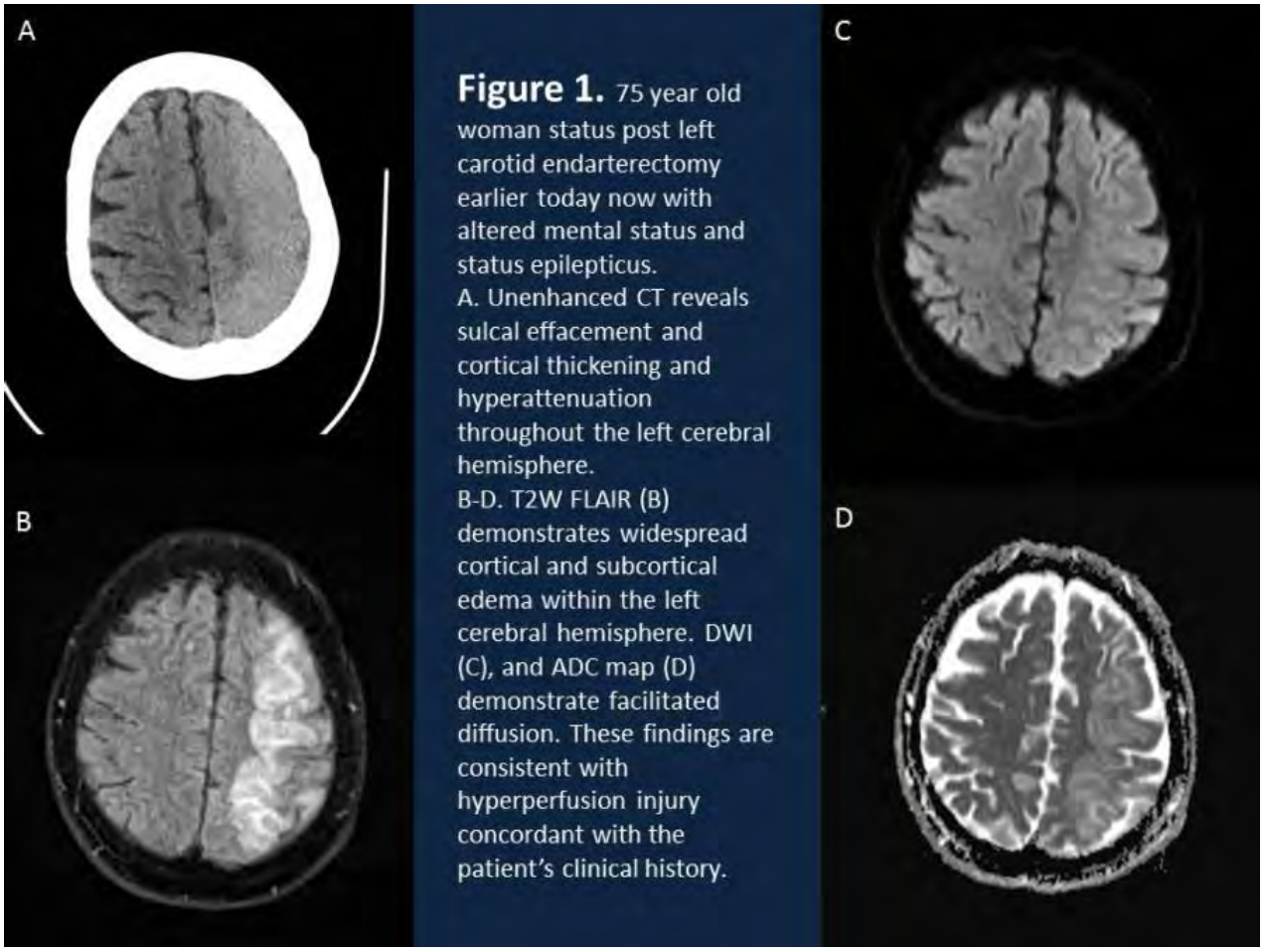
A clinical and imaging review was performed of post-CEA cases in our institution. Representative cases will illustrate the normal expected post-CEA imaging findings and a spectrum of complications, emphasizing appropriate utilization and imaging findings of US, CT, MRI and angiogram.

Results

Carotid endarterectomy is not without risks and the accurate and prompt clinical and imaging diagnosis of peri-operative complications is paramount to patient's outcome. Carotid US and CTA are utilized to quickly identify acute occlusive thrombus, compressive hematoma, and pseudoaneurysm that may require swift intervention. Postoperative neck swelling from parotitis, seromas and abscesses are best delineated by CT for identification of large collection amenable to drainage procedure. Neurological deficit expedites clinical and imaging algorithm to evaluate for ischemic stroke and intracranial hemorrhage. Cerebral hyperperfusion syndrome rarely occurs with clinical headache, deterioration of mentation, focal deficit and seizure, and demonstrates characteristic brain imaging findings on CT and MRI. Cranial nerve injury is clinically evident and occasionally can be identified on neck CT or MRI as end-organ denervation. Restenosis, especially in late 2-3 years after CEA, frequently is associated with irregular plaques that may serve as an embolic source.

Conclusions

Radiologists need to be familiar with normal post-CEA findings, and promptly recognize rare complications of CEA, utilizing the most effective imaging method in clinical management paradigm to contribute to best patient's outcome.



(Filename: TCT_eEdE-14_ASNRabstractjpg.jpg)

eEdE-77

6:30AM - 3:00PM

Power up! The Power of Post-Contrast 3D FLAIR on 3T

J Yetto[1], A Germana[1], K Soderlund[2], D Hawley[1], M Cathey[1]
[1]Naval Medical Center San Diego, San Diego, CA, [2]Naval Medical Center, San Diego, San Diego, CA

Purpose
At times, certain intracranial lesions can be surprisingly difficult to appreciate with conventional imaging sequences. This exhibit will highlight the utility of postcontrast 3D FLAIR in increasing the conspicuity of significant intracranial lesions, emphasizing its utility across a broad spectrum of clinical scenarios using a case-based approach. This presentation will emphasize the inclusion of postcontrast 3D FLAIR sequence as an essential component to any MRI brain with contrast.

Materials and Methods

Case-based educational presentation which illustrates the strengths of postcontrast 3D FLAIR. Relevant anatomy is reviewed with specific attention to normal and pathologic findings. Tips for avoiding certain pitfalls unique to this sequence are suggested. Finally, a review of the current literature on postcontrast FLAIR imaging will be summarized.

Results

Postcontrast FLAIR is best known for highlighting leptomeningeal abnormalities but can be useful in a variety of scenarios. With experience, we have found that only the postcontrast FLAIR is necessary for study interpretation and does not otherwise lengthen study time. This exhibit is divided into the following sections: 1. Physics of postcontrast FLAIR. 2. Case-based comparison of pre and postcontrast 3D FLAIR. 3. Power of postcontrast 3D FLAIR. 4. Subtleties and pitfalls of postcontrast 3D FLAIR at 3T. 5. Protocol Considerations.

Conclusions

Postcontrast 3D FLAIR is a highly sensitive technique which can markedly increase the conspicuity of a variety of inflammatory, infectious, and neoplastic neuropathologic entities. Accordingly, it is critical for neuroradiologists to be familiar with this technique and consider instituting in protocols involving contrast, as a matter of routine.

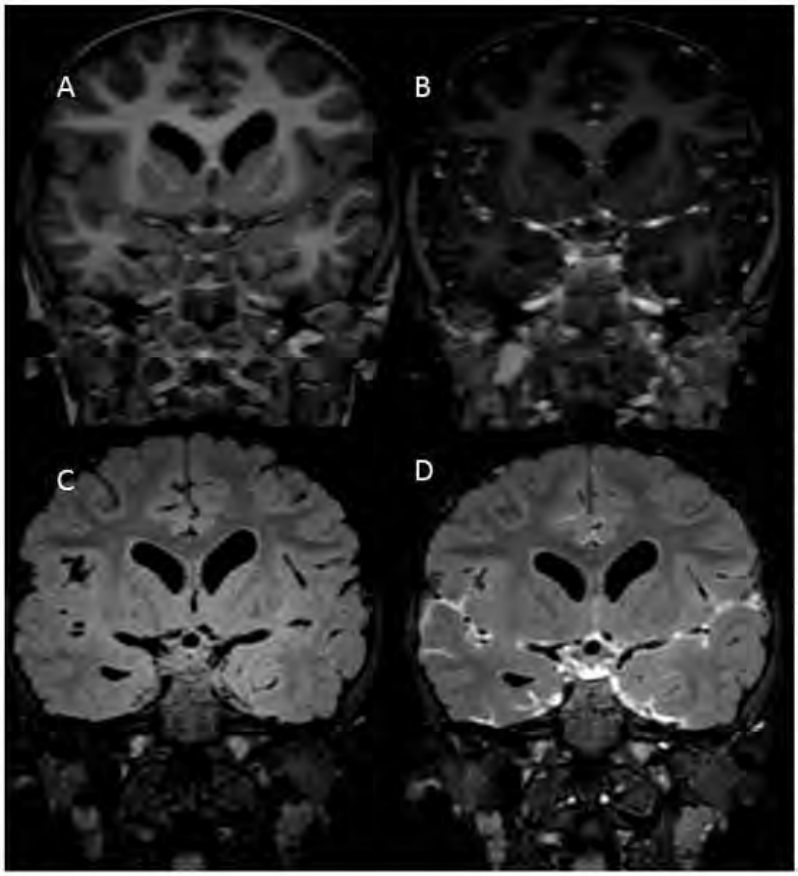


Figure 1. 4-year-old with visual changes and papilledema on exam. High-resolution 3T MRI coronal images through the level of the suprasellar cistern, including (A) pre-contrast 3D T1WI, (B) post-contrast 3D T1WI, (C) pre-contrast 3D FLAIR, and (D) post-contrast 3D FLAIR.

The post-contrast 3D FLAIR highlights markedly abnormal increased signal intensity involving the leptomeninges, particularly at the basal cisterns, which is not apparent standard FLAIR imaging and is relatively subtle on post-contrast T1W imaging. These findings can be seen in the setting of infectious/inflammatory leptomeningitis versus carcinomatosis. This proved to be a case of disseminated primitive neuroectodermal tumor (PNET).

(Filename: TCT_eEdE-77_postgadflairimage2.jpg)

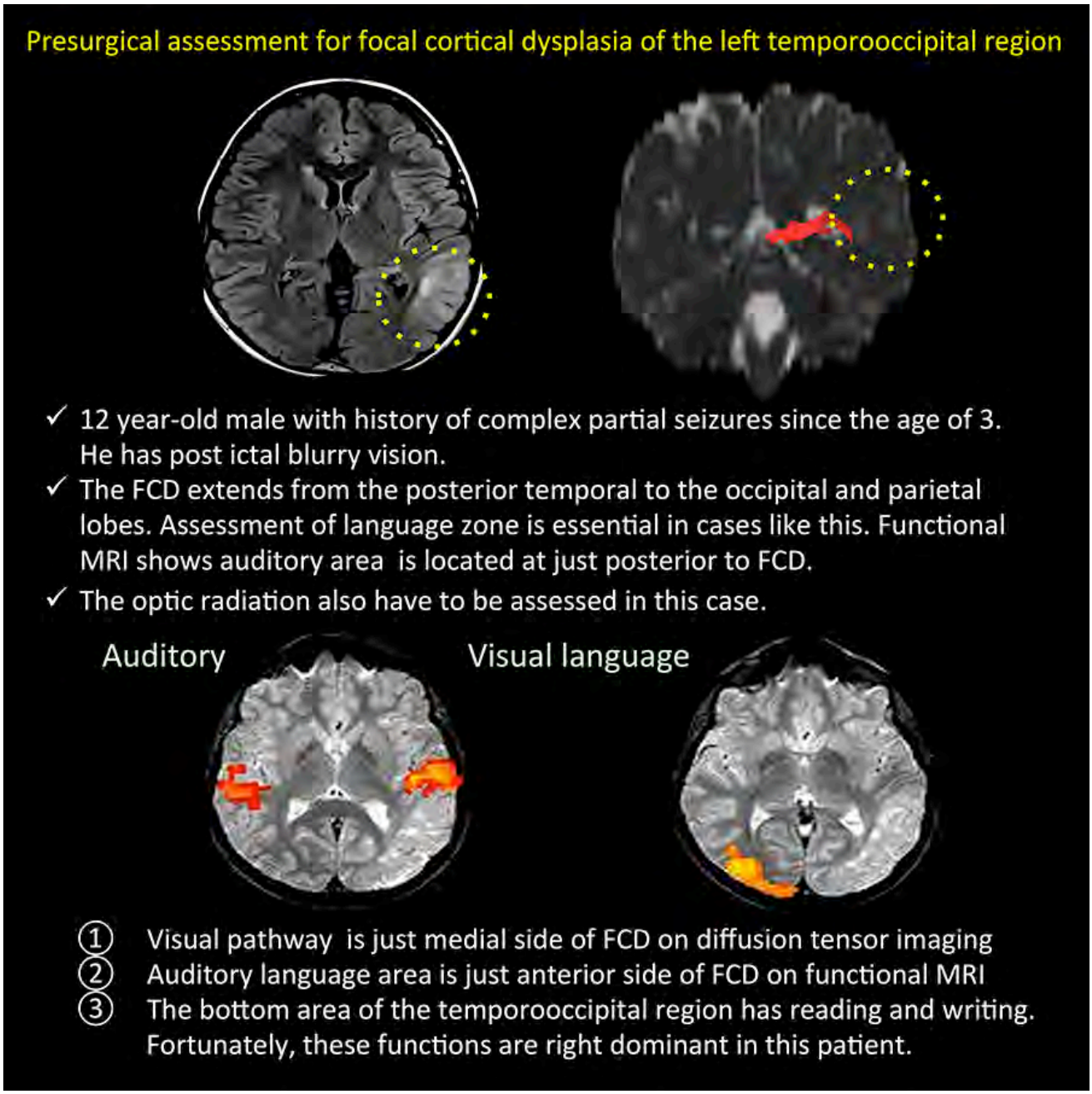
eEdE-12

6:30AM - 3:00PM

Presurgical Assessment of Focal Cortical Dysplasia: How to Approach Functional Assessment?

H Yokota[1], E Morimoto[2], M Cekic[3], N Salamon[4]
[1]David Geffen School of Medicine at UCLA, Los Angeles, CA, [2]David Geffen School of Medicine, UCLA, Los Angeles, CA, [3]UCLA Medical Center, Los Angeles, CA, [4]UCLA, Los Angeles, CA, David Geffen School of Medicine at UCLA, Los Angeles, CA, Los Angeles, CA

Purpose
Focal cortical dysplasia (FCD) is a common cause of intractable epilepsy that may be surgically curable. Magnetic resonance imaging (MRI) findings of FCD can be relatively obvious (type II) or subtle (type I). Presurgical assessment of FCD requires detailed neurophysiological and functional evaluation. The purpose of this exhibit is to revisit presurgical planning for epilepsy surgery to obtain better postsurgical outcome.
Materials and Methods
This exhibit includes: 1. Clinical semiology and location of the lesion. - Example: Visual hallucination, auditory aura, fear, lip smacking, motor component, humming and corresponding white matter tracts. 2. Presurgical Assessment: - How Neuropsychological testing, functional MRI and Wada test can help surgical planning? - What you need to know when FCD is located in eloquent cortex? 3. Clinical cases. - Motor cortex FCD and surgical planning and outcome. - Language zone FCD and surgical planning and outcome.
Results
- Semiology accompanied by aura reflects epileptogenic zone and its propagation pathway. Knowledge of functional anatomy is useful to understand the location. - Eloquent area and FCD can be overlapped. Different surgical approach other than resection to control seizure includes responsive neurostimulation, laser ablation will be presented. - For the child brain may have plasticity. Functional MRI can be used to follow the reorganization of motor and language function. Example will be presented.
Conclusions
Focal cortical dysplasia presurgical assessment is challenging. Understanding propagation pattern of epilepsy and presurgical mapping of lesion, epileptogenic zone and eloquent area can help neurosurgery and patients to obtain better outcome. Precise knowledge of functional neuroanatomy is fundamental for neuroradiologists. Neuroradiologists should take leadership on multimodality approach functional presurgical assessment.



(Filename: TCT_eEdE-12_fig2.jpg)

eEdE-07

6:30AM - 3:00PM

Primary Progressive Aphasia Subtype of Frontotemporal Dementia: The Importance of Integrating Clinical and Neuroimaging Correlates

S Franczak[1], E Ulmer[2], D Sabsevitz[3], A Klein[4]

[1]Divine Savior Holy Angels High School, Milwaukee, WI, [2]University Lake School, Hartland, WI, [3]Medical College of Wisconsin, Milwaukee, WI, [4]Medical College of Wisconsin - Froedtert Hospital, Milwaukee, WI

Purpose

An understanding of clinical criteria for the diagnosis of primary progressive aphasia (PPA) is important in distinguishing the condition from otherwise seemingly nonspecific imaging features. The goal of the exhibit is to improve the accuracy of neuroimaging diagnosis through a knowledge-based approach.

Materials and Methods

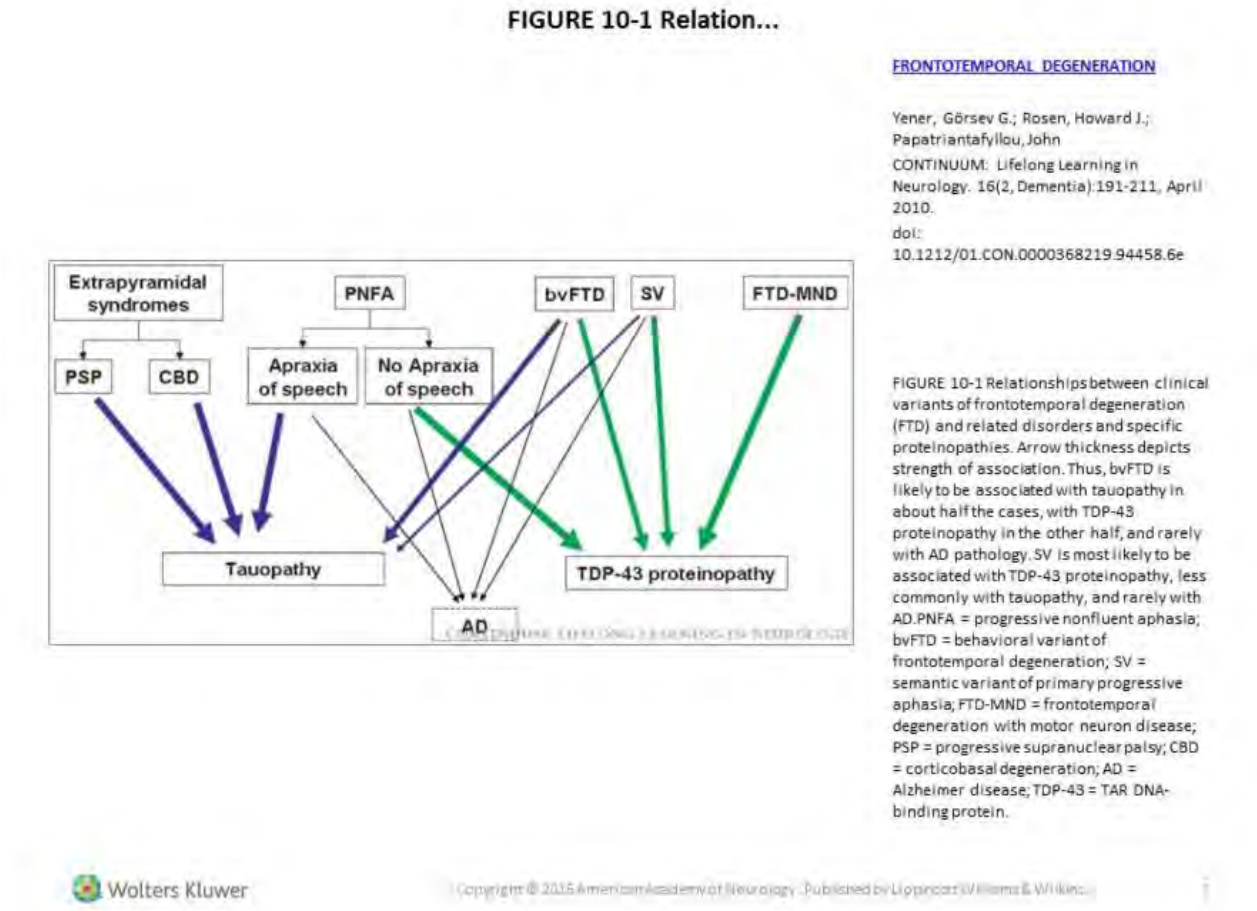
The exhibit classifies and distinguishes clinical presentations, diagnostic imaging data, and therapeutic strategies for PPA. Clinical presentations that reveal dysfunctions of semantic and phonological language networks are discussed and categorized in algorithmic form. Key neuroimaging patterns are illustrated for each subtype through case presentations, and shown how they impact the clinical algorithm. The importance of distinguishing imaging data in supporting the diagnosis of PPA is emphasized.

Results

Primary progressive aphasia is a degenerative dementia, which is characterized by slowly progressive loss of language function in a setting of relatively preserved memory and visuospatial skills. Three major variants of progressive language disorders have been described: primary progressive nonfluent aphasia (PNFA), semantic dementia (SD), and logopenic or phonological aphasia (LPA). Nonfluent PPA and semantic dementia are included in the frontotemporal lobe d pathology, most often tau-positive or TAR-DNA binding protein 43 (TDP-43) positive neuronal inclusions, whereas logopenic aphasia often has an underlying Alzheimer disease pathology. All of the variants have distinct patterns of cortical atrophy on neuroimaging in the language network. The SD subtype usually presents between 55-70 years of age with semantic language dysfunctions. Clinical symptoms include selective disruption of conceptual knowledge, dysnomia with loss of word and object (or face) meaning, and poor confrontation naming. PNFA generally presents in patients older than SD, is more common in women, and is the second most prevalent subtype of FTD. Clinical symptoms differ from SD, characterized by speech apraxia, effortful nonfluent speech with agrammatism, and phonemic paraphasias or anomia. Single word comprehension and object knowledge is spared, but syntactic comprehension is impaired. Episodic memory, executive functions, visuospatial functions are preserved early in the course of the disease in contrast to early AD. LPA, which is usually associated with Alzheimer-type pathology, can often be confused with the other forms of PPA, usually PNFA. Like PNFA, speech in LPA can be hesitant and slow, mostly due to profound word-finding difficulties. Articulation of words is usually intact, and patients have periods of normal fluent speech in between their periods of hesitancy which is not as common in PNFA.

Conclusions

Understanding both the clinical and neuroimaging patterns associated with PPA is critical in diagnosing the condition, and distinguishing PPA from LPA (AD). Accurate, early diagnosis establishes prognosis and provides for the appropriate early treatment strategies and supportive care.



(Filename: TCT_eEdE-07_FTDimage_download.jpg)

eEdE-99

6:30AM - 3:00PM

Quandary of Etiologies in Clinically Suspected Stroke with Dizziness/Vertigo: A review of Vascular and Non-vascular Conditions Comprising the Differential Diagnosis List

M BHALLA[1], J Ulmer[2], A Klein[2], N BHALLA[3], L Mark[2], S Quinet[4], K McAvoy[5]
[1]MEDICAL COLLEGE OF WISCONSIN, Brookfield, WI, [2]Medical College of Wisconsin - Froedtert Hospital, Milwaukee, WI, [3]Froedtert Hospital, Brookfield, WI, [4]Medical College of Wisconsin, MILWAUKEE, WI, [5]MEDICAL COLLEGE OF WISCONSIN, MILWAUKEE, WI

Purpose

Dizziness and vertigo is one of the most common presentations in the emergency department (ED). Some of these patients may have underlying posterior fossa stroke, or can have associated symptoms that raise the suspicion of stroke, which can potentially have profound implications in terms of management and prognosis. However, not all turn out to have infarct or hemorrhage as the etiology for dizziness and vertigo. Our review encompasses the possible causes (vascular and nonvascular) of dizziness that can clinically present with symptoms suspicious for stroke.

Materials and Methods

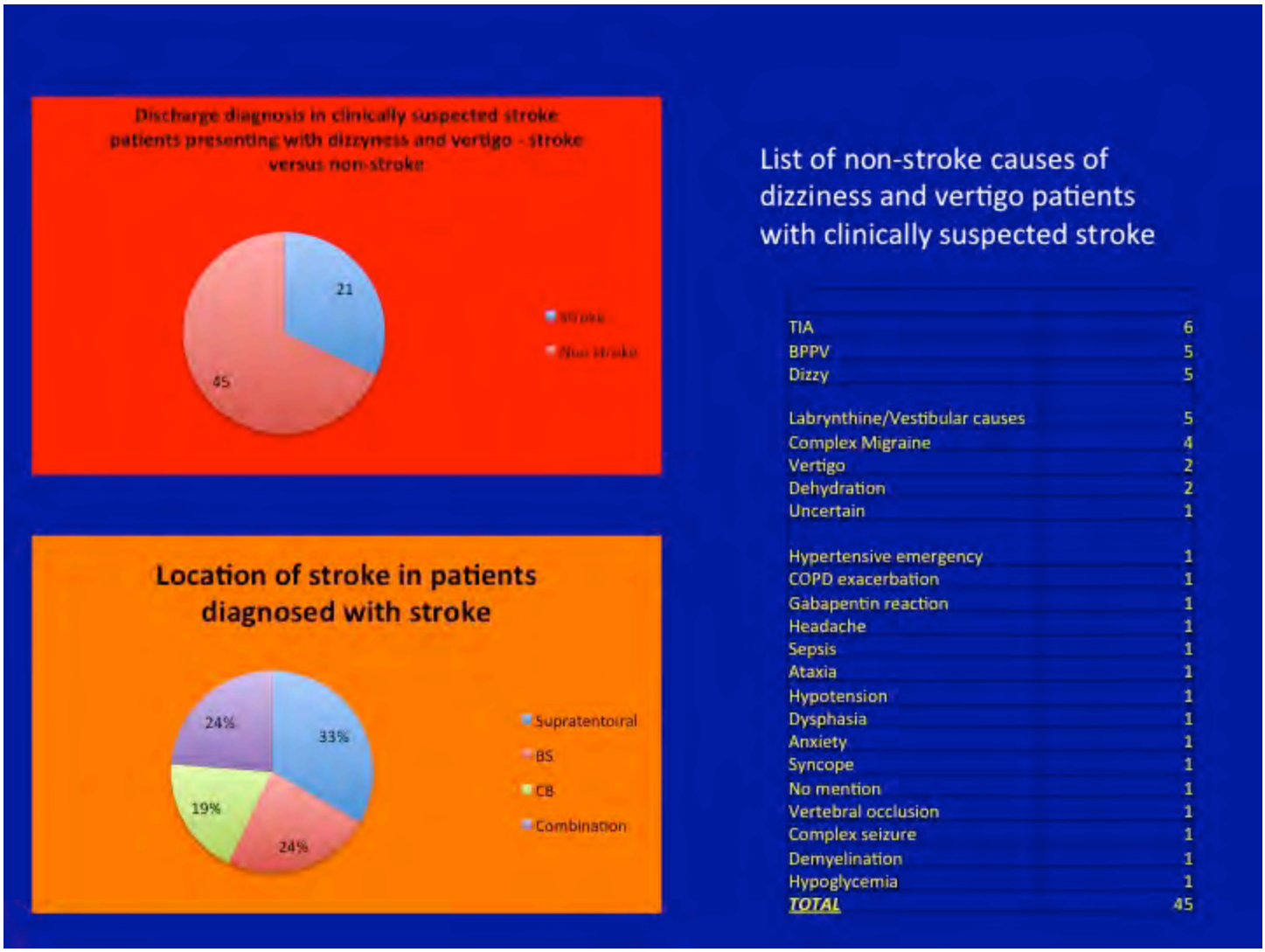
Following the Institutional Review Board (IRB) approval from our institution, electronic medical records (EMR) of clinically suspected stroke patients, who had both the computed tomography (CT) and magnetic resonance imaging (MRI) exams (performed within 24 hours of each other), were reviewed retrospectively. Patients who had either one of the exams (CT or MRI), or both the exams greater than 24 hours apart were excluded. Patients who had dizziness and vertigo as part of their clinical presentation then were reviewed for their final discharge diagnosis mentioned in discharge summary. For those patients who had stroke, location of infarct/hemorrhage was identified. The conditions comprising nonstroke etiologies were enlisted.

Results

A review of 500 patients revealed 66 patients (13.2%) with clinically suspected stroke presented with dizziness and/or vertigo. Thirty-one percent of these patients had MR positive stroke. Only 42.9% of these strokes were purely localized in posterior fossa, 33% were in supratentorial location, and the rest of them were scattered or in combination of supratentorial and infratentorial locations. Sixty-two percent of these strokes were not identified by CT exams, which preceded the MR exam. For the 68.2% of patients who did not have stroke, a total of 23 different etiologies were enlisted in the final diagnoses, transient ischemic attack (TIA) being the single largest cause (see table). Most of the patients presenting within the 0-3 tPA (tissue plasminogen activator) window period had cerebellar strokes, with only 9% being detected by CT.

Conclusions

Dizziness and vertigo can be the presenting symptom in myriad of conditions. Since stroke can be one of the possible etiologies for this presentation, and considering the significant mortality and morbidity associated with cerebellar and brainstem strokes, quick and definitive diagnosis is warranted. While MR predictive values are robust for stroke imaging, CT fails to pick up more than half of these strokes. The list of causes of nonstroke causes can be surprisingly long, which may not be evaluated for by the ED physicians in acute settings. These confounding etiologies all the more favor preferential utilization of MRI as the initial imaging tool in ED.



(Filename: TCT_eEdE-99_Slide1.jpg)

eEdE-16

6:30AM - 3:00PM

Resting-state fMRI and its Application to Presurgical Planning: A Review

J Kramer[1], S Peltier[1], C Gradinaru[1], G Shah[1]
[1]*University of Michigan Health System, Ann Arbor, MI*

Purpose
This review will survey the application of resting-state fMRI in presurgical planning; including summarizing recent clinical examples and outlining the methodological challenges.
Materials and Methods
In this image-rich presentation, high quality examples of fMRI exams from the authors'

institution will be demonstrated and their application to presurgical planning will be discussed. The methodological challenges of this important imaging technique will be highlighted along with proposed suggestions about how to overcome these challenges.
Results
Resting-state low frequency oscillations have been detected in many functional magnetic resonance imaging (MRI) studies. Multiple functional systems have consistent patterns of coherent activity in large subject studies (Biswal 2010), including the motor, visual, and language systems (Biswal 1995; Hampson 2002), as well as the default-mode, attention and executive control networks (Greicius 2003; Fox 2005). Further, these patterns of functional connectivity have been shown to be altered in pathological states, and can be used to monitor physiological changes in the short, medium, and long term (Peltier & Shah, 2011). Resting-state fMRI thus offers an alternative way to clinically assess brain networks. It offers potential advantages over task fMRI in presurgical planning: 1) Task fMRI typically probes a single system for each session, while resting-state fMRI can evaluate multiple functional networks at once; 2) Resting state-fMRI requires a much lower degree of subject compliance; and 3) Resting state networks can persist in sleep or anesthesia (Horovitz 2008; Martuzzi 2010), allowing greater utility in clinical populations.
Conclusions
After viewing this presentation, the observer will gain further understanding of resting-state fMRI, its application to presurgical planning, and measures that can be taken to overcome inherent methodological challenges associated with this clinically important imaging modality.

eEdE-25

6:30AM - 3:00PM

Review of CNS Complications of Oncologic Therapy

C Gradinaru[1]
[1]*Univ. of Michigan Health System, Ann Arbor, MI*

Purpose
Neurotoxicity is a widely recognized adverse effect of cancer treatment and can result from radiation therapy (RT), traditional chemotherapeutic agents, as well as newer biologic and immuno-therapeutic agents. As therapy for cancer has become more innovative and aggressive over the years it has led to patients with cancer living longer. Although the exact incidence of neurotoxicity related to cancer therapy is not known, it is thought to be increasing in frequency. The aim of this presentation is to offer radiologists a brief and concise description of potential CNS complications of oncologic treatment and mimics of cancer progression/recurrence providing several case-based examples with clinical and imaging findings. Radiologists need to be familiar with potential early and late CNS adverse effects of cancer therapy including: toxic effects, infection, endocrine or sensory

dysfunction, neuropsychologic impairment, as well as secondary malignancies. Being aware of these potential adverse effects can accelerate imaging diagnosis and reduce the associated morbidity. In addition, knowledge about these adverse effects will enable the development of more appropriate therapeutic trials and more effective patient surveillance.

Materials and Methods

Magnetic resonance imaging (MRI) is the main imaging modality used to evaluate patients with cancer with new symptoms attributed to the CNS. The presentation provides a brief description of each cancer treatment modality as well as hypothesized pathophysiology for each agent accompanied by case-based examples of CNS adverse effects. To facilitate understanding of potential CNS side effects of oncologic therapies, the side effects can be classified based on timing since the onset of treatment. Each such case will include relevant clinical and imaging findings.

Results

One distinct category of CNS complications is related to radiation therapy (RT). Radiation therapy-related brain injury typically is classified into three phases based on time of onset. Acute post-radiation therapy CNS side effects can present with nonspecific symptoms such as headache, nausea, vomiting and lethargy. However, the incidence and severity has decreased secondary to careful treatment planning and prophylactic steroid use. Imaging is usually negative in this scenario. An important subacute/early-delayed CNS side effect of RT for high-grade glioma, particularly in combination with temozolamide, is tumor pseudo-progression which can be present on follow-up imaging within the first 2-3 months after onset of therapy. Late-delayed CNS side effects of RT can manifest as radiation necrosis, diffuse leukoencephalopathy, vasculopathies, and secondary tumors. Some of these effects can be accelerated by concomitant use of chemotherapy. Early-delayed and late-delayed myelopathy changes also can occur within the spinal cord following RT. Compared with RT induced CNS complications, the neurotoxic effects of chemotherapy and other treatment options are less well characterized, however are increasingly being recognized. Central nervous system side effects can occur in early following therapy initiation. They include postoperative complications, PRES and other vasculopathies, infections and acute toxic effects of chemotherapy agents. Many of these side effects can present as oncologic emergencies. On the other hand, late side effects of these other treatment options can result in permanent endocrine dysfunction, neurologic and neurosensory deficits, as well as neuropsychologic impairment.

Conclusions

When patients with cancer develop new neurologic symptoms, it is important to distinguish symptoms related to the cancer itself from those related to other causes, such as paraneoplastic syndromes, infection, or treatment-related toxicity. Although attributing patient's symptoms to neurotoxicity is generally a diagnosis of exclusion, it is important to recognize so that further injury is prevented by dose adjustment or treatment cessation. Magnetic resonance imaging of the brain and spine is the modality of choice for patients with cancer who develop neurologic symptoms. In some cases conventional MRI might not

be able to differentiate post-treatment effects from disease progression and advanced imaging techniques may be helpful.

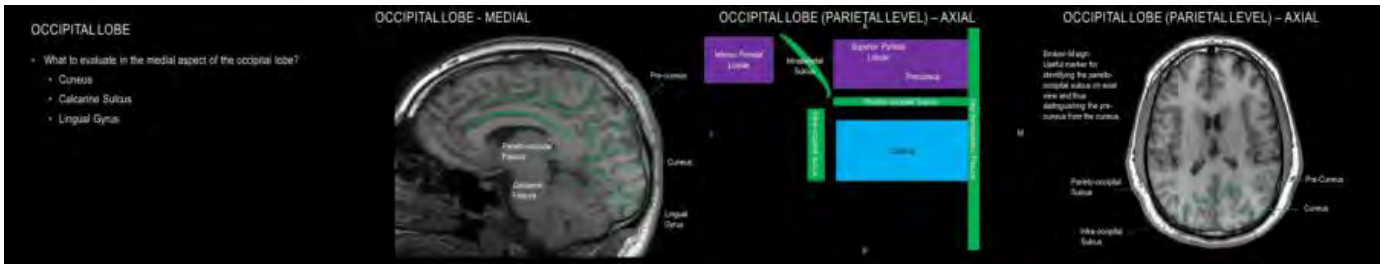
eEdE-15

6:30AM - 3:00PM

Review of Cortical Neuroanatomy

R Chaudhari[1], P Shen[2]
[1]*Stanford / UC Davis, Stanford, CA,* [2]*Kaiser / UC Davis, Santa Clara, CA*

Purpose
The purpose of this educational exhibit is to present a practical review of cortical neuroanatomy for the neuroradiologist. Emphasis is placed on demonstrating the imaging planes and anatomical landmarks that are best utilized for identifying particular sulci and gyri.
Materials and Methods
An extensive review of lobar, gyral, and sulcal neuroanatomy was performed using gross imaging references, neuroanatomical texts, and radiological anatomy atlases. Particular attention was given to various signs which have been established for determining key sulci. High resolution, T1-weighted, 3D SPGR images in a normal patient were used to label cortical sulci and gyri. Additionally, once sulci and gyri were clearly delineated, critical neuro-functional territories were identified.
Results
Neuroanatomy, despite being an inherently complex topic, can be simplified by a commitment to understanding the relationship between sulcal and gyral anatomy. Using various well established signs we were able to consistently reproduce critical cortical sulci (such as the bracket sign for pars marginalis and the broken-m sign for the parieto-occipital and intra-occipital sulci, just to name two). Upon identifying the critical sulci for a given lobe, identifying the gyri was simplified. We attempt to depict the sulci as the outline of a puzzle with the gyri simply fitting between the borders. After clearly labeling the cortical sulci and gyri we turned our attention to identifying the key functional neuroanatomical structures. This allows for not only a demonstration of cortical neuroanatomy but also a review of which of those neuroanatomical structures have functional significance. Finally, we present our information in such a way as to be relevant to the practicing neuroradiologist. Not all anatomical structures are shown in each plane. Rather, we determined which planes are best for identifying particular anatomical landmarks. This allows for a more focused approach that is tailored to clinical practice.
Conclusions
In this educational exhibit we demonstrate the relationship between sulci and gyri both using diagrams and labeled MRI images. The information is presented in such a way as to be applicable and reproducible for the clinical neuroradiologist.



(Filename: TCT_eEdE-15_Abstract.jpg)

eEdE-44

6:30AM - 3:00PM

Review of the Epidemiology, Pathology, Clinical Presentation, Imaging Features, Prognoses, and Management Options of the Arteriovenous, Cavernous, Developmental Venous Anomaly, and Capillary Telangiectasia Intra-Cranial Vascular Malformations

L Dawson[1], N Lambert[1], R Murtagh[1]
[1]*University of South Florida, Tampa, FL*

Purpose
Elucidate the differing CT and MR radiographic presentations of the arteriovenous, cavernous, developmental venous anomaly, and capillary telangiectasia intracranial vascular malformations.
Materials and Methods
Detailed in the exhibit are the general signs and symptoms, epidemiology, unique CT and MRI imaging characteristics, prognoses, and current treatment options for each intracranial vascular pathology.
Results
The intracranial vascular malformations have been well documented in the literature. However these vascular anomalies are still of clinical importance secondary to risk of rupture and intracranial hemorrhage. The most clinically significant vascular malformation is the arteriovenous (AVM) entity. AVMs are congenital vascular anomalies consisting of a nidus of vessels which is fed by one or more arteries that drain directly into the venous circulation. The annual risk of hemorrhage from an AVM is estimated to be 2% to 4% per year which most commonly is seen in the second through fourth decades of life. Traditionally, these lesions have been treated by open resection. Recent advances in neurological endovascular techniques including endovascular embolization techniques and stereotactic radiosurgery, have become useful tools in the treatment of this disease. Cerebral cavernous malformations (CMs) are a relatively common disease entity which is composed of a compact bundle of pathologic capillaries without intervening brain parenchyma. CMs rarely cause hemorrhage. However, CMs located infratentorially carry an increased risk of hemorrhage. Surgical resection is the only curative treatment. CMs are concomitantly seen with deep venous anomalies (DVA) as a mixed vascular malformation. DVA is the most

common vascular malformation accounting for approximately 55 percent of cases. It is a congenital vascular anomaly composed of dilated medullary veins converging centripetally into a large collecting venous system that drains into the superficial or deep venous system. DVA is usually an incidental finding but can present as intracranial hemorrhage 1-5 percent of the time. Capillary telangiectasia is the second most common vascular anomaly. The vast majority are asymptomatic and are found as an incidental finding in middle age and elderly patients demonstrated as a cluster of capillary vessels interspersed with normal brain parenchyma. No treatment is warranted at this time.

Conclusions

In the era of multispecialty collaboration it is extremely important for the radiologist to be familiar with the presentation and management options of the differing dysplastic intracranial vascular malformations. Although, many of these lesions are asymptomatic and appear as incidental findings, they can be associated with hemorrhagic and nonhemorrhagic radiologic and clinical findings.

eEdE-79

6:30AM - 3:00PM

Role of Contrast Enhanced 3D CISS in Imaging Extracranial Segments of the Cranial Nerves

J Wen[1], N Aygun[2], A Blitz[1]
[1]*Johns Hopkins Hospital, Baltimore, MD,* [2]*Johns Hopkins University, Baltimore, MD*

Purpose

Constructive interference in steady state (CISS) sequence acquires high signal, high resolution isotropic 3D images which can be reconstructed in multiple planes to visualize complex cranial nerve (CN) anatomy. Administration of contrast further highlights the presence of pathology and can evaluate for evidence and extent of cranial nerve involvement. The ability of contrast-enhanced 3D CISS (CE-CISS) sequences to demonstrate such anatomical detail exceeds that of conventional and even high resolution T1-weight MR sequences. In this educational exhibit, we will illustrate the utility and superiority of high resolution CE-CISS in visualization of the extracranial segments of cranial nerves and characterization of pathology.

Materials and Methods

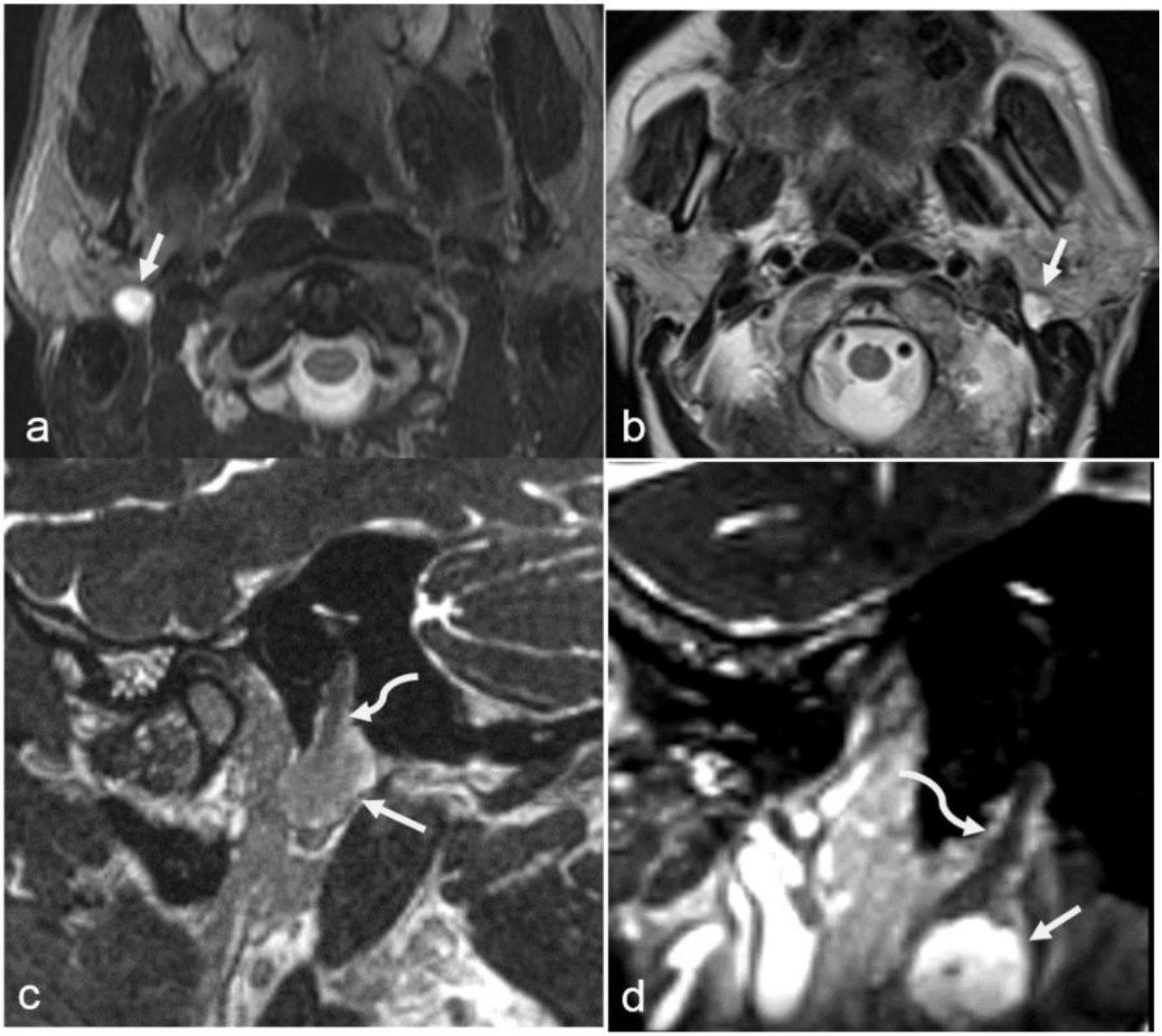
We will briefly discuss the technical details of 3D CE-CISS sequences and our clinical imaging protocol, as well as the basic mechanism of contrast enhancement. We will present case examples of extracranial cranial nerve pathology to systematically demonstrate the added value of CE-CISS images compared to conventional and high resolution T1-weighted MRI sequences. Specifically, cases are organized to cover pathology of the intra-orbital branches of the oculomotor nerve, lingual and inferior alveolar branches of the mandibular nerve, and intraparotid branches of the facial nerve.

Results

High resolution imaging of the extracranial nerves is feasible in routine clinical settings. With isotropic data sets and the ability to reconstruct images in any plane, visualization of small extracranial branches of the 3rd, 5th and 7th cranial nerves is more consistently possible in CE-CISS compared to conventional and high resolution contrast-enhanced T1-weighted sequences. This allows for better characterization of cranial nerve pathology, and more importantly distinguishing intrinsic cranial nerve pathology from secondary involvement of cranial nerves (Fig.1). Fig. 1: Comparison of conventional and CE-CISS imaging. Well defined mass lesions (arrows, 1a and 1b) in the stylomastoid foramen region in two different patients, possibly reflecting facial nerve schwannomas or parotid gland tumors. High resolution CE-CISS image 1c shows an enhancing mass (straight arrow) arising from within the right facial nerve (curved arrow), compatible with a schwannoma. CE-CISS image 1d demonstrates displacement of the left facial nerve (curved arrow) by a mass (straight arrow) suggesting a tumor originating from the salivary gland; subsequent biopsy was consistent with a pleomorphic adenoma.

Conclusions

Contrast-enhanced CISS sequences provide imaging detail that is not otherwise available in the evaluation of small extracranial branches of the cranial nerves, thus increasing the precision and accuracy of lesion detection, localization and differential diagnosis. The improved performance is attributable to the unique contrast provided by CE-CISS.



(Filename: TCT_eEdE-79_fig1.jpg)

eEdE-69

6:30AM - 3:00PM

Sellar Meningiomas and Pituitary Macroadenomas: A Radiologist's Role in Surgical Planning

R Tade[1], R Peterson[1], S Rohatgi[1], A Corey[1]
[1]*Emory University, Atlanta, GA*

Purpose
Describe and discuss radiographic features aiding in differentiating tuberculum/diaphragma sellae meningiomas and pituitary macroadenomas.

Materials and Methods
This educational exhibit will briefly review the complex anatomy of the sella, define imaging protocols to adequately evaluate the skull base and discuss the MR and CT features of each of these tumors. We will discuss classifications and types of skull base meningiomas, tumor enhancement patterns, sellar size/expansion, and the involvement of the pituitary gland, stalk and carotid arteries.
Results
The majority of intrasellar masses are pituitary macroadenomas with only 5% of space occupying lesions of nonpituitary origin. Differentiating sellar meningiomas and pituitary adenomas is difficult both clinically and radiographically. Patients often present with similar clinical features, visual symptoms or endocrine abnormalities. Pre-operative diagnosis of these two lesions dictates the surgical approach. Trans-sphenoidal resection is preferred for pituitary adenomas while a transcranial approach is necessary for adequate hemostasis and mobilization of a meningioma.
Conclusions
Imaging is necessary in identifying and differentiating sellar masses prior to surgery. The surgical approach is often dictated by radiographic findings. This exhibit will help radiologists identify subtle radiographic features which will help differentiate sellar meningiomas and pituitary macroadenomas.

eEdE-65

6:30AM - 3:00PM

Solitary Fibrous Tumor & Hemangiopericytoma: Two Sides of the Same Coin

M Hamidi[1], M Lester[1], E McComb[1], T Hijaz[1]
[1]*Feinberg School Of Med., Northwestern Univ., Chicago, IL*

Purpose
Solitary fibrous tumors and hemangiopericytomas demonstrate overlapping pathologic features and recently have been found to express identical molecular markers. Thus, the 2016 World Health Organization (WHO) classification has been updated to combine the two as "solitary fibrous tumor/hemangiopericytoma." This pictorial essay will review the imaging features of this newly unified entity, including the characteristics that may aid in predicting tumor grade.
Materials and Methods
Cases of solitary fibrous tumor/hemangiopericytoma exemplifying a range of presentations within the central nervous system, including the head and neck, were selected retrospectively. Correlation with pathologic findings was reviewed.
Results
Solitary fibrous tumor/hemangiopericytoma has a wide range of appearances from small lesions with benign features to large, aggressive-appearing or even metastatic lesions.

Distinguishing these lesions from other etiologies, such as meningioma or head and neck carcinoma, can be challenging on the basis of imaging alone, and tissue sampling is required for a definitive diagnosis. The presence of osseous erosion or frank invasion, vascular flow voids, or metastases may help to suggest the diagnosis and the tumor grade.
Conclusions
The entities formerly known as solitary fibrous tumor and hemangiopericytoma are now classified as a single entity, the radiographic features of which are widely varied and overlap with more common diagnoses.

eEdE-59

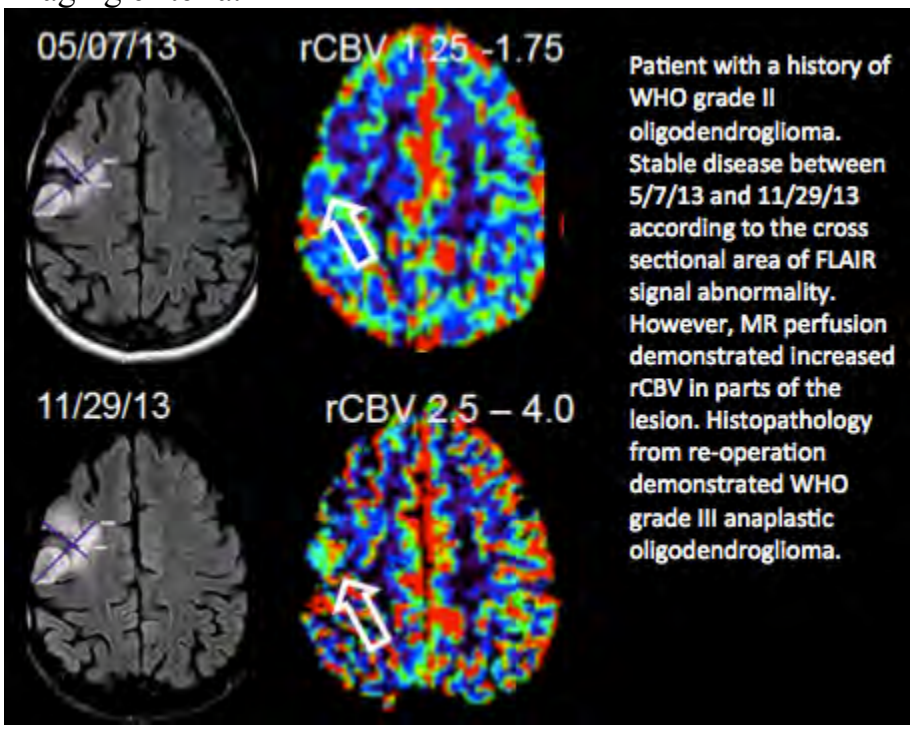
6:30AM - 3:00PM

State of the Art Imaging Surveillance of Gliomas

S Margiewicz[1], R Jain[2]
[1]New York University Langone Medical Center, New York, NY, [2]NYU School of Medicine, New York, NY

Purpose
To review and evaluate the different imaging methods and criteria utilized for glioma surveillance with an emphasis on the current state and role of advanced MRI techniques.
Materials and Methods
A review of the literature will be performed to describe and analyze the different imaging techniques and criteria used in glioma surveillance. Conventional criteria based mostly on two-dimensional measurements, such the Macdonald and RANO criteria will be reviewed and evaluated. Advanced imaging techniques and methods, including MR perfusion, diffusion-weighted imaging, MR spectroscopy, and positron emission tomography then will be reviewed and evaluated. A particular emphasis will be placed on MR perfusion and how it can help overcome shortcomings seen in other methods. Multiple illustrative personal examples of complex cases that demonstrate the benefits of MR perfusion over that of conventional imaging will be provided.
Results
Traditional methods of glioma surveillance, based mostly on two-dimensional measurements of contrast enhancing regions or nonenhancing T2/FLAIR signal abnormalities face a number of limitations when tasked with glioma surveillance. Increased enhancement and abnormal T2/FLAIR signal in the regions of treated tumor can both be due to a number of different causes, not always related to tumor progression or recurrence, and therefore can be misleading. Two-dimensional measurements also can be inaccurate or difficult to reproduce. Advanced imaging methods, particularly MR perfusion, utilize physiologic and metabolic characteristics of gliomas and show great promise in overcoming some of these challenges.
Conclusions
Advanced imaging methods of glioma surveillance, particularly MR perfusion, hold great

promise in providing useful and accurate information about tumor recurrence and progression, and can help overcome some of the limitations associated with conventional imaging criteria.



(Filename: TCT_eEdE-59_ASNR2017.jpg)

eEdE-33

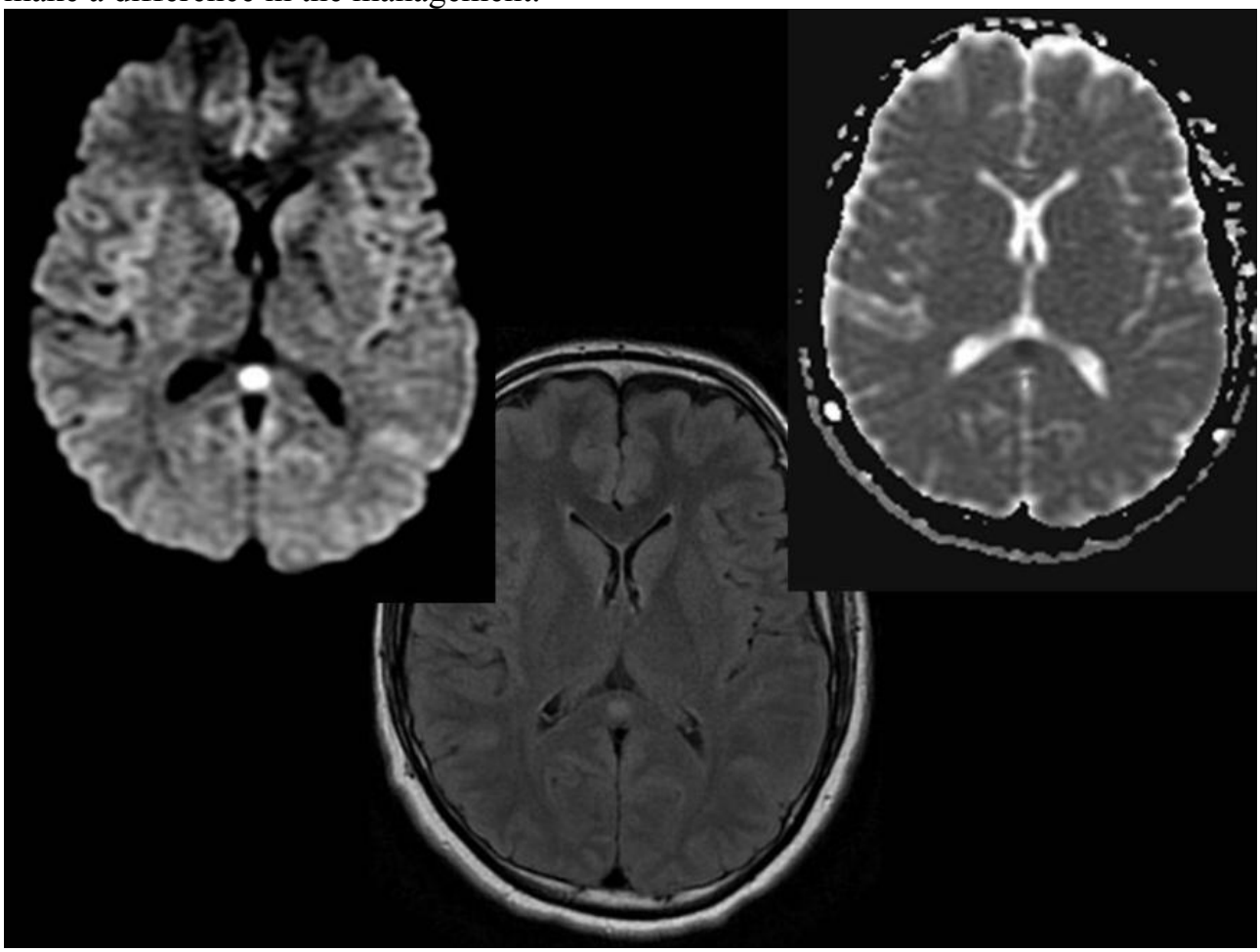
6:30AM - 3:00PM

The Disappearing Act! Transient Lesions of the Splenium, a Pictorial Review

A Patel[1], A Aggarwal[1], K Nael[1], A Doshi[1], P Pawha[1]
[1]*Icahn School of Medicine at Mount Sinai, New York, NY*

Purpose
The objective of this pictorial review is to illustrate the imaging findings and predisposing clinical scenarios which are associated with the transient lesions of the splenium. The background, presentation and the natural history of this entity will be discussed also.
Materials and Methods
The transient lesion of the splenium of the corpus callosum (SCC), also known as mild encephalitis/encephalopathy with a reversible isolated SCC lesion (MERS), is an infrequently encountered entity on MRI. This pictorial review demonstrates cases of transient lesions of the splenium of the corpus callosum occurring in a variety of clinical settings, with follow-up imaging in some cases to highlight their natural progression.
Results
These lesions demonstrate splenial diffusion restriction and T2 hyperintensity which is

reversible. There are two distinct patterns seen: a well circumscribed midline ovoid lesion, and a more diffuse irregular lesion that extends throughout the splenium and sometimes into the adjacent cerebral parenchyma. It is important to distinguish this transient phenomenon from ischemia and other irreversible pathologies which could potentially change treatment plan. Clinical features also will be discussed, such as lack of striking clinical signs and symptoms or hemispheric disconnect often seen with irreversible lesions. Recognizing the complete reversibility of this entity without a specific intervention is essential.
Conclusions
The reader will be able to recognize this entity as a transient, reversible lesion associated with specific known predisposing clinical settings, and knowledge of this phenomenon can make a difference in the management.



(Filename: TCT_eEdE-33_file.jpg)

eEdE-13

6:30AM - 3:00PM

The Temporal Lobe - Not All Restricted Diffusion is Infarction

A Momeni[1], F Choudhry[1], S Mukherjee[1]

[1]*University of Virginia Health System, Charlottesville, VA*

Purpose

This electronic exhibit aims to demonstrate the wide spectrum of temporal lobe pathology. Although mesial temporal lobe abnormalities often have overlapping imaging features we present characteristic imaging and clinical findings, with focus on diffusion-weighted imaging and relevant clinical history, to help differentiate pathology and form a meaningful differential diagnosis. The exhibit is directed towards trainees but also serves as a refresher for practicing neuroradiologists.

Materials and Methods

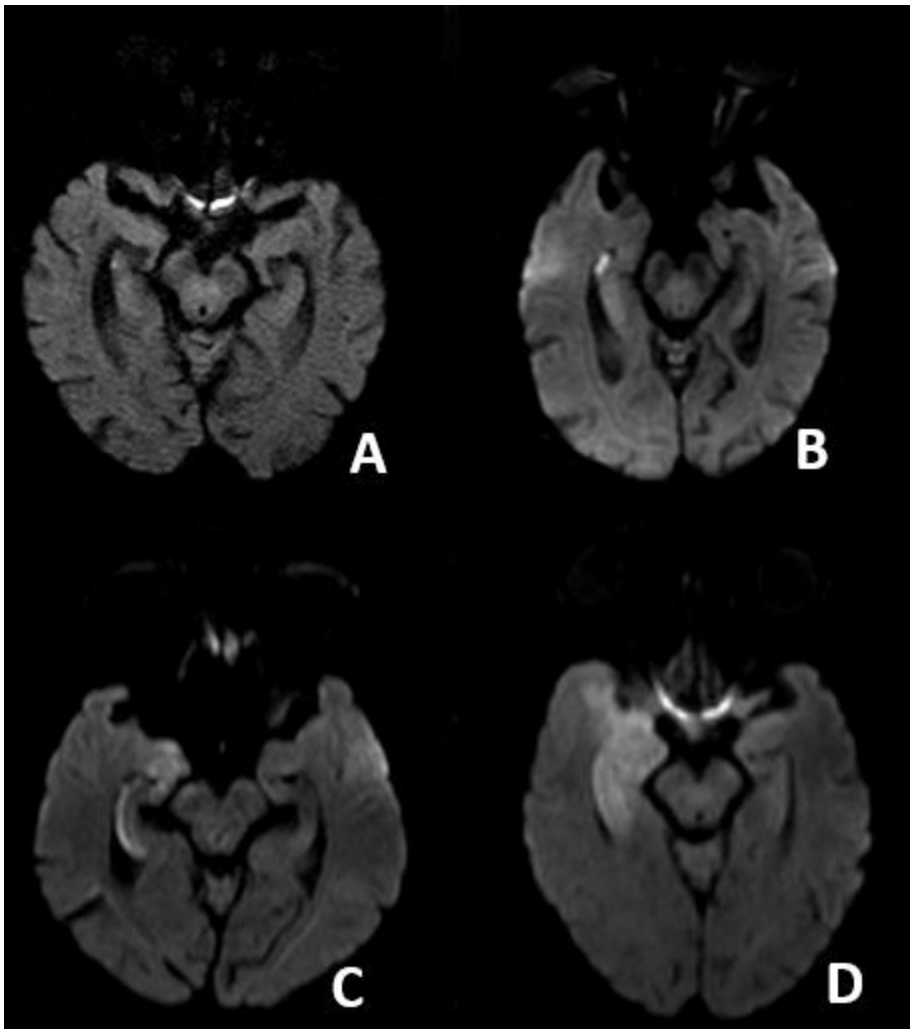
Common causes of restricted diffusion within the mesial temporal lobe are reviewed including transient global amnesia, infarction, post-ictal states, and encephalitis in addition to neoplastic pathology and cystic lesions. All cases presented and clinical data are provided in accordance with the institutional review board. Patients underwent multi-sequence multi-planar brain MRI examinations on either a 1.5T or 3.0T Siemens scanner with or without gadolinium contrast agent (Gadavist).

Results

Figures A-D demonstrate findings from four patients: Images illustrate the differences in morphology of hippocampal restricted diffusion. Patient 1 (A) is a 90-year-old male with transient amnesia and punctate right hippocampal restricted diffusion. Patient 2 (B) is an 84-year-old female with syncope and ovoid focal right hippocampal restricted diffusion. Patient (3) is a 62-year-old male with seizure history and right linear hippocampal gyrus restricted diffusion. Follow up of the same patient revealed abnormal hippocampal signal and atrophy. Patient 4 (D) is a 68-year-old female with altered mental status and diffuse mesial temporal lobe restricted diffusion. Additional cases (not shown) illustrate cystic lesions, both benign perivascular spaces and neoplastic lesions.

Conclusions

Abnormalities of the temporal lobe have both overlapping and individually characteristic imaging features. Knowledge of these imaging features in context of the clinical history aide in forming a meaningful differential diagnosis.



(Filename: TCT_eEdE-13_MomeniTemporallobe.jpg)

eEdE-37

6:30AM - 3:00PM

The Wonderful Net - Rete Mirabele A Case Series

A Verma[1], H PENDHARKAR[2], A Gupta[3], S TIWARI[4]
[1]National Institute of Mental health & Neuro Sciences, Bangalore, Karnataka, [2]NATIONAL INSTITUTE OF MENTAL HEALTH & NEUROSCIENCES, BANGALORE, KARNATAKA, [3]National Institute of Mental Health and NeuroSciences (NIMHANS), Bangalore, Karnataka, [4]National Institute of Mental Health and Neurosciences, BANGALORE, Karnataka

Purpose
To depict the rare vascular condition of rete mirabele.
Materials and Methods
Three cases of rete mirabele were encountered in the last year at our institute. All three

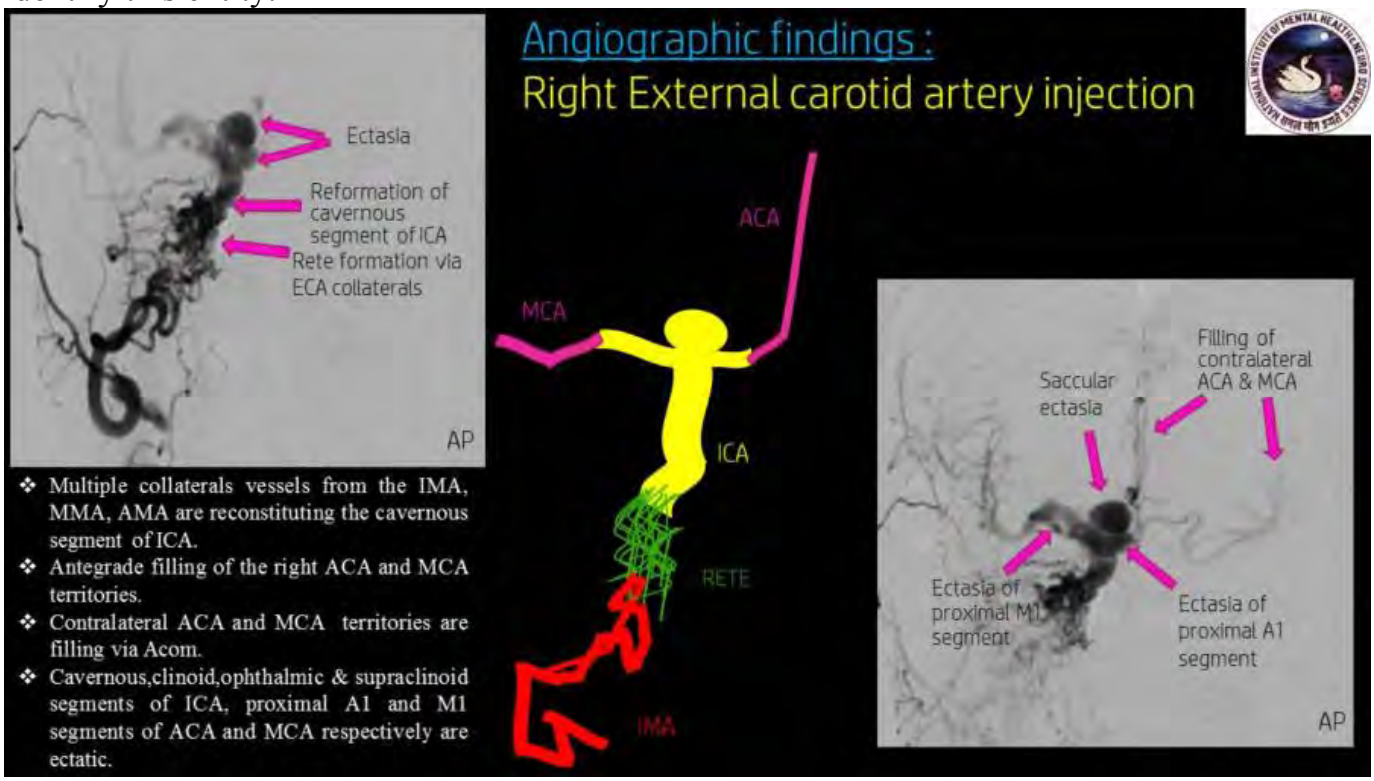
patients were females between 20 - 59 years. Two presented with subarachnoid hemorrhage and one with headaches. Digital subtraction angiography (DSA) was done to look for the cause which revealed rete mirabele in all 3 patients.

Results

Digital subtraction angiography revealed rete mirabele in all 3 patients. One patient had dysplastic vessels with multiple aneurysms. Another patient had a basilar top aneurysm while the third had no other associated vascular anomaly.

Conclusions

Rete mirabile means "wonderful net" in Latin and is a kind of arterial plexus. Carotid rete mirabile (CRM) is a transdural arterial network classically defined to be present at carotid cavernous portion and fed by external carotid artery branches, especially internal maxillary artery (IMA). Knowledge of embryological variants of intracranial vessels is essential to identify this entity.



(Filename: TCT_eEdE-37_RETEMIRABELE.jpg)

eEdE-103

6:30AM - 3:00PM

Thin Section Multiplanar Reconstructions of the Temporal Bone from Standard Head CT's: Can They Replace Dedicated Temporal Bone CT's in the Setting of Trauma?

M Cho[1], A Lerner[1], J Go[2], O Boyko[1]

[1]University of Southern California/Keck Medical Center, Los Angeles, CA, [2]University of Southern California, Los Angeles, CA

Purpose

Since the introduction and widespread adoption of multidetector computed tomography (MDCT), there has been increased use of spiral scanning technique for CT of the head (CTH) over sequential "step and shoot" scanning technique. Studies have shown that thinly collimated multidetector spiral CT of the brain is superior to thickly collimated sequential CT in terms of reducing streak artifacts, visualizing of brain tissue near the skull, and overall image quality. Additionally, spiral CT allows reconstruction of data into axial, sagittal and planes for multiplanar analysis. The latter benefit can be leveraged for the construction of thin section, high resolution imaging of the temporal bone. The purpose of this exhibit is to explore the ability of such reconstructed images from standard CTH studies to depict temporal bone fractures and normal temporal bone anatomy and to discuss the clinical significance of this postprocessing technique.

Materials and Methods

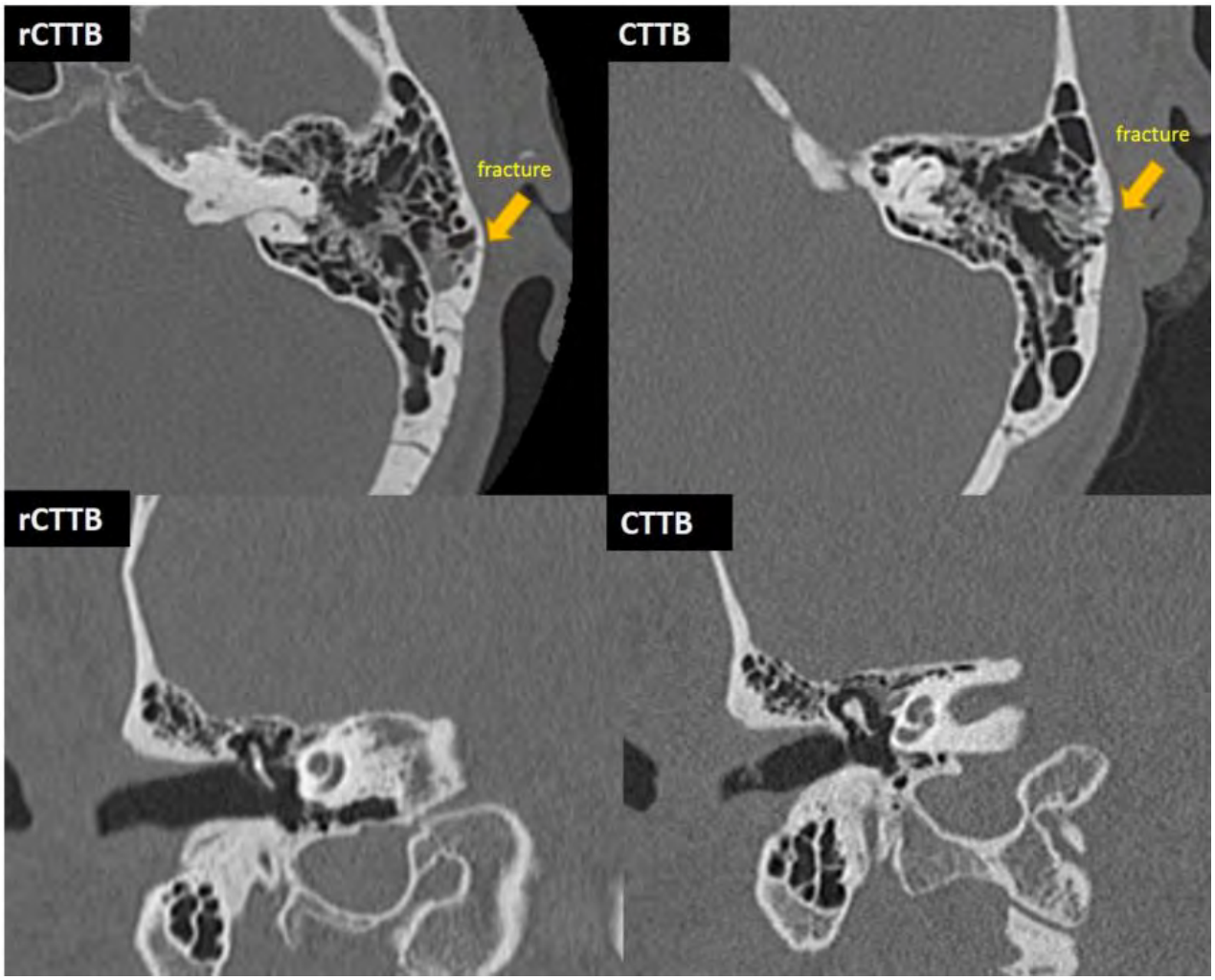
CT of the head and CTTB (CT of the temporal bone) studies were performed at our Level 1 trauma center using helical technique on a 64 slice MDCT, with a scan slice thickness of 0.5 mm, mA of 120, and kVp of 120. Standard CTH studies are reconstructed into 5 mm axial slices, but in cases of possible temporal bone fractures, 1 mm reconstructions were obtained in multiple planes targeted to the temporal bone (rCTTB).

Results

Given their essentially identical technique including helical acquisition, equivalent mA/kVp, FOV, and pitch, rCTTB and CTTB studies are nearly identical in terms of resolution and image quality compared to dedicated CTTBs. Intricate anatomic structures of the temporal bone such as the ossicles and inner ear structures are depicted in clear detail. Temporal bone fractures are clearly seen and complications can be confidently ruled out. Computed tomography of the temporal bone studies often are ordered in the setting of trauma when there is a suspected temporal bone fracture when interpreting a standard CTH. Using thin section reconstructions, there is no longer a need to bring the patient back to the CT suite to rescan. This reduces scanning time, radiation exposure to the patient, and eventually cost to the patient. More routine use of rCTTB could potentially increase efficiency in a radiology department if they are performed in lieu of dedicated CTTB.

Conclusions

With the increasing use of helical MDCT technique for CTH, thin section multiplanar reconstruction of the temporal bone is available at many institutions on a routine basis. Such imaging features may be useful in the setting of suspected temporal bone pathology, especially fractures. Reconstructions of the temporal bone may obviate the need for dedicated CTTB studies, thereby reducing radiation, cost, and time of scanning for the patient.



(Filename: TCT_eEdE-103_tboneasnr.jpg)

eEdE-104

6:30AM - 3:00PM

Traumatic Vertebral Artery Injuries: What the Clinician Wants to Know and What the Radiologist Needs to Know

R Tade[1], R Peterson[1], S Rohatgi[1]
[1]*Emory University, Atlanta, GA*

Purpose
Blunt traumatic vertebral artery injury is a common finding in trauma patients, with an increased incidence in those with head and neck injuries. Early diagnosis and treatment often can prevent or limit serious cerebellar and brainstem infarction. We review common mechanisms of arterial injury, relevant clinical anatomy, illustrate common imaging patterns, diagnostic pitfalls and management from a clinical perspective.

Materials and Methods
We review currently accepted guidelines and common imaging practices for traumatic vertebral artery injury. Illustrative cases from our institutional practice, which includes University affiliated hospitals and level 1 trauma centers.
Results
Traumatic vertebral artery injury has a wide variation in clinical presentation and there is no widely accepted consensus on diagnosis and management. Some reports have found that evidence for traumatic vertebral artery injury can be found in up to 20% of patients with head injuries. While traumatic vertebral artery injury has the potential to lead to serious posterior circulation ischemia, there remains debate on if, and how, it should be actively screened for. Here we will review common mechanisms of traumatic vertebral artery injury including: hyperflexion, hyperextension, distraction, facet dislocation and fractures of the cervical spine. In addition, relevant vertebral artery will be discussed. Common imaging patterns and techniques of evaluation of vertebral artery injury including mimics and diagnostic pitfalls will be reviewed, as well as current screening and appropriate management recommendations.
Conclusions
Imaging plays a crucial role in the diagnosis of traumatic vertebral artery injury. By appropriately identifying and grading these injuries, the radiologist can make key management and follow-up recommendations. This exhibit will highlight common mechanisms of injury, relevant anatomy, imaging patterns as well as screening and management recommendations that are crucial for the radiologist to understanding blunt traumatic vertebral artery injury.

eEdE-57

6:30AM - 3:00PM

Trigeminal Neuralgia-Pictorial Essay

R Glikstein[1], C Torres[1], N Berkovitz[1], J Davila[1]
[1]*University of Ottawa, Ottawa, Ontario*

Purpose
To show different pathologies causing trigeminal neuralgia.
Materials and Methods
We present in this paper patients with clinical history of trigeminal neuralgia, who had an MRI of the brain in order to identify the cause and/or to direct a possible change in treatment. Our trigeminal protocol includes high resolution axial T2 centered on the cisternal segment of the trigeminal nerves, axial FLAIR of the brain, coronal and axial T1, coronal T2 from the brainstem to the orbits and post Gd on axial and coronal planes. The pathologies presented include multiple sclerosis at the entry point of CN V, leptomeningeal

carcinomatosis, atypical choroid plexus papilloma, Neurosarcodoisis, lymphoma, acoustic schwannoma causing compression, vascular loop crossing over CN V.
Results
Trigeminal neuralgia presents as a result of a pathology that affects one of the three divisions of the trigeminal nerve. The prevalence is variable, between 0.01 and 0.3% of the population, more common in women, generally appears at the age of 40. It is classically divided in typical or atypical, the first one characterized by spontaneous acute burning pain on the trigeminal nerve (CN V) distribution which may last few seconds up to few minutes, and the atypical type which is a constant stabbing pain. Magnetic resonance imaging (MRI) is the elective method for diagnosis of this entity.
Conclusions
Magnetic resonance imaging studies including high resolution T2 imaging centered on the cisternal segment of the trigeminal nerve proved to be extremely sensitive to identify small lesions, mass effect or atrophy of the trigeminal nerve, and should be included on the protocol of exploration. Thin slice post Gd T1 following the trigeminal nerve and branches of division is required to reassure the presence or absence of pathology, in coronal plane, preferably with fat saturation.

eEdE-53

6:30AM - 3:00PM

Typical and Atypical Imaging Findings of Chordomas with Pathologic Correlation.

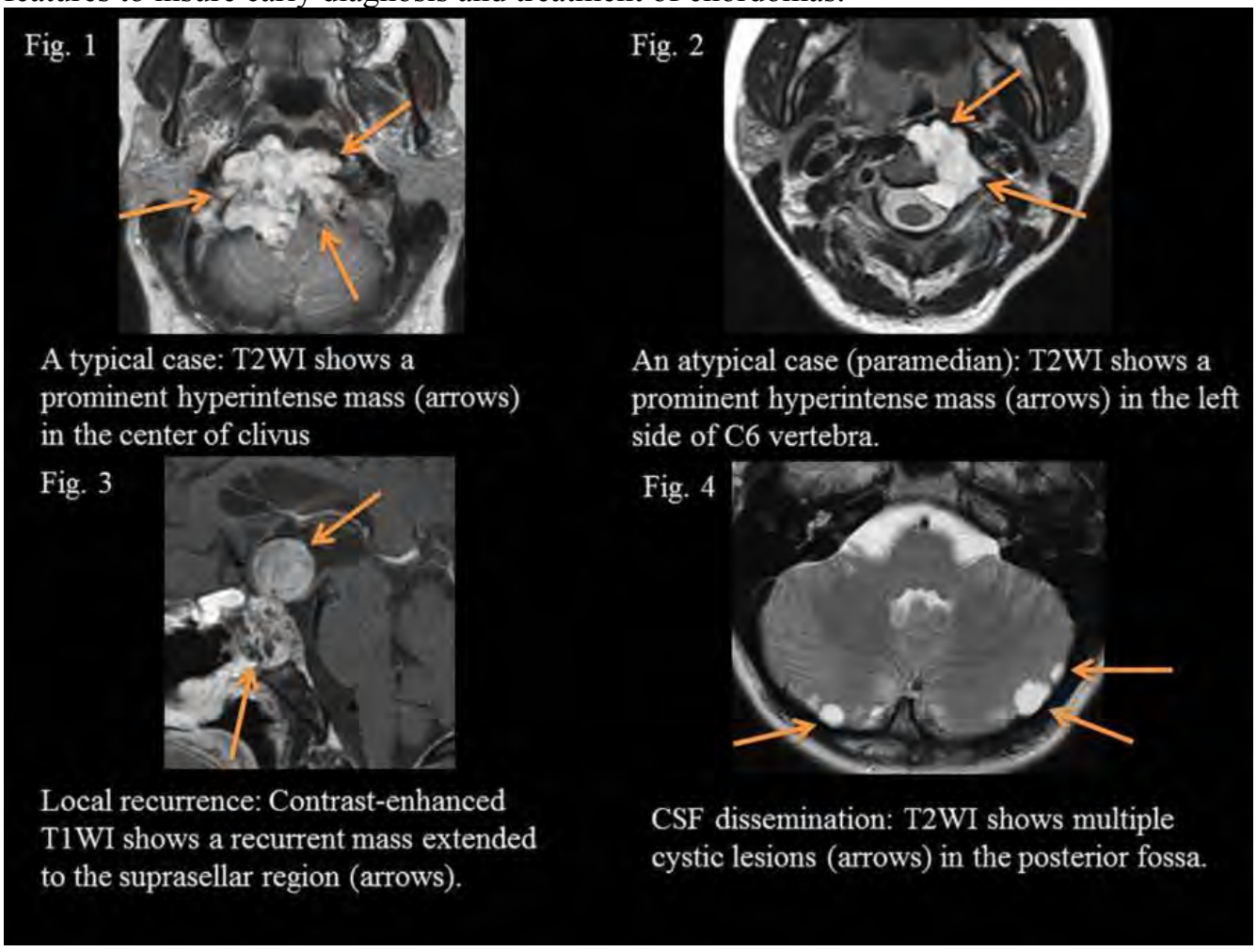
T Sasaki[1], T Moritani[2], T Sato[1], A Capizzano[2], J Hodgson[2], U Shafique[3], Y Sato[1], A Oya[4], M Toda[4], P Kirby[2]
[1]University of Iowa, Iowa City, IA, [2]University of Iowa Hospitals and Clinics, Iowa City, IA, [3]University of Iowa, Hospitals and Clinics, Iowa City, IA, [4]Asahikawa Medical University, Asahikawa, Hokkaido

Purpose
Chordomas are a rare malignant tumor which can involve the skull base, spine, and sacrococcygeal bone. Imaging findings have been reported in typical cases of chordomas, but atypical chordomas can be difficult to distinguish from other tumors. It is important to be familiar with the imaging characteristics of both typical and atypical chordomas to allow for early diagnosis and treatment.
Materials and Methods
1) Overview and WHO classification, 2) typical imaging findings, 3) atypical imaging findings, 4) features of diffusion-weighted imaging, 5) patterns of recurrence or metastasis, and 6) prognostic factors.
Results
1) WHO classification identifies the following three types of chordomas: "Chordoma NOS", "Chondroid chordoma", and "Dedifferentiated chordoma." 2) CT of typical chordomas

demonstrate a well-circumscribed expansile mass with bone destruction often centered in the clivus and sacrococcygeal bone. T1-weighted images show low- or iso-intensity to spinal cord, while T2-weighted image shows prominent hyperintensity (Fig. 1), and postcontrast T1-weighted imaging reveals avid enhancement. 3) In atypical chordomas, T1-weighted images depict a hyperintense component, while T2-weighted images show low- or iso-intensity. Chordomas occasionally can develop paramedian to the vertebrae (Fig. 2). 4) Diffusion-weighted imaging shows lower apparent diffusion coefficient (ADC) in chordoma compared to chondrosarcoma. Furthermore, among the chordomas the dedifferentiated type may reveal lower ADC than classical type. 5) Local recurrent masses can extend to adjacent structures (Fig. 3). Chordomas can metastasize to the lung or bone or disseminate into the arachnoid space (Fig. 4). 5) A recent study demonstrated older age at surgery, recurrent chordoma, and lack of the A variant at rs2305089 are adverse prognostic factors.

Conclusions

We review the typical and atypical imaging findings as well as pathology and prognostic features to insure early diagnosis and treatment of chordomas.



(Filename: TCT_eEdE-53_forasnrabstract.jpg)

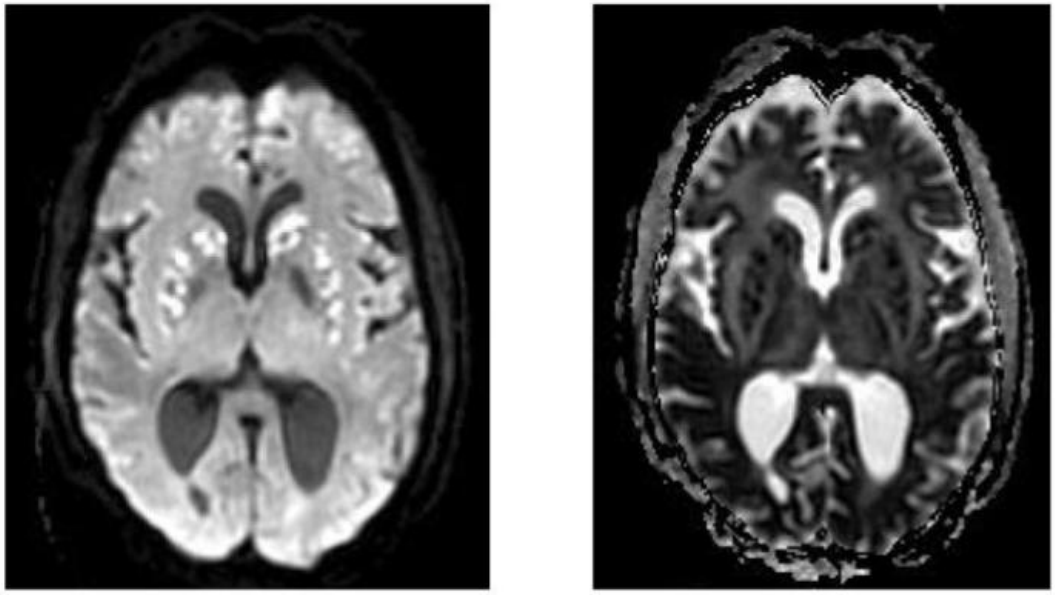
eEdE-98

6:30AM - 3:00PM

Uncommon Patterns of Diffusion Restriction in the Basal Ganglia

A Iqbal[1], A Bhatt[2], J Almast[3]
[1]University of Rochester, Rochester, NY, [2]University of Rochester Medical Center, Rochester, NY, [3]Univeristy of Rochester, Rochester, NY

Purpose
The purpose of this educational exhibit is to show that diffusion restriction in the basal ganglia does not always mean stroke. While stroke is a common etiology, there are other causes which can result in uncommon patterns of diffusion restriction in the basal ganglia. These will be demonstrated and discussed.
Materials and Methods
The presentation will begin with a review of the anatomy of the basal ganglia on imaging. Next typical presentations of stroke will be shown. This will be followed by several cases with unusual patterns of diffusion restriction in the basal ganglia. Differential diagnoses will be suggested based on the imaging findings with a review of the diagnosis and its imaging findings.
Results
This educational exhibit will review the anatomy of the basal ganglia. A quick review of typical findings of stroke of the basal ganglia then will be followed with several cases of uncommon patterns of diffusion restriction in the basal ganglia. A discussion of etiologies of the imaging findings will follow. Etiologies which result in uncommon patterns of diffusion restriction in the basal ganglia will include hemolytic uremic syndrome/thrombotic thrombocytopenic purpura, hyperesonophilic syndrome, and fat embolism as well as others. A discussion regarding the different etiologies and their typical imaging findings will follow.
Conclusions
Uncommon patterns of diffusion restriction in the basal ganglia should make the interpreter think of a few certain etiologies. This educational exhibit will discuss these etiologies, providing several images of findings and review the typical imaging findings in those cases. Clues that may help differentiate certain cases also will be included.



(Filename: TCT_eEdE-98_Images.jpg)

eEdE-86

6:30AM - 3:00PM

Unrestrict Your Differential of Restricted Diffusion

J Weisiger[1], D Durand[2], I Mills[1], K Eng[1], A Malhotra[3]
[1]Yale-New Haven Hospital, New Haven, CT, [2]Yale University School of Medicine, New Haven, CT, [3]Yale New Haven Hospital, New Haven, CT

Purpose
Since its introduction into mainstream radiology in the 1990s, diffusion-weighted imaging (DWI) has become the mainstay for stroke imaging. However, utilization of DWI has proven to be a powerful and essential tool for allowing radiologists to solve complex cases. The purpose of this educational exhibit is to review common, as well as uncommon pathology that can be distinguished utilizing diffusion-weighted imaging.
Materials and Methods
This educational exhibit will review the multivariable role of diffusion-weighted imaging in neuroradiology. Through a case-based approach, we will review several common and uncommon examples in which diffusion-weighted imaging helped narrow the differential and secured the diagnosis.
Results
Cases within the educational exhibit will include:This versus that: •Acute versus chronic

stroke. •Abscess versus necrotic tumor, •Tumor recurrence versus postradiation changes, •Epidermoid cyst versus an arachnoid cyst, •Herpes encephalitis versus diffuse gliomas. Other examples will include: •Demyelination, •Diffuse axonal injury, •Methotrexate toxicity, •Cytotoxic edema secondary to seizures, •Fat embolism, •Cortically-based lesions in CJD, •Neurosarcoidosis, •Amongst others.
Conclusions
The proper utilization of diffusion-weighted imaging is essential for accurate diagnosis and improving patient care. It is indispensable for any practicing neuroradiologist to have a strong working knowledge of diffusion-weighted imaging and its relation to neuropathology.

eEdE-92

6:30AM - 3:00PM

Unrestrict Your Differential of Restricted Diffusion

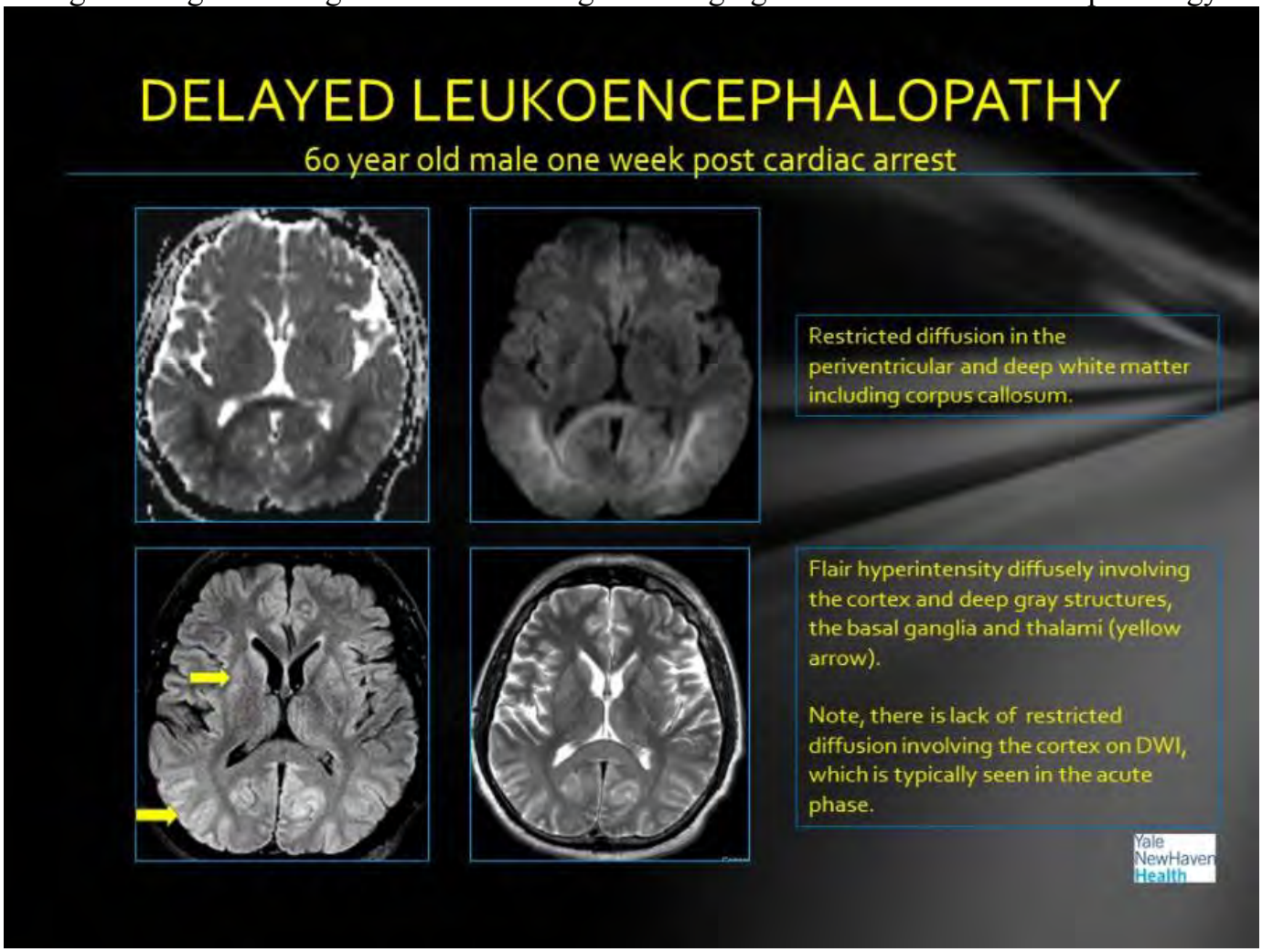
J Weisiger[1], D Durand[2], I Mills[1], K Eng[1], X Wu[2], A Malhotra[3]
[1]Yale-New Haven Hospital, New Haven, CT, [2]Yale University School of Medicine, New Haven, CT, [3]Yale New Haven Hospital, New Haven, CT

Purpose
Since its early development in 1985 and entry into clinical imaging in the early 1990s, diffusion-weighted imaging (DWI) has revolutionized neuroradiology for its role in stroke imaging. As technique and methods improved, DWI has proven to be a powerful and essential technique in solving complex cases. The purpose of this educational exhibit is to review the application of DWI in diagnosing common and uncommon neurological diseases and conditions, highlighting particular situations outside of stroke imaging where it is invaluable.
Materials and Methods
This educational exhibit will review the multivariate role of diffusion-weighted imaging in neuroradiology. Through a case-based approach, we begin with a concise review of diffusion-weighted technique and image acquisition, followed by several examples of common and uncommon pathologies for which DWI can be harnessed to narrow the differential and often secure a diagnosis.
Results
Cases within this educational exhibit will include: ·Acute versus chronic arterial infarcts. ·Venous infarcts. ·Postoperative versus spontaneous abscess. ·Epidermoid cyst versus arachnoid cyst. ·Herpes encephalitis. ·Tumor recurrence versus postradiation changes. ·Subacute hematoma versus high grade hemorrhagic glioma. ·Cholesteatoma. ·Transient global amnesia. ·Lymphoma. ·Hypoglycemic and hyperglycemic encephalopathy. ·Retraction injuries. ·Methotrexate and vigabatrin toxicity. ·White matter diseases: migraines, demyelination and dysmyelination, Susac's disease, and CADASILE. ·epileptogenic foci. ·Traumatic injuries: diffuse axonal injury, contusions, and deep gray

matter injury. ·Fat embolism. ·Carbon monoxide poisoning. ·Creutzfeldt–Jakob disease. ·Hypoxic ischemic encephalopathy. ·Hepatic encephalopathy. ·Neurosarcodosis.

Conclusions

The proper utilization of diffusion-weighted imaging is essential for accurate diagnosis and improving patient care. It is indispensable for any practicing neuroradiologist to have a strong working knowledge of diffusion-weighted imaging and its relation to neuropathology.



(Filename: TCT_eEdE-92_DelayedleukoencephalopathyASNR2017.jpg)

eEdE-61

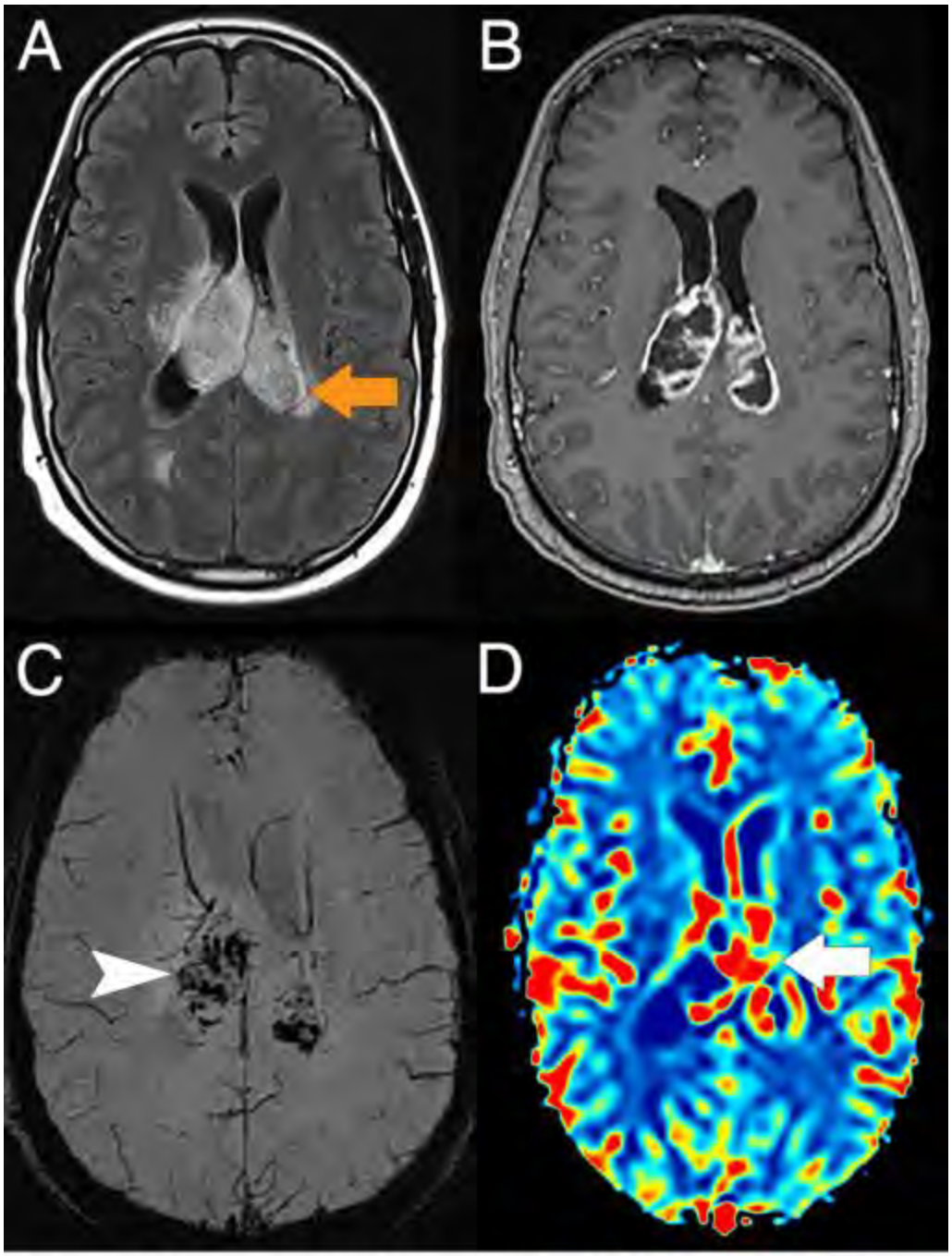
6:30AM - 3:00PM

Unusual Intraventricular Masses: Beyond Choroid Plexus Tumors, Meningiomas, and Ependymomas

C Zamora[1], M Kontzialis[2], M Castillo[3]

[1]University of North Carolina, Chapel Hill, NC, [2]Rush University Medical Center, Chicago, IL, [3]Univ. Of North Carolina School Of Medicine, Chapel Hill, NC

Purpose
The differential diagnosis of intraventricular neoplasms is broad and many lesions present with overlapping imaging and clinical features. The purpose of this review is to present a spectrum of intraventricular masses and mass-like lesions focusing on the imaging characteristics of unusual entities as well as potential mimics and pitfalls for diagnosis.
Materials and Methods
We searched our teaching file over the past 12 years and collected cases of patients who presented with intraventricular masses that were regarded as unusual given their infrequent intraventricular location or which posed a diagnostic challenge due to overlapping characteristics with other lesions including non-neoplastic etiologies.
Results
We identified various intraventricular neoplasms including glial (pilocytic astrocytoma, glioblastoma, pleomorphic xanthoastrocytoma), glioneuronal (dysembryoplastic neuroepithelial and mixed tumors), embryonal (rhabdoid tumors), epithelial (intraventricular craniopharyngioma), and germ cell tumors and primary central nervous system lymphoma. Non-neoplastic intraventricular masses including congenital/developmental (cerebrospinal fluid cysts, dermoid/epidermoid, lipomas, hamartomas), vascular (intraventricular aneurysms), and infectious lesions (neurocysticercosis and intraventricular abscess) also were identified as potential pitfalls for diagnosis.
Conclusions
Outside of the usual etiologies for intraventricular masses, the differential diagnosis of an intraventricular lesion is varied and includes non-neoplastic pathologies that can potentially represent a diagnostic challenge.



Intraventricular glioblastoma. **(A)** Axial FLAIR image shows bright intraventricular masses occupying the lateral ventricles bilaterally (orange arrow) with mild surrounding parenchymal edema. **(B)** Post-contrast T1 image demonstrates irregular and predominantly peripheral enhancement. **(C)** Susceptibility-weighted imaging shows internal foci of signal loss (arrowhead) consistent with hemorrhage and/or vascular flow voids. **(D)** MRI rCBV map shows increased perfusion within the masses (white arrow).

(Filename: TCT_eEdE-61_FIGUREwlegend.jpg)

eEdE-35

6:30AM - 3:00PM

USPIO-Enhanced MRI for Microvascular Imaging – Update of New Concepts

Y Ge[1], E Haacke[2]
[1]New York University School of Medicine, New York City, NY, [2]Wayne State University, Detroit, MI

Purpose
To describe several novel imaging concepts for developing the next generation of microvascular imaging, which we refer to as microvascular in vivo contrast revealed origins (MICRO) MRI. We believe MICRO will serve as a significant predictive marker of disease development and progression in a number of neurological disorders.
Materials and Methods
We have reviewed and tested 4 novel concepts to take us closer to imaging the microvasculature of both the arterial and venous systems with an in-plane resolution of roughly 50 to 100μm. These concepts are based on susceptibility-weighted imaging (SWI) with modifications to increase the speed of acquisition, they involve: 1) using an ultra-small-superparamagnetic-iron-oxide (USPIO) contrast agent (a blood pool agent) [1] to image the microvasculature, including both micro-arterial and microvenous systems (down to 50 to100μm level), through the susceptibility (T2*) blooming effect and a sub-voxel diffraction strategy (super-resolution imaging); 2) using a new quantitative susceptibility mapping (QSM) approach to both image and separate the arterial/venous systems; 3) creating a cerebral microvascular architecture print (cMAP), based on ultra-high resolution MR arteriogram and venogram (MRAV) imaging for 3D visual inspection of the vascular architecture; and 4) generating regional vascular density (VD) and capillary density (CD) measures derived from MICRO data to quantify regional microvascular abnormalities. Ferumoxytol, which is a FDA-approved USPIO for human use, is the contrast agent used in this study.
Results
With acquired data, it clearly demonstrates the feasibility of each concept. These concepts can be integrated into one powerful MICRO MRAV, which can be a new tool in clinical diagnosis and disease monitoring. Adding Ferumoxytol to the blood leads to an increase of the susceptibility, blooming, vascular contrast, and quantification capabilities of both arteries and veins at the micro level. Specifically, a distinctive 3D cMAP (vessel atlas) can be generated for direct visual inspection of the microcirculation network. Quantitative VD and CD maps can be used to measure regional microvascular density from the MICRO imaging data.

Conclusions
Using a low dose of Ferumoxytol, MICRO has the potential to yield the next generation of vascular imaging to unveil underlying microvascular abnormalities in neurovascular diseases.

eEdE-17

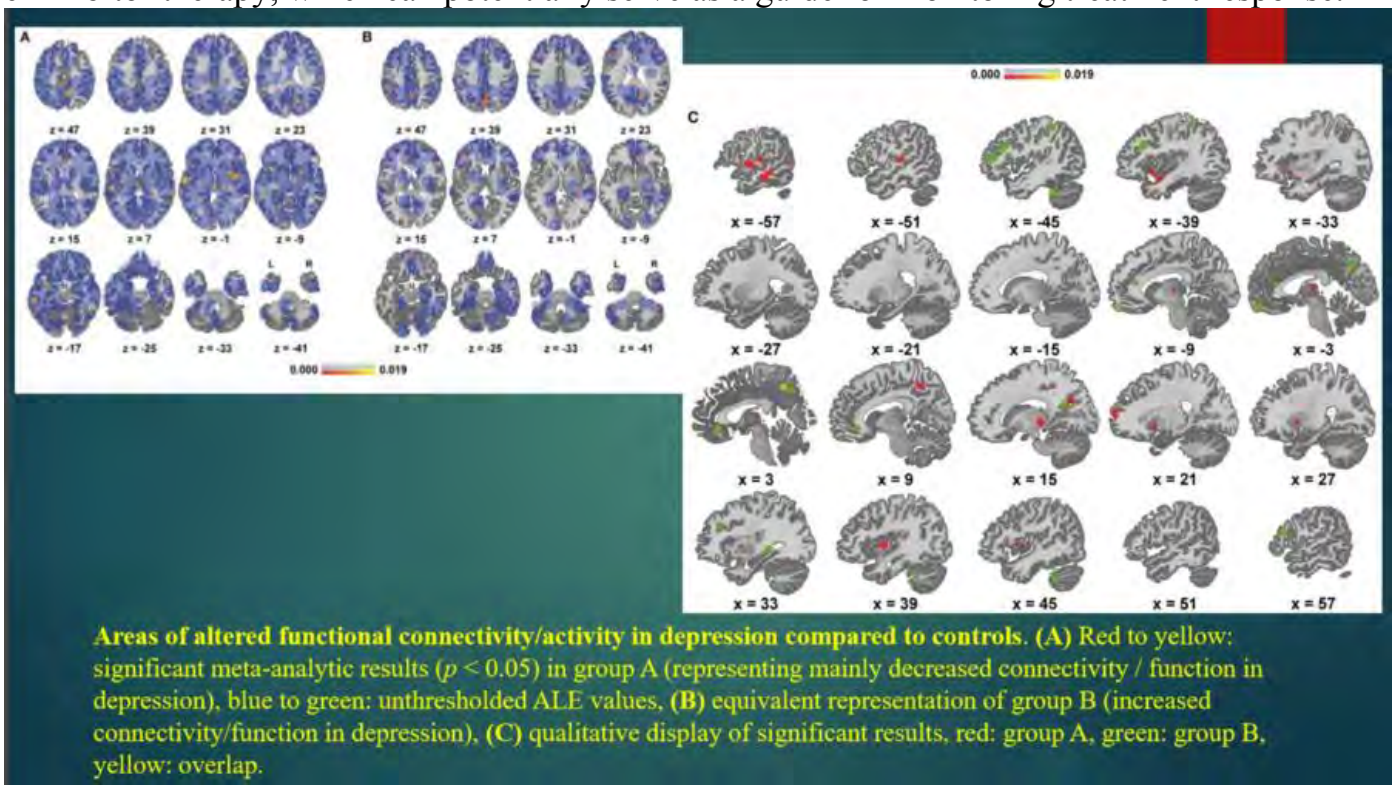
6:30AM - 3:00PM

Utility of fMRI in Depression

A Chaudhry[1], H Sair[2]
[1]Johns Hopkins Medicine, Elkridge, MD, [2]Johns Hopkins Medicine, Baltimore, MD

Purpose
Major depressive disorder (MDD) is a prevalant clinical condition with huge socioeconomic burden on society.
Advancement in understanding of pathophysiology and underlying neuromechanisms have l ed to improved clinical
diagnostic criteria and development of a multitude of treatment regimens. Imaging has gener ally played a
secondary role in evaluation of these patients. However, with the rapid evolution of function al magnetic resonance
imaging (fMRI), neural systems associated with depression have been uncovered. In this revi ew, we aim to
discuss the role of subcortical as well as cortical (particularly prefrontal and cingulate) brain regions (modulated by serotonin and dopamine neurotransmission) as evaluated on resting-state fMRI (rsfMRI).
Materials and Methods
Discuss patholophysiology of MDD, review role of support emotion processing, reward seek ing, regulate emotion and its role in MDD. Review principals of rs-
fMRI as well as common pearls and pitfalls of this imaging technique.
Discuss role of default mode network subregions, lateral frontal areas (within a frontoparieta l network associated
with cognitive control), basal ganglia, hippocampus, frontal lobe (including the orbitofrontal cortex) and less
consistently the cingulate cortex and thalamus as well as the insula, and cerebellum.
Results
Role of dopamine and serotonin pathways in depression Pictorial review of rsFMRI findings within the DMN,
frontotemporoparietal lobes, as well as deep gray nuclei and cerebellum Discuss rsFMRI acti vation patterns used in evaluation of patients pre-
and post serotonin reuptake inhibitor therapy

Conclusions
Resting-
state fMRI studies in depression can identify pattern of brain regions associated alterations in neuronal connectivity especially within the posterior DMN components (related with self-referential processing), within the lateral frontal areas (associated with externally-directed cognition), insula and basal ganglia. Additionally, rsFMRI
can demonstrate alterations in neuronal activity in patients before and after serotonin reuptak e inhibitor therapy, which can potentially serve as a guide for monitoring treatment response.



Areas of altered functional connectivity/activity in depression compared to controls. (A) Red to yellow: significant meta-analytic results ($p < 0.05$) in group A (representing mainly decreased connectivity / function in depression), blue to green: unthresholded ALE values, **(B)** equivalent representation of group B (increased connectivity/function in depression), **(C)** qualitative display of significant results, red: group A, green: group B, yellow: overlap.

(Filename: TCT_eEdE-17_depressionfmri.jpg)

eEdE-20

6:30AM - 3:00PM

Utility of PET-MRI in NeuroOncology

A Chaudhry[1], M Gul[2], A Chaudhry[3], R Matthews[4]
[1]Johns Hopkins Medicine, Elkridge, MD, [2]National Institute of Health, Elkridge, MD, [3]Stony Brook University, Westbury, NY, [4]Stony Brook University Medical Center, Stony Brook , NY

Purpose
The aim of this exhibit will be to provide a comprehensive overview of the clinical utility of the emerging hybrid modality: PET-
MRI (positron emission tomography magnetic resonance imaging) in neurooncology.

Materials and Methods

1. Review physical principles and techniques of PETMRI. 2. Clinical applications of PET-MRI including neuro-oncology. 3. Discuss key imaging findings that help exclude mimics resulting from neurodegenerative disorders and inflammatory conditions. 4. Review common pearls and Pitfalls of PETMRI. 5. Future role of PETMRI in neuroradiology.

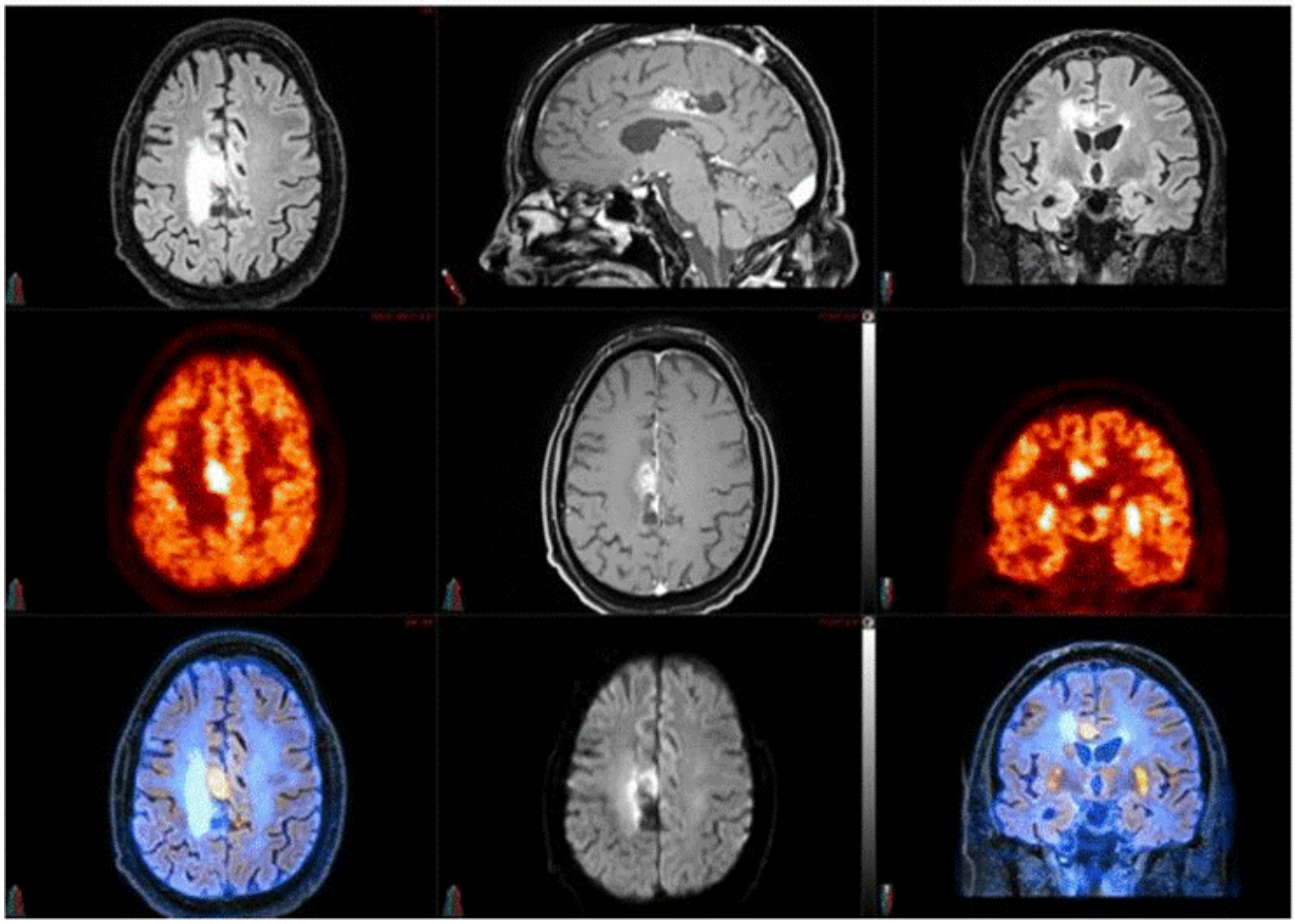
Results

1. Physical principles and techniques of PET-MRI: Relevant concepts involving image acquisition, postprocessing and interpretation will be provided. 2. Overview of clinical applications of PETMRI in neuro-oncology patients: An overview of initial tumor diagnosis, discussion of tumor biology and its effect on tumor imaging (e.g., tumor metabolism, angiogenesis, cellularity, etc.), post-treatment followup imaging evaluation and its role in therapy selection will be provided. 3. Role of PET-MRI in evaluation of neurodegenerative and inflammatory conditions (including MS). 4. Pearls and Pitfalls: Common pitfalls and controversies regarding PET-MRI in neuroradiology will be discussed. 5. Future of PETMRI: A discussion of future applications and challenges facing PETMRI in neuroradiology, specifically neuro-oncology and neurodegenerative disorders will be provided.

Conclusions

PET-MRI is an emerging hybrid imaging modality offering detailed functional and structural imaging with promising clinical applications especially in the field of neuro-oncology, neurodegenerative and inflammatory CNS conditions. This case-based exhibit provides the viewer an indepth review of the relevant concepts underlying the technical and clinical aspects along with common pearls and pitfalls of PET-MRI allowing for better integration and relevant usage of this modality in clinical practice.

GBM s/p Resection Now With Multifocal Recurrence Recurrence



(Filename: TCT_eEdE-20_PETMRIGBM.gif)

eEdE-105

6:30AM - 3:00PM

Vertebral Artery Trauma – Findings and Pitfalls Essential for Emergency Radiologist or Resident

P Sharma[1], P Kochar[2], S Sharma[3], A Ghasemiesfe[2], M Adeb[2], Y Kumar[4]
[1]Yale New Haven Health System at Bridgeport Hospital, Milford, CT, [2]Yale New Haven Health Bridgeport Hospital, Bridgeport, CT, [3]Yale New haven health Bridgeport Hospital, Bridgeport, CT, [4]Yale New Haven Health at Bridgeport Hospital, Bridgeport, CT

Purpose

The purpose of the presentation is to delineate the imaging findings in vertebral artery injuries, its stigmata and most common mimics imaging pitfalls on computed tomography (CT) angiography and magnetic resonance (MR) angiography. Identifying these will help the emergency radiologist or resident to better evaluate vertebral artery injuries.

Materials and Methods

Reviewed the imaging findings of cases of suspected vertebral artery trauma from our emergency department on CT angiography and MR angiography. Review of literature.

Results

The vertebral artery injuries should be suspected in cervical spine trauma to the facet joints or the transverse foramina or symptoms of vertebrobasilar ischemia. The incidence of vertebral artery injuries is more with C5 fracture extending into foramen transversarium or fractures of upper cervical spine. Anatomy: The vertebral artery is anatomically divided into 4 segments: V1 (extraosseous segment), V2 (foraminal segment), V3 (extraspinal segment) and V4 (intradural segment). Digital subtraction angiography: Most common patterns are dissection and occlusion of the vertebral artery. On angiography the vertebral artery injuries are graded into 5 grades. DSA gold standard for evaluation of vertebral artery injuries but being invasive it is less commonly done as a screening procedure. Computed tomography angiography: On CTA the vertebral artery dissection can be smooth or tapered narrowing of the lumen, concentric intramural hematoma or intimal flap narrowing the lumen or total occlusion of the lumen. Other imaging signs like double lumen, intimal flap dilation of artery, string of pearls appearance or stenosis of the lumen are visualized more frequently. Most common finding is nonspecific stenosis of vertebral artery and the most definite sign is double lumen or an intimal flap. Studies have shown that CT angiography has better sensitivity in diagnosing dissections than MR angiography or ultrasound relative to conventional angiography. MR angiography: There could be loss of flow void within the vessel due to thrombosis or occlusion on T2 or hyperintense signal within the vessel wall due to intramural hematoma on T1 fat-sat images. The time-of-flight MR angiography is used to diagnose steno-occlusive disease. However, in cases of trauma the background suppression is not complete due to tissues having short T1 relaxation times like fat or hematoma or thrombus or slow or turbulent blood. Vertebral artery anomalies like fenestration or duplication can mimic injury.

Conclusions

In the setting of cervical trauma the common signs of vertebral artery injury like smooth tapered narrowing of the lumen, double lumen, intramural hematoma, stenosis or complete occlusion should be kept in mind. Pitfall on MRI like loss of flow void, inappropriate signal suppression due to blood or fat or slow or turbulent flow can be challenging in interpretation. Various congenital anomalies like fenestrations or duplication should be seriously considered when calling in vertebral artery injury.



(Filename: TCT_eEdE-105_Picture21.jpg)

eEdE-06

6:30AM - 3:00PM

Wallerian and Transneuronal Degeneration: a Pictorial Review

O Kohannim[1], N Salamon[1]
[1]*University of California, Los Angeles, Los Angeles, CA*

Purpose
Wallerian degeneration refers to degeneration of an axon and its myelin sheath secondary to proximal injury within a nerve. Transneuronal degeneration refers to degeneration of afferent

or efferent neurons in response to injury within a synapsing neuron. Recognition of these two patterns of degeneration in various neuronal tracts is important for every neuroradiologist. We aim to provide an overview of the neuroanatomical basis of commonly encountered cases of Wallerian and transneuronal degeneration and present a pictorial review of their various types.

Materials and Methods

We present a diagrammatic review of neuroanatomic pathways commonly involved in transneuronal and Wallerian degeneration; these include the corticospinal tract, limbic system connections, spinal cord tracts, the corticopontocerebellar pathway, and connections within the Guillain-Mollaret triangle. We then display several interesting and representative images from our institution's cases, demonstrating degeneration of these neural pathways secondary to various types of pathology.

Results

An image-rich review of Wallerian and transneuronal degeneration is provided with neuroanatomic correlates. The primary pathology in our selected cases includes infarction, craniotomy, hemispherectomy, and neoplasm. Relevant teaching points and clinical scenarios are presented.

Conclusions

Wallerian degeneration is recognized most commonly in the corticospinal tract in the setting of middle cerebral artery infarction. Our aim is to offer a more comprehensive, pictorial review of both Wallerian and transneuronal degeneration in several neuronal pathways secondary to a variety of insults. Signal changes caused by degeneration often mimic tumors or nonspecific white matter processes. Precise knowledge of this phenomenon will avoid unnecessary examinations. In addition, new modalities such as DTI tractography can help identify entire pathways more easily and provide better learning tools.

eEdE-94

6:30AM - 3:00PM

When Mirror Images Betray You: Symmetric Imaging Patterns of Stroke Subtypes and Its Common Mimics

V Yedavalli[1], A Thaker[2]

[1]Advocate Illinois Masonic Medical Center, Chicago, IL, [2]University of California San Francisco, San Francisco, CA

Purpose

Radiologists rely heavily on imaging patterns to narrow a differential diagnosis to the most likely entities. Many neurological conditions manifest with asymmetric imaging findings which allows rapid visual detection of pathology. Symmetric imaging patterns are less commonly encountered and pose a diagnostic dilemma, both in terms of visual perception and diagnostic classification. Acute ischemic stroke is a common and debilitating entity that

commonly presents with asymmetric imaging findings, but has specific subtypes which may present with symmetric findings. In addition, there are a number of ischemic stroke mimics that present with characteristic symmetry on imaging. These mimics vary in pathophysiology and can have significantly different clinical management. Therefore, it is crucial to differentiate ischemic stroke subtypes from common mimics when encountering symmetric patterns on imaging.

Materials and Methods

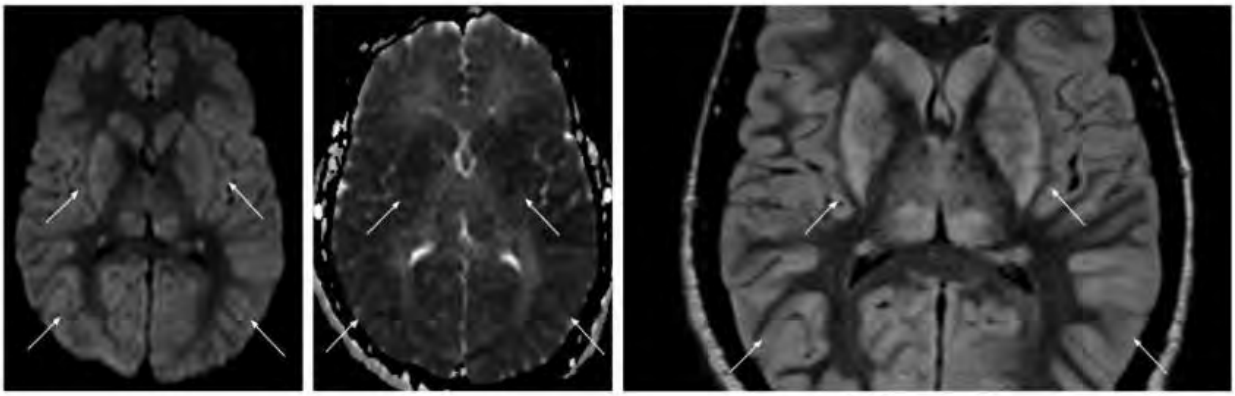
As stroke has several mimics of various etiologies, we hope to elucidate both stroke subtypes and specific subset of stroke mimics that demonstrate symmetry. Because of the nonspecific clinical picture of stroke, it is essential to delineate whether the pathology is truly stroke or one of its many mimics as it could drastically change patient management and timely treatment. We focus on the most common symmetric infectious, ischemic, and metabolic mimics along with symmetric stroke subtypes with an emphasis on the imaging characteristics of each entity.

Results

Stroke, with its nonspecific clinical features, has a number of different symmetric subtypes and mimics which can obfuscate diagnosis. We focus on the symmetric stroke subtypes and stratify the symmetric stroke mimics into infectious, ischemic, and metabolic. The most common entities in each category then are further subdivided into more specific categories such as infectious-neurodegenerative, ischemic-hypoxic, and ischemic-embolic. We also stratify metabolic into vitamin, mineral, and toxic subcategories. We focus on this systematic approach with additional emphasis on distinguishing imaging features of each entity in order to facilitate accurate diagnosis when encountering symmetric imaging patterns.

Conclusions

In this exhibit, we differentiate stroke subtypes from infectious, ischemic, and metabolic stroke mimics which demonstrate symmetry on imaging. With the nonspecific clinical picture with which stroke frequently presents, it is integral to include these common symmetric stroke mimics within differential diagnoses while utilizing a systematic approach to distinguish each entity when encountering symmetric patterns on imaging. Given the vastly different treatments and overall patient management based on each entity, timely and accurate diagnosis is essential for patient management.



Hypoxic Ischemic Encephalopathy

Left Image: DWI sequence demonstrating high signal within the deep grey matter and cortex compatible with restricted diffusion.

Middle Image: ADC sequence demonstrating low signal within the deep grey matter and cortex. Coupled with the high signal shown on the DWI, this is compatible with restricted diffusion.

Right Image: FLAIR sequence illustrating subtle high signal primarily in the basal ganglia and cortices corresponding to the areas of restricted diffusion.

(Filename: TCT_eEdE-94_SymmetricStrokeMimicsPPT2.jpg)

eEdE-41

6:30AM - 3:00PM

Why so Big Blue? Review of Jugular Foramen Lesions

Z Fulton[1], A Singh[2], W Smoker[3]
[1]University of Texas Health Science Center San Antonio, San Antonio, TX, [2]UT Health Science Center San Antonio, San Antonio, TX, [3]University Of Iowa Hospitals & Clinics, Iowa City, IA

Purpose
1. Understand the complex anatomy of the jugular foramen and the surrounding skull base. 2. Recognize the CT/MR imaging characteristics and differential diagnosis of jugular foramen lesions in an interactive quiz based format. 3. Identify anatomic variants that cause pathology and/or mimic neoplasms.

Materials and Methods

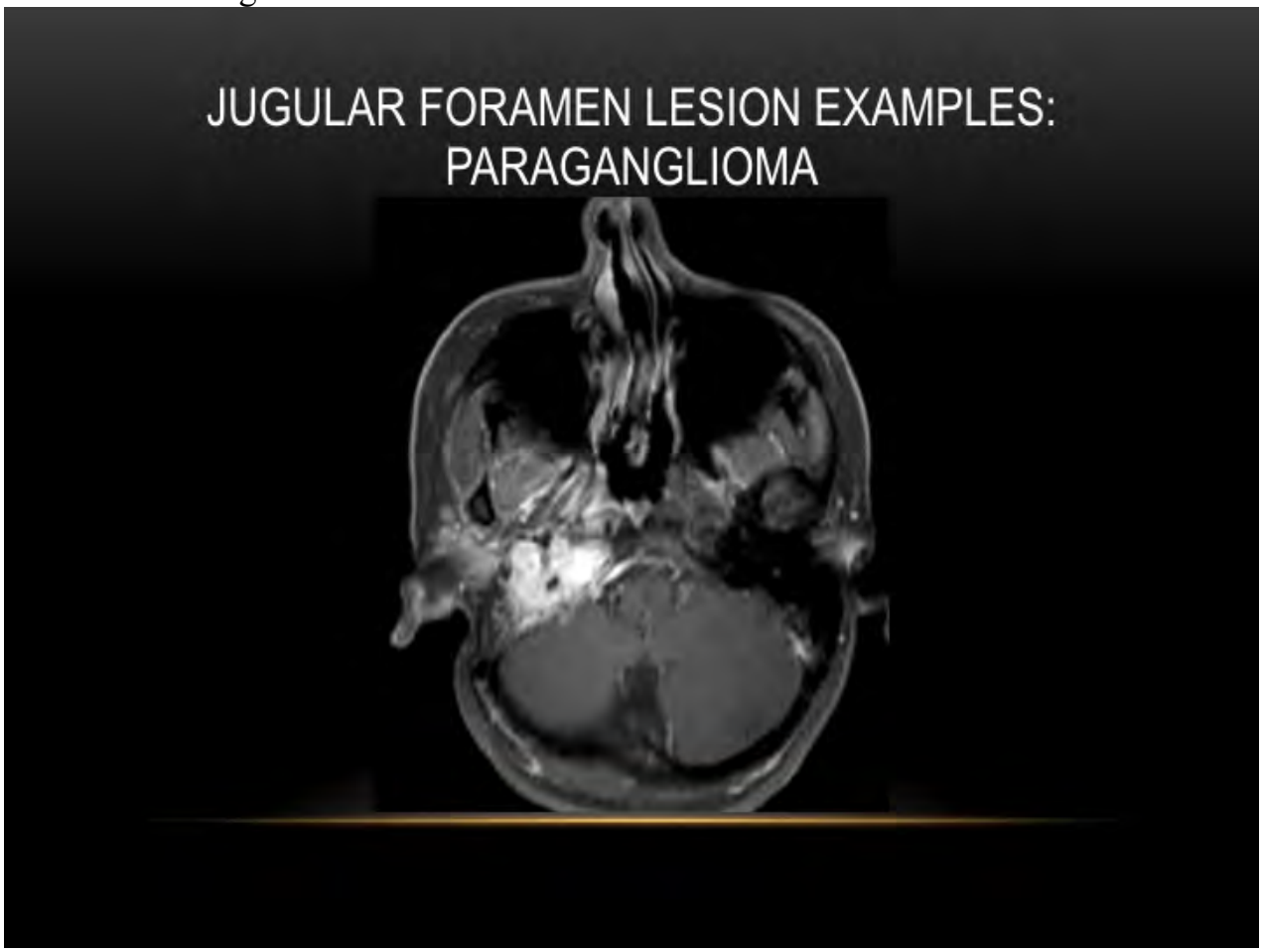
1. Review of jugular foramen anatomy. 2. Cases presented in sequential interactive quiz format with associated answer/discussion slides (including brief clinical overview, key imaging characteristics, and differential diagnoses). 3. Summary with key educational points.

Results

Computed tomography and MR cases collected from patients at our institution will be used to provide examples of benign and malignant jugular foramen lesions. Lesions to be presented/discussed: Jugular and vagal paragangliomas, Schwannoma, Meningioma, Cholesterol granuloma, Metastatic disease, Jugular megabulb, High riding jugular bulb, Jugular dehiscence Chordoma, Paget disease, Fibrous dysplasia, Chondrosarcoma, Langerhans cell histiocytosis, Infection.

Conclusions

The jugular foramen demonstrates complex anatomy with a broad differential for benign and malignant lesions that arise there. Our electronic educational exhibit provides CT and MR cases collected from patients at our institution in order to facilitate a fascinating review for the neuroradiologist.



(Filename: TCT_eEdE-41_FultonJFExamples001.jpg)

eEdE-22

6:30AM - 3:00PM

Zika Virus Infection: MRI Imaging Findings in Adults

D Galheigo[1], I da Silva[2], O Nascimento[2], M Law[3], L da Cruz[4]
[1]Clinica de Diagnostico por Imagem (CDPI), Rio de Janeiro, Rio de Janeiro, [2]Universidade Federal Fluminense (UFF), Niteroi, Rio de Janeiro, [3]Keck Medical Center of USC, Los Angeles, CA, [4]CDPI-Clinica de Diagnostico por Imagem, Rio de Janeiro, RIO DE JANEIRO

Purpose
Zika virus (ZIKV) is a neurotropic mosquito-borne flavivirus that has caused major infection outbreaks in the Americas since 2015, mainly in French Polynesia and in Brazil. Several reports showed microcephaly and other brain malformations in newborns with congenital ZIKV infection. In adults, there was an increase of reported cases of other neurological disorders which include Guillain–Barré syndrome (GBS), encephalitis, and myelitis, what is speculated to be secondary to the ZIKV infection outbreak. The purpose of this retrospective study is to characterize and to illustrate imaging patterns in adults with ZIKV infection presenting acute neurological syndromes.
Materials and Methods
We retrospectively reviewed 34 cases of ZIKV infection with neurological symptoms. ZIKV was detected in serum and cerebral spinal fluid (CSF) by reverse transcription polymerase chain reaction (RT-PCR). The patients were subjected to brain and whole spine magnetic resonance imaging (MRI) at 1.5T and 3T scanners (Siemens). These patients presented several neurological syndromes: 26 with GBS and variants, four cases of encephalomyelitis and four cases of myelitis.
Results
From the 26 cases of GBS and variants, 24 showed nerve root enhancement at the cauda equina without ventral predominance and two had normal exams. We found four cases of encephalomyelitis, presenting with T2W abnormalities in the cortical spinal tract, middle cerebellar peduncle, anterior horns and ventral nerve roots of the spinal cord, as well as in the central portion of the spinal cord. Isolated myelitis was seen in four cases, showing diffuse T2W abnormalities and enhancement at the spinal cord.
Conclusions
ZIKV-related neurological complications have a vast and still unknown spectrum (2). Therefore, we should be familiar with the different imaging patterns in these patients, since some of these neurological complications require an early treatment. Even though some clinical syndromes such as GBS, encephalitis, and myelitis have been associated to recent ZIKV outbreaks, there is still a need for prospective studies to better evaluate such relationship.

eEdE-09

6:30AM - 3:00PM

“Don’t Forget” Dementias: An Imaging Review of Dementias and Cognitive Neurodegenerative Disorders

A Capps[1], P Rajagopalan[1], R Seltman[1], W Fischer[1], A Kamer[1], N Koontz[1]
[1]*Indiana University School of Medicine, Indianapolis, IN*

Purpose
We provide a comprehensive review of the characteristic imaging findings of dementia complexes and cognitive neurodegenerative disorders.
Materials and Methods
We performed a HIPAA-compliant retrospective review of our institution's electronic medical record for illustrative cases of dementias and neurodegenerative disorders, highlighting multimodality (CT, MRI, and nuclear medicine) imaging findings. We also provide a review of the current medical literature.
Results
Dementia and cognitive decline are common features of several neurodegenerative diseases, which may demonstrate some overlap in clinical presentation. Imaging is a tool that, together with clinical presentation, is fundamental to establishing the correct diagnosis and assessing disease progression. Furthermore, early and accurate identification is vital for developing treatments. In this exhibit, we highlight the most common causes (Alzheimer dementia, vascular dementia, frontotemporal lobar degeneration, Lewy body dementia, Parkinson disease, Parkinson-plus syndromes, normal pressure hydrocephalus, and cerebral amyloid angiopathy), as well as less common neurodegenerative diseases (progressive supranuclear palsy, Creutzfeldt-Jakob disease, multiple system atrophy, Huntington disease, chronic hypertensive encephalopathy, corticobasal degeneration, and chronic traumatic encephalopathy) that neuroradiologists should be familiar with, detailing the typical clinicoradiological features, differential considerations, and important diagnostic pitfalls.
Conclusions
Recognizing characteristic imaging features and typical clinical presentations of dementias and cognitive neurodegenerative disorders may enable neuroradiologists to add value to their work by improving diagnostic accuracy and providing an earlier diagnosis.

Monday
6:30AM - 3:00PM

Electronic Education Exhibit (eEdE)-Head & Neck

eEdE-149

6:30AM - 3:00PM

A Minor League of the Same Players: Minor Salivary Glands. A Pictorial Review

J Steinklein[1], K GILL[2], D Shatzkes[1]
[1]*Lenox Hill Hospital, New York, NY,* [2]*LENOX HILL HOSPITAL, NEW YORK, NY*

Purpose

This exhibit aims to familiarize the reader with the minor salivary glands of the head and neck, and imaging findings of benign and malignant minor salivary gland tumors, especially those that may mimic more common neoplasms. The imaging features of some of the more common or interesting etiologies are discussed in depth.

Materials and Methods

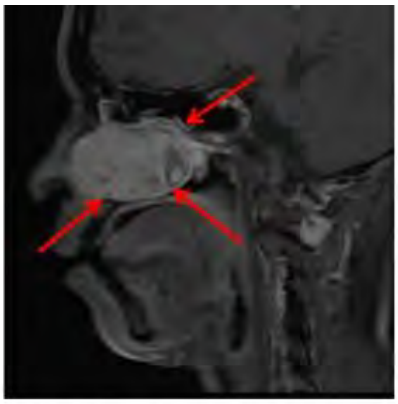
Major objectives of this exhibit are to familiarize the reader with: -Embryology and location of minor salivary glands. -Highlighting the most common malignant and benign minor salivary gland (MSG) tumors and their imaging characteristics. -Case- based imaging review. -Discussing behavior of certain lesions, such as perineural invasion, with discussion of such imaging findings and clinical importance. -Other MSG entities such as non-neoplastic conditions or inflammatory diseases. -Case-based imaging review of multiple example cases.

Results

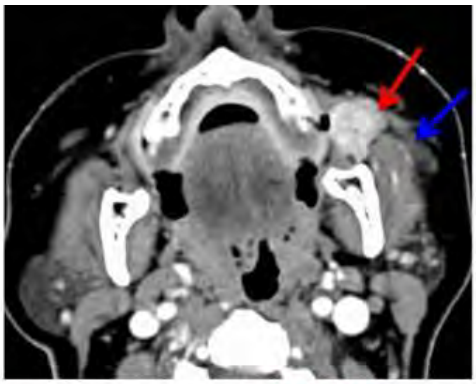
Neoplams will be discussed as below and subsequent case examples will highlight certain imaging features: Malignant Neoplasia: -The smaller the salivary gland, malignancy is more likely. -Adenoid cystic and mucoepidermoid carcinomas are the most common malignant MSG tumors. -ACC has predilection for the sinonasal tract. -Mucoepidermoid prefers the oral cavity. Perineural Tumor Spread: -Bad prognostic indicator. -Adenoid cystic carcinoma is most notorious for perineural spread. -Pain and paresthesia are the most common symptoms. Benign Neoplasia: -Benign Mixed Tumor (BMT) is the most common. -As is the case with BMT of the parotid gland, there is 2-5 % chance of harboring malignancy or degeneration into carcinoma "ex" pleomorphic adenoma (PA). Inflammatory/other causes: -Sjogren's syndrome, IgG4 deposition, sarcoidosis. -HIV

Conclusions

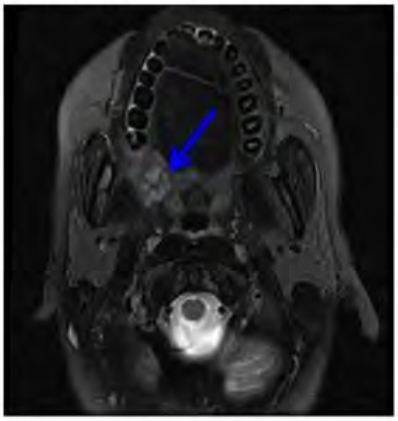
1) Tumors and non-neoplastic diseases of the minor salivary glands are comprised of similar pathological diagnoses as their major salivary gland counterparts. 2) The smaller the gland, the higher rate of malignancy, reported at 50-80% in minor salivary glands. 3) Depending on location and tumor histology, there is preponderance of perineural tumor spread, most notoriously with adenoid cystic carcinoma. This is crucial for accurate prognostication. 4) While imaging features can be helpful, they are nonspecific. Precise tumor localization and detailing spread of disease is the radiologist's role in surgical and potentially oncologic treatment of these diseases. 5) As with other imaging of the oral cavity, MRI is the preferred imaging modality for best soft tissue contrast resolution. Computed tomography (CT) is complementary to assess bony invasion.



Nasal cavity adenoid cystic carcinoma



Buccal space adenoid cystic carcinoma (red arrow) at level of the maxillary molar teeth, with intimate association to Stensen's duct (blue arrow).



Mucoepidermoid carcinoma



Oropharyngeal Benign Mixed Tumor

(Filename: TCT_eEdE-149_ASNRabstract.jpg)

eEdE-151

6:30AM - 3:00PM

A Proclivity for Clinical Evasion: Lesions of the Clivus

M McDonald[1], J Bykowski[1]
[1]*University of California at San Diego, San Diego, CA*

Purpose
This educational exhibit will outline the major important diseases of the clivus and help the participant to build a differential based on contrasting imaging features using multiple imaging modalities. Lastly, a self-assessment quiz will be presented at the end of the exhibit to facilitate knowledge consolidation. At the end of this exhibit the attendee will be able to: 1. Describe the basic anatomy of the clivus and its relationship to adjacent structures and cranial nerves. 2. Describe the time course of clival marrow conversion during development. 3. Correctly identify common benign primary lesions of the clivus, including fibrous dysplasia, Paget's disease and intraosseous hemangioma. 4. Evaluate primary malignant

lesions of the clivus, such as chordoma, chondrosarcoma and osteosarcoma. 5. Recognize the importance of clival involvement in nasopharyngeal carcinoma, lymphoma, metastases and invasive macroadenoma. 6. Complete a post-exhibit self-assessment quiz to consolidate learning.

Materials and Methods

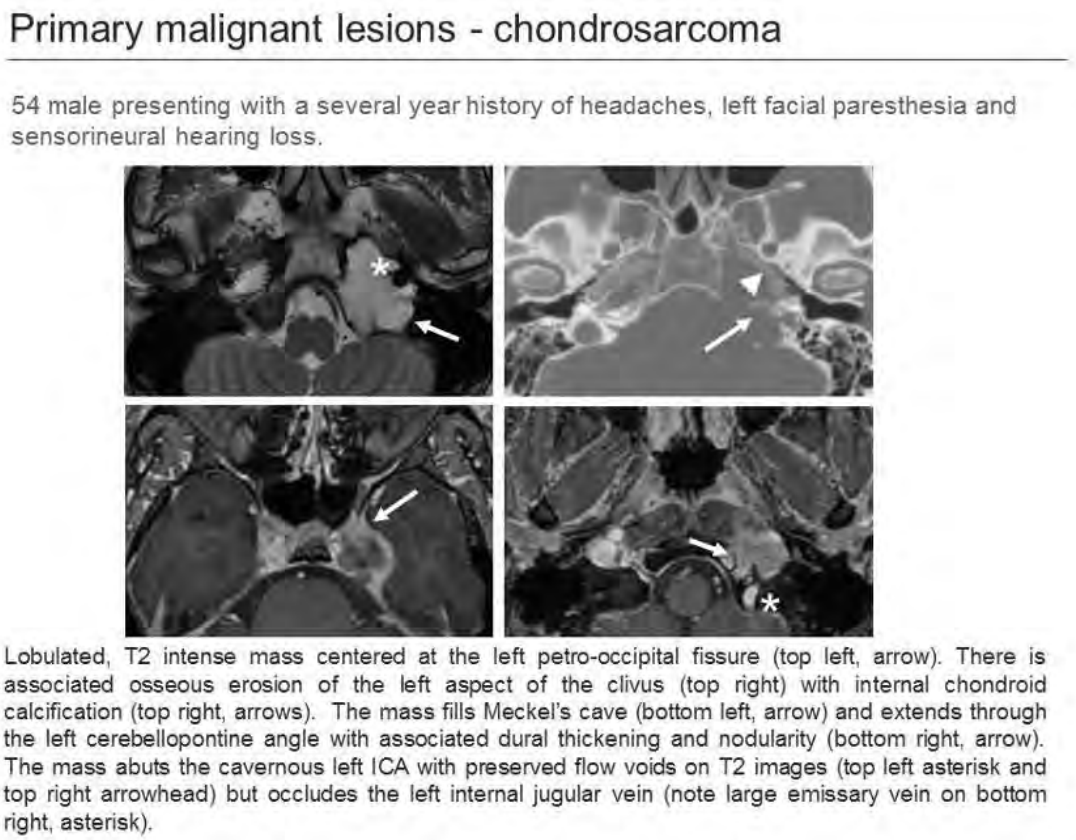
Illustrative cases with computed tomography (CT) and magnetic resonance imaging (MRI) will define the relationship of the clivus to the paranasal sinuses, sella turcica, petrous apex and cranial nerves. We will visually describe the normal time course of marrow conversion in the clivus with attention to the identification of benign marrow processes that have altered appearance on anatomic and PET imaging, underlying marrow disease and malignancy. This framework then will be used to compare and contrast the imaging hallmarks of a variety of benign, primarily and secondarily malignant clival lesions using multiple cross-sectional modalities.

Results

The clivus forms the bony strut of the central skull base at the intersection of the basisphenoid and basiocciput. As such, the clivus is affected by primary marrow neoplasms as well as secondary extension from processes involving the nasopharynx, cranial nerves, sinuses, sella and petrous apex. While many diseases have overlapping appearances on both CT and MRI, there are several features that can aid in forming a specific diagnosis. This clinical case series is focused on the common imaging appearances of primary and reactive clival processes with highlights of the anatomic relationships of the skull base to aid in the identification of locoregional patterns of spread and clinical complications.

Conclusions

A working understanding of the anatomy and developmental marrow changes of the clivus is essential to the identification of a variety of pathologies that commonly affect the skull base, both benign and malignant. This knowledge not only allows the radiologist to accurately describe primary clival lesions, but also to offer critical insight into local disease extension that is critical to the accurate staging and treatment of both skull base pathology and metastatic disease.



(Filename: TCT_eEdE-151_ASNRclivus.jpg)

eEdE-152

6:30AM - 3:00PM

A Sniff of Fresh Air: A Case Based Review of What the Surgeons Want to Know Regarding Sinus Pathology

K Owens[1], M Higgins[1], C Pinheiro-Neto[1], A Narayan[2], S Narayan[1]
[1]Albany Medical Center, Albany, NY, [2]Community Care Physicians, Albany, NY

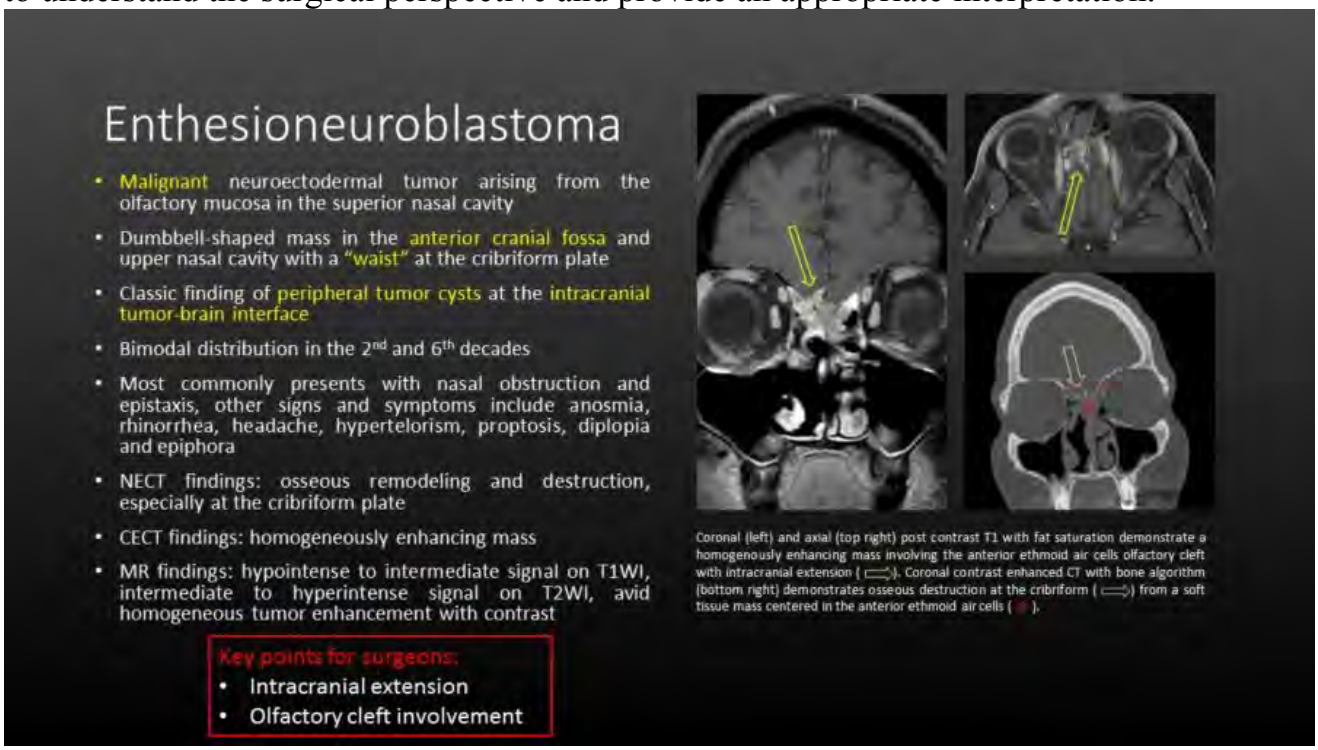
Purpose
The purpose of this educational exhibit is to review the normal paranasal sinus anatomy, learn the imaging features benign and malignant sinus pathology, and determine the salient features for which the surgeon is seeking radiologic consultation.
Materials and Methods
Following a brief review of the normal sinus anatomy, a variety of cases will be presented and discussed, including esthesioneuroblastoma, squamous cell carcinoma, juvenile angiofibroma, lymphoma, mucocele, as a case-based review, demonstrating the salient radiologic features for the referring otolaryngologist. When appropriate, correlate intra-operative images also will be provided.

Results

The paranasal sinuses are comprised of the maxillary, sphenoid, ethmoid, and frontal sinuses. The paranasal sinuses provide a variety of functions, including humidifying and heating inhaled air, immunologic defense, insulating sensitive structures from temperature fluctuations in the nasal cavity, buffering against facial trauma, and decreasing the relative weight of the front of the skull. While acute rhinosinusitis affects greater than 15% of the U.S. population annually, it is not the only cause of a "stuffy nose". When the patient's symptoms persist, nasal endoscopy is the initial method for evaluating sinus disease. However, when pathology is discovered, the radiologist plays a vital role in providing the otolaryngologist with salient information they cannot visualize directly with the endoscope. The salient features can be categorized by the location of the lesion and the presence of osseous, vascular, and/or neuronal involvement.

Conclusions

As demonstrated in this exhibit, there are a variety of benign and malignant pathologies affecting the paranasal sinuses; however, there are key features that the otolaryngologist really wants to know. As a consultant for the otolaryngologist, it is the role of the radiologist to understand the surgical perspective and provide an appropriate interpretation.



(Filename: TCT_eEdE-152_SinustumorsASNR2017esthesioslide.jpg)

eEdE-130

6:30AM - 3:00PM

Advanced MRI Characterization of Orbital Masses

G Avey[1], J Yu[2], T Kennedy[3]

[1]University of Wisconsin, Madison, WI, [2]University of Wisconsin-Madison, Madison, WI, [3]University Of Wisconsin Hospital, Madison, WI

Purpose

A wide array of entities can present as orbital masses, encompassing both indolent and aggressive processes. The closed confines of the orbit and the critical indwelling neurovascular structures often preclude direct tissue sampling. Advanced MRI imaging allows the noninvasive examination of these masses and often can provide either definitive tissue characterization or a limited differential diagnosis, thus enabling appropriate clinical care. However, effective characterization of these masses requires radiologists to be familiar with these MRI techniques and the imaging appearance of these masses and pseudomasses.

Materials and Methods

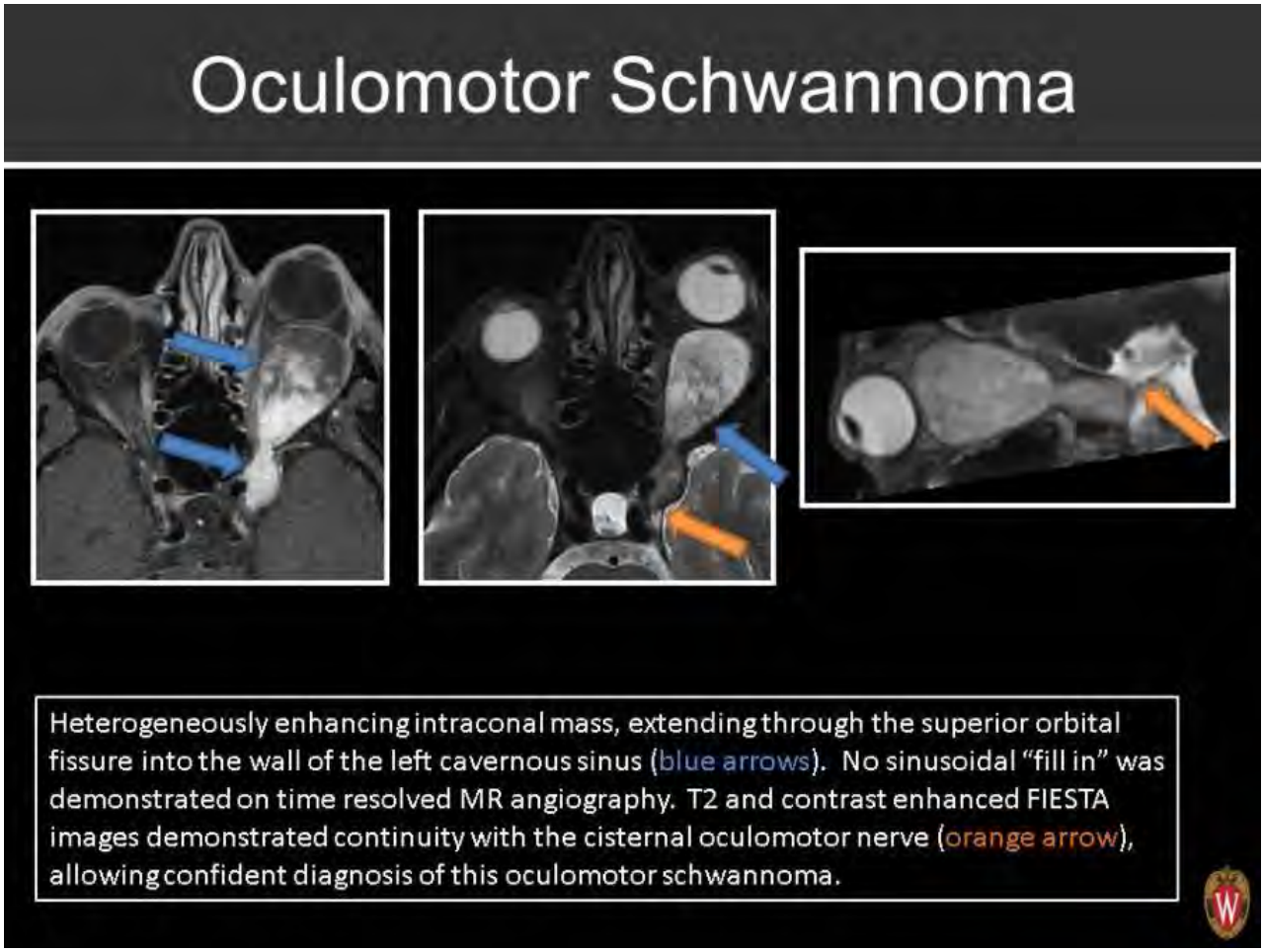
This exhibit teaches users the efficient classification of orbital masses based primarily on lesion location and morphology. This exhibit also demonstrates the utility of advanced techniques such as time-resolved MR angiography, diffusion, and simultaneous PET/MRI for more definitive tissue characterization in challenging cases.

Results

Specific differential diagnoses can be generated from single site disease, such as masses arising from the globe, lacrimal gland, lacrimal duct, optic nerve/sheath complex, extraocular muscles, and cranial nerves. When masses cannot be discretely localized to a specific site of origin, they more generally can be classified as intraconal or extraconal in location. However, these more generic classifications are less helpful for narrowing the differential diagnosis. In these cases advanced MRI imaging can help to narrow the differential. Time-resolved MR angiography allows for characterization of the vascularity of orbital masses, effectively separating cavernous malformations from other bulky orbital masses such as lymphoma and solitary fibrous tumor. Specific morphologic features, such as the teardrop shape of a venous varix, fluid/fluid levels within a lymphatic malformation, or the lobulated contour and highly restricted diffusion of lymphoma can also provide useful diagnostic specificity.

Conclusions

Orbital mass characterization is an important, but challenging imaging scenario. However, with careful attention to MRI technique and lesion characteristics the radiologist can provide vital information to guide appropriate patient care.



(Filename: TCT_eEdE-130_OculomotorSchwannoma.jpg)

eEdE-133

6:30AM - 3:00PM

An Interactive and Digital Educational Exhibit Integrating Modern Imaging Software to Illustrate Anatomical Landmarks and Orbital Pathology of the Orbital Apex via a Series of Cases

B SOON[1], P GOH[2]
[1]NATIONAL UNIVERSITY HOSPITAL, SINGAPORE, SINGAPORE, [2]National University Hospital, Singapore, Singapore

Purpose
The main purpose of this education exhibit is to familiarize the reader with the anatomical landmarks of the orbital apex and to correlate and categorize orbital pathology occurring in these structures.
Materials and Methods
Illustrating key anatomical landmarks and structures around the orbital apex using a series of

cases. Computed tomography (CT) and magnetic resonance (MR) will be used to illustrate the anatomical structures of the orbital apex. Description of the disease entity with CT or MR modality or both will be covered in interactive manner using new media formats beyond text and precisely annotated illustrations. Reviewer of this educational poster would be able to experience a dynamic presentation and enhance learning with scrollable image stack of CT or MR images integrating modern imaging software.

Results

The orbital apex is formed by the osseous component of superior orbital fissure and the optic canal in the posterior portion of the pyramidal-shaped orbit. It consists of complex anatomical structures from which a variety of pathologies can occur, affecting the osseous, neurovascular structure, soft tissue and muscles of the orbital apex. Pathologies that can occur in this area can range from neoplastic, infectious, inflammatory and vascular in etiologies. Furthermore, pathological processes also can extend intracranially into middle cranial fossa through the orbital apex or vice versa. As a broad range of pathologies can occur in this anatomical landmark, categorization of pathologies according to osseous, neurovascular, soft tissue and extra-ocular muscle structures will be beneficial to help generate focused differential diagnosis. Combining a systematic anatomical approach with the clinical presentation and demographic data, as well as key imaging features will also be helpful to further narrow down the differential diagnosis.

Conclusions

The orbital apex is an important anatomical landmark that hosts diverse orbital pathology. A structured anatomical approach will ease the diagnostic which then would guide the clinician's management.

eEde-174a

6:30AM - 3:00PM

Anatomy and Common Pathology of the Parotid Space: What The Radiologist Needs To Know.

O Deochand[1], N Anand[2], J Giampa[3]
[1]Morristown Medical Center, Morristown, NJ, [2]morristown medical center, morristown , NJ, [3]Atlantic Health- Morristown Medical Center, MORRISTOWN, NJ

Purpose

The purpose of this exhibit is to make radiologists aware of the anatomy and common pathology of the parotid space. The parotid spaces are bilateral suprahydoid neck spaces extending from the external auditory canal and mastoid tip superiorly, to below the angle of the mandible. This space is enclosed by the superficial layer of the deep cervical fascia. Adjacent spaces within the neck include the parapharyngeal space directly medially, masticator space anteriorly, and the carotid space which is separated from the parotid space superiorly by the posterior digastric muscle. Internal contents include the parotid gland,

cranial nerve 7, external carotid artery, retromandibular vein, lymph nodes, and parotid duct. An extensive disease spectrum involve the parotid spaces which include benign and malignant tumors, congenital anomalies, and infectious / inflammatory processes.

Materials and Methods

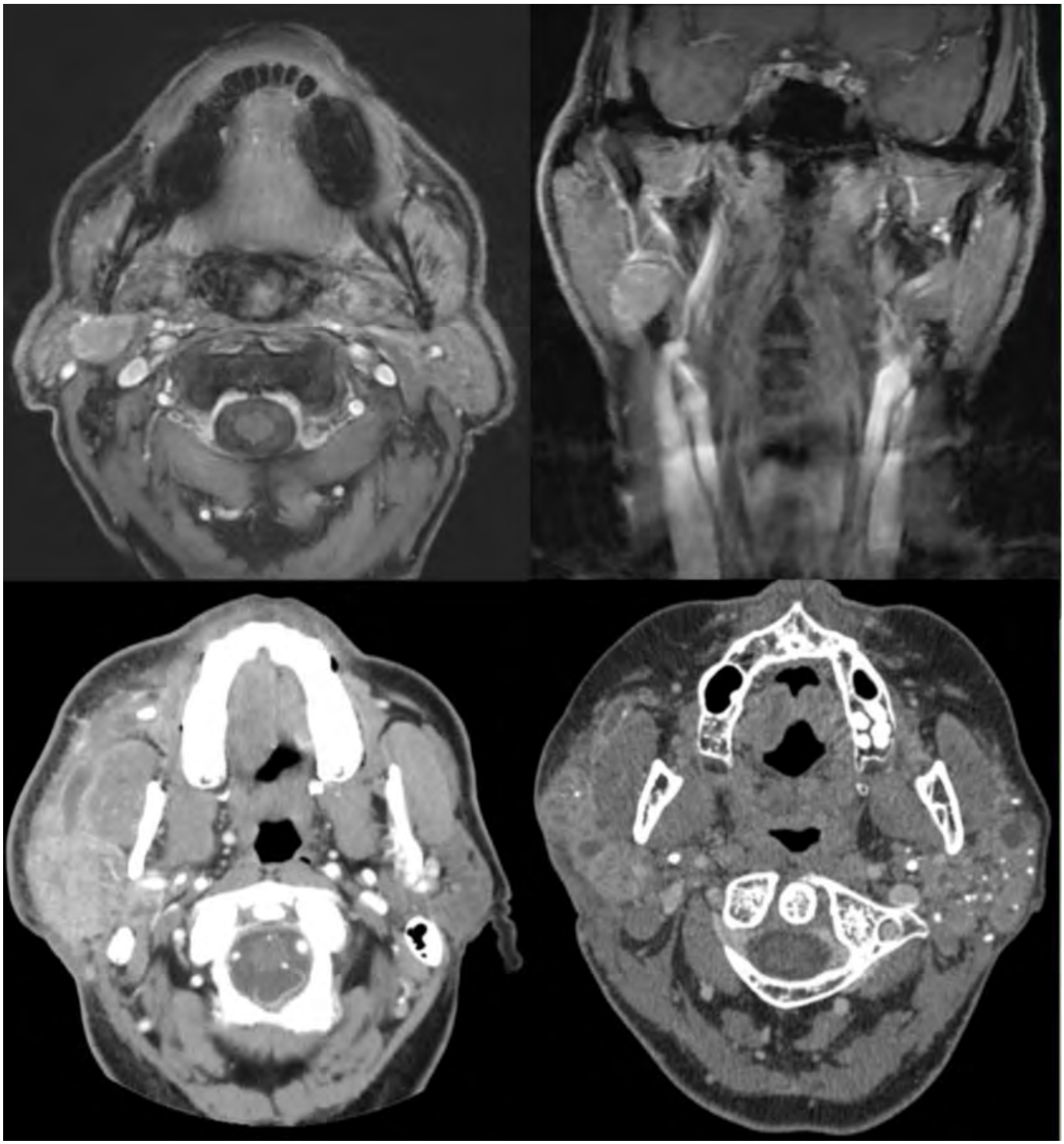
Initially, a list of different parotid space lesions were made. These were subsequently entered into a search of all radiology reports at our institution from January 8, 2008 to January 1, 2016. This method yielded hundreds of different reports in which the searched terms were used. All applicable radiology reports were read and pertinent pathological cases were compiled for use in this exhibit.

Results

Our search yielded hundreds of radiology reports across CT, ultrasound, and MRI modalities. The topics for discussion and review of original images include, but are not limited to: • Acute parotitis • Sjogrens Syndrome • Benign Lymphoepithelial Lesions of HIV • Benign Mixed Tumor • Warthin Tumor • Schwannoma • Mucoepidermoid Carcinoma • Adenoid Cystic Carcinoma • Acinic Cell Carcinoma • Non-Hodgkin Lymphoma • Oncocytoma • Adenocarcinoma • Squamous Cell Carcinoma • Metastatic Disease • 1st Branchial Cleft Cyst • Venous Malformation • Lymphatic Malformation • Infantile Hemangioma Pertinent anatomy and pathology of the parotid space are to be discussed. Additionally, various pathological abnormalities categorized into: Infectious/Inflammatory, benign tumors, malignant tumors, and congenital abnormalities are to be discussed.

Conclusions

To conclude, we would like to make radiologists and clinicians aware of the anatomy and pathology of the parotid space. An extensive disease spectrum involves the parotid spaces, which include benign and malignant tumors, congenital anomalies, and infectious / inflammatory processes. We aim to educate the audience by utilizing the aforementioned pathological cases.



(Filename: TCT_eEde-174a_1.jpg)

eEdE-174

6:30AM - 3:00PM

Bones, Stones, Groans and Moans? Ultrasound, 4D-CT and Sestamibi may help!

m bajaj[1], A Reddy[2], M Abu-yousef[1], B Policeni[3]
[1]University of Iowa Hospitals and Clinics, Iowa City, IA, [2]Univ of Iowa Hospitals and Clinics, Iowa city, IA, [3]University of Iowa hospitals and Clinics, iowa city, IA

Purpose
This educational exhibit aims to describe the role and relative value of various imaging modalities in evaluation of hyperparathyroidism.
Materials and Methods
Imaging findings on various imaging modalities of the patients with hyperparathyroidism will be presented in the form of an educational exhibit organized as follows: 1. Embryology of parathyroid development and basis for location for superior versus inferior parathyroid adenomas. 2. Salient features of parathyroid adenoma on neck ultrasound. 3. Role of 4D-CT as a problem-solving tool to search for parathyroid adenoma. 4. Value of Sestamibi Scan and correlation with pertechnetate imaging to characterize suspicious lesions. 5. Recognition of pertinent differentials and pitfalls in evaluation of parathyroid adenomas.
Results
Ultrasound is the most frequently used modality in localization of parathyroid adenomas with advantages of low cost and lack of Ionizing radiation. Nuclear scan using Sestamibi in two phases (early and late) may help identify parathyroid adenomas that retain radiotracer. Comparison with 99m-Tc Pertechnetate can help differentiating from dubtful thyroid nodules. 4D-CT utilizing anatomical localization on 3-dimensional CT images complemented with functional information provided by perfusion of suspected adenoma over time leads to improved sensitivity and plays a complimentary role with ultrasound.
Conclusions
• A knowledge of normal anatomy and embryology of parathyroids is pertinent to accurate diagnosis in hyperparathyroidism. • Clinical judgement is important to direct appropriate laboratory and imaging investigations. • Ultrasound, 4D-CT and Sestamibi Scan play a complimentary role in identifying parathyroid hyperplasia vis-a-vis adenomas. • A knowledge of mimics and potential pitfalls is necessary to ascertain diagnosis and guide appropriate management.

eEdE-154

6:30AM - 3:00PM

Central Skull Base Landmarks: An "Inside-Out" Approach for Teaching Skull Base Anatomy to Trainees

F Choudhry[1], A Momeni[1], J Donahue[1]
[1]University of Virginia, Charlottesville, VA

Purpose
Rather than dividing central skull base anatomy as osseous components/foramina and

musculature/deep soft tissue spaces, we present 3 landmarks to teach anatomy and common pathways of tumor spread.

Materials and Methods

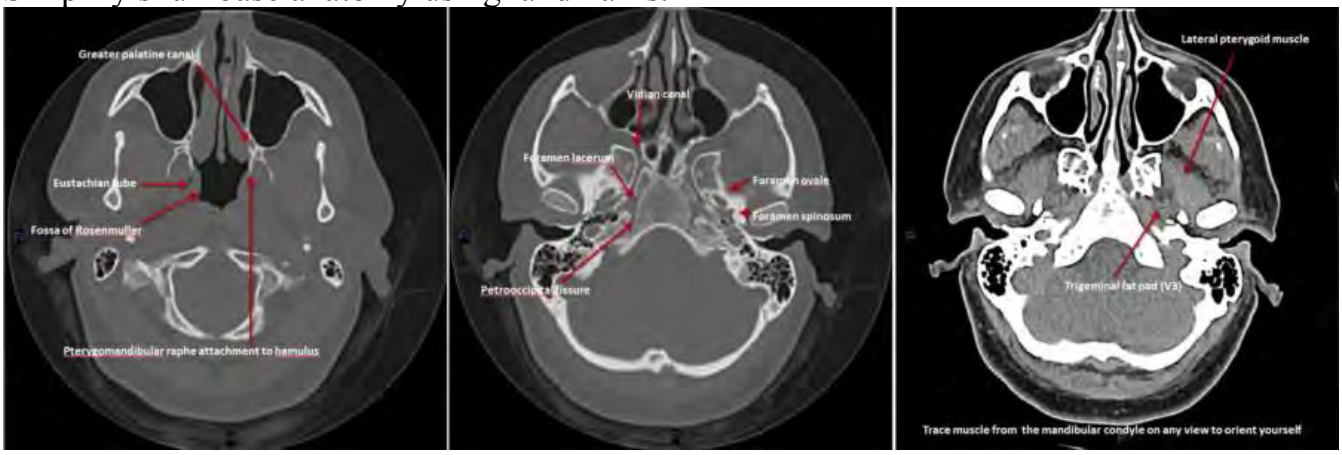
Use carotid canal, medial plate of pterygoid process, and mandibular condyle as computed tomography/magnetic resonance imaging (CT/MRI) landmarks to localize smaller structures: Trace carotid canal superior to inferior to the precavernous genu and foramen lacerum. Note carotid canal opens anteriorly to Vidian canal (via foramen lacerum) and posteriorly to petro-occipital fissure. Note foramina ovale and spinosum of sphenoid greater wing lateral to horizontal petrous carotid canal. Medial plate of pterygoid process is crux for anatomy of palate and pharynx. Learner finds: greater palatine foramen and canal anteriorly, pterygomandibular raphe inferiorly from hamulus, eustachian tube posteriorly, Vidian canal and nasopharyngeal canal cephalad via pterygoid process, PPF above pterygoid process. Find lateral pterygoid muscle from mandibular condyle. Learner finds pterygoid venous plexus and trigeminal fat pad medially. Thus V3 is localized and followed to foramen ovale in multiple planes. Use foramen spinosum and middle meningeal artery to approximate auriculotemporal nerve origin from V3.

Results

Note junction of greater superficial petrosal nerve and deep petrosal nerve at foramen lacerum forming Vidian nerve; note auriculotemporal nerve near parotid gland--potential routes of perineural spread between CN5 and CN7. Note petrooccipital fissure as potential site of skull base chondrosarcoma. Find pars nervosa of jugular foramen by tracing fissure posteriorly. Note pterygomandibular raphe as path of direct tumor spread from oral cavity to buccinator, superior pharyngeal constrictor and buccal space. Note anterior nasopharynx and eustachian tube near medial plate. Note posterior nasopharynx (fossa of Rosenmuller) posterosuperior to torus tubarius, emphasizing site of nasopharyngeal carcinoma. Additional discussion of PPF, tissue spaces, and perineural tumor spread are provided. Correlation of landmarks on CT and MRI is emphasized.

Conclusions

Simplify skull base anatomy using landmarks.



(Filename: TCT_eEdE-154_ASNRabstractpic5.JPG)

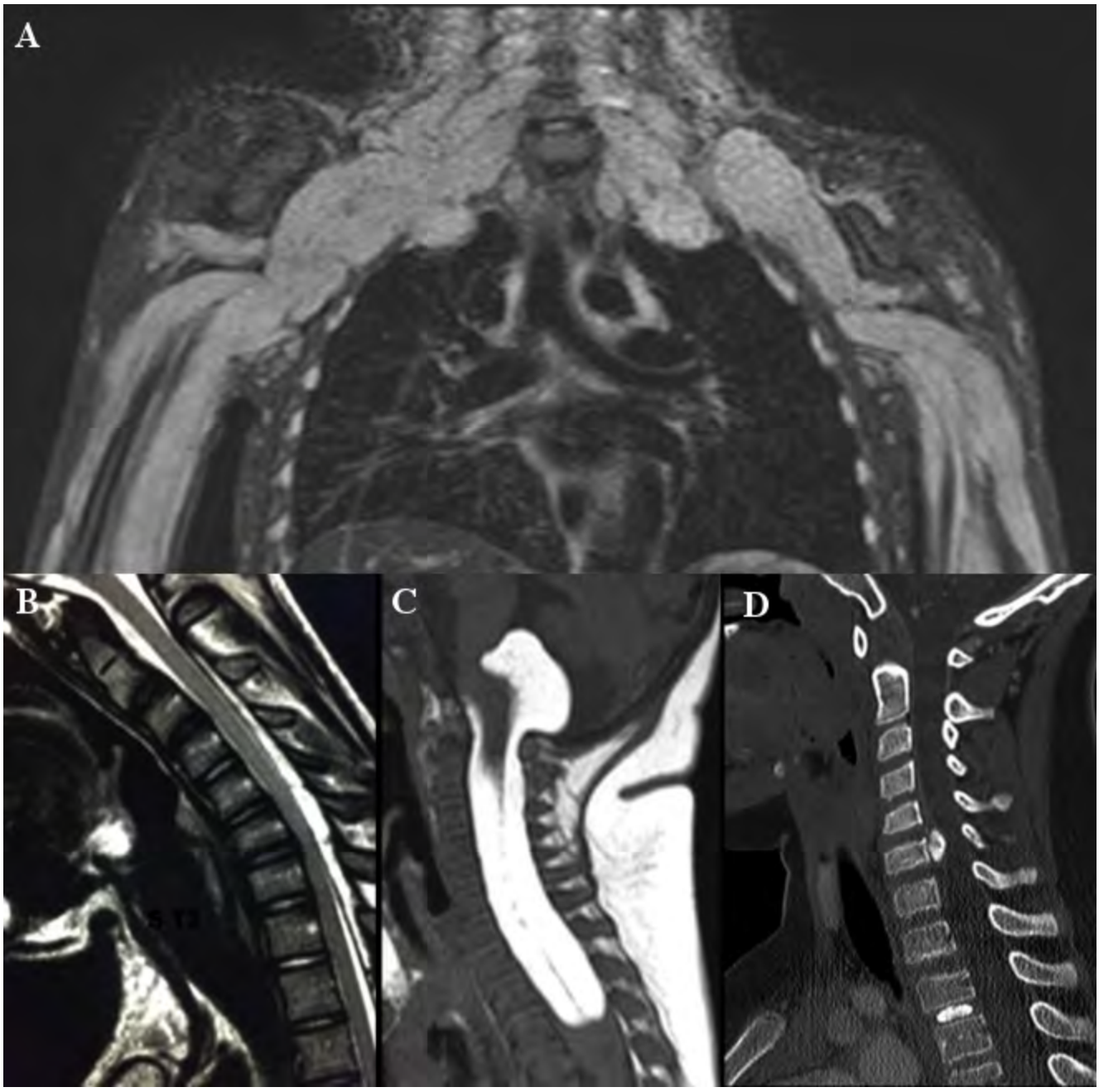
eEdE-142

6:30AM - 3:00PM

Challenging Cases of Pediatric Cervical Spine and Neck Pathology

H Dharmarajan[1], J Rivera[1], H Tran[1]
[1]*Baylor College of Medicine, Houston, TX*

Purpose
The complexity of pediatric cervical spine and neck pathology requires a thorough approach in imaging interpretation and fundamental knowledge of congenital malformations. This exhibit reviews the clinical and radiographic presentations of some rare, complex pediatric pathologies in the head and neck region.
Materials and Methods
Ten rare conditions are reviewed in terms of clinical presentation, pathognomonic imaging findings, and mimics: kaposiform hemangioendothelioma, idiopathic intervertebral disk calcification, congenital fibrosarcoma, Langerhans cell histiocytosis (LCH), fibrodysplasia ossificans progressiva, osteoid osteoma, Hirayama's disease, encephalocraniocutaneous lipomatosis, NF1-Noonan syndrome, and lupus transverse myelitis.
Results
Imaging pearls with pertinent history allow for distinct characterization of these ten rare conditions. NF1-Noonan syndrome may present with unique extreme enlargement of all nerve roots (Figure 1A). Insidious onset of oblique amyotrophy with sparing of brachioradialis is unique to Hirayama's disease; MR flexion view establishes the diagnosis (Figure 1B). Spinal lipoma in conjunction with nevus psiloliparus is pathognomonic for encephalocraniocutaneous lipomatosis (Figure 1C). Fibrodysplasia ossificans progressiva presents with first metatarsal abnormalities and diffuse heterotopic ossifications; biopsy should be avoided due to misdiagnosis with sarcoma. One should consider LCH in the setting of vertebra plana with diabetes insipidus. Endplate preservation differentiates idiopathic intervertebral disk calcifications from infectious etiologies (Figure 1D). Absence of thyroid gland involvement differentiates congenital fibrosarcoma from teratomas. Preservation of the vertebral cortex distinguishes osteoid osteoma. Kaposiform hemangioendothelioma should be strongly considered in the setting of Kasabach-Merritt syndrome with cervical mass. Lupus transverse myelitis is a diagnosis of exclusion; however, peripheral enhancement with rapidly progressive spinal cord atrophy differentiates this entity.
Conclusions
Identification of specific clinical and radiographic presentations of these ten rare entities may drastically alter clinical management. After viewing this presentation, one should be able to generate a focused differential diagnosis for each case through linking clinical presentation with imaging pearls.



(Filename: TCT_eEdE-142_Figure1.jpg)

eEdE-158

6:30AM - 3:00PM

Chew on These: Common and Uncommon Lesions of the Jaw. A Case-Based, RAD-PATH Tutorial

J Mueller[1], L Gentry[2], A Rajan KD[3], W Smoker[4]

[1]University of Iowa, Iowa City, IA, [2]University of Wisconsin Hospitals, Madison, WI, [3]University of Iowa Hospitals and Clinics, Iowa City, IA, [4]University Of Iowa Hospitals & Clinics, Iowa City, IA

Purpose

Lesions of the mandible and maxilla can be a diagnostic challenge for the radiologist. It is important to consider both common and uncommon entities when faced with these cases. One needs to consider a variety of cystic odontogenic, osseous, fibro-osseous, and miscellaneous lesions. The purpose of this tutorial is to educate the reviewer as to several uncommon lesions of the jaw, the main differential diagnoses, and discriminating imaging features of these entities.

Materials and Methods

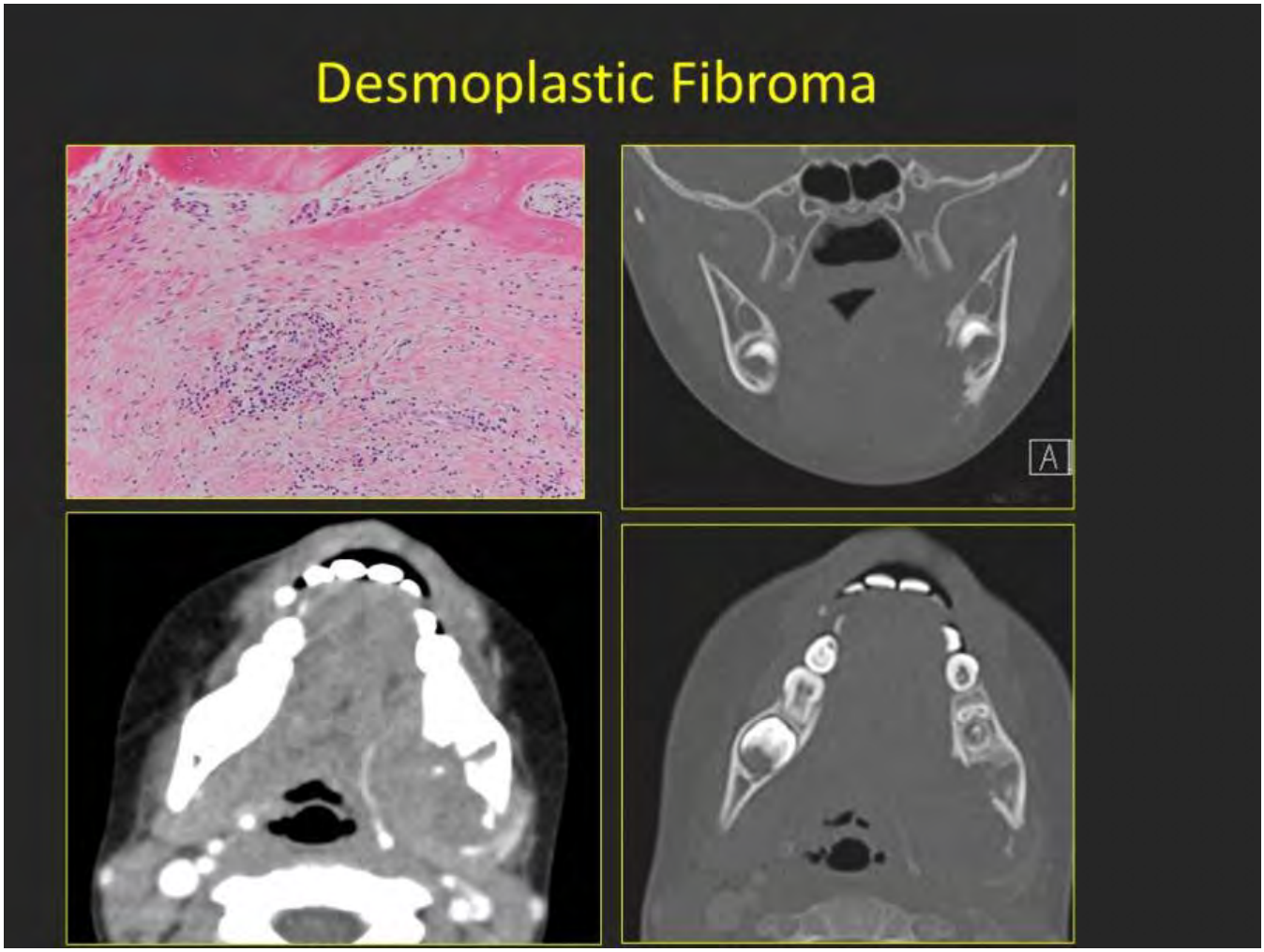
Reviewers are challenged with both common and uncommon osseous jaw lesions utilizing a case-based, computer-interactive, tutorial approach. A series of unknown cases is presented. Each case includes representative images that illustrate key diagnostic findings. A multiple choice question accompanies each case. The reviewer then is given the correct answer, followed by a brief discussion highlighting salient clinical and imaging features, as well as correlation with accompanying pathology images. When available, other examples illustrating the variable appearance of the lesion also are provided, as well as examples of main differential entities.

Results

Cystic odontogenic lesions include ameloblastoma, cemento-ossifying fibroma, keratocystic odontogenic tumor (KOT, including Gorlin syndrome), dentigerous cyst, and radicular cyst. Osseous lesions include desmoplastic fibroma, Gardner syndrome, and osteosarcoma. Fibro-osseous lesions include fibrous dysplasia and cemento-ossifying fibroma. Finally, miscellaneous lesions include aggressive fibromatosis, malignant fibromyxoid tumor, and Safne cyst.

Conclusions

After reviewing this interactive, case-based, educational exhibit, the reviewer will be able to identify common and uncommon osseous lesions of the jaw and describe their discriminating imaging features. Such lesions offer a diagnostic challenge to the radiologist. When faced with these cases, a working knowledge of the most common lesions and their imaging appearances is essential in order to arrive at the correct diagnosis or sufficiently narrow the differential.



(Filename: TCT_eEdE-158_ASNR4images.jpg)

eEdE-137

6:30AM - 3:00PM

Common and Uncommon Disease of the Medial Canthus of Orbit : A Pictorial Review of Findings at CT and MR Imaging

M ISHIKAWA[1], A Ohara[1]
[1]*Kyorin University School of Medicine, Mitaka, Tokyo*

Purpose
The purposes of this exhibit are 1) To understand the normal anatomy of lacrimal sac region. 2) Review of CT and MR findings of the medial canthal mass. 3) To improve the understanding of wide spectrum of tumors and tumor-like conditions.
Materials and Methods
We present malignant and benign nature of the medial canthus of orbit as follows: 1) Infection of lacrimal sac region: dacryocystitis, myositis with orbital cellulitis. 2) Malignant

tumor of lacrimal sac region: sebaceous carcinoma, carcinoma with neuroendocrine differentiation. 3) Miscellaneous: basal cell carcinoma, squamous cell carcinoma, hemangioma, epidermoid, neurofibroma, squamous cell papilloma. 4) Paranasal sinus: ethmoid sinus mucocele, olfactory neuroblastoma. 5) Systemic disease: malignant lymphoma, IgG4-related disease.
Results
The most common disease of the medial canthus of orbit is acute or chronic dacryocystitis. Benign and malignant tumors of the medial canthus of orbit are relatively rare neoplasm. The lacrimal sac region also may be involved secondary by tumor from skin, eyelid, paranasal sinuses.
Conclusions
We illustrate the CT and MR findings of diseases that can manifest as a medial canthal mass. Knowledge of their basic clinical and radiologic features would help differentiate between tumors and tumor-like conditions.

eEdE-153

6:30AM - 3:00PM

Cross Sectional Imaging of Odontogenic Tumors

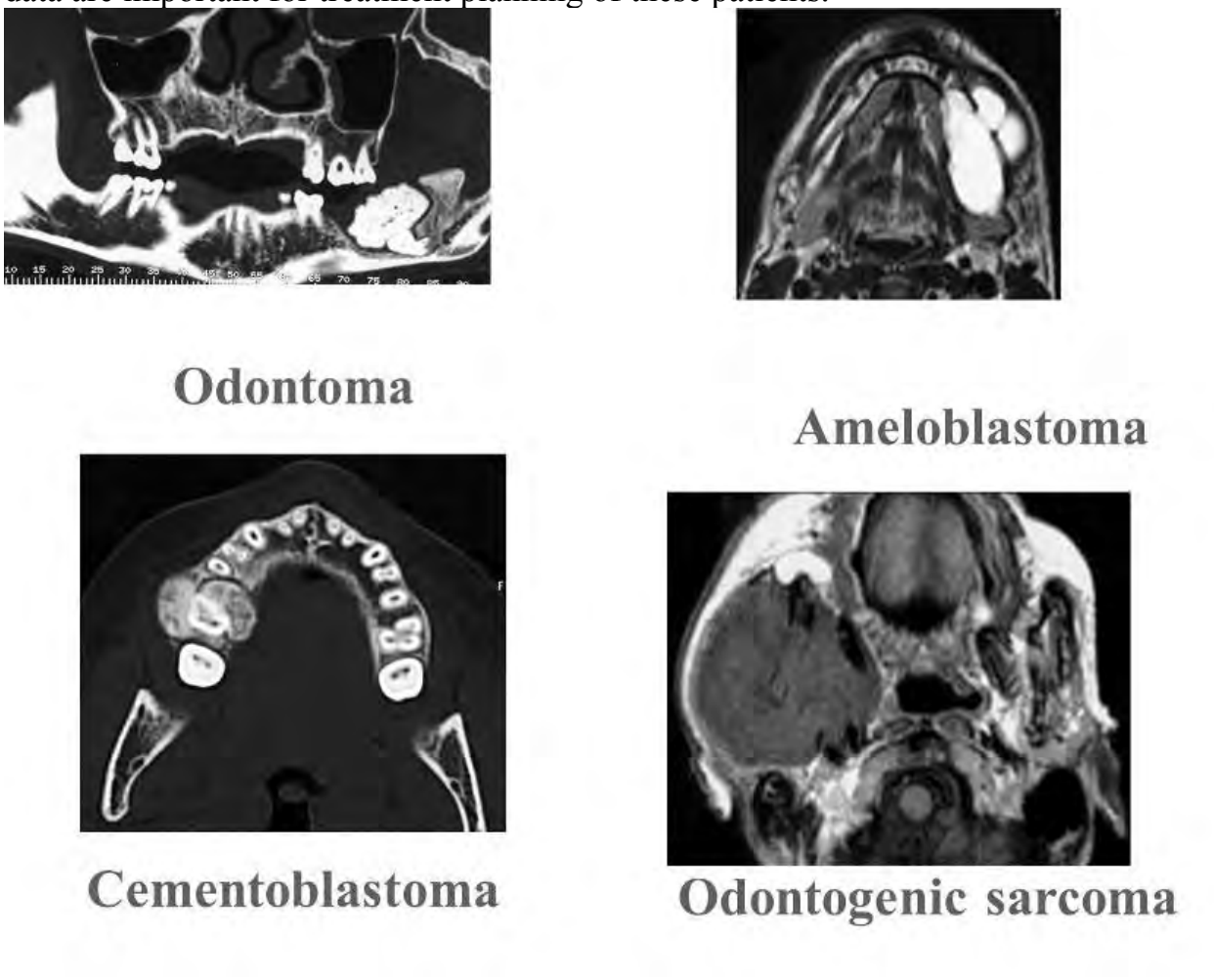
a abdel razek[1]
[1]*Mansoura faculty of medicine, mansoura, WY*

Purpose
1- To review WHO classification, demographic and clinical presentations of odontogenic tumors. 2- To demonstrate typical and atypical imaging appearance of odontogenic tumors at multi-imaging modalities. 3-To discuss the role of advanced computed tomography (CT) and magnetic resonance imaging (MRI) in assessment of odontogenic tumors.
Materials and Methods
1- Basic background about odontogenic tumors. 2- Updated WHO classification of odontogenic tumors. 3- Methods of examination include panorama, CT scan, CBCT and MRI of odontogenic tumors. 4-Role of diffusion-weighted MRI in characterization of odontogenic tumors. 5- Computed tomography and MRI appearance of epithelial tumors as ameloblastoma, keratocystic odontogenic tumor and calcifying epithelial odontogenic tumor. 6- Imaging of mixed epithelial and mesenchymal tumors as odontomas and ameloblastic fibromas. 7- Imaging of mesenchymal tumors as cementomas and odontogenic myxoma. 8- Imaging appearance of malignant odontogenic tumors either carcinoma or sarcoma. 9- Imaging of fibro-osseous lesions of the jaw as fibrous dysplasia and cherubism. 10- Imaging appearance of ossifying fibroma and central giant cell lesion. 11- Summary and conclusion.
Results
Cross-sectional imaging can help in accurate localization, extension and characterization of odontogenic tumors of the jaw. Diffusion-weighted MRI helps in characterization of some

odontogenic tumors. Imaging can suspect malignancy and predict fibro-osseous lesions and simulating lesions. This information is important for treatment planning and prognosis of the patients.

Conclusions

We concluded that cross-sectional imaging is important for accurate localization, characterization and extension of different subtypes of odontogenic tumors of the jaw. These data are important for treatment planning of these patients.



(Filename: TCT_eEdE-153_Picture1.jpg)

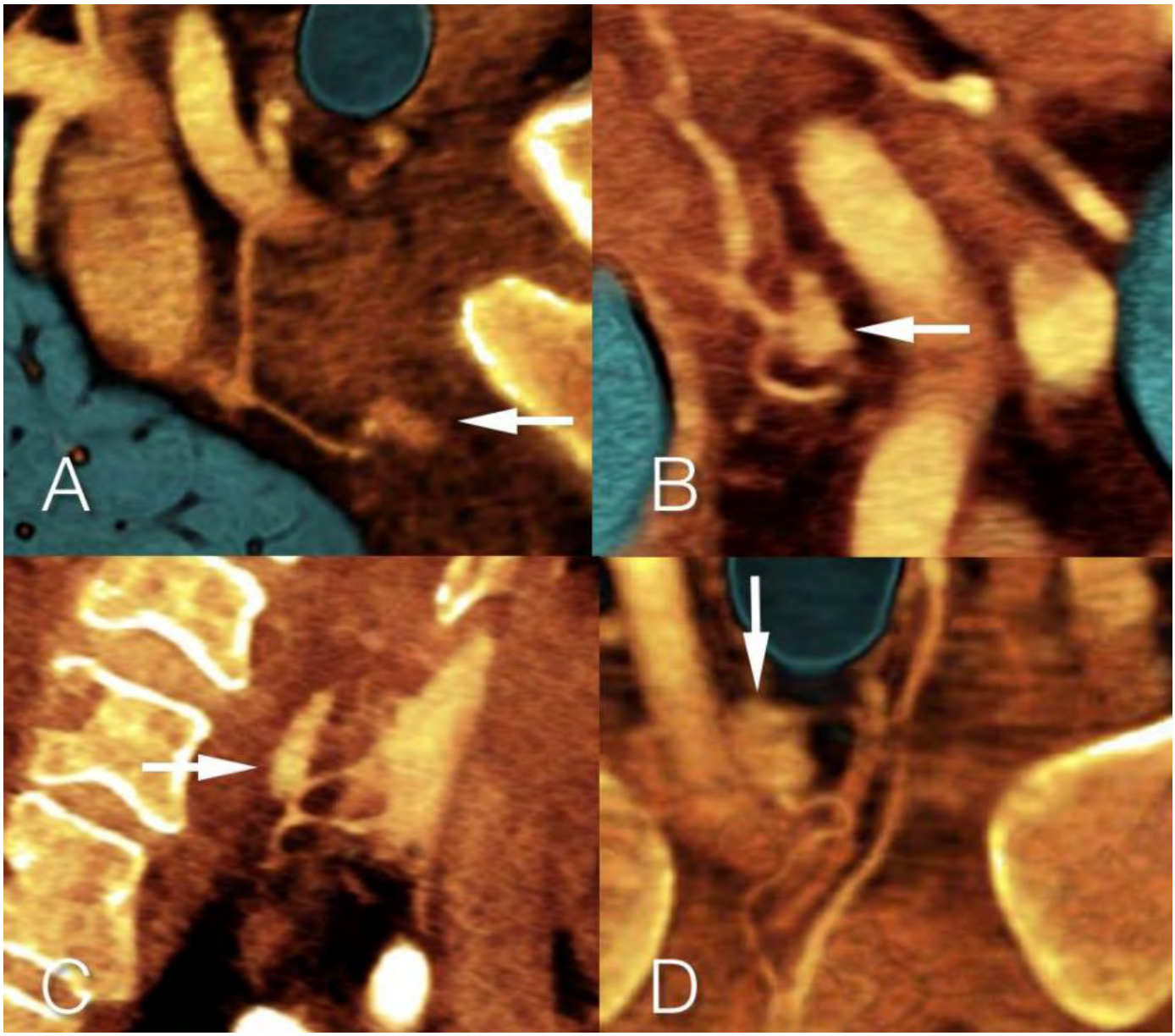
eEdE-125

6:30AM - 3:00PM

CT Angiography Using Radiation Dose Reduction Techniques in the Evaluation of Occult Parathyroid Adenomas

A DeChambeau[1], M Cathey[1], D Hawley[1], T Johnson[1], G Boswell[1]
[1]*Naval Medical Center San Diego, San Diego, CA*

Purpose
It is common practice for patients with hyperparathyroidism to undergo imaging evaluation to assist with a more targeted surgical resection. The current standard of care utilizes a multimodality approach with 4D CT, in addition to ultrasound and scintigraphy. We present our experience using a novel CT angiography technique with radiation dose reduction to evaluate patients with parathyroid adenomas that were occult on scintigraphy and ultrasound. We demonstrate our technique using a case-based approach, and correlate with surgical outcomes.
Materials and Methods
We demonstrate our experience with CT evaluation of occult parathyroid adenoma with a novel CT angiography technique using techniques that result in significant radiation dose reduction. In this review we describe the optimal patient positioning to mitigate the "bone box" at the thoracic inlet. We elaborate on noncontrast, test bolus, and CT angiography technique to perform the examination with just two scans at a significant radiation dose reduction than the current standard of care. We instruct on interpretative skills in discriminating between adenoma versus lymph node or thyroid tissue with numerous case examples.
Results
Utilizing our novel CT angiography technique, we were able to achieve excellent quality examinations at a significant dose savings relative to the current standard of care that correlated well with the clinical and pathologic postoperative findings. The median estimated radiation dose was 4.35 mSv, compared to previously described dosages ranging from 21 to 29 mSv utilizing standard techniques. Radiation dosages using the current standard of care can cause an estimated 0.19% increased attributable cancer risk for a 55-year-old woman and 1.05% increased cancer risk for a 25-year-old woman. A notable finding discovered during our experience utilizing this novel technique is that parathyroid adenomas enhanced to more than 100 HU during individually timed arterial phase imaging, whereas lymph nodes did not. Previously reported polar vessels often can be seen attached to the parathyroid adenoma. Unenhanced parathyroid adenomas were generally a lower density than the thyroid gland, and soft tissue attenuation above 100 HU on the precontrast exam was consistently thyroid tissue.
Conclusions
Computed tomography parathyroid imaging can be performed at low radiation doses with high accuracy using specialized protocols with modern CT scanners. Consideration of using 100 HU on the angiography scan as a potential discriminating threshold for parathyroid adenoma diagnosis is a promising area for future investigation.



(Filename: TCT_eEdE-125_Abstractimage.jpg)

eEdE-114

6:30AM - 3:00PM

Demystifying Vascular Malformations of the Head and Neck

B Dillon[1], M Conti[1], M Johnson[2], R Antaya[1]
[1]Yale University School of Medicine, New Haven, CT, [2]Yale University School Of Medicine, New Haven, CT

Purpose
To demonstrate an anatomic approach to imaging analysis of vascular anomalies of the head

and neck that can improve diagnostic confidence through precise reporting of findings which have specific relevance to diagnosis, prognosis and treatment strategies. Vascular anomalies of the head and neck are not uncommon but frequently are misunderstood and poorly defined. Classification schemes for vascular anomalies of the head and neck include those that are based on imaging and those that are primarily based on pathology. Not every vascular lesion is a hemangioma! This illustrative review will explore common and uncommon vascular anomalies of the head and neck according to clinical presentation and imaging characteristics. Using a simple methodical strategy for image analysis, vascular lesions of the head and neck can be accurately characterized and findings clearly communicated to the treating physician, facilitating patient management.

Materials and Methods

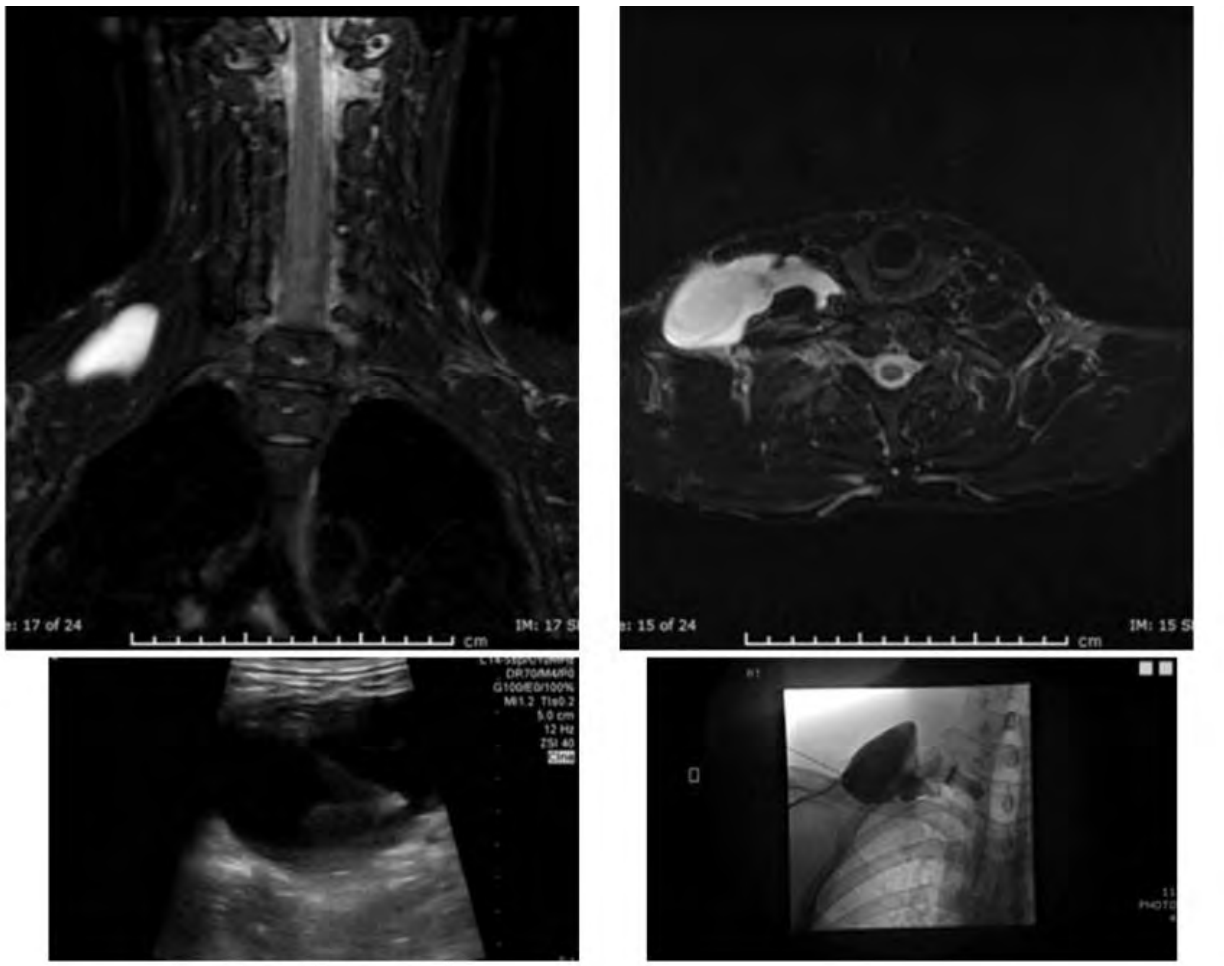
A retrospective review of adult and pediatric cases from our Multidisciplinary Vascular Anomalies Conference Database was performed and selected cases chosen to illustrate a variety of pathologies and treatment strategies. Cases were stratified by clinical presentation and by interrogating the images for the answers to the following questions: Is the lesion cystic, solid or mixed? (single, multiple, large or small). Is the lesion space occupying or infiltrative? (deform or insinuate between normal structures). Are there associated findings? (enlarged vessels, phleboliths). These imaging findings were recorded. Management strategies including expectant, surgical, endovascular and sclerotherapy were correlated with both clinical presentation and imaging characteristics.

Results

By analyzing specific imaging features of vascular anomalies of the head and neck, one can reliably make the correct diagnosis and appropriately direct patient management. Characteristic clinical presentations such as focal masses, skin discoloration, pain or functional loss along with imaging features reliably led to accurate diagnoses. Cystic, solid or mixed lesions whether single or multiple, space-occupying or infiltrative, may deform or insinuate between normal structures. They may erode, resorb or remodel bone or teeth. Associated imaging features such as phleboliths or enlarged vessels may impact diagnosis. Analysis of these cases in a structured fashion permits accurate diagnosis and facilitates patient management.

Conclusions

Vascular anomalies of the head and neck are uncommon lesions that may sometimes defy diagnosis and classification. The application of a structured analytic strategy for imaging analysis including clinical presentation and imaging characteristics will facilitate accurate diagnosis and further optimal patient management and treatment.



(Filename: TCT_eEdE-114_abstract.jpg)

eEdE-124

6:30AM - 3:00PM

Dual Energy CT of the Neck: A Pictorial Review of Normal Anatomy and Pathology Using Different Energy Reconstructions and Material Decomposition Maps

A Perez-Lara[1], M Bayat[2], G Melki[1], A Mandalenakis[1], R Forghani[2]
[1]Jewish General Hospital, Montreal, Quebec, [2]Jewish General Hospital & McGill University, Montreal, Quebec

Purpose
There is increasing use of dual energy computed tomography (DECT) for the evaluation of head and neck pathology. Optimal application and use of DECT requires familiarity with the appearance of normal tissues or pathology on different reconstructions. The purpose of this exhibit is to provide a practical, pictorial review of the normal anatomy and different head and neck pathology on commonly used DECT reconstructions.

Materials and Methods

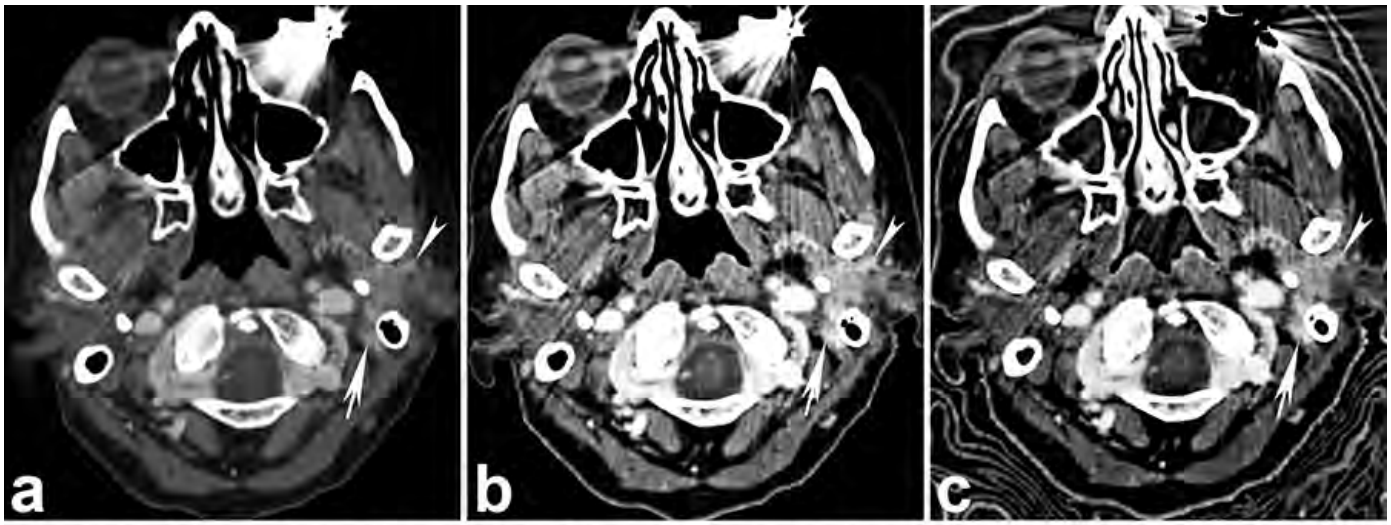
The presentation will begin with a brief overview of fundamentals of virtual monochromatic images (VMIs) and material decomposition maps using a fast kVp switching DECT scanner. Thereafter, a pictorial review of normal anatomy and pathology will ensue using low energy and high energy VMIs, iodine material decomposition maps, and virtual unenhanced images. Both neoplastic and non-neoplastic lesions will be reviewed.

Results

The major anatomical structures of the neck will be reviewed on different reconstructions followed by a review of different pathology including (1) malignant and benign tumors (e.g., head and neck squamous cell carcinoma, thyroid cancer, lymphoma, salivary gland tumors, parathyroid adenomas), (2) infectious and inflammatory disorders (e.g., soft tissues infections and abscesses, sialolithiasis), (3) malignant and inflammatory lymphadenopathy, and (4) miscellaneous pathology (e.g., perineural spread of tumor, thryoglossal duct cyst, skull base lesions). In addition to reviewing the appearance of the lesions on different reconstructions, the exhibit also will highlight reconstructions that may enhance diagnostic evaluation and review the advantages and disadvantages/pitfalls of different reconstructions based on the pathology and location in the neck, when appropriate.

Conclusions

Dual energy computed tomography is a useful tool for evaluation of head and neck pathology and is used increasingly in the clinical setting. The exhibit will provide an overview of the appearance of major anatomical structures and diverse neck pathology on commonly used DECT reconstructions and discuss potential advantages and pitfalls of different reconstructions for lesion evaluation.



DECT of the neck. Axial 65 keV virtual monochromatic image (single energy CT equivalent)(a), 40 keV virtual monochromatic image (b), and iodine-water decomposition map (c) are shown. There is a parotid adenocarcinoma (arrowhead). The associated perineural spread along the VII nerve (white arrow) is better seen on 40 keV and iodine-water decomposition map (c), confirmed by MRI and pathology.

(Filename: TCT_eEdE-124_Figv2.jpg)

eEdE-129

6:30AM - 3:00PM

Evaluation of Oculomotor Palsy and its Mimics

C Miah[1], W Smoker[2], G Avey[3], T Kennedy[4], D Reede[5], L Gentry[6]
[1]Albany Medical Center, Albany, NY, [2]University Of Iowa Hospitals & Clinics, Iowa City, IA, [3]University of Wisconsin, Madison, WI, [4]University Of Wisconsin Hospital, Madison, WI, [5]SUNY downstate University Hospital, Brooklyn, NY, [6]University of Wisconsin Hospitals, Madison, WI

Purpose
The third cranial nerve provides somatic motor innervation to the extraocular muscles, aside from the lateral rectus and superior oblique muscles, as well as parasympathetic innervation to the pupillary constrictors. Knowledge of the course and appearance of the nerve and its branches, as well as knowing the types of lesions that occur along the course of the nerve, can help the radiologist diagnose the various etiologies of oculomotor palsies.
Materials and Methods
We review the normal anatomy of oculomotor nuclei, brainstem fascicles, and the different peripheral segments of the nerve. Clinical description of different types of third nerve palsies including pupillary sparing and pupil involving lesions, as well as mimics of CN3 palsy, are

discussed. Representative cases then are used to demonstrate various etiologies of third cranial nerve palsy including lesions that can occur along the entire course of the nerve.
Results
The oculomotor nerve has a complex anatomic course, originating from the midbrain, exiting ventrally into the interpeduncular cistern, travelling between the posterior cerebral and superior cerebellar arteries in the suprasellar cistern, into the occulomotor cistern, within the lateral wall of the cavernous sinus into the medial limb of the superior orbital fissure, and subsequently ramifying into different branches within the orbit. Clinical cases involving leptomeningeal, neuromuscular, ischemic, compressive, restrictive, and neoplastic processes are presented.
Conclusions
Occulomotor palsy can result from lesions anywhere along its path between the origin nuclei in the midbrain and the extraocular muscles within the orbit. A comprehensive understanding of the anatomy and knowing where the nerve is susceptible to various processes can aide in making the diagnosis.

eEdE-167

6:30AM - 3:00PM

Everything You Need to Know About Inverted Papilloma: A Comprehensive Review

Y Pekcevik[1], I Arslan[2], I Cukurova[2], H Sahin[2]
[1]Tepecik Training and Research Hospital, Izmir, Turkey, Turkey, [2]Tepecik Training and Research Hospital, Izmir, Turkey

Purpose
Inverted papilloma is a benign sinonasal tumor that has a bad reputation. It is a local aggressive tumor that has a high rate of recurrence, multicentricity and an association with synchronous or metachronous squamous cell carcinoma. Endoscopic approaches to resect sinonasal inverted papilloma is the treatment of choice, and appropriate pre-operative assessment of these tumors is crucial for successful treatment. The purpose of this exhibit is to comprehensively review clinical and imaging features of inverted papilloma and to provide a practical approach for pre-operative evaluation of the tumor.
Materials and Methods
Clinical findings and CT and MR images of different cases will be demonstrated to give: - Key imaging findings of inverted papilloma and its differential diagnosis. - Accurate pre-operative mapping of tumor locations using CT and MR imaging. - Findings related to an association with squamous cell carcinoma. - Postoperative, follow-up imaging and recurrence of inverted papilloma.
Results
Relevant clinical and imaging features, additional advanced diagnostic tests help in

differential diagnosis, appropriate pre-operative evaluation for determining tumor origin and extension, follow up in postoperative period for tumor recurrence will be discussed.
Conclusions
Inverted papilloma is an uncommon benign epithelial tumor of the sinonasal tract that needs to be treated due to its local aggressiveness, high rate of recurrence and probable association with squamous cell carcinoma. We should be familiar with imaging findings for diagnosis and appropriate pre-operative assessment of these tumors.

eEdE-157

6:30AM - 3:00PM

FD or NOT FD? That is the Question

A Wright[1], J Courtier[1], R Jordan[1], C Glastonbury[2]
[1]UCSF, San Francisco, CA, [2]University Of California, San Francisco, San Francisco, CA

Purpose
Fibrous dysplasia (FD) classically is described as appearing as a "ground glass" expansile lesion of bone. Too often however, any expansile or "ground glass" bone lesion is diagnosed as FD without consideration of other possibilities.
Materials and Methods
We review the current understanding of the histology, genetics and imaging manifestations of fibrous dysplasia and its associated syndromes in neuroradiology. We illustrate it with typical cases and contrast it with examples of maxillofacial, skull base and calvarium bone abnormalities which initially were thought to represent fibrous dysplasia but which on subsequent review or histological or genetic evaluation were determined to be alternate diagnoses.
Results
There are many different imaging manifestations of FD on computed tomography (CT). It may appear of "ground glass" density or heterogeneous with areas of markedly low density (and enhancing), or markedly high density. In the HN it may be asymptomatic and incidentally found, or it may present because of head or facial asymmetry or from cranial neuropathies. Particularly in the jaw where there are many odontogenic lesions with overlapping imaging appearances, there is a tendency for radiologists to 'lump' together all expansile and/or ground glass bone lesions as "FD". Such lesions may include better known entities such as ossifying fibroma, cemento-osseous dysplasia, intraosseous meningioma and even chronic sinusitis; but also less well known entities including ossifying cephalohematoma, chronic recurrent multifocal osteomyelitis (CRMO) and gigantiform cementoma.
Conclusions
There are specific syndromes associated with FD with which neuroradiologists should be familiar. However, there are many other entities with which FD often is confused and we

present a better understanding of FD and important differentials for the neuroradiologist to minimize surgical intervention.

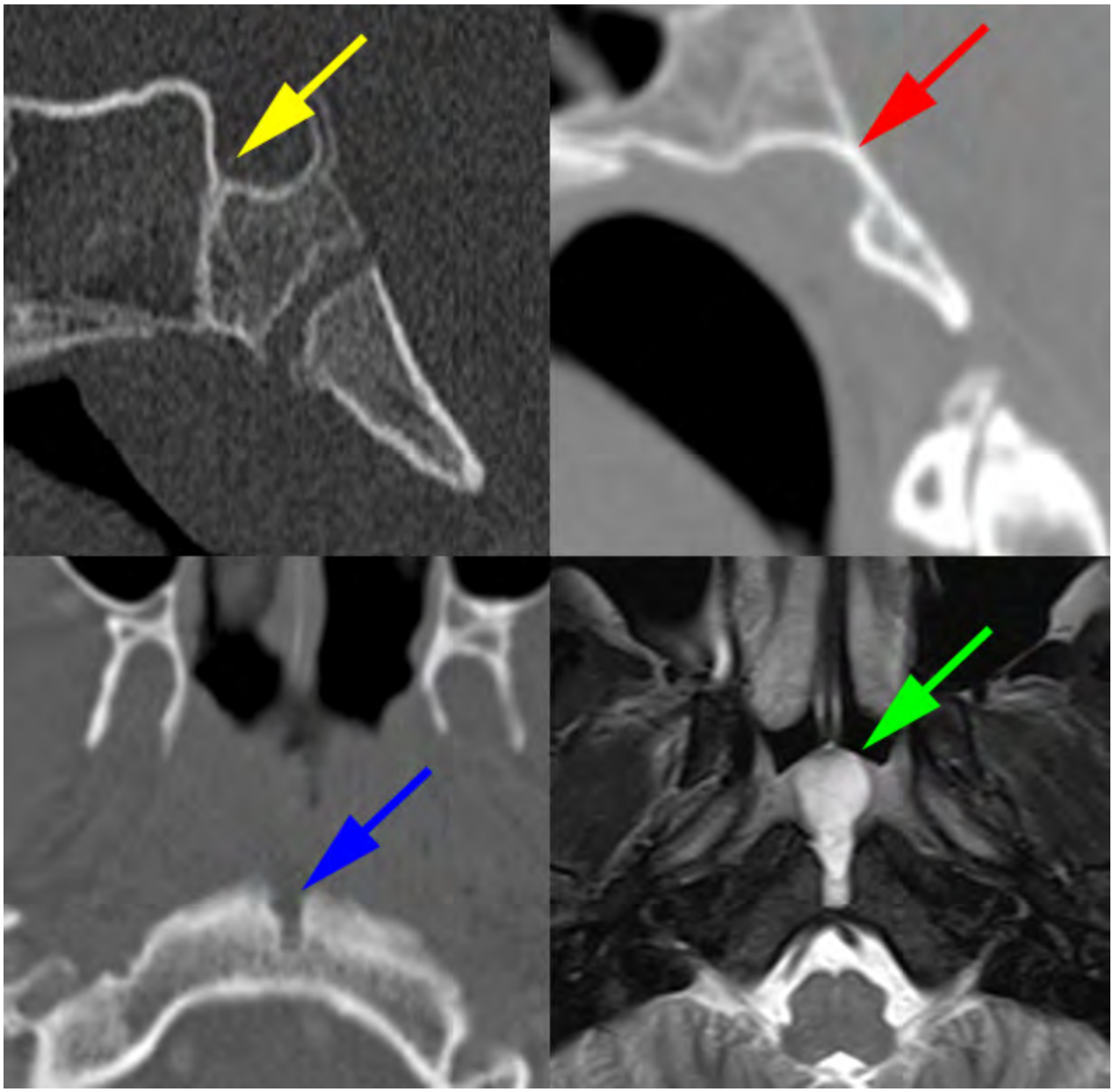
eEdE-160

6:30AM - 3:00PM

Fossa Navicularis Magna and Median Basal Canal: Comprehensive Review of Skull Base with a Focus on Rare Anatomic Variants and Pathology

L Eisenmenger[1], H Harnsberger[1], R Wiggins[2]
[1]*University of Utah, Salt Lake City, UT,* [2]*University Of Utah, Salt Lake City, UT*

Purpose
The purpose of this exhibit is to review for the imager the most important normal skull base anatomy, be able to accurately and concisely describe anatomic variants, and be aware of rare but important pathologic lesions that can occur in the skull base.
Materials and Methods
This exhibit will comprehensively review the skull base, covering skull base anatomy and pathology. Normal skull base development will be discussed such as the normal ossification centers and synostoses as well as normal developmental canals such as the craniopharyngeal canal (Image 1, yellow arrow). Important anatomic variations will be highlighted with case examples such as a fossa navicularis magna (Image 2, red arrow) and median basal canal (Image 3, blue arrow). The underlying developmental causes for these anatomic variations also will be discussed. Common skull base pathologic lesions will be reviewed with case examples such as chordomas, chondrosarcomas, pharyngeal cysts, meningiomas, osseous lymphoma, and metastatic disease. Rare pathology will be focused on, including multiple case examples of extraosseous chordomas (Image 4, green arrow). This exhibit will review the best imaging protocols for different pathology including when the radiologist should recommend additional imaging as well as how imaging directly effects intervention in these lesions.
Results
Accurate recognition and diagnosis of skull base normal anatomy, anatomic variations, and pathology can greatly affect patient care through guiding the need for additional imaging, treatment, and predicting prognostic outcomes. An understanding of this anatomy also will avoid unindicated surgeries and biopsies.
Conclusions
Skull base anatomy and lesions can be complex with involvement of many structures but an ordered approach to skull base evaluation can help the radiologist provide the most relevant information to the clinicians as well as reduce the chance of missing important findings. This exhibit will review what a radiologist needs to know about the skull base.



(Filename: TCT_eEdE-160_skullbase.jpg)

eEdE-121

6:30AM - 3:00PM

Head and Neck Paragangliomas: Review of Classification and Imaging Findings

A Rovira[1], C Tortajada[1], J Cabero[1], M Prenafeta Moreno[2], S Siurana[1], A Rovira Gols[2], C Auger[1]

[1]Vall d´Hebron University Hospital, Barcelona, Spain, [2]UDIAT-CD, Corporació Sanitària Parc Taulí, Sabadell, Spain

Purpose
• To review the spectrum of paragangliomas of the head and neck (HNPS). • Learn the common locations and the different classifications of HNPS. • To illustrate the common imaging features of HNPS.
Materials and Methods
Review of different imaging methods required for an accurate diagnosis and safe management of HNPs, based on the experience of two academic institutions, and on extensive literature research.
Results
Head and neck PGLs (HNPGLs) originate from the sympathetic and parasympathetic paraganglia. The most common HNPGLs locations in descending order are the carotid body, jugular, tympanic, and vagal paragangliomes, and usually are noncatecholamine secreting. Imaging hallmarks of HNPGs include an enhancing soft-tissue mass in the carotid space, jugular foramen, or tympanic cavity at CT or MRI; a salt-and-pepper appearance at MRI; and an intense blush at x-ray angiography or time-resolved contrast-enhanced MR angiography. Imaging studies are essential for precisely depicting their location and extent, the relation with vascular structures, and the presence of unsuspected multiplicity. All of this information will help to determine the surgical approach, and predict operative morbidity and mortality. HNPs typically show avid uptake with different functional nuclear medicine techniques, such as 18F-FDOPA and 18FFDA PET/CT, and 123IMIBG scintigraphy. These functional imaging studies are particularly required in patients with malignant HNPs or in patients with high risk of multiple paragangliomas (gene mutations).
Conclusions
Paragangliomas of the head and neck demonstrate distinctive imaging characteristics, based on topographical and morphological features, and vascularization and vessel displacement patterns. Radiologist must be familiar with the different classifications of these rare tumors, which are based on their origin and topography (relevant for diagnosis and management), and more recently on genetics (relevant for predicting multiplicity and malignancy).

eEdE-127

6:30AM - 3:00PM

Holes, Lumps and Bumps: A Pictorial Review of Calvarial Lesions

I Khodarahmi[1], S Slasky[2], P Thomas[3]
[1]Rutgers The State University of New Jersey, Newark, NJ, [2]Rutgers- New Jersey Medical School, Newark, NJ, [3]Rutgers New Jersey Medical School, Newark, NJ

Purpose
To review the imaging characteristics of various lesions of the calvarium.
Materials and Methods
Calvarial lesions often are incidentally discovered during CT or MR imaging of the brain for

unrelated reasons. Traditionally, these lesions are classified into neoplastic (benign or malignant) and non-neoplastic categories; the latter group including congenital, traumatic and iatrogenic, metabolic, infectious, and idiopathic conditions. Retrospective review of our institution's imaging database identified various skull pathologies from which a pictorial review has been provided in this exhibit.
Results
Patient's age and clinical and laboratory findings are valuable factors in establishing a radiological diagnosis of skull lesions. Imaging characteristics of such lesions often can suggest a specific diagnosis or limit the differential diagnosis. Important imaging features to consider include lesion site, size, multiplicity, pattern of bone destruction, margins, periosteal reaction, local extension, and type of matrix. In this exhibit, imaging characteristics of different entities from each category are provided which include: neoplastic (fibrous dysplasia, osteoma, ossifying fibroma, intraosseous meningioma, hemangioma, plasmocytoma, skull metastasis), congenital and normal variants (epidermoid and dermoid cysts, cephalocele, parietal foramina, arachnoid granulations, venous lakes), traumatic and iatrogenic (burr holes, leptomeningeal cyst, calcified cephalohematoma, flap osteonecrosis), metabolic (renal osteodystrophy), infectious (osteomyelitis) and idiopathic (Langerhans cell histiocytosis, Paget's disease).
Conclusions
There is a wide spectrum of neoplastic and non-neoplastic skull lesions which show different radiologic features on CT and MRI. Although establishing a definitive diagnosis for calvarial lesions based solely on imaging can be sometimes challenging, the recognition of their radiologic appearances usually allows a prospective diagnosis, which can guide optimal clinical management which includes biopsy, surgery, or follow-up imaging.

eEdE-150

6:30AM - 3:00PM

Imaging Evaluation of Facial Pain

v kunam[1], L Gentry[2], W Smoker[3], R Holliday[4]
[1]SUNY Downstate University hospital, Brooklyn, NY, [2]University of Wisconsin Hospitals, Madison, WI, [3]University Of Iowa Hospitals & Clinics, Iowa City, IA, [4]Mount Sinai Beth Israel, New York, NY

Purpose
1. To review pathophysiology of facial pain and facial sensory innervation. 2. To learn common and uncommon causes of facial pain. 3. To demonstrate the role of imaging in the diagnosis and management of patients with facial pain.
Materials and Methods
Pain is classified into nociceptive or neuropathic pain. Nociceptive pain is caused by stimulation of primary afferent nociceptors (pain receptors) as a result of local tissue damage

such as trauma, inflammation or an aggressive neoplastic process. Nociceptive pain typically is described as sharp, aching or throbbing pain. Neuropathic pain is due to lesions involving the peripheral nerves or central nociceptive (neural) pathways. Causes of peripheral neuropathic pain include diabetes, trauma, and vitamin B deficiency. Causes of central neuropathic pain include lesions in the spinal cord, brainstem, thalamus or cerebral cortex. Neuropathic pain typically has a burning, tingling or electric-shock-like quality and is triggered by light touch. For the purpose of this presentation we divided this type of pain into neuralgia (typically not associated with the sensory deficit or another cranial nerve (CN) finding) and FP with motor and /or sensory deficits. Facial pain can be the only presenting complaint in patients with intracranial, facial or neck pathology. Clinical history and physical examination are the key components of the initial evaluation. However, imaging plays a pivotal role in identifying the source of FP when clinical findings are ambiguous due to an overlap of symptoms from different pathologies or inability to perform a proper clinical exam due to soft tissue swelling or trismus. Clinical presentation should be taken into consideration to tailor imaging when looking for underlying pathology. For example malignant parotid lesions presenting with pain should prompt radiologist to explore the possibility of perineural tumor spread (PNTS) along the auriculotemporal branch of trigeminal (CNV) nerve whereas parotid lesions presenting with facial palsy suggest PNTS along the facial (CNVII) nerve.

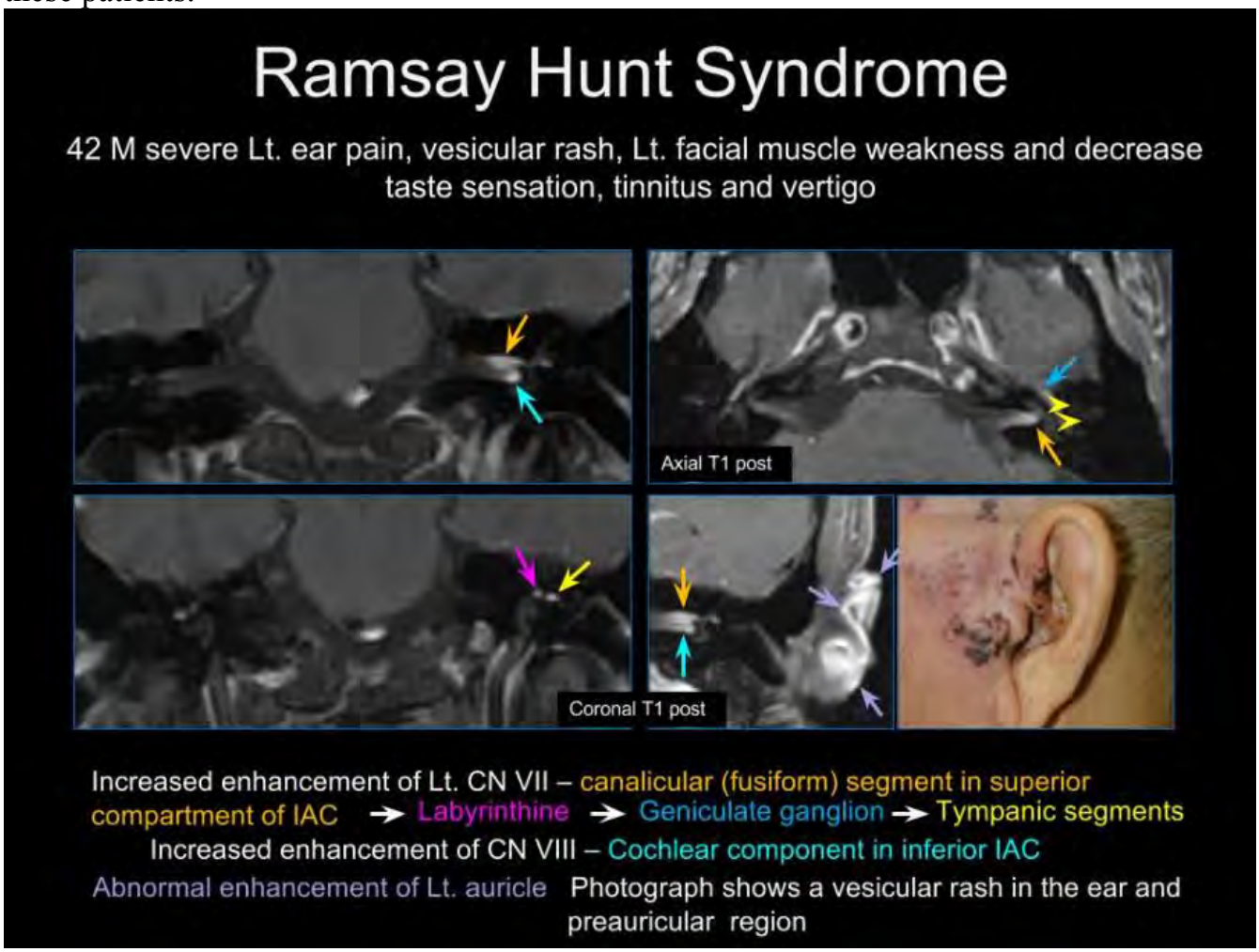
Results

After a brief review of the pathophysiology of pain and sensory innervation of the face, representative cases of pathologies with nociceptive, and neuropathic pain are presented. The etiology of nociceptive pain can be identified based on the location of pain and anatomic correlation: Central (sinonasal disease, orbital inflammatory disease without CN involvement and malignancies of the oral cavity); lateral (mastoiditis, salivary gland, TMJ and masticator and submandibular space pathology) or combined (dental disease). Identification of the source of neuropathic pain requires an imaging of the course of the involved CN. Neuropathic pain cases presented include: • Neuralgia – trigeminal and glossopharyngeal neuralgia. • Facial pain with orbit sensory deficit (CNII - optic neuritis: multiple sclerosis, sarcoidosis). • Painful ophthalmoplegia (CN III, IV and VI) nerves: Tolosa-hunt syndrome, cavernous sinus thrombosis). • Facial pain with facial sensory deficit (CN V: Herpes Zoster, MS, perineural tumor spread). • Facial pain with sixth nerve plasy (CNV and CNVI: Gradenigo syndrome due to petrous apicitis). • Facial pain with motor deficit, hypoacusis and disturbed balance (CN VII and VIII nerves: Bell's palsy, Ramsay-hunt syndrome). • Facial pain with dysphagia, dysphonia or dysarthria (CN IX and X nerves: skull base lesions, brain stem infarction). The role of imaging in the diagnosis and clinical management of the above pathologies is discussed. A summary imaging algorithm for the evaluation of FP is provided to facilitate appropriate imaging and increase diagnostic accuracy.

Conclusions

Understanding the pathophysiology, clinical presentation and imaging findings of

nociceptive and neuropathic causes of FP enables the radiologist to play a major role in the evaluation and management of these patients. After viewing this module, you will be able to localize the etiology of FP and play a significant role in the diagnosis and management of these patients.



(Filename: TCT_eEdE-150_ASNR41.jpg)

eEdE-141

6:30AM - 3:00PM

Imaging Findings Related to Craniosynostosis Surgery

D Ginat[1], A Kuhn[2], R Reid[1]
[1]*University of Chicago, Chicago, IL,* [2]*Rush University, Chicago , IL*

Purpose
The goal of this exhibit is to familiarize the radiologist with the various types of surgical procedures used to treat craniosynostosis.

Materials and Methods
Accurate depiction of the cranial sutures and morphology using high-resolution, but low-dose CT, particularly with 3D surface renderings, is imperative for surgical planning and postoperative assessment.
Results
The following topics will be included in this exhibit: • Describe the standard clinical and imaging work up for patients with craniosynostosis. • Review the types of craniosynostosis, including associated conditions, such as Apert syndrome, Crouzon syndrome, and premature closure of sutures from ventricular shunting. • Discuss the various types of surgeries that can be performed to correct craniosynostosis and depict the corresponding expected imaging findings. • Discuss the potential complications of craniosynostosis surgery with imaging correlates.
Conclusions
There are many types of procedures that can be used to treat craniosynostosis. Imaging is sometimes performed after treatment for evaluating potential complications and for planning additional surgery.

eEdE-116

6:30AM - 3:00PM

Imaging of Airway Compromise: A Pictorial Review

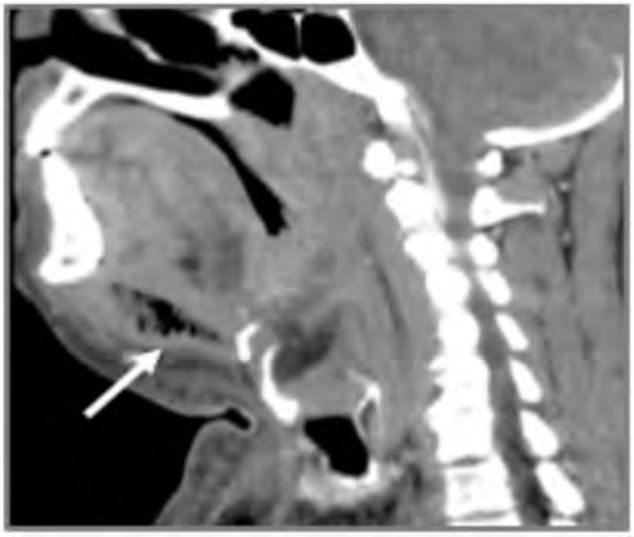
V Nguyen[1], B Tantiwongkosi[1]
[1]*University of Texas Health Science Center at San Antonio, San Antonio, TX*

Purpose
Imaging plays an important role in the work up of airway compromise. It is particularly useful in the emergency department where clinical history and physical examination may be limited or delayed until the exclusion or treatment of more life-threatening conditions. The purpose of this educational exhibit is to: 1. Review head and neck anatomy relevant to the airway; 2. Illustrate characteristic imaging features of each emergent entity with a systematic approach; and 3. Discuss the role of imaging modalities, diagnostic pearls and pitfalls relevant to diagnosis, treatment planning and outcome.
Materials and Methods
A retrospective review of airway emergent cases imaged over a 6-year period (2010-2016) at a tertiary referral center was performed with radiological and clinical correlation. The cases were classified by causes, location/compartments, unique imaging features, and imaging appearance of airway management and their complications.
Results
Based on a retrospective review of airway emergent cases imaged over a 6-year period (2010-2016) at a tertiary referral center, the following entities will be discussed: Causes: foreign bodies, infections (epiglottitis, croup, etc), tumors, angioedema, trauma, radiation

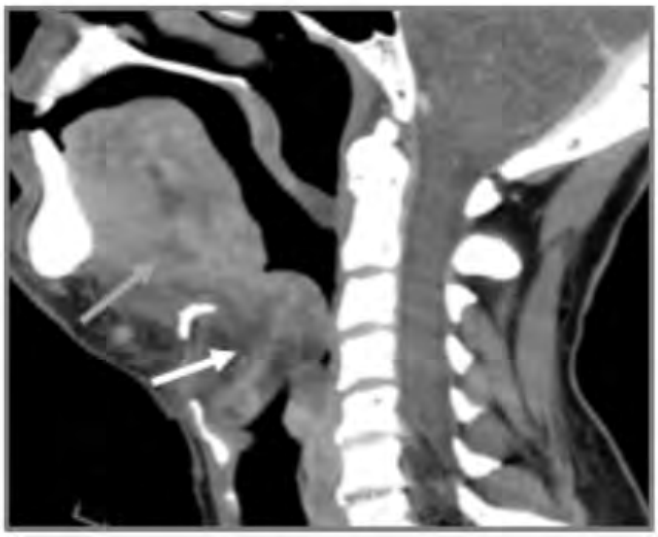
induced, vocal cord paralysis, etc. Compartments: Nose, oral cavity, pharynx, larynx, and trachea. Imaging appearance of airway management and their complications: ET tube, laryngeal mass, tracheostomy, laryngectomy, endoscopic laser, botox, filler injection, etc.

Conclusions

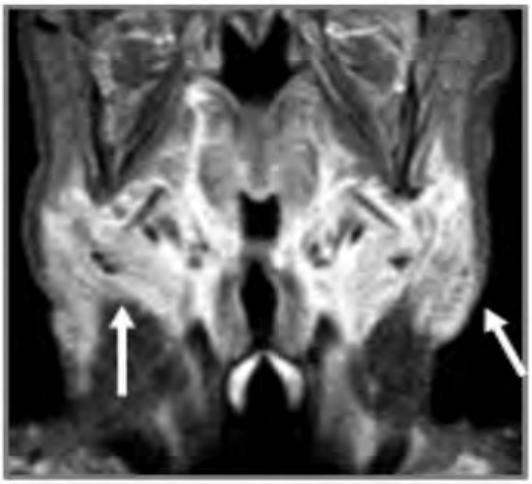
A systematic approach to evaluating airway compromise may assist the radiologist with identifying immediate threats and facilitate prompt clinical management. Recognition of the radiological spectrum of airway compromise also will assist the radiologist in making an accurate diagnosis.



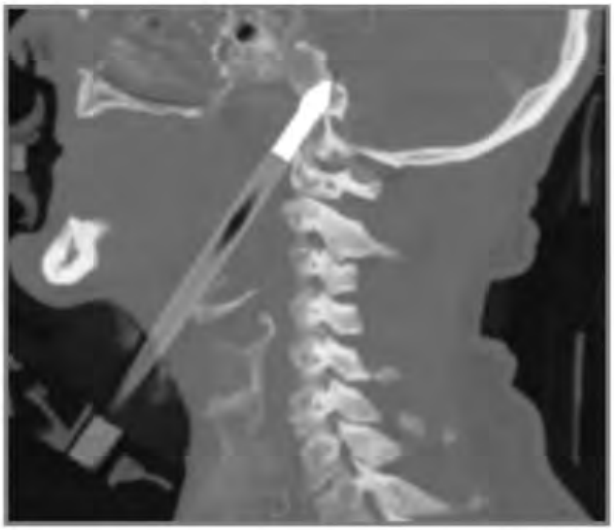
Ludwig's Angina with airway compromise



Epiglotitis with base of tongue abscess



Angioedema due to iodinated IV contrast



Arrow penetrating the pharynx & clivus

(Filename: TCT_eEdE-116_image.jpg)

eEdE-169

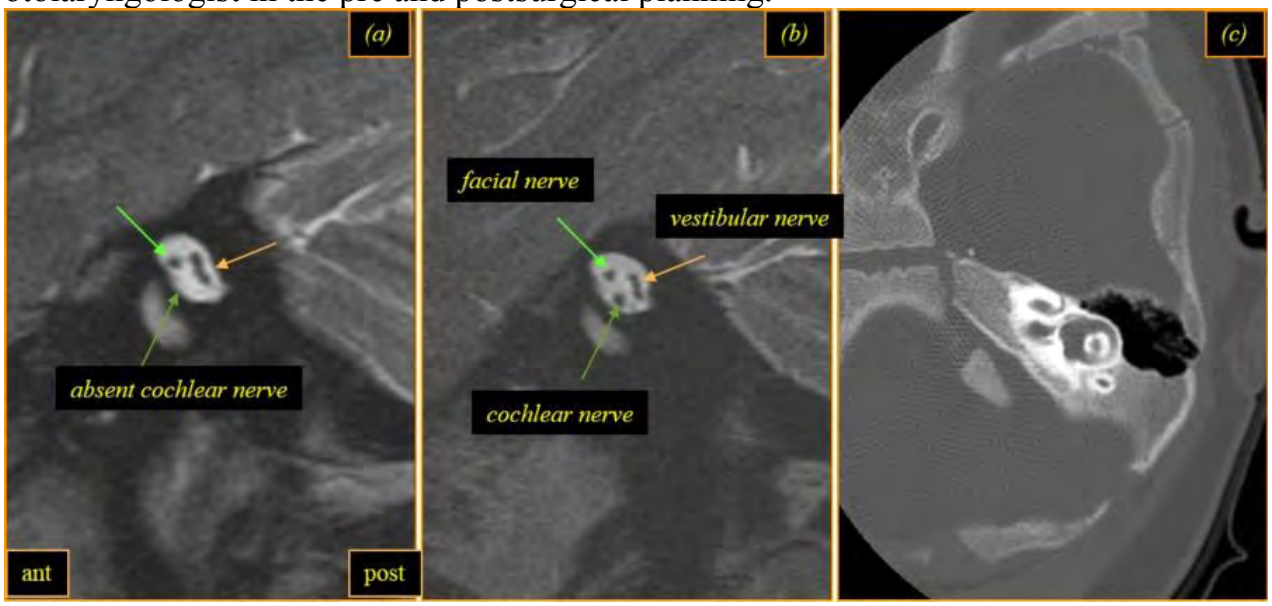
6:30AM - 3:00PM

Imaging of Cochlear Implants: Otolaryngologist Expectations from Neuroradiologist

S Kanekar[1], A Agarwal[1]
[1]*Hershey Medical Center, Hershey, PA*

Purpose
1. To discuss with illustrations the pre, intra and postoperative imaging findings in patient with cochlear implant. 2. To review with illustrations the important radiologic findings which influence the otolaryngologist's decision on the surgical approach. 3. To evaluate the postcochlear implant complications.
Materials and Methods
Hearing function depends on the anatomical and physiological function of the auditory pathway. Hearing loss may be acute or chronic which in turn may affect the linguistic and the communicative development, their cognitive process and subsequently the social integration, especially in children. Today various devices are available to improve the hearing loss. Main indication for use of such devices is patients with severe to profound sensorineural hearing loss in both ears who cannot benefit adequately from the use of hearing aids, having a functioning auditory nerve, without medical reason to avoid surgery and having a high motivation for rehabilitation. With the wider use of these devices it is important to understand the pre-, intra- and postoperative imaging findings. Retrospective review of the imaging studies of 53 patients with cochlear implant surgery for hearing loss forms the basis of this exhibit. All patients had presurgical MRI-IAC and CT temporal bone and 51 had follow-up CT scan of the temporal bone.
Results
Exhibit is presented in three parts, namely: (A) Pre-operative review of HRCT-T bone, and MRI-IAC; (B) Intra-operative assessment (assessment of implant placement) and (C) Postoperative follow up. (A) Pre-operative review includes: evaluation of the cochlear nerve, cochlear and vestibular malformations (cochlear aplasia/ hypoplasia common cavity); Anatomical variations and associated pathologies: Middle ear and mastoid cells (aeration of the mastoid and of the middle ear, mastoiditis); Vascular supply variants (prominent/dehiscent jugular bulb, aberrant carotid artery); cranial nerves (variants anomaly of the pathway of the VII nerve, facial nerve dehiscence, the size of the internal auditory meatus); Vestibular aqueduct and endo-lymphatic duct; Ossifying labyrinthitis and otosclerosis (C) Postoperative follow up: CSF fistula, facial nerve lesions, electrode malpositing; infection/meningitis bleeding, mastoiditis, migration of the electrode guide and extrusion of the receptor/stimulation.

Conclusions
1. Imaging plays an important role in the assessment of the cochlear implant especially in deciding the contraindication and the surgical approach depending on the anatomical and pathological variation within the temporal bone. With the wider use of the multiple hearing aid devices it is important for radiologist to become familiarized with imaging appearances and otolaryngologist expectations. Radiologist plays an important role in guiding the otolaryngologist in the pre and postsurgical planning.



(Filename: TCT_eEdE-169_Picture2.jpg)

eEdE-170

6:30AM - 3:00PM

Imaging of Labyrinth: Application of High Definition 3D CT and High Resolution MRI

P Devgun[1], A Agarwal[2], S Kanekar[3]
[1]Penn State Milton Hershey Medical Center, Hershey, PA, [2]Hershey Medical Center, Hershey, PA, [3]Penn State MiltonHershey Medical Center, Hershey, PA

Purpose
1) To discuss the normal anatomy of the labyrinth. 2) Discuss the technique and application of the high resolution 3D computed tomography (CT) and magnetic resonance imaging (MRI) in the imaging of inner ear. 3) To discuss with illustrations the imaging findings of the various pathologies involving the labyrinth.
Materials and Methods
The labyrinth is the important component of the sensorineural hearing pathway and part of the balancing apparatus. It consist of an osseous labyrinth that encloses the membranous labyrinth and hence the HRCT and higher resolution MRI are complimentary to each other in the imaging of this anatomical structure. Today with better definition of high resolution

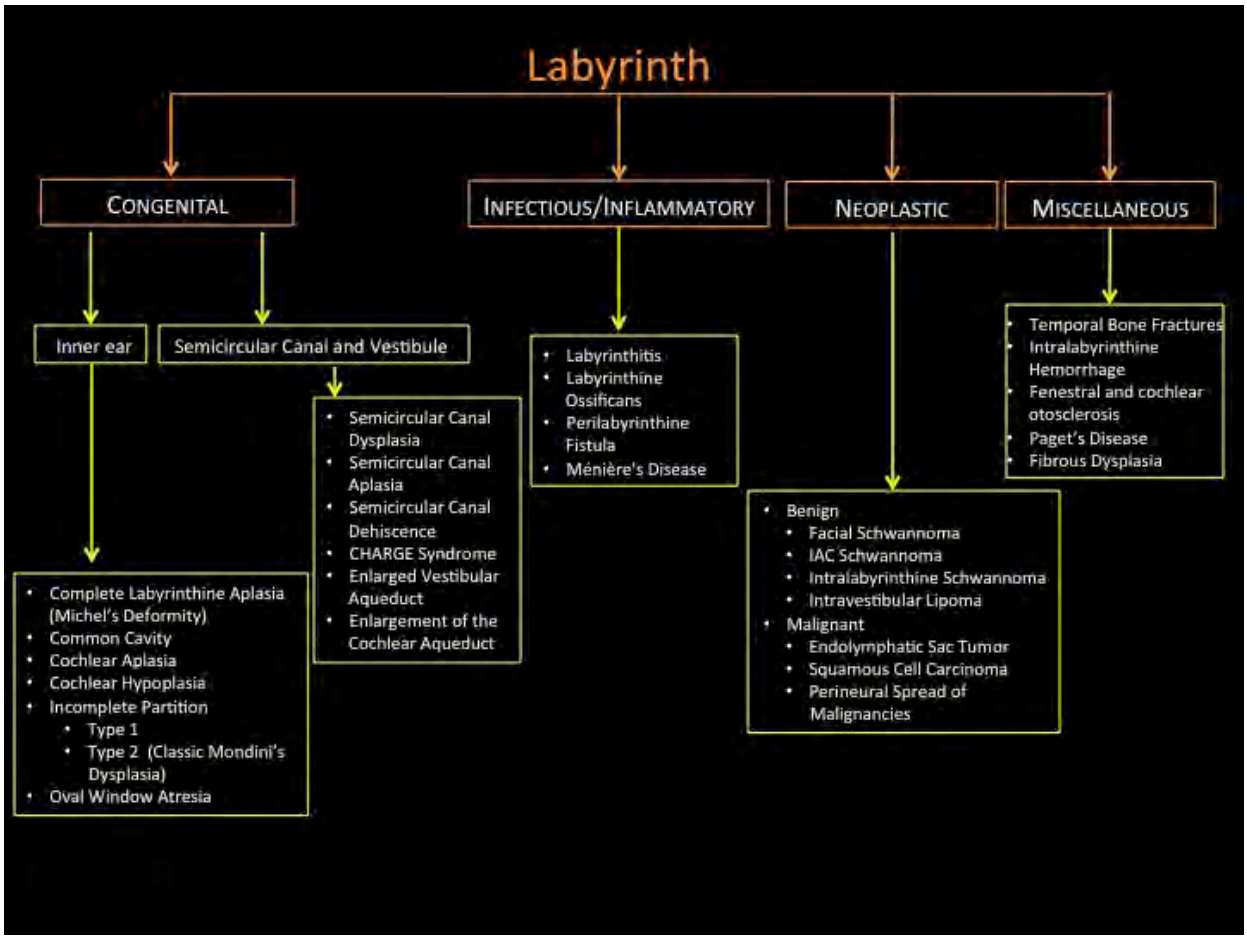
and 3D CT has significantly improved the finer structure details. High resolution MRI with dedicated surface coils and 3T magnet allows the excellent spatial resolution in differentiating the endolymphatic from perilymphatic contents. Retrospective review of imaging studies of 223 patients with acute and slowly progressing sensorineural hearing loss (SNHL), forms the basis of this exhibit. Appropriate cases were selected that illustrate the intended learning points, de-identified, and captured for the inclusion into this presentation. All patients had HRCT and high definition MRI IAC and brain stem protocol imaging with and without contrast. In addition 124 patients also had 3D reconstructed images of the inner ear, as per the requirement.

Results

The recognition of the complex anatomy and pathology of the inner ear can place the radiologist in a unique position in the diagnostic evaluation of common and uncommon inner ear abnormalities. For ease of understanding, this exhibit is reviewed under following categories: 1. Anatomy of the labyrinth. 2. Imaging techniques. 3. Pathologies of the labyrinth. Pathologies are subdivided into: (a) Congenital anomalies: Complete labyrinthine aplasia, Cochlear aplasia, Common cavity, Type I incomplete partition, Cochlear hypoplasia, Type II incomplete partition, Oval window atresia, Malformations of the vestibule and semicircular canals: Semicircular canal aplasia/dysplasia, CHARGE syndrome, Enlarged endolymphatic sac anomaly, Semicircular canal dehiscence (b) Infection and inflammation: Labyrinthitis, Labyrinthine ossificans, Ménière's disease, Perilabyrinthine fistula (c) Inner ear tumors: Schwannoma, Lipoma, Endolymphatic sac tumor, Squamous cell carcinoma, and Perineural spread of malignancies. (d) Miscellaneous: Temporal bone fractures, Labyrinthine hemorrhage, Fenestral and cochlear otosclerosis, Paget's disease, and Fibrous dysplasia.

Conclusions

Imaging plays an important role in defining the anatomy and in the diagnosis of the various inner ear pathologies. For participants, this exhibit will be a core learning module to understand the anatomy, imaging techniques, and an algorithmic approach in evaluation of common and uncommon inner ear abnormalities and their clinical significance.



(Filename: TCT_eEdE-170_Slide1.jpg)

eEdE-135

6:30AM - 3:00PM

Imaging Spectrum of IgG4-related Disease Effecting the Head and Neck

A Chaudhry[1], M Gul[2], A Chaudhry[3]
[1]Johns Hopkins Medicine, Elkridge, MD, [2]National Institute of Health, Elkridge, MD, [3]Stony Brook University, Westbury, NY

Purpose
We aim to present a case-based review series of IgG4-related disease involving the head and neck region.
Materials and Methods
1) Brief review of CT and MRI temporal bone anatomy.
2) Review clinicopathologic spectrum of IgG4related disease.
Discuss spectrum of imaging and pathologic findings in IgG4-related disease in the head and neck region.

4) Review mimics with emphasis on key findings differentiating these entities. 5) Treatment , prognosis and follow-up recommendations will be discussed.

Results

IgG4-related disease is a systemic inflammatory process with a spectrum of presentation depending on specific organ involvement. A significant proportion of patients have years of asymptomatic disease involvement until they present with signs of organ injury secondary to compressive mass lesions, frequently termed "pseudotumor." We will present a case-based series of IgG4-related disease involving the head and neck region highlighting key clinical and imaging features.

Conclusions

First recognized in the early 2000s for its presentation as a form of autoimmune pancreatitis, IgG4-related disease spectrum is now known that the disease can affect nearly every organ system. Involvement of the head and neck is still seldom reported in literature perhaps because affected patients are labeled as having an "inflammatory pseudotumor". Recognizing this presentation of IgG4-related disease is critical as early treatment allows for prompt patient cure and prevents complications such as vision loss, vestibular dysfunction, etc.



(Filename: TCT_eEdE-135_IgG4case.jpg)

eEdE-115

6:30AM - 3:00PM

Inadvertent Radiation Effects on Normal Tissues in Head and Neck Cancer Patients

E Lotan[1], B Conti[2], B Griffith[3], K Hu[4], M Persky[2], M Hagiwara[2], R Jain[5]

[1]NYU Langone Medical Center and Tel-Aviv University, New-York, NY, [2]NYU Langone Medical Center, New York, NY, [3]Henry Ford Health System, Detroit, MI, [4]NYU Langone Medical Center, New-York, NY, [5]NYU School of Medicine, New York, NY

Purpose

In patients with head and neck cancer post-treatment imaging can be challenging, because of the complexity of the postirradiation changes; however, such imaging is critical for post-treatment surveillance and for tumor control. The purpose of this study is to describe potential complications caused by irradiation in order to differentiate these findings from tumor recurrence.

Materials and Methods

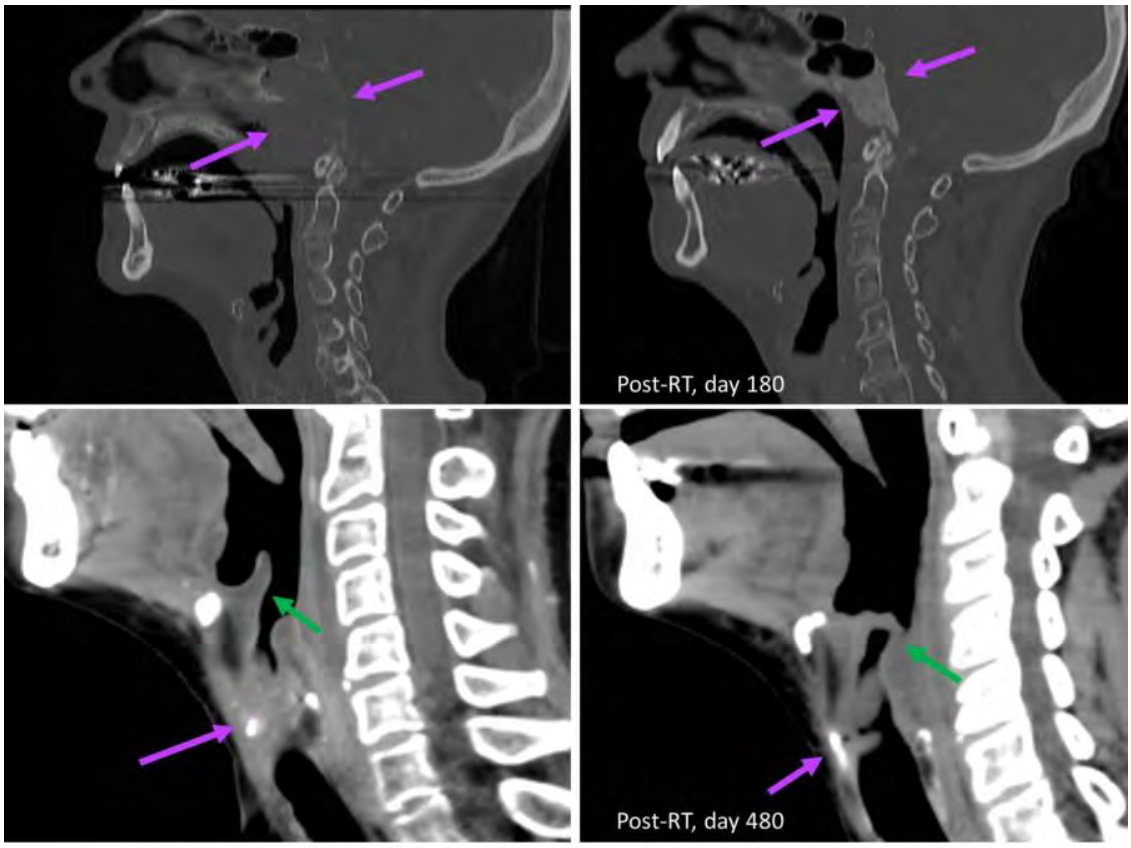
Imaging plays an important role in the early detection of recurrence, to allow early intervention of salvage treatment. CT, MRI and PET are the cornerstone imaging modalities for tumor follow up and the differentiation of recurrence versus postirradiation changes, which commonly are divided into early and late complications. Early complications are observed during the course of radiation therapy or within 90 days after treatment and are reversible in most cases after completion of radiation therapy. Late complications, defined as effects of treatment that manifest more than 90 days after the completion of radiation therapy, may take months to years to emerge, and often are irreversible. They can affect the mucosal surfaces and salivary glands, bones and cartilage, vascular structures, nervous system and reconstruction flaps.

Results

Potential postirradiation complications include mucosal necrosis, osteoradionecrosis, chondronecrosis, radiation-induced vasculopathy, radiation-induced optic neuropathy, radiation-induced plexopathy, radiation-induced labyrinthitis, radiation-induced fibrosis, radiation-induced lung disease, radiation-induced brain necrosis, and radiation-induced secondary malignancies. The severity and duration of these radiation complications are related to the irradiation technique, the total cumulative dose, and the field size of irradiated structures, and may be exacerbated by smoking and alcohol consumption habits and the inherent radiosensitivity of the patient.

Conclusions

Normal tissues of patients with head and neck cancer frequently are affected by irradiation therapy. A familiarity with the imaging characteristics of postirradiation potential complications and an ability to differentiate these findings from tumor recurrence are essential for post-treatment surveillance and follow-up management, and help to avoid unnecessary further diagnostic work up.



(Filename: TCT_eEdE-115_Osteonecrosis_300dpi.jpg)

eEdE-144

6:30AM - 3:00PM

Invasion and Distortion of Tongue Muscles in Oral Cavity Cancer

J Acevedo[1], M McDonald[2], J Bykowski[2]
[1]University of California, San Diego, San Diego, CA, [2]University of California at San Diego, San Diego, CA

Purpose
Identification of the depth of invasion and any involvement of extrinsic tongue muscles are important features in the imaging evaluation of oral cavity squamous cell carcinoma; however evaluation can be degraded due to dental artifact. This educational exhibit reviews the anatomy and function of the intrinsic and extrinsic tongue muscles, risk factors for local lymphatic spread, limitations and alternatives for CT and MR imaging, illustrative cases of distortion and invasion of the tongue muscles, and implications for operative planning and reconstruction.
Materials and Methods
A review of the institutional imaging database and electronic medical record was performed at a NCI Designated Comprehensive Cancer Center to identify recent cases of patients with

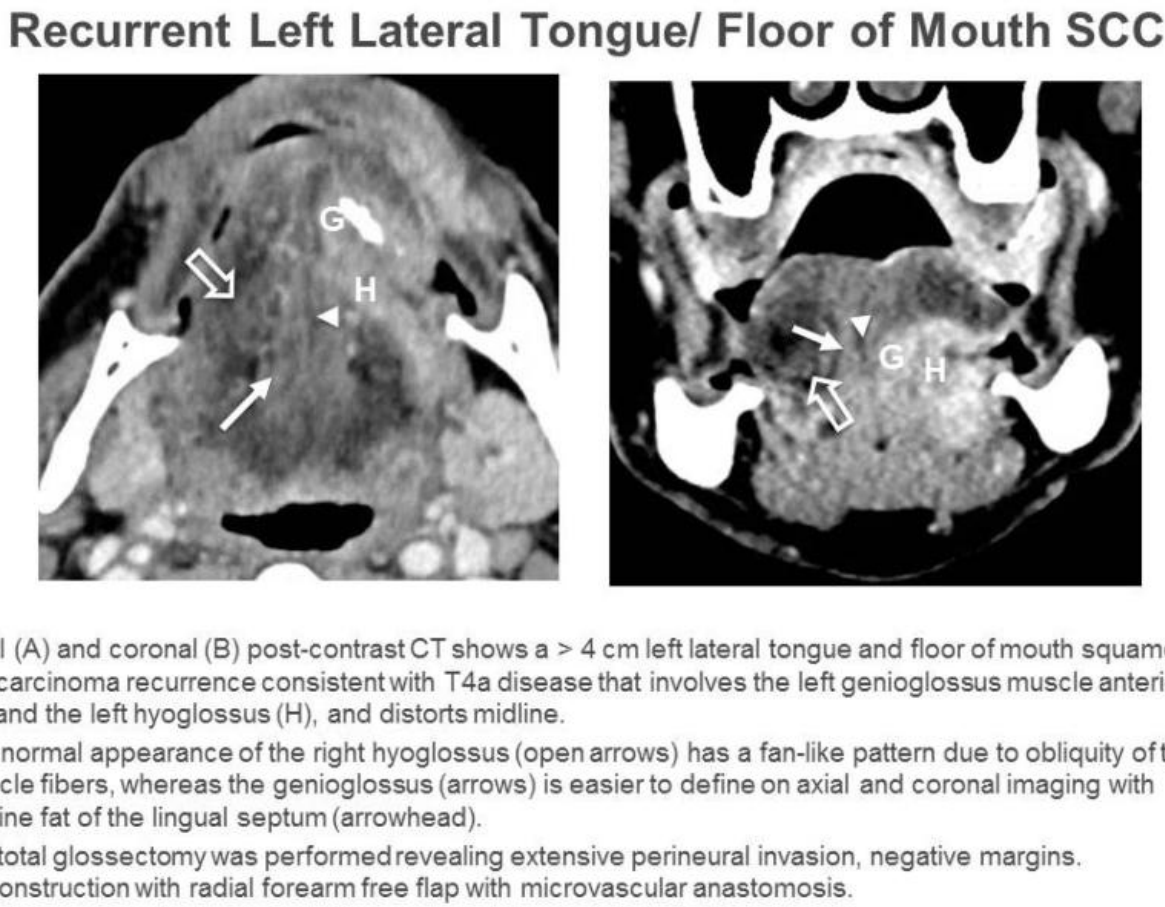
oral cavity squamous cell cancer. Illustrative cases are used to define superficial versus deeply invading masses, and examples of sparing, displacement/distortion, and invasion of the extrinsic tongue muscles on multiplanar CT and MR imaging, as well as issues regarding appropriate imaging and technique. Imaging findings are correlated with the resection and reconstruction performed, pathologic margins and ultimate staging.

Results

By the end of this educational exhibit the attendee will be able to: 1. Describe the normal appearance and function of the 4 intrinsic vs 4 extrinsic tongue muscles on CT and MR imaging in multiple planes. 2. Identify features of extrinsic muscle invasion on CT and MR imaging. 3. Detail the implications of depth of invasion and extrinsic tongue muscle involvement on tumor staging and implications for surgical treatment and reconstruction. 4. Consolidate knowledge via a brief self-assessment quiz.

Conclusions

Accurate characterization of the extent of tumor involvement of the extrinsic muscles and the depth of tongue invasion are key features of tumor staging and risk of regional nodal metastasis. Evaluation should not be deferred due to artifact in the oral cavity.



Axial (A) and coronal (B) post-contrast CT shows a > 4 cm left lateral tongue and floor of mouth squamous cell carcinoma recurrence consistent with T4a disease that involves the left genioglossus muscle anteriorly (G) and the left hyoglossus (H), and distorts midline.

The normal appearance of the right hyoglossus (open arrows) has a fan-like pattern due to obliquity of the muscle fibers, whereas the genioglossus (arrows) is easier to define on axial and coronal imaging with midline fat of the lingual septum (arrowhead).

Subtotal glossectomy was performed revealing extensive perineural invasion, negative margins. Reconstruction with radial forearm free flap with microvascular anastomosis.

(Filename: TCT_eEdE-144_ASNRabstractTongueinvasion2.jpg)

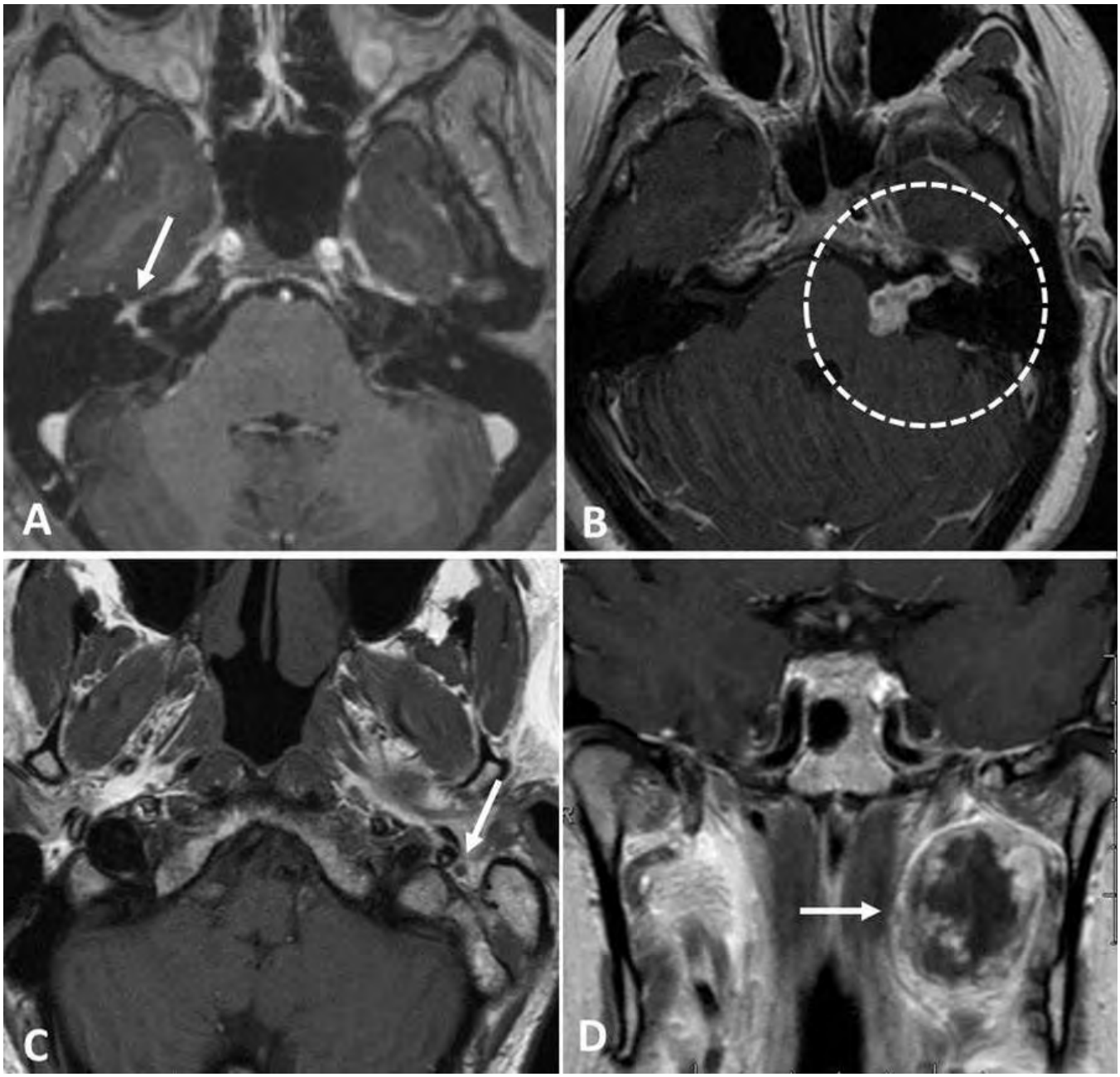
eEdE-172

6:30AM - 3:00PM

Just Face It, We Could All Use a (Pictorial) Review: Anatomy, Variants, and Pathology of the Facial Nerve

T Capobres[1], J Corrigan[1], H Marin[1], S Patel[1], B Griffith[1]
[1]*Henry Ford Health System, Detroit, MI*

Purpose
Imaging plays a central role in the work up of patients presenting with suspected facial nerve pathology. Imaging evaluation, however, can be quite challenging due to the complex anatomy and function of the facial nerve, as well as the diversity of pathology affecting it. The purpose of this exhibit is to provide a pictorial review of the normal anatomy, function, and imaging appearance of the facial nerve, as well as review the numerous pathologic processes affecting it with emphasis on key differentiating imaging features.
Materials and Methods
• Using representative case files, we will review the anatomy of the facial nerve on both computed tomography (CT) and magnetic resonance imaging (MRI) focusing on its course and imaging appearance. Facial nerve branches and vascular anatomy also will be reviewed.
• We will review a broad spectrum of facial nerve pathology, including: Bell's palsy (Fig. 1A), Herpes zoster oticus/Ramsay Hunt; facial nerve schwannoma (Fig. 1B); leptomeningeal and perineural spread of tumor (Fig. 1C, D); geniculate ganglion pathology including ossifying hemangioma/venous malformation, meningioma, and diverticulum; temporal bone fracture, direct laceration; and pitfalls such as exophytic IAC glioma and persistent stapedial artery. Key imaging features of each entity will be emphasized.
Results
Understanding the normal anatomy and appearance of the facial nerve on imaging is key to recognizing and evaluating pathologic processes involving it. This exhibit will use a case-based approach to provide a succinct yet comprehensive review of these concepts.
Conclusions
From a clinical perspective, facial nerve pathology often can be identified due to impaired function. However, from an imaging perspective, the causative abnormalities can be more subtle, necessitating a detailed understanding of the normal facial nerve anatomy and appearance to appropriately assess. This exhibit offers a pictorial review of the anatomy, function and pathology of the facial nerve, which are key concepts for any neuroradiologist or radiology trainee.



(Filename: TCT_eEdE-172_FinalFacialNerve.jpg)

eEdE-163

6:30AM - 3:00PM

Magnetic Resonance Imaging (MRI) of the Pituitary Gland: Pathology and Spectrum; Common and Uncommon Findings with Pitfalls

C Dixon[1], A Wang[2], R Silbergleit[1], K Tech[3], A Krishnan[4], K Barry[5], J FOX[6]
[1]William Beaumont Hospital, Royal Oak, MI, [2]Beaumont Health System, Royal Oak, MI, [3]Beaumont Health - Royal Oak, Royal Oak, MI, [4]Beaumont Health, Royal Oak, Royal

oak, MI, [5]Beaumont Heatlh System, Royal Oak, MI, [6]Beaumont Health System, ROYAL OAK, MI

Purpose

To present magnetic resonance imaging (MRI) findings of common and uncommon pituitary gland pathology; some of which are mistakenly diagnosed as abnormal but are normal within certain patient populations.

Materials and Methods

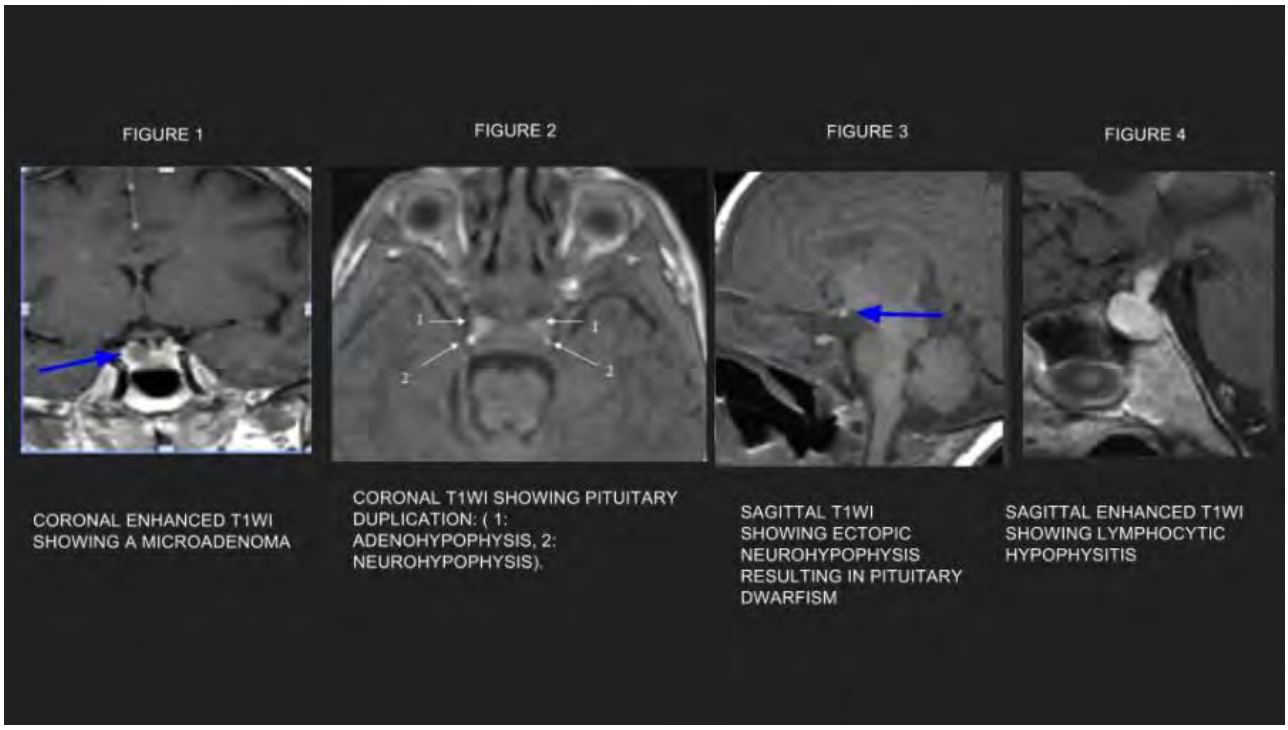
This was a retrospective review of abnormal pituitary gland MRI exams at our institution obtained within the past ten years. Images were obtained on either a 1.5 or 3.0 Telsa MRI unit. The following sequences were obtained; Axial T2WI, coronal and sagittal T1W with and without gadolinium, and dynamic postcontrast images were obtained in select cases.

Results

Multiplanar MRI is the exam of choice for evaluation of the sellar region; specifically the pituitary gland for potential abnormalities. We are presenting the MR imaging findings of pituitary gland abnormalities as correlated with clinical history, pathology if available, and literature review. Cases include common diseases such as pituitary microadenoma, macroadenoma (Figure 1), craniopharyngioma, Rathke's cleft cyst, empty sella, and arachnoid cyst. We also will highlight less commonly seen diseases, such as congenital anomalies, pituitary duplication (Figure 2), and pituitary dwarfism (Figure 3); inflammatory/granulomatous diseases, such as sarcoidosis and lymphocytic hypophysitis (Figure 4); pituitary apoplexy; langerhans cell histiocytosis and metastasis. We also will show cases of temporary enlargement of the pituitary gland, which may mistakenly lead to the diagnosis of pituitary gland tumor. We will briefly discuss technical pitfalls in imaging of the pituitary gland, which can result in abnormal studies being misread as normal.

Conclusions

It is very important to be familiar with the multitude of imaging findings that may be visualized within the pituitary gland and have a grasp of normal imaging findings in order to detect potential abnormalities. Unfamiliarity unfortunately can lead to misdiagnosis and/or delayed diagnosis. This poster will serve as a source of common and uncommon pituitary gland findings with the hope of increasing the interpreters comfort level when assessing the pituitary gland for pathology.



(Filename: TCT_eEdE-163_PIT.jpg)

eEdE-162

6:30AM - 3:00PM

Masses, Malignancy and Mimics in the Masticator Space

J Acevedo[1], M McDonald[2], J Bykowski[2]
[1]University of California, San Diego, San Diego, CA, [2]University of California at San Diego, San Diego, CA

Purpose
The masticator space can be distorted by benign masses, malignant spread of tumor or mass effect from processes in the adjacent parapharyngeal space, paranasal sinuses, and skull base, or have an altered appearance due to post-treatment edema and denervation atrophy. This exhibit uses computed tomography (CT), magnetic resonance imaging (MRI) and positron emission tomography (PET) images to illustrate common and unusual processes of the masticator space to emphasize a structured search pattern and implications for treatment planning.
Materials and Methods
A review of our institutional imaging database and electronic medical record was performed to identify recent cases of patients with benign and malignant processes centered in or involving the masticator space. When available, serial imaging inclusive of the initial presentation and post-treatment surveillance is included. Illustrative cases are used to highlight the regional anatomy, issues regarding appropriate imaging and technique,

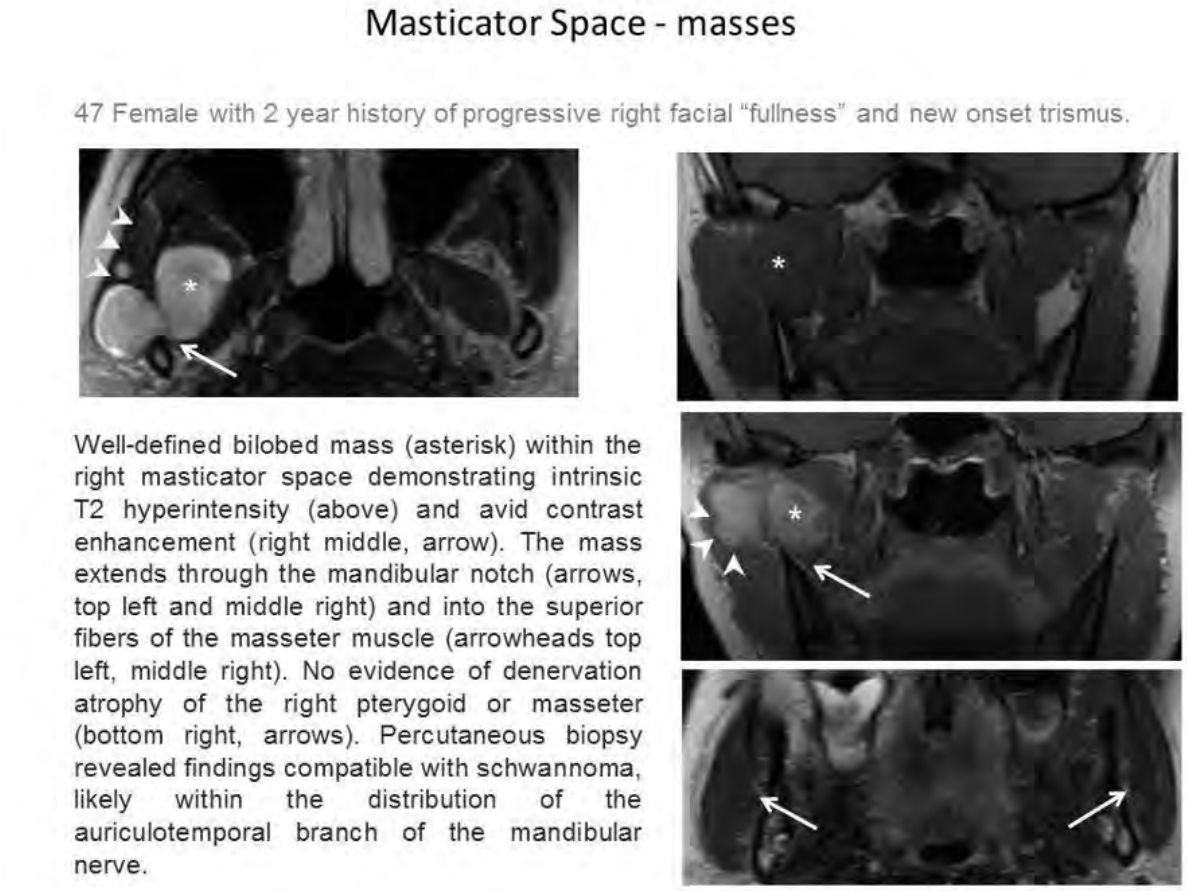
implications of contrast bolus timing, and the importance of margin assessment for treatment planning.

Results

By the end of this educational exhibit the attendee will be able to: 1. Describe the normal contents and boundaries of the masticator space. 2. Identify benign masses and space-occupying processes of the masticator space such as: schwannoma, neurofibroma, hemangioma, abscess, venolymphatic malformation, engorged pterygoid venous plexus. 3. Detail features of primary malignancy (rhabdomyosarcoma, malignant PNST, perineural spread) versus post-treatment changes (edema and muscle atrophy) and local recurrence. 4. Differentiate above processes from mass effect due to large masses of the pre-styloid parapharyngeal space (minor salivary tumors), carotid space (schwannoma), mucosa (nasopharyngeal squamous cell carcinoma), temporomandibular joint (PVNS), intracranial space/skull base (perineural extension, intra-extracranial meningioma, gliosarcoma). 5. Consolidate knowledge via a brief self-assessment quiz.

Conclusions

Knowledge of the contents and common processes of the masticator space is crucial to avoid misdiagnosis of processes given the relative inaccessibility of this space for pre-operative sampling and implications for treatment planning.



(Filename: TCT_eEdE-162_DocumentsMasticatorSpace3.jpg)

eEdE-140

6:30AM - 3:00PM

MR imaging of Soft Tissue Vascular Anomalies in the Head and Neck in Children: An Update with 2014 ISSVA Classification

E Snyder[1], K Puttgen[2], M Pearl[2], S Mitchell[3], A Tekes[1]
[1]Johns Hopkins University, Baltimore, MD, [2]Johns Hopkins University School of Medicine, Baltimore, MD, [3]Johns Hopkins Hospital, Baltimore, MD

Purpose
Vascular anomalies comprise both vascular tumors and vascular malformations, which are found most commonly in the head and neck. Accurate identification of these anomalies is important for proper clinical evaluation and management, particularly since these patients often require multidisciplinary care. The International Society for the Study of Vascular Anomalies (ISSVA) classification, recently updated in 2014, is widely accepted and offers comprehensive classification for all medical subspecialties involved in the care of these complex anomalies, thus providing common language among caregivers. The purpose of this educational exhibit is to highlight the most important MRI and MRA imaging findings in order to identify these lesions according to the 2014 ISSVA classification.
Materials and Methods
Conventional contrast-enhanced MRI and dynamic time-resolved MRA are vital to establishing the correct diagnosis in children with vascular anomalies. In this review article, we present a state-of-the-art MRI imaging protocol with exemplary cases of vascular anomalies in the head and neck, using the updated 2014 ISSVA classification. Clinical pictures, conventional arteriogram/venogram and genetic correlation will be presented as it relates to the particular anomaly presented.
Results
We provide the updated 2014 ISSVA classification system, which delineates vascular anomalies into vascular tumors and vascular malformations, and those that are associated with other anomalies. Cases will highlight vascular tumors including infantile and congenital hemangiomas and vascular anomalies including lymphatic, venous and arteriovenous malformations focusing on infiltration pattern, the presence of a solid or cystic mass, contrast enhancement pattern and hemodynamic characteristics. We also include examples of syndromes associated with vascular anomalies including PHACES syndrome.
Conclusions
In this exhibit we will address the most critical conventional contrast-enhanced MRI and dynamic MRA features of vascular anomalies in the head and neck in children following 2014 ISSVA classification. Multidisciplinary approach is crucial for these patients, thus using a common language as offered by ISSVA is essential to avoid miscommunication, misdiagnosis and delayed or inappropriate treatment.

eEdE-113

6:30AM - 3:00PM

Multimodality Approach to Neoplastic Involvement of Superficial Head and Neck Lymph Lymphatic System

R Assadsangabi[1], Y Chen[2], D Pechersky[3], L Loevner[4], A Nabavizadeh[1]
[1]University of Pennsylvania, Philadelphia, PA, [2]University of Pennsylvania Perelman School of Medicine, Philadelphia, PA, [3]Northwestern Memorial Hospital, chicago, IL, [4]University of Pennsylvania, Philadelphia , PA

Purpose
Unlike deep cervical lymph nodes which are well known to both radiologists and clinicians and are uniformly described by a well-recognized nodal classification system, superficial head and neck lymph nodes are less familiar. The purpose of this exhibit is to illustrate these nodal groups on imaging and illustrate associated malignancies.
Materials and Methods
Superficial head and neck lymph nodes include those in the sub-occipital, parotid, mastoid, pre-auricular, infra-orbital, malar, mandibular, buccinator, and external jugular vein locations. Imaging findings will be demonstrated on multiple imaging modalities including CT, MRI, PET, and ultrasound.
Results
Multiple patients with pathologic superficial head and neck lymph nodes will be illustrated in this educational exhibit. These cases fall into three major categories: 1) Superficial head and neck lymph nodes associated with primary head and neck squamous cell carcinoma most often in the oral cavity and sinonasal cavity; 2) Superficial head and neck lymph nodes in the setting of lymphoma; and 3) Superficial head and neck lymph nodes associated with primary skin malignancies.
Conclusions
Superficial head and neck lymph nodes often are overlooked in the clinical setting and in radiologic evaluations/reports. Familiarity with these important nodal groups and their typical drainage pathways will aid radiologists and clinicians in their detection.

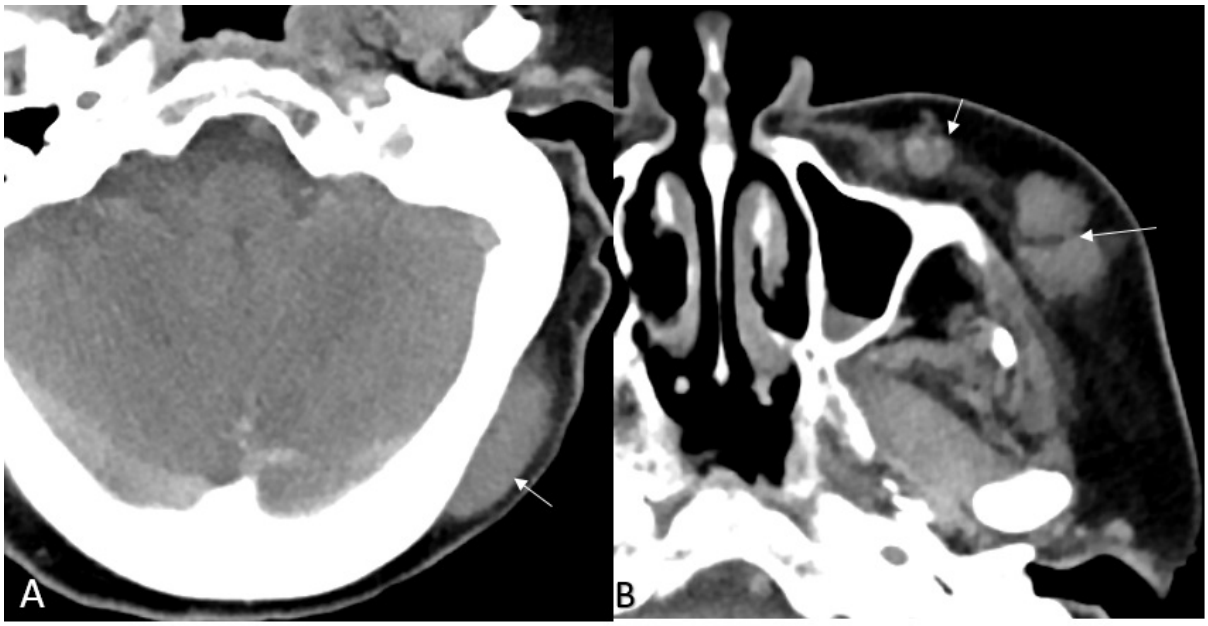


Figure 1.74 year old female with diffuse B-cell lymphoma involving left suboccipital (A, arrow), left malar (B, long arrow) and left infraorbital (B, short arrow) group of lymph nodes.

(Filename: TCT_eEdE-113_Lymphnodesfacefinalfigure.jpg)

eEdE-126

6:30AM - 3:00PM

Neck Imaging Reporting and Data System: An Atlas of NI-RADS Categories for Head and Neck Cancer

B Cavazuti[1], P Hudgins[1], T Rath[2], K Baugnon[1], A Corey[1], A Aiken[1]
[1]Emory University, Atlanta, GA, [2]University of Pittsburgh Medical Center, Pittsburgh, PA

Purpose
The recently published NI-RADS (Head and Neck Imaging and Reporting Data System) surveillance template for head and neck (H&N) cancer includes a numerical assessment of suspicion for recurrence (1-4) for the primary site and neck with linked management recommendations. We aim to create an imaging atlas of examples of NI-RADS categories 1 through 4 for both the primary site and the neck in a number of different subsites of head and neck cancer.
Materials and Methods
A case-based presentation will provide imaging examples of the NI-RADS categories 1 through 4 for the subsites of H&N cancer. We will illustrate the imaging features most useful in determining the correct category and introduce readers to a lexicon of useful descriptors to use in their reports. By demonstrating the findings associated with each category, we hope to

empower radiologists less comfortable with head and neck imaging to utilize this system as a means of effective communication with their referring clinicians.

Results

NI-RADS was introduced as a novel surveillance tool for H&N cancer with the aim to reduce interobserver variability, improve performance and report comprehension, and standardize management recommendations and surveillance protocols through data-driven optimization of H&N cancer imaging. • At our institution, the first follow-up study following H&N cancer treatment is a 12-week post-treatment PET/contrast-enhanced CT (CECT). While this is our preferred algorithm, not every patient receives the PET portion, thus NI-RADS can be used with or without the 18F-fluorodeoxyglucose (FDG) findings. • Category 1: No evidence of recurrence. • Category 2: Low suspicion of recurrence, defined as ill-defined areas of abnormality with only mild differential enhancement and/or mild/moderate FDG uptake. The linked management recommendation is direct inspection for mucosal abnormalities or short interval follow up with CECT or an additional PET. • Category 3: High suspicion of recurrence, defined as discrete, new, or enlarging lesions with marked enhancement and/or intense focal 18F-FDG uptake. The linked recommendation is biopsy. • Category 4: Known recurrence, defined as pathologically proven or definite radiologic or clinical progression. The NI-RADS categories 1-4 are the same for CECT or CECT/PET. However, there are separate surveillance legends for CECT alone and CECT /PET as the linked management recommendations and lexicon are slightly different (as FDG avidity is included in the latter).

Conclusions

Our atlas provides imaging examples of the NI-RADS categories 1 through 4 for both the primary site and the nodes for the different subsites of H&N cancer. This imaging atlas also outlines and provides examples of the specific imaging findings differentiating each category. We hope to familiarize radiologists with the NI-RADS system and its value in guiding everyday practice.

Table 1. NI-RADS Category descriptors, imaging features, and management

Category	Descriptor & Risk	Classification	Imaging findings	Management
No evidence of recurrence	*Low risk* with benign appearance or behavior	1	- Expected post-treatment changes - Non mass-like distortion of soft tissues - No abnormal FDG uptake	Routine surveillance
Low suspicion	*Intermediate risk* finding for which short term follow up or additional testing is recommended	2a	- Focal superficial/muscoal differential enhancement - Focal mucosal FDG uptake	Direct visual inspection
		2b	- Deep ill-defined soft tissue - Borderline FDG uptake	Short interval follow up; repeat PET
High suspicion/definite recurrent	*High risk* findings for which tissue sampling is recommended	3	- New or definitely enlarging primary mass or lymph node - Discrete nodule/mass with differential enhancement - Intense focal FDG uptake	Image guided biopsy or clinical biopsy if clinically needed
Known recurrence	Biopsy proven recurrence or clinical progression	4	- Soft tissue mass at primary site with FDG uptake	Clinical management

(Filename: TCT_eEdE-126_Table1.jpg)

eEdE-165

6:30AM - 3:00PM

Non-Traumatic Facial Swelling: A Pictorial Review of Common and Uncommon Causes

C Chan[1], S Yoon[1], J Rodulfa[1], J Li[2], B Devenney-Cakir[1]
[1]Einstein Medical Center, Philadelphia, PA, [2]Einstein Healthcare Network, Philadelphia, PA

Purpose

Nontraumatic facial swelling is a common complaint that often leads to cross-sectional imaging of the head and neck. Underlying causes for nontraumatic facial swelling encompass a broad spectrum of etiologies and range from benign etiologies such as brachial cleft cysts to more life-threatening causes which demand prompt attention, such as angioedema. Therefore, familiarity with the myriad of head and neck pathologies and a systematic approach to evaluate for the cause is important to the radiologist. Early recognition of the underlying pathology will improve patient care. We present a wide variety of head and neck pathologies with the initial clinical presentation of nontraumatic facial swelling.

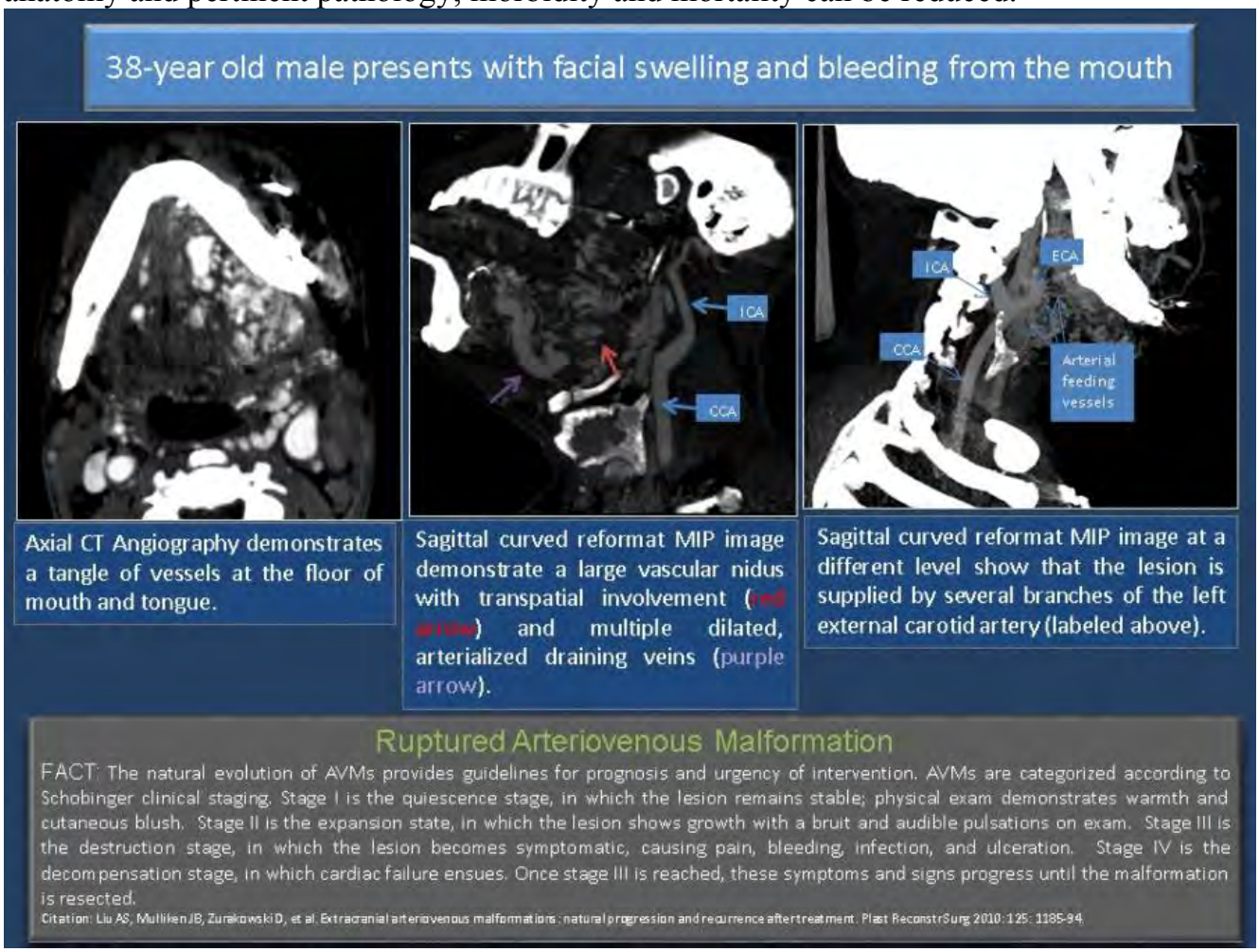
Materials and Methods

A retrospective, pictorial review of a wide variety of imaging findings of facial swelling at our institution will be presented. Cases will be organized by level of acuity and subcategorized by etiologies, including infection, vascular, iatrogenic, inflammatory and neoplastic. Multiple modalities will be presented, with emphasis on computed tomography (CT) and magnetic resonance imaging (MRI).

Results

Our exhibit includes a wide spectrum of head and neck causes of facial swelling and will be presented by level of acuity. Acute causes that will be presented are largely infectious etiologies, such as orbital cellulitis and subperiosteal abscess of odontogenic origin, sialoadenitis, Pott's puffy tumor, septic arthritis of the temporomandibular joint, folliculitis, and Ludwig's angina associated with dental infection. Other acute causes of facial swelling that also will be included are vascular etiologies ranging from a ruptured large arteriovenous malformation of the floor of the mouth and neck, inflammatory etiologies such as angioedema, and iatrogenic causes such as postoperative hematomas. Causes of gradual progressive facial swelling will include inflammatory etiologies such as Graves' orbitopathy and orbital pseudotumor, vascular tumors including lymphatic and vascular malformations and hemangiomas, developmental causes such as nasolabial cysts, osseous lesions such as fibrous dysplasia, neoplasms such as neurofibromas, and slow growing malignancies such as esthesioneuroblastoma. Cases of nonprogressive swelling are usually of congenital or development causes and will include congenital causes such as frontoethmoidal cephaloceles, nasal gliomas, and nasal dermoid/epidermoid cysts, brachial cleft cysts, and plunging ranulas. Lastly, cases of rapidly progressive facial swelling, are usually caused by malignancy, especially if there is an associated cranial nerve deficit, and include lymphoma, Langerhans cell histiocytosis, and osteosarcoma.

Conclusions
Head and neck causes of nontraumatic facial swelling encompass a wide spectrum of pathology. With prompt and accurate diagnosis via recognition and understanding of anatomy and pertinent pathology, morbidity and mortality can be reduced.



(Filename: TCT_eEdE-165_facialswelling.jpg)

eEdE-155

6:30AM - 3:00PM

Normal and Pathological Appearances of the Hypoglossal Nerve: A Pictorial Review

A Madhavan[1], R Siripurapu[2], A Herwadkar[2]
[1]Salford Royal NHS Foundation Trust, Manchester, United Kingdom, [2]Salford Royal NHS Foundation Trust & Greater Manchester Neurosciences Centre, Manchester, United Kingdom

Purpose
To demonstrate the normal anatomical course of the hypoglossal nerve (cranial nerve XII)

and review the imaging appearances of the various pathological processes which can affect it.
Materials and Methods
We present a detailed pictorial review describing the segmental anatomy of the hypoglossal nerve from the medulla oblongata to the tongue. We also will discuss the diverse pathological conditions that can affect each segment and correlate the imaging manifestations.
Results
Solitary disease of the hypoglossal nerve is rare but has unique presenting features. Sound understanding of its anatomy is essential to localizing the pathology and correlating the clinical and radiological manifestations to determine the diagnosis. The hypoglossal nerve innervates the intrinsic and extrinsic muscles of the tongue. It has five divisions as it courses from the medulla oblongata to the tongue: the medullary segment, cisternal segment, skull base segment, nasopharyngeal/oropharyngeal carotid space segment and the sublingual segment. Having a methodical approach to reviewing each segment is vital in identifying the specific underlying pathology. Examples of conditions affecting the hypoglossal nerve include glioma, infarction, aneurysm, glomus tumor, metastasis and infection.
Conclusions
In this educational exhibit, we provide an informative review of the imaging anatomy and the spectrum of pathological conditions affecting the hypoglossal nerve.

eEdE-139

6:30AM - 3:00PM

Orbital Cellulitis Classification and Complications

C Lincoln[1], K Wang[1], N Nguyen[1], S Mukhi[2], T Uribe[1]
[1]Baylor College of Medicine, Houston, TX, [2]Michael E. DeBakey VA Medical Center, Houston, TX

Purpose
Orbital cellulitis requires prompt diagnosis and treatment due to potentially permanent, debilitating effects on vision as well as grave intracranial complications. Imaging is most helpful in cases of atypical presentations or when symptoms worsen inferring a more ominous complication. A collaborative approach among surgery, medicine, and radiology practitioners allows prompt diagnosis and subsequent treatment that may prevent significant patient morbidity and mortality. This exhibit seeks to provide the imaging findings, classification, and spectrum of complications of orbital cellulitis.
Materials and Methods
The imaging findings and complications associated with orbital cellulitis in pursuance of the best management of the patient is reviewed in this exhibit. These topics will be elucidated through illustrative examples.

Results
Chandler et al revised the first classification system introduced by Smith and Spencer for orbital inflammation (1, 2). Revised classification now encompass 5 discrete groups, not necessarily representing different stages of the same disease process. The groups are: preseptal cellulitis, orbital cellulitis, subperiosteal abscess, diffuse orbital abscess and cavernous sinus thrombosis. Imaging findings related to more complex processes of cellulitis including subperiosteal abscess, cavernous sinus thrombosis and additional complications such as meningitis, intracranial abscess, cerebritis, and cavernous internal carotid artery pseudoaneurysm are crucial to be aware of in order to assist in the multidisciplinary management of orbital cellulitis.
Conclusions
The radiologist should be aware of the revised classifications and appropriate use of specific verbiage when communicating findings of orbital cellulitis and its complications to ensure the gravity and implications of such findings are conveyed effectively to ensure prompt, appropriate patient management.

eEdE-131

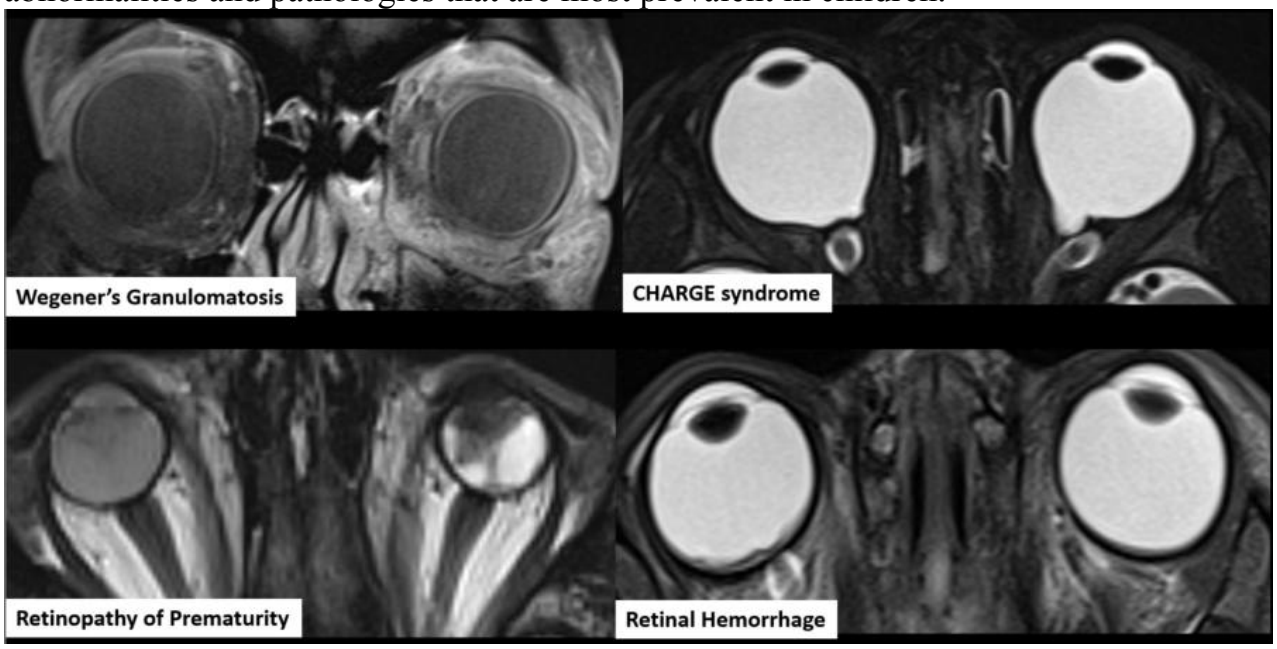
6:30AM - 3:00PM

Orbital Pathology in Pediatric Patients: Looking Beyond Orbital Tumors

S Curran-Melendez[1], J Vaughn[2], K Mullen[1]
[1]Brigham and Women's Hospital, Boston, MA, [2]Boston Children's Hospital, Boston, MA

Purpose
To illustrate the imaging features of pediatric orbital pathology with a focus on nontumorous lesions.
Materials and Methods
We reviewed orbital pathology cases presenting to our institution, with particular focus on the MR imaging characteristics of nontumorous orbital lesions and disease processes. Evaluated etiologies include inflammatory diseases, infection, trauma, acquired and congenital abnormalities of the orbits, globes, lacrimal glands and extra-ocular muscles.
Results
The presentation provides a targeted review of orbital anatomy and optimization of imaging technique of the orbital contents, followed by a case-based review of orbital pathology primarily found in pediatric patients. Discussion is focused on imaging findings and underlying mechanisms, with cases including acquired abnormalities (Coats' disease, persistent hyperplastic primary vitreous, retinopathy of prematurity, papilledema), congenital abnormalities (Duane's retraction syndrome, congenital fibrosis of the extra-ocular muscles, septo-optic dysplasia, staphyloma), infections (chororetinitis, orbital cellulitis, subperiosteal abscess, dacryoadenitis), autoimmune/inflammatory abnormalities (orbital pseudotumor,

sarcoidosis, Wegener's granulomatosis), orbital trauma (Terson syndrome, orbital floor fracture, globe rupture) and abnormalities (coloboma, lens dislocation, orbital infarction).
Conclusions
Orbital pathology is an important area of study as conditions and anomalies involving the globes, muscles and nerves can lead to significant morbidity and mortality with life-altering consequences, including blindness. Often the focus of orbital education is on orbital tumors, which comprise a small subsection of orbital abnormalities. We seek to improve awareness of the more common nontumorous causes of orbital pathology with an emphasis on those abnormalities and pathologies that are most prevalent in children.



(Filename: TCT_eEdE-131_ASNRorbit.jpg)

eEdE-132

6:30AM - 3:00PM

Orbital Trauma: Bringing the Surgically Relevant Findings into Focus

T Richards[1], J Anderson[1], C Lanzieri[1]
[1]*University Hospitals Cleveland Medical Center, Cleveland, OH*

Purpose
The exhibit will demonstrate the relevant anatomy of the orbit on both computed tomography (CT) and magnetic resonance imaging (MRI). The different types of orbital traumatic injuries will be discussed along with findings that indicate emergent surgical intervention. The indications for urgent and emergent surgery in orbital trauma will be discussed to guide the radiologist in providing the surgically relevant findings in their radiology report.

Materials and Methods

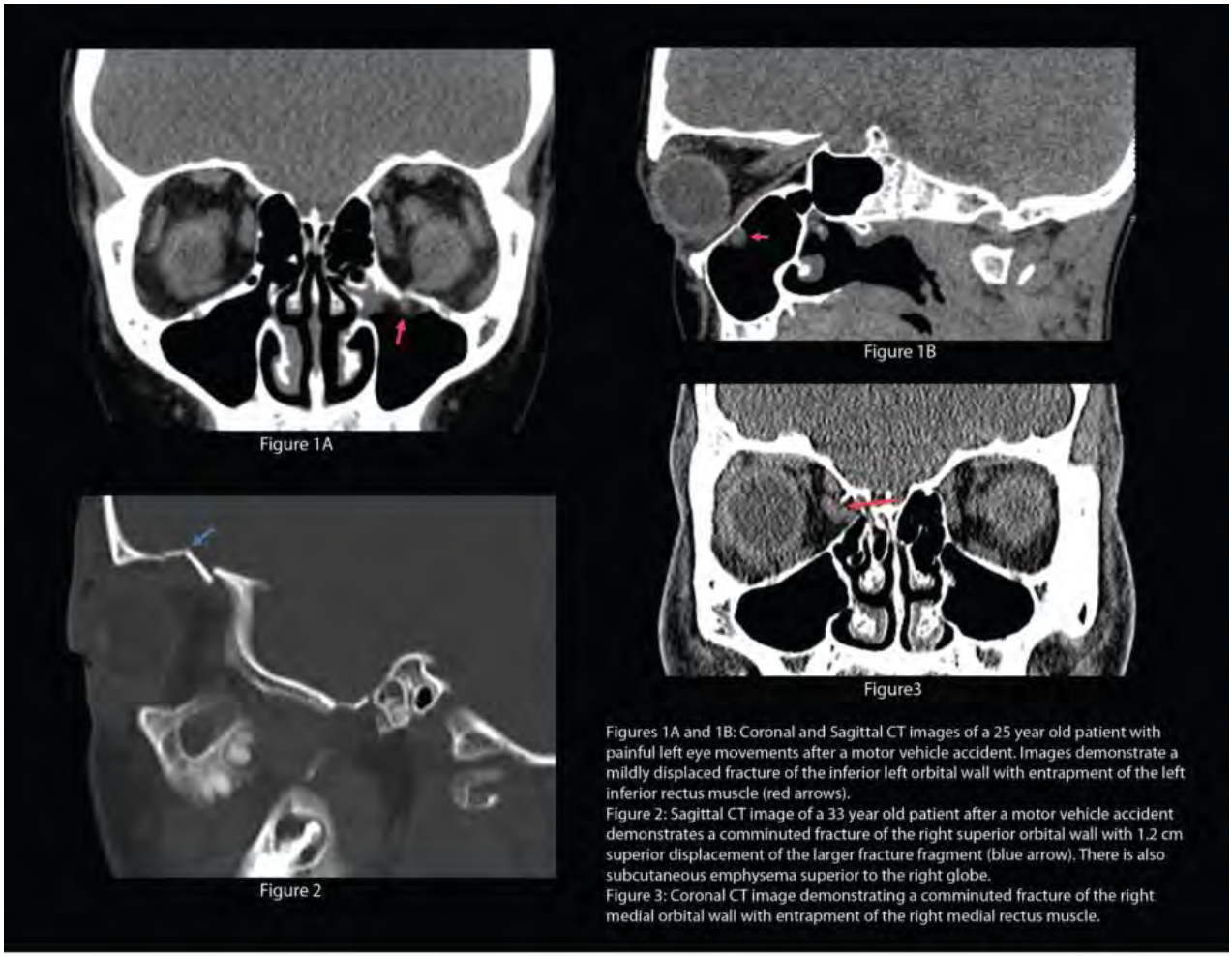
Intermittently throughout the educational information provided in the educational exhibit, cases of orbital trauma will be presented in an interactive fashion. The user will be asked a multiple-choice question such as "Which bones are fractured in this patient?" Then they will click on an answer and be provided with feedback based on the answer that was chosen. Other interactive quiz questions will be formatted so that the user will be prompted to click on a certain finding on the image such as "Click on the finding that requires urgent surgical intervention". If they click on the correct location, it might say something like "Correct! There is entrapment of the inferior rectus muscle which is a criteria for urgent surgical intervention". The outline of the educational material to be included is as follows: I. Overview of role of different types of imaging: A. Radiographs, B. MDCT, C. MRI, D. Ultrasound. II. Types of injuries with imaging examples: A. Anterior chamber injuries, B. Lens injuries, C. Globe rupture, D. Ocular detachments, E. Intraorbital foreign bodies, F. Optic nerve injuries, G. Hemorrhages/hematomas, H. Orbital wall fractures: i. Orbital Floor, ii. Orbital roof, iii. Medial Wall, iv. Lateral Wall. III. Indications for emergent, urgent, and delayed surgical repair. IV. Imaging examples of late complications from orbital trauma.

Results

Orbital trauma is a relatively common occurrence. Studies have reported up to 16% of the major trauma patients have ocular or orbital trauma (3). The clinical evaluation of orbital trauma has many limitations due to the nature of the trauma. Many times the patient is unable to follow commands or cooperate with the examiner due to their altered mental status from head trauma. If the orbital trauma is severe, preseptal edema limits the ability of the patient and the examiner to open the patient's eyelids and perform the eye examination. Other times, there are many other distracting injuries that delay consultation of ophthalmology. Additionally, sometimes surgical emergencies due to orbital trauma are not apparent or detected on physical examination. Studies have reported approximately 43% of pediatric orbital floor fractures were not associated with grossly visible signs on physical examination (1). Because of all of this, imaging evaluation of the orbits with multi-detector computed tomography (MDCT) remains critical in the evaluation of these patients. The radiologist plays a very important role in guiding their surgical colleagues in the detection of injuries requiring intervention.

Conclusions

In many cases, patients with orbital trauma present difficult challenges for the examining clinician. Pathology requiring surgical invention can be difficult to detect without imaging evaluation. The radiologist can help provide important information to their surgical colleagues to help guide them in their clinical and surgical management. Because of this, it is crucial for the radiologist to have an understanding of orbital trauma and the relevant imaging findings that must be communicated with the referring surgeons.



(Filename: TCT_eEdE-132_Orbital-Trauma-Abstract-Images.jpg)

eEdE-164

6:30AM - 3:00PM

Osseous Lesions of the Face: the Incidental, the Bad, and the Ugly

C Chan[1], S Yoon[1], J Rodulfa[1], J Li[2], B Devenney-Cakir[1]
[1]Einstein Medical Center, Philadelphia, PA, [2]Einstein Healthcare Network, Philadelphia, PA

Purpose
Osseous lesions of the face encompass a wide variety of pathologies and are of various clinical significances. While many are simply incidental findings, others are more concerning and demand prompt attention. Therefore, familiarity with the imaging appearances as well as knowledge of their clinical significances and management options is important for a radiologist.

Materials and Methods

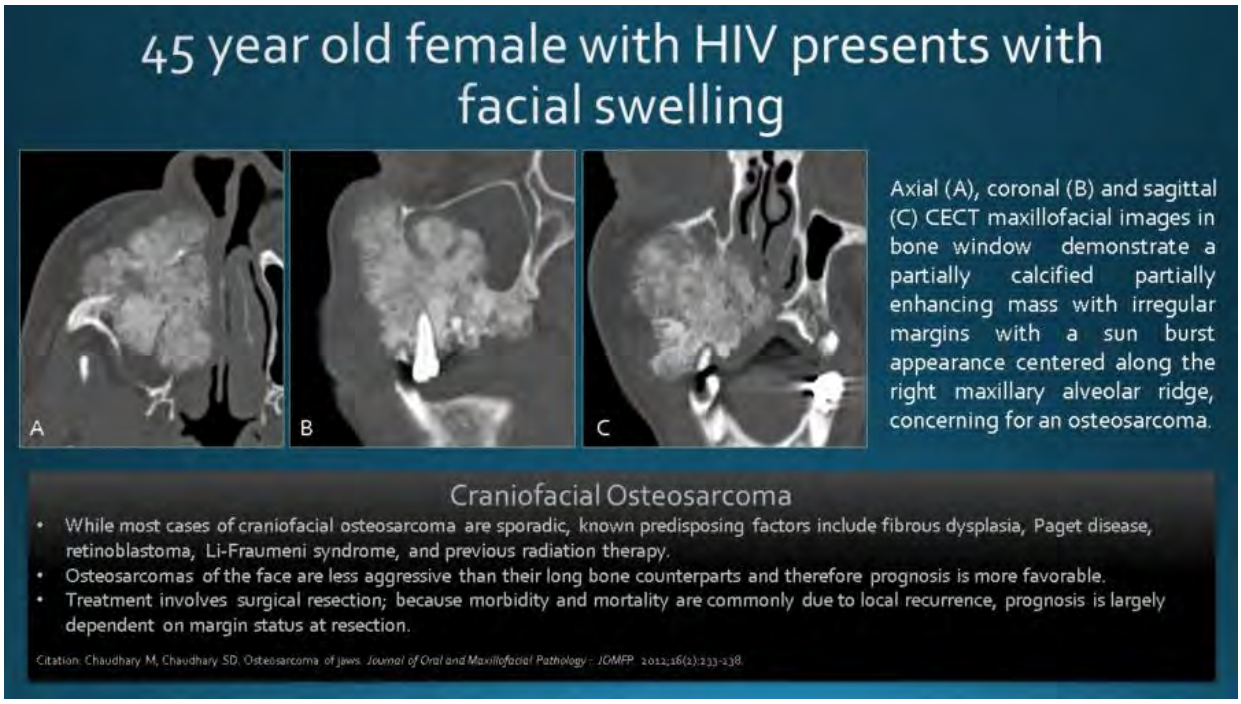
We will present a spectrum of osseous lesions of the face from our institution, ranging from incidental findings to life threatening conditions, focusing on possible clinical implications and management options. Cases will be organized by etiology. At the end of this activity, the radiologist will be able to accurately diagnose bony facial abnormalities as well as discuss possible underlying clinical implications, complications, and treatment options.

Results

Our exhibit includes a spectrum of facial bony lesions of various clinical significance. The cases include common and uncommon benign neoplasms such as osteomas, osteoid osteomas, fibrous dysplasia, chondromas, osteochondromas, aneurysmal bone cysts, intraosseous meningiomas, ameloblastomas, cementoblastomas, odontoma, odontogenic keratocyst; malignant tumors such as osteosarcoma, chondromsarcoma, chordoma, and plasmacytoma; infectious processes such as osteomyelitis and septic arthritis of the temporomandibular joint, radicular cysts, rhinocerebral mucormycosis, and Pott's puffy tumor; inflammatory processes such as granulomatosis with polyangiitis and cemento-osseous dysplasia; metastatic lesions from breast and colon malignancies and malignant melanoma; congenital/developmental lesions such as tori mandibularis, Stafne bone cyst, nasopalatine duct cyst, and dentigerous cysts; and iatrogenic causes such as osteonecrosis in the setting of radiation and steroids. Discussion of underlying clinical implications, potential etiologies and complications as well as an overview of the pertinent facial anatomy will be included.

Conclusions

Osseous lesions of the face encompass a broad spectrum of pathologies and range from incidental to life threatening. The exhibit provides discussion of multiple examples in this variety, encouraging the radiologist to play a paramount role in management guidance.



(Filename: TCT_eEdE-164_osseous.jpg)

eEdE-148

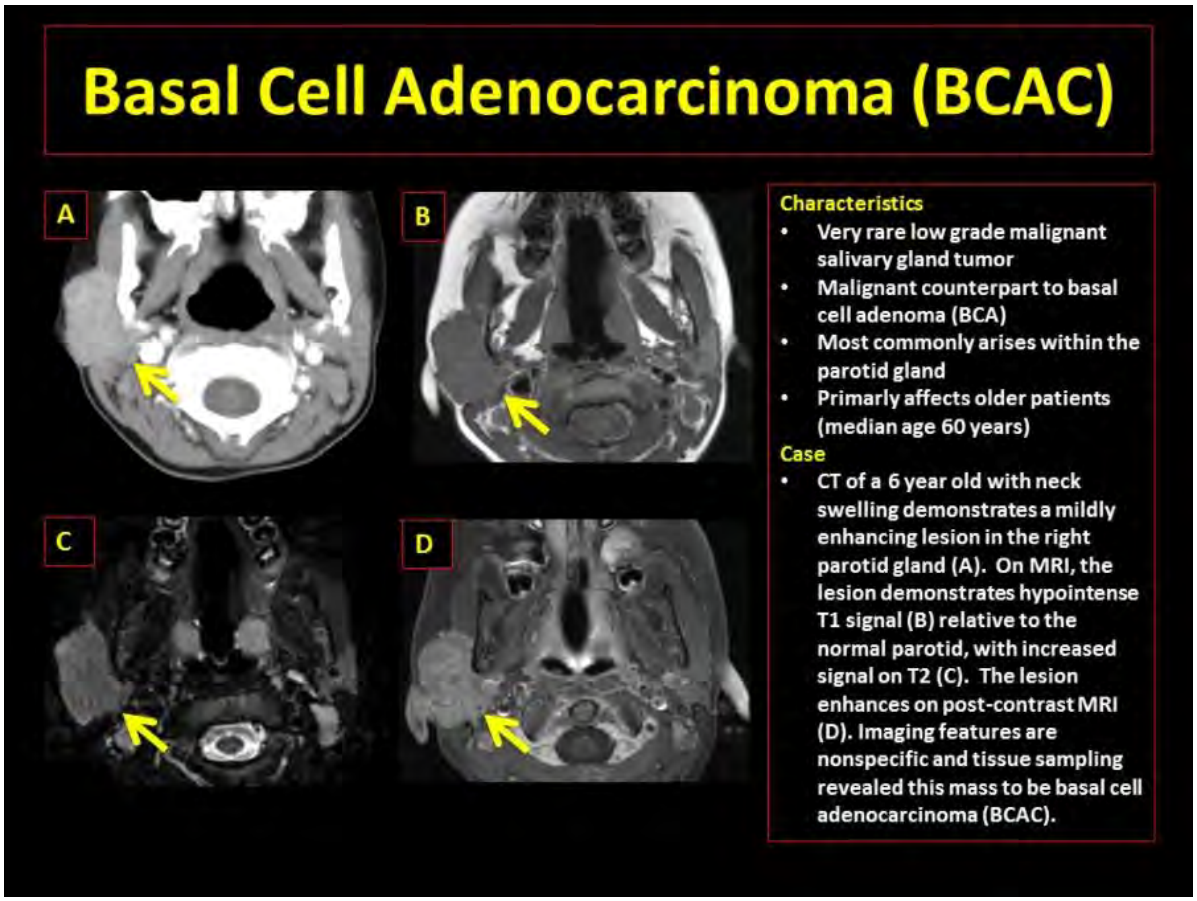
6:30AM - 3:00PM

Pediatric Parotid Pathology: A Pictorial Potpourri

I Mills[1], J Weisiger[2], D Durand[3], A Malhotra[1]
[1]Yale New Haven Hospital, New Haven, CT, [2]Yale Department of Radiology, New Haven, CT, [3]Yale University School of Medicine, New Haven, CT

Purpose
Parotid lesions affect children of all ages, and represent a wide range of pathologies. While some lesions have a nonspecific imaging appearance, others have features which can suggest a specific diagnosis. We review normal parotid space anatomy, followed by a review of the various pathologic entities affecting the pediatric parotid gland. Imaging examples emphasize characteristic appearances of certain pathologic entities.
Materials and Methods
Pediatric parotid lesions are presented according to their pathologic category. The normal parotid space will be reviewed first, followed by infectious/inflammatory conditions, congenital/developmental lesions, and benign and malignant neoplastic conditions. Imaging modalities shown will include ultrasound, CT, MRI, and MR sialography.
Results
Pediatric parotid lesions can be classified as inflammatory/infectious, congenital/developmental, and benign and malignant neoplasms. Inflammatory/infectious etiologies are far more common than neoplastic conditions in children compared to adults.

Diffuse bilateral gland enlargement can be seen in acute viral or bacterial parotitis; however lymphoma rarely may have a similar appearance. Juvenile recurrent parotitis, presenting in mid-childhood and frequently resolving by puberty, has characteristic ultrasound and MR imaging appearances of multifocal punctate sialectasis. This condition can be distinguished from HIV sialopathy with serologic testing. Autoimmune inflammatory conditions present in children as well as adults, with Sjogren's syndrome being the most common. Adenopathy is common in children and frequently involves intraparotid lymph nodes.
Congenital/developmental lesions presenting in and around the parotid gland include venolymphatic malformations and branchial cleft cysts. Lymphangiomas are frequently multispatial, crossing fascial planes. Branchial cleft cysts can present with parotitis when infected. A fistuolous tract to the external auditory canal may be seen on imaging. Benign and malignant neoplasms in children overlap with those affecting adults. In addition, hemangiomas are common in children and characteristically present as a trans-spatial enhancing mass with phleboliths. Mesenchymal neoplasia includes neurofibroma and rhabdomyosarcoma. Similar to adults, pleomorphic adenoma is a common benign neoplasia and mucoepidermoid carcinoma is the most common malignant neoplasia. Rare malignancies such as basal cell adenocarcinoma, more common in adults, also must be considered in children.
Conclusions
This presentation will review the normal parotid gland and the spectrum of parotid pathology in pediatric patients. Parotid lesions represent a variety of pathological diagnoses, and are categorized into infectious/inflammatory, congenital/developmental, and benign/malignant neoplasms. Ultrasound, CT, MRI, and MR sialography will be used to demonstrate characteristic imaging findings and specific pearls for certain lesions.



(Filename: TCT_eEdE-148_UpdatedBCAC.jpg)

eEdE-166

6:30AM - 3:00PM

Perineural Spread of Head and Neck Malignancies: What Radiologists Should Know

M Razmjoo[1], S Jubouri[1], N Agrawal[1], H El Khudari[1], P Prakash[2]
[1]Saint Vincent Hospital, Worcester, MA, [2]St Vincent Medical Center, Worcester , MA

Purpose
Perineural spread of tumor frequently is encountered in various head and neck malignancies. The associated findings are, however, subtle; especially in early stages while the patient remains asymptomatic. Hence, high level of suspicion and radiology acumen is needed to appropriately diagnose the early stages of perineural spread. The purpose of our abstract is to discuss the normal anatomy of the cranial nerves V and VII, and the computed tomography (CT) and magnetic resonance imaging (MRI) features of perineural spread of head and neck malignancies along these nerves.
Materials and Methods
We will use CT and MRI images to demonstrate the normal pathway of trigeminal nerves (CN V) and its branches including the maxillary (V2) and mandibular divisions (V3) and the

facial nerve (CN VII). Subsequently, CT and MRI images from patients with perineural tumor spread along these cranial nerves will be used to illustrate the various findings while keeping the tumor subtype and location in mind.

Results

Perineural spread of tumor implies direct neoplastic extension from the primary lesions to noncontiguous areas along the nerves (1, 3). Adenoid cystic carcinoma and squamous cell carcinoma are the most notorious for perineural spread. Perineural spread is associated with high rate of recurrence, metastasis, and decreased survival (4, 5). Computed tomography and MRI imaging features of perineural spread include: 1. Foraminal enlargement and destruction. 2. Obliteration of fat planes at foraminal opening. 3. Nerve enlargement and enhancement.

Conclusions

Identifying perineural spread of tumor is crucial for accurate staging of head and neck tumors. Knowledge of normal anatomy and the imaging features of tumor spread is, therefore, imperative for diagnosing perineural involvement.

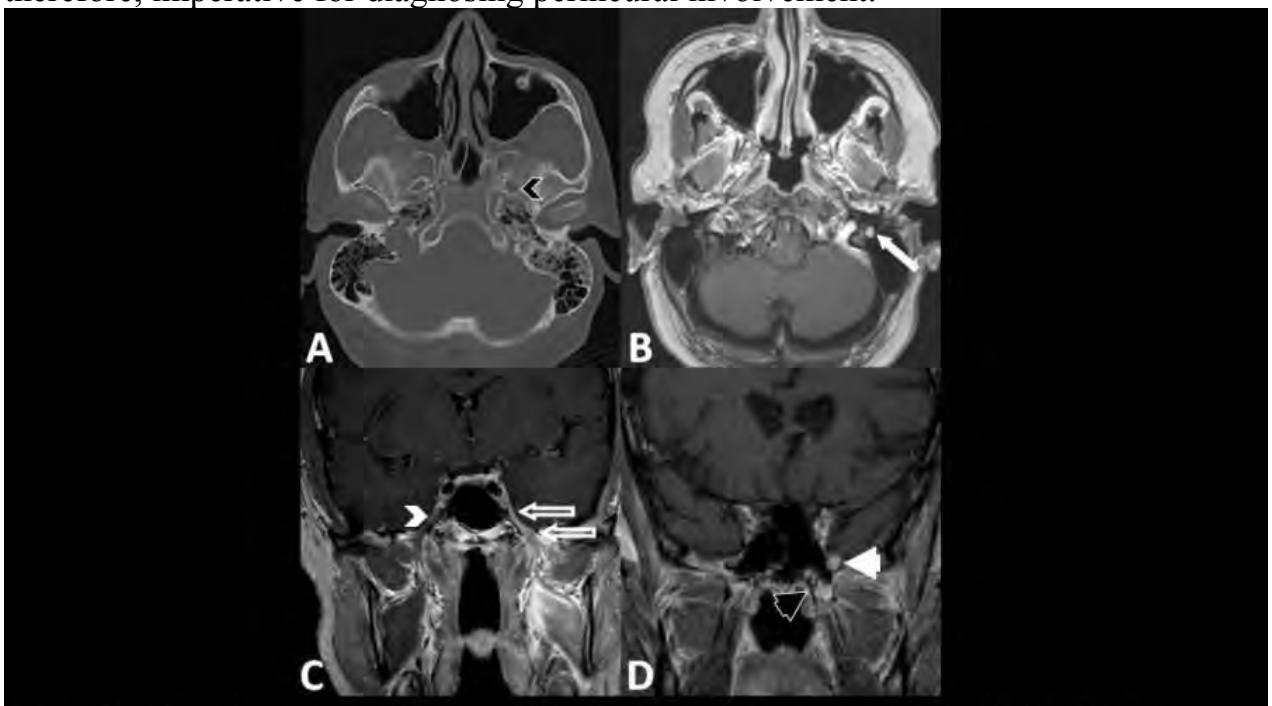


Figure: (A) Axial CT bone window at the level of skull base. Enlarged left foramen ovale (black arrowhead) secondary to perineural spread of SCC along the left V2. (B) MRI of the brain, axial T1 post gadolinium. The left facial nerve is enlarged and enhancing (white solid arrow) secondary to perineural spread of adenoid cystic carcinoma of the left parotid gland. (C) MRI of the brain, coronal T1 post gadolinium. Thickening and enhancement of left V3 secondary to perineural spread of SCC (white open arrow). Note normal right V3 (white arrowhead). (D) MRI brain, coronal T1 post gadolinium. Melanoma patient with perineural spread along the left infraorbital nerve extending to left V2 in foramen rotundum (white short arrow) and left vidian nerve (black short arrow).

(Filename: TCT_eEdE-166_perineuralspread-300.jpg)

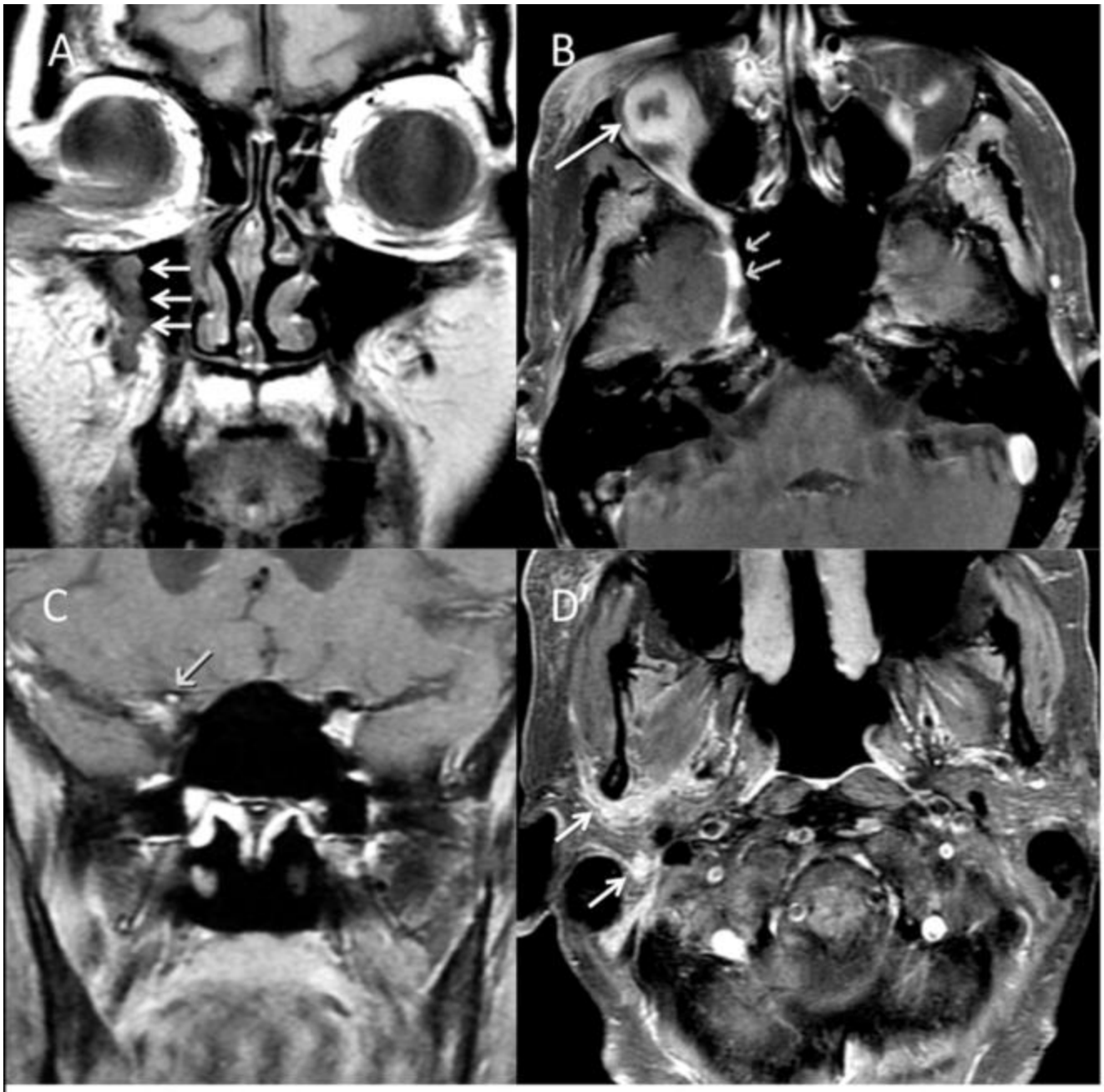
eEdE-159

6:30AM - 3:00PM

Perineural Tumour Spread in the Head and Neck: A Pictorial Review and Review of Literature

M Chan[1], Y Chen[1], E Yu[2]
[1]*University of Toronto, Toronto, Ontario,* [2]*University of Toronto, Toronto, Ontario*

Purpose
The purpose of this educational exhibit is to review the phenomenon of perineural spread in head and neck tumors by reviewing normal cranial nerve anatomy and using a series of illustrative cases to provide practical tips for diagnosing perineural spread. A review of the current literature also will be performed, with a focus on the underlying pathobiology and molecular mechanisms.
Materials and Methods
A pictorial review showcasing the normal anatomy and imaging appearance of cranial nerves in the head and neck will be provided, followed by a series of cases from our institution illustrating the common pathways of perineural spread in the head and neck, including the divisions of trigeminal nerve and facial nerve, as well as less common pathways, such as the glossopharyngeal nerve and vagus nerve. The cases also will highlight various primary tumors with a propensity towards perineural spread. There will be a review of the current literature regarding the current understanding of the pathobiology and molecular mechanisms underlying perineural tumor spread.
Results
Perineural tumor spread is an important finding that is correlated with poorer outcomes including increased local recurrence and decreased disease-free survival. The nerves most commonly associated with perineural spread are cranial nerves V and VII due to their anatomic relationship to various sites in the head and neck where tumors tend to arise. Other nerves represent much less frequently involved routes of spread. The pathogenesis of perineural tumor spread is incompletely understood, although the most commonly cited theory is that there is an interaction between the nerve and tumor cells with signals that activate trophic and chemotactic pathways leading to tumor growth.
Conclusions
Perineural spread in head and neck cancer is an important findings with prognostic implication. A firm understanding of head and neck cranial nerve anatomy and common routes of perineural spread is crucial for the recognition and diagnosis of this phenomenon.



69-year-old female with squamous cell carcinoma of the right upper cheek presents with worsening right eye deviation due to tumour infiltration of the right infraorbtial nerve. This is demonstrated by nodular masses in the premaxillary fat (arrows in A) and a necrotic rim-enhancing mass in the right inferior orbit (Long arrow in B). Abnormal thickening and enhancement extends posteriorly to involve the right pterygopalatine fossa, inferior orbital fissure and foramen rotundum (short arrows in B) along the course of CNV2 (maxillary branch). There is also enhancement of the precavernous right CNIII (arrow in C) as well as the intraparotid right facial nerve and the right auriculotemporal nerve (arrows in D). This constellation of findings is consistent with extensive perineural spread along cranial nerves III, V2, V3, and VII.

(Filename: TCT_eEdE-159_Figure.jpg)

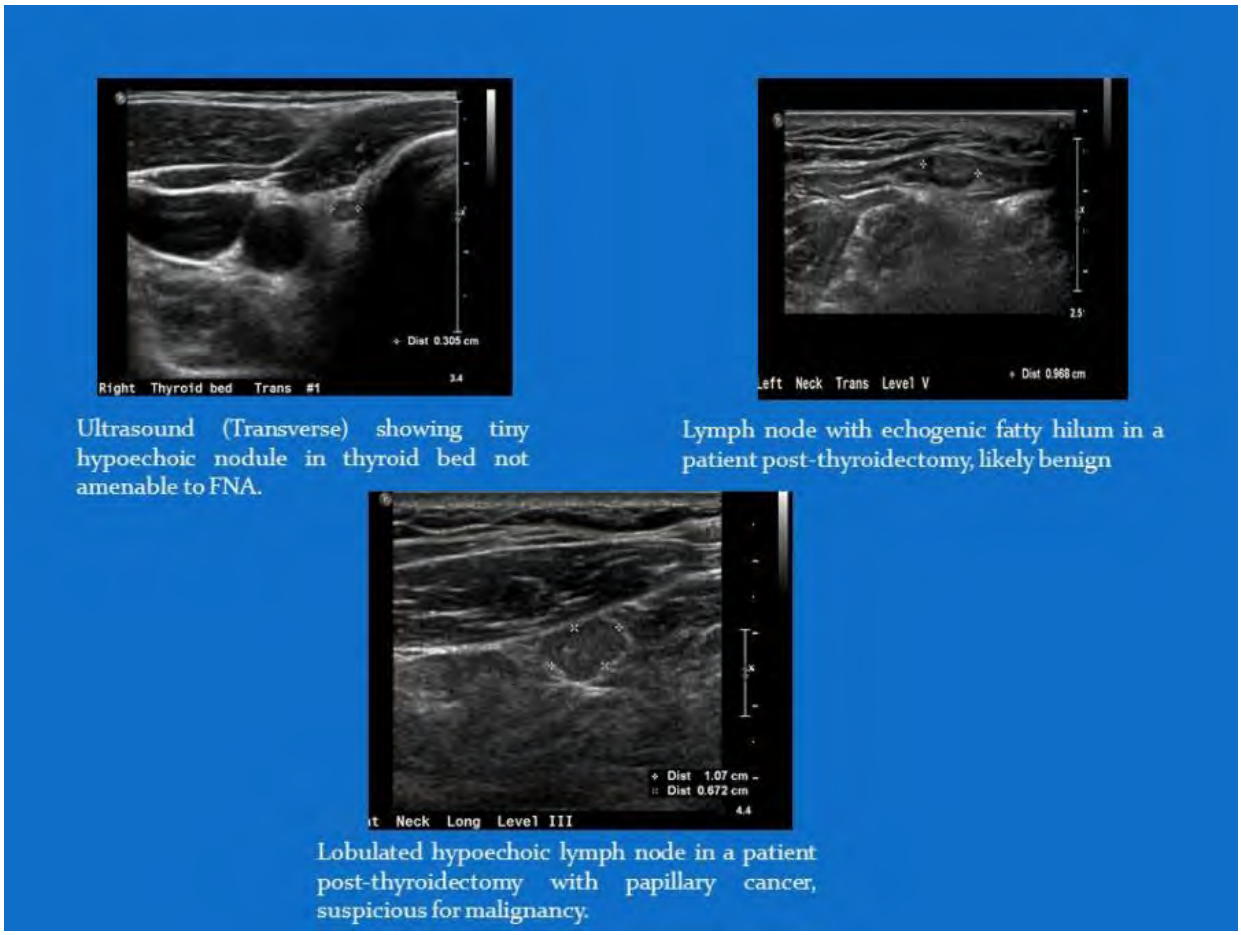
eEdE-173

6:30AM - 3:00PM

Post Thyroidectomy Neck: Role of Imaging

m bajaj[1], M Crain[2], M Abu-yousef[1], R Harris[3], Y Menda[4], B Policeni[5]
[1]University of Iowa Hospitals and Clinics, Iowa City, IA, [2]University of Iowa Hospitals and Clinics, IOWA CITY, IA, [3]University of Iowa Hospital and Clinics, Iowa City, IA, [4]University of Iowa Hospitals and Clinics, Iowa city, IA, [5]University of Iowa hospitals and Clinics, iowa city, IA

Purpose
This educational exhibit aims to describe the role of imaging in the evaluation of neck post-thyroidectomy for cancer emphasizing on relative strengths of different modalities and complimentary role they play in deciding management.
Materials and Methods
Imaging findings on ultrasound, computed tomography (CT) and/or nuclear scans in patients presenting for post-thyroidectomy evaluation were evaluated to create an educational exhibit to: 1. Describe normal appearance of neck post-thyroidectomy for thyroid cancer. 2. Discuss the evolution in appearance of thyroid bed and cervical lymph nodes after surgery. 3. Illustrate the imaging features of postsurgical scar/fibrosis, surgical bed recurrence and reactive/benign versus metastatic lymphadenopathy on ultrasound, CT and nuclear medicine studies. 4. Emphasize on common pitfalls in evaluating post-thyroidectomy neck.
Results
Ultrasound provides many advantages in evaluation of postoperative neck over CT, particularly in patients who may need radioiodine therapy. These include real time evaluation, better depiction of internal architecture of surgical bed lesions and lymph nodes as well as absence of need for intravenous iodinated contrast which may negatively affect subsequent radioiodine therapy. Certain imaging findings, particularly on ultrasound, can be virtually diagnostic of recurrence/ metastaic involvement even in absence of histopathology.
Conclusions
Interpreters of post-thyroidectomy neck must be aware of normal appearance of postsurgical neck as well as the normal evolution of postoperative scarring and reactive/benign lymphadenopathy. Certain imaging features are classical in predicting recurrence or lymph node metastases. Optimal interpretation of these findings on ultrasound, CT and nuclear medicine studies is very important for timely intervention and management.



(Filename: TCT_eEdE-173_Thyroid.jpg)

eEdE-145

6:30AM - 3:00PM

Pre - TORS Imaging Assessment of Oropharyngeal Carcinoma: What the Surgeon Needs to Know

A Vijayasarathi[1], A Sepahdari[2]
[1]*University of California Los Angeles, los angeles, CA,* [2]*UCLA, Santa Monica, CA*

Purpose
Squamous cell carcinoma of the oropharynx is increasing in incidence, particularly in younger/healthier populations, likely due to rising rates of human papilloma virus. Traditionally, treatment for oropharyngeal carcinoma (OPC) included large surgeries such as transmandibular or transpharyngeal resection. More recently, there has been a paradigm shift towards the goal of preservation of functional status, particularly swallowing and speech. Concurrent chemotherapy and radiation thus have become the mainstay of treatment for OPC; however they are not without their own drawbacks. The recent advent of transoral robotic surgery (TORS) for oropharyngeal carcinoma, first described in 2006, allows for

several potential advantages over either open surgery or chemoradiation. Chiefly, the transoral approach preserves the swallowing mechanism, does not require pre-operative tracheostomy, and may obviate the need for chemoradiation in certain cases. The objective of this exhibit is to present cases of OPC and highlight the features most important to the surgeon planning for TORS.

Materials and Methods

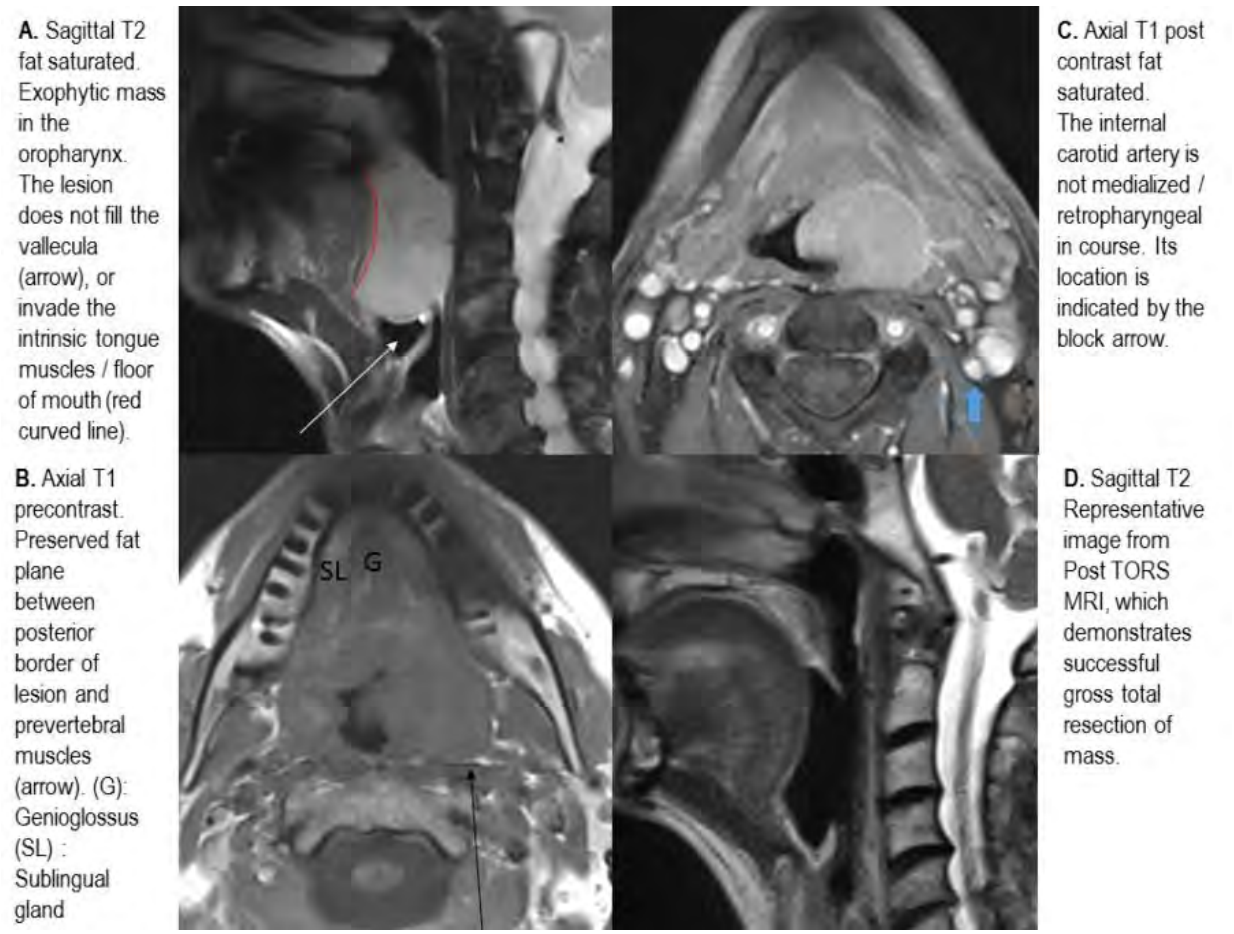
The PACS and departmental teaching files at a large academic medical center were queried for instructive sample of cases of OPC. Through collaboration with the Head and Neck Surgery Department, imaging characteristics salient to preprocedural planning will be highlighted, intra-operative correlation and postoperative cases will be demonstrated.

Results

The slides included in this interactive educational exhibit will include a review of normal anatomy of the oropharynx including important landmarks, cases of OPC treated with TORS, findings that make a lesion challenging or unresectable by TORS (i.e., involvement of the vallecula, medialization of the internal carotid arteries, and an endophytic growth pattern), intra-operative and postoperative appearance, and findings suggestive of disease recurrence.

Conclusions

Transoral robotic surgery represents an opportunity to both preserve quality of life and provide a potential cure for patients afflicted by OPC. High quality pre- and postoperative imaging interpretation is crucial to successful patient selection and outcomes. Understanding the features presented herein may help interpreting radiologists play a major role in caring for this growing patient population.



(Filename: TCT_eEdE-145_figurefortorspresentation.jpg)

eEdE-171

6:30AM - 3:00PM

Radiological Assessment for Intracranial and Extracranial Complications Associated with Mastoid Pathology

U Shafique[1], A Capizzano[2], T Sato[3], T Sasaki[3], Y Sato[3], T Moritani[2], U Chaudhry[4]
[1]University if Iowa, Hospitals and Clinics, Iowa City, IA, [2]University of Iowa Hospitals and Clinics, Iowa City, IA, [3]University of Iowa, Iowa City, IA, [4]Northwestern University, Chicago, IL

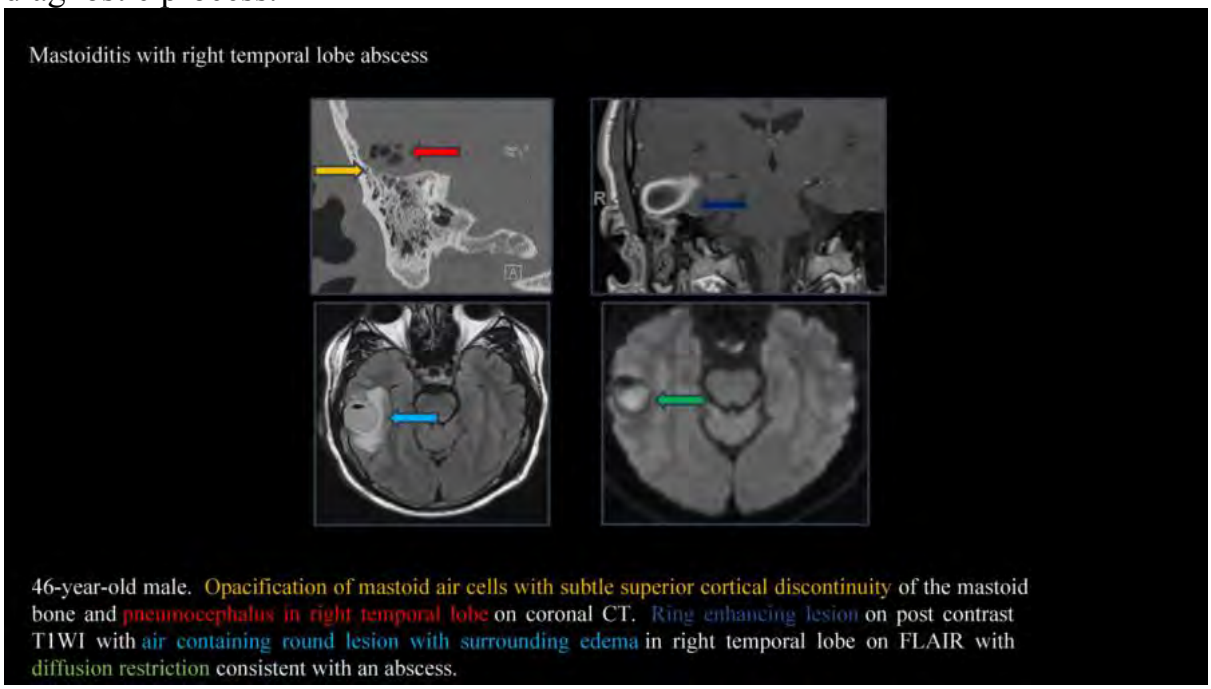
Purpose
To assess clinical and imaging findings in patients with mastoid pathology and potential association with intracranial and extracranial complications.
Materials and Methods
Retrospective evaluation of clinical features and imaging findings on CT, MRI including GRE, SWI, DWI with ADC map, and MRV of mastoid pathology and associated intracranial and extracranial complications based on past 15 years of our institutional experiences.

Results

We will demonstrate anatomy of mastoid antrum, mastoid air cells and middle ear cavity to explain the root of intracranial or extracranial extension. We will discuss the etiology and pathophysiology of mastoid findings and associated intracranial and extracranial complications. Mastoid pathologies include acute mastoiditis, simple vs coalescent mastoiditis, and latent indolent mastoiditis involving mastoid antrum without evidence of middle ear infection. Associated intracranial complications include acute meningitis/cerebritis/ventriculitis, brain abscess, subdural empyema, subdural empyema, and dural sinus thrombosis. Associated extracranial complications include subperiosteal abscess and Bezold abscess. Reactive effusion in mastoid also may be seen in cases of dural sinus thrombosis and post-thrombolysis of dural sinus thrombosis.

Conclusions

Mastoid bone is a crucial anatomical part of temporal bone which should be assessed carefully for pathological process. Due to its close proximity to middle ear, temporal lobe, meninges and dural sinuses it is involved in varying disease processes causing both intracranial and extracranial complications. However it may show reactive effusion in cases of deep sinus thrombosis and head trauma. CT, MRI and MRV play a crucial role in the diagnostic process.



(Filename: TCT_eEdE-171_Mastoiditis.jpg)

eEdE-117

6:30AM - 3:00PM

Review of Fat Stripes in Soft Tissues of the Neck and Impact of Their Involvement on Patient Management and Prognostication

A Singhal[1], D Milner[1], C Hadley[1], S Gaddamanugu[1]
[1]*University of Alabama at Birmingham, Birmingham, AL*

Purpose

Head and neck anatomy is complex. Multiple soft tissue density, neurovascular and osseous structures are in close proximity and detailed anatomical knowledge is essential to provide value-added interpretations. Within the neck, parapharyngeal space fat is the most commonly described fatty space, careful analysis of which helps in localizing neck masses. However, there are several other named or unnamed fat spaces, stripes or pads. Recognizing them not only helps elucidate anatomy better and identify otherwise difficult to detect malignancies, especially when compared to the contralateral side but also has prognostic implications. The goal of this exhibit is therefore to enlist different fat stripes/pads in the head and neck and demonstrate with examples the advantage of this anatomical knowledge in diagnosis and prognostication of head and neck pathologies.

Materials and Methods

A detailed anatomy of the different fat stripes/pads will be discussed utilizing correlation with computed tomography (CT) and magnetic resonance imaging (MRI). The imaging techniques used for head and neck oncologic imaging would be discussed briefly. Individual fat spaces will be discussed with illustration of pathology and discussion of any prognostic and surgical implications of involvement of the region. The main fat spaces to be discussed include: - Parapharyngeal fat, - Retroantral fat, - Buccal fat, - Lingual septum, - Lingual neurovascular bundle, - Carotid space fat, - Pre-epiglottic fat, - Paraglottic fat, - Retropharyngeal fat, - Pterygopalatine fossa and other skull base foramina, - Additional unnamed fat stripes/spaces.

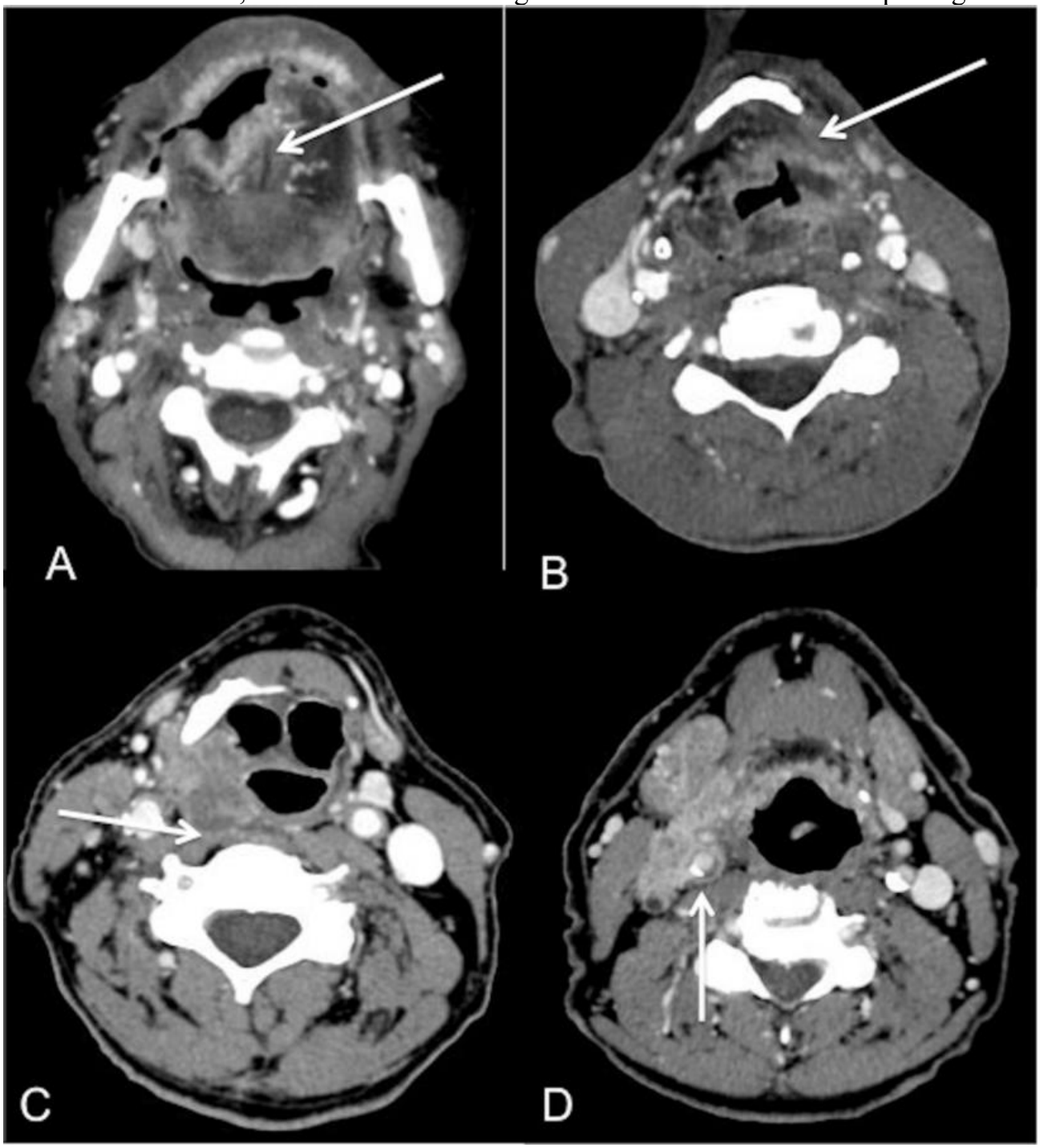
Results

Recognizing involvement of various neck fat stripes is important not only for anatomic localization of a lesion but also due to the effect on surgical approach or management. In addition, there are prognostic implications of involvement of some of the sites in the resectability of head and neck cancer. Some examples include involvement of the lingual septum, which makes the patient unsuitable for hemiglossectomy [1] (Figure A). Invasion of the pre-epiglottic fat (Figure B) increases risk of hyoid bone infiltration and cervical adenopathy. It also raises the possibility of resection of tissue from the tongue base with resultant swallowing dysfunction and poor airway control [2]. Paraglottic fat involvement by a glottic tumor usually precludes laser resection or cordectomy and by a supraglottic tumor precludes a supraglottic laryngectomy [3]. Preservation of the retropharyngeal fat stripe is a relatively specific finding for excluding prevertebral muscle invasion, which would otherwise classify tumors as T4b and render them unresectable [2, 4] (Figure C). Studies have shown that involvement of circumference of the carotid artery by 270° or more is accurate in predicting unresectability and intra-operative inability to remove the tumor from the carotid artery [5] (Figure D). Replacement of normal fat signal in the pterygopalatine

fossa and other skull base foramina suggests perineural tumor spread. It is seen most commonly with squamous cell carcinoma and adenoid cystic carcinoma.

Conclusions

In conclusion, knowledge of different fat stripes/pads in the head and neck is important for providing value-added interpretations to the referring clinician. Involvement of the various fat spaces has surgical and prognostic implications in the resectability of head and neck cancer and therefore, this anatomic knowledge can be crucial for accurate reporting.



(Filename: TCT_eEdE-117_ASNR_fat_labels_a.jpg)

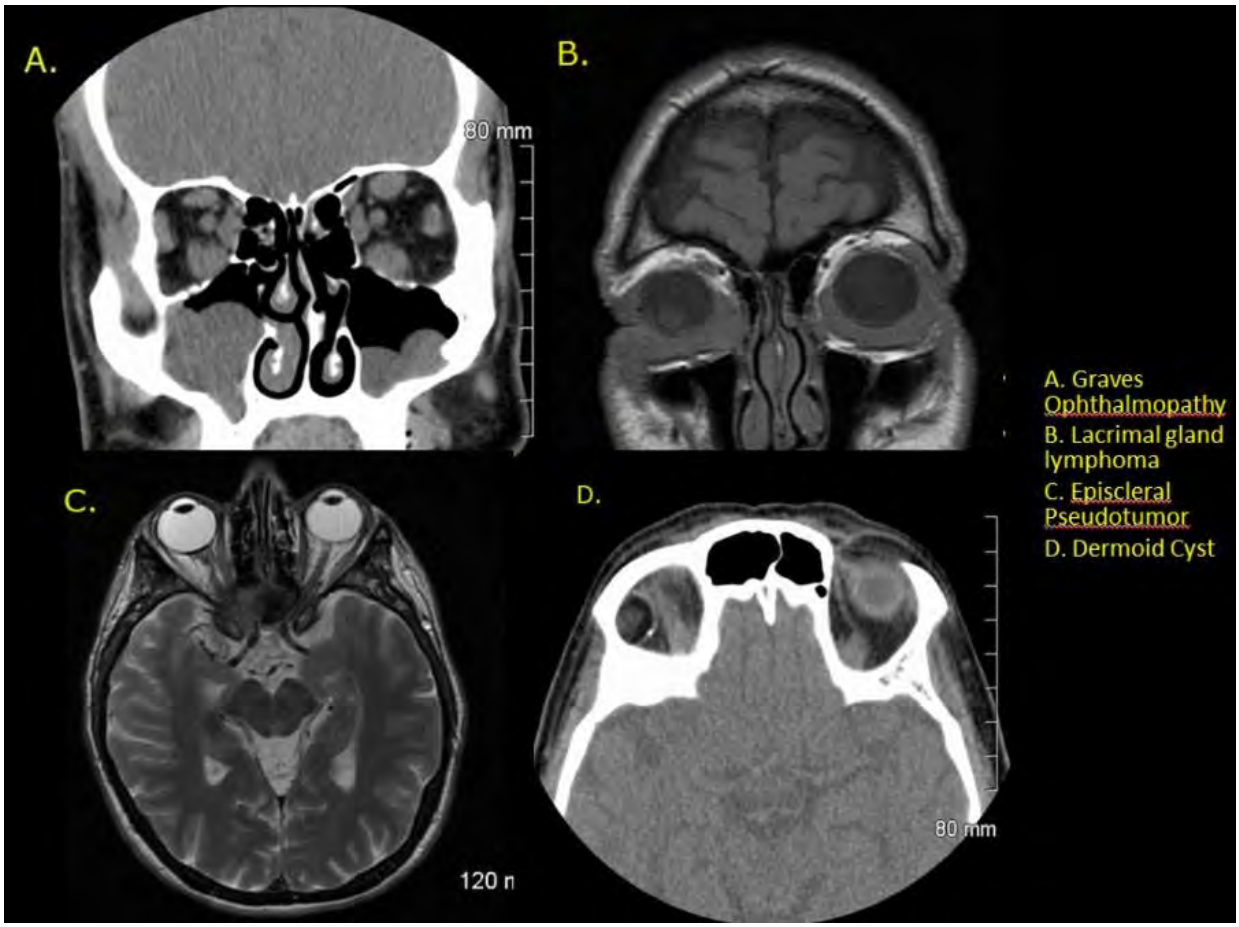
eEdE-136

6:30AM - 3:00PM

Test Your Knowledge of Orbital Anatomy and Pathology

C Quintero[1], V Pandika[1], P Ravenna[2], J QUINTERO[3], M Scanlan[4]
[1]Bryn Mawr Hospital, Bryn Mawr, PA, [2]Associates in Eye Care, philadelphia, PA, [3]Bronx-Lebanon Hospital, Bronx, NY, [4]Main Line Health System, Bryn Mawr , PA

Purpose
-Review orbital anatomy with special attention to pertinent relationships for radiologists in order to facilitate the accurate description of orbital pathology. -Review diverse cases of common and uncommon ocular pathology and apply the anatomy. -Highlight imaging features of common and uncommon orbit pathology. -Propose a checklist for radiologists to use when evaluating orbits.
Materials and Methods
-Pictorial review in which we will discuss orbital anatomy boundaries with pertinent relationships for radiologists. -Case-based pictorial review of common and uncommon ocular pathologies in a quiz format, followed by a discussion of each case.
Results
-Review of orbital anatomy: Bony margins, ocular spaces, orbital foramina, orbital contents and lacrimal apparatus. Pictorial review of diverse cases of ocular pathology presented in a case-based quiz format in which the learner will be able to apply the anatomy and answer multiple choice questions regarding each case. After the correct answer is revealed, we will proceed to review the imaging characteristics of each case and discuss key differential diagnosis and clinical points. Some of the cases included will be: orbital lymphoma, Graves' ophthalmopathy, metastatic disease, Pseudotumor, trauma, infection, foreign body, dermoid, etc. -Checklist of items for the radiologists to identify when evaluating the orbits.
Conclusions
The orbit is a site in which we can encounter a large number of pathologies of diverse etiologies so it is important for radiologists to understand basic orbital anatomy, improve image interpretation skills and familiarize with the clinical presentation of orbital pathologies so they can provide an accurate description and tailor the imaging findings to the patient's clinical presentation in order to improve diagnostic confidence.



(Filename: TCT_eEdE-136_Orbitalanatomypics.JPG)

eEdE-122

6:30AM - 3:00PM

The Added Value of Contrast Enhanced MRA in the Assessment of Head and Neck Paragangliomas: Just Two Minutes of Your Time

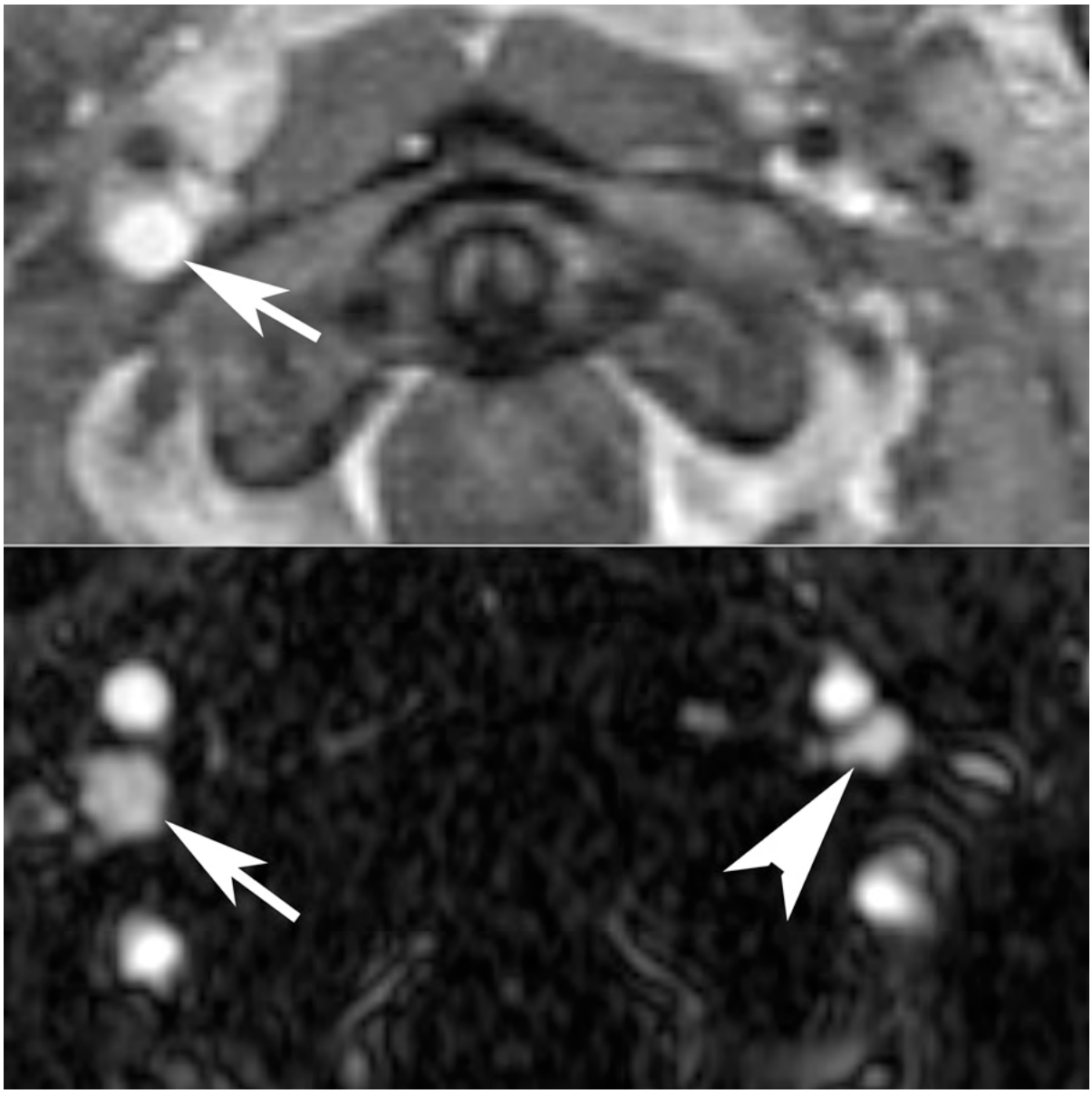
A Johnsen[1], L Davis[2], J Aulino[3]
[1]Vanderbilt University, NASHVILLE, TN, [2]Vanderbilt University, Nashville, TN, [3]Vanderbilt Univ. Medical Center, Nashville, TN

Purpose
To demonstrate the utility of contrast-enhanced magnetic resonance angiography (CE-MRA) as a complement to conventional MR imaging in the assessment of head and neck paragangliomas.
Materials and Methods
A series of illustrative cases is provided.
Results
Paragangliomas are neuroendocrine tumors that occur in characteristic locations in the head

and neck. Like other neuroendocrine tumors, these display characteristic contrast enhancement, with prompt enhancement during the arterial phase. Contrast-enhanced magnetic resonance angiography greatly aids in the diagnosis and assessment of these tumors as an adjunct to conventional MR imaging. Prior to treatment, CE-MRA helps to fully delineate the extent of primary tumors. This technique also is useful for detecting additional paragangliomas, and also may be useful for screening purposes. Finally, CE-MRA also helps to refine a location-based differential diagnosis of head and neck masses, distinguishing paragangliomas from other non-neuroendocrine tumors. Figure. Patient with carotid body tumor (not pictured). Axial MR images through C1-2. Top, post-Gd fat-sat T1WI, and bottom, CE-MRA MPR. 7 mm right vagal paraganglioma visible on both images (arrows), smaller 5 mm left vagal paraganglioma (arrowhead) only identifiable on CE-MRA image.

Conclusions

As a complement to conventional MR imaging, the CE-MRA sequence increases both sensitivity and specificity in the diagnosis of head and neck paragangliomas, with a relatively short acquisition time.



(Filename: TCT_eEdE-122_PGLCEMRAJohnsen.jpg)

eEdE-156

6:30AM - 3:00PM

The Clinical Implications of Failing to Recognize Aberrant Arachnoid Granulations

K Cavallo Hom[1], J Ulmer[2], M Agarwal[3], A Klein[2], L Mark[2]
[1]Medical College of Wisconsin, Milwaukee , WI, [2]Medical College of Wisconsin - Froedtert Hospital, Milwaukee, WI, [3]Medical College of Wisconsin, Milwaukee, WI

Purpose
Failure to recognize or misdiagnose aberrant arachnoid granulations can result in

unnecessary and potentially harmful testing and procedures. This exhibit illustrates the spectrum of aberrant skull base arachnoid granulations as they appear on computed tomography (CT) and magnetic resonance imaging (MRI) and aims to educate the neuroradiologist about the clinical implications to ultimately promote timely accurate end diagnosis.

Materials and Methods

The exhibit discusses the embryologic origins, micro-structure, and natural history of aberrant skull base arachnoid granulations (AbAG). The display illustrates the wide spectrum of appearance of AbAG on CT and MRI, with an emphasis on distinguishing imaging features that allow an accurate diagnosis (Figure 1). A case series is presented, demonstrating real life clinical implications of recognizing or failing to recognize AbAG. In doing so, the exhibit seeks to enhance the understanding of this phenomenon by neuroradiologists, to avoid misinterpretations and to readily recognize the clinical significance of aberrant arachnoid granulations.

Results

Aberrant arachnoid granulations are granulations that penetrate the dura but fail to reach the dural sinus, and most commonly occur within the greater wing of the sphenoid bone (1). They generally measure 5 to 15 mm in diameter, but may enlarge over time due to cerebrospinal fluid (CSF) pulsations generating significantly larger bony defects. They may cause extensive bony expansion as well as erosion of the inner table, outer table, and regional structures including the orbit and the sphenoid sinus. The location in the sphenoid wing predisposes to potentially significant clinical sequelae. There are three main clinical implications that the practicing neuroradiologist should be aware of in recognizing the presence of AbAG. These include misdiagnosis as skull base neoplasms, CSF leak and meningitis, and encephaloceles that may result in seizure activity.

Conclusions

A thorough understanding of the wide spectrum of imaging appearances of aberrant skull base arachnoid granulations is important to clinical practice. Neuroradiologists should be well versed in the clinical implications and natural history of the phenomenon, to promote diagnostic accuracy.

Figure 1:

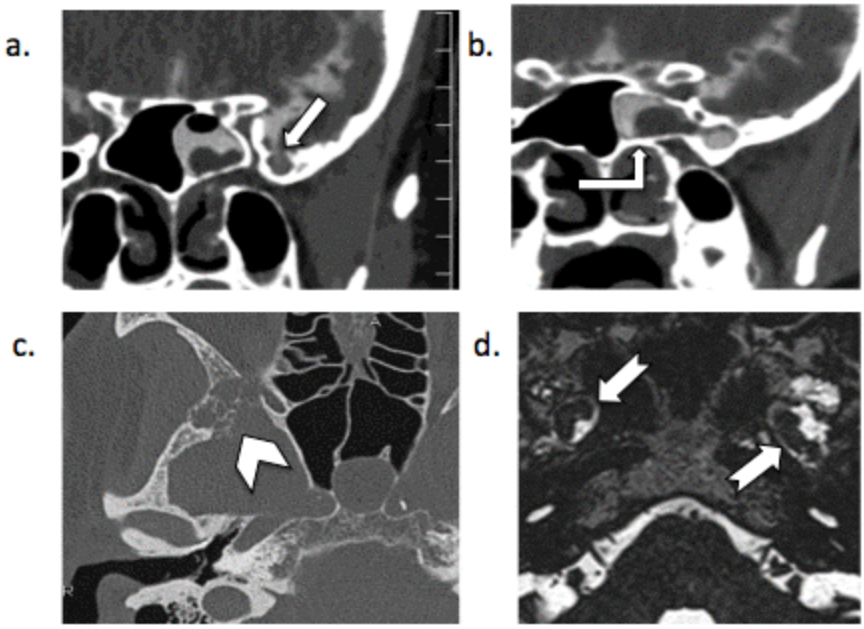


Figure 1 - The spectrum of skull base arachnoid granulations includes a.) cerebrospinal fluid leak into the left lateral recess of the sphenoid sinus ⇨, b.) with extension into the sphenoid sinus in the same patient ⇦, c.) lytic, tumor-like appearance ⇨, and d.) encephalocele (bilaterally) ⇨.

(Filename: TCT_eEdE-156_Figure-arachnoidgranulations.gif)

eEdE-168

6:30AM - 3:00PM

The Other Sinus Cancers: a Tour of the Tumors Not Named Squamous Cell

R Khan[1], J Chokr[2], G Choudhary[3], B Winegar[4], S Ahmed[5]
[1]University of Arizona Medical Center, Tucson, AZ, [2]Banner University Medical Center, tucson, AZ, [3]Banner university medical center, Tucson, AZ, [4]University of Utah, Salt Lake City, UT, [5]UT MD Anderson Cancer Center, Houston, TX

Purpose
To familiarize the reader with the computed tomography (CT) and magnetic resonance imaging (MRI) findings of nonsquamous cell cancers in the sinonasal region, to discuss staging criteria, and the patterns of tumor spread.
Materials and Methods
Electronic Education Exhibit
Results
This educational exhibit will review the CT and MRI findings of nonsquamous cell cancers

on CT and both 1.5T and 3T MRI. Supporting PET/CT images also will be included. The AJCC staging criteria will be discussed as they pertain to sinonasal cancers and specific staging criteria unique to each imaging case will be discussed. Cases to be presented include: inverted papilloma, dedifferentiated inverted papilloma, esthesioneuroblastoma, adenocarcinoma, melanoma, non-Hodgkins lymphoma, sinonasal undifferentiated carcinoma (SNUC), adenoid cystic carcinoma, chondrosarcoma, and osteosarcoma. Patterns of spread including direct extension, perineural tumor spread, nodal and distant metastatic disease also will be discussed.
Conclusions
After the reader has reviewed the presentation, they will be able to appreciate the imaging features of nonsquamous cell cancers in the sinonasal region. They also will be familiar with the AJCC staging criteria, through both discussion and demonstrated case-based examples, in addition to patterns of sinonasal tumor spread.

eEdE-128

6:30AM - 3:00PM

The Radiology of Enophthalmos

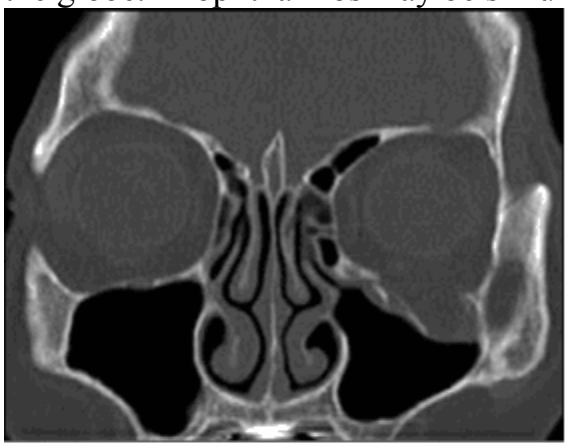
K GILL[1], D Shatzkes[2]
[1]LENOX HILL HOSPITAL, NEW YORK, NY, [2]Lenox Hill Hospital, New York, NY

Purpose
While enophthalmos is a less frequently encountered imaging finding than exophthalmos, there is a similarly wide differential diagnosis. This exhibit offers a classification scheme for entities that may cause enophthalmos and familiarizes the reader with imaging features of some of the more common or interesting etiologies.
Materials and Methods
We categorized the causes of enophthalmos as those that expand the bony orbital volume, those that result in diminished retrobulbar fat and those that result in posterior retraction of the globe. In addition to providing examples of entities within each of these categories, we included a variety of causes of pseudo-enophthalmos, where enophthalmos is simulated by a small globe or ptotic eyelid.
Results
1) Expanded orbital volume- Structural alteration of the bony orbit may result in an increase in orbital volume, which leads to posterior displacement of the globe: -Trauma, -Silent Sinus Syndrome, -Silent Brain Syndrome, -NF1, -Iatrogenic (e.g., post maxillectomy). 2) Orbital fat atrophy: - Fat atrophy leads to reduction in retrobulbar soft tissue volume, allowing the globe to displace posteriorly within the bony orbit. -Anorexia/cachexia, -Senile enophthalmos, -Hemifacial atrophy (Parry-Romberg syndrome, linear scleroderma), -Marfan syndrome, -Radiation. 3) Globe retraction-. Posterior traction of the globe occurs due to fibrosis or contracture of retrobulbar soft tissues. -Scirrhous metastases (breast), -Duane

retraction syndrome, -Post-inflammatory (e.g., Wegener's, TB), -Radiation. 4) seudo-enophthalmos- Enophthalmos may be simulated clinically when there is a small globe or ptotic eyelid. -Microphthalmia, -Phthisis bulbi, -Contralateral exophthalmos, -Ptosis (Horner's syndrome).

Conclusions

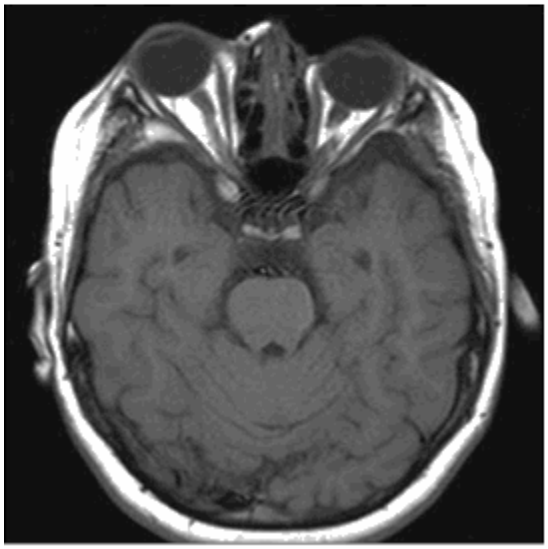
Enophthalmos refers to posterior displacement of the normal-sized globe. It may occur because of expansion of bony orbital volume, atrophy of orbital fat, or posterior retraction of the globe. Enophthalmos may be simulated when there is ptosis or a small globe.



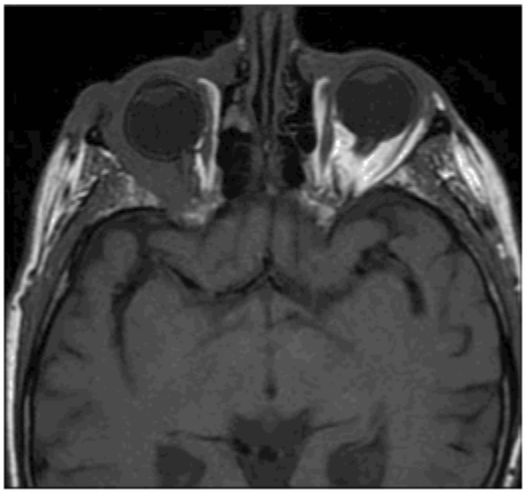
CHRONIC ORBITAL FLOOR FRACTURE



CACHEXIA



BREAST CANCER



PARRY-ROMBERG

(Filename: TCT_eEdE-128_Slide1.gif)

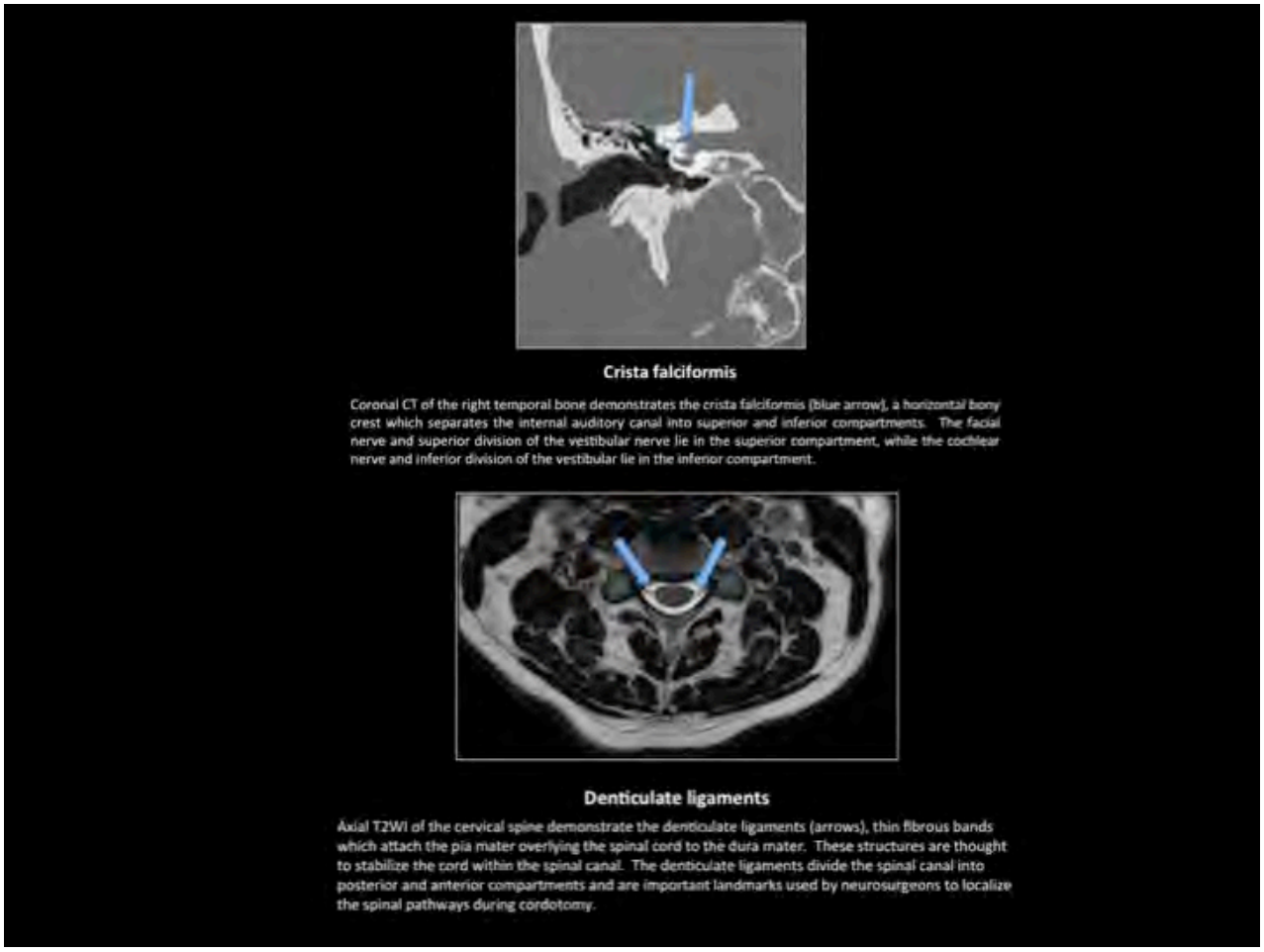
eEdE-120

6:30AM - 3:00PM

The Road Less Traveled: Review of Uncommon Anatomical Terms That the Neuroradiologist Should Know

J Kramer[1], A SRINIVASAN[2]
[1]University of Michigan Health System, Ann Arbor, MI, [2]UNIVERSITY OF MICHIGAN, ANN ARBOR, MI

Purpose
Neuroanatomy is an extensively complex subject that requires years of study for even the most dedicated and brightest to master. Even the tiniest of neuroanatomical structures can have drastic clinical significance. In this presentation, we will discuss several uncommon neuroanatomical terms that the neuroradiologist should know, highlight their clinical importance and treatment implications, and enhance the viewers' ability to assess these structures, therefore adding value to their imaging interpretations.
Materials and Methods
We will present a case-based review of several uncommon anatomical terms using a categorized approach including the brain, head/neck, and spine anatomy. The presentation will be image-rich using high quality imaging examples from the authors' institution. Original illustrations also will be provided to further highlight the salient findings and facilitate learning.
Results
Several uncommon neuroanatomical terms in the brain, head/neck, and spine will be described. Structures to be discussed include psalterium/lyra, induseum griseum, Bill's bar, crista falciformis, buccopharyngeal fascia, pharyngobasilar fascia, sinus of Morgagni, septum posticum of Schwalbe, denticulate ligaments, coronary veins, and fasciculus cuneatus and gracilis.
Conclusions
After viewing this presentation, the observer will gain familiarity with several uncommon neuroanatomical terms, understand their clinical significance, and learn their relevance to surgical interventions. With this knowledge, the neuroradiologist can better evaluate these important structures and add further value to radiologic interpretations.



(Filename: TCT_eEdE-120_Slide1.jpg)

eEdE-161

6:30AM - 3:00PM

Top Ten Frequently Missed Diagnoses in the Head & Neck

B Patel[1], D Shatzkes[1]
[1]*Lenox Hill Hospital, New York, NY*

Purpose
The head and neck is an anatomically complex region where diagnoses may be missed because of a variety of cognitive or systemic errors. The purpose of this presentation is to review and classify the spectrum of cognitive errors, and to apply this classification to 10 frequently missed diagnoses in the head and neck.
Materials and Methods
We classified cognitive errors as follows: 1. Failures of detection (perceptual errors): a. Findings are subtle. b. Not part of visual inspection scheme. 2. Failures of interpretation (errors of diagnosis): a. Unfamiliar diagnosis. b. Imaging features confusing. We then

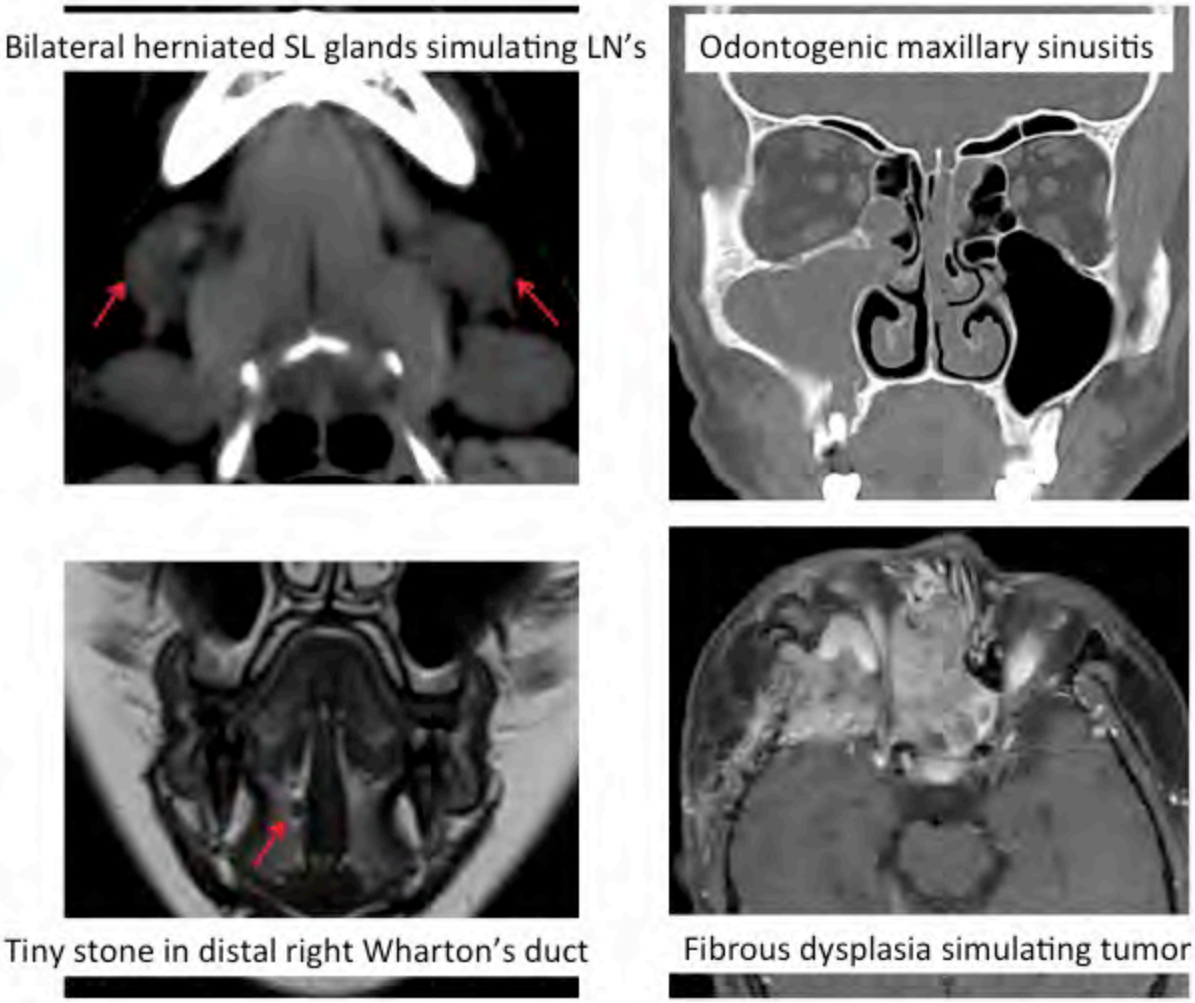
applied this classification scheme to ten commonly missed diagnoses in the head and neck, with a discussion of each entity. Additionally, we recommended practical "fixes" to avoid missing these diagnoses.

Results

The following is a list of the ten frequently missed diagnoses that we have included in this presentation. The numbers that follow refer to the types of cognitive errors, as presented in the Approach/Methods section. Each entity is illustrated with several examples, and suggested fixes accompany the specific descriptions of associated cognitive errors. 1. Labyrinthitis (1a, 1b). 2. Mylohyoid defect with herniation of salivary tissue (2a, 2b). 3. Odotogenic maxillary sinusitis (1b). 4. Submandibular sialolithiasis(1a). 5. Perineural tumor spread (1a, 1b). 6. Fibrous dysplasia on MRI (2b). 7. Sphenoid arrested pneumatization (2a, 2b). 8. Intraosseous meningioma (1a, 2a). 9. Cystic lymphadenopathy called branchial cleft cyst (2b). 10. Fenestral otosclerosis (1a).

Conclusions

We broadly classified cognitive errors as failures of perception and failures of interpretation, and applied this classification scheme to ten commonly missed diagnoses in the head and neck. Application of the recommended fixes, which included modification of existing image interrogation schemes as well as knowledge of common variants that may be mistaken for disease, should help reduce the frequency of these misses. Additionally, a general understanding of the sources of radiology errors should help improve overall diagnostic performance.



(Filename: TCT_eEdE-161_Slide1.jpg)

eEdE-147

6:30AM - 3:00PM

Tumor Board: What the ENT Surgeon Wants to Know About Salivary Gland Malignancies

M Uzee[1], t huynh[1], S Joglekar[1], R Raju[1], Y Kreitman[1]
[1]*Scott and White Medical Center- Temple, Temple, TX*

Purpose
Malignant salivary gland tumors are uncommon tumors, representing 3-5% of all head and neck cancers, as well as 0.3% of cancers overall. According to the WHO classification of salivary gland tumors, there are 24 distinct types of salivary gland malignancy. Although the extensive pathological possibilities may seem daunting when interpreting imaging findings,

the surgical approach is dependent on extent, lymph node metastases, and perineural involvement, as opposed to specific histology. Giving an accurate description of the tumor extension, as well as the possibility of perineural or lymph node involvement, is more valuable to the surgeon than trying to narrow down the specific pathology by imaging alone. Knowledge of relevant tumor extension to certain areas can significantly impact the surgical management and/or approach and is, therefore, of extreme importance to the ENT surgeon. The neuroradiologist thus plays a vital role in the work up of these tumors. This presentation will present both MRI/CT images and corresponding intra-operative photographs detailing a variety of salivary gland tumor spread that affects surgical management. Brief overviews of the staging of salivary gland malignancies and the most common pathology seen in both the major and minor salivary glands also will be included with attention to impact on management. An interactive powerpoint presentation will be utilized to enhance the learner's experience.

Materials and Methods

From a retrospective review of neuroradiology cases performed in the Baylor Scott & White Healthcare system, multiple cases of salivary gland malignancy were identified. In collaboration with ENT surgeons at our institution, the pertinent tumor characteristics that can affect surgical management are identified and presented in this exhibit. Representative cross-sectional images with corresponding intra-operative photographs, when available, will be presented to illustrate the variations of salivary gland malignancy extension and demonstrate how each variation affects the surgical management/approach. An abbreviated summary of the most common histological types of malignancy seen in both the minor and major salivary glands, as well as specific imaging features that can aid diagnosis, will be discussed. Additionally, a brief review of staging of salivary gland malignancies will be provided with attention to the imaging features that define each stage and how staging affects treatment strategy.

Results

Salivary gland malignancies are relatively uncommon head and neck tumors. Surgical management generally does not change significantly with changes in histology; however, certain imaging findings can significantly change the surgical management/approach. In the case of a parotid neoplasm confined to the superficial lobe of the parotid gland, a superficial parotidectomy generally is performed. However, if the tumor extends significantly into the parapharyngeal space, a cervical approach will expose the deep lobe of the parotid gland. Thus, the surgeon needs to be aware of that finding prior to surgery. Salivary gland malignancy staging and a brief discussion of the most common histological types of malignancy seen in the major and minor salivary glands also are reviewed with emphasis on how the treatment strategy changes with variations in each. Given the relative uncommon nature of these tumors, this presentation is meant to highlight the specific imaging findings that the ENT surgeon needs to know. With this knowledge, the learner will be able to confidently relay the necessary information that can potentially make a significant impact on patient care.

Conclusions
Although the malignant pathology that can be encountered in the salivary glands is extensive, only with rare exception is the surgical management decided by a histologic diagnosis. Instead, the treatment strategy is formed based on tumor extension, presence of perineural spread, and evidence of lymph node metastases. Thus, knowledge of the pertinent imaging that can significantly alter the surgical approach is very important. After participating in this cross-sectional imaging and intra-operative photograph rich review, the learner should have a better understanding of the imaging findings and subsequent changes in staging that need to be brought to the attention of the surgeon, so that the most appropriate treatment strategy can be pursued. Also, demonstration of imaging findings that can suggest a specific diagnosis which can potentially alter the treatment plan will increase the learner's confidence in reporting these findings.

eEdE-134

6:30AM - 3:00PM

Understanding Orbital Cellulitis, A Disease that Has Been Changing in the Last 2 Decades

N Hatch[1], K Pflug[1], M Matheus[1]
[1]*Medical University of South Carolina, Charleston, SC*

Purpose
In the last two decades, the presentation of orbital cellulitis has been changing. Several factors may contribute to this change, one of which is the increase in Methicillin-resistant staphylococcus aureus infection. As a result, we are most likely seeing a possible drift in the clinical presentation of orbital cellulitis that may carry more frequent morbid and potentially lethal consequences. This case-based educational review aims to illustrate the most characteristic imaging findings of the benign and complicated course of orbital cellulitis as well as discuss the changes in presentation seen at our institution over the last 2 decades.
Materials and Methods
Using a large series of illustrative orbit CT and brain/orbit MRI cases from our didactic imaging files, we will show the most characteristic imaging features of isolated preseptal cellulitis, postseptal cellulitis, and its complications. Key imaging features such as bone dehiscence and erosion with postseptal cellulitis, orbital abscesses, phlegmonous mass, ophthalmic vein thrombosis, signs of rapid increase in intra-orbital pressure, cavernous sinus thrombosis, meningitis and cerebritis will be illustrated. Microbiological etiology, patient's demographics, as well as patient's comorbidities will be concomitantly presented and discussed.
Results
This case discussion in conjunction with literature review will provide a thorough learning experience highlighting the potential aggressive course of orbital cellulitis focusing on

findings that lead to changes in clinical management. These cases have been observed over the last 2 decades at our institution and will be reviewed. We also will discuss the observed tendency of increasingly complicated orbital cellulitis presentations over the last 2 decades at our institution. It is speculated that this could be due to changes in microbiological etiologies over that time period.
Conclusions
This case-based didactic presentation will review complicated and uncomplicated orbital cellulitis as well as discuss the tendency towards increasingly complicated orbital cellulitis cases presenting at our institution over the last 2 decades.

eEdE-143

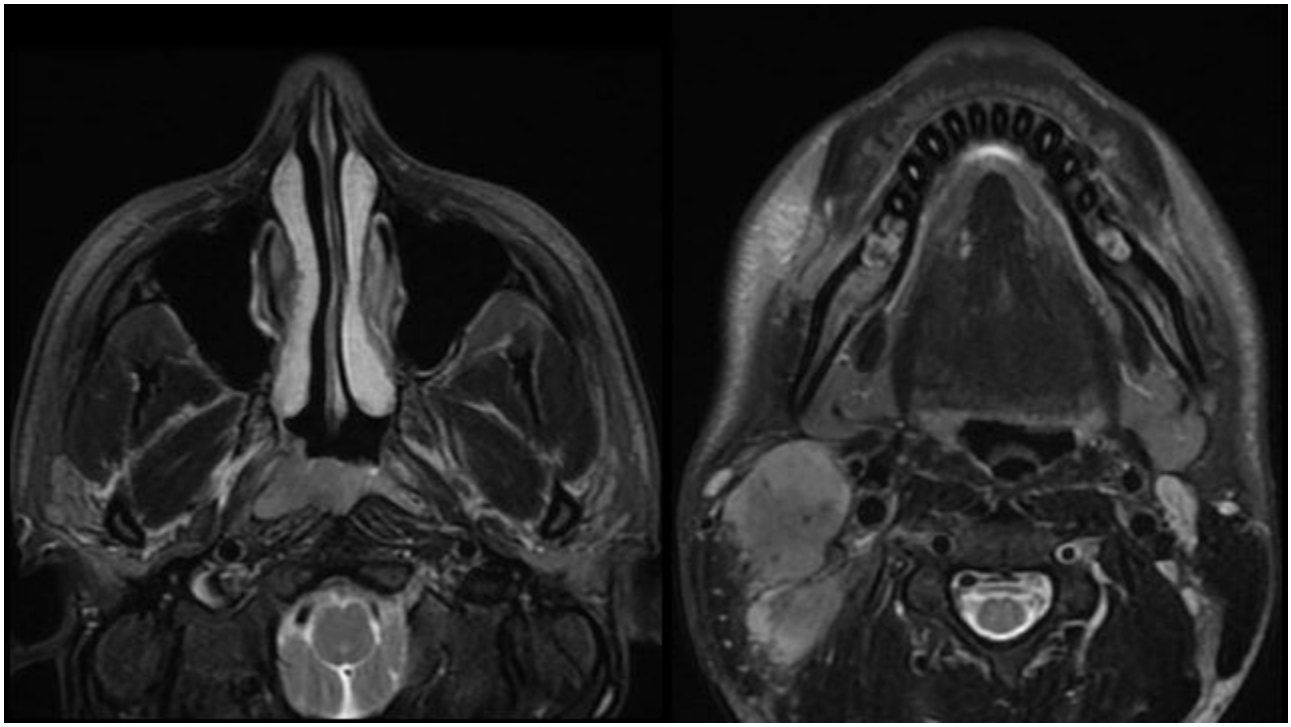
6:30AM - 3:00PM

Update on Head and Neck Viral Carcinogens HIV, HTLV, KSHV, EBV, HPV, MCV

A Uzelac[1], B Rehani[1], C Glastonbury[1]
[1]*University of California, San Francisco, San Francisco, CA*

Purpose
An association of specific viral agents and human malignancies has been well established. In November 2016, the U.S. Department of Health and Human Services released the 14th Report on Carcinogens adding seven new substances to the list of known carcinogens (1). Five of these substances are viruses and all five are associated with malignancies occurring in the head and neck (HN). The purpose of this presentation is to update the readers on these oncogenic viruses and to highlight their manifestations in HN imaging.
Materials and Methods
We present key information about these viral agents, their method of spread, demographics and mechanisms of inducing inflammatory changes and tumorigenesis. The typical and variant imaging manifestations, complications and recommendations for imaging modality choice also are presented.
Results
Viruses are considered causative of up to 15% of human cancers (2). Long-established oncogenic viruses include hepatitis B and C, and human papilloma virus (HPV) which is responsible for most anogenital neoplasms and oropharyngeal squamous cell carcinoma (SCCa). Other viruses have long been recognized to be associated with malignancy (3), but only recently were they designated as carcinogens. These oncogenic agents are human immunodeficiency virus type 1 (HIV-1), human T-cell lymphotropic virus type 1 (HTLV-1), Epstein-Barr virus (EBV), Kaposi sarcoma-associated herpesvirus (KSHV), and Merkel cell polyomavirus (MCV). All of these viruses are associated with HN malignancies with mucosal, skin and/or lymphatic involvement of neck structures. Some also may manifest with inflammatory changes.

Conclusions
Six viral agents have been determined to be oncogenic and associated with HN malignancies, with five only recently declared as carcinogens in November 2016. Neuroradiologists should be cognizant of these viruses, their method of spread and their manifestations of infection and tumor induction in the HN.



(Filename: TCT_eEdE-143_Capture.JPG)

eEdE-118

6:30AM - 3:00PM

Utility of the Color/Gross Appearance and Biochemistry of Fine-Needle Aspiration Specimens in the Differential Diagnosis of Cystic Neck Lesions

M Prenafeta Moreno[1], V Pérez Riverola[1], J Branera[1], V Cheranovskiy[1], L Rivera[1], A Rovira Gols[1]
[1]*UDIAT-CD, Corporació Sanitària Parc Taulí, Sabadell, Barcelona*

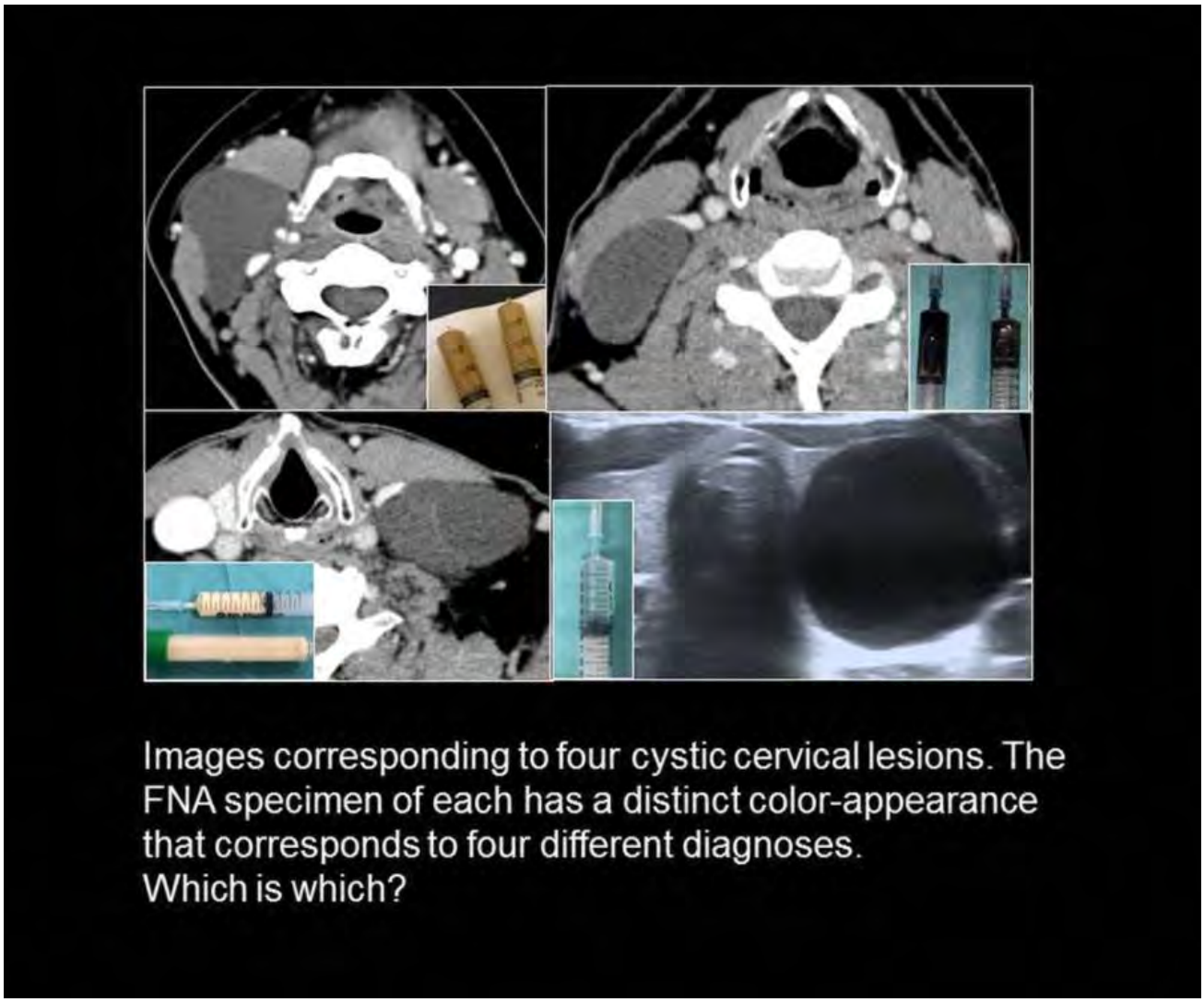
Purpose
To show the clinical and radiologic findings for different cystic and cyst-like neck lesions and the utility of the color/gross appearance and biochemistry of fine-needle aspiration (FNA) specimens in their differential diagnosis.
Materials and Methods
We include all patients with cystic and cyst-like neck lesions studied by US and/or CT with FNA between 2006 and 2016. All patients in the exhibit underwent surgery, and all specimens underwent histopathologic study.

Results

Cystic and cyst-like neck lesions are common, representing a wide spectrum of congenital and acquired diseases. Ultrasound (US) is usually the first imaging study, and it is ideal for determining the cystic nature of the lesion. Computed tomography (CT) and magnetic resonance imaging (MRI) can help characterize these lesions and are especially useful for determining the lesion's exact location and its relation to neighboring structures. Cysts and cyst-like neck lesions (e.g., branchial cysts, cystic metastatic lymph nodes from oropharyngeal carcinomas or papillary thyroid carcinomas, cystic lymphatic malformations, colloid nodules, parathyroid cysts, cystic parotid lesions, and tuberculous lymphadenitis) often represent a diagnostic challenge. Patients' clinical history, physical examination, and imaging work up often can reach the correct diagnosis. However, some of these lesions that share the same anatomic space can have overlapping imaging findings, and it can be difficult to establish the diagnosis in certain locations, such as the posterior thyroid; in these cases US-guided FNA is necessary. Although FNA's performance is not as good in cystic neck lesions as in solid masses, evaluating the imaging findings together with the biochemistry and color/gross appearance of the aspirate greatly improves the performance.

Conclusions

Analyzing the gross appearance, especially the color, and the biochemistry of FNA specimens can be very useful in the diagnostic management of cystic neck lesions.



(Filename: TCT_eEdE-118_NeckQuists.jpg)

eEdE-119

6:30AM - 3:00PM

What Could Be Wrong When Your Head and Neck Muscles Go "Kaput"?

N Wilson[1], B Setty[2], V Andreu[1], M Clement[1], O Sakai[2]
[1]Boston Medical Center, Boston, MA, [2]Boston Medical Center, Boston University School of Medicine, Boston, MA

Purpose
Muscular anatomy of the head and neck is very complicated and comprises of both skeletal and smooth muscles which allow for the different voluntary and involuntary actions necessary for maintenance of life and various daily activities. In this exhibit, we illustrate

with examples the various intrinsic muscle abnormalities encountered in the head and neck in both the pediatric and adult population.

Materials and Methods

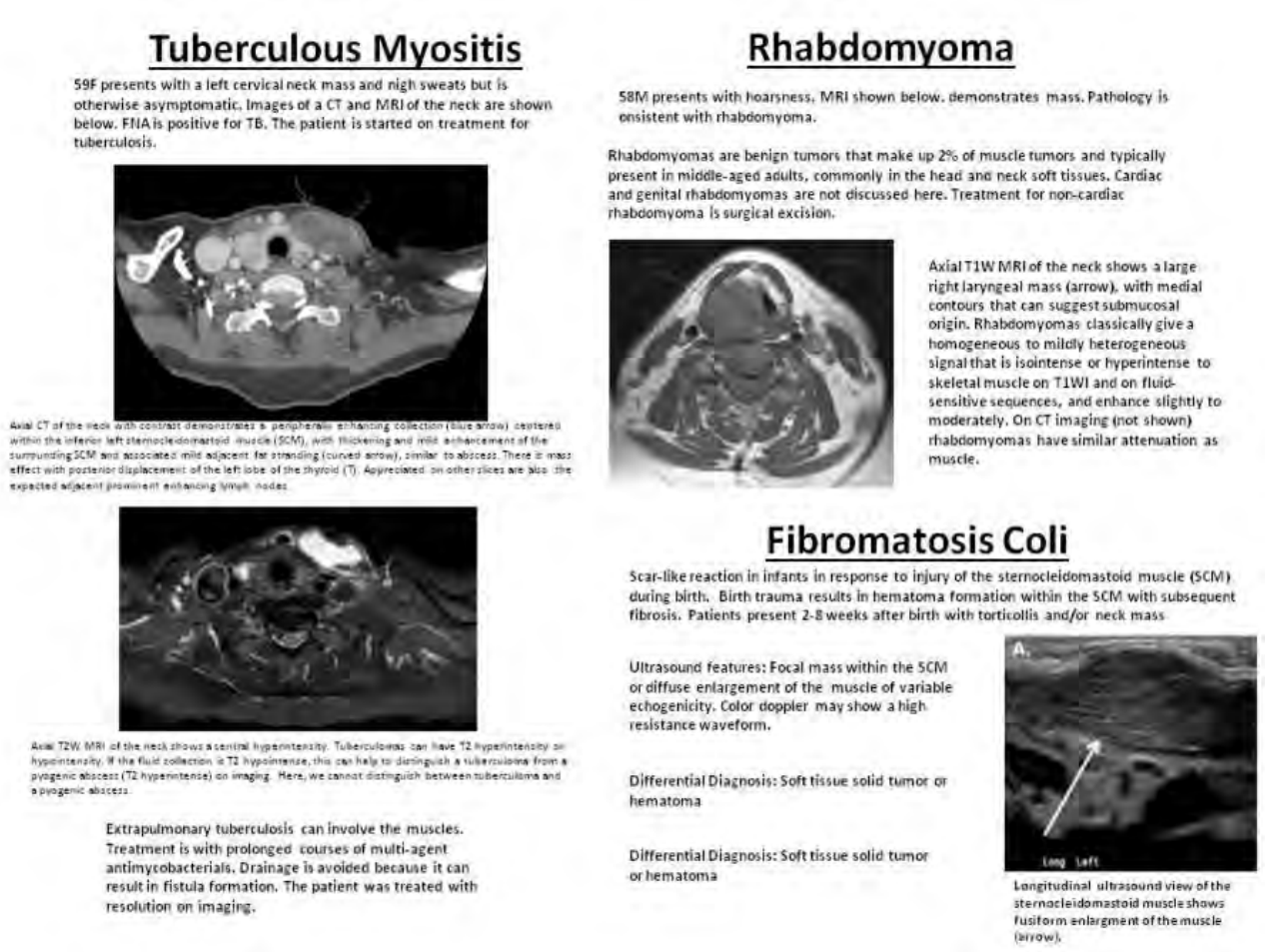
We retrospectively reviewed cross-sectional images of the head and neck from 2001-2016 to identify cases with abnormalities pertaining to the muscles. We excluded masses which invade the musculature or arise from other structures within the musculature but not intrinsic to the muscle fibers.

Results

The majority of muscle pathology is benign and ranges from symmetric and asymmetric hypertrophy of the muscles to atrophy, or rarely congenital absence. Hypertrophy can be seen in Grave's disease or in masseteric hypertrophy. Atrophy of the muscles can result from denervation, often in cases of injury, and can be seen in the muscles of the tongue and those of mastication, in the vocal cords, in the paraspinal muscles, and in cases of perineural involvement from tumors themselves as sequelae of treatment. Focal muscular injury often can lead to infarction, sometimes seen in cases of traumatic herniation into the orbit, whereas severe injury can result in rhabdomyolysis. Idiopathic infiltration of fibrous tissue or inflammation of the muscles can be seen in a range of entities including fibromatosis colli in infancy, longus colli tendinitis or orbital pseudotumor. Infection/inflammation of the musculature can lead to myositis and/or abscess formation. Tumors of the muscles include leiomyoma/leiomyosarcoma involving the smooth muscle, and rhabdomyoma/rhabdomyosarcoma in the skeletal muscle, but these are rare.

Conclusions

Evaluation of the musculature is important in head and neck imaging as it may be affected by different disease processes but also provide indirect clues to the involvement of the cranial nerves.



(Filename: TCT_eEdE-119_HNMusclePathologyExhibitComplete.jpg)

eEdE-146

6:30AM - 3:00PM

What's Black and White and Hoarse All Over?: Unilateral Vocal Cord Paralysis Cases Presented with an Anatomic and Radiologic Review

J Ball[1], A Blanchard[1], J Gupta[1], N Gupta[1]
[1]*Tulane University School of Medicine, New Orleans, LA*

Purpose
Vocal cord paralysis (VCP) is a well-known complication of surgeries involving the neck. Routine surgeries such as thyroidectomy and carotid endarterectomy are common etiologies. Vocal chord paralysis can affect a patient's quality of life from producing hoarseness to dyspnea to dysphonia. Other etiologies of VCP include trauma, infection, inflammation, and mass infiltration or compression, with up to 20% of unilateral VCP cases idiopathic (1). Vocal chord paralysis may be the first symptom of a tumor within the neck as seen in one of the cases reviewed in this presentation.

Materials and Methods

This presentation approaches VCP comprehensively starting with an anatomic review of the nerves involved in normal vocal cord function as well as normal neck structures, especially those of the larynx. A review of common VCP etiologies and associated imaging findings will follow. Finally, common and uncommon cases of VCP from our institution will be presented and discussed.

Results

The right and left recurrent laryngeal nerves (RLN) innervate the right and left vocal cords, respectively. The RLNs originate from their respective vagus nerves. A lesion anywhere along the vagus nerves before the branchpoint of the RLNs as well as a lesion involving the RLNs themselves may result in VCP. Therefore, anomalies in the expected course of those nerves may provide an explanation for the symptoms of VCP and the imaging findings suggestive of VCP.

Conclusions

Vocal chord paralysis may present as a surgical complication or as the first symptom with an unknown etiology at the time of presentation. Prompt imaging evaluation can aid in the diagnosis and identify the underlying etiology. Those imaging findings may dictate treatment plans and options. This presentation will provide an in-depth understanding of the anatomy, pathophysiology, imaging findings, and differential diagnoses of VCP. That understanding will benefit the radiologist's diagnostic accuracy and aid in decisions regarding patient care.



(Filename: TCT_eEdE-146_Figure1.jpg)

eEdE-138

6:30AM - 3:00PM

What's Wrong with My Vision? Anatomical and Neuroimaging Perspective of Orbital Apex Syndrome

R Patel[1], R Jacob[2], A Kamali[1], O Adesina[1]
[1]The University of Texas Health Science Center, Houston, Houston, TX, [2]UMC Health System, Lubbock, TX

Purpose
Orbital apex acts an osseous tunnel for various neurovascular structures entering the orbit from the cranial vault and is formed by the union of the lesser and greater wings of the sphenoid bone. A broad range of lesions of the orbital apex are clinically important as they can have an adverse effect on visual function. Our purpose is to organize the pathologic processes which occur at the orbital apex into imaging differentials, establish an organized approach to imaging analysis, and present examples of representative lesions.
Materials and Methods
We review the anatomy of the orbital apex and categorize and describe the pathologic entities that are encountered most frequently in this anatomically compact region, and identify imaging patterns that can help to narrow the differential diagnosis.
Results
Categories of orbital apex lesions include: neoplasms, inflammatory processes, infections, trauma, and vascular lesions causing extrinsic compression. This categorization provides an organized framework to facilitate a reasonable differential diagnosis. Computed tomography (CT) and magnetic resonance imaging (MRI) are the modalities of choice to evaluate and characterize orbital apex lesions, and imaging examples utilizing these modalities will be presented.
Conclusions
The orbital apex is a clinically important anatomical region and hosts diverse pathologic processes, and an awareness of common imaging patterns can help to generate a focused differential diagnosis. The viewers of this exhibit will gain refreshed information about the anatomy of the orbital apex and also will gain an appreciation for the wide radiographic spectrum of common and uncommon disease processes that affect the orbital apex causing orbital apex syndrome.

eEdE-123

6:30AM - 3:00PM

Workflow Implications of Routine Dual Energy CT Scanning of the Neck in Clinical Practice: A Single Institution Experience

A Perez-Lara[1], G Wing[1], M Levental[2], L Rosenbloom[3], R Forghani[2]

[1]Jewish General Hospital, Montreal, Quebec, [2]Jewish General Hospital & McGill University, Montreal, Quebec, [3]Jewish General Hospital, McGill University, Montreal, AK

Purpose
The availability and use of dual energy computed tomography (DECT) is increasing with multiple emerging clinical applications in head and neck imaging. In the long-run, widespread adoption of DECT in clinical practice likely will depend not only on demonstration of added diagnostic value but also seamless workflow integration. The purpose of this exhibit is to review the practical workflow implications of routine DECT scanning based on the experience at a single institution where most of elective neck CTs are acquired in DECT mode.
Materials and Methods
The exhibit will begin with a brief overview of DECT systems and then focus on the workflow using a fast kVp switching DECT scanner. Dual energy computed tomography workflow will be reviewed with special emphasis on factors that impact technologist and radiologist workflow, current challenges, and potential solutions and improvements where needed.
Results
The exhibit will begin with a brief overview of different DECT systems. Different modes of acquisition and the need for prospective (or pre-planned) DECT acquisition will be discussed with exceptions such as with scanners based on sandwich detectors that always acquire in DECT mode. Thereafter, the entire workflow will be reviewed, with special emphasis on factors that impact workflow on the (1) technologist side (e.g., preset protocols with generation of special DECT reconstructions; scan acquisition and processing times and their impact on patient scheduling) and (2) radiologist side (use of preset reconstructions, sampling of frequency of use, etc.). The exhibit will conclude with a discussion of remaining challenges and potential solutions for seamless workflow integration.
Conclusions
Widespread adoption of DECT in routine clinical practice will likely depend on seamless workflow integration. A number of steps can be taken that improve workflow with current systems, and these are reviewed in this exhibit. Although some challenges remain, these can likely be resolved with future technical innovations.

Monday
6:30AM - 3:00PM

Electronic Education Exhibit (eEde)-Informatics

eEdE-178

6:30AM - 3:00PM

Common Artifacts in Neuroimaging: What Every Resident Should Know

o eissa[1], r eldaya[1], H Al-Jadiry[2], S Gatzert[3], k Raj[4], J Heymann[5]
[1]University of Texas Medical Branch, Galveston, TX, [2]UTMB Galveston, Galveston, TX, [3]The University of Texas Medical Branch, Galveston, TX, [4]UTMB, Galveston, TX, [5]University of Texas Medical Branch at Galveston, Galveston, TX

Purpose

An artifact is a distortion or error in an image that is unrelated to the subject being imaged. Artifacts are common in neuroimaging and often pose a challenging dilemma and lead to misdiagnosis. The purpose of this exhibit is to familiarize radiology residents and general radiologists with the common artifacts in different neuroradiology imaging modalities that are common to every day practice, while offering clues to differentiate them from true pathology. The exhibit also will emphasize and simplify the physics behind those artifacts and offer multiple practical solutions to overcome those artifacts and optimize neuroimaging.

Materials and Methods

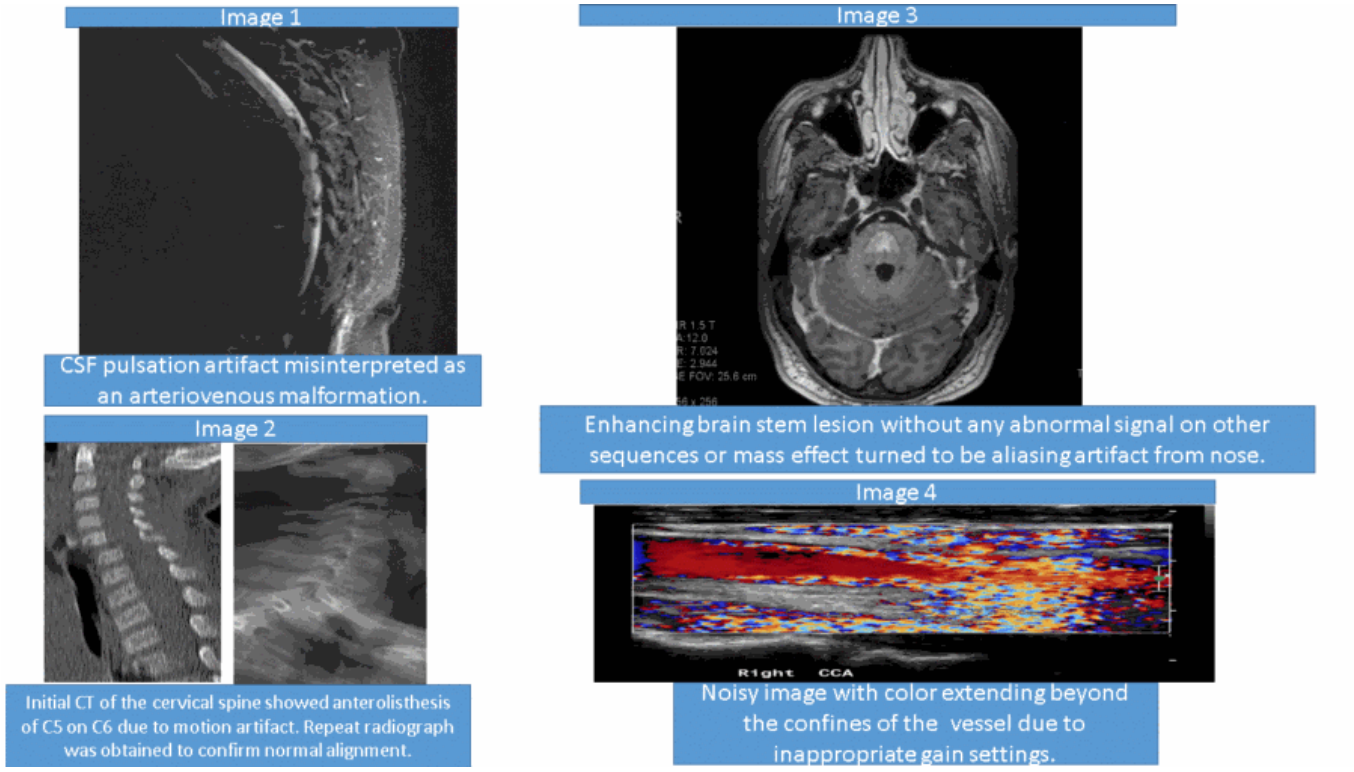
Ultrasound (US) common artifacts; computed tomography (CT) common artifacts; magnetic resonance imaging (MRI) common artifacts.

Results

US Artifacts: Aliasing; Mirror image; Doppler gain. CT Artifacts: Motion; Noise; Beam hardening; Ring artifact. MRI Artifacts: Ghosting; Aliasing; Truncation; Metal artifact. Flow artifact: Magnetic susceptibility; Chemical shift; Zipper.

Conclusions

Artifacts in imaging can be difficult to identify. By recognizing common neuroimaging artifacts and correctly identifying the cause, radiologists can improve image quality. This exhibit describes the appearances of major artifacts encountered in clinical neuroimaging, explains their physical basis, and offers simple strategies for reducing or eliminating them.



(Filename: TCT_eEdE-178_Slide1.GIF)

eEdE-175

6:30AM - 3:00PM

Contextual Radiology Reporting: A New Approach to Structured Templates

M Mamlouk[1]
[1]*Kaiser Permanente, University of California, San Francisco, Santa Clara, CA*

Purpose
Recent literature and several radiology organizations advocate for the use of structured templates as a new standard for radiology reporting. Proponents of this format have expressed improved clinician and radiologist satisfaction, decreased report variability, and improved clarity. Despite this impetus, one limitation of existing structured report formats is that they are modality or exam-based rather than designed for specific diagnoses. In addition, this method of structured reporting is not applicable to every study and does little to guide the interpreter to the specific imaging findings germane to the diagnosis. The purpose of this project is to develop a collection of contextual reporting templates for common diagnoses within neuroradiology.
Materials and Methods
Develop contextual structured templates for common diagnoses/entities encountered in neuroradiology, including: - Neurodegenerative; -Epilepsy; -Multiple Sclerosis; -Pituitary; -CT sinus disease; -Temporal bone; -Developmental delay; -Fetal MRI. Radiologic images

will be shown to highlight findings where contextual structured templates can help ensure important items are discussed, including pertinent positives and negatives, appropriate differential diagnoses, anatomic variants that may impact surgery, and observance of national consensus guidelines when appropriate.

Results

1) Neurodegenerative MRI Report: FINDINGS: BRAIN VOLUME: (No age-significant|Mild|Moderate|Severe) atrophy. (Global without lobar predilection or asymmetry|regional-specify). HIPPOCAMPAL VOLUME: (Normal|Mildly reduced|Moderately reduced|Severely reduced). BRAINSTEM/CEREBELLUM: (Normal volume and signal intensity|abnormal-specify). (No imaging findings of progressive supranuclear palsy, multiple system atrophy, or other primary cerebellar neurodegenerative condition.). CORTEX/BASAL GANGLIA: (No evidence of abnormal mineralization, prion disease, or autoimmune encephalitis.|Abnormal-specify). SCHEMIA: • Infarction: (None.|Yes-specify with attention to strategic infarcts: angular gyrus, thalamus, basal forebrain, PCA territory, ACA territory). • Chronic small vessel disease: (absent|mild|moderate|severe). CEREBRAL MICROHEMORRHAGES: MASS: (None|mass-specify). VENTRICLES: (No hydrocephalus|Ex-vacuo dilatation|Hydrocephalus-specify). 2) Pre-operative Pituitary MRI report: FINDINGS: LESION: []. Cavernous sinus invasion: (None|Abuts|Encases ICA approximately [] degrees|circumferentially encases) the (right side|left side|both sides). NATIVE GLAND: (Normal|Not identified)Identifiable within the (right|left|posterior|anterior) aspect of the sella. Neurohypophysis: (Normal intrinsic T1 signal|Not present). PITUITARY INFUNDIBULUM: (Midline|Rightward deviated|Leftward deviated) Infundibulum thickness: (Normal). OPTIC CHIASM: (Normal position|Prefixed over tuberculum sellae|Postfixed over dorsum sellae).Chiasm signal: (Normal). VASCULATURE: (Normal caliber|Markedly ectatic). Aberrant vasculature: [No aberrant vasculature.|Aberrant vasculature (e.g. persistent trigeminal artery)]. Intercarotid distance [] mm (normal 12-30 mm). SPHENOID SINUS PNEUMATIZATION: [Present anterior and inferior to the sella (most common)|Decreased (solely anterior)|Absent (conchal)]. Intersphenoid septum: [Midline|Rightward|Leftward|Absent].

Conclusions

Contextual structured radiology reporting represents a tailored report specific to the requesting diagnosis or indication. Contextual reports can guide the radiologist to ensure essential items are included for a specific diagnosis. This method of structured reporting may improve clinician satisfaction of radiology reports and serve as the next generation of structured reporting beyond the current exam-based or anatomic reporting model.

eEdE-176

6:30AM - 3:00PM

Development of a Smartphone-based Augmented Reality Technology for Neuroradiology Education

B Xavier[1], K Wong[1], S Bhadola[2], G Grillone[3], K Shaffer[3]
[1]Boston University School of Medicine, Boston, MA, [2]University of Massachusetts Medical School, Worcester, MA, [3]Boston Medical Center, Boston, MA

Purpose

Augmented reality (AR) combines the real-world environment with computer-generated imagery. Current uses in medical education require high-end virtual reality viewers; however, we hypothesize that mobile smartphones are a cost-effective and accessible way for displaying AR anatomic models. This technology allows students to visualize 2-dimensional (2D) radiographic imaging juxtaposed with 3-dimensional (3D) anatomic renderings to allow real-time correlations of pathology. Herein, we describe our experience designing an AR environment to aid medical students and radiology residents to learn neuroradiology.

Materials and Methods

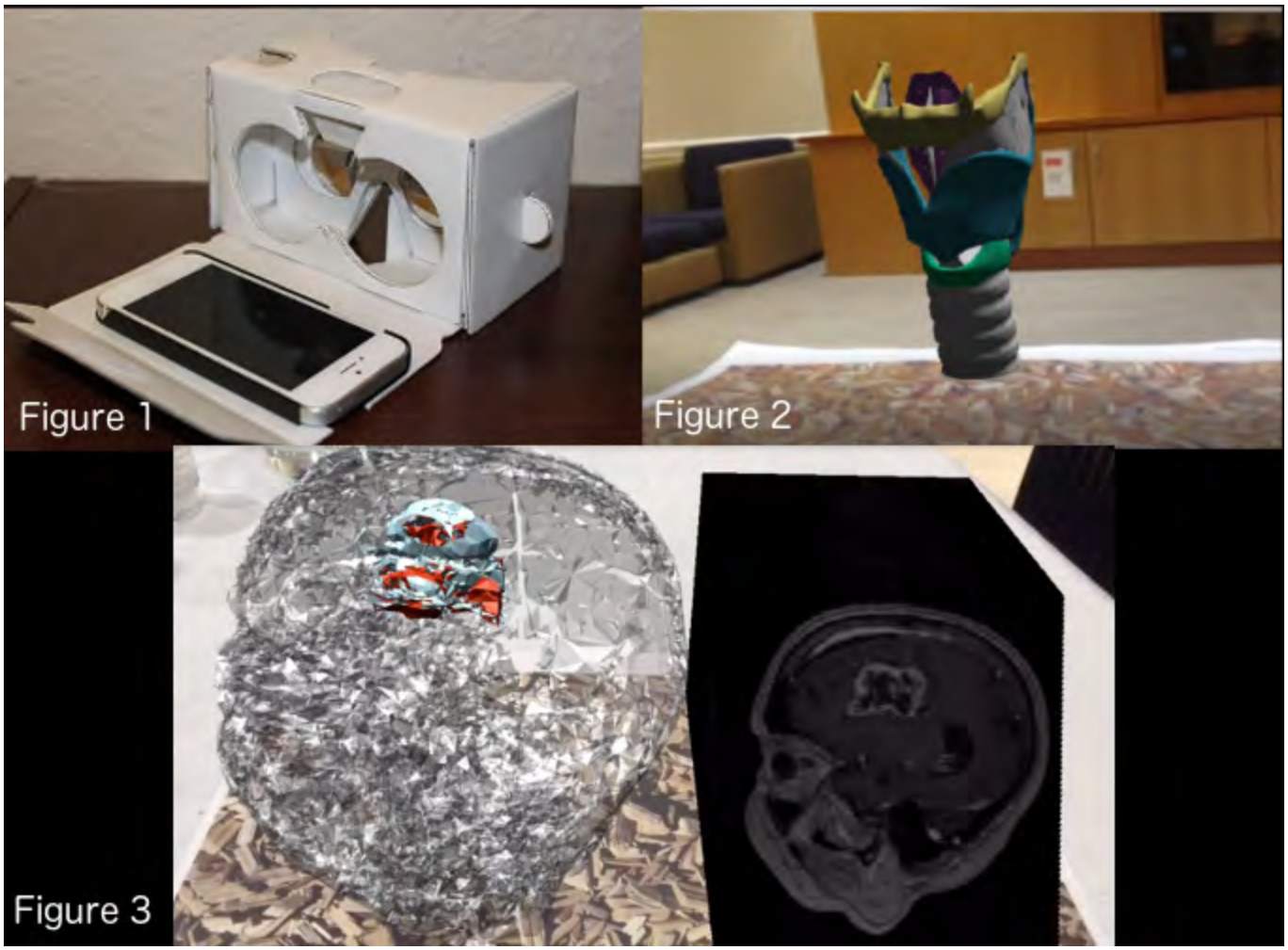
Computed tomography (CT) and magnetic resonance imaging (MRI) of complex neuroradiology were opened in DICOM format by 3D Slicer (www.slicer.org) and surface rendered into 3D models. The 3D models and 2D DICOM images were exported into the Unity 3D game engine (Unity Technologies, San Francisco, CA) and converted into stereoscopic augmented reality using the Vuforia software development kit (PTC Inc., Needham, MA), which positioned models in space based on the user's orientation towards real world images such that a user's perspective of the virtual models corresponded to their orientation towards the real-world image. Data were exported onto an iPhone 6 (Apple Inc., Cupertino, CA) and fitted into a modified cardboard virtual reality viewer (Unofficial Cardboard, La Jolla, CA) worn by the user.

Results

Figure 1 displays the cardboard viewer and mobile phone device setup. Figure 2 demonstrates a user's perspective of a larynx model in augmented reality. Figure 3 depicts the parallel view of a brain tumor with its presentation on sagittal MRI images.

Conclusions

An augmented reality application was created to allow medical students and radiology residents to visualize radiographic imaging in 3D using a smartphone and cardboard viewer. The ability to view 2D and 3D radiologic imaging in parallel may prove beneficial to the learning and application of radiology.



(Filename: TCT_eEdE-176_ASNRAbstractFigure.jpg)

eEdE-177

6:30AM - 3:00PM

Keeping Up with the Ever Expanding Practice

M Wong[1], Y Lui[2], M Hagiwara[3], J Sanger[3], M Borja[3]
[1]New York University Langone Medical Center, New York, NY, [2]NYU School of Medicine, New York City, NY, [3]NYU Langone Medical Center, New York, NY

Purpose
The purpose of this abstract is to emphasize the importance of supportive information, such as schedules and contact numbers, in improving the radiologist's workflow as well as the management of a large and diverse department. Through intentional design and particular goals in mind, we have successfully created a collaborative website that comprehensively hosts and organizes all relevant information that pertains to our neuroradiology department.

We raise several principles that are important in guiding our approach and share our experiences to illustrate these points.

Materials and Methods

After compiling documents and information that are relevant and identifying existing scheduling workflows, we sought the support of our information technology (IT) department and created an intra-network community site under the already available Microsoft SharePoint 3.0 environment. The site was constructed based on guidelines and principles that we have established previously. After beta-testing, a trial-feedback phase was initiated to further identify needs and issues with the website. Statistical data were obtained by analyzing traffic data. Surveys were collected at launch and later at regular intervals to obtain objective and subjective data to monitor the vitality and efficacy of the website. This remains an ongoing project.

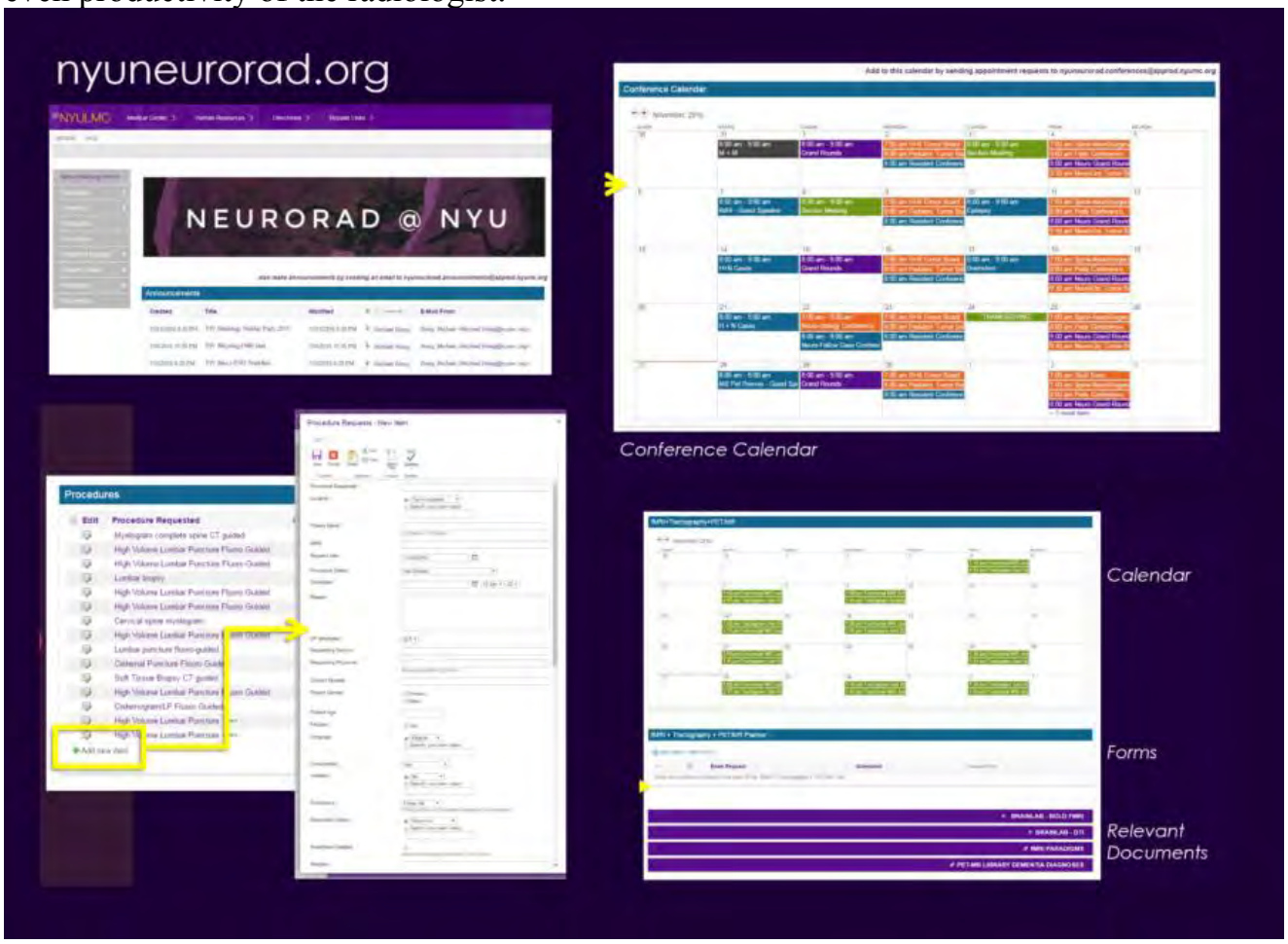
Results

"Information is knowledge, knowledge is power." We are currently in a healthcare environment that accumulates clinical data at a rapid rate, and having that data at our fingertips has proven to be important for the care of our patients. Much emphasis and discussion has gone into handling the ever accumulating "big data" on our patients. Supportive information, such as schedules and contact numbers, plays a secondary role and often is overlooked perhaps due to its lack of direct clinical impact. However, its importance is not any less to our daily workflow and we argue that it plays a bigger role than most of us are aware of. As practices and institutions grow larger and more complex, the more documents, emails, and calendars that tend to accumulate – to a point where navigating through the piles of information becomes inefficient and cumbersome. We have identified that demand in our department. With the support of our IT department, we created a community site to centralize supportive information as well as clinical references and educational material, organized into an easy-to-navigate format. We were able to achieve predetermined goals and maintain privacy, safety, and account integration without disrupting our department's normal workflow. Our project remains ongoing and data are still being collected. However, reception of the website has been positive since its announcement. We continue to collect feedback and incorporate additional functionality and data into the website. There remains obstacles and foreseeable issues that need to be addressed, but there are more applications to the website that we are currently investigating. Our ultimate goal is to make this a low-maintenance, collaborative digital "one-stop-shop" for everything related to neuroradiology at our institution. We hope our focus on comprehensiveness and user-friendliness may provide the information, control, and power to our neuroradiologists simply through their browser window.

Conclusions

In addition to "big data" in the modern healthcare environment, we emphasize the importance of handling "big supportive data" as well. Through our experiences, we have identified the need, concerns, and practical means related to addressing this problem. Our design principles pertain to a large and diverse department and provided a clear guideline to

our approaches. We argue investing into such efforts would improve efficiency, control, and even productivity of the radiologist.



(Filename: TCT_eEdE-177_ASNRImage2017.jpg)

Monday
6:30AM - 3:00PM

Electronic Education Exhibit (eEdE)-Interventional

eEdE-181

6:30AM - 3:00PM

A Pictorial Review of Deep Brain Stimulator Electrode Placement and Associated Complications

S Mehta[1], J Masur[2], K Learned[3]
[1]Pennsylvania Hospital, University of Pennsylvania, Philadelphia, PA, [2]Pennsylvania Hospital, Philadelphia, PA, [3]Univ. Pennsylvania Health System, Philadelphia, PA

Purpose

- To briefly review pathophysiology of Parkinson's disease and other movement disorders and rationale for deep brain stimulation (DBS). - To describe the role of neuroimaging in pre-operative and postoperative evaluation of patients undergoing placement of DBS electrodes, including MR safety considerations and MR imaging protocols. - To review imaging findings of normal DBS placement. - To review imaging findings of potential complications of DBS placement such as hemorrhage, infection, and infarction.

Materials and Methods

- Literature analysis of MRI safety protocols regarding DBS placements will be reviewed and presented. - A radiology data mining and analytics software (Montage Healthcare Solutions Inc, Philadlephia, PA) will be used to collect cases demonstrating normal DBS placements, DBS placements complicated by infection, DBS placements complicated by infarction, and DBS placements complicated by hemorrhage, etc.

Results

- Indications for DBS electrode placement: patients with medication refractory on–off fluctuations, dyskinesia or tremor. - Overview of DBS placement procedure: A stereotactic frame is used to localized the target region. For non-Parkinsonian essential tremor, the lead is placed in the ventrointermediate nucleus (VIM) of the thalamus; for dystonia and symptoms associated with Parkinson's disease (rigidity, bradykinesia/akinesia, and tremor), the lead may be placed in either the globus pallidus internus or the subthalamic nucleus; for depression to the nucleus accumbens. A burr hole is made into the skull. Once the burr hole is made, an electrode is inserted. Small electric currents from the electrode are used to more precisely locate the target. This may cause twitching, light flashes, or other sensations. The electrode then is connected by a wire to an implanted pulse generator. - Review of imaging findings of postoperative hemorrhage, infarct, and infection: Hemorrhage is hyperdense on CT and is usually along the path of the newly placed electrode. Infarct is hyperintense on DWI and hypointense on ADC. Infection can restrict diffusion and peripherally enhance. Correlation with clinical and laboratory findings can help in distinguishing the different complications.

Conclusions

- There is a favorable risk/benefit ratio of brain MRI for patients with DBS stimulators. - There are certain protocols to use to decrease risk of MRI in patients with DBS. - Complications are rare and include infection, infarction, and hemorrhage.

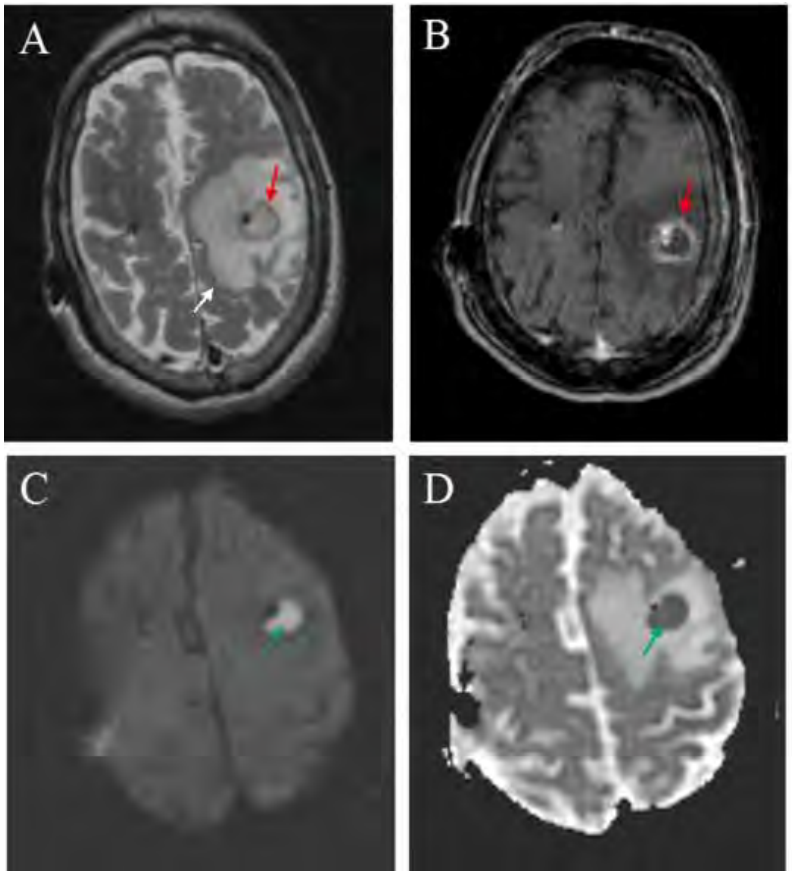


Figure 5. A 68 year old patient with Parkinson Disease presenting with confusion 7 months after DBS placement Axial T2W image (*A*) and postcontrast T1W image (*B*) demonstrate a peripherally-enhancing fluid collection (red arrow) in the left frontal lobe adjacent to a DBS lead with surrounding vasogenic edema (white arrow). *C* and *D*. Axial DWI (*C*) and ADC map (*D*) demonstrate central restricted diffusion in the ring-enhancing collection (green arrows), consistent with abscess.

(Filename: TCT_eEdE-181_ASNRgraphic.jpg)

eEdE-180

6:30AM - 3:00PM

Cerebrovascular Malformations: Imaging Review and Syndromic Associations

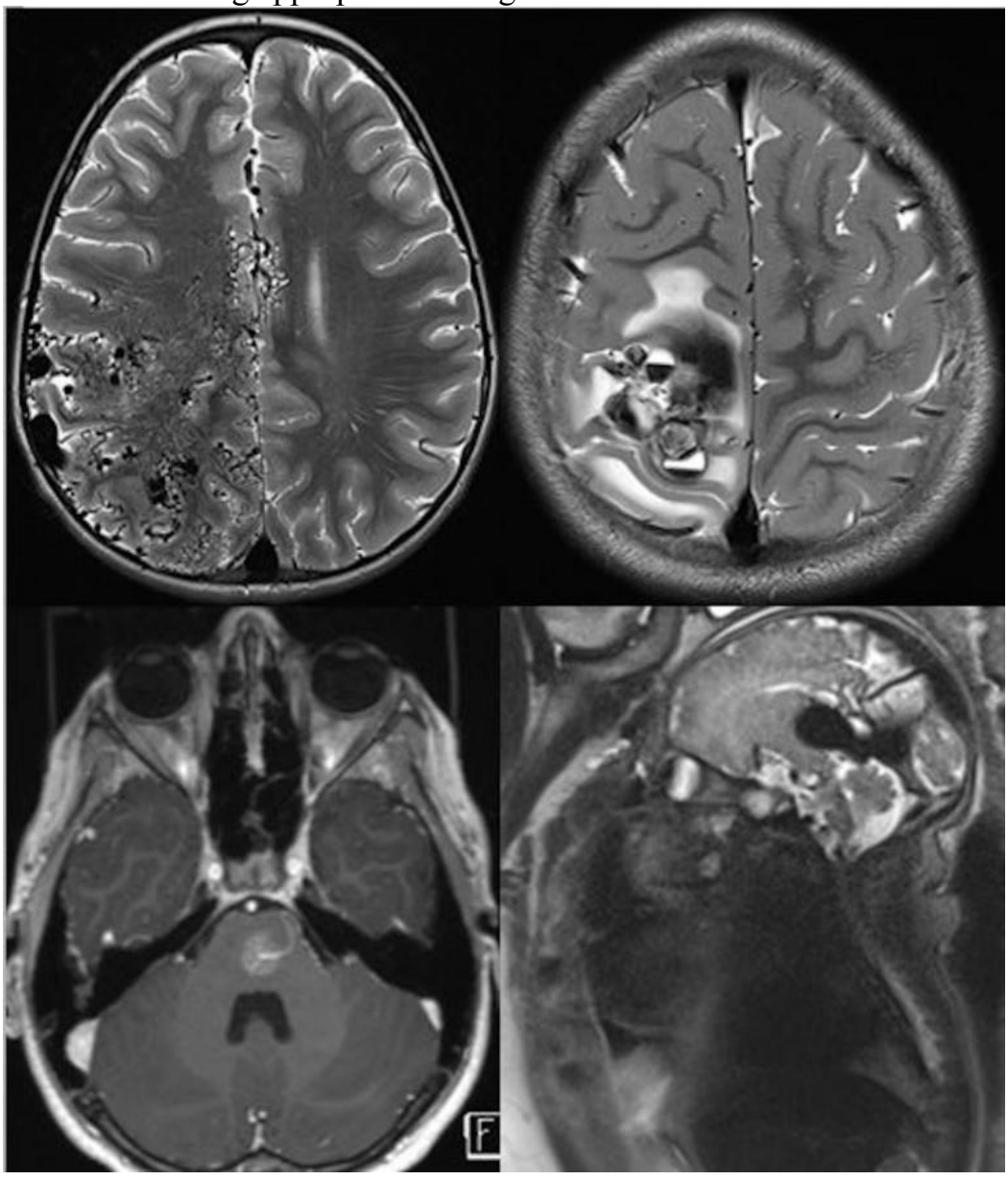
A Schneider[1]
[1]*Brigham and Women's Hospital, Boston, MA*

Purpose
1. Review typical clinical presentation and imaging appearance of cerebral vascular malformations. 2. Emphasize critical imaging findings that help direct appropriate management of cerebral vascular malformations. 3. Detail related syndromic associations.
Materials and Methods
An overview of cerebrovascular malformations is provided, followed by information regarding the clinical presentation and typical imaging findings of the various vascular malformations. Supporting case examples and related syndromic associations are presented.
Results
Case examples include arteriovenous malformations, cerebral proliferative angiopathy, Vein of Galen aneurysmal malformation, pial arteriovenous fistula, dural arteriovenous

malformation, cavernous malformation, developmental venous anomaly, sinus pericranii, and capillary telangiectasia. Syndromes presented include hereditary hemorrhagic telangiectasia, Wyburn-Mason syndrome, cerebrofacial arteriovenous metameric syndrome, familial cavernous malformations, blue rubber bleb nevus syndrome, ataxia telangiectasia, and Sturge-Weber syndrome.

Conclusions

Cerebral vascular malformations can be broadly categorized based on presence or absence of arteriovenous shunting. Knowledge of related syndromic associations and critical imaging findings of vascular malformations can help radiologists provide a meaningful report that can aid in making appropriate management decisions.



(Filename: TCT_eEdE-180_figure.JPG)

eEdE-182

6:30AM - 3:00PM

Flow-Diversion for Intra-cranial Aneurysms with Pipeline Stents: What the Neuroradiologist Needs to Know

P Sajedi[1], P Raghavan[2], G Jindal[2], T Miller[3], D Gandhi[2]
[1]University of Maryland Medical Center, Baltimore, MD, [2]University of Maryland School of Medicine, Baltimore, MD, [3]University of Maryland Medical Center, BALTIMORE, MD

Purpose

The purpose of this educational exhibit is to review the construct, therapeutic applications, potential complications, and follow-up imaging methods of flow-diverting pipeline stents which the neuroradiologists should be familiar with.

Materials and Methods

Over 200 cases of pipeline stenting have been performed at our institution, the majority of which have been subsequently followed with noninvasive cross-sectional imaging, including computed tomography angiography (CTA) or magnetic resonance angiography (MRA), as well as digital subtraction angiography (DSA). We present a thorough review of the clinical applications and imaging appearances of pipeline stents based on our institutional experience as well as the literature. We have organized several representative cases that exemplify characteristic findings on post-intervention imaging, including complications. We also provide considerations for follow-up imaging, including both noninvasive and interventional measures.

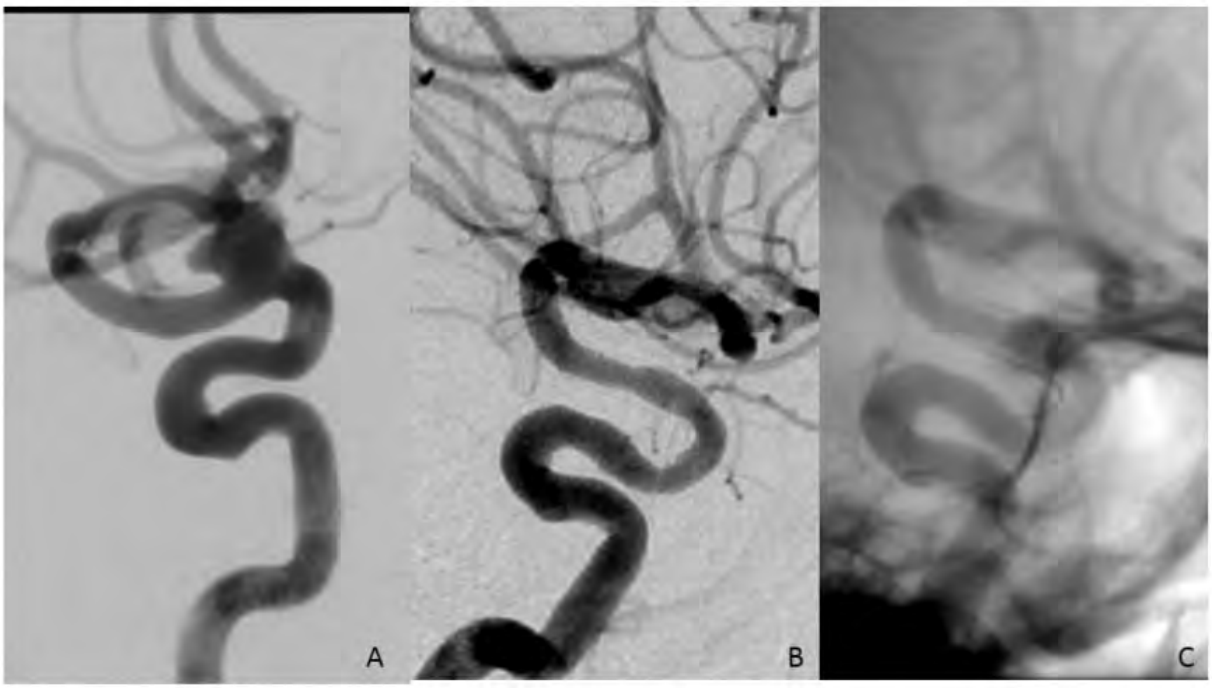
Results

Pipeline flow-diverting stents are an exciting therapeutic advance in the treatment of intracranial aneurysms. Previously described untreatable intracranial aneurysms, such as those with a wide-neck, fusiform, or giant in size, now are potentially managed with pipeline stenting. The construct of a pipeline stent across the parent vessel of an aneurysm allows for adequate flow remodeling, resulting in eventual thrombosis of the aneurysm, while still allowing continued perfusion of branch vessels. Prior studies have demonstrated a high rate of success, with up to 70% of aneurysms occluded at 6 months postintervention and nearly 90% at 1 year (D'Urso et al. 2011). At our institution, pipeline stents have become the preferred form of management in the setting of intracranial aneurysms proximal to the ICA terminus and along the intradural segment of vertebral arteries, as well as select intracranial branch vessel lesions. Possible complications of pipeline stenting include occlusion of the parent vessel, aneurysm rupture, intracranial hemorrhage, and peri-aneurysmal edema. Occasionally, transient in-stent narrowing can be seen on imaging in the early postintervention period which normalizes over time. In our academic practice, follow-up surveillance typically is performed 3-6 months following stent placement with CTA or MRA. Follow-up DSA often is performed between 6-12 months, though can be performed earlier in the case of high risk aneurysms and those that have previously ruptured. Computed

tomography angiography has become the preferred method for follow up of pipeline stents at our institution, though ultra-short TE MRA and contrast-enhanced MRA may prove useful in the setting of adjacent postsurgical clips and coil material which may result in streak artifact on CT.

Conclusions

This exhibit serves to help familiarize neuroradiologists with the role and application of flow-diverting pipeline to better understand its imaging features and potential complications.



Digital subtraction angiography (A) demonstrates a 9 mm irregular wide-necked lobulated left ICA para-ophthalmic aneurysm which was subsequently treated with pipeline stenting across the parent vessel. Follow-up DSA performed at 6 month follow-up (B) demonstrates interval complete thrombosis of the previously identified left para-ophthalmic aneurysm with patency of the ophthalmic artery. Non-subtracted angiogram (C) performed at the same time better demonstrates development of mild narrowing involving the stented portion of the left ICA which ultimately resolved following revision of patient's antiplatelet therapy.

(Filename: TCT_eEdE-182_Slide1.JPG)

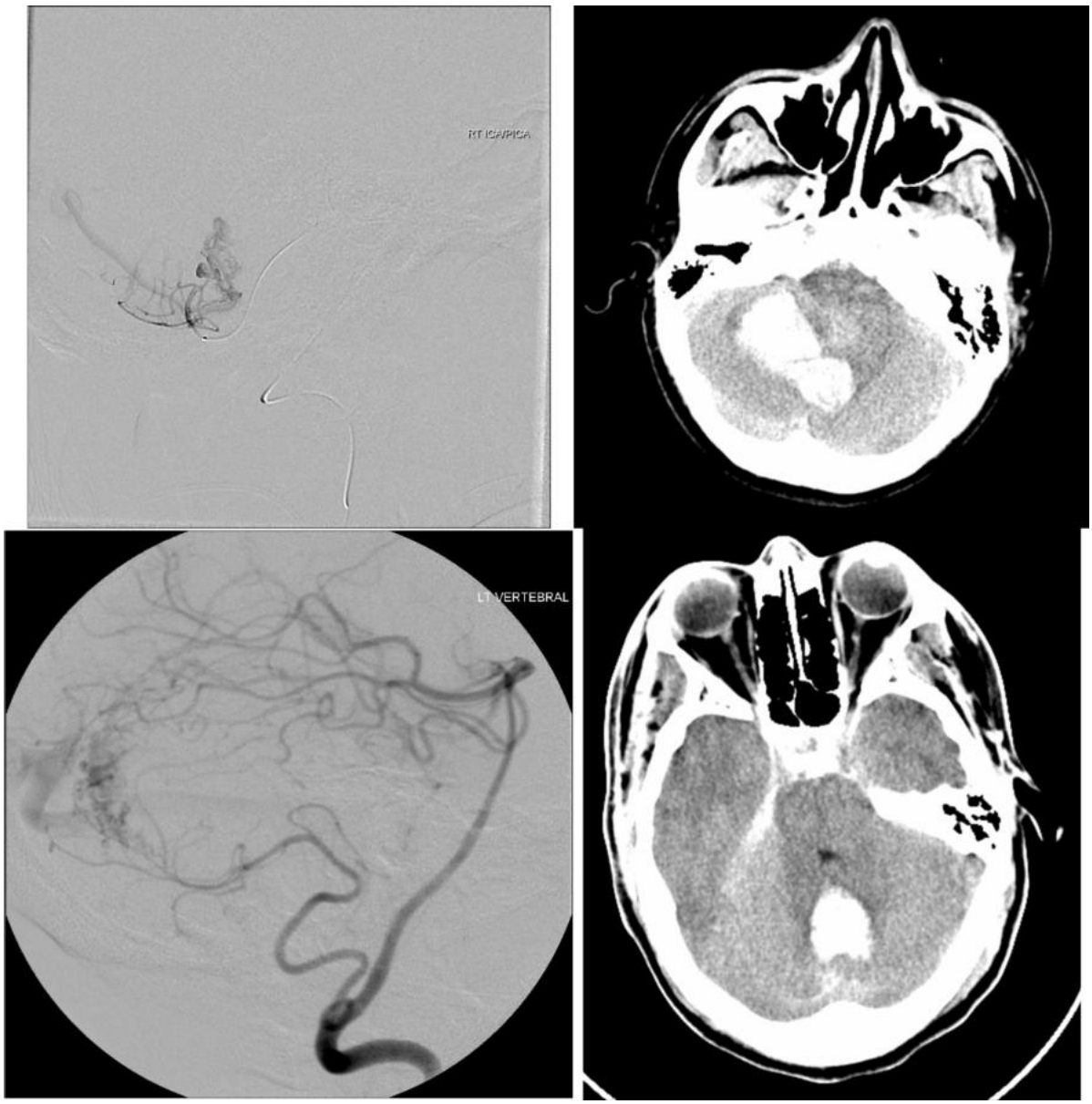
eEdE-179

6:30AM - 3:00PM

Posterior Fossa Arteriovenous Malformations' Angiographic Risk Factors for Hemorrhage and Different Patterns of Hemorrhage Associated with Posterior Fossa Arteriovenous Malformations

G Cruciata[1], E Greif[2], B Barrett[3], J Shah[1], A Derman[1], E Stein[1], R Buciuc[1]
[1]Maimonides Medical Center, Brooklyn, NY, [2]Maimonides Medical Center, Huntington , NY, [3]Maimonides Medical Center,, Brooklyn, NY

Purpose
Posterior fossa arteriovenous malformations (AVMs) make up 7 to 15% of all intracranial AVMs, and have a higher mortality rate than supratentorial AVMs due to the increased risk of hemorrhage and the presence of vital structures in a confined area. The purpose of this abstract is to demonstrate the angiographic factors associated with risk of hemorrhage in posterior fossa AVMs, which can guide endovascular treatment and help reduce the risk of rebleeding. In addition, the various risk factors can present with different patterns of hemorrhage.
Materials and Methods
We will display our experience with cases of posterior fossa AVMs, demonstrating the different patterns of hemorrhage and different angiographic risk factors for hemorrhage, guiding treatment.
Results
Aneurysm formation and venous outflow restriction increase posterior fossa AVMs' risk of hemorrhage, and can be assessed angiographically. The location of the aneurysm can lead to different types of hemorrhage, with arterial aneurysms causing subarachnoid hemorrhage and AVM nidus aneurysms and venous outflow restriction causing parenchymal hemorrhage. These factors can not only determine the risk of bleeding, but help guide the targets as well as timing for treatment and decrease the risk of rebleeding.
Conclusions
Posterior fossa AVMs present a high risk of mortality due to their location and high risk of hemorrhage. By assessing different patterns of hemorrhage, and different angiographic risk factors, prompt endovascular treatment can be guided to decrease the risk of rebleeding and decrease the morbidity and mortality.



(Filename: TCT_eEdE-179_Images.jpg)

eEdE-183

6:30AM - 3:00PM

The Pipeline Embolization Device in the Treatment of Intracranial Aneurysms

R Rimer[1], C Moran[2], D Cross[3], A Kansagra[1]
[1]Washington University School of Medicine, St. Louis, MO, [2]Washington Univ. School Of Medicine, St. Louis, MO, [3]Washington University Medical Center, St. Louis, MO

Purpose
Introduction and brief review of the Pipeline Embolization Device (PED) in the treatment of

intracranial aneurysms. Discuss imaging appearance of the PED using several cases involving intracranial aneurysms of both the anterior and posterior circulation using the following format: brief history, preprocedural imaging, intraprocedure imaging, and postprocedure imaging. Discuss the use of PED in the treatment of intracranial aneurysms.

Materials and Methods

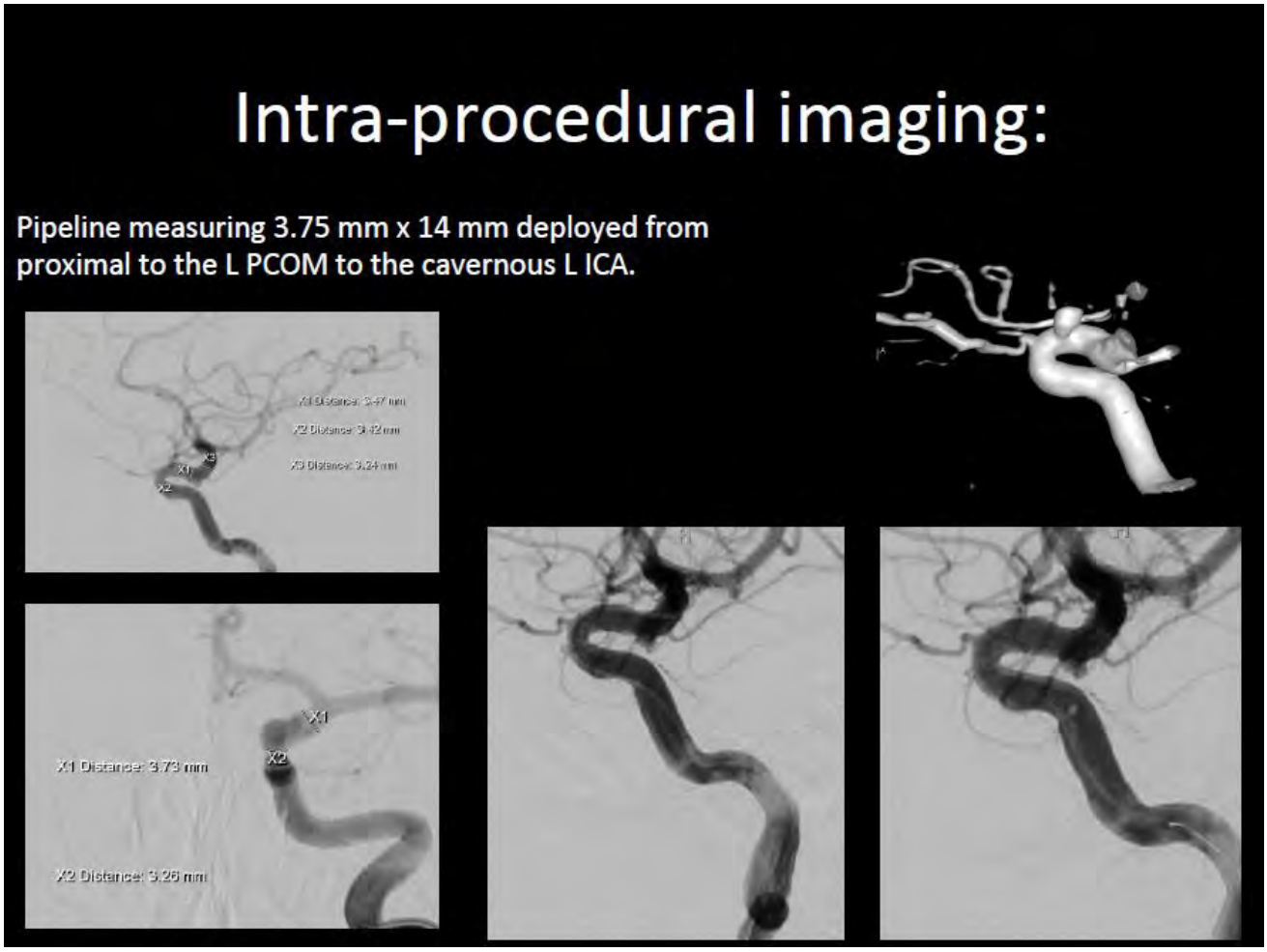
Will review the literature to provide background information on the PED and its various uses. Multiple cases will be presented to review the use of the PED in clinical practice.

Results

Flow diversion using devices such as the PED is a relatively new option for endovascular treatment of intracranial aneurysms, including those that are not amenable to coil embolization or open microsurgical clipping. Flow diverters provide an endoluminal scaffolding intended to redirect blood flow and induce aneurysm thrombosis. Though PED was initially approved for the treatment of intracranial aneurysms of the internal carotid arteries, flow diversion has been used to treat aneurysms of both the anterior and posterior circulation. Here we describe the pre-, intra-, and post-treatment imaging characteristics of PEDs and the aneurysms they are used to treat.

Conclusions

Flow diversion using devices such as the PED is a relatively new endovascular treatment option for intracranial aneurysms. The use of flow diverters has gained tremendous popularity in the treatment of complex secular and fusiform aneurysms. An understanding of the pre- and post-treatment imaging is essential in the management of these complex patients.



(Filename: TCT_eEdE-183_PED.JPG)

Monday
6:30AM - 3:00PM

Electronic Education Exhibit (eEdE)-Pediatrics

eEdE-190

6:30AM - 3:00PM

A Pictoric Essay of Pre and Postnatal CNS Imaging Findings in Congenital Zika Virus Infection

D Galheigo[1], B Guedes[1], T Fazecas[2], R Nogueira[1], H Werner[1], L Hygino da Cruz[3]
[1]Clinica de Diagnostico por Imagem (CDPI), Rio de Janeiro, Rio de Janeiro, [2]Clinica de Diagnóstico por Imagem (CDPI), Rio de Janeiro, Rio de Janeiro, [3]CDPI-Clinica de Diagnostico por Imagem, Rio de Janeiro, RIO DE JANEIRO

Purpose
Zika virus (ZIKV) congenital infection has been associated with an increased number of

central nervous system (CNS) impairment on fetuses and newborns, with some features, which will be described and illustrated in this article.
Materials and Methods
We performed ultrasound and fetal MRI in 49 pregnant patients with ZIKV infection at different gestational ages. They were subjected to RNA-PCR in blood and/or urine exams, and all of them were confirmed with ZIKV infection. After birth, the newborns performed transfontanellar US, CT and MRI of the head, with posterior 3D reconstructions of the skull. We quantified and illustrated the most frequent findings in the patients who had CNS changes and also the less frequent findings. The findings of CNS abnormalities will be illustrated extensively in this presentation.
Results
The main findings of our cases were: excessive hypersignal in the white matter preferentially of frontal lobes and posterior peritrigonal region bilaterally, quite similar to the diffuse excessive high signal intensity (DEHSI) described in extreme preterm infants. Microcephaly, such as multiple calcifications with cortical and mainly subcortical distribution, thinning of the brain parenchyma, which have extensive periventricular areas of hyperintensity on T2 MR-WI also were reported. Other findings were: neuronal migration anomalies, dysgenesis of the corpus callosum, ventriculomegaly probably secondary to cortical/subcortical atrophy, cerebellar hypoplasia, and brain stem sharpening.
Conclusions
Brain calcifications detected prenatally was a finding suspicious with a intrauterine infection. Moreover, perinatal imaging by MRI and CT scan enabled diagnosis of pachygyria, corpus callosum dysgenesis, small anterior fontanel with premature closure of cranial sutures. However, in the patients without microcephaly we have seen an excessive hypersignal in the white matter that resembles that previously described in extreme preterm patients, called DEHSI. The meaning of this finding is still unknown, but we speculate that this alteration may somehow be related to ZIKV and may not have the same prognostic behavior that DEHSI has for premature infants. Thus, we believe there may be some relationship between this finding and the recent reports of change in the development of patients without microcephaly.

eEdE-193

6:30AM - 3:00PM

A Quick Guide to Decoding Pediatric Hypomyelinating Disorders on Brain MR

N Nguyen[1], H Tran[2]
[1]BCM, Houston, TX, [2]Texas Children's Hospital, Houston, TX

Purpose
Hypomyelinating diseases are a fascinating group of white matter disorders, which researchers only recently began to unravel. The purpose of this electronic exhibit is to review

the pathophysiology behind common hypomyelinating diseases in pediatric population and to provide the audience with a quick guide to assess pediatric brain MR for hypomyelinating disorders.

Materials and Methods

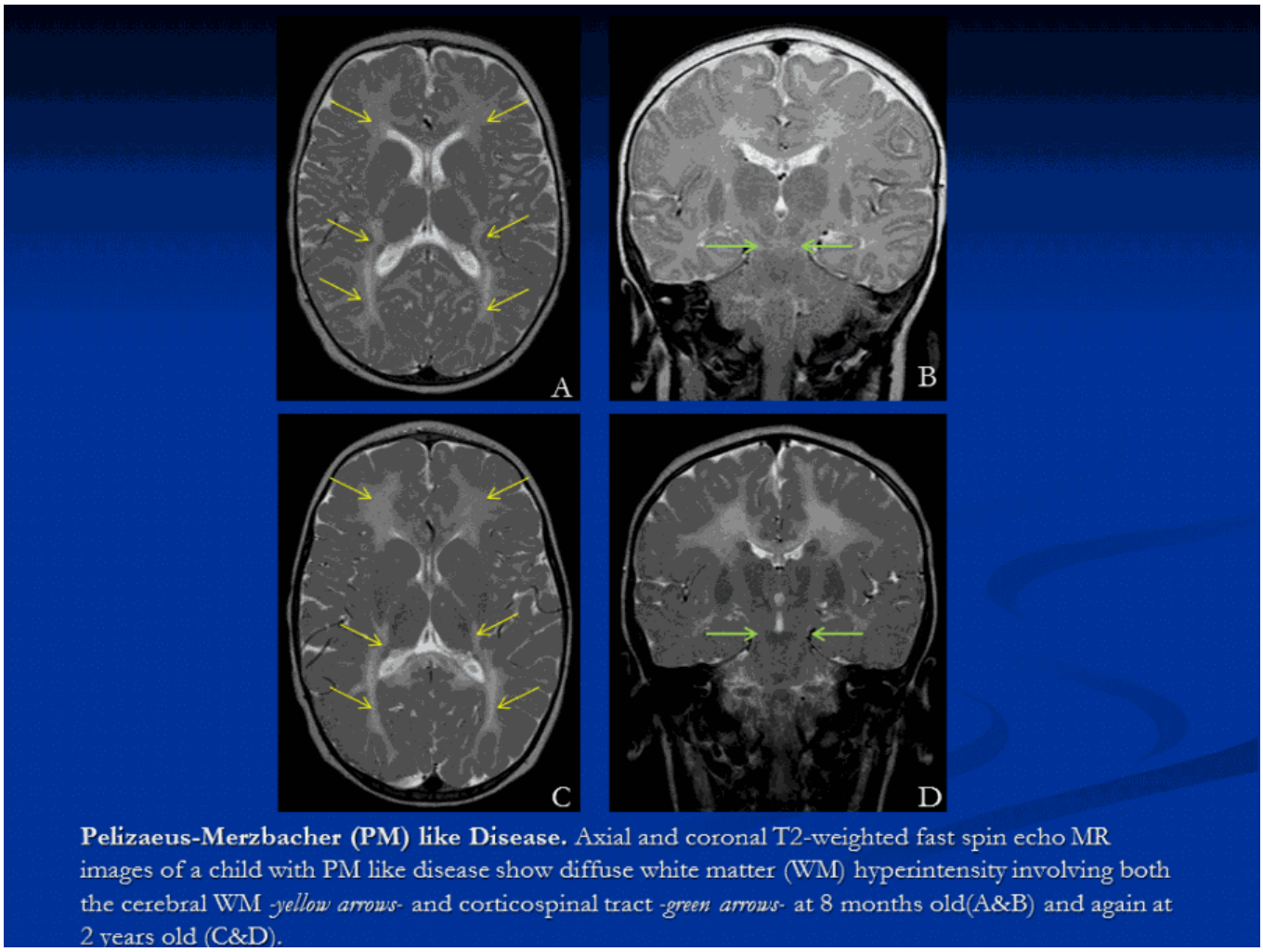
The exhibit begins with a review of the normal myelination and its MR appearance. This is followed by a discussion about the pathophysiology of hypomyelination. The audience then has the opportunity to apply the knowledge toward diagnosing common hypomyelinating disorders via an interactive case-based approach.

Results

The process of axonal myelination by oligodendrocytes requires an intricate network of gene expression and function. A mutation in one these genes could derail this physiologic process and lead to hypomyelination. For example, Pelizaeus-Merzbacher-like disease (PMD-like) is caused by mutations of the gap junction protein encoded by gamma-2 gene in chromosome 1q42.13 that is expressed in oligodendrocytes (1). Affected patients develop movement disorders, dysarthria and nystagmus. MR imaging of PMD-like include diffuse hypomyelination of the cerebral and brainstem white matter (attached image). Diagnosing hypomyelinating disorders is further complicated by overlapping MR imaging findings. We propose a systematic approach to decoding and categorizing hypomyelinating disorders, which starts with gathering patient's age, gender, and clinical presentation. This is followed by image scrutinization especially on T2-weighted spin-echo sequence for pattern of white matter hypomyelination, basal ganglia and cerebellar atrophy, and the evolution of these findings over time.

Conclusions

As illustrated above, diagnosing hypomyelinating disorders is complex and appears daunting to an unfamiliar radiologist. Our exhibit aims to educate the audience about the pathophysiology of hypomyelinating disorders and to provide them with a quick guide to decoding these disorders utilizing clinical information and MR imaging appearance.



Pelizaeus-Merzbacher (PM) like Disease. Axial and coronal T2-weighted fast spin echo MR images of a child with PM like disease show diffuse white matter (WM) hyperintensity involving both the cerebral WM *-yellow arrows-* and corticospinal tract *-green arrows-* at 8 months old(A&B) and again at 2 years old (C&D).

(Filename: TCT_eEdE-193_AttachedImage_PMLikeDisease.gif)

eEdE-202

6:30AM - 3:00PM

Arterial Spin Labeling: Pediatric Applications

M Ho[1], N Campeau[1], M Patterson[1]
[1]*Mayo Clinic, Rochester, MN*

Purpose
Arterial spin labeling (ASL) is a noncontrast MR perfusion technique that enables noninvasive and repeated measurements of absolute cerebral blood flow (CBF). Arterial spin labeling demonstrates special promise in the pediatric population, with clear safety advantages over nuclear medicine radioactive tracers and MR gadolinium-enhanced techniques. This pictorial review will discuss ASL physics, normal variants, and pathology in pediatric neuroimaging.

Materials and Methods

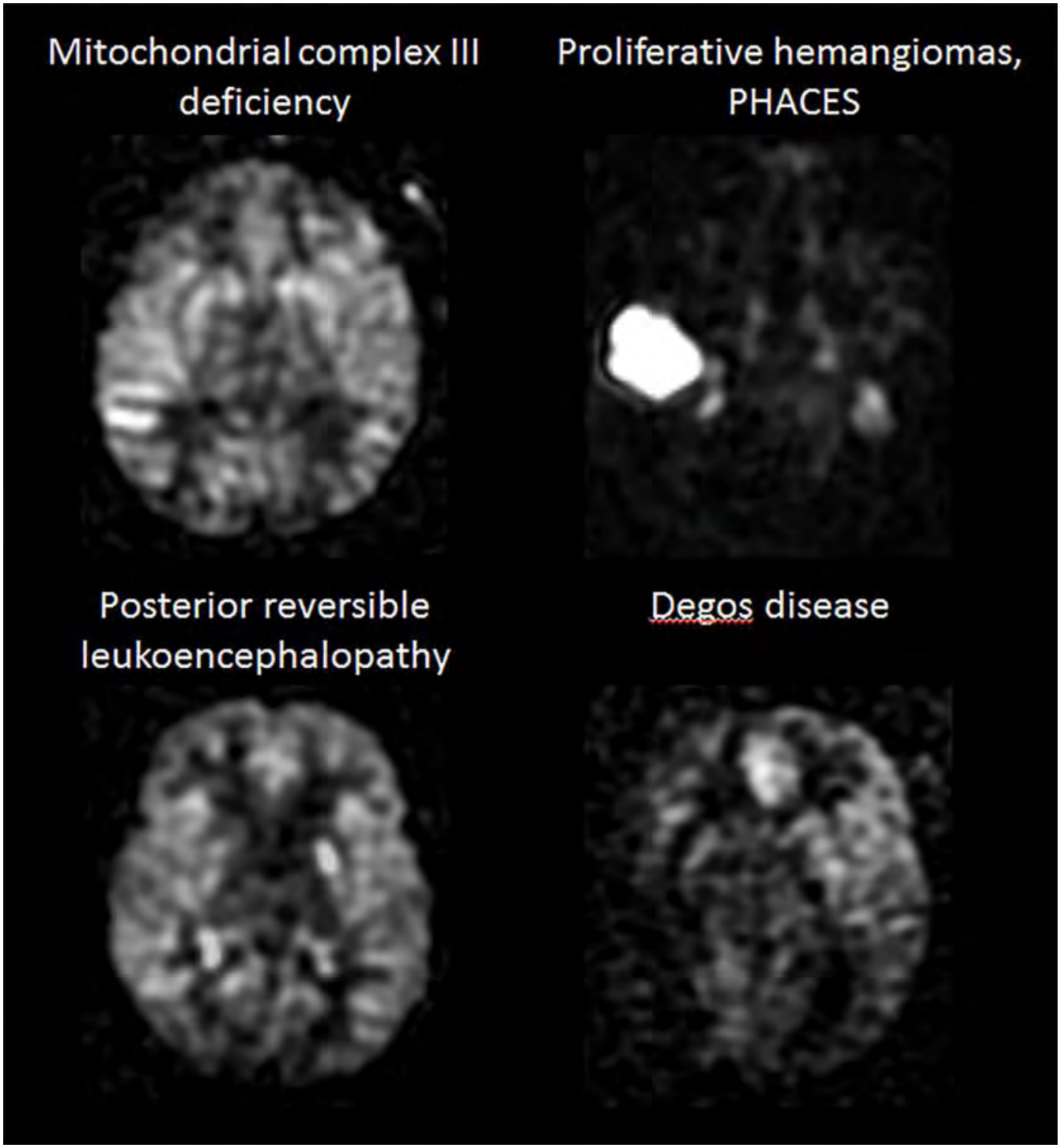
1. Review physics and technical considerations for ASL. 2. Illustrate spectrum of age-dependent variants and artifacts in pediatric ASL. 3. Demonstrate the added value of ASL for diagnosing diverse pathologies involving pediatric brain, head, and neck.

Results

Technical considerations: - Labeling pulse, - pCASL, S-ASL, - Postlabel delay(s). Normal variants. Age dependence: regional, global. Physiologic activity: - Frontal/visual cortex, limbic, DMN, - Nasal mucosa. Artifacts: - Spin tag decay,- Selective/failed excitation, - Coil heterogeneity, - Motion, - Susceptibility, - Tissue masking, - Arterial transit artifact. Imaging Cases Ischemia/Vasculopathy: Involved vessels, core infarct, ischemic penumbra, collateralization, - Arterial infarct, - Long tract signs, - CHD, - CVST, - Dysautoregulation: PRES, RCVS: - Hemiplegic migraine, - TGA, - TCA, - Moyamoya, - Vasculitis: lupus, lymphocytic, drugs, Degos; - HIE: preterm/term, child, adolescent, - Fat, septic emboli, - Global hypoperfusion, Vascular malformations: -Vascular supply, shunting, extravasation, ischemic steal, - VGAM, - DVA, - AVM, - DAVF, - CCF, - HHT, - Sturge-Weber, - Parry-Romberg, - Hemangioma, PHACES. Epilepsy, Ictal-interictal localization, propagation/lateralization, migrational, multifocal/systemic: - MTS,- FCD,- Heterotopia,- PMG, - Schizencephaly, - HME, - TS, - Temporal intermittent rhythmic delta activity, - Febrile infection-related epilepsy syndrome,- Autoimmune epilepsy. Genetic/metabolic, Subclinical, disease distribution: - Serotonin syndrome, - Wernicke, - X-ALD, - Leigh disease, - Complex III deficiency, - Biotin-thiamine responsive basal ganglia disease, - Dynamin-1-like protein mutation, - Fatal familial insomnia. Tumors: Microvascular density, histologic grading, biopsy, follow-up, - JPA, AA, - GG, - PMA, - PXA, - DIA, - DIPG, - Optic glioma, - Medulloblastoma, - Ependymoma, - ATRT, - Schwannoma, - Lymphoma, - Metastasis, - Radiation necrosis. Infection/Inflammation: Vascularity, secondary ischemia, multifocal disease, - Mastoiditis with subdural empyema, - Pott puffy tumor, - Invasive fungal sinusitis, - Multiple sclerosis, - ADEM, - Weston-Hurst, - Opsoclonus-myoclonus, - Rasmussen, - Hypertrophic pachymeningitis.

Conclusions

Arterial spin labeling is a convenient and noninvasive technique for CBF assessment, with special considerations and applications in the pediatric population. Labeling parameters and postlabel delay should be tailored to the patient's age and disease category. Images should be interpreted in conjunction with anatomic sequences, and with knowledge of age-dependent variation and technical artifacts. Arterial spin labeling perfusion data provide added value for a variety of applications including ischemia/vasculopathy, vascular malformations, epilepsy, genetic/metabolic disorders, tumors, and infection/inflammation.



(Filename: TCT_eEdE-202_Figure.jpg)

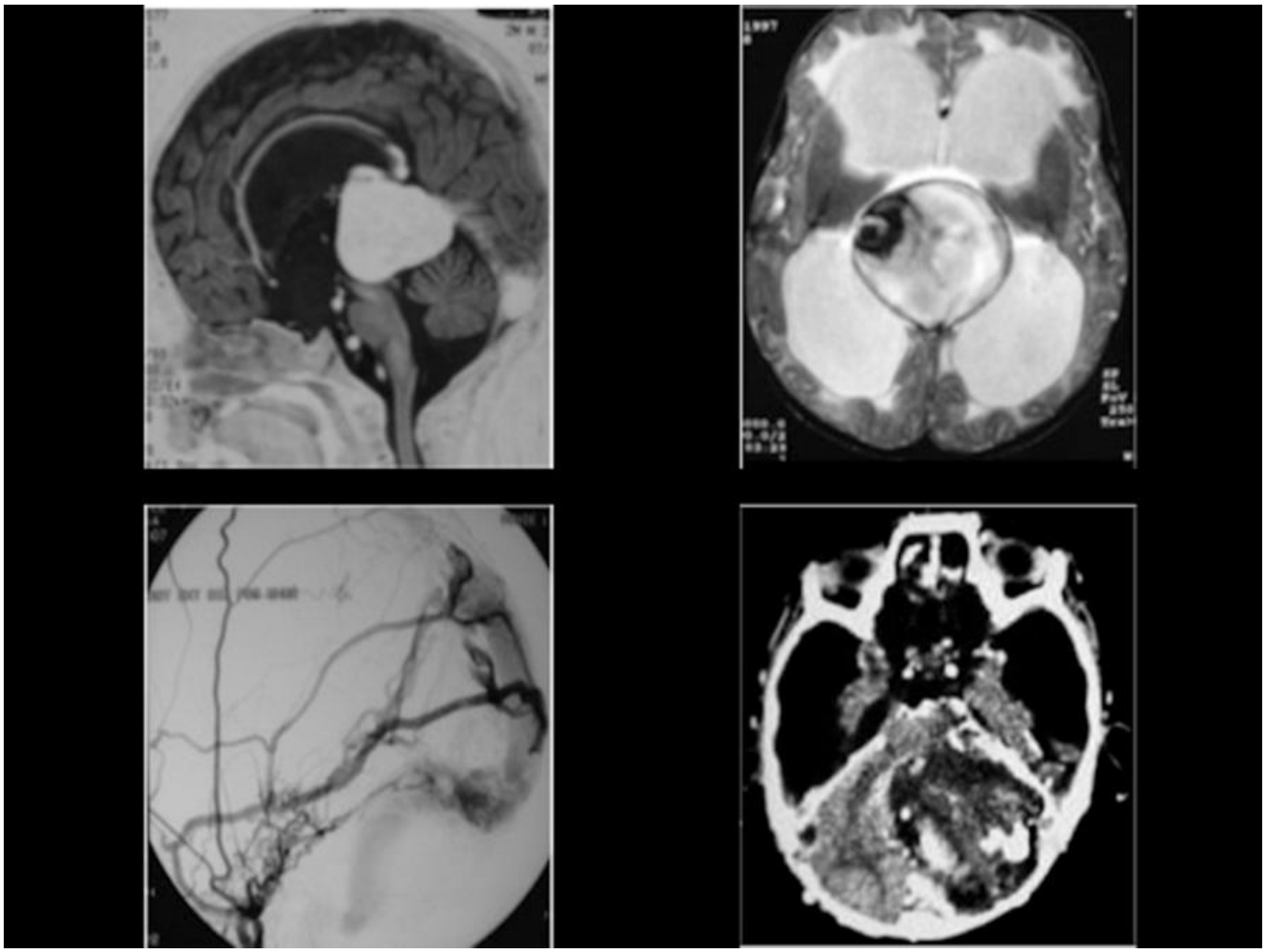
eEdE-184

6:30AM - 3:00PM

Brain Arteriovenous Malformations of the Childhood : What the Radiologist Should Know

L Estacia Ambros[1], F SCORTEGAGNA[2], F Landeira[1], C Campos[1], L Garcia[1], L Amaral[3]
[1]Beneficiencia Portuguesa, SAO PAULO, AK, [2]HOSPITAL BENEFICIÊNCIA PORTUGESA, SAO PAULO, São Paulo, [3]Beneficiencia Portuguesa, SAO PAULO, São Paulo

Purpose
The purpose of this exhibit is: a. To review the anatomical and radiological peculiarities of brain arteriovenous malformations in children. b. To distinguish the vein of Galen aneurysmal malformation (VGAM) types from dural arteriovenous shunt and pial arteriovenous malformation (AVM). c. To evaluate the complications of brain AVM, mainly VGAM. d. The importance of differing these pathologies for adequate management.
Materials and Methods
We reviewed several common and uncommon cases of brain arteriovenous malformations in children at our neuroradiology department, focusing on the importance of an accurate diagnosis and the implication of that on the proper treatment and possible complications.
Results
We analyzed several cases of brain arteriovenous malformations in children, reviewing the literature and focusing on the differential diagnosis. The most frequent subtypes were mural fistula type of Vein of Galen, Aneurysmal Malformation (VGAM), Vein of Galen aneurysmal dilatation secondary to parenquimal AVM, Mural fistula type of VGAM, Choroidal type of MAVG and Childhood dural arteriovenous fistula. We also considered the importance of detecting the most prevalent complications regarding these pathologies, one of the most frequent being MAVG spontaneous thrombosis and also uncommon ones but with drastic prognosis as melting brain syndrome.
Conclusions
In summary, brain arteriovenous malformations in children are uncommon pathologies with a large amount of differential diagnosis and possible serious complications. We have described the classic imaging features of brain AVMs in children and its possible complications. Because the natural history and treatment options differ among these pathologies it is crucial that the radiologist be able to differentiate them.



(Filename: TCT_eEdE-184_Slide1.jpg)

eEdE-203

6:30AM - 3:00PM

Brain Injury in Children Undergoing ECMO: Comprehensive Review of Neuroimaging Findings with Head US, CT and MRI

J Wen[1], E Snyder[2], T Huisman[3], M Bembea[4], A Tekes[2]
[1]Johns Hopkins Hospital, Baltimore, MD , [2]Johns Hopkins Hospital, Baltimore, MD, [3]Johns Hopkins, Baltimore, MD, [4]Johns Hopkins Hospital, Department of Anesthesiology and Critical Care Medicine, Baltimore, MD

Purpose

Extracorporeal membrane oxygenation (ECMO) is a rescue therapy successfully employed in children with respiratory and cardiac failure since 1975. Although survival of neonates with congenital diaphragmatic hernia, congenital heart disease, meconium aspiration, pulmonary hypertension and severe respiratory distress has significantly improved,

neurologic injury remains a significant morbidity and risk factor for mortality in these critically ill children undergoing ECMO. In this educational exhibit, our purpose is to show the diagnostic value and the utility of head ultrasonography (HUS) and Doppler, computed tomography (CT), and magnetic resonance imaging (MRI) in neonates undergoing ECMO. The spectrum and unique features of brain injury related to ECMO will be highlighted in each imaging modality.

Materials and Methods

Optimized imaging techniques for HUS, CT and MRI will be displayed. Intracranial injuries related to ECMO will be categorized as hemorrhagic or ischemic injuries. Intracranial hemorrhages in the extra-axial spaces and within the brain parenchyma (small petechial to large focal and multifocal hemorrhages), and ischemic injuries (punctate infarctions and large territorial infarctions) will be displayed in the acute, subacute and chronic stages.

Results

Head ultrasonography is the first line of imaging as it is radiation free and can be performed daily at the bedside, therefore it is frequently the first modality to demonstrate the presence of brain injury. Head CT can be used when suspected injury needs to be confirmed or when there is a mismatch with a patient's clinical status and HUS findings. Magnetic resonance imaging is performed only after cessation of ECMO, as the equipment of ECMO is not MRI compatible. Magnetic resonance imaging offers the highest image resolution with multiple different contrast settings which can map out the full extent of hemorrhagic injury with the use of susceptibility-weighted imaging (SWI), and ischemic injury with diffusion tensor imaging (DTI). Unique features of hemorrhagic and ischemic injuries will be highlighted as they are quite variable and differ with their presentation in children undergoing ECMO.

Conclusions

Neonatal patients on ECMO therapy are at risk of developing intracranial hemorrhages and/or infarction. The major cause of death in the newborn ECMO population is cerebral injury. Timely identification of these injuries is critical in management of these patients. Neuroimaging is a crucial component in diagnosis, monitoring of these patients, as well as potentially identifying those at higher risk of injury or downstream neurodevelopmental complications. In this exhibit, reviewers will get a comprehensive review of the spectrum and unique features of brain injury and utility of each neuroimaging modality in children undergoing ECMO.

eEdE-196

6:30AM - 3:00PM

Congenital Cystic Neck Masses

J Rivera[1], H Dharmarajan[1], H Tran[1]
[1]*Baylor College of Medicine, Houston, TX*

Purpose

To provide a platform for differentiating the most common congenital cystic neck masses based on clinical presentation, embryologic correlates, and pathognomonic radiographic findings.

Materials and Methods

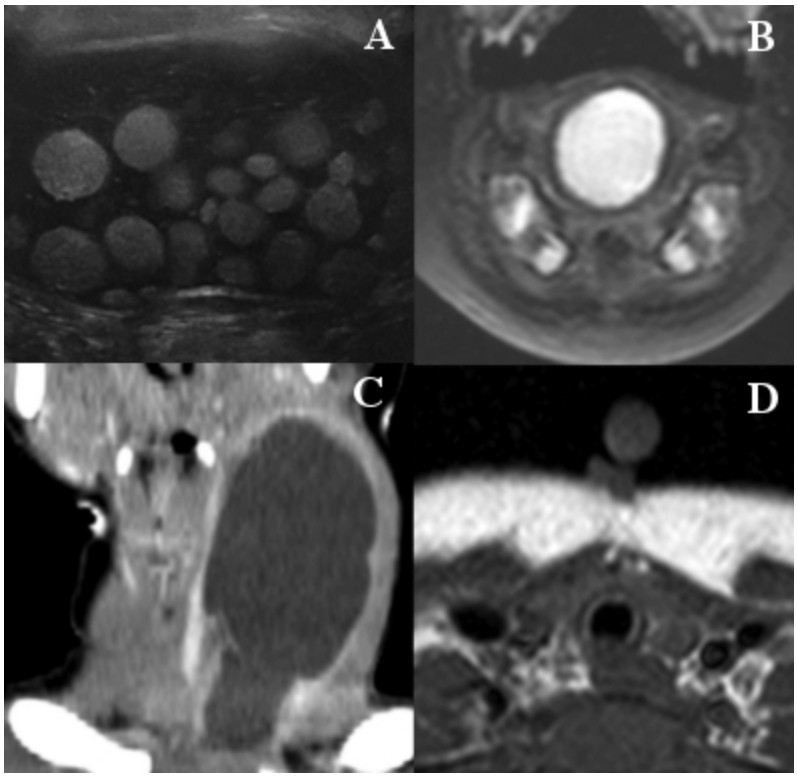
Ten different congenital cystic neck masses are reviewed in terms of characteristic clinical presentation, imaging findings, embryologic relationships, and mimics: thyroglossal duct cyst, branchial cleft cyst, dermoid, lymphatic malformation, foregut duplication cyst, cystic teratoma, laryngocele, ranula, thymic cyst, and congenital midline cervical cleft.

Results

Differentiation between congenital cystic neck masses requires interpretation of unique imaging findings in conjunction with pertinent history. A congenital cyst with associated irregularity of the anterior hyoid bone may indicate a thyroglossal duct cyst. Branchial cleft cysts are classified based on proximity to the parotid gland, insinuation into carotid and submandibular spaces or involvement of the pyriform sinus. A "bag of marbles" ultrasound pattern is pathognomonic of dermoid cysts (Figure 1A). Foregut duplication cysts may present in midline at the floor of the mouth without the "bag of marbles" pattern (Figure 1B). Lymphatic malformations typically cross multiple fascial planes without extension into the spinal canal or remodeling bone. Thyroid gland involvement and intralesional calcifications or fat distinguish cervical teratomas. Laryngoceles appear contiguous with the airway. Ranulas disrupting the mylohyoid membrane require an alternate course of surgical management. Thymic cysts mimic lymphatic malformations; however, carotid space involvement or proximity to the thymus differentiates this entity (Figure 1C). Congenital midline cervical clefts have a unique nipple-like skin tag with a sinus tract between the chin and sternal notch (Figure 1D).

Conclusions

The diagnosis of congenital cystic neck masses is challenging due to variability in clinical presentation, pathogenesis, and anatomic involvement. By reviewing this electronic exhibit, one should be able to differentiate between common congenital cystic neck masses through correlation of pathognomonic clinical and imaging presentations.



(Filename: TCT_eEdE-196_Figure1.jpg)

eEdE-186

6:30AM - 3:00PM

Congenital Disorders of Cerebral Vasculature in Pediatrics

R Assadsangabi[1], S Nabavizadeh[1], A Vossough[2]
[1]University of Pennsylvania, Philadelphia, PA, [2]Children's Hospital of Philadelphia, Perelman School of Medicine of the Uni, philadelphia, PA

Purpose
Cerebral vascular malformations are rarely diagnosed in utero. While most prenatal imaging of intracranial vascular malformations relates to Vein of Galen aneurysmal malformations, they only constitute up to 30% of intracranial vascular abnormalities in the pediatric population (1). Several other vascular malformations and disorders may present in utero or early in life which are less known to the radiologists. The purpose of this exhibition is to describe these entities and discuss their various clinical manifestations and complications.
Materials and Methods
Key examples of different types of vein of Galen aneurysmal malformations, malformations of the fetal dural sinuses and their complications, intracranial hemangiomas, PHACE(S), arteriovenous malformations, venous anomalies, sinus pericranii, atretic cephaloceles, pial vascular malformations, hereditary hemorrhagic telangiectasia, and Sturge-Weber syndrome

will be described. Imaging of both prenatal and postnatal findings will be demonstrated using various imaging modalities, including ultrasound, MRI, and CT.
Results
Clinical presentations, various imaging morphologies, potential complications, and treatments of each disease will be discussed.
Conclusions
Congenital cerebral vascular malformations can produce a variety of morphological and clinical presentations dependent on the cause, localization, extension, and time of development. Familiarity with varied presentation would aid early diagnosis and direct appropriate treatments.

eEdE-218

6:30AM - 3:00PM

Congenital Spine Anomalies: An Embryologic Approach

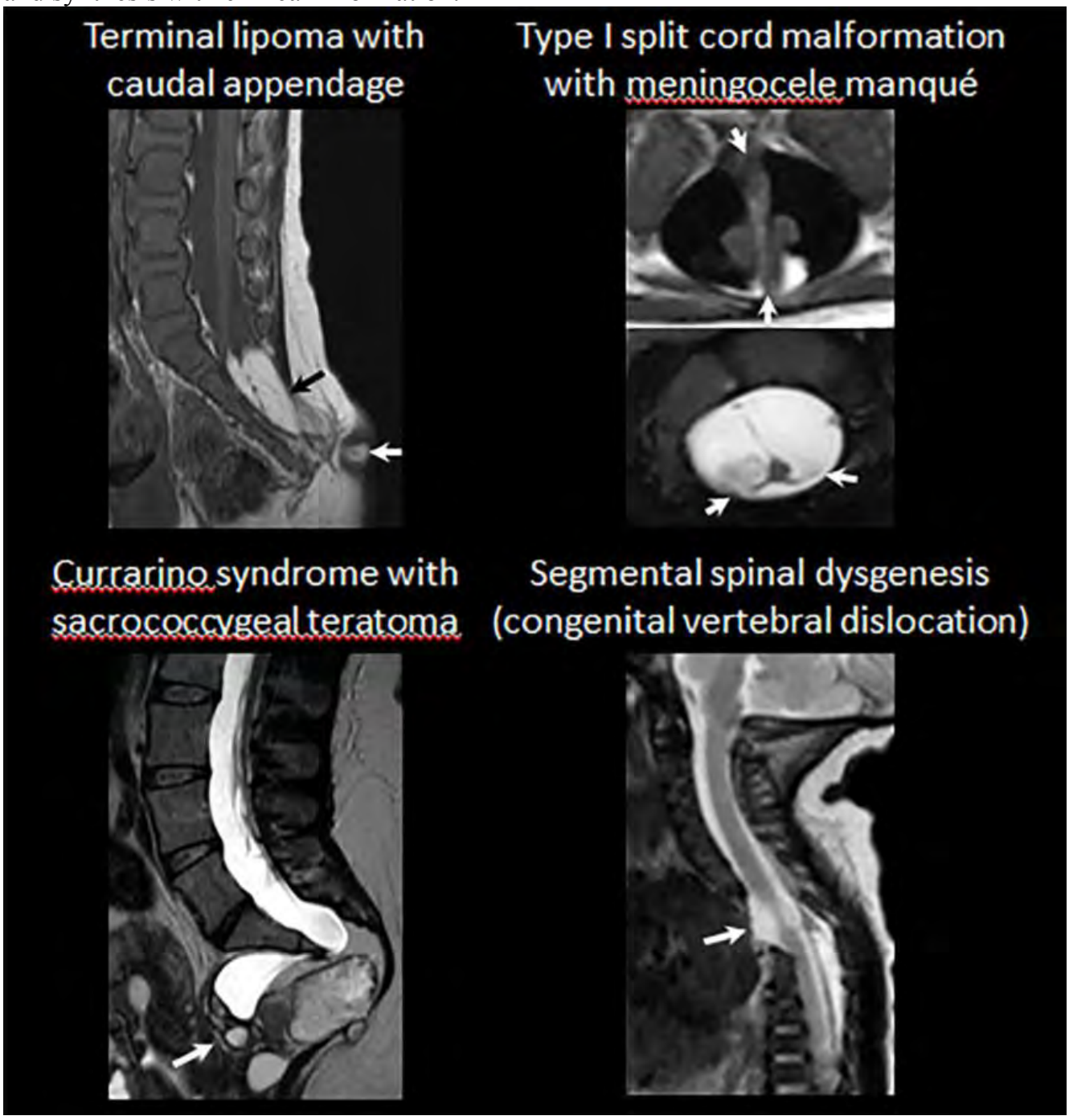
M Ho[1], N Wetjen[2]
[1]Mayo Clinic, Rochester, MN, [2]Mayo Clinic, Rochester , MN

Purpose
Utilize embryologic concepts to understand, describe, and classify congenital spine anomalies.
Materials and Methods
In this exhibit, we will highlight vital steps in prenatal/postnatal spine development that are key to understanding the pathogenesis of congenital spine anomalies. Important terminology for describing spine/cord malformations will be introduced, with an emphasis on the interdependence of clinical and imaging features. Subsequently, we will present a rich case collection of developmental spine anomalies from basic to advanced, highlighting the key anatomic and pathophysiologic features in each process.
Results
Spine Embryology: - Gastrulation. - Primary neurulation: disjunction. - Secondary neurulation: canalization, retrogressive differentiation. - Vertebral segmentation. - Vertebral development: chondrification, primary ossification, secondary ossification, Terminology. Vertebral numbering and transitional anatomy, - Vertebral alignment: disorders of formation, segmentation. - Open vs. closed dysraphisms. - Neural placode: terminal, segmental; Clinical features. - Low-risk vs. high-risk. Imaging Cases: Tight filum terminale: retrogressive differentiation. Open spinal dysraphisms: segmental nondisjunction. - Myelocele, yelomeningocele, Closed spinal dysraphisms, Meningocele, myelocystocele, Congenital spine masses: progenitor cells. - Lipoma, dermoid/epidermoid, sacrococcygeal teratoma, neurenteric remnant, hamartoma, Lipomatous malformations.- Lipomyelocele, lipomyelomeningocele: premature disjunction. - Terminal lipoma: caudal cell mass. - Transitional malformations, caudal appendage Split cord malformations: gastrulation. - Type

I, II. - Hemi-OSD, meningocele manqué, Dorsal tracts. - Dermal sinus tract: disjunction. - Pseudo-dermal sinus tract: atretic fibrovascular stalk, Segmental spinal dysgenesis: notochordal encoding, - Klippel-Feil. - Congenital vertebral dislocation. - Caudal agenesis type I, II, Multisystem anomalies. - VACTERL, OEIS, Currarino. - Skeletal dysplasias.

Conclusions

We illustrate an integrated approach to assessment of congenital spine malformations including application of embryologic concepts, utilization of accurate anatomic terminology, and synthesis with clinical information.



(Filename: TCT_eEdE-218_Spine.jpg)

eEdE-194

6:30AM - 3:00PM

Craniopagus: Role of Neuroradiology in Defining the Challenges and Designing the Treatment

A Spiro[1], J Farinhas[2], J Goodrich[1], J Bello[1]
[1]Montefiore Medical Center, Bronx, NY, [2]Montefiore Med. Ctr./Albert Einstein College Of Medicine, Bronx, NY

Purpose
The purpose of this exhibit is: 1. To review classification of craniopagus twins. 2. To discuss challenges and optimization of patient imaging. 3. To demonstrate the utility of CT angiography/venography and MRI in the evaluation of conjoint vascularity and brain parenchyma in guiding clinical decision making and neurosurgical approach.
Materials and Methods
Content will be presented in several different categories which include: 1. Craniopagus classification. 2. Challenges to imaging. 3. What the neurosurgeon needs to know. 4. Procedural involvement by neuroradiology. 5. The value of teamwork to diagnostic efficiency and patient outcome.
Results
Reviewed topics include: 1. Craniopagus classification: a) Craniopagus nomenclature, b) Prevalence. 2. Challenges to imaging: a) Differing anesthesia requirement based on individual physiology, b) Patient positioning for CT, MRI, c) Correct patient identification throughout imaging acquisition and interpretation. 3. What the neurosurgeon needs to know: a) Variant vascular anatomy in craniopagus twins, b) Vascular dominance, bridging/shared vascularity, c) Parenchymal bridging; meningeal integrity, d) 3D-modeling…making the most of it. 4. Procedural involvement by neuroradiology: a) Pre-operative diagnostic cerebral angiography, b) Pre-operative intravascular embolization, c) Intra-operative imaging guidance. 5. The value of teamwork.
Conclusions
A multi-disciplinary approach is "mission critical" in the evaluation and treatment of craniopagus twins.

eEde-219a

6:30AM - 3:00PM

Craniosynosthosis & Cranial Vault Reconstruction

N Anand[1], T Chao[2], S Sosin[2], N Gowali[2], J Rios[3]

[1]morristown medical center, morristown , NJ, [2]Morristown Medical Center, Morristown, NJ, [3]Morristown Medical Center, Morristown , NJ

Purpose

The purpose of this exhibit is to make radiologists and clinicians aware of the different disease entities, which involve craniosynostosis. Craniosynosthosis refers to premature closure of the cranial sutures. Additionally, we will discuss the different sutures, which may be involved, with respect to their corresponding subtype of craniosynostosis. We aim to educate radiologists and clinicians regarding the imagining characteristics, epidemiology, clinical presentation, differential diagnosis, associated syndromes, and treatment options (cranial vault reconstruction) of the varying types of craniosynostosis.

Materials and Methods

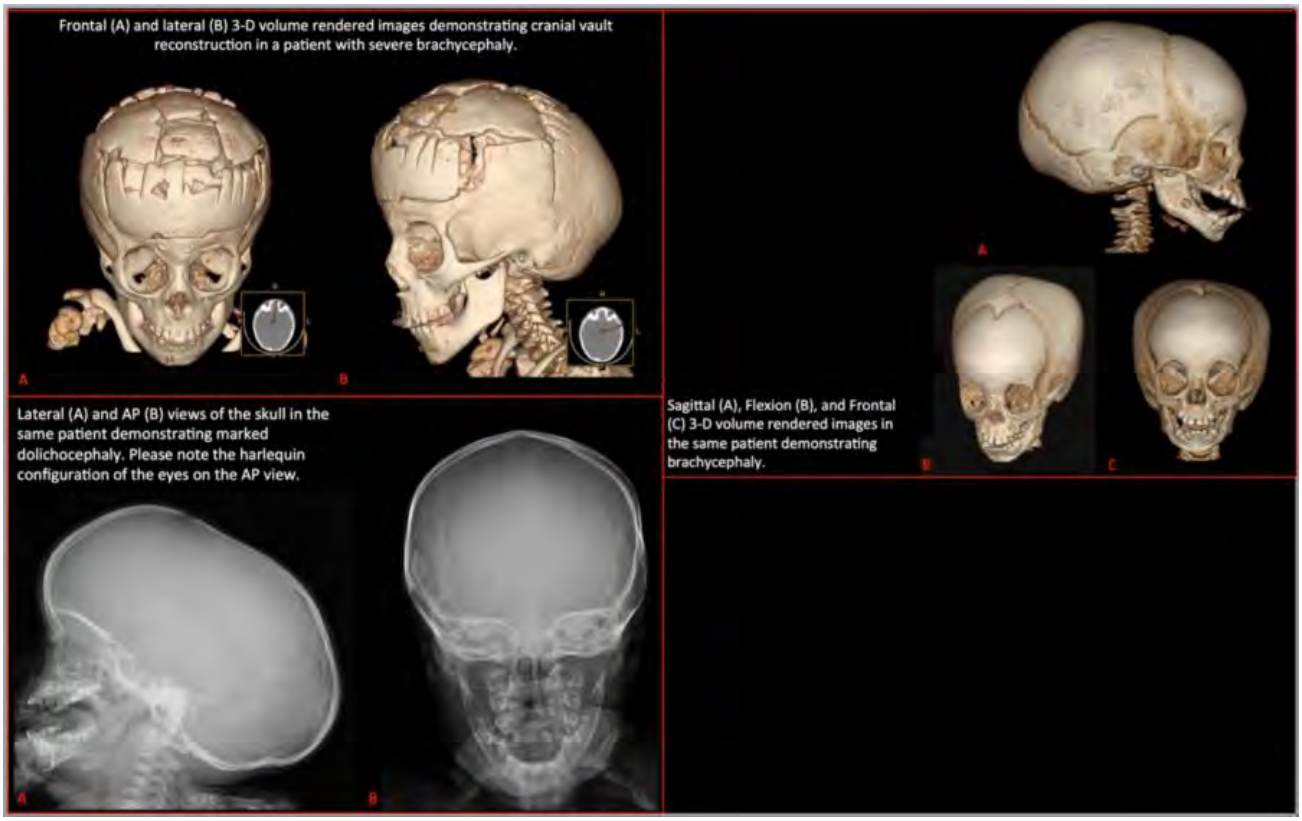
Initially, a list of different forms of craniosynostosis was made. These were subsequently entered, into a search of all radiology reports at our institution from January 8, 2008 to January 1, 2016. This method yielded hundreds of different reports in which the searched terms were used. All applicable radiology reports were read and pertinent pathological cases were compiled for use in this exhibit.

Results

Our search yielded hundreds of radiology reports across X-ray, Ultrasound, CT, and MRI modalities. The topics for discussion and review of original images (including volume rendered 3-D images) include, but are not limited to: - Brachycephaly - Dolichocephaly - Plagiocephaly - Trigonocephaly - Pachycephaly - Oxycephaly - Harlequin eyes - Crouzon syndrome - Apert syndrome - Cranial vault reconstruction

Conclusions

To conclude, we would like to make radiologists and clinicians aware of the different disease entities, which involve craniosynostosis. We aim to educate radiologists and clinicians regarding the imagining characteristics, epidemiology, clinical presentation, differential diagnosis, associated syndromes, and treatment options (cranial vault reconstruction) of the varying types of craniosynostosis.



(Filename: TCT_eEde-219a_CranialVaultReconstruction.jpg)

eEdE-209

6:30AM - 3:00PM

Disseminated Oligodendroglial-like Leptomeningeal Tumour Of Childhood: A Case Series

B Gilmartin[1], C Williamson[2]
[1]The Royal Children's Hospital, Melbourne, VIC, [2]The Royal Children's Hospital, Melbourne , VIC

Purpose
We aim to describe our institution's experience of disseminated oligodendroglial-like leptomeningeal tumor (DOLT) of childhood. We will outline the clinical and radiological findings and discuss the histopathological features of each case in our series. We will discuss the natural history of this disease including the propensity for high-grade transformation as shown in one of our cases.
Materials and Methods
Ethical approval was obtained to gather clinical information from the Electronic Medical Record (EMR) for all patients, identified through our pathology database, who presented to our institution with disseminated neoplasms with an oligodendroglial/leptomeningeal component. The relevant imaging was reviewed.

Results
The relatively novel tumor most commonly known as disseminated oligodendroglial-like leptomeningeal tumor (DOLT) of childhood is classified under neuronal and mixed neuronal glial tumors in the latest 2016 World Health Organization (WHO) classification of central nervous system tumors although the nosological status of this entity is not entirely elucidated. Patients with this rare neoplasm tend to present with acute or subacute hydrocephalus. Characteristic radiological features include leptomeningeal enhancement and subpial, T2 hyperintense lesions usually involving the basal cisterns and spinal cord. Another distinctive finding is discrete intraparenchymal lesions, which are seen more typically in the spine rather than in the brain. A disseminating, slowly progressive course has commonly been described; however, a subset of these patients demonstrates aggressive tumor biology. Histologically these neoplasms display predominant oligodendroglioma-like features with neuronal differentiating capacity and extensive leptomeningeal dissemination.
Conclusions
This educational exhibit describes our insitution's experience and reviews the current radiopathological understanding of this novel tumor.

eEdE-210

6:30AM - 3:00PM

Dynamic MR Imaging (MR fluoroscopy): Clinical Applications in Pediatric Neuroradiology

C Lacroix[1], A Shifrin[2], A Pollock[3], T Feygin[1]
[1]Children's Hospital of Philadelphia, Philadelphia, PA, [2]University of Massachusetts Medical School, Newton, MA, [3]Children's Hospital of Philadelphia, Philadelhia, PA

Purpose
To describe the technique and present the varied applications of dynamic MR imaging (MR fluoroscopy) in pediatric neuroradiology.
Materials and Methods
Dynamic cine magnetic resonance imaging (MR "fluoroscopy") is a rapidly developing technique. The dynamic sequences are based on a fast acquisition and organization of images in a sequential-loop, which results in a display of images providing the impression of observing a real-time movie of the process being studied. The sequences vary slightly between the different manufacturers, but almost any sequence sensitive to flow may be employed. These sequences are easily obtainable from a technical standpoint, and they also are easily tolerated by patients due to their short acquisition time.
Results
Dynamic cine magnetic resonance imaging (MR fluoroscopy) is designed to reveal some of the physiologic/pathologic processes in almost real time, and can be of high value in this context in imaging of physiologic and pathologic processes in the brain, spine and neck. MR

fluoroscopy offers many advantages over other dynamic imaging modalities, due to its lack of ionized radiation and short acquisition time. Both these features are particularly important in pediatric and prenatal imaging. These dynamic sequences are valuable tools in the functional assessment of intracranial or intraspinal cerebrospinal fluid (CSF) flow dynamics and in evaluation of effectiveness of endoscopic procedures. They also are useful in the evaluation of the swallowing mechanism and of phonation in children with suspected velo-pharyngeal dysfunction, sleep apnea, etc. In prenatal imaging, dynamic cine MR imaging is a valuable tool for assessment of CSF flow and swallowing patterns in fetuses with head and neck lesions.
Conclusions
We provide a comprehensive review of dynamic MR techniques with numerous examples of the utilization of dynamic MR imaging (MR fluoroscopy) in pediatric neuroradiology.

eEdE-187

6:30AM - 3:00PM

Dys-myelination, Dat-myelination: Radiologic-Pathologic Considerations in Pediatric White Matter Disorders

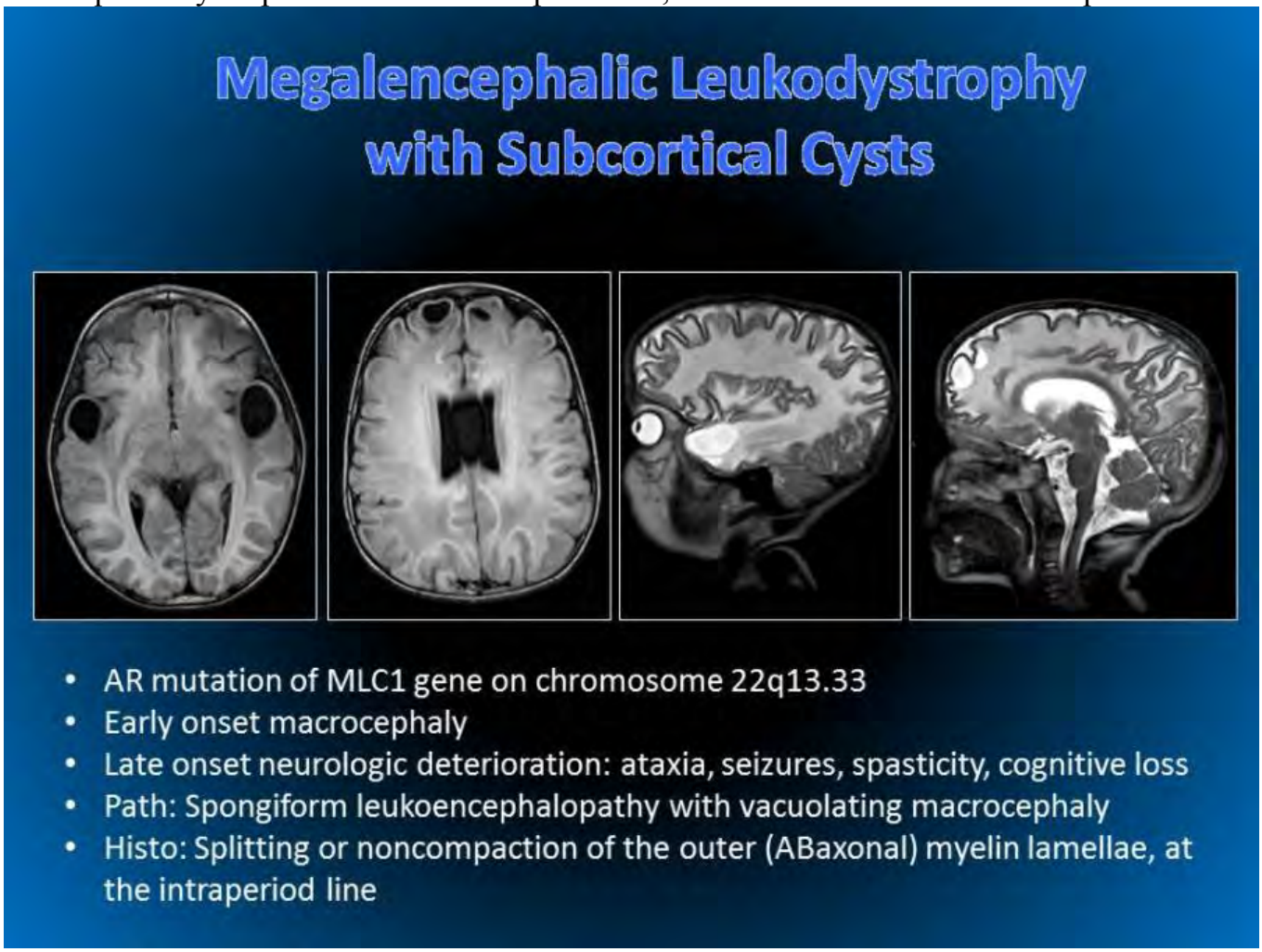
J Brucker[1], T Kennedy[2]
[1]University of Rochester Medical Center, Rochester, NY, [2]University Of Wisconsin Hospital, Madison, WI

Purpose
The purpose of this exhibit is four-fold: 1) To review the cellular/molecular processes of normal myelination, with respect to their resultant effects on MR signal change throughout white matter development. 2) To discuss the biochemical and ultrastructural causes of white matter signal abnormality in various dysmyelination syndromes, thereby correlating radiologic and pathologic mechanisms. 3) To provide the reviewer with a comprehensive overview of a wide variety of childhood white matter disorders, including classic illustrative examples and diagnostic pitfalls. 4) To propose a new conceptual framework for approaching leukodystrophy cases.
Materials and Methods
The exhibit covers three main topics: 1) Normal myelination, 2) Abnormal myelination, 3) Imaging techniques/approaches. It primarily utilizes a case-based approach for reviewing the imaging and clinical features of numerous leukodystrophy cases.
Results
Magnetic resonance imaging (MRI) is the imaging modality of choice for evaluating white matter disease. However, white matter tissue is structurally complex, and its overall signal intensity on classic MR sequences is dependent upon innumerable simultaneous proton interactions occurring at the molecular, cellular, and macroscopic levels. Furthermore, myelination and white matter development is a complicated dynamic process that

continually evolves throughout early childhood. Therefore, clinical evaluation of suspected myelination disorders usually requires molecular and genetic analysis, in addition to radiologic evaluation. In our exhibit, we review the classic (and atypical) imaging features of multiple childhood white matter disorders, specifically in relation to their histochemical mechanisms. In doing so, we hope to strengthen the reviewers' clinical knowledge of these diseases, as well as to help them anticipate the MR appearances of these disorders prospectively.

Conclusions

Myelination is a dynamic process, resulting in the creation of various discrete microenvironments within the tissue ultrastructure that ultimately affect proton interactions and MR signal. The integrity and functionality of white matter also is dependent on the very specific arrangement and composition of myelin lipids and proteins throughout the intracellular and extracellular domains. Alterations of these components result in MRI signal abnormalities, which in some cases can be traced back to cytoarchitectural flaws and cellular processes of specific myelination disorders. Additional quantitative and myelin-specific MRI techniques may help characterize these processes, in addition to standard MR sequences.



(Filename: TCT_eEdE-187_JBruckerASNR2017c.jpg)

eEdE-205

6:30AM - 3:00PM

Embryonal Tumor with Multilayered Rosettes, C19MC-altered: Clinical, Pathological and Radiological Correlation with Advanced Imaging

B Wang[1], L Ketonen[2]
[1]MD Anderson Cancer Center, Houston, TX, [2]M.D. Anderson Cancer Center, Houston, TX

Purpose

1. To illustrate the imaging findings of embryonal tumor with multilayered rosettes (ETMR) with fiber tracking and MR spectroscopy (MRS), which to our knowledge has not been systematically evaluated in the radiological literature. 2. Raise awareness of radiologists concerning this rare central nervous system (CNS) tumor.

Materials and Methods

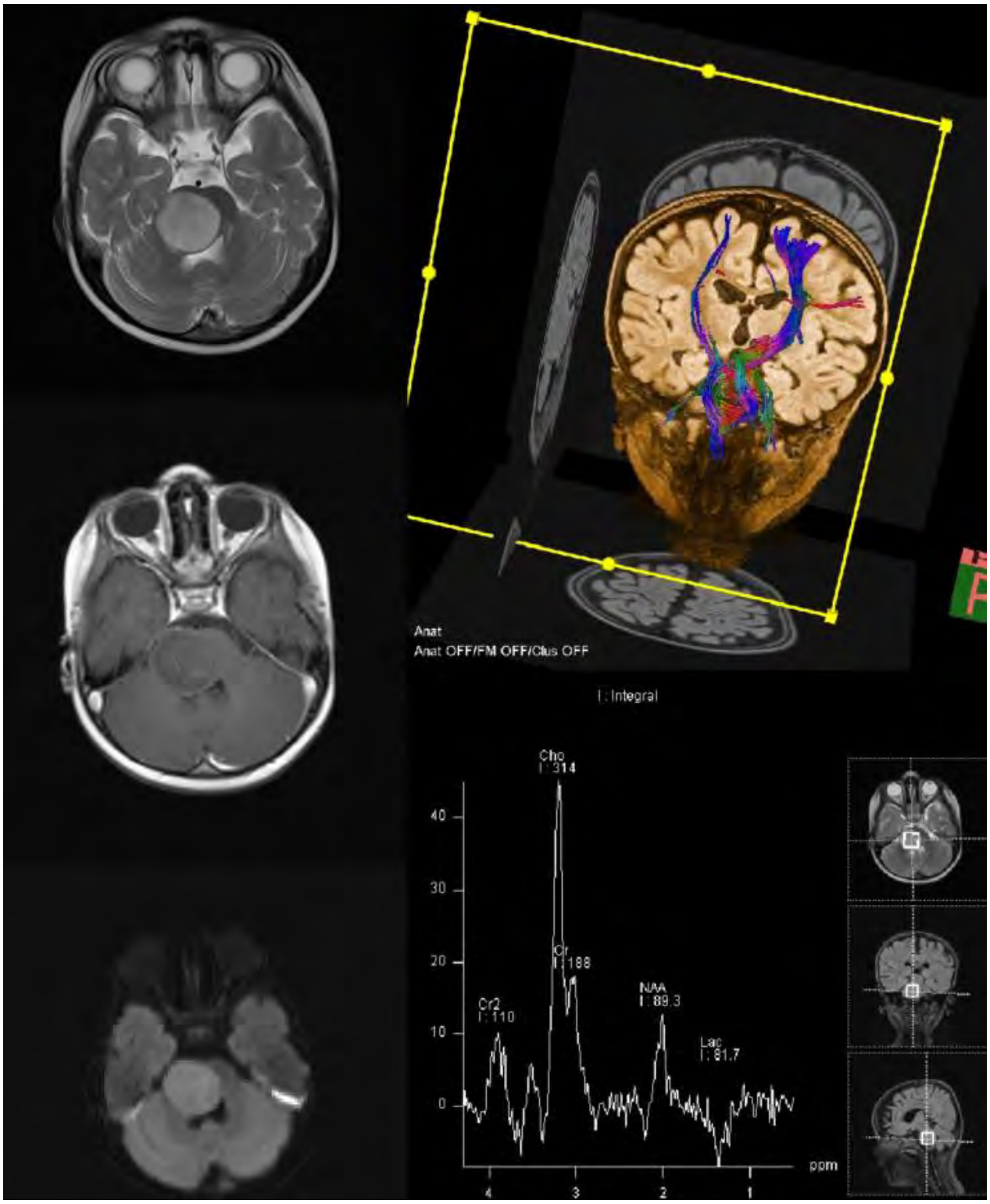
We report here a series of at least 6 tissue-confirmed cases referred to our institution between 2007 to 2015 of ETMR, which is a rare subtype of embryonal tumor of the CNS with histological spectrum led to description under 3 different tumor names: medulloepithelioma, ependymoblastoma, and embryonal tumor with abundant neuropil and true rosettes (ETANTR), originally reported in 2000. These tumors share a common molecular signature, C19MC alteration. It is formally codified in the newly revised 2016 WHO Classification of Tumors of the Central Nervous System as a single, molecularly-defined entity under the unification name of Embryonal Tumor with Multilayered Rosettes, C19MC-altered. Fewer than 100 cases of ETMR have been reported. We present here the MRS features of these tumors, together with CT and conventional MRI with diffusion-weighted imaging (DWI) and diffusion tensor imaging (DTI) with selected perfusion.

Results

All of our cases are in children (2-12 years old). There were 3 males and 3 females. Of the 6 cases, 3 were in brain stem, 1 in frontal lobe, and 2 in spinal canal. On MRI, contrast enhancement often is minimal and has no significant surrounding T2 FLAIR hyperintensity to suggest edema. The lesions are expansile in 3 of 6 case, with no imaging evidence of infiltration on fiber tracking in instances where fiber bundles were displaced. Diffusion-weighted imaging demonstrates restricted diffusion within the tumor, reflecting dense cellularity. On MRS, the choline/creatine ratio is increased with low NAA, or NAA/Cho ratio, high myoinositol, and a lipid/lactate peak. ETMRs are WHO Grade IV. MR spectroscopy and diffusion imaging patterns are typical of high-grade tumors.

Conclusions

We presented a case series of ETMR, C19MC-altered, a rare newly classified CNS tumor with advanced imaging. The knowledge gained may potentially impact patient management, especially in inoperable cases and in locations where it is risky to perform a biopsy.



(Filename: TCT_eEdE-205_ETMRabstractASNR2017Image.jpg)

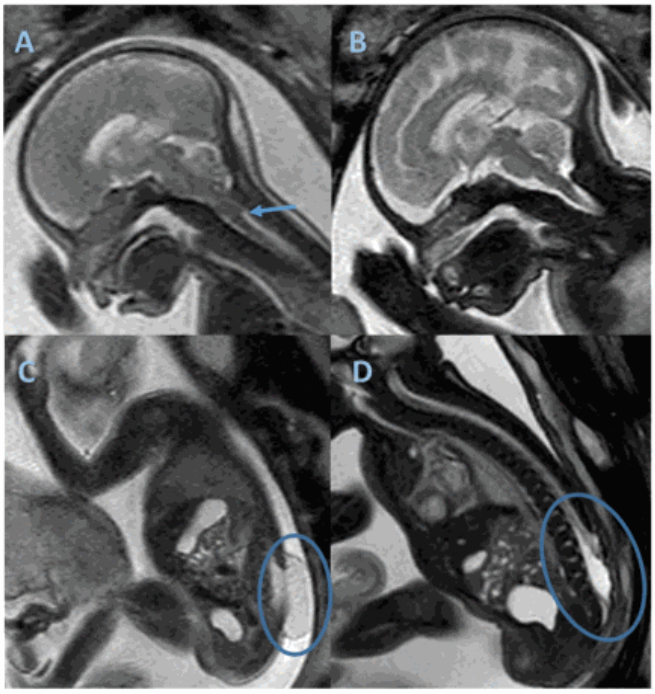
eEdE-213

6:30AM - 3:00PM

Fetal MRI Before and After in Utero Repair of Myelomeningocele: What the Neuroradiologist Should Know?

L Vidal[1], C Guimaraes[2], A Mehollin-Ray[2]
[1]Texas Children's Hospital, Houston, TX, [2]Texas Childrens Hospital, Houston, TX

Purpose
Myelomeningocele (MMC) is a congenital abnormality of the central nervous system that is diagnosed accurately in the prenatal period. Since the Management of Myelomeningocele Study (MOMS) trial demonstrated an improvement in neurological outcomes after in utero repair of MMC, the number of fetal MRIs being performed for pre- and postsurgical evaluation has increased. The purpose of this exhibit is to illustrate the fetal MRI findings in MMC before and after surgical repair.
Materials and Methods
A review of the current literature and retrospective review of typical fetal MRI imaging findings in prenatally-diagnosed MMC was performed. Illustrative cases from before and after in utero repair of MMC were selected and important findings were documented.
Results
Initially, an overview of myelomeningocele pathogenesis and findings will be provided. A review of the MOMS trial inclusion and exclusion imaging criteria for prenatal MMC surgical repair will be available in conjunction with illustrative images. The viewer then will be provided with a series of paired pre and postsurgical fetal MRI examples of both common and critical imaging findings. Areas of special attention such as ventriculomegaly, hindbrain herniation, club foot, and the repair site will be reviewed, along with dynamic evaluation of lower extremity motion. Finally, a discussion regarding optimal imaging protocol, report template and relevant report information will be available.
Conclusions
In utero repair of myelomeningocele has proven to change postnatal fetal outcome, increasing the need for fetal MRI evaluation in this population. It is important for neuroradiologists to be familiar with the prenatal imaging findings of MMC. An accurate, detailed radiology report is vital to the fetal care team for counseling and management decisions.



A - Sagittal T2-weighted pre-surgical Fetal MRI demonstrating severe hindbrain herniation into the cervical canal (arrow). **B** – Sagittal T2-weighted postoperative fetal MRI demonstrating marked interval improvement of the hindbrain. Note the posterior fossa remodeling. **C** - Sagittal T2-weighted pre-surgical Fetal MRI demonstrating a long segment of lumbosacral open neural tube defect extending from L3 to the sacrum (circle). **D** – Sagittal T2-weighted postoperative fetal MRI demonstrating interval closure of the open neural tube defect with no associated fluid collection to suggest surgical repair failure (circle).

(Filename: TCT_eEdE-213_ASNR_fetal_2017-2.gif)

eEdE-192

6:30AM - 3:00PM

From Morphological Phenotype to Genotype: Brain Abnormalities Associated with Alterations in the mTOR Pathway in Children

S Shrot[1], S Calloni[2], A Poretti[3], M Hwang[1], T Huisman[4], B Soares[2]
[1]Johns Hopkins University School of Medicine, Baltimore, MD, [2]Johns Hopkins Hospital, Baltimore, MD, [3]The Johns Hopkins University School of Medicine, Baltimore, MD, [4]Johns Hopkins, Baltimore, MD

Purpose
We review the neuroimaging findings in brain abnormalities related to alterations in the mTOR (Mammalian Target of Rapamycin) pathway, with the goal of illustrating the emerging translational trend from morphology towards genetics in the classification of malformations of cortical development.
Materials and Methods
The current classification of malformations of cortical development (MCD) is based on the interrupted embryological processes (cell proliferation, migration or cortical organization/postmigrational development) and the resulting morphological pattern. Nevertheless, the ideal developing classification will rely on knowledge of biological pathways allowing precise diagnoses and targeted therapies. It recently has been understood

that alterations affecting the mTOR signaling pathway result in diverse abnormalities such as hemimegalencephaly, ganglioglioma, focal cortical dysplasia type IIB, polymicrogyria and brain findings associated with tuberous sclerosis. We will review the mTOR pathway and the neuroimaging findings in these related entities.
Results
The mTOR signaling pathway functions as a controller of cell growth and homeostasis. There are similar neuroimaging findings in various disorders related to dysmorphic excessive neurons in hamartomatous malformations: Subcortical tubers in tuberous sclerosis, localized enlargement of dysmorphic and dysplastic brain in hemimegalencephaly, dysplastic neurons in ganglioglioma and dysmorphic neurons and balloon cells in focal cortical dysplasia type IIb, one of the most frequent lesions found in focal intractable epilepsy requiring surgical resection.
Conclusions
The landscape of classification of malformations of cortical development is evolving from a morphological description based on embryology/neuroimaging, to grouping disorders based on alterations of specific genes of genetic pathways. This approach will not only lead to improved understanding of brain development, but it also will allow precise diagnosis and potentially targeted therapies that may inhibit the mTOR pathway such as everolimus.

eEdE-216

6:30AM - 3:00PM

Getting Real with Phakomatoses: What the Neuroradiologist Needs to Know

T Richards[1], J Anderson[1], M Wien[1]
[1]*University Hospitals Cleveland Medical Center, Cleveland, OH*

Purpose
The purpose of the exhibit will be to demonstrate the role of the neuroradiologist in providing aid in diagnosis, medical and surgical management, and surveillance for complications and neoplasms in patients with phakomatoses.
Materials and Methods
The content of the presentation will be focused on education about the classic and clinically important neurological features and neuroimaging. The bulk of the educational content will be focused on the relatively common phakomatosis disorders including neurofibromatosis types I and II, tuberous sclerosis, Sturge-Weber syndrome, and Von Hippel-Lindau syndrome. Before each syndrome is discussed the imaging will be presented in a multiple-choice quiz format to make the presentation more interactive. I. Overview of phakomatoses: A. Importance of neuroimaging, i. Diagnosis, ii. Monitoring for malignant processes. B. Phakomatosis disorders, i. Relatively common, a. Neurofibromatosis type I; b. neurofibromatosis type II; c. Tuberous sclerosis; d. Sturge-Weber syndrome; e. Von Hippel-Lindau syndrome. ii. Rare, a. Ataxia Telangiectasia; b. Neurocutaneous Melanosis; c.

Meningiomatosis; d. Cowden disease. iii. Extremely rare; a. Incontinentia pigmenti; b. Wyburn-Mason syndrome; c. Haberland syndrome; d. Hypomelanosis of Ito; e. Nijmegen breakage syndrome; f. Epidermal nevus syndrome; g. PHACE syndrome; h. Progressive facial hemiatrophy; i. Gomez-Lopez-Hernandez syndrome. For all disorders under Rare and Extremely rare, basic characteristics of each disease and organ systems involved will be provided. Neuroimaging examples will be several of the rare syndromes as well.

Results

Neuroimaging plays important role in diagnosis and surveillance in many of the phakomatosis syndromes. In neurofibromatosis type 2, bilateral acoustic schwannomas are pathognomonic for the syndrome and can be identified easily on brain imaging. In von Hippel-Lindau (VHL), findings such as bilateral endolymphatic sac tumors are considered diagnostic for VHL. The diagnosis in this syndrome is very important to make early due to all of the tumors in multiple organ systems for which they are predisposed and need surveillance imaging. Surveillance neuroimaging in tuberous sclerosis is crucial to the detection of subependymal giant cell astrocytomas, which are generally treated with mTor inhibitor medical therapy and sometimes require surgical excision.

Conclusions

The neuroradiologist has a crucial role in guiding the diagnosis, surgical and medical management, and surveillance of patients with phakomatosis syndromes. Therefore, it is very important for the neuroradiologist to be able to recommend appropriate imaging and be aware of the key neoplastic and other pathologic processes for patients with these syndromes.

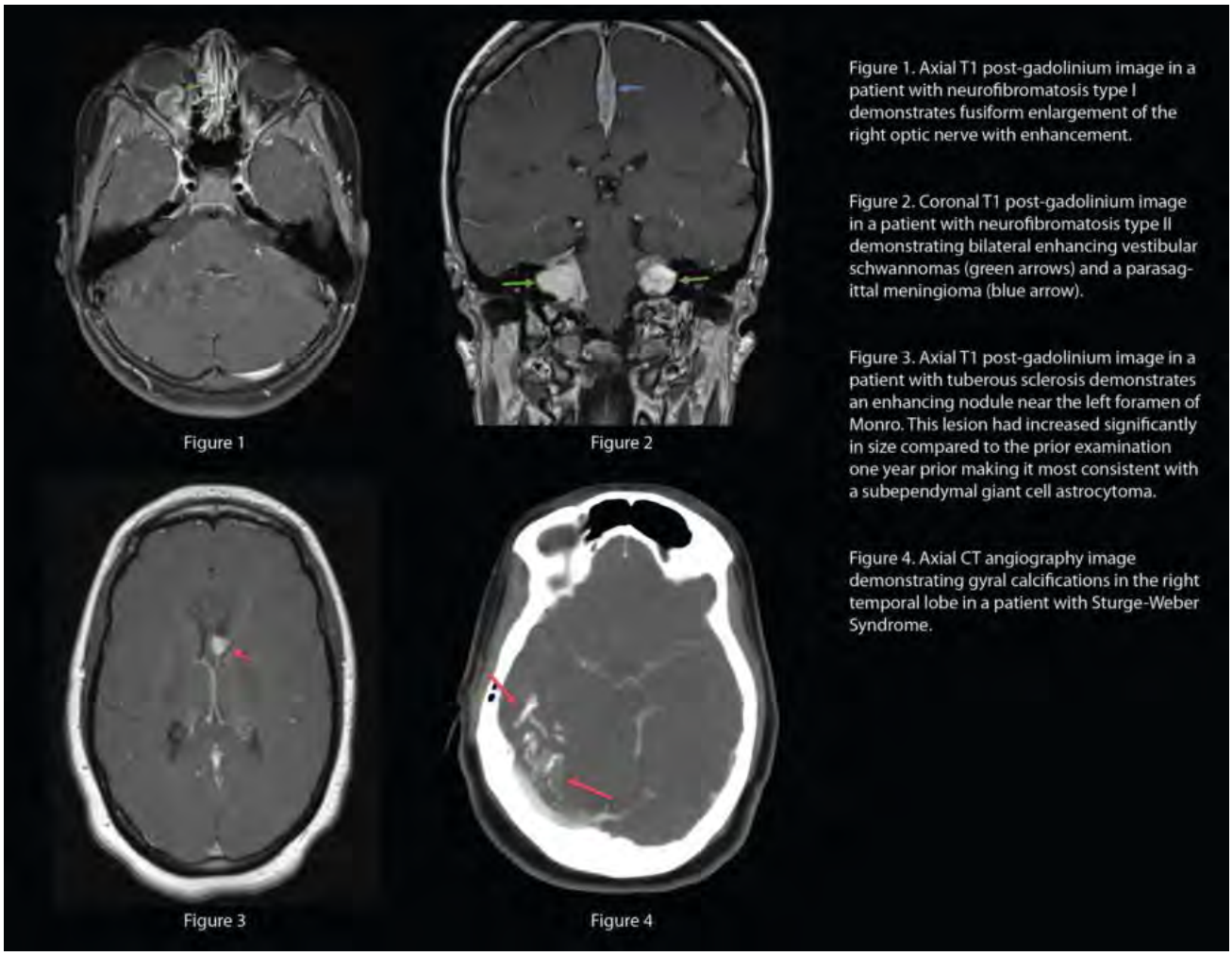


Figure 1. Axial T1 post-gadolinium image in a patient with neurofibromatosis type I demonstrates fusiform enlargement of the right optic nerve with enhancement.

Figure 2. Coronal T1 post-gadolinium image in a patient with neurofibromatosis type II demonstrating bilateral enhancing vestibular schwannomas (green arrows) and a parasagittal meningioma (blue arrow).

Figure 3. Axial T1 post-gadolinium image in a patient with tuberous sclerosis demonstrates an enhancing nodule near the left foramen of Monro. This lesion had increased significantly in size compared to the prior examination one year prior making it most consistent with a subependymal giant cell astrocytoma.

Figure 4. Axial CT angiography image demonstrating gyral calcifications in the right temporal lobe in a patient with Sturge-Weber Syndrome.

(Filename: TCT_eEdE-216_Phakomatoesabstractimagesfinal.jpg)

eEdE-188

6:30AM - 3:00PM

Imaging and Genetics of Mitochondrial Disorders in Children: It's Not Just Leigh's Disease

R Clarke[1], J Pascual[1], N Rollins[1]
[1]*UT Southwestern Medical Center, Children's Health Dallas, Dallas, TX*

Purpose
Mitochondrial disorders may be due to defects in nuclear or mitochondrial DNA with diverse phenotypes. The purpose of this exhibit is to describe key imaging findings and their differential diagnosis, and to discuss the genetics of the multiple disorders affecting mitochondrial function.

Materials and Methods

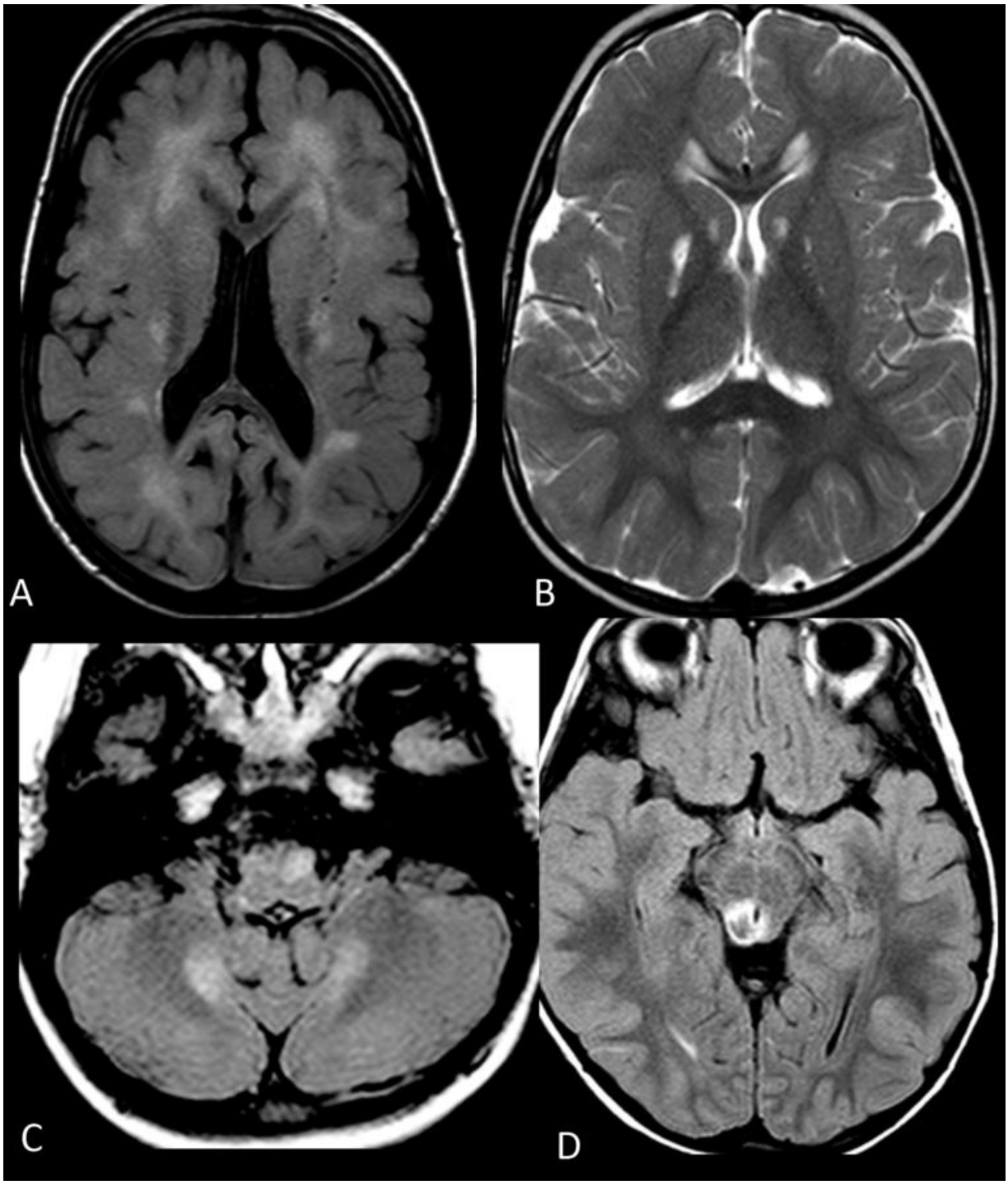
We reviewed the imaging findings and genetics of 40 children with metabolic disorders due to mitochondrial dysfunction imaged at our tertiary pediatric referral center over a decade.

Results

Single site 10-year experience with children ages newborn-16 years presenting with seizures and developmental delay with or without developmental regression for MR imaging. We report the imaging findings for mitochondrial disorders related to both nuclear and mitochondrial DNA, including D-2-hydroxyglutaric aciduria (Fig. A), Leigh Syndrome associated disorders (Figs. B, C, D), Kearns Sayre, MELAS, glutaric aciduria type 2, etc.

Conclusions

With an understanding of the imaging appearance and genetics of mitochondrial disorders, the radiologist can provide essential information that may help to direct further testing.



(Filename: TCT_eEdE-188_mitochonasnr2017.jpg)

eEdE-217

6:30AM - 3:00PM

Imaging Perinatal Spinal Dysraphisms: Clinical Conundrums and Diagnostic Dilemmas

M McDonald[1], J Bykowski[1]
[1]*University of California at San Diego, San Diego, CA*

Purpose

In the course of this educational exhibit, we will review basic developmental anatomy of the fetal spine and spinal cord and highlight the imaging hallmarks of the spectrum of spinal dysraphisms, with an eye on key radiological features aiding early detection and diagnosis. After reviewing this educational exhibit, the reviewer will be able to: 1. Review the appearance of the fetal spine during development using both ultrasound and MRI, with attention to normal anatomic variants. 2. To discuss the imaging hallmarks of the most common spinal malformations encountered in the fetal setting, including: - Myelocele and myelomeningocele, - Lipomyelomeningocele and intraspinal lipoma, - Thickened filum and tethered cord, - Neurenteric cysts and dermal sinuses, - Caudal regression/sacral agenesis, - Hemivertebrae and other bony malformations, - Syndromic constellations (e.g.,VACTERL) associated with spinal dysraphisms. 3. To correlate prenatal findings on ultrasonography (US) and magnetic resonance imaging (MRI) with imaging appearances on postnatal MRI and clinical outcomes.

Materials and Methods

Ultrasonography is a well established method of investigating the spinal canal and cord in the prenatal setting and infancy, as incompletely ossified spinal arches create an acoustic window permitting transmission of the ultrasound beam. In recent years, fetal MRI also has served as a useful adjunct in the evaluation of known or suspected prenatal/neonatal spine malformations, with a particularly vital role in delivery planning and surgical management. In the course of this exhibit, basic fetal US and MRI protocols will be reviewed, with special attention on the necessary views to evaluate the sacral skin and to localize the neural placode and conus medullaris. Examples of protocolling pitfalls and associated artifacts on both MRI and US will be provided to highlight technical considerations that limit early identification of spinal dysraphisms. Then, we will use a longitudinal case series to highlight the appearance of common spinal dysraphisms on both fetal US and MRI with attention to the time course of presentation and evolution over the course of development.

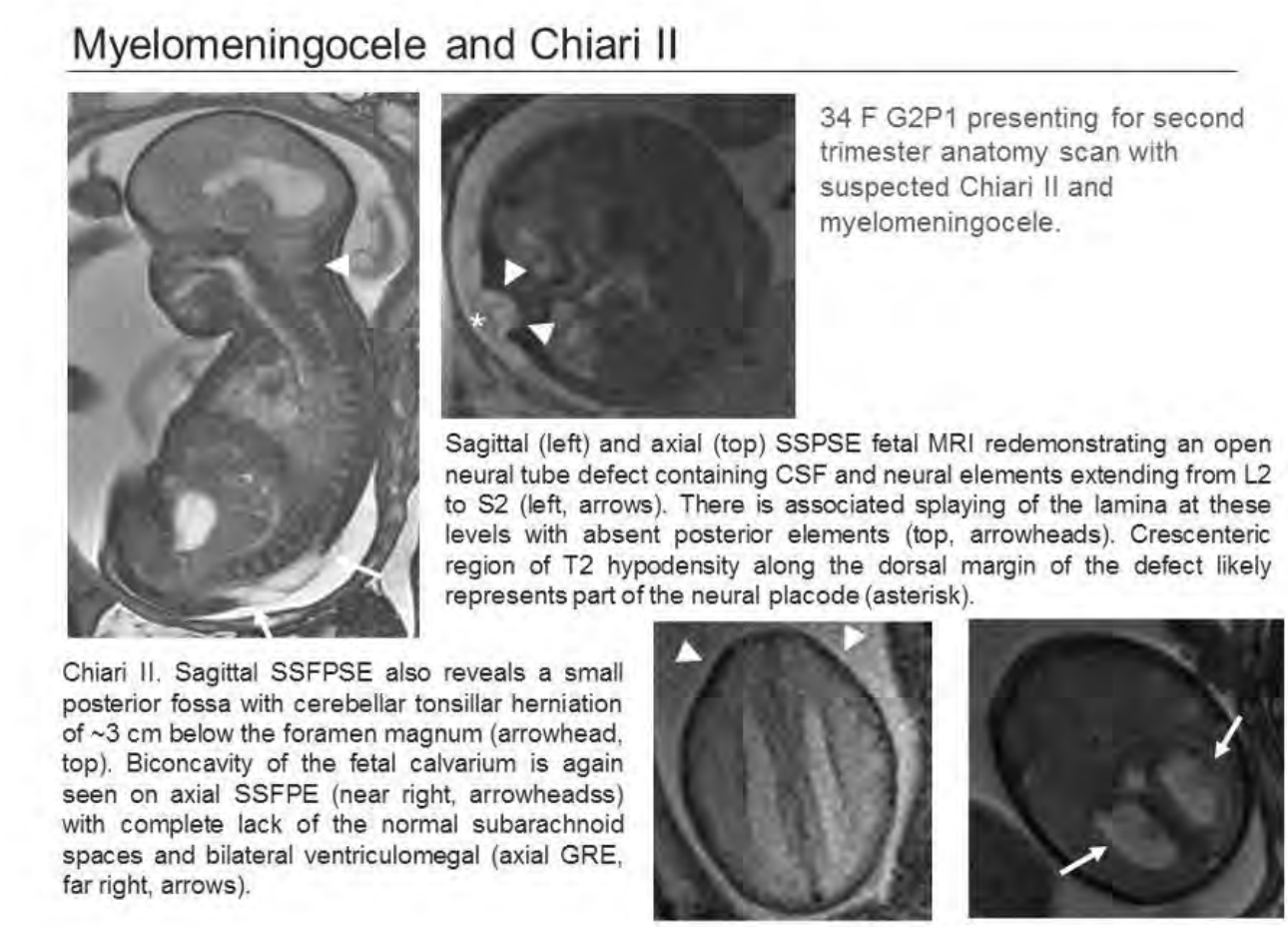
Results

Spinal dysraphism refers to a spectrum of congenital anomalies resulting in a defective neural arch through which meninges or neural elements are herniated. Dysraphism, in some form, is estimated to involve 1-3 per every 1000 live births in the United States. At the most basic level, dysraphisms are divided into two broad categories: aperta (visible external lesions) and occulta (no external lesion). As each type of dysraphism lends itself to different management approaches, and carries disparate clinical outcomes, early and accurate diagnosis is of critical importance in the prenatal setting. Ultrasonography is a well established method of investigating the spinal canal and cord in the prenatal setting and infancy, as incompletely ossified spinal arches create an acoustic window permitting transmission of the ultrasound beam. In recent years, fetal MRI also has served as a useful

adjunct in the evaluation of known or suspected prenatal/neonatal spine malformations. Familiarity with the common sonographic and MRI appearances of spinal dysraphisms enables the clinician to provide early and accurate diagnosis of developmental anomalies of the spinal cord, which in turn can be crucial for both delivery planning and surgical management.

Conclusions

Prenatal imaging with US and MRI allows for precise examination of the spinal canal and aids the radiologist in the identification of significant pathologic conditions. Detection is predicated upon a complete understanding of the normal developmental anatomy of the spinal cord and associated structures, as well as a familiarity of the imaging hallmarks of dysraphism on both US and MRI. Early and accurate diagnosis facilitates appropriate clinical management, involving anything from delivery planning to neonatal surgical techniques, which reduces patient complications and improves overall clinical outcomes.



(Filename: TCT_eEdE-217_asnrfetal3.jpg)

eEdE-204

6:30AM - 3:00PM

Imaging, Pathology and Molecular Biology of Pediatric Intra-Axial Brain Tumors

T Sasaki[1], T Moritani[2], T Sato[1], A Capizzano[2], Y Sato[1], P Kirby[2], M Sato[1]
[1]University of Iowa, Iowa City, IA, [2]University of Iowa Hospitals and Clinics, Iowa City, IA

Purpose

To assess WHO classification, genetic profile and imaging features in pediatric patients with intra-axial brain tumors.

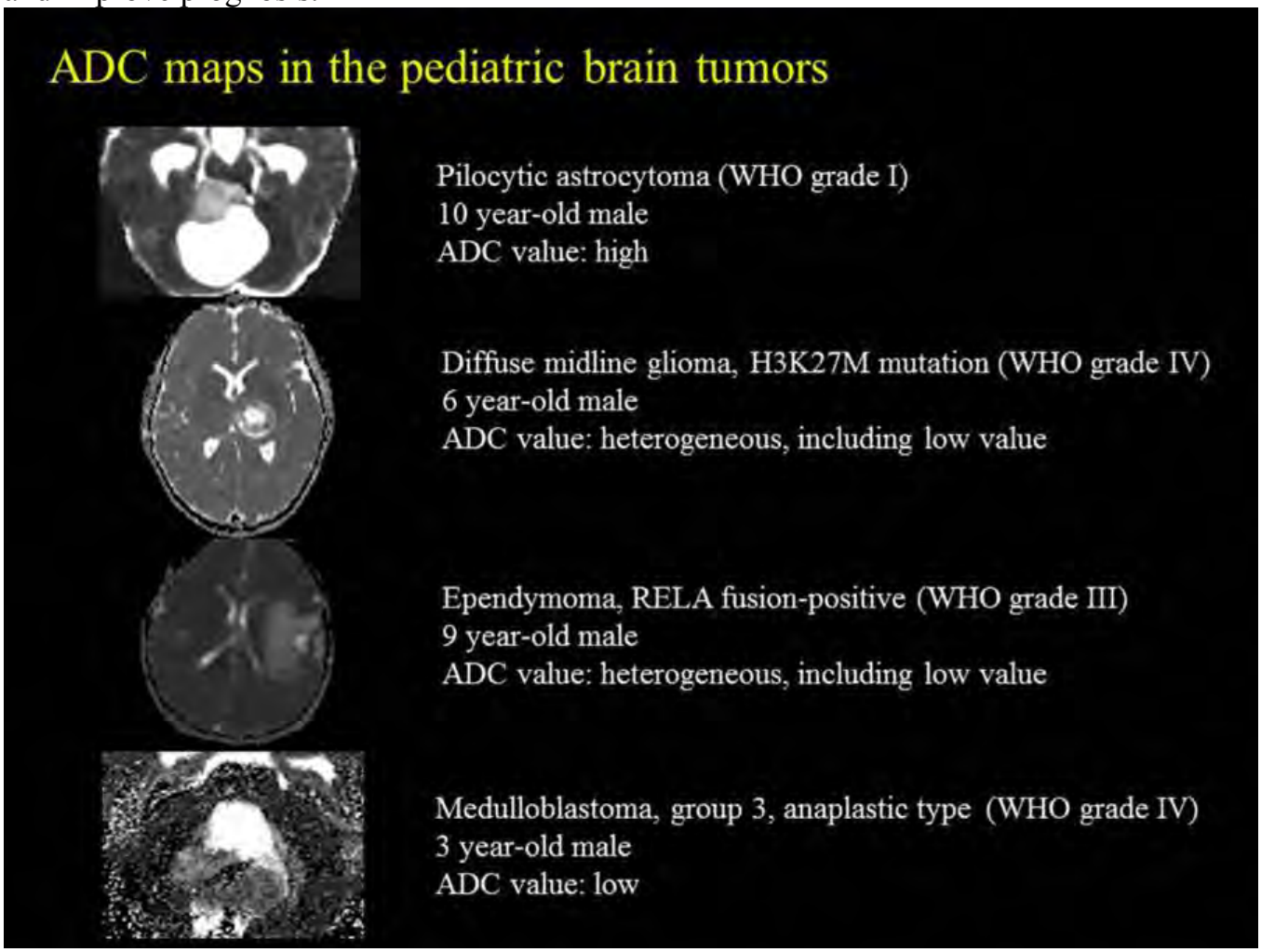
Materials and Methods

We assessed genetic profile and imaging features on magnetic resonance imaging (MRI) in pediatric patients with pilocytic astrocytoma (PA), subependymal giant cell astrocytoma (SEGA), pleomorphic xanthoastrocytoma (PXA), Diffuse midline glioma, H3 K27M-mutant, glioblastoma (GBM), ependymoma/anaplastic ependymoma, medulloblastoma (MB), atypical teratoid-rhabdoid tumor (ATRT), and embryonal tumor with multilayered rosettes (ETMR).

Results

Pilocytic astrocytomas could develop in the infratentorial or supratentorial regions. Pilocytic astrocytomas are correlated with the development of KIAA1549:BRAF fusion gene, which frequently appears in the infratentorial tumors. MR imaging shows both cystic and well-enhanced solid components in the tumors, and apparent diffusion coefficient (ADC) could be high. Subependymal giant cell astrocytoma has a strong association with tuberous sclerosis, which shows well-enhanced mass commonly in the lateral ventricles. Plepomorphic xanthoastrocytoma is related with BRAF point mutation, and the imaging features are cystic and solid components within the mass in the supratentorial regions. Diffuse midline glioma, H3 K27M-mutant is defined as an infiltrative midline high-grade glioma with a H3K27M mutation, which can develop in the pons, thalamus, or spinal cord. MR imaging shows T2 hyperintensity occasionally accompanied with necrosis or hemorrhage. Lower ADC in the tumor could be an adverse prognostic factor. Both primary and secondary GBMs in the pediatric patients could develop based on genetic susceptibility, such as p53 mutation. Ependymoma and anaplastic ependymoma develop more frequently in the posterior fossa than the supratentorial region. MR imaging shows well-circumscribed heterogenous enhancement with moderate ADC values. Ependymoma, RELA fusion-positive is an independent supratentorial lesion which shows an adverse prognostic factor. Medulloblastomas are classified into subgroups according to a combination of the genetic profile (WNT-activated, SHH-activated, group 3, group 4) and histology (classic, desmoplastic/nodular, extensive nodularity, large cell/anaplastic). Apparent diffusion coefficient values in the MBs usually decrease. SHH-activated types could locate in the cerebellar hemisphere compared with other subtypes. ATRT which has inactivation of SMARCB1 or SMARCA4 genes and ETMR with altered of the C19MC gene show low values in the ADC maps.

Conclusions
Understanding genetic point-of-view and imaging features might make an early diagnosis and improve prognosis.



(Filename: TCT_eEdE-204_FigureforASNR3.jpg)

eEdE-185

6:30AM - 3:00PM

Intracranial Arteriovenous Malformation and Arteriovenous Fistula in Children: Review of Radiologic Findings

L Yen[1], H Lee[2]
[1]*Rutgers- New Jersey Medical School, West Orange, NJ,* [2]*New Jersey Medical School, Rutgers University, Newark, NJ*

Purpose
Intracranial arteriovenous malformation (AVM) and arteriovenous fistula (AVF) in children are two different causes of intracranial hemorrhage. Arteriovenous malformation is the more

common disease with prevalence from 0.04% to 0.5% of general population. Congenital dysregulated angiogenesis is the cause and peak incidence is around 20-40 years. The usual presentation is intracranial hemorrhage. Treatment options for AVM include surgical resection, endovascular embolization, gamma knife radiosurgery and proton beam therapy. Arteriovenous fistula is rarer with incidence 10 times rarer than AVM. Peak age for AVF is 40-60 years. Various etiologies have been associated with AVF, including trauma, postsurgery, and venous thrombosis. Hemorrhagic risk of AVF varies depending on venous drainage pattern and it is more often associated with symptoms due to shunting such as heart failure and intracranial hypertension. Arteriovenous fistula usually is treated by endovascular embolization with n-BCA glue or Onyx. In this exhibit, we will review the distinguishing radiologic features of intracranial AVM and AVF.

Materials and Methods

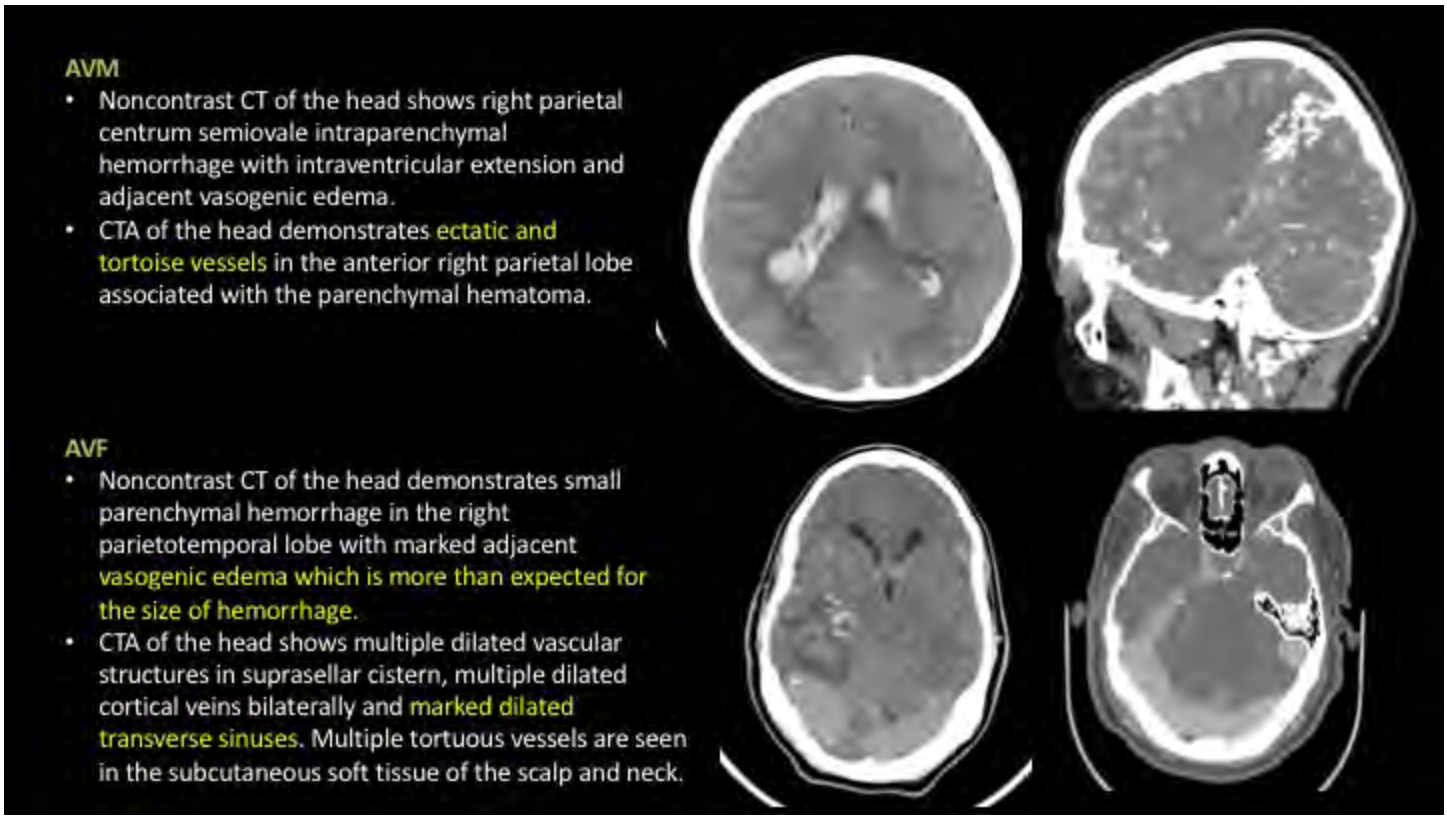
Angiographic proven cases of intracranial AVM and AVF will be used to illustrate different radiologic features between the two entities. The patients underwent noncontrast CT of the head, CT angiogram (CTA) of the head and digital subtraction angiography. The CT examinations were performed with 64 slice scanner with high volume bolus of intravenous contrast material. Digital subtraction angiography was performed utilizing biplanar fluoroscopy.

Results

Arteriovenous malformation presents with tangling blood vessels between the supplying artery and drainage vein. In AVF, the supplying artery and the drainage vein are connected directly without intervening vessels. Detection of tangling blood vessels within brain parenchyma associated with area of hemorrhage is hallmark of AVM, while AVF presents as dilated vessels in the sulci and cistern. Marked dilatation of venous sinus and vasogenic edema out of proportion to the size of hematoma are additional character of AVF. Arteriovenous fistula is graded according to Spetzler-Martin grading system, which consists of size of nidus, eloquence of involved brain, and venous drainage. Arteriovenous fistula is classified based on Borden or Cognard classification system. Both classification take into account of direction of flow and presence of cortical venous drainage. Deep cerebral venous drainage of AVM is associated with poorer prognosis while cortical venous drainage is associated with more aggressive form of AVF.

Conclusions

Intracranial arteriovenous malformation and fistula are two different entities with different radiologic feature and classification systems. Prompt recognition is important to stratify patients into different prognostic groups and for treatment planning.



(Filename: TCT_eEdE-185_Figure.jpg)

eEdE-206

6:30AM - 3:00PM

Intracranial Manifestations of Pediatric Leukemia

S Zheng[1], N Desai[2], A Kamali[1], E Bonfante[1], R Riascos[1], R Patel[1]
[1]The University of Texas Health Science Center, McGovern Medical School, Houston, TX, [2]Texas Children's Hospital Baylor College of Medicine, Houston, TX

Purpose
1. Describe the direct central nervous system (CNS) manifestations of leukemia in pediatric patients. 2. Describe the common CNS findings as results of the toxic effects of therapy (chemotherapy, radiation, bone marrow transplantation). 3. Describe the imaging features of metabolic alterations, coagulopathies, and opportunistic infections in children with leukemia.
Materials and Methods
Retrospective chart review at two major children's hospital in Houston, TX was undertaken. Pediatric patients with leukemia were identified and relevant neuroimaging studies were reviewed and correlated with clinical presentations and relevant pathologies when available. Cases of leukemic meningitis, leukemic spinal and ocular involvement, chloroma, stroke, cerebral hemorrhage, parenchymal volume loss, metabolic disturbances, dural venous sinus

thrombosis, opportunistic CNS infections, and chemotherapy related CNS toxicities were presented.
Results
Many pathological conditions affect the CNS in pediatric patients with leukemia. These conditions may be direct manifestations of the primary disease, related to toxic effects of therapies (radiation, chemotherapy, and bone marrow transplantation), or reflective of opportunistic CNS infections due to profound immunosuppression.
Conclusions
Leukemia in pediatric patients often produce various CNS manifestations as well as related often nonspecific neurological symptoms. Recognition of the neuroimaging features of these conditions is crucial for timely and appropriate clinical intervention to reduce morbidity and mortality.

eEdE-195

6:30AM - 3:00PM

MRI Atlas of Normal Fetal and Pediatric Brain Development

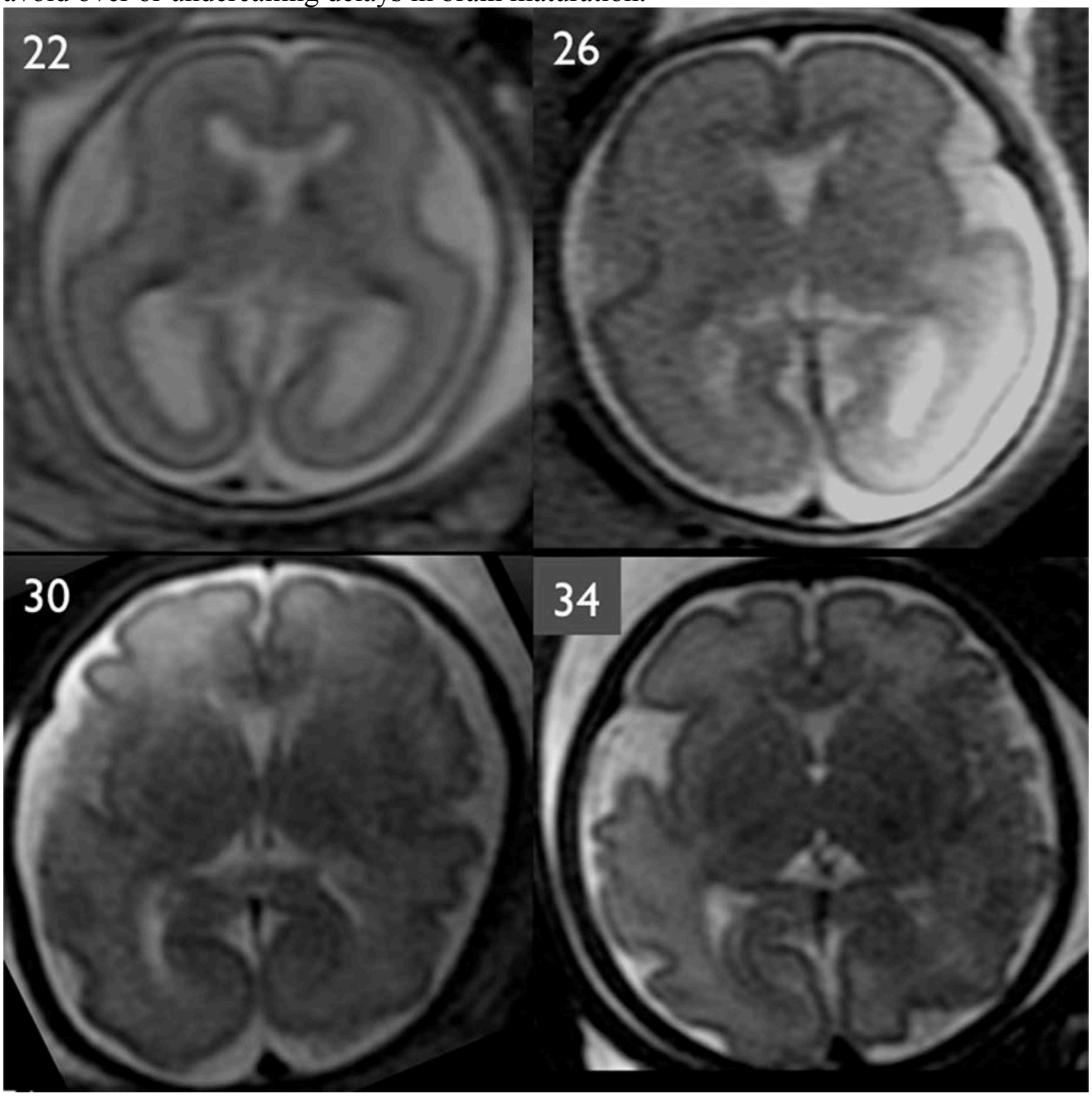
L Lai[1], M Shiroishi[1], T Sato[2], K Yeom[3], J Acharya[1]
[1]University of Southern California, Keck School of Medicine, Los Angeles, CA, [2]University of Iowa, Iowa City, IA, [3]Lucile Packard Children's Hospital, Palo Alto, CA

Purpose
Recognizing the dynamic, varied appearance of the normal fetal and pediatric brain on magnetic resonance imaging (MRI) is one of the most challenging aspects of pediatric neuroradiology given the brain's rapid development during the early years of life. The goal of this educational exhibit is to provide a stepwise illustrative atlas in movie format of the normal MRI appearance of the brain from age 17 weeks to 2 years old. Our goal is to provide a reference normal brain MRI atlas and identify key milestone features that can help radiologists differentiate normal versus abnormal (i.e. delayed sulcation or delayed myelination).
Materials and Methods
We retrospectively collected cases of patients with normal brain MRIs in the fetal and newborn/infant periods. We excluded patients that were pre-term. For the fetal brains, which ranged from 17 weeks to 38 weeks gestational age, we included 3-plane T2-weighted MRI sequences. For the pediatric brains, which ranged from 1 day to 2 years old, we included axial diffusion-weighted imaging (DWI), T1-weighted, T2-weighted, and T2-weighted FLAIR MRI sequences.
Results
A pictorial MRI atlas of the evolving brain from the fetal to infant period will be presented. Characteristic landmark features of the developing brain will be highlighted, including landmark milestones of sulcation, myelination, and corpus callosum development. We will

also review the rationales behind the dynamic imaging characteristics of myelination. In the example figure, axial single-shot fast spin-echo T2 images of fetuses ranging from 22 to 34 weeks gestational age (wga) demonstrates the progressive increase in sulcation. At 22 wga, the T2 hypointense germinal matrix can be seen lining the ventricles and caudate head. The germinal matrix regresses in the third trimester.

Conclusions

After reviewing this exhibit, the reader will become familiarized with varied MRI appearances of the fetal and pediatric brain over different ages. Recognizing key MR features of the normal brain development over these dynamic ages can help radiologists avoid over or undercalling delays in brain maturation.



(Filename: TCT_eEdE-195_fetalbrain.jpg)

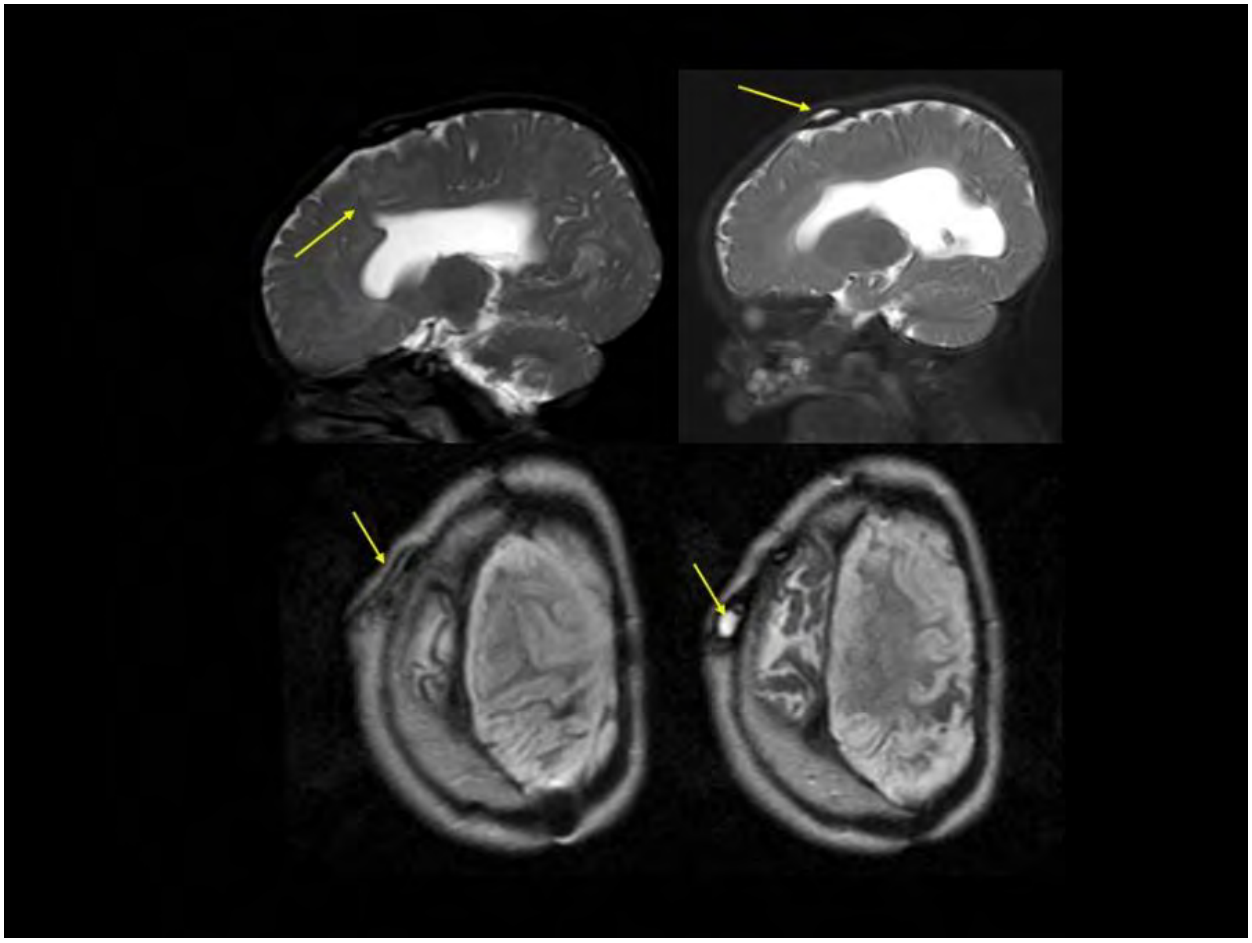
eEdE-198

6:30AM - 3:00PM

New Trends on Treatment of Pediatric Hydrocephalus. The Information that the Neurosurgeons Need

E Bonfante[1], R Riascos[2], R Patel[3]
[1]The University of Texas Health Science Center Houston UTHealth, Houston, TX, [2]UTHSC-Houston, Houston, TX, [3]University of Texas Health Science Center, Houston, Houston, TX

Purpose
To present a pictorial review of imaging findings in treated pediatric hydrocephalus. To discuss optimal imaging protocols in pediatric patients with hydrocephalus. To review the treatment modalities used by neurosurgeons to treat pediatric hydrocephalus.
Materials and Methods
Using a case-based approach, we illustrate the imaging findings of patients with treated hydrocephalus and discuss tips to provide the neurosurgeons with the relevant information while limiting radiation exposure and the need for sedation/anesthesia.
Results
Pediatric hydrocephalus is caused by a variety of conditions including intraventricular hemorrhage, infection, central nervous system (CNS) tumor, neural tube defects, aqueductal stenosis, and idiopathic intracranial hypertension. Treatment options depend on the etiology. Temporary treatment is based on medical therapy or on transient surgical maneuvers such as lumbar tapping, subcutaneous reservoir with repeated tapping, and external ventricular drainage. Endoscopic third ventriculostomy (ETV), choroid plexus cauterization, and stented ETV are moderately invasive surgical techniques. Many patients still need a definitive treatment with ventriculoperitoneal shunting. Goals of the imaging evaluation include the determination of the etiology, the assessment of changes in the ventricular size, and the evaluation of the shunt catheters. Both CT and MRI have advantages and disadvantages. Strategies that limit exposure to ionizing radiation, limit motion artifact, and avoid anesthesia are preferred.
Conclusions
The radiologists play an important role in the evaluation of patients with treated pediatric hydrocephalus. Knowledge of the specific information that the surgeons need in a given time in the evolution of this condition is essential to optimize the imaging modalities used.



(Filename: TCT_eEdE-198_Pedihydro.JPG)

eEdE-207

6:30AM - 3:00PM

Pediatric Leukocoria: What are we looking for?

N Supakul[1], S Kralik[2], C Ho[1]
[1]Indiana University School of Medicine, Indianapolis, IN, [2]Indiana University, Indianapolis, IN

Purpose
To demonstrate a step-by-step approach of interpreting ophthalmologic pathologies causing leukocoria based on specific magnetic resonance imaging (MRI) pulse sequences.
Materials and Methods
Leukocoria is an abnormal pupillary light reflection, resulting from loss of the normal red reflex due to light reflection from the blood-rich retina. All causes of leukocoria are a serious threat for vision loss and for specific pathologies, mortality. The most common cause of leukocoria is retinoblastoma. Other causes include persistent hyperplastic primary vitreous (PHPV), Coats disease, toxocaral endophthalmitis, retinopathy of prematurity (ROP), retinal

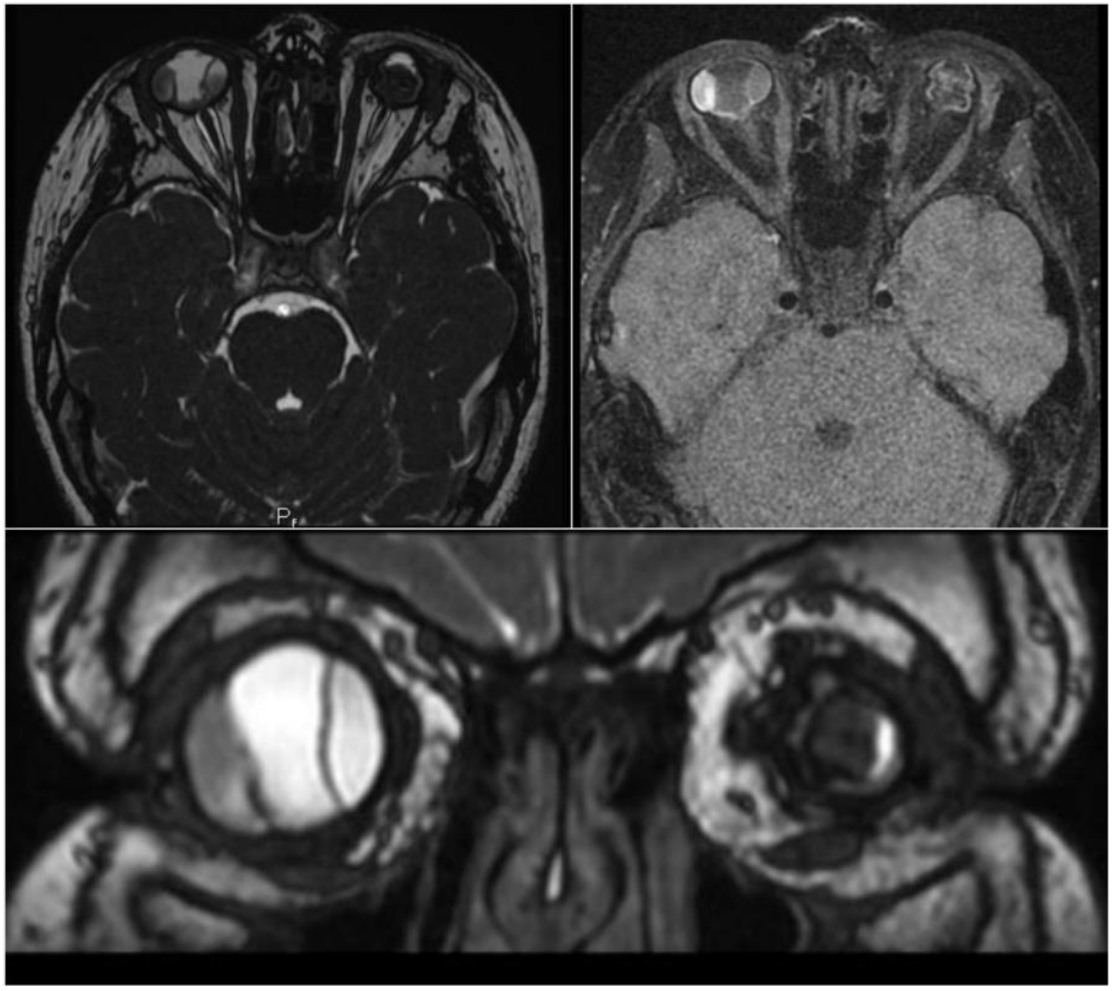
astrocytic hamartoma, choroidal colobomas, and vitreous hemorrhage. Magnetic resonance imaging plays an important role for the work up and differential diagnosis as well as further management.

Results

We will demonstrate several cases of congenital and acquired pathologies causing pediatric leukocoria. Imaging checklists and key imaging findings in each MRI pulse sequences will be highlighted as a tool for interpretation. T1 image checklists include subacute blood products, proteineous content and fat. T2 image checklists include shape and contour of the globe, optic nerve and pathway, detailing size, shape and symmetry. SWI/GRE image checklists include hemosiderin and calcification. DWI checklist includes potential tumor grading. Additional technical factors which reduces field inhomogeneity during SWI/GRE/DWI sequences and higher resolution T2 3D sequences to increase sensitivity of lesion detection will be discussed. The various pathologies we will demonstrate using this method include retinoblastoma, PHPV, Coats disease, toxocaral endophthalmitis, ROP, retinal astrocytic hamartoma, choroidal colobomas and vitreous hemorrhage.

Conclusions

Cross-sectional imaging, especially MRI, is a valuable adjunct to ophthalmoscopy in diagnosing pediatric leukocoria. Understanding the importance of different imaging sequences and having a diagnostic checklist in each sequence can improve accuracy in interpretation, assisting clinicians in optimizing patient counselling and management.



(Filename: TCT_eEdE-207_choroidal.jpg)

eEdE-215

6:30AM - 3:00PM

Phakomatoses: An Imaging Review

M Campbell[1], R Murtagh[1]
[1]*University of South Florida, Tampa, FL*

Purpose
To review the cutaneous and neurologic pathology of selective neurocutaneous syndromes with an emphasis on neuroimaging.
Materials and Methods
Neurocutaneous syndromes, also called phakomatoses, are a diverse group of more than 30 distinct entities. The central nervous system (CNS), skin, viscera, and connective tissue are primarily affected. Here we provide a review of select phakomatoses, including the most common disorders such as neurofibromatosis type 1 (NF1), neurofibromatosis type 2 (NF2), tuberous sclerosis complex (TSC), Von Hippel-Lindau (VHL) syndrome and Sturge-Weber

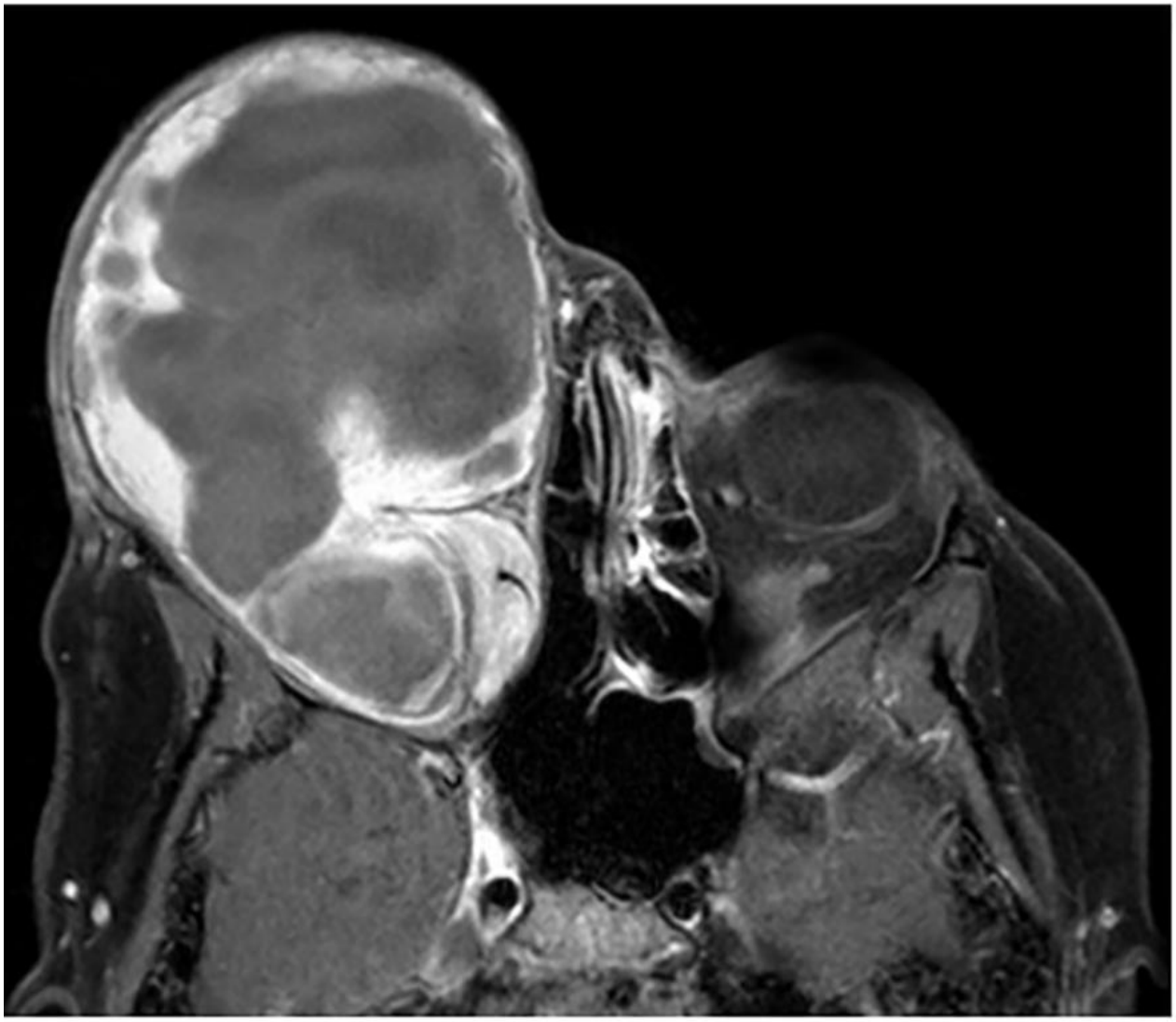
syndrome (SWS). Other entities such as neurocutaneous melanosis, Hereditary Hemorrhagic Telangiectasia (Osler Weber Rendu), and Basal cell nevus syndrome (Gorlin's disease) also will be reviewed.

Results

Phakomatoses are a diverse group of congenital disorders arising from abnormalities of neuroectodermal and mesodermal development. This results in skin, visceral, connective tissue and central nervous system abnormalities. They have varying inheritance patterns and often present in early childhood or adolescence. Many of the syndromes confer an increased risk of neoplastic formation. Of the many purposes for neuroimaging, its main role is its diagnostic utility, owing to the pathognomonic appearance of some cases and it may confirm clinical suspicion of a particular entity. Neuroimaging also is of paramount importance in excluding family involvement and in monitoring the course of disease.

Conclusions

The presentation and imaging of the different neurocutaneous syndromes are highly variable. Neuroimaging techniques including CT and MRI are important in not just the diagnosis of phakomatosis patients, but also to help guide their treatment and subsequent follow up. Screening programs may help curtail late diagnosis, which may improve outcomes.



(Filename: TCT_eEdE-215_phakomatosisgiantong.jpg)

eEdE-214

6:30AM - 3:00PM

Phakomatoses: Molecules to Morphology

M Ho[1], D Babovic-Vuksanovic[1], M Tollefson[1], J Chen[1], M Patterson[1]
[1]*Mayo Clinic, Rochester, MN*

Purpose
Utilize genetics as a framework for understanding multisystem manifestations of the

phakomatoses. Demonstrate the value of multispecialty clinical/imaging expertise in evaluation of these patients.

Materials and Methods

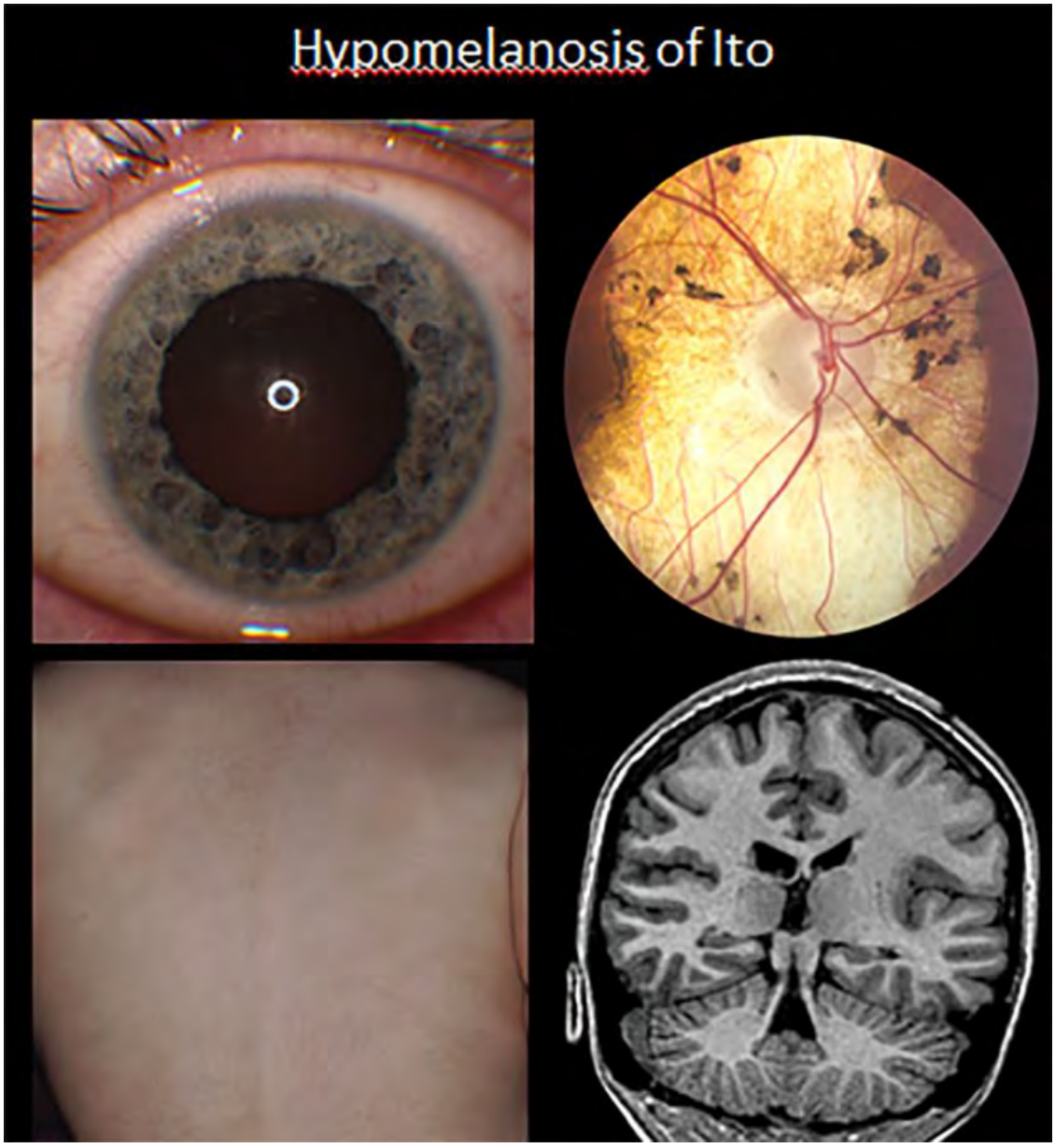
The phakomatoses are complex multisystem ectodermal disorders, the diverse manifestations of which are best understood from a developmental/embryologic perspective. Multidisciplinary clinical and imaging assessment are key for patient diagnosis and follow up. We present several illustrative examples of the common and rare neurocutaneous syndromes, with integrated interdisciplinary discussion including genetic etiology, dermatologic/ophthalmologic manifestations, central nervous system malformations, and other pertinent multisystem findings.

Results

Common syndromes: - Neurofibromatosis type 1: neurofibromin. - Neurofibromatosis type 2: schwannomin. - Tuberous sclerosis: hamartin + tuberin. - Von Hippel-Lindau: cell cycle, VEGF. Vascular syndromes: - Sturge-Weber, - Parry-Romberg, - Wyburn-Mason, - Diffuse neonatal hemangiomatosis, - PHACES. Rare syndromes: - Ataxia-telangiectasia: ATM, - Basal cell nevus: PTCH1, SUFU, - Neurocutaneous melanosis: NRAS, - Mosaic hypopigmentation: incontinentia pigmenti, ypomelanosis of Ito. - Encephalocraniocutaneous lipomatosis: FGFR1. Overgrowth syndromes: PI3K-AKT, RAS/MAPK pathways: - Epidermal nevus, - PIK3CA: macrocephaly-capillary malformation, Klippel-Trenaunay-Weber, CLOVES. - PTEN: Cowden, Bannayan-Riley-Ruvalcaba, - AKT1-3: Proteus, - RASA1: capillary malformation-arteriovenous malformation, Parkes-Weber

Conclusions

Phakomatoses are multisystem abnormalities that initially can be recognized by their cutaneous and ophthalmologic manifestations. Genotype-phenotype correlation plays a central role in diagnosis, prognosis, and treatment. Targeted imaging should include the neuraxis, and is important for initial patient assessment as well as surveillance.



(Filename: TCT_eEdE-214_Figure.jpg)

eEdE-211

6:30AM - 3:00PM

Post-mortem High Resolution Magnetic Resonance Imaging of the Fetal Brain: Characterization of Normal and Pathological Development

E Scola[1], S Avignone[1], C Cinnante[1], G Palumbo[1], G Conte[1], S Boito[2], N Persico[2], F Triulzi[1]
[1]Fondazione Irccs Ca' Granda Ospedale Maggiore Policlinico Milano, Milan, Italy, [2]Fondazione Irccs Ca' Granda Ospedale Maggiore Policlinico Milano, Milano, Italy

Purpose
To describe the use of post-mortem high resolution magnetic resonance imaging (HRpmMRI) in the assessment of fetal central nervous system (CNS) development and in the validation of prenatal MRI findings of CNS malformations.
Materials and Methods
We collected HRpmMRI of 35 fetuses (mean gestational age (GA) = 22 weeks (w); range = 17-33 weeks) after a voluntary termination of pregnancy (TOP) or after a spontaneous intrauterine death (IUD). The HRpmMRI was performed on a 3T scanner without any fixation and without removing the brain from the skull within 33 hours from delivery. The specimens preservation status was assessed based on CNS swelling and transitional layers identification and correlated with obstetric data. Fetuses referred for extracranial abnormalities and without CNS anomalies were used to describe normal fetal brain development with a particular focus on 19 and 22 w of GA. In fetuses with CNS malformations the HRpmMRI findings were compared with prenatal MR findings.
Results
A positive correlation between brain swelling and time from delivery was observed; fetuses scanned more than 24 hours from delivery or after IUD were inadequate for diagnostic evaluation. HRpmMRI allowed the identification of fetal brain laminar organization and the depiction of changes in contrast properties of CNS structures from 19 to 22 w of GA. HRpmMRI confirmed prenatal MRI findings in 13/13 cases with CNS anomalies with a more precise characterization of CNS malformations in 6/13.
Conclusions
HRpmMRI performed on unfixed in situ fetuses preserves the natural tissue contrast and the skull integrity and is a reference to correctly assess fetal brain development. The HRpmMRI overcomes the technical and diagnostic limitations of prenatal MRI (1, 2) allowing the precise depiction of the structural and signal changes involved in normal and pathological brain development. HRpmMRI do not replace conventional autopsy but shows advantages as it is less sensitive to brain autolysis (3).

eEdE-219b

6:30AM - 3:00PM

Posterior Fossa Tumors, A Case Based Review

J Saini[1], N Anand[2], L Kriger[3], K Scherer[1], P Manvani[1], J Rios[3]
[1]Morristown Medical Center, Morristown, NJ, [2]morristown medical center, morristown , NJ, [3]Morristown Medical Center, Morristown , NJ

Purpose
The purpose of this exhibit is to make radiologists and clinicians aware of the different posterior fossa tumors in children. Additionally, we will discuss the different locations (supratentorial vs. infratentorial), pathologies, grading systems, imaging characteristics, and

prognoses. Posterior fossa tumors have a different differential in children than in adults. Brain tumors are the second most common pediatric malignancy overall.

Materials and Methods

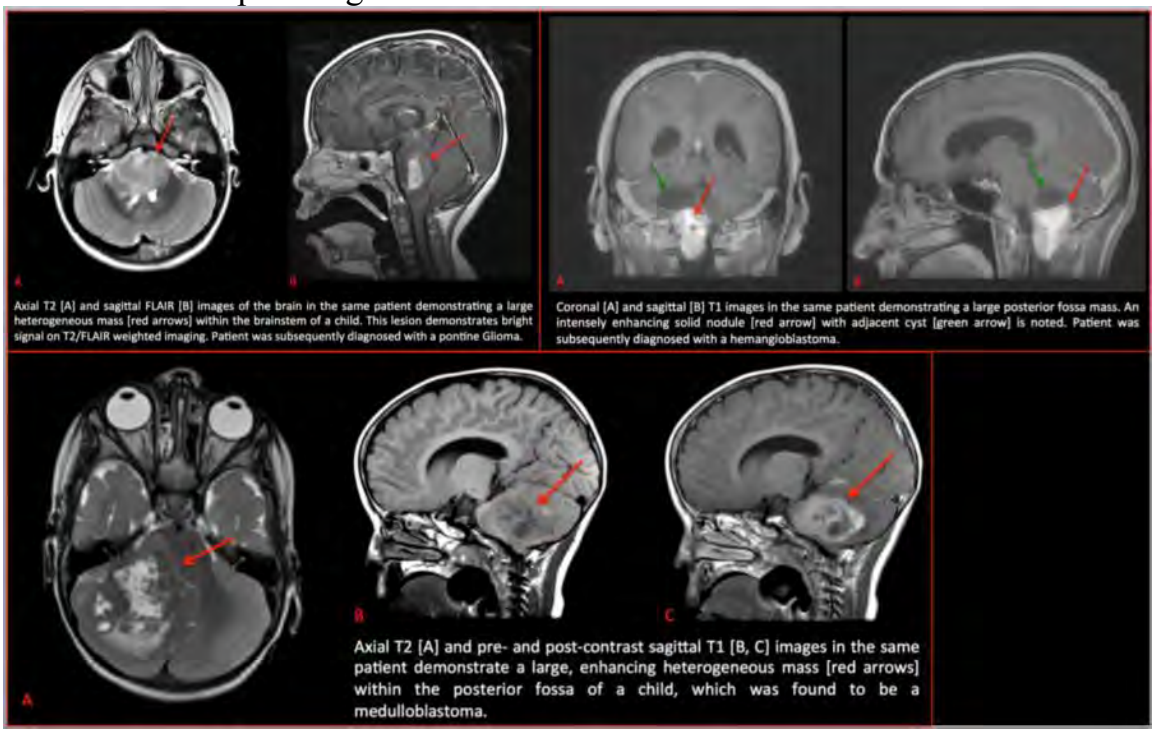
Initially, a list of different posterior fossa tumors were made. These were subsequently entered into a search of all radiology reports at our institution from January 8, 2008 to January 1, 2016. Filters were placed to exclude adolescent and adult patients. All applicable radiology reports were read and pertinent pathological cases were compiled for use in this exhibit.

Results

Our search yielded hundreds of radiology reports across CT and MRI modalities. The topics for discussion and review of original images include, but are not limited to: - Pilocytic astrocytoma - Brainstem/pontine gliomas - Medulloblastoma - Ependymoma - Atypical teratoid/rhabdoid tumor - Hemangioblastoma - Teratoma

Conclusions

To conclude, we would like to make radiologists and clinicians aware of the different posterior fossa tumors in children. We aim do educate the audience regarding imagining characteristics and pathology of different posterior fossa tumors, by utilizing the aforementioned pathological cases.



(Filename: TCT_eEdE-219b_PosteriorFossaTumors.jpg)

eEdE-200

6:30AM - 3:00PM

Radiographic Findings of Tuberous Sclerosis and Implications for Surgical Treatment of Epilepsy

N Beachy[1], C Ho[1]
[1]*Indiana University School of Medicine, Indianapolis, IN*

Purpose

To describe characteristics of brain lesions in tuberous sclerosis complex (TSC) patients that can be used to reliably predict the epileptogenic zone.

Materials and Methods

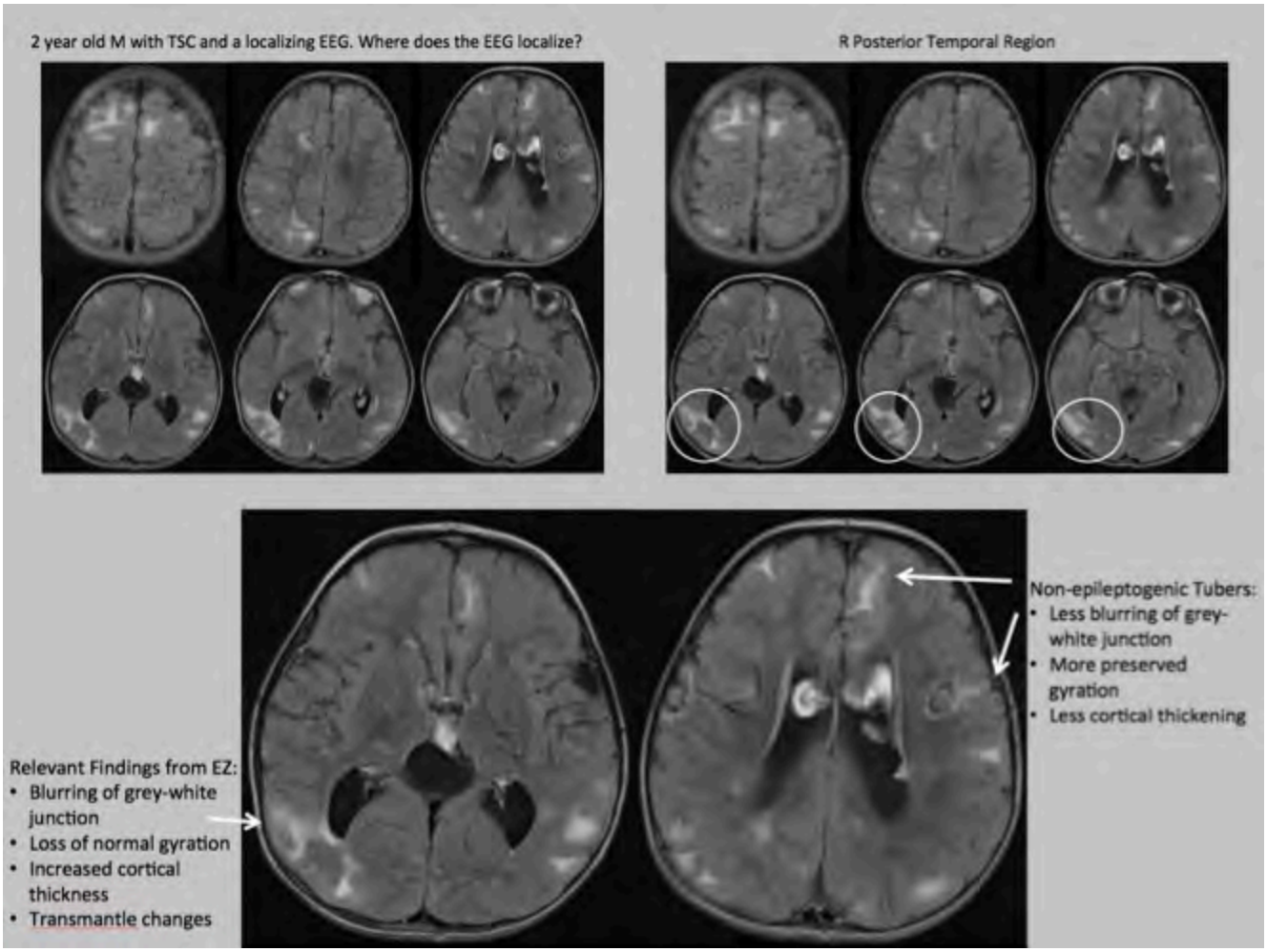
A brief review of the pathogenesis of TSC will be performed. Illustrative cases will be presented focused on localization of the epileptogenic zone in TSC and surgical management from a literature review.

Results

In TSC patients who underwent surgical resection for management of epilepsy, findings of focal cortical dysplasia in areas of resected cortex were more predictive of a successful resection than were tuber size, cystic lesions, or calcifications. Specifically, increased cortical thickness, gray/white matter junction blurring, abnormal gyration, and transmantle changes were predictive of successful resection of epileptogenic foci. Additionally, tubers demonstrating hyperperfusion on pulsed arterial spin labeling (PASL) correlated to seizure frequency, while no correlation was found between number of tubers and seizure frequency. Similarly, increased alpha-methyl tryptophan (AMT) uptake on PET scanning, which is a marker of serotonin synthesis, predicted successful epileptogenic resection.

Conclusions

Seizures are a highly prevalent and debilitating sequela of TSC. In many of these patients, surgery has been shown to improve seizure frequency and quality of life. It is possible to pre-operatively identify epileptogenic foci with MRI and functional imaging. Areas of cortex that demonstrate gray/white junction blurring, increased cortical thickness, abnormal gyration, and transmantle changes are more likely to be epileptogenic. Using multimodality imaging such as hyperperfusion on PASL and increased AMT PET uptake, pre-operative imaging is a valuable tool alongside EEG and clinical presentation for optimal localization of the resection site.



(Filename: TCT_eEdE-200_Graphic.jpg)

eEdE-189

6:30AM - 3:00PM

Resting-State fMRI Utility in Seizure Disorders

A Chaudhry[1], H Sair[2]
[1]Johns Hopkins Medicine, Elkridge, MD, [2]Johns Hopkins Medicine, Baltimore, MD

Purpose
Epilepsy is a prevalent clinical condition with huge socioeconomic burden on society. Advancement in understanding of pathophysiology and underlying neuromechanisms have led to improved clinical diagnostic criteria and development of a multitude of treatment regimens. Imaging generally has played a secondary role in evaluation of these patients. However, with the rapid evolution of functional magnetic resonance imaging (fMRI), neural systems associated with seizure disorders have been uncovered. In this review, we aim to

discuss the role of advanced imaging including task- and resting-state fMRI (rsfMRI) in seizure disorders.
Materials and Methods
1- Discuss patholophysiology of epilepsy. 2- Review principals of task- and rs-fMRI. 3- Discuss role of various connectomes in epilepsy and discuss role of default mode network subregions, lateral frontal areas (within a frontoparietal network associated with cognitive control), basal ganglia, hippocampus, frontal lobe (including the orbitofrontal cortex) and less consistently the cingulate cortex and thalamus as well as the insula, and cerebellum. 4- Discuss common pearls and pitfalls of functional MRi.
Results
1- Role of various neurotransmitters including GABA and acetylcholine as they relate to pathways in epilepsy. 2- Pictorial review of rsFMRI findings within the DMN, frontotemporoparietal lobes, as well as deep gray nuclei and cerebellum. 3- Discuss rsFMRI activation patterns used in evaluation of patients pre and postictal states.
Conclusions
Task- and Resting-state fMRI can help identify pattern of brain regions associated with alterations in neuronal connectivity, can provide clues to alterations in neuronal activity in pre and postictal states and also can potentially serve as a guide for monitoring treatment response.

eEdE-219

6:30AM - 3:00PM

Revisited Imaging Findings and Pathophysiology of Abusive Head Trauma with Emphasis on Diffusion-Weighted Imaging

I Elhelf[1], R Oral[1], T Sato[1], A Capizzano[1], Y Sato[1], M Amarneh[1], T Sasaki[1], T Moritani[1]
[1]*University of Iowa Hospitals and Clinics, Iowa City, IA*

Purpose
To provide an update on the pathophysiology and magnetic resonance imaging (MRI) findings of abusive head trauma (AHT), with emphasis on diffusion-weighted imaging (DWI).
Materials and Methods
We conducted a literature review of recent publications regarding AHT, focusing on pathophysiology, MRI findings and prognostic features of imaging findings. We then reviewed our institutional AHT investigation group database for representative cases.
Results
Main mechanisms of AHT include impulsive or impact loading as well as strangulation. There are many imaging findings associated with AHT. Subarachnoid hemorrhage, subdural or epidural hematoma/fluid collection can occur due to damage of subarachnoid, intradural and extradural vessels,and meninges. Parenchymal injuries include brain contusions, hypoxic

ischemic encephalopathy, diffuse axonal injury, and excitotoxic brain injury. Brain contusions can occur due to forces transmitted to the brain parenchyma. Hemorrhagic contusions such as those seen in adult head injuries are less common in infants due to physiologic differences such as a thin, soft calvarium with smooth inner skull table and differences in mechanism of trauma. Cerebral blood flow may be compromised due to vascular injuries in the neck. Superimposed apnea may lead to HIE. Brain injury may additionally result from excitotoxic response to release of glutamate. On MRI, temporal evolution of SDH is slower compared to that of intraparenchymal hematomas due to increased oxygen content in the CSF. Diffusion-weighted imaging is more sensitive in detecting cytotoxic edema and delineating the extent of brain injury and is useful to evaluate the timing of injury. SWI and GRE are sensitive to detect hemorrhagic lesions. Recent research has linked specific imaging findings on DWI, SWI, DTI and MRS to the early diagnosis and prognostication.

Conclusions

Neuroradiology plays an important role in evaluation of AHT. Recent research links imaging findings to the more detailed diagnosis and clinical outcomes of AHT. Neuroradiologists need to be familiar with imaging findings of AHT and prognostic imaging features when caring for these patients.

eEdE-197

6:30AM - 3:00PM

Taking a Wrong Turn Somewhere: Neuronal Migrational Anomalies

S Wright[1]
[1]*University of Arkansas for Medical Sciences, Little Rock, AR*

Purpose

Most practicing neuroradiologists have a treasure trove of cases which feature these unfortunate neuronal migrational anomalies. The trainees lucky enough to spend a sufficient amount of time may have the opportunity to peruse such a database and familiarize themselves with the ins and outs of the topic. For the rest of the trainees, or for the neuroradiologist who finds herself far from a pediatric patient population, a good primer of the topic may be very useful. This would serve to provide an overview of the cortical migration pathways, what "normal" looks like, and several characteristics of the "abnormal" patterns. Hopefully, after a brief presentation, practitioners of many training levels might come away with something helpful.

Materials and Methods

These cases come from the teaching file of a 359-bed pediatric referral center. High-quality imaging examples of several anomalies with be presented, some of them illustrated via multiple modalities, such as computed tomography (CT), magnetic resonance imaging (MRI), and ultrasound (US).

Results
Conditions discussed (and for which pictures will be included) include: lissencephaly, a normal premature brain with immature sulcation, schizencephaly, pachygyria, polymicrogyria, gray-matter heterotopia, band heterotopia, migrational anomalies brought on from TORCH infection, and more.
Conclusions
This brief overview of the normal development of the cerebral cortex will serve as a succinct refresher to the radiology trainee or neuroradiologist. For those that do not often encounter neuronal migrational anomalies, spending a few minutes looking at high-quality examples of them while reviewing the underlying embryology will be time well spent before the next time they are encountered in practice.

eEdE-201

6:30AM - 3:00PM

Temporal Lobe Epilepsy Tumors and their Mimics

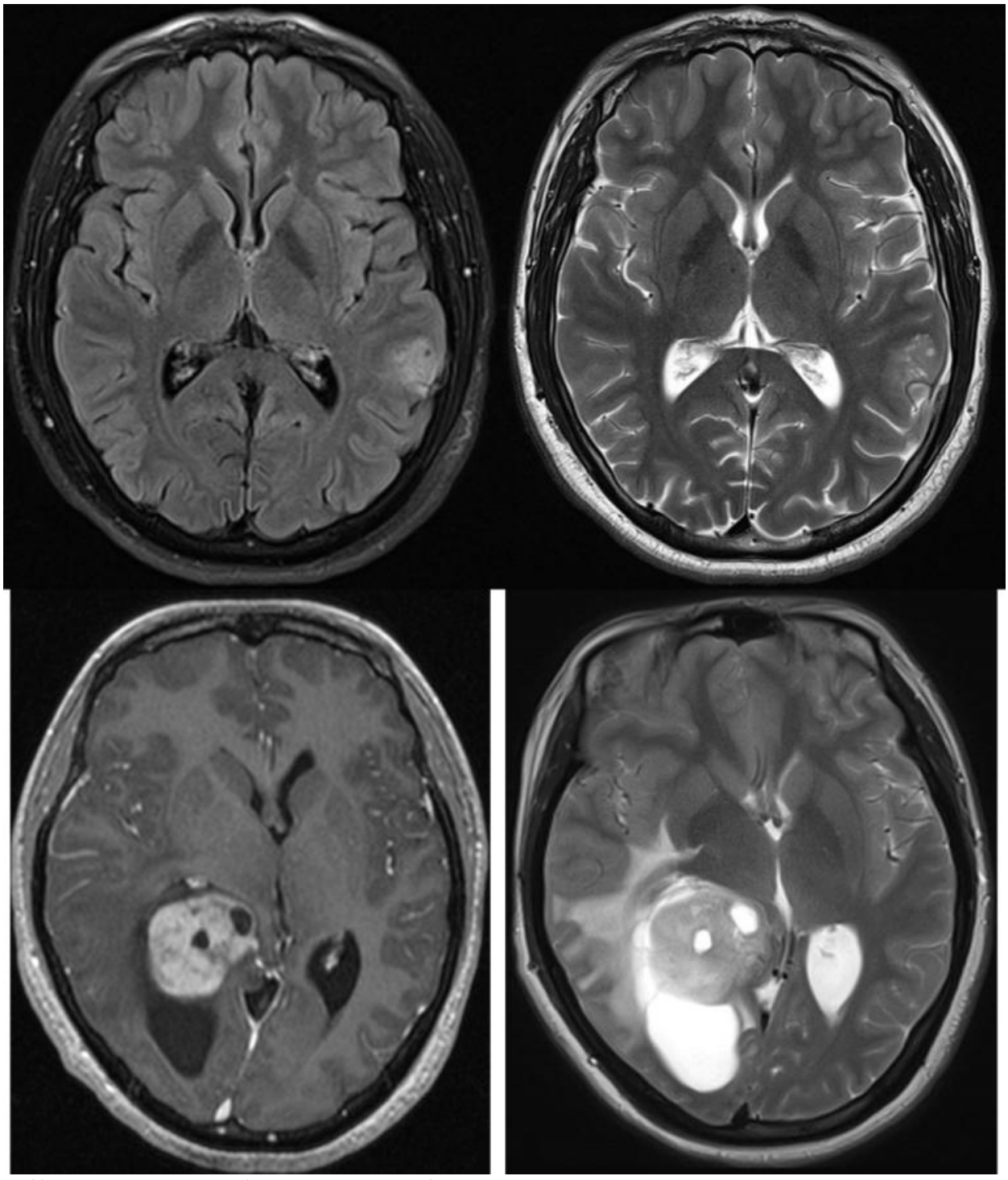
E Greif[1], B Barrett[2], G Cruciata[1], L Portnow[1], J Shah[1], E Stein[1]
[1]Maimonides Medical Center, Brooklyn, NY, [2]Maimonides Medical Center,, Brooklyn, NY

Purpose
The purpose of this presentation is an educational review of both benign and malignant temporal lobe neoplasms associated with the presentation of epilepsy in both adult and pediatric patients and differential diagnoses such as stroke, post-ictal changes, herpes encephalitis, and mesial temporal sclerosis.
Materials and Methods
We present a pictorial review of neoplasms occurring in the temporal lobe and resulting in epileptic events. Tumors include both benign and malignant pathologies, including gangliogliomas, oligodendrogliomas, pilocytic astrocytomas, desmoplastic infantile gangliogliomas, dysembryoplastic neuroepithelial tumors (DNET), and pleomorphic xanthastrocytomas. We also will discuss potential mimics in diagnosis including post-ictal changes, mesial temporal sclerosis, and HSV-2 with case representations from our institution. An accompanying literature review highlights key features regarding neoplastic causes of temporal lobe epilepsy.
Results
Neoplasms of the central nervous system, particularly those located in the temporal lobe, often present to the clinician as medically-intractable epilepsy. Most epileptogenic tumors commonly are seen in children and young adults and include gangliogliomas, oligodendrogliomas, pilocytic astrocytomas, desmoplastic infantile gangliogliomas, dysembryoplastic neuroepithelial tumors (DNET), and pleomorphic xanthastrocytomas. These epilepsy-associated developmental tumors share similar histologic and imaging characteristics. The neoplasms are composed of both glial and neural elements. They are

most often benign with slow growth patterns but can rarely undergo malignant transformation. Characteristic imaging features are well circumscribed, slow-growing, and cortically-based masses that exhibit minimal-to-no surrounding vasogenic edema. Magnetic resonance imaging (MRI) features among each tumor type differ, but overall tend to be contrast-enhancing, T1 hypo-to isointense, and T2 hyperintense masses with or without a cystic component. Non-neoplastic conditions of the temporal lobe are more common causes of intractable epilepsy. Pathologies include post-ictal changes, focal cortical dysplasia, limbic encephalitis, mesial temporal sclerosis, and HSV-2. These entities may respond initially to medical management but often require specialized neurosurgical techniques and approaches to treatment. Therefore, radiologist interpretation with advanced cross-sectional imaging is crucial to appropriate diagnosis and treatment of epilepsy-associated developmental tumors. Partial resection leads to drastic improvement and complete resection of the neoplasm is curative.

Conclusions

Overall, cortically-based or associated temporal lobe tumors can cause medically-intractable epilepsy. Prompt management may lead to improvement or resolution of symptoms. We are presenting a review of cases from our institution displaying the various types of cortically-based or associated temporal lobe neoplasms and their differential diagnoses.



(Filename: TCT_eEdE-201_Images.jpg)

eEdE-212

6:30AM - 3:00PM

Texture Analysis: An Objective Tissue Characterization Method in Neuroradiology

M Wagner[1], A Becker[2], T Huisman[3], A Boss[2], A Poretti[4], M Wurnig[2]
[1]Johns Hopkins Hospital, Baltimore, MD, [2]University Hospital Zurich, Zurich, AK, [3]Johns Hopkins, Baltimore, MD, [4]The Johns Hopkins University School of Medicine, Baltimore, MD

Purpose
Texture analysis (TA) refers to an objective and quantitative set of metrics calculated for quantifying textural patterns of images. TA converts radiological images into a multi-dimensional mineable feature space using automatically extracted data characterization algorithms. Here, we will outline 1) the process of TA as applied in recent literature and 2) provide examples of neuroimaging applications.
Materials and Methods
After normalization and requantization of an image, TA algorithms analyze every voxel with regard to 1) its nearest neighbor voxel and 2) a run length of voxels with the same gray level. These calculations are performed for four directions differing from each other in a 45 degree angle. To make use of the spatial characteristics of 3D texture, this process is repeated twice to account for the remaining directions in 3D space. In comparison to first order features (histogram analysis), second and higher order texture features have a fundamental advantage: instead of summarizing values within percentiles and measuring the peakedness or skewness of a histogram, TA takes advantage of each voxel's integer location with regard to the neighboring voxels.
Results
Texture analysis detects distinct quantifiable phenotypic differences of tissues that are not depicted by qualitative assessment of CT or MRI studies. These TA features are calculated based on gray-level co-occurrence matrices (GLCM), run-length matrices (GLRLM), and size zone matrices (GLSZM). The sequential arrangement of algorithms is crucial for TA. We will discuss pitfalls in the process of TA. We will provide a framework on how to interpret TA features in neuroimaging studies (e.g., hypoxic-ischemic injury).
Conclusions
Texture analysis is the core method of cutting-edge Radiogenomics research. Features like short- and long-run emphasis are being investigated for their potential to predict outcome in hypoxic-ischemic injury. Performed in a standardized setting, TA also could help in the clinical decision making.

eEdE-199

6:30AM - 3:00PM

The Mesial Temporal Lobe: A 7T MRI Pictorial Review

O Clerk-Lamalice[1], E Boyd[2], A Stevens[2], L Tirrell[2], B Buchbinder[1], P Caruso[1], B Fischl[2]
[1]Massachusetts General Hospital, Boston, MA, [2]A.A. Martinos Center of Biomedical Engineering, Boston, MA

Purpose

The mesial temporal lobe is one of the most complex regions of the brain. This portion of the limbic system contains multiple substructures that are not always conspicuous in our patients imaged on magnetic resonance imaging (MRI) at 1.5T or 3T. Here, we propose to use formalin-fixed ex vivo neural tissues imaged on a 7T scanner to demonstrate this complex, yet beautiful anatomy. The relationship between the multiple structures within the mesial temporal lobe and the anatomical correlations at high and lower MRI fields will be demonstrated. Examples of pediatric and adult pathologies occurring in this region also will be shown.

Materials and Methods

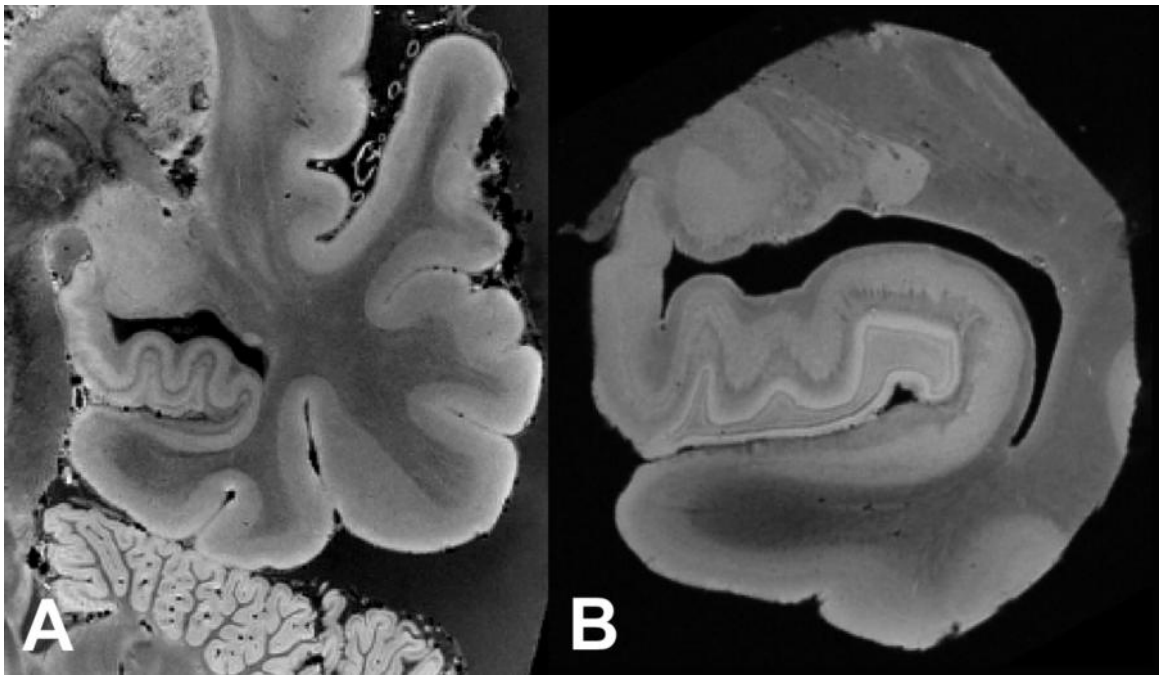
A literature review will be performed in order to accurately discuss the anatomy, function and connections between the structures of the mesial temporal lobe. MR images acquisition: One ex vivo whole-hemi specimen and two left hippocampus specimens were obtained in male patients who died of non-neurologic causes (age range: 50-58 year old). Data were acquired on a clinical 7T whole-body MRI scanner (Siemens Healthcare, Erlangen, Germany). The neural tissues to analyze (either: cerebral hemispheres + cerebellum + brainstem or hippocampus) were positioned in a custom air-tight brain holder containing Fomblin (Solvay Group, Bruxelles, Belgium). We acquired 200 µm and 100 µm isotropic data respectively for the whole brain (1) and for the hippocampus [4-turn small solenoid coil (2); single echo 3D FLASH scan; TR=54ms; TE=25ms; flip angle=20 degrees; Matrix: 400 rows and 650 columns; bandwidth: 25 Hz/px; acquisition time=1.9h]. The 7T anatomic image analysis was done with FreeSurfer (3)(Boston, USA).

Results

The mesial temporal lobe contains a number of structures that are critical for memory, emotion, and olfaction. This region is divided in the hippocampus, the parahippocampal gyrus, the primary olfactory cortex and the amygdala. The multiple subdivisions of the hippocampus [the cornu ammonis (CA), the dentate gyrus and the subiculum] will be demonstrated on 7T. Extrinsic afferents and efferents to the hippocampus also will be detailed. This review will focus not only on the anatomy and functional importance of the mesial temporal lobe but also will review interesting clinical cases of developmental, tumoral and infectious origin.

Conclusions

At the end of this presentation, the viewer should be familiar with the detailed anatomy, function and pathologies of the mesial temporal lobe.



(Filename: TCT_eEdE-199_Figure1_JPG.jpg)

eEdE-208

6:30AM - 3:00PM

Typical and Atypical MR Imaging Findings of Choroid Plexus Tumors with Genetics and Pathologic Correlation

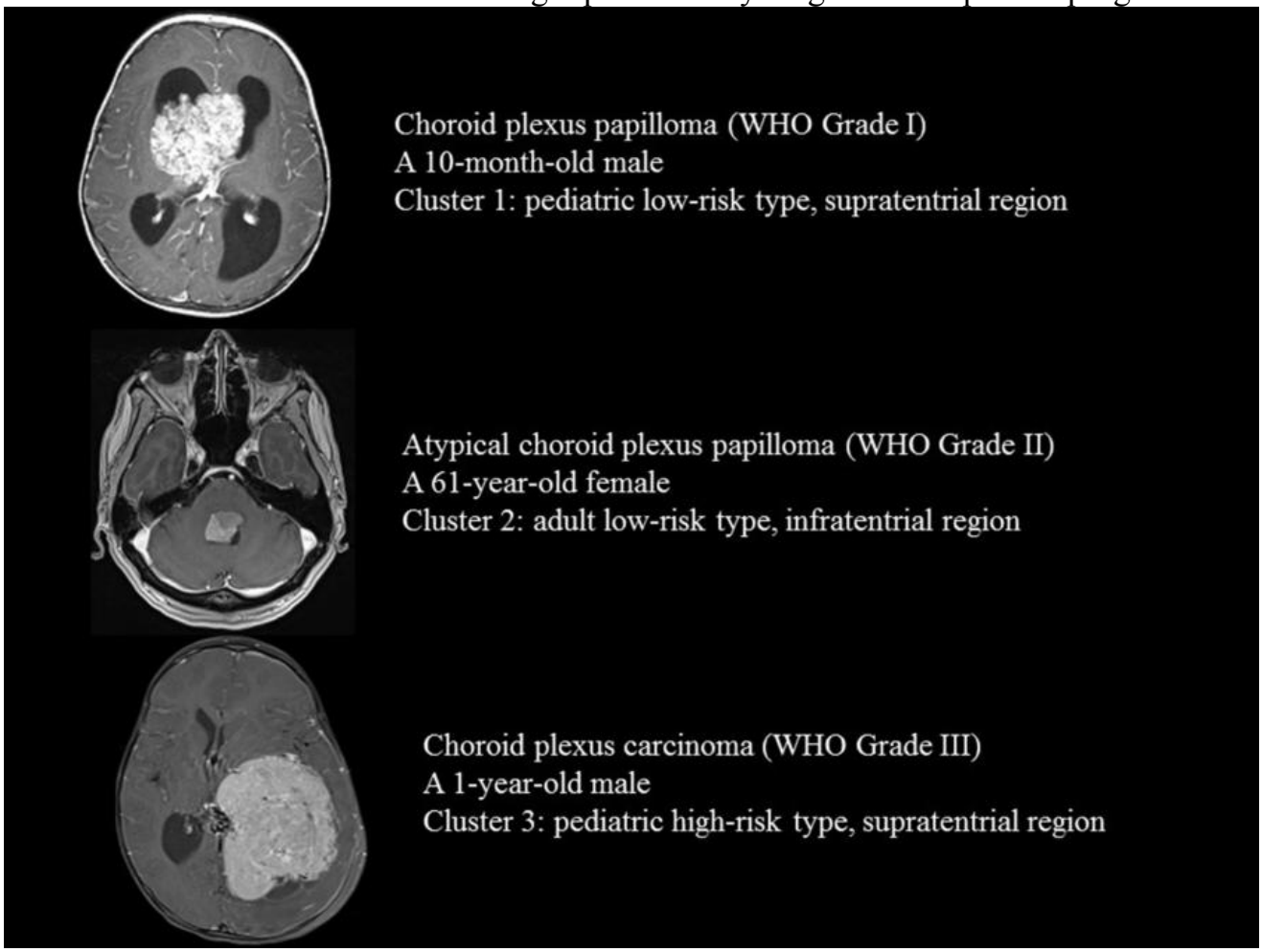
T Sasaki[1], T Moritani[2], T Sato[1], A Capizzano[2], Y Sato[1], I Elhelf[1], J Guan[2], A Oya[3], M Toda[3], P Kirby[2]
[1]University of Iowa, Iowa City, IA, [2]University of Iowa Hospitals and Clinics, Iowa City, IA, [3]Asahikawa Medical University, Asahikawa, Hokkaido

Purpose
WHO 2016 classification categorizes choroid plexus tumors into choroid plexus papillomas (CPP) (grade I), atypical choroid plexus papillomas (aCPP) (grade II), and choroid plexus carcinomas (CPC) (grade III). The WHO classification reflects prognosis of the tumors, but recent advancement genetic classification has potential to reflect morphology and predict prognosis. The aim of this exhibit is to understand the current classification of choroid plexus tumors and explore a possibility of radiogenomics.
Materials and Methods
Review WHO classification of choroid plexus tumors with typical and atypical radiological features. Review clinical expression according to the new methylation profile.
Results
1) CPP: Pathological examination demonstrates similarity to normal choroid plexus tissue with absent or very low mitotic activity. T1-weighted imaging (T1WI) often demonstrates an

iso-intense lobulated mass in the lateral or fourth ventricles with avid enhancement. T2-weighted imaging (T2WI) typically show iso- to hyperintensity with flow voids. Diffusion-weighted imaging (DWI) can show mild to moderate diffusion restriction with heterogeneity. Hemorrhagic change and hydrocephalus are common. 2) aCPP: MR imaging shows similar imaging features to CPP, but occasionally some of the features of CPC could be observed. 3) CPC: At least four of the five histological features are required for diagnosis: frequent mitosis, increased cellular density, nuclear pleomorphism, blurring of the papillary pattern, and necrosis. T2WI shows heterogenous hyperintensity with flow voids frequently in the lateral ventricles, with irregular contrast enhancement with adjacent brain edema, hydrocephalus, and dissemination. Diffusion-weighted imaging may demonstrate heterogeneity. 4) The methylation cluster 1 is often seen in pediatric CPP and aCPP of mainly supratentorial region; cluster 2 in adult CPP and aCPP of mainly infratentorial region; cluster 3 in pediatric CPP, aCPP, and CPC of supratentorial region. The cluster 3 could be an adverse prognostic factor.

Conclusions

To understand these classifications might predict early diagnosis and predict prognosis.



(Filename: TCT_eEdE-208_abstractforasnr.jpg)

eEdE-191

6:30AM - 3:00PM

Zika-Virus Associated CNS Injury

L Brandao[1], A Barkovich[2]
[1]Clinica Felippe Mattoso-Grupo Fleury, Rio De Janeiro, Brazil, [2]University of California at San Francisco, San Francisco, CA

Purpose
To present the most common imaging findings in the central nervous system of babies diagnosed with microcephaly at birth, born to mothers infected with Zika virus at different times during gestation.
Materials and Methods
We retrospectively reviewed the clinical charts and neuroimaging studies in 38 babies (ages 24 gestational weeks to 5 postnatal months) diagnosed with microcephaly at birth in the last 11 months. Magnetic resonance imaging (MRI) was performed on a 1.5T GE Signa Horizon and 1.5 Tesla (T) General Electric (GE) Excite. Available sequences included sagittal T1 3D SPGR, axial T1, T2, FLAIR, GRE, SWAN and DWI, as well as coronal T2. Two neuroradiologists with 20 (BL) and 35 years experience (BAJ) evaluated all the images.
Results
The most common neuroimaging findings were: 1- Microcephaly in all patients (38/38 = 100%) usually > 3 standard deviations below mean; 2- Significant reduction or absence of cortical sulci, named undersulcated pattern (38/38 = 100%); 3- Malformations of cortical development (38/38 = 100%) mainly cobblestone cortex with appearances of atypical polymicrogyria, as well as areas of larger, lissencephaly-like cobblestone cortex; 4- Calcifications (38/38 = 100%), mainly in the subcortical white matter (38/38 = 100%); 5- Thin or hypogenetic corpus callosum (38/38 = 100%); 6- Diminished cerebral white matter, resulting in thin cerebral mantle, with ex vacuo enlargement of the ventricles in all patients (38/38 = 100%); 7- Small thalami in 30/38 patients (78.9%); 8- Small pons in 22/38 = 57.9%; 9- Small cerebellum in 28/38 = 73.7%; 10- Some cases developed hydrocephalus; 11- Very severe cases had fetal brain disruption with profound microcephaly/overlapping sutures at birth. All babies in this study suffered severe fetal brain injury and MRI findings were very similar among them.
Conclusions
There is a recognizable pattern of fetal brain disruption and cortical malformation that defines a specific congenital Zika syndrome, that can be recognized even without laboratory confirmation.

Monday
6:30AM - 3:00PM

Electronic Education Exhibit (eEde)-Socioeconomics

eEdE-221

6:30AM - 3:00PM

Framework for Just Culture in an Academic Radiology Department

J Burns[1], S Goldberg-Stein[1], A Erdfarb[2], K Shifteh[1], T Miller[3]
[1]Montefiore Medical Center, Bronx, NY, [2]Montefiore Medical Center / AECOM, Bronx, NY, [3]Montefiore North Medical Centre, Bronx , NY

Purpose
To describe the approach of using a Just Culture framework towards peer review in an academic radiology department. To highlight the nonpunitive, systems-focused aspects of a Just Culture framework.
Materials and Methods
We will use a didactic approach to outline the structure of the Just Culture framework. Using clinical case examples, we will outline the use of a Just Culture framework in the departmental peer review process. Specifically, we will highlight examples in which best practice is not followed, and how the review process considers the nature of the physician role in these incidents.
Results
1. RadPeer – Similarities and key differences. 2. Structure of a Peer Review process using the Just Culture framework: -Focus on context in which errors occur; -Human error vs. poor judgment; -Identifying systems issues; -Non-punitive outcomes; -Follow-up with individuals, teams, systems. 3. Tools of the Just Culture review: -Substitution test; -Test of intention. 4. Possible Outcomes of a Just Culture review: -Standard of Care; -At risk behavior -> coach; -Reckless behavior -> discipline; -Human error -> console; -Question of competence -> coach. 5. Case Examples.
Conclusions
Adoption of a Just Culture framework shifts the focus of peer review away from physician error towards a nonjudgmental assessment which highlights systems-associated factors that may contribute to medical error.

At Risk Behavior - Coach	Reckless Behavior - Discipline
• Interpretive: o Reporting studies without reviewing all images o Failure to sign reports in a timely manner • Non-Interpretive: o Improper protocol without checking medical record o Approving unknown implant for MRI without checking safety profile • Procedural: o Allowing trainees to routinely begin procedures unobserved o Failure to follow departmental pre-procedure protocols (i.e. Time Out) o Performing a new/difficult procedure without sufficient training or support	• Interpretive: o Remote image interpretation using substandard equipment o Signing preliminary cases without reviewing images o Documenting communication that did not occur • Non-Interpretive: o Inappropriate access of medical records o Failure to properly communicate an identified emergent finding (i.e. tension pneumothorax) o Inappropriate delegation of responsibility to an unsupervised trainee • Procedural: o Performing a non-credentialed procedure o IR procedure without full sterile barrier o Instructing a trainee to begin a procedure when you are not available to supervise
Human Error - Console	**Question of Competence - Coach**
• Interpretive: o Reporting prior exam as the current study o Report typos/template issues causing medical error o Incorrect determination of laterality on an exam • Non-Interpretive: o Forgetting to communicate an unexpected, non-urgent finding (i.e. renal mass, pulmonary nodule) • Procedural: o Procedural complication due to incorrect operator decision o Wrong implant placement (i.e. side hole vs end hole catheter)	• Interpretive: o Failure to compare to prior exam o Failure to understand implication of an imaging finding (i.e. intramural hematoma) • Non-Interpretive: o Inappropriate protocol for CT/MRI o Improper selection of contrast agent for MRI o Approving MRI for non-conditional pacemaker • Procedural: o Incorrect procedure due to poor team communication o Performing high risk procedure unnecessarily o Incomplete documentation of rationale to perform/defer procedure

(Filename: TCT_eEdE-221_JustCultureFramework.jpg)

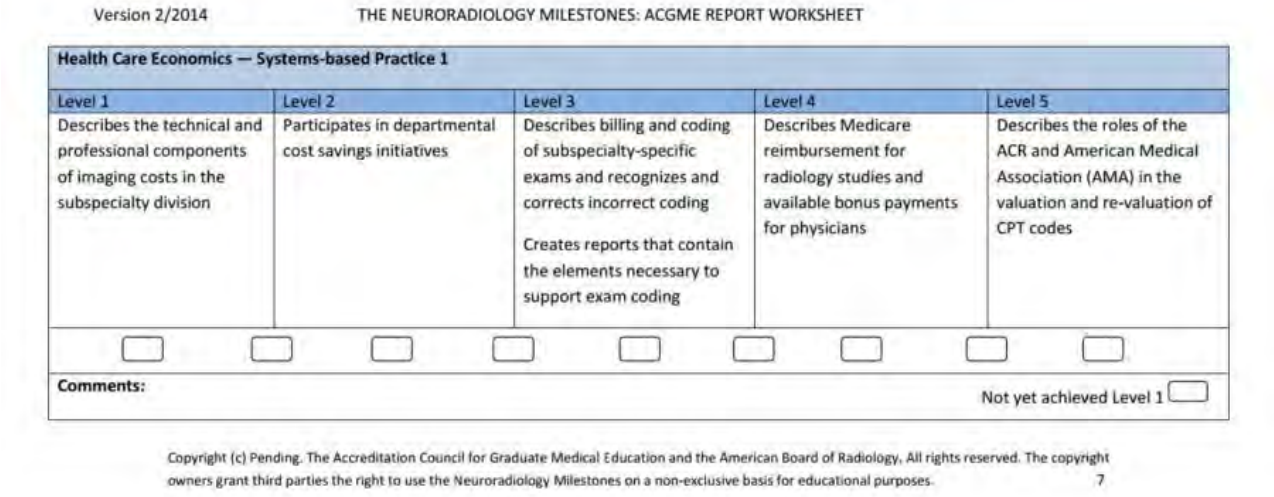
eEdE-220

6:30AM - 3:00PM

Measuring Competence in Healthcare Economics: A Practical Guide for Neuroradiology Program Directors and their Fellows

S Weiner[1], R Tu[2], R Javan[1], M Taheri[3]
[1]George Washington University Hospital, Washington, DC, [2]Progressive Radiology, Washington, DC, [3]George Washington University, Washington, DC, DC

Purpose
Little to no resources are available in the medical literature on healthcare economics as it relates to neuroradiology program directors assessing a fellow's competence in this often overlooked area of medical training. Therefore we present a tailored discussion and a pre/post test questionnaire that program directors can utilize in the preparation and assessment of fellows.
Materials and Methods
Using the PubMed MeSH terms "diagnostic imaging/economics" and "radiology/economics," a nonexhaustive compilation of review articles, identified from roughly the last 5 years on the topic of healthcare economics and its rapidly changing landscape with respect to radiology/neuroradiology, was synthesized into a cogent compendium of useful assessment tools with the ACGME neuroradiology milestones serving as a framework.
Results
Ten questions from the aforementioned review articles regarding healthcare economics relating to radiology/neuroradiology were distilled from each of the following five topics taken from the current ACGME neuroradiology fellowship milestones, 1 for pre-test purposes and the other for post-test: 1) technical and professional components of imaging costs, 2) departmental cost savings plans, 3) creation of reports containing necessary exam coding components for successful billing, 4) current and upcoming (value-based) Medicare reimbursement models, and 5) roles of the ACR and AMA in the ongoing valuation of CPT codes and their impact on our specialty.
Conclusions
By condensing ten focused review topics on healthcare economics as they relate to the practice of radiology/neuroradiology into a single document, the authors' aim is to not only assist fellows in meeting the current ACGME neuroradiology milestones for healthcare economics, but also to construct a useful foundation upon which program directors and their trainees can build upon as policy evolves legislatively over time, facilitating their basic implementation in real world practice.



Version 2/2014 THE NEURORADIOLOGY MILESTONES: ACGME REPORT WORKSHEET

Health Care Economics — Systems-based Practice 1				
Level 1	Level 2	Level 3	Level 4	Level 5
Describes the technical and professional components of imaging costs in the subspecialty division	Participates in departmental cost savings initiatives	Describes billing and coding of subspecialty-specific exams and recognizes and corrects incorrect coding Creates reports that contain the elements necessary to support exam coding	Describes Medicare reimbursement for radiology studies and available bonus payments for physicians	Describes the roles of the ACR and American Medical Association (AMA) in the valuation and re-valuation of CPT codes
☐	☐	☐	☐	☐ ☐ ☐ ☐ ☐
Comments:				Not yet achieved Level 1 ☐

Copyright (c) Pending. The Accreditation Council for Graduate Medical Education and the American Board of Radiology, All rights reserved. The copyright owners grant third parties the right to use the Neuroradiology Milestones on a non-exclusive basis for educational purposes. 7

(Filename: TCT_eEdE-220_EconomicsMilestones.jpg)

eEdE-222

6:30AM - 3:00PM

Safely Imaging the Pregnant Patient

K Hoque[1], W Gibbs[2], P Colletti[3]
[1]USC, Los Angeles, CA, [2]University of Southern California, Keck School of Medicine, Los Angeles, CA, [3]University of Southern California, Los Angeles, CA

Purpose
This educational exhibit reviews current data and recommendations on imaging the pregnant patient using nonionizing radiation, ionizing radiation and nuclear medicine tracers.
Materials and Methods
Using both case-based review and literature review, this exhibit will detail both animal and human studies pertaining to effects of multimodal imaging techniques on the pregnant patient. Trimester-based discussion will explore associated risks with different imaging modalities. In the case of contrast materials and nuclear medicine tracers, fetal and placental distribution and dosemitry will be detailed.
Results
Understanding risks associated with imaging the pregnant patient is critical for counseling referring physicians and patients and facilitating an informed decision.
Conclusions
This exhibit will enable to reader to understand the risks of using multimodal imaging techniques in neuroradiology and nuclear medicine to image the pregnant patient. Current recommendations for imaging the pregnant patient using these techniques will be detailed.

Monday
6:30AM - 3:00PM

Electronic Education Exhibit (eEdE)-Spine
eEdE-238

6:30AM - 3:00PM

"My Head Explodes When I Stand Up!" Understanding Cerebrospinal Fluid Flow Dynamics in Spinal CSF Leaks is Key to Image Guided Diagnosis and Management

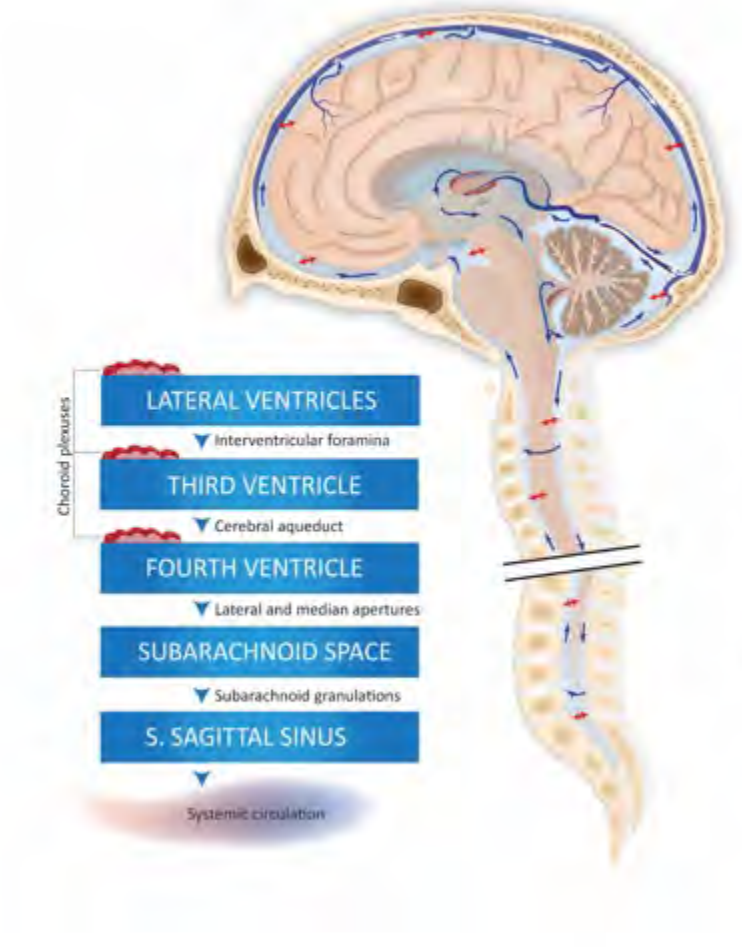
D Franjic[1], B LeSar[1], C Thomas[1], R Messina[1], C Gottschalk[1], M Johnson[1]
[1]*Yale University School of Medicine, New Haven, CT*

Purpose
The purpose of this educational exhibit is to examine normal cerebrospinal fluid (CSF) dynamics in relation to congenital/acquired disorders that disrupt normal CSF dynamics and result in cerebrospinal fluid leaks beyond the subarachnoid space. We review normal CSF flow dynamics and use archival case material to highlight disrupted CSF flow and subsequent CSF leaks whether spontaneous or secondary to iatrogenic causes (LP, surgery), trauma, degenerative disease or underlying congenital features. Spinal imaging utilizing magnetic resonance imaging (MRI) as well as conventional film and computed tomography (CT) myelography play an important role in understanding the etiology and defining subsequent treatment strategies including epidural blood patch, fibrin glue and surgical repair.
Materials and Methods
Case material from clinical and teaching file archives were utilized as the basis of the teaching material in this educational exhibit. Anatomic and physiologic aspects of cerebrospinal fluid dynamics are reviewed and illustrated. Multimodality imaging and clinical features from the electronic medical record of 38 patients with spinal cerebrospinal fluid leaks were reviewed. Patients were divided into 5 groups based on CSF leak etiology: trauma, congenital, iatrogenic (post LP), spontaneous, and postoperative.
Results
Cerebrospinal fluid leaks occur when there is a dural defect, commonly a weakness (congenital or acquired) often accompanied by minor or chronic trauma that results in CSF leakage from the subarachnoid space into the epidural space or into loculated extradural fluid compartments. Clinical sympotms classically feature chronic headache with or without neck pain and exacerbated by standing, sitting, and Valsalva. Brain MRI is often the first study performed and may demonstrate thickened and enhancing meninges, depression of the cerebellar tonsils and flattening of the pituitary - all features of intracranial hypotension. The clinical diagnosis is often long delayed unless an obvious pre-existing iatrogenic cause is present. Noninvasive spinal imaging may be normal, demonstrate meningeal enhancement or demonstrate extradural fluid collections. Knowledge of the normal aspects of cerebrospinal

fluid dynamics including CSF production and absorption and the relationships between the cerebral and spinal subarachnoid spaces is critical to the understanding of the imaging findings that can be present with cerebral hypotension. Archival case examples, divided into 5 etiologic groups (including trauma, congenital, iatrogenic (post LP), spontaneous, and postoperative) with clinical and imaging and treatment details, are used to illustrate the variety of disruptions in flow that may lead to this condition.

Conclusions

The classic postural headache syndrome that occurs in the setting of a CSF leak and cerebral hypotension, etiologies of such leaks, associated imaging findings in the brain and spine and potential treatment strategies are all better evaluated with improved understanding of the anatomy and physiology of cerebrospinal fluid flow dynamics. Knowledge of these features will help the spine radiologist to better identify possible causes of CSF leaks and direct appropriate treatment.



Overview of cerebrospinal fluid (CSF) production and flow. CSF is represented by the light blue area and flows (blue arrows) from the site of production (choroid plexus in each ventricle), through the subarachnoid space to the site of reabsorption at the subarachnoid granulations. Some recent hypotheses postulate that CSF can be secreted and reabsorbed anywhere in the system (red double-arrows).

(Filename: TCT_eEdE-238_Slide1.jpg)

eEdE-228

6:30AM - 3:00PM

Age Related Changes of Normal Spinal Marrow as Segregated by Gender and Age using Common MRI Imaging Sequences

J Choi[1], G Punch[1], B Hicks[1], L Mitchell[1]
[1]*Tripler Army Medical Center, Honolulu, HI*

Purpose

To present representative magnetic resonance imaging (MRI) images of lumbar vertebral body bone marrow in patients 10-80 years of age of both male and female gender. Accounting for the large degree of individual variability, general trends and patterns of fatty replacement will be presented. Increasing familiarity with the normal distribution and maturation of hematopoietic and fatty marrow will improve the ability to identify abnormal bone marrow.

Materials and Methods

A random sampling of lumbar spine MRI exams was collected in a closed health care system from one institution over a 20-year period. All exams were acquired using common imaging techniques (Sagittal T1 fast spin echo and T2 fat-saturated fast spin echo sequences obtained with GE 1.5 Tesla or Siemens 3 Tesla MR suites). The exams were segregated by gender and decade such that a representative group of 20 exams was created for men and women 10-80 years of age. The L1-L3 vertebral levels were selected for analysis given the increased prevalence of degenerative disk disease at the thoracolumbar and lumbosacral junctions. Patients with advanced adjacent level degenerative disease, prior surgery, tumors (both local and metastatic), infection, or diffuse marrow infiltrative disease were excluded from analysis. Within each subgroup, the fatty replacement of red marrow was categorized into three broad categories: bandlike along the endplates (in the absence of significant adjacent degenerative disk disease); scattered foci of fatty replacement (less than 10% as determined by largest area of involvement on single sagittal image); or larger globular areas. When involvement was globular, degree of fatty involvement of the vertebral body was subcategorized as mild (between 10 and 33% area on single sagittal image), moderate (33-66%), or diffuse (greater than 66%). Two board certified radiologists with additional certificates of added qualification in neuroradiology, one general radiologist, and one senior radiology resident independently scored each exam. Raters were blinded to the age and gender of the patient. For each exam, the most common descriptor was used to categorize the degree of red marrow replacement. For each subgroup (e.g., women 30-39 years of age), the most common marrow pattern was determined. A representative exam, as defined by greatest inter-observer consistency, was provided to illustrate typical age-related change.

Results

Sagittal T1-weighted images demonstrate a gradual trend of marrow replacement with increasing age. Red marrow tends to be uniform and diffuse within the spine between the

second and fourth decades with greatest rate of change typically occurring in patients 40-50 years of age. Women tend to have a greater degree of red marrow with increasing fat to red marrow distribution in the postmenopausal period. Some men demonstrate decline in red marrow as early as the second decade. Even when diffusely consisting of red marrow, vertebral bodies retain a small amount of yellow marrow around the venous plexus which is useful as an internal standard. Sagittal T2-weighted images show the least amount of variation in bone marrow signal. These images are useful in categorizing patterns of marrow distribution and determining when pathologic states may exist.

Conclusions

Trends in bone marrow signal change may be challenging to assess in the absence of representative images. We provide representative images from each decade of life to assist in the care and assessment of the lumbar spine.

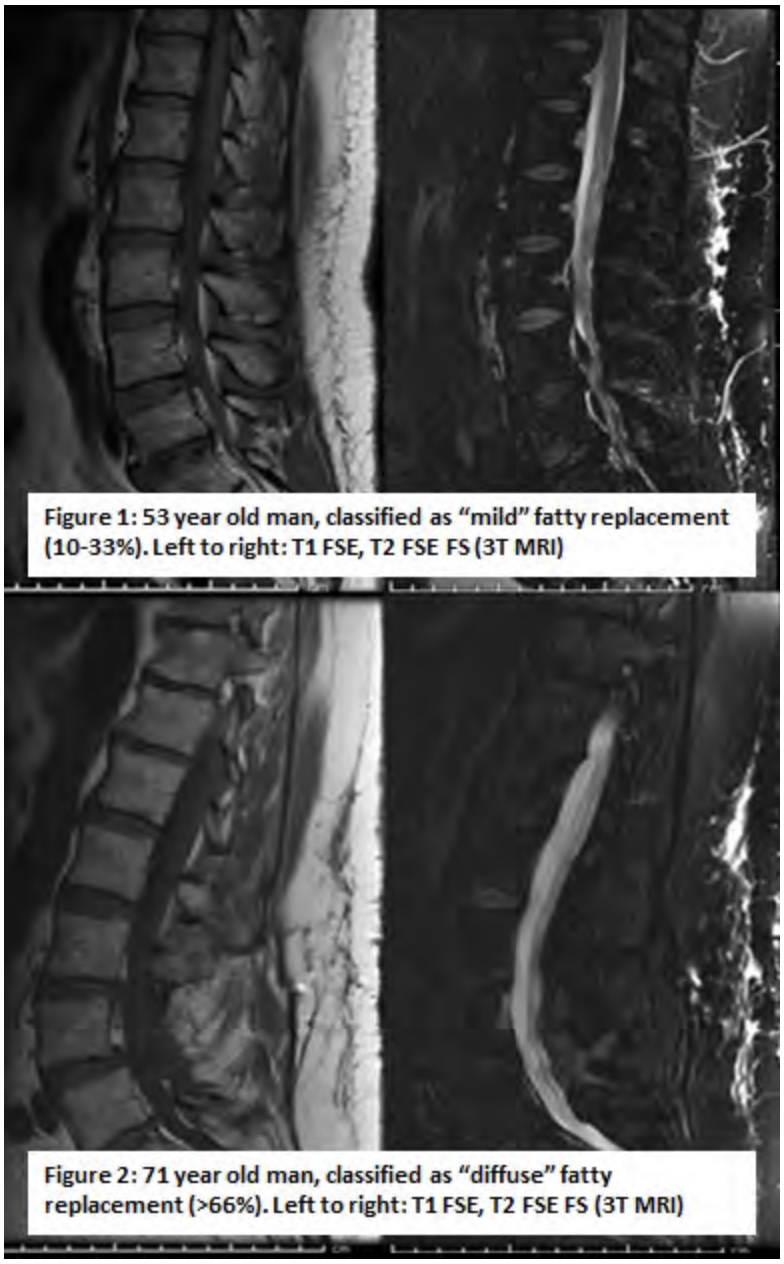


Figure 1: 53 year old man, classified as "mild" fatty replacement (10-33%). Left to right: T1 FSE, T2 FSE FS (3T MRI)

Figure 2: 71 year old man, classified as "diffuse" fatty replacement (>66%). Left to right: T1 FSE, T2 FSE FS (3T MRI)

(Filename: TCT_eEdE-228_Fattymarrowreplacementexamples.jpg)

eEdE-247

6:30AM - 3:00PM

An Illustrated Guide to Intraspinal Cystic Lesions

M Skalski[1], W Gibbs[2], G Matcuk[3]
[1]Palmer College of Chiropractic, San Jose, CA, [2]University of Southern California, Keck School of Medicine, Los Angeles, CA, [3]University of Southern California, Los Angeles, CA

Purpose

To assist the radiologist in differentiating the variety of cystic and cyst-like lesions that are encountered in the spine.

Materials and Methods

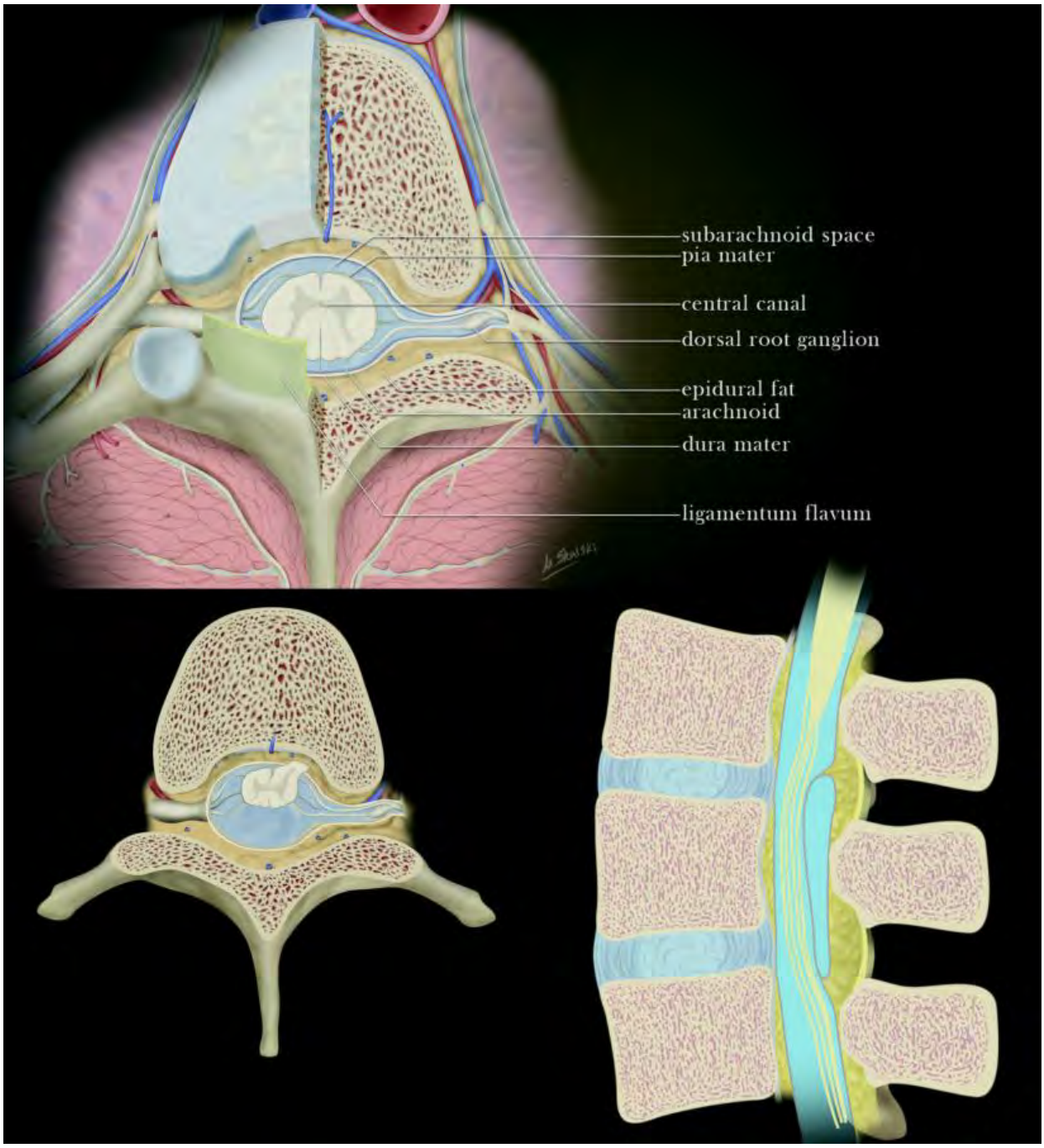
This exhibit will utilize multi-modality imaging and original medical illustrations to review the variety of cystic lesions encountered in the spine and their imaging features (excluding dysraphisms). Distinguishing features and pitfalls in assessment will be highlighted, with a discussion of management strategies for each.

Results

This exhibit will review spinal anatomy and how to assess lesion location, and then review individual cystic entities, and management strategies for each. The following topics are covered: -Spinal meningeal cysts and their classification. -Epidermoid/dermoid cysts, -Epidural abscess and hematoma. -Degenerative spinal synovial cysts, -Syringohydromyelia, -Ventriculus terminalis, -Cystic neoplasms, -Mimics of cystic lesions, -Cord herniation, -Dural ectasia, -Conclusion, -References.

Conclusions

A variety of cystic, cyst-like, and other fluid-signal lesions occur in the spine which can be confusing and difficult to diagnose. Having reviewed this presentation, the radiologist should be more confident in making these often difficult diagnoses.



(Filename: TCT_eEdE-247_SpinalCystssamplegraphics.jpg)

eEdE-254

6:30AM - 3:00PM

Brachial and Lumbosacral Plexus: Practical Imaging and Intervention

M Patel[1], A Rajamohan[1], W Gibbs[1]
[1]*University of Southern California, Keck School of Medicine, Los Angeles, CA*

Purpose

To discuss the anatomy, imaging techniques, pathology and relevant pain procedures involving the brachial and lumbosacral plexus.

Materials and Methods

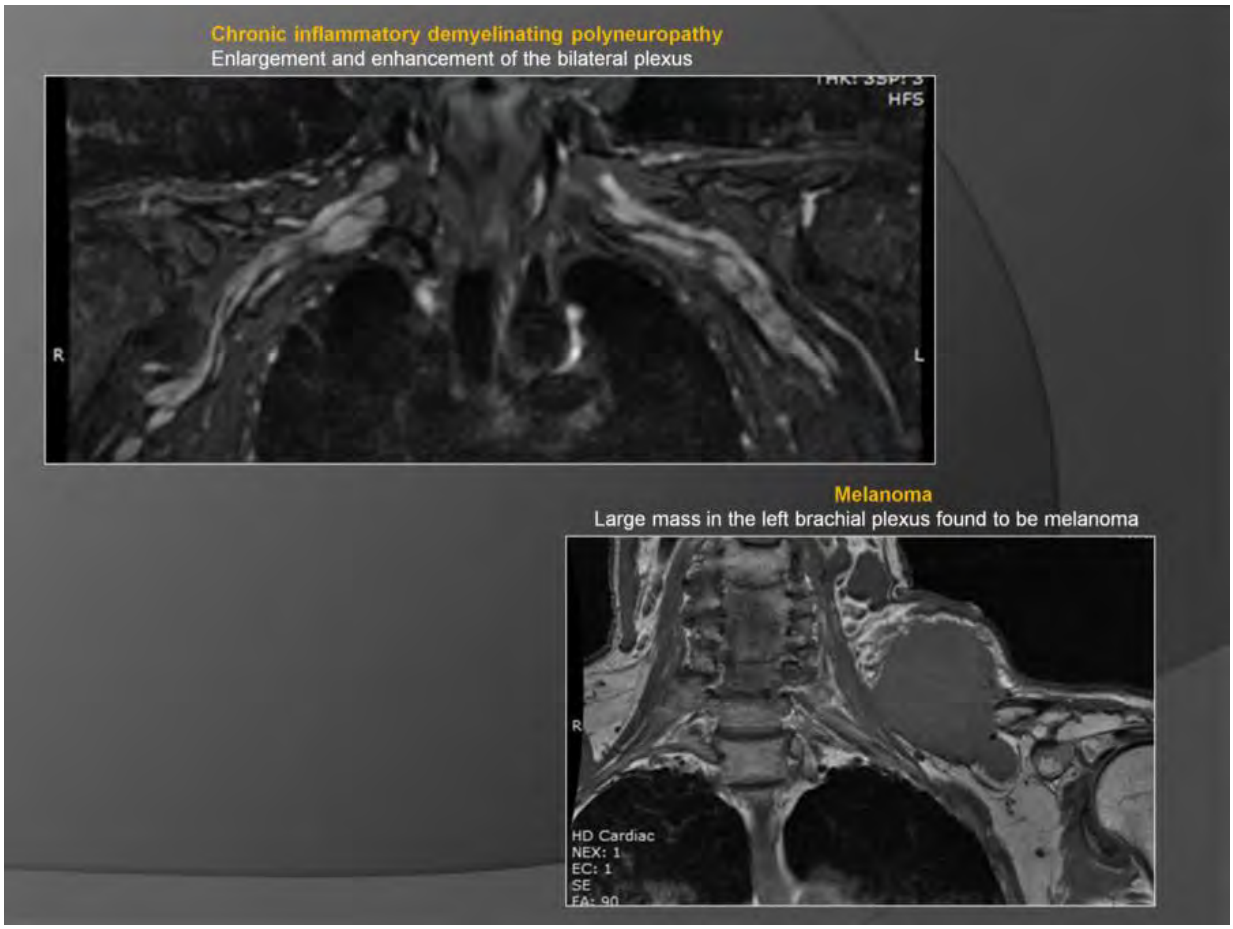
1. Illustrate normal anatomy. 2. Provide a standard imaging protocol, describe advanced imaging techniques, and suggest trouble-shooting tips. 3. Present various cases of brachial and lumbosacral pathology. 4. Discuss techniques to perform brachial plexus and lumbosacral plexus blocks.

Results

The brachial and lumbosacral plexus provide sensory and motor innervation to the extremities. Plexopathy can be caused by trauma, inflammation, infection, neoplasm, and postradiation changes. While clinical history, physical exam and electromyography (EMG) can help localize the source of symptoms, imaging plays a crucial role in diagnosis and determining extent of pathology. Knowledge of normal anatomic landmarks is essential for technical success in pain procedures involving the brachial and lumbosacral plexus.

Conclusions

Imaging of the brachial plexus is a commonly ordered test, but dedicated imaging of the lumbosacral plexus is less commonly performed. This exhibit will provide the readers with knowledge of anatomy and pathology, enable optimization of imaging techniques, and provide a basic understanding of brachial and lumbosacral plexus blocks.



(Filename: TCT_eEdE-254_BPLSASNR2017abstractpictures.jpg)

eEdE-232

6:30AM - 3:00PM

Candida Albicans Spondylitis: Clinical Case Series, Imaging Characteristics, and Overview

D Hill[1], W Slone[2], X Nguyen[3], J Mangino[4], E Bourekas[5], J Fritz[6]
[1]The Ohio State University Wexner Medical Center, Columbus, OH, [2]The Ohio State University Wexner Medical, Columbus, OH, [3]Ohio State Wexner Medical Center, Columbus, OH, [4]The Ohio State University, Columbus, OH, [5]The Ohio State University, Columbus, OH, [6]Wexner Medical Center at The Ohio State University, Columbus, OH

Purpose
Demonstrate the imaging appearance of Candida spondylitis on computed tomography (CT) and magnetic resonance imaging (MRI), and present key imaging findings that may favor this diagnosis.
Materials and Methods
A case series of five patients with biopsy proven Candida albicans spondylitis will be

presented. Computed tomography and MRI imaging findings will be reported and will be correlated with the underlying cause of the Candida infection.

Results

Candida albicans is an uncommon cause of spondylitis that is increasing with the increasing incidence of IV drug abuse. Five cases of biopsy proven Candida albicans spondylitis are presented. Three of these cases were Intravenous drug users. The intravenous drug users showed an atypical appearance lytic osseous involvement, which showed a well defined margin on CT. Remaining cases were immunocompromised, with an appearance resembling pyogenic spondylitis.

Conclusions

Intravenous drug users and immunocompromised patients are more likely to present with infectious spondylitis. Magnetic resonance imaging findings of nonpyogenic spondylitis frequently are distinct from pyogenic spondylitis, although this is not always the case. Biopsy frequently is needed to differentiate the two entities. In this case series there are imaging findings that appear to favor Candida infection in the intravenous drug user population. Given the current opioid epidemic, this can be helpful in guiding clinical management in this growing population, and increase confidence that biopsy results represent true Candida infection rather than contamination.



(Filename: TCT_eEdE-232_Candida.jpg)

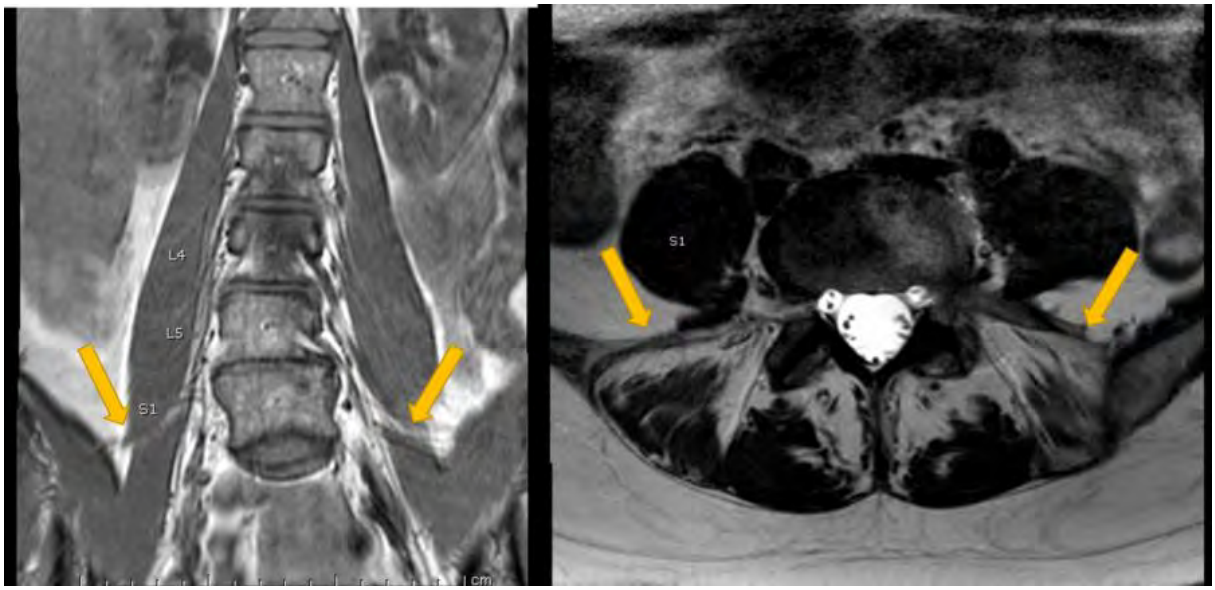
eEdE-224

6:30AM - 3:00PM

Caveat Emptor: Using the Iliolumbar Ligament to define Lumbosacral Transitional Anatomy

M Cho[1], C Liu[1]
[1]*University of Southern California/Keck Medical Center, Los Angeles, CA*

Purpose
The iliolumbar ligament was thought to always arise from L5 and had been thought of as a reliable marker to assign lumbar levels in patients with lumbosacral transitional vertebrae (LSTV). It was shortly thereafter reported that the iliolumbar ligament actually denotes the lowest lumbar vertebra, not necessarily L5. The purpose of this exhibit is to demonstrate variable appearances and attachments of the iliolumbar ligament in the setting of LSTV and reaffirm that it does not solely attach to L5. We also discuss the clinical relevance of such variable attachment.
Materials and Methods
Cases of LSTV were analyzed for attachment of the ILL. The cases all had imaging of the entire spinal axis so that confident numbering of the lumbar spine could be achieved. The attachment of the ILL was assessed by its appearance on axial MR imaging.
Results
The ILL demonstrated variant attachments to the lumbar spine, attaching to the L4, L5, and S1 vertebrae in various cases. In several cases, the ILL was difficult to identify. ILL has variable attachment to the lumbar spine depending on the appearance and anatomy of the LSTV. Numbering of the lumbar spine is further complicated by effects of transitional anatomy at the thoracolumbar junction, with some patients only having 11 thoracic segments. Embryogenesis of the spine is variable, as it derives from para-axial mesenchyma surrounding the neural tube, segmenting cranio-caudally based on position. Although 92% of humans have 24 presacral segments, 5% have 23 segments and 3% have 25 presacral segments.
Conclusions
The ILL does not consistently attach to L5 in LSTV. The identification of the ILL is not sufficient to accurately denote the L5 vertebra. Confident numbering of the lumbar spine can only be accomplished by counting caudally from C2.



(Filename: TCT_eEdE-224_ILL.jpg)

eEdE-226

6:30AM - 3:00PM

Cervical Spine Alignment, a Concept of Balance

M Pejic[1], R Shah[1], R Murtagh[1]
[1]*University of South Florida Morsani College of Medicine, Tampa, FL*

Purpose
The purpose of this exhibit is to recognize the concept of balance within the cervical spine (C-spine) which plays a key role in overall spinal alignment and maintenance of horizontal gaze. An understanding of C-spine alignment is critical to the understanding and management of C-spine deformity which can be debilitating to function and quality of life.
Materials and Methods
This exhibit provides an overview to cervical alignment including column theory. Traditional methods of measuring lordosis are discussed including Cobb Angles, the Jackson Physiological Stress Line Method, and the Harrison Posterior Tangent Method. A pictorial review of regional and global spinal vertical alignment (SVA) is described. The Chin-Brow to Vertical Angle (CBVA) is discussed as an indicator of horizontal gaze. The relationship between new alignment parameters including T1 slope (T1S), thoracic inlet angle (TIA), and neck tilt are covered including their impact on cervical lordosis (CL). Patient examples with abnormal cervical alignment will be given in order to provide a practical example.
Results
Spinal deformity is a three-dimensional pathology and it is important to understand the concept of balance and recognize compensatory maneuvers that attempt to restore balance. Multiple publications have described important thoracolumbar and pelvic radiographic

parameters, but the literature on C-spine alignment is more limited. Spinal vertical alignment can be approached similarly as in the thoracolumbar spine. Abnormalities in SVA are related to a decreased quality of life. The CBVA, as an indicator of horizontal gaze, affects perceived quality of life and its consideration positively affects postoperative outcomes. New C-spine parameters including TIA and T1S affect the degree of CL needed for neutrality. These parameters evaluate sagittal balance, predict physiological alignment, and may provide guidance in the correction of the C-spine.
Conclusions
The C-spine and its management are complex. Cervical lordosis acts as a compensatory mechanism to maintain neutral SVA (regionally and globally) and to maintain normal CBVA. New C-spine parameters may serve as a guide for optimal C-spine alignment management.

eEdE-237

6:30AM - 3:00PM

Complications of Lumbar Spine Surgery

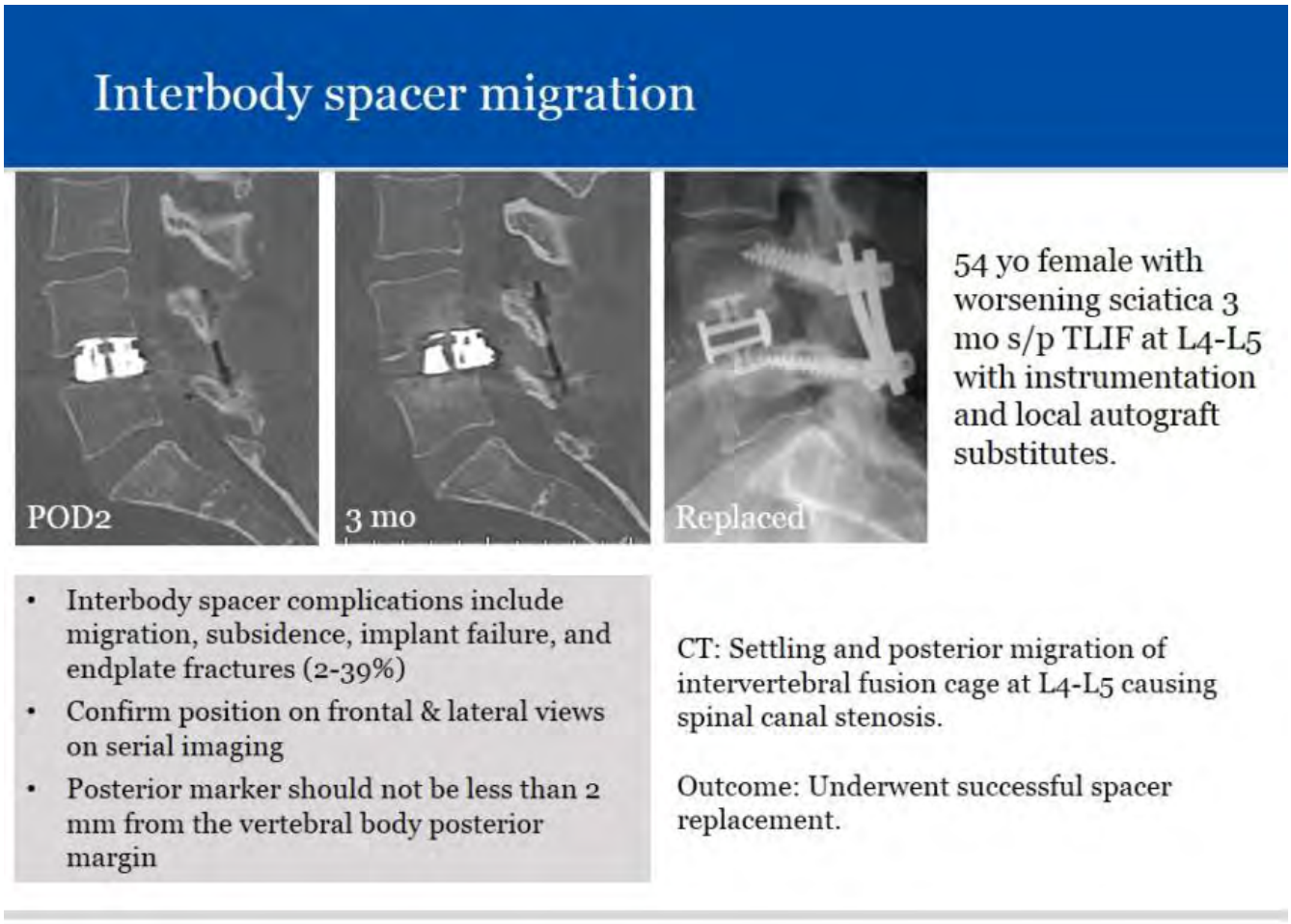
D Durand[1], K Seifert[2], V Kalra[3], A Malhotra[4]
[1]Yale University School of Medicine, New Haven, CT, [2]Yale New Haven Hospital, Milford, CT, [3]Yale University School of Medicine, Tampa, FL, [4]Yale New Haven Hospital, New Haven, CT

Purpose
Back pain affects 80% of the population in their lifetime, and the frequency of complex lumbar spine surgery for spinal stenosis is increasing. Complication rates are closely related to the extent and complexity of surgery. Compared to simple decompression, complex fusions have higher rates of life-threatening complications and rehospitalizations within 30 days. Cross-sectional imaging techniques play a central role in evaluation after lumbar surgery. Utilization of optimal techniques to reduce metallic hardware artifacts is necessary to evaluate hardware placement, fusion and alignment, and to detect complications arising in the postoperative course.
Materials and Methods
This exhibit presents several imaging examples of common and uncommon lumbar spinal surgery complications in a pictorial format. A discussion of each type with imaging correlation follows, with emphasis on diagnostic pitfalls.
Results
Several complications may present intra-operatively or in the early postoperative period. Malpositioned hardware most often involves improper screw depths and intracanalicular screw placement, which can injure nerve roots or radicular arteries, or result in spinal stability and malalignment. Postoperative fluid collections include seromas, hematomas, abscesses, and cerebrospinal fluid (CSF) collections which include pseudomeningoceles,

CSF fistulas, and nerve root herniation with incidental durotomy. In the case of retroperitoneal/abdominal approaches during laparoscopy or anterior fusion, injury to the vessels, lumbosacral plexus, or bowel may occur, which can rarely cause pseudoaneurysm, hemorrhage, erectile dysfunction, and fistulas. Delayed surgical complications include hardware loosening, infection, pseudoarthrosis, and abnormal motion/strain which can lead to hardware failure/fracture and injury to adjacent vertebral levels. New or recurrent symptomatic disk herniation, bone marrow graft extrusion, heterotopic bone formation, peridural/epidural fibrosis, arachnoiditis, and radiculitis also may occur and can contribute to failed back surgery syndrome. Imaging techniques to reduce metallic artifact during computed tomography (CT) image acquisition include increasing tube voltage, decreasing pitch, and decreasing slice thickness; all of which increase patient radiation dosage. Postprocessing options include use of soft tissue kernels, thicker section reconstructions, and adjustment of the Hounsfield scale. New techniques include dual-energy CT and sinogram inpainting. Magnetic resonance imaging metallic artifact reduction techniques include use of a lower-Tesla magnet, fast spin echo and STIR sequences rather than frequency selective fat suppression, decreasing FOV, thinner sections, and use of a high-resolution matrix. Advanced techniques include view angle tilting and slice encoding for metallic artifact correction.

Conclusions

Early detection of lumbar spine surgery complications is critical for patient management. This exhibit serves to review several common and uncommon complications to promote confident diagnoses and prompt recognition of abnormal postoperative findings.



(Filename: TCT_eEdE-237_Slide1.JPG)

eEdE-241

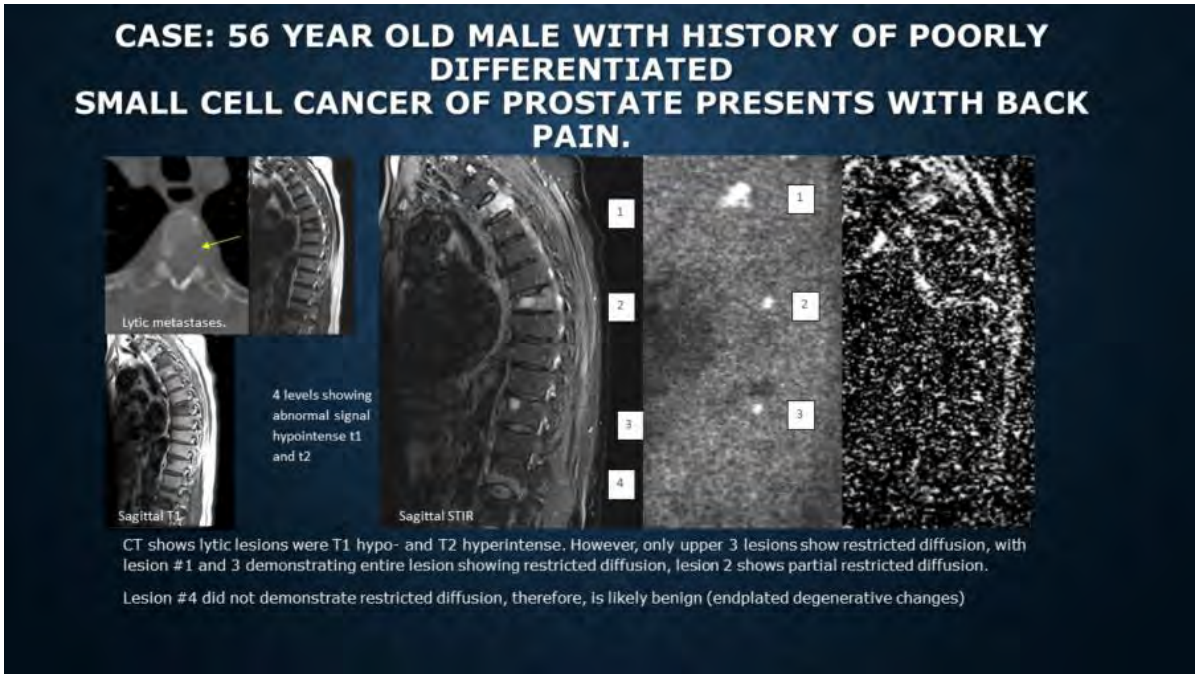
6:30AM - 3:00PM

Diffusion-Weighted Imaging for Evaluation of Benign and Malignant Spinal Tumors

A Chaudhry[1]
[1]*Johns Hopkins Medicine, Elkridge, MD*

Purpose
Radiologists frequently encounter tumor and tumor-like lesions as incidental findings on spine Magnetic resonance imaging (MRI). These can result from a number of processes which can be benign or malignant. Deciphering between the 2 can be challenging and is critical for patient care as miss of a malignant lesion can prove to be fatal. This educational exhibit will be a case-based presentation of common and uncommon causes of benign and malignant processes that result in lytic and/or sclerotic lesions in the skeletal system on CT

and have variable appearance on routine T1 and T2 sequences. We will focus on the utility of diffusion-weighted imaging in these cases in deciphering benign from malignant lesion.
Materials and Methods
1. Case-based presentation will include clinical features, key imaging findings, radiology-pathology correlation, treatment and prognosis of common and uncommon causes of benign and malignant spinal column neoplasms. 2. Case examples include: fibrous dysplasia, enchondroma, chondrosarcoma, sarcoma, lymphoma, metastasis (carcinoid, prostate, lung, melanoma, etc). 3. Chart of salient features for quick reference.
Results
1. Review physics of diffusion-weighted imaging (B-values: 50, 400, and 800 s/mm2) with ADC mapping. 2. Review imaging findings of various spinal tumors. 3. Discuss limitations and pitfalls of diffusion-weighted imaging in the musculoskeletal system.
Conclusions
Osseous spinal tumors frequently are encountered incidentally on radiologic imaging and nonspecific imaging findings cause a diagnostic dilemma. Being familiar with discriminating imaging findings including diffusion-weighted imaging (DWI) can help characterize a tumor as benign or malignant thus assisting radiologists in guiding clinical management of the lesion.



(Filename: TCT_eEdE-241_dwispinetumor.jpg)

eEdE-236

6:30AM - 3:00PM

Epidural Steroid Injections: Complex Topic, Continuing Controversy

W Gibbs[1], B Johnson[2]

[1]University of Southern California, Keck School of Medicine, Los Angeles, CA, [2]Center for Diagnostic Imaging, Minneapolis, MN

Purpose
Epidural injection of steroid for the treatment of back pain is the most widely used pain management procedure worldwide. Extensive literature exists on the subject, but despite decades of research, the safety and efficacy of this procedure remains controversial. Media coverage of recent studies questioning the utility of steroid injections has widened the scope of this debate.
Materials and Methods
(1) Provide an overview of the scientific basis for treatment of back pain and/or radiculopathy with epidural steroid injections. (2) Review the most current literature concerning efficacy and safety of epidural steroid injections, as well as controversy surrounding disparate results and recommendations. (3) Describe investigative targeted therapies that may provide an alternative to steroid treatment.
Results
The 2014 LESS trial, and the 2015 U.S. AHRQ Technology Assessment questioned the effectiveness of epidural steroid injections. This was quickly picked up by the popular press, with numerous headlines claiming steroid injections were no better than placebo for treatment of back pain. The studies were criticized by groups who perform these procedures, and there was concern that patients who might benefit from epidural steroid injections would lose access based upon these publications. Subsequent systematic reviews have demonstrated the effectiveness of the injections. These studies have not been widely covered by the press, and there is a continued threat of loss of coverage. The debate over efficacy, safety, and cost effectiveness of epidural steroid injections continues. In the meantime, investigators pursue alternative treatments. Our knowledge of cellular mechanisms of the pain cascade is rapidly advancing, allowing identification of specific steps that may prove to be therapeutic targets.
Conclusions
This exhibit describes the scientific basis for epidural steroid injections, reviews the literature and current debate over their efficacy, and discusses advances that may produce alternative, targeted treatments for back pain.

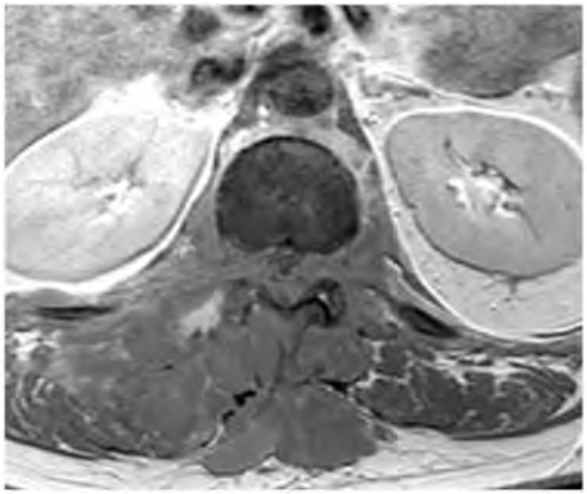
eEdE-242

6:30AM - 3:00PM

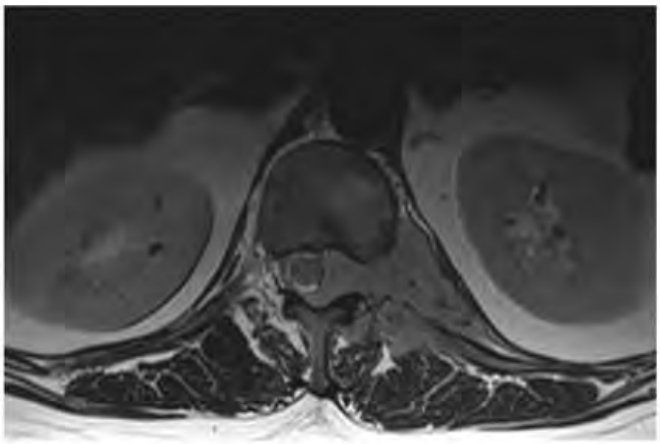
Imaging Findings in Spinal Lymphoma- A Single Centre Experience

P Menon[1], M Puthuran[2], M Bhojak[2], K Das[2], S Niven[2], S Biswas[2]
[1]North Wales School of Radiology, Wales, United Kingdom, [2]The Walton Centre, Liverpool, Merseyside

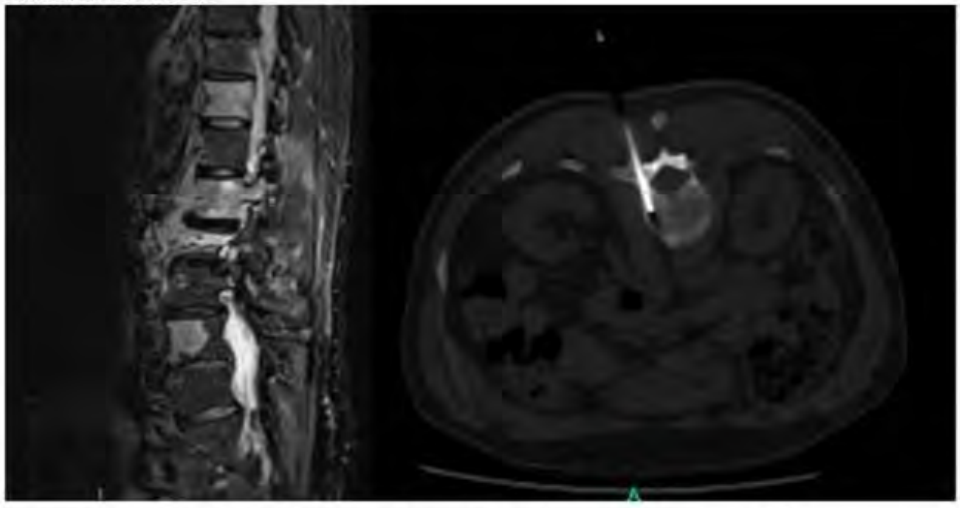
Purpose
To present a spectrum of imaging findings [Magnetic resonance imaging (MRI) and computed tomography (CT)] of spinal lymphoma as demonstrated in our patients who had undergone CT-guided biopsy. To emphasize the salient features of spinal lymphoma in the light of data from our patients.
Materials and Methods
A RIS search of all the CT-guided biopsies of spine was performed. Histopathology results of all these cases were retrieved. Confirmed cases of spinal lymphomas were selected (n=12) and the imaging (CT and MRI) was analyzed for imaging findings.
Results
On CT, most lesions were in the vertebral body and were either lytic, sclerotic or mixed. STIR imaging was most sensitive in picking up bony involvement and identified infiltration in vertebrae that looked normal on CT. T2-weighted sequences demonstrated cases with paravertebral soft tissue involvement, including epidural disease with cord compression. Postcontrast imaging demonstrated homogenous enhancement of most lesions. Most biopsies were performed using a trans-pedicular approach and a Jamshidi bone biopsy needle.
Conclusions
Lymphoma of the spine can have a varied appearance on imaging and CT and MR are complimentary in assessing the extent of disease. Differential diagnoses would include plasmacytoma, metastases and tuberculosis.



Extensive enhancing soft tissues in the epidural region causing thecal stenosis, right paraspinal muscle and subcutaneous fat



T2W image. Epidural soft tissue extending through the left intervertebral foramen and also causing destruction of adjacent rib.



Involvement of multiple vertebrae. Bone biopsy- transpedicular approach.

(Filename: TCT_eEdE-242_ASNRpicture.JPG)

eEdE-246

6:30AM - 3:00PM

Imaging the Spine with Sodium Fluoride F18 Positron Emission Tomography Computed Tomography (NaF PET CT)

K Hoque[1], W Gibbs[2], P Colletti[3]
[1]USC, Los Angeles, CA, [2]University of Southern California, Keck School of Medicine, Los Angeles, CA, [3]University of Southern California, Los Angeles, CA

Purpose
This educational exhibit will enable the viewer to gain an understanding of use of NaF PET CT to image osseous metastatic disease in the spine.
Materials and Methods
This review will detail proper technique for acquiring NaF PET CT images. Using case-based review, this exhibit will first detail normal findings and artifacts in NaF PET CT spine imaging. A discussion of non-neoplastic etiologies, including both degenerative changes and infectious findings will be explored. Next, both classic and rare presentations of osseous metastatic disease in the skull base, cervical, thoracic and lumbar spine as well as the pelvis will provide a complete spectrum of potential imaging presentations. Both qualitative and quantitive imaging analysis techniques will be discussed.
Results
NaF PET CT has emerges as a diagnostic technique which provides excellent sensitivity in the detection of osseous metastatic disease in the setting of prostate cancer. However, this relatively new imaging modality requires careful attention to acquisition parameters and in depth understanding of non-neoplastic imaging findings.
Conclusions
This case-based review guides the reader through proper technique, and the spectrum of neuroradiology findings attributed to both neoplastic and non-neoplastic processes.

eEdE-248

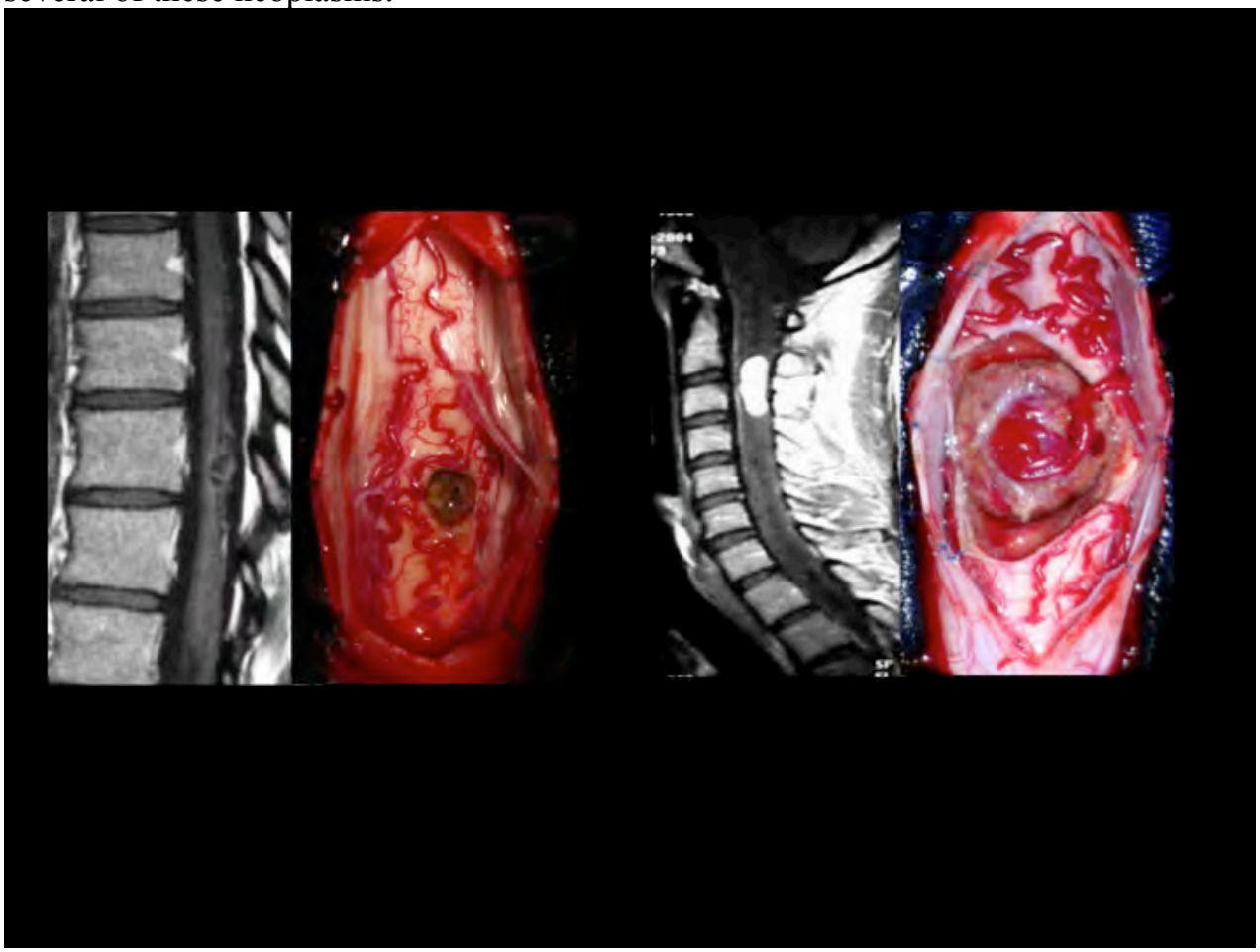
6:30AM - 3:00PM

Intramedullary Neoplasms: A Pictorial Review with Radiologic-Pathologic Correlation

F SCORTEGAGNA[1], L Amaral[2], L Estacia Ambros[2], A Maksoud Piccolo[2]
[1]HOSPITAL BENEFICIÊNCIA PORTUGESA, SAO PAULO, São Paulo, [2]Beneficiencia Portuguesa, SAO PAULO, AK

Purpose
The purpose of this abstract is to review common and uncommon intramedullary neoplasms with transoperatory, radiologic and pathologic images.
Materials and Methods
Pictorial review analyzing images from our neurosurgery, neuroradiology and pathology departments.
Results
We reviewed several intramedullary neoplasms that went to surgery in our hospital, focusing on the ones that had transoperatory pictures, correlating these with the radiologic findings.
Conclusions
As a group, intramedullary spinal neoplasms have limited distinguishing features on radiologic images. In adults, ependymomas are the most common intramedullary spinal neoplasms; astrocytomas are the second most common. In children, the relationship is

reversed. Although there are no pathognomonic imaging findings that allow flawless differentiation of an ependymoma from an astrocytoma in all cases, the combination of MR imaging findings often permits one most likely diagnosis to be posted. Features that favor an ependymoma include a central location; a well circumscribed mass; the presence of hemorrhage; a location in the conus medullaris or filum terminale; and focal, intense, homogeneous enhancement. Astrocytoma is favored when the mass is eccentric, is ill-defined, and enhances in a patchy, irregular fashion. Myxopapillary ependymoma is the most common neoplasm of the conus medullaris or filum terminale. Gangliogliomas characteristically involve 8 or more vertebral segments and have mixed signal intensity on T1-weighted images, a finding unique among spinal cord tumors. Hemangioblastomas are highly vascular lesions, may have prominent flow voids near the mass and may manifest with the cap sign, which classically is associated with ependymomas. Less common intraspinal neoplasms include metastases, lymphoma, cavernoma and PNET. The unique feature of this work is try to correlate radiologic, transoperatory and pathologic findings in several of these neoplasms.



(Filename: TCT_eEdE-248_Slide1.jpg)

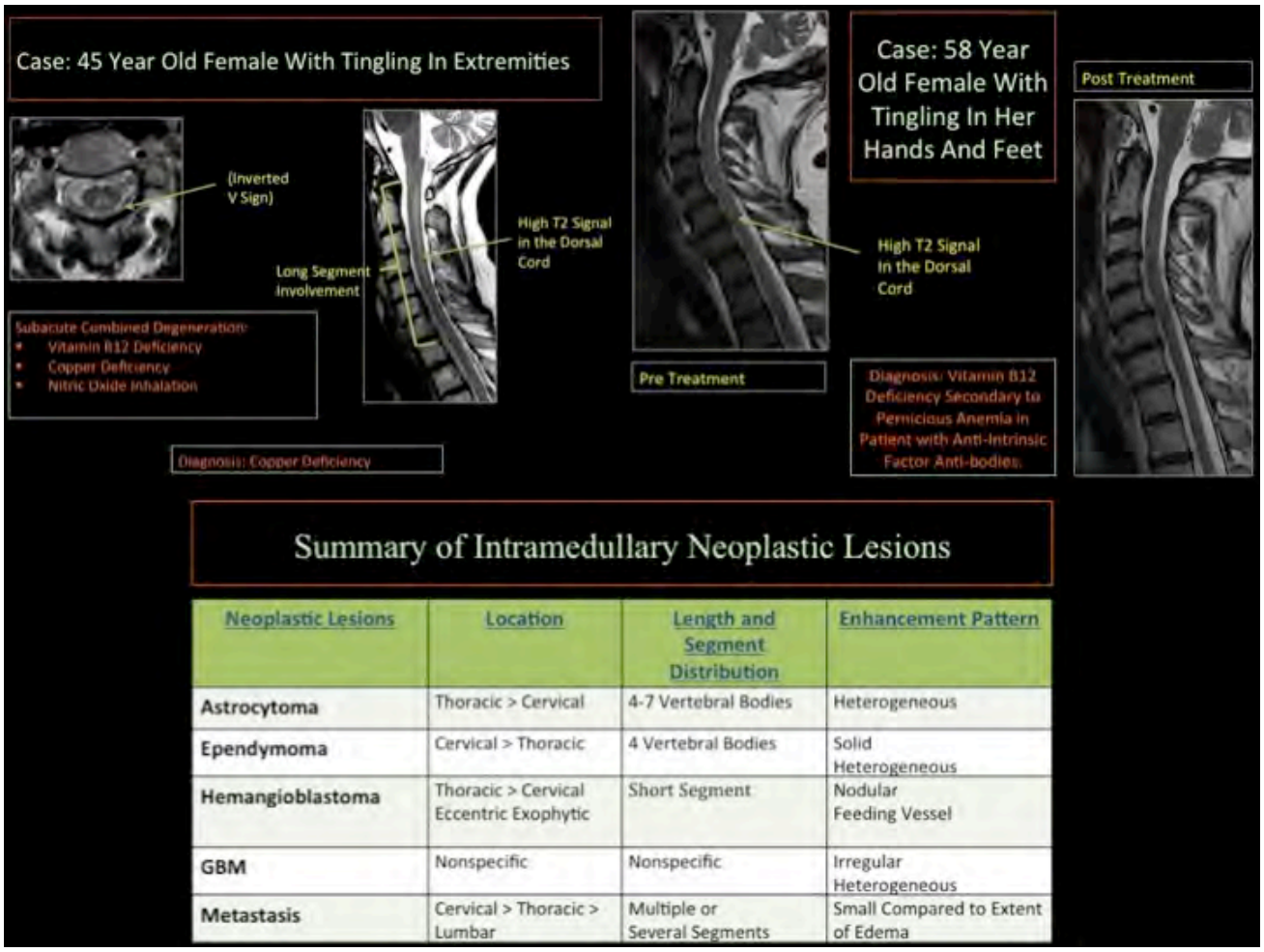
eEdE-253

6:30AM - 3:00PM

Location, Length, and Enhancement: A Systematic Approach to Differentiating Intramedullary Spinal Cord Lesions

S Mohajeri Moghaddam[1], A Bhatt[2]
[1]University of Rochester Medical Center, Rochester, NY, [2]University of Rochester Medical Center, Rochester , NY

Purpose
Intramedullary spinal cord abnormalities often are challenging to diagnose. Spinal cord biopsy is a high-risk procedure with potential to cause long lasting neurological injury, and therefore, it is imperative for the neuroradiologist to narrow the differential diagnosis of a spinal cord lesion. Careful attention to certain characteristics can even lead one to the correct diagnosis. The purpose of this presentation is to review the key imaging findings of various intramedullary spinal cord lesions.
Materials and Methods
We will review the normal anatomy and physiology of the spinal cord, with particular attention given to intramedullary structure and function. This presentation will review a systematic approach for the evaluation of intramedullary spinal cord lesions-with emphasis on location, length, segment distribution, and enhancement pattern-to help narrow the differential diagnosis. Location: Central versus Eccentric, Anterior versus Posterior, Exophytic Component, Conus Medullaris. Length and Segment Distribution: Short versus Long Segment, Single versus Multiple Segments. Enhancement Pattern: Non-enhancing versus Enhancing, Homogenous versus Heterogeneous Enhancement, Rim versus Nodular, Solid versus Patchy Enhancement.
Results
We will describe and differentiate the following spectrum of intramedullary spinal cord pathology using the aforementioned approach (selected examples are given): Demyelinating Diseases: Multiple Sclerosis, Neuromyelitis Optica (Devic Disease), Guillian Barre, ADEM. Metabolic Conditions: Subacute Combined Degeneration. Neoplastic: Astrocytoma, Ependymoma, Hemangioblastoma, Glioblastoma Multiforme, Metastases. Vascular: Infarction, Arteriovenous Malformation, Cavernoma. Other: Compressive Myelopathy.
Conclusions
Although intramedullary spinal cord abnormalities can be a challenge for the neuroradiologist, a systematic approach with focus on lesion location, cord length and segment involvement, as well as enhancement pattern, can help narrow the differential diagnosis and even synch the diagnosis. The radiologist can play a key role in patient care by obviating the need for an invasive approach to diagnosis, as well as help guide treatment.



Neoplastic Lesions	Location	Length and Segment Distribution	Enhancement Pattern
Astrocytoma	Thoracic > Cervical	4-7 Vertebral Bodies	Heterogeneous
Ependymoma	Cervical > Thoracic	4 Vertebral Bodies	Solid Heterogeneous
Hemangioblastoma	Thoracic > Cervical Eccentric Exophytic	Short Segment	Nodular Feeding Vessel
GBM	Nonspecific	Nonspecific	Irregular Heterogeneous
Metastasis	Cervical > Thoracic > Lumbar	Multiple or Several Segments	Small Compared to Extent of Edema

(Filename: TCT_eEdE-253_Slide1.jpg)

eEdE-227

6:30AM - 3:00PM

Lumbar Disc Nomenclature: Version 2.0 – A Pictorial Essay

J Yetto[1], M Bauer[1], J Dryden[1], K Soderlund[1], D Hawley[1], M Cathey[1]
[1]*Naval Medical Center San Diego, San Diego, CA*

Purpose
In 2014, the combined task forces of the North American Spine Society, the American Society of Spine Radiology, and the American Society of Neuroradiology published the review article, Lumbar Disc Nomenclature: Version 2.0 which updated and detailed the recommended verbiage for describing lumbar disc pathology. Furthermore, this article provided updated graphics to illustrate the new lumbar disc glossary of terms. Familiarity with this article avoids unnecessary communication errors on the part of both trainees and credentialed staff while providing a valuable service to our referring clinicians. The purpose

of this exhibit is to review and depict the lumbar disc glossary of terms from this consensus review paper using high-resolution 3T MR imaging.
Materials and Methods
Electronic resource that presents high resolution cross-sectional images which accurately depict the "Version: 2.0" glossary of terms. Images were obtained by performing a retrospective review of 3T MRI spine examinations over the past year. Relevant anatomy is reviewed. Additionally, a literature review on lumbar disc nomenclature was completed.
Results
Didactic electronic reference for clinicians, radiologists, and trainees that expounds upon the graphics included in the consensus paper, Lumbar disc nomenclature: Version 2.0, and clearly depicts the glossary of terms with high resolution cross-sectional imaging. Electronic teaching resources are helpful in familiarizing trainees with imaging findings and diagnoses. Such content is also helpful to radiologists as a reference. Divided into: 1. Introduction of Lumbar Disc Nomenclature. 2. Normal Lumbar Anatomy. 3. High-resolution 3T MRI examples of Version 2.0 nomenclature.
Conclusions
Radiologists play a critical role in the diagnosis of lumbar disc pathology and a comprehensive knowledge of the appropriate lumbar disc nomenclature is a critical component to effective communication of findings. Additionally, familiarity with the appropriate nomenclature provides a beneficial service to patients and referring clinicians.

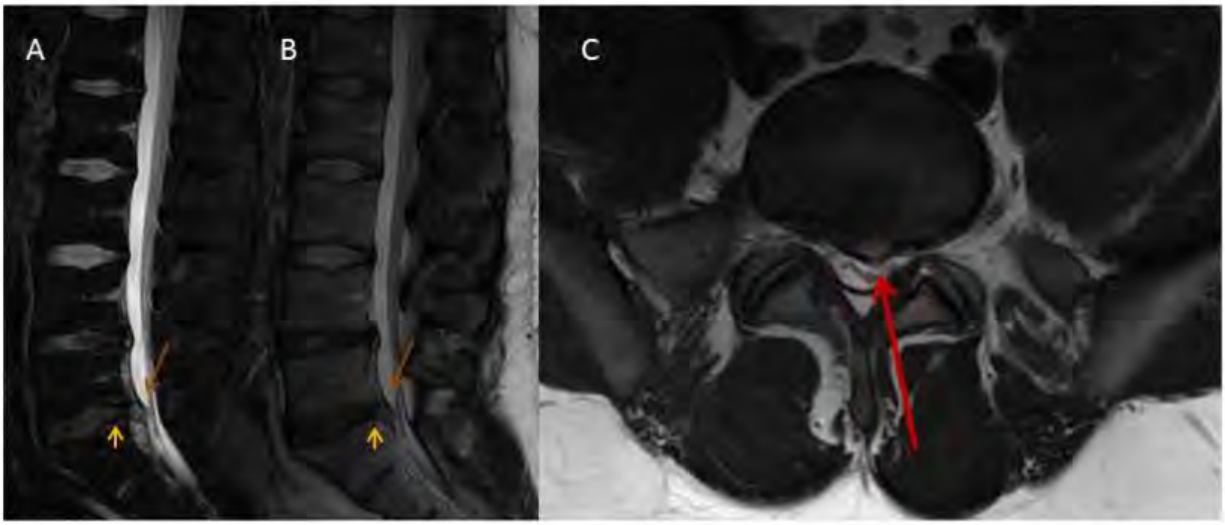


Figure 1. Disc Extrusion in a 29-year-old male with left lower extremity radicular symptoms. Sagittal T2W mDixon with (A) and without fat saturation (B) with axial T2W without fat saturation (C) images.

(A, B) Sagittal MR images demonstrate that the amount of disc material (*orange arrows*) beyond the disc space is greater than the amount of disc material at the base of the disc space of origin (*yellow arrows*).

(C) Axial MR image reveals the left central location of the disc extrusion within the spinal canal. A T2 hyperintense annular fissure (*red arrow*) is present.

(Filename: TCT_eEdE-227_lumbardiscnomenclatureKASedits.jpg)

eEdE-245

6:30AM - 3:00PM

Minimizing Radiation Dose During Lumbar Punctures and Myelograms - Simple Steps

R Downs[1]
[1]*University Of Louisville Hospital, Louisville, KY*

Purpose
This study demonstrates how the implementation of a few simple techniques significantly reduced fluoroscopy time/radiation dose during lumbar punctures and myelography.
Materials and Methods
At our hospital most lumbar punctures and lumbar myelograms are performed in the interventional suite. Cervical myelograms typically are performed in the GI fluoro suite via lumbar puncture and table tilt. The fluoroscopy time was obtained for all lumbar punctures and myelograms performed from 1/1/14 to 3/1/15 (94 performed either with a resident or

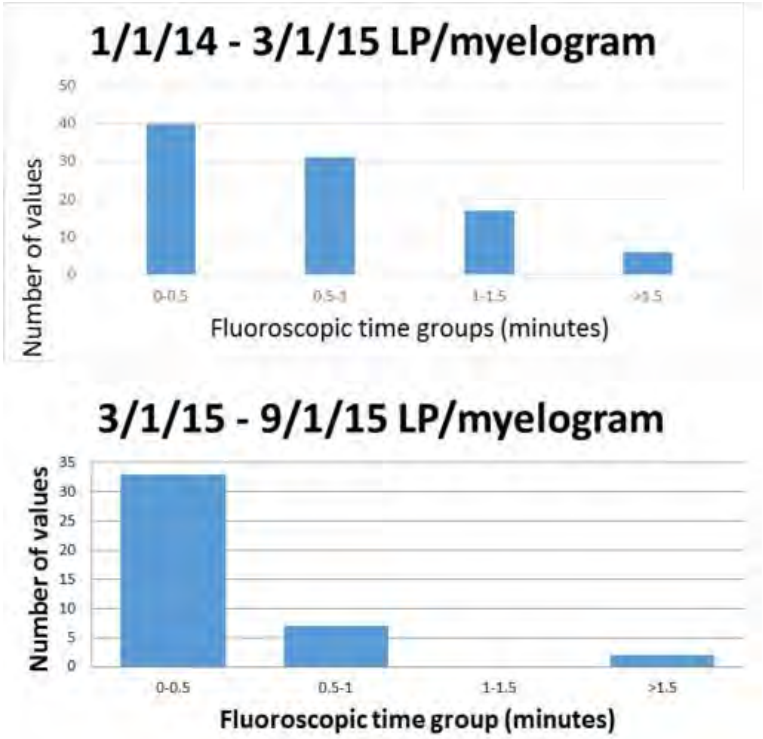
alone). Data were compared with typical published doses. To reduce fluoroscopy time/radiation dose the following 3 procedural points were emphasized: 1. Don't take a fluoroscopic image if you know the needle is not positioned properly. Instead reposition to where you think it is close and then image to check it. 2. When you do image, just step on the fluoroscopy pedal long enough for the picture to be taken and then stop and look at the saved image. Keeping the fluoro on longer does not add more information unless you are simultaneously moving the needle to speed up the procedure due to an unco-operative/altered mental status patient. 3. When the needle is in good position and near the spinal canal just advance the needle 2-3 mm and check for CSF, only checking with fluoroscopy every 3rd or 4th time. This was implemented on 3/1/15. The fluoroscopy times for lumbar punctures and myelograms were recorded from 3/1/3015 to 9/1/15 (42 performed with a resident or alone).

Results

Findings: 1/1/14 to 3/1//15 (see table): 94 exams average fluoro time = 0.8 minutes (0.7 minutes if remove top 5%). Boddu SR, et al. "Fluoroscopic-guided lumbar puncture: fluoroscopic time and implications of body mass index-a baseline study" AJNR, 35:8, 1475-1480, 2014. This article separated fluoroscopic time by BMI with an overall average of 0.65 minutes. Exams from 3/1/15 to 9/1/15 after implementation of the 3 steps: 42 exams average fluoro time = 0.4 minutes (0.3 minutes if remove top 5% with 17 out of 42 measured as 0.1 minute).

Conclusions

Implementation of these 3 simple procedural steps can result in significant reduction in fluoroscopic time/radiation dose during lumbar punctures and myelograms as well as during other interventional procedures. While this is important for the patient who is there once or a few times, it is far more important for the radiologist who will be performing the procedures hundreds to thousands of times over the course of their career.



(Filename: TCT_eEdE-245_Tables1and2jpeg.jpg)

eEdE-255

6:30AM - 3:00PM

Morel-Lavallee Lesion – Spinal Degloving Injury

D Gandhi[1], Y Kumar[2], N Gupta[1], T Jeyakumar[1]
[1]St. Vincent's Medical Center, Bridgeport, CT, [2]Yale New Haven Health at Bridgeport Hospital, Bridgeport, CT

Purpose
The purpose of this exhibit is to describe offbeat Morel-Lavallée lesion, which is traumatic soft tissue spinal injury. This educational exhibit discusses the imaging features and management of Morel-Lavallée lesions.
Materials and Methods
Five patients (mean age 51 years; range, 44–65 years) with either history of significant trauma were included in this retrospective study. Patients were assessed with MRI using a 1.5T unit (GE) and a phased array body coil. Different neuroradiologists reviewed the MR images. Various magnetic resonance imaging (MRI) features were taken into consideration for the diagnosis of the lesion, including site of involvement, existence or nonexistence of capsule. Further characterization of capsule, shape of the lesion, mass effect, contrast enhancement and signal intensities on different sequences. Additionally, various clinical

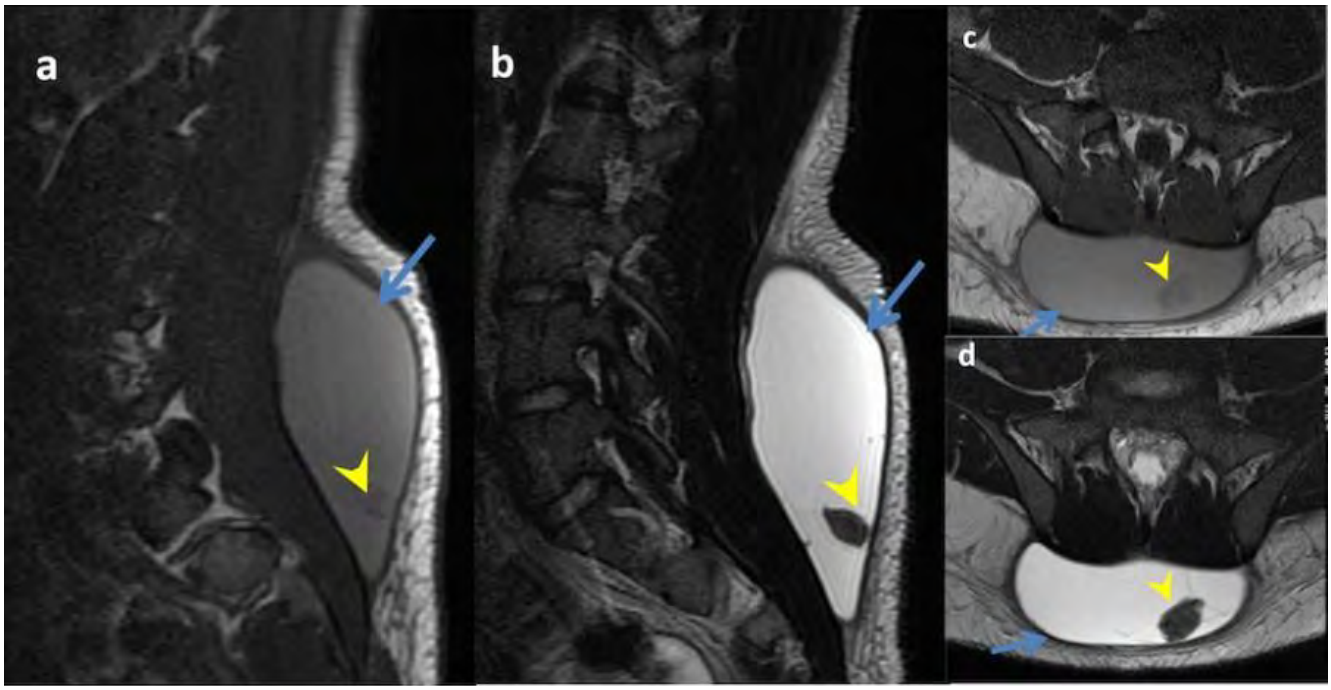
parameters were taken into consideration like type of trauma, location of lesion, delay in diagnosis, pain, etc.

Results

Morel-Lavallée lesion is a post-traumatic soft tissue degloving injury. This is commonly associated with sports injury caused by a shearing force resulting in separation of the hypodermis from the deeper fascia. Generally it occurs in few hours to days after the trauma, however sometimes they present in months to years after the trauma, which manifests the importance of the awareness of the findings of the lesion as well as the detailed clinical history evaluation of the patient. Most common at the greater trochanter, these injuries also occur at flank, buttock, lumbar spine, scapula, and the knee. Separation of the tissue planes result in a complex serosanguinous fluid collection with areas of fat within it. The imaging appearance is variable and nonspecific, potentially mimicking simple soft tissue hematoma, superficial bursitis or necrotic soft tissue neoplasms. It also is named as Morel-Lavallée hematoma, Morel-Lavallée extravasation, Morel-Lavallée effusion, ancient hematoma or organizing hematoma, chronic expanding hematoma, pseudolipoma, pseudocyst. Sonographic appearance is nonspecific. It either appears anechoic, hypoechoic and hyperechoic. Hyperechoic nodules of fat may be seen. CT can show hypodense subcutaneous fluid collection or fluid-fluid levels with different densities or fluid with varying amounts of internal debris including internal fat lobules, and may show a peripheral capsule. Six types of lesions can be seen in MRI like laminar shaped, oval shaped, oval shaped with thick capsule, linear shaped, pseudonodular round shaped or variable. If not treated in the acute or early subacute settings, these collections are at risk for superinfection, overlying tissue necrosis and continued expansion. In this review article, we will discuss the clinical presentation, pathophysiology, imaging features and differential diagnostic considerations of Morel-Lavallée lesions. Role of imaging in guiding prompt and appropriate treatment also will be discussed.

Conclusions

Magnetic resonance imaging is helpful to characterize Morel-Lavallée lesions and its various types. The lesions are typically oval, fusiform, or crescentic, consistent with fluid dissecting along the interfascial planes. It reflects the concentration of hemolymphatic fluid, the heterogeneous debris, the presence of fat, the presence or absence of a capsule, and varying degrees of enhancement. It is frequently associated with underlying fractures and degloving injury, and often is diagnosed within few hours to few days of trauma, but few patients may presents in months or years after the injury. It can mimic soft tissue tumor when present after months or years but interfascial location, shape, capsule, morphology, signal characteristics, and enhancement pattern can help to identify these lesions and guide appropriate therapy. The presence of a capsule is an important finding which is useful for the management of the lesion in surgery versus conservative therapy.



(Filename: TCT_eEdE-255_Figure1.jpg)

eEdE-231

6:30AM - 3:00PM

MR and CT Imaging of Typical and Atypical Infections of the Spine

J Dorr[1], A Chiu[1], J Dorr[1]
[1]*Santa Clara Valley Medical Center, San Jose, CA*

Purpose
Magnetic resonance imaging (MRI) is the most sensitive and specific modality for evaluating spinal infection. The goal of this exhibit is to describe imaging characteristics and present example cases of common and uncommon infections of the spine, with an emphasis on MRI.
Materials and Methods
1. Review locations of infection in the spine. 2. Review risk factors and associated infections. 3. Examine sample cases and describe unique imaging characteristics of specific entities.
Results
Introduction to infections of the spine. Classification of infection by location: spinal cord and canal, vertebral column, intervertebral disk space, and surrounding tissues. Types of infectious processes: -Soft tissue abscess, -Vertebral osteomyelitis, -Diskitis, -Epidural abscess, -Pachymeningitis, -Arachnoiditis, -Myelitis. Risk factors: Sample cases of specific disease entities are presented, including: - Figure 1: Axial (left) and sagittal (right) T2-weighted MR slices of the lumbar spine. -The level of the axial slice is indicated by the thin

line through the inferior L1 level on the sagittal slice. -There is a cystic lesion effacing the anterior cord (arrows) at the L1-L2 levels. -The patient has known neurocysticercosis, and these lesions represent additional foci of disease. - Figure 2: Sagittal T1-weighted postcontrast image of the cervical spine in a patient with tuberculosis. There is a ring-enhancing lesion in the cord (arrow) at the superior aspect of the C7 level, consistent with a tuberculoma. A punctate focus of enhancement in the cord at the C2-3 level with associated cord edema is an additional focus of infection. - Figure 3: Sagittal T1-weighted postcontrast image of the lumbar spine in a poorly controlled diabetic admitted for sepsis with MRSA growing in the blood. There are changes consistent with diskitis-osteomyelitis, most prominent at the L5-S1 level. There is also a large anterior epidural abscess which compresses the thecal sac extending from the inferior L4 through mid-sacral spine levels. - Figure 4: Sagittal T1-weighted postcontrast image of the lumbar spine in a patient with disseminated coccidioidomycosis, who has an intrathecal pump for treatment. The image shows diffuse enhancement of the thecal sac, as well as leptomeningeal enhancement along the inferior aspect of the spinal cord (arrows).

Conclusions

Infections of the spine may be categorized broadly by location, including: spinal cord and canal, vertebral column, intervertebral disk space, and surrounding soft tissues. The infectious etiologies affecting the spine are associated with certain risk factors such as IV drug use, immunocompromised state, and antecedent surgery. In recent years, the incidence of spinal infections has increased, in part due to the increasing incidence of these risk factors. In this study, a review of the locations and types of infections involving the spine is presented, followed by sample cases with MR imaging of typical and atypical infections. Using the reviewed material, a complete description of the findings and unique characteristics in each sample cases is provided.


1


2


3


4

(Filename: TCT_eEdE-231_CombinedImages.jpg)

eEdE-240

6:30AM - 3:00PM

Multimodality Management of Hypervascular Vertebral Lesions: Biopsy, Preoperative Embolization, Decompressive and Reconstructive Surgery and Radiation Therapy

L Kolb[1], V Zohrabian[1], J Camara-Quintana[1], K Abbed[2], J Grauer[1], M Laurens[3], J Yue[1], M Johnson[4]
[1]Yale University School of Medicine, New Haven, CT, [2]Yale School of Medicine, New Haven, CT, [3]Yale University, New Haven, CT, [4]Yale Univ. School Of Medicine, New Haven, CT

Purpose
To review imaging features of hypervascular spinal masses as well as the available imaging, interventional and surgical tools and techniques available for diagnosis and management of lesions requiring surgical decompression. To utilize a case-based approach to review the diagnostic imaging, biopsy, angiography, histology and operative imaging. To demonstrate effective pathways of multidisciplinary care coordination in the management of these complex patients.
Materials and Methods
Retrospective review of imaging and clinical/surgical records was performed on a series of neurosurgical and orthopedic patients with hypervascular spine lesions requiring pre-operative embolization and decompressive surgery. Patient demographics, symptoms, imaging diagnosis, biopsy, embolization and embolic agent, surgery site and type, blood loss, histology and radiation, if utilized, were recorded and both short and long term clinical outcome were assessed.
Results
Magnetic resonance imaging (MRI) was the mainstay of the diagnostic imaging evaluation supplemented by computed tomography (CT) and plain films when instability was an issue. The majority of biopsies were performed using CT guidance although fluoroscopy-guided biopsy at the time of vertebral augmentation was also performed. Myelography was used only for initial diagnosis when there was a contraindication to MRI (pacemaker, etc). Angiography and pre-operative embolization using particles, coils or liquid acrylic embolic agents was employed between 24 and 2 hours prior to surgery. Same day procedures allowed a single intubation and a single anesthetic session requiring care coordination between the angiography suite and the operating room. Surgical procedures included minimally invasive and traditional decompressive surgical methods with instrumentation as needed for stabilization. For benign hypervascular lesions, no further therapy was employed, however conventional and stereotactic radiation therapy for hypervascular metastatic lesions was added when residual tumor remained in the region.

Conclusions
Understanding the role of imaging and minimally invasive interventions in the management of patients with hypervascular vertebral lesions is important for the neuroradiologist and is best exemplified in the Spine Tumor Board model where cases are discussed and optimal management plans devised. Efficient coordination of diagnostic imaging, CT-guided biopsy, pre-operative embolization, and surgery with or without an operative radiation can minimize patient delays and optimize patient care. Spine Tumor Board is a great forum for development of these management plans and fosters multidisciplinary cooperation.

eEdE-251

6:30AM - 3:00PM

Name that Tumor: Spine Challenge

J Fritz[1], A Ajam[2], D Boulter[2], W Slone[3]
[1]Wexner Medical Center at The Ohio State University, Columbus, OH, [2]The Ohio State University Wexner Medical Center, Columbus, OH, [3]The Ohio State University Wexner Medical, Columbus, OH

Purpose
Degenerative changes are the most frequent finding in spinal imaging. Intradural masses are an uncommon but significant finding, and the imaging diagnosis has considerable influence on choice of therapy. The purpose of this exhibit is to provide an interactive review of common and uncommon spinal tumors, with inclusion of common mimics in a quiz format.
Materials and Methods
Imaging-based quiz with multiple choice questions of spinal tumors, both spinal column and cord. The images will be presented as unknowns, with 1-2 multiple choice questions regarding the diagnosis and key clinical features.
Results
Following each question, there is a brief discussion of the correct answer, including key imaging findings and treatment. This exhibit will present a broad spectrum of imaging appearance, from dural-based lesions to intradural, intramedullary lesions. A focused differential based on the images will be presented. Common mimics will be included in the quiz to better simulate routine reading and emphasize the differences, to prevent misdiagnosis of malignancy.
Conclusions
This exhibit with provide an interactive review of spinal tumors and common mimics. This will allow the viewer to test their knowledge of spinal tumors and increase their confidence in appropriate diagnosis and limited differential.



(Filename: TCT_eEdE-251_Spinetumor.jpg)

eEdE-250

6:30AM - 3:00PM

Neurosarcoidosis of the Spine: A Pictorial Review of its Many Appearances

J Gupta[1], H Marin[1], S Patel[2], J Corrigan[1], B Griffith[1]
[1]Henry Ford Health System, Detroit, MI, [2]Henry Ford Hospital, Detroit, MI

Purpose
Neurosarcoidosis occurs in approximately 5-25% of patients with systemic sarcoidosis and isolated spinal involvement is exceptionally rare. In the spine, the disease can involve the

bone, nerve roots, leptomeninges, dura matter and parenchyma. Magnetic resonance imaging (MRI) is a useful tool in diagnosis and used for disease follow up because of the high rate of progression and recurrence. The purpose of this exhibit is to provide a pictorial review of imaging features seen in cases of neurosarcoidosis, specifically within the spine.

Materials and Methods

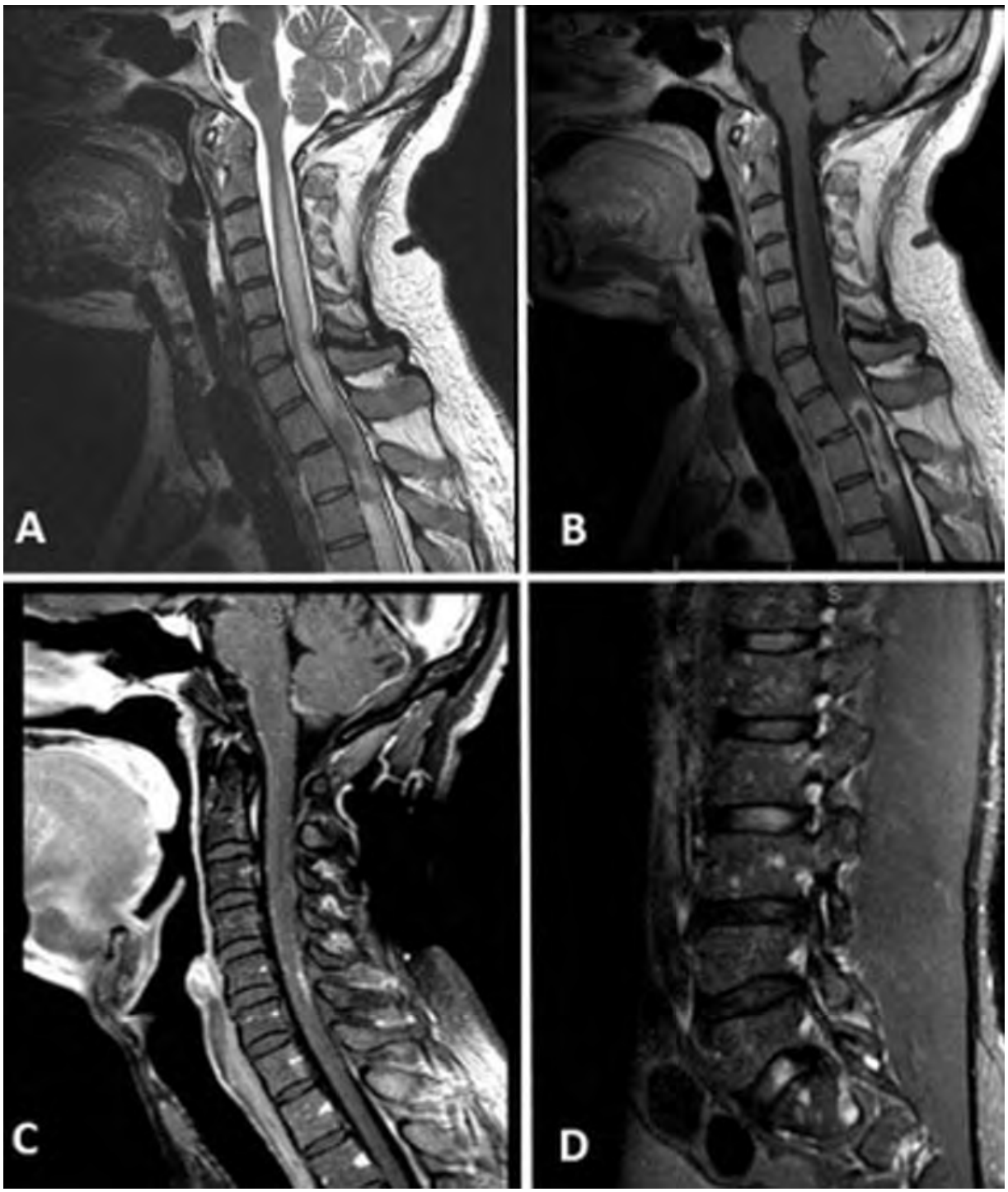
•We will show cases of neurosarcoidosis of the spine, including: intramedullary cord lesions (Figs. 1A and 1B), leptomeningeal involvement (Fig. 1C), peripheral nerve sarcoidosis, focal dural masses and bony involvement (Fig. 1D). •We will discuss clinical features and additional diagnostic tests that can help in formulating an appropriate differential diagnosis. •We will illustrate the potential mimickers of neurosarcoidosis involving the spine.

Results

The initial diagnosis in patients with spinal neurosarcoidosis can be challenging. This exhibit will display key imaging features seen in spinal neurosarcoidosis, demonstrating common lesion locations, signal characteristics, and enhancement patterns.

Conclusions

Neurosarcoidosis occurs in a significant portion (5-25%) of patients with systemic sarcoidosis. Neurologic symptoms are the most common presentation and less than 1% of patients have isolated central nervous system (CNS) disease. However, the first manifestation of sarcoidosis appears with CNS involvement in approximately 50% of cases. The typical imaging finding is leptomeningeal enhancement, but the disease can involve varying tissues within the spine. Due to the high rate of progression and recurrence, familiarity with the MRI findings is necessary for all radiologists. This exhibit will provide images of the multiple different locations spinal neurosarcoidosis can affect.



(Filename: TCT_eEdE-250_Sarcoid.jpg)

eEdE-252

6:30AM - 3:00PM

Onco-Pathology of the Spinal Canal

R Glikstein[1], C Torres[1], F Essbaiheen[1], J Davila[1]

[1]*University of Ottawa, Ottawa, Ontario*

Purpose

To show a series of patients with different oncology pathologies within the spinal canal with compromise of the cord.

Materials and Methods

This retrospective study is done after PACS review of patients with magnetic resonance imaging (MRI) of the spine with symptoms of cord compression and cauda equine syndrome performed in our institution between January 2010 and December 2016. Traumatic injuries, infection, vascular or primary intramedullary tumors were excluded from this work. Imaging included sagittal T1 and T2 sequences of the entire spine, axial T2 and postgadolinium sagittal and axial T1 sequences, performed on a 1.5 or 3T magnet. Among the different cases seven adult patients were selected in particular due to the extent of disease. The pathologies presented in this paper include intradural metastasis of glioblastoma, leptomeningeal carcinomatosis of lung cancer (ca), intradural metastasis of esophageal ca, intramedullary and leptomeningeal metastasis of breast ca, atypical choroid plexus papilloma with compromise of the cord, intramedullary metastasis of endometrial ca, epidural and cauda equine multiple myeloma.

Results

Leptomeningeal carcinomatosis of the spine is uncommon, less than 5% of the patients with primary tumors present with this manifestation of disease; the prognosis is very poor, with an average of 2 or 3 months of survival with very aggressive therapy and less than 15% may survive 1 year after diagnosis. Clinical manifestations may vary from weakness to symptoms of cord compression. Hematogenous spread, drop metastasis from primary brain tumor or perineural spread are considered the different mechanisms of extension to spinal canal. Some articles also make reference to possible iatrogenic spread on neurosurgical patients. Intramedullary metastasis represent 5% of all cord tumors, more commonly lung, breast, prostate and melanoma. Some patients consult because of pain, weakness, urinary incontinence, Brown-Sequard syndrome or other symptoms of cord compromise. These are hematogenous spread lesions, with poor prognosis after diagnosis, approximately 2 months survival. These lesions generally are solitary, eccentric and small. Uncommonly they are multiple, necrotic or hemorrhagic at first presentation. A known primary tumor generally precedes the intramedullary presentation; however, some patients may need biopsy of the lesion to confirm diagnosis.

Conclusions

Oncology patients with clinical manifestations of cord compression or cauda equine syndrome are seen in our daily practice. Due to acute or rapidly progressive symptoms MRI spinal studies are critical and should be performed on emergency basis.

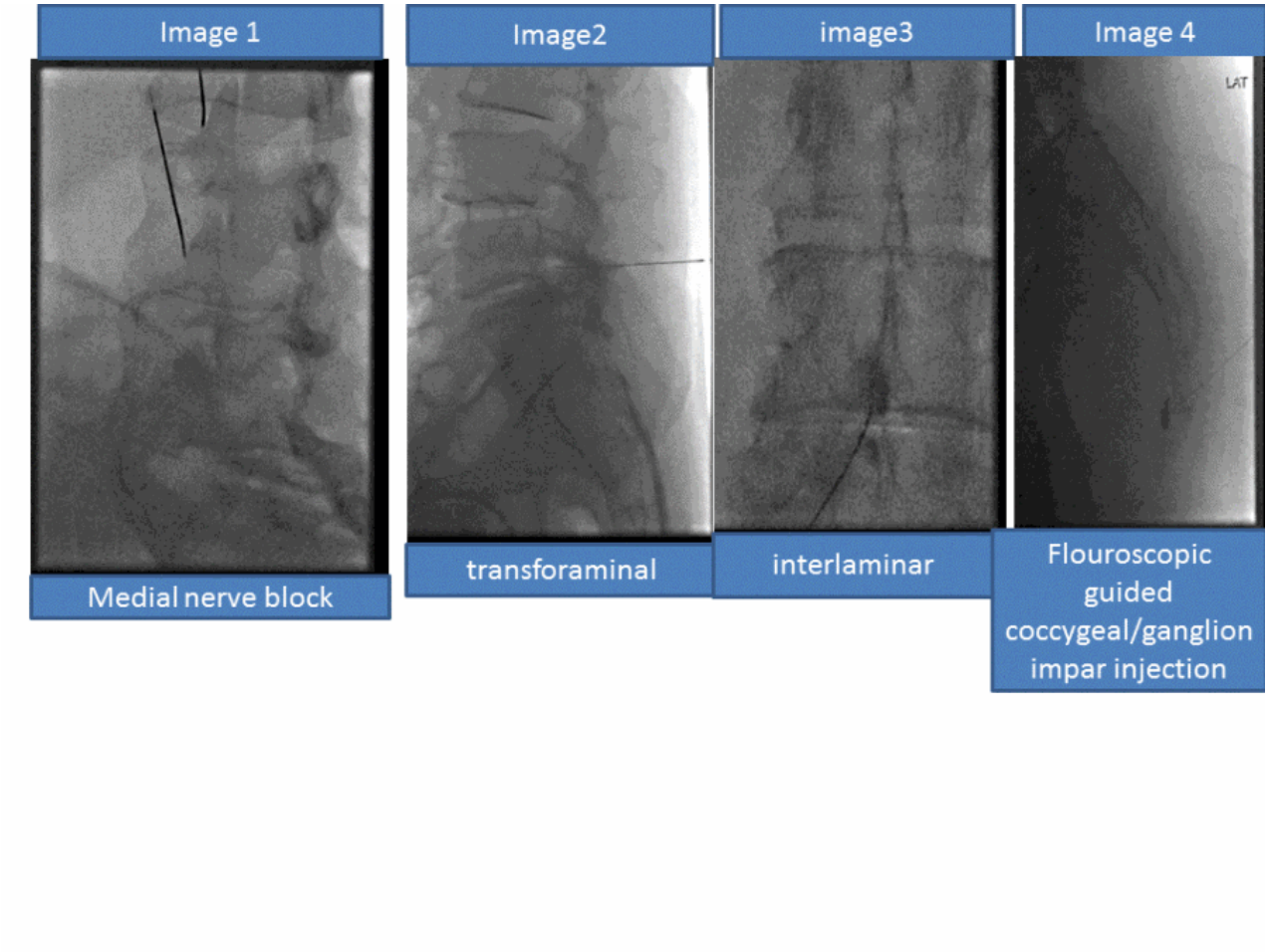
eEdE-239

6:30AM - 3:00PM

Ouch?!! Watch out Where you Put that Needle: Pearls and Pitfall in Image Guided Spine Intervention

o eissa[1], r eldaya[1], H Al-Jadiry[2], K Raghuram[3], S Gatzert[4]
[1]University of Texas Medical Branch, Galveston, TX, [2]UTMB Galveston, Galveston, TX, [3]UTMB, Galveston, TX, [4]The University of Texas Medical Branch, Galveston, TX

Purpose
Low back pain is a major medical problem that affects quality of life and productivity. Multiple therapies, including surgery, have been used to control low back pain. Given the invasive nature, prolonged recovery time, and failure rate of surgical procedures, a surge in noninvasive, image-guided procedures performed by neuroradiologists has occurred. Knowledge of the indications, contraindications, and possible complications of these procedures is an integral component of radiology resident education.The purpose of this educational exhibit is to familiarize radiology residents and general radiologists with the imaging findings and practical, performance "tips" associated with frequently performed neurointerventional procedures.
Materials and Methods
1-Anatomy. 2-General Principles and Tips. 3-Medications. 3-Epidural Steroid Injection: Interlaminar approach. 4-Epidural Steroid injection: Transforaminal approach. 5-Facet Joint Block. 6-Medial Branch block. 7-Sacroiliac Joint Steroid injection. 8-Coccygeal Steroid Injection.
Results
1-Indications. 2-Description. 3-Imaging Findings. 4-Contraindications. 5-Procedure SpecificTips.
Conclusions
Low back pain is a major health problem associated with multiple ER visits, disability, prolonged absence from work, and dramatic reduction in quality of life. Image-guided spine intervention can relieve low back pain, and result in postponement or obviation of invasive surgical procedures. Knowledge of the indications, contraindications, and imaging findings associated neurointerventional procedures is crucial to their proper execution, and to ensure alleviation, rather than exacerbation, of low back pain.



(Filename: TCT_eEdE-239_Slide1.GIF)

eEdE-243

6:30AM - 3:00PM

Practical Applications of Constructive Interference in Steady State (CISS) MRI in Spine Imaging

Y Chen[1], D Chow[1], V Shah[1], C Glastonbury[1]
[1]*University of California, San Francisco, San Francisco, CA*

Purpose
Constructive interference in steady state (CISS) magnetic resonance imaging (MRI) has been used to assist in the assessment of the cisternal spaces in the brain. In particular, it has proven beneficial in the detection of subtle lesions such as cranial nerve abnormalities or cerebrospinal fluid (CSF) leaks due to higher contrast between CSF and solid structures compared to routine spin echo images. This lends its use in the evaluation of multiple pathologies within the spinal canal. To better utilize CISS imaging in the spine, it is important for radiologists to be familiar with its applications as well as its limitations and

potential pitfalls. The purpose of this educational exhibit is to present a pictorial review of clinical applications of CISS imaging in the spine.

Materials and Methods

Our institution's imaging teaching file was queried for spine imaging with added CISS sequences. In this exhibit, content is organized by: (1) Description of CISS physics, (2) Case based review, (3) Challenges and pitfalls, (4) Post quiz.

Results

An organized and illustrative spectrum of CISS imaging in the spine is provided. The clinical scenario, representative imaging, and radiologic teaching points will accompany each case. Examples of spinal pathologies delineated by CISS MRI include complex syringomyelia, traumatic root avulsion injury, arachnoiditis, arachnoid web/band, leptomeningeal drop metastasis and intradural cystic lesions. Familiarity with these imaging features may aid the radiologist as a troubleshooting tool in certain scenarios.

Conclusions

High resolution CISS MRI imaging has important applications in the detection and evaluation of subtle pathologies in the spinal canal. An understanding of its applications and limitations will prove highly useful for the practicing radiologist.



Sagittal T2W with fat saturated (A) vs. Sagittal 3D FIESTA image (B) through the thoracic spine demonstrates the superior delineation of cystic syringomyelia in the thoracic cord of a patient with remote history of posterior surgical decompression from an episode of osteomyelitis-disciitis and epidural abscess.

(Filename: TCT_eEdE-243_Slide1.jpg)

eEdE-233

6:30AM - 3:00PM

Revisiting Infectious Spondylodiskitis And Its Mimics: Multimodality imaging approach

S Gaddikeri[1], M Matesan[2], M Jhaveri[3], P Minhas[4], M Nagarajan[4]
[1]Rush University Medical Center, Chicago, IL, [2]university of washington, Seattle, WA, [3]Rush University Medical Center, chicago, IL, [4]Rush University Medical Center., Chicago, IL

Purpose
Infectious spondylodiskitis confirmation and localization is dependent of imaging findings. Magnetic resonance imaging (MRI) is the imaging modality of choice due to very high sensitivity and specificity. However, diagnosis is not always straightforward particularly

when the MRI features are atypical or in the setting where MRI is contraindicated for various reasons. Many noninfectious inflammatory and degenerative process can mimic spinal infection.

Materials and Methods

1. Discuss the relevant spinal vascular anatomy and clinical findings in infectious spondylodiskitis. 2. Describe various typical and atypical MRI findings of infectious spondylodiskitis. 3. Briefly describe role of other imaging modalities including radiographs, computed tomography (CT), Technitium-99m three phase bone scan, Gallium-67 scan and Indium-111 WBC scan. 4. Describe various mimics of infectious spondylodiskitis.

Results

Early diagnosis of infectious spondylodiskitis is essential to prevent serious complications particularly spinal deformity, instability and neurological deficits. Various clinical and lab features may not be consistent with infectious process all the time. In most cases involvement of 2 consecutive vertebrae and the intervening disk is virtually diagnostic of infectious spondylodiskitis on MRI. The diagnosis may be delayed either due to atypical MRI features or inability to perform a MRI due to various contraindications. Hence, awareness of atypical MRI findings of spinal infection and imaging findings of other imaging modalities including radiographs, CT, Tc-99m triple phase bone scan, Ga-67 citrate and In-111 WBC scans may help the interpreting radiologist to raise suspicion for any early infection and make further recommendations for confirmation. Simultaneously, awareness of the mimics of infectious spondylodiskitis and the imaging features to differentiate them is essential to avoid over-diagnosis of this entity.

Conclusions

Understanding typical and atypical MR imaging features are essential for early diagnosis of infectious spondylodiskitis. Familiarity of mimics and their differentiating features is necessary to avoid over-diagnosis. Awareness of specific radionuclide imaging studies can useful in the setting where MRI is contraindicated or inconclusive.



51 year old male patient with neck pain due to spondylodiskitis. End plate erosions, vertebral sclerosis and prevertebral soft tissue swelling at C6/7 on lateral radiograph (A) and sagittal reformats of CT (B). Corresponding STIR (C) and post contrast T1W (D) MR images demonstrate marrow edema and enhancement. Enhancement is also seen extending along perivertebral and epidural region.

(Filename: TCT_eEdE-233_SPIneinfection.jpg)

eEdE-230

6:30AM - 3:00PM

The Shrinking Spine: Unusual Suspects for Multilevel Vertebral Height Loss

J Whang[1], F Priamo[2], N Chauvin[3], S Mohan[4]
[1]Hospital of the University of Pennsylvania, Philadelphia, PA, [2]Mount Sinai Beth Israel, New York, NY, [3]The Children's Hospital of Philadelphia, Philadelphia, PA, [4]University of Pennsylvania, Philadelphia, PA

Purpose
To present in an interactive manner a series of challenging cases with multilevel vertebral compression/destruction in order to improve diagnostic accuracy.
Materials and Methods
The myriad pathology to consider for multilevel vertebral height loss not typical for osteoporosis or neoplasm will be presented with multimodality imaging and relevant clinical data in a case-based format. Key differential diagnostic and therapeutic points will be highlighted in the discussion of each case. The cases to be discussed include: atypical infections (in immunocompromised patients, in sickle cell patients, and tuberculous spondylitis), dialysis spondyloarthropathy, Charcot spine, avascular necrosis, Paget's disease, Langerhans cell histiocytosis, renal osteodystrophy, and more.

Results

Vertebral destruction occurs with both acute and chronic pathology. In the acute setting, diskitis/osteomyelitis can be multifocal with immunocompromised, drug abuse, or sickle cell disease. Infection also can be slowly progressive, as with tuberculosis/Pott's disease. For patients with end stage renal disease, destructive spondyloarthropathy related to amyloid or crystal deposition can cause multilevel vertebral destruction mimicking infection (Figure 1a). This may co-exist with the characteristic findings of hyperparathyroidism. In patients with sickle cell disease or chronic steroid use, avascular necrosis causes endplate collapse with typical MRI findings (Figure 1b). Steroids also can weaken bone and cause H-shaped vertebrae without frank avascular necrosis. Other entities which weaken bone without destruction include Paget's disease and osteomalacia. Paget's disease has characteristic imaging findings. In children, Langerhan's cell histiocytosis is the most common cause of vertebra plana. A variety of congenital and metabolic disorders including Gaucher disease and mucopolysaccharidoses also should be considered in the pediatric population.

Conclusions

While most commonly associated with osteoporosis, metastasis, and myeloma, there is a wide differential diagnosis for multilevel vertebral height loss. In this review, we provide a comprehensive description of the typical imaging pattern with clinical context and stress important pointers to narrow the differential.



(Filename: TCT_eEdE-230_SpineASNRFigure.jpg)

eEdE-225

6:30AM - 3:00PM

Update on Spinal Fixation Hardware and Complications

E Sung[1], A Mian[1], G Barest[1]
[1]*Boston University/Boston Medical Center, Boston, MA*

Purpose
Neuroradiologists frequently review radiographs and computed tomography (CT) images in patients who have undergone spinal surgery. Therefore, they must be familiar with the various types of spinal hardware, both newer and older device, and potential complications related to the hardware. The purpose of this educational exhibit is to review the various types of spinal hardware that are commonly encountered, and provide a pictorial review of the potential complications related to the hardware.
Materials and Methods
Retrospective review of radiographs and CT scans in patients following placement of various types of spinal hardware. We will present a brief review of various types of more recent and older spinal fixation hardware, as well as examples of different types of hardware complications.
Results
Patients undergo spinal open reduction and internal fixation for various indications, including pain or instability related to degenerative joint/disk disease, traumatic or pathologic fractures, or neoplasms. Various types of hardware complications include component fracture, malfunction, migration, or loosening. Recent advances in new spinal hardware bring additional challenges in recognition of complications due to unfamiliarity. Accurate diagnosis of hardware failure requires an understanding of new developments in minimally invasive surgical (MIS) techniques and associated hardware, as well as familiarity with legacy hardware that currently is not utilized in clinical practice.
Conclusions
Spinal hardware commonly is encountered by neuroradiologists in daily practice. Knowledge of the various types of spinal hardware, as well as the potential complications and malfunctions is important for quality patient care. Familiarity with more recent developments in surgical techniques and devices also is important for accurate diagnosis. Prompt identification of complications can lead to more rapid surgical revision, minimizing further compromise of the intended function of the hardware.

eEdE-235

6:30AM - 3:00PM

Vertebral and Spinal Cord Sarcoidosis: the Many Faces of a Great Mimicker

B Bigjahan[1], F D'Amore[1], M Law[1]
[1]*Department of Radiology, Keck School of Medicine, University of Southern California, Los Angeles, California, U.S.A.*

Purpose
To review the highly variable imaging findings of spine and spinal cord sarcoidosis as well as discuss its pertinent clinical features and diagnostic challenges. This educational exhibit

will emphasize unique clinical background where comorbidities and ongoing treatment at the time of magnetic resonance imaging (MRI) often complicate further the imaging assessment in the daily clinical practice.

Materials and Methods

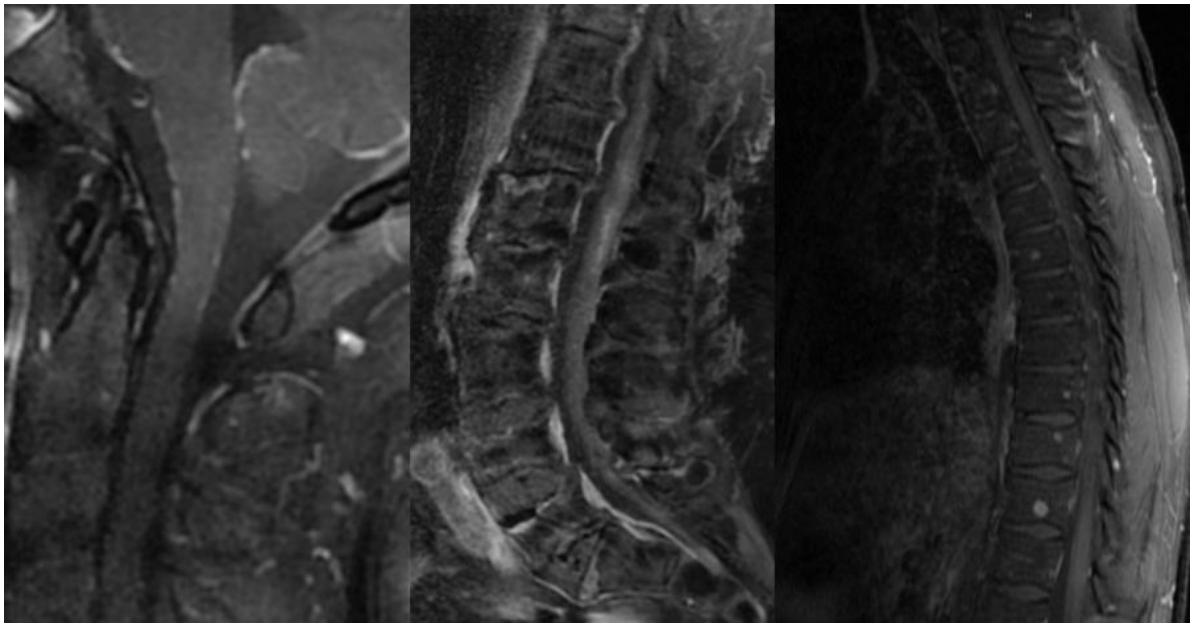
We conducted a retrospective search in our RIS-PACS database for MR scans of the spine performed at our institution between 2005 and 2015. We retrieved 42 patients whose MR reports contained keywords such as sarcoidosis and similar terms in the "clinical indication" field. Afterwards, clinical charts were systematically browsed for each patient to recompile their clinical and diagnostic history. Patients with incomplete history, clinical and diagnostic tests findings weakly supporting the hypothesis of sarcoidosis and low quality MRI scans were excluded.

Results

Our final sample consisted of 10 patients with either a biopsy proven (6 patients) or a combination of clinical/laboratory/radiographic diagnosis of systemic sarcoidosis with spinal involvement. One patient showed only brain and cord findings of sarcoidosis, hence was considered as a case of primary neurosarcoidosis. Three patients had vertebral/paravertebral tissues or other osseous involvement, 7 patients had variable extent of intramedullary and meningeal involvement. Brain findings compatible with sarcoidosis were found in 3 patients. The most frequent symptoms were related to myeloradiculopathy and cauda equina syndrome. Sarcoidosis is a rare cryptogenetic, multisystemic granulomatous disease that most frequently involves the lungs and lymphatic system. Central nervous system (CNS) involvement occurs in 5-13% of cases and the incidence of spinal cord involvement is 1%. Three criteria are used for diagnosis: clinical/radiological presentation, evidence of noncaseating granulomas and no evidence of alternative cause. Its imaging features may overlap with other disease such as tumor (intramedullary neoplasm, lymphoma, metastases), cord infarction, multiple sclerosis, idiopathic transverse myelitis and infection (tuberculosis). Moreover, therapy affecting the immune system (corticosteroids, disease modifying drugs) may alter the most common appearance of typical sarcoidosis findings on MRI.

Conclusions

Spine and spinal cord sarcoidosis is very uncommon. The imaging diagnosis can be very challenging given its variable imaging features that overlap with many other, often more common, diseases. It is important for neuroradiologists to be familiar with the many faces of spinal sarcoidosis.


(Filename: TCT_eEdE-235_Fig_Sarcoidosis_ASNR_2017.jpg)

eEdE-244

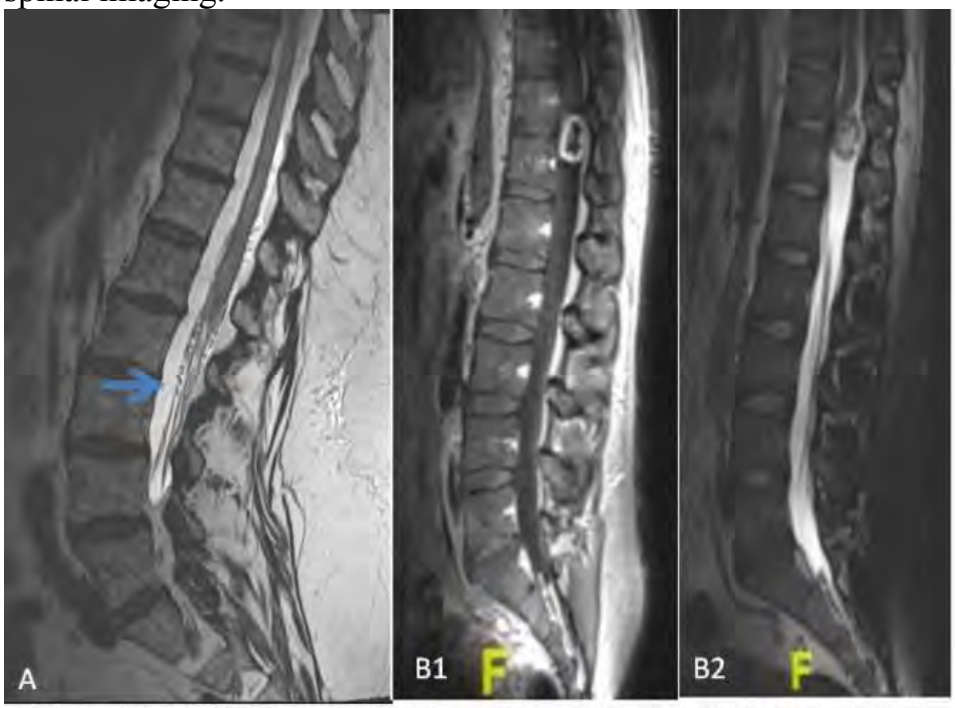
6:30AM - 3:00PM

Volumetric 3D Spinal MR Imaging: Advantages and Applicability

D Poliak[1], J Chazen[2], A Tsiouris[3]
[1]NewYork Presbyterian- Weill Cornell, New York, NY, [2]Weill Cornell Medicine, New York, NY, [3]New York-Presbyterian - Weill Cornell Medical Center, New York, NY

Purpose
Volumetric 3D spinal magnetic resonance imaging (MRI) is a helpful and efficient MRI technique for evaluating the spinal axis with applications including clinical problem-solving and intra-operative guidance. This exhibit will demonstrate its specifications, applicability and advantages.
Materials and Methods
This educational exhibit will highlight the following aspects of volumetric 3D spine imaging: Literature review of spinal 3D imaging. MR imaging techniques, tips, and tricks. Technical considerations (e.g., time efficiency, data processing). Clinical case examples including: -Problem-solving in difficult diagnoses (e.g., subtle migrated disk fragments, spinal dural arteriovenous fistula, intradural extramedullary masses). -Operative planning and intra-operative navigation. -Volumetric co-registration with high-resolution computed tomography (CT).
Results
Magnetic resonance imaging is a critical tool in a diagnostic spine imager's armamentarium. Volumetric 3D imaging is a developing technique for MR acquisition that assists patients

and physicians alike. Clinical diagnostic certainty and operative planning benefits can be realized from these techniques. 3D imaging also has the potential to decrease overall scan times using multiplanar reformations and advanced post-processing.
Conclusions
This exhibit will demonstrate the technical aspects and clinical benefits of 3D volumetric spinal imaging.



(A) Type I Dural AV-Fistula. Sagittal image from volumetric T2 image showing the conus edema and innumerable subarachnoid flow voids in great detail (arrow). Imaging was performed at high-resolution (640x640 pixels) yielding excellent multiplanar reformations. B1.
(B1) Sagittal high resolution T1 post-contrast SPACE and (B2) T2 SPACE volumetric 3D images demonstrating an intradural extramedullary mass at the level of the conus with internal T2 hyperintensity and enhancement. Images were used for intraoperative surgical navigation.

(Filename: TCT_eEdE-244_Slide1.JPG)

eEdE-249

6:30AM - 3:00PM

What's at the Back of the Back? A Review of the Spectrum of Dorsal Spinal Cord Lesions

A Hussein[1], A Carlton Jones[1], S Davda[1], A Krishnan[1], A Adams[2]
[1]Barts Health NHS Trust, London, London, [2]Barts Health NHS Trust, London, -

Purpose
To present a series of cases highlighting the spectrum of dorsal spinal cord lesions and their

various etiologies as well as clinical mimics. Combined with a literature review we also will discuss the pathophysiology of these entities.

Materials and Methods

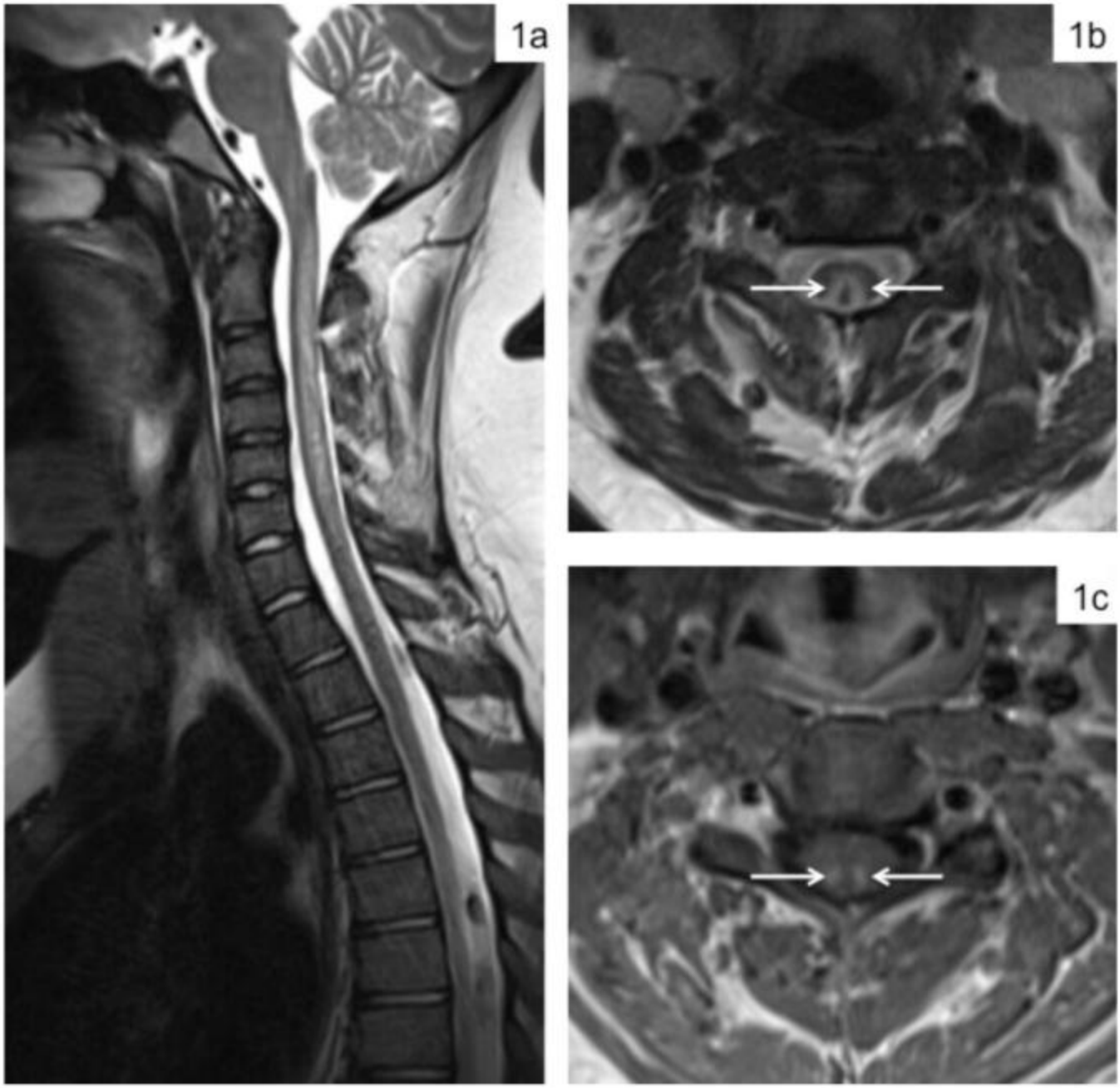
Clinicoradiological review of a series of adult and pediatric cases between 2014 and 2016 of dorsal column myelopathy/subacute combined degeneration of the cord at a central London neurosciences teaching institution, with correlative magnetic resonance imaging (MRI) spinal imaging. These cases are combined with a literature review.

Results

We present a variety of cases demonstrating dorsal spinal cord lesions. This will include cases of both mild and severe subacute combined degeneration of the cord secondary to nitrous oxide use, as well vitamin B12 and copper deficiency myelopathy. Rarer etiologies including HIV, syphilis and HTLV-1 myelopathies also will be reviewed. The clinical presentation and pathophysiology behind these will be recapped. Awareness of the role of nitrous oxide is of particular importance given the widespread medical use of nitrous-oxide containing Entonox gas for analgesia, and increasing illicit recreational use. Myelopathies resulting from the aforementioned metabolic deficiencies, secondary to the increasing use of bariatric surgery, are also rising in prevalence and are important to consider. The reader will understand the importance of how prompt treatment may prevent irreversible complications with lasting neurological impairment. Key aids to differentiating between clinical mimics, such as demyelinating disease and transverse myelitis, will be demonstrated with radiological examples.

Conclusions

The reader will understand the various etiologies and pathophysiology of dorsal column myelopathy, will have reviewed a large series of these examples and be able to differentiate between clinical mimics. Armed with this knowledge, the reader will feel confident in the diagnosis of such lesions and understand that prompt diagnosis and therapy may prevent progression or even reverse neurological deficit.



Case 1: 19 year old girl with illicit nitrous oxide use presenting with rapidly progressive arm and leg numbness. 1a) MRI T2 sagittal and 1b) T2 axial of the cervical spine demonstrates long segment symmetrical abnormality involving the dorsal columns (arrows) of the cervical spinal cord. 1c) Post gadolinium enhanced images show enhancement of the involved dorsal columns (arrows) suggestive of a degree of cord necrosis, which is uncommonly seen in dorsal column myelopathy.

(Filename: TCT_eEdE-249_IMG_0618.JPG)

eEdE-234

6:30AM - 3:00PM

What's in Your Sac? Imaging of the Lumbosacral Thecal Sac

F Essbaiheen[1], R Glikstein[2], C Torres[3]
[1]University of Ottawa and King Saud University, Ottawa, Ontario, [2]University of Ottawa, Ottawa, Ontario, [3]The Ottawa Hospital, Ottawa, Ontario

Purpose
Magnetic resonance imaging (MRI) of the lumbosacral spine is one of the most commonly ordered examinations in the assessment of low back pain. This is likely related to the fact that low back pain is one of the most common reasons to see a physician (1). Although most pathologies may seem obvious on imaging, knowledge of the normal anatomy of the lumbosacral thecal sac and its contents is important to rule out subtle findings that can be easily overlooked by the inexperienced eye.
Materials and Methods
In this educational exhibit, we emphasize the normal radiological anatomy of the lumbosacral thecal sac, describe the commonly used imaging techniques and highlight the different pathologies that can be seen. We categorize these pathologies into 3 major groups; 1. Extradural pathologies compressing the sac, 2. Intradural pathologies or pathologies that expand the sac and 3. Pathologies of the sac contents. Under each group we show common and infrequent imaging examples and we highlight key teaching points.
Results
Normal anatomy; Imaging techniques: (MRI, CT, myelogram); Extradural pathologies compressing the sac: Degenerative spine disease (Protruded disk, Synovial cysts), Spine neoplasia (Metastasis, Myeloma, Giant cell tumor, Hemangioma), Epidural pathologies (Hematoma, Abscess, Lipomatosis, Extramedullary hematopoiesis) and Normal variants (Congenital short pedicles); Intradural pathologies or pathologies that expand the sac: Dural ectasia (Marfan syndrome, Neurofibromatosis), Neoplasia (Drop metastasis, PNET, Lymphoma) , Infectious (Tuberculosis, Abscess) and Hemorrhage (Subarachnoid hemorrhage); Pathologies of the sac contents: Sac (CSF leak, Superficial siderosis), Filum terminale (Tight filum, Fatty filum, Myxopapillary ependymoma), Cauda equina (Focal: Schwannomas, Paragangliomas and Metastasis and Diffuse: Guillain-Barré syndrome, Arachnoiditis, Lymphoma, Sarcoid, TB).
Conclusions
In this educational exhibit we describe the normal anatomy, imaging techniques and pathologies of the lumbosacral thecal sac.

eEdE-223

6:30AM - 3:00PM

Why does my back always hurt? The Evolution of Human Bipedalism and its Effects on Spinal Form, Function, and Pathology

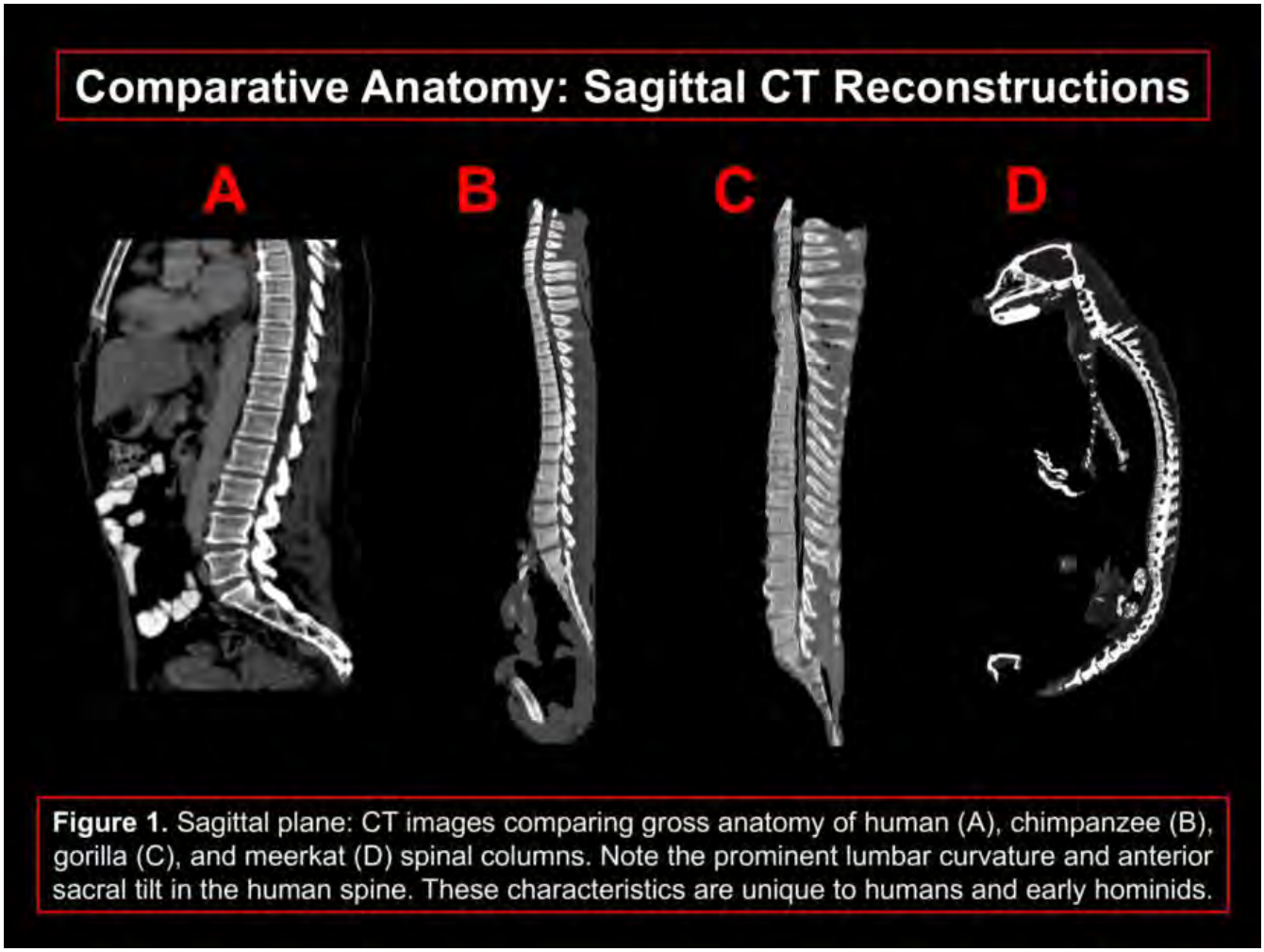
G Santoro[1], M Ramchand[1], S Lev[1]
[1]*Nassau University Medical Center, East Meadow, NY*

Purpose
To discuss the development of bipedalism using a comparative anatomical approach. We demonstrate how advanced imaging can elucidate the many adaptations to the central neuraxis required for an upright gait. Additionally, we explain how rapid evolutionary transitions resulted in postural benefits, but produced significant disadvantages as well, namely an inherent human predisposition to back pain.
Materials and Methods
Freely available CT datasets from the online Digital Morphology Museum of the Kyoto University Primate Research Institute (KUPRI) were uploaded in to our PACS software. DICOM files of an adult human, chimpanzee, gorilla, squirrel monkey, house cat, meerkat and prairie dog were used to create 2D axial, sagittal, and coronal images, as well as 3D reconstructions. Reconstructed CT images from the Adam P. Summers Open Science Framework fish CT database also were obtained. We visited several natural history museums to photograph skeletons of vertebrates, both living and extinct. These images, models, and photographs were used to characterize the gross anatomical distinctive features of each species and to acquire a variety of comparative measurements, particularly those pertaining to regional spinal curvature and vertebral morphology.
Results
The bony spinal column both protects the central neural structures and facilitates locomotion. Early evolutionary vertebrates, namely fish, have biconcave vertebrae, a feature that promotes lateral flexibility. Though their spines are segmented, like in humans, there is minimal cephalocaudal variation. This reflects the fact that fish, supported by a buoyant aquatic environment, have relatively few forces acting on their bodies. The transition to land introduced compressive, tensile, and torsional forces associated with postural support. Quadruped gait necessitated subsequent adaptive changes. Supportive zygapophyses and fibrocartilaginous disks developed to mitigate the constant minute trauma associated with land locomotion. Terrestrial species developed spinal curvatures and regional vertebral characteristics. As cranial mass increased in mammals, a prominent cervical curvature and enlarged cervical vertebrae were necessary to maintain head and neck posture, important for forward gaze. A prominent rib cage and pelvis promoted lateral stability and protected vulnerable abdominal viscera. In humans and primate relatives, a reduction in the number of presacral vertebrae from the mammalian average further approximated these regions, providing additional protection. Mammalian evolution of upright posture and gait gradually led to a stacked vertebral column susceptible to the compressive force of gravity. This

resulted in thicker intervertebral disks, a lumbar curvature, and an anterior sacral tilt. These features are unique to humans and early hominids, but are absent in our closest living ancestor, the chimpanzee, who has a stiff, straight lower back more adapted for support when climbing trees.

Conclusions

Facultative bipedalism is observed in several mammalian species. Meerkats and prairie dogs stand on hind legs to survey surroundings, bears fight upright, while bonobos and chimpanzees walk on hind limbs when carrying objects or when injured. Humans are unique in that they exhibit habitual bipedalism. This evolutionary transition afforded early hominids several advantages. Hands were free for carrying food, fighting, hunting, and manipulating tools, paving the way for higher intellectual activities. A higher head meant better visibility. Our upright posture and new center of gravity allowed for long distance travel and superior thermoregulation. This relatively rapid evolutionary transition required that early hominid morphology and physiology adapt, however imperfectly, to the major redistribution of forces. This might explain the prevalence of radiculopathy, stenosis, disk desiccation, herniation, spondylosis, and spondylolisthesis in humans. Upright posture relies particularly on lumbar lordosis and is affected by factors including spinal musculature strength and vertebral wedging. Often, the signs of an aging spine are a flattened lumbar lordosis and a prominent thoracic kyphosis, features characteristic of our primate ancestors. A comparative anatomical approach applying the unique perspectives provided by radiological imaging can facilitate our understanding of human gait and the effects of bipedalism on degenerative spinal pathologies.



(Filename: TCT_eEdE-223_ASNR_Figure.jpg)

eEdE-229

6:30AM - 3:00PM

"Hot and Bothered": An Imaging Review of the Inflammatory Spondyloarthropathies for Neuroradiologists

P Rajagopalan[1], A Capps[1], R Seltman[1], W Fischer[1], A Kamer[1], L Ladd[1], N Koontz[1]
[1]*Indiana University School of Medicine, Indianapolis, IN*

Purpose
We provide a comprehensive guide to the imaging characteristics of inflammatory spondyloarthropathies geared toward neuroradiologists.
Materials and Methods
We performed a HIPAA-compliant retrospective review of our institution's electronic medical record for illustrative cases of inflammatory spondyloarthropathies, highlighting multimodality (radiographic, CT, MRI, and nuclear medicine) spine imaging. We describe

nonspine imaging findings that may confer additional specificity to the diagnoses and review the current medical literature.
Results
Early manifestations of inflammatory spondyloarthropathies on spine imaging may be easily overlooked, especially when viewed without appropriate clinical context. When viewed solely from a neuroradiology lens, spine findings can be nonspecific and yield a broad differential diagnosis, including inflammatory seropositive spondyloarthropathy (rheumatoid arthritis), inflammatory seronegative spondyloarthropathies (psoriatic arthritis, reactive arthritis, ankylosing spondylitis, and enteropathic spondyloarthropathy), and other arthropathies affecting the spine (SAPHO syndrome, gout, and calcium pyrophosphate dihydrate deposition). We highlight clinicoradiologic features of each entity, demonstrate imaging discriminators that improve the specificity of each diagnosis (including cardiothoracic and musculoskeletal imaging findings that may be overlooked by neuroradiologists), detail important differential considerations (including osteoarthritis, diffuse idiopathic skeletal hyperostosis, neurogenic arthropathy, and spondylodiskitis), and report important diagnostic pitfalls.
Conclusions
Recognizing characteristic imaging features of inflammatory spondyloarthropathies may enable neuroradiologists to add value to their work by improving diagnostic accuracy and providing an earlier diagnosis. This often requires neuroradiologists to look beyond the spine for clues found on cardiothoracic and musculoskeletal imaging.

Monday
6:30AM - 3:00PM
Long Beach Convention Center, Exhibit Hall B-(Lower Level) eP

Electronic Scientific Poster (eP)-Adult Brain

eP-65

6:30AM - 3:00PM

AIRP 2016 Best Case in Radiologic Pathologic Correlation: Neuroradiology. Diffuse Brain Meningitis, Abscess, and Ventriculitis

A Mahammedi[1], S Bachir[1], J Purdy[1], T Lewis[1], O Ashour[1], J Schroeder[1], A Medhkour[1], M Buehler[1]
[1]*University of Toledo, Toledo, OH*

Purpose
During the February, 2016 American Institute for Radiologic Pathology (AIRP) meeting (previously known as Armed Forces Institute of Pathology - AFIP), this case was selected as the best case in Neuroradiology, as it perfectly illustrated strong radiologic pathologic correlation. With each issue of RadioGraphics, the best AIRP cases are selected for

publication, written by the winning resident. Radiologic pathologic correlation is emphasized, and the causes of the imaging signs of various diseases are illustrated. This case demonstrates brain abscesses which ruptured and evolved into ventriculitis with meningitis resulting in a sudden and dramatic worsening of the clinical presentation. Multiple imaging modalities including CT scan and MRI were correlated with gross specimen and histological images.

Materials and Methods

History: A 57 year old Caucasian male with a past medical history of splenic injury who was transferred from an outside facility and presented after being brought in by his sister for progressed confusion and a one day history of fever, random abnormal movements of his extremities. On admission, he was found to have blood pressure 50s/40s and heart rate in the 50s. He also had 6 to 7 mm nonreactive pupils. Initial brain CT showed two mass lesions, left frontal and parietal. Initially, there was concern that these lesions were metastatic; however, MRI confirmed these lesions to be abscesses. Lumbar puncture showed many white blood cells but no organisms or yeast elements. Chest xray demonstrated left lower lobe pneumonia. Patient was empirically treated with broadspectrum antibiotics with vancomycin, ceftriaxone, and Flagyl. Neurosurgery was rapidly involved. He was given: Levophed, mannitol, IV fluid resuscitation and stress dose steroids. His vital signs improved but his pupils became small at 2 mm bilaterally, though still sluggishly and minimally reactive. He also improved to have trace decerebrate posturing on the left side and had left corneal reflex, a gag and cough. A repeat head CT one day after initial study showed significant interval ventriculomegaly with bilaterally dilated temporal horns. Bilateral frontal ventriculostomy drained cloudy fluid and ultimately drained purulent material. Despite management of his sepsis, ventriculitis, respiratory failure and what appeared to be brainstem herniation secondary to mass effect from brain abscesses, his neurological status was very poor and continued to worsen throughout his stay. After review and consultation with neurology and neurosurgery, it was determined that his neurological status and brain function status was not salvageable. On 5 DAA, with no additional treatment options, family decided to withdraw support. Patient expired shortly thereafter and postmortem examination was conducted.

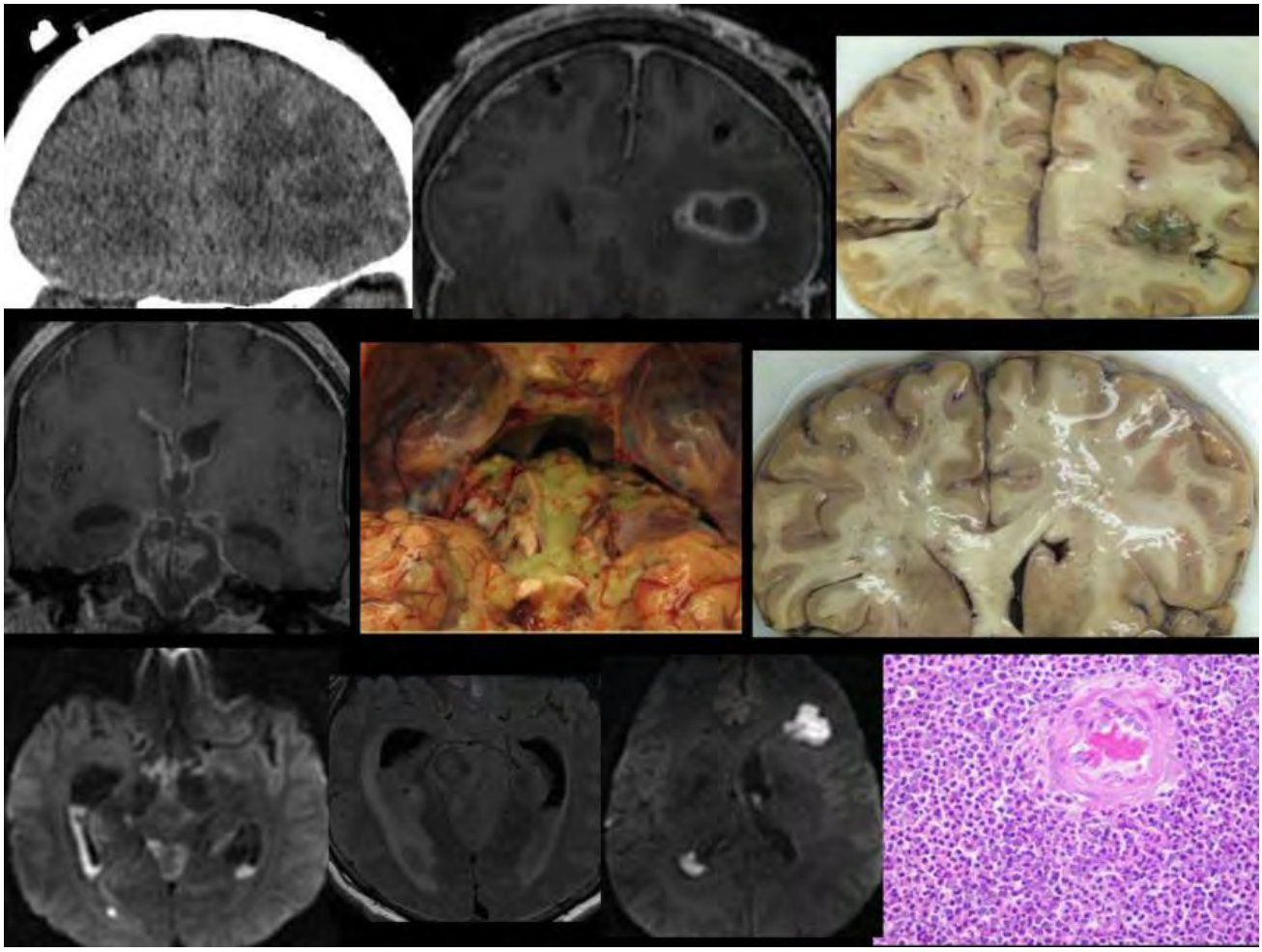
Results

* Imaging: Multiple CT scans with and without IV contrast. MRI with IV contrast. * Pathology: High power views (H&E x 40) tissue sections. Gross specimen and histological images correlated to multiple imaging modalities. Image Findings: Top row, left to right: - Coronal CT without IV contrast shows left frontal lobe abscess. - Coronal MR T1 postcontrast shows left frontal lobe ring enhancing abscess. - A coronal gross section demonstrates a 2.5 x 1.5 x 1.1 cm purulent lesion in the left frontal lobe white matter at a level 1 cm anterior to the genu of the corpus callosum. This lesion appears to have ruptured into the lateral ventricle in the inferior lateral frontal lobe. Middle row, left to right: - Coronal T1 Postcontrast RT ventricultis and brainstem leptomeingeal enhancement. - Gross: Large amount of purulent material in the subdural space surrounding the brainstem,

cerebellum and throughout the ventricular system. - A coronal gross section demonstrates some purulent material in the right lateral ventricle with minimal periventricular extension. Bottom row, left to right: - ADC Axial: diffusion restriction in the brainstem and along the occipital/temporal horns consistent with ventriculitis and meningitis. - Axial Flair: Left pons and ependymal hyperintense signal along the perioccipital/temporal horns of the ventricles. - DWI axial: Two areas of diffusion restriction in the left frontal lobe and right parietal lobe, greater in the left. - Tissue section from hippocampus, high power view(H&E x 40) shows the dense inflammatory infiltrate within the meninges consists mostly of neutrophils. These findings are consistent with meningitis

Conclusions

Brain abscesses are a potentially life threatening condition requiring rapid treatment, and prompt radiological identification. Fortunately MRI is usually able to convincingly make the diagnosis, distinguishing abscesses from other ring enhancing lesions. Ventriculitis is most often due to intraventricular rupture of brain abscess, meningitis (both pyogenic and viral), and shunt/EVD related. Clinical presentation is nonspecific with many cases having no convincing inflammatory or septic symptoms. Symptoms of raised intracranial pressure, seizures and focal neurological deficits are most common forms of presentation. Eventually many abscesses rupture into ventricular system, which results in a sudden and dramatic worsening of the clinical presentation and often heralds a poor outcome. In cases where the abscess cavity does not completely obliterate, followup with MRI including DWI is useful and lack of restricted diffusion is reassuring. Demonstration of ongoing restricted diffusion in a cavity suggests persistent infection. The mainstay of treatment for cerebral abscesses is neurosurgical drainage which can be performed either by stereotactic aspiration or craniotomy. Broad spectrum intravenous antibiotics are also needed and can later be changed to agents tailored to the specific organisms.



(Filename: TCT_eP-65_Slide1.JPG)

eP-15

6:30AM - 3:00PM

Altered Functional Connection in Patients with Classical Trigeminal Neuralgia

Y TSAI[1], B BISWAL[2]
[1]Chang-Gung Memorial Hospital, Chiayi, Taiwan, [2]New Jersey Institute of Technology, Newark, NJ

Purpose
Classical trigeminal neuralgia is a specific type of chronic neuropathic orofacial pain without any apparent cause other than neurovascular compression (1). It has distinct clinical presentation and pathophysiology comparing to other chronic pain disorders. Changes of brain connectivity which may represent functional plasticity in chronic classical trigeminal neuralgia patients have remained largely unknown (2). We aimed to investigate the alteration of connectivity between pain-associated brain regions in classical trigeminal neuralgia and to see the correlation between brain connectivity and duration of pain.

Materials and Methods

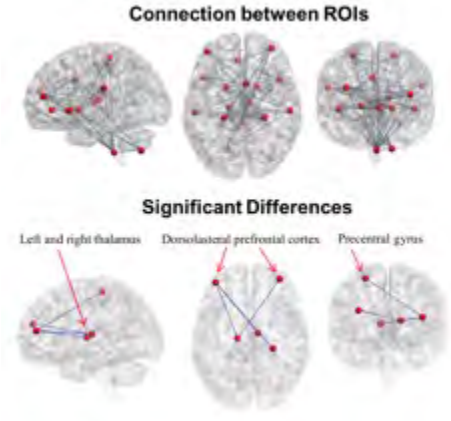
A total of 45 patients with classical trigeminal neuralgia and 20 matched healthy subjects were included and referred to magnetic resonance imaging (MRI) scans. The study was approved by the Institutional Review Board of our institution and all patients gave their written informed consent prior to participation in the study. All MRI data were collected with a 3 Tesla Siemens Verio MRI system (Siemens Medical System, Erlangen, Germany). Functional images were obtained using a gradient EPI sequence that is sensitive to blood-oxygen-level dependent contrast (TR = 2500 ms, TE = 27 ms, FOV = 220 mm, matrix = 64 × 64 × 36, slice thickness = 4 mm. Each scan consisted of 240 image volumes). Functional images were motion corrected, and co-registered to the individual anatomical image using the AFNI package (http://afni.nimh.nih.gov/afni/). By searching the keyword "pain" in the Neurosynth dataset (http://www.neurosynth.org/), the pain related network was obtained (3). The peak point of each cluster was detected and defined as regions of interest (ROI). The average time series were extracted from each ROI and the correlations between time series from each ROI was calculated using age as covariate. The analysis was performed by Network Based Statistic Toolbox (https://sites.google.com/site/bctnet/comparison/nbs).

Results

The connections of the right dorsolateral prefrontal cortex with the bilateral thalamus and the left precentral gyrus, as well as between left dorsolateral prefrontal cortex and right thalamus, are higher in the trigeminal neuralgia group as compared to the healthy controls (Figure 1). The connectivity between left precentral gyrus and right dorsolateral prefrontal cortex is moderately negatively correlated with pain duration ($p = 0.003$). Other networks that are significantly different between trigeminal neuralgia and normal subjects, including the connections between thalamus to dorsolateral prefrontal cortex and to precentral gyrus show modest correlation with pain duration but do not reach statistically significance.

Conclusions

The classical trigeminal neuralgia is due to neurovascular compression of the trigeminal nerve and can result in functional changes of brain. These results have clinical implications regarding the etiology of trigeminal neuralgia as well as the cortical plasticity that can be the target of treatments aimed at reversing cortical reorganization.



(Filename: TCT_eP-15_2.jpg)

eP-18

6:30AM - 3:00PM

Altered Microstructure of Normal Appearing White Matter in Multiple Sclerosis: Prediction of Neurological Disability

N Hatch[1], M Yazdani[2], M Kocher[3], M Spampinato[4]
[1]Medical University of South Carolina, Charleston, SC, [2]Medical University of South Carolin, Charleston, SC, [3]Medical University of South Carolina, Charleston , SC, [4]Medical University Of South Carolina, Charleston, SC

Purpose
To evaluate whether diffusional kurtosis imaging (DKI)-derived metrics for the corticospinal tract (CST) can predict disability in patients with multiple sclerosis (MS).
Materials and Methods
We retrospectively evaluated forty-one patients with MS who underwent a brain MRI including DKI (twice-refocused echo planar sequence with 3 diffusion weightings, b = 0, 1000 and 2000 s/mm2, along thirty diffusion encoding directions) and a baseline neurological evaluation. A 12-month follow-up neurological evaluation also was available for twenty-nine subjects (70.7% of patients). The following diffusion metrics were estimated for the CST using DKI: fractional anisotropy, mean diffusivity, radial diffusivity, axial diffusivity, mean kurtosis, radial kurtosis, and axial kurtosis. Disability was quantified using the extended disability score scale (EDSS) at the time of the MRI (Baseline EDSS) and 12 months after the MRI (12-month EDSS). Linear regression analyses were conducted to evaluate whether diffusion metrics were able to predict the degree of neurological disability.
Results
Significant correlations were found between baseline EDSS and the following variables: CST radial diffusivity ($r = 0.380$, $p = 0.007$), CST radial kurtosis ($r = -0.387$, $p = 0.006$), age ($r = 0.470$, $p = 0.001$), and T2 lesion volume ($r = 0.370$, $p = 0.009$). Significant correlations also were found between 12-month EDSS and the following variables: age ($r = 0.381$, $p = 0.021$), radial diffusivity ($r = 0.352$, $p = 0.031$), and radial kurtosis ($r = -0.486$, $p = 0.004$). We also found that radial kurtosis ($p = 0.034$) and age ($p = 0.005$) were significant predictors of baseline EDSS, radial kurtosis ($p = 0.001$) and axial diffusivity ($p = 0.032$) were significant predictors of 12-month EDSS.
Conclusions
Radial kurtosis of the CST may prove useful as a predictor of neurological disability in MS. DKI-derived metrics provide information about brain tissue microstructure that may be complementary to DTI and conventional MRI techniques in guiding the management of patients with multiple sclerosis (1).

eP-25

6:30AM - 3:00PM

Amplitude of Low-Frequency Fluctuations During Resting State is Associated with Anxiety and Depression in Multiple Sclerosis

J Puig[1], G Blasco[2], C Biarnes-Duran[3], J Gich[4], M Rivero[4], J Salavedra[4], A Alberich-Bayarri[5], M Marti-Navas[1], P Daunis-i-Estadella[6], S Thio-Henestrosa[6], M Wintermark[7], K Nael[8], S Pedraza[2], L Ramio-Torrenta[4]

[1]Research Unit of Diagnostic Imaging Institute (IDI), IDIBGI, University Hospital Dr Josep Trueta, Girona, Girona, [2]Imaging Research Unit, IDI-IDIBGI, Hospital Dr Josep Trueta, Girona, None, [3]Research Unit of Diagnostic Imaging Institute (IDI), Girona Biomedical Research Institute (IDIBGI), Girona, Girona, [4]Department of Neurology-IDIBGI, University Hospital Dr JosepTrueta, GIRONA, GIRONA, [5]Hospital Universitario y Politecnico La Fe-QUIVIM, Valencia, None, [6]Department of Computer Science, Applied Mathematics and Statistics, University of Girona, Girona, Girona, [7]Stanford University, Stanford, CA, [8]Icahn School of Medicine at Mount Sinai, New York, NY

Purpose

We investigated the differences in amplitude of low-frequency fluctuations (ALFF) by resting-state functional MRI (rs-fMRI) among cohorts of patients with multiple sclerosis (MS), and their impact on anxiety and depression scores.

Materials and Methods

We prospectively studied consecutive patients with radiologically isolated syndrome or clinically isolated syndrome (n=23; 18 female; age 35±9.1 years), primary or secondary progressive (PP/PS) (n= 35; 19 female; age 53.5±7.2 years), or relapsing-remitting (n= 24; 16 female; age 43.9±11.3 years) MS and thirty healthy controls (18 female; age 41.4±10.9 years) on a 1.5T scanner. Imaging included 10 minutes of rs-fMRI acquisition and anatomic T1-weighted turbo field echo sequence. We used the Data Processing Assistant for rs-fMRI to compute and normalize ALFF maps. White and gray matter volumes also were calculated. We used the hospital anxiety and depression (HAD) scale to measure anxiety and depression. To avoid confounding effects of age or schooling on cognitive performance, we used unstandardized residual values of the regression between cognitive scores and these factors for all analyses. Analysis of variance and Bonferroni test were used to evaluate differences between groups. To analyze the impact of ALFF on HAD score, we used analysis of covariance (ANCOVA) on variables associated with cognitive scores ($p<0.05$).

Results

Hospital anxiety and depression-depression subscale differed between PP/PS and controls ($p<0.018$); no other differences in HAD scores were found between study groups. Differences in HAD-anxiety scores among groups were explained by mean ALFF in the left posterior cingulate gyrus ($p=0.004$). The best ANCOVA model to explain HAD-depression scores among groups ($p<0.001$) included mean ALFF in the left middle cingulate ($p=0.029$),

left inferior frontal gyrus (p=0.011), left medial frontal gyrus (p=0.001), and right superior temporal gyrus (p=0.033).
Conclusions
Our preliminary results suggest ALFF on rs-fMRI is associated with anxiety and depression scores in subjects with MS.

eP-03

6:30AM - 3:00PM

Analysis of Small Vessel Disease Using Axial CT Head Images and its Association with Obstructive Sleep Apnea

F Kayali[1], M Mantello[1], A Wolfe[1]
[1]*Richmond University Medical Center, Staten Island, NY*

Purpose
Obstructive sleep apnea (OSA) has been associated with an increased incidence of hypertension (HTN) and diabetes. As HTN and diabetes have been associated with small vessel disease (SVD), we aim to investigate the association of SVD with OSA as well.
Materials and Methods
Computed tomography (CT) images of seventy-eight patients between August 2014 and March 2015 were reviewed. All subjects were over the age of 40, participated in an OSA risk assessment questionnaire (STOP-BANG) within 24 hours of CT examination, and consented to a review of their laboratory values. A combination of a STOP-BANG score ≥3 and a bicarbonate level ≥ 28 mmol/L served as the cut-off for high OSA risk (previously shown to have a specificity ~ 85%).
Results
Patients were separated into 2 groups based on the presence of SVD. Group 1 did not demonstrate SVD (n=36, 19F:17M) and had an average age of 57 years (42-80). Group 2 had CT findings consistent with SVD (n=42, 25F:17M) and had an average age of 71 years (41- 94). The incidence of diabetes, hypertension, and increased risk for OSA were higher in patients with SVD (22%±14 vs. 40%±15, $p = 0.087$; 33%±16 vs. 71%±14, $p < 0.0001$; and 22%±14 vs. 48%±15, $p = 0.037$ respectively).
Conclusions
Despite the small number of patient's participating in this prospective study, our data suggest a statistically significant increase in incidence of patient's who are at high risk of OSA when stratifying patients based on who develops small vessel disease. Furthermore, an increase in number of participants to this study is needed to further characterize OSA as a risk factor for SVD independent of HTN and diabetes.

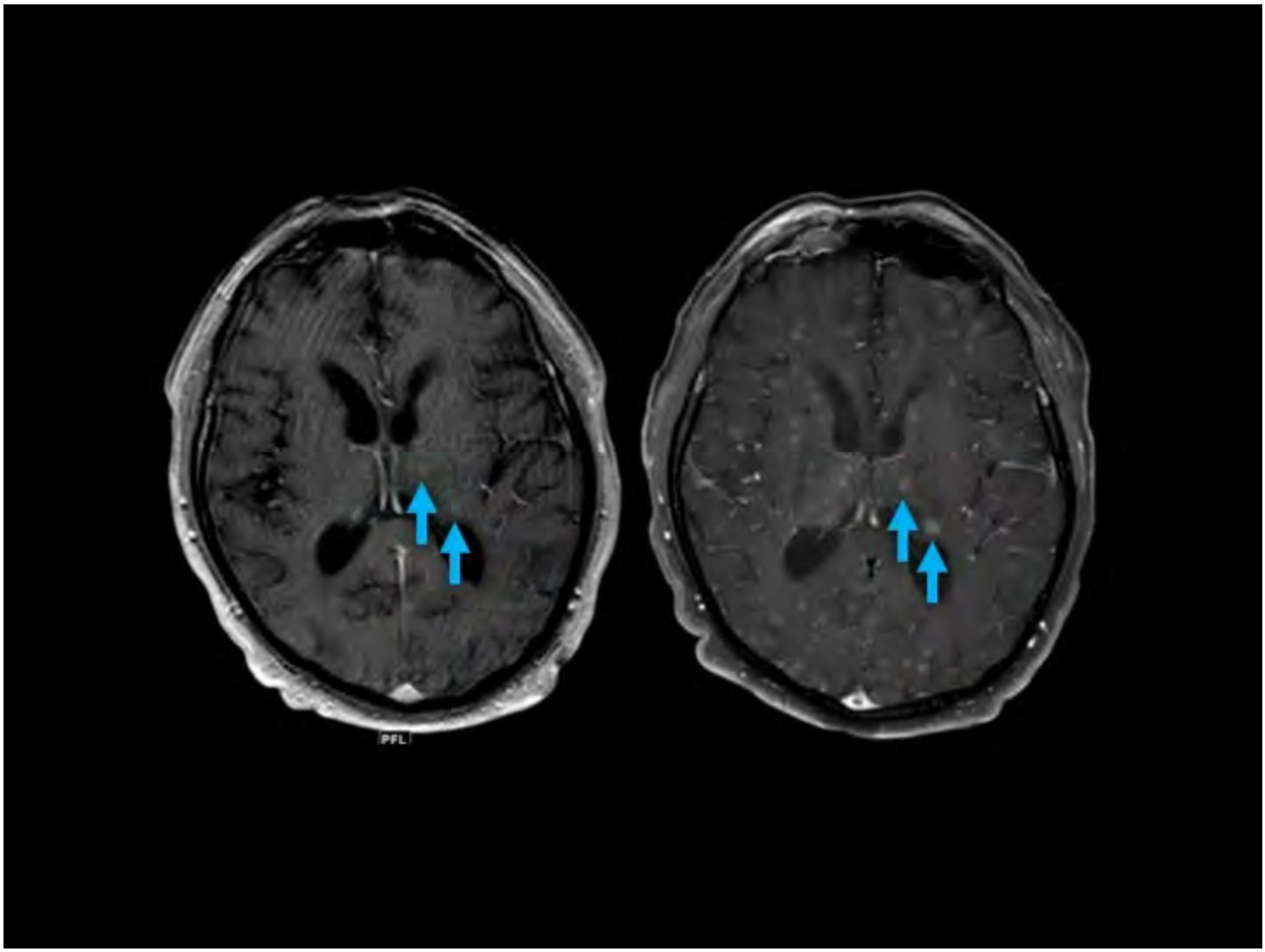
eP-67

6:30AM - 3:00PM

Assessing the Potential Impact of Patient Motion on the Detectability of Intracranial Metastases.

M Dalesandro[1], d haynor[2], T Amthor[3], C Hall[4], D Hippe[1], J Andre[1]
[1]University of Washington, Seattle, WA, [2]university of washington, seattle, WA, [3]Philips Research Europe, Hamburg, Germany, [4]Philips Healthcare, Bothell, WA

Purpose
We sought to evaluate the impact of motion artifacts on the diagnosis and management of intracranial metastases (ICM), a disease process that often relies on the detectability of small lesions using high-resolution, motion-vulnerable sequences.
Materials and Methods
Patients who underwent a standard clinical protocol MRI on one of two identical 3T Philips Ingenia scanners between July 2013 and July 2014 were retrospectively identified and eligible for study inclusion using the following criteria: 1) MRI exam included a whole brain high-resolution axial post-gadolinium 3D inversion-recovery spoiled gradient (IR-SPGR) T1-weighted sequence (TR=25, TE=3.5, matrix=300x296, slice thickness=1.6mm, FOV=240x240mm) ; and, 2) the MRI was performed for the detection of, and/or treatment planning for, ICM or Gamma Knife planning/monitoring. The subset of patients with identifiable and/or known ICM were confirmed on manual image review at a PACS station. In these select patients, all brain MRIs from Jan 1, 2013 - March 2016 were evaluated and re-reviewed by one reader (R1) for the presence of detectable, gadolinium-enhancing ICM that were 1) not mentioned in the official radiologic report, or 2) were initially interpreted as "no new lesion(s)" in which a new lesion was detected upon retrospective image re-review. A second, experienced reader (R2) evaluated the "missed" lesions to identify possible major contributors to the oversight. Missed lesions were categorized as "Perceptual" when there was no significant motion or other artifact obscuring the lesion, "Motion" when moderate to severe motion artifact obscured a lesion (using a predefined clinical scale [1]) , and "Other" when other artifacts (susceptibility, physiological/pulsation artifact, low signal-to-noise, etc.) obscured a lesion.
Results
In 240 reviewed patients, 171 met inclusion criteria, including 21 with "missed" lesions. Of these, six had multiple reasons for missed ICMs, either due to multiple lesions being missed, or the same lesion being missed on multiple exams. The most common reason for missed lesion(s) was perceptual (n=17, 81% of 21 patients with missed lesion), followed by motion (n=7, 33%) and "other" reasons (n=3, 14%). In 1 case (~5%), a de novo diagnosis of ICM was missed due to motion artifacts and resulted in a 9-month delay in the correct diagnosis.
Conclusions
Motion artifacts may impact the detectability of new metastatic lesions and thereby alter appropriate patient care, but appear to be less likely to do so than are perceptual errors.



(Filename: TCT_eP-67_mets.jpg)

eP-61

6:30AM - 3:00PM

Blood in Brain: Usual and Unusual Causes of CNS Hemorrhage

L De Abreu Jr.[1], A Wolosker[2], M Borri[3], A Torres[4]
[1]Fleury Group Hospital, Sao Paulo, Brazil, [2]Fleury Group, Hospital Sao Luiz, Sao Paulo, SAO PAULO, [3]Fleury Group, Hospital Sao Luiz, Sao Paulo, Brazil, [4]FLEURY GROUP,HOSPITAL SAO LUIZ, sao paulo, SAO PAULO

Purpose
The objective of the authors is to review, through daily practice case images, the usual and unusual causes of central nervous system (CNS) hemorrhage, describing particular aspects that lead to correct diagnosis.

Materials and Methods

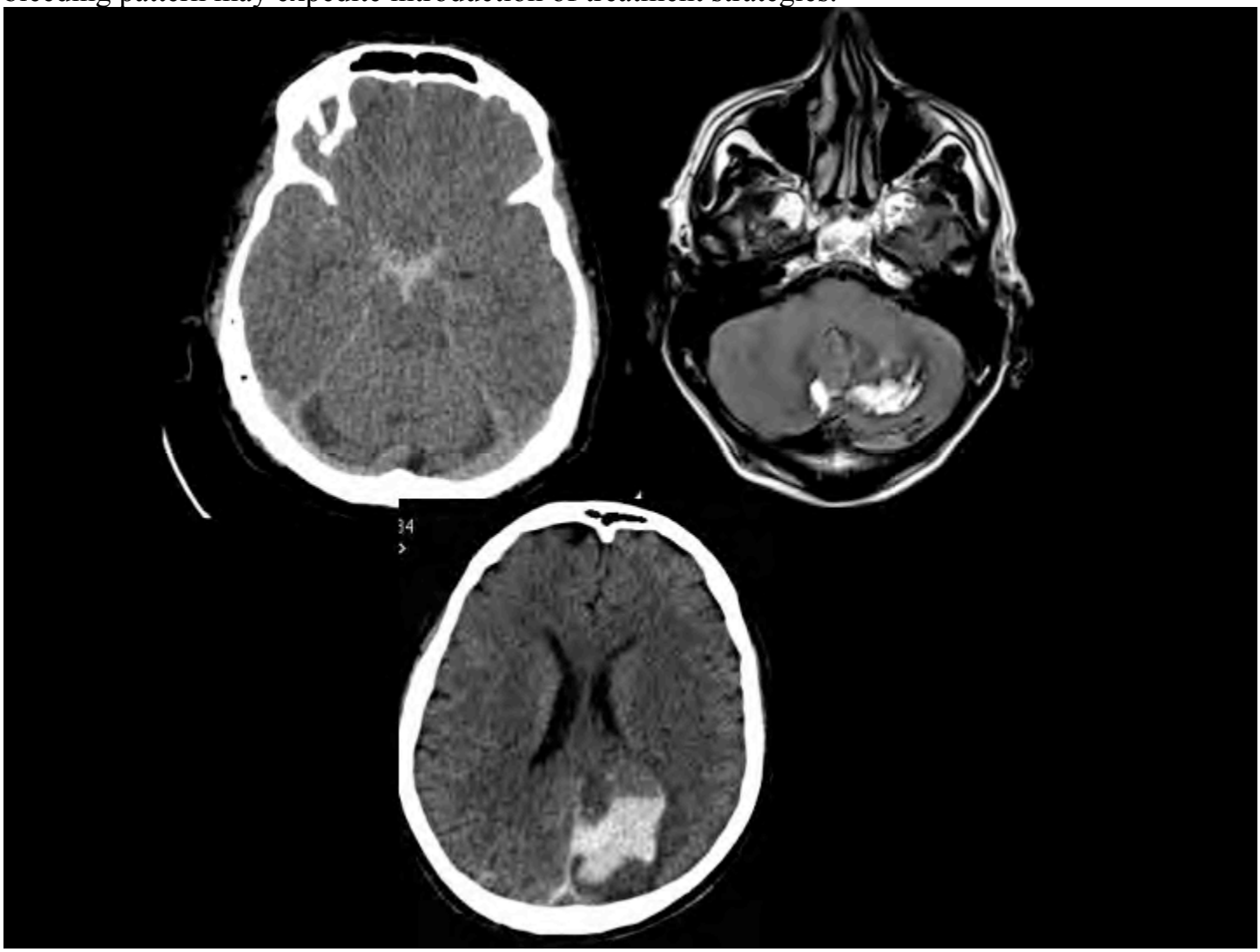
We evaluated the teaching files of our institution, looking for computed tomography (CT) and magnetic resonance imaging (MRI) images of cases of CNS hemorrhage, reviewing their location and specific imaging aspects for each diagnosis.

Results

Among the usual causes of intracranial hemorrhage we demonstrate hypertensive hemorrhage and amyloid angiopathy. Among unusual causes, we demonstrate cases of nonaneurysmal perimesencephalic hemorrhage, remote cerebellar hemorrhage, coagulopathy hemorrhage and subarachnoid hemorrhage associated with posterior reversible encephalopathy syndrome. Each condition is illustrated with CT and/or MRI images, stressing relevant aspects that ensure the diagnosis.

Conclusions

Knowledge of usual and unusual causes of CNS hemorrhage is of paramount importance to both training neuroradiologists and general radiologists, since early recognition of the bleeding pattern may expedite introduction of treatment strategies.



(Filename: TCT_eP-61_SlideASNR.jpg)

eP-14

6:30AM - 3:00PM

Brain Mapping of the Language Network Using Resting State fMRI at Ultrahigh Field Strength (7T) MRI: Comparison to Task-Based fMRI

B Vachha[1], M Hibert[2], B Buchbinder[3], S Stufflebeam[3]
[1]Memorial Sloan Kettering Cancer Center, New York, NY, [2]MGH/HST Martinos Center for Biomedical Imaging, Charlestown, MA, [3]Massachusetts General Hospital, Boston, MA

Purpose
Studies optimizing rsfcMRI for the identification of eloquent cortex have been performed mainly at clinical strength (3T) systems. Recently, ultrahigh field 7T MRI systems have been installed in many clinical centers. Advantages for BOLD fMRI mapping at 7T (increased sensitivity to the BOLD effect, increased functional contrast-to-noise ratio and possibly strengthened measures of rsfcMRI connectivity) co-exist with limitations related to thermal noise, physiological noise, susceptibility-related signal loss, B1 field inhomogeneity, and scanner instability. This study investigates language mapping using rsfcMRI compared to tb-fMRI. Specifically, we compare rfcMRI maps of language networks to tb-fMRI maps of language activation at 7T in healthy subjects.
Materials and Methods
IRB approved study. Six healthy right-handed subjects underwent rsfcMRI and tb-fMRI to localize the language areas at 7T MRI system (Siemens Healthcare, Erlangen, Germany) with a 32-channel head-coil. Resting-state time series (no stimulus, subjects fixated on a cross hair) were obtained using a single-shot gradient echo EPI sequence (TR/TE/flip angle = 5000ms/20ms/90 degrees, 103 measurements). Tb-fMRI was obtained using a verb generation task (TR/TE = 5000ms/20ms, 45 measurements). The spatial correspondence between rsfcMRI and tb-fMRI was assessed.
Results
Overall the language cortex localized based on rsfcMRI matched the regions defined by tb-fMRI, although rsfcMRI showed additional areas of activation such as angular gyrus activation not seen on the tb-fMRI.
Conclusions
This study demonstrates the feasibility of using ultrahigh field strength (7T) MRI to map clinically relevant functional anatomy in healthy subjects using a task-free paradigm. The greatest impact will be for presurgical mapping in patients who cannot tolerate traditional tb-fMRI, such as young children and patients with developmental delay.

eP-73

6:30AM - 3:00PM

Brain White Matter Micro-Structural Changes in Patients with Primary Hyperparathyroidism: Diffusion Tensor Imaging Study Using Tract-Based Spatial Statistics

K Aslan[1], H Gunbey[1], S Cortcu[1], O Ozyurt[2], U Avcı[3], C Polat[4], l incesu[5]
[1]Ondokuz Mayis University Faculty of Medicine Department of Radiology, Samsun, Turkey, [2]Bogazici University, Institute of Biomedical Engineering, İstanbul, Turkey, [3]Ondokuz Mayis University Faculty of Medicine, Department of Endocrinology and Metabolism, Samsun, Turkey, [4]Ondokuz Mayis University Faculty of Medicine, Department of Surgery, Samsun, Turkey, [5]Ondokuz Mayıs University Faculty of Medicine Department of Radiology, Samsun, Turkey

Purpose
Alterations in regional cerebral blood flow in patients with primary hyperparathyroidism (PHP) have been shown. However, PHP microstructural changes in white matter (WM) related with neurological deficits have not been studied so far. The purpose of this study is to assess microstructural changes in WM before parathyroidectomy in patients with PHP by using diffusion tensor imaging (DTI).
Materials and Methods
In this study, we used tract-based spatial statistics (TBSS) DTI analysis to investigate whole-brain WM microstructural changes in 19 PHP patients and 18 age-matched healthy controls.
Results
This study showed significant decrease in FA values in corpus callosum, anterior limb of the internal capsule, external capsule, superior, anterior and posterior corona radiata, posterior thalamic radiation and inferior fronto-occipital fasciculus besides superior and inferior longitudinal fasciculus and cingulum, closely related with default mode network in patients with PHP ($p < 0.05$).
Conclusions
Our study showed decreases in FA values which represent degradation in WM integrity in regions associated with neuropsychiatric symptoms in patients with PHP through TBSS analysis. These results suggested that microstructural changes in WM can give information about the underlying neuropathological process in patients with PHP.

eP-24

6:30AM - 3:00PM

Brainstem Lesions: Meeting the Diagnostic Challenge with Multiparametric MRI

W Muhammad[1], S Jacob[1], G Mattar[2], M Harley[1], V SAWLANI[3]
[1]University Hospitals Birmingham, Birmingham, West Midlands, [2]Queen Elizabeth Hospital, Birmingham, Birmingham, West Midlands, [3]UNIVERSITY HOSPITALS BIRMINGHAM, BIRMINGHAM, United Kingdom

Purpose

Brainstem lesions often can pose a significant diagnostic challenge. Lesions here have a wide differential diagnosis on conventional magnetic resonance imaging (MRI), and biopsy carries a significant risk of morbidity and mortality. Multiparametric MRI can aid in reaching the correct diagnosis and can accurately differentiate between neoplastic, inflammatory or vascular lesions, avoiding the need for invasive biopsy. Very few studies combine information from multiparametric MRI to increase diagnostic confidence and current evidence is confusing and sometimes conflicting. We demonstrate the utility of multiparametric MRI in establishing the diagnosis of brainstem pathology.

Materials and Methods

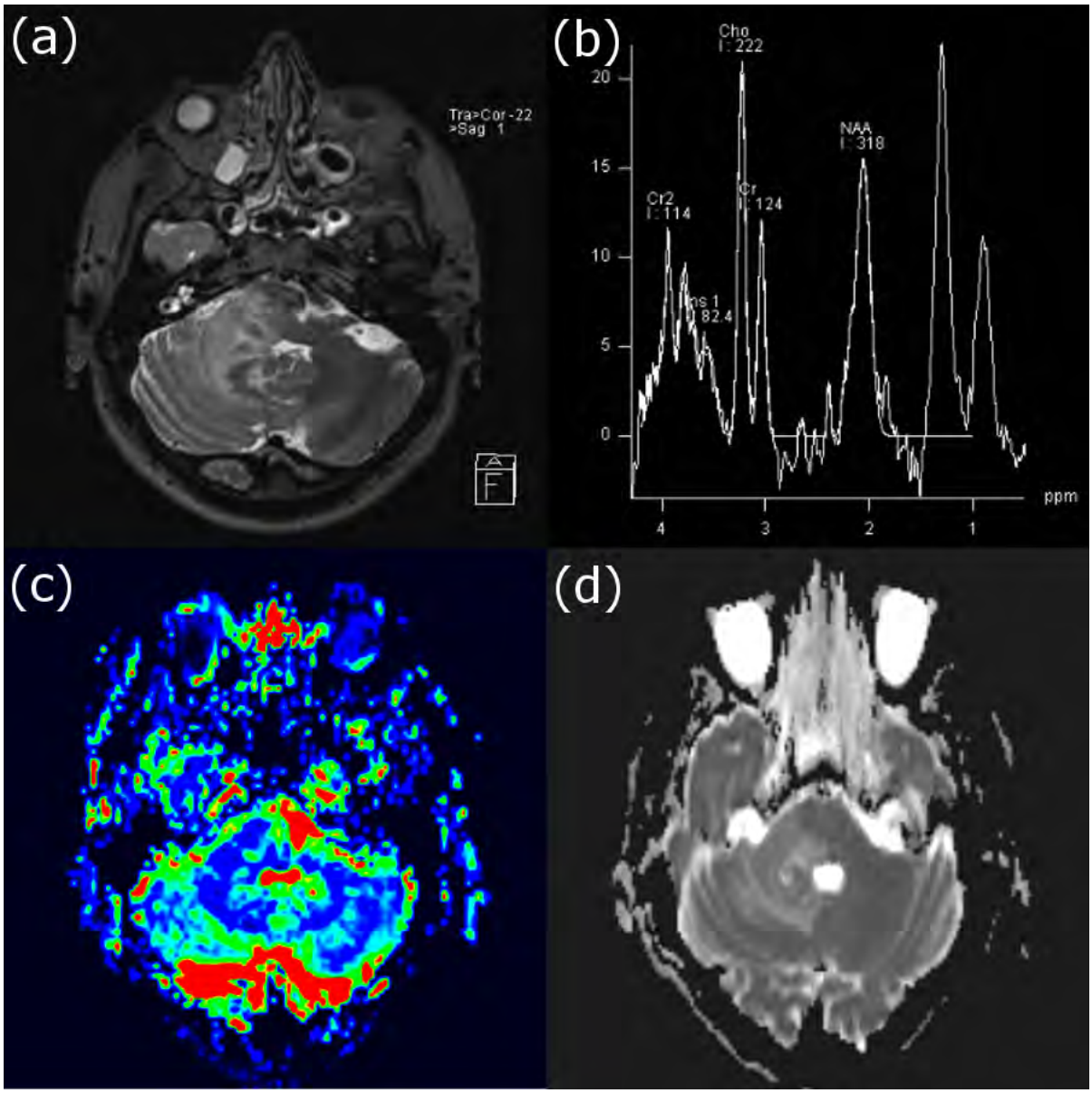
We performed a retrospective review of 4 patients with brainstem lesions who presented between 2015-16 at the Queen Elizabeth Hospital Birmingham, a tertiary neurosciences center. Definitive diagnosis (inflammatory vs. neoplastic) was not established through conventional imaging, and all patients underwent multiparametric MRI prior to definitive diagnosis. Multiparametric MRI examination consisted of T1- and T2-weighted structural imaging, dynamic susceptibility contrast (DSC) perfusion imaging, diffusion-weighted imaging (DWI) and both single- and multi-voxel MR spectroscopy (MRS) (TE = 30 ms). All imaging was acquired on a Siemens Verio 3T MRI scanner. rCBV and ADC maps were analyzed using Siemens syngo.via. Magnetic resonance spectroscopy analysis was performed using Tarquin and peak area ratio of choline to creatine (Cho:Cr) was calculated. Correlations between rCBV ratio, ADC, Cho:Cr and radiological/clinical follow-up were recorded.

Results

In all four patients, multiparametric MRI was successful in predicting diagnosis, which subsequently was confirmed through either biopsy (n=1, Figure 1), specific serological markers (n=1) or evidenced by response to treatment (n=2). Three cases were diagnosed accurately as inflammatory while one case as neoplastic. It was found that a multiparametric approach was more helpful than individual MRI features.

Conclusions

Brainstem lesions are diverse and can present a significant diagnostic challenge. The distinction between an inflammatory or neoplastic etiology is not always possible using conventional MRI. Multiparametric MRI can reduce diagnostic uncertainty in these cases, potentially avoiding the need for invasive biopsy. In cases where tissue diagnosis is essential, multiparametric MRI can be helpful in identifying optimal biopsy target for maximal yield. Clinical and laboratory findings along with careful interpretation of multiparametric MRI findings can aid in establishing an accurate diagnosis.



(Filename: TCT_eP-24_Fig1.jpg)

eP-59

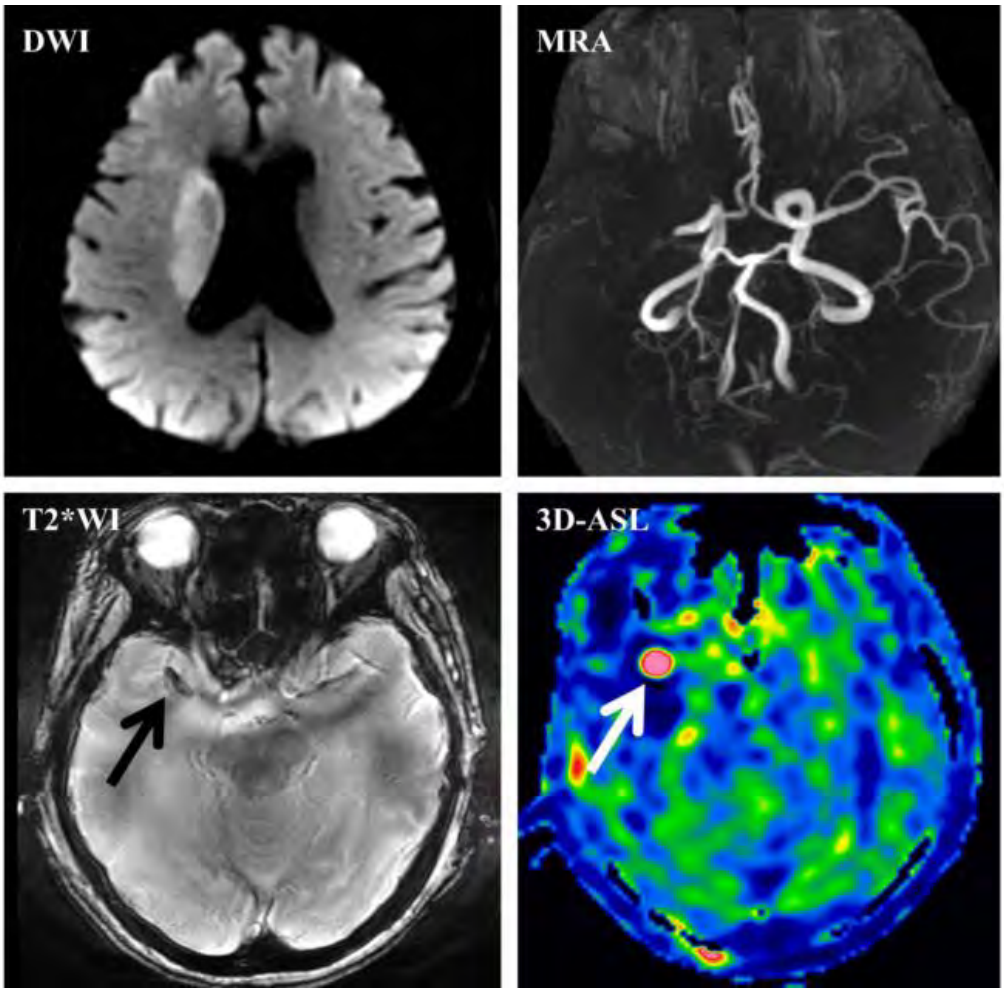
6:30AM - 3:00PM

Bright Vessel Appearance on 3D Pseudo-Continuous Arterial Spin-Labeling Perfusion MR Imaging in the Patients with Acute Cardioembolic Cerebral Infarction

A Kato[1], Y Shinohara[1], K Kuya[1], F Miyoshi[1], M Sakamoto[1], H Kowa[1], T Ogawa[1]
[1]*Tottori University, Faculty of Medicine, Yonago, Tottori*

Purpose
The congestion of spin labeled blood at large vessel occlusion can present as hyperintense

signals on perfusion MR imaging with 3D pseudo-continuous arterial spin labeling (3D ASL), which are called bright vessel appearance (BVA). The purpose of this study was to clarify the difference between BVA and susceptibility vessel sign (SVS) in acute cardioembolic cerebral infarction (CEI).
Materials and Methods
Forty-two patients with CEI in the anterior cerebral artery territory were enrolled in this study. They underwent MR imaging including diffusion-weighted imaging, 3D ASL, T2*-weighted imaging and 3-dimensional time of flight MR angiography by using 3-tesla MR scanner (Discovery MR750w 3T, GE Healthcare). Stroke subtypes were determined according to the Trial of Org 10172 in Acute Stroke Treatment classification. Visual assessments of BVA and SVS were performed by the consensus of the 2 experienced neuroradiologists (A.K. and Y.S.). We also investigated the relationship between the presence of BVA/SVS and the occlusion site of MR angiography.
Results
Twenty-four patients demonstrated BVAs (57.1%) and 25 showed SVSs (59.5%) in 42 patients with CEI. There were 19 BVA/SVS positive and 12 BVA/SVS negative cases. The other 11 mismatched patients had 6 BVA negative/SVS positive and 5 BVA positive/SVS negative cases. Four of 6 BVA negative/SVS positive patients revealed distal MCA occlusion (M2) and 2 of 5 BVA positive/SVS negative patients revealed no occlusion on MR angiography.
Conclusions
Bright vessel appearances are almost compatible with SVSs in the patients with CEI. In the patients with distal MCA embolism, BVAs may be less sensitive to detect occlusive findings than SVSs. Moreover, radiologists should keep in mind the fact that focal intra-arterial high intensity on 3D ASL may not always indicate arterial occlusion as BVAs, but delayed transit time effects.



(Filename: TCT_eP-59_BVA.jpg)

eP-42

6:30AM - 3:00PM

C-11 Methionine PET/CT Versus F-18 FDG PET/CT in Evaluation of Residual or Recurrent Atypical / Anaplastic Meningioma After Treatment

N Tomura[1], T Saginoya[2], H Goto[3]
[1]Southern Tohoku Research Institute for Neuroscience, Southern Tohoku General Hospital, Koriyama, Japan, [2]Southern Tohoku Research Institute for Neuroscience, Southern Tohoku General Hospital, Koriyama, Fukushima, [3]Southern Tohoku Research institute for Neuroscience, Southern Tohoku General Hospital, Koriyama, Fukushima

Purpose
Background: Positron emission tomography-computed tomography using F-18 fluorodeoxyglucose (FDG-PET/CT) has been used to characterize various malignancies, including neoplasms in the brain. Positron emission tomography/CT using C-11 methionine (MET-PET/CT) also has been used to characterize tumors of the brain and to differentiate

between recurrent tumors and radiation necrosis following treatment. Both FDG-PET/CT and MET-PET/CT have not been used to image meningiomas, because most meningiomas are benign. However, meningioma is not always curable. Atypical and anaplastic meningiomas carry a high risk of recurrence. Positron emission tomography/CT might be an effective tool to evaluate residual or recurrent tumors in cases with atypical and anaplastic meningioma after treatment such as surgery and radiotherapy. Purpose: The present study compared MET-PET/CT to FDG-PET/CT in the imaging of residual or recurrent tumors in cases with atypical or anaplastic meningioma.

Materials and Methods

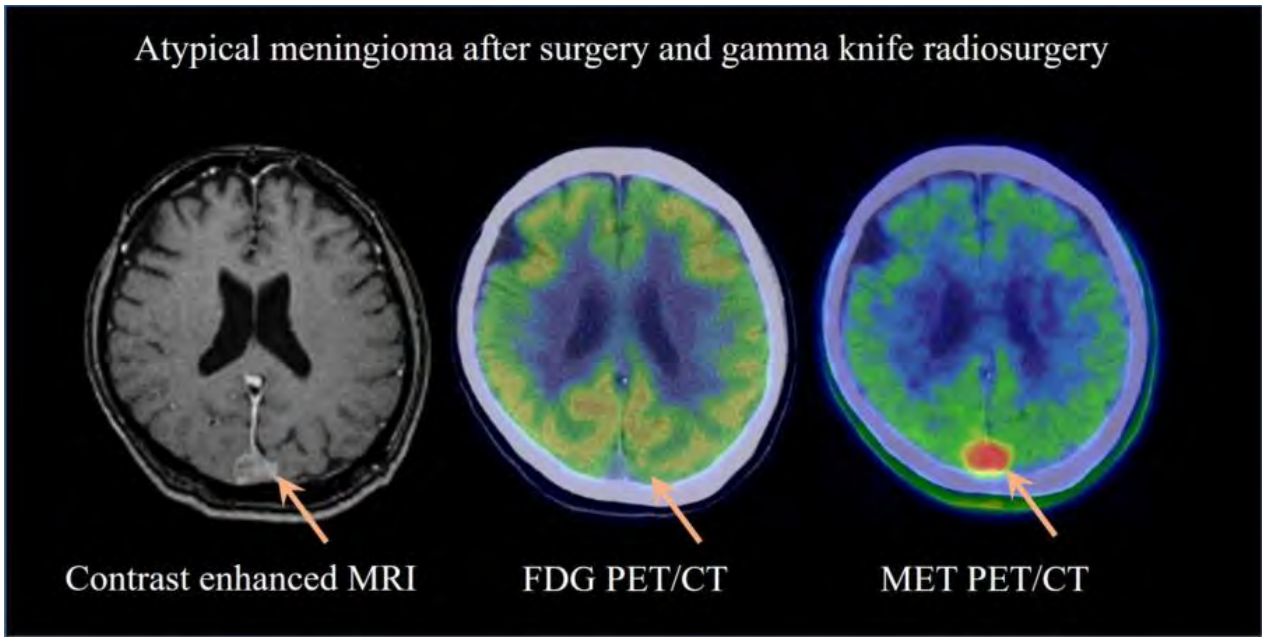
Both MET-PET/CT and FDG-PET/CT were performed in thirteen patients (6 males, 7 females; mean age, 68.8±12.2 years) with histologically proven atypical (n=11) or anaplastic meningioma (n=2). Nineteen tumors (16 atypical, 3 anaplastic) were included. In all cases, pathology was determined by surgery. After surgery, 5 cases received gamma knife radiosurgery, and 1 case received proton therapy. Every patient underwent both FDG-PET/CT and MET-PET/CT on the same day. The protocol of PET/CT was as follows: after CT, MET-PET was performed 20 min after injection of MET. FDG-PET was injected 60 min after MET-PET. Fluorodeoxyglucose-PET was performed 90 min after injection of FDG. Coregistered images were displayed on a workstation. Images were reviewed visually and independently by two reviewers. For qualitative analysis, inter-rater agreement between reviewers was measured. For semiquantitative evaluation, tumor-to-normal brain uptake (T/N) ratios were calculated by dividing the maximum standardized uptake value (SUVmax) for the tumor by the SUVmax of the normal temporal lobe. The difference in T/N ratio between FDG-PET/CT and MET-PET/CT was analyzed for statistical significance.

Results

On qualitative evaluation, inter-rater agreement was better for MET-PET/CT than for FDG-PET/CT. Methionine uptake was interpreted as positive by both reviewers in every tumor. Tumor-to-normal ratio brain uptake was significantly higher for MET-PET/CT (2.81±1.31) than for FDG-PET/CT (0.89±0.42, $p<0.001$).

Conclusions

Methionine PET/CT showed superior inter-rater agreement and had higher uptake for atypical and anaplastic meningiomas than FDG-PET/CT. The present study suggests that MET-PET/CT has superior potential for imaging of atypical and anaplastic meningiomas.



(Filename: TCT_eP-42_ASNRfig.jpg)

eP-09

6:30AM - 3:00PM

Carotid Webs: Innocent Bystanders or Perpetrators of Ischemic Stroke?

P Sajedi[1], J Nunez Gonzalez[1], C de la Houssaye[1], N Kohler[1], O Thompson[1], C Cronin[1], S Kittner[1], D Gandhi[2], P Raghavan[2]
[1]University of Maryland Medical Center, Baltimore, MD, [2]University of Maryland School of Medicine, Baltimore, MD

Purpose
Carotid webs are inherited, intraluminal shelf-like filling defects at the carotid bulb which recently have been theorized to be linked with recurrent ischemic stroke. Given the recently increased awareness of this association, the purpose of our study was to determine the prevalence of this entity in the setting of ischemic stroke and transient ischemic attack (TIA).
Materials and Methods
A retrospective review was performed on consecutive patients who presented to our institution from September 1, 2015 to November 20, 2016 with ischemic stroke or transient ischemic attack (TIA) to assess for presence of a carotid web. Inclusion criteria for included patients 18 years of age and above; documented CT or MR imaging presence of ischemic stroke or clinical exam findings of stroke-like symptoms; as well as presence of CT angiographic (CTA) of the neck during the same admission. A carotid web was defined as an intraluminal shelf-like protrusion arising from the posterior wall of the carotid bulb (Figure 1). Each imaging study was reviewed by a fellowship trained neuroradiologist with over 8 years of experience. The reader was blinded to patient age, sex, and laterality of stroke, if

present. Subsequently, a chart review of patients with positive findings of carotid webs was performed for demographic analysis as well as follow-up management.

Results

Fifteen patients with ischemic stroke demonstrated imaging features consistent with a carotid web. Each of these patients had a web ipsilateral to the side of stroke symptoms. The mean age of the patient population was 42.5 years (range 28-54 years) and mostly comprised of African Americans (86%) (Table 1). Both of these characteristics were comparable to our recent results and those of Choi et al.(2015) and Joux et al.(2014), which showed an average age of patients between 45 and 50 years as well as African American predominance (Joux 2014 and Joux 2016). However, in our study, a greater number of males (n=9, 60%) than females (n=6, 40%) demonstrated webs. These findings are in contrast to our initial review and prior studies which have shown a female preponderance. For example, the carotid web population in our initial review consisted of 86% females (n=7), while a 2014 study by Joux et al. consisted of 64% females (n=25). Thus far, one patient in our current review has undergone carotid endarterectomy, with histopathology demonstrating features of atypical fibromuscular dysplasia (FMD) with superimposed thrombus.

Conclusions

Carotid webs are an under-recognized phenomenon with strong, likely causal association with ischemic stroke. Despite the conventional understanding that these lesions are primarily seen in African American females, our current review shows a much higher rate in the male population than initially thought.

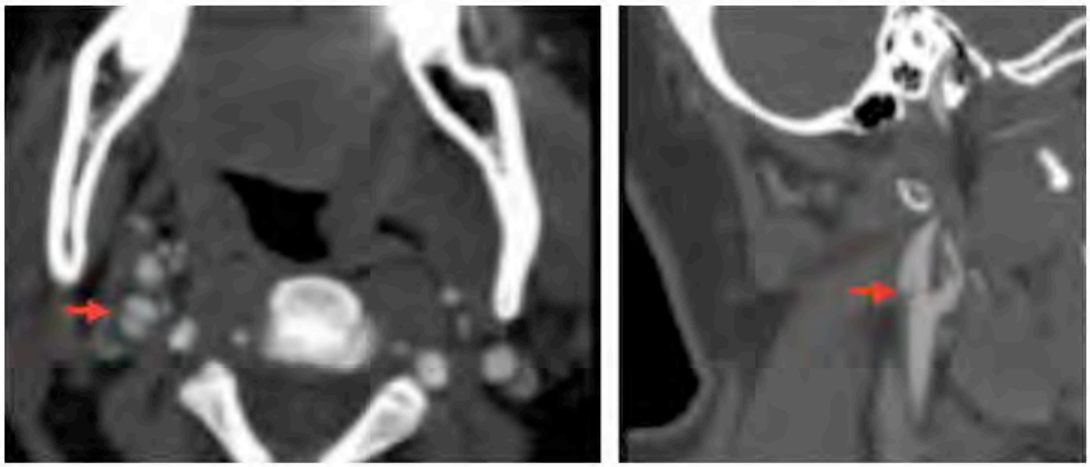


Figure 1: A patient presenting with left-sided weakness and MR imaging compatible with MCA territory infarct. Axial and sagittal CTA neck images (A and B) reveal a shelf-like intraluminal protrusion arising from the posterior wall of the left carotid bulb (red arrows), compatible with a carotid web.

Patient Characteristics (n=15)	
Age (in years), mean +/- SD	42.5, 7.4
Gender	
Male, # (%)	9 (60)
Female, # (%)	6 (40)
Ethnicity	
African American, # (%)	13 (86)
Caucasian, # (%)	1 (7)
Hispanic, # (%)	1 (7)

Table 1. Demographic features of carotid web patients with ischemic stroke

(Filename: TCT_eP-09_WebImage.jpg)

eP-64

6:30AM - 3:00PM

Cervical Epidural Venous Congestion Following Cranioplasty: An Uncommon Postoperative Pitfall Mimicking Hemorrhage

J Hungerford[1], M Antonucci[2], M Spampinato[3], E Duffy[2]

[1]MUSC, Mt Pleasant, SC, [2]MUSC, Charleston, SC, [3]Medical University Of South Carolina, Charleston, SC

Purpose

Overall purpose: Describe an interesting and uncommon postoperative finding to help prepare radiologist for a potential pitfall which could significantly alter patient management.
Introduction: Decompressive craniectomy is a neurosurgical procedure in which part of the skull is removed to relieve elevated intracranial pressure and prevent downward brain herniation in patients with brain swelling (for instance, from trauma, stroke, tumor). This results in vulnerable, uncovered brain parenchyma and a cosmetic deformity. As such, following resolution of the edema, a cranioplasty usually is performed to restore the skull contour. While relatively routine, a cranioplasty is not without risks. Reported complications include hematoma, infection, seizure, herniation, and death. Many patients will undergo a brain computed tomography (CT) following cranioplasty both to assess surgical outcome and to identify any potential early complications. We have identified 3 patients in which a postcranioplasty CT revealed a previously undescribed finding: transient dilatation of the cervical epidural venous plexus. We explore the significance of this finding and underscore the importance of not mistaking it for a new hematoma.

Materials and Methods

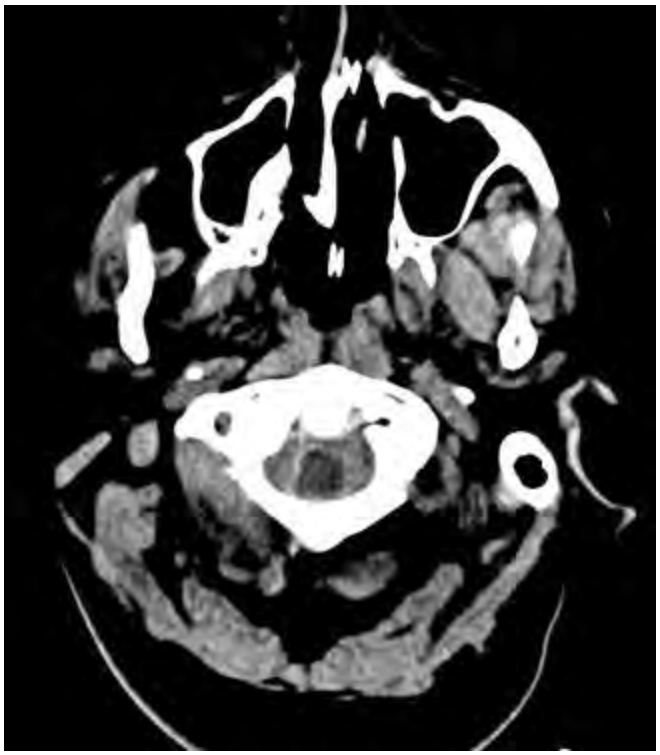
This project is comprised of a retrospective review of the imaging studies and medical charts of 3 patients who demonstrated this unusual postcranioplasty imaging finding.

Results

Three patients who underwent emergent craniectomy and subsequent cranioplasty demonstrated hyperdensity surrounding their upper cervical spinal cord on postoperative brain CT. No referable symptomatology was reported and follow-up imaging demonstrated prompt resolution. Each patient had a constellation of additional findings suggesting impaired cerebrospinal fluid hemodynamics.

Conclusions

Our findings suggest that a small subset of cranioplasty patients develop venous congestion, from altered intracranial fluid dynamics following acute restoration of the confines of the bony calvarium. The sudden change in intracranial volume results in a transient pressure shift and drives a temporary increase in volume draining venous structures. This cervical epidural venous engorgement can be mistaken for a hematoma on CT, but ultimately reflects a rapidly changing physiologic process. Future study is warranted to identify predisposing conditions and the lack of ultimate clinical significance.



(Filename: TCT_eP-64_epiduralvenousplexu2.jpg)

eP-17

6:30AM - 3:00PM

Characterizing the Relationship Between Lesion-Activation Distance Using fMRI and Verbal Measures in Brain Tumor Patients

S Riley[1], V Nair[1], J Kuo[2], M Meyerand[3], V Prabhakaran[4]
[1]University of Wisconsin School of Medicine and Public Health, Madison, WI, [2]University of Wisconsin Department of Neurosurgery, Madison, WI, [3]Department of Medical Physics, University of Wisconsin School of Medicine and Public Health, Madison, WI, [4]University of Wisconsin Department of Radiology, Madison, WI

Purpose
This study focuses on characterizing the relationship between lesion-activation distance (LAD) to Wernicke's and Broca's areas, the primary language centers, and language measures.
Materials and Methods
This study included a sample population of brain tumor patients (age 21-78 years) that received language fMRI [verbal fluency (VF), sentence verification (SV) for pretreatment assessment (n=51)]. The LAD to the nearest language area was measured and divided into those ≤10mm and >10mm. The VF scores, which were adjusted based on age and education level using the FAS COWA scale, were compared between groups. The patients also were

divided into similar groups based on LAD to either Broca's (n=50) or Wernicke's (n=50) areas alone and the VF scores were similarly compared between groups. Patients were similarly divided into groups based on LAD ≤10mm or >10mm to the nearest language area and SV accuracy was compared between groups (n=30).
Results
Brain tumor patients with an LAD ≤10mm to either language center had significantly lower adjusted VF scores than those with LAD >10mm (p=0.028). The percentage of those with LAD ≤10mm to either language area who scored VF scores below one standard deviation compared to patients with LAD >10mm trends toward significance (p=0.091). The difference in VF scores between groups with LAD ≤10mm and >10mm to Wernicke's area alone trends toward significance (p=0.067). The SV accuracy was significantly lower in patients with LAD ≤10mm to either language area (p=0.039).
Conclusions
These findings suggest that there exists a significant relationship between LAD to primary language centers and language measures. Specifically, greater language deficits are seen when LAD is ≤10mm.

eP-20

6:30AM - 3:00PM

Childhood Physical Activity Correlates with Thalamus Volume and Verbal Memory in Healthy Adult Subjects

G Blasco[1], C Biarnes-Duran[2], M Rivero[3], M Puig-Parnau[4], B Roman-Vinas[4], A Prats-Puig[4], J Gich[3], L Ramio-Torrenta[3], S Pedraza[1], J Puig[5]
[1]Imaging Research Unit, IDI-IDIBGI, Hospital Dr Josep Trueta, Girona, None, [2]Research Unit of Diagnostic Imaging Institute (IDI), Girona Biomedical Research Institute (IDIBGI), Girona, Girona, [3]Department of Neurology-IDIBGI, University Hospital Dr JosepTrueta, GIRONA, GIRONA, [4]EUSES University School, University of Girona, Salt, Girona, [5]Research Unit of Diagnostic Imaging Institute (IDI), IDIBGI, University Hospital Dr Josep Trueta, Girona, Girona

Purpose
To study the association between physical activity during childhood and measures of thalamus volume and verbal memory in healthy adults.
Materials and Methods
We studied 24 healthy adults (14 female; age 40.2±11.4 years) with a 1.5T magnetic resonance imaging (MRI) scanner. Imaging included anatomic T1-weighted turbo-field echo sequence with a spatial resolution of 1x1x1 mm. Thalamic volumes were automatically segmented using Freesurfer (Martino Center for Biomedical Imaging, Department of Radiology, Massachusetts). We estimated verbal memory by the long term storage (LTS) subtest of the selective reminding test (SRT) and the Rey auditory verbal learning test

(RAVLT). Physical activity in childhood was assessed with self-reported questionnaires. We analyzed the relation between regular sports practice before 16 years of age with thalamus volume and verbal memory by Spearman correlation followed by multiple regression using the "enter" method.
Results
Regular sports practice before 16 years of age correlated positively with thalamus volumes [left (r=0.672; p=0.002) and right (r=0.646; p=0.003)] and verbal memory [scores from SRT (r=0.502; p=0.024) and false-positive responses on the RAVLT (r=-0.675; p=0.001)]. Moreover, false-positive responses correlated negatively with the volume of the thalamus proper (left: r=-0.543; p=0.013 and right: r=-0.549; p=0.012). The associations between sports practice before 16 years of age with left thalamus volume (β=0.474; p=0.036; R2= 0.469) and false-positive responses on the RAVLT (β=0.381; p=0.013; R2=-0.622) remained significant after correcting for confounding variables such as age, gender, and educational level.
Conclusions
Physical activity during childhood positively affects the volume of the thalamus, a structure involved in motor and cognitive functions as well as in verbal memory in adulthood.

eP-55

6:30AM - 3:00PM

Clinical Information Provided to Radiologists Interpreting Acute Stroke Imaging: How Consistent are Clinicians?

H Fleming[1], S Clifford[1], A Smyth[1], G Healy[1], R Killeen[1]
[1]*St Vincent's University Hospital, Dublin, Ireland*

Purpose
To facilitate a prompt and accurate radiological diagnosis, it is essential that relevant, succinct and standardized clinical information is provided as it is beneficial for the radiologist's interpretation of CT angiographic studies (1, 2). We aimed to assess whether appropriate clinical information was provided to the reporting radiologist in patients presenting with acute stroke who underwent CT angiography for assessment of suitability for mechanical thrombectomy.
Materials and Methods
We retrospectively reviewed all patients who received a CT intracranial and neck angiogram who presented to the ED over a 7-month period with symptoms of acute stroke. We recorded the clinical information provided by the triaging physicians, including the time of symptom onset, side of symptoms and National Institute of Health Score (NIHSS) (3).
Results
Two hundred eight-one CT intracranial and neck angiograms were performed over the 7 month period in patients presenting with acute stroke. The referring clinicians provided the

time of symptom onset in 40% of cases, the side of symptoms in 77% of cases and the NIHSS in 37% of cases.
Conclusions
Referrals for acute stroke imaging rarely provided all three indicators (time of symptom onset, side of symptoms and NIHSS). This lack of relevant request information could hamper speed and accuracy of CT angiogram interpretation in the setting of acute stroke.

eP-41

6:30AM - 3:00PM

Clinical Utility of Arterial Spin Labeling MR Imaging for Cerebellar Hemaniogblastoma: Differentiation from Isolated Cerebellar Metastasis and Postoperative Follow-up

K Kang[1], C Sohn[1], J Kim[1], S Choi[1], T Yun[1], R Yoo[1]
[1]*Seoul National University Hospital, Seoul, Korea, Republic of*

Purpose
To evaluate the clinical utility of arterial spin labeling (ASL) perfusion magnetic resonance (MR) imaging in the differentiation of cerebellar hemangioblastoma from isolated cerebellar metastasis and in the follow up of postoperative patients.
Materials and Methods
This retrospective study included a total of 31 patients with isolated cerebellar tumors including 15 with 52 hemangioblastomas, 13 with 23 metastases, and 16 patients whose hemangioblastoma were removed. For visual analysis, the tumors were graded into 3 categories on CBF map: hypointense, isointense and hyperintense compared with the normal cerebellum. For hyperintense tumors, the size of tumor on the postcontrast T1-weighted image (CET1), the size of the tumor on the cerebral blood flow (CBF) map of ASL MR imaging and absolute CBF were measured at the largest section of them. Normalized tumor blood flow (nTBF) was obtained by normalizing the absolute CBF to the contralateral gray matter. In addition, the size ratio (CBF map to CET1) was calculated. For statistical analysis, linear regression analysis, Mann-Whitney test, and ROC comparison were used.
Results
Thirty-three of fifty-two (62%) hemangioblastomas showed hyperintensity on CBF map and the size of the largest invisible one was 0.5cm. For the cerebellar metastases, 12 of 23 (52%) revealed hyperintensity and the largest invisble one were 4.5cm. None of sixteen whose hemangioblastoma were removed showed hyperintensity. In the hemangioblastoma, there was a significant positive correlation between nCBF and tumor size ($P < .0001$). Hemangioblastoma revealed significantly larger size ratio and nTBF than metastasis ($P < .0001$, $P = .0001$). In the ROC analysis, nTBF and size ratio revealed high sensitivity (69.7% and 81.8 %) and specificity (91.7% and 100%).

Conclusions

Arterial spin labeling perfusion MR imaging can aid in the differentiation of hemangioblastoma from isolated cerebellar tumors and postoperative follow up.

Figure 1. Contrast-enhanced T1WI (A, C) and TBF maps derived from ASL (B, D) in two representative cases. A-B, a residual hemangioblastoma in a 43-year-old man shows hyperintensity on CBF map. C-D, 46-year-old man whose hemangioblastoma was removed shows hypointensity in the tissue defect.

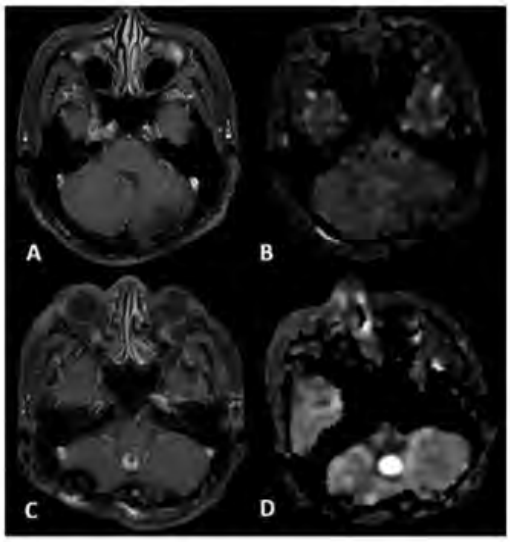


Figure 3. Contrast-enhanced T1WI (A, C) and TBF maps derived from ASL (B, D) in two representative cases. A-B, a cerebellar hemangioblastoma in a 36-year-old woman has high size ratio of 1.92 (1.3cm/2.5cm) and nTBF of 6.16. C-D, a cerebellar metastasis in a 42-year-old woman with breast cancer has relatively low size ratio of 0.71 (1.9 cm/8.5cm) and nTBF of 2.1.

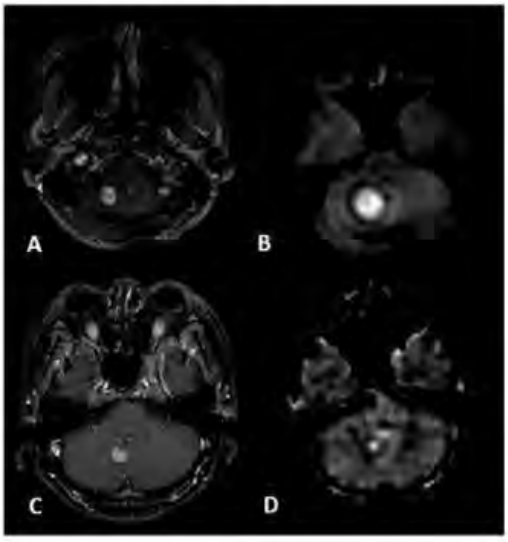


Figure 2. Scatter diagram of the correlations between nTBF and tumor size of post-contrast T1 weighed image. The nTBF and tumor size exhibited a significant positive correlation (Coefficient: 0.431, Standard Error: 0.086, 95% confidence interval: 0.255 to 0.607, $P < .0001$).

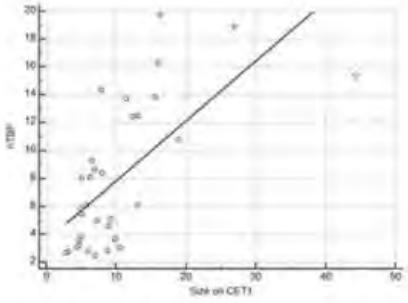


Table 1 . Comparison of nTBF and size ratio between hemangioblastoma and metastasis

	Hemangioblastoma (n=33)	Metastasis (n=12)	*P* - value†
nTBF	6.11 (3.45, 12.44)	2.16 (2.01, 3.39)	.0003
Size ratio	1.29 (1.03, 1.67)	0.73 (0.52, 0.82)	< .0001

† Mann-Whitney U test

Note - Values are median (interquartile range)

(Filename: TCT_eP-41_FiguresandTable.jpg)

eP-08

6:30AM - 3:00PM

Comparative Evaluation of Multi-vendor Semi-automated CT Angiography and Digital Subtraction Angiography for Internal Carotid Artery Stenosis Measurements

J Bai[1], M Comito[1], K Chen[1], L Bangiyev[2], R Peyster[1]

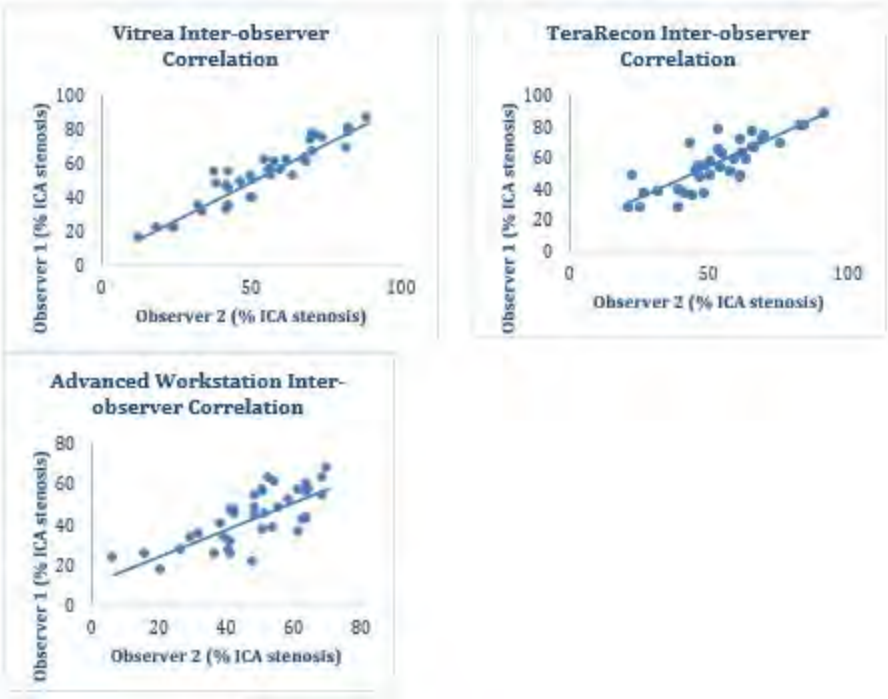
[1]Stony Brook University Hospital, Stony Brook, NY, [2]Stony Brook University Hospital, Stony Brook , NY

Purpose
Assessment of internal carotid artery (ICA) stenosis is essential in guiding the clinician at patient management. However, there have been discrepancies in degree of ICA stenosis measured across vendor-specific semi-automated workstations. The aim of this study is to evaluate potential differences in estimation of the severity of internal carotid artery stenosis using semi-automated technique developed by different vendors on computed tomography angiography (CTA) of the neck and to compare to the gold standard digital subtraction angiography (DSA).
Materials and Methods
Clinically performed CTAs from 30 patients who subsequently underwent DSA were reviewed retrospectively in this IRB approved study. We identified 38 ICAs which demonstrated different degree of stenosis. Two neuroradiologists independently measured the degree of stenosis in a blinded protocol on 3 semi-automated vendor specific workstations in 3 separate sessions: GE Healthcare (Advantage Workstation v7), TeraRecon (v4.4.1.11), and Vital Images (Vitrea Core v6). The vessel analysis software calculates the percentage of ICA stenosis using NASCET methodology. Degree of ICA stenosis on DSA was performed by manually measuring the narrowest diameter of stenosis and distal ICA, and percent of stenosis was calculated using NASCET methodology.
Results
Vitrea demonstrates excellent interobserver correlation with Pearson correlation coefficient of 0.94 ($p<0.01$). TeraRecon and Advantage Workstation demonstrate good inter-observer correlation with Pearson correlation coefficient of 0.83 ($p<0.01$) and 0.75 ($p<0.01$) respectively. Furthermore, Vitrea demonstrates the best correlation with DSA among the 3 workstations ($R=0.74$, $p<0.01$). Two sample paired t test demonstrates no significant difference comparing Vitrea and TeraRecon with DSA. The null hypothesis that no significant difference between measurements on Advantage Workstation and DSA barely holds ($p=0.07$).
Conclusions
The study shows good interobserver correlation and inter-technique correlation with DSA on all 3 semi-automated vessel analysis software in quantifying the degree of ICA stenosis. Out of the three tested workstations Vitrea demonstrates the best correlation with DSA and reproducibility.

Table 1: Interobserver Correlation Coefficient			
	TeraRecon	Vitrea	Advantage Workstation
R	0.83	0.94	0.75
P-value	<0.01	<0.01	<0.01

Table 2: Correlation with DSA		
	Pearson Correlation Coefficient	P-value
TR vs DSA	0.60	<0.01
Vitrea vs DSA	0.74	<0.01
AW vs DSA	0.54	<0.01

Table 3: t-Test: Two-Sample Assuming Unequal Variable			
	TR vs DSA	Vitrea vs DSA	AW vs DSA
P(T<=t) two-tail	0.71	1.67	0.07
t-stat	0.37	-0.02	-1.85
t Critical two-tail	2.00	0.98	2.00



(Filename: TCT_eP-08_Results.JPG)

eP-11

6:30AM - 3:00PM

Comparing Functional and Anatomical Language Networks in Healthy Controls and Glioma Patients: a Combined fMRI and Q-ball Tractography Study

F Sanvito[1], A Castellano[1], K Jordan[2], E Caverzasi[2], G Cerri[3], S Crespi[1], L Altabella[1], M Riva[3], V Ferpozzi[3], L Fornia[3], L Bello[3], R Henry[2], A Falini[1]

[1]*Vita-Salute San Raffaele University, Milan, Italy,* [2]*University of California San Francisco, San Francisco, CA,* [3]*Università degli Studi di Milano, Milan, Italy*

Purpose

This study aimed to identify the subset of anatomical language pathways, depicted by q-ball tractography, underlying specific functional MRI (fMRI) tasks by comparing tractography from fMRI activations (functional tractography, fMRI-T) with the classical anatomical approach (anatomical-T) in healthy controls and glioma patients.

Materials and Methods

3T MR was performed in 16 controls and 19 left-hemisphere glioma patients. The protocol included high angular resolution diffusion imaging (HARDI, 60 directions, b-value=3000 s/mm2) and language fMRI using auditory verb generation, picture naming, and verbal fluency paradigms. On healthy controls, q-ball anatomical-T was performed and overlap between tract terminations and fMRI activations were evaluated. A normalized MNI atlas of functional pathways was obtained by keeping only the fiber subset related to each task-specific activation (Figures 1A and B). On glioma patients, pre-operative q-ball fMRI-T and anatomical-T was performed. Only fMRI-T streamlines representing language pathways were included.

Results

On healthy controls, the atlas showed that functional pathways were a subset of the anatomical network: a considerable part of the network was common to all three fMRI tasks, although some tracts were more task-specific (Figures 1A and B). Preliminary results on glioma patients were consistent with these findings, as fMRI-T was able to identify specific subsets of anatomical-T tracts. Seeding fMRI-T from different tasks enabled representation of different groups of tracts (Figures 1C and D).

Conclusions

Functional MRI-T may be useful to depict language pathways as an alternative to the classical anatomical-T approach. An accurate selection of the appropriate fMRI task is advocated to highlight specific parts of the network. Preliminary fMRI-T results on glioma patients will be validated with intraoperative direct electrical cortico-subcortical stimulation data and functional resection margins on postoperative MRI to assess the robustness and accuracy of this method in depicting the eloquent subsets of language pathways and its sensitivity with respect to the classical anatomical approach.

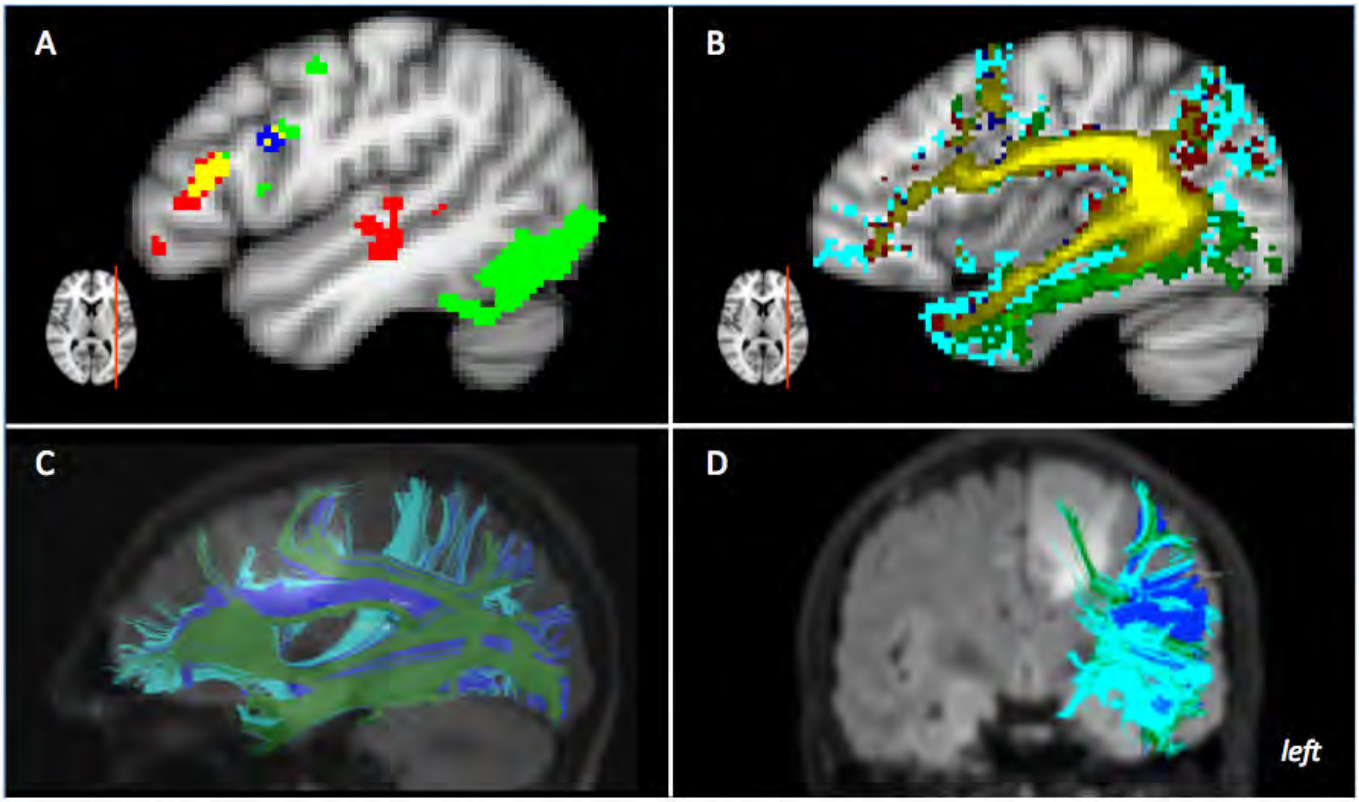


Figure 1. (A) Grey matter fMRI activations from 16 healthy controls: picture naming in green, fluency in blue, auditory verb generation (AVG) in red. Areas activated during two or three tasks are displayed in yellow. (B) White matter functional atlas from 16 healthy controls. A considerable subset of the network is common to two or three tasks (yellow), inferior longitudinal fasciculus (ILF) and other ventral branches are exclusively related to the picture naming task (green), subsets of the parietal and dorsal branches support exclusively the fluency (blue) and the AVG task (red). Other streamlines belong solely to the anatomical pathway (light blue) and are not related to fMRI activations. (C, D) Anatomical-T (light blue), fMRI-T from picture naming task (green), fMRI-T from fluency task (blue) performed on a patient. FLAIR MRI were registered to the diffusion space in order to illustrate the relationships with the tumor. Consistently with results on healthy controls, the functional pathway is a subset of the anatomical pathway, and different tasks can depict different subsets of the tracts.

(Filename: TCT_eP-11_Fig1.jpg)

eP-51

6:30AM - 3:00PM

Computer-aided Detection of Hyperacute Stroke Using Custom Color-lookup Tables and Adobe Photoshop

H Chengazi[1], Z Nuffer[1], S Bhatt[1], J Brucker[1]
[1]*University of Rochester Medical Center, Rochester, NY*

Purpose
Findings of hyperacute stroke on noncontrast head CT (NCCT), such as loss of gray matter-white matter differentiation, can be subtle, and often are not appreciated while the patient is still a candidate for thrombolytic therapy. For this reason, we developed a computer-aided detection (CAD) technique to increase sensitivity of NCCT for hyperacute stroke, which may inform clinical decision making in equivocal cases of stroke, and may aid in calculating Alberta stroke program early CT scores (ASPECTS).
Materials and Methods
This was a retrospective study of 10 adults diagnosed with acute stroke both clinically and radiographically, with MRI. Each patient had an initial NCCT that was reported to be without acute abnormality; however, in each case, this initial NCCT was retrospectively found to have areas of decreased gray-white differentiation which corresponded to areas of restricted diffusion on brain MRI. The first ten patients meeting these criteria identified during the routine clinical workflow in the Neuroradiology section were selected. A custom color-lookup table (CLUT) was applied to the DICOM images using OsiriX, such that conspicuity of the gray-white interface was enhanced, allowing for better appreciation of changes in gray-white differentiation. Adobe Photoshop then was used to divide the brain parenchyma into 4 quadrants and to compare the pixel intensity values between the quadrants via histogram analysis to evaluate gray-white symmetry.
Results
Our process correctly identified each of 4 cases of middle cerebral artery territory infarct and the 1 case of posterior cerebral artery territory infarct, but could not identify the 1 case of anterior cerebral artery territory infarct or 4 cases with small multifocal infarcts.
Conclusions
A CAD tool using a custom CLUT and pixel intensity analysis would be useful to increase interpreter accuracy for MCA and PCA stroke.

eP-71

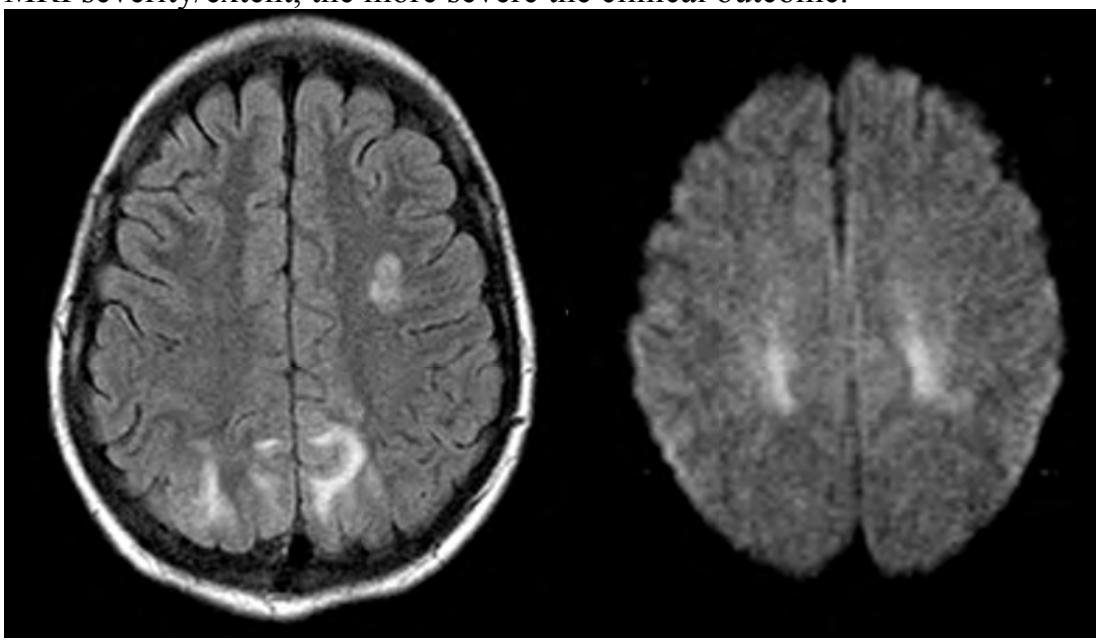
6:30AM - 3:00PM

Concomitant Acute Toxic Leukoencephalopathy and Posterior Reversible Encephalopathy Syndrome

C Ozutemiz[1], S Khanipour Roshan[1], J Rykken[1], F Ott[1], A McKinney[1]
[1]*University of Minnesota, Minneapolis, MN*

Purpose
Although their MRI findings differ, both acute toxic leukoencephalopathy (ATL) and posterior reversible encephalopathy syndrome (PRES) may occasionally simultaneously occur on MRI in acutely encephalopathic patients. Our aim is to describe a series of such patients with MRI findings, and their underlying etiologies or common risk factors.

Materials and Methods
The PACS and radiology information systems were searched for patients with either "acute toxic leukoencephalopathy" (ATL) or "posterior reversible encephalopathy syndrome" (PRES), which yielded 97 adults with PRES and 81 adults with ATL. Of these two groups, five patients were identified with simultaneous imaging features of both PRES and ATL. The MRI severity and clinical outcomes were then scored based on previously described systems.
Results
The mean age was 45; there were 1 male and 4 females. The etiologies/risk factors for developing combined ATL-PRES were: hypertension (n=2) and immunosuppressive and/or chemotherapy medication (n=3). Mean max systolic and diastolic blood pressures were 159 and 97. MRI severity scoring for the ATL and PRES severity score was 1 for four of the patients and in one patient MRI severity score of PRES was 3 and ATL severity score was 2. Regarding clinical outcomes, the severity ranged from 0 to 4 (mean=1.4). The patient with the worst outcome score of 4, demonstrated PRES and ATL scores of 3 and 2 respectively. The rest of the patient's clinical outcome score was either 0 or 1.
Conclusions
This preliminary series describes that ATL and PRES may occur in conjunction with each other in patients with varying risk factors and medications. Regarding outcomes, the preliminary finding in this small study population seems to be that the greater the degree of MRI severity/extent, the more severe the clinical outcome.



(Filename: TCT_eP-71_Fig115y-oM15T.jpg)

eP-10

6:30AM - 3:00PM

Coronary Artery Calcium Score Correlation with Quantity of White Matter Lesions on MRI

S Dissanayake[1], J Acharya[1], A Rajamohan[1], M Sondag[1], C Liu[1]
[1]*University of Southern California, Los Angeles, CA*

Purpose

Coronary artery calcium score predicts hemodynamically significant coronary artery stenosis and is used for myocardial infarction risk stratification (1). Similarly, white matter lesions are associated with increased risk of cerebrovascular accident (2). Previous studies have demonstrated an association between coronary artery calcium volume and volume of white matter lesions in older patients and families with early-onset coronary artery disease (3, 4). We provide an investigation into the correlation between both coronary artery calcium volumes and Agatson scores and quantity of white matter lesions on magnetic resonance imaging (MRI) in patients of all ages who underwent calcium scoring for myocardial infarction risk stratification.

Materials and Methods

Fifteen noncontrast coronary CT studies were performed on 64- or 256-slice CT and evaluated using Vital Vitrea software to semi-automatically quantify coronary artery calcium and Agatson scores with standard calcium threshold of 130 HU for myocardial risk stratification (average at 54.6 years +/- 10.9 years, 8 female). The measurements were performed by a board-certified radiologist with fellowship training in cardiothoracic Imaging. Brain MRIs performed for these patients within a 2-year time interval from the coronary CT study were evaluated for extent of white matter disease. Both Fazeka score and the quantity of discrete T2 hyperintensities were measured by a neuroradiologist. Spearman correlations were used to test relationships between coronary calcium volumes and Agatson scores, Fazeka score (5), and quantity of T2 hyperintense lesions.

Results

Seven of 15 patients (46.7%) had a nonzero calcium score. Mean calcium volume was 315.3 mm3 and mean Agatson score was 402.9. Mean Fazeka periventricular white matter score was 1.2 and Fazeka deep white matter score was 1.1. Fourteen patients (93.3%) had at least 1 white matter lesion. A significant correlation was found between coronary calcium volume ($r = 0.56$, $p < 0.05$) and Agatson score ($r = 0.54$, $p < 0.05$) and quantity of white matter lesions. A significant correlation was not found between coronary calcium volume ($r = 0.5$, $p = 0.05$ and $r = 0.5$, $p = 0.05$) and Agatson score ($r=0.5$, $p = 0.07$ and $r = 0.05$, $p = 0.06$) and Fazeka deep and periventricular white matter scores, respectively. Three patients (20%) had a severe coronary calcium score (Agatson score >300) and the average number of white matter lesions for these patients was 82.

Conclusions

Coronary artery calcium volume and Agatson scores are a significant predictor for quantity of white matter lesions on MRI. Given the correlation between white matter lesions and risk

of cerebrovascular accident, coronary artery calcium score may predict risk of both myocardial infarction and cerebrovascular accident.

eP-04

6:30AM - 3:00PM

Correlating Neuroimaging Findings with Clinic Scoring Inventories in Patients with Amyotrophic Lateral Sclerosis

M Kiczek[1], S Jones[1], J Bullen[1], E Pioroe[2]
[1]Cleveland Clinic, Cleveland, OH, [2]Cleveland Clinic, Cleveland , OH

Purpose
A role for magnetic resonance imaging (MRI) in the diagnosis of amyotrophic lateral sclerosis (ALS) has been sought after in the literature. It has been shown that abnormal signal intensity can be seen along the corticospinal tracts (CST) in patients with ALS on proton density (PD) and T2 sequences (1). Imaging findings have been hypothesized to correlate with clinical symptoms related to upper motor neuron degeneration (2). A few studies also have sought to correlate T2 hypointensity along the precentral gyrus with the diagnosis of ALS. It is postulated that iron deposition may contribute to this finding and play a role in neurodegeneration (3). The purpose of this study is to correlate the extent of CST and precentral gyrus imaging findings with the El Escorial and ALS functional rating system (ALSFRS) clinical inventory scores as well as presence of bulbar, upper or lower motor neuron onset. The goal is to explore the utility of MRI as a clinical tool in the diagnosis and monitoring of ALS patients.
Materials and Methods
The study included a total of 94 patients (56 male and 38 female) with ALS and MR examinations performed at or around the time of diagnosis. All MRI images were reviewed on a standard IMPAX workstation, with scoring of CST signal abnormalities, and any hypointensity along the precentral gyrus on both T2 and PD sequences. The presence of CST hyperintensity was evaluated at 6 standardized anatomic locations (pons, cerebral peduncles, internal capsule, centrum semiovale, corona radiate and motor cortex). Signal findings were recorded on a 3-point scale as 0 (not present), 1 (equivocal), or 2 (present). Complete El Escorial and ALSFRS inventories were obtained for each patient. The correlation between these clinical inventories and the MRI variables was characterized using Spearman's rank correlation coefficient. For each correlation, the null hypothesis that Spearman's rho was equal to zero was evaluated. A significance level of 0.05 was used for each test. A 95% confidence interval for the correlation coefficient also was computed, using the percentile bootstrap method (with 10,000 bootstrap replicates).
Results
Patient diagnoses for ALS using the El Escorial inventory were distributed as follows: 41% (n=39) were 'possible', 6% (n=6) 'suspected', 9% (n=8) 'probable with lab support', 24%

(n=23) 'clinically probable', and 19% (n=18) 'clinically definite'. Of the 94 patients, 22% (n=21) had bulbar onset, 37% (n=35) had upper extremity onset, and 47% (n=44) had lower extremity onset. The ALSFRS total was known for 23 patients in the sample. The mean score was 33 (range: 24-39). The El Escorial variable was significantly correlated with four MRI variables; and the total ALSFRS was significantly correlated with three MRI variables (Table 1). Figures 1 and 2 show the rank correlation coefficients and 95% confidence intervals. There was no statistically significant correlation between any of the MRI variables and the location of onset (Table 2). The presence of signal hypointensity in the precentral gyrus did not correlate with any clinical inventories (Table 1).

Conclusions

T2 and PD hyperintensity along segments of the CST (pons, cerebral peduncles, internal capsule and centrum semiovale) correlated with higher El Escorial and ALSFRS scores in patients with ALS. These findings represent a step towards a standardized imaging scoring system that can aid the diagnosis and monitoring of disease progression. There was no significant correlation with location of onset (bulbar, upper or lower motor neuron), but the sample size may be underpowered and benefit from further investigation.

Figure 1 – Correlation between the Escorial variable and various MRI variables. The points are the rank correlation coefficient estimates and the lines are the associated 95% confidence intervals. The CIs for the correlation coefficients that were statistically significantly different from zero are drawn in red.

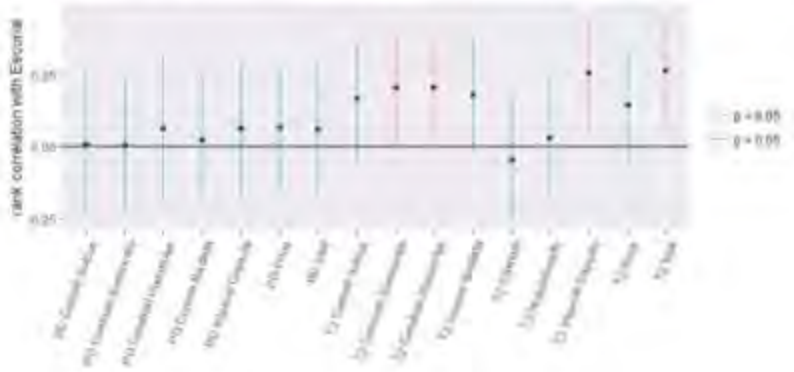


Figure 2 – Correlation between ALSFRS (total) and various MRI variables. The points are the rank correlation coefficient estimates and the lines are the associated 95% confidence intervals. The CIs for the correlation coefficients that were statistically significantly different from zero are drawn in red.

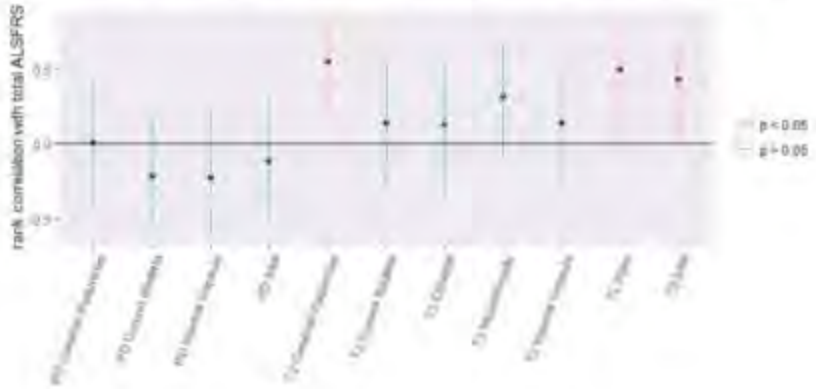


Table 1 – Estimates of Spearman's rank correlation coefficient between various MRI variables and two clinical variables (Escorial and ALSFRS total). Some estimates could not be calculated because there was not enough information (indicated with a dash in the table). Statistically significant correlations are bolded and have an asterisk next to the p-value.

[Note: In the analyses with a dash, there were fewer than three patients marked as abnormal with respect to the MRI variable in question. A correlation coefficient could not be calculated when all but one or two patients were considered normal.]

	Correlation with Escorial			Correlation with ALSFRS total		
MRI variable	n	Estimate	p-val	n	Estimate	p-val
PD Pons	84	0.07	0.554	22	-	-
PD Cerebral Peduncles	84	0.06	0.558	22	0.01	0.963
PD Internal Capsule	84	0.06	0.563	22	-0.23	0.312
PD Corona Radiata	84	0.02	0.833	22	-0.22	0.329
PD Centrum Semiovale	84	0.01	0.959	22	-	-
PD Central Sulcus	84	0.01	0.929	22	-	-
PD total	84	0.06	0.577	22	-0.11	0.614
PD Hypointensity	84	-	-	22	-	-
T2 Pons	93	0.14	0.168	**22**	**0.50**	**0.018***
T2 Cerebral Peduncles	**93**	**0.21**	**0.047***	**22**	**0.55**	**0.007***
T2 Internal Capsule	**93**	**0.26**	**0.013***	22	0.14	0.537
T2 Corona Radiata	93	0.18	0.082	22	0.14	0.523
T2 Centrum Semiovale	**93**	**0.20**	**0.049***	22	-	-
T2 Central Sulcus	93	0.17	0.104	22	-	-
T2 Hypointensity	93	0.03	0.766	22	0.32	0.152
T2 total	**93**	**0.26**	**0.010***	**22**	**0.43**	**0.043***

(Filename: TCT_eP-04_TableandFigures.jpg)

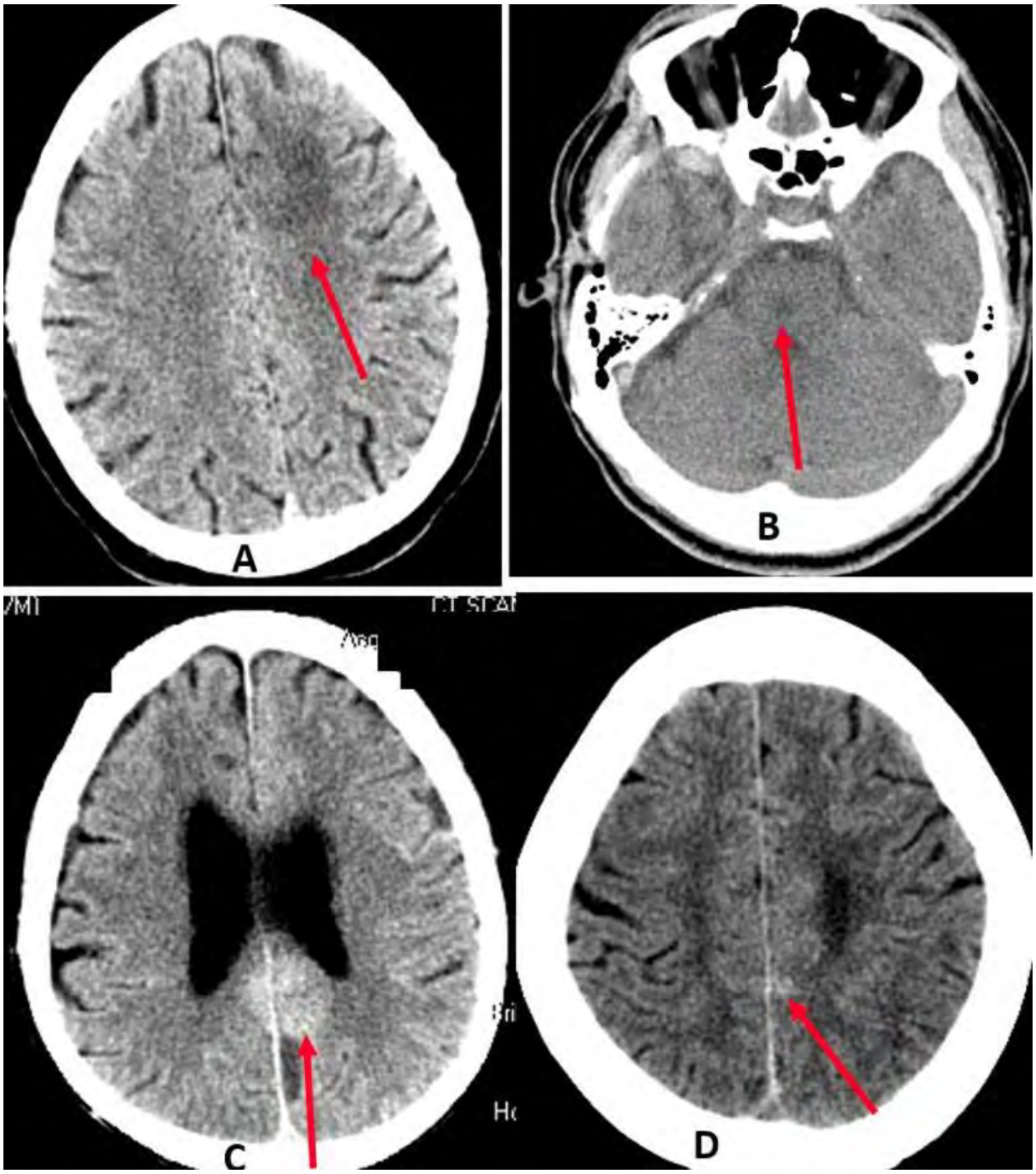
eP-53

6:30AM - 3:00PM

CT Artifacts Mimicking True Intracranial Lesions

M TENG[1]
[1]*Cheng Hsin General Hospital, Taipei, Taiwan*

Purpose
To report different artifacts encountered on cerebral CT images that mimics a true lesion.
Materials and Methods
Different types of CT artifacts were encountered in cerebral CT images. These suspected lesions were proved to be artifacts because of the following reasons: 1. The suspected lesion disappeared on a repeat study using different CT scanner, 2. A phantom study confirmed same kind of artifact, 3. Disappearance of the suspected lesion on a repeat study after calibration or change of parts in the same CT scanner, 4. The suspected lesion disappeared on a repeat study on the same CT scanner using a different mode (sequential mode or spiral mode). Some of these artifacts were discovered because these patients received CT scan examination at the same time period using the same examination mode on the same CT scanner.
Results
Many of these artifacts were reported as a true lesion in the radiological CT reports because some radiologists were not aware of these artifacts. Artifacts mimic different kinds of true lesions, such as low grade glioma or infarct (Figure A), lacunar infarct (Figure B), meningioma (Figure C), subarachnoid hemorrhage or TB (Figure D), metastasis, hemorrhagic infarct will be presented in this report.
Conclusions
Understanding different kinds of CT artifacts is important for making a correct diagnosis and providing neuroradiology service of good quality.



(Filename: TCT_eP-53_Fig.jpg)

eP-19

6:30AM - 3:00PM

Discovery of Concussion Biomarkers using fNCI

B Tucker[1], T Burnham[2], A Fong[2], M Allen[2], E McIff[3]

[1]Case Western Reserve University School of Medicine, Cleveland, OH, [2]Cognitive FX, Provo, UT, [3]COGNITIVE FX, Provo, UT

Purpose

Advanced clinical functional brain imaging requires diagnostic predictive power; i.e., the ability to identify specific abnormal patterns of activation which reliably correlate with a particular pathology, such as postconcussion syndrome (PCS), and show sensitivity to changes over time in an individual (e.g., with treatment) (1). We demonstrate here PCS "neuromarkers" that have been validated on large samples of concussion patients and healthy controls. Having also shown sensitivity with change via treatment as well as spontaneous recovery, these neuromarkers provide the basis for a computation of a PCS severity as expressed in neural activation disruption, which we refer to as the Severity Index Score (SIS). The SIS has proven highly useful in making pretreatment decisions, monitoring treatment efficiency, and assessing long-term stability of outcomes.

Materials and Methods

Sixty-nine patients underwent functional NeuroCognitive imaging (fNCI), using a 6-exam task battery measuring BOLD signal changes in fifty-seven pre-identified brain regions relevant to PCS. The results from each test were analyzed by a qualified neuroanatomist using individual anatomical boundaries. Results were compared to a reference atlas norm to generate neuromarker values and SIS. Additional sets of seventy and one hundred and twenty concussed patients confirmed reliability of the initial discovery group. Sixty-two healthy control subjects and twenty-seven nonconcussion patients also were assessed to provide diagnostic and differential values.

Results

Three successive cohorts of concussion patients revealed 5 reliable neuromarkers, consisting of statistically independent patterns of hyper-/hypo-activation. The 5 identified neuromarkers with true and false positive rates are provided in Table 1.

Conclusions

The use of fNCI in the assessment of fifty-seven functional brain regions has generated reliable neuromarkers that aid in the assessment of concussion. Discovery of these 5 neuromarkers support the utility of fMRI in localization and quantification of concussion pathology, providing a guide to develop individualized therapy for patients.

Neuromarker	True Positive Rate	False Positive Rate
1 Medial Prefrontal Dysregulation	88%	0%
2 Subcortical Hypoactivation	88%	0%
3 Visual Hyperactivation	79%	0%
4 Verbal Hypoactivation	65%	4%
5 Frontal/ Parietal Hyperactivation	41%	2%

(Filename: TCT_eP-19_Table1-Results.jpg)

eP-38

6:30AM - 3:00PM

DKI of the Subventricular Zone in Glioblastoma

A Chatterjee[1], C Swift[1], S Creeden[1], G Bolles[1]
[1]*Medical University of South Carolina, Charleston, SC*

Purpose
There is increasing evidence that glial cells lining the lateral ventricles in the subventricular zone (SVZ) play a role in gliomagenesis, as gliomas often occur in close proximity to the ventricular system and the SVZ. Diffusion kurtosis imaging (DKI) is an MRI technique that provides a clinically feasible extension of diffusion tensor imaging (DTI) that recapitulates DTI metrics including axial diffusivity, radial diffusivity, and fractional anisotropy (FA). Diffusion kurtosis imaging also allows for calculation of the dimensionless metric quantifying non-Gaussian diffusion, termed diffusional kurtosis (K).
Materials and Methods
Magnetic resonance imaging (MRI) was acquired with clinical DKI sequences on twenty control subjects and ten glioblastoma (GBM) patients. Using established tools developed in Matlab (Mathworks, Natick, Massachusetts), regions of interest (ROIs) including the cerebral hemispheres, genu of the corpus callosum, splenium of the corpus callosum, and SVZ were verified by a neuroradiologist. Diffusion tensor imaging and DKI metrics including FA and K were calculated using Matlab tools for each ROI.
Results
Kurtosis metrics in controls showed no statistically significant difference between hemispheres ($p=0.464$). Glioblastoma patients demonstrated a statistically significant lower mean K on the affected-side SVZ than the unaffected side ($p=0.0312$).
Conclusions
While the small size of the SVZ and relatively low resolution of DKI limits robust interpretation of the results, these findings suggest that early changes of gliomagenesis may be detected as early changes in K in the SVZ. Further prospective studies could help determine if SVZ K value changes precede clinical or current imaging detection of gliomagensis to allow for earlier detection.

eP-21

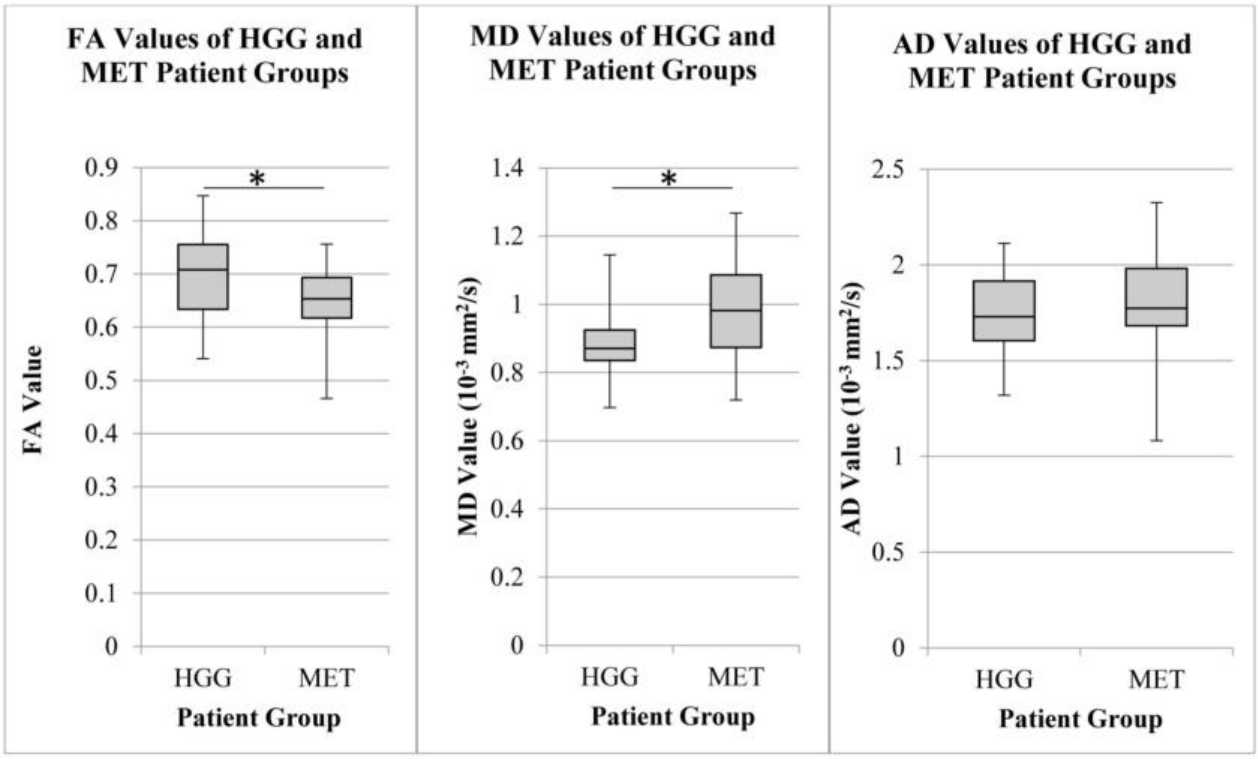
6:30AM - 3:00PM

DTI Characteristics of the Corpus Callosum of Patients with a Brain Tumor: A Comparison Between High-Grade Gliomas and Metastases

N Cho[1], M Jenabi[1], J Arevalo-Perez[1], N Brennan[1], R Young[1], S Karimi[1], A Holodny[2], K Peck[1]
[1]Memorial Sloan-Kettering Cancer Center, New York, NY, [2]Memorial Sloan-Kettering Cancer Center, Weill Medical College Of Cornell Univ., New York, NY

Purpose
We studied the corpus callosum (CC) microstructure in high-grade gliomas and metastases patients through diffusion tensor imaging (DTI) parameters since higher fractional anisotropy (FA) values have suggested more contralateral brain reorganization (1). We hypothesized that DTI would indicate more contralateral brain reorganization in high-grade glioma patients. We also studied if tumor or CC volume had correlations with the DTI parameters.
Materials and Methods
We studied fifty subjects with the following inclusion criteria: 1) diagnosed with a high-grade glioma (n=30) or metastases (n=20); 2) tumor not infiltrating the CC and; 3) tumor located in a region thought to be served by the body CC. For DTI analysis, a neuroradiologist delineated the body CC region of interest (ROI), which included the entire region between the genu and splenium. The ROI then was overlaid onto the FA, mean diffusivity (MD), and axial diffusivity (AD) maps, and the values were averaged per entire ROI. For volume analysis, the ROIs of the tumor, body CC, and entire CC were segmented on 3D T1-weighted scans, and the voxel count was used to calculate volume. We conducted a one-tailed Wilcoxon Rank-Sum test for differences in DTI parameters between the patient groups and a Pearson Correlation test for correlations between the structure volumes and DTI parameters.
Results
There was a significant difference in the DTI parameters of FA [high-grade glioma mean FA=0.691/metastases mean FA=0.646; $p<0.03$)] and MD [(high-grade glioma mean MD=0.894x10^-3(mm^2)(s^-1)]/metastases mean MD=0.992x10^-3(mm^2)(s^-1); $p<0.01$) (Figure 1). There was no statistically significant difference for AD ($p>0.75$) nor correlation for any of the structure volumes with the DTI parameters ($p>0.4$).
Conclusions
Our results suggest that there are structural differences in the body CC due to tumor pathology rather than tumor volume. This suggests that there is more brain plasticity through contralateral brain reorganization within patients with high-grade gliomas than those with metastases.

Figure 1. Box-and-Whisker Plots of FA, MD, and AD Values of Patient Groups



(Filename: TCT_eP-21_CorpusCallosumFigurewithSignificance.jpg)

eP-74

6:30AM - 3:00PM

DVA with and without Associated Cavernous Malformations Show Different Perfusion Patterns.

R Camacaro[1], C Vallejo[1], P Puac[1], A Rodriguez[1], M Castillo[1]
[1]*University of North Carolina at Chapel Hill, Chapel Hill, NC*

Purpose
Developmental venous anomalies (DVA) are the most common intracranial vascular anomaly with a reported incidence of 2.6%. Studies indicate the possible role of DVA in the formation of cavernous malformations (CM). Our aim was to study the MRI post contrast perfusion imaging (PI) findings in DVA without and with CM.
Materials and Methods
In this retrospective study, PI was performed in 30 patients with DVA who were divided in 2

groups: DVA without CM (15) and DVA with CM (15). We calculated rCBV, rCBF and MTT in the brain parenchyma around the DVA excluding the collector veins and compared these parameters with the normal corresponding contralateral side. Perfusion values of peri-DVA tissues were tested for difference between groups with t test. We also reviewed all electronic medical records for any symptoms that could have been associated with all DVA.

Results

When comparing both groups, DVA with CM showed increased rCBV, rCVF and MTT (2.93 vs 1.72, 2.07 vs 1.56, 1.35 vs 1.22) with significant differences only for the rCVB ($p < 0.05$). No associated symptoms were present in any patient.

Conclusions

PI detected significantly increased blood volume in DVA with associated CM. The significance of these findings is uncertain but probably indicates that these dual anomalies are different biologically and hemodynamically from single DVA. Clinically, however, isolated or dual anomalies were silent. Long term follow up of DVA with CM is needed to better determine their clinical behavior.

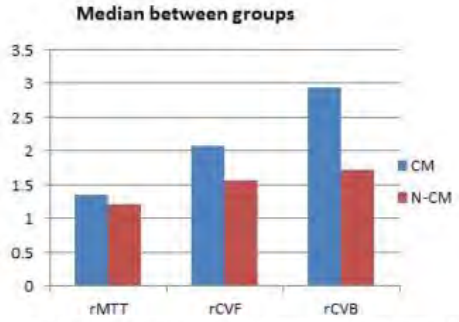


Fig 1 Blue bar represent the group of DVA with CM, and red bar represent the group of DVA without CM

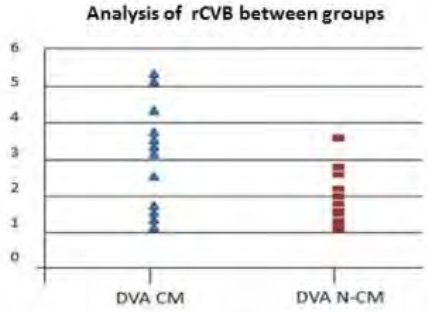


Fig 2 Blue triangle represent the group of DVA with CM, and red square represent the group of DVA without CM

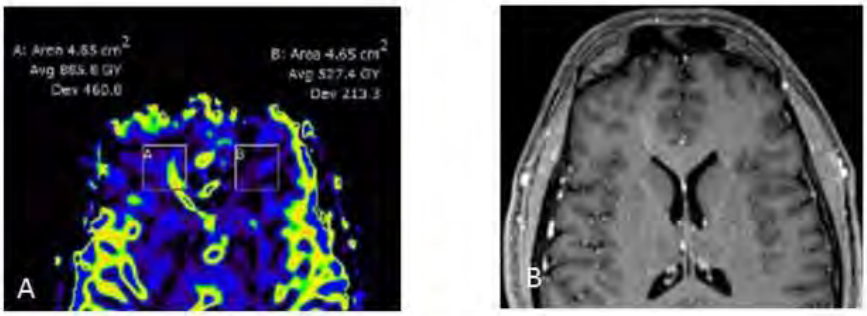


Fig 3 (A) Perfusion maps rCVB showing bifrontal ROI (B) T1 post gad showing a right frontal DVA with cavernous malformation not seen.

(Filename: TCT_eP-74_Slide2.JPG)

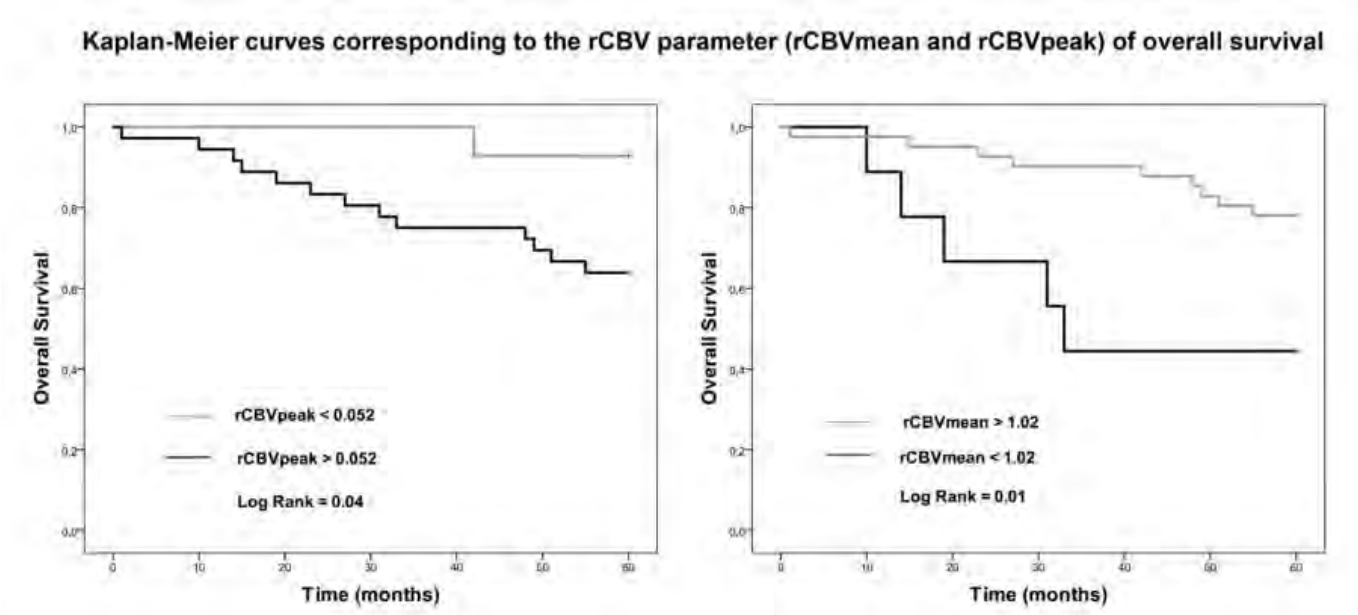
eP-68

6:30AM - 3:00PM

Dynamic Susceptibility Contrast MRI Identifies Favorable Survival Outcome in Patients with Oligodendroglial Tumors

A Latysheva[1], K Emblem[1], J Hald[1]
[1]*OUS-Rikshospitalet, Oslo, Norway*

Purpose
Relative cerebral blood volume (rCBV) and apparent diffusion coefficient (ADC) by MRI are predictive and prognostic biomarkers for patients with gliomas, but also challenged by patients with oligodendroglial tumors possible because of loss of 1p19q heterozygosity 1-3. Our study aimed to evaluate whether rCBV and ADC histogram analyses may stratify survival outcome in patients with oligodendroglial tumor independently of histopathologic grade and genotype.
Materials and Methods
Fifty patients with histologically confirmed oligodendroglial tumors were retrospectively included and analyzed using mean values of ADCmean and rCBVmean, as well as the peak height of normalized whole – tumor histograms, ADCpeak and rCBVpeak 4, 5. Overall survival and progression free survival were analyzed by Kaplan – Meyer and Cox survival analysis adjusted for known survival predictors including age; neurological symptoms; comorbidity; and postsurgery treatment.
Results
rCBVpeak and rCBVmean returned the strongest associations to overall survival. Significant longer overall survival were associated with lower rCBVpeak (median, 59 months for rCBVpeak ≤ 0.052 versus 48 months for rCBVpeak > 0.052, hazard ratio=6.2, p <0,001) and higher rCBVmean (median, 54 months for rCBVmean > 1.02 versus 38 months for rCBVmean < 1.02, hazard ratio =18.0, p = 0,014). ADC parameters (ADCpeak, ADCmean) did not stratify progressive free nor overall survival.
Conclusions
Relative cerebral blood volume histogram analysis can stratify overall survival in patients with oligodendroglial tumor, which may partly explain favorable outcome in tumor with low rCBVpeak and high CBVmean.



(Filename: TCT_eP-68_Kaplan-Meyer.jpg)

eP-46

6:30AM - 3:00PM

Edema is No Reliable Diagnostic Sign to Exclude Small Brain Metastases

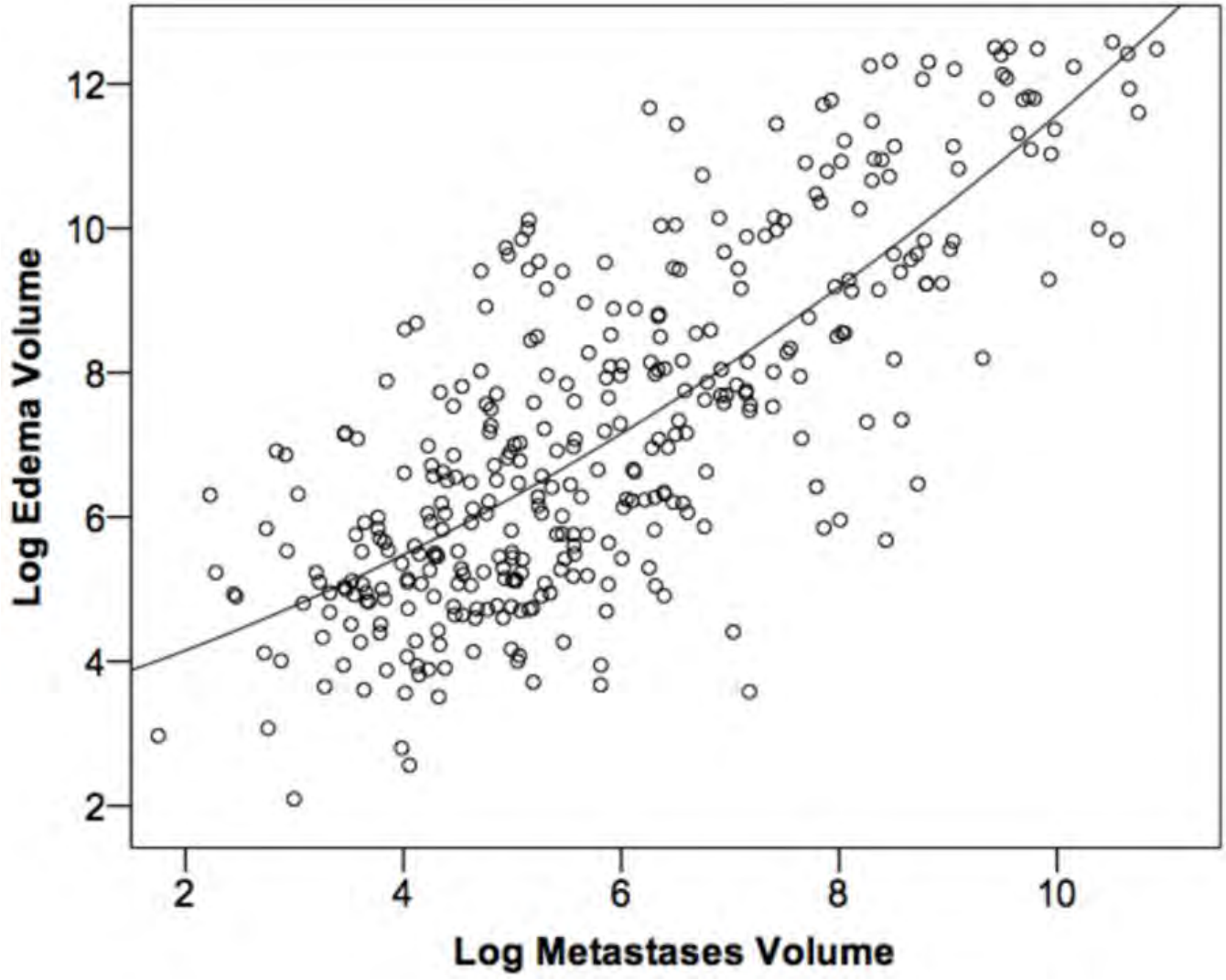
T Schneider[1], J Kuhne[1], J Schröder[1], T Magnus[1], M Mohme[1], M Grosser[1], J Fiehler[1], S Siemonsen[1]
[1]*University Medical Center Hamburg-Eppendorf, Hamburg, Germany*

Purpose
No prior systematic study on formation of a vasogenic edema (VE) in patients with brain metastases (BM) exists. Here, we aim to determine 1) the general volumetric relationship between BM and VE and 2) a threshold diameter above which a BM shows a VE in order to improve diagnostic processes and understanding of edema formation.
Materials and Methods
This monocentric, retrospective study includes 101 untreated patients with histologically proven BM. Semi-manual segmentation of 810 BM on contrast-enhanced T1-weighted images and VE on fluid-attenuated inversion recovery/T2-weighted images was conducted. Statistical analyses were performed using Chi2-test and ROC analysis. A general linear mixed model (GLMM) was used to control the possible effect of nonuniform distributed metastases rates among patients.
Results
For BM with edema, there was a significant positive correlation between volume of BM and volume of VE ($P < 0.001$). Occurrence of VE was less common in the cerebellum and in BM derived from breast cancer. Optimal cut-off for edema formation was a diameter of 5.07mm

for all, 5.07mm for pulmonal, 5.49mm for skin, and 4.01mm for breast BM. In GLMM, only volume had a significant influence on edema formation.

Conclusions

Presence of edema is no reliable diagnostic sign to exclude small brain metastases. Edema size seems to be dependent on the size of underlying BM and therefore might be helpful in native follow-up imaging. Additionally, our findings may help to estimate the potential underlying tumor type in patients in whom diagnosis of BM precedes diagnosis of the primary tumor.



(Filename: TCT_eP-46_Figure.jpg)

eP-72

6:30AM - 3:00PM

EVALUATION of CSF FLOW METRICS in PATIENTS with COMMUNICATING HYDROCEPHALUS and IDIOPATHIC INTRACRANIAL HYPERTENSION

H Toprak[1], t Yilmaz[2], A ARALASMAK[3], E mehdi[2], g kocaman[2], S Kurtcan[2], M KAYA[2], A Alkan[2]
[1]Bezmialem Vakif University, istanbul, turkey, [2]Bezmialem Vakif University, istanbul, istanbul, [3]Bezmialem Vakif University, Istanbul, Turkey

Purpose
To search for CSF dynamics of IIH and communicating hydrocephalus and any correlation between MRI findings, CSF metrics and CSF opening pressure in IIH.
Materials and Methods
Healthy subjects (30) and subjects with IIH (29) and high-pressure communicating hydrocephalus (43) were enrolled. Non-parametric Kruskal-Wallis test (p=0,05) was used to compare three groups, Mann-Whitney U test with Bonferroni correction to compare two groups (p=0,016). Correlation of MRI findings of IIH with CSF metrics and CSF pressure was analysed by non-parametric Mann-Whitney U test (p=0,05). Table 1: Number and age distribution of three groups are given in table 1 (Group 1: Patients with communicating hydrocephalus; Group 2: Patients with IIH.; Group 3: Healthy subjects).
Results
In IIH, no correlation between MRI findings and ASV but a positive correlation with presence of transverse sinus compression and CSF openning pressure was noted. Comparing with healthy subjects, ASV was nonsignificantly lower and standardized diastolic and sum and difference of systolic and diastolic flow durations were statistically significantly lower. Comparing with hydrocephalus, PPC/AS was significantly higher and other CSF metrics with standardized systolic and sum of systolic and diastolic flow durations were significantly lower. In hydrocephalus, ASV and peak velocities were significantly higher. Compared with normal group, PPC/AS and reverse/forward flow duration were significantly lower and other CSF metrcis were significantly higher.
Conclusions
In hydrocephalus, significant increase in ASV and peak velocities were noted. In IIH, CSF openning pressure is positively correlated with presence of transverse sinus compression and standardized diastolic flow durations were statistically significantly short that are probably effects of increased impedance of CSF flow against increased increased intracranial pressure and unchanged or even decreased intraventricular CSF volume.

Group	N	Mean	Std. Deviatiion	Median	Minimum	Maximum
1	43	29,12	21,629	23,00	1	78
2	29	37,28	10,640	37,00	18	57
3	30	36,57	11,413	34,50	20	65
Total	102	33,63	16,685	33,00	1	78

(Filename: TCT_eP-72_table1.jpg)

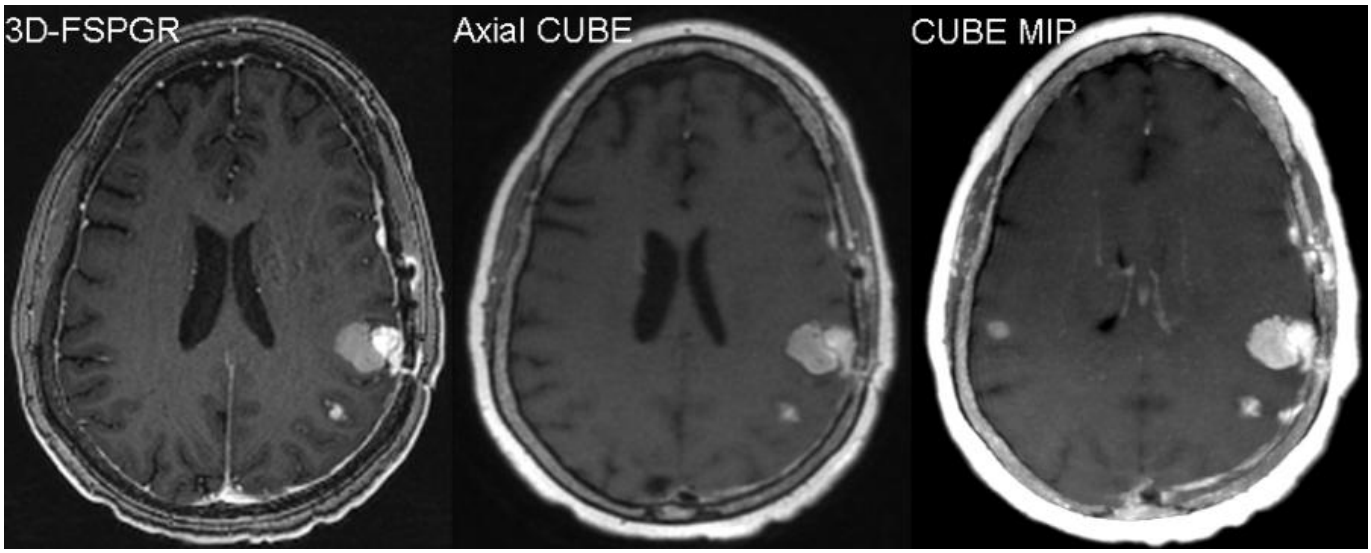
eP-50

6:30AM - 3:00PM

Evaluation of Maximum Intensity Projection (MIP) Images of Contrast-Enhanced 3D T1-Weighted Fast Spin-Echo (CUBE) for Detecting Intracranial Metastases: Comparison of Accuracy and Interpretation Time Compared with 3D-T1-FSPGR

A Saad[1], B Yoon[2], P Rezaii[1], G Zaharchuk[1], M Iv[1]
[1]Stanford University, Stanford, CA, [2]Stanford University, Stanford , CA

Purpose
Maximum intensity projections (MIP) images have shown promise to increase identification of small lesions such as lung nodules and may speed the time of interpretation (1, 2). We undertook this study to determine the performance of MIP images created from contrast-enhanced T1-weighted 3D fast spin-echo (CUBE) MR images for detecting brain metastases.
Materials and Methods
We retrospectively reviewed 20 patients with brain metastases who received MRI (GE Healthcare) at 3T. Each patient underwent the following sequences post-contrast: axial 3D T1 FSPGR (TR 9.2ms, TE 3.7ms,1 mm slice thickness), 1 mm axial reformations from sagittal T1 CUBE (3D fast-spin echo, TR 600ms, TE 13ms, 1.2 mm slice thickness), and axial MIP images (10 mm skip 4 mm) obtained from the T1 CUBE sequence. Two radiologists with differing levels of experience counted the number of brain metastases on each sequence. The time it took for each reader to count the number of lesions was recorded. A comparison of contrast-to-noise ratio (CNR) for T1 CUBE MIP and 3D-FSPGR sequences utilizing the largest lesion in each scan also was performed.
Results
The total number of metastases detected using T1 CUBE MIP images was not significantly different than the number of lesions identified using axial T1 CUBE (reader 1: 156 vs. 165 metastases, P=0.5; reader 2: 148 vs. 143 metastases, P=0.66) and 3D-FSPGR (reader 1: 156 vs. 153 metastases, P=0.58; reader 2: 148 vs. 120 metastases, P=0.08) images. Time of interpretation for T1 CUBE MIP, T1 CUBE, and 3D FSPGR images were as follows: reader 1: mean+SD, 27+6 seconds, 56+12 seconds, 79+16 seconds, respectively; reader 2: 33+22, 50+19 seconds, 81+39 seconds. Lesion CNR was significantly higher with T1 CUBE MIP (mean+SD, 3.78+2.4) than with 3D-FSPGR (1.75+1.47) images ($p<0.05$).
Conclusions
Postcontrast T1 CUBE MIP images allow detection of brain metastases with reduced interpretation time without sacrificing diagnostic accuracy.



(Filename: TCT_eP-50_figure1labeled.jpg)

eP-27

6:30AM - 3:00PM

Evaluation of T1W Dynamic Contrast Enhanced MRI in Tubercular and Cryptococcal Meningitis

A Gupta[1], A Verma[2], j saini[3], S TIWARI[4]
[1]National Institute of Mental Health and Neurosciences, India, Bangalore, Karnataka, [2]national Institute of Mental health & Neuro Sciences, Bangalore, Karnataka, [3]NIMHANS, BANGALORE, Karnataka, [4]National Institute of Mental Health and Neurosciences, BANGALORE, Karnataka

Purpose
To study the blood-brain-barrier (BBB) disruption in tuberculous and cryptococcal meningitis using dynamic contrast-enhanced (DCE) magnetic resonance imaging (MRI) and to compare these with 6 months post-treatment imaging.
Materials and Methods
Fifteen patients, i.e., twelve patients of tubercular meningitis and 3 patients of cryptococcal meningitis were included in the study. The diagnosis was based on clinical features and cerebrospinal fluid (CSF) analysis. All patients underwent MRI Brain with DCE perfusion at the time of initial presentation with a repeat imaging after 6 months of treatment. The pretreatment and post-treatment DCE perfusion indices were evaluated and compared. The DCE model used was the Leaky tracer kinetic model by Sahoo et al. Dynamic contrast-enhanced perfusion analysis revealed 9 maps, i.e., CBV(cerebral blood volume), CBF(cerebral blood flow), Ve(Fractional extravascular extracellular space volume), Vp (fractional blood plasma volume), Ktrans (volume transfer constant), Kep (rate transfer constant), λtr(leakage), CBV corrected for Ve and CBV corrected for Leakage. Area-wise

analysis was done in each lobe of cerebral hemisphere and then global analysis for whole brain for each DCE perfusion indice pretreatment and post-treatment.

Results

The average age of patients was 32.1 years with male:female ratio of 1:1.4. Structural MRI was normal in 4 patients. In rest of the patients of TBM varying imaging features like tuberculomas, hydrocephalus and focal/diffuse leptomeningeal enhancement was seen. In CM patients structural MRI showed crytococcomas with focal leptomeningeal enhancement. Areawise and global analysis showed statistically significant decrease in leakage values post-treatment. Hence the increase in pretreatment values in leakage signified disruption of blood brain barrier (BBB). Blood CSF barrier is more significant in the context of meningitis and the leakage compartment in meningitis is the CSF space. Statistically significant decrease in CBV, CBF, Ve, Vp, CBV corrected for Ve and CBV corrected for leakage was seen post-treatment.

Conclusions

The BBB has been assessed by DCE perfusion. It shows BBB disruption even in those patients where structural MRI is normal. A decrease in leakage post-treatment signifies response to treatment. Dynamic contrast-enhanced MRI holds promise of being a noninvasive tool for monitoring relapse activity and/or treatment effect.

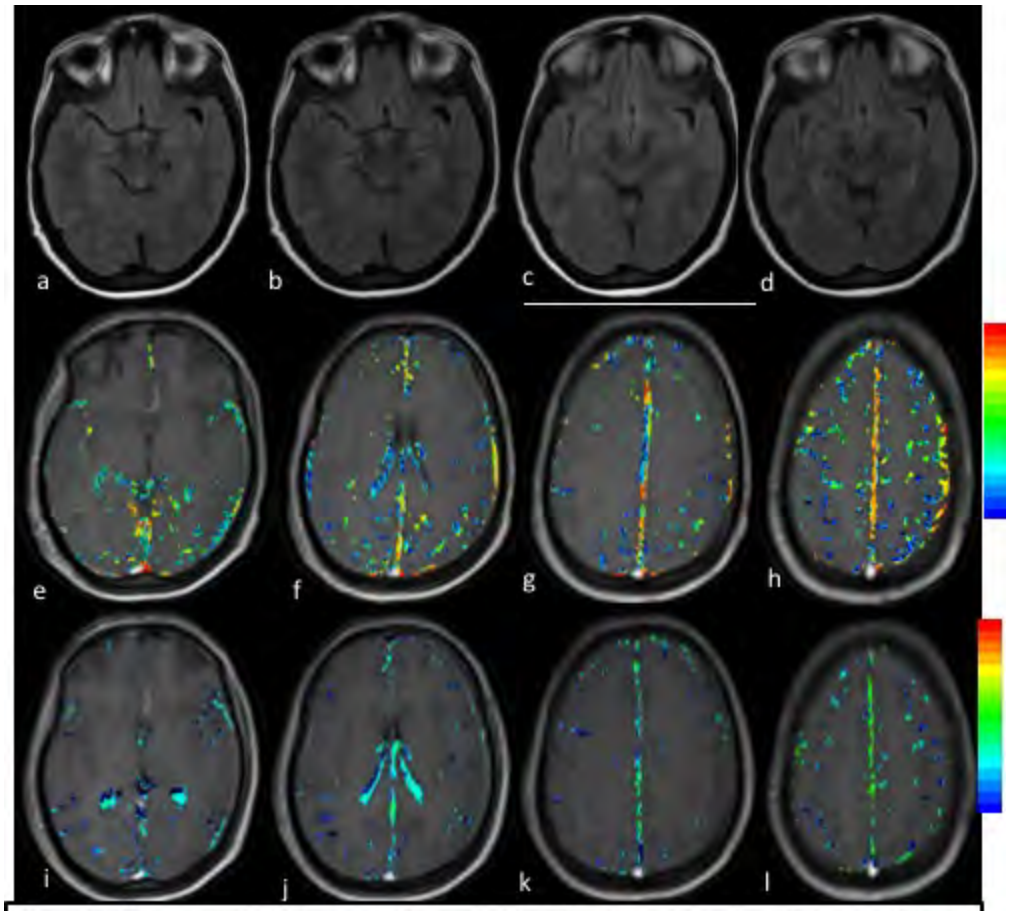


Figure (a): Pretreatment FLAIR sequence shows sulcal hyperintensity in bilateral occipital region. (b): pre-treatment postcontrast FLAIR sequence shows leptomeningeal enhancement in bilateral occipital region. (c) post-treatment FLAIR sequence shows resolution of sulcal hyperintensity. (d) : posttreatment FLAIR sequence shows no leptomeningeal enhancement.(e,f,g,h) : pretreatment leakage maps showing increase in leakage in all lobes of bilateral cerebral hemispheres.(I,j,k,l) : posttreatment leakage maps show decrease in leakage in all areas.

(Filename: TCT_eP-27_ASNR_DCE.jpg)

eP-43

6:30AM - 3:00PM

Extent of Surgery Improves the Overall Survival Independently of Imaging Characteristics in Newly Diagnosed Glioblastoma

J Puig[1], L Oleaga[2], C Balana[3], J Capellades[4]
[1]Research Unit of Diagnostic Imaging Institute (IDI), IDIBGI, University Hospital Dr Josep Trueta, Girona, Girona, [2]Department of Radiology, Hospital Clinic Barcelona, Barcelona, Barcelona, [3]Medical Oncology Service, InstitutCatalàd'Oncologia, Germans Trias i Pujol University Hospital, Badalona, Barcelona, [4]Department of Radiology, Hospital del Mar, UniversitatAutònoma de Barcelona, Barcelona, Barcelona

Purpose
In glioblastoma,the extent of surgery affects neurological condition, survival, and the efficacy of postsurgical systemic treatment. We analyzed the impact of surgical extent on overall survival in function of baseline tumor radiological characteristics (size, eloquence of adjacent brain, and location) and known prognostic factors.
Materials and Methods
Patients received standard radiotherapy and concomitant/adjuvant temozolomide (GLIOCAT Study). We used an MRI-based topographical glioblastoma staging system (stages I, II, and III) integrating tumor location (A, B, C), size (≤5 cm or >5cm), and eloquence of adjacent brain. Evaluations were accepted when kappa was near 1; only evaluations of T1Gd sequences are reported. Surgery was classified as complete resection (CR=disease-free postoperative MRI), partial resection (PR), or biopsy (B). Age, Karnofsky performance score (KPS), Mini-Mental State (MMS), isocitrate dehydrogenase mutations (mIDH), and O6-methylguanine-DNA methyltransferase promoter methylation (methMGMT) were recorded.
Results
In two hundred eighty patients, Location: A=133(47.5%)//B=110 (39.3%)//C=37 (13.2%); Eloquence: No=196 (70%)//Yes=84 (30%); size: ≤5cm: 150(54.5%)//> 5cm: 125 (45.5%); Stage: I: 100 (43.9%)//II: (22.8%)//III: 76 (33.3%). Clinical factors KPS (<70, ≥70), age (<50, ≥50), MMS (<27, ≥27), mIDH,and methMGMT were uniformly distributed across stages. Surgical type: CR 16%//PR 65.7%//B 14.6%. Complete resection was more frequent in stage I (80%) and biopsy in stage III (46.3%) (p=0.000). Univariate analyses found type of surgery (p=0.000), KPS ≥70 (p=0.02), methMGMT(P=0.01), mIDH(P=0.03), stage I vs. II vs. III(P=0.000), location A vs. B vs. C(P=0.000), and size (P=0.005) but not brain eloquence (P=0.39) were associated with longer overall survival. In multivariate analyses, methMGMT, KPS≥70% and resection (CR or PR) were independent prognostic factors, and eloquence, size, and location lost their prognostic value.
Conclusions
In glioblastoma, PR or CR improves overall survival independently of size, eloquence, or tumor location. Overall survival is best in patients with good KPS and methMGMT.

eP-13

6:30AM - 3:00PM

Functional Activation in the Cerebellum Associated with Language Task in Patients with Brain Tumor: Potential for Neurovascular Uncoupling and Functional Reorganization

N Cho[1], K Peck[1], A Holodny[2]
[1]Memorial Sloan-Kettering Cancer Center, New York, NY, [2]Memorial Sloan-Kettering Cancer Center, Weill Medical College Of Cornell Univ., New York, NY

Purpose

The cerebellum exhibits crossed activation with the contralateral cerebral hemisphere during language tasks in healthy subjects (1), so it might indicate cerebral activation when such mapping is difficult. We studied cerebro-cerebellar BOLD fMRI activation for a language task in patients with a tumor affecting left Broca's area to see how lesions would impact cerebro-cerebellar activation. We hypothesized that atypical, uncrossed cerebro-cerebellar activation would be observed.

Materials and Methods

We studied forty-five right-handed patients with a glioma affecting left Broca's area who completed a presurgical fMRI scan with a language task paradigm. Functional MRI data were processed using AFNI. Statistical parametric maps were generated by cross-correlation analysis using a modeled waveform. Voxel region of interest (ROI) masks were drawn on cerebellar hemispheres and left and right Broca's areas using high-resolution anatomical images. The laterality index (LI) was measured from the ROI masks to determine cerebellar and cerebral left-dominance (LD) ($LI \geq 0.2$), co-dominance (CD) ($0.2 < LI < 0.2$), or right-dominance (RD) ($LI \leq -0.2$) (2). We used the Spearman's rank correlation coefficient for relationships between cerebellar and cerebral LI values and the Fisher's exact test for relationships involving atypical cerebro-cerebellar activation frequencies.

Results

Thirty-two of forty-five subjects exhibited atypical cerebro-cerebellar activation (Table 1). Significant differences for atypical cerebro-cerebellar activation were found between cerebral RD and cerebral CD ($p < 0.001$) as well as cerebral RD and cerebral LD subjects ($p < 0.01$). No differences were found when subjects were grouped by cerebellar dominance ($p > 0.75$) or tumor grade ($p > 0.5$). No relationship was found between the cerebellar and cerebral LI values ($\rho = -0.18$; $p = 0.23$).

Conclusions

Atypical cerebro-cerebellar activation was observed in right-handed patients with a tumor affecting left Broca's area during a language fMRI task. Because crossed cerebro-cerebellar activation occurs in patients with brain tumor not affecting the activation area (3), we suggest that cerebellar activation can indicate contralateral reorganization and cerebral false negative behavior from neurovascular uncoupling in cerebral RD and CD subjects.

Table 1. Categorizations of Subject Cerebral and Cerebellar Lateralizations

	Cerebellar LD			Cerebellar CD			Cerebellar RD		
Cerebral LD	Cerebral LI	Cerebellar LI	Grade	Cerebral LI	Cerebellar LI	Grade	Cerebral LI	Cerebellar LI	Grade
	0.99	0.80	Low	0.80	-0.03	High	1.00	-0.95	High
				0.77	0.15	High	0.37	-0.59	High
				0.37	-0.18	High	0.31	-0.37	High
				0.25	-0.15	High	0.71	-1.00	High
				0.52	-0.17	High	0.33	-0.33	Low
				0.41	-0.05	Low			
Cerebral CD	Cerebral LI	Cerebellar LI	Grade	Cerebral LI	Cerebellar LI	Grade	Cerebral LI	Cerebellar LI	Grade
	0.11	0.21	High	0.16	0.00	High	0.10	-0.70	High
				0.07	-0.05	High	-0.05	-0.20	High
				-0.05	0.05	High	-0.17	-0.25	High
				-0.06	-0.02	Low	-0.13	-0.75	Low
				0.09	0.05	Low	-0.06	-0.38	Low
				0.01	0.01	Low	-0.04	-0.32	Low
				-0.16	0.01	Low	0.04	-0.22	Low
				-0.16	0.04	Low			
Cerebral RD	Cerebral LI	Cerebellar LI	Grade	Cerebral LI	Cerebellar LI	Grade	Cerebral LI	Cerebellar LI	Grade
				-0.28	0.00	High	-0.54	-0.33	High
				-0.87	0.06	High	-0.50	-0.70	High
				-1.00	0.07	High	-0.50	-0.28	High
				-0.81	0.10	High	-1.00	-0.37	High
				-1.00	0.02	High			
				-0.73	0.14	High			
				-0.95	-0.14	High			
				-0.28	-0.12	Low			
				-0.62	-0.12	Low			
				-0.33	-0.03	Low			
				-0.26	0.16	Low			
				-0.67	0.13	Low			
				-0.82	-0.17	Low			

(Filename: TCT_eP-13_Table1ASNR.jpg)

eP-33

6:30AM - 3:00PM

High Resolution Imaging of Intracranial Vessel Wall Imaging: Initial Experience in CTA/DSA-negative Acute Subarachnoid Hemorrhage

A Guillonnet[1], J Gentric[2], J Raymond[1], D Roy[1], A Weill[1], L Letourneau-Guillon[1]
[1]CHUM Centre Hospitalier de l'Université de Montréal, Montréal, QC, [2]Centre Hospitalier Régional Universitaire de Brest, Brest, France

Purpose
To report our initial experience using vessel wall MRI (VW-MRI) in CTA/DSA-negative acute subarachnoid hemorrhage (SAH).
Materials and Methods
Retrospective review of consecutive patients admitted to our institution from January 2012 to October 2016 for acute non-traumatic non-perimesencephalic subarachnoid hemorrhage, with negative initial angiographic imaging (CTA in all patients, DSA in all but one patient), and with subsequent acquisition of 3T VW-MRI sequences, including 3D-T1-VISTA (isotropic 0.6 mm3 resolution) pre- and post-gadolinium on a 3 Tesla MR- scan (Achieva X, Philips, Best, Netherlands).
Results
Eight men and 3 women (mean age 54 years) were included. Vessel wall MRI was performed between 1 and 17 days following the first angiography (median time = 6 days). In 4 out of 11 patients, VW-MRI detected a potential hemorrhage source: two small saccular aneurysms (basilar perforating and MCA bifurcation aneurysms) and a partially thrombosed dissecting aneurysm of the superior cerebellar artery. In these 3 patients, follow-up DSA confirmed the VW-MRI findings without other alternative etiologies. In the fourth patient, findings suspicious for a thrombosed arteriovenous malformation were identified. The patient died before the second DSA could be performed. In 7 cases, VW-MRI did not identify a hemorrhage source, and the SAH was considered idiopathic. No rehemorrhage occurred at available clinical follow-up (21-958 days, median = 94 days) in this group.
Conclusions
In the setting of acute nontraumatic and nonperimsencephalic SAH, VW-MRI might prove a useful diagnostic tool in the setting of initial negative angiographic exams. Vessel wall MRI may help target specific anatomic areas on subsequent DSA and increase the diagnostic yield of the latter exam. Whether VW-MRI allows earlier detection of hemorrhage source than standard repeat angiographic imaging needs further study.



Case of pseudoaneurysm secondary to cerebellar superior artery dissection

a. CT-scan: acute SAH in basal cisterns.

b. Negative initial DSA.

c. Post-contrast VW-MRI revealing apparent enhancement within a pseudoaneurysm.

d. Subsequent DSA: confirmation of a left SCA pseudo-aneurysm.

(Filename: TCT_eP-33_modifications.jpg)

eP-07

6:30AM - 3:00PM

Hippocampal Morphology and Seizure Recurrence in a Cohort of First Seizure Patients

M Ghuman[1], C Crocker[1], B Pohlmann-Eden[1], M Schmidt[1]
[1]*QEII Health Sciences Centre, Dalhousie University, Halifax, Nova Scotia*

Purpose
This study examined loss of hippocampal internal architecture (HIA) and hippocampal malrotation (HIMAL) as potential markers of focal epilepsy and predictors of epileptogenesis in patients presenting to a First Seizure Clinic.
Materials and Methods
Fifty-two patients with unprovoked seizures were recruited between May 2010 and February 2014. All patients were imaged on a 1.5T MRI scanner within 6 weeks. Two readers independently examined the images for HIA, using the scoring system of Ver Hoef et al. (1). They also independently scored images for the presence or absence of HIMAL, using the criteria of Tsai et al. (2). Discrepancies were resolved by consensus.
Results
One participant had primary generalized epilepsy and was excluded. Twenty-eight had a first seizure (FS), and 23 had new-onset epilepsy (NOE, defined as ≥ 2 seizures over the past 12 months) at presentation. Ten participants with FS converted to NOE over a 1-year follow-up

period. Fifteen participants had loss of HIA, and 11 participants had HIMAL. There was a statistically significant association between loss of HIA and conversion from FS to NOE ($p = 0.0427$, one-tailed Fisher's exact test). There was no association between loss of HIA and NOE at presentation. There was no association between HIMAL and NOE at presentation, nor between HIMAL and conversion from FS to NOE.

Conclusions

Loss of HIA had a significant association with conversion from FS to NOE in our study, although it did not distinguish FS from NOE at presentation. It may prove a useful predictor of epileptogenesis in FS patients. Loss of HIA has been considered a subtle form of hippocampal sclerosis (3). Its presence in FS patients suggests that it may be a developmental lesion. In keeping with recent findings by others, HIMAL appears to be a normal variant, and not an epileptogenic lesion (2).

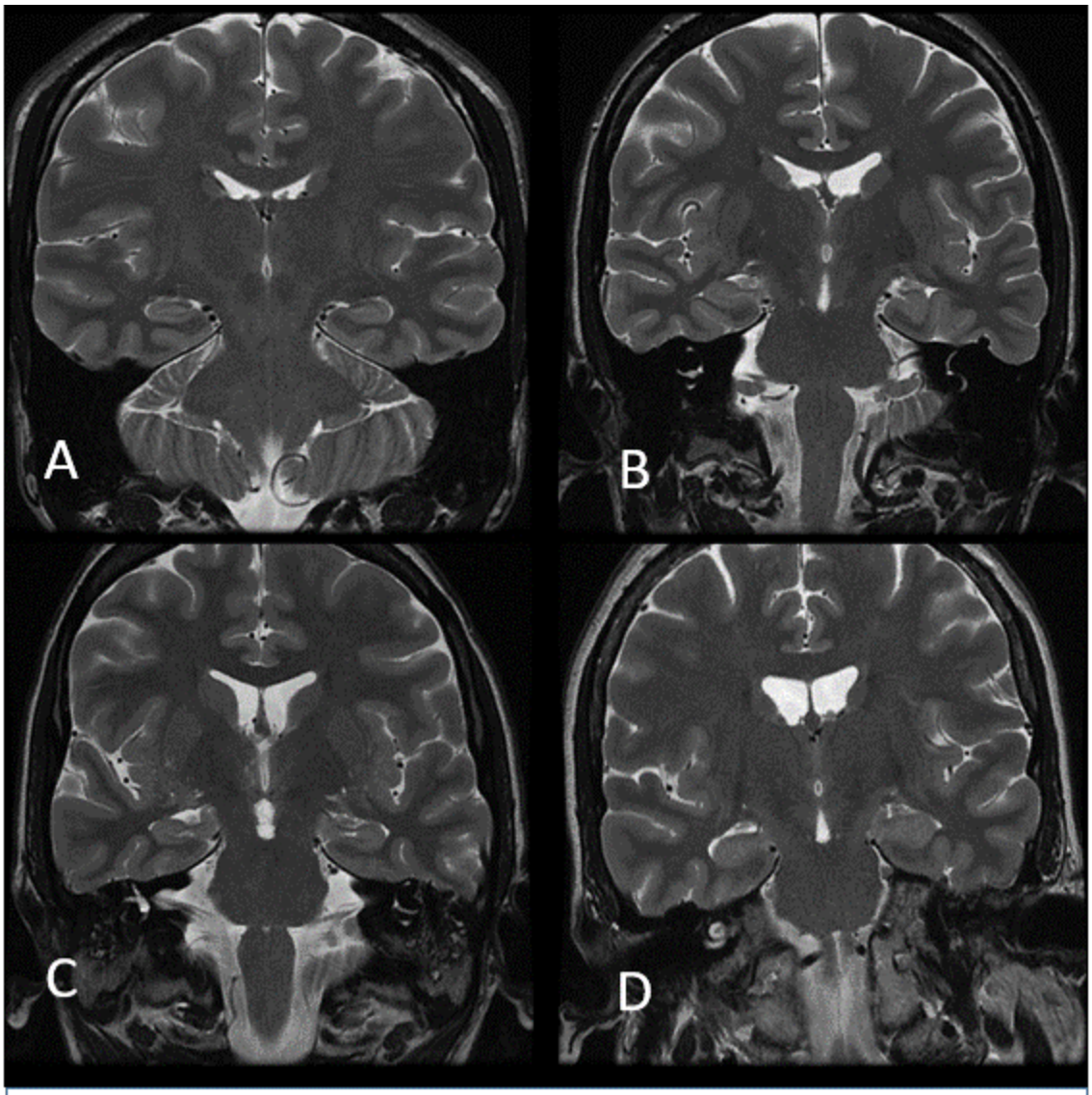


Figure 1: Coronal T2-weighted fast spin echo images with 3 mm slice thickness, angled to the hippocampi. Bilaterally normal hippocampi (A). Left HIMAL (B). Left HIMAL and moderate loss of HIA (C). Bilateral severe loss of HIA (D).

(Filename: TCT_eP-07_GhumanetalASNR2017.gif)

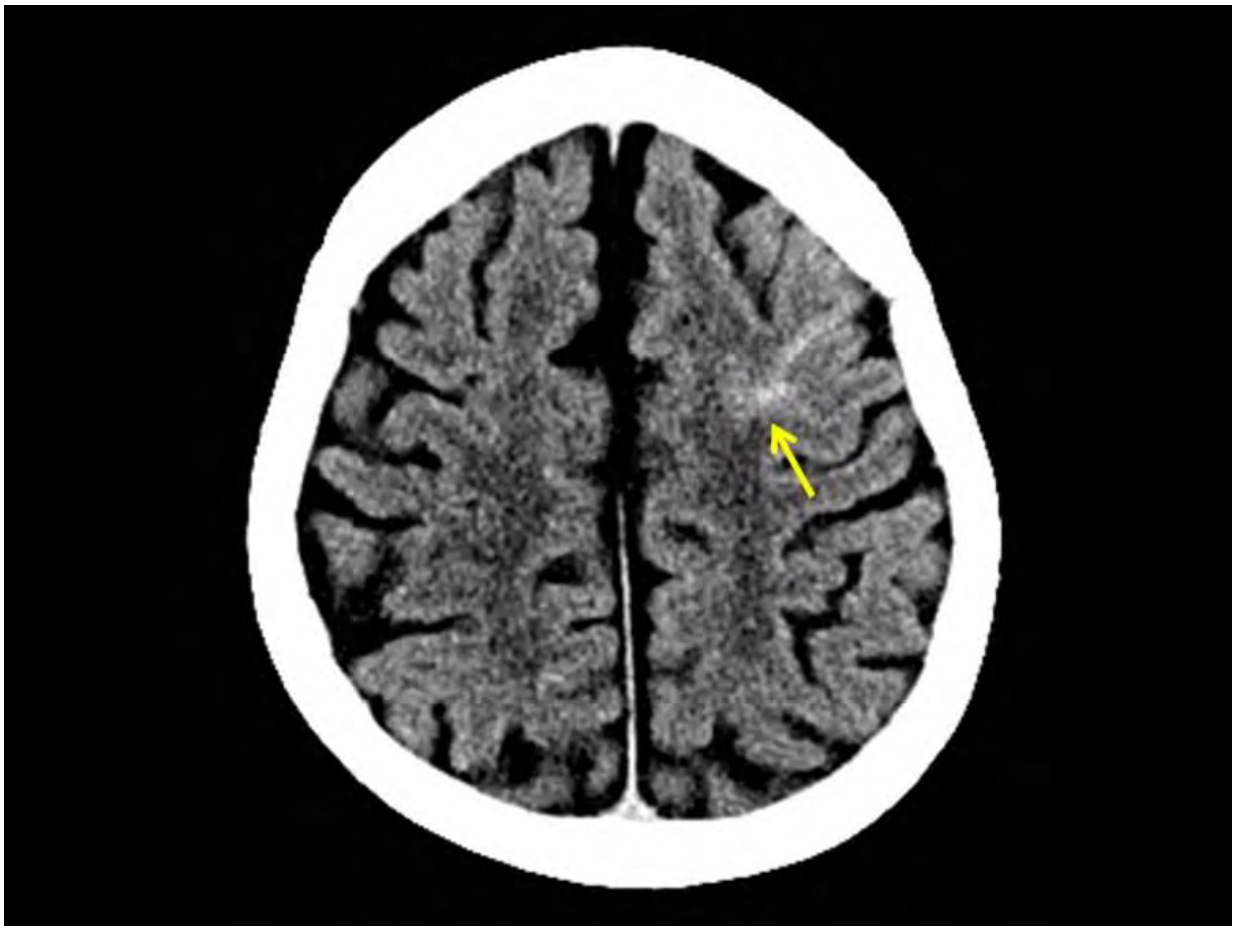
eP-48

6:30AM - 3:00PM

Hyperintense Acute Reperfusion Marker (HARM): The Possibility of Recognizing Early Blood-Brain Barrier Disruption on CT Imaging

J Shah[1], E Greif[2], G Cruciata[1], S Rudolph[3], E Stein[1]
[1]Maimonides Medical Center, Brooklyn, NY, [2]Maimonides Medical Center, Huntington , NY, [3]Maimonides Medical Center, Brooklyn, MI

Purpose
The objective of the study is to present and characterize the findings from blood-brain barrier (BBB) disruption on CT imaging; previously only reported on contrast-enhanced T2-weight FLAIR (MRI) imaging and termed hyperacute reperfusion marker (HARM).
Materials and Methods
This is a case series of 3 patients presenting clinically with CVA. The presence of blood-brain barrier (BBB) disruption was defined by hyperdensity on initial CT imaging with subsequent findings such as gray-white distinction loss and sulcal effacement on follow-up imaging.
Results
Three patients were included in the analysis. Mean age was 69 years 8 months, median NIH Stroke Scale score was 3, the period of symptoms varied (39 min, 10 hours, >24 hours). Imaging findings for the 3 patients included hyperdensity in the subarachnoid space and/or leptomeningeal or subarachnoid space enhancement after iodinated contrast administration.
Conclusions
This series of patients demonstrates a novel finding that has not been described previously. Peripheral and subarachnoid enhancement on contrast-enhanced T2-weighted FLAIR MR imaging has been identified and termed HARM. This is posited to represent a consequence of ischemia-induced transient BBB disruption. We propose here that our series suggests that this finding can be first recognized on both noncontrast and contrast-enhanced CT imaging. This phenomenon may serve as a clinically useful biomarker leading to earlier diagnosis. Future studies are needed to further define the sensitivity of this finding, its time course and the prognostic implications.



(Filename: TCT_eP-48_Slide35.JPG)

eP-45

6:30AM - 3:00PM

Imaging and Management of Skull Base Chordoma and Chondrosarcoma in the Manchester Skull Base Unit

S Masri[1], S Saipriya[2], R Siripurapu[3], K Gnanalingham[3], G Whitfield[4], G Potter[3]
[1]Salford Royal Foundation Trust, Greater Manchester, United Kingdom, [2]National Hospital for Neurology and Neurosurgery, London, United Kingdom, [3]Salford Royal NHS Foundation Trust, Greater Manchester, United Kingdom, [4]Christie NHS Foundation Trust, Greater Manchester , United Kingdom

Purpose
To review postoperative imaging protocols and imaging surveillance of patients with skull base chordomas and chondrosarcomas in the Manchester Skull Base Unit.
Materials and Methods
We reviewed all patients with histologically-proven chordoma or chondrosarcoma from January 2008 to present. Imaging was reviewed using PACS and clinical details obtained

from electronic patient records. We recorded whether postoperative magnetic resonance imaging (MRI) was performed using the standard local skull base protocol (axial T2 head, axial T1 skull base, coronal T2 fat saturation skull base; axial, coronal and sagittal T1 fat saturation with contrast) and any additional sequences or variations from the skull base protocol. We recorded patient demographics, surgical approach, time from surgery to baseline postoperative scans, timing of follow-up imaging and imaging protocols.
Results
Amongst 13 patients, most underwent primary endoscopic transphenoidal resection; 9 had chordoma and 4 chondrosarcoma. Average age was 55 years. All patients had MRI prior to surgery. Sixteen baseline postoperative scans were performed (13 MRI, 3 CT) at between 1 and 9 days following surgery. Seventy-two follow-up MR scans were performed between 2 and 45 months from baseline postoperative imaging. Interval between postoperative scans varied widely between all patients. Postoperative MRI in all patients consisted of the standard protocol, with additional sequences in 13 patients (coronal FLAIR head, DWI skull base, high-resolution T2 skull base, volume T1 with contrast), with the latter two considered helpful in the assessment of residual disease, particularly with regards to radiotherapy planning. A pituitary protocol was used on multiple occasions in 4 patients.
Conclusions
Postoperative interval scanning varied widely depending on surgical and oncological concern regarding site and extent of residual disease. Imaging protocols in postoperative skull base chordoma and chondorsarcoma patients was varied. A standard protocol should be used for postoperative skull base patients with chordoma and chondrosarcoma, to include high-resolution T2 sequences and volume T1 imaging with contrast.

eP-60

6:30AM - 3:00PM

Intracranial 4D CT Angiography More Accurately Predicts Extracranial ICA Patency Than Single-Phase CT Angiography in ICA Terminus Occlusion

A Tarabishy[1]
[1]*West Virginia University, Morgantown, WV*

Purpose
Determining the patency of the extra-cranial internal carotid artery in the setting of carotid-terminus occlusion, is important in the decision process of interventional stroke therapy. It had become more challenging with modern single phase CT angiography(SP CTA), in overestimating the extent of the proximal occlusion. The ability to perform volumetric-head-perfusion CT examinations and including the superior aspect of the cervical internal carotid artery allows for time-resolved (4DCTA) of both the cerebral and distal cervical vessels. In turn, the extent of arterial thrombus proximal to the site of occlusion can be determined more accurately. In turn, the extent of arterial thrombus proximal to the site of occlusion can be

determined more accurately. This information is essential for assessing the need for extra-cranial ICA thrombectomy and/or angioplasty.

Materials and Methods

This retrospective study was approved by the medical center's institutional review board (IRB) and informed consent was waived. Between 2014-2015, three patients were identified retrospectively with internal carotid artery terminus occlusion. These patients underwent multi-modal CT examinations (unenhanced CT of the head, spCTA of the head and neck, and whole-brain VPCT). Image acquisition: Examinations were performed on a 320-slice multidetector CT (Toshiba Aquilion ONE ViSION). Volumetric perfusion CT sequence (VPCT) consisted of 19 consecutive volumetric acquisitions of the brain (160 mm in the z-axis, 7-s delay after start of contrast medium injection, 55-s total imaging duration, 80 kV, 150-300 mAs, rotation time 0.3 s). A 50-ml bolus of contrast medium (Isovue 370) was used at a flow rate of 4 ml/s. For spCTA (120 kV, 120 mAs, rotation time 0.3 s, pitch 0.6, collimation 2 × 64 × 0.6 mm), 50 to 70 ml contrast medium was injected at a flow rate of 4 ml/s, followed by a 30-ml saline chaser at 3 ml/s. Image analysis: Four-dimensional CTA was processed using a commercial software package (Vitrea, Vital) that includes automatic motion correction and automatic definition of the point of peak arterial and venous opacification during the 55 s imaging time identified on the time attenuation curve. Consecutively, axial maximum intensity projections (MIP) were reconstructed from 19 volumetric images with 10 mm slice thickness and 2 to 3 mm increments. In addition, temporal maximum intensity projection (tMIP) reconstructions were obtained that fuse contrast opacification across the entire duration of the 4D CTA.

Results

Patients 1 through 3, with Figures labeled 1 through 3. The single phase CTA demonstrate nonopacification of the extracranial and intracranial internal carotid artery, (on the left in patient 1 and 2 and on the right on patient 3) suggesting tandem occlusion. However, the 4D CTA images (early and delayed phase, middle and last image respectively) demonstrated later filling corresponding to the occluded segment noted on patient 1, and patient 3, while confirming persistent nonfilling and likely tandem occlusion in patient 2.

Conclusions

Four-dimensional perfusion imaging is useful in ruling in cervical carotid artery patency in patients with internal carotid artery terminus occlusion.



Figure 1 (Patient #1) 88-year-old male presenting with right sided weakness with a stroke scale of 11.



Figure 2 (Patient #2): 72 year old male presenting with right sided weakness with a stroke scale of 13



Figure 3 (Patient #3): 61 year old female presenting with left sided weakness with a stroke scale of 8

(Filename: TCT_eP-60_Figure.jpg)

eP-58

6:30AM - 3:00PM

Lesion Location on Diffusion Tensor Imaging Does Not Improve Prediction of Functional Outcomes After Ischemic Stroke Beyond 72-hour Clinical Scores

J Puig[1], G Blasco[2], C Biarnes-Duran[3], S Thio-Henestrosa[4], M Marti-Navas[1], P Daunis-i-Estadella[4], M Rivero[5], J Gich[5], J Figueras[6], A Alberich-Bayarri[7], K Nael[8], M Wintermark[9], S Pedraza[2]

[1]Research Unit of Diagnostic Imaging Institute (IDI), IDIBGI, University Hospital Dr Josep Trueta, Girona, Girona, [2]Imaging Research Unit, IDI-IDIBGI, Hospital Dr Josep Trueta, Girona, None, [3]Research Unit of Diagnostic Imaging Institute (IDI), Girona Biomedical Research Institute (IDIBGI), Girona, Girona, [4]Department of Computer Science, Applied Mathematics and Statistics, University of Girona, Girona, Girona, [5]Department of

Neurology-IDIBGI, University Hospital Dr JosepTrueta, GIRONA, GIRONA, [6]Department of Rehabilitation-IDIBGI, University Hospital DrJosepTrueta, GIRONA, GIRONA, [7]Hospital Universitario y Politecnico La Fe-QUIVIM, Valencia, None, [8]Icahn School of Medicine at Mount Sinai, New York, NY, [9]Stanford University, Stanford, CA

Purpose
Accurate early prediction of long-term outcomes following ischemic stroke would help medical decision-making and rationalize rehabilitation goals. Diffusion tensor imaging (DTI) stroke mapping in the acute setting is promising for predicting some outcomes (e.g., motor and language deficits). We determined whether DTI lesion location is predictive of 3-month functional outcomes in anterior circulation stroke and whether it improves the predictive accuracy of the 72-hour National Institute of Health Stroke Scale (NIHSS).
Materials and Methods
We evaluated 48 consecutive patients within 72 hours of middle cerebral artery stroke onset. We used DTI-derived fractional anisotropy color maps to visually evaluate involvement of white matter tracts (superior longitudinal, superiorfronto-occipital, corticospinal, inferior longitudinal, anterior and posterior limbs of the internal capsule (PLIC), external capsule, uncinate, and corona radiate). We assessed demographic data, infarct volume, lesion side, 72-hour NIHSS subindex scores, 72-hour NIHSS total score, and 3-month modified Rankin Scale (mRS). We used a multiple regression model combining motor deficit, specific tract affected, and imaging data to predict 3-month functional outcome (mRS 0-2, good; 0-5, poor).
Results
Patients with poor outcome (35.4%) had higher median 72-hour NIHSS scores [14 (5-18) vs. 3 (1-5)]; higher best gaze, best visual, and motor leg subindex scores; and PLIC and uncinate involvement ($P<0.001$). The best predictors of 3-month outcome were 72-hour NIHSS total score (AUC 0.85; OR 1.30; 95%CI:1.12-1.58; $p<0.001$) and motor leg subindex score (AUC 0.85; OR 11.99; 95%CI: 1.76-272.12; $p<0.001$), with the best cutoffs for discriminating good vs. poor outcome being 9 and 5, respectively ($p<0.001$).
Conclusions
Our preliminary data indicate that although patients with poor outcome have damage to white-matter tracts, DTI lesion location does not improve prediction of long-term outcome because the 72-hour NIHSS alone strongly predicts outcomes, supporting its use as an early prognostic marker and surrogate of clinical outcome in ischemic stroke.

eP-01

6:30AM - 3:00PM

Mathematical Modeling of Cell Density in Diffusion Weighted Imaging (DWI) - Clinical Application in Crossed Cerebellar Diaschisis

O Kohannim[1], J Huang[1], G Hathout[1]

[1]*University of California, Los Angeles, Los Angeles, CA*

Purpose

Crossed cerebellar diaschisis (CCD) refers to decreased blood flow and metabolic activity in the cerebellum contralateral to supratentorial pathology. This entity is diagnosed most commonly on nuclear medicine studies. We propose an analytical, 2-compartment mathematical model of cell density for detection of CCD on diffusion-weighted imaging (DWI).

Materials and Methods

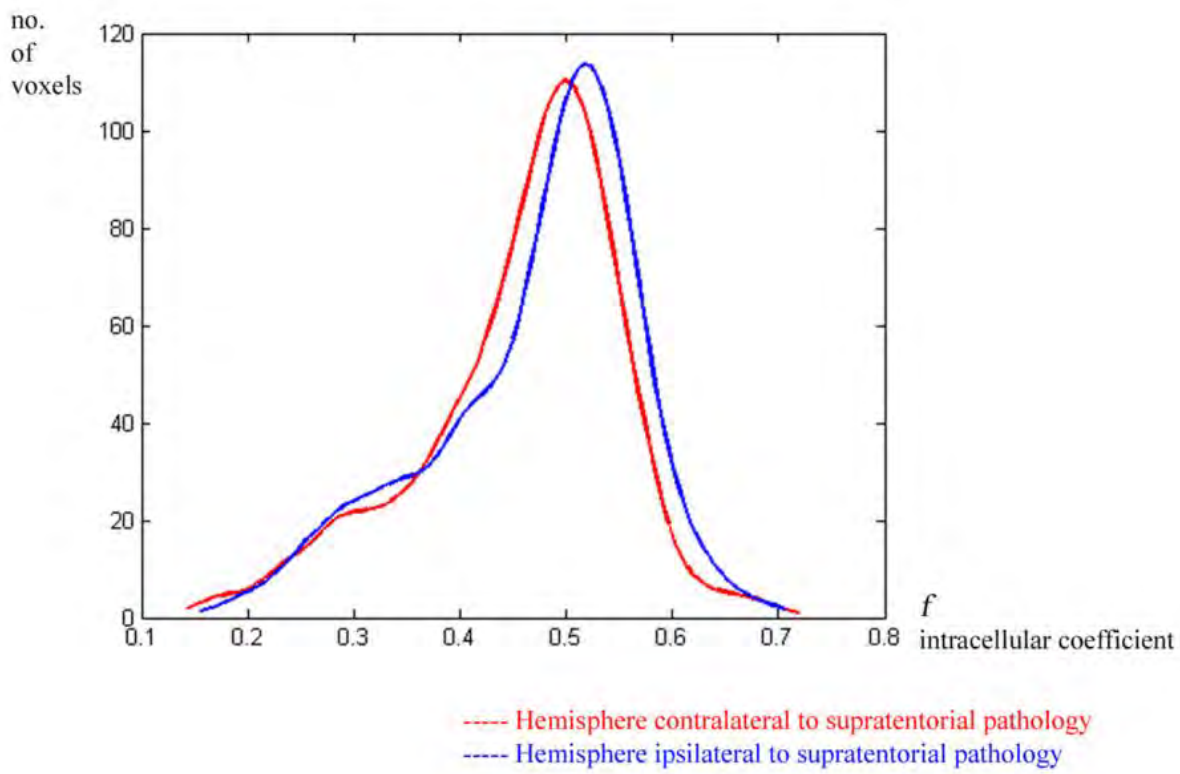
We develop an analytical, biexponential diffusion model with intracellular and extracellular compartments, and apply it to DWI scans of 6 patients with major supratentorial pathology. The model calculates intracellular and extracellular apparent diffusion coefficients with their respective fractions. We solve for voxelwise coefficients for each side of the cerebellum, positing that intracellular fractions reflect cell density. We compare the distribution of coefficients between each side using the Mann-Whitney U test. As proof of principle, we also apply the model to two regions of the brain expected to be rich in gray matter (basal ganglia) and white matter (centrum semiovale).

Results

As expected, we find significantly higher contribution of the intracellular component in the basal ganglia when compared to centrum semiovale ($p < 0.05$). In addition, in all 6 CCD cases, we find the contribution of the extracellular compartment to be significantly higher in the cerebellar side contralateral to supratentorial pathology ($p < 0.01$ in all cases; intracellular coefficient histograms for each cerebellar hemisphere are shown in figure below for an example case).

Conclusions

We apply an analytical, 2-compartment mathematical model to the diagnosis of CCD on DWI scans. Our results are consistent with a decreased intracellular fraction in CCD despite normal-appearing scans, and serve as proof of principle for our model. Our analytical model can be applied to a wide variety of neuropathology to detect subthreshold structural alterations and offers the advantage of applicability to clinical cases, where only 3 DWI beta values are typically available.



(Filename: TCT_eP-01_Figure1.jpg)

eP-76

6:30AM - 3:00PM

MRI Characteristics of Intracranial Breast Cancer Metastasis Based on Tumor Immunohistochemical Subtype

A Chaudhry[1], M Gul[2], A Chaudhry[3], R Matthews[4]
[1]Johns Hopkins Medicine, Elkridge, MD, [2]National Institute of Health, Elkridge, MD, [3]Stony Brook University, Westbury, NY, [4]Stony Brook University Medical Center, Stony Brook , NY

Purpose
Metastasis is the most common cause of a parenchymal brain mass with lung and breast cancer being the two most common causes. As patients with advanced stages of breast cancer are living longer, the incidence of brain metastasis from breast cancer is increasing. Standard of care for breast cancer involves evaluation of immunohistochemistry, which can guide therapy and alter prognosis. We aim to retrospectively evaluate Magnetic Resonance Imaging (MRI) characteristics of breast cancer metastasis to the brain and assess whether imaging findings differ in tumors with different immunohistochemistry.
Materials and Methods
In this retrospective study, we identified 26 patients (mean age, 54.7 years; age range, 34-81

years) who underwent pretreatment MRI at our institution from January 2009 to June 2014 with pathologically proven metastatic breast cancer to the brain. Patients' primary breast cancer immunohistochemistry mutations (Estrogen receptor, progesterone receptor, and HER2-neu receptor etc.) were recorded. The exams were evaluated by two radiologists who were blinded to the pathology data.

Results

Twenty-nine females were identified with metastatic brain cancer, 15/29 were triple negative, 6/29 were triple positive (ER, PR and HER2), 4/29 were ER/PR positive and HER2 negative, 3/29 were only ER-positive and 1/29 were only PR-positive breast cancers. On non-contrast CT, 18/29 (62.1%) of the patients had evidence of a lesion, which were relatively isodense to gray matter. Of these, 13/18 were triple negative, 4/18 were triple positive. On MRI, the lesions relative to gray matter were T1-hypointense in 27/29 (93.1%) of patients. Only 2/29 (6.9%) lesions were T1-isointense and both these cases were triple negative. 24/29 (82.8%) patients demonstrated T2 and FLAIR lesions were isointense to gray matter. Only 5/29 (17.2%) were hyperintense on T2 and FLAIR images, out which four were triple negative. 21/29 (72.4%) patients had heterogeneous post-contrast enhancement. 8/29 (27.6%) had homogenous post-contrast enhancement, out of which four were ER/PR positive and two were triple positive. The lesions varied in size ranging from 3.0 mm up to 4.7cm and average lesion size on post-contrast image was approximately 13.1cm. All lesions on MRI had variable degree of surrounding vasogenic edema. On diffusion-weighted imaging (DWI), 18/29 (62.1%) demonstrated restricted diffusion. 6/11 patients without restricted diffusion were triple negative. On gradient echo sequence, 6/29 patients (20.6%) patients demonstrated susceptibility artifact and none of these lesions demonstrated observable calcium on CT. Five out six of these patients were triple negative.

Conclusions

Our study shows that in patients with metastatic breast cancer to the brain, triple negative breast cancers are the most common subtype. Imaging characteristics of triple negative breast cancers include isodense (relative to gray matter) mass on CT. MRI imaging characteristics of triple negative breast cancer reveals T1 hypointense, T2/FLAIR isointense mass with restricted diffusion and heterogeneous post-contrast enhancement. Also, in patients with history of breast cancer, presence of susceptibility artifact in a potential metastatic brain lesion is more likely to represent triple negative subtype.

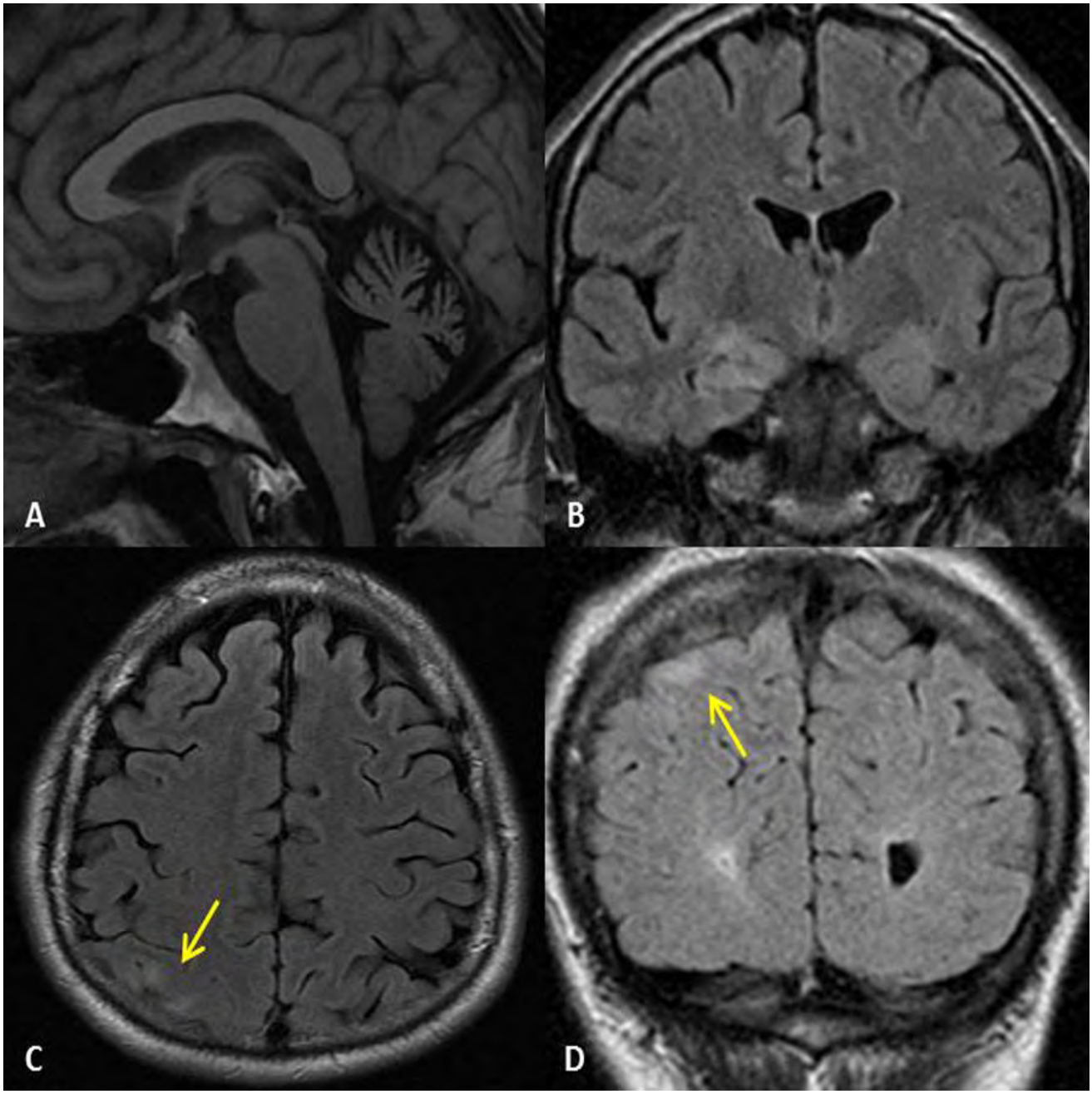
eP-06

6:30AM - 3:00PM

MRI Findings in GAD65+ Autoimmune Epilepsy

J Fredriksen[1], C Carr[2], K Koeller[1], A Kotsenas[3], J Verdoorn[1]
[1]Mayo Clinic, Rochester, MN, [2]Mayo Clinic, Rochester, Rochester, MN, [3]Mayo Clinic, Rochester , MN

Purpose
To review and describe the imaging findings in patients with a clinical diagnosis of autoimmune epilepsy and elevated serum glutamic acid decarboxylase (GAD65+) autoantibodies.
Materials and Methods
An institutional database review was performed to identify patients with both a clinical diagnosis of autoimmune epilepsy and abnormally elevated serum GAD65+ antibodies, who also had undergone MR imaging of the brain. Magnetic resonance imaging (MRI) studies were reviewed independently by 3 neuroradiologists and 1 neuroradiology fellow, with focus on evaluation for parenchymal atrophy, parenchymal signal abnormality, and abnormal enhancement. Discordant findings were reviewed on a consensus basis.
Results
The initial database query identified 702 patients with abnormal serum GAD65+ antibody titers. Of these, a total of 19 patients had a clinical diagnosis of autoimmune epilepsy and had undergone MR imaging of the brain. The majority of patients were female (84%), with an age range of 11 to 66 years. Serum autoantibody titers ranged from 33 to 4,415 nmol/L (normal < 0.02 nmol/L). The most common imaging findings included cerebellar atrophy (A) and abnormal hippocampal signal (B), with a subset of patients also demonstrating abnormal cortical/subcortical T2 hyperintensities (C, D). None of the patients demonstrated abnormal parenchymal or leptomeningeal enhancement, or intrinsic T1 hyperintensity.
Conclusions
Findings of GAD65+ associated autoimmune epilepsy include cerebellar atrophy, hippocampal involvement, and occasionally nonenhancing cortical/subcortical T2/FLAIR hyperintensities. The likelihood and severity of the findings do not appear to be correlated with serum autoantibody titer, likely due in part to the relative rarity of the diagnosis and the presence of overlapping clinical syndromes that are associated with GAD65+ serum positivity. This constellation of imaging findings is important to identify in the setting of de novo epilepsy, and may suggest an underlying autoimmune etiology.



(Filename: TCT_eP-06_MRCollage.jpg)

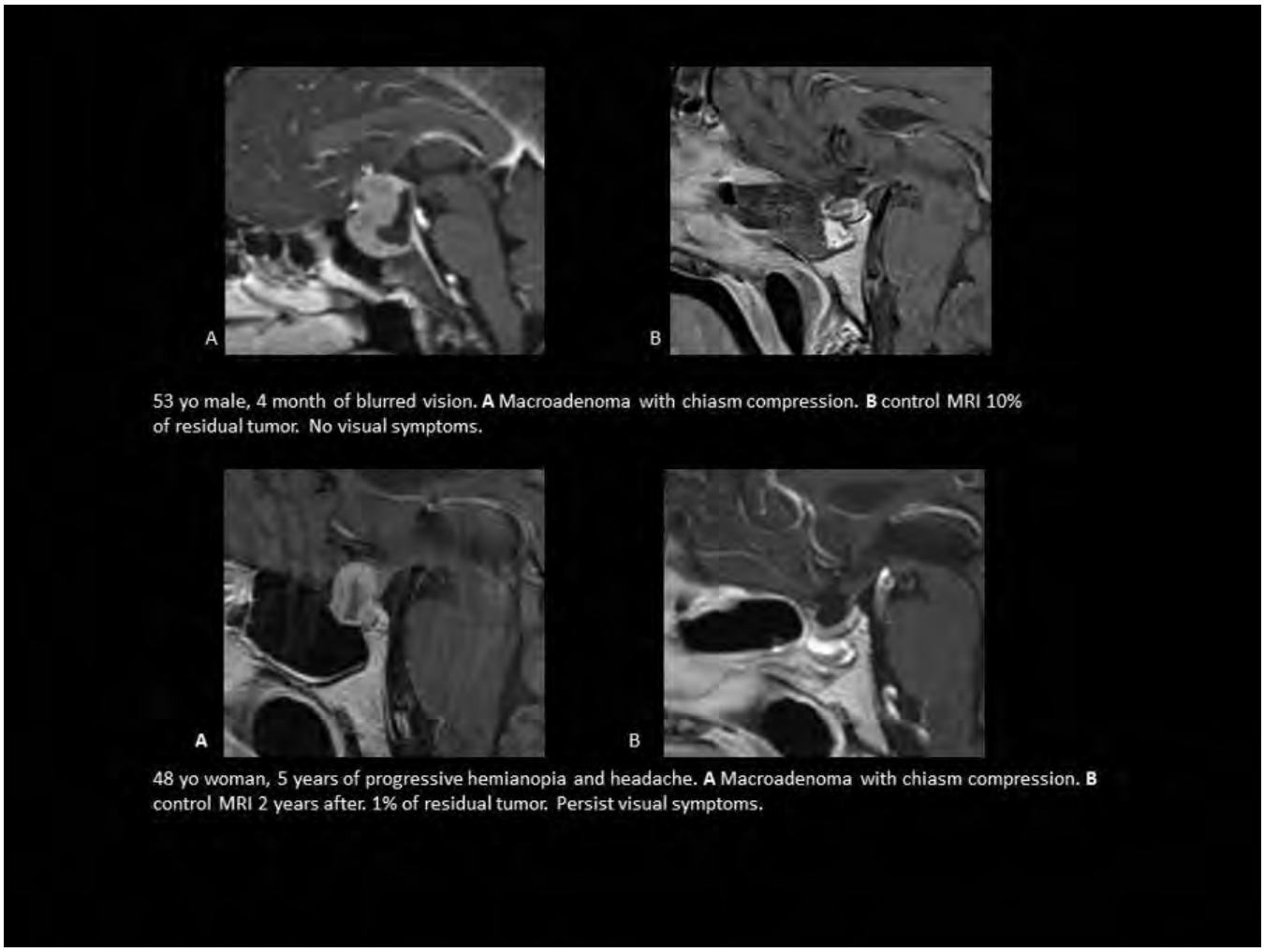
eP-75

6:30AM - 3:00PM

MRI Findings in Pituitary Macroadenoma Post Resection and Symptom Outcome.

C Vallejo[1], R Camacaro[1], P Puac[1], A Rodriguez[1], M Castillo[1]
[1]*University of North Carolina at Chapel Hill, Chapel Hill, NC*

Purpose
Although visual and cranial nerve compression-related symptoms are said to improve nearly immediately after resection of pituitary macroadenomas, our anecdotal experience is that size of tumor in the immediate post-operative period does not correlate significantly with patient's symptoms. Our objectives were to assess the pre- and post-operative volumes of pituitary macroadenomas before, within 24 hours after surgery, and long term and correlated with symptoms.
Materials and Methods
146 patients who underwent surgery for pituitary macroadenomas and had pre- and post-operative (at 24 hours and 3-6 months) MRI studies. Using coronal, axial, and sagittal post contrast T1 images we obtained all tumor volumes before and after surgery. We reviewed all medical records for evidence of symptom improvement including those related to vision and cranial nerves, and headache unrelated to other events. A comparison between symptom improvement or lack of and changes in tumor volume.
Results
The mean tumor volume in pre-operative studies was 24.66 cm3 and the following symptoms were present: visual/cranial nerve abnormalities in 65% and headaches in 56%. Immediately after surgery, tumor volume decreased an average of 65% and all symptoms persisted without significant changes in all patients. On the long term control MRI study, progressive tumor volume decrease was noted in 82% and symptoms improve in 78% of patients. However, 32 patients showed no symptom improvement on long term follow up despite a mean 43% decreased in tumor size and no imaging evidence of chiasmal or cavernous sinus compression.
Conclusions
Despite significant decrease in tumor volume immediately following surgery, symptoms did not change or improve in our patients. Lack of symptom improvement does not mean an inadequate resection. Long term tumor volume decrease correlated with symptom improvement in most but not all patients suggesting that in some patients permanent injuries presumably due to compression had occurred.



(Filename: TCT_eP-75_macroadenomas.jpg)

eP-29

6:30AM - 3:00PM

Neurocysticercosis: a Multifaceted Diagnostic Challenge

A Torres[1], M Borri[2], A Wolosker[3], L De Abreu Jr.[4]
[1]Fleury Group, Hospital São Luiz, São Paulo, São Paulo, [2]Fleury Group, Hospital Sao Luiz, Sao Paulo, Brazil, [3]Fleury Group, Hospital Sao Luiz, Sao Paulo, SAO PAULO, [4]Fleury Group Hospital, Sao Paulo, Brazil

Purpose
The purpose of this pictorial essay is to demonstrate various presentations of cysticercosis in central nervous system (CNS), emphasizing image patterns and evolutionary stages.
Materials and Methods
The pictorial essay was done with images of brain computed tomography (CT) and magnetic resonance (MRI) of patients with neurocysticercosis, collected from our archive. We

reviewed the literature and correlated our images with the presentations and evolutionary stages described.

Results

Neurocysticercosis is characterized by the parasitic involvement of CNS by the larval stage of Taenia solium. The imaging presentation is highly variable, depending on the number, evolution and location of the lesions. This variation may delay and difficult the correct diagnosis. The main clinical findings in our patients were headache, nausea, vertigo and convulsions. All evolutionary phases of neurocysticercosis (vesicular, colloidal vesicular, granular nodular and nodular calcified) were demonstrated with different patterns of lesions, compromising the encephalic parenchyma, subarachnoid space and ventricular system. There were some cases complicated with obstruction of cerebrospinal fluid flow.

Conclusions

Imaging has a critical role for characterize and confirm CNS involvement by cysticercosis.

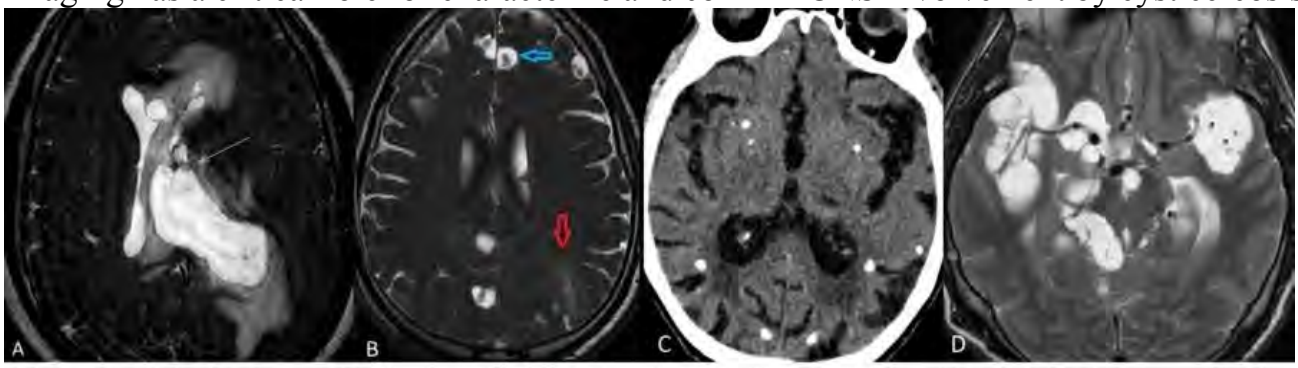


Figure1: Axial CISS image (A): Lesion with internal scolex, in lateral ventricle with extension to interventricular foramen (yellow arrow). Axial CISS image (B): Lesion with internal scolex and lacking adjacent edema is in the vesicular stage (blue arrow) and hyperintense lesion on FLAIR with adjacent edema is in the colloidal vesicular stage (red arrow). Axial CT scan (C): Multiple calcified neurocysticercosis lesions are in the nodular calcified stage. Axial T2-weighted image of subarachnoid neurocysticercosis (D): Multiple fluid-filled lesions lacking internal scolex and filling the basal cisterns and sylvian fissures, with associated mass effect and distortion of adjacent structures.

(Filename: TCT_eP-29_Figure1.jpg)

eP-52

6:30AM - 3:00PM

Neuroimaging in Brain Death: Inter-Rater Reliability of CT Perfusion and Other Ancillary Imaging Tests

D MacDonald[1], J Shankar[1]
[1]*Dalhousie University, Halifax, Nova Scotia*

Purpose

Brain death confirmation usually is clinical. The operational definition of brain death includes permanent loss of brainstem function. Ancillary imaging tests are indicated in patients where clinical decision is not reliable. Use of ancillary imaging modality is highly

variable based on preference of physician, institution, region and even country of practice. The basic principle for ancillary tests for confirmation of brain death is to demonstrate absent cerebral blood flow either in whole brain or just brainstem. The inter-rater reliability has not been studied for the ancillary imaging tests used for confirmation of brain death. The purpose of this study was to demonstrate the utility and interrater reliability of different ancillary imaging tests for confirmation of brain death.
Materials and Methods
We retrospectively analyzed imaging for brain death confirmation in our institution from 2005 – 2016. Studies included 41 CTP scans, 54 computed tomography angiograms (CTA), 15 radionuclide angiograms and 71 nonenhanced CT (NECT) head scans. The reference standard for the diagnosis of brain death was clinical decision in all of these patients. A third year radiology resident and a neuroradiology staff, blinded to clinical information and blinded to each other's results, analyzed all the scans for confirmation of brain death. Interrater agreement was analyzed using kappa statistics for all imaging tests. A p value <0.05 was considered significant.
Results
Data from 71 patients were examined. Kappa values for different modalities for confirmation of brain death were: 1.0 for CTP, 1.0 for radionuclide angiograms, 1.0 for CTA 4-point scale, 0.92 for CTA 7-point scale, and 0.90 for NECT with $p<0.001$.
Conclusions
There was almost perfect interrater reliability (kappa of >0.8) across all imaging modalities for confirmation of brain death and was irrespective of the operator's experience.

eP-02

6:30AM - 3:00PM

Patterns of Neuromyelitis Optica Spectrum Disorders in Patients with Positive Anti-MOG Antibodies

L Resende[1], L Salles[1], S Pereira[1], F Silva[2], D Callegaro[1], L Lucato[1], C Leite[1], D Sato[3], C Rimkus[1]
[1]University Of Sao Paulo, Sao Paulo, Brazil, [2]CDB-Centro de Diagnósticos Brasil, Sao Paulo, Brazil, [3]Pontifícia Universidade Católica do Rio Grande do Sul, Porto Alegre, Brazil

Purpose
A percentage of patients with neuromyelitis optic spectrum disorders (NMOSD) have positive titles for autoantibodies against myelin oligodendrocyte glycoprotein (anti-MOG). However, it is still not clear whether they fulfill the diagnostic criteria for seronegative NMOSD or not and if imaging patterns are similar to the classic forms, which are positive for antiaquaporin-4 antibodies (anti-AQP4). The aim of this study is to describe magnetic resonance imaging (MRI) patterns of NMOSD anti-MOG positive patients and to apply the NMOSD diagnostic criteria in this cohort.

Materials and Methods
Two radiologists blinded for clinical data retrospectively analyzed MRI exams from 25 anti-MOG positive patients who were negative for anti-AQP4. The frequency, distribution and characteristic of lesions were classified according to the Wingerchuk 2015 diagnostic criteria for NMOSD.
Results
Acute optical neuritis (ON) was observed in eleven patients (57.9%), affecting more frequently the anterior segments of the optic nerve (retro bulbar, intraorbital and canalicular in 9 patients), but the optic chiasm was affected in only 2 patients. Five patients (54.5%) had bilateral neuritis and 1 (9.1%) had recurrent neuritis. Ten patients (43.5%) had spinal cord lesions, in which 8 had longitudinal extensive transverse myelitis (LETM). Only 1 patient (4.1%) had lesions in the area postrema. Six patients had brain lesions (27.3%), most frequently localized in the brainstem, fourth ventricle and cerebellum. Only 1 patient had diencephalic and extensive subependymal lesions. Two patients (33.3%) had brain lesions typical for multiple sclerosis (MS). Only 1 patient (4%) fulfilled the Wingerchuk 2015 diagnostic criteria requirements for anti-AQP4 seronegative NMOSD.
Conclusions
Extensive ON and LETM are frequent in anti-MOG positive patients. However, lesions in regions frequently affected in the classic anti-AQP4 positive NMOSD, such as the optic chiasm and area postrema, were less affected in our cohort and MRI findings in most patients did not fulfill the revised diagnostic criteria for NMOSD, suggesting that the pathological mechanisms might be different depending on patient´s immunological profile.

eP-76a

6:30AM - 3:00PM

Perfusion Abnormality in Posterior Inferior Cerebellar Artery Termination of Vertebral Artery on Arterial Spin Labeling and Dynamic Susceptibility Contrast Perfusion MRI

D Park[1]
[1]*Hanyang University Guri Hospital, Guri, Gyeonggi-do*

Purpose
A posterior inferior cerebellar artery (PICA) termination of vertebral artery has been regarded as a normal variation of vertebrobasilar circulation. However, the perfusion condition of PICA territory in the cerebellum has not been evaluated. This study aims to present the perfusion abnormality in PICA termination of vertebral artery (PICA-VA) on arterial spin labeling (ASL) and dynamic susceptibility contrast (DSC) perfusion MRI.
Materials and Methods
Sixteen patients (M:F=8:8, 49-90 years old) who conducted brain MRI including MR angiography, and ASL and DSC perfusion MR studies and are found to have PICA-VA, are

evaluated in this study. PICA-VA are associated with ipsilateral hypoplastic vertebral artery in 14 patients, and bilateral fetal type posterior cerebral artery in 2 patients.
Results
Hypoperfusion in PICA territory is detected on both ASL and time to peak (TTP) map of DSC perfusion MRI in 11 patients (68.7%), on only TTP perfusion MRI in 2 patients (12.5%), on only ASL perfusion MRI in 1 patient (6.3%) and not on both perfusion MRI in 2 patients (12.5%). Any clinical manifestations of vertebrobasilar insufficiency are not accompanied in 2 patients (12.5%).
Conclusions
PICA-VA that is regarded as normal variation, considerably have hypoperfusion in PICA territory of cerebellum. PICA-VA could have the clinical significance, especially in vertebrobasilar insufficiency, so perfusion study such as ASL or DSC perfusion MRI may help to evaluate the clinical status of vertebrobasilar insufficiency.

eP-57

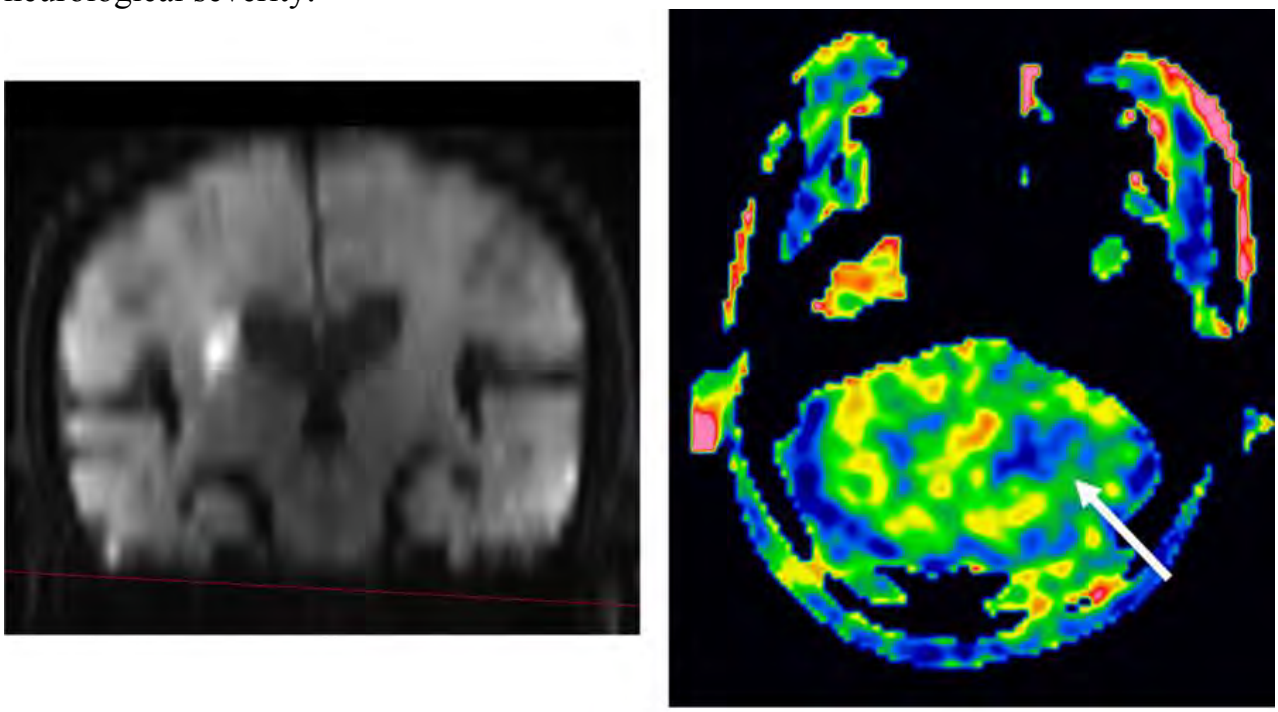
6:30AM - 3:00PM

Perfusion MR Imaging Using Three-Dimensional Pseudo-Continuous Arterial Spin-Labeling Method for Acute Cerebral Infarction Classified as Branch Atheromatous Disease

Y Shinohara[1], A Kato[1], K Kuya[1], F Miyoshi[1], K Okuda[2], M Sakamoto[1], H Kowa[1], T Ogawa[1]
[1]Tottori University, Faculty of Medicine, Yonago, Tottori, [2]Tottori University Hospital, Yonago, Tottori

Purpose
Recent articles have suggested that MR perfusion imaging using 3-dimensional pseudo-continuous arterial spin labeling method (3D ASL) is useful for evaluating cerebral ischemia. However, there were few reports regarding the detectability of crossed cerebellar diaschisis (CCD) on 3D ASL in acute infarction. Additionally, there was no article about 3D ASL findings of branch atheromatous disease (BAD), which is one of the stroke subtypes considered as the risk factors of early neurological deterioration. The aim of our study was to clarify the utility of whole-brain 3D ASL as an imaging biomarker for predicting neurologic severity in BAD.
Materials and Methods
We included 101 patients with acute cerebral infarction in the anterior cerebral artery territory who underwent brain MR examination within 1 week from clinical onset. All patients were performed MR imaging including diffusion-weighted image (DWI), 3D time of flight MR angiography, and 3D ASL by using 3T MR scanner (Discovery MR750w, GE Healthcare). We classified BAD based on the known criteria, and measured DWI infarct volume at lenticulostriate artery territory, asymmetry index of cerebral blood flow in the

affected area (AI-BAD) and contralateral cerebellar hemisphere (AI-CCD). We also compared each parameter with initial NIHSS by using Pearson's correlation coefficient.
Results
Twenty-three patients with BAD were enrolled in this study. There was no correlation between NIHSS and AI-BAD ($r = -0.027$, $p = 0.724$), whereas each DWI infarct volume and AI-CCD had significant correlation with NIHSS ($r = 0.664$; $p = 0.001$, $r = 0.515$; $p = 0.012$, respectively).
Conclusions
3D ASL can detect CCD in the patients with BAD, which are correlated with the degree of neurological severity.



88-year-old male with right branch atheromatous disease-type acute infarction. 3D-ASL shows hypoperfusion signal intensity in the left cerebellum which indicates crossed cerebellar diaschisis (*white arrow*).

(Filename: TCT_eP-57_FIGBADforASNR.jpg)

eP-47

6:30AM - 3:00PM

Perfusion-Permeability-Discrepancy, the Prognostic Factor of Glioma

T Abe[1], M Harada[1]
[1]*Tokushima University Graduate School, Tokushima, Tokushima*

Purpose
We reported that the prognosis of the patient with the arterial spin labeling (ASL) hyperintensity outside the contrast region (ASL-dominant, ASL-d finding) is better than without ones at the 2017 Annual Meeting of the Japan Radiological Society. We performed the Cox proportional hazard model analysis in order to investigate the relationship with other prognostic factors.
Materials and Methods
In this retrospective institutional review board approved study, we included 32 consecutive cases with glioma who received 3T MRI scans including ASL and contrast-enhanced (CE) T1-WI. We examined the effect on ASL-d findings and other factors on prognosis -age, gender, histology (WHO grade, oligodendroglial component), imaging finding (contrast enhancement, ASL-d finding), KPS, operation (tumor location and resection rate), treatment (TMZ, radiation, and other treatment) - using the Cox proportional hazard model increase method.
Results
Arterial spin labeling-dominant (coefficient -3.28), WHO grade (coefficient 2.03), gender (coefficient 1.69) were significant prognostic factors, and the other factors were not significant.
Conclusions
Arterial spin labeling-dominant finding suggests a good prognosis in glioma.

eP-16

6:30AM - 3:00PM

Physical Activity During Childhood Positively Affects Structural Brain Connectivity in Adulthood

G Blasco[1], C Biarnes-Duran[2], M Puig-Parnau[3], B Roman-Vinas[3], A Prats-Puig[3], L Ramio-Torrenta[4], S Pedraza[1], J Puig[5]
[1]Imaging Research Unit, IDI-IDIBGI, Hospital Dr Josep Trueta, Girona, None, [2]Research Unit of Diagnostic Imaging Institute (IDI), Girona Biomedical Research Institute (IDIBGI), Girona, Girona, [3]EUSES University School, University of Girona, Salt, Girona, [4]Department of Neurology-IDIBGI, University Hospital Dr JosepTrueta, GIRONA, GIRONA, [5]Research Unit of Diagnostic Imaging Institute (IDI), IDIBGI, University Hospital Dr Josep Trueta, Girona, Girona

Purpose
To study the association between physical activity during childhood and brain structural connectivity during adulthood.
Materials and Methods
We studied 24 healthy adults (14 female; age 40.2±11.4 years) using a 1.5T magnetic resonance imaging (MRI) scanner. Imaging included diffusion tensor imaging (DTI) with 16

diffusion-sensitized gradients applied along 15 noncollinear directions with a b-value of 1000s/mm2 and anatomical T1-weighted turbo-field echo sequences. We calculated axial diffusivity (AD), radial diffusivity (RD), mean diffusivity (MD), and fractional anisotropy (FA) maps using Olea Sphere 3.0 software (Olea Medical, La Ciotat, France). We used FSL tools (FMRIB, Oxford, UK) to normalize images and the ICBM-Atlas to map white matter tract DTI-metrics. Physical activity in childhood was assessed using self-reported questionnaires. The relation between variables was analyzed by Spearman correlation followed by multiple regression using the "enter" method.
Results
Regular sports practice before 16 years of age correlated positively with mean FA in the right fascicle of posterior corona radiate (r=0.545; p=0.013), the left posterior limb of the internal capsule (r=0.652; p=0.001), and the superior longitudinal fasciculus (r=0.615; p=0.004) and negatively with mean RD in the posterior corona radiate (r= -0.560; p=0.010) and the left superior corona radiate (r= -0.574; p=0.008). All these associations remained significant after correcting for confounding variables such as age, gender, and educational level.
Conclusions
Regular physical activity before 16 years of age positively affects structural connectivity in the brain. In healthy adults, the main regions affected are the corona radiate and the internal capsule, both areas with motor and sensory fibers that carry information to and from the cortex.

eP-39

6:30AM - 3:00PM

Predict Glioblastoma Genetic Features Using DSC Perfusion-Weighted Imaging

J Fang[1]
[1]*Institute of Surgery Research,Daping Hospital, Third Military Medical University, Chongqing, Chongqing*

Purpose
To assess the value of dynamic susceptibility contrast-enhanced perfusion magnetic resonance imaging (DSC-MRI) in predicting major genetic features in glioblastoma (GBM).
Materials and Methods
Sixty patients (36 men and 24 women; mean age 43.00±9.97, age range 35-65 years) with pathologically proved GBM were analyzed from May 2009 to 2015 in our hospital. The conventional MR imaging containing T1-weighted imaging, T2-weighted imaging and fluid-attenuated inversion recovery sequence (FLAIR) and DSC-MRI studies were performed in a 3T MR scanner using a an 8-channel head coil. CBV maps were constructed by using a commercial software package, and then relative CBV values were obtained by drawing region of interest (ROI) based on the enhanced T1-weighted images. The expression of five

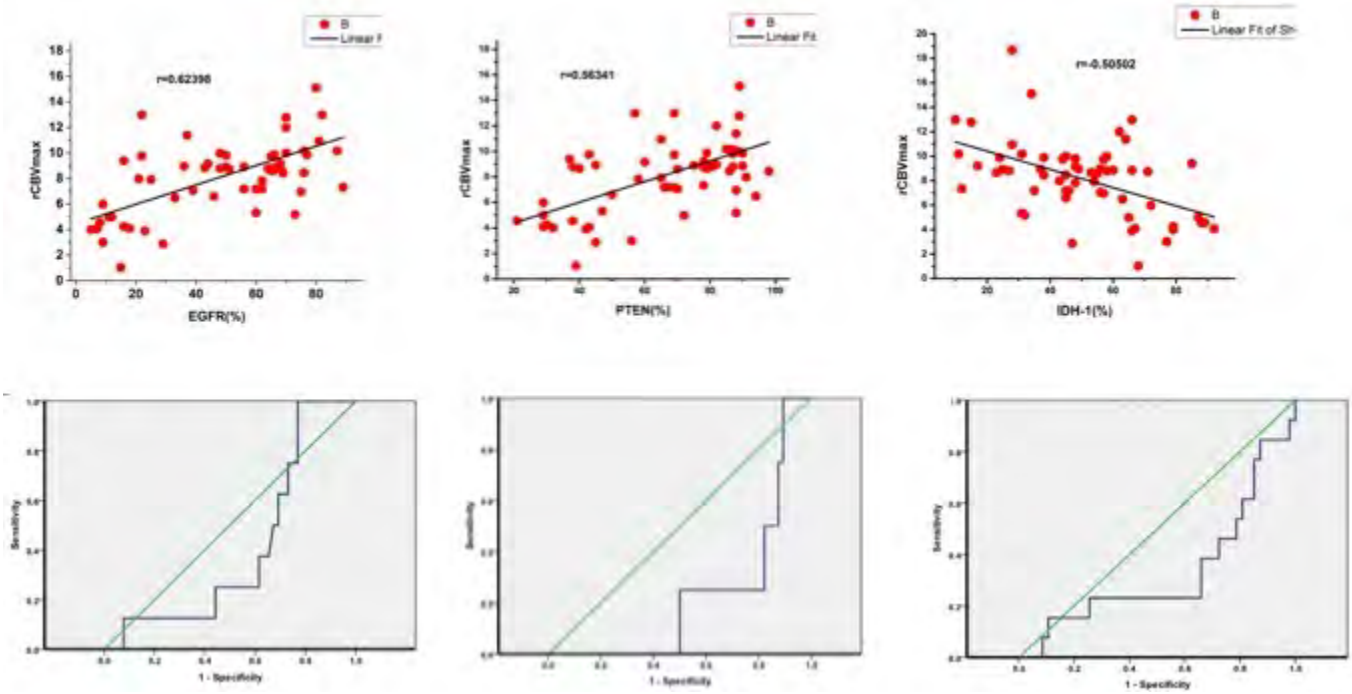
major GBM molecular alterations, including epidermal growth factor receptor (EGFR), p53, isocitrate dehydrogenase-1(IDH-1), neurofilament (NEFL) and Phosphatase and tensin homolog deleted on chromosome ten (PTEN) were confirmed by immunohistochemistry. Statistical analysis was performed using the unpaired Student t test, ROC (receiver operating characteristic) curve analysis and Pearson correlation analysis.

Results

Among the five molecular alterations, the rate of PTEN positive expression was the highest which was about 78 percent (47/60), while, the rate was 76, 52, 33 and 63 percent, respectively for EGFR, p53, IDH-1, NEFL expression. EGFR ($p<0.01$, $r=0.63$) and PTEN ($p<0.01$, $r=0.48$) showed positive correlation with rCBVmax (Figure 1). The optimal cutoff vale for the presence of EGFR was rCBVmax ＞5.98 with an area under the curve of 0.93, a sensitivity of 95.7%, and a specificity of 92.9%. The optimal cutoff vale for PTEN was rCBVmax ＞7.18 with an area under the curve of 0.84, a sensitivity of 76.6%, and a specificity of 84.6% (Figure 1). The rCBVmax of IDH-1 mutant group was lower than that in IDH-1 wild group. IDH-1 was negative correlated with rCBVmax（$p<0.001$, $r=0.-0.56$）, the optimal cutoff vale for the presence of IDH-1 mutant was rCBVmax＜6.63 with an area under the curve of 0.84, a sensitivity of 92.5%, and a specificity of 70% (Figure 1).

Conclusions

rCBVmax could serve as a predictor for the presence of EGFR, PTEN and IDH-1 mutant in glioblastoma. Thus, contrary to conventional MRI, we believe that DSC-MRI could provide more helpful information to make a individual treatment schedule.



(Filename: TCT_eP-39_Fig1.jpg)

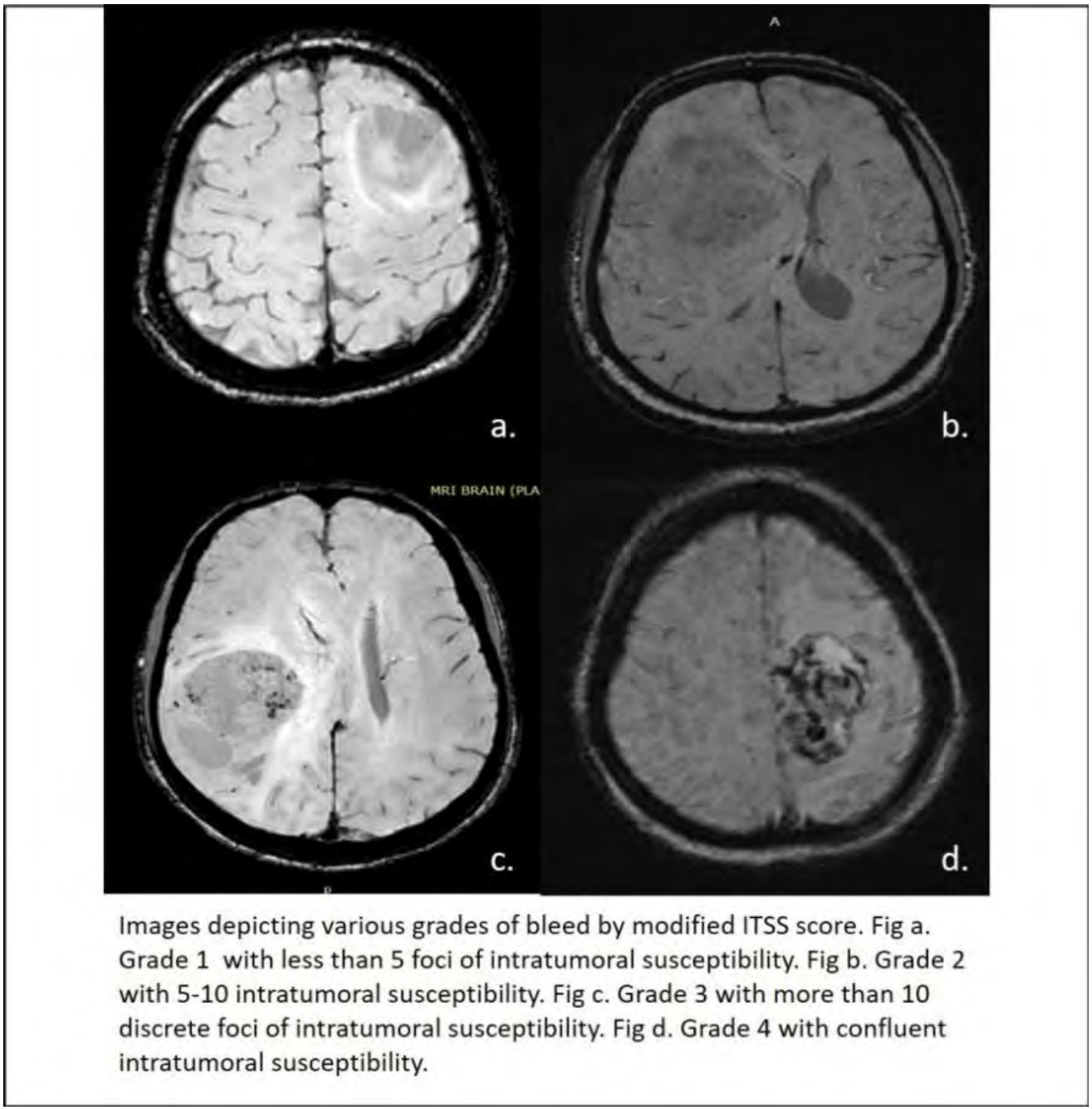
eP-44

6:30AM - 3:00PM

Predicting Tumour Grade and IDH Mutation Status Using Modified ITSS Score in High Grade Gliomas

A Deepesh[1], A Gupta[2], j saini[3], M Bhat[4], S S[1], V Santosh[1], D Chakrabarti[1]
[1]National Institute of Mental Health And Neuro Sciences, Bangalore, Karnataka, [2]National Institute of Mental Health and NeuroSciences (NIMHANS), Bangalore, Karnataka, [3]NIMHANS, BANGALORE, Karnataka, [4]National Institute of Hental Health and Neurosciences, Bangalore , karnataka

Purpose
• To predict grade of the tumor in high grade gliomas using modified Intratumoral susceptibility signal (ITSS) score. • To predict isocitrate dehydrogenase mutation (IDH) status in high grade gliomas using the same modified ITSS score.
Materials and Methods
This is a retrospective study during period of August 2015-November 2016. Forty-seven subjects with MRI and immunohistochemistry results available in hospital records were included in the study. Twenty-eight out of forty-seven were grade 3 gliomas and nineteen were grade 4 gliomas. Among the grade 3 gliomas, nineteen were IDH mutation positive and 9 were negative. Out of the grade 4 gliomas, 10 were IDH mutant positive and 10 were negative. Retrospective review of susceptibility-weighted imaging (SWI)/Venobold images of these subjects were done and modified ITSS score given by 2 experienced neuroradiologists with >10 years of experience. Modified ITSS score. Grade 0: No intratumoral susceptibility. Grade 1: Less than five foci of intratumoral susceptibility. Grade 2: 5- 10 foci of intratumoral susceptibility. Grade3: > 10 foci of intratumoral susceptibility (spotty or scattered). Grade 4: Gross conglomerate areas of intratumoral susceptibility, macroscopic hemorrhage and hemorrhagic tumors. The data were analyzed with Mann Whitney's test for comparing grade 3 and 4 gliomas and IDH mutation status of these tumors.
Results
The modified ITSS score was significantly different between grade 3 (median 1; interquartile range 0 – 2) and grade 4 (3.5; 3 - 4) gliomas ($p < 0.001$) and, also between IDH mutations positive (1; 0.25 -3) and negative (4; 1 - 4) within all cases recruited ($p = 0.009$).
Conclusions
Thus, differentiation between grade 3 and 4 gliomas as well as presence of IDH mutation can be reliably accomplished using the modified ITSS scoring system in SWI/Venobold images. Larger volume samples would be required for validation of robustness of these findings in the future.



Images depicting various grades of bleed by modified ITSS score. Fig a. Grade 1 with less than 5 foci of intratumoral susceptibility. Fig b. Grade 2 with 5-10 intratumoral susceptibility. Fig c. Grade 3 with more than 10 discrete foci of intratumoral susceptibility. Fig d. Grade 4 with confluent intratumoral susceptibility.

(Filename: TCT_eP-44_ComboPic.jpg)

eP-28

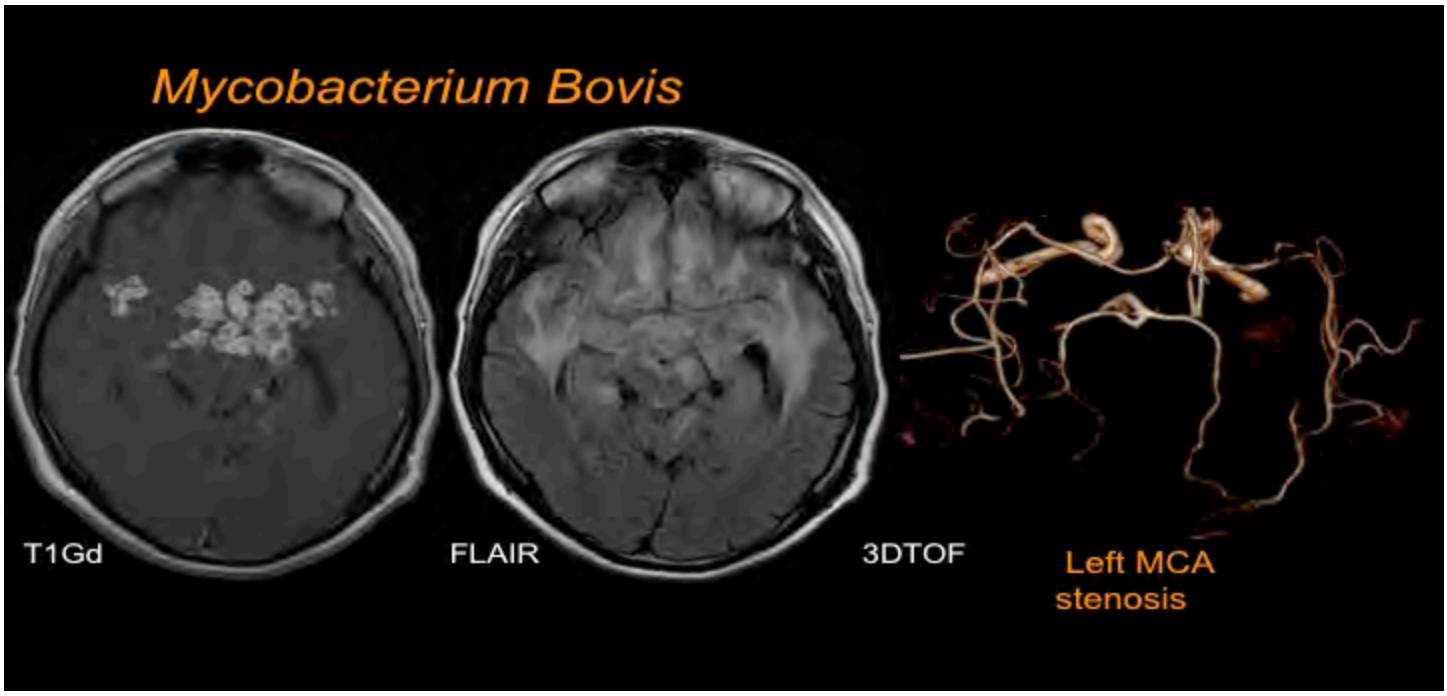
6:30AM - 3:00PM

Predictors and Outcome of Cerebral Vasculopathy in Patients with Tuberculous Meningitis

G Romero-Sanchez[1], J Higuera-Calleja[2], M Gonzalez-Duarte Briseño[3]

[1]Montreal Neurological Institute and Hospital, Montreal, QC, [2]Instituto Nacional de Ciencias Médicas y Nutrición Salvador Zubirán, Mexico city, Tlalpan, [3]Instituto Nacional de Ciencias Médicas y Nutrición Salvador Zubirán, Mexico, Tlalpan

Purpose
To determine the outcome with a 90-day modified Rankin Scale (0-6) in patients with tuberculous meningitis and vasculopathy detected by magnetic resonance imaging (MRI) compared to those with tuberculous meningitis and without vasculopathy.
Materials and Methods
Retrospective and observational study was conducted. Medical records and MRI scans from 2005 to 2015 of patients with tuberculous meningitis confirmed by PCR and culture, and with complete diagnostic criteria of Thwaites (probable and definitive), at the Instituto Nacional de Ciencias Medicas y Nutricion.
Results
A total of 550 MRI scans and medical records of the patients with the diagnosis of tuberculosis were reviewed of which only thirty-one patients met Thwaites criteria. Twenty-four (77.4%) were men and 7 (22.5%) were women. The median age was thirty-three (15.5 SD) years old. Sixteen (52%) patients had poor prognosis, measured by >2 points in the Rankin scale. The presence of vasculopathy was found in twenty-three (74%) patients. Tuberculous meningitis vasculopathy demonstrated various patterns of stenosis, vessel wall thickening, enhancement and vessel occlusion. We found a positive correlation between a higher level in the Rankin modified scale and the infarct volume on DWI ($r = 0.49$), numbers of outbreaks of ischemia on DWI ($r = 0.61$) and number of affected vessels (OR, 0.55), all with significant $p < 0.05$.
Conclusions
1. There is a clear tendency of patients with tuberculous meningitis to present with vasculopathy and stroke. 2. The number of vessels affected and the volume of ischemic tissue should be considered as predictors of poor outcome. 3. In our study, patients with tuberculous meningitis are likely presenting an endothelial dysfunction that result in luminal narrowing and tissue hypoxia. Because of this, a more effective treatment should be proposed, perhaps therapies used in vasospasm or better use of steroids in acute stages will help in these cases. Further studies are necessary.



(Filename: TCT_eP-28_Mycobbovis.jpg)

eP-23

6:30AM - 3:00PM

Prospective Assessment of Brain Iron Deposition and Cognitive Performance in Older Women with Breast Cancer Receiving Adjuvant Chemotherapy

B Chen[1], K Ghassaban[2], S Patel[1], T Jin[3], S Sethi[4], D Utriainen[5], E Haacke[2], A Hurria[1]
[1]City of Hope Medical Center, Duarte, CA, [2]Wayne State University, Detroit, MI, [3]City of Hope National Medical Center, Duarte, CA, [4]Magnetic Resonance Innovations, Inc., Detroit, MI, [5]Magnetic Resonance Innovations, Detroit, MI

Purpose
Some patients with breast cancer suffer from subjective and objective cognitive deficits during and after chemotherapy, colloquially termed "chemobrain" (1, 2). Brain iron deposition is associated with cognitive dysfunction (3). The purpose of this study is to evaluate the association between brain iron deposition and cognition in older women with breast cancer receiving adjuvant chemotherapy.
Materials and Methods
This is a prospective longitudinal study of women aged ≥ 60 years with stage I-III breast cancers receiving adjuvant chemotherapy. Fourteen patients (age 68+/- 5.15 years) underwent neuropsychological testing with the NIH Toolbox4 and brain MRI prior to chemotherapy at time point 1 (TP1), and again within 1 month after completion at time point 2 (TP2). Thirteen age-matched healthy controls (HC) (age 65.4+/-5.86 years) underwent the same assessments. The magnetic susceptibility of the thresholded high iron region (RII) in

seven deep gray matter nuclei was measured from the susceptibility maps generated from SWI phase images and compared to regional baselines established from 174 normal subjects (4). Mixed-design ANOVA and Pearson correlation were used for statistical analysis.
Results
Mean iron susceptibilities of both chemotherapy and HC groups at both time points fell within 95% prediction intervals of the normal population (5). There were no significant differences in brain iron susceptibility values in most of the nuclei measured, except right globus pallidus ($p = 0.04$) at TP1 between HC and the chemotherapy group. There were no group differences at TP2 in any of the measured brain regions. There were no significant changes in iron susceptibility values over time when comparing TP2 to TP1 in either the HC group or the chemotherapy group (all P values > 0.05). There were no significant differences in neuropsychological scores between the HC and the chemotherapy groups. Correlative analysis showed that the crystallized cognition composite score (CCC) was negatively correlated with the brain iron susceptibility values in left substantia nigra ($p=0.02$) and right red nucleus ($p=0.03$) in HC group at TP1. In the chemotherapy group, there was a positive correlation between right caudate nuclei and CCC score at TP1.
Conclusions
Our study showed that there were no short-term longitudinal changes in brain iron deposition and cognitive scores in older patients with breast cancer undergoing adjuvant chemotherapy. There were significant correlations between baseline brain iron deposition in some of the measured brain structures and neuropsychological scores in both groups.

eP-69

6:30AM - 3:00PM

Quantifying Intracranial Internal Carotid Artery Stenosis on Magnetic Resonance Angiography

H Baradaran[1], P Patel[2], G Gialdini[3], K Al-dasuqi[1], A Giambrone[3], H Kamel[1], A Gupta[1]
[1]New York-Presbyterian Hosp/Weill Cornell Med Ctr, New York, NY, [2]NewYork-Presbyterian Hospital/Weill Cornell, New York, NY, [3]Weill Cornell Medical College, New York, NY

Purpose
Intracranial atherosclerosis is a common cause of ischemic stroke. Intracranial stenosis is most commonly quantified by the Warfarin-Aspirin Symptomatic Intracranial Disease (WASID) method, which involves calculating a ratio of luminal diameter measurements on catheter angiography. While accurate assessment of luminal stenosis is important for both assigning stroke etiology and selecting patients for aggressive medical therapy, the current method is cumbersome and prone to error. Our purpose was to determine whether a single linear measurement of the narrowest caliber of the intracranial internal carotid artery (ICA)

on magnetic resonance angiography (MRA) can accurately predict WASID stenosis measurements.

Materials and Methods

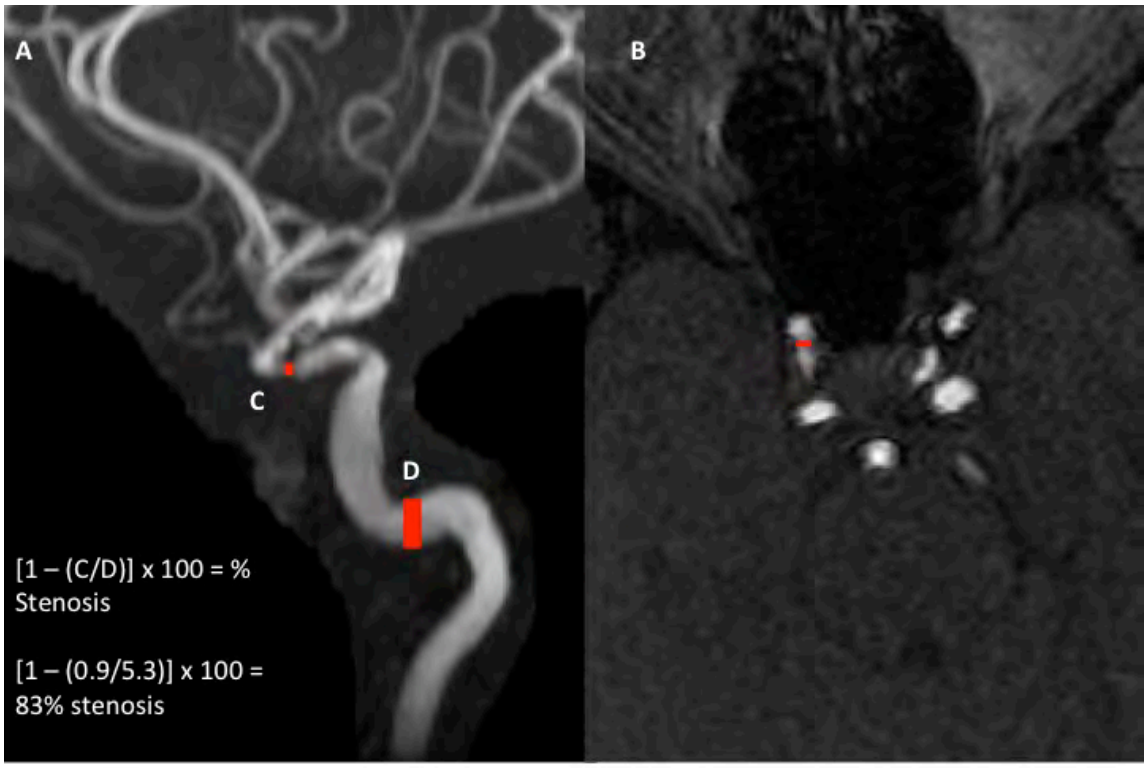
We identified patients from a prospective stroke registry who underwent head MRA to quantitatively evaluate the degree of WASID derived stenosis in each intracranial ICA. We also made single linear millimeter measurements at the site of maximal ICA narrowing (Figure). We calculated a correlation coefficient between the lumen diameter in millimeters and percent WASID stenosis. We performed receiver operating characteristic analysis to determine optimal luminal diameter cutoff values.

Results

In 386 unique intracranial ICAs, we found a strong linear relationship between single lumen measurements and WASID stenosis measurements ($R = -0.84$ [$p < 0.0001$]). We found that ICA lumen diameters of ≤ 2.1 mm and ≤ 1.3 mm were optimal cutoffs for identifying patients with $\geq 50\%$ stenosis and $\geq 70\%$ stenosis, respectively (areas under the curve of 0.96 and 0.99, respectively).

Conclusions

There is a strong linear relationship between the narrowest lumen diameter of the intracranial ICA and WASID stenosis. A single lumen diameter measurement on MRA may allow for accurate estimation of WASID stenosis, which is useful to guide risk stratification and treatment decisions.



(Filename: TCT_eP-69_FigureWASIDQUANT.jpg)

eP-36

6:30AM - 3:00PM

Resolution Limits of Angiography - Fluoroscopic Visualization thresholds in Neuro-Biplane systems: a Comparison of Philips Allura with Clarity and Siemens Artis Zee

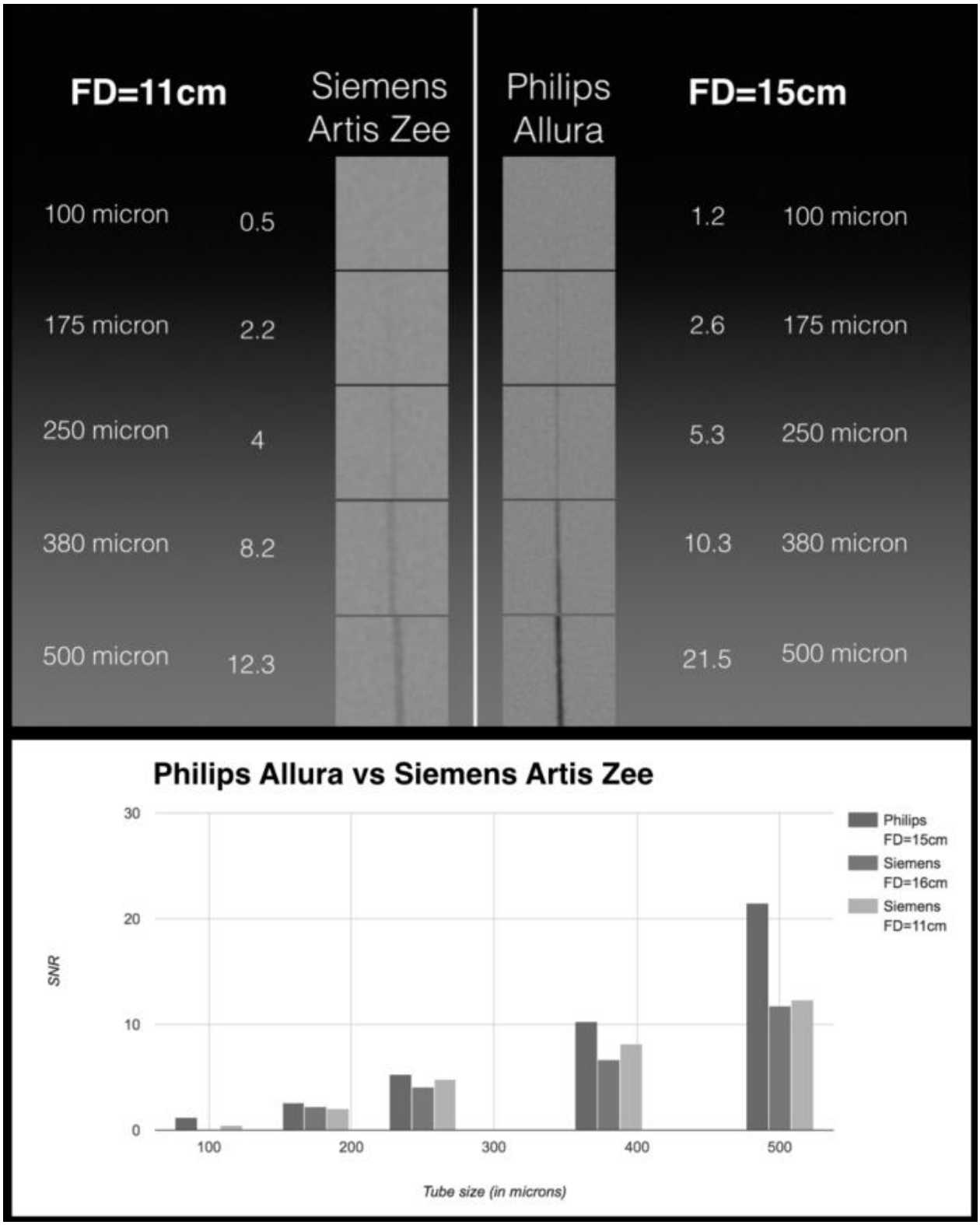
J Mason[1], G Benndorf[2]
[1]Baylor College of Medicine, Bellaire, TX, [2]University of Southern Denmark, Odense, Denmark

Purpose
Accurate angiographic identification of small cerebral vessels which supply important areas of the brain, such as cortical arteries or thalamoperforators is crucial to avoid untoward migration of liquid embolics when performing embolizations of cerebrovascular lesions. Small cerebral vessels like perforating arteries can have diameters as small as 120 microns and range in outer diameters from 330 to 520 microns. In order to maximize diagnostic information during embolization procedures, a so-called "blank Road Map" mode is widely used by most operators. Previous studies in image quality of contrast filled vessels used tubes as small as 230 microns filled with static liquid contrast. In need of a more realistic tool for assessment of angiographic visualization quality of small cerebral arteries, a new dynamic vascular phantom was developed that allows for active visualization of liquid radiopaque agents injected simultaneously into calibrated tubings ranging from 100 to 500 microns. This approach is used to compare 2 state-of-the-art Neuro-Biplane angiographic systems.
Materials and Methods
A previously described linear vascular phantom with step-wise reduced inside diameters ranging from 500 to 100 micron was used. Injections were performed manually using a 5ml syringe and were connected to the phantom via a female luer lock. Injections of undiluted Omnipaque 300mg I/ml were made into the phantom. All injections were performed using a "blank Road Map setting" under optimized conditions for clinical use of each of the 2 systems: Allura with Clarity (Philips Healthcare) and Artis Zee (Siemens Healthcare). Using a previously described method, DICOM pixel data was extracted using region of interest (ROI) tool in Osiris MD version 7.0.4. A previously described formula was used to calculate signal to noise ratios (SNR) using pixel data stored in DICOM images: SNR = (BG – Tube ROI)/[sqrt STD(tube)^2 + STD(BG)^2]/2). (BG = mean background value for pixel data, Tube ROI = ROI within a particular tube (separate values measured for each tube, 100 micron to 500 micron), STD (tube)= standard deviation of pixel data for a particular tube size, STD (BG) = standard deviation of pixel data for background data.
Results
The Allura system using Flat detector (FD) size = 15cm demonstrated a superior SNR compared to Artis Zee system, FD = 16cm (21.5 versus 11.8) and FD=11cm (21.5 versus

12.5). In addition, Philips Allura demonstrates superior SNRs at lower diameters compared to Siemens Artis Zee at FD 16cm and FD=11cm.

Conclusions

There was a measurable and significant difference between SNR of Philips Allura and Siemens Artis Zee during injections of Omnipaque 300 using a standardized dynamic linear vascular phantom with inside diameters ranging from 100 to 500 microns under a "blank Road Map" setting. Based on this study, the Philips Allura system may be superior to Siemens Artis Zee system in the visualization of small cerebral arteries during injections under "blank Road Map". Visualization quality of small cerebral arteries plays a key role in guaranteeing highest possible safety standards during embolizations in patients with cerebrovascular lesions where poor visual control could result in inadvertent embolization of non-target vessels. We have described a novel method of objectively comparing visualization of radiopaque liquids allowing for objective comparisons of fluoroscopy and RM quality between different vendors. The results of such comparisons may differ from claims made for marketing purposes.



(Filename: TCT_eP-36_Philips_Siemens.jpg)

eP-37

6:30AM - 3:00PM

Resolution Limits of CT Angiography - a Comparison of 2 State-of-The-Art CT Scanners using a Calibrated Vascular Phantom

J Mason[1], G Benndorf[2]
[1]*Baylor College of Medicine, Bellaire, TX,* [2]*University of Southern Denmark, Odense, Denmark*

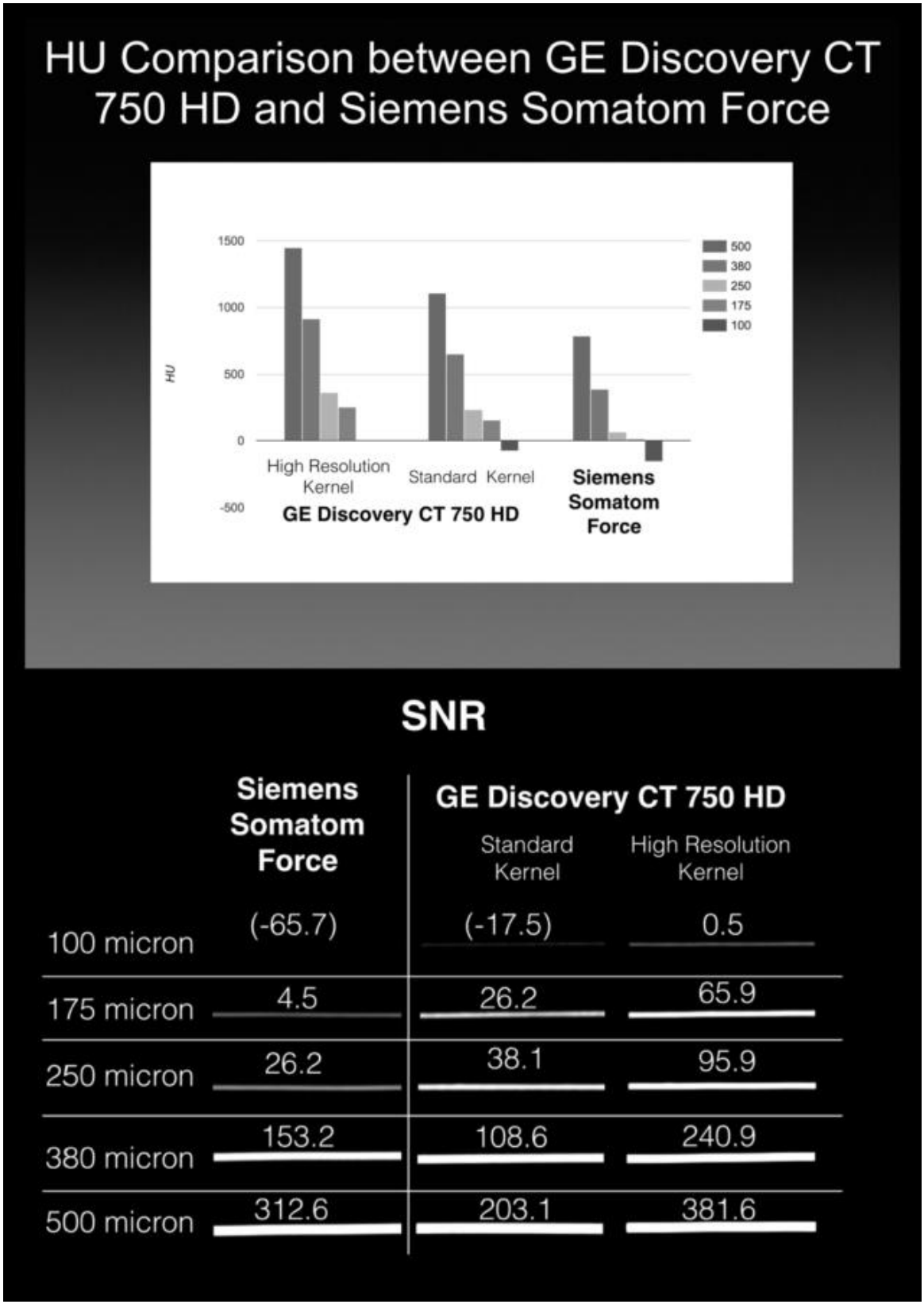
Purpose
Prior research using vascular phantoms has been used to compare visualization under fluoroscopy of contrast and liquid embolic agents, evaluate automated vessel diameter measurements, evaluate automated stenosis measurements, and measure effects of altering kVp on CNR and SNR. The purpose of this study is to evaluate the feasibility of a previously described, injectable vascular phantom with inside diameters ranging from 100 to 500 micron to compare image resolution and quality using 2 state-of-the-art CT scanners.
Materials and Methods
A previously described linear vascular phantom with step-wise reduced inside diameters ranging from 500 to 100 micron was modified to allow for parallel injections. Injections were performed manually using a 5ml syringe and were connected to the phantom via a female luer lock. Injections of undiluted Omnipaque 300mg I/ml were made into the vascular phantom. The phantom then was scanned on 2 different scanners: Siemens Somatom Force (Siemens Healthineers) and GE Discovery CT 750 HD (GE Healthcare Systems) using a standard and a high-resolution kernel. The following settings were used: Siemens Somatom Force: Kernel = Head (H20f), 100mAs, 120 kV, Scan time 4.3s, Rotation 0.5s, Pitch 0.9, Slice = 0.6mm, "Head Angio". GE: HD 750: Standard kernel, 100 mAs, 120 kV, Slice = 0.625mm, Scan time = 4.3s, Pitch = 0.9, Cerebral Angio. GE: HD 750: high resolution kernel, 120 kV, 100 mAs, HD Standard Kernel, Slice = 0.6mm, Scan time = 4.3s, Pitch = 0.9, Cerebral Angio. Using OsiriX MD version 7.0.4, on single axial images a standard circular region of interest (ROI) tool was used to measure maximum mean HU measurable for each tube. The ROI had a radius of ~250microns, and the same ROI was copied exactly to be used for each tube. Regions of interest were manual placed to find the maximum average HU for each tube. Three different areas were measured, and these values were averaged. Signal-to-noise ratios (SNR) were calculated for each tube. Image noise was defined as the standard deviation of background (air) attenuation. HU averages were compared for each tube size between Siemens Somatom Force, GE Discovery standard kernel, and GE Discovery high-resolution kernel using two-tailed student t-test with unequal variance.
Results
GE Discovery CT 750 HD with high-resolution kernel and standard kernel demonstrated statistically significant HU measured for each tube (100-500 micron) compared with Siemens Somatom Force. GE Discovery CT 750 HD with high-resolution kernel demonstrated the highest SNR which ranged from 0.5 to 381, for contrast filled tubes

ranging in size from 100-500 microns. GE Discovery CT 750 HD standard kernel demonstrated higher SNR at 100-250 microns compared to Siemens Somatom Force; whereas Siemens Somatom Force demonstrated higher SNR at 500 and 380 microns.

Conclusions

1) There was a measurable difference in imaging resolution between GE Discovery CT 750 HD and Siemens Somatom Force using the method we have described. The GE Discovery CT 750 HD with high-resolution kernel and standard kernel was superior, and thus may provide better angiographic visualization of small cerebral vessels in cranial CTA datasets.

2) This method may be used to compare various CT systems, as well as other imaging modalities where evaluation of essential small cerebral vessels is important, such as intracranial dissections, moyamoya diseases or vasculitides.



(Filename: TCT_eP-37_CTAIMAGE.jpg)

eP-12

6:30AM - 3:00PM

Resting State Network Dysfunction in Intermittent Explosive Disorder

A Bhattacharya[1], C Conklin[2], M Alizadeh[2], F Mohamed[2], M McCloskey[3]
[1]Lewis Katz School of Medicine at Temple University, Philadelphia, PA, [2]Thomas Jefferson University, Philadelphia, PA, [3]Temple University, Philadelphia, PA

Purpose
Intermittent explosive disorder (IED), defined as the presence of recurrent behavioral outbursts due to a failure to control aggressive impulses, is estimated to affect up to 7% of adults in their lifetime. Studies have shown inconclusive evidence as to the etiology of IED, with suggestions for both genetic and environmental factors cuing the progression of the disorder. As IED often is comorbid with major psychiatric illnesses such as depression and anxiety and also is found in violent criminals, we sought to determine whether individuals with IED have altered resting state brain connectivity that predisposes them to such behavior, and if so, whether early detection and intervention can modify such destructive behaviors and prevent damages to individuals and society.
Materials and Methods
A total of nearly fifty IED subjects and fifty matched controls received MRI resting network connectivity scans over a 2-year period. At the conclusion of the study, differences in connectivity between the 2 populations were analyzed using SPM's Connectivity Toolbox.
Results
As compared to matched controls, IED individuals demonstrated reduced resting state connectivity between the left amygdala and its connections to the frontal medial cortex, posterior cingulate cortex, and posterior cingulate gyrus ($p < 0.05$). These results indicate that when an IED individual gets initially aggravated there is reduced communication between their emotional hubs in the amygdala and their cortical centers for reason and taking action, and thus, they are less likely to be able to process and reason out their emotional aggravation and instead channel it into immediate bursts of violence.
Conclusions
These results lend evidence to the idea that there are organic brain differences in individuals with IED and suggest that detection of these differences early on could be used as a screening tool to promote better behavioral outcomes in these individuals.

eP-70

6:30AM - 3:00PM

Retrospective Review of Cerebral Venous Sinus Thrombosis Cases from The University of Texas Health Science Center at Houston

V Wise[1]

[1]*University of Texas Health Science Center at Houston, Houston, TX*

Purpose

The diagnosis of cerebral sinus thrombosis/cerebral venous thrombosis (CVT) is often initially clinically unsuspected and easily missed on routine screening exam. Our department recognized this difficulty and wished to characterize our own experience. This inquiry was designed as a quality control project with the specific aim of uncovering any patterns underlying our missed imaging diagnoses.

Materials and Methods

Sixteen cases dating from 2015 to 2016 were retrospectively identified by combing our stroke registry for a discharge diagnosis of "venous thrombosis" or a stroke etiology of "venous thrombosis". We found an additional 34 cases by searching our radiology reports, yielding a total of 50 new diagnoses spanning 22 months. Demographics and imaging findings were reviewed and recorded for each case. Imaging findings were recorded as missed, if there were retrospective findings that correlated with the ultimate diagnosis of CVT. Although data was recorded for all imaging modalities, we chose to focus this inquiry on noncontrast CT (NCCT) imaging.

Results

We found 50 new diagnoses of CVT over a period of 22 months, comprised of 24 females and 26 males with an average age of 41 years. Of the 50 cases, 39 underwent NCCT, with 18 cases missed on initial NCCT, 15 cases detected by initial NCCT, and 6 cases with no findings on NCCT. Initial NCCT demonstrated positive findings 85% of the time. Of the 18 missed cases, 10 had suspected hemorrhage adjacent to a sinus, 5 of which could be attributed to actual hemorrhage. The remaining 5 cases were more consistent with hyperdense sinuses misattributed to hemorrhage. Seven cases were missed in the absence of any distractor or misinterpretation. Of those 7 cases, 3 are located at the vertex.

Conclusions

Our demographic data aligns with a recent study from Australia (1), which also used a radiology database to identify cases. The Australian study also detected a high incidence, as others have recently (2), and near equal male to female distribution, which is unusual. Although our exact incidence is difficult to ascertain, our detection of roughly 27 cases per year certainly exceeds the expected number of cases from earlier estimated rates of 4-7 cases per million per year. The most glaring commonality among our misses on NCCT is the suspicion of hemorrhage adjacent to a sinus, usually the transverse sinus, associated with 56% of our misses. Half of these are misinterpretations of the hyperdense thrombosed sinus, with the remainder representing actual adjacent hemorrhage. Another interesting, if less frequent pattern was the incidence of thrombosis at the vertex involving superior sagittal sinus and cortical veins. These findings suggest that there are patterns underlying our misses, which could be used to develop strategies to improve our detection on NCCT. In the future, we would like to use this data to investigate associated delay in diagnosis, misses on other modalities, and further characterize our demographics.

eP-35

6:30AM - 3:00PM

Spectrum of Vascular Events Related to Postpartum Period: Pathogenetic Consideration and Imaging Patterns

A Mironov[1]
[1]*Creighton University Medical Center, Omaha, NE*

Purpose
Postpartum angiopathy as a cause of hemorrhagic events in young women is well known. It is unknown whether this disorder represents a true inflammatory and eventual autoimmune vasculitis, or represents a transient vasoconstriction related to the hormonal events of pregnancy and the postpartum period. Although several previous studies have reported and identified different target factors for events that occur during this specific time period, little has been focused on the morphological imaging versatileness. We describe 5 cases with completely different vascular events in the postpartum period.
Materials and Methods
From a retrospective cohort of 18 patients with vascular events in the early postpartum period we recruited 5 cases representing unique pathologies. They underwent CT, MRI, MRA, and serial catheter angiography.
Results
Mean age of the patients was 29.2 years. All of them had history of comorbid pregnancy-related disorder (hypertension, preeclampsia). The distribution of morphologic pathology included: Case 1- thalamic hemorrhage due to reversible microaneurysm of lenticulostriate artery; Case 2 – ventricular hemorrhage with hemolytic uremic syndrome and kidney failure; Case 3 – spinal, cranial, and abdominal hemorrhage; Case 4 – hemorrhagic ischemia, RCVS; Case 5 – cerebral hemorrhage due to venous thrombosis. All but one (Case 2) had favorable outcome.
Conclusions
It is widely acknowledged the postpartum angiopathy may represent a hormonally mediated effect on the brain vessel intima precipitated by acute hypertension, evidently with affection of other territories (Cases 2, 3). Various hormonal and biochemical factors have been identified playing a role in the deregulation of cerebral vascular tone of both the postpartum period and the RCVS. Some of them are common for both and may activate or lower the threshold for a progressive alteration of the vascular tone, which in turn drives the performance of different degrees abnormalities including vasospasm, ischemia, microaneurysm, or hemorrhage as separated or combined events. The increasing understanding of possible triggers and overlap of features strongly suggests that the postpartum angiopathy and RCVS may represent a common end point of numerous different disease processes.

eP-31

6:30AM - 3:00PM

Structural and Functional Brain Connectivity Biomarkers and Cognitive Impairment in Multiple Sclerosis

J Puig[1], G Blasco[2], C Biarnes-Duran[3], J Gich[4], M Rivero[4], J Salavedra[4], A Alberich-Bayarri[5], M Marti-Navas[1], P Daunis-i-Estadella[6], S Thio-Henestrosa[6], M Wintermark[7], K Nael[8], S Pedraza[2], L Ramio-Torrenta[4]

[1]Research Unit of Diagnostic Imaging Institute (IDI), IDIBGI, University Hospital Dr Josep Trueta, Girona, Girona, [2]Imaging Research Unit, IDI-IDIBGI, Hospital Dr Josep Trueta, Girona, None, [3]Research Unit of Diagnostic Imaging Institute (IDI), Girona Biomedical Research Institute (IDIBGI), Girona, Girona, [4]Department of Neurology-IDIBGI, University Hospital Dr JosepTrueta, GIRONA, GIRONA, [5]Hospital Universitario y Politecnico La Fe-QUIVIM, Valencia, None, [6]Department of Computer Science, Applied Mathematics and Statistics, University of Girona, Girona, Girona, [7]Stanford University, Stanford, CA, [8]Icahn School of Medicine at Mount Sinai, New York, NY

Purpose

Multiple sclerosis (MS) research is fascinating and flourishing. A wide array of advanced neuroimaging techniques are used to study structural abnormalities (e.g., inflammatory lesions and brain atrophy) in attempts to explain the wide clinical heterogeneity. Cognitive impairment, present in 40%–70% of MS patients, correlates poorly with classical imaging measures such aslesion volumes; thus, more sensitive, comprehensive techniques measuring brain function as well as structure are required. Cognitive impairment can derive from local gray matter (GM) damage or from loss of connectivity due to white matter (WM) lesions and degeneration. We explain the roles of structural and functional brain connectivity (SF-BC) biomarkers in assessing brain integrity and its impact on cognition impairment in MS.

Materials and Methods

1. We use cases from our repository (CONNECTIMS Study) to illustrate different SF-BC patterns in groups of patients with radiologically/clinicallyisolated syndrome, relapsing-remitting MS, and progressive MS. 2. We review how SF-BC biomarkers are associated with cognitive impairment.

Results

The concept of anatomical connectivity considers GM and WM parts of an integrated system, with brain function (and dysfunction) relying on neuronal networks, rather than specialized brain areas communicating to each other. Growing evidence suggests that the pathologic substrate involved in cognitive impairment is closely related with GM damage such as cortical atrophy and cortical lesions, and WM damagemay also contribute to the development of cognitive impairment in MS.

Conclusions
Studying the relationship between SF-BC biomarkers and cognitive impairment in patients with MS can help physicians and researchers to understand how neurodegeneration is associated with altered brain connectivity and with cognition impairment. SF-BC biomarkers might be useful for studies on the clinical evolution of MS and for monitoring clinical trials.

eP-22

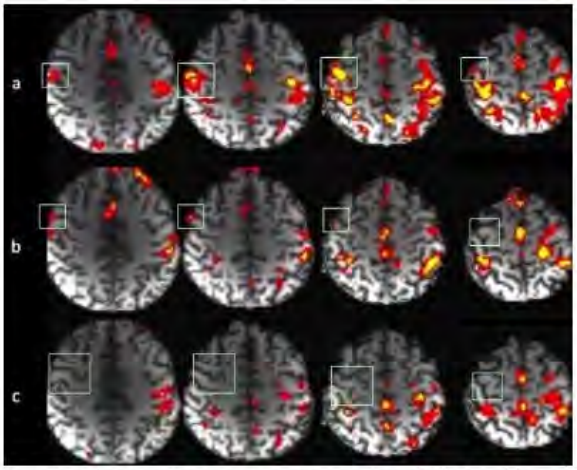
6:30AM - 3:00PM

Structural and Functional Connectivity of Human Hand Motor using Diffusion Tensor Imaging and Resting State Functional MRI

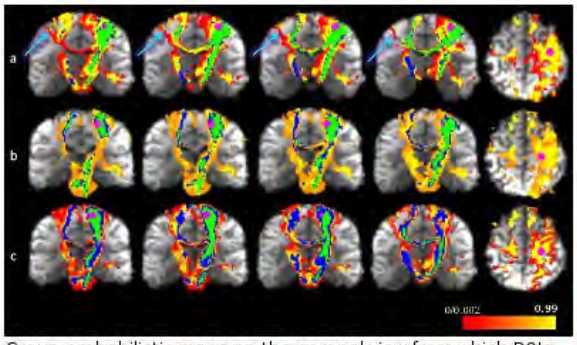
S Hamidian[1], B Vachha[2], R Young[2], S Karimi[2], A Holodny[3], K Peck[2]
[1]MSKCC, New York, NY, [2]Memorial Sloan Kettering Cancer Center, New York, NY, [3]Memorial Sloan-Kettering Cancer Center, Weill Medical College Of Cornell Univ., New York, NY

Purpose
The purpose of this study is to define the hand motor region of interest (ROI) in the precentral gyrus by generating the optimal structural and functional connectivity in the bilateral hemispheres, using resting state fMRI (rfMRI) and probabilistic diffusion tractography (PDT). We hypothesize that the optimal hand-motor ROI may not be limited to the reverse hand omega area in the precentral gyrus (1).
Materials and Methods
Twelve healthy subjects (age range 25-75 years) from the Human Connectome database were studies. Structural data: (T1-weighted 0.8mm isotropic slice thickness, TR/TE=2400/2.12 ms, matrix=300×208, flip angle=8°, slice thickness=1.5mm, FOV=256mm); resting state fMRI data (2mm isotropic slice thickness, TR/TE=720/33.2ms, matrix=104×90, 72 slice, flip angle=52°, slice thickness=2mm, FOV=208×180); and Diffusion tensor imaging data (TR/TE=3730/76.6ms, matrix=140×120mm, 92 slice, slice thickness=1.5mm, b=1000, 80 directions) were obtained. After standard postprocessing procedures, three regions of interest (ROI): (a) lateral from the hand-knob of PCG, (b) within the hand-knob of PCG, (c) just medial from the hand-knob of PCG in the left hemisphere were used to generate resting state and PDT maps.
Results
Using rfMRI, the number of activated voxels ($p<0.002$) in the right PCG was 279, 13, and 9 voxels when an ROI has been placed in lateral, medial, and hand knob respectively in the left. Similarly, using PDT, the highest white matter connectivity resulted from an ROI placed in the lateral portion of PCG (2696 connected voxels versus 948 and 1315 for hand knob and medial ROIs respectively).
Conclusions
Resting state fMRI and PDT show the functional and structural localization of the hand

motor area is not limited to the traditional hand knob. Rather, the lateral portion of PCG demonstrates the optimal structural and functional connectivity to the contralateral hemisphere. Identification of the hand motor area is essential for pre-neurosurgical planning and future studies using intracortical stimulation will be needed to confirm the current findings.



Functional connectivity maps representative of all 12 subjects on the axial view from which ROIs were taken from (a) lateral, (b) hand knob, and (c) medial portions of the left PCG. ROIs are not shown; refer to figure _ to see where they were initially placed. Maps were generated by AFNI's 3dttest program, which ran a t-test that compared each of the 12 images' z-scores to 0.



Group probabilistic maps on the coronal view from which ROIs (shown by the magenta sphere) were taken from lateral (a), hand knob (b), and medial portions (c) of the left PCG. Colored voxels show significant functional connectivity. The warm colors range from 0.02-99% probability of fiber location. The additional blue and green overlays highlight areas with prob=0.95 and prob=0.99, respectively. The teal arrow shows the hand motor tract (shown in red) in (a).

(Filename: TCT_eP-22_asnr2017_FIGURS.jpg)

eP-34

6:30AM - 3:00PM

The Imaging Spectrum of Venous Epidural Hemorrhage: from the Obvious to those Detectable Only with the Help of Reformatting

E Laney[1], A Nemeth[2]
[1]Northwestern Memorial Hospital, chicago, IL, [2]Northwestern University / Feinberg School of Medicine, Chicago, IL

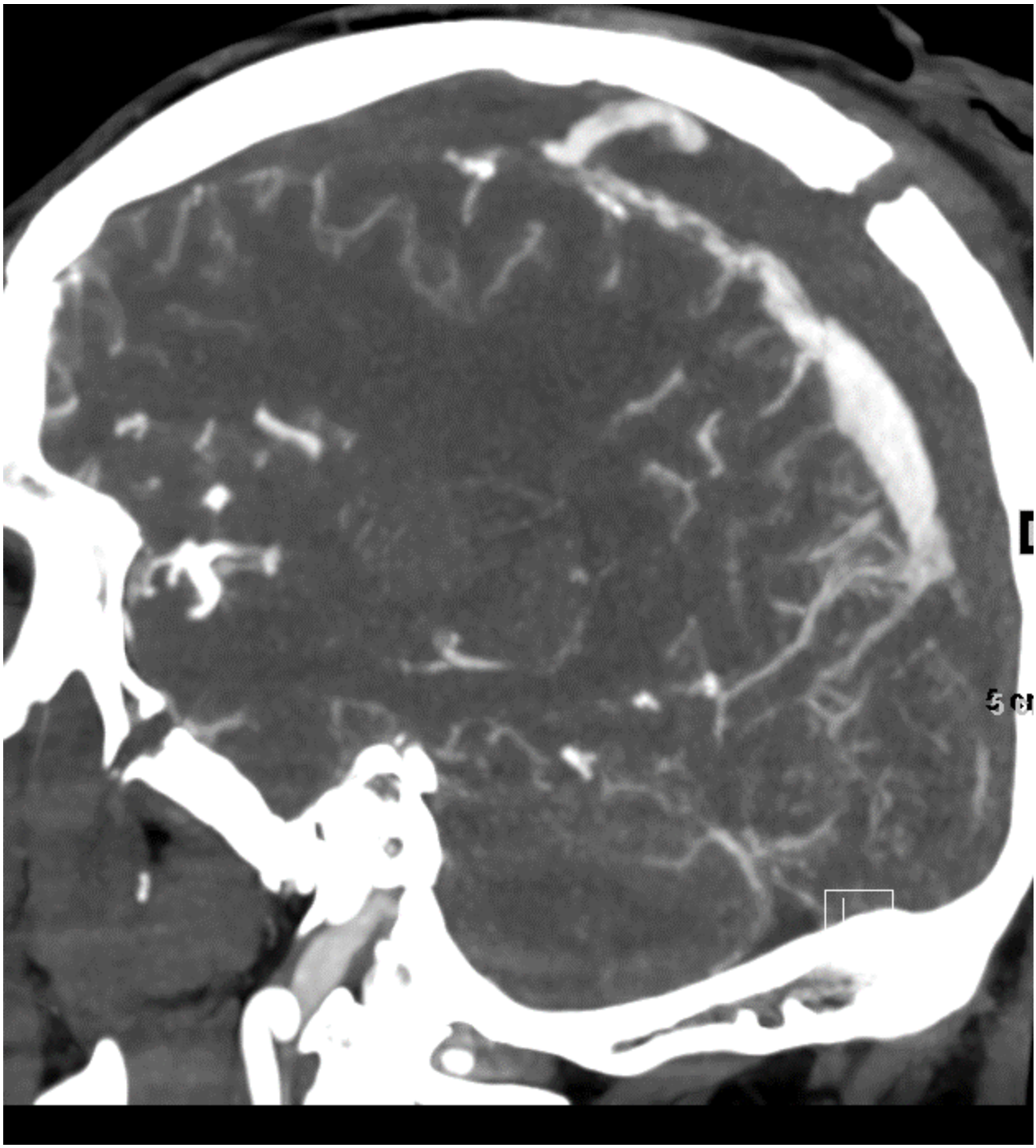
Purpose
To depict the range of venous epidural hemorrhage, with an emphasis on rare, catastrophic venous epidural hemorrhage.
Materials and Methods
Images from several cases of venous epidural hemorrhage will be presented to show the varying degree of presentation and outcome of venous epidural hemorrhage. Both supra-, and the sometimes more subtle, yet still ominous, infra-tentorial examples of venous epidural hemorrhage will be presented. The complete temporal evolution of imaging findings for each patient will be presented, as available.

Results

Venous epidural hemorrhage most frequently occurs after trauma. The imaging findings range from the very subtle appearance of filling defect immediately deep to a dural sinus, resulting in little to no mass effect, to the catastrophic appearance of a large epidural hemorrhage resulting in severe mass effect, parenchymal herniation and/or midline shift. Often, co-existent findings of major trauma (fractures, contusions, subgaleal hematoma, etc.) also are present with the latter. Of note, we report an interesting finding which we have termed a "venous geyser" arising from a tear in a dural venous sinus. This is compatible with acute bleeding into a large venous epidural hemorrhage; it would be analogous to the better known "CTA spot sign" of acute arterial bleeding into a parenchymal hematoma on CT angiography.

Conclusions

Venous epidural hemorrhage has a varied clinical and radiologic presentation, of which many clinicians and radiologists have little familiarity. The range includes a neurosurgical emergency, at one end, to a relatively benign, small, self-limiting bleed, at the other end, the latter often presenting with only vague clinical symptoms such as headache. We present a guided tour through the spectrum of imaging findings of venous epidural hemorrhage.



(Filename: TCT_eP-34_geyser.gif)

eP-40

6:30AM - 3:00PM

The Utility of Dynamic Susceptibility-Weighted and Dynamic Contrast-Enhanced Perfusion MRI-Derived Permeability Parameters in the Pre Surgical Evaluation of Diffuse Gliomas

A Hilario[1], E Salvador[1], P Martin[1], L Koren[2], J Sepulveda[1], A Perez-Nuñez[1], A Hernandez-Lain[1], J Millan[3], A Lagares[1], A Ramos[4]
[1]Hospital 12 de Octubre, Madrid, Spain, [2]Hospital 12 de Octubre, madrid, spain, [3]Hospital Puerta del Sur, Mostoles, Madrid, -- SELECT --, [4]Hospital Madrid Puerta del Sur, Mostoles, Madrid, Spain

Purpose
DSC imaging remains the most commonly used perfusion technique in glioma grading, but may be influenced by contrast leakage from tumor vessels. Leakage parameters extracted from DSC and their relationship to DCE-MRI measures of vascular permeability remains unclear. The aims of the study were in a group of diffuse gliomas: 1) to evaluate diagnostic accuracy of permeability parameters in the discrimination between high- and low-grade gliomas; 2) to assess permeability differences in high-grade tumors classified on the basis of IDH, MGMT and ATRX status; 3) to analyze relationship of permeability with OS and PFS; and 4) to compare DCE and DSC perfusion parameters.
Materials and Methods
Forty-nine patients with histologically proved diffuse gliomas underwent dynamic susceptibility-weighted and T1 dynamic contrast-enhanced perfusion MRI. Post-processing was performed using the Olea Sphere software. Parametric maps of rCBV, rCBV leakage corrected, Ktrans, Vp, Ve, Kep and K2 were calculated. Histopathological evaluation was based on the World Health Organization 2007 criteria. High-grade gliomas also were classified according to IDH, MGMT and ATRX status. Using SPSS software performed statistical analysis. A Mann-Whitney U test was used to test for difference tumor grades. DSC- and DCE-derived parameters were evaluated by using the Pearson correlation. A P value<0.05 indicated a statistically significant difference.
Results
The study included 28 male and 21 female patients, with age ranging from 16 to 78 years. Gliomas were classified into forty-one high-grade and 8 low-grade tumors. Mean leakage was significantly related to OS (p=0.006) and PFS (p=0.012). Leakage showed a linear correlation with Ktrans (310) and Vp (289). We also demonstrated significant differences in the leakage (p=0.01), K2 (p=0.004), Ktrans (p=0.002), Vp (p=0.032) and Ve values (p<0.001) between high- and low-grade tumors. Leakage is the best parameter discriminating high-grade gliomas classified based on IDH and ATRX status.
Conclusions
Both DSC and DCE perfusion parameters can serve as a noninvasive method for approximating tumor grade. Ve was the best parameter distinguishing high- and low-grade gliomas. Leakage was significantly related to OS and PFS and was the best parameter discriminating high-grade gliomas classified based on IDH and ATRX status.

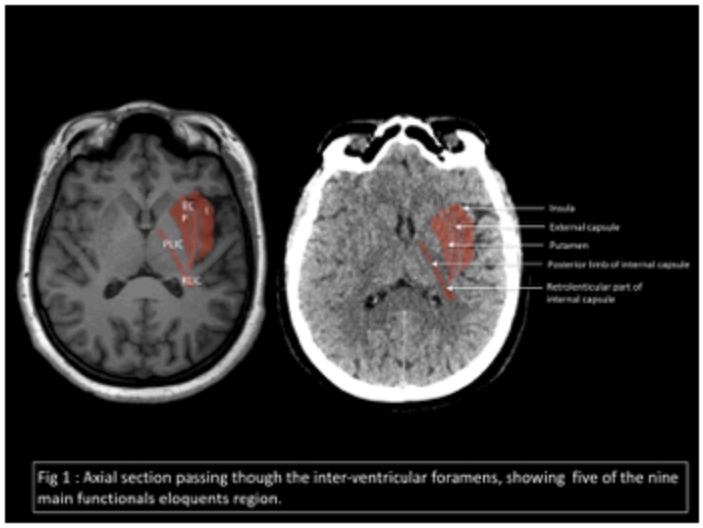
eP-56

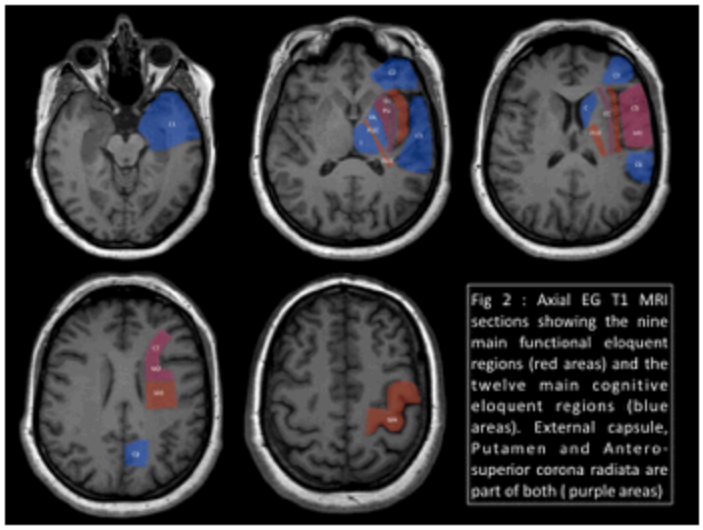
6:30AM - 3:00PM

Tours Stroke Imaging Score (TOSIS): A New Stroke Assessment Model, Incorporating the Concept of Eloquent Brain Areas

B Kerleroux[1], j cottier[1], C Tomasino[1], R Bibi[1], F Domengie[2], k janot[1], M Gaudron-Assor[1], M Annan[1], A Narata[1]
[1]University Hospital of Tours, Tours, France, [2]University Hospital of Tours, Tours, Indre et Loire

Purpose
Patient selection for the treatment of acute ischemic stroke is based on imaging scores that do not integrate the concept of eloquent brain areas nor right/left hemisphere. This study aims to evaluate whether a quantitative score for MRI, integrating the main eloquent functional brain areas, is able to predict functional recovery at 3 months.
Materials and Methods
Radiological images (acute MRI, 24h CT and 3-5 days MRI), demographic and outcome data were acquired for 30 patients with cerebral infraction on anterior vascular territory. Statistical analysis was applied to correlate eloquent brain areas affected by ischemic process with functional recovery based on modified Rankin scale (MRS) and NIHSS. We compared to ASPECT score and we assessed inter-operator reproducibility.
Results
Patients without important neurological impairment (MRS 0-2) were correlated mostly with low TOSIS and those with poor MRS (3-5) were clearly in the high TOSIS group. Correlation rates were not inferior to ASPECT score (Pearson's correlation test).
Conclusions
Tours stroke imaging score could be a very promising new tool for radiological assessment of stroke. A prospective multicenter study with larger sample is necessary to validate our data.





(Filename: TCT_eP-56_5985525658.gif)

eP-49

6:30AM - 3:00PM

Transit Time Corrected Arterial Spin Labeling Predicts Impairments in Cerebrovascular Reserve

H Choi[1], S Choi[2], K Kang[2], J Kim[2], C Sohn[2], R Yoo[2], S You[1], T Yun[1]
[1]Seoul National University Hospital, Seoul, Korea, Republic of, [2]Seoul National University Hospital, Seoul, Seoul

Purpose
Delayed transit time effect is the main source of errors in the quantitative measurement of cerebral blood flow (CBF) using arterial spin labeling (ASL) perfusion MR imaging. In the present study, we evaluated the usefulness of transit time corrected CBF map based on

multi-phase ASL perfusion MRI as compared with basal/acetazolamide stress 99mTc-HMPAO SPECT in prediction of impairments in cerebrovascular reserve (CVR).

Materials and Methods

Transit time corrected CBF maps were acquired in 30 consecutive patients with unilateral ICA or MCA stenoocclusive disease (severe stenosis or occlusion). Internal carotid artery territory-based regions of interest were applied to transit time corrected CBF map and we calculated percent decrease of CBF. And impairments in CVR were evaluated according to both visual diagnosis and measurement of regions of interest on basal/acetazolamide stress 99mTc-HMPAO SPECT. The sensitivity and specificity of transit time corrected CBF were calculated based on the visual diagnosis of decreased CVR as a gold standard. And the correlation between time corrected CBF with calculated CVR was measured.

Results

A transit time corrected CBF decrease cutoff value >10% had a sensitivity of 91.7% and a specificity of 91.7% for diagnosis of decreased CVR in unilateral stenooclusive disease. The calculated CVR based on SPECT shows weak correlation with time corrected CBF value. ($r=0.261$, $p=0.000$)

Conclusions

Our results demonstrate that the transit time corrected CBF maps based on the multi-phase ASL perfusion MRI can predict impairments of cerebrovascular reserve.

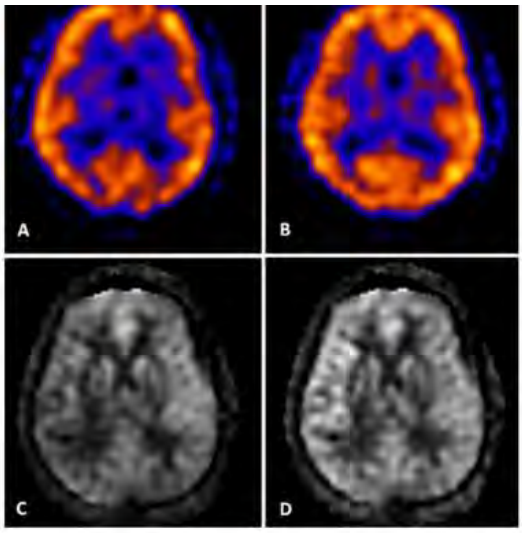


Fig 1. Basal/Acetazolamide stress 99mTc-HMPAO SPECT and single/multiple phase ASL in a 45-years-old patient with right MCA occlusion. A, Baseline. B, ACZ administration. (A) and (B) demonstrate neither basal hypoperfusion nor impairment of vascular reserve in the right MCA territory. (C) Single phase ASL shows decreased CBF in the right MCA territory but, (D) Multiphase ASL shows normal symmetric hemodynamics in the right MCA territory.

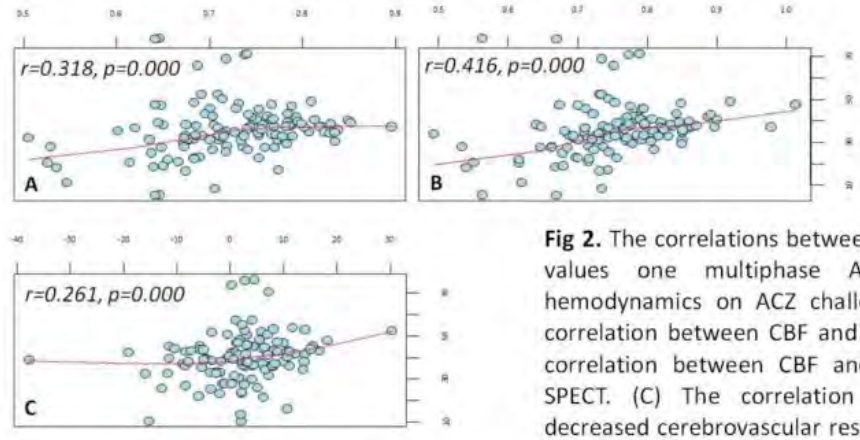


Fig 2. The correlations between time corrected CBF values one multiphase ASL and calculated hemodynamics on ACZ challenge SPECT. (A) The correlation between CBF and basal SPECT. (B) The correlation between CBF and ACZ administrated SPECT. (C) The correlation between CBF and decreased cerebrovascular reserve.

Table 1: Sensitivity and specificity of time corrected CBF

Decrease of transit time corrected CBF	Sensitivity	Specificity
> 10%	91.7%	91.7%
> 20%	68.0%	97.4%
> 30%	48.0%	100%

(Filename: TCT_eP-49_K-063.jpg)

eP-30

6:30AM - 3:00PM

Unusual Presentation of CNS Tuberculoma Mimicking Stroke

S Gupta[1], A Wang[2], S Forseen[3], J Keshavamurthy[3]
[1]Augusta University Medical college of Georgia, augusta, GA, [2]Medical College of Georgia, Augusta, GA, [3]Augusta university, Augusta, GA

Purpose
Intracranial tuberculomas are a rare complication of tuberculosis occurring through

hematogenous spread from an extracranial source, most often of pulmonary origin. About 10% of pulmonary tuberculosis (TB) patients develop central nervous system tuberculosis (CNS TB). It can present as lesions in brain or spine (1-3). Tuberculoma, an uncommon manifestation of CNS TB usually causes seizures and focal signs. The clinical and radiological manifestations of tuberculoma are variable and can cause difficulty in the diagnosis in the absence of systemic tuberculosis or tubercular meningitis (1). Early diagnosis is valuable for decreasing morbidity and preventing mortality.

Materials and Methods

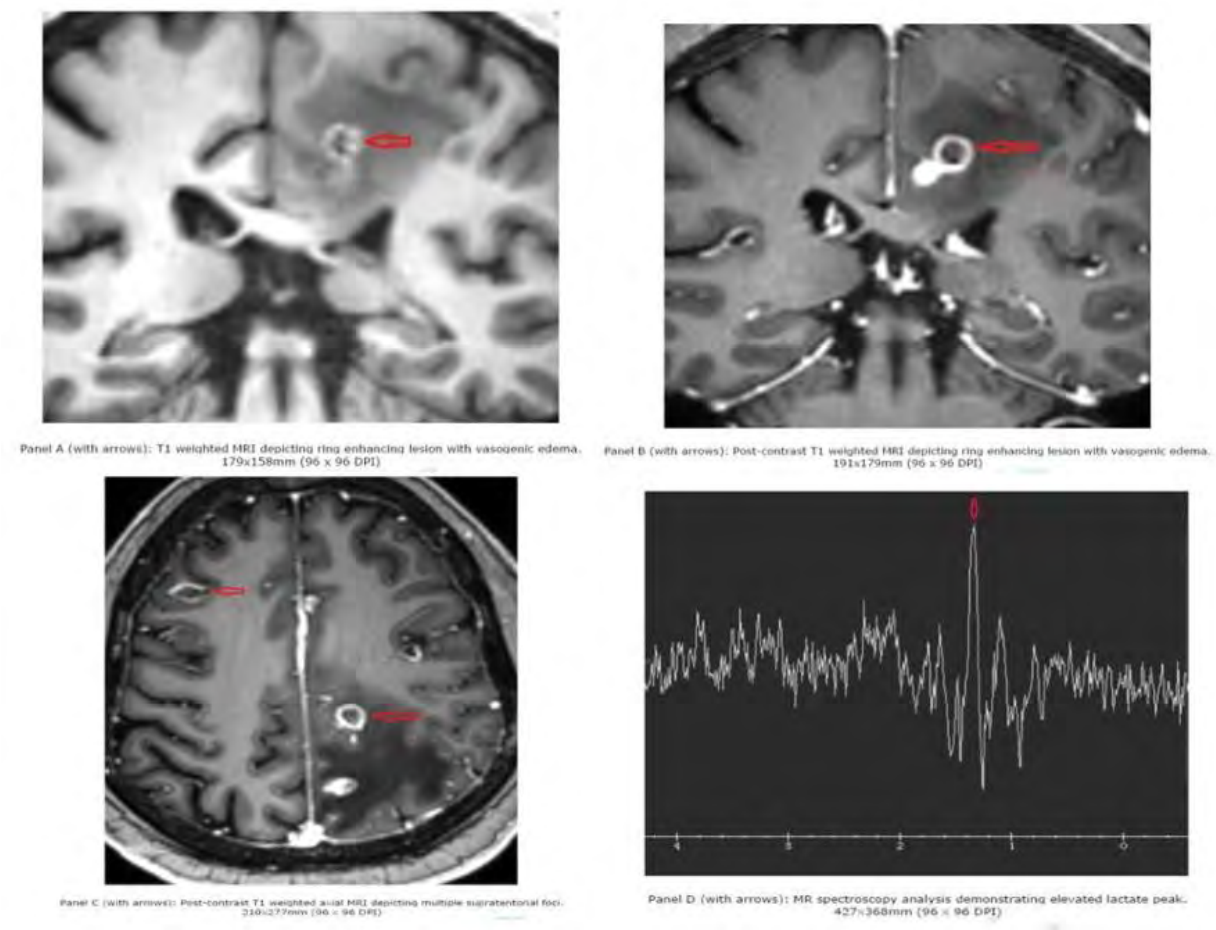
We present the case of a 35-year-old South Asian Indian male with history of treated pulmonary tuberculosis, who presented with slurred speech, right-sided weakness and ataxia. Physical exam revealed oriented patient with intact cranial nerves and sensation, but 3/5 strength in right lower extremity. Initial labs, including CBC and chemistry, were unremarkable.

Results

Computed tomography (CT) imaging demonstrated multiple calcifications and vasogenic edema in left frontal and parietal lobes. T1- (Figure A) and post-contrast T1- (Figure B) weighted MRI depict ring- enhancing lesions with vasogenic edema. Postcontrast imaging revealed multiple foci throughout supratentorial brain (Figure C), the largest ones are marked by red arrow. Magnetic resonance spectroscopy (MRS) analysis demonstrated an elevated lactate in the region of this lesion with surrounding edema, indicative of an infectious etiology (Figure D). Serum quantiferon gold results were positive for tubercular antigen, but pulmonology workup ruled out active TB. Positron emission tomography (PET) scan was performed, revealing possible areas of infection including tonsils, liver, prostate and bowel. Treatment with RIPE therapy, moxifloxacin and injectable aminoglycoside was started.

Conclusions

About 5% of tuberculosis manifests as extra pulmonary disease in United States. Presentation of intracranial tuberculoma can be quite variable. Hence, tuberculoma should be suspected in atypical patients, such as young Asian patients, presenting with stroke-like symptoms especially with history of treated TB. Magnetic resonance imaging of the brain with gadolinium enhancement and MR spectroscopy helps in establishing the diagnosis and distinguishing tuberculomas from the stroke. Early diagnosis and prompt therapy are important in preventing mortality and reducing morbidity.



(Filename: TCT_eP-30_2.jpg)

eP-66

6:30AM - 3:00PM

Use Fluoroscopic Angiography to Quantify Peri-stenting Cerebral Circulation Time in Carotid Stenosis patients: A feasibility Study

H Lee[1], C Lin[2], F Chang[1], C Luo[1], W Guo[1]
[1]Taipei Veterans General Hospital & National Yang Ming University, Taipei, Taiwan, [2]Taipei Veterans General Hospital & National Yang Ming University, Taipei, Taipei

Purpose
Quantitative subtraction angiography (QDSA) facilitates in-angiosuite assessment of hemodynamic changes in various cerebrovascular diseases (Ref 1-5), and improves both diagnostic accuracy and patient safety. The purpose of this study is to compare the peri-stenting cerebral circulation time defined by fluoroscopic angiography (FA) and DSA in carotid stenosis patients.

Materials and Methods

Twenty-one patients with more than 70% carotid stenosis (NASCET criteria) were prospectively included in this study. All patients received DSA and FA before and after carotid stenting using a same angiosuite and software for angiography and post-processing (ArtisZee® and iFlow®, Siemens Healthcare, Forchheim, Germany). The injection protocol for DSA was 12 ml within 1.5 second by a power injector (Liebel-Flarsheim Angiomat®, Illumena), whereas FA was derived with a maximal manual injection of 12 ml done by the operators. Extracranial ICA (eICA), middle cerebral artery (MCA), sagittal sinus (SS), and internal jugular vein (JV) in anteroposterior views; cavernous portion of ICA (cICA), and parietal vein (PV) in lateral views were chosen as ROIs. Time to peak (TTP) of all ROIs were obtained peri-stentingly and compared between FA and DSA. Cerebral Circulation time (CCT) was defined as the differences of TTPs between cICA and PV. (Ref 3)

Results

The correlations between FA and DSA of all ROIs ranged from 0.59-0.82 before stenting and 0.58-0.76 after stenting, except eICA and cICA ($r = 0.07$ and 0.21, respectively). The correlation of CCT was 0.86 before and 0.55 after stenting.

Conclusions

Stenosis facilitates creation of bolus during manual injection and therefore increased the accuracy of cerebral flow quantification in FA. It provides a quicker cerebral hemodynamic assessment with less radiation dose and higher patient safety.

Table 1. Demographic data and angiographic characteristics of the patients

Age (Yrs)	53-91 (Median 67)
M / F (No.)	19/2
Pre-stenting stenosis (No.)	
75-90%	15
90-99%	6
Post-stenting residual stenosis (No.)	
<=30%	15
30-50%	5*
50-70%	1**

**3 patients with in-stent residual stenosis, 2 patients with restenosis at cavernous segment of internal carotid artery*
***1 patient with restenosis at petrous segment of internal carotid artery*

Table 2. Correlation coefficient of time to peak (TTP) and carotid circulation time between digital subtraction angiography (DSA) and fluoroscopic angiography (FA) before and after carotid stenting

	Correlation coefficient between DSA and FA	
	Before Stenting	***After Stenting***
ROI of time to peak		
Extracranial ICA	0.70	0.07
Cavernous ICA	0.67	0.21
M1 of middle cerebral artery	0.60	0.58
Parietal Vein	0.82	0.64
Superior sagittal sinus	0.59	0.65
Internal jugular vein	0.55	0.76
Carotid Circulation Time	0.87	0.55

(Filename: TCT_eP-66_JPG_ASNRAbstract_FAQuantifiesDelayedCerebralCirculationTimeinCarotidStenoticpatients_Table.jpg)

eP-32

6:30AM - 3:00PM

Utilization of Mixed-Reality Visualization for Evaluation of Cerebrovascular Lesions

O Choudhry[1], C Morley[1], S Kelly[2], F Ahmed[1], A Davis[1]

[1]NYU Langone Medical Center, New York, NY, [2]NYU Shanghai, Los Angeles, CA

Purpose

Traditional visualization of cerebrovascular lesions typically is performed utilizing two-dimensional DICOM imaging and desktop-based volume rendering. More recently there has been reporting of use of 3D printing in further assessment of such lesions, especially for surgical planning and patient education. Mixed reality visualization is based on an advancement of augmented reality technology which allows for holographic display of any three-dimensional rendering in real-world space through use of untethered head-mounted display technology such as the Microsoft Hololens. Through this, the visual data can be projected as if it were an object before a user, allowing one to freely move around a volume and observe in true three-dimensional stereoscopy. In this study we describe technique and initial results of mixed reality visualization for cerebrovascular lesions, including technological difficulties, and observer-reported accuracy.

Materials and Methods

Ten cases of cerebrovascular pathology including 5 cerebral aneurysms, 3 arteriovenous malformations, and 2 cavernous malformations were reconstructed in a mixed-reality environment. Computed tomography (CT) angiography, T1- and T2-weight MR, and MR angiography data were utilized, as available, for each lesion. The DICOM-based voxel values were organized in a three-dimensional array and specific C# code was utilized to assign material-based color and opacity values to voxels within the array. Ray-marching-based rendering then was utilized to generate separate stereoscopic imaging. This then was transferred to a head-mounted light field display (Microsoft Hololens, Seattle, Washington). The 10 cases then were compared in mixed reality visualization, desktop-based volume rendering and standard 2D imaging for grading of accuracy and observation of important anatomic nuances (size of lesion, location, direction of aneurysmal dome) between 2 independent observers.

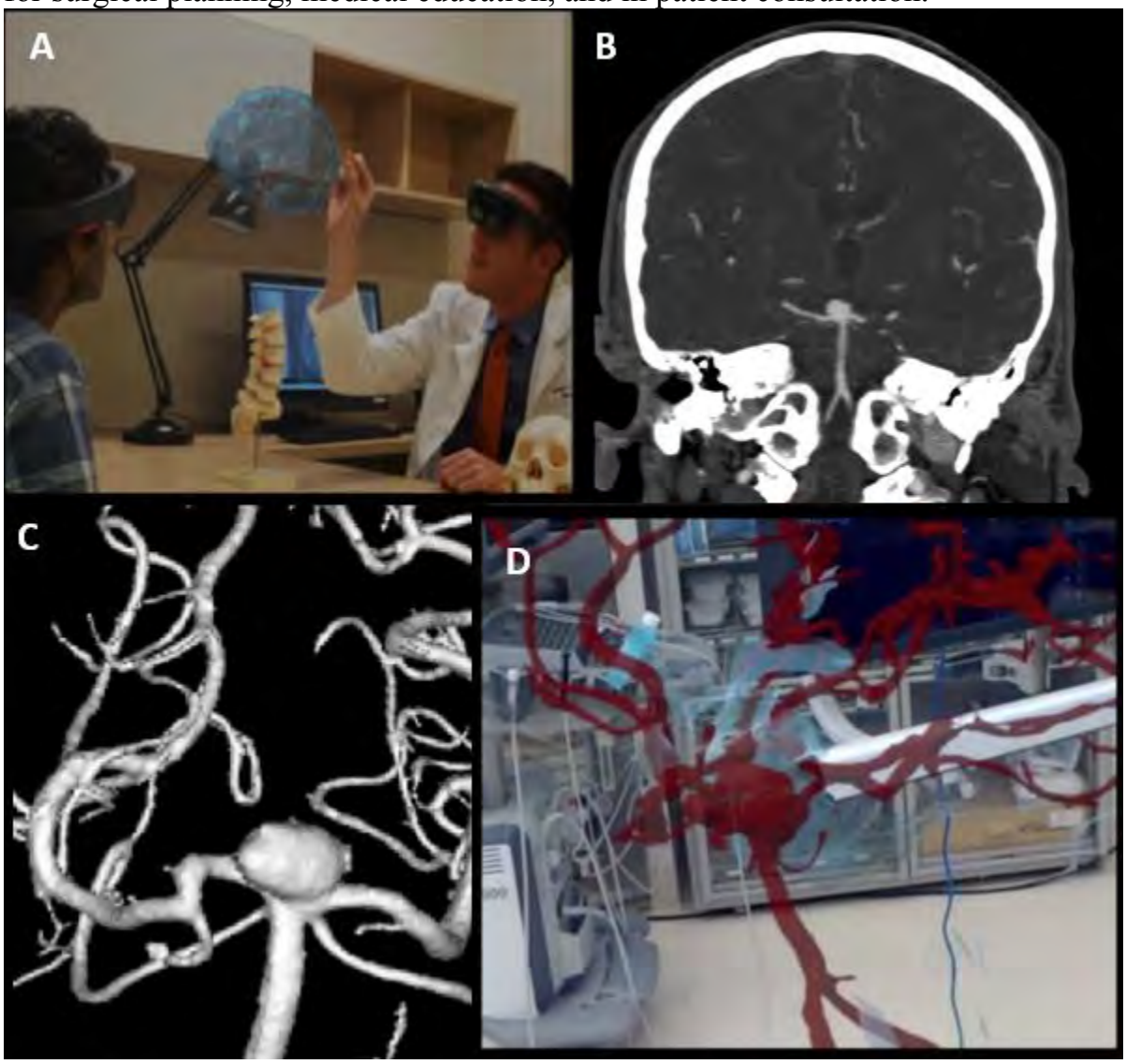
Results

Using the custom-created mixed reality projection environment we were able successfully to render all 10 studies onto a stereoscopic light-field display (Microsoft HoloLens) with the ability to identify and isolate the relevant cerebrovascular lesion using intensity-based transfer functions. The volume rendering was created using a Windows 10 PC with an Core i7 processor and NVIDIA GTX1070 GPU with subsequent transfer to the stereoscopic display. DICOM-based metadata was used to recreate the volume at the exact physical size of the original imaging. We were able to consistently generate 30-40 frames per second of rendering allowing for comfortable three-dimensional analysis and observation of the relevant lesion. Survey studies completed by the independent observers revealed the accuracy of the mixed reality visualization to be equal to that of desktop volume rendering. Observers graded understanding of spatial nuances of cerebrovascular lesions to be highest with mixed-reality visualization, followed by desktop-based volume rendering, and finally 2D imaging. These nuances included perceived size of a lesion, as compared to its actual

size, as well as location of lesion in three-dimensional space and for aneurysms the specific directionality of the dome in three-dimensional space. Users did not report any discomfort during use of the device in evaluation of mixed-reality volume rendering.

Conclusions

We report on the first use of mixed-reality, holographic visualization of cerebrovascular lesions. The modality was found to be as accurate as desktop-based volume rendering with enhanced understanding of key spatial relationships. This technology can become an important tool in true, three-dimensional understanding of intracranial pathology, as needed for surgical planning, medical education, and in patient consultation.



(Filename: TCT_O-28_Figure1.JPG)

eP-54

6:30AM - 3:00PM

Utilization of Mixed-Reality Visualization for Intracranial Tumors

O Choudhry[1], C Morley[1], S Kelly[2], F Ahmed[3]
[1]NYU Langone Medical Center, New York, NY, [2]NYU Shanghai, Los Angeles, CA, [3]NYU Tandon School of Engineering, New York, NY

Purpose

Traditional visualization of intracranial tumors typically is performed utilizing two-dimensional DICOM imaging (MRI and CT derived). Unlike cerebrovascular lesions, for which desktop-based volume rendering has been demonstrated to be an important tool, the same use of three-dimensional (3D) visualization has not been widely utilized for evaluation of intracranial tumors. There have been few recent reports of use of newer technologies such as virtual reality (VR) and 3D printing for surgical planning, resident education, and patient consultation. These technologies, however, have inherent practical limitations including isolation in a VR-based environment and length of time needed to print 3D models. Mixed reality visualization is based on an advancement of augmented reality technology which allows for holographic display of any 3-dimensional rendering in real-world space through use of untethered head-mounted display technology such as the Microsoft HoloLens (Microsoft, Seattle, WA). Through this, visual data can be projected as if it were an object before a user, allowing one to freely move around a volume and observe in true 3-dimensional stereoscopy. In this study we describe technique and initial results of mixed reality visualization for intracranial tumors, including technological difficulties, and observer reported accuracy.

Materials and Methods

Five cases of intracranial tumors including a convexity meningioma, right frontal high grade glioma, posterior fossa hemangioblastoma, right lateral ventricle choroid plexus papilloma, and posterior fossa ependymoma were selected for recreation in a mixed reality environment. Typical MRI sequences, including T1 pre and postconstrast, T2, MR angiography, and CT angiography data were utilized. When needed co-registration of MRI and CT imaging was performed using ITK-SNAP. The DICOM-based voxel values were organized in a 3-dimensional array and specific C# code was utilized to assign material-based color and opacity values to voxels within the array. Ray-marching-based rendering then was utilized to generate separate stereoscopic imaging. This then was transferred to a head-mounted light field display (Microsoft Hololens, Seattle, Washington). The five cases then were compared in mixed reality visualization, desktop-based volume rendering and standard 2D imaging for grading of accuracy and observation of important anatomic nuances (location, size, identification of large adjacent vessels or cerebral venous sinuses, and relevant associated bony anatomy).

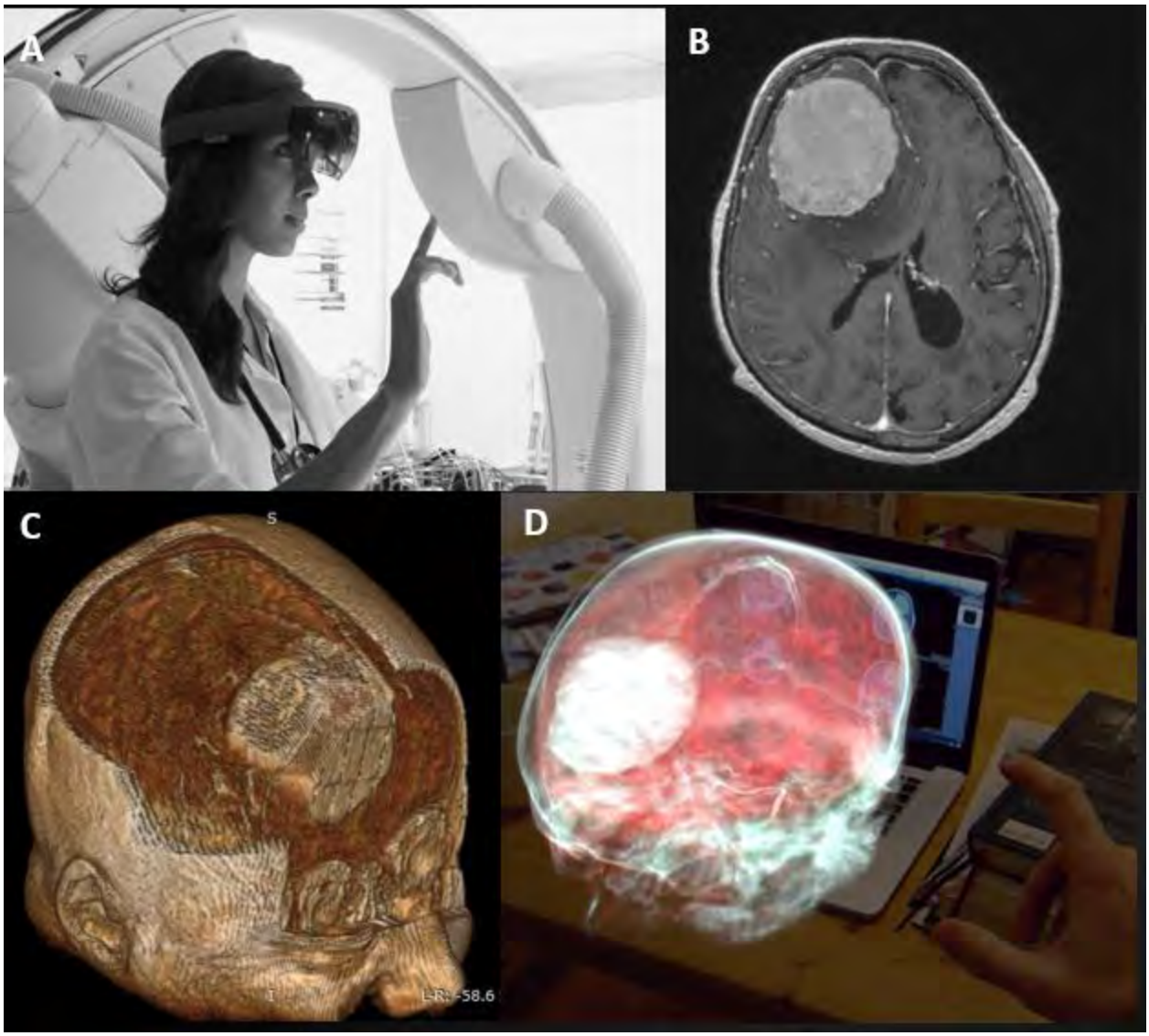
Results

Using the custom-created mixed reality projection environment we were successfully able to render all 5 studies onto a stereoscopic light-field display (Microsoft HoloLens) with the ability to identify and isolate the relevant intracranial lesion using intensity-based transfer

functions. This was done easily with the avid contrast-enhancing lesions such as the parasagittal meningioma, high grade glioma, and choroid plexus papilloma. Computed tomography (CT)-based DICOM data were more readily visualized than MRI-based data given the marked separation in density values between normal and abnormal structures. Magnetic resonance imaging (MRI) postcontrast DICOM imaging was most useful for lesion delineation. The volume rendering was created using a Windows 10 PC with an Core i7 processer and NVIDIA GTX1070 GPU with subsequent transfer to the stereoscopic display. DICOM-based metadata were used to recreate the volume at the exact physical size of the original imaging. We were able to consistently generate 30-40 frames per second of rendering allowing for comfortable three-dimensional analysis and observation of the relevant lesion. Structured surveys completed by the independent observers revealed the accuracy of the mixed reality visualization to be equal to that of desktop volume rendering. Observers graded understanding of specific spatial nuances including precise intracranial location, perceived versus actual lesion size, and visualization of nearby bony anatomy to be highest with mixed-reality visualization, followed by desktop-based volume rendering, and finally 2D imaging. Two-dimensional imaging was found to be of greater use in understanding intra-tumoral characteristics including the presence of cysts, calcification, hemorrhage products, and dural-based attacments (for extra-axial lesions). Users did not report any discomfort during use of the device in evaluation of mixed-reality volume rendering.

Conclusions

We report on the first use of mixed-reality, holographic visualization of intracranial tumors. The modality was found to be as accurate as desktop-based volume rendering with enhanced understanding of key spatial relationships. This technology can become an important tool in true, 3-dimensional understanding of intracranial pathology, as needed for surgical planning, medical education, and in patient consultation.



(Filename: TCT_eP-54_meningomafigure.JPG)

eP-63

6:30AM - 3:00PM

Utilizing Pre-procedural CT Scans to Identify Patients at Risk for Suboptimal External Ventricular Drain Placement with the Freehand Insertion Technique

M Wilson[1], C O'Kelly[2], T Kotylak[3], J Rempel[1]
[1]University of Alberta, Edmonton, Alberta, [2]University of Alberta, Alberta, Alberta, [3]University of Alberta, Allberta, Alberta

Purpose
Freehand insertion remains the mainstay of external ventricular drain (EVD) placement, even though alternative techniques have shown decreased rates of malpositioning.

Limitations in available alternatives when compared to freehand insertion necessitates stratification of patients likely to benefit from an alternative placement technique. The purpose of this study was to retrospectively evaluate which features of the preprocedural CT scan predict malpositioning of EVDs when using the freehand insertion technique.
Materials and Methods
We retrospectively evaluated 193 EVD insertions performed with the freehand technique through a burr hole between January 1, 2014 – December 31, 2015 at a level 1 trauma center in Edmonton, Alberta. Several features of the pre-insertion CT scan were evaluated for risk of malpositioning.
Results
Fifty-two EVD insertions (27%) were positioned suboptimally. Admitting diagnosis, head height-to-width ratio in axial plane, and side of predominant feature were found to be significantly associated with suboptimal placement ($p = 0.006$, 0.012, and 0.019 respectively). A decreased height-to-width ratio also was associated with placement into only eloquent cortex and/or nontarget cerebrospinal fluid spaces ($p=0.005$).
Conclusions
In combination with pre-existing literature, our findings suggest that a propensity for malpositioning occurs with factors which alter the expected ventricular location relative to traditional surface landmarks during freehand technique. In particular, increased head roundedness appears to be a novel and important indicator for malpositioning. Identifying patients with altered ventricular location relative to traditional external landmarks can help stratify patients more likely to benefit from an alternative placement technique.

Demographic and radiographic characteristics of patients by Kakarla Grade (1 vs 2+3)

		Grade 1 (n=141)	Grade 2+3 (n=52)	Difference (95% CI)	P value
Age, Mean (SD)		53.33 (13.61)	50.96 (14.94)	2.37 (-2.34 to 7.08)	0.319
Female		71 (50.4%)	28 (53.4%)		0.667
Diagnosis					0.006
	Trauma	15 (11.0%)	9 (17.3%)		
	Vascular	80 (58.4%)	15 (28.95)		
	Stroke	14 (10.2%)	8 (15.4%)		
	Neoplasm/Cyst	24 (17.5%)	17 (32.7%)		
Glasgow Coma Scale on Admission to ICU, Mean (SD)		9.50 (4.68)	9.55 (4.68)	-0.05 (-1.57 to 1.47)	0.949
Location of EVD insertion					0.677
Diameter of soft tissue external to skull at kocher's point, Mean (SD)		0.46 (0.18)	0.49 (0.27)	-0.03 (-0.05 to 0.11)	0.426
Skull thickness at kocher's point, Mean (SD)		0.75 (0.74)	0.74 (0.24)	0.014 (-0.13 to 0.15)	0.848
Distance from the inner table of the frontal bone to the anterior horn, Mean (SD)		3.35 (0.58)	3.32 (0.59)	0.04 (-0.15 to 0.23)	0.688
Height to width ratio of the skull, Mean (SD)		1.26 (0.07)	1.22 (0.09)	0.04 (0.01 to 0.07)	0.012
Evan's Index, Mean (SD)		0.31 (0.07)	0.30 (0.06)	0.01 (-0.01 to 0.03)	0.324
Ratio of the unilateral ventricle to unilateral hemisphere width from midline, Mean (SD)		0.34 (0.07)	0.35 (0.11)	-0.01 (-0.04 to 0.02)	0.447
Midline shift, Mean (SD)		-0.05 (0.59)	-0.10 (0.56)	0.05 (-0.13 to 0.23)	0.577
Number of different features seen on CT					0.214
Type of predominant feature on CT					0.180
Number of different types of intracranial bleed					0.757
Side of predominant additional feature					0.019
	Ipsilateral	8 (5.7%)	8 (15.4%)		
	Contralateral	26 (18.6%)	14 (26.9%)		
	Both	65 (46.4%)	13 (25.0%)		
	None	41 (29.3%)	17 (32.7%)		
Location of drain insertion					0.432

(Filename: TCT_eP-63_DemographicandradiographiccharacteristicsofpatientsbyKakarlaGrade-page-001.jpg)

eP-26

6:30AM - 3:00PM

Verbal Memory Impairment in Multiple Sclerosis and Brain Structural Damage on Diffusion Tensor Imaging

J Puig[1], G Blasco[2], C Biarnes-Duran[3], J Gich[4], M Rivero[4], J Salavedra[4], M Marti-Navas[1], A Alberich-Bayarri[5], P Daunis-i-Estadella[6], S Thio-Henestrosa[6], M Wintermark[7], K Nael[8], S Pedraza[2], L Ramio-Torrenta[4]

[1]Research Unit of Diagnostic Imaging Institute (IDI), IDIBGI, University Hospital Dr Josep Trueta, Girona, Girona, [2]Imaging Research Unit, IDI-IDIBGI, Hospital Dr Josep Trueta, Girona, None, [3]Research Unit of Diagnostic Imaging Institute (IDI), Girona Biomedical Research Institute (IDIBGI), Girona, Girona, [4]Department of Neurology-IDIBGI, University Hospital Dr JosepTrueta, GIRONA, GIRONA, [5]Hospital Universitario y Politecnico La Fe-QUIVIM, Valencia, None, [6]Department of Computer Science, Applied Mathematics and Statistics, University of Girona, Girona, Girona, [7]Stanford University, Stanford, CA, [8]Icahn School of Medicine at Mount Sinai, New York, NY

Purpose

Although memory impairment in multiple sclerosis (MS) has been studied extensively, its relation to brain changes remains unclear. We assessed whether white matter (WM) and gray matter (GM) damage evaluated by diffusion tensor imaging metrics (DTI-metrics) are associated with verbal memory impairment in patients with multiple sclerosis (MS).

Materials and Methods

We performed a cross-sectional analysis in eighty-two patients with radiologically or clinically isolated syndrome [(n=23; 18 female; age 35±9.1 years), primary or secondary progressive (PP/PS) MS (n=35; 19 female; age 53.5±7.2 years), or relapsing-remitting (RR) MS (n=24; 16 female; mean age 43.9±11.3 years)] and 30 matched healthy controls (18 female; age 41.4±10.9 years) on a 1.5 T scanner. Imaging included DTI with 16 diffusion-sensitized gradients applied along 15 noncollinear directions with b-value of 1000s/mm2 and anatomic T1 turbo-field echo sequence. We used (a) Olea Sphere 3.0 (La Ciotat, France) to map axial diffusivity (AD), radial diffusivity (RD), mean diffusivity, and fractional anisotropy (FA); (b) FSL tools to normalize images; and (c) Juelich's Atlas to identify WM tracts. We also calculated total WM and GM volumes. We estimated verbal memory by the long-term storage (LTS) subtest of the selective reminding test (SRT). We analyzed the covariance (ANCOVA) between DTI-metrics and SRT. To avoid confounding by age or schooling on SRT, unstandardized residual values of the regression between SRT and DTI-metrics were used.

Results
Multiple sclerosis groups differed on SRT-LTS ($p<0.001$). The best ANCOVA model demonstrated that right acoustic radiation AD ($p=0.001$), corpus callosum AD ($p=0.004$) and RD ($p=0.005$), left fornix FA ($p=0.004$), right optical radiation RD ($p=0.028$), right superior longitudinal fascicle RD ($p=0.006$), and total GM volume ($p=0.006$) were associated with verbal memory.
Conclusions
Structural WM damage and GM volume loss were associated with verbal memory impairment in MS patients. This study improves the neuropsychological understanding of verbal memory in MS.

eP-05

6:30AM - 3:00PM

Yield of Peri-ictal Arterial Spin-Labeling MRI Perfusion in Refractory Epilepsy

A Gupta[1], S TIWARI[2], j saini[3], C Prasad[4], R Bharath[5], A Verma[6], S Mangalore[7], C Nagaraj[7]
[1]National Institute of Mental Health and Neurosciences, India, Bangalore, Karnataka, [2]National Institute of Mental Health and Neurosciences, BANGALORE, Karnataka, [3]NIMHANS, BANGALORE, Karnataka, [4]National Institute of Mental Health and Neurosciences, Bangalore, Karnataka, [5]National Institute of Mental Health & NeuroSciences, Bangalore, Karnataka, [6]national Institute of Mental health & Neuro Sciences, Bangalore, Karnataka, [7]National Institute of Mental Health & NeuroSciences (NIMHANS), Bangalore, Karnataka

Purpose
To evaluate potential role of arterial spin labeling (ASL) in localization of seizure focus and study perfusion changes during early post ictal period and to study the concordance of ASL perfusion changes with structural magnetic resonance imaging (MRI) and video electroencephalogram (EEG).
Materials and Methods
Twenty-eight consecutive patients with drug resistant localization related epilepsy with positive video EEG findings were included. Structural MRI (sMRI) with pseudocontinuous ASL was performed in immediate peri-ictal period. ASL changes were classified into hypoperfusion, hyperperfusion and normal or visual analysis. The regional cerebral blood flow maps were compared with the epileptogenic zone determined by the other tests and the strength of concordance was assessed with the kappa coefficient (k). FDG-PET studies whenever available also were included in evaluation.
Results
Of 28 patients [equal gender distribution and mean age 20.8 years (10- 36 years)], 25 patients had lesions on structural MRI. Arterial spin labeling showed perfusion changes in 26 patients (9 hyperperfusion, 17 hypoperfusion and 2 normal) with mean seizure to ASL scan

duration of 6 hours (range 1-20 hours). Arterial spin labeling had good concordance with sMRI (k= 0.66), moderate concordance with VEEG (k= 0.46) and good concordance with FDG-PET (k= 0.60).

Conclusions

Arterial spin labeling, noninvasive perfusion technique, could be incorporated into the presurgical evaluation of all patients with localization-related epilepsy as it may reveal seizure-induced alteration in brain perfusion and may help identifying the location and extent of the epileptogenic zone.

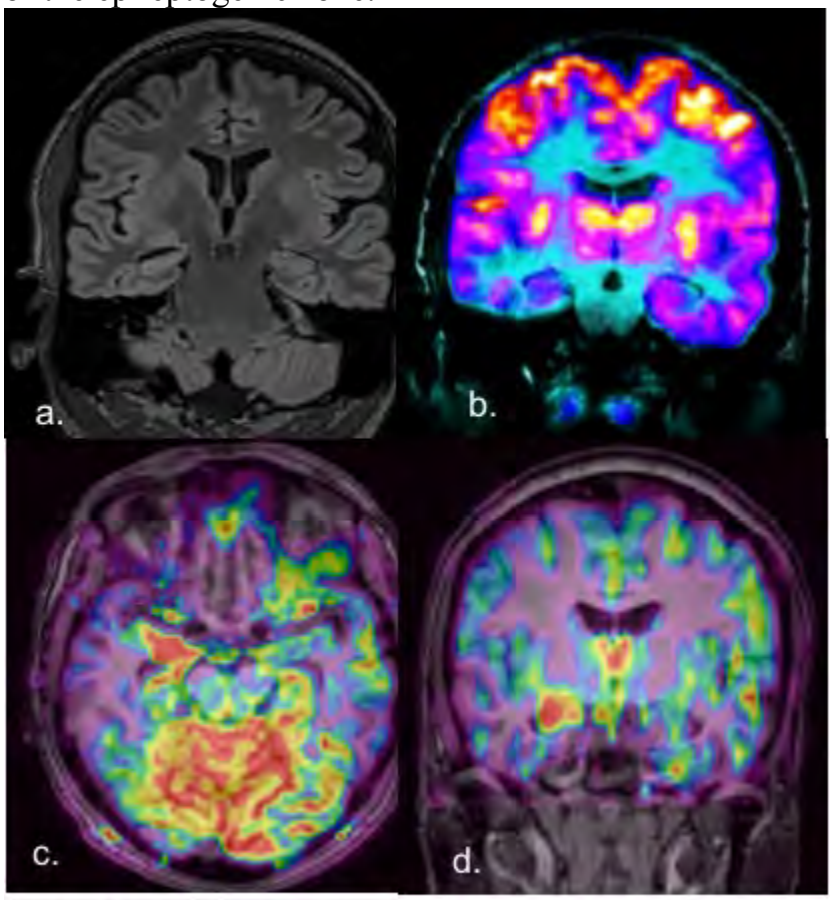


Fig : (a). sMRI shows right hippocampal atrophy with FLAIR hyperintensity suggestive of mesial temporal sclerosis. (b). FDG-PET MR Shows hypometabolism at right temporal lobe. (c) & (d) ASL – T1MPRAGE coregistered images shows hyperperfuson at right medial temporal structure with hypometabolism at right lateral temporal lobe. Good concordance between ASL , sMRI & PET-MR

(Filename: TCT_eP-05_ASL_peri-ictal1.jpg)

Monday
6:30AM - 3:00PM
Long Beach Convention Center, Exhibit Hall B-(Lower Level) eP

Electronic Scientific Poster (eP)-Head & Neck

eP-88

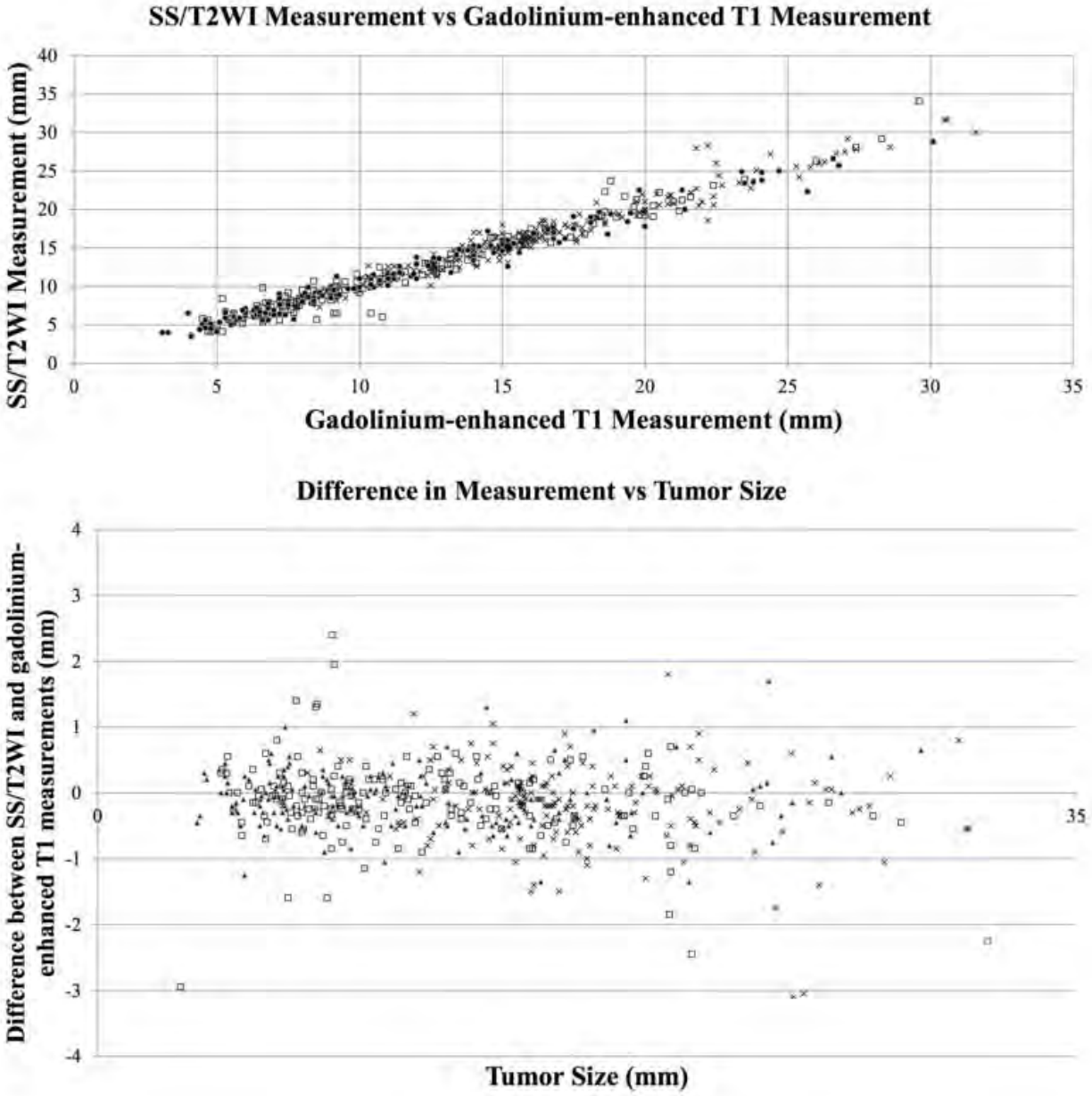
6:30AM - 3:00PM

A Comparison of Steady State/T2-Weighted MRI to Gadolinium-Enhanced MRI for Follow-up of Vestibular Schwannomas Treated with Gamma Knife Radiosurgery

J Whang[1], J Lazor[2], R Assadsangabi[3], S Thompson[4], J Lee[1], L Loevner[5], K Learned[6]
[1]Hospital of the University of Pennsylvania, Philadelphia, PA, [2]The Hospital of the University of Pennsylvania, Philadelphia, PA, [3]University of Pennsylvania, Philadelphia, PA, [4]Pennsylvania Hospital, Philadelphia , PA, [5]University of Pennsylvania, Philadelphia , PA, [6]Univ. Pennsylvania Health System, Philadelphia, PA

Purpose
To compare thin section steady state/T2-weighted imaging (SS/T2WI) to gadolinium-enhanced T1-weighted imaging for follow up of vestibular schwannomas treated with Gamma Knife radiosurgery.
Materials and Methods
We retrospectively reviewed 180 follow-up MRI examinations for fifty-six patients with vestibular schwannoma treated with Gamma Knife at our institution from January 2009-December 2014. All studies utilized thin section gadolinium-enhanced, and precontrast SS/T2WI techniques (CISS, FIESTA, T2 SPACE/DRIVE/RESTORE). Tumor size was measured in 3 orthogonal planes on both the SS/T2WI and gadolinium-enhanced images. Observers also recorded the presence of cystic change and heterogeneous signal of the tumor, presence of additional findings that can only be seen with contrast. Steady-state/T2WI and gadolinium-enhanced images and clinical status were reviewed independently, avoiding bias which would exaggerate the correlation.
Results
The difference in tumor dimension on SS/T2WI was a mean of -0.26 mm, or 1.40% smaller than on gadolinium-enhanced images, with 95% of measured differences between -2.46 mm and +1.94 mm. Steady-state/T2WI and gadolinium-enhanced measurements correlated well with each other in all three planes (correlation coefficient r 0.980). Compared to gadolinium-enhanced images, SS/T2WI correctly demonstrated the presence/absence of cystic content in the tumors in 86.1% of cases. Noncystic but heterogeneously increased SS/T2WI signal also correlated with heterogeneous enhancement, agreeing in 72.4% of cases.
Conclusions
Unenhanced SS/T2WI techniques offer high resolution tumor surveillance of vestibular schwannomas after Gamma Knife, equivalent to gadolinium-enhanced T1 technique. Steady-state/T2WI measurements tend to slightly underestimate tumor size, although the average effect of the bias is negligible without clinical implication. Moreover, alteration of tumor signal on both techniques agrees well, and such changes are expected after treatment without clinical significance. The accuracy of SS/T2WI may obviate the use of contrast in these

patients, reducing healthcare costs and adhering to ALARA principles for contrast administration.



(Filename: TCT_eP-88_TablesandFigures.jpg)

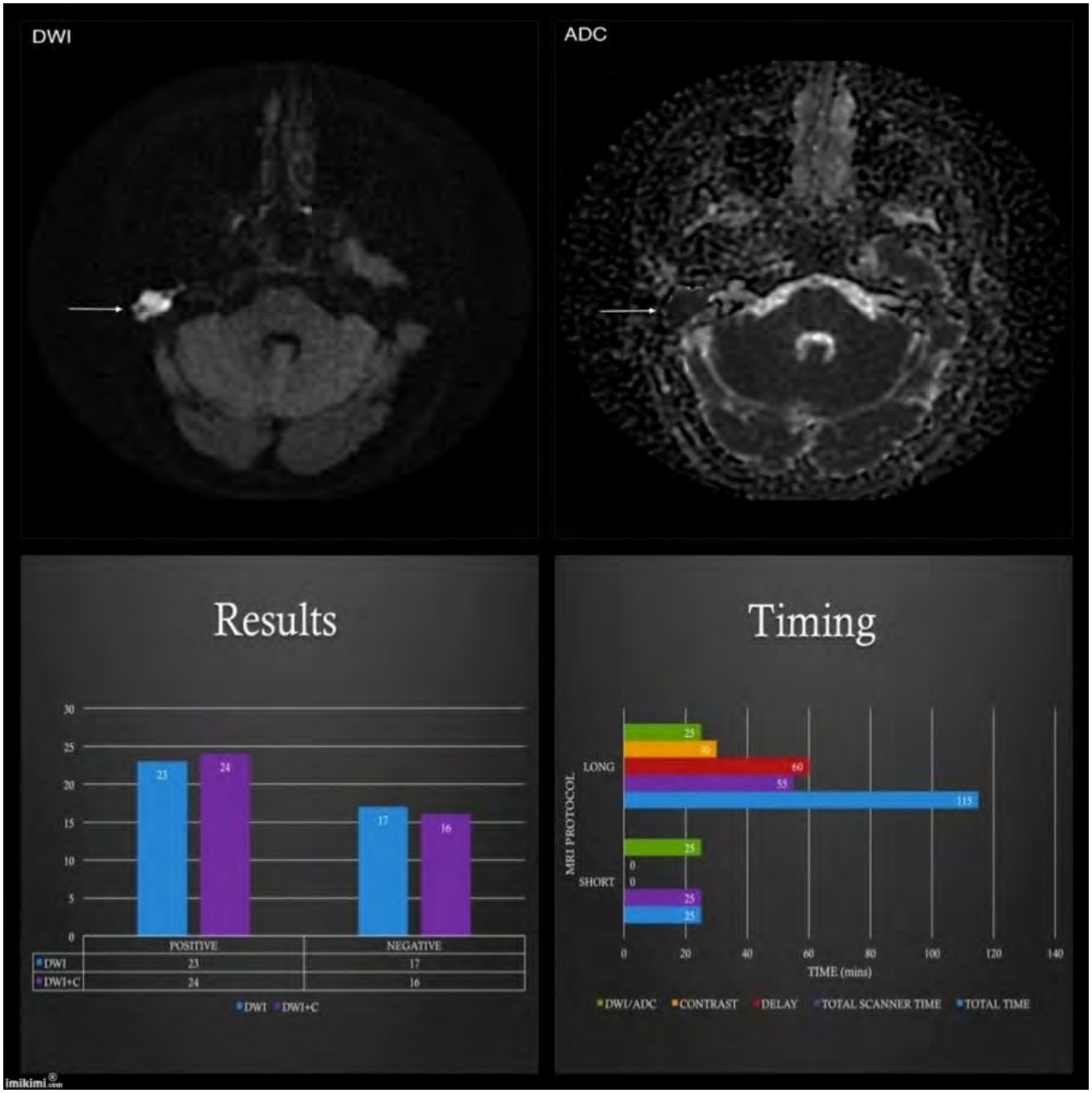
eP-87

6:30AM - 3:00PM

An Assessment of Diffusion-Weighted Imaging and Contrast-Enhanced MRI in the Diagnosis of Cholesteatoma Recurrence

R Kavanagh[1], A Carroll[1], Y Purcell[1], R Killeen[2], A Smyth[3]
[1]St Vincent's University Hospital, Dublin 4, Ireland, [2]St. Vincent's University Hospital, Dublin, Dublin 4, [3]Saint Vincents University Hospital, Dublin, Ireland

Purpose
A cholesteatoma is an abnormal growth of squamous epithelium in the middle ear and mastoid. The mainstay of therapy for cholesteatoma is surgical resection. After surgery there is a high recurrence rate, which ranges between 6% and 27%. Detection of cholesteatoma recurrence is vital so that further treatment can be instituted at an early stage to avoid complications, which can include pain, otitis media, mastoiditis, meningitis and neurological dysfunction. Magnetic resonance imaging (MRI) is the modality of choice in the assessment for cholesteatoma recurrence and our current practice is to perform a number of sequences including diffusion-weighted imaging (DWI) and contrast enhanced MRI (CE MRI). The aim of this study was to assess the accuracy of a DWI compared to DWI with CE MRI in the diagnosis of cholesteatoma recurrence.
Materials and Methods
This was a retrospective cohort study of forty consecutive patients who underwent an MRI for the investigation of cholesteatoma recurrence that were performed in the St. Vincent's Hospital Group. Magnetic resonance imaging was assessed by a fellowship-trained head and neck radiologist and a radiology specialist registrar. Initially, the "short-sequence" MRI (with non-EPI DWI but without CE MRI) was assessed. Subsequently and separately, the "long-sequence" MRI (with DWI and CE MRI) was assessed. A determination of the presence or absence of a cholesteatoma recurrence was made at each assessment. Statistical analysis was performed, using Stata Statistical Software: Release 12 (StataCorp LP, College Station, TX, USA), to assess the agreement between the two MRI protocols.
Results
There was excellent agreement between the short and long sequence MRI protocols in the diagnosis of cholesteatoma recurrence with a Cohen kappa value of 0.95. Taking the long sequence as the gold standard, we found that the DWI imaging without additional contrast-enhanced sequences had a sensitivity of 96%, a specificity of 100%, and accuracy of 97.5%, a positive predictive value of 100% and a negative predictive value of 94% in the diagnosis of cholesteatoma recurrence. Implementation of these findings would result in a saving of 30 minutes of scanner time per patient and the consequent financial benefits.
Conclusions
Magnetic resonance imaging in patients with suspected cholesteatoma recurrence can be performed using diffusion-weighted sequences without the need for further contrast-enhanced sequences. Implementation of this will result in significant time and financial savings.



(Filename: TCT_eP-87_CHOLESTEATOMA1.jpg)

eP-84

6:30AM - 3:00PM

Approaches for Biobank Specimen – Preoperative Imaging Correlation for Radiogenomic Studies of Head and Neck Cancer: Review of a Single Institution Experience

M Bayat[1], F DeBlois[1], A Perez-Lara[2], R Forghani[1]

[1]*Jewish General Hospital & McGill University, Montreal, Quebec,* [2]*Jewish General Hospital, Montreal, Quebec*

Purpose
There is increasing interest in using texture or radiomic analysis for prediction of tumor molecular features. For such radiogenomic investigations, the best achievable correlation of site of tumor specimen collection with the pre-operative images is desired. In this study, we review our single institution experience using different approaches for image-pathology specimen sample correlation and discuss the advantages and pitfalls of the different approaches.
Materials and Methods
This technical exhibit is based on a single institution experience from an ongoing prospective study of head and neck squamous cell carcinoma with informed consent. During operative resection, surgical sutures were used for proper orientation of the resected tumor specimen in the pathology suite. For biobank specimen – image correlation, 3D printing and video-recordings were used. 3D printing was performed pre-operatively with creation of "positive" tumor molds (based on segmented tumor contour) and "negative" molds (based on estimated resection margin). Video recordings were performed in the pathology suite at the time of biobank specimen harvesting for live replay during post-operative tumor segmentation for future radiomic analysis.
Results
Live video recording in the pathology suite replayed during segmentation was most helpful for biobank specimen – image correlation and targeting of a subarea within the tumor on pre-operative imaging. Positive 3D molds provided good visual representation of the tumor but were not helpful for biobank specimen – image correlation. Negative molds with slots, previously used for other organs such as prostate, did not work well for HNSCC because of complex shape of tumors and need for preservation of tumor margins for appropriate clinical-pathologic evaluation of the tumor margins.
Conclusions
Video recordings performed during biobank specimen harvesting are most useful for guiding tumor segmentation for future radiomic analysis.

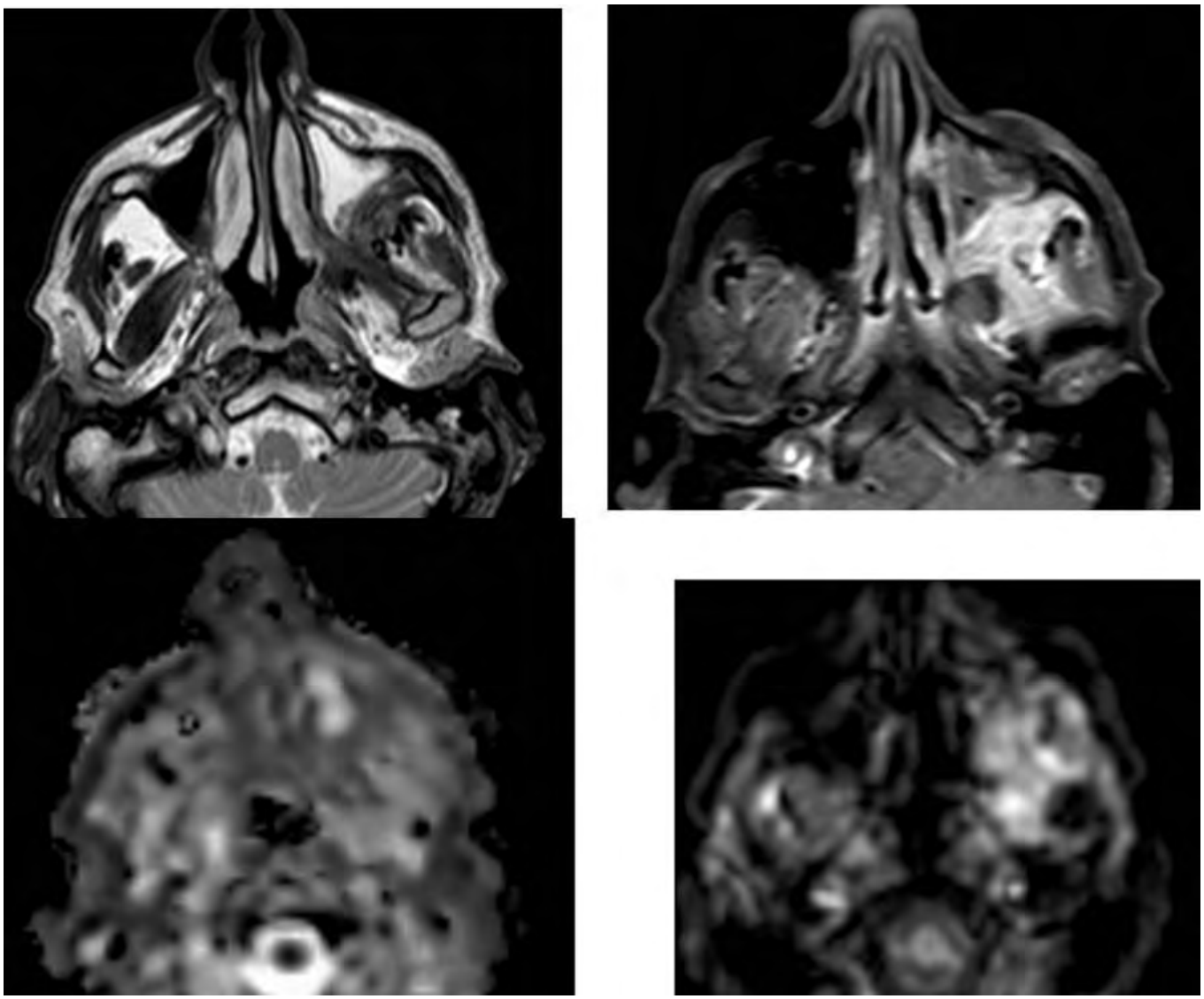
eP-79

6:30AM - 3:00PM

Arterial Spin Labeling Perfusion-Weighted MR Imaging and Diffusion-Weighted MR Imaging in Differentiation of Recurrence Head and Neck Squamous Cell Carcinoma from Post-Radiation Changes

a abdel razek[1]
[1]*Mansoura faculty of medicine, mansoura, WY*

Purpose
To assess arterial spin labeling (ASL) perfusion-weighted MR imaging and diffusion-weighted MR imaging in differentiating recurrent head and neck cancer from postradiation changes.
Materials and Methods
Retrospective study done upon 41 patients with head and neck cancer after radiotherapy underwent ASL perfusion-weighted MR imaging and diffusion-weighted MR imaging. The tumor blood flow (TBF) and apparent diffusion coefficient (ADC) value of the lesion was calculated. The final diagnosis was done with biopsy.
Results
There was significant difference (P = 0.001) in TBF of recurrent cancer (30.9±5.16 mL/100 g/min) and postradiation changes (12.1±3.06 mL/100 g/min). There was significant difference (P = 0.001) in ADC between recurrent cancer (0.94±0.16X10-3mm2/s) and postradiation changes (1.37±0.12X10-3mm2/s). Selection of TBF of 22.2 mL/100 g/min and ADC of 1.07X10-3mm2/s to predict recurrence has area under the curve of 0.822, 0.900 and accuracy of 92.7%, 95.1% respectively. Combined ADC and TBF are under the curve of 0.992 and accuracy of 97.6%.
Conclusions
Combined ADC and TBF are noninvasive imaging parameters that can play a role in differentiation recurrent head and neck cancer from postradiation changes.



(Filename: TCT_eP-79_Picture1.jpg)

eP-82

6:30AM - 3:00PM

Arterial Spin Labeling Perfusion-Weighted MR Imaging of Head and Neck Tumors: A Pilot Study

a abdel razek[1]
[1]*Mansoura faculty of medicine, mansoura, WY*

Purpose
To evaluate the utility of arterial spin labeling (ASL) perfusion-weighted MR imaging in differentiating malignant from benign tumors of head and neck.

Materials and Methods

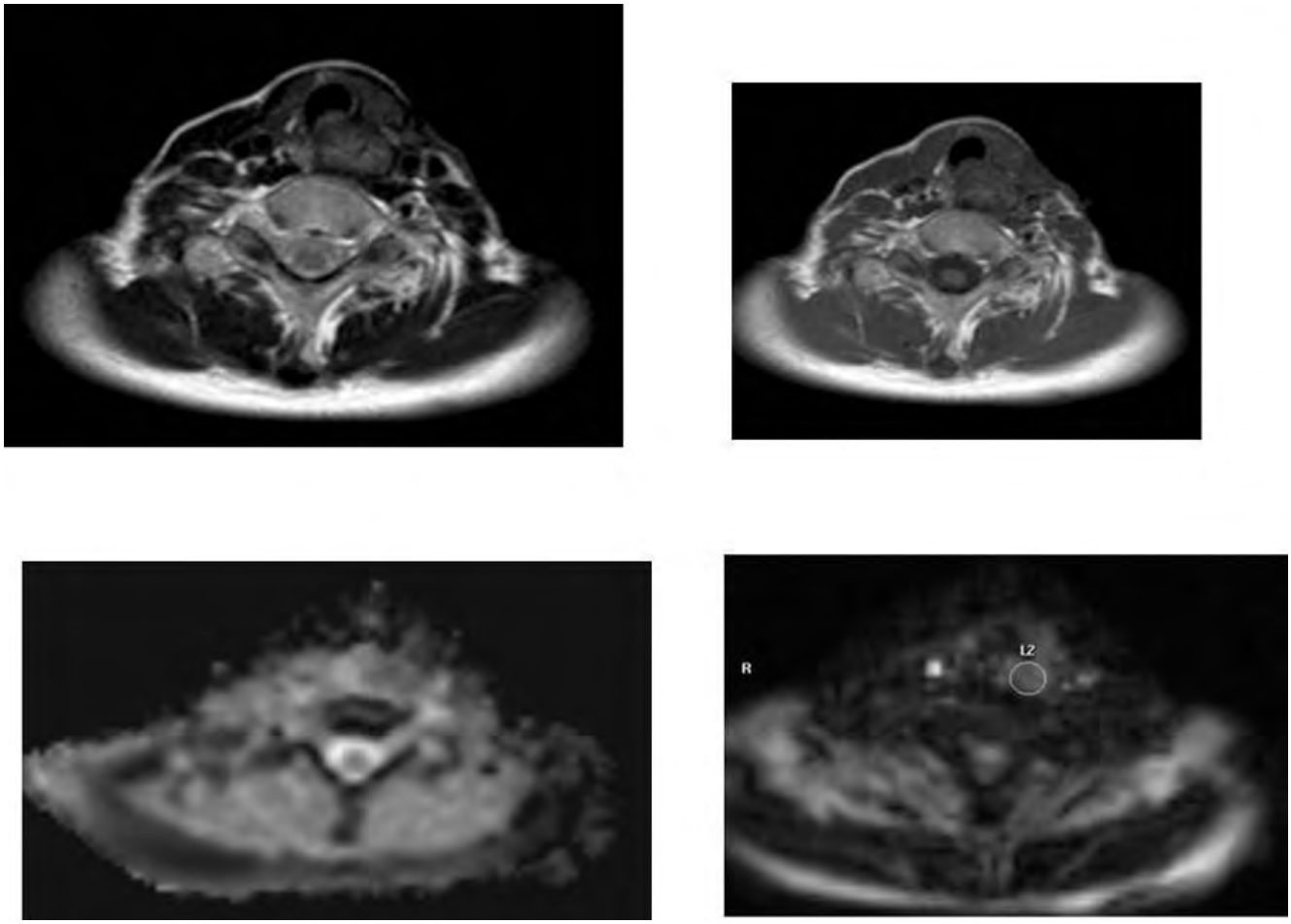
This study was done upon sixty-six patients (43M, 23F aged 28-72 years: mean 49 years) with head and neck solid tumors. Routine postcontrast and diffusion-weighted MR imaging (DWI) of head and neck were done for all patients. Arterial spin labeling with FEEPI sequence applied. There was reconstruction of 1200 source images. Tumor blood flow (TBF) was calculated from ASL and apparent diffusion coefficient (ADC) was calculated from diffusion-weighted MR images.

Results

The TBF of malignant tumors (mL/100g/min) was significantly different (P=0.001) than that of benign tumors (mL/100g/min). There was significant difference in ADC between malignant tumors and benign lesions (P=0.001). Selection of a threshold of TBF and ADC for differentiating malignant from benign tumors results in area under curve of 0.863 and 0.781 and accuracy of 87% and 78% respectively. There was significant difference (P =0.001) in TBF between well and moderately differentiated malignancy versus poorly and undifferentiated head and neck malignancy. The TBF was well correlated with ADC value (r=0.879).

Conclusions

Arterial spin labeling perfusion-weighted MR imaging is a noninvasive imaging technique that can play a role in differentiation malignant tumors of head and neck from benign lesions.



(Filename: TCT_eP-82_Picture23.jpg)

eP-78

6:30AM - 3:00PM

Brachial Plexus MR Neurography using a 3D Dixon-TSE Pulse Sequence with Blood Vessel and CSF Signal Suppression: Preliminary Experience in Children

P Cornejo[1], B Cervantes[2], A Pokorney[1], H Hu[1], D Karampinos[2]
[1]Phoenix Children's Hospital, Phoenix, AZ, [2]Technische Universität München, Munich, Bavaria

Purpose
There has been growing interest in high-resolution MR neurography (MRN) exams of the brachial plexus to complement the diagnosis of neurological pathologies. Three-dimensional TSE sequences combined with an improved T2- and motion sensitized driven equilibrium (iMSDE) preparation have been proposed for lumbar and brachial plexus imaging with blood signal suppression (1-4). Recently, Cervantes, et al., using extended phase graph analysis, optimized the 3D TSE refocusing flip angle train to improve the delineation of small lumbar plexus nerves (5) and showed that the optimized train can further reduce cerebrospinal fluid

(CSF) signal when submillimeter resolution voxels are used (6). These works also have shown that spectral adiabatic inversion recovery (SPAIR) was adequate in providing uniform fat suppression in lumbar plexus imaging. In this work, we modify the previous 3D TSE MRN sequence (5) for brachial plexus imaging, and showcase our experience in 25 children (age range: 6 months-21 years), some with suspected nerve pathology. Since the brachial plexus region is highly sensitive to B0 inhomogeneity, we employ a 2-echo chemical-shift-encoded water-fat Dixon method to achieve uniform fat suppression in the head, neck and chest.

Materials and Methods

Typical imaging parameters used for brachial plexus imaging in children are shown below: 100 overcontiguous coronal 0.7-0.9 mm slices; 0.7-1.4 mm in-plane resolution; 2 signal averages; TR/TE effective = 1500/200 ms; 2 RF pules for T2-preparation with a TE of 35 ms; TSE factor = 60; TSE echo spacing = 6 ms; maximum refocusing flip angles = 100 and 125 degrees; linear phase encoding view order; parallel imaging 2.5x in right-left direction; approximate scan time = 6 minutes. The 2 echoes needed for Dixon water-fat separation were acquired in separate TRs. In contrast to the previously developed protocols used for lumbar plexus imaging, the brachial plexus technique herein used a lower TSE factor and a nerve signal ratio equal to 1 (nerve signal constant for 50% of the flip angle train duration) in order to maintain adequate nerve signal, as the requisite Dixon echo sampling lengthens the echo spacing in the 3D TSE MRN sequence. We imaged the brachial plexus of 25 pediatric patients (12 males, 13 females, 8.1±6.0 years). All patients were referred for a clinically indicated MRI exam of the head and neck, cervical spine, or total spine. All imaging was implemented on 2 similar 3 Tesla platforms (Philips Ingenia) using a 32-channel head coil array and a 12-channel posterior spine coil built into the MRI table. Volume-based B0 shimming of the imaging region was performed by the operator. A pediatric neuroradiologists assessed the conspicuity of the brachial plexus nerves in the resultant data, including the rami and the nerve roots, trunks, divisions, and cords. A 3-point scale was used: "0-not visible or poorly visualized", "1-moderately visualized", "2-well visualized". The neuroradiologist also commented on the presence of artifacts and blurring, the quality of fat suppression, and the degree of blood and CSF suppression.

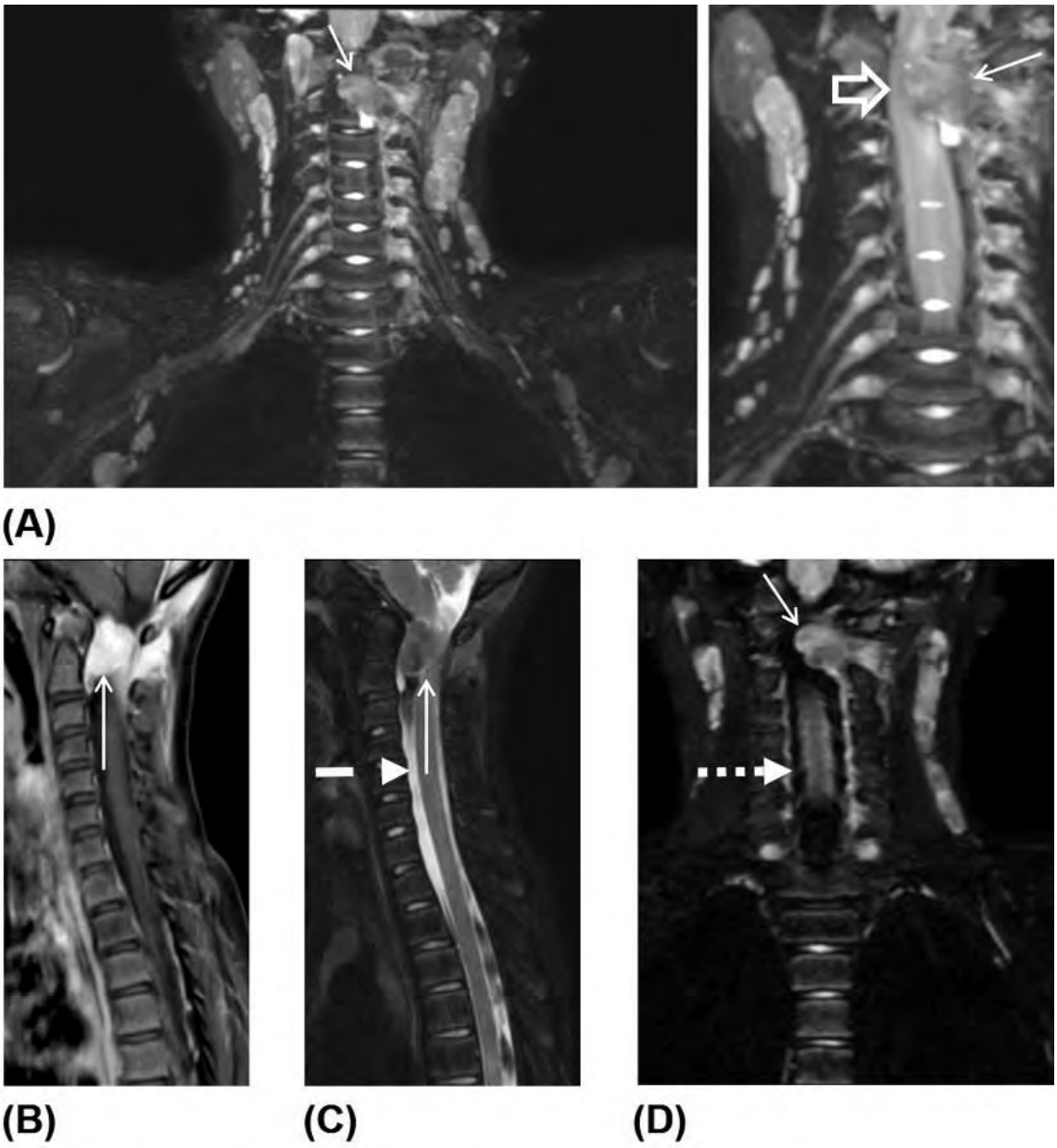
Results

A representative case is shown in Fig. 1, highlighting the diagnostic utility of the 3D TSE MRN technique. Note the consistent and uniform suppression of signals from fat, CSF, and vessels, the strong signal contrast between the brachial plexus nerves and surrounding tissue, and the clear visualization of nerve structures. In the figure, exemplary data in a 10.2-year-old female are shown. (A) Coronal projection depicts an extramedullary soft tissue mass (solid thin arrows in all panels) centered at the C2 vertebrae, causing high grade compression of the spinal cord (open arrow, inset). Also note clear delineation of the C5-C8 and T1 nerve ramus. (B) Postgadolinium T1-weighted fat-suppressed TSE acquisition shows avid enhancement of the mass. (C) Routine sagittal fat-suppressed T2-weighted TSE acquisition. Note high signal intensity from CSF (dash thick arrow). (D) Single slice from

the 3D TSE neurography sequence showing suppressed CSF signal surrounding the spinal cord (dotted thick arrows). Image evaluation identified 1 case with poor fat suppression that significantly impacted nerve visualization. Four additional cases were rated as having poor diagnostic image quality due to improper image planning. These cases received a score of "0", due primarily to their low SNR and poor nerve background CNR. In the remaining 20 cases that were deemed diagnostically useful, 14 cases received a score of "2", while 6 cases received a score of "1".

Conclusions

A blood and CSF-signal suppressed 3D Dixon TSE sequence that enables clear delineation of the brachial plexus nerves has been demonstrated in children at 3 Tesla, with promising data supporting clinical adoption. The employed iMSDE preparation achieved good suppression of the large thoracic blood vessels in agreement with previous works. The optimized flip angle train maximized nerve signals without inducing blurring due to T2-decay apodization of signals in k-space, and enabled the suppression of pulsating CSF signal in all cases. The 2-echo Dixon approach enabled uniform fat suppression in the head-neck region, without the SNR penalty associated commonly with inversion-recovery TSE (i.e., STIR) sequences. Therefore, the brachial plexus imaging technique proposed in this work can assist in the diagnostic assessment of neonates, infants, children who have birth-related injuries, traumatic cervical spine injuries from trauma, genetic disorders such as neurofibromatosis, and cervical spine tumors.



(Filename: TCT_O-428_Fig1_400dpi.jpg)

eP-77

6:30AM - 3:00PM

Comparison between Whole Body and Head and Neck Neurovascular Coils for 3T Magnetic Resonance Proton Resonance Frequency Shift Thermography Guidance in the Head and Neck Region

D Ginat[1], G Anthony[1], G Christoforidis[2], A Oto[1], L Dalag[1], S Sammet[2]
[1]University of Chicago, Pritzker School of Medicine, Chicago, IL, [2]University of Chicago, Chicago, IL

Purpose
To compare the image quality of magnetic resonance (MR) treatment-planning images and proton resonance frequency (PRF) shift thermography images and inform coil selection for MR-guided laser ablation of tumors in the head and neck region.
Materials and Methods
Laser ablation was performed on an agar phantom and monitored via MR PRF shift thermography on a 3T scanner, following acquisition of T1-weighted (T1W) planning images. PRF shift thermography images and T2-weighted (T2W) planning images were also performed in the neck region of five normal human volunteers. Signal-to-noise ratios (SNR) and temperature uncertainty were calculated and compared between scans acquired with the whole body coil and a head and neck neurovascular coil.
Results
T1W planning images of the agar phantom produced SNRs of 4.0 and 12.2 for the body coil and head and neck neurovascular coil, respectively. The SNR of the phantom MR thermography magnitude images obtained using the whole body coil was 14.4 versus 59.6 using the head and neck coil. The average temperature uncertainty for MR thermography performed on the phantom with the body coil was 1.1°C versus 0.3°C with head and neck coil. T2W planning images of the neck in five human volunteers produced SNRs of 28.3 and 91.0 for the body coil and head and neck coil, respectively. MR thermography magnitude images of the neck in these volunteers obtained using the whole body coil had a signal-to-noise ratio of 8.3, while the SNR using the head and neck coil was 16.1. The average temperature uncertainty for MR thermography performed on the volunteers with the body coil was 2.5°C versus 1.6°C with the head and neck neurovascular coil.
Conclusions
The whole body coil provides inferior image quality for both basic treatment-planning sequences and MR PRF shift thermography compared with a neurovascular coil, but may nevertheless be adequate for clinical purposes.

eP-80

6:30AM - 3:00PM

Comparison of 2D Single-Shot Turbo-Spin-Echo and Spin-Echo Echo-Planar Diffusion Weighted Brain MRI at 3.0 Tesla: Preliminary Experience in Children with Orthodontia and Shunts

C Pfeifer[1], A Pokorney[1], H Hu[1], J Miller[1]
[1]*Phoenix Children's Hospital, Phoenix, AZ*

Purpose
Diffusion-weighted magnetic resonance imaging (DWI) has matured into a powerful clinical technique for assessing pathologies in the brain (1, 2). One of the most common DWI pulse

sequences is 2D multi-slice single-shot spin-echo echo planar imaging (SE-EPI). SE-EPI acquisitions are fast and are quite robust to patient motion. However, the SE-EPI approach, which plays only a single 180 degree refocusing radio-frequency (RF) pulse per TR to acquire the entire k-space of an imaging slice, has limitations. Spin-echo-EPI techniques are highly sensitive to inhomogeneous magnetic fields, which can lead to geometric distortions and spatially-dependent loss of signal, especially near areas of air and tissue interfaces. Another common artifact is the chemical-shift between water and fat along the phase encoding direction, making fat suppression an integral requisite in DWI. An alternative DWI pulse sequence is the single-shot turbo spin echo (ssTSE) approach. It is commonly known as the single-shot fast spin echo or HASTE (Half-Fourier Acquisition Single-Shot Turbo-Spin-Echo) method. Since a ssTSE pulse sequence utilizes one 180 degree refocusing RF pulse to acquire each individual phase-encoded echo in k-space, the technique is significantly less sensitive to magnetic susceptibility, geometric distortions, and chemical shift artifacts. In the literature, ssTSE DWI has been described, validated, and compared to SE-EPI at 1.5 Tesla in evaluating a variety of pathologies. There is however a paucity of publications reporting on the diagnostic image quality and performance of ssTSE DWI at 3 Tesla, particularly in pediatrics. The purpose of this work was to determine whether a ssTSE DWI pulse sequence should replace our institution's conventional SE-EPI DWI for pediatric brain imaging at 3 Tesla, and whether the ssTSE DWI technique should be deployed in cases where large magnetic susceptibility-induced artifacts are anticipated, such as from dental braces and shunts.

Materials and Methods

This prospective study was approved by our institution's research and ethics board under expedited review as a minimum-risk project. The ssTSE DWI sequence utilized in this work is a commercially available product from Philips HealthTech. Informed consent and assent, if applicable, were obtained from all participants. Fifteen pediatric patients (8 boys, 7 girls, age range: 0.4-19.0 years, average age: 10.6±6.0 years) were involved in this pilot study. All MRI data were acquired on 2 identical 3 Tesla scanners (Ingenia® multi-RF-transmit platform, software version R5.1.7, Philips HealthTech, Best, The Netherlands) using a pair of 32-channel head coil arrays. Figure 1a summarizes the pertinent pulse sequence parameters. Images were assessed by a board-certified pediatric neuroradiologist. The data were rated in 2 categories using analog scales. In the first category assessing the presence and impact of susceptibility and geometric distortion artifacts, the radiologist reviewed the SE-EPI and ssTSE DWI data and assigned to each image set a score of either 3 for "acceptable with minimal or no artifacts", 2 for "acceptable with clinically irrelevant artifacts", 1 for "marginally acceptable with potentially clinically relevant artifacts", or 0 for "unacceptable/non-diagnostic". Therefore, a total of thirty scores (15 patients x 2 scores) were given. In the second review category assessing overall diagnostic image quality, the paired SE-EPI and ssTSE DWI data from each patient were viewed together, and the rater assigned a -1, 0, or +1 to denote preference for SE-EPI, equivalency, and preference for ssTSE, respectively. The STATA software was used for statistical analysis. We used a one-

way analysis of variance followed by a Tukey-Kramer test to compare SE-EPI and ssTSE scores. In the second review category, we used the nonparametric one-sample Wilcoxon signed-rank test. A p-value of 0.05 was used to reflect statistical significance.

Results

Figure 1b summarizes the rating scores from the image review. SE-EPI was deemed to have unacceptable and nondiagnostic images in 6 cases, 2 of whom had ventriculoperitoneal shunts and 4 had dental braces. In these 6 cases, ssTSE image were however rated to have superior diagnostic image quality with scores of at least "2" (clinically irrelevant artifacts) and "3" (none or minimal artifacts). There were 2 cases where both SE-EPI and ssTSE images were rated to have no or minimal artifacts. Neither of these 2 patients had orthodontia or shunts. In the remaining 7 cases, ssTSE images consistently exhibited fewer artifacts than their SE-EPI counterpart. Out of a maximum possible cumulative score of forty-five (i.e., 15 patients x maximum score of "3"/patient), the SE-EPI data received a score of seventeen, while the corresponding ssTSE data received a significantly higher sum score of forty-two. The Tukey-Kramer test of the scores was statistically significant ($p<0.01$). Scores from the evaluation on diagnostic image quality also are summarized in Figure 1b. There were no cases where the SE-EPI images were preferred over ssTSE data. In 6 cases, images from the 2 pulse sequences were preferred equally. Of these 6, 5 did not have any external devices such as orthodontia or shunts. Overall, a statistically significant improvement in diagnostic image quality with ssTSE over SE-EPI DWI was observed ($p<0.01$). Figure 1c illustrates a representative example.

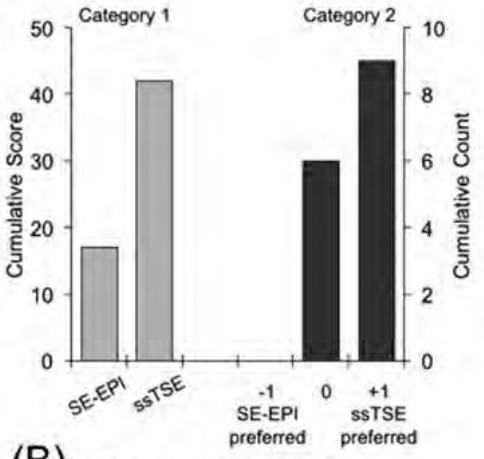
Conclusions

Image artifacts from magnetic susceptibility due to ventriculoperitoneal shunts and orthodontia are one of the common reasons in pediatric brain MRI where the image quality of a DWI scan is deemed compromised or nondiagnostic. Often, the scan must be repeated with imaging slices at a different angulation to minimize artifacts, at the expense of additional anesthesia time in younger patients. In this preliminary work in pediatric patients at 3.0 Tesla, we have demonstrated the potential utility of ssTSE DWI to consistently provide high diagnostic quality brain images from patient to patient, even in the presence of materials that cause magnetic susceptibility. Our findings supporting ssTSE DWI is similar to past literature reports (3-5). We recognize several limitations in our study. First, the sample of fifteen patients is small. However, we believe the presented preliminary data nevertheless clearly demonstrates the potential clinical utility of ssTSE DWI in pediatric brain imaging. The results are visually striking and we do not anticipate an increase in sample size or the involvement of additional blinded raters to significantly alter the study's findings. Second, our study's small cohort size only included only one case with a noticeable brain lesion and thus we did not have the sample size and statistical power to compare quantitative ADC values between SE-EPI and ssTSE DWI data in abnormal pathological tissues, assess intra- and inter-rater variability, and provide a comparison category for lesion conspicuity. Third, we did not design multiple versions of the ssTSE pulse sequence in order to optimize and evaluate impact on signal-to-noise ratio as a balance of spatial resolution,

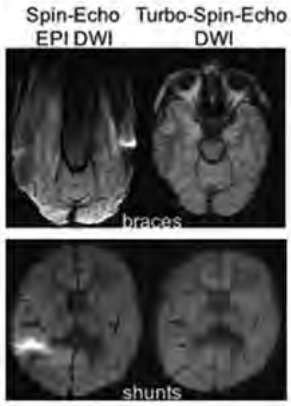
volume coverage, and resultant scan time. In conclusion, ssTSE DWI is robust and provides clinically superior image quality with a very small frequency of irrelevant artifacts.

Parameter	2D SE-EPI	2D ssTSE
orientation	axial	axial
FOV (mm)		
anterior-posterior	200-220	200-220
right-left	200-220	200-220
acquired voxel size (mm)		
anterior-posterior	1.9	2.0
right-left	1.5	2.0
reconstructed voxel size (mm)	1.0	1.0
number of slices	30-35	30-35
slice thickness (mm)	4	4
slice gap (mm)	1	1
fat suppression	SPIR	SPIR
phase encoding profile order	linear	low-high (0, -1, +1, -2, +2)
diffusion b-values (sec/mm^2)	0, 1000	0, 1000
TR (msec)	4,500-5,000	9,000-10,000
TE (msec)	108-116	72-80
Partial echo / partial Fourier	no	no
Excitation flip angle (deg)	90	90
number of signal averages	1	1
readout bandwidth/pixel (Hz)	700-800	400-500
bandwidth along EPI direction (Hz)	1,100-1,400	n/a
EPI factor	50-60	n/a
TSE factor	n/a	40-50
TSE echo spacing (msec)	n/a	5-6
TSE shot duration (msec)	n/a	220-230
parallel imaigng (SENSE)	2x (anterior/posterior)	2.5x (right/left)
scan time (min:sec)	1:00-1:10	1:30-1:50

(A)



(B)



(C)

(Filename: TCT_eP-80_Figure1_300dpi.jpg)

eP-86

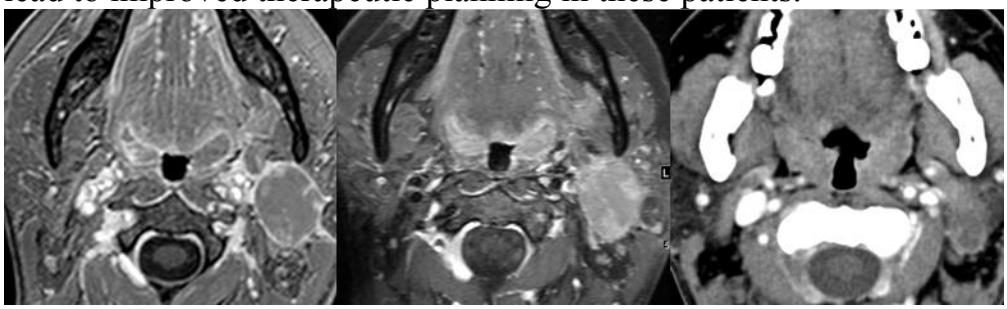
6:30AM - 3:00PM

Detection of Occult Primary Tumors in Patients with Cervical Metastases of Unknown Primary Tumors: Comparison of Three-Dimensional THRIVE MR Techniques with Two-Dimensional Spin-Echo MR or Contrast-Enhanced CT Imaging

J Kim[1], M Yoo[1], J Seo[1], S Bae[2], Y Park[1]
[1]Yonsei University College of Medicine, Seoul, CA, [2]Yonsei University College of Medicine, Seoul , CA

Purpose
To evaluate and compare the diagnostic potential of postcontrast 3D T1-weighted high resolution isotropic volume examination (THRIVE) sequence to spin-echo (SE) T1-weighted sequence or CT imaging in the detection of occult primary tumors in patients with cervical metastasis of an unknown primary tumors (CUP).

Materials and Methods
A total of forty-two patients with initially undetected tumors after endoscopic or physical examination underwent pre-operative contrast-enhanced CT and MR imaging using both SE and 3D THRIVE sequences. Results of guided biopsy with general anesthesia served as the reference standard. Diagnostic values of 3D THRIVE and SE T1-weighted MR, and contrast-enhanced CT imaging were compared with the McNemar test.
Results
Primary tumors were detected in twenty-three (55%) of forty-two patients. There were twelve tumors in the palatine tonsil, 9 in the base of the tongue, and 2 in the nasopharynx. Three-dimensional THRIVE MR technique depicted twenty (87%) of twenty-three primary tumors, but it failed to depict primary tumors in 3 (13%) of twenty-three cases. Overall, sensitivity of 3D THRIVE MR (87%) in detection of primary tumors was higher than that of SE T1-weighted MR (53%) ($P = .042$) or contrast-enhanced CT (24%) ($P < .001$), while specificity of these methods did not differ ($P > .5$). Diagnostic performance (AUC) of 3D THRIVE MR in tumor detection was significantly better than that of SE T1-weighted MR or contrast-enhanced CT imaging ($P = .002$).
Conclusions
Three-dimensional THRIVE MR sequence is more sensitive in detection of primary tumors than SE T1-weighted MR or contrast-enhanced CT in patients with CUP; therefore, it may lead to improved therapeutic planning in these patients.



(Filename: TCT_eP-86_Figure.jpg)

eP-89a

6:30AM - 3:00PM

Do we have Standardized Measurements to be Used Clinically in Inner Ear Malformations: A Literature Review

F D'Arco[1], R Warne[2], R Lakshmanan[2], O Carney[2]
[1]Great Ormond Street Hospital, London , United Kingdom, [2]Great Ormond Street Hospital, London, United Kingdom

Purpose
We conducted an extensive review of the literature relevant to inner ear measurements in

normal and malformative conditions in order to select reproducible measurements and normative ranges that may be used in clinical practice.

Materials and Methods

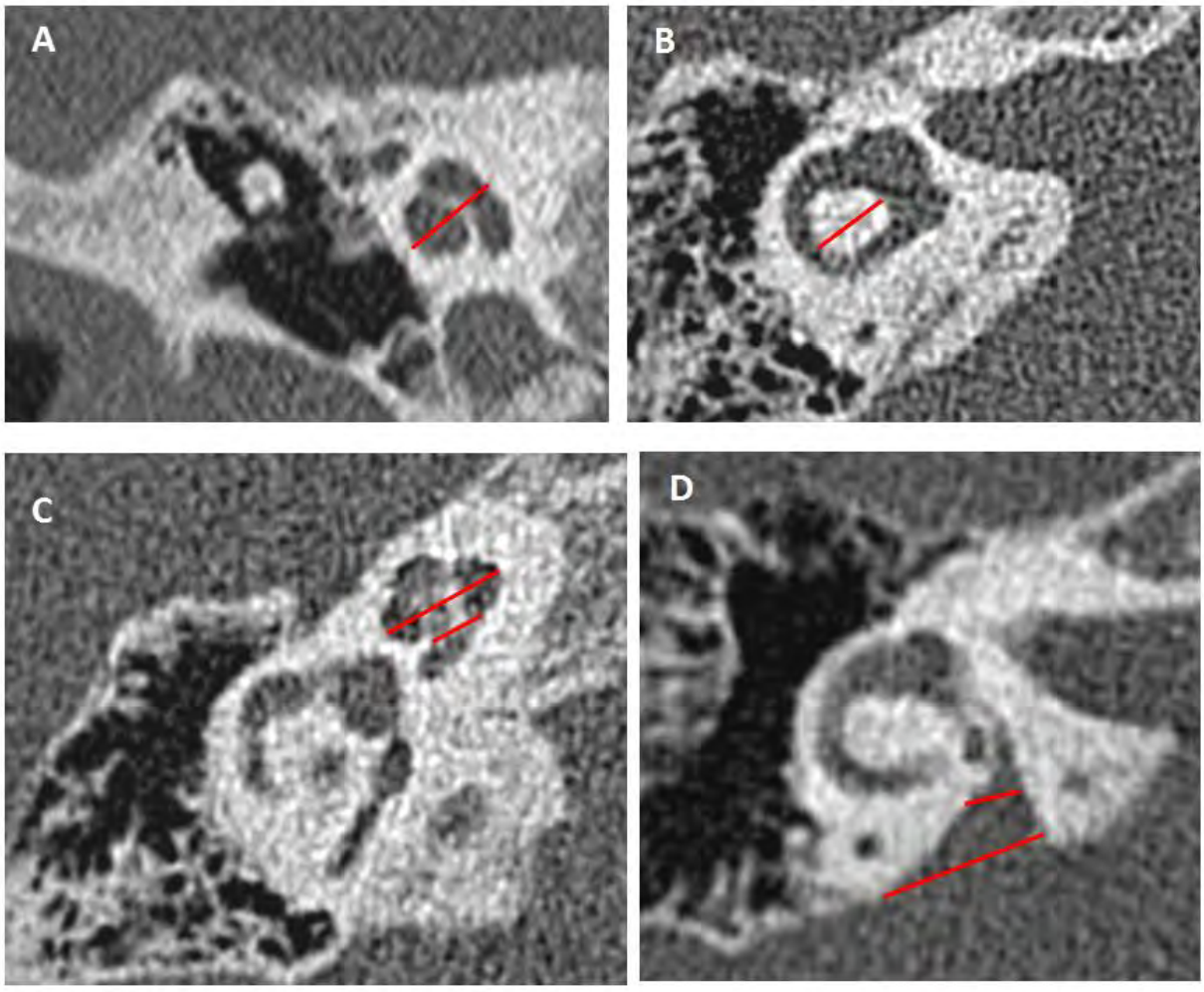
We performed a Pubmed literature search using the following terms: inner + ear + malformations + measurements + normal + values. We found 14 papers from 2003 to 2014 seeking to establish normative values of inner ear structures (all or some of them) by reviewing patients with inner ear malformations and/or disease associated with sensorineural hearing loss. All of the papers where based on computed tomography (CT) measurements. We cross-referenced the measurements obtained and performed a critical analysis of the methods used by different authors.

Results

Based on critical literature review, we propose specific methods for inner ear measurements and cut-off values. The following methods were proposed: Cochlear height (CH): Maximal height in a coronal plane measured perpendicular to the oval window (Shim et al. 2006); Lateral semi-circular canal diameter (LSCC): Maximal diameter of bony island among slices displaying an intact semicircle (Blaser et al. 2006); Vestibular aqueduct (VA): a) midpoint: the part of the VA located half the distance in the petrous bone from its origin in the labyrinth to its aperture in the epidural space. b) operculum: opercular widths of the VA are measured in the same plane as the endolymph sac depths by drawing a line from the opercular edge anterolaterally to form a 90° angle with the posterior wall of the petrous bone (Vijayasekaran et al. 2007); Cochlear canal: Width of the cochlear canal on a MPR axial plane including modiolus and posterior SCC (according to Tessier et al. 2010). Cochlear width: Width of the cochlea on a MPR axial plane including modiolus and posterior SCC (according to Tessier et al. 2010). The following cut-off for normal inner ears: Cochlea height (coronal): > 4.3 mm. Lateral SCC bony island (axial): > 3 mm. Cochlear Canal (axial): > 1.4 mm and < 2.5 mm. Cochlear width (MPR): > 5.4 mm. Vestibular Aqueduct: < 0.9 (midpoint) and < 1.9 mm (operculum).

Conclusions

The reference values for inner ear structures provided in this literature review can serve as an aid for the interpretation of CT images thus increasing sensitivity in detecting inner ear malformations, in particular cochlear hypoplasia which now are considered more common than previously thought (Sennaroglu 2016). In addition, diagnosis of a short cochlea can impact on the choice of electrode used in cochlear implantation by the ENT surgeon. Further prospective studies are required to assess the utility of the proposed cut-off values on a large number of patients and to assess impact on the surgical outcome.



Proposed methods for inner ear measurements: A) Cochlear Height (coronal), B) Lateral SCC bony Island (axial), C) Cochlear Canal and Cochlear Width (MPR), D) Vestibular Aqueduct (axial)

(Filename: TCT_eP-89a_Picture1.jpg)

eP-85

6:30AM - 3:00PM

Dynamic Contrast-Enhanced Magnetic Resonance Imaging of Orbital and Anterior Visual Pathway Lesions

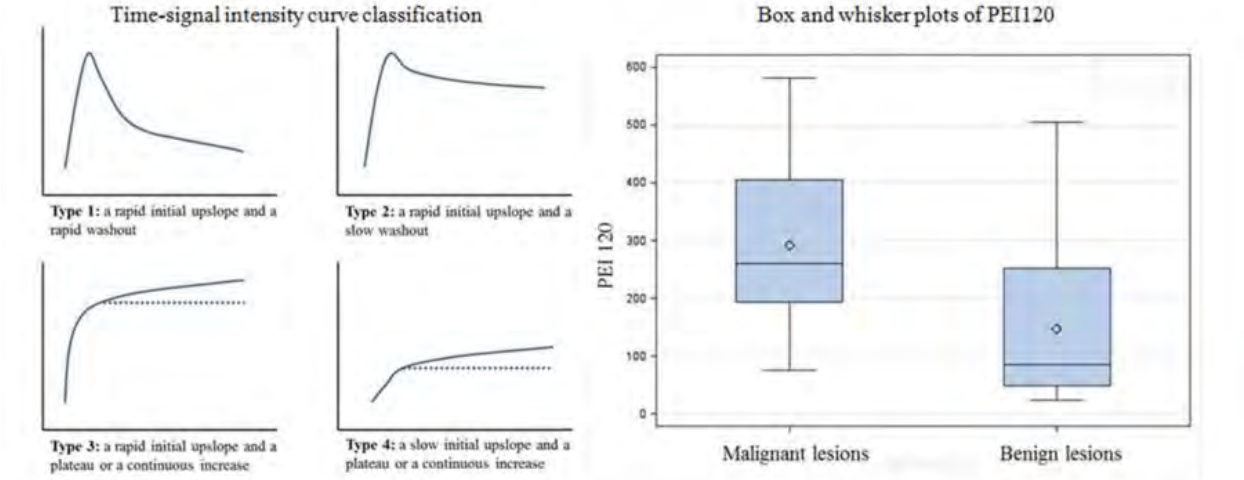
N Jittapiromsak[1], P Hou[1], H Liu[1], J Sun[1], T Chi[1]
[1]*The University of Texas MD Anderson Cancer Center, Houston, TX*

Purpose
The purpose of this study was to evaluate the utility of dynamic contrast-enhanced magnetic resonance imaging (DCE MRI) as an adjunct to conventional MRI in the assessment of

orbital and anterior visual pathway lesions and to explore the best method for DCE data analysis.
Materials and Methods
We retrospectively reviewed DCE MRI of thirty-seven untreated enhancing orbital and anterior visual pathway lesions. The DCE data were processed by 1) model-independent signal intensity with time and 2) model-dependent analysis using a two-compartment model. The time-signal intensity curve (TIC) and semiquantitative parameters from method 1 [positive enhancement integral (PEI) at initial 30, 60, 90, and 120 seconds, time to peak, maximum peak enhancement, maximum enhancement ratio, maximum slope of increase, maximum slope of decrease, and washout ratio] and quantitative parameters from method 2 (Ktrans, kep, vp, and ve) were derived for comparison with the final diagnosis.
Results
The lesions comprised optic pathway glioma (n=9), meningioma (n=6), neurofibroma (n=6), cavernous hemangioma (n=3), schwannoma (n=1), melanoma (n=3), lymphoma (n=1), metastasis (n=3), and radiation optic neuropathy (n=5). The TIC of orbital lesions demonstrated different perfusion characteristics and could be described by 4 types ($P = 0.002$). All of the lesions that demonstrated TIC type-1 were benign lesions. TIC type-4 was significantly associated with benign lesions, whereas TIC type-3 was significantly associated with malignant lesions. The PEI30, PEI60, PEI90, PEI120, and kep were significantly lower in benign lesions than in malignant lesions ($P = 0.027$, 0.020, 0.018, 0.015, and 0.018, respectively). Receiver operating characteristic analysis indicated that the PEI120 yielded the best diagnostic accuracy (AUC, 0.80; 95% CI, 0.64-0.96) in differentiating between benign and malignant orbital lesions.
Conclusions
Dynamic contrast-enhanced MRI is useful in evaluating orbital and anterior visual pathway lesions. A model-independent DCE analysis method is equivalent to model-dependent method in differentiating benign from malignant orbital lesions.

Table. Comparison of dynamic contrast–enhanced MRI parameters for benign lesions and malignant lesions.

Parameter	Method	Benign lesions Mean±SD	Malignant lesions Mean±SD	AUC (95% CI)	Significance (*P* value)	Cut-off value	Sensitivity	Specificity	Accuracy
PEI30	1	82.19±80.68	152.4±85.96	0.77 (0.60-0.94)	0.027	105.7	0.86	0.73	0.76
PEI60	1	117.7±111.87	233.5±129.77	0.79 (0.62-0.96)	0.020	206.0	0.71	0.83	0.81
PEI90	1	136.26±126.98	268.44±146.76	0.79 (0.63-0.95)	0.018	175.4	0.86	0.70	0.73
PEI120	1	147.56±135.19	292.18±161.05	0.80 (0.64-0.96)	0.015	188.6	0.86	0.70	0.73
k_{ep}	2	0.27±0.36	0.43±0.24	0.79 (0.65-0.93)	0.018	0.26	1.00	0.76	0.78



(Filename: TCT_eP-85_GraphicImage.jpg)

eP-81

6:30AM - 3:00PM

Multi-Slice Versus Single Slice 2D Spectral Dual Energy CT Radiomic Analysis of Head and Neck Squamous Cell Carcinoma for Prediction of P16 and Nodal Status

A Perez-Lara[1], B Forghani[2], M Bayat[3], G Melki[1], R Forghani[3]
[1]Jewish General Hospital, Montreal, Quebec, [2]Forghani Medical Services Inc., Cote St-Luc, Quebec, [3]Jewish General Hospital & McGill University, Montreal, Quebec

Purpose

There is increasing use of texture analysis for prediction of molecular or clinical features of interest beyond what typically is done during routine clinical image interpretation. One approach for texture analysis is a 2D texture method evaluating features on a single slice segmented around the largest diameter of the tumor. The purpose of this study was to examine the potential value of multi-slice texture data over single slice by evaluating variations in prediction models based on analysis of different slices in predicting p16 status or presence of lymphadenopathy based on radiomic features of head and neck squamous cell carcinoma (HNSCC).

Materials and Methods
Dual energy CT scans from 30 patients with pathology proven HNSCC were evaluated. Multi-slice segmentation and texture analysis of the entire tumor was performed with a 2D filtration-histogram technique (TexRAD®, Somerset, England, United Kingdom) and Random Forests (RF) was used as the machine learning method. Several RF models were trained from the same set of patients, but each time using a different slice. Given the large number of potential RF models, a finite number (30) was chosen by randomly selecting one slice per patient per model. The prediction performances of the different models then were compared by computing the simple matching coefficient (SMC) between pairs of models.
Results
A SMC value of 0 implies no similarity between the prediction of 2 models, whereas a SMC value of 1 implies complete similarity. For p16, the minimum SMC of the thirty models examined was 0.59 and the average 0.80. For lymphadenopathy, the minimum SMC was 0.34 and the average 0.65.
Conclusions
There were substantial variations in the SMC results of prediction models based. This suggests that multi-slice analysis provides additional potentially nonredundant information and machine learning based on multi-slice analysis may be advantageous to single slice texture analysis.

eP-83

6:30AM - 3:00PM

PET MRI in Head and Neck Cancer

J Bai[1], A Rajput[2], R Gupta[1], L Woroch[1], R Matthews[2], D Franceschi[1], R Peyster[1], L Bangiyev[2]
[1]Stony Brook University Hospital, Stony Brook, NY, [2]Stony Brook University Hospital, Stony Brook , NY

Purpose
In this educational exhibit, we will review the current role and share our initial experience of simultaneously acquired Positron Emission Tomography and Magnetic Resonance Imaging (PET-MRI) as an advanced oncological imaging tool in head and neck cancer.
Materials and Methods
The educational exhibit will demonstrate case based review of the PET-MRI with examples of initial staging, restaging, and assessment of treatment response in various head and neck cancers. The educational exhibit will also incorporate review of the initial clinical trials assessing PET-MRI as an advanced oncological imaging modality into the case discussion.
Results
PET-MRI has recently gained interest in oncologic imaging of head and neck cancer. MRI provides an excellent soft tissue contrast to delineate the complex anatomy of the head and

neck region. The MRI for detecting metastatic lymph node however relies on morphological criteria, which has relatively low sensitivity compared to PET. PET-MRI, which combine the ability of MRI for morphologic delineation and high sensitivity of metabolic imaging, has become a potentially superior advanced oncological imaging tool for head and neck cancer. The discussion will include a brief review of current role of PET-MRI as an advanced oncological imaging tool. Further discussion will also include review of the initial clinical trials assessing this new imaging modality along with its advantages and drawbacks in comparison with other oncological imaging modalities.

Conclusions

PET-MRI has shown promising early results as an advanced oncological imaging modality in staging, restaging, and assessment of treatment response in patients with head and neck cancer. A comprehensive understanding of the advantages and limitations of PET-MRI will help radiologists and clinicians to accurately stage and assess therapeutic response in patients with head and neck cancer.

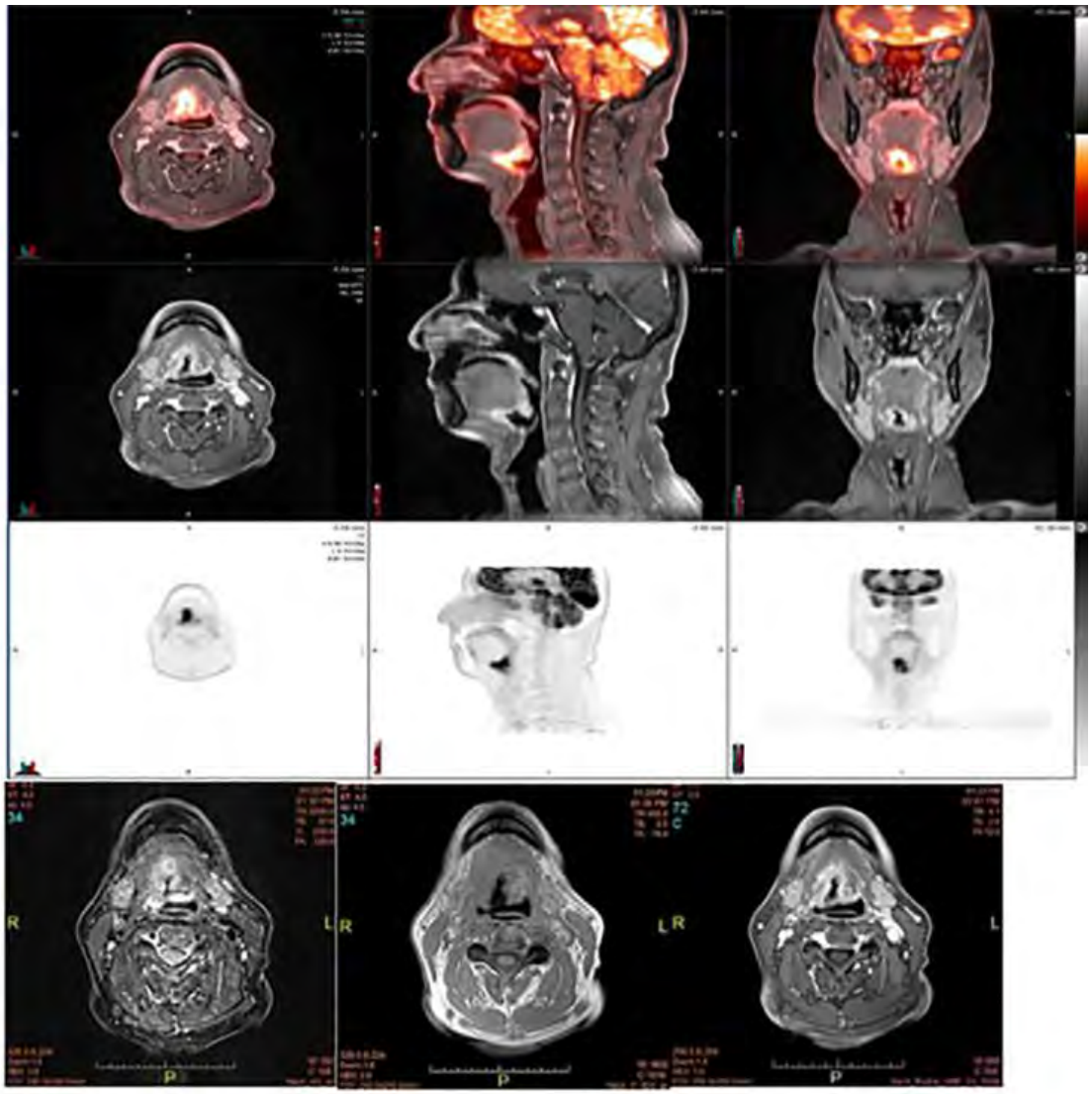


Figure: 62-year-old male with history of tobacco smoking presents with tongue lesion. Biopsy result shows squamous cell carcinoma (SCC) of the tongue. PET-MRI was performed for initial staging. Multi-sequence multiplanar PET-MRI demonstrates STIR hyperintense lesion with heterogeneous enhancement involving the posterior aspect of the tongue, corresponding with increase FDG uptake. PET-MRI demonstrates no hypermetabolic lymphadenopathy.

(Filename: TCT_eP-83_Figure1.jpg)

eP-89

6:30AM - 3:00PM

TMJ MR Imaging Findings in Malocclusion

V Andreu[1], H Kuno[2], M Chapman[3], M Horn[1], V Arya[1], M Pushkar[1], O Sakai[2]
[1]Boston Medical Center, Boston, MA, [2]Boston Medical Center, Boston University School of Medicine, Boston, MA, [3]Boston University Medical Center, Boston, MA

Purpose
To evaluate fossa-condylar-disk morphology and position and other MRI abnormalities in patients with malocclusion after presurgical orthodontic treatment.
Materials and Methods
Eighty-nine patients (13-34 years) with malocclusion undergoing maxillary and/or mandibular osteotomies, near the completion of the presurgical orthodontic treatment phase underwent TMJ magnetic resonance imaging (MRI). Sagittal T2/PD-weighted images in closed and open-mouth positions and coronal T1-weighted images in closed-mouth position of both TMJs (178 TMJs) were obtained.
Results
Disk displacement in closed mouth position was seen in 67% of the joints: anterior (49%), posterior (14%), medial (14%), and lateral (1%), and others (anteromedial, posteromedial, anterolateral, posterolateral) (22%). Disk recapture was seen in 79%. Morphological disk abnormalities (thinning/perforation) were seen in 55%. Osteoarthritic changes (condylar flattening, subcortical cysts, osteophytes) were seen in 55%. Bone marrow signal abnormality was found in 5%. Joint effusion was seen in 5%. Muscle signal abnormality was seen in 1%. In addition, 39% of displaced disks and 18% of normally located disks in closed-mouth position showed morphologic abnormalities (thinning/perforation). Condylar abnormalities were seen in 36% and 20% with and without disk displacement respectively.
Conclusions
TMJ MRI in patients with malocclusion in the pre-surgical phase shows normal joints, internal derangement in various directions, degenerative changes, or a combination of these, which may be relevant to surgical planning.

Monday
6:30AM - 3:00PM
Long Beach Convention Center, Exhibit Hall B-(Lower Level) eP

Electronic Scientific Poster (eP)-Interventional

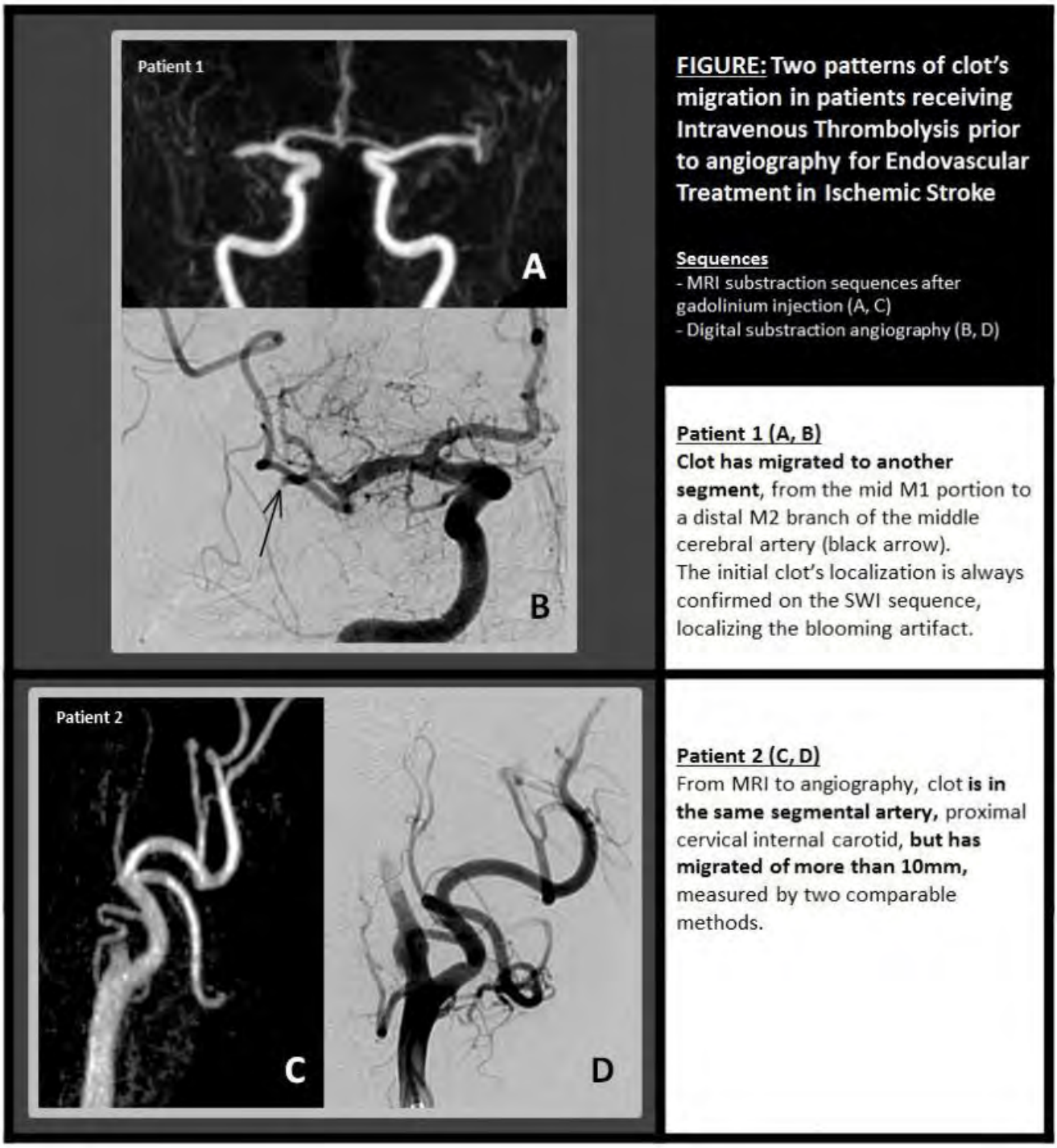
eP-98

6:30AM - 3:00PM

Acute Ischemic Stroke: Comparison of Clot's Localization in MRI and Angiography for Patients with Thrombolysis Prior To Thrombectomy

C Cohen[1], k gaillot[2], j cottier[3], D Herbreteau[4], R Bibi[5], M DEJOBERT[6], A Narata[4]
[1]CHU Tours, Tours, France, [2]chru tours, tours cedex, France, [3]University Hospital of Tours, tours, france, [4]University Hospital of Tours, Tours, France, [5]University Hospital of Tours, Tours, Indre et Loire, [6]CHU TOURS, TOURS, France

Purpose
Intravenous thrombolysis associated to endovascular mechanical thrombectomy is the gold standard treatment for ischemic stroke (IS). We aimed to evaluate clot's migration after thrombolysis using pretreatment magnetic resonance imaging (MRI) and peri-operative angiography.
Materials and Methods
As a preliminary study, we retrospectively collected thirty-three consecutive patients with IS that received thrombolysis before endovascular thrombectomy (ET). Using a curve tool, we measured the distance between vessel origin and the beginning of the clot (D-clot, 2 measurements for each sequence) on MRI (3D TOF and/or contrast-enhanced MRA) and on angiography with the same anatomical parameters. Two methods to convert angiography pixels in millimeters were elaborated: 1) MIPed TOF/MRA was used as a reference, measuring 3 large vessels diameters and determining the ratio from pixels to millimeters. 2) 2D angiography measurements were directly obtained with the field of view scale. Magnetic resonance imaging and angiography D-clot measurements were compared 1 by 1 for each method. Time of onset of the symptoms, time of beginning of thrombolysis/ET and 24 hour secondary bleeding on CT scan were reported.
Results
Displacement ≤5 mm concerned seventeen patients (51,52%) and was not considered relevant. Seven (21,21%) patients presented a migration >5 to ≤10mm, 6 (18,18%) presented a migration >10mm or a very important displacement being characterized as clot fragmentation. No statistical difference for D-clot between the 2 measurements' methods on angiography was shown (Pearson's correlation coefficient r= 0,9928; p<0,01). We could not conclude for 3 (9.09%) patients, because the initial MRI did not cover the clot's origin. Time between thrombolysis and ET was not significantly different in the 4 groups (p=0.14). Eight (24.24%) patients had a secondary bleeding 24 hours after thrombolysis.
Conclusions
More than one-third of the patients presented clot's migration after thrombolysis, including fragmentation; this information can affect ET planning and device choice.



(Filename: TCT_eP-98_ASNRfinalfigure.JPG)

eP-90

6:30AM - 3:00PM

Classification of Pipeline Flow Diverter Endoleaks

N Khan[1], S Georgy[2], F Siddiqui[2], R Burke[3], M Casey[3], A Elias[3]

[1]SIU School Of Medicine, Springfield, IL, [2]SIU School of Medicine, Springfield, IL, [3]Memorial Medical Center, Springfield, IL

Purpose

Pipeline embolization device (PED) is an endovascular device used for the treatment of large or giant wide necked intracranial aneurysms from the petrous to the superior hypophyseal segments (1). Treatment occurs in a 3-step process, reconstruct, remodel and restore. Reconstruction of the parent vessel occurs by the device scaffolding across the aneurysm neck. Pipeline embolization device remodels the parent vessel by allowing endothelization across the aneurysmal neck and flow diversion (2). Ultimately, there is hemodynamic restoration of flow and long-term aneurysmal occlusion. Device leakage post PED deployment is poorly understood and to the best of our knowledge a description of the different types of PED leakages have not been reported in literature.

Materials and Methods

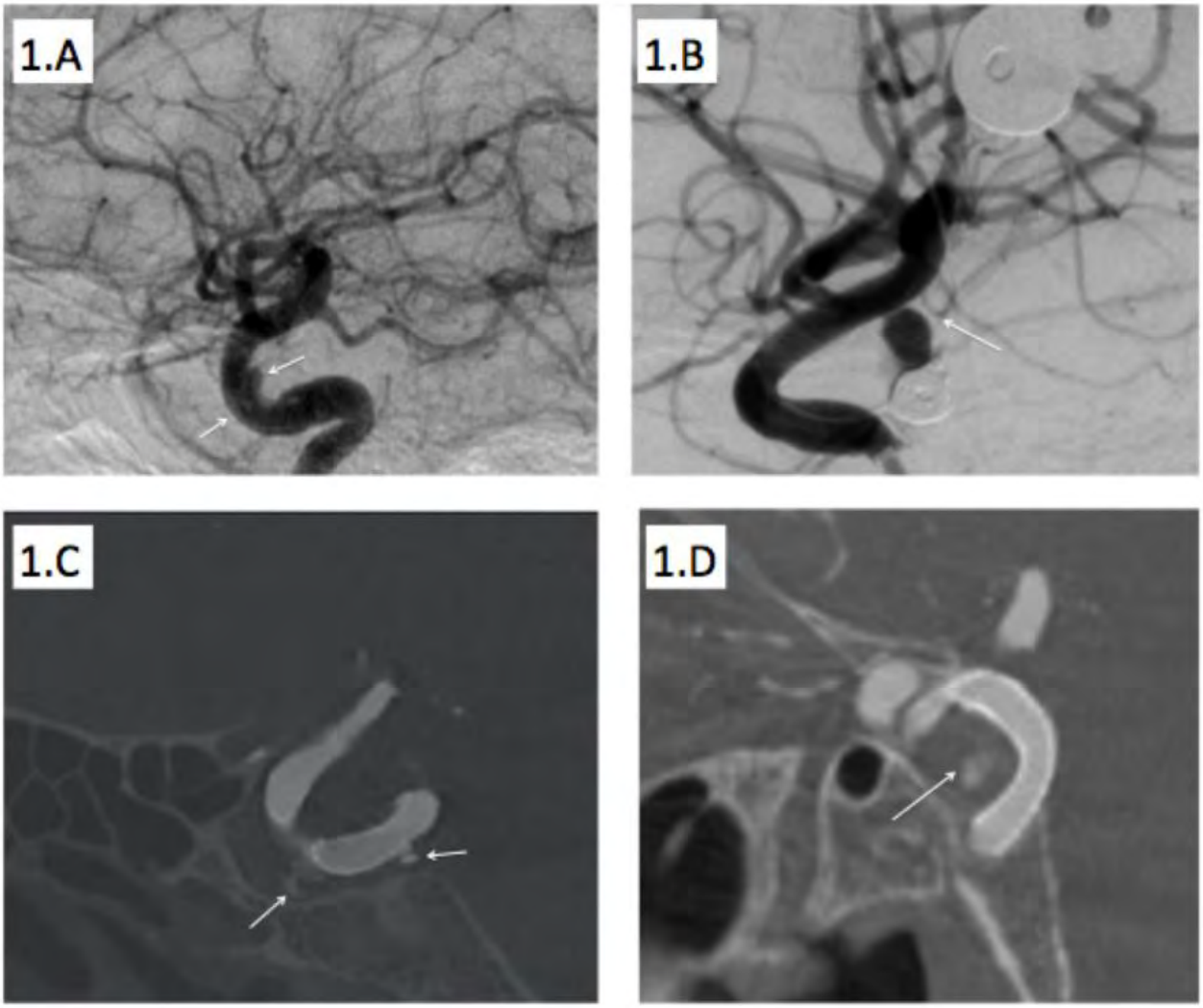
Case Series cases were identified during follow-up cerebral angiograms. Four different types of postpipeline embolization leakages were identified. We utilized an established classification system of the different types of endo-vascular abdominal aortic aneurysm repair endoleaks as reference and adapted it to classify post PED aneurysm repair leaks. We are adapting a well established endovascular leak classification system of abdominal aorta aneurysms to the PED endoleaks.

Results

We identified 4 different types of endoleaks described as follows. Type 1: Endoleak at PED proximal and distal ends (inadequate seal) Fig. 1A. Type 2: Aneurysm sac filling via preferential flow of adjacent branch vessel. Fig. 1B. Type 3: Leak through a defect in the PED. Fig. 1C. Type 4: Leak due to PED intrinsic porosity. Fig. 1D.

Conclusions

We identified 4 different types of endoleaks after PED of intracranial aneurysms, and propose a classification system analogous to an established classification system of endoleak after endovascular aortic aneurysm repair in order to better understand the PED endoleak mechanisms and optimize management of this complication.



(Filename: TCT_O-342_leaks.jpg)

eP-91

6:30AM - 3:00PM

Clinical Presentation, Imaging Diagnosis, and Treatment of PICA Aneurysms

B Chin[1]
[1]*Saint Lukes Health Care System/University of Missouri, Kansas City, MO*

Purpose
To characterize and review the presentation, imaging features, and current endovascular and surgical management strategies of posterior inferior cerebellar artery (PICA) aneurysms.
Materials and Methods
Neurosurgical patients at a large, nonprofit hospital system from 2007 to 2016 were reviewed to identify PICA aneurysms. The patients' presentations, imaging findings (size,

location, and multiplicity), treatments, and outcomes were recorded and reviewed. In addition, a literature review was performed of prior case series regarding presentation and treatment of similar aneurysms.
Results
Fourteen patients with PICA aneurysms were identified, including saccular and fusiform/dissecting aneurysms. Patients presented with a combination of subarachnoid (SAH) and intraventricular hemorrhage and various Fisher grades. Thirty-six percent (5) were detected incidentally. Fourteen percent (2) were seen on digital subtraction angiography (DSA), but not on initial CT or MR angiogram. The patients were treated with various therapies, including microsurgical clip ligations, parent vessel sacrifice, and selective occlusion of the aneurysm with or without stent assistance. Eighty-six percent (12) had complete occlusion/technical success. Fourteen percent (2) had rebleeding during the endovascular treatment.
Conclusions
PICA aneurysms are variable in size and location at presentation. Conventional DSA should be considered for evaluation of regional SAH, even in the setting of trauma, given potential dissecting aneurysms. PICA aneurysms may be treated effectively by different endovascular approaches with favorable clinical and radiologic outcomes, though multidisciplinary consultation is important as surgical treatment may be indicated, particularly for distal PICA aneurysms.

eP-96

6:30AM - 3:00PM

Complications Associated with the Use of Flow Diverters

S Das[1], A Gupta[2], H PENDHARKAR[3], A RAMALINGAIAH[4], C Prasad[5], j saini[6], S TIWARI[7]
[1]National Institute of Health and Neurosciences, BANGALORE, Karnataka, [2]National Institute of Mental Health and NeuroSciences (NIMHANS), Bangalore, Karnataka, [3]NATIONAL INSTITUTE OF MENTAL HEALTH & NEUROSCIENCES, BANGALORE, KARNATAKA, [4]NATIONAL INSTITUTE OF MENTAL HEALTH AND NEUROSCIENCE, NIMHANS, Bengaluru , karnataka , [5]National Institute of Mental Health and Neurosciences, Bangalore, Karnataka, [6]NIMHANS, BANGALORE, Karnataka, [7]National Institute of Mental Health and Neurosciences, BANGALORE, Karnataka

Purpose
One of the most recent endovascular modes of treatment of aneurysms is placement of flow diverter across the neck of the aneurysm. The flow diverter is a low porosity stent placed in the parent artery to reduce blood flow in the aneurysm sac thereby inducing gradual thrombosis without occluding the side branches and perforators. The purpose of our study

was to explore the complications that we have come across with the use of flow diverters over the last 2 years.

Materials and Methods

It was a single institutional retrospective study. Twenty-three patients who had undergone flow diverter placement for management of intracranial aneurysm in the Department of NIIR, NIMHANS, Bangalore from May 2014 to November 2016 were included in this study.

Results

Of the twenty-three patients who were studied, eighteen patients had no complication at discharge – they have been called for follow up. One patient had acute occlusion of parent vessel intraprocedurally for which tirofiban was administered locally and systemically and complete recanalization was achieved – no complication at 6 and 12 months follow-up angiogram. One patient had in-stent thrombosis which was managed with intra-arterial tirofiban, however, subsequently patient developed infarct in right insular cortex and right corona radiata. One patient had kinking of flow diverter with subsequent right MCA infarction. One patient of bilateral ICA aneurysm had aneurysmal rupture on left side and right parieto-temporo-occipital region infarct with eventual fatality. One patient had microwire perforation of M2 segment with eventual fatality.

Conclusions

Even the flow diverters are not free from complications. Early identification and prompt management of complications can however improve the eventual outcome in these patients.

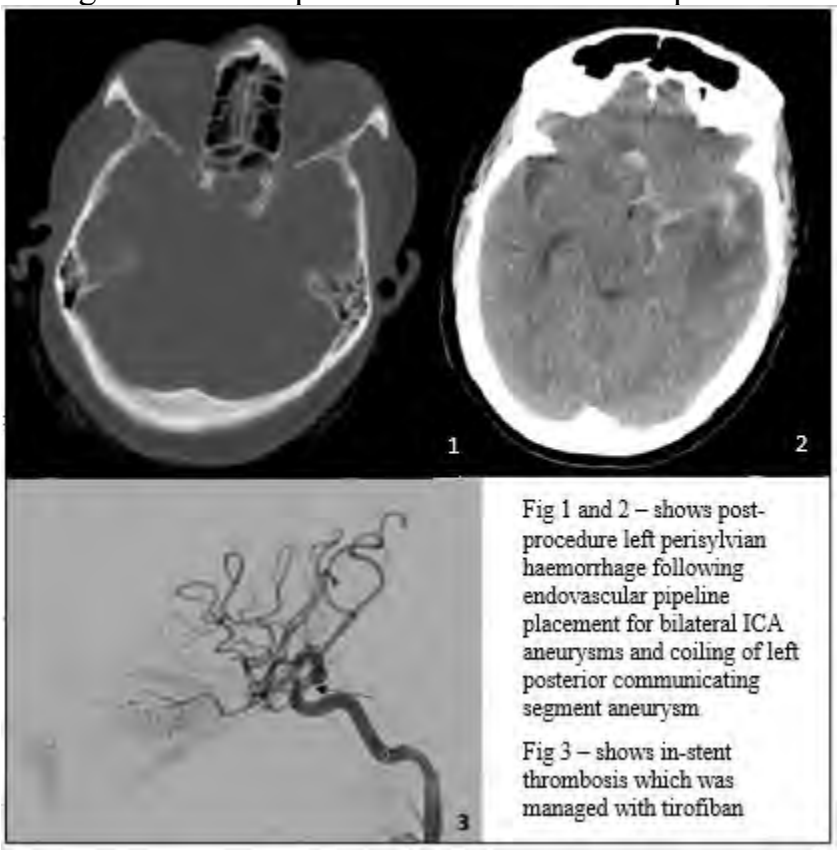


Fig 1 and 2 – shows post-procedure left perisylvian haemorrhage following endovascular pipeline placement for bilateral ICA aneurysms and coiling of left posterior communicating segment aneurysm

Fig 3 – shows in-stent thrombosis which was managed with tirofiban

(Filename: TCT_eP-96_Capture1.JPG)

eP-92

6:30AM - 3:00PM

Cranial Pial Arteriovenous Fistulae - A series of 33 cases

L Sebastian[1], N Jain[2], s shambanduram[3]
[1]All India Institute of Medical Sciences, Newe Delhi, Delhi, [2]All India Institute of Medical Sciences, Noida, Uttar pradesh, [3]All India Institute of Medical Sciences, New delhi , India

Purpose
1.To analyze the angiographic features and their clinical correlates of cranial pial arteriovenous fistulae (CPAVF). 2. To analyze the implications of clinical presentation and angioarchitecture in the management and outcome of our set of CPAVF patients.
Materials and Methods
From our departmental neurovascular database 33 cases of CPAVF who presented during 2005 to 2016 were identified. Details on demographics, clinical presentation, imaging, management and follow up were obtained for each patient. Angiographic records were reviewed independently by 2 neuroradiologists for location, type of fistula, venous varix, arterial feeders,venous drainage, pial venous refflux, venous ectasia/stenosis/thrombosis and status of dural sinuses.
Results
Of the 33 patients (mean age 19.5 years) 22 were males. Sixteen patients were more than 18 years at presentation. Seizures (16/33) were the leading cause of presentation followed by acute intracranial bleed (13). Imaging showed venous varix in 31 cases with 16 of them showing wall calcification. Fresh or old bleed, focal atrophy and local edema were among other imaging findings. Digital subtraction angiography (DSA) showed 42 fistulae (in 33 patients) - 28 single hole and 14 multihole fistulae. Arterial angiopathic changes were seen in a minority of cases (6) in contrast to venous angiopathy (18). Size of the venous varix and presence of calcification were related inversely to presentation with bleed, the correlation reaching statistical significance. Dural sinus thrombosis or stenosis were seen in 12 cases. Transarterial embolization was the preferred treatment modality (28/29) with good angiographic and clinical outcome in 86% of patients. One patient died after embolization. One patient was treated by radiosurgery with good outcome.
Conclusions
Our series is distinctive for the presence of higher number of adults at presentation. Smaller noncalcified venous varix is associated significantly with bleed. Endovascular embolization is safe and effective in the treatment of CPAVF.

eP-93

6:30AM - 3:00PM

Medical Management of Cerebral Arteriovenous Malformations

A Qureshi[1], M Amarouche[1], T Booth[1]
[1]*Kings College Hospital, London, United Kingdom*

Purpose
Arteriovenous malformations (AVMs) are abnormal connections between arteries and veins without an intervening capillary bed. The resulting nidus refers to the tangle of vessels that shunt high velocity arterial blood to the venous system which is normally low pressure. This, together with the presence of intranidal and flow aneurysms, renders AVMs prone to hemorrhage. Various factors increase the risk of hemorrhage, and there is an annual risk of up to 4%. Management of AVMs may aim to definitively eradicate disease through neurosurgical resection, endovascular embolization or stereotactic radiotherapy, or to treat it conservatively by means of medical management. The ARUBA trial (A Randomized Trial of Unruptured Brain AVMs) compared short-term outcomes in patients with unruptured brain AVMs undergoing medical management alone or medical management plus interventional therapy. The researchers found that there was a significantly lower risk of death or stroke in the short term, in patients under the medical management arm compared to those who underwent an interventional therapy. There is no detail in the ARUBA trial as to what constitutes best medical management in AVMs. We describe the evidence surrounding best medical management and the potential future options for therapy.
Materials and Methods
A MEDLINE and PubMed search was performed for journals before September 2016 using search terms 'arteriovenous malformations', 'Hereditary Hemorrhagic Telangiectasia', 'medical therapy'. Relevant articles were reviewed.
Results
The pathophysiology of AVM development is poorly understood, but involved dysregulation of angiogenic factors and cytokines, the net effect of which results in uncontrolled angiogenesis and mural fragility. There is no current medical therapy that specifically targets bAVMs, and medical management is driven towards amelioration of symptoms associated with the disease. Brain AVMs portend a 58% 5-year risk of developing seizures. These tend to be simple or complex partial seizures, and anti-epileptic prophylaxis often is prescribed, although no specific agents are indicated. Maintaining normotension in bAVM patients appears beneficial. High pressures increase the risk associated with aneurysm rupture, or peri-operative edema and hemorrhage, whilst low pressures risk ischemia to surrounding normal parenchyma. Potential targets for more definitive bAVM management include VEGF inhibition, interferon-alpha, beta-adrenergic blockade, tetracyclines, immunomodulators and macrolides. Indeed, a number of these agents have been described to retard nonbAVM growth.
Conclusions
Although surgical, endovascular and radiotherapy form the mainstay of treatment for AVMs,

treatment-related complications are recognized. Early observations from the ARUBA study have suggested a role for conservative management of this disease. We have summarized what this may currently entail, and what agents hold promise for a more definitive role.

eP-94

6:30AM - 3:00PM

Resolution Limits of Angiography - a Comparison of Fluoroscopic Visualization Thresholds of Liquid Embolic Agents

J Mason[1], G Benndorf[2]
[1]Baylor College of Medicine, Bellaire, TX, [2]University of Southern Denmark, Odense, Denmark

Purpose
Liquid embolics are used to treat a variety of cerebrovascular lesions, including brain arteriovenous malformations and fistulas. Though these agents have been used successfully to treat these conditions for > 30 years, their use is not without risks. Reflux beyond safety points or inadvertent embolization of nontarget vessels due to insufficient visual control may cause serious clinical complications. Thus, accurate visualization of liquid embolics is crucial and companies use various radiopaque materials to improve radiographic visualization. This study aims to objectively compare fluoroscopic visualization quality of Omnipaque 300 and four different liquid embolic agents, Onyx® (Medtronic), SQUID® (BALT), and PHIL® (MicroVention), by using a previously described calibrated linear vascular phantom as well as to comparing the sedimentation rates.
Materials and Methods
We 1) measured sedimentation rates and 2) evaluated the visualization of different liquid embolics injected in plastic tubings simulating small cerebral arteries ranging from 100 to 500 microns. The rate of sedimentation of liquid embolics was measured by imaging Onyx 18®, SQUID 12®, SQUID 18®, and PHIL 25® for 30 minutes after preparation. The vials were placed adjacent to each other and images were taken sequentially over 30 minutes. Using a previously described method, DICOM pixel data was extracted using region of interest (ROI) tool in Osiris MD version 7.0.4. The DICOM pixel data then were used to calculate signal to noise ratios (SNR) of the suspension. To compare visualization of the liquid embolics at 500 to 100 microns, we utilized a previously described linear vascular phantom. Injections were performed manually using a 3ml syringe connected to the phantom via a female luer lock. First, injections of undiluted Omnipaque® 300mg I/ml were made into the vascular phantom. Then, Onyx 18®, SQUID 18® and SQUID 12® were injected at 2 and 10 minutes after preparation in the shaker. Injections of PHIL 25® were made into the model immediately. All injections were performed under "blank Road Map" the same way using identical settings on an Allura system (Philips Healthcare). DICOM pixel data were extracted using region of interest (ROI) tool in Osiris MD version 7.0.4. A previously

described formula was used to calculate signal to noise ratios using pixel data stored in DICOM images: SNR = (BG – Tube ROI)/ [sqrt(STD(tube)^2 + STD(BG)^2] / 2); SNR = Signal to noise ratio, BG = mean background value for pixel data, Tube ROI = ROI within a particular tube (separate values measured for each tube, 100 micron to 500 micron), STD (tube) = standard deviation of pixel data for a particular tube size, STD (BG) = standard deviation of pixel data for background data.

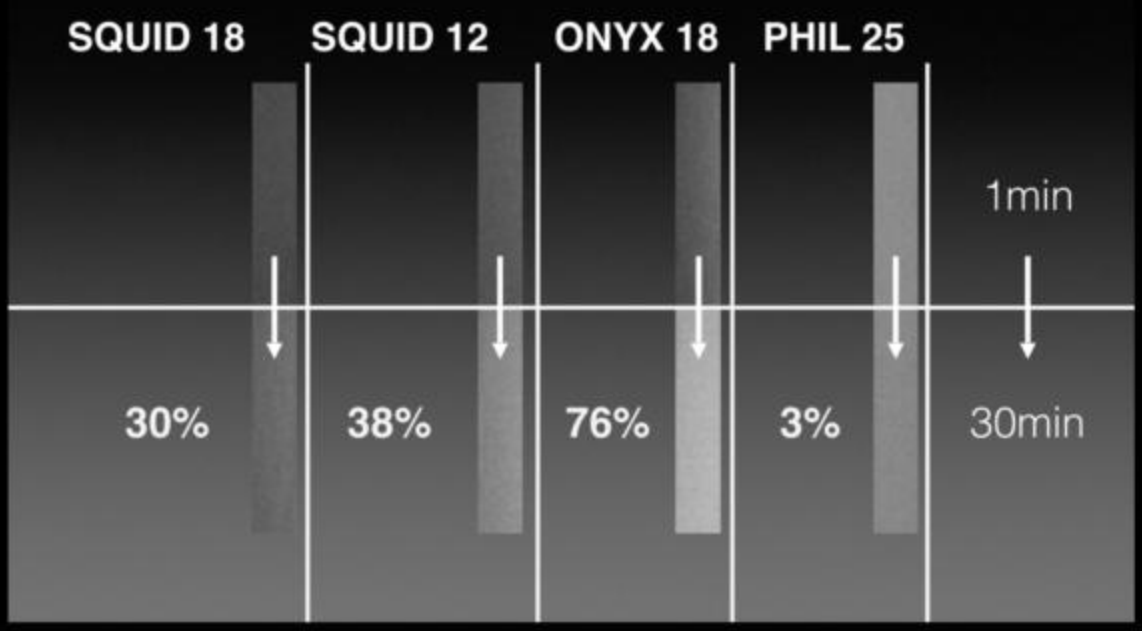
Results

Sedimentation: Onyx® 18 demonstrated the fastest sedimentation rate with 76% drop in SNR over 30 minutes. SQUID 12® and SQUID 18® demonstrated at 38% and 30% drop in SNR over the same time; whereas, PHIL 25® maintained constant SNR – owing to its radiopacity resulting from iodine bonded to its polymer. Visualization: Using a "blank Road Map" setting, Omnipaque 300® had superior SNR compared to all other liquid embolics. Onyx 18® demonstrated the highest SNR from 100 to 500 micron at 2 minutes and 10 minutes postpreparation. SQUID 18® was detectable below 500 microns, but had lower SNR compared to Onyx 18®. Onyx 18® had a higher drop in SNR from 2 minutes to 10 minutes postpreparation compared to SQUID 18®. PHIL 25® was not detectable at 500 micron or below.

Conclusions

There were significant differences in both sedimentation rates and visualization qualities between Omnipaque 300, Onyx 18®, SQUID 12®, SQUID 18®, and PHIL 25®. Onyx 18® demonstrated the highest sedimentation rate, losing nearly 76% of its radiopacity over 30 minutes. There were significant differences in SNRs measured from DICOM pixel data between Onyx 18®, SQUID 18®, and PHIL 25®. Onyx 18® demonstrated the highest SNR of all embolics studied. PHIL 25® was not visualized or measurable at 500 microns or below using pixel data stored in DICOM files. Inaccurate or incomplete visualization of embolics in small cerebral vessels could lead to inadvertent non-target vessel embolization or not recognized reflux. During long injection times, SNR for embolics like Onyx 18® quickly decreases; caution should be taken with injections longer than 10 minutes. We have described a simple technique of evaluating SNRs of varying liquid embolics using a novel vascular phantom with inner diameters ranging from 100 to 500 microns simulating small cerebral arteries. Future studies to include other embolics using various concentrations, including adhesives are warranted.

% Drop in SNR over 30 min - liquid portion of embolics



SNR

	Omnipaque	SQUID18	ONYX18	PHIL 25
100 micron	1.2	0	0	
175 micron	2.6	0.5	2.0	
250 micron	5.3	2.5	3.5	0
380 micron	10.3	5.6	8.3	0
500 micron	21.5	9.8	13.1	0

(Filename: TCT_O-108_emoblics.jpg)

eP-95

6:30AM - 3:00PM

Use Of Pipeline Flow Diverters In Management Of Internal Carotid Blowout Caused By Endonasal Sinus Surgery

N Jahangir[1], N Khan[2], F Siddiqui[3], M Casey[4], A Elias[5]
[1]SIU school of medicine, Springfield , IL, [2]SIU School Of Medicine, Springfield, IL, [3]SIU School of Medicine, Springfield, IL, [4]Memorial Medical Center, Springfield, IL, [5]Memorial Medical Center, Springfield, IL

Purpose
We elaborate role of pipeline flow diverter in cases of ICA injury after endonasal sinus surgery especially in situations when commonly used cover stents can not be deployed due to complexity of vessel anatomy.
Materials and Methods
An online search for case reports, case series and review articles was performed using words "ICA injury, endonasal sinus surgery, pipeline flow, cover stent and endovascular ICA repair". Data on Pubmed and Medline were reviewed and 6 cases of ICA injury after endonasal sinus surgery between 1993 and 2016 were identified. All of these 6 cases were treated with pipeline flow diverter.
Results
A 65-year-old female presented with a 2-month history of sinusitis. Ten days prior to surgical intervention, she developed left facial pain, diplopia, left ptosis and blurred vision. Magnetic resonance imaging (MRI) of the brain with gadolinium demonstrated mass in the left sphenoid sinus measuring 20mm in maximal diameter. The patient underwent imaging-guided endoscopic left sphenoid sinusotomy and drainage of sphenoid sinus mucocele. During the procedure, the patient suffered a left ICA injury leading to massive hemorrhage. Emergent CTA head & neck revealed a contained contrast extravasation, consistent with a 4x3mm pseudoaneurysm, involving the anterior genu of the cavernous segment of the left ICA. Patient was taken to the neurointerventional suite and 2 PED were deployed in a telescoping fashion at the anterior genu of the cavernous portion of the ICA covering the rent. The first PED measured 4.25x20mm and the second PED telescoped within measured 4.5x20mm. Follow-up CTA on postoperative day 10 showed the pseudoaneurysm with no evidence of active bleeding. Postoperatively her symptoms resolved and on 1-month follow up she was neurologically intact.
Conclusions
We present a novel way of endovascular management of ICA injury caused by endonasal sinus surgery with PED. We believe PED can be an alternative modality in the treatment of iatrogenic ICA injury especially when deployment of a cardiac cover stent is challenging due

to large device profile and tortuous course of parent vessel or when the patient is at high risk for an ischemic stroke from vessel sacrifice.

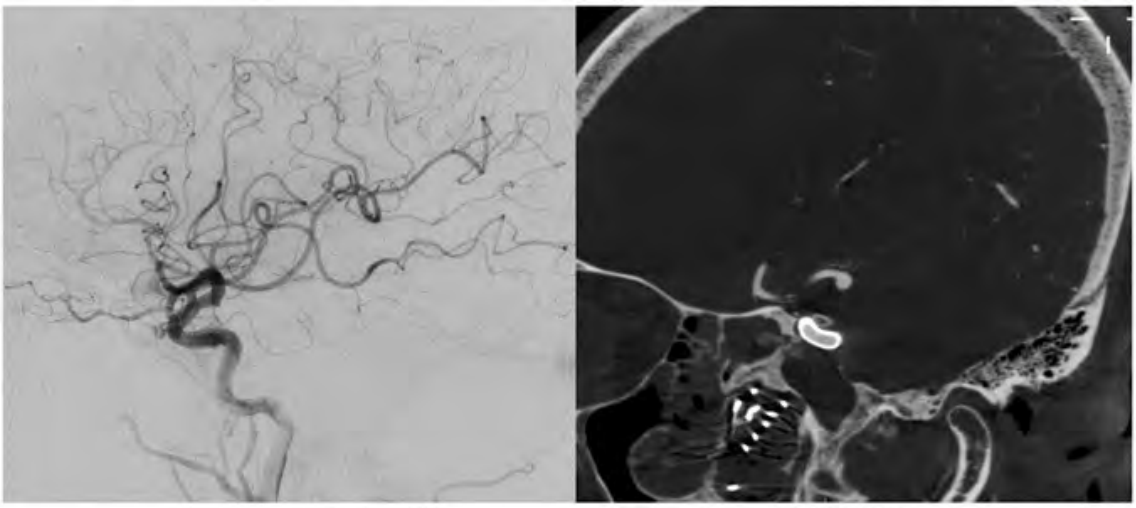
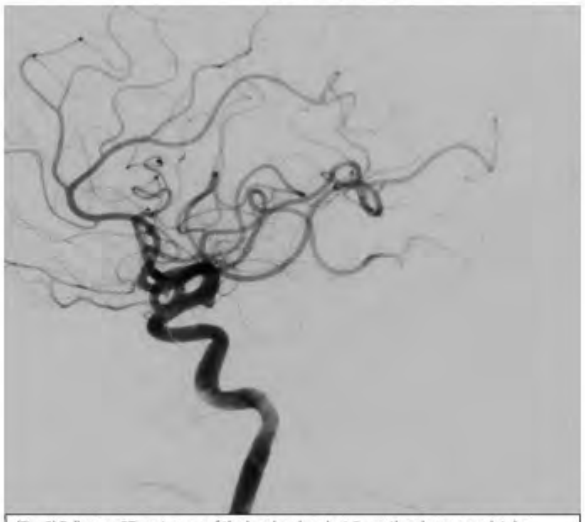


Fig. 1 A

Pre Pipeline Cerebral angiogram showing pseudoaneurysm in the anterior genu of the cavernous left ICA

Fig. 1 B

Post operative Day 10 CTA showed left ICA stent extending from the cavernous segment to the clinoid segment which appeared patent with good flow distally



(Fig. 2) Follow up CT angiogram of the head and neck at 6 months shows completely obliterated PA with patent left ICA demonstrating good distal flow.

(Filename: TCT_O-344_Untitled.jpg)

eP-97

6:30AM - 3:00PM

Vein of Galen Aneurysmal Malformation: Six Years of Treatment at São José Hospital

M Baptista[1], C Perry da Câmara[1], I Fragata[1], J Pamplona[1], c conceicao[2], A SAGARRIBAY[2], J DOS REIS[1]

[1]Centro Hospitalar Lisboa Central, Hospital de São José, Lisboa, Portugal, [2]Centro Hospitalar de Lisboa Central, Hospital Dona Estefânia, Lisboa, Portugal

Purpose
Vein of Galen aneurysmal malformation (VGAM) is a congenital direct arteriovenous fistula characterized by shunting of arterial flow arteries into a persistent median prosencephalic vein. Incidence of this disease is estimated in 1:25000. Most present during infancy either with features of left-to-right shunt and cardiac failure, or with hemorrhage secondary to venous hypertension, and the prognosis is poor, especially for large VGAM left without treatment.
Materials and Methods
Retrospective review of clinical and imaging data of patients referred to Hospital São José between 2011 and 2016, with VGAM for endovascular treatment.
Results
A total of 4 patients were referred for treatment of VGAM. Three were diagnosed in early childhood and 1 antenatally. There were 2 choroidal type VGAM, 1 mural type and a mixed one. The two newborns presented with high-output cardiac failure, 1 infant presented with intracranial hemorrhage and the oldest child was diagnosed after a CT scan with hydrocephalus. Endovascular treatment was performed with intra-arterial cyanoacrylate, aiming to reduce the shunting as much as possible. All patients were treated in several stages, except for 1 newborn, that died from a complication not related to the procedure, after the first treatment. Periprocedural complications included arterial perforation, and distal arterial embolization of cyanoacrylate. All 3 children are still under follow up to this date, with normal neurological development.
Conclusions
Vein of Galen aneurysmal malformation is a rare and serious disease, with reserved prognosis. Endovascular treatment is effective, especially in children with congestive heart failure, where it can be life-saving. Periprocedural complications are frequent, highlighting the importance of technical and clinical experience in managing this rare condition.

Monday
6:30AM - 3:00PM
Long Beach Convention Center, Exhibit Hall B-(Lower Level) eP

Electronic Scientific Poster (eP)-Pediatrics

eP-108

6:30AM - 3:00PM

Characterization of Spinal Cord DTI Metrics in Clinically Asymptomatic Pediatric Subjects with Incidental Congenital Lesions

S SAKSENA[1], M Alizadeh[2], D Middleton[2], L Krisa[1], A Flanders[1], F Mohamed[1], S Faro[3]
[1]Thomas Jefferson University, Philadelphia, PA, [2]Temple University, Philadelphia, PA, [3]Johns Hopkins School Of Medicine, Haddonfield, NJ

Purpose

Hydromyelia and syringomyelia are essentially cystic abnormalities of the spinal cord (SC). Hydromyelia is a dilatation of the central canal of the SC while syringomyelia is defined as a fluid-filled cavity within the SC parenchma (1, 2). Diffusion tensor imaging (DTI) has been shown to assess the microstructural changes in patients with syringomyelia (3). However, the prevalence of these abnormalities in the clinically normal pediatric population is uncommon to rare. Out of 26 healthy typically developing (TD) pediatric subjects scanned in this study, 16% had unexpected incidental findings on conventional MRI. These incidental findings were present in the thoracic SC and represented hydromyelia lesion in 3 subjects and syringomyelia lesion in 1 subject. Since these subjects were healthy and clinically normal, the cord above and below the lesions, normal on MRI would be expected to be normal on DTI as well. The purpose of this study was to quantitatively analyze the cord in these subjects using DTI and comparing to the cord of the TD population. In this study, we performed both group analysis and single-subject analysis to evaluate DTI characteristics of the cord.

Materials and Methods

Out of 26 TD recruited as part of large SC DTI study, 4 subjects (mean age, 11.51±3.62) had incidental findings of hydromyelia and syringomyelia within the thoracic SC. Written informed assent and consent was obtained under the protocol approved by IRB. Subjects underwent scans using a 3T MRI scanner. The protocol consisted of conventional T1- and T2-weighted structural scans and axial DTI scans based on inner field of view sequence (4). Axial diffusion tensor images were acquired by using 2 overlapping slabs to cover the cervical and thoracic SC. The imaging parameters included: 3 averages of 20 diffusion directions, 6 b0 acquisitions, b=800s/mm2, voxel size=0.8x0.8x6mm3, axial slices=40, TR=7900ms, TE=110ms and TA=8:49min. After postprocessing (5), FA, MD, AD and RD were calculated by using regions of interest (ROIs) drawn on the whole cord along the entire SC. Diffusion tensor imaging parameters were quantified at each intervertebral disk level and at the mid-vertebral body level of the cervical and thoracic SC in all subjects. The subjects with hydromyelia had lesions from T3-T4 to T5-T6 levels (subject 1), Mid T6 to T10-T11 (subject 2) and T7-T8 to Lower L1 (subject 3) while subject with syringomyelia had lesion from Mid T3 to T4-T5 (subject 4). In all the subjects, the highest lesion was at Mid T3. Hence, for group analysis, mean values from C1 to T2-T3 were compared to the corresponding levels of the TD subjects. For single subject analysis, the cord above (subjects 1, 2, 3, 4) and below (subjects 1, 2, 4) the lesions was compared to the corresponding levels of the TD subjects respectively. Standard least squares fit model based on restricted maximum likelihood (REML) method was used. A p value ≤ 0.05 was statistically significant.

Results

In the group analysis, MD and AD were significantly different in the cord compared to the TD subjects (Table 1). In single subject analysis, DTI parameters were significantly different in the cord above the subject with syringomyelia lesion compared to the TD subjects (Table

2). However, no significant difference in DTI parameters was found in the cord above the subjects with hydromyelia lesions (Table 2). In the cord below the hydromyelia lesion, no significant difference in DTI parameters was found except for FA in subject 1 (Table 3). In the cord below the syringomyelia lesion, MD, AD and RD were significantly different compared to TD subjects (Table 3).

Conclusions

In the clinically normal pediatric subjects the apriori theory was that the cord above and below the congenital lesions should not be statistically different from the TD population. However, we found that the cord above the syringomyelia lesion demonstrated significant differences in DTI parameters which may correlate to microstructural changes including demyelination, and or axonal loss. Syringomyelia may have a different etiology, in comparison to hydromyelia, possibly representing a combination of congenital and acquired factors such as a subclinical prior demyelinating, traumatic or infectious or inflammatory process. The cord above the hydromyelia lesion showed no significant differences in DTI parameters suggesting that hydromyelia is likely a more benign process than syringomyelia. In the group analysis, MD and AD were significantly different in the cord above the lesion demonstrating that how a single subject (subject 4) can affect the mean of group results which may not correlate to a pathologic process. The limitation of this study is the small sample size. Future work with large number of subjects is needed to assess the DTI differences in the cord above and below these lesions. This study demonstrates that DTI has the potential to be used as an imaging biomarker to evaluate the SC above and below the congenital lesions in asymptomatic subjects and one should use caution while including them into a normative data population.

Table 1: Means of FA, MD, AD and RD in the TD pediatric population and subjects with hydromyelia and syringomyelia grouped together

	DTI Parameters			
	FA (TD, Subjects)	MD (TD, Subjects)	AD (TD, Subjects)	RD (TD, Subjects)
TD vs. Subjects with hydromyelia and syringomyelia	0.57±0.09, 0.52±0.10, p=0.869	1.06±0.22, 1.08±0.25, **p=0.010**	1.80±0.34, 1.73±0.38, **p=0.007**	0.68±0.19, 0.75±0.23, p=0.066

FA, fractional anisotropy; MD, mean diffusivity; AD, axial diffusivity; RD, radial diffusivity; TD, typically developing; DTI, diffusion tensor imaging

Table 2: Means of FA, MD, AD and RD in the cord above the hydromyelia (subjects 1, 2, 3) and syringomyelia (subject 4) lesions and the TD pediatric population

	DTI Parameters			
	FA (TD, Subjects)	MD (TD, Subjects)	AD (TD, Subjects)	RD (TD, Subjects)
TD vs. Subject 1	0.57±0.09, 0.61±0.09, p=0.102	1.04±0.23, 1.00±0.18, p=0.432	1.77±0.36, 1.81±0.37, p=0.193	0.68±0.18, 0.60±0.12, p=0.754
TD vs. Subject 2	0.56±0.09, 0.52±0.06, p=0.953	1.04±0.24, 1.09±0.18, p=0.668	1.76±0.37, 1.73±0.27, p=0.288	0.68±0.28, 0.77±0.17, p=0.060
TD vs. Subject 3	0.57±0.09, 0.53±0.07, p=0.956	1.07±0.24, 1.00±0.16, p=0.880	1.82±0.36, 1.65±0.29, p=0.963	0.68±0.21, 0.68±0.13, p=0.975
TD vs. Subject 4	0.57±0.09, 0.44±0.11, **p<0.0001**	1.05±0.22, 1.10±0.42, **p<0.0001**	1.79±0.35, 1.59±0.55, **p<0.0001**	0.68±0.19, 0.95±0.36, **p<0.0001**

FA, fractional anisotropy; MD, mean diffusivity; AD, axial diffusivity; RD, radial diffusivity; TD, typically developing; DTI, diffusion tensor imaging

Table 3: Means of FA, MD, AD and RD in the cord below the hydromyelia (subjects 1, 2) and syringomyelia (subject 4) lesions and the TD pediatric population. In subject 3, there was no cord below the hydromyelia lesion

	DTI Parameters			
	FA (TD, Subjects)	MD (TD, Subjects)	AD (TD, Subjects)	RD (TD, Subjects)
TD vs. Subject 1	0.55±0.11, 0.50±0.10, **p=0.015**	0.98±0.28, 1.11±0.23, p=0.626	1.64±0.43, 1.79±0.42, p=0.900	0.66±0.24, 0.77±0.17, p=0.239
TD vs. Subject 2	0.48±0.09, 0.48±0.03, p=0.162	0.79±0.23, 1.09±0.14, p=0.587	1.19±0.30, 1.71±0.23, p=0.299	0.60±0.20, 0.78±0.10, p=0.599
TD vs. Subject 4	0.56±0.10, 0.46±0.08, p=0.156	1.00±0.28, 1.05±0.43, **p=0.0006**	1.68±0.43, 1.57±0.63, **p=0.0066**	0.67±0.24, 0.78±0.35, **p=0.0003**

FA, fractional anisotropy; MD, mean diffusivity; AD, axial diffusivity; RD, radial diffusivity; TD, typically developing; DTI, diffusion tensor imaging

(Filename: TCT_eP-108_Image.jpg)

eP-102

6:30AM - 3:00PM

Contralateral Cerebral Volume Growth After Hemispherectomy in Different Childhood Pathologies

P Pan[1], N Salamon[1]
[1]*UCLA, Los Angeles, CA*

Purpose
Hemispherectomy remains the most definitive treatment for refractory epilepsy in childhood when a nonfocal hemispheric structural abnormality is present. Common childhood pathologies requiring hemispherectomy include hemimegencephaly, perinatal cerebral infarction and Rasmussen's encephalitis. While clinicians have observed functional recovery of children as well as physical and mental growth after hemispherectomy, the extent of postsurgical development remains not fully understood. Part of the difficulty lies in the multifactorial nature of child development, which includes nutrition, environmental stimuli, postoperative rehabilitation, education, and probably genetics. While initial data from Functional MRI (fMRI) and diffusion tensor imaging (DTI) have provided some insights of cerebral rewiring after hemispherectomy, currently more data are needed to accurately prognosticate the potential in postop remodeling and recovery. Before these new modalities

became available, researchers had long been using brain volume as a surrogate for evaluating brain growth. In adult brain, it has been well established in various neuropsychological illnesses, that reduction in brain volume, regional or global, correlates well with cognitive impairment. In developing young brains, a similar correlation also has been suggested, for example ex-preterm children were observed to have a smaller cerebral volume and poorer cognitive status when compared to their age-controlled peers. This study aims to provide a foundation in assessing postsurgical growth and recovery of the contralateral hemisphere in patients who received hemispherectomy in childhood by 1) measuring growth of cerebral volume postoperatively, 2) comparing brain growth by underlying pathology, side of hemispherectomy, and age at surgery, and 3) comparing this brain growth with normal healthy subjects of the same age group from existing literature.

Materials and Methods

Patient selection: All patients who received modified hemispherectomy at the UCLA Medical Center in infancy and childhood (prior to age 12) were identified retrospectively. Among these patients, patients who had 1) an underlying pathology of hemimegencephaly, cerebral infarction or Rasmussen's encephalitis, 2) a pre-operative MRI study within 1 month of surgery, and 3) at least 1 follow-up MRI more than 3 years after the hemispherectomy, were selected. All of the selected patients had intractable epilepsy as the indication for surgery, and most of these patients had multiple MRI follow-ups. Magnetic resonance imaging brain studies were queried from the UCLA Department of Radiology picture archiving and communication system (PACS). Measuring contralateral hemispheric volume: Only MRI studies containing a T2-weighted axial sequence covering the entire cerebral hemispheres, and performed as a routine follow-up without an acute indication or finding, were included in analysis. The authors chose to use T2-weighted images due to more optimal tissue contrast. These T2-weighted axial brain images have a maximum slice thickness of 4mm. The total cerebral volume of contralateral (unaffected) hemisphere was measured by manual contouring of individual slices with a 3D software (Visage 7, Visage Imaging, Inc., San Diego, CA) using conventional method in defining the cerebral hemisphere. Comparing brain growth: The growth curve of the contralateral cerebral hemisphere was created for each patient by plotting the hemispheric volume against age. In each curve, the first data point represented the immediate pre-operative hemispheric volume, and the subsequent data points represented volume measured at subsequent follow-up MRI scans. These growth curves were compared to published data of brain volume in healthy individuals, and were grouped and compared by the underlying diagnosis, sex, and age at surgery.

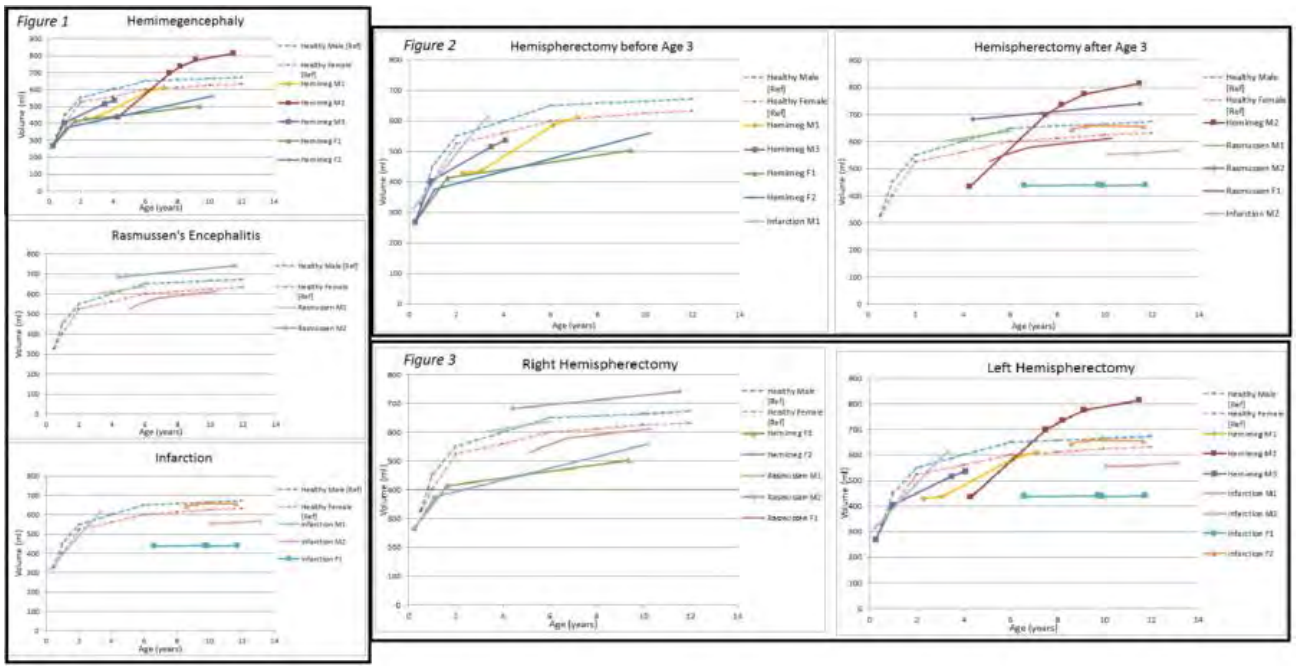
Results

A total of 12 patients were identified with sufficient interval (> 3 years) between the pre-operative scan and follow-up scans. We used the cerebral growth curve of healthy individuals published by Courchesne et al. (Courchesne, E., et al., Normal brain development and aging: quantitative analysis at in vivo MR imaging in healthy volunteers. Radiology, 2000. 216(3): p. 672-682) for comparison. By diagnosis: Among these patients, 3 had hemimegencephaly, 3 had Rasmussen's encephalitis, and 4 had perinatal infarction.

Figure 1 shows the growth curve of contralateral cerebral hemisphere, grouped by diagnosis and compared to the hemispheric cerebral volume in healthy individuals. By Age at Surgery: Among these patients, 5 had hemispherectomy before age 3, and 7 had hemispherectomy after age 3. Figure 2 shows the growth curve of contralateral cerebral hemisphere, grouped by age at surgery and compared to the hemispheric cerebral volume in healthy individuals. By laterality: Among these patients, 5 had right hemispherectomy and 7 had left hemispherectomy. Figure 3 shows the growth curve of contralateral cerebral hemisphere, grouped by side of hemispherectomy and compared to the hemispheric cerebral volume in healthy individuals.

Conclusions

In this study, we confirmed presence of physical growth of contralateral hemisphere after hemispherectomy in all patients. Patients with hemimegencephaly showed the most physical growth after surgery, possibly related to the earlier presentation and thus earlier hemispherectomy. Another potential factor is that presence of an abnormally enlarged hemisphere in hemimegencephaly may deprive space and nutrition for the contralateral hemisphere, and upon removal of the diseased hemisphere, the contralateral hemisphere resumes its growth potential. While in our cohort, many of the hemimegencephaly patients did not quite "catch up" to their peers in the contralateral hemispheric volume within the available follow-up periods of 4 to 10 years, all of these patients showed at least a similar, with some showing a faster, rate of growth when compared to healthy individuals. Patients with Rasmussen's encephalitis and perinatal infarctions showed a noticeably smaller physical growth after hemispherectomy, possibly related to the later timing of surgery in these patients. Nearly all of these patients showed a similar rate of growth, regardless of the initial size of the contralateral hemisphere. Several patients who received left hemispherectomy appeared to have an accelerated growth postoperatively, compared to none observed among patients with right hemispherectomy. While further analysis is limited by the fact that handedness and brain laterality are difficult to evaluate in early childhood, this interesting finding may provide some insight for future research. While timing of the surgery often is dictated by clinical need to protect the contralateral hemisphere, these data provide a foundation in understanding postoperative recovery by reflecting the "potential" for growth. Further studies with advanced imaging and a larger population are needed in order to provide an accurate prognosis in recovery, and to optimize postoperative rehabilitation after hemispherectomy.



(Filename: TCT_O-407_ASNR2017abstractfigure.jpg)

eP-104

6:30AM - 3:00PM

Embryonal Tumours with Multilayered Rosettes (ETMR)- The GOSH Series

D BHATTACHARYA[1], K Mankad[2]
[1]GREAT ORMOND STREET HOSPITAL, LONDON, LONDON, [2]Great Ormond Street Hospital, London, England

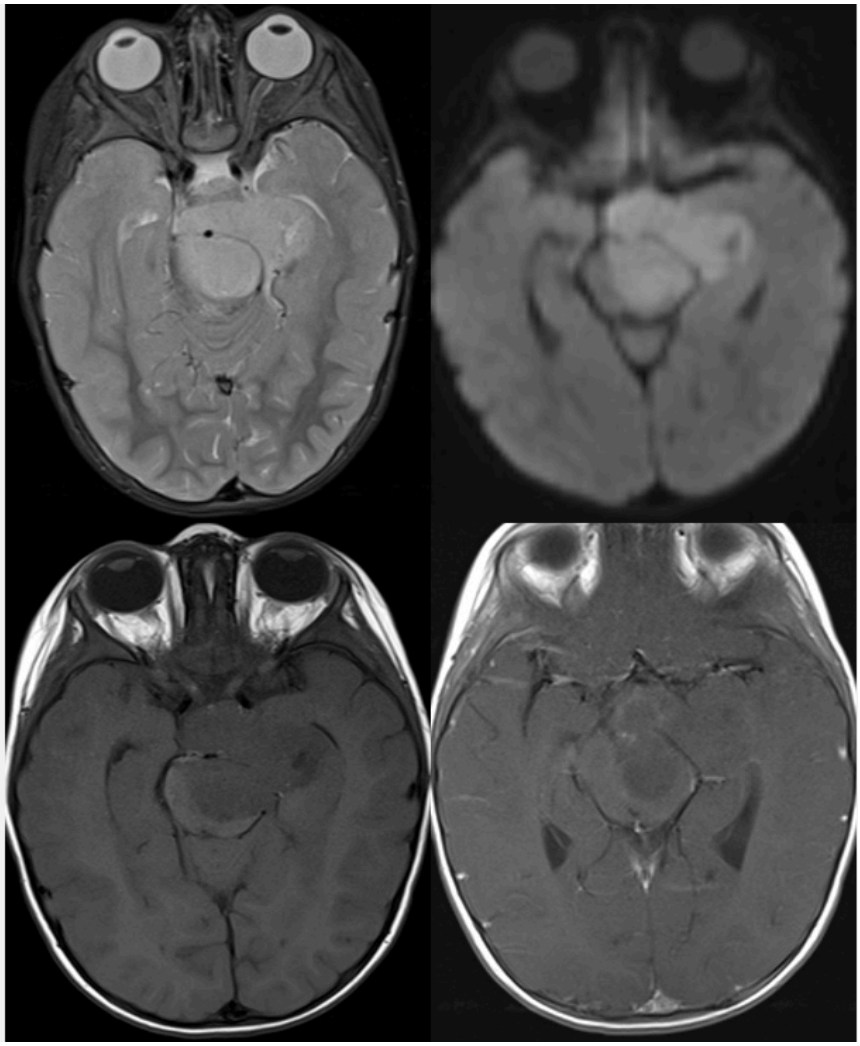
Purpose
Embryonal tumor with multilayered rosettes or ETMR is a recently described malignant neoplasm of the central nervous system. It forms part of the larger embryonal tumor subgroup, as described by the WHO Classification of CNS tumors 2016. Genetic and immune histochemistry markers are Lin28a tumor antibody over-expression and amplification of C19MC locus on chromosome 19q13.421. We describe the imaging features and clinical histories of this relatively rare pediatric tumor in a cohort of patients treated in our institution.
Materials and Methods
We reviewed the clinical histories and imaging of 5 patients, aged between 3-22 months with confirmed histopathological and genetic diagnoses of ETMR diagnosed at the Great Ormond Street Hospital for Children. We also performed a relevant comprehensive review of literature, with special attention to the morphological and imaging features of these tumors. Comparison then was made to the imaging characteristics of our own cohort of patients.

Results

The imaging features in our cohort of patients were relatively uniform, with the tumors deminstrating T1 hypointensity, T2 hyperintensity, diffusion restriction, poor/minimal contrast enhancement and enhancing metastases/recurrent disease. The clinical outcomes also were uniformly poor with a short duration of presenting symptoms, rapid disease progression and recurrent local tumor and neural axis metastases. All the cases demonstrated a fulminant course with mortality.

Conclusions

C19MC amplification in chromosome 19 (19q13.42) with Lin28a antibody overexpression in CNS tumors with characteristic features suggests a diagnosis of ETMR(C19 amplified). In our series of 5 patients, presenting with short clinical histories and rapid disease progression, there were common imaging characteristics as described on initial presentation. All patients had uniformly poor clinical outcome. In cases of CNS tumors presenting in children of this age group, with similar clinical presentation and imaging characteristics, a differential of ETMR should be considered.



(Filename: TCT_eP-104_picture2.jpg)

eP-107

6:30AM - 3:00PM

Feasibility of Fetal MR at 3T: The Final Frontier?

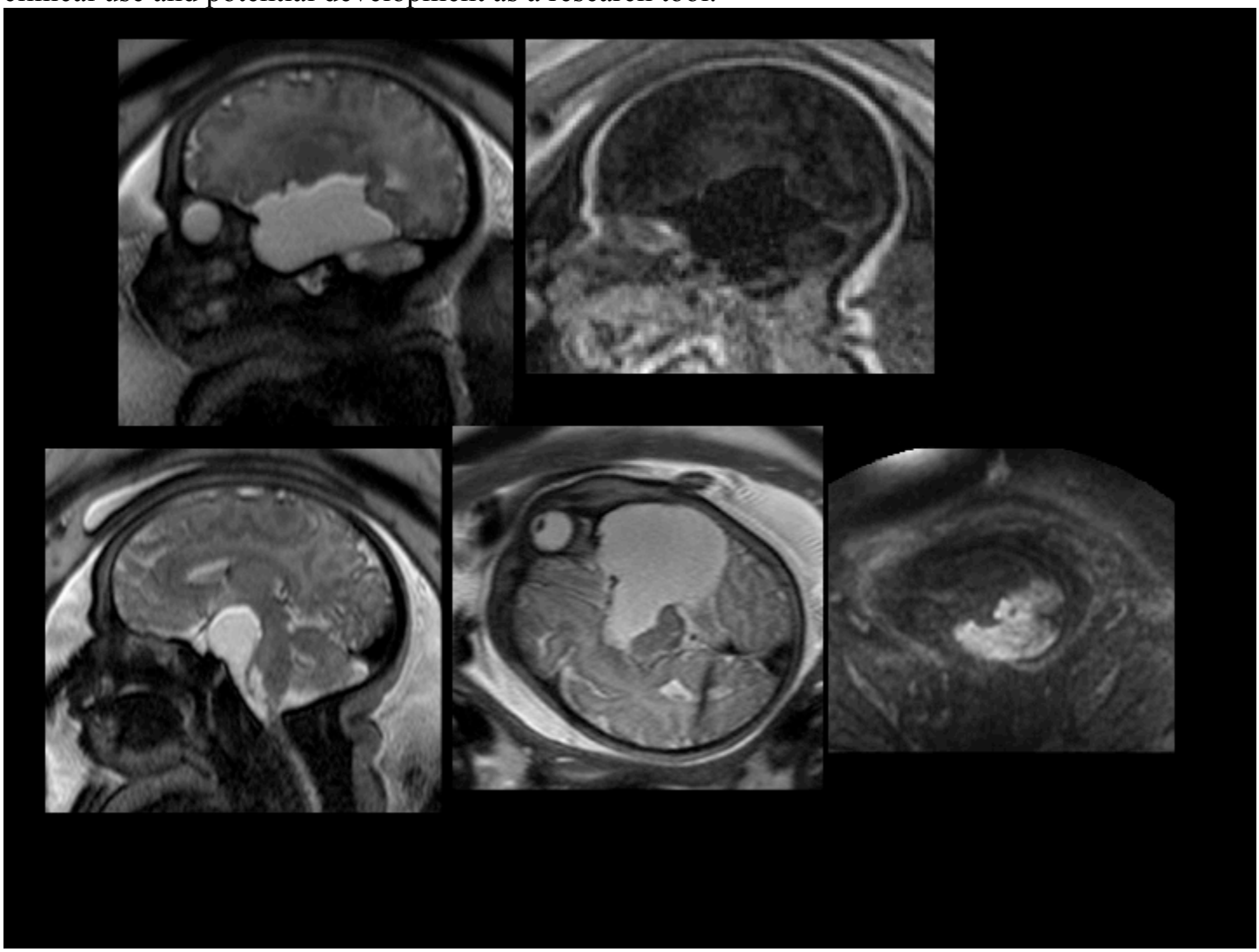
C Filippi[1], B Pramanik[1], J Steinklein[2], J Nickerson[3], R Watts[4]
[1]Hofstra Northwell School of Medicine, New York, NY, [2]Hofstra Northwell School of Medicine, NEW YORK, NY, [3]University of Vermont Medical Center, Burlington, VT, [4]University of Vermont-UVM Medical Center, Shelburne, VT

Purpose
Fetal MR at 1.5T is an established methodology for the delineation and characterization of fetal anomalies detected on prenatal ultrasound, which can be helpful in treatment decisions from planning for fetal surgery, delivery management, and issues around termination. Development of fetal MR at 3T has been limited by concerns regarding focal SAR deposition and B1 inhomogeneity related to dielectric effects, which may limit resolution. Higher field fetal MR imaging potentially allows for better understanding of fetal brain development with diffusion imaging and resting state connectivity that are superior at 3T (1). The purpose of this pilot work is to demonstrate the use of fetal MR at 3T in very selective clinical cases.
Materials and Methods
Nine cases of detected fetal anomalies on ultrasound referred for fetal MR at 1.5T underwent additional imaging at 3T after informed consent was obtained. In all 9 cases, the extent of fetal abnormality would change clinical management with respect to delivery, viability of pregnancy, and/or potential termination. Dual source transmission MR was performed, and the scanner operated in low energy SAR mode, control B1 amplitude of less than 8 microTesla, and flip angle sweep. Average SAR was less than 0.5 W/kg, which is much less than typical SAR values for brain MR performed in premature infants from 24 to 32 weeks. Dual source transmission was used to minimize focal variability in SAR, decrease B1 inhomogeneity, and provide a more uniform flip angle. Single shot TSE sequences (TR 2500/TE 100) with XL-torso coils, FOV 250mm, 4 NEX, and 4mm thickness along with balanced T1 FFE and diffusion-weighted imaging (b value 700) were done. Neuroradiologist with certificate of added qualification evaluated all 1.5T and 3.0T images. In all but 2 cases, fetal age was under 22 weeks gestation.
Results
In all cases, there was concordant diagnosis. Image quality at 3T judged comparable to 1.5T in all cases. Findings included Dandy Walker malformation (n =1), hydrocephalus with ventricles exceeding 15mm in transaxial dimension (n=3), anoxic injury and fetal demise in twin gestation (n =1), Chiari II malformation (n =1), teratoma (n =1), arachnoid cyst (n =1), and intraventricular/parenchymal hemorrhage (n = 1). Figure 1 demonstrates T2W, T1 FFE,

and DWI of a large arachnoid cyst in a scan performed for treatment planning around delivery.

Conclusions

Fetal MR imaging at 3T with dual source transmission is feasible. Future research is needed to more accurately quantify focal SAR to ensure the highest possible safety prior to its clinical use and potential development as a research tool.



(Filename: TCT_eP-107_Slide21.jpg)

eP-105

6:30AM - 3:00PM

Pediatric Supratentorial Glioblastoma - Retrospective Review Of Conventional MR Imaging Features

P HANAGANDI[1], P Krishnan[2], F Gonçalves[3], C Raybaud[4], M Shroff[5]

[1]HOSPITAL FOR SICK CHILDREN, TORONTO, TORONTO, ONTARIO, [2]Hospital for Sick Children, Toronto, Ontario, [3]Hospital da Criança de Brasília José Alencar (HCB), Brasilia, DF, [4]Hospital for Sick Children, Toronto, ON, [5]The Hospital for Sick Children, Toronto, Ontario

Purpose

We intend to selectively analyze the conventional magnetic resonance imaging (MRI) features of supratentorial glioblastoma.The imaging features of pediatric supratentorial glioblastoma exhibit variable features and often resemble some of the commonly encountered pediatric supratentorial brain tumors. Literature elaborates on treatment options and survival outcomes but there is less noteworthy citation about conventional MR imaging features of pediatric glioblastoma.

Materials and Methods

Retrospective review of pediatric supratentorial glioblastoma with an age range of 6 weeks - 18 years was performed from January 2001 to June 2016. Subjects were identified by accessing the ISYS radiology search program with proven histopathology diagnosis of glioblastoma (GBM).

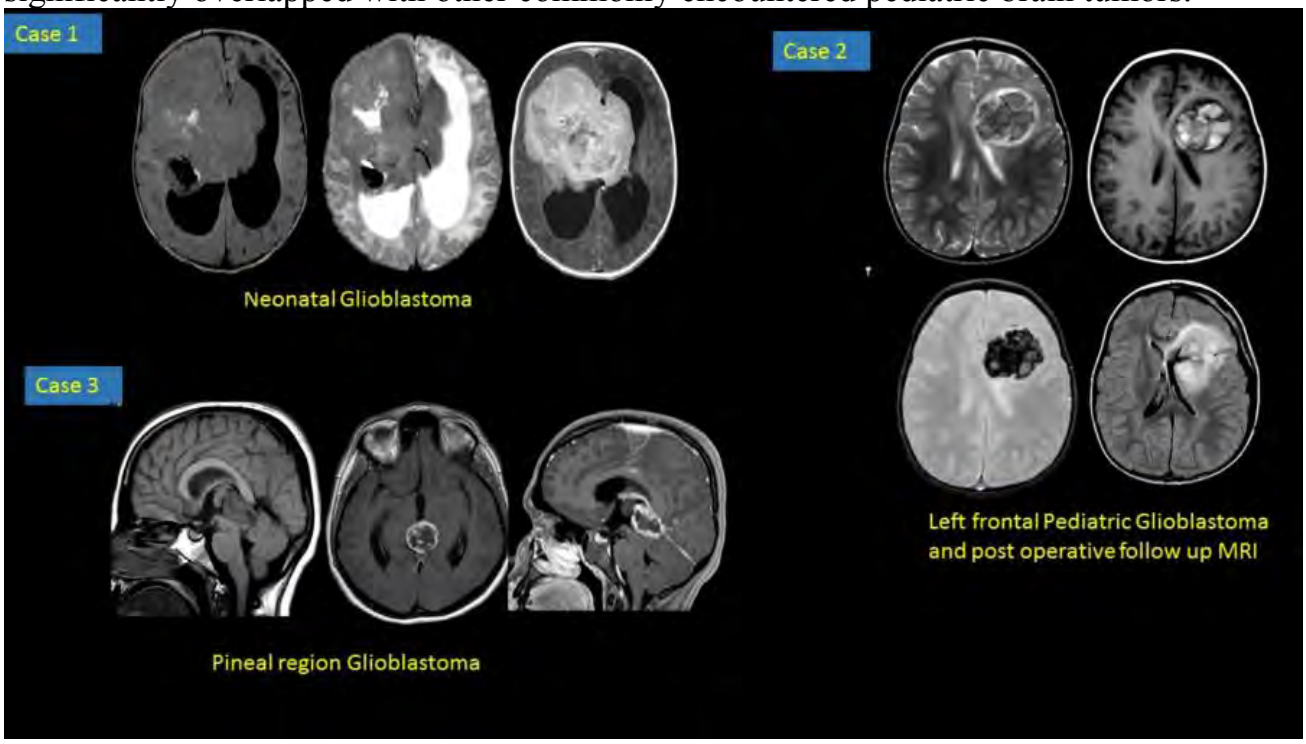
Results

n = 24 patients. Male = 10 (41.66%). Female = 14 (58.33%). Tumor characteristics: Solid tumor – 15 patients (62.5%) (males-6, females -9). Mixed (solid and cystic component) – 7 patients (29.16%) (males-3, females-4). Cystic tumor – 2 patients (8.3%) (male-1, female-1). Intratumoral Hemorrhage - 12 patients (50%) and more common in females (male-3, female-9). Seventeen patients (70.8%) had well defined margins. Eleven patients were less than 10 years of age. Peritumoral edema: 21 patients (87.5%) (males-8, females-13). Absent in 3 patients (males-2, females-1). Minimal in 8 patients (38%) (males-1, females-7). Mild to moderate 3 patients (14.28%) (males-2, females-1). Moderate 4 patients (19.04%) (males-1, females-3). Moderate to marked 6 patients (28.57%) (males-4, females-2). Signal characteristics: n=7 (29.16%) isohyperintense on T1, n= 13 (54.16%) isohypointense on T1 and n=4 (16.66%) hypointense on T1-weighted images. n=19 (79.16%) hyperintense on FLAIR. n=12 (50%) varying degrees of diffusion restriction on DWI. n=8 (33.33%) nodular and peripheral enhancement. n=5 (20.83%) avid enhancement. Rest showed heterogeneous enhancing foci. Location: Single Lobe involvement: n=13 (54.16%). Multilobar involvement: n= 6 (25%). Frontal: 9 (37.5%) (females -6 , males-3). Other locations: n= 4 (16.66%). Thalamus and Basal Ganglia -3 (male-1, female-2). Pineal-1 (female -1, male-0). Differential diagnosis contemplated at the time of initial MRI: Heratoma, Pilocytic Astrocytoma, Ganglioglioma, Pleomorphic Xanthoastrocytoma (PXA). Embryonal tumor, cavernoma or AVM, sarcoma, neuroblastoma. High grade astrocytoma, ATRT, atypical bacterial vs. fungal infection. Desmoplastic infantile ganglioglioma. Cystic glial tumor. Sarcoma, Hemangiopericytoma. Ependymoma. Pineoblastoma, Germinoma.

Conclusions

Single lobe involvement (54.16%) was more common as compared to multilobar prediliction

(25%). Female preponderance for frontal lobe and single lobe involvement in the female subgroup are interesting and new observations from our small cohort. Hemorrhagic lesions were a common feature in female subgroup. Multilobar and infiltrative pattern was observed in the male subgroup. 70.8% had well defined margins. Eleven patients were less than 10 years of age. There were no specific imaging predictors on conventional imaging to make a definitive diagnosis of glioblastoma on initial MRI at presentation. Diverse imaging features significantly overlapped with other commonly encountered pediatric brain tumors.



(Filename: TCT_eP-105_ASNR2017GBMabstract.jpg)

eP-103

6:30AM - 3:00PM

Resistive Index in Neonatal Marked Hydrocephalus: Does It Predict Outcomes?

E Snyder[1], A Jelin[2], E Ahn[2], T Huisman[3], A Tekes[1]
[1]Johns Hopkins University, Baltimore, MD, [2]Johns Hopkins University School of Medicine, Baltimore, MD, [3]Johns Hopkins, Baltimore, MD

Purpose
The resistive index in the cerebral circulation has been proposed as a noninvasive, indirect measure of increased intracranial pressure in neonates with hydrocephalus. Although a few prior studies have suggested that abnormal resistive indices (RI) values may indicate the need for cerebrospinal fluid (CSF) diversion, no studies have evaluated whether these values may be predictive of outcomes in isolated and syndromic hydrocephalus in neonates. The purpose of this study is to evaluate whether changes in resistive indices in the anterior

cerebral circulation may be associated with the need for CSF shunting in neonates with isolated and syndromic hydrocephalus.
Materials and Methods
Fetuses with marked hydrocephalus (ventricular size > 15 mm prenatally) were identified using OBGYN database from January 2008 to June 2016. Hydrocephalus was categorized as isolated versus syndromic. Additional inclusion criteria included postnatal head ultrasound with Doppler evaluation and clinical/surgical follow ups. The resistive index values in the anterior cerebral artery, measured with and without gentle pressure on the anterior fontanelle, on neonatal head ultrasound were recorded and the medical charts were reviewed to determine if and at what age the patient required CSF shunting.
Results
A total of 12 neonates were identified and their resistive index values and outcomes reviewed. Six patients had isolated hydrocephalus and 6 had Chiari II malformation. There was no difference in mean resistive index (p=0.233) without pressure in patients with isolated hydrocephalus (mean= 0.79, range 0.68-0.88, SD=0.08) and in those with Chiari II malformation (mean= 0.76, range 0.65-0.90, SD=0.08). Of those with isolated hydrocephalus, there was no correlation between the change in resistive index and the need for shunt (p=0.98). There was no correlation between change in resistive index and the need for shunting in Chiari II patients, all of whom required drainage in this cohort.
Conclusions
Although RI values may be a noninvasive and indirect way to evaluate cerebral autoregulation, the change in resistive index was not associated with a need for CSF shunting in our small cohort. Future studies with larger sample size and prospective evaluation will be helpful to test this hypothesis.

eP-100

6:30AM - 3:00PM

Retrospective Analysis of Odontoid Cap Thickness in Mucopolysaccharidosis Type I (Hurler Syndrome) after Hematopoietic Stem Cell Transplantation

P Aldinger[1], D Nascene[1]
[1]*University of Minnesota, Minneapolis, MN*

Purpose
There are several musculoskeletal manifestations of mucopolysaccharidosis type I (MPS I) that contribute to narrowing of the craniocervical junction including thickening of the tissues posterior to the dens referred to as odontoid capping. Hematopoietic stem cell transplantation (HSCT) has become the standard of care and has offered extended survival and ameliorated many symptoms of this disease. Hematopoietic stem cell transplantation generally is less effective in treating musculoskeletal manifestations of MPS I. Only a single case report has

quantitatively followed the thickness of odontoid cap following HSCT. We seek to demonstrate that the odontoid cap is stable after successful HSCT in patients with MPS I.

Materials and Methods

Fourteen patients with MPS I who successfully underwent HSCT at our institution between 2002 and 2008 for whom there was sufficient clinical data and follow up were selected. The first brain or cervical spine MRI before HSCT and all subsequent brain and cervical spine MRIs were reviewed. The thickness of the odontoid cap was measured in each to the nearest mm. The amount of change was analyzed.

Results

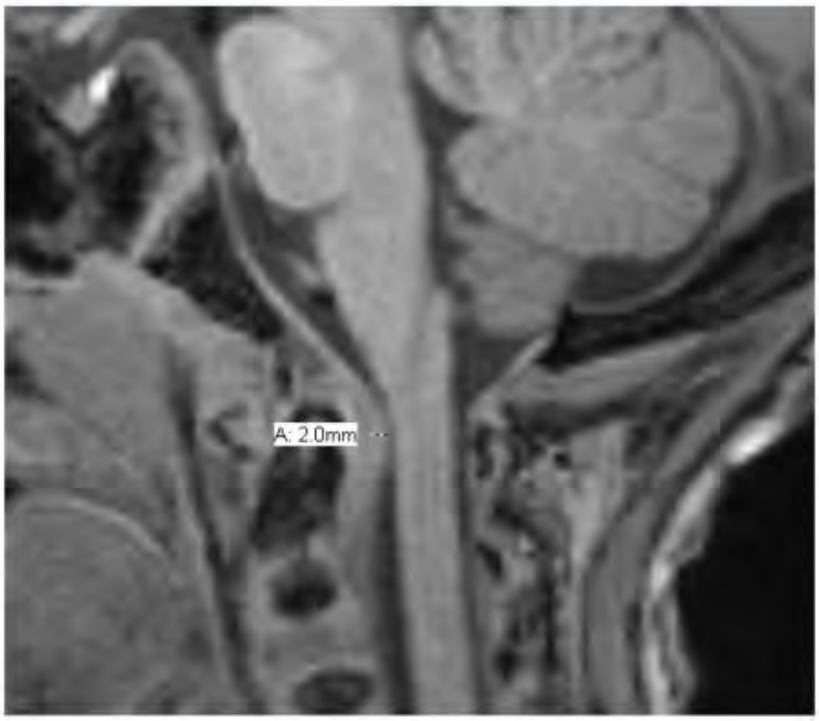
A total of fourteen patients were followed to age 4.7 to 18.8 years of age, average 10.6 years. They were followed from 4 to 14.1 years after HSCT, average 9.9 years. Age of HSCT ranged from 0.7 to 2.8 years, average 1.1 years. The pre HSCT odontoid cap thickness ranged from 2 to 3mm, average 2.4mm. The increase in cap thickness from the first to the last MRI ranged from 0 to 3mm with only single increase of 3mm. The average increase was 0.9mm. The majority of cases had an increase of 1mm between the initial pre HSCT and 1st post HSCT MRIs with relative stability and no clear pattern of growth seen thereafter.

Conclusions

The odontoid cap thickness is stable in patients with MPS I (Hurler syndrome) after HSCT. It is unlikely to be significant contributor to multifactorial craniocervical junction stenosis in patients who have undergone successful treatment.

Table 1: Age of HSCT and MRI scan in years, Corresponding Odontoid Cap thickness in mm.

NO.	HSCT (age)	Pre HSCT MRI (age)	Pre Cap (mm)	1st Post MRI(age)	1st Post Cap	2nd MRI	2nd Cap	3rd MRI	3rd Cap	4th MRI	4th Cap	5th MRI	5th Cap	6th MRI	6th Cap	7th MRI	7th Cap
1	2.8	2.5	3	3.9	4	4.8	4	6.1	4	8.8	3						
2	2.6	2.5	3	5.7	3	6.7	3	8.7	3	10.5	3	11.8	3	14.3	3	16.8	3
3	0.7	0.6	2	4.2	3	4.7	3										
4	1.3	1.2	3	1.7	2	2.3	2	3.6	3	7.7	2	8.7	3				
5	0.8	0.7	3	2.8	4	8.8	2	8.3	2	8.4	3	10.8	4	11.7	4	13.0	3
6	0.9	0.7	2	12.5	4	13.5	5	14.3	5								
7	0.7	0.8	2	1.8	3	3.4	3	5.8	4	9.8	3	10.8	4	12.9	3	14.8	3
8	0.6	0.5	2	1.3	3	3.0	3	4.6	3	9.1	3						
9	1.3	1.1	2	2.8	3	3.8	3	12.8	3								
10	0.6	0.5	3	1.5	3	4.4	3	7.3	3	9.3	4	10.4	4	12.7	3		
11	1.8	1.7	2	2.3	3	2.7	3	4.6	2	6.7	3	7.7	3	12.4	3		
12	1.5	1.3	2	1.4	3	2.5	3	3.7	3	4.8	3	6.8	2	9.2	3		
13	1.6	1.0	2	1.3	3	2.7	2	3.8	3	4.8	3	5.8	3	11.2	3		
14	1.1	0.7	2	1.4	3	1.9	3	2.9	3	4.0	3	5.0	4	5.9	4	7.3	4



(Filename: TCT_eP-100_Hurler6.jpg)

eP-106

6:30AM - 3:00PM

TRANCE (TRiggered Angiography Non Contrast Enhanced) MRI of the Intracranial Vasculature at 3 Tesla: Preliminary Experience in Children

A Pokorney[1], J Chia[2], H Hu[1], J Miller[1]
[1]Phoenix Children's Hospital, Phoenix, AZ, [2]Philips Healthcare, Cleveland, OH

Purpose

In this work, we aim to demonstrate with pilot data the potential clinical utility of a dynamic noncontrast-enhanced angiography technique for imaging blood flow in the intracranial vasculature. The technique, called triggered angiography noncontrast-enhanced (TRANCE) is based on arterial spin labeling (ASL) MRI principles. We showcase the utility of TRANCE in pediatric patients. Background: Over the past year, there has been steadily growing evidence and concerns of intracranial gadolinium deposition in pediatric and adult patients who undergo multiple contrast-enhanced magnetic resonance imaging (MRI) examinations (1). While gadolinium-based MR angiography remains common in both pediatric and adult practices, noncontrast techniques are emerging rapidly as viable alternatives. Recently, a dynamic time-resolved nongadolinium angiography technique (called TRANCE, previously referred to as CINEMA - contrast inherent inflow enhanced multi-phase angiography), based on multi-delay/multi-phase arterial spin labeling MRI, was introduced by Iryo and Nakamura, et al. (2-5) and was made available commercially. Briefly, TRANCE is a subtraction-based ASL angiography technique that utilizes a 3D turbo gradient-echo Look-Locker pulse sequence coupled to a multi-shot echo-planar imaging readout for data acquisition. The technique can be integrated with a variety of ASL labeling schemes (e.g., either a pulsed or pseudocontinuous ASL tagging scheme) and acquires time-resolved data by varying the delay time interval between inversion water-spin labeling and imaging at the more superior slices of interest (i.e., PLD-post labeling delay). In this work, we demonstrate the potential diagnostic utility of nongadolinium dynamic TRANCE in neonates, infants, and children. Specifically, we evaluate TRANCE as a supplemental pulse sequence in addition to conventional time-of-flight (TOF) angiography.

Materials and Methods

Experiments: To date, 36 patients (19 males, 17 females, age range: 1 day to 14 years) were scanned with 4D-TRANCE at our institution. All patients were referred to the radiology department for a clinically indicated brain MRA exam. All MRI data were acquired on a 3T Ingenia scanner (R5.3 software, Philips HealthTech, Best, The Netherlands) using a 32-channel head coil array. Imaging parameters for TRANCE were: 160–220 mm FOV, 1.2 mm in-plane resolution, 80-120 axial 0.65-0.8-mm slices centered around the Circle of Willis, 2-2.5x SENSE acceleration anterior-posterior, 1 signal average, acquisition TR/TE = 11/6 ms, 10° flip angle, 8-12 dynamic phases, first phase at 200 ms PLD, 120-200 ms intervals between consecutive phases, 2 s of cycle duration between control and labeled ASL data

sets, 300 mm labeling slab centered inferiorly just below the carotid bifurcation, a 20-mm gap between the labeling slab and the 3D imaging volume, 1850 ms label duration, and a scan time approximately 5 min. In one patient, we performed TRANCE twice, once by labeling both carotid arteries, and once by labeling only the left carotid artery to visualize inflow of the associated downstream vessels. Preliminary Analysis: A board-certified pediatric neuroradiologist with more than 10 years of experience assessed the TRANCE images in the context of available TOF data. Using a three-point scale, the physician assessed the degree of intracranial vessel conspicuity between TOF and CINEMA and determined whether CINEMA was (−1) inferior, (0) equivalent, or (+1) superior in demonstrating the neural vasculature.

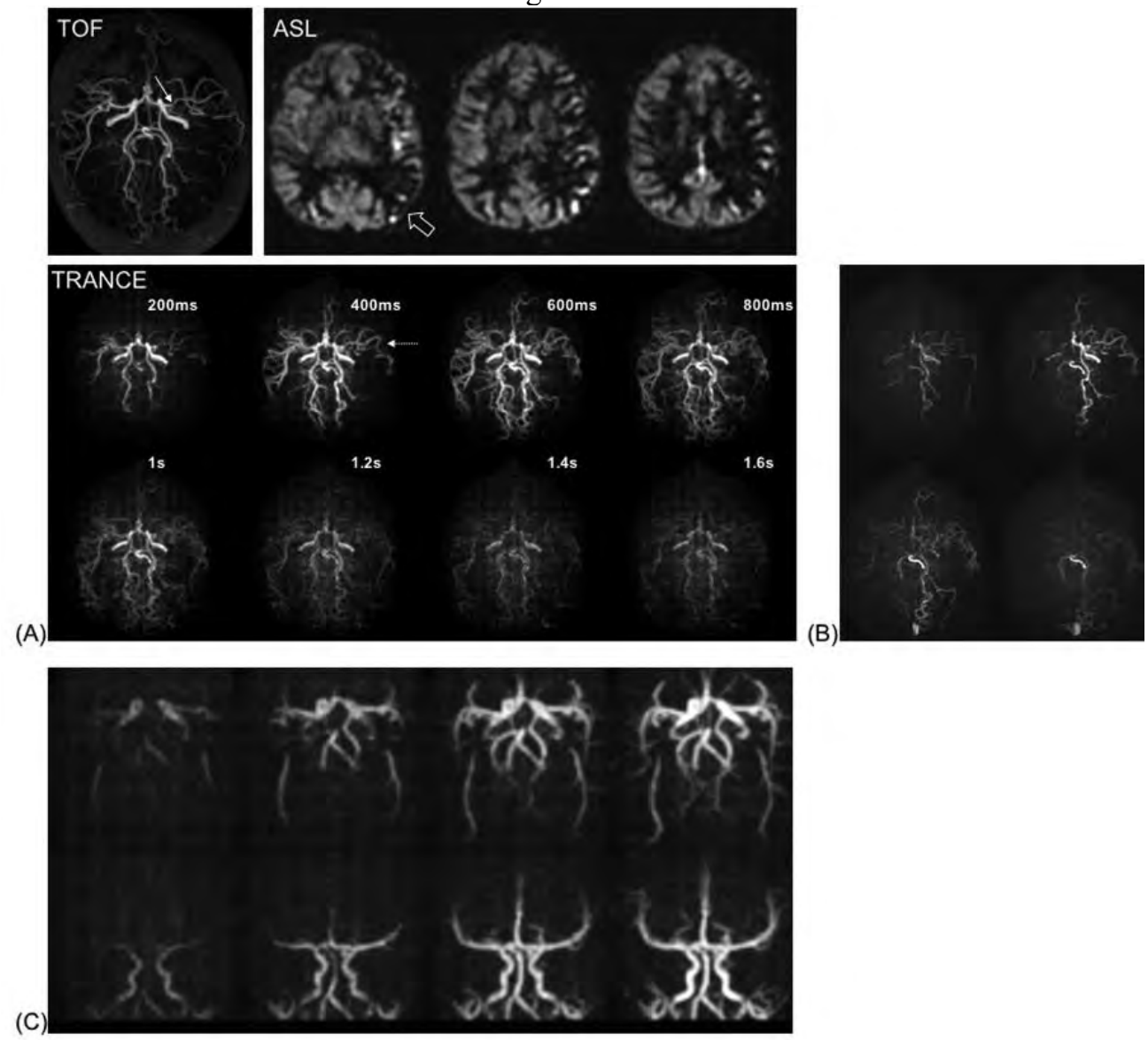
Results

Triggered angiography noncontrast-enhanced data were acquired successfully and reconstructed in all 36 patients with no image artifacts that rendered the dynamic data nondiagnostic. There were no cases where TRANCE was rated inferior (i.e., −1 score) to TOF in depicting intracranial vessel conspicuity. In 24 cases, TRANCE was rated equivalent (i.e., 0 score) to TOF. Sixteen of these 24 cases had normal angiographic findings. In the remaining 12 cases (all with vascular pathologies), TRANCE was rated superior (i.e., +1 score) to TOF in vessel visualization. The neuroradiologist felt that the additional dynamic TRANCE data were complementary to TOF in the normative cases. In cases with vascular pathologies, the time-resolved information from TRANCE supplemented TOF data and potentially provided added diagnostic value. Figure 1a illustrates an example from an 8-year-old female with moyamoya disease. Time of flight data illustrate a stable and diminutive appearance of the left middle cerebral artery (arrow), including a high grade stenosis of the left M1 segment. Conventional ASL cerebral blood flow images show a perfusion defect in the left frontoparietal region (open arrow). Eight frames of TRANCE also are shown, with PLD noted in the inset. There is a slight delay in perfusion to the left side of the brain (dotted arrow). Figure 1b shows the first 4 frames of TRANCE upon labeling only the left carotid artery. Figure 1c illustrates TRANCE data in a 1-month-old female, with normal angiographic findings. Axial (top) and coronal (bottom) projections are shown to highlight the 3D high resolution nature of the data.

Conclusions

Discussion: In our practice, a routine brain MR angiography exam involves a protocol using conventional 3D TOF scans and gadolinium typically is not used. Our preliminary experience suggests that in patients with vascular pathologies and abnormal flow patterns, TRANCE can supplement diagnosis in addition to TOF angiography. We employed an initial PLD of 200 ms in this work in children. Keeping scan time about 5 minutes, we can achieve 8-12 subsequent phases with 120-200 ms phase-to-phase intervals. The shortest achievable PLD given our current 3T system's hardware is 40 ms. A limitation of our current work is that the TRANCE sequence was not evaluated in the context of a corresponding dynamic gadolinium-based contrast-enhanced MRA technique with comparable spatiotemporal resolution. Such a comparison should be performed in the future and maybe

more feasible in adults undergoing scheduled MR angiography exams with gadolinium. Conclusion: In conclusion, our preliminary study demonstrates the potential clinical utility of nongadolinium TRANCE in dynamic intracranial neurovascular imaging. We believe the technique holds promise as a useful supplement to conventional TOF MRA and negates the need for renal function tests or the placement of an intravenous line in pediatric patients. Further evaluations in vessel-selective imaging, as well as in other anatomical regions, including the lower extremities and in the abdomen, and possibly a direct comparison with time-resolved gadolinium contrast-enhanced scans should be considered. We believe one of the most prominent advantages of TRANCE is its ability to be repeated multiple times without limit in a single exam. Triggered angiography noncontrast-enhanced technique therefore may be useful in real-time applications to assess the response of blood flow in the intracranial vasculature to a vasodilator agent.



(Filename: TCT_O-190_ASNR2017_TRANCE_400dpi.jpg)

eP-101

6:30AM - 3:00PM

Vanishing White Matter Disease: Imaging, Clinical and Molecular Correlation in Brazilian Families

M Palmejani[1], G Simão[1], A Mello[1], S Escorsi-Rosset[1], M Cintra[1], C Lourenço[2], A Hamad[2]
[1]Ribeirao Preto School of Medicine - University of Sao Paulo, Ribeirao Preto, São Paulo, [2]Ribeirao Preto School of Medicine - University of Sao Paulo, Ribeirao Preto, Sao Paulo

Purpose
Characterization of vanishing white matter disease (VWMD) cases in relation to brain magnetic resonance imaging (MRI) appearance, clinical and molecular correlation and evolution over the time, comparing with data already described in the literature.
Materials and Methods
Retrospective review of medical records and brain MRI of thirteen patients diagnosed with VWMD disease by molecular tests, during the period from 2001 to 2016. The images were characterized according to the MRI diagnostic criteria described by van der Knaap (2006).
Results
The patients were mostly female (61.5%), white, with mean age of onset symptoms about 10 years. All have mutation in same gene (EIF2B5) and the most prevalent was c.338G> A (p.Arg113His). Trauma or infection as a trigger was described in 38.4%. The most frequent symptoms were ataxia (100%), spasticity (84.6%), seizures (69.2%), headache (53.8%) and vomiting (46.1%). Ovarian failure affected half of the female patients. All MRI of symptomatic patients showed deep white matter involvement, characterized by high sign and cystic degeneration on T2-weighted, with subcortical relatively spared and preference to fronto-parietal region (84.6%), with occipital lobe less involved. Every MRI presented lesions in corpus callosum, diffusely (46.2%) or of the inner rim (53.8%). All showed cerebellar involvement and the majority evidenced brainstem alterations. Optic atrophy was seen in 46.1%. Spectroscopy MRI showed decrease in NAA values and lactate peak. Follow-up exams evidenced white matter lesions and cerebral atrophy evolution, with major involvement of the high convexity and ventricular dilation, without collapsing parenchyma.
Conclusions
Vanishing white matter disease is an important differential diagnosis of leukoencephalopathy both in childhood and in young adults. Clinical and molecular characteristics are variable, making the diagnosis challenging. Magnetic resonance imaging is extremely valuable because it shows typical lesions, which radiologists should be familiar, and helps screening for genetic testing, contributing to the diagnosis and follow up.

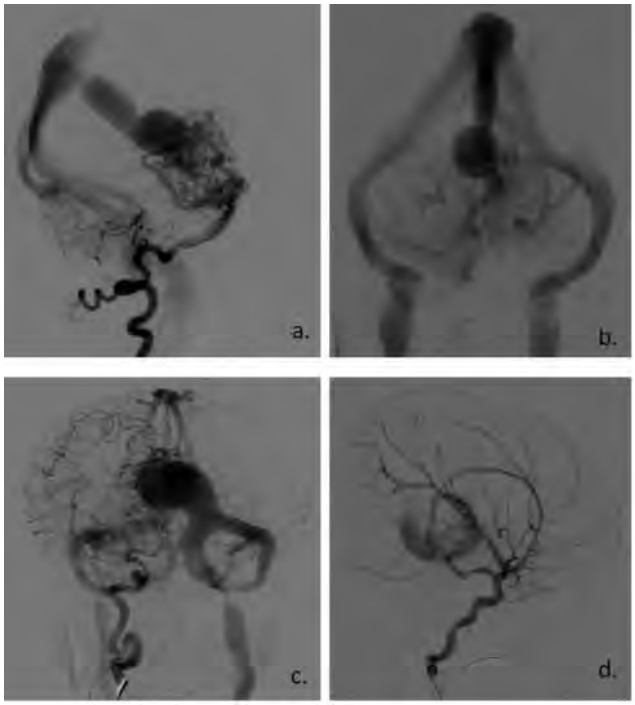
eP-99

6:30AM - 3:00PM

Vascular Abnormalities Associated with Vein of Galen Malformation

K Bhattacharya[1], A Gupta[2], H PENDHARKAR[3], A RAMALINGAIAH[4], C Prasad[5], j saini[6]
[1]National Institute of Mental Health and Neurosciences, India, Bangalore, Karnataka, [2]National Institute of Mental Health and NeuroSciences (NIMHANS), Bangalore, Karnataka, [3]NATIONAL INSTITUTE OF MENTAL HEALTH & NEUROSCIENCES, BANGALORE, KARNATAKA, [4]NATIONAL INSTITUTE OF MENTAL HEALTH AND NEUROSCIENCE, NIMHANS, Bengaluru , karnataka , [5]National Institute of Mental Health and Neurosciences, Bangalore, Karnataka, [6]NIMHANS, BANGALORE, Karnataka

Purpose
To illustrate various vascular abnormalities associated with Vein of Galen malformation and their importance in endovascular management.
Materials and Methods
Twenty patients with ages varying from 2 months to 12 years were evaluated with digital subtraction angiography. All patients were symptomatic presenting with cardiac failure in infants, seizures and epistaxis in young children and low intelligence in older children. Angiograms were reviewed to determine the vascular abnormalities associated with Vein of Galen malformation.
Results
Angiograms of twenty patients including twelve males and 8 females were reviewed. Choroidal type was noted in 7 cases and mural type in thirteen cases. The vascular anomalies were classified as arterial and venous. Arterial anomalies: 1) Limbic arterial arch in 6 patients, 2) Proatlantal artery in 2 patients. Venous anomalies: 1) Falcine sinus in twelve patients, of which 1 showed unusual bifid morphology, 2) Stenosis and occlusion of the sigmoid sinuses in 8 patients, 2 of which showed unilateral involvement, 3) Straight sinus was stenosed/absent in thirteen cases, 4) Sylvian vein capture by the cavernous sinuses in 8 patients, 5) Abnormal torcular dilatation in 2 cases. 6) Absent well formed torcula with malformed posterior part of the superior sagittal sinus in 4 patients, 7) Persistent occipital and marginal sinus in 3 patients, 8) Abnormal venous communication between transverse sinus and sigmoid/marginal sinuses in 2 patients. Endovascular embolization is the treatment of choice in Vein of Galen malformations. Abnormal arterial communications should be kept in mind for complete obliteration of the fistulae. Venous anomalies can provide alternative routes in occlusion or stenosis of normal pathways.
Conclusions
Vein of Galen malformations are a rare group of disorders arising in early embryonic period, and are associated with multiple arterial and venous anomalies. Prior knowledge of arterial and venous anomalies help in proper planning and management of these cases.



- 10-year-old boy presenting with poor scholastic performance Fig. a. Lateral angiogram of right vertebral artery injection shows choroidal type with falcine sinus and absent straight sinus Fig. b. Anteroposterior view of venous phase shows absence of well-formed torcula and bifid posterior part of the superior sagittal sinus
- 7- year- old girl presenting with large head and epistaxis Fig. c. Anteroposterior view of right internal carotid artery showing choroidal type with occipital and marginal sinus. Stenosis noted at bilateral sigmoid-jugular junction.
- 8-month-old baby girl presenting with large head and failure to thrive Fig. d. lateral view of right internal carotid artery injection showing mural type of malformation with limbic arch.

(Filename: TCT_eP-99_VOGM.jpg)

Monday
6:30AM - 3:00PM
Long Beach Convention Center, Exhibit Hall B-(Lower Level) eP

Electronic Scientific Poster (eP)-Socioeconomics

eP-109

6:30AM - 3:00PM

Cognitive Versus Perceptual Errors in Diagnostic Neuroradiology

S Patel[1], J Patrie[1], J Itri[1], T Shepherd[2]
[1]University of Virginia Health System, Charlottesville, VA, [2]NYU Medical Center, New York, NY

Purpose
Radiologic errors can be minimized if we understand the most common types of errors, their underlying causes and situations that present increased risk for error during routine clinical practice (1, 2). This study aimed to characterize the ratio of cognitive to perceptual errors in retrospectively identified neuroradiology errors as a function of study type, underlying abnormality, radiologist experience and time of week.
Materials and Methods
With institutional review board approval, we retrospectively characterized 244 peer-identified diagnostic neuroradiology error cases (with 254 total errors). Errors were

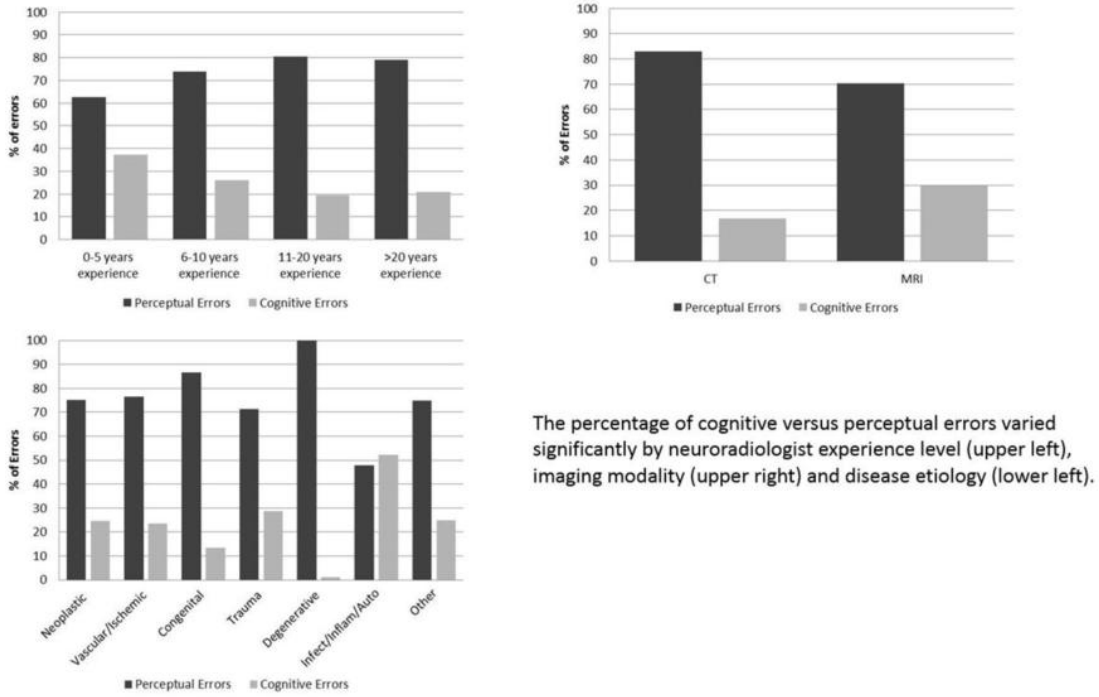
classified as perceptual or cognitive based on missing or misinterpreting the finding respectively. We used logistic regression analysis to identify factors associated the error – these factors included radiologist training and experience, imaging modality, anatomy, disease etiology, and time of week.

Results

Of the 254 diagnostic neuroradiology errors, 190 and 64 were perceptual and cognitive respectively. Logistic regression analysis showed that odds of committing a cognitive error were higher among less experienced neuroradiology attendings [OR = 1.32, 95% CI: (1.00, 1.740), p=0.046]. Cognitive errors were more common during MRI interpretations than CT interpretations [OR 2.10 (1.09, 4.01), p=0.026]. Certain disease categories were associated with more cognitive or perceptual errors (p=0.040).

Conclusions

Among diagnostic neuroradiology errors, the ratio of cognitive to perceptual errors varies significantly with neuroradiologist experience level, imaging modality, and disease etiology. These results may inform efforts towards error reduction in clinical neuroradiology services.



The percentage of cognitive versus perceptual errors varied significantly by neuroradiologist experience level (upper left), imaging modality (upper right) and disease etiology (lower left).

(Filename: TCT_O-18_asnr2017figure.JPG)

eP-111

6:30AM - 3:00PM

Effect of Clinical Decision Support on Appropriateness of Advanced Imaging Use Among Housestaff Physicians in the Emergency Department

L Mao[1], J Poeran[1], N Zubizarreta[1]
[1]*Icahn School of Medicine at Mount Sinai, New York, NY*

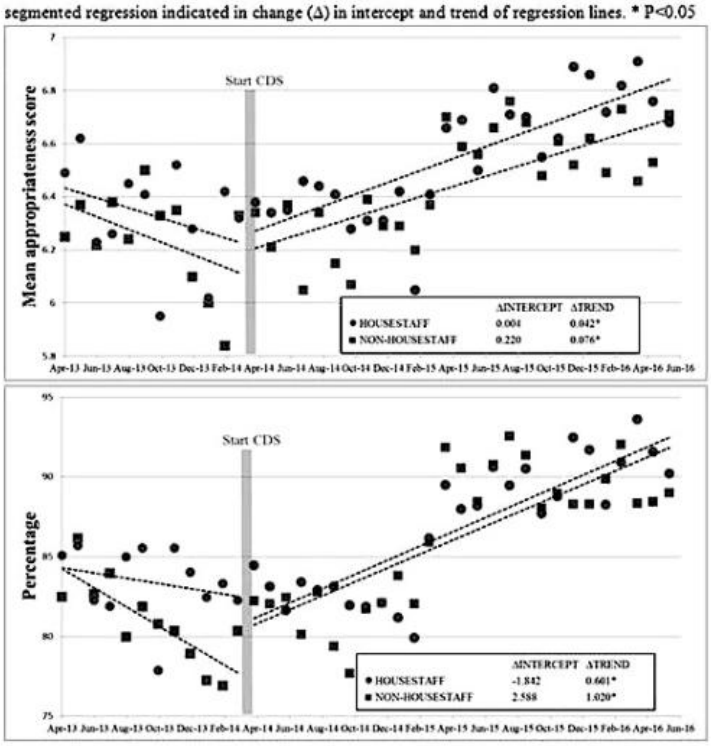
Purpose
Electronic health record-embedded clinical decision support (CDS) tools have been shown to reduce inappropriate scan orders and overall imaging volume. Such tools may be especially effective for housestaff physicians who are prone to overuse of resources. However, data is lacking on the effect of CDS on appropriate imaging use by housestaff and nonhousestaff physicians. Our study will assess this differential effect on advanced imaging orders from the emergency department (ED).
Materials and Methods
Clinical decision support data on all CT and MRI orders placed in the ED of a large urban academic hospital (spanning April 2013-July 2016) with known clinical indication, known order score, and known trainee status of the ordering provider were included. Orders were scored based on the American College of Radiology's (ACR) Appropriateness Criteria (range 1-9; higher scores represent more appropriate imaging orders). American College of Radiology scores were captured in the background for 12 months (baseline period), while CDS with active feedback was initiated in April 2014 (intervention period). Using an interrupted time series design with segmented regression analysis, we estimated changes in appropriateness scores after the implementation of CDS, stratified by housestaff (including residents and fellows) and nonhousestaff physicians (including attendings and physician extenders). In addition, a generalized linear model was fitted (outcome=ACR score) where the modifying effect of the housestaff variable was assessed.
Results
Clinical decision support prospectively generated a score for 62.5% (n=6725; average score 6.3) and 83.2% (n=25938; average score 6.5) of baseline and intervention orders, respectively. The segmented regression analysis showed average ACR scores to significantly increase after active CDS implementation for both housestaff [+0.04/month (95% CI, 0.02 to 0.07), $P<0.05$] and nonhousestaff [+0.04/month (95% CI, 0.02 to 0.07), $P<0.05$], thus demonstrating no difference in CDS effect between housestaff and nonhousestaff cohorts in regard to overall imaging orders and orders stratified based on clinical indication (including headache and abdominal pain). This result was further confirmed in the generalized linear model. Interestingly, orders with headache as an indication were associated with notably low mean ACR scores during both the baseline (average score 1.5) and intervention periods (average score 2.9).
Conclusions
Implementation of active CDS in the ED order entry system increased ACR scores of overall advanced imaging requests and ACR scores of the most common clinical indications. However, there was no significant difference in CDS effect on ACR scores between housestaff and nonhousestaff physicians. The clinical indication of headache resulted in conspicuously low ACR scores for both cohorts, likely reflecting multifactorial challenges in efficacious CDS implementation and utility.

Table 1. Average appropriateness scores and stratification of scores by housestaff/non-housestaff and indication for order.

	PRE-CDS (4/2013 - 3/2014)		POST-CDS (4/2014 - 6/2016)		
	#	%	#	%	P-value*
OVERALL					
Overall mean score	6.3		6.5		0.0038
Score category					
Appropriate (7-9)	4101	61.0	16601	64.0	<0.0001
Uncertain (4-6)	1425	21.2	6008	23.2	
Inappropriate (1-3)	1199	17.8	3329	12.8	
Indication – Mean score					
Abdominal Pain	8.0		7.8		0.0004
Headache	1.5		2.9		<0.0001
HOUSESTAFF					
Score category					
Appropriate (7-9)	2278	60.7	8534	64.7	<0.0001
Uncertain (4-6)	848	22.6	3010	22.8	
Inappropriate (1-3)	629	16.7	1652	12.5	
Indication - Mean score					
Abdominal Pain	8.0		7.8		0.0007
Headache	1.4		2.8		0.0003
NON-HOUSESTAFF					
Score category					
Appropriate (7-9)	1823	61.4	8067	63.3	<0.0001
Uncertain (4-6)	577	19.4	2998	23.5	
Inappropriate (1-3)	570	19.2	1677	13.2	
Indication - Mean score					
Abdominal Pain	8.0		7.8		0.0006
Headache	1.5		3.0		<0.0001

*T-test for continuous variables, Chi2-test for categorical variables

Figure 1. Time series plot; average appropriateness scores and percentage of tests scored 4-9 before and after CDS implementation, stratified by housestaff/non-housestaff. Results from segmented regression indicated in change (Δ) in intercept and trend of regression lines. * P<0.05



(Filename: TCT_eP-111_image2.jpg)

eP-110

6:30AM - 3:00PM

Improving Quality of Clinical Information on Head CT Requisitions from the Emergency Department to Aid Interpretation and Improve Billing Efficiency

D Barron[1], T Spiegel[1], G Katzman[1], S Ali[1]
[1]*University of Chicago, Chicago, IL*

Purpose

Accuracy of radiological interpretations is higher when appropriate clinical information is provided, as is the likelihood of reimbursement for the studies. The purpose of this project is to evaluate and improve the quality of clinical information provided on CT head requisitions from an urban emergency department (ED).

Materials and Methods

Study was prospectively conducted from July 2015 to May 2016. Eleven hundred randomly selected CT head requisitions from the ED were evaluated by attending neuroradiologists for

clinical and billing adequacy on a scale of 0 to 2 (0= inadequate, 1=intermediate, 2= good history including presenting neurological signs/symptoms). Training was provided prior to scoring to ensure consistency among faculty. Following obtaining baseline data (400 studies), an intervention was performed consisting of education to ED residents and faculty on the importance of clinical information on requisitions. Baseline scores for each ED staff member also were provided. A reminder slide also was placed on a large screen in the ED staff working area with examples of what is appropriate history. Post-intervention data (700 studies) subsequently were obtained. Mean pre- versus postintervention scores were calculated and compared using the Wilcoxon rank-sum test.

Results

There was a statistically significant improvement in mean scores following intervention for both clinical (1.32 to 1.43, p=.003) and billing (1.64 to 1.74, p=.02) adequacy categories. The percentage of studies receiving a score of "2" increased for both categories, while the percentages of "0" and "1" scores declined (Table 1).

Conclusions

We demonstrate improvement in clinical information provided on requisitions by ED faculty and residents following a relatively simple intervention. As the literature suggests, we infer that our project may have ultimately enhanced patient care by improving the quality and accuracy of the radiology reports while at the same time increasing reimbursements. Our study can serve as a model for other institutions.

Pre-intervention (July to Oct) 400 cases		Post-intervention (Nov to May) 700 cases	
Billing	**Clinical**	**Billing**	**Clinical**
0 (47/400 12%)	0 (35/400 9%)	0 (51/700 7%)	0 (48/700 7%)
1 (49/400 12%)	1 (204/400 51%)	1 (80/700 11%)	1 (304/700 43%)
2 (304/400 76%)	2 (161/400 40%)	2 (569/700 81%)	2 (348/700 50%)
Mean 1.64	1.32	1.74	1.43

(Filename: TCT_eP-110_cqi-table.jpg)

eP-113

6:30AM - 3:00PM

Inappropriate Skull Radiographs in Pediatric Head Trauma Patients Older than Age Two Years

B Vey[1], K Applegate[2], P Sharp[1], N Kadom[1]
[1]Emory University, Atlanta, GA, [2]Emory University and Children's of Atlanta, Atlanta, GA

Purpose
The scientific literature has proposed several clinical guidelines to aid in decisions regarding the need for initial imaging in acute pediatric head trauma. These guidelines are the CHALICE rule from 2006 [1], the CATCH rule from 2010 [2] and the PECARN rule from 2014 [3]. The imaging modality of choice is a non-contrast head CT. There may be a role for skull radiographs in children under 2 years of age, but not in older children [4]. MRI is currently not yet established as an initial imaging evaluation. Here, we assessed how frequently skull radiographs were inappropriately ordered across our pediatric health care network in children with head trauma over the age of 2 years between 2012 and 2015 and whether the implementation of the PECARN clinical criteria in 2014 had any effect on ordering practices.
Materials and Methods
The study was performed at a dedicated academic children's hospital that serves as a level I trauma center. We used a commercial search tool (Montage Health Solutions Inc., California, USA) to search reports in the radiology information system by study type skull radiograph in children of ages 2-18 years from January 2012 through December 2015. We identified all patients who had a trauma history by using the following Medical Subject Headings (MeSH): Trauma, injury, injuries, wound, fall, MVC, MVA, vehicle, accident, collision, traffic, pedestrian, struck, assault. We included histories of a new or recent "swelling" or "bump" on the head, and excluded any chronic "swelling", "bump", or mass. In children under the age of 2 years, all skull radiographs for a trauma history were rated as "appropriate". In children with trauma who were older than 2 years, skull radiographs were rated as "inappropriate". We analyzed the ratio of "appropriate" to "inappropriate" skull radiographs over time and by ordering provider names and health care facilities.
Results
3746 skull radiographs were performed between January of 20012 and December of 2015. Of these, 2353 (63%) were classified as appropriate and 1393 (37%) were classified as inappropriate. After publication of the PECARN rule in 2014 there was no decrease of skull radiographs performed in children with head trauma. Skull radiographs were ordered from 91 different locations within our affiliated facilities, including emergency rooms, clinics, and outpatient centers. 2608 (70%) skull radiographs were ordered as outpatient exams and 953 (37%) of these were classified as "inappropriate". The emergency room ordered 861 (23%) skull radiographs and 417 (48%) of these were classified as "inappropriate". There were only 277 (7%) inpatient orders for skull radiographs, of which only 23 (8%) were rated as "inappropriate". There were 688 different ordering providers for skull radiographs. Of these, 26 providers had ordered more than 10 skull radiographs and more than 50% of these radiographs were classified as "inappropriate".
Conclusions
Our results show that existence of clinical decision rules does not automatically lead to improved ordering practice. Simple search tools and data analysis can help describe the

magnitude of inappropriate imaging utilization. We conclude from our data that our system would benefit from targeted provider education [5] to achieve a higher percentage of appropriate skull radiograph orders in children with head trauma.

eP-112

6:30AM - 3:00PM

NSsaFe: Observational Study on the Incidence of Nephrogenic Systemic Fibrosis in Patients with Renal Impairment Following Gadoterate Meglumine Administration

j frabizzio[1]
[1]*Abington/Jefferson Health System, abington, PA*

Purpose
To determine the incidence of nephrogenic systemic fibrosis (NSF) in patients with renal impairment after administration of the macrocyclic contrast agent gadoterate meglumine (Dotarem®, Guerbet, France).
Materials and Methods
This worldwide postmarketing study included 540 patients with at least moderate renal impairment (eGFR <60 ml/min/1.73 m2) scheduled to undergo a routine contrast-enhanced magnetic resonance imaging (MRI) using gadoterate meglumine. Medical history, MRI indication(s) and adverse events (AEs) were recorded for each patient. Patients were followed up over 2 years after gadoterate meglumine administration with 3 visits separated by at least 3 months in order to detect any signs of NSF. In case of suspicion of NSF, a biopsy was performed for confirmation.
Results
Among the 540 patients [mean age: 69.6 years (min-max: 21-95); men: 58.5%], renal impairment was evaluated as moderate for 69.3% of patients, severe for 16.1% and end-stage for 12.0%; 2.6% of patients had undergone a previous kidney transplant. Mean eGFR was 37.6 ± 15.7 ml/min/1.73 m2 (4.0-74.2). Main MRI indication was to assess suspected abnormalities of the central nervous system (34.6%). As of 1st September 2016, 434 patients (97.3%) attended the first follow-up visit (between 3 and 12 months after MRI), 343 (76.9%) attended the second (between 13 and 21 months) and 247 (55.4%) attended the third (between 22 and 27 months). Neither AE considered to be related to the administration of gadoterate meglumine, nor NSF suspicion were reported.
Conclusions
Intermediate data of the NSsaFe study show no cases of NSF during 2 years of follow up after gadoterate meglumine administration, confirming its good safety profile in the high risk population of patients with renal impairment.

Long Beach Convention Center, Exhibit Hall B-(Lower Level) eP

Electronic Scientific Poster (eP)-Spine

eP-114

6:30AM - 3:00PM

Differences in the Appearance of the Lumbar Endplates on STIR and T2-/T1-Weighted Images

O Ashikyan[1], B Vettiyil[2]
[1]*University of South Alabama, Fairhope, AL,* [2]*University of South Alabama, Mobile, AL*

Purpose
To compare STIR with T2/T1-weighted images in detecting abnormal endplate signal in patients presenting with back pain.
Materials and Methods
After obtaining IRB exemption, we retrospectively reviewed 50 routine clinical MR studies of patients with back pain. All patients underwent MRI on 1.5T or 3T scanners. All scans consisted of sagittal T1-weighted, T2-weighted and STIR sequences, and axial T2-weighted sequences. Patients with history of lumbar spine surgery, infection, or neoplasm were excluded from this study. We evaluated a total of twelve endplates in each patient from T12-S1 levels. We recorded whether abnormal signal was present on T1/T2, STIR or both sequences. Modic type was recorded for each endplate based on appearance on T2- and T1-weighted images.
Results
There were 24 male and 26 female patients with ages ranging from 25 to 85 years. Abnormal STIR signal in the endplates was seen in 22% of all endplates. Abnormal T2/T1 signal in the endplates was seen in 20.8% of all endplates. 4.7% of all endplates demonstrated abnormal signal only on STIR images. 5.2% of all endplates demonstrated abnormal signal only on T1/T2 weighted images. Overall, 8% of patients had abnormal findings only on STIR images, and 8% of patients had abnormal findings only on T1/T2 images. Abnormal STIR signal was present in 83.3%, 72.3% and 91.7% of endplates that demonstrated Modic type I, II and III changes, respectively.
Conclusions
STIR and T1/T2-weighted images provide complementary, but different information about integrity of endplates. Spine MRI protocols should be designed to include STIR and T1/T2-weighted images to maximize MR sensitivity for detection of endplate pathology.

eP-118

6:30AM - 3:00PM

Fluid-Signal Structures in the Cervical Spinal Cord on MRI in Chiari vs. Non-Chiari Patients

T Tomsick[1], L Wang[2], m zuccarello[3]
[1]University of Cincinnati Hospital, Cincinnati, OH, [2]University of Cincinnati Medical Center, Cincinnati, OH, [3]University of Cincinnati, Cincinnati, OH

Purpose
Hyperintense fluid-signal of the anterior median fissure (AMF) and hyperintense foci (HIF) resembling the central canal or the base of the AMF on cervical spine axial T2 MRI may be associated with a channel-like T2-hyperintense craniocaudad line (SL) on sagittal images, also simulating the central canal. We hypothesize these three structures are seen more frequently in Arnold-Chiari patients.
Materials and Methods
In this exploratory study, we recorded/compared the incidence/frequency of HIF, AMF, and SL in 25 Chiari patients and 25 age-matched controls examined with the same scanner. Incidence/frequency were compared to 356 other non-Chiari cervical MRI previously performed on multiple scanners.
Results
Incidence and frequency of HIF, AMF, and SL are listed in Table 1 for the 3 study groups. Increased incidence/frequency of SL,HIF, and AMF in Chiari patients compared to both the contemporaneous control group and to the earlier study group was identified. HIF and AMF were increased in the non-Chiari control compared to a previous cervical MR scan population, while SL incidence was similar.
Conclusions
The increased frequency of HIF, AMF, and SL in the Chiari population identified in this exploratory analysis is consistent with a hydrodynamic pressure effect created by CSF pulsatile dynamics. Whereas our earlier study had suggested that AMF and HIF are structurally related with the HIF commonly the base of the AMF, we hypothesize that AMF also contribute to the increase incidence of SL in the Chiari population. While such thin channels are usually ascribed to the central canal, we believe some thin SL are not due to the central canal or hydromyelia, but rather the base of the AMF.

	HIF		AMF		SL (%)
	%	HIF/Pt	%	AMF/Pt	
Chiari (n=25)	100%	8.5*	96%	4.0**	14 (56%)***
Control (n=25)	96%	3.9*	88%	2.7**	7 (28%)***
Previous Study (n=356)	65%	3.7	60%	2.3	89/358 (24.8%)

* p=0.0004 ** p=0.04 *** p=0.02

(Filename: TCT_eP-118_Slide1.jpg)

eP-115

6:30AM - 3:00PM

Impact of Needle Parameters on the Measurement of Opening Pressure with Lumbar Puncture

J Dubé[1], m Belair[2], F Ameur[2], D Landry[1]
[1]*University of Montreal, Montreal, Quebec,* [2]*CHUM, Montreal, Quebec*

Purpose
Fluoroscopically guided lumbar puncture commonly is performed in neuroradiology. There is a trend toward using smaller needles (e.g., 25 gauge) when performing lumbar punctures because of concern for postdural puncture headache. The purpose of this study was to

evaluate the technical impact of higher gauge needles on cerebrospinal fluid (CSF) pressure measurements with respect to the time required to obtain an accurate measurement.

Materials and Methods

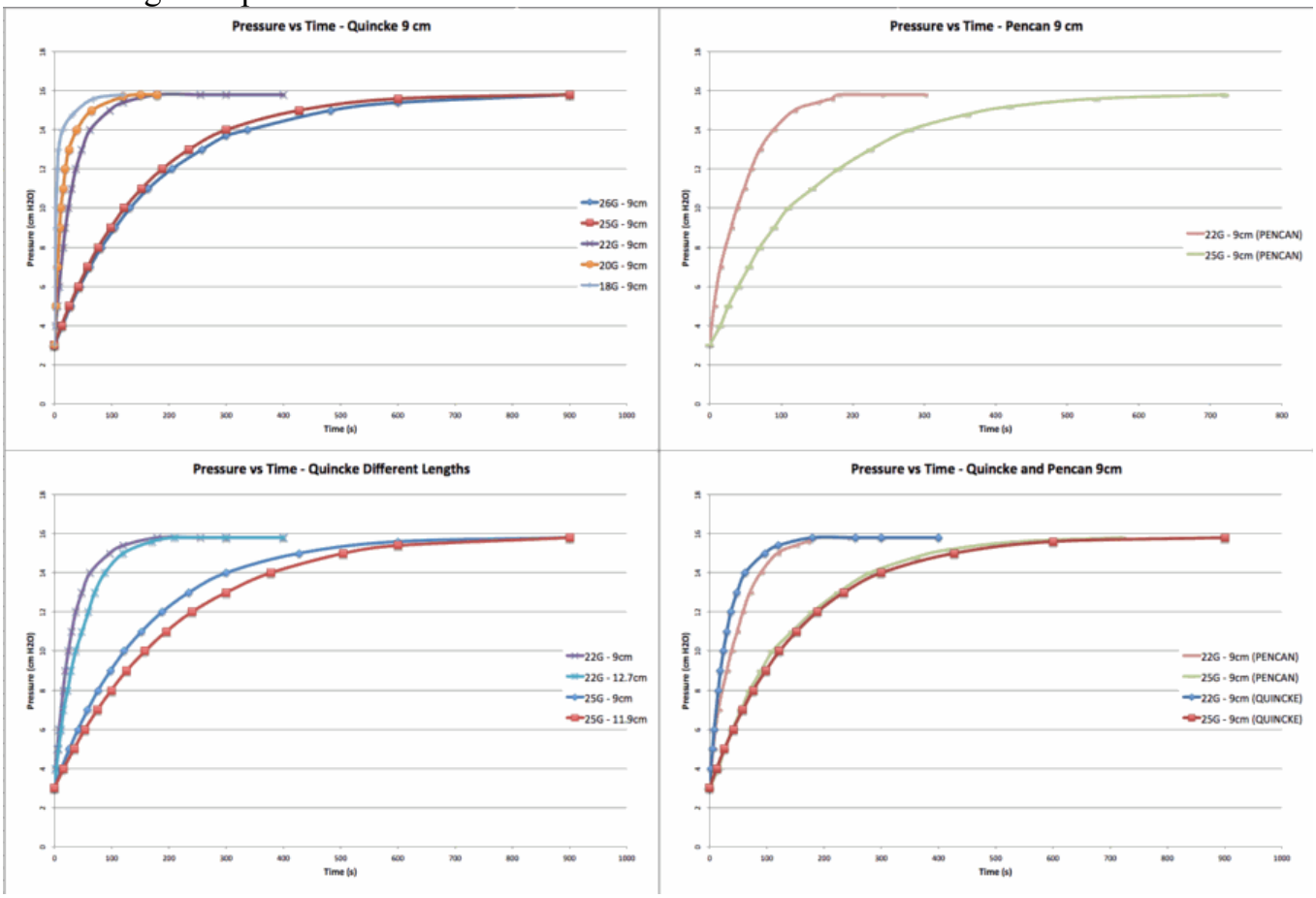
An apparatus was constructed to replicate a patient's opening pressure measurement using a 500mL bag of 0.9% sodium chloride, with a constant pressure applied on the bag, to produce a pressure corresponding to normal cerebrospinal fluid opening pressure (CSF-OP) in a patient. Several needle gauges (18, 20, 22, 24, 25 and 26G) and lengths (9, 10.3, 11.9 and 12.7cm) were tested of Quincke and Pencan type. For each needle, several pressure values were obtained at varying points in time to create a pressure-time plot. The time required to obtain 67% and 99% of the final pressure values subsequently were interpolated from the data.

Results

The largest difference in pressure read-out during this study resulted from different needle gauges. For example, it took 132 seconds to obtain 99% of the final pressure value using the 9cm 22G Quincke, whereas the 9cm 25G Quincke required 571 seconds. The needle length and tip profile yielded only small differences in the pressure-time profile curves.

Conclusions

Our study reveals that needle gauge, when performing spinal taps, is an important factor influencing CSF pressure read-outs.



(Filename: TCT_O-321_GraphicsASNR.gif)

eP-119

6:30AM - 3:00PM

Prospective Assessment of Brain Iron Deposition and Cognitive Performance in Older Women with Breast Cancer Receiving Adjuvant Chemotherapy

Purpose

Brain iron deposition has been proposed as potentially responsible for neural and cognitive impairment in aging and neurodegenerative disease (1, 2). Some patients with breast cancer suffer from subjective and objective cognitive deficits during and after chemotherapy, colloquially termed "chemobrain" (3, 4). We hypothesize that brain iron deposition may play a role in chemotherapy associated cognitive decline in cancer patients. The purposes of this study are 1. To assess the brain iron deposition in older patients receiving adjuvant chemotherapy and age- and sex-matched healthy controls. 2. To correlate susceptibility values of brain iron to neuropsychological testing scores.

Materials and Methods

This is a prospective longitudinal study of women aged ≥ 60 years with stage I-III breast cancers receiving adjuvant chemotherapy. Fourteen patients aged 68+/- 5.15 years underwent neuropsychological testing with the NIH Toolbox (5) for cognition and brain magnetic resonance imaging (MRI) prior to chemotherapy at time point 1 (TP1), and again 1 month after completion of chemotherapy at time point 2 (TP2). Thirteen age-matched healthy controls (HC) aged 65.4+/-5.86 years underwent the same assessments. All brain MRI scans were performed on the same in-house Siemens 3T Verio magnet (Siemens, Erlangen, Germany). The scanning protocol included 3D T1-weighted imaging, 3D T2-weighted FLAIR, and susceptibility-weighted imaging (SWI). Susceptibility-weighted imaging phase images were used to generate the susceptibility maps. The magnetic susceptibility of 7 deep gray matter nuclei was measured. Unpaired student t-test was used to determine if there were any group differences between the healthy controls and patients as well as the paired student.

Conclusions

Our study shows strong correlation of brain iron deposition with age as seen the upward linear extension of the susceptibility-age reference data established in the literature. We concluded that brain iron deposition was not significantly altered by adjuvant chemotherapy in short-term setting. It also has shown that older healthy adults do not have significant changes in brain iron deposition within a short period of time (3 – 6 months). Significant correlations between the susceptibilities and the neuropsychological test scores suggest the iron contents in the deep gray matter nuclei might play a role in the tested cognitive brain functions. The higher brain iron content in the measured nuclei predicts lower cognitive testing scores. There is stronger negative correlation between brain iron content and

cognitive scores in healthy controls than the patients undergoing adjuvant chemotherapy. The less correlation in the chemotherapy group suggests that patients undergoing chemotherapy have a different response or mechanism than the healthy controls. The susceptibilities in substantia nigra are correlated with the most types of the test scores, suggesting its importance in the tested brain function. It is interesting to notice that there is hemisphere specificity in the correlations. Red nucleus, for example, the susceptibilities in the left side is significantly correlated with three test scores, but none for the right side. This study is funded by NIH/NIA grants: R03 AG045090-02 (CHEN) and R01 AG037037-01A1 (Hurria). ClinicalTrials.gov (NCT01992432). Key words: chemotherapy, cognition, quantitative mapping, brain iron susceptibility.

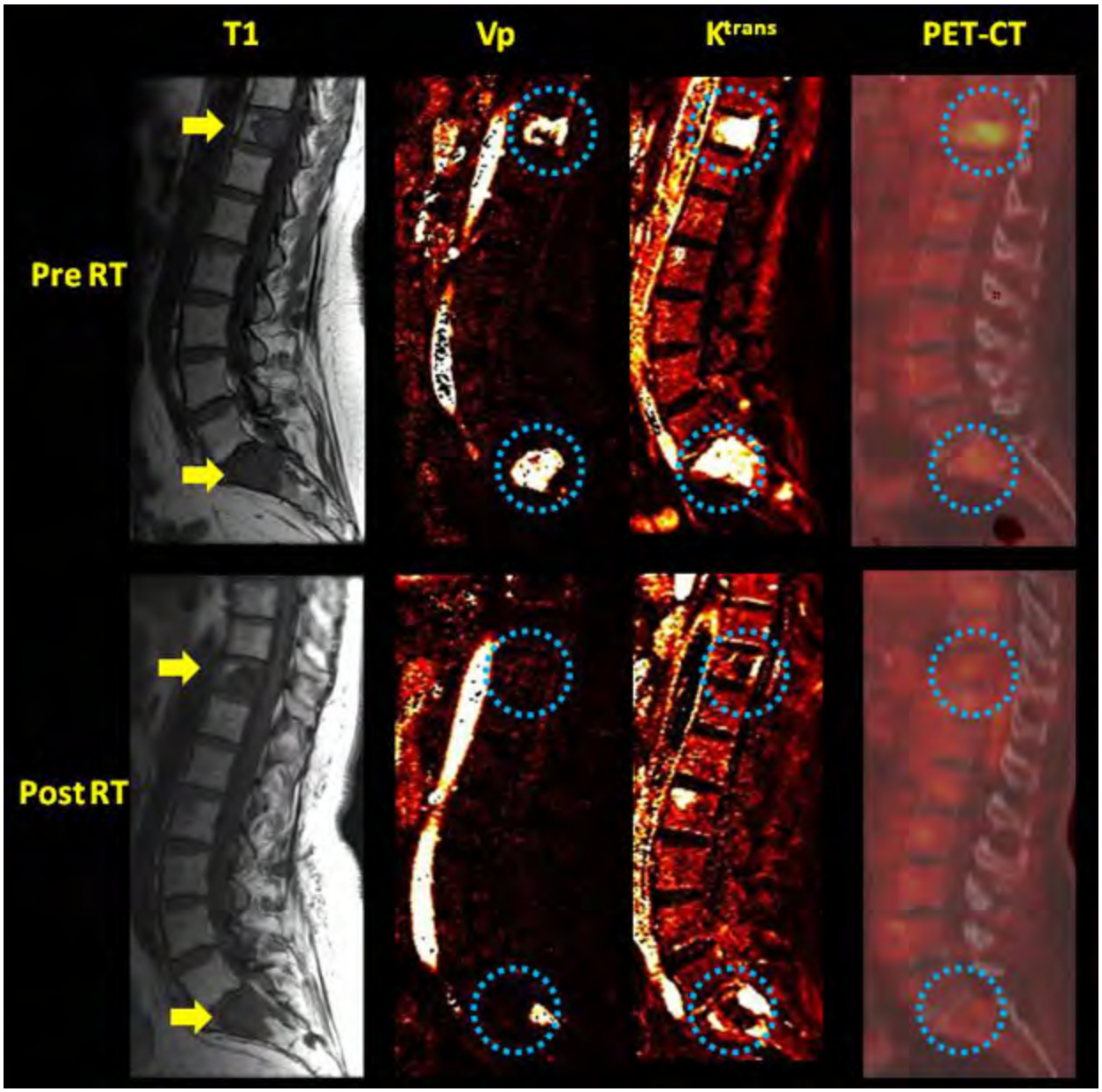
eP-116

6:30AM - 3:00PM

Role of DCE MRI and 18F-FDG PET-CT as Imaging Biomarkers to Evaluate Response to Radiation Therapy in Patients with Spine Metastases

J Arevalo-Perez[1], J Lyo[1], K Peck[1], R Fatovic[1], A Holodny[2], J Osborne[1], S Karimi[1]
[1]Memorial Sloan-Kettering Cancer Center, New York, NY, [2]Memorial Sloan-Kettering Cancer Center, Weill Medical College Of Cornell Univ., New York, NY

Purpose
To evaluate response to radiation therapy using T1-W DCE magnetic resonance imaging (MRI) and F18-FDG PET-CT in patients with spine metastases.
Materials and Methods
Ten patients with a total of 21 metastatic lesions to the spine who were treated with radiation therapy underwent evaluation with DCE-MRI and F18-FDG PET-CT both pre and postradiation therapy. Changes in perfusion metrics, including Ktrans, Vp, and SUV were measured. Percent change and U-tests were used to compare groups. $P<0.01$ was considered statistically significant.
Results
Quantitative perfusion parameters, Vp max and Ktrans max, and SUV max measurements were decreased significantly ($p<0.01$) after radiation therapy as compared to baseline scans (68.6%, 33.8% and 44.5%, respectively). SUV measurements decreased in 21 lesions (100%), Vp decreased in 20 lesions (95.2%) and Ktrans decreased in 18 lesions (85.7%). Vp was the only parameter that was able to detect local progression with 100% accuracy.
Conclusions
Our results show that perfusion parameters, Vp and Ktrans, and PET SUV measurements are optimal imaging biomarkers for the assessment of radiation treatment response. Vp stands out as the best physiologic biomarker for treatment evaluation and early recurrence.



(Filename: TCT_eP-116_Fig1.jpg)

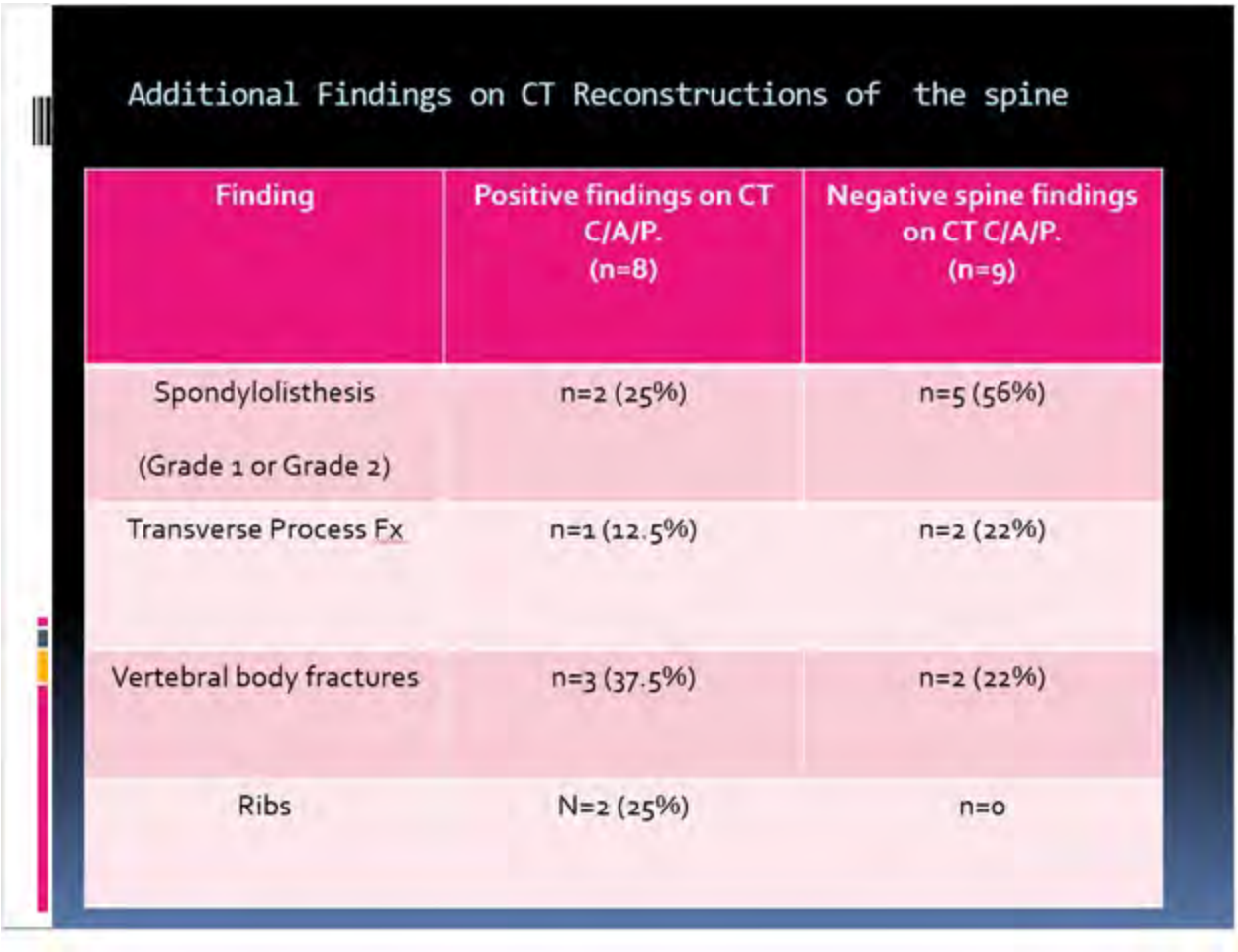
eP-117

6:30AM - 3:00PM

Utility of Obtaining Thoracic and Lumbar Spine Reconstructed Images in the Setting of Trauma

I Russell[1], G Patel[2], Y Rivaud[1], S Slasky[2]
[1]Rutgers-New Jersey Medical School, Newark, NJ, [2]Rutgers- New Jersey Medical School, Newark, NJ

Purpose
To assess the clinical benefit of obtaining reformatted images of the thoracic and lumbar spine from computed tomography of the chest, abdomen, and pelvis (CT C/A/P) in the setting of trauma by ascertaining the value of additional information gathered from these additional images.
Materials and Methods
In our inner city, level I trauma center, all patients who had trauma CT C/A/P from July 2014 - February 2015 with subsequent CT reconstructions of the thoracic or lumbar spine were included. Patients with pathologic fractures were excluded. The protocol for trauma CT C/A/P included a sagittal reformation of the data set with 5 mm slice thickness. The spine reconstruction protocol included 1.25 mm axial small field of view, and 1 mm sagittal and coronal reconstructions. Reports from the CT C/A/P and the CT reconstructions were reviewed for discrepancies, which then were categorized as to how they affected clinical management.
Results
One hundred forty-two patients were evaluated. Of the 90 patients who had no traumatic spine findings on the CT C/A/P, 9 (10%) had additional findings on the reconstructions. Of the 52 patients who had traumatic spine findings on the CT C/A/P, 5 (10%) were found to be false positives and 8 (15%) had additional findings on the reconstructions. When clinically insignificant findings were excluded, only 5 (3.5%) of 142 patients had additional findings on the reconstructions.
Conclusions
In trauma, if the CT C/A/P is negative for thoracic and lumbar spine injury, there is limited utility of spinal CT reconstructions. When additional findings were identified on the reconstructions, the vast majority were clinically insignificant. CT reconstructions of the thoracic and lumbar spine may have specific utility in certain situations, however, their role in trauma evaluation needs to be further investigated with a larger cohort and a prospective, controlled environment.



(Filename: TCT_eP-117_image.jpg)

Monday
6:30AM - 3:00PM
Long Beach Convention Center, Exhibit Hall B-(Lower Level) P

Scientific Poster(P)-Print-Adult Brain

P-06

6:30AM - 3:00PM

7T Brain MRS in HIV Infection: Correlation with Neuropsychological Test Performance

M Mohamed[1], P Barker[1], R Skolasky[1], C Munro[1], N Sacktor[1]
[1]*Johns Hopkins University School of Medicine, Baltimore, MD*

Purpose
Previous brain magnetic resonance spectroscopy (MRS) studies at 1.5 and 3T have shown alterations in the neuro-metabolic profile in HIV+ patients (1, 2, 3). Higher magnetic field

such as 7T provides increased sensitivity, better signal to noise ratio and more reliable measure of the metabolite concentrations. The purpose of this study is to explore the utility of 7T brain metabolite measures as biomarkers for the assessment of cognition and neuropsychological performance (NP) in HIV+ patients.

Materials and Methods

Forty-five HIV+ patients [mean age is 58.9 years ± 5.3 SD; 33 (73%) were male] were included in this study and were stratified according to their HIV associated neurocognitive disorder (HAND) using the Frascati criteria (4). The patients underwent neuropsychological (NP) testing including the Trail Making Test, Grooved Pegboard Test, Digit Symbol, Stroop Test, and Hopkins Verbal Learning Test. 21 HIV+ patients were classified as having symptomatic cognitive impairment [mild neurocognitive disorder (MND) and HIV associated dementia (HAD)] and 24 HIV+ were classified as asymptomatic cognitive impairment [normal cognition and asymptomatic neurocognitive impairment (ANI)]. Unlike symptomatic HAND, the cognitive impairment in ANI does not interfere with everyday functioning, although it also is characterized by cognitive impairment in at least two domains (4). All patients were receiving combination antiretroviral therapy (cART). Using a 7.0T Philips Achieva scanner and 32-channel head coil, brain MRI and single voxel STEAM spectra (TR/TE=3000/14 msec) were acquired from the left frontal white matter (FWM) (Figure), basal ganglia (BG), precuneus (PC), posterior cingulate cortex (PCC) and hippocampus (Hippo) with and without water suppression. The voxel sizes ranged from 8 to 15 cc. Spectra were analyzed using LCModel (5) and quantified in institutional units (i.u., approximately mM) relative to the unsuppressed water signal. Metabolite concentrations and ratios relative to creatine (Cr) were calculated for the 2 groups. Concentration and ratio values were included only if their Cramér-Rao lower bounds (CRB) were 20% or less (5). The data were not normally distributed; therefore, comparisons of the groups' medians and interquartile (IQR) ranges were evaluated for significant differences using a nonparametric median test. Pearson correlations were performed between the metabolites and NP tests. Significance was set at $P< 0.05$.

Results

Metabolite concentrations showed a trend towards significance in the median FWM total N-acetyl aspartate (tNAA) which was lower in the MND group than the ANI group (7.46 vs. 7.81 mM respectively, P=0.06) as well as differences in the median NAA/Cr (1.21 vs. 1.30 respectively, P=0.005), the median tNAA/Cr (1.46 vs. 1.56 respectively, p=.005) and the median myo-inositol/Cr (mI/Cr) (0.97 vs. 1.03 respectively, P=0.02). In the posterior cingulate, there was a difference in median NAA/Cr between the MND vs. ANI groups (1.16 vs. 1.21 respectively, P=0.01), median tNAA/Cr (1.32 vs. 1.40 respectively, P=0.02), and median mI/Cr (0.78 vs. 0.87 respectively, P=0.002). In the precuneus, there were differences in median NAA/Cr between the symptomatic vs. asymptomatic cognitive impairment (1.14 vs. 1.23 respectively, P=0.02) and median glutamate/Cr (Glu/Cr) (1.12 vs. 1.24 respectively, P=0.01). There were no differences in basal ganglia or hippocampus metabolite ratios. In regards to performance on NP tests, lower FWM tNAA/Cr was associated with worse

performance on measures of executive function, fine motor, and psychomotor speed (Trail Making Test, part B, Grooved Pegboard Test, nondominant hand, and Digit Symbol (P= 0.005, 0.01 and 0.001, respectively). Furthermore, lower FWM Glu/Cr was associated with lower performance on delayed recall on the Hopkins Verbal Learning Test (P=0.02). Lower tNAA/Cr in the posterior cingulate was associated with worse performance on tests of psychomotor speed (Digit Symbol and Stroop Test, P= 0.02 and 0.04 respectively). Lower precuneus NAA/Cr was associated with worse performance on the Stroop Test, a test of processing speed (P=0.04); while precuneus Glu/Cr decreases was associated with worse performance in the Trail Making Test Part B, a measure of executive functioning (P=0.04).

Conclusions

In agreement with previous studies, our study showed impaired neuronal integrity across the white and gray matter regions as reflected by the decreased NAA/Cr and Glu/Cr in HIV patients with symptomatic cognitive impairment. Interestingly, this study showed that FWM Glu levels were related more to verbal memory function; the precuneus NAA was more related to processing speed, and the posterior cingulate NAA was more related to executive functioning. In conclusion, 7 Tesla MRS measurements of NAA and Glu are useful indicators of neuronal loss and cognitive dysfunction in patients with HIV infection.

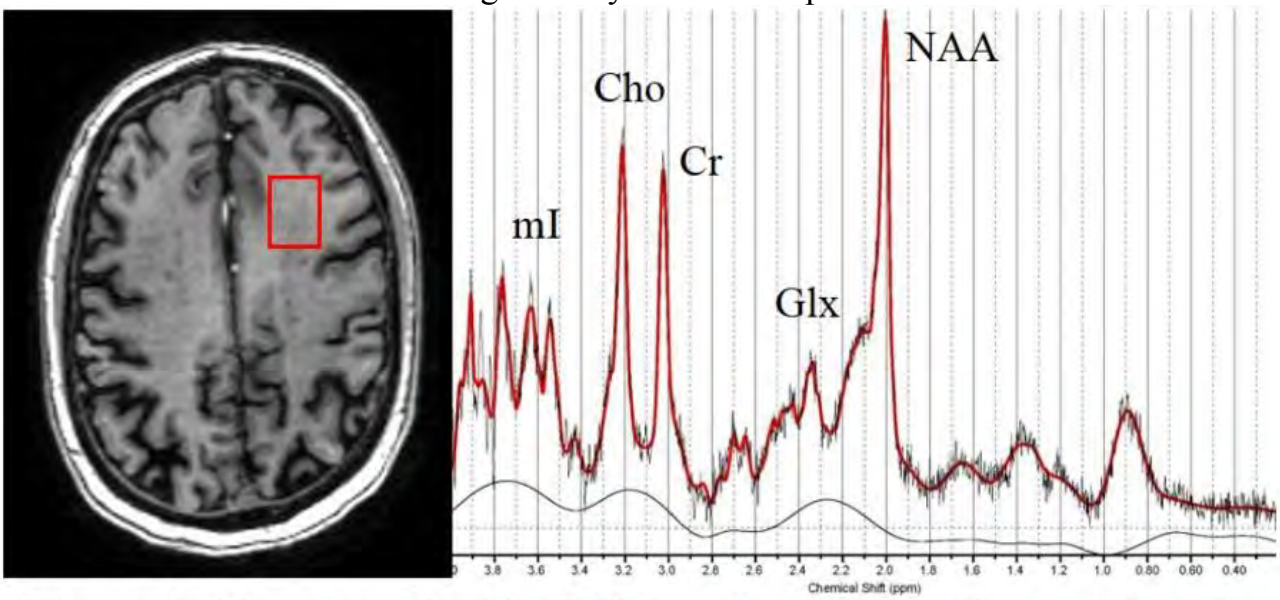


Figure: A 55 years old white HIV+ male patient with asymptomatic neurocognitive impairment (ANI) showing left FWM voxel location and its corresponding spectrum.

(Filename: TCT_P-06_Picture4.jpg)

P-02

6:30AM - 3:00PM

7T MRS on Multiple Brain Metabolites in the First Episode Psychosis: Neuronal Impairment and Neurotransmitter Abnormalities

M Wang[1], S Pradhan[1], A Marsman[1], D Schretlen[1], A Sawa[1], P Barker[1]
[1]*Johns Hopkins University School of Medicine, Baltimore, MD*

Purpose

To investigate neurochemical changes using 7 Tesla MRS in patients with a first episode of psychosis (FEP) and healthy control subjects, and to correlate with a battery of neuropsychological evaluations.

Materials and Methods

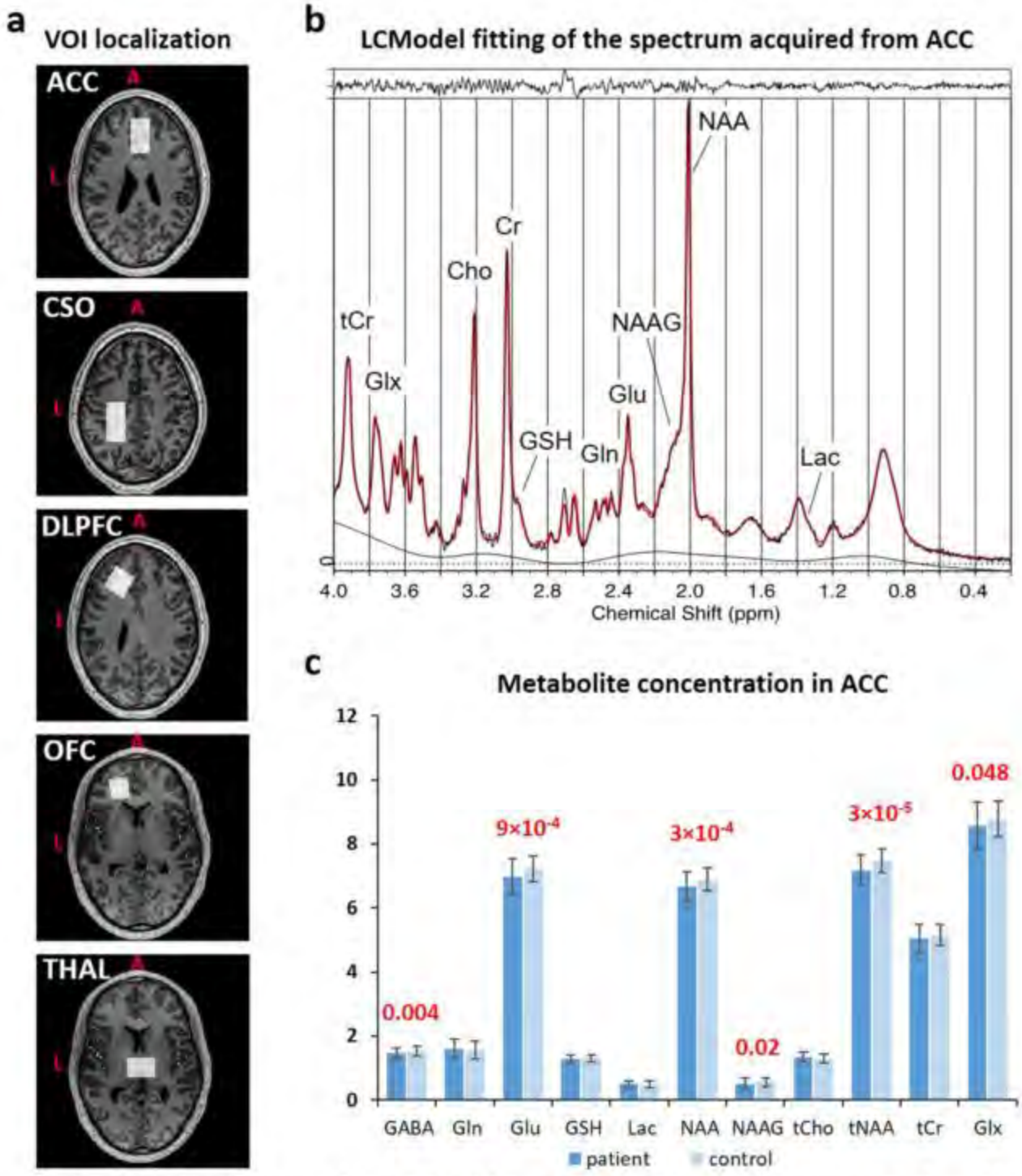
Seventy-five FEP patients (age: 22.2±4.5 years; 53 males) and 94 healthy controls (age: 23.5±4.0 years; 44 males) have been recruited to date. First episode of psychosis patients were evaluated within 2 years after disease onset, and were on antipsychotic medications. All subjects underwent neuropsychological testing [Calibrated Neuropsychological Normative System (CNNS)]. Spectra were recorded from five brain regions (Figure 1a) on a 7T scanner (Philips 'Achieva', Best, Netherlands) using the STEAM sequence (TE/TM/TR = 14/33/3000 ms) and were analyzed using the LCModel software package (1) (Figure 1b). Concentrations of gamma-aminobutyric acid (GABA), glutamate (Glu), glutamine (Gln), glutathione (GSH), lactate (Lac), N-acetylaspartate (NAA), N-acetylaspartylglutamate (NAAG), total choline (tCho), total NAA (tNAA), total creatine (tCr) and the sum of Gln and Glu (Glx) were compared between patients and controls using two-tailed unpaired t-tests. Linear regression was performed between metabolite concentrations and CNNS scores.

Results

A decrease of the neuronal marker NAA (and/or tNAA) was found in all 5 brain regions in the FEP patients, suggesting significant neuronal loss or dysfunction. No significant tissue loss was detected in the anatomical images. In FEP patients, Glx and GABA concentrations significantly decreased in ACC and GSH decreased in THAL while after normalizing by creatine concentration, the glutamine level increased in ACC, CSO and DLPFC (Figure 1c). The CNNS scores were positively correlated with the NAA, tNAA, tCho and GABA levels.

Conclusions

Metabolite levels measured by 7T MRS suggest neuronal damage or dysfunction, and disrupted glutamatergic metabolism in multiple brain regions. Correlations with CNNS scores indicate that these metabolic changes may be associated with deficits in neuropsychological performance.



(a) T_1 weighted images from a healthy subject. White boxes represent the MRS volume of interests (VOIs) of the five brain regions: anterior cingulate cortex (ACC), left centrum semiovale (CSO), left dorsolateral prefrontal cortex (DLPFC), left orbitofrontal cortex (OFC), and bilateral thalamus (THAL). (b) Typical LCModel fitted spectrum from ACC. (c) The summary of metabolite concentrations in ACC in FEP patients and healthy controls. The significant differences ($p<0.05$) were highlighted with the p-value provided above the bar.

(Filename: TCT_P-02_Picture1.jpg)

P-42

6:30AM - 3:00PM

A Comparison of Three Volumetric Software Platforms for Lesion Core Analysis in Ischemic Stroke Patients

S O'Donnell[1], A DeHavenon[2], J McNally[1], L Chung[1], K Mickolio[1], M Peckham[1]
[1]University of Utah, Salt Lake City, UT, [2]Univerity of Utah, Salt Lake City, UT

Purpose
Quantifying lesion core volume in acute ischemic stroke (AIS) is important when deciding on acute intervention such as mechanical thrombolysis. Computed tomography perfusion (CTP) is able to measure lesion core volume, but methods differ. Our aim was to assess the ability of 3 common software platforms to predict clinical and radiologic outcome.
Materials and Methods
We included acute ischemic stroke (AIS) patients from 2010-2014 with CTP and middle cerebral artery (MCA) occlusion. Computed tomography perfusion lesion core was measured with the Olea Sphere (Figure 1), OsiriX, and Siemens syngo.via software using manufacturer recommended settings. Magnetic resonance imaging (MRI) lesion core was measured using Olea Sphere software for patients with MRI 1-3 days from stroke onset. A multivariable ordinal logistic regression was fit to modified Rankin Scale (mRS) at follow-up. The 3 CTP lesion core measurements were compared to MRI lesion volume using linear regression and a correlation coefficient.
Results
We included 61 patients of which 24 also had MRI. The mean±SD age was 61±18 years and 61% were male. Mean NIH Stroke Scale was 14.1±8.0 and median (IQR) follow-up modified Rankin Scale was 3 (1,6). Median days to follow up were 84 (66,125). In the ordinal logistic regression model, all 3 CTP and the MRI volumetric measurements of lesion core correlated well with follow-up mRS (Table 1). All 3 CTP lesion cores underestimated follow-up MRI lesion core (Table 2).
Conclusions
Many stroke centers routinely use CTP to estimate lesion core when deciding whether an AIS patient is eligible for mechanical thrombolysis. This study showed that three CTP volumetric software platforms underestimated follow-up MRI lesion core, but that CTP volumetric analysis is a good predictor of clinical outcome. This underestimation may reflect interval growth of the core, through conversion of peri-infarct ischemia to infarct. Continued tissue infarction after initial infarct represents a potential therapeutic target in future studies.

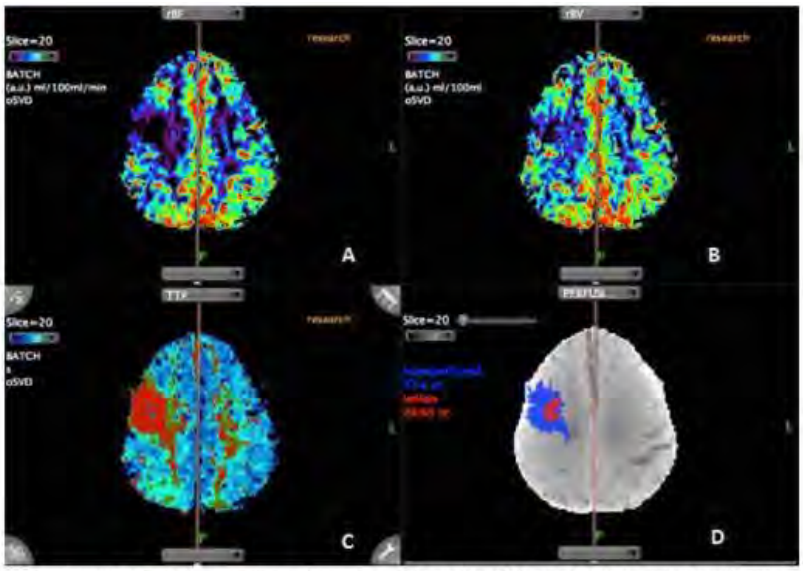


Figure 1: CTP Olea Sphere analysis of a patient with a right middle cerebral artery stroke, showing cerebral blood flow (A), cerebral blood volume (B), time to peak (C) and automated threshold-based volumetric data, with lesion core in red and hypoperfused area in blue (D).

Table 1: Ordinal logistic regression model with odds ratios for a one point increase in follow-up mRS per 10mL shift in CTP and MRI lesion core volume, adjusted for confounders that had p<0.2 in univariate logistic regression.

	Odds Ratio (for one point increase in mRS)	p value
Olea Sphere CTP lesion core (per 10mL increase)*	1.21	0.010
OsiriX CTP lesion core (per 10mL increase)*	1.22	0.002
Siemens CTP lesion core (per 10mL increase)*	1.39	<0.001
Olea Sphere DWI MRI lesion core (per 10mL increase)† (n=24)	1.21	0.018

* Adjusted for patient age, admission NIH stroke scale, history of atrial fibrillation, and hypertension.
† Adjusted for patient age.

Table 2: Linear regression model and correlation coefficient for the outcome of MRI lesion core volume, comparing the 3 CTP lesion core volumetric measurements in the 24 patients with MRI within 3 days of stroke onset.

CTP Volumetric Measure	Coefficient	Std. Error	p value for regression	Correlation coefficient
Olea Sphere CTP lesion core	0.75	0.33	0.033	0.44
OsiriX CTP lesion core	0.82	0.29	0.009	0.48
Siemens CTP lesion core	0.76	0.29	0.017	0.52

(Filename: TCT_P-42_ASNR_CTP_V20.jpg)

P-32

6:30AM - 3:00PM

A Novel Post-Processing Algorithm to Improve Detectability of Brain Hemorrhages in Flat Panel CT Images

J Yu[1], L Pung[2], L Larrabure[1], M Alexander[1], S Hetts[1], D Cooke[1]
[1]University of California, San Francisco, San Francisco, CA, [2]Siemens Healthcare, San Francisco, CA

Purpose
The current treatment protocol of acute ischemic stroke requires CT imaging to determine whether the patients will require endovascular intervention in the angiography suite. Biplane Flat-panel detectors (FP) offer the capability for clinicians to acquire angiography and cone-beam CT images interchangeably in the angiography suite which reduces transport time.

Postprocessing reconstruction algorithms for improving image quality of FP-CT images are under rapid development (1). An advanced postprocessing algorithm (BD) was developed recently to improve the detectability of brain hemorrhage. This algorithm focuses on correcting motion, homogenization and ring artifact, and noise reduction. This study aimed to compare image quality of FP-CT images reconstructed using BD to the FP-CT images reconstructed using a standard postprocessing algorithm (HC).
Materials and Methods
Noncontrast CT and FP-CT images reconstructed with BD and HC of 9 patients who underwent endovascular procedures admitted to our institution were reviewed retrospectively by 3 neuroradiologists. The raters scored the images on the presence or absence of hemorrhage. Using the scores of the noncontrast CT images as standard, sensitivity and specificity were calculated for FP-CT images reconstructed using BD and HC.
Results
BD and HC have an overall hemorrhagic detection sensitivity of 0.933 and 0.824, respectively, and a specificity of 1.00. For subdural hemorrhages (SAHs), BD and HC have a sensitivity 0.875 and 77.98, and a specificity of 1.00 and 0.917, respectively. For intraventricular hemorrhages (IVHs), BD and HC have a sensitivity 0.871 and 0.800, respectively, and a specificity of 1.00. For intraparenchymal hemorrhages (IPHs), BD and HC have a sensitivity 0.851 and 0.545, respectively, and a specificity of 1.00.
Conclusions
FP-CT images reconstructed using the advanced postprocessing algorithm (BD) have higher sensitivity and comparable specificity in detecting brain hemorrhages comparing to FP-CT images reconstructed using the standard postprocessing algorithm (HC).

P-44

6:30AM - 3:00PM

A Novel Voxel-wise Lesion Segmentation Technique on 3.0-T Diffusion MRI of Hyperacute Focal Cerebral Ischemia at 1-hour after Permanent MCAO in Rats

C Choi[1], S Cha[2], K Yi[1], J Kim[1]
[1]Chungbuk National University Hospital, Cheongju, Chungbuk, [2]Chungbuk National University Hospital, College of Medicine and Medical Research Institute, Cheongju, Chungbuk

Purpose
To present a novel lesion segmentation technique for hyperacute focal cerebral ischemia in rats on 3.0T diffusion MRI (DWI) to overcome substantial intra-, and inter-subject variations occurring across the multiple scans.
Materials and Methods
Our novel technique is as follows: 1) intensity normalization including determination of the

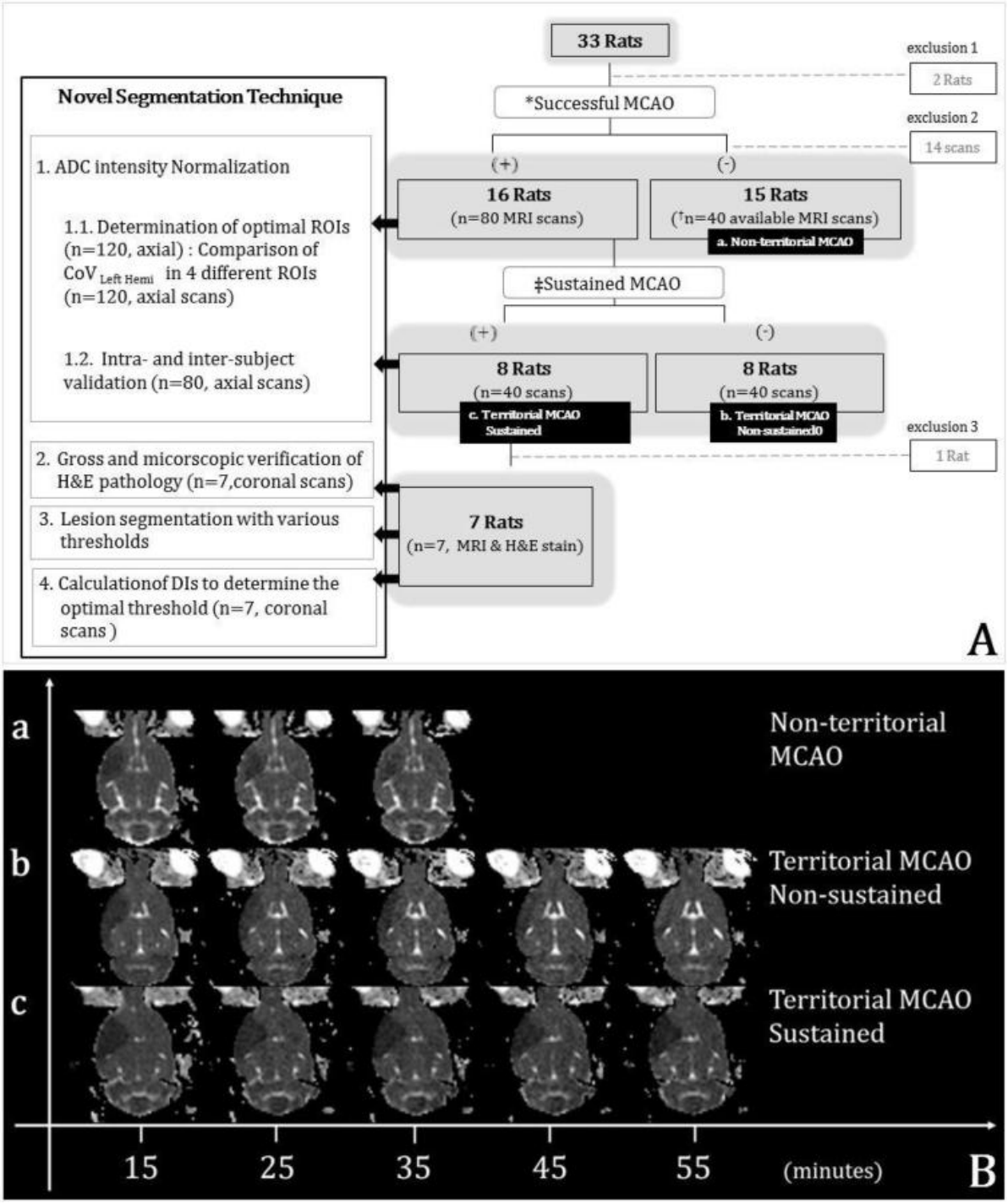
optimal type of region of interest (ROI) and its intra- and inter-subject validation; 2) verification of focal cerebral ischemic lesions at 1 hour with gross and high magnification light microscopy of hematoxylin-eosin (H&E) pathology; 3) voxel-wise segmentation on ADC with various thresholds; 4) calculation of Dice Indices (DIs) comparing focal cerebral ischemic lesions at 1 hour defined by ADC and matching H&E pathology to determine the optimal threshold.

Results

The best was coefficient of variation of mode of left hemisphere after normalization using whole left hemispheric ROI, and it showed lower intra- (2.54%±0.72) and inter-subject (2.67%±0.70) values comparing to the original before normalization (intra-subject, 5.60%±1.28; inter-subject, 6.74%±0.56). Focal ischemic lesion at 1 hour after MCAO was confirmed on both gross and microscopic H&E pathology. Eight-three relative threshold of normalized ADC showed the highest mean DIs (DI=0.820%, $p<0.01$) among others.

Conclusions

We could evaluate hyperacute ischemic lesions at 1 hour more reliably on 3-Tesla DWI in rat brains.



(Filename: TCT_P-44_photo_2016-12-10_09-22-45.jpg)

P-37

6:30AM - 3:00PM

Accuracy and Effectiveness of CTA and CTP in Acute Stroke

V Persaud[1], C Dani[1], M Aftab[2], B Manzer[3]

[1]Michigan State University - Flint Area Medical Education, Flint, MI, [2]Michigan State University College of Medicine, Flushing, MI, [3]MSU COM, East Lansing, MI

Purpose

Conventional nonenhanced CT (NECT) of the brain is the primary imaging modality used to evaluate patients presenting with symptoms of acute stroke, to help determine if there are contraindications to thrombolytic therapy. Computed tomography angiography (CTA) and computed tomography perfusion (CTP) are additional advanced imaging techniques that can be utilized in the evaluation of acute stroke. In particular, CTP is becoming increasingly more common as it allows for differentiation of salvageable ischemic penumbra from unsalvageable core infarct, in addition to helping diagnose acute brain ischemia, which may help clinicians identify which patients will benefit from thrombectomy or thrombolysis. Computed tomography angiography, on the other hand, helps pinpoint the exact location of acute thrombus in the intracranial vessels and if it is amenable to endovascular retrieval. Particular challenges to the diagnosis of acute stroke include patients who present with unknown time of onset or patients who are unresponsive. The purpose of our study was to evaluate the effectiveness of advanced stroke imaging in the setting of acute stroke. It was hypothesized that there is overutilization of advanced imaging in the setting of acute stroke and that the combination of NECT and CTA is sufficient for diagnosis of acute stroke in most cases.

Materials and Methods

A retrospective analysis of the radiologic data (NECT, CTA, CTP) from a total of 135 patients presenting clinically with acute stroke gathered from the last 200 days using PACS. There were a total of 65 male and 65 female patients in the study. The average age of the patients was 67 years old. Patients were made anonymous by being randomly assigned a number from 1 to 135. A total of 5 patients were excluded due to misidentification as stroke patients or absence of appropriate imaging. Parameters found in the patient history in PACS and recorded included: - Age, gender, symptoms, and time of examination. - Presence of absence of intracranial hemorrhage. - Ischemic penumbra. - Major vessel occlusion including middle cerebral artery (MCA) and basilar artery. Parameters found in the electronic medical record (EPIC) and recorded included the following: - Time from Stroke Onset to Advanced Imaging. - Tissue plasminogen activator (IV-tPA). - Endovascular therapy. - National Institutes of Health Stroke Scale (NIHSS) Score.

Results

The data depict that only a minority of patients (25%) had either one or both CTA or CTP positive for stroke despite presenting with stroke-like symptoms. The data was sorted into a predictive value table based on whether the CTA and CTP parameters were positive or negative. The positive predictive value (PPV) was 0.23 and the negative predictive value (NPV) was 0.97. The sensitivity was determined to be 0.67 and specificity 0.82. Additionally, the data from patients who received IV-tPA and CTP or CTA results (positive

or negative) were sorted into a predictive value table. It was determined that, the PPV was 0.57 and the NPV was 0.96. The sensitivity was 0.8 and the specificity was 0.89.
Conclusions
Upon review, we conclude that although CTA is the most appropriate study for assessment of retrievable clot for endovascular therapy, there were many cases (15) when CTA was negative and CTP was positive, which might be seen in the setting of partial territorial infarcts. It is suggested that CTP should only be performed in the real life setting of a community hospital emergency room with unresponsive patients, patients presenting with ambiguous clinical symptoms in which acute stroke is highly suspected or patients who present with unknown time of onset, as it can be useful in detection of acute stroke and guide therapy.

P-33

6:30AM - 3:00PM

Air Bubble Artifact Reduction in Post-mortem Whole Brain MRI: The Influence of Receive Bandwidth

M Scheffler[1], E Kovari[2], E Maturana[1], R Salomir[1], S Haller[3]
[1]Department of Radiology, Geneva University Hospitals, Geneva, Switzerland, [2]Department of Psychiatry, Geneva University Hospitals, Geneva, Switzerland, [3]Affidea Radiologists, Geneva, Switzerland

Purpose
Post-mortem brain magnetic resonance imaging (MRI) plays an increasingly important role in research, where validating studies are conducted that correlate radiological findings such as regional atrophy, ischemic lacunae, leucoaraiosis, strategic infarcts, and cerebral microbleeds (CBM) with those obtained in pathological analysis. However post-mortem MRI, and particularly whole brain studies, are subject to image degradation by air bubble artifacts - most dramatically seen on T2* or susceptibility-weighted imaging (SWI) imaging sequences - to a point where they may impede with a complete analysis of subcortical or paraventricular anatomical regions. We aimed to evaluate, through a double acquisition study, the influence of a higher receive bandwidth in the SWI sequence on the appearance of air bubble artifacts and detectability of CBM.
Materials and Methods
Post-mortem whole brain MRI was performed in ten cases (mean patient age at time of death, 84 years). Cerebral microbleeds were defined as focal hypointensities of ≤5 mm diameter on the SWI imaging sequence. We compared a standard SWI sequence with a receive bandwidth of 120 Hz/pixel to one using a broader bandwidth of 500 Hz/pixel. A neuroradiologist, blinded to the sequence, analyzed the processed SWI magnitude images for the presence of CMB and evaluated susceptibility "halo" artifacts created by air bubbles in

cortical sulci. Simultaneously obtained phase images were assessed for differences in phase contrast at the level of the same artifacts.
Results
Eight CMB were found, all clearly visible on both SWI sequences. On the phase images, air bubble artifacts in cortical sulci were identical in both sequences, butterfly-shaped and of mixed signal intensity, with a hyperintense component aligned with the main magnetic field. In contrast, the magnitude images displayed susceptibility "halo" artifacts which were smaller on the 500 Hz/pixel sequence than on the standard 120 Hz/pixel sequence, thus concealing less of the adjacent cortex and subcortical white matter.
Conclusions
In analyzing post-mortem whole brain specimens by SWI MRI, using a broader receive bandwidth of 500 Hz/pixel is useful in diminishing "halo" artifacts created by air bubbles, without compromising the sensitivity of detecting CBM. Further to ongoing research, the use of a higher receive bandwidth SWI sequence may be even more important in analyses focused on intracortical lesions, such as cortical microinfarcts.

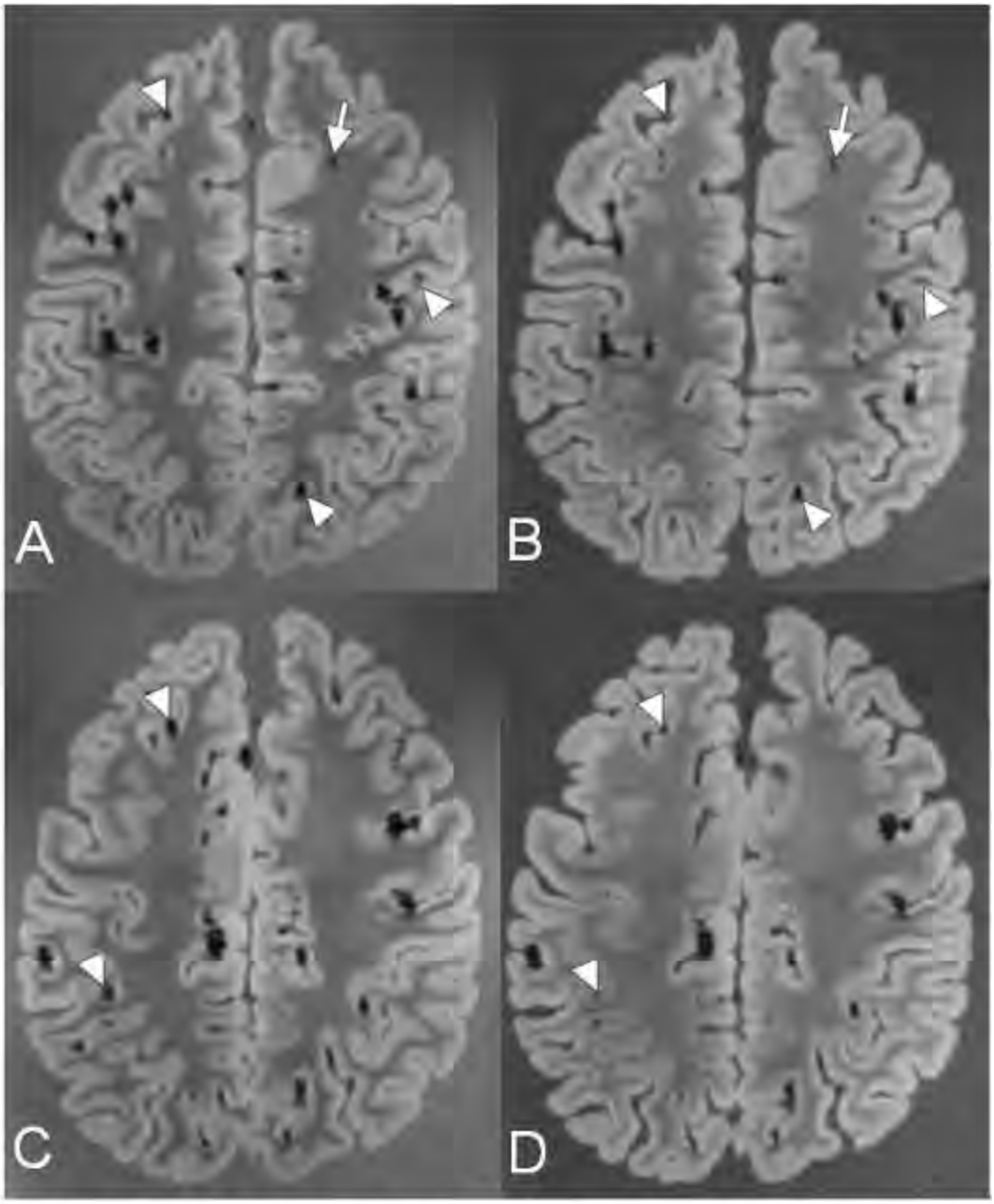


FIG 1. Post-mortem whole brain SWI MRI images of a 79-year-old man (at the time of death). Axial magnitude image acquired with a standard receive bandwidth of 120 pixel/Hz (*A*). A CBM is seen in the left frontal subcortical white matter (arrow). Air bubbles trapped in cortical sulci create "halo" artifacts (arrowheads). Axial image of the same patient at the same imaging level acquired with a broader bandwidth of 500 pixel/Hz (*B*) shows CBM remaining clearly visible (arrow). "Halo" artifacts created by air bubbles (arrowheads) are reduced, allowing for a better analysis of adjacent gray matter. Axial SWI image acquired at a slightly more caudal level with 120 pixel/Hz bandwidth (*C*) shows several cortical air bubbles trapped in frontal sulci (arrowheads). The same air bubbles create less pronounced artifacts on the corresponding 500 pixel/Hz bandwidth image (*D*, arrowheads).

(Filename: TCT_P-33_Figure1.jpg)

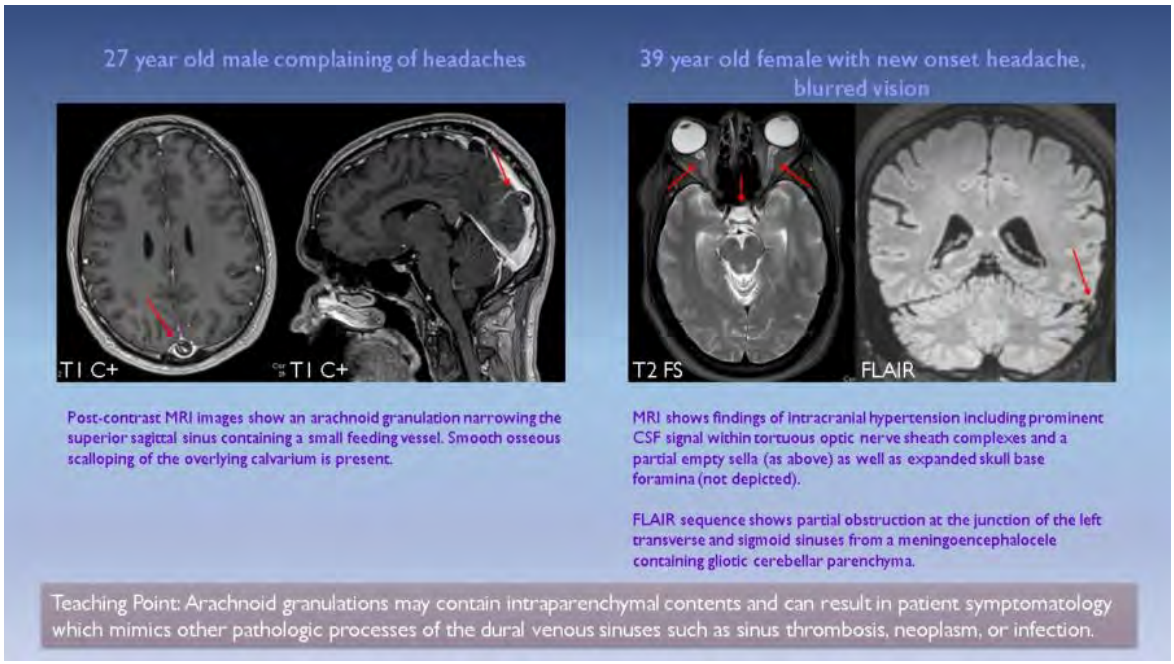
P-17

6:30AM - 3:00PM

Arachnoid Granulations - Not So Innocent

J McCambridge[1], C Cankurtaran[2], S Yoon[3]
[1]Einstein Medical Center, Philadelphia, Philadelphia , PA, [2]Einstein Healthcare Network, Philadelphia, PA, [3]Einstein Medical Center, Philadelphia, PA

Purpose
Arachnoid granulations (AGs) are cerebrospinal fluid (CSF) filled protrusions with a meningo-endothelial lining which extend from the subarachnoid space to the venous sinuses and function to filter CSF to the central venous circulation. Generally, AGs are benign structures; however, recent literature has shown that AGs can be symptomatic and mimic other pathologies of the venous sinuses. The purpose of this exhibit is to describe AGs, present cases in which AGs likely resulted in patient symptomatology, and describe imaging features that can differentiate symptomatic AGs from other pathology of the dural venous sinuses.
Materials and Methods
We present a case series on symptomatic and asymptomatic AGs as well as AGs that contain internal signal abnormality such as brain parenchyma or a feeding vessel. Additionally, we present cases in the differential diagnosis for dural venous sinus pathology including venous sinus thrombosis, trauma, neoplasm, and infection.
Results
Arachnoid granulations are projections of arachnoid villi from the subarachnoid space to the central venous sinuses that allow filtration of CSF into the central venous circulation. Arachnoid granulations occur in close relation to veins penetrating the dural venous sinuses and form a thin dural cap that allow for the passage of CSF. Arachnoid granulations are a common imaging finding occurring in roughly two-thirds of the population. Classically, AGs appear as focal outpouchings near the dural venous sinuses and are isointense to CSF on MRI. Rarely, AGs may contain brain parenchyma or a feeding vessel which have been postulated to cause symptoms indiscernible from other dural venous sinus pathology.
Conclusions
Arachnoid granulations are a common entity by imaging and generally have been considered benign; however, recent research has shown AGs to be symptomatic. Magnetic resonance imaging is a useful tool in characterizing AGs and can be utilized to distinguish symptomatic AGs from other etiologies which result in dural venous sinus symptoms.



(Filename: TCT_P-17_Slide1.JPG)

P-40

6:30AM - 3:00PM

Automated Computed Tomography Perfusion Software is Not Usefull in Evaluating Posterior Circulation Strokes

S Bergamaschi[1], M Law[1], R CORREIA[2], N Calixto[3], K Bezerra[4], P Kim[1], M Kim-Tenser[1], N Sanossian[1], A Amar[1]
[1]University of Southern California, Keck School of Medicine, Los Angeles, CA, [2]BRAIN STATE INSTITUTE PAULO NIEMEYER, RIO DE JANEIRO, CA, [3]Hospital das Clínicas da Faculdade de Medicina de Ribeirão Preto, Ribeirão Preto, SP, [4]Ribeirão Preto School of Medicine, Ribeirão Preto, SP

Purpose
Ischemic stroke is still a leading cause of death and disability worldwide. The selection of patients for intravenous or endovascular treatment remains a challenge. Computed tomography perfusion (CTP) is a technique that provides functional information about the perfusion of tissue, and may show patients with tissue at risk (penumbra), that could benefit from treatment. However, as is the case for conventional CT, the posterior fossa evaluation poses a significant technical challenge to CTP imaging. The purpose of this study was to evaluate the accuracy of an automated postprocessing software for CTP in the evaluation of posterior circulation strokes.
Materials and Methods
We selected patients with acute posterior circulation ischemic stroke, that underwent CTP postprocessed with RAPID software and MRI scan within 24 hours. The RAPID software

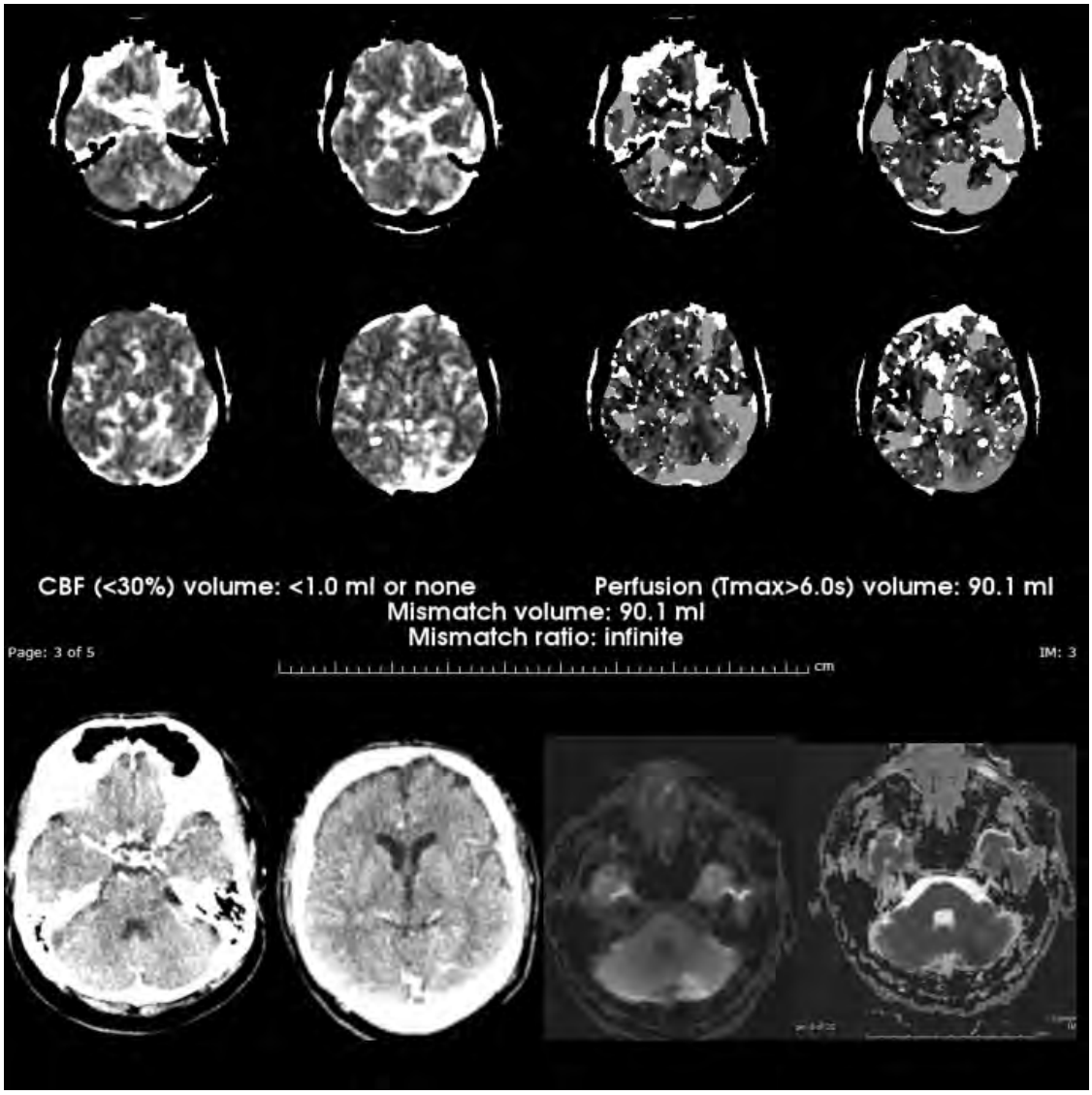
automatically provides the CBF, CBV, Tmax, eTTP maps, as well as the infarct core (CBF <30%), the area of perfusion abnormality (Tmax> 6s) and the mismatch map. We then compared the results with the MRI findings. The CTP maps then were evaluated as being diagnostic versus nondiagnostic. The source images and maps then were reviewed for sources of errors.

Results

From the population of 56 patients with stroke, 9 patients had posterior circulation stroke. There were 3 female and 6 male subjects, the mean age was 64 years (Min 36 Max 87). There was disagreement between the CTP and the MRI findings in 7 patients (77%), and in 2 there was concordance with the MRI. The most common error was incorrect Tmax maps, usually showing overestimated areas of perfusion abnormality, which occurred in 5 patients. In one case there was a pontine infarct which was not shown on the CT; and the other there was a PICA infarct, which was not included in the scanned region. In 2 cases, the CBF demonstrated the infarct core to be in good agreement with the MRI. None of the source images showed excessive motion artifact during the scan time, and the contrast bolus was found to be adequate in all cases. The regions of interest (ROIs) placement for arterial and venous input functions were good in all cases. Review of the anterior circulation evaluation, out of 47 scans, 41 were found to be diagnostic.

Conclusions

Our study demonstrates that the CTP maps of almost all patients with posterior circulation ischemic strokes were nondiagnostic. These usually showed incorrect Tmax maps, even without significant sources of error for incorrect postprocessing. Despite the small sample size the evaluation of the posterior circulation strokes with CTP is less optimal than perhaps MRI, although we continue to review cases of posterior circulation strokes.



(Filename: TCT_P-40_Strokeposteriorcirculation.jpg)

P-25

6:30AM - 3:00PM

Brain Metastases Probability Maps from Different Primary Tumors

T Schneider[1], J Kuhne[1], M Mohme[1], T Magnus[1], J Fiehler[1], S Siemonsen[1]
[1]*University Medical Center Hamburg-Eppendorf, Hamburg, Germany*

Purpose
Prior reports on the location and size of brain metastases almost entirely focus on breast and lung cancer as primary tumors. This is the first study comparing multiple other types of cancer that metastasized to the brain.

Materials and Methods

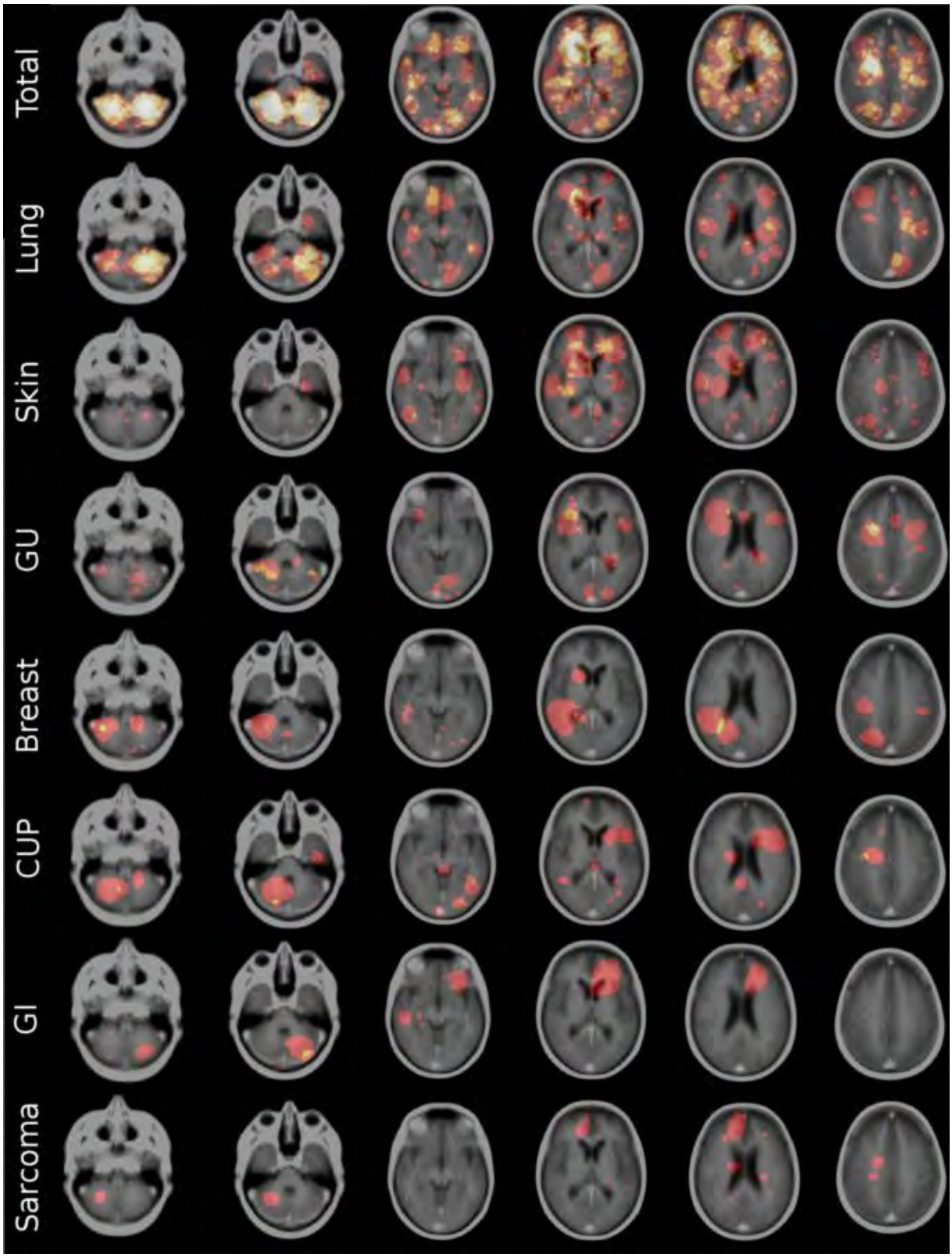
This monocentric, retrospective study includes 101 patients who were first diagnosed with brain metastases in 01/2010-05/2015 by 1.5T or 3T MRI. Region of interest (ROI)-based volumetry and mapping of altogether 810 metastases was performed on 3D-CE-T1W images. After generation of an average whole brain template, cumulative probability distribution maps of metastases were created for all tumor types by 2 independent raters.

Results

Diagnosis of brain metastases was made with a median latency of 11 months (-24-192 months, SD 40.1 months) before or after initial confirmation of the primary tumor (38.5% lung, 24.6% skin, 18.0% breast, 5.8% CUP, 5.2% genitourinary, 5.1% gastrointestinal cancer, and 2.7% sarcoma). There was no significant difference in the number of metastases for the different tumor types. The most frequent locations for metastases were the frontal lobe (30.6%), cerebellum (25.8%), and the parietal lobe (14.9%). The figure shows distribution heat-maps of the tumor groups.

Conclusions

Distribution of brain metastases is heterogenous for the distinct primary tumors. Further pathophysiological studies are needed to elucidate the underlying mechanisms.



(Filename: TCT_P-25_Fig.jpg)

P-05

6:30AM - 3:00PM

Brain Structural Connectivity and Neuroticism in Healthy Adults

I Ueda[1], S Kakeda[2]
[1]University of Occupational and Environmental Health, School of Medicine, Kitakyusyu-shi, Fukuoka-ken, [2]University of Occupational and Environmental Health, School of Medicine, Kitakyushu, Fukuoka

Purpose
The five-factor model organizes personality traits into five factors: Neuroticism, Extraversion, Openness to Experience, Agreeableness, and Conscientiousness. Measures of these personality traits predict people's behaviors and important outcomes of their lives. Because the Neuroticism is a potent risk marker for psychopathology, understanding neural correlates of "neurotic brain" is important. In this study, we examined a correlation between neuroticism scores of NEO Five-Factor Inventory (NEO-FFI) and brain structural networks.
Materials and Methods
Fifty-one healthy participants (18 women, 33 men; mean age, 38.5 ± 11.7 years) underwent the NEO-FFI and MRI including diffusion tensor imaging (DTI) and 3D T1WI (3D-FSPGR). Using MRI data, we constructed whole brain inter-regional connectivity matrices for each participant, and calculated graph theoretical network measures in various brain regions (83 regions from "aparc + aseg" segmentation in FreeSurfer).
Results
Neuroticism correlated positively with nodal clustering coefficient in right superior temporal regions ($p=0.0082$) and negatively with nodal clustering coefficient in right posterior cingulate cortex regions ($p=0.00107$).
Conclusions
Our result suggests that smaller Neuroticism is associated with lowered structural connectivity in the superior temporal regions and greater Neuroticism is associated with lowered structural connectivity in the posterior cingulate cortex regions. The whole brain structural connectome with DTI represents an important technique in further understanding the neural mechanisms underpinning behaviors and mental health conditions related to personality types.

P-10

6:30AM - 3:00PM

Case Report: Aplastic Anemia and Septic Shock Complicated by Micro-hemorrhages in the Corpus Callosum

S Shabbir[1], E Melamed[1], M Milstein[1]
[1]Montefiore Medical Center, Bronx, NY

Purpose

We present an unusual case of a patient with aplastic anemia complicated by septic shock and encephalopathy who was found to have innumerable cerebral microhemorrhages predominantly concentrated in the corpus callosum.

Materials and Methods

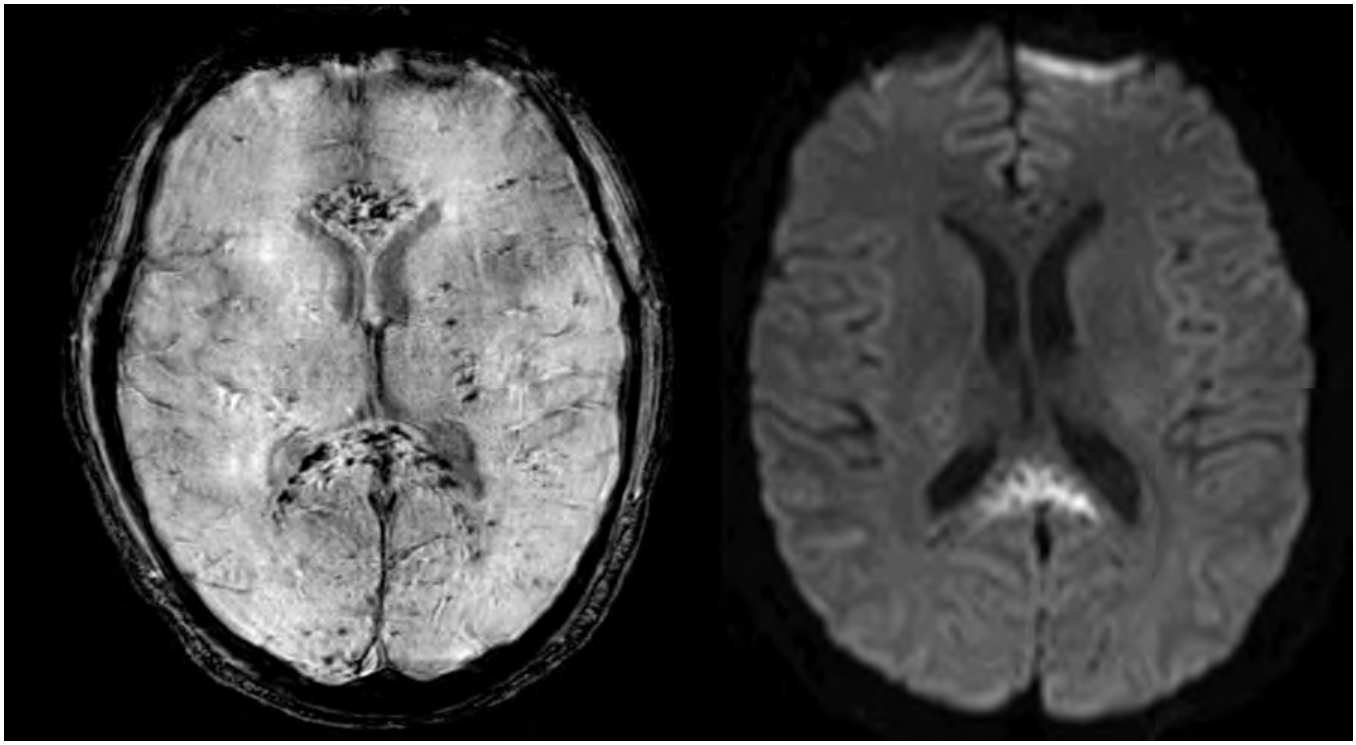
A 33-year-old man, with no known medical history presented to the hospital with bruising and diffuse petechial rash. He was found to have aplastic anemia on bone marrow biopsy and started on anti-thymocyte globulin and cyclosporine. His course was complicated by septic shock requiring intubation, pressors, management with broad spectrum antibiotics and antifungals, and required multiple packed red blood cell and platelet transfusions. Following extubation, patient was noted to be delirious and agitated.

Results

Computed tomography (CT) of the head demonstrated a small amount of linear hyperdensity in the left frontal lobe consistent with subarachnoid hemorrhage. Magnetic resonance imaging (MRI) brain revealed scattered areas of susceptibility artifacts, compatible with microhemorrhages in the subcortical deep white matter and cerebellum, with diffuse involvement of the corpus callosum. The patient's mental status improved over the next several days without intervention.

Conclusions

Very few disease processes are known to predominantly affect the corpus callosum. Similar findings have been reported previously in the setting of sepsis, extracorporeal membrane oxygenation and high altitude cerebral edema, though not to the degree seen in this patient. These findings likely represent leukoencephalopathy stemming from severe disease burden, inflammation, and platelet dysfunction. Our patient had several factors predisposing him to this process, including thrombocytopenia and septic shock, both complications of his aplastic anemia.



(Filename: TCT_P-10_Figure1.jpg)

P-16

6:30AM - 3:00PM

Clinical Imaging of Perivenous Versus Periarterial Spread of Disease : Importance of the Pial Membrane

J Hunter[1], A Hayman[2]
[1]Texas Children's Hospital, Houston, TX, [2]MDAnderson, Houston, TX

Purpose
To re-acquaint the readership with normal venous anatomy and illustrate pathways of perivenous spread in a spectrum of neurological disorders in both children and adults. The circle of Theron (COT), is the venous homologue of the circle of Willis (COW) and like the COW that has peri-arterial spaces the circle of Theron has perivenular spaces that are affected by a variety of pathologies. This poster aims to compare and contrast the pathology in these perivenular spaces with that in the periarterial spaces.
Materials and Methods
Sequential cases from clinical workload and the literature were examined carefully to better understand patterns of perivenous spread based on the existing literature. Imaging of path-proven diagnoses ranging from venous thrombosis and infection through sarcoidosis and multiple sclerosis to glioblastoma multiforme (GBM, n=1250), were examined carefully and commonalities in the pattern of spread of disease noted and correlated with known venous

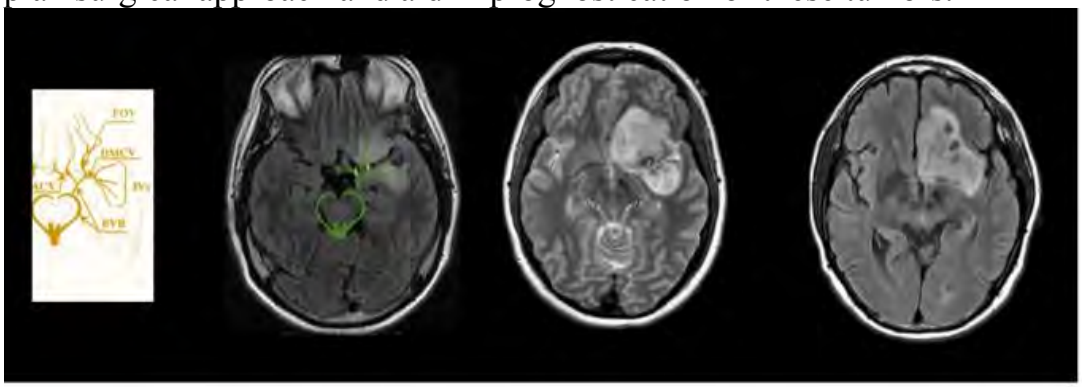
anatomy. This was contrasted with pathologies such as TB and mycosis involving the subarachnoid and periarterial Virchow-Robin spaces.

Results

Predictable patterns of spread and dissemination, including extension through the skull base in the case of GBM, could be explained on the basis of a detailed knowledge of venous anatomy, as illustrated in Figure 1 which demonstrates three different patients with GBM with spread in the perivenous spaces around the inferior striate branches of the middle cerebral vein, which maintain their shape as they enlarge (B-D), with sparing of the cisterns seen in the first case (B). This contrasts with periarterial spread of disease which does not spare the basal cisterns and stays in the subarachnoid space (above the pia) as opposed to the subpial space. The perivenous spaces are continuous with the emissary veins at the skull base, while the periarterial subarachnoid spaces ensheath the exiting cranial nerves.

Conclusions

The pia separates periarterial pathologies in the subarachnoid space from perivenous pathologies in the subpial space. A sound working knowledge of venous anatomy may help understand underlying pathophysiology in a variety of diseases. In the case of GBM an individual's venous anatomy can explain patterns of distribution of disease which can help plan surgical approach and aid in prognostication of these tumors.



(Filename: TCT_P-16_veins.jpg)

P-09

6:30AM - 3:00PM

Comparison of Microfiber Alteration of Fornix in Idiopathic Normal Pressure Hydrocephalus Patient, Alzheimer's Disease and Healthy Volunteers by Diffusion Tensor Imaging

C Ngamsombat[1], A Gonthong[1], J Wongsripuemtet[1], P Charnchaowanish[1], W Muangpaisan[2], T Witthiwej[3], O Chawalparit[1]

[1]Department of Radiology, Faculty of Medicine Siriraj Hospital, Mahidol University, Bangkok, Thailand, [2]Department of Preventive and Social Medicine,Faculty of Medicine Siriraj Hospital,Mahidol University, Bangkok , Thailand, [3]Department of Surgery, Faculty of Medicine Siriraj Hospital, Mahidol University, Bangkok, Thailand

Purpose

The clinical and imaging findings of idiopathic normal pressure hydrocephalus (iNPH) and Alzheimer disease (AD) patients have some overlapping and often are challenging to diagnosis. The fornix is an important structure in memory function and by anatomy is closed to ventricular wall (1). Our study aimed to explore any difference of microstructural change of fornix in iNPH and AD patients as compared with normal control subjects demonstrated by using diffusion tensor imaging (DTI).

Materials and Methods

The ten normal control subjects, 10 iNPH and 10 AD patients underwent MRI scans (Philips 3.0T) and the DTI data were obtained by using a single-shot EPI (echo planar imaging), intra-slice resolution=2x2 mm2, thickness = 2 mm, b-Values 0 and 800 s/mm2 and 32 diffusion-sensitizing directions. Diffusion tensor imaging parameters and diffusion fiber tractography were derived from DSI studio software (2). (Figure 1) The differences in fractional anisotropy (FA), mean diffusivity (MD), axial diffusivity and radial diffusivity data were compared between groups. The receiver operating characteristic (ROC) curve analysis also was evaluated.

Results

There was significant lower mean FA in iNPH and AD patients than in normal control subjects. The mean MD of iNPH patients was significantly higher than that in normal control subjects and AD patients. The best parameter to discriminate iNPH from AD patients was mean FA, using cutoff value of 0.2467 giving the sensitivity, specificity, and accuracy at 90%, 70% and 80%, respectively.

Conclusions

Our study revealed different microstructural change of fornix in iNPH and Alzheimer disease patients by using DTI technique. These results are probably due to difference in pathogenesis of diseases. Furthermore, we have demonstrated possibility to use DTI parameters as a supportive tool in differentiating iNPH from AD patients with high diagnostic accuracy.

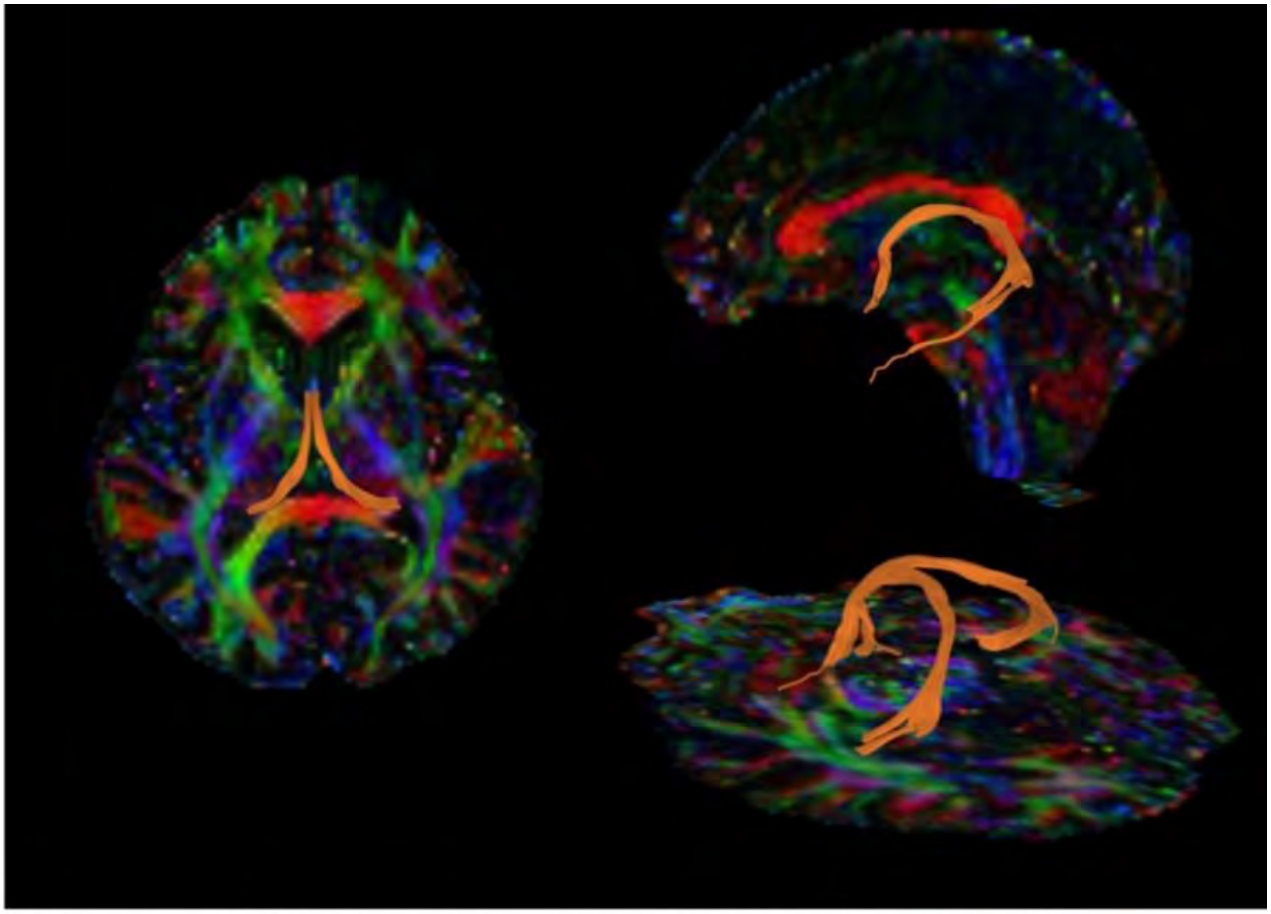


Figure 1 : The fornix was demonstrated by using diffusion fiber tractography.

(Filename: TCT_P-09_Figure1-fornix.jpg)

P-07

6:30AM - 3:00PM

Comparison of Pre-surgical fMRI Language Mapping with Post-surgical Language Deficits

N Thrikutam[1], Z Yetkin[1], T O'Neill[1]
[1]*UT Southwestern, Dallas, TX*

Purpose
The accuracy, reproducibility, and clinical applicability of presurgical imaging evaluation of language in patients with mass lesions near language areas has been demonstrated previously by this group. The accuracy and clinical applicability of presurgical mapping can be confirmed by correlating presurgical imaging to postsurgical imaging and then to any related language deficits. It is hypothesized that if the surgical resection cavity includes areas of

language activation language deficits will result. Correlation of outcomes with language mapping and postsurgical imaging has not been documented in the literature.
Materials and Methods
Presurgical functional maps were created utilizing AFNI and DynaSuite software following fMRI protocol to evaluate language regions. Postsurgical follow up of speech deficits was obtained from the medical charts. A computerized method was used to coregister pre and postsurgical images. The coregistered postsurgical image was used to segment the resection cavity. Overlap in the proximity of activation with the postsurgical resection cavity was documented and analyzed for correlation to outcome.
Results
Thirteen patients with left-sided mass lesions with complete pre and postsurgical clinical imaging and clinical evaluation were included in this retrospective study. Of the thirteen patients only 1 patient was noted to have a severe postoperative language deficit and 4 patients were noted to have moderate postoperative language deficits. Prognostic indicators of language deficits included proximity of activation to the resection cavity and the level of resection.
Conclusions
(1) Presurgical fMRI was accurately coregistered with postsurgical images. (2) Structural and functional images were shown to correlate with postsurgical language deficits.

P-30

6:30AM - 3:00PM

Consistency of Two Common Intracranial Tumors Measured with T1ρ Imaging

M Kitajima[1], S Yano[2], H Uetani[2], Y Yamashita[3]
[1]Kumamoto University, Kumamoto, Japan, [2]Kumamoto University, Kumamoto, Kumamoto, [3]Kumamoto University, Kumamoto, -- SELECT --

Purpose
Knowing the tumor consistency is important for predicting the degree of tumor removal. Several MR indices such as T2 signal intensity have been proposed for predicting the consistency of tumors; however, the results are inconsistent. The purpose of this study was to explore the feasibility of spin-lattice relaxation time in the rotating frame (T1ρ) MR imaging, which is sensitive for detection of collagen and proteoglycans in tissue, for the predicting of consistency in meningioma and pituitary adenoma.
Materials and Methods
This study enrolled 7 patients with meningioma and 6 patients with pituitary adenoma who underwent pre-operative MR imaging including T1ρ sequence. Neurosurgeons intra-operatively assessed the tumors as either soft or hard. We compared T1ρ value with intra-operative assessment of the tumor consistency. In cases with meningioma, we also compared T1ρ value with the connective/fibrotic tissue volume fraction (CVF) defined as the ratio

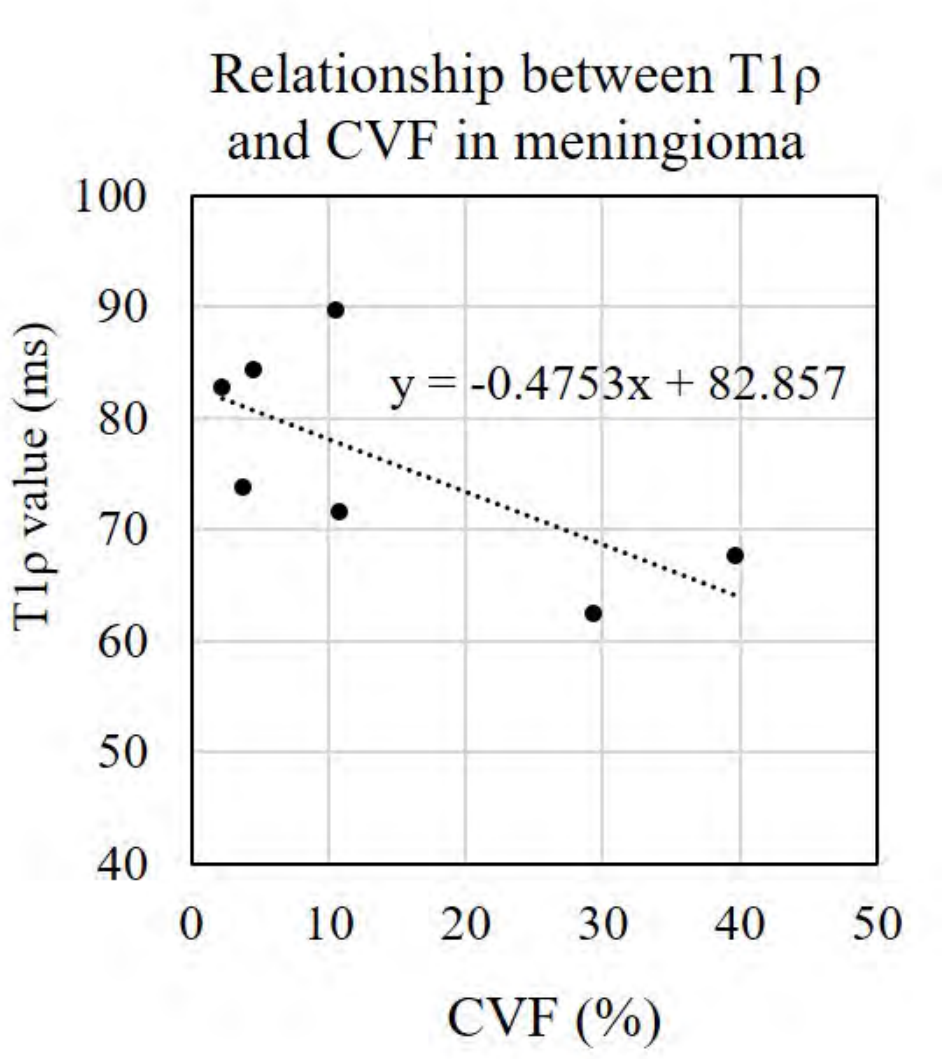
between sum of the connective/fibrotic tissue and total area in the histological specimens stained with Elastica van Gieson method.

Results

Of the 7 patients with meningioma, tumor consistency was classified as hard in 2 patients (29 %) and soft in 5 patients (71 %) at the intra-operative assessment. Of the 6 patients with pituitary adenoma, hard adenoma in 2 patients (33 %) and soft in 4 patients (67 %). The mean T1ρ value for soft meningiomas (80.4 ± 7.5 ms) was longer than those of hard meningiomas (65.1 ± 3.6 ms), and the mean T1ρ value for soft adenomas (80.0 ± 6.1 ms) was longer than those of hard adenomas (70.1 ± 1.8 ms). In cases of meningioma, we found a trend toward shortening of T1ρ value with increase of CVF.

Conclusions

T1ρ may provide pre-operative quantitative information regarding the consistency of common intracranial tumors that appears to be related to the connective/fibrotic tissue content.



(Filename: TCT_P-30_T1rho_fig.jpg)

P-39

6:30AM - 3:00PM

Correlation of Cerebrovascular Reserve Assessed by Acetazolamide-Stress SPECT with Collaterals on Arterial Spin-Labeling MRI in Patients with Carotid Occlusive Disease

H Kang[1], K Roh[1]
[1]*Seoul Veterans Hospital, Seoul, Korea, Republic of*

Purpose
We evaluated the correlation between cerebrovascular reserve (CVR) on acetazolamide-stress single photon emission computed tomography (SPECT) brain scans and collaterals on arterial spin-labeling (ASL) magnetic resonance imaging (MRI) in internal carotid artery (ICA) stenosis.
Materials and Methods
Seventy-four patients with ICA stenosis (>70%) underwent pulsed ASL brain perfusion scan and SPECT brain perfusion scan in the resting and after acetazolamide challenge. We observed the presence of intracranial collaterals, which are manifested by arterial transit artifact (ATA), on ASL. Cerebrovascular reserve based on rest-SPECT and acetazolamide-stress SPECT was calculated. With acetazolamide stress SPECT, the 74 patients were grouped as either showing or not showing evidence of decreased CVR. We assessed the relationship between reduced CVR and intracranial collaterals shown as ATA on ASL.
Results
In 17/74 (23%) of the ICA stenosis patients, ASL showed ATA in ipsilateral to the stenosis. With acetazolamide stress SPECT, the 21/74 (28%) patients showed evidence of decreased CVR. In 7/53 (13%) of the normal CVR group and 10/21 (48%) of the reduced CVR from the SPECT results, ASL showed ATA in ipsilateral to the stenosis. Significant relationship was observed between reduced CVR group and ATA showing group in ICA stenosis patients on ASL brain perfusion ($p=0.004$).
Conclusions
Our results suggest that ICA stenosis patients who had reduced CVR on brain SPECT showed increased dependence on intracranial collaterals shown as ATA on ASL brain scans.

Table 1. Demographic characteristics of the SPECT study population.

Characteristics	ICA stenosis patients with SPECT study (>70%, n=74)
Male / Female	63 / 11
Age (y)*	71.3 ± 6.4

*Data are means ± standard deviations.

Table 2. Results of the analysis of correlation of the ATA and reduced cerebral vascular reserve (CVR) from the SPECT results.

	Normal CVR	Reduced CVR	Total
No ATA	46	11	57
Presence of ATA	7	10	17
Total	53	21	74

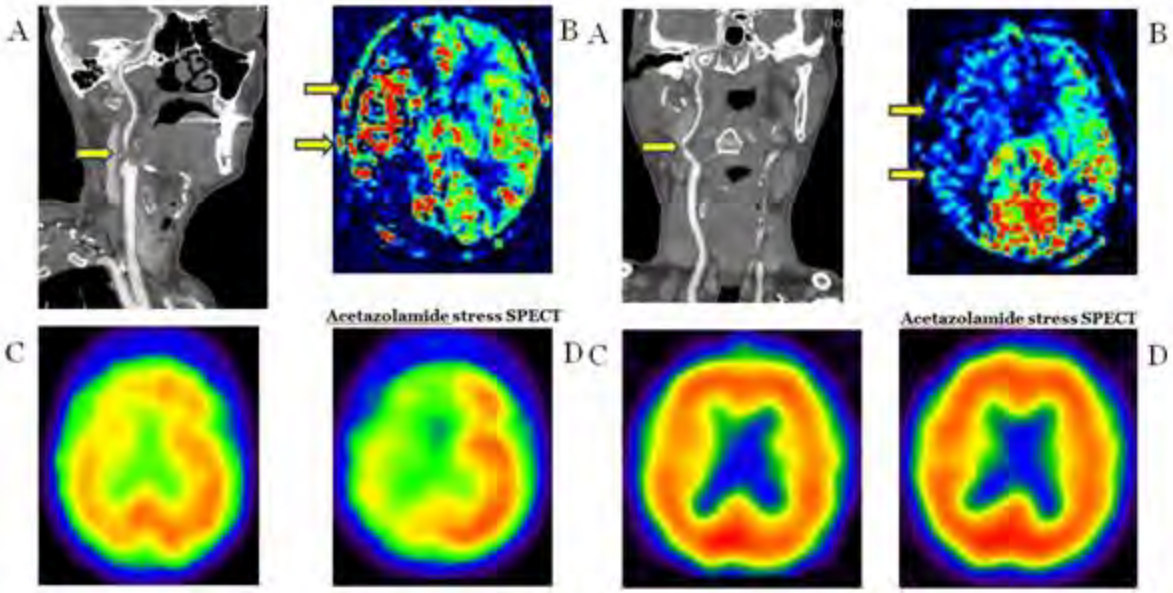
Chi-square test (p=0.004)

Figure 1. 72-year-old male, severe stenosis of the right proximal cervical ICA.

Multiple serpiginous high signal intensity (red) structures were seen in the right frontotemporal area on pulsed ASL with right proximal cervical ICA stenosis patient, and on acetazolamide stress SPECT image, there was reduced CVR change in the right frontotemporal area .

Figure 2. 79-year-old male, severe stenosis of the right proximal cervical ICA.

No ATA in the right frontotemporal area were seen on pulsed ASL with right proximal cervical ICA stenosis patient, and on acetazolamide stress SPECT image, there was no CVR change in the right frontotemporal area.



(Filename: TCT_P-39_s1.JPG)

P-46

6:30AM - 3:00PM

Could Susceptibility-weighted MRI Help Predict the Effect of Anti-coagulation on Dementia Progression?

P Curl[1], N Cornish[2], G Cruciata[1], E Stein[1]
[1]Maimonides Medical Center, Brooklyn, NY, [2]Maimonides Medical Center, Brooklyn,, NY

Purpose
Multiple guidelines and tools exist for balancing the benefit of anticoagulation with the potential harms, none of which currently use MRI evidence of microhemorrhage as factor. In addition to this information having value to predict potential clinical ICH, there is reason to believe anticoagulation could lead to cognitive impairment through an increase in subclinical microbleeds. This review looks into the existing evidence and gaps in knowledge that would be necessary to establish this connection.
Materials and Methods
We performed a comprehensive review of MEDLINE EMBASE and Cochrane databases for the following associations: anticoagulation with microbleeds, microbleeds with dementia, anticoagulation with dementia, and anticoagulation with dementia in patients with pre-existing microbleeds.
Results
There is strong evidence associating microbleeds with dementia (1, 2), some evidence associating anticoagulation with an increase in microbleeds (3), and evidence that anticoagulation does not affect dementia incidence or progression overall (4). There are no currently published studies addressing whether anticoagulation affects dementia incidence or progression in people with pre-existing microbleeds.
Conclusions
The current evidence is consistent with (but not conclusive of) the hypothesis that anti-coagulation may differentially increase the risk of dementia in patients with pre-existing microbleeds. The fact that anticoagulation does not affect dementia incidence or progression on a whole is actually consistent with the hypothesis that it increases the risk of dementia in some patients: it provides an explanation for why findings are not consistent with the expectation that a decrease in ischemic strokes would lead to a decrease in dementia. Considering the large number of patients currently taking anticoagulation have pre-existing microbleeds, further research in this area has the potential to have a large public health impact and is worth pursuing even if the likelihood of a positive result is small.

P-38

6:30AM - 3:00PM

CT Texture Analysis of Clot in Patients Presenting with Acute Ischemic Stroke --- A Preliminary Study

J NAIR[1], Z ASSIS[2], J Khader Eliyas[3], C McDougall[4], M Eesa[5], M Joshi[6], B MENON[7], M GOYAL[8], W Qiu[9]
[1]FootHills Medical Centre, Univesity of Calgary, Calgary, Alberta, [2]FOOTHILLS MEDICAL CENTRE, UNIVERSITY OF CALGARY, CALGARY, ALBERTA, [3]University of

Calgary, Calgary , Alberta, [4]University of Calgary, Calgary, AB, [5]Foot Hills Medical Centre and University of Calgary, Calgary, Alberta, [6]University of Calgary, Calgary, Alberta, [7]FOOTHILLS MEDICAL CENTRE, CALGARY, ALBERTA, [8]FOOTHILLS MEDICAL CENTRE, CALGARY, Alberta, [9]The University of Calgary, Calgary, Alberta

Purpose

To develop and validate CT texture analysis techniques for pretreatment estimation of clot histology, difficulty of endovascular procedure and 90 day mRS.

Materials and Methods

This was a retrospective study of 50 patients (median age 71 years, median NIHSS of 17) presenting with acute stroke (3/2015-7/2016) due to anterior circulation large vessel occlusion presenting within 8 hours of symptom onset and undergoing endovascular stent thrombectomy. All patients had neurovascular imaging in the form of NCCT and multi-phase CTA at baseline. Seventeen of 50 patients received intravenous tPA as standard care. Manual segmentation of the clot was performed on the equilibrium phase of the mCTA. Clots extracted during EVT underwent histopathological analysis. For each segmented clot, 376 texture features were produced using code written in MATLAB. This was repeated for each clot in the chosen data set. The data set then was dichotomized based on the prespecified end points. After the features were produced, a linear discriminant analysis (LDA) was done, which ranked the features in order of "discriminatory Importance". Using the 10 texture features, a logistic regression (LR) was done in which the variable X is a linear sum of all the texture features Xi, with unknown coefficients Bi. The result of the LR is the coefficients Bi for these variables Xi. Areas under the curve (AUC) were reported as appropriate.

Results

Areas under the curve for models with endpoints clot histology, ease of thrombectomy and mRS at 90 days were 0.707, 0.901 and 0.794 respectively.

Conclusions

Computed tomography texture analysis of clot is a promising technique capable of predicting histology, ease of endovascular intervention and clinical outcomes.

Clot Histology

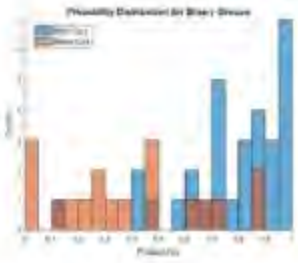


Figure 1

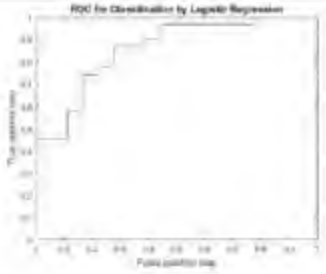


Figure 2

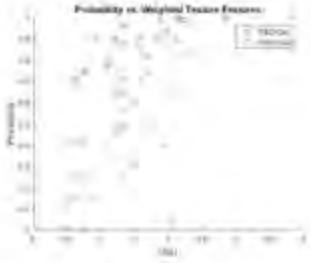


Figure 3

Ease of Thrombectomy

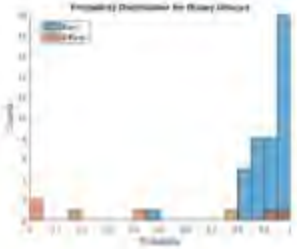


Figure 4

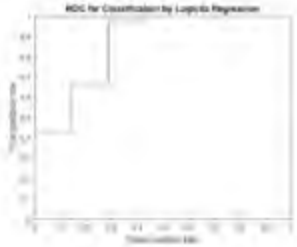


Figure 5



Figure 6

mRS at 90 days

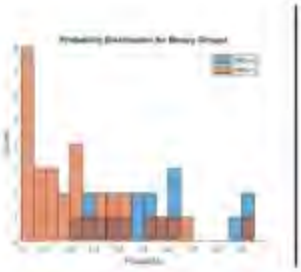


Figure 7

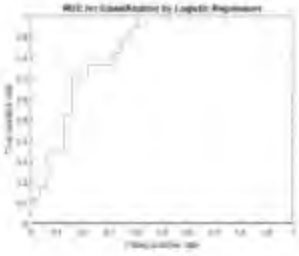


Figure 8

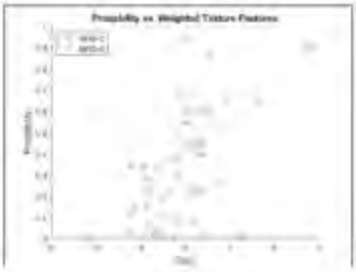


Figure 9

Figures 1,4 and 7show the probabilities as a function of their linear combination of XiBi, for clot histology, ease of thrombectomy and mRS at 90 days respectively.

Figures 2, 5, and 8 show the ROC curve that shows the quality of the LR analysis done for clot histology, ease of thrombectomy and mRS at 90 days respectively.

Figures 3,6 and 9 show the distribution of probabilities within a data set for clot histology, ease of thrombectomy and mRS at 90 days respectively.

(Filename: TCT_P-38_ClotTextureAnalysis.jpg)

P-43

6:30AM - 3:00PM

CTA Collateral Score and NIH Stroke Score Mismatch Predicts Better In-Hospital Improvement in Acute Stroke Patient Treated with IV tPA and/or Mechanical Thrombectomy

K Traylor[1], C Emery[1], B Reznikov[1], J Ahn[1], X Liu[1]
[1]*Christiana Care Health System, Newark, DE*

Purpose
Acute stroke patients with significant NIH stroke score (NIHSS) deficits but relatively good collateral scores (CS) on CTA (NIHSS/CS mismatch) have better outcomes following tPA and/or mechanical thrombectomy. Clinical selection for acute stroke intervention remains very challenging. CTA and noncontrast CT are performed routinely for triage of patients with acute stroke to tPA or endovascular therapy. Assessment of CS in conjunction with NIHSS may help to predict the outcome of the patients who undergo intervention. In this study, NIHSS change between admission and discharge in patients with NIHSS/CS mismatch was assessed and then compared to that in the remaining group, in order to test our hypothesis.
Materials and Methods
We retrospectively identified 51 consecutive patients with acute MCA occlusion who underwent tPA and/or mechanical thrombectomy between 2012-2015. NIHSS at admission and at discharge were reviewed. Collateral scores on CTA were evaluated by two independent neuroradiologists who were blinded to the patient's demographics and NIHSS. Statistical analysis to compare the change of NIHSS in patients with "mismatch" and the remaining group was performed.
Results
The interrater reliability of collateral assessment was very good (r= 14, p <). The patients (n= 19) with NIHSS/CS mismatch showed an average improvement of NIHSS of about 13 compared to 6 in the remaining group (n= 32), statistically highly significant (p<0.001).
Conclusions
Our study reveals that acute stroke patients with NIHSS/CS mismatch demonstrates better in-hospital improvement following tPA and/or mechanical thrombectomy. This information may help clinical triage of stroke patients for intervention.

P-13

6:30AM - 3:00PM

Dentate Nucleus T1 Signal Changes after Linear vs. Macrocyclic Gadolinium Contrast Exposure: Are Multiple Sclerosis Patients at Risk?

K Terashima[1], J Ohayon[1], I Cortese[1], D Reich[1]
[1]*NIH/NINDS, Bethesda, MD*

Purpose
A growing body of evidence has shown that repeated linear gadolinium-based contrast agent (GBCA) administration leads to gadolinium deposition in the dentate nucleus, detectable on T1-weighted magnetic resonance imaging (MRI). Clinical implications of gadolinium retention in the brain remain undefined. Patients with multiple sclerosis (MS) are especially at risk given the importance of contrast imaging in disease diagnosis and management. This study analyzed a closely monitored MS cohort, comparing longitudinal changes in T1 signal intensity of the dentate nuclei and clinical disability measures after repeat administrations of linear or macrocyclic GBCA over a mean of 2.1 +/- 1.5 years.
Materials and Methods
We retrospectively analyzed data from a natural history cohort of MS patients followed at the National Institutes of Health who underwent >4 brain MR examinations with either the linear GBCA gadopentetate dimeglumine (Magnevist), or the macrocyclic GBCA gadobutrol (Gadavist), between 2006 and present. Dentate nucleus-to-pons signal intensity ratio (DPSIR) was calculated from regions of interest generated through automated cerebellar segmentation on non-enhanced T1-weighted scans. A linear mixed-effects model was applied to assess the effect of cumulative GBCA dosage on DPSIR as a function of GBCA type. The model fit subject-level slopes and intercepts; scanner protocol was considered a fixed covariate.
Results
In eighty patients who received linear (n=62) or macrocylic (n=18) contrast, type of contrast and mmol per year improved model fit [Chi-squared (1)=8.54, $p<0.05$]. Patient coefficients of this model did not correlate with change in EDSS over time ($r=0.09$, $p=0.43$).
Conclusions
Although we observed the expected effect of linear GBCA on T1 signal intensity in the dentate nucleus over time, this was not correlated with worsening disease severity, suggestive that dentate nucleus gadolinium deposition could be a benign process. This finding is consistent with human and animal histological studies (1, 2), which thus far have not shown pathological architectural changes in brain.

P-26

6:30AM - 3:00PM

Differentiation Between Glioblastoma and Solitary Metastasis: Morphologic Assessment by Conventional Brain MR Imaging and Diffusion Weighted Imaging

D Shin[1], E Lee[2]

[1]Gongju medical center, Gongju, Chungcheongnam-do, [2]Dongguk University Ilsan Hospital, Goyang-shi, Gyeonggi-do

Purpose
Differentiating between glioblastoma and solitary metastasis is very important for the planning of further workup and treatment. Conventional magnetic resonance imaging (MRI) has been reported to have a limited capacity to differentiate between these two types of tumor. We assessed the ability of various morphological parameters using conventional MRI and diffusion-based techniques to distinguish between glioblastoma and solitary metastasis in tumoral and peritumoral regions.
Materials and Methods
Thirty-eight patients with solitary brain tumors (21 glioblastomas, 17 solitary metastases), who underwent conventional brain MRI and diffusion-weighted imaging (DWI) before surgical resection or stereotactic biopsy, were included. To determine if there were differences in the morphologic parameters of enhancing tumors, we analyzed their shape, margins, and enhancement patterns on postcontrast T1-weighted images, in addition to patients' age and sex, and the presence of intratumoral hemorrhage on T2* gradient echo images. During analyses of peritumoral regions, we assessed the extent of peritumoral edema on T2- and postcontrast T1-weighted images. We also aimed to detect peritumoral neoplastic cell infiltration by visual assessment of T2-weighted and diffusion-based images, including DWI, ADC maps, and exponential DWIs, and evaluated which sequence depicted peritumoral neoplastic cell infiltration most clearly.
Results
The shapes, margins, and enhancement patterns of tumors all significantly differentiated glioblastomas from metastases. Glioblastomas had an irregular shape, ill-defined margins, and a heterogeneous enhancement pattern; on the other hand, metastases had an ovoid or round shape, well defined margins, and homogeneous enhancement. No significant differences in intratumoral hemorrhages were found among tumors. During assessment of peritumoral edema, metastases had significantly more extensive peritumoral edema than glioblastomas. According to receiver operating curve analysis, a cutoff value of 2.21 for the ratio between the maximum diameter of the peritumoral edema and the maximum diameter of the enhancing mass was associated with the optimal combination of sensitivity (76.2%) and specificity (70.6%). In visual assessment of peritumoral neoplastic cell infiltration using T2-weighted and diffusion-based images, all sequences differed significantly between the two groups. Exponential DWI had the highest sensitivity for the diagnosis of both glioblastoma (100%) and metastasis (70.6%). A combination of exponential DWI and ADC maps was optimal for the depiction of peritumoral neoplastic cell infiltration in glioblastoma.
Conclusions
Although advanced MRI techniques provide valuable information for the differentiation of glioblastoma from solitary metastatic lesions, visual morphologic assessment of tumoral and

peritumoral regions using conventional MRI and diffusion-based techniques can also offer diagnostic information.

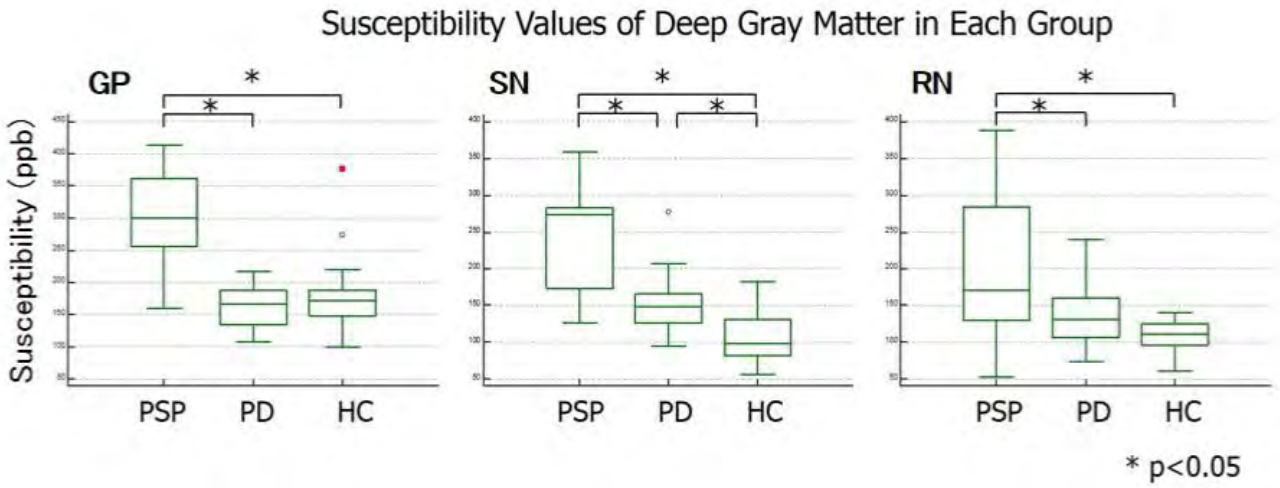
P-01

6:30AM - 3:00PM

Differentiation of Progressive Supranuclear Palsy from Parkinson Disease by Quantitative Susceptibility Mapping

M Kitajima[1], M Azuma[2], S Yamashita[3], M Hashimoto[3], T HIRAI[4], Y Yamashita[5]
[1]Kumamoto University, Kumamoto, Japan, [2]Miyazaki University, Miyazaki, Miyazaki, [3]Kumamoto University, KUMAMOTO, Kumamoto, [4]University of Miyazaki, Miyazaki, Select, [5]Kumamoto University, Kumamoto, -- SELECT --

Purpose
Typical magnetic resonance imaging (MRI) findings of progressive supranuclear palsy (PSP) have been reported; however, the diagnosis and differentiation between PSP and Parkinson's disease (PD) on conventional MR images is challenging, especially in the early stage of the disease. Quantitative susceptibility mapping (QSM) is a useful tool to assess the brain iron levels in patients with neurodegenerative diseases, particularly PD. We compared the susceptibility of the deep gray matter among PSP and PD patients and healthy controls (HC) to determine whether QSM can differentiate PSP from PD and HC.
Materials and Methods
Quantitative susceptibility mapping data were obtained at 3T from 9 patients with PSP, eighteen patients with PD, and eighteen age-matched HC. The clinical diagnoses were made by a neurologist and a psychiatrist. We measured the mean susceptibility values (MSVs) in the bilateral deep gray matter including the globus pallidus (GP), red nucleus (RN), substantia nigra (SN), putamen (PT), and caudate nucleus (CN) in all participants.
Results
The mean MSVs of GP, RN and SN were higher in PSP (300.3 ± 84.8 ppb, GP; 199.8 ± 113.5 ppb, RN; 238.4 ± 75.0 ppb, SN) than PD (160.4 ± 34.0 ppb, GP; 132.7 ± 41.4 ppb, RN; 151.6 ± 44.9 ppb, SN) and HC (183.5 ± 62.3 ppb, GP; 109.1 ± 20.7 ppb, RN; 109.0 ± 36.3 ppb, SN) ($p<0.05$). We found no statistically significant difference in the MSVs of the PT between PSP (122.7 ± 65.7 ppb) and HC (96.7 ± 16.1 ppb), and the CN among PSP (88.5 ± 46.7 ppb), PD (69.9 ± 25.9 ppb), and HC (72.0 ± 16.6 ppb).
Conclusions
Quantitative susceptibility mapping of GP, RN, and SN may help to differentiate PSP from PD and HC.



(Filename: TCT_P-01_PSP_ASNR_last.jpg)

P-48

6:30AM - 3:00PM

Disruption of Thalamo-cortical Tracts is Associated with Post-Concussion Symptoms in mild Traumatic Brain Injury Revealed by Automatic Tract-Based Analysis

C Chen[1], C Lu[2], K Hsieh[1], Y Kao[2], P Tsai[2], H Huang[1]
[1]Taipei Medical University Hospital, Taipei, Taiwan, [2]Taipei Medical University, Taipei, Taiwan

Purpose
Thalamo-cortical (TC) pathways play important role in relaying and integration of memory, cognitive and somatosensory information (1, 2). We aimed to investigate the correlate between the disruption of TC tracts and postconcussion symptoms (PCS) in mild traumatic brain injury (mTBI) using automatic tract-based analysis.
Materials and Methods
This study was approved by the local Institutional Review Board. Seventeen patients with mTBI were recruited according to the criteria by the American Congress of Rehabilitation Medicine Special Interest Group on Mild Traumatic Brain Injury (3), and 31 healthy adults for control (Table 1). A 3D T1-MPRAGE and diffusion tensor imaging with 64 gradient directions were acquired on a Siemens 3T Prisma scanner. The Mini-Mental State Examination and PCS were assessed for each participant. The seventy-six TC tracts between 8 thalamic nuclei and 31 cortical regions were generated automatically based on probabilistic tractography (4) (Table 2 and Fig. 1). A tract-based analysis was applied to assess the fractional anisotropy (FA) along each tract (5).
Results
The mTBI patients showed a mild decline of cognitive performance (MMSE) and significant PCS, especially the somatic and cognitive symptoms (Table 1). Reduced FA values

(reflecting impaired fiber integrities) were found bilaterally between VPL/VPM/LP and somatosensory/parietal regions in mTBI (Fig. 2). Several other TC tracts on the right side, including VA/VL to motor regions and PU to visual/middle temporal cortices, also exhibited declined FA values. The alterations involving the tracts to somatosensory regions may cause the somatic symptoms in mTBI. The left thalamocortical tracts between PU and several temporal regions (vEntorhinal, paraHippo, and Perirhinal areas) showed increased FA which may be acute compensatory effects and associated with the memory and cognitive declines after mTBI.

Conclusions

The alterations of thalamocortical tracts can be efficaciously revealed by the tract-based analysis and correlated to the cognitive and somatic impairments in mTBI.

Table 1 The demography and neuropsychological assessments of study groups.

	HC (n = 31)	mTBI (n = 17)	*p* value
Age	36.16 ± 11.63	43.24 ± 12.24	0.054
Gender	12M, 19F	5M, 12F	0.519
Mini–Mental State Examination (MMSE)	29.50 ± 0.69	28.00 ± 1.35	**0.003****
Rivermead Post-Concussion Symptom Questionnaire (PCSQ)			
Total	3.97 ± 4.76	13.18 ± 12.26	**0.008****
Somatic	1.61 ± 1.89	7.59 ± 6.71	**0.002****
Affective	1.00 ± 1.84	1.88 ± 3.12	0.297
Cognitive	1.35 ± 1.76	3.24 ± 3.38	**0.044***

*p<0.05; **p<0.01

Table 2 The parcellated 8 thalamic nuclei (defined by Thalairach atlas) and their connected 31 cortical regions (defined by Brodmann area) in each hemisphere.

Region Name (Brodmann Area/Thalamus)	Labels	Region Name (Brodmann Area/Thalamus)	Labels
Prefrontal regions ⇔ Mediodorsal Nucleus (MD)			
Frontal Eye Field (BA8)	**FEF**	Dorsolateral Prefrontal Cortex 9 (BA9)	**dlPFC$_9$**
Anterior Prefrontal Cortex (BA10)	**aPFC**	Orbitofrontal Cortex (BA11)	**OFC**
Pars Opercularis (BA44)	**Oper**	Pars Triangularis (BA45)	**Triangularis**
Dorsolateral Prefrontal Cortex 46 (BA46)	**dlPFC$_{46}$**	Pars Orbitalis (BA47)	**Orbitalis**
Parietal regions ⇔ Lateral Posterior Nucleus (LP), Pulvinar (PU)			
Somatosensory Association Cortex 7 (BA7)	**SAC$_7$**	Angular Gyrus (BA39)	**Angular**
Supramarginal Gyrus (BA40)	**SM**		
Occipital regions ⇔ Pulvinar (PU)			
Primary Visual Cortex (BA17)	**V1**	Secondary Visual Cortex (BA18)	**V2**
Associative Visual Cortex (BA19)	**V3-5**		
Motor regions ⇔ Ventral Anterior Nucleus (VA), Ventral Lateral Nucleus (VL)			
Primary Motor Cortex (BA4)	**M1**	Premotor cortex and SMA (BA6)	**PMC & SMA**
Somatosensory regions ⇔ Ventral Posterior Medial Nucleus (VPM), Ventral Posterior Lateral Nucleus (VPL)			
Primary Somatosensory Cortex 1 (BA1)	**PSC$_1$**	Primary Somatosensory Cortex 2 (BA2)	**PSC$_2$**
Primary Somatosensory Cortex 3 (BA3)	**PSC$_3$**	Somatosensory Association Cortex 5 (BA5)	**SAC$_5$**
Temporal regions ⇔ Pulvinar (PU)			
Inferior Temporal Gyrus (BA20)	**ITG**	Medial Temporal Gyrus (BA21)	**MTG**
Superior Temporal Gyrus (BA22)	**STG**	Ventral Entorhinal Cortex (BA28)	**vEntorhinal**
Parahippocampal Gyrus (BA34)	**paraHippo**	Perirhinal Cortex 35 (BA35)	**Perirhinal$_{35}$**
Perirhinal Cortex 36 (BA36)	**Perirhinal$_{36}$**	Fusiform Gyrus (BA37)	**Fusiform**
Temporopolar Area (BA38)	**TempPole**		
Anterior Cingulate Cortex ⇔ Anterior Nucleus (AN)			
Ventral Anterior Cingulate Cortex (BA24)	**vACC**	Dorsal Anterior Cingulate Cortex (BA32)	**dACC**

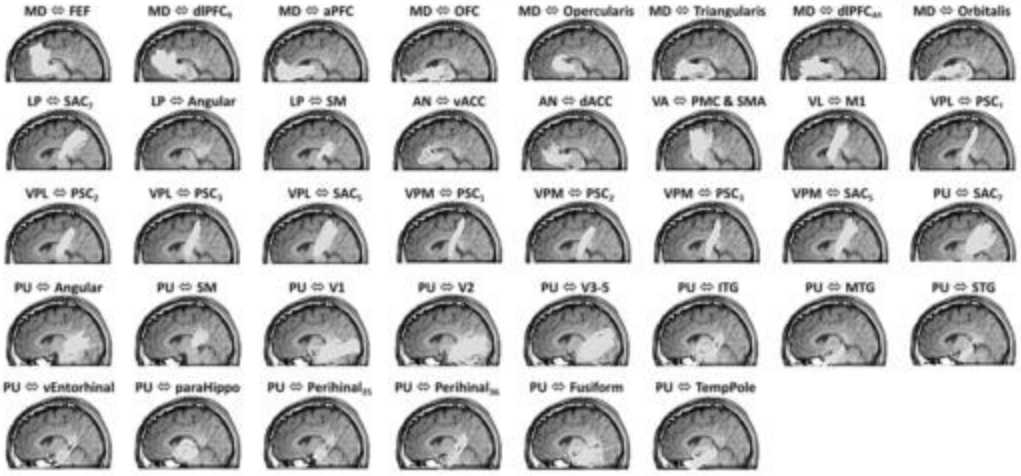


Figure 1 The identified 76 thalamocortical tracts (38 tracts within each hemisphere). The tracts are colored in white.

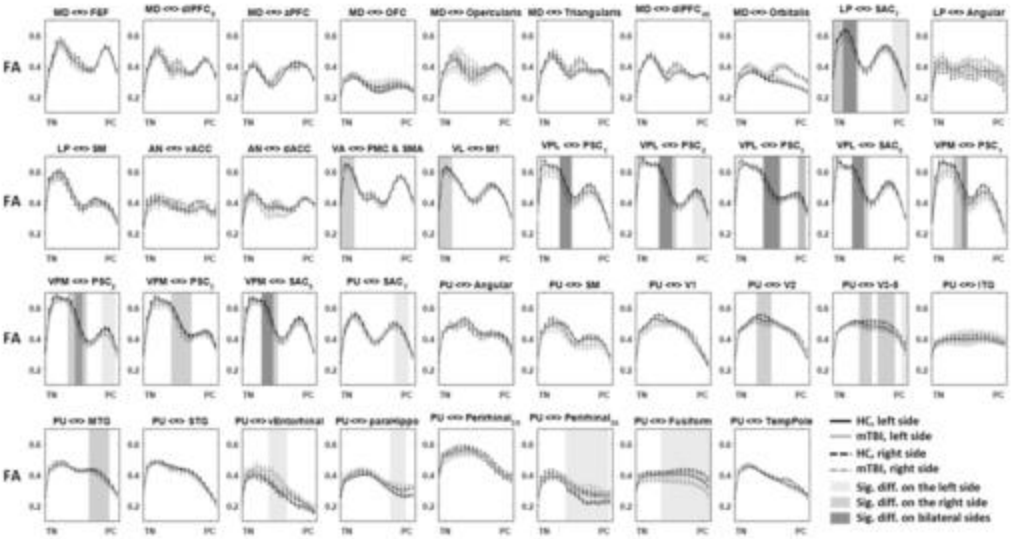


Figure 2 The values of fractional anisotropy (FA) along each thalamocortical tract in mTBI and HC. The significant differences (two-sample *t* test, $p < 0.05$ with a constraint of cluster size larger than 10 steps) of the segments of thalamocortical tracts between groups are labeled by gray boxes. Error bars represent the standard errors of mean. TN: thalamic nucleus; PC: projected cortex.

(Filename: TCT_P-48_Allimage.jpg)

P-21

6:30AM - 3:00PM

Does Patient Age at Glioma Presentation Influence its MRI Phenotype? A Comprehensive Analysis of VASARI Feature-set Criteria in 160 Patients

D Das[1], B Yoon[2], L Golden[3], K Yeom[4], H Vogel[1], P Samghabadi[1], M Iv[5], T Massoud[3]
[1]Stanford Hospital and Clinics, Stanford, CA, [2]Stanford Hospital and Clinics, Stanford , CA, [3]Stanford University School of Medicine, Stanford, CA, [4]Stanford Hospital, Stanford, CA, [5]Stanford University Medical Center, Stanford, CA

Purpose
Several morphological factors besides tumor size and location affect patient survival after glioma diagnosis. The standardized VASARI feature-set criteria are used to qualitatively assess glioma magnetic resonance imaging (MRI) phenotypes. We aimed for the first time to examine whether a large panel of features, including aggressive glioma MRI biomarkers, are more pronounced at different ages. Establishing the role of age as a possible confounder serves as baseline for future more extensive radiogenomic correlations to account for worsening prognosis of glioblastoma with increasing age (>40 yrs).
Materials and Methods
In a retrospective single-center study, we analyzed initial-presentation MRI scans with suspected low- or high-grade gliomas in steroid-naïve patients (n = 160) of all age groups (<20 yrs, 20-40 yrs, 40-65 yrs, and >65 yrs). Three reviewers recorded 30 key imaging features based on VASARI feature-set criteria. We used a chi-square test of independence and a Kruskal-Wallis test to statistically examine the group-wise relation between age and categorical and ordinal VASARI features, respectively. Significance was at $p<0.05$.
Results
The four age groups were equal in numbers. There was no significant difference in short axis ($p=0.32$) or long axis ($p=0.338$) size, necrosis ($p=0.774$), or peritumoral edema ($p=0.118$) between the four groups. However, cortical involvement was highest ($p=0.007$) in >65 yrs; whereas calvarial remodeling ($p=0.002$), deep white matter invasion ($p=0.028$), and proportion of enhancing tumor crossing midline ($p=0.022$) were all highest in those <20 yrs. The latter two features were greater in glioblastoma than in low-grade gliomas ($p=0.027$ and $p<0.0001$), respectively.
Conclusions
Contrary to previous studies, age at diagnosis does not determine tumor size and degree of peritumoral edema or necrosis in gliomas. However, cortical involvement is greatest in the elderly, and several MRI biomarker signatures are more associated with pediatric glioma phenotypes. We will extend this MRI analysis to future correlations with underlying tumor biology and genomic composition to predict patient survival.

P-35

6:30AM - 3:00PM

Evaluation of the White Matter by Magnetic Resonance Diffusion Tensor in Patients After Cerebral Ischemic Event Treated with Physical Rehabilitation

T Andrade[1], G Elizondo-Riojas[1], F Rivera[1], E Garza[2]
[1]University hospital, Monterrey, Nuevo Leon, [2]Psiquiatric hospital, Mexico, Ciudad de Mexico

Purpose
Show the differences in the values of the anisotropy fraction in the white matter in the postischemic patients treated with rehabilitation.
Materials and Methods
It is a longitudinal, comparative, prospective, nonblind observational study. Thirty patients with a diagnosis of cerebral infarction of the middle cerebral artery, older than 18 and younger than 80 years, were evaluated with Rankin clinical scales less than 2 before infarction, NIHSS greater than 6, hemodynamically stable. A 1.5 Tesla GE magnetic resonance was used. RM Protocol: SPGR T1, 65-Way Diffusion Tensor. FSL postprocessing program, Fraction of anisotropy (FA) of the corticospinal tract ipsi and contralateral to infarction. Diffusion toolkit and tracvis. Physical rehabilitation 2 times a week and MR at the beginning and at 3 months. Statistical analysis with SPSS.
Results
To date 30 patients at baseline and 15 at 3 months. Age average of 58 years. Twenty men, smoking history 46% and sedentary lifestyle 50%. NIHSS 9. Rankin 3. Fraction of anisotropy on the side of the lesion 0.52. No association was found between the value of AF and the functional values (NIH and Rankin) for hospital discharge.
Conclusions
These are preliminary results. The values of AF were highly variable. There was a trend in AF on the side of the lesion with respect to the contralateral side.

P-34

6:30AM - 3:00PM

Evaluation of the White Matter Microstructure in PLP1 Mutation Career Using Fiber G-Ratio

Y Takahashi[1], C Takeuchi[2], M Hori[3], Y Tsurushima[4], A Hagiwara[5], S Aoki[6]
[1]Juntendo University School of medicine, Bunkyoku, Tokyo, [2]Tokyo Metropolitan Kita Medical and Rehabilitation Center for Disabled, Kitaku, Tokyo, [3]Juntendo University School of medicine, Bunkyoku, Tikyo, [4]Tokyo Medhial Clinic, Kitaku, Tokyo, [5]Juntendo University School of Medicine, Tokyo, Japan, [6]Juntendo University School of Medicine, Tokyo, Tokyo

Purpose

The fiber g-ratio is defined as the ratio of the inner-to-outer diameter of the myelin sheath (1). It provides advanced information about microstructure not available from other imaging parameters. Fiber g-ratio can provide the distribution of myelin and axon quantitatively. Therefore, white matter assessment in diseases related to myelin formation is essential for this method. Our purpose is to evaluate the change of the axon and myelin distribution in a career of dysmyelinating disease.

Materials and Methods

The objective is a mother of a Pelizaeus-Merzbacher disease patient (male, connatal form). Her son was pointed out PLP1 point mutation and she is heterozygotic career. She was born and brought up healthy in four decades, until she had mild cognitive disturbance at age 44. Myelin volume fraction (MVF) was calculated by T1 mapping (Figure 1). Axon volume fraction (AVF) and g-ratio were calculated by combining MVF and diffusional metrics (Figures 2, 3). Each measurement was performed in the corpus callosum and motor area. MR examinations and MVF, AVF and g-ratio analyses also were demonstrated in 3 healthy volunteers, aged between 24 and 33 (mean age: 27.4) years old.

Results

Table shows the measured AVF, MVF, and g-ratio in a PLP1 career and 3 volunteers. Although AVF and MVF were lower in PLP1 career comparing to volunteers, g-ratio was not much different between PLP1 career and volunteers.

Conclusions

Reduced AVF and MVF in the PLP1 career with minimal symptoms proved potential dysmyelination and axonal impairment. Meanwhile, nearly normal g-ratio could mean maintained neurotransmission function leading clinically asymptomatic course. Fiber g-ratio could potentially evaluate the function of neurotransmission and predict neurological disturbance.

Table

	PLP1 career mean±SD		Volunteers mean±SD (min-max)	
	CC	motor area	CC	motor area
AVF	0.31±0.07	0.33±0.07	0.48±0.04 (0.33-0.48)	0.40±0.07 (0.38-0.41)
MVF	0.30±0.03	0.30±0.03	0.39±0.01 (0.30-0.39)	0.35±0.05 (0.34-0.36)
g-ratio	0.73±0.07	0.74±0.07	0.72±0.02 (0.72-0.74)	0.72±0.03 (0.70-0.74)

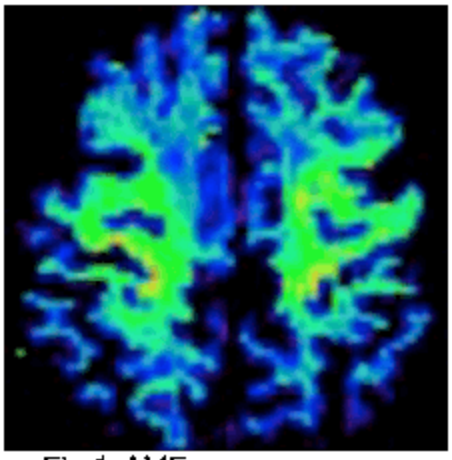


Fig.1 AVF

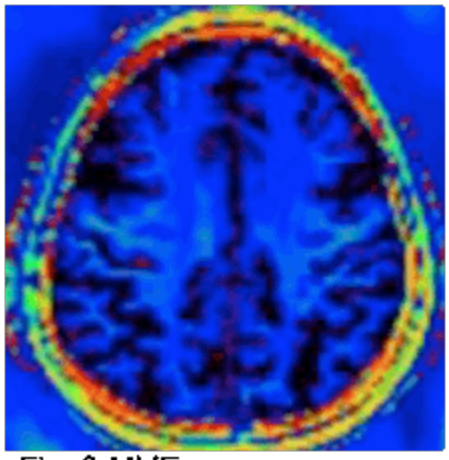


Fig. 2 MVF

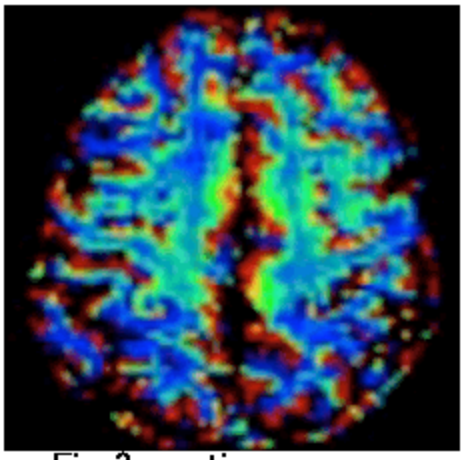


Fig. 3 g-ratio

(Filename: TCT_P-34_ASNR2017.gif)

P-11

6:30AM - 3:00PM

Feasibility study of Language Lateralization using Thai version of Language Paradigm for Functional MRI in Clinical Service

J Wongsripuemtet[1], C Ngamsombat[1], O Chawalparit[1]
[1]*Department of Radiology, Faculty of Medicine Siriraj Hospital, Mahidol University, Bangkok, Thailand*

Purpose
To evaluate the concordance of language lateralization between fMRI using Thai version of language paradigm and Wada test or awake surgery with direct cortical brain stimulation (DCS).
Materials and Methods
Retrospective study of 13 patients (3 males and 10 females with mean age of 33.9 years old) with epilepsy (7 cases) or brain tumor (6 cases) was performed. All underwent both fMRI (word generation, verb generation, naming picture and sentence completion tasks) and Wada test or awake surgery with DCS (defined as the gold standard). The lateralization index (LI)

of fMRI was calculated automatically by using the LI-toolbox on SPM8. The hemispheric lateralization also was evaluated visually. The concordance between fMRI and gold standard was analyzed.
Results
The concordance between the lateralization of fMRI by visual assessment and gold standard was 92.3%. Concordance between the calculated LI by fMRI and gold standard was varied along with the task and regional calculation method. The concordance was good in all tasks (except for naming picture task) when using calculated LI from frontal or whole brain excluded cerebellum and occipital lobe (range 76.92%-88.98% and 76.92-92.31%, respectively).
Conclusions
There was good concordance between fMRI and gold standard. Regional calculation from frontal lobes and whole brain excluded cerebellum and occipital lobes gave the best results. The results supported feasibility to use the fMRI with Thai language paradigm as an alternative way to determine the language dominant hemisphere in Thai patients. In case of language dominant hemisphere is unclear, further invasive investigation of language mapping such as Wada test or DCS is crucial.

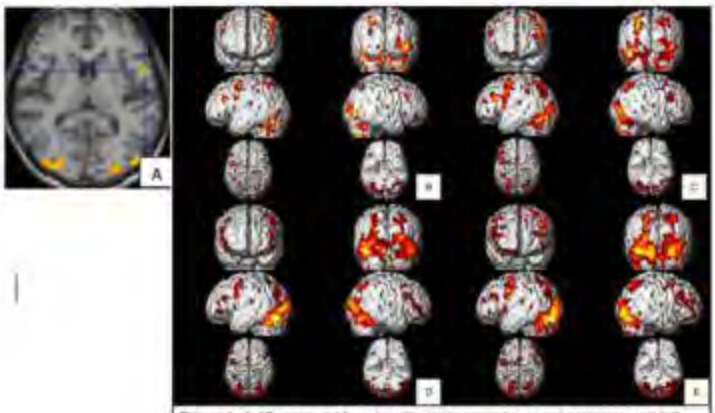


Figure 1. A 48 years old female with right mesial temporal sclerosis and left hemispheric lateralization by fMRI and Wada test. In verb generation paradigm, activation was demonstrated with Broca area at left inferior frontal gyrus (A). Activated areas on SPM overlying with volume rendering T1W image were seen from word generation (B), verb generation (C), naming picture (D) and sentence completion (E) paradigms fMRI.

Table 2 Concordance between fMRI and gold standard in tumor group

Region of interest	Concordance (%)			
	WG	VG	NP	SC
Frontal	5/6 (83.33)	6/6 (100.00)	4/6 (66.67)	3/4 (75.00)
Parietal	5/6 (83.33)	6/6 (100.00)	4/6 (66.67)	1/4 (25.00)
Temporal	3/6 (50.00)	5/6 (83.33)	2/6 (33.33)	3/4 (75.00)
Whole brain	3/6 (50.00)	4/6 (66.67)	2/6 (33.33)	2/4 (50.00)
Whole brain excluded cerebellum	4/6 (66.67)	5/6 (83.33)	2/6 (33.33)	2/4 (50.00)
Whole brain excluded cerebellum and occipital	5/6 (83.33)	6/6 (100.00)	5/6 (83.33)	2/4 (50.00)

Table 3 Concordance between fMRI and gold standard in epilepsy group

Region of interest	Concordance (%)			
	WG	VG	NP	SC
Frontal	5/7 (71.43)	5/7 (71.43)	4/6 (66.67)	4/5 (80.00)
Parietal	5/7 (71.43)	5/7 (71.43)	3/6 (50.00)	5/5 (100.00)
Temporal	2/7 (28.57)	6/7 (85.71)	4/6 (66.67)	1/5 (20.00)
Whole brain	2/7 (28.57)	5/7 (71.43)	2/6 (33.33)	3/5 (60.00)
Whole brain excluded cerebellum	4/7 (57.14)	7/7 (100.00)	2/6 (33.33)	4/5 (80.00)
Whole brain excluded cerebellum and occipital	5/7 (71.43)	6/7 (85.71)	2/6 (33.33)	5/5 (100.00)

(Filename: TCT_P-11_pic.jpg)

P-51

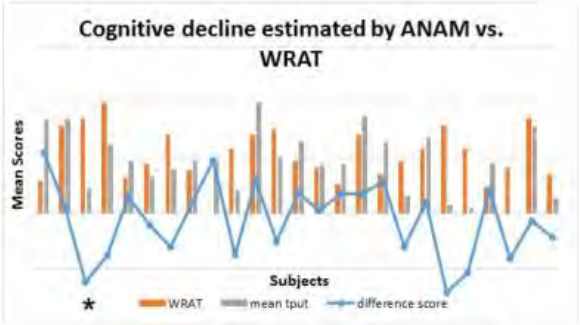
6:30AM - 3:00PM

Global Fractional Anisotropy (FA) in DTI is Correlated with Neurocognitive Impairment in Retired NFL Players

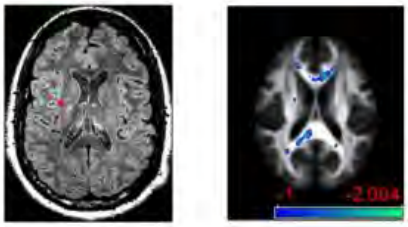
R Benson[1], R Gattu[1], G Trifan[2], J Woodard[3], K Meyers[3], T Halstead[3], V Baragi[1], E Hipple[4], M Haacke[3]
[1]Center for Neurological Studies, Novi, MI, [2]University of Illinois, Chicago, IL, -, -, [3]Wayne State University, Detroit MI, -, -, [4]Eisenhower Center, Ann Arbor, MI, -, -

Purpose
Neuropsychological decline from head trauma in tackle football can augur the onset of diseases such as Alzheimer disease and Chronic Traumatic Encephalopathy. Characterizing the specific findings neuropsychologically and identifying neuroimaging biomarkers in individuals that show decline can serve as the basis for screening and risk assessment (1). This is a report on our ongoing efforts towards evaluating the neurocognitive impairment and neuroimaging findings in former NFL players with demonstrated neuropsychological declines.
Materials and Methods
Twenty-five former NFL players with cognitive and psychiatric symptoms underwent the Wide Range Achievement Test-IV (WRAT-IV) Reading subtest to assess premorbid functioning and the Automated Neuropsychological Assessment Metric-Version 4 (ANAM4™) to assess current cognitive functioning. Subjects were scanned using a 3T Siemens Verio system. Diffusion tensor imaging (DTI) was acquired using 30 directions (1.3x1.3x2 mm; 60 axial slices; TR/TE = 13300/124 ms, and b-values of 0 and 1000 sec/mm2). Scans also included 3D FLASH T1, T2, ASL, MRS, rsfMRI, SWI and FLAIR. We report only the DTI and FLAIR findings currently, which utilized the global white matter (FA) mean and the total white matter hyperintensity lesion count (excluding periventricular lesions), respectively.
Results
There was a high degree of intrasubject inter-task correlation across the ANAM throughput measures so that a single, composite (average), was used to correlate with imaging measures. Twelve of 25 (48%) of the subjects demonstrated some degree of cognitive decline relative to premorbid estimate (Fig. 1). This decline was reflected in almost all the neuropsychological parameters assessed (data not shown). Diffusion tensor imaging analysis revealed a positive correlation between global FA values and the mean throughput scores – a composite assessment of neuropsychological metrics ($r = 0.44$, $P<0.05$). FLAIR, on the other hand, demonstrated a positive relationship between the number of brain lesions and subjects' age ($r = 0.58$, $P<0.01$).

Conclusions
Diffusion tensor imaging has potential utility in identifying neurocognitive impairment in retired NFL players.



Plot: Standard scores for mean ANAM tput and WRAT by subject. Blue line is difference between ANAM tput and WRAT. Decline is thus negative.



Images: FLAIR and DTI for S3 showing a single hyperintensity on FLAIR with DTI revealing many more regions of abnormality shown in blue-green pseudocolor.

(Filename: TCT_P-51_imageforabstractbenson.jpg)

P-20

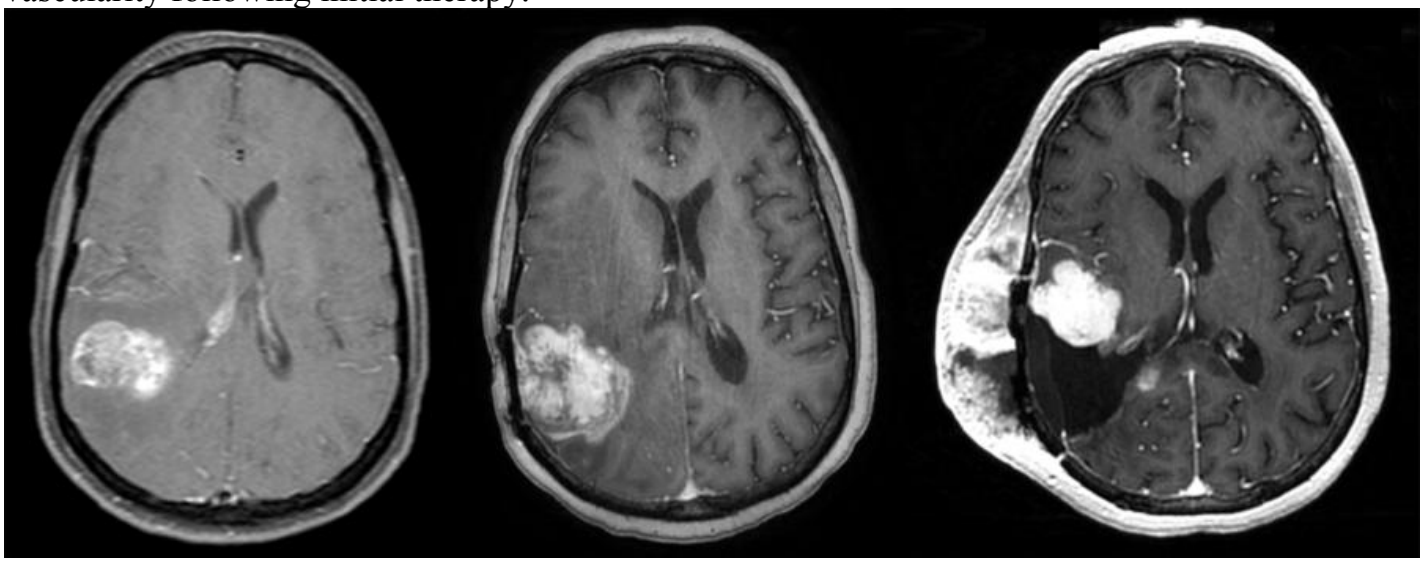
6:30AM - 3:00PM

Imaging Characteristics of Gliosarcoma with Special Emphasis On Dural Involvement At Initial Presentation and At Recurrence

B Merritt[1], T Tihan[1], S Cha[1]
[1]*University of California, San Francisco, San Francisco, CA*

Purpose
Gliosarcoma is a rare and distinct variant of glioblastoma comprised of both malignant glial and sarcomatous components. Few reports have suggested characteristic location of gliosarcoma associated with dura mater (1, 2). The purpose of our study was to investigate MR imaging characteristics of gliosarcoma with particular attention to involvement of dura, recurrence pattern, and quantitative perfusion and diffusion-weighted imaging.
Materials and Methods
Forty patients with histopathologically confirmed gliosarcoma were selected retrospectively from the neuropathology database from 2010 to 2016 at our institution according to IRB-approved protocols. For each patient, detailed clinical history and MR imaging

characteristics were analyzed including dural involvement at initial diagnosis or at recurrence. Apparent diffusion coefficient (ADC) and relative cerebral blood volume (rCBV) were measured prior to surgery.
Results
Of the forty patients included in this study, twenty-three were primary gliosarcoma (PGS) and seventeen were secondary gliosarcoma (SGS). Twenty of twenty-three (87%) PGS demonstrated dural involvement and seventeen of seventeen (100%) SGS showed dural or extradural involvement. Average ADC values for PGS and SGS were 0.608 +/- 0.194 (× 10-3 mm2/sec) and 0.513 +/- 0.234 (× 10-3 mm2/sec), respectively (p=0.19). Average rCBV values for PGS and SGS were 2.82 (+/- 1.25) and 1.97 (+/- 0.35), respectively (p=0.02).
Conclusions
Dural and extradural involvement were highly specific imaging features of gliosarcoma. There was no difference in ADC values between PGS and SGS, however, significantly lower rCBV values were found in SGS when compared to PGS suggesting altered tumor vascularity following initial therapy.



(Filename: TCT_P-20_ASNR.jpg)

P-29

6:30AM - 3:00PM

Imaging Features of Primary Trigeminal Nerve Tumors: Case Series and Review of the Literature

R Valenzuela[1], M Ramirez-Guzman[2], L Ocasio[2], A Cano-Duran[1], R Riascos[1]
[1]The University of Texas, Houston, TX, [2]Memorial Hermann Hospital, CAIP, Houston, TX

Purpose
To present the imaging features of schwannomas, neurofibromas, and neurofibrosarcomas of

the trigeminal nerve. We present the imaging features and their anatomic distribution of 11 cases of primary trigeminal nerve sheath tumors.

Materials and Methods

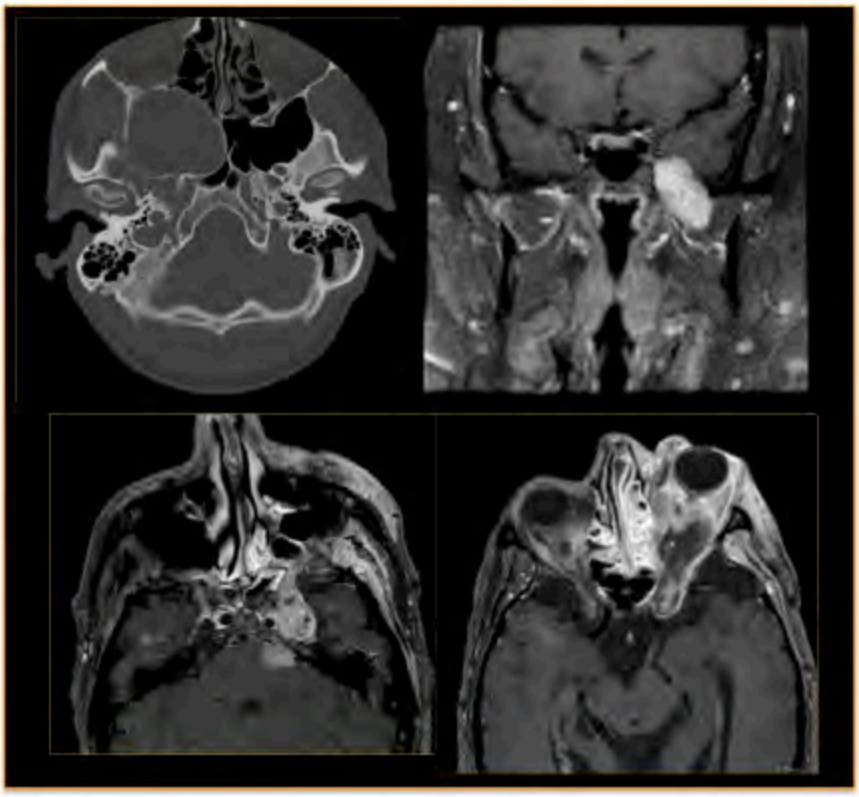
Retrospective study of 11 cases with histological diagnosis of trigeminal nerve sheath tumors is presented. Patient age, gender, tumor distribution, magnetic resonance imaging (MRI) pattern and volume were the analyzed variables.

Results

Patients age ranged from 27 to 81 years old. The average age for neurofibroma and schwannoma patients was 44 years. A single case of a neurofibrosarcoma with medical history of neurofibromatosis type I is presented. Initial imaging diagnosis and differentiation between benign and malignant sheath nerve tumors was performed by MRI interpretation by specialized neuroradiologists. Histopathological analysis showed nine schwannomas (88%), one neurofibromas (9%), one neurofibrosarcoma (9%). Trigeminal nerve tumor distribution in schwannoma was at the main trunk (1), Meckel's cave (1), Meckel's cave with V2 branch extension (1), Meckel's cave with V3 branch extension (2), isolated V2 and V3 branch involvement (2), V2 infraorbital canal and pterigopalatine fossa (1), and V3 pterigopalatine fossa exclusively (1). Tumor distribution in neurofibroma was V2 infraorbital with cavernous sinus extension (1). Tumor distribution in neurofibrosarcoma was V1 branch, intraorbital with cavernous sinus extension (1). Average volume was 33cm3 for schwannoma and neurofibroma, and 61cm3 for neurofibrosarcoma. On MRI, schwannomas and neurofibroma tumors were iso-hypointense on T1-weighted images and hyperintense on T2-weighted sequences. On CT, bone remolding was the main feature. Only the neurofibrosarcoma had low T1 signal because of central necrosis. After contrast administration, all tumors enhanced heterogeneously with intratumoral septa. The neurofibrosarcoma showed ring enhancement.

Conclusions

Low signal on T1, a high signal on T2 and postcontrast enhancement has been proposed as the typical MRI pattern for trigeminal nerve sheath tumors (1, 2). Our results correlate with previous descriptions. Meckel's cave has been proposed as the most common location for schwannomas and a very rare location for neurofibromas (1, 2), helping the differentiation between both of them. Trigeminal nerve schwannomas account for 0.07% to 0.36% of all intracranial tumors. Peripheral trigeminal schwannoma originating from the mandibular branch is a very rare location. Neurofibroma of the trigeminal nerve is a rare entity. Neurofibrosarcoma arising from the first branch of the trigeminal nerve is a rare tumor presentation. Moreover, we describe malignant nerve sheath V1 tumor on a male patient with medical history of neurofibromatosis type 1. The main imaging difference between benign and malignant trigeminal.



(Filename: TCT_P-29_Schwannomafinal.jpg)

P-14

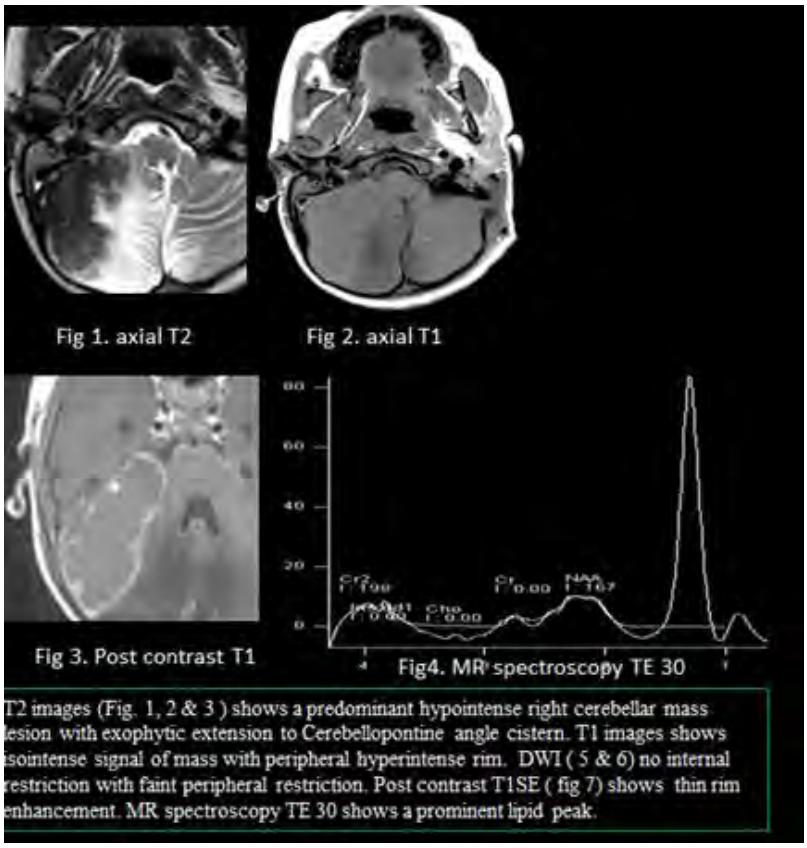
6:30AM - 3:00PM

Imaging of Giant Tuberculoma, a Potential Masquerader

A Gupta[1], S TIWARI[2], j saini[3], R Bharath[4], C Prasad[5], H PENDHARKAR[6], A RAMALINGAIAH[7], A Verma[8]

[1]National Institute of Mental Health and Neurosciences, India, Bangalore, Karnataka, [2]National Institute of Mental Health and Neurosciences, BANGALORE, Karnataka, [3]NIMHANS, BANGALORE, Karnataka, [4]National Institute of Mental Health & NeuroSciences, Bangalore, Karnataka, [5]National Institute of Mental Health and Neurosciences, Bangalore, Karnataka, [6]NATIONAL INSTITUTE OF MENTAL HEALTH & NEUROSCIENCES, BANGALORE, KARNATAKA, [7]NATIONAL INSTITUTE OF MENTAL HEALTH AND NEUROSCIENCE, NIMHANS, Bengaluru , karnataka, [8]national Institute of Mental health & Neuro Sciences, Bangalore, Karnataka

Purpose
Intracranial tuberculosis continues to be a serious problem in both the developing and developed world, with significant morbidity and mortality. A giant and solitary tuberculoma can mimic a neoplasm, both clinically and radiologically. This retrospective case series aims to evaluate the varied imaging spectrum of large intracranial tuberculomas, both the common and uncommon appearances.
Materials and Methods
This retrospective case series includes sixteen patients (12 male, 4 female; age range: 2 – 50 years; median age: 19.5 years) diagnosed and treated at our institute. MR studies were performed on 3 T and 1.5 T clinical MR systems. An arbitrary cut off size of 2.5 cm was taken for giant tuberculomas. All patients were reviewed by 2 experienced neuroradiologists and imaging findings were tabulated.
Results
Ten lesions were located in supratentorial neuroparenchyma (7 in cerebral parenchyma and 3 in Gangliothalamic region) and 6 were infratentorial (4 cerebellar, 1 vermian and 1 pontine). Ten patients presented with solitary lesions. Size varied from 2.5 cm to 7.2 cm. A faint internal T1 peripheral/central hyperintensity (75%), T2 hypointense center (62.5%), irregular peripheral postcontrast enhancement with inner wall projections (93%) and faint peripheral restricted diffusion (50%) were the common imaging findings.
Conclusions
Giant tuberculoma should be suspected in patients with intracranial space occupying lesions who live in geographic areas where tuberculosis is endemic.



(Filename: TCT_P-14_Picture3.jpg)

P-27

6:30AM - 3:00PM

Kink of the Optic Nerve at the Optic Canal Orifice Correlates with Irreversible Visual Impairment in Patients with Pituitary Macroadenoma: A Contrast-Enhanced FIESTA Study

S Hisanaga[1], S Kakeda[1], J Moriya[1], Y Korogi[1]
[1]*University of Occupational and Environmental Health, School of Medicine, Kitakyushu, Fukuoka*

Purpose
To determine whether or not the degree of kink in the optic nerve (ON) at the optic canal orifice on contrast-enhanced fast imaging employing steady-state acquisition (CE-FIESTA) correlates with the subsequent surgical outcome of visual impairment in patients with pituitary macroadenoma.
Materials and Methods
The institutional review board approved this retrospective study. Thirty patients with pituitary macroadenoma who underwent pre-operative magnetic resonance imaging (MRI) and surgery were evaluated retrospectively. All patients had visual acuity disturbance (VAD)

and/or visual field defect (VFD). We measured the ON kinking angle (ONKA) on sagittal oblique CE-FIESTA parallel to the ON; the ONKA was defined as the angle between a line extending across the anterior cranial fossa and a line through the intracranial ON at the optic canal orifice (Figure). We used logistic regression analyses to determine whether or not the clinical (sex, age, and duration of symptoms) and imaging (tumor size, chiasmal compression severity, hyperintense ON on T2WI, and ONKA) characteristics were associated with the postoperative improvement (good vs. little improvement) of the VAD and VFD.

Results

There were 55 impaired sides before surgery: 2 sides with VAD alone, 25 with VFD alone, and 28 with both. After surgery, good improvement was found in 16 of the 30 sides with VAD and in 31 of the 53 sides with VFD. The logistic regression analyses revealed that only increasing ONKA was significantly associated with good improvement of the VAD ($p=0.024$) and VFD ($p=0.010$).

Conclusions

The degree of ONKA was found to be an independent predictor of postoperative improvement, indicating that irreversible damage of the ON may be associated with its kinking at the optic canal orifice.

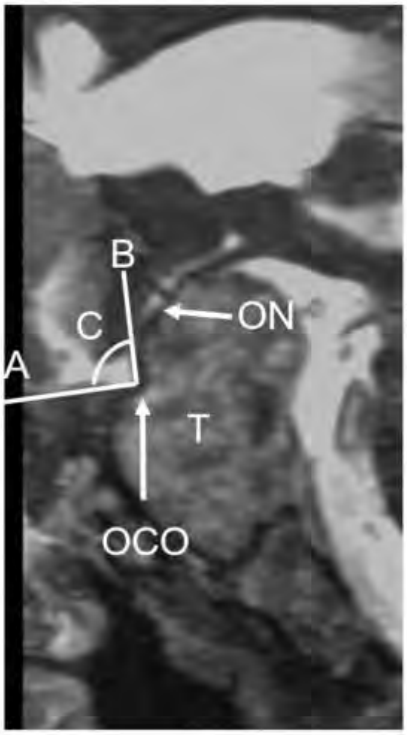


Figure.
A sagittal oblique CE FIESTA images form a patients with pituitary macroadenoma.
A = line extending across anterior cranial fossa, B = line through intracranial optic nerve, C = optic nerve kinking angle, ON = optic nerve, OCO = optic canal orifice, and T = tumor.

(Filename: TCT_P-27_1.jpg)

P-19

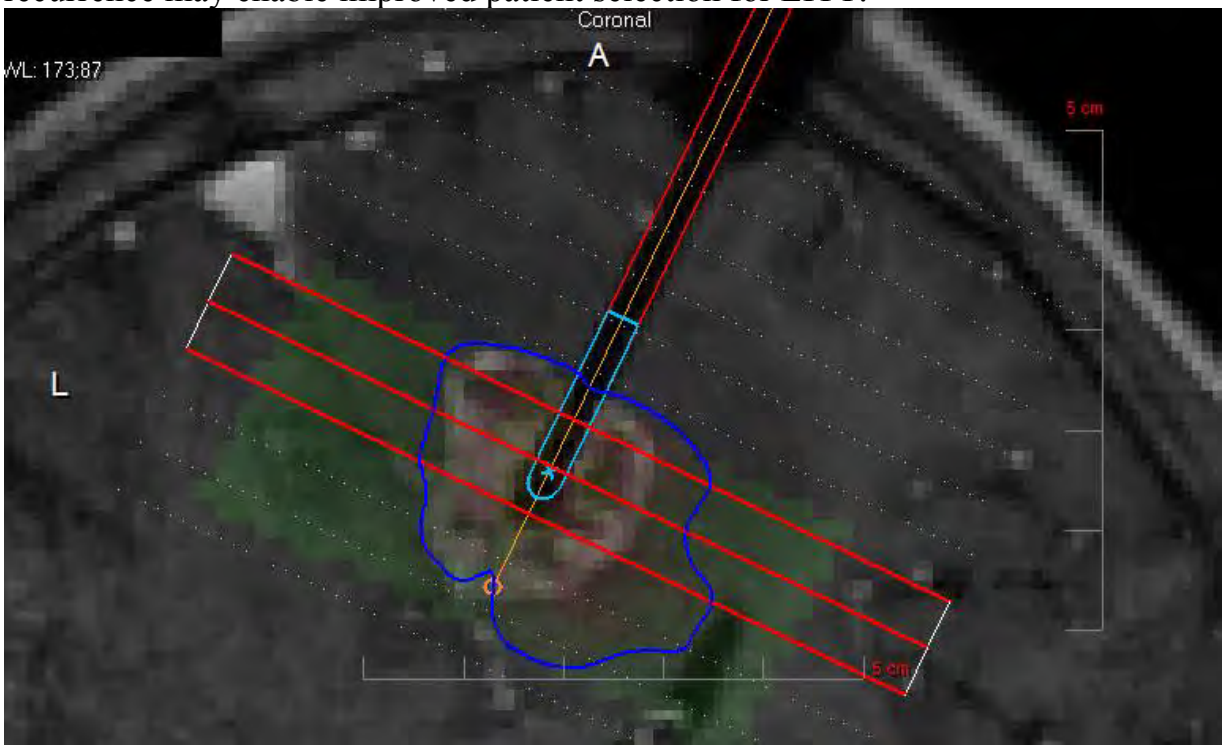
6:30AM - 3:00PM

Laser Interstitial Thermal Therapy for the Treatment of Intracranial Metastasis: An Evaluation of Pretreatment Tumor Features and Posttreatment Outcomes

S Calle[1], D Bastos[1], S Prabhu[2], K Shah[1], V Kumar[3]
[1]MD Anderson Cancer Center, Houston, TX, [2]U.T. MD Anderson Cancer Center, Houston , TX, [3]U.T. MD Anderson Cancer Center, Houston, TX

Purpose
To evaluate the imaging features of brain metastases treated with laser interstitial thermal therapy (LITT) at our institution in order to establish which characteristics may be helpful in predicting success or failure postablation.
Materials and Methods
A retrospective review was made of patients having undergone LITT for the treatment of brain metastases between August of 2013 and October of 2016. Thirty-seven cases were collected for analysis. The following imaging characteristics prior to treatment were recorded: mass size, tumor histology, prior therapy, location of mass, tumor morphology and proportion of internal solid/cystic components. The patients' pretreatment and follow-up imaging studies were reviewed to determine whether there was treatment response or tumor recurrence.
Results
A total of thirteen of thirty-seven patients showed a recurrent enhancing mass developing within a range of 3 months to over a year following ablation. Of these thirteen patients, 6 required surgery for resection of enlarging masses. Pathology revealed viable tumor in 5/6 resected masses and 1 case of radiation necrosis. Of the thirty-seven patients, thirteen showed a favorable response to treatment with reduction in size of the masses on follow-up exams obtained at least 3 months following the procedure and in many cases up to 6 months later. In eleven of the cases the patients did not show clear response or progression and further observation is required. The most common primary tumors were breast (11/37), melanoma (10/37), and lung (9/37). No correlation was made between the primary histology and response to LITT. All patients had received treatment with gamma knife therapy, surgical resection or a combination of both prior to LITT. Preliminary results indicate that superficially located and dural-based masses have a higher tendency for treatment failure. Of the thirteen patients who recurred, 5 had dural-based lesions and 5 were cortically-based, while the remaining 3 were either centrally located within the white matter or adjacent to ventricle. Conversely, of the thirteen patients with favorable response only one was dural-based. The average pretreatment volume was 6.04 cm^3, with tumor volumes that exceed 4 cm^3 serving as a risk factor for postoperative tumor recurrence.
Conclusions
Lesions at locations known to be technically challenging for LITT (cortex and dura) and

larger lesions have a higher tendency for recurrence. Knowledge of factors relevant to recurrence may enable improved patient selection for LITT.



(Filename: TCT_P-19_LITT.jpg)

P-36

6:30AM - 3:00PM

Magnetic Resonance Diffusion-Weighted Imaging in Patients with Migraine and Acute Neurological Deficits

A DeHavenon[1], L Chung[1], K Mickolio[1], S O'Donnell[1], J McNally[1], M Peckham[1]
[1]*University of Utah, Salt Lake City, UT*

Purpose
Complicated migraine is a known stroke mimic. Patients present with focal neurological deficits affecting vision, sensation, language, and motor strength. Areas of localized abnormality on perfusion imaging have been reported, but it is believed that cytotoxicity or tissue infarction is not present in the majority of patients. Our aim was determine if quantitative volumetric analysis of MRI diffusion-weighted imaging (MRI-DWI) could detect abnormalities in patients presenting with complicated migraine who had a negative qualitative interpretation of their MRI.
Materials and Methods
We retrospectively identified consecutive patients who presented to the emergency department from 2013-2015 as an "acute stroke code," but in whom the final diagnosis was complicated migraine with focal neurologic deficits. To be included, patients had an MRI

with DWI at presentation that was negative for true diffusion restriction and therefore without acute infarct. Magnetic resonance imaging was analyzed with the Olea Sphere software, which generated an ADC map from the B1000 DWI images. Magnetic resonance imaging-DWI abnormality was defined as ADC value <600×10−6 mm2/s.

Results

Inclusion criteria was met by 24 patients. The majority of patients, 13/24 (54%), had an MRI interpreted as normal by the neuroradiologist and volumetric software, but 11/24 (46%) had a MRI-DWI abnormality identified only by Olea Sphere volumetric software. In the 11 patients with MRI-DWI abnormalities with Olea Sphere software, the lesion volumes were small (mean±SD volume of 1.79±0.80 mL). Five of eleven (46%) had MRI-DWI abnormalities in a brain region that correlated with the neurologic symptoms (Figure 1) and 6/11 (54%) had MRI-DWI abnormalities in regions that did not correlate with symptoms.

Conclusions

Patients with complicated migraine have initiated a cascade of neurochemical processes that can lead to decreased blood flow and cortical hypometabolism, and may culminate in ischemic stroke. Our data support prior studies that have shown focal perfusion deficits during migraine, and expands that literature to include quantitative MRI-DWI abnormalities in a significant subset of patients, which likely represents a phenotype along the migraine-stroke spectrum. This finding warrants additional study to better understand pathophysiology and prognostic value.

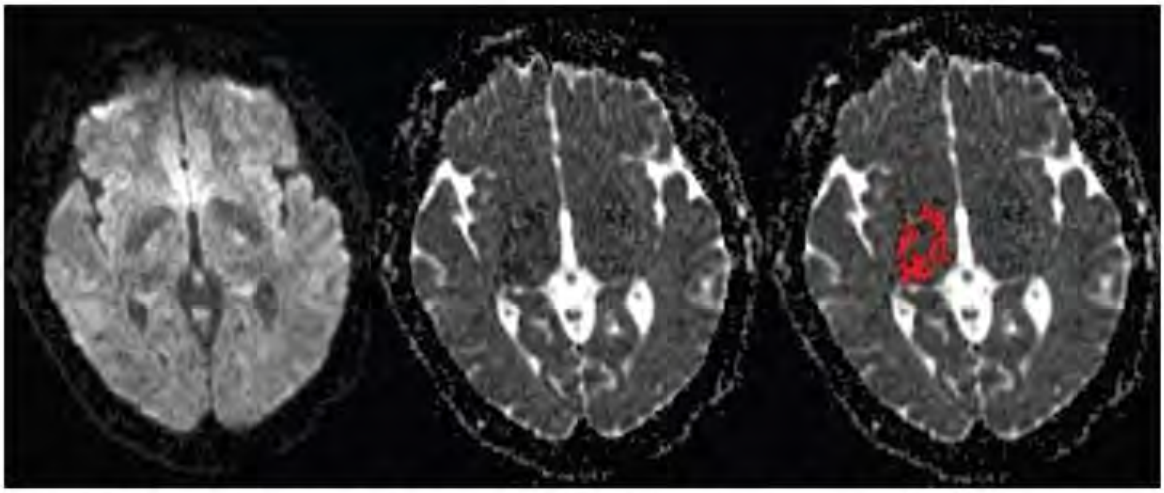


Figure 1: 56 year-old woman presented with acute headache and left-sided numbness. MRI-DWI B1000 and ADC map showed no evidence of diffusion restriction. ADC map analyzed with Olea Sphere software (far right image) revealed right thalamus lesion correlating to patient's clinical presentation.

(Filename: TCT_P-36_ASNR_Figure1_V3.jpg)

P-15

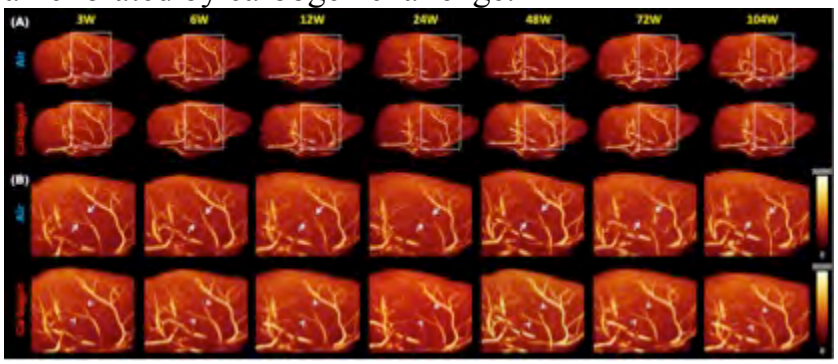
6:30AM - 3:00PM

Normal Senescent Changes of Intracranial Arteries: a Lifespan Longitudinal Time-of-flight Magnetic Resonance Angiography Study in Mice

T Siow[1], C Toh[1], N Yao[2], C Huang[2], C Chang[2]
[1]Chang Gung Memorial Hospital at Linkou, Taoyuan, Taiwan, [2]Institute of Biomedical Sciences, Academic Sinica, Taipei, Taiwan

Purpose
The objective of the present study is to evaluate the lifespan longitudinal changes of intracranial arteries in murine model in order to provide a better understanding of the normal senescent changes of cerebrovasculature.

Materials and Methods
Intracranial arterial changes in normal C57BL/6J mice (n= 6) were characterized over the lifespan (i.e., 2 years) using three-dimensional time-of-flight magnetic resonance angiography (3D TOF MRA) under inhalation of air and carbogen. Carbogen challenge was used as a vasodilatory stimulus to assess cerebrovascular reactivity (1, 2). All animals were scanned for 3D TOF MRA at weeks 3, 6, 12, 24, 48, 72 and 104. The whole-brain vessel length (VL) was calculated by summing the lengths of all the visible vessel lines. Total number of discernible vascular branches (VB) was calculated by summing the branching points. The average vessel diameter (VD) was quantified by computing the average Euclidean distance map of the vasculature.
Results
Figure 1 shows the serial 3D TOF MRA of mouse brain over the lifespan. The VB and VL decreased with age, as indicated by repeated measures ANOVAs [VB: ($F(6, 28) = 50.5$, $p < 0.0001$); VL: ($F(6, 28) = 16.5$, $p < 0.0001$)]. There was a lower VD in aged mice, but the trend was not statistically significant [VD: ($F(6, 28) = 1.142$, $p = 0.3845$)]. The VL and VD increased significantly after carbogen challenge, which occurred during the early life times and persisted to old age. However, significant increase of VB after carbogen challenge was observed only in aged mice.
Conclusions
The current study documented the longitudinal changes of the intracranial arteries in normal aging mice over their lifespan using 3D TOF MRA. The results showed a progressive decline in the visibility of cerebral arteries on 3D TOF MRA, but it can be largely ameliorated by carbogen challenge.



(Filename: TCT_P-15_ASNR.jpg)

P-24

6:30AM - 3:00PM

Prognostic Value of Tumor Volume in Patients with Primary CNS lymphoma: A Preliminary Analysis

G BATHLA[1], G Riesberg[2], U Farooq[2], p watal[3], B Smith[2], T Moritani[4]

[1]University of Iowa hospitals and Clinics, IOWA CITY, IA, [2]University of Iowa hospitals and Clinics, iowa city, IA, [3]university of iowa hospital and clinics, iowa city, IA, [4]University of Iowa Hospitals and Clinics, Iowa City, IA

Purpose

To evaluate the prognostic implications of tumor volumes in patients with primary central nervous system (CNS) lymphoma at the time of initial diagnosis.

Materials and Methods

The patient registry at the authors institute was reviewed to extract immunocompetent patients diagnosed with primary CNS lymphoma (PCNSL) between 2011 and 2014. Prior IRB approval was obtained. This revealed a total of 19 patients. Patients who did not have thin section postcontrast imaging (5), leptomeningeal lymphoma (1), or prebiopsy MR imaging (1) or had concurrent systemic lymphoma (1) were excluded. This revealed a total of eleven patients in which tumor volumes were calculated. 3D volumetric data were acquired using the Vitrea® software (version 6.6.2, Vital images, Toshiba Medical Systems, Minnetonka, MN). In all cases, the tumor was outlined manually on the 1 mm axial postcontrast SPGR images followed by computerized compilation of summated tumor volume. Tumor volumes were analyzed to evaluate correlation with 2-year event-free survival (EFS). Univariable Cox regression was used to estimate the effects of volume on survival.

Results

Mean patient age at diagnosis was 58 years (43-77 years). There were 6 males and 5 females. Mean tumor volume at diagnosis was 20.07 cc (Range: 4.51-36.29 cc). Statistical analysis (Table 1) revealed a trend towards lower 2-year event free survival (EFS) with increasing tumor volumes. The values however did not reach statistical significance, likely due to the small sample size involved.

Conclusions

Semi-automated 3D tumor volumes may be useful to predict 2-year EFS in patients with PCNSL. Our work demonstrates a trend towards lower EFS in patients with higher tumor volumes at diagnosis. The absence of statistical significance is thought to be secondary to a small sample size.

Table-1: Univariable Cox regression shows increased hazard rates for every 10 cc increase in tumor volumes.

	N	Events	HR*	95% CI*	p-value
EFS	11	6	1.22	(0.62, 2.43)	0.5662

(Filename: TCT_P-24_Table-1-1.jpg)

P-12

6:30AM - 3:00PM

Pseudotumoral Brain Lesions: Multimodal MRI Approach

O Telis[1], N Sgarbi[2]
[1]Hospital de Clinicas, Montevideo, Uruguay, [2]Hospital de Clínicas, Montevideo, Montevideo

Purpose
In clinical practice it is relatively frequent to face patients with space occupying lesions of very different origin. In a significant percentage of cases the final diagnosis is complex and magnetic resonance imaging (MRI) plays a key role in the chosen algorithm. Although MRI allows a precise approximation to diagnosis in the majority of cases the functional sequences are the most helpful. Our goal is to highlight the role and contributions of functional MRI techniques, diffusion, perfusion and spectroscopy, to the final diagnosis in pseudotumoral brain lesions.
Materials and Methods
We analyzed in a prospective way the data obtained in a group of 50 patients who were studied in our service between January 2014 and December 2016, with a final histopathological diagnosis of nontumoral lesions with conventional MRI findings of brain tumor. In these cases we obtained the information of functional techniques and highlight their contribution to differential diagnosis.
Results
We found thirty patients with pseudotumoral demyelinating solitary lesions, seventeen infectious lesions, mostly in HIV positive patients, and 3 of vascular origin with atypical behavior. In all patients the functional findings allowed the pre-operative diagnosis of pseudotumoral lesions with perfusion technique having the most significant contributions. In the lesions of infectious nature diffusion technique had fundamental contributions whereas in spectroscopy 35 of 50 patients presented metabolic pattern similar to tumors.
Conclusions
The precise interpretation of the findings in functional sequences in patients with tumor-like lesions is essential and should be included in the routine protocol of these patients.

P-04

6:30AM - 3:00PM

Quantitative Evaluation of Time-dependent Changes between 123I-FP-CIT SPECT Examinations in the Patients with Lewy Body Disease

T Nakatsuka[1], T Inaoka[1], H Terada[1]
[1]Toho University Sakura Medical Center, Sakura, Chiba, Japan

Purpose
To quantitatively evaluate and compare time-dependent changes between 123I-FP-CIT SPECT examinations in patients with Parkinson disease (PD) and dementia with Lewy bodies (DLB).
Materials and Methods
We retrospectively reviewed twenty-five patients with PD (age, 67.0±6.0 years old; 13 male, 12 female; Hoehn and Yahr scale, 2.3±0.6; time interval between 123I-FP-CIT SPECT examinations, 18.3±6.3 months) and seventeen patients with DLB (age, 73.3±7.1 years old; 10 male, 7 female; Hoehn and Yahr scale, 2.9±0.7; time interval between 123I-FP-CIT SPECT examinations, 18.8±5.5 months) who had undergone 123I-FP-CIT SPECT examinations twice from 2014 to 2016. The striatal accumulation of 123I-FP-CIT was measured as the specific binding ratio (SBR) proposed by Tossici-Bolt et al (1). Primary endpoints in this study were 1) ipsilateral and contralateral ΔSBRs between 123I-FP-CIT SPECT examinations and per year in the patients with PD and 2) average ΔSBRs between 123I-FP-CIT SPECT examinations and per year in the patients with DLB.
Results
1) Ipsilateral ΔSBRbe was -0.15±0.50, contralateral ΔSBRbe was -0.05±0.45, ipsilateral ΔSBR1y was -0.16±0.38 and contralateral ΔSBR1y was -0.09±0.31. 2) Average ΔSBRbe was -0.40±0.70 and average ΔSBR1y was -0.20±0.41.
Conclusions
Ipsilateral ΔSBRs were larger than contralateral ΔSBRs between 123I-FP-CIT SPECT examinations and per year in the patients with PD. Average ΔSBRs between 123I-FP-CIT SPECT examinations and per year in the patients with DLB were larger than those in the patients with PD. Our results may indicate the asymmetry striatal accumulation of 123I-FP-CIT is obscured by the progression of PD and resembles that in the patient with DLB.

P-08

6:30AM - 3:00PM

Resting-state fMRI for Preoperative Localization of Supplementary Motor Area: Evaluation in Patients with Brain Tumors

J Wongsripuemtet[1], H Sair[2]
[1]Johns Hopkins Hospital, Baltimore, MD, [2]Johns Hopkins Medicine, Baltimore, MD

Purpose
The supplementary motor area (SMA) is one of the distinct anatomic and functional areas. There are many studies reporting a variety of neurological deficits after SMA surgery or manipulation, including transient motor weakness, aphasia or bradykinesia. For this reason, the pre-operative functional imaging would be of benefit for presurgical evaluation and treatment planning. Resting state fMRI recently has been considered as a possible alternative

or complement to task-based fMRI for surgical mapping. The purpose of this study is to evaluate the utility of resting-state fMRI (rs-fMRI) with seed-based analysis (SBA) method in localization of SMA in patients with intrinsic brain tumors and normal healthy subjects.
Materials and Methods
Pre-operative rs-fMRI studies were performed in 66 patients with brain tumors (38 males and 28 females) and 42 rs-fMRI data of 21 normal healthy subjects (11 males and 10 males) which derived from the datasets of Kirby 21 Multi-Modal reproducibility Study were used in this study. The rs-fMRI data for each patients and subjects then were analyzed with seed-based analysis method using difference seed regions from right hand motor area, left hand motor area, both hand motor areas, right tongue motor area and left tongue motor areas. Identification of the activated connectivity at SMA on postprocessing rsfMRI images were done by experienced neuroradiologists. The number and percentage of positive connectivity at SMA seen by each seed region in patients and normal subjects were analyzed with Mcnemar Chi-square test. Repeatability of the test from left and right motor area seeding in normal subjects were examined. The tumor location and volume were evaluated by conventional MRI.
Results
The group of 66 patients (35/66 are low grade glioma, 25/66 are high grade glioma, 2 cases are metastases and 1 case is myeloid sarcoma), there are 7 lesions involve areas of SMA. The percentage of SMA detection by using seed regions from hand motor area is statistical significant different from those using tongue motor area seeding (75.8% vs 30.3%, p-valute < 0.001). There is statistical significant difference between number of SMA detection when using seed region from single (left or right) hand motor task and both-hand motor area. The percent SMA detection from both-hand seeding is 95.4% (63/66). No statistical significant difference between number of SMA detection in rs-fMRI by using motor hand seeding in patients and normal control subjects. High repeatability of rs-fMRI in term of SMA detection in normal subject (Kappa score = 0.62) is observed.
Conclusions
Resting state fMRI (rs-fMRI) with seed-based analyses is able to identify the areas of SMA in patients with brain tumor and normal healthy subjects. The percent SMA detection is high when using seed region from both hand motor areas. This result shows that it is possible to use rs-fMRI as one of the pre-operative imaging techniques, particularly in the subjects who have difficulties in performing task-based paradigm. Correlation rs-fMRI finding with task-based fMRI and intra-operative electrocortical stimulation might demonstrate the accuracy and feasibility of rs-fMRI in term of localization of the supplementary motor area (SMA) for presurgical planning.

Table1: Number of SMA detection by seeding areas in brain tumor patients and normal subjects

Seeding location	Brain tumor patients		Normal subjects	
	SMA detection	No SMA detection	SMA detection	No SMA detection
Right hand	50 (75.8)	16 (24.2)	34 (80.9)	8 (19.1)
Left hand	50 (75.8)	16 (24.2)	38 (90.5)	4 (9.5)
Both hand	63 (95.4)	3 (4.6)	40 (95.2)	2 (4.8)
Right tongue	20 (30.3)	46 (69.7)	-	-
Left tongue	20 (30.3)	46 (69.7)	-	-

Table2: Comparison of Number of SMA detection between single and both hand seeding

	% SMA detection	P-value*
Brain tumor patients		
Right hand VS Both hand	75.8 and 95.4	**<0.001**
Left hand VS Both hand	75.8 and 95.4	**<0.001**
Normal subjects		
Right hand VS Both hand	80.9 and 95.2	0.041
Left hand VS Both hand	90.5 and 95.2	0.479

Table3: Comparison of Number of SMA detection between hand and tongue motor seeding in brain tumor patients

	% SMA detection	P-value*
Right hand, Left hand	75.8	**<0.001**
Right tongue, Left tongue	30.3	

Table4: Comparison of percent SMA detection in normal subject and brain tumor patients by hand motor seeding

	SMA detection n(%)		P-value*
	Normal subjects	Brain tumor patients	
Total	42	66	
Right hand	34 (80.9)	50 (75.8)	0.637
Left hand	38 (90.5)	50 (75.8)	0.075
Both Hand	40 (95.2)	63 (95.4)	1.000

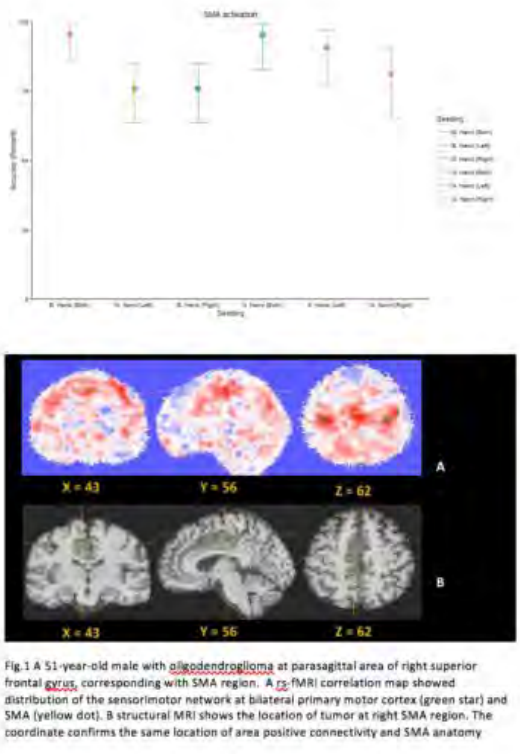


Fig.1 A 51-year-old male with oligodendroglioma at parasagittal area of right superior frontal gyrus, corresponding with SMA region. A rs-fMRI correlation map showed distribution of the sensorimotor network at bilateral primary motor cortex (green star) and SMA (yellow dot). B structural MRI shows the location of tumor at right SMA region. The coordinate confirms the same location of area positive connectivity and SMA anatomy

(Filename: TCT_P-08_Picture.jpg)

P-03

6:30AM - 3:00PM

Role of Multiparametric MRI to Differentiate MCI and Early Dementia due to Alzheimer's Disease

J Chaganti[1]
[1]*St Vincent's Hospital, Sydney, UNSW*

Purpose
To investigate the role of MR spectroscopy (MRS), arterial spin-labelling (ASL) cerebral blood flow (CBF) changes, diffusion and hippocampal volumetric to identify and characterize the minor cognitive impairment and early dementia.
Materials and Methods
Data were obtained from 100 patients with subjective complaints, and classified in to 2 groups based on clinical signs and neuropsychological assessment as mild cognitive impairment and AD. General linear- models were used to assess relationships between the MCI and AD with total and regional CBF, metabolite ratios derived from single voxel short

TE spectroscopy from right hippocampus, volumetric and diffusion tensor imaging and correcting for age and sex.
Results
Decreasing CBF was related to more advanced AD stages in all supratentorial regions (p for trend < 0.05). Posthoc testing revealed that CBF was lower in AD compared to controls in minor cognitive impairment in temporal and parietal regions, whilst there is global reduction in more advanced stages of cognitive impairment. There is more pronounced changes in metabolite ratios (reduced NAA CR and Increase in Choline/Creatine and increase in the myoinositol/ Creatine ratios). Composite score with p=< 0.005). When metabolite levels were compared to the neuropsychological evaluation reduction in glutamates and glutamines appears to be the most sensitive metabolite to measure the CI. Diffusion data (32 directions) showed reduced fractional anisotropy in AD was more generalized while in MCI, the FA was not affected in occipital and frontal white matter (P <0.005). However mean diffusivity was increased in AD in all regions, and in MCI in all but occipital and frontal regions.A composite score generated using volumetry, ASL, spectroscopy, DTI derived metrics demonstrated CI >95% to predict the diagnosis of Alzheimer disease independent to clinical variables.
Conclusions
Multiparametric MRI can characterize and differentiate the MCI and early dementia due to Alzheimer disease.

P-50

6:30AM - 3:00PM

Serial Gray Matter Proton MR Spectroscopy in Mild Traumatic Brain Injury

J Rosenthal[1], A Tal[2], Y Lui[1], O Gonen[1], I Kirov[1]
[1]New York University School of Medicine, New York, NY, [2]Weizmann Institute of Science, Rehovot, Israel

Purpose
Traumatic brain injury (TBI) has been shown to affect white matter (WM) as diffuse axonal injury (1), but recent evidence has suggested that gray matter (GM) is also affected, even in mild TBI (mTBI) (2, 3). In this study, we examine post-TBI longitudinal changes in the concentrations of N-acetyl-aspartate (NAA), creatine (Cr), choline (Cho), and myo-inositol (mI) in cortical GM (cGM) and the deep GM structures: thalamus, lentiform nucleus (LN), and caudate.
Materials and Methods
Fourteen mTBI patients (mean Glasgow Coma Scale=14.5) were scanned at 3T within 43 days of injury, and 373±74 days later (mean±SD) with proton MR spectroscopy (1H MRS) using a 10×8×4.5 cm (AP×LR×IS)=360 cc volume-of-interest, excited with PRESS TE/TR=35/1800 ms, and encoded to 480 voxels, each 1.0×1.0×0.75 cc. High resolution T1-

weighted MRI also was obtained and was used to acquire masks of total cGM and of individual deep GM structures using the longitudinal stream of the atlas-based segmentation software, FreeSurfer. The masks then were registered with the 1H MRS matrix and metabolic concentrations obtained by the phantom replacement method were corrected for partial volume by maximizing the mask voxel fraction (>0.7) and minimizing WM and CSF voxel fraction (both <0.3). We compared the concentration changes between time points 1 and 2 (TP 1, TP 2) using 2-tailed paired t-tests. We also compared the mask volumes between time points to test for atrophy and to correlate any metabolic changes to GM volume.

Results

Our quality control and partial volume constraints eliminated the caudate measurements in 7 patients, and therefore that structure was excluded from the statistical analyses. There was no difference in the NAA, Cr, Cho or mI concentrations between TP 1 and TP 2 in any of the remaining GM regions (all $p>0.09$). We report, however, larger concentration distribution range of the neuronal marker NAA in each region at the later TP, as evidenced by the interquartile ranges (IQR), a measure of distribution spread, being higher at TP 2 relative to TP 1: cGM (IQR, 1.61 vs. 0.49), thalamus (IQR, 1.9 vs. 0.9), and LN (IQR, 2.3 vs. 1.2). These results may represent evolving heterogeneity in neuronal metabolic status at the chronic stage, possibly a result of variable recovery mechanisms. Correlations with clinical outcome measured by neurocognitive testing and postconcussive symptom reports are ongoing to test the hypothesis that NAA changes are reflected of clinical status (these data are expected to be available in the coming months). Finally, there was no difference in GM volumes (normalized to intracranial size) between TP 1 and 2 (all $p>0.3$), indicating no atrophy in the studied regions.

Conclusions

While no changes were found in GM metabolism over 1 year after mTBI, a larger range of NAA concentrations at TP 2 suggests that metabolic recovery in neurons may differ among individual patients. This observation was consistent across all GM regions, warranting ongoing correlations with clinical outcome, which is well known to also vary amongst different patients (4).

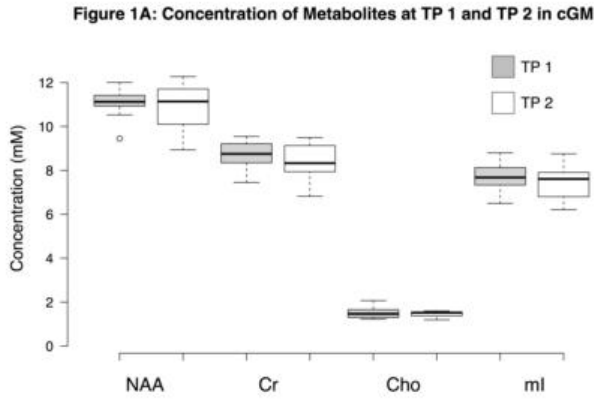
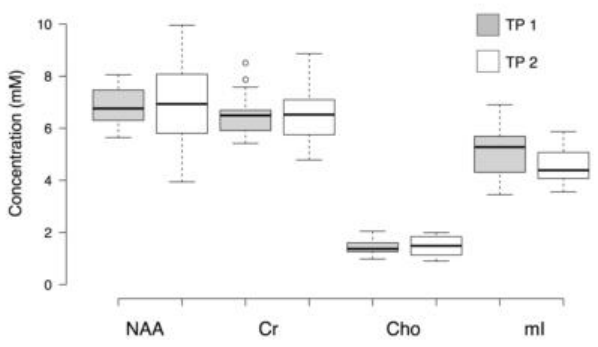
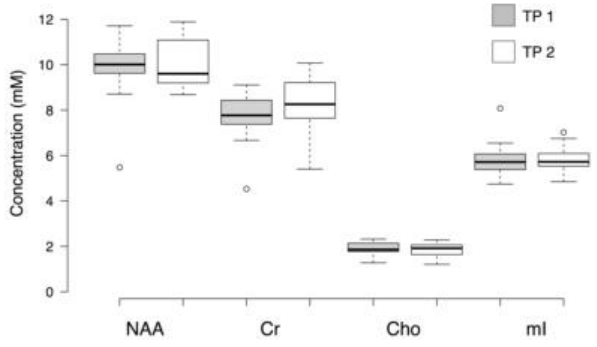


Figure 1: Concentrations of NAA, Cr, Cho, and mI at time point (TP) 1 and TP 2 in cortical gray matter (cGM) (Figure 1A), lentiform nucleus (LN) (Figure 1B), and thalamus (Figure 1C). No difference between time points is significant (all $p > 0.09$). The distribution range of NAA concentrations at TP 2 is larger than at TP 1 in all GM structures.





(Filename: TCT_P-50_ASNRFigure.jpg)

P-41

6:30AM - 3:00PM

SWI Microbleeds: Risks and Consequences

C Yang[1], J Ford[2], S Sten[3], V Jewells[3]
[1]Campbell University School of Osteopathic Medicine, Buies Creek, NC, [2]Moses H. Cone Memorial Hospital, Greensboro, NC, [3]University of North Carolina School of Medicine, Chapel Hill, NC

Purpose
Cerebral microbleeds (CMBs) have been associated with cognitive deterioration and neurodegenerative brain damage. Cerebral microbleeds are small hypointense lesions which can be visualized on susceptibility-weighted imaging (SWI) on magnetic resonance imaging (MRI) scanners. The purpose of this study is to examine the prevalence and determinants of

CMBs with vascular risk factors: age, hypertension, hyperlipidemia, diabetes mellitus type 2 and chronic kidney disease (CKD).

Materials and Methods

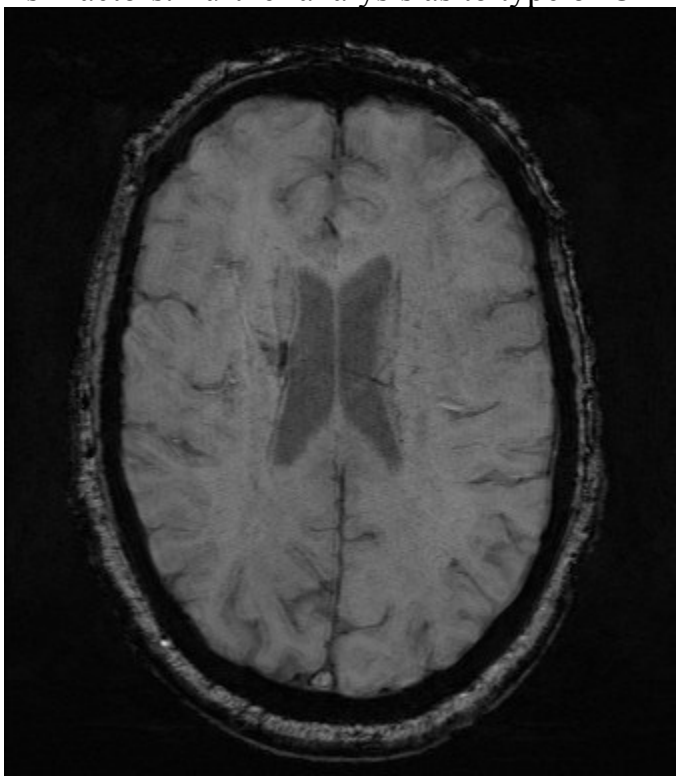
After obtaining an IRB approval, a retrospective study was carried out on 330 patients (164 males and 166 females, median age for both was 61 years) who had a "stroke" or "Brain Circle of Willis (COW)" study logged on the Siemens Skyra 3T MRI scanner. In addition, 4 patients (3 males, 1 female, median age 59 years) who received intra-arterial tPA and subsequent MRI scans did not reveal post-therapy hemorrhage despite CMBs prior to therapy. Vascular risk factors were obtained from the patient's electronic health record.

Results

With the MRI results, a logistic regression was used to model the correlation between CMBs and vascular risk factors. At least 1 CMBs was found in 30% of all of the patients. A statistically significant relationship between CMBs and CKD was determined [P <.001; odds ratio (OR), 4.91; 95% confidence interval (CI), 2.08-11.57], while hypertension had p=.647, diabetes mellitus type 2 had a p=.342, hyperlipidemia had a p=.605, and age had a p=.180. Chronic kidney disease was a strong predictor of CMBs in our logistic regression model. The results of our findings support prior correlation between CMBs and proteinuria as well as cognitive decline and CKD.

Conclusions

These findings may suggest CKD as a prominent pathogenesis for CMBs among vascular risk factors. Further analysis as to type of CKD and CMBs propensity will be performed.



(Filename: TCT_P-41_SWI_ASNR_20161.jpg)

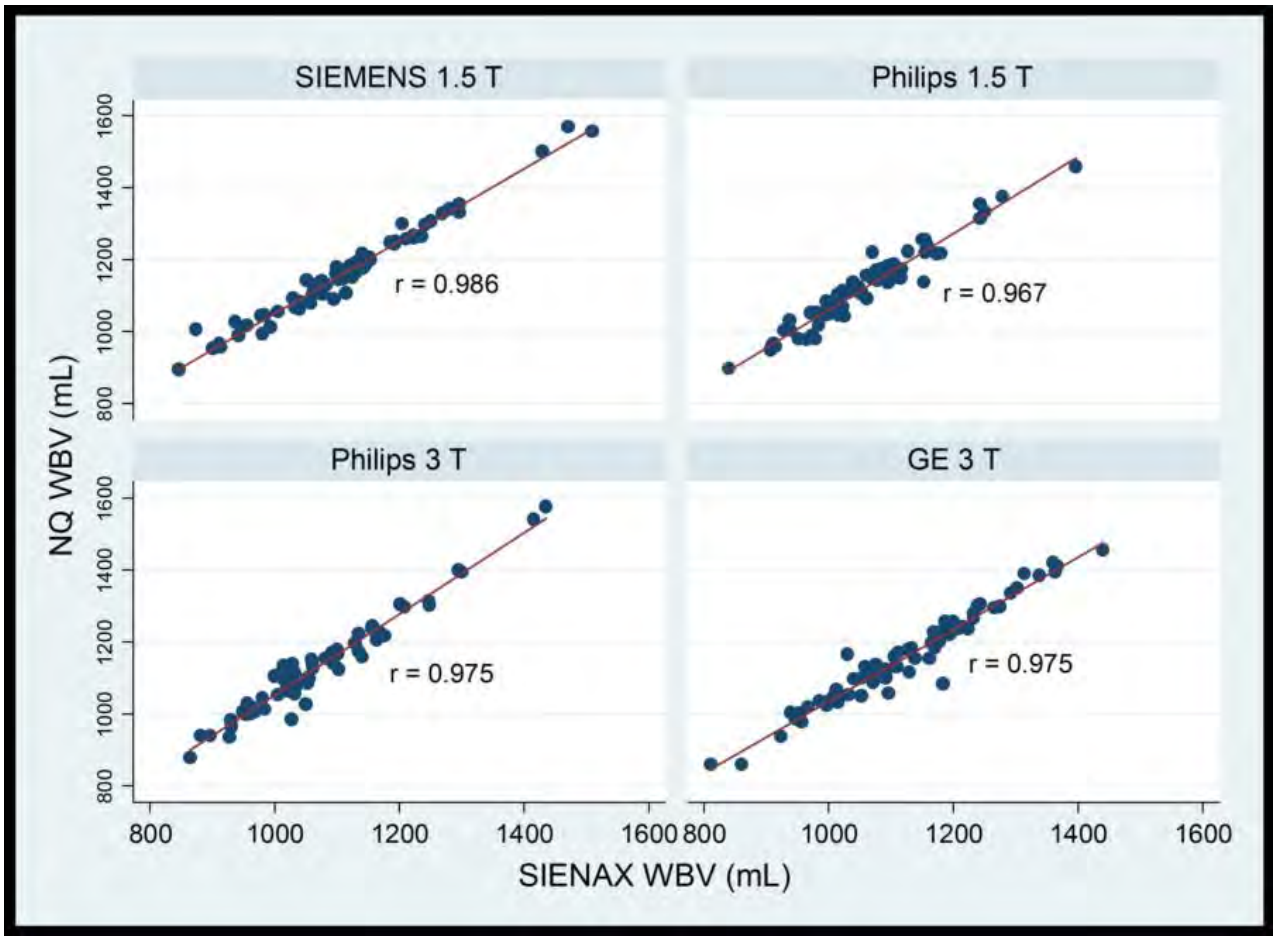
P-31

6:30AM - 3:00PM

Testing the Statistical Agreement of Automated Neuroquant Brain Volumetric Analysis to SIENAX Across Multiple MRI Scanner Manufacturers and Field Strengths

C Rawson[1], J Lin[1], S Sillau[1], E Nyberg[1], L Nagae[1], E Alvarez[1], J Honce[1]
[1]*University of Colorado, Aurora, CO*

Purpose
To evaluate NeuroQuant volumetric software to the reference standard SIENAX across 4 different magnetic resonance scanners by comparing whole brain volume (WBV) and normalized brain volume (NBV) in multiple sclerosis (MS) patients.
Materials and Methods
Two hundred seventy-three standard of care magnetic resonance images (MRIs) from MS patients in 2015-16 were analyzed: 70 patients on Siemens 1.5T, 65 on Philips 1.5T, 61 on Philips 3T, and 77 on GE 3T scanners. Whole brain volume and NBV measurements were calculated using NeuroQuant and SIENAX. Statistical agreement between the methods was evaluated by linear regression and Bland-Altman plots. Precision and accuracy of WBV and NBV measurements were calculated for NeuroQuant using SIENAX as the reference standard. T2 lesion volumes were calculated with the lesion segmentation toolbox.
Results
There were no statistically significant differences in age, gender, type of MS, or lesion volume between the 4 MRI scanner cohorts. Precision (Pearson's r) for WBV estimation for SIEMENS 1.5T, Philips 1.5T, Philips 3T, and GE 3T scanners were 0.986, 0.967, 0.975, and 0.975, respectively, with mean volume differences +4.6%, +6.0%, +5.7%, and +3.1%. Precision of the Neuroquant NBV estimation for SIEMENS 1.5T, Philips 1.5T, Philips 3T, and GE 3T scanners was 0.834, 0.828, 0.767, and 0.819, respectively. Lesion volumes affected the precision of Neuroquant least with the SIEMENS scanner.
Conclusions
Across a wide range of MRI scanners, NeuroQuant derived cross-sectional WBV and NBV shows strong statistical agreement to SIENAX, a standard tool for brain volume measurement in MS studies. However, our results suggest that NeuroQuant does better with WBV than with NBV.



(Filename: TCT_P-31_figure1.jpg)

P-23

6:30AM - 3:00PM

The Diagnostic Value of Postcontrast Susceptibility-Weighted Imaging in the Assessment of Intracranial Brain Neoplasm at 3T

H Kang[1], S Jang[1], K Roh[1], J Kim[1]
[1]*Seoul Veterans Hospital, Seoul, Korea, Republic of*

Purpose
The aim of this study is to estimate the diagnostic value of postcontrast susceptibility-weighted imaging (SWI) in the assessment of intracranial brain neoplasm at 3 Tesla (T).
Materials and Methods
Twenty-five intracranial brain neoplasm patients (nineteen with metastases, and 6 with glioblastomas) were enrolled in this study, They underwent examinations that included SWI and postcontrast SWI in addition to conventional magnetic resonance (MR) sequences on a 3T MR imager. Two radiologists consensually rated the visibility of the tumor margins, the visibility of the internal architecture of the tumors on pre and postcontrast T1-weighted

images (T1WI), and, pre and postcontrast SWIs, and the grade of intratumoral susceptibility signals (ITSS) on SWI and postcontrast SWI.
Results
The postcontrast T1WI was statistically superior to the T1WI and SWI, and the postcontrast SWI was statistically superior to the T1WI and SWI with regard to the visibility of the internal architecture and the visibility of the tumor margins of the brain metastases and glioblastomas ($p < 0.05$, Paired t-test). Statistically significant differentiation was achieved between brain metastases and glioblastomas using the grading of the visibility of the tumor margins in SWI scan ($p < 0.05$, student t-test).
Conclusions
A paramagnetic contrast medium may influence SWI data due to T2 shortening and additional signal loss. However, our results showed that postcontrast SWI clearly visualized the characteristics and the architecture of brain neoplasms with good delineation of the tumor margins. Postcontrast SWI showed both ITSS that was not visible with conventional MR sequences and contrast enhancement that was visible with conventional MR sequences. Postcontrast SWI clearly visualized the internal architecture and tumor margins of brain neoplasms and was useful in differentiating brain metastases and glioblastomas. Intratumoral susceptibility signals and contrast enhancement can be assessed simultaneously in postcontrast SWI.

Table 1. Statistical analysis of the mean score of the grading of the visibility of tumor margins and the internal architec of GBMs ($p < 0.05$, Paired t-test).

	Visibility of tumor margin		Internal architecture of tumor	
	* p value		p value	
T1 vs. T1E	0.000	T1 < T1E	0.000	T1 < T1E
T1 vs. SWI	0.611	** N/S	0.102	N/S
T1 vs. SWIE	0.001	T1 < SWIE	0.000	T1 < SWIE
T1E vs. SWI	0.001	T1E > SWI	0.317	N/S
T1E vs. SWIE	0.363	N/S	0.203	N/S
SWI vs. SWIE	0.001	SWI < SWIE	0.043	SWI < SWIE

Postcontrast T1WI: T1E. Postcontrast SWI: SWIE. * Reference value ; $p < 0.05$. ** N/S: No statistical difference

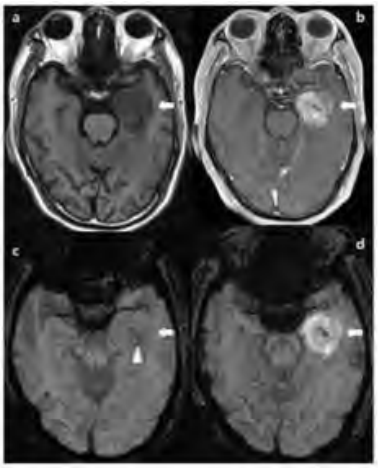


Figure 1. Male 72-year-old patient with glioblastoma.

A: The lesion is barely visible with poor degree tumor margin delineation on T1WI (arrow).

B: Postcontrast T1 shows intratumoral heterogeneity (arrow). Strong enhancement sharply delineates the margins of the lesion (excellent degree).

C: Grade 2 ITSS indicates 6-10 dot-like or linear low intensity structures on SWI (arrow head).

D: Postcontrast SWI shows the internal structure and the margins of the lesion more clearly than noncontrast SWI (arrow).

Table 2. Statistical analysis of the mean score of the grading of the visibility of tumor margins and the internal architectu of solitary brain metastasis ($p < 0.05$, Paired t-test).

	Visibility of tumor margin		Internal architecture of tumor	
	* p value		p value	
T1 vs. T1E	0.000	T1 < T1E	0.000	T1 < T1E
T1 vs. SWI	0.000	T1 < SWI	0.000	T1 < SWI
T1 vs. SWIE	0.000	T1 < SWIE	0.000	T1 < SWIE
T1E vs. SWI	0.000	T1E > SWI	0.331	N/S
T1E vs. SWIE	0.055	N/S	0.130	N/S
SWI vs. SWIE	0.002	SWI < SWIE	0.000	SWI < SWIE

Postcontrast T1WI: T1E. Postcontrast SWI: SWIE. * Reference value ; $p < 0.05$. ** N/S: No statistical difference

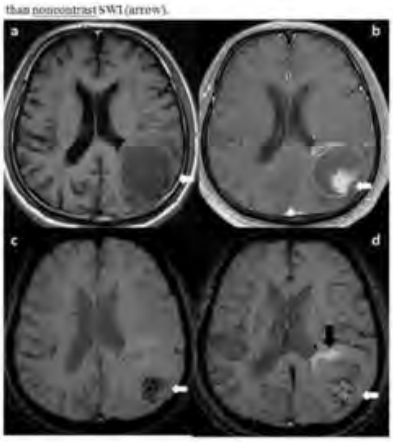


Figure 2. Male 68-year-old patient with metastasis of lung adenocarcinoma.

A: The lesion is barely visible with poor degree tumor margin delineation on T1WI (arrow).

B: Postcontrast T1. Strong enhancement sharply delineates the margins of the lesion (excellent degree). Intense enhancing solid component and no enhancing necrotic portion are seen (arrow).

C: Marked hypointense foci are seen in a solid part of the lesion on SWI, suggesting an increased venous vasculature and hemorrhages (arrow).

D: Postcontrast SWI. Low signal foci are visible, which were interpreted to be hemorrhage with good degree tumor margin (arrow). Moreover, bright enhancement indicating both tumor parenchyma and breakdown of the blood-brain barrier are seen along the tumor (black arrow).

Table 3. Statistical analysis of the pathological comparison of the grading of the visibility of tumor margins, the internal architecture of tumors and ITSS ($p < 0.05$, Student t-test).

	Visibility of tumor margin		Internal architecture of tumor		ITSS	
	* p value		p value		p value	
T1						
GBMs vs. Mets	0.19	** N/S	0.63	N/S		
T1E						
GBMs vs. Mets	0.08	N/S	0.44	N/S		
SWI						
GBMs vs. Mets	0.03	significant	0.58	N/S	0.13	N/S
SWIE						
GBMs vs. Mets	0.18	N/S	0.14	N/S	0.13	N/S

GBMs: Glioblastomas, Mets: Metastases, ITSS: Intratumoral susceptibility signals. T1E: Postcontrast T1WI. SWIE: Postcontrast SWI. * Reference value ; $p < 0.05$. ** N/S: no statistical difference

(Filename: TCT_P-23_31.JPG)

P-28

6:30AM - 3:00PM

The Spectrum of Diffusion Abnormalities in Patients Receiving Bevacizumab for Malignant Brain Tumors

P Shah[1], V Yedavalli[2], S Futterer[3], A Nemeth[4]
[1]Northwestern University, Chicago, IL, [2]Advocate Illinois Masonic Medical Center, Chicago, IL, [3]Northwestern, Chicago, IL, [4]Northwestern University / Feinberg School of Medicine, Chicago, IL

Purpose

Bevacizumab, a monoclonal antibody that inhibits vascular endothelial growth factor A, has been used increasingly for the treatment of malignant intracranial neoplasms. Bevacizumab inhibits angiogenesis, thereby presumably decreasing both tumor growth and peritumoral edema. As its utilization has increased and patients receive more robust imaging follow up, unique imaging abnormalities frequently are observed. Imaging abnormalities include prolonged restricted diffusion within the tumor bed or even within the corpus callosum remote from the tumor bed. It often is difficult to discern whether these imaging abnormalities represent true tumor progression or pseudoresponse, as enhancement characteristics are not always reliable in the setting of Bevacizumab therapy. The purpose of this retrospective case review was to determine how often diffusion abnormalities present after Bevacizumab therapy and establish a temporal relationship between the initiation of Bevacizumab therapy and development of restricted diffusion.

Materials and Methods

Patients with history of malignant brain tumors who received Bevacizumab therapy between April 2015 and July 2016 were identified retrospectively. Demographic data, clinical data, and radiologic data for these patients were collected. Radiologic data included the site of primary tumor, its baseline appearance on contrast-enhanced and diffusion-weighted imaging as well as on follow-up imaging during and after Bevacizumab therapy. Clinical data included duration of Bevacizumab therapy, histology and grade of tumor.

Results

Clinical data and imaging for a total of 47 patients was reviewed. Of these, five patients (10.6%) were found to have increased restricted diffusion in the tumor bed after initiating Bevacizumab therapy that persisted throughout the duration of therapy as well as on subsequent follow-up imaging. Two patients (4.3%) were found to have new diffusion restriction in the corpus callosum remote from the tumor bed after initiating Bevacizumab therapy which also persisted throughout the duration of therapy. One patient (2.1%) was found to have new diffusion restriction remote from the tumor bed without corresponding abnormal enhancement. Of the 47 patients, 44 patients demonstrated restricted diffusion within the tumor bed on baseline pretreatment imaging. Of these patients with restricted diffusion, only one patient had resolution of restricted diffusion while receiving treatment.

Conclusions

New or increased diffusion abnormalities frequently are seen within and away from the primary tumor bed during Bevacizumab therapy and persist after the duration of therapy. These areas of restricted diffusion may represent treatment toxicity given their temporal

relationship with Bevacizumab therapy as opposed to tumor progression, although the association remains to be ascertained.



(Filename: TCT_P-28_avastin.jpg)

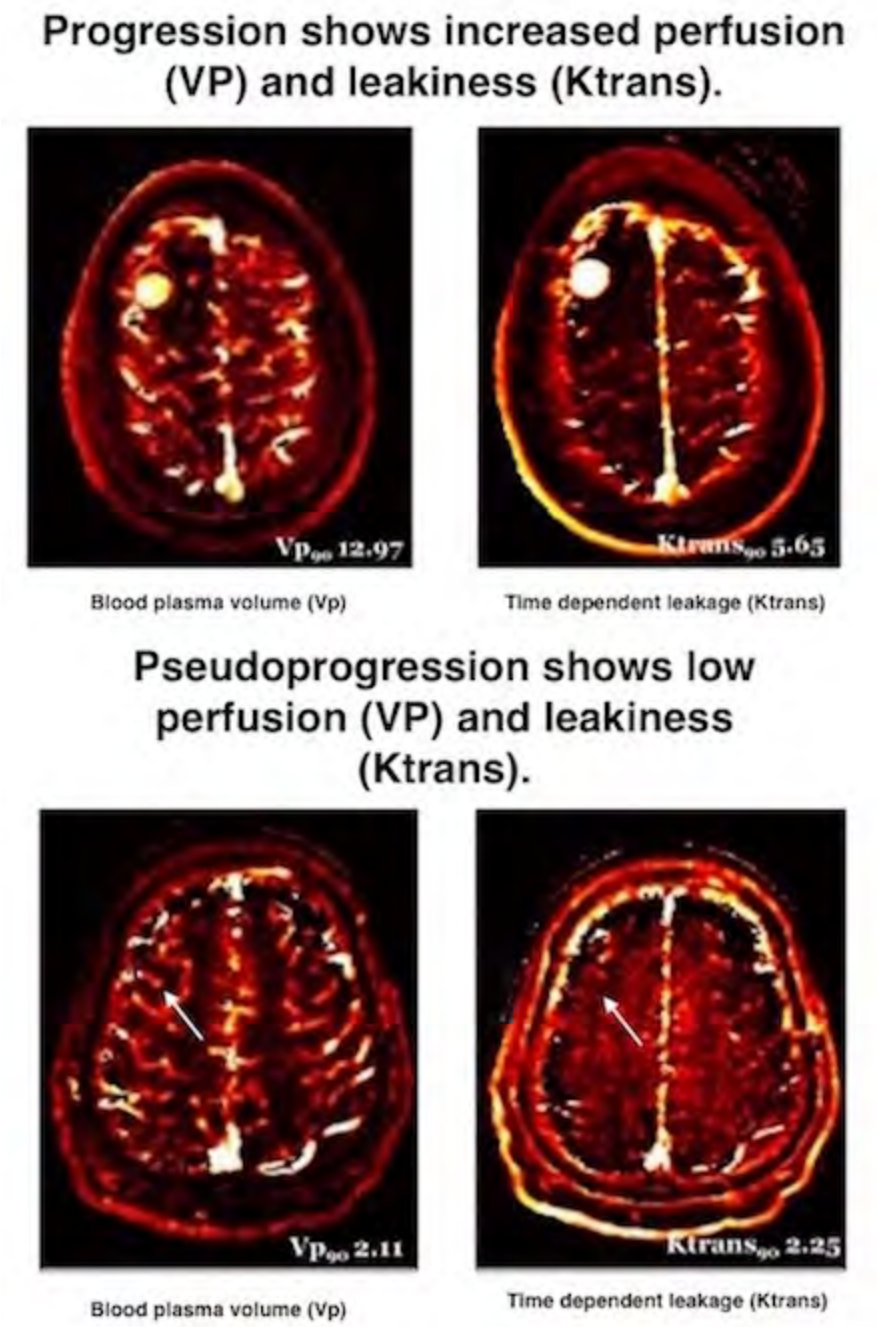
P-22

6:30AM - 3:00PM

Using DCE-MRI Perfusion to Evaluate Possible Immune-related Pseudoprogression in Metastatic Melanoma Brain Metastases

D Wang[1], Y Umemura[2], K Peck[2], W Shi[2], Z Zhang[2], R Fatovic[2], E Anderson[2], K Beal[2], T Kaley[2], R Young[2]
[1]New York University School of Medicine, New York, NY, [2]Memorial Sloan Kettering Cancer Center, New York, NY

Purpose
Immunotherapy is the standard of care for patients with metastatic melanoma. Pseudoprogression, the transient worsening of enhancing lesions, may occur as a result of activating the body's own immune system to help kill cancer cells. DCE-MRI provides information about lesion vascularity and hemodynamics, which are expected to be lower in pseudoprogression than in metastases. The purpose of this study was to evaluate dynamic contrast-enhanced MRI (DCE-MRI) perfusion to predict pseudoprogression in patients with melanoma brain metastases treated with immunotherapy.
Materials and Methods
Forty-four adult patients who had melanoma, brain metastases, received immunotherapy, and underwent MRI perfusion were studied retrospectively. As per the Response Assessment in Neuro-Oncology Brain Metastases (RANO-BM) criteria, up to 5 lesions were measured in each patient. Volumes-of-interest were applied to calculate 90th percentile normalized plasma volume (Vp90) and time-dependent leakage constant (Ktrans90) metrics. Lesion classification was determined by histopathology or follow up with pseudoprogression defined as neurological and radiographic stability or improvement without any new treatment for ≥2 months. Statistical analyses were done using the Wilcoxon rank-sum test.
Results
A total of sixty-four lesions were measured: 9 lesions in 8 patients were PsP, and fifty-five lesions in thirty-six patients were POD. Most patients received ipilimumab (64%) or pembrolizumab (20%). Median immunotherapy course was 9 weeks. The median lesion volume was not statistically different between the PsP group and the POD group ($p=0.82$). Median Vp90 and Ktrans90 were smaller in pseudoprogression than progression ($p=0.02$ and $p=0.047$, respectively), and Vp90 remained significant after multiple comparison adjustment ($p=0.04$). Median overall survival was fourteen months, with no difference between pseudoprogression and progression.
Conclusions
Dynamic contrast-enhanced MRI reveals that immunotherapy related pseudoprogression in melanoma brain metastases has lower Vp and Ktrans in pseudoprogression lesions than in lesions undergoing true progression. Accurate identification of pseudoprogression is essential for making informed clinical treatment decisions.



(Filename: TCT_P-22_Figure.jpg)

P-45

6:30AM - 3:00PM

Visual and Automated Rating for Alberta Stroke Program Early Computed Tomographic Score on Diffusion-Weighted Imaging

J Schröder[1], B Cheng[1], A Kemmling[2], C Malherbe[1], J Fiehler[1], C Gerloff[1], G Thomalla[1]

[1]*University Medical Center Hamburg-Eppendorf, Hamburg, Hamburg,* [2]*Universitätsklinikum Lübeck, Lübeck, Germany*

Purpose
Assessment of ischemic lesions on CT or MRI using ASPECTS is widely used to guide acute stroke treatment. However, it has never been defined how many voxels need to be affected to label an DWI-ASPECTS region ischemic. We aimed to assess the effect of various lesion load thresholds on DWI-ASPECTS and compare automated analysis with visual rating.
Materials and Methods
We analyzed overlap of individual DWI lesions of 315 patients from the previously published PRE-FLAIR study with a probabilistic ASPECTS template derived from 221 CT images. We applied multiple lesion load thresholds per DWI-ASPECTS region (>0, >1%, >10%, >20% in each DWI-ASPECTS region) to compute DWI-ASPECTS for each patient and compared the results to visual reading by an experienced stroke neurologist.
Results
By visual rating, median ASPECTS was 9, 84 patients had an DWI-ASPECTS score ≤7. In contrast, by use of >0, >1%-, >10%-, and >20%-thresholds, median DWI-ASPECTS was 1, 5, 8 and 10; 97.1% (306), 72.7% (229), 41% (129) and 25.7% (81) had DWI-ASPECTS ≤7, respectively. Overall agreement between automated assessment and visual rating was low for every threshold used (>0%: κ=0.020 1%: κ=0.151; 10%: κ=0.386; 20% κ=0.381). Agreement for dichotomized DWI-ASPECTS ranged from fair to substantial (≤7: >10% κ=0.48; >20% κ=0.45; ≤5: >10% κ=0.528; >20% κ=0.695).
Conclusions
Overall agreement between automated and the standard used visual scoring is low. However, dichotomized scoring achieved more comparable results. Varying lesion load thresholds had a critical impact on patient selection by ASPECTS.

Monday
6:30AM - 3:00PM
Long Beach Convention Center, Exhibit Hall B-(Lower Level) P

Scientific Poster(P)-Print-Head & Neck

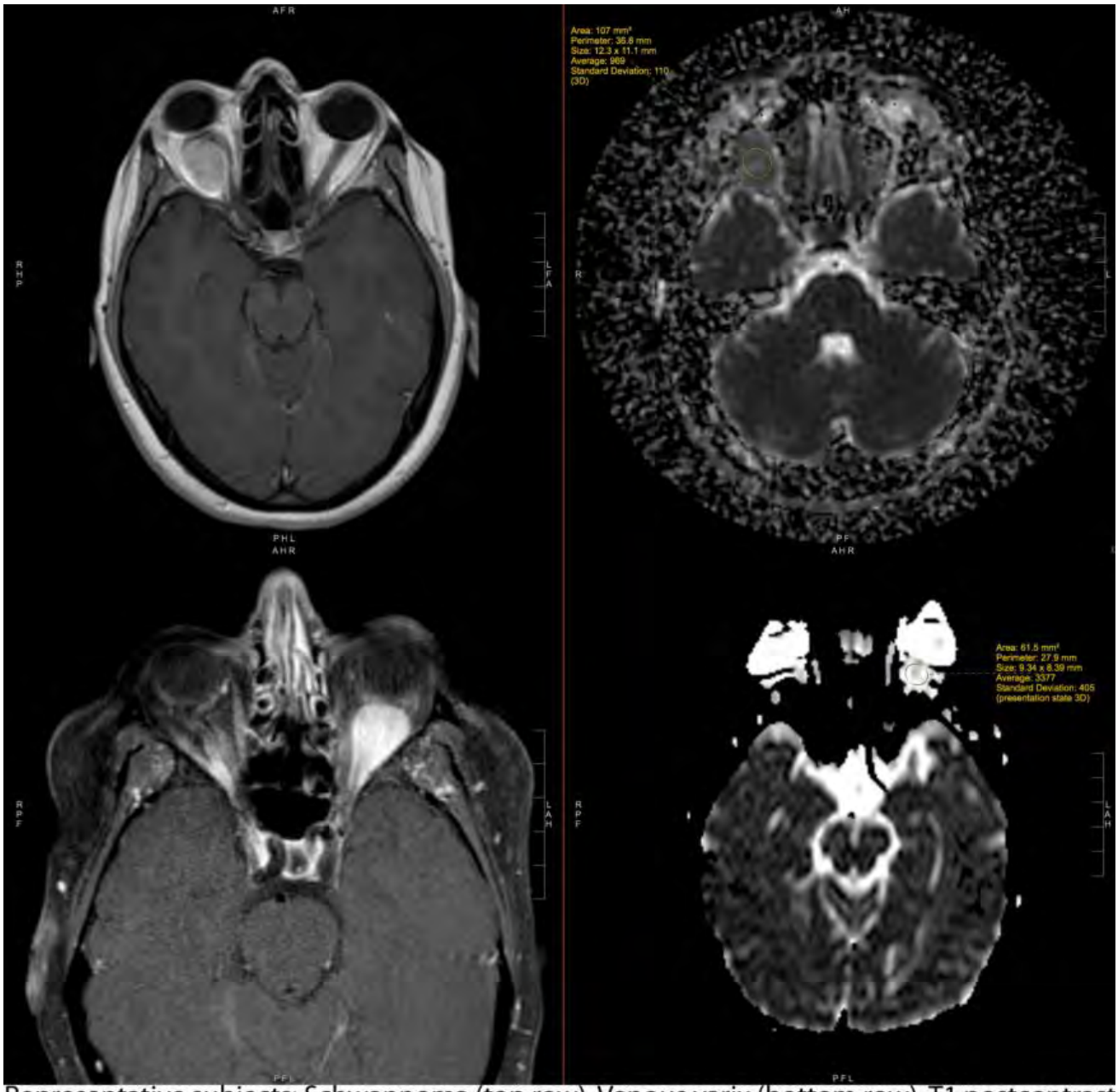
P-56

6:30AM - 3:00PM

ADC Helps Discriminate Venous Varices Among Orbital Masses

J Colby[1], E Kalin-Hajdu[1], C Glastonbury[1], O Idowu[1], M Vagefi[1], R Kersten[1]
[1]*University of California, San Francisco, San Francisco, CA*

Purpose
Imaging characterization of orbital masses is an important pivot point in ophthalmologic management, often determining the course between medical therapy, gross resection, or minimally invasive interventional techniques. While the contribution of diffusion-weighted imaging (DWI) has been well demonstrated in discriminating lymphoma and other malignancy from benign solid orbital lesions, it has not been investigated previously with respect to the often indeterminate and variably described spectrum of slow flow vascular malformations. Here we investigate the utility of apparent diffusion coefficient (ADC, in units x10^-3 mm^2/s) in discriminating orbital venous varices among other vascular and solid orbital masses.
Materials and Methods
In this retrospective cross-sectional analysis, we examined the recent UCSF orbital tumor experience between 2011-2016. This yielded 68 subjects (including 7 nonthrombosed venous varices), who had both DWI/ADC data available as part of routine pre-operative neuroimaging, and histologically proven diagnoses based on surgical pathology. For each subject, ADC was calculated in a hand-drawn region of interest (ROI) placed in the center of the orbital lesion. If heterogeneous in morphology, the ROI was placed in the most fluid-like (i.e., T2 hyperintense) and enhancing component. Three repeat measurements were obtained in order to model intra-rater variability. Inference was performed using linear mixed effects modeling in R.
Results
In the absence of thrombosis, venous varices were typically T1 hypointense, T2 hyperintense, and avidly and homogeneously enhancing on postcontrast images. Apparent diffusion coefficient was significantly higher in nonthrombosed venous varices compared to other lesions (2.8 vs. 1.2, chi^2(df=1) = 53.4, p=2.6e-13). Specifically, while the T1 postcontrast or T2 signal pattern is sometimes equivocal, no other enhancing solid or vascular lesion approached the ADC range of the venous varices, which neared fluid signal around an ADC of 3.
Conclusions
Among the subset of indeterminate orbital lesions, high ADC helps discriminate orbital venous varices from morphologically similar lesions including some avidly enhancing solid lesions and smaller vessel, i.e., capillary/cavernous venous malformations. Routine incorporation of ADC measurement may aid in improving the specificity of our imaging reports with respect to optimal presurgical planning.



Representative subjects: Schwannoma (top row). Venous varix (bottom row). T1 postcontrast (left column). ADC (right column).
(Filename: TCT_P-56_figure1.jpg)

P-54

6:30AM - 3:00PM

Comparison of Fat Suppression Head and Neck MRI: mDixon, STIR, and SPIR Techniques

S Gaddikeri[1], M Mossa-Basha[2], J Andre[2], D Hippe[2], Y Anzai[3]

[1]Rush University Medical Center, Chicago, IL, [2]University of Washington, Seattle, WA, [3]University of Utah, Salt Lake City, UT

Purpose
Reliable and uniform fat suppression is critical for accurate diagnosis of various head and neck pathologies. The goal of this study is to compare multipoint Dixon (mDixon) turbo spin echo (TSE) technique, spectral presaturation and inversion recovery (SPIR), and short tau inversion recovery sequence (STIR) for the quality of fat suppression in the head and neck magnetic resonance imaging (MRI).
Materials and Methods
Imaging records of 72 consecutive patients who underwent head and neck MRI for various clinical indications between July 1st 2014 and September 30th 2014 were reviewed retrospectively. All patients were divided into two groups based on the type of FS techniques used (Group A: STIR and SPIR Gad-T1; Group B: mDixon T2 TSE and mDixon Gad-T1 TSE). Signal intensity ratio between spinal cord to subcutaneous fat was used as an objective measure. In addition, two blinded neuroradiologists graded quality of fat suppression and overall image quality on a 5-point scales (1 being nondiagnostic, 5 being excellent). Scan acquisition times also were compared.
Results
Total of 64 patients were enrolled. No significant difference in patient demographics and body habitus of patients. Signal intensity ratios were significantly higher for mDixon T2W than STIR images ($p< 0.001$) and mDixon Gad-T1 than CHESS Gad-T1 ($p<0.001$). Two blinded readers graded mDixon techniques higher (both T2 and post-Gad T1 TSE) than STIR and SPIR Gad-T1 imaging on overall image quality ($p<0.015$ & $p<0.001$, respectively) and fat suppression homogeneity ($p<0.003$ & $p<0.001$, respectively). Scan acquisition time was less than half on mDixon technique as compared with STIR (2 min vs. 4 min 30 sec), and slightly shorter on mDixon T1TSE than SPIR Gad T1 (4 min vs. 4 min, 30 sec).
Conclusions
mDixon technique offers superior image quality and uniform fat suppression at a shorter scan time as compared to STIR and SPIR Gad-T1W techniques.

Objective signal intensity ratios

		Sequence Group		
Variable		mDixon (N=31)	CHESS/STIR (N=33)	P-value*
T2W spine to fat ratio	Submental level	5.7 ± 1.6	3.5 ± 3.4	<0.001
	Supraclavicular level	7.4 ± 2.4	3.3 ± 3.4	<0.001
Post-gad T1W spine to fat ratio	Submental level	3.7 ± 1.4	0.9 ± 0.7	<0.001
	Supraclavicular level	4.3 ± 2.0	0.5 ± 0.3	<0.001

Subjective assessment of image quality, fat suppression and susceptibility artifacts (two readers averaged)

		Sequence Group		
Variable		mDixon (N=31)	CHESS/STIR (N=33)	P-value*
T2W/STIR Images				
Overall image quality grade		3.9 ± 0.5	3.6 ± 0.7	0.022
Fat suppression grade	Maxilla region	4.6 ± 0.4	4.3 ± 0.5	0.013
	Mandibular region	4.4 ± 0.5	4.0 ± 0.6	0.007
	Lower neck region	4.7 ± 0.4	4.3 ± 0.4	0.001
Post-Gad T1W Images				
Overall image quality grade		4.0 ± 0.4	2.6 ± 0.6	<0.001
Fat suppression grade	Maxilla region	4.8 ± 0.3	3.8 ± 0.7	<0.001
	Mandibular region	4.7 ± 0.3	2.8 ± 0.5	<0.001
	Lower neck region	4.8 ± 0.3	1.4 ± 0.7	<0.001

Values are mean ± SD unless otherwise specified; *Mann-Whitey test

(Filename: TCT_P-54_table.jpg)

P-55

6:30AM - 3:00PM

Computed Tomography and Magnetic Resonance Imaging-based Finite Element Analysis Predicts Current Flow in Labyrinths Implanted with a Multi-Channel Vestibular Prosthesis

A Hedjoudje[1], R Hayden[2], C Dai[1], S Mori[3], C Della Santina[4]
[1]Johns Hopkins University, Baltimore, MD, [2]Massachusetts General Hospital, Boston, MA, [3]Johns Hopkins University School of Medicine,, Baltimore, MD, [4]Johns Hopkins School of Medicine, Baltimore, MD

Purpose
As is true for cochlear implants, current spread beyond the intended target of a given electrode is a key factor determining the pattern of nerve stimulation elicited by a multi-channel vestibular prosthesis. Our goal was to construct a robust, anatomically precise finite element model of current flow in the implanted labyrinth and better understand the biophysics of ampullary, utricular, saccular, cochlear and facial nerves stimulation.

Materials and Methods

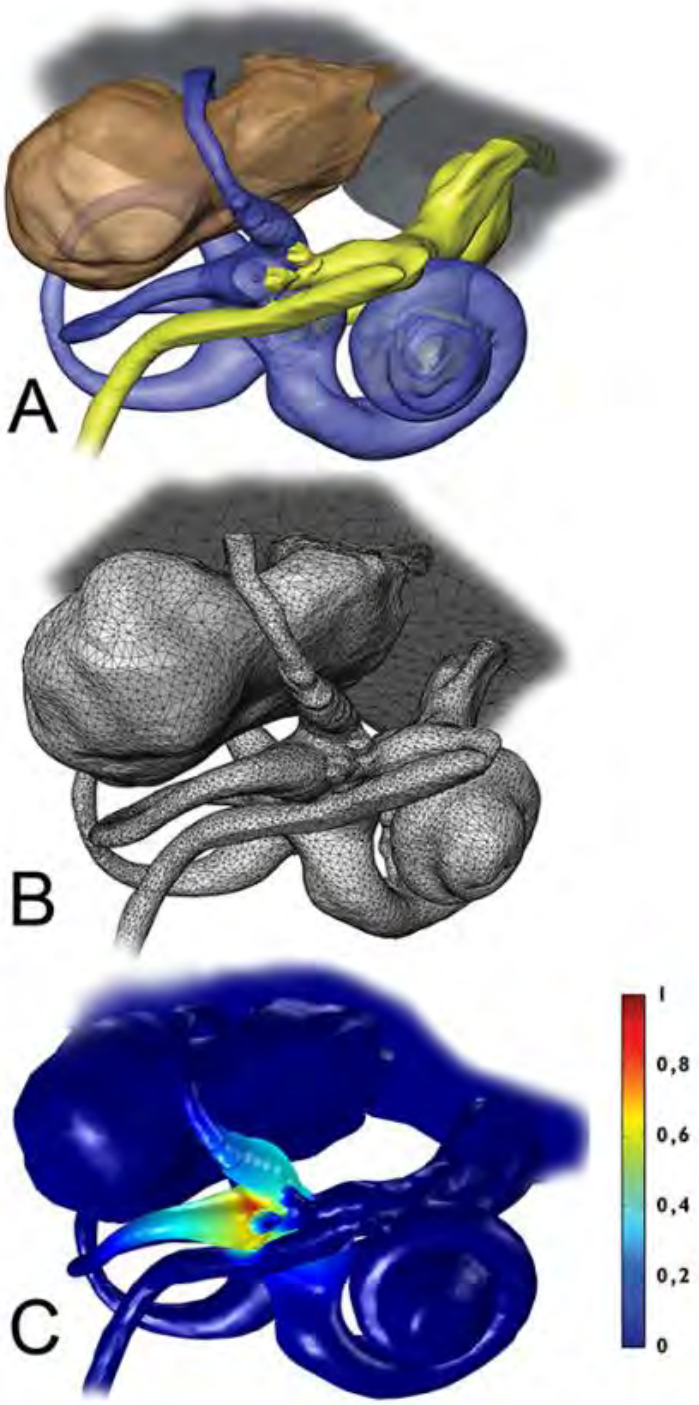
Model geometry was generated through 3-dimensional (3D) reconstructions of a normal rhesus temporal bone imaged using microMRI data obained with a 11.7 Tesla Magnet (48 μm isotropic voxels) and microCT (70 μm isotropic voxels). The extracellular potential field during a biphasic current pulse was computed using finite element methods. Potential field values then served as inputs to stochastic, nonlinear dynamic models for each of 2,415 vestibular afferent axons with spiking dynamics based on a modified Smith and Goldberg model. A well validated model of myelinated fibers implemented action potential propagation. Eye rotation 3D axes were predicted from the relative proportion of model axons excited within each of the ampullary nerves and compared to actual 3D angular vestibulo-ocular reflex axes elicited by prosthetic stimuli.

Results

The model's predicted axis aligned well with the actual axis of eye rotation, with misalignment of 18 ± 6.1 degrees (mean ± SD) for the 234 stimulation conditions examined.

Conclusions

Extension of the model to human anatomy should facilitate optimal design of electrode arrays for clinical application.



(Filename: TCT_P-55_AbstractASNRFig2.jpg)

P-59

6:30AM - 3:00PM

Diagnosis of Endophthalmitis by Computed Tomography: Is it Possible?

B Pfluck[1], H Yamashita[1], R Souza[1], L Abreu Jr.[2], M Borri[3], A Wolosker[3]
[1]Federal University of Sao Paulo, Sao Paulo, SP, Brazil, [2]Fleury Group, Hospital Sao Luiz, Sao Paulo, SP, Brazil, [3]Fleury Group, Hospital Sao Luiz/Federal University of Sao Paulo, Sao Paulo, SP, Brazil

Purpose
The main aspects of endophthalmitis in computed tomography (CT) imaging and the extension and local complications are reviewed based on the presentation of eleven surgically confirmed cases.
Materials and Methods
Retrospective evaluation of eleven confirmed cases of endophthalmitis and correlation with imaging findings in enhanced CT images.
Results
Endophthalmitis is an ophthalmologic emergency. The clinical diagnosis is challenging and the delayed diagnosis can have severe sight-threatening complications. Computed tomography might be useful in the evaluation of disease extent and complications. Computed tomography imaging findings are rarely described in the literature and are correlated to the ocular layers involved. The spectrum of imaging findings vary from uveal thickening, vitreous exudate, retinal and choroidal detachment to chronic stages (phthisis bulbi).
Conclusions
Computed tomography, in many medical centers is the first and more accessible exam, and can help to inform the extension and complications in endophthalmitis. Despite the nonspecificity of endophthalmitis in CT, the radiologist must be familiar with the main findings on clinical suspicion as the disease has a significant morbidness.



Fig. 1 – Axial CT image shows thickening and abnormal enhancement at the anterior aspect of the right globe



Fig. 2 – Axial CT image shows thickening of the preseptal software tissues and the uve-scleral layer in the right globe. In association, choroidal detachment

(Filename: TCT_P-59_endoftalmitefig3.jpg)

P-52

6:30AM - 3:00PM

Differences in Volumetric and Texture Analysis Features of the Buccal Fat Between Young and Old Patient Groups

V Andreu[1], H Kuno[2], M Chapman[3], B Li[2], O Sakai[2]
[1]Boston Medical Center, Boston, MA, [2]Boston Medical Center, Boston University School of Medicine, Boston, MA, [3]Boston University Medical Center, Boston, MA

Purpose
Recent literature suggests that facial fat distribution is complex and changes with age. Buccal fat (also called Bichat's fat pad) is an encapsulated deep fat pad used in different surgeries of the oral and maxillofacial region. The purpose of this study is to evaluate for volumetric changes and textural analysis characteristics of the buccal fat pad with aging utilizing CT.
Materials and Methods
This retrospective study included 45 patients who underwent contrast-enhanced CT, divided into two age groups: young patient group (20-30 years, n = 25) and the elderly patient group (70-80 years, n = 20). The body of the right buccal fat was segmented manually in each patient, and an in-house developed MATLAB-based texture analysis program extracted 42 texture features from each segmented volume. Mann-Whitney U test was used to compare fat volume and each parameter between two groups. A P value of less than 0.05 was considered statistically significant.

Results
There was no significant difference in the volume of the buccal fat pad between the two age groups (the young group, median=8.08 cc vs. the elderly group, median=8.84 cc; P=.167). Texture analysis demonstrated significant differences between these two groups in 5 histogram features [mean (P=.002), median (P=.001), entropy (P=.005), geometric mean (P=.002) and harmonic mean (P=0.002)] and 4 gray-level gradient matrix features [MGR (P<.001), VGR (P<.001), Skewness (P<.001) and Kurtosis (P<.001)].
Conclusions
Texture analysis demonstrated statistically significant differences in the buccal fat between the young and old patient groups despite no significant change in buccal fat volume with age. Therefore, texture analysis may be used as an imaging biomarker for aging, and these results may help explain the morphologic differences during aging.

P-57

6:30AM - 3:00PM

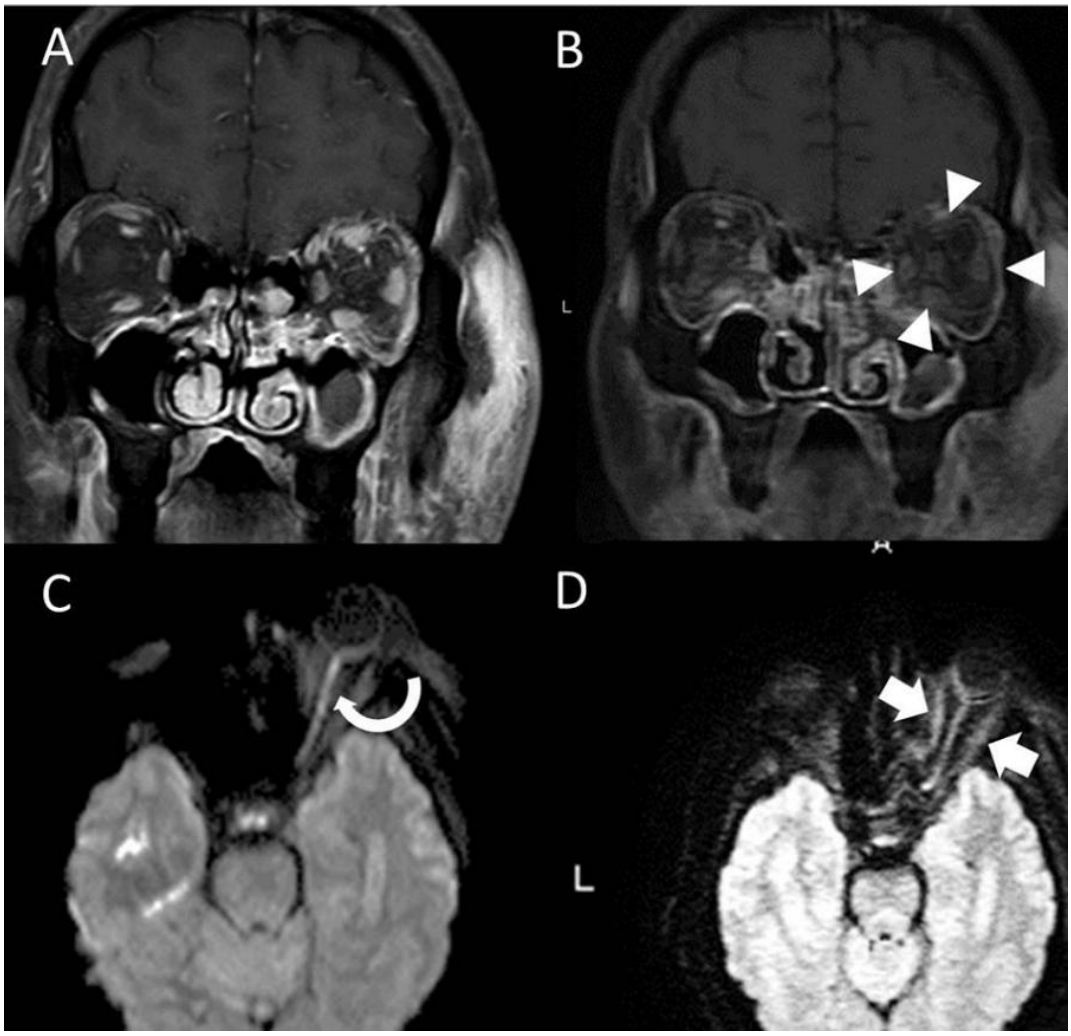
Extraocular Muscle and Optic Nerve Infarction: A Rare Case of Rhino-Orbital-Cerebral Mucormycosis in an Immunocompetent Host

J Hayden[1], S Karnam[1], L Alhilali[2]
[1]Creighton University School of Medicine, Phoenix Regional Campus, Phoenix, AZ, [2]Barrow Neurological Institute, Phoenix, AZ

Purpose
Disseminated mucormycosis is an opportunistic fungal infection with an exceptionally high mortality rate. The purpose of this paper is to describe a rare case of Rhino-Orbital-Cerebral Mucormycosis (ROCM) in an immunocompetent individual, with an uncommon finding of extraocular muscle infarction clearly visualized by diffusion-weighted and contrast-enhanced MRI. This case demonstrates the need to use early diffusion-weighted imaging in order to detect orbital infarction and allow for timely treatment.
Materials and Methods
A literature review of past case reports and studies related to rhino-orbital-cerebral mucormycosis and the radiologic modalities used for diagnosis was performed using PubMed and Web of Science.
Results
Initial T1-weighted postcontrast imaging demonstrated normal enhancement of the left extraocular musculature whereas, 12 hours after admission, the postcontrast imaging illustrated a lack of enhancement of the left extraocular muscles consistent with infarction. Similarly, initial diffusion imaging demonstrating restricted diffusion within the left optic nerve consistent with infarct, while 12 hours after admission the scan showed restricted diffusion not only within the left optic nerve, but also within the extraocular musculature.

Conclusions

Orbital infarction syndrome is a rare finding resulting from ischemia of both the intraocular and intraorbital structures from hypoperfusion of the ophthalmic artery system. As the ophthalmic artery system is not a terminal system, but rather a system rich in anastomoses and collateral circulation between the ophthalmic artery and the external carotid artery, the syndrome is rare, requiring compromise of both the ophthalmic artery itself as well as the collateral blood flow. In mucormycosis, the fungal hyphae have a predilection to both invade and thrombose arteries. Therefore, although blindness is relatively uncommon in ROCM, early detection of orbital infarction is key to both suggest the diagnosis of an angioinvasive infection and prompt aggressive treatment prior to progression into a life-threatening condition.



(Filename: TCT_P-57_Hayden_images_300dpi.jpg)

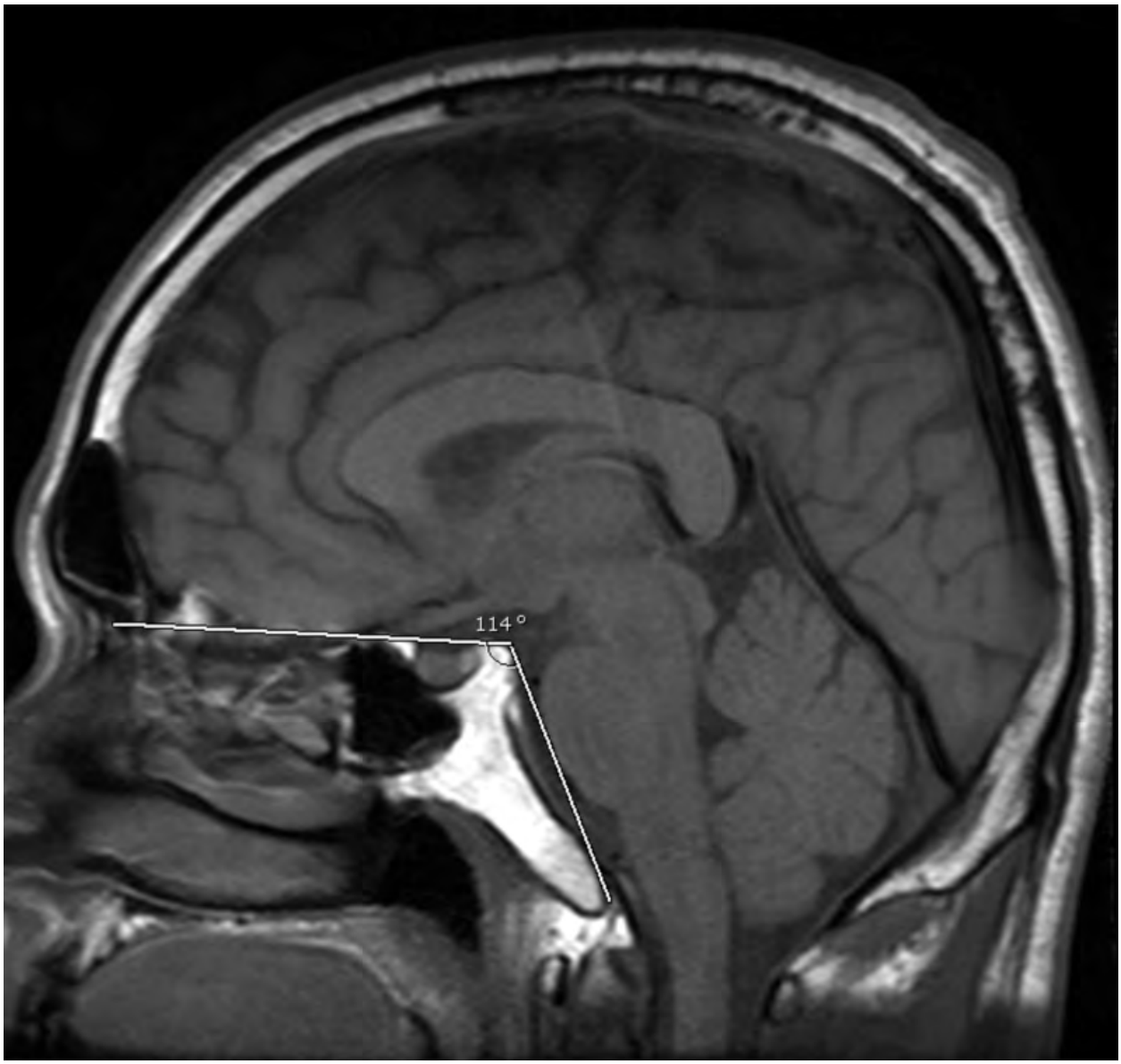
P-63

6:30AM - 3:00PM

Normal Value of Skull Base Angle Using the Modified MR Imaging Technique in Thai Population

S Hirunpat[1], N Wimolsiri[2], N Sanghan[1]
[1]Prince of Sonkla University, Hat-Yai, Songkhla, [2]Mahidol University, Rajthevi, Bangkok

Purpose
To determine the normal value of basal angle measured using the modified MR imaging technique in Thai population compared with the standard value obtained from the Western population.
Materials and Methods
We retrospectively evaluated midline sagittal T1W MR images in 200 adults and 50 children. The basal angle of the skull base was measured using the modified MR imaging technique described by Koenigsberg et al. The angle was formed by a line extending across the anterior cranial fossa to the tip of the dorsum sellae and another line drawn along the posterior margin of the clivus. The mean values of the basal angles among different age groups and sex were calculated and analyzed.
Results
The mean skull base angle of our adult population was 115° (range 100.5°-130°, SD = 5.7) with an inter-observer agreement of 0.85, slightly smaller than the previous study from the USA which was 117°. There was no significant difference between the male and female groups. The mean skull base angle in our children population was 114.7° (range 102 – 130.5°, SD = 6.3) with an inter-observer agreement of 0.89, quite similar to the previous USA study which was 114°. There was no significant difference between adult and children.
Conclusions
The mean adult skull base angle measured using the modified MR imaging technique in Thai population was slightly smaller than the Western population, while the mean skull base angle of children was quite similar. The basal angle range of 103.6°-126.4° may be used as a guide for the potential range of normal skull base angles in Thai population and possibly also the Southeast Asian population.



(Filename: TCT_P-63_11.jpg)

P-58

6:30AM - 3:00PM

Ocular Imaging in Routine Exams: What Radiologist Should Know. A Pictorial Issue

B Pfluck[1], H Yamashita[1], R Souza[1], L Abreu Jr.[2], M Borri[3], A Wolosker[3]
[1]Federal University of Sao Paulo, Sao Paulo, SP, Brazil, [2]Fleury Group, Hospital Sao Luiz, Sao Paulo, SP, Brazil, [3]Fleury Group, Hospital Sao Luiz/Federal University of Sao Paulo, Sao Paulo, SP, Brazil

Purpose
The purpose is to provide a comprehensive review of the appearance of intra-ocular lesions

and potential mimics on computed tomography (CT) and magnetic resonance imaging (MRI).
Materials and Methods
The authors reviewed CT and MR exams of patients referred to diagnostic center of two hospitals in Sao Paulo, Brasil, with different clinical indications, not related to orbital disease, with the exception of facial trauma. There are included cranial, skull base, mastoid and facial exams, that show many different findings of ocular diseases, postoperative, degenerative and mimics. The study included a systematic review of the literature.
Results
The authors discuss the ocular findings in routine head and neck computed tomography and magnetic resonance exams. The different signs which characterize the ocular diseases are shown, allowing recognition by radiologists. Special focus is given to postoperative and mimics that can be mistaken in the diagnosis.
Conclusions
Ocular diseases are common findings in the routine computed tomography and magnetic resonance imaging exams. Sometimes CT is the initial imaging modality of choice, like in traumatic facial injuries. Radiologists should be aware of and need to know the various ocular findings and imaging appearance, that could be crucial for the appropriate diagnosis.

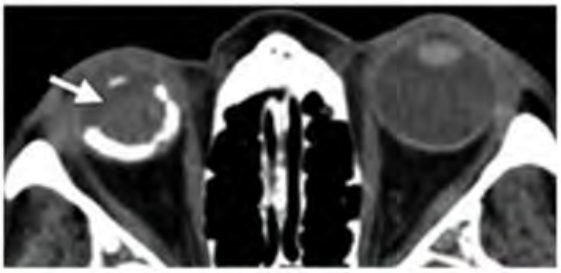


Fig. 1 – Axial CT scan, shows a shrunken globe with thickened and calcified, compatible with Phthisis bulbi

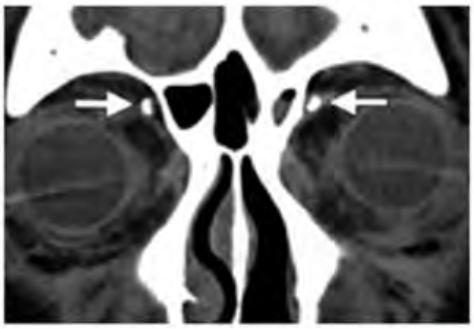


Fig. 3 – Coronal CT image demonstrates bilateral calcification at the superomedial aspect of the orbits, indicative of trochlear calcification

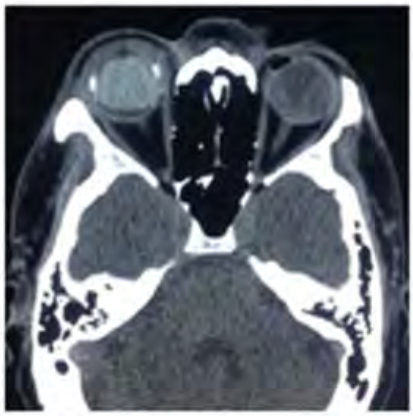


Fig. 2 – Axial CT scan image demonstrates retinal detachment at left globe and circunferencial silicone rubber band (Buckle) at right globe



Fig. 4 – Axial CT image shows fluid acumulation in the subchoroidal space, indicative of choroidal detachment in the right globe

(Filename: TCT_P-58_ASNR2017lesesoculares.jpg)

P-53

6:30AM - 3:00PM

Radiographic Findings in a Series of Brachial Plexopathies

J Rosenblum[1], M Gabbai[2], K Kazmi[2], F Kazmi[3], V Potigailo[2]
[1]Drexel University College of Medicine, Philadelphia, PA, [2]Hahnemann University Hospital, Philadelphia, PA, [3]St. Christopher's Hospital for Children, Philadelphia, PA

Purpose
Radiographic evaluation of a series of brachial plexopathies and comparison to normal anatomy.
Materials and Methods
Evaluation of the cervical spine and brachial plexus was performed using various modalities including PET, CT and MRI. Patients ranged from neonate to 7th decade.

Results

(1) Magnetic resonance imaging (MRI) of the brachial plexus performed on a 63-year-old with history of right breast cancer revealed large heterogeneous elongated mass along the brachial plexus measuring 17 cm x 3.5 cm. CTA and PET/CT also were performed. (2) MRI of the cervical spine and brachial plexus with contrast performed for a patient with facial cellulitis and right arm weakness revealed edema and enhancement of the right anterior and middle scalene muscles as well as the nerve roots of C4, C5 and C6. (3) MRI of the brain and cervical spine performed for a patient with nystagmus and cervical radiculopathy revealed an enhancing, T2 hyperintense lesion originating at the nerve root and extending within the foramen at the level of C5-6. (4) MRI of the brachial plexus with contrast performed for a patient with right upper extremity pain and weakness revealed T2/STIR hyperintensity of the right supraspinatus muscle with a large right disc osteophyte complex at C3-4 with presumed compression of the exiting nerve root. (5) MRI performed on a neonate found increased T2 signal intensity at the exiting nerve root at C5-7. (6) Normal study.

Conclusions

This presentation illustrates a spectrum of brachial plexopathies, including a large brachial plexus malignant nerve sheath tumor, subacute neuritis/Parsonage-Turner syndrome, benign peripheral nerve sheath tumor, muscle denervation due to nerve root compression and Erb's palsy. Normal anatomy and physiology of the brachial plexus is discussed as well.



(Filename: TCT_P-53_erbscoronal.jpg)

P-64

6:30AM - 3:00PM

Skateboard-related Head Injuries are Associated with a High Incidence of Temporal Bone and Skull Base Fractures: A 5-year Retrospective Review

M Booker[1], J Handwerker[1]
[1]*University of California, San Diego, San Diego, CA*

Purpose
Significant head injuries caused by skateboarding have been reported, in part due to a low prevalence of helmet use in younger populations (1, 2). We aim to investigate the incidence, imaging findings and clinical features of skateboard-related head injuries associated with temporal bone and skull base fractures because of their clinical importance.
Materials and Methods
The medical records of patients with a skateboard-related injury imaged by computed tomography (CT) at the University of California San Diego (a level 1 trauma academic medical center) between January 2010 and July 2015 were reviewed. Imaging was reviewed for the presence of temporal bone fracture, intracranial hemorrhage and other head traumatic injuries. Patient demographics, mechanism of injury and complications were analyzed.
Results
Out of 107 patients presenting with skateboard-related injury that underwent a CT head, 8 had temporal bone fractures (7%) and 9 had skull base fractures (8%) (Table 1). These two fracture types accounted for two-thirds of all recorded head and facial fractures. Intracranial hemorrhage accompanied 7 temporal bone fractures (88%) and all 9 skull base fractures. Fifty percent of the temporal bone fractures were mixed type (Table 2). Of those patients with temporal bone fractures, 3 developed hearing loss and 3 required emergency craniotomy. One patient had fracture violation of the otic capsule though none developed a cerebrospinal fluid (CSF) leak. All of the fractures were associated with a lack of helmet use.
Conclusions
Skateboard-related injuries appear strongly associated with temporal bone and skull base fractures. These fractures were associated with a concomitant high incidence of intracranial hemorrhage and lack of helmet use. This fracture association may guide radiologist search pattern and imaging study protocol.

Table 1: Injury Types in Skateboard Head Trauma

Injury Type	Number	Mean Age (SD)	Sex (# Male)
Intracranial Hemorrhage	22	21.9 (7.6)	18
Subdural Hemotoma	13	21.5 (8.3)	10
Intraparenchymal Hemorrhage	12	20.5 (4.6)	9
Subararchnoid Hemorrhage	11	24.9 (8.9)	10
Intraventricular Hemorrhage	4	20.8 (5.0)	4
Epidural Hematoma	4	19.8 (5.1)	3
Head Fracture	25	20.9 (6.9)	22
Skull Base (Occipital, Sphenoid)	9	20.1 (5.3)	6
Temporal bone	8	21.6 (4.9)	6
Calvarium (Frontal, Parietal)	6	20.7 (5.4)	6
Zygomaticomaxillary	6	25.5 (10.8)	5
Mandible	3	19.0 (0.8)	2
Nasal bone	3	22.0 (6.1)	3
Negative	65	24.1 (10.8)	64
Total Patients	**107**	**23.4 (10.0)**	**93 (87%)**

Note: patients with multiple injuries are counted more than once

Table 2: Temporal Bone Fracture Patterns in Skateboard Trauma

Patient	Age	Sex	Mechanism	Laterality	Blunt Force Orientation	Temporal Bone Fracture Orientation	Otic Capsule Involved	Intracranial Hemorrhage	Outcome
1	29	M	vs Car	Left	Head through windshield	Longitudinal	Yes	SAH,IPH,IVH	Hearing loss
2	18	M	Fall	Left	Posterior head	Oblique	No	-	Hearing loss
3	22	M	Fall	Left	Left posterior head	Oblique	No	SDH	Hearing loss
4	16	M	Fall	Right	Right posterior head	Oblique	No	EDH,IPH,IVH	Craniotomy
5	18	M	vs Car	Right	Right head	Oblique	No	SAH,SDH,IPH	None
6	17	F	Fall	Left	Left head	Longitudinal	No	SDH,IPH	None
7	24	M	Fall	Right	Right head	Transverse	No	SAH,IPH	Craniotomy, Death
8	29	F	Fall	Left	Right posterior head	Oblique	No	SAH,SDH,IPH	Craniotomy

SAH = subararchnoid hemorrhage, IPH = intraparenchymal hemorrhage, IVH = intraventricular hemorrhage, SDH = subdural hemorrhage, EDH = epidural hematoma

(Filename: TCT_P-64_tables.gif)

P-61

6:30AM - 3:00PM

The Diagnostic Accuracy of Contrast-Enhanced CT of the Neck for the Investigation of Sialolithiasis

Y Purcell[1], A Carroll[1], R Kavanagh[1], A Cahalane[2], R Killeen[3]
[1]St Vincent's University Hospital, Dublin 4, Ireland, [2]St. Vincent's University Hospital, Dublin, Ireland, [3]St. Vincent's University Hospital, Dublin, Dublin 4

Purpose
The aim of this study is to assess the diagnostic accuracy of contrast-enhanced CT of the neck (CECTN) in the diagnosis of sialolithiasis compared to noncontrast CT of the neck (NCCTN), used as the gold standard.
Materials and Methods
This is a tertiary-referral center, retrospective, case-controlled study of 92 consecutive cases that underwent both NCCTN and CECTN from January 2011 to December 2015 for

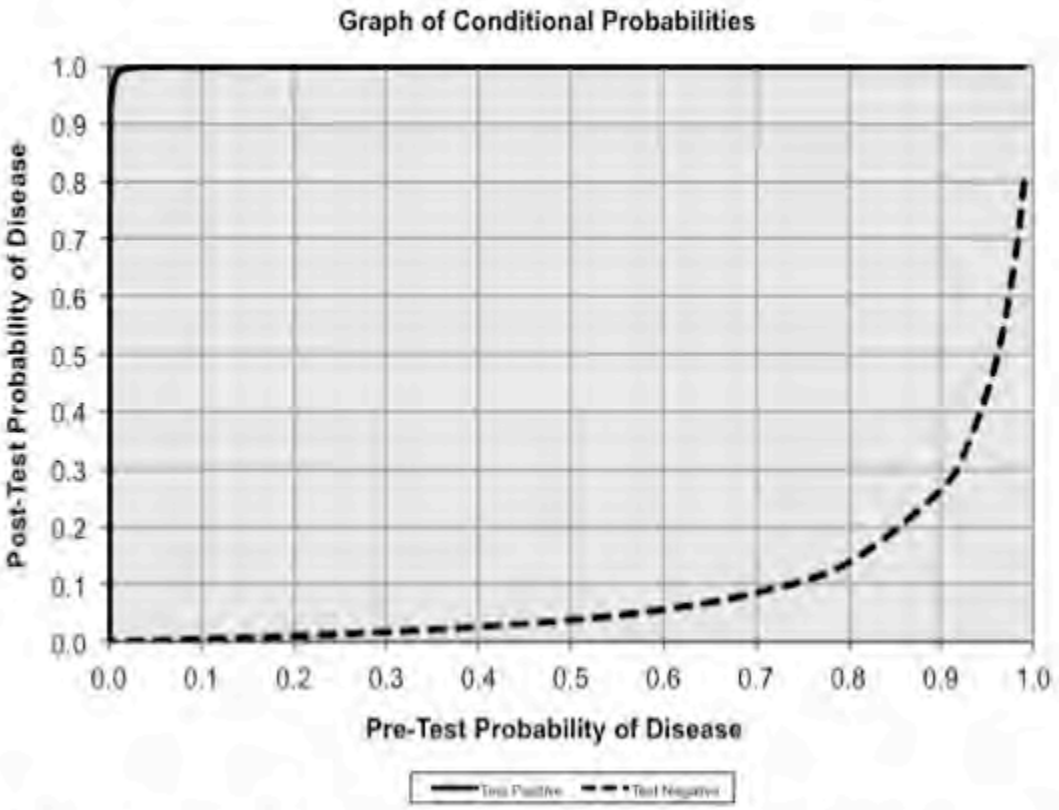
investigation of sialolithiasis. Axial 3 mm slice images were assessed by a fellowship-trained diagnostic neuroradiologist and diagnostic neuroradiology fellow in consensus. Blinded assessment of the CECTN was performed first followed by NCCTN after a 2-week interval. The presence or absence of a stone, stone location and stone size were documented. Statistical analysis was performed to assess the agreement between CT protocols and to calculate the sensitivity/specificity of CECTN.

Results

Fifty calculi were identified on NCCT in 31 cases and 48 calculi in 31 cases on CECTN. The sensitivity and specificity of CECTN in the detection of sialolithiasis is 96% (95% CI 86.3-99.5%) and 100% (95% CI 94.1-100%) respectively. The positive predictive value of CECTN is 100% (95% CI 92.6-100%) and negative predictive value is 96.8% (95% CI 89-99.6%). The accuracy of CECTN in diagnosing the presence or absence of salivary calculi is 98%.

Conclusions

Contrast-enhanced CT of the neck is accurate in the detection of sialolithiasis.



Graph of conditional probability shows the relationship between pre and post-test probabilities for contrast-enhanced CT in the investigation of salivary duct calculi

(Filename: TCT_P-61_Slide1.jpg)

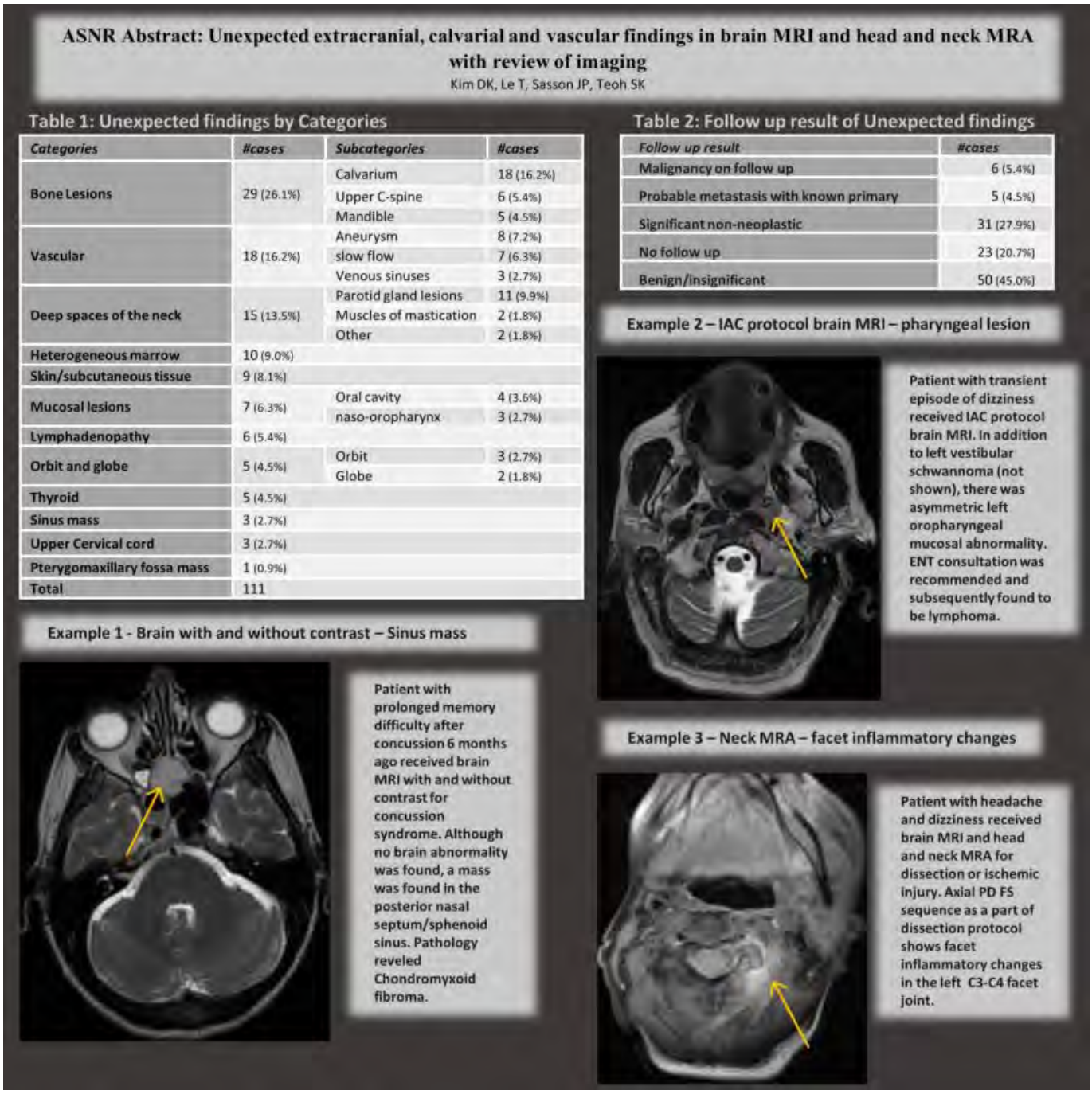
P-62

6:30AM - 3:00PM

Unexpected Extracranial, Calvarial and Vascular Findings in Brain MRI and Head and Neck MRA with Imaging Review

D Kim[1], T Le[2], P Sasson[1], S Teoh[1]
[1]Mount Auburn Hospital, Cambridge, MA, [2]Mount Auburn Hospital, Cambridge , MA

Purpose
Although several prior studies mainly focused on unexpected intracranial findings, there are other unexpected findings in brain MRI which may be of clinical significance. The purpose of our study is to assess the prevalence and pattern of extracranial, calvarial and vascular unexpected findings in routine brain magnetic resonance imaging (MRI) and head and neck magnetic resonance angiography (MRA).
Materials and Methods
A retrospective, HIPAA compliant, IRB approved PACS review of all brain MRI and head and neck MRA studies interpreted by one of two CAQ certified and fellowship trained neuroradiologists from Jan. 1, 2013 to Dec. 31, 2014 was performed at a 213-bed community hospital. Prior and follow-up radiology reports and electronic medical records were reviewed to assess outcomes.
Results
There were 4424 brain MRI and head and neck MRA studies during the two-year period. One hundred eleven unexpected findings were found from 108 different reports (3.5%). There were 29 (26.1%) bone lesions, 18 (16.2%) vascular findings, 15 (13.5%) deep space of the neck lesions, 10 (9%) heterogenous marrow, 9 (8.1%) skin/subcutaneous tissue lesions, 7 (6.3%) mucosal lesions, 6 (5.4%) lymphadenopathy, 5 (4.5%) orbit and globe lesions, 5 (4.5%) thyroid gland lesions, 3 (2.7%) sinus mass, 3 (2.7%) upper cervical cord lesions and 1 (0.9%) pterygomaxillary fossa lesion. There were 6 (5.4%) malignancies on follow up, 5 (4.5%) probable metastasis with known primary without follow up and 31 (28%) significant non-neoplastic findings.
Conclusions
Technical improvements in cross-sectional imaging over the years have enhanced our ability to detect finer anatomic details that may not be related to the primary organ of initial clinical interest. Although several prior studies have focused on incidental intracranial findings, our study focuses on the less recognized calvarial, extracranial and vascular pathology found in routine brain MRI and head and neck MRA. Our study found 3.5% overall rate of unexpected extracranial, calvarial and vascular findings, some of which may have significant consequences if inadvertently overlooked.



(Filename: TCT_P-62_BrainincidentalAbstractJPG.jpg)

Monday
6:30AM - 3:00PM
Long Beach Convention Center, Exhibit Hall B-(Lower Level) P

Scientific Poster(P)-Print-Informatics

P-65

6:30AM - 3:00PM

The Effect of Prenatal MRI on the Newborn Hearing Test

R Hasweh[1], K Raghuram[1], K Jelliffe[1]
[1]*University Of Texas Medical Branch, Galveston, TX*

Purpose
Magnetic resonance imaging (MRI) is a relatively safe modality for imaging acute emergencies in pregnancy when additional detail is needed. Despite not using ionizing radiation and generally recommended as safe for imaging, subliminal effects of the magnetic field and the loud noise generated during scanning, remain unknown. The main source of noise during MRI is vibration produced by gradient of magnetic field which reaches the auditory system particularly affects the hair cells (1). One concern we seek to address is whether the loud noise generated during scanning has any apparent effects on hearing in the fetus. The first hearing response in the fetus has been observed at 19 weeks of gestational age. The number of fetuses responding to each frequency increased with gestational age (2). The purpose of our retrospective study was to determine the effect of prenatal MRI on the newborn hearing test.
Materials and Methods
In our retrospective study, multistep hearing tests performed on newborns exposed to MRI in utero were reviewed. The two types of tests that are commonly used for newborn hearing screening are otoacoustic emissions (OAEs) and auditory brainstem response(ABR). In our institution the primary hearing test for newborns is OAE and ABR is used only when patient fails the multi-step test (3). Otoacoustic emissions are sounds of cochlear origin, which can be recorded by a microphone fitted into the ear canal. They are caused by the motion of the cochlea's sensory hair cells as they energetically respond to auditory stimulation (4). Our screening test starts at day 1, serial follow up is done at day 2, 6 weeks and 6 months in case the baby fails the initial or any subsequent tests.
Results
The medical records of 95 patients that underwent 1.5T MR imaging during their pregnancy were reviewed. Out of the 95 patients, 18 were lost to follow up, one had an abortion during the second trimester and one newborn did not have a hearing test before discharge. The remaining 79 newborn who were tested in our hospital passed their hearing tests either in the initial or the follow-up tests.
Conclusions
Our study concludes that exposure of the fetus to 1.5 T MRI during all trimesters of pregnancy is not associated with neonatal hearing loss as detected by currently available technologies.

Long Beach Convention Center, Exhibit Hall B-(Lower Level) P

Scientific Poster(P)-Print-Interventional

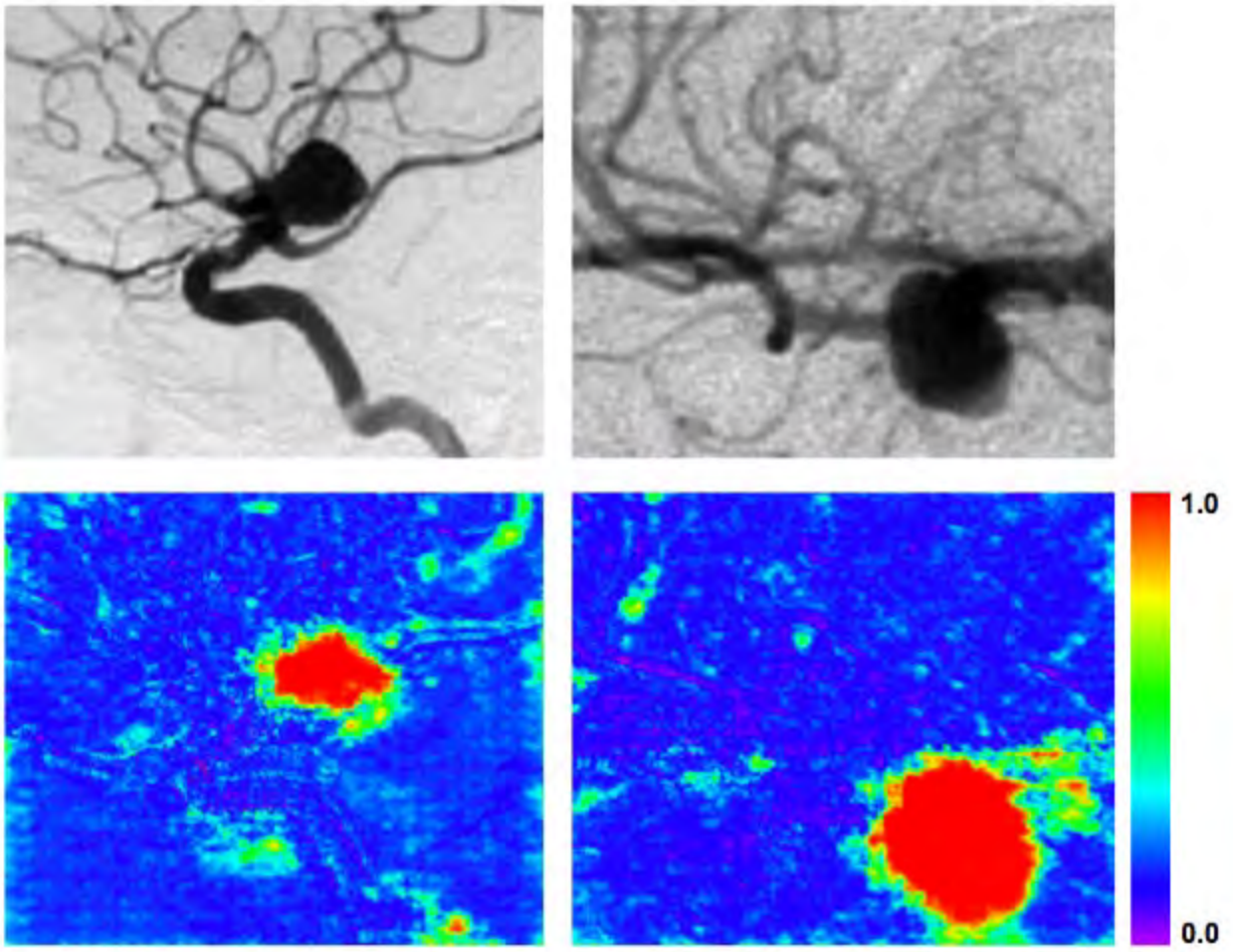
P-67

6:30AM - 3:00PM

A Deep Learning Approach to Automated Cerebral Aneurysm Detection on Conventional Angiograms

J Stember[1], P Chang[1], A Goel[2], C Filippi[3], A Lignelli[4], P Meyers[5]
[1]Columbia University Medical Center, New York, NY, [2]Columbia University Medical Center, new york, NY, [3]Hofstra Northwell School of Medicine, New York, NY, [4]Columbia University Medical Center, New York City, NY, [5]Columbia University, New York, NY

Purpose
Convolutional neural networks (CNNs) have become widely recognized as the best performing method in various image analysis challenges. We seek to demonstrate that a CNN can automatically detect cerebral aneurysms from conventional angiographic images.
Materials and Methods
Twenty conventional angiograms were obtained from publicly available images embedded within teaching or industry web sites as well as peer-reviewed journal article [the first three used being (1-3)]. Images were normalized via z-score standardization (mean=0, S.D.=1). Aneurysms were localized manually by an approximate polygonal ROI. A CNN was developed for aneurysm detection. The 14-layer CNN is implemented via a fully convolutional architecture with contracting/expanding pathways (4) and residual connections (5). Extensive real-data augmentation included: (1) random image rotation by -45 to 45-degrees; (2) random displacement by -20 to 20 voxels; (3) random scaling by 75 to 150%; (4) random addition of a constant between -0.1 and 0.1.
Results
The proposed CNN successfully identified presence and location of aneurysm in 16/20 cases via leave-one-out cross-validation. Upon visual inspection the CNN performed better for larger aneurysms given the over-representation of larger aneurysms in the training set. Example heat maps corresponding to aneurysm localization are shown in Figure 1.
Conclusions
The deep learning approach shows promise as a method to automatically predict and detect cerebral aneurysms. Future applications will focus on MRA and CTA images. Additional training data is expected to permit more accurate identification of smaller and more subtle aneurysms. The approach can be used as a second reader to improve accuracy of radiologist interpretation. Another application is for triage of images with a high likelihood of containing aneurysms for expedited radiologist interpretation.



(Filename: TCT_P-67_image.jpg)

P-71

6:30AM - 3:00PM

Acute Ischemic Stroke Following Interim Stoppage of Anticoagulants in Patients with Atrial Fibrillation Treated with Endovascular Therapy. A Busy Stroke Center's Experience.

I Akhtar[1], K Olds[1], C Martin[1], J Halpin[1], W Holloway[1], N Akhtar[1]
[1]*Saint Luke's Hospital of Kansas City, Kansas City, MO*

Purpose
Atrial fibrillation (AF) remains a significant cause of acute ischemic stroke, with studies demonstrating that patients with AF suffering an acute ischemic stroke are likely to have a more severe stroke and as a result, a poorer outcome when compared to patients who have an ischemic stroke without underlying AF (1). Most commonly either the AF is discovered for the first time in the wake of the stroke on follow-up testing, or is a pre-existing condition in a patient who suffers a stroke despite being on appropriate anticoagulation. A lesser explored

but crucial subset of acute ischemic strokes caused by AF is that of patients with known AF who are on chronic anticoagulation therapy, either with warfarin or the newer novel anticoagulants (NOAC), who stop anticoagulation briefly, and subsequently suffer from an ischemic stroke hours to days after cessation of therapy. We will present data from this subset of patients that were treated with endovascular therapy at our stroke center over the past 4 years, with the purpose of exploring the correlation between time of stoppage of anticoagulant therapy and the onset of the acute ischemic stroke.

Materials and Methods

A comprehensive data collection of all stroke cases treated with stent retrieval at our facility from March 2012 to March 2016 was conducted. Three hundred twenty-five patients were identified. Retrospective chart review of these cases was conducted, and patients with known atrial fibrillation who were receiving treatment with either warfarin or NOAC were selected. Eighty-seven out of 325 patients (27%) had a pre-existing diagnosis of atrial fibrillation and were on treatment prior to stroke onset, although compliance with therapy was varied. Out of these 87 patients, 24 patients (28%) were those in whom anticoagulation was stopped temporarily, either by the physician for an upcoming procedure or due to a complication of use. Our goal in identifying these patients is to discern the correlation with time stoppage of anticoagulation and the onset of stroke.

Results

Demographic: • Gender: o 9 Males (37.5%), o 15 Females (62.5%). • Mean Age at presentation of stroke: 75±10 (range:56-94). Location of Thrombus: (See Table 1). Anticoagulation regime: • Warfarin: 20 patients (83.3%). • Rivaroxaban: 2 patients (8.3%). • Apixaban: 1 patient (4.1%). • Dabigatran: 1 patient (4.1%). Reason for Discontinuation: (See Table 2). • Anticoagulation was stopped in anticipation of a procedure in 17 patients. Of those: o 14 patients developed an ischemic stroke after procedure (post-procedural). o 3 patients developed an ischemic stroke in anticipation of procedure (pre-procedural). Median number of days from stoppage of the anticoagulation to the onset of stroke: 7 days (range: 3-112). Mean INR at presentation±SD: 1.36±.45 (range: 1-2.7). TPA administered in 9/24 (37.5%) patients. Endovascular Parameters: • NIH Scores: o Mean Initial NIH±SD: 16.3±9 (range: 2-34). o Mean 24-hour post IR NIH±SD: 8.5±7 (range: 0-24). Successful Reperfusion (defined by a TICI score of 2b or higher) was achieved in 22/24 patients (91.6%). Complications after endovascular treatment: • 1 patient with symptomatic hemorrhagic conversion. • 1 patient with embolization to different vascular territory.

Conclusions

Our findings illustrate that even a brief stoppage of anticoagulation puts the patient as significant risk for the development of stroke. If anticoagulation is stopped due to an upcoming procedure, the time between the stoppage of anticoagulation therapy and the impending procedure should be minimized and the anticoagulant should be resumed as soon as possible after the procedure to reduce the risk of a stroke developing in that period. Bridging with heparin also may be warranted and should be considered when chronic anticoagulation is stopped in the peri-procedural period. Even more importantly, patients

should be specifically warned about the dangers that can occur following temporary discontinuation of anticoagulant therapy, and be guided by physicians to assess their options and to develop contingency plans in case a stroke develops, such as reaching a stroke center in a timely fashion.

TABLE 1: Location of Thrombus

Location	Number of Patients (n)
Post circulation (basilar/vertebral)	2
ICA terminus	3
M1	14
M2	4
M3	1

TABLE 2: Reason for discontinuation

High risk for side effect of bleeds (i.e. falls, epistaxis, hematuria)	5
Dental procedures	2
Cardiac procedures (i.e. cardiac ablation)	4
Colonoscopy/polypectomy	4
Minor surgery (i.e. biopsy)	6
Physician recently lowered dose (did not stop therapy, lowered dose of anticoagulant)	1
Major surgery (i.e. back surgery)	1
Unable to afford treatment	1

(Filename: TCT_P-71_table1and2.gif)

P-75

6:30AM - 3:00PM

Comparison of Outcome in Endovascular Thrombectomy for Acute Ischemic Stroke Without and With Pre-treatment Intravenous rt-PA: A Single-Center Experience

H Liu[1], C Lee[1]
[1]*National Taiwan University Hospital, Taipei, Taiwan*

Purpose
Intra-arterial thrombectomy becomes one of the standard treatments for acute ischemic stroke (AIS) with large vessel occlusion. This study aimed to compare the outcome between subjects without (group A) and with intravenous t-PA (group B) treatment before intra-arterial thrombectomy from a single-center in Taiwan.
Materials and Methods
Retrospectively, we reviewed the last 60 patients experienced acute ischemic stroke received endovascular thrombectomy in our institute.

Results
Among them, 30 were found in both group A (without intravenous t-PA) and B (with intravenous t-PA). The average age/standard deviation were 74.1/12.9 in group A, and 69.3/10/8 in group B. Sixteen were male in both groups. In group A, 14 involved vessels were on the left side, 12 on right side, 3 in basilar artery, and 1 had bilateral M1. In group B, 10 involved vessels were on the left side, 15 on right, and 6 in basilar artery. M1 lesion alone was in 17 (56.7%) in group A, and 12 (40.0%) in group B. The median NIHSS on admission was 20.2 in group A, and 19.9 in group B. The median time from stroke onset to groin puncture were 245 and 210 minutes in groups A and B respectively. In both groups, 20 (66.6%) patients the final revascularization graded TICI 2b/3. At 90 days, 14 (46.7 %) patients and 12 (40%) achieved favorable outcome (mRS less than 3) in groups A and B respectively. No significant difference in outcome between the two groups.
Conclusions
The study demonstrates a comparable result in both groups of endovascular thrombectomy in AIS with large vessel occlusion in a real world clinical practice.

P-68

6:30AM - 3:00PM

Hemodynamic Factors Associated with Basilar Tip Aneurysm Rupture Determined by Computational Fluid Dynamics

R Blagdon[1], M Bligh[1], A Dias[2], R Vieira[2], J Gasche[2], J Militzer[2], J Shankar[1]
[1]Dalhousie University, Halifax, Nova Scotia, [2]Dalhousie Univeristy, Halifax, Nova Scotia

Purpose
Rupture of intracranial aneurysms carries significant mortality and morbidity. For unruptured aneurysms, rupture prediction currently relies primarily on size and carries significant uncertainty. Refinement of individual aneurysm rupture risk by incorporating computationally determined hemodynamic factors such as intra-aneurysmal pressure and wall shear stress (WSS) has been proposed. There has been no focused investigation of the hemodynamic properties of basilar tip aneurysms, which are common within the vertebrobasilar system and carry major morbidity. The purpose of the current study is to determine hemodynamic variables associated with rupture of basilar tip aneurysms using open source computational fluid dynamics (CFD) software.
Materials and Methods
Three-dimensional models and tetrahedral meshes of eight basilar tip aneurysms (4 ruptured and 4 unruptured) were generated from CT angiograms using Vascular Modeling Toolkit (VMTK, Orobix, Bergamo, Italy). A blinded CFD analysis was performed using OpenFOAM (OpenCFD, ESI Group, Paris, France) to determine the hemodynamic properties at the dome and neck of the aneurysms. Time-dependent pressure and WSS were modeled over 3 cardiac cycles.

Results
The maximum WSS was significantly higher in ruptured than unruptured aneurysms at the dome (m=0.012 m^2/s^2 vs m=0.008 m^2/s^2, p=0.02) but was not statistically different at the neck (m=0.021 m^2/s^2 vs m=0.026 m^2/s^2, p=0.29). Maximum pressure in ruptured aneurysms was not statistically different from that in unruptured aneurysms both at the dome (m=0.52 m^2/s^2 vs m=0.73 m^2/s^2; p=0.13) and the neck (m=0.57 m^2/s^2 vs m=0.92 m^2/s^2; p=0.14).
Conclusions
Ruptured basilar tip aneurysms were associated with significantly higher maximum WSS at their dome compared with unruptured aneurysms. This suggests that dome WSS is a promising metric for determining aneurysm rupture risk and needs to be tested in larger studies.

P-66

6:30AM - 3:00PM

Real-Time Quantitative Changes in Cerebral Perfusion from Intra-Arterial Vasodilator Treatment in Cerebral Vasospasm

J Weng[1], A Tang[2], G Duckwiler[3], D Liebeskind[2], S Sheth[4], F Scalzo[2]
[1]Department of Neurology, David Geffen School of Medicine at UCLA, Los Angeles, CA, [2]Department of Neurology, Neurovascular Imaging Research Core, UCLA, Los Angeles, CA, [3]Department of Interventional Neuroradiology, David Geffen School of Medicine at UCLA, Los Angeles, CA, [4]Department of Neurology, UTHealth, The University of Texas Health Science Center at Houston, Houston, TX

Purpose
Intra-arterial (IA) dilators are key components in the treatment of cerebral vasospasm (CV), yet infusion techniques and protocols vary greatly, due in part to the absence of an established angiographic endpoint against which to titrate treatment. The most commonly used endpoint--proximal vessel caliber--does not predict future ischemia or clinical outcome. Quantitative cerebral blood flow (CBF) measurements from 2D angiographic images may better characterize treatment effect and provide real-time feedback to guide infusion protocols.
Materials and Methods
From our prospectively maintained institutional registry, we identified patients treated with IA verapamil in the internal carotid artery (ICA) for CV between January 2012 and January 2016. Cerebral blood flow maps were calculated automatically for both AP and lateral projections. Wilcoxon Signed-Rank test was used to compare pre versus postinfusion CBF. Spearman correlation was used to calculate correlation of change in CBF and dosage of verapamil.

Results
A total of 80 angiograms from 18 patients treated with verapamil were examined. Median age was 42 years and 66.7% were female. Patients presented with symptomatic vasospasm in 44% (8/18) of cases. The degree of vasospasm varied from mild [10% (8/80)], moderate [33% (26/80)], and severe [57% (46/80)]. Doses of verapamil ranged from 5 mg to 15 mg per ICA. Immediate postinfusion angiograms demonstrated proximal vessel caliber improvement in 34% (27/80) of cases. Total CBF increased on average by 11% postinfusion. Absolute total CBF was significantly increased postinfusion compared to pre-infusion ($p = 0.004$). Changes in CBF did not correlate significantly with dose of verapamil ($p = 0.11$). Mismatch between vessel caliber assessment and change in CBF calculation occurred in 37.5% (30/80) of cases. Among this discordance, 73% (22/30) demonstrated no vessel caliber improvement, but had greater than 11% increase in total CBF.
Conclusions
Vasodilator infusion demonstrated quantifiable increases in CBF in patients with CV. Quantitative angiographic perfusion maps may provide more direct and relevant treatment targets for IA infusion therapy.

P-70

6:30AM - 3:00PM

The Safety of Protected Carotid Artery Stenting in Patients with Unstable Plaque on Carotid High-resolution MR Imaging

H KWAK[1], G Chung[2]
[1]Chonbuk National University Medical School and Hospital, Jeonju-si, Korea, Republic of, [2]Chonbuk National University Medical School and Hospital, Jeonju-si, Korea

Purpose
Based on data from carotid MR imaging, unstable plaques are prone to intraplaque hemorrhage (IPH), thin/ruptured fibrous caps, and ulceration. The aim of this study was to determine the safety of carotid artery stenting (CAS) using an embolic protection device based on the findings of carotid MR imaging in patients with severe carotid artery stenosis.
Materials and Methods
This prospective study assessed 102 consecutive patients with severe carotid stenosis. These patients underwent preprocedural carotid MR imaging, and postprocedural diffusion-weighted imaging (DWI) after CAS. Unstable plaque on carotid Magnetic resonance imaging (MRI) was defined as IPH, thin/ruptured fibrous caps, or ulcers. We analyzed the incidence of postprocedural ipsilateral ischemic events on DWI and the primary outcomes within 30 days of CAS.
Results
Fifty patients (49.0%) had IPH, 84 (82.4%) had thin/ruptured fibrous caps, and 43 (42.2%) had ulcers on carotid plaque MR imaging. Intraplaque hemmorhaging was more common in

the symptomatic group than in the asymptomatic group (58.7% vs. 41.1%, p = 0.12). Overall, DWI was positive after CAS in 25.5% of cases. The combined rate of 30-day stroke, myocardial infarction, or death was 3.9%. New postprocedural ischemic lesions on DWI were observed more frequently in the symptomatic group (17/46; 37.0%) than in the asymptomatic group (9/56; 16.1%)(p = 0.03). There was no significant difference in the primary outcome of CAS based on the type of unstable plaque of IPH, thin/ruptured fibrous caps, or ulcers.
Conclusions
Protected CAS appears to be safe, regardless of unstable plaque findings on carotid MR imaging.

P-69

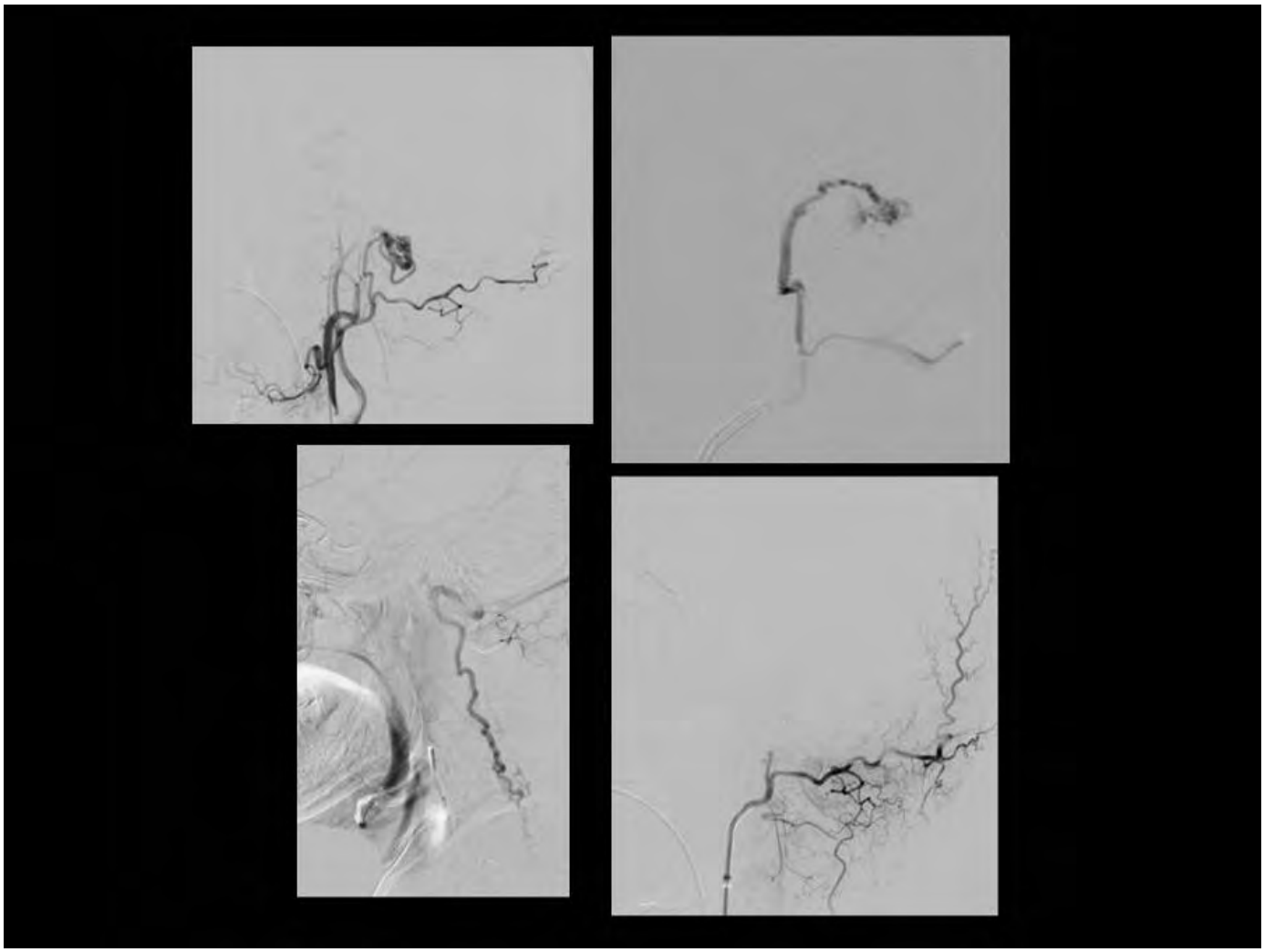
6:30AM - 3:00PM

Type V Dural Arteriovenous Fistula: A Case Series

H PENDHARKAR[1], C Prasad[2], A Gupta[3], A Verma[4], S TIWARI[5]
[1]NATIONAL INSTITUTE OF MENTAL HEALTH & NEUROSCIENCES, BANGALORE, KARNATAKA, [2]National Institute of Mental Health and Neurosciences, Bangalore, Karnataka, [3]National Institute of Mental Health and NeuroSciences (NIMHANS), Bangalore, Karnataka, [4]national Institute of Mental health & Neuro Sciences, Bangalore, Karnataka, [5]National Institute of Mental Health and Neurosciences, BANGALORE, Karnataka

Purpose
To analyze the endovascular management of type V dural arteriovenous fistula at our institute.
Materials and Methods
Five thousand cerebral angiograms done at our department between 2011- 2016 were reviewed. There were 3 patients with Type V DAVF (Intracranial DAVF with perimedullary venous drainage). All were male patients, youngest was 18 years and oldest was 55 years old. All patients presented with bilateral lower limb weakness, one with left upper limb weakness and two with bladder and bowel disturbance. The duration of symptoms varied from 6 months to 1 year.
Results
All patients were subjected to magnetic resonance imaging (MRI) of the spine and brain which revealed cervical perimedullary flow voids. Subsequent DSA revealed type V DAVF in all three patients. In one patient the feeder was from stylomastoid branch of right occipital artery, in the other it was the jugular branch of the left neuromeningeal trunk and in the third it was fed by both stylomastoid branch of the left occipital artery and jugular branch of the left neuromeningeal trunk. Two of three patients underwent embolization with glue with complete closure of the fistula. The third patient is awaiting embolization.

Conclusions
Type V DAVF is a rare vascular malformation. Cervical perimedullary flow voids should raise the suspicion of this entity. A complete six vessel cerebral angiogram is mandatory to delineate the fistula. Endovascular embolization is the treatment of choice.



(Filename: TCT_P-69_ASNR1.jpg)

Monday
6:30AM - 3:00PM
Long Beach Convention Center, Exhibit Hall B-(Lower Level) P

Scientific Poster(P)-Print-Pediatrics

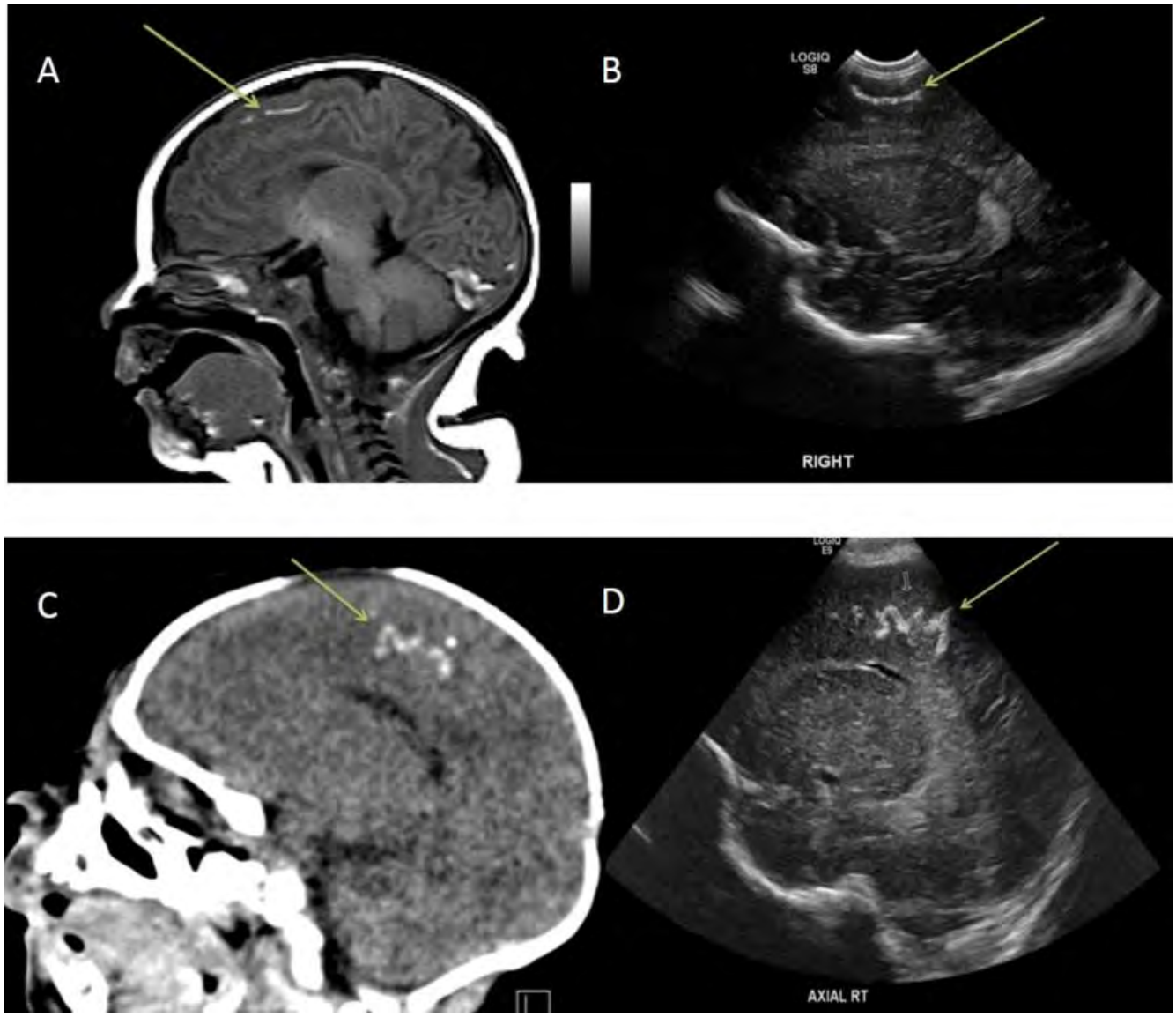
P-77

6:30AM - 3:00PM

Can the Pattern of Intracranial Calcifications be Helpful in Differentiating Zika from Other Congenitally Acquired Infections?

G De La Vega Muns[1], J Mahan[2], R Medvid[3], A de la Vega[4], M Post[5], G Saigal[2]
[1]Jackson Memorial hospital, miami, FL, [2]University of Miami/Jackson Memorial Hospital, Miami, FL, [3]Jackson Memorial Hospital, Miami, FL, [4]University of Puerto Rico School of Medicine, San Juan, PR, [5]Univ. of Miami, Miller School of Medicine, Miami, FL

Purpose
This is a retrospective case review of brain imaging findings in patients who contracted the Zika virus prenatally and were imaged in the University of Miami Miller School of Medicine and in the University of Puerto Rico in 2016. The aim of this study was to identify, if possible, unique imaging patterns which would aid in differentiating Zika infection from other congenitally acquired infections.
Materials and Methods
We identified 6 patients who were exposed to Zika virus prenatally and who subsequently were confirmed to have the virus by PCR analysis. Of these, 4 underwent prenatal ultrasound evaluation, 1 underwent postnatal brain ultrasound and noncontrast brain CT, and 1 underwent postnatal brain ultrasound and brain MRI.
Results
Three (50%) of the patients reviewed were found to have parenchymal calcifications with a characteristic curvilinear, elongated appearance located at the cortical-subcortical gray-white matter junction. Of these, 2 were identified postnatally via ultrasound encephalogram and confirmed with either CT or MRI. The other was identified via prenatal ultrasound at 24 weeks gestation. Two (33%) of the patients were found to have coarse calcifications in the basal ganglia on prenatal ultrasound evaluation.
Conclusions
Several congenitally acquired infections are associated to intracranial calcifications including Toxoplasmosis, Cytomegalovirus, Herpes Simplex, Rubella, among others. Their imaging findings are well documented in the literature and primarily include calcifications in the basal ganglia, periventricular and cortically based calcifications. To our knowledge the pattern observed in some of our patients of elongated curvilinear calcifications in the subcortical white matter has not been described in other prenatally acquired infections and could be unique to Zika virus infection. Therefore, they may help distinguish Zika-infected patients from other congenitally acquired infections. We hope that the illustration of these patients will aid others in identifying Zika-infected patients in the future.



(Filename: TCT_P-77_Image1.jpg)

P-78

6:30AM - 3:00PM

Incidence and Volumetry of Pituitary Cysts in Normal Children

B Pogostin[1], O Bersot[1], N Krasnow[1], J Haigney[1], W Weiler[1], M Kessler[1], R Noto[1], M Tenner[1]
[1]New York Medical College, Sleepy Hollow, NY

Purpose
To assess the incidence and volumetry of pituitary cyst (PC) in a cohort of normal children.
Materials and Methods
Three hundred forty-two patients ages 6-18 who had a high resolution postcontrast MRI

(1mm slices) at the Division of Neuroradiology at NYMC between 2010-2016 were selected randomly to be part of this study. Patients with known pathologic entities were eliminated. Of the 342 patients, 171 (82 male, 89 female) met the criteria for inclusion in this study. The mean age was 12.6±3.37 years with a median of 13.2 years. Pituitary and cyst volumes (CV) were measured using the ellipsoid formula LxWxH/2. Percentage of the gland occupied by cyst (POGO) was calculated as the ratio of CV to pituitary volume. For this study, a POGO exceeding 15% was considered a large cyst.
Results
Twenty-five of 171 patients had a PC, yielding an incidence of 14.6%. Cyst volumes ranged from 2.72-78.41mm3, with a mean of 17.2816.72 mm3 (median 11.52 mm3). POGO ranged from 0.68 - 27.36%, with a mean of 4.875.68% (median 3.07%). One of the 25 patients (4.0%) had a large cyst. The statistical difference between CVs and POGO for males versus females was not significant (p=0.27 and p=0.21 respectively). The difference in CV between children under 11 and children 11 or older was insignificant (p=.15), but the difference in POGO was significant (p=.037).
Conclusions
Our data show a significantly higher incidence of PC than previously reported. Additionally, POGO was significantly lower for all patients older than 11 compared to all patients younger than 11. This suggests that cysts are unlikely to further impinge on the pituitary gland and its function over time. The pathological implications of these findings need to be further investigated.

P-80

6:30AM - 3:00PM

MRI Findings in Children with Spasmus Nutans, a Rare Nystagmus Disorder: Is There Really an Association with Optic Glioma?

M Bowen[1], J Peragallo[1], S Kralik[2], A Poretti[3], T Huisman[4], B Soares[5]
[1]Emory University School of Medicine, Atlanta, GA, [2]Indiana University, Indianapolis, IN, [3]The Johns Hopkins University School of Medicine, Baltimore, MD, [4]Johns Hopkins, Baltimore, MD, [5]Johns Hopkins University School of Medicine, Baltimore, MD

Purpose
Spasmus Nutans (SN) is a rare pediatric ophthalmologic syndrome of nystagmus, head bobbing and abnormal head positioning. Historically, SN has been associated with underlying optic pathway gliomas (OPG). However, evidence of this is association based primarily on a small number of isolated case reports; prior retrospective analyses have found the rate of OPG to be less than 2%. These analyses only intermittently utilized neuroimaging with CT, with its limited sensitivity for detecting small lesions in the optic pathway. The purpose of this study was to evaluate the association of SN with intracranial abnormalities, particularly OPG, utilizing MRI of the brain and orbits.

Materials and Methods

Neuroradiology databases at three institutions spanning January 2010 to May 2016 were queried for examinations ordered for evaluation of SN; magnetic resonance imaging (MRI) of the brain and/or orbits were included and evaluated for OPG and structural abnormalities. At minimum, protocols included sagittal T1 SE or 3D T1 gradient-echo, axial T2 FSE and T2-FLAIR and, if contrast was given, postcontrast coronal and axial T1 SE or sagittal 3D T1 GRE. Medical records were reviewed to confirm a diagnosis of SN, presence of other underlying neurological disease or pre-existing diagnoses.

Results

Forty patients with eligible imaging were identified. Mean (IQR) age at time of imaging was 16.3 (17.4) months. None had optic nerve pathway gliomas. Two children had optic nerve hypoplasia; no other patients had optic pathway abnormalities. None had intracranial or orbital masses. Twenty-five had normal MRI.

Conclusions

This series represents the largest collection of MRI for SN in the literature to date and shows no association between OPG and SN. Given the young age at SN onset and, subsequently, the frequent need for sedation for MRI, in children presenting with SN but no other findings concerning for OPG or neurological abnormalities, neuroimaging may not be required.

Table 1. Intracranial abnormalities on MRI ordered for children with suspected Spasmus Nutans

MRI findings	Medical history, if known
Prominent ventricles, bilateral optic nerve hypoplasia	Unknown
Brachycephaly, ventriculomegaly	Developmental delay
Bilateral optic nerve hypoplasia	Global developmental delay
Ventriculomegaly with paucity of white matter without gliosis	Developmental delay, pre*
Mild periventricular leukomalacia	Unknown
Complex pineal cyst without hydrocephalus	Otherwise healthy
Corpus callosum thinning	Global developmental delay, pre
Mild ventriculomegaly	Otherwise healthy
Delayed myelination	CP, speech delay, pre
Periventricular nodular heterotopia	Otherwise healthy
Mild chronic intraventricular hemorrhage/ germinal matrix hemorrhage	Unknown
Bulging at lateral aspect of bilateral globes	Otherwise healthy; known FH of familial exudative vitreoretinopathy
Corpus callosum thinning, mild ventriculomegaly, diminished periventricular white matter	1p36 chromosomal deletion, resultant seizure disorder
Partial agenesis of posterior body and splenium of corpus callosum, malrotated hippocampi	Trisomy 21, pre
Large frontal lobe subarachnoid spaces	Otherwise healthy

**pre = premature*

(Filename: TCT_P-80_ASNR_Table.jpg)

P-82

6:30AM - 3:00PM

Posterior Fossa Malformations: Accuracy of Fetal ultrasound Versus MRI

E Snyder[1], A Jelin[2], A Poretti[3], T Huisman[4], A Tekes[1]

[1]Johns Hopkins University, Baltimore, MD, [2]Johns Hopkins University School of Medicine, Baltimore, MD, [3]The Johns Hopkins University School of Medicine, Baltimore, MD, [4]Johns Hopkins, Baltimore, MD

Purpose
Accurate prenatal characterization of posterior fossa anomalies is essential for prenatal counseling and postnatal management planning. Use of accurate terminology by all disciplines enables timely diagnosis and guides the management plan. The aim of this study was to assess the accuracy of prenatal ultrasound in diagnosing posterior fossa malformations.
Materials and Methods
From January 2008-October 2016, all patients with abnormal findings in the posterior fossa on prenatal ultrasound were identified from fetal ultrasound database. Patients with Chiari malformations were excluded. The medical records of these patients were reviewed. Cases with all 3 imaging modalities: prenatal ultrasound, prenatal and postnatal magnetic resonance imaging (MRI) were included and diagnoses on prenatal imaging and were compared against postnatal brain MRI.
Results
Abnormalities of the posterior fossa were detected in 106 patients. Only 17 (16.0%) patients had prenatal ultrasound, prenatal MRI and postnatal MRI. All prenatal ultrasonographies were evaluated by Maternal Fetal Medicine specialists, fetal MRI by pediatric neuroradiologists, and postnatal MRIs by adult and pediatric neuroradiologists. Prenatal ultrasound findings were consistent with prenatal and postnatal MRI in only 6 cases (35%), while fetal MRI was consistent with postnatal MRI in an additional 7 cases. In 3 cases, Dandy-Walker malformation was identified by prenatal ultrasound, however milder malformations were visualized on prenatal and postnatal MRI: isolated inferior vermian hypoplasia in 2 cases and mega cisterna magna in the other. In 6 cases, prenatal ultrasound suggested a diagnosis of mega cisterna magna, while the postnatal MRI demonstrated a normal posterior fossa. In two additional cases where prenatal ultrasound suggested the diagnosis of mega cisterna magna, one postnatal MRI diagnosed cerebellar hypoplasia and one revealed an arachnoid cyst.
Conclusions
Prenatal ultrasound does not always correctly identify posterior fossa abnormalities, and may suggest more severe diagnoses than are actually present or may suggest mild abnormalities when the posterior fossa is normal. While prenatal MRI may more accurately identify the diagnosis in an additional subset of patients, postnatal MRI should still be considered for confirmation. Part of the over and under diagnosis may be explained by differences in use of terminology by different subspecialty groups involved in the care of these complex malformations, highlighting the importance of accurate language for counseling.

P-79

6:30AM - 3:00PM

Severity of Brain Injury Score on MRI Correlates with Cerebral Performance Category Scale in Neonatal ECMO

E Snyder[1], J Wen[2], T Huisman[3], A Yiu[4], R Felling[5], W Battarjee[6], J Schwartz[5], S Gutierrez[7], C Salorio[8], M Bembea[1], A Tekes[1]

[1]Johns Hopkins University, Baltimore, MD, [2]Johns Hopkins Hospital, Baltimore, MD, [3]Johns Hopkins, Baltimore, MD, [4]Uniformed Services University of the Health Sciences, Bathesda, MD, [5]Johns Hopkins University School of Medicine, Baltimore, MD, [6]Tufts Medical Center, Boston, MA, [7]Texas Childrens Hospital, Houston, TX, [8]Johns Hopkins Hospital Kennedy Krieger Institute, Baltimore, MD

Purpose

Neonates treated with ECMO are at high risk for cerebrovascular injuries, which can lead to a wide range of adverse neurologic outcomes. We hypothesize that brain injury scoring with MRI correlates with short-term clinical outcomes, which may affect discharge planning.

Materials and Methods

Over a 5-year period from July 2010-2015, neonates treated with ECMO were enrolled in a prospective study and all survivors were followed for at least 42 days following ECMO decannulation. All patients were monitored with serial head ultrasounds during treatment, and those with abnormal ultrasound findings were further evaluated with MRI, per institutional protocols. Magnetic resonance images were interpreted by a pediatric neuroradiologist with 9 years of experience. An imaging severity score was assigned based on the MRI findings as described by Bulas & Glass, et al. (1995) and the severity scores were correlated to discharge location, the patient's pediatric cerebral performance category (PCPC) score and whether the patient required placement of a new gastrostomy tube or discharge to a rehabilitation facility.

Results

Forty-eight neonates met the inclusion criteria. Twenty-seven patients (56.3%) had abnormal neuroimaging findings (petechial/focal/multifocal parenchymal hemorrhage, extra-axial hemorrhage, punctate focal, multifocal or territorial infarct, ventriculomegaly). Those with normal neuroimaging findings had higher death rate during hospitalization (11/21) than those with abnormal neuroimaging findings (3/24, $p<0.01$). Amongst the survivors, however, those with abnormal neuroimaging findings had on average higher discharge PCPC scores (2.17) compared to those with normal neuroimaging (1.5, $p<0.01$), and those with severe neuroimaging findings had higher PCPC scores (2.7) than those with mild abnormalities (2.0). There was no correlation between severity score and whether the patient required gastrostomy tube placement or discharge to a rehabilitation facility.

Conclusions

Although causes of mortality with ECMO may be unrelated to neurologic injury, the severity

score with MRI can help predict short-term functional neurologic outcomes as measured by the PCPC scale.

P-83

6:30AM - 3:00PM

Spinal Abnormalities in Cases of Cloacal Exstrophy

P Patel[1], J Hayden[1], R Richardson[2]
[1]Creighton University School of Medicine, Phoenix Regional Campus, Phoenix, AZ, [2]St. Joseph's Hospital and Medical Center, Phoenix, AZ

Purpose
Cloacal exstrophy is a rare congenital malformation occurring in less than 1 in 100,000 births, and is associated with defects of various organ systems. Early spinal changes seen in a fetus are predictive of a future cloacal exstrophy. A wide spectrum of spinal defects is possible that have not yet been classified thoroughly. This retrospective study on 5 patients with cloacal exstrophy strives to compare the associated spinal abnormalities on MRI and x-ray at a detailed level.
Materials and Methods
We performed a literature search utilizing various journals to scan for reported cases of cloacal exstrophy associated with any spinal malformations. Numerous x-rays, ultrasounds, MRIs, and 3-D CT reconstructions of the 5 patients in our study were compiled and analyzed for any similarities and differences.
Results
Each of the examined 5 patients were noted to have concurrent spinal malformations in addition to their cloacal exstrophies. The most common spinal changes seen were sacral and vertebral defects which were seen to some degree in all 5 patients. Three of the patients had levoscoliosis, while 1 patient had both a conus abnormality and a lipoma of the filum. One patient had both a myelocystocele and a Chiari II malformation. The spinal findings on imaging of 5 pediatric patients as they age are included in the table.
Conclusions
X-ray and MRI are excellent imaging modalities to follow up cloacal exstrophies and determine whether spinal abnormalities are concurrently present. While CT might have been a valid imaging modality to examine bone, exposure to radiation at a young age is not acceptable. It is imperative to continue imaging studies on these patients throughout life to understand whether there are additional spine changes and if they can be remedied. Furthermore, there is a need for future studies to find correlated spinal defects with other cloacal malformations.

PATIENT	AGE	SPINAL ABNORMALITY	RADIOLOGICAL IMAGING
EXSTROPHY 1	unk	47 degree levoscoliosis of the thoracolumbar spine centered at T6-T7. Spinal dysraphism in the sacrum with segmentation.	DX Spine, T/L Standing (Scoliosis)
	unk	Redemonstrates levoscoliosis of the thoracolumbar junction with stable vertebral anomalies including T11 butterfly vertebrae and T12 left hemivertebrae, Sacral hypoplasia	DX Abd Single View
EXSTROPHY 2	6 wks	Large sacral meningocele with a terminal myelocystocele, measures approximately 8.2 x 8.4 x 10.8cm	MRI L-Spine w/o contrast
	16 mo	Levoscoliosis that measures 25 degrees from T1 to T11	DX Spine, T/L Standing (Scoliosis)
	4 yo	The tonsils demonstrate a cone-shope and are low lying with approximately 8mm below the foramen magnum, extending to C1-C2, Findings consistent with Chiari 2 malformation	MR C-Spine wo contrast
	4 yo	Thoracic spinal cord is small in size, abnormal signal at T9-T10 may represent small syrinx	MR T-Spine wo contrast
	4 yo	Loss of normal lumbar lordosis, sacrum is vertically oriented and appears dysplastic, sacral vertebral bodies may be bifid, Spinal dysraphism noted at L4-L5 level and the sacram with adjacent post-op changes consistent with prior repair	MR L-Spine wo contrast
EXSTROPHY 3	11 yo	Hypoplasia of L4 and L5 vertebral bodies as well as of the sacrum and occyx, Dorsal sacral dysraphism with intrasacral meningocele, Low lying conus terminating at L2, lipoma of the filum measuring 5x9 mm axial and 6 cm cranial/caudal	MR L-Spine wo contrast
	11 yo	Same as above	MR T-Spine wo contrast
	14 yo	Same as above/unchanged, unremarkable	MR L-Spine wo contrast
EXSTROPHY 4	12 yo	Only 3 non-rib-bearing vertebral bodies are seen, Cervical rib on the right (13 total ribs right side), 12 ribs left side (normal)	DX Spine IV Thoracic
	12 yo	Levocurvature of the lower lumbosacral region	DX Pelvis w/Lat Hips
	12 yo	Osseous fusion of the right aspect of the L5 and L4 vertebral bodies as wella s butterfly vertebrae at L4, Partial sacral agensesis	CT Pelvis wo contrast
EXSTROPHY 5	0 days	Sacral agenesis and splaying of the pelvis	DX Chest and Abdomen
	1 day	Conus ending at L4-L5 level with a hypoechoic cystic lesion measuring 4 x 9 x 4mm, Only 3 ossified sacral vertebrae are visualized suggestive of sacral agensis	US Echo, Spinal Canal

(Filename: TCT_P-83_ExstrophyChart.jpg)

P-81

6:30AM - 3:00PM

Synthetic MRI in Children: Clinical Utility of Quantitative Segmentation

H West[1], J Leach[2], B Jones[3], A McAllister[3], S Serai[2]

[1]CCHMC, Cincinnati, OH, [2]Cincinnati Children's Hospital Medical Center, Cincinnati, OH, [3]Cincinnati Children's Hospital, Cincinnati, OH

Purpose

Synthetic MRI (SyMRI©) is a method in which a 6-minute multiple-spin echo saturation recovery sequence (QMAP) is used with 4 saturation delays and 5 echoes to create absolute R1, R2, and PD relaxivity maps with associated software which allows for rapid automated intracranial segmentation of tissue types (1). Clinical efficacy of standardized synthetic sequences in children has been evaluated (2, 3), but the utility of the quantitative segmentation capabilities of SyMRI© has not been assessed. We provide a case-based review of intracranial segmentation parameters among children with several clinical scenarios and disease processes compared with normative age-matched data.

Materials and Methods

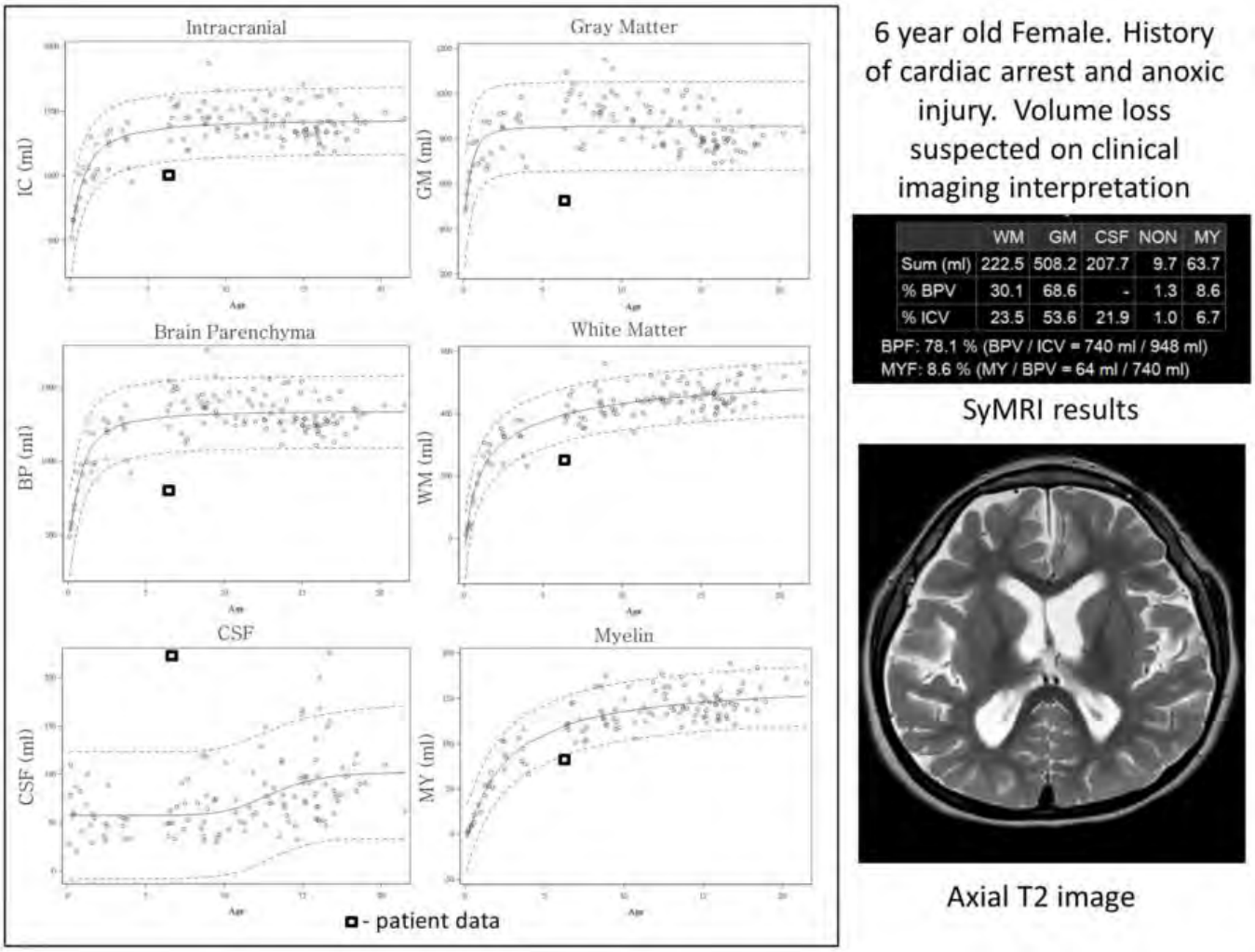
Six hundred twenty patients (ages 0.1 – 22 years) underwent routine clinical brain MRI with conventional and QMap sequences between 12/2013-11/2016. A detailed imaging and clinical chart review was conducted and subjects were divided in to "normal" (N=122) and "abnormal" groups. SyMRI© software (Synthetic MR 8.0) was used to perform segmentation analysis of intracranial (IC), brain parenchymal (BP), gray matter (GM), white matter (WM), CSF, and myelin (MY) volumes (4). Selected clinical scenarios and disease processes were compared with the normal database to examine clinical utility of the segmented volumes.

Results

The QMAP sequence and quantitative analysis using SyMRI© provided useful information in a wide variety of disease states. Case examples presented include: hydrocephalus, benign macrocrania, mitochondrial disorders, disorders of myelination, microcephaly, and perinatal brain injury.

Conclusions

The 6-minute Qmap sequence with rapid processing by SyMRI© can provide enhanced tissue segmentation and volumetric assessment of intracranial tissue components. Understanding the normal trajectory of intracranial volumes during development permits clinical application in children. Quantitative analysis using SyMRI© can provide additional clinically important information in a number of disease states in children.



(Filename: TCT_P-81_ASNRfigureHW02BW.jpg)

P-76

6:30AM - 3:00PM

Utility of Hounsfield Unit and Hematocrit Values in the Diagnosis of Acute Venous Sinus Thrombosis in Unenhanced Brain CTs in the Pediatric Population

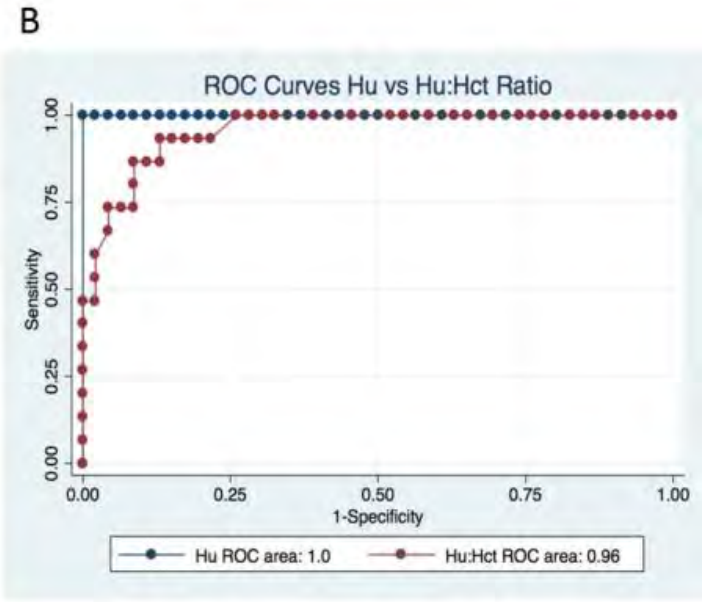
G De La Vega Muns[1], G Saigal[2], R Quencer[3]
[1]Jackson Memorial hospital, miami, FL, [2]University of Miami/Jackson Memorial Hospital, Miami, FL, [3]Univ. of Miami School of Medicine, Miami, FL

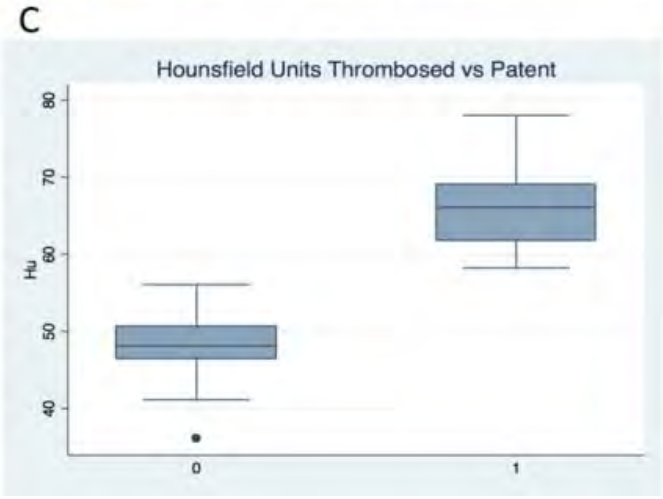
Purpose
Cerebral venous sinus thrombosis (CVST) is a recognized cause of childhood and neonatal stroke with a high morbidity and mortality. It is a challenging diagnosis due to its nonspecific and variable clinical presentation and sometimes subtle imaging findings. The purpose of this study is to investigate the clinical utility of measuring the HU of venous sinuses in noncontrast CT scans of the brain as well as HU/HCT ratio's in the diagnosis of

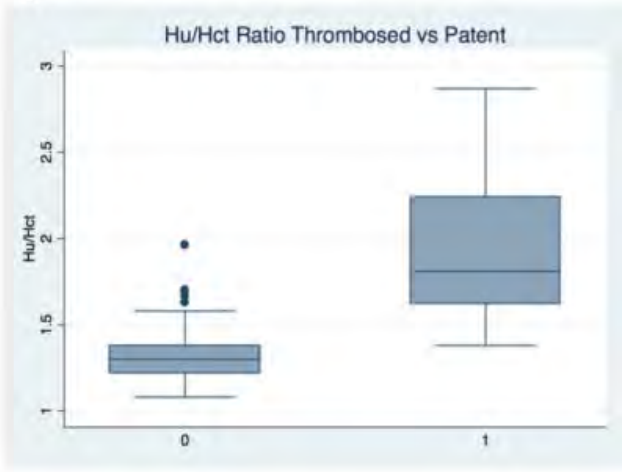
acute CVST in the pediatric population and compare our data with that already available in the literature.
Materials and Methods
This was a retrospective chart review, which studied 15 pediatric patients with acute CVST and 31 control patients without thrombosis. Three radiologists examined each study and plotted ROIs to measure the HU values at various points within the venous sinuses of each patient. In patients with CVST, HU values were determined both in the thrombosed and the nonthrombosed venous sinuses. HU/Hematocrit ratios also were calculated for each patient. Statistical analysis was performed to calculate the differences between each reader and between patient and control groups. Optimal cutoff values for HU and HU:Hct measurements in the diagnosis of CVST on noncontrast brain CTs were determined.
Results
A statistically significant difference in the average sinus attenuation and the HU:Hct ratio was found between the thrombosed (66.2+/- 5.3 HU, 1.96+/- 0.4) and nonthrombosed sinuses (47.2+/- 4.5 HU, 1.38+/- 0.25) in the patient group ($p<0.0001$) , with the average attenuation difference being 19 HU. A statistically significant difference also was found between thrombosed sinuses in the patient group and the sinuses (48.9+/- 3.13 HU, 1.3+/- 0.12) in the control group ($p<0.0001$). Optimal cutoff values of 58 HU and 1.4 lead to sensitivities of 100% in the diagnosis of CVST.
Conclusions
Measuring HU and normalizing HU in relation to Hct improves the detection of CVST. Furthermore, calculating the difference between hyperattenuating and normal appearing sinuses in the same patient may give the reader further confidence in raising the possibility of CVST on an unenhanced brain CT of a pediatric patient.

A

PATIENT	AGE	SEX	THROMBOSED SINUS
1	12Y	F	SS, L TRV, L SIG, R TRV, VG, VR, ICV
2	8 Y	F	SSS
3	11 Y	M	L SIG
4	14 Y	M	SSS, R TRV, TORC
5	16 Y	F	L TRV, L SIG
6	1 M	M	ISS, SS, VG, ICV
7	16 Y	F	R TRV, R SIG
8	16 Y	M	L TRV, L SIG
9	15 Y	F	SSS
10	4 Y	F	R TRV, R SIG
11	9 Y	M	SSS
12	13 Y	F	SSS, R TRV, SS, R SIG, TORC
13	3 M	M	R TRV
14	14 Y	M	SSS, R TRV, R SIG
15	16 Y	M	SS, L TRV, VG, VR







(Filename: TCT_P-76_Image2.jpg)

Monday
6:30AM - 3:00PM
Long Beach Convention Center, Exhibit Hall B-(Lower Level) P

Scientific Poster(P)-Print-Socioeconomics

P-84

6:30AM - 3:00PM

A Picture is Worth a Thousand Words! Factors Increasing Tweet Engagement Rate: Analysis of The AJNR Twitter Feed

V Wadhwa[1], E Latimer[1], K Chatterjee[1], J McCarty[2], R Fitzgerald[1]

[1]University of Arkansas for Medical Sciences, Little Rock, AR, [2]Division of Neuroradiology, Emory University, Atlanta., Atlanta, GA

Purpose
To identify tweet characteristics associated with increased engagement rate on Twitter.
Materials and Methods
Twitter Analytics were obtained from the AJNR twitter account (@AJNR) for August 2015 – July 2016. Twitter calculates an engagement score for each tweet based on numbers of impressions and engagements. Tweets with an engagement score above 75th percentile were considered as high engagement tweets, and tweets below 25th percentile were considered as low engagement tweets. Each tweet was further characterized by the month, time of day (Morning, Afternoon, Evening, Night), weekend versus weekday, the presence or absence of an imbedded image or hashtag, and type of tweet. Logistic regression model was used to identify the tweet characteristics associated with increased engagement rate of a tweet, and p-value <0.05 were considered significant.
Results
A total of 1032 tweets were published during the study period. 405 (39.2%) tweets included an image and 751 (72.8%) tweets had a hashtag. One hundred twenty-two (11.8%) tweets were posted on a weekend. The months of March (106 tweets) and August (100 tweets) had the highest activity on Twitter. Majority of tweets were posted in morning (606, 58.7%) and afternoon (318, 30.8%) hours. Using the logistic model, presence of an image increased the tweet engagement rate 29-fold, and the presence of hashtag increased the rate 3-fold. Tweets published in morning hours were twice as likely to have a high engagement rate compared to afternoon hours. No significant difference was found in tweets published on weekends, evening or night, or according to the month. In an independent analysis, the "Case" tweet type was 140-fold more engaging compared to all other tweet types, due to presence of combination of engaging factors.
Conclusions
Tweets including an image or hashtag and those publishing in morning hours had the highest engagement rate. Our data may allow organizations and individuals to maximize the potential impact of their social media efforts.

P-85

6:30AM - 3:00PM

An Updated Evidence-Based Review of the Safety Profile of Group II Gadolinium Contrast Agents in Renal Failure Patients

B Liu[1], D Pechersky[1], D Cantrell[1]
[1]Northwestern University Feinberg School of Medicine, Chicago, IL

Purpose
In recent years, concern for nephrogenic systemic fibrosis (NSF) has subsided secondary to a combination of specific guidelines for gadolinium contrast use in renal failure patients and newer gadolinium contrast agents. With over 200 million administrations of gadolinium, use of intravenous contrast agents has become nearly ubiquitous in adult MR imaging. New data since 2009 has become available regarding the safety profile of gadolinium administration in the setting of renal failure. This exhibit provides an evidence-based review of the latest literature on gadolinium-based contrast use in renal failure patients and proposes clinical practice considerations based on the available data.
Materials and Methods
A literature search was conducted in PubMed regarding "nephrogenic systemic fibrosis," "renal failure or renal insufficiency," "adverse reactions," and "gadolinium contrast agents." Prospective and retrospective clinical trials since 2009 were included in this evidence-based review. Study data included patients with moderate or severe renal failure, or stages 3 - 5 chronic kidney disease.
Results
No cases of NSF were identified in a prospective study of 870 patients with moderate and severe renal failure over a 2-year follow up exposed to gadobutrol. No cases of NSF was identified in a retrospective cohort of 401 patients undergoing peritoneal dialysis, hemodialysis, or nondialysis but experienced renal failure, after administration of gadobenate when studied with more than 2 years of follow up. No cases of NSF was identified after 2 years of observation in a prospective study of 363 patients with moderate to severe renal failure exposed to gadobenate. No cases of NSF was identified after 2 years of observation in a prospective study of 171 patients with moderate to severe renal failure exposed to gadoteridol. No cases of NSF was identified in 476 patients with moderate to severe renal insufficiency receiving gadoterate after a mean follow up of 148 days.
Conclusions
While there has not been a confirmed case of NSF in the USA since 2009, use of intravenous gadolinium contrast in renal failure patients remains a significant clinical concern. In clinically relevant scenarios, the use of gadolinium contrast in renal failure patients may need to be considered and based on the ACR Manual on Contrast Media, group II gadolinium-based contrast agents should be favored. New and recent data on the safety profile of gadolinium agents in the setting of renal failure continues to become available including the latest data within the past 2 years, raising the question as to whether, when used appropriately, administration of group II gadolinium agents in renal failure patients may be safer than traditionally believed. While the irreversible and devastating effects of NSF cannot be forgotten, the risk of NSF is significantly lower with the use of group II gadolinium contrast agents. However, it is important to remember that administration of gadolinium should not be taken for granted. Each and every MRI study ordered with intravenous contrast should be reviewed to determine if gadolinium administration would be of actual benefit to the management/treatment of the patient. This exhibit provides an

evidence-based review of the latest literature on gadolinium-based contrast use in renal failure patients and proposes clinical practice considerations based on the available data.

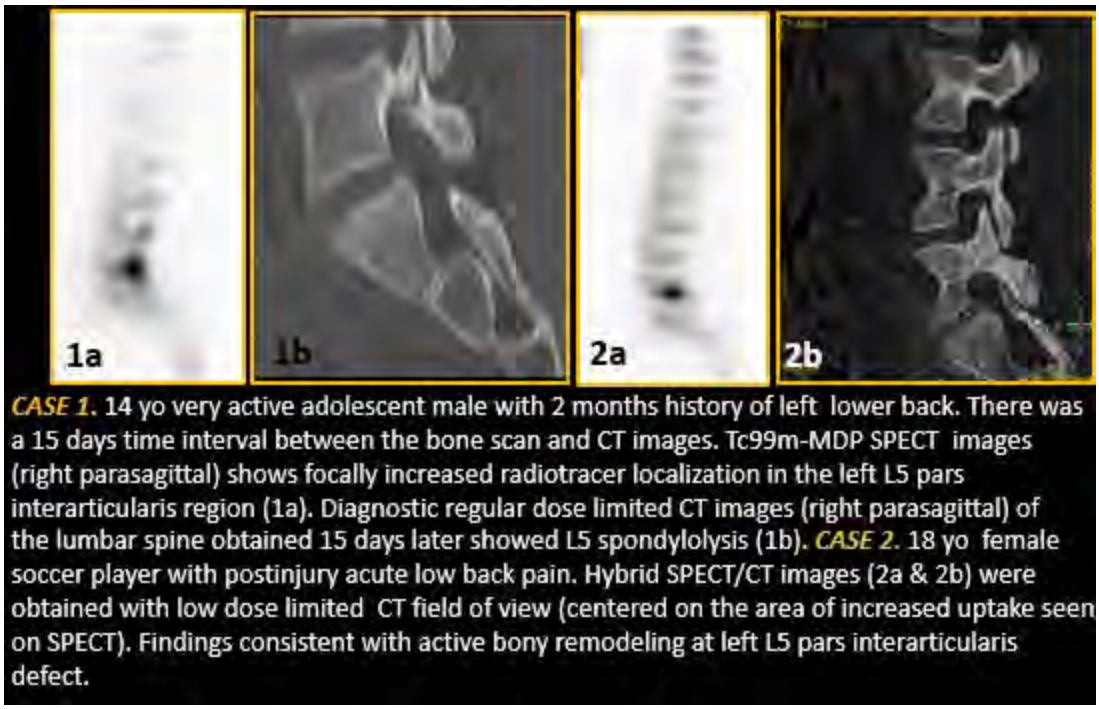
P-86

6:30AM - 3:00PM

Cost Benefits and Other Advantages of Hybrid Imaging Over SPECT Only Imaging in the Initial Diagnosis of Suspected Pars Injury in Young Athletes

S Gaddikeri[1], J Alvarez[2], M Matesan[2], D Hippe[3], H Vesselle[2]
[1]Rush University Medical Center, Chicago, IL, [2]university of washington, Seattle, WA, [3]University of Washington, Seattle, WA

Purpose
To assess benefits of hybrid (combined SPECT/CT)imaging over SPECT only imaging in the management of young athletes with LBP due to suspected pars injury.
Materials and Methods
Retrospective review of medical records of 163 consecutive patients who had radionuclide SPECT imaging for evaluation of LBP between January 2010 and December 2015. All enrolled patients were divided into two groups (Group 1: Patients with radionuclide SPECT imaging only, Group 2: Patients with radionuclide hybrid imaging). Radiation dose, cost benefits, and mean duration of delay in complete diagnosis (both functional and anatomical diagnosis) were assessed and compared using Fischer's exact test between the two groups.
Results
Total 92 patients were enrolled after applying inclusion and exclusion criteria. The CTDIvol and DLP10 [DLP estimated for a scan length of 10 cm (10 x CTDIvol)] were significantly lower for patients in group II ($p<0.006$ and $p<0.006$). Although, the actual DLP was not significantly different between the two groups ($p=0.82$). There was a median delay of 7 days (inter-quartile range 2-10 days) for a complete diagnosis in group I patients. Least expensive imaging for an initial complete diagnosis required for the treatment purpose was in patients who had a radionuclide Tc-99m MDP bone scan with limited lumbar spine planar and SPECT imaging followed by a thin slice, limited CT performed only when SPECT imaging was positive for an active pars injury. No significant difference in the management of patients between the groups ($p=0.43$).
Conclusions
Hybrid imaging should be preferred over SPECT only imaging for initial evaluation of suspected pars injury in young athletes with LBP.



(Filename: TCT_P-86_ImageASNRabstract.jpg)

Monday
6:30AM - 3:00PM
Long Beach Convention Center, Exhibit Hall B-(Lower Level) P

Scientific Poster(P)-Print-Spine

P-90

6:30AM - 3:00PM

Aspiration Assisted Spinal Biopsy: A Step-By-Step Guide

L Lin[1], R Galuppo Monticelli[1], A Alhajeri[1]
[1]*University of Kentucky, Lexington, KY*

Purpose
Percutaneous computed tomography (CT)-guided spinal biopsy is necessary to guide management of vertebral diskitis and osteomyelitis (VDOM). With increasing incidence of VDOM and widespread use of antibiotics, the sensitivity for biopsy for detection has decreased. We present a pictorial guide of an alternative technique to increase the sensitivity of CT-guided spinal biopsy for detecting infection.
Materials and Methods
Computed tomography-guided biopsy of the spine was performed with 18- or 19-gauge coaxial needle into area of interest followed by advancing 19- or 20-gauge Tru-Cut needle for tissue biopsy. Immediately following the core or tissue biopsy, an additional aspiration

biopsy was obtained through the coaxial needle. These specimens were sent for microanalysis in separate containers with preservative-free normal saline. The diagnosis was based on the clinical findings, imaging, and microanalysis.
Results
Usefulness of this technique is demonstrated with a series of 232 patients who underwent CT-guided spinal biopsy. Twenty out of 66 positive cultures were positive in the aspiration sample only. There was no demonstrable increase in morbidity with this additional step.
Conclusions
Approximately a third of culture positive cases were from aspiration culture while the tissue culture was negative. Aspiration following tissue biopsy increases the culture sensitivity compared to standard tissue biopsy alone. The additional sample was obtained easily without significant additional morbidity and should be considered part of standard procedure for spinal biopsy for VDOM.

P-91

6:30AM - 3:00PM

Complications of Synovial Cyst Rupture: A Single Institution Experience

R Brandt[1], S Hauck[1], J McIntyre[1], T Cooke[1]
[1]*Dartmouth-Hitchcock Medical Center, Lebanon, NH*

Purpose
To review the complications of synovial cyst rupture.
Materials and Methods
A retrospective review was performed of synovial cyst ruptures performed at out institution. Imaging obtained following the procedure and follow-up clinic notes were reviewed to identify any complications of the procedure.
Results
Complications of synovial cyst rupture included procedure failure, worsening symptoms and subarachnoid hemorrhage.
Conclusions
Synovial cyst rupture is a well established and safe procedure, but can be complicated by procedure failure, worsening symptoms and subarachnoid hemorrhage. It is important for the radiologist to be familiar with the complications associated with synovial cyst rupture so that the patient can be fully informed about the procedural risks.

P-88

6:30AM - 3:00PM

Correlation Between Lee's MR Grading System for Central Lumbar Spinal Stenosis and the Surgical Intervention

H Park[1]
[1]*Kangbuk Samsung hospital, Seoul, AK*

Purpose
To evaluate the correlation between Lee's grades and surgical intervention for CLSS and to assess whether this grading system can be used as a decision-making tool for the surgical treatment of this condition.
Materials and Methods
This retrospective study included 290 patients (M:F = 156:134; mean age, 46 years) who underwent magnetic resonance imaging (MRI) of the lumbar spine at our institution. Radiologists assessed the presence and grade of CLSS at the stenosis point according to Lee's grading system. Correlation coefficients (rs) between Lee's grades and the operation were calculated with Spearman rank correlation.
Results
In the operated patients, grade 2 was most common (50-58%), grade 3 was less common (35%), and grade 0 was least common (2-3%). In the nonoperated patients, grade 1 was most common (63-65%), grade 0 was less common (15-16%), and grade 3 was least common (8%). The distribution of grades differed between the operated and nonoperated groups ($p < 0.001$). Whereas grades 0 and 1 occurred in less than 25% of patients who underwent surgery, grades 2 and 3 occurred in more than 88%. A moderate correlation between grade and operation was found (rs = 0.632 and 0.583, Table 5). This correlation was moderate to relatively high (rs = 0.670 and 0.754) in young patients and lower than 0.5 in older patient.
Conclusions
Lee's grade was moderately correlated with the surgical intervention. Lee's grading system can be used as a decision-making tool for surgical treatment of CLSS.

P-87

6:30AM - 3:00PM

Inter-Reader Reliability and Clinical Validity of an MRI Grading System for Cervical Foraminal Stenosis

H Park[1]
[1]*Kangbuk Samsung hospital, Seoul, AK*

Purpose
The objective of this study was to evaluate the inter-reader reliability of the Park system among radiologists, residents, and clinicians. This study also assessed the correlations between radiologic and clinical findings.
Materials and Methods
A total of 289 patients (M:F = 155:134, mean age of 50 years) who underwent oblique sagittal MRI of the cervical spine at our hospital were included. According to the MR

grading system suggested by Park et al., two radiologists, two trainees, and two clinicians measured CNFS grade at the most narrow point. A neurosurgeon assessed the associated clinical manifestations. Kappa statistics were used to analyze the inter-reader agreement among the radiologists and clinicians. The clinical correlations between grade and positive clinical manifestations were assessed with Rs using nonparametric correlation analysis (Spearman's correlation).
Results
The overall inter-reader agreements between radiologists, between trainees, between clinicians, and between radiologists and clinicians were almost perfect ($k = 0.80 – 0.96$). There were moderate correlations between grade and clinical manifestations in each group ($R = 0.562$-0.669). There were moderate to relatively high correlations between grade and neurologic manifestations based on cervical level ($R = 0.570$-0.715) (all p-values < 0.05).
Conclusions
Regardless of reader experience, there was substantial to almost perfect inter-reader reliability with the Park system for CNFS based on oblique sagittal MRI.

P-92

6:30AM - 3:00PM

Major Variables Affecting the Yield of Disc and End Plate Biopsy: A 5-year Single Institutional Experience

J Holstad[1], A Radmanesh[1]
[1]*New York University, New York, NY*

Purpose
Image-guided disk/vertebral body biopsy is an occasionally encountered request in many radiology departments. Suspicious or nonconclusive magnetic resonance imaging (MRI) findings usually precede disk biopsy requests which are meant to isolate a specific organism in order to confirm or exclude an infectious process and, in cases of infection, to help formulate optimal antimicrobial therapy. Garg et al. showed that 9.5% of image-guided disk biopsies lead to a change in patient management. In this study, we tried to determine the relationship between different variables (clinical, laboratory, procedure technique) and biopsy yield and to assess the degree by which results affect patient management.
Materials and Methods
Thirty-eight patients with suspected diskitis/osteomyelitis who underwent disk biopsy at NYU Medical Center between Jan 2012 and Dec 2016 were included in this retrospective cohort study, with exclusion of 9 cases that did not have available clinical notes. Chart review was performed with attention to ESR, WBC, needle gauge, culture results, and antibiotic administration before the biopsy. Notes were reviewed to determine how biopsy result affected patient's management.

Results
Of 27 patients included, a noncontaminant organism was isolated successfully in 8 patients (29.6%), none of whom had received antibiotic prior to biopsy. In all 8 cases, biopsy result altered clinical management. Nine of the 19 patients with negative culture results (47.4%) had received antibiotic prior to biopsy. The difference between the two groups was statistically significant (P=0.02). Of note, the average needle gauge in cases of positive and negative biopsies was 14.7 and 12.5, respectively.
Conclusions
Our institutional results are aligned with previously published data and showed isolation of a specific organism in less than a third of all patients who underwent image-guided disk and vertebral end plate biopsy. Knowledge of this rate is important when discussing the biopsy procedure with requesting physician or consenting patients. Antibiotic administration before biopsy may negatively affect the biopsy yield. This is despite other authors' argument that such effect is overstated because hematogenous seeding usually occurs in the subchondral area of the vertebral body before seeding the disk. Interestingly, smaller gauge needles were associated with higher number of positive biopsy results compared to larger gauge needles. This association may be related to operator preference or the appearance of the pre-biopsy MRI study.

P-93

6:30AM - 3:00PM

Plasmablastic Lymphoma in an HIV Negative Patient

M Iqbal[1], R Berger[2], S Iqbal[3]
[1]Kansas University-Wichita, Wichita, KS, [2]University of Kansas - Wichita, Wichita, KS, [3]Kansas University Wichita, Wichita, KS

Purpose
Plasmablastic lymphoma is an uncommon entity commonly presenting with oral/perianal lesions as well as a history of HIV. We present a patient who presents with neither, rather presenting with an HIV negative status and central neuro-axis lesion. A distinguishing feature of plasmablastic lymphoma and plasma cell myeloma is the presence of EBV RNA in the former. We postulate that this patient developed this malignancy following an acquired EBV infection.
Materials and Methods
We present the case of a 53-year-old female who presented with recent onset of vague neck pain one month prior which increased to excrutiating pain a few days before her presentation. She also reported right upper extremity paresthesias. A magnetic resonance imaging (MRI) of the neuroaxis revealed a large exophytic mass centered in the C2 vertebral body with encroachment and mass effect on the right neuroforamina and nerve root of C2-3, as well as encasement of the right vertebral artery at this level. The patient had a subtotal

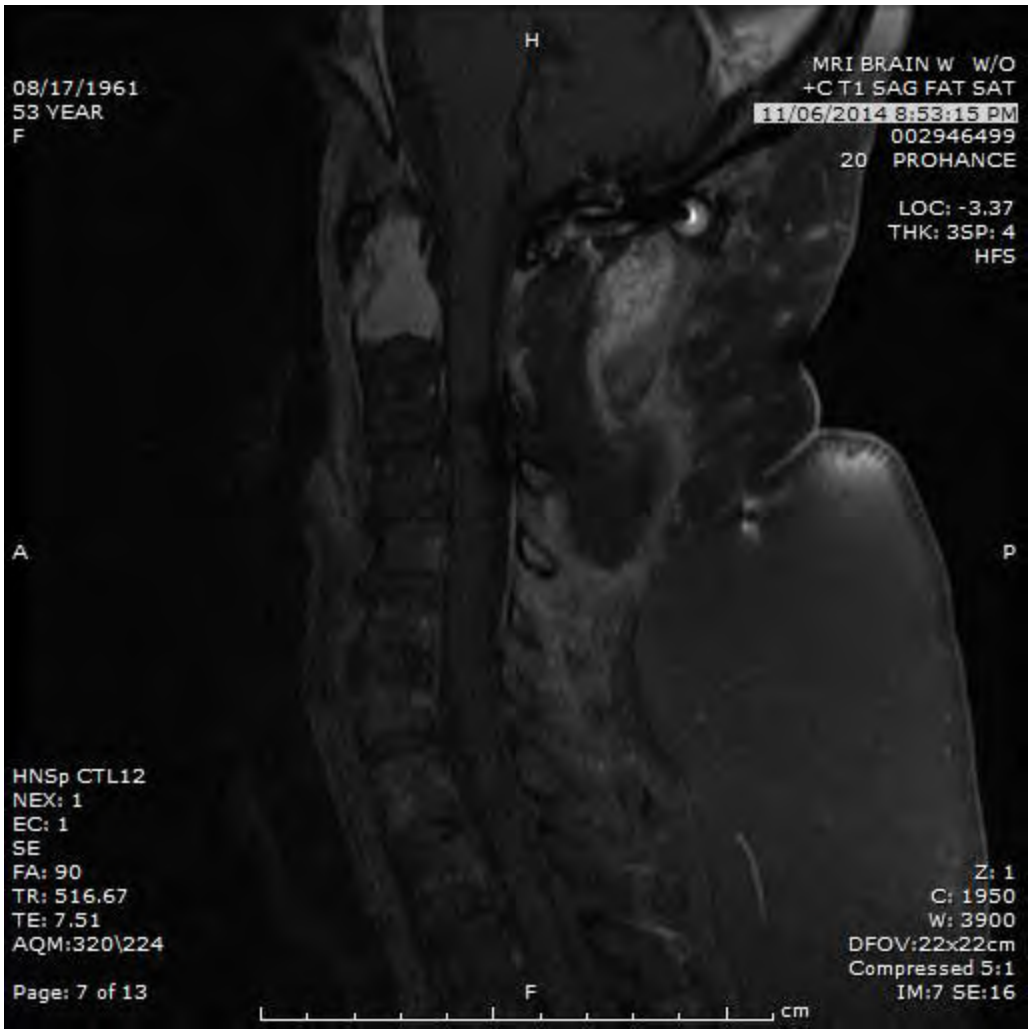
resection/biopsy of the C2 mass which revealed a malignant B-cell lymphoma favoring a plasmablastic lymphoma. She was started on cyclophosphamide, bortezomib and dexamethasone (CyBorD) chemotherapy and radiation. Unfortunately she still had progression of disease with increasing upper and lower extremity weakness and headache. A repeat MRI of the neuroaxsis in 2 months revealed progression of disease with a large exophytic metastatic lesion in the right parietal calvarium resulting in extradural mass effect on the brain parenchyma.

Results

While more common in the immunocompromised, plasmablastic lymphoma is an entity to also consider in a young patient presenting with a neurocentric mass. Multimodality imaging detail an unfortunate and progressive and resistant case in an HIV negative patient. Despite aggressive management, the tumor remained resistant to chemo/radiation therapy with progression to calvarial metastasis in short interval surveillance.

Conclusions

In literature, the vast majority of patients with plasmablastic lymphoma present with oral lesions and a history of HIV (74% in a large case series 1). Our patient was negative for HIV and presented with a C2 vertebral body lesion and subsequent progression to calvarial metastasis. Plasmablastic lymphomas and plasmablastic plasma cell myelomas have a nearly identical immunophenotypic profile with EBV RNA presence distinguishing the former from the latter.



(Filename: TCT_P-93_002946499_CT1SAGFATSAT_7.jpg)

P-89

6:30AM - 3:00PM

Role of MRI Guided Spinal Laser Interstitial Thermotherapy (SLITT) in Treatment of Metastatic Spinal Cord Compression

C Tatsui[1], R Stafford[2], B Amini[2], J Li[2], A Ghia[2], L Rhines[2], J Cata[2], G Rao[2], J Weinberg[3], D Schomer[1], A Kumar[4]
[1]U.T. MD Anderson Cancer Center, Houston, TX, [2]UT MD Anderson Cancer Center, Houston, TX, [3]MD Anderson Cancer Center, houston, TX, [4]Md Anderson cancer center, HOUSTON, TX

Purpose
High grade malignant spinal cord compression is commonly managed with a combination of surgery aimed at removing the epidural tumor followed by spinal stereotactic radiosurgery (SSRS) aimed at local tumor control. The authors introduce the use of magnetic resonance

imaging (MRI)-guided spinal laser interstitial thermotherapy (SLITT) as an alternative to surgery prior to SSRS.
Materials and Methods
Thirteen patients with metastatic spinal cord compression underwent SLITT procedure under anesthesia in an intra-operative suite (BrainLAB™, Feldkirchen, Germany) using 1.5T MRI scanner (MAGNETOM Espree, Siemens Healthcare, Erlangen, Germany). Details of the surgical procedure and MR imaging techniques used during the procedure will be presented in the scientific exhibit. Briefly, MRI was used to localize the target. A mobile C-arm was used to navigate the laser applicators into the target, and MRI thermometry was used to monitor the delivery of laser energy to the target.
Results
Thirteen patients underwent implantation of 47 laser applicators. The mean visual analog scale (VAS) score for pain decreased from 6.18 in the pre-operative period to 4.27 within 30 days and 2.8 within 60 days after the procedure. Significant reduction in mean thickness of the epidural tumor from 8.82 mm before treatment to 6.36 mm after SLITT was achieved.
Conclusions
The authors present an innovative minimally invasive percutaneous procedure alternative to surgery with low morbidity, a short hospital stay and improvement in pain and quality of life in management of metastatic epidural spinal cord compression.

P-94

6:30AM - 3:00PM

Test-Retest and Inter-Reader Reliability of Semi-Automated Atlas-Based Analysis of Diffusion Tensor Imaging Data in Acute Cervical Spinal Cord Injury in Adult Patients

D Peterson[1], D Hippe[1], A Rutman[1], A Wilson[1], J Jarvik[2], W Cohen[1], F Chokshi[3], M Mossa-Basha[1]
[1]University of Washington, Seattle, WA, [2]Univ of Washington, Seattle, WA, [3]Emory University School of Medicine, Atlanta, GA

Purpose
Diffusion tensor imaging (DTI) is a novel tool for the evaluation of acute traumatic cervical spinal cord injury (SCI). Deriving useful measures from DTI of the spinal cord with hand-drawn ROIs can be labor-intensive and may be prone to bias and poor reliability. We evaluated the test-retest reliability of a semi-automated spinal DTI analysis pipeline in the setting of acute traumatic cervical SCI.
Materials and Methods
Thirty participants with clinical suspicion of acute traumatic cervical SCI underwent 2 separate axial DTI scans, during the same imaging session ~5 minutes apart. A sagittal short-tau inversion recovery (STIR) image also was collected. The raw diffusion-weighted images were used as input into an analysis pipeline that uses the Spinal Cord Toolbox

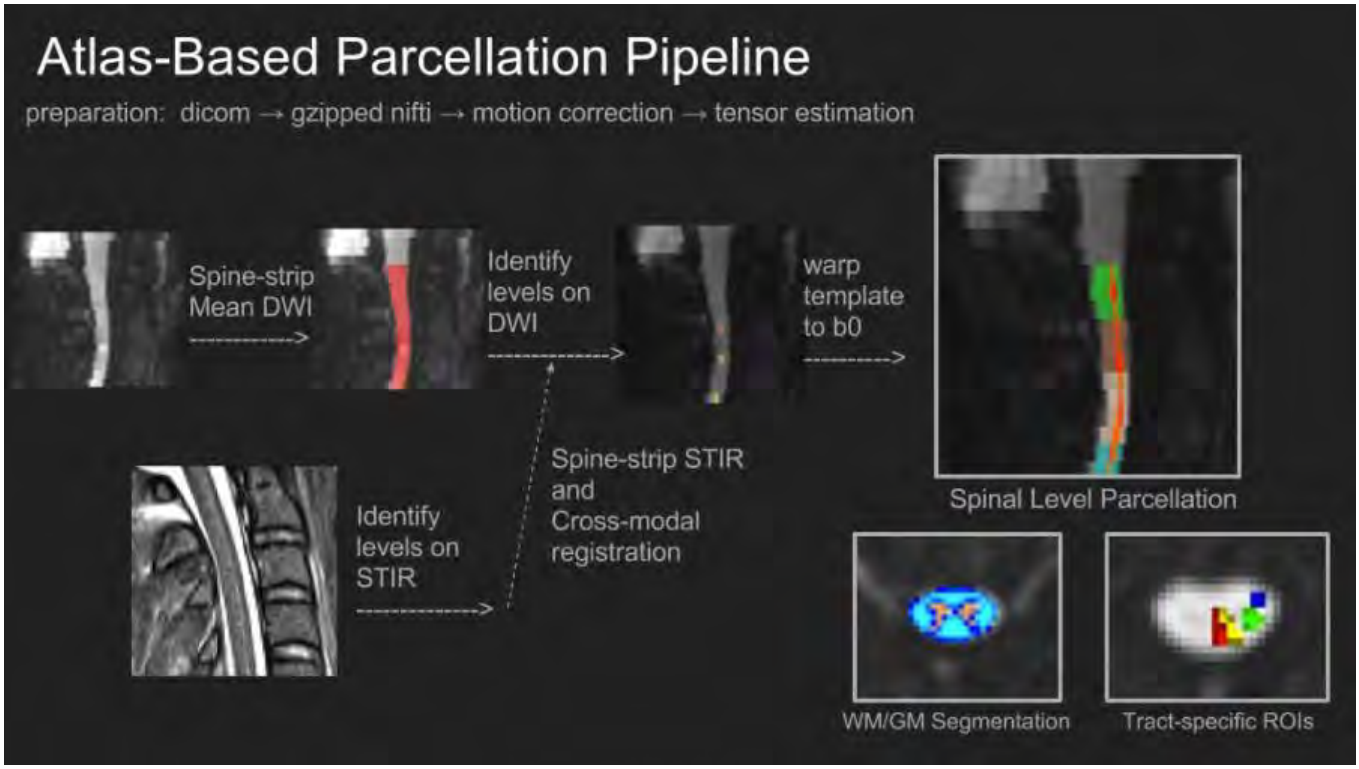
(https://sourceforge.net/p/spinalcordtoolbox/) for atlas-based parcellation of spinal cord images. We placed single-point manual seeds to identify three spinal levels on either the STIR image, or the mean DWI image. This procedure was repeated with another reader after minimal training. Mean diffusivity (MD) and fractional anisotropy (FA) metrics within 13 bilateral atlas regions, as well as gray matter (GM) and white matter (WM) regions of interest (ROIs) were extracted across spinal levels. Reliability was assessed by intraclass correlation coefficient (ICC) r-values, with ICC > 0.6 taken as a threshold of good reliability.

Results

Fractional anistropy and MD metrics within WM and GM all had ICC > 0.6 (0.83 for GM FA, 0.93 for WM FA, 0.66 for GM MD, and 0.64 for WM MD). Fractional anisotropy within individual tracts showed good or better reliability in 10 out of a total of 13 atlas tracts. Inter-reader reliability was good or better across all structures and measures, and 0.7 or greater for all FA measures.

Conclusions

Atlas-based parcellation of spinal DTI data shows good to excellent test-retest reliability, particularly for FA and for measures within WM. Spinal tract-specific diffusion metrics are especially reliable within the larger, major WM tracts. The required manual step introduces minimal variability in the extracted metrics. This work is a step towards using automated parcellation of spinal DTI for cases of acute traumatic cervical SCI. Atlas-based segmentation of cervical spinal DTI generally is reliable, laying the groundwork for automated analyses of tract and level-specific diffusion metrics in cases of acute traumatic SCI.



(Filename: TCT_P-94_sc_DTI_DI-IG.jpg)

Monday
11:00AM - 12:15PM
Long Beach Convention Center, Room 202 (Upper Level)

04B-Parallel Paper Session: Spine Imaging: Trauma and Tools You Can Use

O-01

11:00AM - 11:08AM

5-minute protocol of lumbar spine MRI – initial experience in a clinical setting with SMS TSE

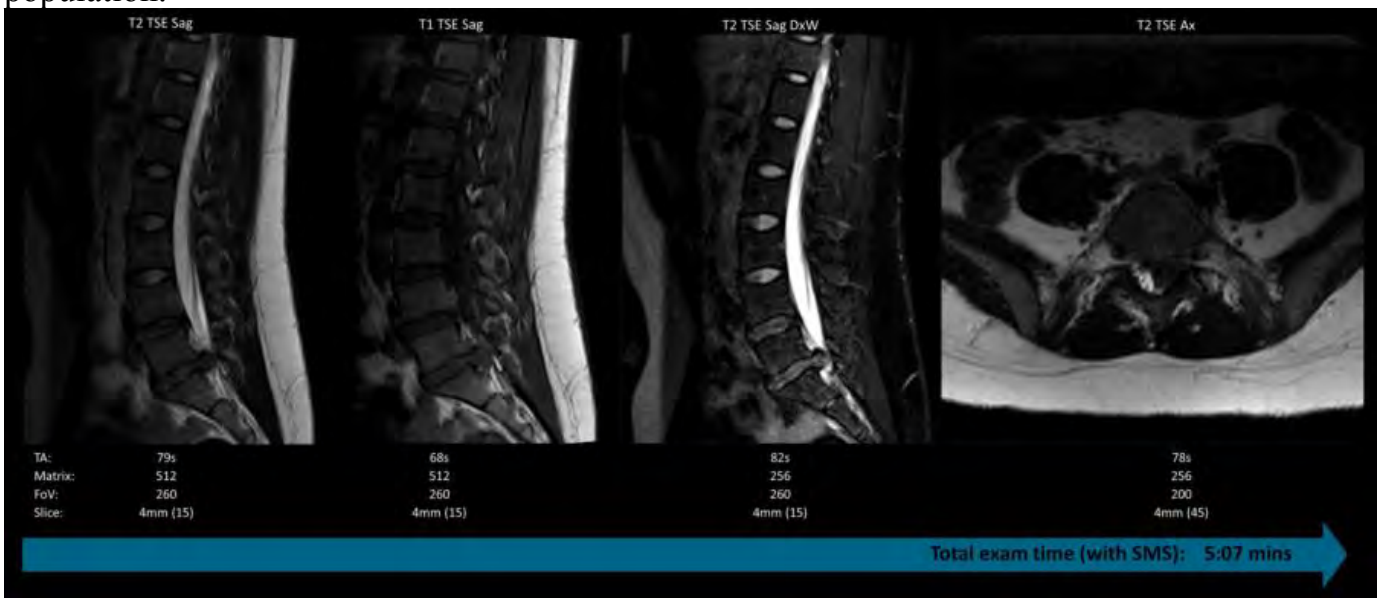
M Longo[1], J Pinto[2], K Setsompop[3], T Witzel[4], B Himanshu[5], P Kollasch[5], K Heberlein[5], S Huang[6], P Schaefer[1], O Rapalino[7]
[1]Massachusetts General Hospital, Boston, MA, [2]CDPI, Rio de Janeiro, Brazil, [3]Harvard Medical School, Boston, MA, [4]Athinoula A. Martinos Center for Biomedical Imaging, Charlestown, MA, [5]Siemens Medical Solutions, Charlestown, MA, [6]Massachusetts General Hospital / Athinoula A. Martinos Center for Biomedical Imaging, Boston, MA, [7]Massachusetts General Hosp., Boston, MA

Purpose
We endeavor to develop a novel 5-minute fast protocol MRI of the lumbar spine using advanced imaging such as SMS TSE and evaluate diagnostic performance versus the standard protocol currently used in our service.
Materials and Methods
Ten inpatients referred for lumbar spine MRI without contrast in our institution were selected prospectively and scanned in a 3-Tesla scanner (MAGENTOM Skyra). Each patient was imaged using both our standard protocol (Sag T1-W, Sag T2-W-FS, Sag T2-W, Ax T2-W) and a novel fast protocol acquiring the same contrasts and planes, however, incorporating advanced parallel imaging with a high-density spine coil (Siemens MR, 30ch spine). The fast protocol used GRAPPA for the sagittal T1-W and T2-W sequences, and simultaneous multi-slice (SMS) for the axial sequence as acceleration methods. Two blinded neuroradiologists independently assessed 3 aspects: (1) anatomical impressions, (2) image quality and (3) diagnostic quality.
Results
The acquisition time of the fast protocol was 5 mins and 7 secs, compared with 16 min and 30 sec of the standard protocol. Regarding the anatomical impressions, each observer considered that the overall level of anatomical detail was similar for both protocols (Obs1 $p=0.317$, Obs2 $p=0.157$). Looking at individual sequences the observers noted decreased image quality in the SMS TSE (Obs1 $p=0.046$, Obs2 $p=0.014$) and the DIXON T2-W-FS (Obs2 $p=0.008$) and otherwise found nonsignificant differences in other individual sequences ($p>0.083$). In terms of diagnostic quality both observers found the protocols

provided similar diagnostic information (Obs1 p=0.317, Obs2 p=0.317), and noted findings which are still under investigation for concordance measures.

Conclusions

The 5-minute protocol for the lumbar spine MRI reduced the acquisition time by 69.5% without significant impact on the overall diagnostic quality even with some compromise in image quality. This pilot study warrants the initiation of a larger study including a broad population.



(Filename: TCT_O-01_ASNRFigure.jpg)

O-02

11:08AM - 11:16AM

Multicontrast Volumetric T2-weighted Spine Imaging with Uniform Fat and Fluid Suppression and 3D Myelography in a Single Acquisition

M Pinho[1], X Wang[1], J Greer[1], J Maldjian[1], R Lenkinski[1], A Madhuranthakam[1]
[1]*University of Texas Southwestern Medical Center, Dallas, TX*

Purpose

Routine MR evaluation of the spine relies heavily on T2-weighted images due to the remarkable anatomical contrast obtained for both intra and extradural structures, allowing high diagnostic accuracy on a wide range of clinical scenarios. However, to fully explore the potential of T2-weighted sequences, it is commonly necessary to obtain separate acquisitions in multiple planes with different contrasts, such as fat or fluid suppression and use of extra long echo times (TEs) for myelographic applications. The purpose of this work was to evaluate a novel approach for comprehensive T2-weighted spinal imaging using a dual-acquisition 3D TSE sequence combined with dual-echo Dixon based approach for uniform fat suppression to generate multiple sets of isotropic images in a single acquisition.

Materials and Methods

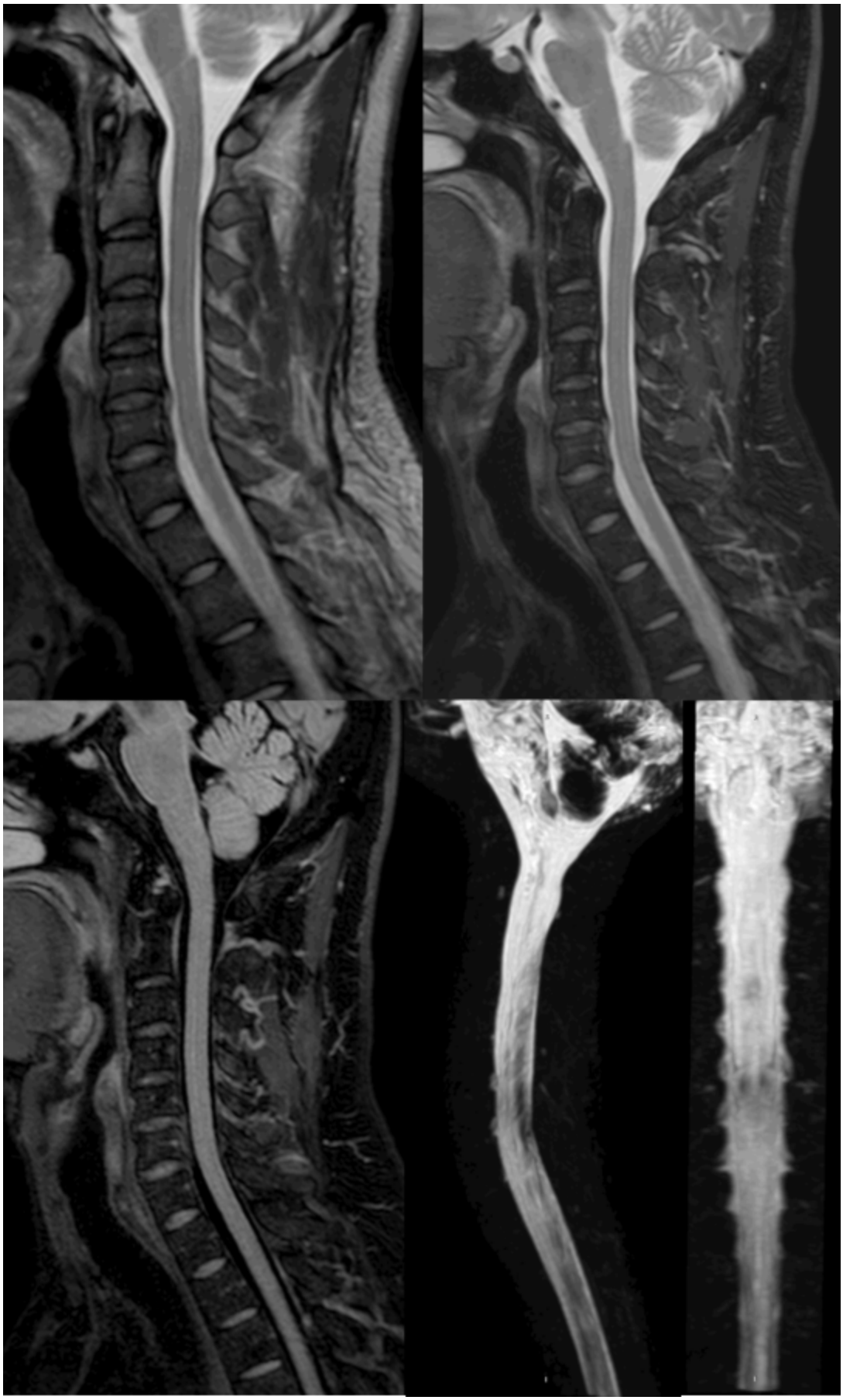
The dual-acquisition (shorter TE and longer TE) 3D TSE sequence with dual-echo Dixon in the sagittal plane was implemented on a 3T Ingenia scanner (Philips Healthcare, Best, The Netherlands). The acquisition and reconstruction methods were evaluated and compared against standard 2D FLAIR and 2D STIR of the spine in 5 healthy volunteers with IRB approval and written informed consent. The typical imaging parameters of the proposed sequence included: sagittal and/or axial orientation; FOV = 360×360×199 mm; Resolution = 1×1×1 mm; SENSE = 2; equivalent TE1/TE2 = 72/304 ms, δt = 1.1 ms for Dixon, partial readout of 0.8, total scan time = 4:05 minutes. The multi-slice 2D T2w, STIR and FLAIR images were acquired using the same parameters except: TR = 2500/6000ms (STIR/FLAIR); TE = 35/120ms (STIR/FLAIR); TI = 240/2000ms (STIR/FLAIR) and a slice thickness of 3mm. The total scan time for the 2D T2-weighted (2:30 mins), 2D T2-STIR (4:15 mins) and 2D T2-FLAIR (4:12 mins) sequences were about 11 mins.

Results

A total of 6 different fully coregistered 3D isotropic datasets (Fig. 1) were reconstructed from the same acquisition: "conventional T2W" corresponding to in-phase images from the first echo, "fat-suppressed T2W" - water only Dixon separated images from the first echo, "fluid suppressed T2W"- in phase images from first echo with subtraction of long TE components of second echo, "fluid and fat suppressed T2W" - water only images from first echo with subtraction of long TE components of second echo, "fat only T2W" - fat only Dixon separated images from the first echo, and "T2-weighted myelogram" - water only Dixon separated images from the second echo. Three-dimensional isotropic datasets were reformatted in axial and coronal planes with a total of 18 available sets of images. All datasets were free from artifacts, fluid and fat suppression was uniform in all subjects and T2W contrast was comparable to standard multi-slice T2W images on qualitative evaluation.

Conclusions

Conclusion: The proposed dual-acquisition 3D TSE with dual-echo Dixon generates perfectly co-registered multi-contrast high resolution volumetric images of the spine with uniform fat and fluid suppression, multiplanar capabilities and myelographic reconstructions in clinically feasible scan times.



(Filename: TCT_O-02_Picture1.gif)

O-03

11:16AM - 11:24AM

Pediatric Head & Neck Injury: Statistical Analysis of Multiple Factors Associated with Blunt Cerebrovascular Injury on CTA.

R Patel[1], K Jobanputra[1], A Kamali[1], E Bonfante-Mejia[1], R Riascos[1], I Ugalde[1]
[1]*The University of Texas Health Science Center, Houston, Houston, TX*

Purpose
Computed tomography angiography (CTA) imaging of pediatric population remains a contentious issue for a concern of unnecessary radiation exposure. There are no specific guidelines for CTA imaging in pediatric population having head and neck trauma and imaging guidelines for adult population usually are followed. In this study we analyze various clinical and imaging factors to establish the most relevant ones which reach level of statistical significance when correlated with cerebrovascular injury on the CTA.
Materials and Methods
A single tertiary level institutional IRB approved study involved retrospective analysis of 473 pediatric patients who underwent CT angiogram based on Denver criteria for blunt cerebrovascular injury in head and neck trauma. The demographic, clinical and imaging factors were evaluated. The demographic factors included age, gender and race; the clinical and imaging factors included Glasgow Coma Scale (GCS), Injury Severity Score (ISS), cerebral hemorrhage, cervical bruit, seat belt sign, infarct on head CT, puncture wound, laceration, penetrating, facial fractures, hanging mechanism, cervical spinal fracture, basilar skull fracture, mechanism of injury, clavicle, thoracic, rib, and scapula fractures. Neurological status evaluation of only 328 cases were available because 145 (30.7%) were under sedation due to endotracheal intubation. Ordinal and nominal variables were evaluated by using the Chi square test or the Fisher's exact test if the count in the contingency table were ≤6. Continuous variables were analyzed by using the Student t-test. Logistic regression was performed. A p-value <.05 (two tailed) was considered statistically significant to all the tests. All analyses were performed with IBM SPSS software (version 23).
Results
Of the 473 patient studied, 82 (17.3%) had cervical vascular injury. The factors associated with cervical vascular injury reaching statistical level of significance ($p< 0.05$) were: GCS (0.01), ISS (<0.001) Cerebral hemorrhage(0.02), infarct on CT (<0.001), puncture wound, laceration/penetrating (0.04), cervical spine fracture (<0.001), basilar skull fracture (<0.01) and focal neurological deficit when evaluated (<0.001).
Conclusions
It was concluded that the factors that reached level of statistical significance were no

different than the ones in the adult cervical spine injury guidelines, hence separate guidelines tailored to the pediatric population are not required as per our institutional experience.

Table 1. Univariate analyses of demographic and clinical factors associated with cervical vascular lesions in children

Characteristic	All N=473 (100%)	Cervical vascular lesion N=82 (17.3%)	No cervical vascular lesion N=391 (82.7)	p-value
Age years, mean (median)	12.4 (14)	13.2 (16)	12.2 (14)	.13
Sex				.17
Male	319 (67.4)	50 (61)	269 (31.2)	
Female	154 (32.6)	32 (39)	122 (66.8)	
Race				.33
White	221 (46.9)	42 (51.9)	179 (45.9)	
Non White	250 (53.1)	39 (48.1)	211 (54.1)	
GCS mean (median)	11.1 (15)	9.8 (13)	11.4 (15)	.01
ISS mean (median)	17.4 (14)	23.9 (22)	16 (14)	≤.001
Cerebral hemorrhage				.02
Yes	189 (40)	42 (51.9)	147 (37.6)	
No	283 (60)	39 (48.1)	244 (62.4)	
Cervical bruit				.17*
Yes	1 (.2)	1 (1.2)	0	
No	472 (99.8)	81 (98.8)	391 (100)	
Seat belt sign				.77
Yes	98 (20.7)	16 (19.5)	82 (21)	
No	375 (79.3)	66 (80.5)	309 (79)	
Infarct on head CT				≤.001
Yes	27 (5.7)	13 (16)	14 (3.6)	
No	445 (94.3)	68 (84)	377 (96.4)	
Puncture wound, laceration, penetrating				.04
Yes	74 (15.6)	19 (23.2)	55 (14.1)	
No	399 (84.4)	63 (76.8)	336 (85.9)	
Facial fractures				.06
Yes	135 (28.5)	30 (36.6)	105 (26.9)	
No	338 (71.5)	52 (63.4)	286 (73.1)	
Hanging mechanism				.15*
Yes	8 (1.7)	3 (3.7)	5 (1.3)	
No	464 (98.3)	79 (96.3)	385 (98.7)	
Cervical spinal fracture				≤.001
Yes	100 (21.1)	31 (37.8)	69 (17.6)	
No	373 (78.9)	51 (62.2)	322 (82.4)	
Basilar skull fracture				.01
Yes	131 (27.8)	32 (39)	99 (25.4)	
No	341 (72.2)	50 (61)	291 (74.6)	
Mechanism				.26
1	212 (44.8)	34 (41.5)	178 (45.5)	
2	80 (16.9)	16 (19.5)	64 16.4)	
3	83 (17.5)	10 (12.2)	73 (18.7)	
4	98 (20.7)	22 (26.8)	76 (19.4)	
Clavicle				.49*
Yes	35 (7.4)	4 (4.9)	31 (7.9)	
No	438 (92.6)	78 (95.1)	360 (92.1)	
Thoracic				.48
Yes	53 (11.2)	11 (13.4)	42 (10.7)	
No	420 (88.8)	71 (86.6)	349 (89.3)	
Rib				.16
Yes	70 (14.8)	8 (9.8)	62 (15.9)	
No	403 (85.2)	74 (90.2)	329 (84.1)	
Scapula				.39*
Yes	22 (4.7)	2 (2.4)	371 (94.9)	
No	451 (95.3)	80 (97.6)	20 (5.1)	
Focal neurological deficit**				≤.001
Yes	43 (13.1)	15 (31.9)	28 (10)	
No	285 (86.9)	32 (68.1)	253 (90)	

*Fisher's exact test
**Only 328 cases were evaluable because 145 (30.7 %) were under sedation due to endotracheal intubation
Missing values (count): race (1), cerebral hemorrhage, (1), cervical bruit (1), infarct on head CT (1), hanging mechanism (

(Filename: TCT_O-03_CTA.jpg)

O-04

11:24AM - 11:32AM

Blunt Cerebrovascular Injury in Patients with Cervical Spine Fractures

S Mahalingam[1], X Wu[2], D Durand[2], F Nautsch[2], R Liu[2], A Malhotra[2]

[1]Yale University School of Medicine, New Haven , CT, [2]Yale University School of Medicine, New Haven, CT

Purpose
Cerebrovascular injury has been reported to occur in up to 2.7% of patients with blunt trauma. Patients with cervical spine fractures are at high risk for blunt cerebrovascular injury (BCVI). We studied patients with cervical spine fractures at our institution over a 6-year period to assess incidence and fracture patterns that predict BCVI.
Materials and Methods
After Institutional Review Board approval, retrospective evaluation of all patients with blunt cervical trauma was performed from 2010 to 2016. Patients with cervical spine fractures were identified and data collected for patients who underwent CT angiography (CTA) or magnetic resonance angiography (MRA) for evaluation of BCVI. The fracture level and patterns were studied in relation to the location and Denver grade of vessel injury.
Results
Over 29,000 cervical spine CTs were performed for trauma and a total of 206 patients were identified with cervical spine fractures over a 6-year period. One hundred forty were evaluated by CTA and 66 patients had an MRA. Blunt cerebrovascular injury was found in 39 of 206 patients. Of these, patients had C1-C3 fractures in 29 patients, C4-C7 fractures in 25 patients and fractures through the transverse foramina in 28 patients. The highest incidence of vascular injury was seen with perched facets (70%) and with subluxations (35%).
Conclusions
Blunt cerebrovascular injury is not uncommon with cervical spine fractures. Although historically C1-C3 fractures have been described to be high risk for BCVI, even subaxial injuries can be associated. Early detection of BCVI is critical to reduce the incidence of stroke in patients with blunt trauma.

Number of Patients with Cervical Fractures and/or Vascular Injuries

	CTA			MRA		
	Vascular Injury (%)	No Vascular Injury	Total	Vascular Injury (%)	No Vascular Injury	Total
Total number of Patients	29 (20.7)	111	140	10 (15.2)	52	66
C1-C3	21 (23.9)	67	88	8 (19.5)	33	41
C4-C7	15 (22.4)	52	67	10 (31.3)	22	32
Foraminal	20 (24.4)	62	82	8 (28.6)	20	28
Subluxation	18 (35.3)	33	51	6 (33.3)	12	18
Perched	7 (70.0)	3	10	4 (66.7)	2	6
Facet Fractures	13 (40.6)	29	32	6 (46.2)	7	13
Ligamentous Injury	11 (40.7)	16	27	4 (40.0)	6	10

(Filename: TCT_O-04_BCVItable.jpg)

O-05

11:32AM - 11:40AM

High Rates of Intrareader Variability in Grade 1 Blunt Cerebrovascular Injury (BCVI)

N Doyle[1], M Ghazarian[2], R Riascos[3], C Sitton[4]
[1]University of Texas Medical School at Houston, Houston, TX, [2]UT Houston Medical School at Houston, Houston, TX, [3]UTHSC-Houston, Houston, TX, [4]The University of Texas Health Science Center at Houston UTHealth, Houston, TX

Purpose
The frequency of Grade 1 blunt cerebrovascular injury (BCVI) varies greatly in the literature. Grade 1 injuries account for 54% of BCVI at our institution. We sought to determine interrater variability in the identification of Grade 1 injury in our own practice.
Materials and Methods
We utilized a database of CT angiograms performed in the setting of trauma between January 2014 to June 2014. A subset cases reported as Grade 1 BCVI were identified and gender and age-matched CTAs with normal reports were selected from the same timeframe as controls. The Grade 1 cases and controls were randomized and reinterpreted by a neuroradiologist with 15 years of experience. Blunt cerebrovascular injuries were graded using the Denver Grading of Vascular Injury Scale. The reinterpreted reports included the grade and location of each BCVI, and were compared to the original reports.
Results
Sixty-seven Grade 1 BCVIs were identified. Seventeen (25%) were read concordantly as

Grade 1 on second interpretation. Forty-five (67%) were read as normal, and 5 (7%) were read as a higher grade (Grade 2-4). There were 512 carotid and vertebral arteries included in these studies, and 427 were originally read as normal. Of the normal vessels, 14 (3%) were re-read as Grade 1, 2 (0.5%) were read as Grade 2, and none were read as Grade 3 or higher. Results were similar to rates of radiographic resolution of Grade 1 injuries at our institution where (64%) patients had a negative follow-up CTA and 9 (36%) remained stable or progressed.

Conclusions

There is a high rate of interrater variability in the interpretation of Grade 1 BCVIs in our practice. Improvement in specificity will be necessary if we are to continue using the Grade 1 designation.



Figure 1: Examples of BCVI grading system. A: Grade 1 vascular injury, with vessel wall irregularity or dissection involving <25% of luminal diameter. B: Grade 2 vascular injury, with raised intimal flap, thrombus, dissection, or hematomas >25% of luminal diameter. C: Grade 3 vascular injury, with pseudoaneurysm. D: Grade 4 vascular injury, with total occlusion of vessel.

(Filename: TCT_O-05_BCVIpic.jpg)

O-06

11:40AM - 11:48AM

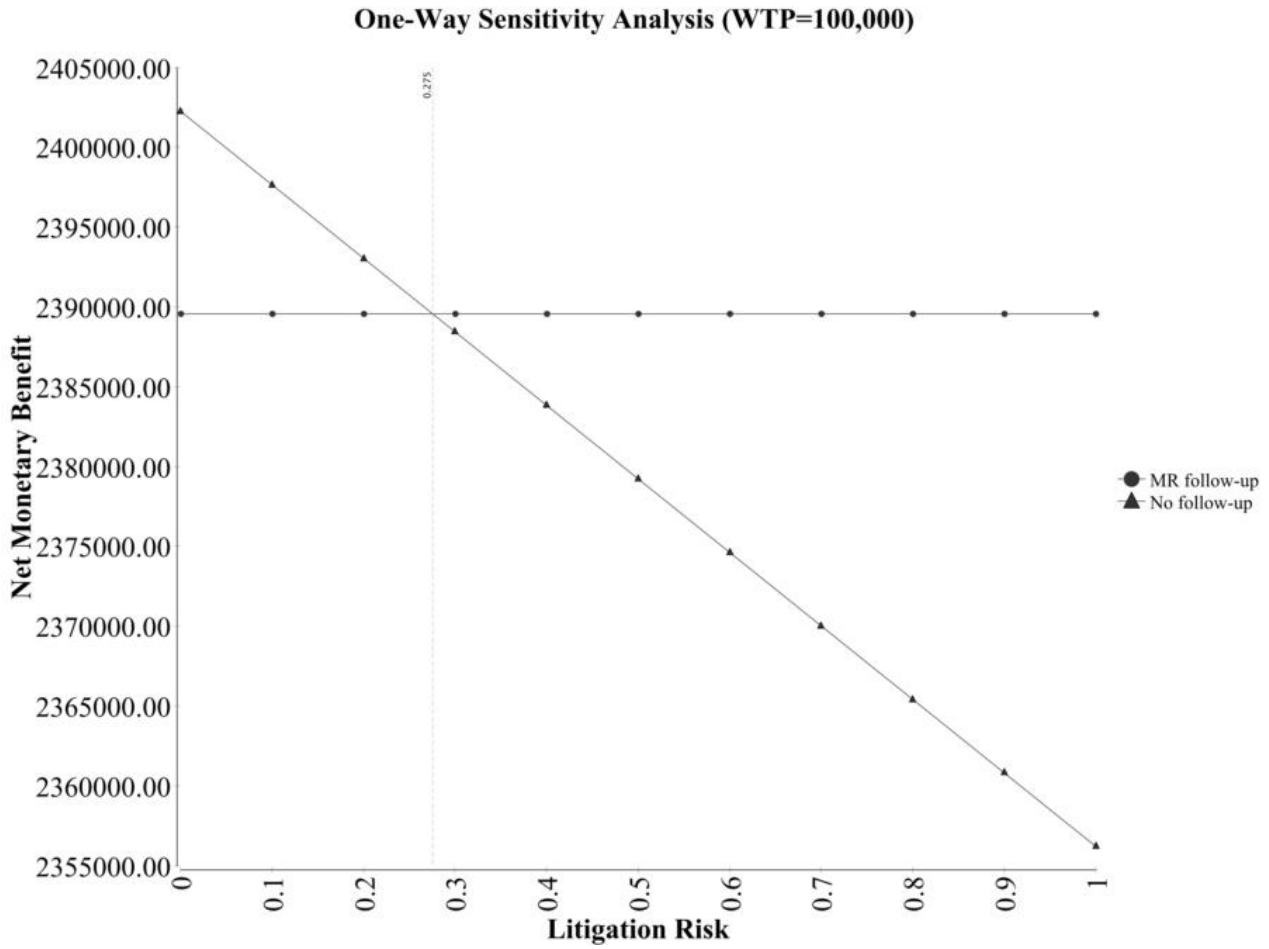
Cost-Effectiveness of MRI in Cervical Spine Clearance of Alert Blunt Trauma Patients

X Wu[1], D Durand[1], V Kalra[1], R Liu[1], H Forman[2], P Sanelli[3], A Malhotra[1]
[1]Yale University School of Medicine, New Haven, CT, [2]Yale University School of Medicine, new haven, CT, [3]Northwell Health, Manhasset, NY

Purpose

Noncontrast cervical spine CT is the imaging modality of choice to assess for acute fracture or rule out injury in blunt trauma patients. Magnetic resonance imaging (MRI) is not recommended for routine use, but is performed for assessment of stability by evaluating soft

tissue injury. Missed unstable injury can lead to permanent neurologic deficits. We studied the cost effectiveness of doing MRI after a negative CT in alert trauma patients.
Materials and Methods
A modeling-based decision analysis is performed over the lifetime of a 40-year-old individual. The 2 strategies compared were no follow up (NFU) and MRI. A Markov model with a 3% discount rate was used with parameters from the literature. Base cases, probabilistic, and sensitivity analyses were performed to assess the cost-effectiveness of the strategies.
Results
In the base case calculation, the cost of MRI follow-up is $11,440 with a utility of 24.01 QALYs; the cost of NFU is $5,649 with a utility of 24.08 QALYs. In the probabilistic sensitivity analysis no follow up is the better strategy in all 10,000 iterations. No follow up is the better strategy when the risk of missed unstable injury turning into permanent neurologic deficits is smaller than 79%. Magnetic resonance imaging would be the more optimal strategy if the percentage of collared patients developing cord injury is lower than 4.8%. When the risk of litigation exceeds 27.5%, MRI follow up should be performed.
Conclusions
Magnetic resonance imaging is not cost effective for further evaluation of unstable injury in alert, blunt trauma patients after a negative cervical spine CT.



(Filename: TCT_O-06_Alertlitigation.jpg)

O-07

11:48AM - 11:56AM

Cost-Effectiveness of MRI in Cervical Spine Clearance of Obtunded Blunt Trauma Patients

X Wu[1], V Kalra[1], R Liu[1], H Forman[1], P Sanelli[2], A Malhotra[1]
[1]Yale University School of Medicine, New Haven, CT, [2]Northwell Health, Manhasset, NY

Purpose
Magnetic resonance imaging (MRI) frequently is performed in obtunded, blunt trauma patients with negative CT results as a reliable clinical examination is difficult. Magnetic resonance imaging is advocated for assessment of stability by further assessment of soft tissue injury, to prevent permanent neurologic injury. We studied the cost effectiveness of doing MRI after a negative CT in obtunded trauma patients.
Materials and Methods
A modeling-based decision analysis is performed from a payer's perspective. The two

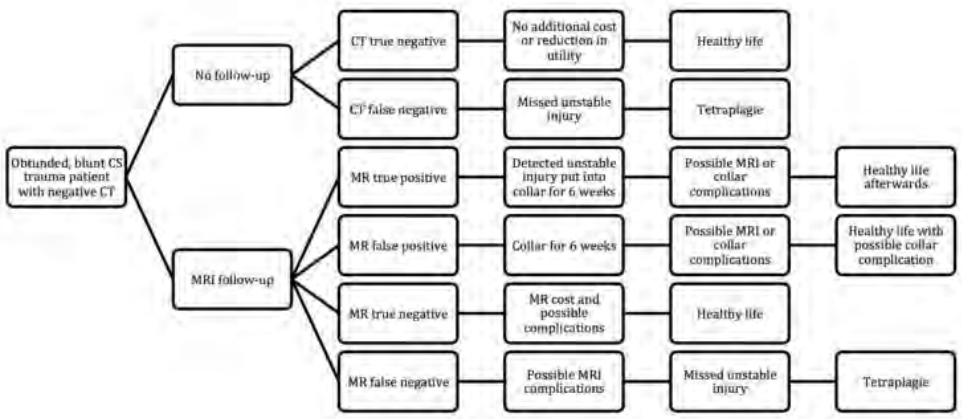
strategies compared were no follow up (NFU) and MRI. A Markov model with a 3% discount rate was used with parameters from the literature. Base cases, probabilistic, and sensitivity analyses were performed to assess the cost effectiveness of the strategies.

Results

In the base case calculation, no follow up is the dominant strategy with a lower cost and a higher utility, and probabilistic sensitivity analysis showed NFU to be the better strategy in all 10,000 iterations. To evaluate the robustness of the conclusions against some key variables and assumptions, we performed multiple one-way and two-way sensitivity analyses. The NPV of the initial CT is assigned to be 99.88% from our previous meta-analysis in the base case calculation. When the value is varied, the resulting graph shows that NFU remains the dominant strategy over MRI follow up throughout 0 to 100% NPV, due to the complication risks, MRI costs, and limited impact on patient outcome after MRI follow-up. No follow up is the better strategy irrespective of the percentage of missed unstable injuries on CT that develop into permanent neurologic injuries, and the percentage of collared patients developing cord injury.

Conclusions

Magnetic resonance imaging is not cost effective for further evaluation of unstable injury in obtunded, blunt trauma patients after a negative cervical spine CT.



(Filename: TCT_O-07_tree.jpg)

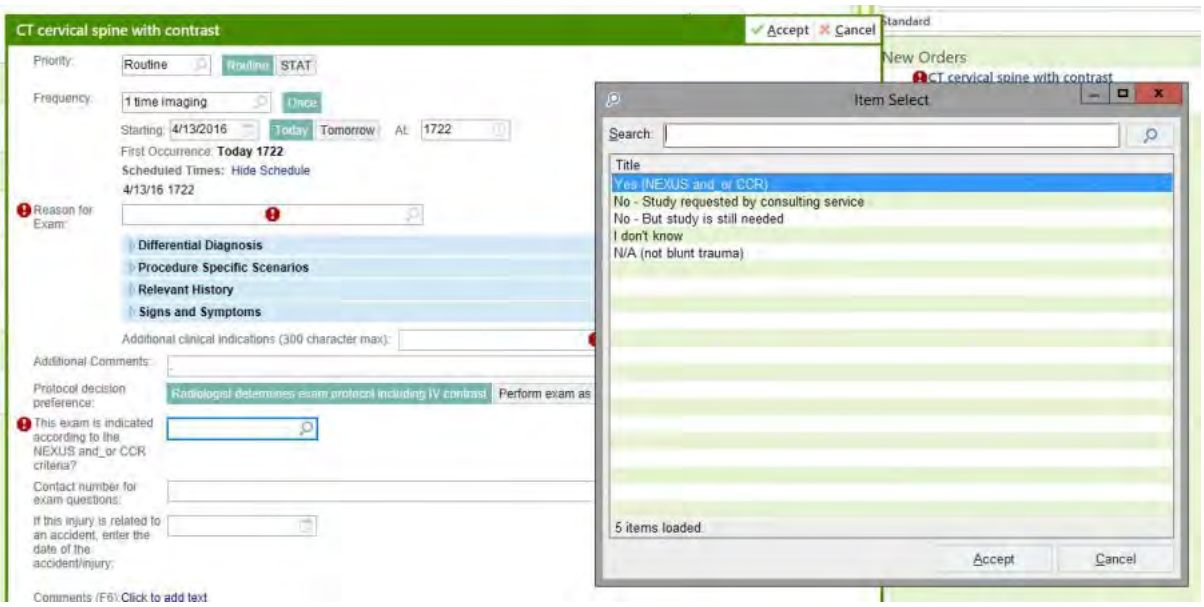
O-08

11:56AM - 12:04PM

Screening Cervical Spine CT in the Emergency Department – Phase Four: Evaluating the Role of Clinical Decision Support – Results of a Prospective Practice Quality Improvement (PQI) Initiative

P Annigeri[1], P Vallee[1], S Krupp[1], D Kastan[1], B Wessman[1], G Tokarski[1], S Patel[2], B Griffith[1]
[1]Henry Ford Health System, Detroit, MI, [2]Henry Ford Hospital, Detroit, MI

Purpose
Improving imaging utilization is an important goal in healthcare. Clinical decision support (CDS) has demonstrated success in reducing imaging utilization in some settings, but its value remains unclear, particularly in the busy emergency department setting. The purpose of this practice quality improvement (PQI) project was to assess whether question prompts during the ordering process improve appropriate utilization of cervical spine (C-spine) CT as evidenced by an increased injury detection rate.
Materials and Methods
All C-spine CT scans ordered for blunt trauma over a 3-month baseline period were identified. Imaging reports were reviewed and classified as positive, negative, or indeterminate for acute injury. A question prompt assessing the presence of clinical indications for imaging then was inserted into the ordering process (Fig. 1) with responses recorded. During a 3-month postintervention phase, imaging reports were reviewed again and classified for presence of acute injury.
Results
Seven hundred seventy-seven C-spine CT scans performed for blunt trauma were identified in the baseline phase. Of those, 0.9% were positive, 97% negative and 2.1% indeterminate for acute injury. During the postintervention phase, 1033 cervical spine CT scans were performed for blunt trauma with 136 excluded due to missing question response. Of the remaining 897, 0.3% were positive, 98.6% negative and 1.1% indeterminate with no statistically significant difference in injury detection rate. Regarding clinician responses, 74.2% responded that imaging was indicated by the decision rule while 13.2% responded that imaging was not indicated and 12.6% did not know.
Conclusions
Insertion of a question prompt into the ordering process did not impact C-spine CT utilization as measured by fracture detection rate. The study did find that in 25.8% of cases, clinicians responded that imaging was either not indicated by clinical criteria or not known. This raises important questions regarding the future direction and success of CDS.



(Filename: TCT_O-08_C-spine.jpg)

O-09

12:04PM - 12:12PM

Utility of Four-dimensional Computed Tomography (4DCT) in Assessing Cervical Spine Instability

K Lim[1], T Goldschlager[2], R Chandra[2], C Daly[3], J Troupis[2]
[1]Monash University, Melbourne, Victoria, [2]Monash Health, Clayton, Victoria, [3]Hudson Institute of Medical Research, Clayton, Victoria

Purpose
Cervical spinal instability (CSI) is a pathological consequence of a variety of spine disorders that may lead to compressive cervical myelopathy, quadriplegia and death. There is no gold standard in diagnosing CSI confidently. Four-dimensional computed tomography (4DCT) is a noninvasive method that assesses functional and dynamic cervical motion in high resolution. This is the first case-series utilizing 4DCT to assess CSI.
Materials and Methods
Nine patients with suspected CSI were included. The mean age of the cohort was 67 years. Three presented after trauma with neck pain. Five had chronic neck pain and/or radicular symptoms, with 2 having had anterior cervical discectomy fusion (ACDF) previously. One patient presented with nondermatomal paresthesia in 4 limbs. Interpretation of findings on MRI, CT and dynamic x-rays by neuroradiologist and neurosurgeon were equivocal for stability. Cervical spine 4DCT was performed using a 320x0.5mm detector multislice CT (Aquilion ONE Vision, Toshiba Medical Systems, Otawara-shi, Tochigi-ken, Japan) with the patient in lateral decubitus position while making full continuous neck motion. Cine movie files were generated from the volume datasets.

Results
Median follow-up duration since 4DCT was 5.5 months (2 months – 19 months), excluding 1 who was lost to follow up. Three patients had CSI on 4DCT. One had cervical spinal myelopathy at C4/C5. Second patient was unstable at the C3/C4 level and incompletely fused from previous ACDF at the C5/C6 level. The third patient with rheumatoid arthritis had facet joint arthropathy and instability at C3/C4. The first patient improved with stabilization procedures, second patient declined surgery while the latter's symptoms improved with corticosteroid injection into C3/C4 facet joints. The remaining stable cases included all trauma cases and an os odontoideum diagnosed on 4DCT. Conservative management was prescribed confidently.
Conclusions
Four-dimensional computed tomography can be used to detect CSI in cervical spinal pathologies. Further studies using cervical spine 4DCT are warranted.

Monday
11:00AM - 12:15PM
Long Beach Convention Center, Room 103 (Main Level)

04C-Parallel Paper Session: Crossroads in Neuroradiology: Progress in Practice

O-10

11:00AM - 11:08AM

Results of the First Biennial Comprehensive Survey of Neuroradiologists' Current Work Effort and Environment

J Chen[1], F Lexa[2]
[1]San Diego VA / UCSD Med. Center, La Jolla, CA, [2]Wharton School, Univ. of Pennsylvania, Philadelphia, PA

Purpose
To report a baseline analysis of the current United States' neuroradiology work environment using the first of a planned series of biennial surveys of the ASNR membership, and to survey perceived trends over the past several years in the setting of continued increases in work productivity.
Materials and Methods
A voluntary online survey was sent to the United States membership of the American Society of Neuroradiology. The survey instrument consisted of 31 questions relating to the neuroradiology work environment. Selected measures included work and call volume, workday length, self-reported burnout symptoms, participation in teaching, mentoring, research/publications, practice building, society volunteering, CME, reading journals; changes in compensation and nonclinical time, effects on perceived interpretation and report

quality, communication of abnormal results, and consideration of early retirement or career changes, among others.
Results
Four hundred thirty-two practicing neuroradiologists responded to the survey, with a broad range in years of practice. 52.8% reported teaching responsibilities with trainees. 62.8% reported increased RVU work-load, while 50% reported longer work-days. Only 7% reported workdays that never extended more than 1 hour beyond expected. 71.9% reported reading more cases per hour. Only 20.5% never or rarely interpreted cases faster than comfortable for optimal interpretation. Only 30.8% never or rarely signed reports faster than needed for optimal clarity. Only 32.4% never or rarely have inadequate time to discuss abnormal results. Symptoms of burnout ranged between 49-75%, with a mean of 62.9% across four measures. For teaching, mentoring, research/publications, a mean of 82.6% reported cut-backs. For practice-building activities, 77.6% reported cut-backs. 51.6% reported considering early retirement. 38.8% reported considering changing career.
Conclusions
Increasing wRVU demands over recent years has had negative effects on the quality of the work environment, the ability and desire of neuroradiologists to perform academic or practice-building duties and the incidence of symptoms of burnout.

O-11

11:08AM - 11:16AM

Worldwide Implementation of Radiology Quality and Safety Programs

C Mutch[1], B Rehani[2], L Lau[3]
[1]University of California, San Francisco, San Francisco, CA, [2]UCSF, San Francisco, CA, [3]International Commission on Radiological Quality and Safety, Melbourne, Austrailia

Purpose
The international radiology community has identified and implemented innovative programs and initiatives to promote more appropriate use, maximize the benefits and minimize the risks of radiological procedures. International, regional, and national organizations, agencies and professional bodies prepare recommendations and guidance tools with the aim to improve appropriate use, quality and safety of radiologic studies as well as reduce the number of unnecessary studies performed. While several well publicized initiatives by the ACR, RSNA and other organizations including Image Wisely, Image Gently and the ACR Appropriateness Criteria are likely familiar to radiologists within North America, there is little available compiled data on the prevalence and role of similar programs throughout the world. In this study we sought to better understand the use and breadth of these types of programs.
Materials and Methods
Surveys were sent to leadership members of national radiology societies. Respondents

answered questions about the creation, adoption, or adaptation of programs addressing quality and safety, referral guidelines, clinical decision support, dose optimization, diagnostic reference levels, incident reporting, and accreditation in their respective countries via web-based survey software.
Results
A total of 46 survey responses representing 40 distinct national entities were obtained. Respondent nations varied from having established programs in all areas queried to none. The majority of countries had programs implemented in some but not all areas. Overall, referral guidelines and national quality and safety programs were the 2 most commonly implemented practices, present in 55.0% and 52.5% of surveyed nations, respectively. Dose reduction training programs and clinical decision support were the least implemented programs, each in only 20.0% of respondents.
Conclusions
Here we have outlined the current state of national and societal radiologic quality and safety improvement measures throughout the world with a goal to share insight and increase future collaborative efforts. Knowledge of the breadth and scope of different national and societal programs may help improve patient care by strengthening awareness, access and more appropriate use of good practice guidance tools.

O-12

11:16AM - 11:24AM

Ecuador International Educational Project in Neuroradiology

Y Zhang[1], K Garcia-Reyes[1], I Brown[1], M Castillo[2], K Shapiro[1], L Luddington[1], M Rawlings-Fein[1], P Espinosa[3], W Dillon[1], B Rehani[1]
[1]UCSF, San Francisco, CA, [2]University of North Carolina at Chapel Hill, Chapel Hill, NC, [3]Hospital de Tena, Ecuador, NA, Tena

Purpose
Improving education in the developing world presents an opportunity to advance radiology and patient care. To provide a sustainable solution for supplementing global education in radiology, an innovative technology platform is needed. Several studies have emphasized the efficacy of interactive real-time virtual classroom education and thus our goal was to implement a web-based pilot educational neuroradiology program via real-time lectures from faculty at academic institutions in the USA.
Materials and Methods
We launched our real-time virtual classroom for neuroradiology in a series of 7 sessions conducted in Spanish from July 25, 2016 to August 30, 2016. We used a low-cost cloud video conferencing platform that supported low bandwidth connections critical for implementation in the developing world. Our audience included medical students, residents, and physicians in pediatrics, internal medicine, emergency medicine, and obstetrics at a

Hospital José María Velasco Ibarra in Tena, Ecuador, which serves as the sole public hospital for approximately 100,000 residents of Napo Province but has no radiologists or neurologists on staff. Our lecturers were neuroradiology experts from academic institutions across the country selected independent of geographical location. Topics were selected by our expert lecturers based on requests from participants in Tena and included the following: Ischemic and Hemorrhagic Cerebral Vascular Accidents; Cerebral Tumors; Neurosonography; Cranioencephalic Trauma; Epilepsy; and Cerebral Congenital Malformations. During the real time virtual classroom teaching, special features like real-time two-way video communication, text chats, advanced interactive whiteboards, desktop application sharing and interactive participation tools on the platform are utilized. Two-way audio and video communication ensures participants abroad can participate, ask questions and respond to quizzes. Efficacy for the virtual live sessions was measured using pre and postlecture quizzes, participant feedback, and quality assessment and evaluations for improvement. Quality assessment in the form of audience feedback were categorized according a grading scale of "1" for positive, "0" for neutral, and "-1" for negative comments.

Results

Pre and postlecture quizzes demonstrate an overall 60-80% improvement in correct responses for materials presented in the respective lectures. We also received individual feedback from participants at the conclusion of our lecture series. Quality assessment of the lectures from 4 participants who provided detailed commentary demonstrated category 1 (positive) reviews.

Conclusions

Our custom designed interactive platform was able to transmit real time live lectures that result in interaction between all audience participants in Tena, Ecuador where only limited internet bandwidth was available. Attendance to these virtual lectures was excellent, pre and postlectures test showed significant knowledge improvement and feedback comments generally were positive.

O-13

11:24AM - 11:32AM

Neuroradiology, a 24/7 Subspecialty!

B Salehi[1], K Spitler[1], R Homer[1], N Salamon[2]
[1]UCLA, Los Angeles, CA, [2]UCLA, Los Angeles, CA, David Geffen School of Medicine at UCLA, Los Angeles, CA, Los Angeles, CA

Purpose

To evaluate the impact of 24/7 neuroradiology coverage on patient care and education.

Materials and Methods

The debate of who should read the after-hours and overnight neuroradiology cases is getting

more challenging in most of the institutes including the academic centers and private practices. Overnight neuroradiology has been manages differently in different institutes with wide range of preliminary reports versus final read, trainee reports versus staff read, local radiology versus teleradiology, and subspecialized neuroradiology versus general or emergency radiology. Different factors are involved in assessment of the ideal protocol for emergency neuroradiology coverage. These factors include but not limited to discrepancy rate, turn around time, emergency physician's satisfaction, stroke team and neurointerventional requirements and guidelines, neurocritical care's need, resident/fellow education, accuracy, sustainability, and cost. Our institute, as a trauma level I center and stroke center with a busy neurocritical care and neurosurgery service, has tried different protocols for overnight neuroradiology coverage over the last years. These protocols experimented final read by emergency/general radiology overnight versus preliminary reads by trainee followed by final read by neuroradiologists the next day. However, recently we extended the day shift hours and also hired 3 fellowship-trained neuroradiologists for night coverage. The consequence of this big change and its impact on the quality of the report, turn around time, patient care, physician's satisfaction, observing the guidelines, and trainee's education seems to be significant and worthy of being discussed with the society of neuroradiology. We compare this new program of neuroradiology coverage with the previous system in our institute, using different indices mentioned above.
Results
The emergency and acute-care neuroradiology overnight coverage by fellowship-trained neuroradiologist produces less discrepancy rate, lower turn around time, higher satisfaction of ER physician, stroke neurology and critical care neurology, but higher cost. Resident's education and satisfaction also showed improvement. The statistics of these results will be included in the presentation. Different strategies that we found to be helpful in increasing the sustainability of this new program will be discussed.
Conclusions
Overnight coverage by neuroradiologists is a superior protocol towards excellence in patient care and education.

O-14

11:32AM - 11:40AM

Non-interpretive, Value-add Tasks During Solo Overnight Coverage in Academic Emergency Neuroradiology.

M Glover[1], M Lev[2], P Schaefer[2], W Mehan[3]
[1]Massachusetts General Physicians Organization/Massachusetts General Hospital/Harvard Medical School, Boston, MA, [2]Massachusetts General Hospital/Harvard Medical School, Boston, MA, [3]Massachusetts General Hospital/Harvard Medical School, Boston , MA

Purpose
Traditional payment models and productivity metrics in radiology often have lacked in accounting for the time and value of noninterpretive tasks. The goal of this study is to systematically quantify the frequency and duration of noninterpretative communication (phone calls) during solo overnight coverage in an emergency neuroradiology setting within a tertiary academic medical center.
Materials and Methods
Retrospective analyses of telecommunications data were performed. Phone logs included dates, times and duration for all phone calls with an origin or destination to one of the phones in the emergency neuroradiology interpretation area. Descriptive statistics were utilized to quantify the time associated with noninterpretive tasks.
Results
Sixty-three hours of solo overnight coverage were analyzed during the study period, resulting in 699 total phone calls. Incoming phone calls represented 73% of total calls, of which 84% were answered. Outgoing phone calls represented 27% of total calls; 40% of outgoing phone calls were not answered. The mean duration of a completed incoming phone call (78 seconds, SD: 115) was significantly longer than the mean duration of an outgoing phone call (33 seconds, SD: 60, $p<0.0001$). Highest call volume nights were Wednesday, Thursday and Friday. Total amount of time spent on the phone was highest on Thursday (175 minutes). The mean time spent on the phone per overnight shift was 109 minutes (SD: 43, range: 51 – 175), representing 20% of total shift time on average.
Conclusions
A significant portion of the time during the neuroradiology fellow's solo overnight shift was dedicated to phone communications. Standardizing the capture of noninterpretive tasks may aid in the development and implementation of strategies that address productivity, communication, value and patient safety.

O-15

11:40AM - 11:48AM

Clinical Access to Reports and Imaging: The Value of Radiology

M Alvin[1], M Shahriari[1], E Honig[2], L Liu[3], D Yousem[4]
[1]Johns Hopkins Hospital, Baltimore, MD, [2]University of Pennsylvania, Philadelphia, PA, [3]Johns Hopkins Hospital, baltimore, MD, [4]Johns Hopkins Medical Institution, Baltimore, MD

Purpose
The value of radiology to the healthcare system is an important topic as hospitals look to curb costs and improve outcomes for patients. Specific to clinicians, prior studies have demonstrated that while most internists believe the radiology report is important, less than half of specialists feel the same. As such, we set out to determine if clinicians actually access

images or radiology reports – do they find the accessibility valuable? We also analyzed the time between when clinicians ordered radiology studies and when they viewed the imaging and radiology reports in the electronic medical record system.
Materials and Methods
Through our institutional clinical data analysis center, data were collected on the top 10 CT, MRI, and other imaging category studies (inpatient, outpatient, and emergency department) ordered from 9/1/2016 through 9/30/2016. Data included patient demographics, timestamps for when imaging study orders were placed and by which provider/department, timestamps for when the patient actually received the imaging study, and timestamps for when the imaging and finalized reports were accessed and by which provider/department.
Results
Of the 5,675 radiology reports accessed in 9/2016, greater than half (54%) of all reports were viewed by providers in either the department of medicine (31%) or surgery (24%). Of the 399 imaging studies viewed in 9/2016, medicine providers remained the most frequent viewers (39%). ENT and radiation oncology providers were more than twice likely to view images rather than reports (16% vs. 8% and 12% vs. 5%, respectively). Surgeons viewed images only 1/3 of the time (8%) compared to reports (24%). Attending faculty viewed images (95%) more often than residents and nurse practitioners (5%). In contrast, residents, nurse practitioners, and physician assistants viewed reports (53%) more often than attending faculty (47%). Six departments (18%), including emergency medicine, did not view any images throughout 9/2016.
Conclusions
Utilization of accessible radiology reports and imaging varies by department and provider level of training. Access to imaging is valued much less than reports by the majority of departments with very few physicians in training viewing images. These findings may allow for targeted value improvement projects to expand the radiologist's role and provide more value to the healthcare system.

O-16

11:48AM - 11:56AM

Time-Activity evaluation in Neuroradiology; a follow-up study

M Salehi Sadaghiani[1], A Al Yassin[2], I Nasrallah[1], S Mohan[1], E Botzolakis[1], R Bryan[1]
[1]University of Pennsylvania, Philadelphia, PA, [2]New York Insitute of Technology, Glen Cove, NY

Purpose
There is constant pressure on radiologists' productivity, with declining reimbursements for imaging in the United States and increasing demands for faster reporting times. Hence, efficiency is the top priority in healthcare related planning. Literature shows a scarcity of report generation timing evaluations. Previously, we presented our results regarding the time

spent by radiologists and radiology trainees from study opening to report signing which was performed during summer 2015. We did a follow-up study and using the same timing methodology during fall 2016. In this abstract we present the aggregation of the data from both studies, along with the comparison of the results between 2 time points. Our data include the independent readings performed by attendings, fellows and residents.

Materials and Methods

This observational study tracked radiologists at different levels of experience and training reporting 227 brain MRIs in an academic practice over a period of 1 year. The cases included outpatient brain MRIs which were timed during summer 2015 (n=100) and fall 2016 (n=118). The radiologists were timed by trained observers using a multitrack digital stop watch. The total reporting duration from study opening to report signing was recorded as well as 5 subactivity times performed during this period: image observation, report transcription, clinical correlation, teaching, and other. Observations were made of attendings, fellows, and residents reading studies independently. ANOVA and t-tests were performed for statistical analysis.

Results

Attendings (n=6), fellows (n=11), and residents (n=12) spent a mean of (11.18 ±6.77), (17.98 ±9.22), and (15.83 ±6.31) minutes reading brain MRIs independently. Mean duration was significantly different comparing attendings to fellows ($p<0.001$) or residents ($p<0.01$), but not between fellows/residents. Transcription duration showed the same pattern and was significantly lower among attendings, in comparison to fellows (3.66 ±2.35 vs. 6.63 ±4.04 $p<0.001$) or residents (3.66 ±2.35 vs. 4.92 ±3.22 $p<0.001$). Image observation time also was significantly lower among attendings in contrast to fellows (4.73 ±2.72 vs. 7.13 ±3.86 $p<0.001$) or residents (4.73 ±2.72 vs. 7.68 ±3.3 $p<0.001$). The comparison of the interpretative times between summer 2015 and fall 2016 did not show statistically different times.

Conclusions

Neuroradiologists interpretation times and subcomponents for clinical brain MRI studies was measured in summer 2015 and fall 2016. The results show a reproducible pattern which establishes a benchmark for future efforts to improve efficiency, perhaps showing opportunity for decreasing the transcription component. Furthermore, our results redemonstrate that additional training is associated with 35 % reduction in overall reading time, as well as individual subcomponents.

O-17

11:56AM - 12:04PM

Virtual Reality Modules for Neuroradiology

Y Zhang[1], K Garcia-Reyes[1], I Brown[1], B Rehani[1]
[1]*UCSF, San Francisco, CA*

Purpose

1. To introduce virtual reality as a technology platform that uses head-mounted stereoscopic displays to create 3D immersive environments. Virtual reality headsets can deliver low-cost smartphone-based neuroradiology educational modules by displaying imaging content in their inherent 3D form. 2. To illustrate user interface design interactions such as gaze-controlled directional motion inside the virtual environment for immersive exploration of 3D models. 3. To illustrate the use of custom programming scripts that specify automatic rotational and translational motion of 3D models in the virtual environment.

Materials and Methods

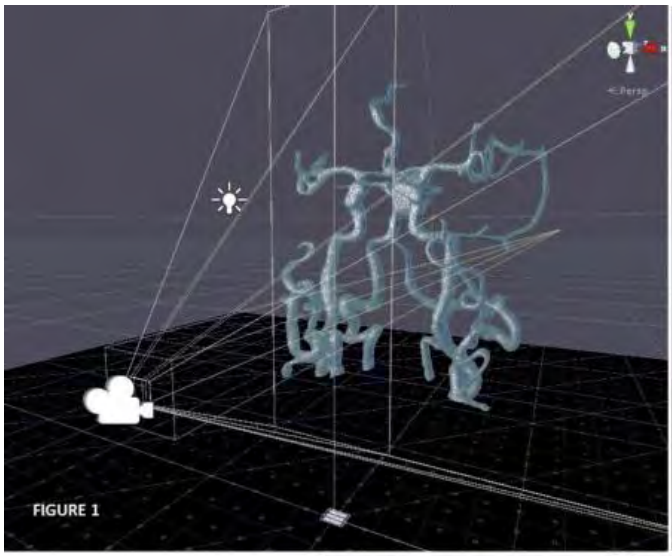
Raw DICOM images were downloaded from the OsiriX DICOM repository made freely available for research and teaching. DICOM datasets containing sample MR cerebral angiography and MR brain images were processed in 3D Slicer, a free open-source software platform for medical image analysis and 3D visualization. Virtual reality interface layout is constructed with Unity, a cross-platform software that interfaces with Google Cardboard to render virtual environments. Neuroanatomy module 1 was created by importing a 3D cerebral angiography model onto a ground plane (Fig. 1a). Neuroanatomy module 2 was created by importing 3D models of brain parenchyma and cerebral white matter onto a ground plane (Fig. 2a). A 3D model of the ventricular system was imported into a Unity scene to construct neuroanatomy module 3 (Fig. 3a).

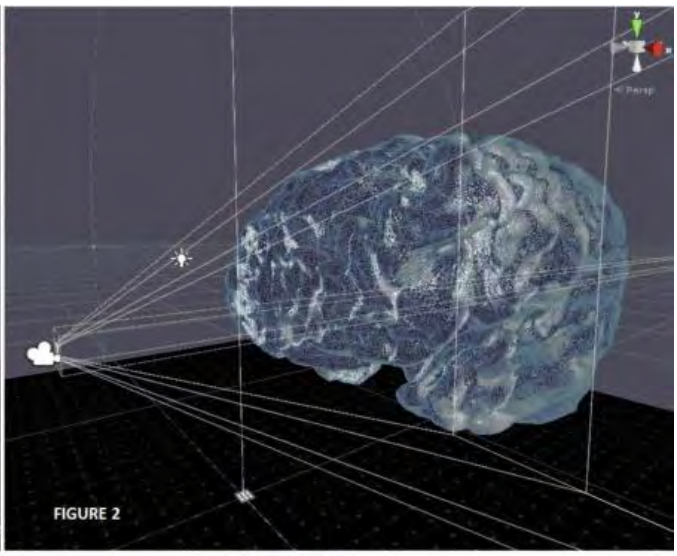
Results

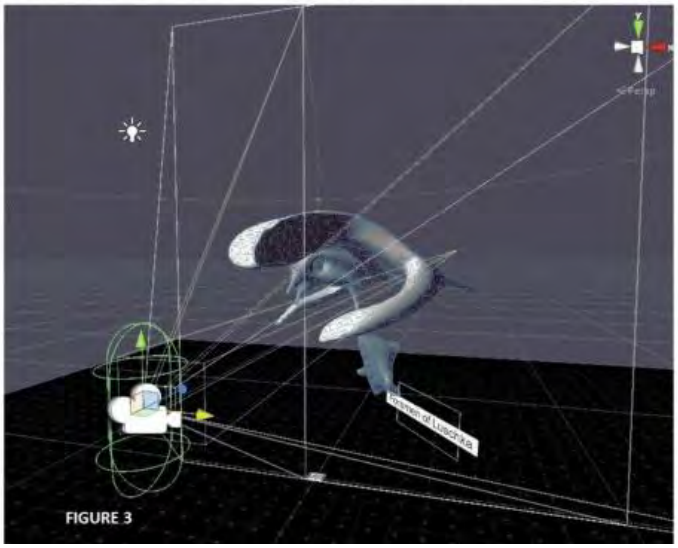
Three neuroanatomy modules are created to illustrate a variety of user-specified inputs to control the rotational and translational movement of 3D models in the virtual space. In addition, a virtual "walk" feature allows users to explore 3D models from any viewing plane with a combination of head tilt and gaze input. A 3D model of the intracranial cerebral vasculature is rendered in the user's field of view at runtime (Fig. 1). A 3D model of the cerebral white matter is embedded within an equivalently scaled model of the whole brain parenchyma (Fig. 2). A 3D model of the ventricular system is rendered in the user's field of view (Fig. 3). To annotate anatomic structures in the virtual environment, a free-text label displaying "Foramen of Luschka" is positioned next to the named structure as an example.

Conclusions

A virtual reality application is constructed for potential use cases in neuroradiology education. Visualization of 3D anatomic structures in a virtual environment adds a new layer of human interaction with medical imaging. Three neuroanatomy modules described here demonstrate example user interaction patterns best suited for particular viewing contexts. Compared to traditional paradigms of viewing stacked 2D images on PACS or 3D models confined to desktop applications, virtual reality increases user interactivity with medical imaging. An intuitive understanding of anatomic structures in 3D space enhances the learning experience for medical students and for residents in diagnostic radiology.







(Filename: TCT_O-17_ASNR.jpg)

Monday
11:00AM - 12:15PM
Long Beach Convention Center, Room 104A (Main Lobby)

04D-Parallel Paper Session: - Pediatrics Neuroradiology: Venturing into Vascular Territory

O-19

11:00AM - 11:08AM

Screening of Intracranial Aneurysms in Children and Young Adults with Familial History of Intracranial Aneurysms or with Personal or Familial History of Polycystic Kidney Disease

C Lacroix[1], A Vossough[2]

[1]Children's Hospital of Philadelphia, Philadelphia, PA, [2]University of Pennsylvania-CHOP, Philadelphia, PA

Purpose
Intracranial aneurysms are considered rare in children. Nevertheless, many screening imaging studies are performed in children and young adults with a familial history of aneurysms, or with a personal or familial history of polycystic kidney disease (PKD), despite unknown effectiveness. The purpose of this study is to assess the prevalence of positive screening studies performed in this population in order to determine the utility and yield of these studies.
Materials and Methods
This retrospective study was approved by our institutional Research Ethics Board. Patients with familial history of intracranial aneurysms or with history of PKD who had a vascular imaging study for screening of aneurysms between June 1993 and September 2016 were included. Relevant demographic and clinical data were recorded, including symptoms and details about familial history of aneurysms (degree and number of relatives affected, ruptured aneurysm versus non-ruptured) or PKD. Images of studies reported as positive or questionable for an aneurysm and their follow-up also were reviewed.
Results
A total of 294 intracranial screening MRA studies were performed in patients with familial history of intracranial aneurysms (267) or with a personal or familial history of PKD (27). Patients included 169 (57%) females, with a mean age of 11.9 years. Most patients presented with headaches (167, 56.8%) or were asymptomatic (71, 24.1%). A total of 289 studies (98.3%) were negative. Five studies (1.7%) were reported as positive. A follow-up brain CTA (2 cases), cerebral angiogram (2 cases), and a second brain MRA study (1 case) were performed in these patients. On further investigation or follow up, all proved to be false-positive.
Conclusions
There is no known or defined benefit of noninvasive imaging methods for aneurysm screening in children or very young adults with a familial history of intracranial aneurysms, or a personal or familial history of PKD. Our results show that the yield is extremely low, if not absent, and does not support routine screening.

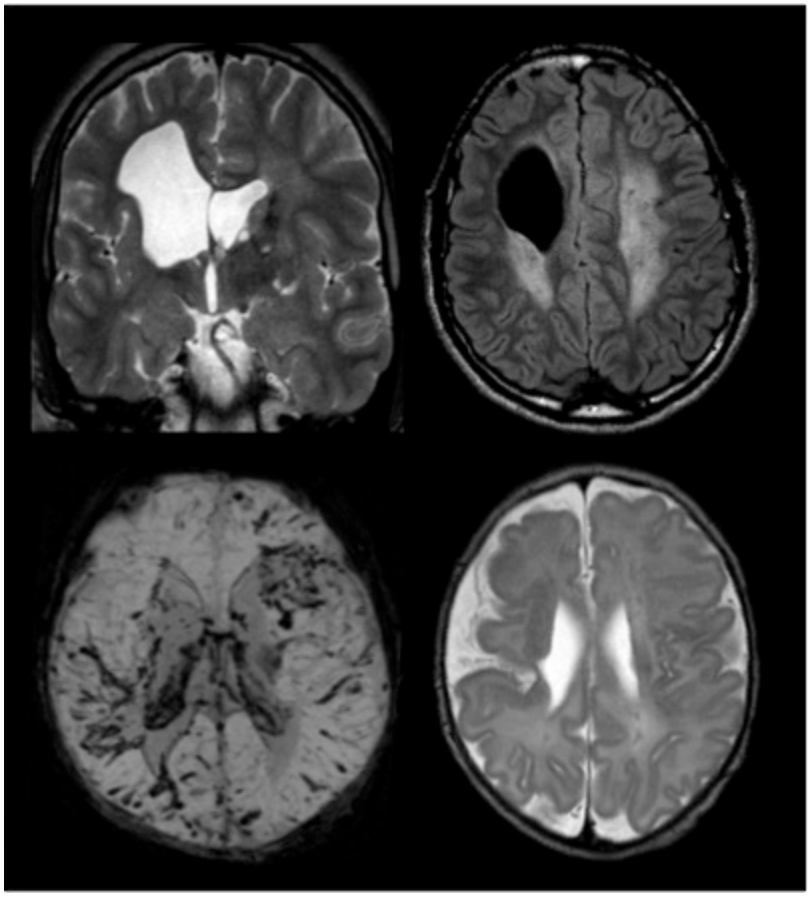
O-20

11:08AM - 11:16AM

Spectrum of diverse neuroimaging findings associated with COL4A mutations

P Krishnan[1], M Shroff[1], P HANAGANDI[1], H Branson[1], S Laughlin[1], N Dlamini[1], M Moharir[1], S MILLER[1], H Faghfoury[2], D Chitayat[3], S Blaser[1]
[1]The Hospital for Sick Children, Toronto, Ontario, [2]University Health Network, Toronto, Ontario, [3]Mount Sinai Hospital, Toronto, Ontario

Purpose
Mutations in the gene encoding type IV collagen, COL4A mutations are associated with weakness of the basement vascular membranes, resulting in small vessel disease and hemorrhage. The spectrum includes cerebrovascular, renal, ophthalmological, cardiac and muscular manifestations with predominance of cerebral and ocular abnormalities. We illustrate the diverse spectrum of neuroimaging findings associated with COL4A mutations in a cohort ranging from a fetus 21.1 weeks gestational age to an adult 35 years of age.
Materials and Methods
Patients were identified via a radiology text search program (ISYS ©). Neuroimaging studies were reviewed for hemorrhagic lesions, brain destruction, vascular and ocular abnormalities and change over time.
Results
We identified 11 patients (M:F 4:7) with confirmed COL4A mutations (COL4A1, n = 9, COL4A2, n = 2) and MRI studies. While patients were predominantly infants and children, fetal MR was available in 2 cases and 1 individual was followed with stable cerebral palsy until 35 years of age when testing revealed a COL4A1 mutation. Two cases had positive family history for COL4A mutation. Serial imaging was available in 7, with an interval between studies ranging from 0.2 months to 131.2 months. The clinical presentation in our cohort included in utero hemorrhage, infantile hemiplegia, cerebral palsy, recurrent stroke, epilepsy and ocular abnormalities. Neuroimaging findings included parenchymal hemorrhage, porencephaly, schizencephaly, and ischemia of various ages on the same imaging study, microcephaly, intracranial calcifications, leukoencephalopathy, focal cortical dysplasia and aneurysms.
Conclusions
COL4A mutations should be considered in the presence of in utero brain parenchymal hemorrhages and porencephaly or schizencephaly without obvious etiology.



(Filename: TCT_O-20_1.jpg)

O-21

11:16AM - 11:24AM

Idiopathic Neonatal Leptomeningeal Hemorrhage

D Cain[1], J Armstrong-Wells[2], N Stence[3], A Jensen[4], D Mirsky[3]
[1]University of Colorado Anschutz Medical Campus, Aurora, CO, [2]University of Colorado Denver Anschutz School of Medicine, Aurora, CO, [3]Children's Hospital Colorado, Aurora, CO, [4]University of Colorado, Aurora, CO

Purpose
Awareness of idiopathic neonatal leptomeningeal hemorrhage (INLH) has been increasing (1). The bleeding has been described as between the pia mater and displaced brain parenchyma, although distinguishing subpial and subarachnoid hemorrhage on imaging is difficult. Prior data have suggested an association of birth trauma and INLH (1), although local medullary vein thrombosis also has been implicated. The clinical data and imaging characteristics of INLH in a single institution cohort were characterized to evaluate these potential relationships.

Materials and Methods

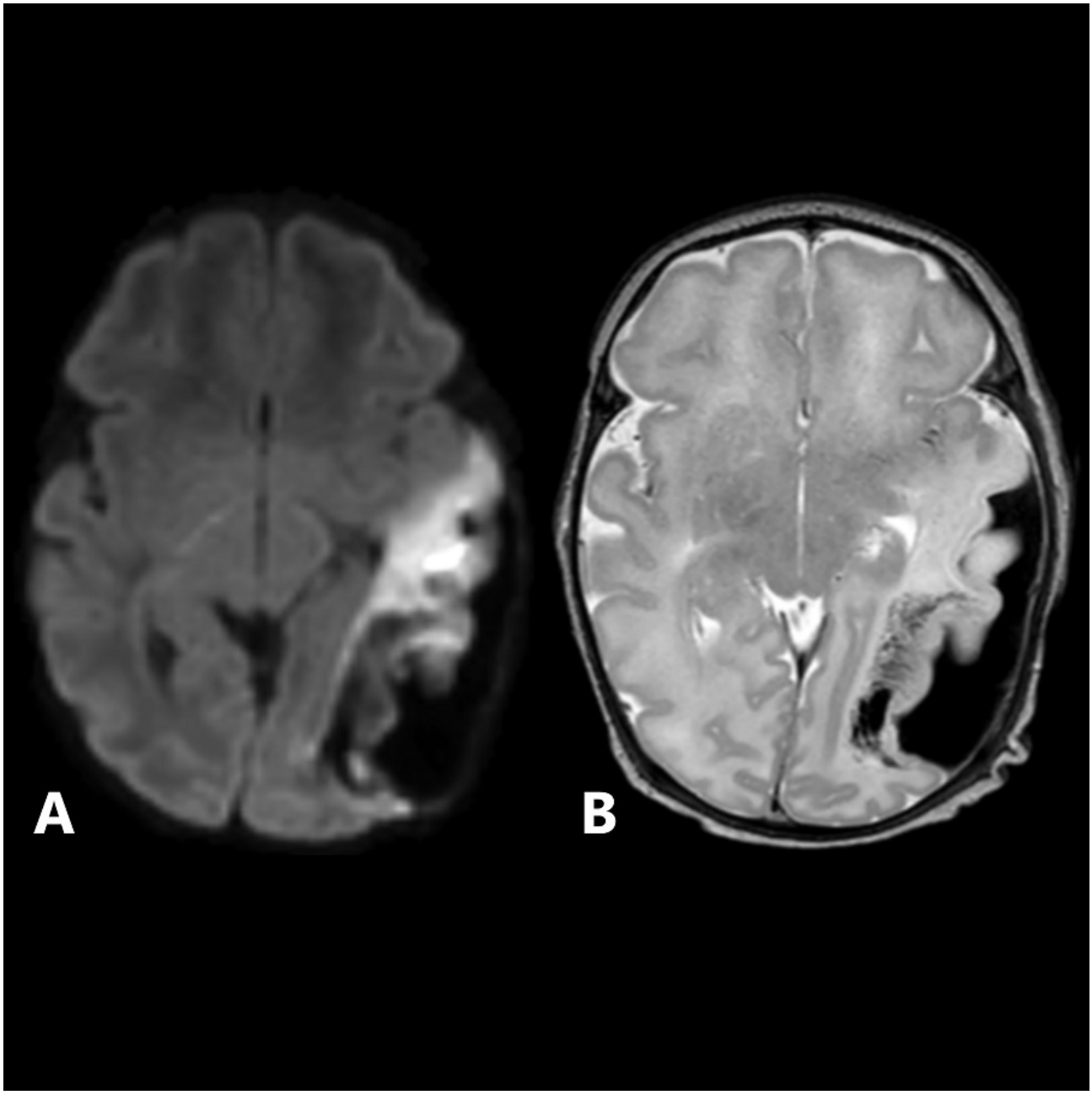
Cases of INLH were identified by performing a keyword search of the radiology database using Montage (TM) Search and Analytics software from 2010 through 2016. Presence of INLH was confirmed by a pediatric neuroradiologist (DMM). The electronic medical records for these cases were reviewed by a radiology resident (DWC) for maternal factors, antenatal and perinatal complications, newborn demographics and NICU course, and clinical outcomes at 6 months. Imaging was reviewed to define hemorrhage location and size, presence of cytotoxic edema, medullary vein prominence, presence of the iris sign [a fan-shaped appearance of restricted diffusion or hemorrhage thought to be an imaging biomarker of deep venous thrombosis (2)], soft tissue swelling, and other findings remote from the primary hemorrhage.

Results

Seventeen patients with INLH and available clinical data were identified. There were no instances of maternal thrombophilia, bleeding disorder, or major maternal infectious episodes during pregnancy. Three deliveries were by cesarean section, all emergent, 2 vaginal deliveries were vacuum/forceps assisted, and there were 3 cases of prolonged labor (>18 hours). Average birth weight was 3.36kg. Sixty-seven percent were male. Apnea was the presenting symptom in most patients (n=16). Focal seizure occurred in the first 48 hours of life in 53% (n=9). No patients were diagnosed with clinical sepsis. Of 11 infants with available 6-month follow-up, 4 had documented clinical or subclinical seizures and remained on anti-seizure medication. INLH was located in the temporal lobe in 80%. Medullary vein prominence subjacent to the hemorrhage was seen in 70% (Fig. 1) and the iris sign was positive in 60%. Magnetic resonance angiography (MRA) was performed in 15 cases, all interpreted as normal. Magnetic resonance venography (MRV) was performed in 12 cases, 11 interpreted as normal, with 1 revealing thrombosis of the ipsilateral right transverse sinus. Additional foci of hemorrhage or ischemia remote from the primary hemorrhage were seen in 9 cases, many of which were felt to be venous in etiology.

Conclusions

In an institutional cohort of 17 neonates with INLH, clinical findings supporting a potential relationship between birth trauma and INLH were infrequent, and no cases had evidence of maternal thrombophilia or bleeding disorder. The imaging in a majority of cases was supportive of medullary venous ischemia as an underlying cause.



(Filename: TCT_O-21_INLHFigure1.jpg)

O-22

11:24AM - 11:32AM

Exposure of cardiopulmonary bypass is associated with presence of cerebral microhemorrhage among pediatric patients with cardiac transplantation.

B Nasman[1], S Harder[2], J Jacobson[1], D Kido[1], P Kim[1]
[1]Loma Linda University Medical Center, Loma Linda, CA, [2]LLUMC, Loma Linda, CA

Purpose
Many children with heart failure from congenital heart disease (CHD) and other acute heart conditions need to undergo cardiac transplantation with cardiopulmonary bypass (CPB) in order to survive. Neurological complications after CPB are a known cause of morbidity and mortality in this population. The contributing factors of the neurological complications include gaseous microemboli, reperfusion syndrome, hypothermic circulatory arrest, and low-flow CPB. Cerebral microhemorrhages (MHs) often are detected in patients after cardiac transplantation. This study was undertaken to estimate the incidence and burden of cerebral microhemorrhage in patients with heart disease or other acute heart requiring cardiac transplantation with CPB, as detected on susceptibility-weighted imaging (SWI).
Materials and Methods
With IRB waiver of consent, MRI scans of a cohort of 128 consecutive pediatric patients who underwent cardiac transplantation evaluation were reviewed retrospectively for MH(s). A nested case-control study was performed including 83 MR brain examinations from 71 patients who met our selection criteria. The transplant (TX) group consisted of 30 pediatric patients requiring cardiac transplantation with CPB who had post-transplant SWI sequences. The control group was comprised of 53 pediatric patients also requiring cardiac transplantation with CPB, but with pre-transplant SWI sequences. Patients in the TX group were imaged at a mean age of 2521 days (13 female; 21 cyanotic heart disease). Control subjects were images at a mean age of 681 days (24 female; 30 cyanotic heart disease). The number of cerebral MH on SWI was counted by an experienced neuroradiologist (SH) who was blinded to the transplantation status. The differences in number of cerebral microhemorrhage between groups were tested for significant using Wilcoxon Rank sum test, $\alpha = 0.05$. Using the logistic regression model, the odds ratio of the presence of >5 cerebral microhemorrhages were also tested between the groups, with adjustment of age at MR imaging, sex, and cyanotic heart condition, $\alpha = 0.05$.
Results
The median number of cerebral MHs was 31.5 (IQR 10, 50) in the TX group and 0 (IQR 0, 1) in the control group, p-value < 0.001. Pediatric patients with heart failure from various cardiac conditions who underwent cardiac transplantation were 21.6 times more likely to have >5 cerebral microhemorrhages, when compared with pediatric patients with similar cardiac conditions who had yet to undergo cardiac transplantation, with adjustment of age at MR imaging, sex, and cyanotic heart condition, 95% CI (5.9-79.6).
Conclusions
Exposure of cardiopulmonary bypass during cardiac transplantation is associated with cerebral microhemorrhage among pediatric patients with heart failure.

O-23

11:32AM - 11:40AM

Predictive Outcome Modeling of Out-of-Hospital Pediatric Cardiac Arrest Using Neuroimaging-guided Supervised Machine Learning Analyses

A Vossough[1], D Licht[1], A Topjian[1]
[1]*University of Pennsylvania-Children's Hospital of Philadelphia, Philadelphia, PA*

Purpose

Prognostication following resuscitation from pediatric cardiac arrest is a clinical dilemma. Prediction of outcome in cardiac arrest is known to be inaccurate, particularly outside of the 2 extremes of severity. Previous attempts at using brain MRI data have suffered from either poor overall accuracy or specificity. The goal of this study was to develop more accurate predictive models and scoring system for postneonatal out-of-hospital pediatric cardiac arrest based primarily on brain MRI measures using supervised machine learning methods.

Materials and Methods

Non-neonate pediatric out-of-hospital cardiac arrest patients admitted to the intensive care unit who had undergone brain MRI during their ICU stay were included in the study. Each of the MRI studies was evaluated by a pediatric neuroradiologist and a pediatric neurologist, and scored for 158 imaging findings based on anatomical location of abnormal findings on diffusion and T2/FLAIR images. Imaging features and demographics were utilized in the analysis. Outcomes included both a binary outcome (dead, alive) and also the change in the standardized Pediatric Cerebral Performance Category (PCPC) score at the time of discharge compared to the patient prearrest status. A number of state-of-the-art supervised machine learning analyses and classification algorithms were used for more powerful predictive modelling, as traditional statistical analyses may fail with large numbers of predictors. In order to prevent over-fitting the predictive models and obtaining falsely high accuracy that would not be applicable in practice across different samples, cross-validation was done where applicable. A validation sample set separate from the model training sample set was also available. Six different machine learning methods were utilized, which included gradient boosted decision trees, random forests, penalized logistic regression with double adaptive elastic net, linear support vector classifiers, radial basis function support vector machines, and simple neural networks.

Results

A total of 78 patients met inclusion criteria. Median age was 3.7 years (IQR 0.6 to 13.1 years) and 65% were male. Median time from return of spontaneous circulation to MRI was 4 days (IQR, 2 to 6 days). The top 3 validated models with the highest accuracy and area under the receiver operating characteristic (ROC) curve for predicting death included the neural network (AUC=0.96), gradient boosted decision trees (AUC=0.94), and random forests (AUC=0.92), based on subsets of the brain MRI abnormalities. Prediction of change in the clinical PCPC score at the time of discharge compared to the pre-arrest clinical state varied between AUC=0.76 and AUC=0.95 depending on the model and degree of PCPC change.

Conclusions

Use of imaging data along with particular supervised machine learning methods can provide

powerful adjunct tools to the neuroradiologist and medical treating team to help with prognostication of out-of-hospital pediatric cardiac arrest ICU patients.

O-24

11:40AM - 11:48AM

Dynamic Arterial Compression in Pediatric Vertebral Arterial Dissection: Diagnosis and Management

N Rollins[1], B Braga[2], M Dowling[3]
[1]UT Southwestern Medical Center, Children's Health Dallas, Dallas, TX, [2]University of Texas Southwestern Medical Center and Children's Health, Dallas, TX, [3]UTSW, Dallas, TX

Purpose
The pathogenesis of spontaneous pediatric vertebral artery dissections (VAD) is poorly understood. Pediatric VAD most often involves the V3 segment where C1 rotates on C2. We studied children with VAD with provocative digital catheter angiography (DSA) and found an association between VAD and rotational compression.
Materials and Methods
Seven male patients (13 months-9 years; mean 4.6 years) presenting with posterior circulation infarcts by MRI and VAD by MRA. Patients were systemically anti-coagulated with heparin upon confirmation of ischemic infarcts by MRI and converted to enoxoprin prior to discharge as per institutional pediatric stroke guidelines. After excluding bony anomalies by CT, the VA were studied with the neck in neutral position followed by repeat VA angiograms with bilateral passive neck rotation.
Results
Vertabral artery dissections were bilateral in 2 patients and unilateral in 5. Provocative DSA showed dynamic V3 compression in 5/7 dissections, most pronounced or seen only with head rotation to the contralateral side. Two patients had VAD without dynamic compression; both returned 4 months later with posterior circulation TIAs due to a new dissection in a previously normal VA and worsening VAD in the other. Dynamic compression also was seen in 3 nondissected VA. Surgical management was C1/2 posterior fusion in 5/7 patients; 1 underwent unilateral C2 decompression with recurrent VAD and subsequently was fused.
Conclusions
The association of dynamic VA compression and VAD at the same level suggests the compression may contribute to the VAD. However, as dynamic compression was observed in nondissected VA and as some VAD were not associated with dynamic compression, VADs may be multifactorial.



(Filename: TCT_O-24_FigVAD.jpg)

O-25

11:48AM - 11:56AM

Age-Related Changes in the Integrity of the Circle of Willis

K Gwal[1], J Edgar[2], R Ichord[2], E Schwartz[2]
[1]UC Davis Health System, Elk Grove, CA, [2]Children's Hospital of Philadelphia, Philadelphia, PA

Purpose
Studies indicate that up to 86% of adults have an incomplete Circle of Willis (COW). Our clinical experience is that the COW is more commonly complete in infants and younger children than adolescents and adults. Determination of the age(s) when "loss" of these arteries occurs can aid in interpreting imaging studies, and also may have implications for neurological conditions such as migraine headache and stroke recovery. The present study determined trends of nonvisualization or small caliber in COW components as a function of age from the neonatal period through 20 years.
Materials and Methods
A retrospective review of intracranial MRA (1.5 or 3T, 3D TOF noncontrast, 0.5mm) (n=300; age range: birth to 20 years). Subjects were stratified into 6 age groups (<1 year, 2-4, 5-7, 8-10, 11-15, and 16-20 years). Circle of Willis was evaluated for components and caliber. A circle was considered incomplete only given nonvisualization of any component. Vessels were considered small caliber when visually less than half the size of commensurate vessels. Age group comparison was performed via chi-square analysis.
Results
Overall, 93.0% (279/300) of subjects demonstrated a complete COW. Comparing children < 5 years to ≥11 years showed a significant difference in the incidence of at least one small

caliber vessel, from <5 years = 10/100 to ≥11 years = 28/100 (p=0.001). Comparing participants with either an absent vessel or a small caliber vessel, showed a significant increase from < 5 years = 13/100 to ≥11 years = 33/100 (p<0.001). The most notable change occurred between the 5-7 and 8-10 year groups: 6/50 and 16/50, respectively.
Conclusions
The presence of a complete COW is greater in our pediatric population than what has been reported previously in adults. The present study demonstrates a significant age-related increase in small caliber and absent vessels. Age-related changes should be considered when interpreting intracranial MRAs in children.

O-26

11:56AM - 12:04PM

Arterial Spin-Labeled Perfusion for PHACE Syndrome

M Mamlouk[1], M Maheshwari[2], I Frieden[3], B Drolet[2], C Hess[3]
[1]Kaiser Permanente, University of California, San Francisco, Santa Clara, CA, [2]Medical College of Wisconsin, Milwaukee, WI, [3]University of California, San Francisco, San Francisco, CA

Purpose
Arterial anomalies are the most common extracutaneous finding in patients with PHACE syndrome. Multiple types of arteriopathy have been described, including stenosis and occlusion, which can produce a moyamoya-like vasculopathy and confer a risk of ischemic stroke. This risk of stroke is increased after propranolol administration for the treatment of hemangioma, as the vasoconstricting properties of the drug can theoretically aggravate the native stenosis. Currently, stroke risk is inferred by the severity of arterial anomalies identified on MRA imaging, although no evidenced-based data exist. The purpose of our study is to determine if arterial spin labeled (ASL) perfusion can detect alterations in cerebral blood flow (CBF) in patients with PHACE syndrome to help prognosticate the risk of infarction.
Materials and Methods
Electronic medical records were reviewed from 2 institutions for all patients with PHACE syndrome that underwent 3D pseudocontinuous ASL MRI from 2000 to 2016. Three neuroradiologists with experience working in a vascular anomalies clinic reviewed the MR images. Cerebral blood flow was qualitatively investigated with ASL to determine if there was decreased or increased perfusion. Arterial anomalies were characterized on MRA imaging, and characterization of the parenchymal brain findings were made on DWI and T2/FLAIR imaging. The location of the hemangiomas also was noted.
Results
Eleven patients with PHACE syndrome had MRI examinations with ASL imaging. There were 10 females and 1 male, with ages ranging from 5 weeks to 15 years. Of the 11 patients,

8 had CBF alterations corresponding to a major arterial territory. Seven of 8 had unilateral decreased CBF, while 1 had unilateral increased CBF. All 7/8 of these patients had decreased CBF corresponding to the anterior circulation, with 1 patient having decreased bilateral anterior circulation CBF and another patient with decreased anterior and posterior circulation CBF. The single patient with increased unilateral CBF likely was related to extensive pial collateralization from a prolonged postlabel delay in ASL acquisition. All 11 patients had at least 1 arteriopathy, and the arteriopathy corresponded to the CBF alteration in all 8 patients. None of the patients had evidence of acute or chronic ischemia. Six of 11 patients had cerebellar dysplasia or hypoplasia. Seven of 11 patients had hemangiomas identified on imaging, while the remaining had involuted by the time of scanning.
Conclusions
Arterial spin labeling perfusion can identify changes in cerebral blood flow in patients with PHACE syndrome. This information can help prognosticate the risk of stroke and potentially guide the referring provider's management of propanol dosage for hemangioma treatment.

O-29

11:08AM - 11:16AM

Utility of Routine Screening with Neuroimaging in Patients with Hereditary Hemorrhagic Telangiectasia

K Seifert[1], X Wu[2], D Durand[2], A Malhotra[3]
[1]Yale New Haven Hospital, Milford, CT, [2]Yale University School of Medicine, New Haven, CT, [3]Yale New Haven Hospital, New Haven, CT

Purpose
Hereditary hemorrhagic telangiectasia (HHT) is characterized by the presence of visceral arteriovenous malformations (AVMs), including brain AVMs (BAVMs). It is estimated that approximately 2% of the general population have BAVMs; however, it is unclear what the true prevalence of BAVMs in HHT patients is, although some studies have reported rates as high as 13%. The risk of BAVM rupture in the population is approximately 4%, with unclear rates in HHT patients. Recent studies have suggested the possibility of screening all HHT patients with CTA/MRA to evaluate for BAVMs in efforts to lower mortality/morbidity in this select group.
Materials and Methods
A retrospective review of patients diagnosed with HHT or with a positive family history of HHT, who also obtained imaging for BAVMs (CT angiography/magnetic resonance angiography) was conducted. Imaging was evaluated for 200 random patients to determine presence of BAVMs, detailed description of size and location, and venous drainage, as well as complications of AVMs.
Results
Brain AVMs were identified in 21 out of 200 patients (10.5%), all of which were

subcentimeter in size. Of these select patients, 2 (9.5%) presented with intracranial hemorrhage, while only 1 (4.7%) was contributed to a ruptured AVM. Only 2 patients with unruptured BAVMs reported neurological complaints of headaches.
Conclusions
Patients in our facility with diagnosis of HHT have a high prevalence of intracranial AVMs. The prevalence of intracranial hemorrhage attributed to ruptured BAVMs in our population approached the general population risk. We will extend the study to include all patients with HHT assessed at our institution in the last 15 years. Based on the preliminary data, the outcome may not be affected and therefore, routine screening of BAVMs in the HHT population may not add significant value.

O-30

11:16AM - 11:24AM

Utility of Intra-Arterial Cone Beam CT Angiography in Detection of Intracranial micro-Arteriovenous Malformations

A Al-Smadi[1], A ElMokadem[2], A Shaibani[3], M Hurley[1], M Potts[4], S Ansari[4]
[1]Northwestern University Feinberg School of Medicine, Chicago, IL, [2]Mansoura University, Mansoura, IL, [3]Northwestern Univ. Medical School, Chicago, IL, [4]Northwestern University, Feinberg School of Medicine, Chicago, IL

Purpose
Micro-arteriovenous malformations (mAVMs) represent about 8-10% of surgically treated brain AVMs, and may be an unrecognized etiology of intracerebral hemorrhages of unknown origin. The aim of our study was to assess the diagnostic value of intra-arterial cone-beam CT angiography (IA-CBCTA) relative to digital subtraction angiography (DSA) in the diagnosis, anatomic identification and localization of intracranial mAVMs. Additionally, we assessed the clinical presentation, radiological features and management of mAVMs.
Materials and Methods
We performed a retrospective review of all diagnosed mAVMSs or AVMs with < 1 cm nidus from our institution's neurointerventional database from 2010-2016. Two blinded interventional neuroradiology observers scored DSA and IA-CBCTA images of mAVMs based on a qualitative scale from 0-2 (2: excellent/good visibility; 1: relevant visibility with restrictions; 0: poor, nondiagnostic) for the following parameters: detection of arterial feeders, venous drainers and subtle nidal components. Interobserver agreement between the 2 readers for qualitative image criteria was assessed using Kendall's τ coefficient. The total grading score was defined as the overall diagnostic value. Differences between CBCTA and DSA scores were defined as the CBCTA efficacy value.
Results
Seven patients (F:M ratio 4:3, mean age 38.2 ±13.97 years) harbored mAVMs with 6/7

patients (86%) presenting with neurological deficits and 5/7 patients presenting with intraparenchymal hemorrhages (71%) with a mean volume of 7 ml (range, 0.5 – 20.3 ml). Following image analysis, both observers assigned significantly higher scores to IA-CBCTA for overall diagnostic value (both observers: $p<0.05$, observer 1: $p = 0.016$, observer 2: $p = 0.017$). Although no significant differences were seen between DSA and IA-CBCTA scores (low relative IA-CBCTA efficacy value) when evaluating venous drainage (both observers: $p=0.317$), both observers assigned significantly higher scores to IA-CBCTA (high relative IA-CBCTA efficacy value) when evaluating arterial feeders (observer 1: $p = 0.02$, observer 2: $p=0.015$) and the micro-nidus (observer 1: $p=0.038$, observer 2: $p = 0.015$). There were interobserver differences in DSA grading with overall good agreement ($\tau=0.6$).
Conclusions
Micro-AVMs often are occult lesions that are diagnosed after presentation with intracranial hemorrhage, and/or neurological deficits. Intra-arterial CBCTA improves the diagnostic identification and anatomic delineation of mAVMs, with the potential to improve treatment planning.

O-31

11:24AM - 11:32AM

Quantification of Arterial Velocity in Cerebral Arteriovenous Malformation by Four-dimensional Digital Subtraction Angiography

C Lin[1], W Guo[2], W Chu[1], C Wu[3]
[1]Taipei Veterans General Hospital, Taipei, Taiwan, [2]Taipei Veterans General Hospital & National Yang Ming University, Taipei, Taiwan, [3]Taipei Veterans General Hospital; School of Medicine, National Yang Ming University, Taipei, AK

Purpose
Current application of quantitative digital subtraction angiography (QDSA) is based on 2-dimensional imaging. Therefore, the accuracy decreases in cases involving complex or high-flow vasculature, as with cerebral arteriovenous malformation (cAVM), which is characterized by overlapping vessels. The purpose of our study was to assess the use of 4-dimensional quantitative digital subtraction angiography (4D-QDSA) to measure intra-arterial velocity in cAVMs.
Materials and Methods
Prospectively, 30 normal subjects and 30 cAVM cases were included. All 4D-QDSA were conducted with the same angiographic machine (ArtisZee, Siemens Healthcare, Forchheim, Germany). The angiocatheter was placed at the common carotid artery with a bolus injection of contrast (total volume: 35-40 c.c.; rate of 5 c.c./sec) while the C-arm rotated 260° to acquire rotational angiography. The dataset was transferred to a workstation (syngo X-Workplace VB21; SiemensHealthcare) equipped with 4D-DSA prototype for voxel-based time density curve analysis. The starting VOI was placed manually in the internal carotid

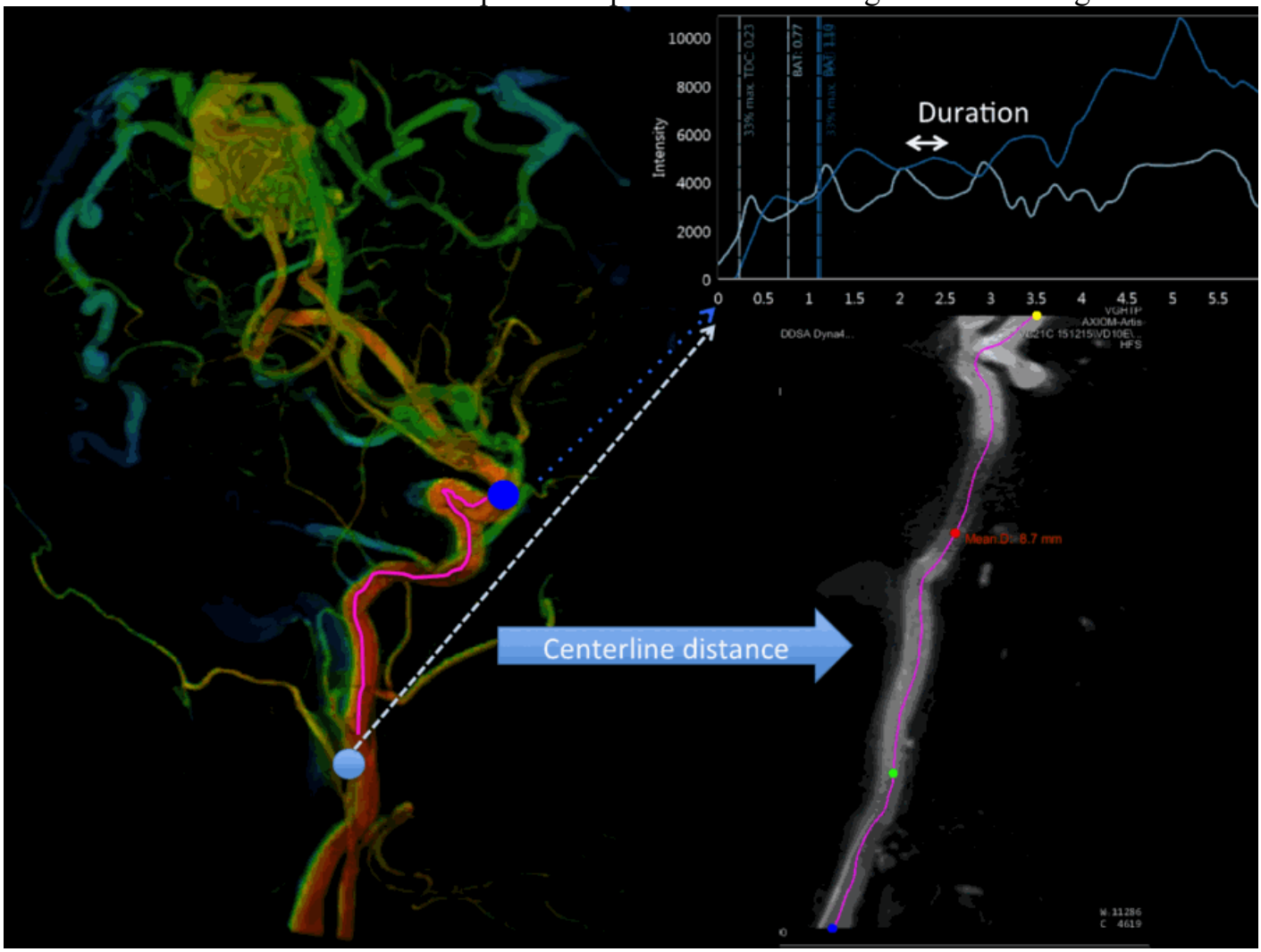
artery, and the ending VOI was placed manually on the supraclinoid internal carotid artery to ensure the TDC demonstrated pulsatile waveform. The distance was determined automatically by the centerline on curve multi-planar reformation. The velocity was equal to the distance between the starting and ending VOI divided by the duration between the 2 waveforms (Fig. 1). Student's t-test was used to compare the difference between the cAVM and control groups.

Results

The distribution of cases by Spetzler-Martin grades for the cAVMs were: I = 5, II = 15, III = 8, and IV = 2). The average velocity in the cAVM group was 65.17 ± 27.40 cm/sec, which was significantly higher than that of the control group (47.99 ±11.18 cm/seconds) ($p < 0.001$). The optimal wave for velocity estimation was usually the 2nd wave.

Conclusions

Our study confirms the feasibility of quantifying the difference in intravascular velocity between cAVM and control groups in a reasonably fast way. It potentially facilitates the safety of endovascular treatment by real-time validating flow changes during embolization to avoid adverse events such as normal perfusion pressure breakthrough or venous stagnation.



(Filename: TCT_O-31_ASNRabstract.gif)

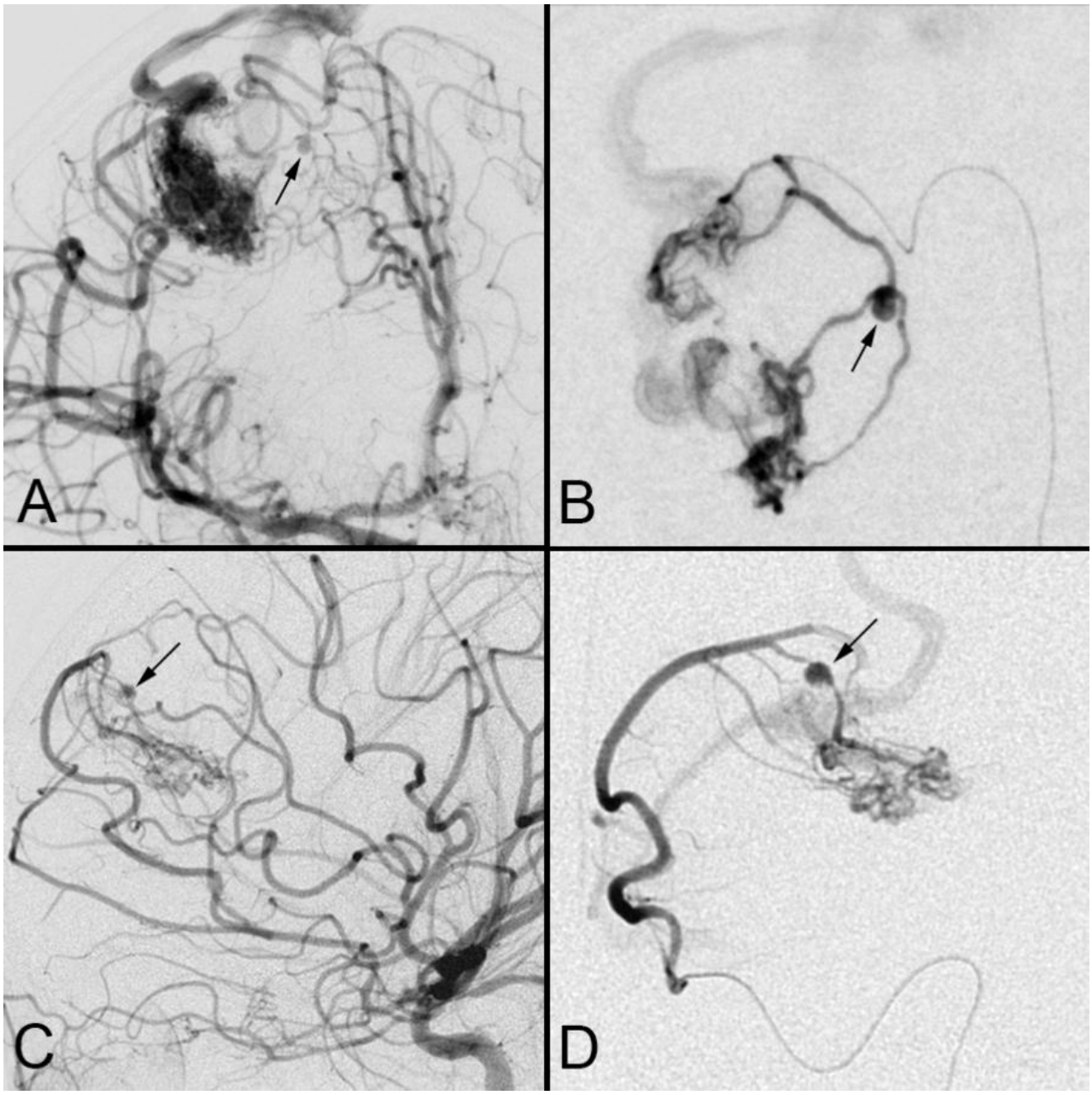
O-32

11:32AM - 11:40AM

Ruptured feeding artery aneurysms in pediatric cerebral arteriovenous malformations

M Pearl[1], M Martinez[1], E Orru[2], P Gailloud[1]
[1]Johns Hopkins University School of Medicine, Baltimore, MD, [2]Johns Hopkins Hospital, Baltimore, MD

Purpose
Pediatric cerebral arteriovenous malformations (AVM) commonly present with intracranial hemorrhage, but the role played by feeding artery aneurysms in these hemorrhagic presentations is not well appreciated (1). We report our experience with children harboring AVM-associated feeding artery aneurysms discovered during diagnostic cerebral angiography at the time of acute intracranial hemorrhage.
Materials and Methods
A prospectively collected database of all children less than 18 years of age undergoing diagnostic cerebral angiography for ruptured cerebral AVM at 2 institutions from July 2010 to December 2016 was reviewed to identify those with ruptured AVMs. Records were reviewed for age, gender, clinical presentation, angiographic findings, and management.
Results
From July 2010 to December 2016, 5 children (4 girls, 1 boy) presented with intracranial hemorrhage due to ruptured AVM-associated feeding artery aneurysms with an average age of 11 years (range: 6 to 17 years). The AVMs were located in the frontal lobe (n = 3), temporal lobe (n = 1), and cerebellum (n = 1). All patients underwent diagnostic cerebral angiography at the time of presentation, and all were treated successfully with transarterial glue embolization of the feeding artery aneurysm at the same time. Fig. 1. Two examples of pediatric patients with cerebral AVMs and ruptured feeding artery aneurysms. A) 16-year-old with a right frontal AVM nidus that was readily apparent on MRI. The presence of the right ACA feeding artery aneurysm (arrows in A, B), however, was only appreciated during diagnostic cerebral angiography. B) Superselective injection of the right internal frontal artery better delineates the ruptured aneurysm. C). Lateral views of a right ICA angiogram (C) and superselective internal frontal microcatheter angiogram (D) in an 8-year-old girl show a small right internal frontal feeding artery aneurysm (arrows in C, D), which was not appreciated by MRI/MRA prior to cerebral angiography.
Conclusions
Diagnostic cerebral angiography performed at the time of presentation provides critical information regarding the angioarchitecture of ruptured pediatric cerebral AVMs, identifying the potential bleeding source and the need for emergent intervention. Importantly, feeding artery aneurysms often are not detected by noninvasive imaging.



(Filename: TCT_O-32_ASNRRupturedAVM.jpg)

O-33

11:40AM - 11:48AM

Comparison of pre-operative Embolization & Surgical Resection vs Surgical Resection Alone for Treatment of Low Grade Pediatric Cerebral Arteriovenous Malformations

T Shokuhfar[1], A Al-Smadi[1], A Malani[1], A Shaibani[2], S Ansari[3]

[1]Northwestern University Feinberg School of Medicine, Chicago, IL, [2]Northwestern University Feinberg School of Medicine, Chicago, IL, [3]Northwestern University, Feinberg School of Medicine, Chicago, IL

Purpose

To compare the safety and efficacy of pre-operative embolization and surgical resection with surgical resection alone in the treatment of Spetzler-Martin (SM) Grades I and II cerebral arteriovenous malformations (AVM) in children.

Materials and Methods

We performed a retrospective review of 38 pediatric patients who received treatment for SM grades I and II AVMs between January 2005 and September 2016. Patients were divided into 2 groups: surgery alone or embolization plus surgical resection. Functional outcome was assessed using the modified Rankin Scale (mRS) before treatment, at discharge, and at 3 months follow-up. Complications were classified as intra-procedural and postprocedural.

Results

Twenty-three males and 15 females with an average age of 10.5 ± 4.3 years were analyzed. Ten patients underwent surgical resection and 28 patients underwent combined embolization and surgery. Twelve AVMs (31%) were S-M grade I and 26 grade II. Of the combined therapy group, the ruptured to unruptured AVM ratio was 15:13. All 10 patients in the resection alone group had ruptured AVMs. Fourteen patients presented with significant deterioration (mRS ≥ 4) prior to treatment. Average mRS scores at different time points are presented in Table 1. Three months follow-up revealed significant improvement regarding mRS scores in both groups ($p < 0.05$). Except for 1 venous hemorrhage with combined therapy, no other intra-operative complication was recorded. One hemiparesis, 1 spastic quadriparesis and 1 change of behavior in combined therapy group and 1 imbalance in resection alone group were recorded postoperatively. All reported complications were among ruptured AVMs and statistical analysis did not show any significant difference between 2 treatment approaches.

Conclusions

There was no significant difference in the outcome and complication rates of pre-operative embolization and surgical resection versus surgical resection alone in the treatment of low grade pediatric cerebral AVMs.

Average of Modified Rankin Score		
	Embolization+ Surgery (mean ± SD)	**Surgery (mean ± SD)**
Pre-operation	3 ± 2	4 ± 1
At discharge	1 ± 1	2 ± 1
At 3 months follow up	1 ± 1	1 ± 1

(Filename: TCT_O-33_Capture.JPG)

O-34

11:48AM - 11:56AM

Early Re-bleeding after Brain Arteriovenous Malformation Rupture: Incidence and Risk Factors

E Shotar[1], S Pistocchi[1], B Bartolini[1], V Degos[1], N Sourour[1], F Clarençon[1]
[1]*Pitié-Salpêtrière Hospital, Paris, France*

Purpose
Brain arteriovenous malformations (AVMs) are a leading cause of intracranial hemorrhage among young people. The aim of this work was to identify risk factors of early re-bleeding after brain AVM rupture.
Materials and Methods
Retrospective monocentric study of clinical and radiological data of patients admitted at the acute phase of brain AVM rupture. Patients with rupture complicating or following a partial embolization procedure within the next 7 days were excluded as well as ruptured brain AVM obliterated by surgery or embolization upon admission. Predictive factors for early re-bleeding demonstrated on imaging studies within 31 days of admission were identified by univariate and multivariate logistic regression.
Results
One hundred and forty-six patients with 153 brain AVM ruptures were included. Nine cases of early re-bleeding events were identified (mean delay of 7 days). Multivariate analysis showed that the presence of distal pedicular arterial flow related aneurysms was the only factor independently associated with early re-bleeding after brain AVM rupture [odd ratio (OR) 27; confidence interval (CI) 95% (3-226), p = 0.003].
Conclusions
In this retrospective cohort, distal pedicular arterial flow related aneurysms are associated with an increased risk of early re-bleeding after brain AVM rupture.

O-35

11:56AM - 12:04PM

Efficacy of the Yakes AVM Classification System that Directs Endovascular Therapies Accurately

W Yakes[1]
[1]*Vascular Malformation Center, Englewood, CO*

Purpose
To determine if AVM angioarchitecture characteristics can be predictive and direct specific curative endovascular procedures accurately and consistently to treat high-flow malformations.

Materials and Methods
Angiographic analysis of high-flow vascular malformations determined 4 major angioarchitectures. Type I: Direct arterial/arteriolar to vein/venule connection; e.g., as commonly seen in pulmonary AVF, congenital renal AVF, etc. Type II: Arterial/arteriolar connections to a "nidus" that then have several out-flow veins with no intervening capillary beds in any of the vascular interconnections. Type IIIa: Arterial/arteriolar connections to an aneurysmal vein ("nidus" is the vein wall) that drains into a dominant out-flow vein with no intervening capillary bed in these connections. Type IIIb: Same angioarchitecture as Type IIIa, except that there are more than 1 (several) out-flow veins. Type IV: "Infiltrative" form of AVM whereby innumerable micro-arteriolar branches fistulize through a tissue (e.g., ear) totally infiltrating it, shunting into multiple out-flow veins. Capillary beds also exist in the tissue and are mixed with the innumerable AVFs. Without the capillaries the tissue could not be viable, therefore must be present.
Results
Type I: Can be effectively treated with mechanical devices; e.g., coils, Amplatzer Plugs, etc. Type II: Can be effectively treated with ethanol embolization. Type IIIa: Can be effectively treated by transcatheter ethanol, retrograde vein catheter access or direct puncture access of the aneurysmal vein and treatment with ethanol and coils, or even by coils alone. Type IIIb: Can be effectively treated as above, but can be more challenging by the vein route as more veins (not a single out-flow vein) require closure. Type IV: Can be effectively treated by transcatheter or direct puncture of the innumerable microfistulous AVFs by embolization with 50% -50% ethanol nonionic contrast mixture.
Conclusions
This never before reported classification system has a direct impact on determining the curative endovascular and direct puncture embolization procedures and also determines the embolic agents that will successfully treat complex AVMS in the body.

O-36

12:04PM - 12:12PM

Intracranial Dural Arteriovenous Fistulae - An Institutional Experience and Proposal of a New Anatomico-Functional Classification System

L Sebastian[1], s shambanduram[2], N Jain[3]
[1]All India Institute of Medical Sciences, Newe Delhi, Delhi, [2]All India Institute of Medical Sciences, New delhi , India, [3]All India Institute of Medical Sciences, Noida, Uttar pradesh

Purpose
1. To retrospectively analyze the angioarchitecture and clinical presentations of cranial dural arteriovenous fistula and their implications in the management and outcome. 2.To develop a new comprehensive classification system which can better explain clinical features and help devise optimal management strategies.

Materials and Methods
Clinical, imaging and angiographic records of all the patients with intracranial dural arteriovenous shunts who presented to the Department of Neuroimaging and Interventional Neuroradiology, AIIMS, New Delhi, in the period between January 2005 and August 2015 were analyzed retrospectively. Clinical presentation was categorized into aggressive, intermediate or benign severity. Digital subtraction angiograms were analyzed for topographic location of the lesions, arterial feeders, venous drainage pattern and the presence of cortical and leptomeningeal reflux and strain. These angioarchitectural features formed the basis for a new classification and were correlated with clinical presentation. Dural sinus shunts (DSS) and extra sinus shunts (ESS) are the major categories based on venous drainage. Focal cortical venous ectasia or congestion indicated cortical venous strain (CVS) while parenchymal venous strain (PVS) was identified by tortuous, engorged pial/medullary veins. Records also were reviewed for treatment modality administered and for angiographic and clinical outcome.
Results
Out of the 59 patients (male: female = 44:15, mean age -42.8 years), 24 (40.66%) presented with aggressive symptoms while 13 (22%) and 22 (37.28%) patients presented with intermediate and benign symptoms respectively. Of the 33 patients (55.9%) with dural sinus shunts 16 patients had cortical venous reflux (CVR). Among them, CVS and PVS were seen in 10 of whom 5 had aggressive clinical presentation. Six patients with PVS only had intermediate symptoms. Six out of 17 patients without CVR had PVS and presented with symptoms of raised pressure. Overall, in DSS presence of CVR had significant correlation with hemorrhage ($p<0.05$) while PVS correlated significantly with raised intracranial pressure. Majority of the 26 patients with extra sinus shunts presented with aggressive symptoms (77%). Treatment and outcome details are available for 42 patients. Thirty-three patients were treated by endovascular embolization and 93% of them showed clinical improvement.
Conclusions
Classification of CDAVFs into dural sinus shunts and extra sinus shunts with consideration of parenchymal and cortical venous strain was more practical and correlated well with clinical severity. Endovascular therapy appears to be effective for the treatment of intracranial dural fistulae with low complication rates.

Monday
11:00AM - 12:16PM
Long Beach Convention Center, Room 104C (Main Lobby)

04F-Parallel Paper Session: Excerpta: "Spine Prime Time"
E-01

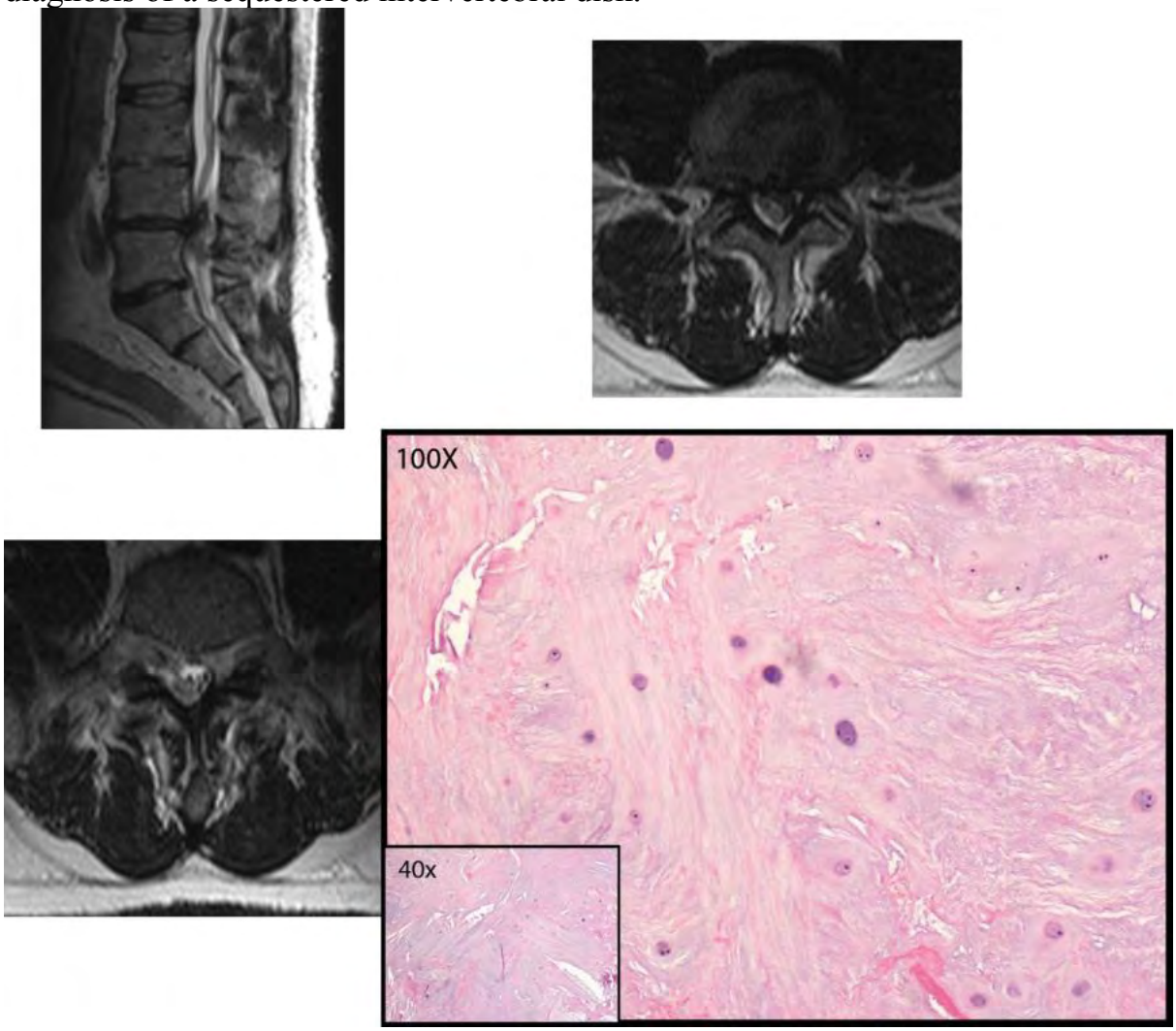
11:00AM - 11:04AM

Lumbar Disc Sequestration with Posterolateral Epidural Migration after Trauma, Mimicking an Epidural Hematoma: Review of Literature and Case Report with Pathologic Correlation

E Greif[1], G Cruciata[1], B Barrett[2], J Shah[1], S Kantharia[1], E Stein[1]
[1]Maimonides Medical Center, Brooklyn, NY, [2]Maimonides Medical Center,, Brooklyn, NY

Purpose
The purpose of this abstract is to identify the magnetic resonance (MR) appearance of a sequestered lumbar disk fragment in the setting of a recent trauma and demonstrate migration causing neurologic symptoms with pathologic correlation.
Materials and Methods
We are presenting a 52-year-old man with progressive lower back pain with left lower extremity paresthesia and weakness over the course of 2 days after being struck at low speed by a motor vehicle. No bladder dysfunction was observed. Physical exam revealed diminished muscle flexion strength and sensation of the left lower extremity with intact strength and sensation of the right lower extremity. A graduated loss of strength in the left lower extremity was observed with more profound deficits noted distally. He also demonstrated left lower extremity radiculopathy and lower lumbar tenderness to palpation. Laboratory tests and vital signs were within normal limits. Initial radiographs of the lumbar spine were unremarkable so MR imaging was performed to assess the etiology of the left lower extremity radiculopathy.
Results
The MR images of the lumbar spine demonstrated a right posterolateral epidural mass measuring 3.3 x 0.5 x 1.0-cm, extending from the lamina of L4 to the lamina of L5. The mass lesion was heterogeneously hyperintense on T2WI and isointense on T1WI. It displaced the thecal sac anteriorly and to the left, effacing the cerebral spinal fluid (CSF) and compressing the cauda equina. There was significant intervertebral disk height loss at L3-4 and T2 hyperintensity of the margin of the annulus fibrosus at this disk level, likely representing edema from the disrupted fibers. Contrast-enhanced imaging was obtained after the administration of intravenous gadolinium (gadobutrol, Bayer, Whippany, NJ) and revealed no abnormal enhancement. Epidural hematoma was the most favored diagnosis originally because of the recent history of trauma. Other possible considerations included synovial cyst but the facet joints did not appear significantly diseased. Sequestered disk was considered but thought less likely considering the posterior location and the distance the extruded disk would have traveled from the disk space.
Conclusions
This is an unusual case of a posterior epidural mass representing a free (sequestered) disk, originally thought to be an epidural hematoma. This finding may also mimic a synovial cyst or tumoral mass on MR imaging. In a patient with imaging findings of an epidural mass, the differential diagnosis includes: extruded disk fragment, epidural hematoma, epidural abscess,

synovial cyst, and neoplasm. In the case of our patient, epidural hematoma was favored because of the recent trauma, and the lack of enhancement. The patient underwent L4-5 laminectomy and surgical removal of the posterior epidural mass. Histopathologic assessment of the specimen revealed degenerated fibrocartilaginous material confirming the diagnosis of a sequestered intervertebral disk.



(Filename: TCT_E-01_Images.jpg)

E-02

11:04AM - 11:08AM

Disc/Osteophyte Induced Dural Tears and CSF Leaks: Spectrum of Imaging Findings

C de la Houssaye[1], P Batchala[2], N Fischbein[3], R Schultz[1], N Kohler[1], P Raghavan[4]
[1]University of Maryland Medical Center, Baltimore, MD, [2]University of Virginia Health System, CHARLOTTESVILLE, VA, [3]Stanford University, Stanford, CA, [4]University of Maryland School of Medicine, Baltimore, MD

Purpose

Disk herniations and/or osteophytes are uncommon causes of dural tears and cerebrospinal fluid (CSF) leaks. In this series, we describe the clinical presentation and imaging findings of 7 patients in whom disk protrusions/osteophytes resulted in dural tears and CSF leaks.

Materials and Methods

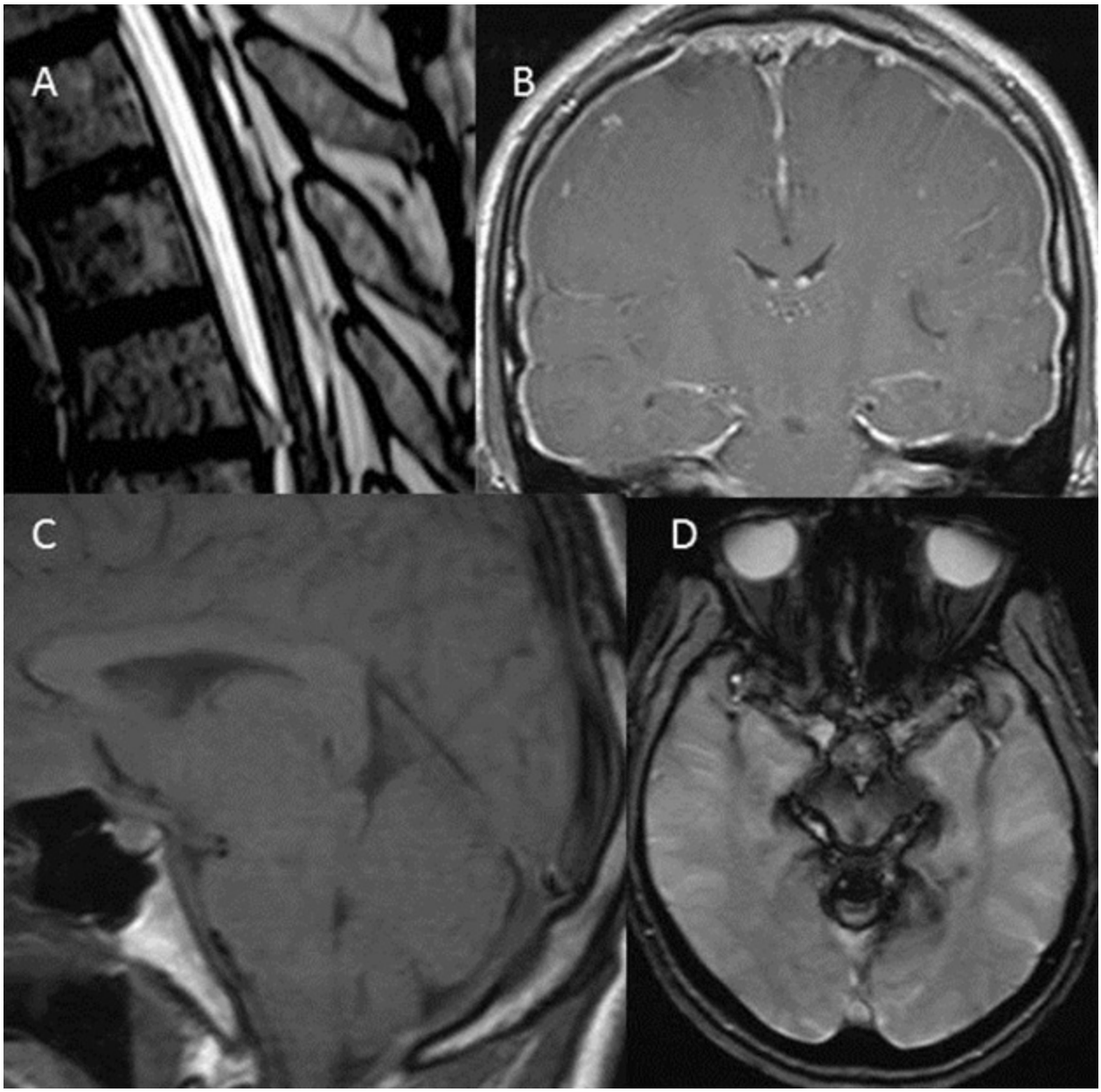
Seven patients (Mean age 51, M: F, 4:3) were included in the study. Four patients presented with postural headache as their chief complaint, while 2 presented with hearing loss and disequilibrium as their main symptom. In 1 patient, cervical radiculopathy was the only complaint. In all patients brain MRI findings suggestive of intracranial hypotension were evident. In all patients a longitudinal ventral epidural intraspinal CSF collection was noted. All patients demonstrated focal tenting of the dura due to a disk (3), osteophyte (1) or both (2), located between the C5-C6 to the T7-T8 levels. No other causes of CSF leak were identified in any patient. Interestingly, striking craniospinal superficial siderosis was evident in 2 cases; engorgement of the spinal pial vasculature also was noted. The presence of a disk/osteophyte-induced dural tear was confirmed at surgery in 3 patients, while 2 others obtained long lasting symptomatic relief after epidural blood patching.

Results

(A) Sagittal T2 space (lumbar spine): T7-T8 disk herniation with tenting of the dura, superficial siderosis (abnormal peripheral T2 hypointensity) and a ventral hygroma. Additionally noted dorsal arachnoid webs. (B) Coronal postcontrast T1: diffuse smooth meningeal enhancement with subtle bilateral frontal subdural hematomas (cortical vessels displaced). (C) Sagittal T1: effacement of the cerebrospinal fluid cisterns, enlargement of the pituitary gland, sagging with tonsillar herniation. (D) Axial SWI: superficial siderosis lining the superior surface of the cerebellum and midbrain.

Conclusions

Cervical and thoracic disks/osteophytes can penetrate the ventral dura and result in CSF leaks and intracranial hypotension. The presence of focal dural tenting by a disk/osteophyte and a longitudinal intraspinal ventral epidural CSF collection are characteristic of this entity, and associated siderosis may be observed. The presence of florid superficial siderosis and marked engorgement of the spinal pial vasculature as seen in some of our patients is reminiscent of the concept of a "Duropathy" as described by Kumar (2012) (4), raising the intriguing possibility that disk/osteophyte-induced dural tears are perhaps the inciting event for this as yet incompletely understood disorder. Surgical removal of the disk/osteophyte and primary dural repair may be necessary, although epidural blood patches may provide symptomatic relief in some patients.



(Filename: TCT_E-02_ASNRosteo.jpg)

E-03

11:08AM - 11:12AM

Intradural Extramedullary Gouty Tophi: A Rare Cause of Spinal Cord Compression

A Galinato[1], S Shaikh[1], B Griffith[1], H Marin[1], J Corrigan[1], S Patel[1]
[1]*Henry Ford Health System, Detroit, MI*

Purpose
Gout is a common cause of acute inflammatory arthritis, which uncommonly can affect the

spine. An intradural location of gout is exceptionally rare with only 2 prior cases reported in the literature. This diagnosis has not been reported in the literature previously in a patient with normal serum uric acid levels. This excerpta describes an unusual case of intradural extramedullary spinal gout, which presented a considerable diagnostic challenge.

Materials and Methods

We present the case of a 69-year-old male who presented with balance difficulty and left lower extremity weakness over the course of 2 weeks. Neurological exam revealed left hip flexion weakness, decreased sensation to pinprick and vibratory sensation, hyperreflexia, and spastic gait. The patient underwent a T11-T12 laminectomy, at which time a heavily calcified intradural extramedullary soft tissue mass was resected. A clear plane was present between the mass and spinal cord. Pathology of the mass demonstrated empty slit-like spaces within an amorphous eosinophilic material, associated histiocytic reaction, and scattered giant cells, characteristic for gouty tophus.

Results

Noncontrast computed tomography (CT) demonstrated multiple densely calcified masses within the spinal canal at T11, T12, and L2 (Figures 1 A, B). Magnetic resonance imaging (MR) demonstrated multiple irregular, rounded intradural, extramedullary lesions with intermediate to low T1 signal and isointense to hypointense T2 (Figure 1C) signal with heterogeneous enhancement (Figure 1D). The largest lesion located at the T11-T12 level resulted in severe spinal cord compression with associated cord signal abnormality.

Conclusions

Gout is a common cause of inflammatory arthropathy, mainly affecting peripheral joints and tendons. While uncommon, gout can involve various spinal structures, but an intradural location is extremely uncommon with only 2 reported cases in the literature. Although exceptionally rare, gout should be considered when a calcified intradural extramedullary lesion is encountered and correlation with clinical history of gout should be performed.



(Filename: TCT_E-03_Finalintraduralgout.jpg)

E-04

11:12AM - 11:16AM

Hepatic Myelopathy - Case Report of Unusual MRI findings

D Patel[1], S Mohan[1], M Hoch[1], R Hu[1]
[1]*Emory University, Atlanta, GA*

Purpose

To describe unusual brain and spine findings of hepatic myelopathy that provide correlation with usual pathological findings.

Materials and Methods

A 60-year-old male with end stage liver disease, alcoholic cirrhosis, and resulting splenorenal shunt was admitted for decompensated liver failure and progressive bilateral lower extremity weakness that significantly progressed in last few months. On admission, physical exam was remarkable for 0/5 strength in bilateral lower extremities, mild (4/5) upper extremity weakness and dysarthria. Initial magnetic resonance imaging (MRI) of the brain and cervical spine showed abnormal long-segment intramedullary T2-hyperintense signal involving central cord extending to involve the corticospinal and spinocerebellar tracts of the medulla without enhancement. There also was restricted diffusion in the splenium. Patient's ammonia levels were elevated (113) few days before admission. However, further laboratory investigation yielded normal/negative results for TSH, B12, B6, methylmelonic acid, rheumatoid factor, complement levels, ANCA, CCP, Ro, La, Jo1, SCL70, RPR, anti-RNP antibody, HIV, HTLV and CSF analysis. Diagnosis of hepatic myelopathy was made based on MRI findings combined with lack of other biochemical abnormalities to explain patient's symptoms. Patient was expedited for transplant work up. Over the next few days, patient developed ascending weakness involving bilateral upper extremities resulting in quadriplegia. Patient subsequently underwent IR embolization of the splenorenal shunt. However, he continued to deteriorate neurologically and developed respiratory paralysis resulting in tracheostomy and ventilator dependence. Repeat MRI of the brain and total spine after embolization showed increased signal abnormality throughout the entire cord and brainstem with restricted diffusion extending superiorly in the bilateral corticospinal and spinocerebellar tracts (see image findings). Patient eventually was considered for hospice and discharged to long-term acute care facility.

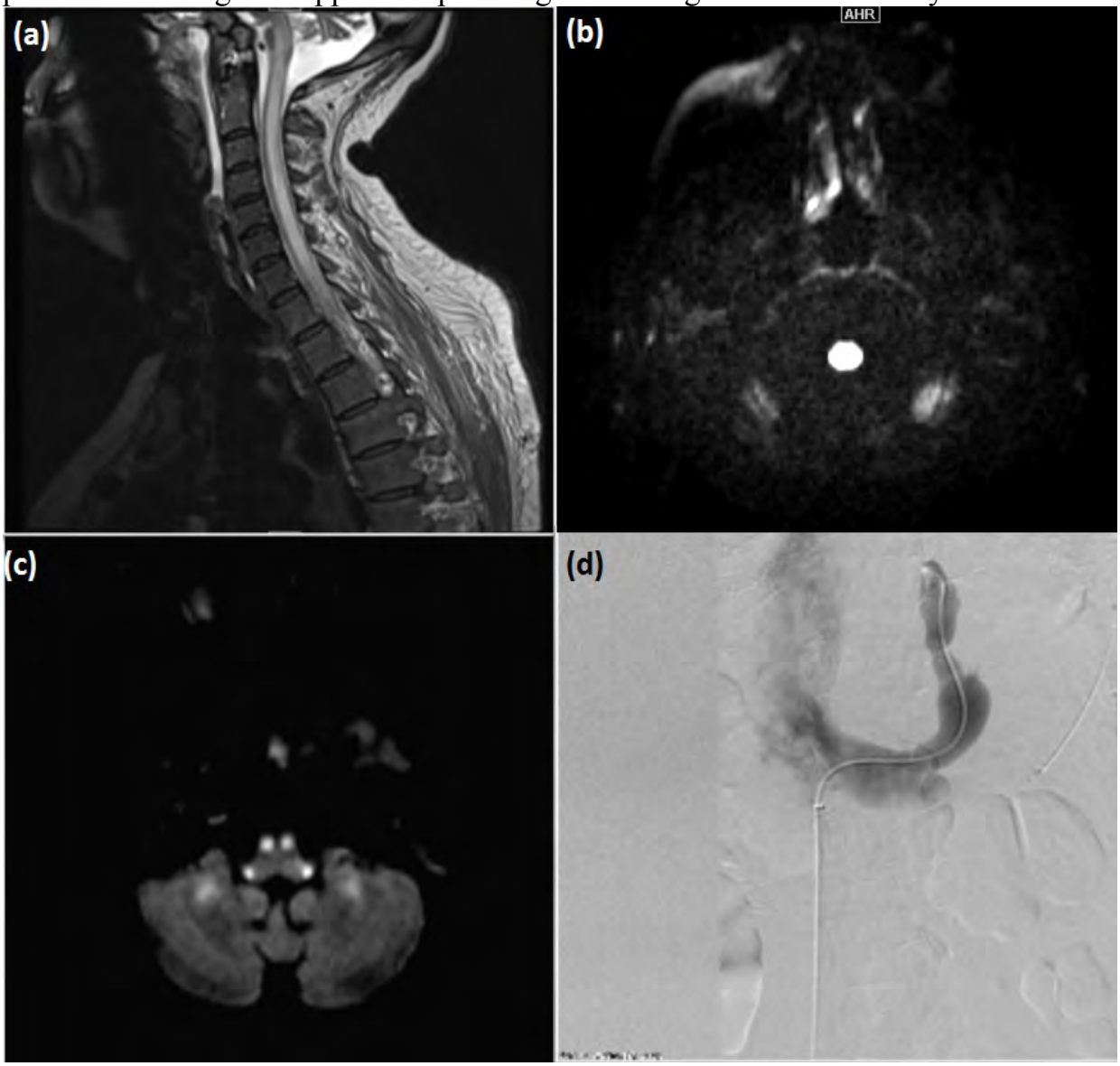
Results

Figure 1: (A) Sagittal T2-weighted image of the cervical spine showing extensive long-segment cord signal abnormality extending from the medulla with cord expansion. Axial diffusion trace images of the (B) upper cervical cord showing total cord restricted diffusion and (C) rostral medulla showing restricted diffusion continuing to involve the bilateral corticospinal and spinocerebellar tracts. (D) Digital subtraction venography depicting the large splenorenal shunt prior to embolization.

Conclusions

Hepatic myelopathy is a rare complication of chronic liver disease resulting in progressive paraparesis and has been associated with portosystemic shunt (1). Patients generally present with progressive spasticity and weakness in lower extremities. However, triparesis/quadriparesis, sensory deficit, urinary/bladder incontinence and nonpyramidal symptoms (dysarthria in our case) also may occur and complicate the diagnosis (1). In vast majority of cases, spine MRI does not show any abnormality but usually is obtained to rule

out other diagnosis such as infarction and compressive myelopathy (1, 2). However, hyperintensity on T2 has been shown in the cervical spine in cases of posterior column involvement (3). Magnetic resonance imaging of the brain may show hyperintense T1 signal within the basal ganglia which is seen in hepatic encephalopathy and is thought to be due to manganese toxicity (1, 4). Findings in corticospinal tracts on MRI is rare, despite symptoms being overwhelmingly pyramidal in nature. On the contrary, pathological findings are usually consistent with demyelination of lateral corticospinal tract. A recent literature review of 98 patients with hepatic myelopathy found that every patient (9/9 patients) who underwent pathological investigation showed demyelination of lateral corticospinal tract on pathology (1). Abnormal findings on T2 and DWI in corticospinal tract in our patient, provides radiological support for pathological findings of this rare entity.



(Filename: TCT_E-04_Figure_1.jpg)

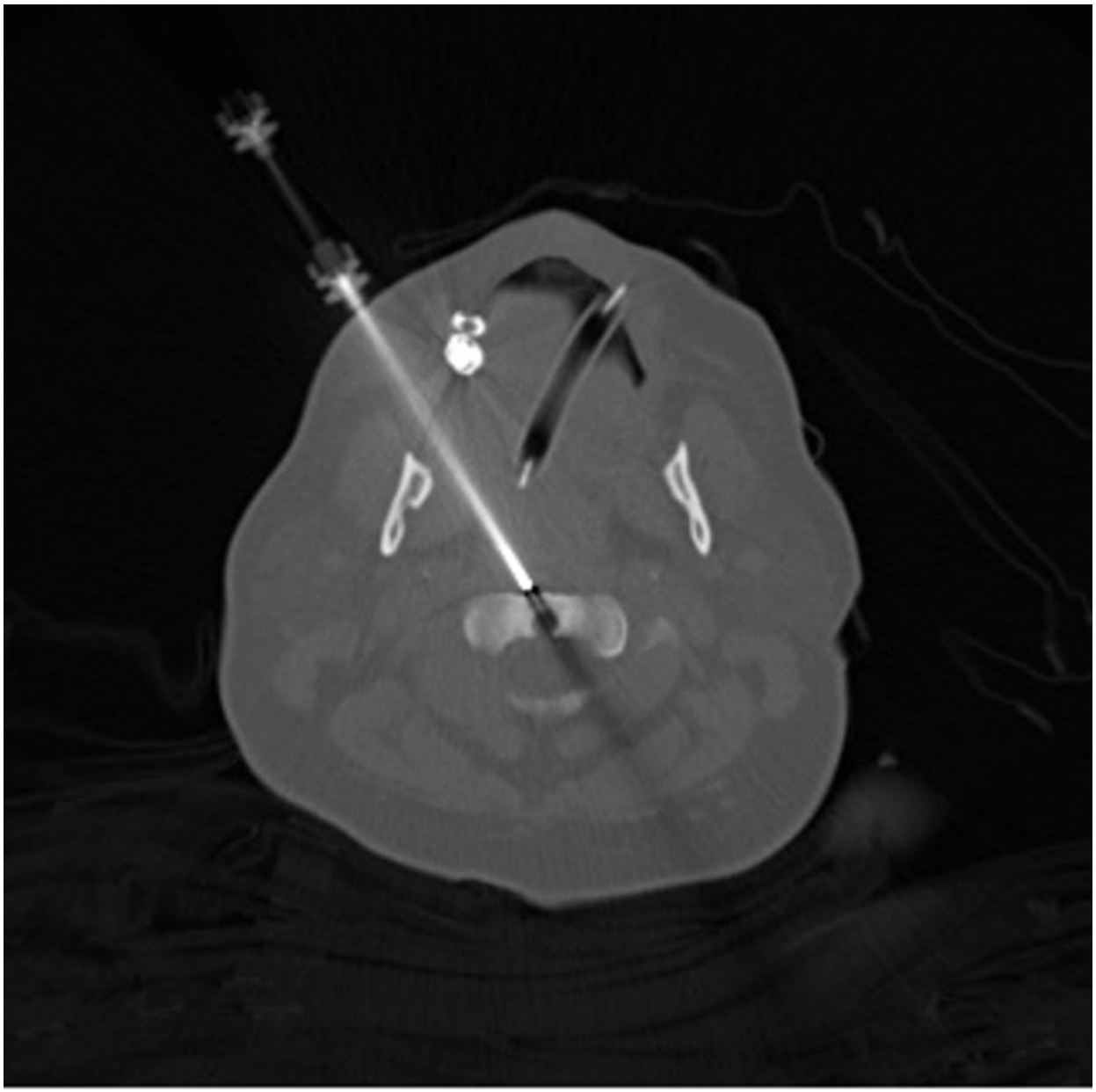
E-05

11:16AM - 11:20AM

Percutaneous anterior transbuccal approach to biopsy and radiofrequency ablation of C2 osteoid osteoma: a case study

N Sterling[1], D Nguyen[1]
[1]*Department of Radiology, Pennsylvania State University - Milton S. Hershey Medical Center, Hershey, PA*

Purpose
Percutaneous biopsy and radiofrequency ablation are commonly used diagnostic and therapeutic modalities in the treatment of vertebral neoplasms. Upper vertebrae such as C2, however, can be technically challenging to access percutaneously due the complexity of surrounding neck anatomic structures and the paucity of literature describing feasible approaches. This case report describes an anterior transbuccal approach to the C2 vertebral body.
Materials and Methods
The patient was a 33-year-old female presenting with progressively worsening neck pain who was found to have C2 vertebral osteoid osteoma. Access to the C2 vertebral body was achieved using a modified transbuccal approach under general anesthesia and computed tomography (CT) guidance. Percutaneous blunt dissection along the parapharyngeal space was utilized to gain access to the anterior cortical region of the vertebral body. The anterior wall of C2 then was penetrated through drill-assisted advancement for biopsy and radiofrequency ablation. The patient's clinical state was improved significantly postoperatively. She had greater range of motion of her neck with less pain. She denied any radicular pattern, weakness, or gait disturbance and was able to resume working full-time while gradually increasing her activities.
Results
The patient was found to have a C2 lytic lesion with a central calcified nidus, surrounding osseous sclerosis, and posterior cortical disruption.
Conclusions
The anterior transbuccal approach may be suitable in situations where more traditional approaches are not an option. The transbuccal approach may, in theory, carry less risk of infection compared to the transoral approach and technically is feasible to perform under CT guidance.



(Filename: TCT_E-05_C2OsteoidOsteomaforASSR-Edited.jpg)

E-06

11:20AM - 11:24AM

Not Your Ordinary Back Pain - Primary Extradural Thoracic Hemangiopericytoma: A Rare Entity

V Yedavalli[1], R Stimpson[1], S Chhadia[1], G Gorelick[1]
[1]*Advocate Illinois Masonic Medical Center, Chicago, IL*

Purpose

Hemangiopericytoma is a hypervascular tumor of mesenchymal origin that is under the spectrum of solitary fibrous tumor. It is seen more commonly in the supratentorial compartment often mimicking other extra-axial lesions. It is extremely rare to find hemangiopericytomas within the spinal canal with only approximately 75 reported cases. We present a very rare case of a primary extradural thoracic hemangiopericytoma.

Materials and Methods

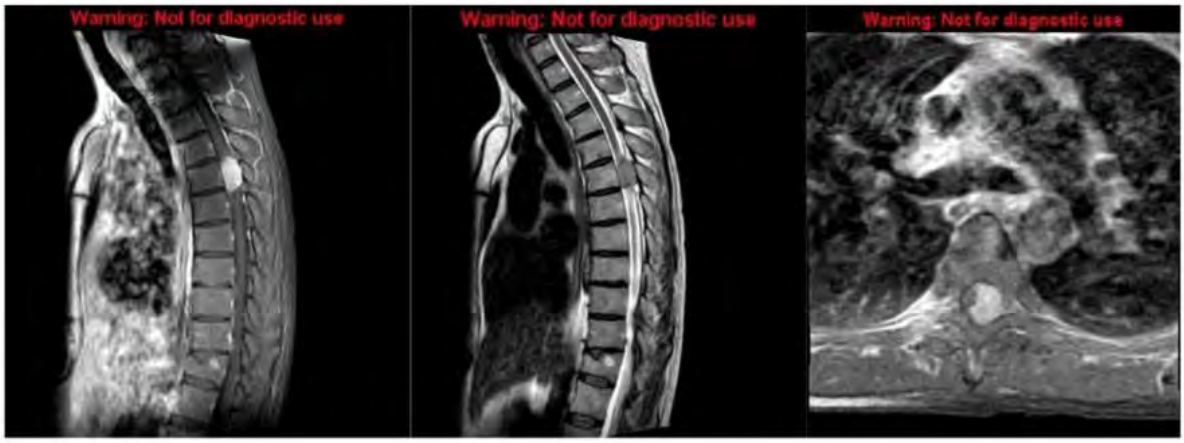
We present a 44-year-old male with increased numbness and tingling of his bilateral lower extremities associated with difficulty with urination over a 3-week period. Due to his worsening symptoms, the patient underwent a magnetic resonance imaging (MRI) of the spine performed which was significant for a T5 mass. The patient was started on IV Decadron and eventually underwent a T5 laminectomy and complete tumor resection. Pathology revealed a cellular tumor with staghorn blood vessels without nuclear atypia. Immunochemistry showed CD31 and CD34 stains highlight the blood vessels with additional blush positivity for CD34. Findings were characteristic of primary hemangiopericytoma. No recurrence was demonstrated on subsequent imaging.

Results

Lobulated intermediate T1- and T2-signal intensity avidly enhancing mass obliterates the central canal at T5 vertebral body level. The mass completely obliterates the central canal, effaces the cerebrospinal fluid (CSF) spaces from the thecal sac, displaces the cord to the far right lateral aspect of the central canal.

Conclusions

We present an exceedingly rare case of a primary thoracic extradural hemangiopericytoma. Even given its rarity, hemangiopericytoma should be a diagnostic consideration for extradural spinal masses. Accurate and timely diagnosis can lead to prompt clinical and potentially surgical management.



(Filename: TCT_E-06_HemangiopericytomaASNRsubmission.jpg)

E-07

11:24AM - 11:28AM

Common Problem, Uncommon Location: MRI and Pathologic Correlation of an Intradural Pyogenic Granuloma

M Bhatt[1], K Barry[1], A Wang[1], R Silbergleit[1], K Donev[1], R Olson[1]
[1]*Beaumont Health System, Royal Oak, MI*

Purpose
Pyogenic granulomas, also known as lobular capillary hemangiomas, are a common subtype of hemangiomas, predominantly involving the cutaneous soft tissues and mucosal surfaces. However, there have been only a handful of case reports of these tumors along the neuraxis, in an intradural extramedullary location. Given its rare occurrence within the spinal canal, it is not readily included in the differential diagnosis. Pre-operative recognition can have value, as these tumors can bleed and thus usually require total surgical resection. Yet imaging characteristics are similar to the more common intradural tumors, including nerve sheath tumors, meningiomas and ependymomas.
Materials and Methods
An 18-year-old male presented with 2 weeks of low back pain radiating to the buttocks and left lower extremity. Clinical symptoms continued to worsen with conservative therapy and magnetic resonance imaging (MRI) revealed an intradural, extramedullary mass at L4-L5. Pre-operative differential diagnosis was a schwannoma or meningioma, and less likely an ependymoma. Patient received steroids and underwent subsequent en-bloc surgical resection.

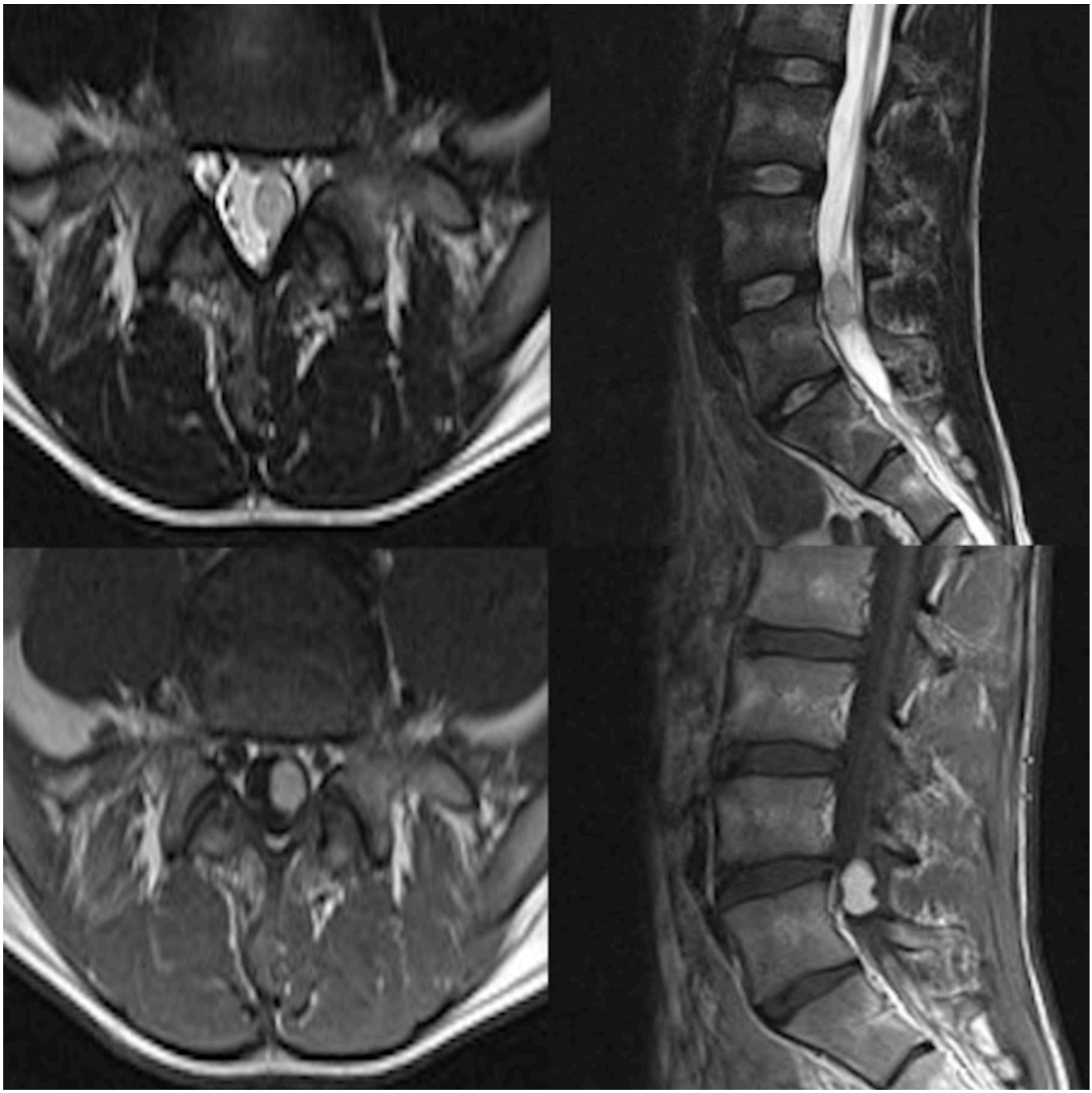
Pathologic evaluation was consistent with a pyogenic granuloma (lobular capillary hemangioma).

Results

Magnetic resonance imaging revealed an intradural extramedullary well circumscribed mass, just to the left of midline at L4-L5. The mass was homogeneous and demonstrated isointense T1 signal, predominantly isointense T2 signal and avid postcontrast enhancement. No osseous or neural foraminal extension was appreciated.

Conclusions

Pyogenic granulomas, or lobular capillary hemangiomas, are relatively common lesions of the cutaneous and mucosal surfaces. Rarely, these lesions can present as an intradural extramedullary mass within the spinal canal. We present a case of an intradural pyogenic granuloma causing mass effect on the cauda equina, with review of the imaging findings and histopathology. Awareness that these lesions can masquerade as an enhancing intradural mass aides in pre-operative planning, as these tumors have the potential for significant bleeding. Pre-operative embolization also may be of clinical benefit; however requires further investigation.



(Filename: TCT_E-07_PyogenicGranuloma.jpg)

E-08

11:28AM - 11:32AM

The Curious Case of an Intraosseous Pseudomeningocele in an Adult

J Huang[1], R Sebro[2]
[1]Pennsylvania Hospital, Department of Radiology, Philadelphia, PA, [2]Hospital of the University of Pennsylvania, Department of Radiology, Philadelphia, PA

Purpose

Intraosseous pseudomeningoceles are extremely rare, with only a handful of cases being reported in the literature. The majority of these cases are pseudomeningoceles that occurred in the skull in children following trauma or in the posterior elements of the spine of adults following surgery. To our knowledge, no cases of the development of an intraosseous pseudomeningocele exists in the vertebral bodies of the mobile spine. We present a case of intraosseous pseudomeningocele of the lumbar spine in an adult patient without prior history of trauma/surgery in the region.

Materials and Methods

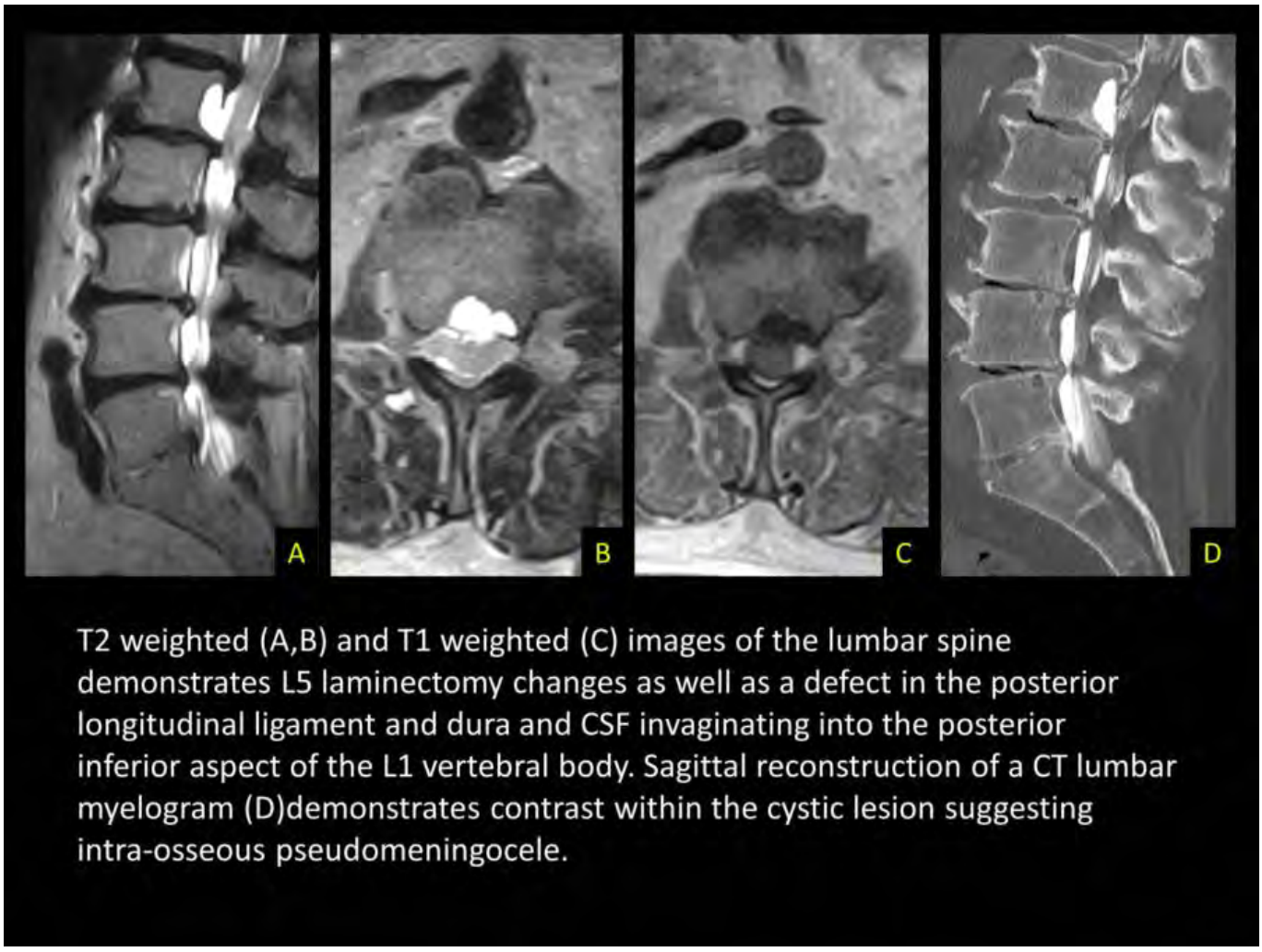
RS is a 65-year-old male with a history of lumbar stenosis status post L5 laminectomy in 1970 who presented with left leg pain. He was scheduled for a lumbar laminectomy when pre-operative magnetic resonance imaging (MRI) demonstrated a T2 hyperintense lesion in the midline inferior endplate of L1 that appeared to communicate with the cerebrospinal fluid (CSF) space through a defect in the dura and a defect in the posterior longitudinal ligament. The operation was deferred and the patient underwent a lumbar computed tomography (CT) myelogram which demonstrated free communication between intrathecal contrast material and the lesion in L1. This finding is confirmatory of a pseudomeningocele. This is a highly curious case as nearly all reported intraosseous pseudomeningocele formations occur in children. Furthermore, those that do occur following surgery typically involve the posterior elements, not the vertebral body. The principle treatment for intraosseous pseudomeningocele is neurosurgical intervention to close the dural defect although this is certainly complicated by proximity of this defect to the conus medullaris/spinal cord and the concomitant injury to the posterior longitudinal ligament.

Results

Magnetic resonance imaging. Sagittal T2-weighted MR of the lumbar spine demonstrates L5 laminectomy changes as well as a defect in the posterior longitudinal ligament and dura with CSF invaginating into the posterior inferior aspect of the L1 vertebral body. Computed tomography. Sagittal images from a CT lumbar myelogram demonstrates contrast freely filling the lesion in the posterior inferior aspect of the L1 vertebral body consistent with an intraosseous pseudomeningocele.

Conclusions

Intraosseous pseudomeningocele is a rare entity and this case is unique in its location, origin and history. One should include pseudomeningocele in the discussion of T2 hyperintense intraosseous structures on spine MR, albeit it is much lower on the differential.



(Filename: TCT_E-08_RS-ASNR-images1.jpg)

E-09

11:32AM - 11:36AM

Percutaneous treatment of metastatic vertebral body lesions with microwave thermal ablation

N Sedora-Roman[1], S Sundararajan[1], M Oselkin[1], B Pukenas[1]
[1]*Hospital of the University of Pennsylvania, Philadelphia, PA*

Purpose
A growing body of literature describes cryotherapy and radiofrequency ablation techniques for palliative treatment of painful metastatic vertebral body fractures. These techniques provide local tumor control, pain reduction and decreased tumor burden. While percutaneous microwave ablation (MWA) is well established for the treatment of various types of nonosseous tumors, few reports exist using this technique for the treatment of metastatic

vertebral body lesions. We report our initial experience and demonstrate the applicability of MWA therapy in the treatment of patients with metastatic vertebral body lesions.

Materials and Methods

We report the use of microwave ablation in the treatment of painful metastatic vertebral body lesions in 8 patients ranging between the ages of 56 and 77 years old. With the exception of 3 cases, all patients presented with vertebral body compression fractures secondary to underlying metastatic lesions. Primary neoplastic sites include breast, nonsmall cell lung, renal cell, prostate and esophageal cancer. Adjunct vertebral body augmentation with polymethylmethacrylate injection was performed in 5 patients whose lesions contained fractures. Microwave ablations were performed under biplane fluoroscopy or computed tomography (CT) guidance using a Neuwave microwave PR20 probe. Burns were created using 30 watts for 30 seconds. No new neurological deficits or complications were encountered during or immediately following the procedures. Magnetic resonance imaging (MRI) follow up was performed in only 1 patient (new symptoms not correlated to level of initially treated metastasis), and demonstrated significant reduction in tumor volume (Figure 1).

Results

Dedicated spinal CT and MR examinations performed prior to percutaneous microwave ablation show known thoracic and lumbar vertebral body metastatic lesions. Associated compression fractures were identified in 5 cases.

Conclusions

Our initial experience suggests microwave ablation is an alternative technique in the management of painful spinal metastasis.

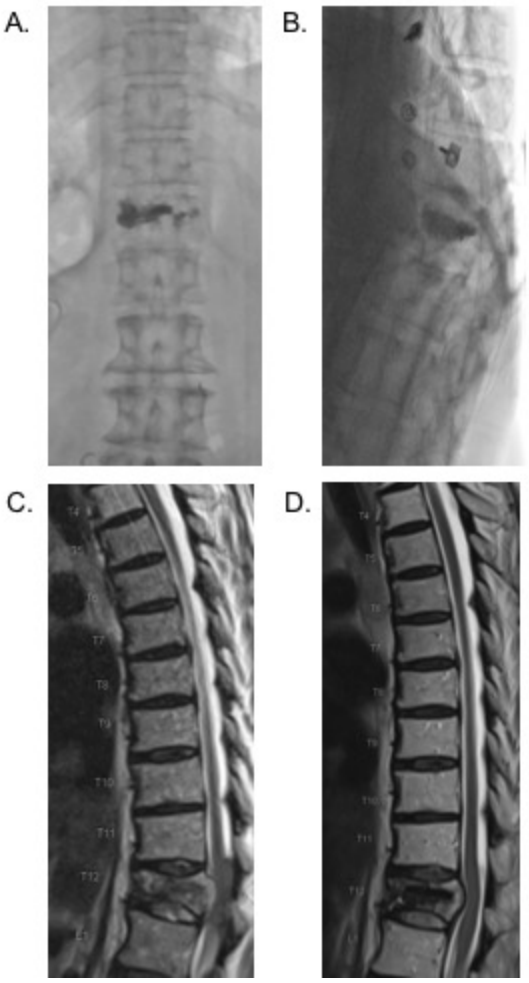


Figure 1. Thoracic metastasis treated with microwave ablation and vertebral body augmentation in a 59 year old female patient with non small cell lung cancer. (A) AP and lateral (B) fluoroscopic views show successful administration of bone cement in the T12 vertebral body. (C) Sagittal T2 weighted sequences of the cervicothoracic spine prior to and post (D) MWA show interval improvement of vertebral body height with decreased compression of the spinal cord.

(Filename: TCT_E-09_Figure1.jpg)

E-10

11:36AM - 11:40AM

Rare Spinal Cord Involvement of Methotrexate-Related Diffuse Necrotizing Leukoencephalopathy in the Setting of Metastatic Breast Cancer

D Cantrell[1], J Raizer[2], C Horbinski[2], Q Mao[3], B Liu[4]
[1]Northwestern, Chicago, IL, [2]Northwestern Memorial Hospital, Chicago, IL, [3]Northwestern University, Chicago, IL, [4]Northwestern University Feinberg School of Medicine, Chicago, IL

Purpose
To describe methotrexate-related diffuse necrotizing leukoencephalopathy in the spinal cord.
Materials and Methods
A 34-year-old woman with stage III (T2, N2A) ER+, HER2- breast cancer underwent bilateral mastectomies followed by 4 cycles of adriamycin and cytoxan, 12 cycles of taxol, chest wall radiation, and tamoxifen. Eighteen months later, she presented with headache, gait instability, dysphagia, and tinnitus due to leptomeningeal disease. The patient received 3

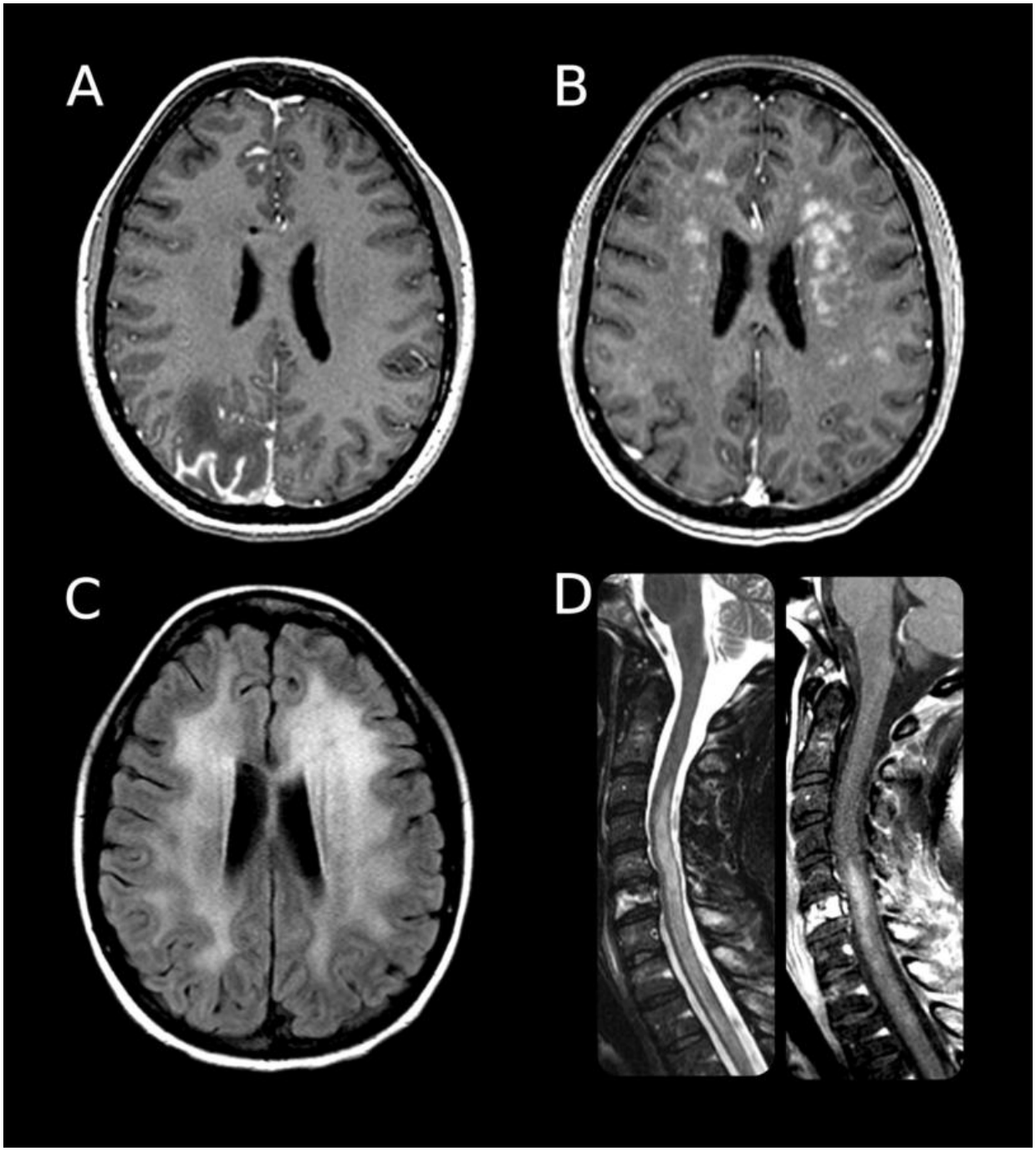
doses of biweekly intrathecal methotrexate and was transitioned to intrathecal topotecan, which achieved a favorable radiological response and conversion to negative cerebrospinal fluid (CSF) cytology. She continued with intrathecal topotecan for another 18 months before malignancy was detected in her CSF samples, and she was transitioned to alternating weekly doses of intrathecal topotecan and methotrexate. Five months later, she presented with a 3-week history of progressive gait imbalance, reduced sensation in her lower extremities, and urinary incontinence due to diffuse necrotizing leukoencephaloapthy. Leptomeningeal disease had improved and CSF cytology was negative for malignancy. The patient received a 5-day trial of steroids followed by 5 days of plasma exchange, but clinical symptoms continued to worsen. To guide further therapy, biopsy was obtained from a portion of the abnormal white matter in the right temporal lobe. Pathology was consistent with methotrexate toxicity. Methotrexate was discontinued, but steroid therapy remained ineffective, and the patient died 6 months later.

Results

Initial magnetic resonance imaging (MRI) demonstrated extensive intracranial and spinal leptomeningeal disease (Figure 1A), confirmed with CSF cytology. Follow-up MRI showed decreased leptomeningeal disease, but revealed new, extensive T2/FLAIR hyperintensity in the supratentorial white matter with small, scattered foci of associated enhancement (Figures 1 B and C). Extensive, expansile T2/STIR hyperintensity and enhancement also was seen throughout the cervical and thoracic cord (Figure 1D).

Conclusions

Methotrexate-related necrotizing leukoencephalopathy involving the spinal cord is extremely rare, and our case expands on the spectrum of methotrexate neurotoxicity previously reported in the literature.



(Filename: TCT_E-10_ASNRFigure.jpg)

E-11

11:40AM - 11:44AM

Rare case of subacute combined degeneration of the spinal cord secondary to nitrous oxide abuse

A Simonetta[1], R Riascos[2], R Valenzuela[3], M Ramirez[4], L Ocasio[4]

[1]University of Texas, Health Science Center- Houston, Houston, TX, [2]UTHSC-Houston, Houston, TX, [3]The University of Texas, Houston, TX, [4]Memorial Hermann Hospital, Houston, TX

Purpose

We present a rare case of subacute combined degeneration of the spinal cord secondary to nitrous oxide abuse diagnosed after magnetic resonance imaging (MRI) of the cervical spine.

Materials and Methods

A 19-year-old female presented to the emergency department with progressive descending bilateral lower extremity weakness, numbness, tingling, and gait disturbance for 1 week after attending a concert where she used recreational substances, including nitrous oxide. The patient denied radiating pain or sphincter dysfunction. On physical examination, light touch and pin-prick sensation were diminished and strength of 3/5 of her lower extremities was noted, as well as loss of vibration and position sense in bilateral toes with preserved reflexes. A drug screen was negative. Spinal MRI was ordered and linear posterior cord T2-hyperintensity was noted, confined to the dorsal columns. The diagnosis of subacute combined degeneration was made. Serum laboratories documented low vitamin B12 levels and macrocytic anemia. Vitamin B12 supplementation was instituted and the patient's symptoms improved.

Results

T2-weighted images demonstrate longitudinal hyperintensity in an "Inverted V-shape" configuration involving the dorsal spinal cord from C2 through C4 in correspondence with the dorsal columns. T1-weighted images demonstrate relatively decreased signal with no enhancement after gadolinium administration.

Conclusions

Nitrous oxide exposure produces oxidation of cobalt ions in vitamin B12 causing its inactivation. As a consequence of the latter, a demyelinating syndrome ensues as a result of reduced recycling of homocysteine to methionine with consequent prevention of methylation of myelin proteins. The role of imaging is crucial in the diagnosis of this rare cause of subacute combined degeneration, particularly in cases like this, when there is no way to quantify the degree of nitrous oxide use aside from its toxic effect on the peripheral and central nervous system. Prompt diagnosis is critical for institution of appropriate supplementation to avoid permanent injury.



(Filename: TCT_E-11_asnrdpi20.jpg)

E-12

11:44AM - 11:48AM

Epidural Hemangioma: A Unique Case

G Venkataraman[1], S Koenig[2], C Bazan[2]
[1]UTHSCSA, San Antonio, TX, [2]University of Texas Health Science Center at San Antonio, San Antonio, TX

Purpose
Vertebral body hemangiomas are a common and often incidental, benign imaging finding. They may, however, display aggressive features and cause significant neurologic symptoms,

necessitating treatment. One common aggressive feature on imaging is the extension of the hemangioma into the extradural space, causing radiculopathy and/or myelopathy. In contrast, primary extra-osseous extradural hemangiomas are rare, often published only in isolated case reports. Our purpose is to present a unique case of one such epidural hemangioma with atypical imaging findings, along with a brief review of typical imaging findings for epidural hemangiomas, as well as the importance of including this rare diagnosis in approaching symptomatic epidural spinal lesions.

Materials and Methods

Patient M.Q. was a 44-year-old female with history of HTN, PID, who presented with approximately 1 year of progressively worsening bilateral lower extremity numbness and paresthesia, progressing to 4 months of ataxia and multiple falls, and about 2 weeks of urinary/bowel incontinence. Initial imaging and clinical presentation (fever, leukocytosis, and bacteriuria/ pyuria) were concerning for PID and appendicitis, and she was initiated on broad spectrum antibiotics. Even though the initial noncontrast computed tomography (CT) image of her thoracic spine showed no spinal abnormalities, follow-up magnetic resonance (MR) spine revealed an epidural lesion. Her fever and leukocytosis responded to antibiotics (for presumed UTI secondary to urinary retention). She subsequently was taken to the OR for spinal cord decompression and resection of the large epidural lesion. Biopsy of the lesion was consistent with a hemangioma. She continued to clinically improve postoperatively and discharged to rehabilitation, with eventual resolution of her symptoms.

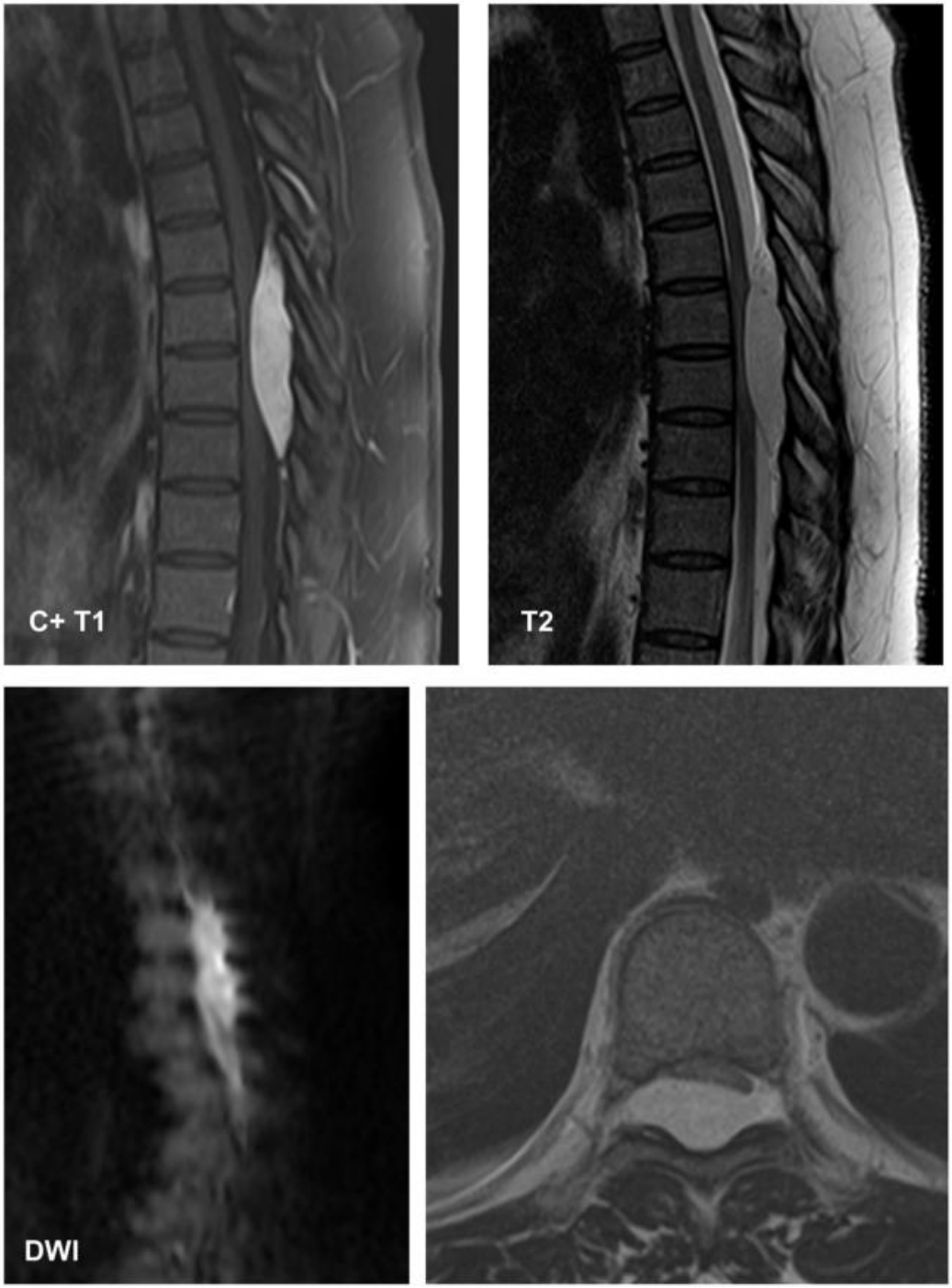
Results

In this patient with initial concern for spinal abscess and associated cord abnormalities, an initial noncontrast CT study of the thoracic spine did not reveal any spinal or cord abnormalities. Subsequent MR study of the spine revealed a large fusiform 1.5 x 1.7 cm x 10 cm extradural lesion spanning the T6-T9/T10 level posteriorly. This lesion appeared homogeneously T2 hyperintense, T1 hypointense, with homogeneous contrast enhancement, without fat suppression. Diffusion restriction in this lesion was noted. Nerve root impingement secondary to neural foraminal extension was seen at the T6-T7, T7-T8, and T8-T9 levels, with cord signal changes at the T7 and T8 levels. Given the involvement of the neural foramen and the diffusion restriction, initial differential diagnoses included lymphoma versus extradural nerve sheath tumor versus metastatic disease. Imaging of the rest of the spine and brain showed no other lesions to suggest metastatic disease.

Conclusions

Spinal epidural hemangiomas are a rare entity, and most of the previously reported imaging findings of spinal epidural hemangiomas describe the cavernous type. These are typically iso-hyperintense T1, and hyperintense T2, and show strong contrast enhancement. Some of these spinal epidural hemangiomas have been reported to demonstrate MR features of a hematoma. Much less commonly reported are the capillary type (solid hypervascular mass on MR) and the arteriovenous type (cystic mass on the MR). In our patient, the biopsy proven hemangioma was somewhat consistent with a cavernous hemangioma in appearance, but was atypical in its hypointense appearance on T1, and restricted diffusion, making the

initial set of differential diagnoses unlikely for a hemangioma. These atypical imaging findings, along with lack of fat suppression suggest fat-poor and vascular rich composition, with a possible hemorrhagic component that also may explain the rapid acute on chronic progression of symptoms for the patient. This case highlights the importance of understanding the varied appearance of a spinal epidural hemangioma, and the importance of considering it in the differential diagnosis since this greatly impacts patient management.



(Filename: TCT_E-12_epi.jpg)

E-13

11:48AM - 11:52AM

Conus Glioblastoma Multiforme in an Adult

R Ahmed[1], U Tariq[1], G Mongelluzzo[1], S Kazmi[1], K Cauley[1], W Millar[1]
[1]*Geisinger Medical Center, Danville, PA*

Purpose
Glioblastoma (GBM) of the spine cord is a rare intramedullary glioma with an aggressive course and a poor prognosis, mostly reported in pediatric patients. We present a rare case of glioblastoma multiforme (GBM) in an adult patient arising within the conus medullaris.
Materials and Methods
A 53-year-old male with history of L3-4 and L4-5 laminectomies presented with a broad-based gait, progressive weakness and numbness in the right leg for 9 months. In the last few days, his weakness progressed and he started using a walker. He also complained of intermittent difficulties with bowel and bladder regulation. On examination, there was decreased muscle strength in both legs, variable sensory loss to both pin and touch in both legs, weak reflexes in bilateral knee and ankle joins. Magnetic resonance imaging (MRI) of the spine revealed a spinal cord mass. Patient subsequently underwent laminectomy and biopsy of spinal cord lesion. Neuropathology was consistent with GBM.
Results
Sagittal T1, T1 post-contrast, STIR and T2 images demonstrate an intramedullary conus medullaris mass with fusiform cord enlargement. The lesion demonstrates T1 isointensity, T2 hyperintensity with cystic components and diffuse peripheral enhancement on postcontrast images.
Conclusions
We describe the clinical and neuroimaging features of a GBM arising within the conus medullaris in an adult. Consideration of this pathologically rare spinal cord tumor may facilitate prompt diagnosis and early therapy.


(Filename: TCT_E-13_GBM.JPG)

E-14

11:52AM - 11:56AM

A Case of Infiltrative Spinal Glioma with "Sugar Coating" of the Spinal Cord

R Koff[1]
[1]*Santa Barbara Cottage Hospital, Santa Barbara, CA*

Purpose
-To present a unique spinal cord neoplasm. -Discuss the imaging findings associated with an infiltrative/aggressive intramedullary spinal cord neoplasm and "sugar coating" of the spinal cord. -Review treatment options and post-therapy imaging.
Materials and Methods
We present the case of a 46-year-old female with progressive right lower extremity numbness and weakness. Her symptoms progressed to generalized lower and upper extremity weakness and paresthesias. Spine magnetic resonance maging (MRI) demonstrated

an expansile intramedullary mass in the cervical and thoracic cord. Also noted was extensive leptomeningeal enhancement of the cervicothoracic cord and cauda equina. A biopsy of the lesion revealed an infiltrative glial neoplasm, with a differential diagnosis of astrocytoma or oligodendroglioma. Given the osseous remodeling of the cervical and thoracic vertebral bodies suggesting a long-standing tumor, it was felt that the leptomeningeal spread may have resulted from aggressive transformation of a lower grade intramedullary glial neoplasm. She improved symptomatically with steroids. She then underwent radiation therapy followed by chemotherapy with temozolomide. While she has significant residual lower extremity weakness, symptoms have mildly improved with physical therapy.

Results

Initial MRI spine survey was performed with and without gadolinium contrast. Images revealed an expansile, intramedullary mass in the mid cervical to mid thoracic spine, with subtle osseous remodeling of the posterior cervical and thoracic vertebral bodies. The mass demonstrates heterogenous T2 hyperintensity and irregular foci of intrinsic contrast enhancement. Nodular enhancement of the surface of the upper cervical cord and cauda equina (sugar coating) suggests leptomeningeal spread of tumor.

Conclusions

We present a case of infiltrative spinal glioma with "sugar coating" of the spinal cord in a 46-year-old female presenting with progressive lower extremity weakness and paresthesias. An expansile and enhancing intramedullary mass of the cericothoracic cord was identified by MRI. Diffuse leptomeningeal enhancement of the upper cervical cord and cauda equina suggest leptomeningeal spread of neoplasm. A subsequent biopsy revealed glial neoplasm, with pathologic consultation suggesting astrocytoma versus oligodendroglioma. High grade astrocytomas and spinal cord glioblastomas in particular have been described with leptomeningeal spread of tumor at time of diagnosis. Given the osseous remodeling of the cervical and thoracic vertebral bodies suggesting a long-standing tumor, it was felt that the leptomeningeal spread may have resulted from aggressive transformation of a lower grade intramedullary glial neoplasm. The patient reported symptomatic improvement with steroid administration. The tumor regressed following radiation therapy and chemotherapy with temozolomide.









(Filename: TCT_E-14_ASNRspinalglioma.jpg)

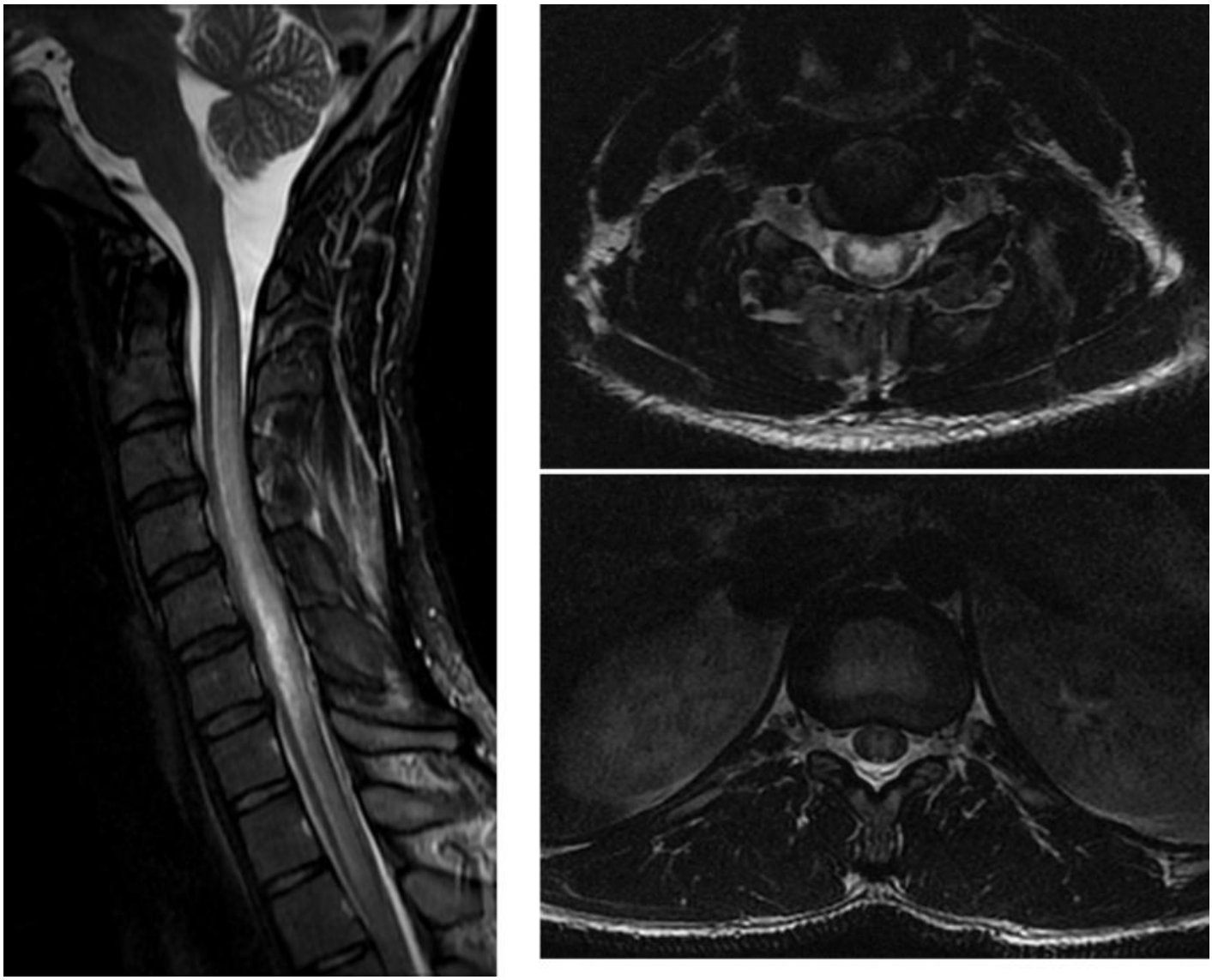
E-15

11:56AM - 12:00PM

Opiate Overdose Leading to Flexion Myelopathy and Quadriparesis

K Covey[1], M Hughes[1], N Zwagerman[1], J Mettenburg[2], V Agarwal[1]
[1]University of Pittsburgh Medical Center, Pittsburgh, PA, [2]UPMC, Pittsburgh, PA

Purpose
Opiate abuse is an epidemic in the United States with overdoses becoming increasingly common. A rare complication of drug overdose is severe flexion myelopathy, with only 3 prior cases reported in the English literature. We present a patient status postopiate overdose and prolonged neck flexion resulting in flexion myelopathy and quadriparesis.
Materials and Methods
A 21-year-old male with a history of opiate abuse was found unconscious, slumped with his neck in a flexed position. He was last seen normal approximately 7 hours before overdosing on oral opium. On initial examination, the patient was found to have no motor or sensory function below C5. Brain and total spine magnetic resonance imaging (MRI) as well as a spinal angiogram were performed. No surgical intervention was performed. Upon discharge on hospital day 8, he could move his toes against gravity and had normal sensation.
Results
Magnetic resonance imaging of the cervical spine demonstrated holocord abnormal increased T2 signal of the gray matter and cord swelling, most severe at C5-C6 without associated restricted diffusion or evidence of hemorrhage. Brain MRI and spinal angiogram were unremarkable.
Conclusions
Vascular and neuronal mechanisms are the 2 leading theories regarding potential mechanisms of spinal cord injury following prolonged flexion. The vascular theory suggests blood flow to neuronal structures during prolonged flexion is impaired. The neuronal theory suggests the cord is mechanically injured by stretching or direct pressure. In the flexed positioning, as this individual was found, the greatest curvature is present at the level of C5–C6; correspondingly C5-C6 was the level of greatest signal abnormality and cord swelling in our patient. Given the current opioid epidemic, radiologists should be familiar with the common and uncommon imaging findings following overdoses including the nontraumatic spinal cord injury of flexion myelopathy.



(Filename: TCT_E-15_Myelopathy.jpg)

E-16

12:00PM - 12:04PM

Radiologic manifestation of the malignant peripheral nerve sheet tumor involving the brachial plexus.

S Aran[1], G Suarez Duran[1], A Kim[1]
[1]*Hahnemann university hospital, Philadelphia , PA*

Purpose
Malignant peripheral nerve sheath tumors (MPNST) are rare. With usual involvement of the sacral plexus, brachial plexus involvement is not seen so frequently. These tumors are aggressive and unfortunately have poor prognosis. Patients usually present with nonspecific

symptoms which usually causes delay in diagnosis. Radiology plays an essential role in early diagnosis which is crucial. The purpose of this case report is to describe characteristic findings and the role of imaging in diagnosis of MPNST and tissue sampling. In addition, even though MPNST are rare, physicians should keep MPNST in their differential diagnosis list when initial work up is nondiagnostic and to choose an appropriate imaging not to delay diagnosis and management.

Materials and Methods

Patient is a 63-year-old African American female with history of osteoporosis and bilateral breast cancer status postlumpectomy of right and left breast in 2008 and 2005, respectively. In 2009 patient presented with complaint of right wrist and hand pain. She initially was managed conservatively for mild osteoarthritis found on x-ray with no improvement. Therefore, she underwent cubital tunnel release surgery on the right side with suspicion of cubital tunnel syndrome. She experienced no improvement of her symptoms and later she was also complaining of neck pain and right upper extremity pain and weakness. Therefore, her cervical spine was evaluated by cervical spine x-ray and magnetic resonance imaging (MRI) in March 2016 which showed mild multilevel spondylosis of the cervical spine with no significant central canal or neural foraminal stenosis. Also, she had a shoulder MRI without gadolinium which showed abnormal high T2, and low T1 soft tissue signal within the region of the neurovascular bundle measuring 2.4x3.9x5.5 cm displacing the vasculature. On 4/2016 an MRI of the shoulder with and without gadolinium was performed which showed right axillary mass splaying the vessels and encompassing the region of the brachial plexus, strongly suggestive of soft tissue mass. On 5/2016 ultrasound-guided biopsy of the axillary mass was performed and was sent to pathology. The results came back as malignant peripheral nerve sheath tumor. Following this diagnosis, a postcontrast computed tomography (CT) of the body and chest were obtained which showed no definitive evidence of metastatic disease. A follow-up shoulder MR with and without gadolinium was obtained again to evaluate extension of disease. Patient later received chemotherapy. On 9/2016 a positron emission tomography (PET) CT was performed for staging which showed FDG avid heterogeneous mass with indistinct margins along the brachial plexus with SUV of 9.49.

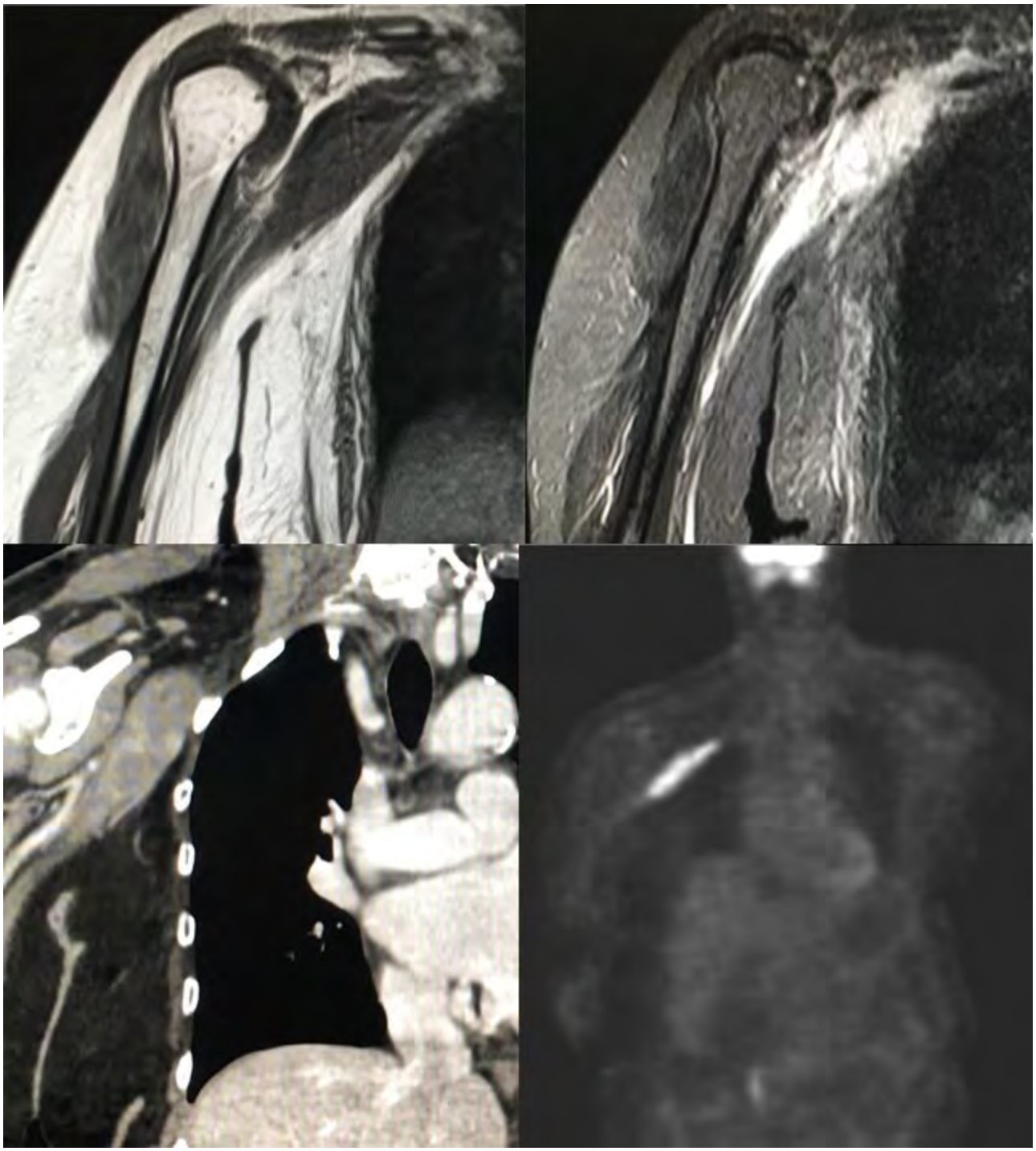
Results

Malignant peripheral nerve sheath tumor involving the right brachial plexus. Magnetic resonance images of the shoulder obtained with coronal T1, and coronal STIR sequences are demonstrated. The MPNST appears as a heterogenous solid mass with T1 hypo intense, STIR hyper intense and avid enhancement on postcontrast images. The CT coronal postcontrast image shows heterogeneously enhancing solid mass involving the brachial plexus and splaying the vessels. The coronal PET attenuated corrected images demonstrated a very hypermetabolic mass involving the right brachial plexus.

Conclusions

Malignant peripheral nerve sheath tumors are rare (reported incidence: 0.001-0.1%) tumors that are associated with neurofibromatosis type-1. Nearly 50% of MNST are from NF-1

patients. In the case report by Redzepagic et al. only 9 cases have been reported in the English literature that describe MNST whose primary location is the breast. Only 2 of those cases were NF-1 patients, but none had a previous history of breast cancer from non-neuroepithelial tissue. Although they are from the same origin as benign tumors such as neurofibromas or schwannomas, malignant nerve sheath tumors are known for their aggressiveness and poor prognosis. These tumors tend to originate adjacent to nerve roots such as the sacral or brachial plexus, with the sciatic nerve being the most commonly affected nerve However, brachial plexus neoplasms are extremely rare. Out of the many neoplastic processes that can occur in this anatomical region, only 5.59% are MPNST, per study performed by Jia et al. Signs and symptoms are nonspecific and include pain, palpable mass, numbness and paresthesia. Morphologically, these tend to have irregular borders and have a tendency to be larger than 5cm, as would be expected on CT imaging. Radiologically, these tumors have distinct appearances in different modalities. On ultrasound, these appear heterogeneously echogenic with posterior acoustic enhancement. On T1MR, these tend to be isointense to adjacent muscle and heterogeneous but may be high intensity on fluid sensitive sequences. As is characteristic of many malignant tumors, MPNST enhance avidly on postcontrast CT and MRI, and have increased metabolic activity on Tc-99m and F-18 FDG PET imaging. Definitive diagnosis is made by tissue sampling which can be performed under guidance of ultrasound. Treatment includes surgical excision with wide margins. There is no need for local lymph node excision due to the tumor's hematogones spread. Other treatment options include radiation and chemotherapy.



(Filename: TCT_E-16_ASNR.jpg)

E-17

12:04PM - 12:08PM

Atypical Imaging Presentation of Spinal Cord Ependymoma

M Ghazarian[1], M Gule-Monroe[2], L Ketonen[3]

[1]UT Houston Medical School at Houston, Houston, TX, [2]The University of Texas MD Anderson Cancer Center, Houston, TX, [3]M.D. Anderson Cancer Center, Houston, TX

Purpose

Present a very atypical imaging presentation of an intramedullary cord tumor. Differentiate the 2 most common spinal cord tumors, ependymoma and astrocytoma, based on imaging characteristics.

Materials and Methods

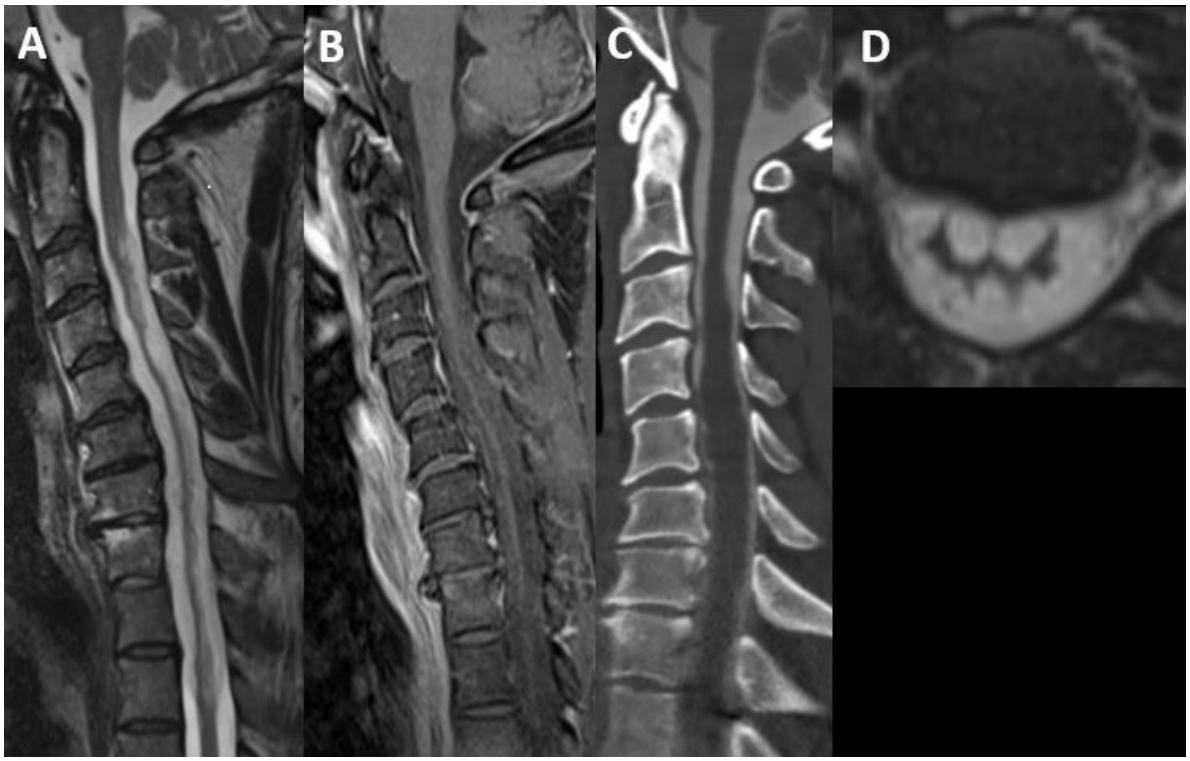
A 48-year-old gentleman initially began having bilateral lower extremity paresthesias and sensory loss 10 years ago. Whole spine magnetic resonance imaging (MRI) revealed a longitudinally extensive spinal cord lesion. Biopsy at an outside facility was consistent with glial neoplasm, NOS. After second opinion at our institution, the patient underwent biopsy/resection of intramedullary spinal cord tumor followed by definitive radiation. Pathology revealed ependymoma.

Results

Sagittal T2-weighted image (A) of the cervical and upper thoracic spine demonstrates irregular, thinned appearance of the spinal cord from C3 to T3. Hazy, intermediate signal is seen surrounding the cord, with preservation of normal CSF signal in the subarachnoid space inferiorly. Sagittal fat saturated, postcontrast T1-weighted image (B) shows no striking abnormal enhancement. Axial T2-weighted image (D) at the level of C4-C5 shows scalloped appearance of the cord parenchyma. Sagittal computed tomography (CT) myelogram (C) depicts masslike expansion of the spinal cord.

Conclusions

This case represents an unusual imaging presentation of spinal cord ependymoma. Typically, ependymomas are centrally located, well defined masses on postcontrast MR imaging. Homogeneous enhancement and tumor-related cyst(s), including syrinx, also are typical features. Peripheral involvement of the cord and no significant enhancement makes this case of ependymoma unique. It also is difficult to assess whether the mass is intramedullary or extramedullary by MR. Ependymomas and astrocytomas account for over 90% of all intramedullary tumors, with ependymomas representing 60% of all cord tumors. Reliable imaging differentiation of these tumors is difficult, but important, as ependymomas typically can be cured surgically, and carry an improved prognosis as compared to astrocytoma.



(Filename: TCT_E-17_joinedpicture.jpg)

E-18

12:08PM - 12:12PM

Spontaneous Regression of a Large Calcified Thoracic Disc Extrusion

H Oligane[1], J Rongo[2], V Agarwal[3], B Branstetter[3]
[1]University of Pittsburgh Medical Center, pittsburgh, PA, [2]St. Petersburgh General Hospital, St. Petersburgh, FL, [3]University of Pittsburgh Medical Center, Pittsburgh, PA

Purpose
While spontaneous regression of herniated disk material has been reported in the lumbar and cervical spine, reports of complete regression of thoracic disk extrusion are exceedingly rare (1, 2). In symptomatic patients surgical intervention typically is the treatment of choice. Conservative therapy with surveillance may however allow time for spontaneous resolution and potentially avoid high-risk surgery.
Materials and Methods
A 40-year-old female with "burning sensation" across her abdomen and lower back pain for 1 week. Past medical history was positive for depression and anemia. She denied any history of trauma or surgery. A noncontrast computed tomography (CT) of the thoracic spine showed a large calcified disk extrusion at the T10-T11 level resulting in severe central canal stenosis. Follow-up magnetic resonance imaging (MRI) of the thoracic spine demonstrated spinal cord signal changes at the level of the calcified disk extrusion. Surgical intervention

was discussed on the assumption that the calcified disk extrusion was unlikely to resolve and could potentially cause further damage. The patient opted for conservative measures with rest and close clinical follow up. Over the next 6 months, her symptoms gradually improved with limits on activity. Eight months after the patient's initial presentation, follow-up MRI showed complete resolution of the calcified disk extrusion.

Results

Computed tomography of the thoracic spine: Calcified disk extrusion at the T10-T11 level resulting in severe central canal stenosis (Figure 1). T2-weighted axial MRI of the thoracic spine: Severe canal stenosis at T10-T11 with increased cord signal at the level of the calcified disk extrusion (Figure 2). T2-weighted axial MRI of the thoracic spine (8 months after initial presentation): Complete resolution of the calcified disk extrusion with resolution of cord signal abnormality (Figure 3).

Conclusions

We report a case of a calcified thoracic disk herniation that resolved with conservative management. Even densely calcified disk extrusions may respond to conservative therapy, and these patients do not necessarily need to undergo immediate surgery.



Figure 1 (left) Sagittal CT Thoracic Spine. Figure 2 (middle) Sagittal T2 MRI of the thoracic spine. Figure 3 (right) Sagittal T2 of the thoracic spine 8 months after presentation.

(Filename: TCT_E-18_figures-page-001.jpg)

E-129

12:12PM - 12:16PM

Inadvertent Intracranial Placement of Foley Catheter Following Severe Craniofacial Trauma

J Dorr[1]
[1]*Santa Clara Valley Medical Center, San Jose, CA*

Purpose
The purpose of this case report is to review a case of inadvertent intracranial placement of a Foley catheter balloon. The use of Foley catheters in the setting of severe posterior epistaxis is discussed, as are a number of complications including that which occurred in this case.

Materials and Methods

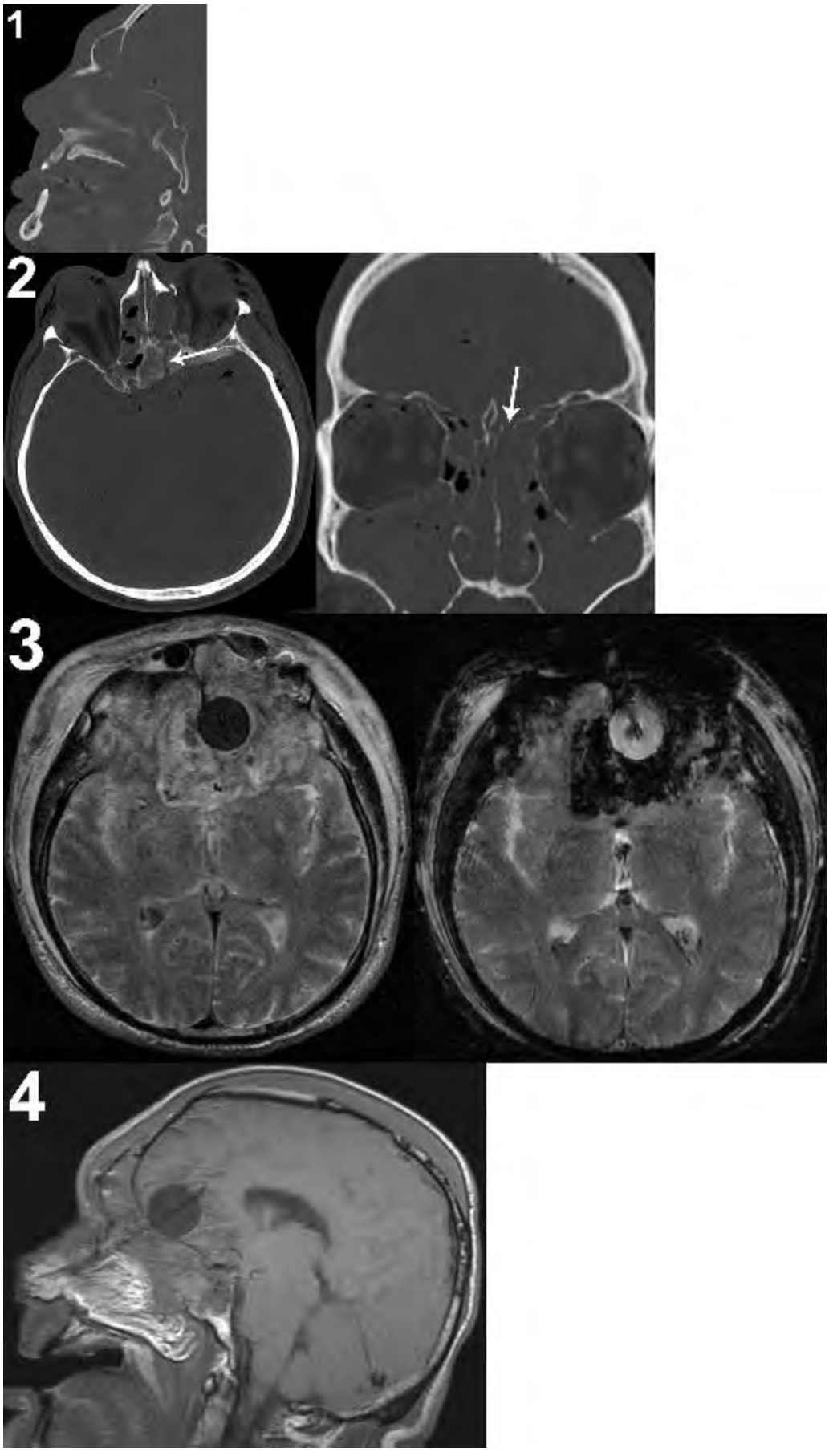
This 52-year-old male was a bicyclist involved in a major trauma when he was hit by a car. Physical exam revealed traumatic depression deformities of the calvarium, facial and globe edema, and epistaxis. Trauma computed tomography (CT) scan revealed intracranial hemorrhage and pneumocephalus, as well as facial and skull base fractures. A Foley catheter was placed for emergent stabilization of hemorrhage from the nose. Subsequent imaging demonstrated the tip of the Foley catheter to be within the frontal lobe. The catheter was removed and then replaced with adequate positioning.

Results

Fig. 1: Sagittal CT image demonstrating comminuted fractures involving the frontal sinus, cribriform plate, and sphenoid sinus. Fig. 2: Axial (left) and coronal (right) CT images demonstrating pnemocephalus and extensive maxillofacial fractures, including fracture through the cribriform plate (arrow). Fig. 3: Axial T2 FLAIR (left) and GRE (right) MR images through the brain after placement of Foley catheter for treatment of posterior epistaxis. Images demonstrate the Foley balloon is within the left frontal lobe, with surrounding edema and blood products. Fig. 4: Sagittal T1-weighted MR image shows the catheter past the skull base, and having entered the inferior anterior cranial fossa.

Conclusions

Placement of a Foley catheter with balloon inflation is an accepted technique for treatment of posterior epistaxis, particularly in the setting of trauma. However, one of the potential complications of the procedure is misdirection of the tip of the catheter as illustrated in this case. Some techniques offered in the literature for avoiding this complication are described.


1
2
3
4

(Filename: TCT_E-129_CombinedImages.jpg)

Monday
11:00AM - 12:20PM
Long Beach Convention Center, Room 203AB (Upper Level)

04G-Parallel Paper Session: Acute Stroke: Tools for Triage...Omens for Outcome?
O-37

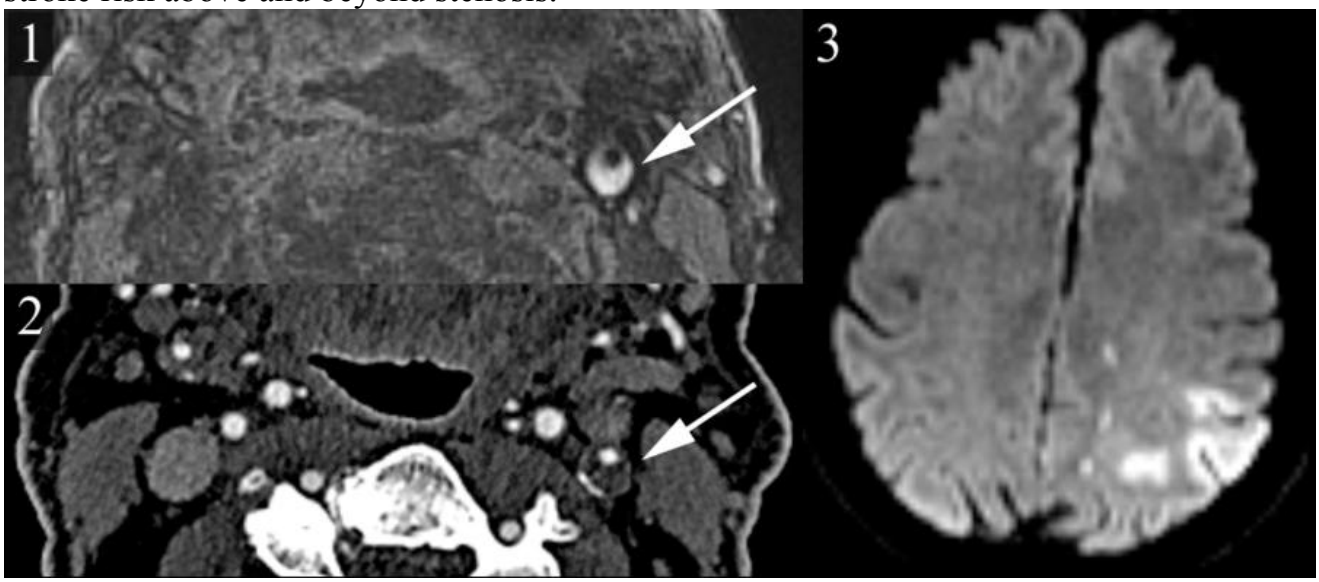
11:00AM - 11:08AM

The CTA Rim Sign: Soft plaque and adventitial calcification predicts stroke.

L Eisenmenger[1], P Hinckley[1], A de Havenon[1], D Parker[1], J McNally[1]
[1]*University of Utah, Salt Lake City, UT*

Purpose
Previously, we found that MRI/MRA markers of vulnerable carotid plaque included intraluminal thrombus, intraplaque hemorrhage (IPH, Image 1), and maximum plaque thickness. Recently, soft plaque, and adventitial calcification (a 'rim-sign,' Image 2) on CTA was found to predict IPH. Because MRI is not used in all patients undergoing stroke workup, our goal was to determine if the CTA rim-sign is an essential imaging marker of vulnerable plaque and ipsilateral stroke (Image 3).
Materials and Methods
In this IRB-approved retrospective cross-sectional study from 2009 to the present, 323 patients met inclusion criteria having undergone CTA neck and MR brain examinations within a 1-month period. After excluding 76 patients with known noncarotid plaque stroke sources (e.g. atrial fibrillation, trauma) we were left with 247 patients (494 carotids). After 11 carotid occlusions and 1 prior carotid stent were excluded, 482 carotid artery and ipsilateral brain pairs were left to analyze. We recorded CTA markers of vulnerable carotid plaque including percent diameter stenosis, mm stenosis, maximum plaque thickness, ulceration, intraluminal thrombus, and the rim-sign defined as thin adventitial calcification (<2mm thick) with internal soft plaque (≥2mm in thickness). Clinical covariates included age, male sex, diabetes, smoking, hypertension, hyperlipidemia, and body mass index. Cardiovascular medication confounders included antihypertension, antiplatelet, anticoagulation, and statin medication classes. A mixed effects multivariable Poisson regression model was used, accounting for 2 vessels per patient. We used backwards elimination to determine the final model with a threshold $p<0.10$ and prevalence ratios (PRs) were reported. Receiver operating charateristic (ROC) analysis was used to determine discriminatory power measured by area under the curve (AUC).
Results
The CTA rim-sign is highly associated with ipsilateral stroke (unadjusted PR=4.3, $p<0.001$, 95%CI: 2.9, 6.3). After multivariable regression and backward elimination, the final model

for CTA stroke prediction included the rim sign (PR=1.8, p=0.024, 95%CI: 1.1,3.1), maximum plaque thickness (PR=1.3, p<0.001, 95%CI: 1.1,1.4), and intraluminal thrombus (PR=3.1, p<0.001, 95%CI: 1.7,5.4). NASCET stenosis and ulceration were eliminated from the model with p>.20. The discriminatory value of our final model (AUC=78.7%) was significantly higher than the rim-sign alone (70.0%, p<0.001), thickness alone (76.7%, p=0.005), and intraluminal thrombus (56.9%, p<0.001).
Conclusions
The CTA rim-sign, previously shown to predict IPH, is highly predictive of ipsilateral stroke. Prospective studies are needed to determine if the rim-sign indicates high future stroke risk above and beyond stenosis.



(Filename: TCT_O-37_potentialcaselabel1.jpg)

O-39

11:08AM - 11:16AM

CT based imaging of voxel wise lesion water uptake in ischemic brain: relationship between density and direct volumetry

G Broocks[1], S Kamalian[2], T Faizy[3], F Flottmann[3], M Ernst[3], J Fiehler[3], S Siemonsen[3], A Kemmling[4]
[1]University Medical Center Hamburg-Eppendorf, Hamburg, Germany, [2]Massachusetts General Hospital and Harvard Medical School, Boston, MA, [3]University Medical Center Hamburg-Eppendorf, Hamburg, Hamburg, [4]University Medical Center Schleswig-Holstein, Luebeck, Luebeck

Purpose
Computed tomography (CT) density reduction has been correlated with the degree of increased tissue water in ischemic infarct lesions in a linear relationship; however, physiologically, the attenuation coefficient cannot change linearly. The purpose was to 1)

prove a corrected theoretical relationship between ischemic edema and CT density in order to 2) establish voxel wise imaging of lesion water uptake.

Materials and Methods

We developed a theoretical rationale to calculate the net water uptake in ischemic lesions based on a densitometric assessment. The precision for those equations was tested in vitro in a set of increasingly diluted iodine solutions with successive CT density measurements. Furthermore, the method was evaluated in a retrospective multicentric study. In 50 edematous infarct lesions, the net water uptake by direct measurement (=volumetric difference between ischemic and normal hemisphere) was correlated with relative density decrease.

Results

In the in vitro study, the correlation of relative density decrease and the ratio of added water was significant ($r=0.995$, $p<0.0001$). The mean uptake of water in the in vivo study, measured by volumetry, was 45.9 ml (± 27.9 ml) and the mean %-water increase within lesion volume was 23.0% (± 7.8%). This was equivalent to %-water increase obtained from relative density: 21.5 (± 6.7 %). Both methods for measuring net water uptake were highly correlated ($r = 0.91$, $p<0.0001$) and Bland-Altman plot revealed significant agreement (Mean= 0.02).

Conclusions

Volume of water uptake in infarct lesions can be calculated from relative CT density measurements. Voxel wise imaging of water uptake depicts lesion pathophysiology and especially should be examined as possible biomarker of lesion age.

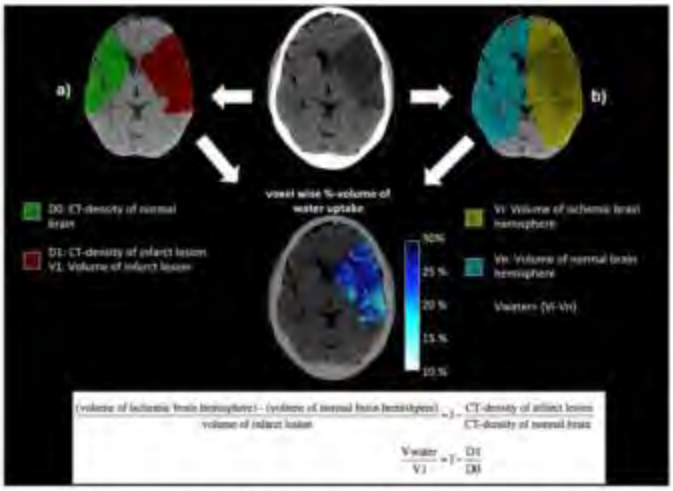


Figure 1: The quantification of net water uptake using densitometric measurements (a) in comparison to a volumetric approach (b).

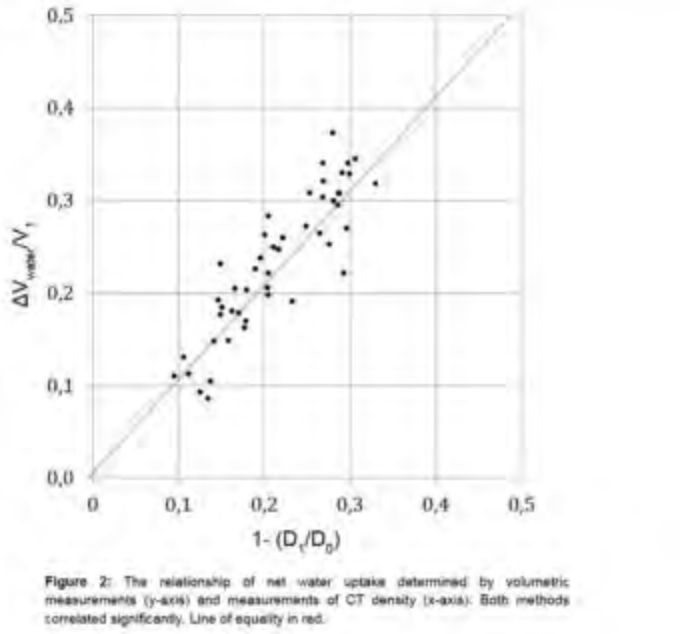


Figure 2: The relationship of net water uptake determined by volumetric measurements (y-axis) and measurements of CT density (x-axis). Both methods correlated significantly. Line of equality in red.

(Filename: TCT_O-39_figures_final_abstract1.jpg)

O-38

11:16AM - 11:24AM

Prediction of Malignant Middle Cerebral Artery Infarction Using Computed Tomography-Based Quantification of Net Water Uptake per Time

G Broocks[1], F Flottmann[2], T Faizy[2], A Aigner[2], S Christiansen[3], C Thaler[2], S Siemonsen[2], J Fiehler[2], A Kemmling[4]
[1]University Medical Center Hamburg-Eppendorf, Hamburg, Germany, [2]University Medical Center Hamburg-Eppendorf, Hamburg, Hamburg, [3]Friedrich-Ebert-Hospital Neumuenster,

Neumuenster, Neumuenster, [4]University Medical Center Schleswig-Holstein, Luebeck, Schleswig-Holstein

Purpose
Early selection of patients with acute middle cerebral artery (MCA) infarctions at risk for malignant edema has a high clinical relevance in order to initiate timely decompressive surgery which improves outcome. It was shown that water uptake per volume contributing to space-occupying ischemic edema can be quantitatively measured in computed tomography (CT) by relative density changes. We hypothesize that net water uptake per time interval from onset to imaging can predict malignant edema.
Materials and Methods
In a pilot study, 40 acute stroke patients with M1-MCA infarctions and complete admission multimodal CT protocol were analyzed retrospectively. Twenty of these patients developed a malignant edema and underwent decompressive surgery. The net water uptake (NWU) within the acute infarct was quantified using relative (to unaffected hemisphere) density measurements and the relation to 'onset to imaging' time was examined in a linear and a nonlinear model. The optimal cut-off values for distinguishing malignant and nonmalignant infarctions subsequently were calculated.
Results
The mean %- NWU per hour for nonmalignant infarctions was 2.4% (± 2%) and 6.1% (± 2.4%) for malignant infarctions ($p<0.0001$). The area under the curve (AUC) for distinguishing these patient groups according to %-NWU per hour was 0.85 (95% Cl, 0.7-0.94) with an optimal cut off value of 2.7% (100% Sensitivity, 65% Specificity) when using the nonlinear approach and slightly superior to the linear approach (AUC 0.83, 95% Sensitivity, 70% Specificity).
Conclusions
Water uptake per hour is a suitable surrogate marker for malignant edema and could help to predict malignant and nonmalignant infarctions. This imaging biomarker might improve the early stratification of malignant MCA infarctions and may identify patients with fast progressing edema.

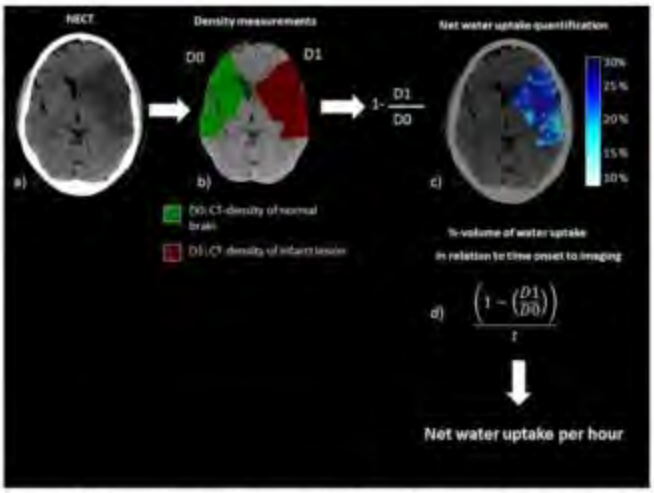


Figure 1: The quantification of net water uptake using densitometric measurements

$$P(\text{Malignant}_{\text{Wateruptakepertime}}) = \frac{1}{1+e^{-(\beta_0+\beta_1 \cdot \text{Wateruptakepertime})}}$$

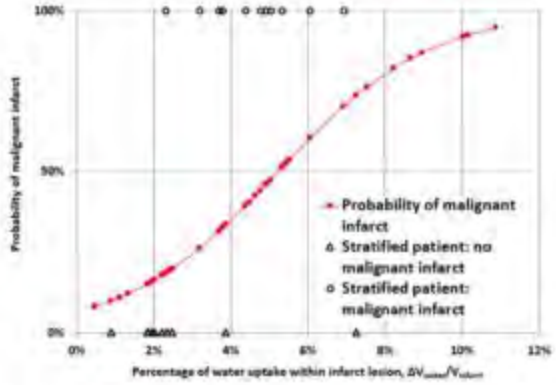


Figure 2: Probability graph
Stratification of patients using water uptake within infarct lesion per hour

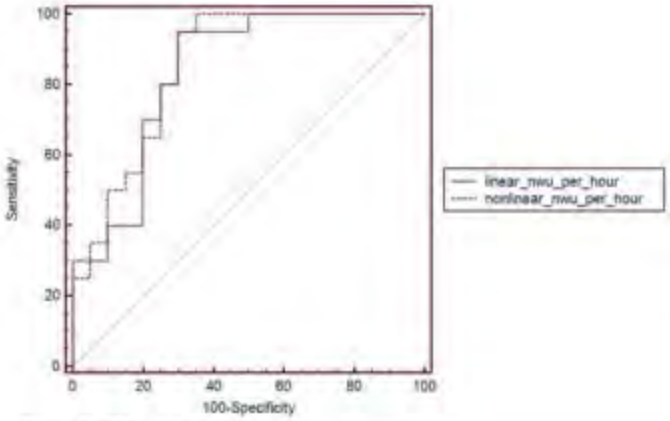


Figure 3: ROC curve analysis
Net water uptake per hour predicts malignant infarctions. The nonlinear approach improves sensitivity.

(Filename: TCT_O-38_figures_final_abstract.jpg)

O-40

11:24AM - 11:32AM

Proof of Principle: Using Dual Energy CT Iodine Mapping to Visualize Acute Cerebral Ischemia in Large Vessel Occlusion

A Khokale[1], C Weimar[1], A Ringelstein[2]
[1]*University Hospital Essen, Essen, NRW,* [2]*Institute of Diagnostic and Interventional Radiology and Neuroradiology, University Hospital Essen, Essen, NRW*

Purpose
Dual Energy CT technique allows to differentiate materials with high atomic numbers, such as iodine, from those with lower atomic numbers by acquiring data with high and low peak voltages from 2 different tubes at the same time. By means of material decomposition exploiting different attenuation levels at different energy levels it is possible to generate color coded iodine maps, visualizing iodine distribution and virtual noncontrast scans (VNC) with a single Dual Energy CTA (DECTA) scan. We hypothesize that lack of blood supply in cerebral ischemia due to large vessel occlusion should translate into hypoattenuation of the affected vascular territory on iodine maps due to decrease in iodine distribution.
Materials and Methods
We acquired 9 CT data sets comprising a nonenhanced scan (NECT), DECTA and CT perfusion scan (CTP) in the setting of acute ischemic stroke with no early stroke signs on native scan but DECTA-proven vessel occlusion and corresponding perfusion lesion. Data were acquired using a Siemens Definition Flash scanner (Siemens Healthineers, Erlangen Germany). Iodine maps and virtual noncontrast scan (VNC) were generated in postprocessing using Syngo Via 3.0 Dual Energy software (Siemens Healthineers).
Results
The generated iodine maps showed cortical hypoattenuation corresponding to the vascular territory that was affected by the vessel occlusion. The hypoattenuation correlated with the CBV deficit measured by CTP. In 2 cases when no iodine deficiency was visible although a CBV lesion was present on CTP good collateral supply was visible on DECTA. Iodine mapping can become a valuable tool in visualizing ischemia already in the acute phase of stroke. It might give insights into collateralization of the affected vascular territory and therefore can become a tool to predict outcome, e.g. for thrombectomy.
Conclusions
Iodine mapping with DECTA data is a promising "one stop shop" technique in acute stroke setting to visualize vessel occlusion (DECTA), ischemia (Iodine maps) and exclude acute bleeding (VNC) with 1 single scan. This would cut down radiation dose, the necessary amount of contrast medium, shorten scan time, and might help to select patients for thrombectomy by evaluating collateral support of the ischemic area.

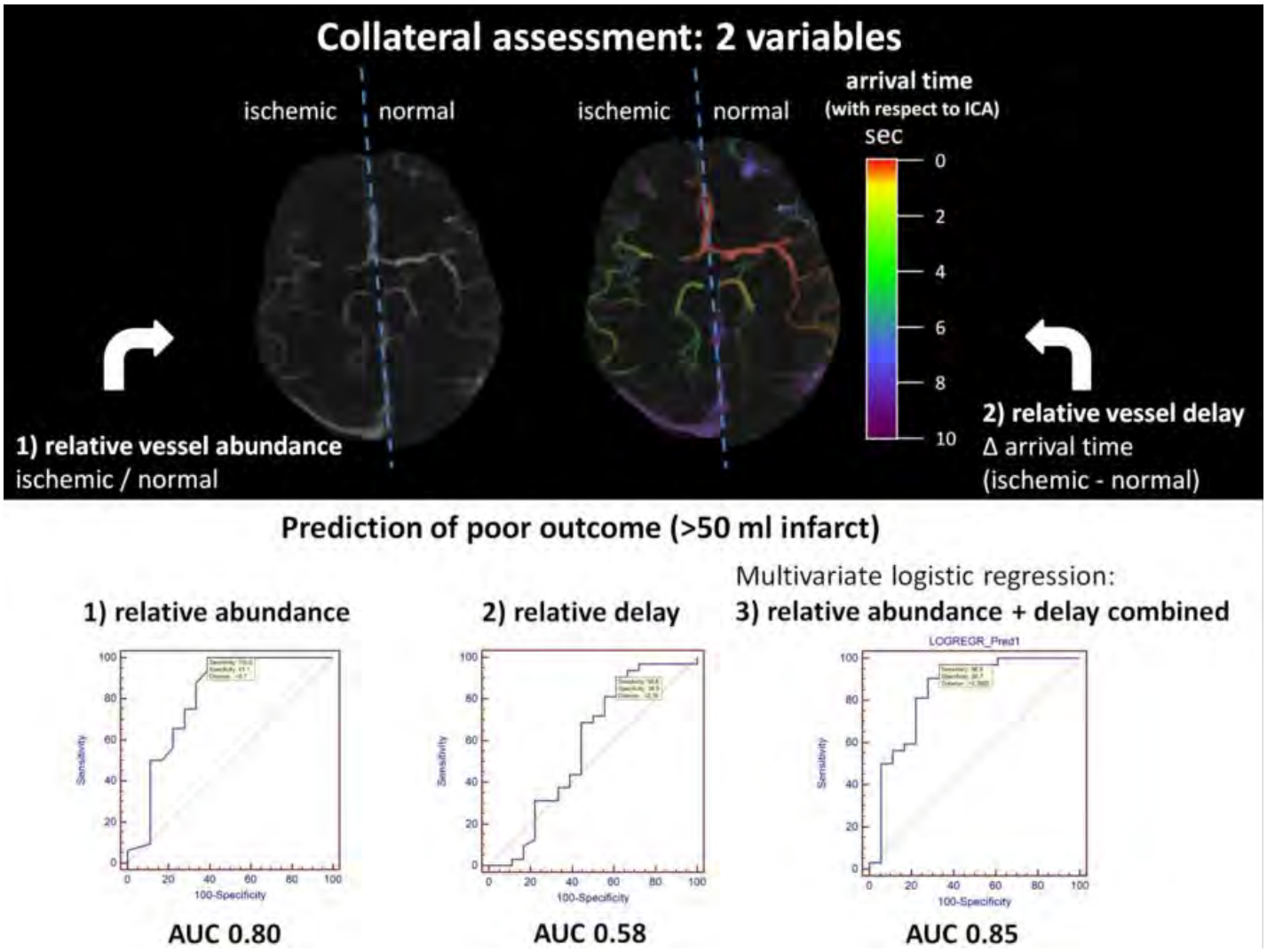
O-41

11:32AM - 11:40AM

Color coded Time Index of Collaterals improves Predictive Power of Good Outcome in Acute Ischemic Stroke

A Kemmling[1], L Aulmann[2], K Busch[2], G Broocks[3], P Schramm[1]
[1]Universitätsklinikum Lübeck, Lübeck, Germany, [2]Universitätsklinikum Lübeck, Lübeck, DEUTSCHLAND, [3]University Medical Center Hamburg-Eppendorf, Hamburg, Germany

Purpose
We employed a prototype software that converts 4D CTP whole brain perfusion data to 3D timing invariant CTA MIPs for collateral assessment with the addition of time delay information by color coding. We hypothesize, that infarct prediction by assessing vascular abundance of collateralized vessels in time MIPs may be enhanced by the additional component encoded by the delay of collateral supply. We therefore evaluated the independent contribution of each collateral component to infarct outcome.
Materials and Methods
In 45 proximal MCA occlusive strokes (recanalized within 6 h), 2 quantitative imaging features of collateral supply were assessed within the MCA territory in stroke patients with proximal anterior occlusion and tested in a multivariate predictive model of infarction: A) cumulative vascular abundance relative to the normal side which is directly related to collateral supply (Fig. 1) and B) delay of vascular intensity relative to normal side (Fig. 2). Vascular collateral abundance and delay of collaterals within the MCA territory were assessed visually and quantitatively by rater independent voxel-based analysis. Quantitative collateral measures were tested against further established univariate predictors of infarction including multiple CT perfusion parameters, time and degree of recanalization, age, sex and admission NIHSS score. The independent contribution of each variable to predict tissue infarction was evaluated in a large multicentric stroke database using a previously employed and published logit model for voxel wise infarct probability.
Results
Receiver operating characteristic (ROC) curve analysis showed that collateral assessment in CTA based on relative abundance of MCA vessels had a higher predictive power for poor tissue outcome (infarct >50 ml) than assessment by color coded delay of collaterals. In multivariate logistic regression analysis both, collateral vascular abundance as well as delay of vascular intensity relative to the normal side, were independent predictors for poor tissue outcome (beta coefficients 3.8 and 2.0, respectively, $P<0.0001$).
Conclusions
The power to predict tissue infarct and favorable outcome after thrombectomy by collateral assessment in ischemic stroke is improved using color-coded delay that encodes the collateral arrival time component.



(Filename: TCT_O-41_Fig.jpg)

O-42

11:40AM - 11:48AM

Multiparametric CT Perfusion Model for Prediction of Infarct Core: A Voxel-based Regression Analysis Using Machine Learning

S Tadayon[1], N Swinburne[1], K Nael[1]
[1]*Icahn School of Medicine at Mount Sinai, New York, NY*

Purpose
In patients with acute ischemic stroke (AIS), reduced CT perfusion parameters such as CBF and CBV have been shown useful for identification of infarct core (1-2); however, others have shown relatively poor correlation between these measures and DWI assessment of infarction (3). In this study we sought to develop a multi-parametric CTP model to predict infarction core using MRI as standard of reference. We performed a voxel-based logistic

ridge regression analysis utilizing machine-learning techniques to classify infarcted vs. noninfarcted voxels.
Materials and Methods
Acute ischemic stroke patients with anterior circulation stroke who had baseline CTP and follow up MRI were included. Computed tomography perfusion data were processed using a Bayesian probabilistic method (4). The extracted brain from CTP was registered linearly to FLAIR-brain. The brain extractions and registrations were refined manually for all subjects. An infarction mask and 2 noninfarcted masks (1 on ipsilateral and the other on contralateral cerebral hemisphere) were manually drawn on FLAIR. In order to build our model, we used the voxel values from five CT perfusion parameters including delay, TTP, MTT, CBV and CBF. Five additional features were generated (difference maps) by subtracting the mean of a cube (27 voxels) on the contralateral side of each voxel. We constructed a simple and a complex logistic ridge regression model to classify voxels into infarcted or noninfarcted voxels. The simple model had the initial 5 CT perfusion parameters plus difference maps (total of 10 features). For the complex model we also included the interaction terms between features resulting in a total of 55 features. To find the optimal ridge regularization parameter, we used a 2 nested 10-fold cross validation. Model performance was measured using receiver operating characteristic (ROC) and by calculating the area under curve (AUC).
Results
The top 5 individual features with highest AUC were: Delay*TTP_diff (AUC=0.728), CBF (AUC=0.724), MTT*TTP_diff (AUC=0.720), TTP*TTP_diff (AUC=0.719), Delay*Delay_diff(AUC=0.715). Both simple and complex multiparametric models significantly improved diagnostic accuracy compared to individual classifiers. Compared to CBF (commonly used as a determinant of infarction core), simple model improved the AUC by 13% (P value = 1.13 * 10-6) and 18.8% (P value=8.9*10-9) and complex model improved AUC by 16.9% (P value= 5.9*10-8) and 20.7% (P value= 2.17 * 10-9) for ipsilateral and contralateral noninfarcted masks, respectively. The complex model improved simple model by 3% (P value = 7.9*10-5) and 2% (P value= 0.0043) for ipsilateral and contralateral noninfarcted masks, respectively. The complex model had higher AUC in all subjects compared to simple model.
Conclusions
Using voxel-based machine learning approach, we showed CT perfusion parameters collectively can delineate infarction core more accurately than any single classifier. The CT perfusion parameters that carry information regarding infarction core differ across subjects. Future studies are needed to assess and define individualized CTP criteria for infarct core identification.

O-43

11:48AM - 11:56AM

Perfusion CT-derived permeability surface area in predicting hemorrhagic transformation after intravenous thrombolysis in acute stroke

J Puig[1], G Blasco[2], C Biarnes-Duran[3], P Daunis-i-Estadella[4], J Serena[5], M Marti-Navas[1], K Nael[6], M Wintermark[7], P Salvador[2], M Castellanos[8]
[1]Research Unit of Diagnostic Imaging Institute (IDI), IDIBGI, University Hospital Dr Josep Trueta, Girona, Girona, [2]Imaging Research Unit, IDI-IDIBGI, Hospital Dr Josep Trueta, Girona, None, [3]Research Unit of Diagnostic Imaging Institute (IDI), Girona Biomedical Research Institute (IDIBGI), Girona, Girona, [4]Department of Computer Science, Applied Mathematics and Statistics, University of Girona, Girona, Girona, [5]Hospital Dr Josep Trueta, IDIBGI, Girona, None, [6]Icahn School of Medicine at Mount Sinai, New York, NY, [7]Stanford University, Stanford, CA, [8]Department of Neurology, A Coruna University Hospital, A Coruna, Galicia

Purpose
Hemorrhagic transformation (HT) is a devastating complication of acute ischemic stroke; parenchymal hematoma type 2 (PH-2) is the most severe type. Blood-brain barrier permeability is a potential predictor of HT after tissue plasminogen activator (tPA) administration; however, perfusion computed tomography (PCT) permeability imaging's reliability for predicting HT is uncertain. We determined the performance of PCT-derived permeability surface area (PCT-PSA) in predicting HT after intravenous tPA in patients with acute stroke.
Materials and Methods
We used a 128-slice CT scanner to prospectively study acute stroke patients treated with tPA. We included patients with symptoms onset ≤4.5 hours, middle cerebral artery territory infarct, an alteration on permeability maps, and CT follow-up at 24 hours. We excluded patients referred for mechanical thrombolysis from the final analysis. To calculate permeability maps, we used delayed acquisition with 5 PCT-PSA thresholds (3, 4, 5, 6, and 7 mL/100g/min). We graded HT on 24-hour follow-up CT using the European-Australasian Acute Stroke Study II criteria. Receiver operating characteristics (ROC) curves selected the optimal volume threshold, and multivariate logistic regression analysis identified predictors of HT.
Results
Of 357 patients treated with tPA, 156 met the inclusion criteria. Of these HT occurred in 37 (23.6%),12 (7.7%) of whom developed PH-2. At admission, patients with HT had lower platelet and fibrinogen levels, higher NIHSS scores, increased ischemic lesion volumes, higher PCT-PSA, and poorer collateral status. The negative predictive value of PCT-PSA at a threshold of 7mL/100g/min was 0.846 for HT and 0.94 for PH-2. The multiple regression analysis selected PCT-PSA combined with baseline platelets and NIHSS score as the best model for predicting HT (area under curve 0.77). Perfusion computed tomography (PCT)-PSA was the only independent predictor of PH-2 (odds ratio 1, area under curve 0.68, p=0.045).

Conclusions
Permeability surface area (PSA) predicts HT after tPA, and is particularly useful in identifying patients with low risk of developing HT.

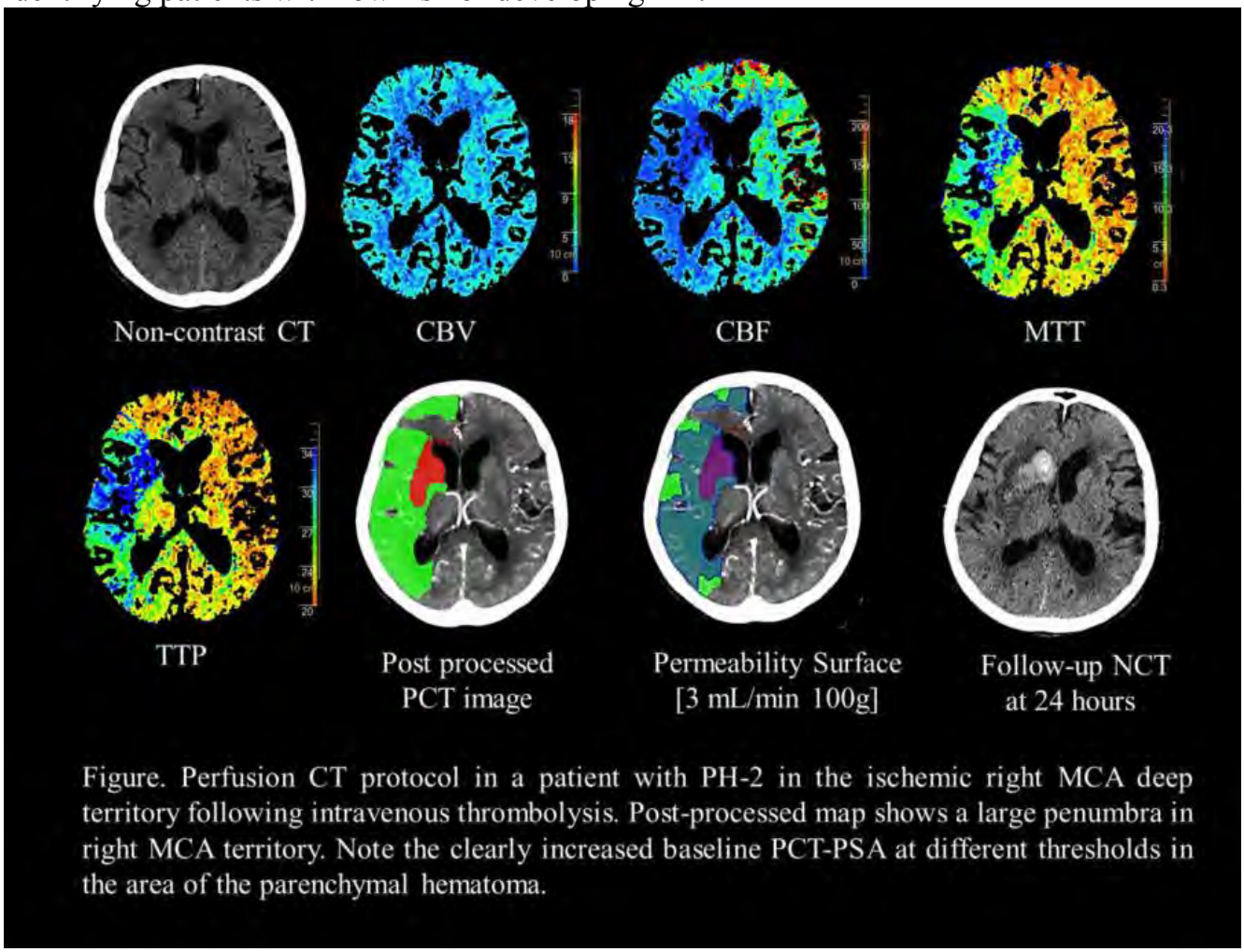


Figure. Perfusion CT protocol in a patient with PH-2 in the ischemic right MCA deep territory following intravenous thrombolysis. Post-processed map shows a large penumbra in right MCA territory. Note the clearly increased baseline PCT-PSA at different thresholds in the area of the parenchymal hematoma.

(Filename: TCT_O-43_PCT-PSA.jpg)

O-44

11:56AM - 12:04PM

Comparison of Multiphase CTA and CT Perfusion for Triage of Acute Ischemic Stroke: A Single Center's Experience

G Bennett[1], J Lavie[1], A Albar[1], S Arndt[1], J Record[1], M Al Hasan[1], G Vidal[1], J Milburn[1]
[1]*Ochsner Clinic Foundation, New Orleans, LA*

Purpose
Multiphase CTA (MCTA) recently has been advocated as an acceptable alternative to whole brain CT perfusion (CTP) for identifying patients with intracranial large vessel occlusion (LVO) who may benefit from thrombectomy (1). Our institution recently transitioned from

CTP to MCTA for triage of acute stroke patients. The purpose of the study is to determine how this has influenced patient selection for thrombectomy and clinical outcomes.
Materials and Methods
The imaging database was queried for all patients evaluated for thrombectomy at our comprehensive stroke center from the implementation of MCTA in August 2016 through November 2016. Rates of thrombectomy, TICI scores, and admission and discharge NIHSS for patients who underwent MCTA were compared to our prior database of CTP of thrombectomy candidates from January to December 2015.
Results
Thirty-six out of 101 patients who underwent MCTA were found to have anterior LVO (35%), compared to 162 out of 401 patients who underwent CTP (40%). The rate of inclusion for thrombectomy of the MCTA cohort with LVO (53%) was significantly higher than the CTP cohort (36%; $p<0.0001$). Successful reperfusion rates (TICI 2B or greater) were similar between CTP and MCTA (86% and 79% respectively). Patients triaged with MCTA had a significantly lower discharge NIHSS than those who underwent CTP (9.6 and 10.7 respectively; $p=0.0002$). There was no statistically significant difference between the initial NIHSS of patients who underwent MCTA versus CTP (18 and 17 respectively; $p=0.55$), or between the improvement in NIHSS from admission to discharge compared to the CTP cohort (8.3 and 6.7 respectively; $p=0.52$).
Conclusions
Using MCTA for triage of patients with acute stroke due to LVO led to more patients being selected for intervention when compared to CTP with similar clinical scores for both groups at discharge.

O-45

12:04PM - 12:12PM

Influence of CT ischemic lesion location on functional outcome measured by the modified Rankin Scale

M Ernst[1], A Boers[2], A Aigner[1], A Yoo[3], J Fiehler[1], H Marquering[4]
[1]University Medical Center Hamburg-Eppendorf, Hamburg, Hamburg, [2]Academic Medical Center, Amsterdam, Netherlanss, [3]Texas Stroke Institute, Plano, TX, [4]AMC, Amsterdam, Noord-Holland

Purpose
Ischemic lesion volume assessed by computer tomography (CT) correlates only moderately with clinical end points, such as the modified Rankin Scale (mRS). We hypothesized that the association between CT ischemic lesion volume and outcome as assessed with mRS 3 months after stroke is strengthened taking into account both the infarct location and the assumed mRS relevance of the affected brain area. In contrast to previous studies, the current study, as a substudy of MR CLEAN*1, adjusts for several important factors that are known

to be associated with long term outcome after stroke such as baseline patient characteristics, treatment modality and recanalization status.

Materials and Methods

An anatomical atlas was registered to the follow-up CT images 3 to 9 days after stroke of 254 patients from the MR CLEAN trial to assess infarct location and determine ischemic lesion volume in each brain area. Computed tomography scans were excluded because of poor quality due to beam hardening or motion artifacts or technical errors, precluding automatic registration or segmentation. We excluded patients with hemicraniectomy, huge old infarcts, bleeding, and brainshift. By calculating the overlap of segmented ischemic lesion with anatomical brain areas in the registered atlas, the ischemic lesion volume for each brain area was determined for each patient. Based on previous studies (2, 3) the 66 brain areas were ordered by their mRS-relevance, i.e. their strength of association with a high 3 months mRS and unfavorable outcome. Hereafter, the 66 brain areas were subdivided into brain areas of high, moderate and low mRS relevance. Based on this distinction, the ischemic lesion volume in the brain areas of high, moderate and low mRS relevance was assessed for each patient. Multiple regression analyses with and without adjustment for known confounders were performed to assess the association between the ischemic lesion volumes of different mRS relevance and outcome. Akaike information criterion was determined for each regression model.

Results

Figure 1 shows the different ischemic lesion volumes for each mRS score at 90 days. The risk for an unfavorable outcome (i.e. mRS>2) was twice as high given an increase of ischemic lesion volume in brain areas of high mRS relevance (OR 1.99, CI 1.58-2.61), while there was no significant risk given an increase in brain areas of moderate and low mRS relevance (OR 1.04, CI 0.88-1.25; OR 1.06, CI 0.75-1.55). The best model fit is obtained by the use of ischemic lesion volume in brain areas of high mRS relevance with an AIC of 235.7 compared to a model using the total ischemic lesion volume with an AIC of 253.2 (Tables 1 and 2).

Conclusions

The association between CT ischemic lesion volume and outcome as assessed with mRS 3 months after stroke is strengthened by accounting for the assumed mRS-relevance of the affected brain area. Future prediction models should account for the ischemic lesion volume in brain areas of high mRS relevance.

Figure 1 Ischemic lesion volumes (mean, 95%-confidence interval) by mRS at 90 days

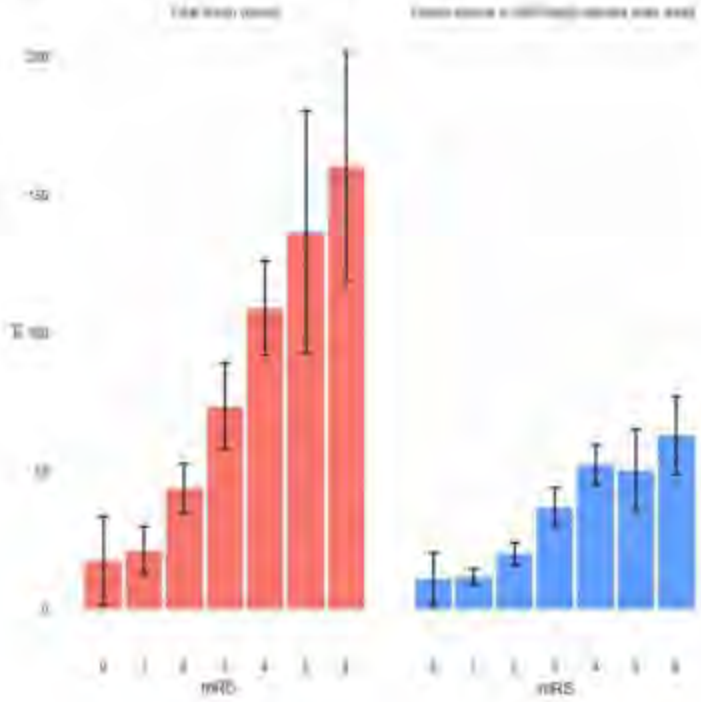


Table 1 Ischemic lesion volumes (mean, 95%-confidence interval) by mRS 90 at 90 days

mRS	0 (n=5)	1 (n=23)	2 (n=56)	3 (n=55)	4 (n=60)	5 (n=24)	6 (n=31)
Total ischemic lesion volume (mL mean)	17.3 (1.2-33.3)	21.1 (12.6-29.5)	43.3 (34.3-52.4)	73.2 (57.8-88.6)	108.5 (91.6-125.4)	136.0 (92.2-179.9)	159.5 (117.9-201.1)
Ischemic lesion volume in brain areas of high mRS-relevance (mL mean)	10.8 (1.4-20.2)	11.4 (8.5-14.3)	19.7 (15.8-23.7)	36.5 (29.4-43.6)	51.9 (44.7-59.1)	49.8 (35.0-64.7)	62.4 (48.3-76.6)

Table 2: Association between ischemic lesion volume and unfavorable outcome (mRS>2) at 90 days

		No adjustment			Adjusted*		
Binary Logistic regression		OR	95% CI	AIC	OR	95% CI	AIC
Model 1	Total ischemic lesion volume	1.30	1.20-1.42	253.2	1.17	1.04-1.34	179.6
Model 2	Ischemic lesion volume in brain areas of high mRS-relevance	2.12	1.73-2.67	235.7	1.57	1.18-2.15	177.0
Model 3	Ischemic lesion volume in brain areas of high mRS-relevance	1.99	1.58-2.61	239.0	1.52	1.11-2.15	180.5
	Ischemic lesion volume in brain areas of moderate mRS-relevance	1.04	0.88-1.25		1.08	0.86-1.35	
	Ischemic lesion volume in brain areas of low mRS-relevance	1.06	0.75-1.55		0.98	0.56-1.81	

* Additionally adjusting for sex, age, atrial fibrillation, diabetes mellitus, previous stroke or mRS>0, occlusion site, collateral score, time to treatment, treatment modality, recanalization status

AIC = Akaike information criterion

(Filename: TCT_O-45_GraphicFile.jpg)

Monday
11:00AM - 12:15PM
Long Beach Convention Center, Room 102BC (Main Level)

04H-Parallel Paper Session: TURBO & TOUR: Head and Neck, and High Tech

T-01

11:00AM - 11:03AM

Clinical Characteristics can Differentiate Peritonsillar from Intratonsillar Abscesses: A Retrospective Imaging Study

W Stewart[1], M Rohrbach[1], J Yu[1], G Avey[1], T Kennedy[1]
[1]*University of Wisconsin, Madison, WI*

Purpose
Intratonsillar abscesses typically are treated conservatively whereas peritonsillar abscesses often require incision and drainage. The purpose of this study is to determine the clinical signs and symptoms that can differentiate a peritonsillar from an intratonsillar abscess as validated by contrast-enhanced computed tomography.
Materials and Methods
This retrospective HIPPA compliant study has been approved by our Institutional Review Board. A 10-year retrospective chart review was performed from 2006 through 2016 to identify patients who (1) presented to our hospital with either a peritonsillar (PTA) or intratonsillar (ITA) abscess and who (2) received imaging at the time of initial presentation; 91 abscesses were identified. Individual patient medical records then were reviewed for the following clinical signs and symptoms: muffled voice, drooling, trismus, tonsillar abnormality, uvular deviation, uvular edema, peritonsillar or soft palate fullness, tonsillar erythema or exudate, and soft palate erythema. The patient's imaging by CT at their initial encounter then was reviewed by 3 experienced board-certified neuroradiologists to establish an imaging diagnosis of either a PTA or ITA; abscesses with imaging findings suggestive of a combined PTA and ITA were excluded from our study. Logistic regression analysis determined statistically significant associations between clinical characteristics and an imaging diagnosis of a PTA or ITA.
Results
Contrast-enhanced imaging of the neck identified 51 PTAs and 26 ITAs; 14 abscesses possessed imaging characteristics of both PTA and ITA and were excluded from our study. The odds of a PTA versus an ITA is 15.60 times greater with soft palate or peritonsillar fullness [95% CI (2.25, 108.11)], 7.12 times greater with uvular deviation [95% CI (1.39, 36.50)] and 4.57 times greater when a muffled voice is clinically present [95% CI (1.18, 17.68)].

Conclusions
Peritonsillar abscess is associated with muffled voice, soft palate or peritonsillar fullness, and uvular deviation. These clinical signs can be used to guide clinicians in differentiating between peritonsillar and intratonsillar abscess and to prospectively identify those patients that may benefit substantially from additional imaging.

T-02

11:03AM - 11:06AM

Foreign Body or Giant Cholesteatoma? A Case Report of a Cholesteatoma not resembling known Imaging Appearance

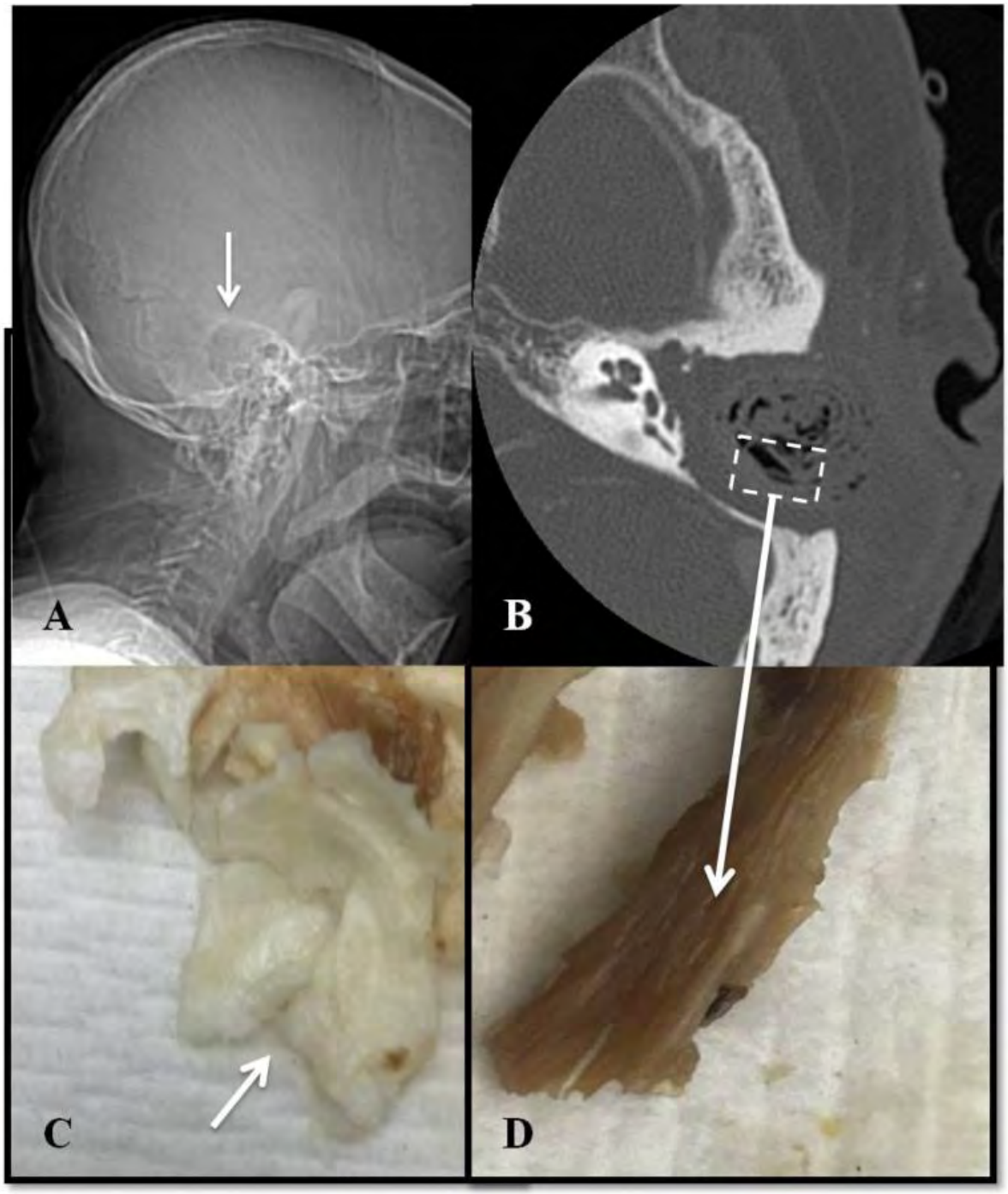
S Kamel[1], M Wolf[2], K Talekar[2]
[1]Thomas Jefferson University Hospital, Philadelphia , PA, [2]Thomas Jefferson University Hospital, Philadelphia, PA

Purpose
Many studies have described the radiologic appearance of a cholesteatoma, which generally is seen on CT as a homogeneous soft tissue density with characteristic surrounding bony erosion. We present a case of a late stage giant cholesteatoma which does not resemble known radiologic appearance.
Materials and Methods
Case Report: A recently immigrated 87-year-old Chinese male with a history of dementia presented with several weeks of progressively worsening left ear pain. The patient was a poor historian but denied any past medical or surgical history related to his ear. Physical exam demonstrated foul-smelling bloody and thick purulent discharge within the left external auditory canal. The posterior auricular region was erythematous and edematous with fluctuance. Cranial nerve exam demonstrated left hearing loss and facial asymmetry consistent with deficiency of the left facial nerve.
Results
Imaging - A contrast-enhanced CT of the temporal bones was obtained for further evaluation. Lateral scout view demonstrated a large translucent cavity in the mastoid with a thin rim of sclerosis (Fig. 1A). Within this bony defect of the left temporal bone was a 2.5 x 2 x 2 cm lamellated, isodense lesion containing multiple curvilinear foci of air (Fig. 1B). Associated with the mass was erosion of the lateral semicircular canal resulting in labyrinthine fistula and a large defect of the sigmoid plate. The scutum was destroyed. The tegmen tympani and mastoideum were dehiscent. There was ossicular chain erosion with partial preservation of the incus. The mastoid bone was sclerotic with a paucity of air cells and opacification of the few remaining mastoid air cells. There was no involvement of the transverse sinus. There was a hypoattenuating collection surrounding the primary mass extending into the subgaleal space with peripheral enhancement, consistent with abscess.
Surgery and Pathology - Intra-operatively, a posterior auricular incision was made with

anterior dissection over the periosteum where extensive purulence was encountered. A large pearly gray lesion characteristic of a cholesteatoma (Fig. 1C) was eroding through the middle ear causing dehiscence of the posterior and middle fossa bony plates, dehiscence of the bony canal of the tympanic and descending mastoid segments of the facial nerve. Gross specimens of portions of the inner cholesteatoma wall demonstrated easily separated thin layers of keratin, similar to the CT appearance of a lamellated air filled lesion (Fig. 1D). Microscopic evaluation of the lesion detailed the keratinized, enucleated, stratified epithelial cells consistent with cholesteatoma. Microbiology and culture data from the subgaleal abscess demonstrated a polymicrobial infection.

Conclusions

Although cholesteatomas are histologically composed of layering keratinized squamous epithelium, they generally resemble a homogeneous soft-tissue density mass on CT.2-4 There are no previous reports demonstrating this lamellated appearance of a cholesteatoma which so closely mirrors the thin layers of epithelium seen on pathology. Prior to the operative procedure, this lesion was thought to be packing material given its isodensity and structural resemblance to manmade gauze which may retain pockets of air. The unreliable clinical history and poor medical follow up given recent immigration clinically supported our initial theory. On retrospective consideration, pathogenesis of air within the cholesteatoma separating the layers of keratin may be secondary to gas tracking from the nearby polymycrobial infection. Air also may have tracked into the cholesteatoma via communication with mastoid air cells. Or, perhaps this appearance may represent partial autolysis with delamination of the keratin sheets as the cholesteatoma continued to grow to a significant stage. Although the internal architecture of this lesion is not what one typically associates with a cholesteatoma, the bony erosion shown by this lesion is more characteristic as cholesteatomas frequently demonstrate tegmen and ossicular erosion. Upon surgical exploration of the gross appearance and pathology review, it was apparent that this lesion was indeed a cholesteatoma. Postoperatively, the patient recovered from the infection with appropriate healing of the surgical bed. Unfortunately, hearing was not recovered in the left ear. Conclusion - This CT appearance of a cholesteatoma which so closely resembles macroscopic appearance is a unique demonstration of radiopathologic correlation. Radiologists should keep pathology in mind when considering a differential diagnosis and additionally how infection or significant growth may change the radiologic appearance of a lesion.



(Filename: TCT_T-02_FIG1.jpg)

T-03

11:06AM - 11:09AM

Treatment of Branchial Cleft Cyst Using Ethanol Ablation

H Lee[1]
[1]*Inha University Hospital, incheon, Korea, Republic of*

Purpose
To evaluate the efficacy and safety of ethanol ablation (EA) for branchial cleft cyst (BCC).
Materials and Methods
Between July 2013 and October 2016, 11 patients with BCC (8 female and 3 male, age: 13-39 years) underwent EA who refused surgical treatment. Benign cystic lesions were confirmed cytologically in all patients before treatment. After aspiration of the cystic fluid, absolute ethanol (99%) was injected. The injected volume of ethanol was 80-100% of the volume of the aspirated fluid. The volume of injected ethanol did not exceed 20 ml. Clinical and US follow-up was performed serially every 1-3 months after treatment. Initial and final lesion volume was compared for the treatment response.
Results
All patient had unilocular cysts, and the initial volume of cysts ranged from 9.9 – 39.1 ml (mean, 22.19 ± 10.11 ml). The number of treatment sessions was single in 9, 2 in 2 patients (mean, 1.2 sessions). Follow-up US was performed in all patients from 1 to 24 months (mean, 5.6 months). The mean volume of the cyst was 6.69 ± 9.82 ml and volume reduction rate was -53 – 100% (mean, 58.39%) at last follow up. Treatment success was achieved in 8 patients (72.7%), and improvement of cosmetic-grading scores was observed at last follow up. Two patients with treatment failure underwent surgery. There were no significant complications during the procedure or follow-up periods.
Conclusions
Ethanol ablation seems to be an effective and safe treatment modality for BCC, and may be considered before surgery.

T-04

11:09AM - 11:12AM

Diffusion-weighted imaging using a readout-segmented, multi shot EPI sequence at 3T distinguishes between morphologically differentiated and undifferentiated subtypes of thyroid carcinoma

S Schob[1]
[1]*University Hospital Leipzig, Leipzig, WY*

Purpose
Thyroid carcinomas represent the most frequent endocrine malignancies. Recent studies were able to distinguish malignant from benign nodules of the thyroid gland with diffusion-weighted imaging (DWI). Although this differentiation is undoubtly helpful, presurgical discrimination in between well differentiated and undifferentiated carcinomas would be crucial in order to define the optimal treatment algorithm. Therefore the aim of this study was to investigate if readout-segmented multi shot echo planar DWI is able to differentiate between differentiated and undifferentiated subtypes of thyroid carcinomas.

Materials and Methods

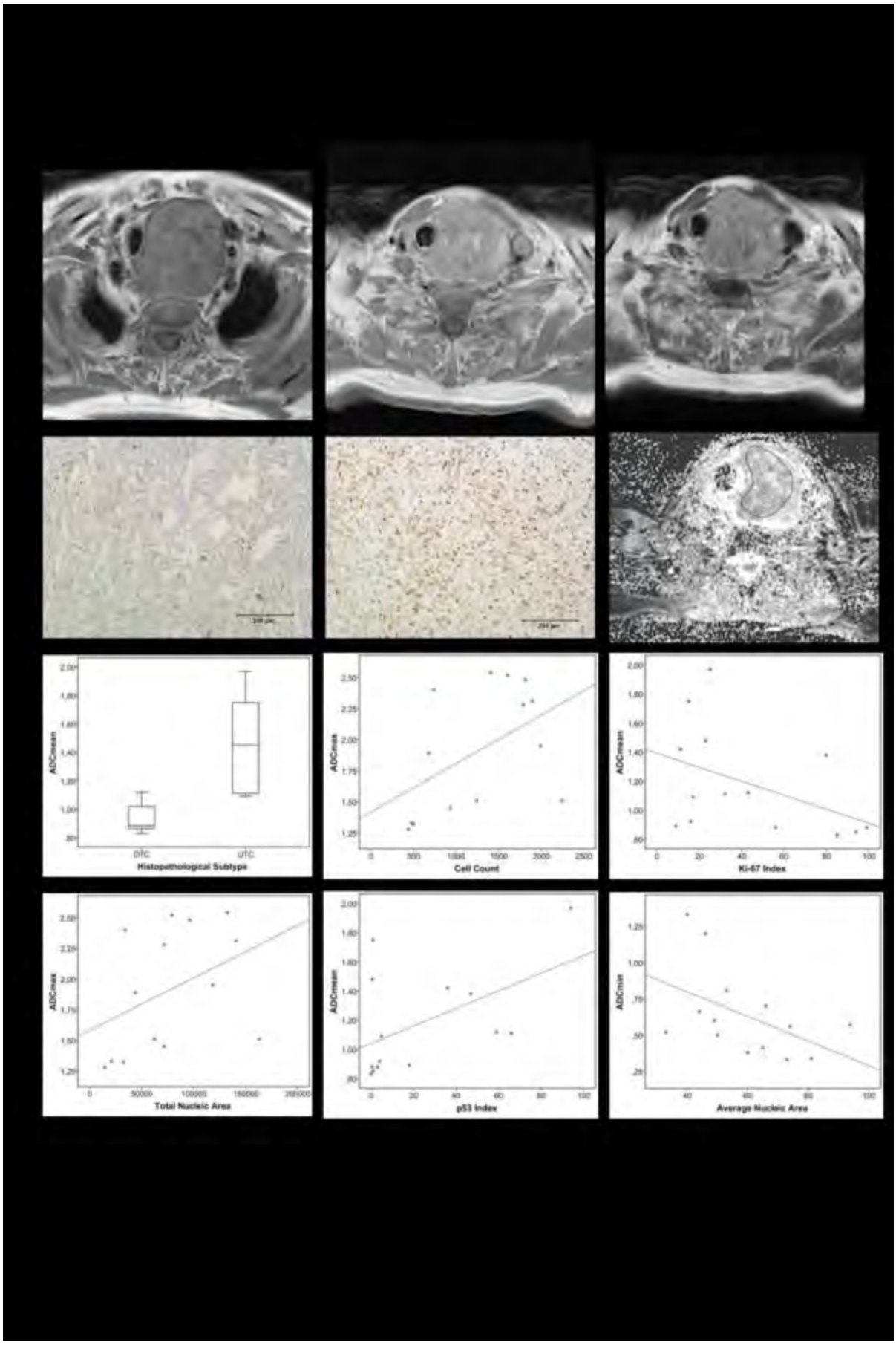
Fourteen patients with different types of thyroid carcinomas who received pre-operative DWI were included in our study. In all lesions ADCmin, ADCmean and ADCmax and D were estimated on basis of region of interest (ROI) measurements after coregistration with T1-weighted, postcontrast images. All tumors were resected and analyzed histopathologically. Ki-67 index, p53 synthesis, cellularity, total and average nucleic areas were estimated using ImageJ version 1.48.

Results

ANOVA revealed a statistically significant difference of ADCmean values between differentiated and undifferentiated thyroid carcinomas ($p= 0.022$). Spearman-Rho calculation identified significant correlations between ADCmax and cell count ($r= 0.541$, $p= 0.046$) as well as between ADCmax and total nuclei area ($r= 0.605$, $p= 0.022$).

Conclusions

Diffusion-weighted imaging can distinguish between differentiated and undifferentiated thyroid carcinomas and therefore aids the thyroid surgeon to identify the optimal treatment algorithm.


ADCmean
DTC
UTC
Histopathological Subtype
ADCmean
Cell Count
ADCmean
Ki-67 Index
ADCmean
Total Nucleic Area
ADCmean
p53 Index
ADCmin
Average Nucleic Area

(Filename: TCT_T-04_thyroidfigure001.jpg)

T-05

11:12AM - 11:15AM

Multi-modality, multi-material 3D printing: visualizing an expansile trigeminal schwannoma obliterating Meckel's cave and foramen ovale, at a glance.

J Shin[1], D Poliak[2], J Chazen[3]
[1]Weill Cornell Medicine, New York, NY, [2]NewYork Presbyterian- Weill Cornell, New York, NY, [3]Weill Cornell Medicine, New York, NY

Purpose
The purpose of this work is to illustrate novel applications of existing postprocessing techniques, in service of maximizing the perceptual and thus clinical utility of diagnostic neuroimaging as patient-specific 3D printed models.
Materials and Methods
Computed tomography image data were acquired on a GE Lightspeed Optima 660 (120kVp AEC postprocessed at 0.625mm collimation in standard kernel). Magnetic resonance image data were acquired on a GE Sygna HDxT (3.0T T1 3D FSPGR post 6.5 mL Gadavist postprocessed at 1.0mm collimation). Image data were postprocessed in 3D Slicer v4.6 (https://www.slicer.org/). Threshold segmentation and fiducial registration techniques were used to create a multi-assembly surface model of the skull (calvaria and skull base components) and tumor (hyperenhancing and hypo-enhancing components). Accuracy of registration was ensured by manual inspection/correction of orbitonasal, clivus, tentorium, corpus callosum, and ventricular alignment. Models were fabricated on a Stratasys Connex3 Objet260 printer, with the skull in VeroClear, hyperenhancing components in VeroMagenta, and hypo-enhancing components in VeroWhite. Fabricated models were validated quantitatively against corresponding digital models and original binary segmentations.
Results
Fabricated assembly is depicted in the included image, and demonstrates tight correspondence between tumor and adjacent osseous margins. Suboptimal clarity of prepolished VeroClear precluded meaningful tumor visualization when wholly encased within the skull, although it is adequate to convey the entire volume of tumor within the skull base. The tumor components are well visualized by direct inspection, and areas of enhancement relative to osseous landmarks are depicted clearly.
Conclusions
Multimodality, multimaterial 3D printing enhances the perceptual benefits of diagnostic neuroimaging, by distilling clinically useful information available in a variety of imaging studies into a single, relatable physical object. The techniques applied here to a dramatic presentation of trigeminal schwannoma are analogously useful wherever multimodal imaging may apply.


(Filename: TCT_T-05_2016-12-07130949.jpg)

T-06

11:15AM - 11:18AM

Dynamic Contrast Enhanced MRI to Differentiate Benign Versus Malignant Parotid Neoplasms Utilizing Golden-angle Radial Sparse Parallel MRI

J Mogen[1], M Hagiwara[1], G Fatterpekar[2], E Zan[3], N Bansal[4], T Block[1], S Patel[5]
[1]NYU Langone Medical Center, New York, NY, [2]NYU School of Medicine, New York, NY, [3]Johns Hopkins Hospital, Baltimore, MD, [4]New York University, New York, NY, [5]University of Virginia Health System, Charlottesville, VA

Purpose
Pre-operative determination of the malignant status of parotid lesions is clinically important, determining future local excision versus total parotidectomy. Benign and malignant lesions often have overlapping appearances on conventional imaging (1). Dynamic contrast-enhanced MRI to differentiate salivary neoplasms is described, however the most useful parameters remain questioned (2). Adding to discussion of semiquantitative parameters (3), our aim was to determine if qualitative analysis of time intensity curves (TIC) can prospectively distinguish benign lesions.

Materials and Methods

Twenty-six patients with a total of 30 parotid neoplasms were recruited. Dynamic contrast-enhanced MRI utilizing Golden-angle Radial Sparse Parallel (GRASP) MRI technique was analyzed and TIC created by region of interest traced around the largest enhancing portion of the tumor. Time intensity curves were created and qualitatively assessed by 2 independent observers. They assigned each TIC to 1 of 4 categories: 1, continuously rising; 2, gradual rise with subsequent plateau; 3, sharp rise with subsequent plateau; 4, sharp rise with washout. Inter-rater agreement was measured by kappa with linear weighting. Diagnostic performance for prediction of malignancy based on curve analysis was assessed.

Results

Inter-rater κ was 0.763 (95% CI 0.639-0.886). One hundred percent of type 1 curves for both readers corresponded to benign neoplasms. Segregating type 1 and 2 curves from type 3 and 4 curves yielded a negative predictive value (NPV) for malignant neoplasm from 93.8% (95% CI 69.8-99.8) to 100% (78.2-100), and a positive predictive value (PPV) from 57.1% (28.9-82.3) to 60% (32.3-83.7). Thirteen of the correctly predicted benign lesions represented pleomorphic adenomas with one Warthin tumor.

Conclusions

Qualitative analysis of GRASP DCE-MRI demonstrates a high NPV for malignant parotid neoplasms. This noninvasive imaging technique may add value in the presurgical diagnostic work up of parotid neoplasms.

Pathologic Diagnoses of Salivary Gland tumors

Diagnosis	Number of lesions
Benign	*21*
Pleomorphic adenoma	14
Cellular pleomorphic adenoma	1
Oncocytoma	2
Warthin tumor	4
Malignant	*9*
Acinic cell carcinoma	2
Adenoid cystic carcinoma	1
Carcinoma ex pleomorphic adenoma	1
Mucoepidermoid carcinoma	1
Salivary duct carcinoma	1
Spindle cell carcinoma	1
Squamous cell carcinoma metastasis	2

(Filename: TCT_T-06_Table1400dpismall.jpg)

T-07

11:18AM - 11:21AM

A Retrospective DTI Study on the Effect of Proximity of Brain Tumor to Superior Longitudinal Fasciculus or Cingulum on Perioperative Language Outcomes

M Turek[1], S Riley[1], V Nair[1], J Kuo[1], M Meyerand[1], V Prabhakaran[1]
[1]*University of Wisconsin School of Medicine and Public Health, Madison, WI*

Purpose
Investigate the utility of diffusion tensor imaging (DTI) as a pre-operative planning tool by analyzing the effect of lesion to tract distance (LTD) for the superior longitudinal fasciculus (SLF) and cingulum on pre-operative verbal fluency (VF) scores and peri-operative language deficits.
Materials and Methods
The study included patients with primary brain tumors who underwent surgical resection (n=43). Pre-operative phonemic VF scores were collected before pre-operative MRI, and deficits retrospectively. For LTD, color coded fractional anisotropy DTI images were overlaid onto contrast-enhanced T1- or T2-weighted images.
Results
Dominant language hemisphere SLF LTD's were correlated to pre-operative VF (Pearson's r=0.31, p=0.045). Language dominant SLF LTD values were categorized into <1, 1-2, and >2 cm groups. Significant differences were observed between these LTD groups with respect to stable, new, and persistent postoperative deficits (chi-square; p=<0.0001, p=0.0089, p=0.00037). The percentage of patients who developed new deficits in the <1, 1-2, and >2 cm LTD groups were: 36%, 56%, and 5.0% respectively. Stable and persistent deficits followed this trend. Average cingulum LTD values organized by SLF LTD of <1, 1-2, and >2 cm were: 10.11, 10.23, and 22.39 mm. Patients grouped by presence of SLF or cingulum LTD of <1 cm versus no LTD of <1 cm showed a significant difference in incidence of new deficits: all new deficits occurred in the <1 cm group (p=0.00062).
Conclusions
Verbal fluency correlated to SLF LTD, supporting the utility of DTI use for presurgical planning. While the SLF LTD comparison to deficits was significant, we unexpectedly found the greatest percentage of deficits in the 1-2 cm category for all 3 measures. This analysis may be affected by a small study size and similar average cingulum LTD values for both <1 and 1-2 cm SLF LTD categories. Still, no significant effect of cingulum LTD alone was shown, so this parameter requires further study.

T-08

11:21AM - 11:24AM

Use and Radiological Interpretation of a Rapid-SWI Acquisition Based on the Wave-CAIPI Technology in a Clinical Setting.

M KIMURA[1], K Setsompop[2], S Cauley[2], B Gagoski[2], E Gasparetto[3]
[1]CDPI-Clinica de Diagnostico por Imagem, RIO DE JANEIRO, Rio de Janeiro, [2]Harvard Medical School, Boston, MA, [3]CDPI-Clinica de Diagnostico por Imagem, UNIVERSIDADE FEDERAL DO RIO DE JANEIRO, RIO DE JANEIRO, RIO DE JANEIRO

Purpose
To verify the results of the use and radiological interpretation of a rapid-SWI acquisition based on the Wave-CAIPI technology in a clinical setting.
Materials and Methods
A work-in-progress study in which we have applied rapid-SWI (9x acceleration) and traditional SWI (3x acceleration) sequences in brain scans of patients with random pathologies. The other conventional diagnostic sequences have been analyzed by 2 senior radiologists. Our research has been conducted in a 3 Tesla MR scanner. The rapid-SWI ultilizes a multi-echo Wave-CAIPI acquisition with 2 echo times to help boost the SNR of this highly accelerated acquisition. All MR images are interpreted in a picture archiving and communication system (PACS).
Results
Rapid-SWI sequence takes 1 minute and 17 seconds, which is nearly 3 times faster than the conventional sequence at 3 minutes 25 seconds. The current online image reconstruction/processing of the rapid-SWI is 4 minutes and 27 seconds. Both the rapid and traditional acquisitions achieve good quality SWI images. The rapid-SWI images show a somewhat lesser degree of susceptibility of the magnetic effect, when compared to the conventional ones. This is due to the rapid-SWI being a 2 echoes sequence, with a slightly lower effective TE. However, all areas demonstrating enhanced magnetic susceptibility effect, related to the presence of deoxygenated blood or calcifications products, have been detected similarly by both sequences, the SWI and rapid-SWI sequences. The image processing of the rapid-SWI Phase map currently is being improved.
Conclusions
Rapid-SWI sequence, in comparison to the SWI sequence, has demonstrated enough susceptibility effect contrast in the brains we have studied. This new technique seems to be feasible for diagnostic purposes in our daily clinical setting.

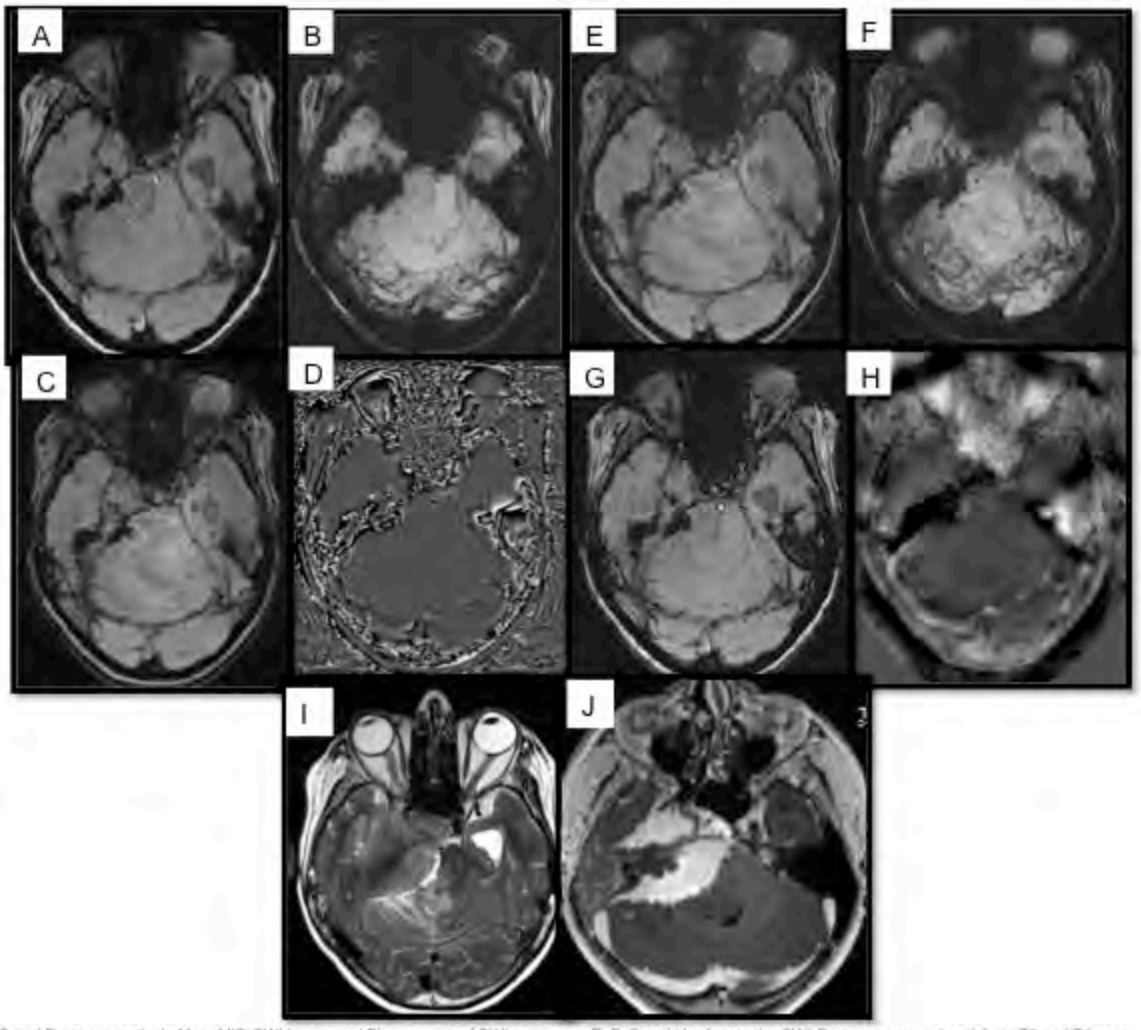


Image- A,B,C and D are respectively Mag, MIP, SWI image and Phase maps of SWI sequence. E, F, G and H refers to the SWI-Fast maps ones. I and J are T2 and T1 post-contrast sequences of the same patient who has a large meningioma centered at the right petrous apex , extending to the posterior and middle cranial fossa's. This tumor contains calcifications and has promoted bone alterations including hyperostosis and erosions, which were well-demonstrated in both SWI and SWI-Fast sequences.

(Filename: TCT_T-08_9001739.jpg)

T-09

11:24AM - 11:27AM

Increased Speed and Soft-Tissue Contrast in Single-Shot Fast Spin Echo Imaging Utilizing Tailored Refocusing Flip Angles for Fast Brain MRI

J Darsie[1], A Field[2], H Rowley[3], S Rebsamen[4], J Holmes[1], D Litwiller[5], K Vigen[6]
[1]University of Wisconsin, Madison, WI, [2]Univ. Of Wisconsin Hospital, Madison, WI, [3]Univ. Of Wisconsin, Madison, WI, [4]U of Wisconsin, Madison, WI, [5]GE Healthcare, New York, NY, [6]University of Wisconsin, Madision, WI

Purpose
Single-shot fast spin echo (SSFSE) MRI, because of its speed and motion robustness, is appealing to avoid both sedation and radiation in pediatric patients, such as those needing

frequent follow-up of shunted hydrocephalus (1). However, radiofrequency energy deposition at 3.0 Tesla forces long pauses between slices due to specific absorption rate (SAR) limitations, leading to longer scans and more between-slice motion. We tested the feasibility of using tailored refocusing flip angles in SSFSE brain imaging to reduce SAR, shorten acquisition times and potentially improve soft tissue (gray-white) contrast (2).

Materials and Methods

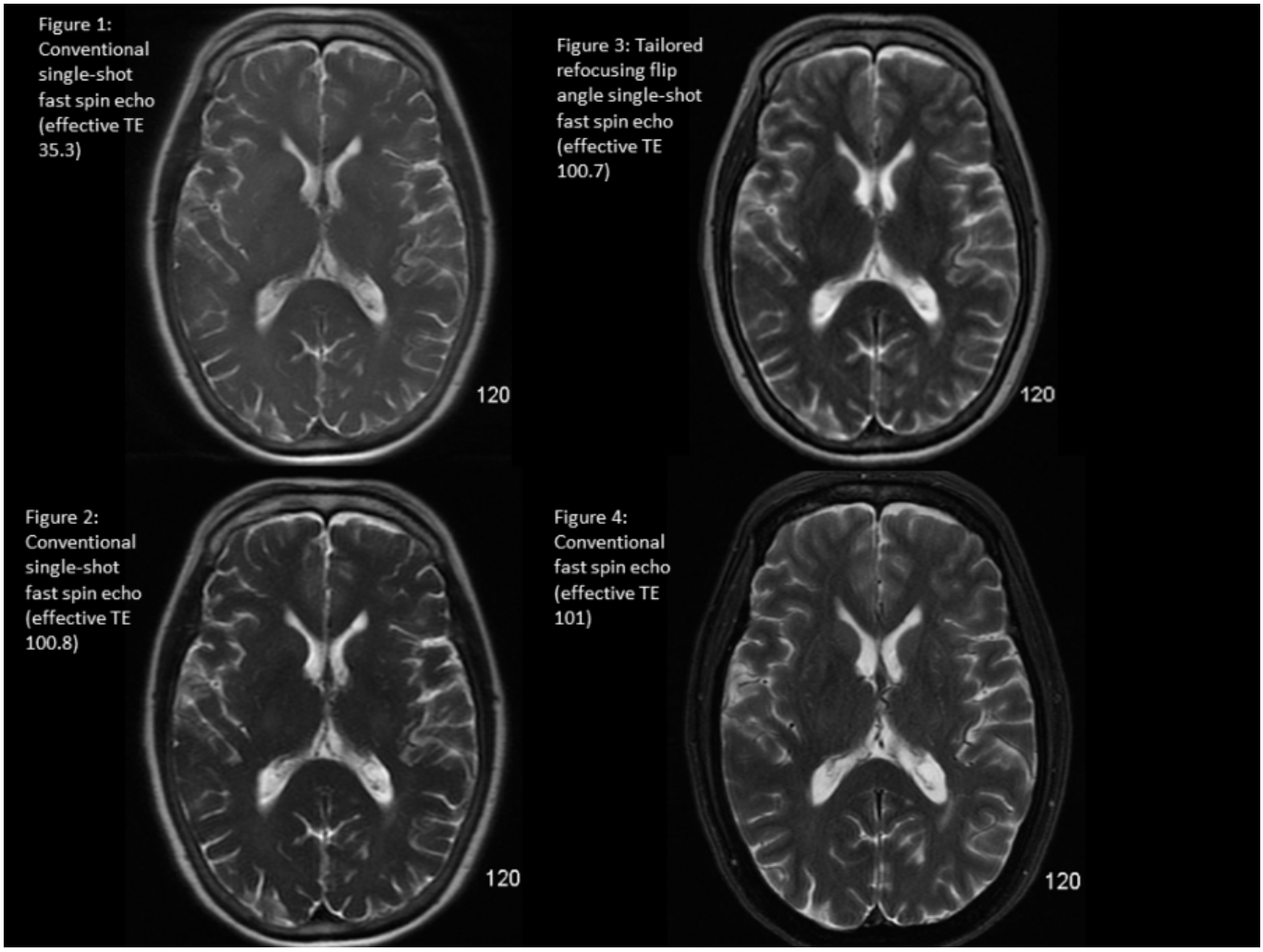
We compared SSFSE sequences with conventional refocusing flip angles (cSSFSE) to tailored refocusing flip angles (trfSSFSE) in volunteers at 3.0T (GE Discovery 750w). Scan parameters and image matrices were matched to the extent possible to minimize differences unrelated to the refocusing flip angles. The effective echo time (TE) on the cSSFSE sequence was modulated from our institution's current protocol to match the effective TE on the trfSSFSE sequence as an additional comparison. Imaging times were compared. A conventional T2-weighted fast spin echo sequence also was performed as a reference for comparison of gray-white contrast.

Results

The acquisition times for a typical adult volunteer from the cSSFSE (effective TE 35.3, top right image), cSSFSE (effective TE 100.8, bottom right image) and trfSSFSE (effective TE 100.7, top left image) were 28, 29 and 8 seconds respectively. The trfSSFSE sequence provided gray-white contrast superior to that of cSSFSE (compare conventional FSE reference image, bottom left image, 84 seconds).

Conclusions

Tailored refocusing flip angles sequences allow for greater than 3-fold reduction in scan time on 3.0T scanners compared to a conventional SSFSE sequence without significant degradation of signal to noise; as an added benefit, trfSSFSE yields superior gray-white matter contrast, presumably owing to the longer effective TE provided by the tailored refocusing flip angles. The combination of increased speed, decreased motion artifacts, and improved gray-white contrast argue for trfSSFSE to be the preferred sequence for fast screening brain MRI applications, including unsedated pediatric patients.



(Filename: TCT_T-09_ASNRabstractfigurefinal1.gif)

T-10

11:27AM - 11:30AM

Ultrafast Brain MRI: results of a 10-minutes brain protocol with contrast

J Pinto[1], M Longo[2], K Heberlein[3], T Witzel[4], S Huang[5], P Schaefer[2], O Rapalino[6]
[1]CDPI, rio de janeiro, Brazil, [2]Massachusetts General Hospital, Boston, MA, [3]Siemens Medical Solutions, Charlestown, MA, [4]Athinoula A. Martinos Center for Biomedical Imaging, Charlestown, MA, [5]Massachusetts General Hospital / Athinoula A. Martinos Center for Biomedical Imaging, Boston, MA, [6]Massachusetts General Hosp., Boston, MA

Purpose
To develop a 10-minute gadolinium-enhanced brain magnetic resonance imaging (MRI) protocol using accelerated sequences and to evaluate its diagnostic performance compared to the standard clinical protocol in a motion-prone inpatient population.

Materials and Methods

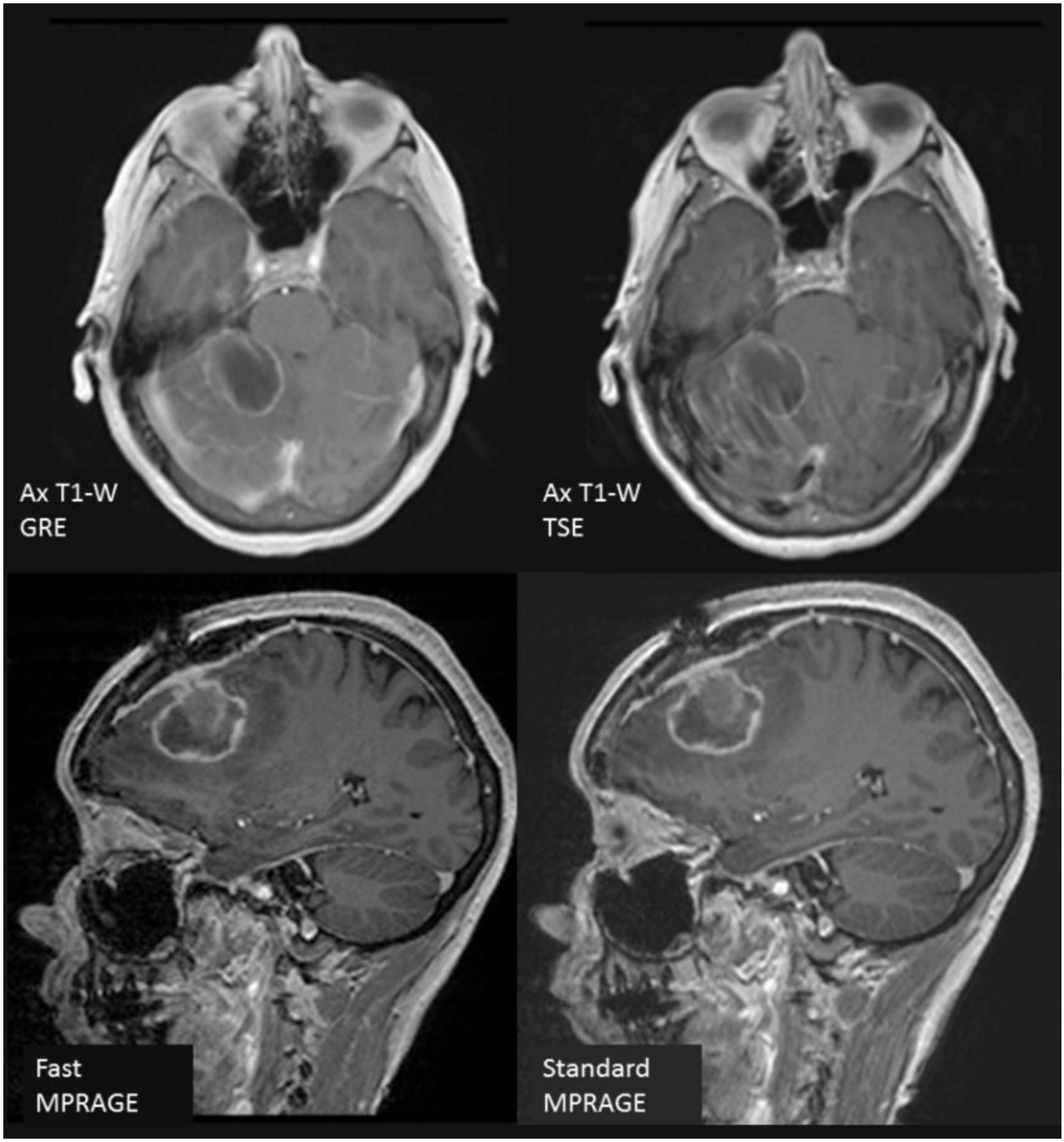
Fifty-three patients referred for brain MRI with contrast in our institution were selected prospectively and scanned using a 3-Tesla scanner (MAGNETOM Skyra, Siemens Healthcare). Each MRI scan consisted of 5 basic fast precontrast sequences plus standard and accelerated versions of the same postcontrast T1-weighted sequences: The standard postcontrast sequences included sagittal 3D-MPRAGE (GRAPPA=2, acquisition time = 5:21) and axial SE sequences. The fast postcontrast T1-weighted sequences incorporated accelerated 3D-MPRAGE (GRAPPA=3, acquisition time = 3:03) and axial T1W GRE sequences. Two blinded neuroradiologists independently assessed image quality regarding artifacts and diagnostic performance.

Results

The acquisition time of the combined accelerated pre and postcontrast sequences was 10:15 (compared to 19:03 for the standard commercially available protocol); the acquisition time of the accelerated postcontrast sequences was 3:36, 46% of the standard sequences acquisition time. The postcontrast axial T1-W sequence included in the accelerated protocol presented less image artifact ($p<0.001$) and better overall diagnostic quality ($p<0.001$). Although the accelerated protocol MPRAGE showed more artifacts than the standard sequence (Obs1 $p=0.027$, Obs2 $p=0.371$), the overall number of scans of diagnostic quality was similar (Obs1 $p=0.680$, Obs2 $p=1.000$). Moreover, there was no significant difference in the diagnostic performance between the standard and accelerated (10-minute) protocols. The sensitivity, specificity, and accuracy values for the 10-minute protocol were 97.8%, 77.8%, and 94.3%, respectively, compared with 97.8%, 87.5% and 96.2% respectively for the standard protocol ($p=1.000$).

Conclusions

The 10-minute brain MRI protocol with contrast is comparable in terms of diagnostic performance with the standard protocol in the setting of an inpatient motion-prone population, with the additional benefits of reducing acquisition times and image artifacts.



(Filename: TCT_T-10_FiguresASNR.jpg)

T-11

11:30AM - 11:33AM

Preoperative and Postoperative Whole Brain Diffusion Tensor Tractography Quantification in Temporal Lobe Epilepsy

M Alizadeh[1], L Kozlowski[2], J Riley[2], F Mohamed[2], A Sharan[2], C Wu[2]

[1]*Temple University, Philadelphia, PA,* [2]*Thomas Jefferson Hospital University, Philadelphia, PA*

Purpose

Diffusion tensor imaging (DTI) allows the reconstruction of white matter tract bundles by modeling the direction of water diffusion. There has been increasing application of tractography techniques to study DTI scalar metric alterations from reconstructed white matter tracts in patients with temporal lope epilepsy (TLE). However, there is a paucity of data on the relationship between pre-operative DTI tractography and postoperative seizure outcome after surgical treatments including anterior temporal lobectomy (ATL) and selective laser amygdalohippocampectomy (SLAH).

Materials and Methods

A total of 10 subjects ranging in age from 20-66 years old [46.78±14.45 (mean ±standard deviation)] were scanned using 3.0T Philips Achieva MR scanner before and at least 6 months after surgery. All patients have medial temporal lobe epilepsy with unilateral hippocampal sclerosis according to MRI criteria with ipsilateral seizure onset during noninvasive/invasive EEG monitoring and underwent epilepsy surgery afterwards. Seven patients were treated based on ATL and 3 patients underwent SLAH. First, eddy current compensation was performed on the diffusion dataset using FSL FDT diffusion toolbox and then FSL FLIRT for motion correction, using the B0 image as the stationary image. Streamline deterministic tractography was generated based on preprocessed DTI data using scan specific gradient table and image orientation information. Streamline deterministic tractography then was applied to pre-operative DTI in patients with TLE who underwent surgical treatment and postoperative follow up. Finally, white matter DTI scalars were calculated from whole brain fiber tracts. In order to exclude background fiber fragments, fiber tracts were only limited to the whole brain ROI generated from FSL BET toolbox. Various DTI indices were calculated: fractional anisotropy (FA), mean diffusivity (MD), axial diffusivity (AD), radial diffusivity (RD), relative anisotropy (RA) and volume ratio (VR). Geometric diffusion measures also were calculated: spherical anisotropy (Cs), planarity anisotropy (Cp) and linearity anisotropy (Cl). Coefficient of variation (CoV) was used to measure relative variability of DTI scalars and to see if they are consistent within subjects in both pre-operative and postoperative scans.

Results

The experimental findings show that there are significant differences in DTI scalars including FA and ADC (using two-tailed t test) between pre-operative TLE and patients who underwent to SLAH surgical treatment. However, no significant differences of DTI values have been shown in patients who went through ATL surgery. Fig. 2 shows the consistency of the DTI scalars measured using CoV within pre- and postoperative TLE scans. In overall, subjects treated by SLAH showed less variability than those who underwent ATL surgery.

Conclusions

This study shows white matter fibers generated from DTI data slightly altered in TLE

patients who had surgical treatments. These alterations were higher in patients with SLAH and consequently has the potential to compete with ATL in improving overall patient health quality if pathological/clinical correlates are further confirmed. However, these preliminary results are very encouraging and warrant further studies with a larger population. Coefficient of variation indicates that laser is a more consistent therapy that results in similar changes across patients. Selective laser amygdalohippocampectomy appears to have greater global wide spread effects throughout the brain compared to ATL.

Table 1: DTI scalars of white matter tracts in patients with TLE before and after surgery.

DTI Scalars	Preoperative (n=10)	ATL (n=7)	SLAH (n=3)	Prob>|t|	
	Mean± Std	Mean± Std	Mean± Std	ATL	SLAH
FA	0.46±0.03	0.47±0.04	0.44±0.01	0.52	**0.03**
ADC($10^{-3}mm^2/s$)	2.07±0.09	2.13±0.09	1.98±0.03	0.18	**0.004**
AD	1.07±0.05	1.11±0.06	1.02±0.06	0.16	0.32
RD	0.5±0.03	0.51±0.03	0.51±0.03	0.7	0.9
RA	0.34±0.03	0.36±0.04	0.32±0.02	0.33	0.13
VR	0.028±0.001	0.027±0.001	0.029±0.001	0.17	0.18
Cs	0.56±0.03	0.55±0.03	0.59±0.02	0.46	0.1
Cp	0.22±0.01	0.22±0.01	0.2±0.02	0.44	0.22
Cl	0.22±0.03	0.23±0.03	0.2±0.00	0.85	0.17

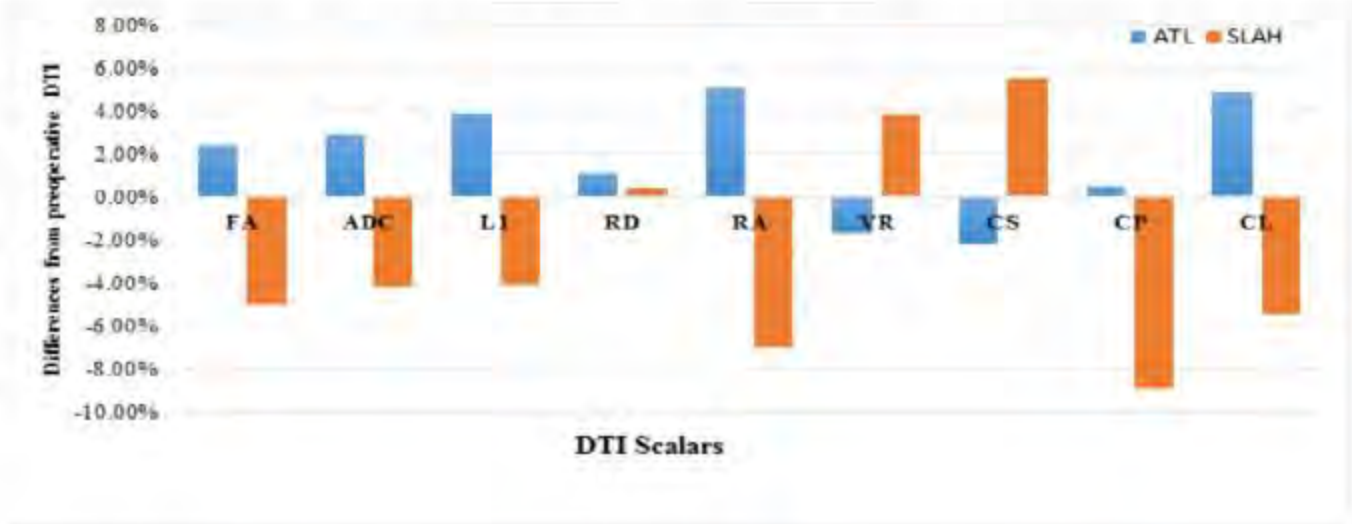


Figure 1. The differences of DTI indices from patients underwent ATL and SLAH surgical treatments.

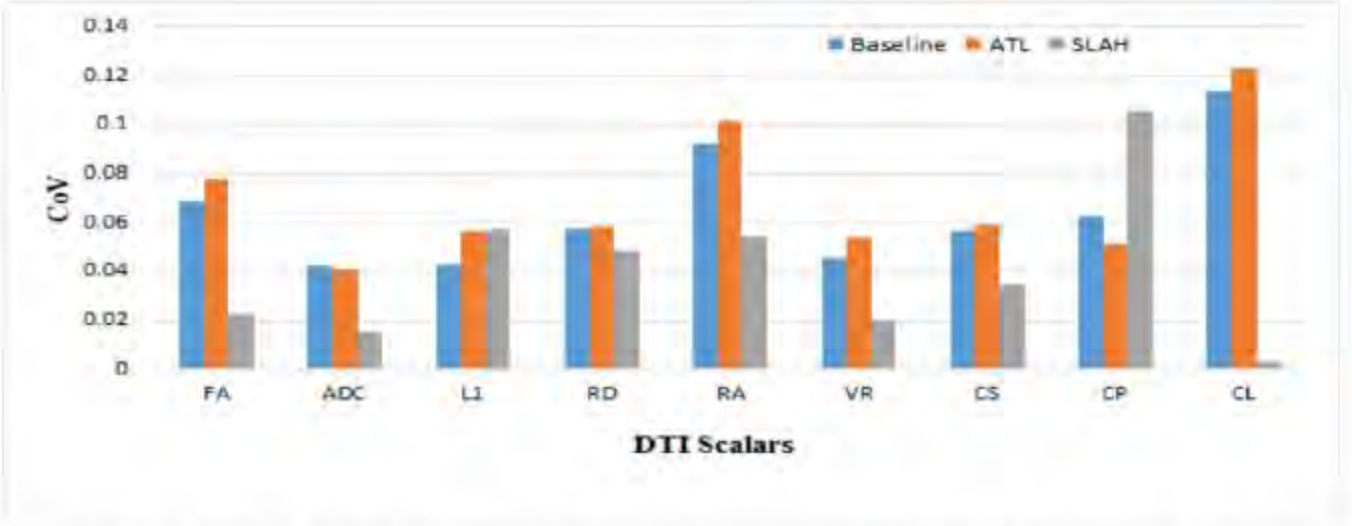


Figure 2. CoV of DTI scalars within bassline (preoperative) scans and postoperative scans.

(Filename: TCT_T-11_final.jpg)

T-12

11:33AM - 11:36AM

Age Related Diffusion and Tractography Changes in Typically Developing Pediatric Cervical and Thoracic Spinal Cord

M Alizadeh[1], Y Sultan[2], S Saksena[3], C Conklin[3], D Middleton[1], J Fisher[3], K Atsina[3], L Krisa[3], S Faro[4], M Mulcahey[3], F Mohamed[3]
[1]Temple University, Philadelphia, PA, [2]Drexel University, Philadelphia, PA, [3]Thomas Jefferson Hospital University, Philadelphia, PA, [4]John Hopkins University, Baltimore, MD

Purpose
Diffusion tensor imaging (DTI) and diffusion tensor tractography (DTT) have been shown to measure white matter integrity of spinal cord (1, 2). Recently DTI indices have been shown to change with age. The purpose of this study is (a) to evaluate the maturational states of the entire pediatric spinal cord using DTI and DTT indices including fractional anisotropy (FA), apparent diffusion coefficient (ADC), mean length of white matter fiber tracts and tract density and (b) to analyze the DTI and DTT parameters along entire spinal cord as a function of spinal cord levels.
Materials and Methods
A total of 23 typically developing (TD) pediatric subjects ranging in age from 6-16 years old [11.94±3.26 (mean ±standard deviation)] were recruited, and scanned using 3.0T Siemens Verio MR scanner (Siemens Healthcare, Erlanger, Germany) with 4-channel neck matrix and 8-channel spine matrix coils. Reduced FOV diffusion tensor images were acquired axially in the same anatomical location prescribed for the T2-weighted images to cover the entire spinal cord (C1-mid L1 levels). The DTI parameters used were: FOV=164 mm, phase FOV=28.4% (47 mm), number of directions=20, b=800s/mm2, voxel size=0.8×0.8×6.0mm3, matrix size= 36×208, axial slices=40, TR=7900ms, TE=110ms, number of averages=3 and acquisition time=8:49min. Initially, diffusion directional images were aligned with the reference image (B0) using a rigid registration algorithm and a scaled least square cost function performed by in-house software developed in Matlab (MathWorks, Natick, Massachusetts) (1, 2). After motion correction, diffusion tensor maps (FA and ADC) and streamline deterministic tractography were generated from DTI data (https://med.inria.fr/) (Fig. 1) with the scan specific gradient table and image orientation information. Diffusion tensor imaging and DTT parameters were calculated by using ROIs drawn on the whole cord along the entire spinal cord being localized anatomically by an independent board-certified neuroradiologist (1, 2). These indices then were compared between 2 age groups [age group A=6–11 years (n=11) and age group B=12–16 years (n =12)] based on similar standards and age definitions used for reporting spinal cord injury in the pediatric population (4). Standard least squared linear regression model based on restricted maximum likelihood (REML)

method (using JMP pro 13.0 software) was used to evaluate the relationship between age and DTI and DTT parameters.

Results

An increase in FA (group A=0.42±0.097, group B=0.49±0.116), white matter tract density (group A=368.01±236.88, group B=440.13±245.24) and mean length of fiber tracts (group A=48.16±20.48mm, group B=61.56±35.65mm) and a decrease in ADC (group A=3.19±0.69×10-3mm2/sec, group B=2.45±0.73×10-3mm2/sec) were observed with age along the entire spinal cord. Statistically, significant increases have been shown in FA ($p=0.016$), tract density ($p<0.0001$), mean length of fiber tracts ($p=0.0004$) and significant decrease has been shown in ADC ($p=0.0078$) between group A and group B. Also, it has been shown DTI and DTT parameters vary along spinal cord as a function of spinal cord level (Fig. 2).

Conclusions

This study provides an initial understanding of DTI values as well as DTT of the spinal cord. The results show significant differences in DTI and DTT parameters which may result from decreasing water content, myelination of fiber tracts, and the thickening diameter of fiber tracts during maturation process. Consequently, when quantitative DTI and DTT of the spinal cord are undertaken in pediatric population; age- and level-matched normative data should be used to accurately interpret the quantitative results.

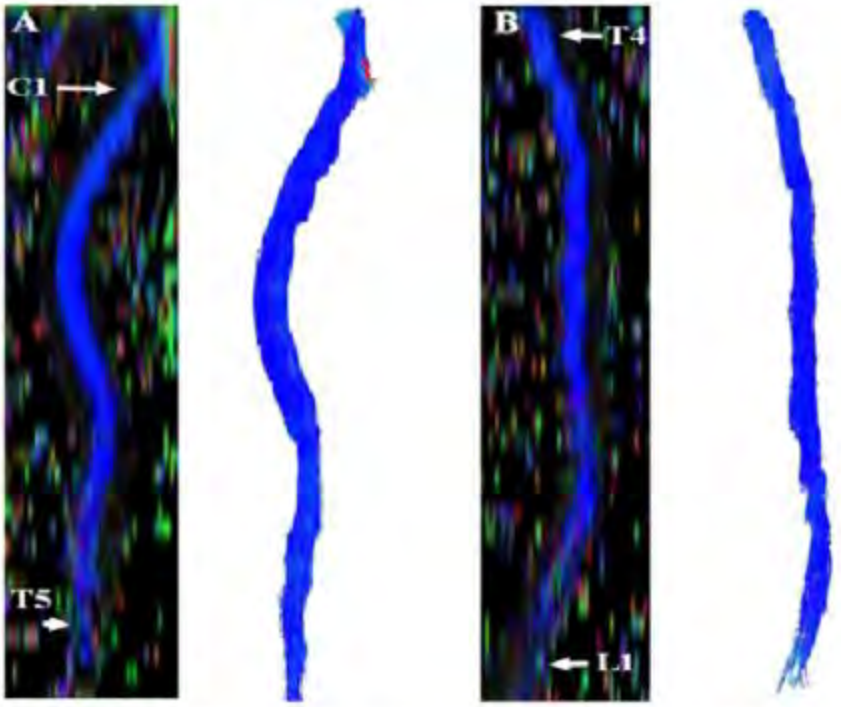


Figure 1. Sagittal reconstruction of the FA color maps and tractography of the entire spinal cord. *A*, The cervical and upper thoracic regions. *B*, The upper thoracic-through-lumbar regions.

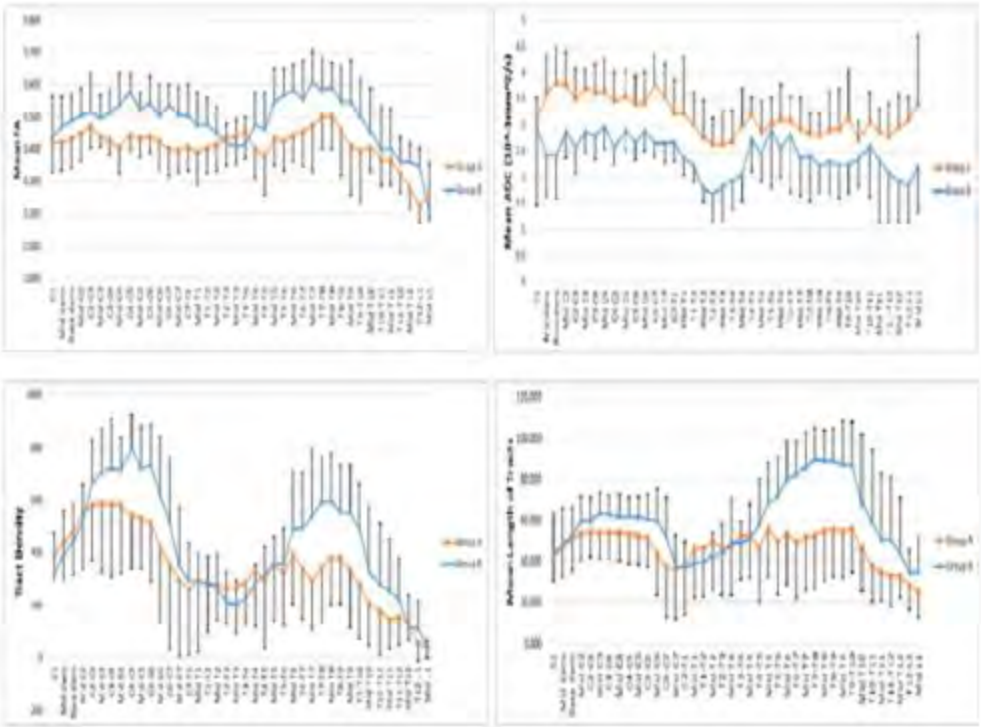


Figure 2. DTI and DTT parameters averaged across all the controls per age groups and plotted as a function of cord levels. The error bars represent the standard deviations.

(Filename: TCT_T-12_Age.jpg)

T-13

11:36AM - 11:39AM

Challenges in interpretation of Pediatric Functional MRI studies

K Shekdar[1], D Zarnow[1], A Vossough[2], T Roberts[3], E Schwartz[1]
[1]Children's Hospital of Philadelphia, Philadelphia, PA, [2]Children's Hospital of Philadelphia, Perelman School of Medicine of the Uni, philadelphia, PA, [3]The Children's Hosp. Of Philadelphia, Philadelphia, PA

Purpose
To discuss the challenges encountered in interpretation of pediatric functional MRI studies with illustrative case examples.
Materials and Methods
We retrospectively reviewed clinical fMRI studies performed at our institute from 2008 to 2016 and evaluated some of the commonly encountered challenges, highlighting the detection of false positives and false negatives, common artifacts and potential clinical impact of these pitfalls. Correlation was made with posttreatment (surgical and/or medical) follow-up of cases whenever available. All fMRI studies were performed on a 3T Siemens Verio™ scanner. Primary fMRI postprocessing was done on Siemens Leonardo postprocessing workstation. A commercially available postprocessing software with augmented motion correction/GLM capabilities also was used in conjunction.
Results
A total of 32 clinical fMRI studies were performed in the time period of the study. Of the 32 studies 15 studies were for mass lesions predominantly tumors and 3 were for vascular lesions. The other main indication was medically refractory epilepsy being considered for surgery. The fMRI evaluation was for motor mapping and language function. The majority of the challenges were due to artifacts encountered due to motion (n=26). Some challenges were related to stimulus correlated subtle motion (n=6) and others due to altered morphology either from vascular structures, prior surgery, tumor or dysplasia presumably resulting in neurovascular uncoupling (n=8).
Conclusions
Performing fMRI studies in the pediatric population presents similar and also unique challenges compared to application in an adult setting. It is important to be familiar with some of the common challenges to avoid misinterpretation of both apparently positive and negative findings, particularly in the setting of potential cortical reorganization in the pediatric population.

T-14

11:39AM - 11:42AM

Case-in-point: Role of Golden-Angle Radial Sparse Parallel MR imaging (GRASP) in identifying tumor recurrence in brain metastasis from lung adenocarcinoma treated with stereotactic radiosurgery

I Littig[1], T Shepherd[2], D Kondziolka[3], G Fatterpekar[4]
[1]New York University, New York, NY, [2]NYU Medical Center, New York, NY, [3]NYU Medical Center, New York , NY, [4]NYU School of Medicine, New York, NY

Purpose

Distinguishing tumor recurrence from radiation-induced change utilizing conventional imaging following stereotactic radiosurgery (SRS) is challenging. The purpose of this case is to illustrate the role of permeability parameters using GRASP imaging in identifying tumor recurrence in SRS treated metastasis.

Materials and Methods

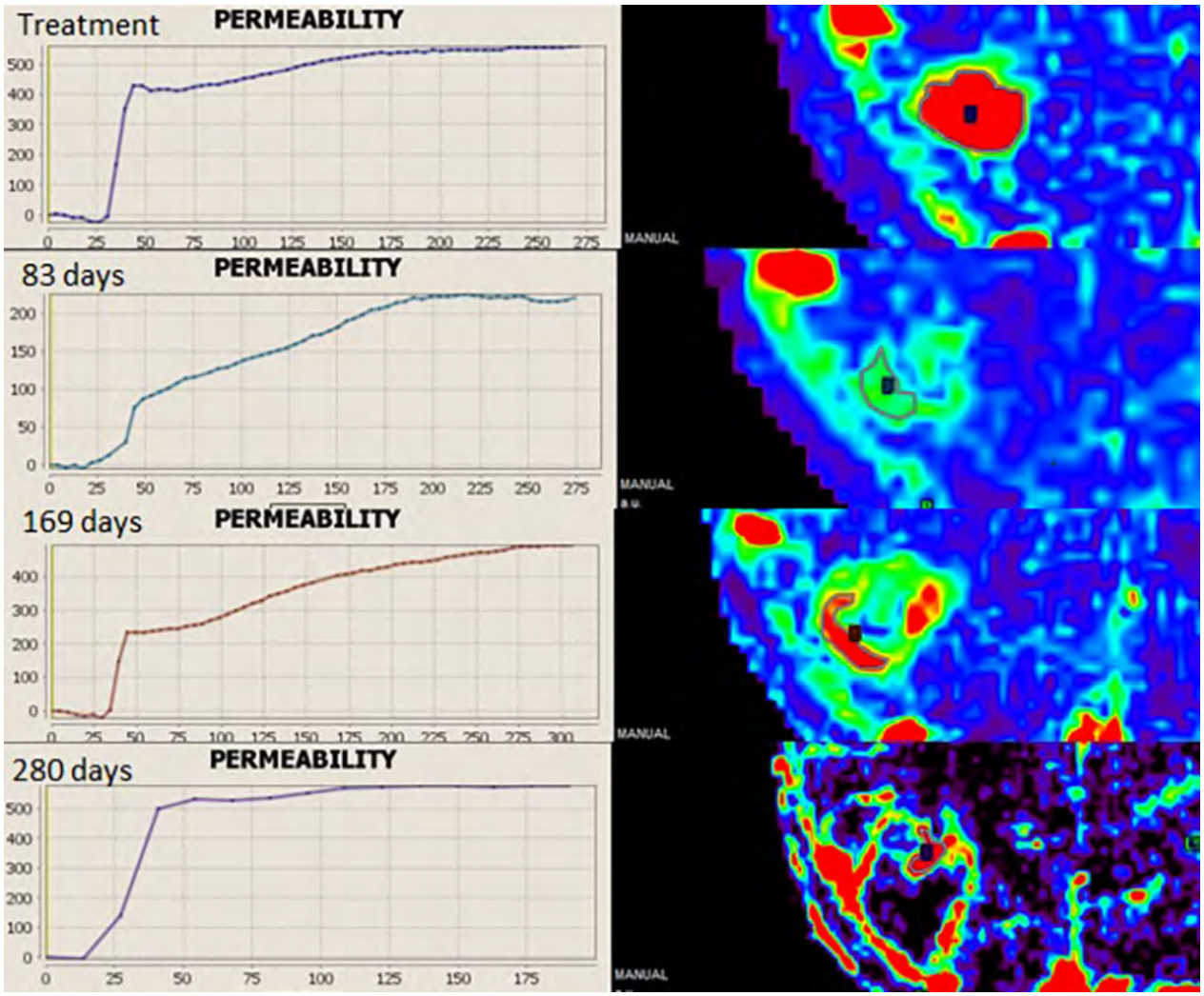
A 1.5 x 1.2 cm sized heterogeneously enhancing lesion was treated using GKRS, and subsequently followed after 83 days, 169 days, and 280 days using GRASP imaging. GRASP images obtained were postprocessed using Olea Sphere software (Olea Medical, LaCiotat). An ROI-based enhancement-time graph analysis of the solid component of the lesions was performed, pre and posttreatment.

Results

Conventional imaging demonstrated a continued increase in the size of the heterogeneously enhancing metastatic lesion. Treatment-induced change versus recurrence were considerations. GRASP assessment demonstrated an initial rightward shift of the enhancement time curve. This likely reflects increasing breakdown of the blood-brain barrier following GKRS. Subsequent GRASP assessment however demonstrated a leftward shift of this curve (please see Fig. below), proven at this point on biopsy as tumor recurrence. This leftward shift of the curve likely reflects neoangiogenesis and is therefore suggestive of tumor recurrence.

Conclusions

This case illustrates the role played by GRASP imaging in assessing GKRS treated lesions, and evaluating for tumor recurrence. Conventional imaging plays a very limited role in identifying tumor recurrence in patients treated with SRS. Since metastatic lesions can be scattered over the brain, and are close to the cortex, DSC-perfusion imaging also has only a limited role in assessing for tumor recurrence. GRASP imaging allows evaluating the entire brain, overcoming all such limitations and therefore should be used when evaluating SRS-treated lesions.



(Filename: TCT_T-14_FINALFIGURE.jpg)

Monday
3:30PM - 4:45PM
Long Beach Convention Center, Grand Ballroom (Upper Level)

06A-Parallel Paper Session: Neurointerventional: Acute Stroke Treatment-Timeline and Technique

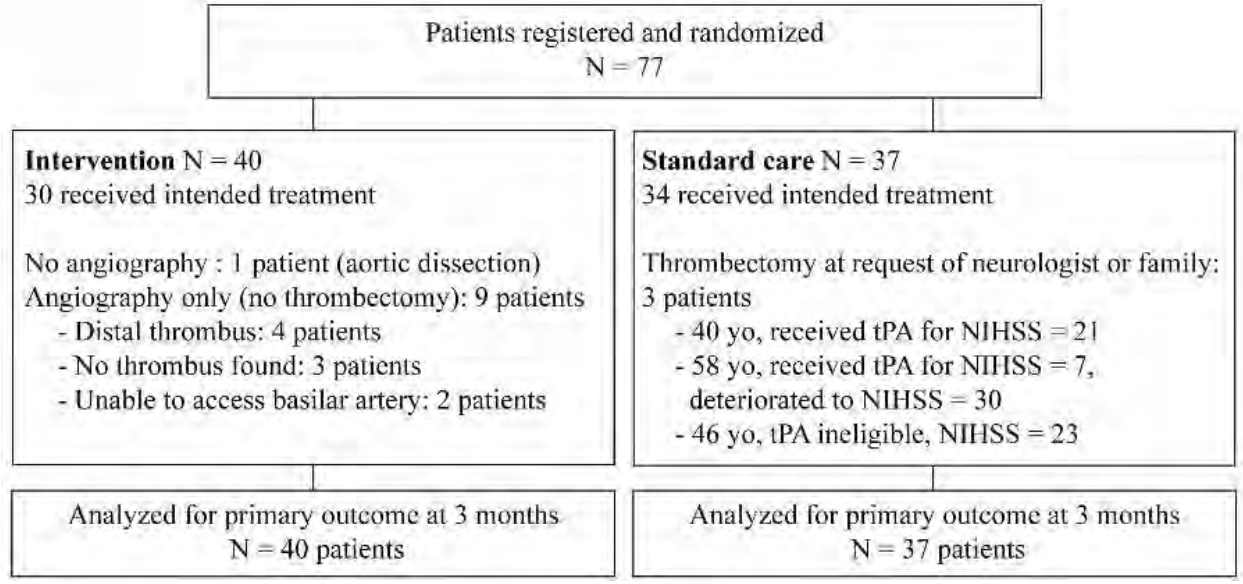
O-46

3:30PM - 3:38PM

Endovascular Thrombectomy and Medical Therapy Versus Medical Therapy Alone in Acute Stroke: a Randomized Care Trial

J Raymond[1], M Kotowski[2]
[1]CHUM Centre Hospitalier de l'Université de Montréal, Montréal, QC, [2]University of Montreal, Montreal, Quebec

Purpose
Until recently, the benefits of endovascular treatment in stroke were not proven. Care trials have been designed to simultaneously offer yet-to-be validated interventions and verify treatment outcomes. Our aim was to implement a care trial for patients with acute ischemic stroke.
Materials and Methods
The study was offered to all patients considered for endovascular management of acute ischemic stroke in one Canadian hospital. Inclusion criteria were broad: onset of symptoms ≤ 5h or at any time in the presence of clinical-imaging mismatch and suspected or demonstrated proximal large vessel occlusion. Exclusion criteria were few: established infarction or hemorrhagic transformation of the target symptomatic territory and poor 3-month prognosis. The primary outcome was mRS ≤ 2 at 3 months. Patients were allocated randomly to standard care or standard care plus endovascular treatment. ClinicalTrials.gov: Identifier NCT02157532.
Results
Seventy-seven patients were recruited in 19 months (March 2013 - October 2014) at a single center. Randomized allocation was interrupted when other trials showed the benefits of endovascular therapy. At 3 months, 20 of 40 patients (50·0 %; 95% C.I.: 35%-65%) in the intervention group had reached the primary outcome, compared to 14 of 37 patients (37.8%; 95% C.I.: 24%-54%) in the control group (P=0·36). Eleven patients in the intervention group died within 3 months compared to 9 patients in the standard care group.
Conclusions
A care trial was implemented to offer verifiable care to acute stroke patients. This approach offers a promising means to manage clinical dilemmas and guide uncertain practices.



(Filename: TCT_O-46_fig1_FC.jpg)

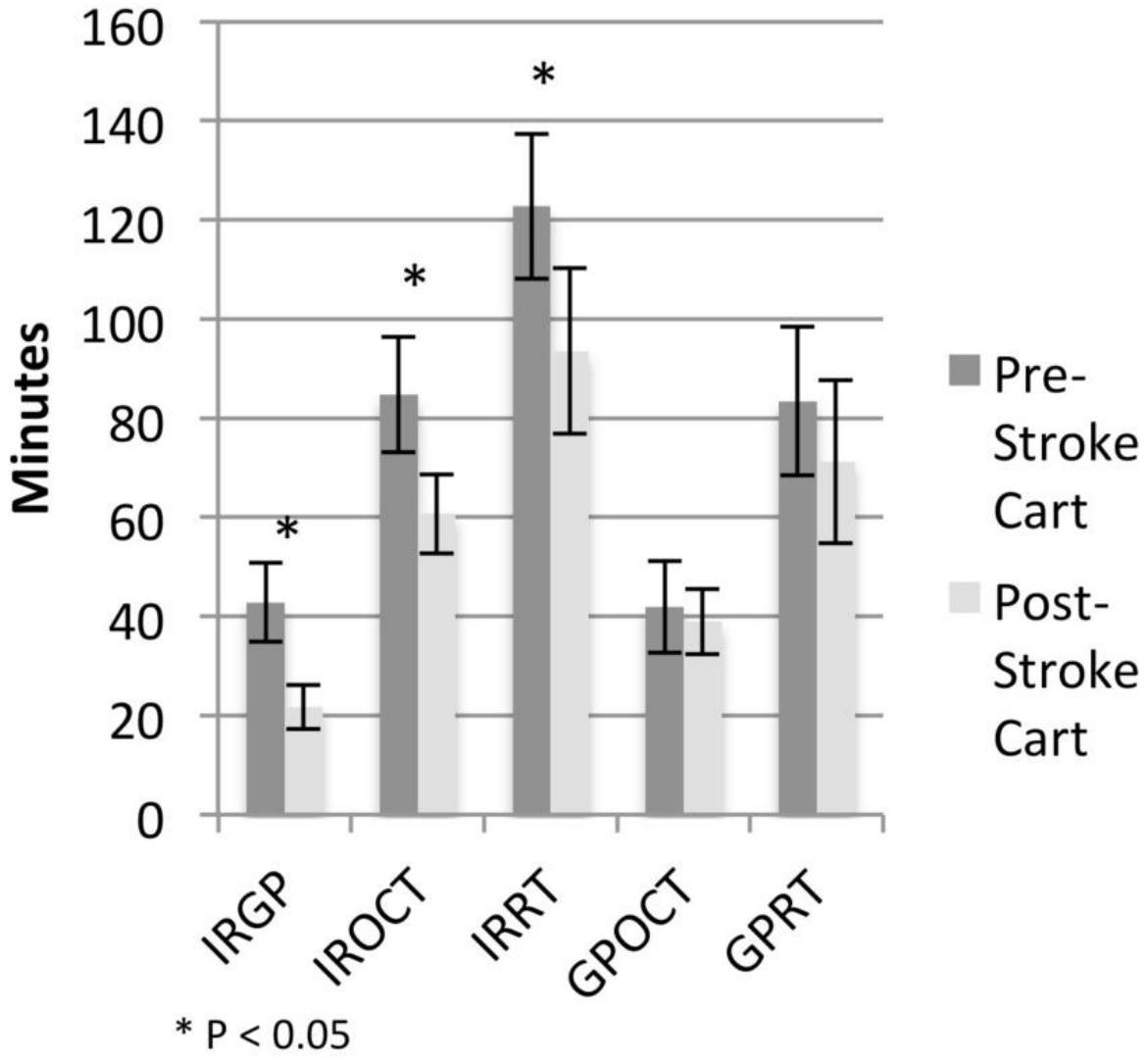
O-47

3:38PM - 3:46PM

Improving Time Metrics During Mechanical Thrombectomy: Use of Stroke Cart in Angiography Suite

F Settecase[1], D McCoy[1], R Darflinger[1], M Alexander[1], A Nicholson[1], D Cooke[1], S Hetts[2], C Dowd[3], V Halbach[1], R Higashida[1], M Amans[1]
[1]UCSF, San Francisco, CA, [2]University of California, San Francisco, San Francisco, CA, [3]Univ. Of California San Francisco, San Francisco, CA

Purpose
Early and rapid reperfusion improves functional outcomes in large vessel occlusion acute ischemic stroke (LVOAIS). We hypothesize that implementation of a Stroke Cart, a self-contained mobile unit that contains all of the equipment required to perform endovascular treatment of LVOAIS, improves procedural efficiency and facilitates faster reperfusion.
Materials and Methods
We identified 47 consecutive patients with LVOAIS who underwent mechanical thrombectomy at our center, retrospectively and prospectively from Stroke Cart implementation in April 2015, (19 prestroke cart and 28 poststroke cart). The following time metrics were recorded: in-room time to groin puncture (IRGP), in-room time to on-clot time (IROCT), in-room time to recanalization time (IRRT), groin puncture time to on-clot time (GPOCT), and groin puncture time to recanalization (GPRCT). A multiple regression analysis was performed which included: stroke cart presence, endotracheal tube placement in the angiography suite (ETTIA), type of anesthesia, arterial line placement by anesthesia team vs arterial pressure transduction via femoral sheath, patient age, large-vessel occlusion (LVO) location, and number of passes required.
Results
Stroke cart presence resulted in significant decreases in time metrics (Fig. 1), independent of other variables, with a 15.8 min decrease in IRGP [40.0 (30.6-49.5) min vs. 24.2 (16.9-31.5) min, p = 0.033], a 32.1 min decrease in IROCT [90.1 (75.3 – 104.9) min vs. 58.0 (46.6 – 69.5) min, p = 0.007], 37.5 min decrease in IRRT [131.2 (114.6-147.8) vs. 93.7 (81.5 – 105.9) min, p = 0.004]. Trends to decreasing GPOCT (-16.3 min, p = 0.095) and GPRT (-19.8 min, p = 0.087) also were seen with stroke cart use. ETTIA was found to significantly increase IROCT and IRRT.
Conclusions
Use of a Stroke Cart in the angiography suite improved treatment times, and significantly decreased time to reperfusion for LVOAIS patients. The Stroke Cart may be helpful to other institutions looking to maximize intraprocedural efficiency.



(Filename: TCT_O-47_FigureASNRabstract.jpg)

O-48

3:46PM - 3:54PM

Benefits of Transbrachial Access For Carotid Artery Stenting with Guide-Sheaths Specifically Designed for Transbrachial Carotid Cannulation

T Mori[1]
[1]*Shonan Kamakura General Hospital Stroke Center, Kamakura, Japan*

Purpose

Transfemoral access usually is used for carotid artery stenting (CAS). However, aortic arch or peripheral artery conditions occasionally limit its access. Transbrachial access has been developed as a routine one for neuroendovascular intervention. The purpose of our retrospective study was to investigate whether or not transbrachial access for carotid artery stenting (CAS) with guide-sheaths (MSK-guide, Medikit) specifically designed for transbrachial carotid cannulation (TCC) was seldom limited by aortic arch or peripheral arterial conditions.

Materials and Methods

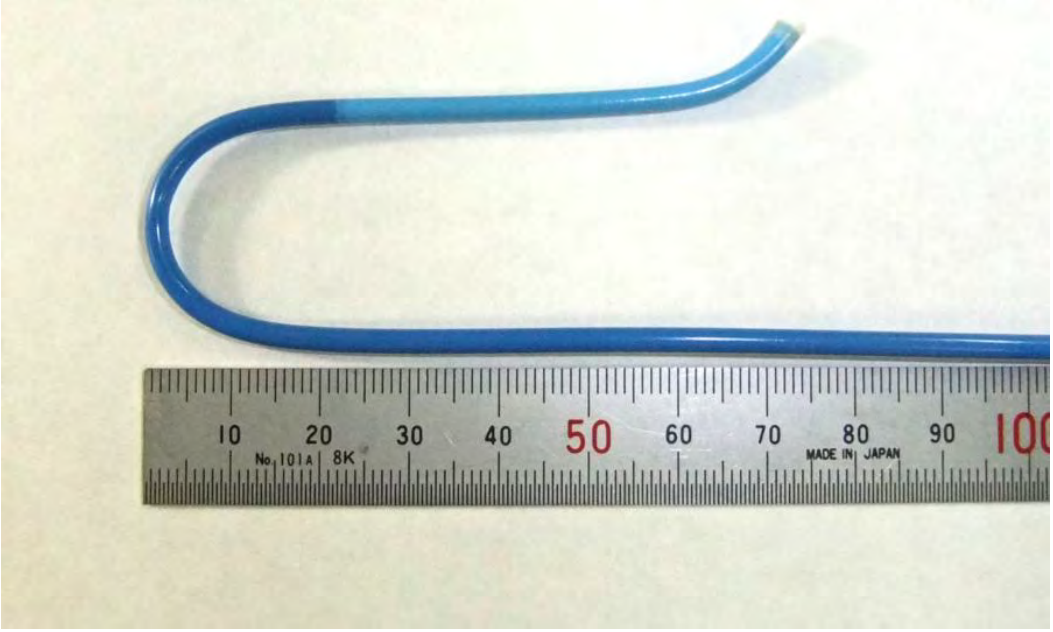
We included in our retrospective study patients who underwent elective CAS with the guide-sheaths between June 2011 and April 2016, and evaluated devices we used and procedural success rate.

Results

One hundred sixty-nine patients were analyzed. The right brachial artery (BA) was punctured in 152 cases and the left BA in others. Successful TCC and stable positioning was achieved in 106 cases of the right common carotid artery (CCA) and in 63 cases of the left CCA. The Spider filter was used in 103 and the Filterwire EZ in 55 and the Angioguard in 11 cases. The Shiden balloon was used in 158 and the RX-Genity in 4 and the Gateway in 1, the Aviator in 1, Coyote in 1 and none in 4 for predilatation. The CarotidWallstent was used in 129, the Precise in 29, the Protégé in 10 cases and the Driver in 1 case. The bovine type or type 3 aortic arch did not limit TCC. Peripheral artery conditions such as aortic aneurysms or iliac artery occlusions did not affect it.

Conclusions

Transbrachial CAS with guide-sheaths specifically for TCC was not limited by the arch type nor peripheral arterial conditions and can be a routine access.



(Filename: TCT_O-48_MSK-guide75.jpg)

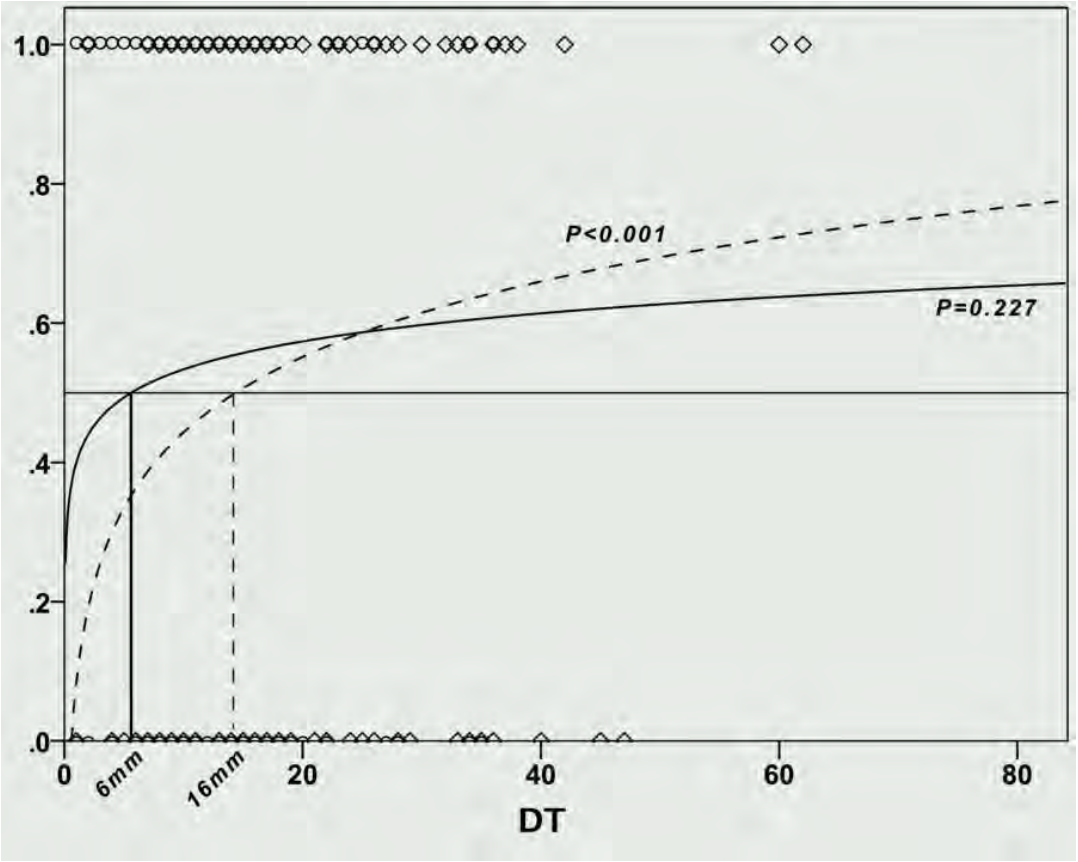
O-49

3:54PM - 4:02PM

Clinical outcome after endovascular MCA stroke treatment is independent of exact occlusion site.

B Friedrich[1], J Kaesmacher[1], S Wunderlich[1], C Maegerlein[1], C Zimmer[1], D Lobsien[2]
[1]Klinikum rechts der Isar, Technical University Munich, Munich, Germany, [2]University Hospital Leipzig, Leipzig, Germany

Purpose
Endovascular mechanical thrombectomy in combination with intravenous thrombolysis (MT) has become the de facto standard in the treatment of ischemic stroke due to large vessel occlusion in the anterior circulation. In previous works a clear correlation between the chances of good clinical outcome and the exact occlusion site, measured by the 'distance to thrombus' (DT) after Intravenous thrombolysis alone (IVT) could be shown. In the present study, we analyze the differences between the chances of a good clinical outcome in respect of DT between patients treated with IVT alone vs. MT.
Materials and Methods
A dual center database analysis including all consecutive patient with ischemic stroke due to isolated occlusion of the middle cerebral artery (MCA) was performed. Distance to thrombus was measured in pre-treatment images. Distance to thrombus was correlated with the mRS at 90 days in respect to the different treatment methods.
Results
A total of 321 patients could be included. Like in previous studies, we were able to show a clear correlation between the chances of good clinical outcome defined by 90d mRS ≤ 2 and the exact occlusion site measured by DT after IVT. Only beyond a DT of 16mm the chances of a good outcome exceed the chances of a bad outcome ($p<0.001$). In contrast to that, the outcome after MT showed no correlation to DT ($p=0.227$). After a DT of 26 mm the chances of a good clinical outcome after IVT alone exceeded those after MT.
Conclusions
In isolated MCA occlusion, the chances of a good clinical outcome after endovascular stroke treatment are independent of the exact occlusion site. Interestingly, if the occlusion occurred in the periphery of the M2 region, expressed by a DT >26 mm, IVT alone was superior to MT in achieving a good clinical outcome.



(Filename: TCT_O-49_FigureAbstract.jpg)

O-50

4:02PM - 4:10PM

Acute Occlusions of New Generation Dual Layer Carotid Stents after Endovascular Emergency Treatment of Tandem Occlusions

U Yilmaz[1], H Körner[2], R Mühl-Benninghaus[2], A Simgen[2], C Kraus[2], w reith[3], M Unger[2]
[1]Saarland University Hospital, Homburg, Germany, [2]Saarland University Hospital, Homburg, Saarland, [3]University clinic saarland, homburg, saarland

Purpose
A new generation of carotid artery stents that uses a second micromesh layer to reduce embolic events during carotid artery stenting has been introduced recently. At the same time emergency carotid artery stenting recently is gaining attention since a series of randomized trials demonstrated the benefit of mechanical thrombectomy in acute large vessel occlusions of the anterior circulation and up to 30% of those are accompanied by an additional occlusion or high grade stenosis of the extracranial ICA that requires PTA and/or stenting in order to gain access to the intracranial clot. Yet, it has not been investigated whether the new stent design influences complication rates in the emergency setting. The purpose of this

study was to compare acute occlusion rates of the new double layer stents with those of classic single layer stents in acute stroke.
Materials and Methods
Patients with acute tandem occlusions of the anterior circulation who were treated endovascularly at our institution were identified from our registry of neuroendovascular interventions. Clinical, angiographic and neuroimaging data were analyzed. Endpoints included acute occlusions of the carotid stents and symptomatic ICH.
Results
Forty-seven patients were included. Double layer stents (n = 20) had a significantly higher rate of acute occlusions than classic single layer stents (45% vs. 3,7%, P = .001, OR 21.3, 95% CI 2.4-188.4).
Conclusions
In this retrospective analysis we report that the recently introduced double layer stents have a higher risk of acute occlusion compared to the classic single layer stents in the treatment of acute stroke. For the time being classic single layer stents should be used in the emergency setting.

O-51

4:10PM - 4:18PM

Contrast Extravasation during Thrombectomy for Acute Ischemic Stroke: Incidence, Endovascular Management and Clinical Outcome

M Kotowski[1], L Nico[2], A Weill[3], J Raymond[1], D Roy[1]
[1]CHUM Centre Hospitalier de l'Université de Montréal, Montréal, QC, [2]CHUM Université de Montréal, Montréal, Quebec, [3]CHUM Montreal QC, Montreal, QC

Purpose
Intracranial vessel perforation is a rare complication of thrombectomy for acute ischemic stroke. To review our database of patients that underwent mechanical thrombectomy complicated by vessel perforation with particular emphasis on endovascular management and clinical outcome.
Materials and Methods
All patients, from March 2015 to December 2016, that underwent thrombectomy for acute ischemic stroke and had contrast extravasation during the procedure were included. Clinical data, details of the procedure, rescue strategies, radiographic findings and clinical outcome were collected.
Results
Contrast extravasation occurred in 13 (3.6%) of 364 patients during a mechanical thrombectomy procedure. Mean age was 67 years, median NIHSS 21. Eight patients recieved iv thrombolysis, 4 patients were on anticoagulants and 1 patient was on Aspirine. The median ASPECTS score before thrombectomy was 8. Clot location was: carotid-T in 4

patients and M1 in 9 patients. Two distinct contrast extravasations occurred in different locations during the same procedure in 1 patient. We suspected that the perforation was due to manipulation of the microwire in 8 cases and to manipulation of the microcatheter in 2 cases. The cause for extravasation could not be determined in 4 patients. Reperfusion (TICI 3 and 2b) was achieved in 5 patients, TICI 2a in 4, and no reperfusion (TICI 1 and 0) in 4 cases. Suspected perforation site was: distal ICA in 1 case, proximal M1 in 1 case, M2 in 5 cases, M3 in 2 cases and A2/A3 in 1 case. Twelve perforations occurred distal to or at the level of the clot and 2 proximal to it. We observed spontaneous resolution of contrast extravasation in 5 cases without any specific management. Rescue strategies, when needed, were: balloon hemostasis in 1 case and coiling of the perforated branch in 6 cases. One microcatheter was left in the subarachnoid space. The mRS at 1-5 months was: 4 (31%) patients had good outcome (mRS 0 to 2), 4 (31%) patients had significant disability (mRS 3 to 5) and 4 (31%) patients died. One (7%) patient was lost for follow up. Despite perforation, thrombectomy was continued in 6 (46%) patients. Of those, 4 had a favorable outcome, 1 patient died and one 1 was lost to follow up. Thrombectomy was abandoned in 7 (54%) patients. In this group, no patient had a favorable outcome, 4 patients had significant disability and 3 patients died, presumably from causes of ischemia. All patients underwent a head CT after the thrombectomy procedure. No patient suffered from significant intracerebral hemorrhage with mass effect.
Conclusions
Vessel perforation during thrombectomy is not necessarily associated with bad outcome. Abandoning thrombectomie with the idea of decreasing blood flow at the level of the perforation remains questionable (1). In this short case series bad outcomes were related more often to ischemia than hemorrhage. The limited number of cases in our series precluded any statistical analysis.

O-52

4:18PM - 4:26PM

The Penumbra Aspiration System in Acute Ischemic Stroke: ACE 64 versus ACE 68 – Does it Change the Outcome?

M Baptista[1], C Perry da Câmara[1], I Fragata[1], J Pamplona[1], C Ribeiro[1], J DOS REIS[1]
[1]*Centro Hospitalar Lisboa Central, Hospital de São José, Lisboa, Portugal*

Purpose
In acute stroke every minute delay is associated with a 2.5% reduction in probability of good clinical outcome. The increasing use of large-bore aspiration catheters has shown to be an effective alternative approach for intra-arterial stentriever thrombectomy, possibly leading to a high degree of recanalization in a shorter time. To determine the superiority of ACE 68 catheter by comparing with ACE 64 in terms of trackability through vessels of acute stroke patients, effectiveness of aspiration, recanalization rates, and, finally, time to recanalize.

Materials and Methods
A retrospective observational study was conducted in patients with anterior circulation acute ischemic stroke who were admitted to a Cerebrovascular Unit between January and November 2016. All patients were submitted to intra-arterial recanalization with primary direct aspiration system and whenever not effective combined with stentriever. Puncture to recanalization time, rate of successful recanalization (TICI 2b/3) and good clinical outcomes (4-point or more NIHSS improvement) were evaluated.
Results
Eighty-six patients were included, with the mean age of 71 years. The ACE 64 catheter was used as primary choice in 43 patients (50%), in the other half ACE 68 was used. Mean of puncture to recanalization time with ACE 68 was 37 minutes, 27.9 minutes, lower when compared to ACE 64, 43 25.3 ($p<0.05$). Successful recanalization was achieved in 41 patients (95.3%) in the arm of ACE 68, and in 39 (90.7%) with ACE 64 ($p=0.36$). At the time of discharge, good clinical outcomes were accomplished in 29 patients (67.4%) with ACE 68 and in 22 (51.2%) with ACE 64 ($p=0.10$).
Conclusions
ACE 68 catheter seems to be more effective in our clinical practice, with shorter times to recanalization and slightly better recanalization outcomes. Although not adjusted for other variables, there was a trend to achieve better clinical outcome with ACE 68, not reaching statistical significance in this small sample.

O-53

4:26PM - 4:34PM

The use of stent-retreivers to treat delayed cerebral vasospasm secondary to sub-arachnoid haemorrhage

P Bhogal[1]
[1]*Klinikum Stuttgart, Stuttgart, Germany*

Purpose
Traditionally intra-arterial vasodilators and/or balloon angioplasty have been the available options for the endovascular management of delayed cerebral vasospasm secondary to subarachnoid hemorrhage. We present cases in which stent retrievers have been used successfully to treat cerebral vasospasm.
Materials and Methods
We present our initial cases (10 patients) treated with commercially available stent retrievers. We demonstrate the radiological improvement in the caliber, improvement in perfusion and clinical status where relevant. We evaluated the safety of this technique, degree of vasodilation and longevity of the vasodilatation effect.
Results
In all treated cases there was successful vasodilatation of the vasospastic segments. CT

perfusion was performed in selected patients and this demonstrated improvement alongside delayed CT angiography that demonstrated a persistent dilatation.
Conclusions
Stent retriever can be used to successfully treat delayed cerebral vasospasm. The use of stent retrievers may have several potential benefits over balloon angioplasty and dedicated stent retrievers should be designed for this particular pathology.

O-54

4:34PM - 4:42PM

Balloon Guide Catheter vs Distal Access Catheter: What Is the Most Effective Technique for Mechanical Thrombectomy in Acute Ischemic Stroke?

J Madjidyar[1], L Pineda Vidal[1], O Jansen[1]
[1]*University Clinic Schleswig-Holstein, Kiel, Schleswig-Holstein*

Purpose
The currently most promising thrombectomy techniques were compared with each other under standardized conditions in an almost physiological flow model.
Materials and Methods
Two different clot models were made of human blood: an erythrocyte rich (red) and a fibrin rich (white) (1). Each clot was placed in the middle cerebral artery of a transparent silicon vascular phantom. Physiological flow and blood pressure was maintained by a precise piston pump (2). The following thrombectomy techniques were performed under direct visual control using an aspiration pump: 1. Trevo Stent Retriever (SR) and distal aspiration (DA) by 5F SOFIA Catheter (3), 2. Trevo Stent Retriever and proximal aspiration by 7F Cello Balloon Catheter (BGC) (4), 3. Direct aspiration by 5F SOFIA Catheter (ADAPT) (5). The results were analyzed statistically.
Results
Six experiments were made for each technique and clot model (n=36). ADAPT showed the shortest procedure time (Table 1), especially in white clots ($p<0.005$). In white clots 1 pass was necessary to achieve full recanalization using BGC+SR and ADAPT, an average of 1.5 passes using DA+SR. In red clots an average of 1.5 passes was necessary with any technique. ADAPT showed the lowest rate of distal embolism in red clots (vs DA+SR $p=0.02$; vs BGC+SR $p=0.25$) and BGC+SR in white clots (vs DA+SR $p=0.007$; vs ADAPT $p=0.21$). Embolism in new territories occurred in only 2/36 experiments retrieving red clots and using ADAPT and BGC+SR, respectively.
Conclusions
In this experimental study ADAPT was the most effective technique. BGC+SR had a significantly longer procedure time in white clots, but aside from that, it was almost equal in safety and efficiency, actually showing a nonsignificant advantage in the rate of distal embolism in white clots. In red clots DA+SR was the only technique with no embolism in

new territories, apart from that, the performance was inferior to the other techniques. The efficiency and safety depended on the composition of the clots.

Table 1: Results

Clot model	Technique	Average procedure time [min]	Average number of passes (n)	Rate of distal embolism	Rate of embolism in new territories
Red (erythrocyte rich)	DA+SR	24.9	1.5	6/6	0/6
	BGC+SR	11	1.5	4/6	1/6
	ADAPT	11	1.5	2/6	1/6
White (fibrin rich)	DA+SR	17.8	1.5	6/6	0/6
	BGC+SR	9.8	1	1/6	0/6
	ADAPT	5.3	1	3/6	0/6

(Filename: TCT_O-54_Table1.jpg)

Monday
3:30PM - 4:45PM
Long Beach Convention Center, Room 202 (Upper Level)

06B-Parallel Paper Session: Practical Points in Diagnosis – Vascular Spine and CSF Imaging

O-55

3:30PM - 3:38PM

Delay to Radiological Diagnosis of Spinal Dural Arteriovenous Fistulas. A 10 Year Retrospective Analysis of Referrals to a Tertiary Neurosciences Centre in the South West of England.

R Hunt[1], R Roberts[1], A Mortimer[1]
[1]*Southmead Hospital, Bristol, UK, Bristol, Bristol*

Purpose
Spinal dural arteriovenous fistulas (SDAVF) are rare, extramedullary vascular malformations which commonly present with an insidious onset of sensory disturbance and lower limb weakness, particularly on exertion. The nonspecific nature of symptoms frequently leads to a significant delay in diagnosis (1). Radiological features on magnetic resonance imaging (MRI) are characteristic and often allow an accurate diagnosis to be made. These appearances frequently are overlooked or mistaken for an alternative pathology, resulting in further delay to definitive management.
Materials and Methods
We identified all patients who had an angiographically confirmed SDAVF over a 10-year period at our institution (2006 – 2016). All available preceding imaging of the spine was

reviewed for characteristic radiological features, including cord expansion, cord edema and extramedullary serpiginous vessels. Each radiology report was scrutinized and information regarding presenting symptoms, imaging findings and differential diagnosis recorded. The diagnosis was considered delayed if classic imaging features were present, but these were either not identified or were misinterpreted within 7 days of image acquisition.
Results
Angiographically confirmed SDAVF were identified in 37 patients. There was a clear male predominance with 27 men diagnosed (76%). The mean population age was 65 years (range 44-85 years). The majority of fistulas were located in the thoracic spine (n=23, 62%). The diagnosis was delayed in 22 (59%) cases, with a mean delay to radiological diagnosis of 184 days (8 – 1135 days). When abnormal cord signal was identified, the differential diagnoses included ischemia (14%), neoplasia (11%), inflammation (11%) and a syrinx (8%).
Conclusions
Spinal dural arteriovenous fistulas are rare, but can be diagnosed readily on MRI of the spine if the characteristic imaging appearances are appreciated. Timely identification of the radiological features is imperative for prompt definitive management and the prevention of potentially irreversible neurological sequelae.

O-56

3:38PM - 3:46PM

The yield of initial MRI in 115 cases of angiographically confirmed spinal vascular malformations

A El Mekabaty[1], P Gailloud[1]
[1]*Johns Hopkins University School of Medicine, Baltimore, MD*

Purpose
Spinal vascular malformations (SVM) represent a heterogeneous and underdiagnosed group of vascular lesions currently estimated to account for about 10% of all vascular malformations of the central nervous system. Magnetic resonance imaging (MRI) - the primary screening tool for patients with myelopathic symptoms - is heavily relied upon when assessing the need for further investigation with spinal digital subtraction angiography (SpDSA). However, findings specific for SVMs on MRI – notably the presence of intra- or perimedullary flow voids – can be absent while intramedullary T2 signal abnormality, cord expansion and parenchymal enhancement also are seen with conditions, for example transverse myelitis. Early recognition of SVMs is necessary for favorable treatment outcome, yet accurate diagnosis often is delayed for months or years even in patients undergoing multiple MRI studies. The purpose of this study was to analyze the yield of initial MRI as a screening tool in a cohort of 115 patients with SVMs subsequently diagnosed by angiography.

Materials and Methods

The charts of patients with angiographically confirmed SVMs seen at our institution between 2006 and 2016 were reviewed. Patients were included in this study when the imaging data and initial report of at least 1 MRI study obtained prior to the angiographic diagnosis of SVM were available for analysis; 115 patients satisfied these inclusion criteria. An initial MRI study was classified as "positive" when the report mentioned a SVM or when SpDSA was recommended, or "negative" when the study was either considered normal or a diagnosis other than SVM was suggested. Spinal vascular malformations were separated in "high-flow" or "low-flow" lesions based on angiographic characterization.

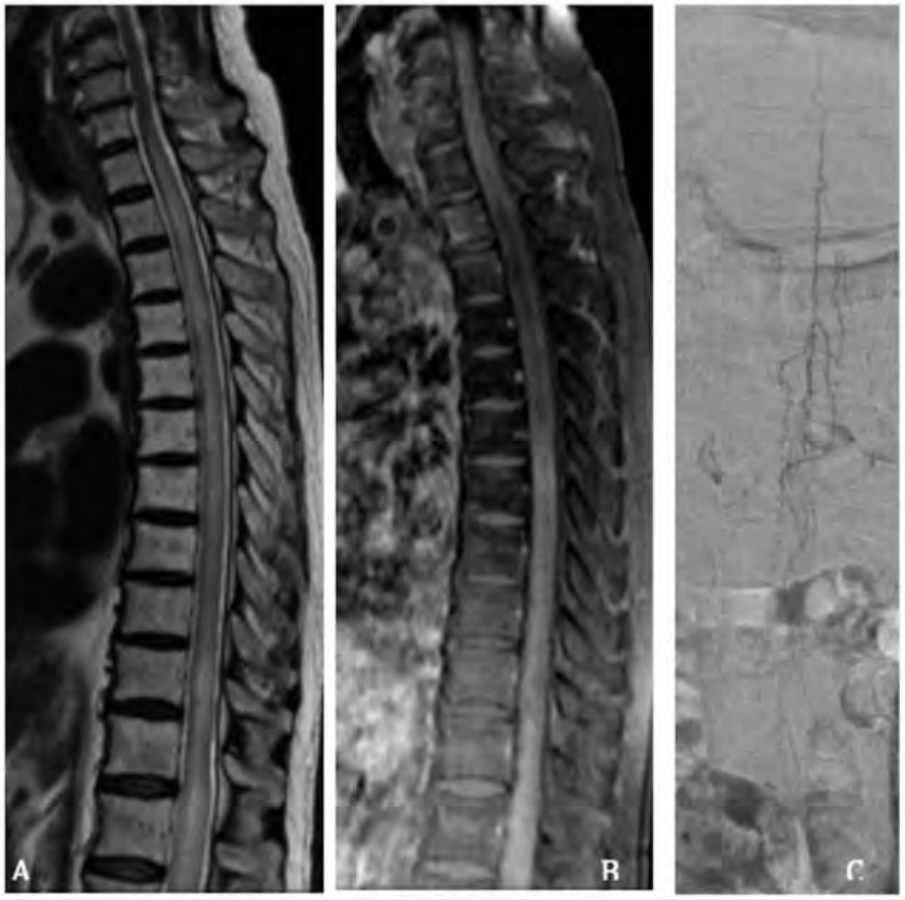
Results

Eighty-five (73.9%) patients had low-flow lesions, including 40 spinal dural arteriovenous fistula (AVF), 35 low-flow spinal epidural AVFs, and 10 perimedullary AVFs (type 1). Thirty patients (26.1%) had high-flow lesions, including 10 perimedullary AVFs (type 2), 8 spinal arteriovenous malformations, 6 high-flow spinal epidural AVFs; 5 perimedullary AVFs (type 3), and 1 paravertebral AVFs. Overall, initial MRIs were positive in 61 patients (53%) and negative in 54 (47%). Magnetic resonance imaging correctly identified 28 high-flow lesions (93.3%) but only 33 low-flow SVMs (38.8%). Flow voids were noted in 39.3% (33/84) of the low-flow lesions and 93.3% of the high-flow ones. T2-signal anomalies were more common with low-flow SVMs (77.1% versus 50%), with a tendency to be extensive in that group and focal with high-flow lesions. Parenchymal enhancement also was more common with low-flow lesions (56.9% versus 33.3%). Patients with an initial negative MRI had an average delay of 111 days before angiography (median: 70, range: 0 to 618) and - for those treated - 239 days before therapy (median 160, range: 0 to 1197); these intervals were respectively of 27 days (median 13, range: 0 to 131) and 76 days (median: 32, range: 0 to 761) for those with initial positive MRIs.

Conclusions

Initial MRI has a very high yield for high-flow SVMs, i.e., those characterized by the presence of prominent flow voids on T2-weighted images. On the other hand, initial MRI misdiagnosed more than 60% of low-flow SVMs in our series. The percentage of correctly identified lesion matched the percentage of studies showing flow voids in both groups. This finding indicates an over-reliance upon this MRI characteristic for the diagnosis of slow-flow lesions. Magnetic resonance imaging findings in that group are commonly nonspecific (T2 signal hyperintensity, parenchymal enhancement), overlapping with other conditions, notably transverse myelitis (TM), which initially was misattributed to 39% of the slow-flow SVMs in our cohort.

A 73-year-old woman with a 10-month history of lower extremity weakness and urinary incontinence with new and acutely worsening truncal ataxia. MRI showed extensive central T2 high signal intensity from T1 to conus with cord expansion, diffuse cord enhancement after contrast media application but no flow voids (Figure-2A-B). The MRI reported transverse myelitis (TM) as a possible diagnosis. SpDSA performed due to progressive myelitis revealed a SEAVF supplied through the left L4 intersegmental artery (Figure-2C). Successful glue embolization of the feeding branches was performed 2 days later.



(Filename: TCT_O-56_ASNRAbstract_Figure.jpg)

O-58

3:54PM - 4:02PM

Cognitive, technical and anatomical pitfalls in spinal angiography

P Gailloud[1]
[1]*Johns Hopkins University School of Medicine, Baltimore, MD*

Purpose
Diagnostic errors in medicine are defined as "those diagnoses that are missed, wrong, or delayed, as detected by some subsequent definitive test or finding" (1). Diagnostic errors can lead to misdiagnosis-related harm, either from delay or failure to treat a condition that

actually was present or from a treatment provided for a condition not actually present; they result in preventable mortality and morbidity as well as increased healthcare costs (2). Cognitive, technical and anatomical pitfalls are reducing the diagnostic accuracy of spinal digital subtraction angiography (SpDSA), leading to falsely negative studies and inadequate patient management. The purpose of this abstract is to illustrate a few correctible operator-dependent pitfalls that can prevent the documentation of critical findings during SpDSA.

Materials and Methods

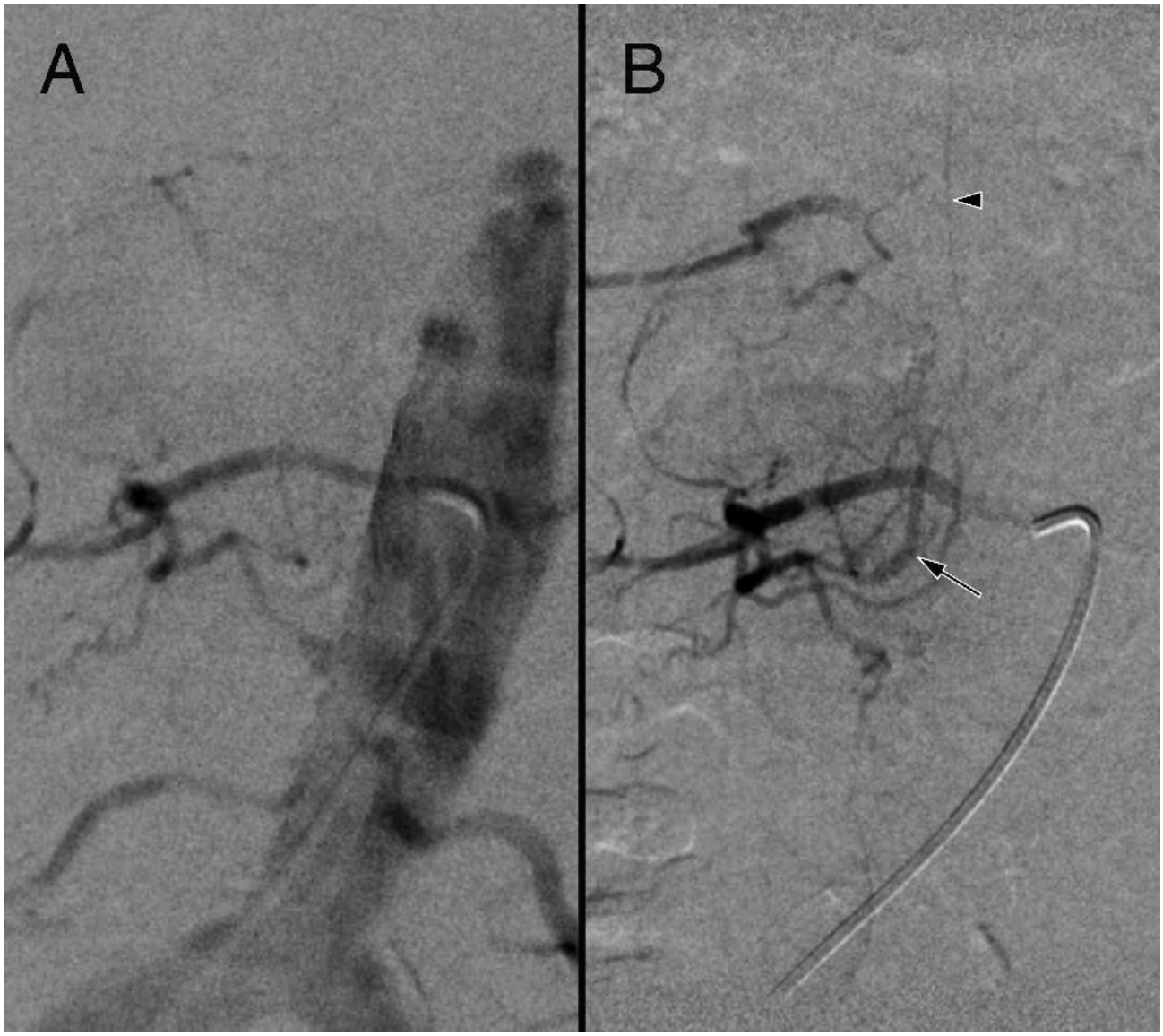
Selected clinical observations have been chosen to illustrate each pitfall category.

Results

The pitfalls most commonly identified during spinal angiography include: Cognitive factors – nonidentification of actually documented anomalies, decision to prematurely interrupt a study based on false premises (e.g., documentation of a normal venous phase); Technical factors - incomplete angiographic studies, nonselective angiography (nonostial injections (Fig. 1), flush aortograms), inadequate injections (premature or inadequate contrast injections); Anatomical factors - in particular, pitfalls related to the second thoracic intersegmental artery, pelvic branches and incomplete intersegmental trunks.

Conclusions

Spinal vascular malformations typically are characterized by a "narrow therapeutic window". Early diagnosis therefore is essential to a favorable endovascular or surgical treatment outcome. Patients in whom a diagnostic spinal angiogram is falsely negative will either receive an inadequate and potentially hazardous therapy (e.g., medical management of transverse myelitis) or receive the appropriate treatment with significant delay, if at all. This abstract illustrates several correctible operator-dependent pitfalls that can result in falsely negative studies. Figure 1. A 75-year-old man with progressive myelopathy A, DSA, nonselective injection at the level of L3, posteroanterior projection, arterial phase, showing no evidence of vascular malformation. The contrast opacification resulting from a nonselective injection may falsely appear sufficient and hide important findings. In addition, the volume used during nonselective injections significantly increases the contrast load. B, DSA, right L3 ISA injection, posteroanterior projection, arterial phase. Continued progression of his symptoms led the patient to consult for a second opinion. A new angiogram was performed, during which a selective injection of right L3 showed a spinal epidural arteriovenous fistula consisting of an epidural venous pouch (arrow) supplied by a right L3 radicular branch and draining into a radiculomedullary vein (arrowhead).



(Filename: TCT_O-58_Figure1.jpg)

O-59

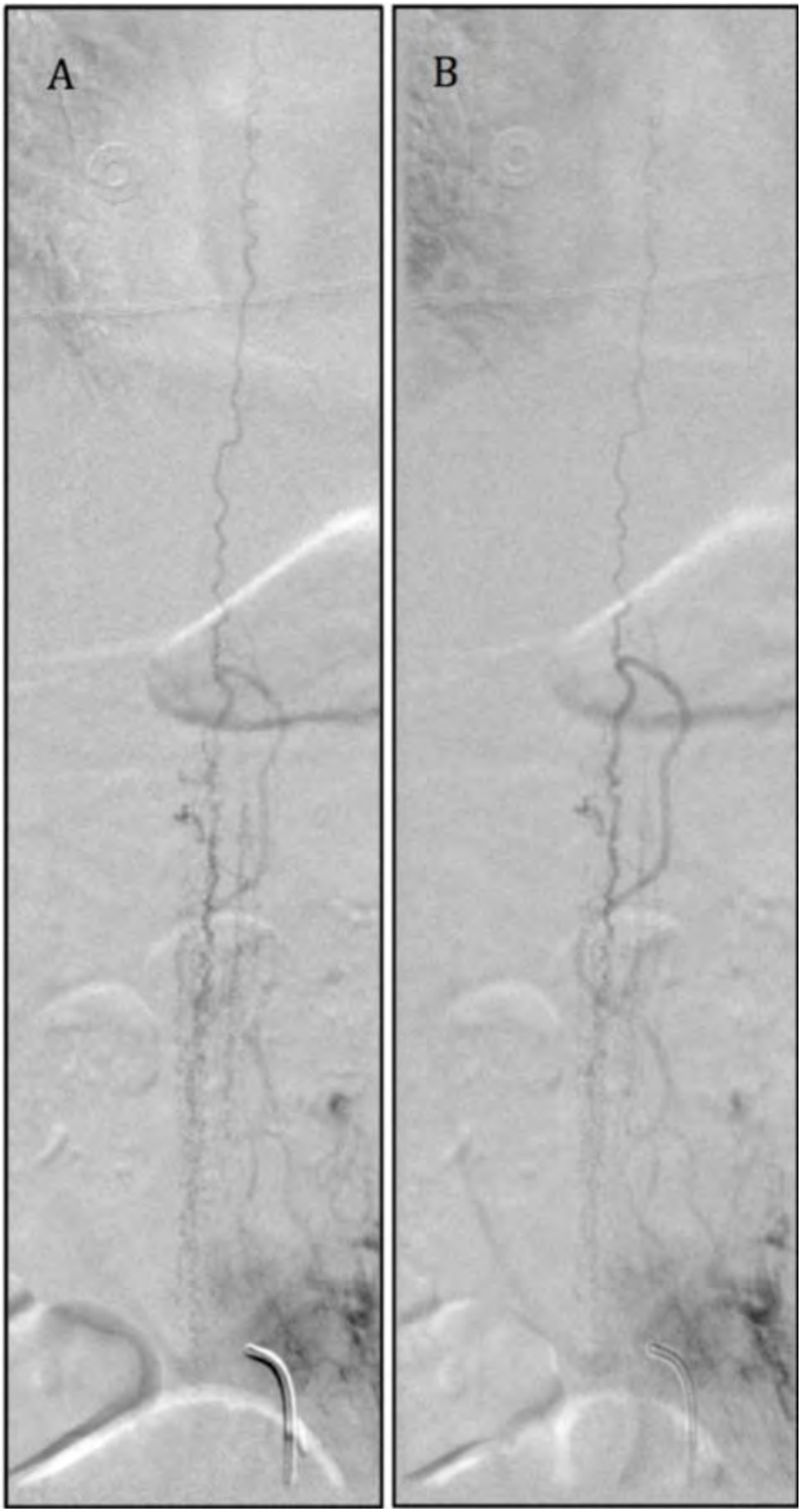
4:02PM - 4:10PM

The Impact of Anti-Scatter Grid Removal on Radiation Dose Reduction During Spinal Angiography

E Orru[1], A El Mekabaty[1], P Gailloud[1]
[1]*Johns Hopkins University School of Medicine, Baltimore, MD*

Purpose
Spinal digital subtraction angiography (SpDSA) requires a high number of acquisitions and potentially can expose the patient and caring team to relatively high radiation doses. Various radioprotection techniques currently are used in our practice to limit radiation exposure

during angiography, including removal of the anti-scatter grid (ASG). We present a prospective evaluation of the impact of ASG removal on dose reduction during SpDSA.
Materials and Methods
The study enrolled adult patients investigated between January and December 2015. The decision to keep or remove the ASG during the clinical part of the angiogram was based essentially on patients' habitus, as customary in our practice. After study completion, each patient was subjected to 1 additional acquisition, either with the ASG installed or removed depending on the technique used for the clinical part of the study. All injections were performed by the same operator using identical parameters (same volume of contrast, number of acquired images, electronic and geometric magnification and collimation). Air kerma and dose area product (DAP) for both acquisitions were recorded.
Results
Sixty-five patients participated in the study. Twelve patients were excluded for clinical or technical reasons. In total 53 patients (32 men) were included in this analysis. The average age was 51 years (range 20-83 years) and average BMI was 27.6 (range 16.4-40.7). The acquisitions without ASG showed a lower air Kerma: 24 mGy (8.3-48.1) versus 35.1 mGy (11.3-68.2) with the ASG (p-value <0.001). The DAP also was lower without ASG: 135.6 µG/m2 (31.5-319.6) versus 201.7 µG/m2 (38.6-548.5) (p-value <0.001).
Conclusions
Anti-scatter grid removal significantly reduces radiation exposure during SpDSA. In our cohort, both the air kerma and the DAP were decreased by more than 30%. The potential of this dose-reduction technique extends beyond the field of spinal angiography, as it has the potential to decrease radiation exposure for patients and operators during intervention performed in the thoracic and abdominal regions.


A
B

(Filename: TCT_O-59_Abstract_Figure20A_B.jpg)

O-60

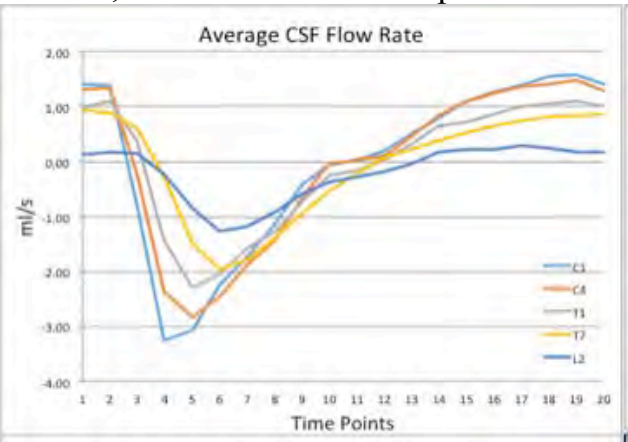
4:10PM - 4:18PM

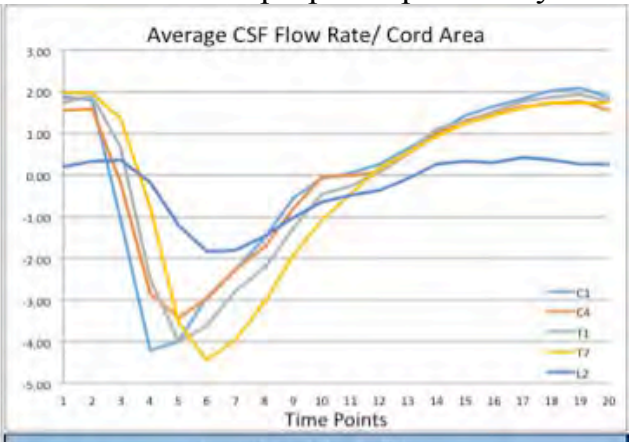
Cervical, Thoracic and Lumbar CSF Flow Pulsation Temporal Correlations with Major Arterial and Venous Flow Pulsation and Inverse Correlations with Cross Sectional Cord Area and Caudal Residual Length

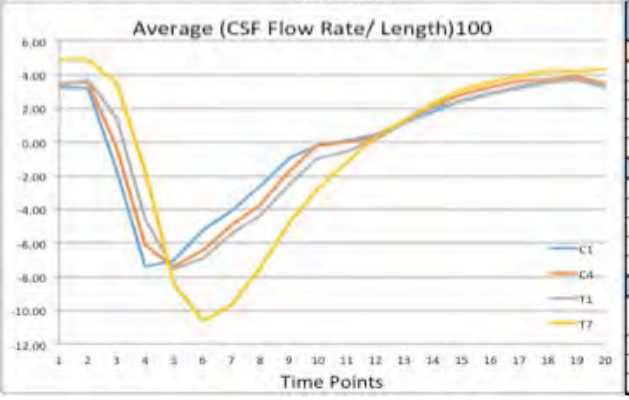
R Bert[1], E Tiwana[1], N Settipalle[1], B Wellman[2], M Boakye[1]
[1]University of Louisville, Louisville, KY, [2]University of Louisville, Louisvlle, KY

Purpose
The origins of recumbent CSF pulsations in the spinal canal have been debated (1-5) and previously we have presented data demonstrating that a portion of the fluid pulsation is generated from within the spinal canal. We have acquired high temporal resolution, through-plane CSF flow curves from 15 normal human volunteers using retrocardiac-gated MR cine acquisition and correlated the curves with major arterial and flow curves from the same patient. We also compared adjusted flow curves, dividing flow by the cord cross-sectional area and the cord length distal to the imaged level.
Materials and Methods
With IRB approval, 15 healthy volunteers ages 23-46 years were scanned. Scanner parameters: TR=60/TE=6/FA=70/thickness=6mm/FOV=160mm/Phases=20/cycle, external retrocardiac-gated, 3T (Siemens Skyra). VENCs were customized and set at 3(L2)-100 (CCA)cm/s to avoid aliasing. Transverse CSF, arterial and venous scans were performed at C1, C4, T1, T7 and L2. Data were analyzed with custom software based on Matlab. The mean flow, velocity, ROI area were measured at each cine timepoint for the CSF, arterial (descending aorta, CCA, ICA and VA) and venous (IJ and IVC) flow.
Results
Average mean CSF flow decreased craniocaudally at each time point (Fig.). In diastole, CSF flow decreased proportionally to cross-sectional area and length of cord below the level. This finding was less consistent in systole, where T7 was the greatest outlier. At C1, CSF and ICA correlation was .937 in systole and 0.761 in diastole, but dropped to 0.356 systole and 0.440 diastole at L2 (table). Interestingly, CSF flow at T7 and L2 were better correlated with the aorta during systole, but uncorrelated in diastole. L2 in diastole demonstrated low correlation with all arteries and veins.
Conclusions
We previously have verified presented data, now with a larger data set of 15 individuals. The data clearly show cranial-caudal attenuation of the flow related to the cord length caudal to a cross section, and to cross-sectional area of the cord. Correlation with arterial and venous flow varies substantially throughout the cord, as blood flow to and from the cord changes at different levels. Accounting for diastolic flow reversal, recent publications (5) and the

minute pressure di erences occurring in CSF during the cardiac cycle, the data support local vascular pulsatility and compliance as sources and sinks generating CSF pulsations in supine humans, rather than dural compliance models that have been proposed previously.







Averaged Correlation Coefficients

		ICA	CCA	VA	Aorta (T7)	U	IVC	Aorta (L2)
Systole	L2	0.356	-0.017	0.072	0.179	0.575	0.572	0.390
	T7	0.551	0.096	0.228	0.298	0.600	0.571	0.498
	T1	0.810	0.410	0.500	0.642	0.708	0.437	0.727
	C4	0.875	0.540	0.599	0.731	0.653	0.342	0.764
	C1	0.937	0.707	0.736	0.835	0.618	0.260	0.779
Diastole	L2	0.440	0.365	0.295	0.110	0.239	0.343	0.062
	T7	0.739	0.694	0.534	0.101	0.445	0.537	-0.001
	T1	0.726	0.714	0.548	-0.026	0.361	0.401	-0.173
	C4	0.665	0.677	0.469	-0.096	0.322	0.380	-0.211
	C1	0.761	0.721	0.566	-0.034	0.389	0.400	-0.160
Whole Cycle	L2	0.495	0.238	0.310	0.336	0.559	0.457	0.441
	T7	0.679	0.362	0.455	0.458	0.617	0.454	0.548
	T1	0.858	0.608	0.660	0.708	0.682	0.332	0.703
	C4	0.889	0.685	0.708	0.762	0.658	0.261	0.723
	C1	0.940	0.800	0.805	0.844	0.644	0.217	0.750

(Filename: TCT_O-60_Graphs.jpg)

O-61

4:18PM - 4:26PM

Fluid-Signal Structures in the Cervical Spinal Cord on MRI in Chiari I Patients: The Mystery and Myth of the Median Sagittal Lines – Syringohydromyelia or Not?

L Wang[1], R Scott[2], T Tomsick[1]
[1]University of Cincinnati & University of Cincinnati Medical Center, Cincinnati, OH, [2]University of Cincinnati, Cincinnati, OH

Purpose

The anterior median fissure (AMF) and central canal of the spinal cord may be seen on MRI with variable frequency (diagram 1). Hyperintense foci (HIF) on axial T2-weighted images in the central spinal cord can be the base of AMF or central canal. Channel-like T2 hyperintense craniocaudad line (SL) on sagittal images can be due to the base of the AMF or central canal from our previous study. Patients with Chiari I have a higher incidence of

syringohydromyelia than the general population. We hypothesize a higher incidence of AMF, HIF and SL on MRI in Chiari I patients than controls.

Materials and Methods

Two neuroradiologists retrospectively analyzed cervical MRI of 85 patients from 6 MR scanners (2 3T, 4 1.5T) for a hyperintense (HI) fissure and central canal (HIF) on axial T2-weighted images, and for a linear channel (SL) on sagittal images. Data from 356 controls and 85 Chiari I patients were analyzed in Excel with Chi square, Student's T, and kappa statistic tests.

Results

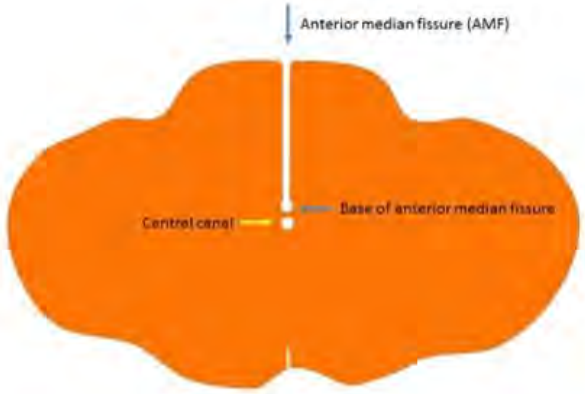
Incidence and frequency of HIF, AMF, and SL for Chiari I patients without syringomyelia are compared to a non-Chiari control group from an earlier study population in Table 1. HIF and AMF per patient were increased in Chiari I patients without syrinx compared to the non-Chiari control study group. The overall incidence of HIF, AMF, and SL also was increased in nonsyrinx Chiari patients compared to the control group. For all Chiari patients, agreement between neuroradiologists was moderate for determining HIF (κ=0.44) and AMF (κ=0.52), and excellent for SL (κ=0.90). In the previous study investigating non-Chiari patients, agreement was substantial for HIF (κ=0.64) and AMF (κ =0.75), and moderate for identification of SL (κ=0.55).

Conclusions

There is a higher incidence of SL in Chiari population compared to control population. Not all SLs in Chiari are syringohydromyelia or central canal. The base of the AMF can cause SL. Our earlier study had suggested that AMF and HIF are related structurally with the HIF commonly the base of the AMF. We postulate that the base of AMF also contributes to the increase incidence of SL in the Chiari population: SL on sagittal images can resemble syringohydromyelia and not all SL represent syringohydromyelia in Chiari patients.

	HIF		AMF		SL (%)
	%	HIF/pt.	%	AMF/pt.	
Chiari I without syrinx (n=121)	97%***	9.10***	66%*	3.55**	39%***
Control (n=356)	65%	3.7	60%	2.3	25%

*significant at p < 0.002; **significant at p < 0.001; ***significant at p < 0.0001



(Filename: TCT_O-61_ASNR2017figure.jpg)

O-62

4:26PM - 4:34PM

Ventriculomegaly in Hydrocephalus Estimated by an Uni-Dimensional and a Two-Dimensional Approach on Magnetic Resonance Images is Associated with Alterations of Rheologically Active Proteins in Cerebrospinal Fluid

S Schob[1]
[1]*University Hospital Leipzig, Leipzig, WY*

Purpose
Surfactant proteins (SPs) are involved in the regulation of rheological properties of body fluids. Concentrations of SPs are altered in the cerebrospinal fluid (CSF) of hydrocephalus patients. The common hallmark of hydrocephalus is enlargement of the brain ventricles. The relationship of both phenomena has not been investigated yet. The aim of this study was to evaluate the association between SP concentrations in the CSF and enlargement of the brain ventricles.

Materials and Methods

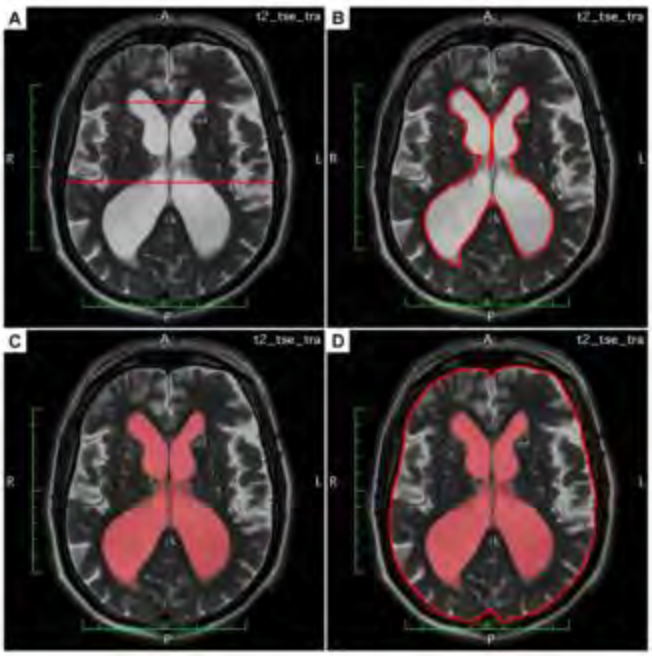
Ninety-six individuals (41 healthy subjects and 55 hydrocephalus patients) were included in this retrospective analysis. Cerebrospinal fluid (CSF) specimens were analyzed for SP-A, SP-B, SP-C and SP-D concentrations by use of enzyme linked immunosorbent assays (ELISA). Ventricular enlargement was quantified in T2-weighted magnetic resonance imaging sections using an uni-dimensional (Evans' Index) and a 2-dimensional approach (Lateral Ventricles Area Index).

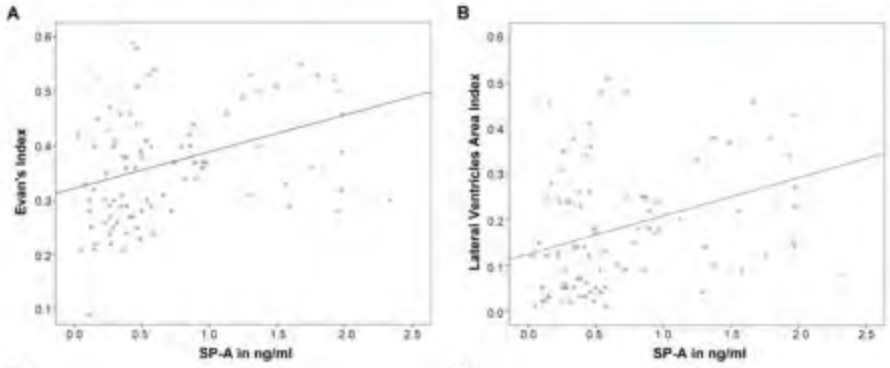
Results

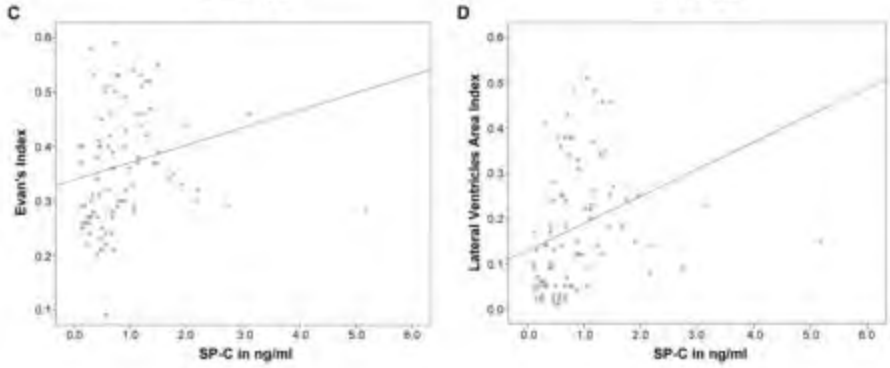
Cerebrospinal fluid-SP concentrations (mean ± standard deviation in ng/ml) were as follows: SP-A 0.71 ± 0.58, SP-B 0.18 ± 0.43, SP-C 0.89 ± 0.77 and SP-D 7.4 ± 5.4. Calculated values of Evans' Index were 0.37 ± 0.11, a calculation of Lateral Ventricles Area Index (LVAI) resulted in 0.18 ± 0.15 (each mean ± standard deviation). Significant correlations were identified for Evans' Index with SP-A ($r=0.388$, $p<0.001$) and SP-C ($r=0.392$, $p<0.001$), LVAI with SP-A ($r=0.352$, $p=0.001$), SP-C ($r=0.471$, $p<0.001$) and SP-D ($r=0.233$, $p=0.025$). Furthermore, SP-C showed a clear inverse correlation with age ($r=-0.357$, $p=0.011$).

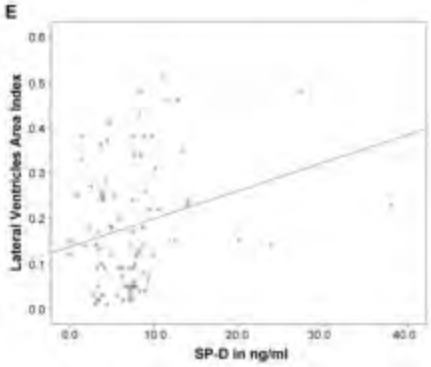
Conclusions

The present study confirmed a clear correlation between SP-A and SP-C in the CSF with enlargement of the inner CSF spaces. Furthermore, a moderate correlation between SP-D in CSF with ventricular enlargement was identified by using a more accurate, 2-dimensional approach compared to the simplistic uni-dimensional approach. This possibly indicates that SP-D also is regulated differently in hydrocephalic conditions, but in a more subtle manner than SP-A and SP-C. In conclusion, SPs clearly play an important role for CSF rheology. Cerebrospinal fluid rheology is profoundly altered in hydrocephalic diseases; however, diagnosis and therapy of hydrocephalic conditions are still almost exclusively based on ventricular enlargement. Until now it was unclear, whether the stage of the disease, as represented by the extent of ventricular dilatation, is somehow related to the changes of SP levels in the CSF. Our study is the first to provide evidence that increasing ventriculomegaly is accompanied by enhanced changes of rheologically active compounds in the CSF and therefore introduces completely new aspects for hydrocephalus testing and conservative therapeutic approaches.


A
B
C
D
t2_tse_tra
A
P
R
L


A
Evan's Index
SP-A in ng/ml
B
Lateral Ventricles Area Index
SP-A in ng/ml


C
Evan's Index
SP-C in ng/ml
D
Lateral Ventricles Area Index
SP-C in ng/ml


E
Lateral Ventricles Area Index
SP-D in ng/ml

(Filename: TCT_O-62_figureevanasnrII.jpg)

O-63

4:34PM - 4:42PM

Predicting Decrease in Cerebrospinal Fluid Pressure Based on Opening Pressure and Volume Removed During Lumbar Puncture

T Capobres[1], L Poisson[1], H Marin[1], S Patel[1], B Griffith[1]
[1]*Henry Ford Health System, Detroit, MI*

Purpose
In patients with idiopathic intracranial hypertension (IIH) and elevated opening pressure (OP), a "high volume" lumbar puncture (LP) may be performed for therapeutic purposes. However, removal of too much fluid can result in post-LP headaches with considerable morbidity. Unfortunately, there is no well established correlation between CSF volume removed and CSF pressure change leading to a trial-and-error approach. The purpose of this study is to determine whether a correlation exists between CSF volume removed and change in CSF pressure, as well as how this relationship is affected by opening pressure.
Materials and Methods
Imaging records of patients with suspected or established IIH who underwent LP at our institution between 2006-2016 were reviewed. Two hundred twenty-six LPs were identified and opening/closing pressures and CSF volume removed were recorded. Analysis of variance, for patients grouped according to opening pressure, and linear regression, for continuous measure, were used to assess the association between opening pressure and pressure change.
Results
Mean pressure change (cm H2O per ml CSF removed) according to OP group was: 0.56 +/- 0.35 for OP <20 cm; 0.57 +/- 0.19 for OP of 20-29 cm, 0.85 +/- 0.30 for OP of 30-39 cm, and 1.09 +/- 0.34 for OP of >40 cm (Fig. 1A). A one-way ANOVA of pressure change per mL indicates a statistically significant difference between groups. Regression analysis demonstrates a positive linear association between OP and pressure change per mL (Fig. 1B) with an estimate that for every 10 cm increase in OP, there is a 0.21 cm/mL increase in pressure change (SE=0.0196, $p<0.0001$) This is a moderately strong correlation with Pearson's coefficient 0.58 (95% CI: 0.49, 0.66).
Conclusions
There is a correlation between CSF volume removed and change in pressure, which is dependent on opening pressure. Understanding this is essential when performing LPs on patients with IIH.

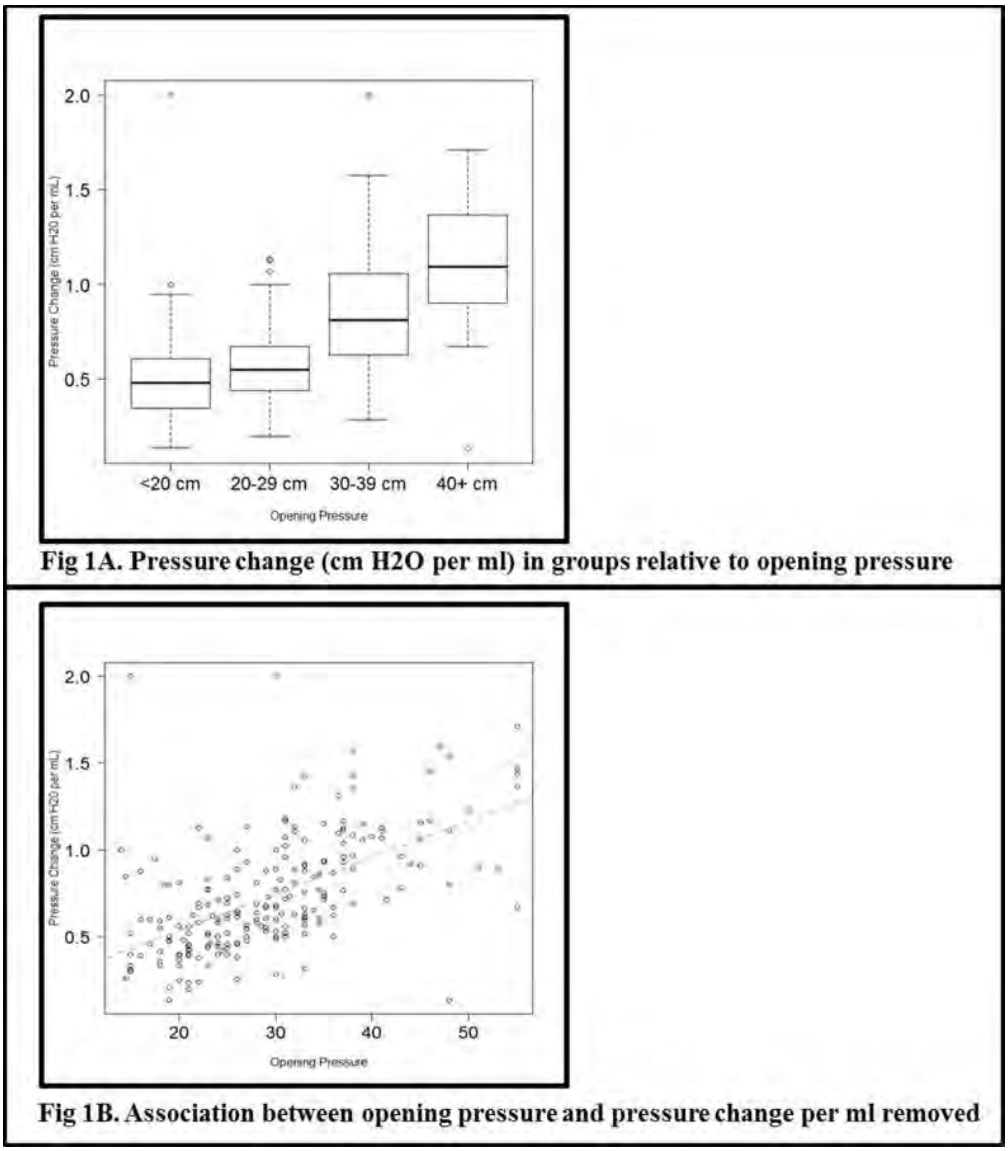


Fig 1A. Pressure change (cm H2O per ml) in groups relative to opening pressure

Fig 1B. Association between opening pressure and pressure change per ml removed

(Filename: TCT_O-63_LPfinal.jpg)

Monday
3:30PM - 4:45PM
Long Beach Convention Center, Room 103 (Main Level)

06C-Parallel Paper Session: Pediatric Neuroradiology: Early Brain Imaging and Injury

O-64

3:30PM - 3:38PM

Gadoterate Meglumine Pharmacokinetics, Safety and Efficacy in Pediatric Subjects Aged <2 Years

I Lazar[1]
[1]*Borsod County University Teaching Hospital, Miskolc, Hungary*

Purpose
To evaluate the pharmacokinetics profile in plasma of gadoterate meglumine (Dotarem®, Guerbet, France) in children aged less than 2 years.
Materials and Methods
This study included pediatric subjects aged less than 2 years with normal estimated Glomerular Filtration Rate (eGFR), scheduled to undergo a routine gadolinium-enhanced MRI of any body region, at the dose of 0.1 mmol/kg. A population pharmacokinetics approach was used. For each pediatric subject, blood samples were collected at 3 time points allocated by randomization, ranging from 10 min to 8 hours after injection. Adverse events (AEs) were recorded. Quality of images and lesion visualization were assessed as efficacy criteria in subjects who underwent MRI for CNS indication.
Results
A total of 45 children received gadoterate meglumine (male: 48.9%; mean age: 9.9 months). Five children were less than 1 month old, 9 children were 1 to 3 months old and 31 children were more than 3 to less than 24 months old. Mean (±SD) baseline eGFR was 129.7±41.5 mL/min/1.73 m² (52-217). Magnetic resonance imaging (MRI) indication was CNS examination for 28 subjects (efficacy subgroup). Median area under the curve was estimated at 1591 h.µmol/L and median terminal half-life was 1.35 h. Median total clearance and volume of distribution at steady state were 0.06 L/h per kg and 0.047 L/kg, respectively. Only 1 child (2.2%) experienced 1 AE related to gadoterate meglumine: a moderate rash. Overall quality of images was good for all 28 subjects and lesion visualization was improved with gadoterate meglumine. Lesions were identified in 15 subjects with precontrast images and in 16 subjects with pre and postcontrast images.
Conclusions
Pharmacokinetics of gadoterate meglumine in children less than 2 years old is similar to that observed in older children or adults. Good safety and efficacy profiles of this contrast agent were confirmed in this pediatric population.

O-65

3:38PM - 3:46PM

A fast screening brain MRI protocol reduces need for sedation and time out of the NICU

C Lacroix[1], J Flibotte[1], S Elshenawy[1], U Nawab[1], E Schwartz[1]
[1]*Children's Hospital of Philadelphia, Philadelphia, PA*

Purpose
Many neonates in the NICU have neurological complications requiring brain MRI. The fragility of these patients prompted implementation of a neonatal brain MRI screening protocol (aka FastNICUs), which includes: sagittal T1 TSE, axial and coronal T2, axial SWI

and axial DWI. Additional sequences can be added, as neuroradiologists monitor in real-time. Goals were to decrease scanning time, time out of the NICU, and need for sedation, while maintaining diagnostic quality.

Materials and Methods

Between 1/1/16 and 10/30/16, 51 FastNICUs (22 females) and 87 routine brain MRIs were performed. Retrospective review was performed for total time in Radiology (not scanning time), sedation, and patient temperature upon return to NICU. Studies for which motion-degraded sequences needed repeating, additional sequences requested, nondiagnostic studies, or those needing repeat study with sedation also were recorded. All parameters were compared against routine brain MRI, with Mann-Whitney U (noncategorical data) and Pearson's chi-squared (categorical data).

Results

FastNICUs were significantly more likely to be performed without sedation than routine protocol, 33 (64.7%) vs 24 (27.6%), (p0.0001). Average time for FastNICUs was significantly less than routine protocols, 27:54 min 10:32 (median 25) vs 48:42 min 19:44 (median 43:30), a decrease in average time by 20:48 min (43%), (p0.0001), despite 17 (33.3%) FastNICUs having additional sequences added. Sequences were repeated due to motion in 19 (37.3%) of FastNICUs and 26 (29.9%) of routine. FastNICUs were interpreted as overall degraded by motion in 2 (3.9%) vs 1 (1.1%) routine protocol. No MRI was interpreted as nondiagnostic, or required repeating with sedation. There was no significant difference in temperature.

Conclusions

Brain MRIs in NICU patients following a tailored protocol resulted in a significant decrease in time away from the NICU and use of sedation, thereby maximizing safety without adversely affecting image quality.

FastNICU Protocol (lower resolution sequences)	**Routine Brain Protocol**
Sagittal T1 (1:43)	Axial DWI (3:11)
Axial T2 (1:41)	Sagittal T1 (5:23)
Axial SWI (2:27)	Axial T2 (4:45)
Coronal T2 (1:53)	Axial FLAIR (3:38)
Axial DWI (0:57)	Coronal T2 (5:02)
	Axial ASL Perfusion (3:52)
	Axial DTI (3:05)
Total time: 8:41 min	**Total time: 28:56 min**

(Filename: TCT_O-65_FastNICUvsRoutineBrainMRIProtocols.jpg)

O-67

3:54PM - 4:02PM

Antenatal Factors that Affect the Severity of Postnatal Brain Injury in Congenital Diaphragmatic Hernia

R Radhakrishnan[1], S Merhar[2], B Zhang[1], P Burns[1], F Lim[1], B Kline-Fath[1]
[1]Cincinnati Children's Hospital Medical Center, Cincinnati, OH, [2]Cincinnati Children's Hospital Medical Center, Cincinanti, OH

Purpose
Approximately 60% of infants with congenital diaphragmatic hernia (CDH) have evidence of brain injury or delayed brain maturation on pre-discharge MRI(1, 2). Identifying factors that cause brain injury is important as they could affect future neurodevelopmental outcome (3). Postnatal clinical factors can influence brain injury in CDH (2); however the role of antenatal factors, and presence of antenatal brain injury is unclear. Here, we identify fetal MR imaging findings that may be associated with postnatal brain injury in CDH to understand the pathogenesis and timing of brain injury in this population.
Materials and Methods
After IRB approval, we retrospectively identified 36 cases of CDH (from 2009 to 2014) with fetal and postnatal MRI available for review. Fetal imaging and postnatal brain MR imaging was reviewed by 2 pediatric neuroradiologists. Postnatal brain injury was graded on a previously published scale (2) and included ventriculomegaly; extra-axial space enlargement; injury to cortex, white matter and basal ganglia; and intraventricular, parenchymal and cerebellar hemorrhage. Using this scale, a composite postnatal brain injury score was obtained. Fetal MRI findings of brain injury including maturational delay, extra-axial space enlargement, engorged venous sinuses, ventriculomegaly, intracranial hemorrhage and parenchymal signal abnormality were recorded. Congenital diaphragmatic hernia severity markers were lung volumetry, side of CDH, intrathoracic liver (ITL), observed to expected total lung volume (o/e TLV), and associated congenital heart disease. Correlations between brain abnormalities on fetal and postnatal brain MRI were analyzed. Postnatal brain injury findings correlating with severity of CDH also were assessed. Scans at < 28 weeks and >28 weeks were analyzed separately. P value <0.05 was considered significant.
Results
In 36 infants (17 girls) with CDH, there were a total of 62 fetal MRIs available for review. Twenty-six patients had 2 fetal MRIs, and 10 had one fetal MRI. Fetal MRI was performed between 20w1d and 36 weeks postmenstrual age. On fetal MRI, the most common imaging abnormality was enlarged extra-axial spaces seen in 22/36 MRIs, always seen at > 28w fetal MRI. Other less common findings were presence of venous sinus distention and ventriculomegaly. There were no cases of maturational delay, intracranial hemorrhage or

brain parenchymal injury identified on fetal MRI. On postnatal MRI, 24/36 infants had findings of brain injury. Average brain injury score was 1.8 (0-6). Most common postnatal MRI finding was enlarged extra-axial spaces. Right sided diaphragmatic hernia was associated with greater brain injury score compared to the left (p=0.05). Presence of intrathoracic liver was associated with postnatal evidence of white matter injury (p = 0.028). Lower o/e TLV was associated with greater total postnatal brain injury score (p = 0.04). No prenatal brain imaging abnormalities were associated with postnatal evidence of brain injury except the presence of mild fetal ventriculomegaly, which was associated with mild postnatal ventriculomegaly (p = 0.047).
Conclusions
We provided a detailed assessment of the association of prenatal brain MRI findings and CDH severity with postnatal MRI evidence of brain injury. Postnatal brain injury is influenced by a measure of prenatal pulmonary hypoplasia (o/e TLV). Although enlarged extra-axial spaces in the third trimester was found to be the most common abnormality prenatally, this surprisingly did not correlate with postnatal brain injury. Absence of maturational delay or parenchymal injury on fetal MRI suggests that these forms of brain injury are likely related to perinatal/early neonatal events rather than in utero injury.

O-68

4:02PM - 4:10PM

Early MRI Evidence of Brain Injury is Associated with Adverse Neurodevelopmental Outcome in Children with Congenital Diaphragmatic Hernia

R Radhakrishnan[1], S Merhar[2], B Zhang[1], P Burns[1], F Lim[1], B Kline-Fath[1]
[1]Cincinnati Children's Hospital Medical Center, Cincinnati, OH, [2]Cincinnati Children's Hospital Medical Center, Cincinanti, OH

Purpose
Sixty percent of infants with congenital diaphragmatic hernia (CDH) have evidence of neuroimaging abnormalities on early MRI (1). While it has been shown that at least half of the CDH survivors have neurodevelopment impairment in early childhood, most studies have described outcome in the context of clinical factors or ultrasound abnormalities (2-4). It is unclear how brain injury on MR relates to neurodevelopmental outcome. In this study, we compare postnatal MRI neuroimaging abnormalities with neurodevelopmental outcome in infants with CDH.
Materials and Methods
After IRB approval, this study was performed in a cohort of longitudinally followed CDH infants. Between 2009 and 2016, 39 infants with CDH had postnatal brain MRI prior to discharge from the NICU and neurodevelopmental follow up with Bayley Scales of infant development 3rd edition (BSID-III) . Magnetic resonance imaging (MRI) findings of brain injury were graded by 2 pediatric neuroradiologists as previously described (1). A composite

MRI brain injury score was obtained. Clinical and demographic data including gestational age, size of diaphragmatic defect, need for ECMO, and presence of sepsis were recorded. BSID-III were scored in each of the 3 domains (language, motor and cognitive). BSID-III scores of less than 85 in any domain were considered abnormal (2). Statistical analyses were aimed at identifying the relationship between MRI brain injury scores, clinical data, and BSID-III scores. For clarity, statistical significance was assumed when $p<0.05$.

Results

Of the 39 infants (20 male) who were enrolled, 24 (62%) had evidence of brain imaging abnormality on early MRI performed before discharge. Median age at early MRI was 35 days of life (11-192 days). Average brain injury score was 2.2 (0-12). Median age at BSID-III evaluation was 24 months (22-36 months). Overall, there was neurodevelopmental delay in 36% (14/39) in any of the domains tested. Total brain injury score was associated with cognitive ($p = 0.027$) and motor (0.039) scores, but not with language scores. Looking at individual brain injury patterns, presence of ventriculomegaly was associated with cognitive, language and motor outcome (all $p <=0.05$). Extra-axial space enlargement was associated with cognitive and motor outcome ($p <=0.02$) and parenchymal hemorrhage was associated with disability in all 3 domains ($p<0.01$). Presence of cerebellar hemorrhage, white matter injury, cortical injury, basal ganglia injury were not associated significantly with cognitive scores. For the clinical variables, ECMO, Apgar at 5 minutes, need for g tube, blood stream or endotracheal infection, need for O2 at discharge, days on parenteral nutrition, days on ventilator, length of NICU stay, and lack of oral feeding at discharge were all significantly associated with neurodevelopmental outcomes in the various domains. Side of hernia, patch repair, and the need for inotropes were not associated with neurodevelopmental outcome.

Conclusions

This is the first comprehensive evaluation of MRI evidence of brain injury associated with neurodevelopmental outcome in infants with CDH. The results of this study would suggest a benefit of early initiation of neurobehavioral intervention in the setting of early MRI evidence of brain injury for this population.

O-69

4:10PM - 4:18PM

Superficial Siderosis after Germinal Matrix Hemorrhage

U Yilmaz[1], H Körner[2], A Simgen[3], w reith[4], R Mühl-Benninghaus[3]
[1]Saarland University Hospital, Homburg, Germany, [2]Saarland University Hospital, Homburg, AK, [3]Saarland University Hospital, Homburg, Saarland, [4]University clinic saarland, homburg, saarland

Purpose

Germinal matrix hemorrhage is a frequent complication of prematurity and can be associated with adverse neurodevelopmental outcome depending on its severity. In addition to

parenchymal damage, intraventricular residues of hemorrhage and hydrocephalus MRI findings include superficial siderosis. The purpose of this study was to investigate the prevalence and location of superficial siderosis in patients with a history of germinal matrix hemorrhage.
Materials and Methods
We retrospectively identified patients with a history of germinal matrix hemorrhage who underwent MRI in our institution between 2008 and 2016. Imaging was evaluated regarding the presence and location of superficial siderosis. The presence of subependymal siderosis and evidence of hydrocephalus was assessed.
Results
Thirty-seven patients with a history of germinal matrix hemorrhage were included. 86.5% were preterm births. The mean age at the first MRI was 386 days (range 2-5140). The prevalence of superficial siderosis was 67.6%. Superficial siderosis was detected significantly more often when MRI was performed within the first year of life (82.8% vs. 12.5%, $P < 0.000$). When present superficial siderosis was located infratentorially in all cases while additional supratentorial superficial siderosis was detectable in 27%.
Conclusions
Here we report that superficial siderosis is a common MRI finding in the first year of life of patients with a history of germinal matrix hemorrhage, but it dissolves and has a low prevalence thereafter. A prospective analysis of its initial severity and speed of dissolution during this first year might add to our understanding of the pathophysiology of neurodevelopmental impairment after germinal matrix hemorrhages.

O-70

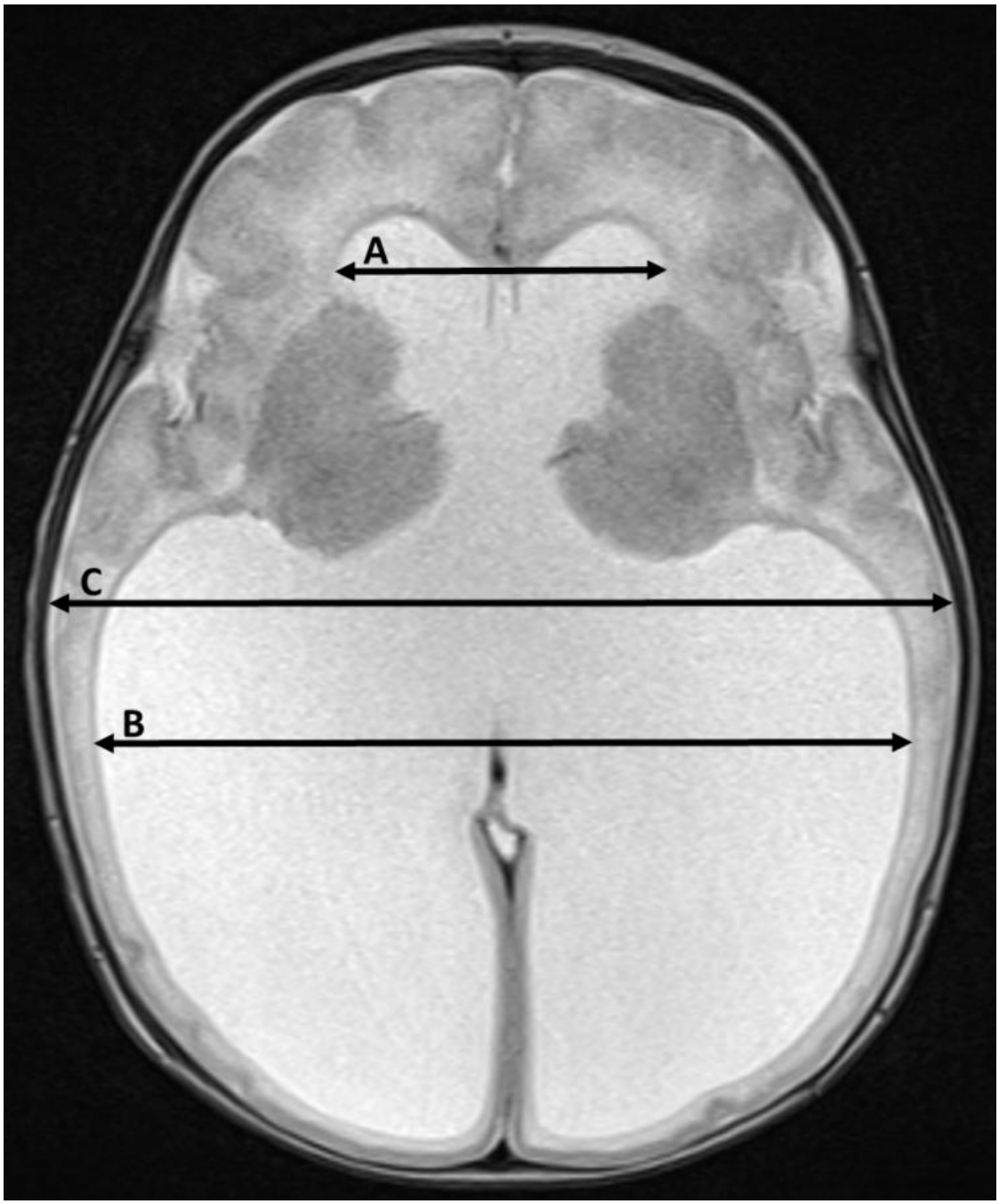
4:18PM - 4:26PM

Frontal to Occipital Horn Ratio is Associated with Multifocal Intraparenchymal Hemorrhages in Neonatal Shunted Hydrocephalus

S Oushy[1], J Parker[2], C Wilkinson[1], N Stence[3], M Handler[1], K Campbell[4], C Palmer[5], D Mirsky[3]
[1]Department of Neurosurgery, University of Colorado School of Medicine, Aurora, CO, [2]Department of Neurosurgery, Stanford University, Palo Alto, CA, [3]Department of Radiology, Children's Hospital Colorado, Aurora, CO, [4]Colorado School of Public Health, Aurora, CO, [5]Department of Pediatrics, University of Colorado School of Medicine, Aurora, CO

Purpose
Placement of a cerebrospinal fluid diversion device (i.e. shunt) is a routine pediatric neurosurgical procedure, often performed in the first weeks of life in congenital hydrocephalus. In the peri-operative period, shunt placement may be complicated by subdural, catheter tract, parenchymal, and intraventricular hemorrhages. We observed a

subset of infants and neonates who developed multifocal intraparenchymal hemorrhages (MIPH) following shunt placement and sought to determine any predisposing peri-operative variables.
Materials and Methods
A retrospective review of the electronic medical record at a tertiary care children's hospital was performed between 1998 and 2015. Inclusion criteria consisted of shunt placement, less than one 30-days of age, and available pre- and postoperative brain imaging. For each patient, ventricular size ratios, laboratory values, clinical presentation, shunt and valve type, as well as operative timing and approach were collected and analyzed.
Results
In our series, of the 121 neonates that met the inclusion criteria, 11 patients (9.1%) had MIPH following shunt placement. Pre-operative frontal to occipital horn ratio (FOR) was significantly higher in patients with MIPH than those without, mean (SD): 0.65 (0.06) vs 0.57 (0.01); ($p<0.001$). The change in FOR (ΔFOR) after shunt placement was significantly greater in the MIPH group, mean (SD): 0.14 (0.08) vs 0.08 (0.08); ($p = 0.04$). Among neonates who developed MIPH, aqueductal stenosis was the most common etiology (45%). Type of shunt valve was associated with incidence of MIPH ($p<0.001$). Pre-operative clinical parameters including head circumference, bulging fontanelle, and coagulopathy were not significantly associated with developing MIPH.
Conclusions
Multifocal intraparenchymal hemorrhages represents a not infrequent complication of neonatal shunted hydrocephalus. Markers of severity of ventriculomegaly (FOR) and ventricular response to CSF diversion (ΔFOR), were associated significantly with developing MIPH. The choice of shunt and etiology of hydrocephalus also was significantly associated with MIPH. After adjusting for corrected age, etiology of hydrocephalus, and shunt setting, the difference in FOR was associated with MIPH. A prospective study of MIPH prevention strategies and assessment of possible implications for patient outcome is needed.



(Filename: TCT_O-70_FIG2.jpg)

O-71

4:26PM - 4:34PM

Neonatal hypoxic-ischemic brain injury with hypothermia therapy: pre-hypothermia ultrasound measurement predicts post-hypothermia white matter injury

N Reddy[1], J Salas[2], K Carson[3], F Northington[4], T Huisman[5], A Poretti[4]

[1]Johns Hopkins Hospital, baltimore, MD, [2]The Johns Hopkins University School of Medicine, Baltimore, Baltimore, MD, [3]The Johns Hopkins Bloomberg School of Public Health, Baltimore, MD, [4]The Johns Hopkins University School of Medicine, Baltimore, MD, [5]Johns Hopkins, Baltimore, MD

Purpose
Hypoxic-ischemic injury (HII) of the brain occurs in 1 to 3 newborns per 1000 live full-term births in developed countries, and is a major cause of neonatal death and neurodevelopmental disability. In HII, head ultrasound usually shows white matter hyperechogenicity with increased gray/white matter differentiation. We aimed to assess the significance of white matter hyperechogenicity to predict white matter structural integrity as measured by diffusion tensor imaging (DTI) in neonates with HII.
Materials and Methods
We performed a quantitative region of interest-based analysis of gray and white matter echogenicty within the cingulate gyrus on pre and posthypothermia paramedian sagittal head ultrasound images and a quantitative analysis of fractional anisotropy (FA) and mean (MD), axial (AD), and radial (RD) diffusivity within the bilateral anterior and posterior centrum semiovale (CSO) on posthypothermia brain magnetic resonance imaging. For head ultrasound studies, we calculated a white to gray matter echogenicity ratio. A Spearman correlation was used to compare ultrasound and DTI measurements.
Results
Forty-two term neonates (27 males) with HII and hypothermia therapy were included. Posthypothermia DTI data have been acquired between 5 and 11 days of age. Spearman correlation revealed a positive, statistically significant correlation between prehypothermia white-gray matter ratio and MD, AD, and RD values in the bilateral anterior and posterior CSO. No statistically significant correlation was found between prehypothermia white-gray matter ratio and FA values in the bilateral anterior and posterior CSO as well as between posthypothermia white-gray matter ratio and all DTI scalars in the bilateral anterior and posterior CSO.
Conclusions
Prehypothermia head ultrasound white-gray matter ratio may predict post-hypothermia white matter structural integrity and may be a potential very early biomarker of severity in neonatal HII which can be acquired easily bedside.

Monday
3:30PM - 4:52PM
Long Beach Convention Center, Room 104B (Main Lobby)

06E-Parallel Paper Session-Excerpta: Miscellaneous Excerpta: A Magical Mystery Tour

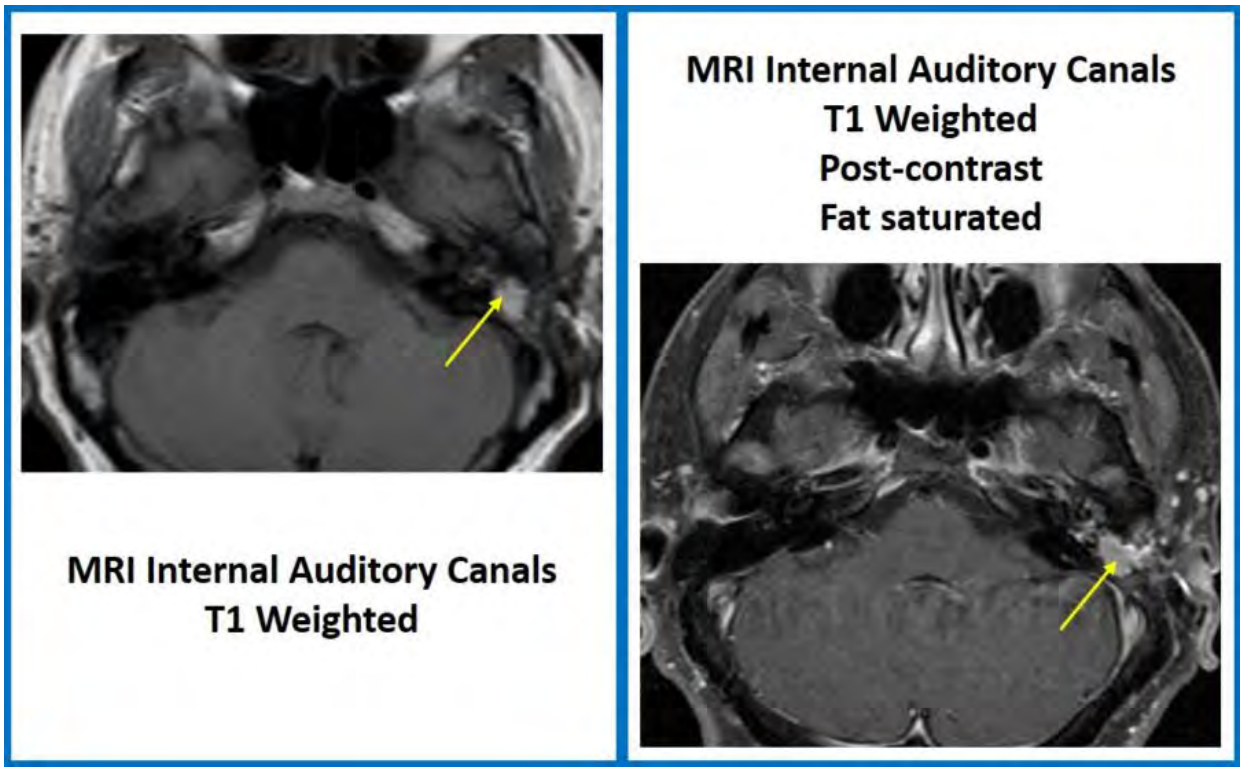
E-57

3:30PM - 4:52PM

Cholesterol granuloma post-mastoidectomy revision for recurrent cholesteatoma.

D LOPEZ GARCIA[1], K Kazmi[2]
[1]HAHNEMANN UNIVERSITY HOSPITAL, Philadelphia, PA, [2]Hahnemann University Hospital, Philadelphia, PA

Purpose
The purpose of this study is to describe the imaging findings of the rare occurrence of a cholesterol granuloma in a postmastoidectomy cavity.
Materials and Methods
A 33-year-old male with a history of chronic left otitis media underwent a left tympanomastoidectomy for cholesteatoma approximately 3 years prior to presentation. After 2.5 years, he presented with eustachian tube dysfunction and mixed hearing loss and was found to have a cholesteatoma recurrence. He then underwent tympanomastoidectomy revision, external auditory canal canaloplasty and eustachian tube dilation. Another 7 months later he presented with a left middle ear mass.
Results
Computed tomography (CT) of the temporal bone was performed which demonstrated changes of left-sided mastoidectomy and a soft tissue opacity in the surgical bed. The primary considerations included cholesteatoma recurrence, granulation tissue or chronic otitis. On MRI the mass was measured at 1.4 x 0.9 cm (transverse x AP). It was hyperintense on T1 and on T2 weighted images and did not demonstrate restricted diffusion. On postcontrast T1-weighted fat saturated images the mass remained hyperintense without demonstrable enhancement. The constellation of imaging findings was consistent with a cholesterol granuloma.
Conclusions
A cholesterol granuloma is a foreign body reaction in response to cholesterol crystals from rupture of red blood cells and breakdown of lipid bilayer in cell membrane. It is a benign lesion that can be locally aggressive by causing expansion, osseous erosions and extending into adjacent structures. It is usually located in the mastoid bone, middle ear cavity or petrous apex. This lesion must be differentiated from other masses of the temporal bone, such as cholesteatoma, chronic otitis media, paraganglioma and encephalocele. Cholesterol granuloma may develop on its own or it can coexist with cholesteatoma. It is however quite rare to present in a postmastoidectomy cavity. Based on our review, fewer than 5 cases have been reported in the published literature. We believe that this is first report of a cholesterol granuloma in a postmastoidectomy revision for cholesteatoma.



(Filename: TCT_E-57_2images.jpg)

E-19

3:30PM - 3:34PM

Simultaneous Collaboration with Colleagues to Make a Lecture Presentation Using Google Slides

I Ikuta[1], A Malhotra[1]
[1]*Yale University School of Medicine, New Haven, CT*

Purpose
The creation of a lecture can be a laborious task, and made much more complicated when multiple contributors are involved. E-mailing an electronic lecture presentation back-and-forth for editing can be a laborious task, interruptive to the process, and is minimally collaborative. Using cloud storage sometimes creates corrupted files when simultaneously accessing the same file, and is still a rather static collaboration. Using Google Slides has great potential for real-time editing, allowing multiple users to simultaneously access and improve presentations in a more fluid manner, allowing more dynamic collaborations.
Materials and Methods
A journal club presentation is used as a case example. In general, the neuroradiology fellow is tasked with creating a presentation to give background information on a topic, present the journal article, and list article strengths and weaknesses. The fellow may collaborate with the attending responsible for journal club, reviewing the presentation in advance so the attending

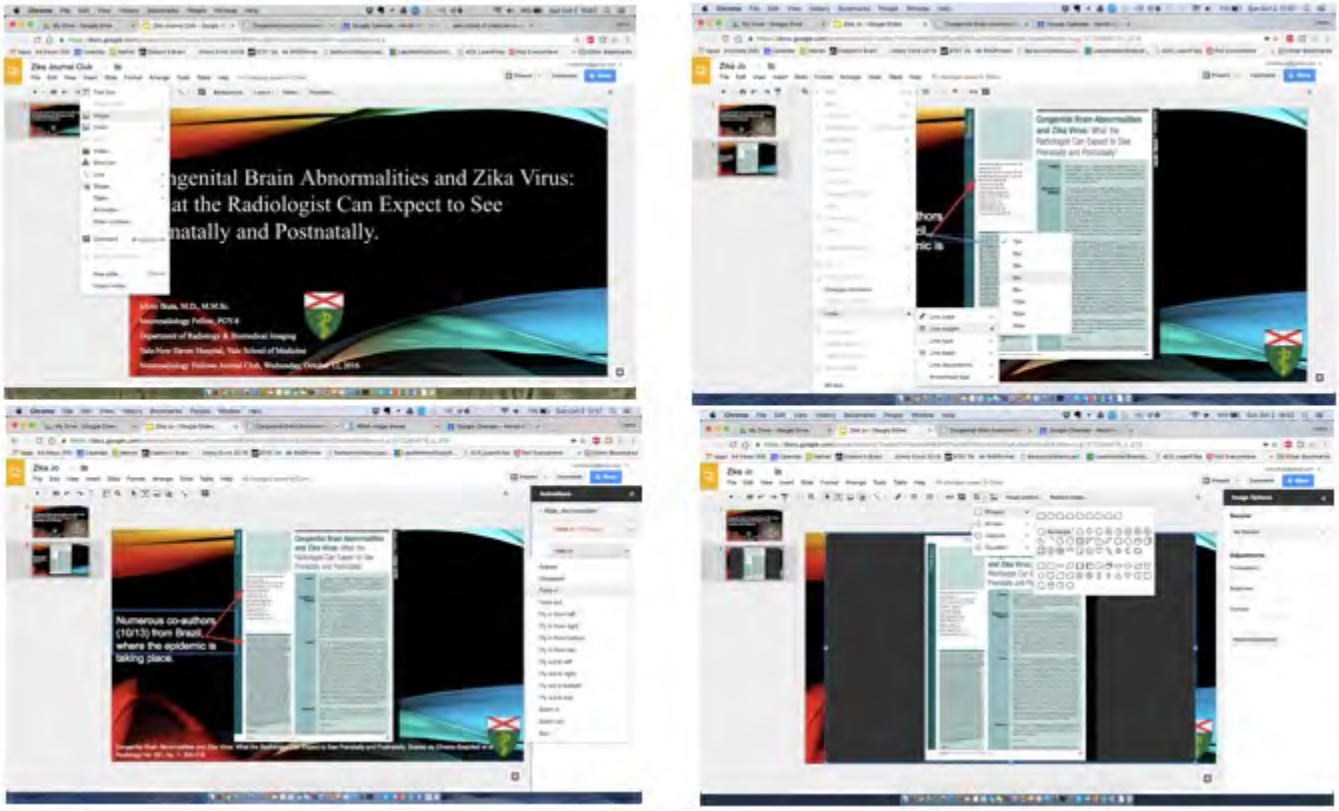
can give feedback on how to improve the journal club presentation. Access was made using both desktop computers, laptops, handheld devices, tablet device, and mobile smartphone.

Results

We present a series of screenshots to demonstrate the basic features and collaborative enhancements provided by using Google Slides. We show how presentations can be accessed simultaneously by multiple users, changes tracked, and presentations exported to whatever format may be desired in order to deliver the final presentation. In our case, we exported the presentation as a Microsoft PowerPoint presentation and saved it to a USB drive. However, that was not necessary since the lecture room had internet access, and the presentation could be downloaded from the cloud storage on Google Drive.

Conclusions

Google Slides provides real time collaboration for the production of lecture presentations such as for our academic institution's neuroradiology fellows journal club. We show how multiple users can interact simultaneously, allowing for dynamic collaborations from almost anywhere around the world.



(Filename: TCT_E-19_ASNR17_abstract_GoogleSlides.jpg)

E-21

3:38PM - 3:42PM

Percutaneous Embolization of Periorbital Arteriovenous Malformation with Bleomycin

M Pearl[1], M Martinez[1], A Dorafshar[1], S Merbs[1]

[1]*Johns Hopkins University School of Medicine, Baltimore, MD*

Purpose

To demonstrate the feasibility and efficacy of percutaneous embolization using bleomycin for a high-flow periorbital arteriovenous malformation (AVM).

Materials and Methods

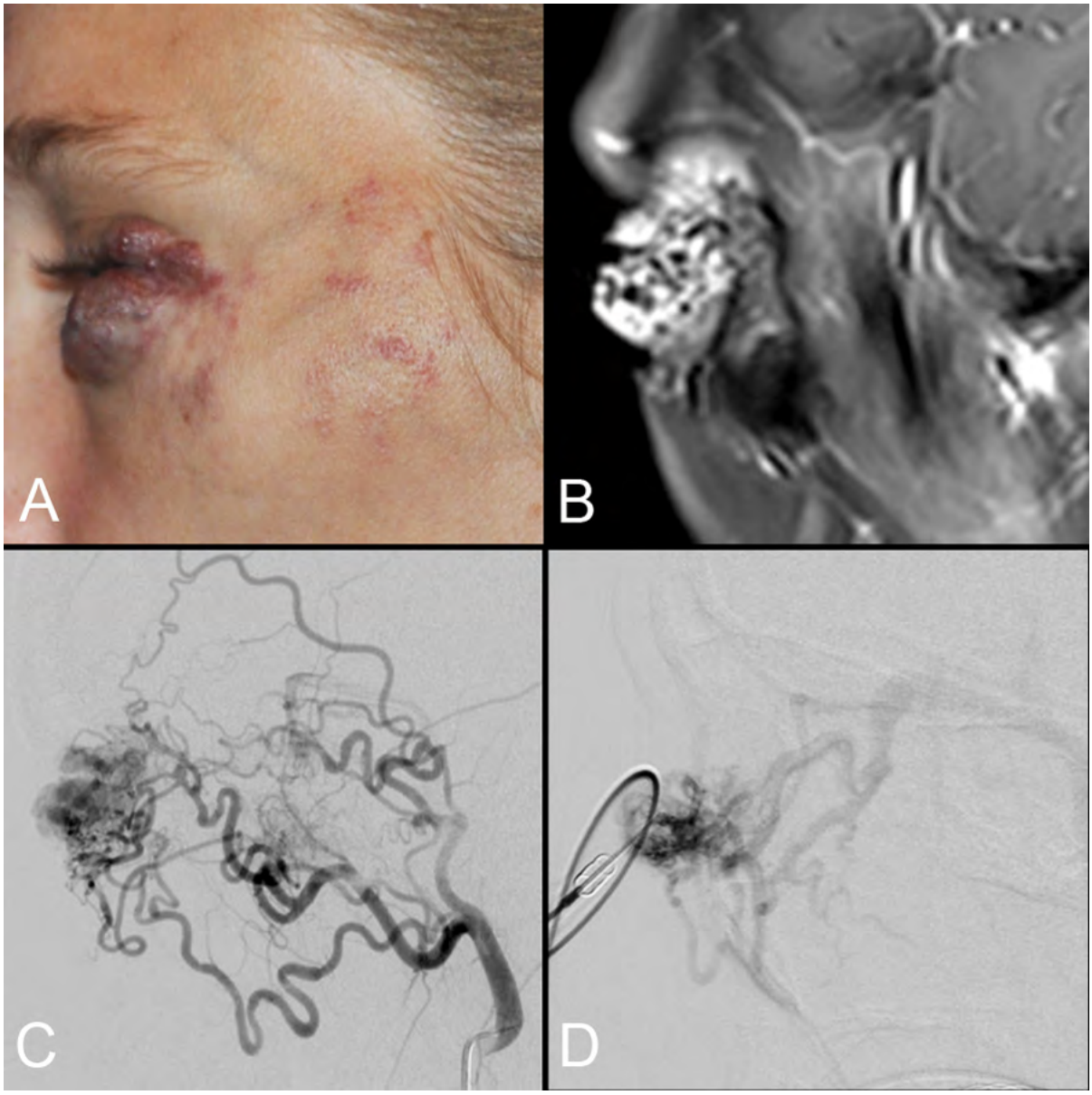
A 30-year-old woman presented with a left periorbital AVM that rapidly increased in size during puberty causing pulsating discomfort. She underwent painful and ineffective laser therapy when she was 16 years old.

Results

Magnetic resonance imaging (MRI)/magnetic resonance angiography (MRA) of the face showed prominent flow voids involving the left preseptal soft tissues and inferolateral periorbital region extending laterally to involve the soft tissues overlying the zygoma. Diagnostic cerebral angiography identified 2 separate areriovenous malformations (AVM) foci, 1 involving the left lower more than upper eyelids and a second distinct focus more laterally involving the soft tissues overlying the left cheek. After multidisciplinary discussion, percutaneous embolization with bleomycin was performed in an effort to decrease lesion size prior to surgical resection in an attempt to preserve any normal surrounding tissue. Percutaneous embolization of both upper and lower eyelid components of the AVM was performed with 15 IU of bleomycin. Two weeks later, her postprocedure swelling resolved and she noted decrease in size of the lesion. She underwent a second percutaneous embolization session with bleomycin 6 weeks later. She tolerated the procedures well without evidence of procedural complication or skin necrosis. Figure 1. Lateral views of preprocedure clinical photo (A), sagittal T1-postcontrast MRI, and lateral selective ECA cerebral angiogram (C) demonstrate the periorbital and left zygoma region AVM. Angiography through a 21G butterfly needle (D) confirms intralesional position for subsequent slow bleomycin embolization.

Conclusions

Percutaneous embolization of high flow AVMs with bleomycin can be performed safely and is efficacious for decreasing AVM size prior to surgical resection and reconstruction. Bleomycin embolization should be considered as an adjunct therapy prior to standard embolization techniques and surgery particularly for AVMs located in critical regions in the face where preserving any normal tissue prior to reconstruction is optimal.



(Filename: TCT_E-21_HMFig1.jpg)

E-22

3:42PM - 3:46PM

A Rare Case of Complex Intraosseous Cranial Arteriovenous Malformation with Successful Multidisciplinary Management

A Al-Smadi[1], T Shokuhfar[1], A Johnston[1], A Shaibani[1], S Ansari[2], M Hurley[1]
[1]Northwestern University Feinberg School of Medicine, Chicago, IL, [2]Northwestern University, Feinberg School of Medicine, Chicago, IL

Purpose

Intraosseous cranial arteriovenous malformations (AVMs) are very rare and challenging entities. We report a case of extra-dural perieto-occipital vascular lesion. A 12-year-old boy who presented with accelerated growth of right scalp lesion over few months. Digital subtraction angiography (DSA) showed a large right parieto-occipital intraosseous AVM with multiple and complex arterial feeders. Treatment of those lesions is challenging and requires a multi-disciplinary approach. In this case we performed 6 embolization procedures over 1 year, including both transarterial and transvenous approaches, followed by a total surgical resection. To the best of our knowledge, we report the second case of an AVM originating in the cranial bones, and the first one with successful multidisciplinary approach management.

Materials and Methods

A 12-year-old male presented to clinic with a right parieto-occipital mass that began 2 years earlier as a small hard bump on the right side. Three months prior to presentation, the mass progressively increased in size. A new posterior auricular mass developed a few weeks before the visit, and the mother noted bluish discoloration of the ipsilateral ear. Family history was negative for vascular malformations and he was otherwise asymptomatic. Physical examination revealed a large right-sided, subcutaneous, soft, pulsatile, nontender mass with a thrill that extended from mid-parietal bone down towards the mastoid and then medially extending to the inion. Due to its large size, the AVM required six embolization procedures over a 1- year (Figures 2, 3). Ten arterial pedicles were embolized and 2 transvenous embolizations were performed. This resulted in a 70-80% reduction in size of the nidus and was followed by complete surgical resection. AVMs are dynamic and tend to progress before adulthood (2). The main area of skeletal involvement of extra-dural AVMs is in teeth bearing bones (4). Expansion of AVMs is the main cause of morbidity. Advancement in the clinical presentation of AVM into a higher Schobinger stage (Table1) is considered a progression (2). They may enlarge due to multiple factors, including increased blood flow, thickening and dilatation of vessels, and neovascularization. Ischemia and circulating hormones in puberty may stimulate AVM enlargement (1, 2, 4) In the few reported cases of intraosseous AVMs, most of them were treated using a combined management(3).The previous reported case of cranial bone was managed by embolization only and was complicated by facial paralysis and hoarseness (5). Diffuse AVMs (Table 2), as in our case, are more challenging to treat, which requires extensive embolization procedures to control. Total resection of the nidus is critical to reduce regrowth rate (4). Resection within 24-48 hours of embolization is ideal (1).

Results

Head CT revealed a right parieto-occipital extracranial vascular lesion, and widening/overgrowth of the subjacent skull. A diagnostic angiogram was performed, including 3D and Dyna CT (Figure 1). Careful analysis of the images revealed a large AVM (8 x 10 cm) with the nidus centered within the calvarium, involving the right parietal bone. As is often seen with hyperemic lesions within or adjacent to bone, there was consequent

growth and increased thickness of the calvarium. Direct supply to the AVM was noted from the right occipital artery (OccA), the right superficial temporal artery (STA), both middle meningeal arteries, a meningeal branch of the right anterior deep temporal artery and the right-sided posterior falcine and meningeal arteries (arising from PICA as an anatomic variant). Indirect supply was seen from the left OccA and left STA. Venous drainage was initially into osseous veins which then converged into a dilated tortuous network of scalp veins. The most dominant scalp vein extended from the right parietal region, inferiorly, to the right mastoid region with an attenuated connection with a branch of the right external jugular vein. Additional scalp veins were noted along the posterior aspect of the scalp, the right temporal region, the left side of the scalp extending to the forehead and left angular vein and retrograde into the superior ophthalmic vein and cavernous sinus with antegrade drainage down the left inferior petrosal sinus. The right occipital artery showed multiple flow-related aneurysms (at least nine) along its course. A small flow-related aneurysm also was associated with the right superficial temporal artery.

Conclusions

Intraosseous AVMs are rare events. To the best of our knowledge, we report the second case of an AVM originating in the cranial bones. In our case, the role of circulating hormones during puberty could explain the rapid progression in the AVM size. Moreover, neovascularizaztion and increased in nidus size was noticed by the senior author after the third embolization procedure, which may be explained by the stimulant effect of ischemia after embolizing feeding arteries. Complete surgical resection after embolization, when feasible, has become the most accepted and optimum treatment, as embolization aids in the achievement of total resection and decreases the risk of recurrence, additionally it significantly reduce the risk of bleeding intra-operatively (1). Given the potential side-effects of treatment, interventional management for AVMs often is reserved for progressive lesions of Schobinger stage two and above (1). In the case reported in this paper, 6 pre-operative embolization procedures were performed and included both transarterial and transvenous approaches. The last embolization procedure was done within 24 hours of total AVM surgical resection.

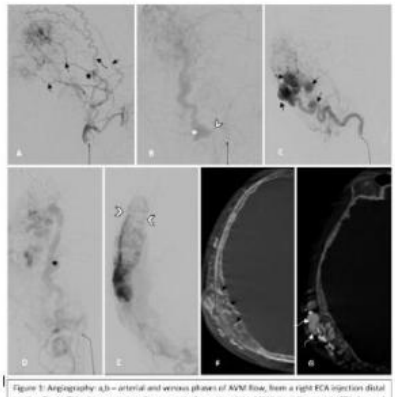


Figure 1: Angiography: a,b – arterial and venous phases of AVM flow, from a right ECA injection distal to the OccA. This demonstrates direct supply from the right MMA (small arrows), STA (curved arrows), as well as a flow-related aneurysm associated with the STA. Part of the AVM nidus is seen (star). The dominant draining scalp vein is seen, extending to connect with a branch of the right ECA via a stenotic connection (arrowhead). The dilated portion of the vein just proximal to the connection was visible as a bluish bump behind the external ear (star). C,D – Right OccA angiography in arterial and venous phases of the AVM, demonstrating multiple flow-related aneurysms along the course of the right occipital artery (small arrows). Again noted are multiple draining scalp veins, most of which converge on the dominant draining vein (star). E – Oblique view of right OccA angiogram demonstrating the nidus within the bone. Inner and outer tables are marked by arrowheads. F,G – Dyna CT axial reconstructions with injection of 30% contrast in the right ECA. Multiple nidal channels are noted within the skull (small arrows). The draining veins are seen in the scalp (curved arrows). There is bony overgrowth and thickening of the involved portions of the skull. (AVM: arteriovenous malformation, ECA: external carotid artery, MMA: middle meningeal artery, OccA: occipital artery, STA: superficial artery)

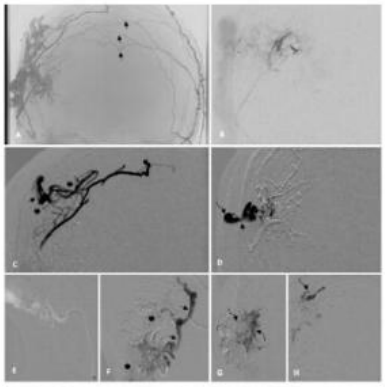


Figure 2: Embolization – A- AP unsubtracted view of a left ECA injection, demonstrating enlarged branches of the left MMA connecting across the midline (small arrows) with distal branches o f the right MMA, supplying the AVM. Onyx is seen within portions of the AVM nidus and some draining veins (curved arrows). B – microcatheter angiography of a distal branch of the right MMA, demonstrating supply to the AVM nidus in the skull, with venous drainage into scalp veins. C,D – Roadmap images during injection of Onyx via MMA approach, demonstrating filling of the nidus (star), and extension of Onyx trans-osseously (arrow) into a draining scalp vein (curved arrow). E-H – Trans-arterial embolization from a right OccA approach, using a scepter balloon-tipped microcatheter . E – demonstrates the roadmap image and position of the microcatheter before inflation of the balloon. The Onyx cast is seen filling multiple flow-related aneurysms (stars), extending into distal arterial branches (arrows), and the intra-osseous nidus (curved arrows). (AVM: arteriovenous malformation, ECA: external carotid artery, MMA: middle meningeal artery, OccA: occipital artery)

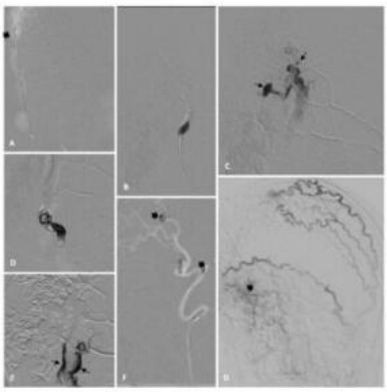


Figure 3: Embolization – A-C – Transvenous embolization of the AVM through the dominant draining scalp vein. This was performed twice. A – roadmap image demonstrating two 7 mm scepter balloon-tipped microcatheters placed proximally in the main draining vein(star). B – Roadmap image after inflation of both balloon, in order to achieve relative flow obstruction down stream and push the embolizate up-stream towards the nidus. C- Onyx cast partway during trans-venous retrograde embolization, extending into more proximal draining veins(arrows). D, E – Second session of transvenous embolization, more distally in the dominant draining veins. Coils have been delivered distal to the microcatheter to achieve some downstream flow obstruction and facilitate retrograde injection of embolizate (arrows). F – Final pre-operative particle embolization of scalp collateral supply. Road map image showing proximal coil occlusion of right STA branches not involved in AVM supply, to protect the scalp and subcutaneous soft tissues (star). G – left OccA angiogram in AP view, during particle embolization of collateral scalp supply to the AVM as the final pre-operative embolization. This demonstrates the enlarged OccA branches extending across the midline to supply residual nidus (star). (OccA: occipital artery, STA: superficial artery)

Table 1: Schobinger staging of AVMs [2]*

Stage	Clinical Finding
I - quiescence	Warm, pink-blue, shunting on Doppler examination
II – expansion	Enlargement, pulsation, thrill, bruit, tortuous veins
III – destruction	Dystrophic skin changes, ulceration, bleeding, pain
VI - decompensation	Cardiac failure

* Liu, A.S., et al., *Extracranial arteriovenous malformations: natural progression and recurrenc treatment*. Plast Reconstr Sura. 2010. **125**(4): p. 1185-94.

Table 2: Revised Richter–Suen classification system for extracranial arteriovenous malformati

Focal AVM	Diffuse AVM
Central Nidua	Nidus difficult to detect or multiple
Single arterial feeder	Two or more arterial feeders
Firm	Compressible, rapid rebound
Single of skin if present	Diffuse skin involvement in affected regio

Uller, W., A.I. Alomari, and G.T. Richter, *Arteriovenous malformations*. Semin Pediatr Surg, 201 p. 203-7.

(Filename: TCT_E-22_Graphs.jpg)

E-23

3:46PM - 3:50PM

Treatment of hemorrhagic head and neck lesions by direct puncture and n-BCA embolization

G Deib[1], M Pearl[1], A El Mekabaty[1], P Gailloud[1]
[1]*Johns Hopkins University School of Medicine, Baltimore, MD*

Purpose
Life-threatening head and neck hemorrhages require urgent management. While the lesions

responsible for the hemorrhage, e.g., a ruptured pseudo-aneurysm, often are treated by transarterial embolization (TAE), prior intervention or surgery, inflammation, anatomic variants and vessel tortuosity may render an endovascular approach challenging, time-consuming and sometimes impossible. We report 2 cases of successful embolization of life-threatening head and neck hemorrhages with n-butyl cyanoacrylate (n-BCA) via direct puncture as an alternative approach to TAE.

Materials and Methods

Case 1. A 56-year-old man with a history of recurrent squamous cell carcinoma of the tongue and mouth floor managed with extensive surgical resection and adjuvant radiotherapy underwent covered stent placement for a right carotid blow out. He came back to the ER 3 months later with a new life-threatening hematemesis. Emergent angiography revealed occlusion of the right common and internal carotid arteries and of the previously placed carotid stent. The trunk of the external carotid artery (ECA), only opacified by vertebral injections via multiple small collateral channels, was ruptured, with significant contrast extravation. Considering the lack of straightforward path for TAE, direct puncture of the ECA trunk was performed under fluoroscopic guidance using the road-map technique. The ruptured ECA then was embolized with n-BCA(TRUFILL n-BCA Liquid Embolic System, Codman Neurovascular, Raynham, MA). The patient recovered and was discharged home a few days later. Case 2 - A 65-year-old woman with a history of lingual tonsillectomy for squamous cell carcinoma of the tongue base was admitted to the ER for life-threatening hematemesis. Emergent angiography demonstrated a ruptured distal lingual artery pseudoaneurysm; the proximal segment of that artery was markedly irregular, likely from tumoral involvement. Initial attempts to pass the microcatheter beyond the irregular segment were unsuccessful, and the branch was embolized from a proximal position with n-BCA glue. The patient was brought back to the angiography suite the next day following a recurrent hemorrhage. At this time, direct puncture and n-BCA embolization of the lingual pseudoaneurysm was performed, leading to complete eradication of the lesion.

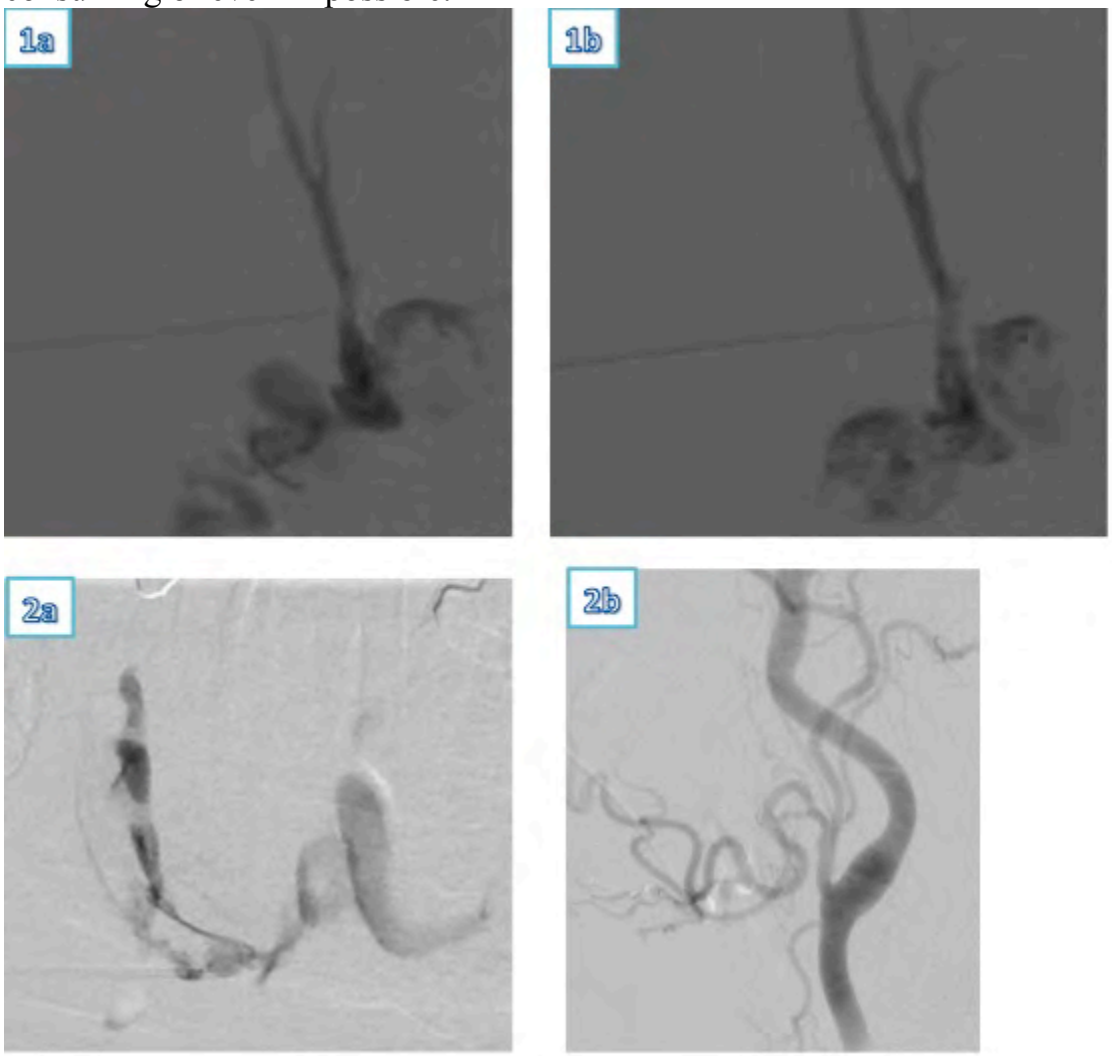
Results

Case 1. Figure 1a: Under roadmap guidance provided by a right vertebral artery injection, a 21G needle was advanced percutaneously into the proximal right ECA. Angiography performed through the needle shows extensive contrast extravasation. Figure 1b: This image documents the cast of n-BCA with the needle still in place. Case 2. Figure 2a: Angiography performed through a 21-gauge needle advanced directly into the pseudoaneurysm, demonstrating opacification of the pseudoaneurysm and adjacent right lingual branches as well as contrast extravasation. Figure 2b. Left common carotid artery angiography obtained after n-BCA embolization, demonstrating new glue cast filling the right lingual artery pseudoaneurysm with no evidence of residual pseudoaneurysm or contrast extravasation. The left lingual artery is patent.

Conclusions

We present 2 cases that demonstrate the safety and efficacy of n-BCA embolization of ruptured vessels by direct puncture under fluoroscopic guidance. This technique seems

particularly interesting when addressing life-threatening hemorrhages in patients with locoregional anatomical and pathological conditions that render TAE challenging, time-consuming or even impossible.



(Filename: TCT_E-23_Slide1.jpg)

E-24

3:50PM - 3:54PM

Post-embolization Peri-aneurysmal Brain Inflammation after Flow Diversion: Late Complication and Stroke Mimic After Aneurysm Treatment

S Raymond[1], M Koch[1], C Stapleton[1], P Schaefer[1], A Patel[1]
[1]*Massachusetts General Hospital, Boston, MA*

Purpose
Flow diverting stents are the preferred treatment option for unruptured large internal carotid

artery (ICA) aneurysms and are being adopted for ruptured, posterior circulation, and distal anterior circulation aneurysms (1). Postembolization peri-aneurysmal inflammation is a lesser known complication occurring late after aneurysm embolization that has been described after coil embolization and after flow diversion using the Silk flow diverting stent (2). It is believed that thrombosis of the aneurysm results in endothelial necrosis, inciting a florid inflammatory response that extends into the adjacent brain parenchyma resulting in clinical deterioration and stroke-like mimic. We present a case of postembolization peri-aneurysmal inflammation after Pipeline embolization device for treatment of a giant basilar tip aneurysm.

Materials and Methods

Two months after combined coil and Pipeline embolization of a giant basilar tip aneurysm, a 57-year-old woman presented with progressive dysarthria, dysphagia and right-sided weakness that had developed over 2 weeks. Computed tomography angiography (CTA) demonstrated hypodensity in the left thalamus adjacent to the aneurysm. Magnetic resonance imaging (MRI) demonstrated FLAIR hyperintensity and elevated ADC in the same distribution that was interpreted as a subacute to chronic infarct. She was treated with corticosteroids with initial gradual improvement but subsequent neurologic deterioration.

Results

Patients present with T2/FLAIR hyperintensity involving the brain parenchyma in contact with and extending out from the thrombosed aneurysm wall. There is characteristic peripheral enhancement of the thrombosed aneurysm on postcontrast imaging. Apparent diffusion coefficient (ADC) values usually are elevated in contradistinction to acute ischemic stroke.

Conclusions

Postembolization peri-aneurysmal inflammatory syndrome is a recognized complication from embolization of giant aneurysms with coils or flow diversion. Misdiagnosis as subacute infarct can delay administration of corticosteroids, which is thought to be the optimal therapy.

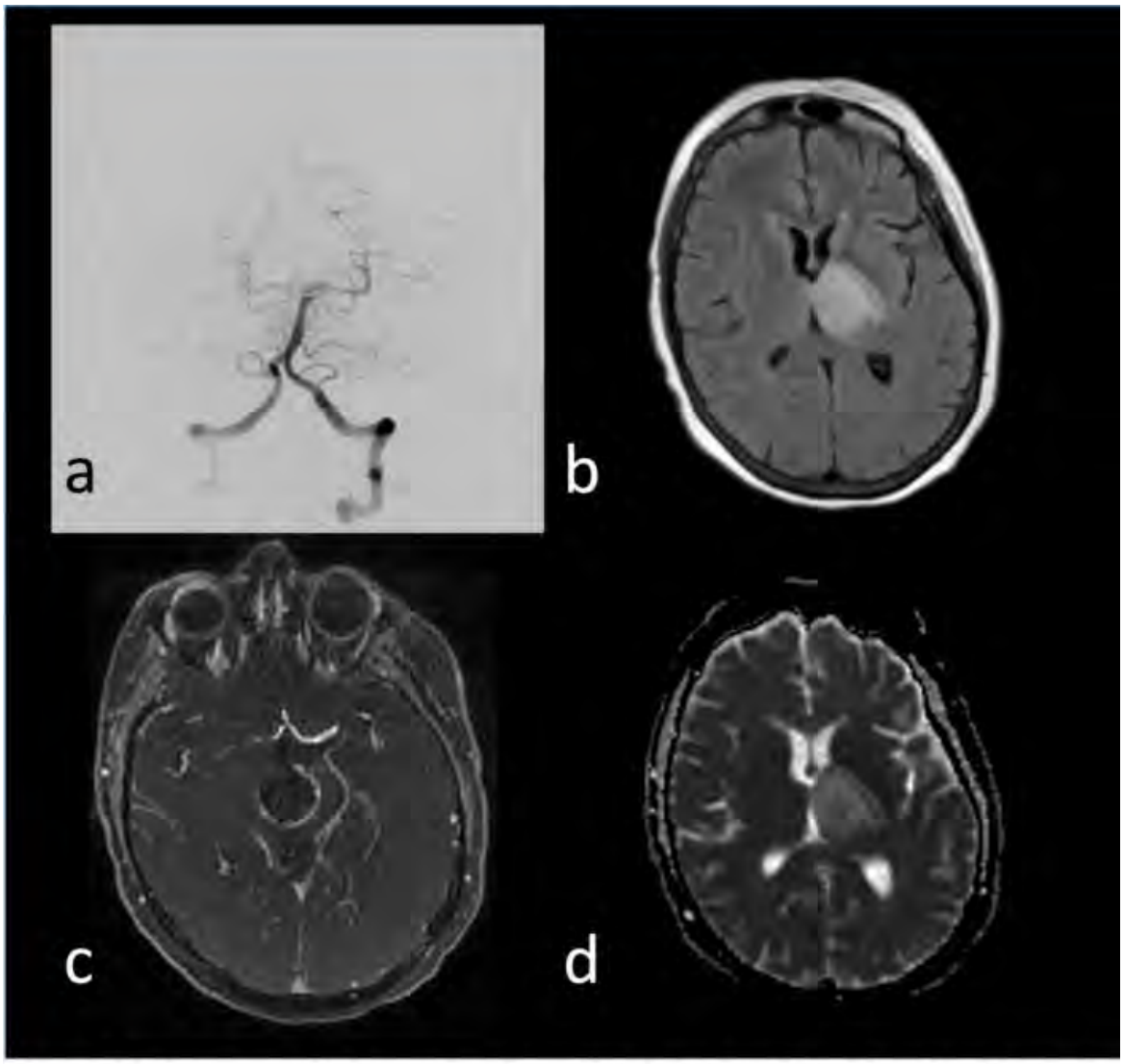


Figure 1. Perianeursymal inflammation 2 months after coil and flow diversion (Pipeline) embolization of a giant basilar tip aneurysm. (a) Immediate post-treatment catheter angiography demonstrates coils within the large superiorly projecting basilar tip aneurysm and a flow-diverting stent (Pipeline) within the distal basilar and proximal left P1 arteries; there is residual contrast opacification at the aneurysm neck extending into the body (Raymond Roy Class 3). (b) Axial FLAIR at time of presentation 2 months after treatment shows mildly expansile abnormal FLAIR hyperintensity involving the left thalamus abutting the coiled aneurysm. (c) Axial post-gadolinium T1 weighted image demonstrates circumferential enhancement of the aneurysm wall. (d) ADC map shows no diffusion restriction in the involved left thalamus

(Filename: TCT_E-24_Fig1.jpg)

E-25

3:54PM - 3:58PM

Kinking of flow diverter – a case report

S Das[1], A Gupta[2], H PENDHARKAR[3], A RAMALINGAIAH[4], C Prasad[5], j saini[6], K Bhattacharya[7], A Swaminathan[8]
[1]National Institute of Health and Neurosciences, BANGALORE, Karnataka, [2]National Institute of Mental Health and NeuroSciences (NIMHANS), Bangalore, Karnataka, [3]NATIONAL INSTITUTE OF MENTAL HEALTH & NEUROSCIENCES, BANGALORE, KARNATAKA, [4]NATIONAL INSTITUTE OF MENTAL HEALTH AND NEUROSCIENCE, NIMHANS, Bengaluru , karnataka , [5]National Institute of Mental Health and Neurosciences, Bangalore, Karnataka, [6]NIMHANS, BANGALORE, Karnataka, [7]National Institute of Mental Health and Neurosciences, India, Bangalore, Karnataka, [8]National Institute of Mental Health And Neuro Sciences, Bangalore, Karnataka

Purpose

In this case study, we present postprocedure kinking of flow diverter. This is a rare complication that we have come across in one of our cases.

Materials and Methods

A case of 28-year-old female presented with 4 months' history of headache and vomiting. Initial MR imaging showed giant right supraclinoid internal carotid artery (ICA) aneurysm with hydrocephalus. Left ventriculo-peritoneal shunt was done outside and the patient was referred to us. Initial digital subtraction angiography (DSA) confirmed the presence of giant ICA aneurysm. It was planned for flow diverter placement and the patient was loaded with prasugrel. Informed consent was taken.Through the right femoral route using 7F long sheath, Headway 27 microcatheter was taken over Traxcess 14 wire and navigated distally into right middle carotid artery (MCA). Few long coils were deployed into aneurysmal sac. FRED flow diverter (4x44 mm) was deployed across aneurysm neck from the M1 segment of MCA to the distal cavernous ICA on the right side. Check injection showed patency of FRED with slowing of circulation in the aneurysm sac. Intravenous infusion of Tirofiban was given @ 0.4 μg/kg/min. Second postop day, patient developed weakness of left side with altered sensorium and immediately was shifted to DSA which showed kinking of flow diverter at the neck of the aneurysm with poor distal flow. Attempts to straighten it by passing a balloon failed. Fifth post-op day, patient worsened in sensorium (E1M3VT) and MRI done showed multifocal infarcts in right MCA territory. All anti-platelet medications were stopped and she was taken for emergency decompressive hemicraniectomy. She improved to M4 status with persisting pupillary asymmetry and left-sided paucity of movements. Subsequent CT scans revealed right MCA infarct. Current neurological status is E4M3 with spontaneous breathing on tracheostomy tube.

Results

Fig. 1 shows giant right supraclinoid ICA aneurysm. Fig. 2 shows immediate postdeployment check. Angiogram shows opening of flow diverter. Figs. 3 and 4 show kinking of flow diverter leading to right MCA infarct for which decompressive right hemicraniectomy was done.

Conclusions

Kinking of flow diverter is a rare complication and we have presented our experience in this case.

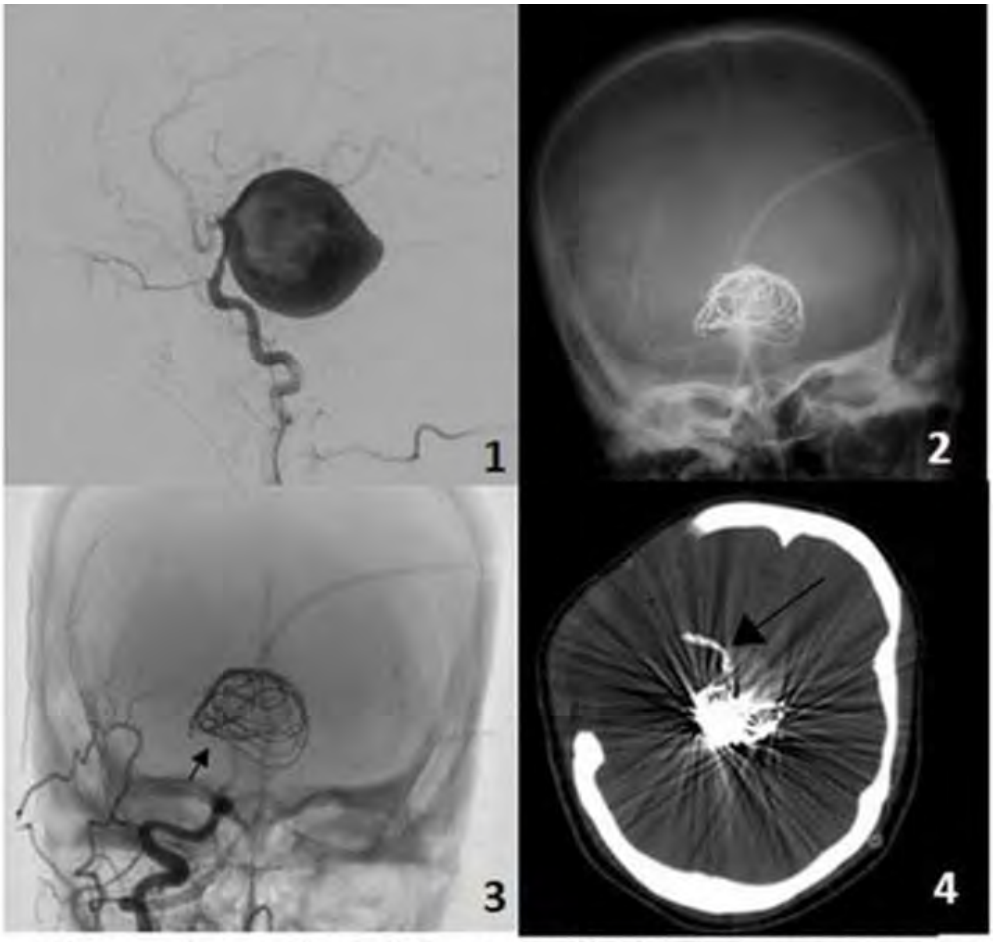


Fig 1 – shows giant right supraclinoid ICA aneurysm
Fig 2 – shows immediate post-deployment check angiogram shows opening of flow diverter
Fig 3 and 4 – shows kinking of flow diverter leading to right MCA infarct for which decompressive right hemicraniotomy was done.

(Filename: TCT_E-25_Capture5678.jpg)

E-26

3:58PM - 4:02PM

Cholesterol Embolization Following Carotid Artery Stenting- a Case Report

K Kulanthaivelu[1], A RAMALINGAIAH[2], A Gupta[3], j saini[4], H PENDHARKAR[5], C Prasad[6]

[1]NIMHANS, Bengaluru, Karnataka, [2]NATIONAL INSTITUTE OF MENTAL HEALTH AND NEUROSCIENCE, NIMHANS, Bengaluru , karnataka , [3]National Institute of Mental Health and NeuroSciences (NIMHANS), Bangalore, Karnataka, [4]NIMHANS, BANGALORE, Karnataka, [5]NATIONAL INSTITUTE OF MENTAL HEALTH & NEUROSCIENCES, BANGALORE, KARNATAKA, [6]National Institute of Mental Health and Neurosciences, Bangalore, Karnataka

Purpose

To discuss the clinical course and imaging findings of a case of cholesterol embolization following carotid artery stenting.

Materials and Methods

A 67-year-old gentleman, diabetic, presented with sudden onset paresthesias in right upper limb. Magnetic resonance imaging (MRI) revealed infarct in the left thalamus. Carotid Doppler demonstrated hypoechoic, smooth, atherosclerotic plaque in the right carotid bulb and proximal internal carotid artery (ICA) causing 90% luminal compromise with spectral broadening. Computed tomography (CT) angiogram showed significant stenosis in the right carotid bulb and moderate degree of stenosis in the left carotid bulb. It was decided to stent the right ICA. Transfemoral access injection showed narrowing of the ICA up to 90%. A Spider FX distal protection filter device was taken over a 0.014 Syncro microwire and positioned across C2. Subsequently, a tapered self-expanding nitinol stent (Protégé 10-7mm x 30mm) was deployed against the stenosis. Check angiogram revealed adequate stent apposition with minimal residual stenosis. No postprocedure deficits were seen. Post filter removal check injection showed normal filling of the right distal ICA branches. Antiplatelets were continued. Ten hours later, he developed insidious left hemiparesis. Check angiogram revealed mild slowing of flow in the right middle carotid artery (MCA), however, with no filing defect. Computed tomography (CT) showed no infarct. Magnetic resonance imaging (MRI) showed diffusion restriction in the right MCA territory and watershed regions with decreased perfusion on arterial spin labeling (ASL). Repeat CT and MRI next day showed infarct in the right MCA territory. No interruption of flow on MRA. He was treated with anti-edema measures. Speech and sensorium improved, however weakness persisted.

Results

Angiography revealed stenosis of right proximal ICA up to 90%. Poststent deployment angiogram showed normal endoluminal contrast opacification with no distal filling defect. Magnetic resonance imaging demonstrated diffusion-weighted imaging (DWI) abnormalities in the right MCA territory.

Conclusions

Cholesterol embolization following carotid artery stenting is a potential complication masquerading as normal angiogram despite confluent areas of ischemia.

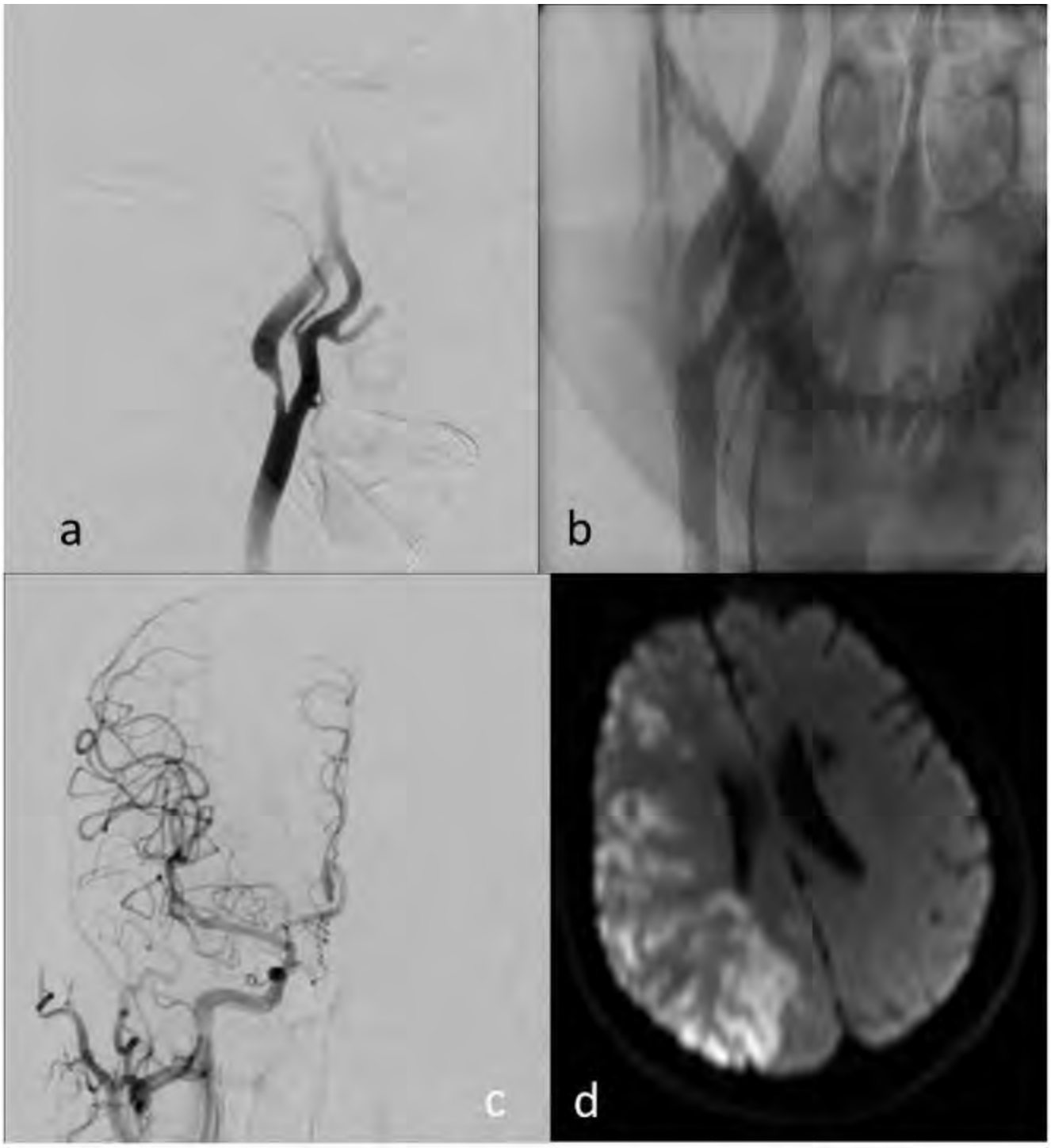


Fig (a) – Right common carotid artery injection reveals 90 % stenosis of right internal carotid artery. (b) Shows deployment of 10 mm x 30 mm self expanding nitinol stent with mild waisting at the site of maximum narrowing. (c) Right CCA injection AP projection 10 hours post stenting shows normal filling of the ACA & MCA. (d) Shows infarct in right MCA territory.

(Filename: TCT_E-26_kkabstract.jpg)

E-27

4:02PM - 4:06PM

Gyriform parenchymal enhancement on Dyna CT helps decision making during acute stroke mechanical thrombectomy

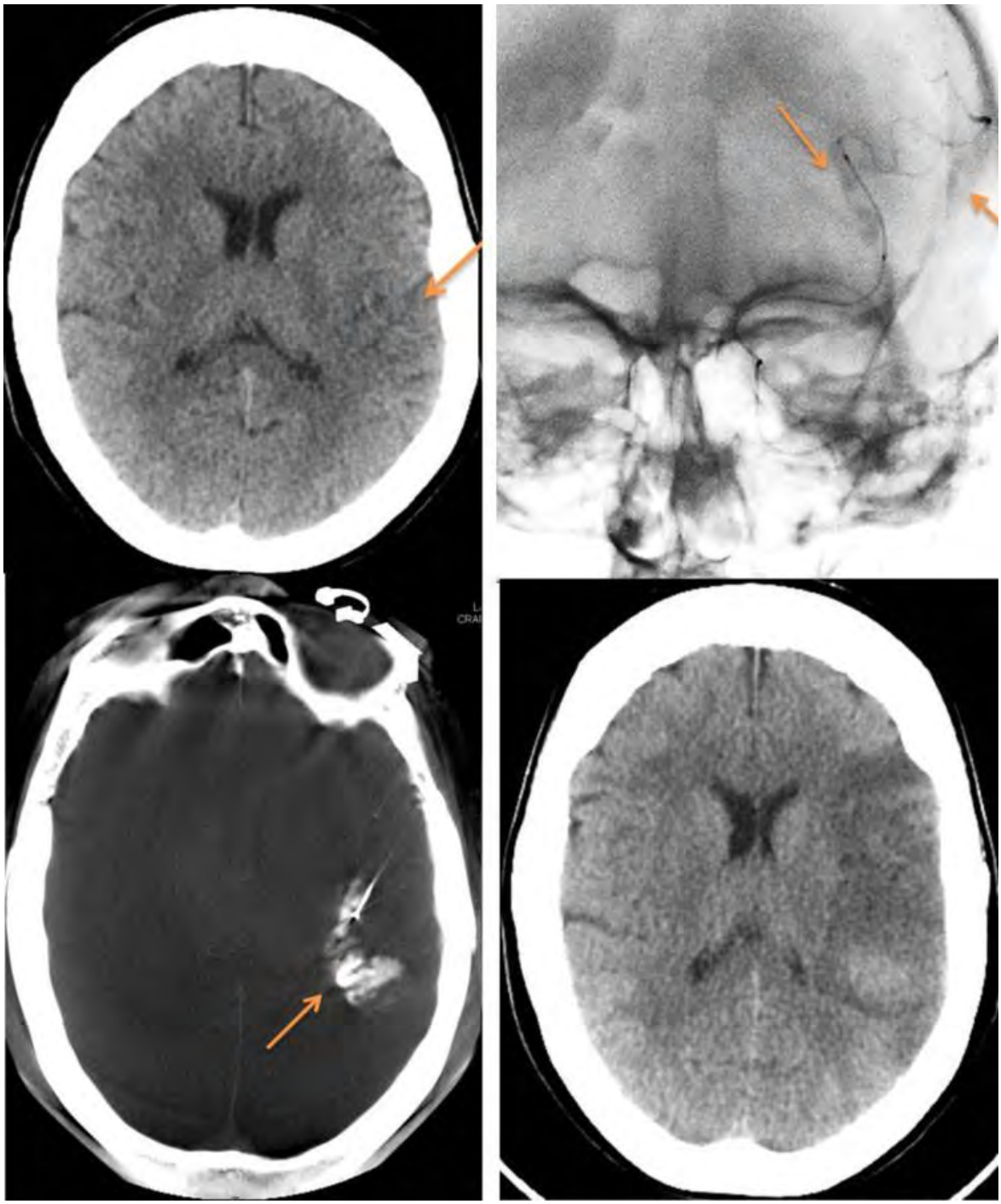
Z ASSIS[1], J NAIR[2], S DEY[3], W MORRISH[3]
[1]FOOTHILLS MEDICAL CENTRE, UNIVERSITY OF CALGARY, CALGARY, ALBERTA, [2]McGill University Health Centre, Montreal, Quebec, [3]UNIVERSITY OF CALGARY, CALGARY, Alberta

Purpose
Intraprocedural Dyna computed tomography (CT) in the angio suite is currently a well established add-on in decision-making during endovascular therapy, especially in ruling out intracranial hemorrhage and significant mass effect. Procedural complications during stroke therapy like iatrogenic subarachnoid hemorrhage and poststent retrieval parenchymal hemorrhage can be evaluated fairly well using this technology. The value of prestent deployment Dyna CT to look for established infarct has not been studied in literature to the best of our knowledge. We report a case of acute stroke endovascular thrombectomy where a midprocedure Dyna CT altered the course of endovascular treatment.
Materials and Methods
A 47-year-old, previously healthy female was brought to the emergency department by EMS, after being found collapsed in her backyard. She was last seen well the night before. On examination, she was found to be drowsy but arousable, had global aphasia, dysarthria, right upper motor neuron facial palsy and right-sided weakness. Her NIHSS score was 21. NCCT head showed a few areas of early ischemic changes involving the posterior insular cortex, temporal and frontal cortex (ASPECT 6-7) (Figure 1a). Multiphase CT angiogram demonstrated a left M2 occlusion with poor collaterals. Intravenous tPA was not administered due to unknown time of onset. Patient was immediately transferred to angio suite for endovascular thrombectomy. The procedure was performed with local anesthesia and conscious sedation. After obtaining right femoral access, the left internal carotid artery was selectively catheterized using a balloon guide catheter. Initial angiogram demonstrated a left M2 occlusion. A microcatheter (027 Prowler select plus) was taken over a 014" Transcend Platinum tip wire into the occluded M2 branch distal to the clot.
Results
A routine pre-stent deployment super-selective microcatheter angiogram to confirm intravascular position showed delayed patchy contrast staining surrounding the tip of the microcatheter (Figure 1b). This prompted an immediate Dyna CT to look for subarachnoid hemorrhage due to vessel perforation. The axial Dyna CT head images demonstrated a well

defined "gyral pattern" of contrast enhancement of the left posterior insular cortex and temporal lobe (Figure 1c).

Conclusions

We interpreted the "gyral pattern" of contrast enhancement to be consistent with blood-brain barrier (BBB) disruption due to established ischemia in these regions. It was felt rapid revascularization in this context would carry a significantly increased risk of hemorrhagic complication, potentially worsening the clinical deficits and outcome. Hence, based on the Dyna CT findings, the decision was made to terminate the procedure at this stage. Patient was transferred to Stroke unit for further care. Next day, patient showed transient clinical worsening. Follow-up CT head in 24 hours demonstrated temporal evolution of the ischemic areas seen as wedge-shaped areas of hypodensities involving the left frontal and temporal lobes (Figure 1d). She had gradual improvement in speech and power and was transferred to the rehabilitation unit with NIHSS-7 and mRS 3. We believe that abstaining from mechanical thrombectomy to avoid an elevated risk of parenchymal hemorrhage was beneficial for this patient, and may have improved the overall patient outcome. Intraprocedural Dyna CT is a potentially useful tool during stroke thrombectomies, with "Gyriform enhancement" a sign of blood-brain barrier leakage.



(Filename: TCT_E-27_ASNRimage1.jpg)

E-28

4:06PM - 4:10PM

Post Traumatic Occlusive Internal Carotid Artery Dissection and Stroke Treated with Mechanical Thrombectomy and Stenting – A Case Report

F ALNASER[1], D Tampieri[1], M Cortes[2]
[1]*Montreal Neurological Hospital and Institute, Montreal, Quebec,* [2]*McGill University, montreal, Quebec*

Purpose

We report an uncommon case of wake-up stroke caused by a carotid dissection and occlusion of the carotid and middle cerebral artery, treated with combination of thrombectomy and angioplasty. The combination of thrombectomy and stenting in patients presenting with carotid dissection is debated in the literature due to the possible complication which may occur during catheters placement through dissected vessels. On the other hand, the use of carotid stent in case of atherosclerotic stenosis during thrombectomy has been advocated as low risk and feasible technique to facilitate thrombectomy and improve cerebral circulation. Our case was managed successfully with thrombectomy and stenting of the carotid dissection which led to a good clinical outcome. The aim of this presentation is to describe the case and some technical features of the procedure that we recommend in order to reduce complication.

Materials and Methods

This is a 61-year-old right-handed male, who had a trauma to the right side of the neck by a puck during hockey game the evening before. The next morning, he woke up with left hemiparesis. On arrival in the emergency room he showed left-sided hemiparesis and left homonymous hemianopia, NIHSS 8. Nonenhanced CT showed ASPECTS score 6 with hyperdense sign at the right middle cerebral artery (MCA). Computed tomography (CT) angiography revealed a right carotid artery complete occlusion extending to the M1 segment of the right MCA. Computed tomography perfusion illustrated an area of penumbra of the right MCA territory. The patient was transferred to the angio-room for mechanical thrombectomy under general anesthesia. The angiogram demonstrated complete occlusion with a short stump of the right internal carotid artery (ICA). Initially thrombectomy was performed using a Solitaire 4x40mm, deployed across the clot in the right M1 segment. The stent was left for 5 minutes then retrieved after balloon inflation in the common carotid artery (CCA). Complete recanalization of the ICA and MCA at M1 was achieved. Residual occlusion of the posterior branch of the right MCA was noted. Irregular stenosis of 14 mm length was noted at the proximal aspect of the cervical segment of right ICA, in keeping with a focal dissection. Therefore, a 7 x 30 mm Wallstent was deployed at the area of dissection. Then a second thrombectomy pass in the occluded posterior branch of the right MCA was performed. A final angiogram showed complete recanalization of the right ICA and right MCA (TICI) scale 3. In the next day, the patient showed improvement of the clinical condition with recuperation of his sensory symptoms and he denied any visual abnormality. Eventually he was discharged home with modified Rankin Scale 1 (mRS) on double antiplatels medication for 6 months.

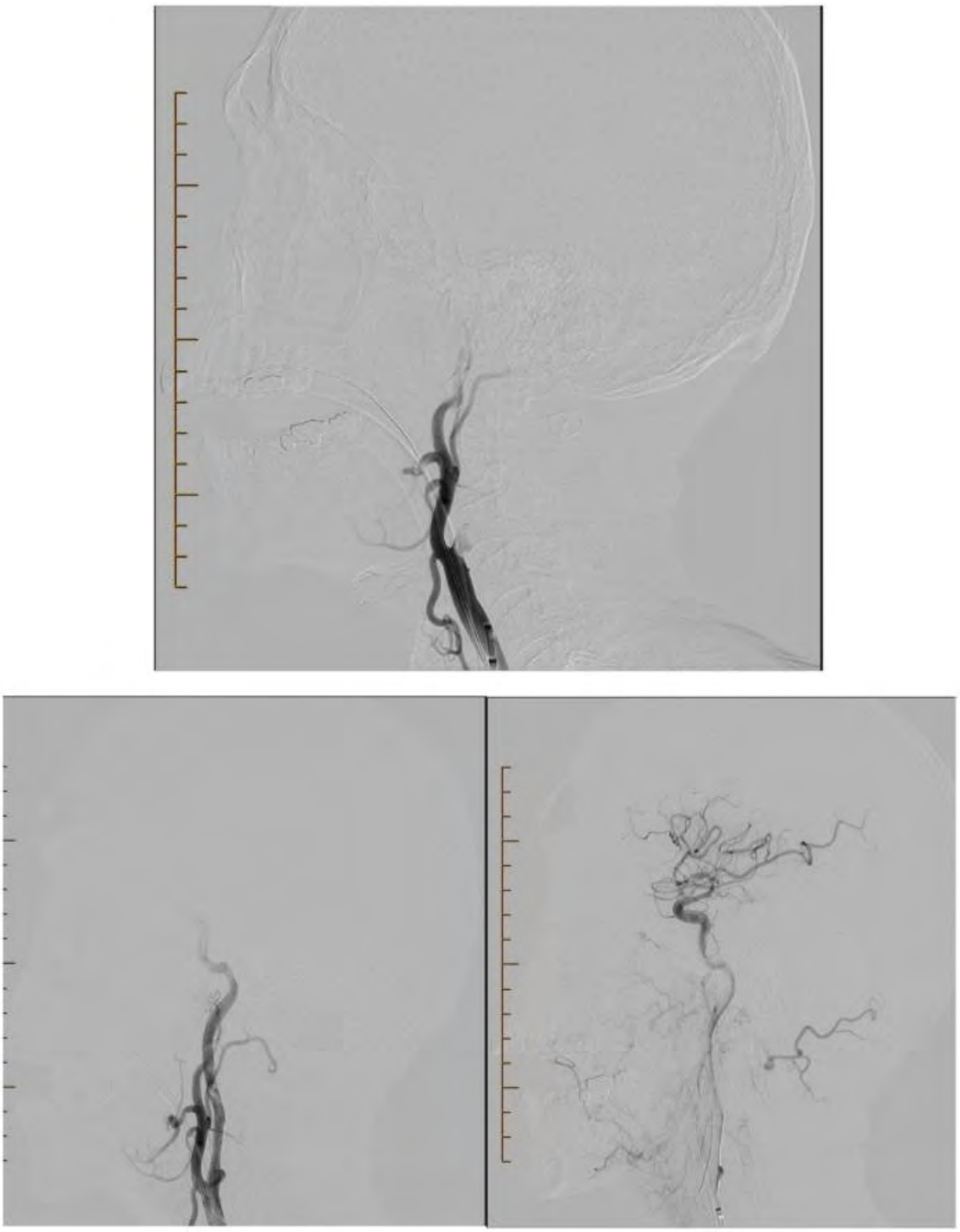
Results

Fig. 1. Complete occlusion of the right common carotid artery with a short stump. Fig. 2.

After the second thrombectomy pass with complete recanalization of the right internal carotid and right middle cerebral artery (TICI) scale 3. A 7 x 30 mm Wallstent was deployed at the area of dissection with satisfactory wall apposition of the stent.

Conclusions

This case illustrates the feasibility of thrombectomy in cases with carotid dissection. Although we understand the implications of navigating a catheter and performing a thrombectomy through a dissected artery, the severe carotid stenosis would not have maintained antegrade circulation and ultimately could have led to complete carotid occlusion hence aggravating the clinical condition of the patient. We perceive that the initial thrombectomy pass was necessary to re-establish rapid brain circulation and also enabling visualization of the length of the dissection, allowing then to perform the correct placement of the Wallstent. The second thrombectomy pass led to complete recanalization of the middle cerebral artery branches and during retrieval there was no damaged to the dissected carotid which was protected by the Wallstent. Finally in these cases we recommend to inflate the balloon, during stent retrieval, in the common carotid artery to avoid additional possible damage to the dissected artery.



(Filename: TCT_E-28_DissectionandThrombectomyNov2016last1copy.jpg)

E-29

4:10PM - 4:14PM

Subarachnoid Fat Embolism Following Traumatic Fracture Of A Sacral Spinomeningeal Cyst

M Sondag[1], J Go[1], W Gibbs[2], J Acharya[1], P Kim[2]
[1]University of Southern California, Los Angeles, CA, [2]University of Southern California, Keck School of Medicine, Los Angeles, CA

Purpose

To present a case of intracranial and intrathecal subarachnoid fat embolism following traumatic sacral fracture.

Materials and Methods

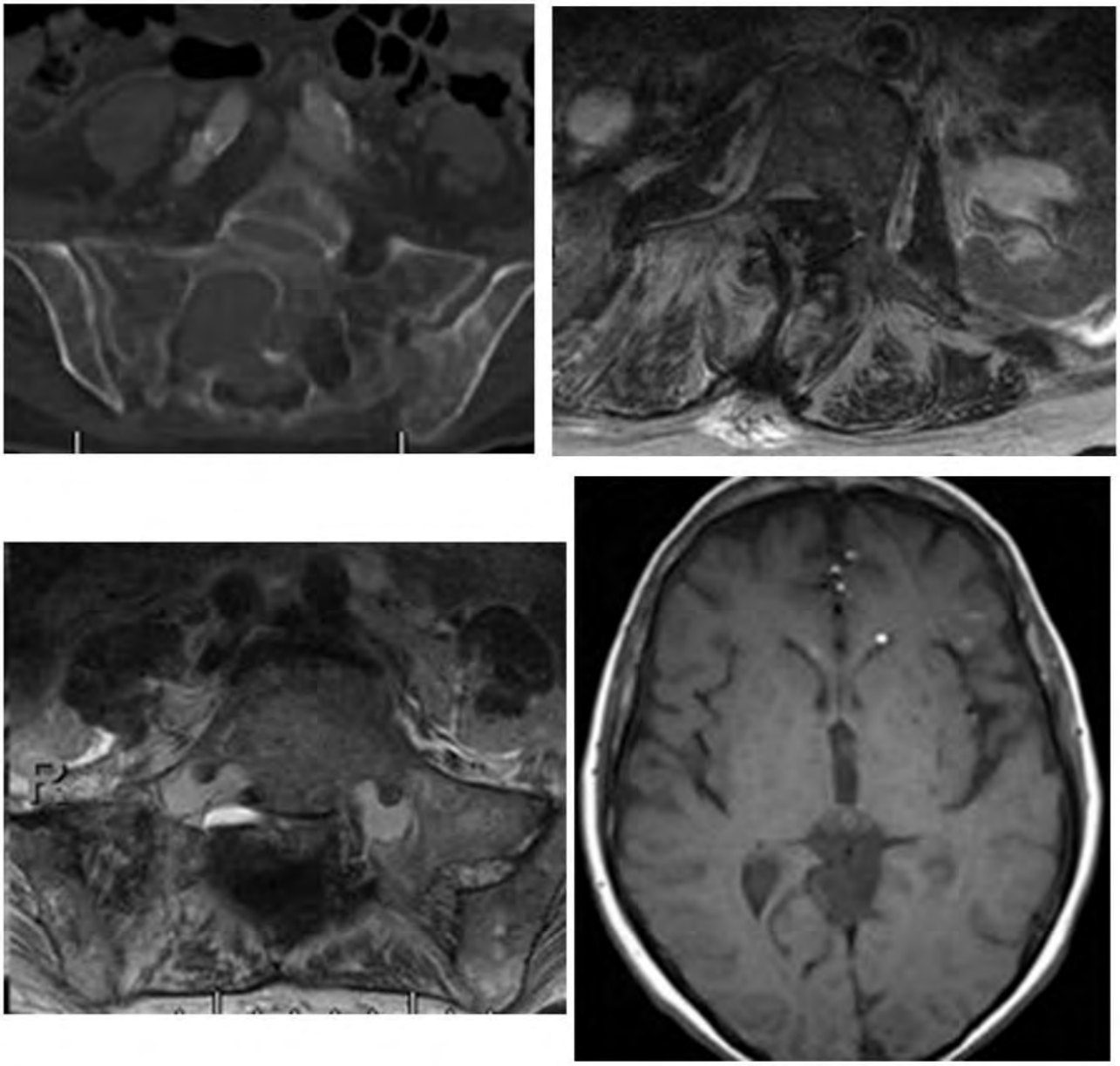
An 80-year-old woman presents to the emergency department after an unwitnessed fall. The patient reports back and hip pain. On physical exam, the patient demonstrated tenderness over the back and right pelvis, and was alert and oriented.

Results

Computed tomography (CT) Pelvis: A fracture extends through a spinomeningeal cyst in the right sacral ala. Magnetic resonance imaging (MRI) Spine: T2 images of the lumbosacral spine demonstrate extensive subarachnoid hemorrhage expanding the thecal sac. A fat-fluid level is visualized within the nondependent aspect of the thecal sac and within a spinomeningeal cyst in the right sacral ala. Magnetic resonance imaging Brain: Scattered foci of intrinsic T1 hyperintensity within the subarachnoid space are compatible with fat emboli.

Conclusions

Intracranial fat emboli are seen most commonly in the setting of long bone fractures (1). We present a rare case of intracranial fat emboli following traumatic fracture of a sacral spinomeningeal cyst. Traumatic intrathecal fat embolism demonstrating dissemination into the intracranial subarachnoid space has rarely been described previously (2, 3). The imaging findings in the presented case are challenging, as extensive intrathecal subarachnoid hemorrhage alters the expected signal intensity and contour of the thecal sac. The presence of fat-fluid levels within the thecal sac and sacral spinomeningeal cyst should prompt the radiologist to search for a vertebral body or pelvic fracture. The presence of fat within the intrathecal subarachnoid space is important for radiologists to recognize in the trauma patient, as this finding warrants additional imaging of the brain to evaluate for the presence of intracranial fat emboli.



(Filename: TCT_E-29_spinetrauma.jpg)

E-30

4:14PM - 4:18PM

Spinal Subarachnoid Hemorrhage: A Rare Case of Spinal Aneurysm Rupture

Z Voronovich[1], C Sanchez[1], A Carlson[1], D Sorte[1]
[1]*University of New Mexico, Albuquerque, NM*

Purpose

Spinal artery aneurysms are rare. We are presenting a case of a ruptured spinal artery aneurysm, visible on magnetic resonance imaging (MRI), with extensive spinal subarachnoid hemorrhage and myelopathy. We hope to educate the audience about the appearance of spinal subarachnoid hemorrhage on MRI, present the angiographic findings of spinal artery aneurysms, and discuss the evaluation and surgical versus endovascular management using an illustrative case. Indocycanine green video angiography was performed and corresponding intra-operative images will be shown.

Materials and Methods

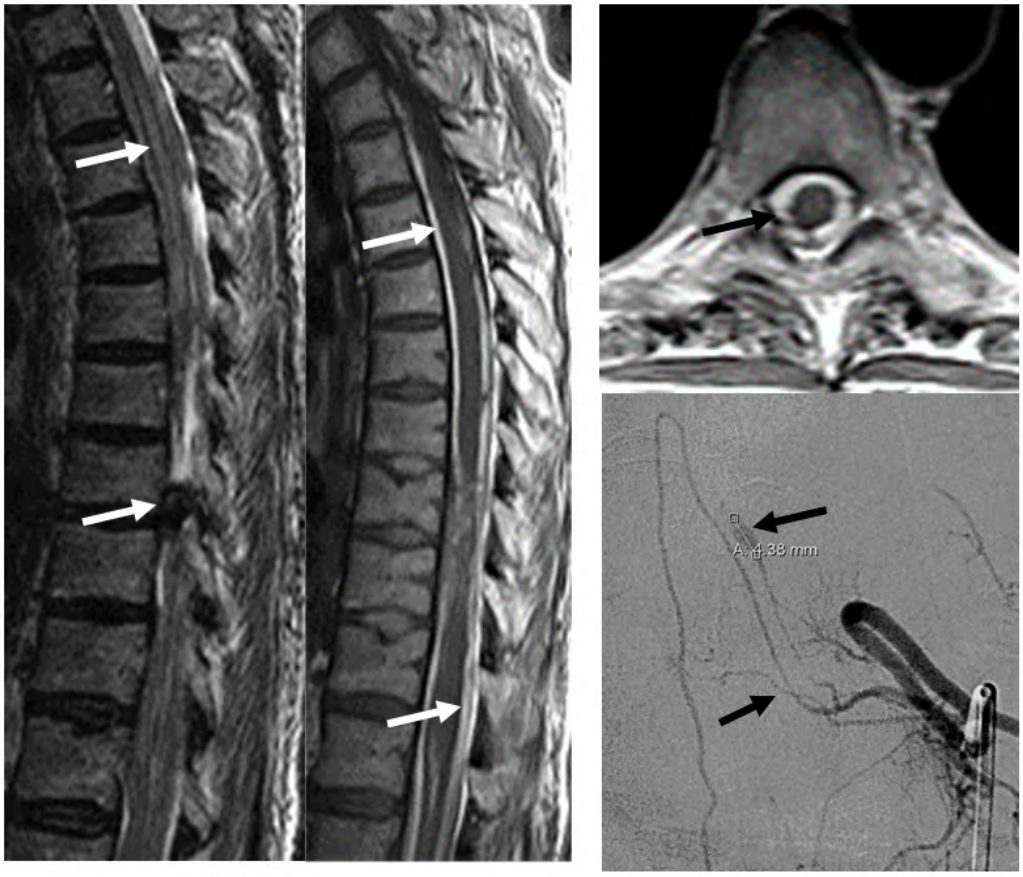
A 71-year-old woman presented with sudden onset of nonradiating back pain, a mildly elevated troponin, and an elevated lactate. She was treated for a non-ST elevation myocardial infarction at an outside hospital with aspirin when she developed bilateral lower extremity flaccid paralysis, a mid-abdominal sensory level, and decreased lower extremity reflexes. She was transferred to our facility on day 8 after presentation after treatment with IV immunoglobulin and steroids for "idiopathic transverse myelitis" was unsuccessful. She underwent an MRI which showed spinal subarachnoid hemorrhage and intramedullary spinal cord signal abnormality. She was taken for spinal angiography which showed a dissecting pseudoaneurysm of the left T10 radiculomedullary artery which supplied a posterior spinal artery. Interestingly, the artery of Adamkiewicz also arose at this level. Hence, she was not a candidate for endovascular treatment. Therefore, the pseudoaneurysm was trapped and excised with use of intra-operative indocyanine green video angiography. A portion of the hematoma was evacuated. After surgery, she failed to improve, probably because her diagnosis was delayed.

Results

Magnetic resonance imaging spine: Extensive spinal subarachnoid hemorrhage was seen, hyperintense on T2 and heterogeneous, but primarily hyperintense on T2. A round T2 dark mass at T10 was seen, later found to represent a ruptured spinal aneurysm. There was longitudinally extensive, intramedullary T2 hyperintense signal abnormality within the thoracic spinal cord. Spinal digital subtraction angiography: The left T10 segmental artery gave rise to both the artery of Adamkiewicz and a radiculomedullary feeder supplying a posterior spinal artery. A 4 mm dissecting pseudoaneurysm of the posterior spinal artery radiculomedullary feeder was visible.

Conclusions

Spinal artery aneurysms are rare. Spinal subarachnoid hemorrhage can present with sudden onset back or neck pain. A high index of suspicion and rapid spinal angiography should be performed for spinal subarachnoid hemorrhage on MRI. We present a case of a ruptured spinal artery pseudoaneurysm with missed diagnosis on initial evaluation. Ultimately, the pseudoaneurysm could not be treated endovascularly due to close proximity to anterior and posterior spinal arteries. Surgical trapping and excision was performed due to anatomic considerations.



(Filename: TCT_E-30_SpinalAneurysmFig300.jpg)

E-31

4:18PM - 4:22PM

Subarachnoid Hemorrhage from a Cervical Dural Arteriovenous Fistula: an Easily Misinterpreted Presentation of an Uncommon Disease

E Orru[1], F Hui[2], C Trimble[1], G Deib[1], I Izbudak[2]
[1]Johns Hopkins Hospital, Baltimore, MD, [2]Johns Hopkins University, Baltimore, MD

Purpose
Cervical dural arteriovenous fistulas (DAVFs) represent a minority of spinal DAVFs. As opposed to the more common thoracolumbar fistula, which often present with an insidious slowly progressive myelopathy, cervical DAVFs can lead to a much more variable clinical picture including hemorrhage, myelopathy, radiculopathy, posterior fossa venous hypertension and a constellation of findings similar to that of an aneurysmal subarachnoid hemorrhage (SAH). Subarachnoid hemorrhage is a relatively common manifestation of cervical DAVFs, reported to be present in as many as 45% of cases. Although cervical DAVFs are rare, they should be considered in the differential diagnosis of posterior fossa and craniocervical canal SAHs without a clear aneurysmal cause. Whilst cerebral DSA is the

gold standard evaluation study and ultimately the only modality able to provide a complete depiction of the malformation, modern cross-sectional vascular imaging (CTA/MRA) serve as excellent first line study. They provide detailed anatomical information that may reveal the vascular lesion. If cervical DAVF are not considered in the differential, the SAH may be erroneously labeled as a perimesencephalic SAH and managed conservatively, exposing the patient to a risk of re-bleeding and further neurological damage. Particular attention also should be paid on cross-sectional vascular imaging to not mistaking possible perimedullary venous varicosities with posterior circulation aneurysms. Subarachnoid hemorrhages from cervical DAVFs usually have better clinical outcomes than aneurysmal SAHs, with more than 90% of cases resulting in minimal or no deficits after surgical or endovascular repair of the lesion. We report a patient presenting with a SAH due to a cervical DAVF initially misdiagnosed as an AICA aneurysm at an outside hospital who eventually died after rehemorrhage, cord infarction and withdrawal of care.

Materials and Methods

An 80-year-old male with past medical history only remarkable for previous unexplained syncopal episodes in the past years presented to an outside hospital following a transient episode of atraumatic syncope with diaphoresis and lightheadedness followed by loss of consciousness. The patient underwent a head CT and CTA, which showed supra and infratentorial SAH, particularly prominent in the prepontine cistern and in the foramen magnum surrounding the cervical cord. CTA demonstrated an enlarged perimedullary vascular structure, initially interpreted as an AICA aneurysm. The patient was transferred to our institution for further management of the aneurysm. Further review of the images suggested that the enlarged vascular structures were not in continuity with the arteries of the vertebrobasilar system. These vessels were instead more in keeping with varicose perimedullary venous structures, most likely representing dilated draining veins from a high flow dural or perimedullary arteriovenous fistula with drainage into anterior medullary veins. Findings were confirmed by cerebral DSA, which showed a high flow DAVF of the right C1 nerve root with extensive perimedullary drainage and multiple venous varicosities, likely the origin of bleeding. Endovascular embolization of the lesion was performed, reducing flow to the lesion, however, there was an infarction of the right hemicord that resulted in hemiplegia. In the following days the patient experienced multiple subarachnoid and intraventricular re-bleeds with development of hydrocephalus that required positioning of an intraventricular catheter. The neurological status of the patient quickly deteriorated and he eventually passed away 11 days after admission and withdrawal of care.

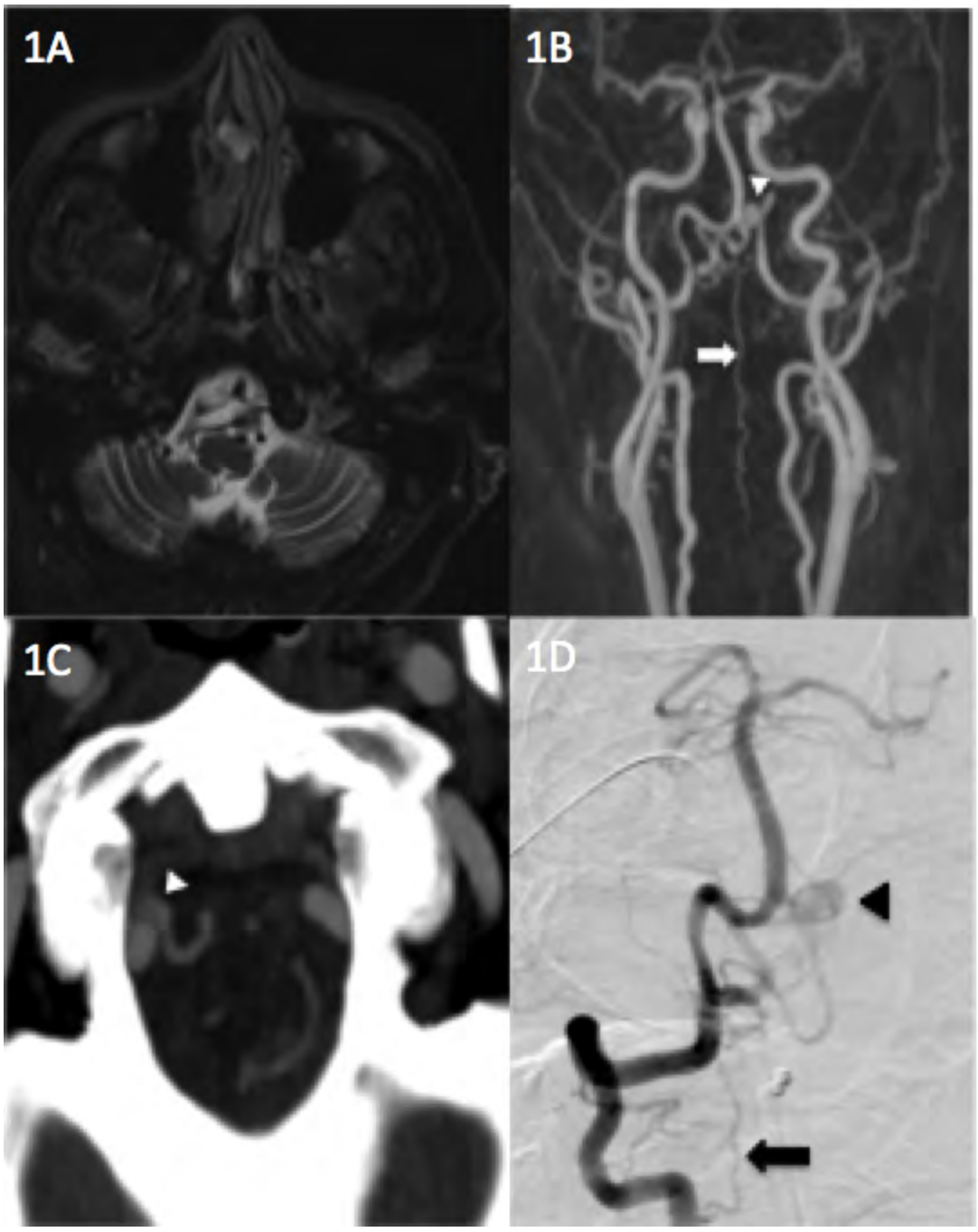
Results

Fig. 1A: Axial T2-weighted MRI shows prominent flow voids at the craniocervical junction along the course of the vertebrobasilar vessels. Fig. 1B: Coronal MIP reconstruction of an MRA of the head and neck with gadolinium demonstrates the suggested dilated vessels at the level of the craniocervical junction with a large venous aneurysm (arrowhead) and perimedullary drainage into the anterior perimedullary vein (white arrow). These anomalous vascular structures do not appear in continuity with the vertebrobasilar arterial vessels. Fig.

1C: CTA axial MIP at the level of the craniocervical junction showing a dilated venous structure abutting the right V4 segment with blurred posterior margins, likely indicating the fistulous point along the course of the right exiting C1 nerve root (arrowhead). Fig. 1D: Right vertebral artery DSA shows a high flow arteriovenous malformation without an intervening nidus with the fistulous point corresponding to the area presumed on CTA. The malformation drains into dilated perimedullary veins with a large aneurysmal pouch, likely the site of the bleeding (black arrowhead). Additional small arterial feeders directed to the fistula arise from the cervical V2 segment of the vessel (black arrow).

Conclusions

Cervical DAVFs are less common than their thoracolumbar counterparts but are more likely to present with SAH. It is important that neuroradiologists keep this entity in the differential diagnosis of a nonaneurysmal SAH in order not to miss a potentially fatal entity. Subarachnoid hemmorhages from bleeding cervical DAVF usually follow a more benign course compared to aneurysmal SAHs. Our case represents an exception to this trend as the patient re-bled multiple times and developed hydrocephalus, eventually passing away shortly after admission. Cross-sectional imaging is useful to rule out an arterial aneurysm and delineate the dilated venous structures and most likely drainage collectors, as well as demonstrate mass effect from hemorrhage or venous varicosities. Careful assessment of vascular wall profiles on CTA and MRA allows detection of a likely fistulous point. Cerebral DSA is still the gold standard however, confirming or refuting the diagnosis and defining the DAVF angio-architecture and flow dynamics, to allow for optimal neurointerventional and/or open surgical planning.



(Filename: TCT_E-31_Image1.jpg)

E-32

4:22PM - 4:26PM

Double Trouble: Preoperative Imaging of Pygopagus Conjoined Twins

A Arneja[1], A Tong[2], Y Sun[3], K Golden[4], S Bobra[1], M Tenner[1], H Mehta[5]
[1]Westchester Medical Center, Valhalla, NY, [2]New York Medical College, Valhalla, NY, [3]New York Medical College - Westchester Medical Center, Valhalla, NY, [4]New York Medical

College- Westchester Medical Center, Valhalla, NY, [5]New York Medical College-Westchester Medical Center, Valhalla, NY

Purpose

To present the pre-operative imaging for pygopagus conjoined twins, twins joined at the sacrum and conus medullaris.

Materials and Methods

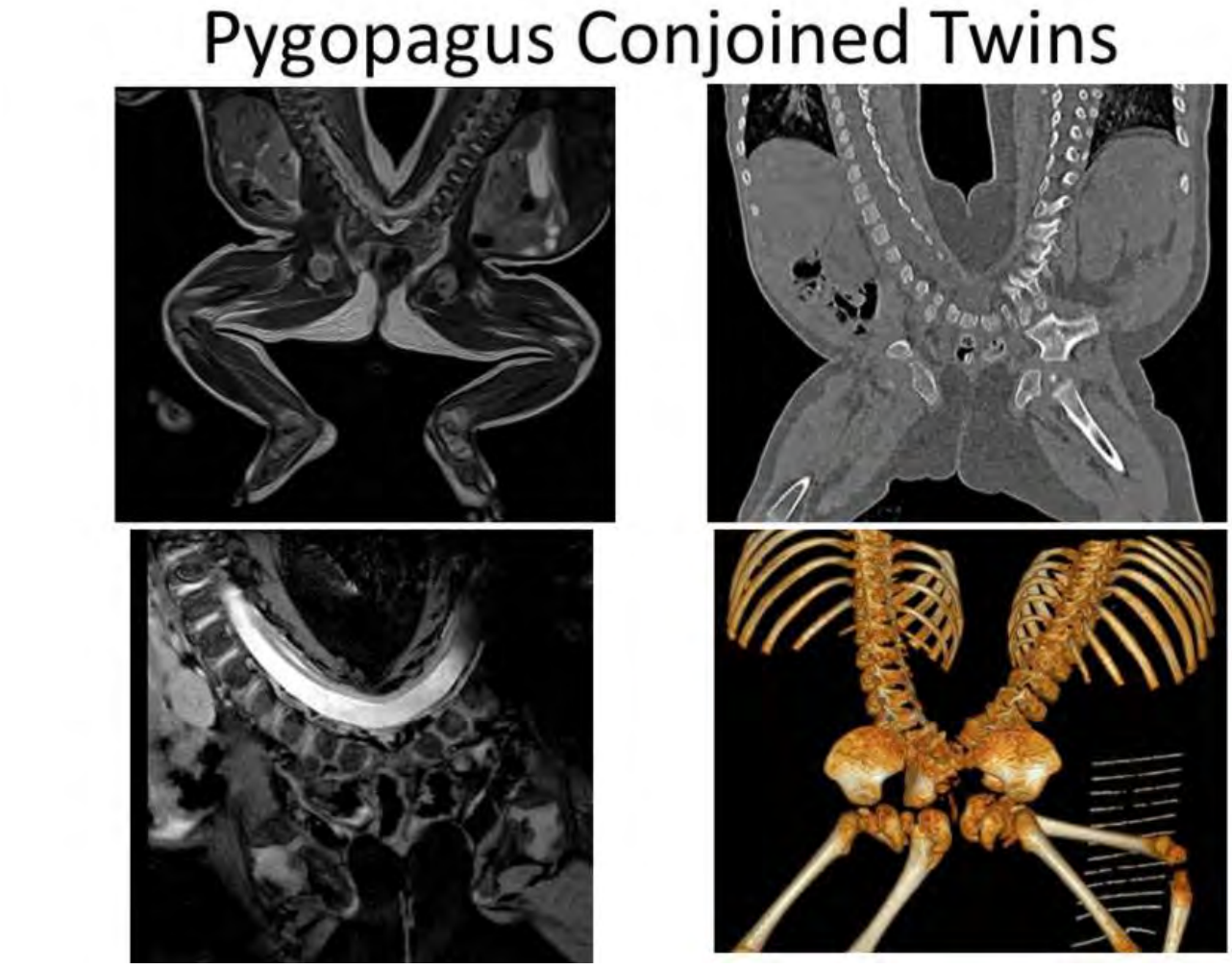
Six-month-old female conjoined twins from the Dominican Republic present for pre-operative workup for separation. The twins are conjoined in a pygopagus configuration, at the sacrum and conus medullaris. Comprehensive radiologic imaging is performed, including, renal and bladder ultrasound, ultrasound of the perineum, magnetic resonance imaging (MRI) of the abdomen and pelvis, MRI urogram, VCUG, vaginogram, MRI Pelvis, barium enema, MRI brain, MRI CTLS spine, computed tomography (CT) abdomen, pelvis and plain films of spine and pelvis, and MRA and MRV of abdomen and pelvis. We present a review of the imaging features of these conjoined twins, focusing on neurologic evaluation of the conjoined sacrum and conus medullaris. Three-dimensional imaging and sagittal T2-gradient sequences were particularly helpful in delineating the joined conus and for pelvic reconstructive planning.

Results

Computed tomography (CT) demonstrated conjoined twins in pygopagus configuration with syndesmotic and fused lower sacrum and coccyx. Magnetic resonance imaging of the spine showed there was hydromyelia of Twin A greater than Twin B with a low-lying conjoined and tethered cord with a single filum terminale. Magnetic resonance imaging of the pelvis demonstrated that the twins also had a common internal iliac artery, prominent sacral venous plexus, and a large right internal iliac vein of twin A. Barium edema and pelvic MRI confirmed that the twins also had 2 rectosigmoid colons and 1 anal opening,

Conclusions

Separation of conjoined twins requires extensive pre-operative planning and imaging with a multidisciplinary approach to ensure a positive outcome. We present the pre-operative CT, MRI and fluoroscopic imaging prior to separation of a pair of 6-month-old pygopagus conjoined twins, twins joined at the sacrum and conus medullaris, including the imaging challenges.



(Filename: TCT_E-32_PygopagusConjoinedTwins.jpg)

E-33

4:26PM - 4:30PM

Metastatic Choroid Plexus Carcinoma in a Patient with Li Fraumeni

s lee[1], A Ozturk[2], B Dahlin[3], M Bobinski[1], J Chang[4]
[1]UC Davis, sacramento, CA, [2]University of California, Davis Medical Center, Sacramento, CA, [3]University of California Davis, sacramento, CA, [4]UC Davis medical center, Sacramento, CA

Purpose
In pediatric patients presenting with multiple primary malignancies, recognizing the constellation of imaging findings in Li Fraumeni may lead to earlier identification and treatment of primary malignancies afflicting these patients.

Materials and Methods

Five-month-old female with history of adrenal cortical neoplasm status postresection presents with several weeks of emesis, fussiness, and irritability. Family history was revealing for a maternal grandfather who was deceased from an unknown cancer, and mother with breast cancer. Birth history was unremarkable, and the patient met normal developmental milestones. Physical exam revealed an inconsolable infant with bulging fontanelles. Laboratory testing was unrevealing. Magnetic resonance imaging (MRI) of the brain and spine demonstrated a right lateral ventricular mass and leptomeningeal enhancement throughout the brain and spine. The patient underwent genomic sequencing which demonstrated a mutation in the TP53 tumor suppressor gene compatible with Li Fraumeni. The patient underwent resection of ventricular mass with pathology confirming diagnosis of choroid plexus carcinoma and meningeal metastases.

Results

Fig 1a. Axial T1 postcontrast MRI demonstrates a large enhancing mildly lobulated mass within the right atrium of the lateral ventricle (white arrow). Ependymal enhancement is seen along the posterior and lateral occipital horn (black arrow). Enlarged third and lateral ventricles compatible with hydrocephalus. Fig 1b. Axial T1 postcontrast MRI at the level of the midbrain showing diffuse leptomeningeal thickening and enhancement surrounding the midbrain (arrow) extending into the interpeduncular cistern. Fig. 2. Axial CT of the abdomen demonstrates a large heterogeneously enhancing mass separate from the left kidney (*) compatible with biopsy proven adrenal cortical carcinoma. Fig. 3. Sagittal T1 fat saturated postcontrast MRI of the lower spine demonstrates leptomeningeal enhancement of the lower thoracic cord and conus medullaris (white arrow) with layering enhancement within the distal thecal sac (black arrow).

Conclusions

Differential diagnostic considerations for a ventricular mass and leptomeningeal enhancement in a pediatric patient with a history of malignancy includes metastatic disease, choroid plexus papilloma with infectious meningitis, and choroid plexus carcinoma with leptomeningeal carcinomatosis. Choroid plexus tumors represent 1-5% of CNS tumors in patients under the age of 15, with choroid plexus carcinomas comprising 20% of such tumors and choroid plexus papillomas comprising the other 80%. However, in patients with Li Fraumeni, choroid plexus carcinomas are much more common with an incidence of 36-64%. Choroid plexus tumors tend to arise within the supratentorial brain in the pediatric population versus infratentorial brain in adults. Clinical criteria for Li Fraumeni was fulfilled in this patient with 1st and 2nd degree relatives with typical Li Fraumeni carcinomas, childhood adrenal cortical carcinoma, and childhood choroid plexus carcinoma. Li Fraumeni is an autosomal dominant cancer syndrome characterized by a mutation of the TP53 tumor suppressor gene and lifelong risk of developing primary brain tumors, adrenal cortical neoplasms, bone sarcomas, and breast cancer. Primary neoplasms of the central nervous system include astrocytomas, choroid plexus carcinomas, and less commonly primitive neuroectodermal tumors. Many patients are diagnosed before the age of 10, with a second

peak between the age of 30 and 50. A strong family history of multiple primary malignancies should raise suspicion for a syndromic disease such as Li Fraumeni. Treatment depends on the type of malignancy but usually involves early detection, resection, and chemotherapy. Preventative measures include genetic counseling and a combination of screening strategies depending on patient age. Pediatric patients may have yearly abdominal ultrasounds and urine screens to evaluate for adrenal tumors. Yearly whole body MRI for CNS tumors, sarcomas, and adrenal tumors also has been advocated.



(Filename: TCT_E-33_asnr.jpg)

E-34

4:30PM - 4:34PM

Imaging findings of meningioangiomatosis in pediatric patients.

J Ndolo[1], W Chow[1], C Carducci[2], G Colafati[2], A Bhatia[1]
[1]Monroe Carell Jr Children's Hospital at Vanderbilt, Nashville, TN, [2]Bambino Gesu Children's hospital, Rome, Italy

Purpose

Meningioangiomatosis (MA) is a rare meningiovascular malformation or hamartomatous lesion in the central nervous system that typically present with seizures. Few case reports are available in literature, with limited data in the pediatric population. The objective is to describe the magnetic resonance imaging (MRI) findings in 3 pediatric patients of MA at our institution.

Materials and Methods

We present 3 cases of MA in our institution. In case 1, a 4-year-old female presented with intractable epilepsy. In case 2, a 7-month-old male presented with intermittent low muscle tone in the right upper limb which progressed to intractable seizures. Case 3 was a 10-year-old male who initially was diagnosed with medulloblastoma and underwent resection, chemotherapy and radiotherapy, and developed MA 4 years after the initial diagnosis. After resection, all the cases were proven to be meningioangiomatosis by pathology.

Results

Case 1: MRI demonstrated a lesion in the subcortical white matter of the right frontal lobe with abnormal FLAIR hyperintensity without enhancement (Fig. 1). CT head performed was normal. PET imaging demonstrated decreased metabolic activity of the lesion. Case 2: MRI demonstrated T2 hyperintense, nonenhancing, cystic lesion in the subcortical white matter of the left parasagittal frontal lobe, which was stable for 3 years (Fig. 2). Case 3: MRI follow-up imaging 4 years after medulloblastoma diagnosis showed development of leptomeningeal enhancement in the right temporal lobe with associated subtle FLAIR hyperintensity in the cortex (Figs. 3 and 4). There were no other imaging findings to suggest additional lesions and the patient never had metastatic or recurrent disease.

Conclusions

The differential diagnosis of the imaging findings reported in our case series and in literature is wide and includes low-grade neoplasms, infectious etiology, and vascular malformations (1). The imaging findings demonstrated a wide spectrum including abnormal FLAIR signal, cystic, nonenhancing lesions, and leptomeningeal enhancement. However, the cases did demonstrate similar findings of location within the cortex and subcortical white matter of the frontotemporal lobes.

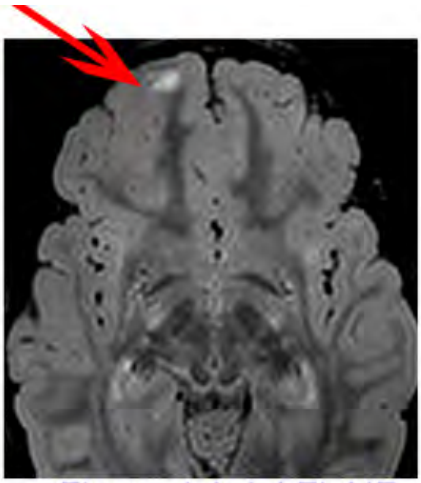


Figure 1 Axial FLAIR



Figure 2 Coronal T2

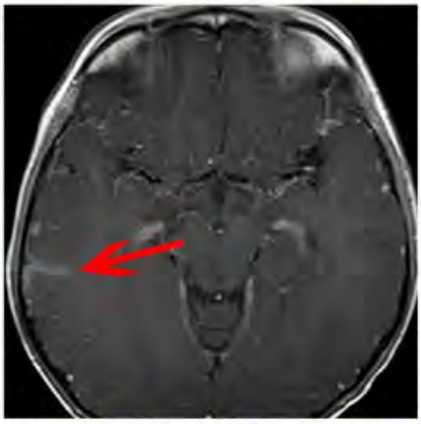


Figure 3 Post Contrast T1

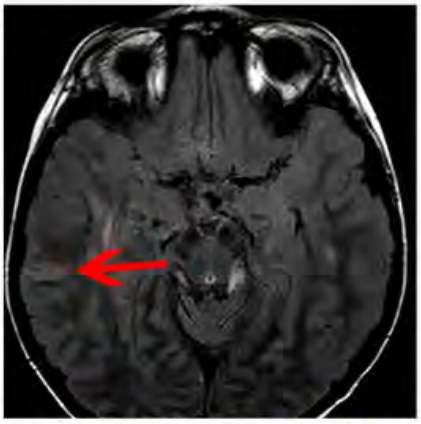


Figure 4 Axial FLAIR

(Filename: TCT_E-34_Graphic.jpg)

E-35

4:34PM - 4:38PM

The Great Oligodendroglioma Mimicker: Supratentorial Astroblastoma Containing a Single Macrocalcification in a 31-year-old Woman

W Carson[1], S Cha[2]
[1]University of California, San Francisco, San Francisco, CA, [2]University of California San Francisco, San Francisco, CA

Purpose
We report a case of supratentorial astroblastoma containing a large coarse macrocalcification in a 31-year-old woman. Computed tomography (CT) and MR imaging (MRI) findings of astroblastoma will be discussed, including a special emphasis on ways to differentiate it from other similar appearing supratentorial tumors (most notably oligodendroglioma).

Materials and Methods

A 31-year-old woman presented to our hospital with gradually worsening bifrontal headaches and temporary alexia. An unenhanced CT of the head was obtained and demonstrated a large left supratentorial intracranial mass. Magnetic resonance imaging subsequently was performed confirming a circumscribed intraparenchymal mass with avid enhancement and areas of reduced diffusion abnormality. Due to the presence of intratumoral calcium, oligodendroglioma was favored in the pre-operative diagnosis. She then underwent a left parietal craniotomy for tumor resection. Intra-operatively, a good plane of separation was appreciated between the tumor and the surrounding normal brain tissue without gross macroscopic invasion of the brain parenchyma. However, surgical pathology demonstrated a malignant glioma with histologic features suggestive of astroblastoma, at least WHO grade III. Molecular analysis of SSTR2a and STAT6 stains were negative, arguing against a diagnosis of meningioma or solitary fibrous tumor, respectively. Stains for IDH1, R132H and BRAF V600E mutant proteins were similarly negative, but the Ki-67 labeling index was focally greater than 50% indicative of a highly proliferative neoplasm. After discussion of her case at our multidisciplinary tumor board, a consensus recommendation was made for adjuvant chemoradiation given the aggressive histologic appearance of the tumor. However, given the rarity of the histologic tumor subtype, further molecular and genomic analyses also were recommended to better categorize and classify her tumor. The patient recovered well from her surgery and currently is undergoing fractionated radiation therapy with concurrent and adjuvant temozolomide.

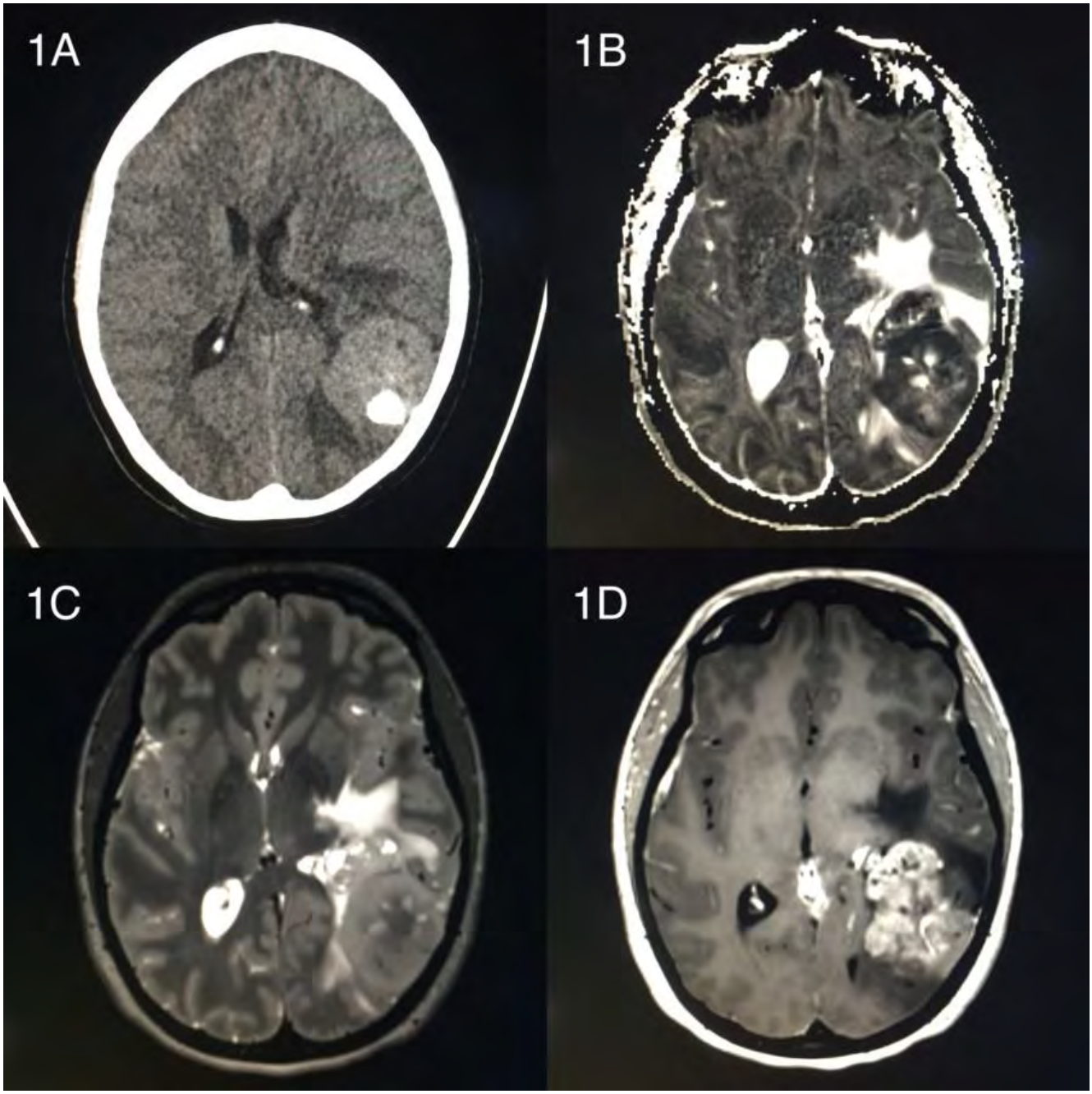
Results

1A: Noncontrast head CT demonstrates a large hyperdense mass in the left parietal lobe with extensive surrounding vasogenic edema, effacement of the left occipital horn, and rightward subfalcine herniation. A single globular macrocalcification is evident within the mass. 1B: Apparent diffusion coefficient (ADC) image demonstrates low ADC values within the mass, indicative of hypercellularity. 1C: T2-weighted fast spin-echo image shows the mass to be isointense to gray matter, expand the cortex of the left inferior parietal lobule, and extend to the subependymal margin of the left occipital horn which is compressed. Foci of cystic change at the deep margin of the mass are better demonstrated. 1D: Contrast-enhanced T1-weighted image demonstrates marked enhancement and hypervascularity of the mass.

Conclusions

Astroblastoma is an exceedingly rare glial neoplasm. According to the 2016 WHO classification, astroblastoma is listed under "other gliomas" without a numeric grade due to the lack of sufficient clinicopathological data (1). However, the tumor is histologically grouped into low-grade and high-grade subtypes, which correlate with prognosis (2). Astroblastoma occurs most commonly in adolescent females (female:male ratio 8:1, median age of 14 years at diagnosis) and is almost exclusively supratentorial (3). Imaging features include superficial location, well-circumscribed margins, mixed cystic and solid components, and presence of contrast enhancement. On CT, astroblastomas classically are hyperattenuating and have calcifications which are usually punctate, however 5 cases of

extensive macrocalcifications have been reported (3). Calvarial remodeling also can be seen, indicative of slow growth in low-grade subtypes. On MR, key findings include iso- or hypointensity on T2-weighted images, reduced diffusion, mixed cystic and solid morphology, heterogeneous enhancement, and peritumoral edema. Differential diagnoses include other hypercellular tumors such as lymphoma and primitive neuroectodermal tumor; other superficially located tumors such as pleomorphic xanthoastrocytoma and ganglioglioma; and other partially calcified tumors such as oligodendroglioma and ependymoma. Oligodendroglioma in particular can closely resemble an astroblastoma as both can present as a well circumscribed supratentorial mass with internal calcifications and calvarial remodeling; however, astroblastoma may be suggested when CT hyperattenuation, punctate calcifications, T2 hypointensity, and reduced diffusion are seen. Prognosis depends on histologic grade and extent of resection, with low-grade astroblastoma having a 95% 5-year survival rate after gross total resection (4). Optimal management has yet to be defined, however adjuvant chemoradiation has been advocated for high-grade cases (5).



(Filename: TCT_E-35_astrocombined.jpg)

E-36

4:38PM - 4:52PM

Childhood Cervical Spine Glioblastoma

C Vallejo[1], R Camacaro[1], A Rodriguez[1], P Puac[1], M Castillo[1]
[1]*University of North Carolina at Chapel Hill, Chapel Hill, NC*

Purpose

Spinal cord glioblastoma (SCGB) in children is rarely reported. Spinal chord glioblastoma most frequently involves the cervical and thoracic regions with a predilection for the 2nd and 3rd decades of life with an average of survival of 15 months This report describes a case of cervical cord glioblastoma in a child with rapid progression.

Materials and Methods

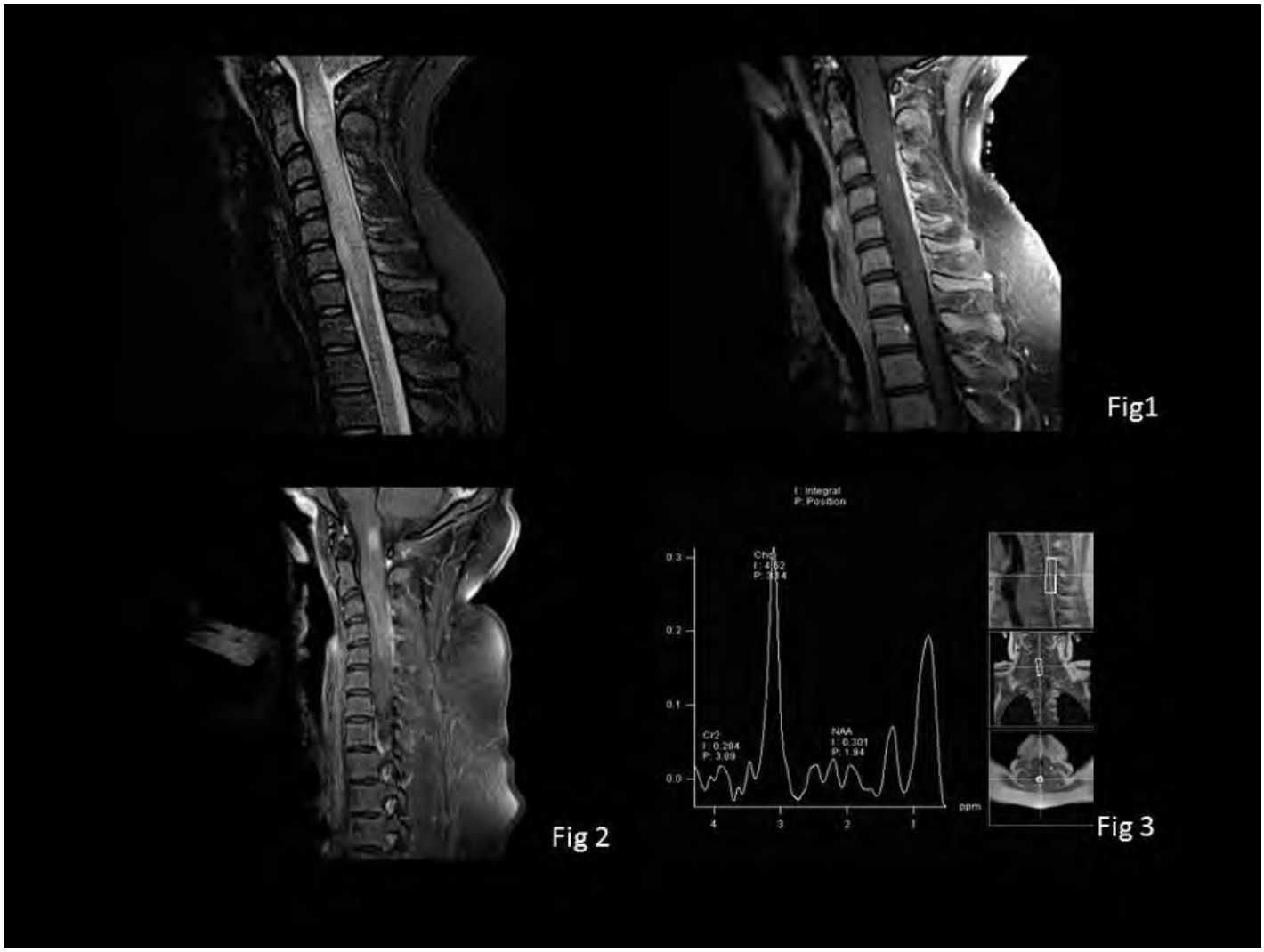
A 13-year-old male with severe posterior neck pain, headache and paresthesias of left hand 2 weeks duration presented to our hospital. History included a questionable viral illness 3 weeks previously and there was no history of recent vaccinations. On physical examination abnormal coordination of the left hand was noted. Magnetic resonance imaging (MRI) showed an intramedullary T2 bright lesion extending from the pontomedullary junction to about C7 with little to no contrast enhancement. A provisional diagnosis of inflammatory myelitis was given and patient was placed on steroids. One month later the patient developed difficulty walking and urinating and repeat MRI showed mild lesion progression and more contrast enhancement. Cord MRS showed markedly elevated choline and absence of creatine and N-acetyl aspartate (NAA) as well as presence of lipids. Biopsy was performed and showed a grade 4 astrocytoma.

Results

Magnetic resonance imaging showed a large infiltrative and expansile cervical cord lesion from C1-C7 with high signal on T2 and FLAIR (Fig. 1) and little contrast enhancement. The size increase on a 2-week follow-up study which showed extension to brainstem and more central enhancement (Fig. 2). Magnetic resonance spectroscopy (MRS) showed very high choline and lipids/lactate (Fig. 3).

Conclusions

Spinal cord glioblastoma is a rare entity which our patient presented with rapid progression simulating acute disseminated encephalomyelitis (ADEM), NMO and other inflammatory processes.



(Filename: TCT_E-36_Spinalglioblastoma.jpg)

Monday
3:30PM - 4:45PM
Long Beach Convention Center, Room 104C (Main Lobby)

06F-Parallel Paper Session: Acute Stroke Management Decisions: Answers from Advanced Imaging?

O-73

3:30PM - 3:38PM

Machine Learning Improves Prediction of Patient Outcomes

S Arndt[1], G Bennett[1], A Albar[1], R Hebert[1], M Al Hasan[1], J Lavie[1], J Milburn[1]
[1]*Ochsner Clinic Foundation, New Orleans, LA*

Purpose
Logistic regression was used to assess mechanical thrombectomy patient outcomes in major trials, but machine learning has not been appropriately assessed for patient outcomes based on mRS. This abstract will compare machine learning models to logistic regression and provide a framework for predictive modeling to aid the interventionalist with patient selection.
Materials and Methods
Seven hundred consecutive patients evaluated with CT perfusion for stroke were analyzed retrospectively. Patients were included if thrombectomy was attempted and excluded if the pre-intervention dataset was incompletely documented. Ninety-one patients were included in the study. Using data available prior to intervention, machine learning models including artificial neural network (ANN), support vector machine (SVM), decision tree, naive bayes, and multivariate logistic regression were created with bootstrap sampling. T-test with Sidak multiple testing correction was used to compare models for accuracy and receiver operating characteristic curves area under the curve (AUC) generated from model application to unseen data.
Results
For the classification of good outcomes defined as mRS 0 or 1, ANN (accuracy 57.6% +/- 6.2) SVM (58.7% +/- 5.3) and naive bayes (63.5 +/- 5.3%) and decision tree (59.2% +/- 5.4) models significantly outperformed logistic regression, (54.1.+/-8.5%) with $p<.001$ for all comparisons to logistic regression. For the classification of good outcomes defined as mRS 0, 1, or 2, all machine learning models significantly outperformed logistic regression with $p<.005$ for accuracy at outcome classification. Analysis for ROC AUC showed that significant improvement in comparison to traditional logistic regression for comparable models ($p<.001$) for either definition of good outcome.
Conclusions
Machine learning methods outperform multivariate logistic regression at the prediction of dichotimized patient outcomes. These methods could help the interventionalist predict and avoid poor outcomes as assessed by mRS prior to thrombectomy, though prediction remains imperfect.

O-74

3:38PM - 3:46PM

DCE-MRI Blood-Brain Barrier Assessment in Acute Ischemic Stroke

K Villringer[1], B Sanz cuesta[2], A Ostwaldt[1], U Grittner[1], P Brunecker[3], A Khalil[1], K Schindler[1], O Eisenblätter[1], H Audebert[1], J Fiebach[1]
[1]Charité Universitätsmedizin Berlin, Berlin, N/A, [2]Autonomous University of Madrid, Madrid, N/A, [3]Berliner Institut für Gesundheitsforschung, Berlin, N/A

Purpose

Evaluation of quantitative blood-brain barrier (BBB) assessment in ischemic stroke patients within 48 hours after symptom onset using dynamic contrast-enhanced (DCE) MR.

Materials and Methods

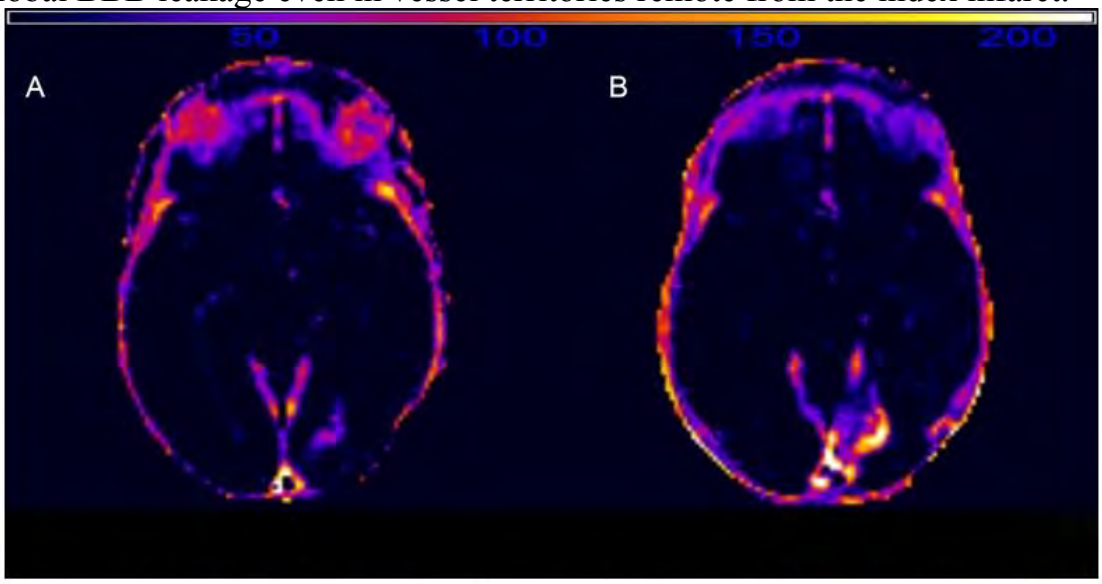
We examined 54 stroke patients (clinicaltrials.gov NCT00715533, NCT02077582) in a 3 Tesla MR scanner. Twenty-eight patients had a follow-up examination on day 5-7. The DCE protocol comprised precontrast T1 measurements with 4 different flip angles (2°, 10°, 20°, 35°) for T1 mapping, as well as continuous serial acquisitions of 60 volumes after administration of 10 ml contrast agent at a flow rate of 1 ml/s. Patlak analysis was employed to assess BBB permeability changes using TOPPCAT (https://sites.duke.edu/dblab/toppcat/) (1) which utilizes Patlak analysis (2).

Results

Median stroke Ktrans values (0.7*10-3 min-1, (IQR: 0.4-1.8)*10-3 min-1) were more than 3 fold higher compared to median mirror Ktrans values (0.2*10-3 min-1, IQR: 0.1-0.7*10-3 min-1, $p<0.001$) and further increased at follow up (n=28, 2.3*10-3 min-1, IQR: 0.8-4.6*10-3 min-1, $p<0.001$). By contrast, mirror Ktrans values decreased over time with a clear interaction of time point and stroke/mirror side ($p<0.001$, Fig. 1). Median stroke Ktrans values were 2.5 times lower than in hemorrhagic transformed regions (0.7 versus 1.8 10-3 min-1; $p=0.055$). There was no association between stroke Ktrans values and the delay from symptom onset to baseline examination, age and presence of hyperintense acute reperfusion marker.

Conclusions

Blood-brain barrier in acute stroke patients can be successfully assessed quantitatively. The decrease of BBB permeability in unaffected regions at follow up may be an indicator of global BBB leakage even in vessel territories remote from the index infarct.



K^{trans} maps in a left sided PCA infarct at baseline, 47 hours after symptom onset (left panel) and follow-up, 5 days after symptom onset (right panel)

(Filename: TCT_O-74_Ktrans_PCA.jpg)

O-75

3:46PM - 3:54PM

Utilizing low b-value DWI sequences to rapidly assess perfusion in the setting of acute stroke.

M Peckham[1], U Rassner[1]
[1]*University of Utah, Salt Lake City, UT*

Purpose
Intravoxel incoherent motion (IVIM) has been applied to evaluation of brain tumors, head and neck tumors, and for acute stroke. At low b-values, diffusion-weighted imaging (DWI) becomes more perfusion weighted. However, IVIM requires substantial post-processing time and is not in widespread use. We present a method to more rapidly acquire perfusion information with diffusion-weighted imaging.
Materials and Methods
Acute stroke patients with MRI or CT perfusion and low b-value diffusion imaging within 24 hours were identified with a free text report search tool. The diffusion images were acquired with a b-value of 50 s/mm2 in 3 planes, and with a b-value of 1000 and 2000 s/mm2 in 10 to 20 planes. Only patients with tissue at risk, defined as cerebral blood flow (CBF) or mean transit time (MTT)/cerebral blood volume (CBV) for CT and CBF or MTT/DWI mismatch, were included.
Results
Regions of perfusion restriction on b50 sequences correlated with regions of low CBF on perfusion sequences in 7 of 9 patients and with MTT in 6 out of 9 patients, 2 of them demonstrated CBF/b50 mismatch. The areas of CBF/b50 or MTT/b50 mismatch showed elevated CBV which likely accounting for the discrepancy, as b50 ADC is affected by both CBF and CBV. None of the areas that were abnormal on CBF/MTT but appeared normal on b50 ADC map went on to infarction.
Conclusions
Low b-value sequences can be acquired rapidly without contrast and provide gross estimation with high specificity of perfusion deficit in the stroke setting. Elevated CBV in the region of stroke can mask areas of decreased flow on the b50 sequence. These sequences can be acquired as a modified routine sequence without new software or hardware.

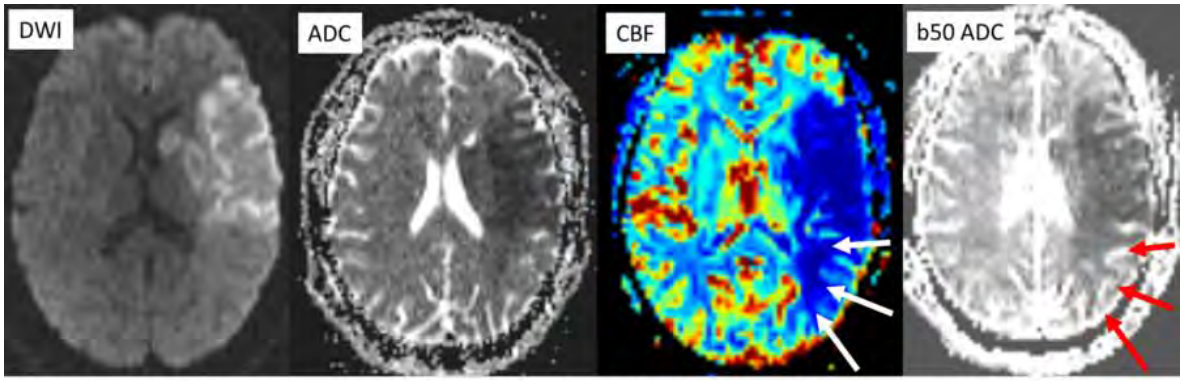


Figure 1: Patient with acute anterior MCA territory infarct with posterior MCA tissue at risk seen on DSC CBF (white arrows). Territory of perfusion restriction on b50 mirrors CBF (red arrows).

(Filename: TCT_O-75_b50figurenew.jpg)

O-76

3:54PM - 4:02PM

A Novel Approach to Measuring Cerebral Oxygen Extraction Fraction and Vascular Reserve Using MRI

C Cantrell[1], S Ansari[2], Y Jeong[3], K Midlash[4], T Carroll[4]
[1]northwestern university, Chicago, IL, [2]Northwestern University, Feinberg School of Medicine, Chicago, IL, [3]Northwestern, Chicago, IL, [4]University of Chicago, Chicago, IL

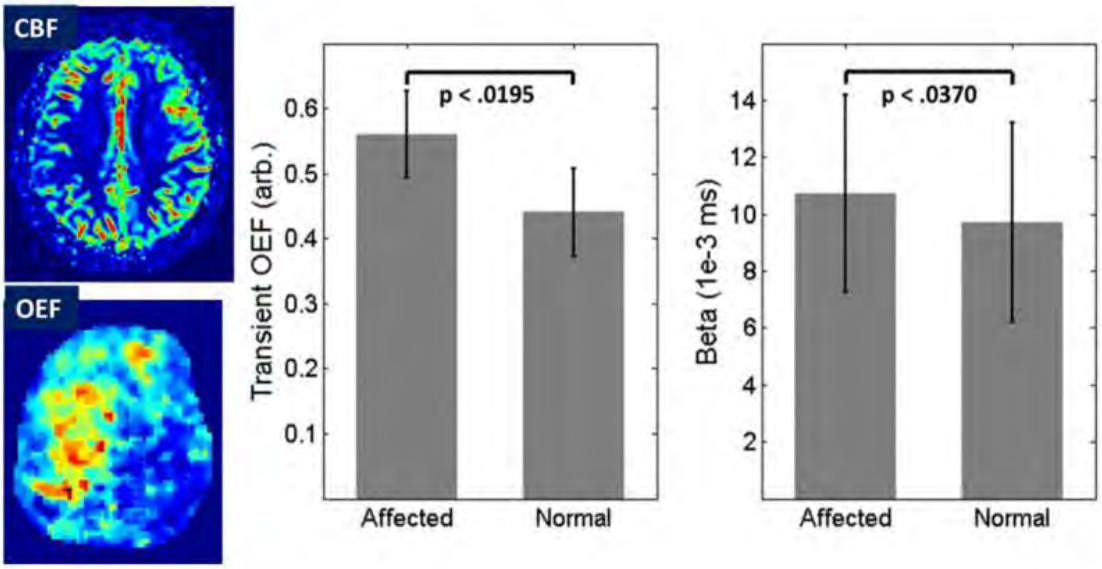
Purpose

The length scales associated with parenchymal oxygen extraction fraction (OEF), coupled with the near uniformity of normative OEF across the brain dictate the development of an imaging approach that is sensitive to low spatial frequency imaging behavior. Previous approaches to measure OEF using MRI have utilized high pass-filters effectively removing much of the signal. We propose a new method to filter out geometric field inhomogeneity, by imaging temporally through the cardiac cycle. In a study in 11 patients with intracranial atherosclerotic disease, we found elevated OEF on the compromised hemisphere as compared to the healthy contralateral side ($p<0.0195$).

Materials and Methods

We acquire 20 parameter assessment by retrieval from signal encoding (PARSE) images at successive times after the cardiac QRS complex. The goal is to measure the change in frequency shift as oxygenated blood is metabolize into deoxygenated blood. The dynamic signal changes acquired with PARSE were decomposed into constant components which contain all the local magnetic field inhomogeneity and dynamic components which represent the change in local susceptibility which occur as oxygen is extracted from fresh blood supplied to the parenchyma: The PARSE acquisition consisted of a single slice, 5.0 mm thick, 210 mm x 210 mm FOV, 108 x 108 matrix, resolution = 1.94 x 1.94 x 5 mm3 2D images. Each 2D slice was acquired 25 times, at 25 ms increments from the R-trigger throughout the cardiac cycle (25 ms to 625 ms delay).

Results
In a series of 11 consecutive ICAD patients (M/F 5/6) OEF in the normal hemispheres was (44%±6.7%) which is in agreement with historical reference PET-OEF and significantly increased in impaired regions (56 % ± 6.7%, p<0.0195).
Conclusions
In this pilot study, we present the first evidence of an MR-based OEF technique that requires no contrast.



(Filename: TCT_O-76_OEFfig.jpg)

O-77

4:02PM - 4:10PM

The Effect of Scan Length on the Assessment of Cerebral Perfusion Using Resting-state Functional MRI: A Comparison Between Sequences in Acute Stroke

A Khalil[1], E Kirilina[2], K Villringer[1], A Villringer[3], J Fiebach[1]
[1]Charité Universitätsmedizin Berlin, Berlin, Germany, [2]Free University Berlin, Berlin, Germany, [3]Max Planck Institute for Human Cognitive and Brain Sciences, Leipzig, Germany

Purpose
Delays in the propagation of low frequency blood-oxygen-level-dependent (BOLD) signal oscillations through the brain provide a useful, noninvasive, measure of hypoperfusion (1). Relatively long scanning times are, however, a potential barrier to the routine use of this method in acute stroke patients, where time-to-treatment is a crucial issue. We investigated

whether scan time could be reduced using newly developed high temporal resolution echo planar imaging (EPI) sequences with multiband acquisition (2).

Materials and Methods

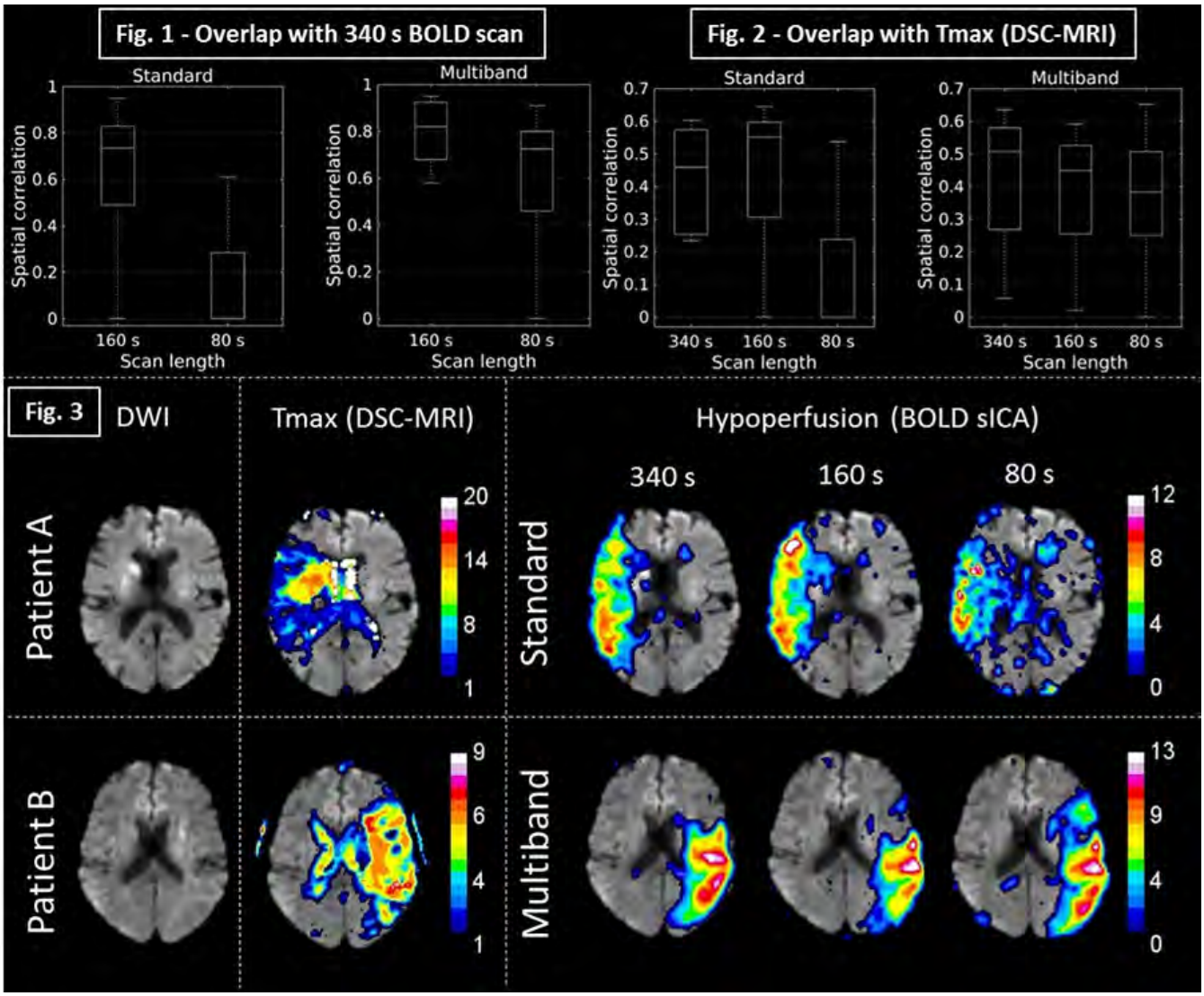
Eight patients with acute stroke (within 24 hours of symptom onset) received a multiband BOLD sequence (TR=0.4 s, TE=30 ms, FA=43, acquisition time=340 s) and another 8 received a standard BOLD sequence (TR=2.3 s, TE=30 ms, FA=90, acquisition time=340 s) as part of a stroke MRI protocol. All of the standard group and 5 patients of the multiband group also received a dynamic susceptibility-contrast MRI (DSC-MRI) scan. Each full BOLD acquisition was shortened to 160 s and 80 s, was preprocessed (motion correction, spatial smoothing), and underwent spatial independent component analysis (sICA) to identify areas of hypoperfusion (3). Spatial overlap between hypoperfusion identified using the shortened and full datasets, and between hypoperfusion on each BOLD dataset and hypoperfusion on DSC-MRI, was calculated.

Results

Hypoperfusion was visible in all 16 patients when the 340 s BOLD data were used. In the multiband group, all patients showed hypoperfusion with the 160 s scan (versus 7 out of 8 in the standard group) and 7 out of 8 showed hypoperfusion with the 80 s scan (versus 2 out of 8 in the standard group). Figs. 1 and 2 show quantitative results and Fig. 3 shows example cases.

Conclusions

Multiband EPI sequences provide a robust assessment of hypoperfusion, even with short scan times. This is likely due to effective separation of perfusion-related low-frequency oscillations (4) from higher frequency sources of noise that are aliased when using standard EPI sequences. These quick, noninvasive sequences are potentially well suited for routine perfusion assessment in acute stroke.



(Filename: TCT_O-77_ASNR17_fig_highres.jpg)

O-78

4:10PM - 4:18PM

Resting-state fMRI delay maps for measurement of the penumbra in acute ischemic stroke patients undergoing endovascular triage.

J Heit[1], T Christen[2], G Zaharchuk[1]
[1]Stanford University, Stanford, CA, [2]Stanford, Stanford, CA

Purpose

The neuroimaging evaluation of acute ischemic stroke (AIS) patients for endovascular therapy often includes measures of cerebral perfusion to identify brain tissue that is ischemic, but viable (termed the "penumbra"). The penumbra is identified most commonly using gadolinium-based perfusion-weighted imaging (PWI) (1, 2) but recent studies

demonstrating gadolinium deposition cerebral tissue has raised gadolinium safety concerns (3). Spontaneous fluctuations of the blood oxygen level dependent (BOLD) signal may be used to generate resting-state functional MRI (rs-fMRI) delay maps that correlate well with regions of impaired cerebral blood flow in cerebrovascular steno-occlusive disease and subacute stroke patients (4, 5). We determined the feasibility of acquiring rs-fMRI delay maps representing the penumbra in AIS patients being considered for endovascular treatment.

Materials and Methods

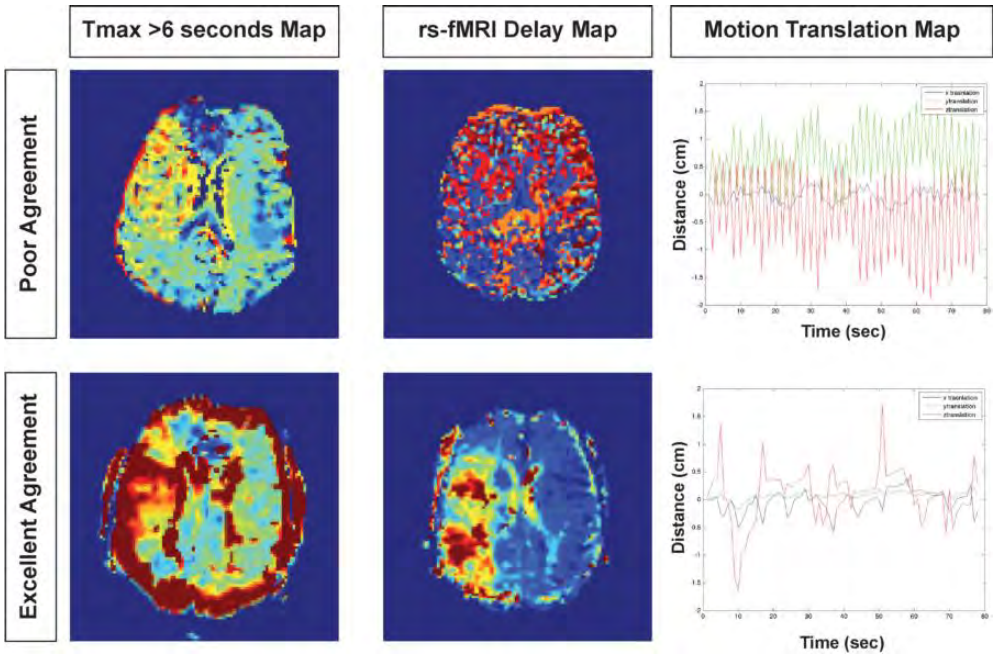
Eleven patients with AIS symptoms underwent endovascular therapy triage by MRI that included DWI, GRE, MRA, PWI, arterial spin labeling, and rs-fMRI (3-minute acquisition). Three were excluded due to excessive motion artifact, and 8 underwent analysis. Rs-fMRI delay maps (4) penumbra volumes were compared to time-to-maximum >6 seconds (Tmax >6s) map penumbra volumes and scored for agreement (excellent, good, or poor). Rs-fMRI motion plots were correlated to delay map interpretability. Clinical data were obtained from electronic medical records.

Results

Eight patients (4 males, 4 females; mean age 68 years) had an average National Institutes of Health Stroke Scale Score of 7 (range 0-17). Mean time from symptom onset to imaging evaluation was 5.2 hours (range 3-7 hours). Four patients received intravenous tPA prior to evaluation, and 3 patients underwent endovascular therapy. Rs-fMRI delay map and Tmax >6 map agreement was excellent in 1 patient, good in 1 patient, and poor in 6 patients. Motion greater than 1 mm on rotation and translation plots was associated with rs-fMRI delay map signal loss that significantly impaired interpretability.

Conclusions

Noncontrast rs-fMRI delay maps that correlate with Tmax >6 seconds maps may be obtained in AIS patients presenting within 6 hours of symptom onset. Artifacts due to patient motion appears more significant in this hyperacute stroke population, and better motion correction techniques will be required.



(Filename: TCT_O-78_rs-fMRIFigure.jpg)

O-79

4:18PM - 4:26PM

Three-Direction Fractional Anisotropy for Improved Infarct Volume Calculation in Acute Stroke.

K Midlash[1], G Christoforidis[1], C Cantrell[2], Y Jeong[3], T Carroll[1]
[1]University of Chicago, Chicago, IL, [2]northwestern university, Chicago, IL, [3]Northwestern, Chicago, IL

Purpose
To develop an accurate, automatic method to measure infarct volume in acute stroke.
Materials and Methods
We compared level-set ADC values to fractional anisotropy (FA) and approximated FA with the fewest number of orthogonal directions. We estimated fractional anisotropy (pseudo fractional anisotropy, pFA) as: where the mean and standard deviations of the signal intensity (SI) were determined by 3 orthogonal diffusion directions. The pFA were normalized by the whole brain average and compared to a level-set threshold on ADC values (1), first using a previously reported value (Th1=0.620e-03), then the optimal value based on direct comparison with reference values (Th2=0.490e-03). In a canine (n=20, 4 experiments, 5 time points) model of MCA occlusion, serially acquired DTI images were subjected to an optimization process to automatically quantify infract volume (2). The minimum number of diffusion directions and automated level-set segmentation were determined. Reference standard mean diffusivity volumes determined by 2 independent reviewers serves as

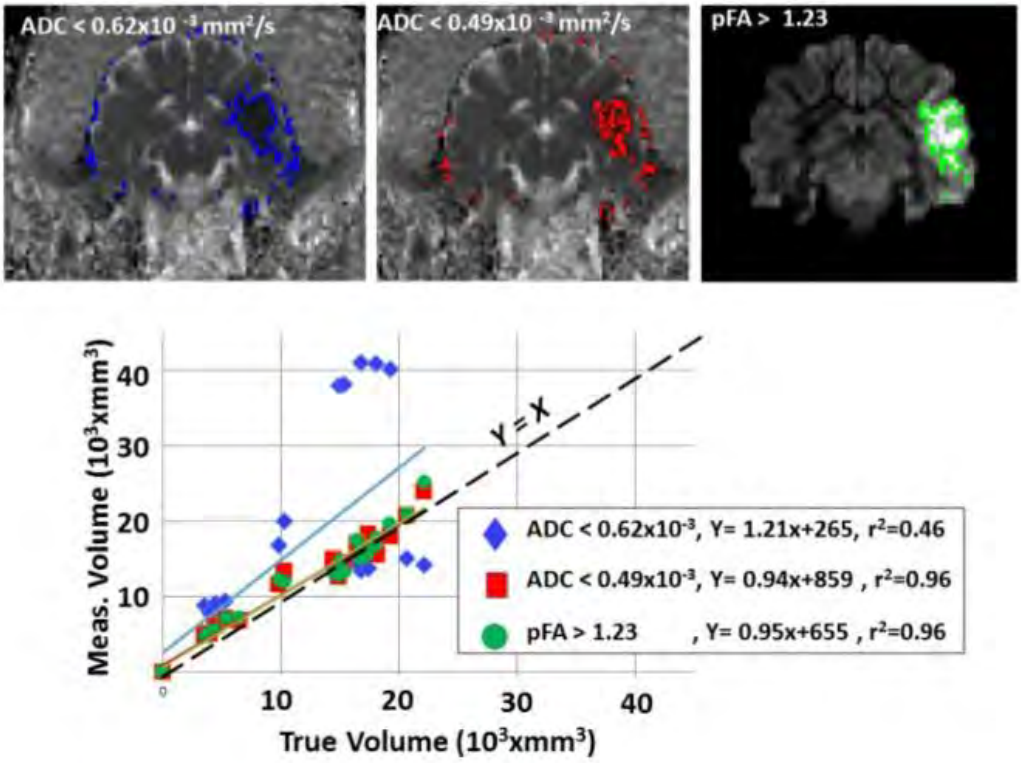
reference values using DWI (FOV/matrix=140/128, 5.0 mm thick, TR/TE= 2131/71, B=0,1000) were acquired at 60, 90, 120, 240 min postocclusion.

Results

Figure 1 shows representative image for ADC and pFA with contours representing infarcted tissue. Both optimized ADC and pFA were strongly correlated with true infarct volume (r^2 =0.96) with pFA yielding slight better visual representation of the infarct. A comparison of Dice's similarity coefficient (DSC) showed significant differences in voxels define as infarcted (DSC=0.384).

Conclusions

Rapid, accurate quantification of (b=100, 3-direction acquisition) and pFA level set segmentation more strongly correlated throughout the growth of an infarct and had less error than volume calculation based on ADC values.



(Filename: TCT_O-79_pFA_compositeImage.jpg)

O-80

4:26PM - 4:34PM

Diffusional Kurtosis Imaging and Prediction of Motor Outcome in Acute Ischemic Stroke

M Spampinato[1], N Hatch[2], J Helpern[3], J Jensen[3], M Yazdani[4]

[1]Medical University Of South Carolina, Charleston, SC, [2]Medical University of South Carolina, Charleston, SC, [3]MUSC, Charleston, SC, [4]Medical University of South Carolin, Charleston, SC

Purpose
To evaluate whether diffusional kurtosis imaging (DKI) can detect corticospinal tract (CST) microstructural changes in the acute phase for patients with first-ever ischemic stroke and motor impairment, and to assess the correlations between DKI-derived diffusion metrics for the CST and motor impairment 3 months poststroke.
Materials and Methods
We evaluated 17 stroke patients who underwent a brain MRI including DKI within 4 days after the onset of symptoms. Neurological evaluation included the Fugl-Meyer Motor Upper Extremity scale (FM-UE) in the acute phase and 3 months poststroke. For the CST in the lesioned and contralateral hemispheres, we estimated with DKI both pure diffusion metrics, such as the mean diffusivity and mean kurtosis, as well as model-dependent quantities, such as the axonal water fraction. We evaluated the correlations between CST diffusion metrics and FM-UE at 3 months. Comparisons of the ipsilateral and contralateral CST diffusion metrics were performed using the paired Wilcoxon Signed-Rank test. Associations between average CST diffusion metrics and 3-month NIHSS were evaluated using Spearman's Rank Correlation tests. Results were considered significant when $p < 0.05$.
Results
Among all the diffusion metrics, the largest percent signal changes of the lesioned hemisphere CST were observed using axial kurtosis, with an average 12% increase compared to the contralateral CST. The strongest associations between 3-month FM-UE and diffusion metrics were found for the lesioned/contralateral hemisphere CST mean kurtosis (rho = - 0.85) and radial kurtosis (rho = - 0.78) ratios.
Conclusions
Diffusion metrics related to the kurtosis were found to be more sensitive than conventional diffusivity metrics to early poststroke CST microstructural changes and may have potential value in the prediction of motor impairment at 3 months.

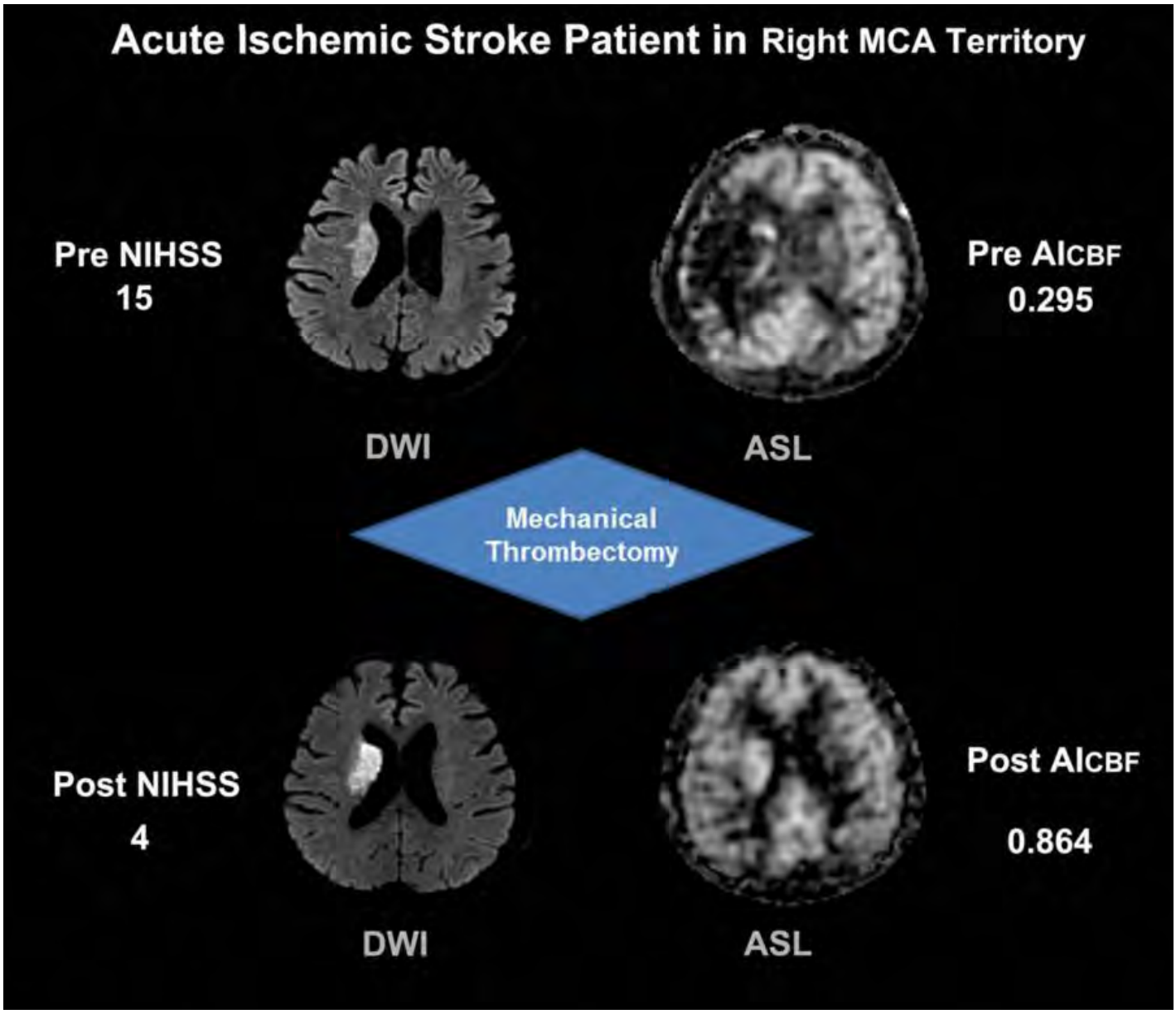
O-81

4:34PM - 4:42PM

Utility of Arterial Spin Labeling Technique for Monitoring Cerebral Blood Flow Change in Acute Ischemic Stroke Patients after Endovascular Thrombectomy

R Yoo[1], K Kang[1], T Yun[2], S Choi[1], J Kim[1], C Sohn[1]
[1]Seoul National University Hospital, Seoul, Seoul, [2]Seoul National University Hospital, Seoul, Korea, Republic of

Purpose
In acute ischemic stroke patients with proximal arterial occlusion, endovascular thrombectomy with a stent retriever within 6 hours after onset has been shown to be safe and effective. Our aim was to evaluate the clinical utility of arterial spin labeling perfusion-weighted imaging (ASL-PWI) in monitoring cerebral blood flow change in acute ischemic stroke patients who underwent thrombectomy.
Materials and Methods
A total of 67 acute ischemic stroke patients, who underwent ASL-PWI before and after endovascular thrombectomy between October 2012 and October 2016, were included in this retrospective study. Asymmetric index (CBF of the lesion normalized with respect to that of normal contralateral brain parenchyma) before and after endovascular thrombectomy (AICBFpre and AICBFpost) were calculated. Linear regression and Pearson correlations were used to evaluate correlations between AICBF values [AICBFpre, AICBFpost, and ΔAICBF (change in AICBF after endovascular thrombectomy)] and NIHSS scores [NIHSSpre, NIHSSimmediate, NIHSS24 hr, NIHSS5-7 days, ΔNIHSS values (change in NIHSS after endovascular thrombectomy)].
Results
Mean AICBFpost was significantly higher than mean AICBFpre (0.88 ± 0.35 vs.0.28 ± 0.21, $P < .001$). AICBFpre had a significant correlation with NIHSSpre ($r = -0.395$, $P = .001$). AICBFpost had significant correlations with NIHSSimmediate, NIHSS24 hr, and NIHSS5-7 days ($r = -0.327$, $P = .017$; $r = -0.343$, $P = .015$; $r = -0.681$, $P < .001$, respectively). ΔAICBF also was significantly correlated with ΔNIHSS5-7 days ($r = -0.316$, $P = .029$). Statistical significance was not achieved between ΔAICBF and ΔNIHSSimmediate ($r = -0.230$, $P = .100$) or between ΔAICBFpost and ΔNIHSS24 hr ($r = -0.188$, $P = .196$).
Conclusions
Arterial spin labeling has the potential to be used as a noninvasive imaging tool to monitor cerebral blood flow change and to predict neurologic outcome in acute ischemic stroke patients after endovascular thrombectomy.



(Filename: TCT_O-81_thrombectomy1.jpg)

Monday
3:30PM - 4:45PM
Long Beach Convention Center, Room 203AB (Upper Level)

06G-Parallel Paper Session: Tracking Tumors: Meningiomas and More!

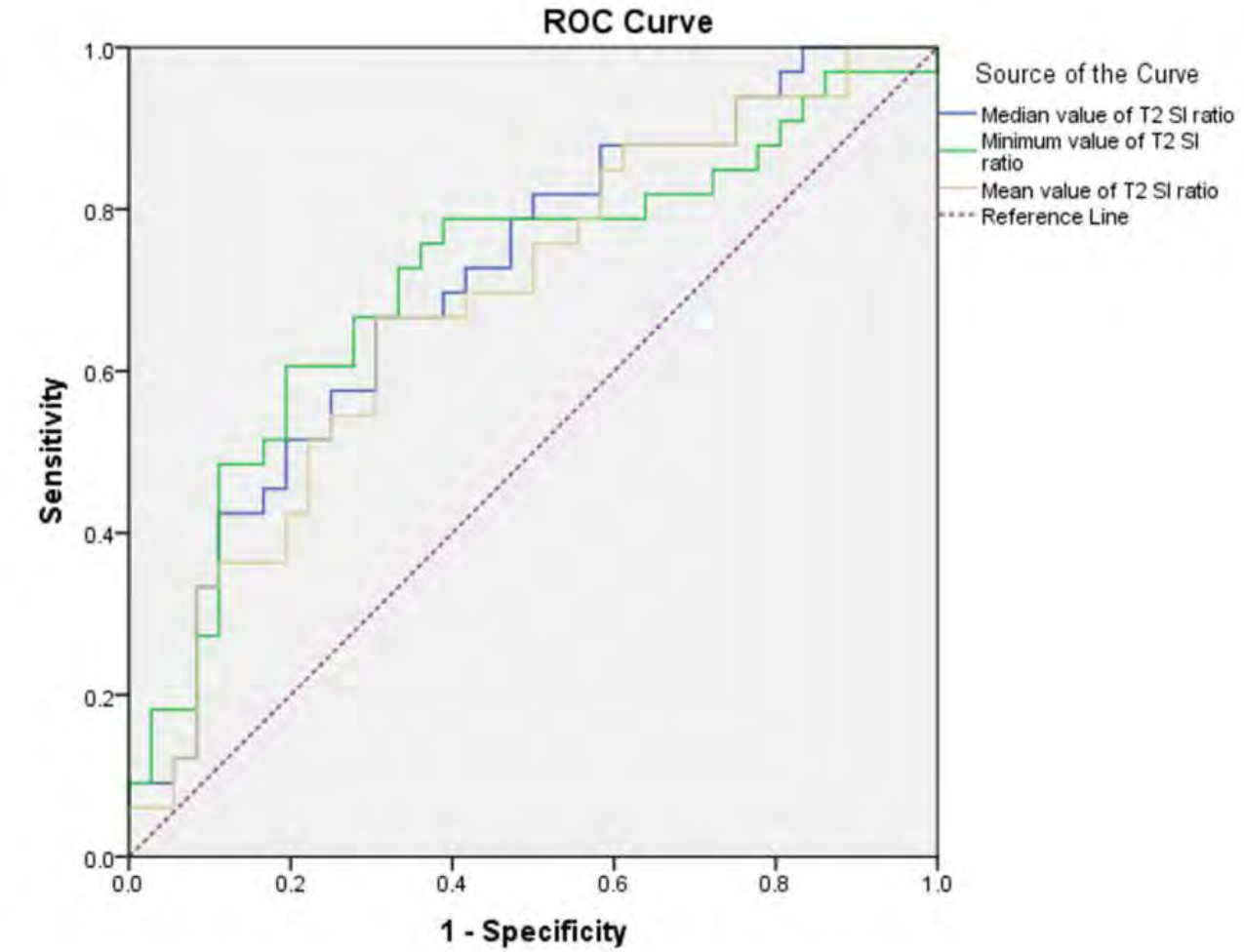
O-83

3:38PM - 3:46PM

Is diffusion tensor imaging superior to conventional magnetic resonance imaging in predicting the consistency of meningioma? : Preliminary results

A Yogi[1], D Higa[1], T Watanabe[1], Y Iraha[1], S Takehara[1], A Nakamata[1], Y Tamashiro[1], S Murayama[1]
[1]*Graduate School of Medical Science, University of the Ryukyus, Nakagami-gun, Okinawa*

Purpose
It is challenging to predict the meningiomas' consistency presurgically (1-5). This study aims to measure the signal intensities (SIs) of T1-weighted image (T1WI) and T2-weighted image (T2WI), and diffusion tensor image (DTI) values, including mean diffusivity (MD), fractional anisotropy (FA), axial diffusivity (AD) and radial diffusivity (RD) of meningiomas, and to correlate them with meningiomas' consistency, in order to evaluate which measurements are more useful in predicting the meningiomas' consistency.
Materials and Methods
We retrospectively selected consecutive 69 meningiomas, which were resected at our institute between 2011and 2016. All cases underwent pre-operative MR examinations, including T1WI, T2WI and DTI. A neurosurgeon evaluated the consistency of meningioma as soft or hard, according to whether the meningioma was resected by suction probe only. Two observers, who were blinded to the consistency, contoured meningiomas on T2WI in consensus, to generate the regions of interest (ROIs) of meningiomas. The ROIs of pons also were generated to calculate T1 and T2 SI ratios of meningioma to pons. T1WI and DTI maps were linearly registered to T2WI, so that the generated ROIs were applied to all images in each case. We measured minimum, maximum, mean and median values of all parameters and compared them between soft and hard groups using nonparametric test. The diagnostic performance was evaluated by receiver operating characteristic curve (ROC) analysis.
Results
Thirty-three meningiomas were defined as soft. Minimum, median and mean T2 SI ratios were significantly higher in soft meningiomas ($p = 0.002$, 0.002 and 0.008, respectively). None of the other measurements showed the significant difference (p values > 0.52). Receiver operating characteristic (ROC) curves for T2 SI rations in predicting soft meningiomas are shown in the figure. AUC values in minimum, median and mean T2 SI rations were 0.71, 0.71 and 0.69, respectively.
Conclusions
A quantitative assessment using conventional T2WI may be more useful in predicting the consistency of meningioma than DTI indices.



(Filename: TCT_O-83_ROC_t2.jpg)

O-84

3:46PM - 3:54PM

Imperfection of Dynamic Susceptibility Contrast Perfusion-Weighted Imaging (DSC-PWI) Time-Intensity Curve in Differentiating Typical from Atypical Meningioma.

S Hussain[1], k Sandougah[2], H AlKhalidi[2], I Alorainy[3]
[1]King Saud University, Riyadh, Central Province, [2]King Saud University, Riyadh, Riyadh, [3]King Saud University, Riyadh, Saudi Arabia

Purpose
Differentiation of typical from atypical meningioma often is a difficult task on conventional MR sequences. Histopathologic differentiation is based on vascular pattern, necrosis, mitoses and cellularity. MR perfusion has been used to examine tumor vascularity, however, previous studies showed significant overlap in rCBV values between typical and atypical

meningiomas. We explored the possibility of differentiating the 2 types of meningioma using various parameters of DSC-PWI time-intensity curve.

Materials and Methods

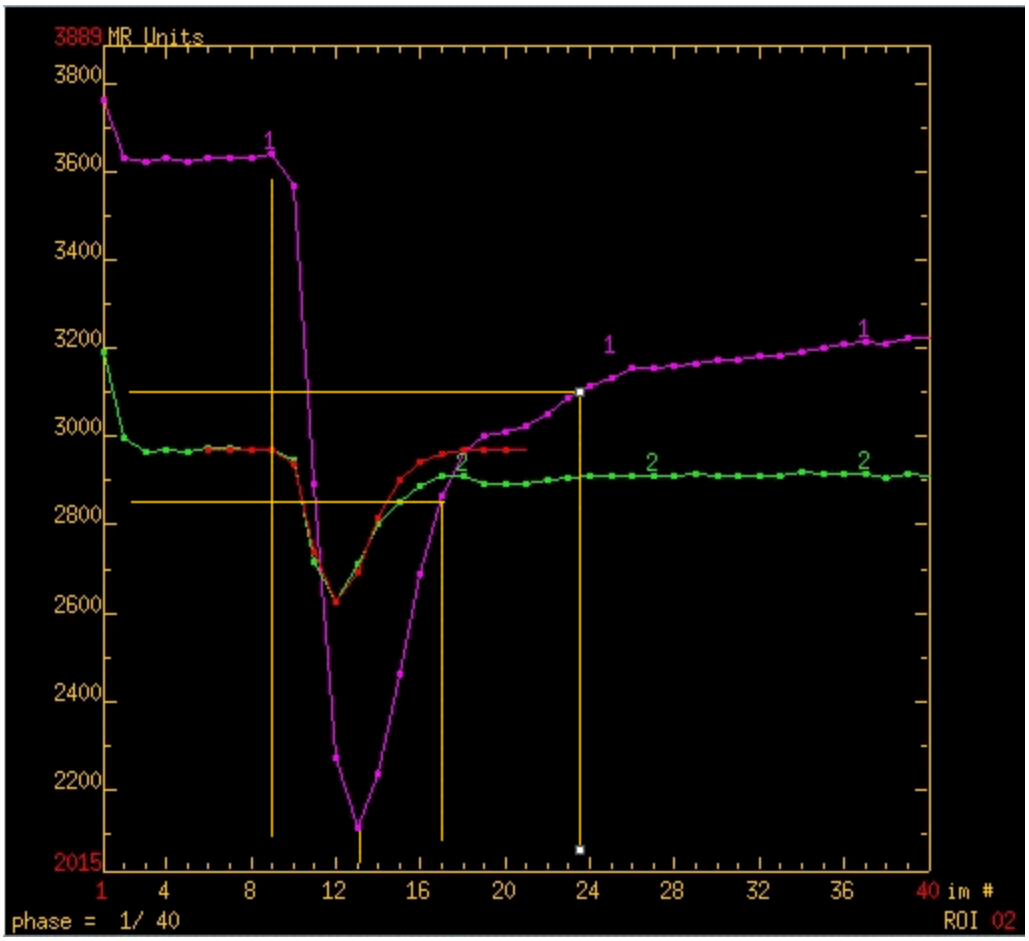
This is a retrospective cross-sectional study of histopathologically-proven typical and atypical meningiomas at a University hospital from October 2010 to June 2015. We analyzed cerebral blood volume (rCBV) maps and time-intensity curves of tumors on DSC-PWI and compared both types of meningioma. Time-intensity curves were used to calculate percentage of signal intensity recovery (SIR) and time to peak (TTP). T- test was used for significance. See figure attached (here is explanation). Time intensity curve with time on x-axis and intensity on y-axis is shown for an atypical meningioma. Each number on x-axis represents 3 seconds as total 40 volumes were acquired over 120 seconds. The initial flat curve indicates images acquired before the arrival of bolus (precontrast images). A very brief dip of the curve before this flat curve is likely due to technical reasons. There is brisk drop of signal intensity after arrival of bolus of contrast, from frame # 9 – 13 representing TTP of 12 seconds. This is immediately followed by a similarly brisk phase of signal intensity recovery from frames # 13 – 19 (18 seconds) in early phase with 50% SIR occurring over 12 seconds during frames # 13 – 17. This is followed by very slow further SIR that continued throughout the time data were being collected. However, the intensity did not return back to baseline. Total SIR at frame # 40 representing 80 seconds after peak drop was about 75%. Note that the curve for white matter shows slower and less remarkable downward and upward slopes, with signal recovering nearly completely back to baseline in about 20 seconds. 1 - Purple – meningioma. 2 - Green – white matter.

Results

A total of 25 typical and 10 atypical meningiomas were included. Mean rCBV value was 11.7 for typical meningiomas and 9.2 for atypical meningiomas. Mean percentage of SIR for atypical meningiomas at 10, 20, 30, 40 and 80 seconds was 49, 64, 71, 77 and 82, respectively. Values obtained for typical meningiomas showed no significant difference. Mean TTP value was 10.8 seconds for atypical meningiomas and 9.5 seconds for typical meningiomas with no statistically significant difference.

Conclusions

Dynamic susceptibility contrast perfusion data cannot reliably differentiate typical from atypical meningioma using SIR and TTP from time intensity curve.



(Filename: TCT_O-84_figure.gif)

O-85

3:54PM - 4:02PM

Incidence and volume of acute post-operative hemorrhage after resection of grade 1 vs. grade 2 meningiomas

O Shearkhani[1], S Symons[2], A Chan[1], P Maralani[2]
[1]University of Toronto, Toronto, Ontario, [2]Sunnybrook Health Sciences Centre, Toronto, Ontario

Purpose
Meningiomas form 13–30% of primary intracranial neoplasms, making them the second most common only after gliomas. Of those, 90% are classified by the World Health Organization (WHO) as Grade I (Gr1), defined as benign tumors without atypia or mitosis, and 5–7% are Grade II (Gr2), defined as tumors with rare mitosis or some cellular atypia. Although various treatment options are available, the most common primary management of meningiomas is surgical resection as over 90% of cases are benign and can be removed completely. Acute hematoma (AH) is a common imaging finding after resection of

meningioma. Postoperative hematoma (POH) is a subset of AH that requires surgical evacuation, and is the most significant risk factor for increased morbidity and mortality in these cases. Two previous studies did not identify differences in POH rate among histological subtypes of meningiomas. In regards to clinical decision making, however, the meningioma WHO grading is more important than their architectural pattern. Furthermore, it is unclear whether the recent WHO changes to diagnosis criteria of Gr2 meningioma tumors - where brain invasion is now a sufficient criterion for diagnosing atypical Gr2 meningioma - would have an effect on previous studies. Moreover, the literature lacks studies that have assessed differences in intracranial AH volume on postsurgical resection scans based on meningioma tumor grade. Tumor grade usually is unknown at the time of surgery but this information potentially can affect postoperative care on cases with known recurrent grade 2 meningioma or primary radiation-induced meningiomas that usually are of higher grade. Therefore, the objective in this study was to assess the differences between Gr1 and Gr2 meningiomas in POH rate and AH volume on post-surgical resection CT scan.

Materials and Methods

All cases of Gr1 and Gr2 meningiomas that underwent surgical resection and had both pre- and postoperative scans during a 24-month timeframe (June 2014 and June 2016) immediately prior to initiation of our data collection were retrieved from the PACS at our institution. To investigate AH volume, postoperative scans were limited to those obtained less than 24 hours after surgery. Computed tomography (CT) scans were performed as routine protocol with the following parameters: slice thickness 5 mm, 0.3 mm gap, 4i mode, diagonal field of view 25 cm, matrix 512 x 512, kV=120, mA=280–300. Regions of interest (ROIs) were drawn manually around the tumor on pre-operative images and around the AH on postoperative images by a neuroradiologist blinded to tumor grade. A Matlab (MathWorks Inc., Natick, MA) code was used to analyze ROIs and calculate tumor and AH volumes, based on number of voxels and their volume. In order to restrict analysis to acute hemorrhagic material, only voxels with Hounsfield unit of 55–75 were counted. Our institution's Electronic Medical Records wee searched to identify the tumor WHO grade and histological subtype, based on their associated pathology reports. Furthermore, as either brain invasion or a mitotic rate greater than or equal to 4 alone are sufficient to classify the neoplasm as Gr2, we collected tumors' maximum mitotic rate and presence/absence of brain invasion to assess their potential effect on AH volume. Other relevant information such as patients' demographics, and number of POH events were collected. Our final patient cohort consisted of 48 patients, 34 with Gr1 and 14 with Gr2 meningiomas. For more accurate comparison of Gr1 and Gr2 groups, Gr2 cases were matched to the Gr1 cases based on previously reported factors associated with increased POH rate after surgical resection of meningiomas: the patient's age, as well as platelet count and prothrombin time immediately after surgery.

Results

Postoperative hematoma rate and AH volume in the Gr2 group was higher than the Gr1 group (p-value = 0.024 and < 0.001, respectively). There were no differences between

groups' tumor volumes or between AH volumes based on tumors' maximum mitotic rate (p-value = 0.917 and 0.229, respectively). Compared to Gr1 tumors, AH volume was similar in Gr2 tumors without brain invasion (p-value > 0.999), but higher in Gr2 tumors with brain invasion (p-value = 0.039).

Conclusions

Here, we have demonstrated the potential effect of meningioma tumor grade and presence of brain invasion on AH volume on postoperative scan and POH rates. Determination of meningioma grade and brain invasion is not done at the time of frozen section, and it has been demonstrated that it is difficult to separate Gr1 from Gr2 meningioma on crush preparation during frozen section. However, awareness of these factors can be useful at the time of surgery for recurrent tumors, as knowledge that Gr2 meningiomas have higher risk of POH may prompt more rigorous imaging and clinical follow-up.

Feature		Grade I (n=5)	Grade II Without Invasion (n=3)		Grade II With Invasion (n=3)	
		Value	Value	p-value	Value	p-value
Tumour Volume (mm^3)						
	Average	19181.01 ± 13589.22	34193.05 ± 23622.71		23963.83 ± 11253.72	
	Median	14737.01	21962.17	0.67	21305.06	>0.999
Age (days)						
	Average	66.62 ± 9.20	49.68 ± 12.94		74.38 ± 6.03	
	Median	61.70	45.24	0.47	76.49	0.757
Platelet Count						
	Average	202.2 ± 67.35	236.67 ± 27.39		210.71 ± 46.11	
	Median	194	254	0.473	198	0.757
Prothrombin Time						
	Average	0.98 ± 0.08	1.07 ± 0.06		0.97 ± 0.04	
	Median	0.99	1.11	0.243	0.97	>0.999
POH Volume (mm^3)						
	Average	116.58 ± 112.69	183.98 ± 236.16		5495.69 ± 4578.13	
	Median	100.14	34.57	>0.999	2502.17	0.039

(Filename: TCT_O-85_Table4.jpg)

O-86

4:02PM - 4:10PM

Radiologic Differential Diagnosis between Typical and Atypical Meningiomas: Added Value of Non-Model Based Dynamic Contrast Enhanced (DCE) MRI

K Ahn[1], J Jang[2], H Choi[2], S Jung[2]

[1]Seoul St. Mary's Hospital, The Catholic University of Korea, Seoul, Korea, Republic of, [2]Seoul St. Mary's Hospital, The Catholic University of Korea, Seoul, IA

Purpose

Predicting the histological grade of meningiomas has important clinical significance because high-grade meningiomas have a poorer prognosis, and they frequently require additional treatment, including postoperative adjuvant radiotherapy. Our purpose was to assess whether there are different characteristics of typical and atypical meningiomas visible on MR images and to determine the added value of non-model based DCE MRI when differentiating between typical and atypical meningiomas.

Materials and Methods
A total of 81 patients with meningioma were divided into training (64 patients: typical 35, atypical 29 patients) and test (total 17 patients) sets. Two radiologists evaluated tumors in terms of size, heterogeneity in signal intensities, peri-tumoral edema, necrotic or cystic changes, lobulation contour, interface irregularity and invasion into bone or large sinuses. As functional studies, DSC, DCE, and diffusion MRI were performed. The ability to discriminate between the 2 entities was evaluated using multivariate analysis and receiver operating characteristic (ROC) curve analysis.
Results
Presence of interface irregularities (p=0.023), necrotic or cystic changes (P = 0.048), and increased time to peak (P = 0.002) from non-model based DCE MRI were independent variables for discrimination of atypical from typical meningiomas. The area under the curve (AUC) value of the combination of 2 parameters (interface irregularities and necrotic or cystic changes) was 0.796 on ROC curve analysis. The combination of all 3 parameters including time to peak further increased diagnostic performance (AUC = 0.881). Comparison test of the 2 AUCs revealed the 2 compared areas are significantly different (P = 0.0474). In the test set, the diagnostic accuracy was improved by using time to peak and was significant (P = 0.001).
Conclusions
In differentiating atypical from typical meningiomas, the presence of interface irregularities, necrotic or cystic changes, and increased time to peak were diagnostically accurate and the time to peak calculated from DCE MRI could be a supportive tool.

O-88

4:18PM - 4:26PM

3D guided direct puncture therapeutic embolization of intracranial tumors

J Caroff[1], l spelle[2]
[1]Hôpital Bicêtre, Le Kremlin Bicêtre, France, [2]Hôpital Bicêtre, Le Kremlin-Bicêtre, Ile de France

Purpose
To assess the feasibility, safety, efficacy, and advantages over the traditional transarterial route (1, 2, 3), of using 3D DSA-guided direct puncture to pre-operatively devascularize intracranial lesions in particular clinical situations, paying special attention to any correlation with surgical observations. Direct punctures of intracranial tumors rarely have been described in the literature (4, 5); we present here the largest series to date.
Materials and Methods
Between July 2015 and July 2016, data from all presurgical embolizations performed in our institution were collected prospectively. Information on tumor type, location, size, eventual

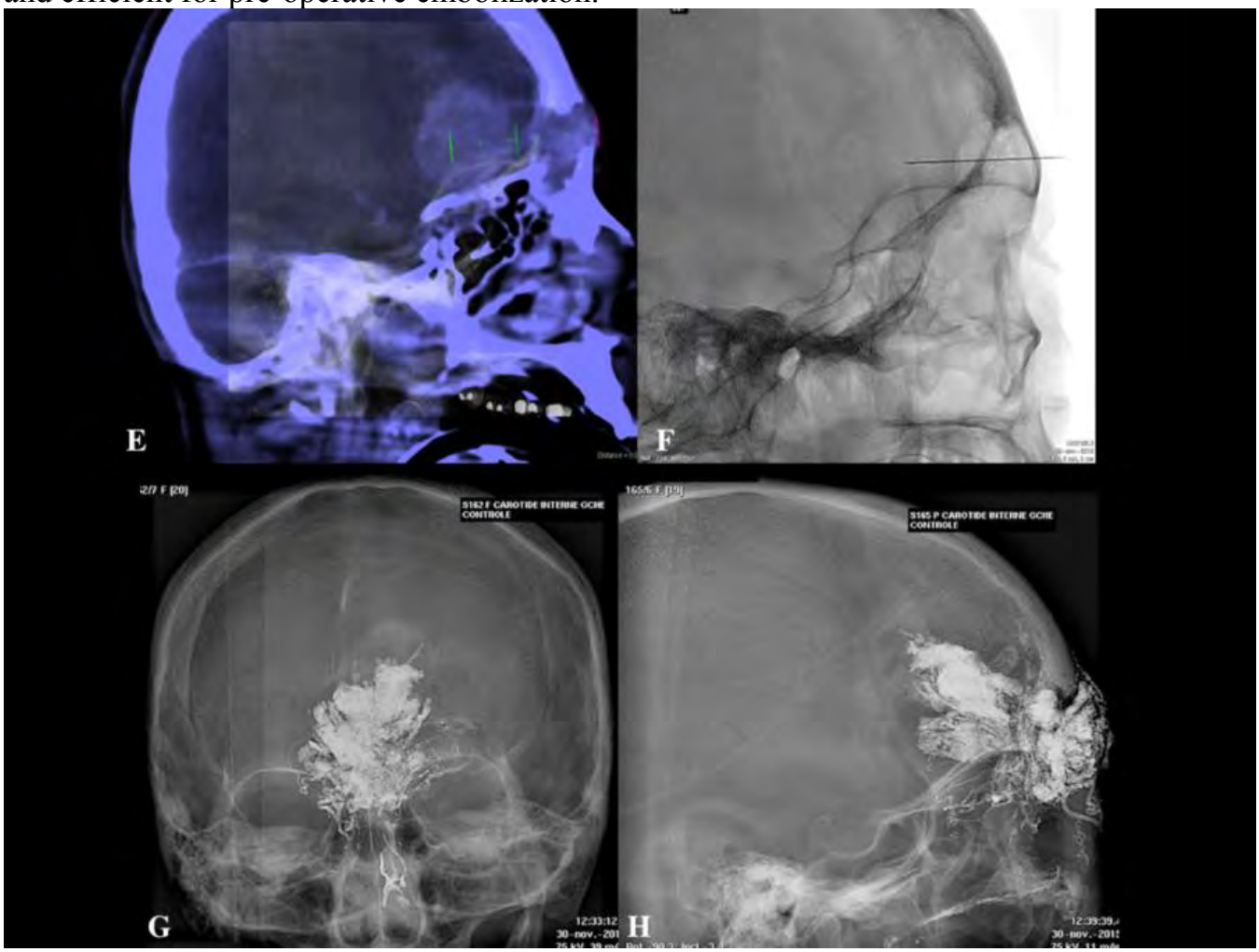
bone erosion, complications, devascularization percentage, and estimated blood loss was analyzed.

Results

Tumors of 4 patients (2 meningioma, 2 endolymphatic sac tumor) were embolized using direct puncture. 3D XperGuide planning software was used in all procedures. Embolization was feasible in all cases. In 1 case, a small craniotomy was performed specifically to allow needle positioning. In all cases n-butyl cyanoacrylate was used. No ischemic or hemorrhagic complications related to embolization occurred. Complete or near complete devascularization was obtained in all cases. In 1 case, surgery was not performed and the patient was monitored. Resection was complete without significant blood loss in 2 cases, and resection was incomplete but satisfactory in 1 case.

Conclusions

In selected cases, 3D-guided direct puncture of intracranial tumors appeared safe, feasible, and efficient for pre-operative embolization.



(Filename: TCT_O-88_Sanstitre001.jpg)

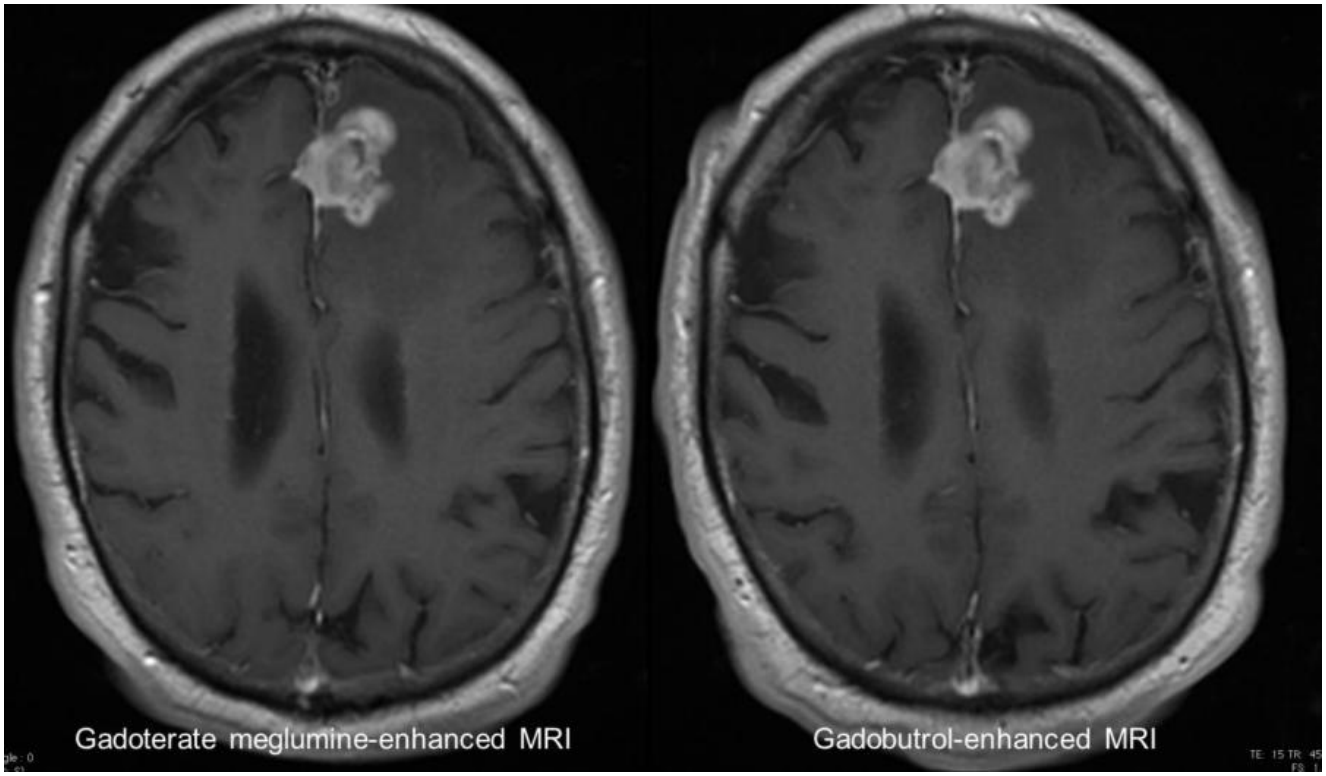
O-89

4:26PM - 4:34PM

Comparison of gadoterate meglumine and gadobutrol in MRI diagnosis of brain tumors: a double-blind randomized intra-individually controlled in cross-over study (the REMIND study)

D Roberts[1]
[1]*Medical University of South Carolina, Charleston, SC*

Purpose
To demonstrate the noninferiority of gadoterate meglumine (Dotarem®, Guerbet, France) vs. gadobutrol (Gadovist®/Gadavist®, Bayer, Germany/New Jersey, United States) in MRI diagnosis of primary intracranial tumors.
Materials and Methods
This double-blind, randomized, controlled, intra-individual, cross-over, study included 279 patients. The primary endpoint was overall lesion visualization and characterization, assessed by 3 independent off-site neuroradiologists on a 4-point scale ranging from "poor" to "excellent". Secondary endpoints were related to efficacy (qualitative criteria and quantitative signal intensity measurements) and safety (adverse events). Contrast agents were assessed with 2 identical MRIs (dose: 0.1 mmol/kg) at a time interval of 2 to 14 days.
Results
Mean (±SD) age was 53.6±15.1 years (range: 18-98 years); 64.2% of patients were female. Most frequent diagnoses at previous imaging prior to inclusion were meningioma (49.3%) and glioma (14.9%). Overall lesion visualization and characterization was "good" or "excellent" in more than 90% of patients for all 3 readers and noninferiority of gadoterate meglumine vs. gadobutrol was demonstrated statistically. No significant differences were observed between the 2 contrast agents regarding lesion border delineation, internal morphology and degree of contrast enhancement. Quantitative mean percentage enhancement was on average 14% higher with gadobutrol ($p<0.001$). Diagnostic confidence was high or excellent for the 3 readers in >81% of the patients with both contrast agents. The good safety profile was confirmed with similar percentages of patients with postinjection adverse events related to contrast agents (7.8% related to gadoterate meglumine vs. 7.3% related to gadobutrol). No serious adverse reactions were encountered.
Conclusions
Noninferiority of gadoterate meglumine vs. gadobutrol in MRI diagnosis of brain tumors was demonstrated. Although quantitative signal intensity measurements showed a small difference in favor of gadobutrol, this did not result in any clinical benefit since no differences were demonstrated for overall diagnostic evaluation of the images for any of the blinded readers.



(Filename: TCT_O-89_RemindFigure.jpg)

O-90

4:34PM - 4:42PM

MRI-based Fractal Analysis and Diffusion-weighted Imaging for Pre-operative Prediction of Atypical Meningiomas

C Filippi[1], A Demopoulos[2], R Goyal[2], J Li[2], J Steinklein[3], B Pramanik[1], M Schulder[2], J Boockvar[4], M Czyz[5]
[1]Hofstra Northwell School of Medicine, New York, NY, [2]Hofstra Northwell School of Medicine, Manhasset, NY, [3]Lenox Hill Hospital, New York, NY, [4]North Shore-LIJ Health System, New York, NY, [5]Notthingham University Hospital-NHS, Nottingham, none

Purpose
Fractal geometric analysis of MR images is an emerging tool for a more quantitative analysis of imaging features. There is no reliable way to objectively predict meningioma grade pre-operatively although research has suggested that mean diffusivity from diffusion-weighted imaging may identify atypical and/or malignant meningioma pre-operatively. The purpose of this study was to use fractal MR analysis and diffusion-weighted imaging to differentiate WHO I benign meningiomas from atypical WHO II meningiomas.
Materials and Methods
Twenty-seven patients diagnosed with atypical meningioma (WHO II) and 27 patients diagnosed with typical, benign meningioma (WHO I) were recruited from institutional

database and retrospectively analyzed (total of 54 patients (34 female, 20 male, mean age 62 +/- 15 years). All patients had standard contrast-enhanced pre-operative brain MR exams including diffusion-weighted imaging. Mean diffusivity was quantified for the tumor core using GE Functool and Philips Extended Brilliance Workstations. Fractal analysis with box-count method was performed on the postcontrast images to determine average (FDa) and maximum (FDm) fractal dimension of the enhancing portions of the tumor, and Image J1.49 software was used for MR fractal analysis.
Results
Ki-67 was significantly higher in atypical meningioma group (10.0, interquartile range or IQR 7.0) than the benign group (3.0, IQR 3.0) ($p < .0001$). Both the FDa and FDm were significantly higher in the atypical groups ($p < .0001$) and correlated with the Ki-67 index. Mean diffusivity quantified from the apparent diffusion coefficient (ADC) maps did not differ significantly from these 2 groups. Isointensity of signal qualitatively was significantly associated with benign WHO I meningiomas (odds ratio 0.17; 95% CI .44-.62, $p < .008$). Multivariate regression model using MR fractal analysis and DWI isointensity reached significance, $P = .001$ and AUC 0.87 (95% CI 0.74-0.94). The maximum fractal dimension, FDm, > 1.31 was a significant predictor of atypical WHO II meningioma (OR 12.30, $p < .02$). Mean diffusivity and signal characteristics on DWI were not confirmed to be reliable predictors of atypical meningioma.
Conclusions
Tumor fractal dimension analysis on pre-operative MR reliably correlates with atypical WHO II meningioma. Mean diffusivity from ADC maps does not reliably distinguish WHO I from WHO II meningioma but qualitative isointensity of signal correlates with the benign phenotype of WHO I meningioma.

Monday
3:30PM - 4:45PM
Long Beach Convention Center, Room 102BC (Main Level)

06H-Parallel Paper Session: TURBO & TOUR: Evaluating Headaches...and Avoiding Them in Practice!

T-16

3:33PM - 3:36PM

Keeping Up with the Ever Expanding Practice

M Wong[1], M Borja[2], M Hagiwara[2], J Sanger[2], Y Lui[3]
[1]New York University Langone Medical Center, New York, NY, [2]NYU Langone Medical Center, New York, NY, [3]NYU School of Medicine, New York City, NY

Purpose
As practices and institutions grow larger and more complex, the more documents, emails,

and calendars accumulate. Individuals may find themselves utilizing multiple various means and resources to gather the much needed but basic information for their own day-to-day tasks and navigating through the overabundance of information may become inefficient and cumbersome. With the complex structuring in our academic center, a centrally organized system that adheres to HIPAA requirements to address this challenge is optimal. Here we describe our pilot experience creating and implementing a safe, tailored and dynamic intranet resource within the neuroradiology section of a busy urban academic practice, aggregating relevant information from multiple existing systems, presenting needed information to individuals in a user-friendly format.

Materials and Methods

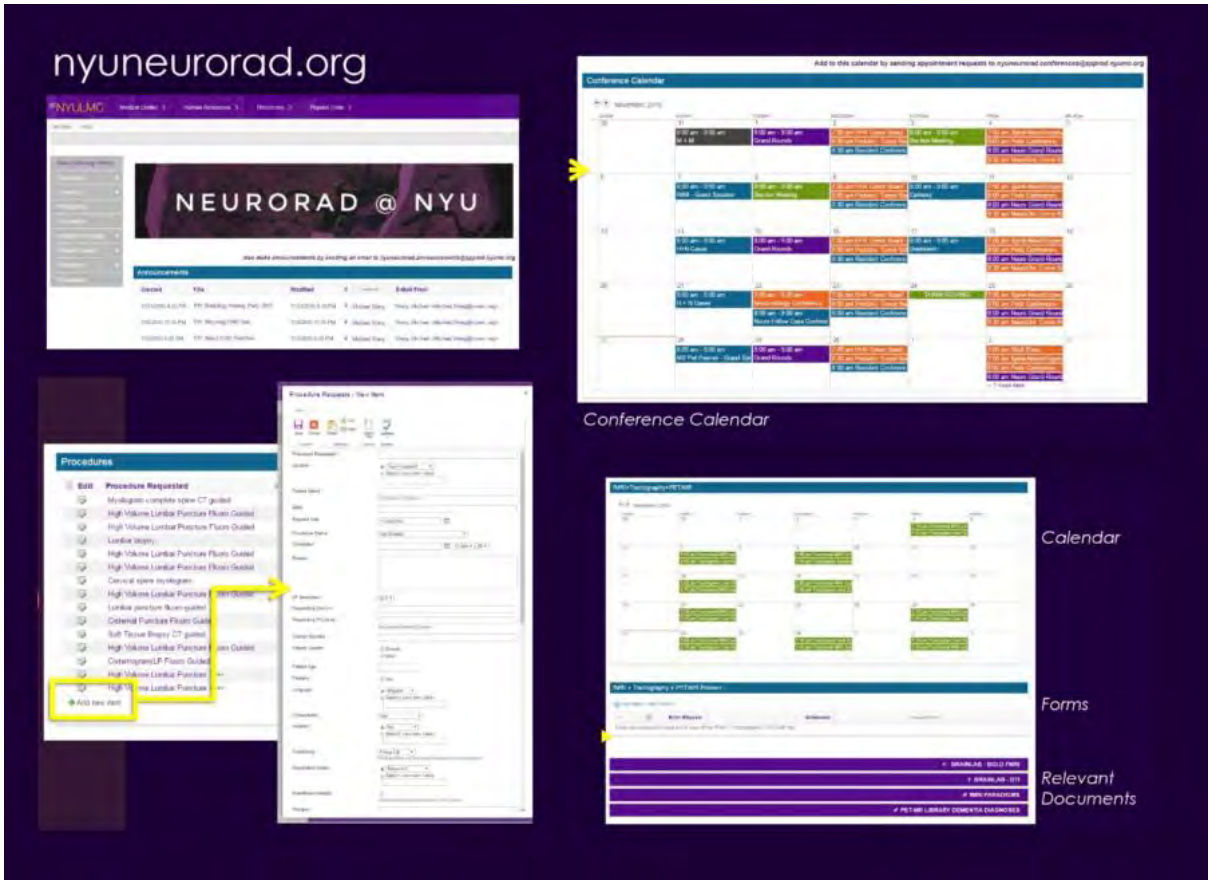
Existing methods for extracting important information for attending and fellow neuroradiologist workflow were compiled. Consideration of HIPAA compliance was made. An intranetwork community site under an existing Microsoft SharePoint 3.0 environment (Redmond, Washington) provided by the information technology (IT) department was constructed in keeping with institutional guidelines. Information extracted from multiple existing systems include schedules, contact information, description of protocols, procedures planning, advanced imaging schedules, conference calendars and postprocessing analysis methodology guides.

Results

Schedules for attending and fellow clinical coverage, upcoming inpatient and outpatient procedures, fetal MRI studies, and functional brain mapping studies encompassing 4 hospitals and 16 outpatient imaging sites were prioritized and incorporated in the site as a main feature. Additional tools included centralized planning of imaging-guided procedures and hosting up-to-date contact information, references documents, educational material, and links to various other resources. The positive features of an intranetwork site provided at our institution include 1) out-of-network accessibility by means of individual account login requirements and virtual private network (VPN) encryption, 2) control of user accessibility within the network, 3) familiar format uniformity for easier navigation, 4) medical center IT support and 5) integration with Microsoft Office services. Limitations include 1) slower network speeds, 2) the requirement for VPN login to access site contents, and 3) restrictions implemented by the institutional IT department.

Conclusions

Here we demonstrate the potential and feasibility of creating an intranetwork web-based site to centralize supportive information for our radiologists and staff that is tailored and dynamic, providing a one-stop-shop for critical practice information that implements itself seamlessly into existing departmental workflow all while maintaining privacy and security.



(Filename: TCT_T-16_ASNR.jpg)

T-17

3:36PM - 3:39PM

Radiology as a Champion in Efforts in Realizing a Culture Change in Patient and Referring Clinician Access in a Large Academic Medical Center Through Development of a Successful Comprehensive Centralized Scheduling Department

T Donovan[1], J Gross[2], S Osborn[1], C Harvey[1], S Williams[3], J Bisanti[1], D Moore[4], M Keiper[5]
[1]University of Nebraska Medical Center, Omaha, NE, [2]University of Nebraska, Omaha, NE, [3]University of Nebraska Medical Center, omaha, NE, [4]Unmc, Omaha, NE, [5]UNMC, Omaha, NE

Purpose
To demonstrate a radiology department's role as an expert and champion in the development, implementation and success of a centralized scheduling call center in a large academic medical center.
Materials and Methods
Radiology has a unique perspective and expertise with high volume patient scheduling and the application of protocols erasing barriers to patient and referring clinician access. By

demonstrating this expertise in a large medical center, a radiology department may apply this knowledge and become a key leader in developing a successful centralized scheduling department for a more comprehensive list of specialties. Alternative staffing models, streamlined scheduling processes, and application of customer first service initiatives will be discussed as some of the value-added approaches well known to radiology that can be applied to a more comprehensive centralized call center. Established call center indicators including abandoned call rates, time to answer and overall talk time as well as referring clinician and patient satisfaction surveys were followed before and after interventions to assess for change.

Results

Radiology leadership was successful in recommending and implementing alternative staffing models utilizing medical assistants as an alternative to nursing staff for medical center scheduling. Scheduling processes also were streamlined by reducing excessive requirements for scheduling, limiting follow-up phone calls and inquiries to referring clinician offices and patients and reducing the steps necessary in scheduling an event in the medical center electronic health record. In addition, a new culture of a customer service first approach to scheduling was instilled through mini-retreats and strategic movement of the scheduling department from the domain of the Revenue Cycle personnel to the domain of the Chief Experience Officer and Patient Access personnel. Implementing alternative staffing models, streamlining the scheduling processes, and shifting leadership to those individuals in radiology and the medical center with expertise in customer relations combined to effect a significant improvement in call center parameters and customer satisfaction surveys. Abandoned call rates decreased from 12% to below 4%, overall talk times decreased from 180 seconds to 100 seconds and time to answer decreased from 66 seconds to below 30 seconds. Customer satisfaction surveys also improved with significant increase in responses in the highest category of "Very Good" after implementation of changes.

Conclusions

Radiology is in a unique position to effect change in patient and referring clinician access to an academic medical center through knowledge and expertise applied to the development of a customer centric medical center scheduling department. These changes may be successful in improving call center metrics and patient and referring clinician satisfaction with access and use of the services of a large academic medical center.

T-18

3:39PM - 3:42PM

Delivering the Message to a Large Academic Medical Center: Portable Tablet Surveys to Outside Referring Clinicians are Effective in Identifying Service Barriers and Ultimately Increasing Referrals from this Valuable Source

T Donovan[1], J Gross[2], S Osborn[1], C Harvey[1], S Williams[3], J Bisanti[1], D Moore[4], M Keiper[5]

[1]University of Nebraska Medical Center, Omaha, NE, [2]University of Nebraska, Omaha, NE, [3]University of Nebraska Medical Center, omaha, NE, [4]Unmc, Omaha, NE, [5]UNMC, Omaha, NE

Purpose

To determine the feasibility and utility of using portable tablet surveys for referring clinicians outside of the health system of a large academic radiology department in order to engage outside referring clinicians and increase radiology referrals.

Materials and Methods

A portable tablet-based survey was developed for referring clinicians who were outside of the healthcare system of a large academic radiology department. The questions on the survey were developed to investigate the success of delivery of radiology services to outside referral sources in order to improve radiology referrals from this source. A tablet survey was utilized in order to increase the response rate of outside referring clinicians over traditional mail and web-based surveys. A radiology physician liaison traveled to outside referring clinician offices as a part of a normal schedule of sales and marketing office visits. At the time of the visits, the physician liaison offered a survey on a tablet that was submitted by the referring clinician to a web server anonymously. Surveys were distributed for a 1-month period and compared with average monthly submissions utilizing the traditional method of survey distribution.

Results

In a 1-month period, 57 tablet-based surveys were submitted anonymously by outside referring clinicians. This is in contrast to 6 surveys per month average submitted via the traditional method. The surveys identified substantive service issues creating barriers for outside referring clinician referrals. This consisted primarily of institutional requirements for exam scheduling and pre-authorization that were burdensome to outside physician offices. Subsequently significant changes in policy in the scheduling call center and pre-authorization department were instituted. Within 1 month of the instituted changes, the academic radiology department received referrals from 67 new outside clinicians, thereby doubling outside referral revenue for that time period.

Conclusions

Tablet directed surveys of outside referring clinicians are a more effective tool for accumulating business intelligence than traditional mail or web-based survey tools. Given the increase in survey response rates, a more representative sample of potential issues in substandard service delivery may be identified, allowing the academic radiology department to improve service and engage outside referring clinicians and thereby increase outside imaging referrals.

T-19

3:42PM - 3:45PM

Advanced Imaging in the Evaluation of Headache in the Emergency Department: When is it Appropriate After a Negative Head CT?

M Lanfranchi[1], K Buch[2], R Hakimelahi[2], P Schaefer[2]
[1]Massachusetts General Hospital, Boston , MA, [2]Massachusetts General Hospital, Boston, MA

Purpose
To investigate the diagnostic value of advanced imaging (MRI/MRA and CTA) in the emergency department (ED) evaluation of nontraumatic headache after a negative nonenhanced head CT (NECT), and to determine if any clinical factors may predict its utility in this patient population.
Materials and Methods
This is an ongoing study with active data collection. To date, we have reviewed the neuroimaging studies and clinical data in the electronic medical records of 101 consecutive patients presenting to our ED with headache during a 14-month period. Acute abnormalities on all modalities were recorded. Clinical data were extracted from the medical record. Descriptive statistics and Fisher's exact test were performed.
Results
A total of 143 imaging studies were performed on the 101 patients. Eighteen patients had positive findings on NECT, including mass lesions and intracranial hemorrhage. The remaining 83 patients (82%) had negative NECTs, 26 (31%) of which underwent advanced imaging, including 9 CTA, 17 MRI and 9 MRA. Only 1 (3.8%) had a positive acute finding (1 case with embolic infarcts). Two had small, incidental unruptured aneurysms. There was no statistically significant difference between patients with and without advanced imaging in age, gender, sinus disease, vision changes, systolic blood pressure >180, history of malignancy, migraine, or anticoagulation (Table 1). However, admission rate was marginally significantly higher among patients with advanced imaging ($p=0.044$).
Conclusions
Our preliminary results suggest those ED patients with nontraumatic headache and a negative NECT rarely benefit from emergent advanced imaging. In the 1 case with a positive acute finding on advanced imaging despite a negative NECT, the infarcts were not clearly responsible for the headache symptoms. Ongoing evaluation of more cases will be useful to determine which clinical characteristics are predictive of additional diagnostic value of advanced imaging in the ED.

Table 1

	All	No advanced imaging	Advanced imaging	P value
Negative head CT	82	56	26	0.015
Age (mean±SD)	53±20	54±22	53±17	0.86
Female	49 (60%)	33 (59%)	16 (61%)	1.0
Sinus disease	15 (18%)	11 (20%)	4 (15%)	0.76
Vision change	11 (13%)	9 (16%)	2 (8%)	0.49
SBP>180	4 (5%)	3 (5%)	1 (4%)	1.0
Malignancy	9 (11%)	4 (7%)	5 (19%)	0.13
Migraine	6 (7%)	6 (11%)	0 (0%)	0.17
Anticoagulation	4 (5%)	3 (5%0	1 (4%)	1.0
Admission	17 (21%)	8 (14%)	9 (35%)	0.044

Stats: Two tailed T-test and Fisher's exact test

(Filename: TCT_T-19_Table1.jpg)

T-20

3:45PM - 3:48PM

Headache Imaging in Children: When and How?

A Trofimova[1], K Kim[1], D Kishore[1], L Urquia[1], N Kadom[1]
[1]*Emory University, Atlanta, GA*

Purpose
Childhood headaches are a source of great parental and clinician concern regarding the possibility of an underlying brain neoplasm. It is very common therefore for children with headaches to undergo brain imaging. To protect children from radiation exposure, providers frequently order magnetic resonance imaging studies to evaluate children with headaches. The literature, however, has shown that the incidence of brain tumors in children and adolescents ages 3-20 years is only 4% and that all of these patients had abnormal clinical exams (1). Performing cross-sectional imaging studies in children can pose a significant burden to patients; for example, sedation may be necessary, or computed tomography may confer radiation exposure. Scientific data also suggest that there may be overuse of cross-

sectional imaging studies (2). Imaging utilization may be improved through adoption of clinical decision rules, such as the SNOOPY criteria (3) and use of imaging appropriateness criteria (4, 5). The purpose of this presentation is to review the SNOOPY criteria for pediatric headache imaging, list causes of secondary headaches in children, and discuss imaging options for emergent and nonemergent imaging.

Materials and Methods

The IRB designated this quality assurance review as exempt. We also performed a comprehensive Medline search for articles related to primary and secondary headache disorders in pediatric population using the PubMed search engine. The search was limited to English-language articles. Additional relevant articles were selected from the references of reviewed articles and published guidelines. We have used the following search criteria: frequency of specific primary or secondary headache disorders in pediatric population, associated significant clinical findings, clinical diagnostic algorithms, relevant imaging modalities or inappropriateness of imaging for a clinical diagnosis, special protocols/MRI sequences required to make a diagnosis.

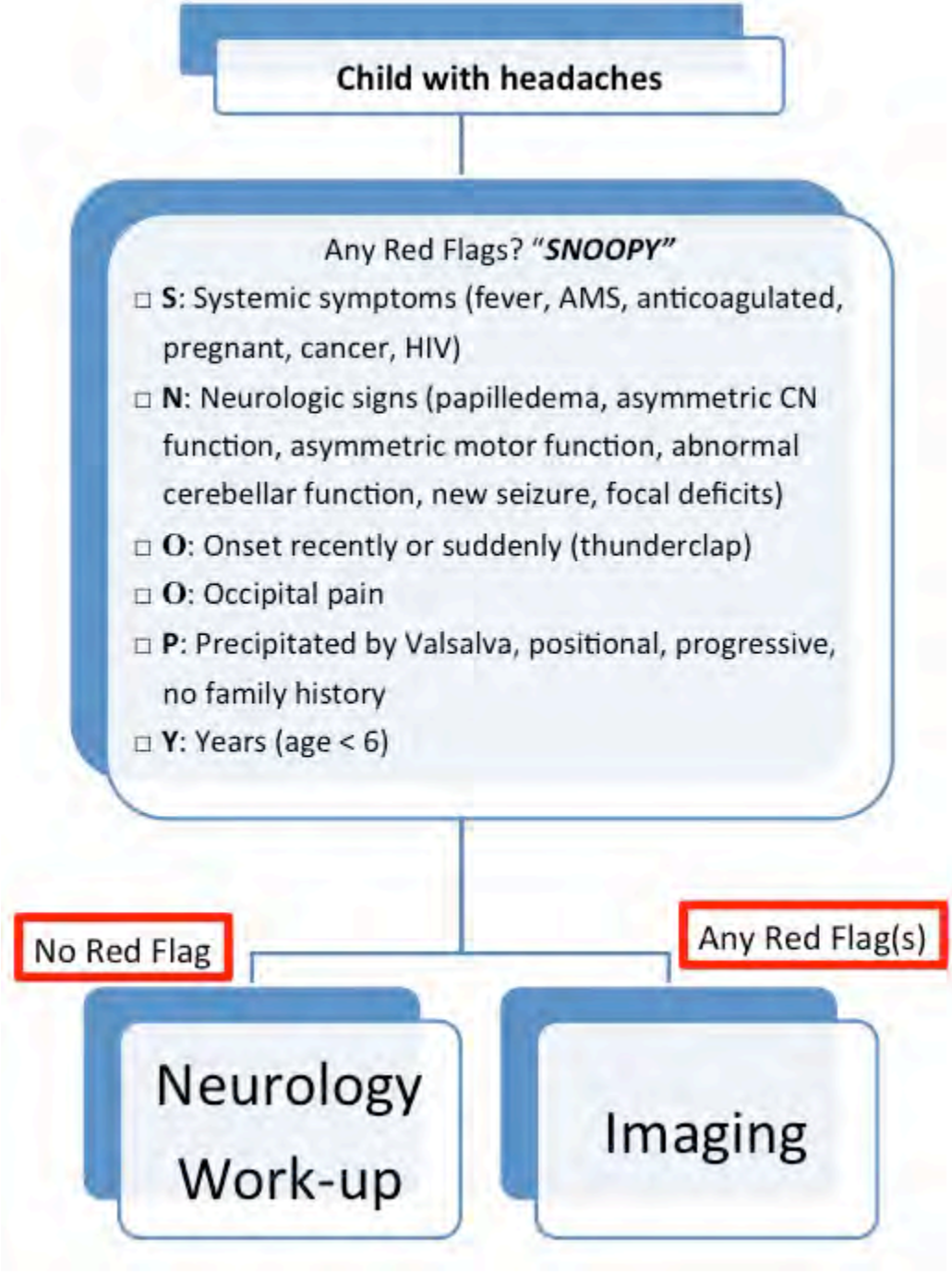
Results

In 2015 our institution performed 5989 brain MRI, 519 noncontrast head CTs, and 107 radiographs in children for headaches or migraine. A set of clinical criteria can help gauge the need for imaging work-up in children with headaches (Fig. 1). The criteria help determine whether a child has a primary headache (imaging work-up either not needed immediately) or a secondary headache (imaging indicated). The criteria can be remembered by the acronym "SNOOPY": Systemic symptoms (e.g. fever, altered mental status, cancer, HIV infection), Neurologic signs (e.g. papilledema, asymmetric cranial nerve function, asymmetric motor function, new seizure, focal exam findings), Onset (recent or sudden), Occipital pain, pattern (precipitated by Valsalva, positional, progressive, lack of parental headache history), Years (patient age <6 years). In the emergency setting CT imaging may be indicated in patients prior to undergoing a lumbar puncture, in patients who are shunted, in patients with suspected hemorrhage, and for suspected intracranial mass (ACR). Most acute etiologies of headaches are benign. Causes of nonemergent secondary headaches are manifold (Table 2, not submitted): Systemic infection, sinusitis, meningitis/encephalitis, inflammatory process (ADEM, CNS vasculitis), abnormal intracranial pressure (elevated and low), space occupying lesion, Chiari 1 malformation, stroke, spontaneous intracranial hemorrhage, venous sinus thrombosis, acute trauma, posttraumatic headache, substances causing headaches (illicit drug use, carbon monoxide poisoning, lead toxicity), metabolic derangements and endocrine disorders (fasting, sleep apnea, hypothyroidism, neuromuscular disorders), headaches of oro-maxillofacial origin.

Conclusions

Headache imaging plays a large role in pediatric neuroimaging. Utilization of imaging in the work up of pediatric headache can be optimized by promoting clinical decision rules, delineating best imaging pathways based on most likely underlying causes, and using

optimized MRI protocols, such as ultrafast sequences that may allow for imaging of the brain without sedation.



(Filename: TCT_T-20_SNOOPY.jpg)

T-21

3:48PM - 3:51PM

Issues with determining appropriateness of MR imaging in pediatric headache

K Kim[1], D Kishore[1], L Urquia[1], A Trofimova[1], N Kadom[1]
[1]*Emory University, Atlanta, GA*

Purpose

Many children presenting with headaches undergo MRI brain imaging at our institution, regardless of whether their headaches are primary or secondary headaches (1). Subjectively, many MRI studies for pediatric headache imaging at our institution have no significant findings, and the literature states a low rate of malignancies found in children with headaches (2). In addition, it is known that children with relevant imaging, such as brain tumors, usually have clinical symptoms besides headaches indicating that they have a secondary headache. In fact, there are well defined clinical criteria that can be used to guide the decision for imaging with children in headaches (1). Here, we analyzed MRI imaging studies performed for headaches and reviewed patients' medical histories for the SNOOPY criteria (1) to determine which patient had a primary or secondary headache. Our hypothesis was that most patients have a primary headache and therefore do not need to undergo imaging.

Materials and Methods

The IRB designated this quality assurance review as exempt. We searched our institution's database of radiology reports (Montage Health Solutions Inc., California, USA) for all studies of MRI brain without contrast performed between January 1, 2015 and December 31, 2015 that contained terms "Headache" and "Migraine" in the indication section. Of these, we accessed the medical records of 100 randomly selected patients and reviewed the clinical documents generated between 1 year before and 1year after the imaging for presence of any findings suggestive of a secondary headache using the SNOOPY criteria (1): Systemic symptoms (e.g. fever, altered mental status, cancer, HIV infection), beurologic signs (e.g. papilledema, asymmetric cranial nerve function, asymmetric motor function, new seizure, focal exam findings), Onset (recent or sudden), Occipital pain, Pattern (precipitated by Valsalva, positional, progressive, lack of parental headache history, family history of cerebral aneurysm), Years (patient age <6 years).

Results

We found that at our institution in 2015 we performed 5989 brain MRI in children with an indication of "Headache" or "Migraine". A random sample of 100 patients was analyzed further. This sample had 59 females and 41 males with a mean age of 11.9 years (ranging from 3-19 years). The majority of MRI studies was obtained as outpatient studies (n=92), followed by studies from the emergency room (n=4) and inpatient studies (n=4). Among the 100 patients whose medical records were retrieved, 48 patients (48%) did not have any clinical documentation, so we could not determine whether the SNOOPY criteria for secondary headaches were met. The remaining patients had at least 1 medical record entry. There were 52 patients (52%) who had a documentation of at least 1 SNOOPY criterion, justifying the imaging exam. There was family history of aneurysm reported for 5 patients, but all of them had at least one SNOOPY criterion documented. The MRI brain study was

normal in 68 patients (68%). Of the 32 patients with an imaging finding, 6 patients showed definitely attributable causes of headache (signs of hemiplegic migraine, signs of intracranial hypotension, venous sinus thrombosis, acute otitis); 17 cases had potential causes of headache (sinus disease, Chiari I, arachnoid cysts, NF1); and 9 cases had likely unrelated incidental findings (volume loss, heterotopia, developmental venous anomaly).
Conclusions
Our data assessment showed that, contrary to our subjective assessment, the majority (52%) of brain MRI studies for pediatric headache were indicated based on the SNOOPY criteria. There was, however, a considerable number of patients (48%) in whom we could not ascertain whether they met SNOOPY criteria because their medical records were inaccessible to us. The majority of imaging studies was normal (68%) and only in a small number (9%) did the imaging study offer a clear-cut etiology for the headaches. We conclude from our analysis that an initiative to document SNOOPY criteria in the medical record and/or on the MRI order form could be helpful to better assess the appropriateness of provider imaging ordering practices in the work-up of pediatric headache.

SNOOPY CRITERIA	Number of patients		
	Only 1 criterion	>1 criteria	Total
Systemic symptoms (e.g. fever, altered mental status, cancer, HIV infection)	4	3	7
Neurologic signs (e.g. papilledema, asymmetric cranial nerve function, asymmetric motor function, new seizure, focal exam findings)	8	6	14
Onset (recent or sudden)	7	9	16
Occipital pain	0	2	2
Pattern			
1. Precipitated by Valsalva/Positional	2	3	5
2. Progressive	3	7	10
3. Lack of parental headache history	0	2	2
Years (patient age <6 years)	2	3	5

(Filename: TCT_T-21_HeadacheMRI.jpg)

T-22

3:51PM - 3:54PM

Radiographs in Pediatric Headache

D Kishore[1], L Urquia[1], K Kim[1], A Trofimova[1], N Kadom[1]
[1]*Emory University, Atlanta, GA*

Purpose
Many children presenting with headaches undergo imaging at our institution. We observed that some children undergo inappropriate radiographic imaging for headaches. Our rationale

for determining whether radiographs were inappropriate is as follows: For primary headaches, imaging is not indicated. For secondary headaches, a cross-sectional imaging study should be obtained because intracranial pathologies are not detectable with radiographs (1). Sinus disease is diagnosed predominantly based on clinical criteria and should be worked up with cross-sectional imaging if the disease recurs or does not respond to medical treatments (2, 3). In this study, we assessed the number and types of radiographs obtained in children with headache or migraine as a basis for launching an improvement intervention.

Materials and Methods

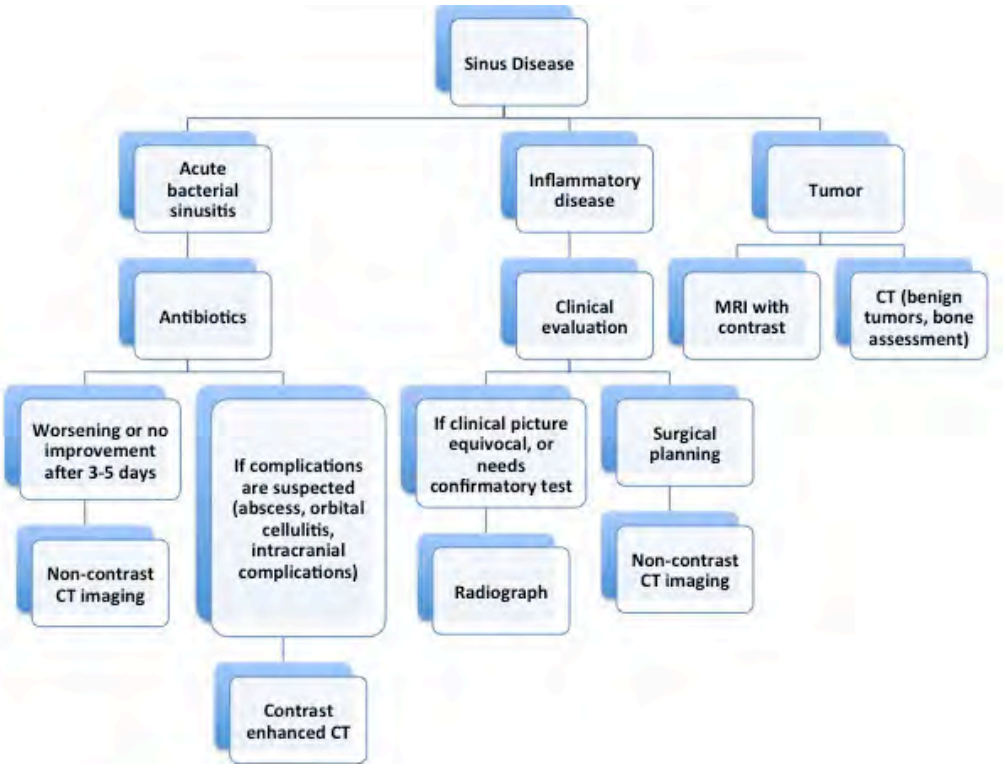
The IRB designated this quality assurance review as exempt. We searched for radiographs in children performed between January 1, 2015 and December 31, 2015 who had an indication of "headache" or "migraine" (Montage Health Solutions Inc., California, USA). We excluded patients with trauma, those under the age of 2 years, and shunted patients, as they probably met criteria for appropriate imaging. We included only radiographs of the head and neck. We assessed the frequency of each type of inappropriate imaging study.

Results

We found that, at our institution in 2015, we performed 107 radiographs for headaches and migraine in patients without trauma and patients who are not shunted. The majority of these imaging studies were radiographs of the sinuses (n=80, 75%), followed by skull radiographs (n=15, 14%), cervical radiographs (n=8, 7%), soft tissue neck films (3%), and facial bones (n=1, 1%).

Conclusions

Our data assessment shows that the majority of radiographs for headache in children at our institution are sinus radiographs. Recent diagnostic criteria for pediatric sinusitis work up strongly discourage the use of imaging for differentiating acute bacterial sinusitis from viral upper respiratory infection (2, 3). A possible intervention to improve imaging ordering practices at our institution could be a collaboration among the departments of pediatrics, otolaryngology, and emergency medicine to design an evidence-based clinical and imaging algorithm (see algorithm proposal in Fig. 1) for children with headaches and suspected sinus disease.



(Filename: TCT_T-22_SinusitisAlgorithm.jpg)

T-23

3:54PM - 3:57PM

Inappropriate Skull Radiographs in Pediatric Head Trauma Patients Older than Age Two Years

B Vey[1], K Applegate[2], P Sharp[1], N Kadom[1]
[1]Emory University, Atlanta, GA, [2]Emory University and Children's of Atlanta, Atlanta, GA

Purpose
The scientific literature has proposed several clinical guidelines to aid in decisions regarding the need for initial imaging in acute pediatric head trauma. These guidelines are the CHALICE rule from 2006 (1), the CATCH rule from 2010 (2) and the PECARN rule from 2014 (3). The imaging modality of choice is a noncontrast head CT. There may be a role for skull radiographs in children under 2 years of age, but not in older children (4). Magnetic resonance imaging (MRI) is currently not yet established as an initial imaging evaluation. Here, we assessed how frequently skull radiographs were ordered inappropriately across our pediatric health care network in children with head trauma over the age of 2 years between 2012 and 2015 and whether the implementation of the PECARN clinical criteria in 2014 had any effect on ordering practices.
Materials and Methods
The study was performed at a dedicated academic children's hospital that serves as a level I

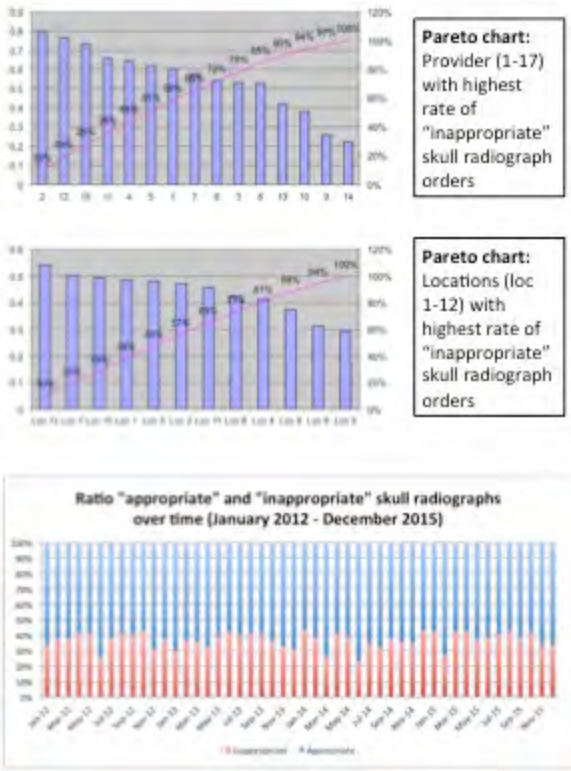
trauma center. We used a commercial search tool (Montage Health Solutions Inc., California, USA) to search reports in the radiology information system by study type skull radiograph in children of ages 2-18 years from January 2012 through December 2015. We identified all patients who had a trauma history by using the following Medical Subject Headings (MeSH): Trauma, injury, injuries, wound, fall, MVC, vehicle, accident, collision, traffic, pedestrian, struck, assault. We included histories of a new or recent "swelling" or "bump" on the head, and excluded any chronic "swelling", "bump", or mass. In children under the age of 2 years, all skull radiographs for a trauma history were rated as "appropriate". In children with trauma who were older than 2 years, skull radiographs were rated as "inappropriate". We analyzed the ratio of "appropriate" to "inappropriate" skull radiographs over time and by ordering provider names and health care facilities.

Results

Three thousand seven hundred and forty-six skull radiographs were performed between January of 2012 and December of 2015. Of these, 2353 were rated as appropriate and 1393 were rated as inappropriate. After publication of the PECARN rule in 2014 there was no decrease of skull radiographs performed in children with head trauma. There was a trend for an increased number of skull radiographs preformed between 2012 and 2015. Skull radiographs were ordered from 91 different facilities, including emergency rooms, clinics, and outpatient centers. The majority of skull radiographs were ordered as outpatient exams (n=2608) and 37% (n=) of these were rated as "inappropriate". The emergency room ordered n=861 skull radiographs, and 48% of these were rated as "inappropriate". There were only n=277 inpatient orders for skull radiographs, of which only 8% were rated as "inappropriate". There were 688 different ordering providers for skull radiographs. Of these, 26 providers had ordered more than 10 skull radiographs and more than 50% of these radiographs were rated as "inappropriate".

Conclusions

Our results show that existence of clinical decision rules does not automatically lead to improved ordering practices. Simple search tools and statistical analysis can help describe the magnitude of inappropriate imaging utilization. We conclude from our data that our system would benefit from provider education (5) to achieve a higher percentage of appropriate skull radiograph orders in children with head trauma.



(Filename: TCT_T-23_TBIcompliance.jpg)

T-25

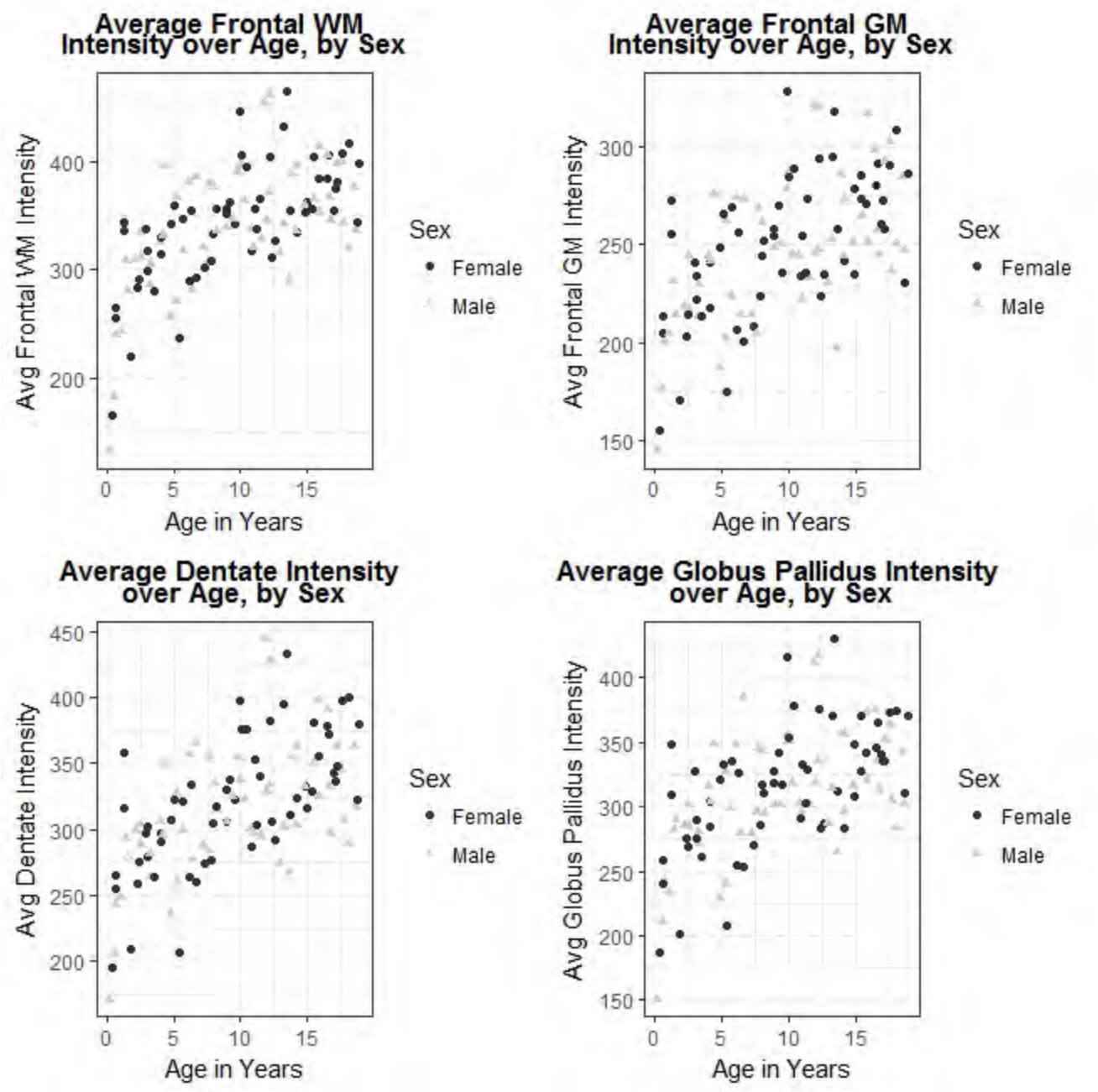
4:00PM - 4:03PM

Age-Dependent Signal Intensity Changes in the Clinically Normal Pediatric Brain on Unenhanced T1-weighted MR Imaging

T Flood[1], P Bhatt[2], A Jensen[3], J Maloney[4], N Stence[4], D Mirsky[4]
[1]University of Colorado Denver - Anschutz Medical Campus, Aurora, CO, [2]University of Colorado, Denver, CO, [3]University of Colorado, Aurora, CO, [4]Children's Hospital Colorado, Aurora, CO

Purpose
Various pathologic and nonpathologic disease states result in brain parenchymal signal intensity changes on unenhanced T1-weighted MR imaging. However, the absence of quantitative data to characterize normal age-related signal intensity values limits evaluation. We sought to establish a range of normal brain parenchymal signal intensity values in a sample of individuals under 18 years of age on unenhanced T1-weighted MR imaging.
Materials and Methods
A single center retrospective study was performed. Pediatric patients with normal MR brain examinations were analyzed. Region of interest signal intensity measurements were obtained from the globus pallidus, thalamus, dentate nucleus, pons, cortical gray matter, and

subcortical white matter. Multivariable linear regression was used to analyze the relationship between signal intensity values and age, controlling for sex and signal intensity of the CSF.
Results
One hundred fourteen normal MR brain examinations in pediatric patients were analyzed (age range: 68 days – 18 years). Results demonstrated a statistically significant association between signal intensity values and linear age (in months) in all neuroanatomical areas tested ($p<0.001$ for all). There were no statistically significant differences attributable to patient sex in any of the models.
Conclusions
Normal age-dependent pediatric brain signal intensity values were determined on unenhanced T1-weighted MR imaging. Increased age was found to be associated with increased signal intensity values in all brain locations tested, irrespective of sex. The biological mechanisms underlying our results remain unclear, and may be related to chronological changes in myelin density, synaptic density, and water content. Establishing normal signal intensity parameters in the pediatric brain will help clarify developmental aberrations and enhance gadolinium deposition research by providing an improved understanding of the confounding effect of age.



(Filename: TCT_T-25_ASNR_Plot_v3.jpg)

T-26

4:03PM - 4:06PM

Is Contrast Needed in Routine Intracranial MR Surveillance Imaging in Pediatric Neurofibromatosis Type -1 Patients? Gadolinium Deposition and Considerations for Surveillance Scanning

B Connolly[1], M Tamber[2], G Zuccoli[2]
[1]UPMC, Pittsburgh, PA, [2]Children's Hospital of Pittsburgh of UPMC, Pittsburgh, PA

Purpose
To determine whether neurofibromatosis type-1 (NF-1) patients undergoing serial MR scans with a gadolinium-based contrast agent (GBCA) for glioma follow up develop increased T1 signal intensity (SI) in deep brain nuclei suggestive of gadolinium retention.
Materials and Methods
An IRB approved retrospective chart review was performed. Seventy-four patients met the inclusion criteria of a clinical diagnosis of NF-1 and at least 3 contrast-enhanced MRI brain exams performed at the home institution. Surveillance imaging was measured in the dentate nucleus (DN), globus pallidus (GP), thalamus (thal), and pons on the first and most recent exams on axial T1-weighted sequences as previously described. DN-pons and GP-thal ratios were calculated on the first and last exams and compared using the paired sample t-test. Univariate and multivariate linear regression was used to determine if age at first scan, total number of scans and total cumulative dose of gadolinium were significant predictors of DN-pons and GP-thal ratios on the last exam. Treatment decisions were reviewed with particular attention to whether a change in size and/or enhancement pattern of the glioma prompted the decision to treat.
Results
Patient age at first exam was 2.53±2.52 years (mean±SD). The mean number of contrasted exams was 10.74±8.10 and the mean cumulative gadolinium dose was 26928.1±27847.8mg. Compared to the respective ratios at their first scan, NF-1 patients demonstrated an increase in their last mean GP-thal ratio (1.01±0.07 vs. 1.06±0.08, $p=0.0004$) but not in their last mean DN-pons ratio (1.03±0.05 vs 1.04±0.06, $p=0.17$). In univariate analysis, the total number of contrasted exams performed ($p=0.032$) and the total cumulative gadolinium dose ($p=0.039$) were found to be significant predictors of the GP-thal ratio at the time of the last exam. In multivariate analysis, only the total number of contrasted exams remained significant at the $p<0.05$ level. Forty-six of 74 (62.1%) patients harbored NF-1 associated gliomas. Of the 17/46 (36.9%) who required chemotherapy, the treatment decision was based on clinical/ophthalmological progression in 5/17 (29.4%) and radiologic progression in 12/17 (70.5%). All 12 patients with radiologic progression demonstrated both increased tumor size and contrast enhancement.
Conclusions
A significant dose-dependent T1 SI increase was demonstrated in pediatric NF-1 patients undergoing serial GBCA-enhanced MRI in the GP but not in the DN, suggestive of gadolinium deposition. Glioma surveillance in these patients without intravenous contrast could be considered, as changes in tumor size and enhancement appear to happen concurrently.

T-27

4:06PM - 4:09PM

The Clinical and Imaging Spectrum of Hypertrophic Olivary Degeneration in Children

D Streicher[1], M Nguyen[2], S Palasis[3], N Kadom[1], B Weissman[1], S Milla[3]
[1]Emory University, Atlanta, GA, [2]University of Maryland School of Medicine, Potomac, MD, [3]Children's Healthcare of Atlanta, Atlanta, GA

Purpose

Hypertrophic olivary degeneration (HOD) is an uncommon phenomenon resulting from injury to the dento-rubro-olivary pathway (also known as the Guillain-Mollaret triangle). The incidence in children is unknown. Most reports of HOD in children are the result of a posterior fossa tumor resection (1-4). Few case reports have described pediatric HOD in the setting of neurodegenerative disorders including mitochondrial diseases (5). There is, however, no systematic investigation of the diverse etiologies of pediatric HOD. We performed a retrospective chart review at a freestanding pediatric hospital to identify patients with HOD and recorded demographics, etiologies, clinical findings, and temporal course.

Materials and Methods

In this institutional review board-approved study, we performed a search of our institution's radiologic report database spanning a 10-year period from 2007-2016. Search terms for brain magnetic resonance imaging (MRI) studies included: "hypertrophic olivary degeneration", "HOD", "olivary", and "inferior olivary degeneration". Magnetic resonance imaging scans of the brain were reviewed retrospectively to confirm the presence of HOD and to document the temporal course of the process on follow-up studies. Detailed review of the electronic medical record (EMR) also was performed. Upon review of the EMR, 1 additional case was discovered in the twin of a patient with Leigh's disease not captured by our search terms and also was included in the analysis.

Results

Our search yielded 27 patients with MRI findings of HOD, 10 females and 17 males. There was bilateral involvement in 24 patients and unilateral involvement in 3 patients. The most common etiologies were (Table 1): sequelae of posterior fossa tumor resection (48%), mitochondrial diseases (19%), tumors without surgical intervention (11%), multiple sclerosis (4%), infection (4%), post-traumatic (4%), and neurofibromatosis type 1 (4%). Clinical symptoms were seen in most patients with imaging findings of HOD (24/27). Twenty patients had imaging follow-up with median follow-up duration of 28 months (range 1-96 months). Of these, 30% showed lesion improvement on imaging, 55% showed stable imaging appearance, and 15% showed worsening.

Conclusions

Our study showed significant increased frequency of bilateral as compared to unilateral HOD with the most common etiology following midline posterior fossa tumor resection. The majority of patients in our cohort demonstrated clinical signs and symptoms of HOD but lacked the characteristic symptoms of palatal tremor and ocular symptoms consistent with prior reports in children (3). The imaging findings typically improved or remained stable on

follow-up examinations. Larger cohort studies will be helpful in further evaluating HOD in the pediatric population.

Table 1: Causes of hypertrophic olivary degeneration in our cohort

	Bilateral HOD (n)	Unilateral HOD (n)
Overall	24	3
Post tumor resection	15	0
Medulloblastoma	7	0
Pilocytic astrocytoma	3	0
Pineoblastoma	1	0
Ependyoma	1	0
Craniopharyngioma	1	0
Mitochondrial diseases	5	0
Leigh's disease	2	0
POLG gene mutation	2	0
Presumed mitochondrial disorder	1	0
Tumor without surgery	1	2
Brainstem glioma	0	1
Germinoma	0	1
Pineal choriocarcinoma	1	0
Other	5	1
Multiple sclerosis	1	0
Neurofibromatosis type 1 (possible gliomas)	1	0
Premature with bilateral cerebellar encephalomalacia	1	0
Post-traumatic	1	0
Necrotizing encephalitis	1	0
Unknown (history of congenital myasthenia gravis)	0	1

(Filename: TCT_T-27_HODabstractTable1-final.jpg)

T-28

4:09PM - 4:12PM

Enhanced Cortical Lesion Detection in Multiple Sclerosis Using Z-Score Methodology to Surface-based Cortical Myelin Mapping

J Nickerson[1], C Filippi[2], R Watts[3]
[1]University of Vermont Medical Center, Burlington, VT, [2]Hofstra Northwell School of Medicine, New York, NY, [3]University of Vermont-UVM Medical Center, Shelburne, VT

Purpose
Cortical myelin mapping is an emerging MR technology (1), and the purpose of this study is to use Z-score methodology (2) to improve the sensitivity of MR at 3T for the detection of cortical lesions in MS patient, as cortical plaque burden is an independent predictor of cognitive dysfunction and strongly correlated with long-term disability (3). Cortical plaque detection is challenging even with advances in MR at 3T such as double inversion recovery and volumetric FLAIR sequences at isotropic resolution. Reliable detection of cortical disease burden in patients with multiple sclerosis is a critical, unmet need. Developing quantitative MR methodology with increased sensitivity to cortical plaque detection would

have an impact on the management of disease progression and evaluation of therapeutic interventions in MS patients.

Materials and Methods

Twenty patients with MS and a control group of 10 patients with chronic migraine were studied using 3D volumetric SPGR T1-weighted (0.8mm isotropic resolution) and volumetric FLAIR (1.0mm isotropic resolution) images on a Philips Achieva dStream 3T MRI scanner with a 32-channel head coil. Cortical myelin maps were generated using the Human Connectome Project pipelines (4) (version 3.16.1) derived form the T1 and FLAIR sequences. Each myelin map was converted to a Z-score based on the mean and standard deviation of all subjects except for one individual (leave-one-out approach). Regions of unusually low cortical myelin content were defined based on a threshold $Z<-3$. The total number of cortical gray ordinates beyond this threshold was used as a measure of disease burden. Differences between the MS and control groups were assessed using a nonparametric Mann-Whitney U-test (SPSS v24).

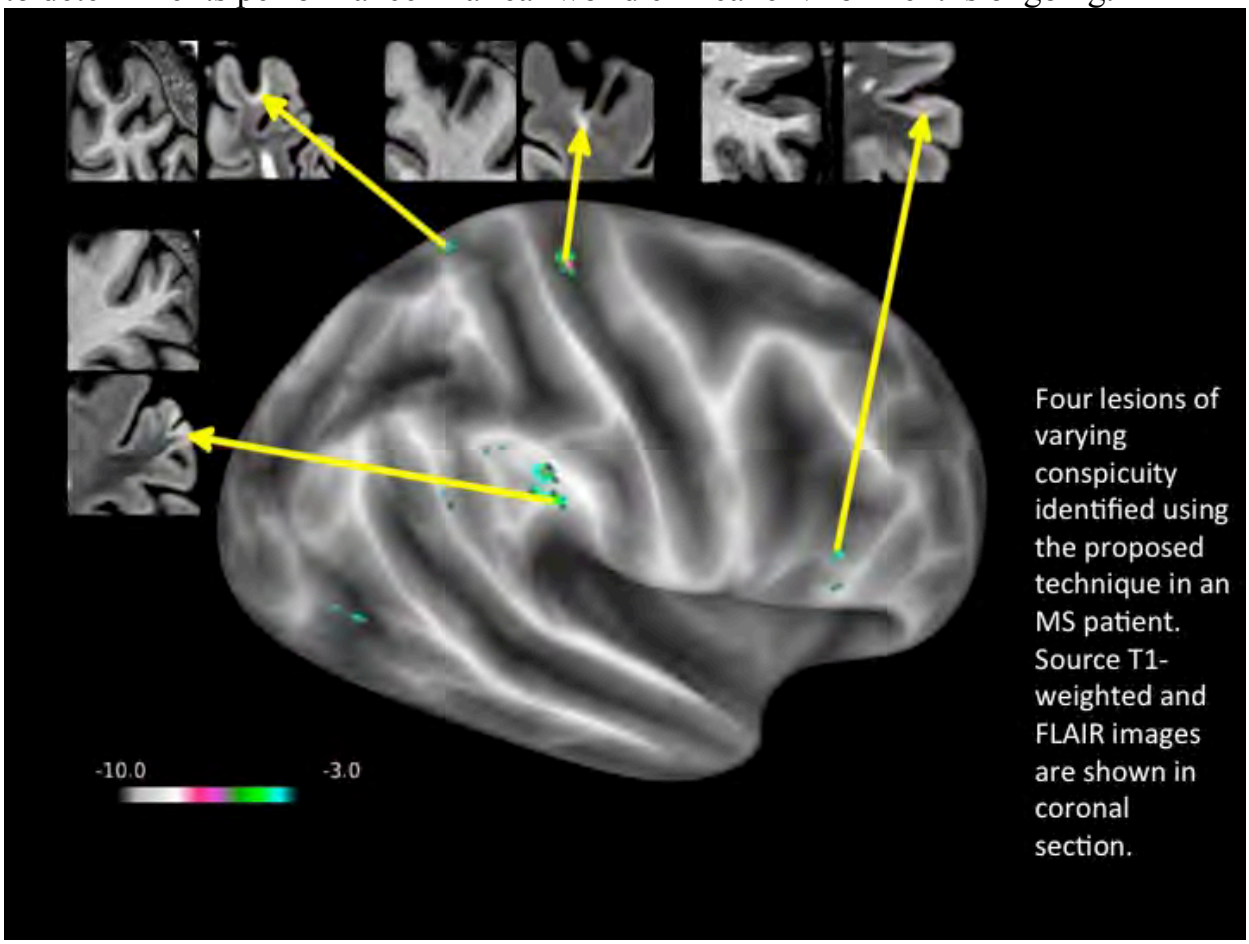
Results

Compared to the cohort of migraine patients, the MS patients had a significantly larger number of regions of decreased cortical myelin ($p = .002$). ROC analysis resulted in an AUC of 0.837, and both a sensitivity and specificity of 0.8. Visual inspection of the raw volumetric T1 and FLAIR cortical segmentation and myelin maps resulted in the exclusion of a single MS patient for the analysis. Cortical lesion detection using this Z-score approach identified many apparent lesions that were not identifiable on the routine MR source images, even retrospectively. There were only a few lesions that could be prospectively identified in the cortex on source MR images, all of which were identified on the Z-approach method (Fig. 1). Without a "gold standard" for cortical plaque detection, it is impossible to know whether all Z-score identified lesions represent real plaque, as it is possible to score false positive lesions. Double inversion recovery acquisitions, albeit with lower SNR, could be used in future studies for comparison. Comparing to high field 7T MR or direct histopathologic confirmation may be better but more difficult to achieve. The use of a leave-one-out approach is not ideal in that the reference population includes MS patients with known cortical lesions, which would be expected to increase the standard deviation in the reference group. However, patients with migraine were chosen as the control group because they share many of the same clinical symptoms and radiographic findings as MS although the pathophysiology is different. A larger, independent healthy control population to define "normal" would be preferable and increase sensitivity. However, with the small number of subjects in this study, the leave-one-out approach avoids the potential for introducing bias between the groups, which has been a problem in previous studies (5).

Conclusions

A new technique combining surface-based cortical myelin maps derived from routinely acquired 3D volumetric T1-weighted and FLAIR techniques with Z-score methodology is being proposed to better identify cortical lesions in patients with multiple sclerosis given that cortical disease burden correlates with cognitive dysfunction and long-term disability. This

technique detects significant cortical abnormality in the cohort of MS patients compared to a control group of migraine patients (p=0.002). Regions of unusually low myelin content sometimes correspond to lesions visible on the source T1-weighted and FLAIR images, but in most cases, these lesions were occult on either individual scan. The technique is clinically applicable and feasible, requiring only 3D T1 and FLAIR acquisitions that are already routinely acquired, and from that data, just a novel, automated way to generate the myelin maps to detect cortical lesions. Future studies using a large database of diverse clinical cases to determine its performance in a real-world clinical environment is ongoing.



(Filename: TCT_T-28_Slide3.jpg)

Tuesday
3:30PM - 4:45PM
Long Beach Convention Center, Grand Ballroom (Upper Level)

14A-Parallel Paper Session: Pediatric Neuroradiology: Infection and Inflammation . . . Information

O-91

3:30PM - 3:38PM

Causes and Patterns of Leptomeningeal Enhancement on Brain MRI in a Pediatric Population

J Maloney[1], D Mirsky[1], C White[1], N Stence[1]
[1]*Children's Hospital Colorado, Aurora, CO*

Purpose
Leptomeningeal enhancement (LE) is a common neuroimaging finding, and has been described in association with numerous disease entities. Its presence may help guide the radiologist to a specific and accurate diagnosis, although in challenging cases, this finding also can lead to confusion given its lack of specificity. The available literature tends to focus on LE in the setting of a specific diagnosis, and there is little information regarding the relative frequency of different diagnoses within a subset of patients with this finding. We seek to further clarify the incidence and patterns of the various causes of LE within a pediatric population.
Materials and Methods
This was a single-institution IRB-approved retrospective study. The institutional PACS database was searched using Montage (Montage Healthcare Solutions, Philadelphia, PA) for reports of brain MRIs with and without contrast performed in patients less than 18 years of age between July 2012 and June 2015 containing the keywords "enhancement" in combination with "leptomeningeal," "pial," "arachnoid," and "sulcal." The MRIs were reviewed by 2 pediatric neuroradiologists to confirm the presence of LE. Patient age, gender, and diagnosis; the distribution of LE; and the MRI sequence(s) showing the enhancement were recorded.
Results
Sixty-six patients (40 males and 26 females) met inclusion criteria, with an average age of 6.2 years (range 3 days – 18 years). As expected, the 2 most common etiologies of LE were neoplasm (26) and infection (24). The most commonly encountered neoplasms were medulloblastomas/PNETs (5), leukemia (5), and astrocytomas (any grade; 4). The most common infection was bacterial meningitis (10), of which pneumococcus and E. coli were most frequent (2 cases each). An additional 8 cases of infectious meningitis arose in the setting of acute sinusitis and were localized to the anterior cerebrum. Other causes of LE included Sturge-Weber syndrome (4 cases), infarcts or hypoxic-ischemic injury (3), and radiation effects (2). Supratentorial involvement was more common than infratentorial. A diffuse LE pattern was encountered in 5 cases, with confluent enhancement along the cerebral hemispheres, cerebellum, brain stem, and cranial nerves, 4 of which represented disseminated neoplasm. Patchy bilateral involvement was seen in cases of posterior reversible encephalopathy syndrome, mitochondrial disease, and autoimmune encephalitis. Leptomeningeal enhancement was identified readily on both T1-weighted and FLAIR images following contrast administration.

Conclusions
Leptomeningeal enhamcement has myriad causes in the pediatric brain, and knowledge of the potential etiologies and associated patterns can help guide an appropriate differential diagnosis.

O-92

3:38PM - 3:46PM

CNS Imaging Findings in Congenital Zika Virus Infection: a Prospective Study

D Galheigo[1], B Guedes[2], T Fazecas[3], R Nogueira[2], H Werner[2], L Hygino da Cruz[4]
[1]Clinica de Diagnostico por Imagem (CDPI), Rio de Janeiro, Rio de Janeiro, Brazil, [2]Clinica de Diagnostico por Imagem (CDPI), Rio de Janeiro, Rio de Janeiro, [3]Clinica de Diagnóstico por Imagem (CDPI), Rio de Janeiro, Rio de Janeiro, [4]CDPI-Clinica de Diagnostico por Imagem, Rio de Janeiro, RIO DE JANEIRO

Purpose
Zika virus (ZIKV) has tropism for the central nervous system (CNS) that has caused major infection outbreaks in the Americas since 2015, mainly in French Polynesia and in Brazil. Several retrospective studies demonstrated microcephaly associated with cortical malformations, calcifications, ventriculomegaly and other abnormalities. The purpose of this prospective study is to quantify and to illustrate the spectrum of neuroimaging features of congenital ZIKV infection, sequentially using fetal ultrasound and magnetic resonance imaging (MRI) and newborn ultrasound, CT and MRI.
Materials and Methods
We performed a prospective study with 48 pregnant patients with ZIKV infection at different gestational ages. They were subjected to ultrasound and fetal MRI. After birth, the newborns performed transfontanellar US, CT and MRI of the head, with posterior 3D reconstructions of the skull. We compared the cases with and without CNS involvement in the patients with intrauterine ZIKV infection. We quantified and illustrated the most frequent CNS findings in these patients such as diffuse excessive high signal intensity (DEHSI), corpus callosum dysgenesia, calcifications, microcephaly, cortical malformations and brain stem abnormalities.
Results
From the 48 cases of ZIKV infection, 38 showed brain abnormalities and 10 had normal exams. Only 3 cases demonstrated microcephaly. We found in 36 cases a hypersignal in the white matter preferentially of frontal lobes and posterior peritrigonal region bilaterally, quite similar to the signal modification DEHSI described in extreme preterm infants. Multiple calcifications with cortical and mainly subcortical distribution were seen in 4 cases. Significant thinning of the brain parenchyma, which have extensive periventricular areas of hyperintensity on T2 MR-WI were reported in 2 cases. Neuronal migration anomalies were reported in 3 cases. Dysgenesis of the corpus callosum were detected in 2 cases and

ventricular enlargement secondary to cortical/subcortical atrophy also were detected in 2 cases. The cerebellum was affected in 1 case. Brain stem was not affected in these 48 cases.
Conclusions
Brain calcifications detected prenatally was a finding suspicious with a intrauterine infection. Moreover, perinatal imaging by MRI and CT scan enabled diagnosis of pachygyria, corpus callosum dysgenesis, small anterior fontanel with premature closure of cranial sutures. However, in the patients without microcephaly we have seen an excessive hypersignal in the white matter that resembles that previously described in extreme preterm patients, called DEHSI. The meaning of this finding is still unknown, but we speculate that this alteration may somehow be related to ZIKV and may not have the same prognostic behavior that DEHSI has for premature infants. Thus, we believe there may be some relationship between this finding and the recent reports of change in the development of patients without microcephaly.

O-93

3:46PM - 3:54PM

Neuroimaging findings on the congenital ZIKA virus outbreak in Brazil: the value of ultrasonography as a screening tool

S Teixeira[1], J Elias Jr[2], M Zotin[3], G Simão[4], K Souza[5], O Moritsugu[6], M Mussi-Pinhata[7], A Yamamoto[8], C Caldas[5], A Hamad[8], A Santos[9]
[1]Hospital das Clínicas, RIbeirão Preto Medical School - University of São Paulo, Ribeirão Preto, São Paulo, [2]Ribeirao Preto Medical School, University of Sao Paulo, Ribeirão Preto, SP, [3]Clinics Hospital of Ribeirão Preto school of Medicine -Univesity of São Paulo (HCFMRP USP), Ribeirão Preto, São Paulo, [4]Clinics Hospital of Ribeirão Preto´s School of Medicine - University of São Paulo (HCFMRP USP), Ribeirão Preto, São Paulo, [5]Hospital das Clínicas, RIbeirão Preto Medical School - University of São Paulo, Ribeirao Preto, SP, [6]Clinics Hospital of Ribeirão Preto School of Medicine, Ribeirão Preto, SP, [7]Ribeirao Preto Medical School, University of Sao Paulo, Ribeirao Preto, SP, [8]Clinics Hospital of Ribeirão Preto School of Medicine - São Paulo University, Ribeirão Preto, SP, [9]University of Sao Paulo, Ribeirao Preto, Brazil

Purpose
To investigate the prevalence of neuroimaging findings in neonates and infants with congenital Zika virus infection.
Materials and Methods
These are preliminary data of a cohort during the Zika virus outbreak from June1st to October 31st 2016. Inclusion criteria were: neonates and infants with laboratorial evidence of intrauterine exposure to the zika virus and available ultrasonography (US). In 29 cases, magnetic resonance imaging (MRI) was available.

Results
We included 172 cases. Twenty-five cases were exposed in the first trimester of gestation, 107 in the second trimester and 39 in the third trimester. For the cases infected in the first trimester, US showed abnormalities consistent with the ZIKA virus syndrome (ZIKA) in 6 cases, lenticulostriate vasculopathy (V) in 3 cases, subependymal cysts (C) in 2 cases, V and C in 2 cases and hyperechoic areas in the cerebral parenchyma in 1 case. In those exposed in the second trimester, 38 out of 107 had abnormal findings on US (5 V and C, 16 V, 13 C, ventriculomegaly in 1 case, periventricular calcifications in 1 case). Two cases with associated CMV infection had findings suggestive of CMV. In the third trimester, US showed 4 V and C, 2 V, 11 C and hyperechoic areas in the brain in 1 case. Nineteen cases had normal US. In 3 cases with abnormalities consistent with ZIKA, gestational age of exposure was not known. Ten out of 29 cases who underwent MRI had abnormalities consistent with ZIKA, 8 had white matter lesions (2 with ventriculomegaly), 2 white matter volume loss, 1 partial thalamic fusion, 2 CMV imaging findings and 6 were normal.
Conclusions
The most common US findings were V and C, whereas the most common MRI findings were white matter lesions. Ultrasonography is useful as a screening tool for children exposed to intrauterine ZIKA virus infection.

Summary of ultrasonography findings according to the trimester of exposure to the zika virus

	1st trimester	2nd trimester	3rd trimester	Unknown
Normal	10	69	19	0
Lenticulostriate vasculopathy	3	16	2	0
Subependymal cyst	3	13	11	0
VC	2	5	4	0
White matter lesions	1	0	1	0
ZIKA	6	0	0	3
Others	0	4	0	0

VC, Lenticulostriate vasculopathy and subependymal cyst; ZIKA, Zika syndrome

(Filename: TCT_O-93_Table.jpg)

O-94

3:54PM - 4:02PM

Posterior Reversible Encephalopathy Syndrome in Cerebral Malaria: Clinical Risk Factors and Prognosis

S Mohajeri Moghaddam[1], M Potchen[2], S Kampondeni[3], S Sherazi[2], G Birbeck[2]
[1]University of Rochester Medical Center, Rochester, NY, [2]University of Rochester Medical Center, Rochester , NY, [3]University of Malawi College of Medicine, Blantyre , Malawi

Purpose
Recent research has identified cerebral edema as the cause of death in pediatric cerebral malaria. Posterior reversible encephalopathy syndrome (PRES) also was present in a significant subset of children with cerebral malaria. The pathophysiology of PRES is controversial. Various clinical risk factors for PRES have been identified from populations in developed settings. We investigated clinical risk factors and outcomes associated with PRES in pediatric cerebral malaria.
Materials and Methods
Our cohort consisted of children with retinopathy-positive cerebral malaria admitted to the Blantyre Malaria Project from 2009-2014 with brain MRIs at admission. Images were interpreted independently by 2 radiologists using NeuroInterp. A case definition of PRES was developed based on the most widely reported patterns of imaging findings in the literature. Demographic and clinical factors including relative hypertension, having received a blood transfusion, severe lactic acidosis, dehydration, a history of convulsions prior to admission, and admission temperature and heart rate were evaluated as possible risk factors for PRES.
Results
Two hundred sixty-nine children had brain MRIs with 91 (34%) demonstrating PRES. There was no difference between the PRES and non-PRES groups in age, gender, weight and height. Severe lactic acidosis was less common with PRES (OR= 0.9; 0.83-0.96) when corrected for a history of convulsions prior to admission. The remaining clinical factors, including hypertension and seizures were not associated with PRES. Among children with PRES, 75 (82%) completely recovered, 8 (9%) had neurologic sequela at discharge, and 8 (9%) died. There was no difference in mortality.
Conclusions
Hypertension and seizures are not risk factors for cerebral malaria-associated PRES. Posterior reversible encephalopathy syndrome is less likely to be seen in malaria-infected children with hyperlactatemia, a marker of severe and often fatal malaria. Future investigations should assess whether malaria-associated PRES is related to parasite burden (i.e. Histidine Rich Protein-2) or malaria-induced endothelial injury (Angiopoetin-2).

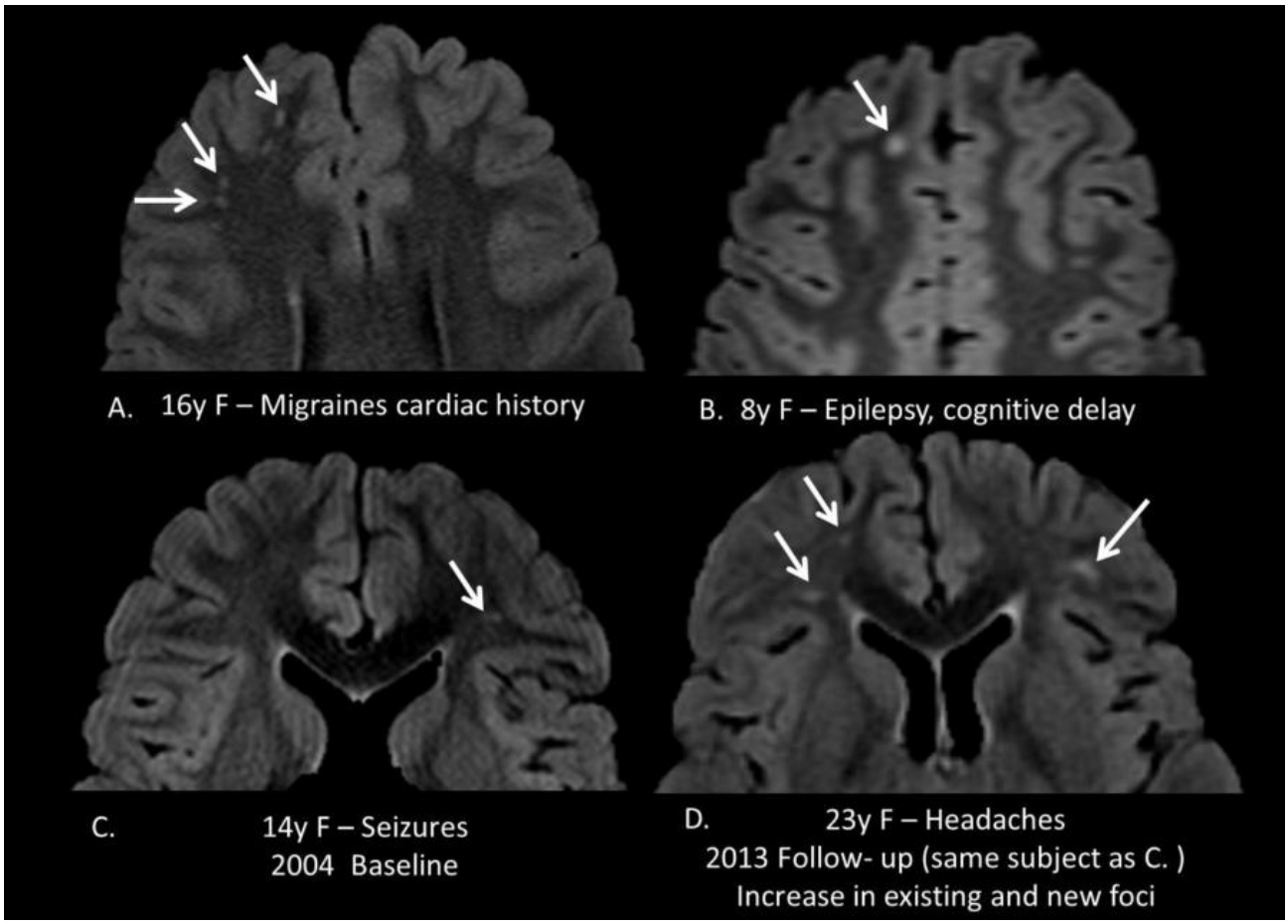
O-95

4:02PM - 4:10PM

Non-specific foci of white matter signal identified on brain MRI in children: Clinical significance and imaging follow-up

D Mihal[1], J Leach[2]
[1]University of Cincinnati Medical Center, Cincinnati, OH, [2]Cincinnati Children's Hospital Medical Center, Cincinnati, OH

Purpose
Nonspecific, small foci of white matter signal are a common finding in the evaluation of brain MRIs in children. Unlike in adults, when small vessel arteriopathy often is evoked as a cause, in children the etiology often is obscure and clinical significance uncertain. This can lead to diagnostic uncertainty and confusion regarding need for follow up. A small number of prior investigations have focused on specific clinical scenarios, including only small subpopulations with imaging demonstrating these white matter lesions. We evaluated a large number of children with these lesions, assessed their distribution, and evaluated change on follow up in order to inform a consistent recommendation on their significance in a wide range of clinical indications and scenarios.
Materials and Methods
Brain MRI reports were searched (Softek Illuminate Insight) for the terms nonspecific, punctate, and white matter (common terms for these foci at our institution). A preliminary group of 271 subjects were identified, from which 62 were excluded. Exclusions included: known disorders causing white matter signal changes, diffuse or ill-defined white matter abnormalities, lesions with associated susceptibility or diffusion restriction, age greater than 21 years at initial imaging, and those with no clinical information, providing a final group of 210 subjects. Initial imaging, follow-up imaging, and clinical information documented in the electronic medical record were reviewed for each subject. The number and location of WM foci tabulated.
Results
The mean age was 10 years old (48% M, 52% F) in the 210 included subjects. The most common clinical indications for imaging were for seizures (28%) and headache (27%). Foci were T2 hyper intense, not suppressed on T2 FLAIR, and predominately frontal (frontal 96%, parietal 51%, temporal 16%, occipital 4 %), and subcortical in location (subcortical 89%, periventricular 18%, deep 10%). Sixty-eight subjects had follow-up imaging (mean interval: 695d). In 90% the foci remained stable, 6% (4) developed new or more conspicuous lesions, and 4% became less conspicuous or resolved. Imaging follow up was recommended by the radiologist in 29% (64% completed follow up imaging, all stable). In the 4 subjects with new or more conspicuous lesions all re-imaging was performed for other clinical reasons. No subjects were subsequently diagnosed with a demyelinating disorder. Discussion of potential etiologies and comparison with prior literature will be performed.
Conclusions
Nonspecific punctate areas of white matter signal on pediatric brain MRI are most often frontal and subcortical in location. They rarely change on follow-up exams, and in the vast majority of cases they have no identifiable clinical significance.



(Filename: TCT_O-95_MihalASNR2017Image.jpg)

O-96

4:10PM - 4:18PM

Acute brain injury following illicit drug abuse in adolescent and young adult patients: Spectrum of neuroimaging findings

S Shrot[1], A Poretti[2], B Soares[3], T Huisman[4]
[1]Johns Hopkins University School of Medicine, Baltimore, MD, [2]The Johns Hopkins University School of Medicine, Baltimore, MD, [3]Johns Hopkins Hospital, Baltimore, MD, [4]Johns Hopkins, Baltimore, MD

Purpose
The use of illicit drugs is currently a major medical problem among adolescents. The clinical manifestation of adolescents with acute drug-induced neurotoxicity is often characterized by nonspecific symptoms and findings. We report on clinical and neuroimaging findings in 5 adolescents with acute brain imaging following illicit drug intoxication.
Materials and Methods
Clinical data and results of laboratory investigations were collected from review of the

clinical history. All imaging studies were evaluated retrospectively for supra- and infra-tentorial abnormalities.

Results

All patients presented with acute altered mental status, 2 patients showed extrapyramidal signs and 1 patient had spinal cord related symptoms. Opiates were the most common substance including 2 cases of heroin and 1 case of methadone intoxication. Neuroimaging findings included symmetric subcortical white matter involvement in 3 patients, multiple foci of acute ischemic infarctions in 1, and both patterns of brain injury in 1. All patients had cerebellar involvement including diffuse symmetrical cerebellar edema in 4 patients and multiple foci of cerebellar ischemic infarctions in 1. Supratentorial cerebral edema also was common (n=5), but with variable extent. In 3 patients there was involvement of the basal ganglia, either as diffuse edema or multiple foci of acute ischemic infarctions. The thalami and cerebral cortex were spared in all patients. When diffusion-weighted imaging was obtained, white matter T2 edema also showed restricted diffusion, both in infra- and supratentorial white matter.

Conclusions

Our patients reveal 2 main neuroimaging patterns of brain injury: diffuse symmetric subcortical white matter injury with preferential cerebellar involvement (leukoencephalopathy pattern) or multiple foci of ischemic infarctions in a nonarterial territory distribution (ischemic pattern). Familiarity with these 2 neuroimaging patterns of findings in the evaluation of MRI studies in adolescents with acutely altered mental status, may suggest the correct diagnosis and narrow the differential diagnosis.

O-97

4:18PM - 4:26PM

Reversible Hyper Intense Foci on T1-weighted Images in Acute Disseminated Encephalomyelitis

Y Kawanaka[1], K Ando[2], J Taniguchi[1], Y Kawanaka[1], T Katsuura[1], Y Wakata[1], R Ishikura[3]
[1]Hyogo College of Medicine, Nishinomiya, CA, [2]Hyogo College of Medicine, Nishinomiya, Japan, [3]Hyogo College of Medicien, Nishinomiya, CA

Purpose

Acute disseminated encephalomyelitis (ADEM) is an inflammatory demyelinating disorder of the central nervous system that usually occurs in children after viral infections or vaccinations. Neuroimaging shows focal or multifocal hyperintense lesions on T2-weighted and FLAIR images on MRI. But findings on T1-weighted images (T1WI) have not been evaluated in detail in the literature. The aim of this study is to evaluate the radiological and clinical features of reversible hyperintense foci on T1WI in acute disseminated encephalomyelitis (ADEM).

Materials and Methods

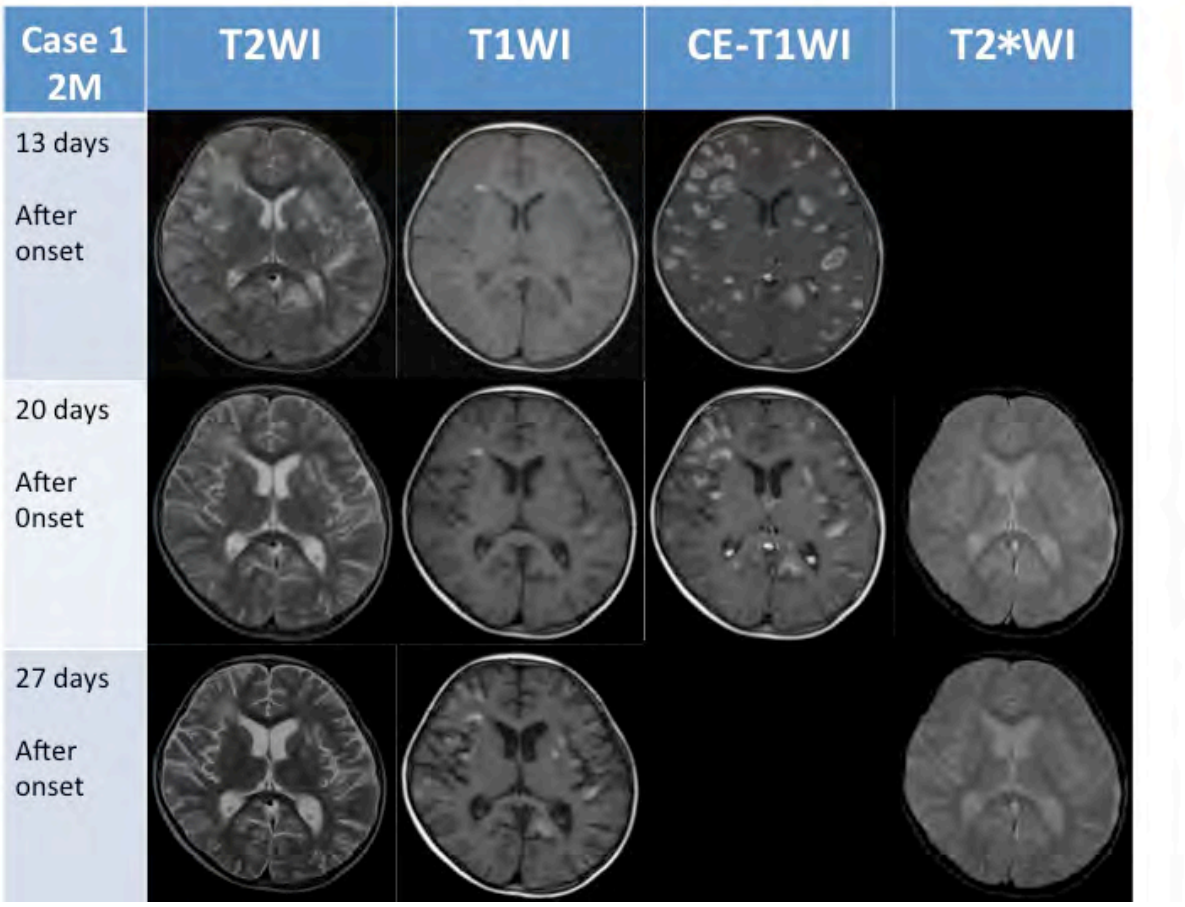
Twelve patients were diagnosed as ADEM in our hospital and affiliated hospital between November 2007 and September 2016. Six patients underwent MRI only 1 time at onset and 6 patients underwent MRI multiple times. Two neuroradiologists (with 26 and 5 years of experience in radiology, respectively) blinded to the clinical and neuroradiological outcomes evaluated all images.

Results

Hyperintense foci on T1WI were observed in none of the MRI at onset. In 4 of 6 cases of ADEM with follow-up MRI, hyperintense on MRI appeared in 2 weeks to 3 months after the onset when patients' clinical symptoms have resolved and when abnormal intensities on T2WI/FLAIR on MRI have diminished. All hyperintense foci on T1WI disappeared in 3 months to 2 and a half years after onset. When compared with the MRI at onset, hyperintense foci appeared where hyperintense areas were observed on T2WI and FLAIR images. None showed hypo signal intensity on T2*WI. Apparent diffusion coefficient (ADC) values were increased in all lesions. Contrast enhancement was observed in 1 case.

Conclusions

Delayed appearance of reversible hyperintense foci on T1WI in ADEM is not a rare finding and does not suggest poor prognosis. Because none of the foci showed T2* shortenings, hyperintense may not reflect hemorrhage. We suggest transient accumulation of inflammatory cells such as macrophages might be the etiology of T1 shortening (1, 2).



(Filename: TCT_O-97_Figure1.jpg)

O-98

4:26PM - 4:34PM

Pediatric Onset Multiple Sclerosis: Evaluation of Sequential Brain MR Imaging to Study the Disease Evolution and Predict Outcomes.

K Jobanputra[1], F Nelson[1], J Lincoln[1], A Kamali[1], R Patel[1]
[1]*The University of Texas Health Science Center at Houston, Houston, TX*

Purpose
Multiple sclerosis (MS) occurs more commonly in adults; however about 2-5% of all patients with MS have a history of symptom onset before age 18. Pediatric onset multiple sclerosis is a less understood disease, hence a more challenging diagnosis to make and subsequently manage. Though MR imaging plays a major role in diagnosis and follow up of the patients, there is paucity of scientific imaging-based temporal evaluation of the disease process. In this study we quantitatively evaluate temporal apparent diffusion coefficient (ADC) values and correlate it with disease evolution on the conventional contrast-enhanced MR imaging.

Materials and Methods

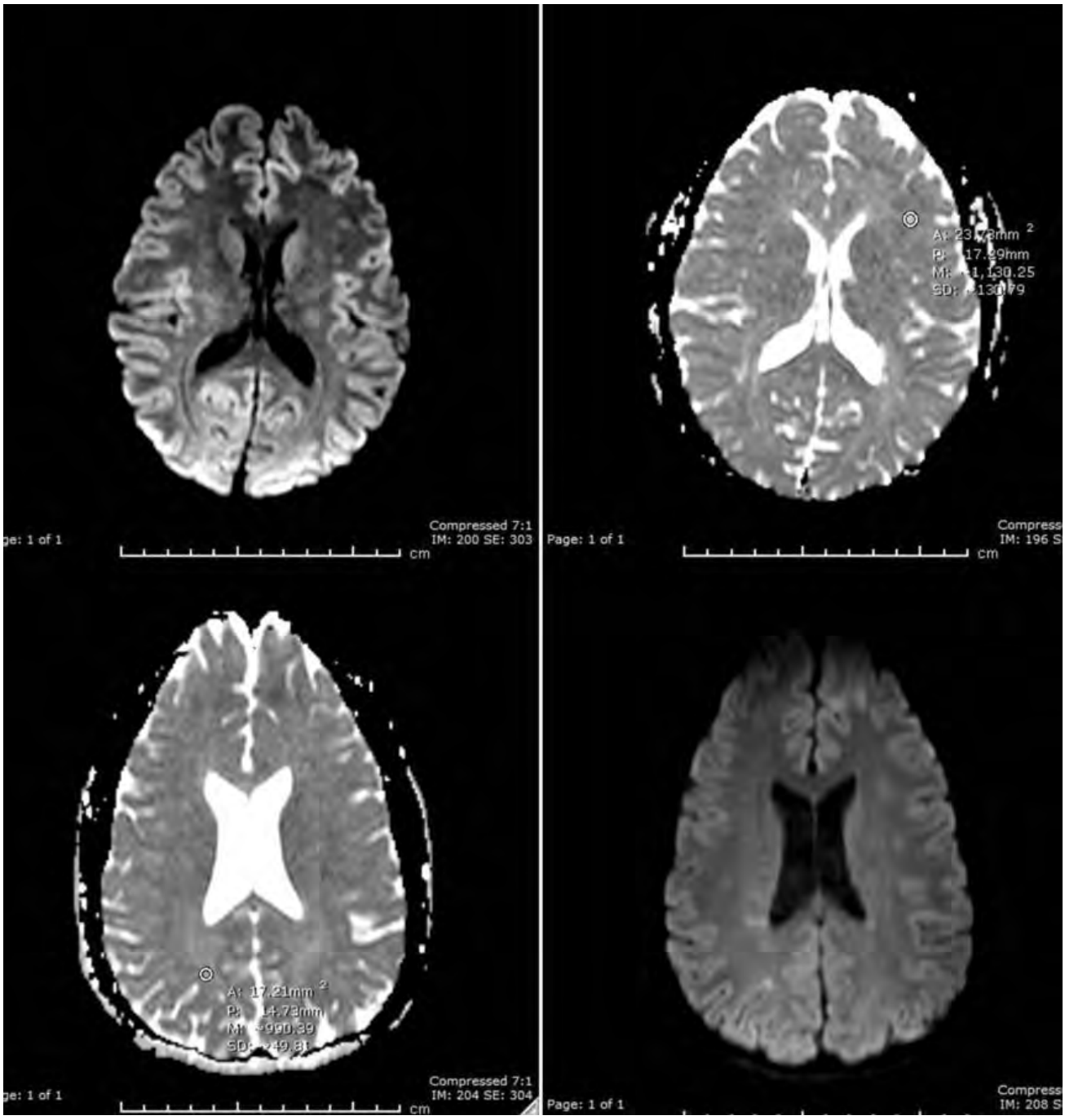
Single institutional, retrospective evaluation of 12 patients with an established diagnosis of pediatric onset multiple sclerosis is being performed. A total of 60 conventional brain MR studies are under evaluation. Apparent diffusion coefficient values of all of the acute as well as chronic demyelinating plaques showing hyperintense signal characteristics on DWI are calculated. These are followed temporally to study their correlation with T2 hyperintensities, enhancing lesions on the contrast-enhanced T1 images and the overall disease process.

Results

On preliminary evaluation of the data set, many of the T2 hyperintense lesions had hyperintense signal on DWI but no contrast enhancement or obvious T1 hypointensity. The ADC values of these DWI hyperintense foci appear to be more sensitive than contrast enhancement as an indicator of disease process. The patients having development of new T2 hyperintense foci or contrast enhancing lesions demonstrate lesser mean ADC values at presentation (1000 x 10^-6 mm^2/ s) as compared to the patients having stable or resolving lesions (1150 x 10^-6 mm^2/s).

Conclusions

In the patients with pediatric onset multiple sclerosis DWI appears to be more sensitive indicator of disease activity than the contrast enhancement, the mean ADC values may prove to be an index for predicting the outcomes.



(Filename: TCT_O-98_PEDMS.jpg)

O-99

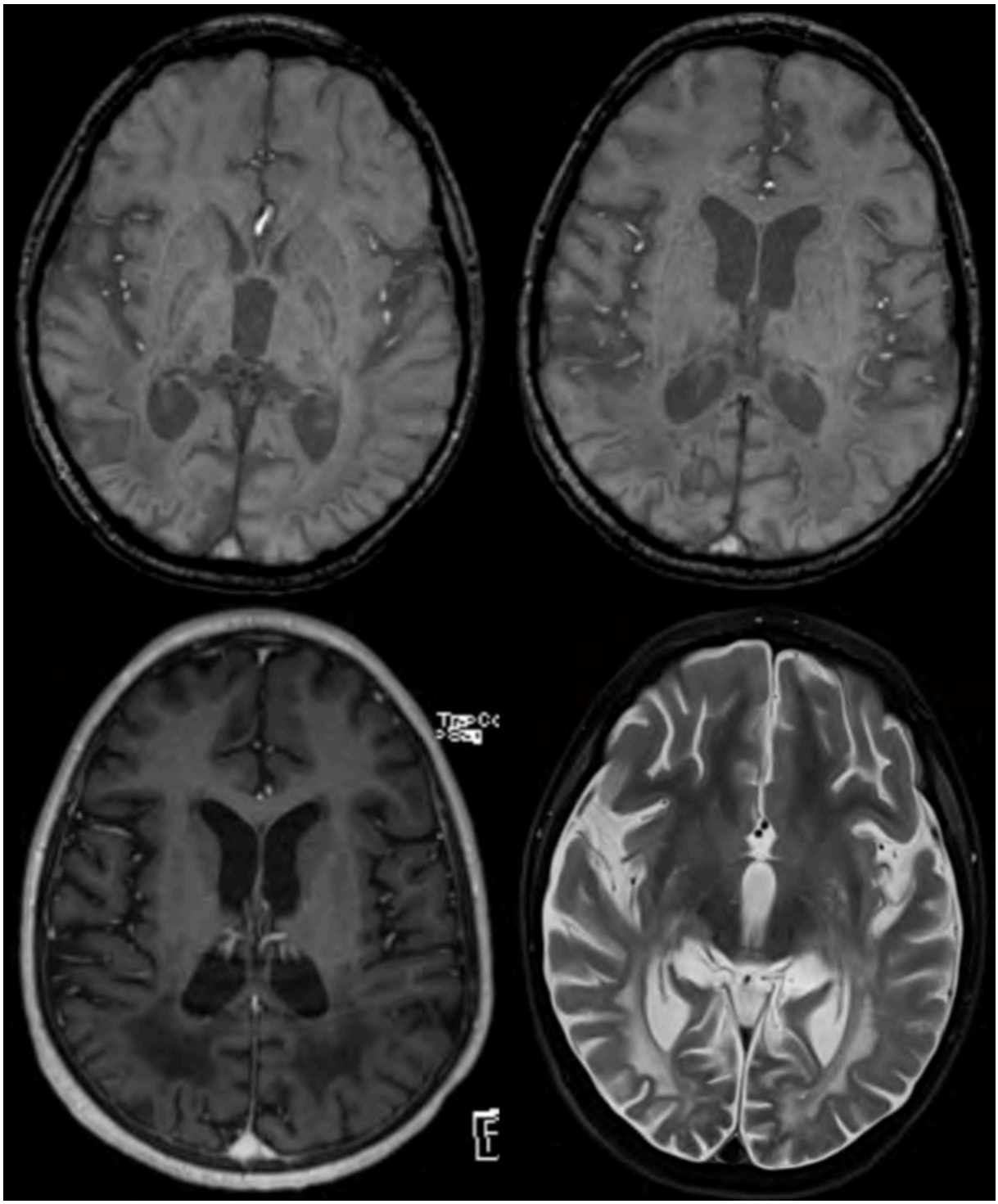
4:34PM - 4:42PM

Susceptibility weighted imaging in adrenoleukodystrophy: correlation of findings with disease severity and clinical outcome

J Benson[1], D Nascene[1], L Zhang[2], W Miller[1]

[1]*University of Minnesota, Minneapolis, MN,* [2]*Clinical and Translational Science Institute, University of Minnesota, Minneapolis, MN*

Purpose
Cerebral variant adrenoleukodystrophy (cALD) is an X-linked peroxisomal disorder characterized by severe demyelination of the cerebral white matter. No comprehensive study has assessed imaging features of cALD on susceptibility-weight imaging (SWI).
Materials and Methods
Patients were included with: 1) biochemically confirmed diagnosis of ALD, 2) SWI imaging of the brain, 3) posterior-type (typical) ALD, and 4) <18 years old at time of hematopoietic stem cell transplantation (HSCT), if completed. Up to 3 MRIs were analyzed for patients who underwent HSCT: 1) pre-transplantation closest to HSCT, 2) first MR after HSCT, and 3) most recent MR. For patients not treated with HSCT, up to 2 MRIs were analyzed: the oldest, and most recent studies. Number and location of SWI foci were noted on each study. MR and clinical severity were assessed using Loes scores and neurologic function scores, respectively. Both the lowest platelet count and the presence or absence of prolonged thrombocytopenia were recorded.
Results
Thirty patients with cALD were included. Twenty-three of 30 (76.7%) patients had abnormal SWI foci observed on at least 1 imaging study. Of patients with findings on SWI, the most common location of abnormal foci were: 13/23 (56.5%) in the dorsal thalami, 8/23 in the parieto-occipital white matter, and 8/23 (56.5%) in the leading edge of enhancement. New and/or more prominent foci were discovered after HSCT in 8/23 (34.8%) of patients; foci resolved following HSCT in 1/20 (5.0%) of patients. Macroscopic intracranial hemorrhage was not observed in any of the patients. Susceptibility-weighted imaging foci were identified as iron in all (5/5) patients for which phase sequences were available.
Conclusions
Susceptibility-weighted imaging foci are present in most patients with cALD, although they do not appear to portend macroscopic hemorrhage. In the minority of patients, microhemorrhagic foci worsen after HSCT; improvement following HSCT is rare.



(Filename: TCT_O-99_Imageabstract.jpg)

Tuesday
3:30PM - 4:45PM
Long Beach Convention Center, Room 202 (Upper Level)

14B-Parallel Paper Session: Vascular Issues and Interventional: Variety Show

O-100

3:30PM - 3:38PM

Head and Neck Diagnosis and Endovascular Repair of Vascular Malformations

W Yakes[1]
[1]*Vascular Malformation Center, Englewood, CO*

Purpose
To determine the efficacy of ethanol embolotherapy of extracranial head and neck vascular malformations of all types, particularly after failure of other endovascular and surgical treatments.
Materials and Methods
One hundred and sixty-six patients (64 males, 102 females; mean age: 38 years) presented with extracranial arteriovenous malformations (AVMs) of the head and neck area. Over half of the patients had undergone previous failed therapies. All patients underwent ethanol embolotherapy under general anesthesia. Forty-five patients had AVMs and 121 patients had venous malformations (VM).
Results
Of 45 AVM patients, 36 patients are cured (mean follow up 2½ years); of 121 venous malformation patients, 65 are at end-therapy (mean follow up 4½ years). The remaining patients are not at end-therapy and are being treated for their residual malformations. In AVM follow-up, arteriography is the main imaging modality to determine cure or residual AVM as MR is less sensitive in the evaluation of residual AVM. In VM follow-up, MR is the main imaging tool, particularly with T- 2 fat suppression and/or STIR imaging. All patients demonstrated improvement post-therapy. Complications were 4.5%, to include bleeding (self-limited), partial 7th nerve palsy (with recovery), skin injury (not requiring skin grafts), infection, and pain.
Conclusions
Ethanol has proven its consistent curative potential at long-term follow up for high-flow AVMs and low-flow VM lesions at long-term follow up as lesions in the periphery. Complication rates remain low. The procedures are tolerated well by the patients and done on an out-patient basis. Prior surgery and embolization procedures can cause difficulty in lesion access, but does not obviate further ethanol endovascular treatment.

O-101

3:38PM - 3:46PM

Auricular Arteriovenous Malformation Diagnosis and Management

W Yakes[1]

[1]*Vascular Malformation Center, Englewood, CO*

Purpose
To determine the efficacy of ethanol endovascular repair of ear arteriovenous malformations (AVMs).
Materials and Methods
Ten patients (7 female, 3 males; age range 6-39 years; mean age: 22 years) with ear AVMs presented for therapy. Two patients had failed prior embolizations (PVA/coils/nBCA/steroids) and 2 patients had other therapies (laser/excisions/grafting). All presented with a grossly enlarged painful ear, and 5 patients had intermittent bleeding. All patients underwent transcatheter and direct puncture ethanol treatments (86 procedures).
Results
All 10 patients were cured of their AVM at long-term follow up (mean follow up: 52 months). One patient had transient partial VII nerve palsy. Two patients had minor blisters and ear injuries that healed on the outer tragus.
Conclusions
Ethanol endovascular repair of ear AVMs can achieve cures in this vexing lesion that previously was treated with resection of the ear and with high recurrence rates. This series documents long-term cures of AVMs of the ear and scalp that were not treatable by endovascular approaches as previously documented in the world's literature. Permanent treatment of the auricular AVMs is documented and no recurrence occurred in any patient. Only one article is published (group from Shanghai, China) emulating this technique, that I taught them.

O-102

3:46PM - 3:54PM

Mandibular AVM Diagnosis and Curative Endovascular Treatment

W Yakes[1]
[1]*Vascular Malformation Center, Englewood, CO*

Purpose
To determine optimal management strategies for the treatment of mandibular arteriovenous malformations (AVM).
Materials and Methods
Thirteen patients (10 females, 3 males), age 9 -14; mean age 10, underwent endovascular therapy to treat their mandibular AVMs. Nine patients had distinct intraosseous AVMs. Three had multiple facial and intramaxillary AVMs requiring treatment. Outside institutions recommended massive hemi-facial resections in these patients. Four patients had prior PVA and gel foam embolization, 1 patient had a lip graft, 1 had prior mandible surgery, all that had failed.

Results
All 13 patients have demonstrated MR and angiographic cure of their AVMs. One patient's therapy is not completed and is on-going. The patient's mandibular AVM is cured, a third AVM in this patient in the infratemporal fossa is still undergoing treatment. The follow-up range is 11 months – 41 months, with a mean follow up of 29 months. No complications were noted in treatment of mandibular AVMS. One patient required a minor gingival surgery after treatment of an additional intramaxillary AVM.
Conclusions
Endovascular approaches to manage mandibular AVM can be curative. The intraosseous variety is largely a fistula between artery and vein within the bone. All respond well to endovascular ethanol therapy alone. Surgery was not required in any patient. Surprisingly no complications were encountered in this patient series. Long-term cures are noted in this patient series with endovascular approaches alone. No massive surgical resections in any patient, even in patients with multiple AVMs of the soft tissues, mandible and maxilla, was required to effect cure. In patients who suffered hemorrhages from floating teeth, bone formed and stabilized the teeth and no further hemorrhages occurred. Ethanol sclerotherapy proved curative in mandibular intraosseous AVMs in patients who had additional facial soft-tissue AVMs and intramaxillary AVMs that were cured as well at long-term follow up.

O-103

3:54PM - 4:02PM

Alternative Routes for Intra-arterial Chemotherapy Delivery for Treatment of Retinoblastoma

C Quinn[1], B Jagadeesan[1], R Tummala[1]
[1]*University of Minnesota, Minneapolis, MN*

Purpose
Retinoblastoma (Rb) is the most common primary ocular malignancy of childhood. The development of new chemotherapy and endovascular techniques led to intra-arterial delivery of these agents as first line treatment in selected cases (Yousef, 2017). Typically, intra-arterial chemotherapy (IAC) is infused through a microcatheter following selective catheterization of the ophthalmic artery on the affected side. In some cases, the ophthalmic artery may not provide viable vascular access to the tumor, forcing the interventionist to find alternative routes. We discuss a subset of our Rb patient population that received IAC through routes other than the ophthalmic artery.
Materials and Methods
We reviewed records and imaging studies of Rb patients who received IAC between 2011 and 2016. We analyzed their imaging and examined their treatment course, which includes number and type of IAC treatments, routes of delivery, outcomes, and complications.

Results
We identified 13 patients who received IAC for Rb treatment, and 46 total treatments were performed. Of these, 5 patients required alternative methods of chemotherapy delivery other than through the ophthalmic artery, which totaled 19 treatments. Four of the 5 patients had group D or E retinoblastoma classification. Two patients needed balloon-assisted infusion through the distal internal maxillary artery. Two patients required selective catheterization of the middle meningeal artery. One patient had anomalous anatomy and no internal carotid supply to the choroidal blush. In this patient the superficial temporal artery provided the vascular access for IAC. This patient experienced the 1 complication in this series, a forehead burn which was treated surgically. Reasons for using alternative routes included anomalous orbital supply, loss of ophthalmic artery from previous procedures, additional vascular supply to the tumor by the external carotid branches, and prohibitive vasospasm of the ophthalmic artery. There were no neurological complications in this series. Two of the patients ultimately required enucleation.
Conclusions
Alternatives to the ophthalmic artery may be necessary to deliver IAC for selected cases of Rb. These routes can be safe and effective. However, thorough understanding of the orbital blood supply and potentially dangerous extracranial-intracranial anastomoses is essential. Whether these alternative IAC methods result in similar outcomes to ophthalmic artery infusions has not been established.

O-104

4:02PM - 4:10PM

Primary Report on the Application of Mynxgrip Vascular Closure Device in Pediatric Neuro-Interventional Procedures

T Shokuhfar[1], A Al-Smadi[1], A Malani[1], M Hurley[1], A Shaibani[1], S Ansari[2]
[1]Northwestern University Feinberg School of Medicine, Chicago, IL, [2]Northwestern University, Feinberg School of Medicine, Chicago, IL

Purpose
The application of arterial closure devices has been investigated broadly and previously approved in adults but their feasibility and safety have not been approved in pediatric patients and any application of such devices in children is considered off-label. The decision to use the Mynxgrip in our practice has been made based on the low reported rate of complications in adults and the fact of no intraluminal component regarding the usage of Mynxgrip.
Materials and Methods
A retrospective review of all pediatric patients undergoing diagnostic or interventional neurovascular procedures was conducted. Mynxgrip was applied to any pediatric patient with adequate depth of subcutaneous tissue and common femoral artery (CFA) diameter.

Patients' demographic and procedural data were recorded. Hemostasis status and complication reassessment for outpatients and pre-operational inpatients were documented.

Results

During the period of 36 months, a total of 83 Mynxgrip was deployed on 53 children (23 male and 30 female, mean age = 14.5 years) undergoing diagnostic/interventional neuro-endovascular procedures through CFA access site. About 46% procedures were diagnostic angiography and the remaining were angiography with embolization. CFAs' diameter ranged between 4mm to 8.5mm with the average diameter of 6.24 (SD± 1.16). Deployment of Mynxgrip was successful in 82 procedures (98.8%). There was a single (1.2%) device failure but no other immediate or delayed major complications were recorded.

Conclusions

Comparing with the manual compression as the current standard of care, the application of Mynxgrip in our practice brought immediate hemostasis at common femoral artery access site, along with earlier ambulation and shorter duration of hospitalization.

Table 1: patients' demographics and procedure characteristics	
Variable	Mean (SD) or n (%)
Age (years) (mean (SD))	14.52 ± 3.08
Gender (n (%))	
Male	23 (43.3%)
Female	30 (56.7)
Age-adjusted BMI (Mean (SD))	23.48 ± 4.95
Underweight (BMI≤18.5) (n (%))	4 (7.5)
Overweight (25≤ BMI <30) (n (%))	13 (24.5)
Obese (BMI ≥ 30)	5 (9.4)
Status (n (%))	
Inpatient	40 (48.2)
Outpatient	43 (51.8)
Common Femoral Artery Diameter (mm) (Mean (SD))	6.24 (1.16)
Side of arteriotomy (n (%))	
Right	82 (98.7)
Left	1 (1.3)
Type of interventional procedure (n (%))	
Diagnostic Angiography	38 (45.7)
Angiography + embolization	45 (54.4)
Time between initial and subsequent procedure (days) (Mean (SD))	21± 16.97

(Filename: TCT_O-104_Capture.GIF)

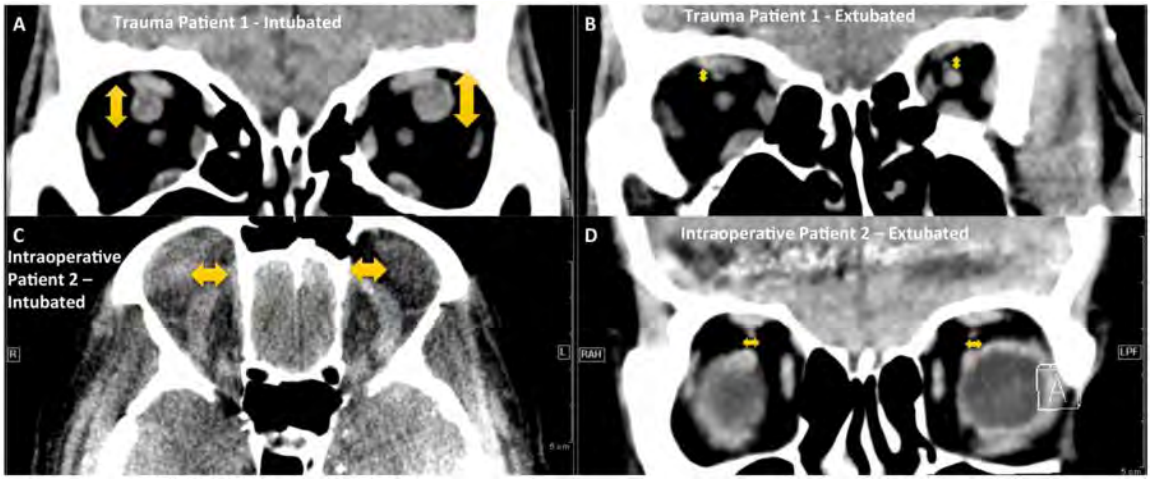
O-105

4:10PM - 4:18PM

Diameter of the Superior Ophthalmic Vein in Relation to Intubation

S Sundararajan[1], L Loevner[2], A Nabavizadeh[3]
[1]Hospital of the University of Pennsylvania, Philadelphia, PA, [2]University of Pennsylvania, Philadelphia , PA, [3]University of Pennsylvania, Philadelphia, PA

Purpose
Unilateral and bilateral superior ophthalmic vein (SOV) enlargement occurs in a spectrum of disease. Bilateral SOV enlargement has been associated with diffuse cerebral swelling and other causes of increased intracranial pressure. We have observed SOV enlargement in intubated patients without underlying intracranial pathology that is reversible after extubation. This study evaluates the incidence of SOV enlargement in post-traumatic and intra-operative intubated patients without pre-existing intracranial or intra-orbital pathologies.
Materials and Methods
An IRB approved retrospective search was performed in 2 cohorts of intubated patients with head imaging: 1) trauma patients, and 2) epilepsy patients with intra-operative scans for stereotactic localization of subdural electrodes. All patients also had head imaging following extubation. Airway maintenance in our trauma cohort was established with or without positive pressure ventilation (PPV). All intra-operative imaging was acquired during PPV. No patient had intracranial pathology that would contribute to elevated intracranial or intra-orbital pressure. Superior ophthalmic vein diameter was recorded in all patients just caudal to the superior rectus. Paired student T-test was performed to analyze differences in intubation and postextubation SOV caliber. Dilated SOVs were considered ≥ 2.5 mm (Lirng et al).
Results
Trauma cohort consisted of 70 patients (48 men, 22 women, mean age 58 years). Intra-operative cohort consisted of 45 patients (24 men, 21 women, mean age 56 years). At the time of intubation, 70% of the 115 patients had dilatation of the bilateral SOVs. From this subset of patients, 79% of trauma patients and 97% of intra-operative patients showed reversal of SOV dilatation to <2.5 mm following extubation. In the intra-operative cohort with dilated SOVs, the mean and maximum SOV diameter were 3.6 and 7.5 mm respectively. This decreased to a mean of 2.2 mm and maximum of 2.4 mm after extubation. In the trauma cohort with dilated SOVs, the mean and maximum SOV diameter were 3.6 mm and 10 mm respectively. This decreased to a mean of 3.6 mm and maximum of 2.4 mm after extubation. Changes in SOV size between intubation and extubation were statistically significant ($p<0001$) in both cohorts.
Conclusions
Our results indicate that bilateral dilatation of the SOV is common in intubated patients, and that it often is reversible following extubation. Patients receiving PPV exhibited significantly larger and more frequent changes in SOV caliber, perhaps as a result of venous back flow into the head and neck. In the appropriate clinical setting, this knowledge may help prevent misinterpretation of prominent SOVs as automatically indicative of underlying pathology.



(Filename: TCT_O-105_ProperSOVFigure.jpg)

O-106

4:18PM - 4:26PM

Dural AV Fistula: Developing Osseous Changes in the Setting of Sinus Thrombosis

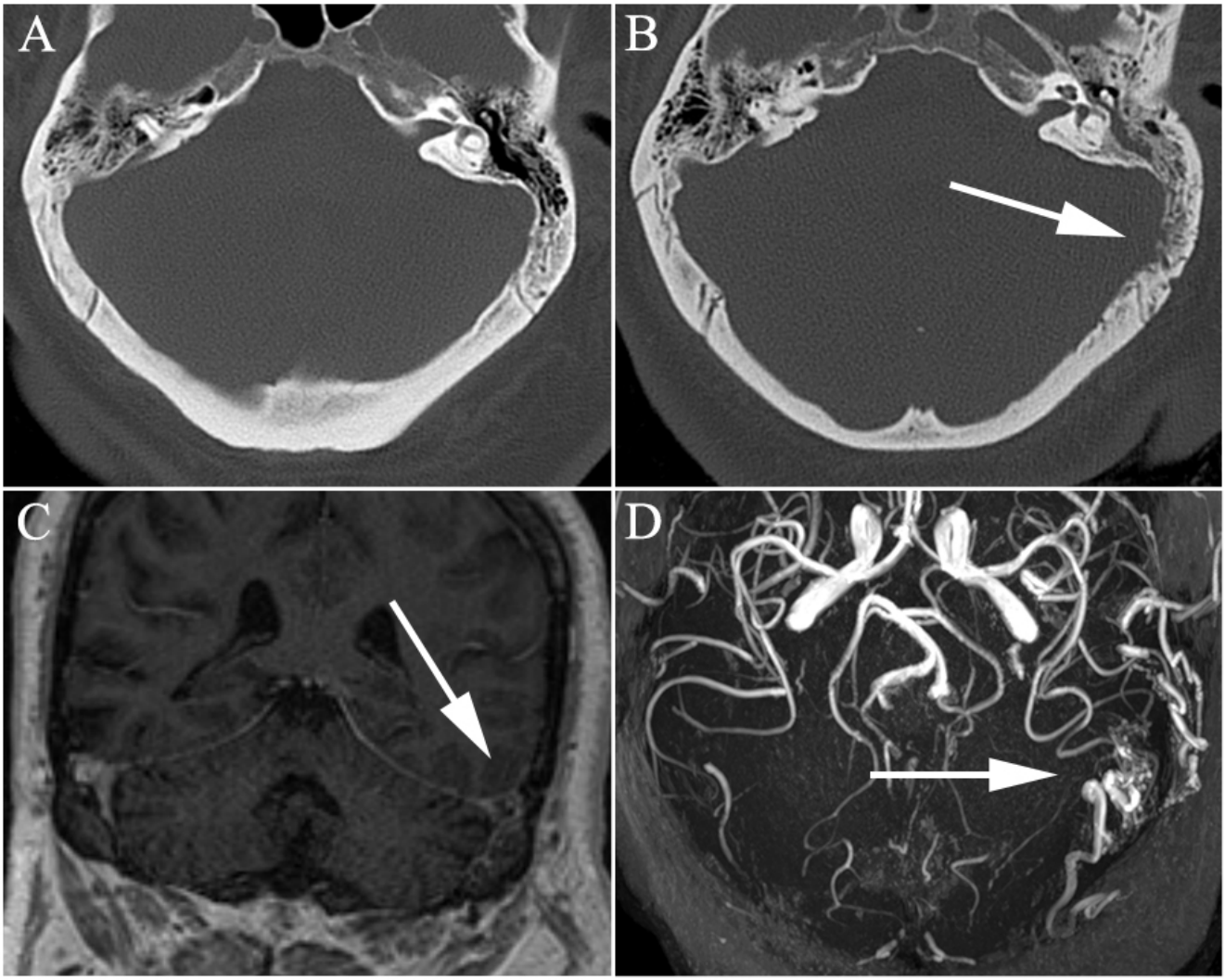
B Putbrese[1], R Wiggins[2], H Harnsberger[3], E Stevens[3], J McNally[3]
[1]University of Utah, Salt Lake City , UT, [2]University Of Utah, Salt Lake City, UT, [3]University of Utah, Salt Lake City, UT

Purpose
Prior studies have shown dural arteriovenous fistulas (dAVF) are associated with venous sinus thrombosis and development of transosseous vessels (1, 2). Our goal was to determine the prevalence of neovascular osseous changes as a diagnostic tool for dAVFs.
Materials and Methods
On retrospective review, we found 17 patients with dAVF in the last 2 years with associated noncontrast CT scans. Six patients had history of sinus thrombosis, 2 of which had progressive osseous permeative changes (Figs. 1A-1D). Two observers classified the presence or absence of permeative changes in 3 locations per patient. Osseous changes were evaluated at the right and left transverse/sigmoid sinus junction as well as along the superior sagittal sinus. Interrater reliability was calculated using kappa analysis and test characteristics were recorded.
Results
Interrater reliability for the site of permeative osseous findings was high (kappa = 0.80). Specificity was 97% (95% CI: 83-99), sensitivity was 75% (95% CI: 51-91%), positive predictive value was 94% (95% CI: 70-99%), and negative predictive value was 86% (95% CI: 70-95%). Area under the curve was 0.86 (95% CI: 0.76-0.96) consistent with high discrimination for identifying the site of dAVF using bone changes. Fig.: A) Initial CT showing normal bone at the left transverse/sigmoid sinus junction. B) Follow-up CT showing development of permeative osseous changes at the left transverse/sigmoid sinus

junction (arrow). C) Contrast MRV showing filling defect within the left sigmoid sinus (arrow) consistent with thrombosis. D) Time-of-flight MRA MIP showing dAVF with transosseous vessels at the left transverse/sigmoid sinus junction (arrow).

Conclusions

Permeative osseous changes have a high interrater reliability and may assist in identifying the presence and location of dAVF. In cases of patients with known prior thrombosis, osseous changes may signal transformation to dAVF and could select patients for further work up including MRA or conventional angiography.



(Filename: TCT_O-106_BryndAVFfigure120616.jpg)

Tuesday
3:30PM - 4:45PM
Long Beach Convention Center, Room 103 (Main Level)

14C-Parallel Paper Session: Spine Imaging: Lesion Detection and Infection . . .Ready, Set, PET!

O-109

3:30PM - 3:38PM

Expert-based Artificial Intelligence Tool for Diagnosis of Spine Pathology using Bayesian Networks

N Cross[1], I Nasrallah[1], S Mohan[1], E Botzolakis[1]
[1]*University of Pennsylvania, Philadelphia, PA*

Purpose
Bayesian networks (BN) are a promising form of artificial knowledge representation capable of providing radiology diagnosis support. To explore their potential utility for assisting spine MRI interpretation, we developed a BN that integrates imaging features with patient demographics and pertinent clinical history to discriminate a challenging set of diseases affecting the spinal cord and canal.
Materials and Methods
Using commercially available software (Netica), a naive BN was generated consisting of a parent "disease" node connected to multiple child "feature" nodes. The disease node contained a comprehensive list of 40 entities affecting the spinal cord and canal. Feature nodes included MR signal and spatial characteristics, plus clinical features such as patient age, 16 features in total. Disease pretest probabilities and conditional probabilities (i.e., the probability of a feature given a disease) were generated from a combination of neuroradiologist expert opinion and literature review. Bayesian network performance was evaluated using 10,000 randomly generated test cases derived from the expert-provided conditional probabilities. By comparing BN prediction to ground truth, a confusion matrix was generated and used to evaluate diagnostic performance.
Results
Overall BN sensitivity and specificity were 0.74 ± 0.16 and 0.99 ± 0.01, respectively, with an overall accuracy of 0.79. Sensitivity was highest for dural AVF (0.96), lipoma (0.92), and subdural hematoma (0.90), reflecting relatively distinct features including flow voids, T1 hyperintensity, or hyperdensity, respectively. Based on sensitivity analysis, the 5 most discriminating imaging features were (in decreasing order of entropy reduction): axial location, number of lesions, craniocaudal extent, CT density, and enhancement.
Conclusions
A comprehensive expert-based BN was developed successfully with high discriminatory capacity for diseases affecting the spinal cord and canal. Although further validation will be needed with radiologist-extracted imaging features from clinical cases, these preliminary results demonstrate the potential utility of BNs for neuroradiology diagnostic support.

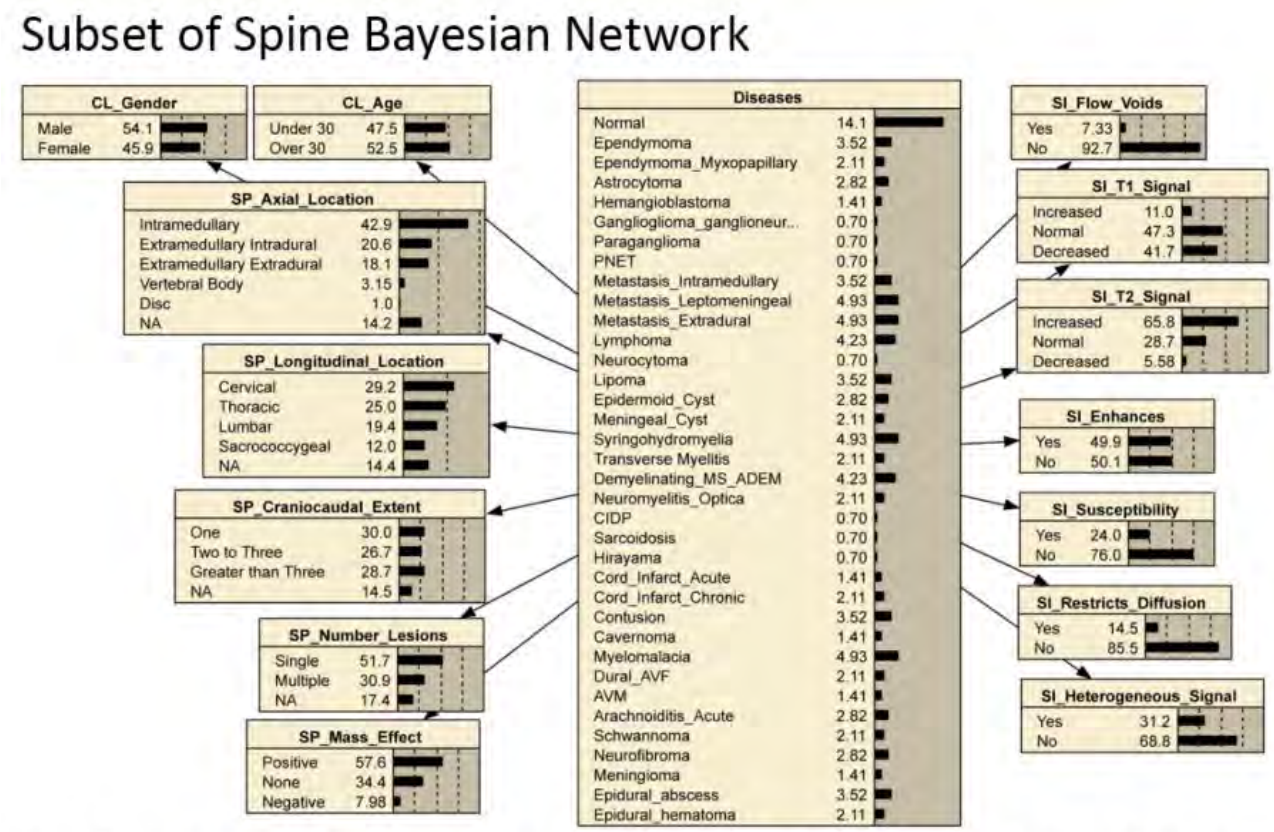


Figure 1: Subset of the spine bayesian network demonstrating the clinical (CL_), signal (SI_), and spatial (SP_) nodes and their attributes. Displayed probabilities represent calculated pretest probability before any attribute is input.

(Filename: TCT_O-109_SubsetBayesianNetwork.jpg)

O-110

3:38PM - 3:46PM

Detection of spinal cord lesions in clinically isolated syndrome patients: comparison of sagittal short T1 inversion recovery (STIR), T2-weighted, proton density and combined T2-STIR sequences

C Auger[1], A Salerno[2], J Gutierrez[2], E Huerga[2], F Aymerich[2], J Corral[2], M Alberich[1], M Tintore[2], G Arrambide[2], X Montalban[3], A Rovira[2]
[1]Vall d'Hebron University Hospital, Barcelona, [2]Vall d´Hebron University Hospital, Barcelona, [3]Vall d'Hebron University Hospital, barcelona

Purpose
To compare the sensitivity in the detection of spinal cord (SC) lesions of different sagittal sequences [short T1 inversion recovery (STIR), T2 and proton density (PD)-weighted, and combined T2-STIR sequences] acquired at 3.0T, in patients presenting with a clinically isolated syndrome (CIS).

Materials and Methods
Magnetic resonance imaging (MRI) of the whole SC of 84 patients presenting with a CIS (age 34.7+7.4 years; 66.7% females; 17.9% with a SC syndrome) were analyzed retrospectively by 2 independent observers (O1, O2). Presence of SC lesions was evaluated on sagittal STIR, T2, PD and combined T2-STIR sequences. The reference standard (RS) was obtained by a third experienced neuroradiologist using all sequences available, in order to calculate a definitive lesion counts. Sensitivity, specificity and interobserver agreement were assessed for each sequence.
Results
A total of 84 image sets, which included all 4 types of images, were analyzed. The RS detected 107 lesions, and 35.7% patients with at least one SC lesion. In the independent analysis, the total lesion count was 84 (O1) and 128 (O2) on STIR, 103 (O1) and 90 (O2) on T2-STIR, 75 (O1) and 97 (O2) on PD, and 71 (O1) and 78 (O2) on T2. The percentage of patients with at least 1 SC lesion was 31% (O1) and 59.5% (O2) on STIR; 45.2% (O1) and 46.4% (O2) on T2-STIR images; 34.5% (O1) and 50% (O2) on PD; while 36.9% (O1) and 41.7% (O2) on T2 images. Sensitivity detecting lesions by observers were 72.0% (O1) and 72.0% (O2) for STIR; 72.0% (O1) and 60.8% (O2) for T2-STIR; 51.4% (O1) and 60.8% (O2) for PD, and 54.2% (O1) and 57.0% (O2) for T2. Sensitivity and specificity in detecting patients with at least 1 SC lesion were 83.3% and 98.2% (O1) and 96.7% and 61.1% (O2) for STIR; 96.7% and 83.3% (O1) and 90% and 77.8% (O2) for T2-STIR; 80.0%, and 90.7% (O1) and 93.3% and 74.1% (O2) for PD; and 76.7% and 85.2% (O1) and 80.0% and 79.6% (O2) for T2. The interobserver (O1, O2) agreement (weighted kappa value) for the detecting patients with at least 1 SC lesion was moderate to good: 0.423 (STIR), 0.502 (T2), 0.69 (PD), and 0.64 (T2-STIR).
Conclusions
Highest sensitivity for detecting SC lesions and patients with at least 1 SC lesion, was achieved with STIR and combined T2-STIR images, although the first sequence showed only a moderate level of interobserver agreement. The combination of STIR, T2 and combined T2-STIR images is probably the best strategy for detecting SC lesions in CIS patients.

O-111

3:46PM - 3:54PM

Neurographic Imaging as a Biomarker for Detecting Radiation Injury to the Spinal Cord

D Schellingerhout[1], D Grosshans[1], L Le Roux[1]
[1]*UT MD Anderson Cancer Center, Houston, TX*

Purpose

The goal of this study was to detect changes in the spinal cord in response to radiation injury by means of molecular imaging.

Materials and Methods

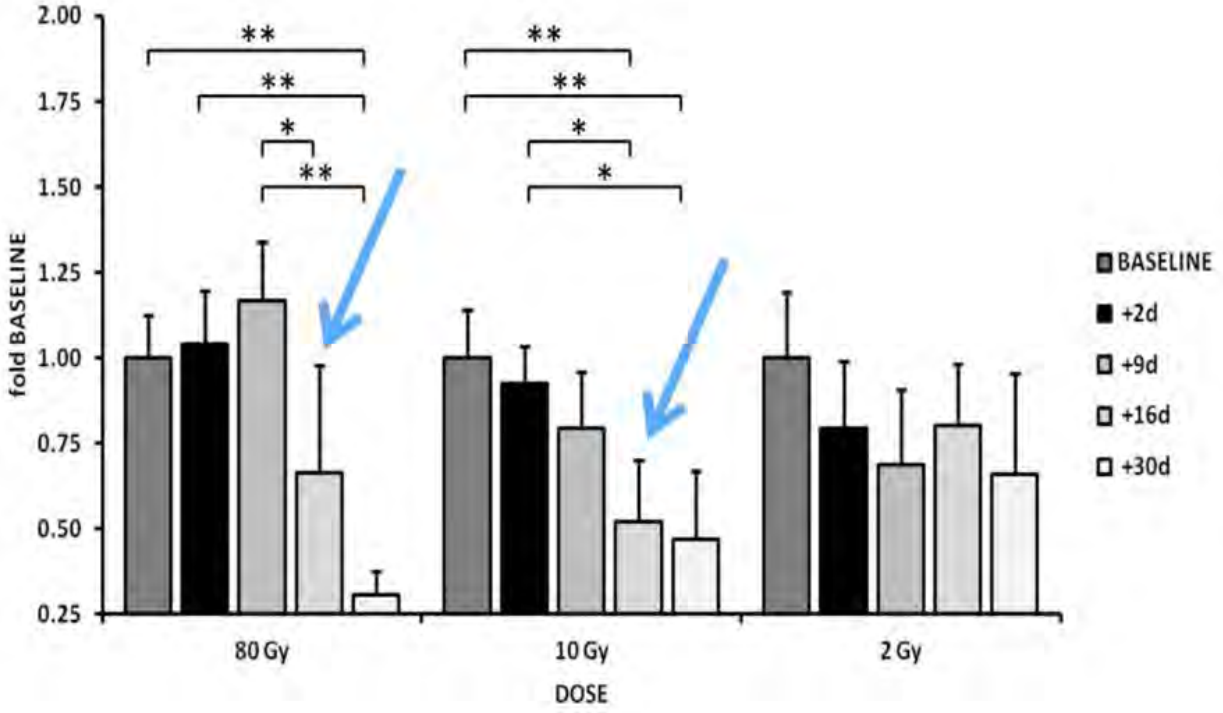
The lower thoracic spinal cord of adult female BALB/c mice was irradiated with single doses of 2, 10, and 80 Gy. Fluorescently labeled Tetanus Toxin C-fragment (TTc) was used to evaluate changes in the retrograde axonal transport mechanism by means of optical imaging. Hematoxilin-Eosin staining served to assess pathologic changes in radiated cords.

Results

Transport of TTc in the spinal cord was impaired in a dose-dependent manner as early as 2 days after radiation. Transport was significantly decreased by 16 days in animals exposed to either 10 or 80, while animals exposed to 2 Gy remained unaffected (See Fig.). Further, animals exposed to the highest dose also experienced significant weight loss by 9 days and developed posterior paralysis by 45 days. Pathologic changes of radiation damage could be seen in radiated cords after 30 days in mice exposed to 80 Gy.

Conclusions

Radiation of the spinal cord induces dose-dependent changes in the axonal transport mechanism which can be monitored by molecular imaging. This approach suggests a novel diagnostic biomarker to assess radiation induced cord injury and monitor therapeutic interventions aimed at preventing such injury.



(Filename: TCT_O-111_RadiationLeRoux12_08_16.jpg)

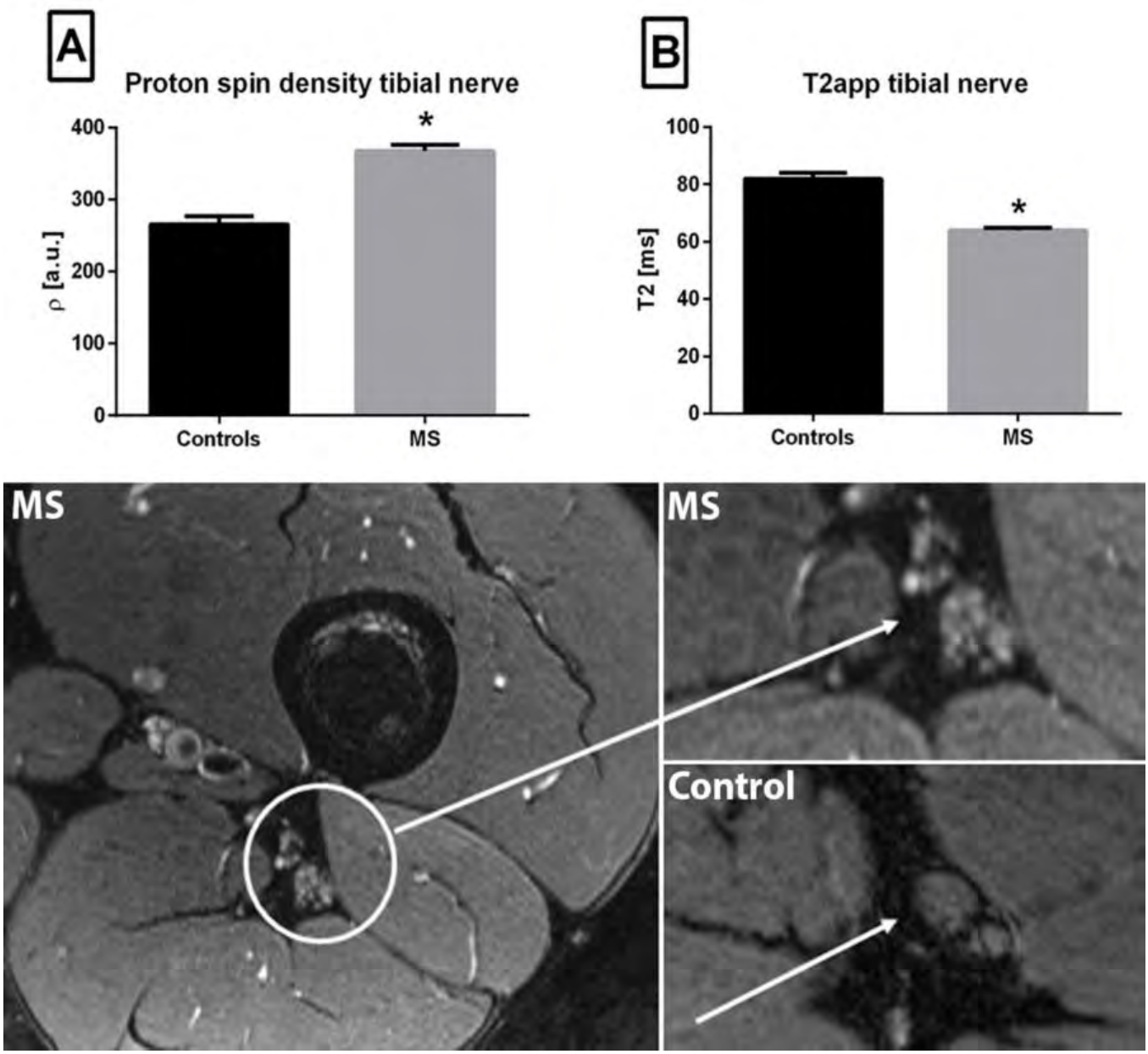
O-112

3:54PM - 4:02PM

Involvement of the peripheral nervous system in multiple sclerosis detected in vivo by high-resolution MR-Neurography

G Hauck[1], M Weiler[1], S Heiland[1], B Wildemann[1], W Wick[1], M Bendszus[1], J Kollmer[2]
[1]University Hospital Heidelberg, Heidelberg, Baden-Wuerrtemberg, [2]University Hospital Heidelberg, Heidelberg, Germany

Purpose
To detect, localize and quantify peripheral nerve lesions in patients with multiple sclerosis (MS) by high-resolution magnetic resonance neurography (MRN) with large anatomical coverage, in combination with electrophysiological and neurological evaluations.
Materials and Methods
We prospectively investigated 32 patients (18-45 years) with confirmed MS (>3 years) and compared them to 35 healthy volunteers matched for gender and age. All MS patients received detailed neurological and electrophysiological examinations. Magnetic resonance neurography at 3 Tesla magnetic field strength and with large anatomical coverage from lumbar plexus and spinal nerves down to ankle level was performed in all participants by using fat-saturated, T2-weighted turbo-spin-echo (TSE) sequences (repetition-time/echo-time 5970/55 ms) and a dual echo TSE sequence for T2-relaxometry (repetition-time 5210 ms; echo-times 12/73 ms). Furthermore we used a 3D T2-weighted inversion-recovery sequence (repetition-time/echo-time 3000/202ms) for evaluation of the lumbar plexus. Manual segmentation of spinal/sciatic/tibial/peroneal nerves was performed on a total of 16,080 axial slices. Besides evaluation of nerve T2-weighted signal, detailed quantification of nerve impairment by morphometric (nerve caliber) and microstructural markers (1, 2) (proton-spin-density and T2-relaxation-time) was conducted.
Results
Nerve proton-spin-density was higher in MS patients (tibial/peroneal: 367.9±7.9 / 364.4±8.5) vs. controls (tibial/peroneal: 266.0±11.0 / 276.8±9.7; $p<0.0001$). In contrast, T2-relaxation-time was significantly higher in controls (tibial/peroneal: 82.0±2.2 / 78.3±1.7) vs. MS (tibial/peroneal: 64.0±1.0 / 61.0±0.9; $p<0.0001$). Proximal nerve diameter also was significantly higher in the MS group (tibial: 53.0±2.1) vs. controls (tibial: 45.2±1.4; $p<0.0007$). Electroneurographic and F-wave results were completely normal in all MS patients.
Conclusions
For the first time, we visualized and quantified peripheral nerve lesions in MS patients in vivo by high-resolution MRN. Lesions are defined by an increase of proton-spin-density and not by an increase of the T2-relaxation-time. Nerve caliber as a morphometric criterion also showed a significant increase. The proof of a PNS involvement in MS may offer new insights into the pathomechanism and might have future implications on therapeutic approaches.



(Filename: TCT_O-112_Figure_ASNR.jpg)

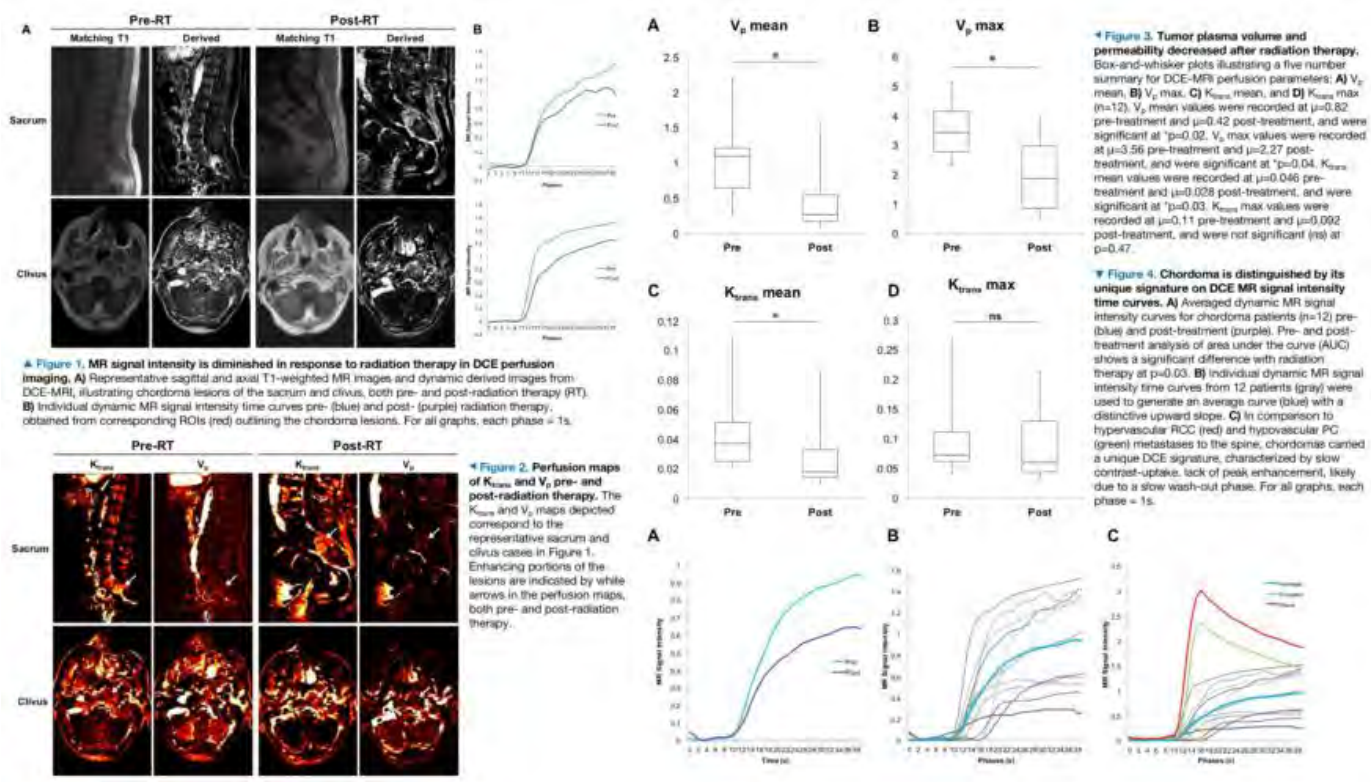
O-113

4:02PM - 4:10PM

Using Dynamic Contrast-Enhanced Magnetic Resonance Perfusion Imaging to Monitor Tumor Response to Therapy in Chordoma.

P Santos[1], K Peck[2], J Arevalo-Perez[2], S Karimi[2], E Lis[2], Y Yamada[2], A Holodny[3], J Lyo[2]
[1]Perelman School of Medicine at the University of Pennsylvania, Philadelphia, PA, [2]Memorial Sloan Kettering Cancer Center, New York, NY, [3]Memorial Sloan Kettering Cancer Center, Weill Cornell Medical College, New York, NY

Purpose
Highly aggressive and locally invasive, chordoma is characterized by a paradoxically low-grade, heterogeneous histology that limits discrimination between chordoma and other spinal tumors via conventional magnetic resonance imaging (MRI). In this study, we show that dynamic contrast-enhanced (DCE)-MRI quantitative parameters [i.e. plasma volume (Vp) and vascular permeability (Ktrans)] can be used to characterize tumor response to radiation--detecting subsequent changes in chordoma vascularity before parallel changes in tumor volume are detected with conventional MRI.
Materials and Methods
Eleven patients with DCE-MRI perfusion before and after radiation therapy (RT) were enrolled. Kinetic enhancement of tissue before, during and after injection was obtained using 3D T1-weighted fast spoiled-gradient echo sequence. Voxel-by-voxel estimates of quantitative perfusion parameters, specifically Ktrans and Vp, were determined using Tofts' 2-compartment pharmacokinetic model. Area under the curve (AUC) was obtained via semi-quantitative analysis. We used Mann-Whitney U tests at a significance of $P \leq 0.05$ to assess differences between dynamic response curves, pre- and post-RT and Wilcoxon rank-signed tests at a significance of $P \leq 0.05$ to assess the difference between Vp and Ktrans values, pre- and post-RT.
Results
Post-treatment, there was decreased enhancement across dynamic derived images, and Vp and Ktrans maps. Plasma volume mean showed the most significant (*p=0.02) difference, followed by Vp max and Ktrans mean, which also were also significant at *p=0.04 and *p=0.03, respectively; however, Ktrans max showed no significant difference. Semiquantitative AUC analysis of the aggregate pre- and post-RT curves, showed a significant difference (p=0.03) in MR signal decreasing from μ=3.56 pretreatment to μ=3.56 post-treatment.
Conclusions
Dynamic contrast-enhanced parameters such as Vp, Ktrans, and AUC are decreased significantly after post-treatment, reflecting the extent of vascular damage induced by radiation therapy. Of the 3 parameters studied, Vp was the most significant indicator of tumor response. Collectively, these findings demonstrate the capacity of DCE-MRI to accurately reflect underlying tumor physiology in response to therapy.



▲ Figure 1. **MR signal intensity is diminished in response to radiation therapy in DCE perfusion imaging. A)** Representative sagittal and axial T1-weighted MR images and dynamic derived images from DCE-MRI, illustrating chordoma lesions of the sacrum and clivus, both pre- and post-radiation therapy (RT). **B)** Individual dynamic MR signal intensity time curves pre- (blue) and post- (purple) radiation therapy, obtained from corresponding ROIs (red) outlining the chordoma lesions. For all graphs, each phase = 1s.

◂ Figure 2. **Perfusion maps of K_{trans} and V_p pre- and post-radiation therapy.** The K_{trans} and V_p maps depicted correspond to the representative sacrum and clivus cases in Figure 1. Enhancing portions of the lesions are indicated by white arrows in the perfusion maps, both pre- and post-radiation therapy.

◂ Figure 3. **Tumor plasma volume and permeability decreased after radiation therapy.** Box-and-whisker plots illustrating a five number summary for DCE-MRI perfusion parameters: **A)** V_p mean, **B)** V_p max, **C)** K_{trans} mean, and **D)** K_{trans} max (n=12). V_p mean values were recorded at μ=0.82 pre-treatment and μ=0.42 post-treatment, and were significant at *p=0.02. V_p max values were recorded at μ=3.56 pre-treatment and μ=2.27 post-treatment, and were significant at *p=0.04. K_{trans} mean values were recorded at μ=0.046 pre-treatment and μ=0.028 post-treatment, and were significant at *p=0.03. K_{trans} max values were recorded at μ=0.11 pre-treatment and μ=0.092 post-treatment, and were not significant (ns) at p=0.47.

▾ Figure 4. **Chordoma is distinguished by its unique signature on DCE MR signal intensity time curves. A)** Averaged dynamic MR signal intensity curves for chordoma patients (n=12) pre- (blue) and post-treatment (purple). Pre- and post-treatment analysis of area under the curve (AUC) shows a significant difference with radiation therapy at p=0.03. **B)** Individual dynamic MR signal intensity time curves from 12 patients (gray) were used to generate an average curve (blue) with a distinctive upward slope. **C)** In comparison to hypervascular RCC (red) and hypovascular PC (green) metastases to the spine, chordomas carried a unique DCE signature, characterized by slow contrast-uptake, lack of peak enhancement, likely due to a slow wash-out phase. For all graphs, each phase = 1s.

(Filename: TCT_O-113_Figures.jpg)

O-114

4:10PM - 4:18PM

Direct Comparison of T1-Dixon and STIR in the Identification of FDG PET Avid Metastases in the Spine on Dedicated PET-MRI

J Varghese[1], J Bai[1], R Matthews[2], L Bangiyev[2], a chimpiri[3], D Franceschi[1]
[1]Stony Brook Medicine, Stony Brook, NY, [2]Stony Brook Medicine, Stony Brook , NY, [3]Stony Brook Medicine, stony brook, NY

Purpose
Positron emission tomography-magnetic resonance imaging (PET-MRI) is playing an increasing role in the staging and restaging of malignancy. However, no standardized MRI sequence is accepted for evaluation of the spine on PET-MRI. Dixon technique imaging is promising due to its ability to identify lesions containing microscopic fat, thought generally to be exclusive to benign lesions. This study aims to compare T1-Dixon imaging with STIR imaging in the evaluation of spine metastases on PET-MRI.
Materials and Methods
We retrospectively identified 10 patients from September to December 2016 who underwent fluorodeoxyglucose (FDG) PET-MRI imaging of the spine with both T1-Dixon and STIR sequences. Each sequence was reviewed separately and blindly by a board-certified

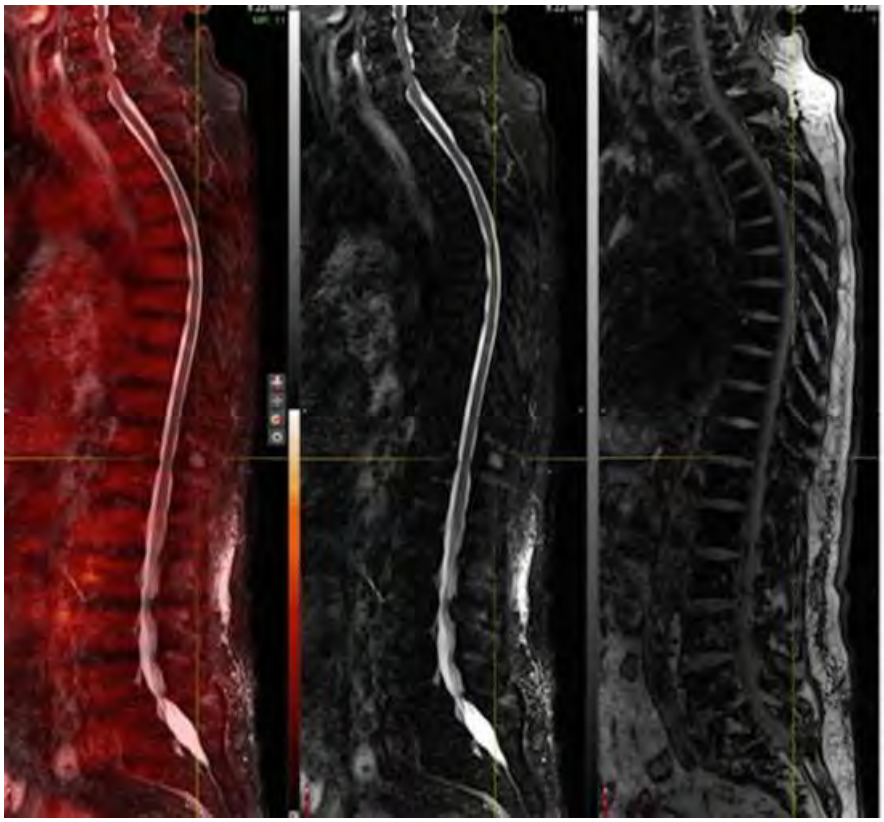
neuroradiologist and a board-certified nuclear medicine physician by consensus reading. Lesions identified on T1-Dixon images were classified as either benign or malignant. This was repeated for STIR images. Finally, a diagnosis of benign or malignant was given to each lesion based on FDG PET activity, clinical history, pathological findings, and complete radiology record. T1-Dixon and STIR characterization of each lesion then was compared with the final lesion diagnosis. Statistical analysis was performed on Excel.

Results

One hundred fifty-four lesions were identified on T1-Dixon and STIR sequences. T1-Dixon sequence demonstrated higher specificity (78% vs 43%), PPV (53% vs 31%), and NPV (82% vs. 72%) in identifying metastases when compared to STIR (Table 2). STIR showed slightly higher sensitivity in identifying FDG avid lesions (61% vs. 59%). Chi-square analysis demonstrated no statistically significant difference between T1-Dixon sequence and FDG-PET in identifying the number of metastases ($p= 0.54$). The null hypothesis was rejected in Chi-square analysis between STIR and PET ($p<0.01$).

Conclusions

T1-Dixon sequence demonstrated superior PPV, NPV, and specificity over STIR in the identification of FDG PET avid metastases in the spine. It also was noted incidentally that T1-Dixon demonstrated superior ability in discriminating between treated metastases and active metastases.



Data Analysis

Table 1

	PET (positive)	PET (negative)
DIXON(positive)	27	24
DIXON(negative)	19	84
STIR(positive)	28	61
STIR (negative)	18	47

Table 2

	Sensitivity	Specificity	PPV	NPV
DIXON	0.59	0.78	0.53	0.82
STIR	0.61	0.43	0.31	0.72

Table 3

	Chi Square
DIXON and PET	0.54
STIR and PET	<0.001

Figure 1: (From left to right) Midline sagittal fused PET-MRI, STIR, and T1-Dixon (opposed phase) images of the spine. STIR sequence demonstrates a hyperintense lesion in the T11 spinous process (crosshairs) and was concerning for metastasis. On T1-Dixon opposed phase images, however, the lesion dropped signal and was therefore called benign. The lesion was indeed not FDG PET avid and was finally determined to be benign in nature.

(Filename: TCT_O-114_dixonstirpetmri1.jpg)

O-115

4:18PM - 4:26PM

PET Imaging of Infection Using Metabolic Labeling of the Bacterial Cell Wall

J Villanueva-Meyer[1], K Neumann[1], C Mutch[1], T Kwak[1], R Sriram[1], O Rosenberg[1], D Wilson[1]
[1]*University of California - San Francisco, San Francisco, CA*

Purpose
Radiologic differentiation between degenerative and infectious bony changes often presents a diagnostic dilemma. Current methods of imaging bacterial infection rely on detecting morphologic changes or host immune response (1). As these strategies often are nonspecific, several new approaches aimed at detecting gram negative bacterial metabolism have been studied (2). However, the causative organisms often are gram positive and a reliable imaging technique to probe bacterial metabolism in vivo is needed. Most bacteria produce and incorporate D-amino acids (DAA) into the peptidoglycan cell wall (3). The central hypothesis of our study was that radiolabeled DAAs could be used as a specific marker of bacterial infections in vivo.
Materials and Methods
D-amino acids retention in bacterial cultures was studied with 14C-enriched D-alanine, D-met, and D-phenylalanine using liquid scintillation. Using an analogous method to that employed for 11C L-methionine, a mirror image D-homocysteine thiolactone precursor was synthesized and used to generate 11C D-met with improved conditions to minimize racemization (4). Uptake of the resulting 11C D-met was assessed in E. coli culture studies. Subsequently, a murine myositis model, similar to one recently described in the literature, was prepared with both E. coli and S. aureus and PET imaging was performed on a micro PET/CT system with dynamic imaging over 60 minutes (2).
Results
In our 14C-enriched DAA studies we found that D-met had 4 times greater uptake than the other studied DAAs. Therefore, D-methionine was selected as the lead candidate for PET radiotracer synthesis. Radiosynthesis was optimized and resulted in greater than 95% D-methionine. E. coli culture studies performed with 11C D-met recapitulated observed results from liquid scintillation studies of emitting nuclei including cell uptake that demonstrated blocking with cold product and significantly decreased uptake using heat-killed bacteria. In vivo PET imaging in a murine infection model demonstrated greater than 2-fold tracer accumulation within muscle for live versus heat-killed E. coli and S. aureus.
Conclusions
We demonstrated radiosynthesis, in vitro evaluation, and initial PET imaging evaluation of 11C D-met in a murine model of both gram positive and gram negative infection. This, along with other DAAs, represent a promising class of compounds for imaging bacterial infection in vivo and may have useful applications in differentiating spinal infection from other common pathologies.

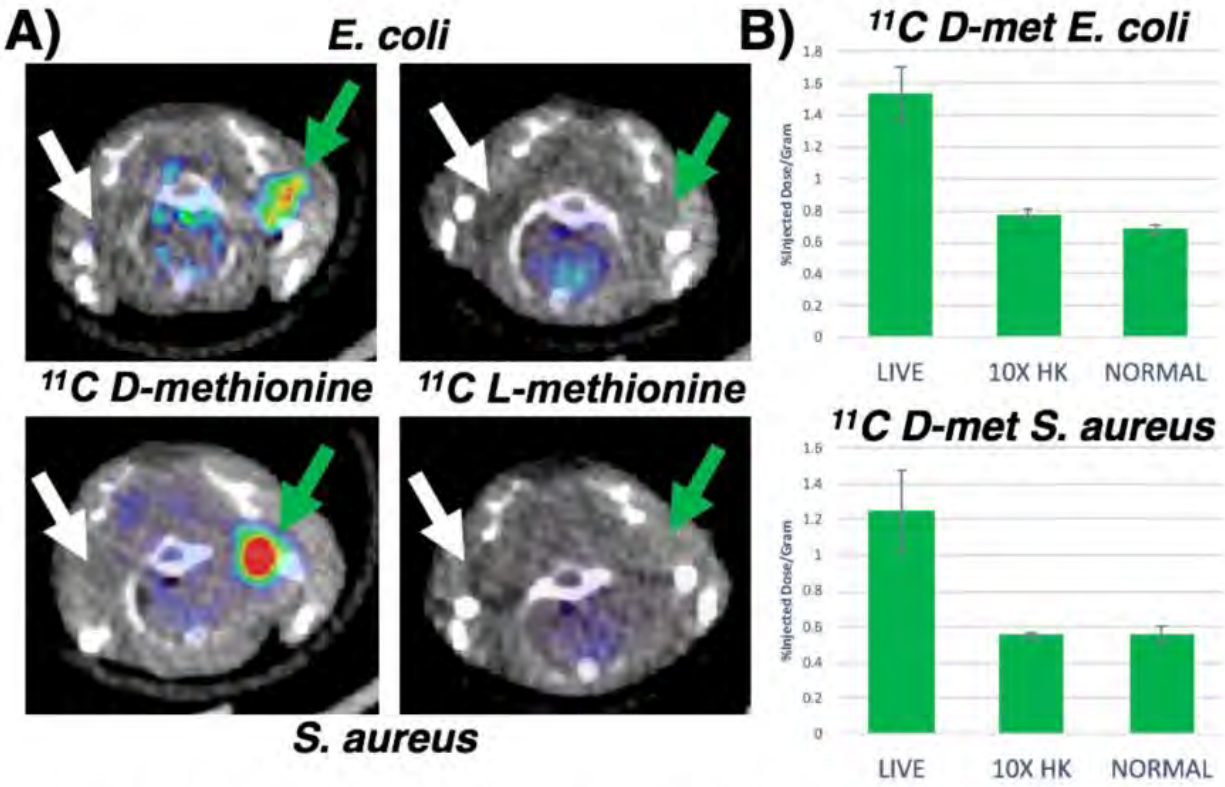


Figure 1. (A) Micro PET/CT following intravenous injection of 1 mCi ^{11}C D- and L-met in mouse *E. coli* and *S. aureus* myositis model. Significantly increased tracer accumulation is demonstrated in the live bacteria inoculated shoulder (green arrow) versus heat-killed control shoulder (white arrow) with ^{11}C D-met. No significant uptake is seen in either live or heat-killed shoulders with ^{11}C L- met. (B) Uptake of ^{11}C D- and L-met at 45 minutes following injection shows greater than 2-fold uptake of D-met as compared to L-met in shoulders injected with live *E. coli* and *S. aureus* and no significant difference between heat-killed control shoulder and normal muscle background uptake.

(Filename: TCT_O-115_D_met_fig_ASNR_2016.jpg)

O-116

4:26PM - 4:34PM

PET Imaging of Spinal Infection by Targeting Folate Metabolism

C Mutch[1], K Neumann[1], J Villanueva-Meyer[2], J Blecha[3], D Wilson[3]
[1]University of California, San Francisco, San Francisco, CA, [2]University of California - San Francisco, San Francisco, CA, [3]UCSF, San Francisco, CA

Purpose
Spinal infections including vertebral osteomyelitis and diskitis are a common indication for spinal imaging. There can be significant overlap in the appearance in infectious and

noninfectious spinal pathology, particularly in postoperative patients. Existing imaging techniques rely on secondary changes of infection, though; most of these also are seen in cases of sterile inflammation. Recently there has been increased interest in metabolic imaging of infection. A recent report by Weinstein et al. described imaging of gram-negative infection with FDS. As spinal infections often arise from both gram negative and gram-positive organisms, there is an unmet need for imaging probes that detect both. Folate metabolism is an attractive target for bacterial imaging because mammals unlike bacteria are unable produce endogenous folate. Here we describe synthesis of a new PET tracer and a novel approach to directly image both gram positive and gram-negative bacterial spinal infections by using radiolabelled folate precursors.

Materials and Methods

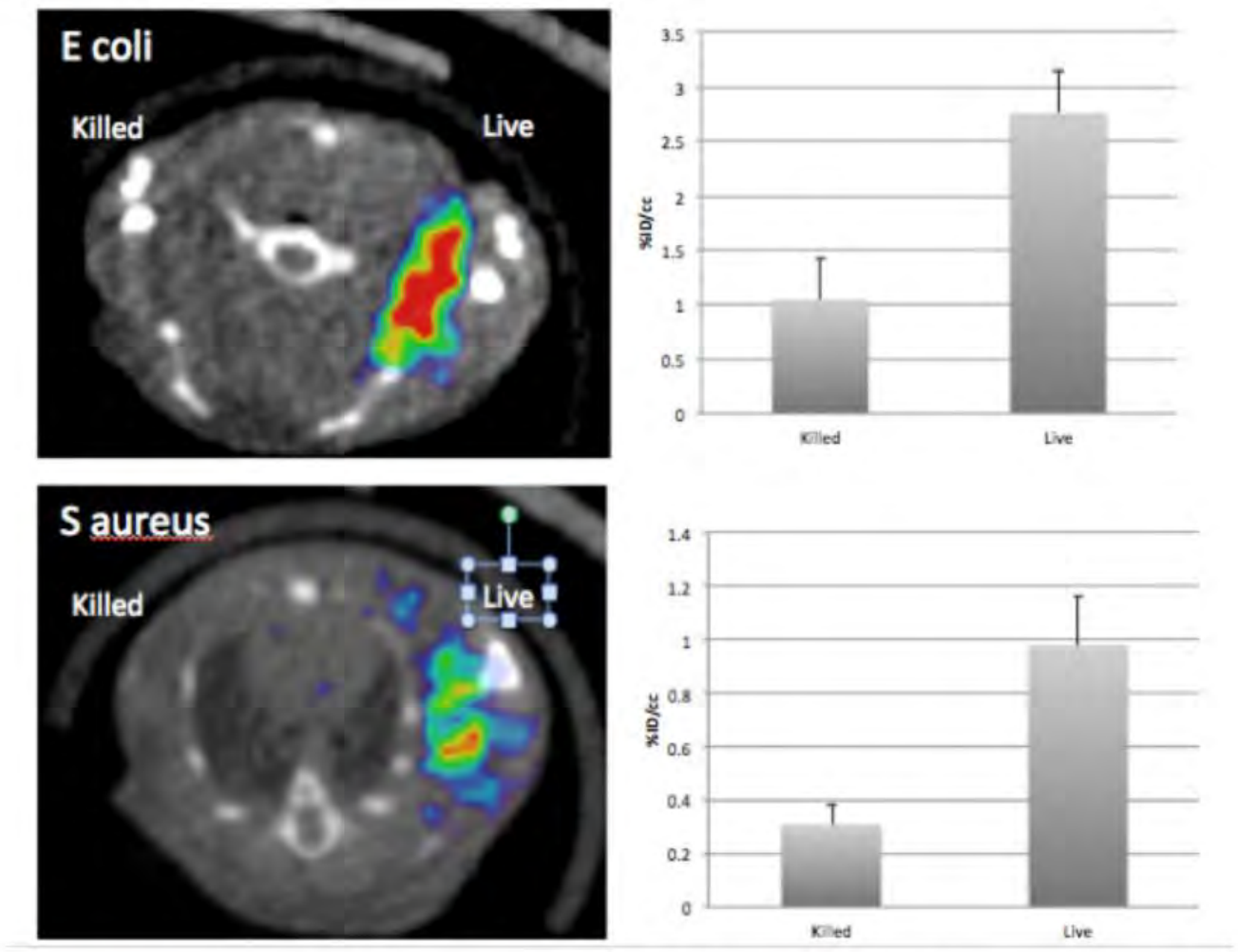
We developed a novel method for efficient and rapid production of 11C labeled para-aminobenzoic acid, a direct precursor to folate using a commercially available Grignard reagent. The 11C-PABA was purified with cation exchange cartridges and radiochemical purity was verified with HPLC. Radiotracer was administered to bacterial cultures (1 uCi/ml) shaking at 37 degrees for in vitro studies. For in vivo studies a murine myositis model was used as described previously. Radiotracer was administered via tail vein injection into mice (1 mCi) 45 minutes prior to imaging on a Siemens microPET/CT scanner.

Results

HPLC analysis revealed synthesis of 11C-PABA with greater than 95% radiochemical yield. In vitro studies revealed that 11C-PABA was rapidly and specifically incorporated into both gram positive (S aureus) and gram-negative (E coli) bacteria. In vivo, assays with murine myositis model revealed significantly increased focal uptake 11C-PABA in infected limbs as compared to sterile inflammation.

Conclusions

11C-PABA is a novel PET tracer for specific imaging gram-positive and gram-negative bacteria.



MicroPET/CT image generated following intravenous injection of 1000 μCi ^{11}C PABA in mouse *E. coli* and S aureous abscess model. Significantly increased tracer accumulation is demonstrated in the live bacteria-inoculated flank versus heat-killed control flank. Uptake of ^{11}C PABA at 60 minutes following injection of 1000 μCi [1] shows greater than 2-fold uptake in the flank inoculated with live bacteria as compared to heat-killed bacteria.

(Filename: TCT_O-116_PABAASNR.jpg)

O-117

4:34PM - 4:42PM

Percutaneous Spinal Biopsy: Is Aspiration Crucial in Detecting Infection?

R Galuppo Monticelli[1], L Lin[1], A Alhajeri[1]
[1]*University of Kentucky, Lexington, KY*

Purpose
Percutaneous computed tomography (CT)-guided spinal biopsy is necessary to guide management of vertebral diskitis and osteomyelitis (VDOM). With increasing incidence of VDOM and widespread use of antibiotics, the sensitivity for biopsy for detection has

decreased. We want to determine if technique, specifically aspiration aided biopsy versus traditional tissue biopsy, and location of biopsy would affect sensitivity of cultures. To our knowledge, this is the largest series of patients who have undergone spinal biopsy for infection.

Materials and Methods

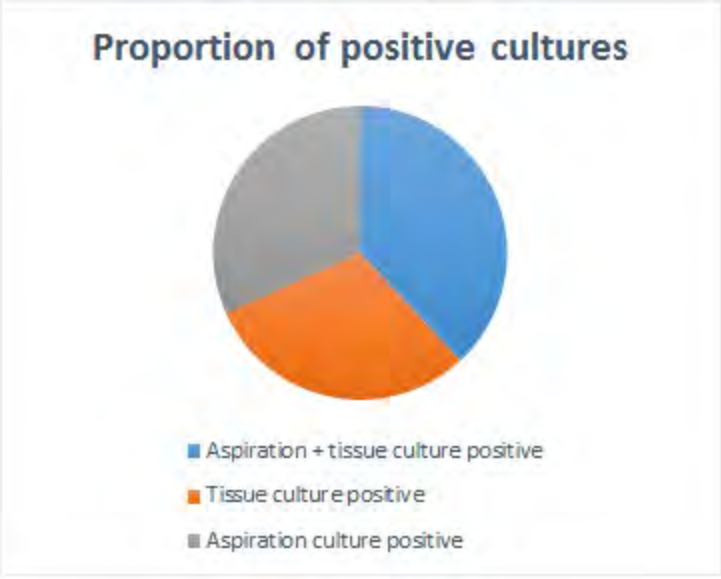
We retrospectively reviewed 232 patients with suspected VDOM. Computed tomography (CT)-guided biopsy of the spine confirmed the findings, utilizing 18/20G coaxial temno needle biopsy system. Immediately following the core biopsy, an aspiration biopsy was obtained through the coaxial needle. These specimens were sent for microbiology analysis. The diagnosis was based on the clinical findings, imaging, and microanalysis.

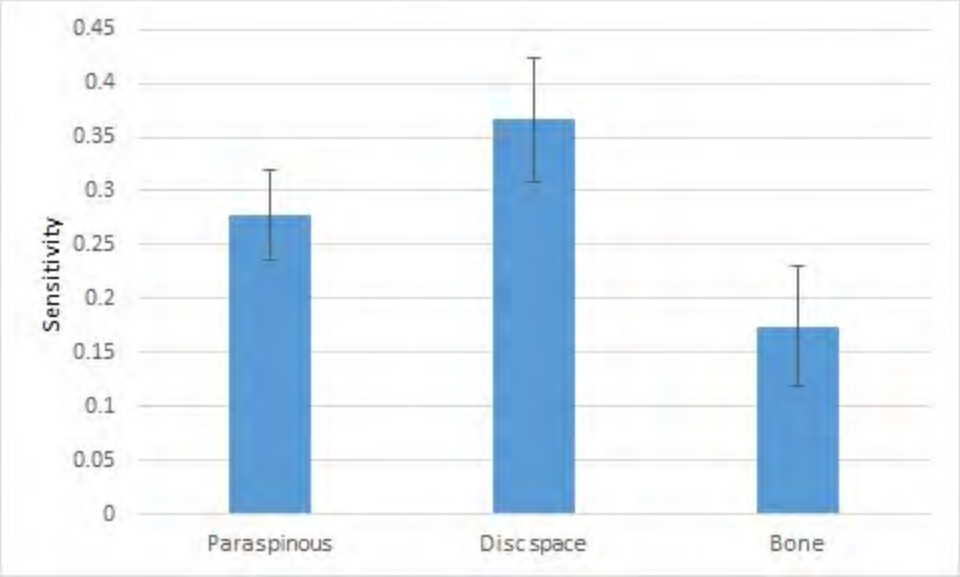
Results

Two hundred thirty-two patients underwent CT-guided spinal biopsy. Sixty-six patients had positive microanalysis, 24 had positive aspiration and tissue microanalysis, 19 had positive tissue microanalysis only, and 20 had positive aspiration microanalysis only. Thus, the aspiration aided biopsy increased the examination sensitivity from 18.8% to 27.5%, relative to the standard tissue biopsy. There is a trend for a higher sensitivity with disk space biopsy versus bone biopsy, 36.6% versus 17.4% respectively, with paraspinous biopsy yielding intermediate sensitivity at 27.8%.

Conclusions

Approximately a third of culture positive cases were from aspiration culture while the tissue culture was negative. Aspiration following tissue biopsy increases the sensitivity relative to standard tissue biopsy alone. Additionally, the data supported higher sensitivity if the sample was obtained from the disk space relative to the bone. This suggests aspiration after tissue biopsy should be considered as part of standard procedure and disc space biopsy should be obtained if possible for maximal sensitivity.





(Filename: TCT_O-117_SpineBxv1.jpg)

Tuesday
3:30PM - 4:50PM
Long Beach Convention Center, Room 104A (Main Lobby)

14D-Parallel Paper Session: Stroke Management: Viable Outcomes for Vascular Occlusions

O-118

3:30PM - 3:38PM

DSA Cerebral Circulation Time for Assessment of Symptomatic Carotid Stenosis

Y Hu[1], C Lin[1], F Chang[1], C Wu[1], H Lee[1], C Luo[1], W Guo[1]

[1]*Taipei Veterans General Hospital; School of Medicine, National Yang Ming University, Taipei, Taiwan*

Purpose
Current strategy for carotid stenosis management primarily relies on the internal carotid artery (ICA) stenotic degrees (based on NASCET criteria) and clinical symptoms. Other factors such as collateral circulation might influence the brain perfusion, and theoretically make the stenotic degree less reliable to reflect cerebral ischemic burden. This study aimed to compare the cerebral circulation time (CCT) and the ICA stenotic degree defined on digital subtraction angiography (DSA) in terms of their association with the presence of symptomatic carotid stenosis.
Materials and Methods
Eighty-three patients with a unilateral carotid stenosis, 29 symptomatic and 54 asymptomatic, were retrospectively (2011–2016) enrolled. All patients underwent DSA evaluation with fixed contrast injection protocols and acquisition parameters. The CCT was defined as the time difference of the maximal intensity between the 2 target points at the ICA and the parietal vein on lateral view DSA. The CCT and ICA stenotic degrees of the symptomatic and asymptomatic groups were compared. Logistic regression analysis was performed to estimate the odds ratio in the presence of symptomatic carotid stenosis with the CCT, ICA stenotic degree and antithrombotics use.
Results
The symptomatic group had significantly longer mean CCT, greater mean ICA stenotic degree, and less frequent antithrombotics use. The CCT (odds ratio 1.9; $P = 0.015$) was significantly more associated with symptomatic carotid stenosis than the ICA stenotic degree (odds ratio 1.0, $P = 0.170$) after adjusting for antithrombotics use.
Conclusions
The CCT derived from DSA may be more highly associated with symptomatic carotid stenosis than the ICA stenotic degree, and thus can serve as a more reliable objective parameter for assessment of patients with carotid stenosis. Antithrombotics may help to reduce risk of ischemic symptoms.

Table l: Comparison of demographics and DSA parameters between carotid stenosis with and without symptoms

	Symptomatic (n = 29)	Asymptomatic (n = 54)	*P* Value
Demographics			
Age (yr)	69 ±15	73 ± 12	0.142
Sex (male)	24 (83%)	44 (81%)	>0.999
Coronary arterial disease	7 (24%)	16 (30%)	0.620
Hypertension	24 (83%)	41 (76%)	0.582
Diabetes	12 (41%)	20 (37%)	0.814
Hyperlipidemia	13 (45%)	27 (50%)	0.818
Intermittent claudication	3 (10%)	6 (11%)	>0.999
Cigarette smoking	15 (52%)	25 (46%)	0.653
Antithrombotics	**10 (34%)**	33 (61%)	**0.021**
Symptoms at entry [a]			
Transient ischemic attack	15 (52%)	NA	NA
Nondisabling stroke	14 (48%)	NA	NA
DSA parameters			
ICA stenotic degree (%)	**78.3 ± 13.0**	70.8 ± 13.4	**0.017**[b]
CCT (sec)	**5.6 ± 1.4**	4.7 ± 0.9	**0.003**[b]

Note:—CCT indicates cerebral circulation time. [a] Symptoms within the **180 days** before entry.
[b] Statistically significant (*t* test, $P < 0.05$).

Table 2: Multivariate analysis of variables associated with symptomatic carotid stenosis

Variables	OR	95% CI	*P* value
ICA stenotic degree	1.0	0.9-1.1	0.170
CCT	**1.9**	1.1-3.1	**0.015**[a]
Antithrombotics	0.3	0.1-0.9	0.043[a]

[a] Statistically significant (logistic regression analysis, $P < 0.05$).

(Filename: TCT_O-118_ASNRgraphic.jpg)

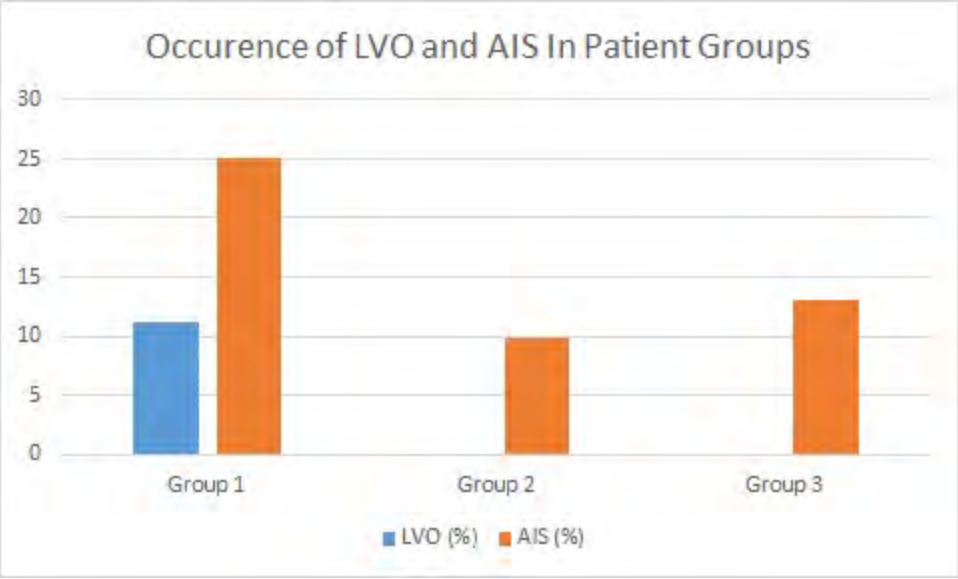
O-119

3:38PM - 3:46PM

Correlation of Large Vessel Occlusion with Types of Neurologic Symptoms in Acute Ischemic Stroke

C Rawson[1], M Boehnke[2], M Leppert[3], S Poisson[3], E Nyberg[3]
[1]University of Colorado Medical Center, Denver, CO, [2]University of Colorado Denver School of Medicine, Aurora, CO, [3]University of Colorado, Aurora, CO

Purpose
Triage of patients with suspected acute ischemic stroke (AIS) is based primarily on presenting neurological symptoms. Activation of the AIS triage pathway ('stroke alerts') involves considerable resources and patient radiation, particularly when CTA head and neck and CT perfusion are obtained. Optimization of patient selection for stroke alerts is important for both safety and sustainability. Our goals were to correlate types of presenting symptoms with the occurrence of large vessel occlusion (LVO) and likelihood of AIS.
Materials and Methods
IRB approval was obtained. We reviewed the database of stroke alerts performed at our comprehensive stroke center. All patients received a brain noncontrast CT and were examined by a stroke neurologist. Patients were divided into 3 groups: Group 1 with focal objective symptoms (e.g. hemiplegia), Group 2 with focal subjective but not objective symptoms (e.g. paresthesia), and Group 3 with nonfocal symptoms only (e.g. dizziness). NIHSS, final diagnosis, and findings on additional imaging (CTA, MRI, or MRA) were recorded.
Results
One hundred eighty-nine consecutive stroke alerts were evaluated. Twenty-one patients with intracranial hemorrhage were excluded. Of the remaining 168 patients, 104, 41 and 23 patients were in Groups 1, 2, 3, respectively. Mean NIHSS in the 3 groups were 5.5, 0.9, and 2.7, respectively (all pair-wise comparisons $p< 0.05$). LVO in the 3 groups were found in 11.2%, 0%, and 0%, respectively ($p=0.019$). Final diagnosis of stroke was made in the 3 groups in 25%, 9.8%, and 13%, respectively. Odds ratio of AIS in Group 1 was 2.714 (95% confidence 1.10 to 6.688, $p=0.026$).
Conclusions
Patients presenting with focal objective neurological symptoms were significantly more likely to be diagnosed with AIS. In the absence of a focal, objective neurological deficit, the likelihood of LVO is very low. This should help inform triage and imaging decisions in patients with suspected AIS.



(Filename: TCT_O-119_bargraph.jpg)

O-120

3:46PM - 3:54PM

Relationships Between the National Institute of Health Stroke Scale (NIHSS) and Predictive Values of CT and MRI in the Identification of Stroke in ED Patients: Can Clinical Presentations Improve Efficacy in the Selection of Competing Imaging Modalities?

M BHALLA[1], J Ulmer[1], A Klein[1], B NAMRATA[2], K McAvoy[3], S Quinet[1], B Fitzsimmons[1]
[1]Medical College of Wisconsin - Froedtert Hospital, Milwaukee, WI, [2]Froedtert Hospital, Milwaukee, WI, [3]Medical College of Wisconsin, Milwaukee, WI

Purpose
The National Institute of Health (NIH) stroke scale (NIHSS, 0-42) is the most accurate and widely used clinical functional assessment tool in the initial management of stroke. On an average, an increase of 1 point in an NIHSS score decreases the likelihood of an excellent outcome by 17%. Outside of the thrombolytic therapeutic window, CT and MRI are competing or complementary modalities used to aid the clinical diagnosis of stroke in emergency departments (ED). The advantages of easy access and speed of CT must be weighed against the high accuracy of MRI. Our study seeks to investigate the utility of the NIHSS as a clinical guide to select the most efficacious imaging modality to diagnose stroke. Specifically, we sought to determine the relationships between NIHSS score and predictive values of CT and MRI.
Materials and Methods
Following Institutional Review Board (IRB) approval, 500 electronic medical records (EMR) of patients presenting to the ED who had CT and MRI brain examinations for

clinically suspected stroke were retrospectively reviewed. A clinical discharge diagnosis was considered the gold standard for the presence of stroke. Inclusion criteria were patients between the ages of 18 and 89 who had both CT and MR performed within 24 hours of each other. Final reports of CT and MR brain examinations were reviewed, and predictive value data (sensitivity, specificity, negative predictive value (NPV), positive predictive value (PPV), and accuracy) of CT and MRI for stroke diagnosis were assessed. Clinical data pertaining to the NIHSS score of patients at the time of presentation were reviewed. NIHSS data were recorded for each score ranging from 0 to 10. NIHSS scores were also grouped: A (0-6), B (7-10), C (11-15) and D (>16). Category A has the best prognosis, while D indicates a high probability of death or significant functional impairment. The predictive values of CT/MRI for each of the NIHSS score and for groups were compared, seeking associations that may enhance the selection criteria of CT or MRI for patients with clinically suspected stroke. The duration between symptom onset and NIHSS designation was recorded for each patient.

Results

Out of 500 patients with clinically suspected stroke, 356 had presentation NIHSS scores documented in the EMR. NIHSS scores ranged from 0 to 42. Seventy-five percent of stroke patients presented outside of the thrombolytic therapeutic window. There was no significant difference in clinical symptoms between CT and MRI examinations. Across all NIHSS groups (A-D), the predictive values and accuracy of MRI remained superior to CT (Table). Surprisingly, NIHSS scores did not correlate with higher CT predictive values or accuracy. There was no significant change in CT PPV or accuracy across all NIHSS groups. There was an inverse relationship in CT NPV across groups A and B, after which CT NPV plateaued (graph top left). An expanded view of the NIHSS data showed that CT accuracy and NPV was inversely related to scores ranging from 0 to 7, peaking at the score of 0 with 80% accuracy and NPV (graph top right). There was no correlation between the duration of symptoms and predictive values of CT; this was not a confounding variable in our results.

Conclusions

In our evolving era of value-based imaging, clinical decision-making should emphasize the most efficacious use of imaging modalities for ED stroke workups, where both CT and MRI are designated as appropriate. Computed tomography (CT) is used as an initial diagnostic modality to aid the clinical diagnosis of stroke. Its ease of access makes it ideal for quickly excluding hemorrhage in patients within the thrombolytic therapeutic window. Magnetic resonance imaging (MRI) equally diagnoses hemorrhage, but has limited access with longer acquisition times at most institutions. Seventy-five percent of our patients fell outside of the thrombolytic therapeutic window. In this scenario, the ED physician must weigh the clinical certainty of stroke against the expediency and convenience of CT versus the high accuracy of MRI. We originally sought to determine if higher NIHSS scores would yield higher predictive values of CT in identifying stroke. Surprisingly, we found this not to be true, with an actual inverse relationship identified across scores ranging from 0-7. Highest CT accuracy (80%) was observed in patients with NIHSS scores of 0. NIHSS scores above 7 provide no

estimate of CT predictive values. The reason for this phenomenon is likely the higher comorbidities and associated chronic white matter disease that may hinder detection of acute or subacute stroke, in patients with more severe symptoms. Clinical relevance: Where speed of ED stroke diagnosis necessitating CT is not a critical factor, MRI should be considered as the initial most efficacious diagnostic imaging modality, thereby avoiding duplicate imaging examinations and unnecessary delays in characterizing stroke.

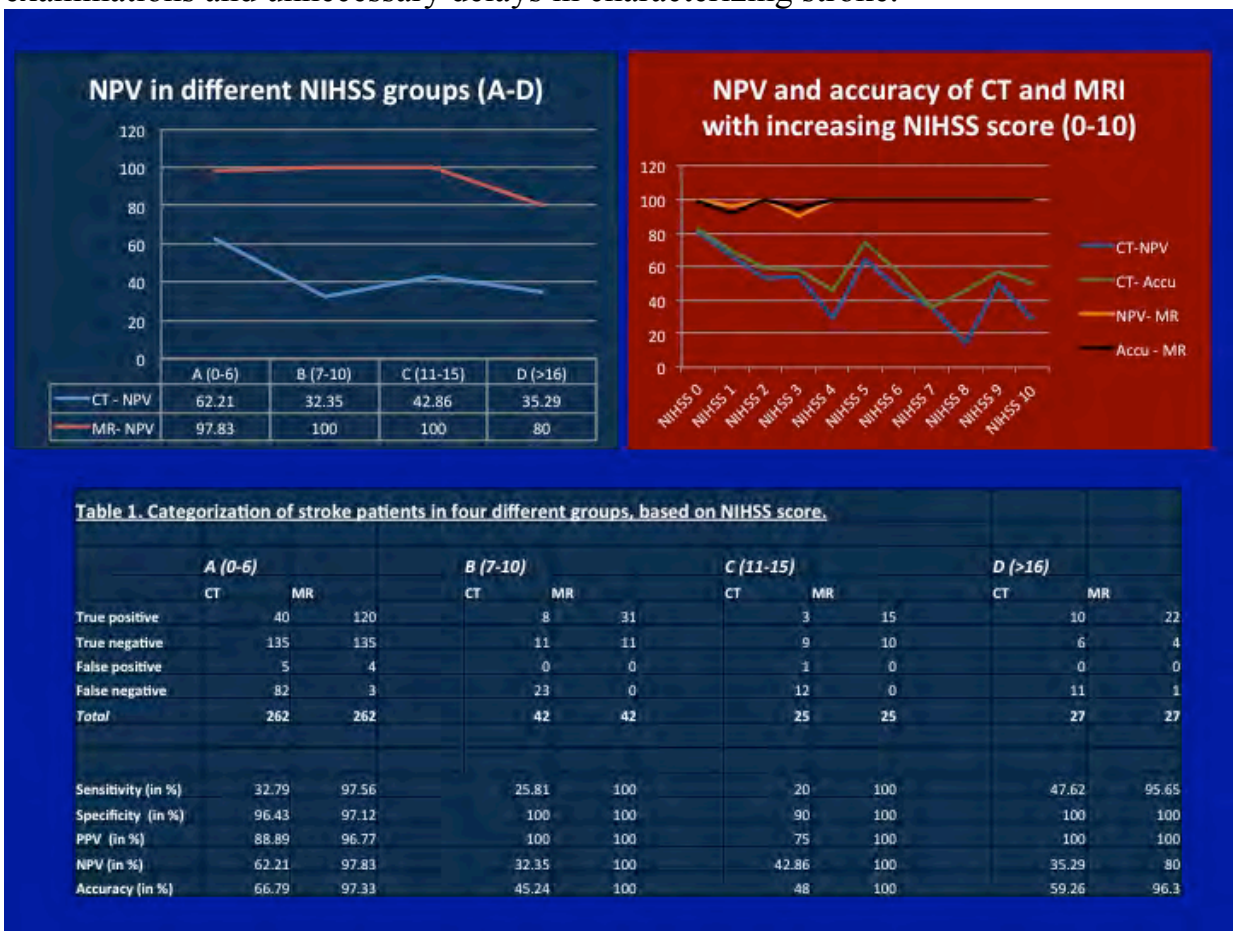


Table 1. Categorization of stroke patients in four different groups, based on NIHSS score.

	A (0-6)		B (7-10)		C (11-15)		D (>16)	
	CT	MR	CT	MR	CT	MR	CT	MR
True positive	40	120	8	31	3	15	10	22
True negative	135	135	11	11	9	10	6	4
False positive	5	4	0	0	1	0	0	0
False negative	82	3	23	0	12	0	11	1
Total	262	262	42	42	25	25	27	27
Sensitivity (in %)	32.79	97.56	25.81	100	20	100	47.62	95.65
Specificity (in %)	96.43	97.12	100	100	90	100	100	100
PPV (in %)	88.89	96.77	100	100	75	100	100	100
NPV (in %)	62.21	97.83	32.35	100	42.86	100	35.29	80
Accuracy (in %)	66.79	97.33	45.24	100	48	100	59.26	96.3

(Filename: TCT_O-120_Slide1.jpg)

O-121

3:54PM - 4:02PM

Clinical scores and imaging-based venous biomarker for predicting recanalization and functional outcome after thrombolysis

J Puig[1], M Hernandez-Perez[2], G Blasco[3], P Daunis-i-Estadella[4], C Biarnes-Duran[5], M Marti-Navas[1], J Munuera[2], J Serena[6], K Nael[7], M Wintermark[8], P Salvador[3]
[1]Research Unit of Diagnostic Imaging Institute (IDI), IDIBGI, University Hospital Dr Josep Trueta, Girona, Girona, [2]Hospital Universitari Germans Trias i Pujol, Badalona, None, [3]Imaging Research Unit, IDI-IDIBGI, Hospital Dr Josep Trueta, Girona, None, [4]Department of Computer Science, Applied Mathematics and Statistics, University of

Girona, Girona, Girona, [5]Research Unit of Diagnostic Imaging Institute (IDI), Girona Biomedical Research Institute (IDIBGI), Girona, Girona, [6]Hospital Dr Josep Trueta, IDIBGI, Girona, None, [7]Icahn School of Medicine at Mount Sinai, New York, NY, [8]Stanford University, Stanford, CA

Purpose
Intravenous thrombolysis (tPA) after ischemic stroke results in timely recanalization in only 50% of occluded arteries; the reasons for treatment failure are not fully understood. Being able to predict the success of tPA would probably help in choosing other recanalization strategies such as mechanical thrombectomy.We aimed to identify predictors of recanalization and functional outcome after intravenous thrombolysis in patients with acute ischemic stroke.
Materials and Methods
We used multimodal CT to prospectively study acute stroke patients treated with tPA. Inclusion criteria were symptoms onset ≤4.5 hours, middle cerebral artery territory infarct, and CT follow-up at 24 hours. Patients referred for mechanical thrombolysis were excluded. Demographics, stroke severity (NIHSS score), stroke origin, time to thrombolysis, ASPECTS scores, thrombus characteristics [occlusion site, density, length, clot burden score (CBS)], internal cerebral vein ratios (rICV), CT-perfusion indexes, vascular recanalization (thrombolysis in myocardial infarction criteria) after tPA, and 3-month Modified Rankin Scale (mRS) were recorded. Receiver operating characteristic (ROC) curves selected optimal thresholds, and multivariate logistic regression analysis identified predictors of vascular recanalization and functional outcome (mRS 0–2 good; 3-5 poor).
Results
Of 552 patients, 483 met the inclusion criteria. Recanalization was successful in 169 (35%) patients. Functional outcome was poor in 267 (55%). At admission, patients with persistent occlusion had higher NIHSS scores, ASPECTS scores, ischemic lesion volumes, and thrombus lengths and lower CBS, lower rICV, and poorer collaterals status. Patients with persistent occlusion had higher 3-month mRS scores The best independent predictors of vascular recanalization and functional outcome were NIHSS scores at admission and rICV($P<0.001$).
Conclusions
Combining clinical scores and the imaging-based venous biomarker rICV is useful for predicting recanalization and functional outcome after tPA administration.

O-122

4:02PM - 4:10PM

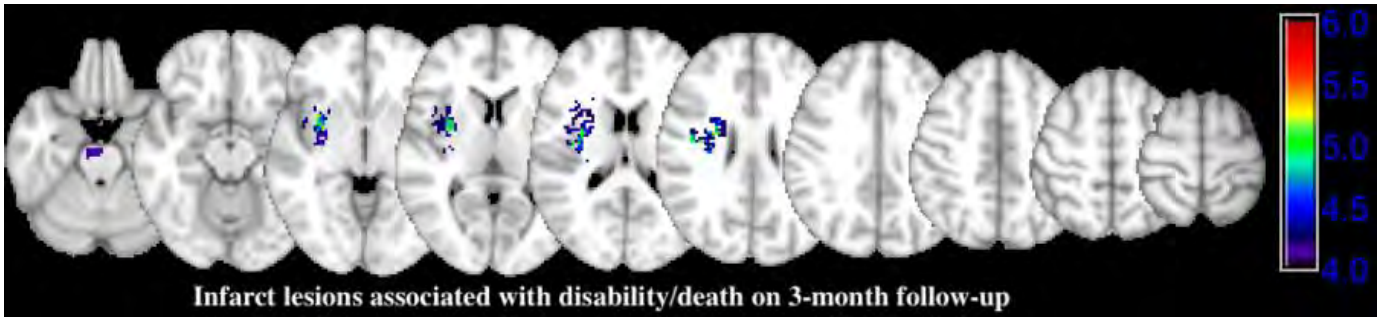
Multivariate Prognostic Model of Acute Ischemic Stroke Combining Admission Infarct Location and Symptom Severity: a Proof-of-Concept Study

S Payabvash[1], J Benson[2], A Tyan[3], S Taleb[4], A McKinney[4]

[1]University of California, San Francisco, San Franciscon, CA, [2]University of Minnesota, St. Paul, MN, [3]Johns Hopkins Medicine, Baltimore, MD, [4]University of Minnesota, Minneapolis, MN

Purpose
Although both ischemic infarct volume and location affect the stroke presentation and outcome, the infarct topography is evaluated far less commonly in predictive models compared to the lesion volume. We developed a multivariate model for stroke prognostication, combing admission clinical and imaging variables, including the infarct topology.
Materials and Methods
Acute ischemic stroke patients without baseline functional disability who had MRI within 24 hours of onset or last-seen-well were included. The admission stroke severity was determined using the NIHSS score. The relation between infarct location and outcome was assessed using both voxel-based and visual atlas-based analyses. The mRS score>2 at 3-month follow-up defined the disability/death.
Results
A total of 198 patients were included. Higher admission NIHSS score, larger infarct volume, and presence of major arterial occlusion (particularly MCA) were associated with disability/death at 3-month poststroke follow-up. The voxel-based analysis showed that infarct lesions in the middle centrum semiovale, insula, and mid pons were associated with higher rates of disability/death and mRS scores at the 3-month follow-up. In atlas-based analysis of images, the infarction of insula, caudate, M1 and M2 cortical regions are associated with higher rates of disability/death at 3-month follow-up, after applying Bonferroni correction for multiple comparisons. In multivariate logistic regression, the only independent predictors of clinical outcome were admission NIHSS score ($p<0.001$), infarction in insula ($p=0.005$), and brainstem ($p=0.006$). Then, we developed a 0-to-3 multivariate model, where 1 score was added for each of (1) an admission NIHSS greater than 5, (2) infarction in insula, and (3) brainstem. The ROC curve showed an area under the curve of 0.812 (95% confidence interval of 0.741 to 0.883) for this simple multivariate model for prediction of disability/death ($p<0.001$).
Conclusions
Using voxel-based as well as atlas-based visual assessment of infarct distribution in consecutive acute ischemic stroke patients with anterior and posterior circulation territory lesions, we found that infarction of insula and brainstem along with admission NIHSS scores were independent predictors of clinical outcome; and a simple scoring tool using these three variables can be applied for prognostication of stroke with high accuracy. Our results support the hypothesis that infarct location, and not just its volume, impact clinical outcomes and provide additional prognostic value in multivariate predictive model. Keeping with the theme of proof-of-concept, we emphasize the methodology and concept of current study design; these results should not be seen as the final model for clinical practice but rather

suggest that such a methodology can be used to allow prognostication and potentially treatment triage in stroke patients based on the infarct location and clinical findings at the time of admission.



(Filename: TCT_O-122_DDmRs.jpg)

O-123

4:10PM - 4:18PM

A simple prognostic tool for predicting 3-month functional outcome 24 hours after ischemic stroke

J Puig[1], M Hernandez-Perez[2], S Thio-Henestrosa[3], G Blasco[4], C Biarnes-Duran[5], M Marti-Navas[1], P Daunis-i-Estadella[3], J Serena[6], K Nael[7], M Wintermark[8], P Salvador[4]
[1]Research Unit of Diagnostic Imaging Institute (IDI), IDIBGI, University Hospital Dr Josep Trueta, Girona, Girona, [2]Hospital Universitari Germans Trias i Pujol, Badalona, None, [3]Department of Computer Science, Applied Mathematics and Statistics, University of Girona, Girona, Girona, [4]Imaging Research Unit, IDI-IDIBGI, Hospital Dr Josep Trueta, Girona, None, [5]Research Unit of Diagnostic Imaging Institute (IDI), Girona Biomedical Research Institute (IDIBGI), Girona, Girona, [6]Hospital Dr Josep Trueta, IDIBGI, Girona, None, [7]Icahn School of Medicine at Mount Sinai, New York, NY, [8]Stanford University, Stanford, CA

Purpose
Scoring systems to predict 3-month functional outcome after ischemic stroke treated with tPA usually are based on clinical variables (e.g., age, sex, baseline NIHSS score, blood glucose, and onset-to-treatment time) or imaging variables [e.g., stroke extent using the Alberta Stroke Program Early CT Score (ASPECTS)]. Accurate early prediction of long-term outcome would enable clinicians and patients to set realistic goals. We aimed to develop a prognostic tool that integrates clinical- and imaging-based scoring systems for predicting the 3-month clinical outcome 24 hours after stroke onset.
Materials and Methods
We studied 192 consecutive patients within 24 hours of middle cerebral artery stroke onset with noncontrast CT. Two readers blinded to clinical outcome reviewed all images. We used classification and regression tree analysis to construct a model considering demographics, 24-hour NIHSS score, vessel occlusion, infarct volume, ischemic changes in each of the 10

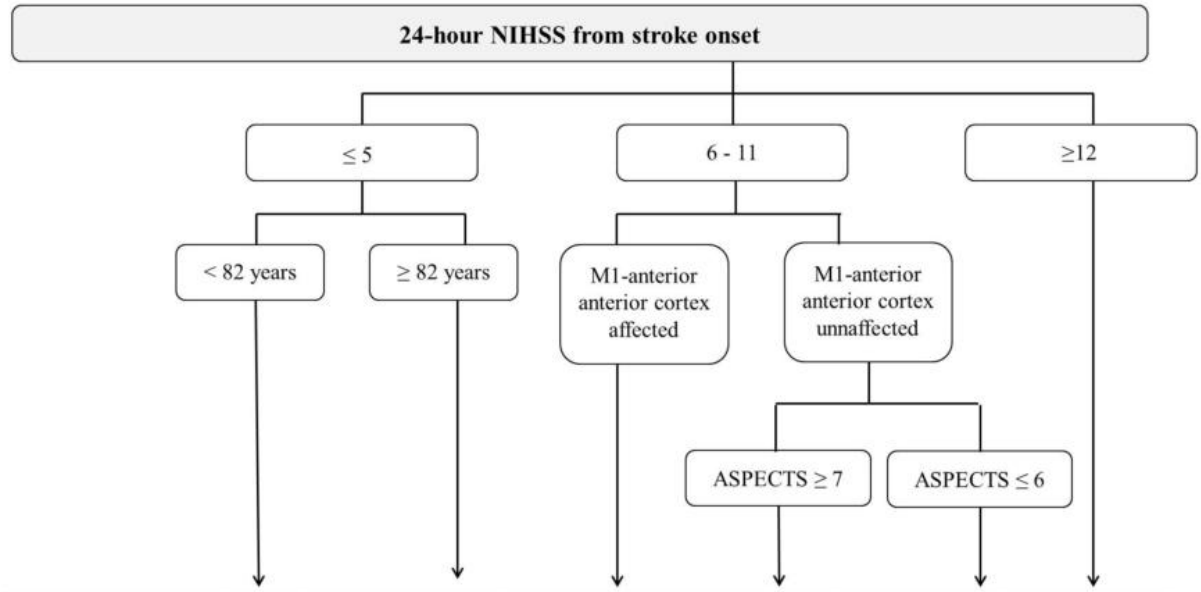
ASPECTS regions (caudate, lentiform nucleus, insula, internal capsule, and M1 to M6 regions), and hemorrhagic transformation to predict 3-month modified Rankin Scale (mRS) score, dichotomized into good (0–2) or poor (3-5) outcomes.

Results

The analyses revealed 4 prognostic subgroups in a decision tree where the explanatory nodes were 24-hour NIHSS score, age, ASPECTS region M1-anterior cortex, and ASPECTS total score.Split-sample validation found classification accuracy of 87.9% for the training dataset and 78.7% for the testing dataset (1000-fold cross-validation). Interobserver reliability for ASPECTS assessment was good (intraclass correlation coefficient=0.86).

Conclusions

The classification tree generated seems to predict 3-month functional outcome. Its ease of application and good reliability would support its use as an early prognostic marker and surrogate of clinical outcome in ischemic stroke. These preliminary results need to be validated in other studies.



3-months mRS 0-2 [%]	89	45	86	71	30	4
3-months mRS 3-6 [%]	11	55	14	29	70	96

(Filename: TCT_O-123_ASPECTSalgorithm.jpg)

O-124

4:18PM - 4:26PM

Endovascular management and outcomes in acute ischemic stroke with tandem occlusions of cervical ICA and intracranial arteries - Insights from the ESCAPE Randomized Controlled Trial

Z ASSIS[1], B MENON[2], J Rempel[3], D Roy[4], C Lum[5], J Shankar[6], B Baxter[7], D DOWLATSHAHI[8], H CHOE[9], V YANG[10], P Burns[11], M HILL[12], A Demchuk[12], M GOYAL[12]
[1]FOOTHILLS MEDICAL CENTRE, UNIVERSITY OF CALGARY, CALGARY, ALBERTA, [2]FOOTHILLS MEDICAL CENTRE, CALGARY, ALBERTA, [3]University of Alberta, Edmonton, Alberta, [4]CHUM Centre Hospitalier de l'Université de Montréal, Montréal, QC, [5]University Of Ottawa, Ottawa, ON, [6]Dalhousie University, Halifax, Nova Scotia, [7]Tennessee Interventional Associates, Chattanooga, TN, [8]OTTAWA HOSPITAL RESEARCH INSTITUTE, OTTAWA, ONTARIO, [9]ABINGTON HOSPITAL, Abington , PA, [10]Sunnybrook Health Sciences Centre, Toronto, ONTARIO, [11]Royal Victoria Hospital, Belfast, United Kingdom, [12]FOOTHILLS MEDICAL CENTRE, CALGARY, Alberta

Purpose

Tandem occlusions are defined as simultaneous presence of intracranial arterial occlusions with extracranial cervical ICA severe stenosis (near complete occlusion) or complete occlusion as seen on CT angiogram. Tandem occlusions generally have poorer prognosis (1). Nonetheless, they seem to benefit most from EVT (2). Various strategies have been used to manage tandem occlusions in the past. Also, if treating both the occlusions in the same setting, the sequence of treating these occlusions is not well established. In this study, we analyze patient demographics, treatment strategies and clinical outcomes in patients with tandem occlusions enrolled in the ESCAPE trial.

Materials and Methods

We performed a retrospective evaluation of patients receiving endovascular treatment (EVT) in the ESCAPE trial (3). Data on patient demographics, vascular risk factors, workflow and endovascular technique along with any co-interventions, complications and final clinical outcomes were analyzed.

Results

Of 165 patients randomized to endovascular treatment, 30 (18.1%; median age 66 years, Males 66.7%) patients had tandem extracranial and intracranial occlusions. Patients with tandem occlusions were more likely to be younger, male and diabetic (all $p < 0.05$). They also were less likely to have a history of atrial fibrillation ($p=0.04$). There was no difference in baseline NIHSS or NCCT ASPECTS ($p>0.05$). Patients with tandem occlusions were more likely to have intracranial ICA occlusions vs. M1 occlusions ($p<0.01$). No statistically significant difference was noted between patients with or without tandem occlusions in time from onset to CT, reperfusion rates at end of procedure, rates of PH at end of procedure, NIHSS at 24 hrs or mRS at 90 days. Seventeen of 30 patients (57%) underwent emergency endovascular treatment of the extracranial occlusion. Of these 17 patients, 10 (59%) underwent recanalization of the extracranial occlusion first, followed by intracranial thrombectomy. The most common technique used for treating extracranial stenosis/occlusion was angioplasty with stenting (7/17), followed by angioplasty alone or thrombo-aspiration (5 each). In the remaining 13 patients, residual stenosis after the endovascular procedure ranged

from 30% to 100%. Only 4/13 patients underwent invasive treatment of the cervical occlusion subacutely (2 underwent carotid artery stenting vs. two carotid endarterectomy). Reperfusion rates at the end of the procedure were higher in patients whose extracranial lesions were treated acutely (12/17, 70.5%) compared to those in whom only the intracranial occlusion was treated acutely (6/12, 50%), although the difference was not statistically significant (p=0.21).

Conclusions

Tandem occlusions are common in patients eligible for EVT. Younger males with diabetes are more likely to have tandem occlusions. Workflow, complication rate and clinical outcomes are similar to patients without tandem occlusions. Management is yet to be standardized.

TABLE: EFFICACY AND SAFETY OUTCOMES IN TANDEM GROUP VERSUS NO-TANDEM GROUP IN THE ENDOVASCULAR TREATMENT ARM

VARIABLES	TANDEM GROUP	NO TANDEM GROUP	p value
Reperfusion (TICI 2b/c)	65.50%	74%	0.36
CT TO RECANALIZATION TIME (MIN)	87 (50)	84 (52)	0.91
NIHSS AT 24 HOURS (Median, IQR)	6 (6)	6 (11)	0.73
Any Parenchymal Hemorrhage on follow-up Imaging (%)	6.70%	5.20%	0.67
mRS AT 90 DAYS	2 (2)	2 (3)	0.4
MORTALITY	10%	10.50%	1

(Filename: TCT_O-124_Picture1.jpg)

O-125

4:26PM - 4:34PM

Stent retrievers prevent distal embolism effectively during mechanical thrombectomy

C Riedel[1]
[1]*UKSH Kiel, Kiel, Schleswig-Holstein*

Purpose

The purpose of this study was to determine whether mechanical thrombectomy by distal aspiration alone is more likely to result in peripheral embolism compared to distal aspiration used with retriever stents.

Materials and Methods

We analyzed the initial nonenhanced CT (NECT) images, Computed tomography angiograms and interventional DSA images of 118 patients with an acute ischemic stroke in the anterior cerebral circulation who were treated using mechanical thrombectomy with

either distal aspiration alone or with distal aspiration during retriever stents maneuvers. Clot representations were first segmented from thin-slice NECT reconstructions and superimposed on the CTA images in order to determine the initial position of the clot. In the next step, the DSA images were registered with the CT angiograms using a 3D/2D registration technique. Using these image registrations, distal emboli that occurred during thrombectomy were separated from those that were already identifiable before the intervention.
Results
Forty-seven of our patients were treated with distal aspiration alone, the remaining 71 patients were treated with distal aspiration during retriever stent maneuvers. In 13 (27%) of the patients treated only with distal aspiration distal emboli not present in the initial CT angiograms were identified. In the patients treated with stent retrievers and distal aspiration, only 6 patients (8%) had distal emboli that were attributed to the recanalization procedure. In 4 of these patients it was shown that the stent retriever position did not reach the distal end of the clot.
Conclusions
Stent retrievers do not only have the purpose to attach to the clot in order to retrieve it into the aspiration catheter. They additionally form a barrier for clot fragments that form during the retrieval maneuver. Thus, they are effective protection devices preventing distal embolism during mechanical thrombectomy. It is therefore necessary to place them in an optimal position with respect to the location of the clot. Even if this procedure is time consuming, it prevents the neurointerventionalist from having to switch to additional thrombectomy devices for reaching distal emboli.

O-126

4:34PM - 4:42PM

Penetration depth of stent retrievers into clots is highly dependent on stent design

S Lamprecht[1], C Riedel[1]
[1]*UKSH Kiel, Kiel, Schleswig-Holstein*

Purpose
The aim of this study was to investigate the interaction between retriever stents and clots of different composition regarding the penetration depth of stent struts into the clot.
Materials and Methods
We designed 4 different clot types from human whole blood that histologically resembled clot categories found in acute ischemic stroke patients. These experimental clots were filled into vascular models of the proximal middle cerebral artery and we flushed the remaining inner lumen of these vessels with contrast medium. Finally, these occluded vessel segments were recanalized using 5 different stent retrievers (Trevo, Solitaire, Aperio, Separator 3D and Preset LT) during constant high resolution biplane angiographical imaging in order to

obtain negative contrast images of the clot and the interaction with the stent struts. These images subsequently were analyzed by measuring the penetration depth of stent struts into the clot.
Results
In 4 stent retrievers (Trevo, Solitaire, Aperio, Separator 3D) we observed only partial penetration of stent struts into the clots with a mean penetration depth of 1.1 mm (± 0.3mm), even after waiting for 5 min after deployment. Only the Trevo and Solitaire devices were capable of penetrating 1 clot model that was rich in red blood cells and built under conditions of blood stasis. The Preset LT stent retriever penetrated nearly all clots completely. We measured a mean penetration depth of 1.9 mm (±0.4 mm) for this device. The complete penetration of the clot by stent struts is observed to be associated with a higher number of clot fragments.
Conclusions
Four of our 5 investigated retriever stents fix most of the clot volume on the outer stent surface due to the fact that the stents struts penetrate only less than 50% of the clot diameter. Only the Preset LT retriever with very thin stent struts is capable of enclosing the entire thrombus due to complete penetration. While a complete entrapment of the clot seems more safe for clot retrieval, more clot fragments might even out this advantage.

O-413

4:42PM - 4:50PM

Infarct Growth Rate Depends on Collateral Quality in Acute Ischemic Stroke Patients

R Hakimelahi[1], K Buch[1], T Leslie-Mazwi[2], J Rabinov[1], J Hirsch[1], R Gonzalez[1], P Schaefer[1]
[1]Massachusetts General Hospital, Boston, MA, [2]massachusetts general hospital, Boston, MA

Purpose
Multiple studies have demonstrated no statistically significant association between time after stroke onset and initial infarct volume. Factors other than time may play a role in infarct growth. We sought to investigate association between collateral status and infarct growth rate in acute ischemic stroke (AIS) patients.
Materials and Methods
We included 130 consecutive patients with CTA showing ICA and/or proximal MCA occlusions who had DWI within 8 hours of stroke onset. Collateral status was categorized into 3 groups: poor (none or minimal), intermediate (present but < contralateral side) and good (≥ contralateral side). Diffusion-weighted imaging (DWI) lesion volumes were measured and infarct growth rate was calculated using MRI time after stroke onset. Mann-Whitney test and correlation coefficient were used for statistical analysis.
Results
In our 130 patients, 62 female (48%), the average values (mean ± SD) were: age 70 ± 17 years, NIHSS 16 ± 6, DWI volume 59 ± 65 mL, time after stroke onset 4 ± 2 hours, and

infarct growth rate 17 ± 23 mL/hour. Nineteen (14.6%) had poor, 75 (57.7%) had intermediate, and 36 (27.7%) had good collaterals. Infarct growth rate and DWI lesion volume were significantly increased with decreased collateral quality ($p<0.0004$ for all group comparisons). Patients with good collaterals were younger ($p=0.004$ and $p=0.018$ compared to poor and intermediate groups respectively) and had lower NIHSS scores ($p< 0.001$). Time after stroke onset, gender, or occlusion site (ICA vs MCA) were not significantly different among different collateral groups. There was no correlation between time and DWI volume ($r2=0.02$, $p=0.8$) or collateral status ($r2=0.05$, $p=0.6$). There was significant correlation between collateral status and infarct growth ($r2=-0.6$, $p<0.0001$).

Conclusions

Acute ischemic stroke patients with good collaterals have small initial DWI lesion volumes and slower infarct growth rates. These patients may be candidates for treatment options outside traditional time windows.

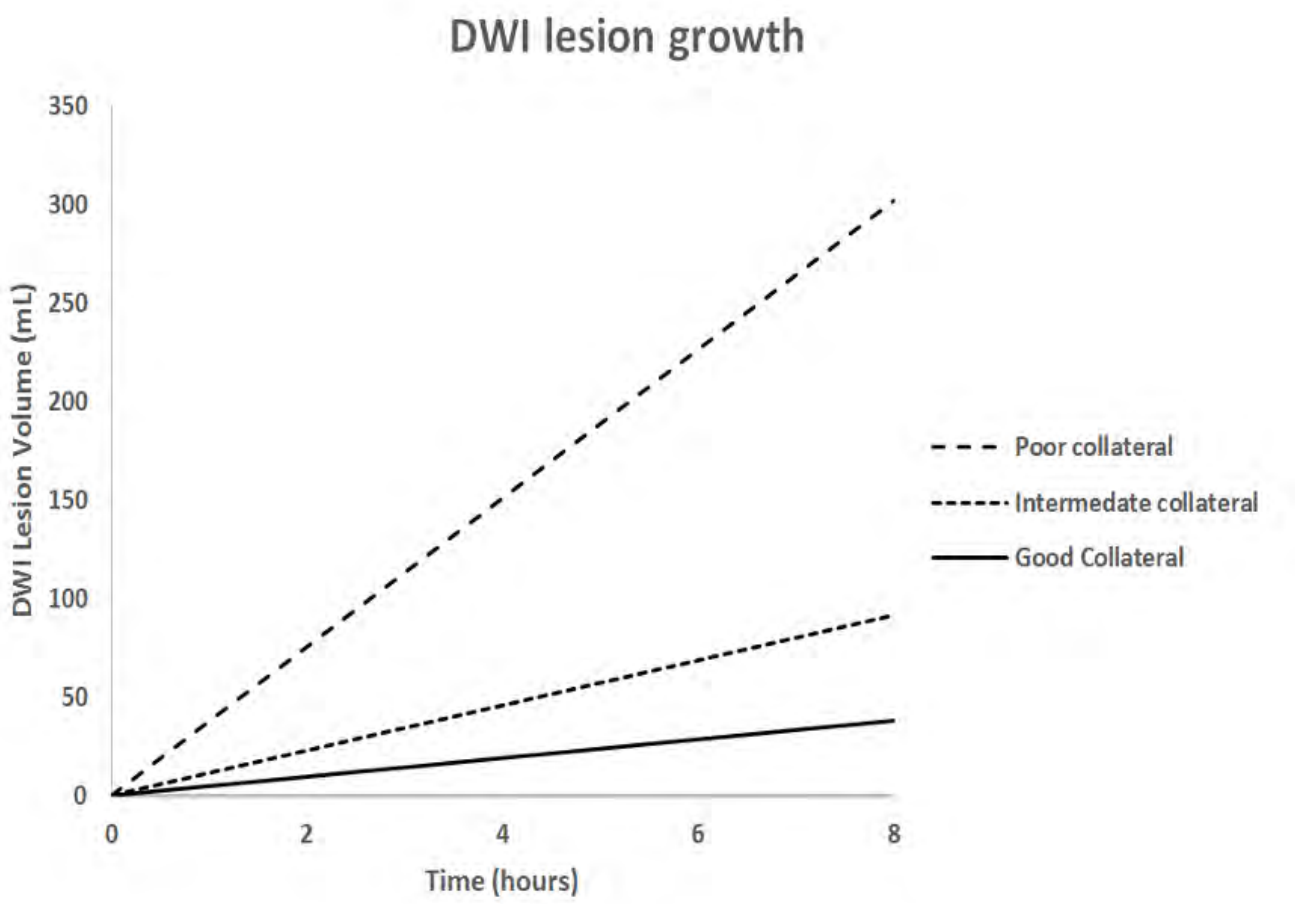


Figure. Depicted are estimated infarct growth rates assuming linearity for each collateral group using average DWI lesion volume and time after stroke values. The infarct growth rates are (mean±SD) 49.2±38.6, 14±15.7 and 5.4±6.1 mL/hour for poor, intermediate and good collateral groups.

(Filename: TCT_O-413_ASNR2017-infarctgrowth.jpg)

Tuesday
3:30PM - 4:45PM
Long Beach Convention Center, Room 104B (Main Lobby)

14E-Parallel Paper Session-Excerpta: "Brain Teasers". . .Try to Untangle!
E-37

3:30PM - 3:34PM

Sagging Eye Syndrome

M Maher[1], P Chang[1], L Ghadiali[1], M Bernieri[2], g moonis[3]
[1]Columbia University Medical Center, New York, NY, [2]University of Rome, La Sapienza, Rome, RM, [3]Columbia University Medical Center, south orange, NJ

Purpose
Sagging eye syndrome is a recently recognized sequelae of orbital connective tissue degeneration which results in an esotropia and diplopia for distance. The lateral rectus-superior rectus band is a ligament connecting the superior rectus and the lateral rectus extraocular muscles. The band thins and tears with age, leading to inferior displacement of the lateral rectus. The inferior displacement of the lateral rectus causes a mechanical disadvantage for the muscle, resulting in divergence paresis diplopia which can be clinically mistaken for a sixth nerve palsy. Careful attention to lateral rectus muscle positioning on orbital magnetic resonance imaging (MRI) can diagnose sagging eye syndrome.
Materials and Methods
A 52-year-old woman presented with new double vision accentuated at distance which worsened over several months. Physical exam revealed divergence paresis. Orbital MRI revealed symmetrical rupture of the lateral rectus-superior rectus band and inferior displacement of the inferior recti. The patient was prescribed spectacle prisms which significantly reduced her symptoms.
Results
A routine orbital MRI was acquired on a 1.5T scanner with the patient focusing on a central object and without a surface coil. The position of the lateral rectus muscle was analyzed on a 3D volumetric gradient echo sequence in 3 mm-thick cuts. The interpreting physician performed 3D advanced postprocessing at an independent workstation to generate oblique coronals of the orbits, using the optic nerve as the central axis.
Conclusions
Sagging eye syndrome is a clinically significant disease entity with reliable diagnostic changes seen on orbital MRI. Awareness of this disease will allow early diagnosis, avoid more advanced neuro-ophthalmology work up, and guide therapy.

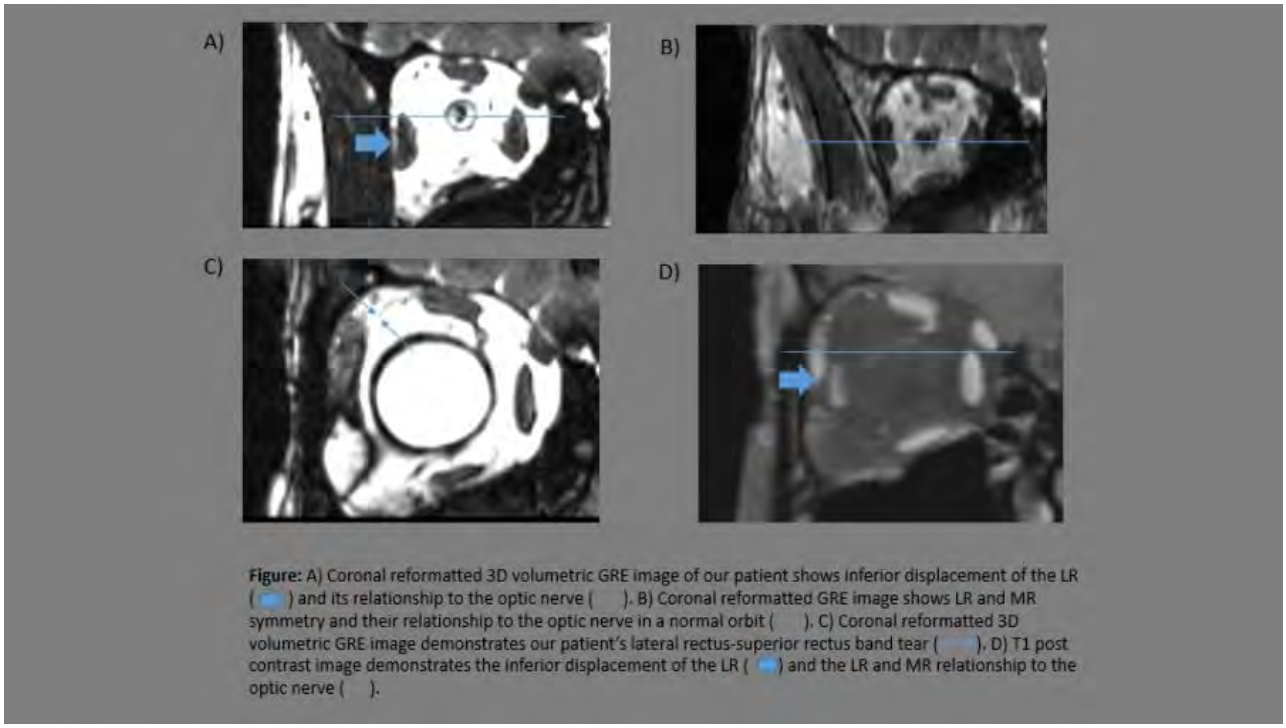


Figure: A) Coronal reformatted 3D volumetric GRE image of our patient shows inferior displacement of the LR ( ) and its relationship to the optic nerve ( ). B) Coronal reformatted GRE image shows LR and MR symmetry and their relationship to the optic nerve in a normal orbit ( ). C) Coronal reformatted 3D volumetric GRE image demonstrates our patient's lateral rectus-superior rectus band tear ( ). D) T1 post contrast image demonstrates the inferior displacement of the LR ( ) and the LR and MR relationship to the optic nerve ( ).

(Filename: TCT_E-37_Maherabstractimages.jpg)

E-38

3:34PM - 3:38PM

Heidenhain variant Creutzfeldt-Jakob Disease: another cause for Posterior Reversible Encephalopathy Syndrome?

J Guan[1], B Policeni[2], A Capizzano[1], T Sasaki[3], T Moritani[1]
[1]University of Iowa Hospitals and Clinics, Iowa City, IA, [2]University of Iowa hospitals and Clinics, iowa city, IA, [3]University of Iowa, Iowa City, IA

Purpose

Heidenhain variant Creutzfeldt-Jakob disease (HvCJD) is characterized by predominant visual symptoms preceding other clinical manifestations of CJD. Prior case reports have described how magnetic resonance imaging (MRI) findings of HvCJD may mimic those of posterior reversible encephalopathy syndrome (PRES). Although CJD is not yet proven to be related to development of PRES, prion invasion to the endothelium has been shown to change blood-brain barrier permeability. We present a case of HvCJD that had associated findings of PRES, raising the question of whether CJD instead represents another cause for the development of PRES.

Materials and Methods

A 59-year-old female presented to ophthalmology clinic with 1-week history of blurry vision. Repeat evaluations including visual acuity test, Goldmann Visual Fields, and orbital MRI found no clear neuro-ophthalmic cause. She was admitted to inpatient neurology 1

month later with worsening ataxia, aphasia, and near-complete vision loss. Throughout admission patient's alertness decreased and she became progressively more disoriented. She developed myoclonic jerks, increased startle response, and generalized hyperreflexia. Findings on repeat MRI after admission revealed diffusion restriction in the right caudate nucleus and bilateral fronto-parieto-occipital cortex consistent with CJD with associated posterior vasogenic edema compatible with PRES. There was no history of hypertension or other known causes of PRES. Electroencephalogram (EEG) revealed diffuse cerebral dysfunction with triphasic waveforms. Tau, 14-3-3, and paraneoplastic panel were negative. Patient eventually was discharged to hospice after 10 days, where she passed away 3 days later. Family declined brain biopsy or autopsy.

Results

Initial orbital MRI at 1 week of visual symptoms was negative. Repeat MRI after admission demonstrated diffusion restriction involving the right caudate nucleus as well as the bilateral fronto-parieto-occipital cortices, right more than left, best demonstrated on high-b-value diffusion-weighted imaging (DWI) (Fig. 1a, 1b). These findings were consistent with CJD. Additionally, there were areas of marked hyperintensities on FLAIR (Fig. 1c) and T2-weighted images involving the cortical and subcortical regions of bilateral posterior occipital lobes correlating with increased signal on apparent diffusion coefficient (ADC), as well as focal areas of blooming on gradient recall echo (GRE) and susceptibility-weighted imaging (SWI) (Fig. 1d) in the right occipital lobe, reflecting superimposed vasogenic edema from PRES. T2, ADC, and GRE images are not shown.

Conclusions

We present a patient who had concurrent MRI findings of both CJD and PRES. Although pathologic confirmation of CJD via biopsy was not possible, this patient's clinical and imaging findings fulfill both the MRI-CJD Consortium Diagnostic Criteria and the WHO Diagnostic Criteria for probable CJD. While CJD is not yet proven to be related to development of PRES, prion invasion to the endothelium has been shown to change blood brain barrier permeability. Along with prior case reports detailing how MRI findings of CJD may mimic those of PRES, this case raises the question of whether CJD, and specifically HvCJD, may in fact be a cause for PRES.

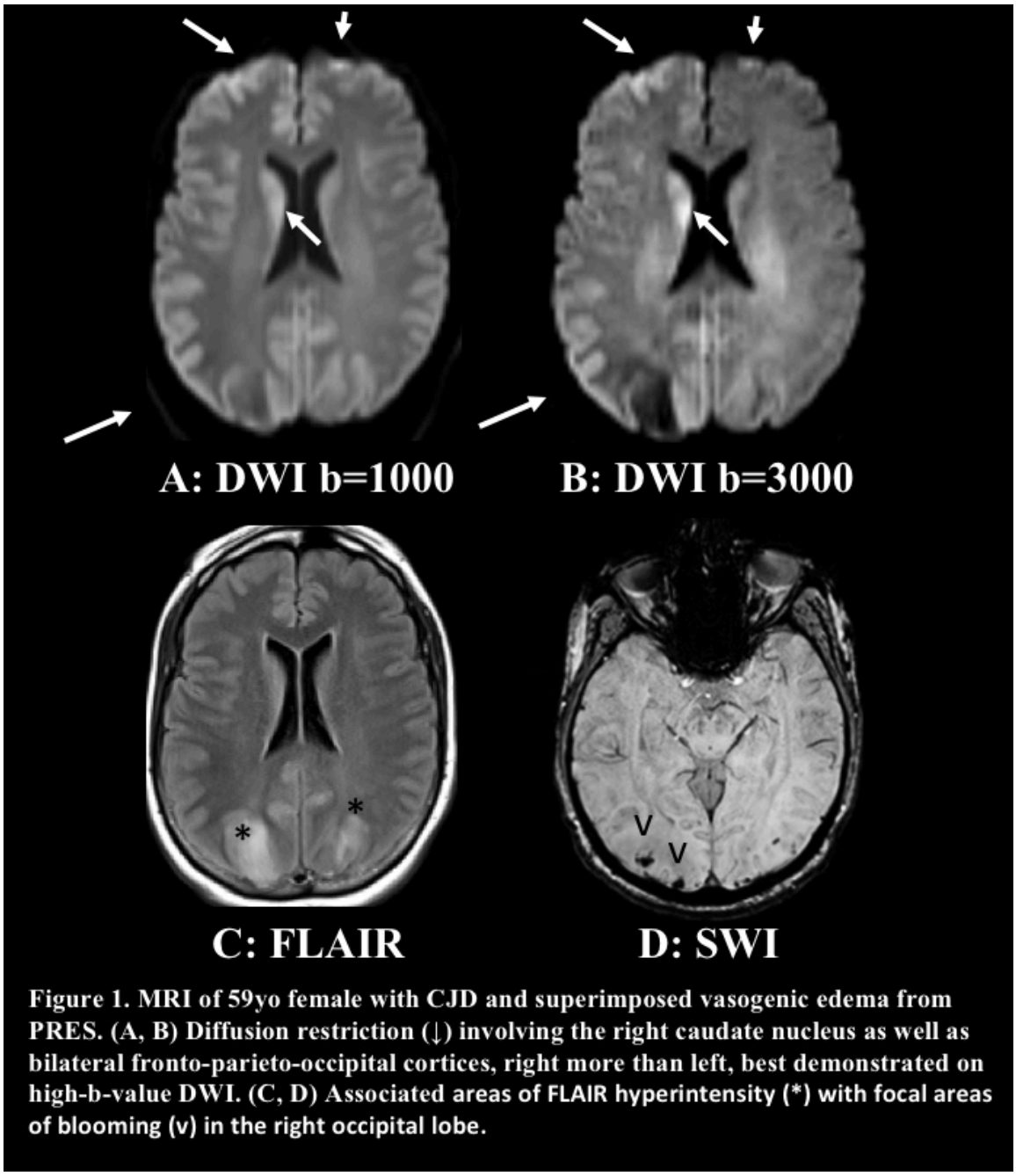


Figure 1. MRI of 59yo female with CJD and superimposed vasogenic edema from PRES. (A, B) Diffusion restriction (↓) involving the right caudate nucleus as well as bilateral fronto-parieto-occipital cortices, right more than left, best demonstrated on high-b-value DWI. (C, D) Associated areas of FLAIR hyperintensity (*) with focal areas of blooming (v) in the right occipital lobe.

(Filename: TCT_E-38_Figure1JPEG.jpg)

E-39

3:38PM - 3:42PM

CT, MRI, and FDG-PET findings in Adult Onset Adrenoleukodystrophy; advanced neuroimaging of this classic entity.

A Germana[1], J Yetto[1], M Cathey[1]
[1]*Naval Medical Center San Diego, San Diego, CA*

Purpose

Adrenoleukodystrophy (ALD) is an X-linked disorder that involves mainly the nervous system white matter and the adrenal cortex. It is associated with abnormal accumulation of very long chain saturated fatty acids in the brain and adrenal gland. The phenotypic expression of ALD is widely variable and ranges from the most severe childhood cerebral form, which often is fatal in the first decade of life, to milder adult forms that are compatible with life into the eighth decade. Awareness of this disease and recognition of its suggestive imaging features is important in order to prompt early counseling and management. The purpose of this presentation is to revisit this classic entity using the full complement of state of the art neuroimaging techniques including high-resolution 3T magnetic resonance (MR), MR spectroscopy, and MR perfusion as well as Brain FDG-PET.

Materials and Methods

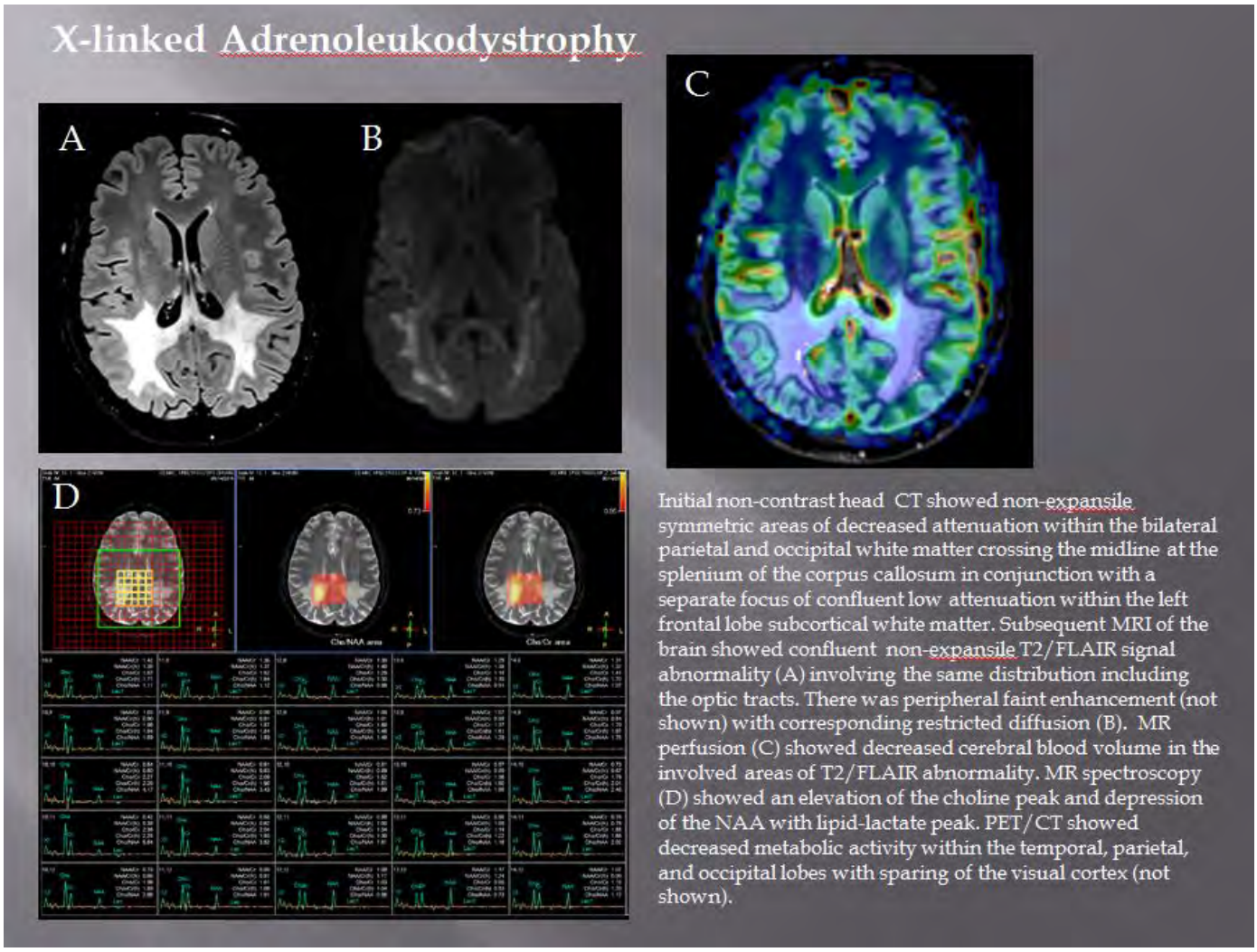
A 44-year-old male without a significant past medical history presented to the emergency department with gradually progressive bilateral painless loss of vision for the past 3 months. Neurological examination showed reactive pupils with no afferent pupillary defect. Visual acuity was 20/20 bilaterally. There were bilateral visual field defects consistent with left homonymous hemianopsia. Extra-ocular muscles were intact bilaterally. Lumbar puncture revealed normal opening pressure. Cerebrospinal fluid (CSF) analysis showed 10 RBCs, 4 WBCs, glucose was 56 mg/dl, and protein was 41 mg/dl. Oligoclonal bands were not detected. Microbiology studies were negative. Comprehensive serum laboratory work up was significant for markedly elevated very long chain fatty acids.

Results

Initial noncontrast head computed tomography (CT) showed nonexpansile symmetric areas of decreased attenuation within the bilateral parietal and occipital white matter crossing the midline at the splenium of the corpus callosum in conjunction with a separate focus of confluent low attenuation within the left frontal lobe subcortical white matter. Subsequent MRI of the brain showed confluent nonexpansile T2/FLAIR signal abnormality involving the same distribution including the optic tracts. There was peripheral faint enhancement with corresponding restricted diffusion. MR perfusion showed decreased cerebral blood volume in the involved areas of T2/FLAIR abnormality. MR spectroscopy showed an elevation of the choline peak and depression of the NAA with lipid-lactate peak. PET/CT showed decreased metabolic activity within the temporal, parietal, and occipital lobes with visual cortex sparing.

Conclusions

Adrenoleukodystrophy has characteristic imaging findings across several imaging modalities. This case report re-exams the typical imaging findings of ALD in the context of today's high resolution and advanced techniques.



(Filename: TCT_E-39_XlinkedAdrenoleukodystrophy.JPG)

E-40

3:42PM - 3:46PM

Young female with Fragile X-associated tremor/ataxia syndrome

I Mark[1], L Eckel[1], C Carr[1]
[1]*Mayo Clinic, Rochester, Rochester, MN*

Purpose
Present a case of Fragile X-associated tremor/ataxia syndrome (FXTAS) in a young female and review the magnetic resonance imaging (MRI) findings that may be seen in this disease.
Materials and Methods
A 26-year-old female with a history of an uneventful birth, but by age 3 was developmentally delayed, diagnosed with Asperger's syndrome, and developed an action tremor of the hands. At age 15, the tremor worsened and began to affect her activities of

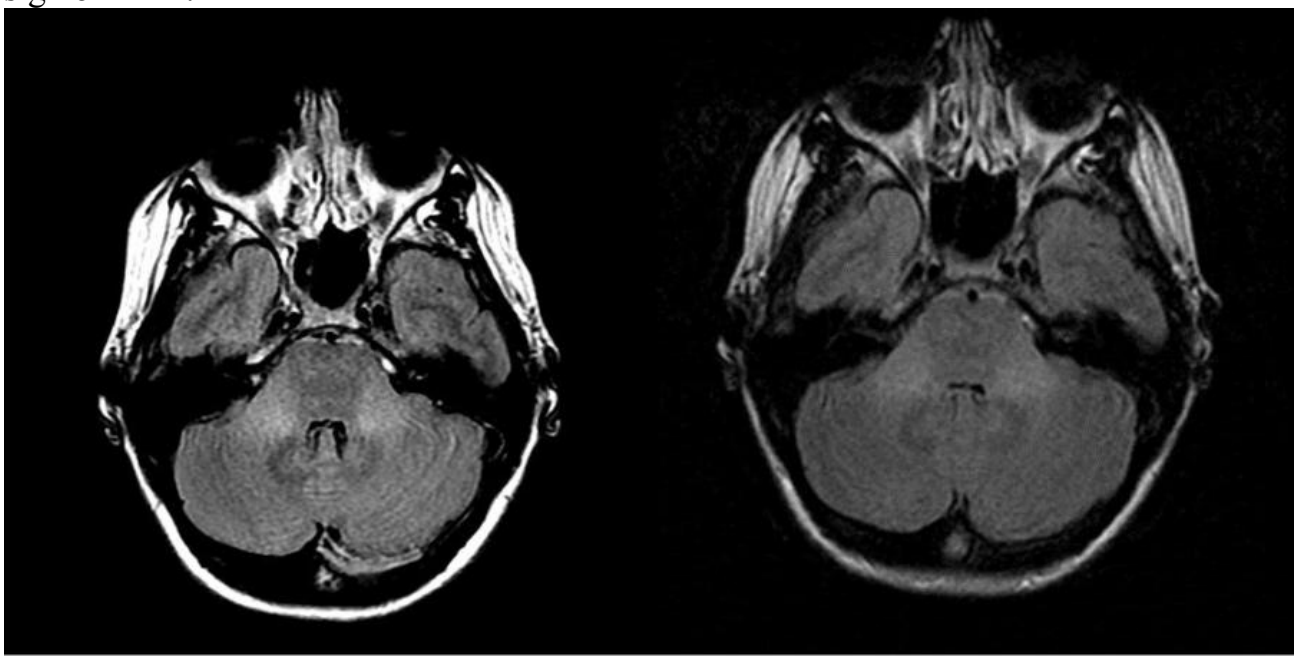
daily living. During evaluation for a movement disorder, she also was found to have ataxia with tremor. Genetic testing revealed an abnormality of the FMR1 gene with one X chromosome containing 30 CGG repeats and one containing 60 CGG repeats. The patient's action tremor currently is managed medically with a beta blocker. Her family history includes 2 brothers who are negative for the mutation and 1 sister who also tested positive for 60 CGG repeats but remains asymptomatic. Her father was positive for the premutation, but is asymptomatic. Her paternal grandmother also has the premutation, but only developed a hand tremor in her mid-80's and was diagnosed with Parkinson's.

Results

An MRI of the brain demonstrated subtle T2 hyperintensity within the middle cerebellar peduncles. Cerebral and cerebellar volumes are within normal limits for age. The T2 hyperintensity in the middle cerebellar peduncles also were seen on an MRI 10 years prior, when the patient was 16 years old.

Conclusions

Fragile X syndrome is defined as >200 CGG repeats on the fragile X intellectual disability 1 (FMR1) gene, while individuals with 55-200 repeats are classified as having a Fragile X premutation. This premutation can affect up to 1/250 women, of which 8% of women (as opposed to 40% of males) will develop an action tremor and cerebellar ataxia, consistent with FXTAS. FXTAS typically presents in males, ages 50-60 as a consequence of progressive degenerative movement disorder. This condition has not been described in the literature of a female patient this young. She presented with the classic action tremor, genetic testing positive for the Fragile X premutation, and the typical middle cerebellar peduncle sign on MRI.



(Filename: TCT_E-40_Combined.jpg)

E-41

3:46PM - 3:50PM

Cerebellar Herniation into an Arachnoid Granulation – Does it Matter? A Report of Two Cases and Review of the Literature

P Annigeri[1], S Patel[1], J Corrigan[2], H Marin[2], B Griffith[2]
[1]Henry Ford Hospital, Detroit, MI, [2]Henry Ford Health System, Detroit, MI

Purpose
Brain herniation into an arachnoid granulation – while rare – is an increasingly recognized entity. Although typically considered an incidental finding, signal abnormalities within the herniated brain parenchyma have been described and postulated to represent strangulation and infarction of herniated tissue. This excerpta describes two cases of cerebellar herniation into arachnoid granulations and reviews the literature associated with this entity.
Materials and Methods
We present 2 cases of cerebellar herniation into arachnoid granulations. Case 1 was an 84-year-old male undergoing cervical spine magnetic resonance imaging (MRI) for worsening peripheral neuropathy. The second was a 66-year-old female undergoing MRI brain for burning foot pain and difficulty walking. In both cases, the findings were present on prior imaging and considered unrelated to the clinical presentation.
Results
Case 1: Cervical spine MRI shows cerebellar tissue herniating into a large arachnoid granulation. Encephalomalacia within the herniated cerebellar tissue was present and unchanged from 12 years prior. Head computed tomography (CT) showed large arachnoid granulations within the occipital calvarium at the site of herniation. Case 2: MRI demonstrates linear regions of cerebellar tissue extending into arachnoid granulations within the diploic spaces of the occipital bone bilaterally. The cerebellar tissue within the granulations extends from the vermis with a traction type appearance and increased T2/FLAIR hyperintensity.
Conclusions
Arachnoid granulations are normal protrusions of arachnoid membrane through gaps in the dura into dural venous sinuses or calvarium. Brain herniation into arachnoid granulations, although rare, is an increasingly recognized entity. Associated signal changes within the herniated brain parenchyma can occur, possibly due to strangulation and infarction of the herniated tissue. While likely representing an incidental finding, awareness of this entity is important to avoid incorrect diagnosis, including intraluminal clot when present within a dural venous sinus. This excerpta describes 2 cases and provides a brief review of the literature on this under-recognized entity.



(Filename: TCT_E-41_Finalcerebellarherniation.jpg)

E-42

3:50PM - 3:54PM

Restricted DWI in Acute Wernicke's Encephalopathy

G Romero-Sanchez[1], R La Piana[2], M Cortes[3], D Tampieri[4]

[1]Montreal Neurological Institute and Hospital, Montreal, QC, [2]Montreal Neurological Institute, Montreal, Quebec, [3]McGill University, montreal, Quebec, [4]Montreal Neurological Hospital and Institute, Montreal, Quebec

Purpose
There are few data regarding the appearance of Wernicke's encephalopathy lesions in acute phases. The aim of this project is to demonstrate a case of acute Wernicke's encephalopathy and the reversible lesions on diffusion-weighted imaging (DWI) after the adequate treatment.
Materials and Methods
A 56-year-old female presented with an acute internuclear ophthalmoparesis, ataxia and a malnourished state caused by chronic alcoholism, hence the classic triad of Wernicke's encephalopathy. She received Thiamine 100 mg daily for 5 days. She was re-evaluated at the end of the first cycle of treatment and showed a significant improvement of the symptoms. The patient was maintained with the treatment and was asymptomatic at the most recent follow-up.
Results
The first magnetic resonance imaging (MRI) showed bilateral symmetric restricted DWI lesions and corresponding low-levels in the ADC maps in the periventricular region of the thalamo-mesencephalic junction associated with slight increase in the T2 signal. No abnormal enhancement was noted. A follow-up MRI 30 days after the onset of symptoms demonstrated the complete resolution of the findings previously noted.
Conclusions
Our case suggests that specific areas of the brain might be sensitive to thiamine concentrations. In case of rapid decrease of thiamine levels, this can result in metabolic breakdown documented as cytotoxic edema in the diffusion sequences. The reversibility of the imaging findings further supports this hypothesis.

E-43

3:54PM - 3:58PM

The Claustrum Sign: A Case Report and a Discussion its Significance

M Cho[1], S Hazany[1], E Raff[1], W Gibbs[1]
[1]University of Southern California/Keck Medical Center, Los Angeles, CA

Purpose
The "claustrum sign" is associated with a rare, aggressive form of status epilepticus. In adults, it has been seen with a rare entity called new-onset refractory status epilepticus (NORSE), a form of seizure activity that typically follows a febrile illness. We describe a case illustrating the claustrum sign and explore its clinical significance. We review specific imaging findings, acute and chronic, and discuss the proposed functions of the claustrum possible explanations linking it to seizure propagation.

Materials and Methods

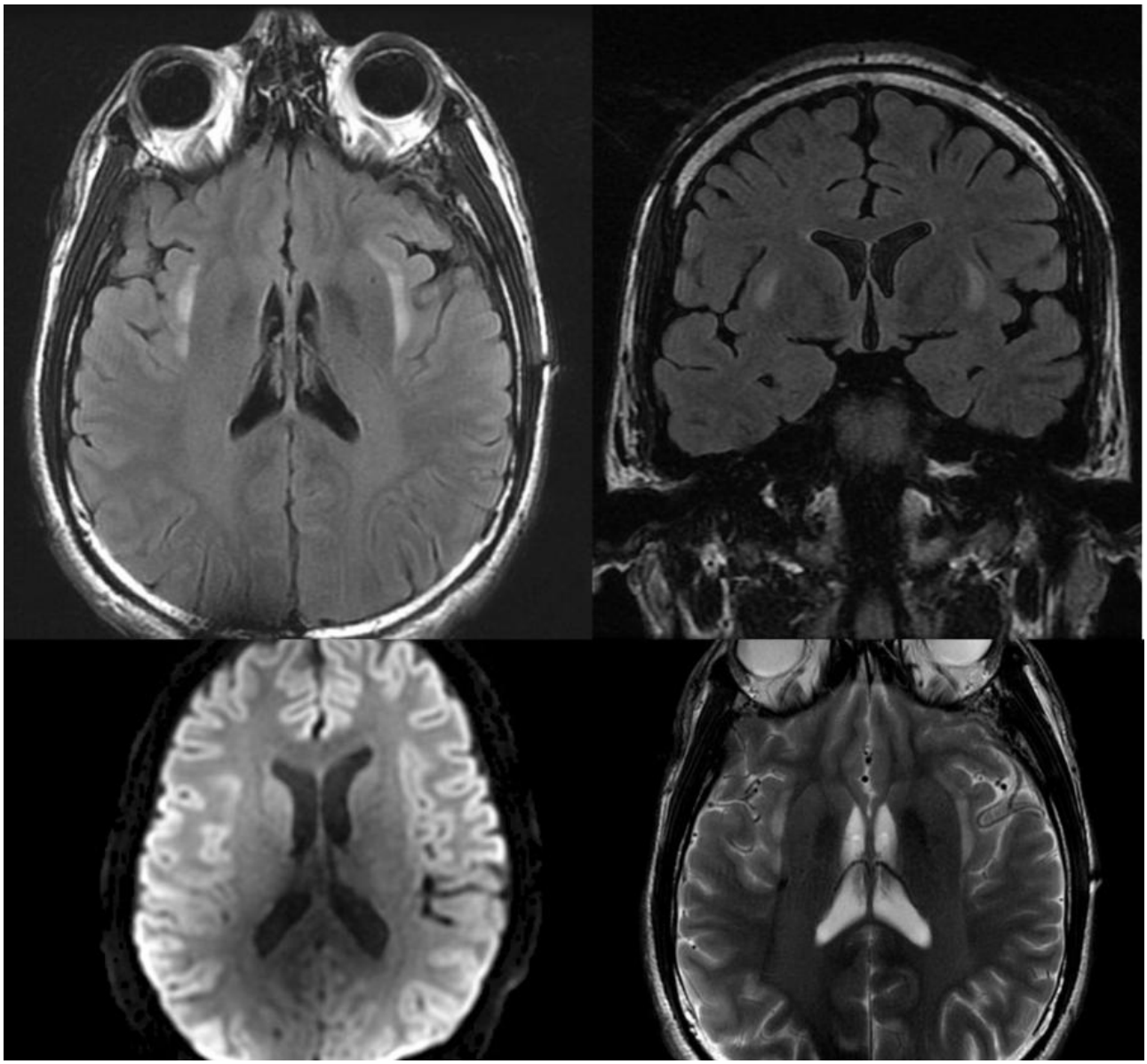
A 22-year-old male with a history of febrile seizures presented with a cluster of tonic clonic seizures approximately 1 week after a viral illness. The patient was hospitalized and started on anti-epileptic medications. Magnetic resonance imaging (MRI) demonstrated symmetric bilateral T2/FLAIR signal abnormality within the claustra. Electroencephalogram (EEG) showed generalized slowing in the delta range throughout the study. The patient improved within a week and was discharged home.

Results

Magnetic resonance imaging revealed isolated, symmetric bilateral T2/FLAIR signal abnormality with the claustra. There was no diffusion restriction of contrast enhancement.

Conclusions

The "claustrum sign" is a recently described imaging finding associated with an entity called NORSE in adults. It is associated with a very aggressive form of status epilepticus, with focal motor seizures and myoclonus, often requiring ICU admission and anesthetic drugs. During the acute phase, there is bilateral claustrum T2/FLAIR signal hyperintensity with elevated signal on diffusion-weighted imaging, but normal signal on the ADC map. In the chronic phase, the claustral imaging findings typically resolve. There may be parenchymal atrophy in some cases. The claustrum sign is likely under-recognized: the findings can be described incorrectly as peri-insular or external capsule lesions. The function of the claustrum remains incompletely understood. Animal models have shown that some subcortical structures act as modulators of seizure propagation. The claustrum may act as such a structure, as a hub for neural synchronization. Damage to the claustrum could result in persistence of epileptogenic activity. In summary, the rare, recently described claustrum sign is associated with a severe form of status epilepticus associated with febrile illness. Radiologists must be aware of these imaging findings, in order to better stratify and treat affected patients.



(Filename: TCT_E-43_claustrumsign.jpg)

E-44

3:58PM - 4:02PM

Atypical Language Representation and Multimodal Preoperative Assessment in a Trilingual Patient with Epilepsy

M Cekic[1], P Walshaw[2], N Salamon[3]
[1]Ronald Reagan UCLA Medical Center, Los Angeles, CA, [2]Ronald Reagan UCLA Medical center, Los Angeles, CA, [3]UCLA, Los Angeles, CA, David Geffen School of Medicine at UCLA, Los Angeles, CA, Los Angeles, CA

Purpose
Multilingual language representation in the brain remains an open scientific question that gains significant importance in the context of surgical treatment for brain disorders such as epilepsy. Here we discuss variable cortical representation of multiple languages and the importance of multimodal pre-operative functional mapping in a trilingual patient with intractable epilepsy.
Materials and Methods
We report the case of a 32-year-old early trilingual (Portuguese, Spanish, English) female with atypical language representation undergoing pre-operative mapping for epilepsy surgery.
Results
Magnetoencephalography (MEG) showed a focal cluster of dipoles in the left frontal operculum, with corresponding hypometabolism on positron emission tomography (PET) consistent with the epileptogenic focus. This was confirmed by monitored subdural electrocorticography (ECoG). Pre-operative functional MRI (fMRI) demonstrated bilateral representation for all languages, with additional distinct activation in the left pars opercularis for Spanish and Portuguese. Intracarotid amobarbital (Wada) test showed qualitative indication of stronger left hemispheric receptive language with unequivocal right hemispheric dominance for expressive language. Awake intra-operative ECoG showed distinct cortical representation in the left frontal operculum for each language, with a common area corresponding to the seizure focus. Electrode stimulation of this area caused complete speech arrest for all languages, which was in contrast to findings on other pre-operative imaging. These findings suggest the need for multimodal approaches to patients who are multilingual or demonstrate atypical patterns of language organization.
Conclusions
We present a case of a trilingual patient undergoing functional brain mapping prior to neurosurgical intervention for epilepsy. Imaging assessment demonstrated atypically distributed cortical language processing, with some areas of language overlap as well as areas of distinct processing for each language. Some discrepancy was noted among different imaging modalities, emphasizing the importance of multimodal preoperative functional assessment in patients with atypical language representation. These findings are discussed in the more general context of language representation in multilingual individuals.

E-45

4:02PM - 4:06PM

Fully Autonomous Bilateral Language Processing in a Patient with Right Temporal Epilepsy

M Cekic[1], P Walshaw[2], N Salamon[3]

[1]Ronald Reagan UCLA Medical Center, Los Angeles, CA, [2]Ronald Reagan UCLA Medical center, Los Angeles, CA, [3]UCLA, Los Angeles, CA, David Geffen School of Medicine at UCLA, Los Angeles, CA, Los Angeles, CA

Purpose
Language processing is thought to occur predominantly in the left hemisphere of the brain, with more than 95% of right-handed and approximately 70% of left-handed individuals demonstrating left language dominance. Recent developments in neuroimaging suggest that the picture may be more complicated than traditionally assumed, especially in patients with pathological states such as epilepsy. We consider language lateralization and the importance of pre-operative language mapping in patients with epilepsy in the context of an individual with independent bilateral language processing.
Materials and Methods
We report the case of a 33-year-old ambidextrous male with right mesial temporal epilepsy with bilateral language processing as determined by functional magnetic resonance imaging (fMRI) and intracarotid amobarbital (Wada) test. Each hemisphere was independently capable of maintaining language function and memory.
Results
Functional MRI demonstrated fully bilateral expressive language function with receptive function that was mostly left-sided with some right-sided representation. The basal temporal language area was left-sided. The supplementary motor area also was bilaterally represented, consistent with ambidexterity. Wada test confirmed independent hemispheric support for both language and memory function, with slight right hippocampal predominance for memory encoding and consolidation.
Conclusions
We present an unusual case of bilateral language processing in a patient with right mesial temporal epilepsy in whom each hemisphere was capable of independently supporting language and memory function. This example provides support for the view of language as a distributed network with differences in specific regional involvement that are likely to be dependent on genetics and clinical history. These findings are discussed in the broader context of preoperative functional assessment for patients undergoing neurosurgical intervention.

E-46

4:06PM - 4:10PM

Vessel Wall Imaging can be Used to Detect and Monitor Treatment Response in the Setting of Deep External Carotid Artery (ECA) Vasculitis

A Mallik[1], M Peckham[1], C Koening[1], R Wiggins[2], A DeHavenon[1], S Kim[1], D Parker[1], J McNally[1]
[1]University of Utah, Salt Lake City, UT, [2]University Of Utah, Salt Lake City, UT

Purpose

Our goal was to use combined computed tomography angiography (CTA) and high resolution 3T magnetic resonance imaging (MRI) to detect vessel wall inflammation and monitor treatment effect in a case of temporal artery biopsy proven, deep and superficial external carotid artery (ECA) eosinophilic vasculitis.

Materials and Methods

A 67-year-old female was referred to rheumatology with 3-4 weeks of gradual onset headaches and jaw claudication, and 1 week of ageusia. A temporal artery biopsy 3 weeks after symptom onset demonstrated active vasculitis with chronic inflammation most consistent with eosinophilic temporal arteritis. Computed tomography angiography of the head, neck, chest and abdomen were performed to evaluate the extent of vasculitis. The patient was recruited to an IRB-approved study, underwent informed consent and 2 week follow-up high resolution vessel wall MRI was performed. Two months after starting immunosuppressive treatment, the headache and jaw claudication had resolved but ageusia remained as the patient's primary complaint.

Results

Head CTA (A) demonstrated marked wall thickening along ECA branches, most prominent along the bilateral internal maxillary arteries. Concurrent abdomen CTA (D) demonstrated multisegmental, medium-sized abdominal vessel narrowing and dilatation, consistent with systemic vasculitis. Follow-up 3T high resolution MR vessel wall imaging (B, C) demonstrated ECA branch vessel wall enhancement with decreased thickening, consistent with treatment response.

Conclusions

Deep ECA branch vasculitis can demonstrate wall thickening and enhancement on CTA and vessel wall MRI. Furthermore, vessel wall imaging can be used to monitor treatment response in these patients and allow future studies with noninvasive imaging endpoints. These imaging techniques offer clues to the patient's chief complaint of ageusia, which may reflect downstream ischemia of the vasa nervorum of cranial nerves VII and IX.

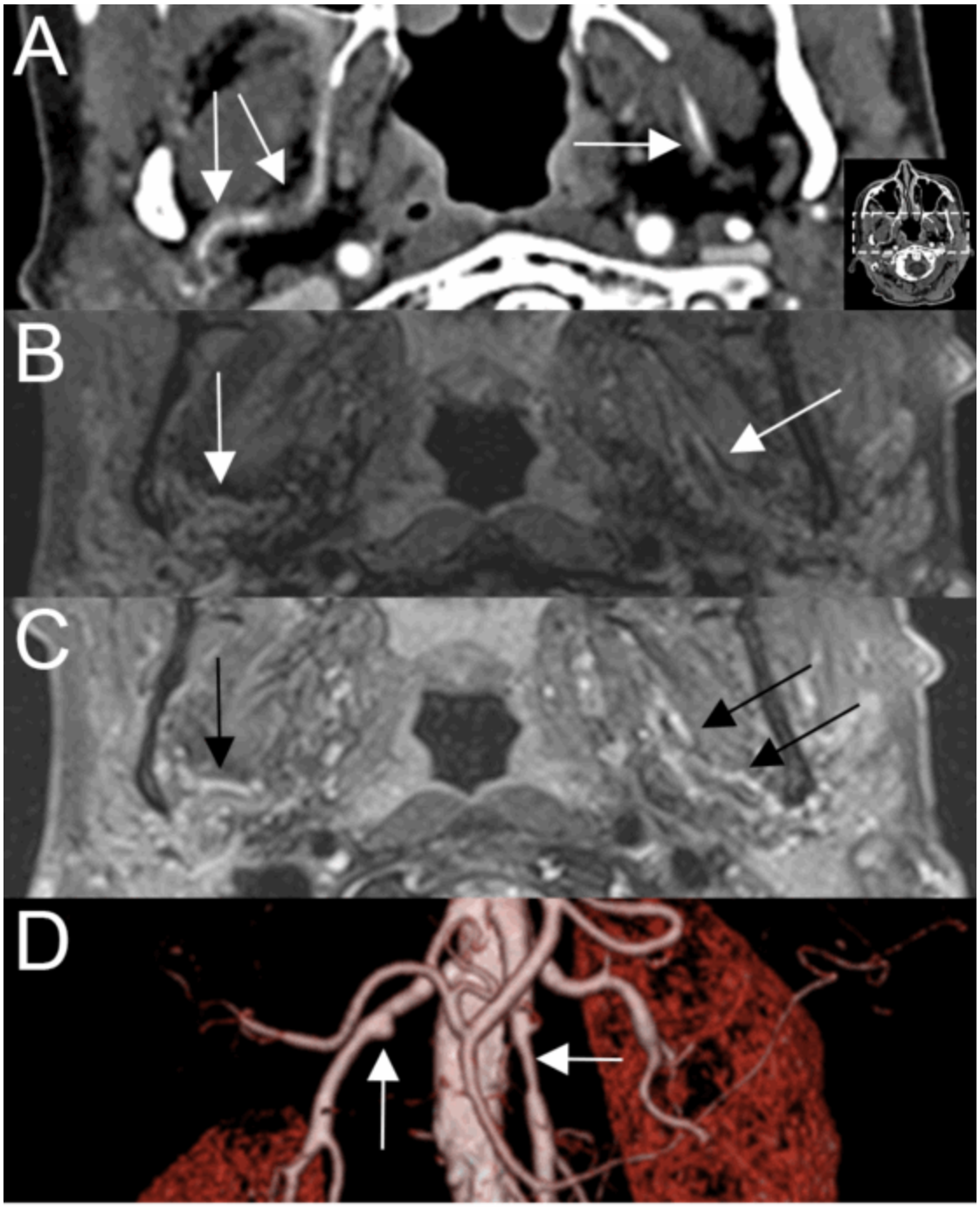


Figure: 67 year-old female with gradual onset headaches, jaw claudication and loss of taste (ageusia). Head and neck CTA (A) demonstrated marked wall thickening along the ECA branches, most prominent along the bilateral internal maxillary arteries (and including the superficial temporal arteries, not shown). Follow-up pre- (B) and postcontrast (C) 3T axial DANTE T1 high resolution vessel MR images demonstrated ECA branch vessel wall enhancement with decreased thickening. Abdomen CTA (D, 3D reconstruction) concurrent with the head CTA demonstrated multisegmental, medium-sized, abdominal vessel narrowing and dilatation, including at the superior mesenteric and right renal arteries.

(Filename: TCT_E-46_eosin_vasc_fig_v2b.gif)

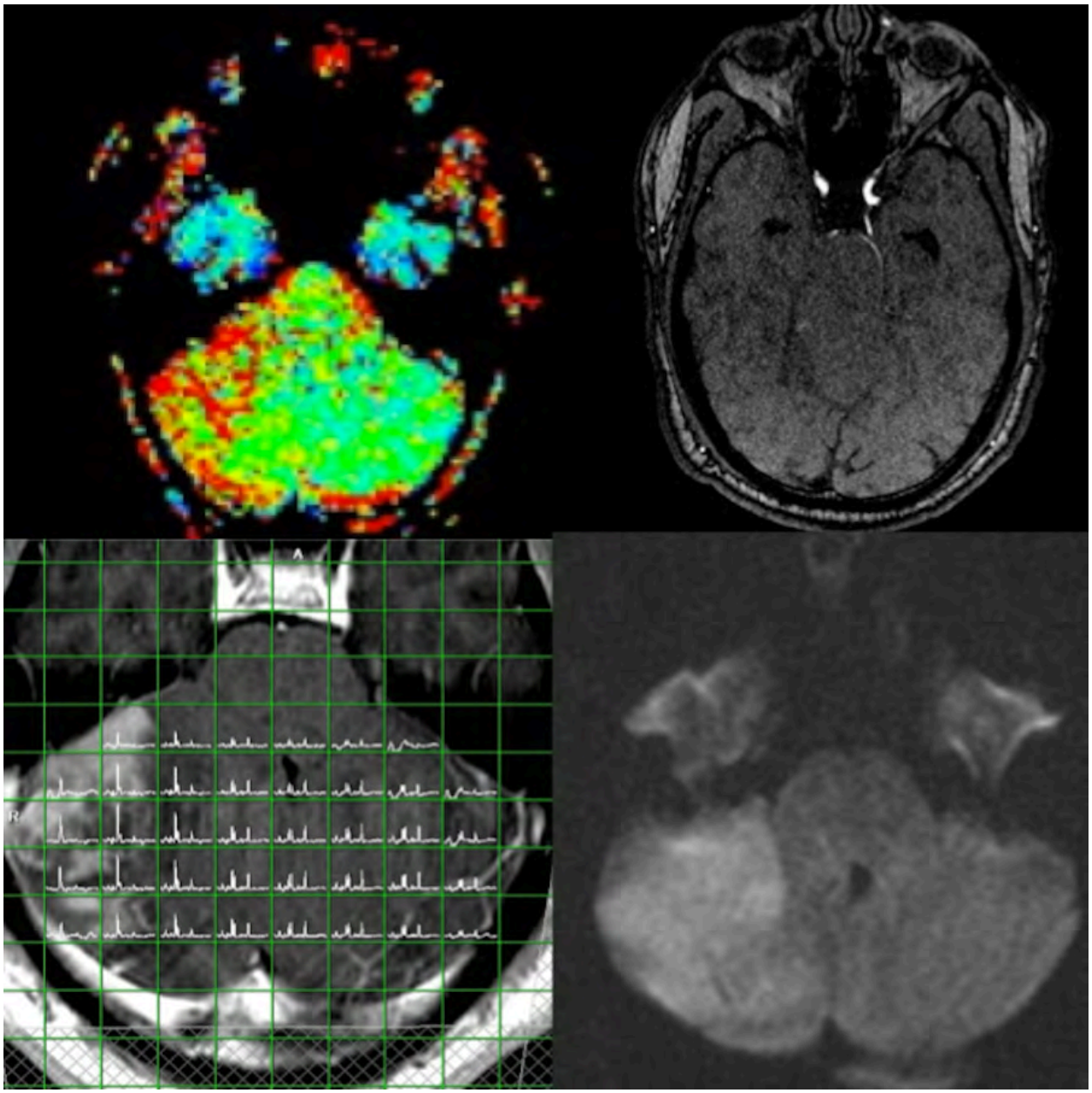
E-47

4:10PM - 4:14PM

Hidden in Plain Sight: Unusual Case of Medulloblastoma in an Adult, Masquerading as Subacute Infarction with MRI and Pathologic Correlation

M Bhatt[1], A Wang[1], A Krishnan[1], R Silbergleit[1], R Olson[1], N Cao[1], K Donev[1], M Juan[2], E Olariu[1], K Welker[1]
[1]Beaumont Health System, Royal Oak, MI, [2]Michigan State University College of Osteopathic Medicine, East Lansing, MI

Purpose
Medulloblastoma is a rare entity in adults. We present a case of medulloblastoma in an adult, with initial imaging findings that were suggestive of subacute infarction with occlusion of the distal right superior cerebellar artery (SCA). Our purpose is to show and discuss a spectrum of magnetic resonance imaging (MRI) findings with pathologic correlation in this atypical case, of tumor with arterial occlusion impersonating ischemia.
Materials and Methods
A 30-year-old male presented with dizziness and headaches. Initial imaging was concerning for subacute infarction involving the right superior cerebellar artery territory with occlusion of the right SCA. Patient was medically managed, however returned after 1 month with worsening symptoms. Repeat imaging was concerning for underlying tumor. Patient underwent resection for a suspected right cerebellar mass, with a pathologic diagnosis of medulloblastoma.
Results
Initial MRI demonstrated a geographic area of FLAIR and T2 hyperintense signal within the superior right cerebellar hemisphere with marked diffusion restriction, edema and irregular, peripheral gyriform enhancement. There was cut off of the right SCA just distal to its origin. Magnetic resonance spectroscopy (MRS) showed elevated choline peak, decreased NAA and creatine peaks, a lactate peak and absence of a taurine peak. Prolonged time to peak and mean transit time with decreased cerebral blood flow and blood volume were appreciated on MR perfusion. Repeat MRI 1 month later demonstrated similar findings with persistent diffusion restriction.
Conclusions
Our case illustrates a constellation of findings on conventional MRI, MRS and MR perfusion that can be seen with subacute infarction. Additionally there was occlusion of the right SCA just after its origin. However these findings were due to underlying tumor. We believe this phenomenon, of tumor, specifically medulloblastoma causing vascular compression and findings of ischemia is incredibly rare. If follow-up imaging is not obtained, this mimic of infarction may lead to a delay in patient care.



(Filename: TCT_E-47_Medulloblastoma.jpg)

E-48

4:14PM - 4:18PM

Neurosyphilis as Important Imaging Mimic of Limbic Encephalitis

O Foesleitner[1], M Skoll[1], R Höftberger[1], D Prayer[1], G Kasprian[1]
[1]*Medical University of Vienna, Vienna, Austria*

Purpose
Bilateral mesiotemporal T2/FLAIR-hyperintensity on magnetic resonance images is highly

suggestive of limbic encephalitis, with potentially fatal outcome. Clinical and radiologic findings in infectious (mostly herpes simplex virus, HSV) and noninfectious (autoimmune, among others) limbic encephalitis can be very similar. Neurosyphilis is an important imaging mimic of limbic encephalitis and should be considered as it is not routinely tested for but early treatment is essential.

Materials and Methods

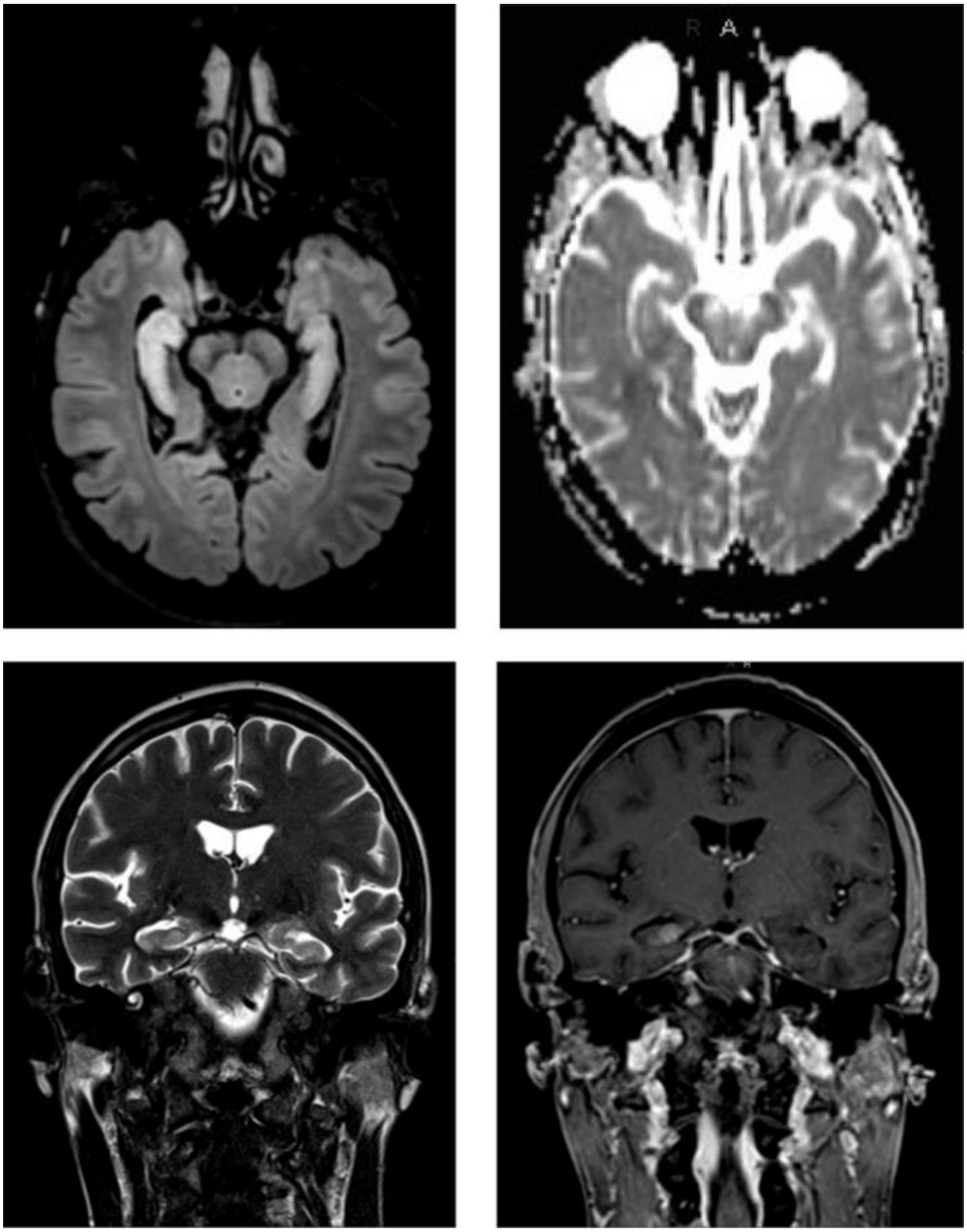
A 36-year-old MSM was admitted to hospital with acute partial disorientation and 1 week progressive cognitive deficits. Neurological examination revealed partial disorientation to time, place and situation, and a short-term memory of 10-15s (Mini-Mental State Examination-score 14/30) but otherwise no neurological deficits and no seizures. The patient was HIV-positive for 9 years with recently infrequent drug intake and had presumably untreated primary syphilis 3 years ago. Lumbar puncture showed pleocytosis (87 cells/µl, 93% lymphocytes), intrathecal IgG, IgM and IgA production, positive oligoclonal bands and HIV-1 RNA (2.77x10^2). EEG showed generalized slowing with intermittent bursts of theta waves. With imaging compatible to herpes encephalitis (see Imaging Findings), empirical treatment with IV acyclovir was started on day of admission. However, polymerase chain reaction for HSV 1-2 turned out to be negative. Further laboratory workup revealed positive blood and cerebrospinal fluid (CSF) venereal disease research laboratory test (blood titer 1:64, CSF titer 1:8), Treponema pallidum particle agglutination and fluorescent treponemal antibody-absorbed, leading to the final diagnosis of neurosyphilis and treatment with IV penicillin. On 1-month follow-up the patient still suffered from severe memory deficits.

Results

Computed tomography (CT) scan on day of admission was normal. Magnetic resonance imaging (MRI) on the same day showed bilateral mesiotemporal T2/FLAIR-hyperintensity (including hippocampi, parahippocampal gyri, insulae), no diffusion restriction (ADC-map), contrast enhancement in the right pes hippocampi and no hemorrhage on susceptibility-weighted imaging (SWI).

Conclusions

Neurosyphilis can mimic limbic encephalitis and should be considered in a patient with subacute temporal T2/FLAIR-hyperintensity to ensure early diagnosis and treatment.



(Filename: TCT_E-48_neurosyphilis.jpg)

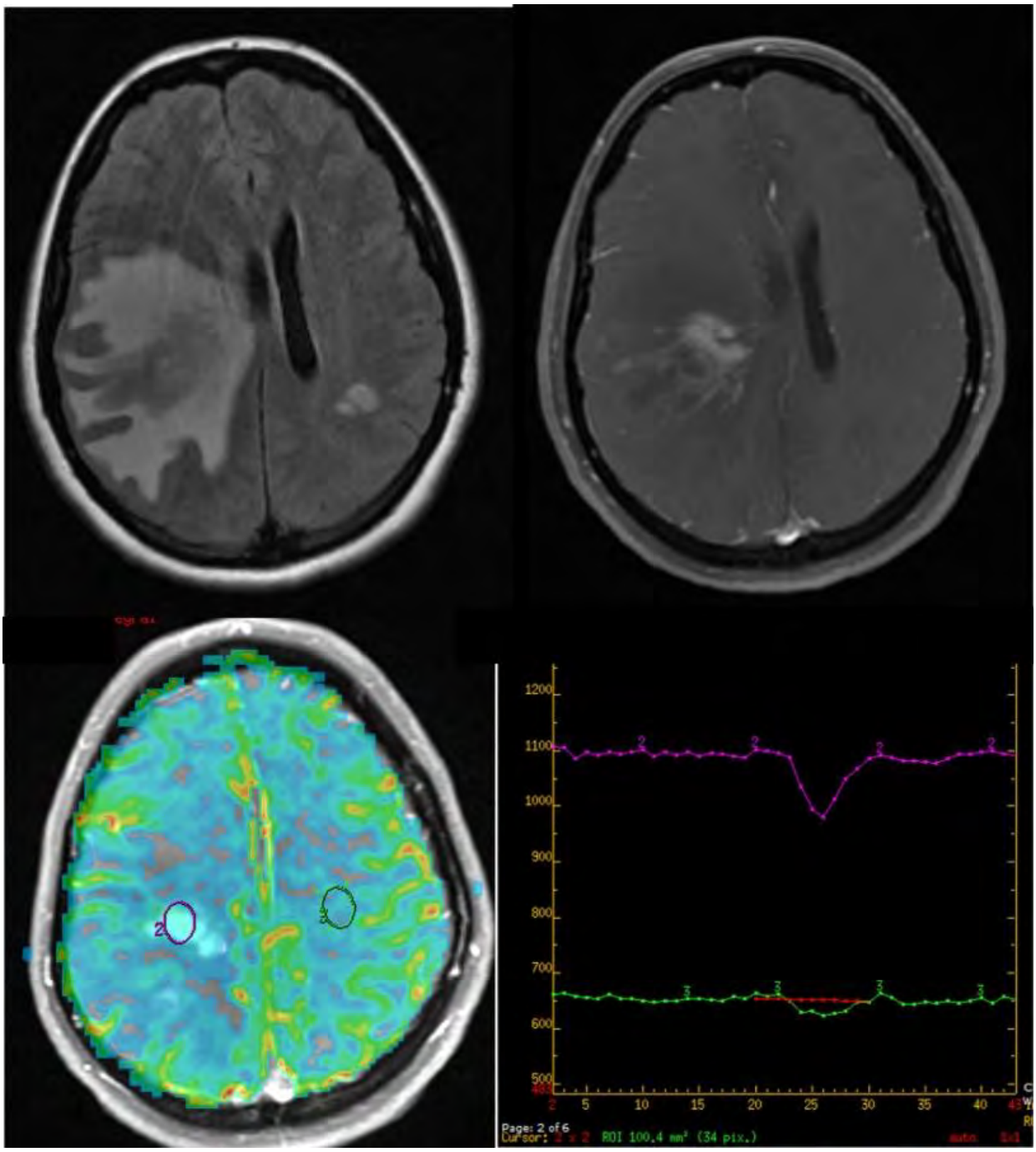
E-49

4:18PM - 4:22PM

A Challenging Case of Tumefactive Demyelinating Lesion: Atypical Findings on Conventional and Advanced Imaging

M Cho[1], A Lerner[1], W Gibbs[1]
[1]*University of Southern California/Keck Medical Center, Los Angeles, CA*

Purpose
On occasion, differentiating a tumefactive demyelinating lesion (TDL) from tumor can be a diagnostic challenge. We describe a pathology proven case of TDL that showed both conventional and advanced imaging features suggestive of tumor. We review expected findings of TDL and discuss pitfalls of advanced imaging in such a scenario.
Materials and Methods
A 47-year-old woman presented with a 1-week history of left arm and leg weakness. Magnetic resonance imaging (MRI) revealed a large, enhancing mass in the right cerebral hemisphere and several smaller lesions in the left hemisphere. A surgical biopsy was consistent with a demyelinating lesion. The patient was started on steroids. Short term follow-up demonstrated marked improvement in the right hemispheric mass effect. The patient's clinical symptoms improved.
Results
Conventional MRI showed an enhancing, partially necrotic mass with marked perilesional edema and several T2 hyperintense, non-enhancing lesions in the contralateral hemisphere. Magnetic resonance spectroscopy demonstrated increased choline, diminished NAA, and increased lipid/lactate. Magnetic resonance perfusion demonstrates elevated cerebral blood volume in comparison with normal contralateral white matter, with a ratio of 3.1.
Conclusions
Often, advanced imaging techniques such as MR perfusion and MR spectroscopy can add valuable information in cases of tumefactive demyelination versus tumor. We describe an atypical case in which imaging findings were not typical for TDL, and were in fact, more suggestive of a high grade glioma. Prior studies have shown that the rCBV of TDL tends to be lower than the rCBV of neoplasms, typically below 1.7. Studies have also shown that NAA/Cr ratio for TDL tend to be lower than that of gliomas. In this case, both rCBV and NAA/Cr ratio were values typically seen in gliomas. Recent studies have demonstrated vascular changes in TDL that may offer possible explanations for our atypical findings. In summary, not all lesions, tumefactive or neoplastic, "read the textbook" in terms of conventional or advanced imaging.



(Filename: TCT_E-49_tdl.jpg)

E-50

4:22PM - 4:26PM

Cerebral schistosomiasis mimicking brain tumor.

S Suthiphosuwan[1], A Lin[1], A Gao[2], D Munoz[2], J Spears[3], A Bharatha[1]

[1]Department of Medical Imaging, St. Michael's hospital, University of Toronto, Toronto, Ontario, [2]Department of Laboratory Medicine and Pathobiology, St. Michael's hostpital, University of Toronto, Toronto, Ontario, [3]Department of Surgery, St. Michael's hostpital, University of Toronto, Toronto, Ontario

Purpose

Schistosomiasis is the second most common parasitic infection worldwide. North America is a nonendemic area. However, there are occasional case reports among travelers and immigrants from endemic regions. We describe a case of active cerebral schistosomiasis in a North American patient, mimicking a brain tumor, with pathological correlation.

Materials and Methods

A 55-year-old Canadian female presented with first episode of seizure. Magnetic resonance imaging (MRI) scan showed a mass-like lesion with linear and nodular enhancement in left temporal lobe associated with brain edema. Initially, the lesion was thought to be a malignant tumor. She underwent left anterior temporal lobe resection. Histological examination showed parasitic eggs with characteristic lateral spine consistent with Schistosoma mansoni infection. Upon subsequent questioning, it was revealed that the patient did live in Ghana at the ages of 8-10 and she went back to Ghana again 10 years ago, for 2 weeks. She recalls swimming in beaches and rivers. No recent travel history to endemic regions after that.

Results

Magnetic resonance imaging revealed a mass-like lesion involving anterior left temporal lobe. The lesion showed T1 hypo- and T2 hyperintense with perilesional brain edema. On postgadolinium enhanced T1-weighted sequence, the lesion showed multiple small nodular and linear enhancements (Figure). Our case showed a classic appearance of cerebral schistosomiasis similar to that reported in previous literatures (1-4). A unique enhancement pattern of clusters of central linear enhancement surrounded by multiple enhancing punctate nodules also called "arborized" appearance (Figure) has been reported specific to cerebral schistosomiasis (1-4). Latent disease like in our case with presentation many years or decades after presumed exposure is rare but has been reported (5).

Conclusions

Cerebral schistosomiasis is rare. The history of exposure to endemic areas is helpful but can missed especially if remote from the time of presentation. Characteristic MRI findings may suggest the diagnosis and facilitate noninvasive work up.



(Filename: TCT_E-50_120.jpg)

E-51

4:26PM - 4:30PM

Optic Neuritis Related to Varicella Zoster Vaccination

A Rodriguez[1], P Puac[1], C Vallejo[1], R Camacaro[1], M Castillo[1]
[1]*University of North Carolina at Chapel Hill, Chapel Hill, NC*

Purpose
Optic neuritis is characterized by inflammation or demyelination of the optic nerve. Symptoms usually include pain, limited eye movements and visual impairment. Different viral diseases and vaccines have been associated with optic neuritis. We describe a case of optic neuritis following Varicella Zoster vaccination.
Materials and Methods
A 44-year-old healthy female, was seen in our emergency department with 3 days of pain

around and behind her right eye followed by blurriness of vision that appeared one day before. The patient denied other symptoms. Past medical history included chicken pox at age 23 and a shingles vaccine 3 weeks prior consultation. Physical examination on the slit lamp showed 1x1 mm confluent corneal staining in her right eye. Complementary studies revealed a positive PCR for varicella zoster.

Results

Magnetic resonance imaging (MRI) of the orbits showed blurriness and mild enlargement of the right intra-orbital optic nerve with patchy enhancement on T1 postgadolinium images. These findings were consistent with a right optic neuritis. In absence of any history of demyelinating disease and laboratories supporting that diagnosis, the cause of the optic neuritis was believed to be an ADEM-like reaction and the patient was successfully treated conservatively with steroids.

Conclusions

Although there are no specific imaging findings for post-vaccination optic neuritis, the temporal association with the immunization in this patient and PCR results suggest optic neuritis due to varicella zoster vaccination. In such cases, it is important to rule out disorders that include multiple sclerosis and neuromyelitis optica as these patients are at higher risk of chronic visual impairment and have a different prognosis.



Fig 1. MRI of the orbits. There is blurring and thickening of intraorbital portion of the right optic nerve with increased enhancement in the postcontrast images, consistent with the diagnosis of optic neuritis.

(Filename: TCT_E-51_VZ.jpg)

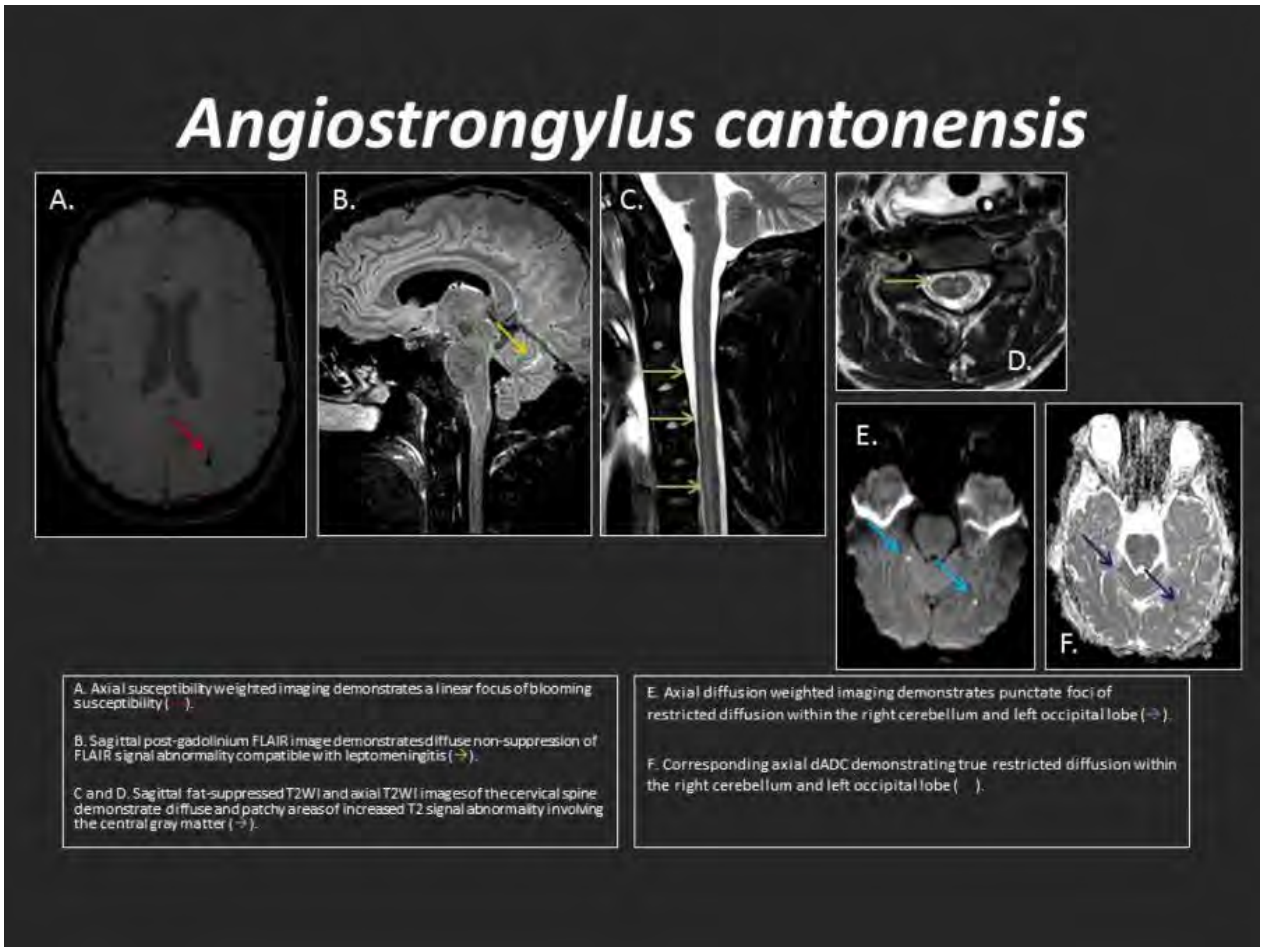
E-52

4:30PM - 4:34PM

Just Say No to Giant Escargot! A Case of Eosinophilic Meningomyelitis caused by Angiostrongylus cantonensis After Ingestion of a Giant African Snail

S Sasovetz[1], J Yetto[2], A Germana[2], M Cathey[2]
[1]NMCSD, San Diego, CA, [2]Naval Medical Center San Diego, San Diego, CA

Purpose
The purpose of this presentation is to demonstrate high resolution 3T MR imaging findings compatible with eosinophilic meningomyelitis which, in this case, was caused by Angiostrongylus cantonensis after ingestion of a giant African snail.
Materials and Methods
The patient is a 20-year-old male located in Southeast Asia who presented to the local hospital with bilateral thigh myalgias, dysuria, and constipation. His initial workup was unremarkable and he was discharged home. The patient re-presented to the local hospital approximately 10 days later after acute onset of a headache and neck stiffness. Upon further questioning, the patient reported that, following a "dare", he ate a raw giant African snail approximately 2 weeks earlier which led to immediate hospitalization and empiric treatment for a suspected diagnosis of eosinophilic meningitis likely from Angiostrongylus cantonensis which often is present in snails, the parasite's intermediate host. The patient's symptoms progressively worsened to include diminished deep tendon reflexes, urinary retention, and ultimately overt quadriparesis with need for intubation. Ultimately, PCR of obtained cerebrospinal fluid (CSF) samples proved positive for the suspected organism.
Results
Magnetic resonance imaging (MRI) of the brain demonstrated abnormal leptomeningeal enhancement and nonsuppression of CSF FLAIR signal in a pattern consistent suggesting inflammatory leptomeningitis. Additional linear foci of blooming susceptibility thought to represent petechial hemorrhagic migratory tracks from the offending organism. Scattered punctate foci of restricted diffusion suggestive of cerebral ischemia were presumably secondary to cytotoxic infectious/inflammatory mediated vasculitic insult versus secondary to direct parenchymal injury by the infectious agent. Magnetic resonance imaging of the spine showed diffusely increased T2 signal involving cord with a predilection for the central gray matter in conjunction with diffuse abnormal leptomeningeal enhancement. In light of the clinical history, the overall constellation of findings are those of eosinophilic meningomyelitis secondary to Angiostrongylus cantonensis.
Conclusions
Although Angiostrongylus cantonensis is the most common cause of eosinophilic meningoencephalitis in Southeast Asia, this case report is unique because it demonstrates findings compatible with eosinophilic meningomyelitis on 3T MR imaging.



(Filename: TCT_E-52_Angiostrongyluscantonensissub1.jpg)

E-53

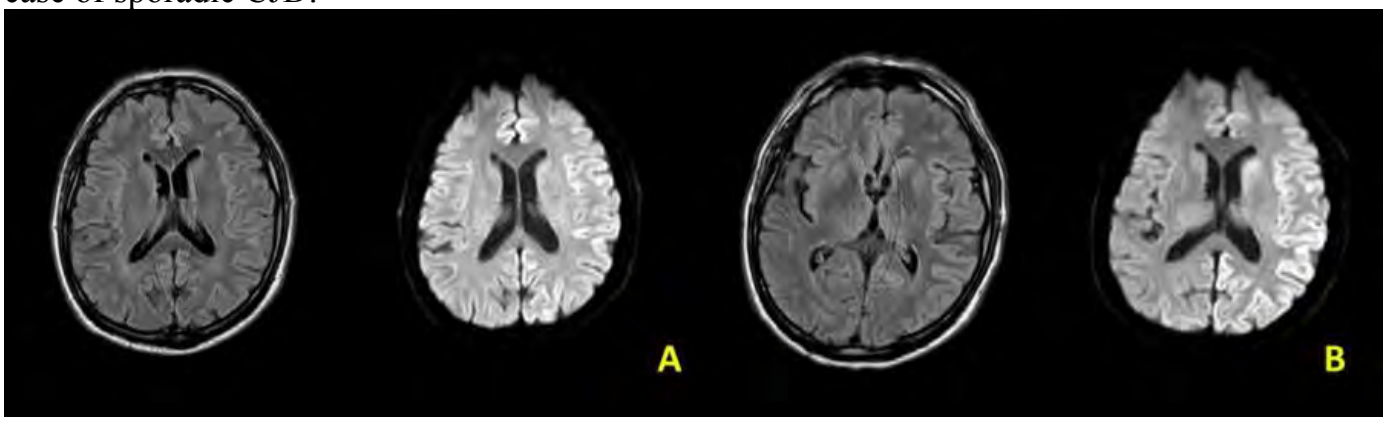
4:34PM - 4:38PM

Atypical Clinical and Neuroradiologic presentation of a Sporadic Form of Creutzfeld-Jacob Disease

A Stecco[1], E Soligo[2], A Trisoglio[2], C Varrasi[3], R Cantello[4], A Carriero[2]
[1]SCDU Radiologia, Novara, Italy, [2]SCDU Radiologia, Novara, ITALY, [3]SCDU Neurologia, Novara, ITALY, [4]Aou Maggiore Carita' - UPO University, Novara, ITALY

Purpose
Creutzfeld-Jacob disease (CJD) is a rare and incurable condition determined by prionic proteins. Characteristic EEG patterns, symptoms and high values of specific proteins in the cerebral fluid are considered important diagnostic markers but only brain biopsy make definitive diagnosis. Magnetic resonance imaging (MRI) can play an important role to identify this condition: our case exhibits unusual MRI findings and onseft of movements disorders associated with a specific subtype of CJD.

Materials and Methods
A 68-year-old man with an unremarkable past medical history, rapidly developed visual impairment and dizziness. During 1 month, he progressively showed dementia, associated with impairment of speech. Only before his death the patient presented characteristic movement disorders. Magnetic resonance imaging findings with a strongly elevated titer 14-3-3 proteins in cerebral fluid suggested a diagnosis of Creutzfeld-Jacob disease, confirmed as sporadic form after patient's death.
Results
At the onset of symptoms, patient underwent brain MRI: on diffusion-weighted imaging (DWI) only a small part of left occipital lobe presented cortical hyperintensity. When dizziness and visual impairment exacerbated, second MRI, done after 8 days, has shown progressive extension of the left cortical abnormal signal. At the end stage of the disease, when EEG reported periodic synchronous discharges, MRI showed in DWI an abnormal cortical hyperintensity of the complete left hemisphere. Also left caudate nucleus and right thalamus were involved with the same MRI abnormalities.
Conclusions
There are 4 major categories of CJD: sporadic is the most common documented form (80% of cases), other forms are variant, familial and iatrogenic. Sporadic presents, since at the early stage, movements disorders, and our case showing atypical manifestation of the disease and also clinical findings are not common. Actually specific MRI criteria do not exist, but literature demonstrate abnormalities in different and discrete areas: insula, cingulate gyrus, frontal gyrus and occipital gyrus. Our case had complete and progressive involvement of left hemisphere and, with the unusual clinical manifestations, it represent an atypical and curious case of sporadic CJD.



(Filename: TCT_E-53_FLAIRDWI30days.jpg)

E-54

4:38PM - 4:42PM

Miliary Neurotuberculosis

M Nguyen[1], B Addicott[1], J Anderson[1]

[1]*Oregon Health & Science University, Portland, OR*

Purpose

Central nervous system (CNS) tuberculosis (TB) accounts for 1% of all cases of Mycobacterium tuberculosis (MTb), yet stands out as the most lethal form of this disease. MTb may invade the CNS following primary infection by way of inhalation, filtering by regional lymph nodes, bacteremia, and metastatic seeding. Similarly, reactivation of dormant TB may seed the CNS resulting in various nonspecific syndromes that can mimic other neurological diseases. Diagnosis of CNS TB often is delayed or missed, giving way to devastating neurological sequelae despite the existence of effective anti-tuberculous treatment. Herein we present the rare case of miliary neurotuberculosis in the setting of disseminated TB in an immunocompetent patient.

Materials and Methods

A 55-year-old non-smoking male with no significant past medical history was admitted to our hospital for evaluation of chronic cough, night sweats, anorexia, generalized weakness and 9-lb weight loss over several months. He had returned to the U.S. from a week-long trip to Mexico just 1 week prior to admission, and recalled traveling to his native home in Mexico on at least 2 prior occasions in the past 3 years. Physical exam was remarkable for an ulcer in his left lower extremity, which he first noticed 4 weeks prior to admission. There was no known associated trauma. Neurological exam was negative for focal deficits, although the patient endorsed intermittent headaches at baseline. CT imaging revealed scattered miliary nodules in both lungs (A), osteomyelitis and diskitis predominantly involving the L4-L5 levels (B) and bilateral right-greater-than-left psoas abscesses, altogether most consistent with disseminated TB infection. Additional imaging findings of asymmetrically enlarged right seminal vesicles and prostate, along with striated nephrograms bilaterally, were concerning for dissemination to the genitourinary system. Tuberculosis infection was confirmed with findings of MTb in 1 of 3 separate acid-fast sputum smear stains, MTb growth from the left lower extremity lesion biopsy with histologic findings of nodular, suppurative granulomatous dermatitis, and lumbar puncture yielding MTb-positive CSF samples verified by PCR. MRI of his brain demonstrated extensive enhancing foci throughout the supra- and infratentorial parenchyma, some of which demonstrated FLAIR and subtle T2 hyperintensity (C,D), consistent with miliary brain TB. The patient was initiated on 4-drug antituberculosis therapy and high-dose steroids, and a drain was placed in his right psoas collection. HIV-testing was negative. Given continued clinical improvement, the patient was discharged on hospital day 15. His drain was removed, and he was continued on TB therapy with steroid taper.

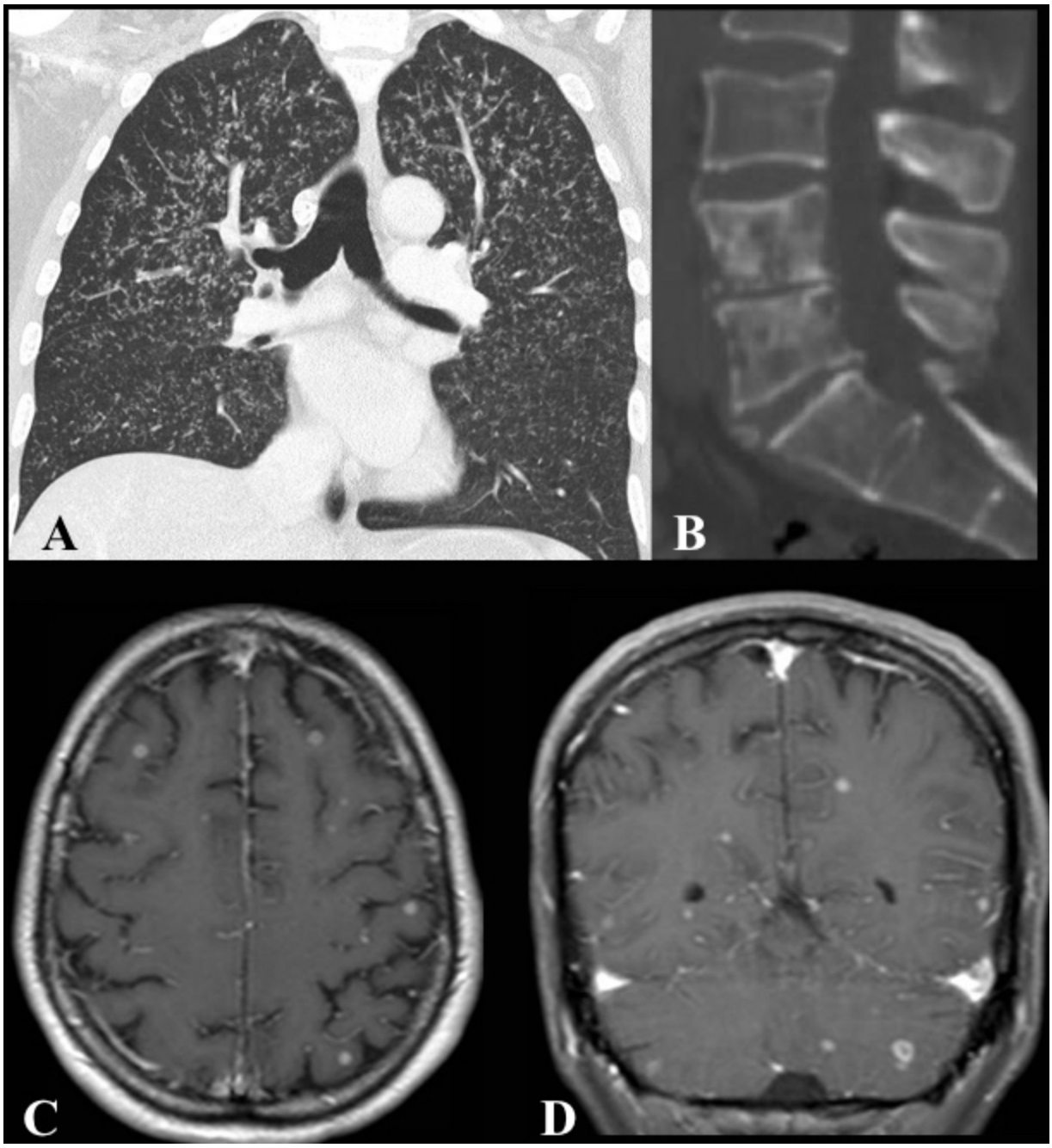
Results

Coronal contrast-enhanced CT of the chest (Fig. A) demonstrates innumerable sub-3mm lung nodules scattered throughout the bilateral lungs. Noncontrast CT of the lumbar spine (Fig. B) reveal patchy lytic foci, scattered sclerosis and multifocal osseous destruction with loss of the L4-5 disk space and destructive endplate changes. Axial and coronal MR T1-

weighted images of the brain postcontrast (Figs. C, D) demonstrate extensive sub-5mm round, enhancing foci throughout the supra and infratentorial parenchyma.

Conclusions

Tuberculosis is a worldwide health problem, resulting in an estimated 1.5 million deaths per year. Primary infection occurs through inhalation of droplet nuclei containing MTb, an aerobic, nonspore forming acid-fast bacillus that interacts with alveolar macrophages thereby triggering a type 1 T-helper cell mediated immune response. Although TB is known most commonly for its pulmonary manifestations, MTb can infect any organ as it gets filtered into regional lymph nodes, with hematogenous seeding occurring most frequently in highly oxygenated areas of the body. CNS TB begins with development of small caseating vascular foci ("Rich foci") in the brain, spinal cord, or meninges. The specific location of the foci, stage of tuberculoma (eg. caseating versus noncaseating), as well as a complex interplay of host immune factors all contribute to the various possible forms of CNS TB, primarily meningitis and less commonly intracranial tuberculoma, encephalitis, or abscess. Miliary brain TB is rare and seen predominantly in severely immunocompromised patients, unlike the patient in our case. However, widely disseminated TB with multiple primary extracranial sites likely increased the probability of our patient developing Rich foci with subsequent rupture. On imaging, miliary TB manifests as numerous round, sub 5mm lesions with homogenous enhancement on post-contrast T1-weighted imaging. Differential diagnosis includes fungal granulomas, pyogenic abscesses, lymphoma, metastases, healing stages of neurocysticercosis, and rarely glioma. Diagnosis of CNS TB is based on a combination of clinical signs, imaging and CSF findings, with the modified acid-fast staining method being most rapid for identifying MTb. First-line treatment comprises isoniazid, rifampin, ethambutol, and pyrazinamide plus a systemic steroid taper for 2 months. Timely diagnosis and treatment of CNS TB is paramount to preventing the high morbidity and mortality associated with disease progression.



(Filename: TCT_E-54_FIGURESA_D.jpg)

Tuesday
3:30PM - 4:45PM
Long Beach Convention Center, Room 203AB (Upper Level)

14G-Parallel Paper Session: Advanced Imaging for Brain Tumors – Get Out in Front of Gliomas (and more!)

O-127

3:30PM - 3:38PM

Deep Learning and Recurrent Glioblastoma: A New Approach For Imaging Evaluation

P Chang[1], Z Englander[1], J Grinband[2], T Wang[1], A Lassman[1], F Iwamoto[3], J Bruce[1], P Canoll[1], A Lignelli[3]
[1]Columbia University Medical Center, New York, NY, [2]Columbia University, New York, NY, [3]Columbia University Medical Center, New York City, NY

Purpose
In post-treatment glioblastoma patients with areas of new enhancement, current paradigms aim to classify the entire lesion as either recurrent tumor (RT) or treatment effect (TE) (1, 2, 3); however this approach is limited as histologically both components are known to coexist (4). Using a deep learning algorithm calibrated to localized biopsies, we hypothesize that varying proportions of RT and TE will yield distinct MR features that can be used to extrapolate ratios of these components across a tumor volume.
Materials and Methods
After IRB approval, localized biopsies were obtained in post-treatment glioblastoma patients with new enhancement seen on MRI. Each biopsy specimen was rated on a four-point scale based on the observed proportions of RT and TE. Using a corresponding 8x8 voxel patch on ADC, FLAIR, precontrast- and postcontrast-T1, a deep learning algorithm was developed to predict histologic scale based on MR features. The 6-layer neural network consists of 5 convolutional kernels and a single fully connected layer (8438 parameters total including batch normalization).
Results
A total of 106 localized biopsies from 42 post-treatment glioblastoma patients were obtained. Unsupervised learning yielded distinct MR features for each of the 4 histologic classes with 81% accuracy (Fig. 1a). Based on these learned features, the proportion of RT and TE was projected for each tumor volume (Figs. 1b-c). For 28 patients with survival data, the proportion of tumor containing at least a component of RT (score 3 or 4) was inversely correlated with days of overall survival ($r=-0.59$, $p=0.0038$).
Conclusions
A deep learning algorithm calibrated to localized biopsies can quantify varying proportions of RT and TE in post-treatment glioblastoma, yielding a more nuanced assessment of disease progression. Increasing proportions of estimated RT significantly correlated with incrementally worse survival. Notably, the fully automated tool can generate maps from raw images within seconds facilitating ease of clinical implementation.

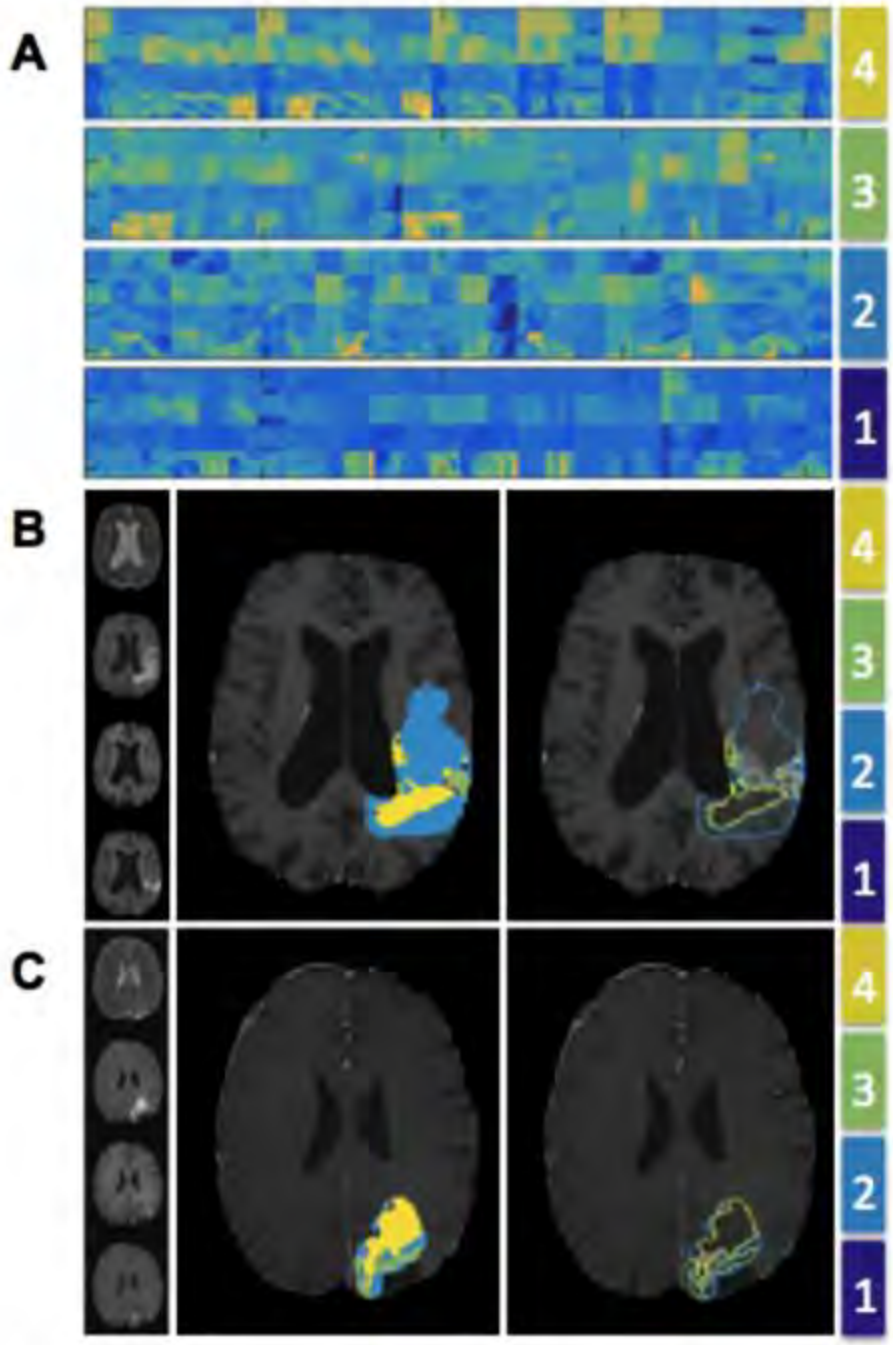


Fig. 1. (a) MR features identified through unsupervised learning associated with histologic class (1 = no RT or TE e.g. necrosis; 2 = TE predominates over RT; 3 = TE and RT both present; 4 = RT predominates over TE; RT = recurrent tumor, TE = treatment effect). Each column represents one 8x8 biopsy patch, with ADC, FLAIR, precontrast-T1 and postcontrast-T1 shown from top to bottom. (b-c) Extrapolation of learned features applied patch-wise over entire tumor volume. Example shown in (b) suggests that the majority of new enhancement and surrounding areas are composed of treatment effect (blue), while example shown in (c) suggests recurrent tumor predominates (yellow).

(Filename: TCT_O-127_Abstract.jpg)

O-128

3:38PM - 3:46PM

Deep Learning and Glioma Radiogenomics: A TCGA/TCIA Project

P Chang[1], J Maffie[2], A Lignelli[3], L Poisson[4], R Jain[5], C Filippi[6]
[1]Columbia University Medical Center, New York, NY, [2]New York Presbyterian, New York, NY, [3]Columbia University Medical Center, New York City, NY, [4]Henry Ford Health System, Detroit, MI, [5]NYU School of Medicine, New York, NY, [6]Hofstra Northwell School of Medicine, New York, NY

Purpose
Deep learning is an emerging branch of artificial intelligence rapidly outperforming conventional benchmarks on various computer vision tasks (1, 2, 3). The present study evaluates this technique in automatically learning MR features capable of predicting IDH mutation, 1p/19q co-deletion and survival in glioma patients.
Materials and Methods
MR imaging data from The Cancer Imaging Archives and corresponding genomic data from (4) were downloaded for glioma patients. Only patients with full pre-operative MRI including T2, FLAIR, precontrast-T1 and postcontrast-T1 were analyzed. A deep learning algorithm was developed for prediction of: IDH mutation; 1p/19q co-deletion; below- or above-average survival (relative to median survival 11.5 months). The 8-layer neural network is comprised of 7 serial convolutional blocks and a single fully-connected layer, and classifies based on a single axial slice cropped to tumor margins. Final classification for each tumor is based on the mode of all slices per volume.
Results
A total of 5,259 axial slices of tumor from 260 glioma patients (WHO Grade II/III = 115, WHO Grade IV = 145) were included for analysis. Unsupervised learning yielded distinct MRI phenotypes based on mutation and survival (Fig. 1). Overall the algorithm correctly predicted IDH mutation (94%), 1p/19q co-deletion (92%) and survival (82%) with high accuracy on five-fold cross-validation.
Conclusions
A deep learning algorithm can identify MRI features that accurately predict IDH mutation, 1p/19q co-deletion and survival in glioma patients. Notably the algorithm can differentiate visually similar cases (Figs. 1a-b) and atypical cases such as high-grade gliomas with IDH mutation, lower-grade gliomas (LGG) with wild-type IDH, and LGG without 1p/19q co-deletion (Figs. 1c-e). Furthermore the algorithm is objective (requires no human interaction) and fast (several seconds from raw imaging data to prediction). Ongoing efforts aim for incorporation into clinical workflow and treatment paradigms.

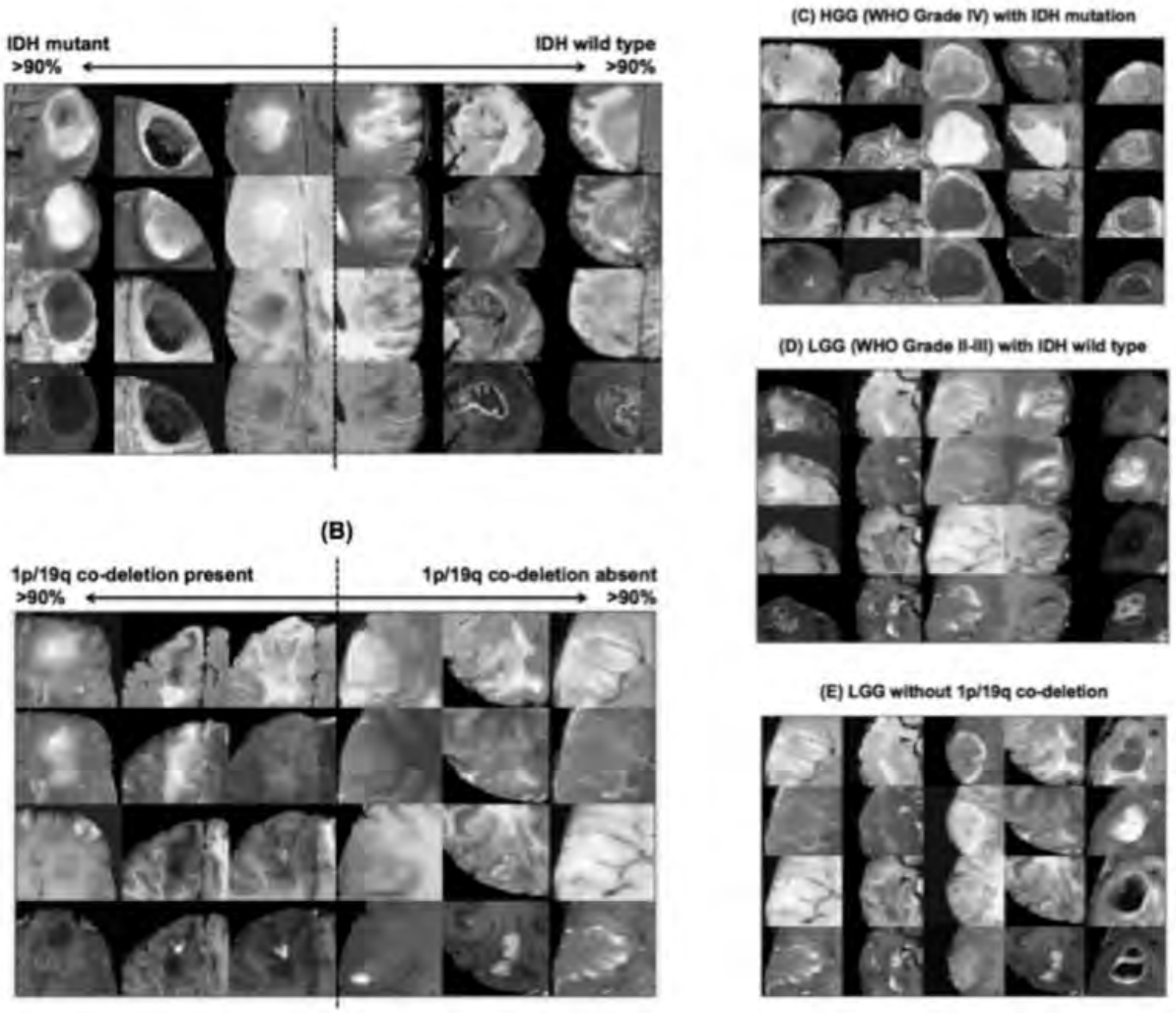


Fig. 1. Prototypical cases as identified by deep learning algorithm showing spectrum of imaging features for (a) IDH mutation and (b) 1p/19q co-deletion. Each column represents a single tumor, with FLAIR, T2, precontrast-T1 and postcontrast-T1 shown from top to bottom. Note that the middle third and fourth columns of (a-b) show visually similar tumors with distinct mutations that the algorithm is able to differentiate with high accuracy. Additional correctly identified atypical cases are shown for (c) HGG with IDH mutation, (d) LGG with wild-type IDH and (e) LGG without 1p/19q co-deletion.

(Filename: TCT_O-128_Figure1.jpg)

O-386

3:46PM - 3:54PM

Analysis of Heterogeneity in T2-Weighted MR Images Can Differentiate Pseudoprogression from Progression in Glioblastoma

T Booth[1]
[1]*Kings College Hospital, London, United Kingdom*

Purpose
To develop an image analysis technique that distinguishes pseudoprogression from true progression by analyzing tumour heterogeneity in T2-weighted images using topological descriptors of image heterogeneity called Minkowski functionals (MFs).
Materials and Methods
Using a retrospective patient cohort (n = 50), and blinded to treatment response outcome, unsupervised feature estimation was performed to investigate MFs for the presence of outliers, potential confounders, and sensitivity to treatment response. The progression and pseudoprogression groups then were unblinded and supervised feature selection was performed using MFs, size and signal intensity features. A support vector machine model was obtained and evaluated using a prospective test cohort.
Results
The model gave a classification accuracy, using a combination of MFs and size features, of more than 85% in both retrospective and prospective datasets. A different feature selection method (Random Forest) and classifier (Lasso) gave the same results. Although not apparent to the reporting radiologist, the T2-weighted hyperintensity phenotype of those patients with progression was heterogeneous, large and frond-like when compared to those with pseudoprogression.
Conclusions
Analysis of heterogeneity, in T2-weighted MR images, which are acquired routinely in the clinic, has the potential to detect an earlier treatment response allowing an early change in treatment strategy. Prospective validation of this technique in larger datasets is required.

O-130

3:54PM - 4:02PM

Texture Analysis of Magnetic Resonance Fingerprinting in Adult Brain Tumors

S Dastmalchian[1], D McGivney[1], O Kilinc[1], D Ma[1], J Barnholtz-Sloan[1], J Sunshine[2], M Griswold[1], V Gulani[3], A Sloan[2], C Badve[2]
[1]*Case Western Reserve University, Cleveland, OH,* [2]*UH Hospitals Cleveland Medical Center, Cleveland, OH,* [3]*UH Hospitals Cleveland Medical Center, Case Western Reserve University, Cleveland, OH*

Purpose
To investigate the utility of statistical texture analysis in characterizing magnetic resonance fingerprinting (MRF)- based quantitative maps to discriminate between adult brain tumors.
Materials and Methods
Magnetic resonance fingerprinting acquisition was performed in 31 patients with untreated

brain tumors: 17 glioblastomas (GBM), 6 lower-grade gliomas (LGG) and 8 metastases (1). Regions of interest (ROI) for the solid tumor (ST) (range: 0.32-12 cm2) and peri-tumoral white matter (PW) (range: 0.25-2.5 cm2) were drawn on quantitative T1 and T2 maps (2). Second-order textural features were computed based on Gray level co-occurrence matrices (GLCMs) using Matlab (The Mathworks, Natick, MA) (3,4, 5). Pearson correlation coefficients were used for further feature selection and removal of the redundant features. Five features including correlation, homogeneity, entropy, cluster-shade, and information measure of correlation 1 (IMC1) were selected for further analysis. These were compared across tumor types using the unpaired Student's t-test and receiver operating characteristic (ROC) analysis.

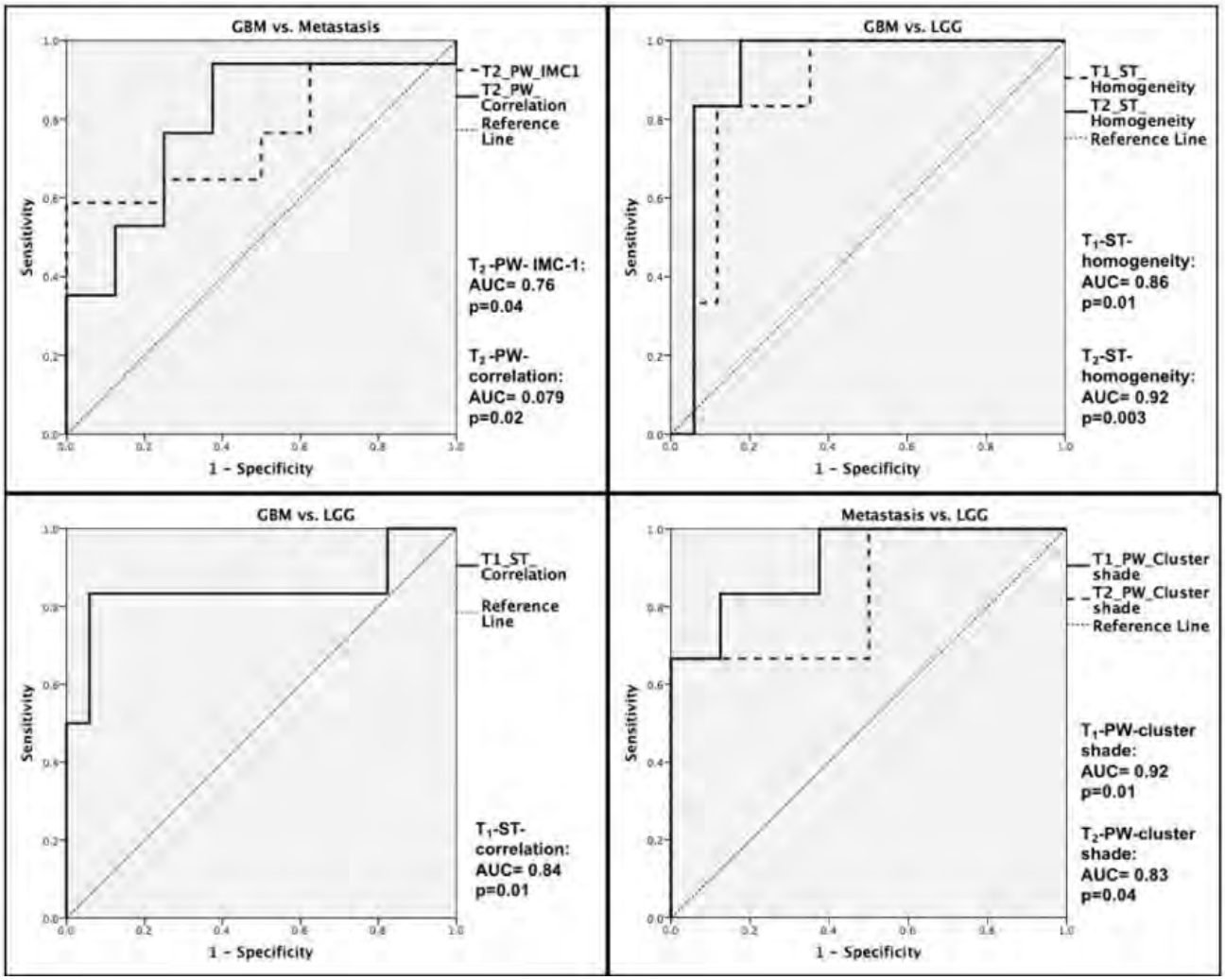
Results

In ST analysis, T1 correlation and T2 homogeneity of LGGs were significantly higher compared to GBMs ($p=0.008$, and $p =0.002$ respectively) while the T2 entropy of GBMs were significantly higher than LGGs ($p=0.02$). The cluster-shade of T1 PW was significantly different between metastases and LGGs ($p= 0.004$). Also, there were significant differences in T2 correlation and T2 IMC1 for PW regions of GBMs compared to metastases ($p=0.03$, and $p=0.03$). Receiver operating characteristic analysis revealed that homogeneity of ST on T2 maps offered best separation between GBM and LGG with AUC of 0.92 ($p=0.003$) (Fig. 1).

Conclusions

This study demonstrates the utility of texture analysis in evaluating MRF derived brain tumor maps. Second order texture features allow differentiation between common brain tumors by improving characterization of tumoral and peritumoral regions. Magnetic resonance fingerprinting-based texture analysis may offer a unique approach to effectively capture the tissue heterogeneity that is characteristic of aggressive brain tumors.

Figure-1: ROC curve analysis of the second-order statistical features in differentiation of adult brain tumors.



(Filename: TCT_O-130_Picture1.jpg)

O-131

4:02PM - 4:10PM

TERT promoter mutation prediction using support vector machine (SVM) in patients with wild-type IDH1 Glioblastoma

K Yamashita[1], A Hiwatashi[1], O Togao[1], R Kamei[1], D Momosaka[1], H Honda[1]
[1]*Kyushu University, Fukuoka, Fukuoka*

Purpose
Glioblastoma (GBM) patients with telomerase reverse transcriptase (TERT) mutations have a poorer clinical outcome than those without such mutations. Computer-assisted diagnosis could provide high reproducibility and reduce human errors in diagnosis. Support vector

machine (SVM) has been proposed as an effective statistical learning algorithm. Our purpose was to investigate whether TERT mutation status in the patients with wild-type IDH1 GBM can be predicted using SVM.
Materials and Methods
We retrospectively studied 43 patients with wild-type TERT (TERTw), and 69 patients with mutant TERT (TERTm). Each patient underwent pre-operative postcontrast T1-weighted images with a 1.5 or 3 T MR scanner. We constructed 9 feature vectors consisted of age, gender, tumor location, subventricular extension, cortical extension, multiplicity, enhancing volume, necrosis volume, and the percentage of necrosis volume as input data. All cases were divided randomly into training (n = 56) and validation data set (n = 56). First, the training data set was used for learning and identifying optimum discriminant model of SVM. Second, developed SVM applied to the validation data set to evaluate the diagnostic performance. The diagnostic performance using conventional multiple linear regression analysis also was evaluated.
Results
Our proposed SVM allowed the differentiation between TERTw and TERTm with sensitivity, specificity, and accuracy of 85.7 %, 47.6%, and 71.4%, respectively. We observed no significant differences between the 2 groups using multiple linear regression analysis.
Conclusions
Support vector machine based on the tumor enhancing/necrosis volume and distribution may be useful for predicting TERT mutation status in the patients with wild-type IDH1 GBM.

O-132

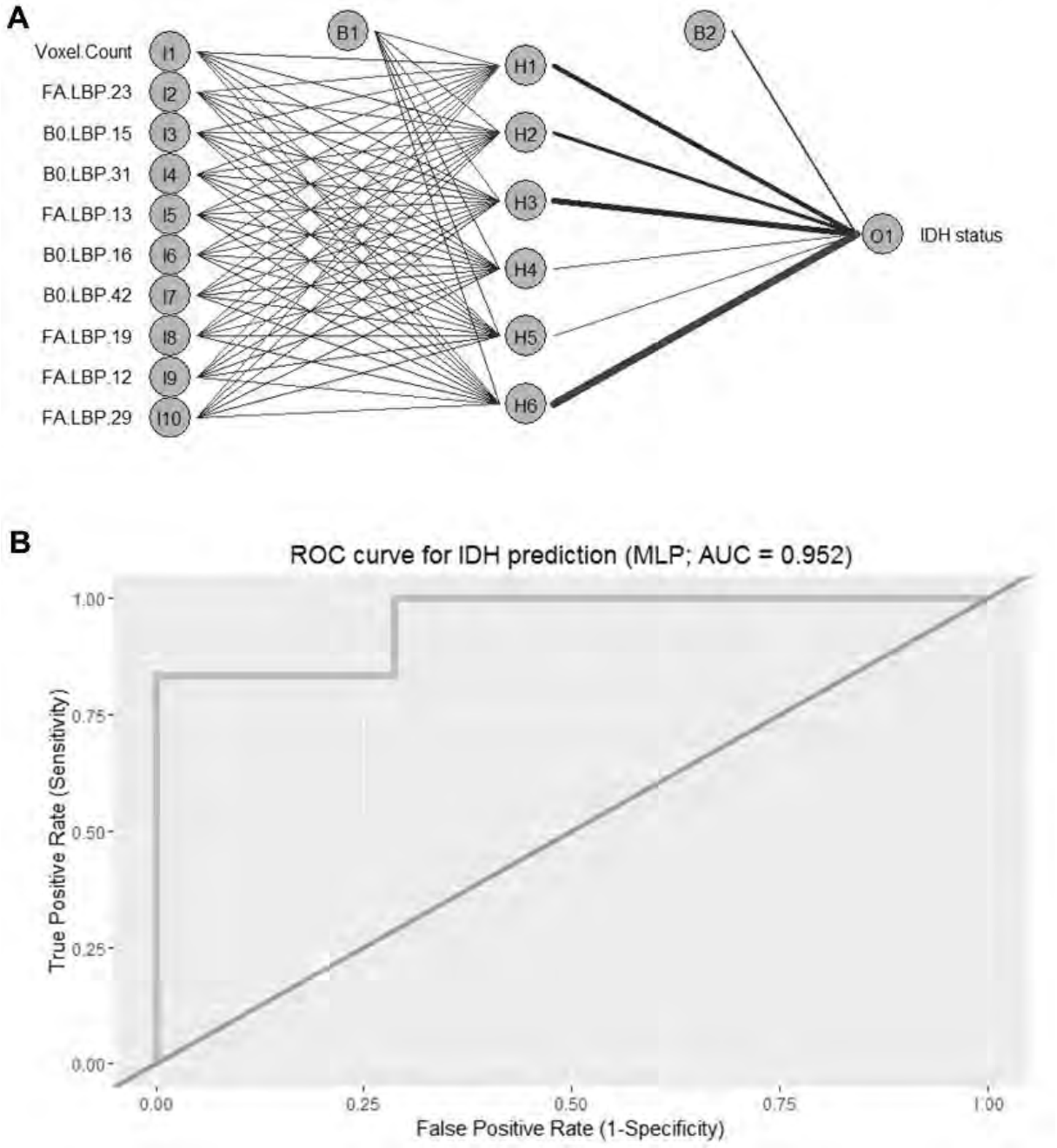
4:10PM - 4:18PM

Diffusion Tensor Image Features Predict IDH Genotype in Newly Diagnosed WHO Grade II/III Gliomas Using a Machine-Learning Classifier

B Wiestler[1], P Eichinger[1], E Alberts[2], C Delbridge[1], S Trebeschi[1], T Huber[1], S Bette[1], J Gempt[1], J Kirschke[1], C Zimmer[1], B Menze[2]
[1]Klinikum Rechts der Isar, TU München, München, Bavaria, [2]TU München, München, Bavaria

Purpose
We hypothesized that machine learning analysis based on texture information from the pre-operative MR imaging phenotype can reliably predict IDH mutational status in newly diagnosed WHO grade II and III gliomas.
Materials and Methods
This retrospective study was approved by the local institutional review board and included in total 79 consecutive patients with a newly diagnosed WHO grade II or III gliomas. Local binary pattern texture features were generated from pre-operative B0 and fractional

anisotropy (FA) diffusion tensor imaging. In a training set of 59 patients, a single hidden layer neural network to generate a model predicting IDH status (determined via immunohistochemistry and sequencing) was trained. Model performance was validated in an independent set of 20 glioma patients.
Results
Seventy-six percent of tumors were IDH mutant. Prediction accuracy of the generated model was 92% (54 / 59 cases; AUC = 0.921) in the training cohort and 95% (19 / 20; AUC = 0.952; Fig. 1A) in the validation cohort. The 10 most important features were comprised of tumor size and both B0 and FA texture information, underlining the joint contribution of imaging data to classification (Fig. 1B). Tumor size was larger in IDH mutant tumors, which was validated in an independent cohort. However, a logistic regression model including only tumor size had a mediocre classification performance (AUC in training cohort = 0.727; AUC in validation cohort = 0.679), underlining the advantage of leveraging the full information contained in the data set through a neural network.
Conclusions
Machine learning analysis of B0 and FA texture information as well as tumor size reliably predicts IDH status in pre-operative MRI of WHO grade II and III gliomas. Such information may in the future increasingly supplement pathological analysis of gliomas, and highlight the potential of radiogenomics.



(Filename: TCT_O-132_Figure1.jpg)

O-134

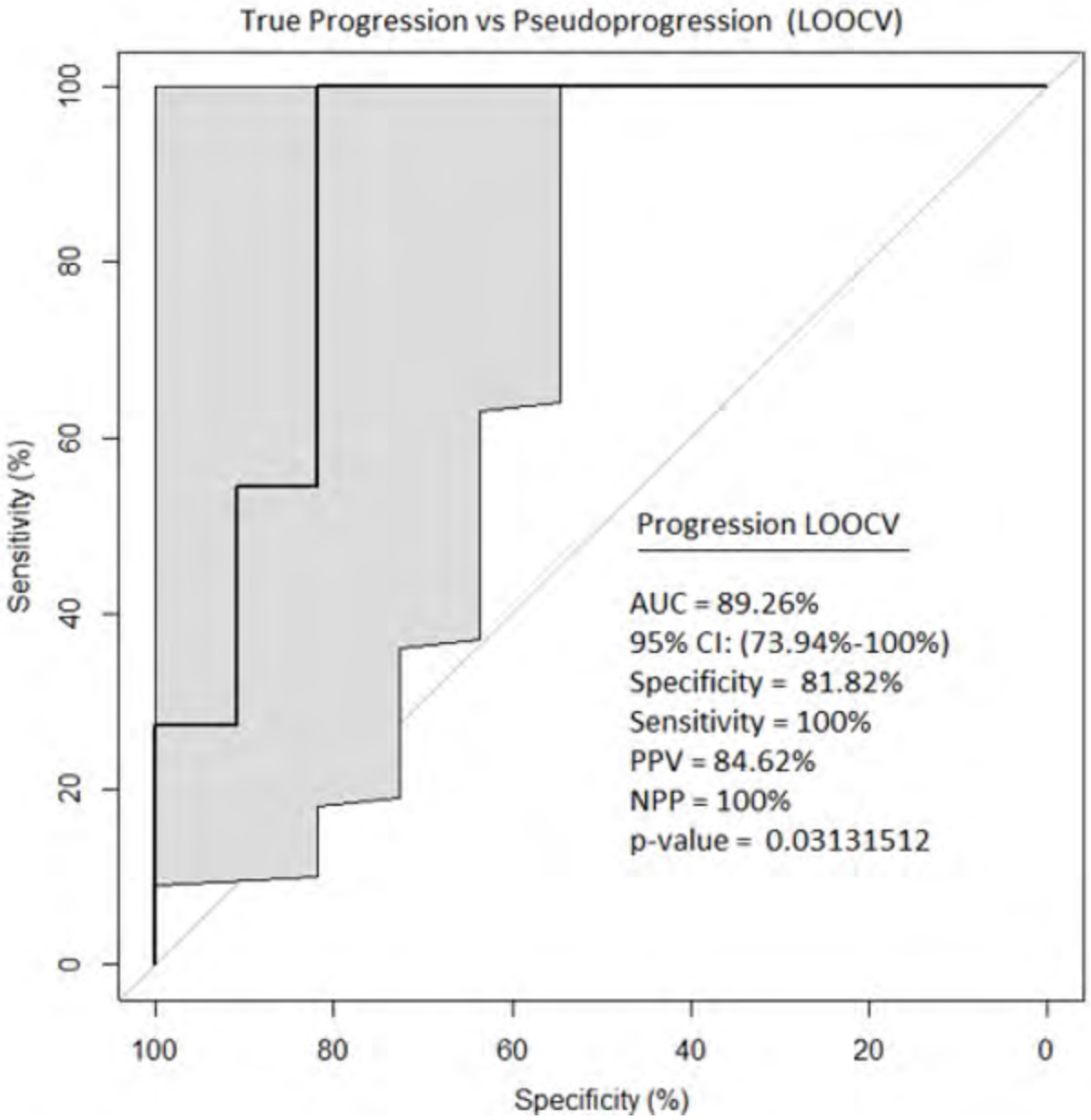
4:26PM - 4:34PM

Multi-center study demonstrates radiomic texture features derived from MR perfusion images predict pseudoprogression from true progression in glioblastoma patients

N Elshafeey[1], A Kotrotsou[1], D Giniebra[1], S Abrol[1], I Hassan[1], K El Salek[1], A Hassan[1], A Shaaban[1], S Bergamaschi[2], F Moron[3], M Law[4], P Zinn[3], R Colen[1]

[1]MD Anderson Cancer Center, Houston, TX, [2]University of Southern California, Los Angeles, CA, [3]Baylor College of Medicine, Houston, TX, [4]Keck Medical Center of USC, Los Angeles, CA

Purpose
To differentiate between pseudoprogression and true progression in patients with glioblastoma using MR perfusion radiomic texture analysis (TA).
Materials and Methods
Ninety-eight patients with pathologically-proven diagnosis of GBM were included retrospectively in this IRB approved HIPAA compliant study. All patients underwent DSC and DCE perfusion MRI as part of their routine clinical care. Images were analyzed using Nordic ICE 2.3 (NordicNeuroLab) ; rCBV and ktrans maps were obtained. Subsequently, 3D slicer 4.3.1(http://www.slicer.org) was used to segment the entire tumor on the different processed maps to create a volume of interest (VOI) for Radiomic TA. Multiple invariant texture features then were extracted from each VOI. Four hundred seventy-five invariant texture features were applied to each map. Leave-one-out cross-validation (LOOCV), receiver operating characteristic (ROC), Kaplan Meier, and multivariate Cox proportional hazards regression analyses were used to assess the relationship between texture feature and pseudoprogression and true progression.
Results
Variance and sum entropy were the 2 most significant radiomic features that discriminated between pseudoprogression and true progression. P value, AUC, specificity and sensitivity were 0.03, 89.26%, 81.82%, and 100% respectively (Fig.).
Conclusions
Radiomic TA derived from perfusion images can be helpful in determining true versus pseudoprogression in GBM. Further, this study illustrates successful application of radiomic TA as an advanced processing step for different MRI perfusion maps (DCE, DSC).



(Filename: TCT_O-134_figure2.jpg)

O-135

4:34PM - 4:42PM

Differentiation of Enhancing Glioma and Primary Central Nervous System Lymphoma by Texture-based Machine Learning

P Alcaide Leon[1], P Dufort[1], A Geraldo[1], L Alshafai[1], P Maralani[1], J Spears[1], A Bharatha[1]
[1]*University of Toronto, Toronto, ON*

Purpose
Accurate pre-operative differentiation of primary central nervous system lymphoma (PCNSL) and enhancing glioma is essential to avoid unnecessary neurosurgical resection in PCNSL patients. The purpose of the study was to evaluate diagnostic performance of a machine learning algorithm using texture analysis of contrast-enhanced T1-weighted (CE T1-W) images for differentiation of PCNSL and enhancing glioma.
Materials and Methods
Seventy-one adult patients with enhancing gliomas and 35 adult patients with PCNSL were included. The tumors were contoured manually on CE T1-W images and the resulting volumes of interest (VOIs) were mined for textural features and subjected to a support vector machine (SVM)-based machine learning protocol. Three readers classified the tumors independently on CE T1-W images. Areas under the receiver operating characteristic curves (AUCs) were estimated for each reader and for the SVM classifier. A noninferiority test for diagnostic accuracy based on paired AUCs was performed with a noninferiority margin of 0.15.
Results
The mean AUCs were 0.877 (95% CI: 0.798-0.955) for the SVM classifier; 0.878 (95% CI: 0.807-0.949) for reader 1; 0.899 (95% CI: 0.833-0.966) for reader 2; and 0.845 (95% CI: 0.757-0.933) for reader 3. The mean AUC of the SMV classifier was significantly noninferior to the mean area under the curve of reader 1 (p= 0.021), reader 2 (p=0.035) and reader 3 (p=0.007).
Conclusions
Support vector machine classification based on textural features of CE T1 images is noninferior to expert human evaluation in the differentiation between PCNSL and enhancing glioma.

Tuesday
3:30PM - 4:45PM
Long Beach Convention Center, Room 102BC (Main Level)

14H-Parallel Paper Session: TURBO & TOUR: Stenosis, Thrombosis and Other Vascular Pathology . . . .Finding It and Losing It!

T-29

3:30PM - 3:33PM

Prevalence and Impact of Aortic Arch Anatomy Variants in Patients Undergoing Mechanical Thrombectomy for Emergent Large Vessel Occlusion (ELVO).

A Spiro[1], A Erdfarb[2], D Edasery[1], J Nakhla[1], N Haranhalli[1], D Altschul[1], R Zampolin[1]
[1]Montefiore Medical Center, Bronx, NY, [2]Montefiore Medical Center / AECOM, Bronx, NY

Purpose
To evaluate the prevalence of aortic arch variants in patients undergoing mechanical cerebral thrombectomy for large vessel occlusion and assess their impact on recanalization times.
Materials and Methods
Seventy-two consecutive CT angiograms of the head and neck performed on patients at an inner-city, tertiary care, academic medical center subsequently treated with mechanical thrombectomy in the setting of emergent anterior circulation large vessel occlusions from July 2015 through October 2016 were reviewed retrospectively. The aortic arch anatomy was assessed by 2 neuroradiologists and 1 neuroradiology fellow and classified as having a common origin (bovine arch), Type I,II or III arch configuration. Procedural imaging was reviewed to determine the groin puncture to recanalization time.
Results
Of the 72 patients, 27 demonstrated a common origin configuration (37%). Of the remaining 45 (63%) of patients, 22 (49%) had a type I configuration, 6 (13%) a type II, and 17 (38%) a type III. Average time to recanalization in the aggregate type I/II group was 56 min (med 48, SD 31) compared with 103 min (med 105, SD 44) in the type III group and 82 min (med 63, SD 50) in the common origin group.
Conclusions
Our study demonstrated higher prevalence of type III and common origin configurations in our ELVO patients compared to previously reported population studies (1-2). Type III and common origin configurations were associated with longer groin puncture to recanalization times than the aggregate type I/II group. This data suggest that there may be benefit to prospectively choosing alternative access sites, for example from the radial or common carotid arteries, in such patients, particularly in regions such as our own where complex aortic arch variants are more prevalent. Further research is necessary to identify additional factors that may contribute to the increased recanalization times in these patients and to assess the risks and benefits of alternate approaches.

T-30

3:33PM - 3:36PM

ICA “Pseudo-occlusion”: Initial Experience Using A Low-Kv, Low-Contrast CT Angiography Protocol for Acute Stroke and Correlation With Angiography at the Time of Mechanical Thrombectomy.

M Oselkin[1], S Mohan[2], J Woo[2], N Sedora-Roman[2], R Hurst[2], B Pukenas[3]
[1]University of Pennsylvania, Merion Station, PA, [2]University of Pennsylvania, Philadelphia, PA, [3]Hospital Of the Univ. Of Pennsylvania, Philadelphia, PA

Purpose
At our institution, patients with acute stroke who are eligible for mechanical thrombectomy require CTA of the head and neck, followed by catheter-based angiography, and a

postprocedure head CT in rapid succession within the first 24 hours. Efforts to reduce patient radiation and iodinated contrast doses have led to implementation of a low-kV and low-iodinated contrast protocol for CT angiography of the head and neck at our institution. This technique has led to increased diagnosis of cervical internal carotid occlusions. However, subsequent catheter-based angiographic intervention in these cases often has demonstrated patency of the cervical ICA. We report our initial experience using this CTA protocol and highlight the incidence of cervical ICA "pseudo-occlusion."

Materials and Methods

In May of 2016, the new low dose CTA protocol was initiated at our institution. All patients with acute ischemic stroke eligible for mechanical thrombectomy from June – November 2016 were reviewed. Computed tomography angiography of the head and neck was performed using 50 ml Isovue 370 mg/ml and a 50 ml saline chaser with bolus triggering at 100 kV acquisitions.

Results

A total of 3 cases were identified where the CTA reported cervical ICA occlusion in which subsequent angiography demonstrated the occlusion was in the intracranial ICA with a fully patent cervical carotid vasculature.

Conclusions

Use of a low-radiation and low-contrast dose CTA protocol potentially results in false-positive cervical ICA occlusion. Awareness of the ICA pseudo-occlusion on CTA is important when considering treatment of emergent large vessel occlusion, so as not to exclude potential patients from life-saving interventions.

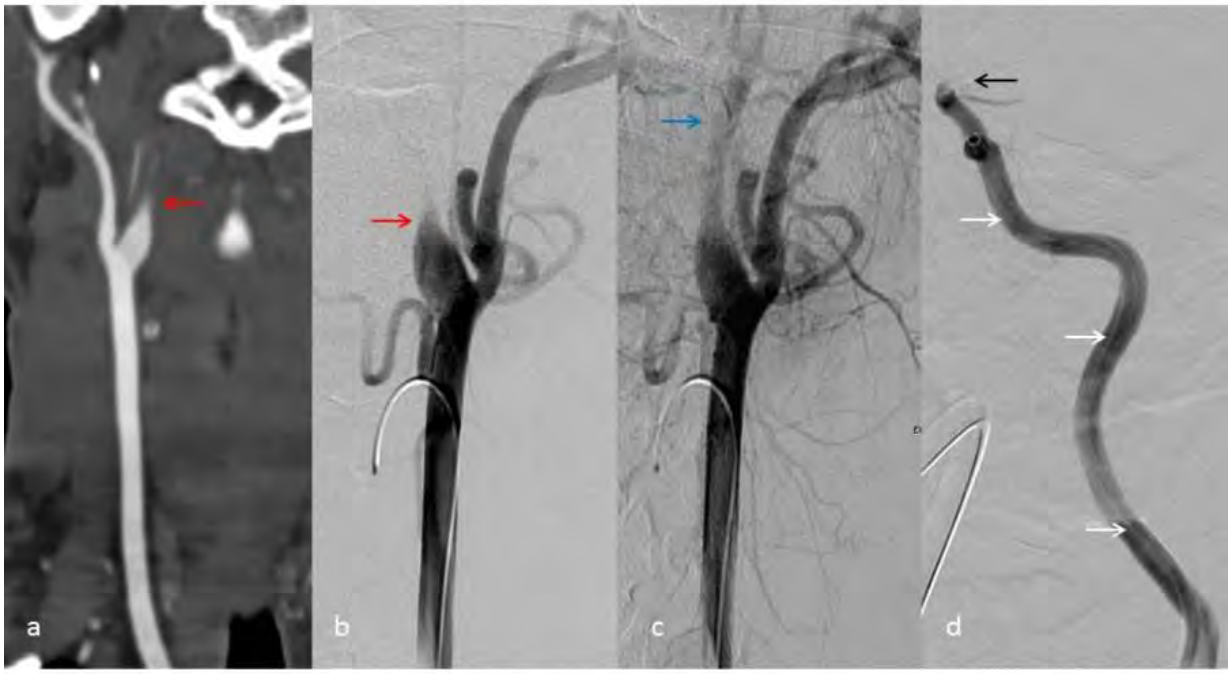


Figure 1. CTA of the neck (a) reveals a flame-shaped abrupt occlusion of the proximal left ICA (red arrow). Early arterial phase DSA (b) following CCA injection demonstrates a correlate to the CTA findings (red arrow). Late arterial phase (c) image shows vessel opacification in an antegrade manner beyond the suspected point of occlusion (blue arrow). The 6 french guide catheter (white arrows) was easily advanced into the intracranial ICA where repeat injection through the guide catheter (d) demonstrates a fully patent cervical ICA with a supraclinoid ICA thrombus (black arrow) responsible for the appearance of the cervical pseudo-occlusion.

(Filename: TCT_T-30_AbstractFigure.jpg)

T-31

3:36PM - 3:39PM

Efficacy and Safety of a New Dual-Layer Micromesh Stent for the Treatment of Carotid Artery Stenosis

F Wodarg[1], J Hensler[1], J Meyne[1], O Jansen[1]
[1]*University Hospital Kiel, Kiel, SH*

Purpose
To evaluate the efficacy and safety of the new double layer micromesh CASPER RX Carotid Artery Stent System in a retrospective single-center experience.
Materials and Methods
We report about 222 internal carotid artery (ICA) stenting procedures with CASPER RX Stents in 206 patients (mean age 70.5, 158 men). Sixty-four (28.8%) of the lesions were asymptomatic, 101 (45.5%) were symptomatic prior to the day of treatment and 57 (25.7) were treated within an acute endovascular stroke procedure. We retrospectively analyzed our data for periprocedural complications, any stroke or death within 30 days after treatment, the

rate of restenosis and secondary stent thrombosis as well as the effect of the tight mesh on the perfusion of the covered external carotid artery (ECA).
Results
Technical success was achieved in all cases. We had major and minor periprocedural complications in 13 (5.9%) cases. Acute thrombosis of the ECA in 3 cases, severe arterial hypertension in 4 cases and severe arterial hypotension in 6 cases. Any stroke or death within 30 days after treatment occurred in 4 of 165 (2.4%) cases (procedures during acute stroke treatment not included). None in asymptomatic stenosis but 4 (4.0%) in symptomatic stenosis. Until now we found 6 (2.7%) cases with in-stent restenosis. A secondary thrombotic stent occlusion (before discharge) occurred in 6 (2.7%) cases. Two in patients with symptomatic stenosis and 4 after acute stenting during stroke treatment.
Conclusions
From our data the CASPER RX double layer micromesh stent is a safe and effective device for the treatment of carotid artery stenosis. The tighter mesh has no negative influence on patients outcome but may offer additional security concerning plaque protection and appearance of embolic events. This needs to be proven in future studies.

T-32

3:39PM - 3:42PM

Correlation between immunohistochemical thrombus analysis, stroke etiology and patient prognosis

k janot[1], I Filipiak[2], j cottier[3], A Narata[4]
[1]University Hospital of Tours, TOURS, FRANCE, [2]Plateform CIRE, Tours, Indre et Loire, [3]University Hospital of Tours, tours, france, [4]University Hospital of Tours, Tours, France

Purpose
University Hospital of Tours started a clinical study to define the composition of thrombi involved in acute ischemic strokes. We hypothesize that there is a correlation between thrombus composition, stroke etiology and patient prognosis.
Materials and Methods
After a few months, all thrombi retrieved after mechanical thrombectomy in the university hospital of Tours were histopathologically analyzed. Clinical and imaging datas also were collected. First, thrombi were classified as fibrin-dominant, erythrocyte-dominant or mixed-pattern. Then, we performed quantitative analysis of CD3+, CD4+, CD28-, CD34+ and vWF+ cells on immunohistochemically-stained thrombi to define platelets, endothelial and white cells clot composition. After, we compared these histopathological results with the initial MR imaging of the patient, his stroke etiology (atherosclerosis or cardio-embolic) and his clinical evolution.

Results
At the moment, few clots were included but histopathological analysis already finds a high content of leukocytes in thrombi. These results support the hypothesis of an important role of inflammation in thrombosis process. High content of CD3+ cells could be correlate with atherosclerosis etiology. On MR imaging, red clots could be correlated with a bleeding artifact. We are waiting for the follow-up neurology consultation to collect clinical evolution data.
Conclusions
This study could enable us to evaluate whether clot composition is correlated to MR imaging, stroke etiology and clinical prognosis of the patients.

T-33

3:42PM - 3:45PM

Endovascular Treatment for Acute Basilar Thrombosis via a Transradial Approach: Initial Experience and Future Considerations

M Oselkin[1], S Sundararajan[2], D Kung[1], S Satti[3], R Hurst[1], B Pukenas[4]
[1]University of Pennsylvania, Philadelphia, PA, [2]Hospital of the University of Pennsylvania, Philadelphia, PA, [3]Christiana Care Health System, Neward, DE, [4]Hospital Of the Univ. Of Pennsylvania, Philadelphia, PA

Purpose
Posterior circulation strokes represent approximately 15% of all ischemic strokes and acute basilar artery occlusion (BAO) secondary to emergent large vessel occlusion (ELVO) has an extremely poor natural history. Cerebrovascular intervention generally is performed via a transfemoral approach; however, a challenging vascular anatomy often can lead to difficulty in achieving successful thrombectomy. Radial access is being explored as an alternative to femoral access and direct carotid access for complex cerebrovascular intervention given growing literature supporting advantages over femoral access in terms of decreased vascular complications including bleeding, pseudoaneurysm formation, and arterial occlusion. We report an initial multi-institutional experience using primary radial access in the treatment of acute BAO in 9 consecutive cases.
Materials and Methods
All patients with acute BAO presenting to a comprehensive primary stroke center between June – October 2016 were reviewed. All radial access procedures were performed with ultrasound-guided single wall Seldinger technique using a micropuncture kit and through a 6 French vascular sheath. Following completion of the procedure, patient hemostasis was achieved utilizing pneumatic compression with the Terumo TR Band device.
Results
A total of 9 cases were included in this retrospective review. All patients presented with complete basilar occlusions, or TICI 0. The average age of the patients was 67.8 years old.

The average NIHSS was 21. Eight out of 9 cases were technically successful with a TICI score of 3 or 2B. The average revascularization time was 35.8 minutes. In one patient, thrombectomy could not be performed due to basilar stenosis precluding microcatheter access to the thrombus. There were no intracranial or radial access site complications.
Conclusions
Radial access is a rapid viable approach to mechanical thrombectomy in selected patients with ELVO and is associated with high technical success and low complications.

Age (Yrs)	Gender	Admission NIHSS	Last Known Normal -> Puncture (Hrs)	Puncture -> Revascularization (Min)	Post TICI Scores	Intervention
57	F	11	5.85	16	2B	STENT RETRIEVER + ASPIRATION
78	M	11	6.25	53	1	N/A
63	M	31	13.40	24	3	STENT RETRIEVER + ASPIRATION
61	M	5	17.57	90	2B	STENT RETRIEVER
61	M	30	2.40	19	2B	STENT RETRIEVER
80	F	8	13.68	60	2B	STENT RETRIEVER + ASPIRATION
82	F	22	4.58	30	3	ASPIRATION
69	F	36	10.17	8	2B	ASPIRATION
58	M	31	6.50	22	3	ASPIRATION

(Filename: TCT_T-33_TabletoEmailforBasilarStrokeASNR.jpg)

T-34

3:45PM - 3:48PM

Safety and efficiency of ticagrelor in interventional neuroradiology : experience of the University Hospital of Tours

k janot[1], R Bibi[2], D Herbreteau[3], A Narata[3]
[1]University Hospital of Tours, TOURS, FRANCE, [2]University Hospital of Tours, Tours, Indre et Loire, [3]University Hospital of Tours, Tours, France

Purpose
In interventional neuroradiology, some procedures can justify the prescription of antiaggregants to prevent thrombosis. There is little data in the literature about ticagrelor in these indications. We present here our results about 40 months of use of ticagrelor.
Materials and Methods
Since September 2013, all patients admitted in our department who required double antiaggregation received aspirin associated with ticagrelor. The loading dose of ticagrelor was 180mg (2cp) the day before and 180mg in the morning of the procedure associated with aspirin. After procedure, ticagrelor was prescribed associated with aspirin during 3 months at 90mg (1cp) in the morning and 90mg in the evening. One hundred fifty-nine patients were included between September 2013 and December 2016 : 102 stent flow diverters, 47 stents associated with coils, 3 intracranial arterial stenoses and 7 extracranial arterial stenoses.
Results
Until now, 2 cases of cerebral ischemia (including 1 with poor observance), 2 delayed asymptomatic flow diverter occlusions, 9 no-surgical punctured hematomas and 2 surgically treated false aneurysms were observed. Two patients reported resolutive asthma when ticagrelor was stopped. However, between September 2013 and December 2014, 4 cerebral hemorrhages were reported. Two of these were fatal and justify decreasing the dose of

heparin administered during procedure from 70 to 50 IU / kg. Since January 2015, only 1 asymptomatic cerebral hemorrhage was observed.
Conclusions
We report our experience of 40 months of use of ticagrelor. It is a safe and effective alternative to clopidogrel in association with aspirin. The decrease of the dose of heparin administered during procedure decreased the number of cerebral hemorrhagic complications.

T-35

3:48PM - 3:51PM

Safety of Combined Intravenous tPA and Endovascular Therapy vs. Intravenous tPA Alone for Treatment of Large Vessel Occlusion in Low Stroke Scale Patients

W Boyce[1], T Tomsick[1]
[1]*University of Cincinnati Hospital, Cincinnati, OH*

Purpose
Mounting data support the use of endovascular therapy (EVT) of acute ischemic stroke in the anterior circulation. However, patients may present with large vessel occlusion (LVO) but a low initial NIHSS (low-NIHSS/LVO), attributed to good collateral flow. Despite the threat of worsening following iv tPA alone, the risks of EVT in all such patients may potentially outweigh its benefits.
Materials and Methods
A meta-analysis was performed to assess the risk of symptomatic intracerebral hemorrhage (SICH) and other major complications associated with EVT of acute ischemic stroke following iv tPA. Retrospective analysis of the complication rates from 4 controlled studies of EVT both with and without imaging selection (IMS III, ESCAPE, EXTEND IA, SWIFT PRIME) was compared to a risk model of SICH of iv tPA based on 2.7% SICH in low-NIHSS 0-5 (NINDS tPA Stroke Study Group), and percent LVO in NIHSSS <5, as estimated based on sensitivity analysis.
Results
Average percent SICH was 4.2% in 498 patients in 4 EVT studies, with estimated 10% additional procedural complication risks (vessel perforation, dissection, and new emboli in an uninvolved territory). With 10-30% estimated incidence of LVO in low-NIHSS patients (EMS study, Lewandowski et al.), and 17% estimated SICH in patients with LVO (NINDS study), a 1.7-5.1% SICH in a low-NIHSS, iv tPA-alone population is anticipated.
Conclusions
Where definition of SICH varies, equal SICH risk with iv tPA alone vs. iv tPA + EVT for LVO in low-NIHSS, with 10% risk of additional EVT complications, recommends a randomized study, allowing rescue EVT in patients who deteriorate after initial iv tPA treatment, with clinical outcome the primary end point.

	Patient #	sICH	New Emboli in Uninvolved Territory	Perforation/ Dissection	Mortality
EXTEND IA	35	0(0%)	2 (6%)	1 (3%)	3 (9%)
IMS III	200	15/200 (7.5%)	26/175 (14.9%)	7/200 (3.5%)	46/200 (23%)
ESCAPE	165	6 (3.6%)	Not reported	1 (0.6%)	17/164 (10.4%)
SWIFT PRIME	98	0 (0%)	Not reported	Not reported	9 (9%)
IV tPA NIHSS 0-5 (NINDS)	42	10% LVO: 1.7% 20%: " 3.4% 30%: " 5.1%	n/a	n/a	?

(Filename: TCT_T-35_Table1.jpg)

T-36

3:51PM - 3:54PM

Venous Phase 3 D Rotational Angiography: A Noble Technique For Transvenous Embolization Of An Indirect Carotid-Cavernous Fistula In An Apparently Inaccessible Cavernous Sinus

M Ghuman[1], A Weeks[2], M Schmidt[2]
[1]QEII Health Sciences Centre, Dalhousie university, Halifax, Nova Scotia, [2]QEII Health Sciences Centre, Dalhousie University, Halifax, Nova Scotia

Purpose
The transvenous route via the inferior petrosal sinus (IPS) is the preferred approach to an indirect carotid-cavernous fistula (CCF) (1); however, sometimes a anatomically variant or hypoplastic IPS may be difficult to identify and roadmap (2). We propose the use of an innovative modification of 3-dimensional rotational angiography (3D RA), venous phase 3D RA, to gain access to the cavernous sinus in this situation.
Materials and Methods
A 70-year-old woman presented with right eye proptosis, chemosis and vision loss. Computed tomography angiogram suggested a CCF. Catheter angiography revealed a Barrow type D CCF (1). Bilateral IPSs could not be demonstrated convincingly. No

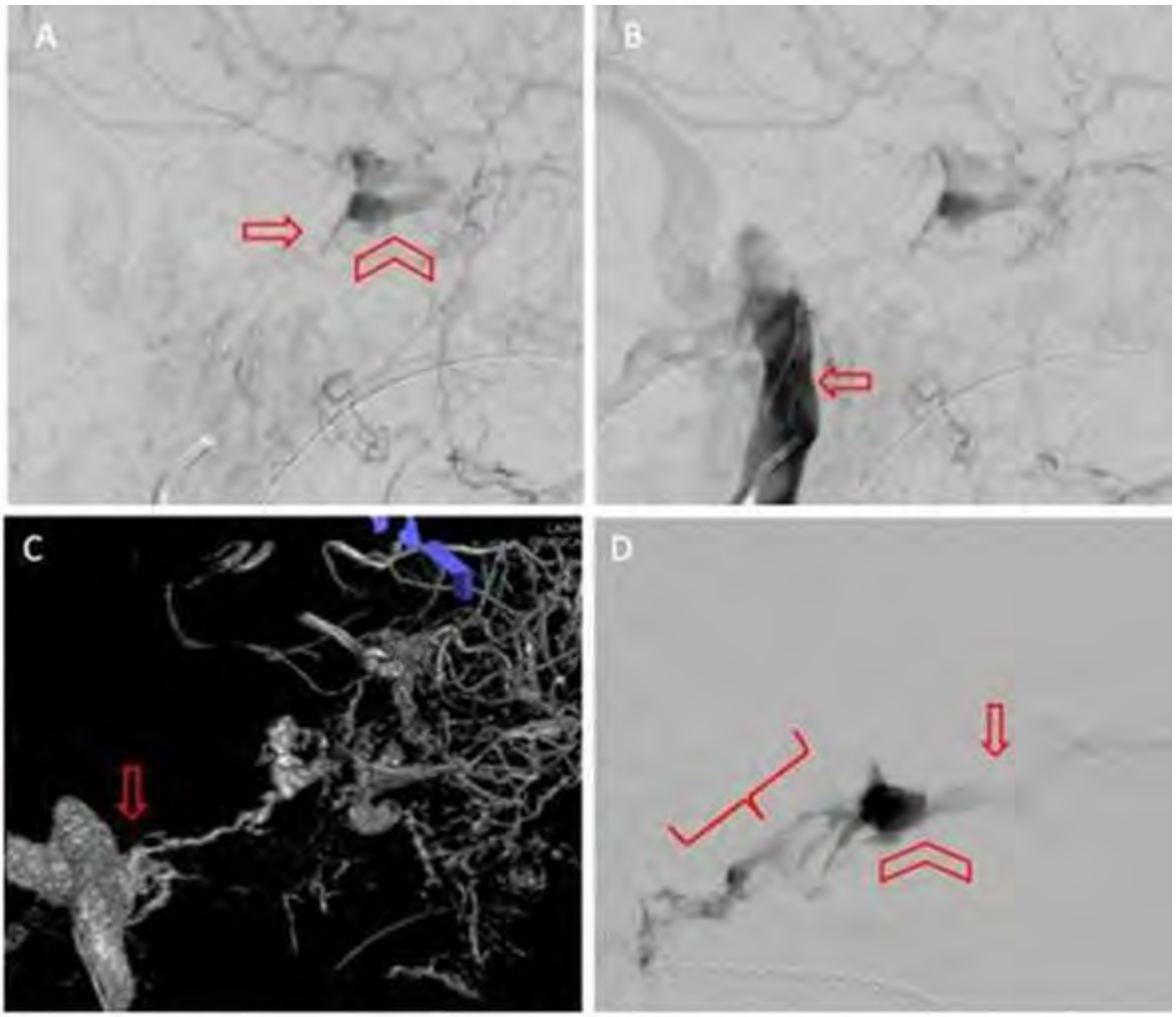
communication between the superior ophthalmic vein (SOV) and facial vein was visible, leaving no alternative route for transvenous access.

Results

To find a hypoplastic ipsilateral IPS and identify its connections to the jugular bulb and cavernous sinus, respectively, a novel variation of 3D RA was attempted. Additional delay of 4 seconds was added between the beginning of contrast injection and the start of image acquisition to capture the venous phase of the internal carotid angiogram. Venous phase 3D RA from the contralateral common carotid artery revealed a thin, tortuous IPS and provided optimal projections for roadmapping. This permitted microcatheter placement in the cavernous sinus, followed by uncomplicated coil embolization. Follow-up angiogram at 3 months showed no residual fistula.

Conclusions

Anatomical variations and thrombosis commonly are encountered in the treatment of indirect CCFs, sometimes necessitating surgical access to the SOV (2). Venous phase 3D RA has the potential to resolve venous channels that are inapparent on biplane angiography. This modification of conventional 3D RA may avoid surgical exposure of the SOV in the treatment of CCFs. In addition, it may prove useful for IPS sampling in the presence of variant anatomy.



A, Late arterial phase of carotid angiogram showing early opacification of cavernous sinus and hypoplastic IPS (arrow). B, Venous phase carotid angiogram and simultaneous IJV venogram fail to reveal any communication between IPS and jugular bulb or IJV (arrow). C, Venous phase 3D RA subtracted image in oblique view depicting the communication of IPS to jugular bulb (arrow). D, Angiogram via microcatheter placed in cavernous sinus (chevron), depicting the IPS (brace), consisting of a rete of small venous channels; in addition, confluence of superior ophthalmic vein and cavernous sinus is seen anteriorly (arrow).

(Filename: TCT_T-36_Figure.jpg)

T-37

3:54PM - 3:57PM

Delayed hemodynamics of normal white matter relative to gray matter demonstrated with DSC perfusion MRI: high temporal resolution TTP maps

A Mian[1], C Farris[2], O Sakai[3], H Jara[1]
[1]Boston University/Boston Medical Center, Boston, MA, [2]Boston Medical Center/Boston University, Boston, MA, [3]Boston Medical Center, Boston University School of Medicine, Boston, MA

Purpose

Currently, the major emphasis in the analysis of dynamic susceptibility contrast (DSC) perfusion exams has been on cerebral blood flow (CBF), cerebral blood volume (CBV) and meant transit time (MTT). Comparatively scarcer information is available on the time-to-peak contrast in brain tissues and in particular of white matter relative to gray matter. The purpose of this work was to study at enhanced temporal resolution the tissue TTPs of white matter versus gray matter.

Materials and Methods

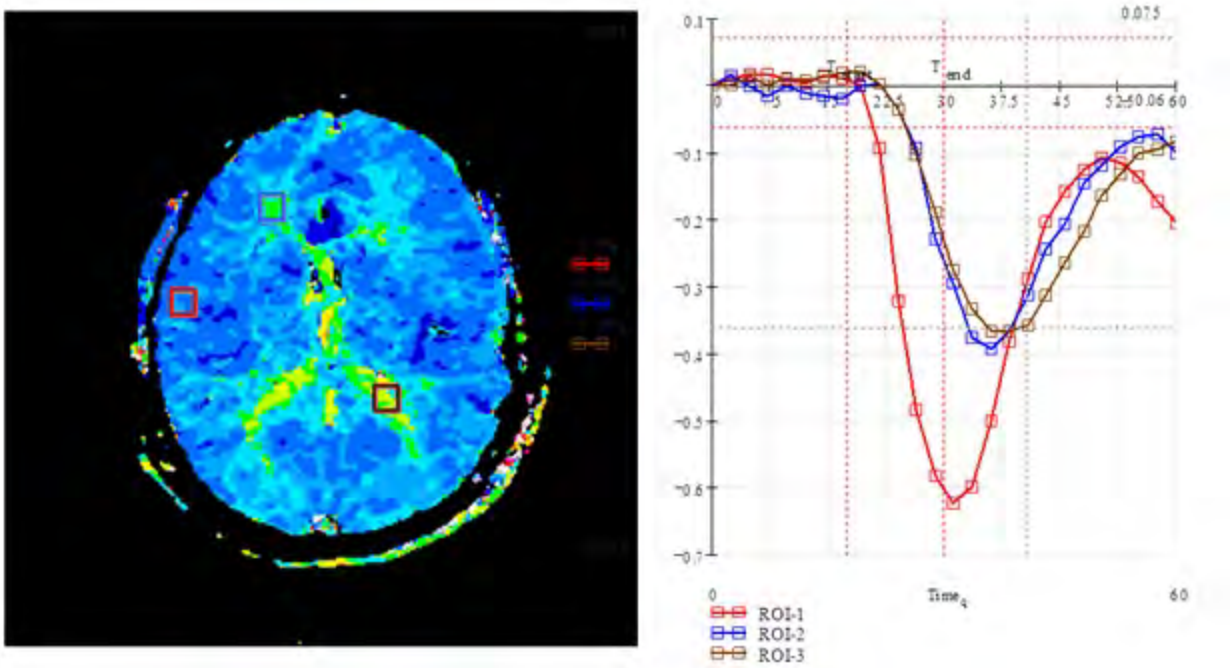
This study was approved by the IRB of our hospital. Magnetic resonance imaging was performed at 1.5T (Achieva, Philips Healthcare): head array and body coil for RX/TX with Gd DSC: 60 dynamics, 16 slices with weight-adjusted Gd dose. A computer program (Mathcad 2001i, PTC Needham, MA) was developed to map TTP at interpolated temporal resolution thus allowing for an accurate estimation of TTP on a pixel by pixel basis. This allows mimicking tissue hemodynamics at a much shorter time scale as limited by computational time. This program was used in selected patients.

Results

As shown in Fig. 1, TTP maps show distinctively delineated white matter architecture with a relative delayed maximum enhancement time relative to gray matter. Observed TTP delays of white matter relative to gray matter ranged between 5-10 seconds.

Conclusions

Maximum perfusion of white matter is delayed relative to gray matter. Temporal resolution enhanced TTP maps could be useful for characterizing various disease states (e.g. stroke, schizophrenia, NPH, neurodegenerative diseases).



(Filename: TCT_T-37_whiteMatterfigASNR_2017.jpg)

T-39

4:00PM - 4:03PM

Intracranial Aneurysms of 1-3 mm Discovered on MRA are Highly Stable Over Time

M Yao[1], Y Numaguchi[2], J Starkey[3]
[1]NYU School of Medicine, New York, NY, [2]St. Luke's International Hospital, Tokyo, Tokyo, [3]St. Luke's International Hospital, Tokyo, FM

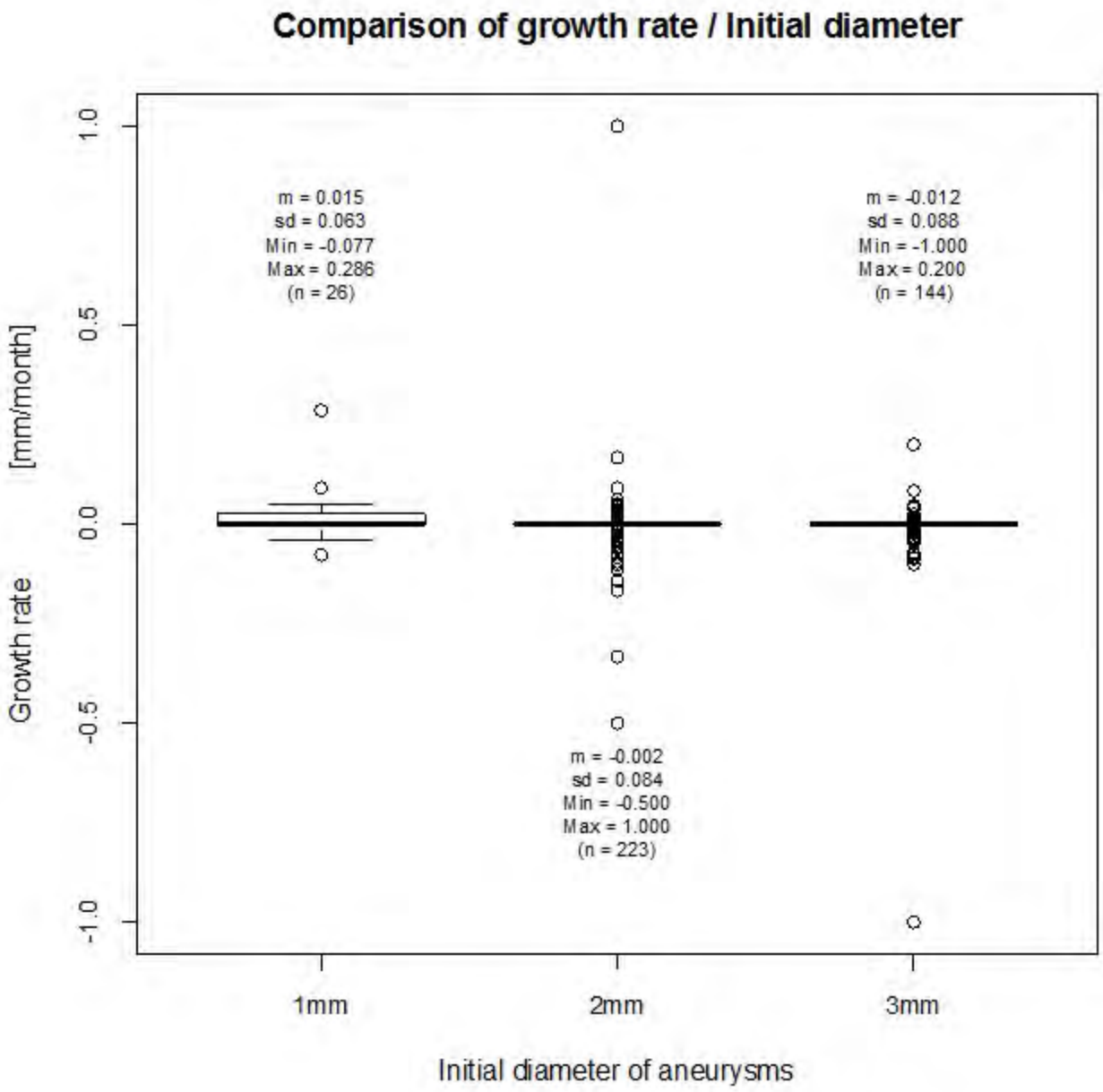
Purpose
Intracranial aneurysms are common and often discovered incidentally. However, there is no consensus on the frequency and duration of surveillance of incidentallydiscovered small aneurysms, and there is a lack of studies focusing on very small aneurysms between 1-3 mm. The aim of this study was to examine growth or rupture of intracranial aneurysms measuring 1-3 mm in diameter found on MRA.
Materials and Methods
Four hundred and three aneurysms of 1-3mm were identified in 394 patients (1 mm n=26, 2 mm n=223, 3 mm n=144). No aneurysms ruptured during the study period. The average monthly growth rate for the aneurysms was 0.015, -0.002, and -0.012 mm for initial diameters of 1, 2, and 3 mm, respectively. The maximum growth rate of all aneurysms was 1.00 mm/month. There was no statistically significant correlation of growth-rate with hypertension or smoking. Growth rate showed mild positive correlation with age only for 2 mm aneurysms (r=0.146, p=0.029).

Results

Four hundred and three aneuryms of 1-3mm were identified in 394 patients (1 mm n=26, 2 mm n=223, 3 mm n=144). No aneurysms ruptured during the study period. The average monthly growth rate for the aneurysms was 0.015, -0.002, and -0.012 mm for initial diameters of 1, 2, and 3 mm, respectively. The maximum growth rate of all aneurysms was 1.00 mm/month. There was no statistically significant correlation of growth-rate with hypertension or smoking. Growth rate showed mild positive correlation with age only for 2 mm aneurysms ($r=0.146$, $p=0.029$).

Conclusions

Most 1-3 mm aneurysms do not change over time. Those that do typically grow very slowly, although 1 patient had an aneurysm that grew at a rate of 1 mm per month. These findings need to be replicated prospectively on a larger sample, but a reasonable approach in patients without significant risk factors may be to follow 1-3 mm aneurysms at 6-months, then 2 years, and finally at 5 years.



(Filename: TCT_T-39_aneu.jpg)

T-40

4:03PM - 4:06PM

Markedly Increased Prevalence of Intracranial Aneurysms in High Risk Sickle Cell Patients.

K Pflug[1], J Kanter[1], M Antonucci[2], S Kuril[1]
[1]Medical University of South Carolina, Charleston, SC, [2]MUSC, Charleston, SC

Purpose
Cerebrovascular complications of sickle cell disease represent a major clinical and public health concern. Increased utilization of technically advanced imaging has not only revolutionized primary stroke prevention in sickle cell patients, but increased awareness of additional intracranial findings, including aneurysms. Our study represents an analysis of high-risk sickle cell patients and reveals markedly higher aneurysm prevalence in this subset than previously reported in the general sickle cell population.
Materials and Methods
This study is comprised of an IRB-approved retrospective chart/imaging review of 67 pediatric and young adult sickle cell patients who met trans-cranial Doppler velocity criteria for prophylactic transfusion therapy and/or underwent secondary stroke prevention. Relevant records and vascular imaging studies were assessed. The majority of studies were comprised of MRI/MRA, though CT and catheter angiography was available in some patients.
Results
In a cohort of 67 high-risk patients, 9 (13.4%) were found to have a total of 19 intracranial aneurysms. Five patients had a single aneurysm, and 4 had multiple (range: 1-4). All aneurysms were subcentimeter, with a propensity for anterior involvement. Three were located in the posterior circulation. Several aneurysms were noted to develop over successive studies, and some smaller aneurysms only were evident prospectively on catheter angiography. Only 1 patient had evidence of significant supraclinoid internal carotid artery (ICA) narrowing.
Conclusions
Our findings demonstrate a striking prevalence of aneurysms in high-risk sickle cell patients, observed primarily in those with little, if any, ICA narrowing. This suggests the etiology of cerebrovascular disease in sickle cell is complex and multifactorial with erythrocyte morphological changes, vessel wall physiology, and intraluminal flow mechanics variably manifesting as specific neuroimaging findings. This underscores the need for a thorough and systematic approach to interpreting subtle cerebrovascular findings and may prompt additional assessment using vessel wall imaging and other advanced imaging techniques.

T-41

4:06PM - 4:09PM

HHT Revisited : MR Imaging–based Evaluation of Underlying Structural and Vascular Anomalies in Patients with Hereditary Hemorrhagic Telangiectasia

S Gupta[1], S Forseen[2], B Gilbert[3]
[1]Augusta University Medical college of Georgia, augusta, GA, [2]Augusta university, Augusta, GA, [3]Augusta University, Augusta, GA

Purpose
HHT is an autosomal dominant genetic disorder that leads to abnormal blood vessel

formation in several organs, including brain. Previous studies have identified an increased incidence of arteriovenous malformations (AVM), developmental venous anomalies, and cerebral aneurysms in HHT. Our purpose was to assess frequency and imaging characteristics of nonclassified brain malformations in HHT. We also evaluated for possible associated structural brain parenchymal abnormalities.

Materials and Methods

IRB approved ongoing retrospective analysis of gadolinium-enhanced brain MR was performed in clinically diagnosed HHT patients by 2 board-certified subspecialty staff radiologists. For each MR exam, patient demographics (age, gender), clinical information (subtype of HHT, HHT-related symptoms), imaging characteristics (date of study and imaging findings) and follow up (imaging vs. embolization vs. observation) were recorded. SAS Analytics software was used to calculate kappa to assess for interobserver agreement and Microsoft Excel statistical software was used to calculate the prevalence of imaging findings in our database.

Results

The study found 18.3% of cases (11/60) positive for pial-based AVMs and 6.67% of cases (4/60) demonstrated polymicrogyria. The interobserver agreement was excellent (kappa=1). The pial AVMs found in our study were located predominantly in the frontal and postcentral gyri in 10 out of the 11 patients (see attached figure). There was no evidence of statistically significant gender predilection for pial AVMs. None of the patients with polymicrogyria were symptomatic. The number of patients with polymicrogyria were too small to result in any statistical significant differences.

Conclusions

Our study demonstrated a significantly increased number of pial AVMs in patients with HHT which may manifest as acute intracranial hemorrhage. Pre-existing knowledge of these findings can aid in patient management and improve survival.HHT continues to be an important and evolving topic as more and more people survive this diagnosis. Although not statistically significant we found cases of polymicrogyria, previously unknown in some of the patients. The study raises an important possibility of previously nondocumented underlying structural brain abnormalities in HHT patients. Our knowledge and understanding of the disease process is very limited and advanced imaging techniques can help us understand underlying structural and developmental anatomy better in such patients.

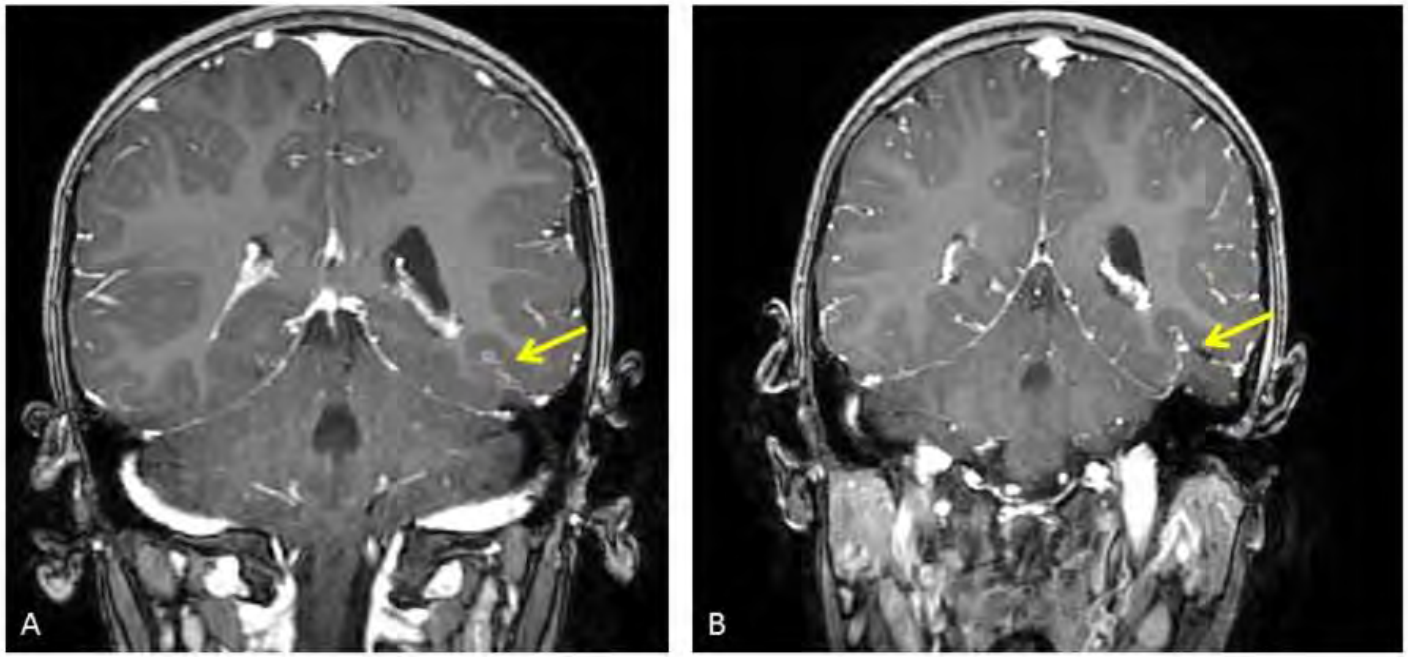


Image A displaying an incidentally found pial-based AVM in one of the patients (yellow arrow), Image B demonstrates post coiling appearance of the AVM (Yellow arrow)

(Filename: TCT_T-41_1.jpg)

T-42

4:09PM - 4:12PM

Unexpected Findings from 10,391 Brain Magnetic Resonance Imaging Exams in Research Volunteers

P Rowley[1], A Field[1], E Simcock[1], T Chandereng[1], H Rowley[1]
[1]*University of Wisconsin, Madison, WI*

Purpose
Our neuroradiology group has reviewed 10,391 consecutive research brain MRIs as part of an IRB protocol intended to discover clinically relevant unexpected findings. Herein we describe the incidence and characteristics of the unexpected findings for which clinical referral was recommended.

Materials and Methods
N = 10,391 consecutive scans were prospectively collected in our database, with scans spanning 2002-04-12 to 2016-05-11 Most studies recruited volunteers with no history of neurologic conditions while some specifically recruited patients with known diagnoses such as multiple sclerosis or Down syndrome. Magnetic resonance imaging scan protocols were variable and dependent on research scan needs, but all available images were sent to a clinical PACS system for interpretation. Readings were performed by a neuroradiologist using a structured reporting form. Any concerns on the part of scanning technologists or researchers also were prospectively collected in the database. A forced final interpretation placed results into 3 possible categories: normal, abnormal but no follow up recommended, or abnormal with follow up recommended.
Results
Among the 10,391 exams, 8510 (82%) were normal, 1522 (15%) were abnormal but for which follow up was not recommended (e.g. known disorder or common minor changes, such as sinus inflammation), and 359 (3%) were flagged by the neuroradiologist for clinical follow up. Amongst those for which clinical referral was recommended, the most common findings were vascular abnormalities (23%, 86/359), white matter lesions (19%, 71/359), and suspected neoplasms (18%, 68/359). Congenital abnormalities accounted for 15% (56/359) of clinically significant findings. Lesions found outside the skull but discovered on brain MRI accounted for 8% (32/359) of abnormalities. Less common were indications of post-traumatic injury (3%, 14/359), severe inflammatory disease (1%, 7/359) or atypical degenerative processes (1%, 6/359). Only 6 percent (20/359) of all clinically significant abnormalities were prospectively flagged by scanning technologists or research staff.
Conclusions
Three percent of 10,391 research subjects were found to have an abnormality prompting clinical referral due to potential or overt clinical significance. Only 6% of the significant abnormalities were detected prospectively by scanning technologists or research staff, highlighting the need for routine expert neuroradiology review in the research setting.

Tuesday
5:00PM - 6:30PM
Long Beach Convention Center, Room 104A (Main Lobby)

15D-Parallel Paper Session: Pediatric Neuroradiology: Brain Tumors Beware!

O-136

5:00PM - 5:08PM

Combined Use of Permeability and ADC Histogram Metrics for Classification of Pediatric Brain Tumors

S Vajapeyam[1], D Brown[1], P Johnston[1], K Ricci[2], M Kieran[3], T Poussaint[1]

[1]Boston Children's Hospital, Boston, MA, [2]Massachusetts General Hospital, Boston, MA, [3]Dana Farber Cancer Institute, Boston, MA

Purpose
To differentiate between low and high grade pediatric brain tumors using tumor permeability and ADC histogram metrics, and explore correlations between these metrics.
Materials and Methods
Diffusion-weighted imaging (b-values 0,1000) and T1 permeability imaging using T1 mapping with flip angles of 2, 5, 10 and 15°, followed with 0.1 mmol/kg bw of Gd-based bolus were performed on all patients in addition to standard MR imaging. Permeability data were processed using automated iCAD® OmniLook software (iCAD Inc., Nashua, NH) and k_trans (transfer constant from the blood plasma into the extracellular extravascular space, EES), k_ep (rate constant from EES back into blood plasma), and v_e (extravascular extracellular volume fraction) were calculated (1). Apparent diffusion coefficient (ADC) histogram metrics were calculated (2) for 3 separate tumor volumes derived from FLAIR, enhancement and permeability maps, respectively.
Results
Thirty-three patients (ages 0.3-17 years; mean 6.68 years) with newly diagnosed brain tumors (15 low grade; 18 high grade) were included in the IRB approved retrospective analysis. Wilcoxon tests showed that high grade tumors had higher k_trans and k_ep and lower v_e ($p<0.001$). The mean, median and mode values of the ADC histograms were lower in high grade tumors when compared to low grade ($p<0.001$). Spearman rank correlations showed that k_trans, k_ep and v_e all highly correlated with mean, median and mode of the ADC histograms for the entire cohort (0.5 in absolute value, $p<0.0005$) but not within low and high grade groups. Receiver operator characteristic (ROC) analysis showed that when the permeability metrics (k_trans, k_ep and v_e) were combined with the location and dispersion ADC histogram metrics (mean, coefficient of variation) the probability of correctly classifying high and low grade tumors was over 0.99.
Conclusions
Apparent diffusion coefficient histogram metrics combined with permeability pharmacokinetic metrics can differentiate between low and high grade pediatric brain tumors with almost perfect sensitivity and specificity.

O-137

5:08PM - 5:16PM

Differentiation of the Fourth Ventricular Primary Brain Tumors Using the ADC Histogram Analysis

S Payabvash[1], T Tihan[2], S Cha[3]
[1]University of California, San Francisco, San Franciscon, CA, [2]UCSF, San Francisco, CA, [3]University of California San Francisco, San Francisco, CA

Purpose

Differentiation of posterior cranial fossa tumors based on conventional MRI features can be challenging. In current study, we used the ADC histogram analysis of the solid component of the tumor, for differentiation of the main fourth ventricle tumors. We specifically applied the results for differentiation of those tumors extending through the foramina of Luschka and/or Magendie.

Materials and Methods

A total of 159 patients with intra-axial/intraventricular tumor in the posterior cranial fossa, with final surgical pathology diagnosis, were evaluated. For the ADC histogram analysis, the solid component of the tumor was segmented manually; then, the ADC percentile values, histogram skewness, kurtosis, and average were analyzed for differentiation of tumors using logistic regression and ROC curve analyses.

Results

A total of 51 fourth ventricle tumors were identified. The ependymoma (n=16, 31%), medulloblastoma (n=11, 22%), and pilocytic astrocytoma (n=10, 20%) were the most common tumors comprising 73% of cases. Among the 3 most common fourth ventricle tumors (n=37), the logistic regression and ROC curve analysis showed that a 5th percentile ADC value <570 ×10-6mm2/s can best differentiate medulloblastomas; whereas, a 35th percentile ADC value >1300 ×10-6mm2/s can best differentiate pilocytic astrocytomas (Table). Notably, in 21/37 (57%) patients, the tumor extended through the fourth ventricle exit foramina. In this subgroup of patients, a 5th percentile ADC value <570 ×10-6mm2/s correctly identified the 2 medulloblastoma tumors (100% sensitivity) with 1 false positive ependymoma; and a 35th percentile ADC value >1300 ×10-6mm2/s correctly identified all 7 pilocytic astrocytoma tumors (100% sensitivity) with 1 false positive ependymoma.

Conclusions

The ADC histogram analysis can help with differentiation of the fourth ventricle tumors, offering higher accuracy compared to the ADC average value based on the logistic regression analysis. The ADC histogram analysis can be especially helpful for accurate diagnosis, in challenging cases like medulloblastomas and pilocytic astrocytomas extending through the foramina of Luschka and/or Magendie.

	Sensitivity	Specificity	p value
5^{th} percentile ADC value <570 $\times 10^{-6} mm^2/s$ for medulloblastomas	91%	96%	<0.001
5^{th} percentile ADC value ≥570 $\times 10^{-6} mm^2/s$ & 35^{th} percentile ADC value ≤1300 $\times 10^{-6} mm^2/s$ for ependymoma	88%	90%	<0.001
35^{th} percentile ADC value >1300 $\times 10^{-6} mm^2/s$ for pilocytic astrocytomas	90%	96%	<0.001

(Filename: TCT_O-137_4thvent.jpg)

O-138

5:16PM - 5:24PM

The Diagnostic Utility of Balanced Steady-State Free Precession (bSSFP) Sequences in the Imaging of Pediatric Posterior Fossa Ependymoma.

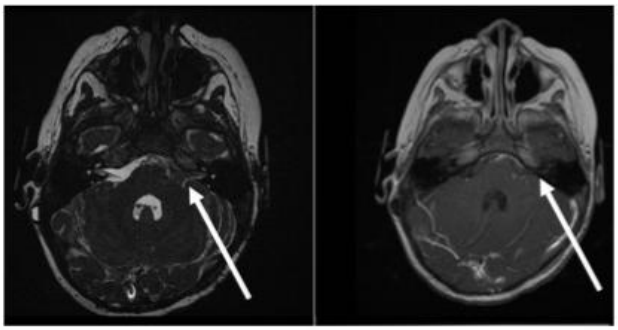
S Sotardi[1], K Buch[1], P Caruso[2], S Rincon[1]
[1]Massachusetts General Hospital, Boston, MA, [2]MGH, Boston, MA

Purpose
Magnetic resonance imaging (MRI) is the standard of care for preradiation planning of pediatric patients with resected posterior fossa ependymomas. Balanced steady-state free precession (bSSFP) sequences (CISS/FIESTA/3D-DRIVE) provide excellent contrast resolution for the evaluation of residual tumor that invests cranial nerves, neural foramina, cisterns, and brainstem. We hypothesize that the addition of bSSFP sequences increases diagnostic yield and diagnostic confidence in the detection of residual tumor.
Materials and Methods
This was an IRB-approved, retrospective study, performed on 15 patients with resected posterior fossa ependymomas undergoing preradiation MRI evaluation for residual tumor. Two neuroradiologists reviewed MRIs with the bSSFP sequences, and 2 neuroradiologists reviewed MRIs without bSSFP sequences. All 4 neuroradiologists reviewed the preradiation planning MRI, which included T2, FLAIR, DWI, GRE/SWI, T1 precontrast and postcontrast T1 sequences. The presence of tumor was assessed in the following locations: foramen magnum, foramen of Luschka, internal auditory canal (IAC), petrosal fossula, 4th ventricle, perimedullary, and prepontine cisterns.
Results
Patients ranged in age from 2-13 years (mean 5.6, SD 3.6), with 8 males and 7 females. Neuroradiologists reviewing the MRI with bSSFP sequences detected 14 sites of residual disease, compared to 6 sites by neuroradiologists without bSSFP sequences (Table 1). Specifically, detection of tumor improved with bSSFP sequences when assessing the: IAC, 4th ventricle, petrosal fossula, prepontine and perimedullary cisterns. Figure 1 demonstrates an example of IAC tumor involvement, where detection improved with bSSFP sequences. Higher diagnostic confidence was seen in the group using bSSFP, (mean 90%), compared to the group without bSSFP, (mean 53.3%).
Conclusions
The addition of bSSFP sequences is an important adjunct to the MRI evaluation of residual tumor in pediatric patients with intracranial ependymomas, providing increased diagnostic yield and diagnostic confidence. The benefit of these sequences varies by location, with improved detection within the IAC, 4th ventricle, petrosal fossula, prepontine and perimedullary cisterns.

TABLE 1. Ependymoma by Location. Number of cases called positive by both reviewers in the group with bSSFP sequences versus the group without bSSFP sequences.

Location	Group	# Positive Cases
IAC	With bSFFP	4
	Without bSSFP	2
Foramen Luschka	With bSFFP	2
	Without bSSFP	2
Foramen Magnum	With bSFFP	0
	Without bSSFP	1
Perimedullary Cistern	With bSFFP	2
	Without bSSFP	1
Petrosal Fossula	With bSFFP	1
	Without bSSFP	0
Prepontine Cistern	With bSFFP	4
	Without bSSFP	0
Intraventricular	With bSFFP	1
	Without bSSFP	0
TOTAL	With bSFFP	14
	Without bSSFP	6

Figure 1. Patient with left IAC tumor extension, where detection was improved with the addition of a bSSFP sequence. bSSFP images (left) demonstrates tumor within the IAC. Post-contrast T1 images (right) demonstrate mild asymmetric enhancement within the left IAC, which underestimated tumor burden.



(Filename: TCT_O-138_FigureTable.jpg)

O-139

5:24PM - 5:32PM

Pediatric medulloblastoma: does apparent coefficient value predict the molecular subtypes?

N Reddy[1], D Ellison[2], B Soares[3], K Carson[4], T Huisman[1], A Poretti[5], Z Patay[2]
[1]Johns Hopkins Hospital, Baltimore, MD, [2]St. Jude Children's Research Hospital, Memphis, TN, [3]Emory University, Atlanta, GA, [4]The Johns Hopkins Bloomberg School of Public Health, Baltimore, MD, [5]The Johns Hopkins University School of Medicine, Baltimore, MD

Purpose
Molecular subgroups based on gene-expression profiling have been recognized recently in pediatric medulloblastomas. The subgroups wingless (WNT), sonic hedgehog (SHH), group3, and group4 are biologically and clinically distinct disease entities. We aimed to evaluate the role of apparent diffusion coefficient (ADC) values in the differentiation of the medulloblastoma subgroups.
Materials and Methods
We retrospectively measured the ADC values of the 1) enhancing, solid part of the tumor (EST) and 2) whole tumor (WT) and compared the absolute tumor ADC values and cerebellar and thalamic ratios across 3 molecular subgroups (SHH, WNT, and group3/group4) using the Kruskal-Wallis test.
Results
Ninety-three children (65 males) were included. The median age at presurgical MRI was 7

years (interquartile range [IQR] 4-10 years). Fifty-seven (61%) children had group3/group4, 27 (29%) had SHH, and 9 (10%) had WNT medulloblastomas. The median (IQR) absolute ADC values in EST and WT were 0.719 (0.632-0.818) x10-3 mm2/s and 0.864 (0.788-1.068) x10-3 mm2/s for group3/group4, 0.660 (0.574-0.797) x10-3 mm2/s and 0.965 (0.735-1.130) x10-3 mm2/s for SHH, and 0.594 (0.573-0.675) x10-3 mm2/s and 0.728 (0.617-0.841) x10-3 mm2/s for WNT medulloblastomas (p-values=0.02 and 0.13). The median (IQR) of the cerebellar ratio in EST and WT were 1.017 (0.874-1.104) and 1.258 (1.090-1.411) for group3/group4, 0.895 (0.826-1.024) and 1.291 (1.038-1.625) for SHH, and 0.888 (0.815-0.928) and 1.029 (0.902-1.184) for WNT medulloblastomas (p-values=0.03 and 0.09). The median (IQR) of the thalamic ratio in EST and WT were 0.922 (0.800-1.066) and 1.126 (0.991-1.342) for group3/group4, 0.791 (0.744-0.933) and 1.155 (0.979-1.381) for SHH, and 0.754 (0.661-0.839) and 0.936 (0.808-1.015) for WNT medulloblastomas (p-values=0.02 and 0.06).

Conclusions

Apparent diffusion coefficient analysis of the EST may contribute to the pre-operative molecular classification of pediatric medulloblastomas and may help to plan optimal treatment, hence reduce surgery-induced morbidity.

O-140

5:32PM - 5:40PM

Group 3 and 4 medulloblastomas originate from the nodulus of the cerebellar vermis

Z Patay[1], C Okuma[2], S Hwang[3], L Pinkard[4], D Ellison[5]

[1]St. Jude Children's Research Hospital, Memphis, TN, [2]Institute of Neurosurgery Dr. Asenjo, Santiago, -, [3]St. Jude Children's Research Hospital, Memhis, TN, [4]The University of Illinois Chicago, Chicago, IL, [5]St Jude Children's Research Hospital, Memphis, TN

Purpose

Over the past years, the origins of medulloblastoma and its dysfunctional signaling pathways leading to neoplastic transformation in the WNT and SHH molecular groups have been progressively elucidated, but our understanding of the tumorigenic process in Groups 3 and 4 is still incomplete. We conducted a review of the brain MRI data in a cohort of patients that were diagnosed with small Group 3 and 4 tumors in an attempt to identify their putative anatomical points of origin.

Materials and Methods

Eleven patients (mean age: 12 years, range: 5-20 years, gender: 5F/6M) treated in our institution between January 1, 2000 and July 20, 2015 with small tumors (defined as the sum of the perpendicular diameters of the tumor <8.5 cm) at initial MRI work-up were found to have adequate histopathological, molecular and additional cytogenetic data to classify their tumors as "non-WNT/non-SHH medulloblastoma", i.e. Group 3 and 4 combined.

Results
All 11 small non-WNT/non-SHH tumors were midline intraventricular and attached to the nodulus of the cerebellar vermis. Histopathologically 9 tumors were classic and 2 were large cell/anaplastic variants. Despite the small size of the primary tumor, 4 of 11 patients (38%) had CSF seeding with metastatic disease at initial diagnosis.
Conclusions
Group 3 and 4 medulloblastomas, regardless of their size, are consistently midline and intraventricular. The origin of these tumors is still unknown, but since different streams of cells migrate out of the upper rhombic lip of the primitive hindbrain at different developmental stages, Group 3 and 4 tumors, similar to SHH medulloblastomas, may originate from upper rhombic lip-derived granule neuron precursor cells, but at a later stage when the cerebellar vermis is formed. The results of our research allow us to submit a unifying theory for the cellular origins of Group 3 and 4 medulloblastomas.

O-141

5:40PM - 5:48PM

MRI Characteristics of Metastatic Lesions to Differentiate Molecular Subgroups in Pediatric Medulloblastoma

D Mata-Mbemba[1], V Ramaswamy[2], M Zapotocky[2], S Laughlin[3], M Taylor[4], C Raybaud[3]
[1]Department of Diagnostic Imaging, The Hospital For Sick Children, University of Toronto, Toronto, ON, Canada, [2]Department of Neurooncology, The Hospital for Sick Children, University of Toronto, Toronto, ON, Canada, [3]Department of Diagnostic Imaging, The Hospital for Sick Children, University of Toronto, Toronto, ON, Canada, [4]Department of Neurosurgery, The Hospital for Sick Children, University of Toronto, Toronto, ON, Canada

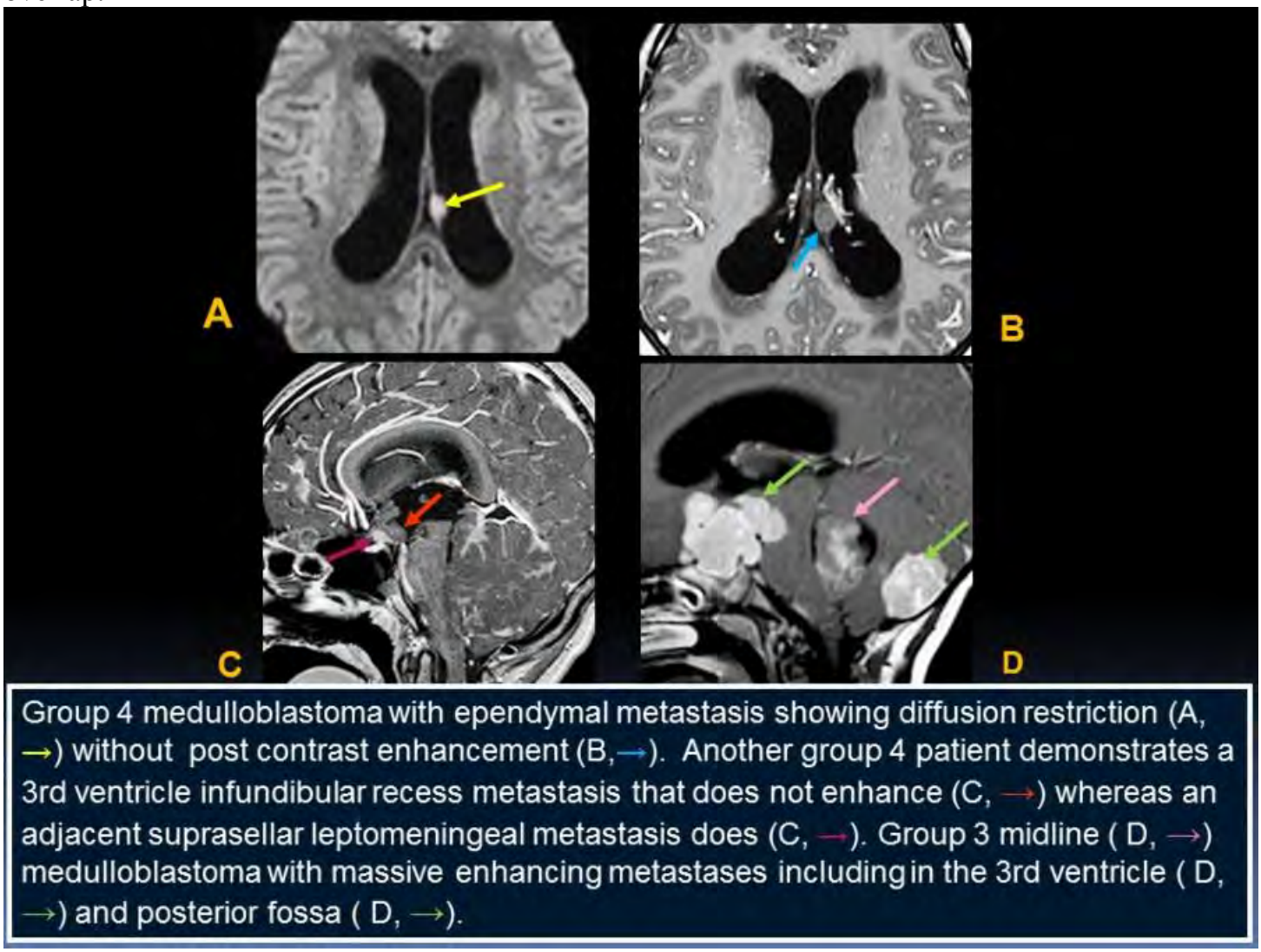
Purpose
Molecular subgrouping of medulloblastoma correlates with prognosis and should be used to determine the therapeutic strategy. Recent reports investigate the possibility of using imaging features of the primary tumor to identify the different subgroups. We hypothesize that metastatic patterns also correlate with the molecular classification.
Materials and Methods
One hundred seventeen consecutive patients [age: 7.3 ±3.8 years at diagnosis; male, 78 (67.2%)] with a confirmed diagnosis of medulloblastoma and interpretable pretherapeuthic MRIs were retrieved from our database from January 1999 to November 2016. All were assigned to one medulloblastoma subgroup: WNT, SHH, group 3 or group 4. Magnetic resonance imaging (MRI) studies were evaluated for early (at diagnosis) or late metastases, as well as for specific locations of metastases: lateral ventricular ependyma, 3rd ventricular infundibular recess, supratentorial convexity, skull base, infratentorial and spinal leptomeninges. Signal patterns were evaluated as restricting (D+) or not (D-) and enhancing (C+) or not (C-). Findings then were correlated with the molecular subgroups.

Results

Thirty-two of 117 (27.4%) showed metastatic disease: 1/15 (1 late) WNT; 2/25 (late) SHH, 14/29 (8 early, 6 late) group 3; 15/48 (14 early, 1 late) group 4. Ependymal metastases D+/C-, especially in the third ventricular infundibular recess, were significantly associated with group 4 (P=0.0031) with 60% sensitivity, 100% specificity, negative predictive value 100%, and positive predictive value 81% for group 4 (Figs. A to C). In group 3 all ependymal or nfratentorial/spinal meningeal metastases were D+/C+ like the principal tumor (all P<0.05), and often massive (Fig. D).

Conclusions

Magnetic resonance imaging metastatic patterns correlate well with molecular subgroups of pediatric medulloblastoma. This supports the biologic validity of the classification. It also may help in differentiating groups 3 and 4 when the characteristics of the primary tumor overlap.



Group 4 medulloblastoma with ependymal metastasis showing diffusion restriction (A, →) without post contrast enhancement (B,→). Another group 4 patient demonstrates a 3rd ventricle infundibular recess metastasis that does not enhance (C, →) whereas an adjacent suprasellar leptomeningeal metastasis does (C, →). Group 3 midline (D, →) medulloblastoma with massive enhancing metastases including in the 3rd ventricle (D, →) and posterior fossa (D, →).

(Filename: TCT_O-141_ASNRdefinitefigure.jpg)

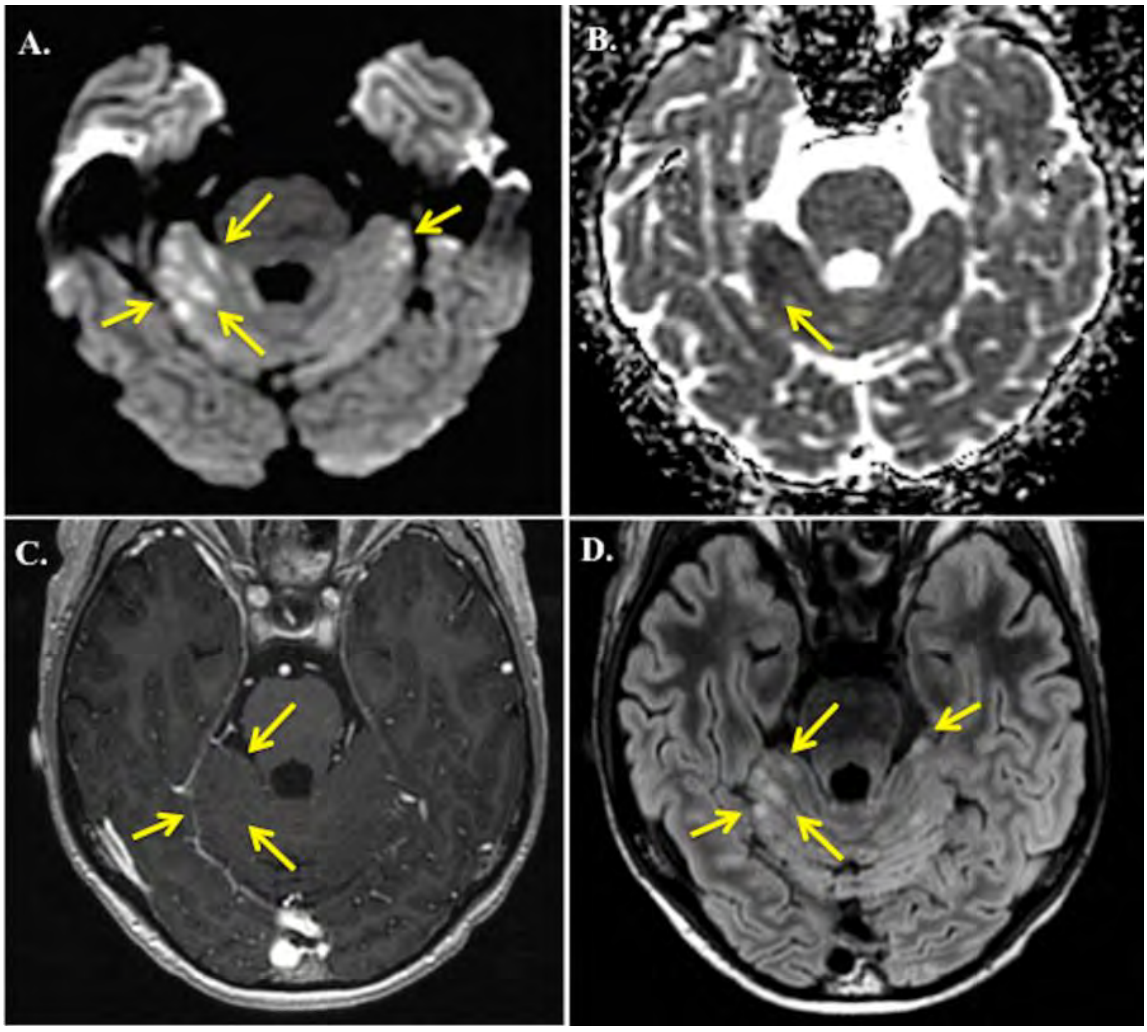
O-142

5:48PM - 5:56PM

Detection of non-enhancing recurrent medulloblastoma on diffusion weighted imaging

M Aboian[1], C Kline[1], D Solomon[1], S Mueller[1], S Braunstein[1], W Dillon[2], S Cha[1]
[1]University of California San Francisco, San Francisco, CA, [2]UCSF, San Francisco, CA

Purpose
Medulloblastoma recurrence historically has been diagnosed based on identification of new contrast-enhancing lesions on surveillance imaging. We propose that reduced diffusion is a more sensitive imaging marker than contrast enhancement in identifying recurrent metastatic medulloblastoma.
Materials and Methods
We identified 40 pediatric patients with medulloblastoma at our institution. Seventeen of these patients went on to develop definitive disease recurrence. In these patients, MR imaging at the time of diagnosis of recurrence and for 6 months prior to diagnosis was evaluated for presence of contrast-enhanced lesions, size of contrast-enhanced lesions, presence of lesions with reduced diffusion, and quantitative measurement of ADC within the recurrent lesions. Apparent diffusion coefficient was measured in 10^-3 mm2/s.
Results
All patients with recurrent medulloblastoma demonstrated reduced diffusion within the recurrent lesions. Apparent diffusion coefficient measurements were 0.658±0.072 for the recurrent lesion as compared to 0.923±0.146 for contralateral normal white matter region of interest (ROI) measurements ($p = 0.00001$). Only 11 patients with disease recurrence (65%) demonstrated contrast enhancement within the recurrent lesions. All 6 patients with nonenhancing recurrence demonstrated reduced diffusion with mean ADC of 0.680±0.097, which was significantly lower compared to contralateral normal brain with ADC values 0.894±0.089 ($p = 0.003$).
Conclusions
In our cohort of patients with recurrent medulloblastoma, recurrent lesions did not uniformly demonstrate contrast enhancement on MR imaging, but all lesions demonstrated reduced diffusion. Our findings support that diffusion-weighted imaging is more sensitive than contrast enhancement alone and as such should be considered part of standard of care imaging for medulloblastoma surveillance.



(Filename: TCT_O-142_Figure1.jpg)

O-143

5:56PM - 6:04PM

Quantitative ADC to predict histone H3 K27M mutational status in pediatric diffuse midline gliomas

M Aboian[1], D Solomon[1], E Felton[1], C Kline[1], M Mabray[2], J Villanueva-Meyer[3], S Mueller[1], S Cha[1]
[1]University of California San Francisco, San Francisco, CA, [2]University of New Mexico, Albuquerque, NM, [3]University of California - San Francisco, San Francisco, CA

Purpose
Diffuse midline gliomas with histone H3 K27M mutation are a new diagnostic entity defined by the 2016 WHO CNS tumor classification. The purpose of our study was to measure apparent diffusion coefficient (ADC) values of tumor to distinguish histone H3 K27M mutant gliomas from wildtype high grade gliomas.

Materials and Methods

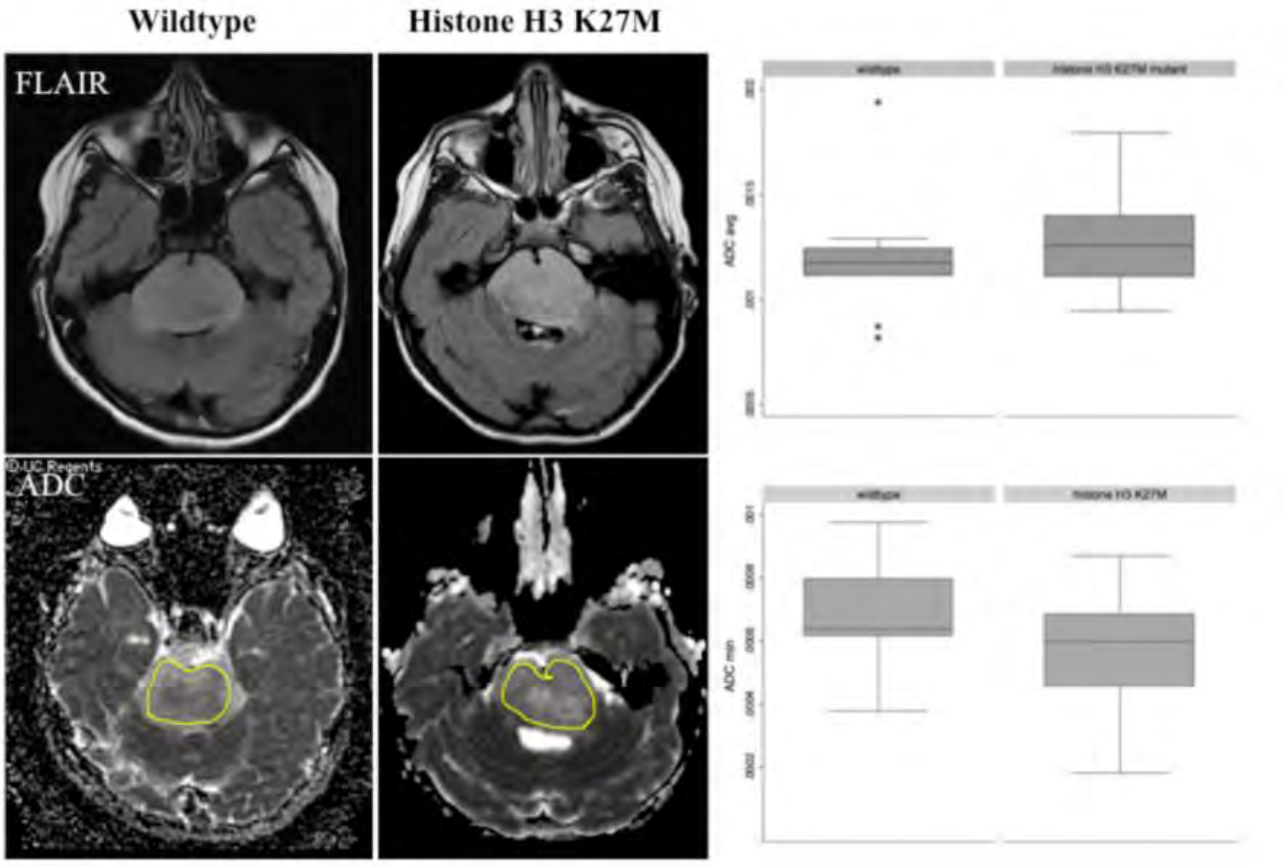
We identified 26 pediatric patients (<21 years old) with diffuse gliomas with pre-operative MRI imaging including DWI and histone H3 K27M mutational status. Average and minimum ADC values of tumor and histogram of voxel based intensities were measured using FuncTool software (GE Healthcare, version 9.4.05a).

Results

There were 16 infratentorial and 9 supratentorial gliomas, with 84% (22) of the tumors being midline and 15% (4) being hemispheric. Seventeen (77%) midline tumors were histone H3 K27M mutant. All (4) of the supratentorial hemispheric tumors were glioblastomas and were histone H3 wildtype. There was no difference between the K27M mutant and wildtype midline gliomas with respect to their ADCaverage and ADCmin means. Subgroup analysis based on tumor location also did not identify a difference in means. When comparing hemispheric histone H3 wildtype glioblastomas to K27M mutant tumors, there was a difference in ADCaverage values ($p<0.048$) but not ADCmin. Hemispheric glioblastomas also were associated with high amount of necrosis ($p<0.003$) and underwent either gross total resection or subtotal resection, while midline gliomas were only biopsied.

Conclusions

Analysis of quantitative ADC measurements in diffuse midline gliomas originating in the thalamus and pons did not identify a difference in ADCaverage or ADCmin means based on presence of histone H3 K27M mutation. In contrast, histone H3 wildtype hemispheric glioblastomas had lower mean ADCaverage values as compared to midline gliomas.



(Filename: TCT_O-143_Figure1.jpg)

O-144

6:04PM - 6:12PM

Leukoencephalopathy and Diffusion Tensor Imaging in Survivors of Childhood Acute Lymphoblastic Leukemia Treated with Chemotherapy Only

N Sabin[1], Y Cheung[1], W Reddick[1], D Bhojwani[2], W Liu[1], J Glass[1], T Brinkman[1], D Srivastava[1], C Pui[1], L Robison[1], M Hudson[1], K Krull[1]
[1]St. Jude Children's Research Hospital, Memphis, TN, [2]Children's Hospital Los Angeles, Los Angeles, CA

Purpose
Survivors of childhood acute lymphoblastic leukemia (ALL) are at risk for neurocognitive deficits and white matter changes in the brain referred to as leukoencephalopathy. We examined the relationship between leukoencephalopathy and diffusion tensor imaging (DTI) in previously demonstrated susceptible areas of the brain, and report associations between

neuroimaging and neurocognitive outcomes in survivors of pediatric ALL treated with chemotherapy only.
Materials and Methods
One hundred seventy-three survivors of childhood ALL treated on a uniform protocol with chemotherapy alone, underwent magnetic resonance imaging of the brain at 1.5 Tesla and neurocognitive testing at a mean age of 14.4 years (SD=4.6) and at a mean time of 7.7 years (SD=3.9) years post diagnosis. Among these, 163 completed DTI. Demographic data, treatment factors, and neurocognitive outcomes were analyzed for associations with leukoencephalopathy identified on T2-weighted and FLAIR images. Diffusion tensor imaging parameters for white matter in the periventricular and supraventricular regions were assessed for associations with neurocognitive performance and leukoencephalopathy.
Results
There were no associations between demographic data or treatment factors and leukoencephalopathy. Survivors with, compared to those without, leukoencephalopathy performed worse on long-term memory [mean(SD) Z-scores: -1.71 (1.35) vs. -1.11 (1.35); p=.02}. On DTI, lower fractional anisotropy (p<.001) and higher radial diffusivity (p<.001) values were demonstrated in the periventricular and supraventricular white matter of patients with leukoencephalopathy than in those without it. Diffusion tensor imaging parameters were associated with multiple neurocognitive deficits. For example, higher fractional anisotropy was associated with better verbal fluency (Est. 69.0; P=0.007), memory recall (Est. 56.1; P=0.01) and motor processing speed (Est. 132.6; P=0.02).
Conclusions
Although leukoencephalopathy is an MRI biomarker of loss of white matter structural integrity based on its association with abnormal DTI parameters, it was only associated with one type of neurocognitive deficit in our subjects. Diffusion tensor imaging appears to be more specific to neurocognitive deficits and may serve as a more sensitive imaging measure for clinically significant loss of white matter integrity in ALL survivors. Diffusion tensor imaging may be a better tool for identifying patients with clinically significant white matter injury during treatment.

O-145

6:12PM - 6:20PM

Methionine PET, MR Spectroscopy, and MR Perfusion Imaging for Assessing Pontine Gliomas

S Hwang[1], M Doubrovin[2], A Edwards[2], Z Patay[2]
[1]St Jude Children's Research Hospital, Germantown, TN, [2]St. Jude Children's Research Hospital, Memphis, TN

Purpose
Volumetric assessment of diffuse intrinsic pontine gliomas (DIPGs) does not adequately

assess response to treatment and clinical outcomes (1). More sophisticated imaging parameters including magnetic resonance spectroscopy (MRS), MR perfusion-weighted imaging (PWI), MR diffusion-weighted imaging (DWI), and C-11 methionine PET/CT (MET-PET) are evaluated as potentially improved predictors of clinical outcomes.
Materials and Methods
Magnetic resonance imaging (MRI) and Methionine PET-CT were acquired on 33 patients (Mean age 9 years, range 2.3 to 17.3 years) with diffuse infiltrating pontine gliomas who were enrolled on several treatment regimens from different study protocols. Imaging was obtained at 3 time points: at diagnosis, 4-16 weeks after the initiation of therapy, and at completion of therapy. Patients were removed from the protocol if the tumor demonstrated progression. Diffusion imaging was available for all of the patients. Adequate MR spectroscopy (MRS) was available for 22 cases. Dynamic contrast-enhanced perfusion imaging was available for 16. The various parameters were correlated with each other and with tumor progression. For correlation with multivoxel MR spectroscopy, the grid of spectroscopy voxels were co-registered with the Met-PET, diffusion, and MR perfusion images. Each voxel was used as an ROI and mean values were determine for all the imaging parameters.
Results
The perfusion parameter ktrans, a marker of capillary permeability, and the choline/NAA ratio from MR spectroscopy were significantly correlated ($p = 0.005$). The choline/NAA ratio was significantly higher in patients who progressed before the second Met PET was obtained ($p = 0.005$).
Conclusions
Magnetic resonance spectroscopy (MRS) may provide a means of predicting progression of diffuse infiltrating pontine gliomas. Tumor volume changes may not accurately reflect response to therapy, suggesting that conventional MRI metrics need to be re-evaluated critically. Advanced quantitative imaging methods such as MET-PET, MRS, PWI, and DWI may provide better assessment of disease progression for patient management and clinical trials.

O-146

6:20PM - 6:28PM

MRI Features and Survival in Diffuse Intrinsic Pontine Glioma (DIPG): Report from the International DIPG Registry

J Roebker[1], J Leach[2], J Baugh[3], A Lane[3], M Fouladi[3], B Jones[4]
[1]University of Cincinnati, Cincinnati, OH, [2]Cincinnati Children's Hospital Medical Center, Cincinnati, OH, [3]Cincinnati Children's Hospital and Medical Center, Cincinnati, OH, [4]Cincinnati Children's Hospital, Cincinnati, OH

Purpose
As part of the International Diffuse Intrinsic Pontine Glioma (DIPG) registry's long term goal of maintaining a robust research infrastructure, we evaluated baseline MR imaging in registry subjects and defined a common imaging lexicon and database for registry approved research. To validate utility we correlated registry defined imaging features to overall survival (OS) in DIPG.
Materials and Methods
Three hundred fifty-two submitted cases were evaluated by 2 radiologists blinded to outcome, treatment and demographics. Twenty-seven cases in which the tumor was primarily exophytic or was not centered within the pons were excluded. Imaging features assessed included size, location/extent, internal signal characteristics, enhancement, diffusion restriction, and spectroscopy. Consensus opinion based on each radiologist's review was used for final classification. Univariate and multivariate analyses of imaging features and basic clinical data relative to OS were performed using Cox proportional hazards regression. Quantitative agreement data between reviewers was assessed with concordance rates, kappa statistics, and paired t-tests.
Results
Mean age in the 325 included cases was 7.3 years, with a 1.27:1 female to male ratio and a median OS of 10.8 months. Imaging features associated with worse overall survival (Odds Ratio) included: extension beyond pons and brachium pontis (1.84), larger craniocaudal tumor dimension (1.01), larger AP tumor dimension/pons dimension (2.27), enhancement (1.38), necrosis (1.46), diffusion restriction (1.33), and distant disease (3.96). Interrater agreement for imaging features was moderate (mean concordance rate: 0.838, mean kappa 0.538). Tumor measurement was not significantly different between reviewers.
Conclusions
Baseline imaging features have been assessed for 325 subjects in the International DIPG registry using standardized imaging features and measurements which will serve as a resource for collaborative research projects. Consensus review is necessary for imaging feature classification, but not tumor measurement. Multiple imaging features correlate with OS, helping validate the utility of the imaging classification scheme.

Tuesday
5:00PM - 6:30PM
Long Beach Convention Center, Room 203AB (Upper Level)

15G-Parallel Paper Session: Vascular Overture – Getting to Know You

O-147

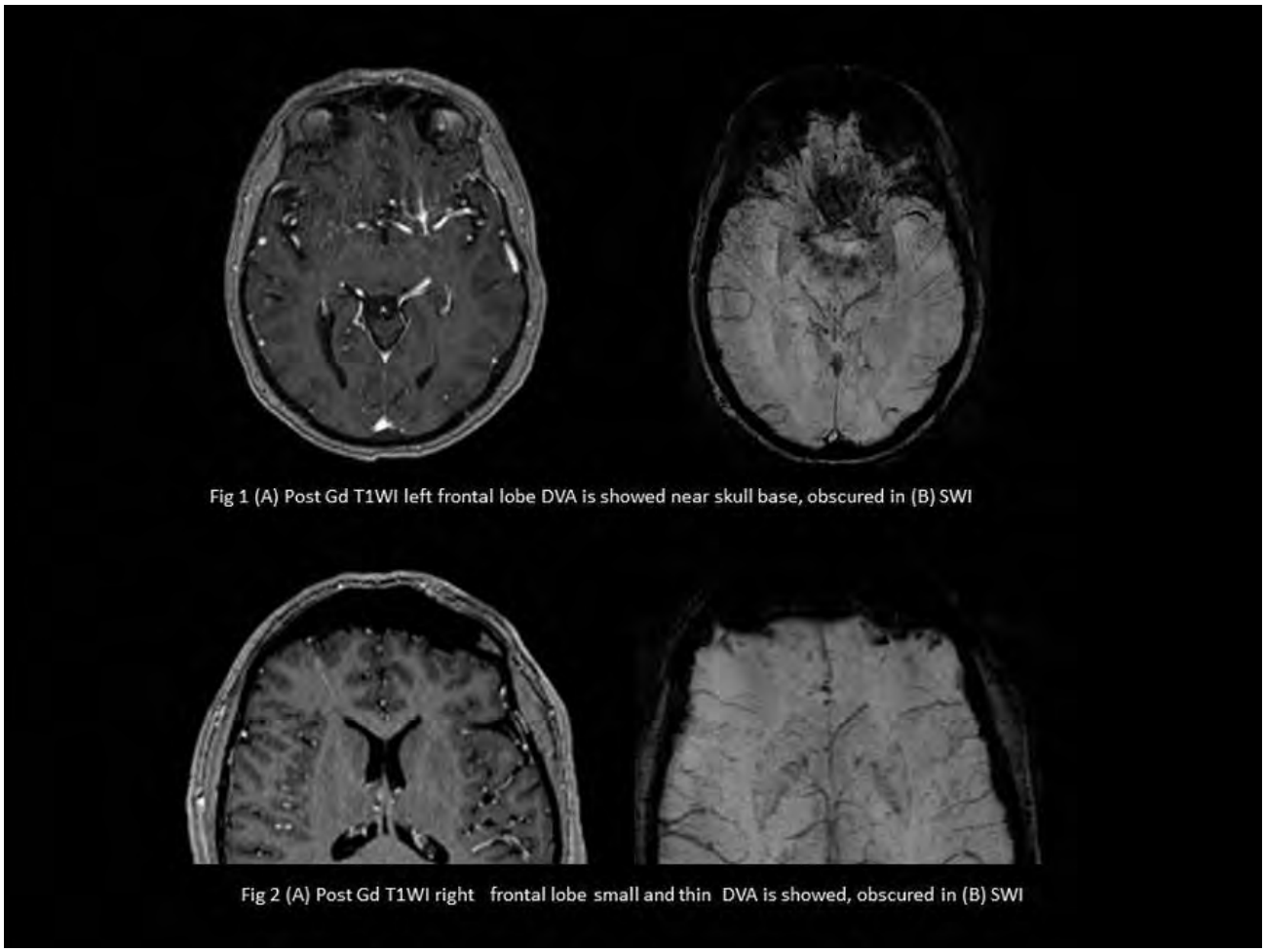
5:00PM - 5:08PM

SWI vs Post Gd T1WI in the Detection of Developmental Venous Anomalies

R Camacaro[1], C Vallejo[1], A Rodriguez[1], P Puac[1], M Castillo[1]

[1]*University of North Carolina at Chapel Hill, Chapel Hill, NC*

Purpose
Developmental venous anomalies (DVA) are the most common intracranial vascular anomalies. Recently, there is evidence that as many as 10% of them have atypical features which may be related to complications. Thus, reliably identifying all DVA and reporting them is desirable. Susceptibility-weighted imaging (SWI) is a sequence that depicts de-oxygenated blood with high sensitivity and should be ideal to identify DVA. Here we retrospectively reviewed all patients with DVA who were imaged with SWI and post Gd T1WI to assess which sequence depicted the most.
Materials and Methods
We retrospectively reviewed MRI in patients with a diagnosis of DVA studied between January 2011 and September 2016 with post Gd T1WI and SWI. We also recorded clinical information including patient demographics, symptoms, and size and location of DVA as well as any additional imaging features appreciated in all other sequences obtained as part of routine contrast MRI brain studies.
Results
A total of 247 patients (male: 83, female: 164) with DVA were identified, 158 were supratentorial (frontal: 110, parietal: 18, occipital: 7, temporal: 23) and 89 were infratentorial. Developmental venous anomalies were classified according to their size as: small (<10 mm) N =16 , medium (10-25mm) N =189 and large (>25mm) N =41. Twenty-seven (11.34%) were associated with cavernous malformations. Developmental venous anomalies with cavernomas (60%) presented high T2 signal intensity suggesting gliosis around their medullary veins. Of the 247 DVA seen on post Gd T1WI, 219 identified on SWI (88.7%). Developmental venous anomalies that were not seen in SWI, all were small or medium in size and 60% were located juxtacortical-subcortical and near the skull base where susceptibility artifacts obscured them.
Conclusions
Post Gd T1WI better depicts DVA as SWI missed small/medium sizied and peripherally located DVA.



(Filename: TCT_O-147_Slide3.JPG)

O-148

5:08PM - 5:16PM

Imaging Findings in Thrombosis of Developmental Venous Anomalies

R Assadsangabi[1], S Mohan[1], A Nabavizadeh[1]
[1]*University of Pennsylvania, Philadelphia, PA*

Purpose
Developmental venous anomalies (DVA) are the most common cerebral vascular malformation, with a reported prevalence of 2.6% (1). Developmental venous anomalies usually are asymptomatic; however, on occasion may give rise to symptoms secondary to various circumstances, including thrombosis of the drainage vein. The purpose of this study is to investigate the imaging findings and clinical outcome of patients with thrombosed DVAs.
Materials and Methods
A retrospective search for patients with thrombosed DVAs during January 2000 to July 2016

at University of Pennsylvania affiliated hospitals was performed. Patients with associated other vascular malformations e.g., cavernomas were excluded.

Results

A total of 6 patients (5 females and 1 male) with thrombosed DVA were identified, with a mean age of 27.66 years. Clinical manifestations varied from asymptomatic to headache, seizure, numbness and visual field cut. Head CT findings ranged from normal, focal hypodensity, transmantle tubular hyperdensity, and hemorrhage. Magnetic resonance imaging (MRI) demonstrated linear T1/T2 shortening with expansile surrounding signal abnormality, nonenhancement of transmantle collecting vein, engorgement of medullary veins, susceptibility blooming in collecting vein and proximal subependymal medullary veins, faint diffusion restriction along the margin of draining vein, varix at the drainage point and hemorrhagic mass mimicking brain tumors (tumefactive venous infarct). In 1 patient, initial imaging was limited to subtle edema and DVA was found only on follow up after resolution of edema. Follow-up imaging displayed resolution of surrounding signal abnormality, decreasing/resolving filling defects in draining vein and restoration of enhancement, reduced susceptibility, local encephalomalacia and cortical laminar necrosis. Clinical outcome was favorable in the majority of patients with complete recovery (n=5) with persistence of mild neurological symptoms (n=1).

Conclusions

Thrombosed DVAs can present with a variety of imaging findings, ranging from subtle venous congestive edema to a frank hemorrhagic mass depending on size, location, extension, drainage pattern and time course of venous occlusion. Thrombosed DVAs may pose a major diagnostic challenge and recognition of imaging findings may provide important clues to the correct diagnosis.

	Age	Sex	Clinical Presentation	Risk factor	Imaging	Location	Drainage	Management	Follow up
1	45	F	Headache, numbness, Seizure	Oral contraceptive pill	Transmantle abnormality, congestive edema	Right parietal	SSS	Anticoagulation	Mild residual numbness
2	17	F	Seizure	Pregnancy	Transmantle abnormality, congestive edema	Left frontal	SSS	Anticoagulation	Total resolution
3	21	F	Headache, left homonymous hemianopia	Crohn's exacerbation	Hemorrhagic mass, DVA on follow up	Right parieto-occipital	Straight sinus	Asacol, antibiotic	Normal visual field, local encephalomalacia
4	16	M	None. Work up for prior concussion	Multiple cavernoma in mother	Transmantle susceptibility	Right frontal	SSS	None	None
5	41	F	Left face clonic seizure	Antiphosph-olipid Syndrome	Congestive edema, DVA on follow up	Right frontal	SSS	ASA, Vimpat	Total resolution
6	26	F	Headache, left homonymous hemianopia	None	Hemorrhagic mass, DVA on follow up	Right medial occipital	Straight sinus	None	Normal visual field, local encephalomalacia

Table 1. Demographics, imaging findings and clinical characteristics of patients with thrombosed DVA.

(Filename: TCT_O-148_TablethrombosedDVA.jpg)

O-149

5:16PM - 5:24PM

Brain Metabolic and Perfusion Abnormalities Associated with Developmental Venous Anomalies

A Nabavizadeh[1], J Lazor[2], J Schmitt[1], L Loevner[3]
[1]University of Pennsylvania, Philadelphia, PA, [2]The Hospital of the University of Pennsylvania, Philadelphia, PA, [3]University of Pennsylvania, Philadelphia , PA

Purpose
Developmental venous anomalies (DVAs) are the most common cerebral vascular malformation and usually are incidental findings on imaging. The purpose of this study is to investigate the metabolic activity of DVAs using FDG-PET imaging and to correlate metabolic activity with conventional and advanced MRI sequences.
Materials and Methods
A retrospective search was performed to identify patients with DVAs that had both dedicated FDG-PET and brain MRI studies. Magnetic resonance imaging scans were analyzed to assess DVA size, location, and associated structural findings. Magnetic resonance imaging and PET images then were coregistered and qualitative and quantitative evaluation of FDG uptake in the region of DVA was performed. Quantitative analysis of DSC perfusion imaging also was performed whenever available. All quantitative measurements were normalized to contralateral normal brain.
Results
Fifty-six DVAs in 53 patients (32 male, 21 female) were included. The indication for PET imaging was epilepsy in 25 (47%), memory loss in 16 (30%) and neoplasm in 12 (22%) patients. Twenty-one (38%) DVAs demonstrated regional metabolic abnormality (20 hypometabolism, and 1 hypermetabolism). Developmental venous anomalies with cortical involvement were significantly more hypometabolic compared to DVAs with only white matter involvement on both qualitative ($p = 0.004$) and quantitative analysis ($p = 0.0092$). In 8 patients, DSC perfusion imaging was available and demonstrated increased relative cerebral blood volume (rCBV) regardless of the metabolic activity which was statistically significant ($P=0.0039$).
Conclusions
Metabolic abnormalities are seen in a significant proportion of patients with DVAs. Increased rCBV was visualized in all DVAs. These findings may increase our understanding of DVAs, beyond just an anatomical variation in the venous drainage system to a vascular lesion with abnormal physiologic features. The constellation of imaging findings indicates that the drainage territory in a significant proportion of patients with DVA is congested and hypometabolic.

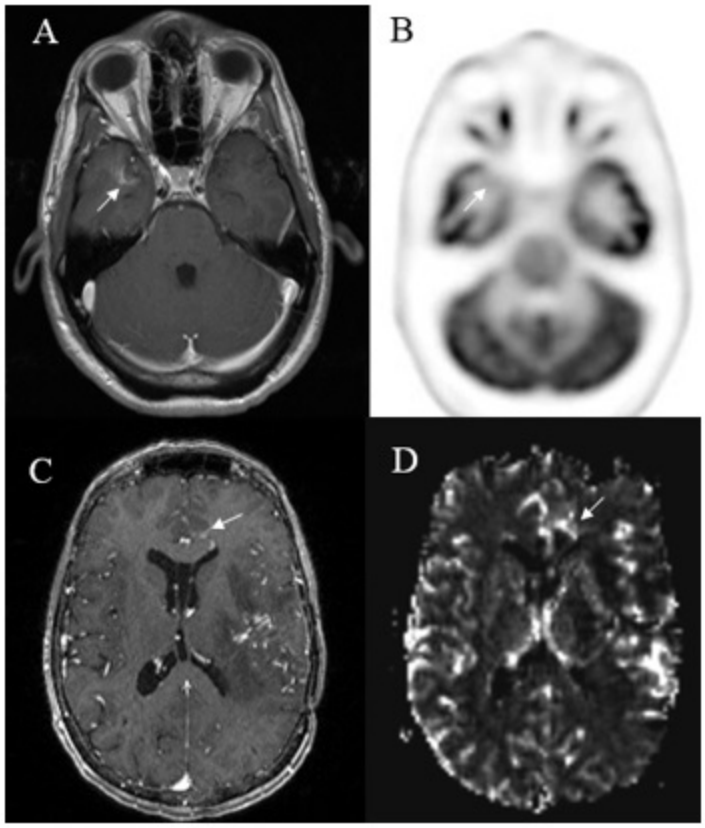


Figure 1. CE T1W MRI (A) and FDG-PET (B) demonstrate right temporal DVA associated with regional hypometabolism. CE T1W MRI (C) and DSC perfusion (D) demonstrate left frontal DVA associated with elevated relative cerebral volume.

(Filename: TCT_O-149_Lymphnodesfacefinalfigure.jpg)

O-150

5:24PM - 5:32PM

Accuracy of SWI Sequences Compared to T2*-Weighted Gradient Echo Sequences in the Detection of Cerebral Cavernous Malformation

G Sparacia[1], A Chan[2], A Anastasi[3], A Iaia[2], C Speciale[3], A Banco[3], F Agnello[1], M Midiri[3]
[1]University of Palermo, Palermo, AK, [2]christianaCare Health, Wilmington, NC, [3]Università degli studi di Palermo- Policlinico P. Giaccone, Palermo, AK

Purpose
To assess the accuracy of SWI sequences compared with GRE T2* sequences in assessing cerebral cavernous malformations (CCV).
Materials and Methods
We retrospectively evaluated 11 patients with familial form of CCV (4 men, 7 women; age: 32 -77 years; mean age, 53,7 years). MR protocol included nonenhanced and contrast-enhanced FSE T1-w sequences, FSE T2-w, FLAIR, GRE T2* w and SWI sequences. Images were reviewed by 2 expert neuroradiologist to assess location, number, size and conspicuity of the lesions on GRE and SWI sequences. Statistical differences of lesions seen on SWI and GRE images were assessed with the nonparametric Wilcoxon signed rank test.
Results
We retrospectively evaluated 11 patients with familial form of CCV (4 men, 7 women; age: 32 -77 years; mean age, 53,7 years). Magnetic resonance protocol included nonenhanced and contrast-enhanced FSE T1 w sequences, FSE T2 w, FLAIR, GRE T2* w and SWI sequences. Images were reviewed by 2 expert neuroradiologist to assess location, number, size and conspicuity of the lesions on GRE and SWI sequences. Statistical differences of lesions seen on SWI and GRE images were assessed with the nonparametric Wilcoxon signed rank test.
Conclusions
Susceptibility-weighted imaging sequence allowed to identify malformations that did not appear in GRE T2 * images. Thus, routine clinical neuroimaging protocols should contain SWI sequences for the evaluation of patients with or suspected cerebral cavernous malformations to assess the true prevalence of lesions in order to improve the diagnosis.

O-151

5:32PM - 5:40PM

Susceptibility Weighted Imaging Improves Detection of Microhemorrhage in Primary Angiitis of the CNS

F Sepulveda[1], P Yañez[2], N Stefanoff[2], R Goñi[2], N Arakaki[2], M Castillo[3]
[1]FLENI, Buenos Aires, NC, [2]FLENI, Buenos Aires, Buenos Aires, [3]University of North Carolina at Chapel Hill, Chapel Hill, NC

Purpose
Our purpose was to assess the ability of SWI to detect microhemorrhages in patients with histological proven primary angiitis of the CNS (PACNS).
Materials and Methods
A retrospective analysis of 10 MRI examinations of patients with PACNS was performed. We compared detection rates of microhemorrhages on SWI with those of conventional MRI sequences (T2, FLAIR, and T1). Additionally, presence or absence of contrast-enhancing lesions on post-gadolinium SPGR was documented and correlated with presence or absence

of microhemorrhages in these regions. Two blinded neuroradiologists reviewed all sequences in a consensus fashion. Posteriorly an independent neuroradiologist and a neuropathologist compared the SWI detection rate with the presence of hemorrhages on brain biopsies.
Results
Susceptibility-weighted imaging sequence yielded an increased detection of microhemorrhages by all readers. For SWI analysis the readers identified microhemorrhages in 9 examinations and in 1 examination with conventional sequences. For contrast-enhanced lesions, readers identified 6 positive examinations. Additionally, the readers found that the contrast-enhanced parenchymal zones contained microhemorrhages on SWI. The 1 case with no microhemorrhages showed only leptomeningeal contrast enhancement. In the histopathology analysis, 6 patients presented hemorrhages.
Conclusions
We found that SWI improved detection of microhemorrhages in the setting of PACNS. Microhemorrhages usually were located in areas where contrast enhancement was seen (active inflammation). The sensitivity of SWI for detection of microhemorrhage was higher than that of the biopsy, but this probably reflects a sampling artifact.

O-152

5:40PM - 5:48PM

National Survey of Radiologic Management of Angiographically-Negative Subarachnoid Hemorrhage

G Sadigh[1], J Allen[2]
[1]Emory University School of Medicine, Atlanta, GA, [2]Emory University, Atlanta, GA

Purpose
Diagnostic algorithms for patients with nontraumatic angiographically-negative SAH (AN-SAH) vary between institutions and the optimal method remains subject to debate. We assessed variations in radiologic management of these patients in academic institutions nationally.
Materials and Methods
Radiology Department Chairs of academic institutions across the nation were contacted via the Society of Chairs of Academic Radiology Departments (SCARD) listserv in October 2016 and asked to complete an online survey with a representative neruoradiogloist in their department. Questions were aimed to assess institutional routine initial, delayed same-admission follow-up and repeat follow-up after discharge imaging tests for management of AN-SAH, as defined by a negative head CTA or DSA, and the degree of compliance with their protocol.
Results
Response rate was 28%. Seventy-four percent of institutions were university hospitals, 3%

community hospitals, and 23% combination of both. Majority of institutions (33%) had 7-9 practicing neuroradiologists, followed by 28% with 4-6 neuradiologists. Eighty percent of institutions reported having a monthly average of 1-3 patients with AN-SAH. In 79% of institutions, there was an established routine radiologic protocol for management of AN-SAH patients, which was developed by a multi-specialty team including neurosurgery (72%), radiology (66%) or neurology (17%) departments. Majority of institutions (76%) reported a high degree of compliance with the protocol (e.g., in more than 75% of cases). Institutional protocols included brain MRI (67%), cervical spine MRI (41%), and repeat, delayed same admission CTA (41%) or DSA (64%). A delayed follow-up test after at least 30 days from presentation was performed in 59% of institutions, with DSA (60%) the most common, followed by head CTA (32%) and head MRA (8%). Fifty-eight percent of delayed follow-up imaging tests were performed within 6-11 months after presentation.
Conclusions
There is high variability among institutions for routine management of AN-SAH, requiring the need for standardization of the radiologic protocols across institutions.

O-153

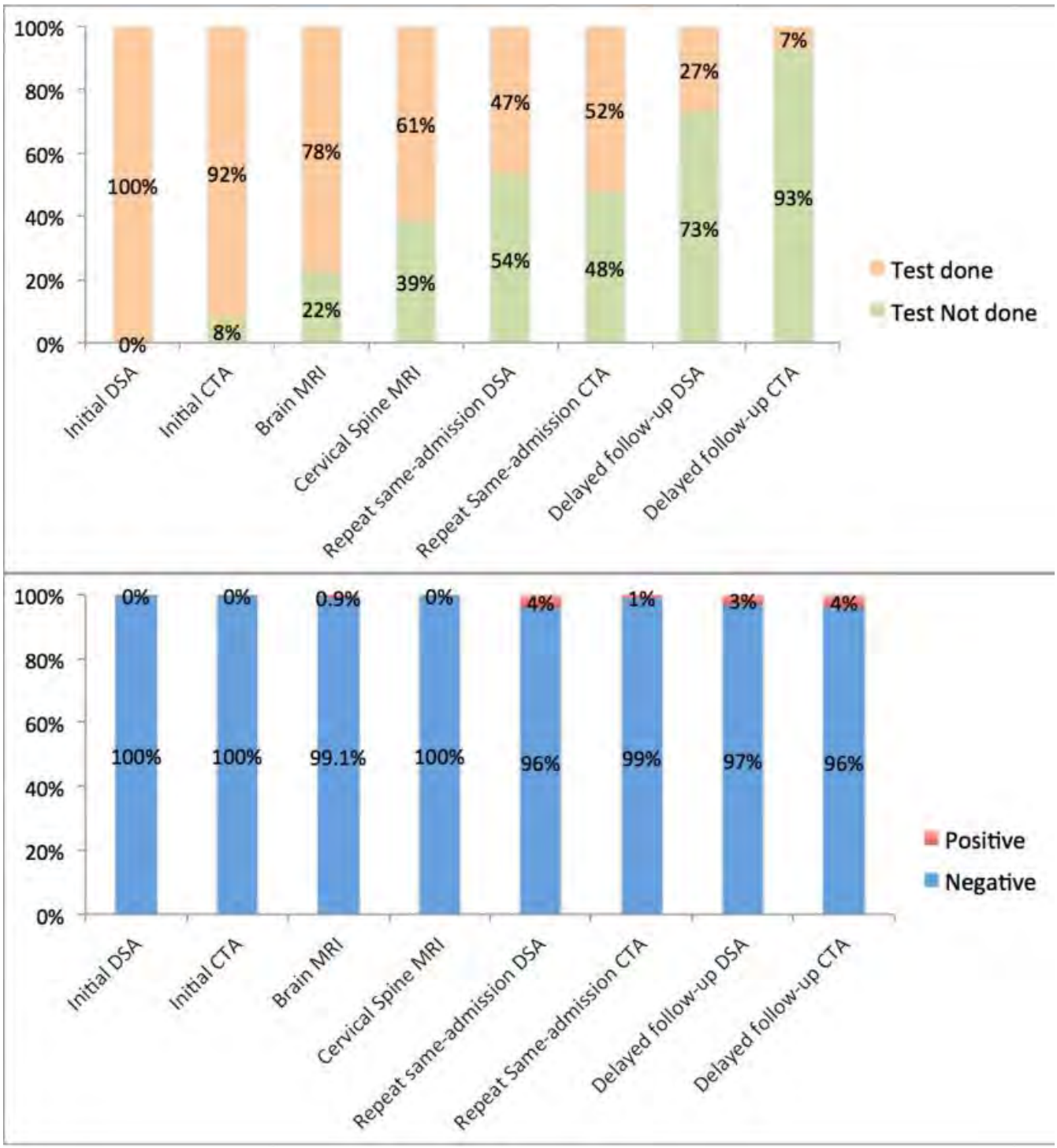
5:48PM - 5:56PM

Radiologic Management of Angiogram-Negative Spontaneous Intracranial Subarachnoid Hemorrhage: A Multi-center Study of Utilization and Diagnostic Yield

G Sadigh[1], R Menon[2], M Bhojak[3], A Aladi[4], M Mossa-Basha[5], L Wu[5], V Lehman[6], W Brinjikji[6], C Holder[7], J Allen[8]
[1]Emory University School of Medicine, Atlanta, GA, [2]The Walton Centre NHS Foundation Trust, Liverpool, United Kingdom, [3]The Walton Centre, Liverpool, Merseyside, [4]Keele University, Stoke-on-Trent, Staffordshire, [5]University of Washington, Seattle, WA, [6]Mayo Clinic, Rochester, MN, [7]Emory University School Of Medicine, Atlanta, GA, [8]Emory University, Atlanta, GA

Purpose
To assess the utilization rate and diagnostic yield of imaging tests routinely obtained in identifying a structural cause for angiographically-negative spontaneous subarachnoid hemorrhage (AN-SAH).
Materials and Methods
In this multi-center retrospective study, consecutive adult patients admitted with nontraumatic, angiographically negative, SAH to 1 of the 5 University Hospitals between 01/2009 and 12/2015 were included. Patients with intraparenchymal, subdural, or epidural hematomas were excluded. Baseline clinical characteristics and posthospitalization outcomes were collected. Outcomes studied included utilization rate, diagnostic yield and median time of the imaging test postadmission for the following imaging tests: initial DSA and CTA,

brain and cervical spine MRI, and repeat DSA and CTA performed during the initial admission and at long-term follow-up.
Results
Seven hundred patients were included (mean age, 54 year; 54% male; 32% with hypertension; 32% with smoking history). Mean Hunt & Hess and Fisher scores were 1.7 and 2.7, respectively. Initial DSA and CTA were performed for 100% and 92% of patients, respectively. Brain MRI was preformed in 78% of patients and identified an etiology for the SAH in 0.9% of cases. Cervical spine MRI was performed in 61% of patients and identified an etiology for the SAH in 0% of cases. Repeat, same-admission follow-up DSA and CTA were performed in 47% and 52% of patients and was positive in 4% and 1% of cases, respectively. Ninety-three percent of patients were discharged home, while 6% were sent to rehab facility and 1% died. Delayed follow-up DSA and CTA after discharge were performed in 27% and 7% of patients respectively at a median of 90 days postadmission. Digital subtraction angiography was positive in 3% of cases and CTA was positive in 4% of cases.
Conclusions
Variation exists in radiologic evaluation of AN-SAH within and amongst institutions. These results suggest that such evaluation could be more standardized without need for MRI of the cervical spine which has a very low diagnostic yield.



(Filename: TCT_O-153_Figure1.jpg)

O-154

5:56PM - 6:04PM

Evaluating the Temporal Patterns of Blood Brain Barrier Permeability after Subarachnoid Hemorrhage

E Weidman[1], A Hoang[2], J Ivanidze[1], O Kallas[1], A Gupta[1], P Sanelli[2]
[1]New York-Presbyterian Hospital/Weill Cornell Medical Center, New York, NY, [2]Northwell Health, Manhasset, NY

Purpose

Delayed cerebral ischemia (DCI) is a major contributor to morbidity and mortality after aneurysmal subarachnoid hemorrhage (aSAH) and may be related to microvascular dysfunction with alterations in blood-brain barrier permeability (BBBP) (1, 2). We evaluate the temporal patterns of BBBP parameters (PS, Ktrans, KEP, E) following aSAH in patients who developed DCI and those who did not.

Materials and Methods

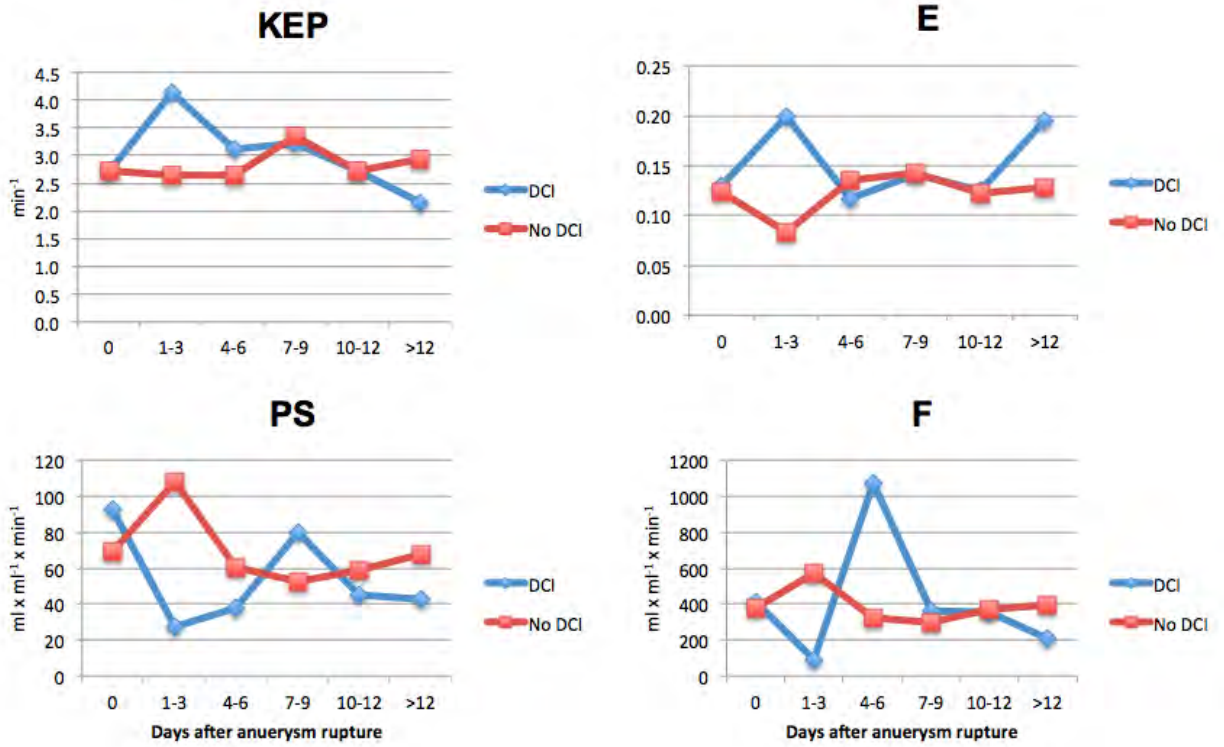
Repeated extended-pass CTP exams performed on consecutive aSAH patients at days 0-21 after aneurysm rupture was reviewed retrospectively. Delayed cerebral ischemia was determined by established criteria defined as infarction on imaging, permanent neurologic deficit distinct from presentation, or symptomatic vasospasm (3). CTP data were postprocessed using standardized methods to assess quantitative permeability (PS, Ktrans, KEP, E) and perfusion (F) parameters. Mean values were generated for each patient. A trend analysis was performed for DCI and non-DCI groups at each time point (days 0-21).

Results

Seventy-nine CTP exams from 43 patients were included; 11 DCI and 32 non-DCI. According to trend analysis, PS and F were significantly lower in the early phase (days 1-3) in DCI compared to non-DCI patients ($p<0.001$). Conversely, KEP and E were higher in DCI patients in the early phase compared to non-DCI patients, although this trend did not reach statistical significance. There was no significant difference in Ktrans between groups.

Conclusions

Permeability parameters may have characteristic temporal patterns after aSAH in patients who develop DCI, with elevated E and KEP representing increased BBBP during the early phase (days 1-3) after aSAH. PS and Ktrans are not elevated at this time point because these parameters are dependent on blood flow conditions, which are decreased at this time in DCI patients. However, during days 7-9, when flow conditions are restored in DCI, PS and Ktrans are elevated. This supports the hypothesis that early microvascular dysfunction, as measured by alterations in permeability over time, may contribute to DCI in patients with aSAH.



(Filename: TCT_O-154_CTPASNR_resize.jpg)

O-155

6:04PM - 6:12PM

Metabolic Dysfunction and Altered Blood-Brain-Barrier Permeability Metrics in Aneurysmal Subarachnoid Hemorrhage.

J Ivanidze[1], A Gupta[2], P Sanelli[3], X Mao[4], D Shungu[5], H Mangat[6]
[1]New York Pres. Hos. Cornell, New York, NY, [2]New York-Presbyterian Hosp/Weill Cornell Med Ctr, New York, NY, [3]Northwell Health, Manhasset, NY, [4]Weill Cornell Medicine, New York, NY, [5]Weill Cornell Medical College, New York, NY, [6]NewYork-Presbyterian Hospital-Weill Cornell, New York, NY

Purpose
Aneurysmal subarachnoid hemorrhage (ASAH) is a devastating condition with high morbidity and mortality. Clinical prognostication utilizing advanced imaging, including CT-perfusion to monitor cerebral blood flow and blood-brain barrier permeability, has been the subject of active research in recent years. Complications including global cerebral edema (GCE) and delayed cerebral infarction (DCI), are related to poor clinical outcomes, and are thought to arise from blood-brain barrier (BBB) dysfunction. However, a possible correlation between BBB dysfunction, as assessed by CTP-derived permeability surface area

product (PS) and metabolic abnormalities, as assessed by MR spectroscopy evaluating NAA, Choline and Lactate spectra, has not been studied previously in a clinical setting. We performed a pilot study to determine possible correlation of BBB dysfunction and metabolic abnormalities in patients with ASAH.

Materials and Methods

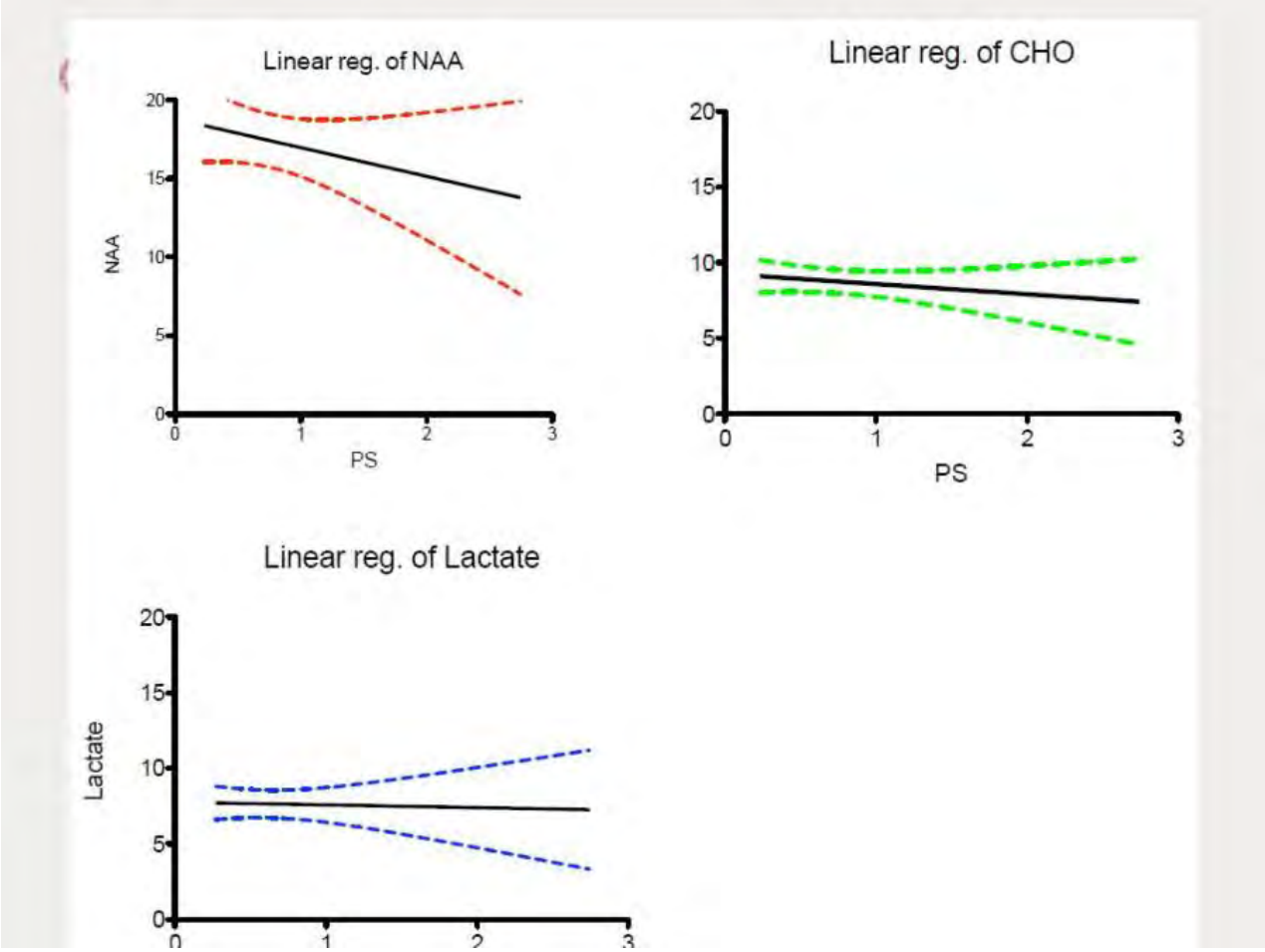
MR spectroscopy (MRS) was utilized to measure regional NAA in 13 ASAH patients who had suffered neither cerebral infarction nor neurological deficits. Only patients who underwent endovascular aneurysm coiling were included. Measurements were made in frontal, temporal, occipital lobes, lateral ventricles, and averaged in each hemisphere from 3 slices. Matching ROIs were placed on the most proximate CT perfusion maps to measure corresponding PS. MR spectra were correlated with PS. Average age was 58 years, Hunt Hess score was 2.43±1.09, modified Fisher score was 2.79±1.05. Three patients had DCI and none had cerebral infarction. Median GCS at discharge was 15. MR spectroscopy was obtained at 9.93±7.73 days from admission. Linear regression analysis was performed to determine correlation.

Results

NAA, Choline and Lactate spectra did not correlate with PS in pooled data, demonstrating R-square of 0.05334, 0.03464, and 0.002289, respectively (p-values were 0.2195, 0.3248, 0.8368, respectively).

Conclusions

In this pilot study, metabolic abnormalities in ASAH did not correlate with BBB dysfunction. This may be reflective of independent mechanisms driving BBB dysfunction and metabolic abnormalities in the early course of ASAH. Further evaluation in a larger cohort is needed to better characterize this potential relationship.



(Filename: TCT_O-155_JIASNR.jpg)

O-156

6:12PM - 6:20PM

Radiogenomics of Blood Brain Barrier Damage – Applications in Aneurysmal Subarachnoid Hemorrhage

J Ivanidze[1], R Ferraro[2], M Jin[2], A Segal[3], A Gupta[4], P Sanelli[5]
[1]New York Pres. Hos. Cornell, New York, NY, [2]NewYork-Presbyterian Hospital - Weill Cornell Medical College, New York, NY, [3]NewYork-Presbyterian Hospital - Weill Cornell, New York, NY, [4]New York-Presbyterian Hosp/Weill Cornell Med Ctr, New York, NY, [5]Northwell Health, New York, NY

Purpose
The lack of quantitative markers is a major limitation for accurate monitoring of aneurysmal subarachnoid hemorrhage (ASAH) complications, including global cerebral edema (GCE) and delayed cerebral infarction (DCI), which are related to poor clinical outcomes. We previously have demonstrated BBBP monitoring with CTP to be a promising biomarker of

GCE, DCI and poor clinical outcomes in ASAH. MicroRNA plays an important role in the epigenetic regulation of a multitude of diseases. However, epigenetic regulation of BBB damage and correlation with advanced BBBP imaging has not been applied to date in a clinical setting. We performed a pilot study to evaluate a possible role for microRNA-driven epigenetic regulation of BBBP in the CSF, which may represent a potential diagnostic and therapeutic target for ASAH, where BBB disruption has been implicated.

Materials and Methods

In this prospective IRB-approved clinical study, we collected CSF from 10 ASAH patients who required ventriculostomy catheter placement for intracranial pressure management, stratified by good (modified Rankin Score (mRS) 0-1) versus poor (mRS 5) clinical outcomes. Patients underwent Shuttle CTP as part of clinical standard-of-care. MicroRNA was evaluated in CSF supernatant utilizing miRCURY LNA Universal RT microRNA PCR (Exiqon, Woburn, MA). A total of 752 assays per sample were analyzed. Statistical analysis was performed to determine differentially regulated microRNA.

Results

There were 8 differentially regulated microRNAs. The most significantly regulated microRNA was found to be microRNA-34 (fold change "mRs 5" versus "mRs 0-1" = -9.0, p-value = 0.014).

Conclusions

MicroRNA-34 was significantly down-regulated in ASAH patients with poor clinical outcomes. MicroRNA-34 is a negative regulator of CD-44, a key signaling protein involved in MMP-2 mediated BBB disruption. This represents the first study linking epigenetic and perfusion-imaging-based analysis of BBB disruption in the clinical setting.

A

MicroRNA Name	Fold Change ("mRS 5" vs "mRS 0-1")	p-value
MicroRNA-34	*- 9.0*	*0.014*
Let-7b	- 5.3	0.0057
MicroRNA-548	- 3.1	0.015
MicroRNA-652	- 2.2	0.023
MicroRNA-21	- 1.7	0.033
MicroRNA-378	- 3.6	0.034
MicroRNA-660	- 2.2	0.036
MicroRNA-7	- 4.2	0.037

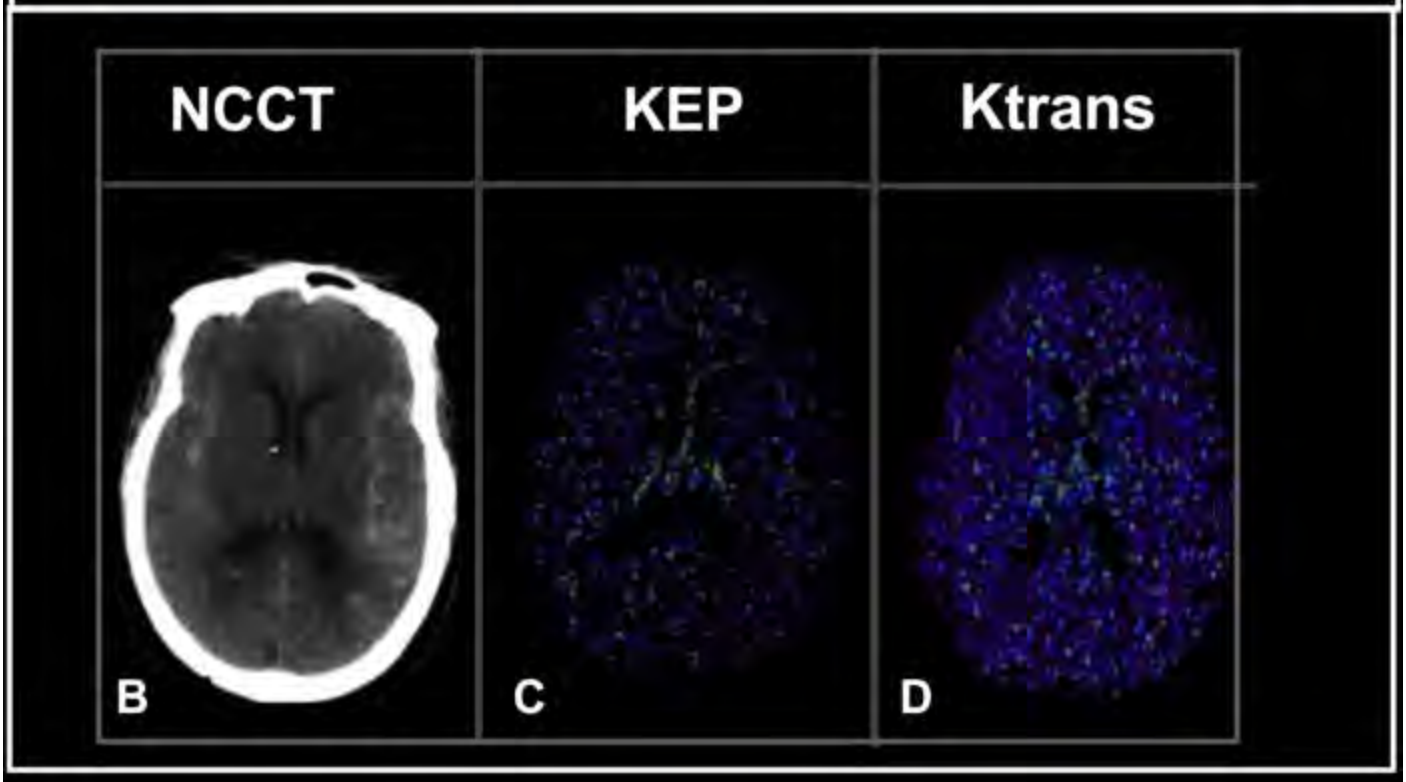


Table 1A. 8 microRNAs were statistically significantly differentially regulated in the CSF of ASAH patients with poor clinical outcomes (mRS 5) compared to patients with good clinical outcomes (mRS 0-1). The highest regulated microRNA was microRNA-34 (fold change: - 9.0, p-value = 0.014).

Figure 1B -1D. Representative ASAH patient evaluated with NCCT demonstrating diffuse ASAH (A); BBBP maps demonstrating abnormal KEP and Ktrans permeability metrics (B and C, respectively).

(Filename: TCT_O-156_JIASNRmicroRNA.jpg)

O-157

6:20PM - 6:28PM

Substance Abuse Effects in the Cerebral Vasculature: A Retrospective Study.

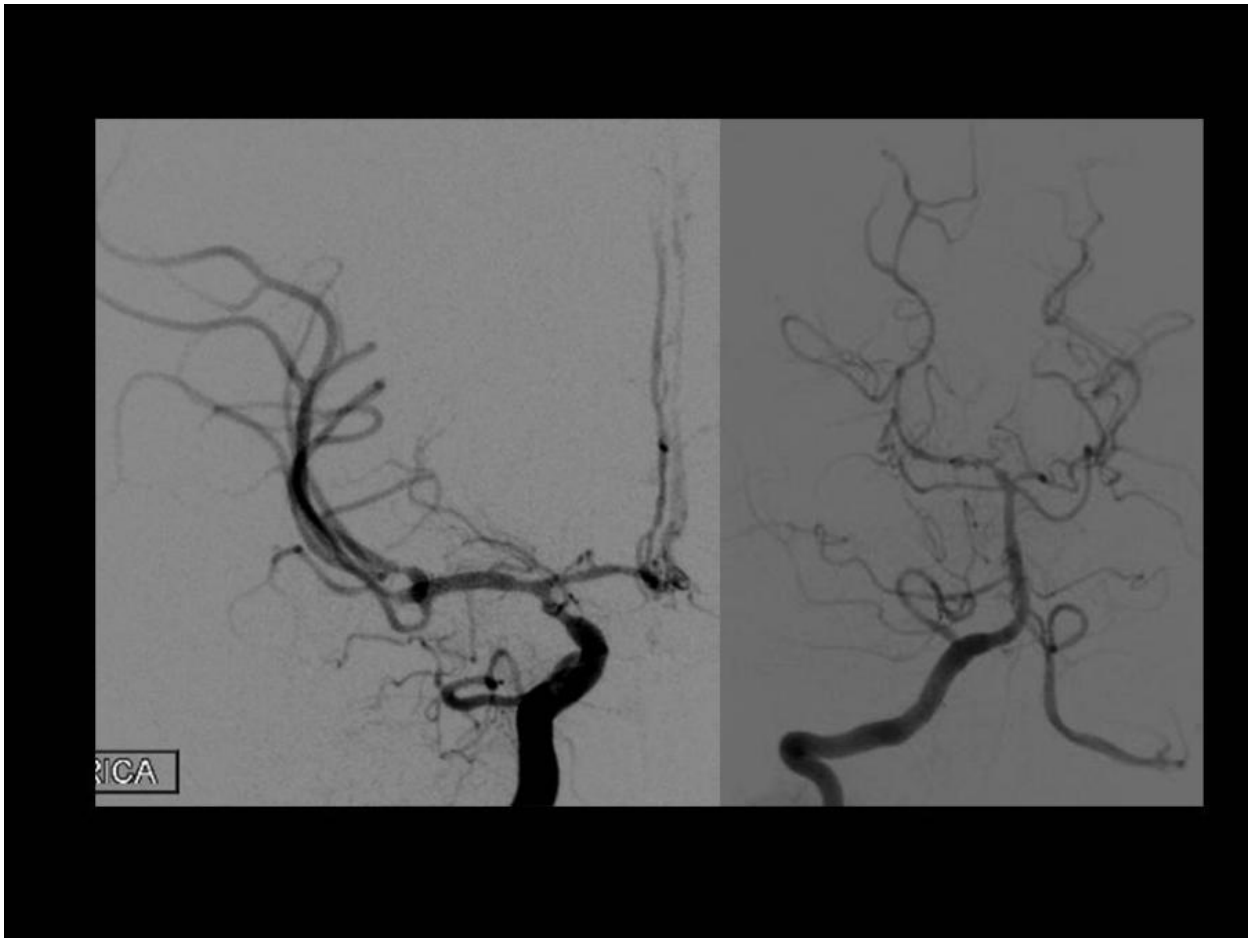
E Bonfante[1], A Jagolino-Cole[2], N Solomon[3], A Tenreiro[1], C Cai[1], R Riascos[4]
[1]The University of Texas Health Science Center at Houston, Houston, TX, [2]McGovern Medical School at the University of Texas Health Sciences Center at Houston, Houston, TX, [3]The University of Texas Health Science Center at Houston UTHealth, Houston, TX, [4]UTHSC-Houston, Houston, TX

Purpose
It is known that illicit drug use and abuse raise the risk for strokes, both ischemic and hemorrhagic. Vascular changes have been described in patients with stroke associated to substance abuse. Cannabis use is associated with arterial disease such as stroke, myocardial infarction, and limbs arteritis. Cocaine-induced stroke has been attributed to a number of factors including vasospasm, cerebral vasculitis, enhanced platelet aggregation, cardioembolism, and hypertensive surges associated with altered cerebral autoregulation. In vascular studies, the distinction between intracranial atherosclerosis and vasculopathy is not always possible. In addition to the extracranial findings, the comorbidities and the clinical evolution following withdrawal are taken into account to favor one or another. In order to optimize management and prevention of acute stroke or recurrent stroke in this population, it is important to understand the pathophysiology of the vascular changes. We sought to describe the pattern of vascular imaging findings in a cohort of patients with ischemic and hemorrhagic stroke associated to substance use.
Materials and Methods
We conducted a retrospective chart review of patients who were admitted from 2005 to 2015 with a diagnosis of acute stroke and had either a positive urine toxicology screen and/or reported drug use in their medical histories. In the reviewed data, we included demographic information (gender, age, race, ethnicity), comorbidities (atrial fibrillation, cardiac heart failure, diabetes I and II, elevated cholesterol, hypertension, coronary artery disease, carotid stent), CT findings, MRI findings, and findings in vascular studies including Neck CTA, MRA, DSA, and intracranial CTA, MRA, and DSA. Extracranial vascular findings were classified as extracranial occlusion, extracranial stenosis, other relevant extracranial finding and normal/nonrelevant findings. Intracranial vascular findings were classified as intracranial occlusion, intracranial stenosis, other relevant intracranial finding, and normal/nonrelevant findings.
Results
Of a total of 424 patients with stroke and positive substance use admitted between 2005 and 2015, 369 had vascular imaging studies. Mean age was 54.5 years ranging from 19 to 83,

24% female, 76% male. Extracranial vascular findings in this group included occlusion in 36 patients (9.7%), and stenosis in 166 patients (44.9%). Intracranial vascular findings in this group included acute vascular occlusion in 96 patients (26%) and vascular stenosis in 71 patients (19%). Of the 369 patients with vascular imaging studies, 210 had a recent ischemic stroke and 74 had intracranial hemorrhage (ICH). Abnormal extracranial findings were present in 132 (62.8%) of the patients with ischemic stroke (including occlusion and stenosis). Of these, 2 were acute occlusion or dissection. Of the 74 patients with ICH, 33 (44.5%) had extracranial stenosis or occlusion, and 16 (21.6%) had intracranial stenosis or occlusion. Fifty-eight (78%) had no intracranial vascular abnormality and 41 (55%) had no extracranial abnormality. The most frequent substances were 1, alcohol found in 142 (67.2%) of the patients with ischemic stroke and in 45 (60.8%) of the patients with hemorrhage; 2, cocaine found in 46 (21.9%) of patients with ischemic stroke and in 18 (24.3%) of patients with ICH; and 3, marijuana, found in 62 (29.5%) of patients with ischemic stroke and in 17(22.9%) of patients with ICH. Amphetamines were found in 7 (9.4%) of patients with ICH. All other substances were found in less than 3% of the ischemia or ICH groups. There were 91 patients with vascular studies who were positive for cocaine. Extracranial occlusion was found on 5 (1.3%), extracranial stenosis on 26 (28.5%), intracranial occlusion in 23 (25.2%) and intracranial stenosis in 15 (16.4%). There were 90 patients with vascular studies that were positive for marijuana. Of them 10 (11%) had extracranial occlusion, 35 (38.8%) had extracranial stenosis, 25 (27.7%) had intracranial occlusion, 9 (10%) had intracranial occlusion.

Conclusions

We found a significant incidence of abnormal vascular imaging findings in patients with stroke associated to substance abuse. Extracranial occlusion and stenosis were found more commonly in patients with marihuana use as compared to cocaine use. These included stenosis (38.8%) and occlusion (11%). Intracranial vascular occlusion and stenosis were found with similar frequency in both groups. Additional analysis of the characteristics of the vascular abnormalities of these subgroups of stroke patients may help elucidate the pathophysiology of stroke and potentially aid in the development of management strategies.



(Filename: TCT_O-157_Vasculopathyimage.jpg)

Tuesday
5:00PM - 6:30PM
Long Beach Convention Center, Room 102BC (Main Level)

15H-Parallel Paper Session: Brain Tumor Imaging: Predicting Pathology, Monitoring Management

O-158

5:00PM - 5:08PM

An "Aerobic Glycolytic Index" derived from simultaneous pH- and oxygen-weighted metabolic MRI correlates with histopathology in human gliomas

B Ellingson[1], R Harris[1], K Leu[1], T Abe[2], W Pope[3], T Cloughesy[1]
[1]University of California Los Angeles, Los Angeles, CA, [2]University of California, Los Angeles, Los Angeles, CA, [3]David Geffen School Of Medicine at UCLA, Los Angeles, CA

Purpose
Abnormal metabolism is a hallmark of cancer. Rapidly proliferating tumor cells increase

extracellular acidosis even in the presence of oxygen due to the downstream effects of aerobic glycolysis via the Warburg effect. In this study we have implemented a simultaneous pH- and oxygen-weighted molecular MRI technique using multi-echo amine chemical exchange saturation transfer (ME-aCEST) to characterize the glycolytic status of human gliomas. When combined with tumor perfusion information, this approach allows estimation of extracellular pH and relative cerebral metabolic rate of oxygen (rCMRO2). The ratio of pH-weighted MR contrast to rCMRO2 allows estimation of an "aerobic glycolytic index", which may be useful for characterizing the metabolic behavior of human tumors.

Materials and Methods

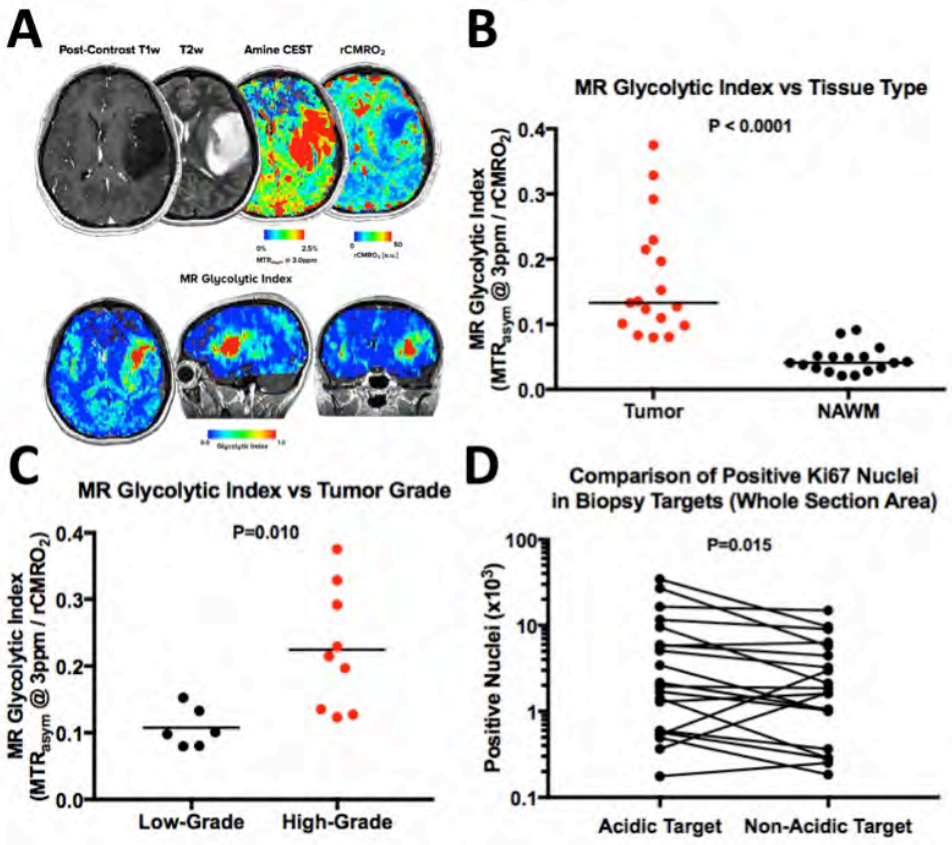
ME-aCEST was applied to 15 glioma patients prior to surgery. Perfusion and anatomical MRI were also acquired. Maps of T2, T2*, R2', CBV, CBF, rCMRO2 and pH-weighted image contrast (MTRasym) were calculated from ME-aCEST and perfusion data. Glycolytic index was then calculated as MTRasym/rCMRO2. Measurements of glycolytic index were obtained in healthy and tumor tissue for all patients. Multiple image-guided biopsies were identified on pH-weighted images and biopsy samples were used to determine tumor grade and Ki67 proliferation index.

Results

Maps of glycolytic index provided unique contrast near the tumor boundaries that may be indicative of metabolically active tumor undergoing high rates of glycolysis (Fig. 1A). Mean glycolytic index was able to dichotomize healthy and tumor tissue with 88% sensitivity and 94% specificity (Fig. 1B). Histologically, glycolytic index was also greater in high-grade tumors than low-grade (Fig. 1C; $P=0.010$) and acidic biopsy targets had significantly elevated Ki67 proliferation index compared with non-acidic targets within the same tumor (Fig. 1D; $P=0.015$).

Conclusions

An "aerobic glycolytic index" derived from simultaneous pH- and oxygen-weighted metabolic MRI provides unique information about tumor metabolism that may be useful for identifying aggressive regions of tumor and for metabolic response assessment in novel therapeutics.



(Filename: TCT_O-158_Fig1.jpg)

O-159

5:08PM - 5:16PM

Brain Imaging Using ROS-sensitive Ascorbate-derived 11C Radiotracers

J Villanueva-Meyer[1], V Carroll[1], R Flavell[1], D Wilson[1]
[1]*University of California, San Francisco, San Francisco, CA*

Purpose
Reactive oxygen species (ROS)-sensitive molecular imaging techniques hold special promise in neuroradiology. For example, successful treatment of both primary and secondary brain tumors relies on ROS-generating therapies. Upon initial diagnosis of glioblastoma (GBM), standard treatment consists of maximal surgical resection, chemoradiotherapy, and adjuvant temozolomide. Radiotherapy delivers a therapeutic cell killing dose to diseased cells by increasing the concentration of ROS above the cytotoxic threshold. This therapeutic mechanism occurs when ROS interacts with DNA, proteins, and lipids causing DNA double strand breaks, loss of protein function, and membrane damage to cancer cells (1, 2). However, in the case of radiation resistance, cells may avoid the cytotoxic effects of ROS by upregulating production of ROS scavenging antioxidants such as GSH, SOD, and catalase. A recent study demonstrated an in-field component of treatment failure in 81% of GBM

recurrences following focal radiotherapy with concomitant temozolomide (3). Redox adaptation has been increasingly implicated in both the resistance of GBM to ROS-generating therapies. Therefore, our goal was to develop an ROS-sensitive radiotracer, to investigate mechanisms of radiation resistance in GBM, and verify ROS-based cell killing following therapy.

Materials and Methods

[11C]Vitamin C (VitC) was synthesized from L-xylosone based on a modification of the previously reported [13/14C] enriched techniques (4). Stability of [11C]VitC was achieved by adding carrier KCN during the radiochemical preparation. With the presence of 0.6 – 1.0 mM (specific activity ≅ 3.0 – 10.0 mCi/μmol) carrier in the final isolated product [11C]VitC is stable at all time points tested. The transport of both [11C]VitC and its oxidized partner [11C]dehydroascorbic acid (DHA) was investigated in U87 human GBM cells using [18F]FDG as a standard radiotracer for GLUT transport. ROS-dependent [11C]VitC accumulation in cells was studied in U87 cells by addition of exogenous H2O2 to the media. Having shown the expected behavior of [11C]VitC and [11C]DHA in vitro, the differential transport of these tracers across the blood-brain barrier (BBB) was investigated in normal rats. It has been well established that DHA (but not VitC) crosses the BBB, transported primarily by GLUT1 (5). Approximately 200 μCi of [11C]VitC (n = 3) and [11C]DHA (n = 3) each were administered to normal rats via tail vein injection and a 40 min dynamic scan was obtained using a microPET/CT scanner. Finally, an orthotropic model of GBM was generated using U87 cells in nu/nu athymic mice. These animals also were studied using [11C]VitC/ microPET/CT.

Results

In vitro results showed that the uptake of [11C]VitC in U87 cells occurred via an oxidation-driven process dependent on the GLUT1 transporter. Consistent with this hypothesis, the uptake of [11C]DHA via GLUT was 10 fold higher than uptake of [11C]VitC. Addition of exogenous H2O2 to the media, resulted in a greater than 2-fold increase in [11C] accumulation when [11C]VitC was applied to cells. Having shown the expected behavior of [11C]VitC and [11C]DHA in vitro, we performed a proof of concept in vivo experiment to demonstrate the differential transport of the 2 tracers. Approximately 200 μCi of [11C]VitC (n = 3) and [11C]DHA (n = 3) each were administered to normal rats via tail vein injection and a 40 min dynamic scan was obtained using a microPET/CT scanner. As anticipated the brain accumulation of [11C]DHA was markedly higher than that of [11C]VitC, confirming our hypothesis that changes in uptake based on oxidized vs. reduced forms of ascorbic acid can be detected using PET. Finally, then we applied the same methods to a cohort of U87 murine orthotopic xenografts. Preliminary studies showed increased accumulation of [11C]VitC in tumor relative to the surrounding brain. This uptake is expected to be increased in the context of ROS generated by radiation therapy.

Conclusions

In conclusion, we have developed a new PET radiotracer, [11C]VitC, that exhibits ROS-dependent cellular accumulation. [11C]VitC and its redox partner [11C]DHA behaved as

anticipated in vitro and in vivo, consistent with their markedly different transport mechanisms. [11C]VitC showed ROS-sensitive accumulation in U87 GBM cells. We hypothesize that the ascorbate recycling mechanism may be used in studying the sequelae of ROS-generating therapies in GBM. Furthermore, as clinical application of high dose VitC in cancer treatment has been known for decades, we anticipate that the radiolabeled PET analogue, [11C]VitC may have rapid clinical translation.

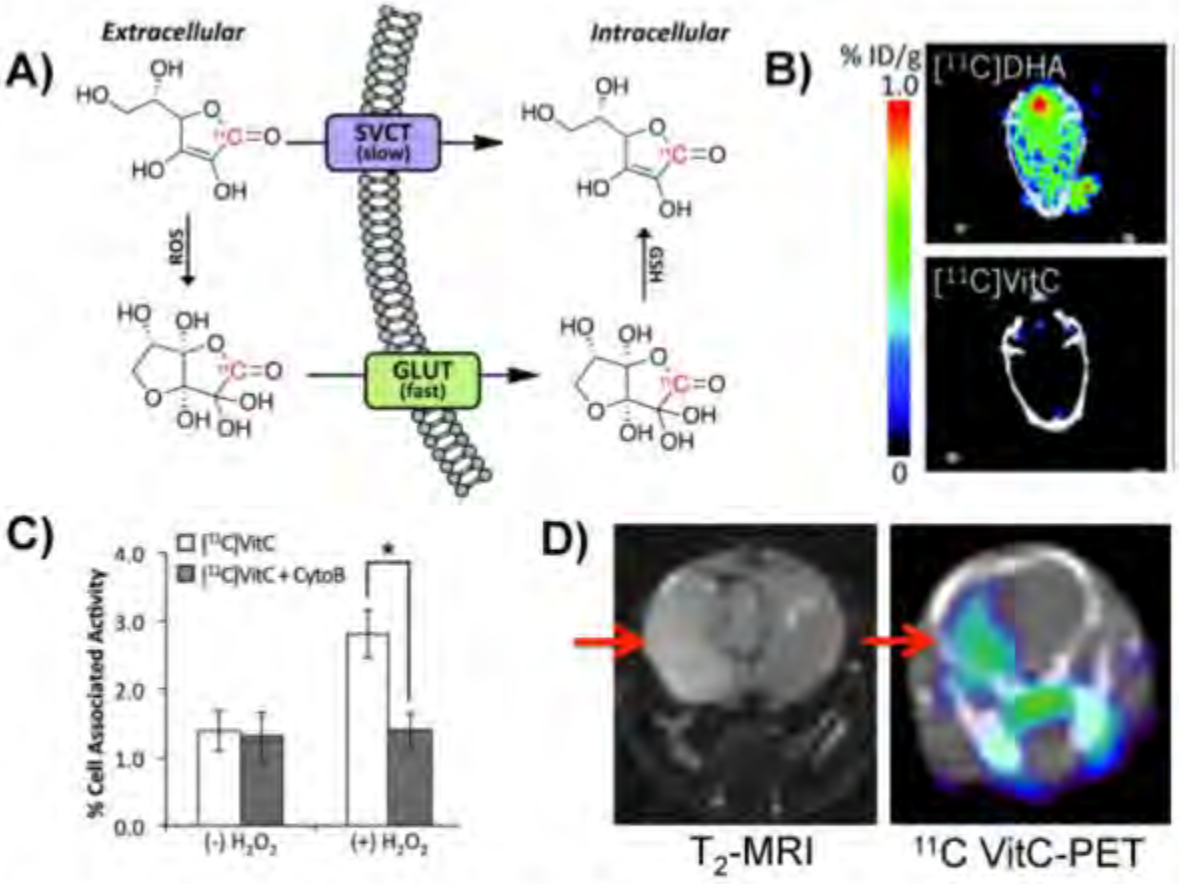


Figure 1. Use of ^{11}C-Vitamin C as an *in vivo* ROS sensor. (A) Ascorbate recycling mechanism, showing ROS-dependent accumulation of the probe (B) Uptake of ^{11}C vitamin C and ^{11}C DHA in the normal rat brain. ROS-generated ^{11}C DHA shows markedly increased uptake. (C) ROS-dependent accumulation of ^{11}C vitamin C in U87 cells *in vitro*. (D) Baseline ^{11}C vitamin C uptake in a U87 orthotopic xenograft.

(Filename: TCT_O-159_Fig_glioma_ASNR.jpg)

O-162

5:32PM - 5:40PM

F-18 FLT PET and MRI as Outcome Predictors in Glioblastomas Following Chemoradiation Therapy

H Nandu[1], M Kijewski[2], S Dubey[2], A Belanger[3], D Reardon[4], P Wen[5], P Mi-Ae[2], S Kesari[6], R Huang[2]
[1]Brigham and Women's Hospital, Brookline, MA, [2]Brigham & Womens Hospital, Boston, MA, [3]Brigham & Women's Hospital, Boston, MA, [4]Center for Neuro Oncology, Dana-Farber Cancer Institute, Boston, MA, [5]Dana Farber Cancer Institute, Boston, MA, [6]Pacific Neuroscience Institute, Santa Monica, CA

Purpose
To evaluate F-18 fluorothymidine (FLT) PET and MRI as pretreatment and post treatment biomarkers predicting progression-free survival (PFS) and overall survival (OS) in patients with glioblastomas, and to discover predictors to improve stratification of patients for treatment.
Materials and Methods
Twelve patients with newly diagnosed glioblastomas who had had biopsy or subtotal resection were enrolled in a prospective clinical trial; they received baseline F-18 FLT PET and brain MRI as well as post-treatment PET and MRI at 4 weeks. Volumetric segmentation of tumor was performed on baseline FLAIR imaging and subsequently applied to T1+gadolinium contrast, T2, apparent diffusion coefficient (ADC), cerebral blood volume (CBV) images of baseline and post-treatment MRI, and to pre and post-treatment FLT-PET images. The 10th, 25th, 75th, and 90th percentile values as well as mean signal intensity within each modality and time point were analyzed individually using the Kaplan-Meir approach to discover the best predictors of OS and PFS.
Results
Several baseline MR parameters (mean and P90 ADC, P25 and P10 FLAIR) were significant predictors of OS (log-rank p = 0.041 ADC; p=0.016 FLAIR). Median survival was 10.07 months for low and 28.17 months for high ADC, and 17.8 months for low and 8.0 months for high FLAIR. Post-treatment ADC (P90 and P75) and normalized PET uptake (mean, P90, and P75) were significant predictors of OS (p=0.037 ADC; p=0.047 PET); median survival was 10.07 months for low and 28.17 months for high ADC, and 28.7 months for low and 10.8 months for high PET uptake.
Conclusions
Volumetric analysis of baseline and post-treatment diffusion MRI predicts progression and survival in patients with high-grade gliomas receiving chemoradiation therapy. Post-treatment F-18 FLT PET also predicts survival.

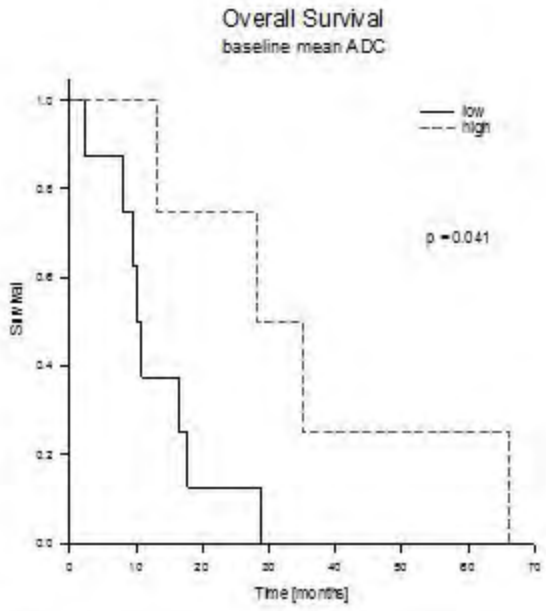


Figure 1:

Kaplan-Meier survival curves for high and low baseline **mean_ADC**; the difference between the curves was significant (log-rank p=0.041).

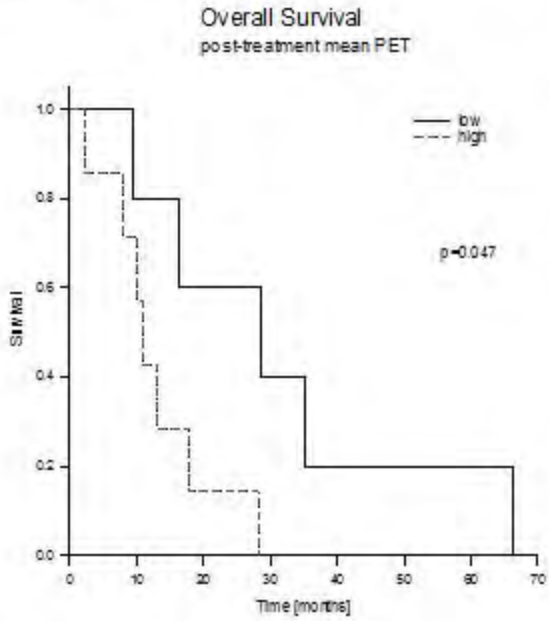


Figure 2:

Kaplan-Meier overall survival curves for high and low post-treatment mean PET uptake; difference of curves was significant (p=0.047).

(Filename: TCT_O-162_Figure1.JPG)

O-163

5:40PM - 5:48PM

18F-FET-PET in the Assessment of Recurrent Glioblastoma receiving Bevacizumab Treatment

E George[1], M Kijewski[1], S Dubey[1], A Belanger[1], D Reardon[2], P Wen[3], S Kesari[4], L Horky[1], P Mi-Ae[1], R Huang[1]

[1]Brigham & Womens Hospital, Boston, MA, [2]Center for Neuro Oncology, Dana-Farber Cancer Institute, Boston, MA, [3]Dana Farber Cancer Institute, Boston, MA, [4]Pacific Neuroscience Institute, Santa Monica, CA

Purpose

Glioblastomas are aggressive primary brain tumors, with a high recurrence rate despite combination therapy of surgery, radiation, and temozolamide. Antiangiogenic therapy with bevacizumab is used increasingly in recurrent glioblastoma (1). Antivascular effects of bevacizumab can be difficult to distinguish from true antitumor effects on contrast-enhanced MRI by conventional criteria (2). The aim of this study is to assess the utility of 18F- flouro-ethyl-tyrosine (FET)-PET in the evaluation of recurrent glioblastoma treated with bevacizumab.

Materials and Methods

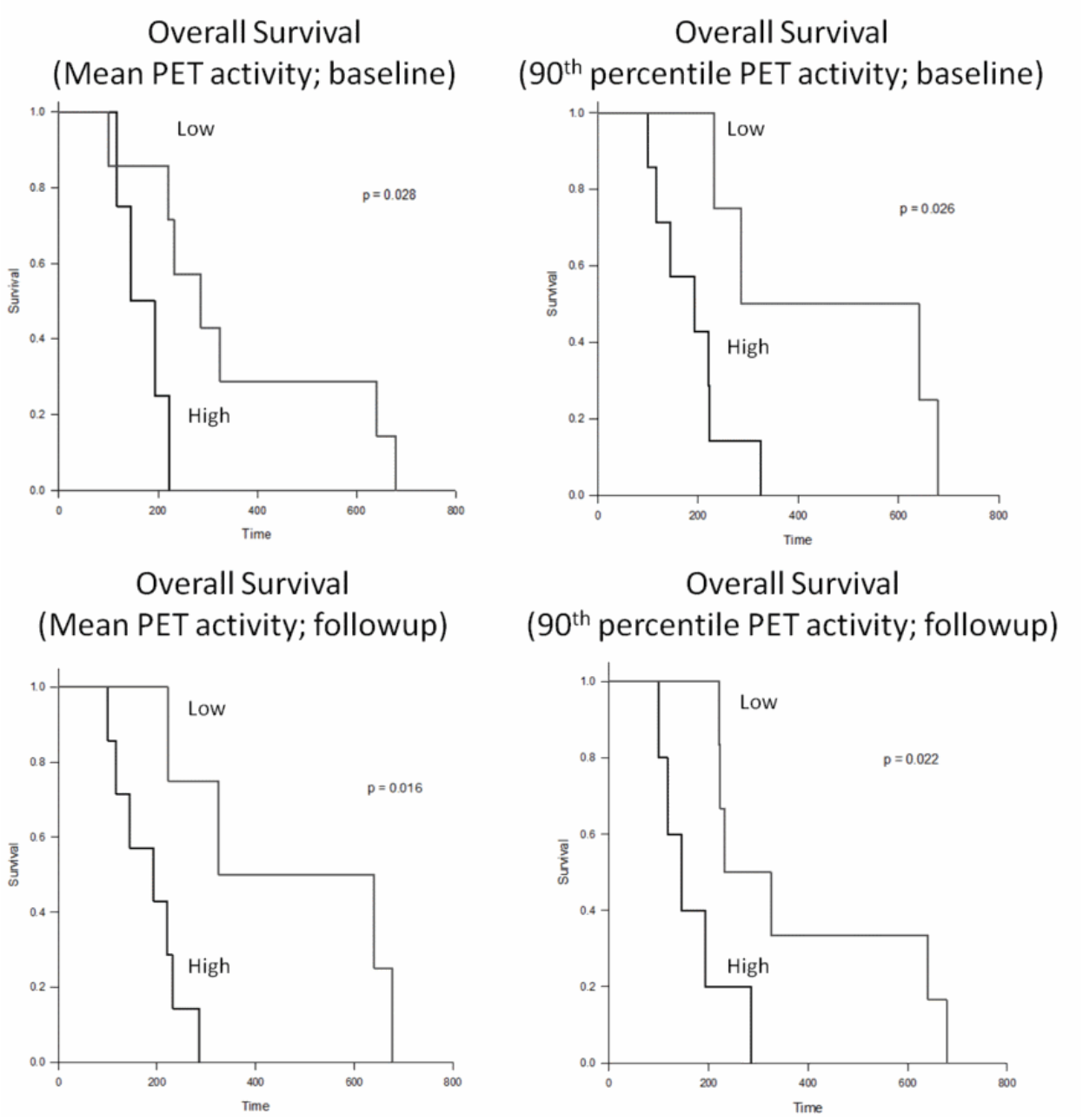
Magnetic resonance imaging (MRI) and FET-PET were performed before and after (range: 3.1-4.7 weeks) the initiation of bevacizumab in patients with recurrent glioblastoma. Volumetric segmentation was performed on pretherapy postcontrast T1-weighted images and subsequently registered to the PET images to calculate FET tracer uptake within enhancing tumor. Mean and 90th percentile FET-PET parameters were calculated and survival analysis was performed for both progression-free survival (PFS) and overall survival (OS) using the Kaplan-Meier approach.

Results

Thirteen patients were enrolled, of which 2 were excluded due to lack of follow-up imaging (mean age: 61.4 years, 64% male). The median PFS and OS after the initiation of bevacizumab therapy were 111 days and 223 days, respectively. Higher baseline FET-PET activity of the tumor was associated with a lower PFS (mean, log-rank p=0.061; 90th percentile, log-rank p=0.085) and OS (mean, log-rank p=0.028; 90th percentile, log-rank p=0.026; Fig. 1). Higher FET-PET activity after ~1 month of bevacizumab also was associated with lower PFS (mean, log-rank p=0.037; 90th percentile, log-rank p=0.113) and OS (mean, log-rank p=0.016; 90th percentile, log-rank p=0.022).

Conclusions

Baseline and follow-up FET-PET activity is associated with progression-free and overall survival in patients with recurrent glioblastoma treated with bevacizumab.



(Filename: TCT_O-163_fig2.gif)

O-164

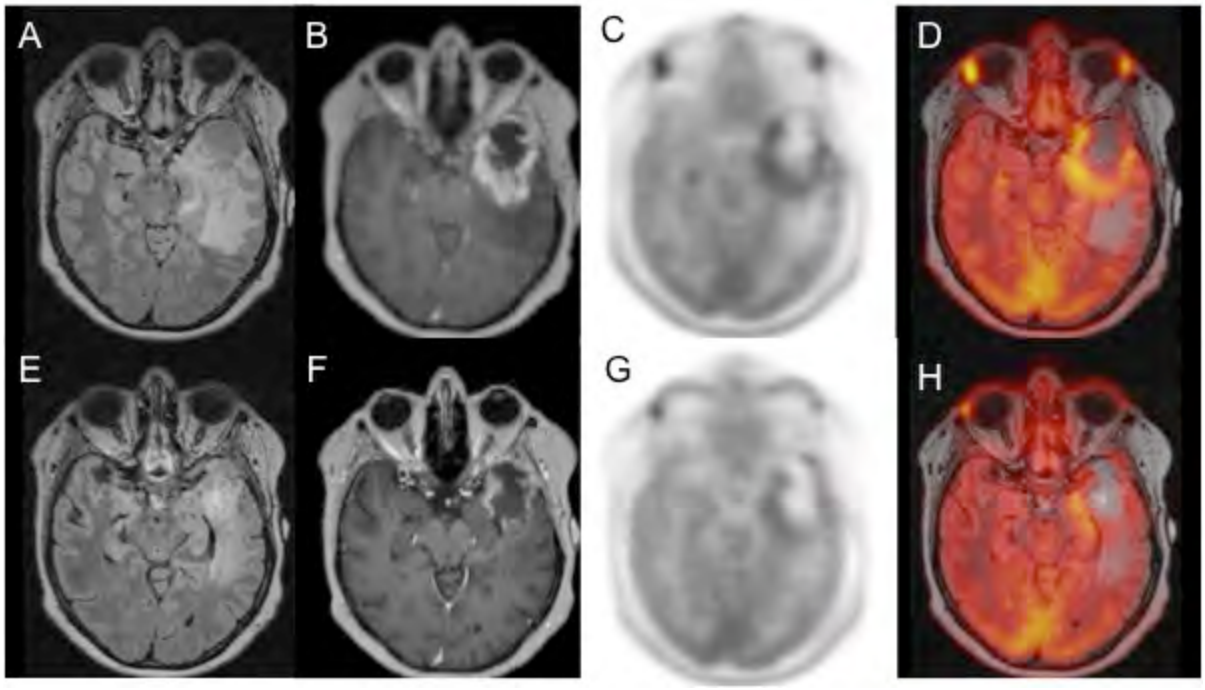
5:48PM - 5:56PM

Response Assessment of Bevacizumab therapy in GBM with integrated 11C-MET-PET/MRI

C Deuschl[1], C Moenninghoff[1], T Poeppel[2], M Forsting[3], L Umutlu[1], K Herrmann[2], J Hense[4], M Schlamann[5]

[1]Institute of Diagnostic and Interventional Radiology and Neuroradiology, Essen, NRW, Germany, [2]Department of Nuclear Medicine, Essen, NRW, Germany, [3]University Hospital Essen, Essen, NRW, Germany, [4]Department of Medical Oncology, West German Cancer Center, Essen, NRW, Germany, [5]Department of Neuroradiology, Giessen, Hessen, Germany

Purpose
Integrated PET/MRI scanners provide simultaneous morphologic and metabolic information with an excellent coregistration in a single hybrid examination, rendering this hybrid imaging modality available for an easy and broad clinical application. The objective of this study was to evaluate the potential of integrated L-[methyl-11C] Methionine (11C-MET) PET/MRI for response assessment of relapsed glioblastoma multiforme (GBM) receiving bevacizumab treatment.
Materials and Methods
Eleven consecutive patients with relapsed GBM were enrolled for an integrated 11C-MET PET/MRI at baseline and at follow up (c1) after start of treatment. Treatment response for MRI was evaluated according to RANO criteria 1 and integrated 11C-MET PET was assessed by T/N ratio, whereas metabolic response was defined by a more than 25% reduction. For further evaluation the results of treatment assessments were related to progression-free survival (PFS) and overall survival (OS).
Results
At time of follow up, MR showed no patient with complete response, 6 of 11 patients with partial response, 4 of 11 patients with stable disease and 1 of 11 patients with progressive disease. Integrated 11C-MET PET revealed metabolic response in 5 of the 6 patients with PR (RANO) (Fig. 1), and in 2 of the 4 patients with SD (RANO). Whereas metabolic nonresponders (defined as T/N ratio reduction 25%) was shown in 1 of the 6 patients with PR (RANO), in 2 of the 4 patients with SD (RANO) and in the 1 patient with PD (RANO). Morphological imaging was predictive for PFS and OS when response was defined as CR, PR, SD and nonresponse as PD (P=0.002 respectively 0.052, log rank). Metabolic imaging was predictive when using T/N ratio reduction of >25 as discriminator (P=0.048 respectively 0.009, log rank). Based on the morphologic and metabolic findings of this study a proposal for applying integrated 11C-MET PET/MRI for treatment response in relapsed GBM was developed, which was significantly predictive for PFS and OS (P=0.010 respectively 0,029, log).
Conclusions
This study demonstrates a high potential of integrated 11C-MET-PET/MRI for response assessment of GBM undergoing antiangiogenic therapy with bevacizumab and the need for a combined assessment of morphologic and metabolic information. The proposal for assessing integrated PET/MRI for treatment response in relapsed GBM needs to be confirmed in larger study cohorts.



(Filename: TCT_O-164_Fig1ASNRAvastin.jpg)

O-165

5:56PM - 6:04PM

Characterization of Glioblastoma Multiforme treated with Bevacizumab using Diffusion Weighted Imaging

F Yu[1], O Rapalino[2]
[1]Massachusetts General Hospital / Athinoula A. Martinos Center for Biomedical Imaging, Boston, MA, [2]Massachusetts General Hosp., Boston, MA

Purpose
Glioblastoma multiforme (GBM) represents the most common primary brain neoplasm in the adult population (Khalifa et al., 2016). Unfortunately, the overall patient survival remains poor with an average life expectancy of approximately 14 months following diagnosis (Chang et al., 2016). Bevacizumab (Avastin®, Genentech) is a monoclonal antibody targeting vascular endothelial growth factor that is FDA-approved for recurrent GBM, and has been shown to increase progression-free survival without increasing overall survival (Nguyen et al., 2016). One potential imaging pitfall during treatment with bevacizumab is that contrast enhancement frequently recedes following its administration, which may lead to an erroneous interpretation of treatment response. This highlights the need for new imaging approaches and techniques in the evaluation of GBM patients treated with this agent. Diffusion-weighted imaging (DWI) has shown promise in tumor imaging, wherein the apparent diffusion coefficient (ADC) can be related inversely to tumor cellularity (Nguyen et al., 2016). However, there are conflicting reports of diffusion restriction seen in

bevacizumab-treated GBM, wherein it may represent either hypercellular tumor or areas of necrosis. The purpose of this study is to review our experience with bevacizumab-treated GBM and the corresponding findings on diffusion-weighted imaging.

Materials and Methods

Approval was obtained from the institutional review board at Massachusetts General Hospital for this retrospective case series. Inclusion criteria included history of pathology-proven GBM, treatment with bevacizumab, and pathology during or after bevacizumab therapy. Exclusion criteria included presence of a CNS tumor other than GBM (i.e. lower grade gliomas, CNS lymphoma, etc). To date, 5 patients with pathological sampling of areas of restricted diffusion following treatment with bevacizumab have been reviewed. Treatment records, pathology reports/slides, and MR images were reviewed.

Results

Five cases with pathological sampling of areas of restricted diffusion during treatment with bevacizumab were obtained, including 4 autopsy cases and 1 patient who had a stereotactic biopsy. Two of these cases demonstrated extensive tumoral infiltration producing abnormal diffusivity. One case had a combination of tumor cells and superimposed post-treatment changes. The 2 remaining cases (including the stereotactic biopsy case in the Figure) had post-treatment changes with extensive areas of necrosis (with minimal viable cells in the periventricular regions in 1 of them).

Conclusions

Our preliminary results highlight the challenges that neuroradiologists face in the interpretation of diffusion abnormalities during antiangiogenic treatment of glioblastoma patients. The literature also has conflicting reports about the nature of these diffusion abnormalities and more research is needed in the identification of imaging markers (e.g. MR spectroscopy or other diffusion metrics) that can differentiate the presence of hypercellular tumor and post-treatment changes. Summary: Areas of abnormal restricted diffusion during antiangiogenic treatment with bevacizumab can represent progressive hypercellular tumor and/or post-treatment changes, and more accurate imaging markers are needed for this differentiation.

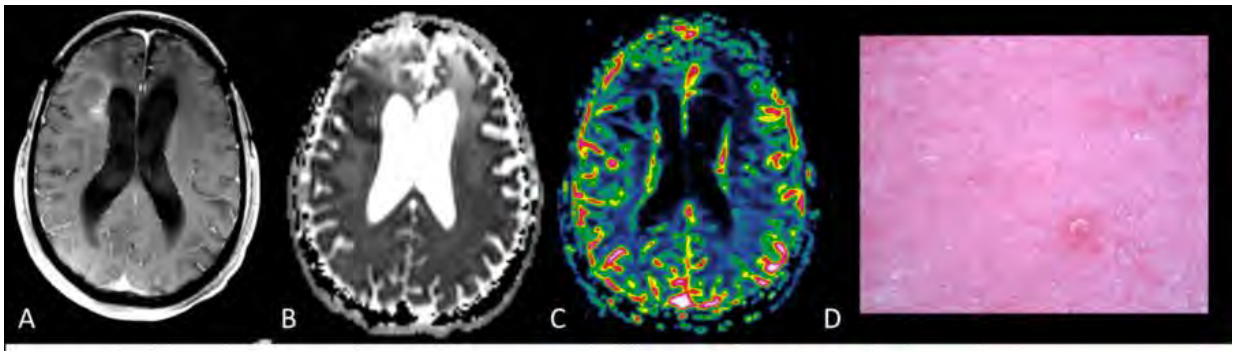


Figure: Ill-defined areas of abnormal restricted diffusion (B) in the right frontal white matter with associated peripheral ill-defined enhancement (A) in a patient with a Glioblastoma with oligodendroglial features, 1p-19q co-deleted, IDH1 (R132H) mutated, KRAS (G12A) mutated, MGMT methylated. The patient has been treated with Bevacizumab for 9 weeks. MR perfusion shows a predominance of relatively low rCBV values within the lesion (C). A stereotactic biopsy of these areas of restricted diffusion demonstrates extensive bland necrosis (D).

(Filename: TCT_O-165_GBM_figure.jpg)

O-166

6:04PM - 6:12PM

Monitoring Cerebral Perfusion in Patients with Glioma Using Arterial Spin Labeling as an Aid in Differentiating Progressive Disease versus Treatment Effect

S Fung[1], C Liang[2], P New[1]
[1]Houston Methodist Hospital, Houston, TX, [2]George Washington University Hospital, Washington, DC

Purpose
Evaluation of patients with high-grade glioma undergoing treatment continues to be a challenge. These tumors are highly vascular with altered endothelium. Treatment with radiation therapy and chemotherapy affects the microvascular environment, resulting in changes in blood-brain barrier permeability, which can confound assessment of response to therapy based on measuring the contrast-enhancing component of the tumor. We hypothesize that cerebral blood flow (CBF) measured using arterial spin labeling (ASL) can provide supplemental information in stratifying risk of progressive disease (PD) given changes seen on routine MRI.
Materials and Methods
Thirteen patients (ages 24-63, M:F 7/6) with glioma (7 glioblastoma, 2 anaplastic astrocytoma, 2 oligodendroglioma, 1 diffuse astrocytoma, 1 optic nerve glioma) were followed during their treatment using serial brain MRIs with ASL. All brain MRIs were performed with 3.0T clinical scanner using an 8-channel head coil. Standard MRI sequences included DWI, T2 FSE, T2 FLAIR, GRE, pre and postcontrast T1 FSE obtained before and after intravenous administration of 0.1 mmol/kg gadopentetate dimeglumine. Additionally,

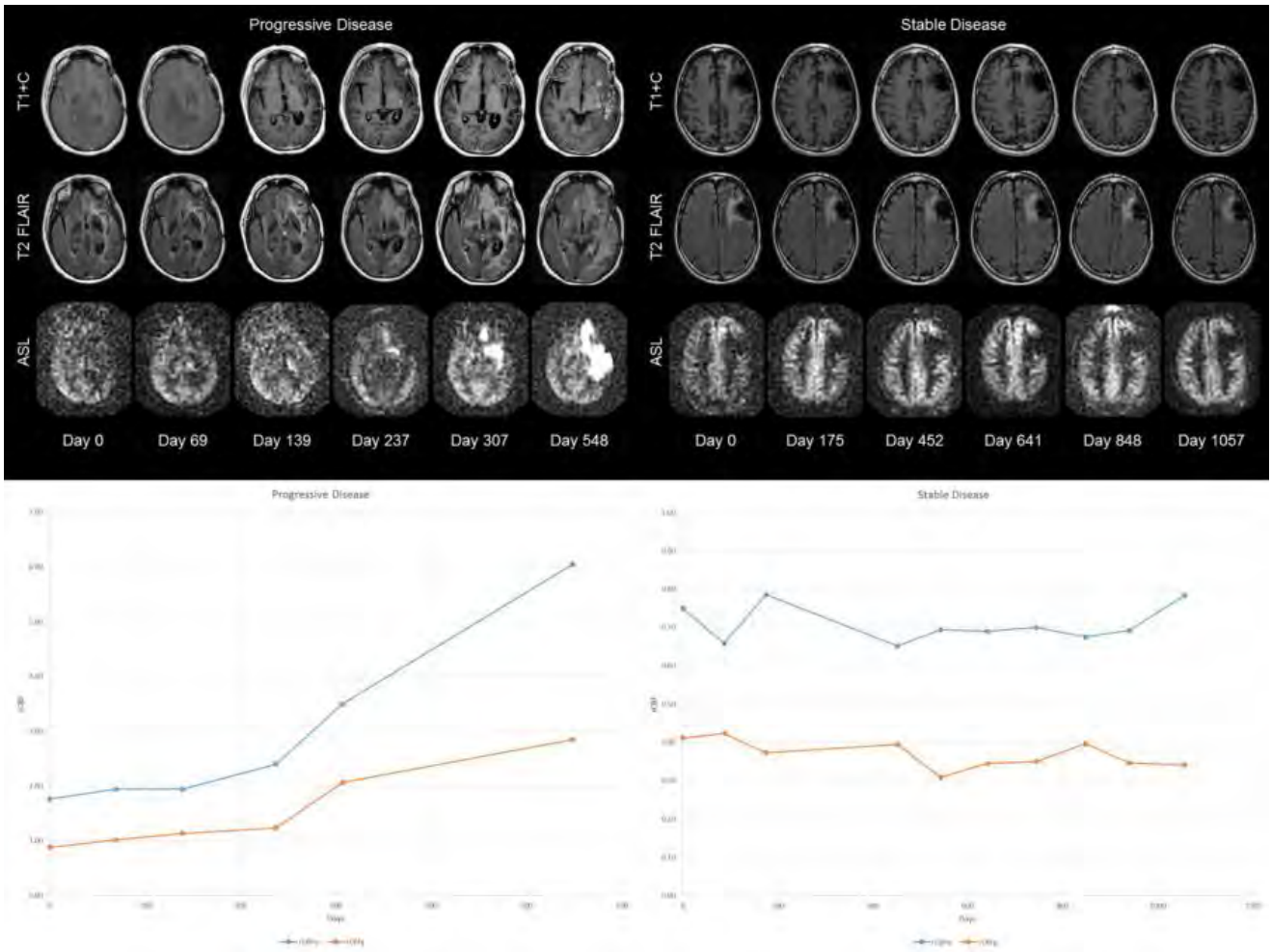
CBF (ml/100g/min) was estimated using pseudocontinuous ASL (pCASL). Evaluation of ASL was performed by visual inspection of color and grayscale cerebral blood flow (CBF) maps as well as placement of standard 1x1 cm2 regions of interest (ROI) to measure max CBF over (1) regions of focally increased CBF irrespective of enhancement, (2) regions of enhancement if no focally increased CBF, and (3) regions of confluent T2-prolongation if nonenhancing and no focally increased CBF. Max CBF of the contralateral gray matter (GM) and white matter (WM) were obtained, and relative CBF was computed, defined as rCBFw = (max CBF of ROI/max CBF of contralateral WM) and rCBFg = (max CBF of ROI/max CBF of contralateral GM).

Results

Low-grade gliomas and treatment effects involving WM generally presented with bland regions of very low CBF, and these regions with rCBFg < rCBFw < 1 were considered as low risk of PD, even though 3/13 patients had some contrast enhancement. Low-grade gliomas and treatment effects involving GM also had relatively low CBF but not as low as that of surrounding WM, and these regions with rCBFg < 1 < rCBFw were considered as intermediate risk since these areas are inherently more difficult to follow given higher background cerebral perfusion. Increasing CBF correlated with tumor progression and at times antedated changes seen on contrast-enhanced T1 or T2 FLAIR images. Regions of focally increased CBF with rCBFw > rCBFg > 1, often surrounded by a halo of relatively decreased CBF, was observed in 5/13 patients and signaled poor prognosis and rapid progression. One patient with oligodendroglioma had focally elevated CBF but stable disease on standard MRI and confirmed by resection, thought probably hyperperfusion from nonconvulsive status epilepticus.

Conclusions

Addition of ASL to routine brain MRI provides supplementary information that is helpful in the evaluation of patients with glioma undergoing treatment. Serial measurements indicating increasing CBF generally portends tumor progression and at times antedates changes seen on standard MRI. Risk of PD is considered low if rCBFg < rCBFw < 1, intermediate if rCBFg < 1 < rCBFw, and high if rCBFw > rCBFg > 1.



(Filename: TCT_O-166_AbstractFigure.jpg)

O-167

6:12PM - 6:20PM

Normalization of ADC does not improve correlation with overall survival in patients with high-grade glioma (HGG)

A Li[1], L Qin[2], A Bryant[2], K Leung[3], G Young[4]
[1]Brigham and Women's Hospital, Boston, MA, [2]Dana-Farber Cancer Institute, Boston, MA, [3]Massachusetts Eye and Ear Infirmary, Boston, MA, [4]Brigham and Women's Hospital, Boston, MA

Purpose
Mixed reports in the literature leave uncertainty whether ADC normalization is necessary in diffusion imaging of high-grade glioma (HGG) patients (1-4). To address this, we assess whether normalization improves the previously reported correlation of resection margin ADC with 15-month overall survival (OS) in HGG patients (5).

Materials and Methods

Magnetic resonance imaging (MRI) from 37 adult patients with newly diagnosed HGG status postmaximal surgical resection, including glioblastoma multiforme (n=25) and anaplastic astrocytoma (n=12), were retrieved retrospectively. Apparent diffusion coefficient (ADC) maps were generated using the FSL DTIFIT tool (Oxford Centre for Functional MRI of the Brain) from axial spin-echo echo-planar (SE-EPI) DWI acquired on immediate postresection, preradiation therapy MRI. Images were acquired on 1.5T and 3T MRI systems from 2 vendors (Siemens Healthcare and GE Medical Systems). Apparent diffusion coefficient analysis was performed independently by 3 neuroradiologists. Regions of interest (ROI) were selected manually in both normal-appearing white matter (NAWM) and in nonenhancing tumor within 2cm of the resection margin or margin of residual enhancing tumor (5). Normalized ADC (nADC) was calculated as the ratio between the mean of tumor ROI and NAWM ROI. Intraclass correlation coefficient (ICC) and coefficient of variation (CV) were used to compare absolute and normalized ADC among the 3 readers. A receiver operating characteristics (ROC) curve was calculated to correlate ADC and nADC with OS. A $p<0.05$ was considered to be statistically significant.

Results

Table 1 demonstrates CV and ICC among the 3 readers were similar for absolute and normalized ADC. Figure 1 illustrates the mean ADC and nADC of patients subgrouped by 15 months OS. Table 2 provides the summary statistics for the correlation between ADC and nADC with 15-month OS. A ROC analysis shows that the nADC correlation with OS is not significantly better than absolute ADC correlation with OS.

Conclusions

Normalization of ADC does not significantly improve correlation between absolute ADC and OS in HGG, suggesting that this is not necessary for clinical or research ADC analysis in HGG patients.

Table 1. Coefficient of Variation (CV) and Intraclass correlation coefficient (ICC) among three readers for absolute ADC ($\times 10^{-3}mm^2/s$), nADC, and NAWM ADC($\times 10^{-3}mm^2/s$)				
	Mean	**Std Dev**	**CV%**	**ICC**
ADC	1.15	0.25	13.5	*0.60*
NAWM ADC	0.76	0.05	3.8	*0.61*
nADC	1.53	0.35	14.0	*0.62*

Table 2. Receiver Operating Characteristics (ROC) curve correlating ADC with 15-month overall survival.			
	ROC AUC	**Std Err**	***p*-value**
Reader1 ADC	0.8794	0.0647	<0.0001
Reader2 ADC	0.8441	0.0708	<0.0001
Reader3 ADC	0.6588	0.0920	0.0844
Mean ADC	0.8206	0.0738	<0.0001
Reader1 nADC	0.8618	0.0690	<0.0001
Reader2 nADC	0.8353	0.0683	<0.0001
Reader3 nADC	0.6235	0.0949	0.1933
Mean nADC	0.7882	0.0781	0.0002
AUC = area under the curve			

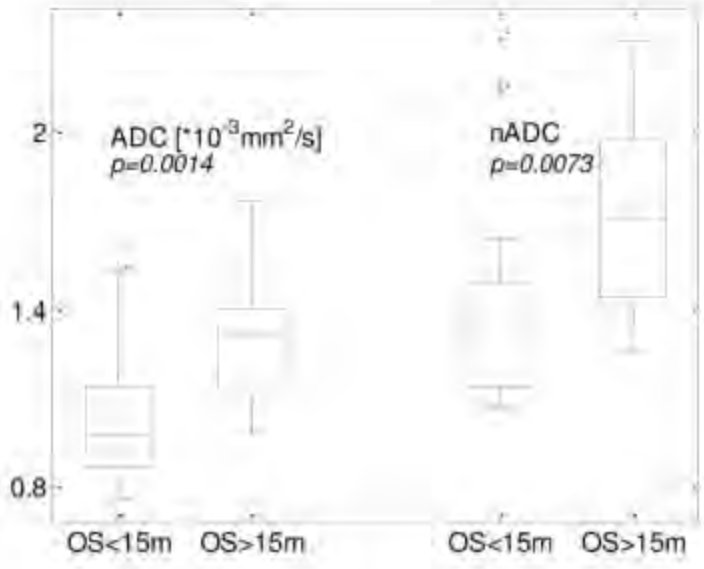


Figure 1. The mean ADC and nADC of patients subgrouped by 15 months OS. T-test shows significant difference between the two groups for both ADC and nADC.

(Filename: TCT_O-167_ASNRimages-001.jpg)

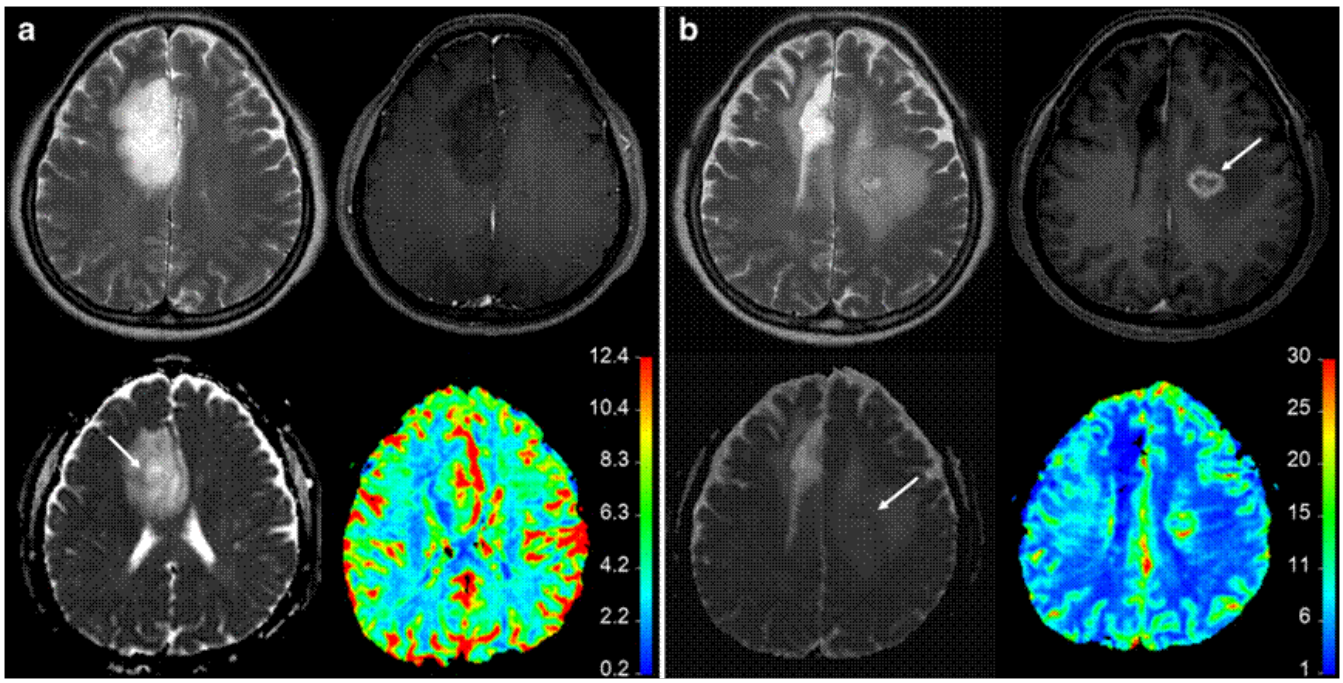
O-168

6:20PM - 6:28PM

Prognostic Relevance of Gemistocytic Grade II Astrocytoma: Gemistocytic Component and MR Imaging Features Compared to Non-Gemistocytic Grade II Astrocytoma

Y Heo[1], J Park[2], H Kim[3], S Kim[2]
[1]Busan Paik Hospital, Inje University, Busan, Korea, Republic of, [2]University of Ulsan College of Medicine, Asan Medical Center, Seoul, -, [3]University of Ulsan College of Medicine, Asan Medical Center, Seoul, NY

Purpose
To determine if gemistocytic grade II astrocytoma (GemA) and its MR imaging characteristics are associated with a shorter time-to-progression (TTP) compared with nongemistocytic grade II astrocytoma (non-GemA).
Materials and Methods
We enrolled 78 patients who were followed up more than 5 years (29 pathologically proven GemA and 49 non-GemA) during a 10-year period. Contrast-enhanced T1-weighted, diffusion-weighted imaging (DWI), dynamic susceptibility contrast (DSC), and MR spectroscopy (MRS) and clinical data were reviewed retrospectively. Clinical and MR imaging features were analyzed as possible prognostic factors of high-grade transformation, and multivariate analysis of TTP was performed using Cox proportional modeling.
Results
GemA showed more frequent high-grade features than non-GemA, including diffusion restriction ($P < .001$), increased choline/creatine ($P = .02$), and increased choline/ NAA ratio ($P = .015$). Patients with GemA had a significantly shorter median TTP (53.1 vs 68 months; $P < .001$). A gemistocytic histopathology (hazard ratio = 3.42; $P = .015$) and low ADC (hazard ratio = 3.61; $P = .001$) were independently associated with a shorter TTP.
Conclusions
GemA can present with MR imaging findings mimicking high-grade glioma at initial diagnosis and transforms to high-grade disease earlier than non-GemA. Low ADC on DWI might be useful in stratifying the risk of progression in patients with grade II astrocytoma.



(Filename: TCT_O-168_GA.gif)

Wednesday
11:00AM - 12:20PM
Long Beach Convention Center, Grand Ballroom (Upper Level)

18A-Parallel Paper Session: Head and Neck Imaging – Can You Hear Me Now?

O-421

11:00AM - 12:20PM

A New Radiological Tool for Diagnosis of Pseudotumor Cerebri (PTC) on Routine Brain CT Study

T Bartsikhovsky[1], T Sigal[2], M Vaiman[3], T Ziv-Baran[4], P Gottlieb[3], I Bekerman[5]
[1]Assaf Harofeh Medical Center, Ramat Gan, Israel, [2]Assaf Harofeh Medical Center, Zerifin, Zerifin, [3]Assaf Harofeh Medical Center, Zrifin, Zrifin, [4]Tel Aviv University, Tel aviv, Tel aviv, [5]Assaf Harofeh Medical Center, Tzrifin, Tzrifin

Purpose
Our purpose was to evaluate the optic nerve sheath diameter (ONSD) to eyeball transverse diameter (ETD) index as a diagnostic sign on brain CT study in cases of PTC.
Materials and Methods
In a retrospective study CT scan data of 20 adult patients diagnosed with PTC were collected and analyzed. As control group we used patients who were referred to brain CT study for symptoms unrelated to elevated ICP and had a negative scan. Computed tomography scans were obtained by the 256-channel CT scanner with initial single slice section of 3mm. All

measurements were held manually on a "spine" window (WW 60, WL 360). Optic nerve sheath diameter was measured on axial images at the point where the ophthalmic artery crosses the optic nerve. Coronal images were used as reference. The ETD was measured from retina to retina on a slice where lens maximal width was identified.
Results
A total of 103 patients were included. Study group population included 20 patients (2 men, 18 women, mean age 32.3 years). Control group included 83 patients (32 men, 51 women, mean age 65 years). There was no significant difference in index value between left and right sides. We found that median and IQR values of ONSD/ETD index in control group (0.2, IQR = 0.18-0.21) was significantly smaller than in study group (0.27, IQR = 0.23-0.29) ($p<0.001$). A strong female predominance in group of PTC patients was observed (90% compared to 61% in control group, $p=0.0015$). The ONSD/ETD index has an excellent discrimination ability between patients with and without PTC with AUC of 0.93. The raised index values were bilateral. No correlation with age was found ($r=-0.132$, $p=0.184$). The ONSD/ETD index of 0.24 is 74% sensitive and 90% specific for elevated ICP in patient with PTC.
Conclusions
In patients with PTC the ONSD/ETD index is significantly enlarged and can be the only sign of elevated ICP on brain CT scan. Implementing this method as a diagnostic tool in cases of suspected PTC may help in early accurate diagnosis, avoiding misdiagnosis and providing appropriate early treatment.

O-169

11:00AM - 11:08AM

Imaging of Tinnitus and Sensorineural Hearing Loss: Less May Be More

A Copelan[1], R Petrossian[2], K Tech[3], R Silbergleit[4], A Wang[1], K Barry[5], C Kazmierczak[4], A Krishnan[6], S Noujaim[4], S Patel[7], J Wilseck[8], J Mick[9], J Wong[1]
[1]Beaumont Health System, Royal Oak, MI, [2]Oakland University William Beaumont School of Medicine, Rochester, MI, [3]Beaumont Health - Royal Oak, Royal Oak, MI, [4]William Beaumont Hospital, Royal Oak, MI, [5]Beaumont Heatlh System, Royal Oak, MI, [6]Beaumont Health, Royal Oak, Royal oak, MI, [7]Beaumont Hospital, royal oak, MI, [8]Beaumont Hospital, Royal Oak, MI, [9]Beaumont Health Sysyem, Royal Oak, MI

Purpose
In the current era of healthcare reform, cost-effective medicine is at the forefront, and in particular, avoidance of over-utilization of medical imaging. We aimed to evaluate the diagnostic accuracy of utilizing a single noncontrast axial CISS sequence for the detection of vestibular schwannomas in patients presenting with sensorineural hearing loss (SNHL) or tinnitus.

Materials and Methods
This single center study included 102 patients (36 with and 66 without vestibular schwannomas) who underwent MRI brain and IAC with gadolinium protocol, considered the gold standard for IAC lesion detection, between March 2012 and August 2015 for SNHL or tinnitus. Ten board-certified neuroradiologists, blinded to both the proportional makeup of positive versus negative pathology as well as the original radiology reports, prospectively evaluated the axial CISS sequence only from the original comprehensive examinations, which was transferred into a dedicated teaching file. Accuracy, sensitivity and specificity were assessed.
Results
The average maximum lesion dimension was 11.7 mm (range, 1.5 - 28 mm) and 21 lesions demonstrated a maximum dimension of ≤10 mm. Among the ten neuroradiologists who reviewed the CISS sequence only, the overall mean accuracy, sensitivity, and specificity were 96.7%, 93.5%, and 98.7%, respectively.
Conclusions
In patients presenting with SNHL or tinnitus, screening noncontrast MR imaging using a single axial CISS sequence can detect vestibular schwannomas with accuracy and with a high degree of sensitivity and specificity. This approach is likely more cost-effective in comparison to the current approach with a comprehensive MRI brain and IAC with and without gadolinium protocol. The authors currently are performing a cost-analysis based on scanner utilization time and reimbursement rates by the Centers for Medicare and Medicaid Services.

O-170

11:08AM - 11:16AM

MRI screening of the internal auditory canal: is gadolinium necessary to detect intrabyrinthine schwannomas?

J Valesano[1], C Carr[1], L Eckel[1], J Lane[1]
[1]*Mayo Clinic, Rochester, MN*

Purpose
Noncontrast MRI of the internal auditory canals (IAC) using high resolution 3D T2WI has been proposed as the primary screening study in patients with asymmetric sensorineural hearing loss. However, concerns have been raised that noncontrast MRI may not detect labyrinthine pathology, specifically intralabyrinthine schwannomas (ILS). The purpose of this study was to determine if noncontrast T2WI alone are adequate to exclude these rare intralabyrinthine tumors compared to the "gold standard" postcontrast sequences.
Materials and Methods
From 2006 to 2015, 31 patients with ILSs detected on contrast-enhanced MR screening examinations were included in this retrospective review. Thirty-six negative examinations

performed during the same time period were selected randomly as controls. Only the T2WI, with MPR and MIP reconstructions, were reviewed retrospectively by 3 blinded neuroradiologists. When an ILS was identified, its laterality, location and greatest axial dimension were recorded. Sensitivity, specificity, and accuracy were calculated using the postcontrast T1WI as the "gold standard". Interobserver agreement was calculated using Fleiss' kappa. After the initial review, a consensus review of all cases with discordant results was conducted.
Results
The sensitivity, specificity, and accuracy were 1.0, 1.0, and 1.0 for observer 1; 0.84, 1.0, and 0.96 for observer 2; 0.90, 1.0, and 0.98 for observer 3. The kappa statistic for interobserver agreement was 0.93. The 5 unique ILSs with discordant results were all identified correctly upon consensus review. All discordant results involved intracochlear lesions. Eighteen of the ILSs were intracochlear, 5 were vestibulocochlear, 3 were intravestibular, 2 were transmodiolar, 2 were transmacular and 1 was transotic in location. The median size of the ILSs was 4.4mm (standard deviation 2.9mm).
Conclusions
This study demonstrates that noncontrast T2WI alone can detect ILSs with up to 100% sensitivity. These results lend support to the contention that noncontrast IAC screening examinations are sufficient to detect intracanalicular as well as intralabyrinthine schwannomas.

O-171

11:16AM - 11:24AM

Diagnostic Utility of Compressed Sensing SPACE for IAC MRI Screening Protocols

M Yuhasz[1], M Hoch[1], M Bruno[1], M Hagiwara[1], E Raithel[2], A Anwar[1], T Roland[1], T Shepherd[1]
[1]NYU Langone Medical Center, New York, NY, [2]Siemens Healthcare, Erlangen, Germany

Purpose
Compressed sensing (CS) reconstruction allows sub-Nyquist sampling of k-space to reduce scan times. This study compared the diagnostic sensitivity and accuracy of T2 SPACE with and without CS for screening MRI examinations in adults with sensorineural hearing loss.
Materials and Methods
With IRB approval, 72 subjects (37 male, 51.4±16.4 years, enriched with 20 positive cases, 12 cases duplicated for intrarater assessment) had 3-T contrast MRI with T2 SPACE (3D TSE) (acquisition time 4:10, TE: 134ms; TR 1000ms, 0.47 x 0.47 x 0.47 mm^3) both with CS (prototype sequence; 4x undersampling, regularization = 0.005, acquisition time = 50 sec) and without CS. Unilateral, multiplanar reconstructions were reviewed in independent, blinded fashion by 3 neuroradiologists. Reviewers indicated if lesion was present. Visualization of clinically relevant structures was rated between 1 ("poor") and 5

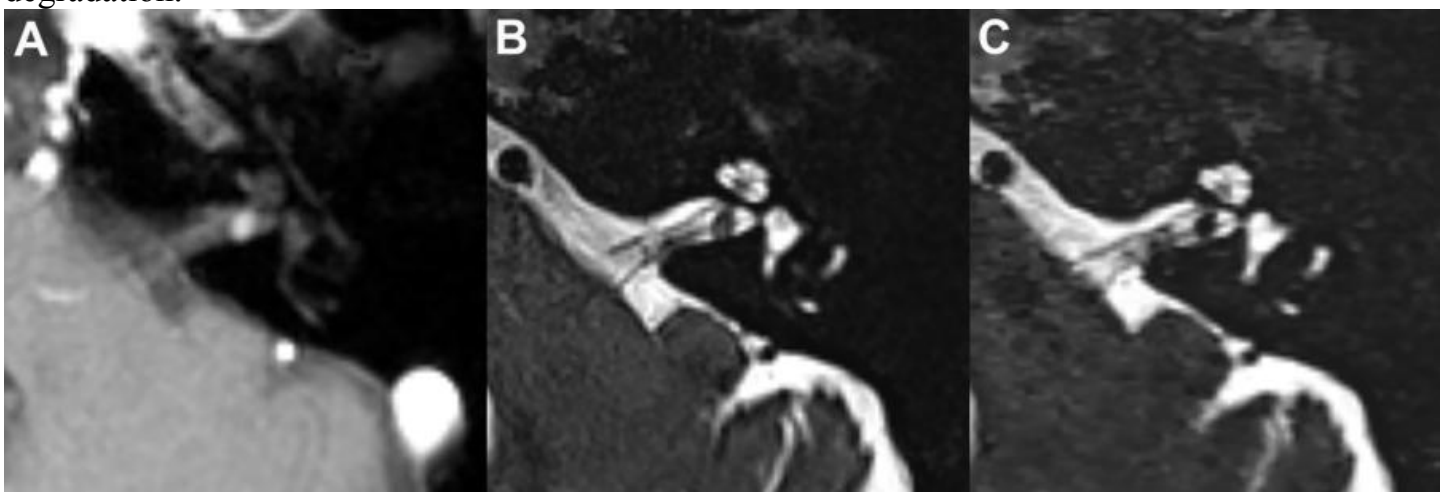
("excellent"). McNemar, Wilcoxon and Mann-Whitney statistical tests characterized accuracy, equivalence and reliability.

Results

Compressed sensing SPACE acquisitions for sensorineural hearing loss screening protocols reduced scan time by 80%. Radiologists visually preferred conventional T2 SPACE with global score of 4.4 vs 3.6 for CS ($P<0.001$). Similar small decreases for visualization of individual structures were reported for CS, however 95% of CS SPACE sequences were rated noninferior using "3" or greater as cutoff score. CS SPACE had less perceived motion degradation compared to 2 of 3 raters ($P<0.03$). Raters' accuracy and specificity were high (97-100% and 90-100%, respectively) for lesion detection using only noncontrast CS SPACE. Inter-rater reliability for lesion detection was high (kappa 0.96). Lesion measurements did not differ between sequences (12.8±7.1 mm), and differences in measurement between sequences did not significantly differ between radiologists (1.14±1.10mm, 0.80±0.78mm, 1.12±1.15mm).

Conclusions

Compressed sensing can accelerate T2 SPACE imaging in screening IAC MRI protocols by 80% while preserving adequate diagnostic image quality. Radiologists found the images slightly less satisfying, but rated them diagnostically acceptable with less motion degradation.



(Filename: TCT_O-171_Figure_1-labels.jpg)

O-172

11:24AM - 11:32AM

Correlation of Quantitative Analysis on FLAIR and enhanced FLAIR with Auditory Test in Sudden Hearing Loss

E Kim[1]

[1]*Hallym University College of Medicine, Anyang, Kyungki-do*

Purpose
Visualization of Meniere's disease has been reported using magnetic resonance imaging (MRI), especially 3D-FLAIR and enhanced FLAIR. The study was to assess the prognostic value of quantitative analyses of region of interest (ROI) magnetic resonance (MR) imaging data, relating with degree of hearing decrease in patients with sudden hearing loss and vertigo.
Materials and Methods
Four hundred and thirty-six patients underwent 3 Tesla (3T) MRI of the temporal area for possible inner or IAC pathology over 3-year period. Three-dimensional-fluid attenuated inversion recovery (3D-FLAIR) sequence imaging and enhanced 3D-FLAIR were included on temporal MRI. Signal intensity (SI) was measured at ROIs in membranous labyrinth of cochlea and quantitatively analyzed. Measured ROI value was compared with available clinical findings, speech audiometry and pure tone audiometry test (PTA). Patients had typical results of auditory testing for Meniere's disease.
Results
Eighty-eight (20.2%) patients were assessed to have sudden unilateral sensory neural hearing loss and tinnitus and take temporal MRI including FLAIR/ enhanced FLAIR within 7 days. There was statistical significance of SI increase of cochlea on FLAIR and enhanced FLAIR with severity of hearing loss ($P < .0001$). The cut off value of SI increase on FLAIR was 20.8 (sensitivity, 64%; specificity, 66%; AUC, 72.9%) and on enhanced FLAIR was 30.4 (sensitivity, 66%; specificity, 68%; AUC, 72.8%) between normal ear and affected ear. There was no statistical significance between prognosis and cochlear SI of FLAIR and enhanced FLAIR.
Conclusions
Quantitative analysis of ROI MR imaging data does not confer a benefit to predict the prognosis of hearing disturbance in Meniere's disease. Increase of signal intensity and inner ear enhancement of 3D FLAIR may be a helpful diagnostic adjunct for Meniere's disease. This may be particularly helpful when the enhanced T1WI are equivocal.

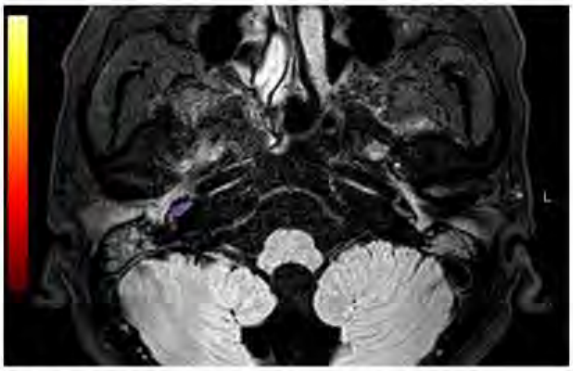


Fig 1: Signal intensity measurement on 3D FLAIR MR imaging. Measurement of signal intensity was performed by drawing a seed growing ROI at middle and basal turn of cochlea at bilateral membranous labyrinths (affected and normal ear). Area: 19.65, Mean: 22.3, SDve: 10.1

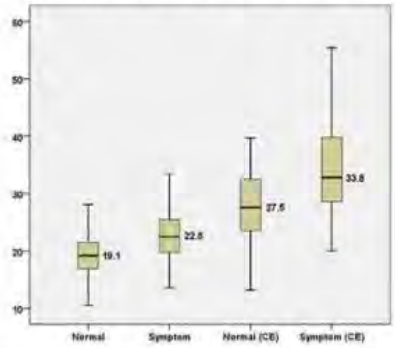


Fig 2: Box plots showing the signal intensity value for normal and symptomatic ear.

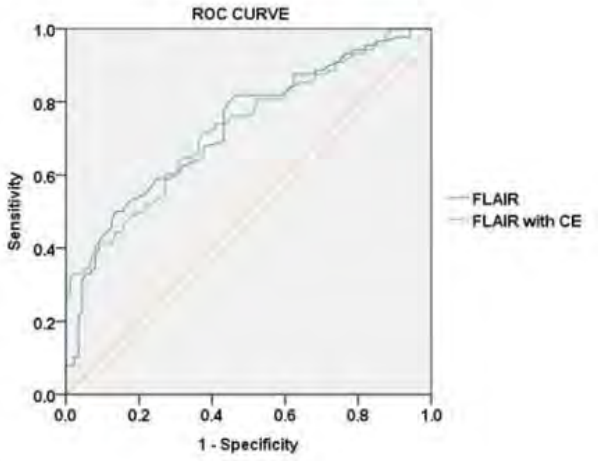


Fig 3: Receiver operating characteristic curve (ROC) for signal intensity of FLAIR and enhanced FLAIR, comparing normal ear to symptomatic ear with sudden sensorineural hearing loss. This curve demonstrates high discriminatory power of increased signal for sudden sensorineural hearing loss. The cut off value of SI increase on FLAIR > 20.8 was 64% sensitivity, 66% specificity, 72.9% AUC and on enhanced FLAIR > 30.4 was 66% sensitivity, 68% specificity, 72.8% AUC for sudden sensorineural hearing loss between normal ear and affected ear.

(Filename: TCT_O-172_2016-12-05TableFigure.jpg)

O-175

11:48AM - 11:56AM

Evaluation of the Cochlear R2 angle and Depth on 3D T2 Weighted Images of the Temporal Bone in Children without Sensorineural Hearing Loss: A Potential Tool for the Diagnosis of Scala Communis

T Booth[1], C Wick[2], J Kutz[2], R Clarke[1], Y Xi[2], M Medina[2], B Isaacson[2]
[1]Children's Health Dallas, UT Southwestern Medical Center, Dallas, TX, [2]UT Southwestern Medical Center, Dallas, TX

Purpose
Scala communis is a developmental abnormality of the cochlea characterized by deficiency of the partition separating the cochlear turns (interscalar septum), which may be isolated or associated with other anomalies of the inner ear. Histopathology, CT and MRI have demonstrated a deficient R2 interscalar septum and or absent or shallow lateral notch between the middle and basal turns of the cochlea. The objective of this study is to evaluate

the size of the R2 depth and angle in cochlea of ears without sensorineural hearing loss (SNHL) on 3D T2-weighted images.

Materials and Methods

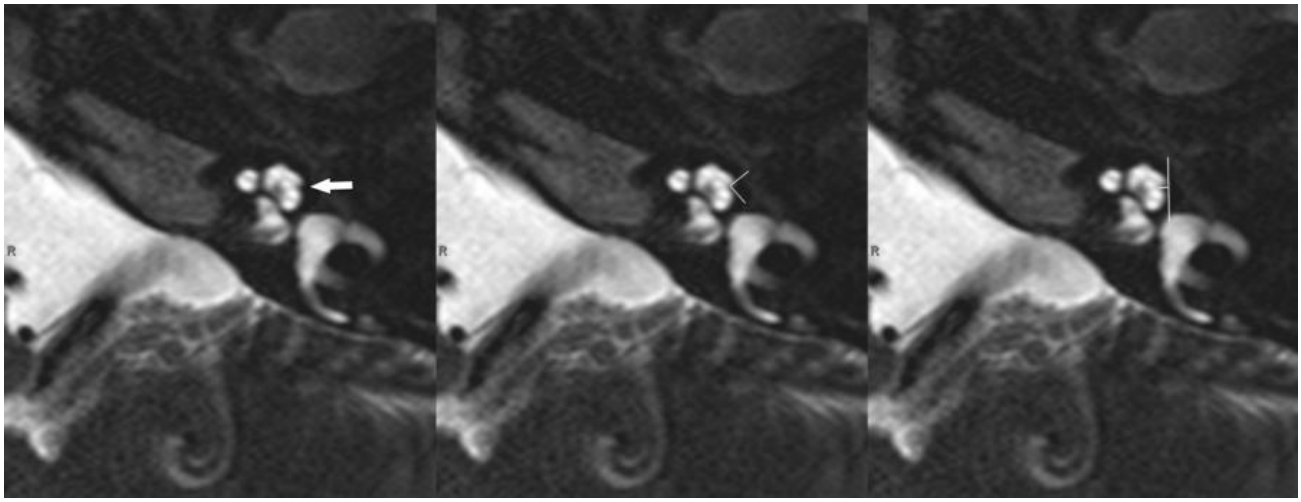
Inclusion criteria included a diagnostic axial 3D T2-weighted sequence through the temporal bone, which was obtained as part of a routine cholesteatoma protocol. A retrospective search of the electronic medical record was performed using this exam code. Patients were excluded if audiogram was not available for review, SNHL was present (>20dB mean bone line), images were nondiagnostic or no 3D sequence was obtained. Measurements were performed using electronic calipers on a PACs station. All audiograms were reviewed by an otolaryngologist.

Results

Sixty-eight diagnostic exams were found with 11 patients not having reviewable audiograms. Of the remaining 57 patients or 114 ears, 13 ears were excluded due to the presence of SNHL. Subjects ranged in age from 2 to 15 years (mean 10.3). There were 41 male and 16 female subjects. In the 101 included ears, the mean R2 angle was 80.86 degrees + 10.91SD and depth was 0.54mm + 0.14SD. Ninety-five percent of the cochlea demonstrated an R2 angle less than 98 degrees and a R2 depth greater than 0.3mm. No significant difference was noted comparing gender, mean depth was significantly different comparing sides (p=0.03), left deeper than right.

Conclusions

Ninety-five percent of ears without SNHL had an R2 angle of < 98 degrees and a depth > than .3mm. This normative data now can be used to compare with a cohort of children with SNHL.



(Filename: TCT_O-175_Fig1composite.jpg)

O-176

11:56AM - 12:04PM

Evaluation of Mid-aperture Measurement of the Endolymphatic Duct on MRI in Children without Sensorineural Hearing Loss with CT Comparison.

T Booth[1], C Wick[2], J Kutz[2], R Clarke[1], Y Xi[2], M Medina[2], B Isaacson[2]
[1]Children's Health Dallas, UT Southwestern Medical Center, Dallas, TX, [2]UT Southwestern Medical Center, Dallas, TX

Purpose
Magnetic resonance imaging (MRI) has been reported to be less sensitive for the diagnosis of an enlarged vestibular aqueduct (VA) as diagnosed on CT. The objective of this study is to evaluate the size of the endolymphatic duct (ELD) on MRI in a population of children without sensorineural hearing loss (SNHL) and also compare the size to the VA on CT as measured on both studies.
Materials and Methods
Inclusion criteria included a diagnostic axial 3D T2-weighted sequence and CT through the temporal bone, which were obtained as part of a routine cholesteatoma protocol. A retrospective search of the electronic medical record was performed using this exam code. Patients were excluded from the normal population, if an audiogram was not available for review or SNHL was present (>20dB mean bone line). Measurements of the mid-aperture ELD on MRI and VA on CT were performed with electronic calipers on a PACS station. All audiograms were reviewed by an otolaryngologist.
Results
Thirty-six patients had diagnostic MRI and CT studies with 6 patients not having reviewable audiograms. Of the remaining 30 patients or 60 ears, 7 ears were excluded due to the presence of SNHL. Subjects ranged in age from 2 to 15 years (mean 10.3). There were 19 male and 11 female subjects. In the 53 included ears without SNHL, the mean diameter of the mid-aperture ELD as measured on MRI was 0.36mm with + 0.3SD and the VA as measured on CT was 0.51mm + 0.18SD. Ninety-five percent of the ELD on MRI and VA on CT measurements were less than 0.8mm. Using the data set of all ears (n=72) that had both CT and MRI regardless of audiogram availability or SNHL, significant correlation was noted between the measurements obtained on CT and MRI with a spearman correlation of 0.65 ($p<0.0001$).
Conclusions
Magnetic resonance imaging tends to underestimate size of the VA, but the measurements significantly correlate. Ninety-five percent of ears without SNHL have a ELD/VAQ size of less than 8mm. This normative data may be used to compare ELD size on MRI with a cohort of children with SNHL.

O-177

12:04PM - 12:12PM

Estimating the Volume of Acoustic Neuromas Using "Ice Cream Cone" Method Compared with the ABC/2 Formula and the Planimetry Method

H Ho[1], Y Li[1], C Wang[1], H Hsu[1], C Juan[1]
[1]*National Defense Medical Center and Tri-Service General Hospital, Taipei, Taiwan*

Purpose

To estimate the volume of acoustic neuromas by a newly proposed "ice cream cone" method in comparison with the ABC/2 formula and the planimetry method.

Materials and Methods

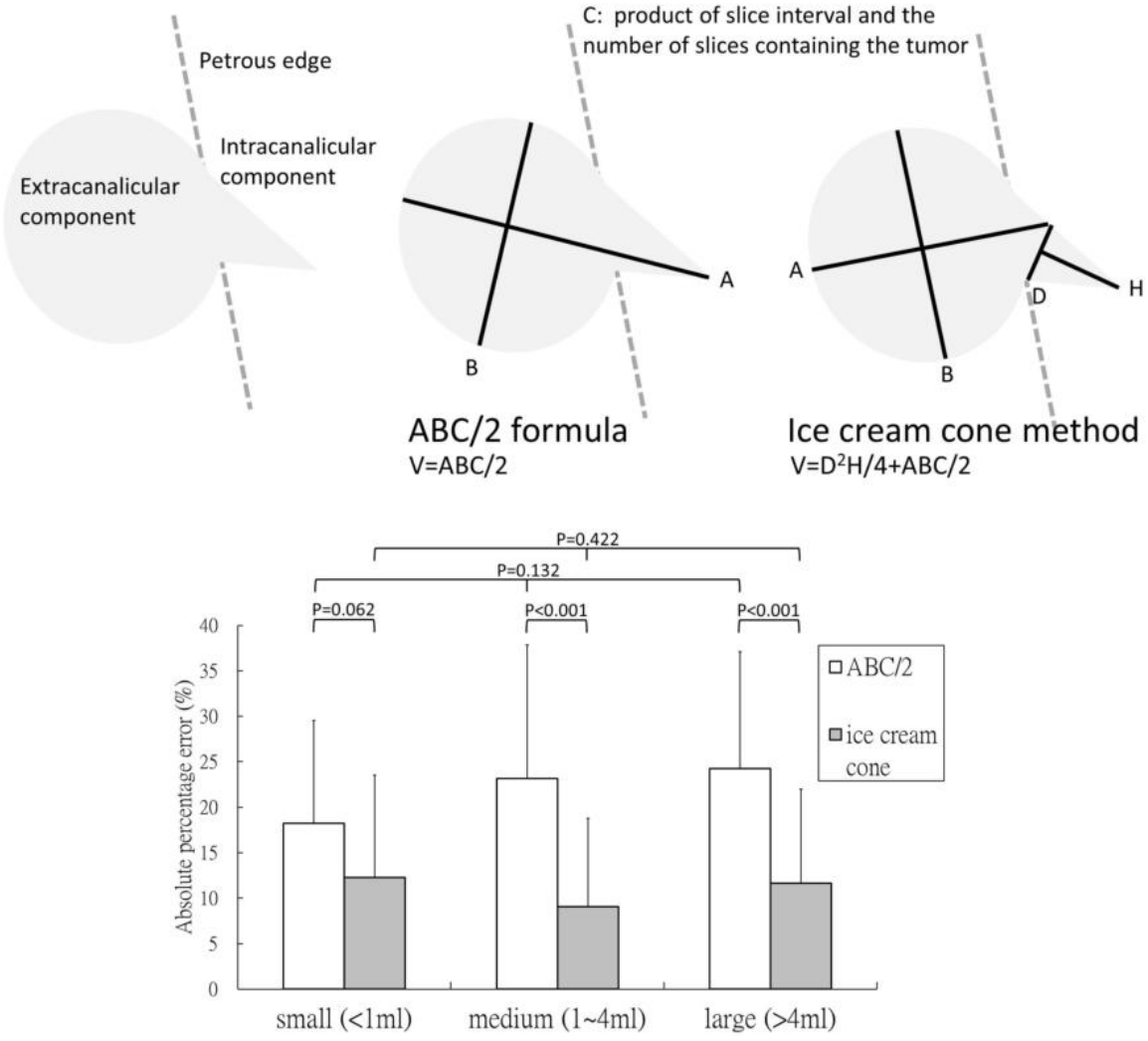
Approved by a local institutional review board, 100 acoustic neuromas examined by MRI during January 2011 to November 2015 were enrolled retrospectively. Informed consent was waived. Volume of acoustic neuromas was estimated by an ice cream cone method (D^2H/4 + ABC/2) and the ABC/2 formula by 2 observers when compared to the volume measured by the planimetry method as gold standard. Patients were further classified into 3 subgroups according to tumor volume, including small (<1 ml; n=34), medium (1 ml ~ 4 ml; n=33), and large (>4 ml; n=33) groups. Estimation error was evaluated. Statistical analysis included intraclass correlation coefficient (ICC), linear regression analysis, one-way analysis of variance, and paired-t test with $P < 0.05$ considered as statistical significance.

Results

The overall tumor size was 4.80 ± 6.8 ml (mean ±standard deviation). All ICCs were no less than 0.992. The tumor sizes estimated ABC/2 formula and the ice cream cone method were both highly correlated with that measured by the planimetry method (both R-squared>0.991, $P<0.001$). The ABC/2 formula overestimated tumor size by 21.85 ± 13.15% than the ice cream cone method (11.01 ± 10.47%) significantly ($P<0.001$). Subgroup analysis showed significant difference between 2 methods only in medium and large size groups ($P<0.001$).

Conclusions

The ice cream cone method allows quantifying the volume of acoustic neuromas more accurate than the ABC/2 formula.



(Filename: TCT_O-177_fig1.jpg)

O-178

12:12PM - 12:20PM

Tumor Volumes in Vestibular Schwannomas: Do the ABC/2 Method and 3D Planimetric Method Correlate?

G BATHLA[1], B Policeni[2], M Hansen[2]
[1]University of Iowa hospitals and Clinics, IOWA CITY, IA, [2]University of Iowa hospitals and Clinics, iowa city, IA

Purpose
To assess the efficacy of the ABC/2 method for calculating the volume of vestibular schwannomas as compared to 3D planimetric method.
Materials and Methods
Post IRB approval, medical records of patients seen by 1 of the otolaryngology surgeons

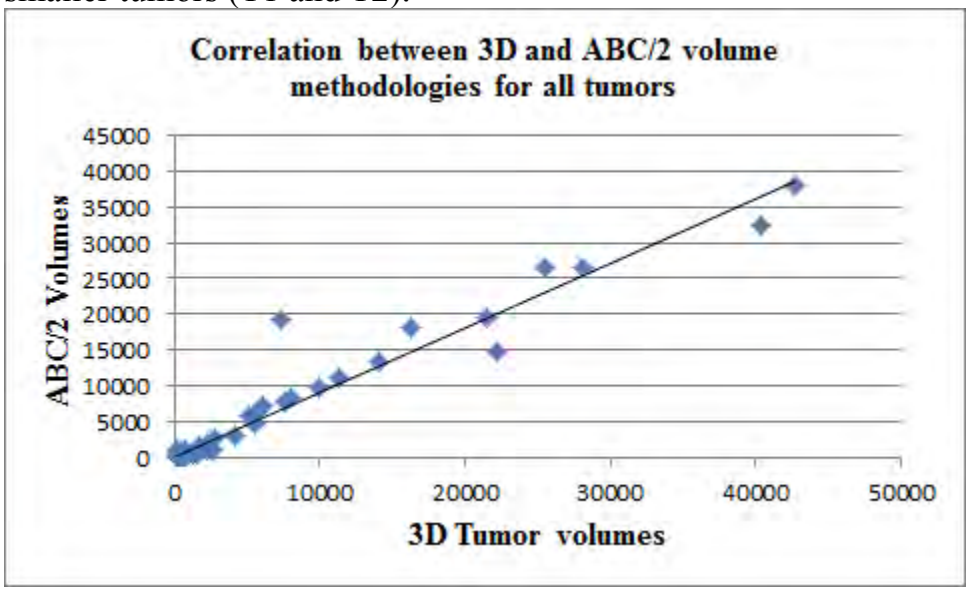
(MRH) were examined and 58 biopsy proven consecutive cases of sporadic vestibular schwannoma (VS) were selected for analysis. There were 36 females and 22 males. Mean age at presentation was 50.8 years (16-80.3 years). The tumor was right-sided in 30 cases and left-sided in 28 cases. Magnetic resonance imaging (MRI) was performed either with 1.5 or 3 Tesla systems. Tumor volumes were obtained on postcontrast fat suppressed T1WI. The maximal anteroposterior (AP), mediolateral (ML) and craniocaudal (CC) dimensions were obtained to calculate volumes through ABC/2 method. Tumors initially were analyzed together (n=58) and subsequently divided in to 3 groups based on Hannover classification. Three-dimensional volumetric data were analyzed using the Vitrea® software (version 6.6.2, Vital images, Toshiba Medical Systems, Minnetonka, MN). In all cases, the tumor was outlined manually on the axial postcontrast images on all sections followed by computerized compilation of summated tumor volume. Nonparametric Spearman correlations were calculated.

Results

Tumor volumes calculated through ABC/2 and 3D methodologies were highly correlated when tumors were analyzed as a group (rho= 0.913, $p < 0.0001$). When using the Hannover classification, subgroup 1 and 2, 3a and 3b and 4a and 4b were grouped together. This yielded 3 groups with n= 26, 15 and 17 respectively. Spearman correlation coefficients were subsequently calculated for each subgroup and revealed correlation coefficients of 0.592 ($p < 0.001$), 0.710 ($P < 0.005$) and 0.918 ($p < 0.0001$) respectively.

Conclusions

1. The ABC/2 method appears to be equivalent to 3D volumetric method for calculating vestibular schwannoma volumes, with high correlation especially for larger (T4) tumors. 2. The correlation is somewhat less strong for intermediate tumors (T3) and even less so for smaller tumors (T1 and T2).



(Filename: TCT_O-178_Correlation_for_all_tumor_volumes.jpg)

Wednesday
11:00AM - 12:20PM
Long Beach Convention Center, Room 202 (Upper Level)

18B-Parallel Paper Session: Pediatric Neuroradiology: Potpourri . . . a "Must See!"

O-179

11:00AM - 11:08AM

Improved Fat Suppression Homogeneity with mDIXON Turbo Spin Echo in Pediatric Spine Imaging at 3 Tesla

C Pfeifer[1], A Pokorney[1], H Hu[1], J Miller[1]
[1]*Phoenix Children's Hospital, Phoenix, AZ*

Purpose
Robust and uniform fat suppression remains essential in routine clinical MR imaging (1-3). In this preliminary work, we demonstrate the robustness of fat suppression with a two-echo mDIXON turbo-spin-echo (TSE) pulse sequence in large field-of-view sagittal total spine pediatric MRI. We compare fat suppression in 3 Tesla MRI of the total spine with a commercially available two-echo mDIXON TSE technique versus conventional frequency-selective and inversion-recovery fat suppression methods. While gradual progress in the development of Dixon-based TSE data acquisition and reconstruction algorithms have occurred over the past 2 decades, 1 of the most significant methodological benefits of mDIXON and similar advances is the operator's ability to select flexible echo times needed for chemical-shift-encoding beyond the traditional practice of choosing only in-phase and opposed-phase pairs (4). Although conventional fat suppression techniques based on T1-relaxation (i.e., STIR: short-TI inversion recovery) and chemical-shift (i.e., frequency) selective techniques remain popular and effective at B0 magnetic field strengths of less than 1.5 Tesla and in anatomical regions where the main B0 magnetic field is relatively homogeneous, the latter's ability to uniformly suppress fat is limited at 3 Tesla and beyond. Fat suppression via frequency-selective methods (i.e., SPIR, SPAIR) is particularly challenging in anatomical regions requiring a large field-of-view, such as total spine imaging, where B0 inhomogeneity can become a significant concern. While STIR techniques can provide uniform fat suppression in most instances where the inversion time is appropriately chosen, its performance also can be variable from patient to patient due to differences in fat T1, and its applications are limited to proton density and T2-weighted imaging due to the method's insensitivity to nonfat species that have similar short T1 values (i.e., gadolinium-enhanced blood and lesions).
Materials and Methods
This prospective, HIPAA-compliant MRI study was approved by the local institutional review board under expedited review as a minimum-risk research project. The two-point 2D mDIXON TSE pulse sequence utilized in this work is a commercially available, medically

approved product in both the United States and Europe, and is implemented with a reconstruction algorithm that uses a 7-peak spectral model of fat (5). The pulse sequence was determined to have minimal risk and its addition to a conventional spine MRI exam was approved. Informed consent and assent were obtained from all study participants, who were referred to our institution for standard MRI of the whole spine. Thirty-six patients (17 males, 19 females, age range: 1 week-22.8 years, average: 5.8±5.4 years) were involved in this pilot study to assess the clinical utility of total spine MRI with mDIXON TSE. All MRI data were acquired on a 3.0 Tesla scanners (Ingenia multi-transmit platform, software version R5.1.7, Philips HealthTech, Best, The Netherlands) using the system's built-in 32-channel posterior coil array embedded within the MRI patient table. Figure 1a summarizes the pulse sequence parameters for the two mDIXON TSE sequences. A total of 42 pairs of images T1- (N=16) and T2-weighted (N=26) scans were acquired. Two board-certified pediatric radiologists reviewed the data sets in a blinded manner, and rated images from each patient using a 3-point scale in 2 categories, including the uniformity of fat suppression and the presence of related fat-suppression artifacts, and overall diagnostic image quality, including conspicuity of lesions, if present. The STATA software was used for statistical analysis. We used the nonparametric Wilcoxon rank-sum test to compare each pulse sequence's scores (i.e., conventional vs. mDIXON) in the 2 categories and the Cohen's kappa coefficient to assess inter-rater agreement. A p-value of 0.05 value was chosen to reflect statistical significance.

Results

Image evaluations results are summarized in Fig. 1b. For fat suppression uniformity, mDIXON TSE images were preferred over conventional SPIR- and STIR- TSE results in 22 out of 42 comparisons by Rater 1 and 25 out of 42 comparisons by Rater 2. In 17 comparisons mDIXON TSE and conventional imaging were rated equally by Rater 1. Rater 2 scored 14 comparisons equally. In 3 of the same cases, the 2 radiologists agreed that conventional fat suppression is superior to mDIXON TSE. The superior fat suppression of mDIXON was more noticeable in the 16 comparisons where postcontrast T1-weighted TSE imaging was compared, where 13 comparisons received a "+1" score from Rater 1 and 14 comparisons received a "+1" score from Rater 2. In contrast, only 9 out of 26 comparisons between mDIXON and STIR T2-weighted TSE imaging received a "+1" score from Rater 1, while Rater 2 gave 11 out of the 26 comparisons a score of "+1". In 17 comparisons where Rater 1 determined both conventional TSE and mDIXON TSE equivalent in fat suppression quality, 14 were in T2-weighted cases. Similarly, for Rater 2 who deemed 14 comparisons equivalent in fat suppression quality, 12 were in T2-weighted cases. Collectively, the preference for mDIXON in yielding more uniform fat suppression was statistically significant ($p < 0.01$). In image quality, mDIXON TSE was preferred in 13 of 42 comparisons from Rater 1. Rater 2 preferred mDIXON TSE in 11 of the 42 comparisons. Rater 1 determined both conventional TSE and water-only mDIXON TSE images equivalent in diagnostic image quality in 28 comparisons. Similarly, Rater 2 determined both conventional and mDIXON TSE results equivalent in diagnostic image quality in 30 comparisons. Collectively, the outcome in the category of diagnostic image quality was

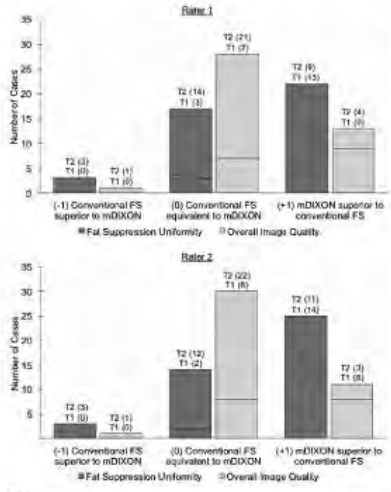
statistically significant ($p < 0.01$), in favor of mDIXON TSE. Figure 1c illustrates representative examples from one of the youngest patients in the cohort, a 1.3-year-old female.

Conclusions

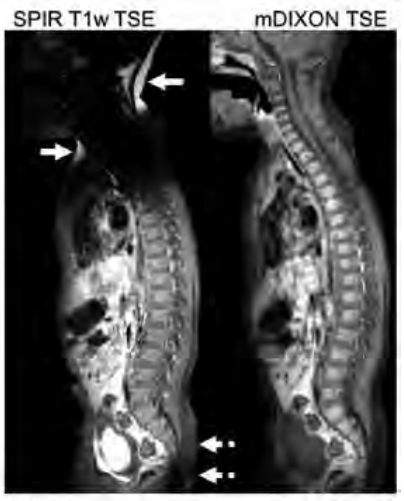
Inadequate or failed fat suppression is one of the most common reasons a MRI scan is rendered nondiagnostic and must be repeated. In pediatric imaging, the additional time needed for a repeat scan often can be coupled with the need for prolonged sedation, potentially increasing patient risk. We have shown in this work that uniform and consistent fat suppression can be achieved with 2D mDixon TSE pediatric spine imaging at 3.0 Tesla across large sagittal FOVs, and that mDIXON should be considered as a permanent replacement of traditional fat suppression methods, in particular frequency-selective techniques in T1-weighted applications. In our cohort of 36 patients, mDIXON TSE provided robust fat-suppressed results in every case, with no need for a repeat scan and minimal patient-to-patient variation in overall image quality. The explicit estimation of a wide dynamic range of B0 inhomogeneity values as a part of the mDIXON data reconstruction algorithm is a key factor in the method's reliability. In our experience, we have measured variations of up to ±500 Hz in B0 inhomogeneity across the sagittal whole-spine volume, and the current mDIXON reconstruction algorithm is able to resolve this off-resonance factor without causing water-fat signal swap artifacts. Although the mDIXON TSE scan times were noticeably longer than their SPIR- and STIR- counterparts for matched spatial resolution and volume coverage, one noteworthy benefit of mDIXON TSE imaging that was not evaluated in this current work is the method's ability to output four separate types of image reconstructions (i.e., signal contrasts) from a single scan acquisition, including water-only (i.e., fat-suppressed), fat-only (i.e., water-suppressed), in-phase (i.e., water+fat, non-fat-suppressed), and opposed-phase (water-fat) series. In conclusion, we have demonstrated the clinical utility of mDIXON TSE in fat-suppressed total spine imaging at 3.0 Tesla, as an alternative to conventional methods.

Parameter	T1-Weighted 2D mDIXON TSE	T2-Weighted 2D mDIXON TSE
Orientation	sagittal	sagittal
Voxel Size (mm)		
Anterior-posterior	0.7	0.7
Superior-inferior	1.4	1.4
Number of slices	13-21	13-21
Slice thickness (mm)	3.1	3.1
Slice gap (mm)	0.5	0.5
Phase encoding order	asymmetric	linear
TR (msec)	623	3500
TE / TE effective (msec)	9/9	90/76
Partial echo	no	no
mDIXON TE shift (msec)	0.8-1	0.8-1
Bandwidth/pixel (Hz)	442	460
TSE factor	6	17
TSE echo spacing (msec)	9	10
Parallel imaigng	no	no
Scan time (min:sec)	3:42	3:44

(A)



(B)



(C)

(Filename: TCT_O-179_Figure1_300dpi.jpg)

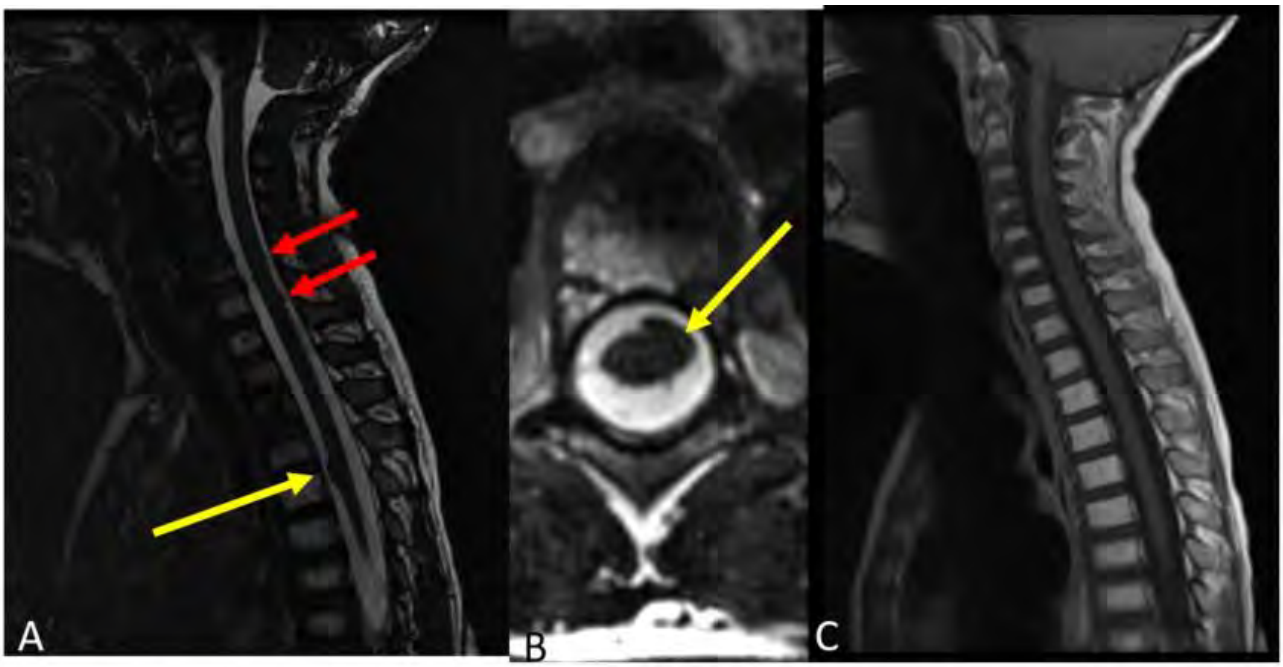
O-180

11:08AM - 11:16AM

The Diagnostic Utility of Isotropic Balanced Steady State Free Precession Imaging (bSSFP) Sequence For the Evaluation of Spinal Drop Metastases

K Buch[1], P Caruso[2], S Rincon[1]
[1]Massachusetts General Hospital, Boston, MA, [2]MGH, Boston, MA

Purpose
The purpose of this study is to assess the diagnostic utility of the bSSFP sequence (CISS/FIESTA/3D DRIVE) for detection of spinal drop metastases in pediatric patients with primary intracranial tumors.
Materials and Methods
This was an IRB-approved, retrospective study, of 39 pediatric patients with primary intracranial tumors undergoing MRI spine evaluation for drop metastases prior to radiation treatment. All patients received a whole spine MRI exam including both a bSSFP and postcontrast T1 sagittal sequences. Two neuroradiologists independently reviewed only the postcontrast T1 sequence, then 1 week later only the bSSFP sequence.
Results
Patients ranged in age 1-18 years (mean 7.3+/-4.8 years) with 24 males and 15 females. Most common primary tumors included medulloblastoma (n=14), ependymoma (n=10), and germinoma (n=7). The bSSFP sequence showed drop metastases in 7 patients (18%). The postcontrast T1 showed drop metastases in 10 patients (26%); in 3 of these, the bSSFP and T1 were concordant. In 7 patients, the lesions were not detected on the bSSFP sequence, these lesions were not seen on follow-up imaging without interval treatment, and thus were considered false-positives. In 4 patients, drop metastases were detected on bSSFP, but not on the T1 sequence including 1 nonenhancing lesion and 3 lesions <3 mm in size. The number of lesions per patient ranged from 1 discrete lesion to diffuse disease, and ranged in size from 2-10 mm. Inter-rater agreement was excellent (0.88) for the bSSFP sequence and excellent (0.85) for the postcontrast T1 sequence.
Conclusions
The bSSFP sequence increased the diagnostic yield for the detection of drop metastases in pediatric patients with primary intracranial tumors. The bSSFP sequence is particularly advantageous for the detection of small drop metastases (<3mm), nonenhancing metastases, and decreases the number of false-positives. These data suggest bSSFP is an important adjunct to postcontrast T1-images.



7 year old male with ependymoma. Image A, sagittal bSSFP sequence demonstrates a dominant, T5 ventral spinal metastasis (yellow arrow) with multiple, additional, smaller metastases (red arrows). Image B, axial bSSFP sequence at the T5 level demonstrates the left ventral metastasis (yellow arrow). Image C, post-contrast T1 sagittal sequence does not demonstrate abnormal enhancement or detectable drop metastases.

(Filename: TCT_O-180_SpinalDropMetsimage.jpg)

O-181

11:16AM - 11:24AM

Reduced FOV Diffusion Tensor Imaging and Fiber Tractography of the Pediatric Cervical and Thoracic Spinal Cord Injury

M Alizadeh[1], S Saksena[2], J Fisher[2], Y Sultan[3], C Conklin[2], D Middleton[1], L Krisa[2], S Faro[4], M Mulcahey[2], F Mohamed[2]
[1]Temple University, Philadelphia, PA, [2]Thomas Jefferson Hospital University, Philadelphia, PA, [3]Drexel University, Philadelphia, PA, [4]John Hopkins University, Baltimore, MD

Purpose
The purpose of this study is to assess the utility and effectiveness of diffusion tensor imaging (DTI) and fiber tractography (FT) of pediatric cervical and thoracic spinal cord towards discrimination of normals and patients with spinal cord injury (SCI).
Materials and Methods
A total of 43 pediatric subjects including 23 typically developing (TD) subjects ranging in age from 6-16 years old [11.94±3.26 (mean ±standard deviation)] and 20 subjects with SCI ranging in age from 7-16 years old [11.28±3.00 (mean ±standard deviation)] were recruited,

and scanned using 3.0T Siemens Verio MR scanner (Siemens Healthcare, Erlanger, Germany) with 4-channel neck matrix and 8-channel spine matrix coils. Reduced FOV diffusion tensor images were acquired axially in the same anatomical location prescribed for the T2-weighted images to cover the entire spinal cord (C1-mid L1 levels). The DTI parameters used were: FOV=164 mm, phase FOV=28.4% (47 mm), number of directions=20, b=800s/mm2, voxel size=0.8×0.8×6.0mm3, matrix size= 36×208, axial slices=40, TR=7900ms, TE=110ms, number of averages=3 and acquisition time=8:49min. Streamline deterministic tractography were generated from preprocessed reduced FOV DTI data (https://med.inria.fr/). For DTI analysis, motion correction was performed by coregistration of diffusion directional images to the reference image (B0) using a rigid body registration algorithm and a scaled least square cost function (using in-house software developed in Matlab) (1, 2). Diffusion tensor imaging and FT parameters including fractional anisotropy (FA), apparent diffusion coefficient (ADC), tract length and relative tract density were calculated by using regions of interests (ROIs) manually drawn on the whole cord along the entire spinal cord being anatomically localized by an independent board certified neuroradiologist. These measures then were compared between TD and SCI groups using standard least squared linear regression model based on restricted maximum likelihood (REML) method (using JMP pro 13.0 software).

Results

Compared to TD subjects a decrease in mean FA (TD=0.46±0.11, SCI=0.37±0.09), white matter tract density (TD=405.93±243.84, SCI=268.90±270.34) and mean length of tracts (TD=55.21±30.18, SCI=43.28±18.56), and an increase in mean ADC (TD=2.81±0.8×10-3mm2/sec, SCI=3.03±0.76×10-3mm2/sec) were observed in SCI subjects along the entire spinal cord. Statistically, significant decreases have been shown in FA ($p<0.0001$) and tract density ($p<0.0001$). However, the mean length of tracts and mean ADC did not show significant differences. Also, as shown in Fig. 1 DTI and FT parameters vary along spinal cord as a function of spinal cord level.

Conclusions

The observed significant DTI and FT changes between TD and SCI subjects suggest that FA and tract density appear to be the most sensitive parameters in assessing the state of the spinal cord in chronic SCI. This study demonstrates that DTI and FT has a potential to be used as an imaging biomarker which may be useful for prognosis as well as possible future treatment planning such as stem cell therapy.

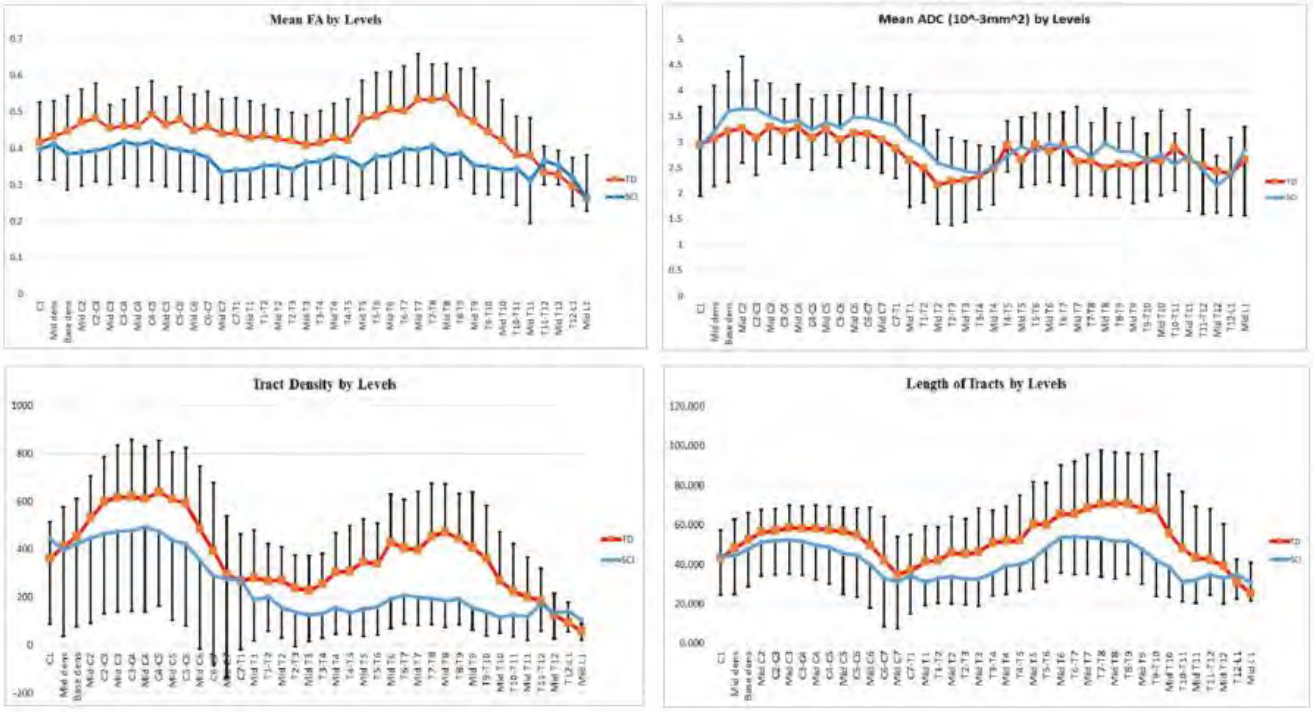


Figure 1. DTI and FT parameters averaged across all TD and SCI subjects and plotted as a function of cord levels. The error bars represent the standard deviations.

(Filename: TCT_O-181_SCI_WHOLE.jpg)

O-182

11:24AM - 11:32AM

Developing Imaging Pulse Sequences for Miniature Swine Traumatic Spinal Cord Injury Model

R Bert[1], D Muddasani[1], M Negahdar[1], L Sherwood[1], B Wellman[2], M Boakye[1]
[1]University of Louisville, Louisville, KY, [2]University of Louisville, Louisvlle, KY

Purpose

Miniature swine have been a well characterized animal model for standardized traumatic spinal cord injury assessment. Currently, however, there are no centers in the U.S.A. that have facilities for pre- and postinjury in vivo assessment to correlated with the histological, physiological and behavioral changes. We have a well tested 3T Siemens Skyra Human and Animal research center in close proximity to the veterinary facilities that have allowed us to become the first center to develop imaging sequences for this purpose.

Materials and Methods

Seven-8 month old female Yucatan miniature swine (23-33 kg) underwent a combination of contusion and compression to the thoracic spinal cord using a weight drop device. Anesthesia was induced with 0.025 mg/kg atropine, 0.04 mg/kg dexmedetomidine and 10 mg/kg ketamine IM. An endotracheal tube then was placed and anesthesia was maintained

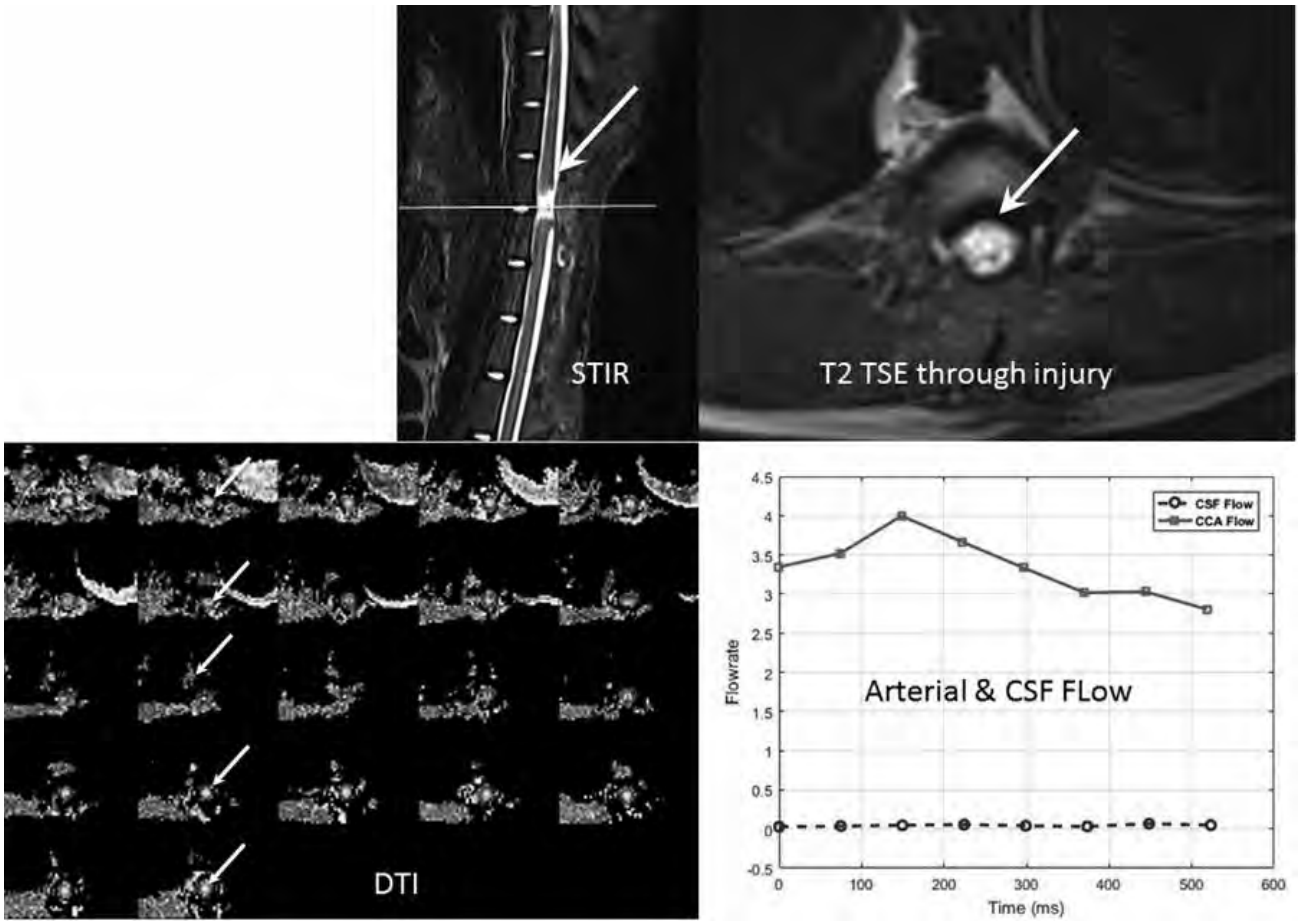
with 3-3.5% isoflurane in 100% oxygen and mechanical ventilation. A 20G intravenous catheter was placed in a marginal ear vein and intravenous Lactated Ringer's Solution with 5% Dextrose was administered to maintain normal blood pressure and blood glucose. Body temperature was supported with a warm air circulating blanket. Heart rate, noninvasive blood pressure, SpO2, and end-tidal CO2 were monitored constantly during the anesthetic procedure.

Results

The following sequences provided interpretable images on 2 swine with TSCI and 2 animals with sham laminectomies: T2_TSE (TR/TE=4500/104/FOV=400*400mm/Matrix=320*192/SliceThickness=3mm/FA=120/NSA=2). T2 STIR (TR/ 6500/TE=98/TI=220/FOV=160x160mm/Matrix=256x180/SliceThickness=4mm/FA=134/NSA=1). T1 Fat saturated (TR/TE=894/13/FOV=120x120mm/Matrix=256x172/SliceThickness=4mm/FA=120/NSA=5). CSF cine flow (TR/TE=95/12/FOV=132*132mm/Matrix=256x256/SliceThickness=10mm/FA=7/NSA=3). Post MR myelographic T1 Fat Saturation (TR/TE=650/9.9/FOV=300x300mm/Matrix=320x224/SliceThickness=2mm/FA=140/NSA=2). Diffusion Tensor Imaging (TR/TE=3700/92/FOV=220x220mm/Matrix=128x128/SliceThickness=4mm/diff_directions=30/NSA=2). Diffusion tensor images demonstrated discontinuity at the levels of injury but not at sham laminectomy levels. MR myelography proved technically challenging because of cord extension to the sacrum. Central gray contrast enhancement occurred in rat and rabbit models but was less conspicuous due to lower field strength than used in small animal magnets. Cine flow measurements were detectable in the carotid arteries but were undetectable in vertebral arteries or CSF.

Conclusions

We found most standard imaging pulse sequences could be used in miniature swine with minor adjustments in parameters. Our MRI research center can now perform structural and advanced imaging on the standardized miniature swine traumatic spinal cord injury model. We are the first center in the U.S.A. that can perform these pre- and postinjury in vivo imaging-physiologic-pathologic-behavioral correlations. The absence of CSF pulsations in normal pigs is attributed to their unique blood supply to the cord. Gray matter interstitial spaces appear to communicate with the SAS as in rats and rabbits.



(Filename: TCT_O-182_Composite.jpg)

O-183

11:32AM - 11:40AM

Connectome Mapping with Edge Density Imaging Separates Persons with Pediatric Mild Traumatic Brain Injury from Controls

C Raji[1], M Wang[2], E Palacios[2], N Nguyen[2], J Owen[2], P Mukherjee[3]
[1]UCSF Medical Center, San Francisco , CA, [2]UCSF, San Francisco, CA, [3]San Francisco VA Med Ctr, San Francisco, CA

Purpose
To determine if structural connectomes using edge density imaging can separate a pediatric group with mild traumatic brain injury from controls.
Materials and Methods
Recruitment and analyses received IRB approval as part of the "Therapeutic Resources for Attention Improvement using Neuroimaging in Traumatic Brain Injury" (TRAIN-TBI) study. A total of 24 adolescents (mean age 14.1 years, standard deviation 1.6 years, range 10-16) were recruited from The Bay Area Concussion and Head Injury Program clinic at

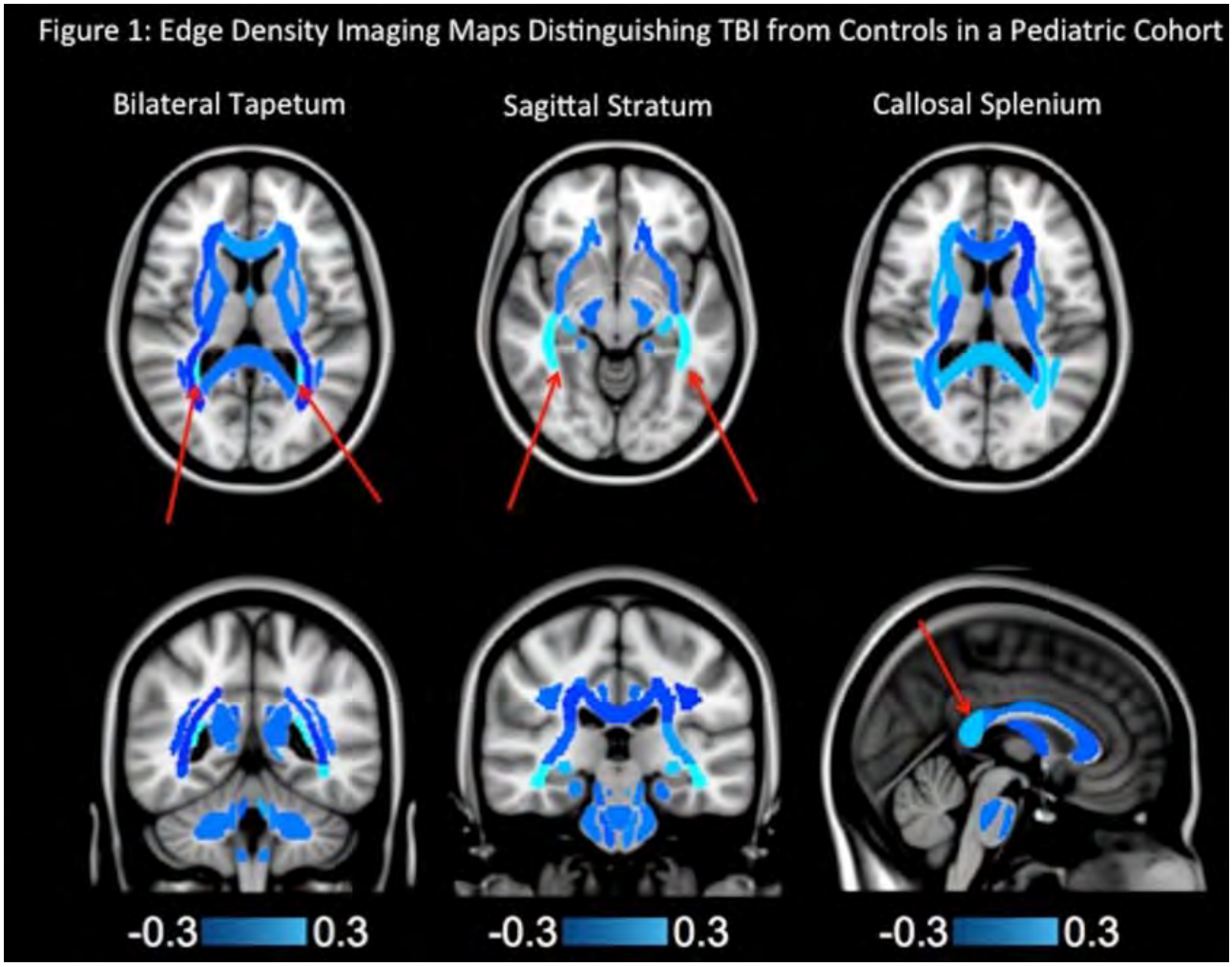
UCSF. Of these, 14 had mild TBI (mTBI) defined by blunt trauma 1 month prior with 1 postconcussive symptom. Age and education equivalent typically developing children (n=10) served as control subjects. Each subject was neurocognitively evaluated with the California Verbal Learning Test (CVLT) and the Attention Network Task (ANT) (1). A 3 T GE MR750 scanner (GE Healthcare, Waukesha, WI) was used to perform MRI using a 32-channel phased-array radiofrequency head coil. High-resolution structural MRI of the brain was collecting using an axial 3D BRAVO T1-weighted sequence [echo time (TE) =1.64 ms, repetition time (TR)=2530 ms, (TI)= 400 ms, flip angle of 11º] with a 256-mm field of view (FOV), and 160 1.2-mm contiguous partitions at a 256x256 matrix. Whole-brain diffusion-weighted images were collected at b = 1300 s/mm2 with 64 directions. DTI data were analyzed in the FMRIB Software Library (FSL) (http://fsl.fmrib.ox.ac.uk/fsl/fslwiki/). All DTI images were first corrected for Eddy current artifacts. Second, images were skull stripped using the FSL brain extraction tool (BET) (5). Third, fiber tractography was done using probtrackx and bedpost (2). Edge density images were generated as previously described by calculating the number of connections passing through each white matter voxel as determined by DTI and fiber tractography (3). We used principal components analysis (PCA) and support vector machines to identify changes in the mean EDI of the 48 JHU white matter tracts on the subject level for binary classification purposes (4). We validated our approach using ROC curves and leave-one-out cross-validation (5).

Results

Principal components analysis of EDI maps identified 3 principal components that distinguished pediatric mTBI cases from controls (Fig. 1). Light blue colors (arrows) denote areas in which low edge densities correlate to mTBI status. These areas are the bilateral tapetum, sagittal stratum, and callosal splenium and provided excellent separation of pediatric TBI from controls. Sensitivity was 85% and specificity was 90%. Overall accuracy from the area under the curve was 87.5%. Neurocognitive testing, by comparison, provided an area under the curve of distinguishing mTBI from controls ranging from 61% with CVLT to 71% with ANT.

Conclusions

Edge density imaging is a new form of connectome mapping that provides good diagnostic delineation between pediatric mTBI and healthy controls.



(Filename: TCT_O-183_Figure_1.jpg)

O-184

11:40AM - 11:48AM

Normal Basion-Cartilaginous Dens Interval (BCDI) in Children

A Singh[1], W Altmeyer[2], R Tiwari[3], X Zhang[2], L Lu[4], Z Fulton[4], B Tantiwongkosi[5]
[1]UT Health Science Center San Antonio, San Antonio, TX, [2]UTHSCSA, San Antonio, TX, [3]University of Texas Health Science Center, San Antonio, TX, [4]University of Texas Health Science Center San Antonio, San Antonio, TX, [5]University of Texas Health Science Center at San Antonio, San Antonio, TX

Purpose
Craniocervical injuries require prompt diagnosis as these injuries may cause devastating morbidity in the pediatric population. Widening of the basion-dens interval (BDI) is an important predictor of craniocervical injury. However, the BDI in children is vastly different than in adults due to incomplete development of the dens. The established adult BDI values

should not be used for the pediatric age group. The current literature on BDI in the pediatric population is sparse and mainly based on bony measurements. Cartilage always is seen around the tip of the dens in younger children and serves as the precursor of future bony dens. In the pediatric population, BDI should be modified to BCDI (basion-cartilaginous dens interval) which is the distance between basion and the cartilaginous tip. Our goal is to establish the normal values of BCDI in the pediatric population.

Materials and Methods

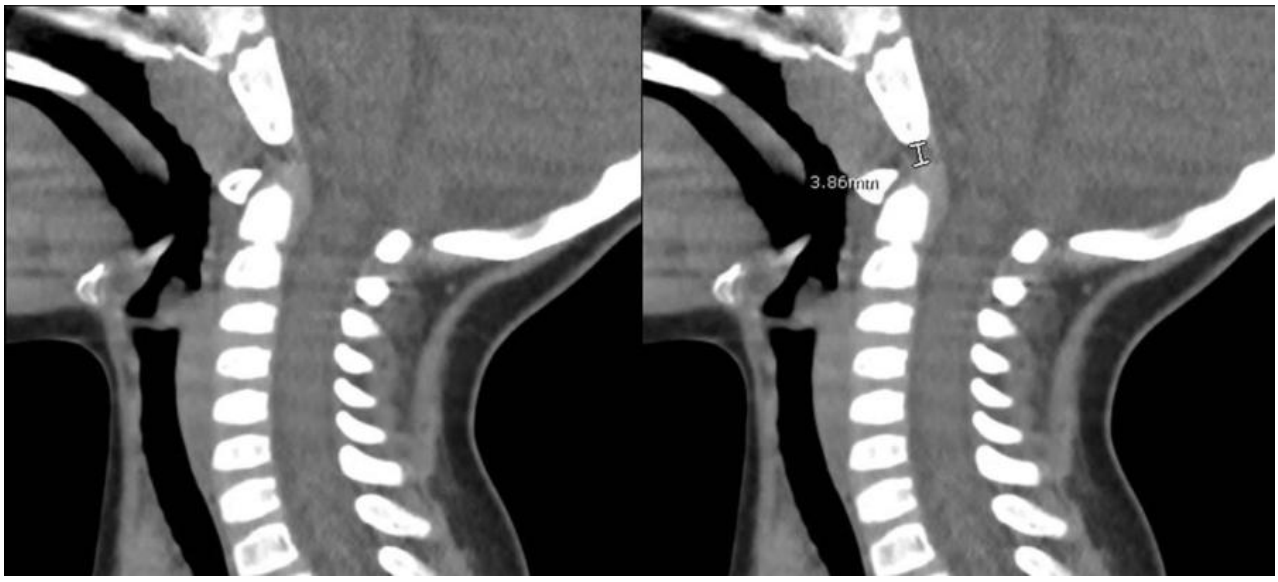
Total of 300 pediatric patients (0-10 years) were selected retrospectively by using the keyword "CT Cervical Spine" in our PACS system. These patients (100 in each group) were divided into 3 different categories: 0-3 years, 3-6 years and 6-10 years. Patients with craniocervical injury, significant intracranial injury, congenital anomalies of the craniocervical junction, and nondiagnostic scan due to artifacts were excluded from the study. Only patients with normal cervical spine were included. The BCDI was measured on the sagittal multiplanar reconstruction (MPR) image of cervical spine CT in the soft tissue window. The mean, standard deviation (SD) and the upper limit of normal (mean + 2SD) of the 3 groups were calculated. The one-way ANOVA and subsequent post-hoc tests were used to check for significant differences of BCDI between these 3 groups. Statistical analysis (t-test) also was performed to check if there is any significant difference of BCDI between males and females in these groups. Data also were gathered regarding os terminale, to check for its presence in 0-6 years age group and its fusion in 6-10 years age group. Descriptive statistical analysis was done in these 2 groups.

Results

The patients range from 3 months to 10 years of age with 172 males (57%) and 128 females (43%). The mean, standard deviation (SD) and the upper limit (mean + 2 SD) of BCDI were calculated for 3 different groups. The mean and upper limit of BCDI were 3.97 and 5.54 mm in the 0-3 years age group, 3.62 and 5.57 mm in the 3-6 years age group and 4.95 and 7.21 mm in the 6-10 years age group. Basion-cartilaginous dens interval CDI values were found to be significantly different between 3 groups (p-value <0.05). Basion-cartilaginous dens interval values were not significantly different between males and females (p-value >0.05) in 3 different groups. The mean age for the appearance of os terminale was 47 months and for fusion was 8.6 years.

Conclusions

This study describes the normal values of basion-cartilaginous dens interval in the pediatric population.



(Filename: TCT_O-184_BCDI.jpg)

O-185

11:48AM - 11:56AM

MRI markers of degenerative disc disease in a population of young patients with Multiple Sclerosis

R Glikstein[1], P HANAGANDI[2], C Torres[1], R Thornhill[3], C Rush[1], T Al Mansoori[1]
[1]University of Ottawa, Ottawa, Ontario, [2]HOSPITAL FOR SICK CHILDREN, TORONTO, TORONTO, ONTARIO, [3]The Ottawa Hospital University of Ottawa, Ottawa, Ontario

Purpose
To determine the presence and extent of degenerative disk disease of the cervical spine (DDD) in young patients with multiple sclerosis (MS).
Materials and Methods
This retrospective study included 82 patients with MS (ages 17 to 29 years; 52 female and 32 male) scanned between January 2009 and June 2012. Each patient underwent an examination on a 3T MR scanner (Trio, Siemens Medical Solutions), which included the following sequences: sagittal T2 FLAIR of the brain and cervical spine with axial MPR reconstruction of the cervical spine, Sagittal T2 of the cervical, axial T2me2d. Patients with known history of trauma or surgery, or infectious/inflammatory diskitis were excluded. Inter agreement was assessed by 2 neuroradiology readers. The presence of DDD was scored as "no DDD" (score=0) or DDD at either single or multiple levels of the cervical spine (score=1 or 2, respectively). The severity of DDD was scored from 0 to 4: normal (0), evidence of disk signal loss, but no evidence of prolapse, osteophyte, or spinal stenosis (1), evidence of disk signal loss, loss of height of the intervertebral disk space, mild osteophyte-disk complex/mild prolapse of the disk, mild anterior indentation of the thecal sac (2), evidence of disk signal loss, loss of height of the intervertebral disk space, large osteophyte-disk

complex/indentation of the spinal cord without signal cord changes (3) and, finally, evidence of disk signal loss, loss of height of the intervertebral disk space, listhesis, indentation of the spinal cord with signal change (4). Signal changes in the cervical spinal cord were scored as "0" : no signal change, "1": signal at the level of the stenosis, "2": signal change at any level of the spinal cord, or "3": signal changes at the level of stenosis, in addition to other levels. Inter-rater agreement was assessed using weighted kappa coefficients (DDD level/severity and spinal cord signal changes). A kappa of 0-20 indicated poor agreement; 20-40 fair agreement; 40-60 moderate agreement; 60-80 substantial agreement and 80-100 indicated very good agreement.
Results
There were 5 patients (6%) with no DDD, 16 patients (21%) with single level of DDD and 57 (73%) with multilevel DDD (Fig. 1).The distribution of DDD severity is depicted in Fig. 2: 5 patients exhibited no DDD (6%), 23 with type 1 (29%), 36 with type 2 (45%), 15 with type 3 (19%), and 1 patient with type 4 (1%). The distribution of cord signal changes is provided in Fig. 3: there were no changes observed in 39 patients (49%), 2 at the level of stenosis (3%), 4 at the level of the stenosis in addition to other levels (4%), and 35 patients with cord changes at any level (44%). There was substantial agreement between readers for the assessment of DDD level (kappa =0.74, 95% CI 0.58-0.91), DDD severity (kappa =0.67, 95% CI 0.54-0.80), and cord signal changes (kappa =0.73, 95% CI 0.61-0.85).
Conclusions
In our study we found a significant number of patients showing various degrees of degenerative disk disease with compromise of the spinal canal. This finding is unusual for the age of the patients and is markedly earlier considering the literature.

O-186

11:56AM - 12:04PM

Why Do Intracranial Germ Cell Tumors Arise in the Pineal Region: A Preliminary Hypothesis

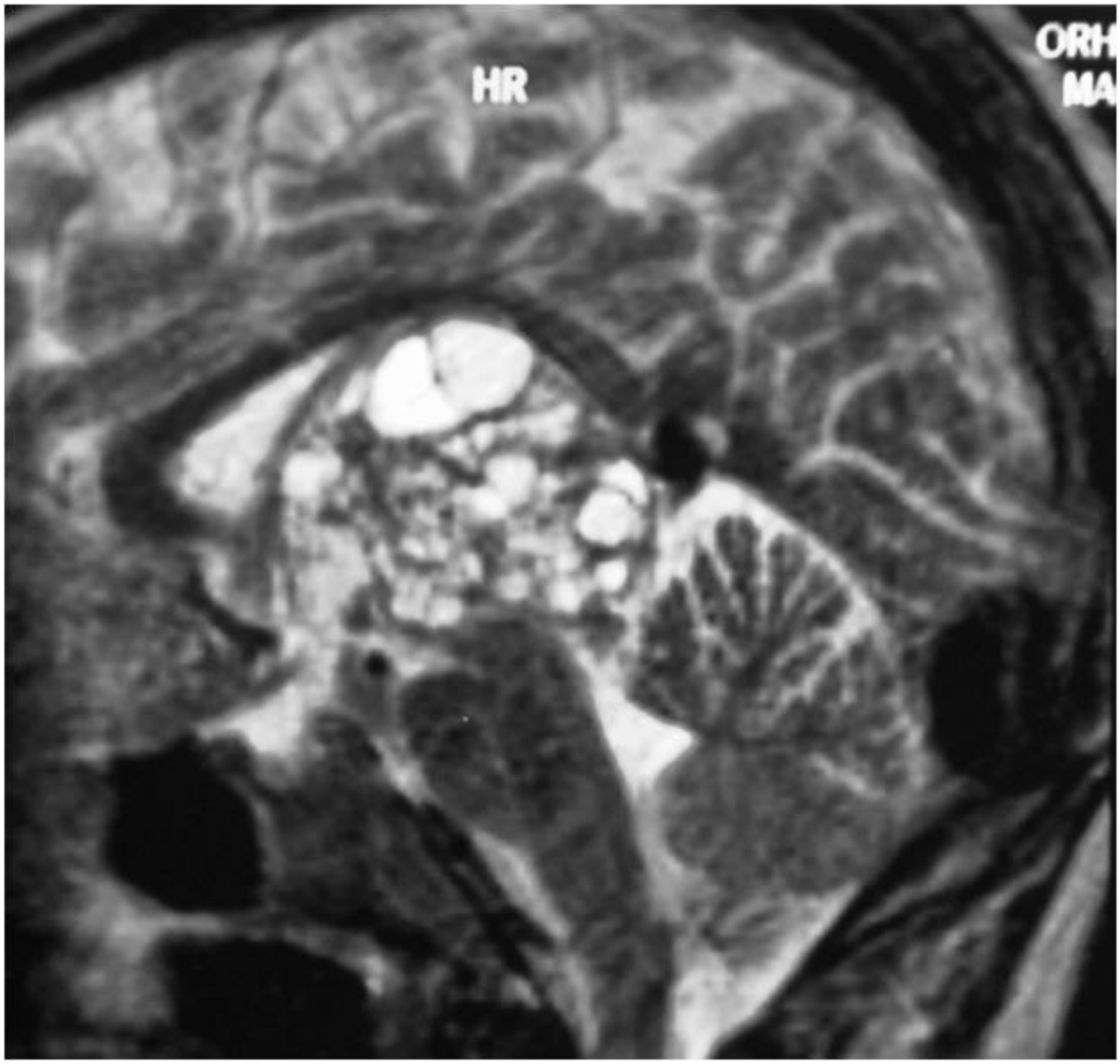
J Rees[1], J Smirniotopoulos[2]
[1]*Georgetown University, Washington DC,* [2]*George Washington University, Bethesda, MD*

Purpose
To present a new hypothesis of intracranial germ cell tumor pathogenesis.
Materials and Methods
We will review current theories of intracranial germ cell tumor pathogenesis, the normal physiology of the pineal gland in humans, and the corresponding functions and pathways in other animals and plants. We will focus on the current understanding of the role of melatonin as a complex multiregulatory molecule in plants and animals.
Results
The primary known function of the pineal gland in humans is to produce and regulate

melatonin. Melatonin is involved intimately in transducing light signals into physiologic activity including regulation of our diurnal cycles and sleep. Sexual development and maturation are regulated by other more specific hormonal systems in humans and other mammals. In plants, melatonin function is more complex and is involved in establishing day/night cycles but also is involved intimately in reproductive functions such as flowering and seed production, which are tied to day light cycles. Melatonin is a multiregulatory molecule all of whose functions are not fully understood. Germ cell tumor pathogenesis has been attributed theoretically to mechanical infolding of germ cell precursors into the pineal region during embryology, some of which then undergo neoplastic transformation. This has not been proven, and does not fully explain the specific frequency of these tumors in the pineal region and secondarily in the suprasellar region.

Conclusions

It is our hypothesis that melatonin has a vestigial neurophysiologic relationship to germ cell differentiation and maturation which can induce undifferentiated stem cells to become germ cell precursors. This induction occurs in the pineal region and secondarily in the suprasellar regions due to melatonin exposure via adjacent venous portal systems. It is this cellular induction rather than mechanical infolding which gives rise to germ cell precursors, a certain number of which then undergo neoplastic transformation and develop into germ cell tumors including germinoma, choriocarcinoma, and endodermal sinus tumors.



(Filename: TCT_O-186_choriocarcinomasagT2.jpg)

O-187

12:04PM - 12:12PM

The Incidence of Pituitary Cysts in Children may be Underreported

J Haigney[1], O Bersot[2], B Pogostin[2], W Weiler[2], N Krasnow[2], M Kessler[2], R Noto[3], M Tenner[2]
[1]New York Medical College, Valhalla, NY, [2]New York Medical College, Sleepy Hollow, NY, [3]New York Medical College, Sleepy Hollow , NY

Purpose
To determine if cysts on MRI studies always are reported, and if not, how cyst volume (CV) and percentage of the gland occupied by cyst (POGO) affects the frequency of reporting.
Materials and Methods
Three hundred forty-two patients ages 6-18 years who had a high resolution postcontrast MRI (1mm slices) at the Division of Neuroradiology at NYMC between 2010-2016 were randomly selected to be part of this study. Patients with congenital anomalies, acute trauma, active metastatic disease, intracranial pressure abnormalities, and active inflammation were excluded. Of the 342 patients, 171 (82 male, 89 female) met the criteria for inclusion in the study. We read all images with particular attention to the pituitary gland for the presence of PC and compared our results with those originally reported by the neuroradiologists. Pituitary and cyst volumes were calculated using the ellipsoid formula LxWxH/2. Percentage of the gland occupied was calculated as the ratio of CV to pituitary volume.
Results
Magnetic resonance imaging (MRI) analysis of 171 subjects determined that 25 cysts (14.6%) were present. Only 4 cysts were reported during the initial neuroradiologist readings (2.3%) ($p<0.001$). For the entire cohort, mean and median CV were 17.28±16.72mm3 and 11.52mm3 respectively with a range of 2.72-78.41mm3. Mean and median POGO were 4.87±5.68% and 3.07% respectively with a range of 0.68-27.36%. The 4 patients reported by the radiologists to have cysts in the initial screening had CVs of 4.54, 23.74, 23.76, and 41.52mm3, and POGO were 0.91%, 6.42%, 8.55%, and 5.97%, respectively. Mean and median CV were 16.1±17.1mm3 and 10.2 respectively. Mean and median POGO were 4.75±6.09% and 2.3% respectively. There was no significant difference in mean CV and POGO between the 2 groups ($p=0.43$ and $p=0.74$, respectively).
Conclusions
Our data demonstrate that PC in normal children may be underreported. Our findings suggest that researchers investigating the prevalence or incidence of radiographic findings should not limit themselves to query searches and instead utilize direct examination.

O-233

12:12PM - 12:20PM

Implications of Regional TSC1 Gene Expression on Cerebellar Development and Behavioral Abnormalities in Patients with Tuberous Sclerosis Complex

Y Li[1], M Barkovich[1], R Desikan[1], A Barkovich[2]
[1]University of California, San Francisco, San Francisco, CA, [2]UCSF Benioff Children's Hospital, San Francisco, CA

Purpose
Autosomal dominant mutations in TSC1 lead to tuberous sclerosis complex; however, the regional brain expression of TSC1 is unknown. Furthermore, there is an increased

prevalence of autism spectrum disorders in patients with tuberous sclerosis complex (1), and little is known about whether the TSC (1) mutation affects behavioral abnormalities in tuberous sclerosis. To date, there is no definite imaging or pathologic determinant of such behavioral abnormalities (2). Studies of cortical tuber number, volume, and location have shown no correlation with the range of clinical phenotypes (2). Of note, many of the abnormalities seen on imaging studies of tuberous sclerosis complex are believed to be the result of later, mosaic mutations. Thus, the underlying mechanism of behavioral abnormalities in the tuberous sclerosis population is still unknown, but may be partially elucidated through the evaluation of regional TSC1 gene expression.

Materials and Methods

We evaluated RNA expression across 160 brain regions in 6 normal adult participants using publicly available gene expression data from the Allen Brain Sciences Institute database (3). We performed a repeated-measures ANOVA across 3 RNA probes (z-score average) to determine if there was a significant difference in gene expression across the 160 brain regions.

Results

We found a strong overall effect (omnibus ANOVA, $F = 7.6$, $p < 2 \times 10^{-16}$) indicating differential regional TSC1 expression. Across all 160 brain regions, highest TSC1 RNA levels were present in various cerebellar regions (Fig. 1). In comparison, lowest TSC1 RNA levels were noted in the cerebral cortex.

Conclusions

In normal adults, TSC1 RNA expression is highest in the cerebellum and lowest in the cerebral cortex. TSC1 RNA levels in the supratentorial brain were not consistent throughout the studied group, which may reflect the known high incidence of mosaicism in this population. Multiple prior studies have described the importance of the cerebellum in cognition, and implicated abnormalities of cerebellar development in the development of autism spectrum disorders (4). Considered together, our findings suggest that selective cerebellar TSC1 gene expression could partially account for autism spectrum disorder and tuberous sclerosis complex co-morbidity.

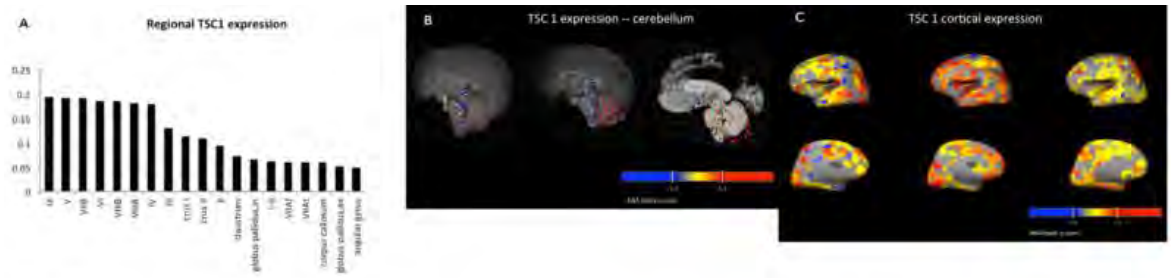


Figure 1.
A) Mean RNA expression across 3 probes and 6 subjects demonstrates largest burden of TSC1 gene expression in the cerebellar lobes.
B) Mean RNA gene expression across 3 probes overlaid on sagittal T1-weighted MRI brain, demonstrating increased gene expression in the cerebellum, with respect to other brain regions. Color scale demonstrates z-score values, with red corresponding to elevated RNA expression in that region of the brain with respect to other regions, and blue corresponding to decreased RNA expression in that region of the brain with respect to other regions.
C) Mean RNA gene expression across 3 probes overlaid on inflated medial and lateral views of the left cerebral hemisphere, demonstrating no predominant area of TSC1 gene expression in the cerebral cortex. Different patterns of expression amongst patients may reflect known mosaicism of gene expression in tuberous sclerosis complex.

(Filename: TCT_O-233_TSCFigure1.jpg)

Wednesday
11:00AM - 12:15PM
Long Beach Convention Center, Room 103 (Main Level)

18C-Parallel Paper Session: Imaging Points of Interest: Practical and Prescient

O-188

11:00AM - 11:08AM

Initial Clinical Experience Utilizing Accelerated Velocity Selective Arterial Spin Labeling for Non-Contrast 3D MR Angiography in Complex Geometries

P Sanan[1], P Turski[1], J Holmes[2], K Johnson[3], T Schubert[4]
[1]Univeristy of Wisconsin, Madison, WI, [2]University of Wisconsin, Madison, WI, [3]University of Wisconsin, Madison , WI, [4]University of Wisconsin Madison, Madison, WI

Purpose
Velocity selective arterial spin labeling (VS-ASL) is a technique for transit time insensitive, noncontrast perfusion and vascular imaging (1-3). Unlike the more common ASL techniques, for VS-ASL the tagging module is targeted to be velocity rather spatially selective. However, VS-ASL tagging is subject to other error sources including eddy currents, B1 heterogeneity, subject motion, and susceptibility artifacts. The goal of this work

is to demonstrate our preliminary experience utilizing a B0, B1, and eddy current insensitive velocity selective ASL preparation for noncontrast 3D RA/MRV.

Materials and Methods

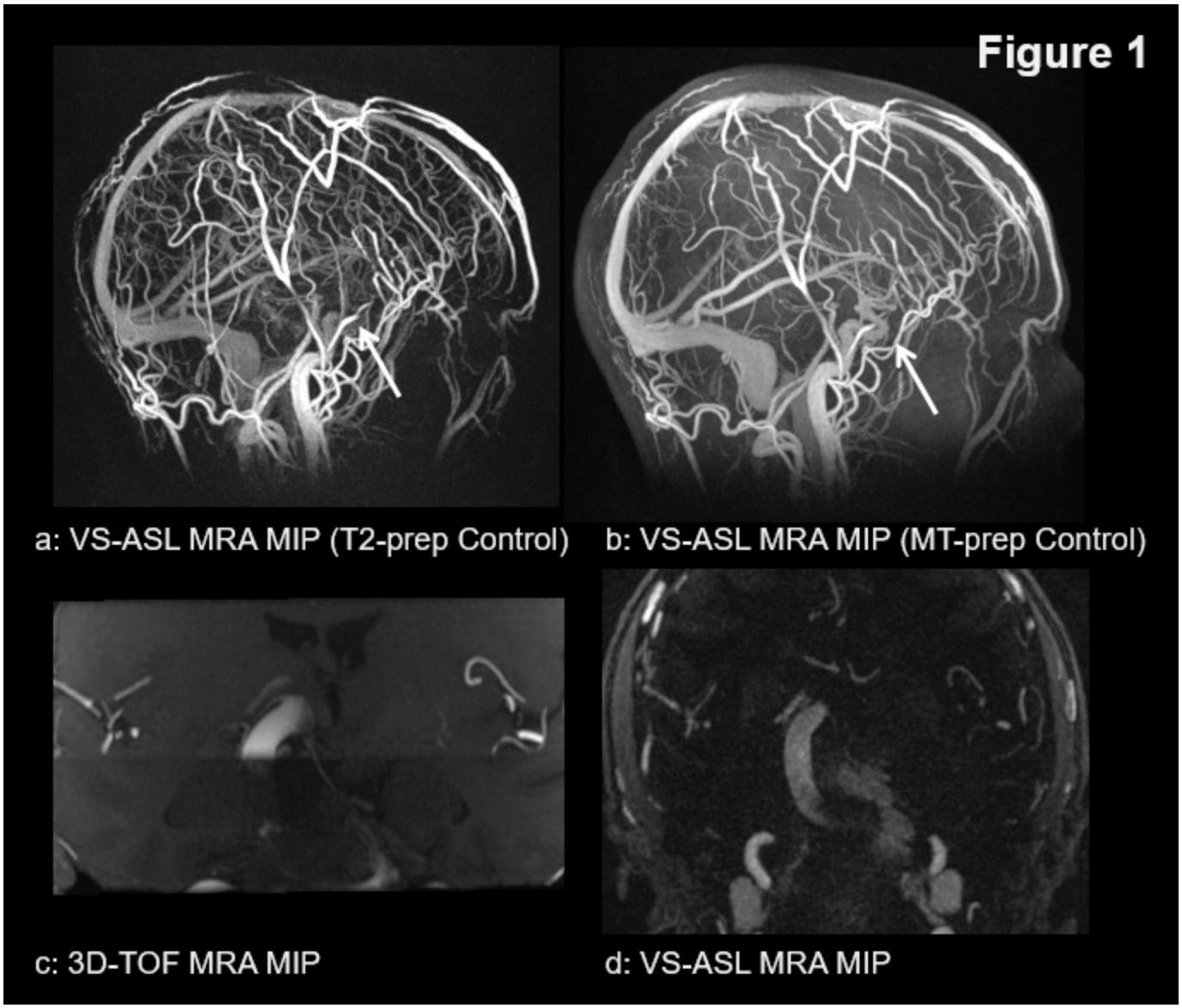
Velocity selective tagging was achieved with an eddy current and B1 insensitive tagging module (4); where images are acquired with motion sensitizing gradients (Venc=2cm/s) inserted into an adiabatic T2-preparation module. Velocity selective imaging was interleaved with a control image acquired without explicit flow sensitization. For this work, control images were collected utilizing either a conventional T2-preparation or a novel magnetization transfer (MT) preparation. Imaging was accelerated by utilizing an undersampled 3D radial trajectory (5), enabling 0.7mm isotropic resolution and whole head coverage in 5-10 minutes.

Results

Figure 1 demonstrates the differences between using a T2-preparation (1a) versus an MT-preparation (1b) as the control sequence in a normal volunteer. Notable findings include marked improvement in signal within/improved depiction of the arterial vasculature near the sinonasal cavity (arrows) utilizing the MT-preparation. Also shown is a comparison between 3D-time of flight MRA (1c) and VS-ASL MRA (1d) in a volunteer with vertebrobasilar fusiform ectasia. Notably, there is improved flow-related signal in the dilated arteries utilizing VS-ASL MRA.

Conclusions

Our initial results using VS-ASL MRA show this method to provide delineation of both arterial/venous flow without the need for intravenous contrast and with limited artifacts related to slow flow/complex geometries. This work demonstrates that signal loss at the skull base due to susceptibility artifacts can be counteracted utilizing an MT-preparation control.



(Filename: TCT_O-188_FigureLast.jpg)

O-189

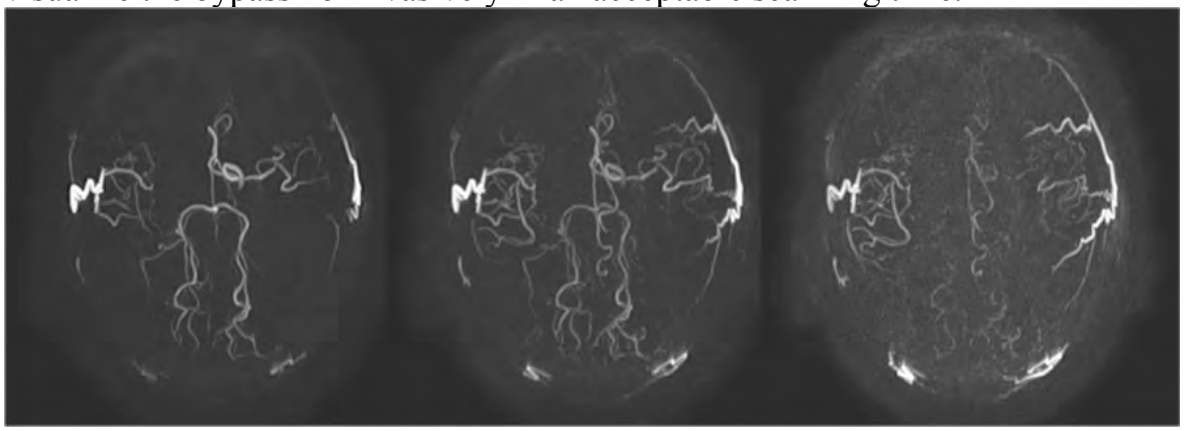
11:08AM - 11:16AM

Assessment of Extracranial-Intracranial Bypass by 3D ASL-based Non-contrast MRDSA

K Tsuchiya[1], M Gomyo[2], A Ohara[2], S Katase[2]
[1]Tokyo Teishin Hospital, Tokyo, Japan, [2]Kyorin University, Mitaka, Tokyo

Purpose
Arterial spin labeling (ASL) recently has been applied to visualize cerebral arteries as noncontrast MR digital subtraction angiography (MRDSA). We assessed the value of an

ASL-based MRDSA sequence that acquires 3D signal data at multiple interval times, which is named multi-TI MRA with signal targeting with alternating radiofrequency with asymmetric inversion slabs ASL technique (mASTAR), at 3T in the postoperative assessment of extracranial (EC) - intracranial (IC) bypass surgery.
Materials and Methods
First, we assessed the contrast-to-noise ratio (CNR) between mASTAR and 3D TOF MRA at the ICA trunk and M1 and M3 of the MCA in 5 volunteers. Then, six-phase mASTAR was performed in patients after bypass surgery using a 3D fast field-echo sequence with an initial delay of 435 ms followed by 5 phases with a 235-ms interval in 5 min 17 sec. Our patient group comprised 14 patients after EC-IC bypass for atherosclerotic occlusion of the internal carotid artery (n = 7) or moyamoya disease (n = 7). They underwent STA-MCA bypass except 1 patient that received encephaloduroarteriosynangiosis (EDAS) for moyamoya disease. We performed comparative visual assessment with 3D-TOF MRA (all 14 patients), DSA (n = 9) and SPECT (n = 13).
Results
In the volunteer group, mASTAR yielded images well demonstrating intracranial arterial branches, but mASTAR was inferior to 3D-TOF MRA in the CNR assessment. In the patient group, mASTAR better depicted the bypass recipient vessels in 11 patients, while the 2 methods were equivalent in 3 patients compared with 3D-TOF MRA. mASTAR equally demonstrated the bypass with DSA in all of the 9 patients assessed. Regional blood flow findings on mASTAR corresponded with SPECT in 11 of the 13 patients.
Conclusions
mASTAR is an effective method to evaluate the status of EC-IC bypass, as it can well visualize the bypass noninvasively in an acceptable scanning time.



(Filename: TCT_O-189_Fig.jpg)

O-190

11:16AM - 11:24AM

TRANCE (TRiggered Angiography Non Contrast Enhanced) MRI of the Intracranial Vasculature at 3 Tesla: Preliminary Experience in Children

Miller, J.
Phoenix Children's Hospital
Phoenix, AZ

O-191

11:24AM - 11:32AM

Ultrafast High-Spatial Resolution MR Angiography of the Head Using Differential Subsampling with Cartesian Ordering (DISCO)

J Drummond[1], J Jani[2], K khokhar[2], A Doshi[1], R Deleacy[1], P Pawha[1], K Nael[1]
[1]Icahn School of Medicine at Mount Sinai, New York, NY, [2]Mount Sinai Hospital, New York, NY

Purpose
The purpose of this study was to evaluate the feasibility of an ultrafast high-spatial resolution contrast-enhanced MRA of the head. Using fast imaging tools such as DIfferential Subsampling with Cartesian Ordering (DISCO) (1) and Auto-calibrating Reconstruction for Cartesian imaging (ARC) (2), we obtained near isotropic submillimeter whole-brain CE MRA during 6 sec acquisition time and compared the results with conventional time-of-light MRA (TOF MRA).
Materials and Methods
So far, 16 patients (2 men, 14 women; age range, 10 – 77 years old) were scanned prospectively by our new CE MRA sequence and TOF MRA using a 3.0T MR scanner (Discovery MR750, GE Healthcare). For CE MRA we used a gradient-echo sequence (TR/TE: 3.241.4 ms, FA 12º). Using DISCO a variable density k-space undersampling strategy was used to generate a pseudo-random distribution of k-space lines. By applying view-sharing, central k-space was sampled every time while peripheral regions sub-sampled with pseudo-random segmentation. ARC (acceleration factor of 2) was enabled in both phase-encoding (ky) and slice-encoding (kz) directions to further accelerate data acquisition. With these settings, a 3D volume with voxel-size of 0.75 x 0.75 x 1 mm3 was obtained during 6 sec acquisition covering the entire head. Time-of-flight MRA was obtained with voxel size of 0.5 x .05 x 1 mm3 during 6-minute acquisition time. We used 0.05 mmol/kg of gadobentate dimeglumine (Multihance) was injected to accomplish our CE MRA (1 cc of this contrast solution was used for timing run). Arterial tree was classified into 17-paired and 2-unpaired arterial segments. Image quality was analyzed with regard to arterial enhancement, presence of artifacts (reconstruction artifact, motion, saturation and flow dephasing), and noise by using a 4 point scoring scale (1: Not Visible, 2: Poor Quality, 3: Good Quality, 4: Excellent Quality). Qualitative image analysis was performed independently by 2 neuroradiologists. In addition arterial diameter of 3-paired arterial segments in each patient and aneurysm size (when present) was quantified. Statistical

analysis was performed using kappa, spearman-rank correlation, regression and bland-Altman analysis.
Results
All CE MRA studies were performed successfully. There was no statistical significance in terms of overall image quality between CE MRA and TOF MRA (p=0.21). Interobserver agreement regarding evaluation of image quality of arterial segments was k= 0.62, 95%CI 0.56-0.69 for TOF and k= 0.59, 95%CI 0.53-0.66 for CE MRA. Intermodality agreement between TOF and CE MRA was r= 0.49 (95% CI, 0.43-0.55) and p<0.0001. The mean ± SD of arterial diameter was 1.75 ± 0.76 mm on CE MRA and 1.98 ± 0.77 mm on TOF MRA with a mean of 0.24 mm, regression analysis showed significant correlation r2=0.81, p<0.001. The mean ± SD of aneurysm diameter was 4.90 ± 3.2mm on CE MRA and 5.2 ± 3.2 mm on TOF MRA with a mean of 0.29 mm, regression analysis showed significant correlation r2=0.94, p<0.001.
Conclusions
Using currently available fast imaging tools such as DISCO and ARC, the described brain MRA protocol provides high spatial resolution images with a 6 sec acquisition time and comparable results to conventional TOF MRA. We demonstrate here the feasibility of this protocol, although a larger prospective study is required to establish its potential clinical application.

O-192

11:32AM - 11:40AM

High Resolution Velocity Encoded PC-MRA (4D Flow): Image Quality Comparison with 3D Time of Flight MRA

W Chang[1], M Loecher[1], A Chien[1], D Ennis[1], J Villablanca[1]
[1]*UCLA, Los Angeles, CA*

Purpose
While time-of-flight (TOF) has been the gold standard for noncontrast MRA, PC MRA techniques offer velocity encoding as well as angiographic images, but are limited by long scan times and lower spatial resolution. Recently, accelerated techniques such as 4D Flow PC MRA have allowed faster scan times with high spatial resolution (1-3). In this study we compare the image quality of 4D Flow PC MRA at 0.5 mm isotropic spatial resolution with 3D TOF in 10 healthy volunteers.
Materials and Methods
Ten healthy volunteers were scanned using a Siemens Prisma 3.0T MRI scanner. Source/MIP images were obtained using 4D Flow and 3D TOF sequences. Two experienced readers scored image quality in the ICA, basilar, ophthalmic, anterior choroidal, P1-3, A1-3, and M1-3 arterial segments, following the protocol used in our previous image quality study (4). Images were scored using a 4-point Likert scale (1=poor visualization; 2=visualized but

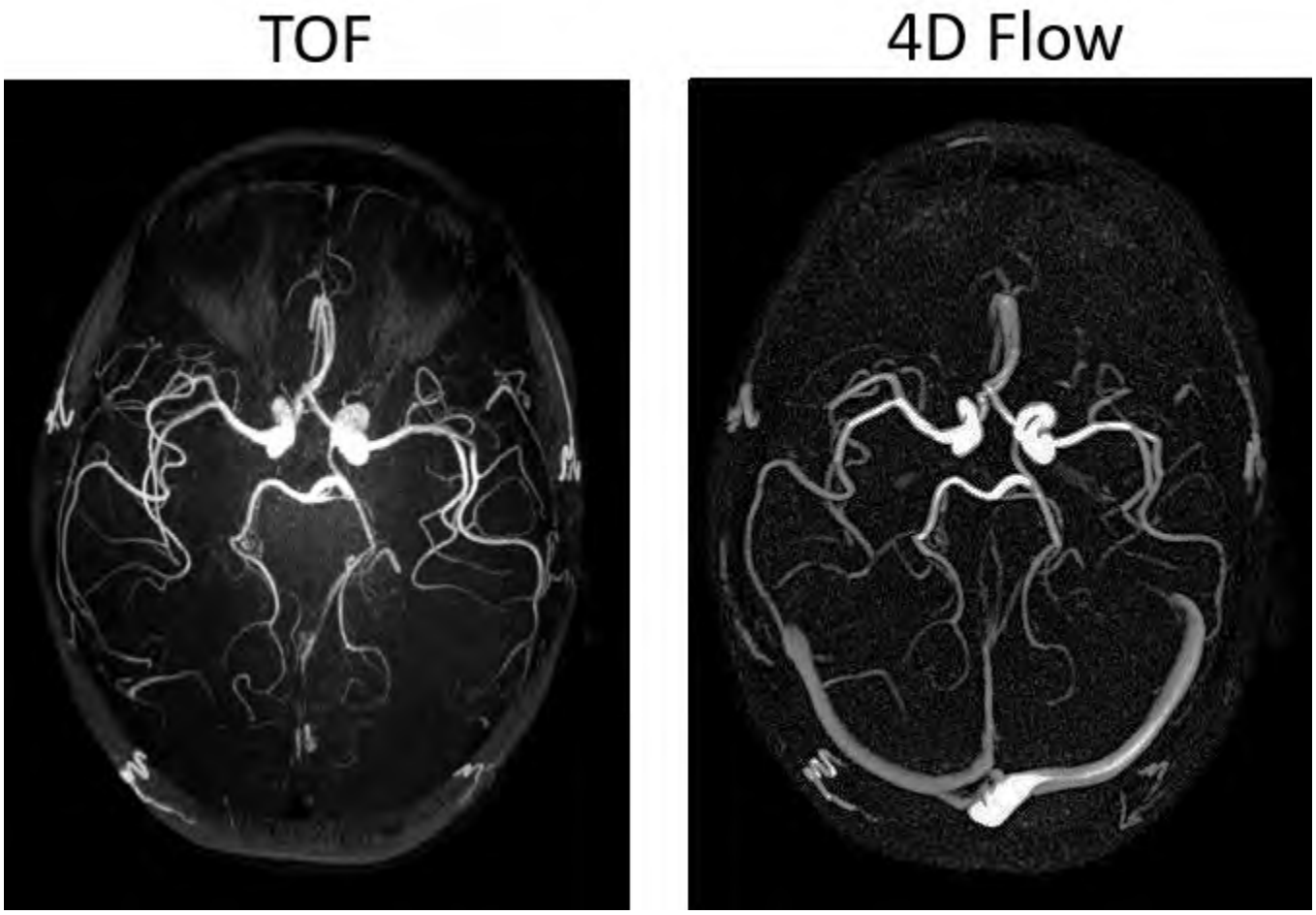
not of diagnostic quality; 3=good visualization of diagnostic quality; 4=excellent diagnostic quality). A Mann-Whitney U-test was performed to compare mean image quality for both source images and MIPs.

Results

Both techniques had excellent visualization of all major vessels on both source images and MIPs (image quality 4.0±0). For source images there was no significant difference between 4D Flow and 3D TOF for all vessels (3.84±0.49 TOF, 3.81±0.55 4D Flow, p=0.87) or 2nd/3rd order branches (3.74±0.60 TOF, 3.71±0.67 4D Flow, p=0.82). For MIPs there also was no significant difference between image quality between 4D Flow and 3D TOF for all vessels (3.75±0.70 TOF, 3.64±0.88 4D Flow, p=0.51) or for 2nd/3rd order branches (3.60±0.85 TOF, 3.43±1.05 4D Flow, p=0.37).

Conclusions

In this study, we demonstrated that 4D Flow showed no significant difference in image quality when compared to 3D TOF in both major intracranial vessels and 2nd/3rd order branches, while simultaneously acquiring velocity information which was used to calculate hemodynamic data such as flow and WSS (5). In the future, 4D Flow techniques may represent viable alternatives to 3D TOF that also acquire hemodynamic data.



(Filename: TCT_O-192_fig1b.jpg)

O-193

11:40AM - 11:48AM

Imaging Characteristics Associated with Clinical Outcomes in Posterior Reversible Encephalopathy Syndrome

A Schweitzer[1], N Parikh[1], G Askin[2], A Nemade[1], J Lyo[3], S Karimi[4], B Navi[5], R Young[3], A Gupta[6]

[1]Weill Cornell Medicine, New York, NY, [2]Weill Cornell Medical College, New York, NY, [3]Memorial Sloan Kettering Cancer Center, New York, NY, [4]Memorial Sloan-Kettering Cancer Center, New York, NY, [5]New York Presbyterian Hospital- Weill Cornell Medical Colelge, New York, NY, [6]New York-Presbyterian Hosp/Weill Cornell Med Ctr, New York, NY

Purpose

Posterior reversible encephalopathy syndrome (PRES) is a disorder of cerebrovascular autoregulation that can result in brain edema, hemorrhage, and infarction. We sought to investigate whether certain imaging characteristics in PRES are associated with clinically significant patient outcomes.

Materials and Methods

We retrospectively reviewed all cases of PRES occurring between 2008 and 2014 at 2 major academic medical centers. Demographic, clinical, and radiographic data were collected. We analyzed imaging studies for vasogenic edema, hemorrhage, and diffusion restriction. We performed univariate analysis and stepwise logistic regression to assess the association between our radiologic findings of interest and clinical outcomes as defined by hospital discharge disposition and modified Rankin scale (mRS) at time of discharge.

Results

We identified 99 cases of PRES in 96 patients. The median age was 55 years (IQR 30-65) and 74% were women. Of the 96 patients, 58% had active cancer, 20% had history of bone marrow or organ transplantation, 15% had autoimmune disease, and 8% were peripartum. Imaging at clinical presentation showed extensive vasogenic edema in 39%, hemorrhage in 36%, hemorrhage with mass effect in 7%, and restricted diffusion in 16%. In our final logistic regression models, the presence of extensive vasogenic edema, hemorrhage with mass effect, or diffusion restriction was associated with worse clinical outcome as defined by both discharge disposition (OR=4.3; 95% CI: 1.4-36.3; p=0.047) and mRS (OR=3.6; 95% CI: 1.2-10.7; p=0.019).

Conclusions

Extensive vasogenic edema, hemorrhage, and restricted diffusion on initial imaging in PRES are associated with worse clinical outcomes.

Multivariable logistic regression model of clinical and radiologic factors associated with discharge disposition after PRES

Variable	OR Crude	OR Adj	95% CI	p-value
History of brain radiation	3.91	11.19	2.03, 61.68	0.006
Presence of sepsis	5.75	4.35	1.13, 16.76	0.033
Presence of diffusion restriction	5.92	8.18	1.94, 34.49	0.004

Note: The following variables were entered into the stepwise regression model: brain radiation (Y/N), sepsis (Y/N), hemorrhage (Y/N), diffusion restriction (Y/N).

Multivariable logistic regression model of clinical and radiologic factors associated with modified Rankin score at discharge after PRES

Variable	OR Crude	OR Adj	95% CI	p-value
Age	1.04	1.07	1.03, 1.11	<0.001
History of brain radiation	11.6	52.89	3.09, 904.79	0.006
Presence of autoimmune condition	0.16	0.15	0.02, 0.99	0.048
Presence of sepsis	2.46	5.29	1.35, 20.70	0.017
Presence of hemorrhage	2.8	3.05	0.96, 39.69	0.059
Presence of DWI restriction	2.81	6.41	1.20, 34.33	0.030

Note: The following variables were entered into the stepwise regression model: age, brain radiation (Y/N), sepsis (Y/N), autoimmune condition (Y/N), edema (Y/N), brainstem edema (Y/N), hemorrhage (Y/N), diffusion restriction (Y/N).

(Filename: TCT_O-193_ASNRPREStablelarge.jpg)

O-194

11:48AM - 11:56AM

Exploring atypical PRES – what is typical?

A McClelland[1], C Ellis[1], E Kuo[2], R Balu[1], S Mohan[1]
[1]Perelman School of Medicine, University of Pennsylvania, Philadelphia, PA, [2]Philadelphia College of Osteopathic Medicine, Philadelphia, PA

Purpose

Posterior reversible encephalopathy syndrome (PRES) is a neurotoxic syndrome with characteristic parieto-occipital subcortical vasogenic edema (1). However, atypical imaging findings may suggest alternative or superimposed diagnoses. While the presence of atypical findings is well documented, characteristic imaging patterns and their relationship to clinical parameters is not. The purpose of this study is to identify common patterns in atypical PRES and assess their relationship to clinical factors.

Materials and Methods
Radiology and clinical databases were searched from 2002 to 2015 for keywords related to PRES. Clinical information was gathered from retrospective review of the electronic medical record and clinical notes, and cases were included after thorough review by an attending neurologist and neurology resident. For each included case, areas of typical subcortical white matter FLAIR edema, as well as atypical involvement of additional brain areas, was identified by consensus review of an attending neuroradiologist and neuroradiology fellow. Chi-squared and Fisher's exact test were used to evaluate proportions of different areas of involvement and their relationship to clinical parameters.
Results
Fifty-five cases of PRES were identified, 45 of which had atypical findings (34 female, 11 male; mean age 51 years). The most common atypical site was the cerebellum (80%), followed by the brainstem (69%), thalamus (56%), basal ganglia (36%), and corpus callosum (27%). Hierarchical cluster analysis identified clustered patterns of involvement including a "posterior circulation" pattern with involvement of the cerebellum with the brainstem and/or the thalami (55%). Other patterns included an isolated cerebellar pattern (22%) as well as "brainstem" and/or "thalamic" predominant (16% each). Interestingly, involvement of the basal ganglia and corpus callosum was never seen in isolation. Severe hypertension on presentation was associated with an overall greater severity of imaging findings and greater likelihood of cerebellar involvement. Basal ganglia involvement was uncommon in patients with history of hypertension or immunosuppression.
Conclusions
Atypical PRES most commonly involves the cerebellum alone or together with other atypical locations. Other patterns include thalami or brainstem predominant with basal ganglia and corpus callosum findings occurring only in combination with other atypical locations. Moreover, some clinical presentations are associated with specific atypical imaging manifestations. Knowledge of atypical PRES patterns and their associations with clinical factors will add diagnostic certainty in cases of PRES in which atypical findings may suggest an alternative or superimposed diagnosis.

O-195

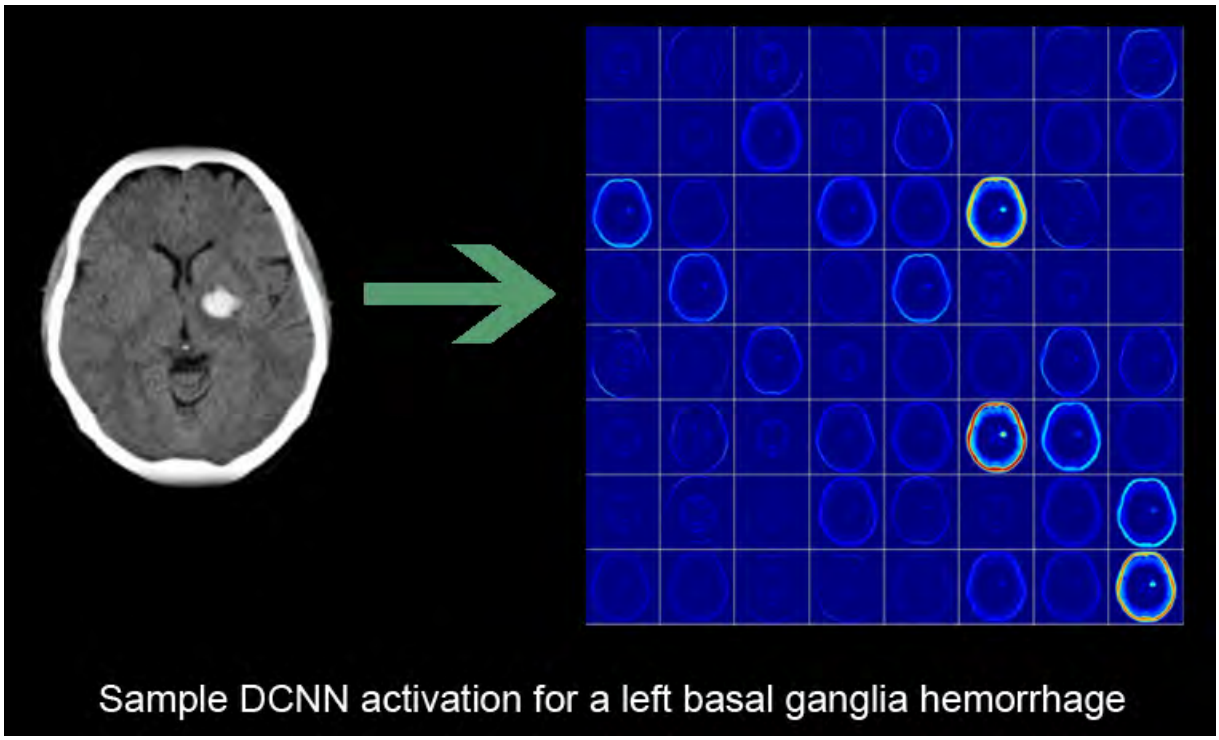
11:56AM - 12:04PM

Application of Deep Learning in Neuroradiology: Automated Detection of Basal Ganglia Hemorrhage

V Desai[1], P Lakhani[1], A Flanders[2]
[1]Thomas Jefferson University Hospital, Philadelphia, PA, [2]Thomas Jefferson Univ. Hosp., Philadelphia, PA

Purpose
Automated triage of emergent imaging studies has been lauded as one of the compelling

applications of machine learning in radiology. This has the potential capacity to improve both the efficiency and value of the neuroradiologist by prioritizing exams with urgent/critical findings. This study evaluates the efficacy of deep convolutional neural networks for detecting basal ganglia hemorrhage on noncontrast head CT.
Materials and Methods
Two de-identified HIPAA-compliant datasets were used in this study, with the primary training dataset consisting of 20 noncontrast head CTs of right basal ganglia hemorrhage, 20 CTs of left basal ganglia hemorrhage, and 20 head CTs without hemorrhage. Several key images at the level of the basal ganglia were stored for each CT (approximately 3-5 per study), resulting in 242 unique DICOM images. Subsequent automated data augmentation was performed in which multiple CT windows, different zoom levels, and various degrees of rotation, blur, and edge enhancement were applied to the images. The resultant large dataset was split into training (75%, 11037 images) and validation (25%, 3678 images). A hold-out test dataset consisting of 76 unique cases (72% basal ganglia hemorrhage, 28% no hemorrhage) was obtained - half from our institutional PACS and the other half, unmodified from internet sources. The size of the hemorrhages for the training and test datasets ranged from 1 cm to larger than 10 cm. Two different deep convolutional neural networks (DCNN) were used to classify the images - AlexNet and GoogLeNet - as having a right basal ganglia hemorrhage, a left basal ganglia hemorrhage, or normal. Both untrained and pretrained networks on ImageNet were utilized. Statistical analysis was performed on the results of the test dataset, which was classified previously by an independent radiologist. Area under the curve (AUC) for the receiver-operator characteristic (ROC) curves were calculated using the pROC package (ver. 1.7.3) for R (ver. 3.3.1), using the DeLong method for statistical comparison of ROCs.
Results
The best performing classifiers were the untrained and pretrained GoogLeNet DCNN, which had an area under the curve (AUC) of 0.99 and 1.0 respectively in identifying bleed versus no bleed. The GoogLeNet classifiers correctly identified 55/55 cases of basal ganglia hemorrhage in the hold-out test dataset, including the laterality of the bleed (sensitivity 100%). The classifiers correctly labeled 20/21 cases without hemorrhage, including 6 cases of basal ganglia calcifications (specificity 95.2%). The one false-positive case demonstrated asymmetric basal ganglia calcifications. The AlexNet classifiers retained a high AUC (0.92), with sensitivity for hemorrhage near 100% but with a lower specificity. The GoogLeNet classifiers had significantly greater accuracy compared to the AlexNet classifiers (p=0.03).
Conclusions
Deep learning with convolutional neural networks achieves state-of-the-art accuracy for identification of basal ganglia hemorrhage, including laterality, on noncontrast head CT with a sensitivity of 100% and AUC of greater than 0.99. With the widespread availability of deep machine learning APIs, classifiers of this type are amenable to being integrated into a PACS workflow engine. The future of deep machine learning to automatically triage and appropriately flag cases is very promising.



(Filename: TCT_O-195_bleed_activation.jpg)

O-196

12:04PM - 12:12PM

Automated Diagnosis of Basal Ganglia Diseases Using a Customized Image-Processing Pipeline Coupled with Bayesian Networks

J Rudie[1], L Xie[1], A Rauschecker[1], Y Ding[1], I Nasrallah[1], P Chen[1], R Bryan[1], S Mohan[1], E Botzolakis[1], J Gee[1]
[1]*University of Pennsylvania, Philadelphia, PA*

Purpose
Despite significant recent advances in computational approaches utilizing massively parallel algorithms and big data, there has yet to be substantial progress in computer-aided diagnosis of complex medical imaging (1, 2). We sought to combine powerful image processing methods and neuroradiology expertise encapsulated within robust Bayesian networks, in order to achieve automated neuroradiology diagnoses. As proof of concept, we focused on a challenging subset of diseases affecting the basal ganglia, as they reflect a wide variety of underlying pathology and require integration of multiple imaging and clinical variables (3).
Materials and Methods
Seventy-three clinically-validated cases representing 22 different basal ganglia diseases were included in the study. This included ischemic and hemorrhagic stroke, carbon monoxide poisoning, high and low grade gliomas, sarcoidosis, toxoplasmosis, CJD, lymphoma, and metastases. Seven clinical MR modalities were incorporated into the image-processing

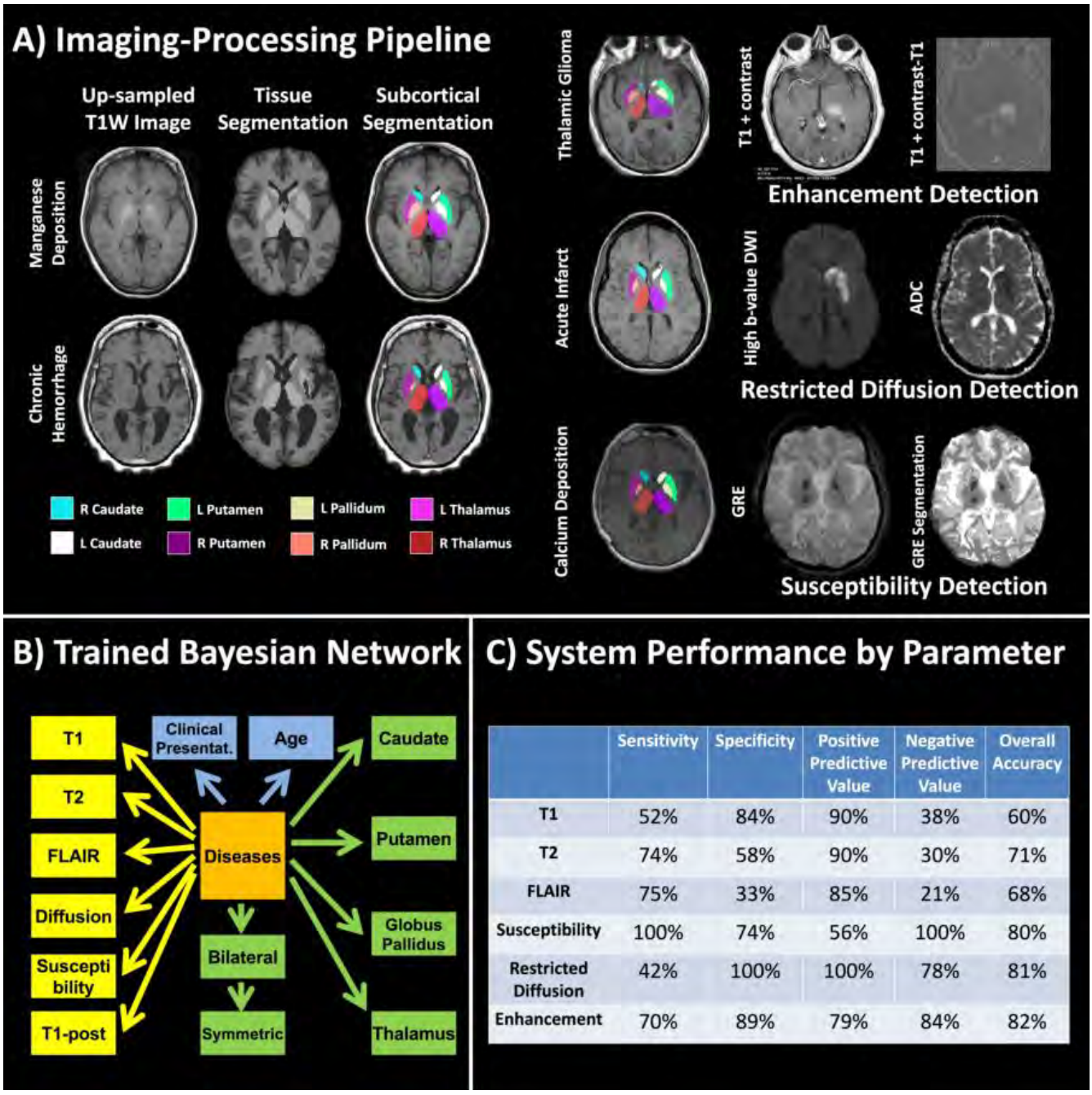
pipeline: T1, T1-postcontrast, T2, FLAIR, GRE, DWI, and ADC. T1 images were normalized, skull stripped, and up-sampled using a super-resolution technique (4) prior to gray/white matter segmentation and subcortical segmentation with freely available ANTs cortical segmentation software (5) (Fig. 1A). Eight subcortical volumes, including left and right caudate, putamen, globus pallidus, and thalamus were segmented and then co-aligned to the other modalities in order to detect signal abnormalities within the regions. The extracted spatial and signal imaging features were combined with clinical information (age, chronicity) and fed into an expert-trained Bayesian network encompassing 53 possible diagnoses to generate a probability-ranked differential diagnosis (Fig. 1B).

Results

Accuracy of the image-processing pipeline was >80% for detecting regions with restricted diffusion, susceptibility and enhancement, while accuracy was 60-71% for detecting abnormal T1, T2, and FLAIR signal (Fig. 1C). The Bayesian network, integrating features extracted by the image-processing pipeline, determined an accurate differential diagnosis in 62% of the cases (within the top of 3 probabilistically ranked diagnoses). It determined the exact diagnosis in 44% of the cases. In comparison, when attending neuroradiologists manually extracted features, the Bayesian network determined an accurate differential diagnosis in 90% of cases and the exact diagnosis in 74% of cases.

Conclusions

Using a hybrid approach that computationally mirrors the 2 fundamental steps to image interpretation, our integrated system automatically diagnoses a diverse array of neuroradiologic diseases. Although the method will require rounds of improvements to be clinically useful, this novel approach shows incredible promise as a first step to harness the power of big data and machine learning methods in clinical imaging.



	Sensitivity	Specificity	Positive Predictive Value	Negative Predictive Value	Overall Accuracy
T1	52%	84%	90%	38%	60%
T2	74%	58%	90%	30%	71%
FLAIR	75%	33%	85%	21%	68%
Susceptibility	100%	74%	56%	100%	80%
Restricted Diffusion	42%	100%	100%	78%	81%
Enhancement	70%	89%	79%	84%	82%

(Filename: TCT_O-196_ASNR_Figure.jpg)

Wednesday
11:00AM - 12:15PM
Long Beach Convention Center, Room 104A (Main Lobby)

18D-Parallel Paper Session: Brain Tumor Imaging: Here and On the Horizon

O-197

11:00AM - 11:08AM

Machine learning algorithms for predicting GBM growth patterns using advanced and delayed-contrast MRI: feasibility demonstration

Y Mardor[1], V Sason[2], D Last[3], D Daniels[4], G Tsarfaty[4], C Hoffmann[5], D Nass[5], S Salomon[2], A Talianski[3], A Kanner[6], D Blumenthal[7], F Bokstein[8], D Limon[9], T Tzuk[10], Z Cohen[11], L Zach[4], D Guez[3]

[1]Sheba Medical Center and Tel-Aviv University, Ramat-Gan, Israel, [2]Sheba Medical Center, Ramat Gan, AK, [3]Sheba Medical Center, Ramat-Gan, AK, [4]Sheba Medical Center and Tel-Aviv University, Ramat-Gan, AK, [5]Sheba Medical Center and Tel-Aviv University, Ramat Gan, AK, [6]Tel Aviv Medical Center and Tel Aviv University, Tel-Aviv, AK, [7]Tel Aviv Sourasky Medical Center, Tel aviv, AK, [8]Tel Aviv Medical Center, Tel Aviv, AK, [9]Rabin Medical Center, Petah-Tikva, AK, [10]Rambam Medical Center, Haifa, AK, [11]Sheba Medical Center and Tel Aviv University, Ramat Gan, AK

Purpose

We recently have presented delayed contrast MRI-based treatment response assessment maps (TRAMs) enabling efficient separation between tumor and treatment effects, validated histologically in 54 resected patients, reaching 100%/93% sensitivity/PPV to active tumor. Here we demonstrate potential prediction of tumor growth patterns using a neural network (NN) and advanced MRI including the TRAMs.

Materials and Methods

Glioblastoma (GBM) patients were followed by advanced MRI (T1-Gd, diffusion, perfusion, T2, FLAIR, TRAMs) acquired every 2 months during periods of no treatment changes. Each patient underwent 2-9 consecutive MRI follow-ups. All MRIs were coregistered. Regions of interest (ROIs) were plotted surrounding enhancing regions on T1-Gd and copied to all the patients' MRIs/maps. Then all pixels within these ROIs were fed into the NN. The NN then was trained to use all the pixels of the various MRI sequences acquired during one MRI exam to predict the tumor spatial distribution (calculated from the TRAMs) of the following MRI exam. Data of 6 patients (2.6x10^6 pixels from 22 follow-ups) were used to train the NN and data of additional 3 patients (0.65x10^6 pixels from 10 follow-ups) served as the test group. The NN was fed with the multidimensional data of each pixel individually and with micro-environmental information consisting of local tumor density per pixel and the distance to the tumor edge per pixel, calculated from the TRAMs.

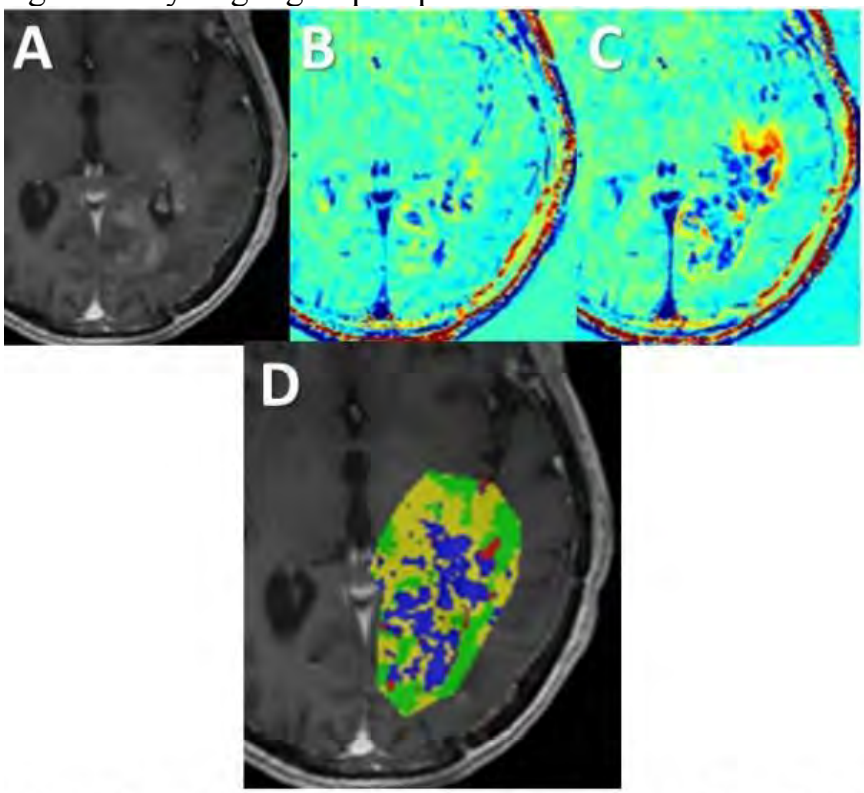
Results

Sixty-eight percent of the tumor pixels in the outcome TRAMs were predicted correctly by the NN for the test group. Receiver operating characteristic (ROC) analysis resulted in AUC=0.70, sensitivity=71%, specificity=58% and F1-score=77%.

Conclusions

These preliminary results demonstrate the potential of this per-pixel based machine learning algorithm to predict GBM growth patterns. The TRAMs high sensitivity/PPV to active tumor provides the essential deterministic definition of input and outcome for the algorithm.

The reliability of such a NN for potential clinical application is yet to be studied in a significantly larger group of patients.



A: T1-Gd of a GBM patient 20 months post chemoRT. B-C: TRAMs of the patient at 20 (B) & 22 months (C) (blue=tumor; red=treatment effects). The color map in D shows preliminary results of the machine learning algorithm: pixels correctly predicting non-tumor are shown in green, falsely predicting non-tumor in red, correctly predicting tumor in purple and falsely predicting tumor in yellow.

(Filename: TCT_O-197_Fig.jpg)

O-198

11:08AM - 11:16AM

Comparison Study of Radiogenomics Association and Prognostic Value Between MR Dynamic Susceptibility Contrast Perfusion Weighted Imaging and Diffusion Imaging in Patients with Newly Diagnosed Glioblastoma

X Liu[1], W Tian[1]
[1]*University of Rochester Medical Center, Rochester, NY*

Purpose

Glioblastoma is the most common malignant primary brain tumor in adults. Magnetic resonance dynamic susceptibility contrast perfusion-weighted imaging (DSC-PWI) and diffusion-weighted imaging (DWI) are advanced imaging techniques investigating

hemodynamic changes and tumor cellularity. The purpose of this study is to evaluate and compare the association between molecular genomic biomarkers and imaging parameters derived from MR DSC-PWI and DWI, and their prognostic value in predicting overall survival time (OS) in patients with newly diagnosed glioblastomas.
Materials and Methods
Forty-one cases (mean age is 62.32±12.09) with new pathology confirmed glioblastomas were enrolled in this study. The mean, maximal relative cerebral blood volume (rCBV) ratio, mean apparent diffusion coefficient (ADC) and minimal ADC of the enhancing tumor (rCBVmean, rCBVmax, ADC mean and ADCmin), maximal rCBV ratio and minimal ADC of peri-enhancing tumor area (rCBVperi-tumor and ADCperi-tumor) were measured. The association between imaging parameters and Ki-67 labelling index, isocitrate dehydrogenase (IDH), mammalian target of rapamycin (mTOR), and epidermal growth factor receptor (EGFR) was assessed, the Cox regression was used to evaluate their implication on OS. The difference of clinical and imaging parameters, and molecular genomic biomarkers between the patients who survived less than 14 months and more than 14 months was compared.
Results
There were 40 cases without IDH mutation, and there was significant difference of rCBVmax, rCBVperi-tumor and OS among three mTOR groups ($p<0.05$). Compared to ADC parameters, the rCBVmax had significant association with mTOR, ($p =0.047$), the rCBVperi-tumor was significantly associated with mTOR after adjustment of age and EGFR. The rCBVperi-tumor showed significant difference in the group comparison between patients survived less or longer than 14 months ($p =0.002$). The Cox regression analysis showed that rCBVperi-tumor and age were the two strongest predictors of OS (hazard ratio= 1.29 and 1.063; $p =0.003$ and 0.005 separately). The combination of rCBVperi-tumor and age improved the predication of OS with specificity of 78.9% and sensitivity of 81.8%.
Conclusions
This study showed significant radiogenomics association between quantitative rCBV parameters and mTOR-EGFR pathway biomarkers, which may suggest that tumor angiogenesis is moderated by mTOR-EGFR pathway. The rCBVperi-tumor had better prognostic value than molecular genomic biomarkers and ADC parameters, which may suggest that tumor angiogenesis plays more important role in role in tumor progression in patients with primary glioblastoma, and the genomics mechanism related with tumor cellularity may be more complicated.

O-199

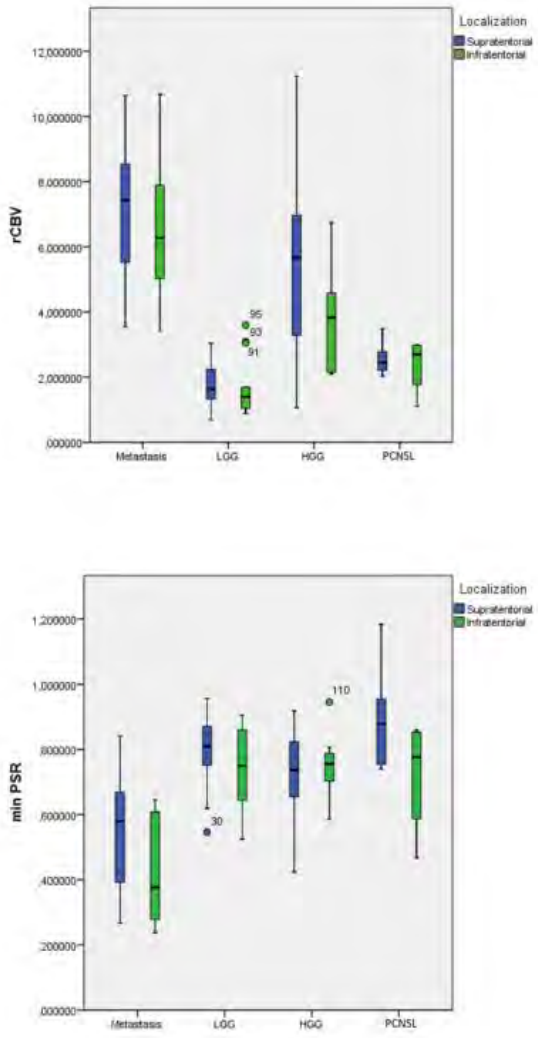
11:16AM - 11:24AM

Investigating Dynamic Susceptibility weighted Contrast enhanced (DSC) Perfusion MR Imaging in Posterior Fossa Tumors: Differences and Similarities with Supratentorial Tumors.

M Martucci[1], S Gaudino[2], A Botto[3], C Colosimo[4]

[1]Institute of Radiology - Fondazione Policlinico Universitario A. Gemelli, ROME, Italy, [2]Institute of Radiology - Fondazione Policlinico Universitario A. Gemelli, Rome, RM, [3]Institute of Radiology - Fondazione Policlinico Universitario A. Gemelli, ROME, ROME, [4]Institute of Radiology - Fondazione Policlinico Universitario A. Gemelli, ROME, RM

Purpose
The analysis of perfusion parameters derived from DSC tissue signal intensity time curves have shown utility in distinguishing adult brain neoplasms, but has limited description in the literature for infratentorial tumors. Thus, the aims of our study were: 1. To assess the accuracy of dynamic susceptibility-weighted contrast-enhanced perfusion-weighted magnetic resonance imaging in glioma grading and brain tumor characterization of infratentorial tumors. 2. To investigate differences from supratentorial tumors.
Materials and Methods
This retrospective study, approved by the institutional review board, included 114 patients with brain tumors (40 infratentorial, 74 supratentorial), grouped by tumor type: high grade glioma (HGG), low grade glioma (LGG), metastases, and primary central nervous system lymphoma (PCNSL). Relative cerebral blood volume (rCBV) and mean and minimum percentages of signal recovery (PSR) were calculated. For statistical analysis lesions were divided according to the location and histology. Mann-Whitney U test was used to test the differences; accuracy, sensitivity, specificity, PPV and NPV for rCBV and PSR were calculated from ROC curves.
Results
For infratentorial tumors, rCBV was highly accurate in differentiating HGG from LGG ($p<0.001$) and PSRs (mean and minimum) were significantly higher in PCNSL and HGG compared to metastases ($p<0.001$; $AUC>0.9$). Infratentorial and supratentorial tumors had similarly high rCBV in HGG, high mean PSRs in PCNSL, and low mean PSRs in metastases. The main differences were the optimum threshold rCBV values (3.05 for supratentorial, 1.89 for infratentorial tumors) and the mean PSR, which was significantly higher in LGG than in HGG in supratentorial, but not infratentorial tumors ($p=0.001$). Applying infratentorial rCBV threshold values for supratentorial tumors decreased both the sensitivity and specificity.
Conclusions
Relative cerebral blood volume and PSRs are useful in grading and differentiating infratentorial tumors. The overall behavior of perfusion parameters was similar between supratentorial and infratentorial tumors, but some differences in rCBV and PSRs were demonstrated. The difference of rCBV threshold value between supratentorial and infratentorial tumors to distinguishing HGG from LGG might be of high clinical relevance, and in our opinion deserves consideration.



(Filename: TCT_O-199_Untitled-1.jpg)

O-200

11:24AM - 11:32AM

Predicting Genomic Features of Lower Grade Gliomas with Diffusion and Signal Intensity Based Compartmentalization to Account for Tumor Heterogeneity

S Hwang[1], R Lee[2], C Holder[3], A Rao[4], A Flanders[5]
[1]St Jude Children's Research Hospital, Germantown, TN, [2]University of Tennessee Health Science Center, Memphis, TN, [3]Emory University School Of Medicine, Atlanta, GA, [4]MD Anderson Cancer Center, Houston, TX, [5]Thomas Jefferson Univ. Hosp., Philadelphia, PA

Purpose
Facilitate the prediction of genomic features in diffuse lower grade gliomas (LGGs) (grades I

to III) of the brain by compartmentalizing tumors on the basis of signal intensity and diffusion to account for heterogeneity.
Materials and Methods
Lower grade gliomas are difficult to manage, secondary to infiltration and malignant progression. Genomic analysis has identified 2 key molecular markers for predicting prognosis and targeting treatment but requires invasive biopsy: isocitrate dehydrogenase gene (IDH) mutation and codeletion of the short arm of chromosome 1 (1p) and long arm of chromosome 19 (19q). Classification of LGGs in The Cancer Genome Atlas (TCGA) database into 3 groups (IDH mutants with 1p19q codeletion, IDH mutants without codeletion, and IDH wild type) was more robust than WHO histopathologic classification in predicting outcome. The role of imaging genomics is to noninvasively predict genomic features. One obstacle is tumor heterogeneity. One method for subdividing tumors is to threshold images into low versus high signal intensity regions. Subtraction (post-precontrast) images were generated to assess enhancement (T1enh). Four compartments are generated by combinations of low and high signal in T2 and T1enh. Otsu thresholds were applied to T2 images while triangle thresholds were applied to T1enh images. FLAIR and diffusion were thresholded to generate more compartments. Eighty image sets of LGGs from TCGA were coregistered and segmented using NIH ImageJ with Weka machine learning software. Mean ADC was computed in tumor compartments and associations with genomic features were investigated with Student t-tests and ANOVA. Receiver operating curve (ROC) analysis also was performed.
Results
The high T1enh/low T2 compartment demonstrated lower ADC ($p<0.001$ compared to high T2 compartments and $p<0.03$ compared to low T2/low T1enh). Associations with genomic markers were identified with the more aggressive IDH-wt tumors exhibiting lower ADC ($p<0.0001$), suggesting greater cellularity. The difference was statistically significant in all of the compartments but a multivariate model provided the best area under the curve (AUC) of 0.78 for the prediction of IDH mutation status based on ROC analysis. Apparent diffusion coefficient (ADC) also was predictive of other mutations such as TERT (AUC = 0.71). However, AUC was only 0.56 for the prediction of 1p/19q co-deletion.
Conclusions
Compartmentalization based on thresholds may provide an efficient method for characterizing heterogeneous tumors and facilitate the prediction of genomic features. Specifically, areas of low T2 signal and more enhancement were confirmed to have lower ADC, especially in the more aggressive tumors with wild type IDH. A multivariate model, however, was most predictive of IDH mutation status based on ROC analysis.

O-201

11:32AM - 11:40AM

Quantitative multimodal MRI improves the predictive power of survival models for glioblastoma patients

J Puig[1], G Blasco[2], A Gimeno[3], C Biarnes-Duran[4], P Daunis-i-Estadella[5], M Marti-Navas[6], S Thio-Henestrosa[5], J Sanchez-Gonzalez[7], A Alberich-Bayarri[8], M Puigdemont[9], M Wintermark[10], K Nael[11], R Jain[12], M Essig[13], P Salvador[2]
[1]IDIBGI-IDI Hospital Dr Josep Trueta, Girona, Girona, [2]Imaging Research Unit, IDI-IDIBGI, Hospital Dr Josep Trueta, Girona, None, [3]Department of Radiology (IDI), University Hospital Dr Josep Trueta, Girona, Girona, [4]Research Unit of Diagnostic Imaging Institute (IDI), Girona Biomedical Research Institute (IDIBGI), Girona, Girona, [5]Department of Computer Science, Applied Mathematics and Statistics, University of Girona, Girona, Girona, [6]Research Unit of Diagnostic Imaging Institute (IDI), IDIBGI, University Hospital Dr Josep Trueta, Girona, Girona, [7]Philips Healthcare Ibérica, Madrid, Madrid, [8]Hospital Universitario y Politecnico La Fe-QUIVIM, Valencia, None, [9]Catalan Institute of Oncology (ICO), Hospital Cancer Registry, University Hospital Dr Josep Trueta, Girona, Girona, [10]Stanford University, Stanford, CA, [11]Icahn School of Medicine at Mount Sinai, New York, NY, [12]NYU School of Medicine, New York, NY, [13]Department of Radiology, University of Manitoba, Winnipeg, Manitoba

Purpose
Accurate survival prediction can be highly beneficial when treating glioblastoma patients. Previous studies have focused on identifying individual predictors of survival. Limited evidence suggests that adding imaging features to clinical predictors (e.g., treatment, clinical status, and age) will improve survival predictions. We retrospectively determined the usefulness of dynamic susceptibility contrast (DSC) permeability maps, diffusion parameters, and many qualitative findings for contrast-enhancing lesion (CEL) and surrounding non-CEL in predicting survival.
Materials and Methods
Before treatment, 72 consecutive patients (45 men; mean age, 64 years) with histologically proven glioblastoma underwent 1.5T MRI (anatomical, first-pass DSC, DWI, and postcontrast T1-weighted sequences). Perfusion maps were computed with the Bayesian approach. We used Olea Sphere V.3.0 software (Olea Medical,La Ciotat, France) to determine cerebral blood volume ratio, cerebral blood flow ratio, mean transit time, time-to-peak, delay time (DT), permeability constant (k2), and apparent diffusion coefficient (ADC) in volumes of interest in CEL, non-CEL, and contralateral tissue. We evaluated 26VASARI descriptors. Patients were classified by survival: 1 year. Complete treatment was defined as surgery, radiotherapy, and chemotherapy.
Results
Survival was <1 year in 49 (68%) patients; 39 (54.16%) underwent complete treatment. Differences between patients surviving 1 year, respectively, were observed image (62.21±12.53 vs.50.63±15.1 years; P<0.001), ADC-CEL (0.98±0.97 vs.0.78±0.05mm2/s; P=0.032), delay-CEL (-0.41±0.82 vs. 0.07±0.54s; P=0.043), DT-nonCEL (-0.26±0.58 vs 0.18±0.47s; P=0.01), and treatment (P<0.001). In the univariate analysis, complete treatment

best predicted survival at 1 year [AUC=0.774, 60.6% sensitivity, 94.3% specificity, 95.6% positive predictive value (PPV), 54.1% negative predictive value (NPV)]. However, DT-CEL plus age yielded the best combined prediction of survival (AUC=0.859, 86.7% sensitivity, 73.3% specificity, 86.7%PPV, 73.3% NPV).
Conclusions
Beyond well known survival factors, our data suggest the perfusion parameter DT might help predict survival in newly diagnosed glioblastoma.

O-202

11:40AM - 11:48AM

Sodium Imaging and Gliomas

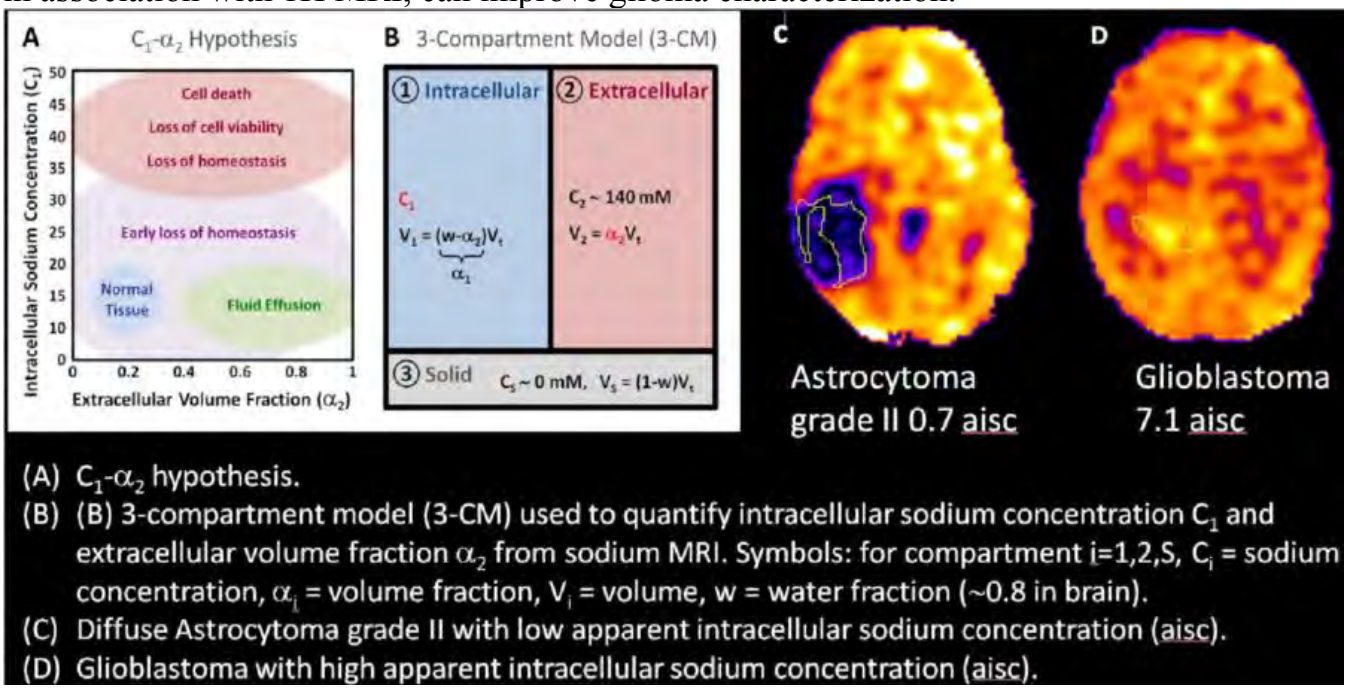
L Nunes[1], G Madelin[1], A Gilles[1], T Pandit[1], I Littig[1], D Placantonakis[2], A Chi[3], R Jain[1]
[1]Department of Radiology, New York University School of Medicine, New York, NY, [2]Department of Neurosurgery, New York University School of Medicine, New York, NY, [3]Division of Neuro-oncology, New York University School of Medicine, New York, NY

Purpose
Sodium MR imaging can provide direct information on tissue viability, disruption of cell packing, changes in vascularization, and cell metabolism (1). Purpose of the study is to measure intracellular sodium concentration (C1), extracellular volume fraction (α2), apparent intracellular and total sodium concentrations (aisc and atsc) in glioma patients using 23Na imaging.
Materials and Methods
Nine glioma patients were scanned at 3 Tesla with an 8-channel transmit-receive 1H/23Na head coil. Two 23Na MRI were performed: (1) FLORET (1, 2): 3 hubs, cone angle 45°, 120 interleaves/hub, FA 80°/1 ms, TE 0.2 ms, TR 100 ms, FOV 320 mm, resolution 5 mm isotropic, 20 averages, TA 12:00 min; (2) FLORET with fluid suppression by inversion recovery (IR): same parameters as (1) except: inversion pulse 180°/6 ms, TI 25 ms, FA 90°/1 ms, 30 averages, TA 18:00 min. Images were reconstructed with 3D regridding and nominal isotropic resolution of 2.5 mm. Both 23Na acquisitions were used to generate C1, α2, atsc, and aisc maps of whole brain using linear regression of gel reference phantoms and 3-compartment model (1, 3). Measurements of C1, α2, atsc, and aisc were obtained in the normal appearing white matter, putamen, and in tumor regions of T2-FLAIR abnormality, excluding areas of edema, cysts, or necrosis.
Results
Average values for normal appearing white matter were 9.7±3.7 mM (C1); 17.2±2.2% (α2); 29.8±3.6 mM (atsc); and 5.8±2.2 mM (aisc). Average values for the putamen were 13.5±5.4 mM (C1); 18.8±2.6% (α2); 34.2±4.5 mM (atsc); and 7.8±3.2 mM (aisc). Average values for the six low grade gliomas were 13.1±5.7 mM (C1); 41±8.3% (α2); 61.5±11.8 mM (atsc); and 4.4±1.9 mM (aisc) (Fig. 1). Average values for the naïve-treatment glioblastoma were

14.8±0 mM (C1); 28.9±0% (α2); 47.4±0 mM (atsc); and 7±0 mM (aisc) (Fig. 1). Average values for recurrent glioblastoma were 4±0 mM (C1); 41.7%±0 (α2); 59.8±0 mM (atsc); and 1.4±0 mM (aisc). Average values for the pleomorphic xanthoastrocytoma were 4±0 mM (C1); 39.9±0% (α2); 57.3±0 mM (atsc); and 1.4±0 mM (aisc).

Conclusions

Brain sodium MRI adds valuable information about physiology and cellular metabolism that, in association with 1H MRI, can improve glioma characterization.



(A) C_1-α_2 hypothesis.
(B) (B) 3-compartment model (3-CM) used to quantify intracellular sodium concentration C_1 and extracellular volume fraction α_2 from sodium MRI. Symbols: for compartment i=1,2,S, C_i = sodium concentration, α_i = volume fraction, V_i = volume, w = water fraction (~0.8 in brain).
(C) Diffuse Astrocytoma grade II with low apparent intracellular sodium concentration (aisc).
(D) Glioblastoma with high apparent intracellular sodium concentration (aisc).

(Filename: TCT_O-202_300dpiimage.jpg)

O-203

11:48AM - 11:56AM

Early Tumor Growth Between Initial Resection and Radiotherapy of Glioblastoma: Incidence and Impact on Clinical Outcomes

J Villanueva-Meyer[1], S Han[1], S Cha[1], N Butowski[1]
[1]*University of California - San Francisco, San Francisco, CA*

Purpose

Current standard-of-care therapy for glioblastoma involves maximal safe resection followed by concurrent chemoradiotherapy and adjuvant chemotherapy. Magnetic resonance imaging (MRI) plays a pivotal role in the monitoring of glioblastoma treatment response. Typically, MRI is obtained pre-operatively as well as within 72 hours of surgery to assess extent of resection and serve as a new baseline for future monitoring. Chemoradiotherapy then usually is initiated 4 to 5 weeks following surgery. Radiotherapy planning is performed with CT and comparison to immediate postoperative MRI. A few small studies of clinical trial patients

have evaluated glioblastoma patients for interval tumor growth between the immediate postoperative period and prior to initiating radiation. Results of these studies show that a certain proportion of patients have new or increased enhancement suggesting progressive disease (1, 2). As glioblastoma has a rapid cell doubling time, several studies have sought to assess the impact of delay in chemoradiotherapy on patient survival (3-5). We sought to investigate the incidence of early tumor growth in glioblastoma in the interval between surgical resection and initiation of radiotherapy, determine the correlation of tumor growth with survival outcome measures, and identify predictors of early tumor growth.

Materials and Methods

We reviewed the records of patients with newly diagnosed glioblastoma who underwent surgical resection and standard-of-care chemoradiotherapy at our institution. Patients with pre-operative, immediate postoperative, and preradiotherapy MRI were included. Conventional MRI and DWI features were assessed. New or increased contrast enhancement on the preradiotherapy MRI was compared to DWI on the immediate postoperative MRI to differentiate postoperative injury from true tumor growth. The correlation between early tumor growth and extent of resection with survival was assessed with Kaplan-Meier analysis. Logistic regression was carried out to evaluate predictors of early tumor growth.

Results

In total, 140 patients were included. Based on immediate postoperative MRI, 67 patients (48%) had a gross total resection of enhancing tumor by MRI. On average, preradiotherapy MRI was obtained 24.5 days (range, 10-45 days) from surgery and radiotherapy was initiated 30.3 days (range, 11-56 days) from surgery. Ninety patients (64%) demonstrated increased contrast-enhancement at preradiotherapy MRI. In 23 of these 90 cases, the increased contrast enhancement was wholly within a region of reduced diffusion noted on postoperative MRI and consistent with postoperative injury. Sixty-seven cases (48%) had new or increased contrast enhancement attributed to early tumor growth. Median progression free survival was 6.5 months (95% CI, 5.7-9.4 months) in patients with early tumor growth and 12.2 months (95% CI, 9.9-13.5 months) in patients without early tumor growth ($p < 0.001$). Median overall survival was 15.2 months (95% CI, 12.9-18.3 months) in patients with early tumor growth and 23.3 months (95% CI, 19.8-28.0 months) in patients without early tumor growth ($p < 0.001$). Additionally, progression free and overall survival were longer in patients who underwent gross total resection of enhancing tumor ($p = 0.016$ and < 0.001, respectively). Of the evaluated predictors of early growth, subtotal resection was most likely to result in early growth ($p < 0.001$).

Conclusions

Imaging evidence of early tumor growth often is observed at preradiotherapy MRI and is associated with shorter survival. Gross total resection of contrast enhancing tumor decreases the likelihood of early tumor growth. Early tumor growth at preradiotherapy MRI has implications for radiotherapy planning, defining the incidence of pseudoprogression, and patient outcomes.

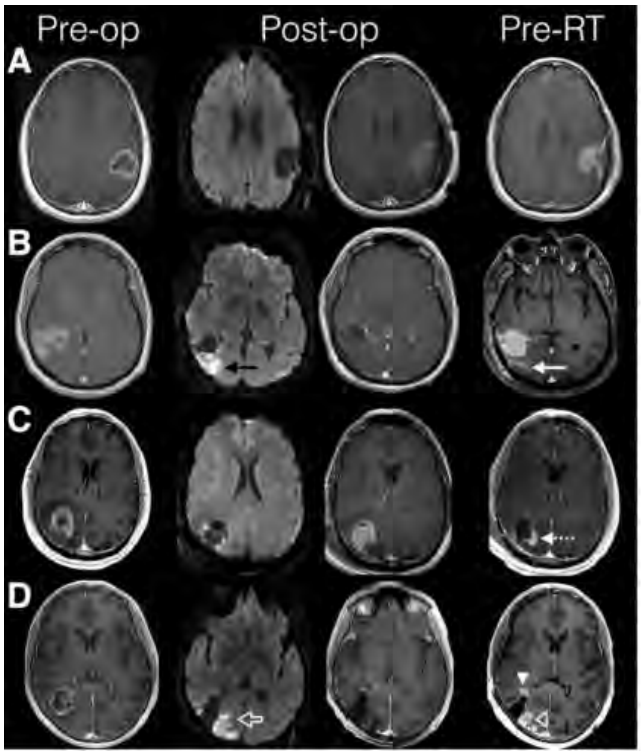


Fig. 1. Preoperative (T1 postcontrast, first column), immediate postoperative (DWI, second column; T1 postcontrast, third column), and preradiotherapy (T1 postcontrast) axial MRI of selected patients.
(**A**) Gross total resection of enhancing tumor without immediate postoperative reduced diffusion and without new contrast enhancement to suggest tumor growth at preradiotherapy MRI.
(**B**) Gross total resection of enhancing tumor with reduced diffusion along the posterior margin of the resection cavity (black arrow) that demonstrates contrast enhancement on preradiotherapy MRI (white arrow) consistent with evolving postoperative injury.
(**C**) Gross total resection of enhancing tumor with minimal pericavity reduced diffusion that demonstrates new nodular contrast enhancement along the posteromedial resection cavity (dashed white arrow), suggestive of tumor progression.
(**D**) Gross total resection of enhancing tumor with reduced diffusion along the posterior resection cavity (open white arrow) that demonstrates contrast enhancement on preradiotherapy MRI consistent with evolving postoperative injury (open white arrowhead) as well as new nodular contrast enhancement not associated with diffusion abnormality (white arrowhead) suggestive of tumor progression.

(Filename: TCT_O-203_ASNR_RT_CE_Fig.jpg)

O-204

11:56AM - 12:04PM

Longitudinal Relationship Between DWI and DTI Parameters in Glioblastoma Following Treatment

K Atsina[1], M Alizadeh[2], F Mohamed[1], D Andrews[1], A Flanders[1], K Talekar[1]
[1]Thomas Jefferson University Hospital, Philadelphia, PA, [2]Temple University, Philadelphia, PA

Purpose
Diffusion-weighted imaging (DWI) and diffusion tensor imaging (DTI) provide vital information in assessing microstructural changes due to brain pathology. Diffusion-weighted imaging, which is routinely obtained as part of conventional MR techniques, provides image contrast by utilizing differences in the magnitude of water diffusion. Diffusion tensor imaging, which employs advanced techniques to DWI, additionally provides information on water anisotropy and the orientation of diffusion. These parameters altogether enable assessment of fiber tracts and tissue cellularity that conventional structural imaging fails to achieve. Preliminary investigations during a phase I trial, which involved the use of an antisense to the insulin-like growth factor type 1 receptor as an integral part of an autologous tumor cell vaccine, indicated that mean water diffusivity may provide utility in tracking microstructural changes that may indicate pseudo-progression versus true progression in

glioblastoma (GBM) patients. Apparent diffusion coefficient (ADC) maps are generated routinely from DWI maps and are used frequently as a measure of diffusivity. However, mean diffusivity (MD) derived from DTI is more rotationally invariant and in theory may convey a more robust measure of microstructural change than ADC. Further studies are needed to elucidate the relationship between DWI and DTI maps. The purpose of this study is to compare DWI (i.e., ADC) with the DTI scalars, including MD, axial diffusivity (AD), radial diffusivity (RD) and fractional anisotropy (FA).

Materials and Methods

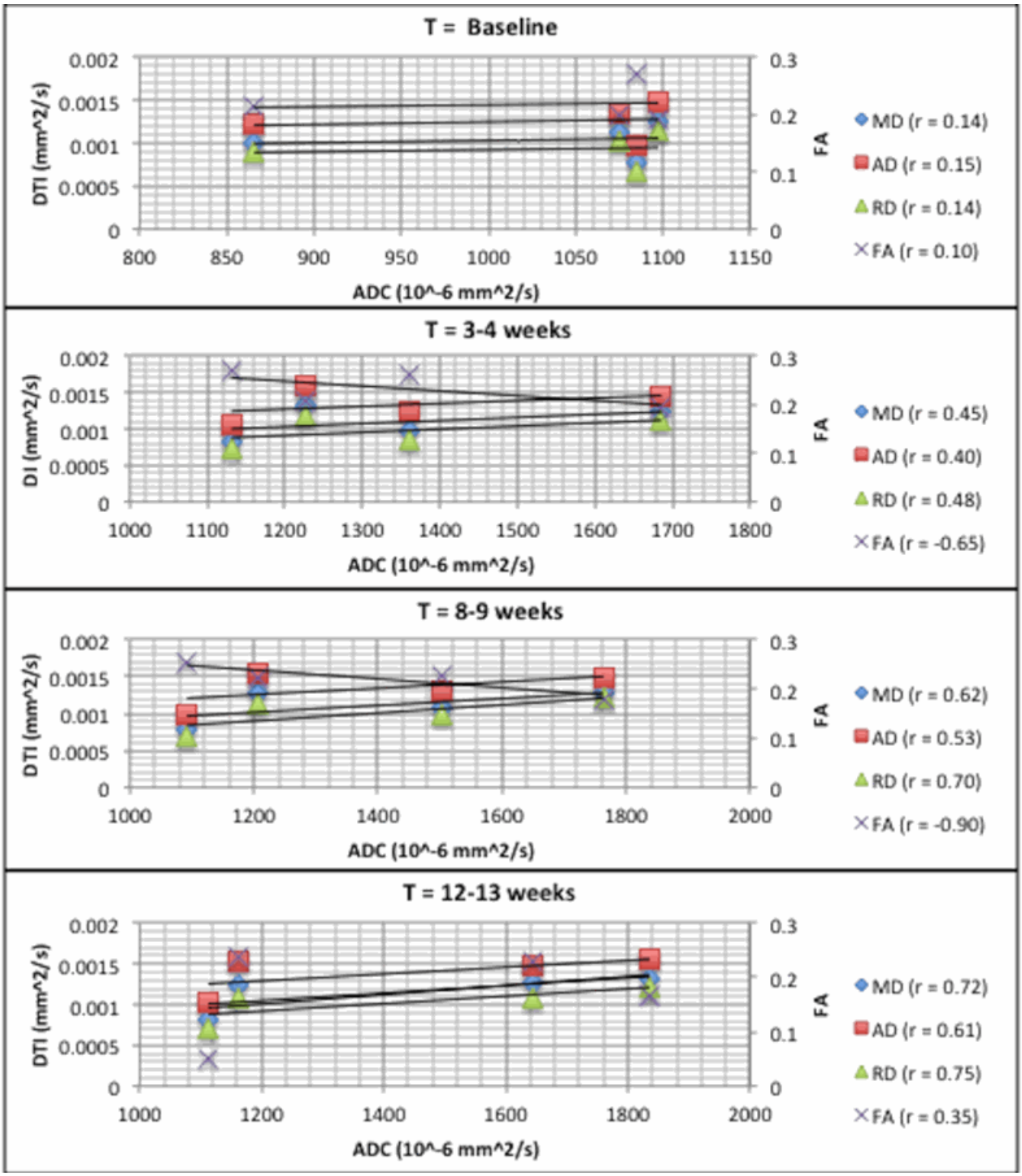
As part of a phase I-II immunotherapy trial at a single institution, DWI and DTI were acquired using a 3.0T Phillips Achieva scanner in 4 patients (age: 52 - 68 years) with glioblastoma (GBM). Patients had pre-operative (baseline) MRI and postoperative MRIs obtained at 3-4 weeks, 8-9 weeks and 12-13 weeks following surgery and immunotherapy. Mean diffusivity, FA, AD and RD maps were computed from raw DTI data with scan specific gradient table and image orientation information, and subsequently preprocessed for magnetic field inhomogeneities and motion-induced artifacts using FSL. These DTI maps were coregistered with conventional ADC maps generated from DWI using SPM12. DWI-ADC and DTI indices were calculated by using manually drawn ROIs of the entire tumor or residual/recurrent tumor in the case of postoperative studies, on fluid attenuated inversion recovery (FLAIR) and contrast-enhanced T1 images coregistered to the same MNI space. Voxel intensities of the tumor were computed using MatLab.

Results

A strong positive voxel-wise correlation (Pearson's correlation coefficient) was seen between ADC and three DTI maps (MD, AD, RD) within each patient before [r (MD) = 0.89 – 0.95, $P < 0.05$; r(AD) = 0.78 – 0.92, $P < 0.05$; r (RD) = 0.89 – 0.94, $P < 0.05$] and after treatment [r (MD) = 0.79 – 0.94, $P < 0.05$; r (AD) = 0.71 – 0.91, $P < 0.05$; r (RD) = 0.80 – 0.94, $P < 0.05$]. However, there was weak or moderate negative voxel-wise correlation between ADC and FA before [r = -0.5 – -0.24, $P < 0.05$] and after treatment [r = -0.65 – -0.04, $P < 0.05$). A very weak correlation was seen between mean ADC and MD, AD, RD values amongst the four patients (r = 0.14, 0.15, 0.14 with P = 0.86, 0.85, 0.86) at baseline. At 3-4 weeks postoperatively, an improved but weak correlation developed (r = 0.45, 0.40, 0.48 with P = 0.54, 0.60, 0.52). A moderate correlation was seen at 8-9 weeks postoperatively (r = 0.62, 0.53, 0.70 and P = 0.38, 0.47, 0.29). This correlation became stronger at 12-13 weeks (r = 0.72, 0.61 0.71 with P = 0.28, 0.39, 0.25) (See Fig.). No trend was observed for correlations between mean values of ADC and FA over time amongst the patients.

Conclusions

The correlations between mean values for ADC-MD, ADC-AD, and ADC-RD are very weak at baseline, improve modestly after treatment, and progressively get stronger with time suggesting stability in the microenvironment, which may reflect posttreatment changes as opposed to tumor recurrence. The correlation of mean values was not statistically significant; thus further studies are needed to corroborate these findings. Diffusion tensor imaging has the potential to be used as noninvasive imaging marker to follow-up prognosis of treatment.



(Filename: TCT_O-204_Slide20.gif)

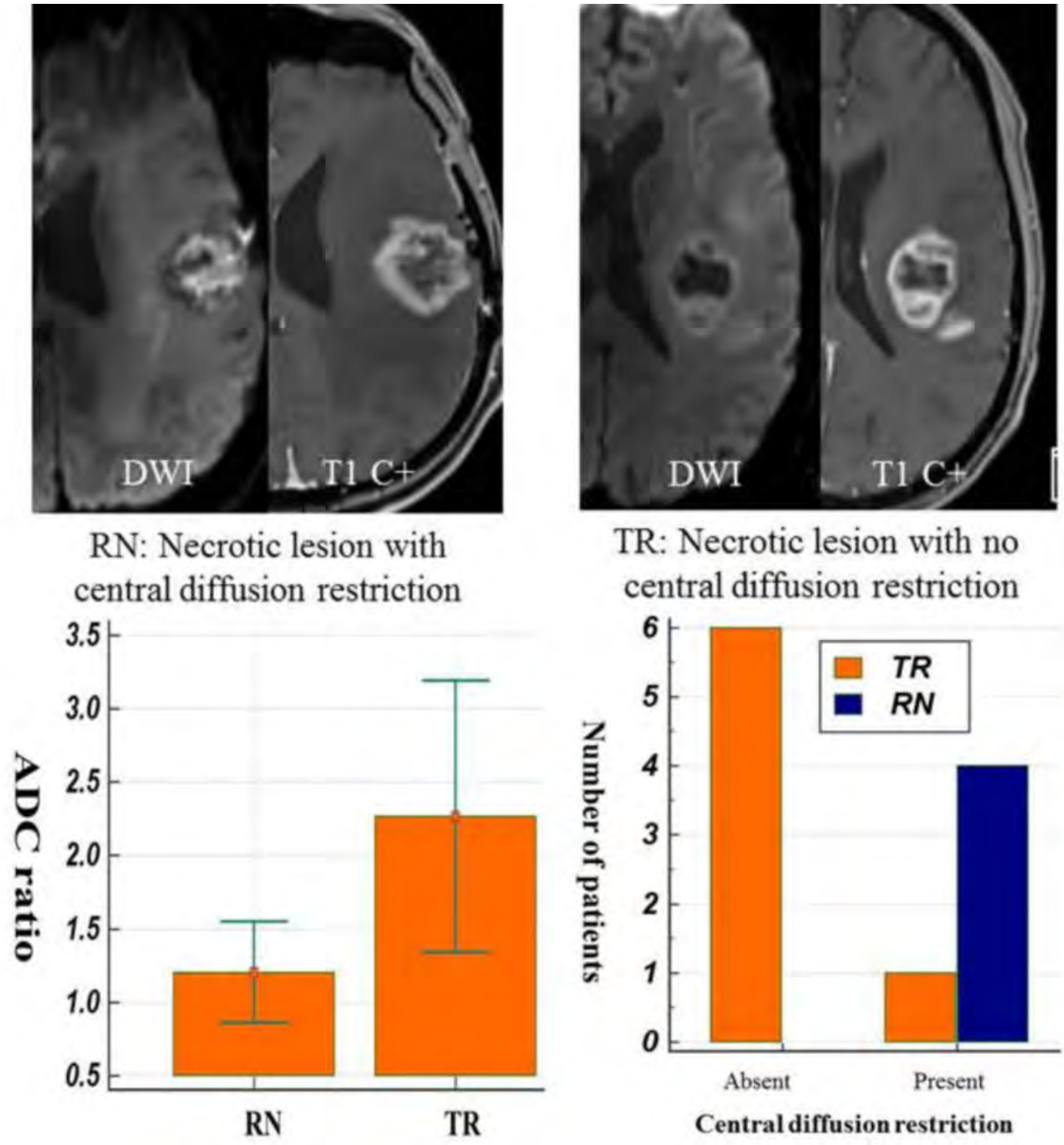
O-205

12:04PM - 12:12PM

Diagnostic Accuracy of Centrally Restricted Diffusion in the Differentiation of Radiation Necrosis from Tumor Recurrence in High Grade Gliomas

N Zakhari[1], T Nguyen[2], C Torres[3], S Chakraborty[4], J Woulfe[2], G Cron[2], R Thornhill[2]
[1]The Ottawa Hospital, Ottawa , Ontario, [2]The Ottawa Hospital University of Ottawa, Ottawa, Ontario, [3]University of Ottawa, Ottawa, Ontario, [4]University of Ottawa, The Ottawa Hospital, Ottawa, Ontario

Purpose
The appearance of a new ring-enhancing lesion after surgery and chemoradiation for high grade glioma (HGG) can be seen in radiation necrosis (RN) as well as tumor recurrence (TR). Centrally restricted diffusion has been demonstrated in recurrent HGG treated with bevacizumab. Our purpose is to assess the accuracy of centrally restricted diffusion in the diagnosis of RN in HGG not treated with bevacizumab.
Materials and Methods
In this prospective study, we enrolled HGG patients who developed a new ring-enhancing necrotic lesion following resection and standard chemotherapy and underwent re-resection. Each patient underwent a pre-operative diffusion tensor imaging on a 3T MR scanner. The presence of a centrally restricted diffusion within the ring-enhancing lesion was assessed visually on diffusion trace images and by ADC measurements. The percentage of TR and RN in each surgical specimen was defined histopathologically. Specimens containing equal proportions or less than 50% of TR and RN were excluded. The association between centrally restricted diffusion and RN was assessed using Fisher exact test. Differences in ADC and ADC ratio between the groups were assessed via Student t-test and ROC curve analysis was performed.
Results
Fifteen patients had a ring-enhancing lesions: 4 RN (>= 50%), 7 TR (>= 50%), and 4 mixed lesions (excluded). There was a statistically significant association between the presence of centrally restricted diffusion by visual assessment and RN (p= 0.015). There was a statistically significant difference in ADC ratio between RN and TR (p= 0.03). Receiver operating characteristic curve analysis for diagnosis of RN: ADC ratio ≤1.41 sensitivity 100.00% and specificity 83.33% (p= 0.004, AUC= 0.875) and ADC ≤821.7 x 106 mm2 /s specificity 100% and sensitivity 50% (p=0.004, AUC=0.857).
Conclusions
The presence of centrally restricted diffusion in a newly ring-enhancing lesion might indicate RN rather than TR in HGG previously treated with standard chemotherapy without bevacizumab.



(Filename: TCT_O-205_FIGURES.jpg)

Wednesday
11:00AM - 12:20PM
Long Beach Convention Center, Room 104B (Main Lobby)

18E-Parallel Paper Session: Excerpta: Adult Brain Topics: “Real and Rare” . . . Really?

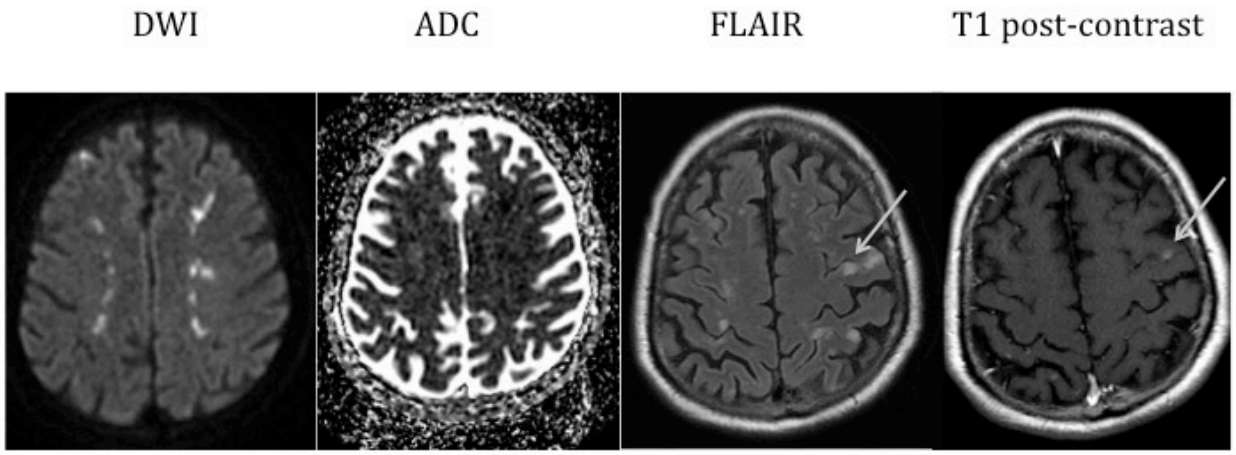
E-55

11:00AM - 11:04AM

CNS Involvement in Hypereosinophilic Syndrome

R Delfanti[1], N Farid[1]
[1]*University of California, San Diego, San Diego, CA*

Purpose
To demonstrate the rare imaging findings of central nervous system (CNS) involvement in a patient with hypereosinophilic syndrome.
Materials and Methods
A 66-year-old male with new-onset of erythemic rash accompanied by progressive fatigue, chest pain, shortness of breath and pruritis which prompted hospitalization. Initial work-up suggested non-ST elevation myocardial infarction and also revealed a leukocytosis with marked eosinophilia of 53,800/mm3 (normal reference < 700/mm3). Both bone marrow biopsy and molecular studies were unrevealing, and the patient was started on therapy to which his leukocytosis and eosinophilia responded. During his hospitalization, the patient experienced intermittent confusion, and subsequent MRI revealed widespread acute and subacute embolic infarcts, many in a borderzone distribution.
Results
Diffusion-weighted imaging from the Brain MRI demonstrates multiple bilateral supra and infratentorial small foci of restricted diffusion, many involving borderzone territories. Corresponding FLAIR imaging demonstrates multiple corresponding foci of hyperintensity, and a few lesions demonstrate enhancement on postcontrast imaging reflecting subacute etiology. Subsequent CT angiography of the head and neck revealed no intracranial or cervical arterial stenosis. The patient's cardiac work-up included an echocardiogram and MRI, which were both suspicious for endomyocardial fibrosis.
Conclusions
Central nervous system involvement in hypereosinophilic syndrome is very rare. While in patients with concomitant endomyocardial fibrosis, thromboembolism may be the postulated pathogenesis, review of the literature reveals that patients with CNS manifestations often do not have concurrent cardiac findings. Therefore, another hypothesis is that hypereosinophilia leads to defective anticoagulation and a prothrombotic state. These CNS emboli have a penchant for a borderzone distribution, hypothesized to be due to delayed and incomplete clearance of the microemboli. Subsequently, in patients with CNS involvement, identifying hypereosinophilia as a possible cause of multiple embolic infarcts involving the borderzone regions can have tremendous clinical implications for guiding clinical work-up and swiftly initiating the appropriate therapy to minimize further end organ damage.



Diffusion weighted imaging (DWI) with corresponding apparent diffusion coefficient (ADC) demonstrate multiple infarcts in a borderzone distribution reflecting emboli. On a more cephalad slice, numerous hyperintense foci are seen on FLAIR, with one (arrow) demonstrating enhancement on the post-contrast sequence, reflecting the acute to subacute temporal duration of the emboli.

(Filename: TCT_E-55_Hypereosinophilia_Final.jpg)

E-56

11:04AM - 11:08AM

Multimodality Imaging of Cerebral Crystal Storing Histiocytosis – distinguishing imaging characteristics and literature review of a very rare entity

V Garg[1], D Mendelsohn[1], C Cai[1], J Raisanen[2], M Pinho[1]
[1]University of Texas Southwestern Medical Center, Dallas, TX, [2]University of Texas Southwestern Medical Center / Parkland Hospital Department of Pathology, Dallas, TX

Purpose
Crystal-storing histocytosis (CSH) is a rare immunoglobulin storage disorder frequently associated with lymphoproliferative diseases. There are few reported cases of CSH involving the neurologic system and only a handful of cases with cerebral involvement as the primary and sole finding. We present a case of CNS crystal-storing histiocytosis with extensive multimodality imaging evaluation, review the available literature and propose how some unique imaging findings distinguish CSH from other brain disorders.

Materials and Methods

Noncontrast computed tomography (CT) demonstrated an irregular area of marked hyperdensity involving most of the white matter of the left frontal lobe with some cortical sparing and no mass effect, which was atypical for hemorrhage, suggesting deposition of calcium or other hyper attenuating material. T2-weighted (T2W) MRI images were remarkable for a large central core of marked hypointense signal matching the CT hyperdensity and peripheral areas of whiter matter hyperintensity. Postcontrast T1W images demonstrated heterogeneous enhancement in the central most aspect of the lesion, with irregular, slightly spiculated margins. Apparent diffusion coefficient (ADC) map had a biphasic appearance such as the T2W images, with central areas of low diffusivity and peripheral increased diffusivity suggesting edema. Cerebral blood volume (CBV) map from dynamic susceptibility contrast (DSC) perfusion (I) demonstrated subtle areas of increased perfusion along the margins of the enhancing component. Spectroscopy demonstrated markedly reduced NAA/Cr ratio, moderately elevated Cho/Cr ratio and a large abnormal peak of mobile lipids/lactate. Other nonspecific subtle white matter focal T2W smaller hyperintense lesions also were identified.

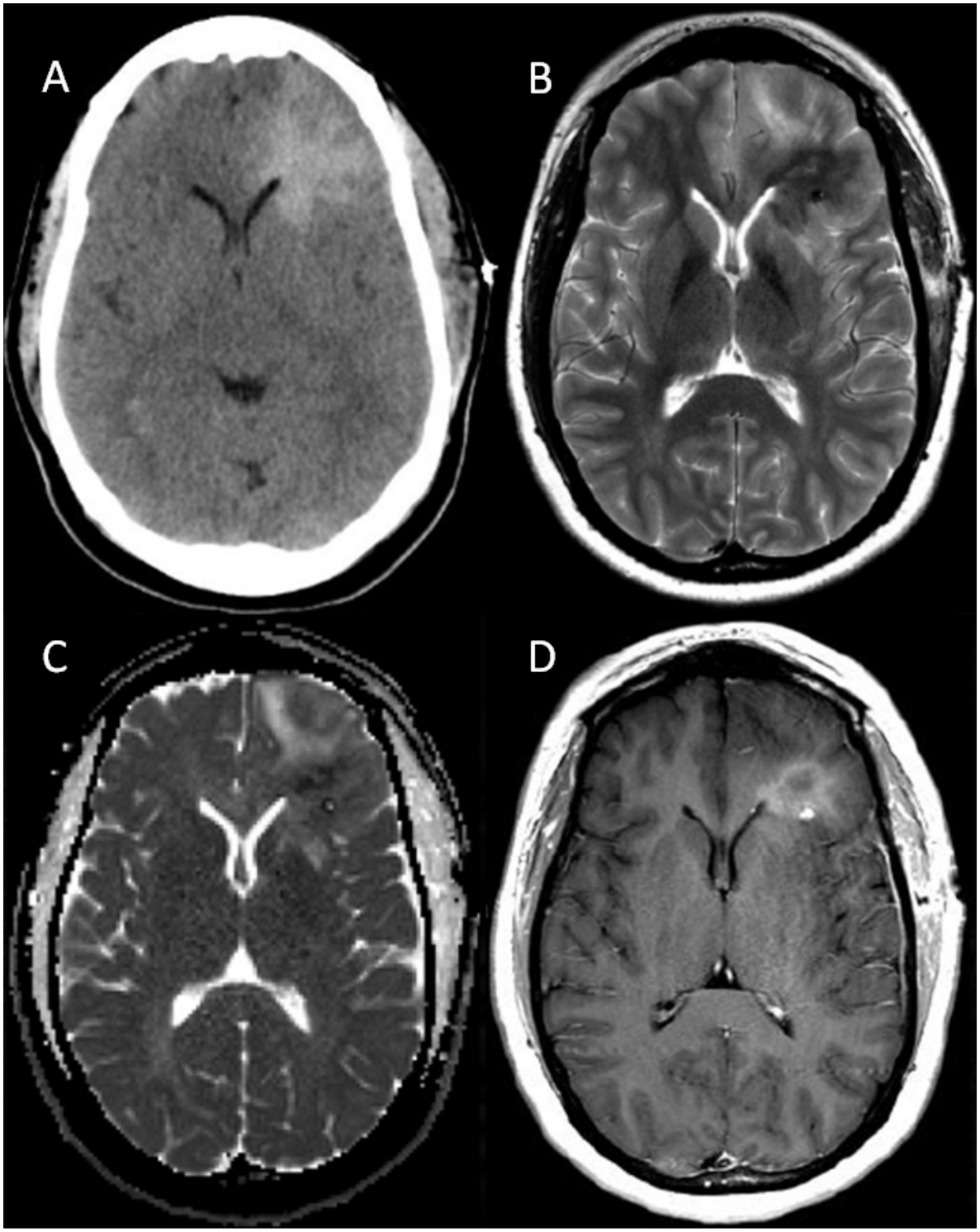
Results

Noncontrast CT demonstrated an irregular area of marked hyperdensity involving most of the white matter of the left frontal lobe with some cortical sparing and no mass effect, which was atypical for hemorrhage, suggesting deposition of calcium or other hyper attenuating material. T2-weighted MRI images were remarkable for a large central core of marked hypointense signal matching the CT hyperdensity and peripheral areas of whiter matter hyperintensity. Postcontrast T1W images demonstrated heterogeneous enhancement in the central most aspect of the lesion, with irregular, slightly spiculated margins. Apparent diffusion coefficient (ADC) map had a biphasic appearance such as the T2W images, with central areas of low diffusivity and peripheral increased diffusivity suggesting edema. Cerebral blood volume (CBV) map from DSC perfusion (I) demonstrated subtle areas of increased perfusion along the margins of the enhancing component. Spectroscopy demonstrated markedly reduced NAA/Cr ratio, moderately elevated Cho/Cr ratio and a large abnormal peak of mobile lipids/lactate. Other nonspecific subtle white matter focal T2W smaller hyperintense lesions also were identified.

Conclusions

The case was presented in our institution multidisciplinary tumor board and a diagnostic hypothesis of pseudotumoral amyloidoma was offered by the neuroradiology team based on previously published case reports. Biopsy performed at the outside institution was reviewed and demonstrated predominant histiocytes and expression of kappa immunoglobulin light chains, indicating CSH. We performed a literature review of published CSH cases with imaging findings and identified the central T2-weighted hypointensity in some previous cases, but the appearance on CT had not been previously described. Imaging findings of a focal parenchymal lesion with marked T2W hypointensity, hyperdensity on CT, spiculated or patchy linear postcontrast enhancement and minimal or no mass effect are unusual for

most common neoplastic and non-neoplastic brain lesions such as primary and metastatic neoplasms, demyelination, vascular disorders and lymphoproliferative disease, creating a diagnostic dilemma. However, these findings seem to be fairly characteristic for both CSH and cerebral amyloidomas. The common pathologic characteristics between the two entities (massive deposition of immunoglobulin light chains with reactive inflammatory changes) likely account for the shared unique imaging characteristics. Despite the rarity of these entities, prospective identification by radiologists is crucial to avoid unnecessary and potentially disabling surgical procedures.



(Filename: TCT_E-56_ASNRabstractCSH.jpg)

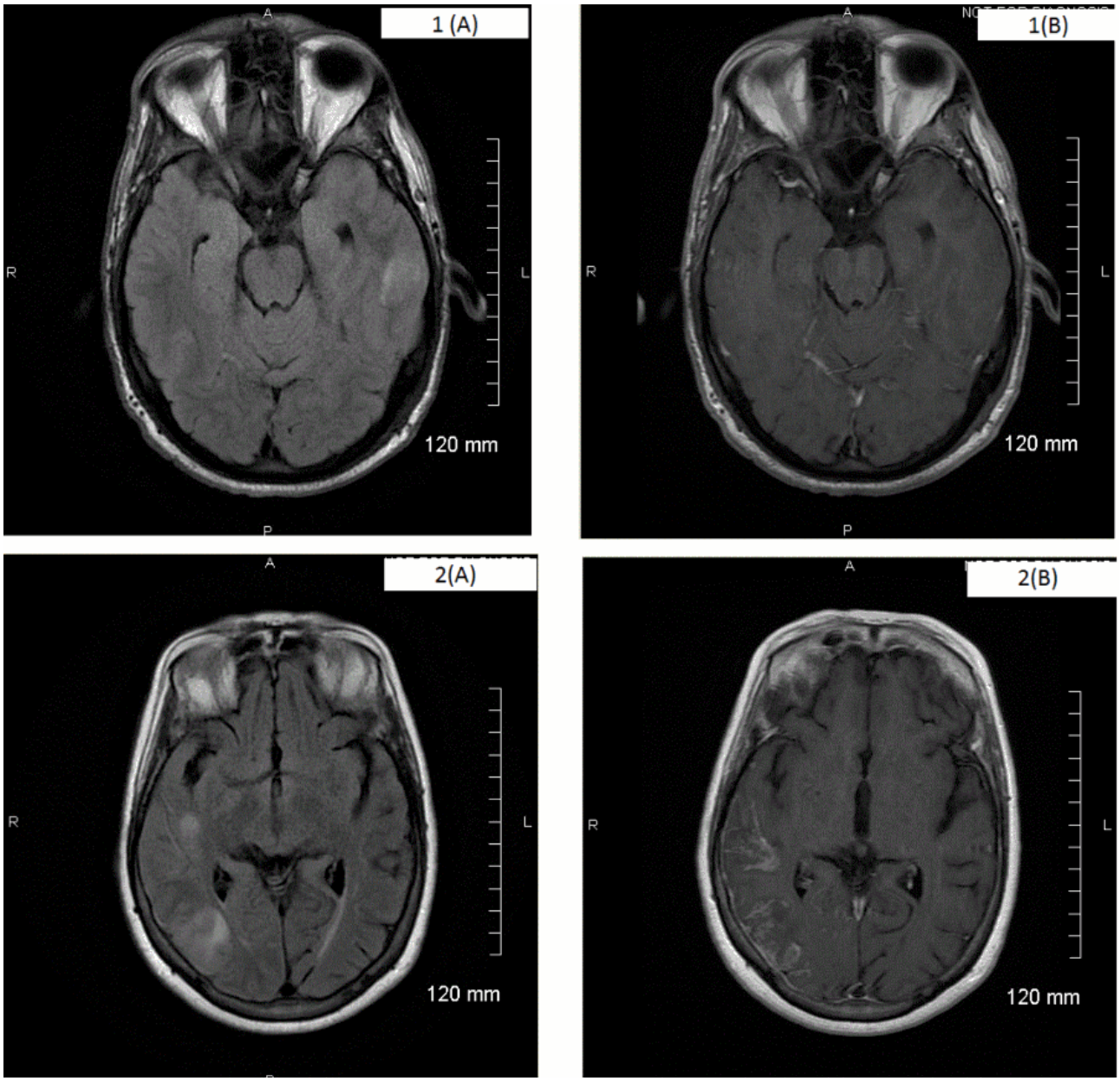
E-58

11:12AM - 11:16AM

Beta-Amyloid Angiitis: An Atypical Radiographic Appearance

T Teo[1], S Lu[1]
[1]*Monmouth Medical Center, Long Branch, NJ*

Purpose
To present two variants of beta amyloid angiopathy.
Materials and Methods
A 39-year-old male present with a first onset of tonic clonic seizure and anti-epileptic medication was initiated. A MRI of the brain shows an ill-defined area of cortical T2-signal abnormality, without enhancement in the left temporal lobe and subsequently was biopsied. A beta-amyloid immunostaining demonstrated widespread intramural vascular deposition and numerous extracellular deposits in the form of diffuse plaques. Immunostains for CD 3, CD68 and CD 20 also were positive. These immunostaining supported the diagnosis of amyloid-beta-related angitis (ABRA). Another case involved a 73-year-old Hispanic female who present with abrupt onset of temporary neurologic deficit of left-sided facial numbness and left hand weakness and subsequently recovered full motor and sensory function. A MRI stroke protocol shows ill-defined area of cortical T2-signal abnormality of the right temporal lobe without enhancement. A biopsy was performed for tissue diagnosis showed amyloid angiopathy involving the leptomeningeal and superficial cerebral vessels.
Results
1. Axial FLAIR image (A) shows the ill-defined left temporal lobe lesion. On the postcontrast sequence, there is minimal enhancement (B). 2. Axial FLAIR image (A) show ill-defined T2 signal abnormality in the right temporal region. On the postcontrast sequence, the lesion is enhancing (B).
Conclusions
Amyloid-β related angiitis (ARBA) is a predominantly granulomatous angio-destructive inflammatory mediated disease affecting leptomeningeal and cortical vessels characterized by meningeal lymphocytosis and abundant amyloid-beta deposition with the vessel walls.(1) ABRA usually presents in the 7th decade of life and without gender predilection. Both of the cases support the diagnosis of ABRA, a distinct variant of cerebral angiopathy (CAA) with associated vasculitis. 2. The clinical features of ABRA include headaches, seizures and focal neurologic deficits. 3. The first patient was young since the mean presentation of ABRA is 67 years old. The most common neuroimaging findings include nonspecific white matter changes, vasogenic edema and intracerebral hemorrhages.



(Filename: TCT_E-58_ABRAFigure1V9.gif)

E-59

11:16AM - 11:20AM

Varicella Zoster Virus Meningoencephalitis

A Iqbal[1], A hussain[2]
[1]University of Rochester, Rochester, NY, [2]University of Rochester Medical Center, rochester, NY

Purpose

The purpose of this project is to discuss a specific case which had atypical MRI findings and changes on imaging over time. A differential diagnosis based on the imaging findings will be reviewed. Next the findings seen with varicella zoster virus meningoencephalitis will be discussed.

Materials and Methods

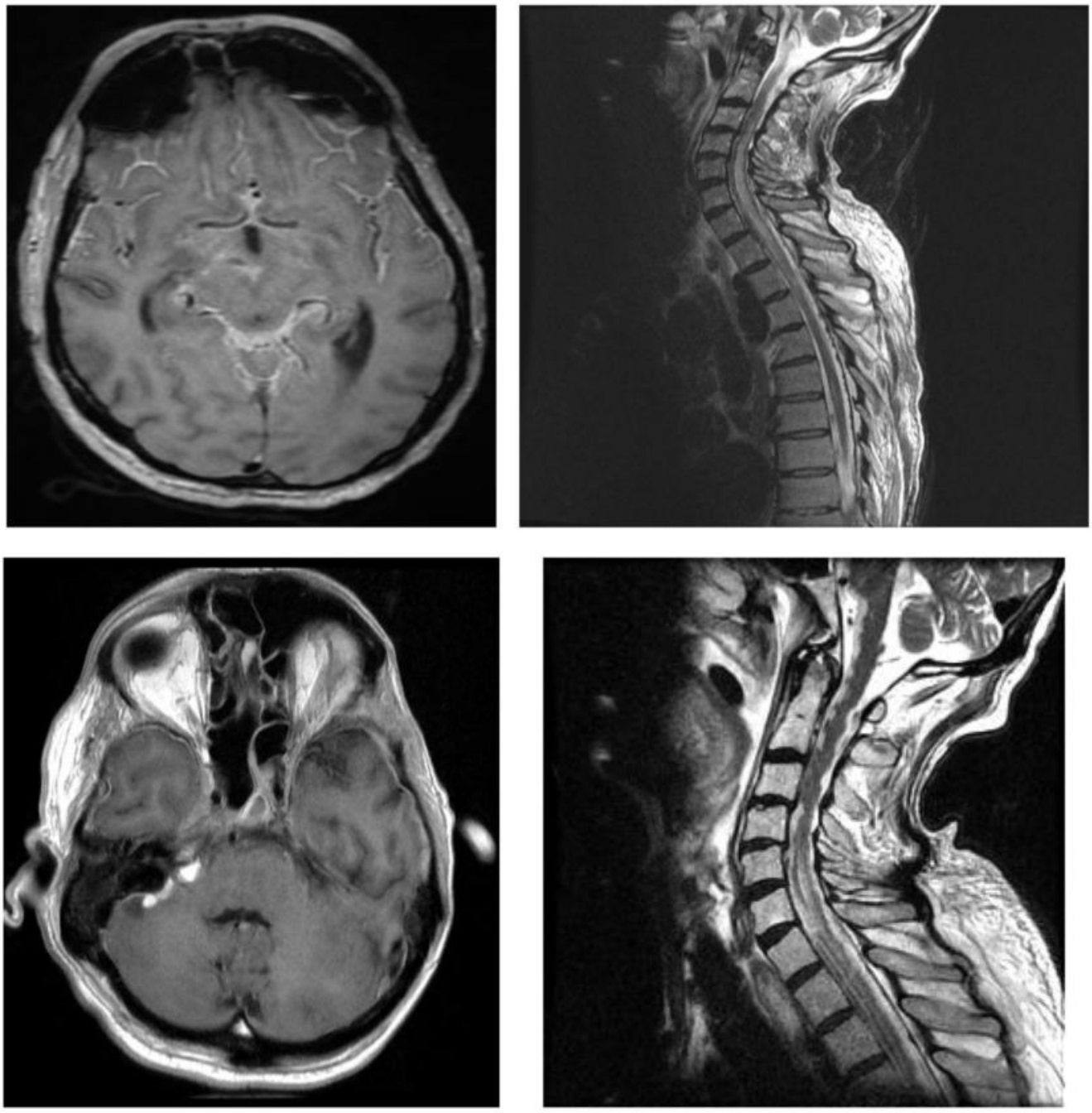
This is the case of a 67-year-old male with PMH significant for CAD, CHF with an AICD, pulmonary HTN, A-Fib, MVR, Hep C, and AKI who was brought into the emergency department with generalized weakness. He was suspected to have a CNS infection and was admitted to the Neuromedical ICU. Patient had a MRI that demonstrated extensive diffuse leptomeningeal enhancement. A follow-up MRI 11 days later demonstrated a decrease in the leptomeningeal enhancement, however there was interval development of pseudocysts in the brainstem and spinal cord. Patient's condition continued to deteriorate clinically and patient's family decided to pursue comfort measures. An autopsy demonstrated that patient had varicella zoster meningoencephalitis.

Results

This is the case of a 67-year-old male with PMH significant for CAD, CHF with an AICD, pulmonary HTN, A-Fib, MVR, Hep C, and AKI who was brought into the emergency department with complaints of right leg weakness. Patient described a generalized weakness and progressive deterioration in his health over the past year. Following a C1-C2 puncture the patient had a decline in his mental status, had increased confusion, became restless and agitated as well as an increase his work of breathing. He was suspected to have a CNS infection and was admitted to the Neuromedical ICU. Patient had a MRI that demonstrated extensive diffuse leptomeningeal enhancement. A follow-up MRI 11 days later demonstrated a decrease in the leptomeningeal enhancement, however there was interval development of pseudocysts in the brainstem and spinal cord. Patient's condition continued to deteriorate clinically and patient's family decided to pursue comfort measures. An autopsy demonstrated that patient had had varicella zoster encephalitis.

Conclusions

This project will show atypical MRI findings in a patient with an unusual presentation. A differential diagnosis of potential etiologies will be discussed. This will be followed by a focus on the imaging findings of varicella zoster virus menigoencephalitis which is what the patient ultimately was diagnosed with at autopsy.



(Filename: TCT_E-59_Images.jpg)

E-60

11:20AM - 11:24AM

Early Hemodynamic Response Assessment of Stereotactic Radiosurgery for a Cerebral Arteriovenous Malformation using 4D Flow MRI

C Li[1], A Hsiao[1], J Hattangadi-Gluth[1], J Handwerker[1], N Farid[1]
[1]*University of California, San Diego, San Diego, CA*

Purpose

To provide a proof of concept application of 4D Flow MRI (3D time-resolved phase-contrast MRI with three-directional velocity encoding) to quantitatively detect changes in blood flow through a cerebral arteriovenous malformation (AVM) treated with stereotactic radiosurgery (SRS).

Materials and Methods

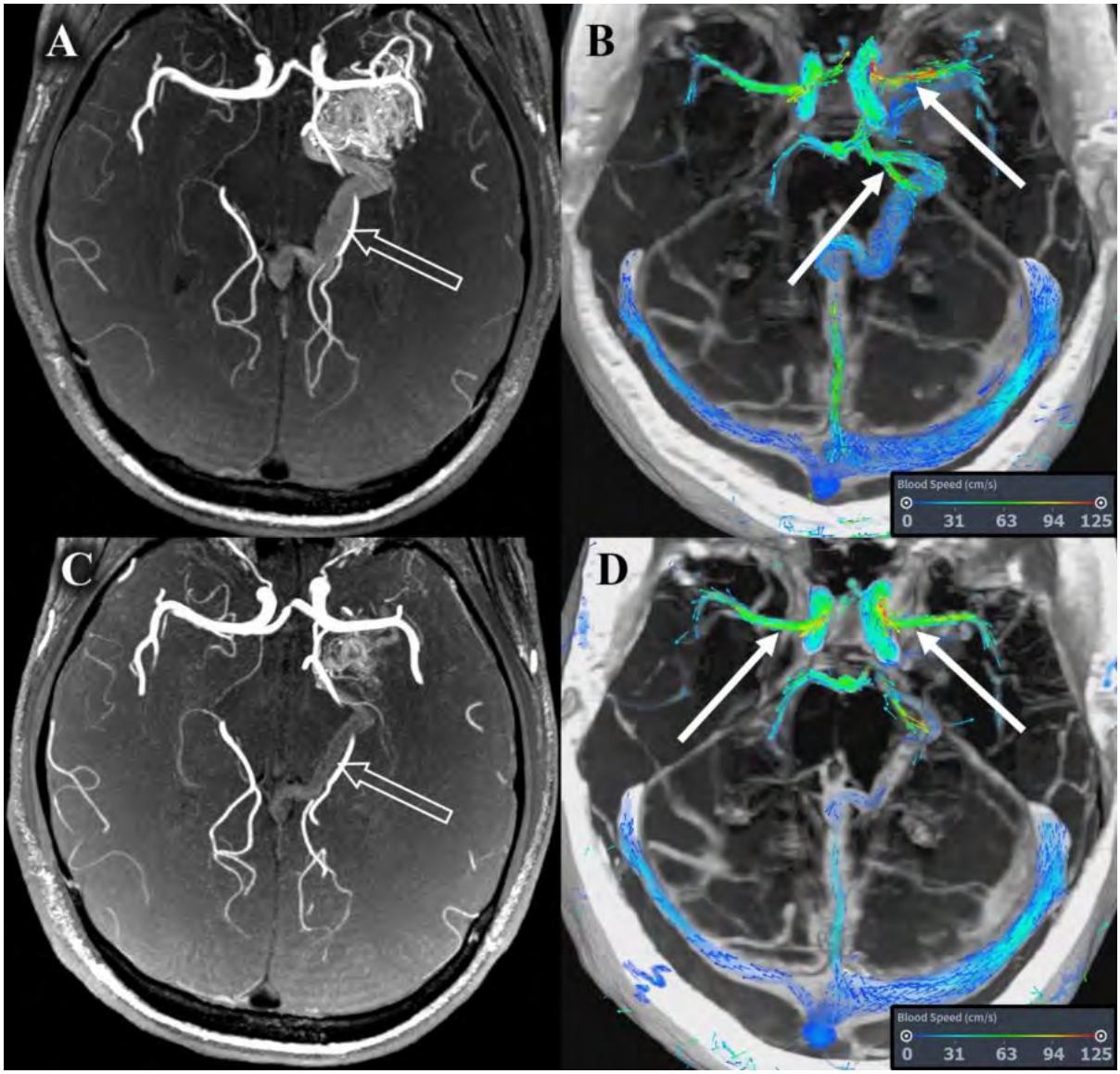
A 20-year-old male was incidentally discovered to have a Spetzler-Martin grade III AVM in the medial left temporal lobe during a trauma workup. He was treated with SRS (single fraction of 1,800 cGy) and has been monitored with 3 follow-up MRIs.

Results

Magnetic resonance imaging (MRI) on a 3T scanner with 4D Flow and MRA sequences was performed 1, 6, and 12 months after SRS. Three-dimensional time-of-flight MRA performed 1 month after SRS (Fig. 1A) demonstrates an AVM with a 3.1 x 3.0 x 2.7 cm nidus centered in the medial left temporal lobe with venous drainage primarily via an enlarged left basal vein of Rosenthal (open arrow). Four-dimensional Flow images (Fig. 1B) reveal increased blood flow velocities in the feeding vessels, denoted by warmer color flow vectors in the M1 segment of the left MCA and more flow in the proximal left PCA compared to the right (solid arrows). Blood flow in the left MCA measured by 4D Flow was 0.51 L/min, compared to 0.24 L/min in the right MCA. MR angiography performed 6 months after SRS showed no significant change in size of the nidus or draining vein, but 4D Flow measurements demonstrated interval reduction in left MCA flow to 0.34 L/min (33% less than prior), while right MCA flow remained stable at 0.28 L/min. MR angiography performed 12 months after SRS (Fig. 1C) demonstrates a decrease in nidus size to 1.8 x 1.7 x 1.4 cm and also decreased size of the draining vein (open arrow). 4D Flow (Fig. 1D) images reveal more symmetric flow in the proximal MCAs (solid arrows) compared to the original study. 4D Flow measurements showed continued normalization of left MCA flow to 0.28 L/min, a reduction of 45% from the immediate post-SRS MRI. Right MCA flow remained stable at 0.25 L/min.

Conclusions

Though SRS can be highly effective for cerebral AVMs, the latency period between treatment and obliteration of the nidus is typically several years (1). The presented case demonstrates not only an unusually rapid decrease in nidus size 1 year after SRS, but also hemodynamic changes (measured by 4D Flow MRI) only 6 months after treatment, which has not been previously reported. While 4D Flow imaging has been used to evaluate hemodynamic changes in brain AVMs after staged embolization, this is the first reported application of 4D Flow to assess response to SRS (2). Our case demonstrates changes in AVM hemodynamics on 4D Flow prior to structural changes evident on conventional MRI/MRA, suggesting increased sensitivity and accuracy of 4D Flow in detecting treatment response.



(Filename: TCT_E-60_abstractcollage.jpg)

E-61

11:24AM - 11:28AM

Computed Tomographic Angiography of the Head in Extracorporeal Membrane Oxygenation

J Acharya[1], A Rajamohan[1], W Gibbs[1]
[1]*University of Southern California, Keck School of Medicine, Los Angeles, CA*

Purpose
The hemodynamic changes produced by extracorporeal membrane oxygenation (ECMO) affect the appearance of computed tomographic angiography (CTA) of the head images, often confounding interpretation if the correct history and understanding of ECMO are not

known. We aim to describe the principles of ECMO, techniques to optimize intracranial CTA imaging, and pitfalls.

Materials and Methods

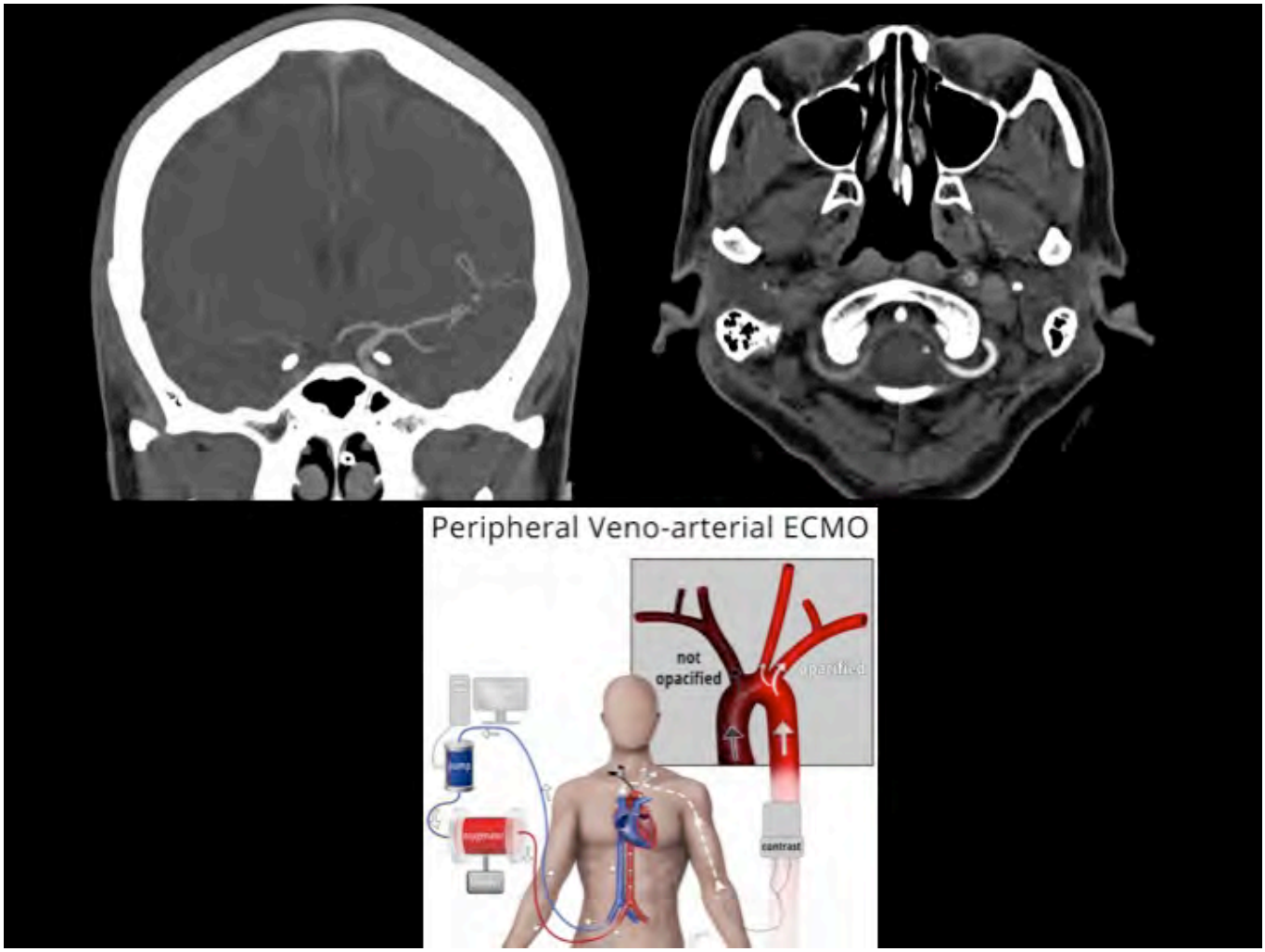
A 45-year-old previously healthy female suddenly collapsed at home after 3 days of cough and shortness of breath. Emergency medical services arrived on the scene finding the patient in ventricular tachycardia. Electrical cardioversion was performed in the field. The patient was intubated, but progressively decompensated en route to the hospital. Upon arrival, the patient coded for 75 minutes, with intermittent return of spontaneous circulation. She was placed on veno-arterial ECMO. The patient's left ventricular ejection fraction was 11%. During the next few days, the patient remained comatose. Multiple noncontrast CT examinations of the head were performed, all of which were negative for CT evidence of acute infarction. As per neurosurgical request, the patient subsequently underwent CTA of the head. On the CTA, there was decreased contrast opacification of the right internal carotid artery and right vertebral artery in comparison to the left internal carotid artery and left vertebral artery. The appearance suggested that the asymmetric vascular opacification was caused by alterations in the distribution of contrast produced by VA ECMO. This case illustrates the need for a detailed history and knowledge of typical hemodynamic changes produced by ECMO so the radiologist can properly protocol and provide an accurate interpretation of subsequent CTA imaging.

Results

In the peripheral veno-arterial ECMO system, the draining cannula tip is near the right atrium and the return cannula tip is in the superior right common iliac artery. When contrast is injected into the left antecubital fossa intravenous line, it travels towards the heart. Once it enters the right atrium, a large proportion of the contrast is sucked out through the draining cannula, then passes through the ECMO circuit, and subsequently returns into the arterial system with a high rate of retrograde flow through the descending aorta. Residual left ventricular function pumps unopacified/poorly opacified blood into the ascending aorta where there is convergence with the contrast opacified blood coming up the descending aorta. Naturally, the unopacified blood will preferentially fill the brachiocephalic artery and thus, the right vertebral and right internal carotid arteries; whereas the left common and left subclavian arteries will be preferentially contrast opacified. Coronal 7.0 mm MIP image demonstrates asymmetric opacification of the distal internal carotid, anterior cerebral, and middle cerebral arteries. Contrast avidly opacifies the distal left ICA, left A1 segment, and left MCA. This is not the sequela of an arterial thrombosis or dissection. Residual left ventricular function pumps poorly opacified blood preferentially into the brachiocephalic artery and to the right internal carotid artery and is the cause of this asymmetric appearance.

Conclusions

Hemodynamic changes produced by ECMO can confound accurate interpretation of CTA head imaging. Radiologists should understand the principles, physiology, and types of ECMO. This knowledge, as well as techniques used for evaluating the pulmonary circulation, may allow for optimized CTA imaging of the intracranial vasculature.



(Filename: TCT_E-61_ASNRECMO.jpg)

E-62

11:28AM - 11:32AM

TEMPI Syndrome Case with Multiple Neurological Findings (Telangiectasias, Elevated erythropoietin level and Erythrocytosis, Monoclonal gammopathy, Perinephric-fluid collections, and Intrapulmonary shunting)

S Bergamaschi[1], J Acharya[2], A Rajamohan[3], W Gibbs[3], M Law[4]
[1]University Of Southern California, Los Angeles, CA, [2]University of Southern California, Los Angeles, CA, [3]University of Southern California, Keck School of Medicine, Los Angeles, CA, [4]Keck Medical Center of USC, Los Angeles, CA

Purpose
To report a case of TEMPI syndrome presenting with neurologic symptoms and multiple brain imaging findings.

Materials and Methods

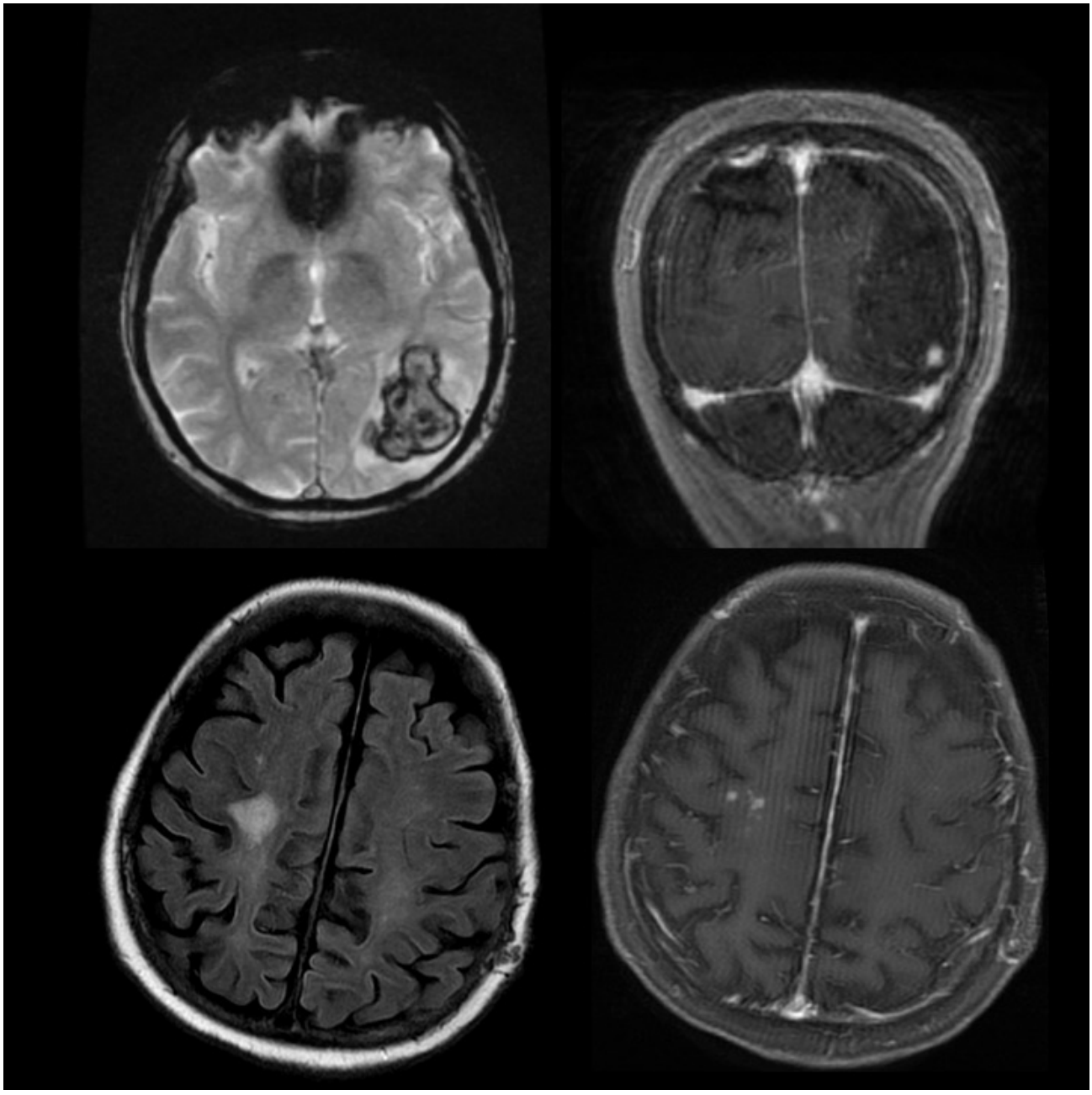
A 55-year-old female with history of perinephric fluid collections and ascites requiring multiple paracenteses, labial telangiectasias, erythrocytosis and monoclonal gammopathy, developed sudden onset severe headache, visual impairment and right hemiparesis. Magnetic resonance imaging (MRI) of the brain revealed a large left hemispheric hemorrhage. Subsequent computed tomography (CT) angiogram (CTA) and catheter angiogram could not identify a source of hemorrhage. The angiograms did show multiple small external carotid arteriovenous fistulas and arteriovenous malformations, without evidence of intracranial vascular malformation. One year later, the patient presented with new onset seizure. The brain MRI showed left frontoparietal vasogenic edema, with multiple contrast enhancing foci. After commencing treatment for monoclonal gammopathy of uncertain significance (MGUS) with a proteasome inhibitor, these areas showed improvement, with regression of the vasogenic edema and decreased enhancement.

Results

Spontaneous left hemispheric parenchymal hemorrhage, multiple small scalp AV fistulas and AV malformations, without signs of trans-diploic drainage, vasogenic edema in the left frontal and parietal lobes and multiple small enhancing foci. Substantial decrease in vasogenic edema and enhancement after treatment.

Conclusions

TEMPI syndrome is a newly described hereditary hemorrhagic telangiectasia-like syndrome, that can present with spontaneous brain hemorrhages, AV fistulas and malformations. The finding of areas of vasogenic edema with small contrast-enhancing foci has not been described previously in the literature, but may be related to small telangiectasias and permeability alterations.



(Filename: TCT_E-62_TEMPI.jpg)

E-63

11:32AM - 11:36AM

Cavernous Sinus Hemangioma: A Case Report

M Cho[1], C Liu[1]
[1]*University of Southern California/Keck Medical Center, Los Angeles, CA*

Purpose

Cavernous sinus hemangiomas are rare vascular malformations consisting of abnormal dilated vessels without normal intervening normal neural tissue. Pre-operative diagnosis is important because of the propensity of these tumors to bleed during resection. The purpose of this exhibit is to describe the imaging characteristics, presentation, and treatment of cavernous sinus hemangiomas.

Materials and Methods

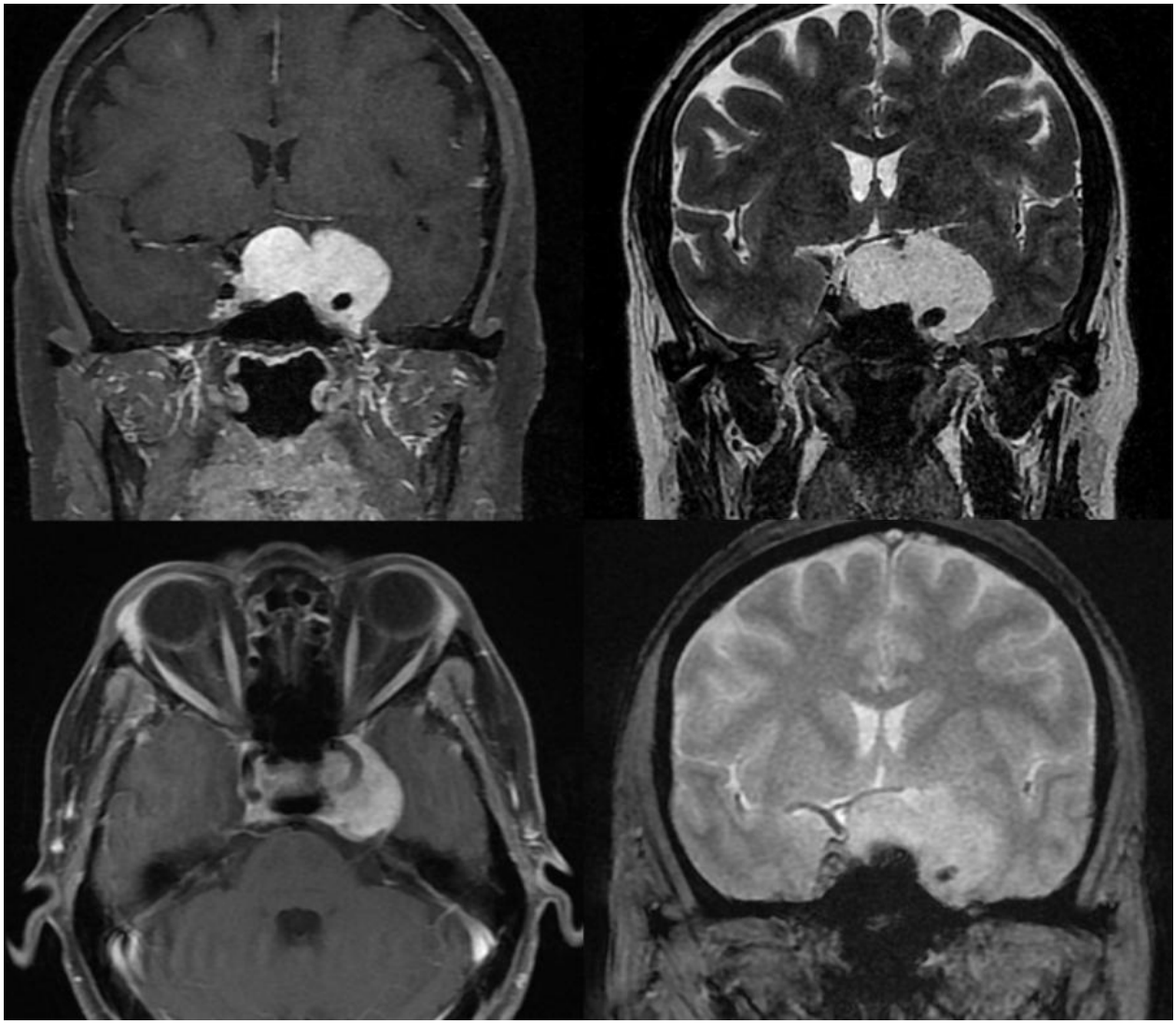
A 58-year-old woman who presented with limb numbness and vertigo. Magnetic resonance imaging (MRI) revealed a large sellar/suprasellar mass centered in the left cavernous sinus. The mass was resected and pathology demonstrated features consistent with a cavernous sinus hemangioma.

Results

Magnetic resonance imaging demonstrates a large lobulated sellar/suprasellar mass centered in the left cavernous sinus encircling the left cavernous carotid artery, abutting the left temporal lobe and producing mass effect upon the optic chiasm. The mass is T2 hyperintense and enhances avidly and homogeneously with intravenous contrast.

Conclusions

This case demonstrates classic imaging findings of a cavernous sinus hemangioma. Such lesions typically have an insidious onset of symptoms due to large size. Headache, dysfunction of cranial nerves passing through the cavernous sinus, and ptosis/diplopia are common presenting symptoms. Facial numnbness/neuralgia can occur if the gasserian ganglion is involved. The mass typically is isointense to hypointense on T1, markedly hyperintense on T2, and enhances homogeneously. Differential considerations include meningioma, which would demonstrate signal intensity that is more similar to gray matter on T1 and T2, and schwannomas, which would be lower signal intensity on T1 than gray matter with more heterogeneous enhancement. The peri-operative mortality rate can be high due to uncontrollable bleeding. Thus, proper diagnosis of the lesions pre-operatively is important.



(Filename: TCT_E-63_cavernoussinushemangioma.jpg)

E-64

11:36AM - 11:40AM

A Rare Presentation of Cerebral Proliferative Angiopathy with Subarachnoid Hemorrhage.

M Bean[1], A Carlson[1], G Lorenzo[1], D Sorte[1]
[1]*University of New Mexico, Albuquerque, NM*

Purpose
We seek to illustrate an unusual case of cerebral proliferative angiopathy which presented with subarachnoid hemorrhage. We will explore the imaging findings on computed tomography (CT), CT angiography, conventional angiography, and magnetic resonance imaging (MRI) in this rare diagnosis and discuss a management dilemma.

Materials and Methods

A 59-year-old woman with cirrhosis and hypothyroidism presented with thunderclap, severe headache and left pronator drift. She was otherwise neurologically intact. She underwent a head CT and was found to have subarachnoid hemorrhage. Computed tomography angiography was performed for presumed ruptured intracranial aneurysm, but showed an atypical vascular lesion. Magnetic resonance imaging was performed to further characterize the lesion and surrounding brain. Next, digital subtraction angiography was performed with flat panel rotational angiotomography. An usual vascular lesion, suspected cerebral proliferative angiopathy (CPA), was evident with a dissecting anterior choroidal artery aneurysm, likely the source of hemorrhage. The decision was made to manage the aneurysm and hemorrhage conservatively due to the good neurologic status of the patient. Vessel sacrifice was not performed despite the risk of re-rupture as a morbid anterior choroidal artery infarct would have occurred. Unfortunately, the patient died of unrelated causes (pancreatitis and ischemic bowel) during her hospitalization.

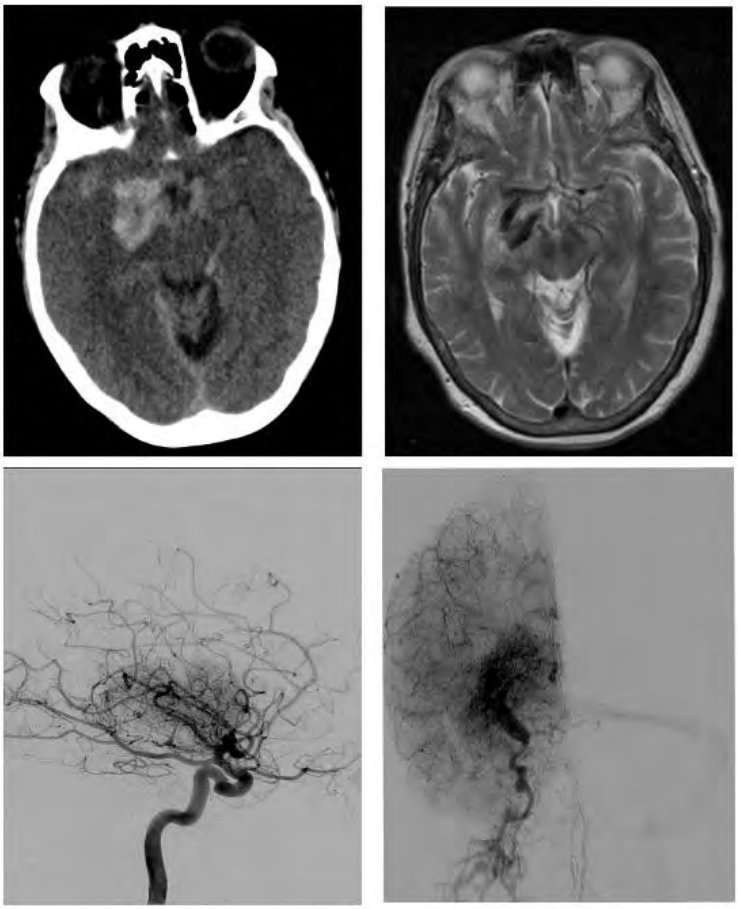
Results

Head CT: Initial head CT demonstrated moderate volume subarachnoid hemorrhage in the basilar cistern, eccentric to the right in the suprasellar cistern, and extending into the right Sylvian fissure. Thick subarachnoid hemorrhage was present in the ambient and quadrigeminal plate cisterns as well. A small amount of hemorrhage along the interhemispheric fissue was noted. Hyperdense material also was visible in the right medial temporal lobe. CTA head: Multiple dilated vessels, predominantly lenticulostriate arteries, were seen in the right medial temporal lobe. A large venous varix drained anteriorly into the cavernous sinus. No definite nidus was identified. Brain parenchyma was interposed between the abnormal blood vessels. This was reported as a probable arteriovenous malformation (AVM), despite atypical features. MRI brain: MRI showed dilated vascular flow voids in the right medial middle cerebral artery (MCA) region with a dominant tubular structure connected to the cavernous sinus. Small volume temporal lobe hemorrhage was confirmed. Again, the vascular malformation contained edematous brain parenchyma between the vessels. DSA head: A mass-like tuft of dilated lenticulostriate and MCA arterial vessels drain into a venous varix. The varix is seen in the capillary phase compatible with shunting. No definite nidus was present. A sessile dissecting aneurysm was seen on the anterior choroidal artery, the likely source of subarachnoid hemorrhage. A flat panel angiotomogram was performed during the angiogram, confirming findings on the CTA, showing brain parenchyma within the vascular lesion.

Conclusions

Cerebral proliferative angiopathy (CPA), described in 2008 by Lasjaunais, et. al, is rare with unknown etiology. The case present herein is most consistent with CPA rather than an arteriovenous malformation or dural arteriovenous fistula, although it has some atypical features. Atypical features include a flow-related aneurysm, presentation with hemorrhage, and intralesional shunting. As is typical for CPA, the presented case demonstrated brain parenchymal interposed within the vascular lesion, absence of a dominant feeder, the size of

the lesion was disproportionately enlarged when compared to the draining vein. There is no true nidus but extensive capillary angioectasia. The feeder vessel anterior choroidal artery aneurysm was managed conservatively without vessel sacrifice as the risk was felt to outweigh the benefit. Knowledge of this rare entity and its imaging features can help in early diagnosis and differentiation of CPA from conventional AVM. Despite the fact that feeder artery aneurysms are uncommon, a high index of suspicion should be maintained in the setting of subarachnoid hemorrhage.



(Filename: TCT_E-64_cpafigure.jpg)

E-65

11:40AM - 11:44AM

Brainstem Venous Congestion from Craniocervical Junction Dural AV Fistula: A Rare Cause of Brainstem Dysfunction

Y Park[1], Y Chng[1], B Yoo[1]
[1]*UCLA, Los Angeles, CA*

Purpose

To present a rare case of brainstem edema from dural arteriovenous fistula (DAVF) at the craniocervical junction.

Materials and Methods

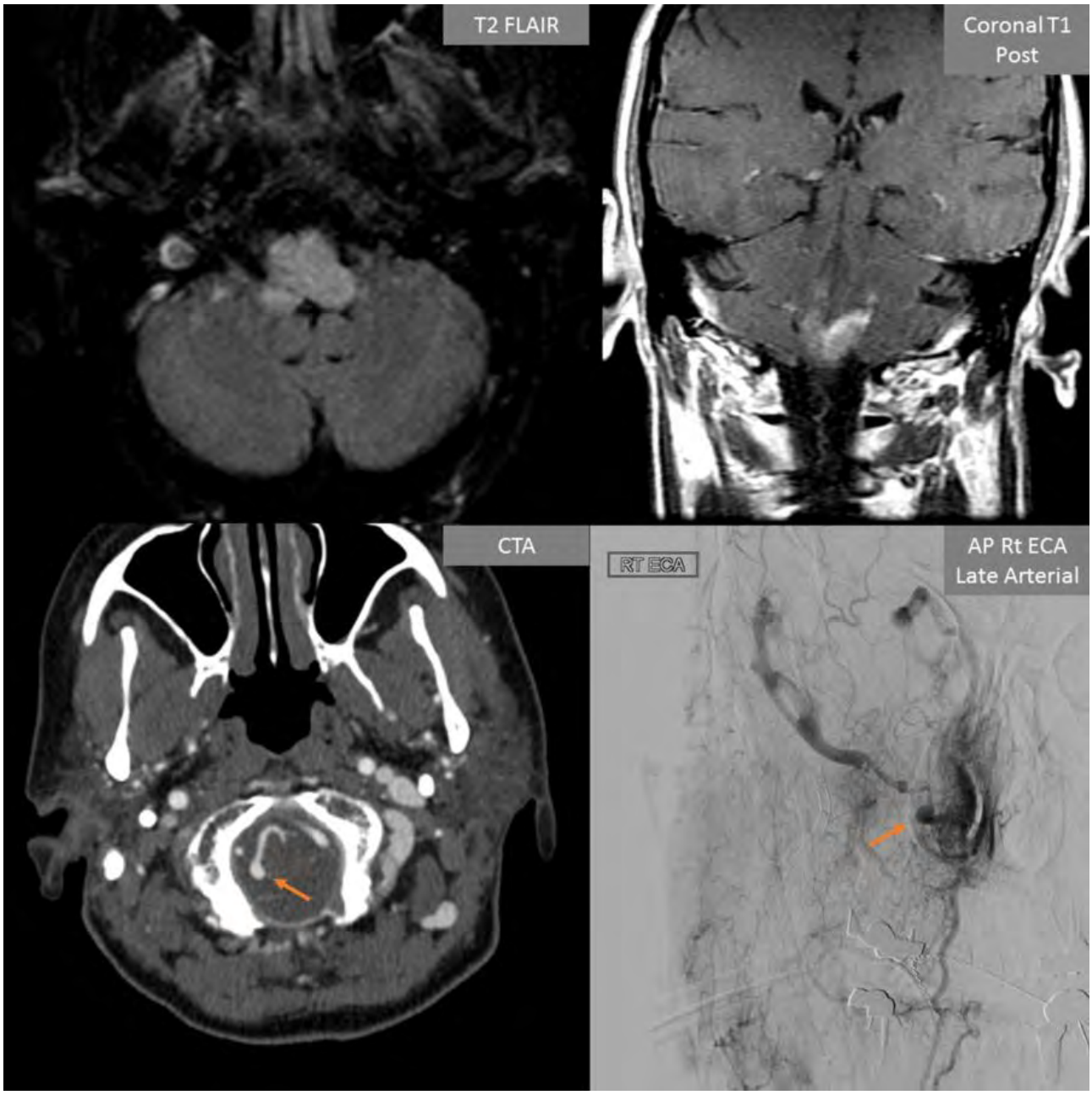
A 57-year-old woman presented to an outside hospital with dizziness, dysphagia, and upper and lower extremity weakness progressing to inability to walk over the course of a week. Initial brain MRI revealed extensive brainstem T2/FLAIR hyperintensity and abnormal enhancement. The patient was treated presumptively for an inflammatory/demyelinating process with a course of corticosteroids, despite nonrevealing cerebrospinal fluid (CSF) analysis and worsening of symptoms. The patient then was transferred to our institution for further evaluation.

Results

Initial outside brain MRI demonstrated extensive T2/FLAIR hyperintensity involving the medulla and upper cervical cord, with associated patchy enhancement in the medulla. Repeat brain MRI upon transfer to our institution 10 days later demonstrated worsening brainstem edema and a new focus of restricted diffusion in the lateral left medulla. There was also suggestion of an abnormal flow void along the surface of the cervicomedullary junction. A CT angiogram of the head and neck confirmed the presence of an abnormal vascular structure contiguous with an engorged anterior spinal vein, raising concern for a vascular lesion such as DAVF. Catheter cerebral angiography showed an isolated arterialized sigmoid sinus pouch draining via the lateral medullary vein, compatible with a Cognard type V DAVF. There was significant venous reflux into the anterior and posterior medullary and spinal veins, accounting for venous congestion seen on MRI. Transvenous embolization was successfully performed using a liquid embolic agent. Post embolization, the patient's symptoms improved, with follow-up MRI demonstrating resolving brainstem edema and enhancement.

Conclusions

Brainstem dysfunction due to venous congestion is a potentially reversible complication of a Cognard type V DAVF. Awareness of this rare presentation of DAVF can allow for prompt diagnosis and appropriate management, improving patient outcomes.



(Filename: TCT_E-65_Imagefull.jpg)

E-66

11:44AM - 11:48AM

A Dissecting Posterior Cerebral Artery Aneurysm Mimicking a Pineal Mass and Causing Obstructive Hydrocephalus.

P Wangaryattawanich[1], H Kale[2]
[1]University of Pittsburgh Medical Center, Pittsburgh, PA, [2]University of Pittsburgh Medical center, Pittsburgh, PA

Purpose

Cerebral aneurysms mimicking intracranial mass are rare, particularly in unusual locations. We report a case with a large dissecting posterior cerebral artery aneurysm mimicking a pineal mass producing obstructive hydrocephalus.

Materials and Methods

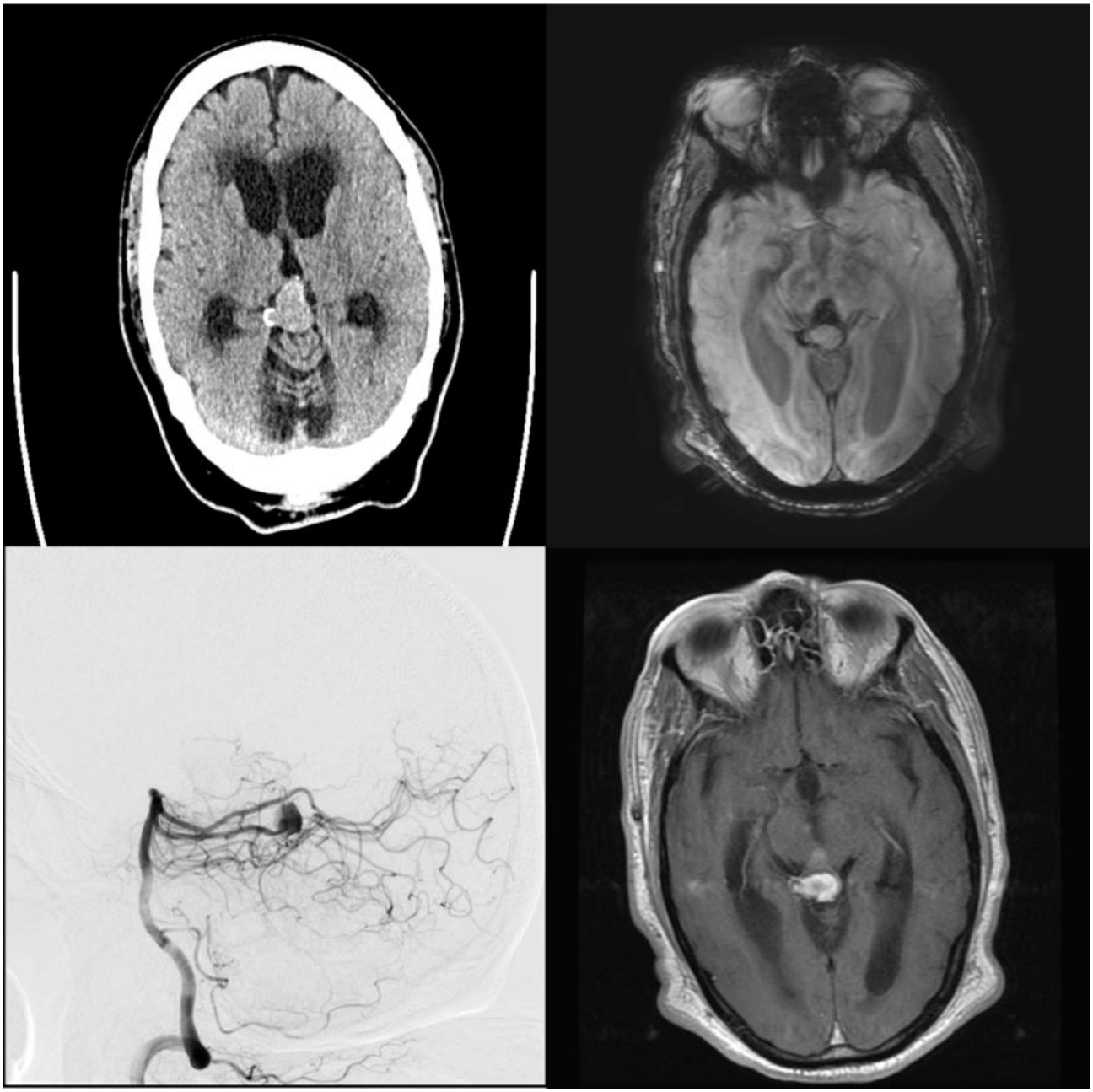
Sixty-year-old male with past medical history of hypertension was transferred to our institution for further evaluation of a newly discovered pineal mass evident on an outside brain CT. The patient presented to an outside hospital with a 2 weeks' history of increasing dizziness and recurrent falls. He had a brief episode of loss of consciousness following the most recent fall. On neurological exam, there was gait instability and balance impairment but, otherwise, he was neurologically intact.

Results

Non-contrast CT scan of the brain demonstrated a 2.2-cm partially peripherally calcified soft tissue mass centered in the pineal region compressing tectum and causing obstructive hydrocephalus secondary to cerebral aqueductal obstruction. MRI revealed the lobulated enhancing pineal mass with heterogeneous signals. At its periphery, there was focal intrinsic T1 hyperintensity and peripheral susceptibility. There was phase-encoded motion artifact associated with the lesion, most notably on post-contrast sequences, raising possibility of vascular etiology. This motion-related artifact is caused by moving tissue/blood such as vascular pulsation and occurs in phase-encoding direction. Given MRI findings, the initial plan of tissue biopsy was deferred and additional CT and catheter cerebral angiography were subsequently performed which showed a fusiform partially thrombosed aneurysm involving the entire P3 segment of the right posterior cerebral artery. The aneurysm was then embolized with coils and liquid embolic material. The patient had thereafter undergone endoscopic third ventriculostomy and extraventricular drain placement. After procedures, the patient has gradually improved and currently receiving an outpatient rehabilitation.

Conclusions

Intracranial vascular pathology occasionally can mimic intracranial soft tissue mass. In our search of medical records, this is the only case we have found of a PCA aneurysm mimicking a pineal tumor. Careful attention to flow (for eg. phase-encoded motion artifact) within such lesions, is of great value in accurate diagnosis and avoiding a potential adverse outcome.



(Filename: TCT_E-66_combined.jpg)

E-67

11:48AM - 11:52AM

Reversible Cerebral Vasoconstriction; an underdiagnosed entity for thunderclap headaches.

R Ahmed[1], J Pitzen[1], O Bronov[1]
[1]*Geisinger Medical Center, Danville, PA*

Purpose

To review clinical presentation, imaging findings, and workup of reversible cerebral vasoconstriction syndrome (RCVS).

Materials and Methods

We present a case of a 35-year-old female who presented with acute onset of severe headache. Patient has a past medical history of migraine headaches/tension headaches, acute frontal sinusitis, Hepatitis C, and chronic drug abuse now in remission. At presentation in emergency department she described her headache as "the worst headache of her life", 10/10 in severity, which started sharply, but then became more diffuse and dull throughout her head and neck, radiating into her occipital area. She denied auras, visual changes, head trauma, photophobia, chest pain, SOB, palpitations, abdominal pain.

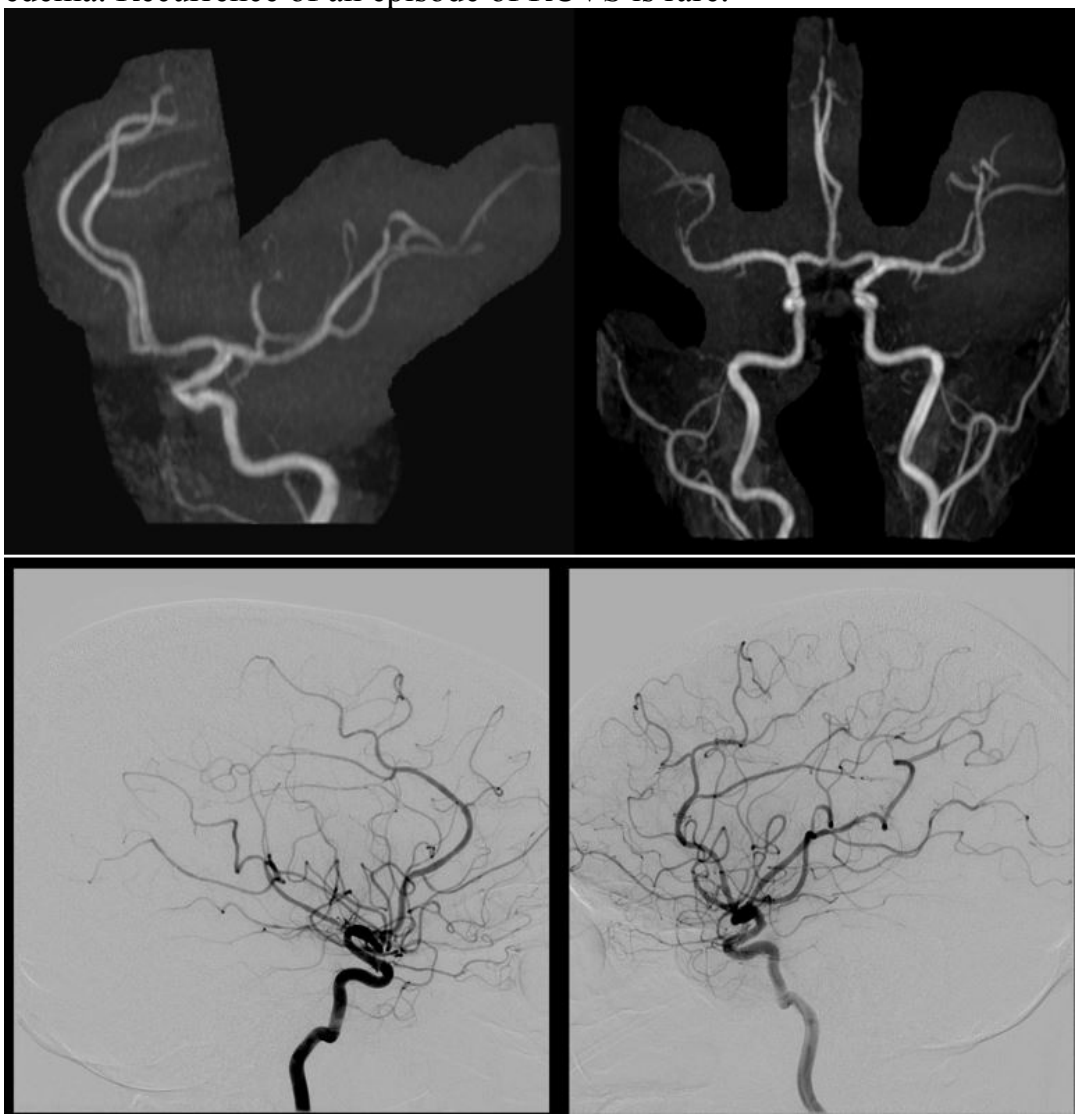
Results

Computed tomography Head without contrast showed no acute intracranial abnormality. Magnetic resonance imaging Head showed small area of abnormal T2/FLAIR hyper intensity within the cortex and possibly the subcortical white matter of the medial left parietal lobe, which may represent a subacute infarction. MRV was normal. Magnetic resonance angiography showed short irregular segments of narrowing involving multiple arteries in different vascular territories. Subsequently digital subtraction angiography (DSA) was performed and showed multifocal areas of irregularity and narrowing involving the distal cerebral arterial vasculature in multiple vascular distributions, nonspecific finding, but in view of clinical history most consistent with RCVS. Follow-up MRI 6 days after presentation demonstrated resolution of parietal signal abnormalities.

Conclusions

The presentation of RCVS usually is dramatic with sudden onset of "thunderclap" headaches, that are sudden, severe, peak within 60 seconds and can start fading after an hour. Many disorders can present as thunderclap headaches. These include subarachnoid hemorrhage, intraparenchymal hematoma, intraventricular hemorrhage, acute subdural hematoma, tumors and sinusitis. Several of these including RCVS, cerebral venous thrombosis, and cervical artery dissection do not show up on CT or through analysis of CSF. MRI to examine the parenchyma as well as cervical and cerebral angiography to visualize the vasculature, is necessary. RCVS is characterized by reversible narrowing of the cerebral vasculature, and neurologic deficits. Approximately 1/3 of patients develop ischemic or hemorrhagic stroke, or reversible brain edema. Headache location is usually diffuse or located in the occipital region or vertex. They often are accompanied with nausea and photosensitivity. A diagnosis of RCVS can only be confirmed when the reversibility of the vasoconstriction is assessed by imaging; 12 weeks from onset of symptoms has been proposed as a cutoff by which reversal should be complete or at least substantial, however complete resolution can be slower in some patients. MRA, CTA, and DSA are crucial for diagnosis. DSA is the most sensitive test, though is not routinely performed if a noninvasive study is diagnostic in the typical clinical setting. Cerebral angiographic abnormalities are dynamic and progress proximally, resulting in a "sausage on a string" appearance of the

circle of Willis and their branches. These abnormalities resolve spontaneously (without specific therapy) over a few weeks. Management is mostly symptomatic and includes supportive care and observation. The clinical outcome is benign in 95% of patients. Rarely patients develop severe irreversible deficits or death from progressive strokes or cerebral edema. Recurrence of an episode of RCVS is rare.



(Filename: TCT_E-67_RCVS.JPG)

E-68

11:52AM - 11:56AM

Vessel Wall Enhancement in Delayed-Onset Intracranial Herpes Zoster Vasculitis

Y Xie[1], S Imbesi[2], J Chen[3]
[1]University of California San Diego, San Dieog, CA, [2]University of California, San Diego, San Diego, CA, [3]San Diego VA / UCSD Med. Center, La Jolla, CA

Purpose

To demonstrate vessel wall enhancement and delayed onset of central nervous system (CNS) vasculopathy associated with herpes zoster ophthalmicus despite antiviral therapy.

Materials and Methods

A 71-year-old male with PMH of childhood chicken pox was diagnosed with left-sided herpes zoster ophthalmicus. He completed a course of valacyclovir with resolution of the cutaneous symptoms. Three months later, he presented with acute RUE and RLE weakness and left V1/V2 distribution numbness. Imaging showed multiple areas of acute lacunar infarcts. One month later, he represented with new word finding difficulty. Given the multiple episodes of recent neurologic events, MRI of the brain without/with contrast and MRA of the head were performed.

Results

Initial imaging: CT and MRI of the brain showed acute lacunar infarcts involving the left putatmen and subinsular region extending into the left corona radiata and left anterior and inferior temporal cortex. The major vascular flow voids, in particular the left M1 and A1, were normal without major wall thickening. Subsequent imaging during word-finding difficulty: Post-contrast brain MRI and MRA showed new, marked segmental, irregular, wall-thickening and diffuse enhancement of the left-sided vessel walls, ipsilateral to the previous zoster ophthalmicus, resulting in marked narrowing of the left supraclinoid ICA, and left M1 and A1 segments, compatible with medium vessel vasculitis. This was also confirmed on CT and catheter angiogram. MRI of brain showed multiple new lacunar infarcts in the left corona radiata and new left anterior temporal lobe infarct.

Conclusions

Despite treatment and resolution of the acute cutaneous manifestations, herpes zoster ophthalmicus patients have a 3-fold increased risk of infarct 6 months after the initial outbreak. This is due to trans-axonal migration of the reactivated virus to the intracranial vessels, causing a delayed onset, medium vessel CNS vasculitis, which can be demonstrated by diffuse vessel wall enhancement and thickening on MRI.



(Filename: TCT_E-68_zoster2on1.jpg)

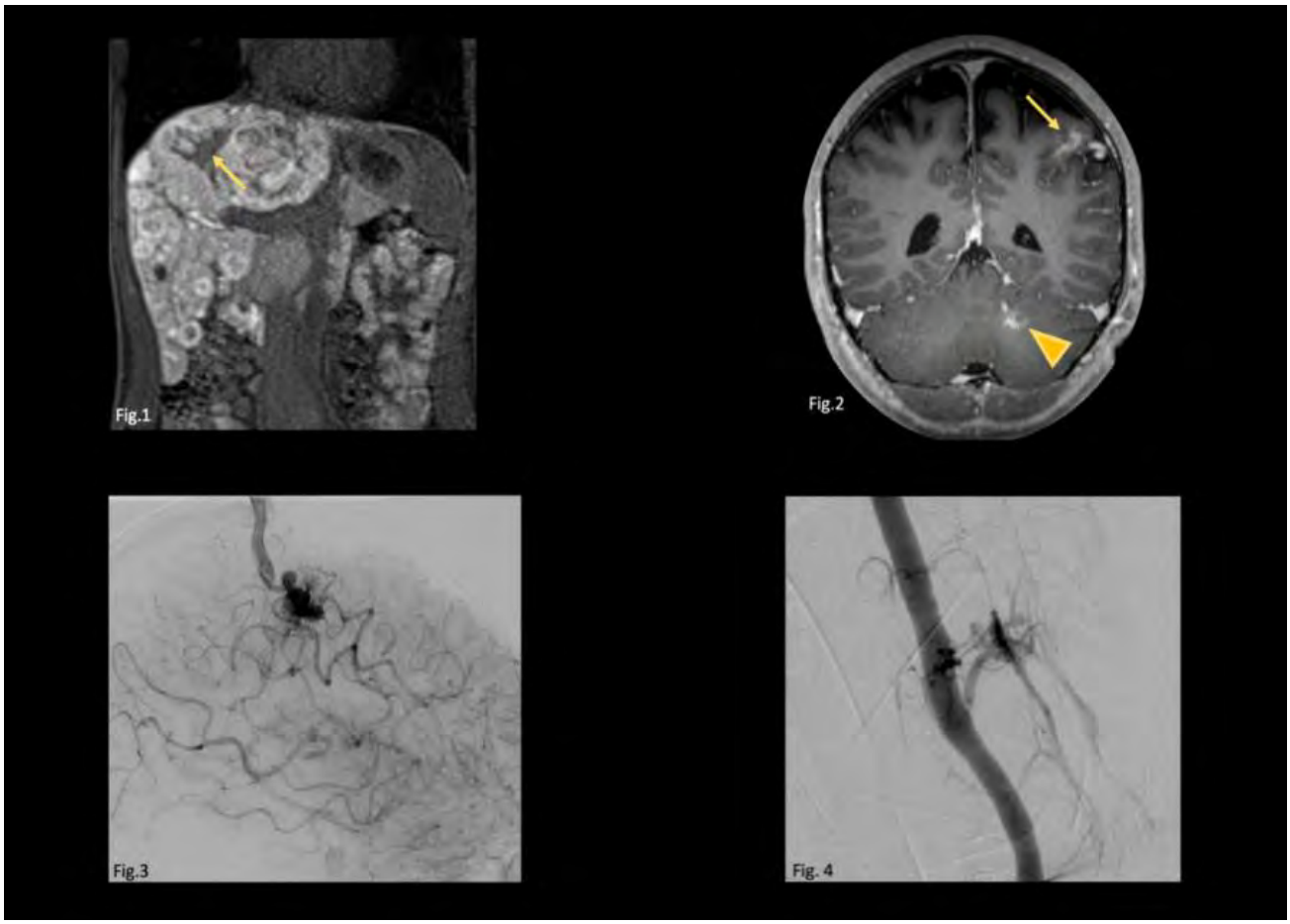
E-69

11:56AM - 12:00PM

Multiple Brain Arteriovenous Malformations (AVMs) associated with Multiple Focal Nodular Hyperplasia (FNH) of the liver: A Rare Syndrome

P Puac[1], A Rodriguez[1], C Vallejo[1], R Camacaro[1], M Castillo[1]
[1]*University of North Carolina at Chapel Hill, Chapel Hill, NC*

Purpose
The purpose of this case report is to show the imaging findings in multiple FNH syndrome.
Materials and Methods
A 18-year-old male presented with acutely periumbilical and epigastric abdominal pain. Imaging workup revealed multiple liver masses and a porto-systemic shunt. Initial labs showed anemia (Hgb 11.3 g/dL) and borderline ammonia (50 umol/L). A liver biopsy was performed and was consistent with multiple FNH. Six months later he complained headaches. A brain MRI revealed multiple AVMs. An arteriogram confirmed them and showed multiple epidural slow flow shunts at the cervical spine. No clinical findings that suggested hereditary hemorrhagic telangiectasia (HHT) or Klinefelter syndrome were present. Genetic tests revealed maternally inherited 10q duplication.
Results
Abdomen MRI (Fig. 1) showed multiple enhancing masses throughout the liver, some of them showing central stellate scars (arrow) compatible with multiple FHN. Brain MRI (Fig. 2) demonstrated multiple AVMs located at left motor cortex (arrow), right occipital lobe, right frontal lobe and medial left cerebellar hemisphere (arrowhead). Digital subtraction angiography (DSA) confirmed them (Fig. 3 precentral gyrus AVM) and also showed multiple arteriovenous shunts (AVS) into the epidural space at the C1,C2 and C5 (Fig. 4 AVS at C5).
Conclusions
Given the combination of multiple FNH of the liver and multiple CNS AVMs the diagnosis of multiple FNH syndrome was given. Multiple FNH is a relatively new syndrome occurring in approximately 20-25% of patients with FNH.



(Filename: TCT_E-69_GraphicFile.jpg)

E-70

12:00PM - 12:04PM

Multifocal Progressive Intracerebral "Aggregomas": Novel Clinical, Imaging and Pathologic Findings

S Khan[1], A Steven[2], P Raghavan[1]
[1]University of Maryland School of Medicine, Baltimore, MD, [2]Ochsner Health System, New Orleans, LA

Purpose
Nonamyloid light chain deposition disease (LCDD) is a rare clinicopathologic entity characterized by a monoclonal gammopathy resulting in nonamyloid immunoglobulin light chain tissue deposition. Only 5 other cases of tumoral intracerebral LCDD (termed "aggregoma") have been reported. The purpose of this presentation is to review multimodality (CT/MR/PET) imaging findings in a patient with a novel clinical, imaging and histologic presentation of progressive multifocal "aggregomas" at time of initial diagnosis and, uniquely, during post-treatment progression.

Materials and Methods

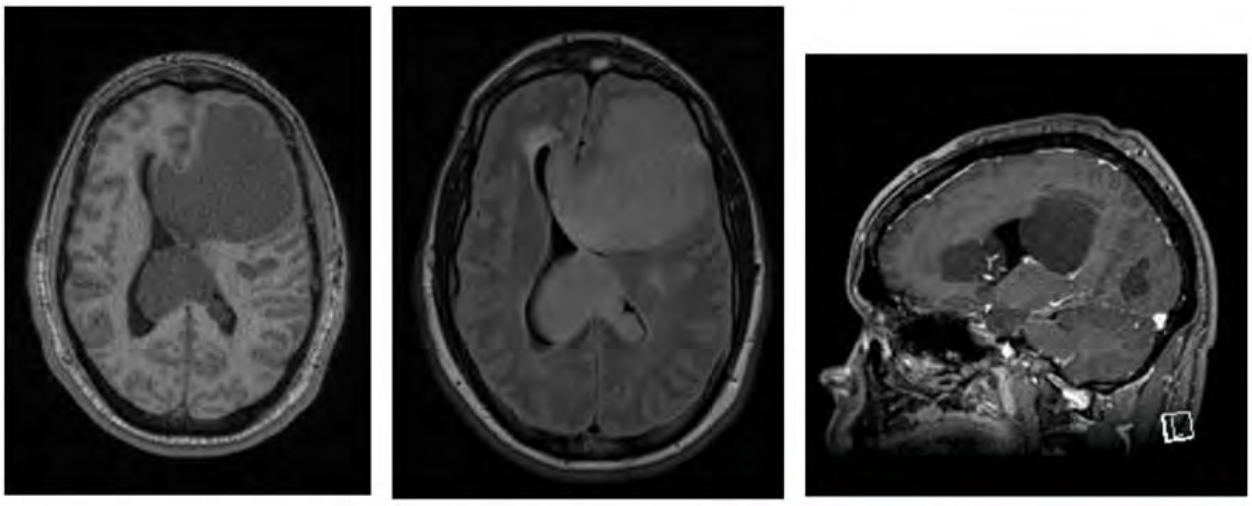
The patient is a 31-year-old African American male who presented with 6 months of blurred vision in the left eye (beginning in late 2012) which the patient attributed to cessation of smoking marijuana. His symptoms of diplopia, disconjugate gaze, and intermittent headaches had been getting progressively worse. The patient eventually sought medical attention in May 2013 and was found to have papilledema on ophthalmologic exam. Initial MRI revealed multiple large brain lesions, the largest in the frontal lobe, resulting in mass effect and suggestive of a primary neoplastic abnormality. The patient underwent subsequent craniotomy and excisional biopsy of the largest tumor in the frontal lobe in May 2013. Postoperatively, the patient's vision improved. Postoperative MRI demonstrated decreased mass effect and re-expansion of the right lateral ventricle. The patient's neurologic exam improved as well, and the patient was discharged home and followed by the neurology, neurosurgical and ophthalmology services. At time of surgery, 3 core biopsies of the largest frontal lobe lesion were obtained. On hematoxylin and eosin (H&E) stain, these samples demonstrated an amorphous, multifocal eosinophilic material arranged predominantly in a perivascular pattern. Congo red stains were negative for signs of amyloid. Interval surveillance MRI examinations showed progressively, minimally enlarging, nonenhancing masses in the brain. The patient underwent total brain radiation of 24 Gray (Gy) over 12 fractions, completed in December 2015. Despite radiation therapy, the patient's lesions continued to progressively enlarge, without recurrence in the resection cavity. Most recently, the patient presented with recurrent diplopia secondary to progressive mass effect from the enlarging lesions, which was temporized by neurosurgical intervention.

Results

Initial presenting magnetic resonance imaging (MRI) examination demonstrated at least 6 nonenhancing lesions involving the bilateral supratentorial white matter, the largest of which measured up to 7.7 centimeters (cm) in the left frontal lobe. Lesions demonstrated intermediate T2/FLAIR signal and hypointense T1 signal. Enhancing vessels, likely veins, appeared to traverse the substance of a few of these lesions, all of which did not enhance on postcontrast images. Marked associated intracranial mass effect, with effacement of the cerebral sulci and basilar cisterns and 1.9 cm of rightward midline shift was noted. Entrapment of the right lateral ventricle with associated periventricular edema was seen. The optic chiasm appeared to be downwardly displaced due to third ventricular dilatation.

Conclusions

Only 5 cases of intracerebral nonamyloid light chain deposition disease (LCDD) have been reported in the literature, with only a single case of disease isolated to the cerebrum reported. This second case of isolated intracerebral nonamyloid LCDD is unique in its presentation of previously undemonstrated imaging findings related to the apparent potential for chronicity and progression of this rare and, thus, limitedly understood disease process. This novel case of progressive isolated intracerebral nonamyloid LCDD further informs a growing understanding of the varied radiologic features of LCDD in the CNS, reflecting a more diverse disease process than currently understood.



Clockwise from left: (a) Axial unenhanced T1 magnetic resonance imaging (MRI) sequence; (b) Axial unenhanced FLAIR MRI sequence; (c) Coronal post-contrast MRI sequence; and (d) High-power hematoxylin and eosin (H&E) stain of frontal lobe mass specimen.

(Filename: TCT_E-70_Slide1.JPG)

E-71

12:04PM - 12:08PM

Melanotic Schwannoma: A Rare Cause of Accessory Nerve Palsy

L Nash[1], S Saipriya[2], D Weinberg[3], F Roncaroli[3], S Rutherford[3], R Siripurapu[3], G Potter[3]
[1]Greater Manchester Neurosciences Centre, Salford, United Kingdom, [2]UCL Institute of Neurology, London, London, [3]Greater Manchester Neurosciences Centre, Salford, Greater Manchester

Purpose
To demonstrate a rare case of melanotic schwannoma of the spinal accessory nerve.
Materials and Methods
A 58-year-old female with shoulder pain underwent magnetic resonance imaging (MRI) cervical spine which showed an incidental posterior fossa lesion. Subsequent MRI brain demonstrated a heterogeneous left cerebellopontine angle cistern mass, T1-hyperintense with mixed T2 signal and enhancement. The patient described dizziness, veering to the right and

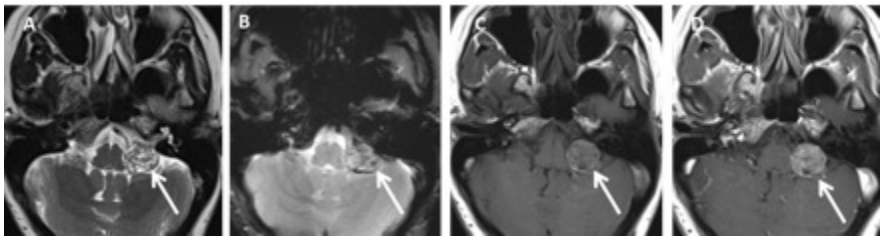
occasional choking episodes. There was no other significant clinical history. Clinical examination showed reduced strength and bulk of the left trapezius and a reduction in left speech discrimination. Pre-operative radiological differential diagnosis included hemorrhagic schwannoma or atypical meningioma. The patient was reviewed at the regional skull base tumor board and subsequently underwent neurosurgical excision. Histology showed a benign epithelioid melanotic tumor with no malignant features, initially felt to be meningeal melanocytoma. Upon further discussion with neurosurgery, the lesion was felt to be subcapsular and intrinsic to the nerve, favoring a diagnosis of melanotic schwannoma.

Results

Magnetic resonance imaging head showing a heterogeneous mass in the left cerebellopontine angle with mixed T2 signal (Fig. 1A), small areas of susceptibility artifact on gradient echo imaging (Fig. 1B) and T1-hyperintensity (Fig. 1C). The lesion demonstrated mild enhancement (Fig. 1D). There was minimal mass effect on the brainstem.

Conclusions

Melanotic schwannomas are rare tumors of neural crest origin believed to arise from a common precursor for Schwann cells and melanocytes. They may be seen as part of Carney complex (cutaneous pigmentation, cutaneous fibromyxoid tumors, cardiac myxoma and endocrine over activity). They have the potential for malignant transformation and for recurrence following excision. Histologically, melanotic schwannomas are characterized by spindle- shaped neoplastic Schwann cells and melanosomes. On MRI, lesions typically are T1-hyperintense and T2-hypointense with enhancement. Radiological differential diagnosis includes pigmented meningioma, primary or metastatic malignant melanoma, melanocytoma and melanoblastosis. Surgical and imaging findings guide histopathological diagnosis, as in this case.



(Filename: TCT_E-71_ASNRMelanoticSchwannoma.jpg)

E-72

12:08PM - 12:12PM

Extraventricular Subependymoma Of The Cerebellopontine Angle In An Adult Patient

M Sondag[1], S Dissanayake[1], P Kim[2]
[1]University of Southern California, Los Angeles, CA, [2]University of Southern California, Keck School of Medicine, Los Angeles, CA

Purpose

To present a rare case of extraventricular subependymoma of the cerebellopontine angle (CPA) in an adult male patient.

Materials and Methods

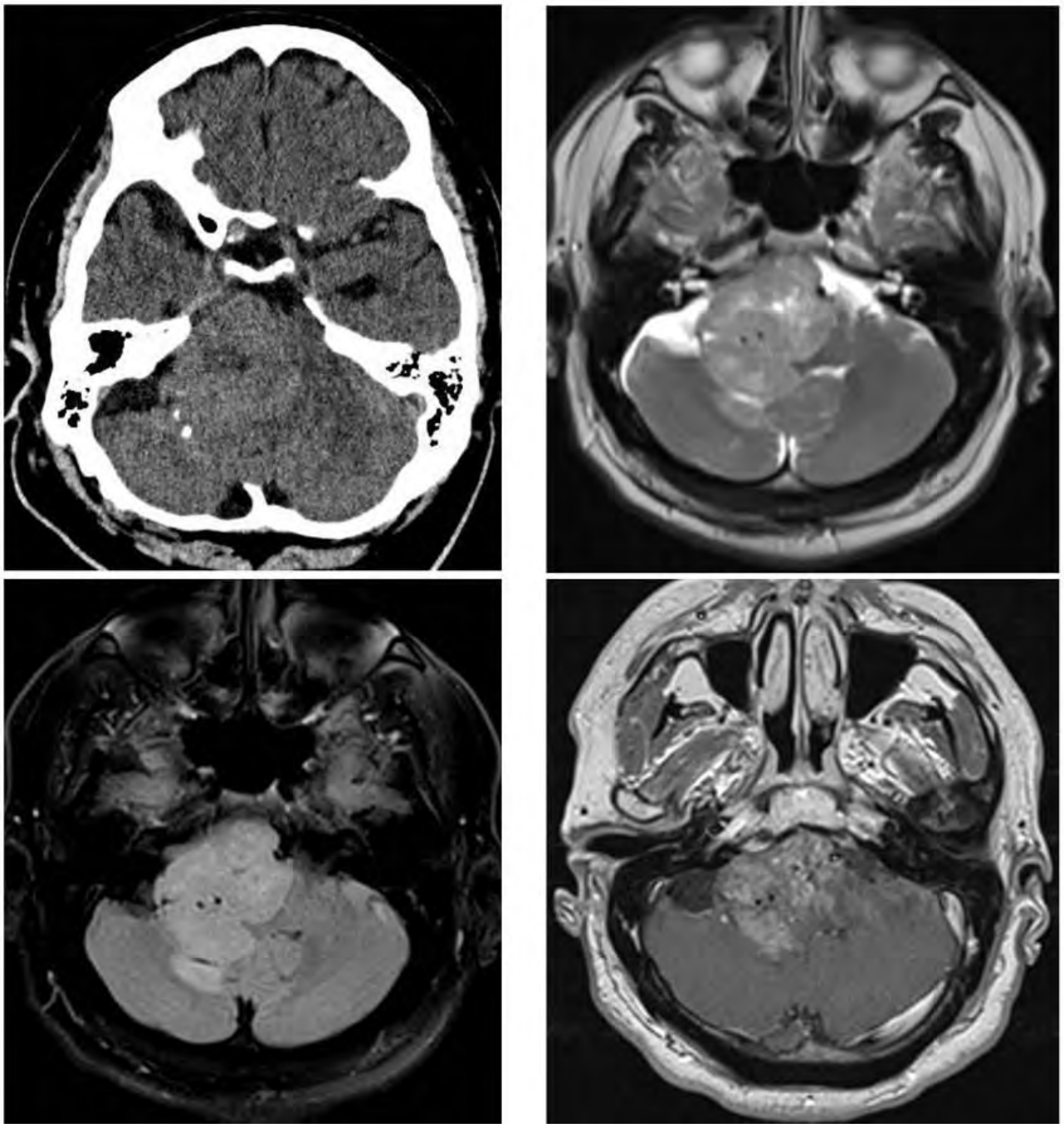
A 62-year-old-man presenting with 3 months of progressive headache, imbalance, ataxia, hearing loss, diplopia, and dysphagia. On physical exam, the patient had mild vertical nystagmus, leftward deviation of the tongue, right-sided hearing deficit, decreased right hemi-facial sensation, and unsteady gait. Magnetic resonance imaging (MRI) demonstrated a large, heterogeneously enhancing mass in the right CPA associated with mass effect and moderate hydrocephalus.

Results

Magnetic resonance imaging (MRI): Heterogeneously enhancing, T2 hyperintense mass centered in the right CPA with mass effect resulting in moderate hydrocephalus and effacement of the right aspect of the CPA cistern. A prominent flow-void courses centrally through the lesion. Computed tomography angiography (CTA): A prominent vessel coursing through the center of the mass corresponds to the right posterior inferior cerebellar artery (PICA). Noncontrast CT: A few coarse calcifications are noted along the periphery of the mass.

Conclusions

Subependymomas are benign WHO grade 1 lesions typically found within the ventricular system (1). We present an exceedingly rare case of a subependymoma located within the CPA without intraventricular extension. In concordance with previously reported intracranial subependymomas, the mass demonstrated mild and heterogeneous enhancement, coarse calcifications, and lack of significant perilesional edema (1, 2, 3, 4, 5). The prominent PICA flow void within the lesion was notable for purposes of surgical planning. Differential diagnoses included schwannoma, ependymoma, and meningioma. However, these diagnoses were considered less likely due to a growth pattern separate from the expected course of cranial nerves, lack of significant perilesional edema, and absence of homogenous enhancement, respectively. Recognizing subependymoma as a potential etiology for CPA mass is important for operative planning. Partial resection may be considered in certain instances, as this is a purely benign lesion (2, 3, 4).



(Filename: TCT_E-72_ASNRsubependymoma.jpg)

E-73

12:12PM - 12:16PM

Calcifying Pseudoneoplasm of the Neuraxis (CAPNON) Involving the Central Skull Base: Uncommon Location for an Uncommon Lesion

M Kontzialis[1], M Alkaphoury[1], M Kocak[1]

[1]*Rush University Medical Center, Chicago, IL*

Purpose

The purpose of this abstract is to highlight calcifying pseudoneoplasm of the neuraxis (CAPNON) as an uncommon diagnosis in the central skull base. Familiarity with the typical imaging findings of this rare condition may allow its inclusion in the differential diagnosis when appropriate.

Materials and Methods

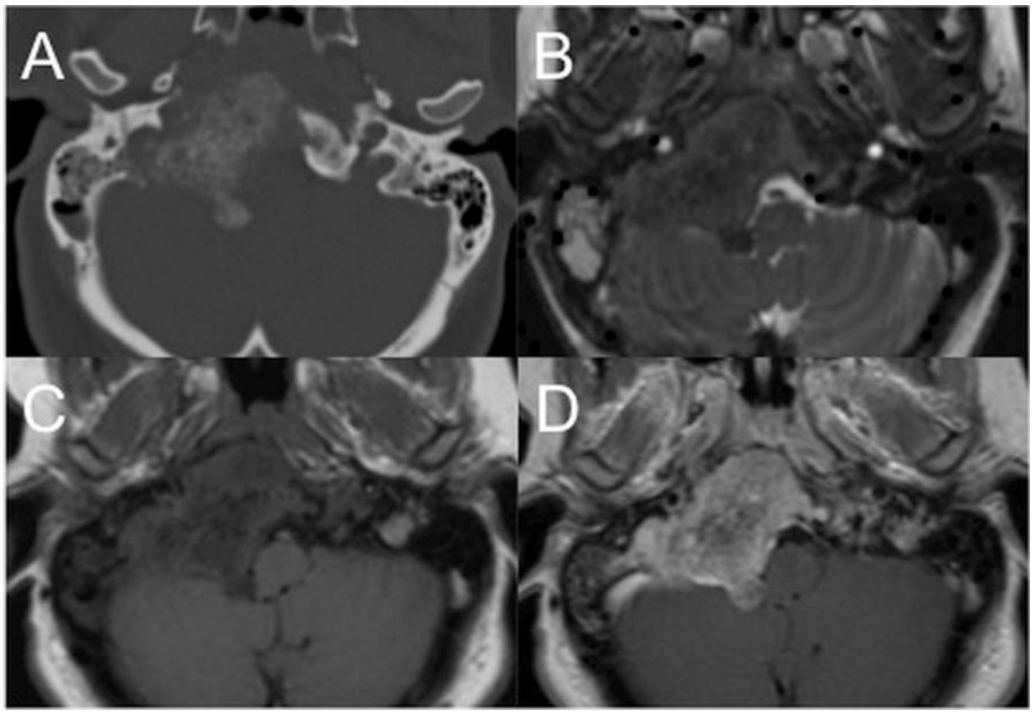
A 31-year-old female presented with sudden worsening of occipital and neck pain, which has been slowly increasing over a period of 2-3 years. The growing pain had been attributed to a cervical sprain/strain in the past. However, physical therapy, massage, anti-inflammatory medications and muscle relaxants had failed to alleviate the pain. Cross-sectional imaging with computed tomography (CT) and magnetic resonance imaging (MRI) revealed a large skull base mass.

Results

On CT, there was a large calcified mass lesion that was eroding the central and right side of the skull base. The lesion was hypointense on T1 and T2 and enhanced heterogeneously following contrast administration. The mass lesion extended into the basal cisterns creating a small indentation on the right side of the cerebellomedullary junction.

Conclusions

CAPNON is a rare benign lesion that can occur anywhere along the neuraxis with most reported cases extra-axial. Extra-axial lesions may be intradural or extradural. Typical imaging findings include a calcified mass with uniform T1 and T2 hypointense signal. A CAPNON may demonstrate no enhancement, rim enhancement or internal enhancement that may be homogeneous or heterogeneous. The main differential considerations for a calcified skull base mass include chordoma, chondrosarcoma and meningioma. The imaging feature that facilitates diagnosis in this case of calcified skull base CAPNON is the T2 hypointense signal, which would be unusual for a chordoma and chondrosarcoma. Lack of substantial dural enhancement excludes meningioma. Solitary mass with calcified matrix and smooth osseous erosions excludes lymphoma, plasmacytoma, and metastatic disease. In summary, we present a unique case of a large CAPNON involving the central skull base and discuss relevant differential considerations as well as imaging findings that point towards the correct diagnosis.



(Filename: TCT_E-73_CAPNONskullbasehighres.jpg)

E-20

12:16PM - 12:20PM

Multiple Peripheral Fusiform Cerebral Aneurysms from Atrial Myxoma: Diagnostic Imaging and Interventional Management

A Malik[1], A Chukus[2], R Dahlgren[1], J Chaloupka[1]
[1]Mount Sinai Medical Center, Miami Beach, FL, [2]Stanford Hospital, Stanford, CA

Purpose
We present a case of multifocal intracerebral fusiform aneurysms arising from atrial myxoma emboli. Our case highlights both classic imaging features and use of advanced neuroendovascular surgical techniques to treat a challenging intracerebral aneurysm morphology prior to required cardiac surgery, thereby reducing operative risk and complications.
Materials and Methods
Previously healthy 40-year-old woman experienced syncope and right hemiparesis on a cruise ship, eventually determined to be a left middle carotid artery (MCA) ischemic stroke at a nearby Mexican hospital. She was airlifted to our institution. Left atrial myxoma was seen on 2D echocardiogram, and a brain magnetic resonance imaging (MRI) revealed multiple embolic subacute infarcts, and dilated peripheral flow voids suspicious for peripheral aneurysms. Diagnostic cerebral digital subtraction angiography (DSA) showed multiple, various-size peripheral myxomatous fusiform aneurysms, 3 of which required

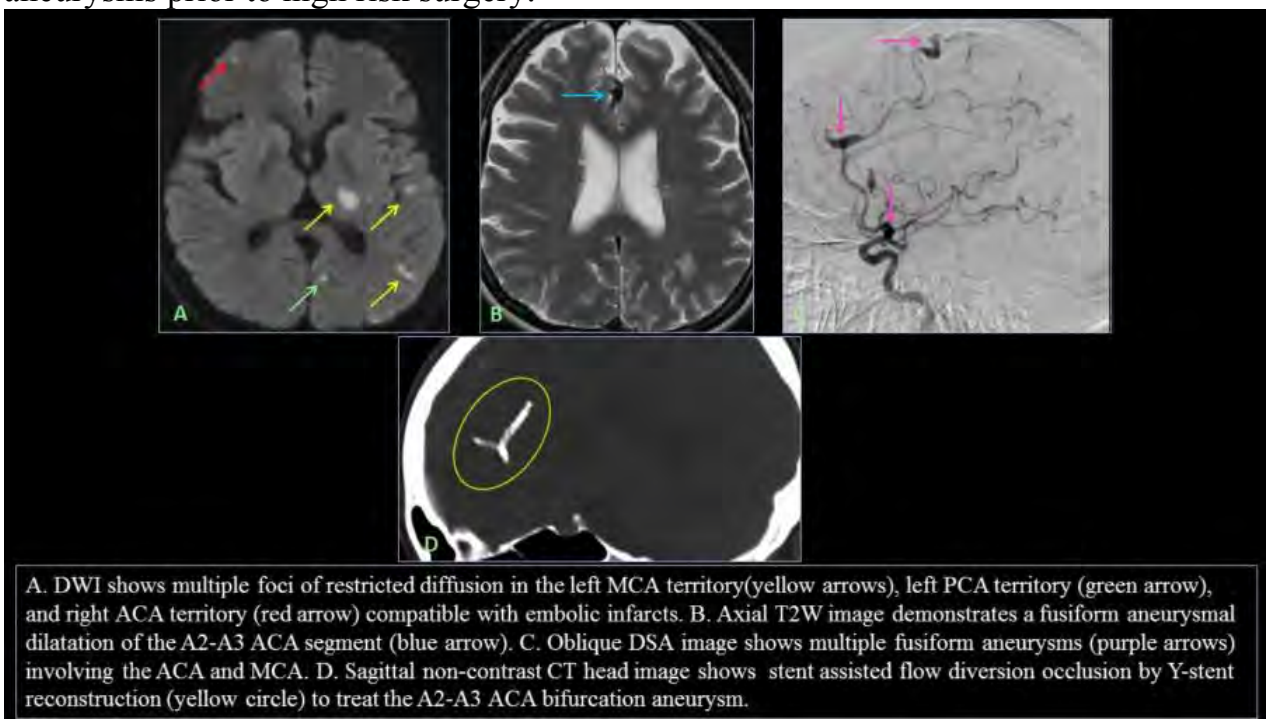
endovascular aneurysm surgery. Four days later, she underwent resection of her left atrial myxoma proven by pathology and was discharged uneventfully. She was asymptomatic at follow up.

Results

Two-dimensional echocardiogram showed EF 65-70% with a large, mobile, lobulated left atrial myxoma (7x4cm). Brain MRI showed multiple predominantly left-sided, cortical/subcortical, subacute embolic infarcts with areas of microhemorrhage, and dilated arterial flow voids on T2. Diagnostic cerebral DSA showed multiple fusiform peripheral myxomatous aneurysms involving bilateral ACA, MCA and left PCA distal segments. Additionally, there was complete thromboembolic occlusion of the mid-cervical right vertebral artery. The patient subsequently underwent microstent-assisted flow diversion occlusion of high-risk right A4-ACA, and right M3-MCA aneurysms. Also, a right A2-A3 ACA bifurcation aneurysm was treated by Y-stent reconstruction to achieve stent-assisted flow diversion occlusion.

Conclusions

Fusiform intracerebral aneurysms, particularly at a bifurcation, are challenging, but can be treated safely and effectively with advanced techniques using flow-diverter devices and Y-stent reconstruction. Risk of fatal subarachnoid hemorrhage can be reduced by treating these aneurysms prior to high risk surgery.



A. DWI shows multiple foci of restricted diffusion in the left MCA territory(yellow arrows), left PCA territory (green arrow), and right ACA territory (red arrow) compatible with embolic infarcts. B. Axial T2W image demonstrates a fusiform aneurysmal dilatation of the A2-A3 ACA segment (blue arrow). C. Oblique DSA image shows multiple fusiform aneurysms (purple arrows) involving the ACA and MCA. D. Sagittal non-contrast CT head image shows stent assisted flow diversion occlusion by Y-stent reconstruction (yellow circle) to treat the A2-A3 ACA bifurcation aneurysm.

(Filename: TCT_E-20_ASNRIMAGESLABEL.jpg)

Wednesday
11:00AM - 12:15PM
Long Beach Convention Center, Room 104C (Main Lobby)

18F-Parallel Paper Session: TBI: Understanding "Undone"

O-206

11:00AM - 11:08AM

Distribution of Subarachnoid Hemorrhage as a Predictor of Diffuse Axonal Injury

D Li[1], A Mensinkai[1]
[1]*McMaster University, Hamilton, Ontario*

Purpose

Diffuse axonal injury (DAI) exists on the traumatic brain injury (TBI) spectrum of disease and carries significant mortality and morbidity. Imaging features of DAI are readily apparent on magnetic resonance imaging (MRI) with susceptibility-weighted images (SWI), however remain inconspicuous and nonspecific on computed tomography (CT). In contradistinction, traumatic subarachnoid hemorrhage (SAH) is a more commonly identified CT finding in cases of traumatic brain injury. Earlier suspicion for DAI improves prognostication and can direct patient management. The purpose of this study is to elucidate the relationship between the distribution of SAH on the initial CT and the diagnosis of DAI on follow-up MRI.

Materials and Methods

Following approval from our institutional research ethics board, we retrospectively reviewed all cases of trauma patients from January 2010 to March 2016 who underwent both a CT of the head at initial presentation and an MRI of the head with the query of DAI within 30 days of the CT. Demographic data, clinical data, the presence of SAH categorized by location on the initial CT, and the presence and grading of DAI on MRI as per the staff radiologist report were documented. Diffuse axonal injury grading was based on the classification system devised by Adams et al (1989). We then performed univariate and multivariate binomial logistic regression on the different locations of SAH with respect to the presence of DAI, followed by sensitivity and specificity calculations.

Results

Of the 72 cases that were included, DAI was present on 42 (56.8%) cases and not present in 32 (43.2%) based on MRI findings. The mean time interval between the initial CT and the MRI was 8.43 (±8.79) days. Within the DAI group, 12 (28.6%) had grade 1, 18 (42.9%) had grade 2, and 12 (28.6%) showed grade 3 disease as per the Adams classification system. Visibly hemorrhagic parenchymal lesions were detected on CT in 19 of the 42 DAI patients (45.2%). Two locations of SAH were significantly associated with DAI on univariate binomial logistic regression: convexal SAH distant from the site of primary injury ("non-primary cSAH") ($p = <0.005$; OR, 5.38) and interpeduncular SAH ($p = 0.0158$; OR, 3.57), detected in 41 (55.4%) and 26 (35.1%) of cases respectively. Non-primary cSAH was the only single location of SAH that was significantly associated with DAI on multivariate binomial logistic regression ($p = 0.0232$; OR, 4.05). These results yielded a specificity of

65.6% and a sensitivity of 73.8% for non-primary cSAH in predicting DAI in this selected subpopulation.
Conclusions
Our retrospective study shows that, in the subpopulation of trauma patients where there is clinical suspicion, convexal subarachnoid hemorrhage distant from the primary site of injury may be associated with increased likelihood of the presence of DAI on follow-up MRI.

O-207

11:08AM - 11:16AM

Prevalence of Microhemorrhages Following Blast-Related Mild Traumatic Brain Injury in Military Service Members Using Susceptibility-weighted MRI

C Morley[1], E Lotan[2], C Marmar[3], D Abu-Amara[1], Y Lui[4]
[1]NYU School of Medicine, New York, NY, [2]NYU Langone Medical Center and Tel-Aviv University, New-York, NY, [3]New York University Langone Medical Center, New York, NY, [4]NYU School of Medicine, New York City, NY

Purpose
Microhemorrhages are a marker for mild traumatic brain injury (mTBI). Non-blast injury is believed to be pathophysiologically distinct from blast-related mTBI. There are a substantial number of individuals (active military and veterans) exposed to blast-related mTBI due to improvised explosive devices. Previous reports in military personnel group individuals with varying severity of head injury and/or blast and nonblast related TBI. The purpose of this study is to characterize cerebral microhemorrhages in military service members with blast-related mTBI, correlating with published literature on nonblast mTBI in the civilian population.
Materials and Methods
Research ethics committee approval and patient written informed consents were obtained. One hundred and forty-seven veterans with a clinical history of blast-induced mTBI underwent MRI performed on a Siemens Skyra 3Tesla magnet (Erlangen, Germany). Included in this study are military service members who experienced mTBI in conjunction to close proximity to a blast explosion. One hundred fourteen participants were included (107 males and 7 females, average age 31 years with standard deviation of 7). Susceptibility-weighted images were assessed by 2 radiologists independently for the presence of cerebral microhemorrhage.
Results
Among 114 veterans with blast-induced mTBI, 46 reported a feeling of being "dazed or confused" and 68 reported loss of consciousness for less than 30 minutes. Cerebral microhemorrhage was identified in one participant (0.9%).
Conclusions
While the frequency of SWMRI-detectable microhemorrhages following blunt-induced

mTBI in the civilian population has been reported to be as high as 20-25%, this study finds a much lower rate of microhemorrhages detected at 3T following blast-induced mTBI in veterans. These results support the idea the underlying pathophysiological mechanisms of injury differ between blast-induced mTBI versus blunt head trauma induced concussion.

O-208

11:16AM - 11:24AM

SWI Patterns of Cerebral Bleeds in Patients with Diffuse Axonal Injury: Correlation with GCS at Admission

A Rodriguez[1], R Camacaro[1], P Puac[1], C Vallejo[1], M Castillo[1]
[1]*University of North Carolina at Chapel Hill, Chapel Hill, NC*

Purpose
Disruption of white matter tracts due to trauma injury may happen as shearing forces are applied to the brain. These abnormalities are seen in susceptibility-weighted images (SWI) as hemorrhages that can be nodular or linear with the latter following white matter tracts. Our goal was to characterize patterns of hemorrhages associated with diffuse axonal injuries (DAI) and compare them with patient's presentation.
Materials and Methods
We reviewed MRI studies in 43 patients who presented with DAI. Patients with cerebral contusions were excluded. Four readers reviewed the images to assess presence of bleeding in SWI and the pattern of hemorrhages (linear, nodular or mixed pattern), DAI were graded based on anatomical distribution as shown in Table 1. Medical records were reviewed for Glasgow Coma Scale (GCS) at admission and classified using the Traumatic Brain Injury (TBI) Scale (Table 2) and compared with imaging findings to determine correlation between initial symptoms and pattern of SWI findings. Statistical significance of the findings was assessed.
Results
Linear microhemorrhages were identified in 1 (2.3%); nodular in 18 (41.8%) and mixed pattern in 24 (55.8%) patients with their distributions shown in Tables 3 and 4. There were no significant differences in DAI patterns and their grades nor in the DAI patterns and traumatic brain injury ratings with P-values of 0.73 and 0.49 respectively.
Conclusions
There were no significant differences between the linear, nodular and mixed patterns of DAI-associated hemorrhages and GCS at admission. Although intuitively, patients with larger and more complex hemorrhagic lesions would be expected to have worse GCS at admission, this was not found and thus other factors not identified by SWI may play a role in the initial presentation of these patients.

Table 1	
Grade DAI	**Location**
I	Grey-White matter interface
II	Corpus Callosum in addition to grade I location
III	Brainstem in addition to grade I and II locations

Table 2	
Grade TBI	**GCS**
1	13-15
2	9-12
3	3-8

Table 3			
PATTERN	**GRADE DAI**		
	I	**II**	**III**
LINEAR	1	0	0
NODULAR	6	5	7
BOTH	9	5	10

Table 4			
PATTERN	**GRADE TBI**		
	1	**2**	**3**
LINEAR	0	0	1
NODULAR	2	3	13
BOTH	0	3	21

(Filename: TCT_O-208_Tables.jpg)

O-209

11:24AM - 11:32AM

Perfusion Deficits Identified in Blast-TBI Subjects

J Andre[1], S Rane[1], C Mac Donald[1]
[1]*University of Washington, Seattle, WA*

Purpose
To prospectively assess perfusion status in active duty U.S. military subjects following a concussive injury, drawn from the Assessment of Long-term Outcome and Disability in Active Duty Military. Prospectively examined following concussive TBI (ADAPT) study.
Materials and Methods
Experiment: Subjects comprised individuals sustaining a concussive blast injury during deployment, while those without history of blast exposure and no diagnosis of brain injury from deployment served as controls. Magnetic resonance imaging (MRI) examination performed at 3T (Philips Achieva) included: sequential 3D T1-weighted images and a

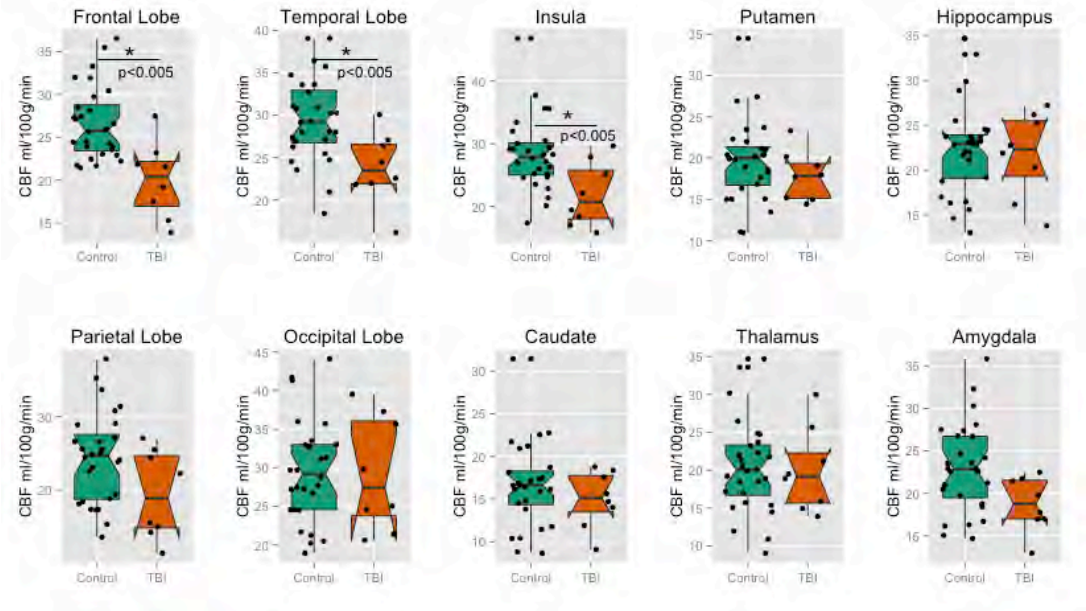
pseudo-continuous arterial spin labeling (pCASL) acquisition. pCASL parameters included: matrix = 96×96×20, TE = 19 ms, TR = 5000 ms, label duration = 1800 ms, post-labeling delay = 2000ms, 30 control/label pairs and a matched M0 image. Analysis: Images were motion-corrected and registered to the M0 image. Pairwise subtraction of the pCASL control and label pairs was performed and CBF was calculated (1). Cerebral blood flow maps were registered to a standard 2mm MNI template in FSL-FLIRT using intramodal registration. Accuracy of registrations was verified, and manually altered in select subjects to improve congruence with the MNI template. Cerebral blood flow was calculated using the MNI and Harvard-Oxford atlases in FSL, compared between the 2 groups using a 1-sided t-test, and corrected for multiple comparison using Bonferroni adjustment (p-value for significance = 0.05/10 = 0.005).

Results

Eight male TBI subjects (age=32±8 years, education = 13±1 years) and 30 gender-matched male controls (age = 34±8 years, education = 15±2 years) underwent pCASL imaging following informed, written consent. All evaluated brain regions showed reduced perfusion in the TBI compared to the control group (Fig.). After correction for multiple comparisons, CBF was significantly reduced in the frontal lobe, insula, and the temporal lobe ($p<0.005$) in the TBI group (20±4, 22±5, 24±4 ml/100g/min, respectively) compared to the controls (26±4, 28±6, 29±5 ml/100g/min respectively).

Conclusions

We have shown the applicability of ASL to identify perfusion deficits in concussive blast injury. Results are in accordance with prior studies reporting decreased perfusion in similar brain regions (2-4).



(Filename: TCT_O-209_Figure1_BLASTnew.jpg)

O-210

11:32AM - 11:40AM

Resting Cerebral Perfusion Deficits and Relation To Cognitive Outcomes in Chronic Traumatic Brain Injury

J Ware[1], S Dolui[1], J Whyte[2], W Choi[2], J Detre[1], J Kim[3]
[1]Hospital of the University of Pennsylvania, Philadelphia, PA, [2]Moss Rehabilitation Research Institute, Elkins Park, PA, [3]City College of New York School of Medicine, New York, NY

Purpose

Traumatic brain injury (TBI) is a leading cause of cognitive morbidity worldwide (1), for which biomarkers are needed to better understand neurobiological manifestations, assess injury severity, and inform prognosis. Research utilizing advanced neuroimaging has begun to elucidate some of the neural mechanisms underlying the cognitive sequelae of TBI. To date, however, the preponderance of investigations have focused on the structural consequences of TBI, despite mounting evidence suggesting that alterations in perfusion and metabolism also mayserve as key pathologic mechanisms (2, 3). The degree to which these mechanisms relate to cognitive outcomes remains poorly understood. Furthermore, the degree to which functional and metabolic consequences of TBI interact with structural damage has not been thoroughly investigated. Ultimately, a detailed mechanistic understanding of post-traumatic cognitive dysfunction is needed to develop more effective rehabilitation strategies. Arterial spin labeling (ASL) is a promising approach to assessment of brain perfusion and metabolism in the post-traumatic setting, with several advantages over alternative methods of brain perfusion assessment, including ability to quantify absolute cerebral blood flow (CBF) and lack of exposure to ionizing radiation. Furthermore, as ASL can be acquired easily as part of routine MRI examination, it is well suited to employ in multimodal assessments, required to assess the breadth of heterogeneous TBI-related neuropathology. In this investigation, we use ASL to examine the chronic effects of TBI on brain perfusion measurements. Furthermore, we examine the relationship of perfusion alterations to important cognitive outcomes across several domains, as well as to structural manifestations of TBI. We hypothesize that TBI is associated with chronic alterations in brain perfusion, and that altered perfusion is in turn related to post-traumatic dysfunction independent of structural gray matter damage.

Materials and Methods

This study included 39 adults with single-event TBI of at least moderate severity, carefully selected to exclude the effects of factors which may potentially confound the relationship between TBI, perfusion, and cognitive outcomes including comorbid psychiatric conditions and substance abuse. Thirty-four healthy controls also were recruited and matched for demographic characteristics. Demographic and clinical information regarding injury severity were recorded for each subject at the time of injury. Demographic data included age, sex, and years of education. Injury severity was assessed using duration of post-traumatic

amnesia. Cognitive outcomes assessed at 3 months after injury included neuropsychological test performance across selected domains frequently impaired in the setting of TBI, including attention, executive function, working memory, and processing speed. Neuroimaging evaluation was completed on a 3T MRI scanner and included a high resolution structural MPRAGE sequence as well as resting ASL perfusion using a 2D pseudo-continuous labelling technique. Cortical thickness and subcortical volume measurements were derived from structural data using FreeSurfer (4). Structural images also were used for manual segmentation of focal lesions. Arterial spin labeling data were processed using in-house software to derive whole-brain maps of CBF (5). Perfusion and structural imaging data were compared between the TBI and control groups in voxel-wise fashion using permutation testing with correction for multiple comparisons. Subsequently, region-of-interest (ROI) measures were extracted and compared with clinical and cognitive measures using multivariate linear regression. Region-of-interest analysis was restricted to regions known to exhibit high metabolic activity and which have been implicated frequently in TBI literature including the thalamus, cingulate cortices, and dorsolateral prefrontal cortex.

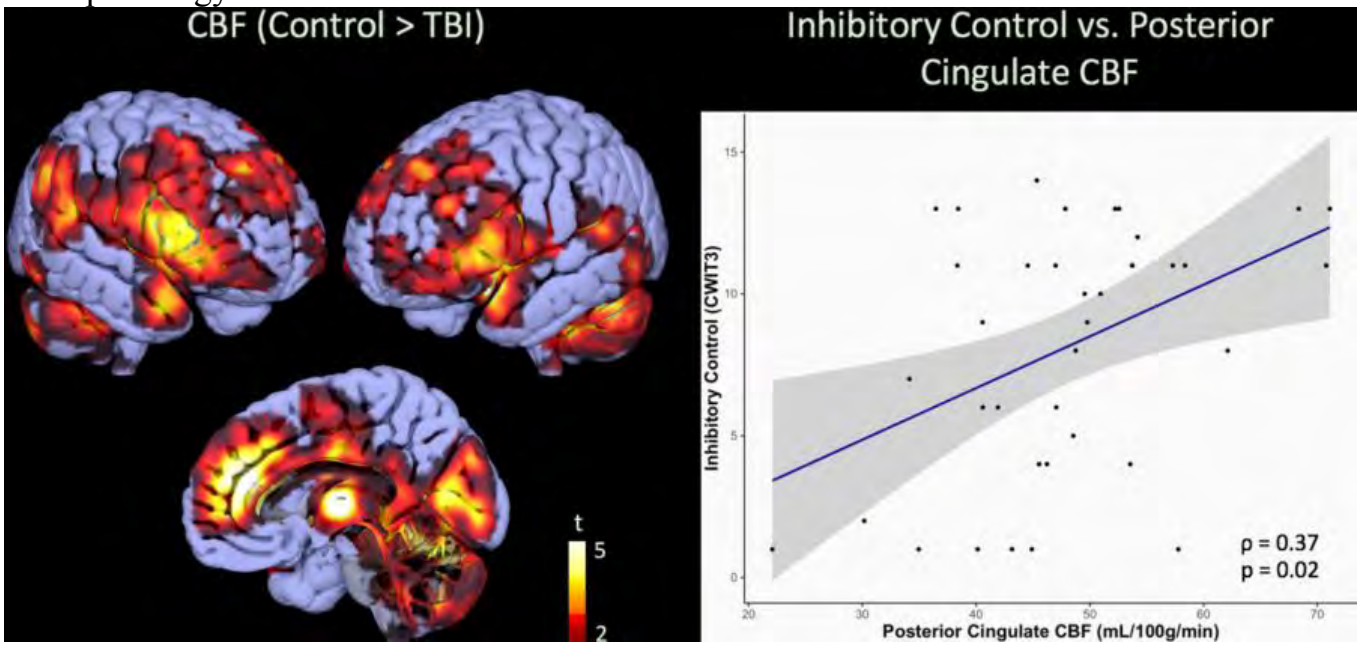
Results

Compared to controls, the TBI group demonstrated several regions of significantly reduced resting perfusion in both cortical and subcortical locations ($p<0.05$, corrected). The TBI group also demonstrated several regions of significantly reduced cortical thickness as well as reduced subcortical volumes ($p<0.05$, corrected). The TBI group demonstrated significantly reduced neuropsychological performance compared to controls across all domains examined ($p <0.05$). Within the TBI group, the distribution of focal encephalomalacia demonstrated a strong predilection for the inferior frontal and anterior temporal regions. The distribution of reduced CBF at the group level overlapped with but was distinct from that of macrostructural lesions and atrophy. In ROI analysis, all regions examined demonstrated reduced CBF in the TBI group compared to controls ($p<0.05$). In linear regression analysis, several significant correlations between CBF and neuropsychological test performance unique to the TBI group were identified. For example, CBF in the posterior cingulate cortex demonstrated a direct correlation with performance on the color-word-interference test, a measure of inhibitory control (=0.37, $p=0.02$). Furthermore, CBF in the dorsolateral prefrontal regions was correlated with performance on the trails B test, a measure of divided attention (=0.35, $p=0.03$). In the multivariate analysis, group-wise differences in CBF in the posterior cingulate cortex were independent of cortical thickness. In contrast, group-wise differences in CBF within the anterior cingulate cortex, dorsolateral prefrontal cortex, and thalamus were no longer significant when accounting for structural measures. Furthermore, the correlation between posterior cingulate CBF and attentional function was independent of cortical thickness. In contrast, the correlation between dorsolateral prefrontal CBF and executive function was no longer significant when controlled for cortical thickness.

Conclusions

Chronic TBI is associated with persistent, widespread cortical and subcortical CBF

reductions 3 months after injury, in a pattern that overlaps with but is distinct from the distribution of macroscopically evident structural pathology as well as that of more subtle atrophy. The extent of CBF reduction in key brain regions is correlated with both injury severity and post-traumatic cognitive dysfunction. While some relationships between CBF and clinical measures may be confounded by structural measures, other relationships appear to be independent of structural damage. The observed dissociation between CBF and atrophy may imply that different mechanisms underlie TBI-related CBF reductions in different regions of the brain. While reductions in neuronal volume may in some cases account for CBF reduction, in other cases CBF differences may represent a direct manifestation of decreased microvascular perfusion or decreased metabolic integrity, as CBF and metabolism are known to be tightly coupled. Arterial spin labeling measurement of CBF is therefore a promising modality for the study of vasculometabolic alterations as they apply to chronic post-traumatic cognitive dysfunction, particularly when employed in a multimodal fashion. Additional research focused on further elucidating the mechanisms of TBI-related CBF reduction and trends over time may yield important insights into the nature of TBI-related neuropathology.



(Filename: TCT_O-210_fig.jpg)

O-211

11:40AM - 11:48AM

Hyperbaric Oxygen Therapy Can Induce Angiogenesis and Regeneration of Nerve Fibers in Traumatic Brain Injury Patients

S Tal[1], S Efrati[2], A Hadanny[2]
[1]Assaf Harofeh MC, Zeriin, Israel, [2]Assaf Harofeh MC, Zerifin, AK

Purpose
Recent clinical studies in patients with chronic neurological impairment due to stroke or traumatic brain injury (TBI) present evidence that hyperbaric oxygen therapy (HBOT) can induce neuroplasticity. The aim of this article is to assess the neurotherapeutic effect of HBOT in patients suffering from prolonged post-concussion syndrome (PPCS) due to TBI using brain microstructure imaging.
Materials and Methods
Fifteen patients afflicted with PPCS were treated with 60 daily HBOT sessions. Imaging evaluation was performed using dynamic susceptibility contrast-enhanced (DSC) and diffusion tensor imaging (DTI) MR sequences. Cognitive evaluation was performed by objective computerized battery (NeuroTrax).
Results
Hyperbaric oxygen therapy was initiated 6 months to 27 years (10.3±3.2 years) from injury. After HBOT, DTI analysis showed significantly increased fractional anisotropy values and decreased mean diffusivity in both white and gray matter structures. In addition, the cerebral blood flow and volume were increased significantly. Clinically, HBOT induced significant improvement in the memory, executive functions, information processing speed and global cognitive scores.
Conclusions
The mechanisms by which HBOT induces brain neuroplasticity can be demonstrated by highly sensitive MRI techniques of DSC and DTI. Hyperbaric oxygen therapy can induce cerebral angiogenesis and improve both white and gray microstructures indicating regeneration of nerve fibers. The micro structural changes correlate with the neurocognitive improvements.

O-212

11:48AM - 11:56AM

Subconcussive Impacts in High School Football Alter MEG Measured Default Mode Network

E Davenport[1], J Urban[2], B Wagner[3], M Espeland[2], A Powers[4], C Whitlow[2], J Stitzel[2], J Maldjian[3]
[1]UT Southwestern Medical Center, Dallas, TX, [2]Wake Forest University School of Medicine, Winston-Salem, NC, [3]University of Texas Southwestern, Dallas, TX, [4]Wake Forest University School of Meidine, Winston-Salem, NC

Purpose
The purpose of this study is to determine if the cumulative effects of head impacts from a season of high school varsity football cause connectivity changes in the magnetoencephalography (MEG) measured default mode network (DMN) in the absence of a clinically diagnosed concussion.

Materials and Methods

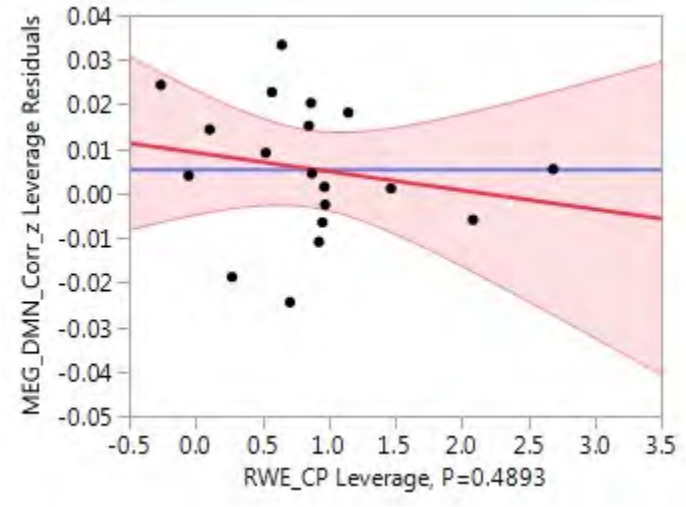
Twenty players from a local high school football team (mean age=16.9; no concussions within the past 6 months; right handed) were instrumented with the Head Impact Telemetry System (HITs) during all practices and games. The biomechanical metric computed from the HITS data was risk-weighted cumulative exposure (RWE). Eight minutes of eyes-open, resting-state MEG data were acquired for each subject using a 275 channel CTF whole-head system, pre and postseason. Structural anatomic MRI was acquired for co-registration with MEG. Using Brainstorm, MEG data were baseline corrected, band-stop filtered (60Hz), down-sampled to 250Hz, and band-pass filtered to 1-100Hz. Eye blinks, and muscle artifacts were removed using independent component analysis. A cortex surface head model was computed using overlapping spheres. Magnetoencephalography data were projected into standard source space using the whitened and depth-weigthed linear L2-minimum norm estimates algorithm (wMNE). A mean time series was extracted from 8 regions of interest (ROIs) representing the DMN: inferior parietal L&R, medial orbitofrontal L&R, posterior cingulate L&R, superior frontal L&R. The correlation was converted to the Fisher's z-scale, the average correlation between all ROIs was computed, and the difference between pre and postseason correlation was computed.

Results

A regression analysis between RWECP and mean DMN correlation did not yield a statistically significant result. However, when corrected for number of previous concussions, years of football played, age, and time between scans, the regression analysis revealed a significant relationship ($p = 0.03$, Adjusted $R2 = 0.03$) between RWECP and mean DMN correlation. One data point was excluded due to outlier analysis (Cook's $D>4/n$).

Conclusions

We demonstrate that a single season of football can produce changes in the MEG measured DMN connectivity in the absence of clinical concussion. These changes were modulated by previous concussion history and years of contact sport play, as has been suggested previously in fMRI literature.



(Filename: TCT_O-212_RWEvsCorrz_19.jpg)

O-213

11:56AM - 12:04PM

Decreased Hippocampus and Amygdala Volumes in Patients with Traumatic Brain Injury Are Associated with Decreased Post-traumatic Stress Disorder Resilience

S Kosaraju[1], J Stevens[2], T Jovanovic[3], J Allen[3]
[1]Emory University School of Medicine, Atlanta, GA, [2]Emory University School of Medicine, Marietta, GA, [3]Emory University, Atlanta, GA

Purpose
Recent clinical data suggest a linkage between traumatic brain injury (TBI) and post-traumatic stress disorder (PTSD). However, there have been a limited number of imaging studies investigating this. The purpose of this study was to assess the effect of the interaction between TBI and PTSD on structural changes in relevant brain areas.
Materials and Methods
Thirty-eight patients were analyzed from a database of 321 who had undergone a recent criterion-A trauma according to DSM-IV. This subset was recruited to undergo a research brain MRI at 3.0 T that included a T1 MP-RAGE (mean time to scan 56 days, SD = 15.9) and in-depth psychiatric measures to determine PTSD symptom severity at 1, 3, 6, and 12 months. Heirarchical linear modeling was used to assign patients to "resilient" or "not resilient" PTSD symptom trajectories. Images were processed and automatically segmented into regions of interest (ROIs) using the previously validated FreeSurfer software. Analysis of ROIs was performed using a series of 2-way ANOVAs followed with Boneferroni correction for multiple comparisons.
Results
Patient demographics for the parent set from which subjects were drawn, as well as the analyzed subset are available in Table 1 (parent set) and Table 2 (subset). A significant interaction effect was noted between PTSD resiliency and head injury on volumes of the right hippocampus, right amygdala, and left amygdala. In addition, simple main effects testing of structures with significant interactions showed that there were significant differences in volumes of the right hippocampus and right amygdala between those who did and did not have head injury in the group of patients who developed chronic PTSD. In the right and left amygdala, a significant difference was noted between PTSD resilient and PTSD prone subjects in those who were exposed to head injury.
Conclusions
The volumes of the right amygdala, right hippocampus, and left amygdala all showed significant interaction effects between PTSD resiliency and head injury. The significant interaction between head injury and PTSD symptom trajectory in the effect on these volumetric measures suggests that structural imaging following TBI or head injury may be of use in targeting therapy to prevent or reduce psychiatric morbidity in the long term.

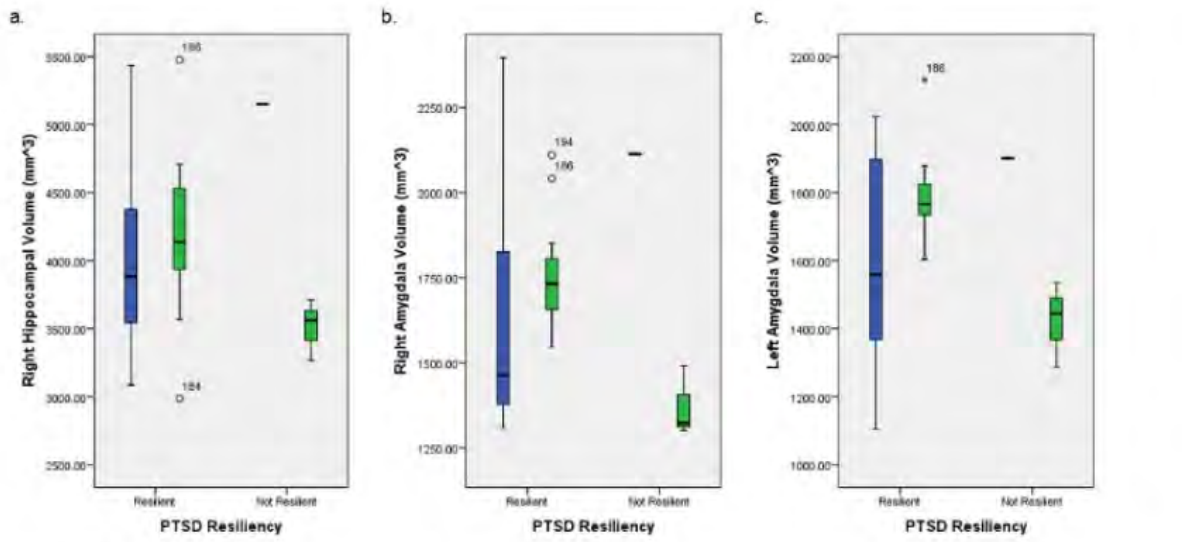


Figure 1. Structural volumes as a function of PTSD resiliency and head injury. Green represents head injury, while blue represents no head injury. Plots show mean (horizontal line), 1st quartile (box), and 3rd quartile (error bars). Outliers represented by circles. **a.** Right hippocampal volume **b.** Right amygdala volume **c.** Left amygdala volume

	SUSPECTED HEAD INJURY	NO HEAD INJURY
N	178	143
AGE	Mean 34.06 St. Dev. 11.783	Mean 35.97 St. Dev. 13.498
GENDER	1.51 0.501	1.44 0.498
EDUCATION LEVEL	5.28 1.242	5.17 1.296
TRAUMA SEVERITY	3.51 1.349	3.85 1.087
PDS SCORE (ED)	8.89 10.056	8.04 9.990
1 MO. PSS SCORE	15.09 11.562	14.16 11.215
3 MO. PSS SCORE	11.76 11.278	10.96 9.537
6 MO. PSS SCORE	11.43 11.647	9.72 9.666
12 MO. PSS SCORE	10.45 11.633	8.42 8.317

Figure 2. Patient Demographics of total cohort (N=321) from which the TBI cohort was drawn.

	SUSPECTED HEAD INJURY	NO HEAD INJURY
N	16	22
AGE	Mean 34.50 St. Dev 10.671	Mean 32.64 St. Dev 13.336
GENDER	1.56 0.512	1.41 0.503
EDUCATION LEVEL	5.31 1.195	5.32 .780
TRAUMA SEVERITY	3.94 1.063	3.77 1.066
PDS SCORE (ED)	5.33 7.345	5.45 8.769
1 MO. PSS SCORE	17.63 12.077	16.55 12.779
3 MO. PSS SCORE	13.33 11.437	12.60 9.522
6 MO. PSS SCORE	12.36 13.148	9.45 9.854
12 MO. PSS SCORE	10.82 13.250	8.25 9.651

Figure 3. Patient demographics of cohort with imaging (N=38) on which volumetric analysis was performed.

(Filename: TCT_O-213_KosarajuTBIPTSDASNR2017figures.jpg)

O-214

12:04PM - 12:12PM

Near term decrease in brain volume following mTBI is detectible in the context of pre-injury stability

A Goldman-Yassen[1], K Chen[1], K Hsu[2], M Lipton[1]
[1]Montefiore Medical Center, Bronx, NY, [2]Stanford University, Stanford, CA

Purpose
Neuroinflammation has been proposed as a mechanism underlying brain structural changes and persistent symptoms following mild traumatic brain injury (mTBI). Head CT is often the first imaging modality used to evaluate mTBI but typically does not demonstrate visible abnormalities. We hypothesize that quantitative analysis of brain volume from CT, obtained during routine emergency department (ED) assessment of mTBI patients, could reveal subtle changes in brain volume and may help illuminate underlying mechanisms of brain injury.
Materials and Methods
We searched our institution's electronic medical records for patients with head trauma indications for noncontrast head CT who also underwent noncontrast head CT 1 month to 1 year both before and after the traumatic event, for a medical indication unrelated to another acute trauma. Brain and intracranial volumes were computed using ITK-SNAP threshold-based semi-automated segmentation software. Brain volume was normalized to intracranial volume. To determine the reliability of our protocol, 20 additional cases were segmented by 2 researchers independently and the intraclass correlation coefficient (ICC) was calculated to assess interrater reliability. Continuous dependent variables were compared with the Wilcoxon rank sum test.
Results
We analyzed 10 patients, with a median age of 52 years, who underwent head CT at the time of mTBI and who also had preceding and subsequent head CTs that were performed for medical reasons other than acute trauma. The ICC between 2 researchers employing the same standardized segmentation protocol was .998 (.995-.999) indicating excellent agreement. The median time from the pre-TBI scan to TBI and from TBI to follow-up scan were 142 days and 120 days, respectively. Adjusted for intracranial volume, mTBI patients demonstrated similar median normalized whole brain volume at time of mTBI compared with their pre-mTBI studies (86.6% versus 86.3%, p=0.88). There was, however, a significant decrease in median normalized whole brain volume on the follow-up study (86.6% versus 80.1% p=0.04).
Conclusions
Semi-automated CT brain volume quantification is highly reliable across users. Decrease in brain volume following mTBI in patients may represent neurodegeneration in the setting of stable brain volume from the pre-trauma CT. Alternatively, as the scans were performed in the acute setting, neuroinflammatory changes may have been present.

Wednesday
11:00AM - 12:20PM
Long Beach Convention Center, Room 203AB (Upper Level)

18G-Parallel Paper Session: “Seizing” Opportunity

O-215

11:00AM - 11:08AM

Quantitative assessment of contralateral hippocampal signal alteration in temporal epilepsy patients with unilateral mesial temporal sclerosis.

K Sargar[1], M Parsons[2], A Sharma[3]
[1]Washington University in St. Louis, St. Louis, MO, [2]Mallinckrodt Institute of Radiology, Saint Louis, MO, [3]Mallinckrodt Institue of Radiology, Saint Louis, MO

Purpose
Evaluate whether signal alteration exists within the contralateral hippocampus in patients with unilateral temporal lobe epilepsy and ipsilateral mesial temporal sclerosis.
Materials and Methods
In this HIPAA compliant retrospective study approved by our institutional IRB, 18 patients with unilateral temporal lobe epilepsy (10 females, 8 males; mean age 41.2 years) and evidence for ipsilateral MTS were included. Using consensus region-of-interest (ROI) measurements performed on coronal FLAIR images, we calculated contrast-to-noise ratios (CNR) for each hippocampus and for normal gray matter in cingulate gyri. We calculated 25th, 50th, and 75th percentiles of extent to which CNR of abnormal ipsilateral hippocampus was elevated relative to that of normal gray matter; and then used these to define arbitrary thresholds for considering contralateral hippocampus abnormal. In addition, a neuroradiologist masked to the side of proven MTS rated intensity of each hippocampus on a 5-point scale ranging from definitely normal to definitely abnormal.
Results
Contrast-to-noise ratio for ipsilateral abnormal hippocampus was 30.01 ±11.03 (mean ± SD), significantly higher than that of normal gray matter within the cingulate gyrus (20.45 ± 8.99; $p<0.0001$). Contrast-to-noise differences between hippocampal and normal gray matter positively correlated with the confidence with which hippocampal signal abnormality was identified (rho=-0.501; p=0.0342). Ipsilateral hippocampal CNR was higher than normal gray matter by 56.5% ± 44.3%. Contralateral hippocampal CNR (24.2 ± 10.09) also was significantly higher than that of normal gray matter (p=0.0141). Contrast-to-noise ratio of contralateral hippocampus was greater than that of normal gray matter in 13/18 (72.2%) cases, with estimated prevalence of contralateral hippocampal abnormality based on increasingly stringent thresholds being 7/18 (38.8%), 4/22 (22.2%), and 2/22 (11.1%) respectively. Qualitative assessment confidently identified contralateral hippocampal signal alteration in 2/18 (11.1%).
Conclusions
In adult patients with unilateral temporal lobe epilepsy and MTS affecting ipsilateral hippocampus, contralateral hippocampi show significant differences from normal gray matter, often to an extent that would be considered abnormal.

O-216

11:08AM - 11:16AM

Determination of Hippocampal Epileptogenicity on the basis of Alteration of Clinical 3T MR Microarchitecture alone in the Absence of Volume or Signal Change

V Gupta[1], P Vibhute[1]
[1]*Mayo Clinic Florida, Jacksonville, FL*

Purpose

Three Tesla brain MR has become standard in clinical imaging of epilepsy. Hippocampus is the most common site of epileptogenesis in localization-related epilepsy. The MR diagnosis of hippocampal sclerosis, the most common lesion responsible for temporal lobe epilepsy, is based upon alteration of volume and signal in the hippocampal formation. The histological layered architecture of normal human hippocampus has been replicated in high field cadaveric MR studies. Microscopic alterations of hippocampus are known to occur in surgical specimens of hippocampi appearing normal on MRI. Yet, in normal appearing hippocampi on clinical 3T MR, there is no systematic attempt to assess subtle alterations of microarchitecture as the sole basis of epileptogenesis. This work investigates if alteration of microarchitecture on clinical 3T MR could help localize epileptogenesis to hippocampus when its volume and signal are normal.

Materials and Methods

One hundred fifty consecutive MRIs of adult epileptic subjects without previous surgical intervention were reviewed. These clinical MR scans were obtained on Siemens Skyra 3T scanner in 32 channel phased-array head coil. Magnetic resonance imaging included 2D FSE: (TR/TE 3600/97, NEX 2, 2mm thickness, 320 x 256 resolution, FOV 170 x 170 mm), and 3D True SPACE IR (phase reconstructed T1 contrast, TR/TE/TI 3600/159/500, 1.8 mm partition thickness, 320 x 288 in-plane resolution, FOV 170 x 170 mm) coronal sequences orthogonal to hippocampal long axis. The images were reviewed independently on ultra-high resolution monitors by 2 experienced neuroradiologists blinded to the semiologic and electrographic data. Twenty-two subjects with MR exams revealing potential temporal or extratemporal epileptogenic abnormality including hippocampal sclerosis were excluded. Developmental variations of hippocampal contour and orientation were not regarded as epileptogenic. Of remaining 128, 19 were excluded due to motion and other artifacts on MR exam. Based upon the suspected seizure onset on the scalp or intracranial depth EEG recording, the 222 eligible hippocampi were divided into 3 groups: Group I. Probably nonepileptogenic: normal EEG or contralateral electrographic onset/interictal spikes. Group II. Possibly epileptogenic: ipsilateral extratemporal, bitemporal or nonlocalized electrographic onset, and ipsilateral interictal spikes. Group III. Probably epileptogenic: ipsilateral temporal electrographic onset. The MR microarchitecture template was established on the basis of previously published* histologic and MR microscopic details including: 1. Detection of the anatomic landmarks including subiculum, cornu ammonis, dentate gyrus and hippocampal fissure/remnants on MR sections, 2. Visualization of the

internal layers in the cornu ammonis and dentate gyrus in MR sections of head, body and tail.
Results
Of the 222 hippocampi analyzed, 156 were in Group I, 47 in Group II, and 19 in Group III. There was 99% interobserver agreement on the identification of landmarks, and MR microscopic layers of the cornu ammonis and dentate gyrus. In all of the hippocampi in Group I (probably nonepileptogenic) and Group II (possibly epileptogenic), the microarchitecture was preserved. In 4 hippocampi in Group III (probably epileptogenic) focal or diffuse abnormalities of unilateral hippocampal microarchitecture were reported independently by both reviewers. One hippocampus reported as altered microarchitecture by 1 observer was considered normal upon joint review. None of the microarchitectural abnormalities were bilateral. These abnormalities included subtle swelling or atrophy of the CA4, loss of distinction between the dentate and CA4, and subtle enlargement of the dentate. In all 4 subjects in group III with altered hippocampal microarchitecture, the epilepsy was medically refractory. All 4 subjects were treated by ipsilateral hippocampal thermal laser ablation. One-year follow up was available in 3 of these subjects; all were seizure free. Fifteen hippocampi showed developmentally incomplete rotation with an oblique or vertical orientation, 14 occurring on the left side. The incomplete rotation of the hippocampus was bilateral in 1 subject. Other than a somewhat unfolded appearance of the end-folium, hippocampal microarchitecture on MR was unaffected by these variations. One of these hippocampi was found to be epileptogenic from depth EEG recordings, and the epilepsy was treated successfully by amygdalohippocampectomy.
Conclusions
On the basis of our observations we conclude that hippocampal microarchitecture: 1. Can be reliably evaluated on dedicated high resolution clinical 3T MR. 2. Should be assessed routinely in addition to its signal and volume on clinical 3T MR of epilepsy subjects, particularly those who present with ipsilateral temporal electrographic abnormalities. 3. Is unaffected by developmental rotation abnormalities.

O-217

11:16AM - 11:24AM

Amygdala and Hippocampal Enlargement in Temporal Lobe Epilepsy

A Capizzano[1], H Kawasaki[1], P Kirby[1], T Moritani[1]
[1]*University of Iowa Hospitals and Clinics, Iowa City, IA*

Purpose
Isolated amygdala enlargement (AE) may represent a subtype of mesial temporal lobe epilepsy (mTLE). The purpose of this study was to assess MRI derived volumes of the amygdala, hippocampus and other brain structures in a series of mTLE patients with AE without mesial temporal sclerosis (MTS).

Materials and Methods

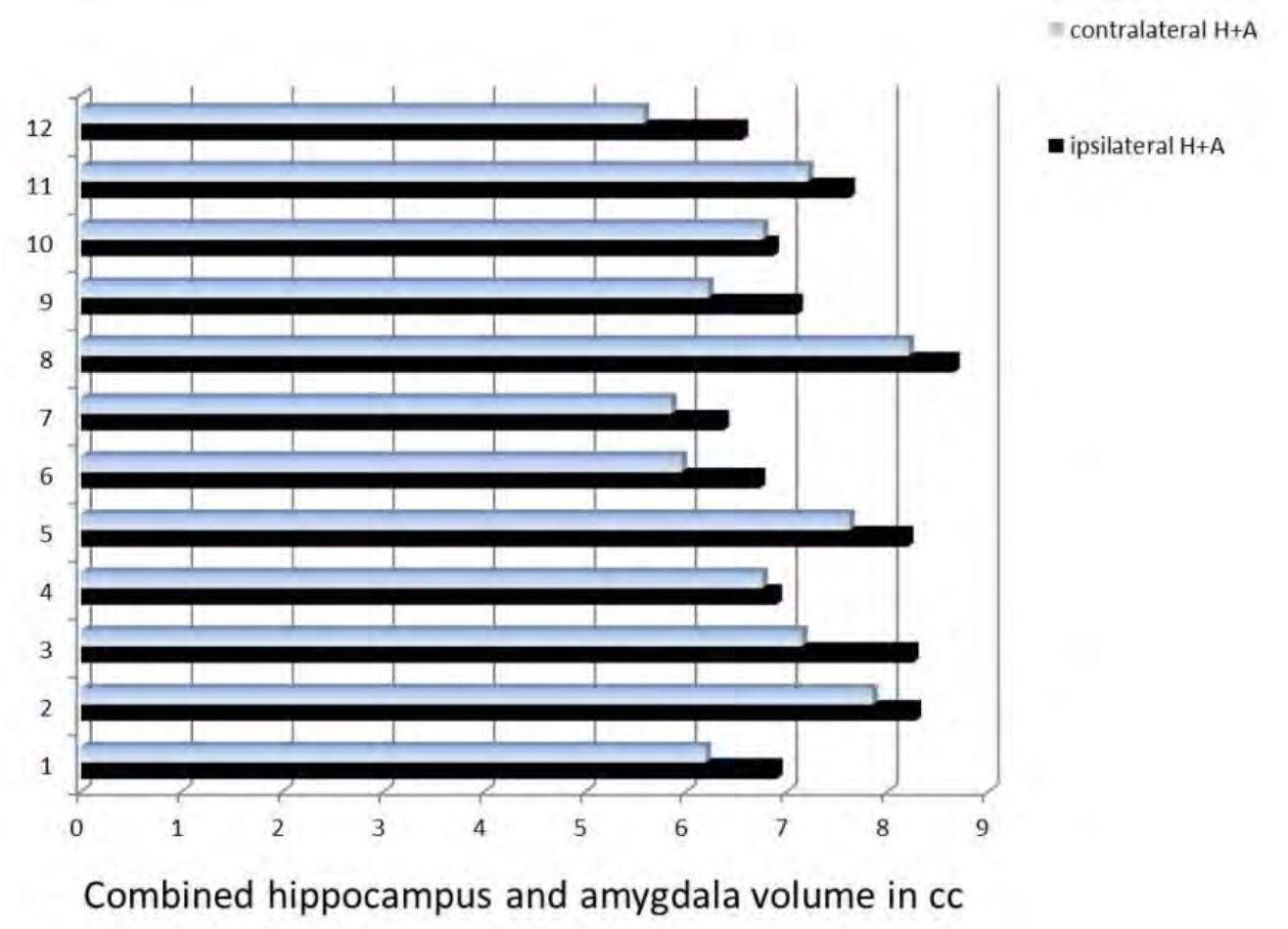
Institutional Review Board approval was obtained for this retrospective study. Twelve AE patients were included (5 women, 7 men; mean age 34.4 years) with clinical diagnosis of mTLE without MTS and enlarged, FLAIR hyperintense uncus ipsilateral to the video EEG defined seizure focus. Patients with mass lesions or MTS were excluded. Volumetric 3D T1-weighted MPRAGE images were fed into the NeuroQuant software to obtain ipsilateral and contralateral brain volumes. Pathologic diagnosis is available in 6 patients.

Results

There were 7 left and 5 right AE patients. Most patients had limbic auras followed by complex partial seizures. Four AE patients are seizure free on medications, while 8 had refractory seizures. Six of the latter underwent ipsilateral anterior temporal lobectomy. Pathology disclosed cortical dysplasia in 3 and gliosis in 3. These 6 patients became seizure free after surgery with mean follow up of 14 months. Statistically significant larger volumes were demonstrated only for the ipsilateral versus contralateral amygdala ($p<0.01$) and hippocampus ($p<0.01$) with no significant differences between sides for the cerebral cortex, white matter, basal ganglia, thalamus, cerebellum or ventricles. Ipsilateral hippocampus plus amygdala volumes (H+A) were 8% larger on average than contralateral volumes and in all 12 cases were larger on the ipsilateral side (Fig.).

Conclusions

Quantitative analysis suggests that the ipsilateral hippocampus also is enlarged in AE cases. Pathologically, both limbic structures show dysplasia and/or astrocytic gliosis. Therefore, AE may not be as isolated as originally thought, but part of an epileptogenic limbic lesion with a dysplastic and a "second hit" component.



(Filename: TCT_O-217_PictureAE2017.jpg)

O-218

11:24AM - 11:32AM

Signal changes of the temporal pole can be seen in non mesial temporal lobe epilepsy

E MORIMOTO[1], H Yokota[2], B Ellingson[3], N Salamon[4]
[1]David Geffen School of Medicine, UCLA, Los Angeles, CA, [2]David Geffen School of Medicine at UCLA, Los Angeles, CA, [3]University of California Los Angeles, Los Angeles, CA, [4]UCLA, Los Angeles, CA, David Geffen School of Medicine at UCLA, Los Angeles, CA, Los Angeles, CA

Purpose
Signal changes in the temporal pole is a commonly seen MR finding in mesial temporal lobe epilepsy (MTLE) which can indicate laterality of the epileptogenic focus. However, this finding is not well analyzed in non - MTLE. The purpose of this study is to evaluate

association between temporal pole signal changes and focal cortical dysplasia (FCD) in the other areas of the mesial temporal lobes.

Materials and Methods

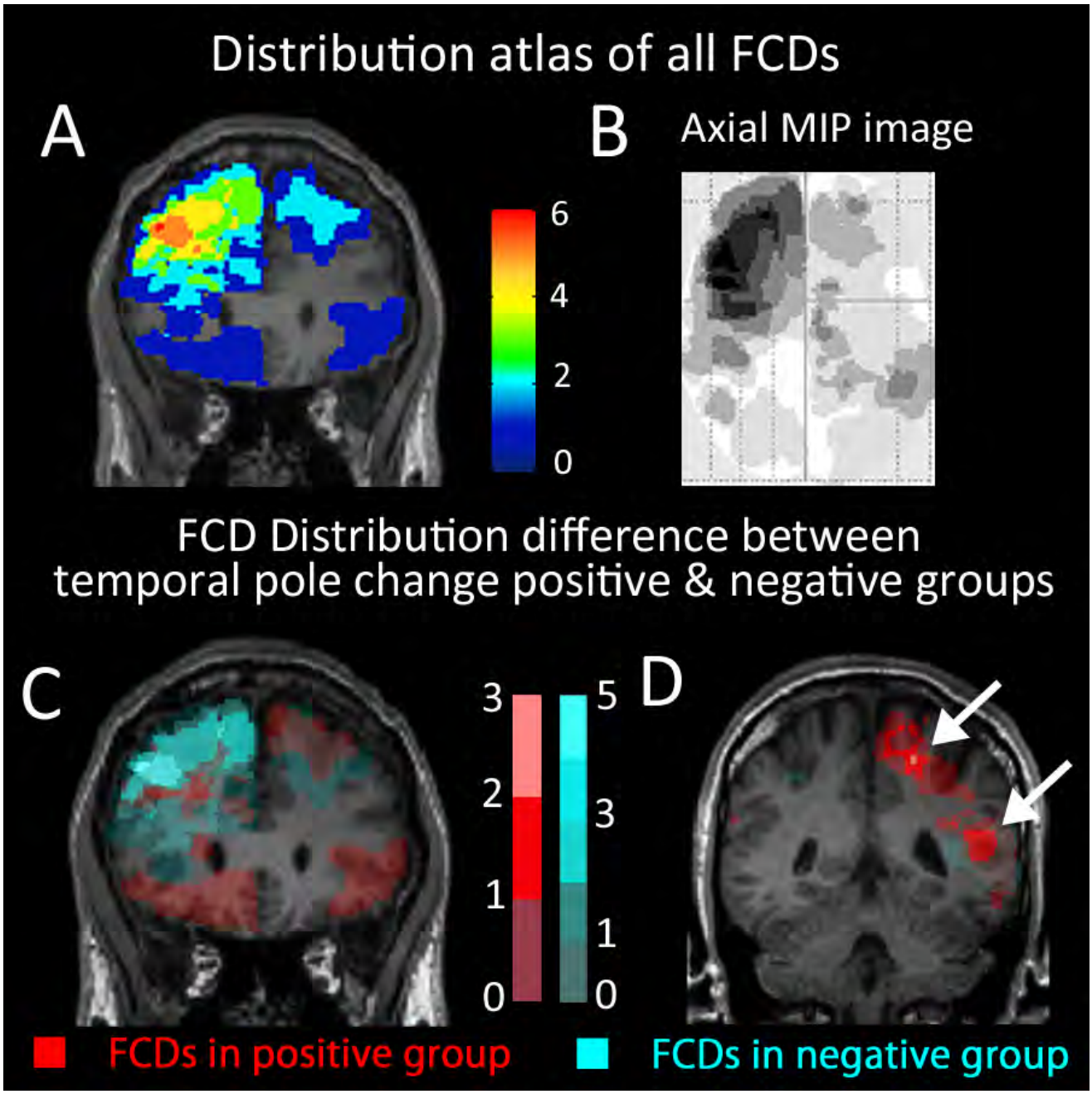
Forty-three patients of pathologically proven isolated FCD cases in non-MTLE were included. Presence and absence of temporal pole changes were assessed visually. Regions of interest were generated manually for all 43 cases using fluid-attenuated inversion recovery (FLAIR) with reference to hypometabolic areas on FDC-PET. All ROIs were spatially normalized and superimposed. Logistic regression analysis was performed to assess the relationship between age of onset, laterality of FCD localization and temporal pole changes.

Results

Temporal pole changes were found in 14/43 (32%) cases. Twenty of 43 FCD located on the left side (Figs. A and B). Seventy-one percent of FCDs in temporal pole change positive group was seen on the left and more often seen in the superior and inferior parietal lobule (Fig. D). The bilateral orbital frontal regions were also involved by FCDs in the group (Fig. C). Logistic regression modelling suggested that laterality of FCD localization ($p = 0.044$) was a significant predictor of temporal pole change.

Conclusions

The temporal pole change can be found not only with mesial temporal lobe lesion, but also FCD in the parietal lobe and orbital frontal region. Superior frontal lobe FCD was not associated with temporal pole changes. This may be related to temporal white matter pathway network.



(Filename: TCT_O-218_figure_MorimotoE2.jpg)

O-219

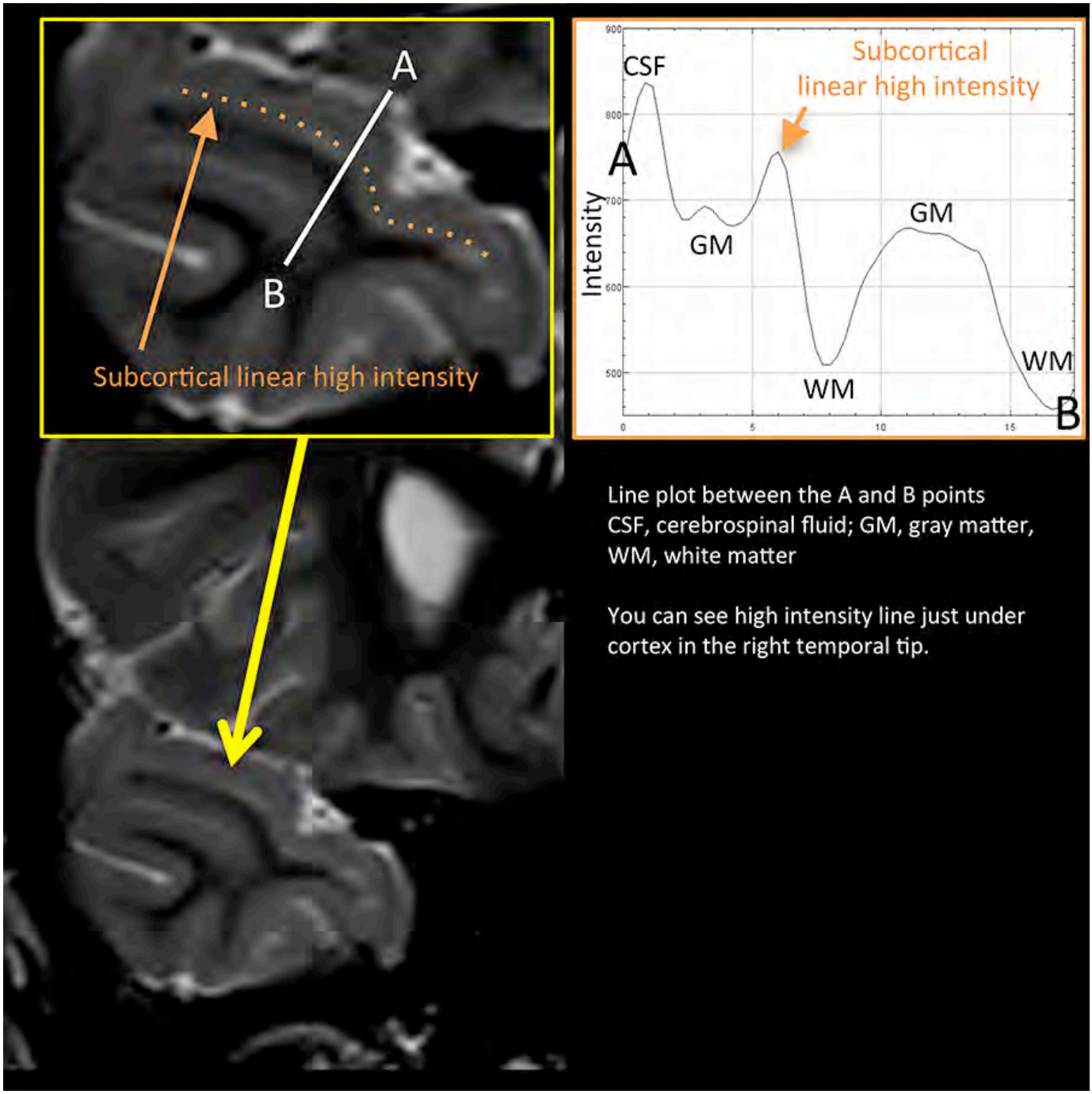
11:32AM - 11:40AM

Subcortical linear high intensity in the temporal pole is related with mesial temporal lobe epilepsy

E Morimoto[1], H Yokota[2], B Ellingson[3], N Salamon[4]
[1]David Geffen School of Medicine, UCLA, Los Angeles, CA, [2]David Geffen School of Medicine at UCLA, Los Angeles, CA, [3]University of California Los Angeles, Los Angeles,

CA, [4]UCLA, Los Angeles, CA, David Geffen School of Medicine at UCLA, Los Angeles, CA, Los Angeles, CA

Purpose
Several types of temporal pole changes have been described in epilepsy patients especially in mesial temporal lobe epilepsy: blurring of the gray white matter demarcation, high intensity of the cortical and white matter on fluid-attenuated inversion recovery (FLAIR) and atrophy. These are useful findings to diagnose seizure focus laterality. One recurrent finding we are aware of is the presence of linear high intensity in the subcortical areas of the temporal pole on T2-weighted imaging (T2WI). The purpose of this study was to evaluate the frequency of subcortical linear high intensity in epilepsy patients with focal cortical dysplasia (FCD) or glioma to investigate the cause and its usefulness to diagnose epileptogenic focus.
Materials and Methods
Seventy-seven epilepsy patients with pathologically proven isolated FCD cases [15 cases in the mesial temporal lobe (FCD mesial) and 43 cases in the other areas than the mesial temporal lobe (FCD nonmesial)] or with pathologically proven primary low-grade glioma (19 cases) in the nontemporal pole areas were included. Presence and absence of subcortical linear high intensity were assessed. Fisher exact test and Mann-Whitney U test with multiple comparison were performed to analyze the frequency of the finding among the 3 groups.
Results
No statistical significant difference for age and sex among the 3 groups. Total of 12, 24 and 5 patients showed subcortical linear high intensity in the groups with FCD mesial, FCD nonmesial and with glioma, respectively. 26.7% of the cases without the other ipsilateral temporal pole changes have stronger subcortical linear high intensity on the ipsilateral to the seizure focus than that on the contralateral side. Focal cortical dysplasia mesial showed significant high frequency of subcortical linear high intensity compared to the cases with glioma (Fisher exact test; $P<0.001$, Pairwise comparison with Bonferroni correction; $P=0.015$).
Conclusions
Mesial temporal epilepsy with FCD frequently showed subcortical linear high intensity in the temporal pole. Strong epileptic damage in the temporal pole might cause the lesion. This finding could be useful to diagnose seizure focus laterality when the other temporal pole changes are not detected.



(Filename: TCT_O-219_fig4.jpg)

O-220

11:40AM - 11:48AM

Hybrid [(18) FDG] - PET/MRI in patients with temporal lobe epilepsy

C Deuschl[1], T Rueber[2], L Ernst[2], T Poeppel[3], S Goericke[1], M Forsting[4], C Elger[2], L Umutlu[1]

[1]Institute of Diagnostic and Interventional Radiology and Neuroradiology, Essen, NRW, Germany, [2]Department of Epileptology, Bonn, NRW, Germany, [3]Department of Nuclear Medicine, Essen, NRW, Germany, [4]University Hospital Essen, Essen, NRW, Germany

Purpose

Integrated PET/MRI scanners provide simultaneous morphologic and metabolic information with an excellent co-registration in a single hybrid examination, rendering this hybrid imaging modality available for an easy and broad clinical application (1). The purpose of this study is to evaluate the diagnostic impact of hybrid 18F-FDG PET/MRI in the diagnostic work up of temporal lobe epilepsy.

Materials and Methods

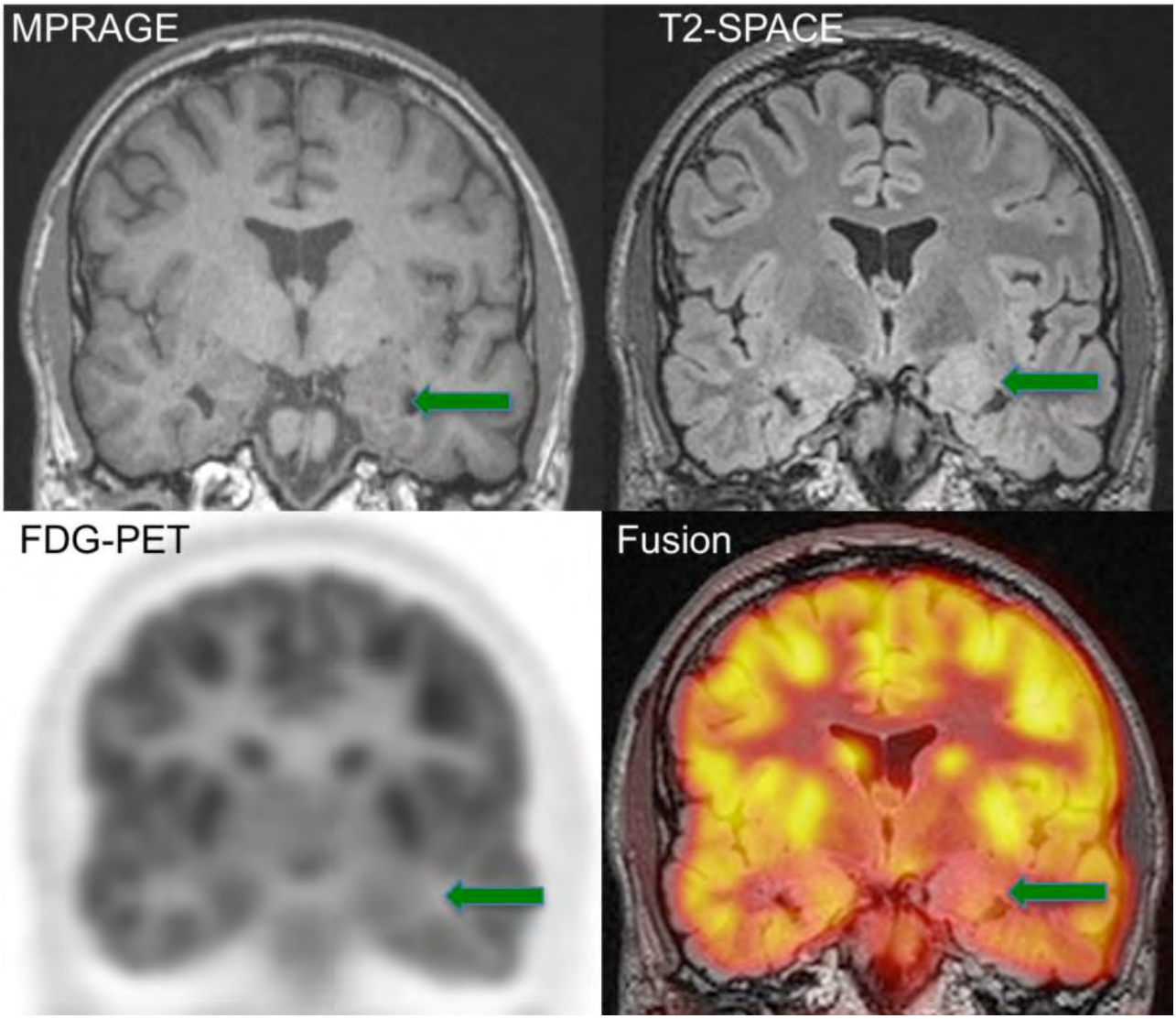
Ten patients with temporal lobe epilepsy were enrolled in this ongoing prospective study (mean age: 42.1 years, range: 19-75 years, 6 female). All patients underwent a hybrid 18F-FDG PET/MRI of the brain, comprising the following sequences: (1) nonenhanced MPRAGE, (2) 3D FLAIR, STIR cor, (4) T2 ax, (5) SWI. Image analysis was performed by a neuroradiologist and a nuclear medicine specialist during consensus reading with subsequent reading of the (1) MRI, (2) PET and fused integrated PET/MRI datasets regarding (a) lesion detection and (b) diagnostic confidence.

Results

All examinations were obtained successfully without any relevant artifacts. Based on morphologic MR readings, 8/10 patients were found to show suspicious lesions. Out of these 8 morphologically suspicious lesions, 5 lesions showed a corresponding lesion in FDG-PET (Fig. 1). Based on the fused image analysis the diagnostic confidence was rated higher (mean 3.1) for PET/MRI when compared to sole morphologic reading (2.7). Two of 10 patients did not show any pathologic findings in MRI and/or PET/MRI.

Conclusions

Our preliminary study results show an added diagnostic value of hybrid 18-F-FDG PET/MRI in temporal lobe epilepsy by improving the diagnostic confidence for lesion detection.



(Filename: TCT_O-220_Fig1EpilepsyASNRfinal.jpg)

O-221

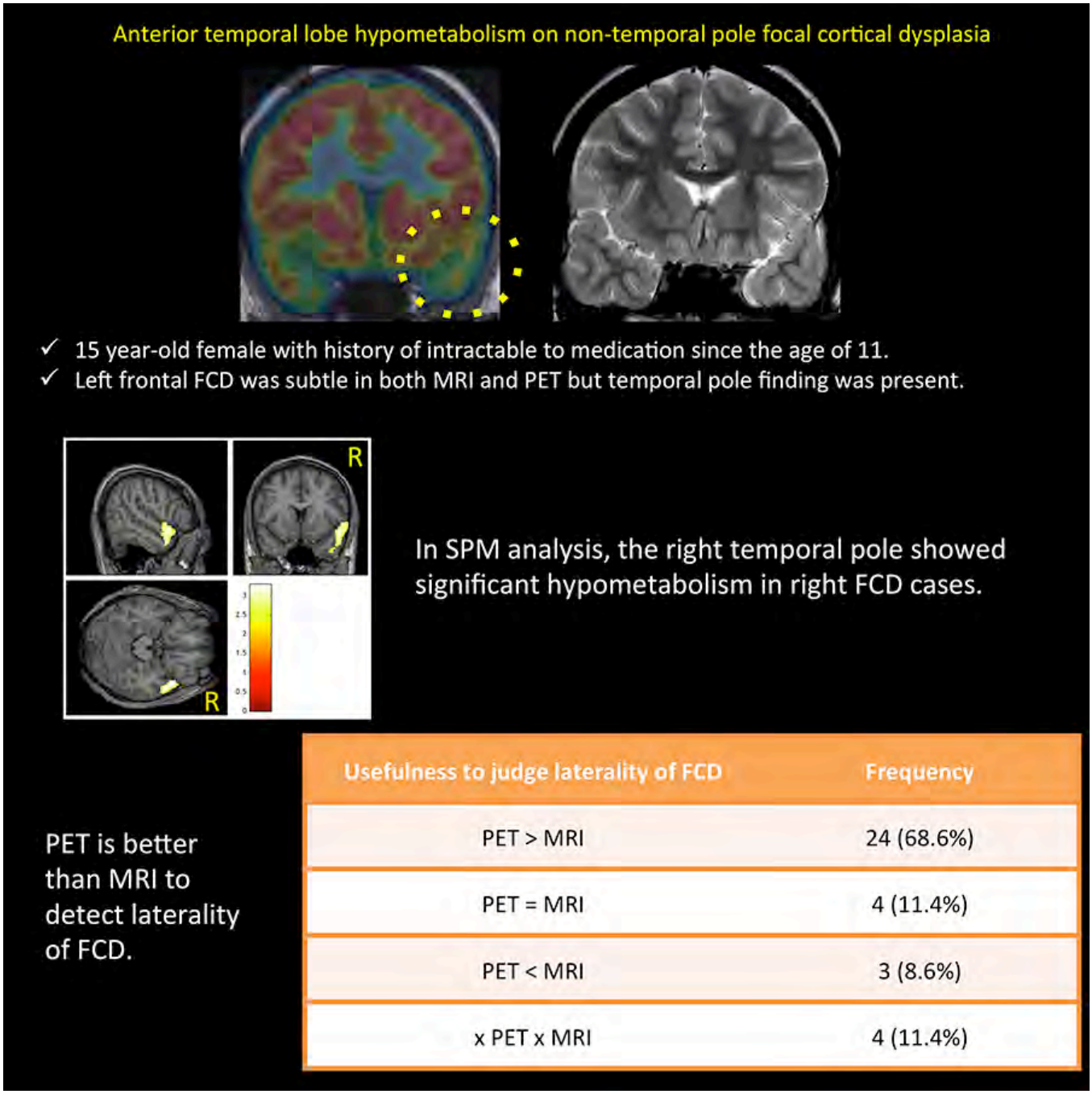
11:48AM - 11:56AM

Laterality of Anterior Temporal Lobe Glucose Metabolism in Extra Temporal Focal Cortial Dysplasia.

H Yokota[1], E MORIMOTO[2], N Salamon[3]
[1]David Geffen School of Medicine at UCLA, Los Angeles, CA, [2]David Geffen School of Medicine, UCLA, Los Angeles, CA, [3]UCLA, Los Angeles, CA, David Geffen School of Medicine at UCLA, Los Angeles, CA, Los Angeles, CA

Purpose
Temporal pole often shows hypometabolism asymmetrically on 18F-fluorodeoxyglucose–positron emission tomography (FDG-PET) even in cases of extra temporal focal cortical

dysplasia (FCD). The purpose of this study is to evaluate frequency and mechanism of anterior temporal lobe hypometabolism on extra temporal focal cortical dysplasia.
Materials and Methods
Pathologically proven 35 extratemporal FCD (2-54 years, mean age, 15.8 years; right 18, left 17) were included. Multilober FCD was excluded. Two experienced neuroradiologists performed visual assessment of the laterality of temporal pole metabolism and presence of T2/FLAIR abnormality of temporal pole. On quantitative evaluation, the PET images were normalized using statistical parametric mapping (SPM) and accumulation value was retrieved using region of interest (ROI) method for anterior temporal lobe. Clusters of significant reduction in metabolism were determined between right and left side FCD cases, thresholding at a minimum size of 2 cm^3 and a P-value 0.005.
Results
In 19 of 35 (54%) cases, hypometabolic laterality of the temporal lobe matched the FCD side in visual assessment. With quantitative analysis, when the threshold was less than 1.0 in accumulation ratio of the FCDside/contralateral side, 28 (80.0%) and 7 (20.0%) cases matched and unmatched laterality of FCD using ROI of the anterior temporal lobe, respectively. Right FCD demonstrated ipsilateral temporal pole hypometabolism more frequently than left FCD (94.4% vs 64.7%, P = 0.041). In SPM analysis, the right temporal pole showed significant reduction in metabolism in right FCD cases. In MRI, temporal pole signal change was demonstrated 11 of 35 (31.1%). In 24 of 35 (68.6%) cases, PET was more useful to obtain laterality of FCD than MRI.
Conclusions
Laterality of hypometabolism on anterior temporal lobe was useful to determine FCD laterality in cases of extra temporal FCD. Fluorodeoxyglucose-PET is more sensitive than MRI to detect temporal pole change. Multimodality approach can increase detectability of FCD.



(Filename: TCT_O-221_fig1.jpg)

O-222

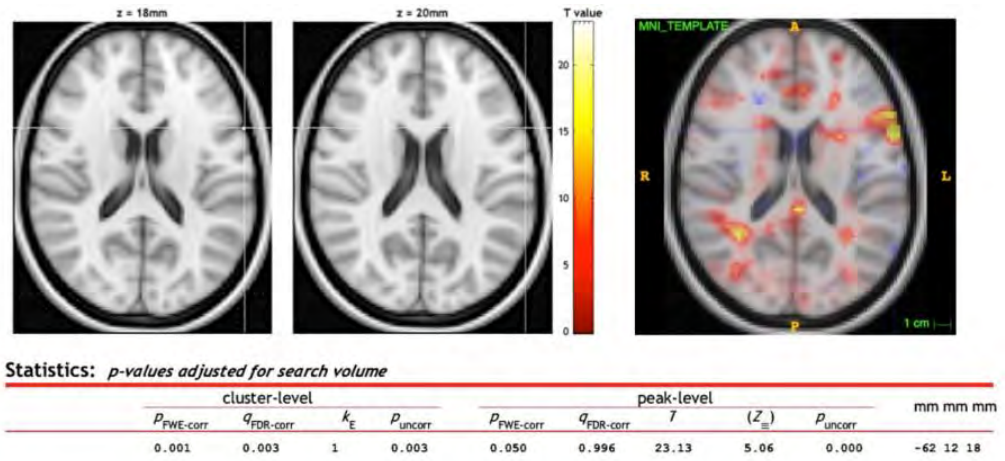
11:56AM - 12:04PM

Language Network Plasticity in Surgical Temporal Lobe Epilepsy Patients - Preliminary Results from a Clinical fMRI-study

O Foesleitner[1], K Nenning[1], S Bonelli[1], S Pirker[2], T Czech[1], D Prayer[1], G Kasprian[1]

[1]*Medical University of Vienna, Vienna, Austria,* [2]*General Hospital Hietzing with Neurological Center Rosenhügel, Vienna, Austria*

Purpose
Our aim was to analyze the reorganization of language networks in temporal lobe epilepsy (TLE) patients with task-based functional MRI (fMRI) before and after anterior temporal lobectomy (ATLR) or selective amygdalohippocampectomy.
Materials and Methods
We performed task-based language fMRI on 14 surgical TLE patients (9 right-hemispheric; 8 female; mean age at surgery: 41 years, range 28-53 years; 9 right-handed; 8 ATLR) before and after surgery (mean latency 25.6 months, range 3-52 months). For fMRI data acquisition the same verb generation and semantic paradigm in block-design and the same protocol in a 3 T scanner were used in patients and 10 healthy right-handed controls (8 male; mean age 38 years; range 31-49 years). For analysis of TLE-triggered plasticity a lateralization index (LI) was calculated and fMRI activation patterns in pre-operative patients to healthy controls were compared. Investigation of surgery-triggered reorganization within patient groups was done by contrasting the LI, pre- to postoperative fMRI activation maps and by functional connectivity analysis.
Results
Postsurgically left-sided TLE patients showed a significantly different LI compared to controls ($p<0.05$), to postoperative right-hemispheric TLE patients ($p\leq0.01$), and to pre-operative fMRI scans ($p\leq0.01$). In patients with right-hemispheric TLE there was no significant difference in LI compared to controls or postoperative scans ($p>0.05$). Functional MRI activation maps in left TLE patients showed a postoperative increase in the inferior frontal gyrus (opercular part, $p=0.001$, FWE corrected at 0.05). Functional connectivity analysis did not result in a statistically significant difference of language networks before and after surgery.
Conclusions
Functional MRI shows reorganization of language networks in epilepsy patients. Epilepsy surgery causes postoperative language network plasticity with more extensive changes in left than right-hemispheric TLE patients.



Statistics: *p-values adjusted for search volume*

cluster-level				peak-level					mm mm mm
$p_{FWE-corr}$	$q_{FDR-corr}$	k_E	p_{uncorr}	$p_{FWE-corr}$	$q_{FDR-corr}$	T	$(Z_{=})$	p_{uncorr}	
0.001	0.003	1	0.003	0.050	0.996	23.13	5.06	0.000	-62 12 18

(Filename: TCT_O-222_lTLE_fMRI.jpg)

O-223

12:04PM - 12:12PM

Semi-Automated Stereo-Electroencephalography Electrode Localization

R Gorniak[1], C Wu[1], S Das[2], J Stein[2], M Sperling[1]
[1]Thomas Jefferson University, Philadelphia, PA, [2]University of Pennsylvania, Philadelphia, PA

Purpose
Stereo-electroencephalography (sEEG) involves the placement of multiple depth electrodes, each with multiple contacts, into the cerebrum to localize epileptogenic regions. Determining the anatomic location of a particular electrode contact by visual inspection of postoperative imaging can be challenging. Manual labeling of sEEG contacts on postoperative CT can be performed but is time consuming and tedious as there usually are more than 100 contacts per implant. The aim of this project was to develop a semi-automated method for labeling sEEG contacts on postoperative CT that did not require prior knowledge of the planned electrode trajectories, could handle crossing electrodes and was resistant to artifacts.
Materials and Methods
A MATLAB script was developed to do this relying on 2 characteristics of sEEG technique: electrode trajectories are relatively straight and a bolt is used to anchor each lead. Electrode contacts are detected along a cylindrical search region extending from the centroid of each bolt along its longest axis. If contacts merge together secondary to crossing electrodes or artifact, k-means clustering is used to separate the contact clumps. The user monitors the process, modifying parameters as needed. Postoperative CTs were acquired from 12 patients following sEEG implantation. The 1898 individual electrode contacts were localized manually using the semi-automated method. Differences in individual electrode co-ordinates between the 2 methods were calculated.

Results
The average distance between the manually labeled electrodes and the semi-automated method was 1.31 pixels (0.53 mm) with standard deviation of 0.58 pixels (0.24 mm). Average difference in x, y, and z (slice) coordinates was 0.24, 0.25 and -0.11 pixels, respectively.
Conclusions
The semi-automated method results in similar electrode coordinates compared to manual labeling with less user effort. Generating electrode labeled images which can be coregistered with pre- or postoperative MRI can be useful in the clinical interpretation of sEEG and for research.

O-505

12:12PM - 12:20PM

FLAIR Fusion in Multiple Sclerosis Follow up : an Unavoidable Tool for Private Practice

E Lamain[1], O Casez[2], M Vaillant[2], V Lefournier[1], P Tourret[1], M Bakir[3], P Roux[4], J Savatovsky[4], S Cantin[1]
[1]Groupe Clinique du Mail, Grenoble, FRANCE, [2]Centre Hospitalier Universitaire Grenoble Alpes, Grenoble, FRANCE, [3]Siemens Healthcare France, Saint-Denis, FRANCE, [4]Fondation A. de Rothschild, Paris, FRANCE

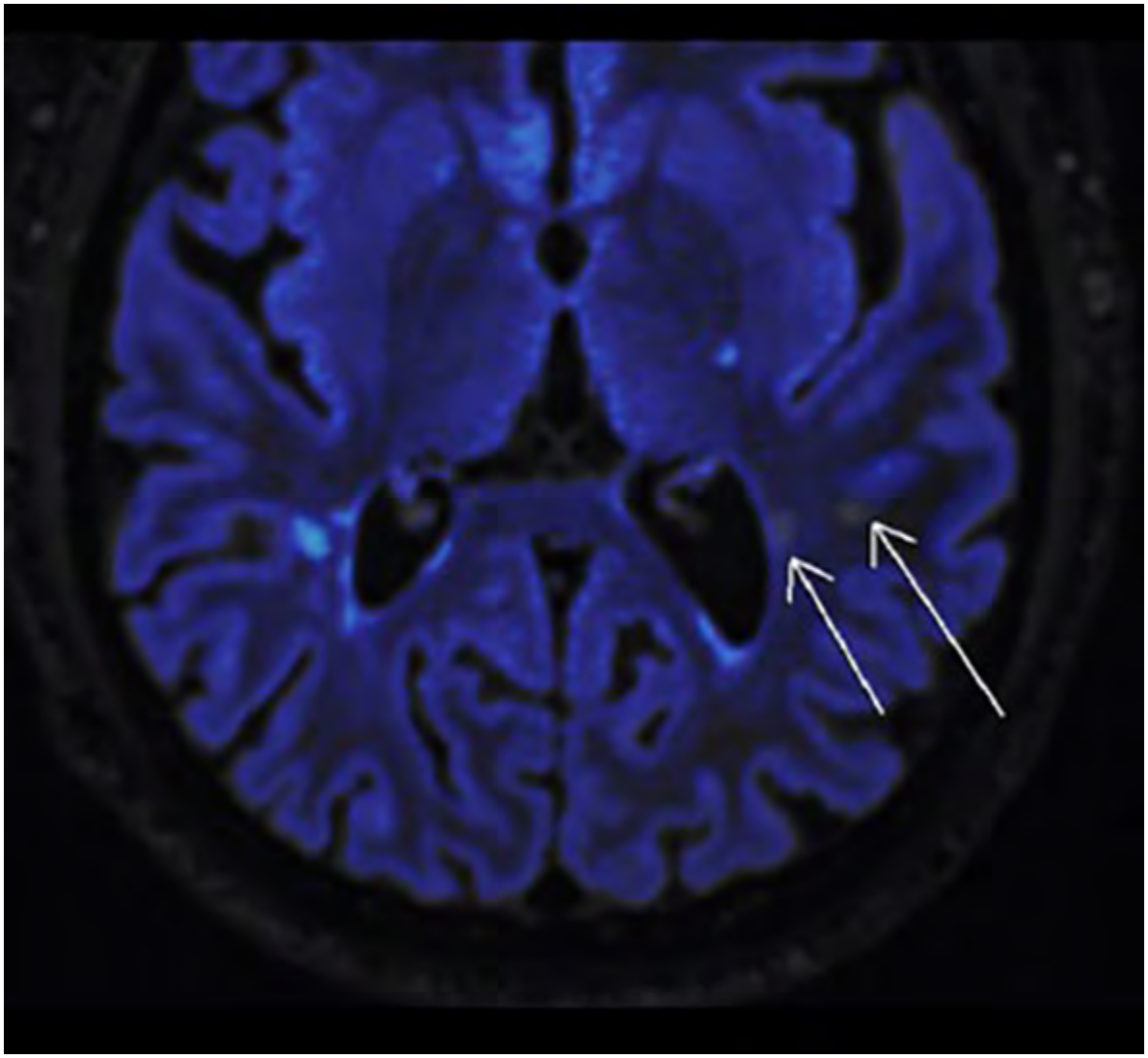
Purpose
Multiple sclerosis (MS) follow up leads to millions of brain MRI scans around the world. According to the number and the size of inflammatory lesions, the comparison between successive exams to assess dissemination in time is challenging and time consuming. The aim of this study was to assess the use of the FLAIR fusion in terms of new lesion detection capacity and interpretation time saving, compared to conventional frame by frame 3D FLAIR comparison.
Materials and Methods
3D FLAIR acquired on 1.5T Siemens MRI of successive exams were coregistered and fused. A colored clot was applied to the oldest scan to differentiate new and old lesions. Post-treatment was done using Siemens Syngovia software. The fused sequence obtained was compared to frame by frame analysis. For each patient and techniques, we measured the time needed to assess the number of new MS lesions. Interpretations were done by a neuroradiologist and a radiology technician quickly formed to MS lesion detection. Nonparametric Man Whitney test was carried out to compare the interpretation time between the 2 methods and the number of new MS lesions detected by the neuroradiologist. Spearman's rho and Kendall's tau were calculated to access the effect of the FLAIR Fusion use on the agreement between readers. Twenty-one patients were analyzed.

Results

Using Man Whitney test at $p<0.05$, the interpretation time with FLAIR fusion for the radiology technician is not significantly different but significantly shorter for the neuroradiologist with a gain of 59%. The number of MS lesions detected also is more than doubled for both readers. Using FLAIR FUSION also increases the agreement between readers (Kendall's tau increasing from 0.56 to 0.74 and Spearman's rho from 0.63 to 0.83).

Conclusions

FLAIR fusion is an unavoidable tool for MS patient follow up, allowing up to 60% interpretation time reduction, and increasing agreement between readers, irrespective of their experience. The mean number of MS lesion detected also was more than doubled for both readers.



(Filename: TCT_O-505_FLAIRFUSION.jpg)

Wednesday
11:00AM - 12:15PM

Long Beach Convention Center, Room 102BC (Main Level)

18H-Parallel Paper Session: TURBO & TOUR: Advanced Imaging: Now and Next

T-43

11:00AM - 11:03AM

Transient Cerebral Injury After A Single Hypobaric Exposure to 25,000 Ft During Routine Aircrew Training? MRI Evaluation of High Altitude Exposure Upon the Brain

J Bernot[1], M Gusman[1], P Sherman[2]
[1]59th Medical Wing, Joint Base San Antonio, Lackland AFB, TX, [2]59th Medical Wing, Department of Neuroradiology, Joint Base San Antonio, Lackland AFB , TX

Purpose
Discover cellular changes occurring after acute hypobaric exposure in hypobaric naïve trainees utilizing magnetic resonance spectroscopy (MRS) and arterial spin labeling (ASL) to offer insight into causes of cerebral white matter hyperintensities (WMH) in high-altitude pilots.
Materials and Methods
Seventy-five U.S. Air Force aircrew trainees were evaluated during their initial occupational hypobaric exposure, which entailed a 30-minute exposure to 25,000 feet. Magnetic resonance imaging was obtained – T-minus 24h, T-plus 24h, and T-plus 72h. Quantitative analysis of ASL and MRS was performed. Thirty-five similar health USAF subjects served as controls without hypobaric exposure. Paired two-tailed t-tests were used for comparison.
Results
Arterial spin labeling showed upregulation of both white and gray matter cerebral blood flow (CBF) at both T+24 and T+72 hours in the exposed subjects with no change in controls (subjects' white matter p=0.004/0.021; gray matter 0.065/0.037). Exposed subjects had decreased N-acetylaspartate (p=0.039), myo-inositol (0.019), creatine (0.076), and glutathione (0.063) at T+24 with no change in controls.
Conclusions
Significant declines in markers of neuronal integrity suggests oxidative stress is evident within 24-hours of hypobaric exposure. Increased CBF measured by ASL in exposed subjects is a response to oxidative damage and evidence of increased metabolic demand. White matter hyperintensities formation may occur because of oxidative stress without adequate time for healing between repetitive exposures. White matter hyperintensities in this population are likely a function of both cumulative effects and frequency of hypobaric exposure.

T-44

11:03AM - 11:06AM

FNCI directed Assessment of NeuroVascular Uncoupling in Concussion Patients

B Tucker[1], T Burnham[2], A Fong[2], M Allen[2]
[1]Case Western Reserve University School of Medicine, Cleveland, OH, [2]Cognitive FX, Provo, UT

Purpose
Current research suggests that a pathological reduction of neurovasuclar coupling efficiency (Hnvc) can be caused by mild traumatic brain injury (mTBI), leading to a likelihood of chronic postconcussion syndrome (PCS) symptomology (1, 2). Functional MRI has sometimes been dismissed as an appropriate imaging tool to identify mTBI pathology on the grounds that it is not a direct measure of neuronal activity (3). However, because fMRI is an effective and reliable means of measuring changes in Hnvc, it is precisely the right tool to assess PCS cases. Functional neurocognitive imaging (fNCI) is a specialized form of fMRI that has the ability to localize neurovascular uncoupling (NVU) post-mTBI by measuring the most relevant characteristics of BOLD signal change during performance of MRI-adapted neuropsychological evaluations. The measurement of Hnvc and NVU via fNCI allows for direct assessment of the neuronal signaling chain most relevant to PCS, namely Hnvc, leading to diagnosis and quantification of mTBI severity and treatment outcomes.
Materials and Methods
Two hundred seventy concussed patients were assessed with fNCI to establish pretreatment NVU benchmarks. Functional NCI and self-reported postconcussion symptom scale (PCSS) findings were used to develop individualized, targeted, sustained, and cyclical week-long enhanced performance in cognition (EPIC) therapy incorporating cognitive, occupational, and neuromuscular modalities. Postconcussion syndrome symptomatology and fNCI-directed measures were used to evaluate post-treatment outcomes.
Results
Functional NCI severity index score (SIS) measurements of NVU reported 80 percent of patients showing 60 percent improvement in Hnvc over their pretreatment scan. Longitudinal reassessment of patients show maintained SIS improvement 8.6 months post-treatment. Eighty-seven percent of patients reported a minimum 50 percent improvement in symptomatic PCSS post-treatment.
Conclusions
Functional NCI provides reliable measurement of NVU allowing for identification of concussion pathology. Additionally, fNCI derived SIS scores direct tailored EPIC therapy to restore Hnvc and subsequently resolve chronic PCS resulting from mTBI.

T-45

11:06AM - 11:09AM

Effects of Sports-Related Head Impact Exposure on Cerebral Blood Flow in Deep Gray Nuclei

Y Nguyen[1], J Urban[1], M Johnston[2], Y Jung[3], L DellaGrotta[1], E Davenport[4], M Espeland[1], A Powers[5], J Stitzel[1], J Maldjian[6], C Whitlow[1]
[1]Wake Forest University School of Medicine, Winston-Salem, NC, [2]Wake Forest University Biomedical Engineering, Winston-Salem, NC, [3]Wake Forest School of Medicine, Winston-Salem, NC, [4]UT Southwestern Medical Center, Dallas, TX, [5]Wake Forest University School of Meidine, Winston-Salem, NC, [6]University of Texas Southwestern, Dallas, TX

Purpose

Deep gray matter nuclei are thought to be vulnerable to injury, especially among pediatric patients, due to intrinsically high metabolic demand and extensive vascularization, as well as high baseline levels of ionic elements that can generate oxygen free radicals (1, 2). This study aimed to characterize the relationship between head impact exposure and basal ganglia cerebral blood flow (CBF) in youth football players without clinical diagnosis of concussion. We hypothesized that higher head impact exposures may be associated with reduced CBF in these potentially vulnerable areas of the brain.

Materials and Methods

Thirty-one male players from local youth football teams (age range, 8-13 years) without history of concussion were recruited as part of an IRB approved NIH funded study. All players were instrumented with the head impact telemetry system (HITS) during all practices and games, and HITS data were processed to compute risk-weighted cumulative exposure (RWE) (3-4). Magnetic resonance imaging (3T Siemens Skyra) data were acquired before and after the season, including pseudocontinuous arterial spin labeling (PCASL) measures of CBF. Regression analysis of the cohort was conducted to characterize the overall relationship between CBF and RWE (adjusted for age, weight, time between scans) for each region within the basal ganglia.

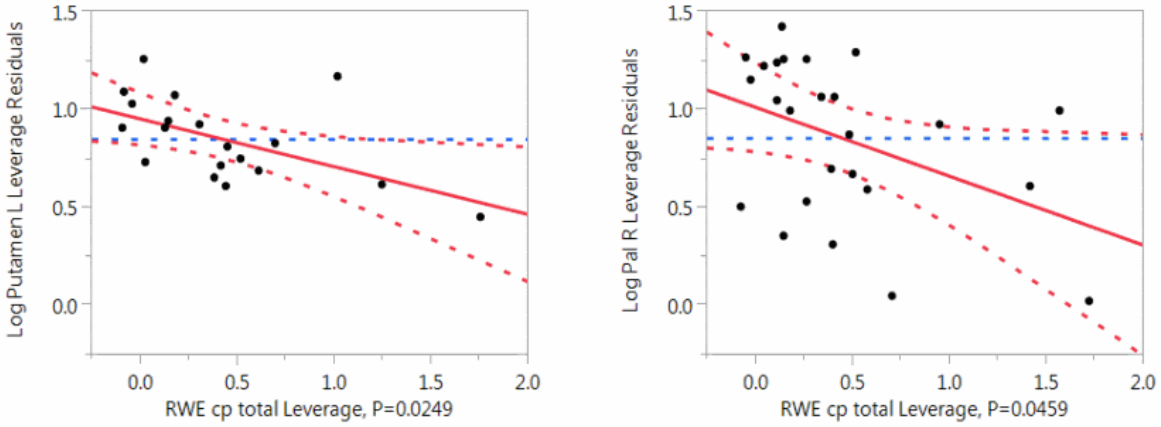
Results

There was a statistically significant linear relationship between CBF and RWE in the left putamen and the right globus pallidus (Table 1). No statistically significant relationship was identified for the right putamen, left globus pallidus, or other deep gray nuclei (caudate and thalamus).

Conclusions

These findings suggest that nonconcussive head impact exposure may be associated with functional changes in deep gray nuclei, which may be vulnerable to injury. Several factors limit the generalizability of our results to the overall population of youth athletes, including the small sample size, single sex (males) and focus on American football.

Area vs RWEcp Total	Sample Size	P value	R^2 Adjusted
Log Left Caudate	n=31	0.9560	-0.2025
Log Right Caudate	n=29	0.3145	0.0416
Log Left Putamen	n=29	**0.0249**	0.6147
Log Right Putamen	n=28	0.1912	-0.0114
Log Left Globus Pallidus	n=29	0.4025	-0.0173
Log Right Globus Pallidus	n=29	**0.0459**	0.0711
Log Left Thalamus	n=29	0.0963	0.0693
Log Right Thalamus	n=29	0.4953	-0.1512
P-values from fully adjusted model, with outliers removed.			



(Filename: TCT_T-45_RWEslopeabstractimages.gif)

T-46

11:09AM - 11:12AM

Occupational Hazards of Flying Pigs: A Swine Model for Hypobaric-Induced Neuronal Injury

M Gusman[1], M Gusman[2], J Bernot[3], P Sherman[4]
[1]59th Medical Wing, San Antonio, TX, [2]59th Medical Wing, Joint Base San Antonio, Lackland AFB, TX, [3]59th Medical Wing, Lackland AFB, TX, [4]59th Medical Wing, Department of Neuroradiology, Joint Base San Antonio, Lackland AFB, TX

Purpose
Human exposure to nonhypoxic hypobaria is associated with increased white matter hyperintensities, degradation of axonal integrity, and neurocognitive processing decrements. We looked to develop an animal model for axonal cerebral injury following nonhypoxic hypobaric exposure utilizing magnetic resonance (MR) diffusion tensor imaging, Q-space, and advanced diffusion kurtosis imaging.

Materials and Methods
Utilizing a revised/improved hypobaric exposure protocol that no longer necessitates intubation or anesthetization of exposure subjects, miniature pigs (Sus scrofa domestica) were exposed repetitively to nonhypoxic hypobaria at 30,000 feet. Controls remained at 5,000 feet altitude. Magnetic resonance imaging was obtained at baseline, immediately postexposure, and 4 weeks postexposure. Advanced diffusion quantification was used to include kurtosis anisotropy, multi-b-value diffusion (Q-space), and fractional anisotropy (FA). Two-tailed t-tests were used for individual and group comparisons.
Results
Perfusion-diffusion index and mean kurtosis anisotropy revealed an increase in unrestricted water immediately after repetitive high altitude exposures. In addition, age-adjusted average FA significantly decreased at 4 weeks postexposure in the high altitude group compared to controls ($p < 0.001/0.547$).
Conclusions
Perfusion-diffusion index and kurtosis demonstrate an increase in unrestricted water after repetitive hypobaric exposure, consistent with injury. The significant decrease in FA at 4 weeks suggests degradation of axonal integrity. This replicates similar MR imaging findings in humans. The study provides evidence that repetitive hypobaric exposure incites axonal damage, and that swine may be a feasible animal model with which to improve our understanding of injury mechanisms and potentially test interventions that could reduce hypobaric neuronal injury.

T-47

11:12AM - 11:15AM

MRI in Mesial Temporal Lobe Epilepsy – is Hippocampal Astrogliosis a Distinct Entity?

E Hattingen[1], A Grote[1], S Enkirch[1], A Jurcoane[1], M Kruse[1], A Becker[1]
[1]*University Hospital Bonn, Bonn, Germany*

Purpose
Hippocampal sclerosis (HS) (1) is the most common histopathological finding in patients with drug-resistant mesial temporal lobe epilepsy (MTLE). Hippocampal sclerosis is defined as segmental nerve cell loss and fibrillary astrogliosis (AG) (2), but in few cases only pronounced AG may be found instead. Our unpublished single center data from MTLE patients with histologically confirmed AG or HS revealed that AG patients are unlikely to become seizure-free postsurgically. Here, we evaluate if MRI morphology differs between HS (3) and AG.
Materials and Methods
We retrospectively analyzed presurgical MRIs of our MTLE cohort and included those with digitalized high-quality 3D-T1 and coronal T2/FLAIR images. Two blinded raters visually

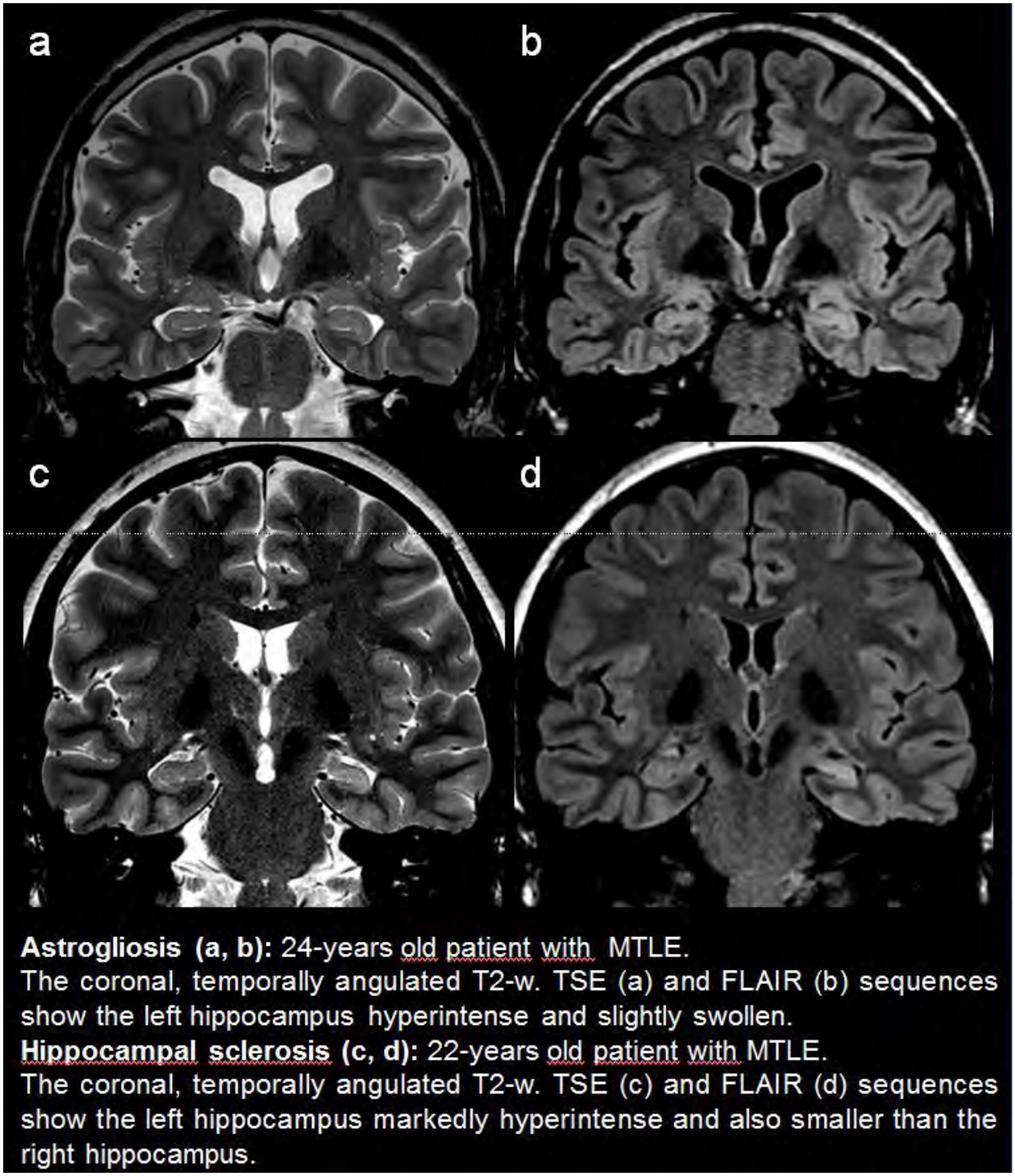
evaluated (1) hippocampal T2/FLAIR signal intensity (SI), (2) hippocampal volume, and (3) contralateral temporomesial alteration. We also compared hippocampal T2-SI in regions of interest and volumes of automatically segmented hippocampus, amygdala and thalamus with Fishers Exact and Kruskal-Wallis test.

Results

Magnetic resonance imaging of 20 AG and 107 HS (40 HS for visual rating) were evaluated. Interrater reliability was high for all visual analyses. Contralateral temporomesial structures were altered in 16 AG (84%) and in 17 HS (43%) ($p=0.01$), but contralateral affection was not related to worse postsurgical seizure outcome. Hippocampus appeared smaller in 38 HS and only in 9 AG; it looked normal or enlarged in the others ($p<0.001$). We rated the hippocampal SI as high in all cases, either as hyperintense (AG 85%; HS 10%) or markedly hyperintense (AG 15%; HS 90%; $p<0.001$), although SI quantification showed no difference between groups. Hippocampal volumes were significantly lower in HS (mean±SD 2.8±0.7 ml) compared to AG (3.5±0.9 ml; $p=0.004$). No volume differences were found for whole brain, thalamus and amygdala.

Conclusions

Astrogliosis patients showed lesser hippocampal volume loss, visual aspect of more contralateral temporomesial affection and less pronounced T2/FLAIR hyperintensity. These results suggest that hippocampal astrogliosis may be a different entity than hippocampal sclerosis.



(Filename: TCT_T-47_asnr.JPG)

T-48

11:15AM - 11:18AM

The Role of MRI in Thermal Laser Ablation for Epilepsy

N Kadom[1], J Cheng[1], A Saindane[1], B Soares[2], Y Bezchlibnyk[1], D Qiu[1], J Willie[1], R Gross[1], D Drane[1]
[1]Emory University, Atlanta, GA, [2]Johns Hopkins University School of Medicine, Baltimore, MD

Purpose

Laser-induced thermal therapy (LITT) is a minimally invasive technology that has been used in the treatment of patients with medically refractory epilepsy (1, 2). For medically intractable epilepsy open resection of well-defined seizure foci results in seizure control for 75-80% of patients and comes with a risk of adverse surgical outcomes, such as permanent neurological deficits, especially for deep-seated lesions (1). Therefore, minimally invasive procedures, such as LITT, could represent a beneficial alternative treatment for patients with medically refractory epilepsy (Wicks 2016). The LITT technology is performed under magnetic resonance imaging guidance (MRgLITT) and pre and postprocedural imaging studies are obtained. The role of imaging for LITT includes: 1) ablation probe localization, 2) thermal monitoring of the ablative zone in real time, 3) assessing the extent of ablated tissue, 4) assessing for procedural complications, and 5) correlating ablation status with clinical outcomes. Here, we provide imaging examples of ablation probe positioning and of ablation extent, MRI appearance of ablated tissue over time, and examples of other procedure-related imaging findings.

Materials and Methods

Retrospective review of imaging studies between 2011 and 2014 in 41 patients who underwent MRgLITT for medically refractory temporal lobe epilepsy. We used an FDA-approved surgical laser ablation system (Visualase Thermal Therapy System, Medtronic, Inc., Louisville, CO). There were 19 females and 21 males. All patients had at least 1 baseline brain MRI (epilepsy protocol, including quantitative assessment) and 1 procedural MRI that included postprocedural postcontrast high-resolution volumetric T1-weighted imaging. Nine patients had repeat ipsilateral ablations.

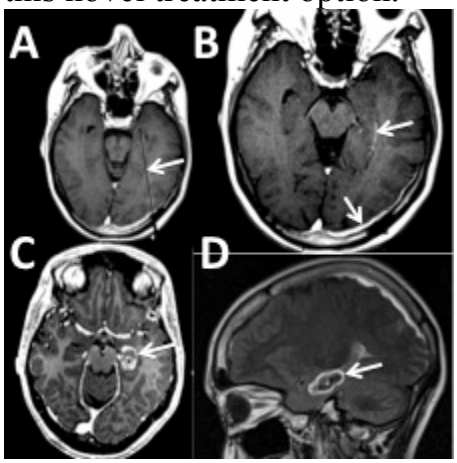
Results

First, the visualase cooled laser assembly system (VCLAS), consisting of a laser diffusing fiber and a cooled catheter system, is positioned. Axial T1-weighted imaging is used to confirm positioning in the medial temporal lobe, traversing the hippocampal formation centrally (Fig. 1A, arrow). The T1-weighted imaging sequence also may demonstrate other changes at this stage of the procedure, such as subdural and intraventricular blood (Fig. 1B, arrows). Postablation, multiple MRI sequences are obtained to evaluate the ablation outcome, including axial and coronal postcontrast T1 (Fig. 1C, arrow), axial T2, axial FLAIR, sagittal FLAIR (Fig. 1D, arrow), and axial DWI/ADC. The typical imaging appearance after ablation shows a central signal void at the level of the probe, surrounded by T1 and T2 iso- to hypointense tissue with restricted diffusion, and a peripheral rim of enhancement (3). Expected radiological imaging findings include small amounts of subdural, subarachnoid and intraventricular blood products (Figs. 1B and D). The vast majority of

these are clinically insignificant. Rare neurological complications include visual field deficits, which may be related to thermal injuries being transmitted to the optic tract or radiations and/or the lateral geniculate nucleus (4). Over time, ablated tissue resolves and appears as cystic encephalomalacia (3).

Conclusions

Magnetic resonance imaging plays a crucial role in the performance of LITT for patients with medically refractory temporal lobe epilepsy. Radiologists with knowledge of this procedure and of the postprocedural appearance of lesions, complications, and long-term imaging outcomes, are more likely to actively participate in a multidisciplinary approach to this novel treatment option.



(Filename: TCT_T-48_ablation.jpg)

T-49

11:18AM - 11:21AM

Imaging temporal Lobe Epilepsy: Beyond the Hippocampus

J Whitlock[1], A Saindane[1], B Soares[2], D Drane[1], D Qiu[1], N Kadom[1]
[1]Emory University, Atlanta, GA, [2]Johns Hopkins University School of Medicine, Baltimore, MD

Purpose

Magnetic resonance brain imaging studies provide essential information in patients with medically refractory temporal lobe epilepsy to identify those that might benefit from laser thermal ablation (1). Radiologists play a crucial role in identifying the nature and extent of temporal lobe pathology. Traditionally, the focus has been on evaluating the hippocampal formation (2). Other structures such as the subiculum, entorhinal cortex, amygdala, uncinate and parahippocampal gyri, collateral white matter, fornix, and mammillary bodies, rarely are reported (3). In this presentation we will review anatomical structures that should be evaluated in patients with epilepsy, including anatomical landmarks for identification of these structures, and examples of normal and abnormal appearances. In addition, the

presentation highlights the value of routine quantitative assessment of the temporal lobes in epilepsy imaging (4, 5).

Materials and Methods

Retrospective review of a cohort of 45 patients presenting with medically refractory temporal lobe epilepsy, with brain MR imaging (epilepsy protocol) between 2012 and 2015, who subsequently underwent hippocampal laser thermal ablation. Of the 45 patients, 27 patients had additional evaluation by volumetric automated computer assessment of hippocampal volume and asymmetry using an FDA approved fully automatic software package (NeuroQuant, CoreTechs Labs, CA, USA). Literature review for anatomical landmarks and value of quantitative imaging of the temporal lobe was performed. For each anatomical structure, at least one imaging example for anatomical landmarks, normal and abnormal appearances are provided.

Results

The structures that play a role in temporal lobe epilepsy are the hippocampus - which is subdivided into head, body, and tail - the subiculum, entorhinal cortex, uncinate and parahippocampal gyri, collateral white matter, amygdala, fornix, and mammillary body. Anatomical landmarks on coronal imaging include: Hippocampus: The hippocampal head is recognized by its digitations. The head/body junction is located at the level of the red nucleus, and the body-tail junction at level of the tectal plate. Subiculum: Transition between the hippocampus and the parahippocampal gyrus. Subiculum represents the superior most cortex of the parahippocampal gyrus, and can be found just below the hippocampus. Entorhinal cortex: Medial and anterior cortex of the parahippocampal gyrus which abuts the subiculum. Parahippocampal gyrus: Medial projection of temporal lobe located inferior to hippocampus. Uncinate gyrus: Medial aspect of amygdala, which connects to the hippocampus head located directly posterior to it. Amygdala: Gray matter nucleus located medial to anterior aspect of the temporal horn of lateral ventricle. Collateral White Matter: White matter in the parahippocampal gyrus directly superior to the collateral sulcus (sulcus in inferior aspect of parahippocampal gyrus). Fornix: White matter efferent tracts arising from fimbria (white matter structure on superior and medial aspect of hippocampus), which course along inferior aspect of third ventricle and connect with the mammillary bodies. Mammillary Body: Paired round bodies in the hypothalamus at the midline, seen at the level of the amygdala.

Conclusions

Knowledge of anatomical landmarks is important to identify structures outside the hippocampus that are functionally connected to the hippocampus and play a role in epilepsy. Once the structures can be identified, it becomes easier to identify pathology. Knowing the exact location of pathology can help target invasive therapies, such as surgery or thermal laser ablation, in patients with medically refractory epilepsy.

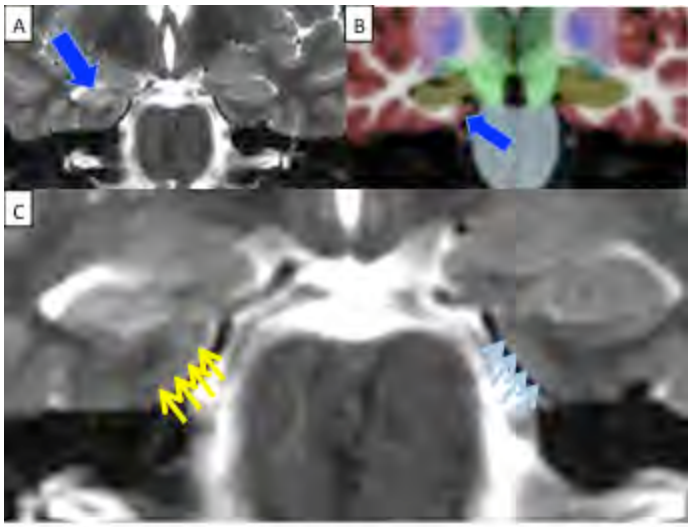


Figure 1: Coronal T2-weighted (A, C) and color coded segmented volumetric T1-weighted (B) MR images showing right-sided hippocampal sclerosis and abnormal right entorhinal cortex. There is volume loss of the right hippocampus (A, blue arrow). The entorhinal cortex can be found in the medial aspect of the parahippocampal gyrus (C, magnified view of image A). Note the volume loss on the right entorhinal cortex (yellow arrows) as compared to the normal left side (blue arrows). The volumetric difference can also be seen of the color-coded segmented scan (B, blue arrow)

(Filename: TCT_T-49_Figure1.jpg)

T-50

11:21AM - 11:24AM

Chorda Tympani and Multifocal Cranial Nerve involvement in CIDP

M McDonald[1], J Bykowski[1]
[1]*University of California at San Diego, San Diego, CA*

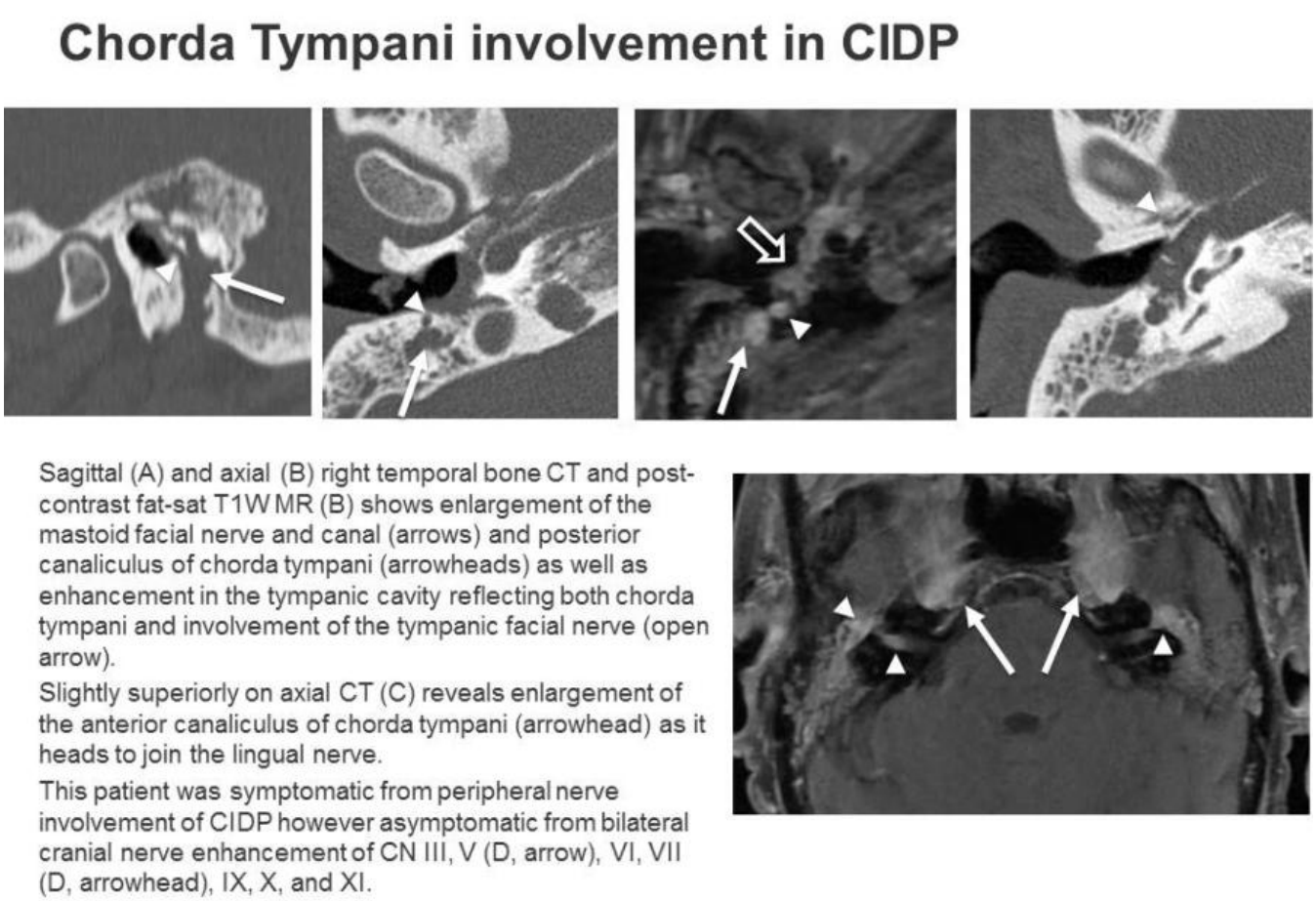
Purpose
Chronic inflammatory demyelinating polyneuropathy (CIDP) is classically a symptomatic process of the peripheral nerves; however cranial neuropathies and abnormal cranial nerve findings have been reported in a small subset of CIDP patients. This exhibit aims to alert the radiologist to the possibility of cranial nerve enlargement, enhancement and symptoms in CIDP as well as the differential diagnosis that must be considered for cranial nerve findings in patients undergoing immunosuppressive therapies.
Materials and Methods
A review of our institutional imaging database and electronic medical record was performed to identify patients with known diagnosis of CIDP who had cranial nerve symptoms, abnormal enlargement and/or expansion of one or more cranial nerves on imaging. Computed tomography and MR images from these cases are used to illustrate multiplanar appearance of abnormal skull base foramina, intra and extracranial involvement of upper and lower cranial nerves, and pitfalls of evaluation when a dedicated skull base protocol is not used. When available, serial imaging studies are included. A summary of the literature is provided.

Results

Imaging confirmed abnormal cranial nerve findings in 4 patients including bilateral CN III enhancement, intra and extracranial enlargement and enhancement of CN V and branches, and multifocal involvement inclusive of upper and lower cranial nerves. To our knowledge, this includes the first described case of enlargement of the chorda tympani, which was present in the setting of asymptomatic multifocal upper and lower cranial nerve enlargement and enhancement (Fig. 1). Literature review is summarized in tabular form, identifying additional cases with imaging and based on symptoms and exam or neuroconduction testing. An additional case reveals cranial nerve enhancement in a patient with CIDP who subsequently was confirmed to have leptomeningeal spread of lymphoma. By the end of this educational exhibit, the attendee will be able to: 1. Describe diagnostic criteria for CIDP and common therapies. 2. Identify abnormal enlargement of skull base foramina on CT in the setting of cranial nerve involvement in CIDP. 3. Identify abnormal enlargement and enhancement of cranial nerves intra- and extra-cranially in the setting of CIDP. 4. Conduct a systematic review to discern above processes from findings suspicious for perineural or meningeal spread of tumor. 5. Consolidate knowledge via a brief self-assessment quiz.

Conclusions

Cranial nerve enlargement and enhancement may be present in patients with CIDP and potentially under-reported in asymptomatic patients. It is crucial for radiologists to be aware of these often multifocal, bilateral findings and have a systematic approach to exclude any other intracranial manifestations of malignancy or infection in the setting of immunosuppressive therapy.



(Filename: TCT_T-50_CIDPASNRabstract2.jpg)

T-51

11:24AM - 11:27AM

Neuroimaging Manifestations of Hematologic Malignancies: A Compartmental Approach

K Buchanan[1], A Chan[1], R Fulbright[2], J Baehring[1], M Johnson[3]
[1]Yale University, New Haven, CT, [2]Yale University Medical Center, New Haven, CT, [3]Yale Univ. School Of Medicine, New Haven, CT

Purpose
Neurologic manifestations of hematologic malignancies (leukemias, lymphomas, myeloma) are common and multifaceted. They can be understood best from a compartmental approach. Significant morbidity can result from hematogenous spread, leptomeningeal dissemination, infiltration along neurovascular structures, peripheral or cranial nerves. Direct tumor invasion can occur from adjacent bone or bone marrow. Indirect effects from leukostasis,

coagulopathy or a resorptive hydrocephalus often are under-reported. Involvement can vary widely with the malignancy subtype; with frequent intraparenchymal involvement by aggressive non-Hodgkin lymphoma, leptomeningeal involvement in acute lymphoblastic leukemia (ALL), and more prominent dural infiltration in myelogenous leukemia. Systematic evaluation of these compartments is fundamental to ensure adequate evaluation for subtle lesions and early detection of asymptomatic involvement. This illustrated review will demonstrate the protean manifestations of hematologic malignancies with a compartmental approach to facilitate accurate diagnosis.

Materials and Methods

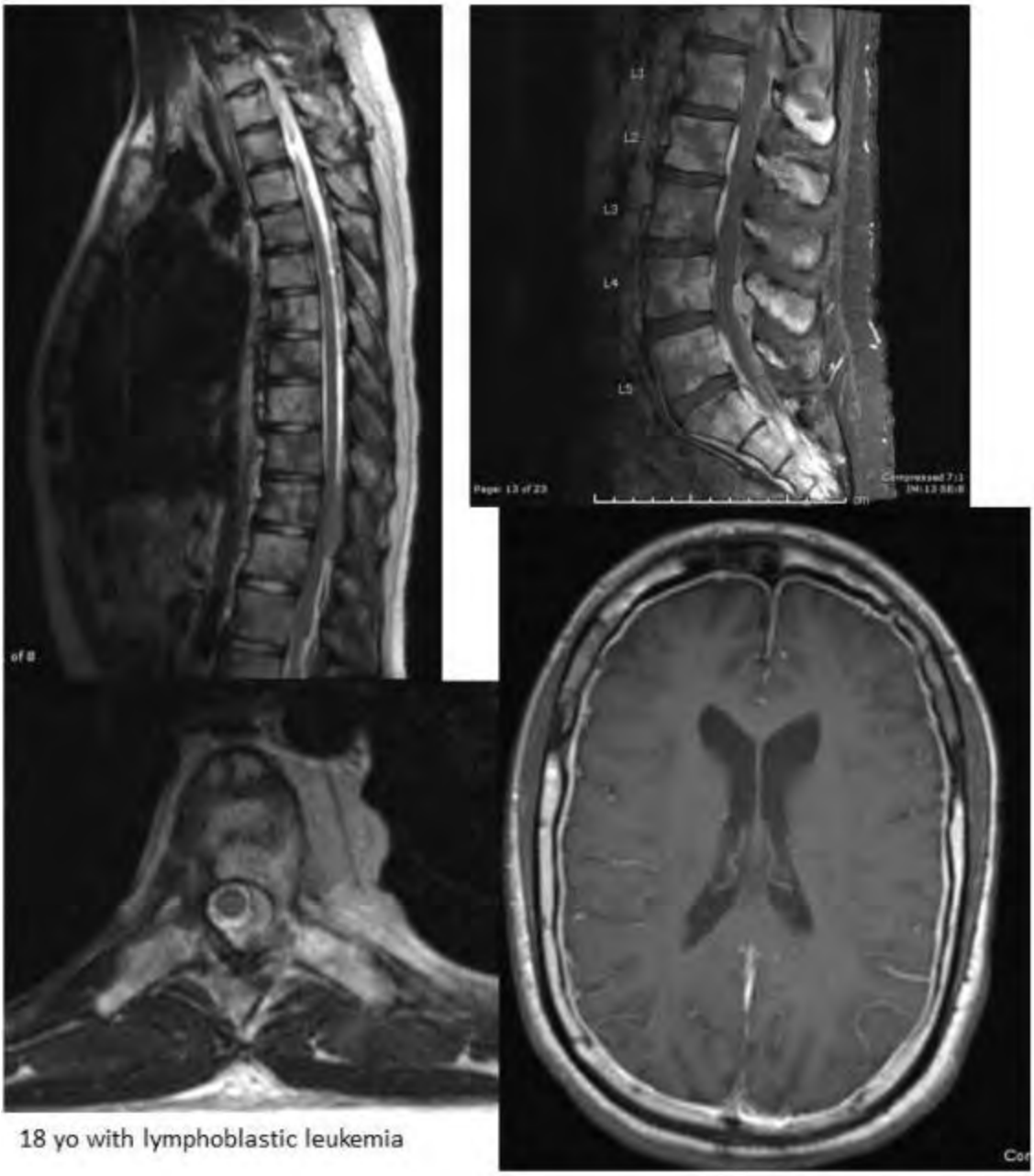
Exemplary cases of hematologic malignancies with neurologic involvement from our clinical archives will be utilized to demonstrate important compartments as follows: Osseous and bone marrow, extradural space, leptomeningeal, parenchymal, intravascular and neuro-lymphomatosis. Indirect effects of hematologic malignancy such as leukostasis, coagulopathy or aresorptive hydrocephalus also will be demonstrated. These imaging findings are correlated with the patient's disease type, prognosis and treatment.

Results

The compartmental approach to the analysis of neurologic findings in hematologic malignancies facilitates recognition and differential diagnosis in this complex group of patients. Detection of pathology is enhanced with a compartmental-based search pattern. Lesions are often in atypical locations as compared with solid neoplasms and may be subtle and possibly be overlooked without a structured approach.

Conclusions

Knowledge of the multiple presentations of hematologic malignancies in the central and peripheral nervous systems coupled with a pattern-based compartmental approach is crucial for accurate recognition and diagnosis. This approach is important and can increase sensitivity and specificity for the protean neurologic manifestations of hematologic malignancy.



(Filename: TCT_T-51_thumbnail_hematologic_malignancies.jpg)

T-52

11:27AM - 11:30AM

Multicenter Study on the Prognostic Utility of Diffusion Weighted Imaging in Patients with Brain Metastases

Y Chen[1], R Zakaria[2], S Wang[1], S Chawla[1], D Hughes[2], A Berghoff[3], M Preusser[3], H Poptani[2], M Jenkinson[2], S Mohan[1]

[1]University of Pennsylvania Perelman School of Medicine, Philadelphia, PA, [2]University of Liverpool, Liverpool, AK, [3]Medical University of Vienna, Vienna, Wien

Purpose

Graded prognostic assessment [GPA (1)] and recursive partitioning analysis [RPA (2)] are used clinically for prognostication in patients with brain metastases. Previous single center studies have shown correlation between apparent diffusion coefficient (ADC) derived from diffusion-weighted imaging (DWI) and survival in this patient population (3-4). In this study, we extend the evaluation of the prognostic utility of DWI to a multi-institutional setting.

Materials and Methods

Magnetic resonance imaging from 223 patients (106 M:117 F, age 59±11 years) diagnosed with brain metastases in 2002-2013 from 3 tertiary care academic centers in United States and Europe were analyzed retrospectively. All patients had brain MRI with ADC derived from DWI prior to treatment specific for brain metastases. Clinical data included primary tumor type, Karnofsky performance scale (KPS), GPA, RPA, whole brain radiation, and overall survival after initial diagnosis of brain metastasis. Mean ADC (ADCmean) was quantified from the dominant metastatic lesion using either a manual region-of-interest method or a semi-automated segmentation method (5). Univariate survival analyses were performed using log rank tests stratified by centers when appropriate. Multivariate survival analysis was performed using Cox proportional hazards model stratified by centers.

Results

Median KPS score was 80 and median overall survival was 278 days. Primary tumor types included lung (115), breast (34), melanoma (18), colorectal (10), renal (7), and other (39). Univariate log rank tests showed significant survival differences by GPA class ($p<0.0001$), RPA class ($p<0.0001$), primary tumor type ($p=0.032$, stratified by centers), whole brain radiation ($p=0.0069$, stratified by centers), and ADCmean ($p=0.0054$, stratified by centers). Multivariate Cox proportional hazards model showed significant survival differences with GPA class, RPA class, whole brain radiation, and ADCmean (see Table). This indicated the independent value of ADCmean, with lower ADCmean predicting shorter overall survival.

Conclusions

Our results demonstrate added prognostic value of ADC that is independent from the clinical GPA and RPA prognostication systems based on age, KPS, number of metastases, and extracranial disease status. Therefore, ADC shows promise as a robust imaging-based biomarker for predicting survival in this patient population useful across different institutions.

Table – Multivariate Cox Proportional Hazards Model Stratified by Centers

	Hazard Ratio	95% Confidence Interval	P-Value
ADC_{mean}	N/A for continuous variable	N/A for continuous variable	**0.0021**
GPA Class II (Relative to GPA Class I)	0.54	0.31 to 0.93	**0.026**
GPA Class III (Relative to GPA Class I)	0.25	0.12 to 0.54	**0.00048**
GPA Class IV (Relative to GPA Class I)	0.43	0.17 to 1.10	0.078
RPA Class II (Relative to RPA Class I)	1.82	1.01 to 3.28	**0.045**
RPA Class III (Relative to RPA Class I)	2.47	0.91 to 6.74	0.077
Whole Brain Radiation (Yes Relative to No)	0.59	0.41 to 0.83	**0.0029**

(Filename: TCT_T-52_Table.gif)

T-54

11:33AM - 11:36AM

Analyzing Imaging Manifestations of Neurosarcoidosis: A Retrosepctive review

S Gupta[1], A Wang[2], A Willis[3], S Forseen[4], B Gilbert[5], R Figueroa[5], J Keshavamurthy[4]
[1]Augusta University Medical college of Georgia, augusta, GA, [2]Medical College of Georgia, Augusta, GA, [3]Medical College of Georgia at Augusta University, Augusta, GA, [4]Augusta university, Augusta, GA, [5]Augusta University, Augusta, GA

Purpose
Neurosarcoidosis is characterized by noncaseating granulomatous disease of the neural axis (1). Unfortunately, studies indicate that only 50% of cases of neurosarcoidosis are diagnosed due to its many clinical and imaging manifestations and its rarity. We evaluated imaging

features of CNS sarcoidosis from our database which could enable disease characterization and prompt diagnosis.

Materials and Methods

Retrospective search of a single institution's pathology records (via PathNet) was performed with parameters for CNS specimen with pathology proven diagnosis of CNS sarcoidosis. The imaging records, predominantly MRI, were obtained from the teaching files and imaging database. Further analysis of these records was performed and following data was recorded: patient demographics (age, sex), location of sarcoid, relevant medical history and treatment history.

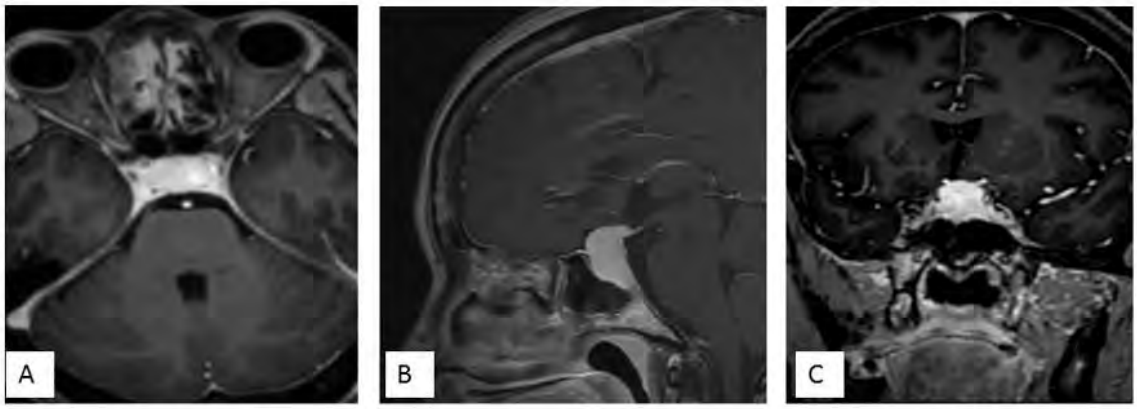
Results

A total of 10 patients met diagnostic criteria for confirmed (n = 4) (positive CNS biopsy), probable (n = 2) (suggestive symptoms, laboratory results of CNS inflammation, exclusion of other diseases), or possible (n = 4) neurosarcoidosis (suggestive symptoms, exclusion of other diseases) based on the criteria of Zajicek et al (2). The patients in this study were found to have leptomeningeal, dural, parenchymal, optic nerve/chiasm, and/or pituitary involvement. Although seizures and headache were common clinical manifestations, other patients presented with pituitary insufficiency, meningoencephalitis, or focal deficits. Five patients were known to have either cutaneous or pulmonary sarcoidosis prior to their diagnosis of CNS involvement. Conversely, 2 patients first diagnosed with neurosarcoidosis were later found to have systemic involvement, and in 3 patients, neurosarcoidosis was the only diagnosis. Neurosarcoidosis has a predilection for the leptomeninges and commonly presents with nodular and/or diffuse infiltrative lesions, as seen in 7 patients (3) (see Fig.). Dural involvement with an enhancing dural mass was seen only in 1 patient. Periventricular and white matter lesions were seen in 3 patients, and cranial nerve involvement was seen in 3 patients, most commonly of the optic nerve. Isolated spinal involvement was seen in 2 patients, both of which were extramedullary lesions. We found 1 case of pituitary sarcoidosis (see Fig.). Of the 5 patients who underwent cerebrospinal fluid analysis, angiotensin converting enzyme was elevated only in 2 patients. First line therapy was initiated in all 10 patients, for which 6 experienced significant short-term improvement. Second line therapy, including infliximab, methotrexate or cyclophosphamide, was started in 3 patients, and 1 patient was lost to follow up.

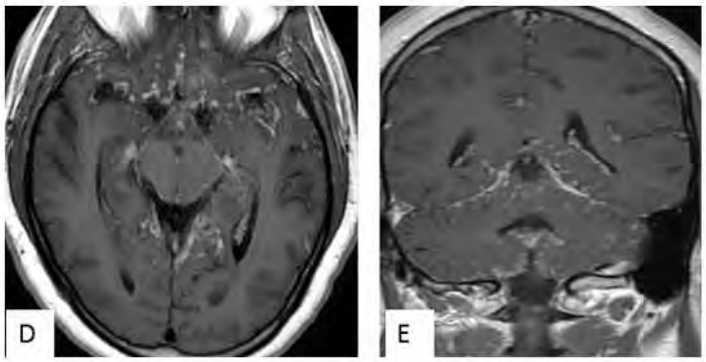
Conclusions

The protean manifestations of neurosarcoidosis include parenchymal, dural, meningeal, and spinal involvement. The prevalence of sarcoidosis can be greater than 50 per 100,000 in the African American population, and approximately 5% of these patients have clinically recognized nervous system involvement. Neurological symptoms were the first manifestation of disease in more than half of patients. The most common presenting feature is cranial neuropathy (especially facial nerve palsy), followed by headaches (4). With treatment, more than 50% of patients can achieve total or incomplete remission with appropriate treatment (5). Thus, it is especially important to be mindful of neurosarcoidosis and its possible presentations in relevant patient populations. Leveraging MR imaging and

CSF analysis could improve clinical outcomes by hastening appropriate treatment and in equivocal cases, direct management toward biopsy for definitive diagnosis.



Figures A-C demonstrate T1- weighted post contrast MRI with avidly enhancing pituitary lesion which was proven to be sarcoidosis on pathology.



Figures D-E demonstrate T1- weighted post contrast MRI with avidly enhancing nodular leptomeningeal lesions consistent with sarcoidosis.

(Filename: TCT_T-54_5.jpg)

T-55

11:36AM - 11:39AM

Management and treatment of headaches based on neuroradiological findings

M Goldust[1]
[1]*Massachusetts general hospital, Boston, MA*

Purpose
The present study aims at determining radiological symptoms, clinical manifestations, and possible risk factors of intracerebral hemorrhages.
Materials and Methods
In this descriptive analytical study, clinical and radiological findings (primary CT-scan) of 80 patients with intracranial hemorrhage were evaluated retrospectively. The study consisted of 300 patients. Radiological findings considering clot age and brain scan of all patients were studied to determine location and extension of hemorrhage.

Results
There were 160 male and 140 female patients with the mean age of 62.24± 12.34 years. The most prevalent clinical manifestation including decrease of consciousness and headache were seen in 51% and 41.6% of cases and only 8.3% of the patients referred while they were in coma. Hematoma was replaced in 36% of lobar and 32.6% in basal ganglia (lenticular). It was observed in 15%, 9%, and 7.3% of thalamus, cerebellum, and other areas, respectively. Additionally, hypertension and consumption of anticoagulation were respectively seen in 60.3% and 9% while there was not any specific risk factor in 30.6% of the patients. Hypertension was regarded as main risk factors and hemorrhage was seen in basal ganglia in most cases of hypertensive patients. Headache and extension of hemorrhage into ventricles often were seen in cerebellum and thalamus hemorrhages, respectively. Subarachnoid hemorrhage often was associated with lobar hemorrhage. Most hypertensive patients suffering from intracerebral hemorrhage were older than 45 years.
Conclusions
The present study referred to hypertension and consumption of anticoagulation drugs as the most important risk factors for spontaneous intracerebral hemorrhage. Although detection and treatment modalities of the disease have progressed significantly, cerebral intraparenchymal hemorrhages have poor prognosis and high mortality rate. Therefore, controlling of blood pressure and observing of different aspects in consumption of anticoagulation drugs may play an effective role in prevention from cerebral intraparenchymal hemorrhages.

Wednesday
1:30PM - 3:00PM
Long Beach Convention Center, Room 104A (Main Lobby)

19D-Parallel Paper Session: Pediatric Neuroradiology: Clinical Development and Imaging Developments

O-224

1:30PM - 1:38PM

Diffusion Tensor Imaging in Horizontal Gaze Palsy with Progressive Scoliosis

I Alorainy[1], M GAHA[2], A Abujamea[1], D Oystreck[3], T Bosley[4]
[1]King Saud University, Riyadh, Saudi Arabia, [2]King Saud University Medical City, Riyadh, Saudi Arabia, [3]IWK Health Centre, Dalhousie University, Halifax, NS, [4]The Johns Hopkins Hospital, Baltimore, MD

Purpose
Horizontal gaze palsy with progressive scoliosis (HGPPS) is a rare disorder characterized by the congenital absence of conjugate horizontal eye movements, preservation of vertical gaze and convergence, and progressive scoliosis developing in childhood and adolescence. It is

caused by mutations in the ROBO3 gene, which are critical for decussation of developing neuronal tracts in the brainstem, particularly the pons. Diffusion tensor imaging (DTI) observations in HGPPS were reported sporadically in only 12 patients. We are documenting DTI details of white matter tracts in the brainstem in a cohort of 5 patients with genetically proven HGPPS from 3 families.
Materials and Methods
A brain MRI protocol, including structural MRI and DTI, was performed on each subject using a Siemens 3T MAGNETOM Tim/Verio scanner (Siemens Medical System, Germany) and a standard 12-channel head coil. Directional sensitized diffusion-weighted single-shot spin-echo echo-planar imaging sequence with 30 gradient directions was used to obtain DTI data. Fiber tracts were generated using a Neuro 3D software provided by Siemens.
Results
All our patients showed the classical structural brainstem changes of HGPPS with pontine hypoplasia, absent facial colliculi, butterfly configuration of the medulla, and a deep midline pontine cleft. In all patients, DTI revealed ipsilateral ascending and descending connectivity in the brainstem without any crossing over of the major tracts. The interhemispheric connections in the corpus callosum were normal. Transverse pontine fibers either were absent or thin and anteriorly displaced. Decussation of superior cerebellar peduncles was absent, while crossing of the middle cerebellar peduncles was normal.
Conclusions
Tractography is a valuable investigative tool to assess neuronal connections in the brain and is a useful adjunct to the structural MR imaging in confirming the diagnosis of HGPPS.

O-225

1:38PM - 1:46PM

Utility of diffusion imaging in detection of gray matter heterotopia

R Ashmawy[1], H Branson[1], W Lee[1], P Krishnan[1], S Laughlin[1]
[1]*The Hospital for Sick Children, Toronto, Ontario*

Purpose
To determine if qualitative and semiquantitative assessment of routine diffusion sequence (DWI) improves detection of gray matter heterotopia (GMH) in cases of pediatric epilepsy. Heterotopia is a common finding on MRI studies in epilepsy. Gray matter heterotopia may represent the epileptogenic focus, hence detection and characterization of these structural malformation is crucial, as surgical resection is considered in refractory cases. However detection of small nodules may be challenging on routine imaging studies. Heterotopic gray matter has been shown to have significant altered anisotropy on diffusion presumably secondary to underlying histological characteristics and embryo-genetic mechanisms.
Materials and Methods
REB approved retrospective study. Diagnosis based on MR using data base retrieval system

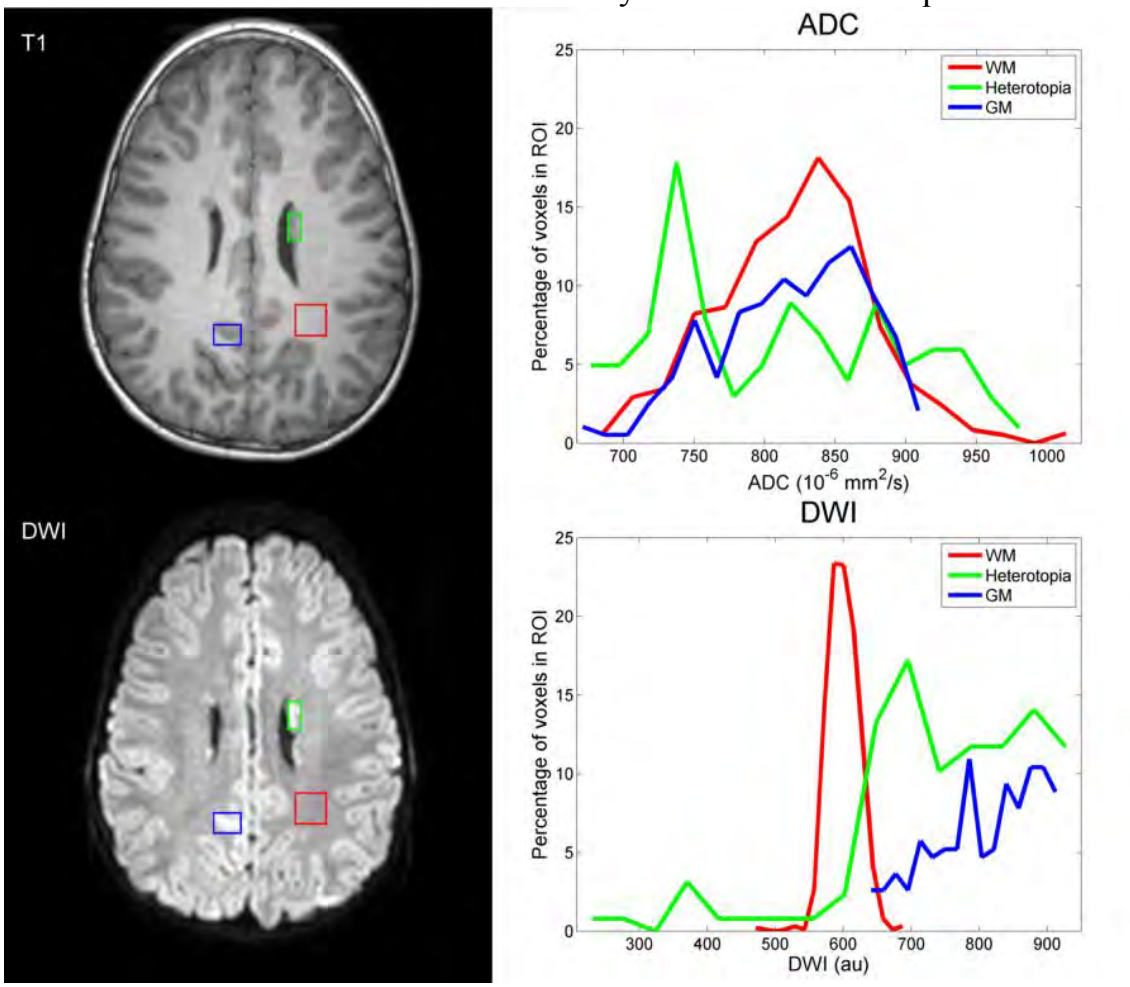
(ISYS tm). Magnetic resonance imaging (MRI) studies done between 2008 and 2013 for seizures were included. A cohort of 45 MRI studies with GMH and 45 studies of age-matched normal controls were included. Two neuro-radiologists, blinded to the reports, assessed the DWI and conventional sequences (3DT1, T2, FLAIR) separately for detection of GMH. Quantitative assessment of GMH on diffusion was performed with manually drawn regions of interest (ROI) and distribution of DWI and ADC values within each ROI were plotted on a curve (Fig. 1).

Results

The sensitivity and specificity for detection of GMH on the diffusion was higher 86.6% (39/45) and 92.7% respectively compared to 83.7% and 86.7% for rest of the conventional sequences with high inter-reader agreement. In 4% cases (2/45) GMH was identified only on the diffusion sequence and not on the conventional sequences. Quantitative assessment demonstrated lower ADC than normal gray matter.

Conclusions

Diffusion sequences can qualitatively and quantitatively improve the detection of GMH in routine imaging for pediatric epilepsy. The utility of this approach is illustrated by the fact that few cases of GMH were identified only on the diffusion sequences.



(Filename: TCT_O-225_ASNRcolor.jpg)

O-226

1:46PM - 1:54PM

MR Imaging Features of Idiopathic Developmental Delay

K Alenezi[1], C Martinez-Rios[2], P Krishnan[1], C Raybaud[1]
[1]The Hospital for Sick Children, Toronto, Ontario, [2]McMaster University, Hamilton, Ontario

Purpose
To assess the presence of unrecognized significant structural abnormalities in children diagnosed with idiopathic developmental delay (IDD) using magnetic resonance imaging (MRI).
Materials and Methods
REB approved retrospective descriptive study of brain MRI performed between January 2015 and December 2015 at our institution, in 100 patients, aged between 18 months to 6 years with clinically diagnosed IDD and no associated disorders accounting for developmental delay (no history of congenital or neonatal meningitis and encephalitis, perinatal asphyxia, creatine deficiency, or syndromes including chromosomal disorders). We correlated with a control cohort of 100 normal cases. The head size and the following structures were assessed systematically: temporal lobes, corpus callosum (thickness, morphology), ventricles and white matter thickness, brainstem and cerebellum.
Results
In 100 patients with IDD only 8/100 (8%) had normal MRI and 92/100 (92%) had abnormal structural MRI findings compared to 70/100 (70%) and 30/100 (30%) respectively in the control group: borderline abnormal head size (micro- or macrocephaly) was present in 36% as opposed to none in control. Anterior hypogenesis of the temporal lobe was seen in 49% compared to 9%, abnormal corpus callosum in 79% compared to 19%; prominent ventricles in 34% compared to 5%; squaring of the angle of the frontal horns 31% compared to 5%. Other MRI findings included abnormalities in the myelination (6%); dysplastic brainstem (6%); and hypoplastic cerebellum (4%) compared to none in control group.
Conclusions
Magnetic resonance imaging findings of abnormal head size, anterior temporal lobe hypoplasia, abnormal corpus callosum or large ventricles were seen in a larger proportion of the patients with IDD suggesting that in a significant number of patients, IDD may result from "minor", often unrecognized structural abnormalities.

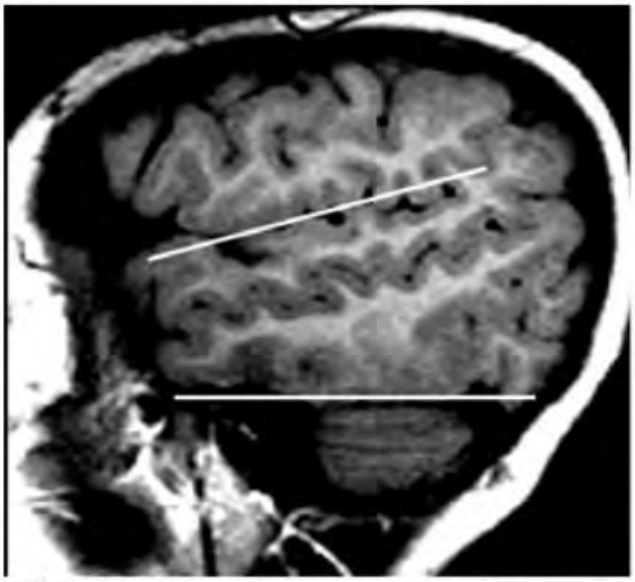


Fig. 1. Parasagittal T1 image shows a triangular temporal lobe indicating an anterior hyopgensis.

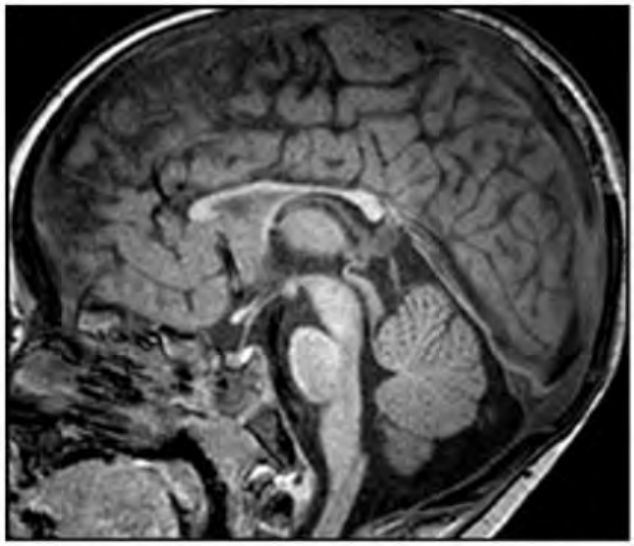


Fig. 2. Sagittal midline T1 image shows thin corpus callosum.

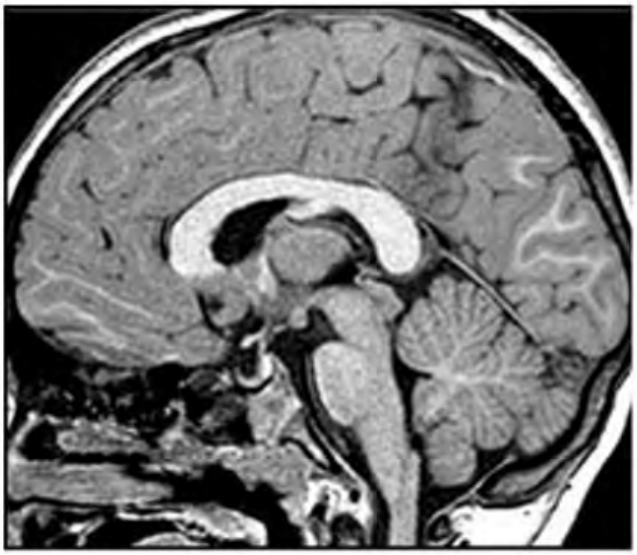


Fig. 3. Sagittal midline T1 image shows thick corpus callosum.

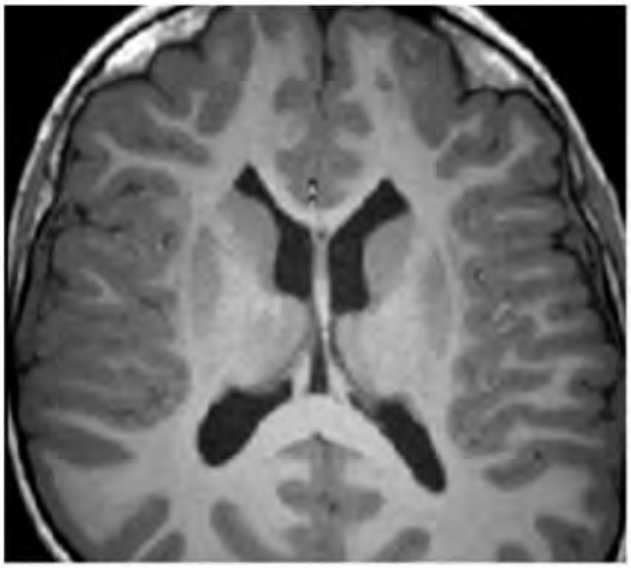


Fig. 4. Axial T1 image shows squaring of the angle of the frontal horns.

(Filename: TCT_O-226_1-4.jpg)

O-227

1:54PM - 2:02PM

Joubert syndrome: Correlation between neuroimaging and cognitive function

A Poretti[1], J Snow[2], A Summers[2], A Tekes-Brady[3], T Huisman[4], N Aygun[5], T Vilboux[6], W Gahl[6], M Gunay-Aygun[6]

[1]The Johns Hopkins University School of Medicine, Baltimore, MD, [2]National Institute of Mental Health, Bethesda, MD, [3]Johns Hopkins Hospital, Baltimore, MD, [4]Johns Hopkins, Baltimore, MD, [5]Johns Hopkins University, Baltimore, MD, [6]National Human Genome Research Institute, Bethesda, MD

Purpose
Joubert syndrome is a clinically and genetically heterogeneous ciliopathy. Neuroimaging findings have not been evaluated systematically in a large cohort of patients with Joubert syndrome in correlation with cognitive function.
Materials and Methods
A comprehensive evaluation of brain magnetic resonance imaging (MRI) studies for infratentorial and supratentorial morphological abnormalities. Genetic cause was identified by whole exome sequencing and cognitive functions were assessed with age-appropriate neurocognitive tests in a subset of patients. For the neurocognitive evaluation, age appropriate versions of the Wechsler intelligence scales or the Vineland Adaptive Behavior Scales-Second Edition were used. In addition, a "level of functioning" score was derived by assigning a score from 0-5 with 0 being the highest function.
Results
Brain magnetic resonance images of 110 patients with Joubert syndrome were included in this study. The cerebellar hemispheres were enlarged in 18% of the patients, mimicking macrocerebellum. The posterior fossa was enlarged in 42% of the patients, resembling Dandy-Walker malformation. Abnormalities of the brainstem, such as protuberance at the ventral contour of the midbrain, were present in 66% of the patients. Abnormalities of the supratentorial brain were present in approximately one-third of the patients, most commonly malrotation of the hippocampi. Mild ventriculomegaly, which typically did not require shunting, was present in 23% of patients. A novel predictor of outcome was identified; the more severe the degree of vermis hypoplasia, the worse the neurodevelopmental outcome was.
Conclusions
The spectrum of neuroimaging findings in Joubert syndrome is wide. Neuroimaging may predict the neurodevelopmental outcome. A high degree of vermis hypoplasia correlates with worse neurodevelopmental outcome. This novel finding is important for prognostic counseling in Joubert syndrome.

O-228

2:02PM - 2:10PM

Diffusion Kurtosis Imaging of the Developing Brain from Childhood to Adult

K Ando[1], R Ishikura[2], J Taniguchi[3]
[1]Hyogo College of Medicine, Nishinomiya, Japan, [2]Hyogo College of Medicien, Nishinomiya, CA, [3]Hyogo College of Medicine, Nishinomiya, CA

Purpose

Diffusional kurtosis imaging (DKI) detects non-Gaussian diffusion effects, providing information of microstructural changes during brain development. Paydar et al. studied age-related changes in mean kurtosis (Kmean) in the developing brain during the first 5 years of life and concluded that Kmean showed age-related increases in all white matter (WM) regions, reflecting progression of diffusional anisotropy, even after the fractional anisotropy plateau. However, DKI of the pediatric brain after the first 5 years is still unknown. Also, other than Kmean, DKI offers other parameters such as radial kurtosis (Krad) and axial kurtosis (Kax), but age-related changes in Krad and Kax are likewise unknown. The output clarify DKI (Kmean, Krad, and Kax) in the developing brain from childhood to adults.

Materials and Methods

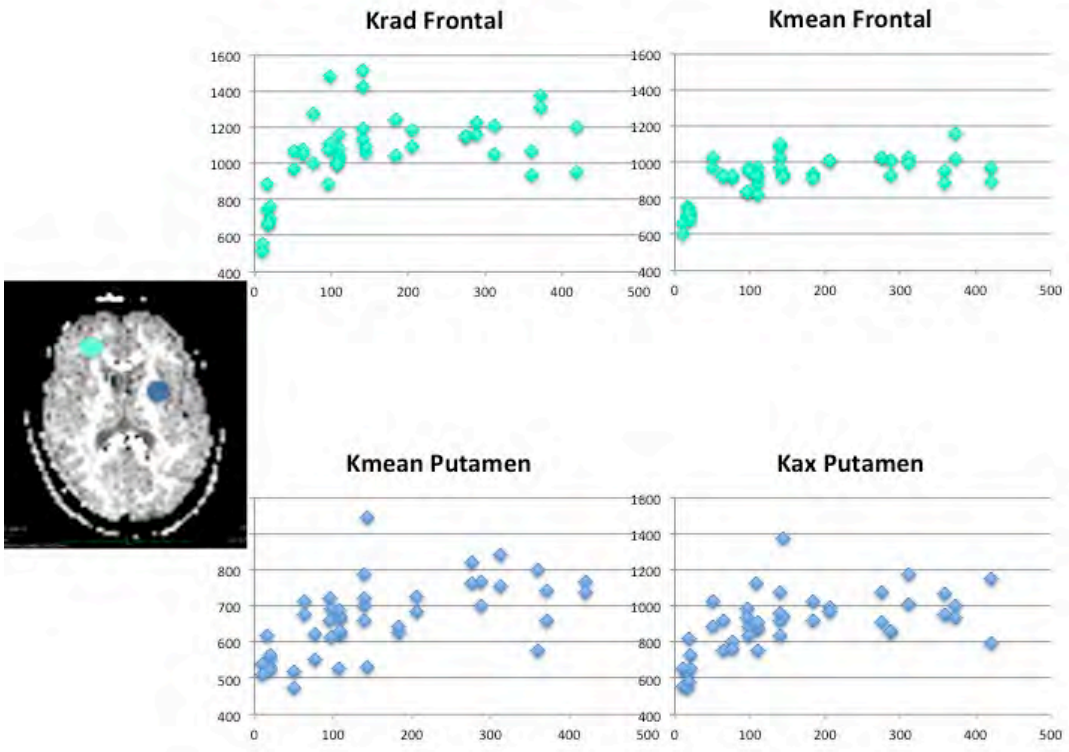
Participants comprised 21 neurologically normal subjects ranging in age from 1 year 5 months to 35 years (mean, 13 years 5 months). All DKI was performed prospectively using a 1.5-T scanner. Imaging parameters were: repetition time, 4500 ms; echo time, 96 ms; matrix size, 78-82 × 78-82 × 28-34; voxel size, 2.2-2.8 × 2.2-2.8 × 4-5 mm3; partially parallel acquisition acceleration factor, 2; acquisition time, 4 min 48 s; diffusion directions, 30; and b-values, 0, 1000, and 2000 s/mm2. Output images from the DKI sequence including fractional anisotropy (FA), Krad, Kax, and Kmean were automatically obtained on the console workstation of the scanner immediately after scan completion. Region-of-interest (ROI) analyses were performed for multiple WM and deep GM regions in each brain, and subsequently analyzed with respect to age (Fig. 1).

Results

For ROIs in frontal and parietal WM, increases in Krad followed by Kmean were prominent in the first decade of life. For ROIs in WM of the corpus callosum, brainstem, middle cerebellar peduncles and cerebellum, slow increases in all three DKI measurements were observed until the fourth decade of life. For ROIs in the putamen and thalami, increases in Kax were observed until the fourth decade of life, whereas increases in Kmean were prominent in the first decade of life.

Conclusions

Diffusional kurtosis imaging detects age-related changes in both white matter (Krad > Kmean) and deep gray matter (Kax and Kmean) of the brain even after the first 5 years of life, possibly reflecting the increasing complexity of the brain matrix.



(Filename: TCT_O-228_Fig1.jpg)

O-229

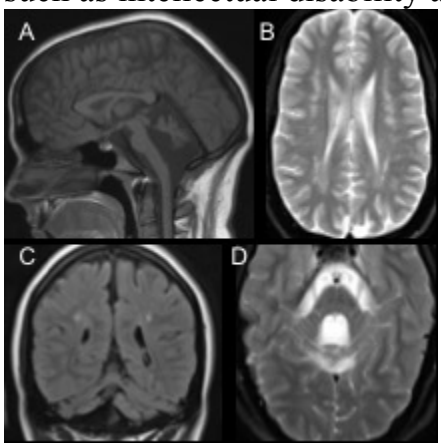
2:10PM - 2:18PM

Cerebral Palsy, Intellectual Disability, Epilepsy, and Cerebellar Hypoplasia Caused by a Novel Homozygous SEPSECS Mutation

A Moreno De Luca[1]
[1]*Geisinger Health System, Danville, PA*

Purpose
To describe the clinical presentation, neuroimaging findings, and identification of the underlying genetic cause of an autosomal recessive type of cerebral palsy.
Materials and Methods
A 22-year-old female with a syndromic form of cerebral palsy was identified from a cohort of subjects recruited to a research study exploring the genetic underpinnings and neuroimaging correlates of individuals with cerebral palsy. She was born prematurely and was diagnosed with cerebral palsy, moderate intellectual disability, generalized convulsive epilepsy, cerebellar ataxia, attention deficit hyperactivity disorder, congenital cataract, retrolental fibroplasia, exotropia, speech disturbance, and hypothyroidism. Magnetic resonance imaging (MRI) of the brain was performed at age 12 and 21. Whole exome sequencing (WES) was performed to identify probable causative genomic variants.

Results
Magnetic resonance imaging of the brain showed marked cerebellar hypoplasia with compensatory enlargement of the cisterna magna and 4th ventricle, as well as numerous nonenhancing foci of high FLAIR/T2 signal intensity in the bilateral periventricular white matter. Whole exome sequencing analysis identified a novel homozygous missense variant (p.Gly45Cys) in the SEPSECS gene, encoding the O-phosphoserine tRNA-selenocysteine tRNA synthase, which was absent from 60,706 control exomes. Mutations in this gene, leading to defective selenocysteine biosynthesis, have been reported in a total of 13 patients with pontocerebellar hypoplasia type 2, progressive cerebello-cerebral atrophy, or progressive encephalopathy (1-4).
Conclusions
These results expand the neuroimaging and clinical spectrum associated with selenocysteine deficiency and highlight the potential of WES to identify causative genetic abnormalities in individuals with cerebral palsy, a neurodevelopmental disorder frequently attributed to birth asphyxia. A growing body of evidence supports the notion that cerebral palsy is probably caused by multiple genetic abnormalities, similar to other developmental brain disorders such as intellectual disability and autism.



(Filename: TCT_O-229_Picture1.jpg)

O-230

2:18PM - 2:26PM

Septo-optic Dysplasia: Revisited, with Special Attention to the Olfactory Sulci and Hippocampi

A McKinney[1], J Benson[2], D Nascene[1]
[1]University of Minnesota, Minneapolis, MN, [2]University of Minnesota, St. Paul, MN

Purpose
Septo-optic dysplasia (SOD) is a rare congenital disorder that consists of bilateral optic nerve hypoplasia combined with absent septum pellucidum. Other anomalies may occur, which include anomalies of the pituitary, schizencephaly ("SOD-plus"), periventricular

nodular heterotopia (PVNH), callosal agenesis/hypogenesis, and hippocampal incomplete rotation (HIR), to name a few. This may or may not include olfactory bulb/tract hypoplasia as well, but the frequency of olfactory sulcus hypoplasia is not well described. Our goal was to describe the frequency of each of these potentially associated anomalies in patients with known SOD, and particularly focus on the presence of olfactory sulcus hypoplasia.

Materials and Methods

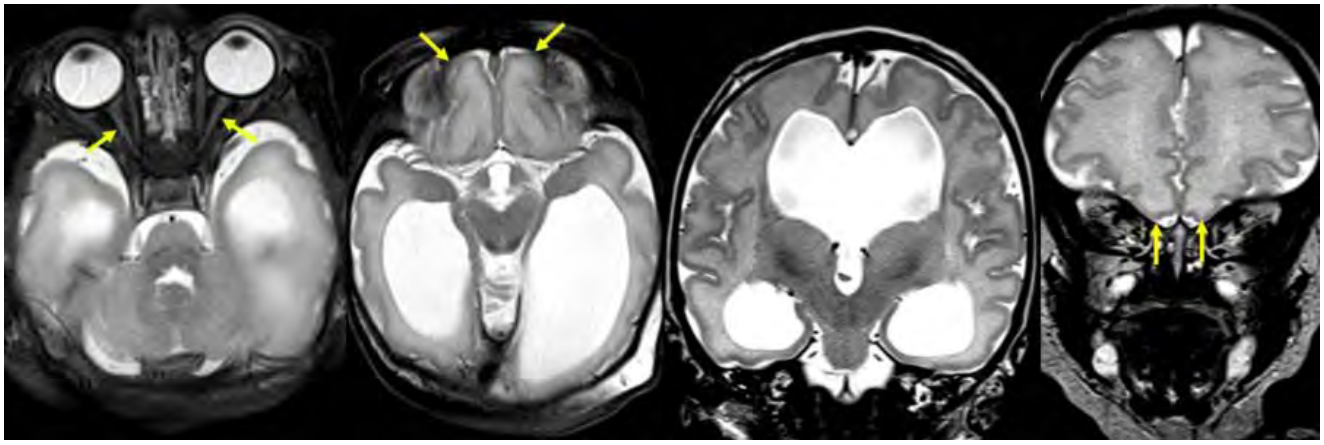
A PACS-RIS search over a 15-year period for patients with a clinical history for SOD yielded 15 patients. The intent was to include only patients with both coronal and axial imaging, and ≤3mm thickness on both sequences. All 15 patients were included, and were reviewed by 2 staff neuroradiologists by consensus. A note was made of associated anomalies, with particular attention to the grade of olfactory sulcus hypoplasia (Grade 0= normal, Grade 1= anterior 1/3 only, Grade 2= anterior 2/3, Grade 3= complete hypoplasia), and each side was graded separately.

Results

The mean age of the 15 included SOD patients was 11.5 months; 9/15 were female. Associated anomalies were: HIR (n=6, 40%), ectopic posterior pituitary (n=4, 26.7%), callosal agenesis/partial agenesis (n=5, 33%), schizencephaly (n=2, 13.3%), PVNH (n=2, 13.3%), polymicrogyria (remote from schizencephaly, n=2, 13.3%), tectal hamartoma (n=1, 6.67%) and a large choroidal fissure cyst >5cm size (n=1, 6.67%). An olfactory sulcus was hypoplastic or incompletely formed on one side or another in 9/15 patients (60%), with 4/9 patients being Grade 2, 3/9 being grade 1, and 2/9 being grade 3 for degree of olfactory hypoplasia. Of these 9 patients, 3 were discordant between sides.

Conclusions

Olfactory sulcus hypoplasia seems to be fairly common in SOD, while HIR is also not uncommon. Future, larger cohorts with thin, ≤3mm imaging may better describe this incidence.



(Filename: TCT_O-230_Fig1.jpg)

O-231

2:26PM - 2:34PM

Regional NF1 gene expression: implications for neurofibromatosis type I pathobiology.

M Barkovich[1], Y Li[1], R Desikan[1], A Barkovich[2]
[1]University of California, San Francisco, San Francisco, CA, [2]UCSF Benioff Children's Hospital, San Francisco, CA

Purpose

The characteristic MRI signal abnormalities in the deep grey nuclei and brainstem in young patients with neurofibromatosis type I (NF1) are a minor diagnostic criteria for the disease and usually resolve by the second decade of life, but their etiology is still not well understood. The underlying genetic mechanism of these findings and their clinical significance may be elucidated better by evaluating regional NF1 gene expression.

Materials and Methods

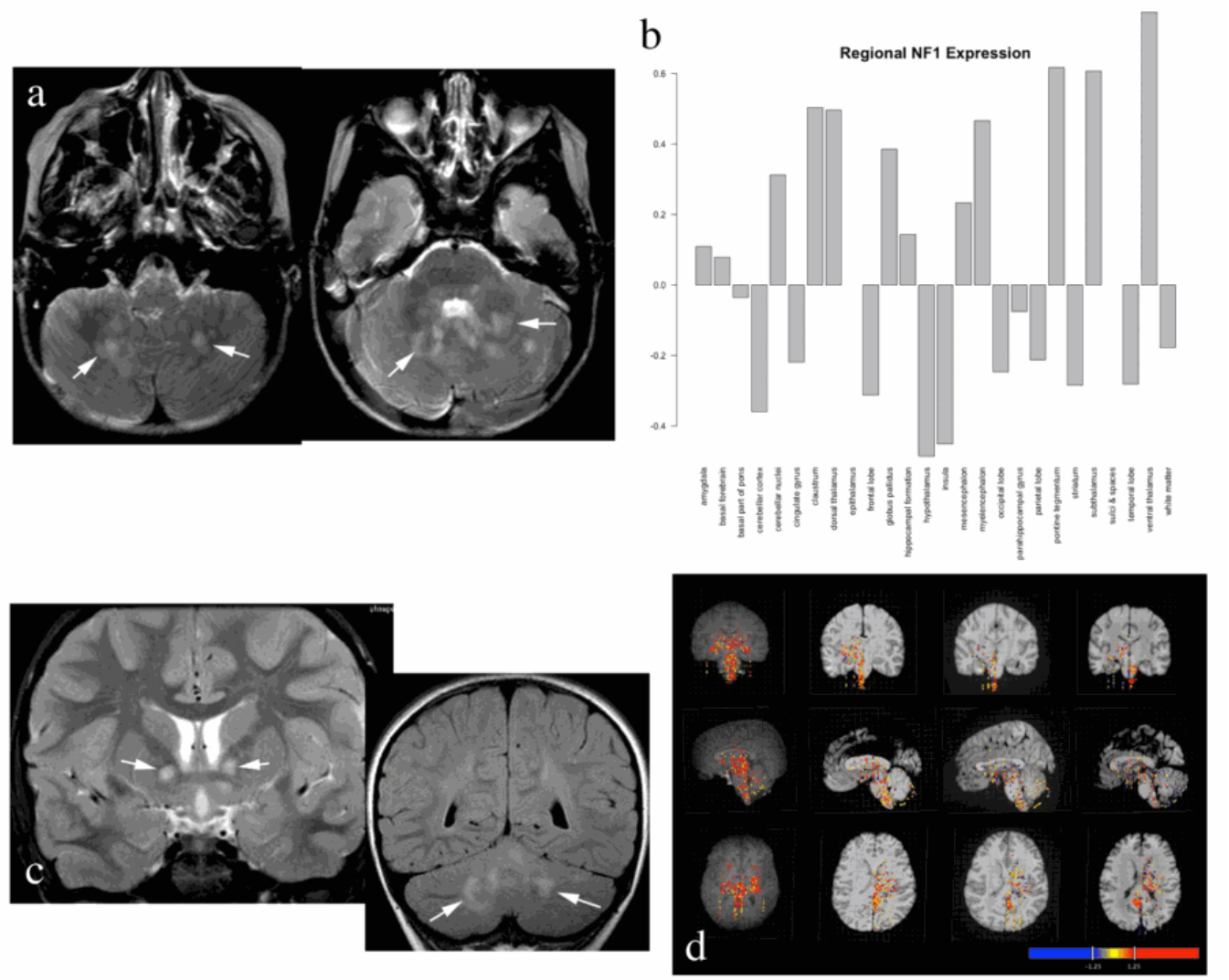
RNA expression across 26 brain regions was evaluated in 6 adult patients using publicly available gene expression data from the Allen BSI database. A repeated-measures ANOVA was performed across 4 RNA probes (z-score average) in the 6 patients to determine if there was a significant difference in gene expression across the 26 brain regions.

Results

There was an overall effect (ANOVA $p < 2 \times 10^{-16}$) indicating differential regional NF1 expression. Across all 26 regions, highest NF1 RNA levels were present in the ventral thalamus, and pontine tegmentum. In comparison, lowest NF1 RNA levels were noted in the cerebral cortex.

Conclusions

In normal adults, NF1 RNA expression is highest in those brain regions where the characteristic myelin vacuolization in patients with NF1 are seen most frequently. Further investigation of changes in the pattern and levels of NF1 expression by age may explain the evolution of the imaging appearance of myelin vacuolization during development.



a) Axial T2 weighted images of characteristic NF1 myelin vacuolization in the deep grey nuclei and hindbrain (arrows)
b) Mean RNA expression across 4 probess and 4 subjects (with error bars and median values)
c) Coronal T2 and T2 FLAIR weighted images of characteristic NF1 myelin vacuolization in the deep grey nuclei and hindbrain
d) Axial, coronal and sagittal T1 images with mean RNA expression (across 4 probes) overlaid
Color scale shows z-score values with yellow/red indicating elevated RNA expression and blue indicating low RNA expression

(Filename: TCT_O-231_fig1.gif)

O-232

2:34PM - 2:42PM

Hybrid Phacomatoses: A Review of four Patients

H Tirumani[1], A Kanfi[1], R Ramakrishnaiah[1], A Rowell[1], C Glasier[2]
[1]University of Arkansas for Medical Sciences, Little Rock, AR, [2]Arkansas children's hospital, Little Rock, AR

Purpose

Hybrid phakomatoses is described as the presence of 2 neurocutaneous syndromes in the same patient. Although neurocutaneous syndromes, such as neurofibromatosis type I and tuberous sclerosis are common inherited disorders, concomitant existence of 2 neurocutaneous syndromes in the same patient is rare and not well described in literature. Phakomatoses have known distinct clinical presentations and well delineated, specific imaging findings. The co-existence of these neurocutaneous syndromes in a single patient often is due to autosomal dominant transmission of 1 disease process with a sporadic mutation in different gene loci leading to a hybrid presentation. Two de novo mutations also have been reported in the literature. The purpose of this scientific exhibit is to provide a review of the imaging findings of hybrid phakomatoses and the potential clinical implications for the patient.

Materials and Methods

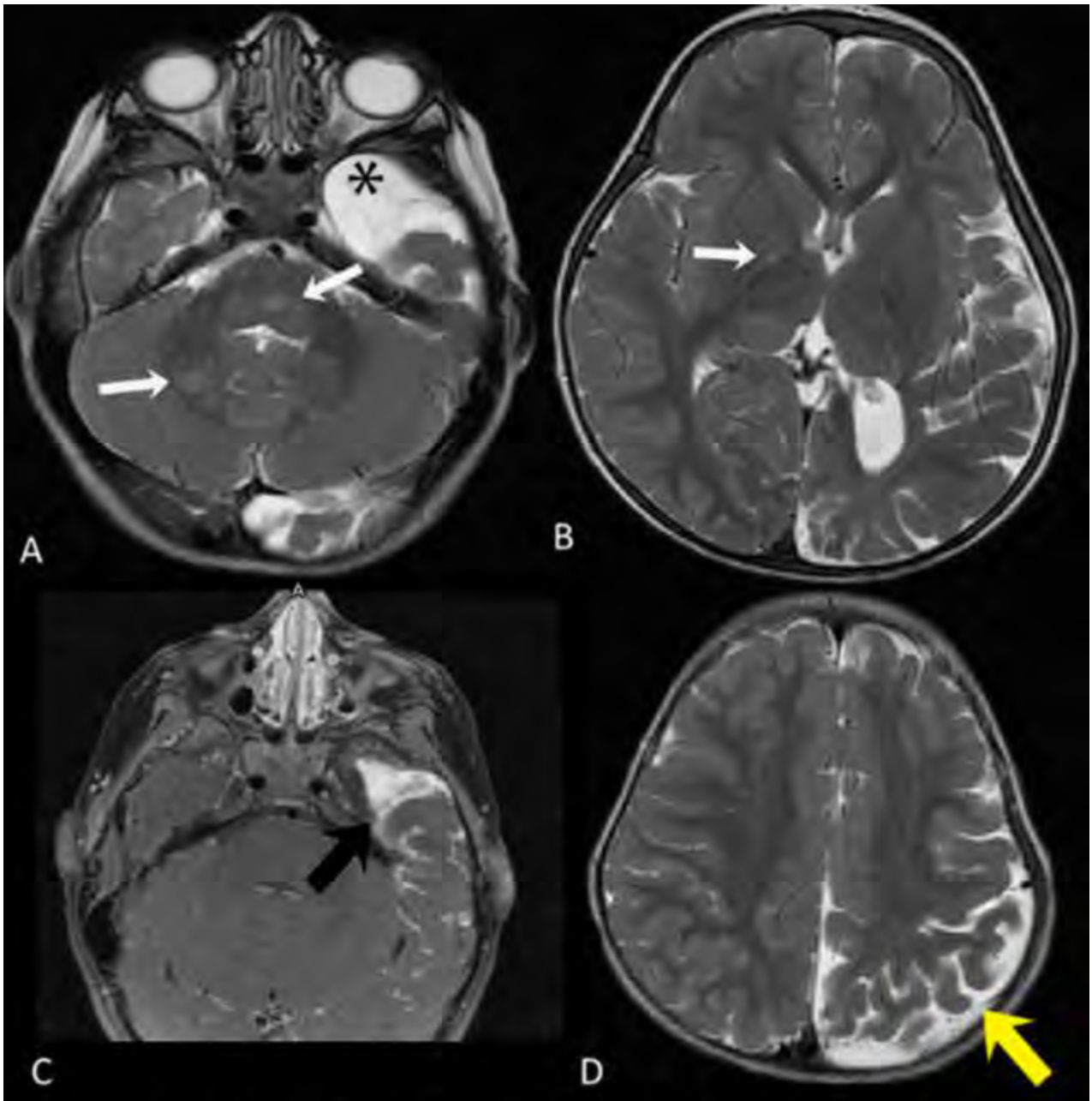
Patients with hybrid neurocutaneous syndromes were selected from a teaching data base at a tertiary care pediatric hospital. Each case was reviewed by 3 pediatric neuroradiologists. A detailed pictorial review and a brief discussion will be displayed under the following headings: Clinical presentation, genetic work up, imaging findings, unusual complications and clinical management.

Results

Listed are the sample hybrid phakomatoses cases to be highlighted: Patient 1: Neurofibromatosis type 1 and Neurofibromatosis type 2. Patient 2: Neurofibromatosis type 1 and Sturge-Weber syndrome. Patient 3: Neurofibromatosis type 1 and Tuberous Sclerosis. Patient 4: Sturge-Weber syndrome and Klippel Trenaunay syndrome.

Conclusions

Hybrid phakomatoses rarely are encountered in neuroimaging practice. Knowledge of the existence of hybrid phakomatoses syndromes and the associated imaging findings are important for accurate diagnosis, avoiding potential pitfalls, and improving patient management.



Patient with Neurofibromatosis type 1 and Sturge-Weber syndrome.

Typical findings of NF I are demonstrated in images A and B: focal areas of signal intensity (FASI) in the basal ganglia, brainstem and peridentate white matter of the cerebellum (thin white arrows), left sphenoid wing dysplasia (asterisk).

Features of Sturge-Weber are identified in images B, C, and D: leptomeningeal enhancement (black arrow) and left hemispheric atrophy (yellow arrow).

(Filename: TCT_O-232_HybridPhakomatoses.jpg)

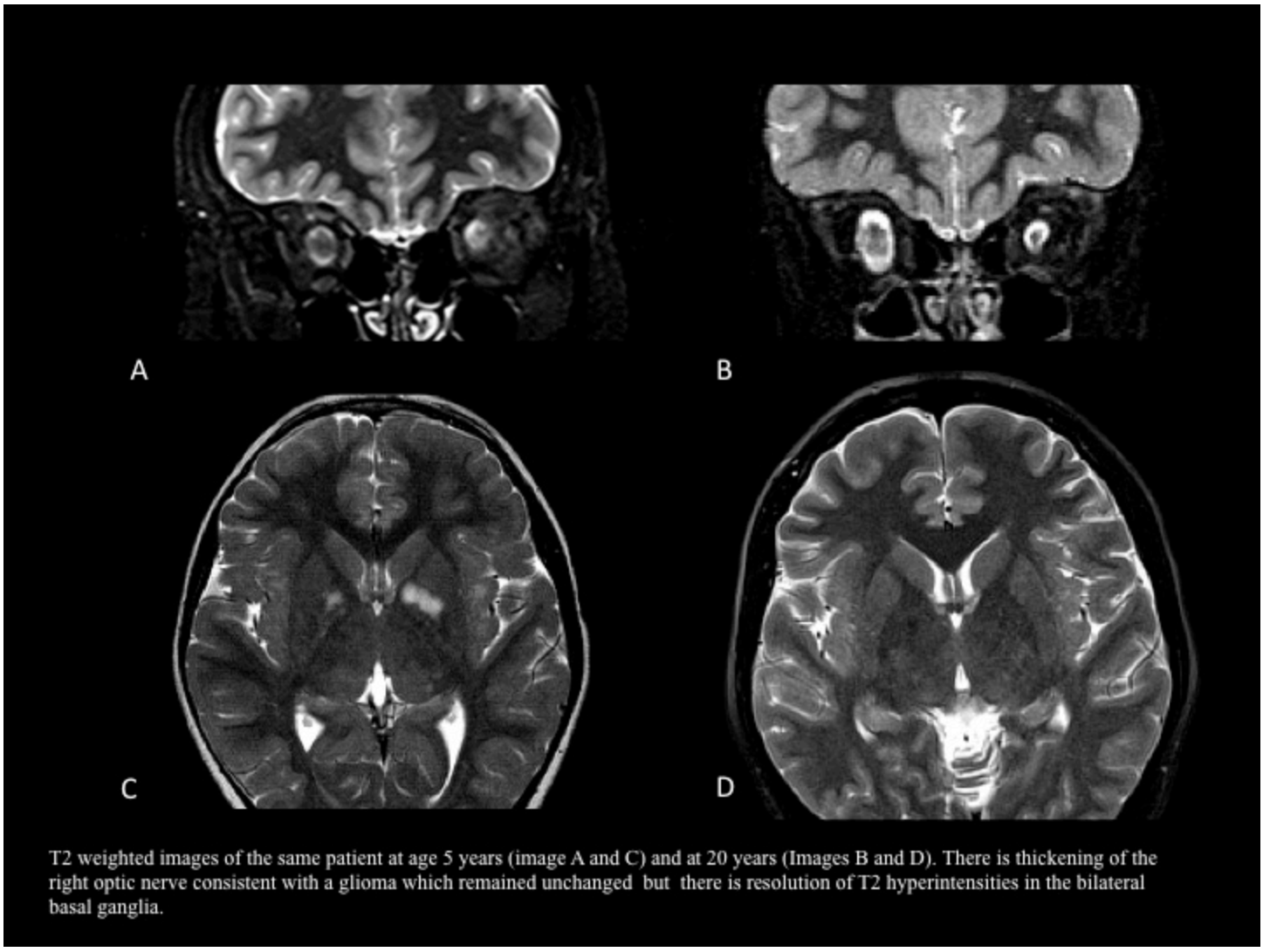
O-234

2:50PM - 2:58PM

Central Nervous System Manifestations of Neurofibromatosis Type 1 in Adulthood

A Rodriguez[1], P Puac[1], R Camacaro[1], C Vallejo[1], M Castillo[1]
[1]*University of North Carolina at Chapel Hill, Chapel Hill, NC*

Purpose
Neurofibromatosis type 1 (NF1) the most common phakomatosis usually presents during the first decade of life and multiple parts of the body are involved showing a wide range of lesions with unpredictable behaviors. Although the severity of the disease and mortality increases with age, there is little information about central nervous system (CNS) NF 1 complications and their natural history in adults. The purpose of this study is to evaluate the cranial/orbital findings in NF1 in adult patients.
Materials and Methods
This is a retrospective study of adult patients with diagnosis of NF1 identified through a query of our electronic medical record system. Magnetic resonance imaging (MRI) findings were analyzed and then compared with the typical findings found in childhood as described in the literature. Once this was done, we search our PACS system for previous MRI studies in these patients.
Results
Twenty-two patients were included in our study. Eleven patients had no intracranial stigmata of NF1 and 11 had myelin vacuolization or gliomas. All patients with vacuolar myelin lesions who had previous studies showed significant decrease in the size of lesions in adulthood or lesion resolution. Of the patients with presumed gliomas, 50% remained stable and 50% enlarged.
Conclusions
Observations in this limited group of NF1 adult patients suggest that healing and/or resolution of areas of myelin vacuolization is common while one-half of presume gliomas increase in size and need careful follow up. Most importantly, 50% of adult NF1 patients show no intracranial or orbital abnormalities.



T2 weighted images of the same patient at age 5 years (image A and C) and at 20 years (Images B and D). There is thickening of the right optic nerve consistent with a glioma which remained unchanged but there is resolution of T2 hyperintensities in the bilateral basal ganglia.

(Filename: TCT_O-234_NF1.jpg)

Wednesday
1:30PM - 3:00PM
Long Beach Convention Center, Room 104C (Main Lobby)

19F-Parallel Paper Session: Spine Imaging: Pain and Procedures

O-235

1:30PM - 1:38PM

Vertebral Augmentation for Multiple Myeloma Patients with Spinal Fractures: A Population Analysis of Mortality Using SEER-Medicare Data.

F Chokshi[1], D Howard[2], R Duszak[1], J Jarvik[3]

[1]Emory University School of Medicine, Atlanta, GA, [2]Emory Rollins School of Public Health, Atlanta, GA, [3]Univ of Washington, Seattle, WA

Purpose

Cohort studies and clinical trials focusing on spinal fractures in myeloma patients have predominantly evaluated pain and functional status, but not mortality. Population level information on mortality associated with vertebral augmentation is lacking. Our purpose was to evaluate the association of vertebral augmentation with 1-year mortality in multiple myeloma patients with spinal fractures.

Materials and Methods

Using 2005-2012 SEER-Medicare data, we used ICD-9 and CPT codes to identify multiple myeloma patients who did (intervention group) and did not (control group) undergo vertebral augmentation within 60 days of an index spinal fracture. Our primary outcome was death within 1 year after intervention. We then matched intervention and control patients in both groups by the following covariates: age, race, gender, poverty level, education level, Medicaid inclusion status, comorbidity count (Elixhauser index), National Cancer Institute (NCI) hospital status, spinal fracture claim before myeloma diagnosis, hospitalization for index fracture, and presence of 2 or more index spinal fractures. A Cox proportional hazards regression model was used to compute hazards ratios (HR) and the Kaplan-Meier method to assess cumulative incidence of time to death. All confidence intervals (CI) were at 95% significance. P-values were significant at <0.05.

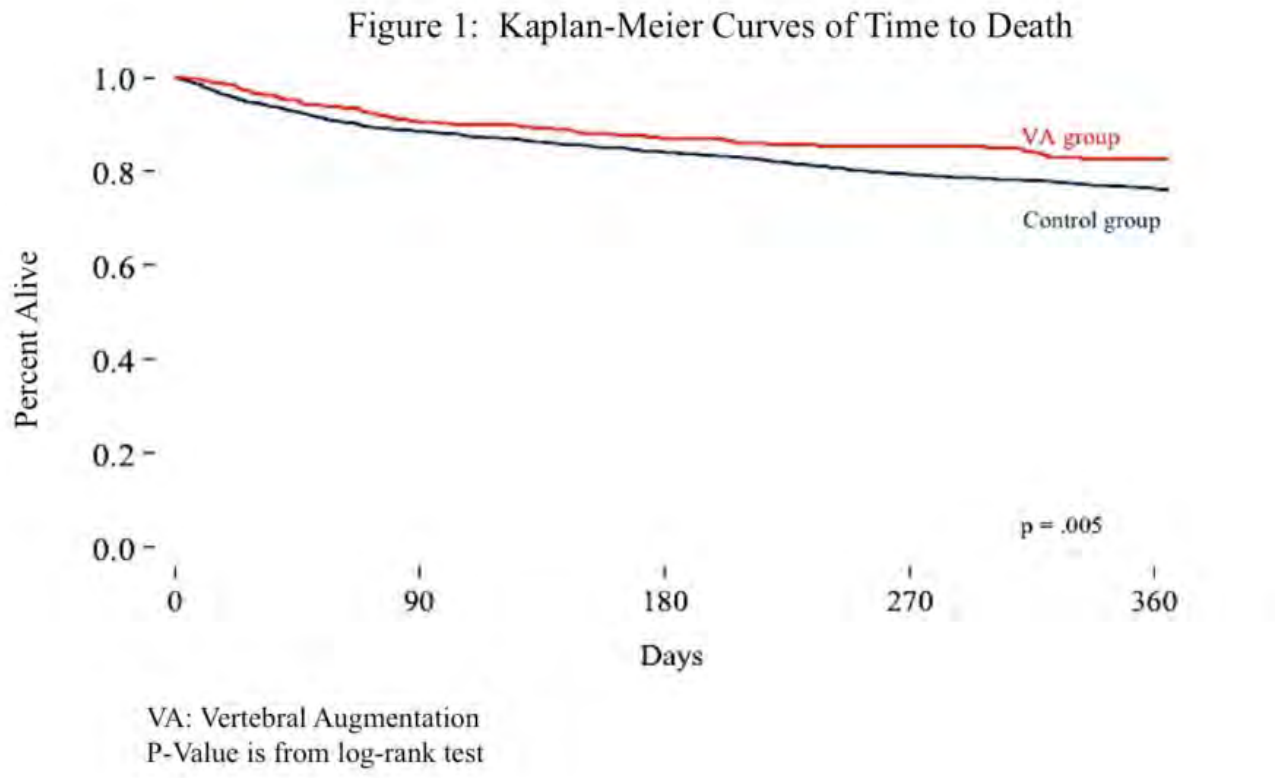
Results

Of 3,492 myeloma patients identified with spinal fractures, 635 (18.2%) underwent vertebral augmentation. Vertebral augmentation was associated with a lower 1-year adjusted relative risk of death compared to the control group (HR 0.67, CI 0.52-0.85, p-value 0.002). Other variables that were associated with a lower risk of death included: spinal fracture diagnosis before myeloma diagnosis (HR 0.65, CI 0.50-0.86, p-value 0.002) and treatment at an NCI cancer center (HR 0.60, CI 0.41-0.86, p-value 0.05). There was a higher risk of death if: 1) patients were between 75-84 (HR 1.58, CI 1.30-1.93, p-value 0.0001) and 85+ in age (HR 2.90, CI 2.30-3.67, p-value <0.0001), of female gender (HR 1.21, CI 1.02-1.45, p-value 0.033), zip code income 20%-100% above the U.S. poverty line (HR 1.36, CI 1.04-1.77, p-value 0.023), not on Medicaid (HR 3.09, CI 1.97-4.85, p-value <0.0001), having 6 or more comorbidities (HR 1.57, CI 1.26-1.96, p-value <0.0001), and hospitalization for index spinal fracture (HR 2.53, CI 2.11-3.02, p-value <0.0001).

Conclusions

1. Compared with controls, myeloma patients with spinal fractures who underwent vertebral augmentation had a lower relative likelihood of dying in the first year following the procedure. 2. Patients treated at an NCI cancer center and whose spinal fracture was discovered before their myeloma diagnosis had lower relative likelihood of mortality. This may be due to more aggressive use of the procedure in these settings. 3. Older patients, females, those of higher socioeconomic status, and those with 6 or more comorbidities had

higher relative likelihood of mortality. These differences in social determinants of health may be related to access to vertebral augmentation; however, this has yet to be investigated. 4. Limitations of this study include: a) possible residual confounding, b) potential spurious associations, c) difficulty demonstrating any causality, and d) difficulty explaining the above-mentioned associations due to the use of an administrative claims oncology database.



(Filename: TCT_O-235_Figure1.jpg)

O-236

1:38PM - 1:46PM

Volume of Epidural Contrast on Post-Myelogram CT of the Lumbar Spine and Rates of Subsequent Blood Patch Treatment

R Yu[1], H Kale[2], B Branstetter[1], V Agarwal[1]
[1]University of Pittsburgh Medical Center, Pittsburgh, PA, [2]University of Pittsburgh Medical center, Pittsburgh, PA

Purpose
Headaches due to cerebrospinal fluid (CSF) leakage are a well known complication of dural

puncture. There still is a lack of knowledge regarding factors that can predict which patients ultimately will require a blood patch. Existing literature has focused on patient demographics, procedural technique and postprocedural care. The purpose of this study is to determine whether the presence and volume of epidural contrast on postmyelogram CTs of the lumbar spine are associated with postdural headaches requiring epidural blood patches.
Materials and Methods
A retrospective case control study of all fluoroscopically guided lumbar myelograms performed over a 5-year period by a single radiology practitioner assistant was performed. Ten patients requiring subsequent blood patches after their myelograms were identified. Forty-six age and gender-matched patients who did not receive blood patches then were selected. CT-myelogram images then were reviewed for the presence of epidural contrast. When present, the volume of epidural contrast then was quantified as "substantial" or "not substantial." Substantial epidural contrast was defined as contrast detected in the anterior epidural space, the extra-foraminal space, a site distant from needle entry, or when a subjective large volume of epidural contrast was present.
Results
Epidural contrast material was present on postmyelogram CTs in both patients who required blood patches and those who did not. The presence of a substantial volume of epidural contrast on postmyleogram CTs of the lumbar spine was associated with an increased risk of postdural puncture headache requiring epidural blood patch (Odds Ratio: 38.00; 4.2526 – 339.56, P = 0.0011).
Conclusions
Epidural contrast on postmyelographic CTs of the lumbar spine was noted in both patients who required blood patches and those who did not. A substantial volume of epidural contrast on postmyelogram CTs of the lumbar spine was associated however with an increased risk of postdural puncture headache requiring epidural blood patch treatment. When present, this finding can alert the proceduralist to the need for early intervention with blood patch.

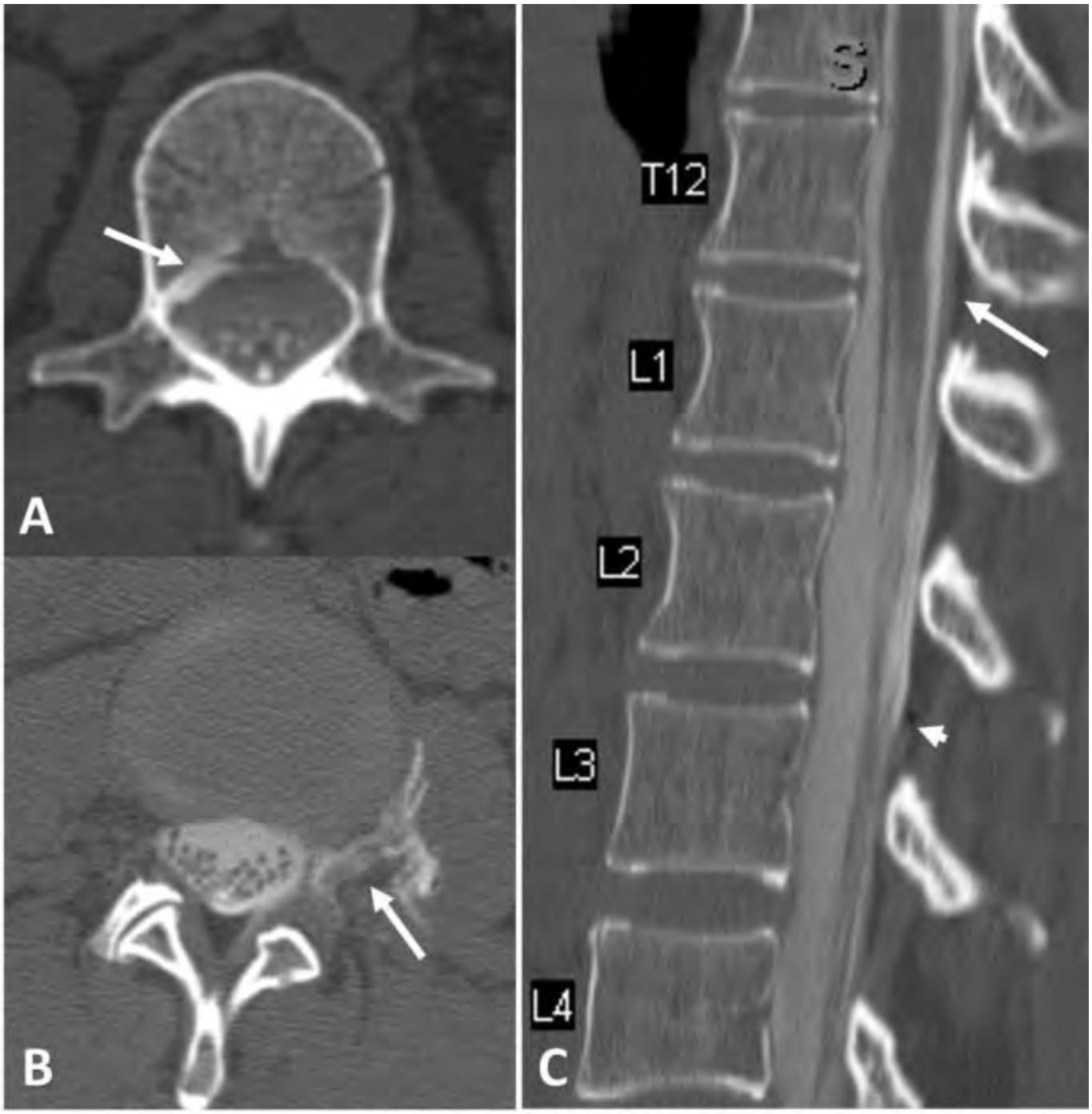


Figure 1. Substantial epidural contrast. (A) Axial CT myelogram demonstrates epidural contrast in the anterior epidural space (arrow). (B) Axial CT myelogram demonstrates epidural contrast in the extraforaminal space. (C) Sagital CT myelogram demonstrates dorsal epidural contrast from T11-L1 (arrow) which is distant from the needle entry at L2-L3 (arrowhead).

(Filename: TCT_O-236_Figure-Myelogram2.jpg)

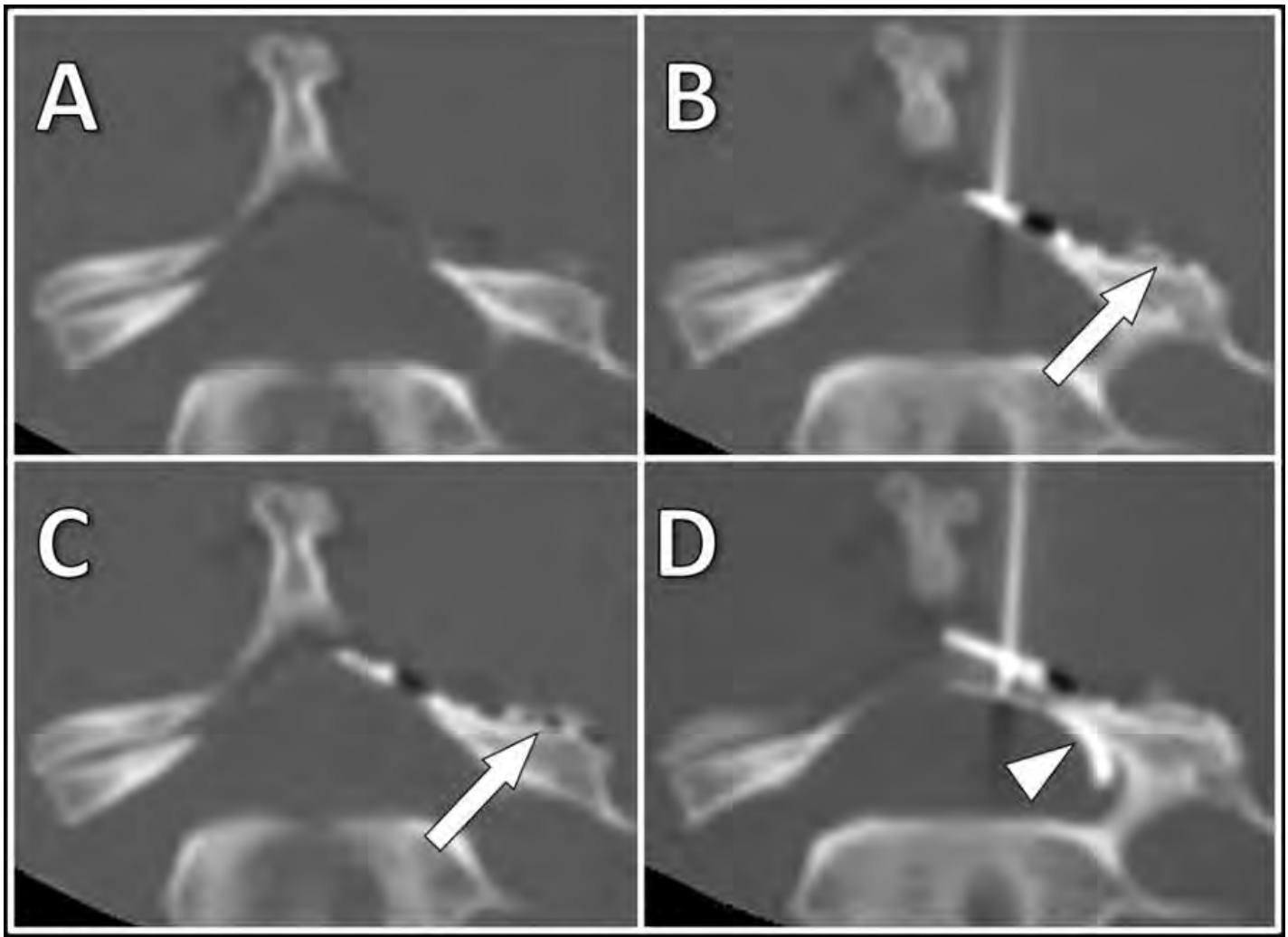
O-237

1:46PM - 1:54PM

CT Fluoroscopy-Guided Cervical Interlaminar Epidural Steroid Injections: Assessing the Rate of Inadvertent Intrafacet Injection

S Parivash[1], P Kranz[1], L Gray[1], T Amrhein[1]
[1]*Duke University Medical Center, Durham, NC*

Purpose
Cervical interlaminar epidural steroid injections (ILESI) commonly are performed for treatment of cervicalgia. However, in 18-32% of cases, patients do not experience symptom relief (1, 2). Inadvertent intrafacet injection during ILESI is known to occur via needle entry into the retrodural space of Okada, a potential space posterior to the ligamentum flavum that connects the facet joints bilaterally (3, 4). Injection into this space results in false-positive loss of resistance, mimicking injection into the target epidural space, potentially causing nontarget injection and reducing efficacy (3, 5). Recent research suggests CT fluoroscopy-guided (CTFG) ILESI may be superior to conventional fluoroscopy in identifying these injections (5). While the rates of such inadvertent injections have been well studied in the lumbar spine, no prior studies have investigated cervical ILESI (5). The purpose of this study is to determine the incidence of inadvertent injection into the retrodural space of Okada during cervical ILESI.
Materials and Methods
We retrospectively reviewed consecutive CTFG cervical ILESI's performed at a single institution from 11/2009 to 11/2015. Procedural images were reviewed by 2 board-certified neuroradiologists with 5 and 8 years CTFG-ILESI experience, respectively. The following was recorded: inadvertent intrafacet injection, injection level, contrast flow extent (ipsilateral facet, interspinous bursa, contralateral facet).
Results
Nine hundred seventy-four CTFG cervical ILESI cases were identified. There were 28 inadvertent intrafacet injections (2.9%), all recognized during the procedure. These cases were distributed throughout the cervical spine: C3/4 (1,2.2%), C4/5 (4,3.9%), C5/6 (18,4.6%), C6/7 (4,1.3%), and C7/T1 (1,0.9%). In nearly all cases, contrast opacified the ipsilateral facet joint (96%) and interlaminar bursa (93%). In 3 cases (11%) contrast reached the contralateral facet joint.
Conclusions
We identified a 2.9% rate of inadvertent intrafacet injection during CTFG cervical ILESI. While all were recognized during the procedure, unrecognized cases may lead to nontarget injection and potential treatment failure.



A) Pre-injection image. No contrast in right facet joint. B) Initial contrast injection after loss of resistance demonstrating opacification of interlaminar bursa and left facet joint (arrow) – i.e. retrodural space of Okada. C) Another image confirming inadvertent intrafacet injection. D) Needled advanced for appropriate epidurogram (arrowhead).

(Filename: TCT_O-237_Figure.jpg)

O-238

1:54PM - 2:02PM

Open Surgical Biopsy of Degenerated Discs with correlation of associated MRI Modic Changes

M Georgy[1]
[1]*University of California San Diego, San Diego, CA*

Purpose
Recent publication had suggested evidence of chronic infection of degenerated disk spaces with Propionibacterium Acnes (PA) as a cause of chronic back pain that linked to type I Modic changes. Researchers had advocated for antibiotic treatment of patients with chronic back pain. This had created extensive debate in the medical community. We are presenting our pilot data as a part of larger NIH prospective study of serial biopsies of degenerative disk spaces during open surgery.
Materials and Methods
An IRB approval was obtained to conduct this retrospective study in a multicenter single neurosurgery practice over a 9-month period. Biopsies were obtained from the disk space during open surgery when possible for all patients who underwent surgery for degenerative disk disease. Biopsy materials were sent for gram stain and culture in all cases. Pre-operative MRI images were evaluated for the presence of Modic changes.
Results
Complete data were available from 21 lumbar disk surgeries, 10 of them (48%) had a positive culture. Five levels were positive for PA, 1 level was positive for S. Aureus, 1 level was positive for Actinomycen and 3 levels were positive for S. Epidermis. There was a total of 7 cases with Modic changes and none of them were positive for PA. Biopsies were collected from 26 cervical cases, and 9 of them (35%) showed a positive biopsy. There were 16 cases with Modic changes that included 6 (37.5%) of the positive cultures. Three of the positive cultures showed no Modic changes. Ten cases with Modic changes had a negative culture.
Conclusions
Our results concur with the published data of high incidence of PA infection of the degenerated nucleus. However we did not show any constant relationship to Modic changes which could be due to the small sample size. The etiology of Modic changes may be related to factors other than infectious processes. Furthermore, the patho-physiology of the Modic changes in the cervical and lumbar spine could be different. Further evaluation of these results with a larger prospective controlled study is underway.

O-239

2:02PM - 2:10PM

Success rates of image guided Botox injection in patients with neurogenic thoracic outlet syndrome: Correlation with MR neurography and Dynamic Ultrasound

V Shah[1], C Chin[2]
[1]University of California San Francisco, San Francisco, CA, [2]University of California, San Francisco, San Francisco, CA

Purpose
Neurogenic thoracic outlet syndrome (TOS) is a painful condition that may be difficult to

distinguish from other cervicobrachial pain syndromes on clinical grounds. It is thought to occur due to brachial plexus compression in the interscalene triangle (most common), costoclavicular, and/or retropectoralis minor spaces. The purpose of this study was to assess the effectiveness of image guided Botox injection into the anterior scalene muscles in helping to alleviate symptoms, confirm a diagnosis of neurogenic TOS, and to correlate with results of electromyography (EMG), dynamic ultrasound, and MR neurography.

Materials and Methods

A search for patients with suspected neurogenic TOS who underwent image-guided Botox injections of the anterior scalene muscle at our institution was performed using an internal search engine. Retrospective review of the medical records was performed and the following was recorded: history and physical exam findings at presentation; results of EMG studies; imaging findings of dynamic ultrasound and/or MR neurography; impact of injection; and surgical outcomes.

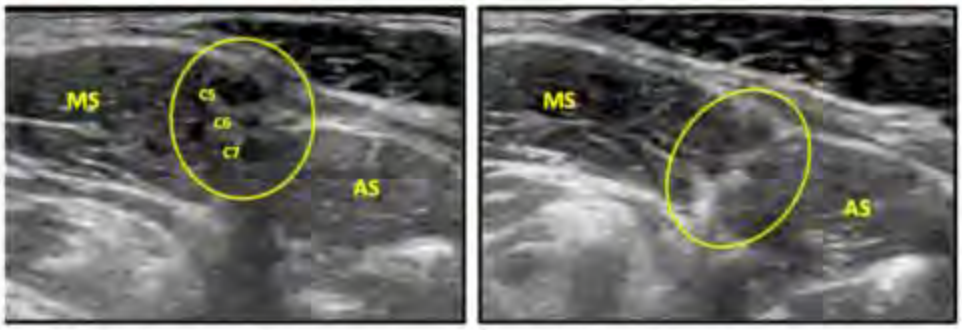
Results

Nine patients (ages 23-73 years, average age 39 years, 6 female and 3 male) underwent a total of 12 image-guided Botox injections into the anterior scalene muscle on the symptomatic side (7 injections performed under US, 5 under CT guidance) between 11/2013 and 11/2016. All of these patients were diagnosed with neurogenic TOS after clinical evaluation by a neurosurgeon who specializes in this condition. All patients complained of pain in the affected extremity. Five patients (56%) had at least partial relief from the procedure and 2 patients (22%) were lost to follow up. No complications were reported. Seven patients (78%) had MR neurograms and 5 patients (56%) had dynamic ultrasounds performed prior to the Botox injection. Three of the 5 patients with positive response to injection had abnormal MRIs demonstrating intraneural edema involving the C8 nerve and lower trunk in 2 cases, and hypertrophic anterior scalenes in 1 case. In the 2 cases with positive response to injection but normal MR neurograms, dynamic ultrasound of the brachial plexus was abnormal and showed at least partial compression of the lower trunk with arm abduction. Of the 2 patients who were lost to follow up, 1 patient had both an abnormal MRI and an abnormal dynamic ultrasound. Electromyographies were performed in a total of 6 patients and were abnormal in 2 patients. One of the patients who had relief from the injection underwent surgical decompression of the brachial plexus with success.

Conclusions

Image-guided Botox injection into the anterior scalene muscle is a safe and minimally invasive procedure that may relieve symptoms in patients with neurogenic TOS. MR neurography and dynamic ultrasound of the brachial plexus may aid in the diagnosis of this challenging condition and can help identify patients who may benefit from a Botox injection. Dynamic ultrasound should be considered in those patients with suspected TOS but normal MRI studies.

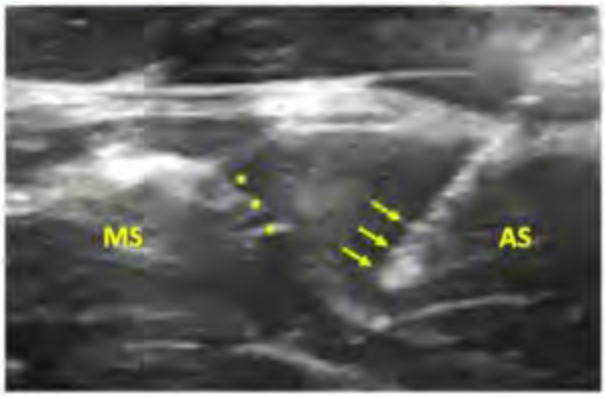
26 year-old-female with right TOS: Dynamic Ultrasound



(a) Neutral Position (b) With Arm Abduction

Dynamic Compression of the Right Brachial Plexus with Abduction (a) Normal appearing hypoechoic C5-C7 nerve roots between the anterior (AS) and middle (MS) scalene muscles. (b) With abduction there is complete effacement of those nerve roots.

26 year-old-female with right TOS: Ultrasound Guided Botox Injection



Ultrasound Guided Botox Injection: Ultrasound image in the transverse plane shows the hyperechoic needle and tip (arrows) within the belly of the anterior scalene muscle (AS). Brachial plexus trunks are seen posterolateral to the anterior scalene muscle (asteriks). Patient's symptoms improved after the Botox injection.

(Filename: TCT_O-239_Document10.jpg)

O-240

2:10PM - 2:18PM

CT Guided Biopsy of Spinal Occult Lesions can be Safely Performed with Reasonable Diagnostic Yield

M Cai[1], A Aggarwal[2], A Doshi[2], K Nael[2]
[1]Icahn Sinai School of Medicine at Mount Sinai Hospital, New York, NY, [2]Icahn School of Medicine at Mount Sinai, New York, NY

Purpose
Computed tomography-guided biopsy of the spine is a well established procedure with the advantages over prior methods of decreased cost, risk, and time while maintaining high diagnostic yield (93%). To our knowledge, there has been limited evaluation of diagnostic yield for lesions present on MRI or PET, but occult on CT. We retrospectively evaluated CT-guided spine biopsies performed at our institution to determine the diagnostic yield for vertebral lesions occult on CT.
Materials and Methods
Following approval of the institutional review board, data from 2008 to 2016 were collected from patients who had undergone percutaneous CT-guided spine biopsy. Anatomy was limited to the cervical, thoracic, and lumboscral spine. Lesions with abnormalities on PET and MRI imaging, but not visible on CT within were included. Lesions demonstrating lucent or sclerotic features on CT imaging were excluded from the study. A total of 22 CT occult lesions were assessed for lesions size, procedural radiation exposure, complications and diagnostic yield (positive histopathology). A total of 331 CT-guided biopsies were reviewed and 22 lesions were found to be CT occult and confirmed to be occult by independent review by 2 neuroradiologists (6.6%).
Results
A total of 22 CT occult lesions were assessed for lesions size, procedural radiation exposure, complications and diagnostic yield. Of the 22 lesions that were CT occult, but had abnormalities on MRI or PET examinations, 13 of them yielded positive pathologic correlation with abnormal histology (59%). The mean short-axis measurement of lesions with negative histology was 0.92 cm (stdev 0.42) as compared to 1.33 (stdev 0.51) for the cases with positive histological correlation. Mean radiation exposure to the patient as a dose length product (DLP) was 941.2 mGym-cm (stdev 453.4). There were no reported complications for biopsy procedures.
Conclusions
Retrospective review of CT-guided biopsies performed at our institution spanning an 8-year period was performed to evaluate the diagnostic yield of CT occult lesions with known MRI/PET abnormalities. Although diagnostic yield of CT-guided biopsies of occult lesions

is reduced compared to previously reported rates in nonoccult lesions, biopsy of occult lesion can be performed safely with a reasonable yield.

O-241

2:18PM - 2:26PM

Numbering the Lumbar Vertebral Segments by Localizing the Exiting L5 Nerve Root.

M Peckham[1], S Stilwill[1], T Hutchins[2], M Mills[1], G Stoddard[1], L Shah[3]
[1]University of Utah, Salt Lake City, UT, [2]University of Utah, Neuroradiology, salt lake city, UT, [3]University Of Utah, Salt Lake City, UT

Purpose
Multiple methods have been used to determine the lumbar vertebral level when images of the full spine are not available. Locating the iliolumbar ligament is a leading method as it most often arises from the L5 vertebral body. Other methods (level of the aortic bifurcation, conus, and renal arteries) have been found less accurate. Post-mortem studies show the lumbar vertebral bodies can be numbered at 95% accuracy by counting the lumbar nerve roots. On axial MRI, the L5 nerve root is medial and inferior relative to L4 and does not split, making it twice the caliber of L4 which splits proximally (Fig. 1). At the sacrum, the lateral component of the L4 nerve root joins L5. These characteristics allow localization of the L5 nerve root on MRI, allowing accurate numbering of lumbar vertebrae when full spine imaging is not available.
Materials and Methods
One hundred cases with full spine imaging available for numbering were evaluated by 2 investigators. The level of the L5 nerve root and iliolumbar ligament on L-spine MRI were documented. Castvelli was documented in transitional states. Numbering by full spine imaging was compared with numbering by nerve morphology. Prevalence and bias adjusted kappa (PABAK) was used to measure interrater reliability. Three additional blinded raters evaluated 10 lumbar MRIs with nerve morphology technique.
Results
The L5 nerve root arose from the 24th presacral vertebral body (L5) in 99/100 cases (CI 95%-100%). Accuracy was preserved in transitional states and cases with numeric variation. This method was more accurate than iliolumbar ligament localization which arose from the 24th vertebral body in 95/100 cases and also had accessory fibers in 8/100. Interrater reliability ranged between 0.8-1.0.
Conclusions
The level of the exiting L5 nerve root can determine accurately the number of lumbar vertebral bodies in cases where full spine imaging is not available. This method has been found to be more accurate for localization than the iliolumbar ligament and has high interrater reliability.

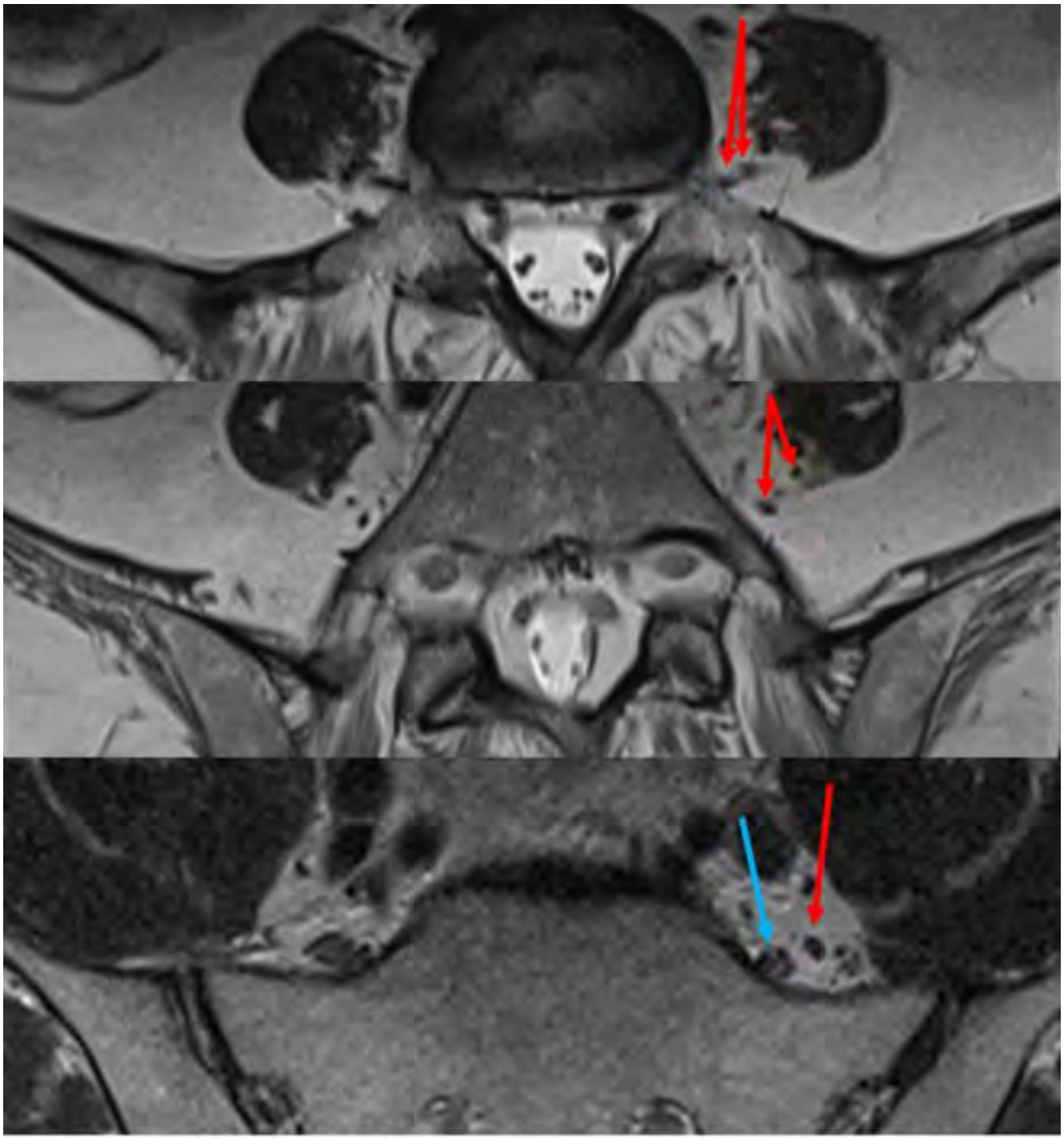


Figure 1: The L4 nerve root splits proximally (red arrows) and its peroneal branch joins the L5 nerve root (light blue arrow) at the level of the sacrum. The L5 nerve root does not split and is twice the caliber of the L4 branch.

(Filename: TCT_O-241_updatednerverootfigurecopy.jpg)

O-242

2:26PM - 2:34PM

Biomechanical influence of pre-existing surgical interventions of the spine and/or lower extremities or scoliosis on sacroiliac joint related pain syndromes and on subsequent sacroiliac joint treatment outcomes.

A Rahman[1], S Islam[2], A Ortiz[1]
[1]Winthrop University Hospital, Mineola, NY, [2]Winthrop-University Hospital, Mineola, NY

Purpose
Sacroiliac joint irritation/inflammation accounts for approximately 16% to 30% of chronic mechanical low back pain cases. Sacroiliac joints (SIJ) connect the spine to the pelvis and lower extremities. As such, they transmit and absorb bi-directional vertical forces from the spine to the lower extremities. Patients with pre-existing conditions including previous history of spine, hip or knee surgeries as well as scoliosis often complain of moderate to severe chronic SIJ pain. Patients with chronic sacroiliac joint pain usually are treated by SIJ steroid injection, physical therapy and/or radiofrequency ablation. We hypothesize that these patients are subjected to altered sacroiliac joint biomechanics because of these pre-existing conditions which in turn causes SIJ pain. Moreover, this patient cohort requires more frequent interventions to control their SI joint pain. Whereas, patients with chronic SIJ pain with no pre-existing conditions would have better outcomes to SIJ injections and/or RF ablation. The purpose of this study is to determine the influence of pre-existing surgical conditions of the lumbar spine, for example spinal fusion, vertebral augmentation or implants in the lower extremities (hip implants, knee implants) or nonsurgical conditions (scoliosis) on the treatment outcomes for sacroiliac joint (SIJ) interventions for SIJ-related pain.
Materials and Methods
Retrospective chart review of 113 patients with SIJ pain syndrome who received either SIJ injection or radiofrequency ablation (preceded by a favorable temporary response to SIJ injection) between April 2014 to March 2015. These patients were stratified into 3 groups: 1) patients with pre-existing implants/surgeries (spine and/or lower extremities), 2) patients with scoliosis and 3) patients with no pre-existing conditions. All patients were followed for 365 days to assess if they needed a second treatment following the first treatment. The time to second treatment and accumulative event rates were compared among the groups using the Kaplan-Meier method. The log-rank test was used to compare Kaplan-Meier failure curves among the 3 groups.
Results
Of the 113 patients, group 1 (pre-existing surgical condition/implants of the spine and/or lower extremities) consisted of 45 patients, group 2 (scoliosis group) consisted of 23 patients

and group 3 (no pre-existing condition) consisted of 45 patients. Time to second treatment was similar between groups (Log-rank p value=0.079). Multiple comparisons revealed that patients with no pre-existing condition (group 3) had a longer time to second treatment event rate as compared to groups 1 and 2 (unadjusted p-value=0.026). However, when adjusted for multiple comparisons, the difference became insignificant (Sidak p-value=0.077). Fourteen patients had sacral RF procedure. Radiofrequency events rates were similar among the groups (13%, 13% and 11% for group 1, 2 and 3 respectively, p=0.064.

Conclusions

Patients without a pre-existing surgical condition or scoliosis showed a tendency to have a longer pain-free interval as measured by time to second treatment. Additionally, pre-existing surgical or medical conditions do not exert a significant adverse effect on SIJ treatment outcomes. An awareness of these conditions may help operators to better counsel their patients with respect to treatment options and prognosis.

Figure-1:

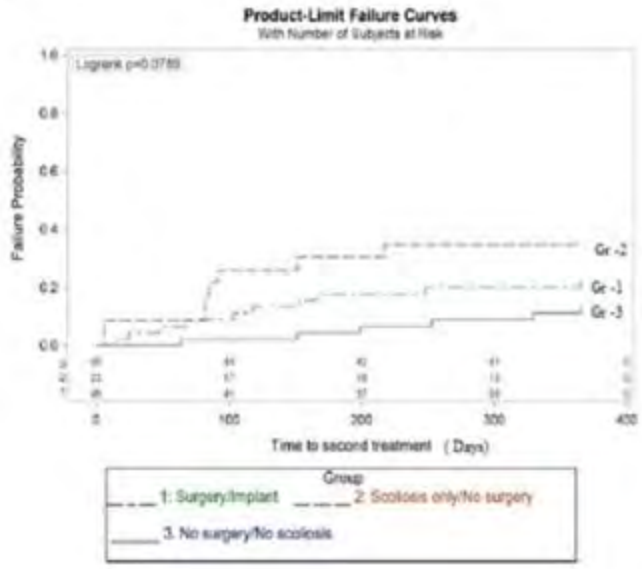


Figure -2:

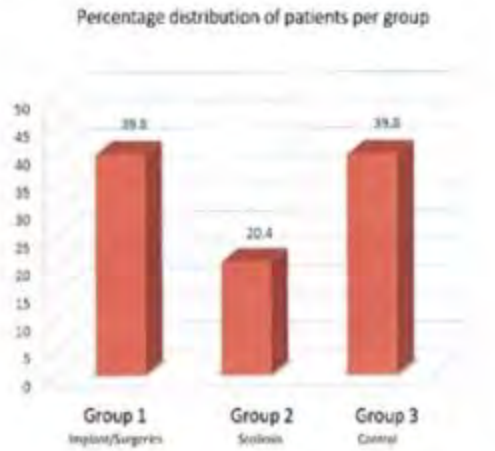
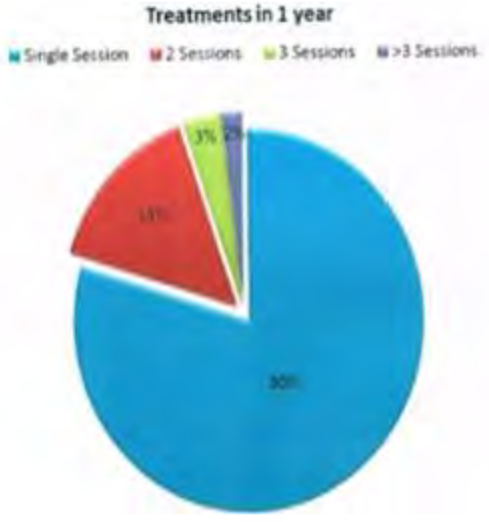


Figure – 3:



(Filename: TCT_O-242_figures.jpg)

O-243

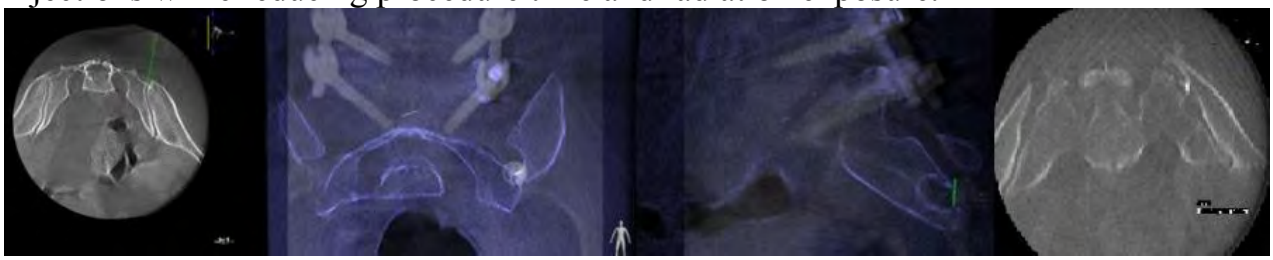
2:34PM - 2:42PM

3D Cone Beam Computerized Tomography (3D-CBCT) guided Sacroiliac (SI) Joint Injection: A Real-time, Interactive, Accurate, Fast and Reduced Radiation Exposure Technique.

S Aftab[1], S Lee[2], S Ali[3], J Mok[4]
[1]University of Chicago, Chciago, IL, [2]University of Chicago Medical Center, Chicago, IL, [3]University of Chicago, Chicago, IL, [4]University of Chicago, chicago, IL

Purpose
To ensure effective therapeutic management of sacroiliac (SI) joint pain, precise needle placement during diagnostic SI joint injection is essential. The reported accuracy of diagnostic SI pain assessment using single or dual blocks is highly variable, with false positive rate of 20% to 54%. Computed tomography (CT) guidance for sacroiliac joint injection has been the preferred imaging technique for needle guidance due to the complex 3-dimensional anatomy of the SI joint, frequent encounter of covering osteophytes and occasionally encountered extremely narrowed SI joint. However, the technique has been challenged due to relatively prolonged procedure time and increased risk of radiation exposure. We evaluated the technical feasibility of the 3D-CBCT guided diagnostic SI joint injection technique.
Materials and Methods
From March to July 2016, 10 consecutive patients (11 SI joints) with clinically suspected SIJ pain were enrolled and underwent diagnostic SIJ injection. Three patients had bilateral lower back pain and 7 had unilateral pain. The patients were queried about the intensity of the pain just prior to the procedure and just after the procedure. The pain was quantified on a scale of 1-10 with 10 being the worst. Informed consent was obtained from each patient before beginning the procedure. The procedure was performed under local anesthesia in a bi-plane neuroangiography suite. With the patient lying in prone position, a 3D-CBCT was obtained in the angiography suite. Using the integrated image guidance system, the lower pole of the SIJ and the point of entry on the skin surface were selected in order to establish a needle trajectory (Fig. 1). Subsequently, the selected images were fused with real-time fluoroscopy for the needle guidance (Fig. 2). The fluoroscopy tube was angled at a cephalocaudal tilt of 10–25 degrees for clear delineation of the SIJ space. The point of entry on the skin surface then was infiltrated with subcutaneous local anesthetic (approximately 0.5 -1.0 ml). A 22-gauge 3.5 inch needle then was advanced under live fluoroscopy to the lower pole of the SIJ. The fluoroscopy tube then was shifted medially and laterally to ensure that the needle was within the SIJ. Approximately 1 ml of Iodinated Omnipaque 300 contrast then was instilled into the joint to verify needle positioning within the joint space. An additional 3D-CBCT is

obtained to confirm needle positioning within the SIJ (Fig. 4). Finally, approximately 1 ml of Bupivicane 0.5 % was administered into the joint space.
Results
The needle placement and diagnostic injection for the target SI joint was successful in all 10 cases (11 SI joints). Success rate was determined by visualization of contrast within the joint space. The mean fluoroscopy time per SI joint was 6.7 min (range: 3.2 min – 15.6 min) and average total DAP was 99308.2mGycm2(range: 23,395 mGycm2– 287,808 mGycm2). Preprocedure mean pain level was 7.1/10 and immediate postprocedure mean pain level was 0.6/10. There was only 1 patient that did not report significant pain reduction and this patient's pain is thought to not be related to the SIJ.
Conclusions
We have demonstrated that 3D-CBCT can be used to increase the accuracy of SI joint injections while reducing procedure time and radiation exposure.



(Filename: TCT_O-243_figure.jpg)

O-244

2:42PM - 2:50PM

A 3D-printed Lumbosacral Spine Simulation Model for CT and Fluoroscopically-guided Spine Procedures

Y Li[1], H Trivedi[1], D Gillan[1], C Chin[1], W Dillon[1], C Hess[1], V Shah[1]
[1]*University of California, San Francisco, San Francisco, CA*

Purpose
To design an anatomically accurate three-dimensional (3D) printed model of the lumbosacral spine with realistic spondylosis that may be visible under both fluoroscopy and CT, for purposes of simulating imaging-guided spine procedures in an academic setting.
Materials and Methods
Images from a computed tomography (CT) of the lumbosacral spine with significant loss of intervertebral disk height, endplate osteophytosis and facet arthropathy were used to reconstruct the osseous anatomy. Materialise Mimics version 19.0 software was used for the 3D segmentation, using both automated and manual segmentation techniques to ensure preservation of fine osseous details, such as the facet joints. The 3D model was exported as a STL file, and additional postprocessing was performed using Materialise 3-matic software. The STL file was printed with calcium sulfate and cyanoacrylate, with minimum detail of

0.8 mm, using a 3D Systems Project 660pro commercial printer. The model can be embedded within a gelatin or silicone mold to simulate soft tissues. Subsequently, the lumbosacral spine model was imaged under both CT and fluoroscopy, with simulation of various needle positions used in facet blocks, medial branch bocks, interlaminar epidural injections, lumbar punctures, and radiofrequency ablations.

Results

A realistic model of a lumbosacral spine with significant degenerative changes was created for purposes of simulating fluoroscopically and CT-guided spine procedures. The spine model is appropriately radiodense, allowing for visualization by both CT and fluoroscopy (Fig. 1). The production of such a model allows for the successful simulation of facet blocks, medial branch bocks, interlaminar epidural injections, lumbar punctures, and radiofrequency ablations.

Conclusions

Computed tomography and fluoroscopically-guided spine procedures are challenging for trainees to learn. Particular challenges include the development of three-dimensional spatial visualization and the development of efficiency in targeting a location with minimum radiation. These challenges are more pronounced in spines with significant degenerative changes. Practicing these techniques on patients carries ethical concerns. Thus, the creation of a realistic lumbosacral spine model allows for the practice of such procedures without concern about repeated needle repositioning and radiation exposure. The ability to practice on a simulation model will increase trainee proficiency and confidence regarding these procedures. Additionally, the ability to visualize needle positioning in a three dimensional format allows for translation of skills between CT and fluoroscopically-guided procedures.

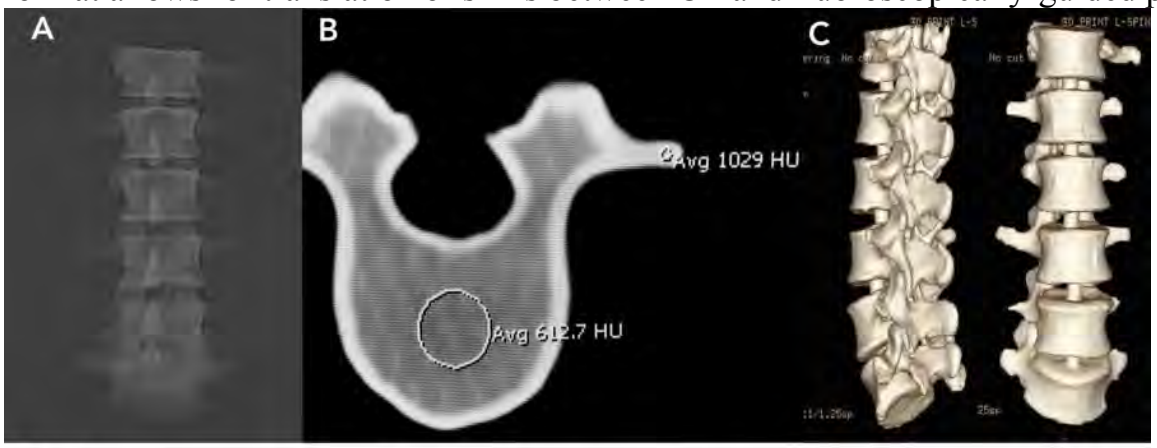


Figure 1.
A) Anterior-posterior (AP) fluoroscopic exposure of the lumbosacral spine model.
B) Axial CT image of lumbosacral spine model in prone position, with cortical bone measuring 1029 Houndsfield Units (HU) and medullary bone measuring 612 HU, similar to human bone.
C) Oblique lateral and AP projections of a 3D rendering of the lumbosacral spine model, obtained through a 3D reconstruction of the CT of the model, which demonstrates preservation of fine bony detail, such as facet joint spaces and endplate osteophytosis.

(Filename: TCT_O-244_ASNRspineFigure1fluoroCT3D.jpg)

O-245

2:50PM - 2:58PM

Use of Trans-visible Wearable Augmented Reality Goggles as an adjunct imaging guide in Spinal Pain Management Interventions: Proof of concept using a 3D printed Phantom

A Gibby[1], S Cvetko[2], M Taheri[3], R Javan[4]
[1]George Washington University, Washington, DC, [2]Novarad, American Fork, UT, [3]George Washington University, Washington, DC, DC, [4]George Washington University Hospital, Washington, DC

Purpose
Augmented Reality is a technology which allows users to overlay computer-generated 3D images onto real space. Applied to radiology, images from cross-sectional studies can be registered to patients in holographic form to outline underlying anatomy. Augmented Reality has been utilized in a variety of surgical procedures. To our knowledge, there are no studies using wearable Augmented Reality goggles utilizing cross-sectional radiologic imaging as an adjunct in image-guided procedures and this work aims to demonstrate its potential.
Materials and Methods
DICOM dataset of a CT scan of a 3D printed phantom of the lumbar spine was translated into the Microsoft Hololens Augmented Reality Headset using 3D surface reconstruction with Novarad software. The phantom was placed on a CT-fluoroscopy table and the 3D surface rendering containing the stacked 2D axial CT images then was projected onto the physical phantom in 3D space by the goggles. A spinal needle then was used to target a specific location in the 3D printed phantom, such as a neural foramen. This was confirmed by CT-fluoroscopy to simulate the procedure.
Results
This "proof of concept" project demonstrates the clinical potential for this technology. This serves as a demonstration for performing image-guided interventions on actual patients who have prior cross- sectional imaging available. Theoretically, this can be applied to other cross-sectional modalities. Future work aims at determining subjective ease of use and whether there are decreased number of needle adjustments, radiation dose, procedure time, as well as potential complications.
Conclusions
Wearable Augmented Reality goggles may serve as an adjunct for image-guided interventions, especially with further developments in accuracy which may be enhanced by the use of fiducial markers. Results are expected to show improvement in number of needle adjustments needed as well as an improved subjective perception for ease of needle placement with Augmented Reality.

Wednesday
1:30PM - 3:00PM
Long Beach Convention Center, Room 203AB (Upper Level)

19G-Parallel Paper Session: Neuroimaging Clues, Reviews, and News to Use

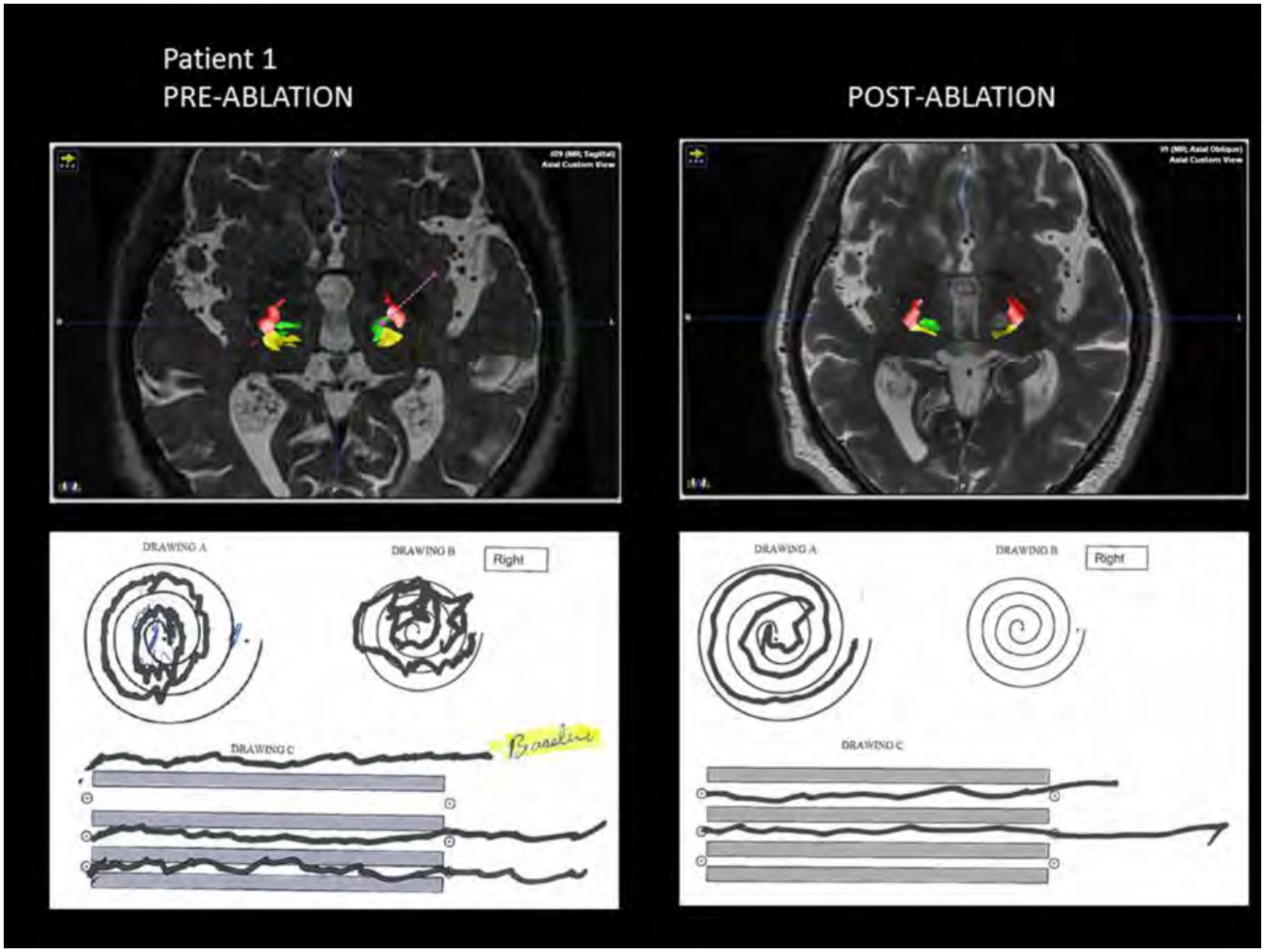
O-246

1:30PM - 1:38PM

Clinical improvement associated with targeted interruption of the cerebellothalamic tract following MR-Guided Focused Ultrasound for Essential Tremor

J Chazen[1], H Sarva[2], M Kaplitt[2]
[1]Weill Cornell Medicine, New York, NY, [2]Weill Cornell Medicine, New York, NY

Purpose
To evaluate the utility of diffusion tensor imaging (DTI)-based targeting of the dentato-rubro-thalamic tract (DRT) for magnetic resonance-guided focused ultrasound (MRgFUS) thalamotomy in patients with essential tremor (ET) and correlate postprocedural tract disruption with clinical outcomes.
Materials and Methods
Four patients received preprocedural and immediate postprocedural DTI imaging in addition to traditional anatomic MRI sequences for MRgFUS thalamotomy. Optimal ablation sites were selected based on the patient-specific location of the DRT as demonstrated by DTI (direct-targeting) and correlated with traditional atlas based measurements for thalamic Vim lesioning (indirect-targeting). Fiber tracts were displayed 3-dimensionally during the procedure and used in conjunction with clinical signs of tremor control for fine-correction of the ablation site. Immediately following the conclusion of the procedure, the MRgFUS head frame was removed and patients were placed in a 32-channel MRI head coil for follow-up DTI and anatomic MR sequences.
Results
All patients had excellent postoperative tremor control and successful pre and postprocedural DTI fiber tracking of the corticospinal tract, medial lemniscus, and DRT. Immediate postprocedure DTI failed to track the DRT ipsilateral to the lesion site with a preserved contralateral DRT, coincident with substantial resolution of contralateral tremor.
Conclusions
Diffusion tensor imaging can reliably identify the optimal ablation target and demonstrates tract disruption on immediate postprocedural imaging. A clinical improvement of tremor was observed immediately following the procedure, correlating with DRT disruption and suggesting that interruption of the DRT is a consequence of clinically successful MRgFUS thalamotomy. These findings may have utility for both MRgFUS procedure planning in surgically-naive patients and retreatment of patients who have failed prior thalamic Vim lesioning.



(Filename: TCT_O-246_ASNR-Fig.JPG)

O-247

1:38PM - 1:46PM

Reduction of Intracranial Clip and Coil Metal Artifacts in Computed Tomography using Iterative Reconstructions.

S Winklhofer[1], R Hinzpeter[2], G Baltsavias[1], D Stocker[2], J Burkhardt[3], A Valavanis[1], H Alkadhi[2]
[1]Department of Neuroradiology, University Hospital Zurich, Zurich, [2]Institute of Diagnostic and Interventional Radiology, University Hospital Zurich, Zurich, [3]Department of Neurosurgery, University Hospital Zurich, Zurich

Purpose
Aim of the study was to assess the value of iterative metal artifact reductions (iMAR) in computed tomography (CT) for metal artifact reduction of intracranial clips and coils of various materials and sizes.

Materials and Methods

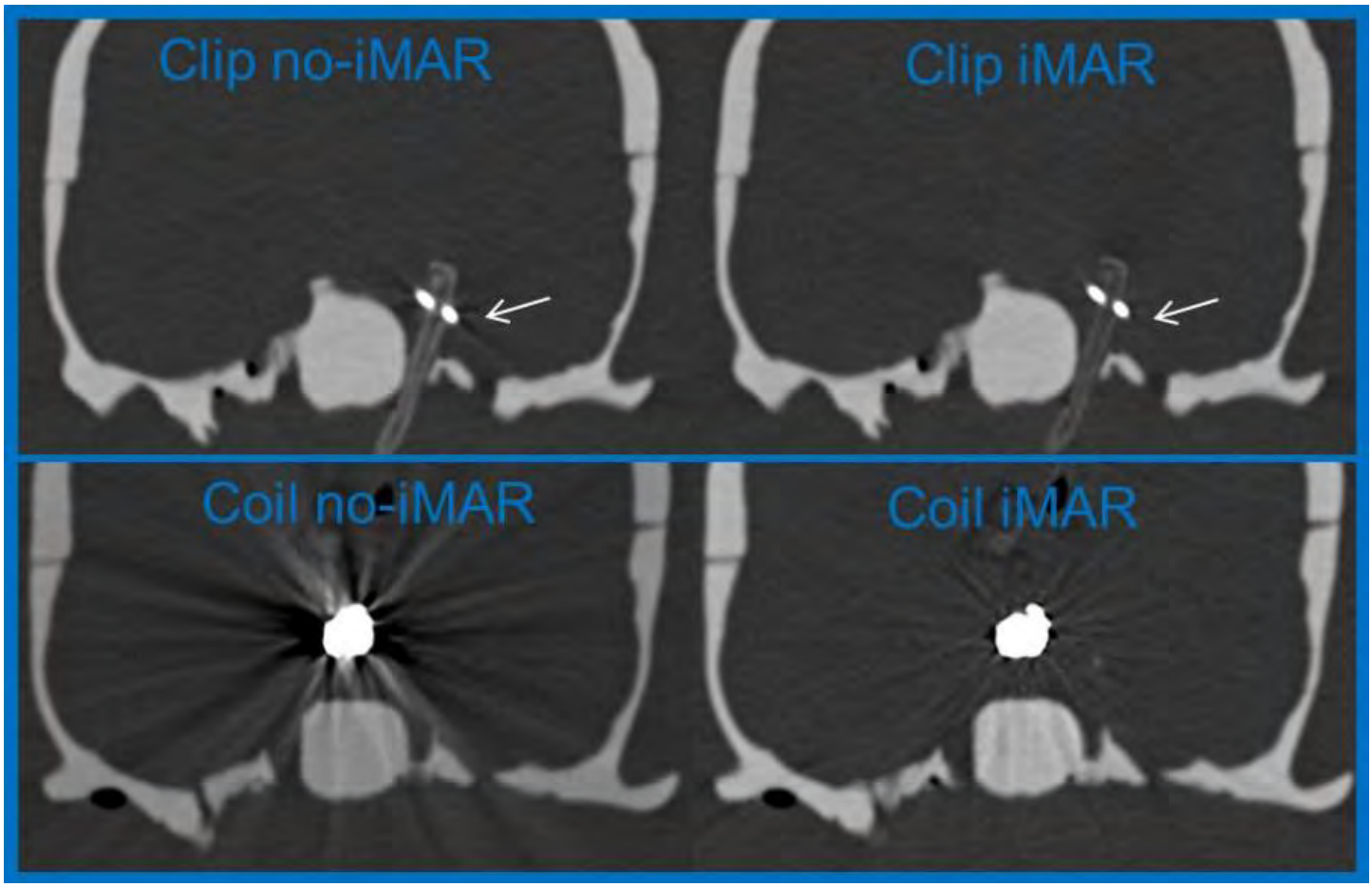
In this experimental CT phantom study, artifacts of 6 titanium clips (straight shape: size mini, small, medium and large; curved shape: size small and medium), 3 Phynox (Cobalt-Chromium-Nickel alloy) clips (straight shape: size small and medium; curved shape: size medium) and 6 coils (small, medium, large size) were examined. Postprocessing included routinely used standard filtered back projections (FBP) images and additional reconstructions using a previously published iMAR algorithm (Ref. 1). Image analysis included the quantitative assessment of image artifacts [Hounsfield units (HU) measurements] as well as the qualitative evaluation of artifact severity and the visualization of contrast media filled adjacent simulated vessels using a four-point Likert scale.

Results

Hounsfield unit values of streak artifacts were significantly ($P<0.05$) different between standard FBP images (mean 430 ± 267 HU) and iMAR images (-214 ± 315 HU). Artifact scores improved significantly from FBP images (median 4) to iMAR (median 2; $P<0.05$). Visualization scores of simulated vessels were significantly ($P<0.05$) better with iMAR (median 2) compared to FBP images (median 3). No significant artifact reduction was visible in large-sized coils when performing subgroup analyses.

Conclusions

Iterative metal artifact reductions postprocessing allows for a significant reduction of clip and coil artifacts and a better assessment of adjacent vessels compared to standard image reconstructions. Nevertheless, it is important to note the limited value of iMAR reconstructions in large-sized coils.



(Filename: TCT_O-247_figure_iMAR_ASNR.jpg)

O-248

1:46PM - 1:54PM

Hyperpolarized 13C Imaging of Infection using Bacteria-specific Metabolite Signatures

D Wilson[1], J Villanueva-Meyer[2], M Ohliger[1], C Mutch[1], O Rosenberg[1], R Sriram[1]
[1]University of California, San Francisco, San Francisco, CA, [2]University of California, San Francisco, San Francisco, CA

Purpose
Central nervous system (CNS) infection is a major concern in clinical neuroradiology, with high morbidity and mortality. Currently, there is no reliable imaging technique to detect living bacteria in vivo. Present clinically viable methodologies either detect morphologic changes in the brain or spine (CT/MR), recruitment of immune cells (111In SPECT white blood cell scan), or the enhanced glycolytic flux seen in inflammatory cells (18F-FDG PET). These strategies often are inadequate to detect bacterial infection during fever workup and are not specific for living bacteria. Our goal is to develop a metabolic technique using

hyperpolarized 13C MR spectroscopy that identifies pathogen-specific metabolic signatures, allowing facile distinction between bacteria and mammalian cells.

Materials and Methods

Cultures of E. coli and S. aureus were inoculated in 20 mL lysogeny broth (LB) from agar plates and were grown overnight at 37°C. Shake flask cultures were inoculated from these precultures and grown to the mid-exponential phase (OD600 = 1). Initial MR studies were performed in centrifuged cell pellets resuspended in 500 mL of 40 mM HEPES buffer at pH 7.3. For comparative metabolic studies, a renal cell carcinoma cell line (UOK262) and activated macrophages (using lipopolysaccharide, LPS) were studied in MR compatible cell culture bioreactors. [2-13C] pyruvate was polarized using dynamic nuclear polarization using a 3T Hypersense (Oxford Instruments) and neutralized in a phosphate buffer. The dissolution buffer was added to the cells for dynamic 13C MR measurement in an 11.7T Varian INOVA NMR using 30° pulses, and 3s interval for 300s.

Results

A 5 mm, NMR-compatible bioreactor was developed successfully, for performing controlled studies of bacteria encapsulated in alginate beads with a perfusion system capable of regulating the cellular involvement. This system was designed to better mimic the behavior of in vivo infection, and test MR-compatible molecular imaging agents. This micro-engineered susceptibility-matched bioreactor system platform showed remarkable spectral resolution (average line-width of 10.9± 0.4 Hz with cell encapsulates or tissue). Hyperpolarized 13C agents were introduced into the system, and their metabolism followed using routine spectroscopic techniques. Figure 1 shows the production of 13C acetate in E. coli following injection of hyperpolarized [2-13C] pyruvate. Acetate production was observed in both E. coli and S. aureus (representative gram positive bacteria). In contrast, UOK262 renal cell carcinoma and the activated macrophages did not demonstrate any acetate production, but [1-13C] lactate was observed as expected. These findings indicate divergent metabolism between bacteria and eukaryotic cells that can be used to differentiate them in a hyperpolarized 13C MRI study.

Conclusions

Acetate plays a key role as a metabolic switch in bacterial growth and survival. In this work, we demonstrated that hyperpolarized acetate production from pyruvate in pathologic bacteria is observable and distinct from the signals observed in mammalian cells. Further experiments are underway to gauge the sensitivity of this technique for in vivo translation. 13C pyruvate is just one of several 13C probes we are currently studying, that may be exploited to identify bacteria-specific metabolic pathways. Our intent is to use this study to diagnose infections frequently encountered in neuroradiology, that are challenging to identify using routine 1H MRI or nuclear imaging techniques.

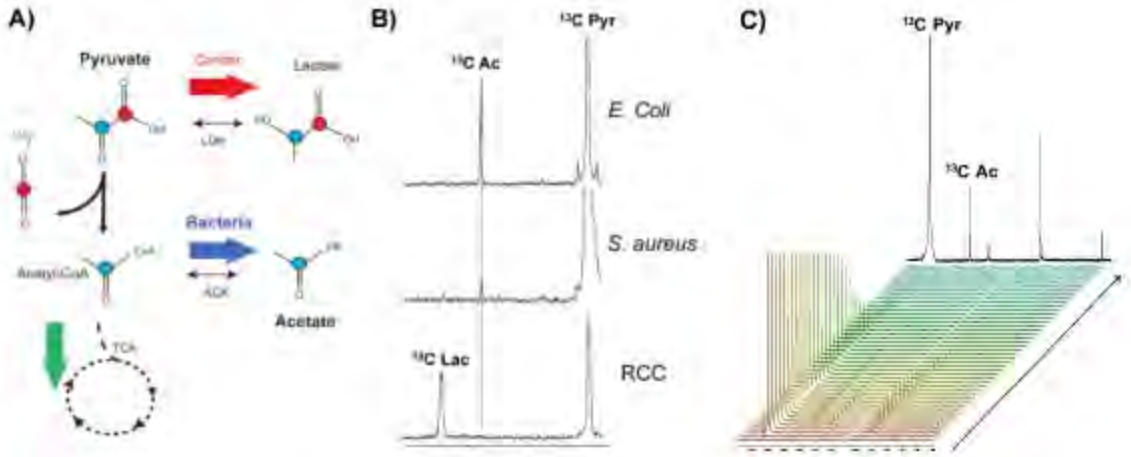


Figure 1. Hyperpolarized ^{13}C investigation of a bacteria-loaded NMR bioreactor shows bacteria-specific metabolism of ^{13}C pyruvate, enabling detection of living microorganisms. (a) Differential metabolism of pyruvate in cancer cells and living bacteria (b) Detection of bacteria-specific metabolite ^{13}C acetate in gram-negative and gram-positive bacteria, but not mammalian cells where ^{13}C lactate is seen. (c) Dynamic generation of ^{13}C acetate in an *E. Coli*- loaded bioreactor.

(Filename: TCT_O-248_ASNR_figure.jpg)

O-249

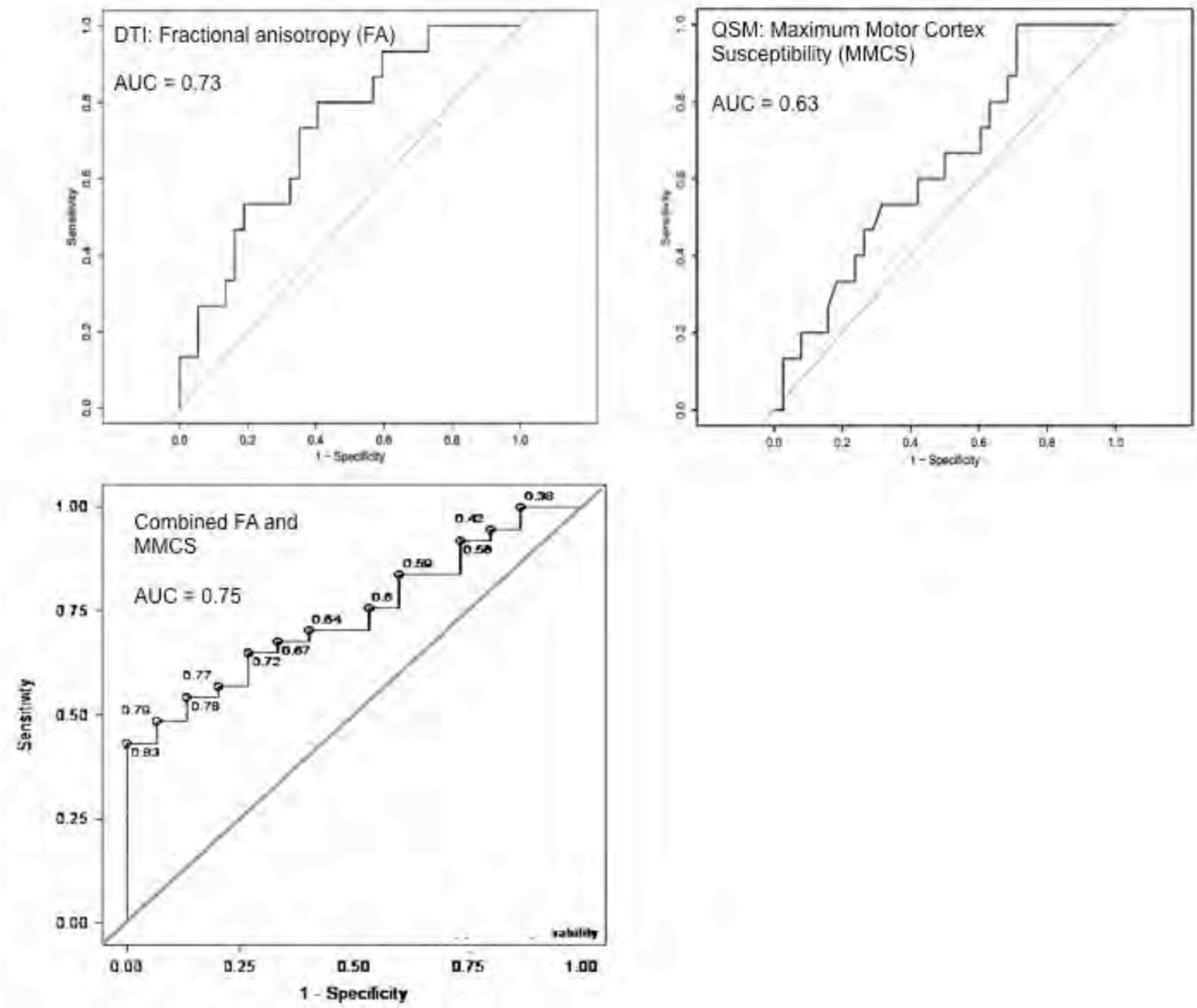
1:54PM - 2:02PM

Diffusion Tensor Imaging and Quantitative Susceptibility Mapping as Diagnostic Tools in ALS and PLS

E Weidman[1], A Schweitzer[1], S Niogi[1], G Askin[2], A Starikov[2], Y Wang[2], D Lange[3], M Shahbazi[3], A Tsiouris[1]
[1]New York-Presbyterian - Weill Cornell Medical Center, New York, NY, [2]Weill Cornell Medical College, New York, NY, [3]Hospital for Special Surgery, New York, NY

Purpose
Diffusion tensor imaging (DTI) and quantitative susceptibly mapping (QSM) have been proposed as quantitative biomarkers to aid in the diagnosis of amyotrophic lateral sclerosis (ALS) and primary lateral sclerosis (PLS) (1, 2). We tested the performance of DTI and QSM in distinguishing ALS and PLS patients from patients with other motor symptom predominant neurologic disorders.
Materials and Methods
For this IRB approved study, MRI exams acquired on a 3T magnet with 33-direction DTI and QSM sequences in patients presenting with a suspected motor neuron disease were reviewed retrospectively. Fractional anisotropy (FA) was measured at 6 regions of interest (ROI) along each side of the corticospinal tract (CST) using a semi-automated technique. Maximum motor cortex susceptibility (MMCS) was generated for each subject by subtracting adjacent white matter signal from the maximum susceptibility of the motor

cortex, determined by semi-automated segmentation. Chart review was performed to ascertain a final clinical diagnosis of ALS or PLS versus other neurologic diseases. Receiver operating characteristic (ROC) analysis was performed using mean CST FA, MMCS, and combined FA and MMCS.
Results
Diffusion tensor imaging and QSM sequences for 58 patients seen in our ALS clinical between June 2012 and April 2014 including 43 patients with a final diagnosis of ALS or PLS and 15 patients with other final diagnoses were analyzed. There was no statistically significant difference in patient age or gender between ALS/PLS and non-ALS/PLS groups. The AUC for mean CST FA was 0.73 and the AUC for MMCS was 0.63. The AUC for combined mean CST FA and MMCS was 0.75.
Conclusions
We demonstrated that combined DTI FA and QSM MMCS parameters are superior to distinguishing ALS and PLS from neurological mimics compared to DTI FA or QSM MMCS parameters alone, which may have clinical utility for diagnosing ALS and PLS. This is the first study to our knowledge to compare the performance of DTI and QSM in diagnosing ALS and PLS.



(Filename: TCT_O-249_ASNRDTIQSMROC.jpg)

O-250

2:02PM - 2:10PM

Altered structural and functional motor cortex connectivity in patients with symptomatic cervical spondylotic myelopathy

B Ellingson[1], D Woodworth[2], N Salamon[2], L Holly[3]
[1]University of California Los Angeles, Los Angeles, CA, [2]UCLA, Los Angeles, CA, David Geffen School of Medicine at UCLA, Los Angeles, CA, Los Angeles, CA, [3]UCLA, Los Angeles, CA

Purpose

Motor symptoms arising from compression of the spinal cord are of particular concern in patients with cervical spondylosis, and previous task-based functional studies of the primary motor cortex (PMC) have demonstrated measurable alterations in these patients (1, 2). In the current study we analyzed the relationship between PMC cortical thickness (CT) and functional connectivity (FC) with the modified Japanese Orthopedic Association score (mJOA) as a measure of neurological impairment in patients with cervical spondylosis.

Materials and Methods

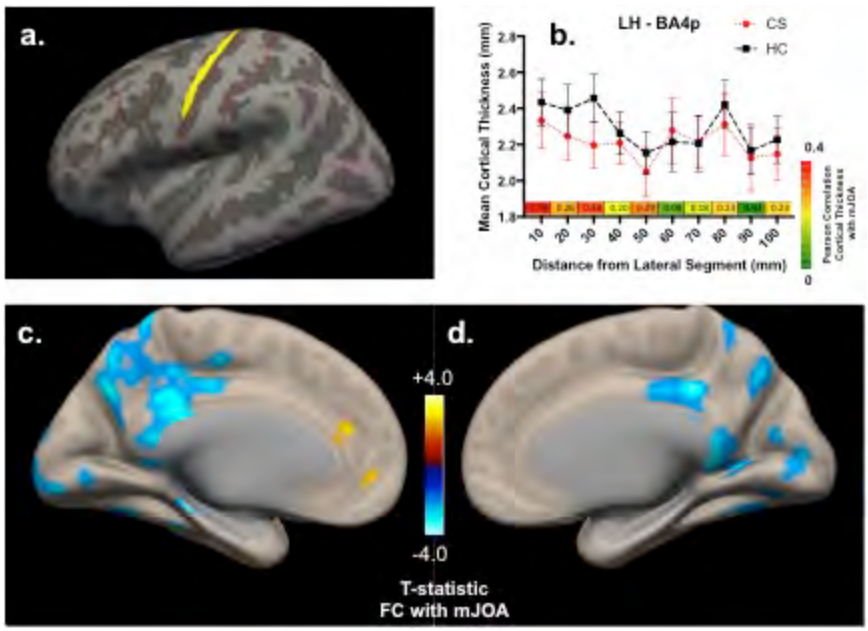
Twenty-six patients with cervical spondylosis with or without myelopathy (mean age 59; mean mJOA of 15) and 17 healthy controls (HC, mean age 31) had brain MRI scans that included a 3D-T1 MRI and resting-state fMRI examinations. An additional 28 HC subjects with similar datasets were included from the PAIN repository (http://uclacns.org/programs/pain-research-program/pain-repository/) for the CT analysis. We evaluated differences in CT between CSM and HC and Pearson correlations of mean CT with mJOA in the PMC Brodmann areas (BA4a, BA4p) using FreeSurfer (3). Analysis of FC with mJOA was performed by seeding the PMC using the CONN toolbox (4). Significance was set at $P<0.05$.

Results

Mean CT in the left and right BA4a were lower in CSM vs HC ($P=0.007$, $P=0.02$). Mean CT of left and right BA4a ($r=0.37$, $P=0.001$; $r=0.30$, $P=0.01$) and left and right BA4p ($r=0.30$, $P=0.01$; $r=0.32$, $P=0.007$) were positively correlated with better mJOA. Figure 1 illustrates the left BA4p (Fig.1a) and the mean CT across the length of the motor strip in 10mm segments for both groups and Pearson correlation coefficients with mJOA (Fig.1b). Functional connectivity analysis of the left PMC displayed decreased connectivity with the precuneus and posterior cingulate with better mJOA in both the left (Fig.1c) and right (Fig.1d) hemispheres; similar results were seen for the right PMC.

Conclusions

The PMC of cervical spondylosis patients displayed structural and functional changes in connectivity, which highlight the importance of the brain in managing insult to the spinal cord. Further, these initial results suggest early intervention may be valuable in order to halt progression of brain structural and functional alterations in patients with cervical spondylosis with or without myelopathy.



(Filename: TCT_O-250_Fig1.jpg)

O-251

2:10PM - 2:18PM

Neurostructural Effects of Age and Serostatus in Treated HIV Infection

T Zeffiro[1], E O'Connor[2], F Renard[3], T Zeffiro[4], J Becker[5]
[1]Neurometrika, Potomac, MD, [2]University of Maryland Medical Center, Baltimore, MD, [3]AGEIS, EA-UGA 7407 Université Grenoble Alpes, Grenoble, Auvergne-Rhône-Alpes, [4]Neurometrika, Potomac , MD, [5]University of Pittsburgh, Pittsburgh, PA

Purpose
Although many studies have documented cortical and subcortical gray matter volume (GMv) changes following HIV infection, Gray matter volume also is known to decline with age and drug use. As the HIV infected population is steadily aging, the effects of age and past drug use may confound attempts to identify specific effects of serostatus on regional GMv, or to use neurostructural measures more generally in HIV diagnostic and treatment assessment contexts. In a cross-sectional study, we examined the effects of serostatus, age and past drug use on regional GMv using voxel-wise linear regression and both linear and nonlinear classification techniques.
Materials and Methods
Participants included 105 seropositive and 90 seronegative men, ages 23-77 years, with 121 reporting past drug use. Seropositive participants all were treated with antiretroviral therapies. Mixed effects models were used to explore effects of serostatus, race, age, intracranial volume and drug use on regional GMv. Following three-fold cross validation for parameter estimation, linear discriminant analysis (LDA) and random forest (RF)

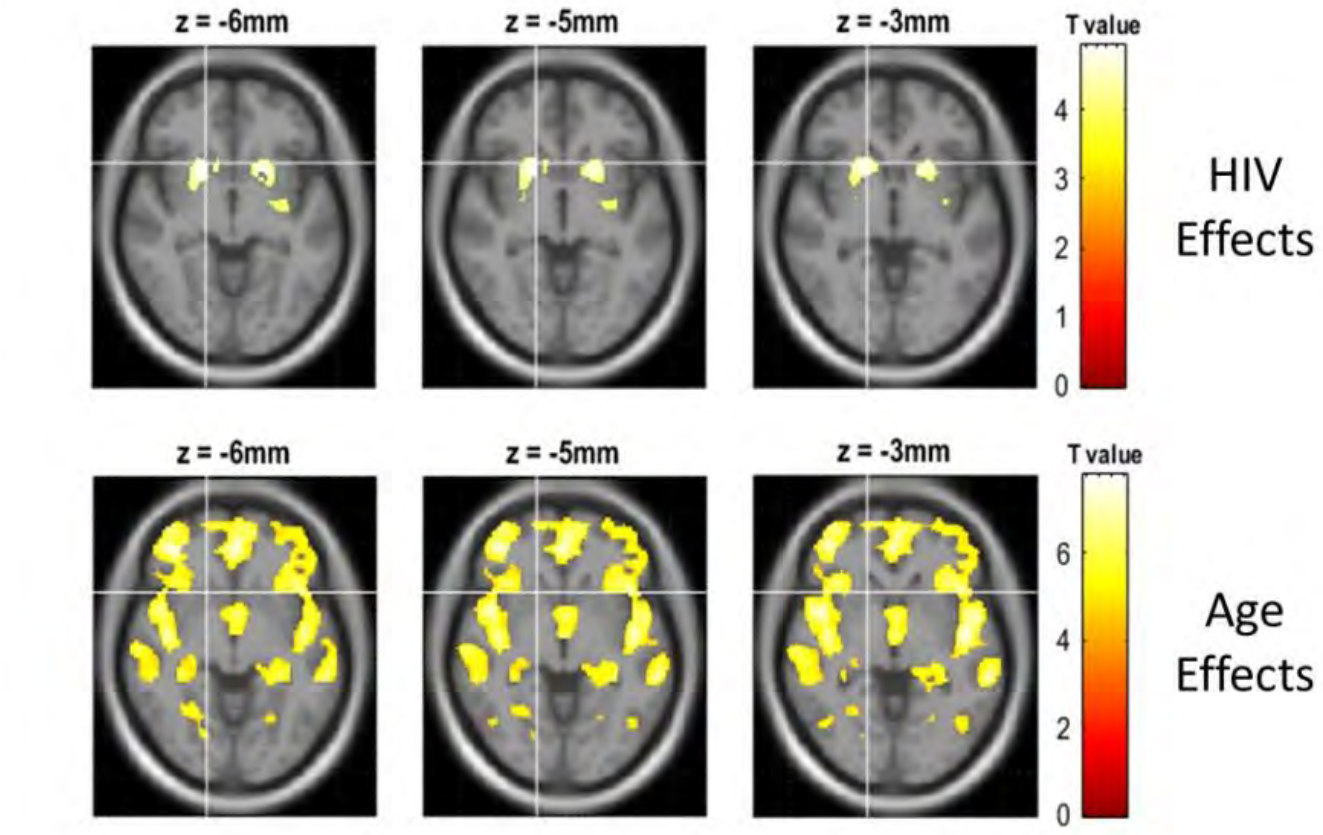
classification techniques were compared to determine if regional GM values could predict serostatus.

Results

Seropositive participants exhibited bilateral decreases in GMv ($p<0.05$ FWE-corrected) in caudate and putamen. Spatially independent effects of age and past drug use were also seen ($p<0.05$ FWE-corrected), with age broadly affecting numerous frontal and temporal cortical regions (Fig. 1). Comparison of linear (LDA) and nonlinear (RF) classification showed that regional GMv features, notably including basal ganglia nuclei, could predict serostatus with 56% and 72% accuracy, respectively.

Conclusions

Regional GMv is subject to spatially separate effects of serostatus, age and past drug use. Serostatus effects had high regional specificity when age and drug use were controlled, suggesting that basal ganglia GMv measured using computational neuroanatomy methods may be a useful biomarker to follow effects HIV infection and its treatment.



(Filename: TCT_O-251_asnr-2017-hiv-structural-figure.jpg)

O-252

2:18PM - 2:26PM

A DTI-equivalent measure of white matter anisotropy based on T2-weighted MRI

Y Zhang[1], S Sharma[1]
[1]*University of Calgary, Calgary, Alberta*

Purpose

Changes in white matter anisotropy occur following neurological damages in both focal lesions and the lesion-free regions. Such abnormalities however are difficult to identify visually. Currently, diffusion tensor imaging (DTI) (1) is one of the main methods that are used to detect alterations in white matter anisotropy, and is only included in dedicated imaging protocols. Here we present an alternative imaging method using standard T2-weighted MRI.

Materials and Methods

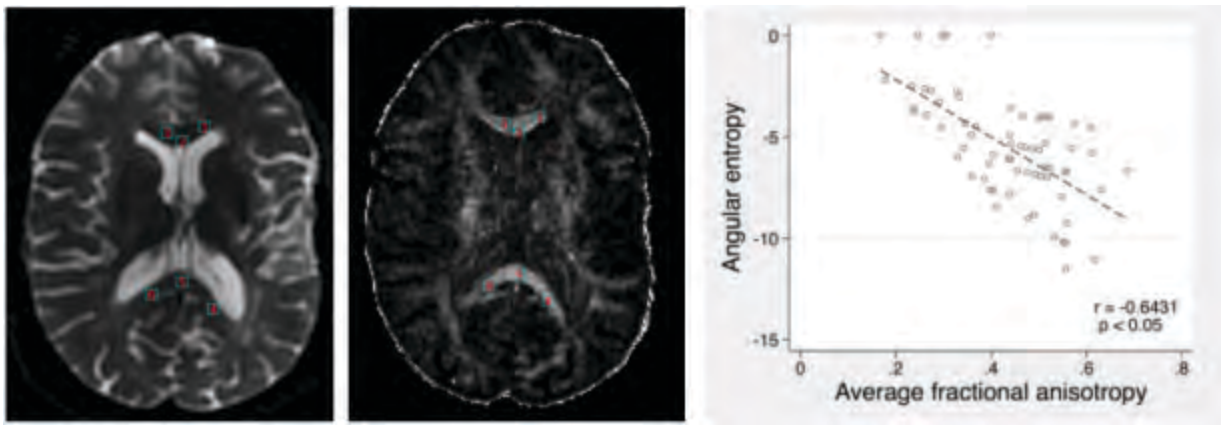
Our method is based on the Fourier transform (FT), the corner stone theorem of CT and MRI. Specifically, we calculate the power spectrum of FT which is shown to be a promising measure of tissue integrity (2). The FT power spectrum was thresholded and normalized to enhance image contrast and reliability, and then was transformed into the polar coordinates. In this way, a distribution profile of tissue alignment at various angles was derived, from which a tissue anisotropy outcome named angular entropy was calculated. In this study, we assessed the brain MRI of 19 patients with multiple sclerosis (MS) and 19 matched controls. Both T2-weighted MRI and DTI was acquired. From DTI, fractional anisotropy was computed. Image analysis was focused on the corpus callosum, with the same regions of interest (ROIs) in both methods.

Results

Angular entropy derived from T2-weighted MRI was significantly higher in MS than in controls, indicating greater loss of tissue anisotropy. This trend is similar to that seen in DTI. Angular entropy was also highly and negatively correlated with DTI fractional anisotropy (Fig. 1, $p<0.05$), when all samples were assessed as a group.

Conclusions

Our findings suggest that advanced analysis of tissue anisotropy is possible using clinical MRI. As opposed to DTI, this method does not require additional imaging time or cost. With further validation, analysis of FT power spectrum may become a useful approach for evaluating white matter anisotropy in diagnostic imaging.



(Filename: TCT_O-252_Fig_ASNR2016.jpg)

O-253

2:26PM - 2:34PM

DTI Parameter Estimation Using Convolutional Neural Networks

E Dickerson[1], C Hess[2]
[1]University of California San Francisco, San Francisco, CA, [2]University of California, San Francisco, San Francisco, CA

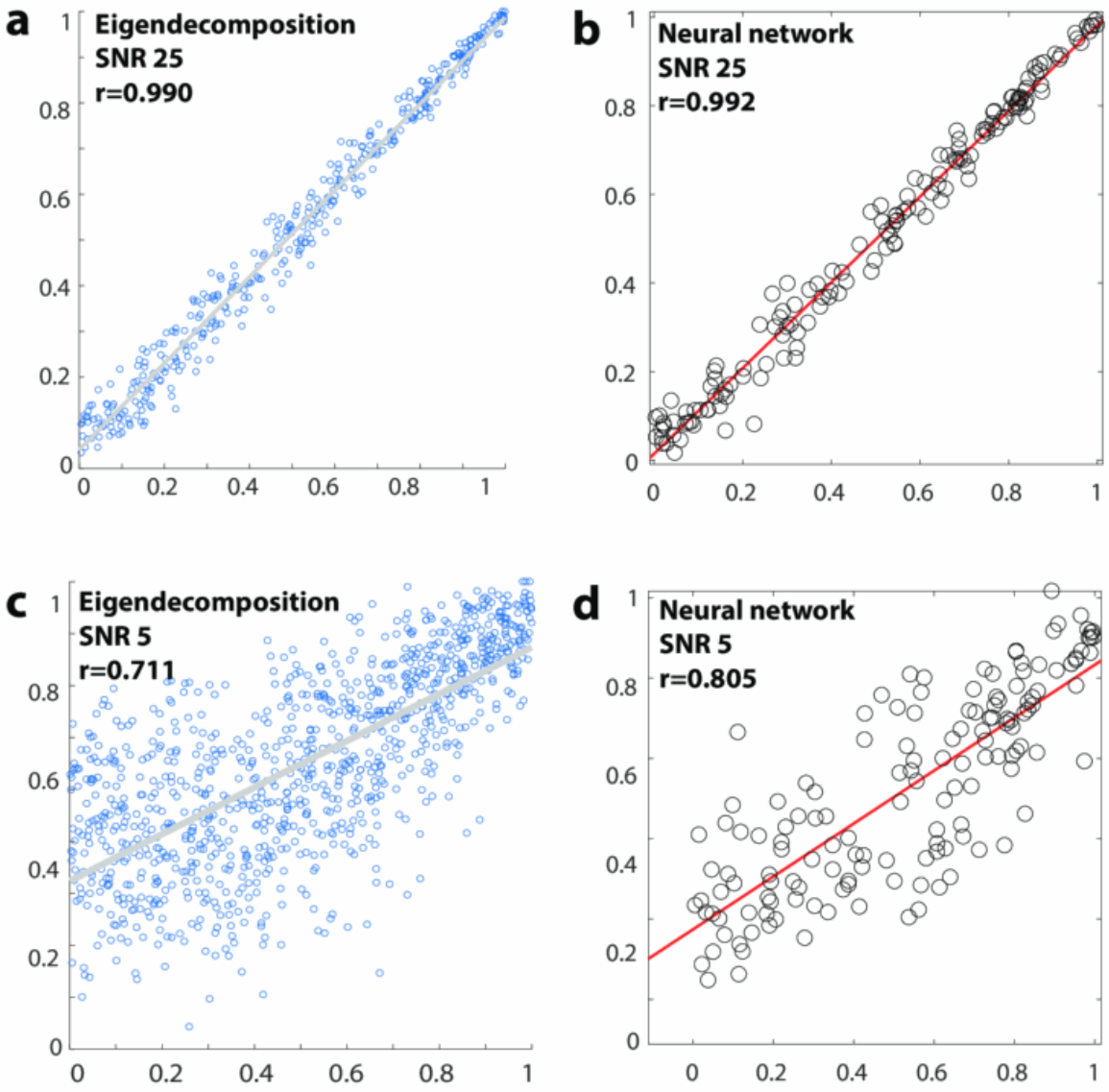
Purpose
Diffusion tensor imaging (DTI) parameters including mean diffusivity (MD), fractional anisotropy (FA) and tensor orientation are used routinely for tissue characterization and fiber tractography. These values traditionally have been calculated from parametric models using eigendecomposition. Noisy, sparse or otherwise corrupted diffusion estimates introduce uncertainty into the estimated parameters (1). In this work, we introduce the concept of nonparametrically estimating of diffusion parameters using feed-forward Neural Networks (NNs) trained on simulated data to overcome these limitations of traditional parametric diffusion estimation.
Materials and Methods
Although this formalism might be used for reconstruction of diffusion spectrum imaging (DSI) probabilities, high-angular resolution diffusion imaging (HARDI) or microstructure characterization methods such as neurite orientation dispersion and density imaging (NODDI), this work used conventional DTI and focused on estimation of FA for proof of concept. Noisy, simulated diffusion measurements from 1000 known, randomized FA values were split into training, validation, and test sets. A feed-forward NN with 2 hidden layers of 10 neurons each was trained using back-propagation. Fractional anisotropy also was calculated using eigendecomposition (2). Effectiveness of both methods was compared using Pearson correlation between 'true' and 'calculated' FA values for the test set. This simulation was repeated at multiple simulated signal-to-noise ratios (SNRs).

Results

At every SNR, NN estimates of FA were more strongly correlated with true values of FA. At SNR of 25, correlation was 0.992 for the NN approach versus 0.991 for eigendecomposition. This difference became more pronounced as image noise increased: at a SNR of 10, the correlation was 0.938¬ for the NN versus 0.934 for eigendecomposition. At a SNR of 5, the correlation was 0.953 for the NN versus 0.935 for eigendecomposition. At a SNR of 5, the correlation was 0.805 for the NN versus 0.711 for eigendecomposition. At a SNR of 2, the correlation was 0.362 for the NN versus 0.160 for eigendecomposition.

Conclusions

Neural Networks are a promising technique for robust nonparametric assessment of DTI parameters affected by noise. Implications include improved mapping of brain white matter structures.



Scatterplots comparing actual fractional anisotropy (horizontal axis) to estimated fractional anisotropy (vertical axis) using both eigendecomposition (figure parts **a** and **c**) and test subset prediction of feed-forward trained neural network (figure parts **b** and **d**) at various signal-to-noise ratios (SNR of 25 in figure parts **a** and **b**, SNR of 5 in figure parts **c** and **d**). Model type, SNR, and Pearson correlation coefficient is superimposed on upper-left region of scatterplots.

(Filename: TCT_O-253_ASNR_Abstract_DTI_Neural_Networks_Figure.gif)

O-254

2:34PM - 2:42PM

Accuracy of Presurgical Functional MRI Language Mapping for Brain Tumors: A Systematic Review and Meta-analysis

H Weng[1], K Noll[2], M Chen[2], J Johnson[2], S Prabhu[2], Y TSAI[1], J Hazle[2], D Schomer[2], H Liu[2]
[1]Chang Gung Memorial Hospital, Chiayi County, Taiwan, [2]U.T. MD Anderson Cancer Center, Houston, TX

Purpose
Functional magnetic resonance imaging (fMRI) is a noninvasive method for mapping cortical language functions to delineate eloquent tissue boundary and guide surgical planning. However, the accuracy of fMRI for localizing language functions varies across studies. To better understand the utility of presurgical fMRI and factors associated with its accuracy, we performed a meta-analysis of studies that compare language fMRI with direct cortical stimulation (DCS) in the patients with brain tumors.
Materials and Methods
PubMed and related databases were searched for articles published between January 1990 and September 2016. Studies included all research comparing fMRI and intra-operative DCS language mapping. Findings were pooled with bivariate random-effects and hierarchic summary receiver operating characteristic (HSROC) curve models to summarize the accuracy of fMRI. Meta-regression and subgroup analyses were performed to evaluate whether significant covariates existed.
Results
Ten studies met inclusion criteria. On a per-patient basis, the pooling results gave sensitivity and specificity estimates for fMRI identification of eloquent cortex of 44% (95% CI, 14% to 78%) and 80% (54% to 93%), respectively. On a per-tag basis, sensitivity and specificity were 67% (51% to 80%) and 55% (25% to 82%), respectively. Meta-regression and subgroup analyses on a per-tag basis showed significantly higher sensitivity for studies that applied statistical threshold and fMRI session time. Significantly higher specificity was found in statistical threshold, fMRI session time, visual presentation of stimuli, and use of expressive language tasks.
Conclusions
Based on advanced meta-analytic modeling, fMRI shows promise as a noninvasive tool for presurgical language mapping, though it cannot replace and only complements the gold-standard intra-operative DCS.

O-255

2:42PM - 2:50PM

Comparison Between Diffusion Weighted and Diffusion Tensor Imaging Using Voxel-based analysis.

K Atsina[1], M Alizadeh[2], F Mohamed[3], D Andrews[1], A Flanders[4], K Talekar[1]
[1]Thomas Jefferson University Hospital, Philadelphia, PA, [2]Temple University, Philadelphia, PA, [3]Thomas Jefferson University, Philadelphia, PA, [4]Thomas Jefferson Univ. Hosp., Philadelphia, PA

Purpose

Diffusion weighted imaging (DWI) and diffusion tensor imaging (DTI) provide vital information in assessing microstructural changes due to brain pathology. The apparent diffusion coefficient (ADC), which is derived from DWI, measures the magnitude of water diffusivity in brain tissue and provides information of the density of cellular tissues. A dense cellular environment provides a lower magnitude of diffusivity. Similarly cerebrospinal fluid (CSF) has a high ADC value because it is acellular. Traditional methods of ADC estimations require obtaining the average of several manually drawn regions of interest (ROI) within the specified area within a given scanner-generated ADC map. However, this strategy can be laborious, with significant potential for human error and thwarts quantitative comparison. Additionally, applying this conventional based technique to high-resolution DTI images can be resource and time intensive, given the significant number of slices to be reviewed. The purpose of this study was to investigate an alternative methodology that utilizes image analysis software to generate voxel-based comparisons of ADC with the DTI scalars, including mean diffusivity (MD), and fractional anisotropy (FA).

Materials and Methods

As part of a phase I-II immunotherapy trial at a single institution, 16 DWI and DTI scans were acquired using a 3.0T Phillips Achieva scanner in 4 patients (age: 52 - 68 years), with a history of glioblastoma (GBM). Four scans were obtained before treatment and the remaining 12 were obtained at varying durations of time after treatment. Mean diffusivity and FA maps were computed from raw DTI data with scan specific gradient table and image orientation information, and subsequently preprocessed for magnetic field inhomogeneities and motion-induced artifacts using FSL. For voxel-based analysis, these DTI maps were co-registered with conventional ADC maps generated from DWI using SPM12. Tumor volumes were estimated by manually drawn ROIs of the entire tumor on fluid attenuated inversion recovery (FLAIR) images co-registered to the same MNI space. The resulting tumor masks were superimposed on ADC and DTI maps and all voxel intensities within the tumor were computed using MatLab. Traditional methods involved calculating average ADC and DTI indices using 4 ROIs planted on ADC and DTI maps in corresponding enhancing portions of the tumor seen on contrasted-enhance T1 images. Agreement between the 2 methods was assessed using Bland-Altman plot and correlation coefficients.

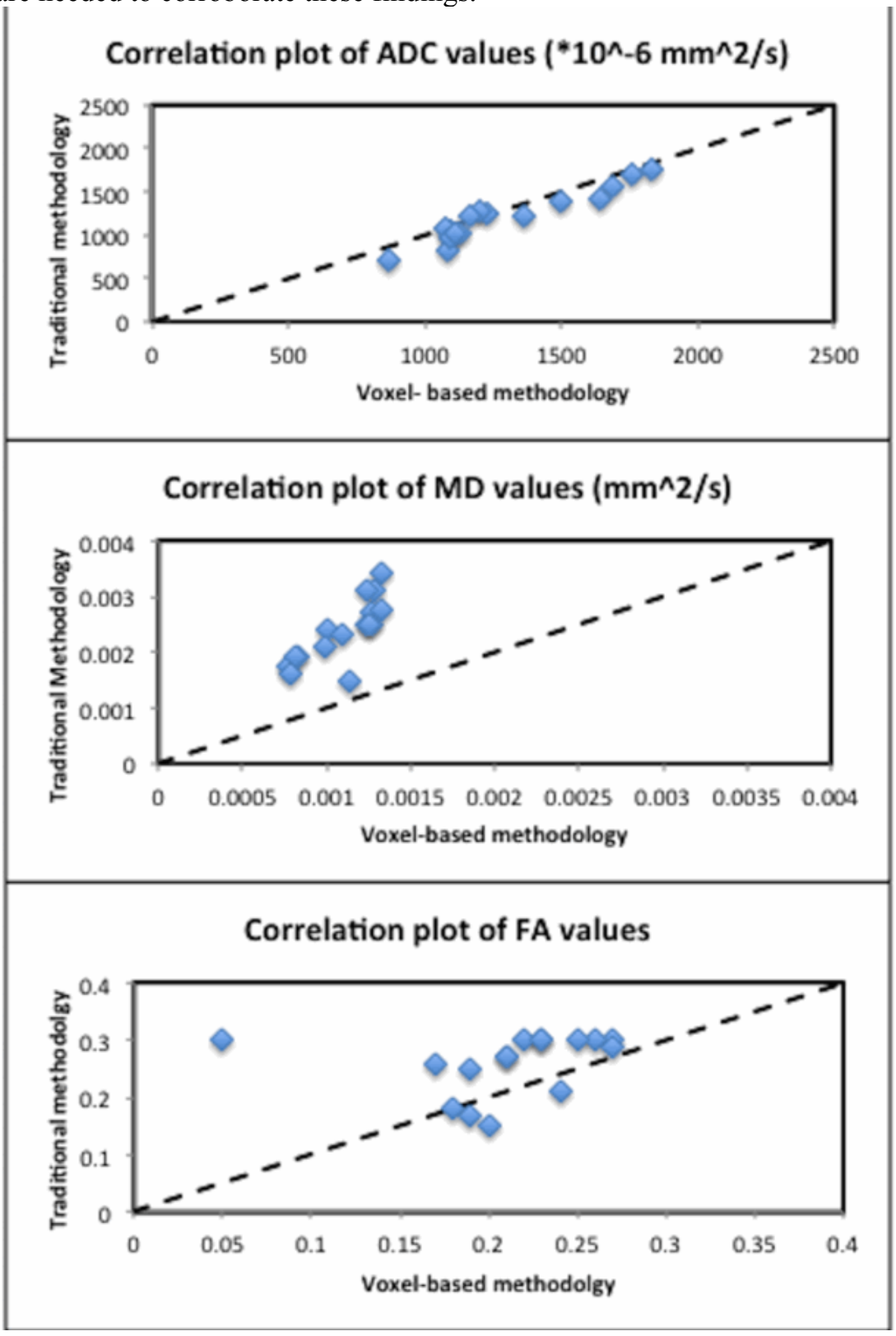
Results

A strong correlation was observed between the 2 methods when measuring ADC values ($r = 0.94$ $P < 0.05$) and MD values ($r = 0.80$, $P < 0.05$). A very weak correlation was seen between the 2 methods for FA measurements ($r = 0.17$), however this was not statistically significant $P = 0.53$. Correlation plots showed good agreement between methods of ADC, MD, and FA (See Fig.).

Conclusions

The voxel-based methodology described above shows good agreement when compared with traditional methods with regard to 2 or 3 measures. The weaker correlation of FA values

between the 2 methods was not statistically significant, likely due to outliers. Further studies are needed to corroborate these findings.



(Filename: TCT_O-255_Slide21.gif)

O-256

2:50PM - 2:58PM

Mapping the Polar Angle Representation of Saccades in Human Superior Colliculus

R Savjani[1], D Ress[2]
[1]Texas A&M University College of Medicine, Houston, TX, [2]Baylor College of Medicine, Houston, TX

Purpose
The superior colliculus (SC) is a layered midbrain structure involved in directing eye movements and coordinating visual attention. Electrical stimulation (1) and neuronal recordings (2) in the intermediate layers of monkey SC have shown a retinotopically organized saccadic eye-movement map. Specifically, saccades along the superior-inferior visual field are mapped along the medial-lateral axis of the SC in monkeys (1, 2). However, its deep subcortical location and vascular noise sources make human SC difficult to image using functional magnetic resonance imaging (fMRI), so the polar angle representation of saccades in human SC has not been well studied. Pathology (e.g., pineal gland tumors, strokes) involving the SC manifests in both visual and motor eye movement deficits. However, the nature of these deficits are not well characterized as the basic vision science of the layered SC in humans has not been elucidated yet.
Materials and Methods
We used high resolution fMRI to map the representation of eye movements in human SC using a phase-encoding approach. Previous human studies of saccadic mapping in cortex used a similar approach (3–5), but with a very low duty cycle (1 saccade every 5 s) and reverse saccades made immediately after forward saccades. To overcome these limitations, we designed a paradigm in which subjects could perform many forward saccades while minimizing the saccades in the opposing direction. Subjects made saccades either to left or right (activating primarily the contralateral SC) while we cyclically varied the vertical component of the saccade to correspond to the lower, horizontal, and upper visual field (Fig. A). We trained 5 subjects using eye tracking to perform visually guided saccades. Subjects performed three 6° saccades guided by a green dot target in a static grid of red dots. The use of a static grid reduces differential contrast effects from retinal slip; the use of green-red color contrast minimizes the effects of bottom-up contrast in target discrimination. After 3 saccades, the subjects then performed a smooth pursuit (1.2 s) back to the first dot. Saccades and the pursuit were continued along the same axis for 9.6 s, and then subjects performed another smooth pursuit to the start of the next axis. Subjects performed 9 cycles in a single run (~4.5 min) and 15 runs per session. Leftward and rightward saccades were run on separate sessions to measure the contralateral response of each SC independently. Eight quasi-axial slices covering SC were imaged on a Siemens 3T Trio (1.2-mm voxels, 3-shot

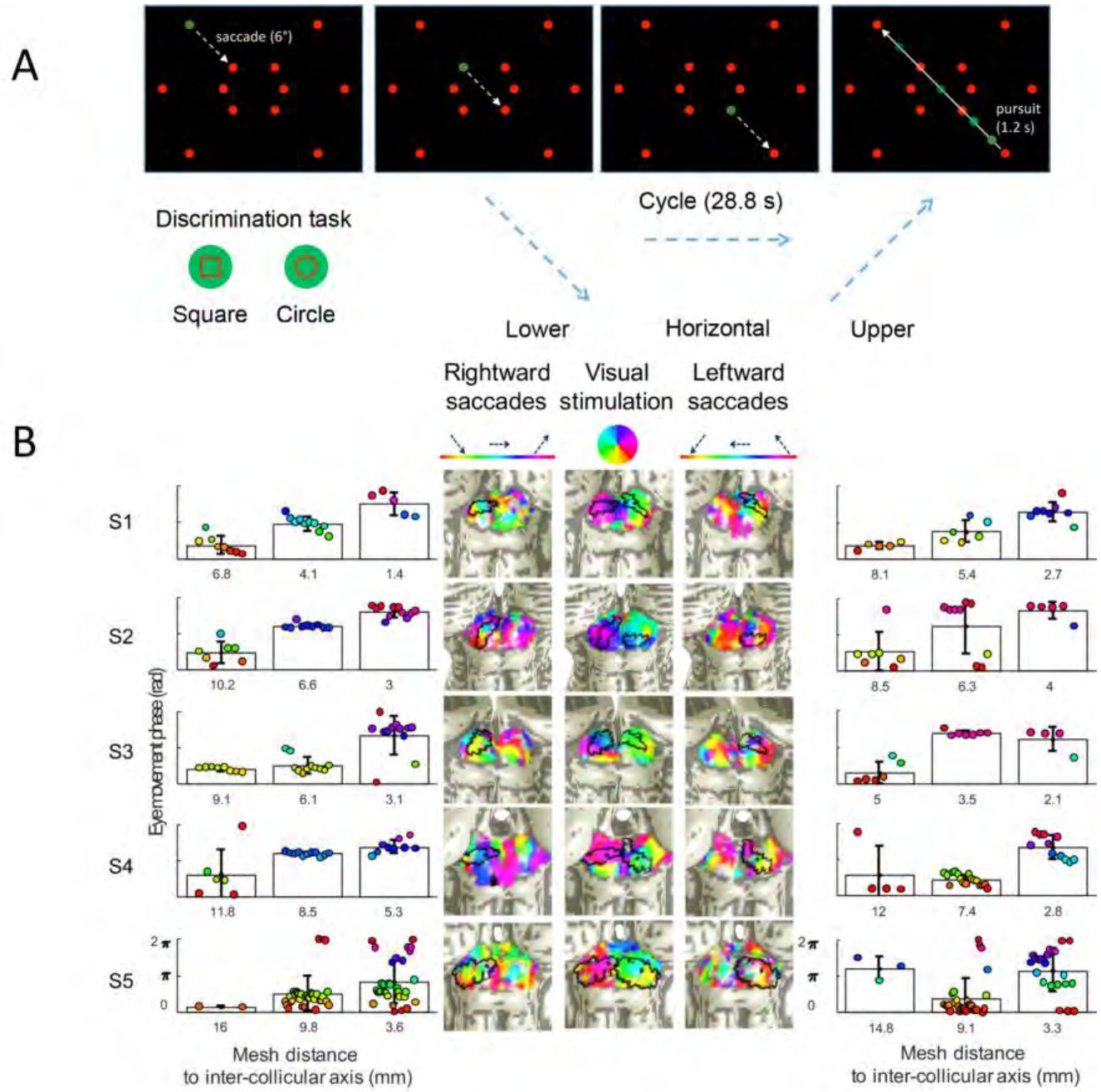
dual-echo spiral), and the functional data were transformed onto surface projections of the SC built from segmented anatomical scans from each individual.

Results

Data from 5 subjects show eye movements along the inferior-superior visual field axis are mapped along the anatomical medial-lateral axis in both SC (Fig. B). Phase maps were depth averaged from 0.6 to 1.8 mm and projected on the surface. Maps were bootstrapped across runs for each SC and thresholded at $p < 0.2$ (transparent) to $p < 0.05$ (opaque). All 5 subjects showed inferior eye movements to be mapped laterally, horizontal mapped centrally, and superior mapped medially in the SC contralateral to the right/left eye movement direction. Some subjects also showed a weaker reversed mapping on the SC ipsilateral to the direction of saccadic eye movements, perhaps due to the unavoidable saccadic anticipation during smooth pursuit.

Conclusions

Our data show the topographic map of eye movements in human SC is consistent with previous studies in alert monkeys: the superior-inferior visual field is roughly mapped along the medial-lateral axis. We previously have obtained visual stimulation maps from these same subjects and are now able to correlate the 2 maps as well as compare depth profiles of the functional response, which lie 1 cm deeper than that evoked by visual stimulation. Our techniques in psychophysics and imaging allow us to better relate findings in nonhuman primates to human SC, strengthening our understanding of subcortical vision. Now that we are able to obtain robust saccadic eye movement maps within the SC using functional MRI, we can begin to study how the maps are altered in a variety of pathologies that involve saccadic eye movement disruptions (e.g., neoplasms, vascular injury, and traumatic brain injury).



(Filename: TCT_O-256_Figure.jpg)

Wednesday
1:30PM - 3:00PM
Long Beach Convention Center, Room 102BC (Main Level)

19H-Parallel Paper Session: Gd, Gd Everywhere . . . . . .Cause for Pause, and Think!

O-257

1:30PM - 1:38PM

Safety and Diagnostic Efficacy of Gadoterate Meglumine in Magnetic Resonance Imaging (MRI) of Central Nervous System (CNS)

A Gottschalk[1], B Kress[2]
[1]Krankenhaus Nordwest, Frankfurt am Main, Germany, [2]Krankenhaus Nordwest, Frankfurt am Main, NY

Purpose
To assess the safety profile and diagnostic efficacy of gadoterate meglumine (Dotarem®) in MRI examinations of the brain, spinal cord and surrounding tissue.
Materials and Methods
As part of a postmarketing surveillance study conducted in 52 centers between 2011 and 2013, 21,959 gadoterate meglumine-enhanced neuroradiological MRI examinations [82% of the brain, 20% of the spinal cord, 4% of surrounding tissue (including multiple examinations)] were evaluated for safety profile (adverse events) and efficacy [diagnostic value (yes/no) and image quality (5-step scale from very poor to very good)]. The patients (58.2% female) had a mean age of 52.8 ± 17.2 years and included 42 children under 12 years of age and 204 adolescents aged 12–17 years.
Results
At least 1 risk factor was reported in 26.0% of patients, mainly allergies (15.6%) and hypertension (6.1%). Adverse events (AEs) occurred in 64 patients (0.3%), including 2 adolescents. In 3 cases (0.01%), the AEs were serious: 1 adolescent (swelling face, urticaria), 2 adults (allergy and renal failure for 1, eye pruritus, cough, nasal congestion, sneezing for the other). All AEs fully resolved. Image quality was good or very good in 99.0% of patients. It was possible to make a diagnosis in 100% of children and adolescents and in 99.8% of adults.
Conclusions
Gadoterate meglumine has proved to be a safe MRI contrast agent in neuroradiology, with high diagnostic value for CNS examinations.

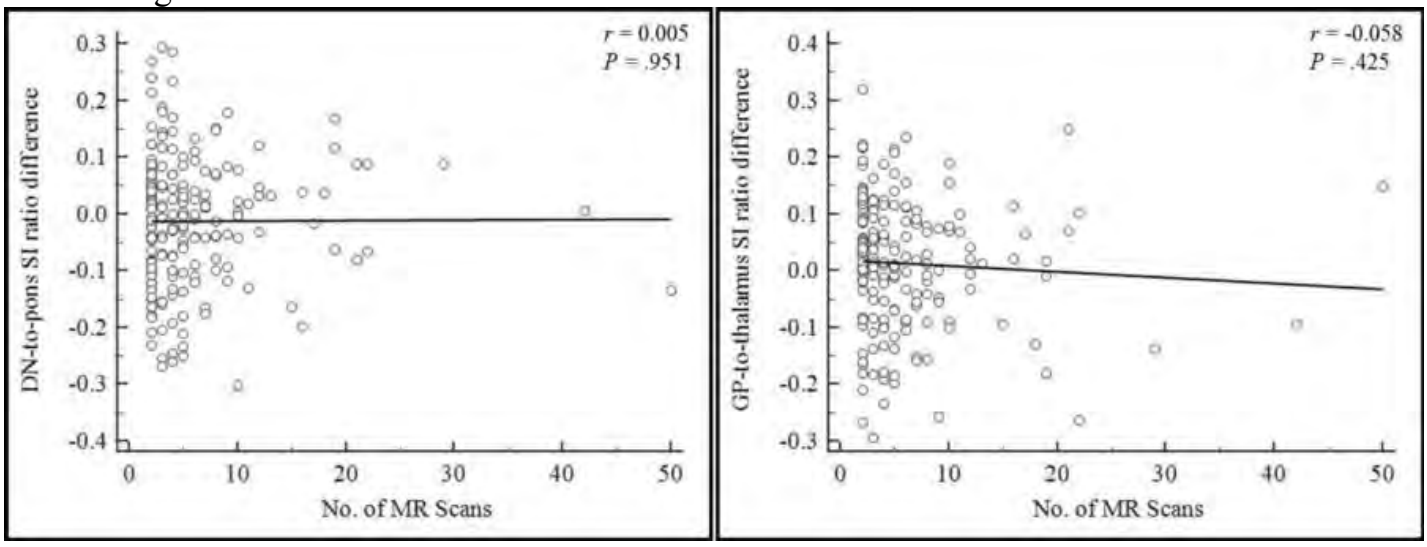
O-258

1:38PM - 1:46PM

Evaluation of Gadolinium Retention after Serial Administrations of a Macrocyclic Gadolinium-Based Contrast Agent (Gadobutrol): A Single-Institution Experience with 189 Patients

R Yoo[1], K Kang[1], T Yun[2], S Choi[1], J Kim[1], C Sohn[1]
[1]Seoul National University Hospital, Seoul, Seoul, [2]Seoul National University Hospital, Seoul, Korea, Republic of

Purpose
Unlike linear gadolinium-based contrast agents (GBCAs), controversial data have been published regarding gadolinium retention after serial administrations of macrocyclic GBCAs. Our aim was to evaluate gadolinium retention in the dentate nucleus (DN) and globus pallidus after serial administrations of gadobutrol in a large number of patients.
Materials and Methods
A total of 189 patients, who had undergone at least 2 contrast-enhanced MR scans using only gadobutrol between August 2009 and August 2016, were included retrospectively. Dentate nucleus-to-pons and GP-to-thalamus SI ratio differences on unenhanced T1-weighted MR images were calculated by subtracting the SI ratios at the first MR images from those at the last MR images. One-sample t tests were used to evaluate whether the SI ratio differences differed from 0. Linear regression and Pearson correlations were performed to evaluate correlations between SI ratio differences and various confounding variables, including the number and mean interval of MR scans, age, sex, history of radiation therapy or chemotherapy, renal and liver functions.
Results
Sixty-three patients underwent 6 or more MR scans, while 126 patients underwent less than 6 MR scans. Both the DN-to-pons SI ratio difference and GP-to-thalamus SI ratio difference did not differ significantly from 0 with mean values of -0.012 ± 0.115 (P = .148) and 0.012 ± 0.111 (P = .126), respectively. Significant but weak correlations were found only between DN-to-pons SI ratio difference and abnormal liver function (r = -0.225, P = .003) and between GP-to-thalamus SI ratio difference and history of whole-brain radiation therapy (r = -0.181, P = .017).
Conclusions
In our study based on a large number of patients, serial administrations of gadobutrol did not result in signal increases in the DN or in the GP.



(Filename: TCT_O-258_Fig_final.jpg)

O-259

1:46PM - 1:54PM

Deposition of Gadolinium in the Organs, Tissue, and Bone of Patients who Underwent Multiple Gadodiamide-Enhanced MR Exams

J McDonald[1], M Jentoft[1], M Paolini[1], D Murray[1], D Kallmes[1], E Williamson[1], L Eckel[2], R McDonald[1]
[1]Mayo Clinic, Rochester, MN, [2]Mayo Clinic, Rochester, Rochester, MN

Purpose
Intracranial gadolinium deposits following intravenous administration of gadolinium-based contrast agents (GBCAs) have led to concerns regarding the safety and biologic activity of these deposits. However, the extent of this deposition in other tissues has not been investigated fully. The purpose of the current study was to identify and quantify the extent of gadolinium deposition in other tissues of patients who underwent multiple gadodiamide-enhanced MR exams.
Materials and Methods
After obtaining antemortem consent, we examined all available organ, tissue, and bone samples from 3 adult patients (2 male, 1 female) who underwent 11-14 gadodiamide-enhanced MR exams (total gadodiamide dose 117-252 cc) at our institution. Formalin-fixed organ, tissue, and bone samples, including heart, kidney, liver, lung, pancreas, spleen, adrenal gland, bone, gallbladder, testicle, ovary, aorta, skin, colon, and thyroid, were harvested from our institutional biospecimen archive. Gadolinium was quantified using inductively coupled plasma mass spectrometry (ICP-MS).
Results
The time between the patient's last gadodiamide-enhanced MR exam and death ranged from 17 to 197 days. All 3 patients had normal renal function (eGFR > 60 ml/min/1.73m2) during the timeframe of gadodiamide administration. Gadolinium was detected in all samples tested, with the highest concentrations detected in bone (37.5-75.1 ug gadolinium/g sample), aorta (0.6-43.7 ug/g), kidney (1.0-66.0 ug/g), and thyroid (12.2-29.5 ug/g) samples. Comparatively, 8.5-25.4 ug/g gadolinium was deposited within dentate nucleus samples and 1.3-5.2 ug/g gadolinium was deposited within globus pallidus samples from these patients. Gadolinium was notably detected in all testicle (0.2 and 1.9 ug/g) and ovary (2.4 ug/g) samples.
Conclusions
Gadolinium deposits in numerous organs, tissues, and bone following multiple intravenous gadodiamide injections for contrast-enhanced MR exam, raising additional concerns regarding the safety of GBCAs. The clinical significance of this deposition is not fully understood and requires additional study.

O-260

1:54PM - 2:02PM

Gadobenate Dimeglumine (Multihance) Deposition in the Dentate Nucleus and Globus Pallidus

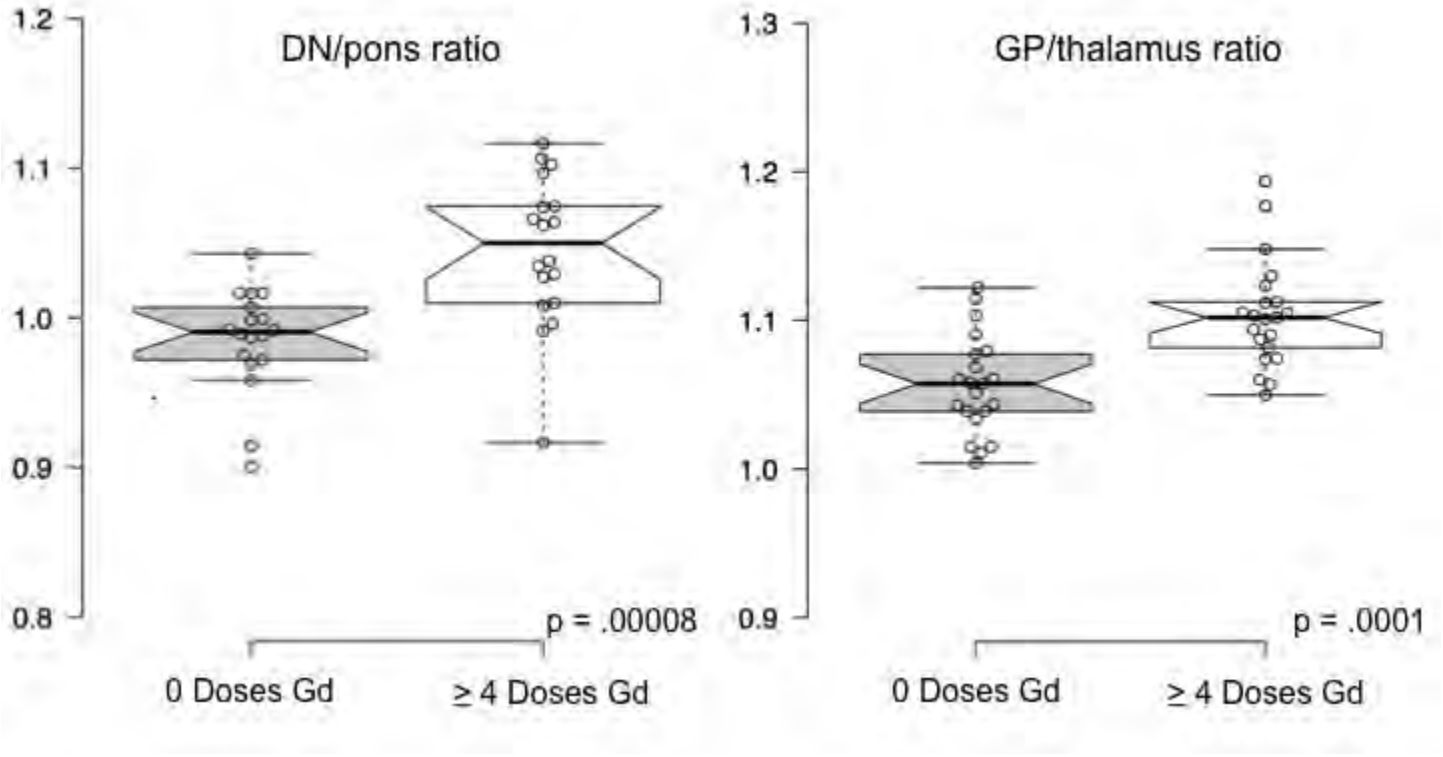
A Mashhood[1], S Barnes[2], K Tong[3]
[1]Loma Linda University Medical Center, Loma Linda, CA, [2]Loma Linda Unversity Medical Center, Loma Linda, CA, [3]LLUMC, Loma Linda, CA

Purpose
Primary aim: Demonstrate abnormal signal hyperintensity on precontrast T1 of the globus pallidus and dentate nucleus in patients who have received multiple doses of gadolinium as Multihance only. Secondary aim: Demonstrate abnormal signal hypointensity on SWI of the globus pallidus and dentate nucleus in patients who have received multiple doses of gadolinium as Multihance only.
Materials and Methods
A search of our institutional image archives was performed over the period of February 2014 to October 2016 for patients who received greater than 4 doses of any gadolinium-based contrast agent. The approximately 500 cases were vetted individually for inclusion on the study based on the following criteria: exposure only to Gadobenate Disodium, greater than 4 doses of Gadobenate Disodium, absence of significant anatomic or surgical defects resulting in deformity of the target tissues, availability of axial precontrast T1 images prior to any Gadobenate Disodium exposure, and availability of precontrast T1 images of 2 mm slice thickness or thinner. Of the reviewed subjects, 21 subjects met the inclusion criteria. Standardized elliptical ROIs were placed in the target structures [dentate nuclei (DN), pons, globi pallidi (GP), and thalami] in axial precontrast T1 sequences and axial SWI sequences (if available) from both the most recent (case) and oldest (control) studies. Signal intensity ratios were calculated for DN/pons and GP/thalamus, and compared between the case and control studies for both sequences. A 2-sample t-test was used to test for a statistically significant difference in mean signal intensity ratios between the case and control calculated from both precontrast T1 and SWI sequences.
Results
In the evaluation of the precontrast T1 DN/pons ratio, there was an average exposure of 5.4 doses. The mean signal intensity ratio before any gadolinium exposure was 0.99, compared to 1.05 after exposure. This corresponds to a signal intensity difference of 6%, and a p-value of <0.001, indicating a statistically significant signal intensity ratio change. In the evaluation of the precontrast T1 GP/thalamus ratio, there was an average exposure of 5.2 doses. The mean signal intensity ratio before any gadolinium exposure was 1.06, compared to 1.10 after exposure. This corresponds to a signal intensity difference of 4%, and a p-value of <0.001, indicating a statistically significant signal intensity ratio change. In the evaluation of the SWI DN/pons ratio, there was an average exposure of 5.4 doses. The mean signal intensity ratio before any gadolinium exposure was 0.86, compared to 0.87 after exposure, and a p-value of

0.80, a statistically insignificant change. In the evaluation of the SWI GP/thalamus ratio, there was an average exposure of 5.2 doses. The mean signal intensity ratio before any gadolinium exposure was 0.80, compared to 0.75 after exposure, and a p-value of 0.27, a statistically insignificant change.

Conclusions

Precontrast axial T1 signal intensity ratios of the globus pallidus to thalamus and dentate nucleus to pons demonstrate a statistically significant increase following exposure to gadobenate disodium. This is consistent with results of other studies examining other linear gadolinium based contrast agents, thus demonstrating the presence of gadolinium deposition after exposure to gadobenate disodium. The clinical implications of this finding are unknown. Susceptibility-weighted imaging does not demonstrate a statistically significant change in signal intensity ratios in the target structures.



(Filename: TCT_O-260_GadoliniumDeposition.jpg)

O-261

2:02PM - 2:10PM

Adult patients demonstrate progressive T1 shortening in the dentate nucleus following multiple doses of gadobenate dimeglumine administration

G Bolles[1], S Stalcup[2], M Yazdani[3], S Creeden[2], H Collins[1], D Roberts[2]
[1]MUSC, Charleston, SC, [2]Medical University of South Carolina, Charleston, SC, [3]Medical University of South Carolin, Charleston, SC

Purpose
Recently, there have been reports of gadolinium accumulation in the brain of patients with normal renal function who have undergone multiple gadolinium-based contrast agent (GBCA) administrations. A progressive increase in T1-weighted signal in the dentate nucleus has been shown to be associated with administration of some, but not all GBCAs. Previously, in patients who received on average 4.6 doses of gadobenate dimeglumine, Ramalho et al. showed no significant increase in DN:MCP (dentate to middle cerebellar peduncle ratio) over time but did show a significant trend toward an increase in relative percentage change for DN:MCP between the first and last examinations. The purpose of this project was to determine if a correlation exists between intrinsic T1-weighted shortening in the DN and number of GBCA doses in patients who received large cumulative doses of gadobenate dimeglumine.
Materials and Methods
In this single center, retrospective study, we measured signal intensity of the DN and MCP on unenhanced T1-weighted images in 35 adult patients with normal renal and liver function who had undergone multiple contrasted MRIs using gadobenate dimeglumine exclusively (mean 9.14 doses ± 3.87 std, range1-19]. Two blinded neuroradiologists separately placed regions of interest within the DN and MCP on unenhanced T1-weighted images. We hypothesized a positive correlation between DN:MCP ratio and tested this with a one-tailed Pearson correlation.
Results
The DN:MCP ratio showed a significant correlation with the number of previous GBCA administrations ($r=0.486$, $p=0.002$). The correlation between relative change in DN:MCP ratio from the first to last scan and number of doses also was statistically significant ($r=0.295$, $p= 0.043$).
Conclusions
At higher doses, as can be experienced by tumor or multiple sclerosis patients, gadobenate dimeglumine is associated with a significant increase in DN:MCP ratio, shown in autopsy studies to represent gadolinium deposition. Research is needed to address the clinical significance, if any, of gadolinium deposition in the human brain.

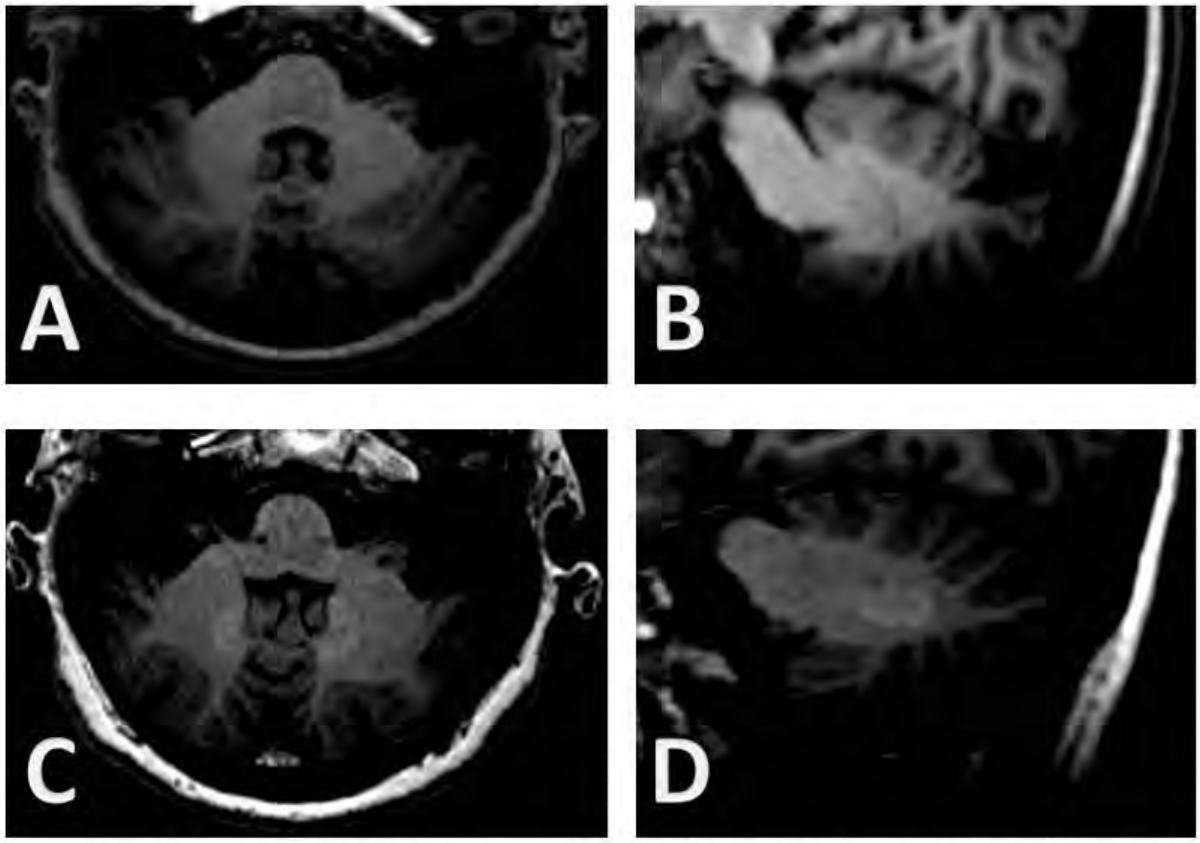


Figure 1: Coned down unenhanced T1 weighted MPRage images of a patient before (A- axial, B-sagittal) any administration of intravenous gadolinium based contrast agent and after (C-axial, D-sagittal) 9 doses of intravenous gadobenate dimeglumine over 600 days. There is intrinsic T1 shortening within the dentate nucleus on unenhanced T1 weighted imaging (C,D) after exclusive administration of intravenous gadobenate dimeglumine in this patient with normal renal and hepatic function without history of posterior fossa radiation.

(Filename: TCT_O-261_Multihanceabstract.jpg)

O-262

2:10PM - 2:18PM

High Signal Intensity In The Dentate Nucleus and Globus Pallidus On Unenhanced T1-weighted MR Images: Comparison Between Gadobutrol And Linear Gadolinium-based Contrast Agents

f moser[1], C Watterson[2], R prasad[2], M Austin[2], S Weiss[2], j mirocha[2]
[1]cedars-sinai medical center, los angeles, CA, [2]cedars-sinai medical center, Los Angeles, CA

Purpose

The ability of a chelating agent to retain the gadolinium - and therefore maintain its safety profile - has been shown to correlate with the chelating molecule's structure and stability. In general, macrocyclic chelating agents are more stable than linear chelating agents. Recent data indicate that patients exposed to multiple administrations of linear GBCA may exhibit dose-related T1 shortening in the globus pallidus (GP) and dentate nucleus (DN) (6-12).

Results regarding macrocyclic agents have been more varied, with some authors demonstrating T1 signal stability over sequential administrations, most commonly studying gadoterate meglumine, and a minority describing T1 changes with gadobutrol. This leads to reason that all macrocyclic GBCAs may not behave identically and further study of individual agents is warranted. Our study compares T1 signal changes following successive doses of only gadobutrol to those seen in a similar patient population receiving linear GBCAs.

Materials and Methods

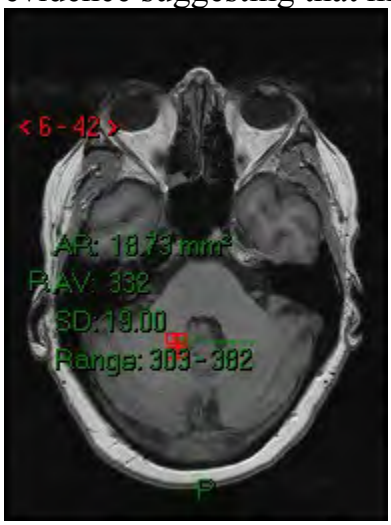
At our institution, prior to 2011, there had been exclusive use of the linear, nonionic contrast agents OptiMARK (gadoversetamide) and, to a lesser extent, Omniscan (gadodiamide). In between 2011 and February 2012, gadobenate dimeglumine (MultiHance), a linear, ionic GBCA, became the primary contrast agent. Following February 2012, we began to exclusively use gadobutrol (Gadovist), a macrocyclic GBCA, for all neuroimaging. This allowed us to have a population of patients who only had received the macrocyclic agent gadobutrol to compare against an earlier population who had received only linear GBCAs. Whole-brain MR imaging was performed by using 1.5T or 3T MR imaging units (Siemens; Erlangen, Germany). Unenhanced T1-weighted MR images (3D MPRAGE) were obtained with the following parameters on 1.5T systems: TR = 1330 msec; TE = 4.8 msec; TI = 800 msec; flip angle = 15 degrees; section thickness = 12.5 mm; matrix size = 256 x 192; echo train length = 1. T1-weighting parameters on 3T systems were: TR = 2100 msec; TE = 3.0 msec; TI = 900 msec; flip angle = 9 degrees; section thickness = 11 mm; matrix size = 256 x 256; echo train length = 1.

Results

Consistent with expectations, a significant percent increase was detected in the DN/Pons ratios when comparing the 1st examination to the 7th of patients receiving linear agents, while no significant change was demonstrated in the gadobutrol group (3.10% for those receiving linear GBCA; -0.8% for patients receiving gadobutrol; $P < 0.0001$) and comparing the 1st to the 8th exam (3.64% for those receiving linear GBCA; 0.14% for patients receiving gadobutrol; $P = 0.0002$). No significant difference was detected in either group when comparing DN/Pons ratios between the 7th and 8th examinations ($P = 0.39$). While a statistically significant increase was seen in the GP/Pons ratio in the linear GBCA cohort between the 1st to 7th examinations (2.47% for the linear GBCA group; -0.30% in the gadobutrol group; $P = 0.033$), the increase between the 1st and 8th examinations was less statistically significant (2.74% for the linear GBCA group; 1.01% increase in the gadobutrol group; $P = 0.141$). Again, no significant T1 signal change was detected in the patients receiving gadobutrol. As with the DN/Pons ratio, no difference was seen in the GP/Pons ratio between the 7th and 8th examinations ($P = 0.74$).

https://ww4.aievolution.com/asn1701/index.cfm?do=att.submitAbstract&style=0&attendeeID=6539&abstractID=1521&abstractField=results. Interestingly, a nonsignificant increase in GP/Pontine signal intensity ratio was seen between the 7th and 8th examinations of the

gadobutrol group (Recall Mean Change = 1.45%; P = 0.067), while there was minimal to no change in the linear agent group between the 7th and 8th exams (0.48%; P = 0.58).
Conclusions
The demonstration of a stable DN/Pons T1 signal intensity ratio over subsequent administrations of gadobutrol supports the growing preponderance of evidence suggesting that macrocyclic GBCAs, as a class, are less likely to deposit gadolinium in the brain. As with previous examinations, the use of linear GBCAs was found to result in T1 shortening. Our study failed to demonstrate a significant difference in T1 shortening over the course of a single examination with either class of agent, supporting the notion that such deposition occurs on a very minute scale. An additional consideration arose during our statistical analysis of the GP/Pons changes in that the T1 shortening seen between the 1st and 8th examinations of the gadobutrol group lost statistical significance when it had been present while comparing the 1st and 7th examinations. The most likely answer for this is wider variation of measurements taken of the 8th examination, favoring a higher T1 signal and thus narrowing the difference between the gadobutrol and linear GBCA groups. Another consideration would be that there are more variable, but lower, rates of deposition in the globus pallidus compared to the dentate nucleus, resulting in more variable measurements. Lastly, it is possible that a macrocyclic agent such a gadobutrol may deposit in such low concentrations that an imaging-apparent threshold may have only begun to be reached by the 8th examination. This potentially would be supported by the fact that a nonsignificant increase in T1 signal was seen between the 1th and 8th examinations of the gadobutrol group. In summary, patients exposed to gadobutrol, a macrocyclic agent, failed to demonstrate a demonstrable change in T1 signal intensity in the regions of the brain classically susceptible to gadolinium deposition. This corroborates in vitro and in vivo evidence suggesting that macrocyclic agents are less likely to deposit Gd than linear GBCAs.



(Filename: TCT_O-262_DNroi.jpg)

O-263

2:18PM - 2:26PM

Administration of multiple (6 or more) doses of a linear gadolinium contrast agent (GBCA) demonstrates no adverse clinical effects or new neurological sequelae in multiple sclerosis (MS) patients with normal renal function.

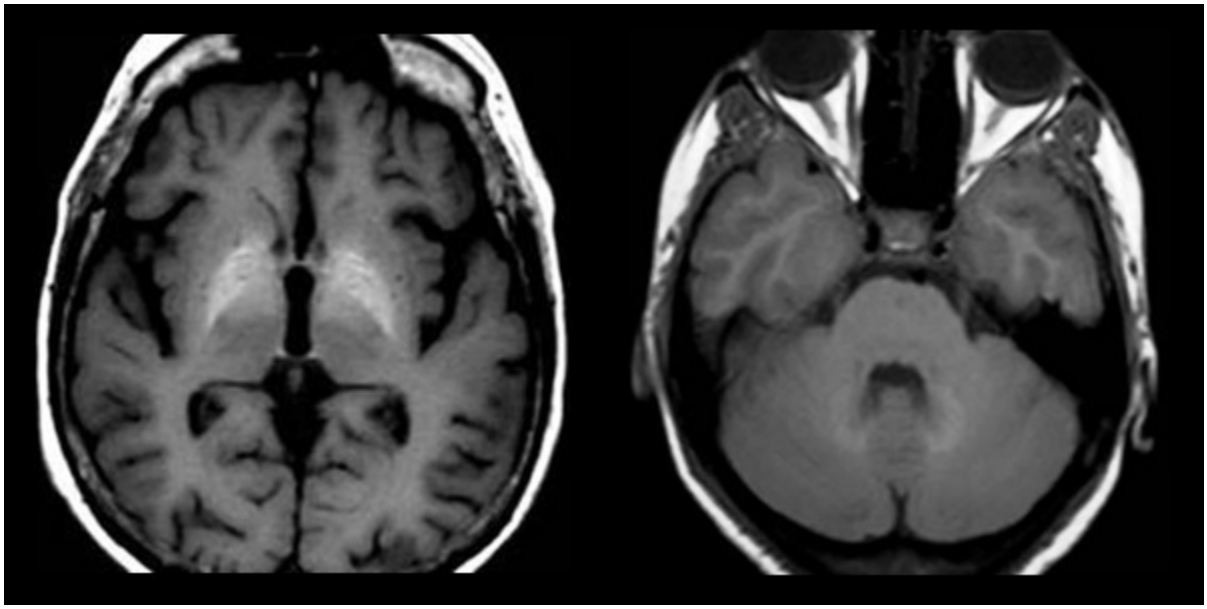
A Lerner[1], B Bigjahan[1], S Bergamaschi[1], O Boyko[1], M Shiroishi[1], W Gibbs[1], M Law[1]
[1]*Department of Radiology, Keck School of Medicine, University of Southern California, Los Angeles, California, U.S.A.*

Purpose
Patients undergoing magnetic resonance imaging (MRI) procedures often are exposed to gadolinium-based contrast agents (GBCA). Gadolinium-based contrast agents are used to improve the visibility of the internal organs and pathologic lesions. Gadolinium-based contrast agents have been reported to be associated with nephrogenic systematic fibrosis (NSF) in patients with renal failure. Nephrogenic systemic fibrosis is a progressive, debilitating, and emotionally distressing disease with early symptoms including but not limited to swelling, redness, pruritus, and pain in the limbs, sometimes with muscle weakness (1). Recent studies have identified T1 hyperintensity in globus pallidus and dentate nucleus in individuals with normal renal function who have received GBCAs (2, 3, 4). McDonald et al. have identified gadolinium in brain tissue and demonstrated a dose dependent relationship between GBCA administration and tissue deposition (5). However, at present, it remains unclear if there is associated adverse clinical effects in these patients. We retrospectively investigated the incidence of symptoms previously described in NSF and other clinical adverse events in multiple sclerosis (MS) patients with normal renal function who had 6 or more contrast MRIs having received manufacturers' recommended GBCA dose.
Materials and Methods
For this study, we reviewed the list of MS patients who underwent MR imaging from January 1, 2000 to December 9, 2016 based on our institution's RIS-PACS database. We identified 28 MS patients with normal renal function who had 6 or more contrast MRI scans with only gadobenate dimeglumine and/or gadopentetate dimeglumine administered. Subsequently, we performed a thorough analysis of the clinical charts and MRI scan reports, in our electronic medical record to identify any potential gadolinium deposition-related symptoms. Furthermore, we checked the administered GBCA dosage to confirm it was within manufacturers' recommended limits. We excluded all patients with renal failure and patients under the age of 18.
Results
Thirty patients (17 females, and 13 males) met the inclusion criteria. The patients received 6-13 doses of GBCAs for routine MRIs. Of the total 245 contrast MRIs included, 80% were gadobenate dimeglumine and 20% were gadopentetate dimeglumine. The mean time of follow up was 6 years, and the mean number of clinical consultations was 8 occurring every 6-12 months. The mean age was 45 and the median age was 43. No significant symptoms

were found in 22 patients. Of the remaining 8 patients, reported symptoms included back pain, hip pain, hand pain, and foot pain which were attributed to trauma, degenerative joint disease, carpal tunnel syndrome, and plantar fasciitis. Two patients reported "foggy mind" which resolved after discontinuing specific medications. One patient also had eye pain without an identified cause, and another patient had lower back pain without an identified cause.

Conclusions

Administration of multiple (6 or more) doses of a linear gadolinium contrast agent (GBCA) demonstrates no significant adverse clinical effects or new neurological sequelae in MS patients with normal renal function. Despite the limitations of our study, a systematic review of the MS patients with normal renal function and at least six GBCA injections could not identify any patients with skin lesions, joint pain nor musculoskeletal findings that did not have a reasonable alternative cause. Further investigations, especially large prospective studies/registries, are needed to determine if there are potential clinical consequences of GBCA administration and deposition. At present, we did not find any significant adverse clinical events.



(Filename: TCT_O-263_Image.jpg)

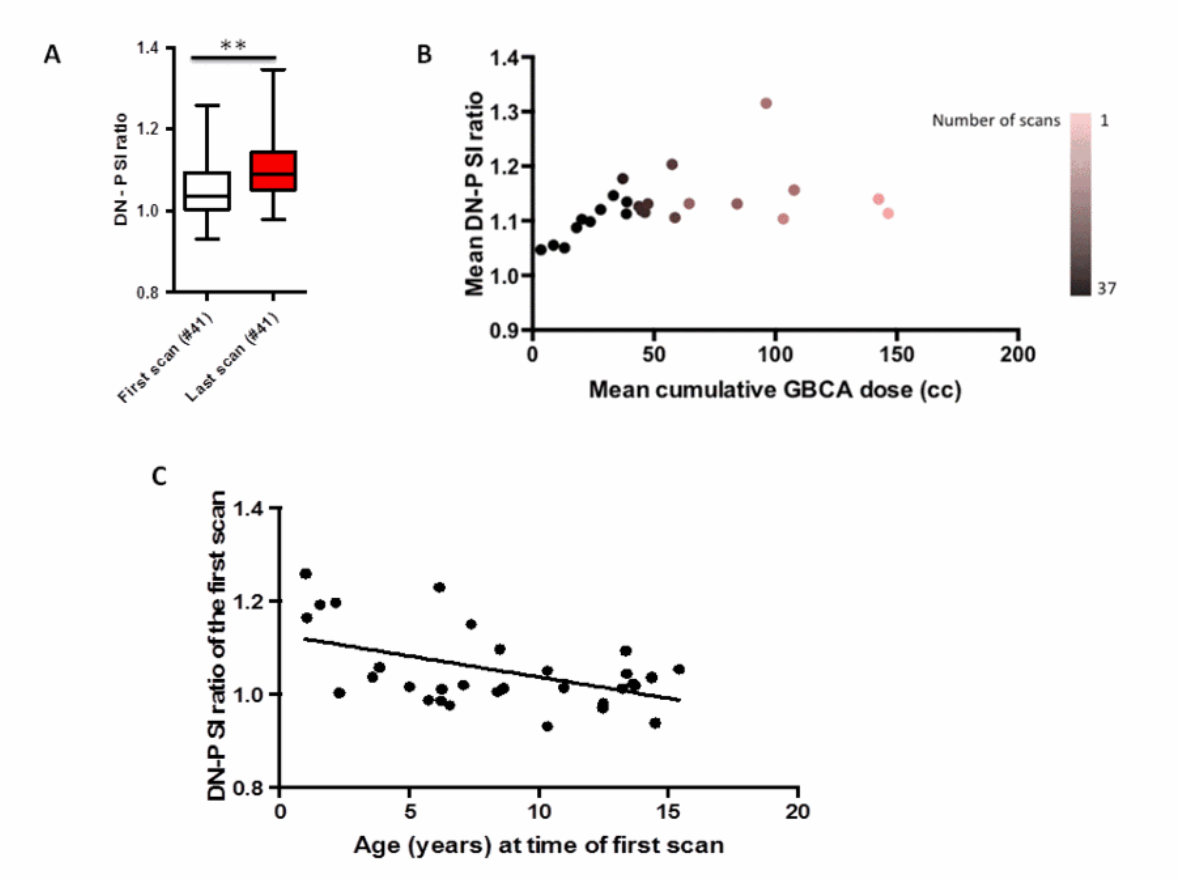
O-264

2:26PM - 2:34PM

Gadolinium Deposition in the Pediatric Brain: T1-Weighted Hyperintensity within the Dentate Nucleus Following Repeated Gadolinium-Based Contrast Agent Administration

J Young[1], I Orosz[1], M Franke[1], H Kim[1], D Woodworth[1], B Ellingson[1], N Salamon[1], W Pope[1]
[1]*David Geffen School of Medicine at UCLA, Los Angeles, CA*

Purpose
To determine whether repeated gadolinium-based contrast agent administration (GBCA) in children is associated with the development of increased T1-weighted signal intensity within the dentate nucleus.
Materials and Methods
With IRB approval for this HIPAA-compliant retrospective study, we identified a cohort of 41 patients under the age of 18 years who underwent at least 4 contrast-enhanced MR examinations of the brain from 2005-2015. For each examination, both dentate nuclei were contoured manually, and the mean dentate-to-pons signal intensity (DN-P SI) ratio was calculated. The DN-P SI ratios from last to first MR examination were compared, and the correlation between DN-P SI ratio and cumulative gadolinium dose was calculated using a linear mixed effect model to control for potentially confounding variables.
Results
For the 41 patients in our cohort, there was a significant increase in the mean DN-P SI ratio from the first MR scan to the last MR scan (1.05 vs. 1.11, p=0.004, Panel A) and a significant positive correlation between DN-P SI ratio and cumulative gadolinium dose (p=0.03). When controlling for patient diagnosis, history of chemotherapy or radiation, sex, and age, a significant positive association between cumulative GBCA dose and the DN-P SI ratio persisted (Spearman correlation r=0.57, p=0.003, Panel B). In patients over the age of 1 year, there was an inverse correlation between age and the DN-P SI ratio on the first MR scan prior to GBCA administration (i.e., before the patient received any GBCA) with a trend toward significance (r= -0.30, p=0.096, Panel C).
Conclusions
Repeated GBCA administration in children is associated with increased T1-weighted signal intensity within the dentate nuclei, an imaging surrogate for gadolinium deposition. Our findings also suggest that without exposure to intravenous GBCA, the DN-P SI ratio may decrease with age. Thus, even a stable DN-P SI ratio across serial MR examinations may reflect gadolinium deposition in the dentate nucleus.



(Filename: TCT_O-264_ASNRAbstract.gif)

O-265

2:34PM - 2:42PM

Longitudinal changes in dentate nucleus-pons and globus pallidus-thalamus signal intensity ratios in multiple sclerosis patients from cumulative gadobenate administrations

A SRINIVASAN[1], M Carter[1]
[1]*University of Michigan, Ann Arbor, MI*

Purpose
The aim of our study was to assess the longitudinal changes in dentate nucleus-pons (DN-P) and globus pallidus-thalamus (GP-T) signal intensity (SI) ratios across 6 cumulative gadobenate doses received for research purposes in a set of multiple sclerosis (MS) patients.
Materials and Methods
An IRB-approved retrospective analysis was performed on 20 MS patients (enrolled in a clinical trial from 2009-2011) who had received 6 contrast-enhanced brain MRIs over a 12-month period. One reader placed elliptical regions of interest (ROI) on the precontrast T1W images (per methods described in the literature) to create DN-P and GP-T SI ratios on each

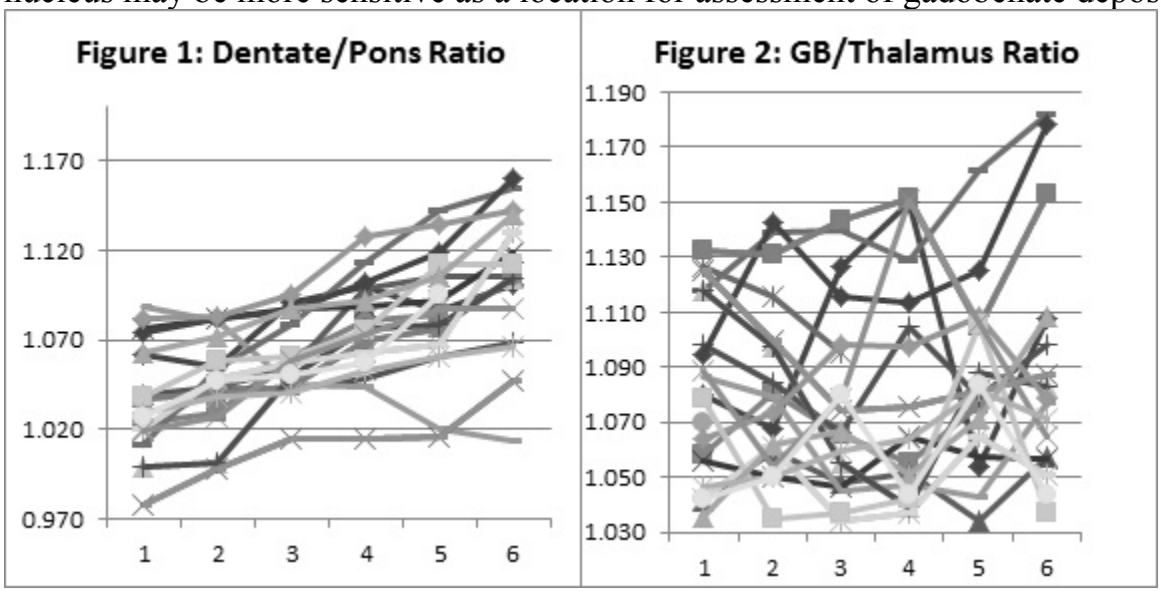
MRI scan. The differences in the SI ratios between the first and last scans were calculated with paired t-test used to study significant changes. Percent changes in SI ratios across each successive scan were calculated and also represented in a graphical fashion.

Results

All patients received 0.1 mmol/kg of gadobenate during each MRI. Of the 20 patients, 18 received 6 MRI scans, 1 only 3 scans, and 1 patient only 1 due to dropout from the trial. Significant differences in DN-P SI ratios between the first and last scan were seen (1.038 versus 1.101, $p<0.000$) but not in GP-T ratios (1.081 versus 1.091, $p=0.242$). Figures 1 and 2 demonstrate the longitudinal trend in SI ratios with a mild increase in DN-P ratios but no trend in GP-T ratios.

Conclusions

Cumulative doses of gadobenate contrast agent for brain MRI were associated with a small but significant increase in DN-P SI ratios but not in GP-T ratios, suggesting that the dentate nucleus may be more sensitive as a location for assessment of gadobenate deposition.



(Filename: TCT_O-265_Figures1and2.jpg)

O-266

2:42PM - 2:50PM

The Effect of a Gadolinium Holiday on MRI Signal Changes in Brain Gadolinium Deposition

A Wu[1], D Cantrell[1], B Liu[2]

[1]Northwestern, Chicago, IL, [2]Northwestern University Feinberg School of Medicine, Chicago, IL

Purpose

To investigate longitudinal signal intensity (SI) change in patients who received serial

administration of linear gadolinium-based contrast agent (GBCA) followed by either the same number of macrocyclic GBCA or a gadolinium-free interval (gadolinium holiday) of at least 3 years.

Materials and Methods

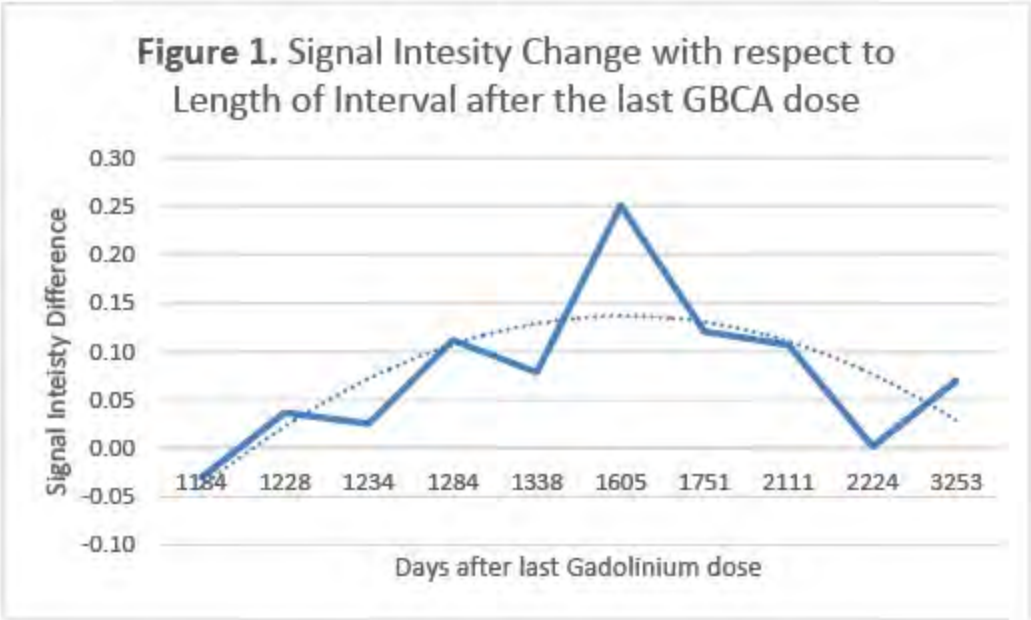
IRB approved, single center, retrospective study, 25 patients with mean age of 51.8 years (range 28-77) included. Contrast group included 15 patients who had 5 or more serial MRIs with a linear GBCA (gadopentetate dimeglumine, Magnevist) followed by the same number of exams with a macrocyclic agent (gadobutrol, Gadavist). The holiday group included 10 patients who had 5 or more serial gadolinium-enhanced MRIs with a linear agent (gadopentetate dimeglumine) followed by a gadolinium-free period (gadolinium holiday) of at least 3 years. On axial noncontrast T1 spin echo sequence, ROIs were drawn over the dentate nucleus (DN) and central pons. Signal ratio of DN:Pons and the difference of the ratios between studies were calculated.

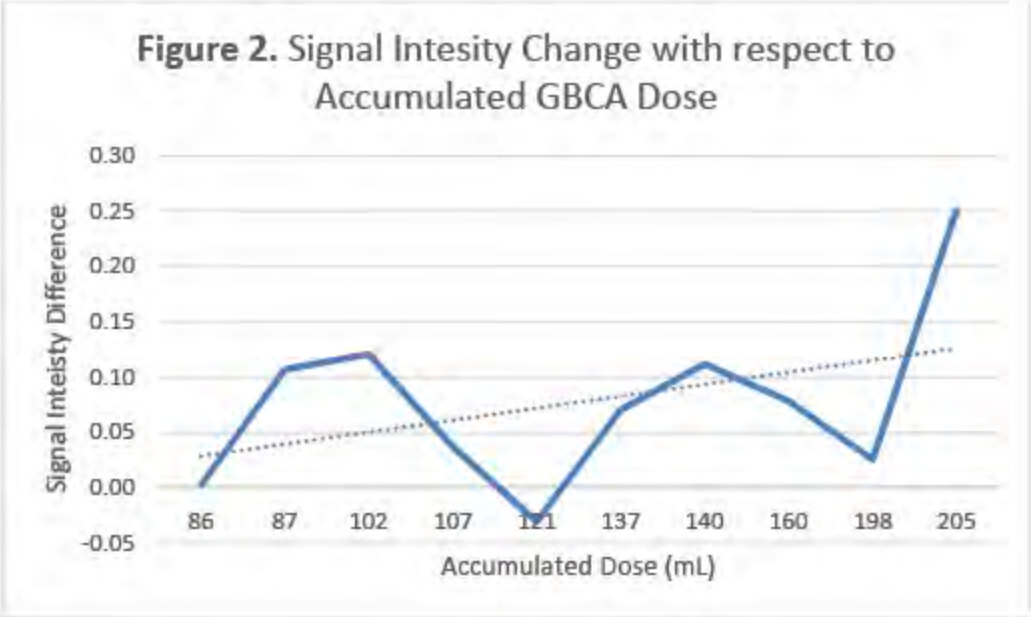
Results

The contrast group had a mean number of 8.67 doses of both linear and macrocyclic GBCA and an average accumulated dose of 195.8 mL of the linear agent over a mean study interval of 2.35 years and 72.9 mL of the macrocyclic agent over 2.83 years. Using linear regression, we observed an increase in SI with increasing number of linear GBCA administration. However, SI change did not correlate with the number of macrocyclic GBCA administration. The holiday group had a mean number of 7 linear GBCA doses with an average accumulated dose of 137 mL followed by a mean gadolinium-free interval of 4.9 years (range 3.2–8.9). Using linear regression, we found an initial increase of SI after multiple linear GBCA administration, peak at approximately 4 years and then decrease thereafter (Fig. 1), which was statistically significant ($p = 0.038$). We also observed a trend of SI increase with increasing accumulated gadolinium dose (Fig. 2) although this was not statistically significant.

Conclusions

Our study confirmed the literature in that SI increase and thus gadolinium deposition occur with linear GBCA and not macrocyclic agents (1-3). In the gadolinium holiday group, evolution of signal change may reflect gadolinium deposition dynamics related to systemic reservoirs in the body such as bone versus other mechanisms.





(Filename: TCT_O-266_Untitled.jpg)

O-267

2:50PM - 2:58PM

Gadolinium Deposition in the Organs, Tissues, and Bone of a Patient Diagnosed with Nephrogenic Systemic Fibrosis

J McDonald[1], M Jentoft[1], M Paolini[1], D Murray[1], D Kallmes[1], E Williamson[1], L Eckel[2], R McDonald[1]
[1]Mayo Clinic, Rochester, MN, [2]Mayo Clinic, Rochester, Rochester, MN

Purpose
Intravenous administration of gadolinium-based contrast agents (GBCAs) has been linked separately to the development of nephrogenic systemic fibrosis (NSF) and deposition of gadolinium in intracranial tissues. However, the extent of gadolinium deposition in NSF patients as compared to patients who received GBCAs but did not develop NSF has not been fully examined. The purpose of the current study was to examine gadolinium deposition in the organs, tissues, and bone of a patient who developed NSF.
Materials and Methods
After obtaining antemortem consent, we identified a male patient seen at our institution with renal failure (median eGFR 26 ml/min/1.73m2) who underwent 2 gadodiamide-enhanced MR exams (total gadodiamide dose 46 cc) and subsequently developed pathology-confirmed NSF. The patient underwent autopsy at our institution, with 1350 days between the patient's last gadodiamide injection and death. Formalin fixed organ, tissue, and bone samples, including heart, kidney, liver, lung, pancreas, spleen, adrenal gland, bone, gallbladder, testicle, ovary, aorta, skin, colon, and thyroid, were harvested from our institutional biospecimen archive. Gadolinium was quantified using inductively coupled plasma mass spectrometry (ICP-MS).
Results
Very high concentrations of gadolinium were detected in the neural tissues of this patient (dentate nucleus 39.8 ug gadolinium/g sample, globus pallidus 43.4 ug/g, thalamus 5.0 ug/g), and thalamus (5.0 ug/g). As a comparison, these intracranial concentrations were similar to concentrations we observed in patients with normal renal function who did not develop NSF who underwent a total of 28-29 gadodiamide-enhanced MR exams (total gadodiamide dose 420-500 cc). High gadolinium concentrations also were observed in all NSF patient organs, tissues, and bone samples that were tested (bone 166.9 ug/g, heart 19.6 ug/g, kidney 63.0 ug/g, lung 94.5 ug/g, pancreas 34.3 ug/g, spleen 32.9 ug/g, aorta 306.7 ug/g, skin 4.4 ug/g, hypodermis 16.4 ug/g, testicle 12.4 ug/g).
Conclusions
A patient who developed NSF after 2 gadodiamide-enhanced MR exams had very high concentrations of gadolinium in his organs, tissues, and bone. These concentrations were comparable to patients who received 28-29 total gadodiamide-enhanced MR exams who did not develop NSF. These findings suggest that NSF patients are particularly susceptible to gadolinium deposition.

Wednesday
3:30PM - 4:45PM
Long Beach Convention Center, Room 202 (Upper Level)

20B-Parallel Paper Session: Fetal and Pediatric Imaging Feats: Way to Grow!

O-268

3:30PM - 3:38PM

Ultrafast brain MRI can be used for indications beyond shunted hydrocephalus

A Tekes[1], S Senglaub[1], E Ahn[1], T Huisman[2], E Jackson[1]
[1]Johns Hopkins University, Baltimore, MD, [2]Johns Hopkins, Baltimore, MD

Purpose
Shunted hydrocephalus evaluation is the most common indication for use of ultrafast brain MRI (UFB-MRI). Radiation and sedation-free imaging capabilities make this protocol more desirable over CT and routine brain MRI. We hypothesize that UFB-MRI can be utilized for selected indications beyond shunted hydrocephalus without adverse outcomes.
Materials and Methods
Ultrafast brain MRI was performed with axial, sagittal and coronal HASTE. Radiology Information Systems (RIS) was used to identify pediatric patients (ages 0 to 18) who received an UFB-MRI between March 2014 and May 2016. A retrospective chart review was completed in these cases to identify the indication other than shunted hydrocephalus such as ventriculomegaly, macrocephaly, or intracranial cyst. All UFB-MRIs were evaluated by a certified neuroradiologist and a neurosurgeon. Ultrafast brain MRI was deemed sufficient diagnostic value for these indications if no further brain imaging was required before the planned next follow-up visit, or additional imaging was required for alternate diagnosis.
Results
Radiology Information System identified 800 patients who received an UFB-MRI during the study period. One hundred and nineteen of these patients had ventriculomegaly, macrocephaly, or intracranial cyst as the study indication. Sixty-five patients did not require any further imaging. Thirty-seven patients were planned for follow-up UFB-MRI. Four patients had a follow-up ultrasound. Twelve patients had additional studies with new or alternate diagnosis. One patient had an aqueductal stenosis protocol done months later as routine follow up.
Conclusions
These results suggest that the UFB-MRI is sufficient to evaluate ventriculomegaly, macrocephaly, or intracranial cyst. As the UFB-MRI is radiation and sedation-free, we recommend its use as the primary screening study for these indications, sparing sedated MRI or CT for patients with indications based on the UFB-MRI results.

O-269

3:38PM - 3:46PM

Brain DSC MR imaging perfusion in children: a clinical feasibility study

S Gaudino[1], M Martucci[2], A Botto[3], P Frassanito[4], M Caldarelli[5], F Triulzi[6], C Colosimo[7]

[1]Fondazione Policlinico Universitario A. Gemelli, Institute of Radiology, Rome, Italy, [2]Fondazione Policlinico Universitario A. Gemelli, Institute of Radiology, ROME, Italy, [3]Fondazione Policlinico Universitario A. Gemelli, Institute of Radiology, ROME, ROME, [4]Fondazione Policlinico Universitario A. Gemelli, Institute of Neurosurgery, Rome, RM, [5]Fondazione Policlinico Universitario A. Gemelli, Institute of Neurosurgery, 00168, RM, [6]Fondazione Irccs Ca' Granda Ospedale Maggiore Policlinico, Milan, Italy, [7]Fondazione Policlinico Universitario A. Gemelli, Institute of Radiology, ROME, RM

Purpose

There is a growing interest in perfusion magnetic resonance (MR) imaging for pediatric tumor, but dynamic susceptibility contrast (DSC) MR imaging perfusion resulted limited in children due to difficulties in reproducing technical standards derived from adults. This prospective multicenter study aims to determine feasibility of DSC MR imaging perfusion in children, and to assess DSC perfusion quality using custom child administration of a standard dose of gadolinium.

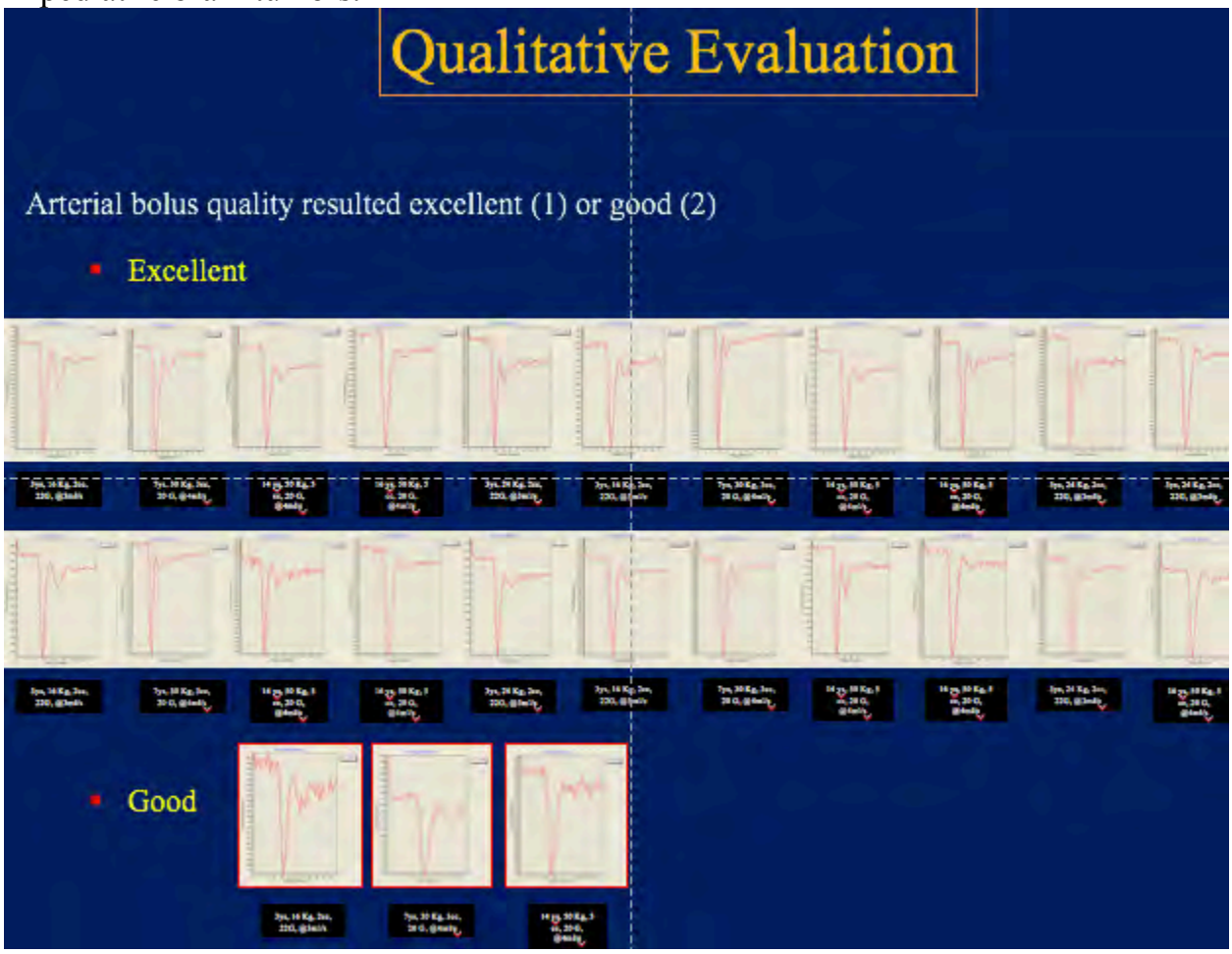
Materials and Methods

Fifty consecutive children (age range from 4 month to 15 years) with brain tumor underwent DSC MRI perfusion at 1,5T (34 patients) and 3T (6 patients). In order to provide a safe administration of contrast, and with the aim to obtain a compact bolus, the choice of IV access, catheter size, and flow rate was performed under the direct supervision of a physician (anesthesiologist, pediatric, neuroradiologist). The standard dose of gadolinium (gadobutrol, 0.1 mL/kg of body weight) was administrated with an automated power injector. The location and size of IV catheters, volume and flow rates were documented, as well as the use of sedation. Catheter site was checked at the end, and 24 hours after MRI exam, and adverse effects recorded. Qualitative evaluations of contrast bolus adequacy (CBV maps, signal intensity-time curves) was performed by 2 independent investigators (radiology resident, senior neuroradiologist) and interobserver agreement was measured (Cohen k). Quantitative assessment (percentage of signal drop, full width half-maximum) was performed by a junior neuroradiologist. Data were compared with the quality DCS standards reported in the literature for adults. Quantitative data also were grouped by flow rate, and differences between flow rate group were evaluated at analysis of covariance and tested for statistical significance with a t test.

Results

Locations of IV catheters were arm (35/50), hand (12/50), and feet (3/50); gauge used was 18G for 4/50, 20G for 30/50, 22G for 13/50, and 24G for 3/50; volume of gadobutrol ranged from 1 to 7 ml, and flow rate from 1 to 5 mL/s (4@5mL/s, 31 Pts @4mL/s, 10@3mL/s, 4 @2mL/s, one @1mL/s. Sedation was used for 18 patients (≤8 years). No access site complication and adverse effects were reported. High quality of CBV maps and signal intensity-time curves were achieved in 50/50, with excellent interobserver agreement (k >0. 75). Quantitative evaluations resulted equal or superior to those reported from the literature. In all cases percentage of signal drop resulted ≥45% and full width half-maximum ranged

from 5s to 8s. No significant differences ($p \geq 0.05$) of percentage of signal drop and full width half-maximum were identified between the 2 conspicuous groups of flow rate (@3ml/s and @4ml/s), and between these groups and data from the literature.
Conclusions
A custom child administration of a standard dose of gadobutrol allows obtaining safe and high quality DSC MR imaging perfusion. Feasibility and reliability of DSC perfusion in children might be the prelude to include DSC in the routinely clinical MR imaging protocol in pediatric brain tumors.



(Filename: TCT_O-269_ImageASNR.jpg)

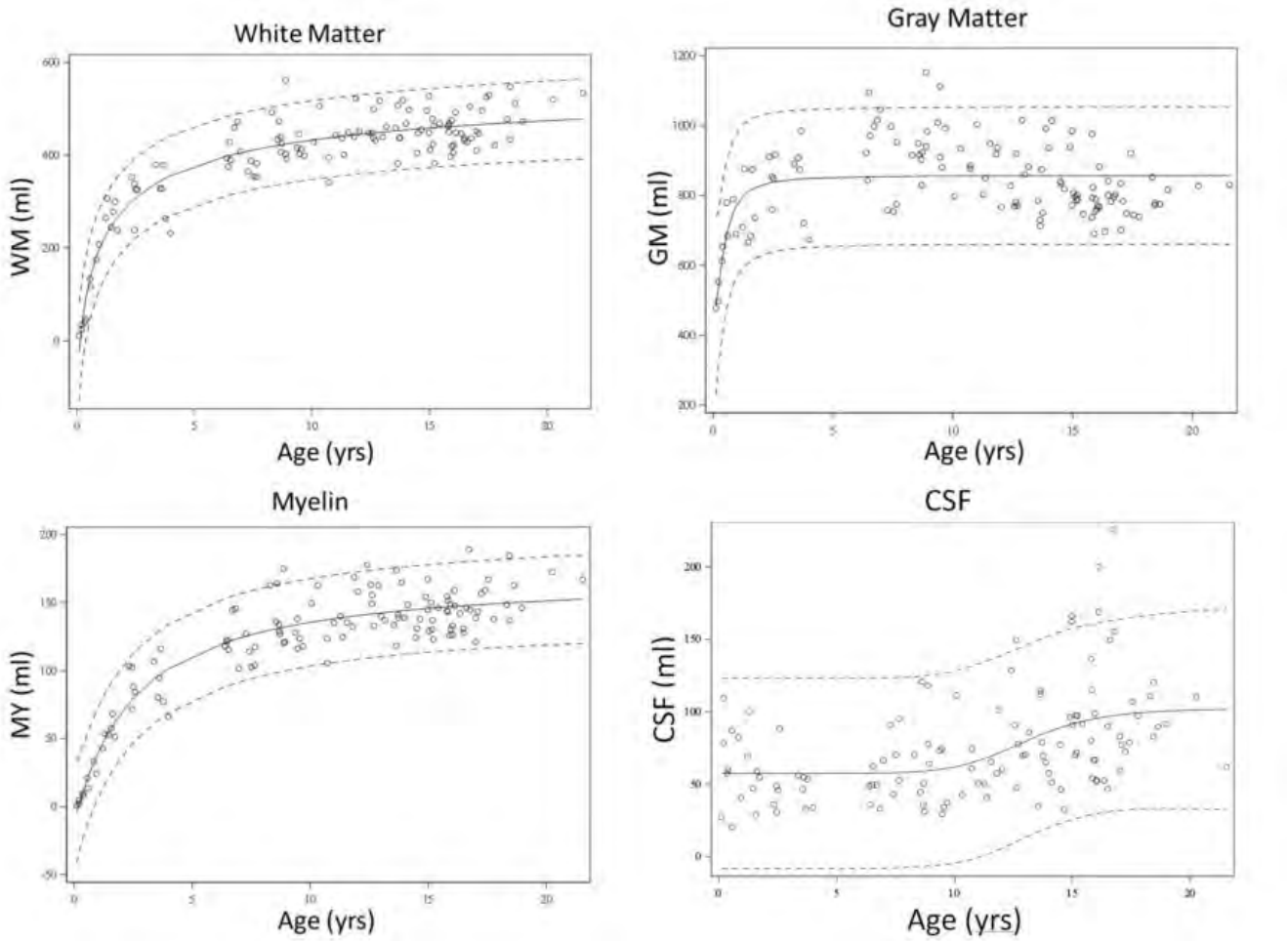
O-270

3:46PM - 3:54PM

Quantitative Synthetic MRI in Children: Normative Intracranial Tissue Segmentation Values During Development

A McAllister[1], H West[1], J Leach[1], B Jones[1], S Serai[1]
[1]*Cincinnati Children's Hospital Medical Center, Cincinnati, OH*

Purpose
Synthetic MRI (SyMRI®) is a method in which a multiple-spin echo saturation recovery sequence (QMAP) is used with 4 saturation delays and 5 echoes to create absolute R1, R2, and PD relaxivity maps with associated software which allows for rapid automated intracranial segmentation of tissue types. We created a normative database of intracranial (IC), brain parenchymal (BP), gray matter (GM), white matter (WM), cerebrospinal fluid (CSF), and myelin (MY) volumes in a pediatric population with normal brain MRIs using SyMRI® in order to demonstrate its potential clinical use.
Materials and Methods
All brain MR studies that were interpreted as normal and in which the QMAP sequence was performed over a 34-month period were reviewed. Examinations in which there was incomplete anatomic coverage on the QMAP sequence, or which had excessive artifact or image noise were excluded. A detailed clinical chart review was conducted on the remaining subjects. Those who were not neurologically normal or had conditions known to affect neurological development or alter brain parenchymal or intracranial volumes were excluded. The remaining normal examinations then were quantitatively analyzed using SyMRI® software (Synthetic MR 8.0). IC, BP, GM, WM, CSF, and MY volumes were calculated and plotted versus age. Selected abnormal exams are compared with these normative curves.
Results
Of 619 MRI examinations performed with the QMAP sequence, 497 examinations were excluded (475- clinical/imaging 22-technical) leaving 122 normal studies for analysis. The subjects ranged in age from 0.1-21.5 years (median 11.8). Resulting normative data plots compare favorably with previously published data using more onerous techniques. Differentiation from pathologic states was possible using quantitative values. Limitations of the automated segmentation will be discussed.
Conclusions
A pediatric database of normal intracranial tissue volumes using a single sequence and rapid software analysis has been compiled and correlates with previously published data. This provides a framework for clinical interpretation of quantitative synthetic MRI scans during development.



(Filename: TCT_O-270_2016-12-08_21-39-34charts300dpi.jpg)

O-271

3:54PM - 4:02PM

Image Processing to Improve Gray-White Differentiation in Pediatric Head CT Images

T Madaelil[1], A Sharma[2], M Parsons[3]
[1]Mallinckrodt Institute of Radiology, St Louis, MO, [2]Mallinckrodt Institue of Radiology, Saint Louis, MO, [3]Mallinckrodt Institute of Radiology, Saint Louis, MO

Purpose

Differentiation of gray and white matter is important in recognition of normal structures as well as identification of pathologic processes on head CTs. Using quantitative measures of conspicuity and contrast-to-noise ratio (CNR), we aimed to test whether an image-processing algorithm could improve gray-white differentiation (GWD) in normal low-dose pediatric head CT images.

Materials and Methods
Sixty baseline normal head CT images were processed using a custom algorithm (Correlative Image Enhancement, CIE) to generate corresponding enhanced images. Using equivalent ROIs placed over normal gray and white matter in baseline and enhanced images, conspicuity and CNR was calculated. In addition, 2 masked radiologists rated ease of gray-white differentiation on a 5-point Likert scale. Baseline conspicuity and CNR were tested for correlation with mean GWD ratings. Conspicuity, CNR, and gray-white differentiation ratings for baseline and enhanced images were compared.
Results
Baseline CNR between gray and white matter was 1.86 ± 0.94 with gray matter conspicuity of 37.3 ± 11.5. Mean qualitative GWD rating score on baseline images was 3.15 ± 0.90. Spearman correlation test revealed a positive correlation of baseline CNR ($r = 0.54092$; $p<0.001$) and conspicuity ($r=0.27$; $p=0.03695$) with GWD ratings. Image processing with CIE had a statistically significant increase in CNR (2.27 ± 1.00; $p=0.02$) and conspicuity (46.4 ± 11.5; $p<0.001$). This quantitative result also was confirmed qualitatively with improvement in qualitative assessment of GWD ratings on enhanced images (4.03 ± 0.79; $p<0.001$).
Conclusions
Correlative Image Enhancement resulted in improvement in both conspicuity of normal gray matter and CNR between normal gray and white matter, with resultant improvement in qualitative perception of GWD. Such processing may prove useful in head CT images with poor inherent CNR.

O-272

4:02PM - 4:10PM

MRI Determination of Normal Pediatric Pituitary Gland Volumes Utilizing Ellipsoid Volumes compared to 3-Dimensional Volumetric Analysis

A Arneja[1], J Haigney[2], A Ferguson[2], S Bobra[1], H Mehta[3], M Tenner[1]
[1]Westchester Medical Center, Valhalla, NY, [2]New York Medical College, Valhalla, NY, [3]New York Medical College-Westchester Medical Center, Valhalla, NY

Purpose
Determination of normal reference range for pediatric pituitary volume as by MRI utilizing length/width/height measurements and 3D volumetric analysis.
Materials and Methods
Magnetic resonance imaging brain examinations of 140 pediatric individuals with clinically normal pituitary function (75 female, 65 male) and age ranging from 5-18 years were reviewed in order to obtain volumetric measurements of the pituitary gland. The height, width, and depth of the pituitary were obtained from mid-sagittal, coronal and axial planes and volume was calculated from these measured parameters utilizing (LxWxH)/2.

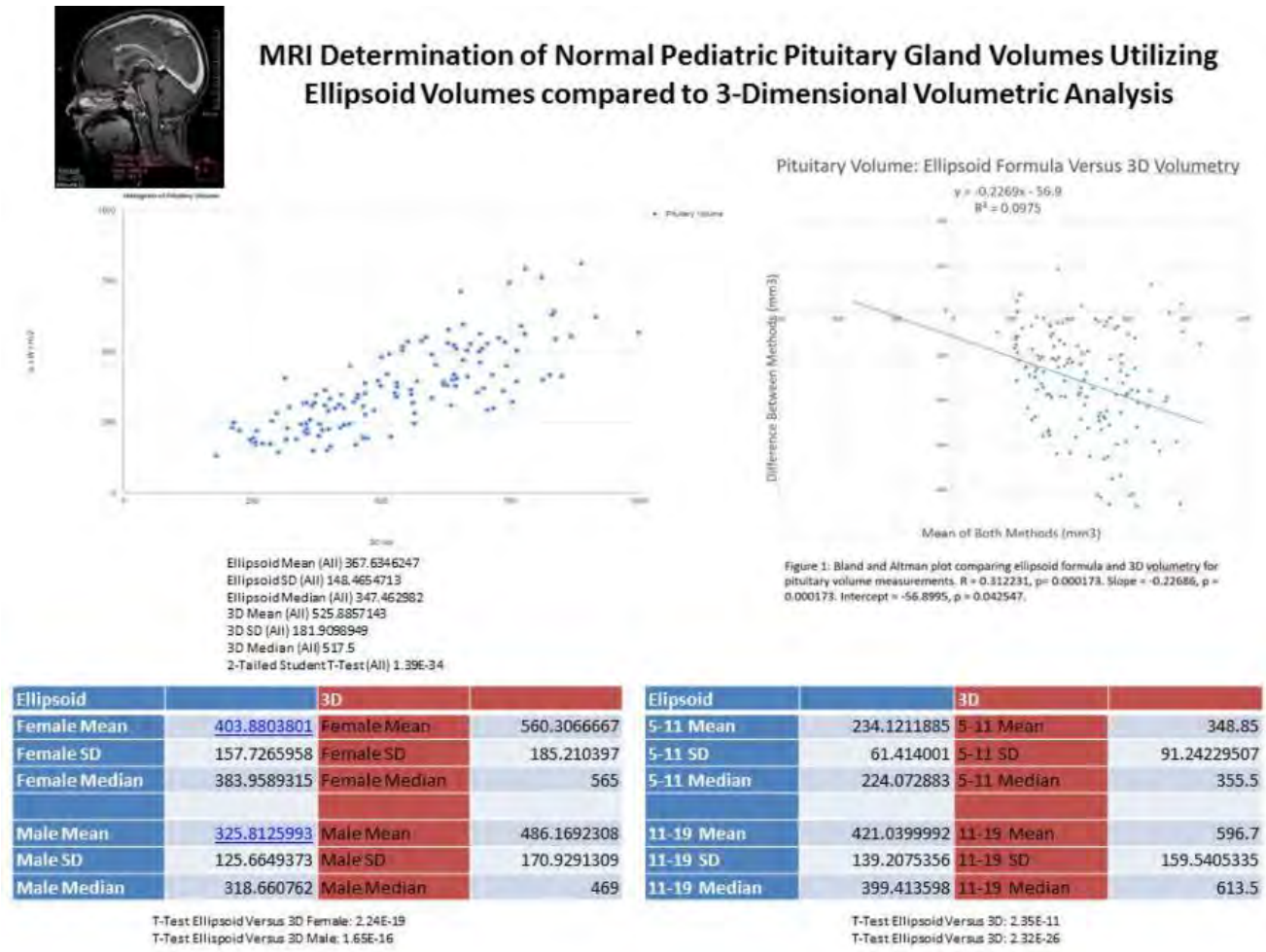
Additionally, 3-dimensional volumes were calculated utilizing the Phillips IntelliSpace advanced imaging software. The data obtained was stratified based on age (5-11 or 11-19 years) and sex (M or F) for analysis. Statistical tests applied included Student's t-test and Bland-Altman correlation. A minimum level of statistical significance was set at $P < 0.05$.

Results

The mean ellipsoid pituitary volumes were 367.6 ± 148.5 mm3 with median of 347.5. The mean ellipsoid pituitary volumes were 403.9 ± 157.7 mm3 and 325.8 ± 125.7 mm3, in females and males respectively. The mean 3D pituitary volumes were 525.8 ± 181.9 mm3 with median of 517.5 mm3. The mean 3D pituitary volumes were 560.3 ± 185.2 mm3 and 486.2 ± 170.8 mm3, in females and males respectively. There was a statistically significant difference between ellipsoid and 3D pituitary volumetric analysis ($P = 0.000$). There also was statistically significant difference between the ellipsoid and 3D pituitary volume in both sexes as well as both age groups ($P = 0.000$). Bland Altman plot also yielded a statistically significant correlation (correlation coefficient $R = 0.312231$, $p = .000173$).

Conclusions

With this study, we have provided reference values in a normal pediatric population for the dimensions of normal pituitary gland utilizing both ellipsoid and volumetric analysis, in order to facilitate assessment and diagnosis in patients with abnormalities of the hypothalamic-pituitary axis. Additionally, we have found statistically significant difference and statistically significant correlation between ellipsoid and 3D volumetric calculations of normal pediatric pituitary glands.



(Filename: TCT_O-272_pit.JPG)

O-273

4:10PM - 4:18PM

Evaluating a new objective indicator of Idiopathic Intracranial Hypertension (IIH) on routine pediatric brain CT scan

T Bartsikhovsky[1], T Sigal[2], S Nagieva[3], M Vaiman[4], T Ziv-Baran[5], P Gottlieb[4], I Bekerman[3]
[1]Assaf Harofeh Medical Center, Ramat Gan, Israel, [2]Assaf Harofeh Medical Center, Zerifin, Zerifin, [3]Assaf Harofeh Medical Center, Tzrifin, Tzrifin, [4]Assaf Harofeh Medical Center, Zrifin, Zrifin, [5]Tel Aviv University, Tel aviv, Tel aviv

Purpose
The aim of this study was to establish optic nerve sheath diameter (ONSD) to eyeball transverse diameter (ETD) index value as sign of elevated ICP on brain CT scan in pediatric patients and correlate this data with papilledema on ophthalmologic examination.
Materials and Methods
We retrospectively reviewed brain CT studies and medical files of pediatric patients for a

period 2014-2015 years. We selected patients who were admitted to the emergency department with complaints of headache and/or one of the signs of elevated ICP, had a normal brain CT scan and underwent ophthalmological evaluation during the same clinical episode. These patients were stratified into 2 groups depending on whether they had signs of papilledema on ophthalmological study. The control group included subjects who underwent brain CT studies for various reasons not related to elevated ICP and had normal results. All measurements were held manually on routine brain CT scan axial images obtained using the 256-channel CT scanner with slice thickness 3 mm. Optic nerve sheath diameter was measured at the point where the ophthalmic artery crosses the optic nerve. The ETD was measured from retina to retina on a slice where lens was identified.
Results
Total study population included 153 patients (75 boys, 78 girls, mean age 11.1±5.2 years). Optic nerve sheath diameter/ETD index had significantly higher values ($p<0.001$) in patients with papilledema (median 0.24, IQR=0.22-0.25) compared to patients with no signs of papilledema (median 0.18, IQR=0.16-0.19) and control group (median 0.17, IQR=0.15-0.18). No correlation with age was found ($r=-0.086$, $p=0.288$). There was a significant female predominance in patients with papilledema comparing to the group without papilledema and control group (76%, 40.5% and 51.1% respectively, $p=0.04$). Optic nerve sheath diameter/ETD index showed to have an excellent discrimination ability (AUC= 0.96, 95%CI, 0.94-0.99). The ONSD/ETD index of 0.21 is 82% sensitive and 93% specific for papilledema and thereby for elevated ICP in pediatric patients.
Conclusions
A strong correlation between papilledema on ophthalmologic examination and elevated values of the ONSD/ETD index was established making it a simple and reliable sign of elevated ICP on otherwise normal brain CT scan in pediatric population.

O-274

4:18PM - 4:26PM

Does a Correlation exist between Placental Volume and Fetal Isolated Ventriculomegaly?

G Shapira[1], D Grynspan[1], D Reddy[1], M Valdez Quintana[1], E Miller[1]
[1]*Children's hospital of Eastern Ontario, Ottawa, Ontario*

Purpose
There is a known correlation that exists between placental insufficiency and neurodevelopmental injury (1, 2) and a reduction in placental volume has been shown in intrauterine growth restriction (IUGR) patients (3, 4). Experimentally, induction of placental insufficiency in animals caused reduced brain weight, ventriculomegaly, and volumetric reductions in the basal ganglia and the hippocampus of the offspring (5). We hypothesized that isolated ventriculomegaly (IVM) is related to placental insufficiency in contrast to other

structural central nervous system (CNS) abnormalities that are more likely due to intrinsic causes (e.g. genetic, metabolic). Based on this hypothesis, the aim was to investigate if differences in placental volume exist between fetuses with IVM, fetuses with other structural CNS abnormalities and controls.

Materials and Methods

Institutional research ethics board approval was obtained. 1.5 T fetal MRI of 75 singleton pregnancies between 20 and 24 weeks of gestational age (GA) were analyzed retrospectively, 49 with CNS morphologic abnormalities, 8 of which had isolated ventriculomegaly (3 mild, 1 moderate, 4 severe), and 26 controls without any detectable structural abnormalities. Placental volume was measured by manually outlining the placenta on all slices in a single plane and the volume subsequently was calculated automatically. Placental volume measurements were compared between normal controls versus fetuses with IVM and fetuses with CNS abnormalities other than IVM. Placental volume assessment also was subdivided by GA (20 - 21+6 weeks, and 22 - 24 weeks) as placental volume increases with GA. Mann-Whitney statistical test was used.

Results

Statistically significant differences were shown in placental volume between normal fetuses and fetuses with IVM, wherein the placentas of the normal fetuses were significantly smaller ($p= 0.03$). When subdividing by GA, significant differences were shown for the older GA group ($p=0.03$) but not for the younger GA group ($p= 0.5$). No significant difference was shown in placental volume between normal fetuses and fetuses with complex CNS abnormalities. Additionally, no significant difference was observed when subdividing by GA ($p=0.79$ for 20-24 weeks GA, $p=0.36$ for 20 to 21+6 weeks GA and $p=0.9$ for 22-24 weeks GA).

Conclusions

Correlation between placental volume and IVM suggests that alterations in the placenta potentially may be related to IVM in human fetuses. Placental volume does not seem to have a use in prediction of other fetal CNS abnormalities which are more likely due to intrinsic etiologies rather than placenta-dependent etiologies. Further evaluation with a larger sample size is needed for substantiation of the results.

O-275

4:26PM - 4:34PM

Volumetry, ADC and T2-weighted values of the Placenta in Fetuses with and without CNS Abnormalities

G Shapira[1], M Valdez Quintana[1], P Caro Dominguez[1], D Grynspan[1], J Davila[2], D Reddy[1], E Miller[1]

[1]Children's Hospital of Eastern Ontario, Ottawa, Ontario, [2]University of Ottawa, Ottawa, Ontario

Purpose
There is a known correlation that exists between placental insufficiency and neurodevelopmental injury (1, 2), yet MRI features of the placentas of fetuses with central nervous system (CNS) abnormalities have not been studied. Decreased apparent diffusion coefficient (ADC) measurements have been observed in placentas of growth-restricted fetuses (3), and differences in placental volume has been demonstrated between fetuses with and without congenital heart disease (4). The ratio of placental and amniotic fluid T2 signal intensities (relative T2 signal intensity) has been shown to correlate with gestational age (GA) (5). The purpose of this study was to investigate if differences in ADC values, placental volume, fast imaging employing steady-state acquisition sequence (FIESTA) signal intensity of the placenta, and placental to amniotic fluid ratio on FIESTA (relative FIESTA) exist between fetuses with and without CNS abnormalities.
Materials and Methods
Institutional research ethics board approval was obtained. 1.5 T fetal MRI of 97 singleton pregnancies were analyzed retrospectively, 64 with CNS morphologic abnormalities and 33 controls without abnormalities. FIESTA measurements were done by averaging 3 regions of interest (ROI) within the placenta. An additional ROI in the amniotic fluid was measured in order to calculate the relative FIESTA (rFIESTA). Placental volume measurements were possible on 75 pregnancies, 49 of which had CNS abnormalities (cases wherein the entire placenta was not scanned on the same sequence were excluded). Placental volume assessment was subdivided further by GA (20 to 21+6 weeks, and 22 to 24 weeks) as placental volume increases with GA. Apparent diffusion coefficient values were assessed in 57 singleton pregnancies, 39 with CNS morphologic abnormalities and 18 controls without morphologic abnormalities. On diffusion-weighted imaging (DWI) (b 1000 s/mm2) the slice that displayed the largest surface of placenta was selected and ADC measurements were performed by averaging 3 ROIs within the placenta blinded to the CNS findings. Measurements were compared with the presence or absence of CNS fetal abnormalities. Wilcoxon tests and t-tests were used.
Results
Significantly lower ADC values ($p = 0.002$) were measured in placentas of fetuses with CNS abnormalities compared to controls. No significant difference was shown in placental volume (also when subdivided by GA), FIESTA signal intensity, and rFIESTA between fetuses with and without CNS abnormalities ($p= 0.636$, 0.712, and 0.488 respectively). No differences in volume were noted also when subdivided by GA.
Conclusions
The quantification of DWI of the placenta in fetal MRI suggests that the presence of fetal CNS abnormalities is associated with restricted diffusion and reduced ADC values of the placenta. Therefore in the pathologic placenta, DWI and ADC mapping have the potential to quantify early neurological changes. Placental volume, FIESTA signal intensity, and rFIESTA do not predict fetal CNS abnormalities in this series.

O-276

4:34PM - 4:42PM

Intensity Profiles of Transient Layers in the Human Fetal Brain on Postmortem MRI and Corresponding Histology, with Special Emphasis on Subplate

I Pogledic[1], C Mitter[1], E Schwartz[2], G Gruber[3], P Brugger[4], P Baltzer[5], G Kasprian[6], D Prayer[6]

[1]Division of Neuroradiology and Musculoskeletal Radiology, Vienna, Austria, [2]Computational Imaging Research Lab, Vienna, Austria, [3]Department of Systematic Anatomy, Vienna, Austria, [4]Medical University of Vienna, Vienna, AK, [5]Department of Biomedical Imaging and Image-guided Therapy, Vienna, Austria, [6]Medical University of Vienna, Vienna, Austria

Purpose

The aim of our study was to delineate transient fetal layers during normal brain development on postmortem MR images and histology in identical subjects between 19 and 24 gestational weeks (GW).

Materials and Methods

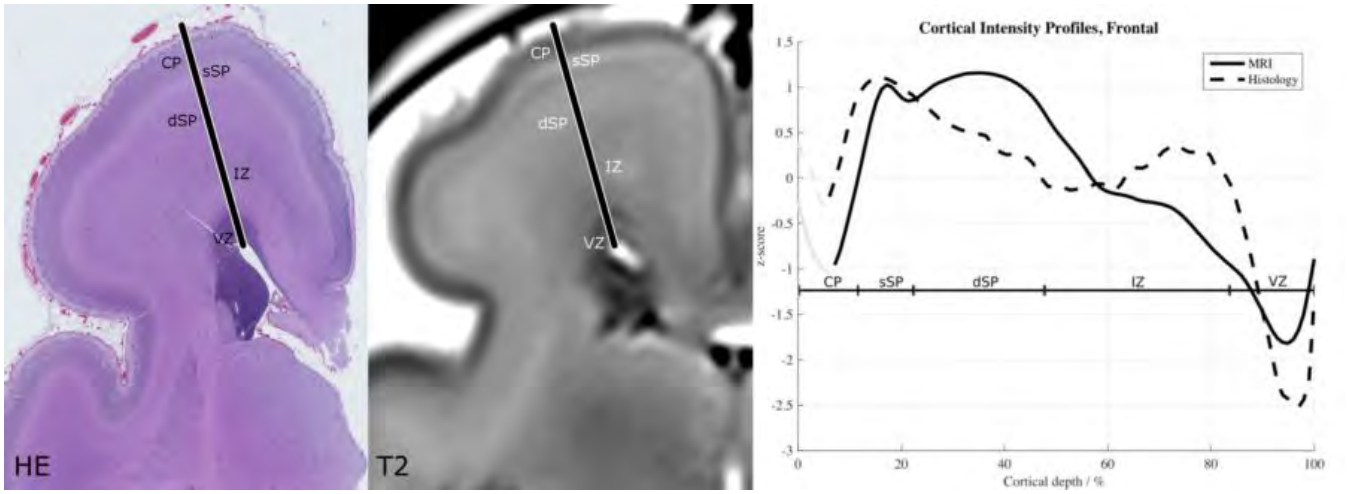
Postmortem human fetal brains without cerebral pathologies between 19 and 24 GW were imaged on 3 Tesla MR scanner (T2-weighted coronar sequence; TR 3180, TE 137, voxel size 0.3mm x 0.4mm x 1.7mm) and 9 cases with existing histology (hematoxillin-eosin staining, HE) were selected for analysis. Three measurements were performed in the frontal lobe perpendicular to the pial surface by the first rater (IP) in agreement with the second rater (CM). Intensity profiles were plotted via Software ImageJ and directly compared to the lamination profiles of corresponding histological sections in identical subjects. All profiles were z-normalized according to the length of the profile. Calculations were performed using MATLAB and Statistics Toolbox Release 2013a, The MathWorks, Inc., Natick, Massachusetts, United States.

Results

The intensity profiles of developmental fetal layers in frontal lobe on MRI match the ones on HE staining (from pia to ventricle): CP (the first hypointense layer), the superficial subplate-sSP (the second hyperintense layer), deep subplate-dSP (the third less hyperintense layer), intermediate zone-IZ (the fourth hypointense layer) and ventricular and subventricular zone-VZ (the fifth extremely hypointense layer). See Figure, the x-axis shows the percentage of the depth of each pixel from the superficial part of the cortical plate-CP (0%) to the ventricle (100%). The average thickness of sSP was 0.805 mm and of the dSP 2.937 mm on MRI. The ratio between dSP and sSP was 3.649.

Conclusions

Brain lamination from GWs 19-24 visible on post-mortem MR images corresponds to histology. This is an important requirement to recognize deviations from normal brain development on MRI.



(Filename: TCT_O-276_FigureASNR2017.jpg)

Wednesday
3:30PM - 4:45PM
Long Beach Convention Center, Room 103 (Main Level)

20C-Parallel Paper Session: Imaging of Cognitive Impairment - Not in the Know?

O-277

3:30PM - 3:38PM

The ERICA-Score (Entorhinal Cortex Atrophy) – A Novel Visual Scoring System for the Assessment of Medial Temporal Lobe Atrophy in Alzheimer's Disease with MRI

S Enkirch[1], A Traschütz[1], M Heneka[1], A Jurcoane[1], A Mueller[1], H Schild[1], E Hattingen[1]
[1]*University Hospital Bonn, Bonn, Germany*

Purpose
Visual evaluation of focal brain atrophy in MRI - precisely medial temporal lobe atrophy (MTA) - is an important part in the diagnostics of dementia. The MTA score is used to assess hippocampal atrophy in Alzheimer disease (AD) on standardized coronal slices. However, volumetric and functional studies have shown that in AD, the entorhinal cortex (EC) is among the first brain structures to show pathological changes, even before the hippocampus. Since these methods are not practical in daily routine, we aimed to establish a novel visual score focused on entorhinal cortex atrophy ("ERICA") and compare its diagnostic value with the MTA score.
Materials and Methods
Two independent raters retrospectively analyzed coronal slices of 3D T1-sequences (3-Tesla) of 60 patients with probable AD vs. 60 age-matched patients with only subjective cognitive complaints (SCC). Medial temporal lobe atophy was assessed visually with the established MTA score and our novel four-step ERICA score (Fig. 1). Diagnostic value to

discriminate patients with AD from those with SCC was assessed according to the Standards for Reporting of Diagnostic Accuracy Studies (STARD).
Results
Patients with AD had significantly higher MTA and ERICA scores than those with only SCC ($p<0.001$). Pathological values were defined as: MTA score ≥ 2 in patient age <75 years; MTA score ≥ 3 in patient age >75 years; ERICA score ≥ 2 regardless of age. With regard to identification of patients with AD, ERICA score performed considerably better than the MTA score (sensitivity 80% vs. 53%, specificity 92% vs. 87%; positive predictive value 91% vs. 80%, negative predictive value 82% vs. 65%; diagnostic accuracy 86% vs. 70%; $p<0.001$).
Conclusions
ERICA score ≥ 2 with moderate atrophy and detachment of the EC from the cerebellar tentorium is an easy and valid marker for AD and proved to be superior to the MTA score. Future studies should investigate if the ERICA score allows an earlier diagnosis of initial stages of AD than other established methods.

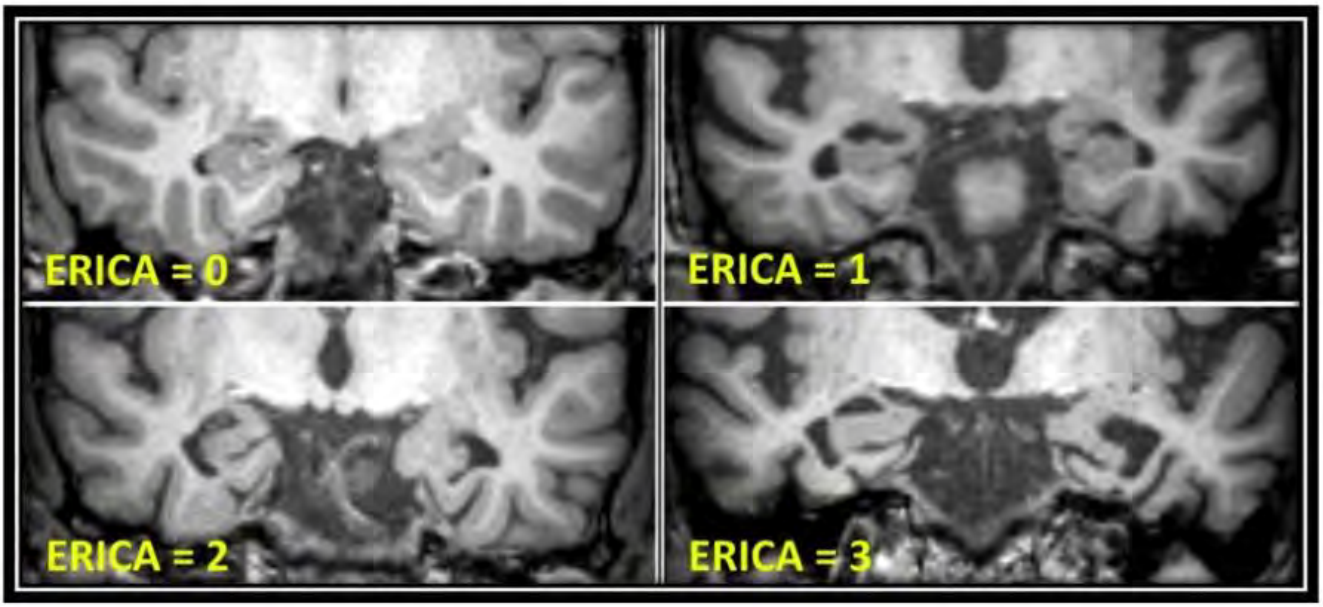


Figure 1. ERICA-Score 0 = normal volume of the EC; 1 = mild atrophy with widening of the collateral sulcus; 2 = moderate atrophy with detachment of the EC from the cerebellar tentorium; 3 = pronounced atrophy with wide collateral sulcus and broad gap between EC and cerebellar tentorium.

(Filename: TCT_O-277_ERICA_final.jpg)

O-278

3:38PM - 3:46PM

The correlation between cerebral microbleed, amyloid uptake and hypometabolism in Alzheimer's disease and mild cognitive impairment

N Sheikh-Bahaei[1], S Sajjadi[2], R Manavaki[3], J O'Brien[4], J Gillard[5]

[1]University of Cambridge, Cambridge , United Kingdom, [2]University of California Irvine, Irvine , CA, [3]University of Cambridge, Cambridge , ,, [4]university of Cambridge, Cambridge , ., [5]University of Cambridge, Cambridge , Cambridgeshire

Purpose

There is a growing body of evidence suggesting strong correlation between vascular pathology and Alzheimer disease (AD). Cerebral microbleeds (CMB), that are foci of amyloid β (Aβ) deposition in the small vessel walls, are one of these vascular manifestations. Although CMBs are significantly more prevalent in Alzheimer disease, compared to healthy controls and other types of neurodegeneration (1), their ultimate role in AD pathogenesis remains unclear. With the recent introduction of immunotherapy for AD, CMBs have attracted even more attention. Nevertheless, there is still lack of quantitative studies investigating the relation between microbleeds and other AD related pathologies. Such studies are essential for increasing our knowledge about the role of CMB in AD. In this study, we aimed to investigate the relationship between lobar burden of CMBs and both Aβ deposition and hypometabolism in AD. We hypothesized that the burden of CMB in each anatomical region is related to neurodegeneration rather than local Aβ deposition.

Materials and Methods

Cases with clinical diagnoses of early AD (n=11), mild cognitive impairment (MCI) (n=10), and healthy control (HC) (n=8) were recruited through memory clinics in the University of Cambridge. All participants underwent 11 C- Pittsburg compound B- (PiB) and 18 F-fluorodeoxyglucose (FDG)-PET followed by high resolution 3T susceptibility-weighted imaging (SWI). Dynamic 90 minute PiB- and 30 minute FDG-PET were performed and images were assessed quantitatively using standard uptake value ratio (SUVR) using cerebellum as reference. The SWI images were assessed by expert neuroradiologists using Microbleed Anatomical Rating Scale (MARS) (2).

Results

Cerebral microbleeds were present in 80% of AD, 33% of MCI, and 12.5% of HC. There was no significant difference in the age and vascular risk factors of participants in the 3 groups. Total cortical PiB uptake was significantly higher in cases with CMB (p-value<0.0001) but there was no association between the lobar PiB uptake and presence of CMB. Also while total cortical FDG SUVRs were not different between cases with or without CMB, lobar FDG uptake was significantly lower in temporal lobes that had CMB (p-value:0.009). Parietal lobe uptake also was trending toward significance (p-value:0.09).

Conclusions

In concordance with previous studies, our data confirmed that while presence of CMB is associated with higher total PiB uptake, amyloid load was not higher in CMB positive lobes. The novel finding of our study is the observed relationship between CMB and hypometabolism in temporal lobes. This suggests that presence of CMB might be an indicator of neurodegeneration. Further studies are needed to elucidate the causal relationship between hypometabolism and formation of CMBs.

O-279

3:46PM - 3:54PM

Cerebral perfusion alterations in amnestic mild cognitive impairment determined by cortisol gene variant: An arterial spin labeling (ASL) cerebral blood flow study

P Rajagopalan[1], E Horgusluoglu[1], K Nho[1], S Risacher[1], A Saykin[1]
[1]*Indiana University School of Medicine, Indianapolis, IN*

Purpose
Stress hormone, cortisol, is linked to cognitive decline and brain atrophy in patients with mild cognitive impairment (MCI) and Alzheimer disease (AD) (1). Plasma cortisol has a moderate-high heritability (30-60%) (2), and therefore, we wanted to determine if gene variants increasing plasma cortisol caused alterations in regional cerebral blood flow, and if so, in what regions.
Materials and Methods
Data for SERPINA6/SERPINA1 locus variant, rs12589136 affecting plasma cortisol (2) were genotyped in 109 subjects with MCI enrolled in the Alzheimer's Disease Neuroimaging Initiative GO/2 study (http://adni.loni.usc.edu). Quantified pulsed arterial spin labeling (ASL) performed on Siemens systems were obtained from University of California San Francisco (3) and a voxel-wise imaging analysis using SPM8 was performed at Indiana University.
Results
One hundred nine MCI patients had ASL and genetic data (Fig. 1). In the region of interest (ROI) analysis, cortisol-associated T allele demonstrated significantly increased cerebral blood flow in left frontal, bilateral (left>right) temporal and left occipital cortex (Fig. 2), after correcting for age, gender, education, handedness and Apoe4 group. A voxel-wise imaging analysis of ASL demonstrates significantly (FDR critical p-value < 0.0005 and q = 0.0001) increased regional perfusion by approximately 4-5 ml/100mg/min in the presence of risk allele, notably in the left inferior parietal lobule (Fig. 3). This region demonstrates altered metabolism early in the course of AD as implicated in prior default-mode network studies involving episodic memory processing and may thus reflect a compensatory mechanism for damage to other memory-related regions (4). Our previous results of predominant right-sided cortisol associated brain atrophy (5) may partly explain the asymmetric preserved perfusion on the left.
Conclusions
Cortisol gene variant carriers show significant cortical hemodynamic alterations in MCI, which may help distinguish them from healthy aging adults, through noninvasive neuroimaging measures. By identifying these vulnerable brain regions early on in MCI, we may further understand the role of genetic risk factors in amyloid and tau pathways and one's

risk for AD, with significant clinical implications towards targeted disease-modifying strategies.

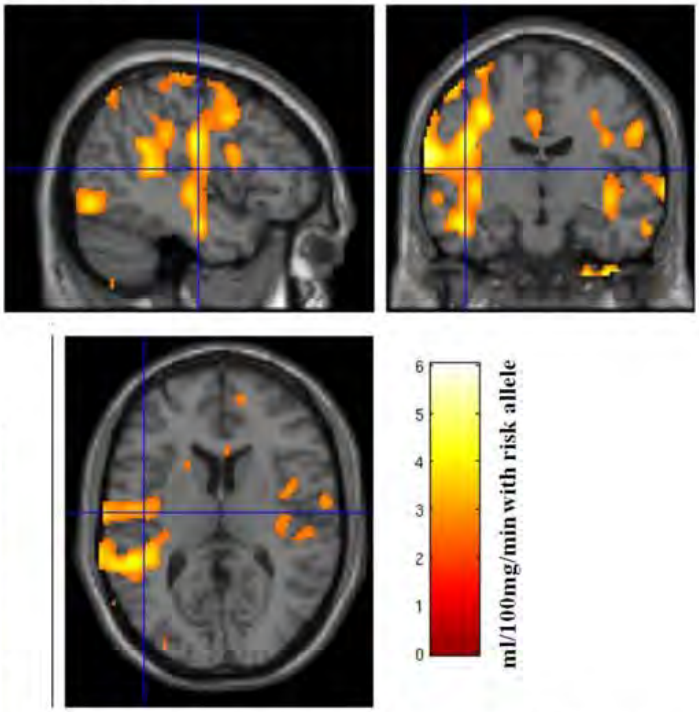
Figure 1.

SERPINA locus variant	GG	GT	TT
No. of MCI subjects	69	36	4
Gender (M, F)	41, 28	19, 17	2, 2
Mean age Years)	71.8	70.3	71.8
Education (Years)	16.6	16.6	16.5
Handedness (Right, Left)	59, 10	30, 6	3, 1
APOE(e4) (Positive, Negative)	34, 35	10, 26	1, 3

Figure 2.

Perfusion ROI	*Beta*-value	*P*-value
Right Frontal lobe	2.93	0.023
Left Frontal lobe	3.45	0.004*
Right Temporal lobe	4.31	0.001*
Left Temporal lobe	4.71	<0.0005*
Right Parietal lobe	4.35	0.001*
Left Parietal lobe	5.72	<0.0005*
Right Occipital lobe	4.52	0.008
Left Occipital lobe	4.86	0.005*

Figure 3.



Cerebral perfusion alterations in ml/100mg/min associated with cortisol gene variant risk allele after controlling for age, sex, handedness, education and Apoe4 group.

(Filename: TCT_O-279_ASNR2017_Rajagopalan_SERPINA.jpg)

O-280

3:54PM - 4:02PM

Noninvasive Detection of Cortical Glutathione using 1H MRS: Associations with Brain Amyloidosis and Hippocampal Volumes

G Chiang[1], X Mao[1], G Kang[1], E Chang[1], S Pandya[1], R Isaacson[1], L Ravdin[1], D Shungu[1]
[1]*Weill Cornell Medical College, New York, NY*

Purpose
Oxidative stress has been reported to be an important pathological mechanism in the development of Alzheimer disease (AD) and may serve as a potential target for disease-modifying interventions. The purpose of this study was to determine whether glutathione (GSH) and other brain metabolite levels, detected noninvasively with proton magnetic resonance spectroscopy (1H MRS), are associated with brain amyloidosis and hippocampal volumes in a community-dwelling cohort of normal older adults.

Materials and Methods

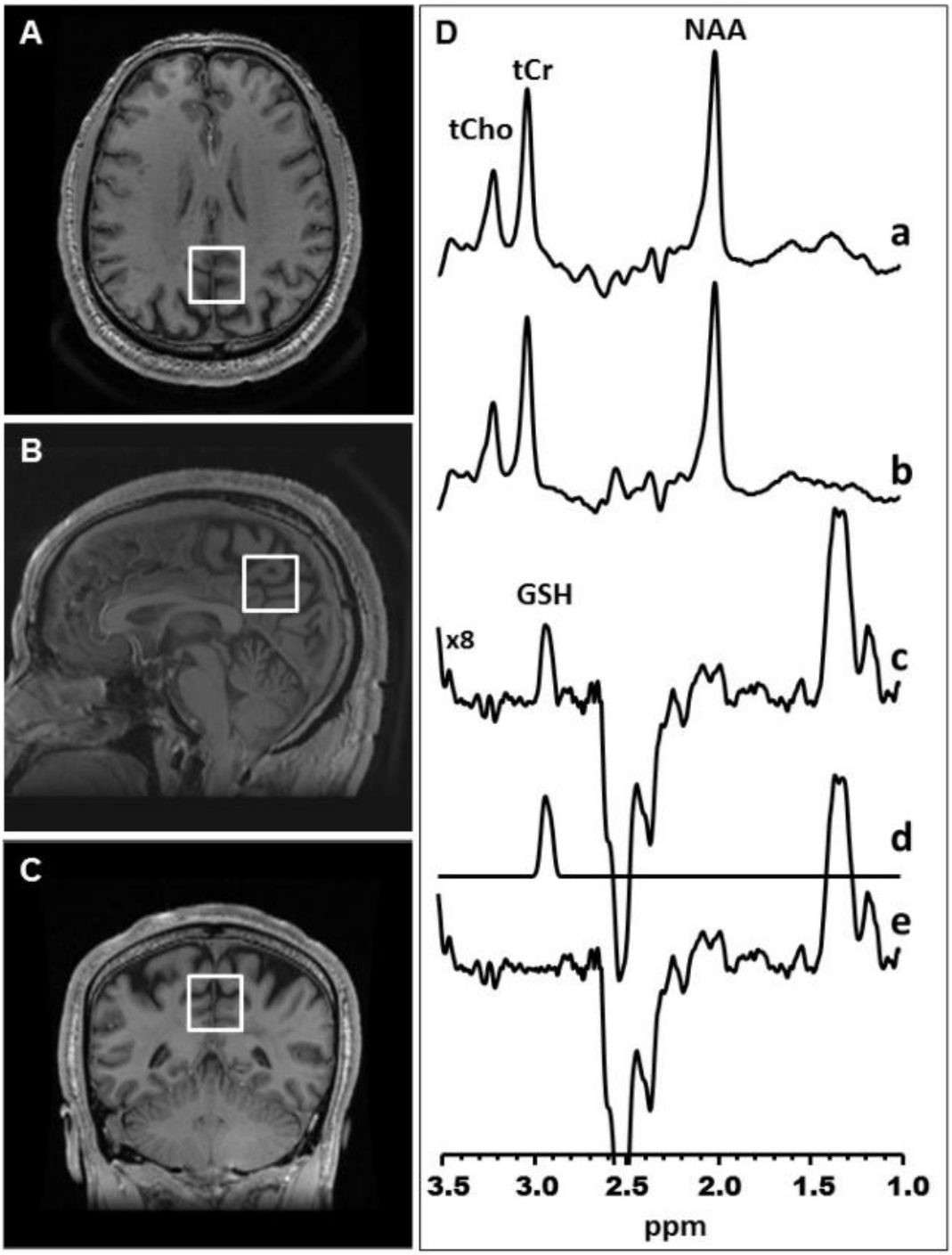
Fifteen cognitively normal subjects were enrolled prospectively in this pilot study. All subjects underwent 1H MRS of GSH, a positron emission tomography (PET) scan with an amyloid tracer, and volumetric MRI. Associations among GSH and other metabolite levels, brain amyloidosis, and hippocampal volumes were assessed using multivariate regression models.

Results

Lower GSH levels, suggestive of higher oxidative stress, were associated with greater brain amyloidosis in the temporal region ($p=0.03$) and, marginally, in the parietal ($p=0.05$) region, adjusted for apolipoprotein E ε4 carrier status. NAA, Cho, Cr, and myoinositol levels were not associated with brain amyloidosis. There was a nonsignificant trend towards larger hippocampal volumes with lower GSH levels ($p=0.08$). Higher creatine levels were associated with large hippocampal volumes ($p=0.02$).

Conclusions

This study found an association between cortical GSH levels and brain amyloidosis in normal older adults, suggesting a potential role for 1H MRS measures of GSH as a noninvasive biomarker of early AD pathogenesis.



(Filename: TCT_O-280_figure1.jpg)

O-281

4:02PM - 4:10PM

PET-Guided MR Spectroscopy Reveals Distinct Relations between Brain Metabolites, Amyloid, and Hypometabolism in Alzheimer's Disease

N Sheikh-Bahaei[1], S Sajjadi[2], R Manavaki[3], M Mclean[4], J O'Brien[3], J Gillard[3]
[1]University of Cambridge, Cambridge , United Kingdom, [2]University of California Irvine, Irvine, CA, [3]University of Cambridge, Cambridge , Cambridgeshire., [4]Cancer Research UK, University of Cambridge, Cambridge , Cambridgeshire.

Purpose
Despite the recent advances in development of imaging biomarkers for Alzheimer disease (AD), there is a lack of translation from research to clinical practice. Most of functional imaging techniques are expensive; require specialised facilities to perform and expertise to interpret them. MR spectroscopy (MRS) is a noninvasive, relatively cheap, and available method that can provide very useful information about the metabolite characteristics of the brain. Neverthless, MRS has not been validated thoroughly, particularly in comparison with other imaging biomarkers. In this study, we used PET-guided spectroscopy to measure the level of brain metabolites in areas of amyloid (Aβ) deposition and hypometabolism in AD. We hypothesized that the patterns of change in some of brain metabolites are correlated with undelying pathology making MRS a valuable surrogate marker to help with AD diagnosis in clinical setting and to monitor response to treatment in therapeutic trials.
Materials and Methods
Cases with clinical diagnoses of early AD (n=11), mild cognitive impairment (MCI) (n=10), and healthy control (HC) (n=8) were recruited through memory clinics in University of Cambridge. Global cognitive function was assessed using both Mini Mental State Examination (MMSE) and Addenbrooke's Cognitive Examination-Reverse (ACE-R) tests. All participants underwent 11 C- Pittsburg compound B- (PiB) and 18 F-fluorodeoxyglucose (FDG)-PET followed by 3T MRI and MRS. Dynamic 90 minute PiB- and 30 minute FDG-PET were performed and images were assessed both visually and quantitatively using kinetic modeling and standard uptake value ratio (SUVR). After co-registration of PET on T1-weighted images, MRS voxels were placed on 2 areas each of maximum Aβ deposition and minimum metabolism. Corresponding regions of interest (ROI) were selected in HC. The ratios of total N-acetyl (tNA) group, myoinositol (mI), Choline (Chol) and Glutamate plus Glutamine (Glx) over Creatine (Cr) were measured in each ROI and compared between groups.
Results
There was no significant difference in the age of participants in the 3 groups. Compared to representative normal regions, the mean of tNA/Cr was significantly lower in areas of hypometabolism (p-value <0.001) and high Aβ deposition (p-value<0.0001). Moreover the level of tNA/Cr correlated with the SUVR values of FDG- (R=0.27, p-value: 0.007) and PiB- (R: -0.36, p-value=0.0002) PET in each ROI. A regression model confirmed that both hypometabolism and Aβ deposition are significant predictors of change in tNA (R2: 0.14,

p=0.03 and 0.003 respectively). The mI/Cr ratio, on the otherhand, was significantly increased in both hypometabolic (p-value:0. 03) and Aβ positive regions (p-value <0.0001) and mI/Cr level correlated with the SUVR values of FDG (R: -0.25, p-value=0.01) and PiB-PET (R: 0.46, p-value<0.0001). Unlike tNA, regression analysis showed that mI increase was only related to amyloid deposition and not hypometabolism. Lastly, the correlation between the level of Chol/Cr and FDG-SUVR was trending toward significance (p-value=0.1).

Conclusions

To our knowledge this is the first study of PET-guided MRS in AD. This technique enabled metabolite measurement in objectively recognized abnormal regions. While previous studies have shown that the level of some of these metabolites alters in AD, there is limited knowledge about how these changes are related to AD pathology or correlated with other imaging biomarkers. Significant association between mI and Aβ in our study is in concordance with previous histopathological findings, which showed mI is associated with accumulation of amyloid β pathology (1). Reduction in tNA, on the other hand has been associated with synaptic dysfunction (1), which is again compatible with our finding that showed the level of tNA correlated with the FDG-PET result. The observed in vivo correlations suggest that MRS can detect early changes of AD and can be used as a more available and cheaper marker to improve the disgnostic accuracy of AD without risk of radiation or imposing significant cost.

O-282

4:10PM - 4:18PM

Data Mining Detects 3 Parkinson Disease Subgroups with Distinct Clinical Features

E Herskovits[1], L Shulman[2], E Nixon[2], R Chen[2]
[1]the University of Maryland, Baltimore, MD, [2]The University of Maryland, Baltimore, MD

Purpose

Patients with Parkinson disease (PD) have diverse symptoms, progression, and outcomes (1). Our overarching goal is the discovery of predictive variables that identify outcome subtypes, and thereby contribute to more accurate prognoses for people with PD. Anatomic brain connectivity, as manifest through DTI tractography, has shown great promise in evaluating patients with psychiatric disorders such as schizophrenia; neurodegenerative disorders such as Alzheimer disease; and for evaluating white-matter development. The majority of research involving anatomic-connectivity disorders has been hypothesis-based, in which investigators compare connectivity in specified tracts or regions among predefined experimental groups. We have developed a complementary data-mining method, which automatically detects subgroups based on tractography; our algorithm is designed to detect the optimal number of subgroups, and to generate clusters of subjects in connectivity space that best separate these subgroups. We applied our approach to data from the Parkinson's

Progression Markers Initiative (PPMI). Our algorithm returned 3 clusters; subjects in these subgroups manifested different clinical and connectivity characteristics at baseline, and at 2- and 4-year follow up. We further found that 4-year clinical outcomes diverged among these groups, potentially indicating their prognostic value.

Materials and Methods

Our approach, unsupervised Connectivity-based SUbtype Detection (CSUD), consists of 3 phases: DTI data preprocessing [as described in (2)], connectivity score generation, and subtype detection. MR preprocessing of T1-weighted and DTI volumes began with parcellation of each T1 volume into 90 seed regions based on the Automated Anatomical Labeling (AAL) atlas. To quantify connectivity between tractography seed regions A and B, we first normalized raw connectivity scores to the volumes of A and B, and defined A↔B connectivity as the average of A→B and B→A connectivity, to enforce symmetry. We log-transformed A↔B connectivity to improve normality, and then removed outliers. Finally, we thresholded connectivity to remove spurious connections, and regressed out age, sex, site, education, and handedness. The core of CSUD is clustering; CSUD models high-dimensional connectivity as a K-component Gaussian mixture distribution. CSUD estimates K based on Affinity Propagation Clustering (3); this approach yielded excellent results with simulated high dimensional, under-sampled data. CSUD then applies the High Dimensional Data Clustering algorithm HDclassif to generate K clusters; this approach has been shown to estimate Gaussian mixtures reliably for high-dimensional data, given K (4). PPMI clinical assessments include a broad range of assessments; for this analysis, we focused on the Movement Disorder Society-sponsored revision of the Unified Parkinson's Disease Rating Scale (MDS-UPDRS; disease severity and motor function), Total score and Parts 2 (ADLs) and 3 (Motor Exam); the University of Pennsylvania Smell Identifier test (UPSIT; olfactory function), and the Hopkins Verbal Learning Test (HVLT; cognitive status). We evaluated CSUD in 2 ways: we compared average values for clinical scales across subgroups; and we determined how well the CSUD-generated connectivity models predict subgroup membership, based on cross validation.

Results

We analyzed the subset of PPMI subjects who had baseline DTI data (142 individuals with PD). We used baseline DTI data, and clinical-assessment data at baseline, 2- and 4-year follow-up visits. To detect PD subtypes, we provided baseline DTI connectivity scores to CSUD; the algorithm returned three clusters or subtypes (N = 68, 44, 30). The connections that best distinguish PD subtypes are from the cortico-limbic system, which has been documented in the PD literature. We compared clinical scales across the 3 subgroups, and found that they differ with respect to UPDRS3 at baseline (ANOVA $p = 0.01$), year 2 ($p = 0.02$) and year 4 ($p < 0.01$), baseline UPSIT (chi^2 $p = 0.02$), HVLT Total Recall year 2 (ANOVA $p = 0.03$), and HVLT Delayed Recall year 4 ($p = 0.01$). We found no subtype differences with respect to handedness, race, education, age, or gender. A support-vector machine model of subgroup connectivity differences predicted group membership based solely on baseline connectivity with cross-validation accuracy = 0.96.

Conclusions
Parkinson disease patients have diverse symptoms and progression, but reliable markers of prognosis are lacking. We have described an unsupervised data-mining algorithm, CSUD, that clusters high-dimensional, severely under-sampled DTI data, in connectivity space. We applied this algorithm to the PPMI data to determine whether PD is a heterogeneous disorder. As expected, we found that $K > 1$; in particular, CSUD generated 3 subtype clusters. Subjects differed across subtypes with respect to commonly employed PD assessment scales. In addition, we found that statistical significance across groups for the UPDRS 3 (the motor exam) increased over time, indicating diverging motor outcomes among subtypes. If validated independently, this would have prognostic implications. Future work includes validation of these subtypes using independently acquired DTI and clinical data. We also plan to evaluate the effects of the atlas on these results; it may be the case that atlas structures derived from connectivity data (e.g., Mori's white-matter atlas) would provide greater statistical power than the AAL atlas used for this analysis. In addition, we plan to apply CSUD to other neuropsychiatric data sets. Finally, we plan to modify CSUD to accommodate genetic data, although this extension would greatly increase the dimensionality, and therefore the complexity, of the data to be clustered. Overall, our results indicate the potential utility of unsupervised data mining for the analysis of high-dimensional, severely under-sampled data.

O-285

4:34PM - 4:42PM

MRI Findings in Patients with Alcohol-Related Encephalopathy Syndromes

M Gencturk[1], S Khanipour Roshan[1], A McKinney[1], J Rykken[1]
[1]*University of Minnesota, Minneapolis, MN*

Purpose
To determine the brain MR imaging findings in patients presenting with either alcohol-related or Wernicke-Korsakoff encephalopathy.
Materials and Methods
Over a 3-year period, the radiology information system was checked for the terms "alcohol", "encephalopathy", "Wernicke's" and "Korsakoff", with a total of 31 patients found. Their electronic health records were reviewed retrospectively for clinical findings, and their acute phase MRI exams reviewed by 2 neuroradiologists in consensus (n=25 at 1.5T, n=6 at 3T).
Results
Of the 31 patients, 29 (94%) had definite alcohol (Etoh) abuse history; 2 (6%) did not. Seven (23%) presented with Wernicke encephalopathy (WE), 5 (16%), with Wernicke-Korsakoff syndrome (WKS), 2 (6%) with Etoh-withdrawal seizure (WDS), and the remaining 17 (55%) presented with nonspecific encephalopathy (NSE) symptoms, such as altered mental status, confusion, tremor or fall. The frequency of imaging findings for each clinical presentation is

in Table 1. The most commonly affected area was the insula in patients with NSE (70%) and WKS (70% and 60% respectively), with the medial thalami (71%) being most common in clinical WE.

Conclusions

In alcohol-related encephalopathies, involvement of the limbic system structures is more common than previously reported. Insular and medial thalamic involvement are also quite common. Notably, the often-reported periaqueductal involvement was found only in a minority.

Table 1. Prevalence of imaging findings according to clinical presentation

Location	NSE(n=17)	WE(n=7)	WKS(n=5)	WDS (n=2)
Hippocampus	11 (64%)	0	2 (40%)	1 (50%)
Cingulate Gyrus	9 (53%)	3 (43%)	2 (40%)	1 (50%)
Insula	12 (70%)	7 (57%)	3 (60%)	1 (50%)
Medial Thalami	4 (24%)	5 (71%)	1 (20%)	0
PVWM	5 (30%)	2 (28%)	1 (20%)	0
CN nuclei	1 (6%)	2 (28%)	0	0
Hypothalamus/MB	1 (6%)	2 (28%)	0	0
Cerebral Cortex	2 (12%)	1 (14%)	1 (20%)	0
Cerebellum	0	1 (14%)	1 (20%)	0

Note: PVWM= periventricular white matter, CN= cranial nerve, MB= mammillary bodies.

(Filename: TCT_O-285_Table1.jpg)

Wednesday
3:30PM - 4:50PM
Long Beach Convention Center, Room 104A (Main Lobby)

20D-Parallel Paper Session: Imaging of MS - White Matter Matters!

O-286

3:30PM - 3:38PM

Correlation Between Cerebellar Volumetry and Cognitive Status in Primary Progressive Multiple Sclerosis.

S Cocozza[1], E Mormina[1], M Petracca[1], N Oesingmann[1], M Heinig[1], K Buyukturkoglu[1], F Lublin[1]
[1]*Icahn School of Medicine at Mount Sinai, NY, NY*

Purpose

Recent evidences suggested that cerebellar atrophy in secondary progressive multiple sclerosis (MS) patients correlates with clinical disability, in particular with cognitive performance (1). However, to date, the association between posterior cerebellar volumetry and cognitive status has never been explored in patients with primary progressive multiple

sclerosis (PPMS). The aim of our study was to evaluate the correlation between global and lobar cerebellar volumes (CbV) and cognitive outcome in patients with PPMS.
Materials and Methods
Cognitive scores and brain MRI scans were obtained in 49 patients with PPMS, along with 36 healthy controls (HC). For all subjects, global and sub-regional CbV were calculated using SPM12 toolbox, Spatially Unbiased Infratentorial Toolbox (SUIT), which perform automatic segmentation of cerebellum in 28 lobules, thus allowing lobes volume computation. Partial correlation analysis, was performed between cognitive scores and CbV, entering age and gender as covariates.
Results
Compared to HC, PPMS patients showed a global reduction of CbV (p=0.03). When evaluating sub-regional anatomy, PPMS patients showed a reduction of the posterior cerebellar lobe volume (p=0.04), while no differences emerged for the anterior portion of the cerebellum (p=0.58). When testing for possible correlations with clinical variables, a significant correlation emerged between cognitive scores and total CbV (p=0.03), with a trend of significance for the posterior cerebellar lobe (p=0.06).
Conclusions
Patients with PPMS showed a reduction of global CbV, mainly involving the posterior lobe. Such cerebellar atrophy correlated with cognitive function. Our results provide further evidence of cerebellum role in cognition and suggest that CbV exploration could improve our understanding of the physiopathological basis of cognitive deficit in MS.

O-287

3:38PM - 3:46PM

Improved precision in Automatic Brain Volume Measurements of Early-Onset Multiple Sclerosis Patients Using Edema Correction

M Warntjes[1]
[1]*CMIV, Linköping, Östergötland*

Purpose
The presence of edema in brain tissue will result in an increased brain volume, which may obscure progressing brain atrophy. Likewise, the reduction of edema due to treatment may appear as accelerated brain tissue loss [pseudo-atrophy (1)]. Recently, there has been a substantial progress in magnetic resonance quantification of patient properties such as T1 relaxation, T2 relaxation rate and proton density (PD). Especially PD is expected to reflect the water content of the brain and hence should be correlated to the extent of edema. The purpose of this study was to measure both PD and brain volume in early-onset multiple sclerosis (MS) patients and to use PD as a correction for brain tissue edema, in order to improve the precision of automated brain volume measurements.

Materials and Methods

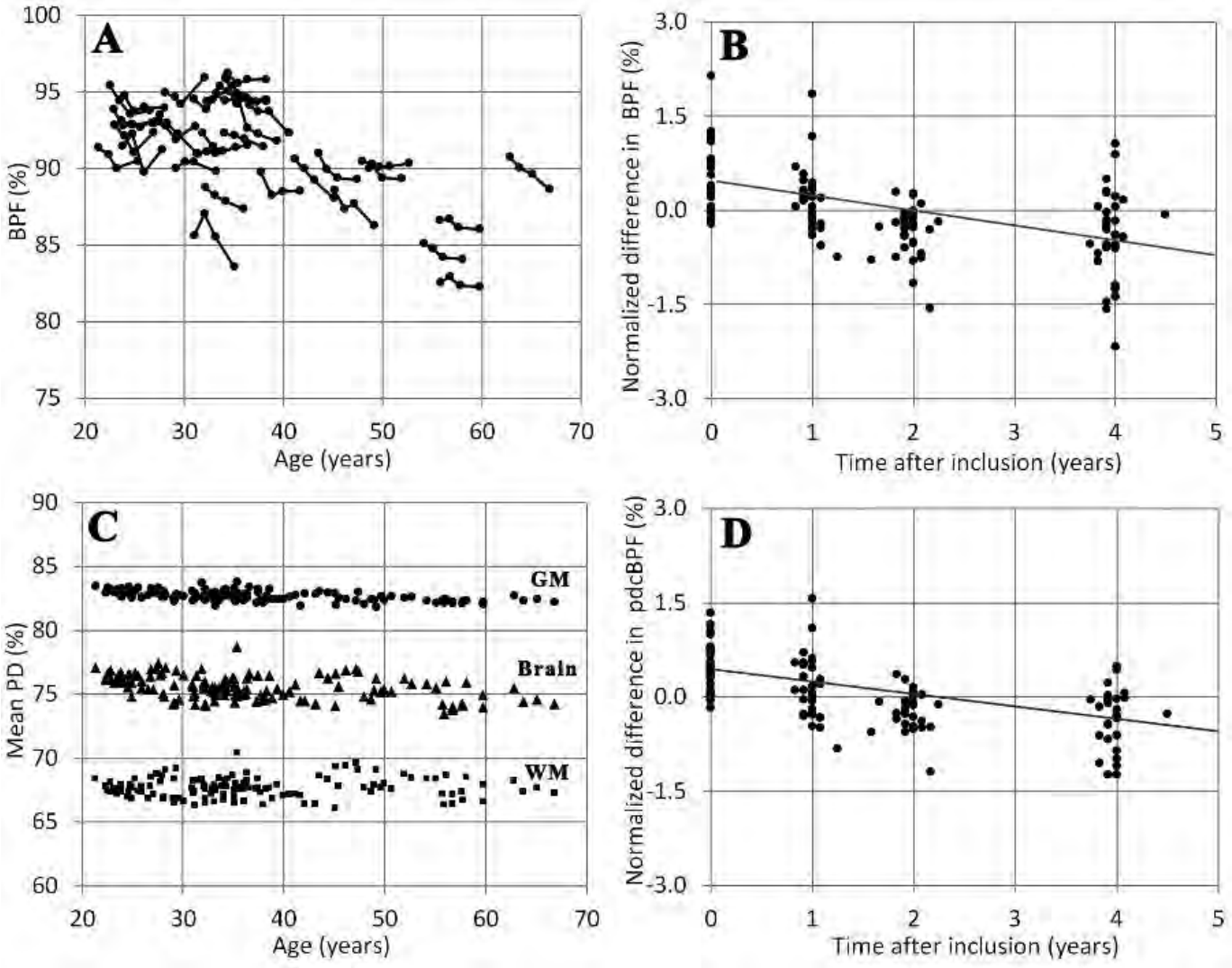
A group of 33 newly diagnosed MS patients were imaged at inclusion, and after 1, 2 and 4 years using a previously described MR quantification sequence (2). The brain parenchymal fraction (ratio of brain volume and intracranial volume) and average proton density (PD) was measured by automated software (SyMRI, SyntheticMR AB, Sweden). The repeatability error of this method to estimate BPF is reported 0.14% (3).

Results

The reduction of BPF of all subjects over age was 0.182%/y (A), whereas the reduction of BPF after inclusion was 0.248%/y (B). The mean standard deviations were 0.538%, 0.505%, 0.398% and 0.710% at baseline, 1, 2 and 4 years. The average PD of all subjects was 75.57±0.92% (C, triangles). Linear regression showed a slope of 0.542 ($p<0.001$) between the relative change of BPF and the relative change of PD. Applying the measured PD as a correction factor for BPF, the mean standard deviations became 0.353%, 0.487%, 0.296% and 0.577% at baseline, 1, 2 and 4 years (D), an improvement of 34.4%, 3.6%, 25.6% and 18.7%, respectively. The measured atrophy rate reduced to 0.235%/y.

Conclusions

Edema correction for brain volume using the mean PD value for the brain improves the precision of brain volume measurements with up to 34%.



(Filename: TCT_O-287_Figure1.jpg)

O-288

3:46PM - 3:54PM

Automated Detection and Characterization of White Matter Lesions on Clinical Brain MRI

A Rauschecker[1], L Xie[1], J Rudie[1], Y Ding[2], S Mohan[1], E Botzolakis[1], J Gee[1]
[1]*University of Pennsylvania, Philadelphia, PA,* [2]*Shandong Normal University, Shandong, China*

Purpose

Progress in computer-aided diagnosis of complex medical images has been sluggish (1, 2). A targeted approach to detect specific types of lesions using advanced computational image analysis methods may prove more successful. Our aim was to develop a highly functioning

prototype system capable of automatically detecting and characterizing lesions on clinical brain MRIs. As proof of concept, we focused on neurological diseases affecting cerebral white matter.

Materials and Methods

Using advanced post-processing algorithms, we developed a novel automated process for identifying and characterizing white matter lesions. First, freely available ANTs cortical segmentation software (3) was modified for accurate white matter (WM) segmentation on clinical-grade MR images in patients with WM signal abnormalities (Fig. 1A). We included MR data of varying resolution, including "high-resolution" (1x1x1mm) and "low-resolution" (0.5x0.5x3mm) T1W data. Second, after WM masking, lesions were identified automatically by applying threshold T2-value and cluster size criteria to the FLAIR brain volume. Third, after alignment with other imaging sequences, a total of 20 key lesion features were extracted, which included signal intensity metrics (relative T1W, T2W, GRE, PD, diffusion, enhancement, and FLAIR signal), lesion volume-related metrics (average size, size range, total lesion volume, # lesions), and spatial distribution metrics (symmetry, periventricular/subcortical/deep location, percent involvement frontal, temporal, parietal, and occipital, and corpus callosum involvement). These imaging features were chosen by expert neuroradiologist consensus for optimal differentiation between WM diseases (4). Brain volumes also were aligned with a standard WM tract template (ICBM) (5) for automated localization of lesions to specific WM tracts. The automated pipeline was applied to 20 exemplars of WM disease representing 10 distinct diagnoses with varying lesion appearances (Fig. 1B), including more and less common entities such as multiple sclerosis, HIV encephalopathy, PML, and adrenoleukodystrophy. Lesion detection was compared to ground truth as determined by a radiologist.

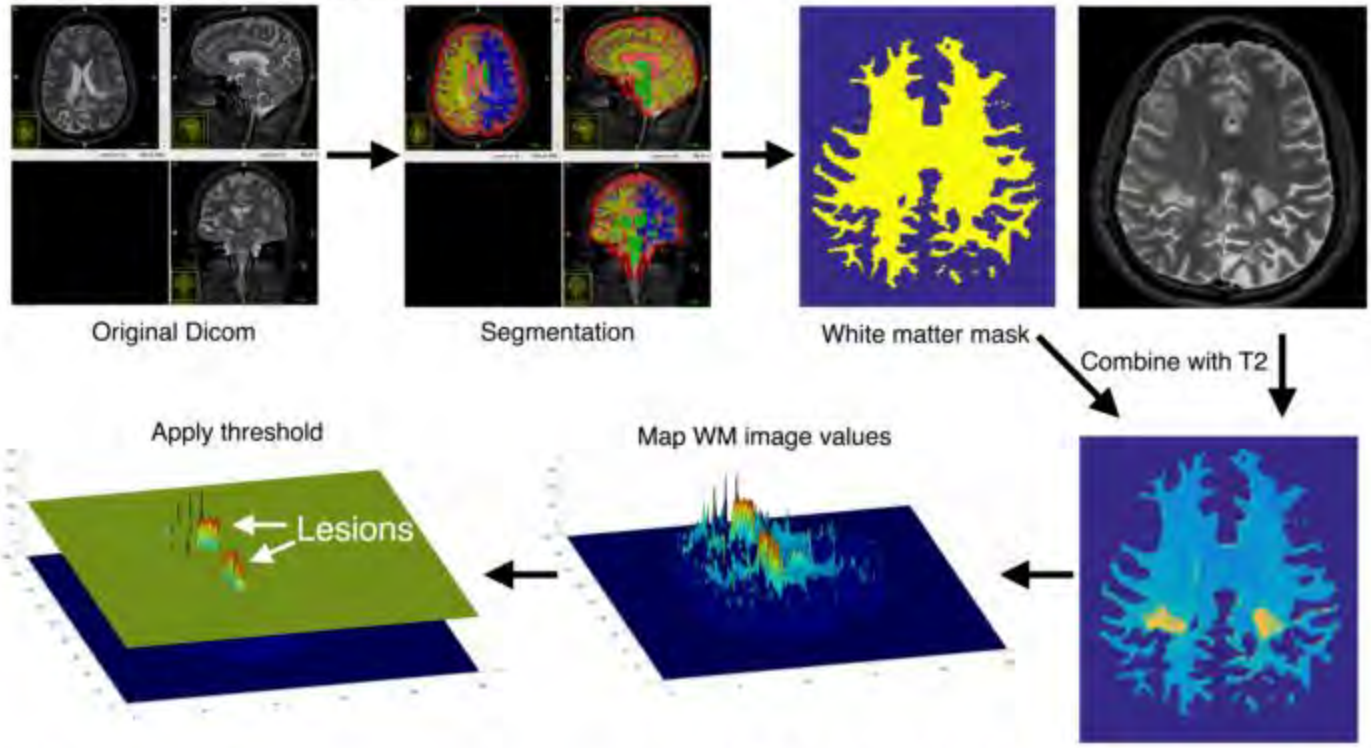
Results

Sensitivity of lesion detection was 73% by number and 90% by involved WM volume (see Fig. 1C representative examples). Positive predictive value reached greater than 80% due a low false positive rate. Following lesion detection, the pipeline reliably extracted 7/7 signal intensity metrics, 4/4 volume-related metrics, and 10/10 spatial distribution metrics without user intervention. There was no significant difference in successful lesion detection or characterization between high-resolution and low-resolution imaging data.

Conclusions

By applying advanced post-processing algorithms to clinical brain MRIs, we have successfully developed an automated pipeline for detecting and characterizing WM lesions. In upcoming work, these extracted imaging features will serve as input for an expert-trained Bayesian network capable of generating probabilistic differential diagnoses, thereby paving the way for a fully automated pipeline for diagnosing white matter diseases.

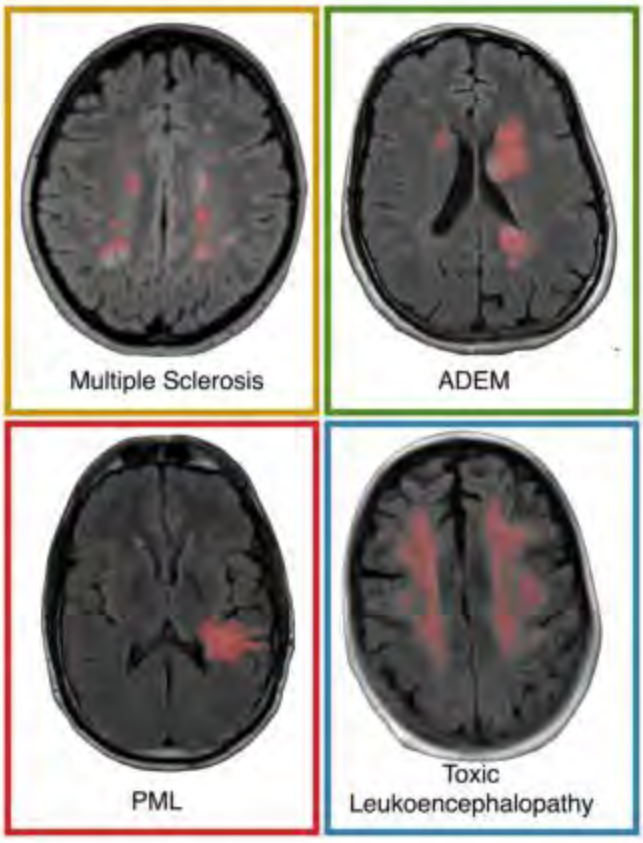
A. Lesion Detection



B. Cases

AGE	SEX	DIAGNOSIS	RESOLUTION
38	M	active MS	High
25	F	active MS	High
40	F	active MS	High
33	F	active MS	High
40	M	ADEM	Low
56	M	adrenoleukodystrophy	Low
64	M	CNS lymphoma	High
49	M	HIV encephalopathy	Low
33	M	inactive MS	High
33	F	inactive MS	High
57	M	inactive MS	High
36	F	inactive MS	High
53	M	inactive MS	High
29	F	inactive MS	High
18	M	inactive MS	High
36	M	PML	Low
23	M	Susac syndrome	High
31	F	Susac syndrome	Low
55	M	SVID	High
48	F	toxic leukoencephalopathy	Low

C. Lesion Detection Examples



(Filename: TCT_O-288_ASNR-Figure.jpg)

O-289

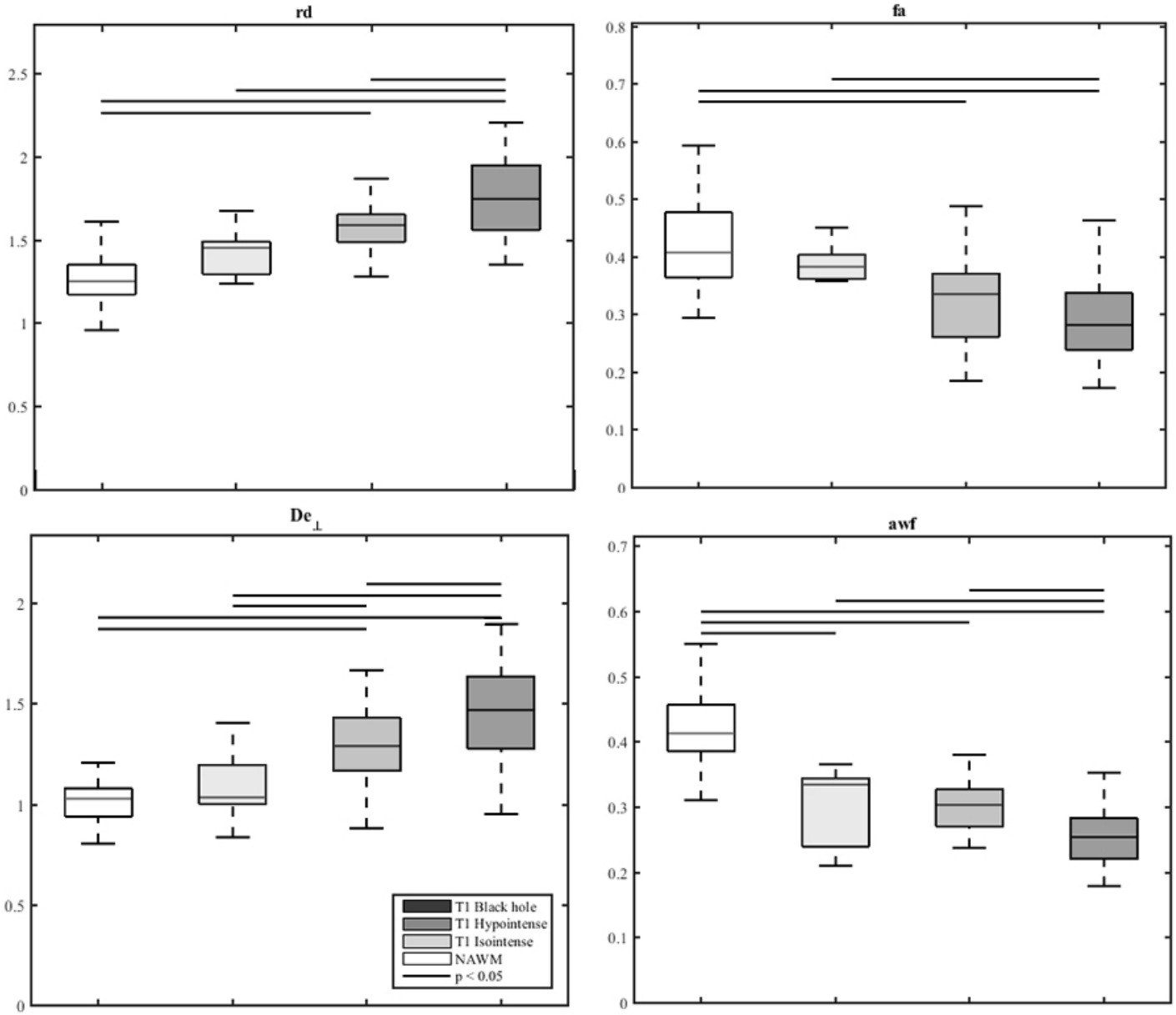
3:54PM - 4:02PM

Characterization of Multiple Sclerosis Lesions with Diffusion Kurtosis Imaging

B Conti[1], B Ades-Aron[2], Y Lui[3], D Novikov[2], I Kister[2], T Shepherd[4], E Fieremans[5]
[1]NYU Langone Medical Center, New York, NY, [2]NYU Langone Medical Center, New York, NY, New York City, NY, [3]NYU School of Medicine, New York City, NY, [4]NYU Medical Center, New York, NY, [5]New York University School of Medicine, New York, NY

Purpose
This study used a validated model of water diffusion to characterize specific axonal and myelination changes in the different chronic lesion types for relapsing-remitting multiple sclerosis (MS) patients. White matter (WM) microstructural integrity was evaluated using diffusion kurtosis imaging (DKI), a clinically feasible extension of diffusion tensor imaging (DTI) that allows for characterizing WM in terms of the extra-axonal radial diffusivity $D_{e,\perp}$ and the axonal water fraction (AWF), specific markers for demyelination and axonal loss (1, 2).
Materials and Methods
Thirty MS patients (8 males; 41.6 +/- 8.9 years; disease duration 14.1 +/- 8.5 years), underwent MRI on a 3T MRI scanner. The protocol included a sagittal 3D MPRAGE, axial FLAIR and diffusion MRI with b=0, 250, 1000, and 2000 s/mm2 (84 directions total). For consistency all 139 centrum semiovale lesions characterized were T2-hyperintense and lacked enhancement. Lesions then were classified as T1 isointense, T1 mildly hypointense and T1 black holes. Two additional normal appearing white matter (NAWM) regions were identified in each subject. Diffusion kurtosis imaging fitting provided parametric maps of fractional anisotropy, radial diffusivity (RD), $D_{e,\perp}$ and AWF (3). Analysis of variance (ANOVA) characterized statistical differences.
Results
Axonal water fraction was decreased significantly between NAWM and T1 isointense lesions (see Fig.), while $D_{e,\perp}$ is increased between T1 isointense and hypointense lesions – these changes may represent early patchy demyelination followed by more global demyelination (1). Axonal water fraction decreased, while RD and $D_{e,\perp}$ both appear increased between T1 mildly hypointense and black holes – these changes may represent axonal loss.
Conclusions
This cross-sectional study suggests DKI-derived WM integrity can provide more specific and sensitive measures of the myelination and axonal changes underlying MS lesion evolution. These data form a foundation for future investigations into lesion differences for

different clinical stages of MS, active versus chronic lesions, and comparisons to MS lesion mimics seen in migraines.



(Filename: TCT_O-289_ASNRv4.jpg)

O-290

4:02PM - 4:10PM

Analysis of White Matter Damage in Patients with Multiple Sclerosis by a Novel In Vivo MR Measurement Method of Axon and Myelin

A Hagiwara[1], M Hori[1], M Nakazawa[2], R Ueda[3], M Horita[4], C Andica[5], Y Takahashi[6], S Aoki[2]

[1]Juntendo University School of Medicine, Tokyo, Japan, [2]Juntendo University School of Medicine, Tokyo, Tokyo, [3]Juntendo University School of Medicine, Tokyo, N/A, [4]Juntendo University School of Medicine, Japan, N/A, [5]Juntendo University Graduate School of Medicine, Tokyo, Tokyo, [6]Juntendo University School of medicine, Bunkyoku, Tokyo

Purpose

To evaluate the white matter damage in patients with multiple sclerosis (MS) by MR imaging for quantifying the myelin volume fraction (MVF), the axon volume fraction (AVF), and the g-ratio, which is equal to the ratio of the inner to the outer diameter of a nerve fiber.

Materials and Methods

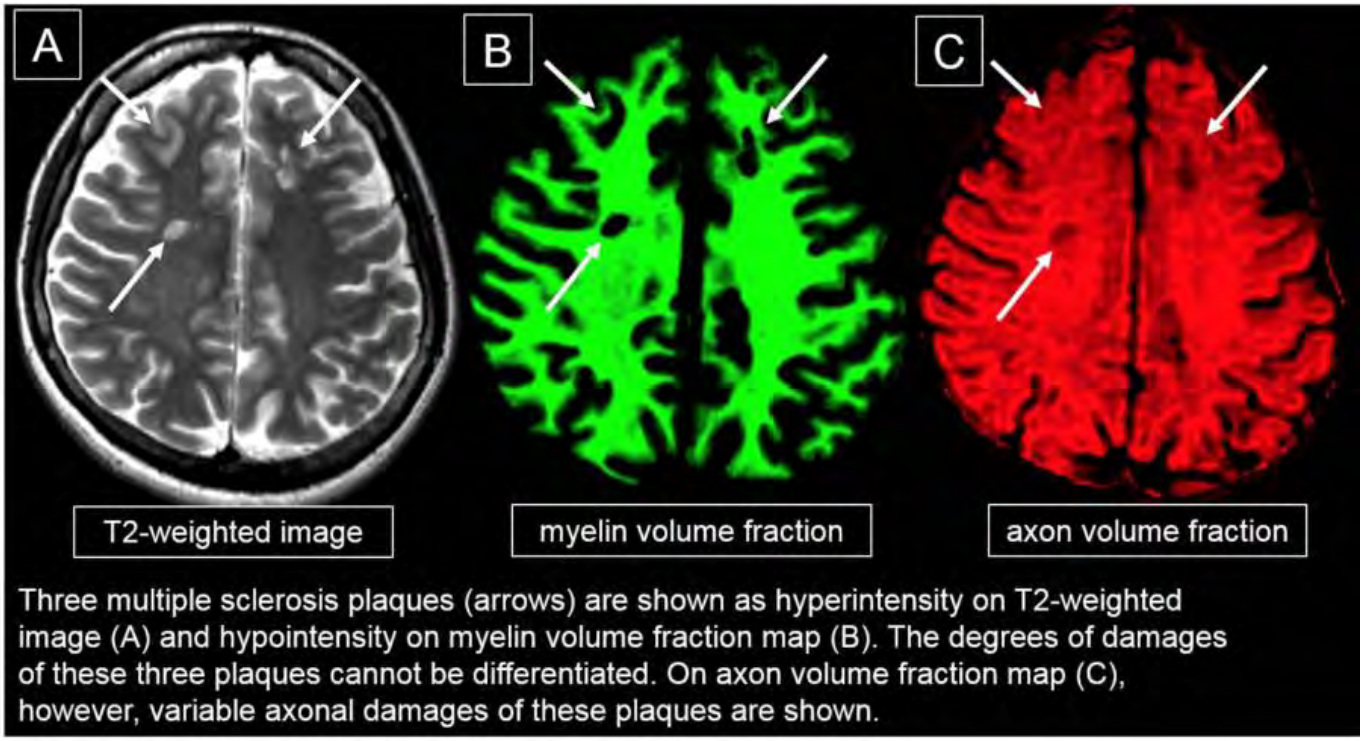
Twenty-five MS patients with a combined total of 148 plaques were analyzed. R1, R2, and proton density were quantified by simultaneous tissue relaxometry (1), and Vicvf and Viso (volume fraction of the intra-cellular and CSF compartments, respectively) were quantified by neurite orientation dispersion and density imaging (NODDI) (2). Myelin volume fraction was calculated by R1, R2, and proton density (3). Axon volume fraction and g-ratio were calculated by combining MVF, Vicvf and Viso (4). Myelin volume fraction, AVF and g-ratio were measured in plaques, periplaque white matter (PWM), and normal appearing white matter (NAWM).

Results

G-ratios of plaques, PWM, and NAWM were 0.926 ± 0.060, 0.768 ± 0.049, and 0.757 ± 0.047, respectively; MVFs of these were 6.48 ± 5.01, 26.4 ± 4.32, and 31.5 ± 3.76; AVFs of these were 19.9 ± 1.65, 21.2 ± 1.07, and 22.1 ± 0.97. All metrics differed significantly across the 3 groups ($P < .001$, except $P = .037$ for g-ratio between PWM and NAWM). Those in plaques differed most from those in NAWM. The percentage changes of the metrics in plaques and PWM relative to NAWM were significantly more different from zero for MVF and AVF than g-ratio, with MVF most different from zero ($P < .001$).

Conclusions

This in vivo MRI study showed myelin to be more damaged than axon in plaques and PWM of patients with MS. Myelin volume fraction, AVF, and g-ratio have potentials to be useful for evaluating white matter damage in patients with MS.



(Filename: TCT_O-290_g-ratio.jpg)

O-291

4:10PM - 4:18PM

Evaluation of Axonal and Myelin Integrity with Advanced MRI Methods in Multiple Sclerosis

F Yu[1], S Huang[2], N Machado[1], J Bireley[3], T Duval[4], J Cohen-Adad[5], L Wald[1], E Klawiter[1]
[1]Massachusetts General Hospital, Boston, MA, [2]Massachusetts General Hospital / Athinoula A. Martinos Center for Biomedical Imaging, Boston, MA, [3]Department of Neurology, Massachusetts General Hospital, Boston, MA, [4]Institute of Biomedical Engineering, Ecole Polytechnique de Montreal, Montreal, Montreal, QC, [5]Polytechnique Montreal, Montréal, Quebec

Purpose
Multiple sclerosis (MS) is a neurodegenerative disorder characterized by demyelination and axonal loss. Demyelination exposes axons to injury, while axonal damage and loss are considered the cause of permanent disability (1). Remyelination and repair occur to a variable extent, and promoting remyelination represents an area of great therapeutic interest. MRI plays an important role in the diagnosis of MS and has high sensitivity for demyelinating lesions. However, conventional MRI fails to reflect the extent of axonal injury and remyelination with high specificity (2). Reliable imaging markers for characterizing the structural integrity of white matter would be invaluable in grading the degree of axonal

damage and remyelination at different stages of disease progression in MS. We recently developed an advanced in vivo diffusion MRI technique known as TractCaliber that measures axon diameter and density in white matter tracts using ultra-high gradient strengths up to 300 mT/m (3). Ultra-high gradient diffusion MRI has been shown to detect axonal loss through quantifying reductions in axon density in MS lesions in the corpus callosum. Myelin volume fraction, based on the macromolecular tissue volume (MTV), can be separately determined using proton density mapping (4). The ability to measure axon density and myelin content in white matter has enabled noninvasive measurements of myelin sheath thickness (5), termed the myelin g-ratio. These novel biomarkers offer the possibility of studying axonal and myelin integrity in chronic and active MS lesions as well as in the major white matter tracts of patients with MS. In this work, we propose a novel multi-modal MRI protocol to study axonal and myelin integrity in MS. We measured the myelin g-ratio in vivo by combining information on axonal volume fraction (AVF) and myelin volume fraction (MVF) in lesions and normal-appearing white matter (NAWM) of MS patients and compare the results with healthy controls.

Materials and Methods

This prospective study was approved by the institutional review board at Massachusetts General Hospital. Five patients with relapsing-remitting MS and 5 matched healthy controls were imaged on a 3T Siemens Magnetom Connectom MR scanner with a 64-channel head coil. Whole brain sagittal 2-mm isotropic resolution diffusion-weighted echo planar imaging was performed using the following parameters: TE 77 ms, TR 3800 ms, 32-64 non-collinear diffusion gradient directions, linearly spaced 8 diffusion gradient increments from 30 to 290 mT/m, parallel imaging factor 2, and simultaneous multislice MB factor 2. Macromolecular tissue volume images were acquired using a spoiled gradient echo 3D FLASH sequence acquired at multiple flip angles (4°, 10°, 20°), TE 2.74 ms, and TR 20 ms at 1 mm3 isotropic resolution. High-resolution T1 MEMPRAGE and FLAIR sequences also were acquired. The diffusion data were preprocessed for eddy current and motion correction, and then fitted using TractCaliber to derive estimates for axon diameter, restricted (fr) and free water (fcsf) volume fractions in white matter. Myelin volume fraction (as determined by MTV) was determined using customized MATLAB scripts based on the approach outlined by Mezer et al. (2). The g-ratio then was calculated as g=[1/(1+MVF/AVF)], where AVF (axon volume fraction) = (1-MVF)*(1-fcsf)*fr 3. Registration to the anatomic T1 image was performed using bbregister (Freesurfer). MS lesions were segmented manually on the FLAIR images by an experienced neuroradiologist using Slicer (www.slicer.org). NAWM masks were created using the results from the Freesurfer segmentation. Statistical analysis was performed using SPSS version 21. The Mann-Whitney U test was used to compare AVF, MVF, and g-ratio in NAWM in MS patients with healthy controls. The nonparametric Wilcoxon matched-pairs signed rank test was used to compare these metrics between lesions and NAWM for MS patients.

Results

The mean g-ratio in healthy subjects was 0.59 (SD 0.04). MS lesions showed significantly

higher average g-ratio (mean 0.57, SD 0.06) compared to NAWM (mean 0.54, SD 0.06) ($p<0.05$). Of note, some MS lesions demonstrated increased g-ratio (>0.8), while others had values similar to the adjacent NAWM (see Fig. 1). Multiple sclerosis lesions had significantly lower MVF (mean 0.19, SD 0.05) compared to NAWM (mean 0.26, SD 0.06) ($p<0.05$). There was a trend for lower AVF in MS lesions and MS NAWM compared to white matter in HC.

Conclusions

We found a statistically significant decrease in mean MVF between MS lesions and NAWM, which would be expected for demyelination/decreased myelin content in lesions. Differences in AVF were not statistically significant, but nevertheless suggest relative white matter axonal loss in MS patients compared to healthy subjects. The increased mean g-ratio of MS lesions compared to NAWM imply overall thinning of the myelin sheath in lesions, consistent with myelin loss. The fact that the g-ratios for individual lesions varied considerably suggests different levels of demyelination, remyelination, and axonal loss within lesions. For instance, lesions with g-ratios approaching that of NAWM may reflect remyelination or demyelination with concomitant axonal loss (i.e. chronic lesions). This could be further delineated with imaging-pathologic correlation. We demonstrate estimates of the myelin g-ratio, AVF and MVF throughout the white matter of MS patients and HC that are consistent with expected trends from histopathology, including increased g-ratio and decreased MVF in MS lesions relative to NAWM. Considering the small sample size, the results are encouraging and warrant further investigation in a larger cohort and in different MS subtypes. Future work will focus on increasing the sample size and obtaining longitudinal imaging data, as well as validating MRI measures of the myelin g-ratio through correlation with histology.

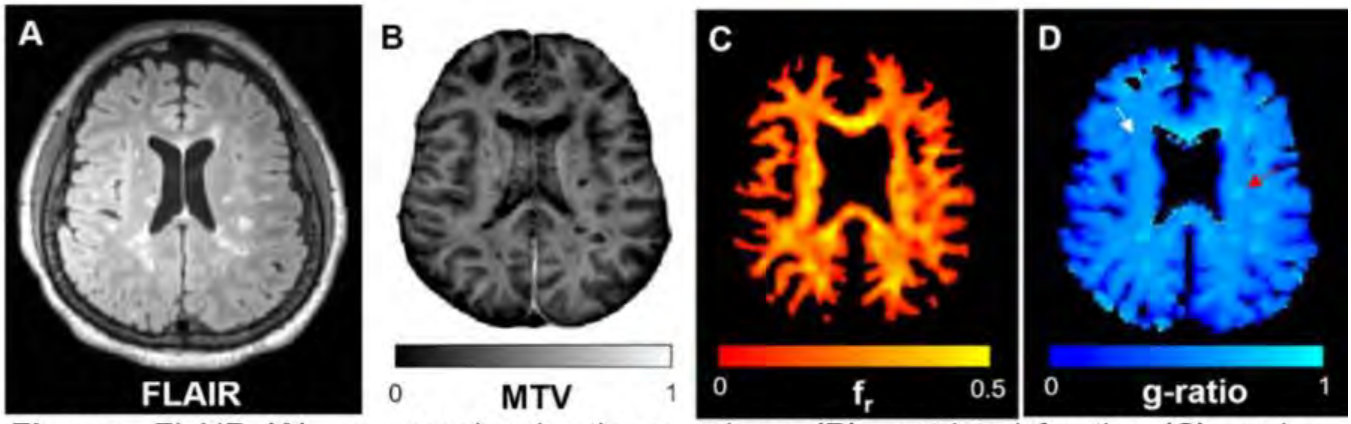


Figure: FLAIR **(A)**, macromolecular tissue volume **(B)**, restricted fraction **(C)**, and g-ratio maps **(D)** calculated for an MS patient. Red arrow (D) shows a lesion with elevated g-ratio>0.8, while white arrow shows a lesion with g-ratio=0.6, similar to surrounding NAWM.

(Filename: TCT_O-291_g_ratio_fig.jpg)

O-293

4:26PM - 4:34PM

Evaluation of Normal Appearing White Matter in Multiple Sclerosis using Quantitative Susceptibility Mapping and Diffusion Tensor Imaging

F Yu[1], F Chiang[2], N Stephens[3], B Tantiwongkosi[2], R Romero[3], S Huang[4]
[1]Massachusetts General Hospital, Boston, MA, [2]University of Texas Health Science Center at San Antonio, San Antonio, TX, [3]University of Texas Health Science Center at San Antonio, SAN ANTONIO, TX, [4]Massachusetts General Hospital / Athinoula A. Martinos Center for Biomedical Imaging, Boston, MA

Purpose

Conventional MR imaging has high sensitivity in the detection of white matter lesions in multiple sclerosis (MS). However, the correlation with long term clinical disability has been moderate, which may be due to the lack of specificity for underlying disease processes (1). This discrepancy highlights a need for more specific MR methods. Pathophysiologic changes in MS lesions include demyelination and axonal damage, as well as concurrent local inflammatory changes. Iron is stored in activated M1 macrophages, and also acts as a promoter of inflammation (2). Accordingly, MR sequences that can assess iron content (magnetic susceptibility) could serve as noninvasive biomarkers for inflammation. Quantitative susceptibility mapping (QSM) is a novel MRI method that is able to delineate tissue-specific susceptibility, in contrast to T2*-GRE and susceptibility-weighted imaging which are affected by nonlocal susceptibility sources. We recently devised a general QSM method for estimating and subtracting streaking artifacts from the susceptibility map for single orientation acquisitions (iLSQR) (3). This provides an unbiased estimate of susceptibility with significantly reduced streak artifact. Although there have been studies looking at MS lesions using QSM as well as iron deposition in subcortical gray matter, other brain regions, including normal appearing white matter (NAWM), have not been thoroughly explored (2). Additionally, although magnetic susceptibility has been treated as a reflection of iron content, it is known that myelin and tissue microstructure also have contributions. Our purpose was to investigate these questions by evaluating the magnetic susceptibility of NAWM in association with diffusion tensor imaging (DTI) metrics for MS patients compared to healthy controls.

Materials and Methods

This prospective study was approved by the institutional review board at the University of Texas Health Science Center at San Antonio. Brain imaging of 16 relapsing remitting MS patients (mean age 38±10 years, 13 females) and 16 healthy controls (HC; mean age 35±9.7 years, 5 females) was performed on a Philips Achieva 3T MR scanner with an 8-channel head coil. A 3D mFFE (multi-echo gradient echo) sequence was acquired with the following parameters: flip angle 20°; TE1 4.2 ms; echo spacing 4.8 ms; TR 36.56 ms; FOV 230 x 230 mm2; matrix size 256 x 256; slice thickness 2 mm; SENSE factor 2. Anatomic images were obtained using a T1-weighted 3D TFE sequence with a 1 mm3 reconstructed resolution.

Diffusion tensor images were acquired using a single-shot echo planar imaging sequence with 15 directions and a maximum b-value of 800 s/mm2. High resolution isometric 3D FSE FLAIR images also were acquired. QSM images were generated from the 3D mFFE images using customized MATLAB (v. R2015b) scripts based on methods previously described (3). The T1 images were processed and segmented using FreeSurfer (v. 5.3.0) (http://surfer.nmr.mgh.harvard.edu). Fractional anisotropy (FA), mean diffusivity (MD), radial diffusivity, and axial diffusivity (AD) maps were generated using the Tracts Constrained by Underlying Anatomy tool (Freesurfer). White matter lesion segmentation was performed using the lesion growth algorithm as implemented in the LST toolbox (v. 2.0.13; www.statistical-modelling.de/lst.html) for SPM12, and verified with visual inspection. NAWM masks were created from the Freesurfer segmentation. Image co-registration was performed using FLIRT (www.fmrib.ox.ac.uk/fsl) and bbregister software (Freesurfer). Statistical analyses were performed in MATLAB. Comparison of MS NAWM versus MS lesion metrics was performed using the Wilcoxson signed rank test. Comparison of MS NAWM versus HC white matter (WM) metrics was performed using the Mann-Whitney U test.

Results

Multiple sclerosis lesions demonstrated increased mean susceptibility (1.3 x 10^-2 ppm, SD 3.5 x 10^-2) compared to MS NAWM (5.5 x 10^-3 ppm, SD 3.5 x 10^-3), although this was not statistically significant versus ($p=0.3$). Multiple sclerosis NAWM showed increased susceptibility compared to HC WM (2.1 x 10^-3 ppm; $p<0.05$). Of note, the susceptibility of individual MS lesions was variable, demonstrating instances in which the susceptibility increased compared to NAWM, and others in which it was not significantly different. The mean FA of MS NAWM (1.3 x 10^-1, SD 3.1 x 10^-2) also was decreased compared to HC WM (1.9 x 10^-1, SD 2.7 x 10^-2; $p<0.05$). On the other hand, the mean MD of MS NAWM (5.7 x 10^-4, SD 1.2 x 10^-4) was lower than that of HC WM (6.5 x 10^-4, SD 5.8 x 10^-5; $p<0.05$). Mean AD was significantly decreased in in MS NAWM compared to HC WM (7.0 x 10^-4 versus 8.3 x 10^-4, $p<0.05$), whereas mean RD was not significantly different between the two groups (5.1 x 10^-4 versus 5.5 x 10^-4).

Conclusions

We found increased susceptibility in MS lesions and MS NAWM compared to HC WM. As has been previously described, the susceptibility pattern varied among individual lesions, which has been associated with lesion age (4). Although demyelination in MS lesions would result in increased local susceptibility (since myelin is diamagnetic), it is thought that iron content has a greater contribution. We also noted increased susceptibility as well as decreased FA and AD in MS NAWM compared to HC WM. On the other hand, RD and MD was not significantly increased, suggesting that myelin integrity was largely preserved in MS NAWM. Correspondingly, the observed increased susceptibility in the white matter of MS patients may be primarily the result of ongoing neuroinflammation (as reflected by increased iron content). Decreased AD, which has been thought of as an axonal metric, suggests concomitant axonal loss. Through this preliminary work, we found evidence suggestive of

axonal damage and inflammation in the NAWM of MS patients. These changes potentially could contribute to the clinical disability observed in patients. However, further work utilizing advanced myelin and axonal imaging markers, such as TractCaliber, along with imaging-pathologic correlation are needed to validate these observations (5).

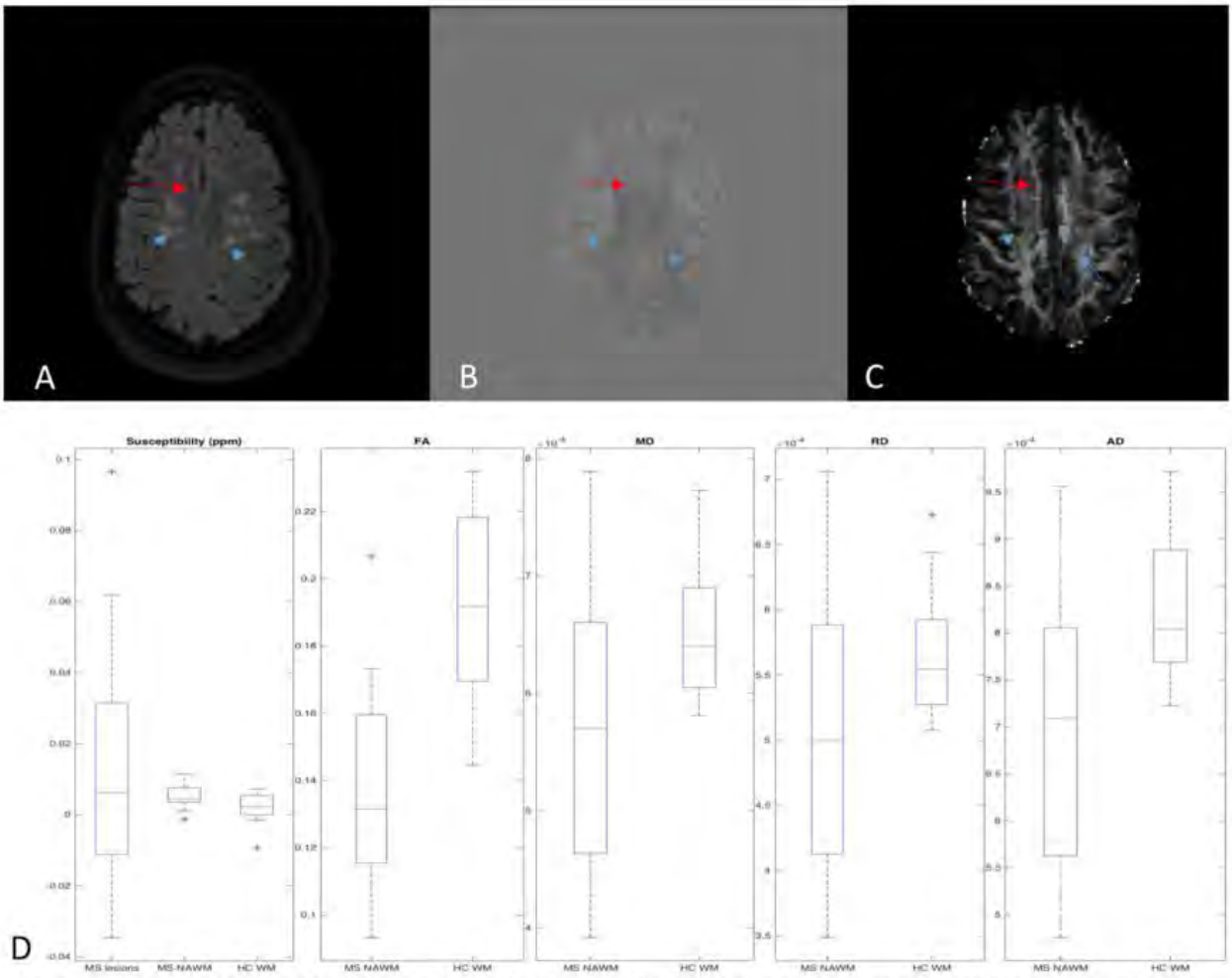


Figure: Axial FLAIR (a), QSM (b), and DTI FA (c) images of the brain in an MS patient. MS lesions can appear hyperintense (dotted blue arrow) or relatively isointense (solid blue arrow) to NAWM (red arrow) on QSM. Boxplots of susceptibility, FA, MD, RD, and AD for MS NAWM and HC WM.

(Filename: TCT_O-293_qsm_figure1.jpg)

O-294

4:34PM - 4:42PM

Assessing the Central Vein Sign in Multiple Sclerosis on different 3T MR scanners

A FECHNER[1], M Absinta[2], J Savatovsky[1], J Sadik[1], D Reich[2], P Roux[1], P Sati[2]
[1]A. de Rothschild Foundation, Paris, Ile de France, [2]NIH, Bethesda, MD

Purpose
The central vein (CV) recently was proposed as a novel MRI biomarker to improve the

accuracy of multiple sclerosis (MS) radiological diagnostic criteria (1), but clinical validation involving large prospective multi-center studies is still required (2). In this study, we compared the CV detection in MS patients scanned on different 3T MRI manufacturers using fast high-resolution T2*-weighted 3D EPI acquisition (3).

Materials and Methods

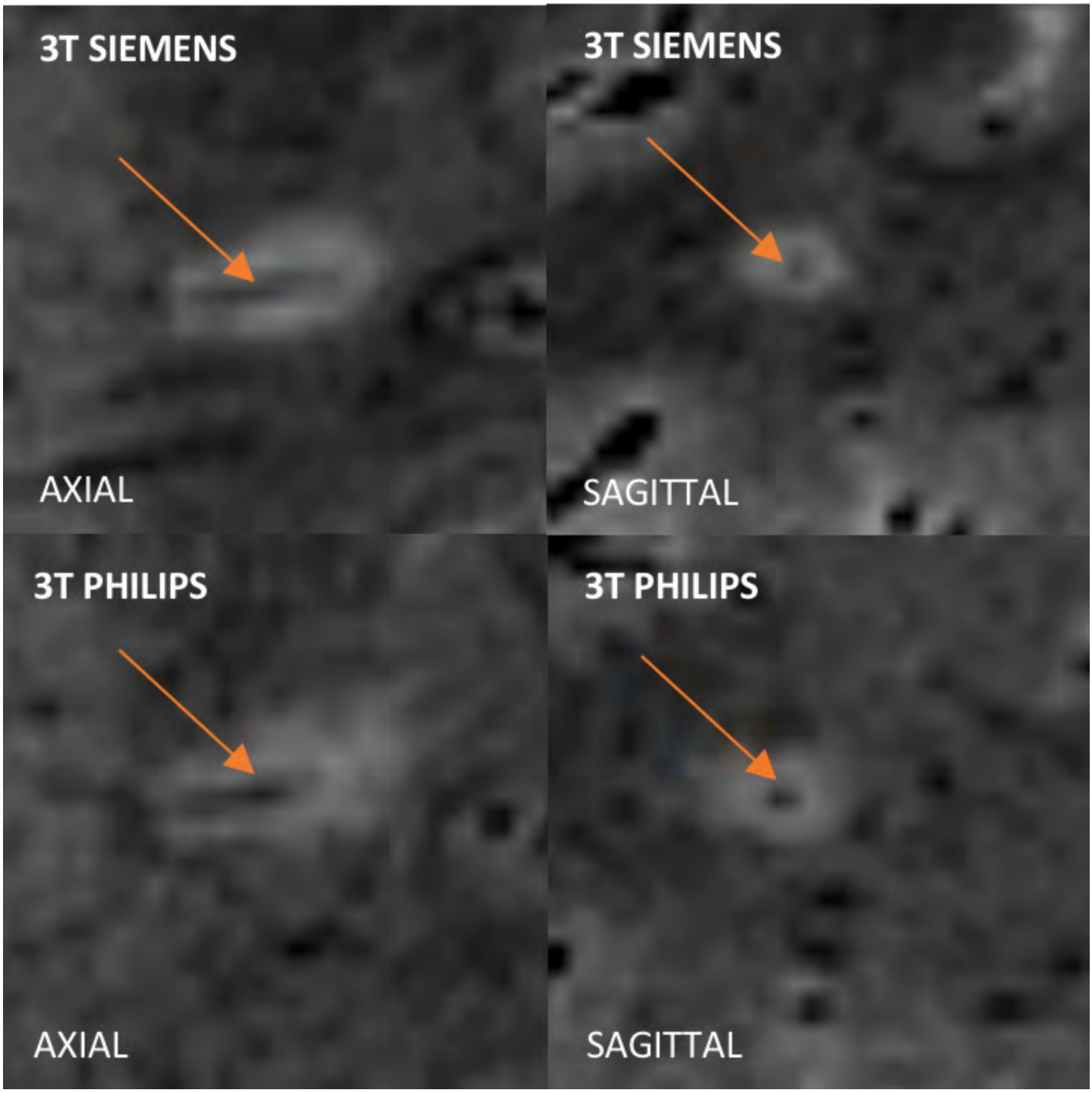
Fifteen MS patients who had brain MRIs acquired on 2 3T MR scanners (3T Philips Achieva and 3T Siemens Skyra) were included in this retrospective study. Whole-brain 3D FLAIR (1 mm isotropic voxel) and T2*-weighted 3D EPI (0.55 mm and 0.65 mm isotropic voxel, respectively) were acquired on both scanners. T2* acquisition was performed during, or shortly after, the injection of gadolinium-based contrast agent (gadobutrol). Based on recent criteria for CV assessment (2), after selection of discrete MS lesions on FLAIR images, 2 raters reviewed independently the T2* images to evaluate the presence (CV+) or absence (CV-) of a central vein within selected lesions.

Results

Sixty-one MS lesions were analyzed: 27 were located in the deep white matter (44%), 16 juxta-cortical (26%), 2 infratentorial (3%), 17 periventricular (28%). Raters agreed on 59/61 lesions (96.7%): 54 lesions (88.5%) were CV+ on both scanners (Fig.), 2 (3.2%) were CV- on both scanners, 2 (3.2%) were CV+ on Philips only, and 1 (1.6%) was CV+ on Siemens only. The slight difference observed between scanners could be due to variations in the timing of the contrast agent injection.

Conclusions

This study demonstrates similar sensitivity for central vein detection in MS patients scanned on 2 different 3T MRI manufacturers using optimized fast high-resolution T2*-weighted 3D EPI acquisition. This work confirms the feasibility of multi-center clinical studies on the central vein for MS diagnosis.



(Filename: TCT_O-294_IconoAbstract_300dpi.jpg)

O-507

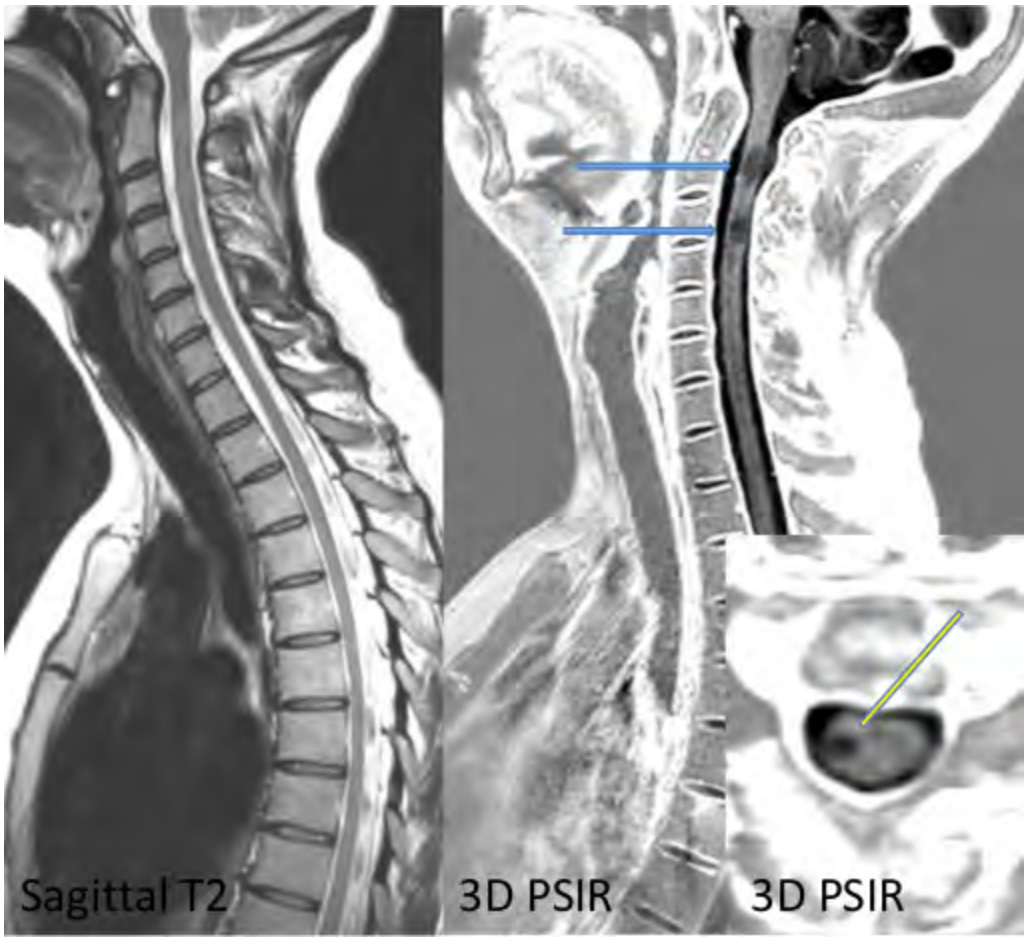
4:42PM - 4:50PM

3D Phase Sensitive Inversion Recovery for Spinal MS lesion detection

A FECHNER[1], J Savatovsky[1], E Saragoussi[1], P Roux[1], J Sadik[1], A Lecler[1]

[1]*A. de Rothschild Foundation, PARIS, Ile de France*

Purpose
Multiple sclerosis is a demyelinating inflammatory disease of the central nervous system. Diagnosis is established with clinical examination and magnetic resonance imaging (MRI). Spine lesions are problematic since many artifacts affect this region. New MRI sequences have proved to detect more lesions in small and medium cohorts. We developed a 3D PSIR sequence for the spine, and compared lesion detectability with sagittal T2 sequences.
Materials and Methods
One hundred MS patients were recruited for this monocentric retrospective study, approved by a local ethics committee. Two raters (a junior and a senior radiologist) analyzed both MRI sequences separately in a random order. The senior radiologist data were considered as the gold standard. A consensus meeting was organized after data collection. Confidence level was assessed.
Results
A total of 480 lesions were described in 3D PSIR (270 in cervical spine, 210 in the dorsal spine) versus 168 on sagittal T2 (83 in the cervical spine and 85 in the cervical spine). 3D PSIR allowed the detection of lesions not seen in sagittal T2 for 13 patients. The inter reader concordance was good (Kappa = 0.7). Confidence levels were higher with 3D PSIR than sagittal T2 ($p = 1.8e-11$).
Conclusions
Detection rate of spinal cord lesions in MS patients was significantly better using a 3D PSIR sequence compared to a sagittal T2 sequence for the cervical and dorsal spine.



(Filename: TCT_O-507_Abstr.jpg)

Wednesday
3:30PM - 4:45PM
Long Beach Convention Center, Room 104B (Main Lobby)

20E-Parallel Paper Session: Imaging of Headache, Across the Pressure Spectrum

O-295

3:30PM - 3:38PM

Gadolinium Contrast Does Not Add Value to Brain MRI in the Evaluation of Primary Headache

T Miller[1], E Lundberg[2], S Ali[3], K Shifteh[4]
[1]Montefiore North Medical Centre, Bronx , NY, [2]Montefiore, Bronx, NY, [3]Maimonides Medical Center, Brooklyn, NY, [4]Montefiore Medical Center, Bronx, NY

Purpose
While most headaches are attributable to benign conditions - primary headache, patients and physicians often are concerned about intracranial pathology. However, the yield of

significant abnormalities on neuroimaging in patients with chronic headaches is 1% to 3%. Given the comparable yield in patients without headaches, multiple guidelines have recommended against routine headache neuroimaging, and efforts to improve the efficiency of health care utilization, such as the Choosing Wisely campaign [ABIM (American Board of Internal Medicine) Foundation; http://www.choosingwisely.org], have identified these tests as a target. The ACR appropriateness criteria for primary headache (chronic headache, without new features) list MRI brain with and without contrast as the most appropriate test (4 - may be appropriate). The references from the appropriateness criteria include large case series. The listed positive findings from the cited studies included abnormalities which would be visible without contrast (AVM, subdural, hydrocephalus, tumor). Given the very low probability of abnormalities on Brain MRI for primary headache, we hypothesize that a review of scans with and without contrast will not yield any clinically significant findings that require contrast to identify. Aims: 1. Use the EMR to identify subjects meeting the criteria of primary headache who had Brain MRI scans at a single health system from 2006-2016. 2. Review these MRI reports to identify those with positive findings. 3. Primary outcome: enumerate total number of findings detectable only with contrast. 4. Secondary outcome: determine if findings only visible on contrast scans were likely to be clinically significant or account for subject symptoms.

Materials and Methods

This is a retrospective review composed of a record search in the computerized Radiology Information System from 2006-2016 for patients with the diagnosis of primary headache or a synonym. The search included all Brain MRI scans with and without contrast. The data collected included: age, sex, clinical indication, radiology report impression. Indications will be classified into 2 groups: primary and secondary headache. Only those with the indication of primary headache will be included. For those subjects where the radiology report impression identifies positive findings on the Brain MRI, the images will be reviewed to determine if the findings can be made without contrast, or if the findings can be made only with contrast. Images will be reviewed by a team of board certified neuroradiologists with at least 10 years' experience. Disagreements will be resolved by consensus. The subject population is expected to include approximately 200/year or 2000 total sample size. The majority will be healthy adult female subjects as reported for this population, but none will be excluded if the referral reason is primary headache. Data analysis: 1-3% positive findings may yield 20-60 positive scans. The total number of these scans with findings only identifiable on contrast scans (expected to be <10) will be reviewed for common factors. It is expected that this will include small lesions which lack clinical significance and are found incidentally. An overall assessment of clinically significant lesions which were likely to account for symptoms will be made.

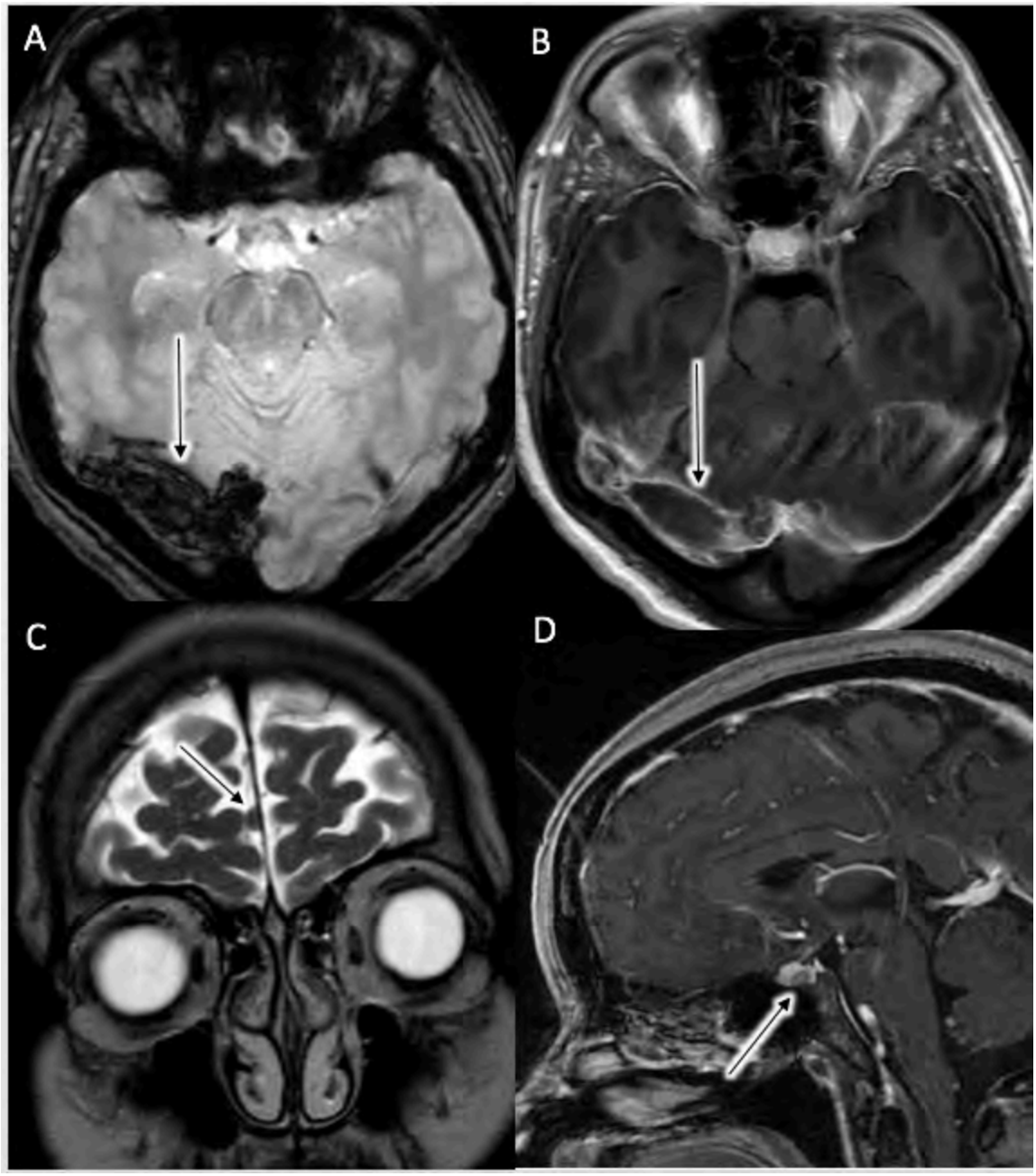
Results

Radiology reports of 3212 met the inclusion criteria. Of these 1937 were excluded based upon incorrect history, or imaging performed for indications other than primary headache. There were 1476 cases analyzed. There were 1009 normal examinations. Reports

demonstrating abnormality included: 429 with abnormal white matter lesions visible on FLAIR sequences, 9 with white matter lesions of atypical variety for which contrast enhancement may indicate active inflammation, 9 demonstrated findings only seen on the sequences with contrast. Of the 9 (0.6%) where a positive finding was seen only after contrast, 6 studies questioned the presence of a microadenoma, and 3 identified meningiomas of <5 mm size. None of these was judged to be of clinical significance after review of the medical record. The included images demonstrate examples of what was seen in the imaging cohort. Examples A and B demonstrate a transverse sinus thrombosis well demonstrated on gradient echo axial (A), and the postcontrast T1 axial (B). Example C, shows a tiny midline meningioma on coronal T2 that was better seen on the contrast-enhanced imaging and might have been missed without contrast - but was judged to be clinically insignificant. Example D shows a pituitary abnormality on sagittal T1 with contrast. This was not demonstrated on any other sequences from the examination. This was in a 58-year-old female with normal endocrine function, and judged to be clinically insignificant.

Conclusions

With a 0.6% rate of positive findings, all of doubtful clinical significance, the use of gadolinium contrast does not add value to the use of Brain MRI in patients with primary headache.



(Filename: TCT_O-295_Examples.jpg)

O-296

3:38PM - 3:46PM

Arterial Spin Labelling Imaging in Migraine with aura: report of a series of 33 adult patients

B Lanseur[1], R Le Bouc[1], C Rosso[2], D Dormont[3], Y Samson[1], A Bertrand[1]
[1]Pitié-Salpétrière Hospital, Paris, Paris, [2]Pitié-Salpêtrière Hospital, Paris, AK, [3]AP-HP, Pitié-Salpétrière hospital, Paris, Ile de France

Purpose
Migraine with aura is a frequent stroke-mimic, and its positive diagnosis may be challenging in cases with no previous history of migraine, no headache or atypical symptoms. Previous studies have reported that arterial spin labeling (ASL) can depict perfusion abnormalities in patients presenting with migrainous aura. The aim of our study was to assess the frequency and the chronology of ASL abnormalities in a series of adult patients with atypical acute migraine with aura.
Materials and Methods
We retrospectively reviewed the prospective database of patients seen in our Stroke Unit. From 2013 to 2016, we found 67 patients referred for acute neurological deficit with a possible diagnosis of migraine with aura. We excluded patients for whom the final diagnosis of migraine was uncertain (n=3), the beginning of symptoms was unknown (n=16), the laterality of symptoms was unavailable (n=9), or the MRI examination did not include ASL sequence (n=6). The final study group comprised 33 patients; among them, 9 underwent a follow-up MRI control from 24 hours to 5 days after the first one. All MRI included the following sequences : FLAIR, T2*, 3DTOF and pcASL with a PLD=2025ms. We collected all clinical data (age, sex, cardiovascular risk factors, type and duration of symptoms) and time of MRI. Two neuroradiologists, blinded from clinical data, reviewed all ASL sequences in order to determine 1) the presence of an area of abnormal perfusion (hypo or hyperperfusion), 2) the location of perfusion abnormalities (cerebral lobes involved). In the few cases of discordance, a consensus was reached during a third lecture.
Results
Among the 33 patients, 18 (55%) had abnormal ASL imaging. Patients with abnormal ASL had longer aura duration (198 min vs. 167 min in the normal ASL group, $p<.05$, Mann-Whitney test) and shorter delay between the beginning of aura and the MRI (16 hours vs. 39.5 hours in the normal ASL group, $p<.01$, Mann-Whitney test). In patients who underwent MRI less than 5 hours after the beginning of aura, ASL showed hypoperfusion (7/11) , no abnormality (3/11) or hyperperfusion in only 1 case. In patients who underwent MRI 5 to 36 hours after the beginning of aura, ASL showed hyperperfusion (10/19), no abnormality (8/19), or hypoperfusion in only 1 case. In patients who underwent MRI more than 36 hours after the beginning of aura, ASL showed hypoperfusion in 2 cases and was normal in all others (10/12). In 4 patients with initial hypoperfusion, follow-up MRI demonstrated hyperperfusion (n=2) or normalization (n=2). In 3 patients with initial hyperperfusion, follow-up MRI demonstrated persistant hyperperfusion (n=1) or normalization (n=2). In 2 patients with normal initial ASL, follow-up MRI was normal.
Conclusions
Half of the patients presenting with atypical migraine with aura display perfusion abnormalities on ASL sequence. These abnormalities are more frequent when the aura duration exeeds 10 min, and when the MRI is performed less than 24h after the beginning of the aura. Our results are consistent with sequential perfusion changes associated with aura,

including initial hypoperfusion (typically from 0 to 5h), followed by hyperperfusion (typically from 5 to 36h) and normalization (typically after 36h).

O-297

3:46PM - 3:54PM

Chief Complaint "Headache" with Initially Normal Imaging and Follow-up within 9 days: Low Yield of Repeat Parenchymal Imaging but Unexpectedly High Rate of Unruptured Aneurysms on Vascular Imaging

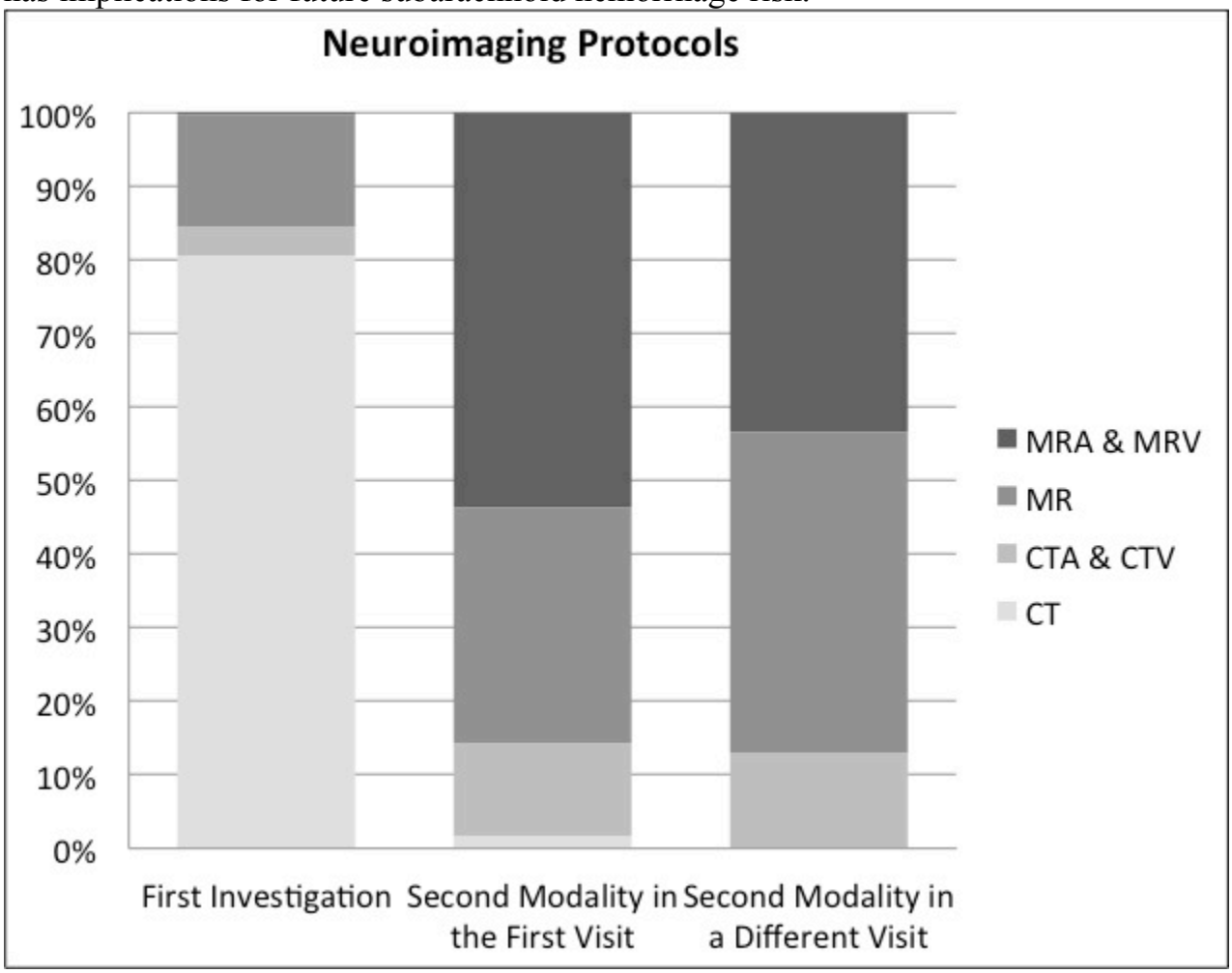
R Almeida[1], M Lev[2], B Bizzo[1], M Mansouri[1], W Mehan[1]
[1]Massachusetts General Hospital, Boston, MA, [2]Massachusetts Gen'l Hosp./Harvard Med. Schl., Boston, MA

Purpose
Headache is a common complaint among patients visiting the emergency department (ED). Imaging is performed frequently in these patients with clinical features suggesting a secondary cause of headache. The value of subsequent neuroimaging studies following an initial normal imaging exam in this cohort remains unclear. Our goal was to assess the frequency and results of follow-up imaging performed in headache patients within 9 days of a normal initial neuroimaging exam.
Materials and Methods
We retrospectively reviewed our radiology database for brain CTs or MRs performed in the ED from January 1st to December 31st 2015, with the term "headache" in the exam indication. Exam protocols and report impressions were reviewed; "important" and "incidental" imaging findings for headache were catalogued. Demographics and final diagnosis were retrieved from the medical records. Fisher's exact test was used to compare number and type of follow-up exams, and imaging findings.
Results
A total of 1687 patients presenting with headache in 2015 underwent neuroimaging. Of these, 985/1687 (59%) were interpreted as normal [107/985 (89%) MR and 878/985 (11%) CT]. Of those with initially normal imaging 142/985 (14.3%) had follow-up within 9 days (83.8%, 119/142 during the same visit and 16.2%, 23/142 in a 2nd visit after discharge). Of patients with initially normal MR, 10/107 (9.3%) had follow up, and with CT, 132/878 (15%) had follow up (p=0.14). There were 23/142 (16.1%) follow-up patients with initially normal imaging who had "important" findings. Of the 10 follow-up patients with initially normal MR, 1/10 (10%) important findings (an unruptured ICA aneurysm) were seen on follow-up CTA, and no important findings 0/10 (0%) were seen on follow-up brain parenchymal MR. Of follow-up patients with initially normal MR, no incidental findings that might be associated with headache were seen (0/10, 0%). Of the 132 follow-up patients with initially normal head CT, 14/132 (10.6%) important findings were seen on follow-up CTA, MRA or MRV only, and 8/132 (6%) important findings were seen on follow-up brain MR

only. These included: 10 strokes, 3 internal carotid artery (ICA) aneurysms, 2 idiopathic intracranial hypertension (IIH, "pseudotumor"), 2 anterior communicating artery (ACA) aneurysms, 1 meningitis, 1 dural sinus thrombosis, 1 ICA dissection, 1 reversible cerebral vasoconstriction syndrome (RCVS), and 1 sinusopathy. Of follow-up patients with initially normal CT, 30/132 (22.7%) incidental findings that might be associated with headache were seen, including atherosclerotic disease. It is noteworthy that 6/23 (26%) of the important findings in follow-up patients with initially normal imaging were unruptured aneurysms.

Conclusions

There were no important parenchymal findings in patients who had follow-up imaging within 9 days of an initially normal MRI; only a single important but non-actionable finding on CTA follow-up was observed, an unruptured ICA aneurysm (1/10, 10%). Of the 22/132 (16%) important findings following initial normal head CT, five were unruptured aneurysms (3 ICA and 2 ACA). The 26% (6/23) rate of unruptured aneurysms among the important findings seen in the follow-up group represents a substantially larger incidence than the 3.2% aneurysm rate seen in the general population (1), although the clinical significance of this observation remains uncertain. We are planning additional studies to determine whether this has implications for future subarachnoid hemorrhage risk.



(Filename: TCT_O-297_ASNR.jpg)

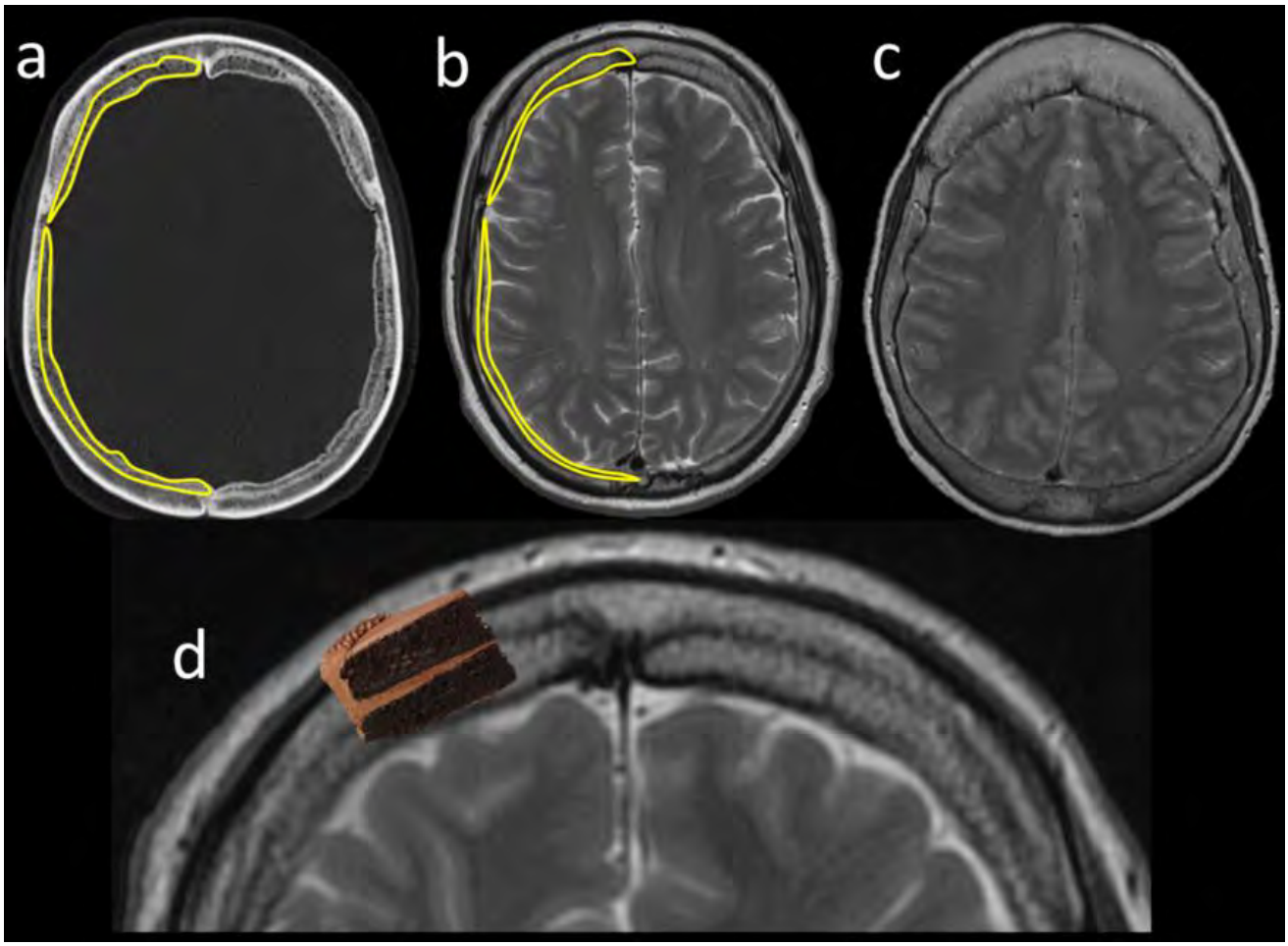
O-298

3:54PM - 4:02PM

Layer Cake Skull in Patients with Spontaneous Intracranial Hypotension

D Johnson[1], C Carr[1], P Luetmer[1], F Diehn[1], V Lehman[1], J Verdoorn[1], K Krecke[1]
[1]*Mayo Clinic, Rochester, MN*

Purpose
Diagnosis of spontaneous intracranial hypotension (SIH) may be delayed due to nonspecific symptoms and variable imaging findings. Cases of hyperostosis in children who are overshunted have been reported. This situation is physiologically analogous to that of adults with SIH, and we have anecdotally observed examples of hyperostosis in SIH. The frequency and characteristic appearance of diffuse hyperostosis in SIH have not been described previously to our knowledge.
Materials and Methods
Brain CT and MRI exams from 311 consecutive patients with SIH who underwent myelography were assessed for the presence of diffuse calvarial thickening or development of a secondary layer of bone. Patients with typical benign frontal hyperostosis were excluded.
Results
Diffuse hyperostosis was observed in 13% (41/311) of patients. The median age of patients with hyperostosis was 53.6 (IQR 46.7 – 59.0) and 63% (26/41) were female. Of the positive cases, 80% (33/41) demonstrated a distinct secondary layer of bone formation extending circumferentially along the inner table of the skull. This finding could be identified on either CT or MRI, as shown in images (a) and (b) of the accompanying figure, where the secondary layer of bone formation is outlined on the left side. The remaining 20% (8/41) of positive cases demonstrated diffuse calvarial thickening, as illustrated by image (c) in the figure.
Conclusions
Development of a secondary layer of bone or diffuse calvarial thickening can be seen in the setting of SIH. The mechanism may be analogous to hyperostosis in the setting of pediatric over-shunting. The most distinctive pattern, which we refer to as "layer cake skull", image (d), involves the presence of a circumferential secondary layer of bone that may be unique to this condition. Further analysis is ongoing to define the relationship of this finding to duration of symptoms, type of leak, brain sag, dural thickening and prognosis.



(Filename: TCT_O-298_Figurewithletters.jpg)

O-299

4:02PM - 4:10PM

Idiopathic Intracranial Hypertension: Cranial MRI Findings In Correlation With Direct Venous Sinus Pressure Measurements.

R Valenzuela[1], R Riascos[2], L Ocasio[3], M Ramirez[4], D Marcus[5], A Cano-Duran[5]
[1]The University of Texas, Houston, TX, [2]UTHSC-Houston, Houston, TX, [3]memorial hermann, Houston, TX, [4]The University of Texas Health Science Center at Houston. Department of diagnostic and intervention, Houston, TX, [5]University of Texas Health Science Center at Houston, Houston, TX

Purpose
To analyze the correlation between intracranial MRI findings and the probability of an increased transverse sinus pressure in a series of patients with direct venous pressure measurements.

Materials and Methods

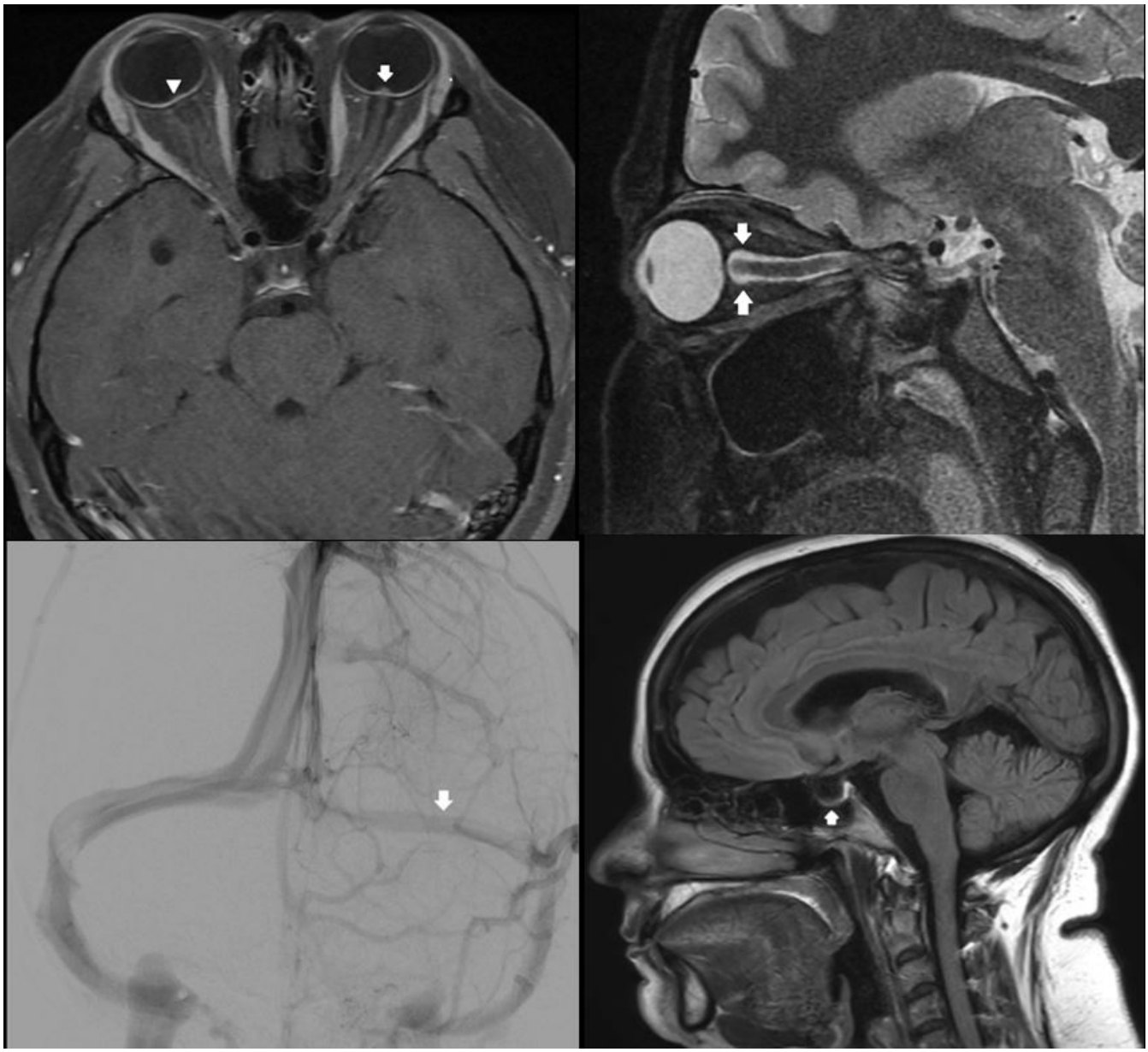
Nineteen cases of clinically diagnosed idiopathic intracranial hypertension (IIH) presented to Memorial Hermann Hospital in Houston Texas, who underwent angiography with direct venous pressure measurements were analyzed. Data regarding lumbar puncture opening pressure, MRI findings and direct venous sinus pressure measurements were collected and subjected to statistical analysis.

Results

The only MR sign that was significantly positively correlated with venous sinus stenosis was the presence of sellar diaphragm depression. Lumbar puncture opening pressure lower than 28cm. H_2O was significantly associated with a high negative predictive value for an elevated venous sinus pressure and trans-stenotic gradient. The number and grade of all other MR findings did not reach a statistically significant correlation with angiographic findings.

Conclusions

The lumbar puncture opening pressure cut-off value lower than 28 cm. H_2O may provide a minimally invasive candidate exclusion criteria for venous sinus stenting, this is to be further evaluated by a larger sample study. No statistically significant correlation was found between the total number of positive MRI findings and increased venous pressure measurements in patients with clinical IIH diagnosis.



(Filename: TCT_O-299_IHHfinal.jpg)

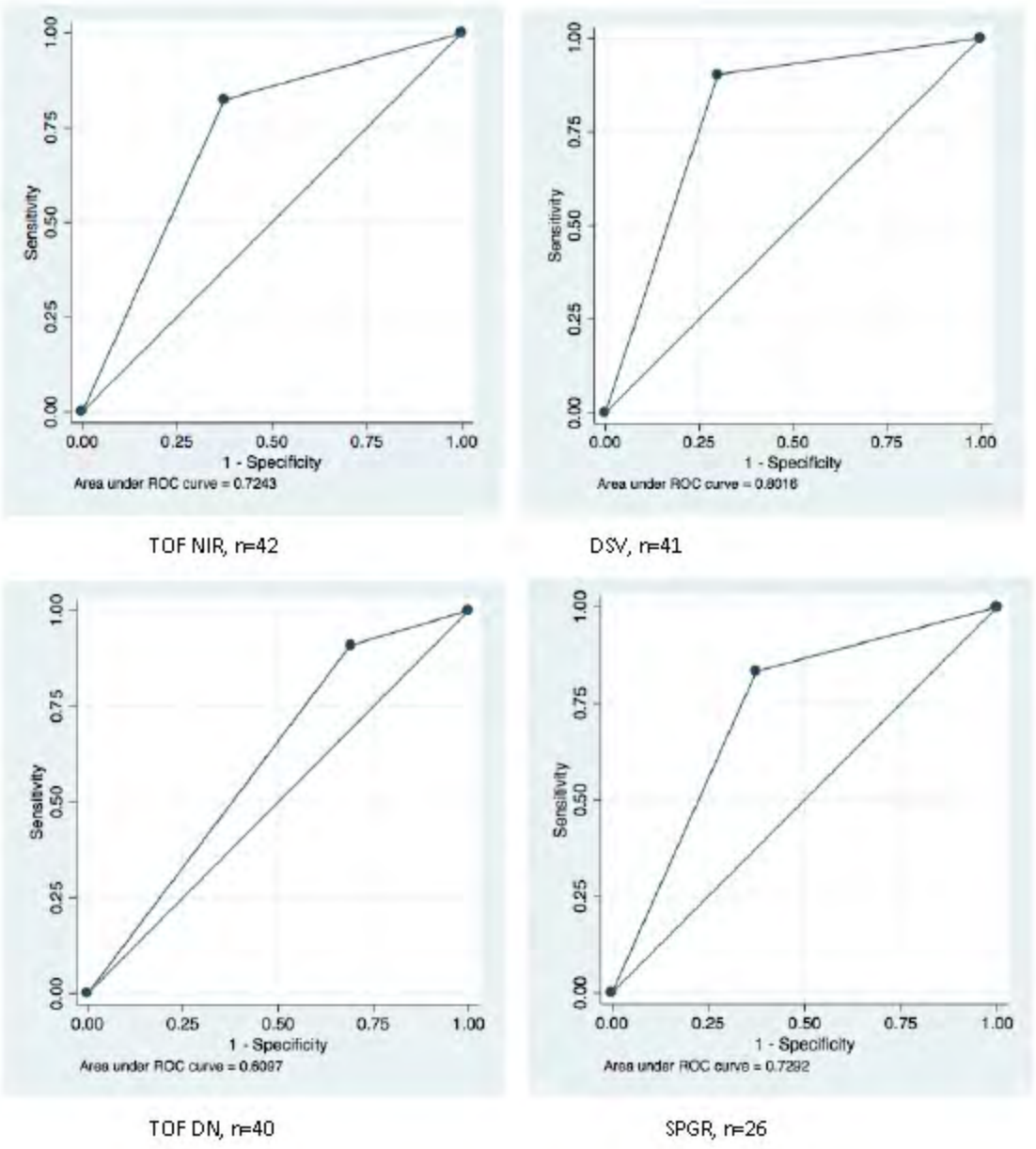
O-300

4:10PM - 4:18PM

The Value of Non Invasive MR Venous Imaging in Idiopathic Intracranial Hypertension: Comparison to Catheter Venography and Manometry

K Chen[1], E Chow[1], C Chung[2], S Jones[3], M Luciano[1], F Hui[1]
[1]Johns Hopkins University, Baltimore, MD, [2]Brigham and Women's Hospital, Allston, MA, [3]Cleveland Clinic, Cleveland, OH

Purpose
Bilateral transverse sinus stenosis abnormalities have been reported in up to 93% of patients with clinically diagnosed idiopathic intracranial hypertension. Increasingly, transverse sinus stenting has been used to treat such patients which often includes venographic manometry to verify a pressure gradient across the stenosis. This study compares the accuracy of MRV (TOF vs. contrast enhanced) and venographic findings against the gold standard of manometry in patients with idiopathic intracranial hypertension.
Materials and Methods
A prospectively maintained database of patients with clinically diagnosed idiopathic intracranial hypertension was accessed including patients that had diagnostic venography and manometry, time of flight magnetic resonance venography (TOF MRV), and spoiled gradient recall echo venography (SPGR) with or without gadolinium. Time of flight MRV images were read by both a diagnostic neuroradiologist and interventional neuroradiologist and stored seperately. Given that a pressure gradient of 8 mm of water is considered the threshold for therapy in the majority of reported series, this was considered the "gold standard" for significant venous stenosis. Post-treatment gradients also were recorded along with symptoms to assess treatment effect. Receiver operating characteristic (ROC) curves were constructed to assess for each diagnostic modality against the gold standard of manometry and area under the curve (AUC) was calculated to compare accuracy across modalities and readers.
Results
Area under the curve was highest for digital subtraction venography. Time of flight MRV and SPGR findings by an interventional neuroradiology trained reader yielded greater AUC than TOF MRV read by a diagnostic neuroradiologist. The difference in accuracy across DSV, TOF MRV by an interventional neuroradiologist, or TOF MRV by a diagnostic neuroradiologist was not statistically significant.
Conclusions
Idiopathic intracranial hypertension patients who fail medical therapy should be evaluated for dural sinus stenosis with dedicated imaging protocols. Stenoses detected on imaging correlate well with venous gradients on manometry during venography and these patients often go to receive symptomatic relief after stenting. However, sensitivity is affected significantly by interobserver variation and modality. With this in mind, radiologists and interventionalists may increase detection with multimodality imaging, reviewing the images themselves. Pretest probability of stenosis in clinically diagnosed IIH is high, and some argument may be made to go directly to venography and manometry, given discordance between noninvasive imaging and invasive manometry.



(Filename: TCT_O-300_IIHMRV.jpg)

O-301

4:18PM - 4:26PM

Pressure Maps of Normal and Variant Dural Sinuses derived from 4D Flow MRI Velocity Measurements (PC VIPR)

Z Clark[1], L Rivera-Rivera[2], K Johnson[3], O Wieben[2], P Turski[4]
[1]University of Wisconsin Hospital and Clinics, Madison , WI, [2]University of Wisconsin Madison, Madison, WI, [3]University of Wisconsin, Madison , WI, [4]Univeristy of Wisconsin, Madison, WI

Purpose

Venous hypertension involving the dural sinuses is implicated in the pathophysiology of dural arteriovenous fistulas (DAVFs). However, normal dural sinus pressure variation is not well established. The goal of this project is to characterize variations in normal dural sinus pressure using 4D Flow MRI (PC VIPR) providing a basis for interpretation of dural sinus pathology.

Materials and Methods

Four-dimensional Flow MRI exams were obtained in 84 healthy subjects using the phase contrast vastly undersampled isotropic projection reconstruction (PC VIPR) method to measure velocity fields, dural sinus cross sectional area, venous flow rate and maps of relative pressure (1). 4D Flow MRI (PC VIPR) has been validated as a method to measure pressure noninvasively (2, 3). Dural venous drainage was classified based on torcular herophili anatomy [type 1= true confluence/symmetric, type 2 = partial confluence/asymmetric, type 3 = isolated drainage of the deep venous system into one transverse sinus, and type 4= absent transverse sinus (4)] and based on differences in cross sectional area of the transverse sinuses (TS).

Results

Greater than 60% difference in cross-sectional area of the TS was associated with higher relative pressure in the smaller TS in 19 of 22 subjects. This group included 14 patients with type 3 anatomy with elevated pressure in the TS draining the deep venous system. Subjects with <60% asymmetry had no pressure differences. Initial clinical experience in DAVF patients revealed higher pressure in the TS on the side of the fistula (Fig. 1).

Conclusions

4D Flow MRI derived relative pressure differences in pathologic conditions such as DAVFs must be interpreted within the context of anatomic variants and normal variations in pressure. Type 3 torcular herophili anatomy and >60% asymmetry in cross-sectional area between transverse sinuses represent important normal variants to recognize given their association with higher relative pressure.

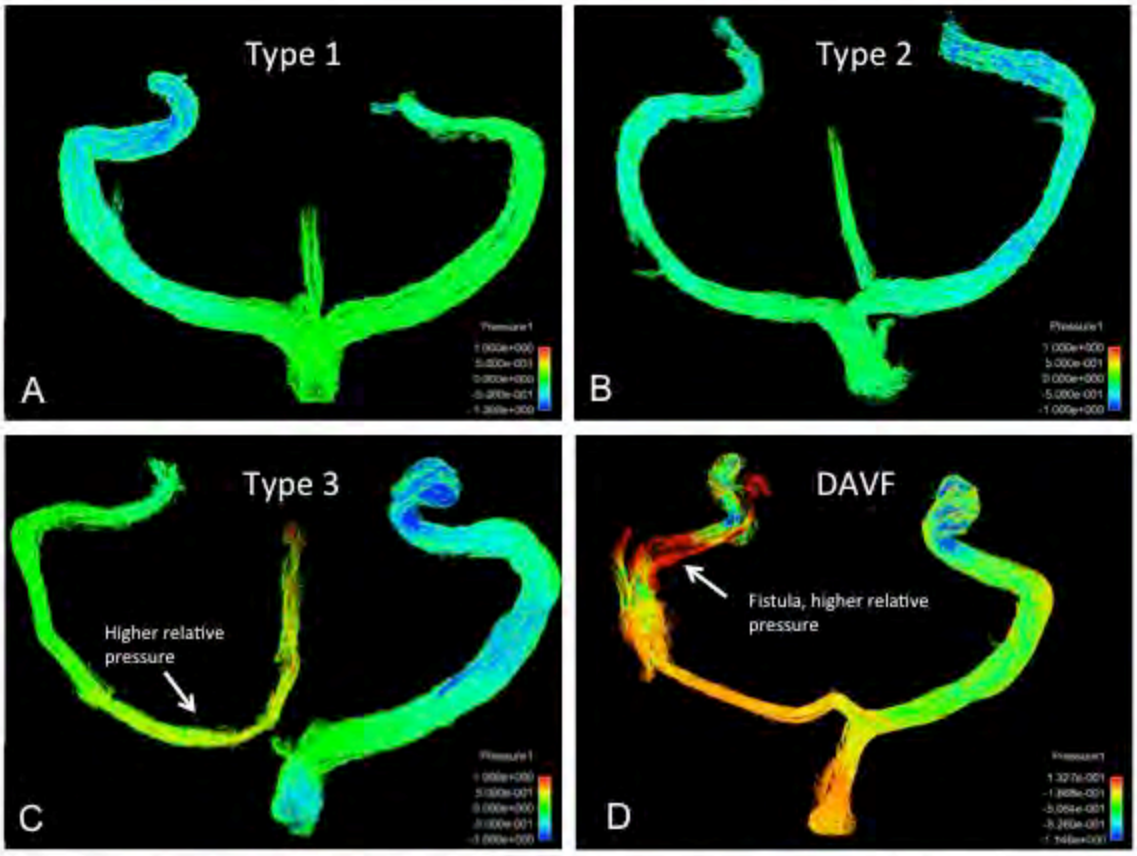


Figure 1. Dural Sinus Pressure Variation. Relative pressure maps demonstrate similar pressure between transverse sinuses in patients with true (A, type 1 anatomy) and partial confluence (B, type 2 anatomy) of the Torcular Herophili which were more likely to have symmetric transverse sinuses (<60% difference in cross sectional area). Higher relative pressure was observed in the smaller transverse sinus in patients with asymmetric transverse sinuses (>60% difference in cross sectional area) as seen in C (type 3 anatomy, separate deep venous drainage of straight sinus into smaller right transverse sinus, arrow) as well as on the side of the fistula in a DAVF patient.

(Filename: TCT_O-301_DuralPressureFigure.jpg)

O-302

4:26PM - 4:34PM

Characterization of Pre/Post Shunt Normal Pressure Hydrocephalus Pathology with Diffusion Kurtosis Imaging

B Conti[1], B Ades-Aron[2], B Conti[1], E Lotan[3], E Fieremans[2], J Golomb[2], A George[2], B Damadian[4]

[1]NYU Langone Medical Center, New York, NY, [2]New York University School of Medicine, New York, NY, [3]NYU Langone Medical Center and Tel-Aviv University, New-York, NY, [4]Jacobs School of Medicine & Biomedical Sciences at the University at Buffalo, Buffalo, NY

Purpose

Normal pressure hydrocephalus (NPH) is characterized by gait impairment, ranging from mild to severely incapacitating, which can show significant improvement following ventricular shunt surgery. However, the physiologic basis for the reversibility of gait impairment is poorly understood. Previous studies have demonstrated significant alterations of diffusion along the corticospinal tract (CST), most prominently at the level of the corona radiata (1). In this study, white matter (WM) microstructure was probed using diffusion kurtosis imaging (DKI), which allows for the computation of specific markers for fiber coherence and axonal loss (2, 3). The purpose of this study is to examine diffusion parameters of the CST in NPH patients before and after shunt surgery in order to identify reversible versus irreversible changes.

Materials and Methods

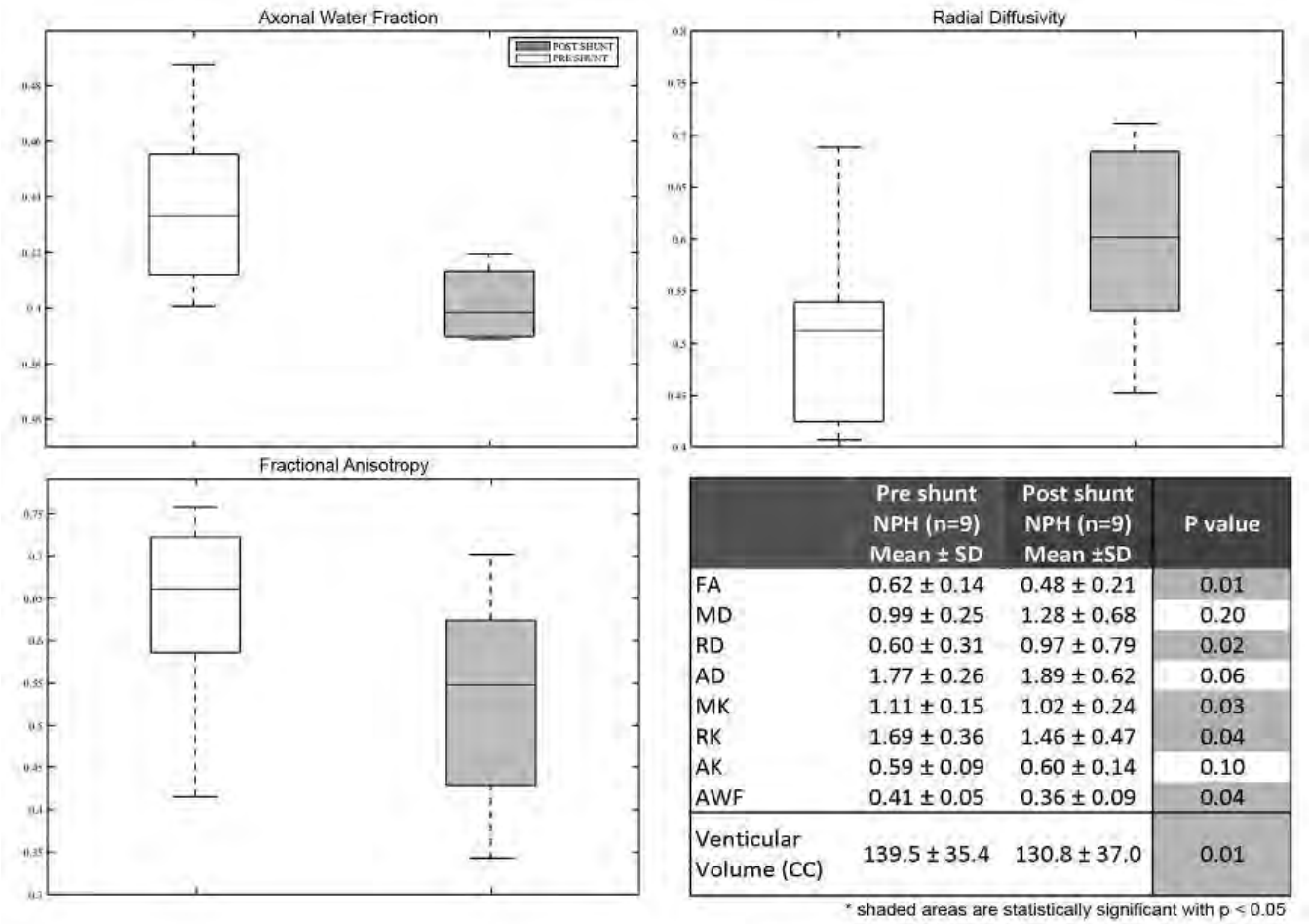
Nine shunt-responsive NPH patients (7 male, mean age = 76 ± 5.5 years) underwent MRI on a Biograph mMR 3T MRI system (Siemens AG, Erlangen, Germany). A monopolar diffusion-weighted EPI sequence was applied with b=0, 1000, and 2000 ms/μm2 along 61 directions in total. Data was acquired in a volume of 32 slices, 88x80 matrix, with voxel size=2.6mm x 2.6mm x 5mm, TE/TR=91/4500ms. Regions of interest (ROIs) were placed symmetrically within the following regions: subcortical white matter of frontal and parietal lobes, motor strip, corona radiata at maximum ventricular diameter, posterior limb of internal capsule, midbrain, and corpus callosum. Diffusion kurtosis imaging fitting provided parametric maps of the axonal water fraction (AWF) (3) in addition to standard kurtosis metrics. Paired Wilcoxon Signed rank tests were used to evaluate statistical differences.

Results

Axonal water fraction and radial diffusivity (RD) were significantly decreased and increased, respectively, in the superior corona radiata of NPH patients after shunt surgery (see Figure). These changes in diffusion may be manifestations of decompression - increased RD implies more space between axons and decreased AWF implies a lower axonal packing density (3). Fractional anisotropy (FA) is decreased in the same region, which may imply lower fiber bundle coherence, pointing towards tissue relaxation in the corona radiata. The lack of significant differences in selected regions outside of the CST validates the hypothesis that this region is the core of NPH disease mechanism.

Conclusions

This study suggests that DKI and derived parameters provide measures of microstructural changes occurring in NPH which will increase our diagnostic accuracy and help define the pathophysiology of this complex but treatable condition.



	Pre shunt NPH (n=9) Mean ± SD	Post shunt NPH (n=9) Mean ±SD	P value
FA	0.62 ± 0.14	0.48 ± 0.21	0.01
MD	0.99 ± 0.25	1.28 ± 0.68	0.20
RD	0.60 ± 0.31	0.97 ± 0.79	0.02
AD	1.77 ± 0.26	1.89 ± 0.62	0.06
MK	1.11 ± 0.15	1.02 ± 0.24	0.03
RK	1.69 ± 0.36	1.46 ± 0.47	0.04
AK	0.59 ± 0.09	0.60 ± 0.14	0.10
AWF	0.41 ± 0.05	0.36 ± 0.09	0.04
Venticular Volume (CC)	139.5 ± 35.4	130.8 ± 37.0	0.01

* shaded areas are statistically significant with p < 0.05

(Filename: TCT_O-302_NPH-ASNR-v2.jpg)

O-303

4:34PM - 4:42PM

Transverse Sinus Stenting for Idiopathic Intracranial Hypertension: A Review of 29 Cases

N Kathrani[1], A Gupta[2], A RAMALINGAIAH[3], j saini[4], C Prasad[5], H PENDHARKAR[6], A Verma[7]

[1]National Institute of Mental Health and Neurosciences (NIMHANS), Bengaluru, Karnataka, [2]National Institute of Mental Health and NeuroSciences (NIMHANS), Bangalore, Karnataka, [3]NATIONAL INSTITUTE OF MENTAL HEALTH AND NEUROSCIENCE, NIMHANS, Bengaluru , karnataka , [4]NIMHANS, BANGALORE, Karnataka, [5]National Institute of Mental Health and Neurosciences, Bangalore, Karnataka, [6]NATIONAL INSTITUTE OF MENTAL HEALTH & NEUROSCIENCES, BANGALORE, KARNATAKA, [7]national Institute of Mental health & Neuro Sciences, Bangalore, Karnataka

Purpose
Idiopathic intracranial hypertension (IIH) has a high prevalence of transverse sinus stenosis. Studies suggest that stent placement within a transverse sinus stenosis which has a significant pressure gradient decreases cerebral venous pressure, improves cerebrospinal fluid (CSF) resorption in the venous system, and thereby reduces CSF pressure and resolves the symptoms of IIH. Purpose of our study was to determine if IIH could be reliably treated by stent placement in transverse sinus stenosis and to look for the complications associated with it.
Materials and Methods
Stenting was carried out whenever pressure gradient across the stenosis was found to be more than 10 mm Hg. The clinical , venographic and CSF pressure data were reviewed before and after the stent placement in transverse sinus stenosis in 29 patients with IIH unresponsive to maximum acceptable medical treatment, treated between 2010 to 2016 in our institution and followed between 1 month and 6 years.
Results
Prior to stenting, the mean superior sagittal sinus pressure was 36 m Hg with a mean pressure gradient of 14 mm Hg across the stenosis. The lumber CSF pressure before stent placement was more than 250 mm water. In 26 patients, stent placement immediately eliminated the pressure gradient, rapidly improved IIH symptoms and abolished papilledema. Two patients had persistent headache, papilledema and giddiness for 15 days followed by slow resolution of symptoms, though pressure gradients were relieved immediately after stent placement. Subdural hematoma was seen in 1 patient during the procedure followed by slow resolution. Recurrent stenosis or symptoms have not been observed until now.
Conclusions
Transverse sinus stent placement is a safe and effective treatment in management of selected patients with IIH.

Wednesday
3:30PM - 4:45PM
Long Beach Convention Center, Room 104C (Main Lobby)

20F-Parallel Paper Session: Excerpta: Pediatric Problems...Can you Solve Them?

E-74

3:30PM - 3:34PM

Quantitative and Qualitative Measurements of Flow in Vein of Galen Malformations using PCVIPR

Y Li[1], Z Clark[2], L Rivera-Rivera[3], P Turski[4], B Aagaard-Kienitz[5]

[1]University of Wisconsin, Madison, WI, [2]University of Wisconsin Hospital and Clinics, Madison , WI, [3]University of Wisconsin Madison, Madison, WI, [4]Univeristy of Wisconsin, Madison, WI, [5]University of Wisconsin Hospital and Clinics, Madison, WI

Purpose

The purpose of this study is to report on a novel application of 3D phase-contrast with vastly under sampled isotropic projection reconstruction (PC-VIPR) magnetic resonance imaging (MRI) sequence to noninvasively assess changes in cerebral arterial flow patterns and venous pressure gradients before and after embolization of Vein of Galen malformations (VOGM).

Materials and Methods

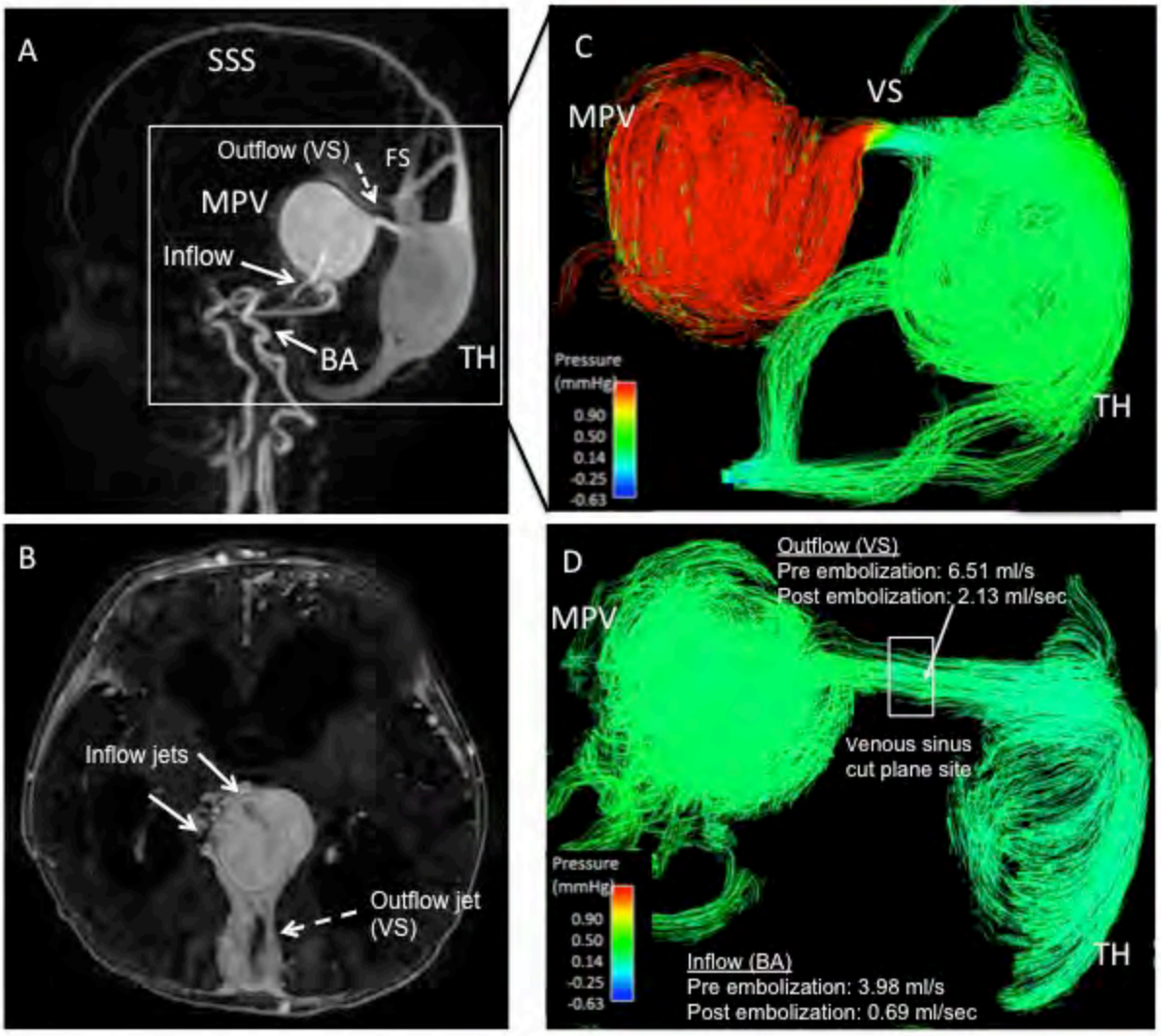
We present the case of a 6-month-old girl with developmental delay found to have a mural VOGM with secondary ventriculomegaly, venous hypertension, and volume loss. The patient was treated with staged transarterial embolizations.

Results

Fig. A. Sagittal time-resolved magnetic resonance angiography (MRA) (TRICKS) demonstrates a mural VOGM with arterial supply from the basilar artery (BA) whose terminal branch (inflow, arrow) feeds a dilated median prosencephalic vein (MPV). Outflow is through a narrowed venous sinus (VS) into an enlarged torcular herophili (TH). A patent falcine sinus (FS) is present. Fig. B. Axial contrast-enhanced T1-weighted images demonstrates arterial inflow jets (arrows) into the MPV with a large outflow jet (dashed arrow) at the VS indicative of elevated velocities and VS stenosis. Fig. C. Pre-embolization PC VIPR relative pressure map demonstrating elevated pressure in the MPV relative to the TH. Fig. D. Postembolization PC-VIPR relative pressure map demonstrating decreased pressure gradient between the VM and TH. Cut planes placed at the BA (inferior arrow from figure A) and VS (arrow) demonstrated reduced blood flow (ml/s) into and out of the MPV, respectively following embolization.

Conclusions

Evidence shows that VOGM hemodynamics cause decreased cerebral blood flow due to cerebral arterial steal and intracranial venous hypertension resulting in poor clinical outcomes. Qualitative and quantitative data from PC-VIPR potentially can be used as additional criteria to assess treatment success, timing of treatments, as well as progressive disease. PC-VIPR could be used to enhance management decisions for treating patients with VOGM.



(Filename: TCT_E-74_VoGFigure.jpg)

E-75

3:34PM - 3:38PM

Brain MRI Findings in Poorly Controlled Homocystinuria

C Li[1], B Barshop[1], A Feigenbaum[1], P Khanna[2]
[1]University of California, San Diego, San Diego, CA, [2]Rady Children's Hospital, San Diego, CA

Purpose
To describe conspicuous magnetic resonance imaging (MRI) findings not previously reported in poorly controlled homocystinuria.
Materials and Methods
A three-year-old female with homocystinuria due to cystathionine β-synthase (CBS)

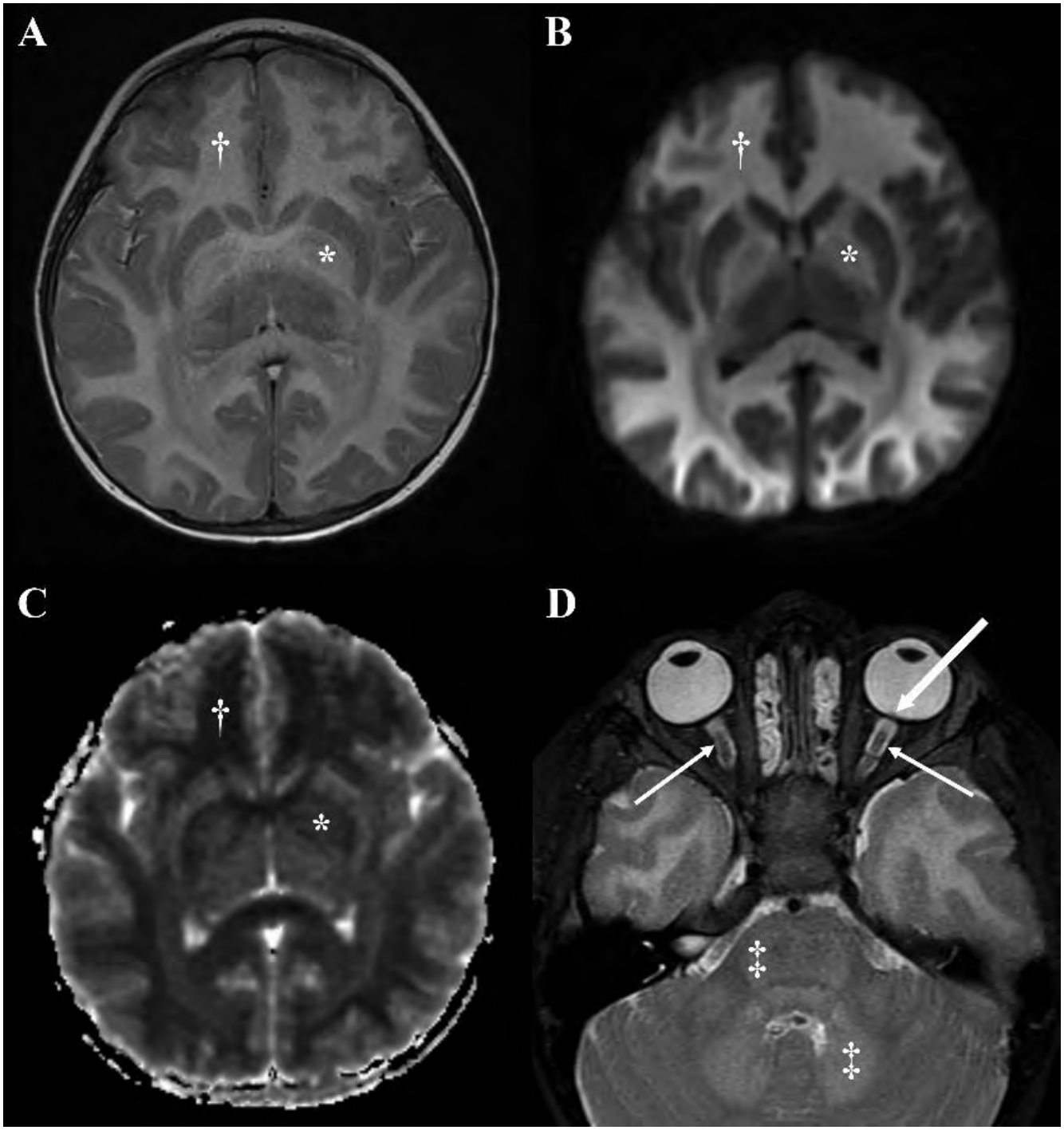
deficiency was admitted for mild asymptomatic bilateral papilledema incidentally detected on routine ophthalmologic examination. Lumbar puncture opening pressure was borderline elevated (28 cm, normal 10–28) and cerebrospinal fluid (CSF) methionine concentration was high (199 μmol/L, normal <5.8). Plasma homocysteine was elevated (203 μmol/L, normal 3.4–11.8) and plasma methionine was markedly elevated for several months prior to admission (>1000 μmol/L, normal 7–47) despite prescription medication and diet.

Results

Brain magnetic resonance imaging (MRI) on admission showed diffuse brain swelling and effacement of the cerebral sulci and lateral ventricles, as well as abnormal signal throughout the white matter (†), bilateral globi pallidi (*), and bilateral dorsolateral thalami (not pictured) on all sequences. These structures were abnormally bright on T2-weighted images (Fig. A) and demonstrated diffusion restriction on diffusion-weighted images (Fig. B) and calculated apparent diffusion coefficient maps (Fig. C). High-resolution T2-weighted images of the orbits (Fig. D) revealed papilledema (thick arrow), dilated optic nerve sheaths (thin arrows), suggestive of increased intracranial pressure (ICP). The white matter of the pons and cerebellum also was abnormally T2-bright (‡). MR spectroscopy of the left basal ganglia showed decreased N-acetylaspartate (NAA) without a lactate peak. No venous filling defects were present on MR venography.

Conclusions

Homocystinuria is an inherited metabolic disorder whose name derives from elevated urine homocystine, the disulfide of homocysteine. Classical homocystinuria is due to CBS deficiency, although other metabolic defects also may result in homocysteine accumulation. Several poorly controlled cases have demonstrated nonspecific white matter T1 and T2 prolongation and diffusion restriction on MRI, sometimes also with brain swelling and clinical manifestations of increased ICP (1–5). While the cellular processes underlying these findings is unclear, they may represent a combination of vacuolating myelinopathy and osmotic cell swelling due to hypermethioninemia and concurrent betaine therapy. Our case not only exhibits a strikingly severe example of such MRI findings, but also similar signal abnormalities in the basal ganglia as well as imaging manifestations of increased ICP (effaced subarachnoid spaces, optic nerve sheath dilation, and papilledema). This combination of imaging findings has not been reported previously and should not be mistaken for other vascular, toxic and metabolic disorders, such as hypoxic-ischemic injury, metachromatic leukodystrophy, Canavan disease, urea cycle defects, or maple syrup urine disease, etc.



(Filename: TCT_E-75_abstractcollage.jpg)

E-76

3:38PM - 3:42PM

Osteopetrosis in a pediatric patient with altered mentation

R Sharma[1], J Felder[2], A Derman[1], G Cruciata[1], E Stein[1]

[1]*Maimonides Medical Center, Brooklyn, NY,* [2]*Maimonides medical center, Brooklyn, NY*

Purpose

To outline a case of osteopetrosis in a pediatric patient and elucidate pertinent radiographic findings.

Materials and Methods

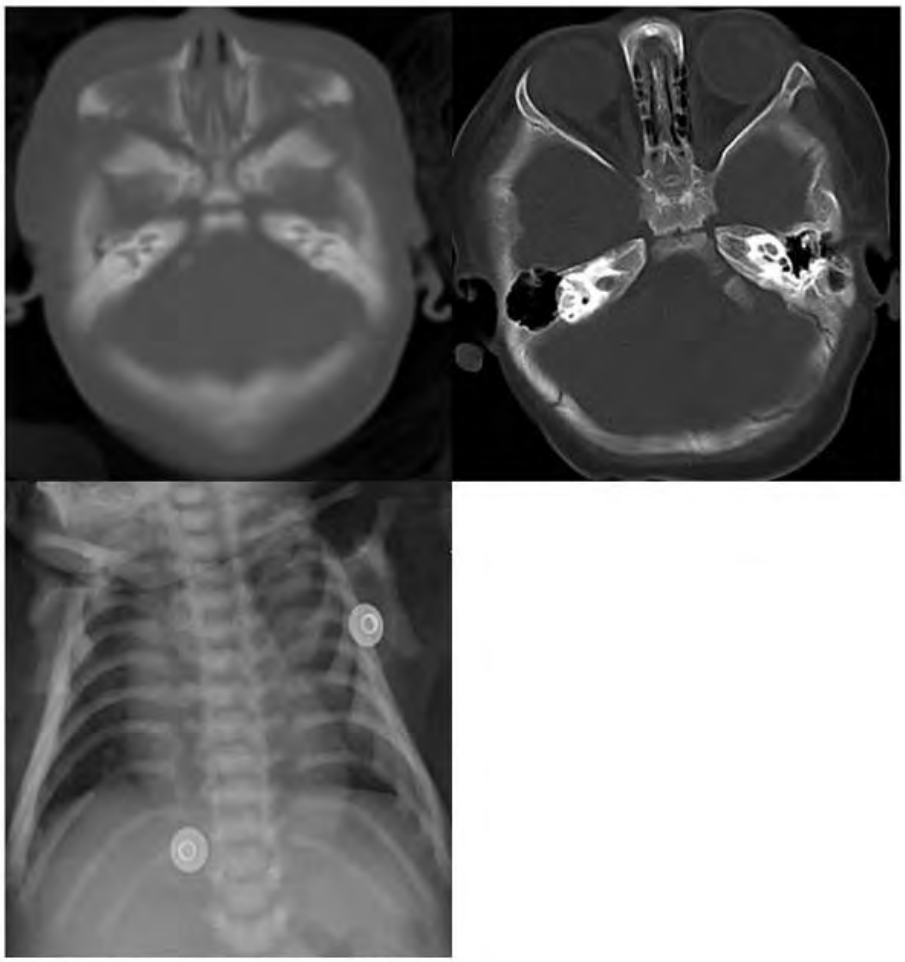
A 2-month-old female presented with lethargy, paleness, and decreased PO intake of several days duration. Physical exam was unremarkable except for a soft but bulging anterior fontanel. The patient also was noted to have an elevated white blood cell count and anemia. Further work up revealed a diffusely dense bony thorax as well as an otic capsule that was equally dense to surrounding bone.

Results

Computed tomography (CT) imaging of the brain without contrast revealed no focal parenchymal abnormality, i.e., hemorrhage or mass. Upon review of images in bone windows, the otic capsule was noted to be the same density as the surrounding bone (normally hyperdense). Further work up revealed diffusely dense rib bones on chest radiograph. These findings were consistent with the autosomal recessive subtype of osteopetrosis.

Conclusions

This case highlights a pediatric patient with altered mentation who was found to have diffusely dense rib bones and isodense otic capsules relative to the surrounding skull. The patient was transferred to pediatric ICU at another institution for further treatment. Osteopetrosis is a genetic disorder resulting in abnormal bone formation due to dysfunctioning osteoclasts. In the autosomal recessive form affecting infants, bony abnormalities of the skull can lead to cranial nerve compression in severe cases.



(Filename: TCT_E-76_OP.jpg)

E-77

3:42PM - 3:46PM

Asymmetric Degos Disease

M Ho[1], B Dewey[2]
[1]Mayo Clinic, Rochester, MN, [2]Mayo Clinic Radiology, Rochester, MN

Purpose
Introduce the pathophysiology, clinical features, and imaging appearances of Degos disease (DD). Discuss a unique case of DD with asymmetric central nervous system (brain and optic nerve) involvement.
Materials and Methods
A 17-year-old male presented to our hospital with a 2-year history of small skin lesions on the abdomen. These started as pink, asymptomatic papules with a small white clearing. Over

time, these increased in number and distribution, spreading from the central abdomen to the back and lower extremities. Over the past several months, the patient also experienced multiple episodes of left-sided neurologic symptoms. This first began with an episode of left arm numbness and slurred speech, which lasted for several hours before resolving. A second episode involved acute painless loss of vision in the left eye. Subsequently, the patient experienced rapidly progressive left-sided weakness, ataxia, dysphagia, and neurogenic bladder. Due to worsening confusion and expressive/receptive aphasia, he underwent electroencephalography, which showed diffuse right hemispheric slowing and rare left frontotemporal spikes. Cerebrospinal fluid studies were unrevealing. Ophthalmologic examination showed left ischemic optic neuropathy with multiple small vessel occlusions and hemorrhages in the optic nerve fundus. Skin biopsies of the abdomen demonstrated dermal necrosis and lymphocytic vasculitis, pathognomonic for Degos disease. Meningeal biopsy showed focal chronic pachymeningitis and subacute organizing subdural membranes. The underlying brain parenchyma demonstrated focal lymphocytic vasculitis with transmural involvement of cortical and leptomeningeal vessels, including nodular collections of chronic inflammatory cells around damaged vessel wall components, and subacute organizing cortical microinfarcts. The patient was placed on an extensive immunosuppressive and anticoagulative regimen including prednisone, cyclophosphamide, aspirin, dipyridamole, pentoxifylline, treprostinil, and eculizumab. Despite aggressive therapy, his neurologic status continued to decline, and he ultimately succumbed to his disease 2 months later.

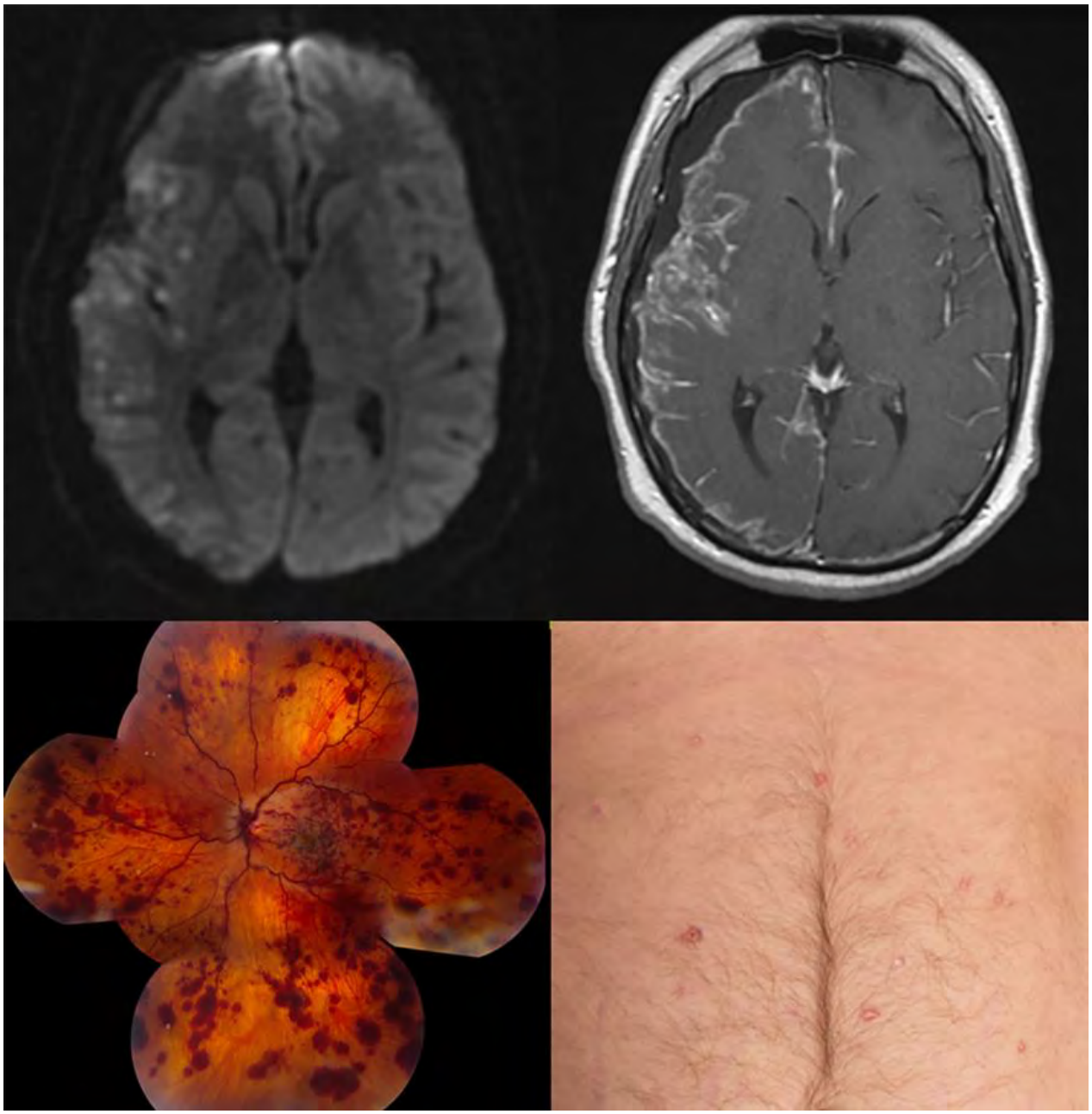
Results

Multiple MR imaging examinations were performed over an 6-month period. Diffusion-weighted imaging (DWI) demonstrated progressive peripheral infarcts in the right cerebral hemisphere. Time-of flight MR angiography (MRA) showed subtle tapering of peripheral right cerebral arteries. Susceptibility-weighted imaging (SWI) demonstrated cortical laminar necrosis and venous congestion. Postcontrast T1-weighted and fluid-attenuated inversion recovery (FLAIR) images showed increasing leptomeningeal nodular enhancement and reactive subdural effusion. Cerebral perfusion was assessed by arterial spin labeling (ASL) MRI and nuclear medicine positron emission tomography (PET). Both modalities confirmed diffuse right cerebral cortical hypoperfusion, as well as early areas of developing hypoperfusion on the left. Follow-up MRI examinations confirmed disease spread to the left hemisphere, although the distribution remained asymmetric throughout the patient's hospital course.

Conclusions

Degos disease (DD) is an obliterative small vessel endotheliopathy of unknown etiology, which overlaps clinically with lupus, dermatomyositis, and other connective tissue disorders. Adolescent males are most commonly affected, but patients can present anywhere between 8 months and 60+ years of age. Skin lesions are stereotypical and begin as rose-colored papules, which umbilicate and heal into atrophic porcelain-white lesions with peripheral erythema and telangiectasias. Degos disease exists in two forms: benign cutaneous, with isolated involvement of the skin; and malignant atrophic papulosis, with systemic

manifestations including neurologic, gastrointestinal, cardiac, pulmonary, and renal. Diagnosis and management of DD requires ongoing communication among subspecialists in radiology, dermatology, ophthalmology, neurology, and internal medicine. Cutaneous lesions are treated with the antiplatelet agents aspirin and dipyridamole, often in conjunction with steroids. Neurologic involvement can diffusely involve brain, optic nerves, spinal cord, and peripheral nerves. Visceral involvement merits more aggressive anticoagulation and immunosuppression with a variety of agents. Prognosis depends on the degree of systemic involvement, with the majority of patients ultimately progressing to fatal neurologic decline and/or bowel perforation. The differential diagnosis for a patient presenting with optic neuritis and worsening episodic neurologic symptoms includes demyelinating, inflammatory/autoimmune, and vasculitic disorders. The asymmetric central nervous system (CNS) involvement demonstrated in our patient has not been reported previously in the literature. In this case, multimodality and advanced MR imaging techniques helped to characterize the extent and progression of neurologic disease for appropriate counseling and management.



(Filename: TCT_E-77_Figure.jpg)

E-78

3:46PM - 3:50PM

Hemophagocytic Lymphohistiocytosis, a rare case with a myriad of MRI findings.

A Heilala[1], P Massa[2], P Doshi[2]
[1]Henry Ford, Detroit, MI, [2]Henry Ford Hospital, Detroit, MI

Purpose

Hemophagocytic lymphohistiocytosis (HLH) is a rare disorder of the immune system characterized by cytokine overproduction and improper immune regulation, most frequently affecting children. Due to the highly variable presentation, imaging can play an important role in in making the diagnosis. We present a case of HLH in a young patient with review of the radiological findings.

Materials and Methods

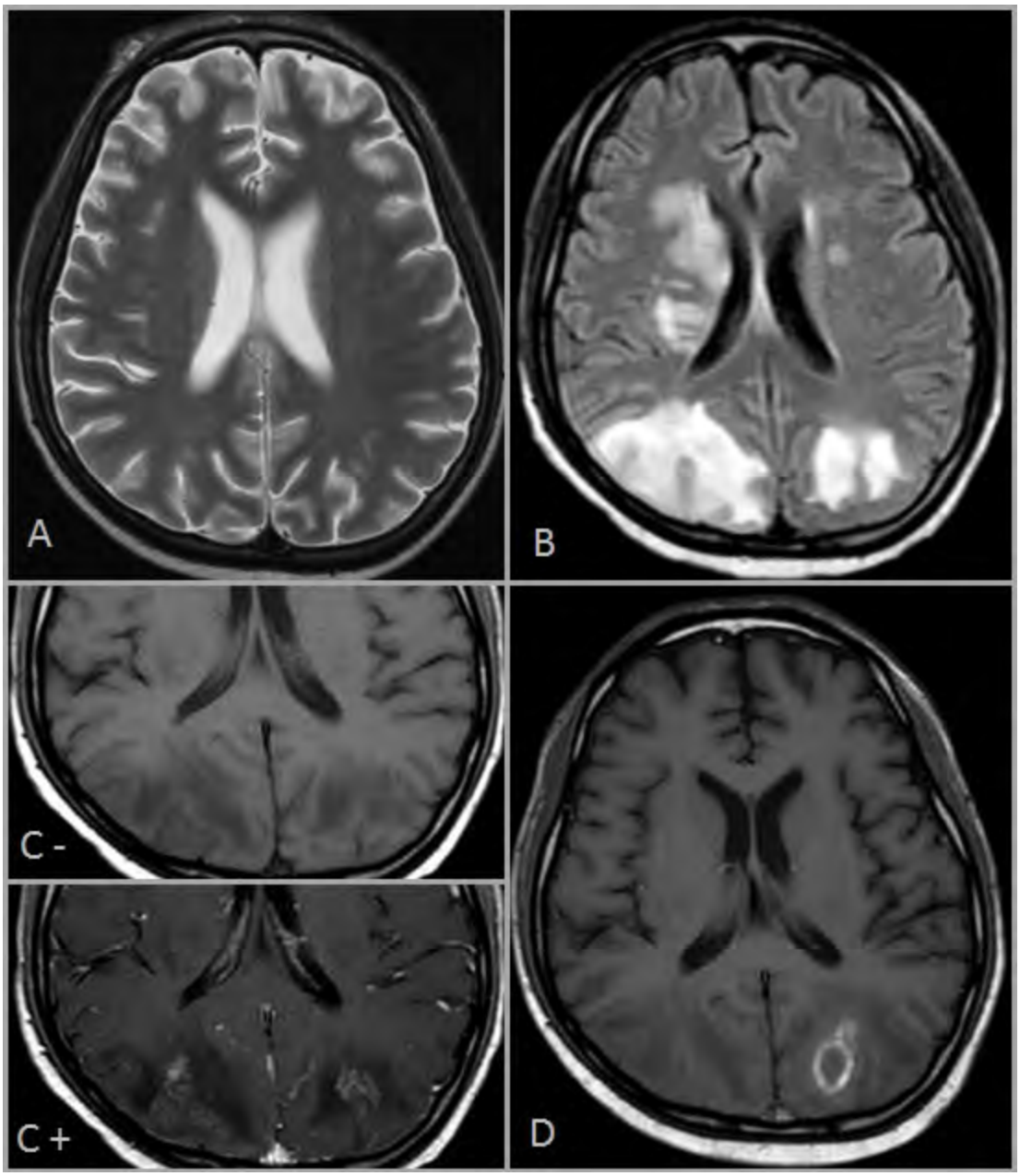
We present the case of an 18-year-old male with a recent diagnosis of HLH by bone marrow and brain biopsy during work up for pancytopenia, presenting with new onset seizure. Initial imaging demonstrated demyelinating lesions with later development of PRES and deep cerebral vasculitis. The patient ultimately succumbed to complications from severe sepsis and multisystem infection.

Results

Initial MRI brain demonstrated scattered hyperintense T2/FLAIR abnormalities in the bilateral parieto-occipital and frontal lobe subcortical white matter, consistent with demyelinating foci (A). Progress MRI demonstrated significant worsening of the T2/FLAIR white matter hyperintensities with new cerebral and basal gangliar foci bilaterally suggesting posterior reversible encephalopathy syndrome (PRES) (B). Pre and postcontrast T1 imaging demonstrated abnormal nodular enhancement along the perforating arteries in the basal ganglia and bilateral parieto-occipital regions (C). Eight day Progress MRI brain demonstrated near complete resolution of the T2/FLAIR hyperintense abnormalities consistent with PRES and resolution of the abnormal nodular enhancement with a residual small hematoma in the left parieto-occiptal lobe after treatment with dexamethasone and IV antivirals (D).

Conclusions

Hemophagocytic lymphohistiocytosis is a rare immune regulation disorder involving T cell and macrophage activation causing overproduction of cytokines and manifests with chronic relapsing infections. Hemophagocytic lymphohistiocytosis can involve the bone marrow, lymph nodes, liver, and CNS. Described MRI findings include delayed myelination, parenchymal atrophy, and diffuse abnormal signal in both gray and white matter. These findings are nonspecific, and differential includes infectious and inflammatory etiologies including acute disseminated encephalomyelitis and neoplastic disorders.



(Filename: TCT_E-78_ASNRHLH1.jpg)

E-79

3:50PM - 3:54PM

Rare Hemorrhagic Complication in a Pediatric Patient With Fatal West Nile Viral Encephalitis

D Leake[1]
[1]*Austin Radiological Association, Austin, TX*

Purpose

The purpose of this case report is to describe a rare hemorrhagic complication on magnetic resonance imaging (MRI) Brain imaging of a pediatric patient with West Nile viral encephalitis.

Materials and Methods

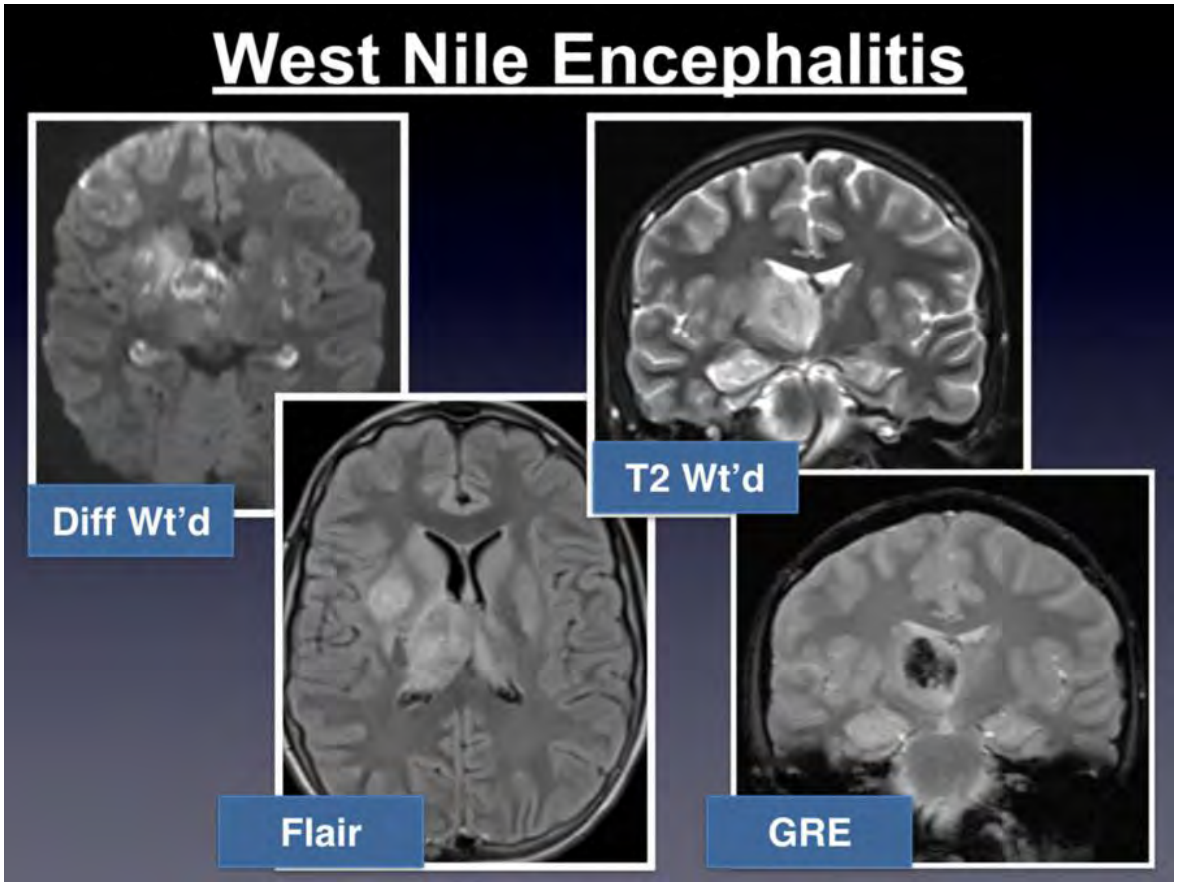
A previously heathy 13-year-old male presented to the emergency room with altered mental status for 24 hours. A recent skin rash was noted. Computed tomography (CT) Head was normal. Lumbar puncture showed pleocytosis with elevated white cells and normal glucose, protein. Initial MRI Brain demonstrated abnormal right basal ganglia with restricted diffusion and T2 hyperintensity on FLAIR images. Clinical and imaging findings were concerning for viral encephalitis or ADEM. Subsequent cerebrospinal fluid (CSF) was positive for West Nile virus. Positive IGM and negative IgG were compatible with active infection. The patient clinically worsened over the next week. A 7 day postadmission MRI Brain demonstrated worsening of abnormal restricted diffusion and T2 hyperintensity of the brain. There was interval hemorrhage involving right basal ganglia and thalamus. The patient clinically worsened over the next 48 hours and died.

Results

9/30/2016, CT Head was normal. 9/30/2016, Initial MR Brain showed abnormal restricted diffusion involving right basal ganglia. T2 FLAIR images showed abnormal hyperintensity involving the right basal ganglia. There was no abnormal enhancement, no hemorrhage, no mass effect. 9/30/2016, MR Spine was normal. 10/6/2016, 8 days after admission, repeat MRI Brain exam demonstrated enlarged area of abnormal restricted diffusion and T2 hyperintensity right basal ganglia and thalamus. There was a new area of hypointensity involving the right basal ganglia on GRE pulse sequence indicating hemorrhage. There also were new areas of T2 hyperintensity involving the left basal ganglia, right frontal lobe, bilateral hippocampi. 10/6/2016, CT head did not show high density hemorrhage, indicating that the hypointensity on MRI Brain represented petechial hemorrhage. There also were areas of T2 hyperintensity involving right basal ganglia, thalami, and bilateral hippocampi. 10/7/2016, 10/8/2016 CT head exams showed progressive edema of these structures with mass effect and poor gray white matter differentiation.

Conclusions

Magnetic resonance imaging findings of West Nile encephalitis may show involvement of lobar gray and white matter, cerebellum, basal ganglia, thalamus, brainstem, and spinal cord.These areas may show restricted diffusion and T2 hyperintensity. However, hemorrhage has been described only rarely in West Nile encephalitis imaging. Radiologists should be aware of all the imaging manifestations of West Nile encephalitis including hemorrhage.



(Filename: TCT_E-79_WestNileEncephalitis.jpg)

E-80

3:54PM - 3:58PM

Callosal Agenesis with Interhemispheric Cyst: Heterogeneous Group of Disorders Not a Single Malformation.

B Brown[1], J Chang[1], M Bobinski[1], M Zwienenberg[2], A Ozturk[1]
[1]University of California, Davis Medical Center, Sacramento, CA, [2]UC Davis, Sacramento, CA

Purpose
Agenesis of corpus callosum (ACC) with interhemispheric cyst (IHC) is not a single malformation, but a heterogeneous group of disorders which have in common callosal anomalies and midline cyst. Our purpose is to demonstrate the magnetic resonance imaging (MRI) findings of a case of ACC with IHC and associated anomalies.
Materials and Methods
We present a 21-month-old male who presented with history of gait abnormalities, increasing frequency of falls and macrocephaly. Magnetic resonance imaging revealed ACC with multiloculated IHC without communication to the ventricles causing obstructive

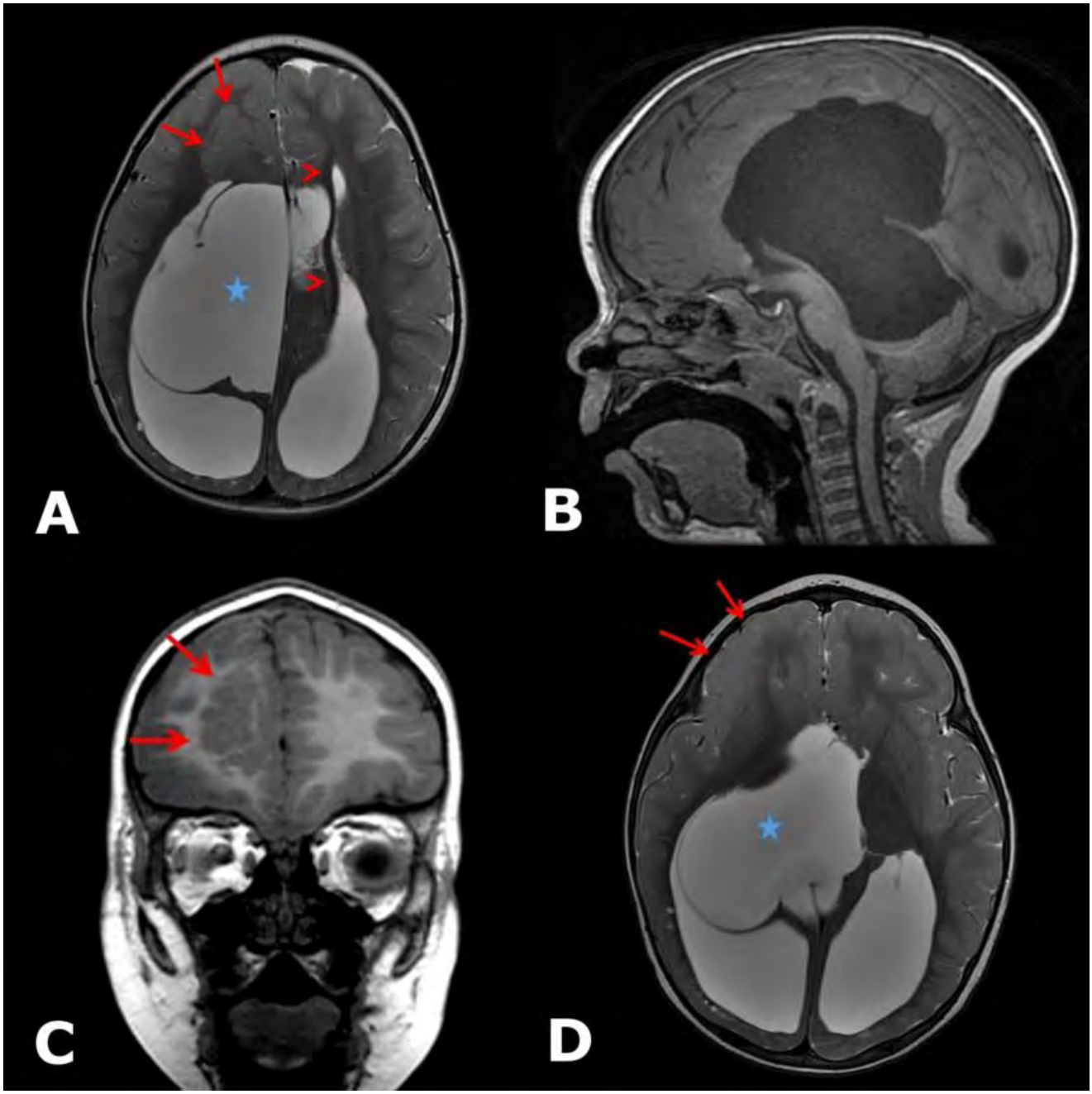
hydrocephalus, and associated subcortical heterotopia and polymicrogyria of right frontal lobe. He underwent cyst fenestration with shunt placement resulting in adequate decompression of cyst and ventricles.

Results

Fig. 1A. Axial T2- weighted image demonstrates large multiloculated IHC (star) with no communication to ventricles, right frontal subcortical heterotopia (arrows), and Probst bundle (arrowheads). Fig. 1B: Sagittal T1- weighted image shows absence of corpus callosum and mass effect of IHC to posterior fossa. Fig. 1C: Coronal SPGR image shows right frontal lobe subcortical heterotopia (arrows). Fig. 1D: Axial T2- weighted image shows right inferior frontal polymicrogyria (arrows) and IHC (star).

Conclusions

Agenesis of corpus callosum with IHC can be classified into 2 major groups based on morphology. Type 1 cysts are extension or diverticulum of the third and lateral ventricles. Type 2 cyst are multiloculated cysts with no communication to the ventricles. They often are associated with anomalies such as thalamic fusion without subcortical heterotopia, small ipsilateral cerebral hemisphere in Type 1; subcortical, subependymal heterotopia, polymicrogyria, and deficient falx cerebri in Type 2 cyst. All types of cysts may not develop or become evident on imaging until late in gestation and frequently associated with macrocephaly and hydrocephalus. Diagnosis of ACC with IHC and associated anomalies is important for patient counseling as well as potential guidance for intervention.



(Filename: TCT_E-80_ACC_Brown_et_al_figures.jpg)

E-81

3:58PM - 4:02PM

Duplicated Pituitary Gland with Multiple Midline Craniofacial Anomalies: A Case Report.

J Wu[1], V Hill[1]
[1]*Cleveland Clinic, Cleveland, OH*

Purpose

To describe the clinical and imaging findings of a rare case of duplicated pituitary gland with associated midline facial anomalies.

Materials and Methods

The patient presented as a full term neonate with spontaneous vaginal delivery with multiple midline defects of a nasal pit, midline tubular tongue mass, hard and soft palate cleft, and a nasopharyngeal mass with inability to pass an endoscope through the left nasal cavity. Her neurological exam was significant for low set ears, cleft palate, torticollis, occipital plagiocephaly, mild hypotonia, and unsustained clonus of the left ankle. A magnetic resonance imaging (MRI) brain and neck was performed, which showed duplicated pituitary glands and infundibula with additional midline facial anomalies including a nasopharyngeal mass extending from the hard palate, cleft palate, bifid tongue and uvula, tongue mass, an apparent hypothalamic mass, and a persistent craniopharyngeal canal. Also noted was a mega cisterna magna. She underwent resection of the tongue mass with repair of the bifid tongue. The pathology was consistent with a tongue hamartoma. The nasopharyngeal mass was biopsied with pathology demonstrating ectodermally derived tissue, including skin, sebaceous glands, and hair follicles, suggesting dermoid versus teratoma.

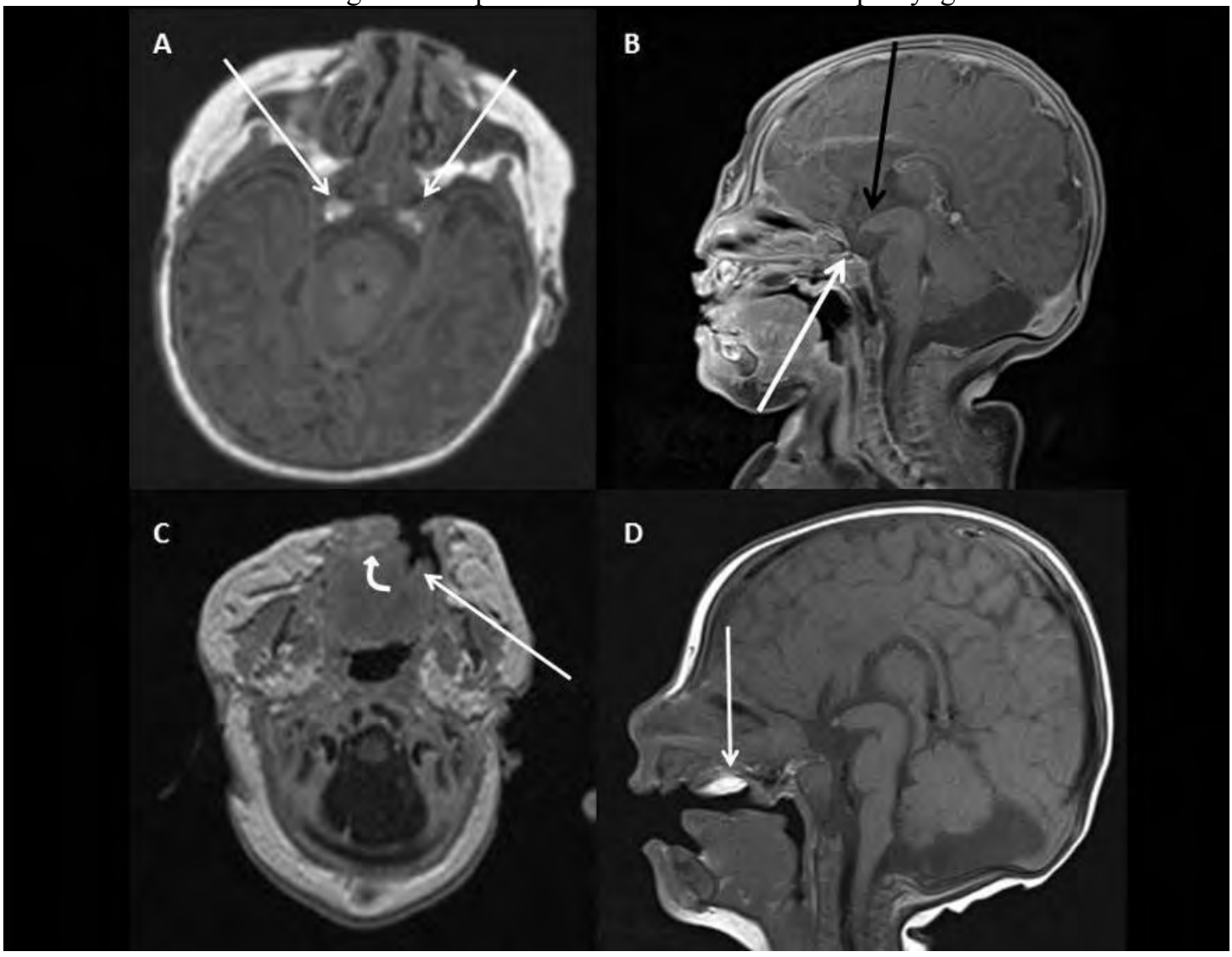
Results

Image A: MRI of the brain at age 1 day with axial T1-weighted sequence demonstrates a broad, shallow sella turcica with no midline pituitary gland or infundibulum. Instead, there are 2 T1 hyperintense pituitary glands along the lateral margins of the sella to which 2 separate infundibula extend (white arrows). Image B: Sagittal T1-weighted postcontrast sequence demonstrates a nodular contour of the hypothalamus with a mass at the floor of the third ventricle (black arrow). There is no associated enhancement of the mass. The mass likely represents "small, tightly packed nerve cells interspersed by glial cells", as described in multiple case reports of pituitary duplication. Additionally, there is a midline, well marginated tract extending from the sellar floor to the roof of the nasopharynx (white arrow) compatible with a persistent craniopharyngeal canal. Incidentally noted is a mega cisterna magna. Image C: T1-weighted postcontrast axial sequence through the oropharynx demonstrates a bifid tongue (straight white arrow). At the anterior aspect of the right hemitongue, there is a T1 heterogeneously hyperintense partially exophytic enhancing mass (curved white arrow). This mass was later resected and compatible with a hamartoma on surgical pathology. Image D: A. T1-weighted sagittal sequence of the brain demonstrates a T1 hyperintense mass within the posterior midline hard palate extending into the floor of the left nasal cavity (white arrow). This was biopsied with pathology demonstrating a dermoid/teratoma.

Conclusions

Duplication of the pituitary gland is a rare entity with less than 20 reported cases in the literature. This anomaly likely occurs during blastogenesis. Often, there are associated midline craniofacial defects of cleft palate, bifid tongue and uvula, nasoseptal mass, commonly a nasopharyngeal teratoma or dermoid inclusion cyst. A tongue/oral mass, as in

this case, also has been reported previously to be associated with duplicated pituitary. Multiple reports have described a hypothalamic bar-like mass at the floor of the third ventricle with pathology showing a "small, tightly packed nerve cells interspersed by glial cells". Additional intracranial anomalies include cerebellar hypoplasia, absence of the anterior commissure and/or septum pellucidum. Extracranial anomalies also have been reported, including a duplicated spine, notched epiglottis, and other vascular, cardiac, diaphragmatic, urinary, and colorectal abnormalities, as well as skeletal abnormalities. In this case, the patient has progressed satisfactorily since resection of the tongue hamartoma although she is unable to feed by mouth and has a percutaneous gastrostomy tube. She currently is being followed by ENT and will eventually have repair of her other midline craniofacial defects including the cleft palate and resection of the nasopharyngeal mass.



(Filename: TCT_E-81_ASNRimages.jpg)

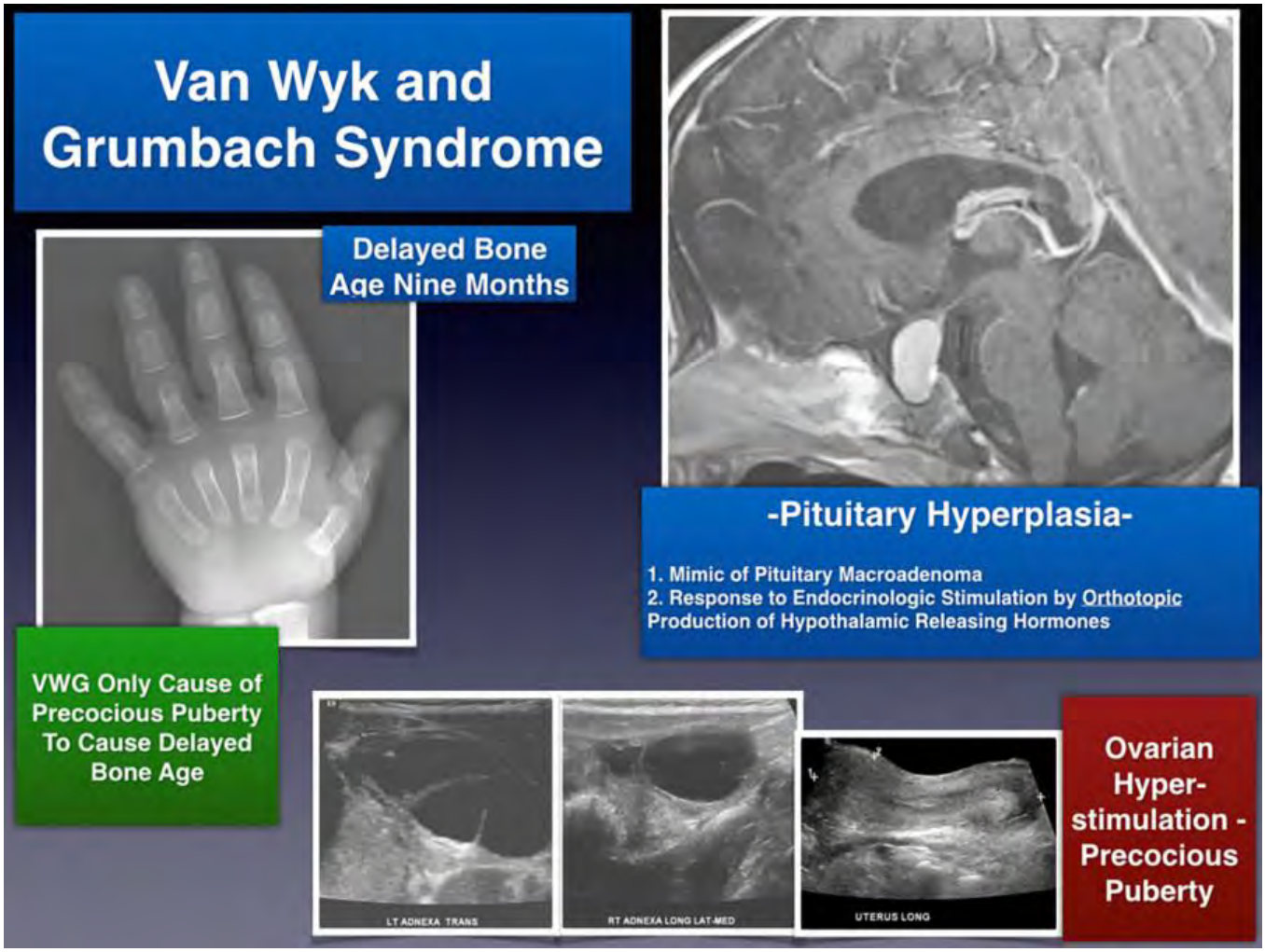
E-82

4:02PM - 4:06PM

Pediatric patient with Van Wyk and Grumbach syndrome: case report including imaging and clinical findings

D Leake[1]
[1]*Austin Radiological Association, Austin, TX*

Purpose
The purpose of this presentation is to describe the significance of imaging and clinical findings of a pediatric patient with Van Wyk and Grumbach syndrome (primary hypothyroidism). This case will show how the neuroradiologist can be extremely helpful in diagnosing this syndrome with the use of the bone age radiograph, pelvic ultrasound findings, and pituitary MR findings.
Materials and Methods
The patient is a 2 1/2 year old female Afghanistan refugee. She presented to our institution with vaginal bleeding. Workup revealed severe developmental delay. Bone age was delayed, 9 months. Pelvic ultrasound demonstrated bilateral enlarged cystic ovaries and a menarche uterus. Magnetic resonance (MR) Brain revealed an enlarged pituitary gland. Endocrine consult found an extremely low thyroid level. The clinical and ultrasound findings were consistent with precocious puberty. The significant finding of delayed bone age also contributed to the final diagnosis of Van Wyk and Grumbach syndrome. Patient was begun on thyroid replacement. Follow-up clinical and imaging were scheduled.
Results
Bone age was delayed, 9 months compared to 2 1/2 years. Pelvic ultrasound revealed bilateral enlarged ovaries and a menarche uterus. Magnetic resonance (MR) Brain showed an enlarged homogenous enhancing pituitary gland.
Conclusions
Van Wyk and Grumbach syndrome consists of primary hypothyroidism, end organ failure. Extremely low thyroid levels are found. This results in high levels of TSH. This causes pituitary hyperplasia/enlargement, which can mimic a pituitary macroadenoma. The high TSH levels also causes precocious puberty. It simulates the ovaries, via FSH receptors. This causes the enlarged ovaries and menarche uterus, vaginal bleeding. Low thyroid levels cause delayed bone maturation. Van Wyk and Grumbach syndrome is the only cause of precocious puberty to cause delayed bone age. The clinical and imaging findings disappear with thyroid supplementation. It is important for the neuroradiologist to be aware of the clinical and imaging findings of VWG syndrome to expedite the diagnosis, and prevent unnecessary pituitary surgery.



(Filename: TCT_E-82_ASNR2017AbstractVWGSyndrome.jpg)

E-83

4:06PM - 4:10PM

Primary Amenorrhea - An Uncommon Presentation of Obstructive Hydrocephalus

P Batchala[1], A Momeni[1], T Eluvathingal Muttikkal[1]
[1]*University of Virginia Health System, Charlottesville, VA*

Purpose
Hydrocephalus is a very rare cause of primary amenorrhea. The entity has been described mainly in Neurosurgery and Obstetrics/Gynecology journals with a paucity of publications in the radiology literature. The purpose of this case report is to highlight primary amenorrhea as an uncommon presenting feature of obstructive hydrocephalus for both practicing neuroradiologists and radiology trainees.
Materials and Methods
A 16-year-old girl with primary amenorrhea presented for interval follow up at our

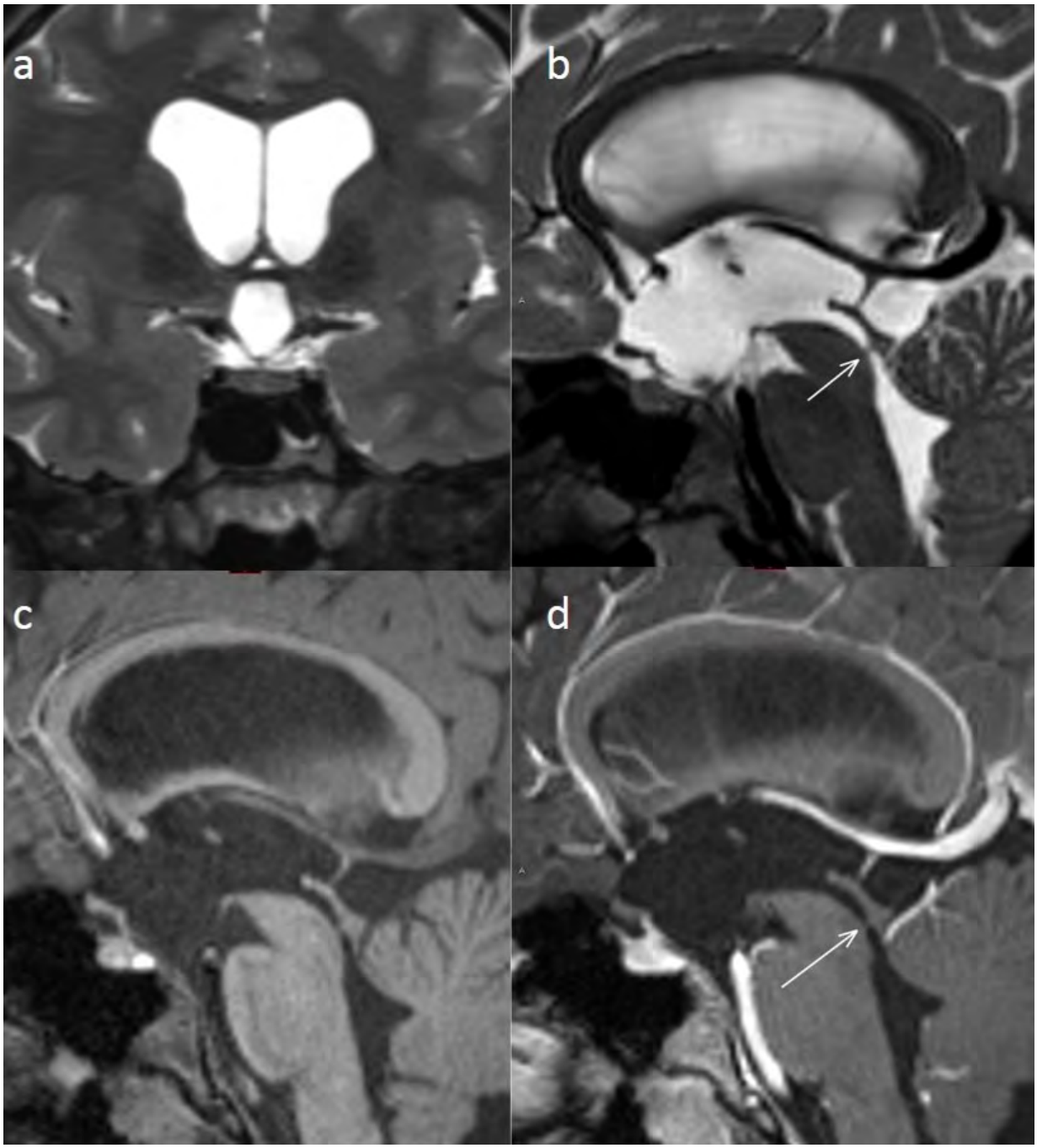
institution. Her height (1.66 m) and body mass index (21.59) were normal. Bone age lagged behind the chronological age by 21 months. Neurological examination was normal. She had Tanner stage IV sexual maturity staging, with a discordant low gonadotropins. Prolactin and thyroid hormones were normal. Past history was significant for uncontrolled diabetes mellitus diagnosed at 5 years of age and episodic migraine without aura for the past 2 years. Constitutional delay was the favored working diagnosis for amenorrhea on prior visits. Persistent low gonadotropins over 2 years raised concern for a central cause, thus a pituitary protocol brain magnetic resonance imaging (MRI) was conducted.

Results

Brain MRI for evaluation of the pituitary gland revealed moderate obstructive hydrocephalus secondary to cerebral aqueduct obstruction. High resolution T2 and MPRAGE (Figs. b and d) sequences were acquired for greater delineation revealing a web-like structure in the distal aqueduct. The third ventricle was ballooned, with mass effect on the pituitary stalk and the hypothalamus (Figs. a, b, c and d).

Conclusions

Hydrocephalus is a very rare, treatable cause of primary amenorrhea, with less than thirty cases described in the English Medical Literature. The mass effect by the dilated third ventricle on the gonadotropin-releasing hormone (GnRH)-containing cells in the periventricular and medial basal regions of the hypothalamus is a postulated cause. GnRH disruption results in loss of pulsatile release of luteinizing hormone which is essential for menstrual cycle. Most of the patients have menstrual cycle within months after surgical treatment of hydrocephalus.



(Filename: TCT_E-83_Fig.jpg)

E-84

4:10PM - 4:14PM

A Multimodality Presentation of Pallister-Hall Syndrome.

E Greif[1], B Barrett[2], G Cruciata[1], J Felder[3], E Stein[1]
[1]Maimonides Medical Center, Brooklyn, NY, [2]Maimonides Medical Center,, Brooklyn, NY, [3]Maimonides medical center, Brooklyn, NY

Purpose

The purpose of this abstract is to demonstrate a multimodality, multisystem presentation of a patient who presented with Pallister-Hall syndrome and its clinical and radiologic manifestations.

Materials and Methods

We are presenting a case of a 2-year-old male born at full term with multiple congenital abnormalities. At birth the patient presented with imperforate anus, polydactyly, and microcephalus. In the neonatal period the patient was operated on for imperforate anus. The patient then had an magnetic resonance imaging (MRI) for delayed physical development, which demonstrated a hamartoma of the tuber cinerum, confirming the diagnosis of Pallister-Hall syndrome.

Results

Magnetic resonance imaging (MRI) of the sella showed a nonenhancing isointense 4.5 x 2.8 x 4 cm (transverse by AP by CC) tuber cinereum mass projecting into the third ventricle, the suprasellar cistern, and the pre-pontine and ambient cisterns with mass effect elevating the floor of the third ventricle and displacing the optic chiasm and pituitary infundibulum. There also was mass effect on the pons and midbrain. Radiograph of the hand showed an accessory 6th digit (polydactyly) as well as syndactyly of the 3rd and 4th metacarpal bones. The patient also had radiographs and fluoroscopic studies demonstrating imperforate anus.

Conclusions

Pallister-Hall is a very rare congenital syndrome of autosomal dominant inheritance or more rarely secondary to de novo mutation of the GLI3 protein, which plays a role in the normal modeling of many organs in utero. The key feature of Pallister-Hall syndrome is the benign hypothalamic (tuber cinereum) hamartoma, differentiating it from other similar congenital syndromes. Other major manifestations of the syndrome include polydactyly, imperforate anus, renal anomalies, pituitary dysplasia, hypopituitarism, and bifid epiglottis. Hypothalamic hamartomas arise from the tuber cinereum, a midline eminence of hollow gray matter situated between the mammillary bodies and the optic chiasm in the suprasellar region. The hamartoma is composed of gray matter and therefore has imaging appearances similar to normal cortex on both CT and MR imaging. Hypothalamic hamartomas do not enhance or have calcifications. The lesion follows gray matter density and signal characteristics on all imaging modalities and therefore isointense to gray matter on MRI T1-weighted images and hyperintense on T2-weighted images. Pallister-Hall associated hypothalamic hamartomas tend to be larger than isolated hypothalamic hamartomas (not associated with the syndrome), and can cause considerable mass affect with posterior displacement of the pons and midbrain, superior displacement of the optic chiasm and third ventricle, and anterior displacement of the infundibulum and compression of the pituitary. The hypothalamic hamartoma can cause some of the signs and symptoms of Pallister-Hall syndrome including endocrine abnormalities, epilepsy, and midline facial defects. Accurate diagnosis of Pallister-Hall syndrome is important for clinical management and future genetic

counseling. Clinical management includes endocrinologic evaluation of the hypothalamic-pituitary axis, ophthalmologic evaluation with visual field testing, serial MR imaging for tumor progression, and an evaluation for associated anomalies.



(Filename: TCT_E-84_Images.jpg)

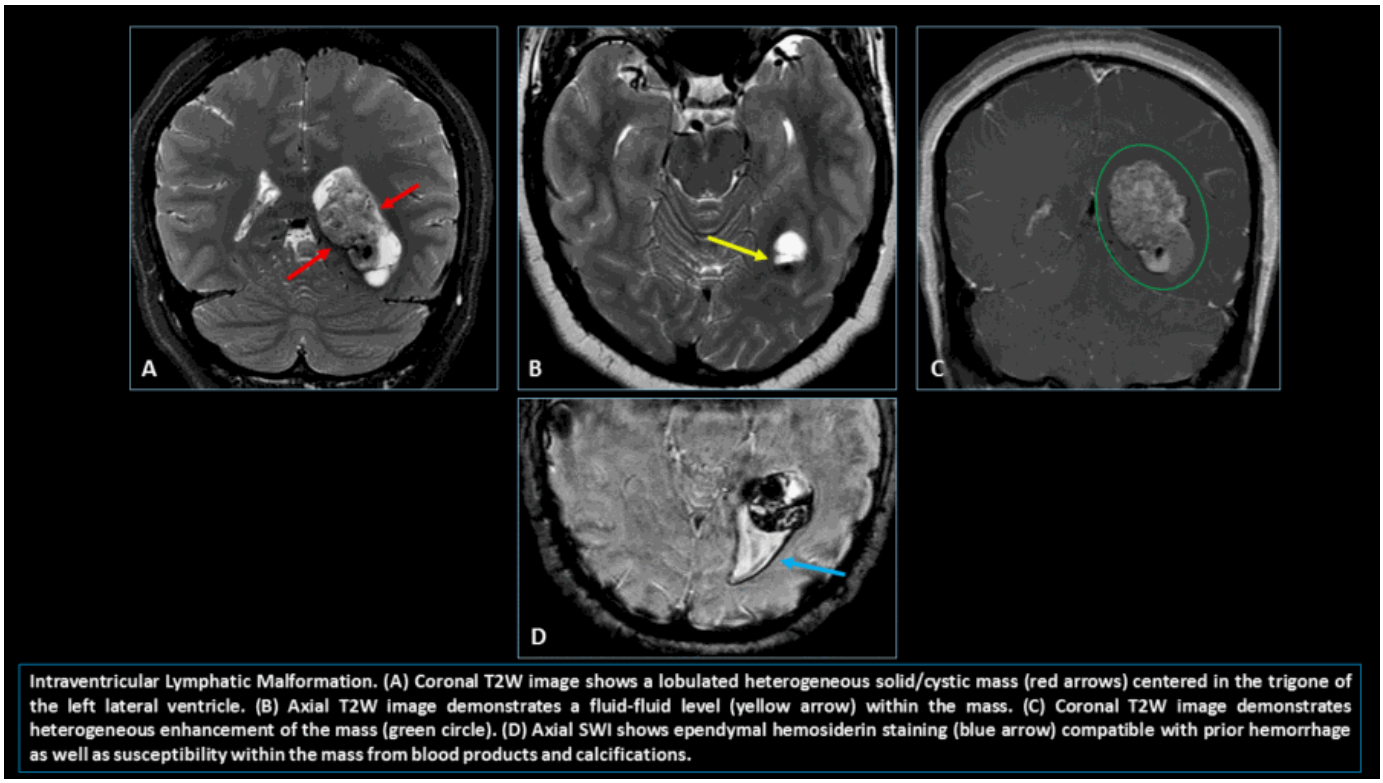
E-85

4:14PM - 4:18PM

The First Reported Case of Intraventricular Lymphatic Malformation

A Chukus[1], K Yeom[1], P Barnes[1], H Dahmoush[1]
[1]*Stanford Hospital, Stanford, CA*

Purpose
We present the first ever reported case of intracranial lymphatic malformation located in the lateral ventricle. Certain imaging features and endothelial markers can suggest the diagnosis among the broad differential for intraventricular masses. Identifying intracranial lymphatic malformations is an important step in our evolving understanding of intracranial lymphatic tissue.
Materials and Methods
A 16-year-old female with ADHD and anxiety suffered a head trauma and underwent a head CT which showed a left lateral ventricular mass. Magnetic resonance imaging (MRI) demonstrated a mass in the atrium of the left ventricle. She underwent a gross total resection. Pathology demonstrated thin-walled vascular spaces containing predominantly proteinaceous material with scattered lymphocytes as well as blood products. This complex vascular lesion had endothelial expression of podoplanin and the transcription factor Prox-1 that support the diagnosis of lymphatic malformation.
Results
Noncontrast computed tomography (CT) revealed a hyperdense mass in the left lateral ventricle with multiple foci of calcifications. Magnetic resonance imaging showed a solid/cystic enhancing mass in the trigone of the left lateral ventricle. Blood products and calcifications were present within the mass. Layering fluid-fluid levels were identified. The mass extended to the brain parenchyma with adjacent mild vasogenic edema. Ependymal hemosiderin staining compatible with prior intraventricular hemorrhage was seen.
Conclusions
Lymphatic malformation is a congenital vascular malformation composed of embryonic lymphatic sacs. We did not find any reports of intracranial lymphatic malformations in a PubMed search. Although functional lymphatic vessels along the dural sinuses have been described recently in the literature, the intraventricular location of our case with characteristic lymphatic endothelial markers helps further our understanding of CNS lymphatics. The best diagnostic imaging clue is a multiloculated macrocystic mass with fluid-fluid levels. In addition to the differential diagnosis for common intraventricular masses, it is important for radiologists to consider vascular malformations, particularly for cystic lesions that demonstrate fluid-fluid levels.



(Filename: TCT_E-85_LM-Images.gif)

E-86

4:18PM - 4:22PM

MRI and MR Spectroscopy Findings of Creatine Deficiency Syndromes

A Reddy[1], T Moritani[2], A Capizzano[3], T Sato[4], Y Sato[4]
[1]Univ of Iowa Hospitals and Clinics, Iowa city, IA, [2]University of Iowa Hospitals and clinics, Iowa city, IA, [3]University of Iowa Hospitals and Clinics, Iowa City, IA, [4]University of Iowa, Iowa City, IA

Purpose
To discuss magnetic resonance spectroscopy (MRS) findings in creatine (Cr) deficiency syndromes (CDS). Creatine deficiency syndromes usually are underdiagnosed and should be considered in the differential diagnosis of children with unexplained mental retardation, seizures and/or speech difficulties. However, milder clinical forms also are possible as in Case 1. Creatine deficiency syndrome results from defective creatine synthesis due to more commonly to guanidinoacetate methyltransferase –GAMT mutations or less common to arginine-glycine amidinotransferase - AGAT mutation. Alternatively, CDS may result from deficiency in transport of Cr into the brain. Creatine synthesis deficits have a favorable response to oral Cr supplementation. Magnetic resonance spectroscopy is useful for initial diagnosis as well as for assessment of Cr supplementation effectiveness.

Materials and Methods

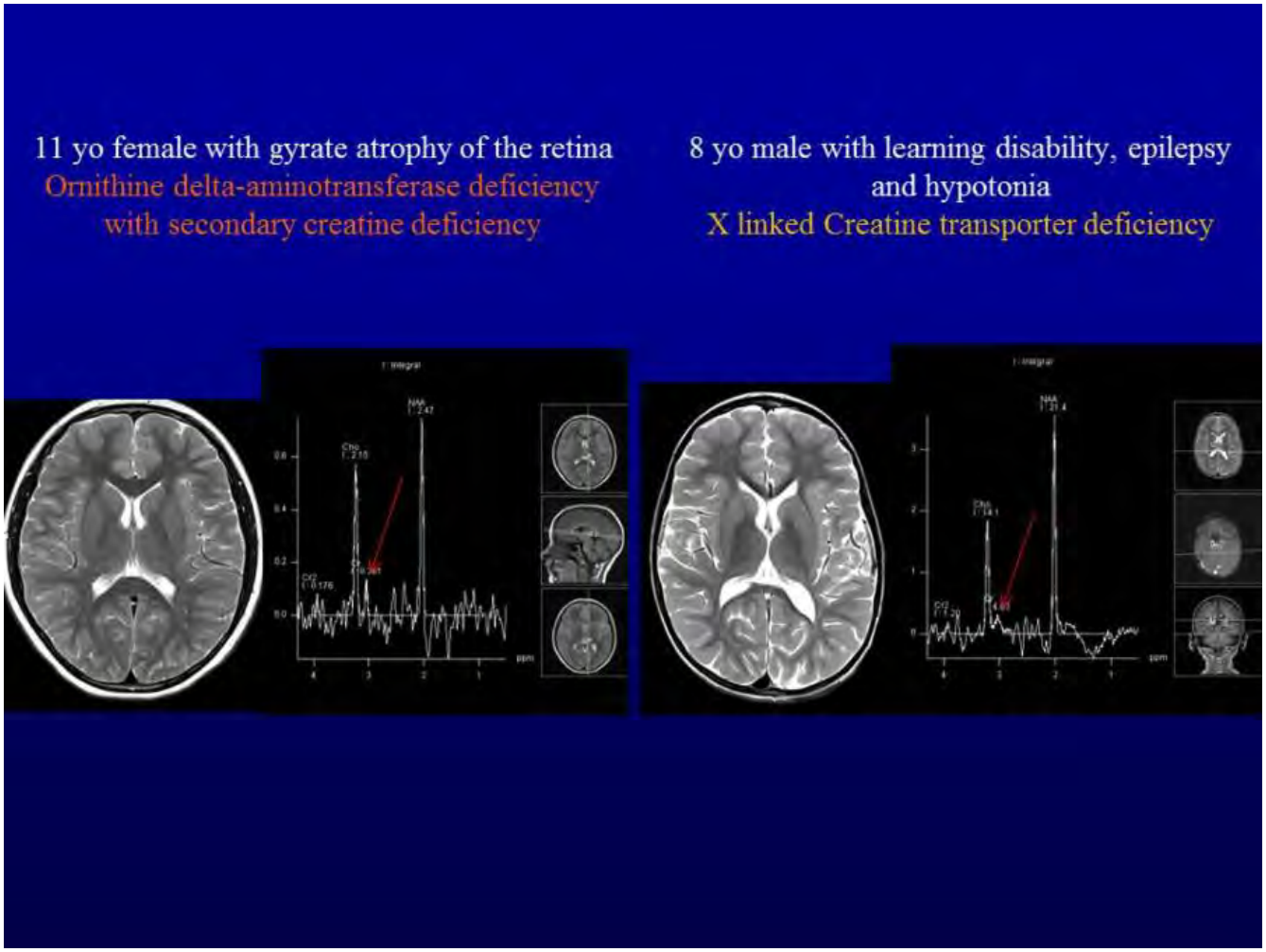
Patient 1: An 11-year-old female presented with loss of visual acuity and was diagnosed with gyrate atrophy of the choroid and retina. Further work up showed her blood ornithine levels were elevated and she was diagnosed with ornithine aminotransferase deficiency leading to Cr deficiency. Magnetic resonance spectroscopy (MRS) was done to confirm the diagnosis and revealed reduced creatine/choline ratio consistent with CDS. She was started on oral Cr replacement and showed improvement in macular edema. Patient 2: An 8-year-old male with medically intractable epilepsy and severe developmental delay, after much extensive work up was negative for other causes of cognitive disability, a multi gene intellectual disability panel showed mutation in Gene SLC6A8 corresponding to X- linked creatine transport disorder was demonstrated.

Results

Patient 1: Brain MRI was normal with no structural defects. Multivoxel PRESS MRS revealed a significantly reduced creatine signal compared to the choline and NAA peaks. Patient 2: Brain MRI displayed mild global volume loss. Magnetic resonance spectroscopy showed severely decreased creatine signal throughout both cerebral hemispheres compared to choline and NAA peaks. The NAA to choline ratio was preserved.

Conclusions

Magnetic resonance spectroscopy is clinically useful and specific in confirming the diagnosis of CDS. Magnetic resonance spectroscopy displaying Cr deficiency will orient the clinician to perform specific genetic tests to diagnose the specific CDS involved. Early diagnosis can limit structural damage by timely Cr supplementation.



(Filename: TCT_E-86_CR.jpg)

E-87

4:22PM - 4:26PM

Newborn Facial Mass as a Rare Presentation of Subcutaneous Fat Necrosis

J Lam[1], G Wrubel[1]
[1]*Hartford Hospital, Hartford, CT*

Purpose
Subcutaneous fat necrosis of the newborn (SFNN) is a rare dermatological disorder found in newborns with predisposing maternal risk factors or who experienced perinatal complications. The palpable and mobile subcutaneous masses associated with SFNN most commonly occur on the trunk, buttocks, and extremities. More atypical locations of SFNN include the malar region, neck, and scalp. Hypothermia during the neonatal period has been reported in association with the development of SFNN. We present characteristic imaging

findings of SFNN in a patient who received therapeutic hypothermia for hypoxic ischemic encephalopathy.

Materials and Methods

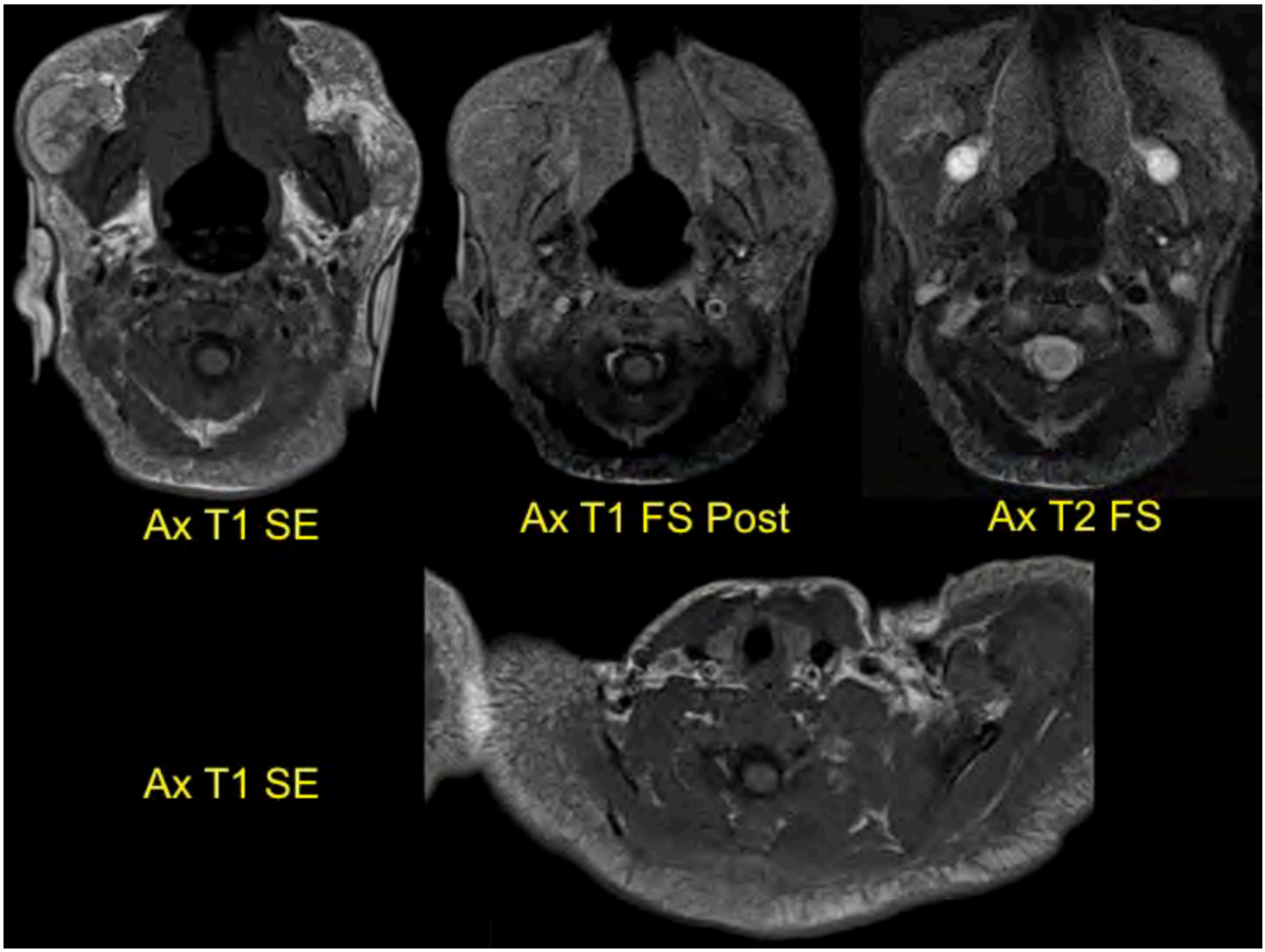
A 39-week-old term infant with a complicated birth history developed hypoxic ischemic encephalopathy requiring intubation and whole body therapeutic cooling, resulting in a 4-week NICU stay. Twenty-six days later, the patient developed palpable nodules over the malar regions and the occipital scalp. The nodules persisted and slowly enlarged. Subsequent magnetic resonance imaging (MRI) of the orbit, face and neck with and without contrast was order to delineate the abnormality.

Results

The MRI of the orbit, face and neck with and without contrast revealed extensive soft tissue nodularity and reticulation with the subcutaneous fat of the entire neck, face, and partially visualized upper chest. These nodules exhibited areas of intermediate signal on T1- and T2-weighted imaging mixed with areas of fat signal intensity demonstrated with fat suppressed series. None of the nodules exhibited contrast enhancement. The largest nodules located within the right and left buccal spaces contained a large amount of fat and were the most readily palpable nodules on physical exam.

Conclusions

Subcutaneous fat necrosis of the newborn is a rare, benign disorder within the adipose tissue found in both premature and full term newborns. Predisposing maternal and newborn risk factors include gestational diabetes, preeclampsia, traumatic delivery, birth asphyxia, meconium aspiration, and therapeutic hypothermia during the neonatal period. SFNN is characterized by mobile plaques and nodules, which may be erythematous to violaceous in color. The nodules appear within the first month of life and slowly resolve within several weeks to 6 months, with some exhibiting residual calcification. Although the pathophysiology is unclear, it is postulated that these lesions occur secondary to tissue hypoperfusion or defects in fat metabolism. Newborns who develop SFNN are predisposed to hypoglycemia, hypertriglycemia, thrombocytopenia, and hypercalcemia, which can be life threatening. The early recognition of this self-limiting process by radiologists is important to minimize invasive surgical procedures for the newborn, alleviate emotional turmoil for the parents when considering alternative malignant processes, and ensuring that the clinical team caring for the patient monitors for potential harmful sequelae of SFNN. In considering other neck masses of the newborn period, congenital neoplasms such as teratomas and sialoblastomas have enhancing solid soft tissue components. Low flow lymphatic malformations may not enhance and may also be trans-spatial but do not exhibit fat signal intensity that suppress on fat suppressed imaging. Low flow venous malformation and high flow vascular malformations are all associated with enhancement unlike SFNN. Nonenhancing subcutaneous nodules and reticulation within the subcutaneous fat of a newborn with the maternal or perinatal risk factors described above in the setting of neonatal hypercalcemia should strongly raise the suspicion for subcutaneous fat necrosis of the newborn which can be confirmed readily with a punch biopsy.



(Filename: TCT_E-87_SFNN.jpg)

E-88

4:26PM - 4:30PM

High Grade Glioma in Children with NF1- Pictorial Review and Discussion

C Spyris[1], R Castellino[1], M Schniederjan[1], N Kadom[1]
[1]*Emory University, Atlanta, GA*

Purpose
Over the past decade, there have been several reports of high-grade gliomas (HGG) in children with neurofibromatosis type 1 (NF1) (1, 2). Brain tumors associated with NF1 are typically LGG, such as juvenile pilocytic astrocytomas, and they most commonly develop along the optic pathway (3). High-grade gliomas in NF1 are rare and the incidence reported in the literature varies. A single institution review of 121 children with NF1 showed that 17

of 121 patients had brain tumors and only 3 of these were HGG (astrocytomas) (4). Magnetic resonance imaging (MRI) can help to some degree in differentiating LGG from HGG. Imaging findings associated with LGG include lack of contrast enhancement, lack of restricted diffusion, and lack of hyperperfusion (5). The purpose of this presentation is a pictorial review of 4 pediatric NF1 patients from our institution with imaging signs of HGG and surgical neuropathology correlation. Our goal is to raise awareness of HGG in children with NF1 so that the diagnosis can be made early and appropriate treatment can be initiated earlier.

Materials and Methods

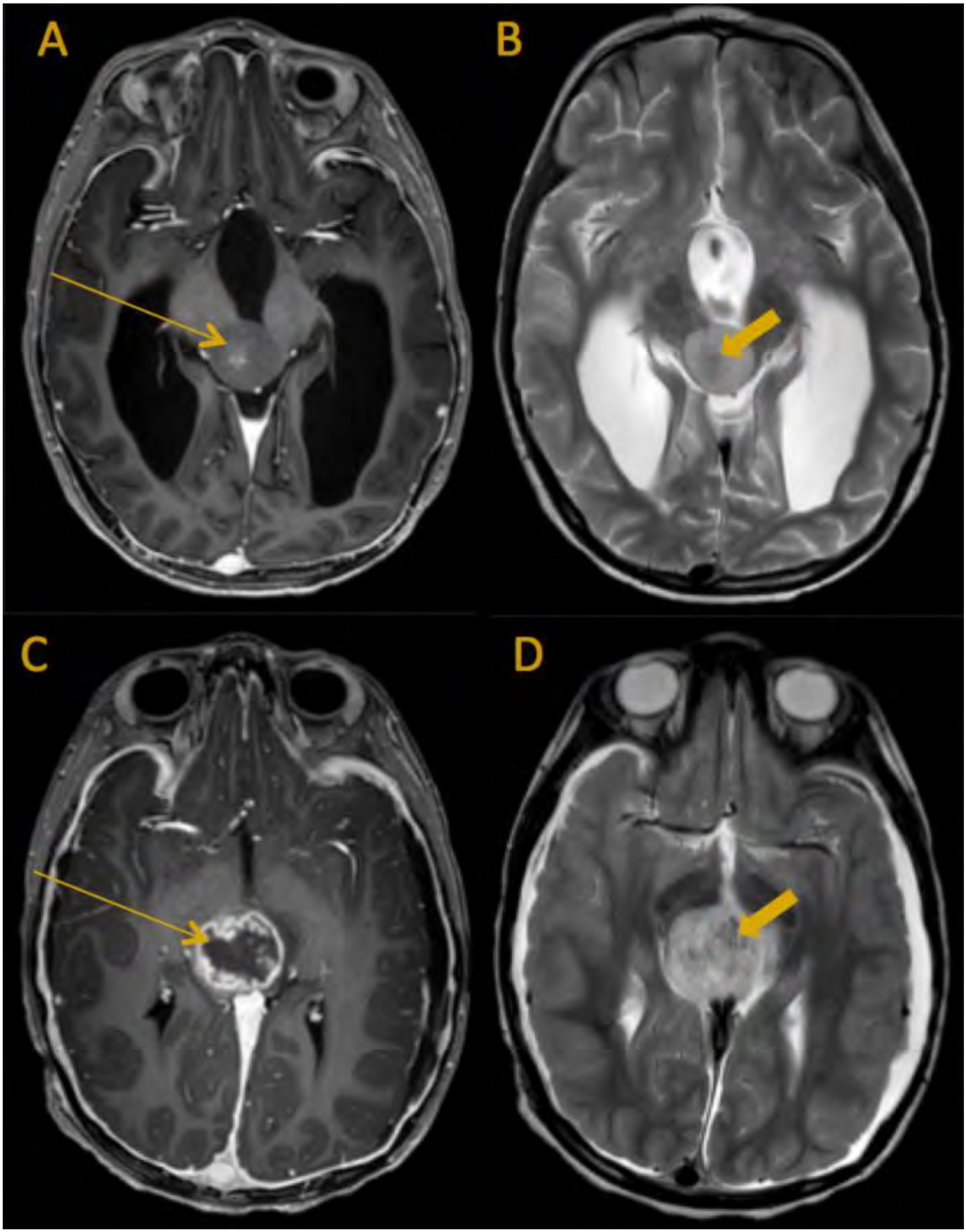
Presentation of up to 4 patient vignettes: Patient 1 with HGG (WHO IV), Patient 2 with HGG (WHO IV), Patient 3 with anaplastic xanthoastrocytoma (WHO III), and Patient 4 with low grade glioma (WHO I). For each patient, the following information is presented: 1. Clinical presentation and course. 2. Magnetic resonance imaging findings (pre/post contrast, MR spectroscopy, perfusion imaging). 3. Surgical neuropathology results.

Results

All patients had imaging signs concerning for malignancy, including lace-like enhancement, central necrosis, growth progression (Patient 1, Figs. 1 A-C), abnormal MR spectroscopy and MR perfusion imaging findings (Figures not submitted). Three patients had a high-grade glioma (WHO grade III and IV) and one patient had a low-grade pilocytic astrocytoma (WHO I). Three patients had new symptoms or symptom progression, only 1 patient with HGG had a stable clinical presentation.

Conclusions

In our small cohort of 4 patients with concerning imaging signs, 3 had a high-grade glioma and 1 had a low-grade lesion mimicking a high-grade mass. This shows that changes in imaging appearance of mass lesions in children with NF1 should be taken very seriously and may require tissue diagnosis. Additional benefits of tissue diagnosis include verification of a high tumor grade and determining molecular markers indicative of high- versus low-grade gliomas that may influence patients' treatment choices and/or surveillance schedules.


A
B
C
D

(Filename: TCT_E-88_Figure1.jpg)

E-89

4:30PM - 4:34PM

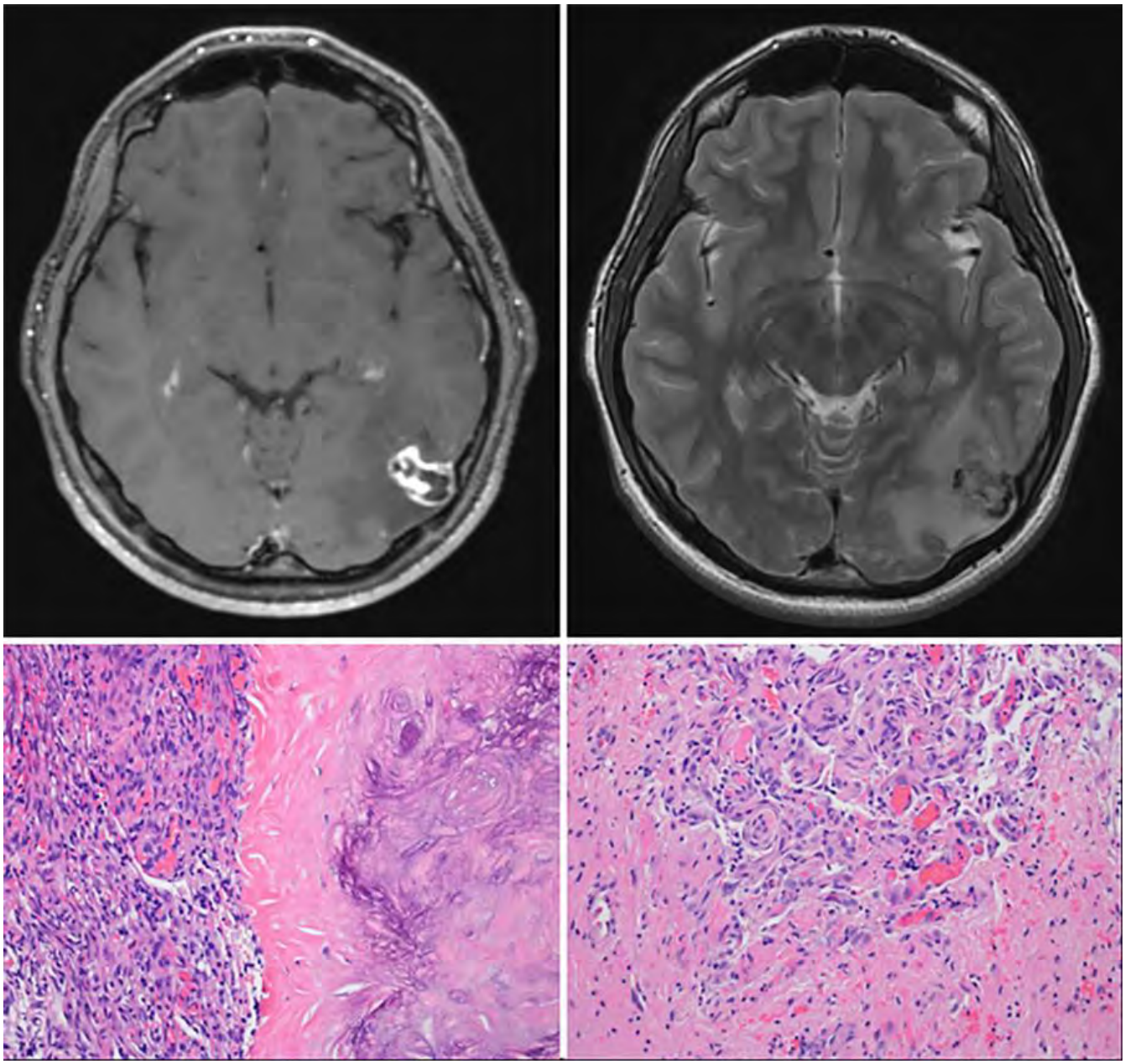
Supratentorial CAPNON + Meningioma: Collision or Collusion?

M Ho[1], M Paolini[1], H Monahan[2], A Raghunathan[1]
[1]Mayo Clinic, Rochester, MN, [2]Mayo Clinic - Rochester, Rochester, MN

Purpose
Review current knowledge regarding the pathogenesis of calcifying pseudoneoplasm of the neuraxis (CAPNON). Correlate radiologic and pathologic findings in a unique pediatric case of supratentorial CAPNON with meningioma.
Materials and Methods
A 17-year-old male presented to our hospital with first-time generalized tonic-clonic seizure, followed by prolonged loss of consciousness and amnesia. The event was preceded by an aura of presyncope and visual obscuration in the left hemifield, which he described as a "spinning wheel of colors." Upon further questioning, he reported episodic recurrent headaches over the past 2 years with similar vision changes, lightheadedness, and fatigue. This had been occurring approximately once per week, becoming more severe and intense in the past 6 months. Birth and developmental history were normal, and neurologic exam was nonfocal. Laboratory values, electrocardiography, and electroencephalography were within normal limits. Brain magnetic resonance imaging (MRI) was performed and revealed a left temporo-occipital extra-axial mass with marked subjacent parenchymal edema. At surgery, the lesion was located immediately beneath and separate from the dura. It was exceedingly firm and hard, with densely calcified portions. En bloc resection was performed along the brain-lesion interface. Portions of the tumor margin were noted to have a slightly irregular border that appeared to cross sulcal interfaces. Pathologic examination revealed a central region with characteristic histological features of CAPNON, including nodular fibro-osseous to chondroid stroma; sparse palisading, spindled to epithelioid cells; and few regions of calcification and ossification. Peripherally, the CAPNON was intimately associated with an atypical meningioma (WHO grade II) that invaded into the adjacent brain parenchyma. Following resection, the patient was placed on Keppra for seizure control. Follow-up imaging showed no evidence of tumor recurrence, and he has remained seizure-free.
Results
Magnetic resonance imaging of the brain showed a 2-cm extra-axial mass at the left temporo-occipital junction, abutting the dura mater without adjacent hyperostosis. This had a solid-cystic appearance, with solid components demonstrating dense calcification, avid enhancement, and normal diffusivity; and cystic components with T2-hyperintense signal, hypoenhancement, and facilitated diffusion. The deep margin of the mass obscured the pial surface, with exuberant surrounding vasogenic edema, concerning for intra-axial invasion.

Conclusions

Calcifying pseudoneoplasm of the neuraxis (CAPNON) is a rare and benign lesion of the central nervous system that has been described in various extra-axial and occasionally intra-axial locations throughout the neuraxis including cerebrum, corpus callosum, posterior fossa, skull base, craniovertebral junction, spine, and nerve roots. Affected patients range in age from children to older adults. Clinical presentation depends on lesion location and size, with resultant mass effect on brain, spinal cord, and/or nerves. These are benign lesions without infiltrative or metastatic potential. Resection is curative and prognosis is excellent, even with subtotal resection. Histologically, CAPNON is characterized by chondromyxoid matrix with varying proportions of dense metaplastic calcification/ossification (psammoma bodies), inflammatory (granulomatous/histiocytic) cell infiltrates, and fibrovascular stroma (palisading spindle/epithelioid cells). The pathogenesis is incompletely understood, with multiple potential etiologies including inflammation, infection, hamartoma, blood-brain barrier derangement, and/or metabolic disorders. There are a few reports of "dual pathology" in which CAPNON has been identified in conjunction with dysembryoplastic neuroepithelial tumor, ependymoma, meningioangiomatosis, callosal agenesis, or neurocysticercosis. This is the first known report of CAPNON arising in association with a meningioma; as meningiomas are also very rare in the pediatric population, the coexistence of these 2 lesions further supports a reactive/dysplastic etiology. At imaging, the diagnosis of CAPNON should be considered whenever an atypical calcified tumefactive lesion is identified along the neuraxis. The imaging differential for calcified lesions of the neuraxis includes meningioma, hamartoma, solitary fibrous tumor, chordoma, glioma, sarcoma, metastasis, heterotopic ossification, and dystrophic or metastatic calcification.



(Filename: TCT_E-89_Figure.jpg)

E-90

4:34PM - 4:38PM

A Rare Case of Pediatric Intracranial Ganglioneuroblastoma

A Chukus[1], H Dahmoush[1]
[1]*Stanford Hospital, Stanford, CA*

Purpose
Ganglioneuroblastomas (GNBs) are primitive neuroectodermal tumors that most commonly

occur extracranially. Intracranial GNBs are extremely rare. We present a case of cerebral ganglioneuroblastoma and discuss the clinical presentation, radiographic appearance, histologic characteristics, staging and prognosis associated with this entity.

Materials and Methods

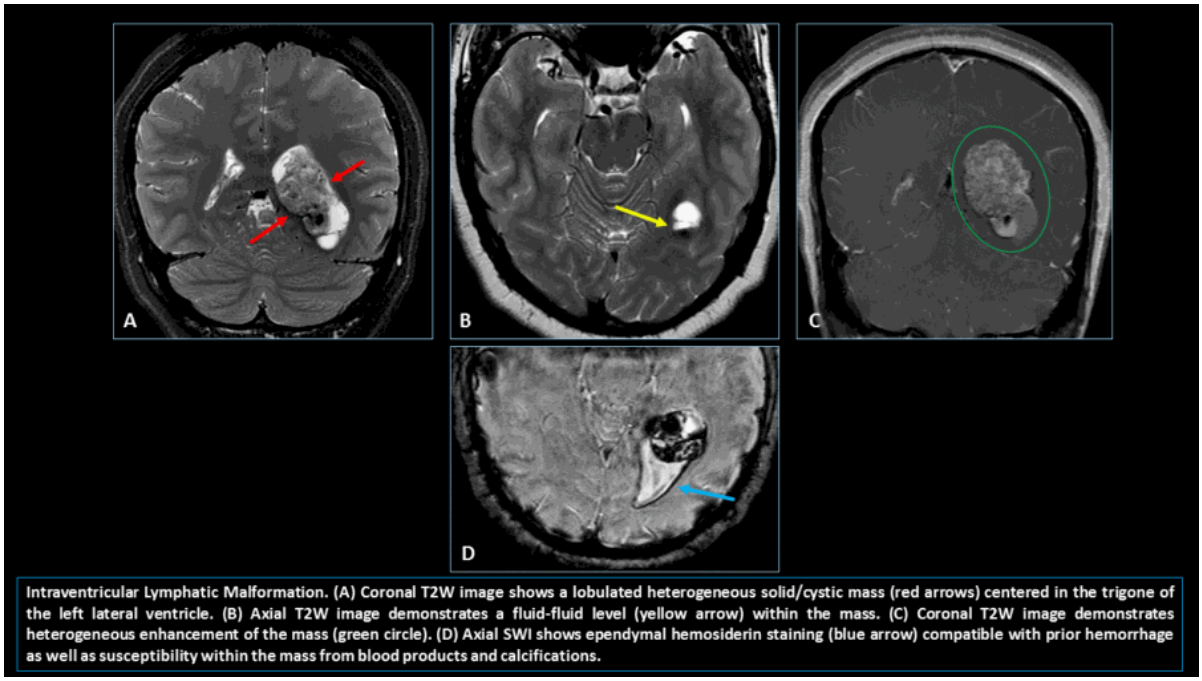
A 3-year-old female with history of intermittent headaches had a fall. Computed tomography (CT) revealed a pathologic skull fracture and a large left parieto-occipital intracranial mass with calcifications. Magnetic resonance imaging (MRI) redemonstrated the large mass. Spine MRI was normal. She underwent subtotal surgical resection. Pathology revealed ganglioneuroblastoma (WHO IV). Whole-body MIBG was negative for MIBG-avid disease. Cerebrospinal fluid (CSF) sampling was negative for metastasis. Postoperatively, the patient had right facial paresis and right hemiparesis, which subsequently improved.

Results

Magnetic resonance imaging showed a huge heterogeneous solid mass with decreased diffusivity, hemorrhage, and necrotic areas in the left parieto-occipital lobes. The mass demonstrated patchy areas of nodular enhancement. Surrounding vasogenic edema was less than expected for the size of the mass. Perfusion demonstrated predominant hypoperfusion of the mass with increased perfusion peripherally. Rightward midline shift, effacement of the cerebral aqueduct, and contralateral ventricular entrapment were present. Abnormal signal and enhancement involving the overlying calvarium was noted.

Conclusions

Ganglioneuroblastoma is a primitive neuroectodermal tumor that occurs in the peripheral and central nervous system composed of mature gangliocytes and immature neuroblasts. It has an intermediate malignant potential; immature tissue indicates potentially malignant behavior. Children under 5 years of age are most commonly affected. The most common sites are the adrenal gland, retroperitoneum, and posterior mediastinum. Cerebral involvement is extremely rare. Treatment for low-risk tumors is surgery alone with additional chemotherapy for high-risk tumors. Early-stage tumors with young age group (less than 1 year) have a 3-year-survival rate of more than 75%, whereas late-stage and age more than 1 year have a 3-year-survival of less than 50%.



(Filename: TCT_E-90_LM-Images.gif)

E-91

4:38PM - 4:42PM

"Primary Diffuse Leptomeningeal Primitive Neuroectodermal Tumor (PDL-PNET)" a Challenging Diagnosis in Pediatric Population: Case Report and Review of Literature.

R Patel[1], K Jobanputra[1], A Kamali[1], R Jacob[2], E Bonfante-Mejia[1], R Riascos[1]
[1]The University of Texas Health Science Center, Houston, Houston, TX, [2]UMC Health System, Lubbock, TX

Purpose
To discuss an extremely rare case of a primary diffuse leptomeningeal primitive neuroectodermal tumor (PDL-PNET) in a 5-year-old child and review of its literature.
Materials and Methods
A 5-year-old female child with 4-month history of progressive headache presented to ER with chief complaint of continuous vomiting. Computed tomography (CT) scan of the head followed by Magnetic resonance imaging (MRI) brain and entire spine with and without contrast were performed. Computed tomography scan of the head demonstrated moderate communicating hydrocephalus. Contrast-enhanced MRI of the brain and entire spine also demonstrated diffuse leptomeningeal enhancement within brain and the spinal cord, in absence of intraparenchymal enhancement. Subsequently patient underwent lumbar puncture and cerebrospinal fluid (CSF) analysis which revealed elevated protein but no malignant cells. Based on this information, primary differential diagnosis included (1) leptomeningeal spread of infectious process such as bacterial, tuberculous or cryptococcal meningitis,

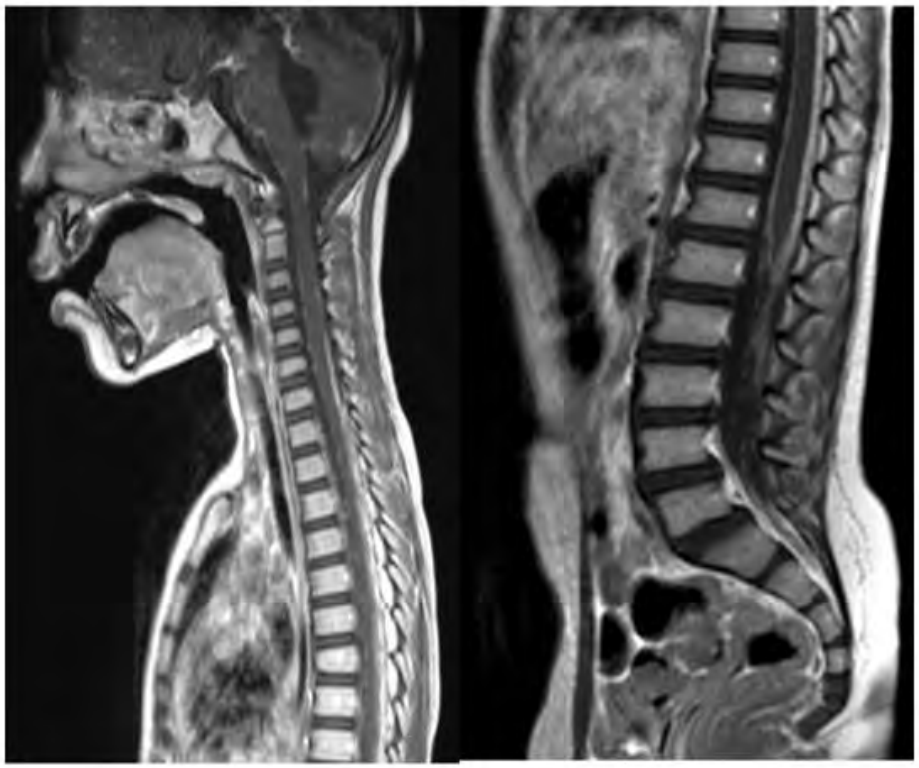
however longer duration of symptomatology and CSF, laboratory findings were not supportive (2) leptomeningeal spread of neoplastic process such as pineal tumors, medulloblastoma, ependymoma, however lack of a primary neoplastic process and lack of malignant cells on CSF made these considerations less likely (3) Inflammatory process such as Neurosarcodoisis. Due to lack of a definitive diagnosis, patient subsequently underwent biopsy of leptomeninges. Pathology of the leptomeningeal biopsy was consistent with neuroepithelial neoplasm. Immunohistochemical stains revealed tumor cells strongly positive for synaptophysin and CD56, retained INI-1, but negative for CD99. Cytogenetical analysis revealed absence of EWS translocation. Based on this information, final diagnosis of primary diffuse leptomeningeal PNET was established.

Results

Computed tomography scan of the head demonstrated moderate communicating hydrocephalus. Contrast-enhanced MRI of the brain and entire spine demonstrated diffuse leptomeningeal enhancement within brain and the spinal cord, in absence of an intra-parenchymal lesion.

Conclusions

Leptomeningeal PNET carries poor prognosis with most patients succumbing to their disease within 1 year after diagnosis (range = 4 weeks to 13 months). There are 8 case reports in the pediatric literature. The rarity of this clinical entity had hindered developing therapeutic guidelines as well as its consideration in the initial imaging differential diagnosis. Prospective studies are needed to understand if the elusive molecular biology of this rare disease differs from other central PNET. This could help in strategizing optimal therapy and provide a meaningful improvement in the survival of these children.



(Filename: TCT_E-91_Slide5.JPG)

Wednesday
3:30PM - 4:50PM
Long Beach Convention Center, Room 203AB (Upper Level)

20G-Parallel Paper Session: Aneurysms: Search and Destroy Mission - to Find, Fix and Follow

O-304

3:30PM - 3:38PM

Optimal timing of Digital Substraction Angiography in Diagnostic Work-up for Acute Non-Traumatic Intracerebral Hemorrhage.

S Jacobs[1], E Jacobs[2], A Bharatha[3]

[1]University of Toronto, Toronto, Ontario, [2]Leiden University Medical Center, Leiden, Zuid-Holland, [3]St. Michael's Hospital, Toronto , Ontario

Purpose
CT angiography (CTA) and MRI/MR angiography (MRA) are noninvasive imaging methods that are performed frequently as initial investigations in acute nontraumatic intracerebral hemorrhage (ICH). When CTA/MRA are negative, patients often undergo digital subtraction angiography (DSA). However, little is known about the optimal timing of DSA in the context of high quality noninvasive angiography. In this study we will review the results of CTA, MRA and DSA (early and delayed) in patients presenting with nontraumatic ICH to determine if DSA done at presentation adds information that influences acute management.
Materials and Methods
We conducted a retrospective study of all patients presenting with acute nontraumatic ICH based on CT from January 1, 2005 to January 1, 2016 at our tertiary neurosurgical center based on search of clinical reports database and cross-referenced against all DSA reports in that time period. Demographics, imaging methods, timing and results based on the reports were reported. Every patient's medical record was reviewed for underlying risk factors and final diagnosis, when available. Patients with a previously identified cause of hemorrhage were excluded.
Results
A macrovascular cause was identified in 129 out of 363 patients (36%). Two hundred ninety patients (80%) underwent CTA; of the 191 patients with a negative CTA, 93 underwent additional MRI/MRA and 75 underwent DSA (of which 65 were early). Computed tomography angiography detected 99 macrovascular causes (yield 34%). Computed tomography angiography combined with MRI/MRA identified 7 additional macrovascular causes (yield 42%). Early DSA at time of ICH detected 17 macrovascular causes after negative CTA/MRA. Out of these, 13 patients underwent immediate treatment. Late DSA and follow-up DSA detected another 4 macrovascular causes.
Conclusions
Early CTA/MRA occasionally can miss macrovascular causes of acute nontraumatic ICH that are visible on DSA and for which up-front treatment may be warranted. Early DSA should be performed in patients with unexplained ICH with negative CTA/MRA studies.

Table 1 | Causes of intracerebral haemorrhage in participants	
Causes	No (%) of patients (n=363)
Macrovascular:	
Arteriovenous malformation	35 (10)
Dural arteriovenous malformation	6 (2)
Cavernoma	3 (1)
Cerebral venous sinus thrombosis	9 (3)
Aneurysm	76 (21)
of which mycotic aneurysm	*7 (2)*
Subtotal	129 (36)
Other:	
Probable cerebral amyloid angiopathy	5 (1)
Hypertensive vasculopathy†	72 (20)
septic Emboli endocarditis	1 (0.3)
Vasculitis	3 (0.8)
Neoplasm	5 (1)
Metastases	4 (1)
Moyamoya	1 (0.3)
Haemorrhagic infarction	7 (2)
Pre-eclampsia	1 (0.3)
PRESS	3 (0.8)
Anticoagulants	2 (0.5)
Unknown	130 (36)
Subtotal	234 (64)
†Intracerebral haemorrhage in basal ganglia, thalamus, or posterior fossa in presence of hypertension.	

(Filename: TCT_O-304_Causesintracerebralhemorrhagesinparticipants.jpg)

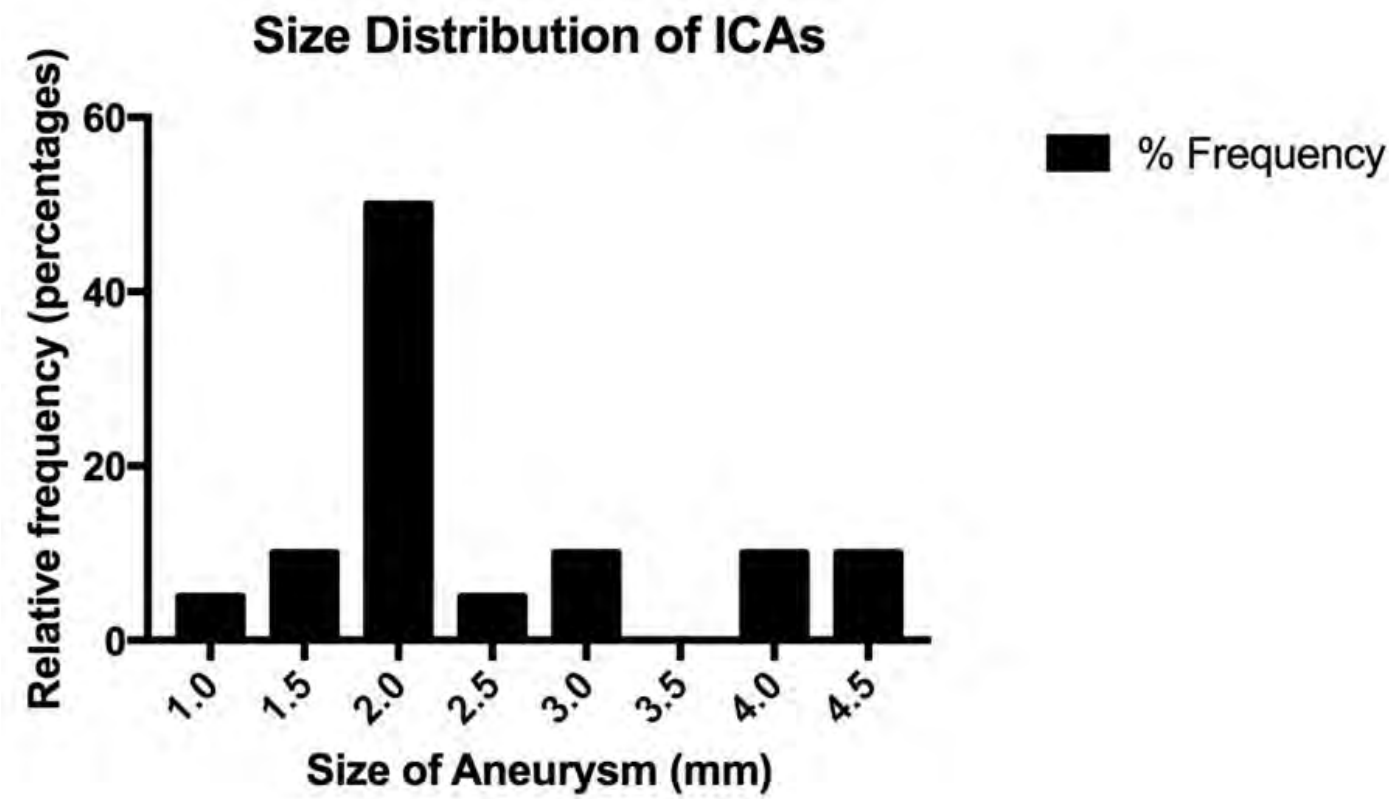
O-305

3:38PM - 3:46PM

Screening for Intracranial Aneurysms in Patients with Aortic Aneurysms

K Seifert[1], X Wu[2], D Durand[2], F Nautsch[2], V Kalra[2], A Malhotra[2]
[1]Yale University School of Medicine, Milford, CT, [2]Yale University School of Medicine, New Haven, CT

Purpose
A higher incidence of intracranial aneurysms (ICA) has been reported in patients with ascending aortic aneurysms in previous retrospective reviews. The purpose of the current study was to prospectively screen patients with ascending aortic aneurysms to detect the incidence of intracranial aneurysms and establish the utility of screening.
Materials and Methods
Patients with thoracic aortic aneurysms (TAA) were prospectively screened with CT angiography (CTA) and magnetic resonance angiography (MRA) over a 7-year period between 2009 and 2016. Each aneurysm was detailed according to its location and maximum diameter. Additional data collected was: age at diagnosis, gender, history of hypertension, diabetes mellitus, hyperlipidemia and previous or current tobacco use. Follow-up results on imaging in patients with ICAs were recorded when available.
Results
A total of 433 patients with TAA were prospectively screened for ICAs between 2009 and July 2016. Nineteen of the 433 patients harbored an UIA (4.39%). There were a total of 20 aneurysms in 19 patients, ranging from 1 to 4.5 mm in size. The average diameter was 2.47 ± 0.98 mm. There were 319 male and 114 female patients. There were 176 patients under 60 years old, and 6 of them had an ICA (3.41%). Out of the 19 UIAs, 4 were extradural aneurysms, arising from the cavernous segment of ICAs. None of the patients with aneurysms had rupture during the available follow up.
Conclusions
The incidence of intracranial aneurysms in patients with aortic aneurysms may not be as high as previously reported in retrospective studies.



(Filename: TCT_O-305_TAAICA.jpg)

O-306

3:46PM - 3:54PM

A CAD System to Track Aneurysms on 3D Time-Of-Flight MRA

M Bilello[1], K Hsieh[2], R Assadsangabi[1], R Hurst[1]
[1]University of Pennsylvania, Philadelphia, PA, [2]Hospital of the University of Pennsylvania, Philadelphia, PA

Purpose
3D time-of-flight (TOF) magnetic resonance angiography (MRA) is becoming an increasing popular modality to monitor treated or untreated brain aneurysms. Interpreting serial MRA studies can be a tedious and error-prone task for the neuroradiologist, in both qualitative and quantitative assessment of aneurysmal recurrence. In particular, studies have reported different interobserver agreement. These limitations highlight the need for the development of an automated system to detect and quantify aneurysm recurrence or growth.
Materials and Methods
3D TOF MRA images were acquired from 22 patients with known aneurysms. An image-processing pipeline was applied to the baseline and follow-up images, including coregistration, skull-stripping, intensity normalization, and bias correction. The system

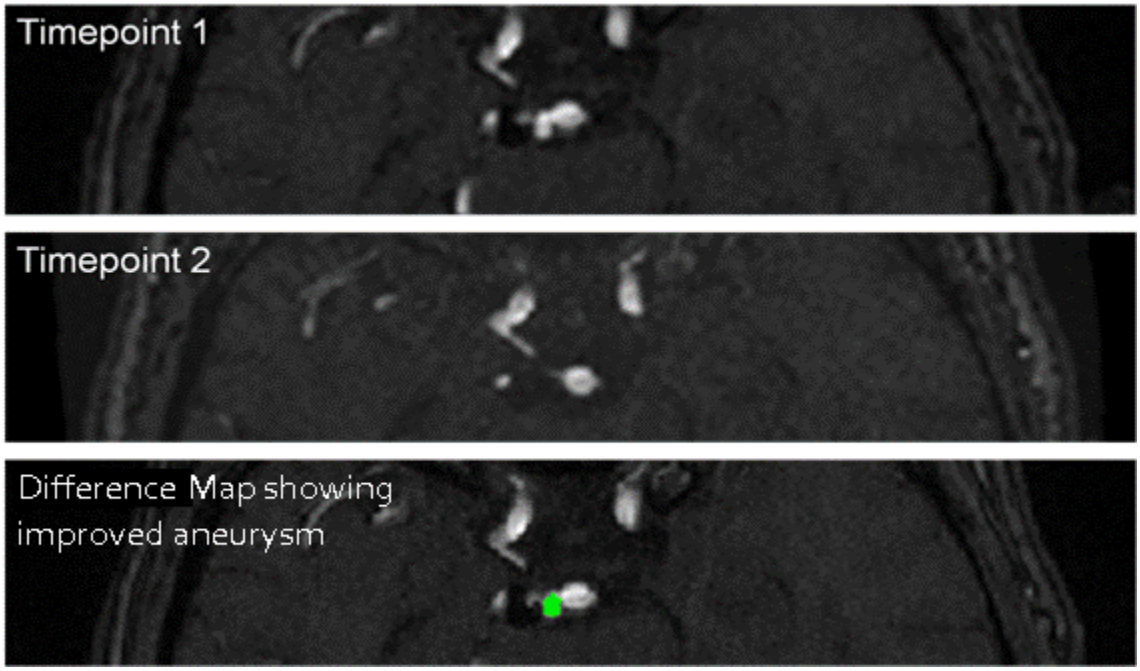
dynamically estimates blood vessel intensities, and then calculates a difference map highlighting interval increase or decrease of aneurysmal size. Color-coded changes are displayed on subtraction maps. Performance was assessed by comparison with a human expert.

Results

Following accurate registration and establishment of consistency with respect to vessel detection, forward and backward difference images across pairs of serial scans were created, using image subtraction that permits detection of aneurysmal change. The two-way subtraction allows tracking of both progressing and regressing aneurysms. Results demonstrate a sensitivity around 90% for aneurysm change. False positives occur mainly at the edges of volumes, and are easily discarded.

Conclusions

This CAD system could help not only neuroradiologists in everyday clinical care of patients with aneurysms through increased reproducibility and accuracy than current tedious methods, but also in research areas, as a large amount of imaging data can be analyzed reliably, accurately, and objectively for aneurysmal change.



(Filename: TCT_O-306_Picture1.gif)

O-307

3:54PM - 4:02PM

Early Detection of Aneurysm Growth by Volume and Surface Area Analysis Using 3D Modeling from CT Angiography

H Yokota[1], A Chien[2], E MORIMOTO[3], J Villablanca[2], N Salamon[4]

[1]David Geffen School of Medicine at UCLA, Los Angeles, CA, [2]UCLA, Los Angeles, CA, [3]David Geffen School of Medicine, UCLA, Los Angeles, CA, [4]UCLA, Los Angeles, CA, David Geffen School of Medicine at UCLA, Los Angeles, CA, Los Angeles, CA

Purpose

Enlargement of unruptured aneurysms indicates an increased risk of rupture. Assessment of aneurysm growth typically is based on aneurysm max diameter. However, this method often is unreliable due to factors such as the degree of contrast enhancement, tilting among studies and artifacts. The purpose of this study is to evaluate usefulness of three-dimensional modeling to judge aneurysm growth.

Materials and Methods

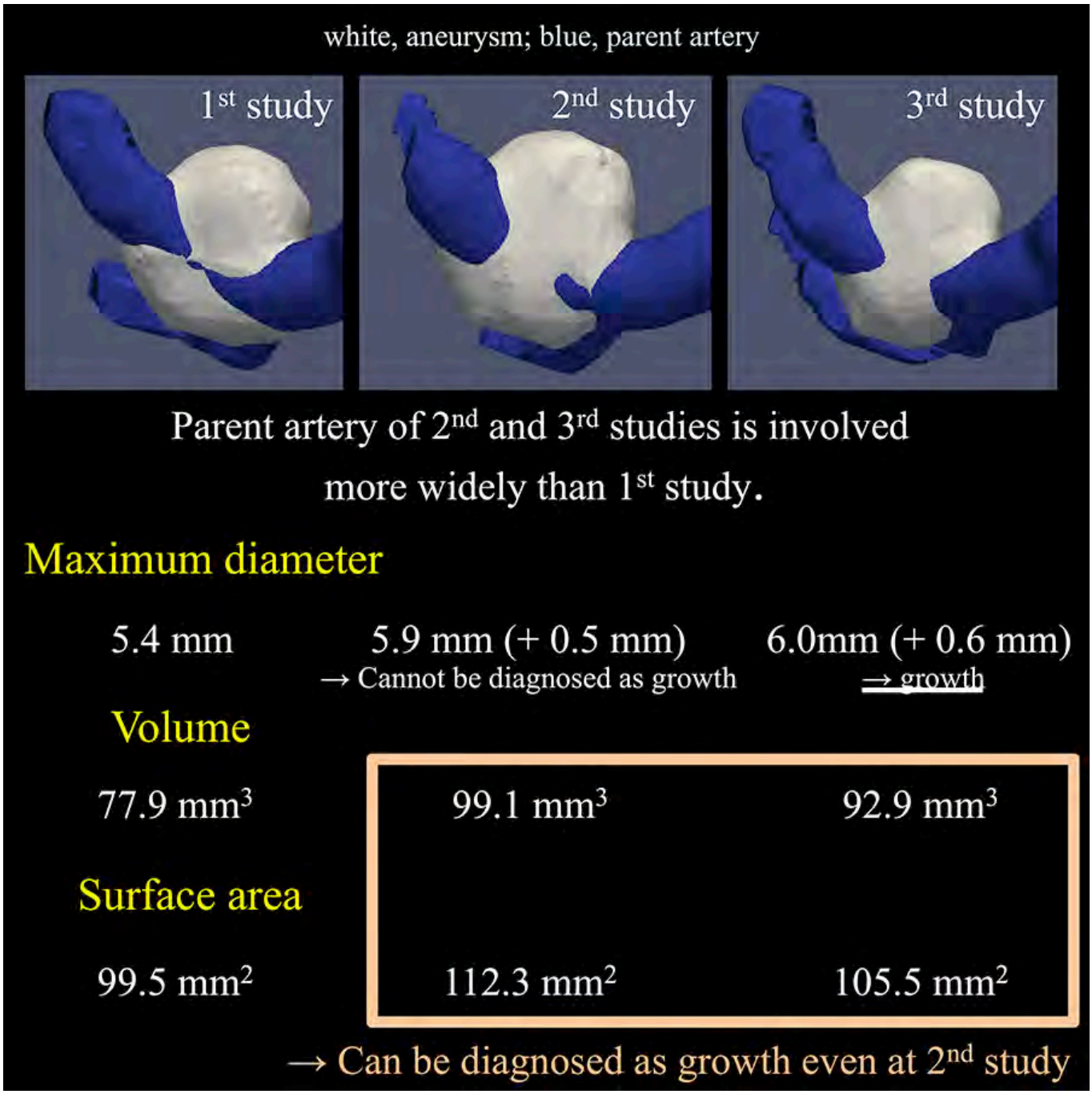
All aneurysm patients who underwent CTA (1.0-mm slice thickness) with at least 1 follow up in 2015, were reviewed. Intracranial saccular aneurysms were selected and fusiform, dissecting and mycotic aneurysms were excluded. Growth was defined as more than a 0.5 mm increase in size compared with the first study. Three-dimensional (3-D) models were created from the source data using 3D-slicer (http://www.slicer.org). Aneurysm extraction from the parent artery was performed semi-automatically and volume and surface area were calculated using vascular toolkit (http://www.vmtk.org). The Mann-Whitney test and ROC curve analysis were applied to compare cases which increased in size with no-change cases.

Results

This research included 59 aneurysms in 51 patients that underwent 250 CTA, with follow-up duration of 50.0 ± 50.5 months. Nine aneurysms increased in size. In 5 of 9 cases, follow-up studies prior to growth detection were available. In these cases, maximum diameter change from the first study was not significant ($P = 0.169$). By contrast, volume and area were significantly different ($P = 0.046$ and 0.046, respectively). On ROC analysis, AUCs of maximum diameter, volume, and area changes were 0.7, 0.772 and 0.772.

Conclusions

Calculating volume and area changes was useful to judge aneurysm growth earlier than size measurement.



(Filename: TCT_O-307_fig3.jpg)

O-308

4:02PM - 4:10PM

Vessel Wall Enhancement and Correlating Histopathological Findings in Unruptured Intracranial Aneurysms

N Larsen[1], D Trick[1], C Flueh[1], J Madjidyar[1], M Synowitz[1], O Jansen[1], C von der Brelie[2]

[1]*University Hospital Schleswig-Holstein Kiel, Kiel, Germany,* [2]*University of Göttingen, Göttingen, Germany*

Purpose
Recent studies have linked intracranial aneurysm wall enhancement in magnetic resonance imaging (MRI) to instability and higher risk of rupture. Understanding the histopathological condition underlying aneurysm wall enhancement would be an important step towards assessing the value of this method for stratifying patient risk. This has not been explicitly subject of investigation yet. We present our first observations of aneurysm wall enhancement in MR vessel wall imaging and underlying histopathologic changes.
Materials and Methods
We retrospectively reviewed patients with unruptured intracranial middle cerebral artery aneurysms who underwent MR imaging and aneurysm clipping. Contrast enhancement of the aneurysm wall was rated visually as none, mild/partial or strong. Histopathologic analysis included assessment of vasa vasorum, myeloperoxidase stain for detection of granulocyte infiltration, and anti-CD34 stain for assessment of neovascularization.
Results
Ten patients were included. Four aneurysms showed strong wall enhancement. MPO staining revealed granulocyte infiltration of the wall in 3. Three showed neovascularization as detected by anti-CD34-staining. In 1 of these aneurysms, vasa vasorum were present In 1 aneurysm, only part of the wall enhanced. In this case, MPO staining for granulocytes was positive and vasa vasorum were present, but there was no evidence of neovascularization. Four aneurysms did not show any wall enhancement, 1 only mild. Neither of these bore evidence of invasion of granulocytes or neovascularization, and they all lacked vasa vasorum. There was a significant difference of estimated 5-year-rupture risks according to PHASES score between aneurysms with wall enhancement and aneurysms without.
Conclusions
Aneurysm wall enhancement as detected by MR vessel wall imaging is associated with inflammatory cell invasion, neovascularization and/or presence of vasa vasorum. Nonenhancing aneurysms did not show these features. Vessel wall enhancement correlates with higher estimated 5-year-rupture risk according to PHASES score.

O-309

4:10PM - 4:18PM

MRI Vessel Wall Imaging Characteristics of the Circle of Willis in Patients with Endovascular Treated Ruptured and Unruptured Aneurysms: Association of vessel wall enhancement with vasospasm and balloon/stent-assisted coiling

T Huynh[1], M Levitt[1], R Morton[1], M Mossa-Basha[1]
[1]*University of Washington, Seattle, WA*

Purpose
To characterize magnetic resonance imaging (MRI) vessel wall imaging (MRI-VWI) findings of the circle of Willis in patients with acutely treated ruptured and unruptured aneurysms and to determine the association with use of intraprocedural balloons/stents and subsequent vasospasm.
Materials and Methods
Magentic resonance imaging-VWI was performed on consecutive endovascular treated unruptured and ruptured aneurysm patients treated by a single neurointerventionalist from Sept. 2015 to Nov. 2016 using a black-blood T1-weighted 3T MR sequence previously described (1). Vessels of the circle of Willis (bilateral A1 ACA, M1 MCA, P1 PCA, terminal ICA, and basilar artery) were evaluated systematically for vessel wall thickening and enhancement on pre and postcontrast T1 sequences. Follow-up imaging was used to determine presence of angiographic vasospasm and/or infarct.
Results
In total 27 patients (median age 58 years, range 34-72 years; 20 female) with treated unruptured (n=7) and ruptured aneurysms (n=20) were evaluated, for a total of 243 vessel segments. Seventeen patients were treated with balloon/stent assistance. Eight (40%) patients had subsequent angiographic vasospasm involving 26 vessel segments and 2 had distal infarcts. Wall enhancement of the vessels of the circle of Willis was only present in cases of ruptured aneurysms ($p<0.05$). Of ruptured cases, 17/20 (85%) demonstrated wall enhancement of which 13/17 (76%) involved 2 or greater vessels. Enhancement was not associated statistically with balloon/stent-assistance or future vasospasm.
Conclusions
Magnetic resonance imaging-VWI enhancement of the vessels of the circle of Willis is common in the setting of treated ruptured aneurysms and not seen in treated unruptured aneurysms. Vessel wall enhancement is not associated significantly with balloon/stent-assisted intervention or vasospasm.

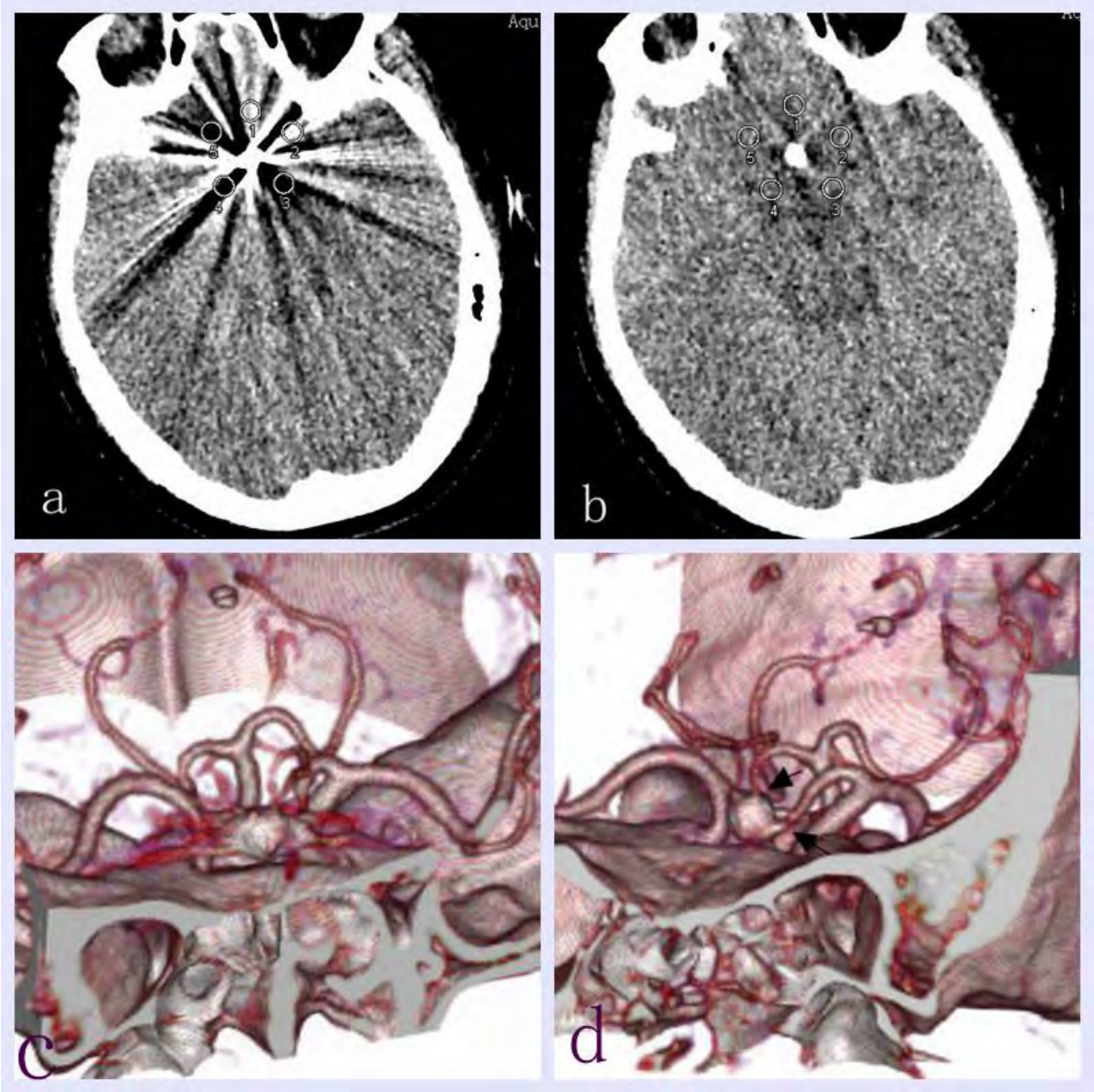
O-310

4:18PM - 4:26PM

Reduction of Artifacts from Implanted metallic Materials in Patients with Intracranial Aneurysms: Effects of A New Single-Energy Metal Artifact Reduction(SEMAR) Algorithm

S Li[1], Y pan[2], B Mattson[3], Z Chen[2], Y Zeng[4]
[1]University of Massachusetts Medical School, Longmeadow, MA, [2]Ningbo First Hospital, Ningbo, Zhejiang Province, [3]University of Massachusetts Medical School - Baystate Medical Center, Springfield, MA, [4]Department of Medical College, Ningbo University, Ningbo, Zhejiang Province

Purpose
As spatial and temporal resolution are continually improving, multidetector computed tomography (MDCT) cerebral angiography has become a primary method for evaluating outcomes and complications after cerebral aneurysm embolization and clipping (1). Beam-hardening artifact from implanted metallic materials in the brain can obscure surrounding anatomical structures and make it difficult to detect postoperative complications and evaluate for aneurysm recurrence (2). In this study, a newly developed artifact reduction technique, the single-energy metal artifact reduction (SEMAR) algorithm, was introduced on a second-generation 320-row CT scanner (3). To the best of our knowledge, this is the first study that evaluates the SEMAR algorithm and its reduction of beam-hardening artifact from implanted metallic materials in the brain.
Materials and Methods
Computed tomography angiography (CTA) was performed on 38 patients of Ningbo First Hospital, with implanted metallic materials in the brain (17 men, 21 women; mean age, 59.7 ± 15.74 years). All CT examinations were performed on a 320-row CT scanner (Aquilion ONE, Toshiba, Japan). Non-SEMAR images were reconstructed with iterative reconstruction alone, and SEMAR images were reconstructed with iterative reconstruction plus the SEMAR algorithm. Noise (N - measured on the image with the most pronounced artifact), contrast-to-noise ratio (CNR), artifact index (AI), maximum diameter of artifact, image quality score, and cerebral perfusion parameters were compared between the 2 groups. Two radiologists visually evaluated the metallic artifacts using a four-point scale and a double blind method: 1 = extensive; 2 = strong; 3 = mild; 4 = minimal artifact.
Results
Compared with non-SEMAR images, noise, artifact diameter, and artifact index were reduced significantly after images were reconstructed using the SEMAR algorithm ($P < 0.01$). The subjective image quality score and contrast-to-noise ratio increased significantly ($P < 0.01$). There was no statistically significant difference in cerebral perfusion parameters (blood flow, blood volume, and mean transit time) between the non-SEMAR and SEMAR groups ($P > 0.05$).
Conclusions
The SEMAR algorithm significantly reduces artifact from implanted metallic materials in the brain and potentially can increase CT image quality without influencing cerebral blood perfusion parameters.



(Filename: TCT_O-310_.jpg)

O-311

4:26PM - 4:34PM

Creation of Larger Elastase-induced Aneurysms with Predilation of the Right Common Carotid Artery before Elastase Incubation

Y Ding[1], S Asnafi[1], D Dai[1], R Kadirvel[1], D Kallmes[1]
[1]*Mayo Clinic, Rochester, MN*

Purpose
The elastase-induced aneurysm model in rabbits typically are relatively small. The purpose

of the study was to determine whether predilation of the right common carotid artery (RCCA) with a noncompliant balloon immediately prior to elastase incubation can result in larger elastase-induced aneurysms in rabbits.

Materials and Methods

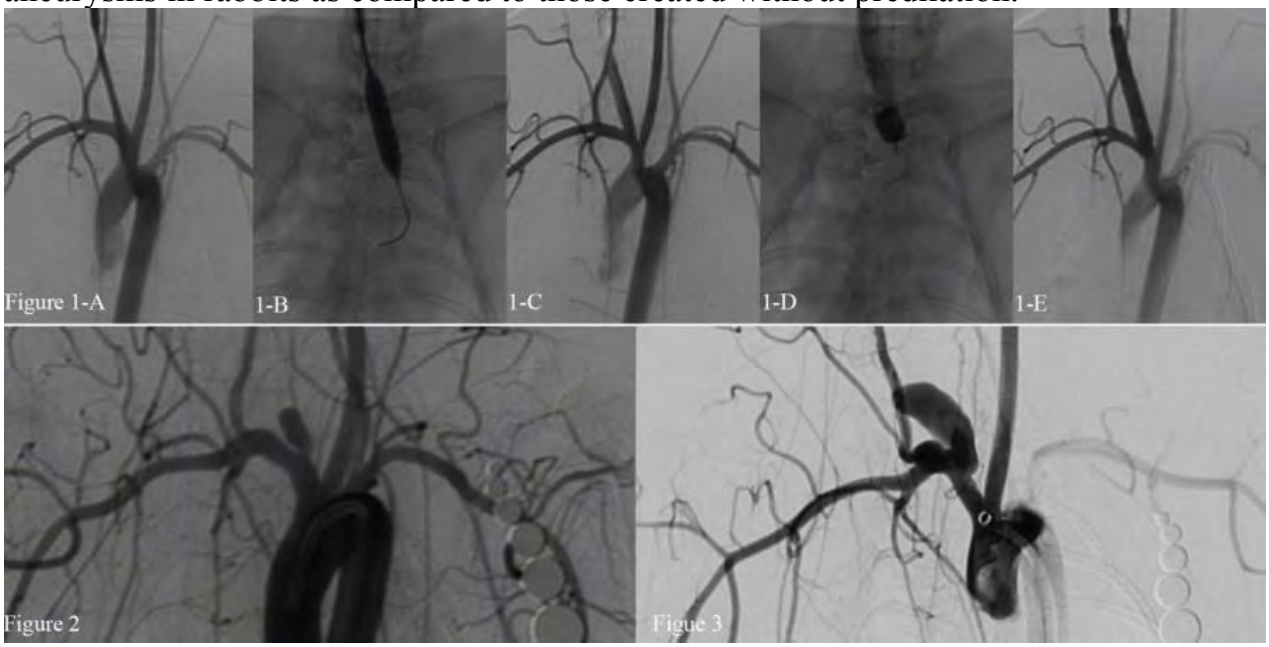
Elastase-induced aneurysm sizes were analyzed retrospectively in 114 New Zealand White rabbits. Two groups were classified: Group 1 (n = 47) in which elastase-induced aneurysms were created without predilation of the RCCA; Group 2 (n = 67) in which predilation of right common carotid artery (RCCA) with an angioplasty balloon (balloon diameter/length: 3.5 mm/2 cm; inflation pressure: 8 atm; inflation duration: 60 seconds; inflations times: 3) was performed before elastase incubation (Figs. 1-A, RCCA before predilation; 1-B, predilation of RCCA; 1-C, wider RCCA after dilation but before elastase-incubation; 1-D, elastase-incubation; 1-E, further enlargement of RCCA after elastase-incubation). Follow-up digital subtraction angiography (DSA) was performed 3 weeks after aneurysm creation. Aneurysm sizes (neck diameter, width, height) in the 2 groups were measured and calculated. Comparison of aneurysm sizes between the 2 groups was compared using the Student's t test.

Results

The mean aneurysm neck for Group 1 (Fig. 2) was narrower than Group 2 (Fig. 3) (2.8 ± 1.0 mm and 4.3 ± 1.1 mm, respectively, $p < .05$). Differences in aneurysm width between the 2 groups were significant (3.1 ± .5 mm and 4.8 ± 1.1 mm, respectively, $p < .01$). Mean aneurysm height for Group 1 was smaller than Group 2 (6.8 ± 1.4 mm and 11.5 ± 1.7 mm, respectively, $p < .0001$).

Conclusions

Predilation of the RCCA before elastase incubation can create larger elastase-induced aneurysms in rabbits as compared to those created without predilation.



(Filename: TCT_O-311_2017asnrimagepredilationYonghongDing.jpg)

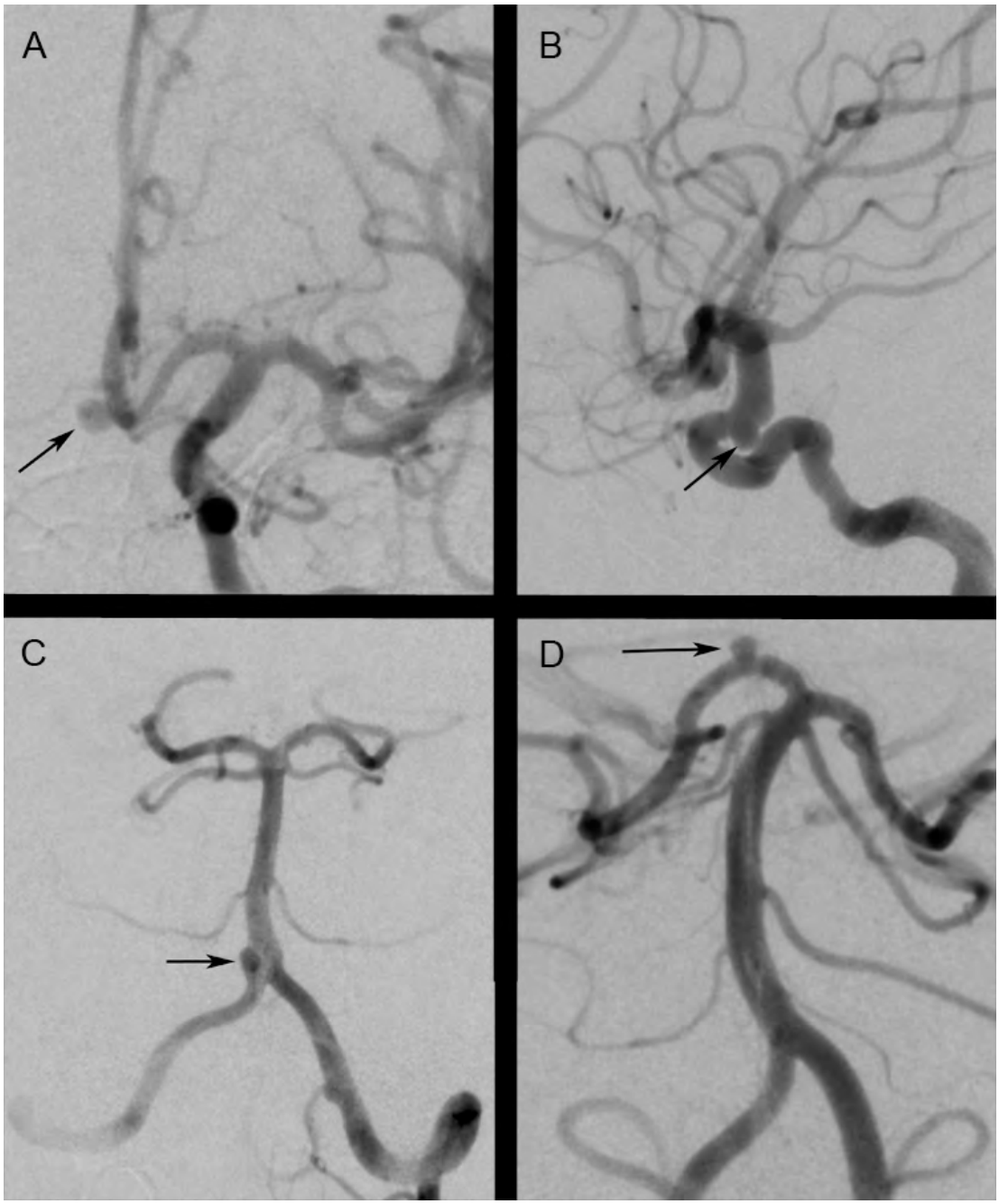
O-312

4:34PM - 4:42PM

Endovascular Treatment of Pediatric Patients with Intracranial Aneurysms and Sickle Cell Disease.

M Pearl[1], P Gailloud[1]
[1]*Johns Hopkins University School of Medicine, Baltimore, MD*

Purpose
Endovascular treatment of intracranial aneurysms (IAs) in patients with sickle cell disease (SCD) has been avoided because of concerns for the potential risks of local sickling and arterial occlusion. Experience is limited to 4 published cases in children (1, 2). We present our series of coil embolization (primary or stent-assisted) for both ruptured and unruptured IAs in 4 pediatric patients with SCD.
Materials and Methods
A prospective database of all children undergoing diagnostic cerebral angiography in children with SCD (HbSS, HbSC) at a single institution from July 2010 to December 2016 was reviewed to identify those with IAs. Records were reviewed for age, gender, sickle cell genotype, clinical presentation, treatment approach, and neurological outcome.
Results
From July 2010 to December 2016, 28 children with SCD underwent cerebral DSA and 9 (3 boys, 6 girls) were found to harbor 23 intracranial aneurysms. Endovascular treatment was performed in 4 patients (2 girls, 2 boys), aged 13 to 18 years and included primary coil embolization (n = 2) and stent-assisted coil embolization (n = 2). One patient presented with subarachnoid hemorrhage. Four aneurysms were treated endovascularly in the following locations: anterior communicating artery (ACOM), left ophthalmic segment, basilar artery fenestration, and right P1 segment (Fig. 1). All patients had homozygous HbSS disease and tolerated their procedures well without immediate or delayed complications (Fig. 1). Four patients with sickle cell disease and intracranial aneurysms. A). AP view of a ruptured 4-mm ACOM aneurysm which was primarily coiled. B). Lateral view of a 4 mm left ophthalmic segment aneurysm which underwent stent-assisted coiling. C). Transfacial view from a left vertebral artery injection demonstrates a 4.8-mm aneurysm involving the right limb of a basilar artery fenestration, which subsequently was coiled. D). Transfacial view from a left vertebral artery injection shows an unruptured 2.5-mm right P1 segment aneurysm prior to stent-assisted coil embolization.
Conclusions
Endovascular treatment of intracranial aneurysms can be a safe and effective treatment alternative for pediatric patients with SCD. Periprocedural precautions and multidisciplinary management are important to reduce the risk of intravascular sickling and its complications.



(Filename: TCT_O-312_ASNRfig1.jpg)

O-511

4:42PM - 4:50PM

CT Angiography (Early and Delayed Phase) Vs. CT Perfusion For the Diagnosis And Treatment Of Stroke

S Tal[1], M Abrahamy[2], S Kalmanovich[2]
[1]Assaf Harofeh MC, Zeriin, Israel, [2]Assaf Harofeh MC, Zerifin, AK

Purpose
Stroke treatment focuses on 3 strategies – conservative treatment, thrombolytic treatment (IV rt-PA) or an endovascular procedure. Our purpose is to evaluate whether information provided by CTA (early and delayed phase imaging) correlates to what is detected on CT perfusion (CTP) prior to endovascular treatment.
Materials and Methods
A retrospective review of 54 consecutive adult brain CT examinations (early and delayed phase CTA, CT perfusion) performed from January 3, 2015 – April 10, 2016 on patients admitted to the ER with acute stroke and were candidates for thrombolytic treatment (arriving within 4.5 hours of symptom onset) or endovascular procedure (arriving within 6 hours) and NIHSS $\geq$ 4 or NIHSS 2 with concomitant major neurological deficit. Independent blind review was performed by a board certified neuroradiologist and invasive neurologist. The ischemic areas were evaluated on axial imaging only according to ASPECT score.
Results
The area measurements of the hypodensities (representing oligemia) on CTA early images were found to be nonequivalent to the penumbra areas seen on MTT/CBF images of the CTP. The area measurements of the hypodensities (representing oligemia) of the CTA delayed images were found to be equivalent to the core infarct areas seen on CBV images of the CTP.
Conclusions
Computed tomography angiography should not be used independently for referring to endovascular treatment when CTP is available, and delayed CTA images show equivalence with CBV images on CTP.

Wednesday
3:30PM - 4:58PM
Long Beach Convention Center, Room 102BC (Main Level)

20H-Parallel Paper Session: Mixture of Interest

O-313

3:30PM - 3:38PM

Corrected Clivo-Axial Angle

A Farley[1], A Sayah[2], F Berkowitz[3]
[1]Medstar Georgetown University, Washington, DC, [2]Medstar Georgetown University Hospital, Washington, DC, [3]Georgetown University Hospital, Washington, DC

Purpose
The clivo-axial angle (CXA) is a measurement used to quantify the severity of cranial cervical instability in cases of basilar invagination. An abnormally decreased CXA has been

associated with neurological changes related to deformative stress to the upper cervical spinal cord. There has been little discussion regarding the alteration in the CXA based on head positioning (flexion and extension). The CXA can vary significantly (up to 30 degrees) depending on the degree of flexion or extension which can result in in both false-negative and false-positive measurements. The aim of this study was to develop a method to correct the CXA based on the degree of flexion or extension of the cervical spine. We devised a novel technique to calculate a corrected clivo-axial angle (CCA) that is independent of head position.

Materials and Methods

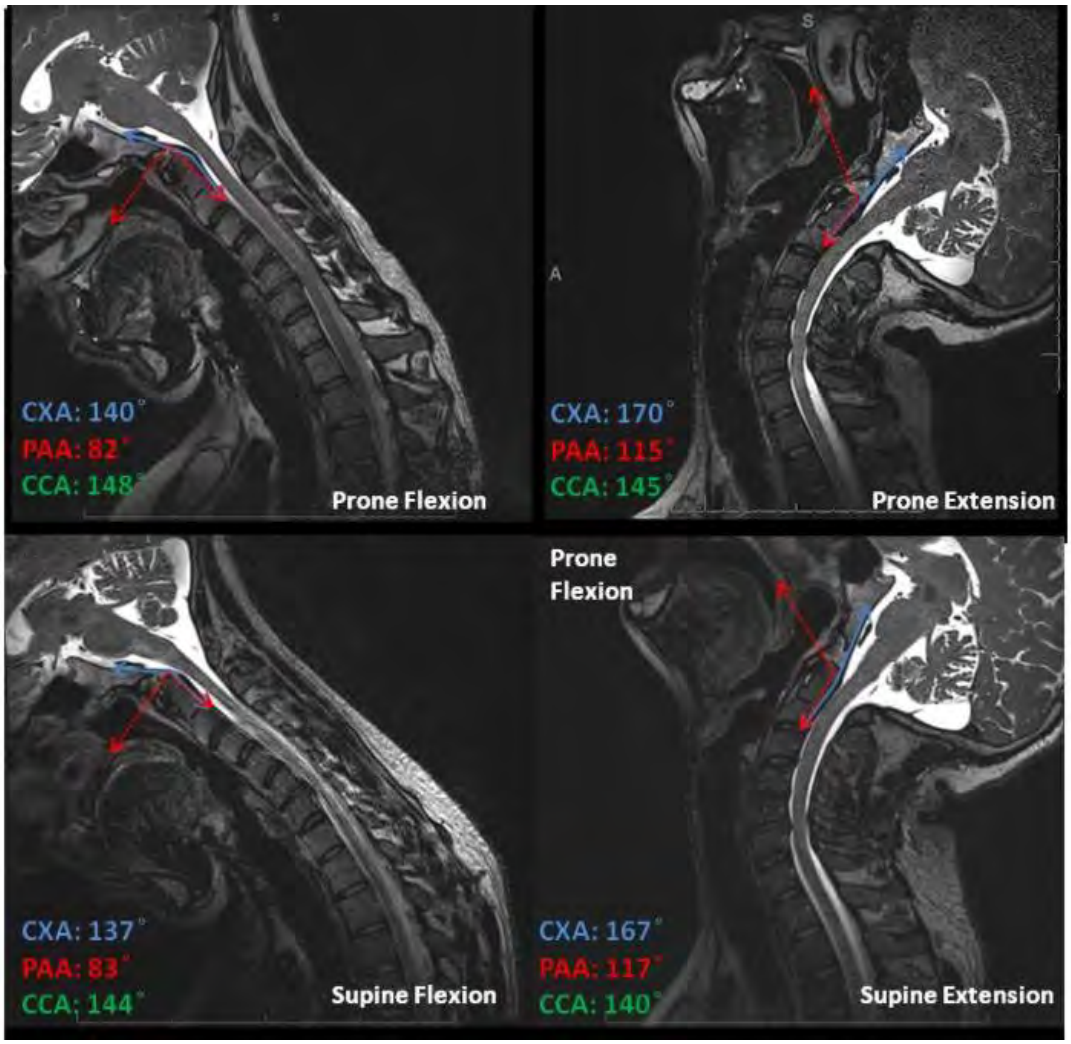
Sagittal T2 SPACE images of the cervical spine of 10 healthy male and female participants were obtained both in flexion and extension. Measurements were performed by 2 individual radiologists. Defining neutral head position as 90 degrees, the palato-axial angle (PAA) (the angle from the hard palate to the posterior cortex of C2 body) is subtracted from 90 degrees and the difference subsequently is added to the measured CXA to determine the CCA. Statistical analysis was performed and the mean, range, variance and standard deviation were measured for both the CXA and CCA in both flexion and extension.

Results

The mean CXA in all positions is 154.76 with a standard deviation of 12.78 and a range of 135-179. The mean CCA in all positions is 148.56 with a standard deviation of 5.64 and a range of 136-158.

Conclusions

This study presents a novel technique for calculating the corrected clivo-axial (CCA). The CCA is more precise than the noncorrected clivo-axial angle (CXA) demonstrated by a lower variance and standard deviation as well as a narrower range. The mean CCA and CXA did not differ significantly. Future directions may include measuring a larger cohort of participants to determine an accurate measurement of the clivo-axial angle.



(Filename: TCT_O-313_CAA.jpg)

O-314

3:38PM - 3:46PM

CT-Fluoroscopic Guided Suboccipital Puncture

S Sundararajan[1], N Sedora-Roman[2], M Oselkin[2], R Hurst[2], B Pukenas[3]
[1]Hospital of the University of Pennsylvania, Philadelphia, PA, [2]University of Pennsylvania, Philadelphia, PA, [3]Hospital Of the Univ. Of Pennsylvania, Philadelphia, PA

Purpose
Suboccipital puncture stemmed from a diagnostic need to obtain cerebrospinal fluid (CSF) after failed lumbar puncture. Reported independently in 1919 by Wegeforth et al in the USA and in 1923 by Eskuchen in Germany, the technique was performed first without imaging guidance. Procedural complications include infection, brainstem injury, and posterior circulation trauma. Despite these risks, suboccipital puncture offers the shortest path to

traverse the blood-brain barrier without calvarial disruption. We review our experience with a reproducible methodology of performing CT-fluoroscopic suboccipital puncture.

Materials and Methods

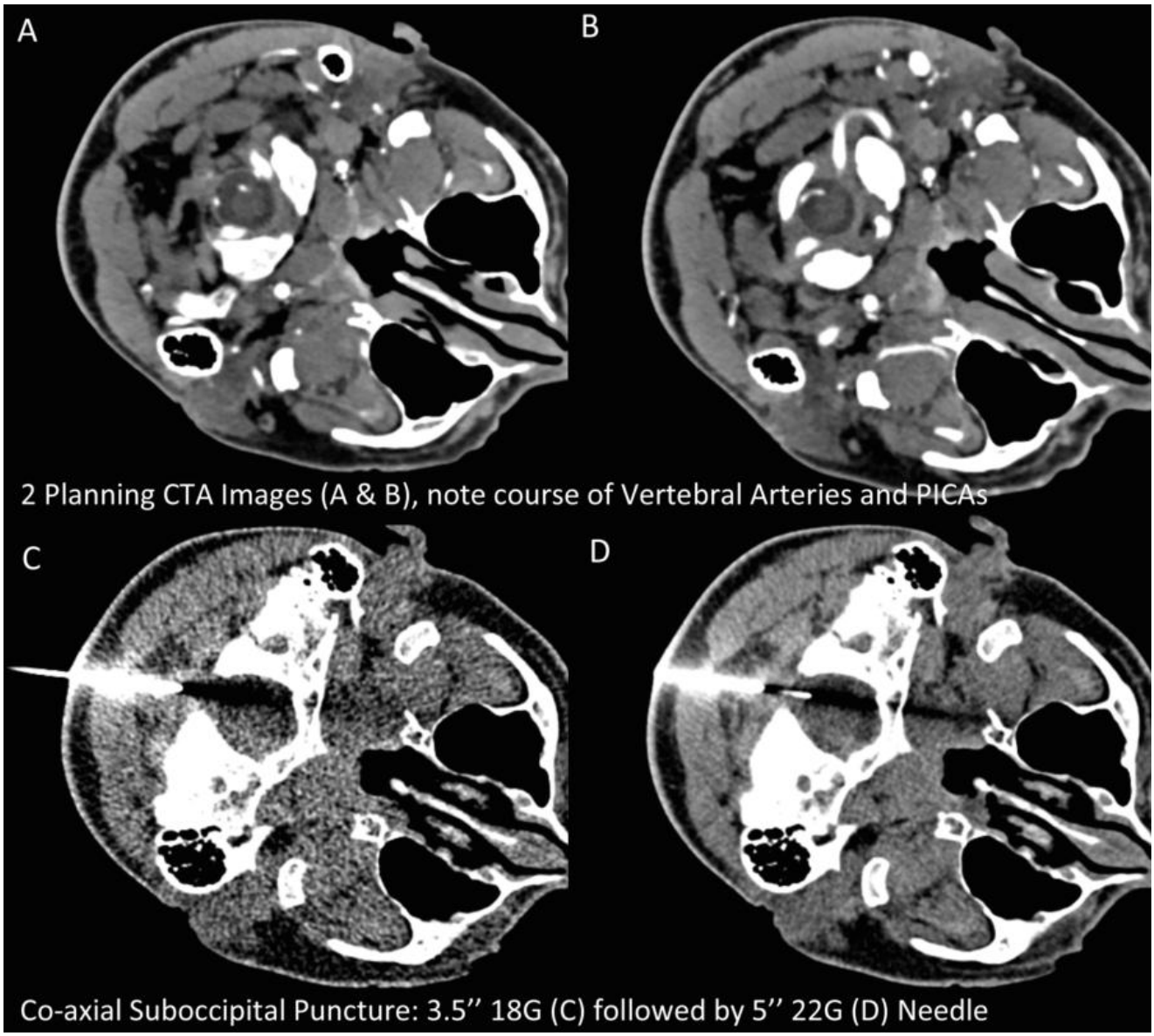
A cadavieric learning session was performed with 4 operators (2 neurointerventional radiologists, 2 neurosurgeons). Success was defined as the ability to withdraw CSF once in the cistern. Operators were instructed to describe their comfort level with the procedure after the session. Under an IRB-approved protocol, this approach then was translated into a human patient who had 2 failed lumbar attempts due to fibrous dysplasia. Technique consists of first performing skull-base CTA to map the vertebral arteries and posterior inferior cerebellar arteries (PICA). Trajectory angle then is mapped, with minor adjustments made according to traversing vessels. A 3.5" 18G spinal needle is advanced under CT just proximal to the occipital membrane. Using coaxial technique, a 5" 22G spinal needle then is inserted into the foramen magnum subarachnoid space.

Results

All session participants achieved 100% success rate of CT-guided suboccipital puncture during the cadaveric learning session. Comparable interoperator levels of comfort and device stability during CT-guided co-axial needle technique implementation were reported. Procedure was translated successfully into our human patient without complication or technical difficulty. Planning CTA allowed for precise needle trajectory calculation between the vertebral arteries and PICAs (Figs. A to D). Clear, colorless CSF was collected. Post-procedural imaging follow-up confirmed no injury to the posterior circulation.

Conclusions

Implementing a cadaveric workshop allowed for appropriate development of operator reproducibility and procedural confidence during CT-fluoroscopic guided suboccipital puncture. While positioning in the posterior and posterior/lateral decubitus positions allow for optimization of atlantooccipital distance, co-axial needle technique provides additional procedural stability. Limited skull base CTA allows for safe needle trajectory mapping. CT guidance allows for safe intracranial subarachnoid space access with improved accuracy. This protocol can be implemented for diagnostic, scientific, and therapeutic indications, including the delivery of targeted intracranial therapies.



(Filename: TCT_O-314_SuboccipitalPunctureASNRFigure.jpg)

O-315

3:46PM - 3:54PM

Unilateral Leukoencephalopathy Is Frequently Associated with Parry-Romberg Syndrome and Linear Scleroderma en Coup de Sabre.

R La Piana[1], D Tampieri[2]
[1]Montreal Neurological Institute, Montreal, Quebec, [2]Montreal Neurological Hospital and Institute, Montreal, Quebec

Purpose
Unilateral leukoencephalopathy is an uncommon finding, generally attributed to a vascular

or infectious origin, unless proven otherwise. The purpose of our study was to review our series of patients with unilateral white matter disorder and no evidence of vascular or infectious diseases in order to clarify the underlying etiology.
Materials and Methods
We retrospectively collected and analyzed the MRI data of a series of patients with unilateral white matter disease referred to our department. The clinical and histopathological data, when available, also were integrated into the analysis.
Results
We collected 8 patients (3 females, 5 males; mean age at MRI 35.8 years) with unilateral leukoencephalopathy. The pattern of involvement was limited to 1 lobe in 2 subjects and it was diffuse to the entire hemisphere in 6 subjects. In 3 subjects with diffuse pattern, the white matter abnormalities were associated with cortical involvement and atrophy. Magnetic resonance imaging (MRI) follow up was available for 7 subjects (mean follow-up duration 4.8 years): white matter changes and/or atrophy were variably progressive in 4 subjects, while remained stable in 3. Five subjects had a diagnosis of Parry-Romberg syndrome (PRS) or linear scleroderma en coup de sabre (LSCS). Five patients (4 with PRS or LSCS) presented with epileptic disorders of various severity, one with headache, and in 2 patients the leukoencephalopathy was an incidental finding. The evolution of the MRI findings correlated with the progression of the clinical status. Histopathological data were available for 3 patients. Reactive astrocytosis, lymphocytic infiltration, vessel damage and demyelination were the main findings.
Conclusions
Our study highlights the association of unilateral leukoencephalopathy with PRS and LSCS. When presented with unilateral white matter disorder, the radiologists and clinicians should assess the patient for even minimal facial soft tissue abnormalities or asymmetry which can clarify the diagnosis and prevent the patient from more extensive and invasive diagnostic workup.

O-316

3:54PM - 4:02PM

Cerebellar Hemispheric Medulloblastoma Molecular Subtypes: Imaging Features and Application of ADC Histogram for Diagnosis

S Payabvash[1], T Tihan[2], S Cha[3]
[1]University of California, San Francisco, San Franciscon, CA, [2]UCSF, San Francisco, CA, [3]University of California San Francisco, San Francisco, CA

Purpose
Classically, medulloblastomas present as midline posterior fossa tumors near the fourth ventricle in pediatric population. Medulloblastomas in adults, on the other hand, tend to occur more commonly within cerebellar hemispheres and are associated with wingless

(WNT) and sonic hedgehog (SHH) molecular variants. The purpose of our study was to identify the conventional MRI findings and ADC histogram characteristics of cerebellar hemispheric medulloblastomas.

Materials and Methods

A retrospective comprehensive review of patient with path-proven posterior cranial fossa tumors was performed. The solid component was segmented manually to determine the voxel-based ADC histogram percentile, kurtosis, skewness, and average values. Logistic regression and ROC curve analyses were applied to identify the independent imaging predictors for accurate diagnosis of medulloblastoma.

Results

Of 159 patients with posterior cranial fossa intra-axial tumors, 85 (54%) had hemispheric lesions. Medulloblastomas comprised 5 (6%) of cerebellar hemispheric tumors (the major tumors included in Table). Of these 5 medulloblastomas, 2 were mostly solid (>80%) and 3 were mixed solid and cystic. All medulloblastomas demonstrated heterogeneous enhancement. Hydrocephalus was found in 2 cases, and 4 had moderate to severe vasogenic edema. Patients with medulloblastoma were younger (33.3±11.0) compared to the rest of patients with hemispheric cerebellar tumor (48.1±20.1, p=0.039). Also, 3/5 medulloblastomas involved cerebellar peduncle compared to 13/80 of other tumors (p=0.044). The only independent predictor of medulloblastoma, among ADC histogram analysis variables, was the voxel kurtosis. The ADC kurtosis>3 and age range of 20-50 years could identify cerebellar hemispheric medulloblastomas with 80% sensitivity, 98% specificity, 67% PPV, and 99% NPP (are under ROC curve of 0.888, p=0.004).

Conclusions

The quantitative ADC histogram analysis and clinical features can help with identification of cerebellar hemispheric medulloblastomas. Specifically, we have shown that "a combination of kurtosis>3 in voxel-based ADC histogram analysis and an age range of 20-50 years" can differentiate medulloblastomas from other cerebellar hemispheric tumors with ~89% accuracy. The leptokurtic (kurtosis>3) distribution of ADC voxel values may represent homogenous and densely cellular characteristics of medulloblastomas.

Cerebellar hemispheric tumor subtypes (n=85)	
Metastasis	34 (40%)
Hemangioblastoma	21 (25%)
Pilocytic Astrocytoma	9 (11%)
Lymphoma	6 (7%)
Medulloblastoma	5 (6%)

(Filename: TCT_O-316_hemisph.jpg)

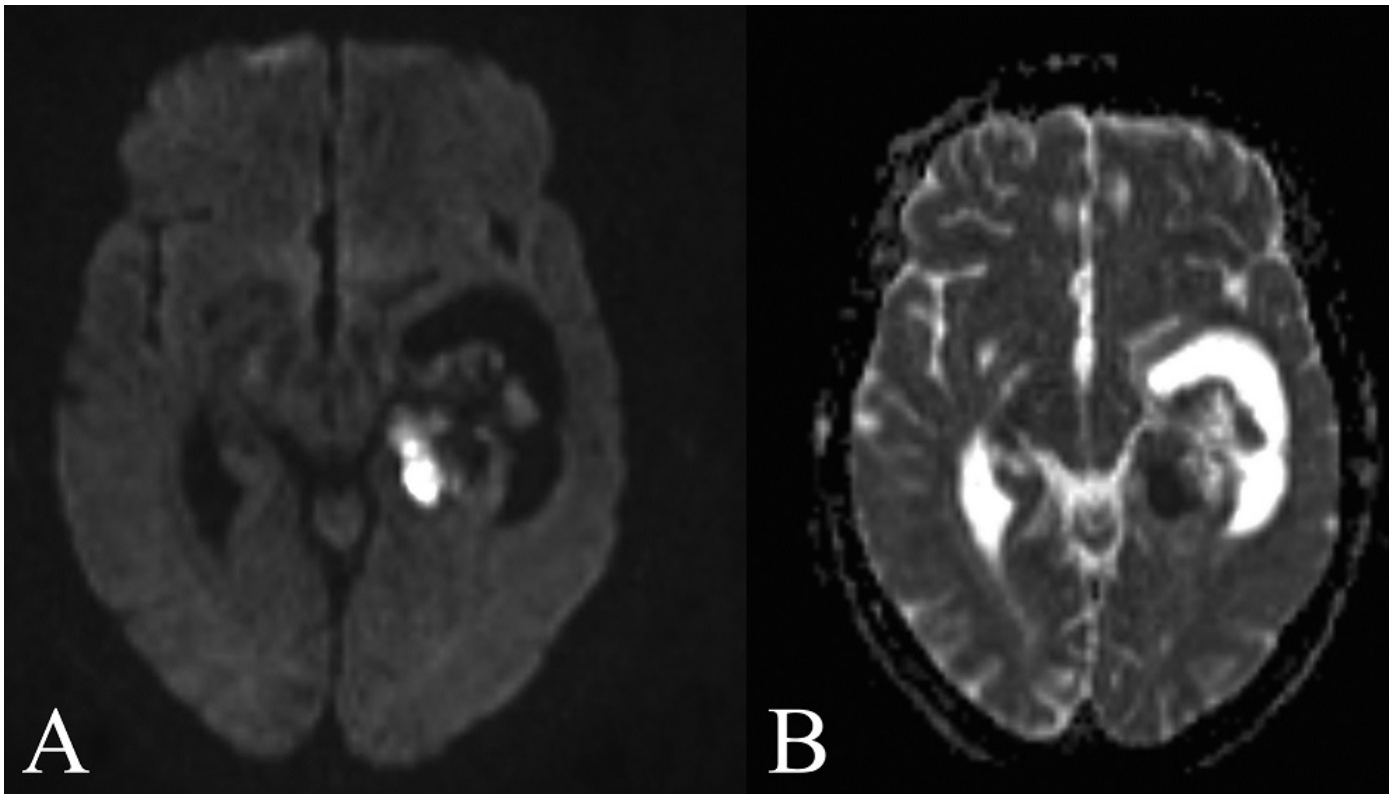
O-317

4:02PM - 4:10PM

Ischemic stroke and intracranial hemorrhage in glioblastoma multiforme patients treated with bevacizumab

Y Tanyildizi[1], T Auer[1], F Marini[1], M Renovanz[1], M Brockmann[1]
[1]*University Medical Center Mainz, Mainz, Germany*

Purpose
Bevacizumab (BVZ), a monoclonal antibody directed against vascular endothelial growth factor (VEGF), has been suspected to increase the incidence of ischemic stroke (IS) and intracranial hemorrhage (ICH) in GBM patients.
Materials and Methods
Vascular events, such as IS and ICH, were analyzed in 364 MRI scans of 82 GBM patients. Out of these 82 patients, 40 were treated with BVZ (178 scans) in addition to basic treatment, whereas 42 patients only received basic treatment (186 scans). Both groups were matched for age and gender. Distribution of typical vascular risk factors between both groups was analyzed retrospectively.
Results
In seven out of 82 patients (8%) vascular events were detected in MRI. Four vascular events were recorded in the BVZ-group (3 IS and 1 ICH), and 3 vascular events were found in the control group (1 IS and 2 ICH; $p>0.05$ between both groups). Likewise, vascular risk factors (arterial hypertension, diabetes mellitus, obesity, former vascular event, hyperlipidemia and/or hypercholesterolemia) did not differ significantly between both groups.
Conclusions
Bevacizumab treatment does not seem to be associated with an increased risk for vascular events in GBM patients.



(Filename: TCT_O-317_ASNR.jpg)

O-318

4:10PM - 4:18PM

Incidence of Dural Venous Sinus Thrombosis in Patients with Glioblastoma Multiforme

A Helmi[1], S Symons[2], P Maralani[2]
[1]University of Toronto, Toronto, Ontario, [2]Sunnybrook Health Sciences Centre, Toronto, Ontario

Purpose
Dural venous sinus thrombosis (DVST) is an uncommon disorder in the general population. More recent imaging studies estimate the incidence at 1.5 to 3 cases per million. A hypercoagulable state, and effects of antineoplastic treatment are potential contributors to increased risk of development of DVST in cancer patients. High-grade gliomas in particular, are associated strongly with thrombotic complications. Intensive screening for venous thrombi often does not improve survival and generally is unwarranted. This is especially true in patients with glioblastoma multiforme (GBM) who generally have poor prognoses and short life expectancies. Clinical diagnoses of DVST often are not made as symptoms are more readily attributed to the cerebral effect of neoplastic disease. In this study, we investigate the incidence of DVST in patients with GBM.

Materials and Methods
Inclusion criteria: 1. Adults (>18 year old) who received radiation for GBM at Sunnybrook hospital in the last 10 years. Exclusion criteria: 1. Prior brain surgery or radiation 2. Other brain tumors. All MRI imaging following diagnosis was studied to detect DVST and measure its incidence in patients with GBM.
Results
Preliminary data collected up to this point includes an examination of all postdiagnosis brain MRI images of 120 gbm patients. Dural venous sinus thrombosis was detected in 5% of the cases examined thus far. This figure is significantly higher than the estimated incidence of 1.5-3 per million in the general population.
Conclusions
Preliminary results suggest a considerable increase in the incidence of DVST in patients with GBM. This is in accordance with the expectation that the hypercoagulable state of cancer patients puts them at increased risk of developing thromboses. The results of this study can help direct future research and guide potential modifications to clinical guidelines with respect to the potential role for the use of thromboprophylactic therapy in this patient group.

O-319

4:18PM - 4:26PM

Radiation Dose at Site of Subventricular Recurrence Predicts Glioblastoma Survival

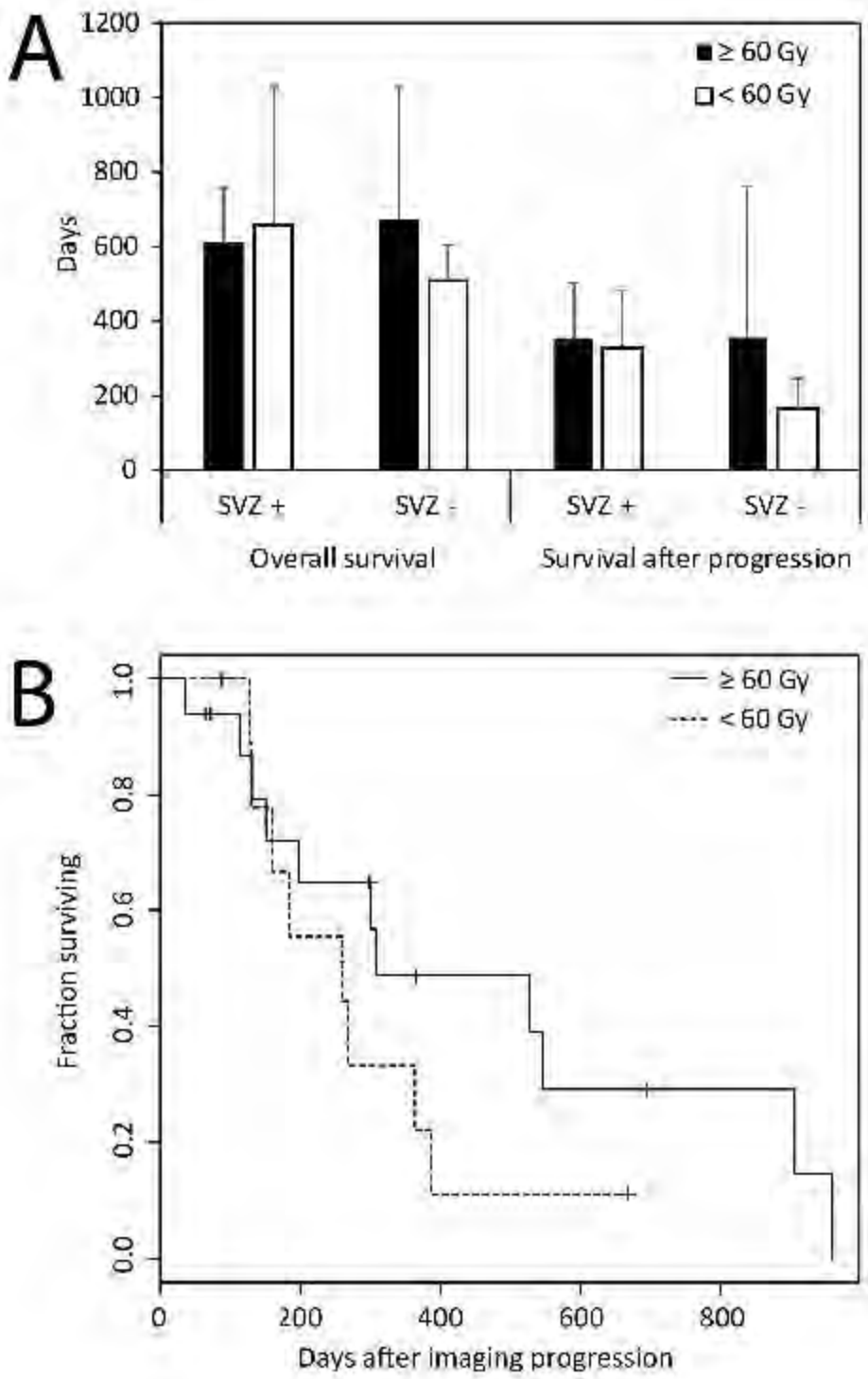
B Weinberg[1], L Boreta[2], S Braunstein[2], S Cha[2]
[1]Emory University Hospital, Atlanta, GA, [2]University of California San Francisco, San Francisco, CA

Purpose
Glioblastomas are the most common and most aggressive primary malignant brain tumor that frequently recur in the subventricular zone (SVZ) despite maximal treatment. The purpose of this study was to evaluate varying imaging patterns of progression and clinical outcome impacted by initial or recurrent SVZ tumor involvement and radiation dose to sites of SVZ recurrence.
Materials and Methods
Review of 50 consecutive patients with irradiated glioblastoma at a single institution from January 2012-June 2013 was performed. Tumors were classified based on location, size, and cortical and SVZ involvement. Progression-free survival, survival after progression, and overall survival were compared based on recurrence type, distance from the initial tumor bed (local ≤ 2 cm, distant > 2 cm), and the radiation dose at the site of recurrence as determined from dosimetry data.
Results
Average progression-free survival was 7.5±2.2 months and overall survival was 18.9±3.1 months. There was no difference in survival measures based on initial tumor involvement of

the SVZ or cortex. Thirty of 45 (67%) patients had disease progression at a local subventricular site where the average radiation dose was 57.6±3.5 Gy, while 19/45 (42%) patients had progression at a distant SVZ which had an average dose of 44.7±7.4 Gy. Patients with distant SVZ progression at a site which received a dose < 45 Gy had worse subsequent survival (Fig. 1).

Conclusions

Glioblastomas frequently recur at SVZ, both local to the initial tumor site and at distant locations. Patient survival is worse when enhancing tumor occurs at sites that received lower radiation doses, which may represent multifocal disease that was undertreated at the time of diagnosis. Further study is needed to determine if altered radiation treatment volumes including the SVZ or other alternative treatment strategies that could help mitigate this risk to improve clinical outcome.



(A) Mean survival after diagnosis and survival after imaging progression (+/- 95% confidence interval) for patients who had distant subventricular recurrence of enhancing disease. (B) Survival plot for patients who had recurrent enhancing disease in a subventricular region that initially received ≥ 45 Gy or < 45 Gy. Plus signs denote censored patients. P = 0.05 for comparison between survival curves.

(Filename: TCT_O-319_ASNRfigure.jpg)

O-320

4:26PM - 4:34PM

Cytoreduction following proton beam radiotherapy for partially resected and unresected oligodendroglioma and oligoastrocytoma.

K Sargar[1], J Vu[1], C Tsien[1], J Huang[1], C Robinson[1], A Salter[1], T Benzinger[2], M Miller-Thomas[3]
[1]Washington University in St. Louis, St. Louis, MO, [2]Washington University in St. Louis, Saint Louis, MO, [3]Mallinckrodt Institute of Radiology, St. Louis, MO

Purpose
To assess the impact of proton beam therapy on the tumor size in patients with partially resected and unresected oligodendrogliomas and oligoastrocytomas treated with combination of proton beam radiotherapy and chemotherapy.
Materials and Methods
Proton beam therapy is becoming widely implemented for the treatment of gliomas. This retrospective study included 7 patients with oligodendroglioma (5 WHO grade III and 2 WHO grade II) and 7 patients with oligoastrocytomas (5 WHO Grade III and 2 WHO Grade II) with either partial resection (11/14) or biopsy only (3/14) who underwent combination of proton therapy and chemotherapy. These patients had baseline MR imaging prior to the combination therapy and subsequent MR imaging every 2 to 4 months after the therapy. Imaging assessment and volumetric measurement of the tumor was performed by consensus of 2 radiologists.
Results
Median follow-up period was 24.6 months (range=12.1 - 31.5 months). Median clinical target volume was 169.5 cc (range, 14.6–918.9 cc). Six of 14 showed no tumor progression, 6/14 developed radiation necrosis without tumor progression and 2/14 developed progressive disease/recurrence. Thirteen of 14 patients showed cytoreduction on follow-up imaging with median reduction in volume measuring 57% (range=3.1-100%). One of 14 showed increase in tumor volume by 16%. In the patients with radiation necrosis or tumor progression, final volumetric measurement was done on the MR study prior to development of radiation necrosis or tumor progression. On the first follow-up MR study after completion of therapy 11 patients showed reduction tumor volume with median reduction in volume measuring 37% (range= 3-78%), and 3 patients showed increase in volume by 12,30 and 50% respectively. Radiation necrosis was observed on median follow-up period of 9 months (range=4.8-13.8 months).
Conclusions
In patients with partially resected or nonresected oligodendrogliomas and oligoastrocytomas

(grade II and III) treated with combination of proton therapy and chemotherapy, majority of the patients showed rapid reduction in tumor size.

Patient	Pathology	Intervention prior to treatment	Baseline volume prior to treatment (cc)	Tumor volume on first follow up study (cc)	Tumor volume of last follow up study (cc)	Volume reduction on first follow up study (%)	Volume reduction on last follow up study (%)
1	Oligoastrocytoma	subtotal resection	205.7239	173.8551382	89.2516755	15.5	57
2	Oligoastrocytoma	subtotal resection	56.97462	29.4052824	18.93700187	48	67
3	Oligodendroglioma	subtotal resection	105.315	101.8754805	102.0607087	3	3.1
4	Oligodendroglioma	subtotal resection	94.11641	42.78828825	25.93897766	55	72.5
5	Oligodendroglioma	subtotal resection	14.65238	3.284008747	Non-measurable	78	100
6	Oligoastrocytoma	subtotal resection	224.0174	140.2204714	127.721132	37.5	43
7	Oligodendroglioma	subtotal resection	106.8769	139.8080854	124.7326338	+30	+16
8	Oligoastrocytoma	subtotal resection	918.9694	704.2188898	704.2188898	23	23
9	Oligodendroglioma	subtotal resection	271.8688	143.0078576	99.8863514	47	63
10	Oligoastrocytoma	Biopsy only	477.7582	537.7276134	50.1308124	+12	90
11	Oligodendroglioma	Biopsy only	349.5347	221.914805	161.7727004	37	54
12	Oligoastrocytoma	subtotal resection	16.92209	25.41787584	Non-measurable	+50	100
13	Oligoastrocytoma	subtotal resection	134.0978	124.1357401	116.5428856	7.5	13
14	Oligodendroglioma	Biopsy only	468.55	400.4415965	318.2533714	15	32

+ indicates increase in tumor volume from baseline.

(Filename: TCT_O-320_Table.jpg)

O-321

4:34PM - 4:42PM

Impact of Needle Parameters on the Measurement of Opening Pressure with Lumbar Puncture

Dubé, J.
Université de Montréal
Montréal, Québec

O-322

4:42PM - 4:50PM

Intradural Extramedullary Cavernous Malformation with Extensive Superficial Siderosis of the Neuraxis: Case Report and Review of Literature

P Golnari[1], S Ansari[2], A Shaibani[3], M Hurley[1], M Potts[2], M Kohler[4], P Sugrue[5], B Jahromi[2]
[1]Northwestern University Feinberg School of Medicine, Chicago, IL, [2]Northwestern University, Feinberg School of Medicine, Chicago, IL, [3]Northwestern University Feinberg School of Medicine, Chicago, IL, [4]Northwestern Memorial Hospital, Chicago, IL, [5]Advocate Good Samaritan Hospital, Downers Grove, IL

Purpose
Spinal cavernous malformations usually affect the vertebral bodies; they are seldom intradural and even less frequently extramedullary. While the latter primarily present with radicular symptoms, we report a rare case of a spinal intradural-extramedullary cavernous malformation presenting with extensive superficial siderosis along the neuraxis.
Materials and Methods
Case Report: A 60-year-old male presented with a 1-2 week history of left-sided lumbar back pain radiating into the buttocks and the posterior aspect of the left leg, preceded by a gradual-onset of diffuse headaches and intermittent fever over several months. Apart from radicular signs, his neurological examination was normal. Laboratory findings were unremarkable. Imaging revealed an intradural-extramedullary lesion just below the conus medullaris. His symptoms resolved after surgical resection. Histopathology confirmed a diagnosis of cavernous malformation.
Results
Imaging Findings: Magnetic resonance imaging (MRI) of the spine revealed a 1.8 x 1.3 x 1.1 cm intradural-extramedullary hemorrhagic lesion below the conus medullaris (at the L2 level), along with moderate subarachnoid hemorrhage (SAH) in the lumbar cistern and superficial siderosis along the conus. Along with history of headaches and fever, these findings prompted an MRI of the brain and cervical/thoracic spine, which identified diffuse superficial siderosis across the neuraxis, consistent with repeat hemorrhagic episodes.
Conclusions
Summary: We summarize the presentation, treatment and results of all cases of spinal intradural-extramedullary cavernous malformations published to date. There have been 56 cases (including the present) of which only 2 were reported previously to present with superficial siderosis. We describe the third such case, unique in the degree of extensive and diffuse superficial siderosis documented across the neuraxis. We hypothesize that the slowly recurring hemorrhages seen with these lesions, along with their location within the spinal subarachnoid space, contributes to development of superficial siderosis remote from the

primary lesion. We recommend consideration of this entity during evaluation and imaging of patients with superficial siderosis.

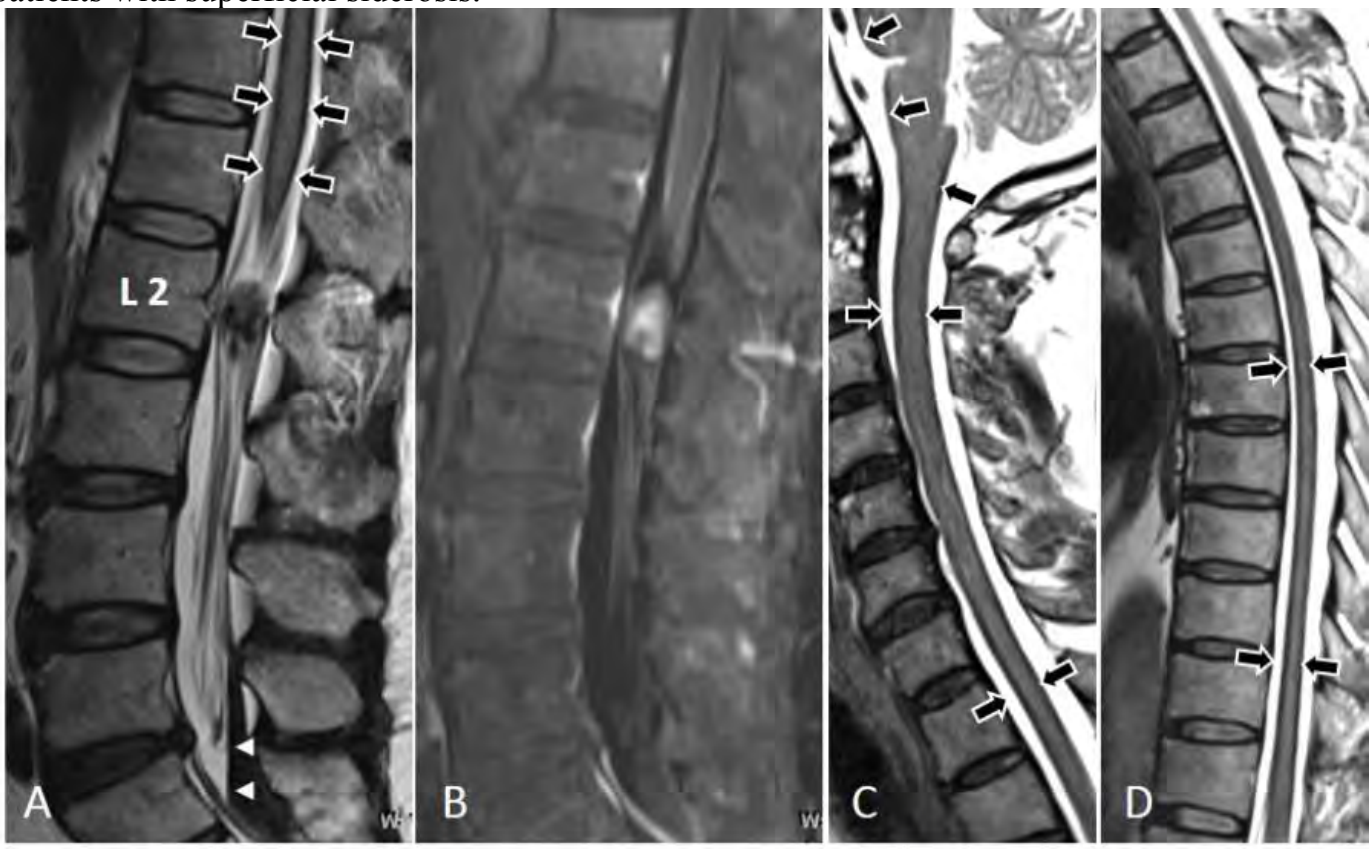


Figure 1: Sagittal T2-weighted (A), fat-suppressed gadolinium-enhanced T1-weighted (B), and T2 short tau inversion recovery turbo-spin echo MRI images show an intradural extramedullary lesion at L2. Hemosiderin deposition is seen along the conus (arrows), and fluid-subarachnoid blood level is layered in the lumbar cistern (arrowheads). Cervical (C) and thoracic (D) T2-weighted sagittal MRI images show superficial siderosis (arrows) across the cervical and thoracic spinal cord.

(Filename: TCT_O-322_Graph1.jpg)

O-465

4:50PM - 4:58PM

Efficacy of Combination Antiretroviral Therapy and CNS Penetration Efficacy Index in Preventing and Assessing Progressive Neurodegeneration in Chronic HIV Infection

J Boban[1], S Brkic[1], R Semnic[1], D Lendak[1], J Ostojic[2], M Bjelan[1], A Todorovic[1], D Kozic[1]
[1]Faculty of Medicine, University of Novi Sad, Novi Sad, Vojvodina, [2]Clinical Center of Vojvodina, Novi Sad, Vojvodina

Purpose
Although highly efficient in peripheral control of the disease, combination antiretroviral

therapy (cART) failed to reduce high prevalence of mild forms of HIV-associated neurocognitive disorder (HAND). The aim of this study was to test the effect of cART on brain metabolites' ratios in chronic HIV infection using 2D multivoxel magnetic resonance spectroscopy (mvMRS).
Materials and Methods
We performed 2D mvMRS study in 50 neuroasymptomatic chronically HIV-infected subjects [31 patients on cART (28 men and 3 women) and 19 cART-naïve (17 men and 2 women)], covering frontal and parietal subcortical white and cingular gray matter, analyzing ratios of NAA/Cr and Cho/Cr on long echo and mIns/Cr on short echo time MRS (differences were analyzed using independent t-test). Using Spearman's correlation test, we tested correlations of obtained MRS parameters with data on cART efficacy, expressed as central nervous system penetration efficacy (CPE) scores.
Results
Groups were age ($p=0.082$), gender ($p=0.687$) and education-matched ($p=0.082$). There were no significant differences in MRS parameters between 2 groups of chronically infected HIV+ patients. HIV+ patients were receiving cART for mean of 5.1 years (1-11), with mean CPE score 8.26±0.89 (6-10). Groups of HIV+ patients did not differ significantly considering self-reported infection duration ($p=0.891$). Central nervous system penetration efficacy scores showed no significant corrrelations with NAA/Cr and mIns/Cr ratios, and some weak positive correlations with Cho/Cr ratios in some observed locations (anterior cingulate gyrus on the right and deep frontal white matter on the left).
Conclusions
Continuous process of neuronal loss and dysfunction in chronic HIV infection remains grossly undisturbed by cART, which failed to confirm its role in preventing neurodegeneration. The use of CPE index in estimating the efficacy of cART in the brain does not adequately reflect changes in neurobiochemistry in observed regions, except the process of disturbed cell membrane metabolism expressed through Cho/Cr ratio.

Region of the brain	Metabolite ratio	HIV+ on therapy vs. HIV+ therapy naïve (p)	Correlations with CPE ρ (p)
Frontal SWM (right)	NAA/Cr	0.989	-0.208 (0.260)
	Cho/Cr	0.927	0.037 (0.845)
	mI/Cr	0.959	-0.019 (0.921)
Ventral ACG (right)	NAA/Cr	0.501	-0.208 (0.260)
	Cho/Cr	0.102	**0.494 (0.005)**
	mI/Cr	0.534	0.150 (0.420)
Ventral ACG (left)	NAA/Cr	0.930	-0.156 (0.402)
	Cho/Cr	0.986	-0.084 (0.652)
	mI/Cr	0.240	-0.197 (0.289)
Frontal SWM (left)	NAA/Cr	0.443	-0.009 (0.962)
	Cho/Cr	0.721	0.209 (0.260)
	mI/Cr	0.470	0.096 (0.609)
Frontal deep WM (right)	NAA/Cr	0.219	0.084 (0.653)
	Cho/Cr	0.575	0.230 (0.213)
	mI/Cr	0.965	-0.079 (0.672)
Dorsal ACG (right)	NAA/Cr	0.329	0.181 (0.329)
	Cho/Cr	0.500	**0.557 (0.001)**
	mI/Cr	0.863	0.046 (0.805)
Dorsal ACG (left)	NAA/Cr	0.929	-0.086 (0.644)
	Cho/Cr	0.780	0.259 (0.159)
	mI/Cr	0.069	-0.024 (0.897)
Frontal deep WM (left)	NAA/Cr	0.751	-0.056 (0.763)
	Cho/Cr	0.347	**0.386 (0.032)**
	mI/Cr	0.344	0.187 (0.313)
Parietal SWM (right)	NAA/Cr	0.996	-0.194 (0.296)
	Cho/Cr	0.992	-0.176 (0.342)
	mI/Cr	0.993	0.097 (0.604)
PCG (right)	NAA/Cr	0.564	-0.138 (0.459)
	Cho/Cr	0.134	0.202 (0.277)
	mI/Cr	0.751	0.230 (0.214)
PCG (left)	NAA/Cr	0.948	0.023 (0.902)
	Cho/Cr	0.628	0.129 (0.487)
	mI/Cr	0.506	-0.187 (0.314)
Parietal SWM (left)	NAA/Cr	0.654	-0.030 (0.871)
	Cho/Cr	0.923	0.255 (0.167)
	mI/Cr	0.661	0.189 (0.309)

SWM= subcortical white matter, ACG= anterior cingulate gyrus, PCG= posterior cingulate gyrus, WM= white matter

(Filename: TCT_O-465_Tabela1ASNR.jpg)

Wednesday
5:00PM - 6:30PM
Long Beach Convention Center, Room 103 (Main Level)

21C-Parallel Paper Session: Cancer of the Head and Neck: Reality Check - from the Rare to the Response

O-323

5:00PM - 5:08PM

Extracranial Esthesioneuroblastoma: Imaging Spectrum.

M Peckham[1], R Wiggins[2], R Orlandi[1], H Harnsberger[1]
[1]University of Utah, Salt Lake City, UT, [2]University Of Utah, Salt Lake City, UT

Purpose
Esthesioneuroblastoma (ENB) is a neuroectodermal tumor arising in the olfactory recess known for its intracranial extension through the skull base. Small ENBs isolated to the nasal cavity can have smooth margins, making them indistinguishable from benign polyps. Location is a differentiating finding in ENB which has a high propensity for originating in the olfactory recess. Though ENB is uncommon compared to other intranasal lesions (3-5%), its propensity for local spread and potential for metastases make it important to exclude prior to polypectomy. Cases of extracranial ENB were collected to evaluate imaging characteristics on CT and MRI.
Materials and Methods
Cases of ENB evaluated in our tertiary hospital from 2007-2016 were obtained using a report search tool. Only cases with histologic confirmation were included. Studies demonstrating skull base involvement or intracranial extension were excluded.
Results
Eight histologically proven cases of intranasal and extracranial ENB were identified and reviewed. All cases had CT imaging demonstrating an intranasal polypoid lesion directly contacting and widening the olfactory recess with osseous remodeling (Fig. 1). Seven of 8 cases included coronal imaging and all tumors extended to the cribriform plate. Five cases showed tumor extension into the paranasal sinuses, confirmed histologically. Five cases included pre-operative MRI with the lesions T2 isointense to gray matter and diffusely enhancing to a lesser degree than the surrounding nasal mucosa. Three cases had DWI which demonstrated mild restriction within the mass. Three patients required additional surgery for skull base resection after ENB was found incidentally during routine nasal polypectomy. Five patients had presurgical biopsies prior to resection.
Conclusions
Esthesioneuroblastoma can present as a well marginated polypoid lesion isolated to the nasal

cavity which contacts and widens the olfactory recess on CT imaging. This diagnosis should be mentioned in the differential for a solitary polyp enlarging the olfactory recess to elicit pre-operative biopsy and avoid routine surgery for polypectomy.

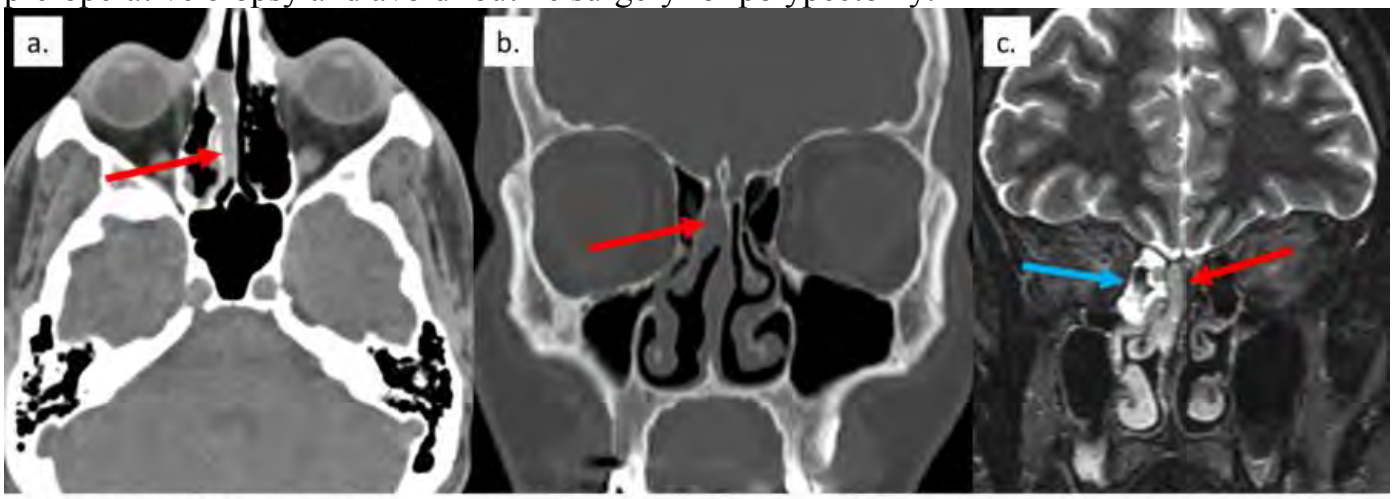


Figure 1: Axial (a) and coronal (b) CT sinus images demonstrate a lesion which opacifies and widens the olfactory recess and contacts the cribriform plate (red arrows). Coronal MRI (c) demonstrates isointensity of this lesion with gray matter (red arrow), differentiating it from adjacent inflammatory sinus disease (blue arrow).

(Filename: TCT_O-323_ENBfigureupdatedcopy.jpg)

O-324

5:08PM - 5:16PM

Unique Trilateral Spread Pattern of Squamous Cell Carcinoma Arising from Inverted Papilloma from the Nasopharynx to the Bilateral Mastoids via Eustachian Tubes

X Wu[1], I El-Sayed[2], C Glastonbury[1]
[1]University Of California, San Francisco, San Francisco, CA, [2]University of California San Francisco, San Francisco, CA

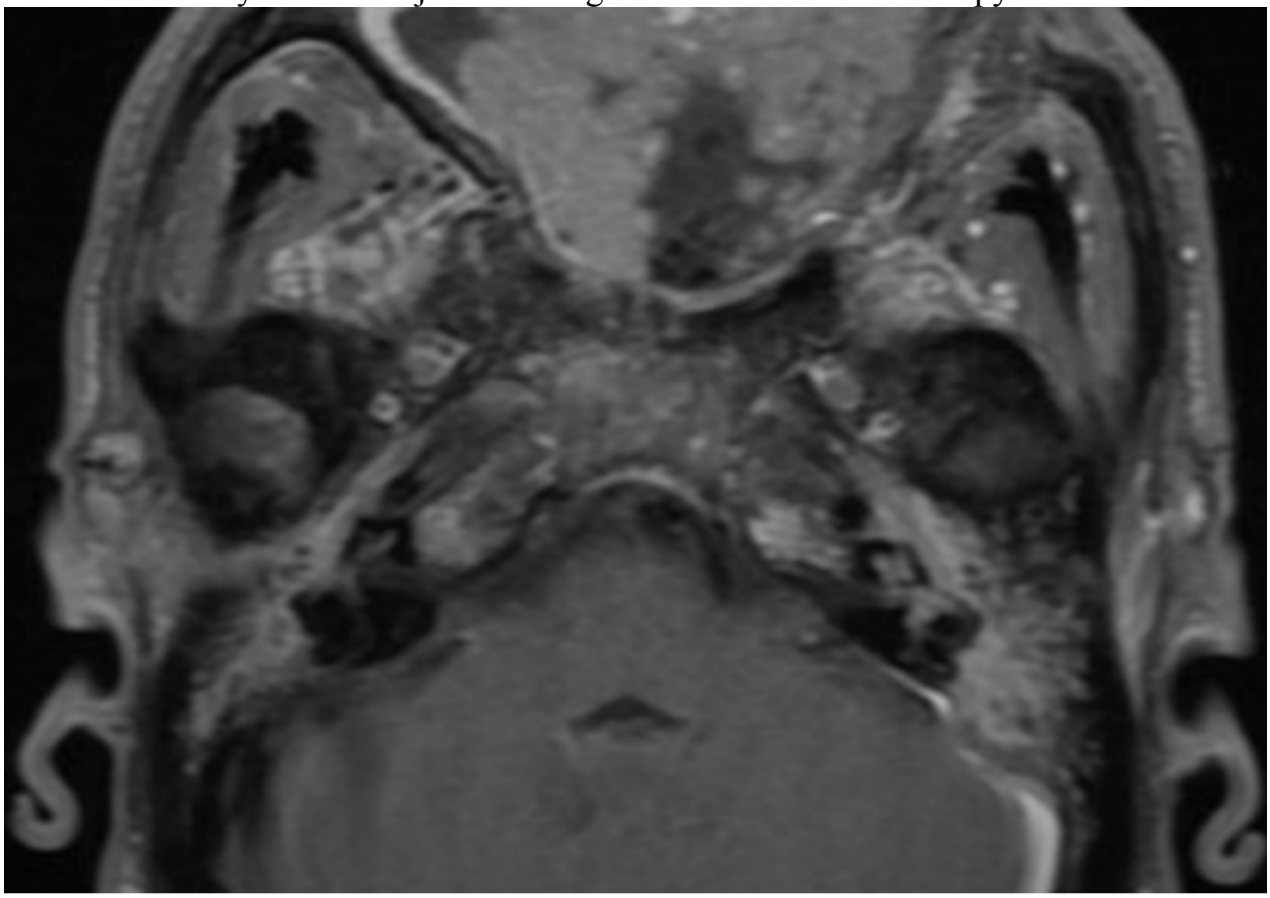
Purpose
Inverted (Inverting, Schneiderian) papilloma (IP) is an uncommon, benign, locally destructive sinonasal epithelial tumor. Squamous cell carcinoma (SCC) is estimated to arise from IP in approximately 10% of cases. There have been limited reports of middle ear or mastoid spread of benign IP, via the Eustachian tube (1), but none of SCC arising from IP spreading along this route. We present 3 cases of this unique route of tumor spread.
Materials and Methods
A HIPPA compliant retrospective search was conducted through the institutional teaching files, identifying pathologically proven head and neck squamous cell carcinoma cases with imaging findings of tumor involvement of the mastoids as well as the sinonasal tract or nasopharynx. These cases were reviewed and their clinical and imaging findings synthesized.

Results

Three male patients are presented. Patient #1 had a history of previously resected IP containing high-grade dysplasia and subsequent development of an aggressive sinonasal SCC that extended into the nasopharynx. A year after this tumor was resected, the patient presented with bilateral mastoid masses, pathologically proven to be SCC. Patient #2 had a history of prior mass removal from the nasal cavity, and presented with bilateral destructive mastoid masses. Pathology demonstrated SCC with morphology suggestive of tumor arising from IP. Patient #3 had a history of prior IP resection and developed a nasal cavity mass with bilateral invasive mastoid masses and eventual intracranial extension, resulting in venous sinus thrombosis and intracranial hemorrhage.

Conclusions

Similar to IP, invasive SCC arising from IP can spread from the nasopharynx along the Eustachian tubes to involve the bilateral tympanic cavities and mastoids, with potentially devastating intracranial involvement. Attention should be paid to these areas, in particular to distinguish by imaging obstructed secretions from tumor extension. Temporal bone involvement may warrant adjunctive surgical and/or radiation therapy.



(Filename: TCT_O-324_Abstract.gif)

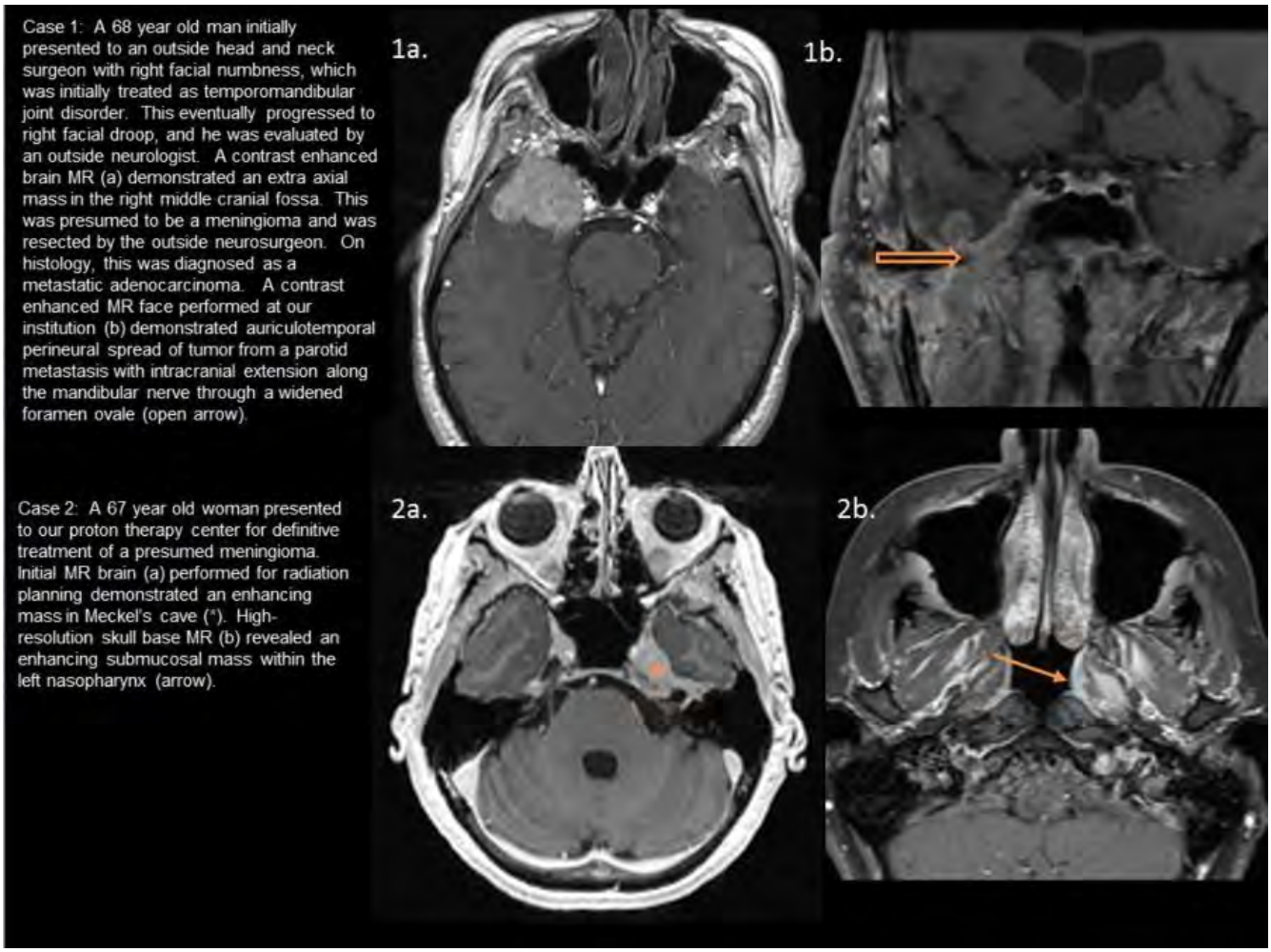
O-325

5:16PM - 5:24PM

Perineural Tumor Spread Mimicking Benign Disease: Contribution of Radiology to Diagnosis versus Misdiagnosis

M Chen[1], P Gidley[1], L Ginsberg[1], S Ahmed[1]
[1]*UT MD Anderson Cancer Center, Houston, TX*

Purpose
Definitive treatment of benign intracranial neoplasms, such as schwannomas and meningiomas, often is based on imaging alone, without histologic confirmation. Radiologic erroneous interpretation of intracranial perineural tumor spread as a benign neoplasm can have devastating consequences. The purpose of this exhibit is to review imaging findings of histologically verified malignant intracranial perineural tumor spread originally misdiagnosed as benign neoplasms.
Materials and Methods
We present a case-based review of 6 malignant intracranial lesions initially diagnosed as benign neoplasm, such as schwannoma or meningioma. Based on an initial benign imaging diagnosis, these patients were referred either directly for proton therapy or for additional therapy after having received surgery or radiation therapy elsewhere. We review the cranial nerve pathways and common routes of intracranial spread of malignant head and neck tumors, such as adenoid cystic carcinoma, nasopharyngeal carcinoma, squamous cell carcinoma and metastases. The treatment of these tumors is discussed.
Results
Cases include: auriculotemporal perineural tumor spread of parotid metastases to Meckel's cave treated as a meningioma; nasopharyngeal adenoid cystic carcinoma spreading to the cavernous sinus and referred for proton therapy of presumed meningioma; and cutaneous squamous cell carcinoma spreading along the ophthalmic segment of the trigeminal nerve resected with presumed diagnosis of schwannoma. Emphasis is placed on examining the entire course of a cranial nerve to arrive at a correct diagnosis. For each case, the factors leading to misdiagnosis are discussed, as well as clues to the correct diagnosis.
Conclusions
Intracranial perineural spread of malignancy can mimic benign conditions, when only the intracranial component is considered. Clinical history can contribute to a more accurate diagnosis. Examining the entire cranial nerve pathway can identify subtle mucosal and submucosal masses critical in making an accurate diagnosis. Radiologists must consider the entire nerve pathway and entertain the possibility of more sinister processes to ensure proper diagnosis and treatment.



(Filename: TCT_O-325_perineuralbenignmimicfinal.JPG)

O-326

5:24PM - 5:32PM

Accuracy of computed tomography (CT) and magnetic resonance imaging (MRI) in determining depth of invasion for squamous cell carcinoma of the oral tongue

J Go[1], G Low[1], C Cheng[1], A Correa[1], U Sinha[1], N Kokot[1]
[1]*University of Southern California, Los Angeles, CA*

Purpose
Depth of invasion (DOI) of squamous cell carcinoma (SCC) of the oral tongue has been shown in literature to correlate with prevalence of nodal metastases. The gold standard for determining DOI is through pathological section. Our objective is to analyze DOI using imaging (CT/MRI) to determine its correlation with DOI on pathology and its usefulness for surgical planning.

Materials and Methods
We retrospectively reviewed T1 and T2 patients undergoing total or partial glossectomy for SCC of the tongue between 2012 to 2015 at a large tertiary care center. All patients had their pre-operative imaging (CT/MRI) reviewed by a senior neuroradiologist with 20 years of head and neck imaging expertise. Depth of invasion was measured as the distance from the mucosal junction line to the deepest margin of the tumor best demonstrated on axial, sagittal, or coronal plane measured radially from the mucosal surface to the deepest depth within the oral tongue.
Results
Forty-two patients with T1 or T2 staging of oral tongue cancer utilizing AJCC criteria based on pre-operative imaging were identified with SCC of the tongue. Of these patients 17 were excluded due to film quality which did not allow for accurate identification of the DOI. Ten patients had MRI imaging pre-operatively and 15 had CT imaging. Magnetic resonance imaging (MRI) was performed including T1- and T2-weighted axial images, T1- and STIR coronal images and postcontrast images with fat saturation in all 3 orthogonal planes with fat saturation were performed. Computed tomography (CT) imaging utilizing a multi-slice CT with 64 or 128 channel scanner was performed with volumetric acquisition and reconstruction to 3mm in all 3 orthogonal planes with contrast administration.The gross and histological pathology were reviewed by a dedicated head and neck pathologist who determined depth of invasion. Linear regression comparing MRI to pathology showed a strong linear correlation that was statistically significant (r =0.798, r 2 = 0.637, p = 0.006). Linear regression comparing CT and pathology showed a moderate linear association that was not statistically significant. (r =0.418, r 2 = 0.175, p = 0.137).
Conclusions
Depth of invasion of SCC of the oral tongue on MRI is highly correlated to the DOI as measured on final pathology. Magnetic resonance imaging is a useful tool for pre-operative surgical planning in patients with SCC of the oral tongue.

O-327

5:32PM - 5:40PM

Calcified Lymph Nodes in Head and Neck Cancer: Predictor of HPV Positivity?

P Shah[1], A Karagianis[2], M Lester[1], R Loomba[3], A Paintal[1], E McComb[4]
[1]Northwestern University, Chicago, IL, [2]Northwestern University, Feinberg School of Medicine, Chicago, IL, [3]Medical College of Wisconsin, Milwaukee, WI, [4]Northwestern memorial hospital, Chicago, IL

Purpose
Human papilloma virus (HPV) positive head and neck squamous cell carcinoma (HNSCC) has been increasing in incidence, despite an overall decline in the incidence of HNSCC. With increasing incidence of HPV-positive HNSCC, efforts have been made to characterize

the distinct imaging features of HPV-positive squamous cell carcinoma. Studies have shown that cystic lymph nodes are strongly associated with HPV-positive HNSCC. Other features have yet to be identified. At our institution, we found several unusual cases of calcified lymph nodes, all of which were HPV positive HNSCC. Nodal calcifications in the neck are infrequent with only a few isolated cases reported in the setting of metastatic HSNCC. With the growing incidence of HPV-positive HNSCC and increasing frequency of nodal calcifications at our institution, a possible association remains to be established. This association could help further radiologic distinction between HPV-positive and negative HNSCC through imaging and thereby help guide management.

Materials and Methods

Patients with history of HNSCC who underwent a CT scan of the neck between January 2013 and August 2016 were identified retrospectively. Demographic data, clinical data, and radiologic data for these patients were collected. Radiologic data included site of the primary tumor and presence of calcified, cystic, and/or necrotic lymph node metastases. As per the study by Goldenberg et al in 2008, cystic lymph nodes are differentiated from necrotic lymph nodes by the presence of a thin wall, homogeneous fluid content, and absence of internal complexity. Clinical data included P16 expression within the nodal metastases/primary tumor as a marker of HPV-positivity. Patients without P16/HPV data were excluded from the final analysis. Univariate analysis was conducted to determine characteristics that differed between those that had tumors that were HPV-positive and negative. A composite score using the odds ratio was derived including characteristics that had a p-value of less than 0.1 in the univariate analysis. A receiver operator curve analysis then was used to determine the sensitivity and specificity of the composite score in predicting HPV-positivity.

Results

Data for a total of 439 patients were reviewed, of which 155 patients were included in the final analysis after exclusion criteria. Of these, 93 (60%) had HPV-positive tumors. Those with HPV-positivity were more likely to be male, have primary oropharyngeal tumors, and have cystic nodal metastases, and they were less likely to have necrotic nodal metastases by univariate analysis. Calcified nodal metastases were found in 5 cases, all of which were present in those having HPV-positive HNSCC. However, the p-value was only 0.063 due to limited statistical power. The median composite score was 1 in those with HPV-negative tumors versus 19 in those with HPV-positive tumors. A composite score of 15.5 was 84% percent sensitive and 74% specific in predicting HPV-positivity.

Conclusions

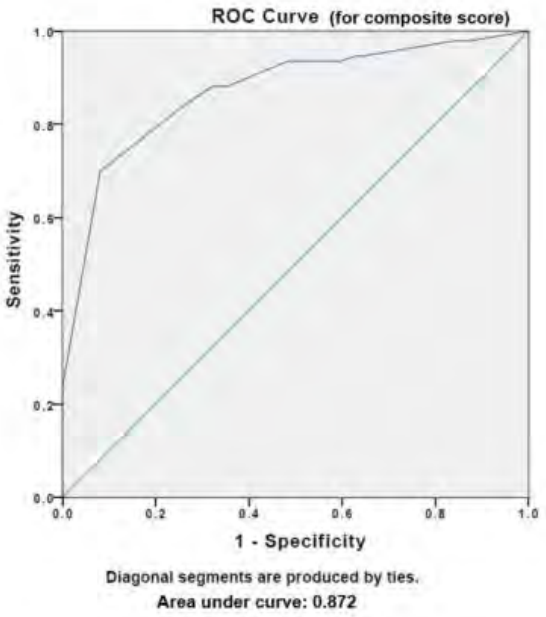
The presence of calcified and/or cystic nodal metastases, male gender, oropharyngeal primary tumor site, and absence of necrotic nodal metastases are helpful in predicting HPV-positive HNSCC. A composite score of these factors may be clinically useful in predicting HPV-positivity.

	HPV/P16 negative (n=62)	HPV/P16 positive (n=93)	Odds ratio (95% Confidence interval)	p-value
Age (years)	61.8 ± 11.4	59.8 ± 9.5	--	0.232
Male	46 (74%)	86 (93%)	4.273 (1.640 to 11.134)	0.002
Race			--	0.146
Asian	1 (2%)	1 (1%)		
African American	11 (18%)	5 (5%)		
Pacific Islander	0 (0%)	1 (1%)		
Caucasian	34 (54%)	69 (74%)		
Other	16 (26%)	17 (19%)		
Primary tumor site				< 0.001
Oral cavity	23 (37%)	5 (5%)	0.096 (0.034 to 0.272)	
Oral tongue	3 (5%)	0 (0%)	--	
Oropharynx	21 (34%)	82 (88%)	14.554 (5.409 to 33.052)	
Hypopharynx	3 (5%)	0 (0%)	--	
Larynx	12 (19%)	6 (7%)	0.287 (0.102 to 0.813)	
Calcifications	0 (0%)	5 (5%)	3.466 (0.395 to 30.409)*	0.063
Cystic	1 (2%)	19 (20%)	15.662 (2.038 to 120.361)	0.001
Necrosis	22 (36%)	13 (14%)	0.295	0.002
Composite score	1 (-10 to 19)	19 (-10 to 38)	--	< 0.001

*odds ratio is null but the provided odds ratio is if 1 case of HPV/P16 negative squamous cell cancer with calcifications is assumed

**composite score= 4 * malrecode - 10 * oralcavityrecode + 15 * oropharynxrecode - 3 * larynxrecode + 3 * CalcsYN + 16*CysticYN - 3*NecrosisYN.





(Filename: TCT_O-327_ABSTRACTASNR.jpg)

O-328

5:40PM - 5:48PM

Head and Neck Squamous Cell Carcinoma: What Is the Necessary Extent of Anatomic Imaging in Patients Undergoing PET-MRI?

D Simpson[1], T Kennedy[1], J Coburn[1], G Avey[1]

[1]*University of Wisconsin, Madison, WI*

Purpose
Distant metastasis is an infrequent finding in head and neck squamous cell cancer (HNSCC), with lungs being the predominant site of metastatic disease. The site and frequency of distant metastases is of interest in developing PET/MRI protocols, as time spent imaging for distant metastasis could be utilized for improved local tumor characterization. The purpose of this retrospective cross-sectional study is to determine the necessary anatomic extent of imaging in a modern cohort of HNSCC patients.
Materials and Methods
This single institution retrospective review identified 2 cohorts of patients with squamous cell carcinoma of the oral cavity, oropharynx, hypopharynx, or larynx. One cohort underwent PET/CT between 6/1/2014 and 5/30/2015. A second cohort of patients was imaged with both PET/MRI and PET/CT from 10/15/2015 to 11/30/2016. The PET/CT report served as the gold standard for determination of distant metastatic disease. The presence of distant metastasis was correlated with pathology reports and subsequent imaging.
Results
A total of 224 patients met inclusion criteria, 215 from the PET/CT cohort, and 9 with both PET/CT and PET/MRI for HNSCC. The oropharynx was the predominant primary site, present in 110 patients (50%). There were 74 patients (33%) initially presenting with T4a disease. Nodal disease was advanced in this cohort, with 139 patients staged with either N2 or N3 nodal disease. There were 70 exams (31%) in which a pulmonary nodule was described in the PET/CT report, with 35 (16%) describing FDG avid nodules. There were 14 exams (6%) with distant metastatic disease. Six exams (3%) demonstrated subdiaphragmatic metastasis. No exams demonstrated isolated subdiaphragmatic metastasis.
Conclusions
Distant metastasis of HNSCC is uncommon, most frequently occurring in the thorax. Subdiaphragmatic metastasis is rare, with no exams in this study demonstrating isolated subdiaphragmatic metastasis. These results support routine anatomic imaging of the chest, but not necessarily the abdomen or pelvis in patients undergoing PET/MRI.

O-329

5:48PM - 5:56PM

Use of Likert scale for Qualitative PET Interpretation of Primary Head and Neck Tumor Response to Radiotherapy

H Tore[1], A Spano[1], S Khanipour Roshan[1], Z Cayci[1]
[1]*University of Minnesota, Minneapolis, MN*

Purpose

Radiation therapy is the treatment of choice in early stage or locally advanced head and neck cancer patients. Positron emission tomography (PET) is used to evaluate the response (1). Semiquantitative SUVmax measurement with PET/CT is the most commonly used method to assess response but it is limited by multiple factors (2, 3).The Deauville criteria is a likert scale used for qualitative assessment of response to treatment in Hodgkin lymphoma (4). Recent studies have shown that the Deauville criteria is an accurate predictor of regional control and remission of tumor and is more accurate than SUVmax in deciphering responders from nonresponders in metastatic cervical lymphadenopathy from primary head and neck tumors (5). The present study aims to apply the Deauville criteria for the assessment of primary tumor response and hypothesizes that the Deauville criteria is predictive of the outcome.

Materials and Methods

We retrospectively evaluated PET/CT studies of patients with HPV positive primary head and neck squamous cell carcinoma who underwent radiotherapy with or without chemotherapy. We evaluated the baseline PET/CT studies prior to radiotherapy, a PET/CT scan 8-12 weeks after radiotherapy, and the most recent PET/CT or CT study alone. FDG uptake of the primary site and ipsilateral lymphadenopathy were evaluated at each time point on a 5-point Likert scale as described before (Table 1) (5). Differences between groups were evaluated using Mann-Whitney U test. A P value < 0.01 was considered significant.

Results

A total of 30 patients met all the inclusion criteria. Baseline PET/CT demonstrated the primary lesion and the metastatic lymph node having either markedly or moderately higher FDG uptake compared to the liver. In the initial follow-up PET/CT after radiotherapy 50% of the primary lesions showed complete response, 27% showed probably complete and 20% showed probably postradiation inflammation. Only 1 primary lesion (3%) showed probably persistent tumor. Two (7%) of the lymph nodes had persistent tumor in the first follow-up PET/CT. One (4%) lymph node showed probably postradiation inflammation. Remaining 89% of the lymph nodes showed either complete or probably complete response. There was complete response in all primary lesions in the latest imaging study except for the one lesion which had shown probably persistent tumor in the initial follow-up PET/CT. Only 2 lymph nodes had persistent tumor in the last follow-up scan. There was statistically significant difference between the baseline scan score and the initial follow-up study for both the primary site ($P< 0.0001$) and the ipsilateral lymphadenopathy ($P< 0.0001$).

Conclusions

Visual evaluation of response to radiation therapy with PET/CT using Likert scale in patients with HPV positive head and neck tumors is a useful method to predict the outcome.

Deauville Score	FDG Uptake	Category
1	No uptake	Complete metabolic response
2	Uptake ≤ mediastinum	Probably complete response
3	Uptake ≤ mediastinum but ≤ liver	Probably post-radiation inflammation
4	Uptake moderately increased compared with the liver at any site	Probably persistent tumor
5	Uptake markedly increased compared with the liver at any site and/or new sites of disease	Persistent tumor

(Filename: TCT_O-329_tablelikert.jpg)

O-330

5:56PM - 6:04PM

Brain Pathology Initially Identified on Whole Body FDG PET-MRI

A Franceschi[1], R Matthews[2], L Bangiyev[2], A Chaudhry[3], N Relan[4], D Franceschi[5]
[1]NYU Medical Center, New York, NY, [2]Stony Brook University Hospital, Stony Brook , NY, [3]Johns Hopkins Medicine, Elkridge, MD, [4]Stony Brook, Stony Brook, NY, [5]Radiology, Stony Brook, NY

Purpose
Routine fluorodeoxyglucose (FDG) PET-CT imaging for oncology is performed from the base of the skull to the mid thighs. Both benign and malignant brain findings can occur in the oncology patient that would be missed on the typical PET scan. In our institution, when performing whole body PET-MRI for cancer patients, we routinely include the entire head. The aim of our study was to characterize both PET and MRI brain findings incidentally detected on the included head portion of the study.
Materials and Methods
We retrospectively identified 235 FDG PET-MRI body scans that included the head. Images were obtained on a dedicated hybrid PET-MRI camera using body coil with sequences for body pathology without IV contrast. Of the 235 studies, 204 individual patients were scanned (125 female, 79 male). Only the patient's first PET-MRI was reviewed. Mean age was 55 years (range 7-89 years). (One hundred ninety-one restaging). Other 14 indications

were for 5 paraneoplastic syndrome, 3 adenopathy, 3 lung nodule, 1 vasculitis, and 2 monoclonal gammopathy. Of these 4 were later diagnosed with cancer. Images of the brain were reviewed by a neuroradiologist in conjunction with a nuclear radiologist.

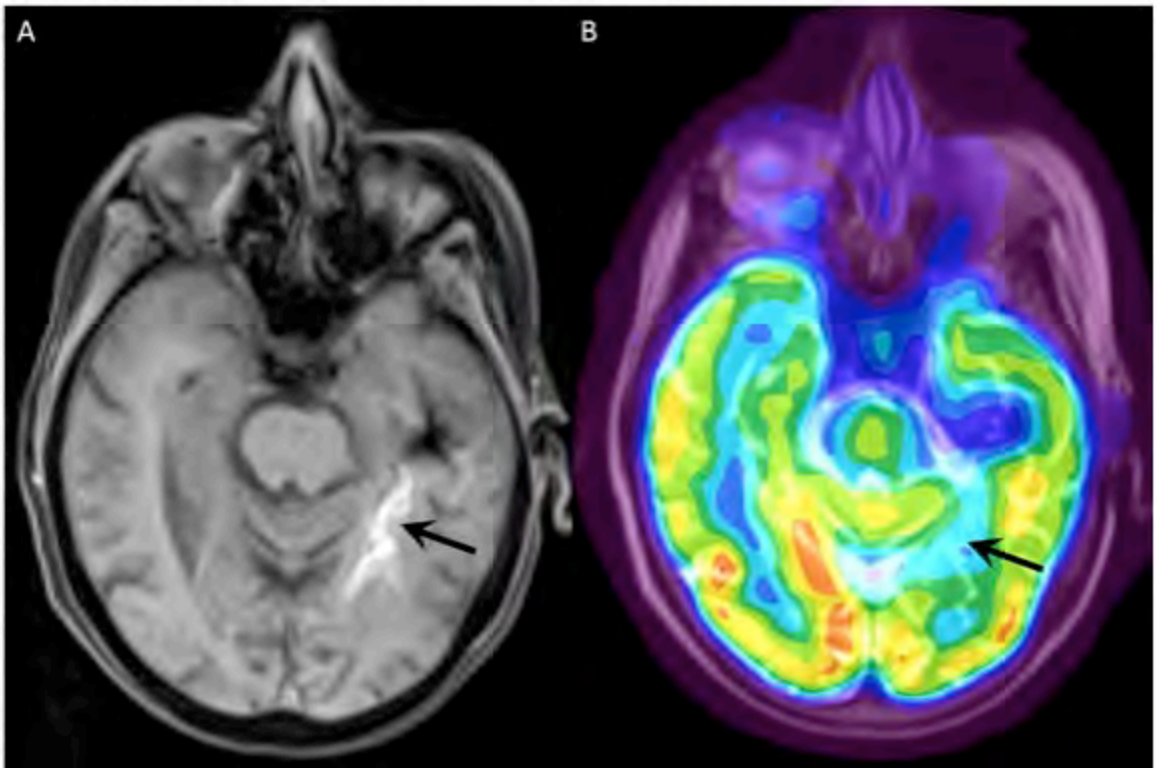
Results

Of the 204 patients, 31 patients (15.2%) had positive brain findings on PET-MRI body sequences. Eleven (5.4%) had vascular disease (average age 72 years) with 7 chronic microvascular ischemic changes and 4 brain infarcts. One infarct was a subacute stroke in a paraneoplastic patient and another a newly discovered infarct in a 38-year-old female. Detection rate for microvascular ischemic changes was likely lower due to the body MRI sequences. Nine patients (4.4%) had post-therapy changes in the brain due to either radiation (n=2), surgery (n=3), or chemotherapy (n=4). Three others had benign cystic lesions. Nine patients (4.4%) had serious brain pathologies including 4 paraneoplastic syndromes (leptomeningeal metastases, metabolic encephalopathy, Creutzfeld-Jakob disease, and lymphoma), 1 metastases, 2 pituitary tumors, 1 chronic and 1 acute subdural collection with mean age in this subset being 63 years old.

Conclusions

Fluorodeoxyglucose PET-MRI imaging is a rapidly evolving modality that is employed most commonly for cancer evaluation. The standardized base of skull to mid thigh imaging may miss many important brain pathologies that are discovered incidentally using MRI body sequences. These pathologies could change patient management or alter patients' prognosis. As a result of this study we would like to advocate other institutions to image the entire brain when performing body FDG PET-MR imaging.

Whole Body FDG PET-MRI. A. Axial VIBE and B. Fused Axial HASTE and PET images demonstrate gyriform T1 hyperintense signal in the left posterior parahippocampal region with corresponding decreased FDG uptake (arrows) compatible with late subacute infarct.



(Filename: TCT_O-330_FigureforASNR.jpg)

O-331

6:04PM - 6:12PM

Significance of new mucosal uptake on post-radiation therapy FDG PET/CT in patients with head and neck squamous cell carcinoma.

N Mallak[1], Y Menda[2], C Anderson[2]
[1]University of Iowa Hospitals and Clinics, Iowa City, IA, [2]University of Iowa Hospitals and Clinics, Iowa city, IA

Purpose
Post-radiation changes on FDG-PET/CT imaging complicate scan interpretation in head and neck squamous cell carcinoma (HNSCC), and are often an important source of false-positives. The purpose of this study is to evaluate the significance of new focal areas of mucosal uptake identified in the head and neck on post-therapy FDG-PET/CT obtained 3 -4 months after radiation therapy (RT).

Materials and Methods
We prospectively enrolled HNSCC patients who completed radiotherapy and underwent 3-4 month post-radiation FDG-PET/CT. Whole-body PET/CT scans were obtained after an approximate 90 minutes uptake period. Post-RT PET/CT images of the neck were reviewed for areas of new mucosal abnormal uptake outside the primary tumor. These areas were evaluated based on their location and maximum Standardized Uptake Values (SUVmax). Correlation with outcome was based on clinical and pathologic follow-up for at least 6 months.
Results
One hundred nineteen patients underwent post-therapy PET/CT scans after a median of 95 days (range of 71 to 122 days) after completion of RT. Forty-five patients demonstrated 55 new mucosal foci of uptake with an SUVmax of 4 or more in areas other than the primary site or surgical margin (range of 4 to 11.6; median of 4.9). Most common areas of new uptake included floor of mouth (n=15), larynx (n=12), tongue (n=8), soft and hard palate (n=9) and oropharynx (n=7). Patients were followed for a median of 27 months (range of 6 to 58 months); No second primary or recurrent tumor developed (0%) at any of these mucosal sites with new abnormal uptake.
Conclusions
New mucosal sites of abnormal uptake on the 3-4 month post-RT FDG-PET/CT scan in patients with HNSCC reflect post-treatment changes and are highly unlikely to represent malignancy.

O-332

6:12PM - 6:20PM

Diagnostic Accuracy of Intraoperative Transoral Ultrasound-Guided Fine-Needle Aspiration Biopsy of Retropharyngeal Masses

T Vu[1], M Kwon[1], M Gule-Monroe[1], J Stewart[1], B Fornage[1], B Edeiken-Monroe[1]
[1]*The University of Texas MD Anderson Cancer Center, Houston, TX*

Purpose
The purpose of this study was to evaluate the diagnostic accuracy of our original technique of intra-operative transoral ultrasound-guided fine-needle aspiration (TOUS-FNA) in diagnosing indeterminate retropharyngeal masses with surgical pathology and imaging follow up used as gold standards.
Materials and Methods
We reviewed the images and medical charts of patients with suspicious retropharyngeal masses detected on CT, MRI and/or PET/CT examinations between November 2006 and January 2015, and which were subsequently sampled by TOUS-FNA. Intra-operative TOUS examination was performed using an endovaginal transducer. TOUS-FNA was performed using a needle guide attached to the transducer shaft and a 20 cm-long 20-gauge needle. The

cytopathologic results were categorized as positive (favor malignant), negative (favor benign) or nondiagnostic.
Results
Twenty-three (8 females and 15 males) patients met the inclusion criteria. The median age was 54 years (range, 3-74 years). Eleven masses were located on the left side and 12 on the right side. The clinical history of the 23 patients included thyroid cancer (n=13), mucosal squamous cell cancer (n=5), olfactory neuroblastoma (n=1), parotid acinic cell cancer (n=1), metastatic colon adenocarcinoma (n=1) and in 2 patients there was no history of cancer. TOUS-FNA yielded a diagnostic specimen in 22 of 23 (95.7%) patients with a sensitivity of 87.5%, a specificity of 87.5% and an overall accuracy of 91.3%. Eleven patients underwent a subsequent transoral resection of the retropharyngeal mass. In 4 patients, the lesion was localized intra-operatively by a TOUS-guided injection of methylene blue.
Conclusions
TOUS-FNA of suspicious masses in the retropharyngeal space is a highly accurate procedure.

Wednesday
5:00PM - 6:30PM
Long Beach Convention Center, Room 104A (Main Lobby)

21D-Parallel Paper Session: Aneurysm Treatment - Conversion to Diversion...When and Why?

O-334

5:00PM - 5:08PM

Predicting Aneurysm Occlusion following Flow Diverter Deployment using Intra-aneurysmal Contrast Kinetics

M Kamran[1], J Finney[2], C Moran[3]
[1]Washington University School of Medicine, St Louis, MO, [2]Siemens Medical Solutions USA, Inc., Hoffman Estates, IL, [3]Washington Univ. School Of Medicine, St. Louis, MO

Purpose
Flow diverters (FDs) alter the intra-aneurysmal flow to induce stasis and thrombosis. We implemented a high frame-rate 2D angiographic imaging protocol with an aim to extract parameters predictive of aneurysm occlusion.
Materials and Methods
Twenty-three patients (3 male, 20 female; mean age 54.2 years) with 29 aneurysms (23 saccular, 6 fusiform; 21 <8mm, 8 >8mm; 8 posterior-circulation; 21 anterior-circulation) underwent FD treatment (Pipeline Embolization Device; PED, Covidien, Irvine, CA, USA) and were studied prospectively. High frame-rate 2D angiographic data (Axiom Artis dBA, Siemens, Germany) was acquired pre and post FD-deployment, using a standard protocol

(A-plane, 30 frames/second, intrarterial Optiray-320 contrast injection at 2ml/second for 8 seconds using a power injector, 0.5 second x-ray delay). Intra-aneurysmal contrast kinetics were analyzed, first by extracting the time concentration curve for each angiographic dataset, from which the following parameters were measured: time-to-peak (TTP), full-width-half-maximum (FWHM), area-under-curve (AUC), inflow-rate, outflow-rate. Flow-diverter-induced change in the parameters then was correlated to the aneurysm occlusion status on 6-month follow-up catheter angiogram. Optimum thresholds for each parameter predictive of aneurysm occlusion were calculated using the receiver operating characteristic (ROC) curve.
Results
For 30-minute post-FD-deployment angiogram, relative to pre-FD-deployment, mean change in the studied parameters was: TTP 62% increase, FWHM 66% increase, AUC 58% decrease, inflow-rate 30% decrease, outflow-rate 42% decrease. The change in parameters reflecting flow alteration was higher for aneurysms < 8mm compared to the aneurysms > 8mm ($p < 0.01$). Of the 29 treated aneurysms, 19 demonstrated complete occlusion, 9 residual filing, and 1 interval growth at 6-months. Full-width-half-maximum was the most sensitive (0.85) and specific (0.81) parameter predictive of complete aneurysm occlusion (accuracy, 0.78) at 6-month follow-up.
Conclusions
High temporal-resolution 2D angiography in conjunction with intra-aneurysmal contrast kinetic analysis offers a unique tool utilizing functional information to quantify flow diversion and predict aneurysm occlusion after FD treatment.

O-335

5:08PM - 5:16PM

Flow Diverter Foreshortening Simulation Sensitivity to Segmentation Threshold

J Blasco Andaluz[1], R Kale[2], H Fernández[3], L San Roman[4], A López-Rueda[5], A Narata[6], O Chirife Chaparro[7], M Cappucci[5], I Larrabide[8]
[1]Hospital Clinic of Barcelona, BARCELONA, -- SELECT --, [2]Galgo Medical, Barcelona, Barcelona, [3]galgo Medical, barcelona, barcelona, [4]Hospital Clinic of Barcelona, Barcelona, Barcelona, [5]Hospital Clinic of Barcelona, BARCELONA, Catalunya, [6]University Hospital of Tours, Tours, France, [7]hospital Clinic of Barcelona, Barcelona, Barcelona, [8]PLADEMA-CONICET, Universidad Nacional del Centro de la Provincia de Buenos Aires, Tandil, Buenos Aires

Purpose
A flow diverter (FD) is a braided device commonly used for the endovascular treatment of intracranial aneurysms (1). Different computational methods have been proposed for the simulation of a braided device released inside the patient vasculature (2). In this study, we determine the variability of the computed FD length inside the vessel for 1 of this methods, namely Braided Device Foreshortening (BDF), presented by Fernandez el al (3). A 3D

surface model of the vasculature is obtained from 3DRA images of aneurysmatic patients. For each patient, 10 meshes were created by using different threshold levels. The BDF is applied to each resulting surface model, and each 1 produces 1 FD length after simulation. These results were analyzed to assess the algorithm sensitivity to this parameter.

Materials and Methods

Ten 3D rotational angiography (3DRA) images of intracranial aneurysms (cases) were used. The images were acquired using either AXIOM-Artis from Siemens, Integris Allura System from Philips or AW4.6_0.5.003_SLED_11 from General Electrics. The FD was selected by means of the 3D vessel model diameter at the proximal region, replicating the criteria followed by the interventionist. Lower and upper thresholds were selected for each image to segment the selected region of interest (ROI). The threshold range is defined manually for each image, ensuring that the upper threshold produced a 3D model completely inside the image vessel contrast in the lower threshold (SU), and the lower threshold a 3D model completely outside it (SU). The FD virtual deployment was done by applying the BDF algorithm to the surface model (3). The FD was selected for each case by means of the diameter at the proximal position, calculated from an intermediate surface model within the threshold range.

Results

Results indicated that the coefficient of variation (Cv) is below 7% in all the cases. Figure 5 - statistical distribution of the Cv values will be shown. The distribution does not present any outlier values, and the interquartile range is narrow (from 2.85 to 4.15%), showing low data spread. The robustness analysis has been extended to test the influence of different FD (with different nominal diameter) on a single case. Table 4 shows the consistency of the relation between the FD length against the threshold segmentation when different FDs are simulated into the vessel models corresponding to case PA007. The Cv is almost the same for the three FDs (4.5x15, 5.0x30 and 6.0x25), indicating a robust final length prediction from BDF algorithm.

Conclusions

Several vessel models were created using different threshold segmentation levels and a morphology analysis and FD simulation were applied to each vessel model. The range of the computed FD lengths for each case was obtained to calculate the variability of the method against the threshold segmentation values. Despite of the wide threshold changes between the vessel models, the average FD Length change (LU – LL) is found to be 9.14% of the total length and, the average coefficient variation is 3.65%, lying within the order of the error reported on previous papers for the simulated change in length (3). Thus, independently of the threshold applied to the vessel images, FD length changes do not vary significantly; showing this tool to be suitable for clinical purposes.

O-336

5:16PM - 5:24PM

Large Basilar Apex Aneurysms treated with Flow-Diverter Stents

J Caroff[1], V Da Ros[2], M Iacobucci[2], l spelle[3]
[1]Hôpital Bicêtre, Le Kremlin Bicêtre, France, [2]Hôpital Bicêtre, Le Kremlin Bicêtre, Ile de France, [3]Hôpital Bicêtre, Le Kremlin-Bicêtre, Ile de France

Purpose
The treatment of broad-neck, large basilar apex aneurysms (BAAs) with either an endovascular or surgical approach is challenging (1,2,3,4,5). The aim of the present study is to evaluate the efficacy and safety profile of flow-diverter stents (FDSs) for the treatment of this specific anatomical condition, in terms of both aneurysm occlusion and covered branch patency, with a midterm follow-up.
Materials and Methods
From the prospective institution database, all large basilar apex aneurysms, treated with flow diverter stents, were collected. Technical issues, immediate post-treatment and follow-up angiographic findings, and clinical outcomes were assessed.
Results
Between January 2011 and January 2015, 5 patients (2 females and 3 males; age range: 44-58 years) were treated with FDSs for broad-neck, large BAAs at our institution. We report clinical and angiographic results, with a mean follow-up of 21 months (range 15-24 months). One patient died on day 31 due to an early postprocedural midbrain hemorrhage. One patient had a right cerebellar hemispheric ischemic lesion, which resulted in a transient cerebellar syndrome that resolved within 24 hours, without neurologic sequelae during follow up. The mRS at last follow up was 0 in 4 patients and 6 in 1 patient.
Conclusions
The use of FDSs is feasible, with efficacy demonstrated at a midterm follow-up, particularly where broad-neck, large BAAs had recurred after previous endovascular treatment. However, concerns remain about their safety profile.

O-337

5:24PM - 5:32PM

The Treatment of Unruptured Anterior Choroidal Artery Aneurysms with Flow Diversion – Dual Centre Experience

P Bhogal[1], P Lylyk[2], H Henkes[3]
[1]Klinikum Stuttgart, Stuttgart, Germany, [2]Clinica ENERI, Buenos Aires, Buenos Aires, [3]Klinikum Stuttgart, Stuttgart, BW

Purpose
Background: The region of the brain supplied by the anterior choroidal artery is exquisitely eloquent. Aneurysms arising at or close to the origin of the vessel are not uncommon and damage or occlusion to the vessel can result in devastating clinical consequences and the

optimal treatment strategy is yet to be determined. Objective: We sought to determine the efficacy of flow diversion for the treatment of unruptured anterior choroidal artery aneurysms.
Materials and Methods
A retrospective review of the databases at 2 neurointervention centers was performed to identify all patients with unruptured aneurysms of the anterior choroidal artery between February 2009 and February 2016. The aneurysm fundus size, number and type of flow diverting stent (FDS), patency of covered branches, complications and both clinical and radiographic follow-up data were recorded.
Results
We identified 42 patients (62% women) with an average age 51.5 years (range, 7-77 years). A total of 43 aneurysms were treated. The aneurysms were generally small with a mean average maximum fundus diameter of 4.5mm (range, 1mm to 25mm). Angiographic follow-up data were available for 30 patients. At delayed follow-up 25 aneurysms were completely occluded. One patient developed transient ischemic symptoms after interruption of the antiplatelet medications and another patient had a small embolic infarct in the periprocedural period. One patient died 3 weeks postprocedure from delayed parenchymal hemorrhage.
Conclusions
Flow diversion can be used to successfully treat aneurysms of the anterior choroidal artery. The treatment carries a high rate of technical and radiological success with a good safety profile.

O-338

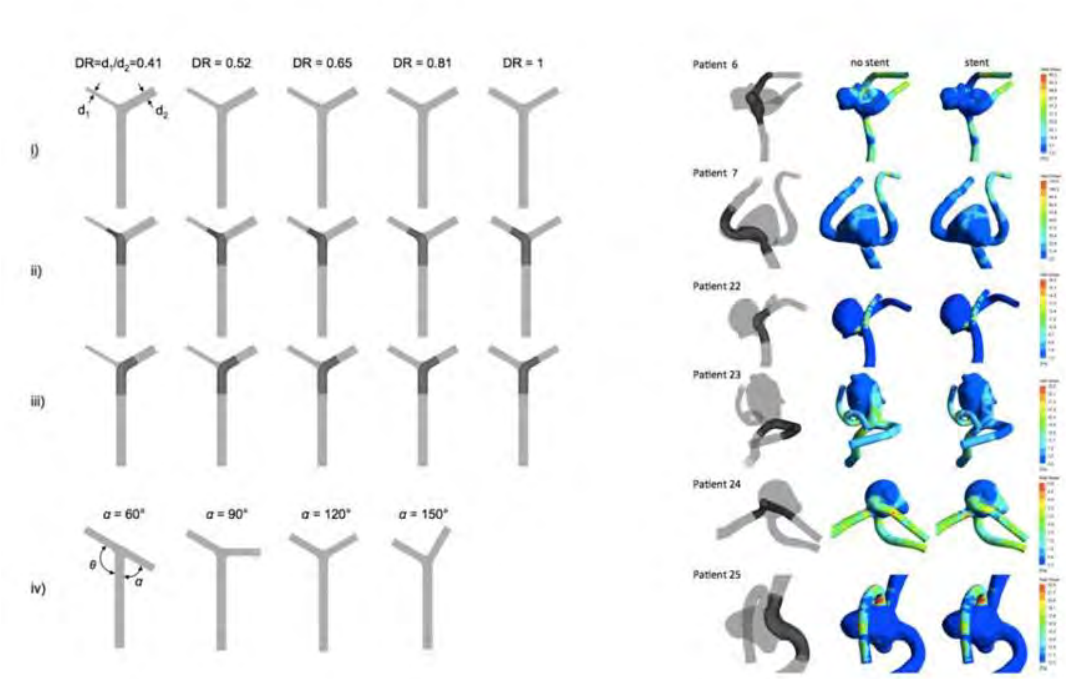
5:32PM - 5:40PM

The Role of Hemodynamics in Intracranial Bifurcation Arteries After Aneurysm Treatment with Flow-Diverting Stents

A Narata[1], F Silva de Moura[2], C Perrault[3], I Larrabide[4], R Bibi[1], S Velasco[5], A Januel[6], C Cognard[7], R Chapot[8], C Sennoga[9], A Marzo[3]
[1]University Hospital of Tours, Tours, France, [2]Engineering, Modelling and Applied Social Sciences Center, Federal University of ABC, Santo Andre, Sao Paulo, Brazil, [3]Mechanical Engineering Department, Insigneo, University of Sheffield, Sheffield, United Kingdom, [4]PLADEMA-CONICET, Universidad Nacional del Centro de la Provincia de Buenos Aires, Tandil, Buenos Aires, Argentina, [5]University Hospital of Poitiers, Poitiers, France, [6]University Hospital of Toulouse, Toulouse, France, [7]University Hospital of Toulouse, Toulouse, Toulouse, [8]Alfried Krupp Krakenhaus, Essen, Germany, [9]UMR Imagerie et Cerveau, Inserm 930, Université François Rabelais, Tours, France

Purpose
Treatment of intracranial bifurcation aneurysms with flow-diverter stents (FDS) can lead to

sub-occlusion/narrowing of the distal vessels. This study investigated how hemodynamics affect arteries surrounding a FDS in this anatomical configuration.
Materials and Methods
Radiological images, demographic and outcome data were acquired for 25 bifurcation aneurysms treated with FDS. Statistical analysis was used to correlate the event of vessel subocclusion or narrowing with anatomical data (diameters ratio=DR=1 symmetric, <1 asymmetric). Computational fluid dynamics (CFD) study was performed on idealized and patient-specific anatomies to identify possible cause-effect mechanisms mediated by hemodynamics.
Results
Statistical analysis identified marked correlation between asymmetric bifurcation and sub-occlusion/narrowing (DR<0.7, DRmedium=0.61). Computational fluid dynamics predictions in both idealized and patient-specific anatomies showed that wall shear stress (WSS) in the jailed vessel is mostly affected when FDS are deployed in nonsymmetric bifurcations (DR<0.65), and least affected when deployed in symmetric anatomies (DR = 1.00).
Conclusions
Analysis of the anatomical data showed statistically significant correlations between occlusion/narrowing and bifurcation asymmetry characterized by DR<0.7. Similarly, CFD results showed that FDS have the highest impact on hemodynamics when deployed in bifurcation with higher degrees of anatomical asymmetry (DR<0.65) with strong changes induced on the WSS fields. This suggests a higher risk associated to FDS-treatment of asymmetric bifurcation together with a possible FDS-induced pathway leading to occlusion/narrowing of arteries and mediated by hemodynamics and vessel wall response.



(Filename: TCT_O-338_models.jpg)

O-339

5:40PM - 5:48PM

Transient in-stent stenosis at mid-term angiographic follow up in patients treated with flow diversion: incidence, clinical significance and long-term follow-up.

F Essbaiheen[1], R Thornhill[2], H AlQahtani[3], T Almansoori[4], S Patro[3], C Lum[3], B Drake[3], H Lesiuk[3], D Iancu[3]
[1]University of Ottawa, King Saud University, Ottawa, Ontario, [2]The Ottawa Hospital University of Ottawa, Ottawa, Ontario, [3]The Ottawa Hospital, Ottawa, Ontario, [4]University of Ottawa, Ottawa, Ontario

Purpose
Little is known about in-stent stenosis (ISS) in patients with aneurysms treated with flow diverter (FD) stents (1). The aim of this study is to assess the incidence and evaluate the severity, distribution, clinical significance and predictors of ISS.
Materials and Methods
We reviewed prospectively collected data of patients treated with FD stents between July 2012-Nov 2015. Cases with mid (3 +/- 3 months) and long-term (> 1 year) follow up with digital subtraction angiograms were included. In-stent stenosis was graded as mild (<25%),

moderate (25-50%) or severe (>50%). We assessed the following predictors for ISS: age, gender, smoking, hypertension, aneurysm location, presence of SAH, post-deployment angioplasty, occlusion status.

Results

Twenty-five of 55 patients met the inclusion criteria. In-stent stenosis was seen in 44% (11/25) of patients at mid-term and 16% (4/25) at long-term follow up (P=0.03). Seven patients (64%) had mild ISS, 2 had moderate and 2 had severe stenosis of which 64% were diffuse and 36% were focal. All 11 patients with ISS were asymptomatic at mid-term follow-up. Complete resolution was seen in 7 patients and significant improvement was seen in 3 patients at long-term follow-up. Of these 10 patients, 9 (90%) were maintained on dual anti-platelet therapy. On univariate analysis, there was no significant predictor for ISS.

Conclusions

In-stent stenosis in FD stents is a common finding on mid-term angiographic follow-up. Complete resolution or improvement at long-term follow-up is seen in patients who are maintained on dual anti-platelet therapy.

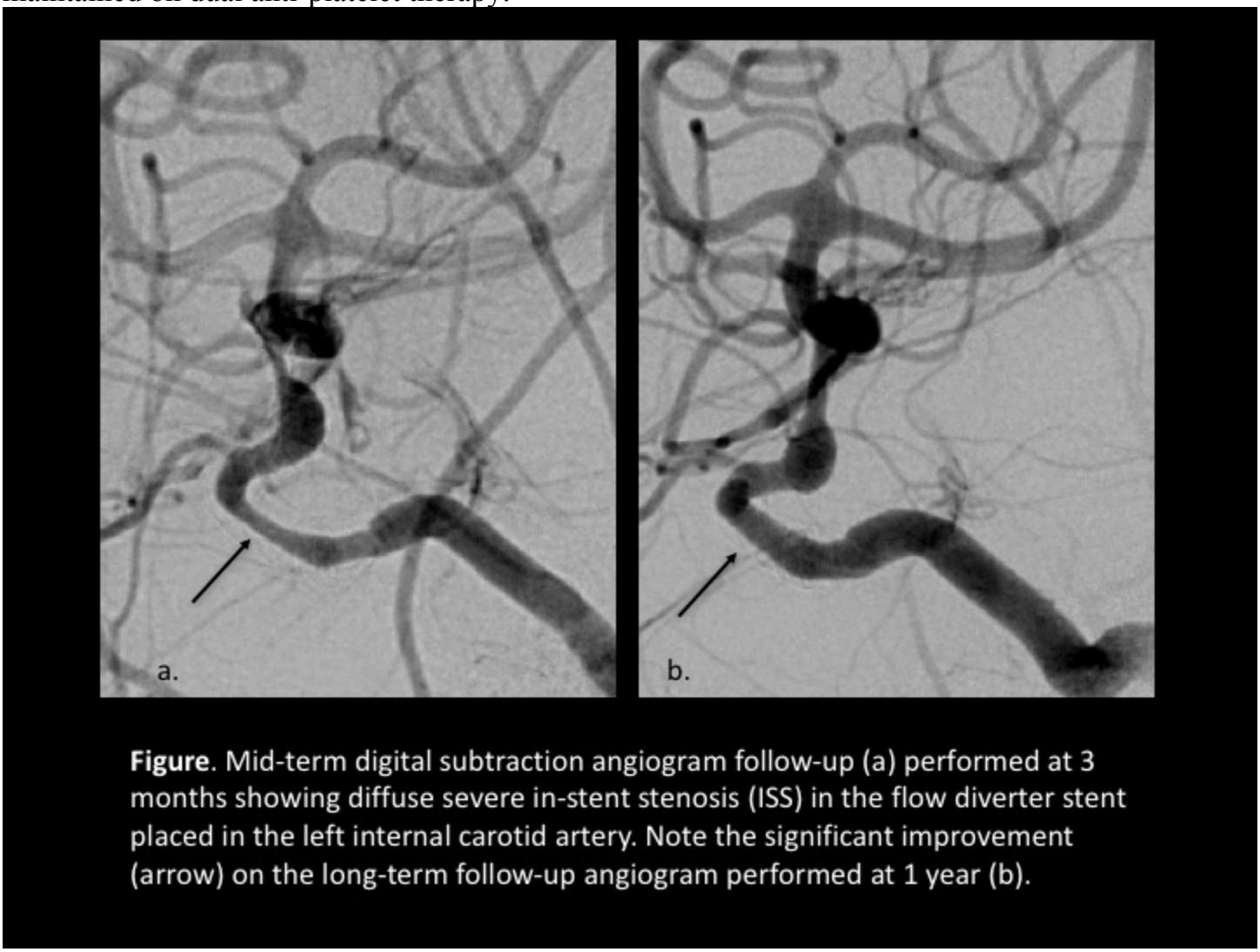


Figure. Mid-term digital subtraction angiogram follow-up (a) performed at 3 months showing diffuse severe in-stent stenosis (ISS) in the flow diverter stent placed in the left internal carotid artery. Note the significant improvement (arrow) on the long-term follow-up angiogram performed at 1 year (b).

(Filename: TCT_O-339_FDFigure.jpg)

O-340

5:48PM - 5:56PM

Optimized 4D pcMRI Protocol for Quantifying Velocity Changes in Cerebral Aneurysms post Flow Diverter Device treatment

C Karmonik[1], J Anderson[1], J Zhang[2], O Diaz[2], R Klucznik[2], R Grossman[2], G Britz[2]
[1]Houston Methodist Hospital Research Institute, Houston, TX, [2]Houston Methodist Hospital, Houston, TX

Purpose
To measure changes in aneurysmal flow velocities after treatment with a flow diverter device (FDD) using 4D phase contrast magnetic resonance imaging (4D pcMRI).
Materials and Methods
Six patients with an aneurysm of the internal carotid artery (ICA) underwent an MRI examination immediately prior to treatment. An optimized 4D pcMRI protocol was developed using 2 3D-printed replicas of ICA aneurysms and a flow loop (Siemens Aera, 1.5 T) (1, 2). From a 3D time-of-flight (TOF) localizer, maximal intensity projections in the axial, coronal and sagittal plane were reconstructed to prescribe the 4D pcMRI acquisition [slice thickness 1.5 mm, number of averages 1, in-plane resolution 0.55 mm, number of cardiac phases 3-4, acquisition time 5 – 7 min, velocity encoding value (VENC) 60 – 80 cm/sec, total duration of the MRI examination 20 -30 min]. The MRI acquisition was repeated in 3 patients within 1 week after FDD (Pipeline Embolization device, Covidien) placement. The 4D velocity field was calculated and its magnitude determined inside the aneurysm as well as in the proximal segment of the parent artery.
Results
Acquired 4D pcMRI images visualized major flow patterns within the aneurysms well (Fig. 1). Little or no image artifact from the FDD device was noticeable. Average flow velocities inside the aneurysm decreased on average by 24%. While there was little change in the inflow velocities (4%) post FDD treatment, outflow velocities increased by about the same percentage (24%) as the aneurysm velocity decreased. Statistical significant correlations were found between the change in inflow velocity and average velocity inside the aneurysm post-treatment ($p<0.05$) as well as between the dome height and the change in outflow velocity ($p<0.01$).
Conclusions
Using an optimized 4D pcMRI acquisition protocol developed with 3D-printed replica of a cerebral aneurysms, velocity changes post FDD treatment were visualized and quantified in vivo.

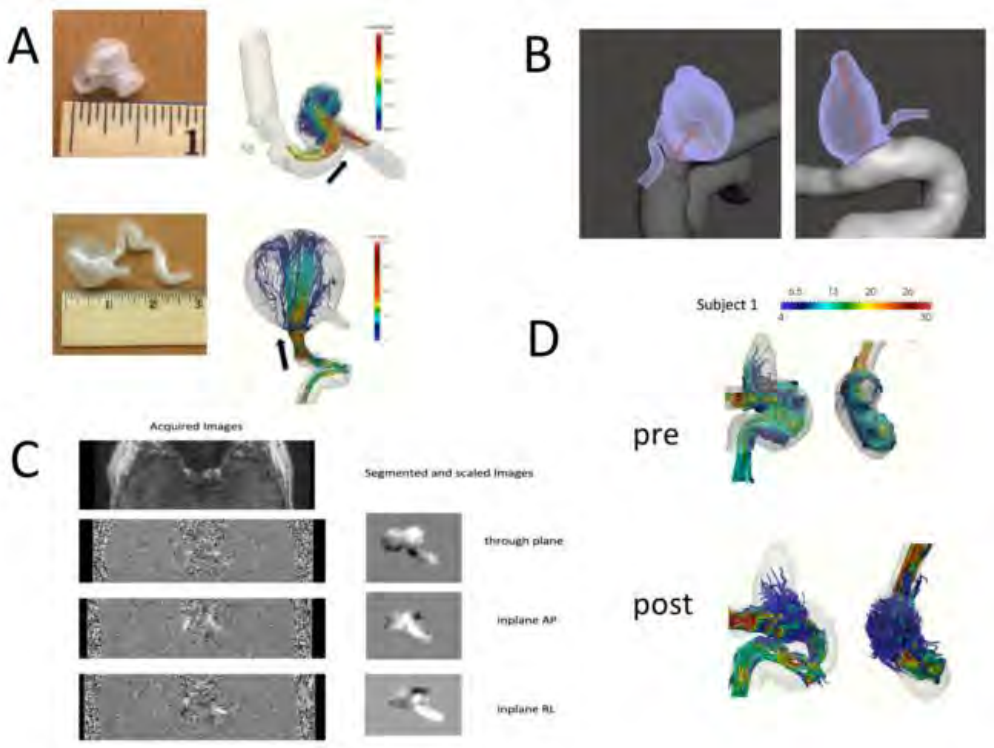


Figure 1: A: 3D-printed replicas and measured velocity field. B: 3D surface reconstruction for subject one illustrating measurements of neck width and dome height. C: 4D pcMRI images acquired in subject 3. D: Pre and post velocity field in aneurysm for subject 1. Disruption of inflow jet and reduced velocities inside aneurysms post treatment can be appreciated.

(Filename: TCT_O-340_ASNR2017_1_figure.jpg)

O-341

5:56PM - 6:04PM

Outcome Study of the Pipeline Embolization Device for Treatment of Intracranial Aneurysms at a Single UK Institution

S Yang[1], T Hampton[2], J Hart[2], J Ashmore[2], C Tolias[2], T Booth[2]
[1]Wan Fang Hospital, Taipei Medical University, Taipei, Taiwan, [2]King's College Hospital NHS Foundation Trust, London, London, London

Purpose
Flow-diverting stent implantation has become an alternative endovascular treatment choice in selected intracranial aneurysms. Through retrospective analysis, we provide a large UK center's experience of Pipeline Embolization Device (PED) treatment with clinical and radiographic outcomes.

Materials and Methods
The electronic patient records, diagnostic and procedural images and written procedural records of PED treatments between August 2009 and April 2014 were reviewed. Unlike other similar studies using angiography for follow up, we performed TOF MRA 6 and 12 months after treatment. The mortality, morbidity events and radiographic outcomes were analyzed and compared with other PED studies.
Results
Twenty-nine patients with 33 aneurysms and 30 attempted PED treatments, which represented a highly selected (3.5%) patient cohort, were reviewed. 63.6% of the aneurysms were wide-necked (> 4 mm), 60.6% were large or giant (≥ 10 mm). The mean aneurysm sac diameter was 12.0 mm, the mean neck width was 4.5 mm. The overall mortality and morbidity rates were 3.3% and 10.0%, respectively. The total adequate occlusion rate was 78.1% at 1 year. The neck width of aneurysms with residual sac filling and complete occlusion differed significantly (P = 0.04).
Conclusions
Highly selected aneurysms treated with a PED in a UK center have similar occlusion and complication rates when compared to non-UK studies, none of which provide evidence for such a refined selection. Follow up with TOF MRA gave similar occlusion results compared to those obtained with DSA in other studies. The clinical outcome analysis showed that delayed aneurysm rupture remained a risk for PED treatment in large or giant aneurysms. The influence of neck size on occlusion rate should be examined in future PED studies.

Wednesday
5:00PM - 6:30PM
Long Beach Convention Center, Room 104B (Main Lobby)

21E-Parallel Paper Session: Cost-Effective Imaging in the Era of the Triple Aim

O-345

5:00PM - 5:08PM

Comparative Effectiveness of CT/MRI Utilization in Stroke Imaging: Does Increasing Duration of Time Between Stroke Onset and Imaging Improve CT Predictive Values ?

M BHALLA[1], K McAvoy[2], A Klein[1], J Ulmer[1], L Mark[1], B Fitzsimmons[1], N BHALLA[3]
[1]Medical College of Wisconsin - Froedtert Hospital, Milwaukee, WI, [2]Medical College of Wisconsin, Milwaukee, WI, [3]Froedtert Hospital, Milwaukee, WI

Purpose
A cornerstone of acute stroke management is thrombolytic therapy, which in the absence of relevant contraindications typically is administered within a few hours of symptom onset. Generally, CT is ideal for quickly excluding hemorrhage in this early symptomatic period. However, many patients present beyond the thrombolytic therapeutic window where a

vascular basis of symptoms may be less certain. In this scenario, emergency department (ED) physicians must weigh the clinical certainty of stroke against the expediency and convenience of CT versus the high accuracy but limited access of MRI. Our study sought to determine if the duration between symptom onset and imaging can help estimate the predictive value of CT for identifying stroke. The goal was to provide ED physicians with information that may aid in selecting the most efficacious imaging tool to support diagnosis or exclusion of stroke, within patient-specific clinical contexts.

Materials and Methods

Following Institutional Review Board (IRB) approval, 501 electronic medical records (EMR) of patients between the ages of 18 and 89 years presenting to the ED who had CT and MRI brain examinations for clinically suspected stroke were reviewed retrospectively. A clinical discharge diagnosis supported by an MRI within 24 hours of the presentation CT was considered the gold standard for the presence of stroke. The time between symptom onset and CT imaging in the ED was used to categorize data into 5 groups: 0-3 hrs, 3-24 hrs, 1-3 days, > 3 days, and unknown. Final reports of CT and MR brain examinations were reviewed, and predictive value data [sensitivity, specificity, negative predictive value (NPV), positive predictive value (PPV), and accuracy] of CT for stroke diagnosis were calculated.

Results

Eighty-one percent of patients presented to the ED with known duration from onset of stroke-like symptoms, while in the remainder time of symptom onset was unknown. For those with known onset, 41% presented within the acute 0-3 hour window, while 42% presented beyond this time-frame but within the first 24 hours. The remaining 17% presented after 24 hours of symptom onset. Nineteen percent of patients presented without definitely known time of symptom onset. Across all time periods, the NPV and accuracy of CT in diagnosing stroke was unaffected by increasing duration between symptom onset and imaging, whereas PPV increased in the first 24 hours and plateaued thereafter (Fig.). Accuracy of CT in identifying stroke ranged from 65% and 70%, while NPV ranged between 58% and 63%. Computed tomography PPV at 0-3 hours was at 75%, but increased to above 90% beyond this window. With the exception of PPV in the first 3 hours after symptom onset, predictive values and accuracy for the "unknown" group were similar to the other groups.

Conclusions

Computed tomography imaging in the ED is necessary for quickly excluding hemorrhage in the early symptomatic period of stroke where thrombolytic therapy is a consideration. However, a significant number of patients present in a time-frame where "speed" of imaging is not a requirement. In this scenario, emergency department (ED) physicians will weigh the expediency of CT against the high accuracy but limited access of MRI. Often, both CT and MRI may be obtained, which can waste resources and delay diagnosis. Neuroradiologists are well aware of the temporal progression of stroke findings at CT, and it is intuitive to believe that CT accuracy increases with time. Outside of PPV in the acute presentation, our results found this not to be true. This is likely due to relatively high frequency of acute or subacute

infarcts involving white matter and/or small regions of gray matter that are difficult to distinguish from chronic microvascular or microembolic phenomena. Beyond the 0-3 hour window, PPV at CT remains high. However, the ability to exclude (NPV) a stroke at CT remains poor irrespective of symptom onset. Emergency department physicians should consider MRI as a first choice for patients presenting beyond the thrombolytic therapeutic window where a vascular basis of symptoms is less certain, with the goal of fostering the efficacious use of modalities in diagnosing or excluding stroke.

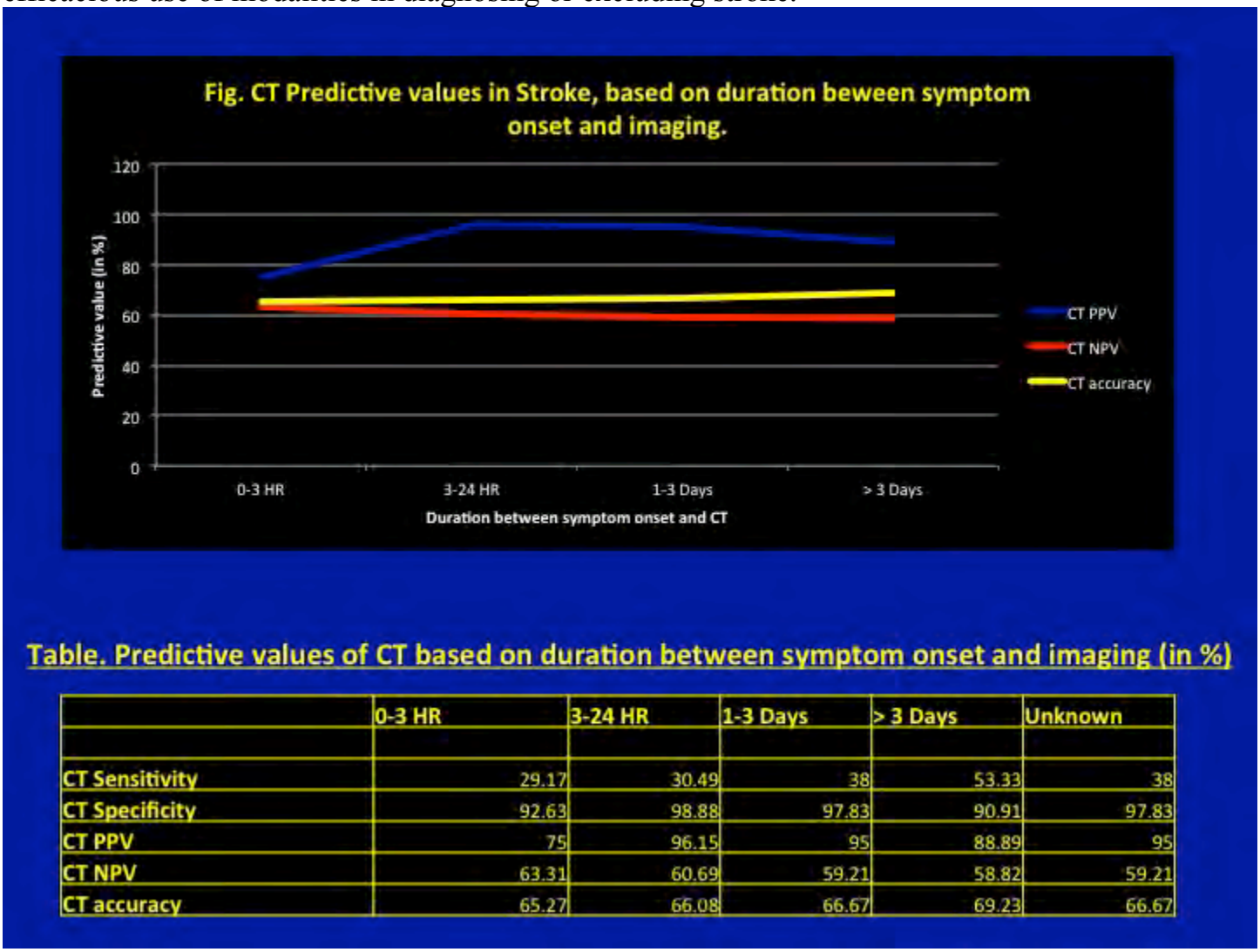


Table. Predictive values of CT based on duration between symptom onset and imaging (in %)

	0-3 HR	3-24 HR	1-3 Days	> 3 Days	Unknown
CT Sensitivity	29.17	30.49	38	53.33	38
CT Specificity	92.63	98.88	97.83	90.91	97.83
CT PPV	75	96.15	95	88.89	95
CT NPV	63.31	60.69	59.21	58.82	59.21
CT accuracy	65.27	66.08	66.67	69.23	66.67

(Filename: TCT_O-345_Slide1.jpg)

O-346

5:08PM - 5:16PM

Economic impact of Intra-Arterial therapy for Acute Ischemic Stroke in the US: Marketscan Database Analysis.

S Lee[1], C Lyttle[2], G Nicola[3], J Hirsch[4]

[1]University of Chicago Medical Center, Chicago, IL, [2]University of Chicago, Chicago, IL, [3]Hackensack Radiology Group, River Edge, NJ, [4]Massachusetts General Hospital, Boston, MA

Purpose
Increased public awareness, utility of advanced imaging, adoption of new interventional technology and sophisticated in-hospital and post-acute care have significantly improved clinical outcome of acute ischemic stroke (AIS) patients. However, composite in-patient cost accounting for active AIS interventions including mechanical thrombectomy is rare. We aimed to review the trend of composite medical expenses and frequency of active interventions for AIS management over last 7 years.
Materials and Methods
Marketscan Commercial Research Database from 2008 to 2014 were used to extract patients who have submitted first in-patient medical claim under the diagnosis of AIS. Patients were categorized into Group 1(18-64 years) and Group 2 (over 64 years) supplemental group. Each group was subcategorized into No treatment (NoT), IV-tPA only (IV), IA therapy (IA) and IV+IA (Both). Composite in-patient claim and the frequency of subcategories over observed period were calculated and compared.
Results
In Group 1 (n=69,897), AIS therapy was performed with IV (n=4,320, 6.18%), IA (n=484, 0.69%) and Both (n=206, 0.29%). The remaining 92.83% of patients did not get any therapy. Mean composite in-patient claim amount of NoT, IV, IA, and Both were $17,922.21, $29,560.39, $68,657.44, and $66,443.27 respectively. The use of IV therapy has increased by 14.7 times, and that of IA therapy by 18.9 times since 2008. In Group 2 (n=92,934), AIS therapy performed with IV (n=4,556, 4.9%), IA (n=370, 0.4%), and Both (n=160, 0.17%). Mean composite in-patient claim amount of NoT, IV, IA and Both were $14,192.05, $24,011.63, $41,012.36 and $42,412.78, respectively. The use of IV therapy has increased by 16.6 times, and that of IA therapy by 4.5 times since 2008.
Conclusions
Both IV and IA therapy for AIS patients have significantly increased since 2008. The in-patient claim costs for AIS using IA therapy, including mechanical thrombectomy, is almost double the costs of IV tPA.

O-347

5:16PM - 5:24PM

Institution of Multidisciplinary Telestroke Program at Multicenter Integrated Health Care System Leads to Marked Improvement in Clinical and Radiological Performance Metrics.

A Kim[1], P Shen[2], J Klingman[1], M Nguyen-Huynh[3]

[1]The Permanente Medical Group, Walnut Creek, CA, [2]The Permanente Medical Group, Santa Clara, CA, [3]Kaiser Permanente Division of Research, Oakland, CA

Purpose

Since the release of several important papers in early 2015 demonstrating efficacy of endovascular therapy for large vessel occlusions, Northern California Kaiser Permanente, a 21 hospital integrated healthcare system serving 3.7 million patients, initiated a system-wide centralized telestroke program with a single teleneurologist working in concert with radiologists to evaluate, diagnose, and treat all possible acute strokes, including: eliminating barriers to prompt IV tPA administration, and rapidly identifying and triaging patients with large vessel occlusions. Overall radiology and clinical performance metrics were reviewed and compared to recommendations by American Heart Association and American Stroke Association (AHA/ASA) "Target Stroke Campaign" 2014 and to the previous year.

Materials and Methods

We performed a detailed analysis of a subset of the total stroke cases, from 3 of the 21 medical centers, representing 177 cases (35% of the total 507) from January 1, 2016 to June 30, 2016. Data points recorded included time of arrival or initiation of the stroke code (door time), NIH stroke scale score, start time of noncontrast head CT and CT angiogram (CTA), time of initiation of tPA administration (needle time), and radiology reporting time for both CT and CTA.

Results

Total number of tPA administrations for acute stroke were 507 for the entire region during this timeframe. Detailed analysis of the 177 subset cases showed an average NIH stroke scale of 8.6. The average door to noncontrast CT and CTA times were 17.6 and 22.5 minutes respectively. The average door to radiology noncontrast CT and CTA reporting time were 29.3 and 48.5 minutes respectively. The median door to needle time for patients requiring IV tPA treatment was 34 minutes, comparing very favorably to the previous year when it was 56 minutes. The average door to noncontrast CT time of 17.6 minutes and door to noncontrast CT reporting time of 29.3 minutes were well below the AHA/ASA recommendations of 25 and 45 minutes respectively. The median door to needle time of 34 minutes also was well below the AHA/ASA recommendation of 60 minutes.

Conclusions

Since unifying our acute stroke response system by having a single teleneurologist work in concert with radiologists to evaluate all acute strokes for all 21 Northern California Kaiser Permanente hospitals, our subset analysis shows we have significantly improved radiologic and clinical performance metrics to well below the recommendations by AHA/ASA "Target Stroke Campaign" 2014, as well as a >30 minute decrease in door-to-needle time over the same period last year. This type of telestroke program has been implemented in single centers and smaller hospital organizations, but to the best of our knowledge has not been attempted in a hospital network of this size or patient population. We expect detailed

analysis of the entire Northern California Kaiser Permanente hospital system (available early 2017) to yield similar results.

O-348

5:24PM - 5:32PM

Mobile Stroke Treatment Unit Effect on Key Time Related Imaging Metrics

J Cox[1], E Nyberg[1], W Jones[2]
[1]University of Colorado, Aurora, CO, [2]Department of Neurology, University of Colorado School of Medicine, Aurora, CO

Purpose
Timely administration of thrombolytic therapy is critical to maximizing the likelihood of a favorable outcome in patients with acute ischemic stroke. A 20% decrease in treatment effect for every 30-minute delay in tPA administration has been reported (Mazighi 2013). Our Mobile Stroke Treatment Unit (MSTU) is a new-generation ambulance with on-board CT and tele-neurology capability which can facilitate tPA delivery in the field. This proof of concept study aims to evaluate the effect of the MSTU on imaging time metrics, including time last seen normal (LSN) to image acquisition and time LSN to actionable CT report.
Materials and Methods
IRB approval was obtained. We reviewed our prospectively maintained database of stroke alerts at our comprehensive stroke center. We then retrospectively compared key time metrics of patients imaged via the MSTU with controls imaged via the conventional in-hospital pathway. Controls were matched for pre-hospital status and time of day. We collected the time LSN, time images were available in PACS, and time of actionable report communication to the stroke neurologist. Imaging and report times for MSTU and in-hospital groups were compared using a Student's t-test.
Results
Sixty-four patients were included, including 32 MSTU patients and 32 controls. Mean LSN to imaging time was 56 vs 162 minutes for MSTU and controls, respectively ($p<0.001$). Mean LSN to report time was 71 vs 178 minutes for MSTU and controls, respectively ($p<0.001$). Mean times from imaging to communication of an actionable report were 14 and 15 minutes for the 2 groups ($p=0.56$).
Conclusions
The MSTU can significantly reduce times from LSN to image acquisition and communication of an actionable report to the stroke neurologist. In this preliminary study, time to actionable report was reduced by 107 minutes. The MSTU thus has the potential to substantially impact the delivery and effectiveness of thrombolytic treatment.


(Filename: TCT_O-348_MSTUpic.jpg)

O-349

5:32PM - 5:40PM

CT Imaging for Pediatric Headache

L Urquia[1], D Kishore[1], K Kim[1], A Trofimova[1], N Kadom[1]
[1]*Emory University, Atlanta, GA*

Purpose
Many children presenting with headaches undergo CT brain imaging at our institution, regardless of whether their headaches are primary or secondary headaches (1). One drawback of CT imaging is radiation exposure; but CT imaging has many advantages, including short exam times, 24/7 access, cross-sectional technique and ability to create multiplanar reformatted views. In addition, CT imaging is a low cost modality relative to MR imaging and can be performed without use of sedation in the majority of patients. In this study we assessed the number of head CT studies performed in children at our institution with headache or migraine at our institution and the diagnostic yield for these imaging studies.
Materials and Methods
The IRB designated this quality assurance review as exempt. We searched for noncontrast and contrast-enhanced head CT imaging studies in children performed between January 1, 2015 and December 31, 2015 who had an indication of "headache" or "migraine" (Montage Health Solutions Inc., California, USA). We excluded the following patients as we felt the imaging was probably justified: patients with trauma, shunted patients, postoperative imaging, patients with a known mass, patients with abnormal coagulation profile (anticoag therapy, thrombocytopenia, etc), immune-compromised patients, prior cerebro-vascular accident, known Chiari, seizures, and documented increased intracranial pressure. Radiologic findings were recorded and categorized as: Normal, infectious, mass lesion, sinus

disease, vascular disease, or "other", which included findings likely not related to headaches (e.g., volume loss).
Results
We found that in 2015 our institution performed 519 head CT studies in children with an indication of "Headache" or "Migraine" that fulfilled our inclusion and exclusion criteria. Of these, n=355 were normal (68%), n=111 (22%) had sinus disease, n=16 (3%) had a mass lesion, n=6 (1%) had a vascular abnormality, n=1 (0.2%) had an infectious process, and n=30 (6%) had other findings that were probably not related to headaches.
Conclusions
Our data assessment showed that the majority (68%) of CT imaging studies in children with headaches or migraine were normal. Providers may not be aware of clinical decision rules that can help differentiate patients with primary headaches (no imaging initially indicated) and secondary headaches (imaging work-up indicated) (1). This represents an opportunity for designing improvement interventions.

O-350

5:40PM - 5:48PM

Overuse of Repeat Noncontrast Head Computed Tomography

D Chow[1], Y Chen[1], B Weinberg[2], L Sugrue[3]
[1]University of California, San Francisco, San Francisco, CA, [2]Emory University Hospital, Atlanta, GA, [3]UCSF, San Francisco, CA

Purpose
Availability and ease have made noncontrast head CT the go-to imaging examination to exclude acute intracranial abnormalities such as hemorrhage, hydrocephalus, herniation, or large infarcts. For this reason noncontrast head CT has become a routine part of the assessment of patients presenting to the emergency room (ER) with neurological symptoms. Anecdotally, many neuroradiologists have observed that head CTs performed in patients presenting without focal neurological deficits are of low diagnostic yield. The purpose of this study is to evaluate the negative predictive value of a negative head CT, and the "risk-free" period that a negative study confers on patients presenting without focal neurological symptoms.
Materials and Methods
We retrospectively evaluated patients who received repeat noncontrast head CTs at our institute over a 3-year period. Repeat examinations were defined as those occurring within 90 days of first imaging. We excluded examinations in patients with acute findings at first examination. Positive repeat examinations were defined as those that showed acute hemorrhage, herniation, hydrocephalus, or interval change.
Results
A total of 12711 noncontrast head CTs were identified during the study period, of which

88.5% (11243/12711) had no acute finding. Of these patients, 9.1% (1160/12711) had a negative CT had a repeat CT within 90 days. Of these 1160 patients with initial negative noncontrast head CTs, the incidence of acute findings on subsequent imaging was 1.5%. When evaluated by duration, rates were 0.8%, 2.3%, and 2.6% at 30, 60, and 90 days. Of the 11 positive patients, 4 had prior history of malignancy, 3 had history of recent trauma, and 4 had a history of new altered mental status.
Conclusions
In the absence of underling malignancy or recent trauma, repeated noncontrast head CT is of limited value in the assessment of emergency room patients.

O-351

5:48PM - 5:56PM

Evaluation of Educational Sessions and the Use of Radiology Support, Communication and Alignment Network Platform in Reducing Inappropriate Imaging for Uncomplicated Low Back Pain

K Wang[1], C Yen[1], M Chen[2], D Variyam[1], T Uribe[1], B Reed[3], C Lincoln[1]
[1]Baylor College of Medicine, Houston, TX, [2]University of Texas MD Anderson Cancer Center, Houston, TX, [3]Baylor College of Medicine, Department of Family and Community Medicine, Houston, TX

Purpose
Low back pain (LBP) is a common, disabling disease in adults (1, 2). The overall trend in the routine and inappropriate use of spine imaging for uncomplicated LBP continues to increase (3). The aim of this study is to evaluate the impact of educational sessions informing referring physicians on current guidelines and the use of the American College of Radiology's Radiology Support, Communication and Alignment Network (R-SCAN) platform (4) on reducing inappropriate use of lumbar spine MRIs for uncomplicated LBP.
Materials and Methods
Educational presentations were given at 3 peripheral county clinics in April and May of 2016. Two additional county clinics without educational sessions served as controls. Presentations highlighted the American College of Physicians (ACP) and Choosing Wisely Campaign imaging guidelines for LBP and the R-SCAN platform using a case-based approach. Pre-implementation time period was from April 1st, 2015 to March 31st, 2016. Postimplementation time period was from June 1st to October 31st, 2016. Wilcoxon-Mann-Whitney rank-sum test was used to compare the reduction in the number of lumbar spine MRI orders per month by requesting clinicians between clinics receiving implementation and controls. Wilcoxon signed rank test was used to compare the number of lumbar spine MRI imaging orders placed per month at each clinic that received implementation between 6/1/2015 to 10/31/2015 (pre-implementation) and 6/1/2016 to 10/31/2016 (postimplementation). A p value < 0.05 was considered statistically significant.

Results
The largest clinic demonstrated significantly lower monthly number of lumbar spine MRI orders during the post-implementation period when compared to the pre-implementation period (15.6 versus 9.4, p=0.0431). No significant differences were noted with remaining clinics, or differences in reduction between clinics and controls.
Conclusions
Multiple and recurring sessions of education, feedback, and dialogue with referring physicians may be necessary to improve the process for sustained change in the appropriate use of lumbar spine MRI for uncomplicated LBP.

O-352

5:56PM - 6:04PM

Imaging Reduction via Blood Pressure Control: Impact of Hypertension on Neuroimaging in a Healthcare Population.

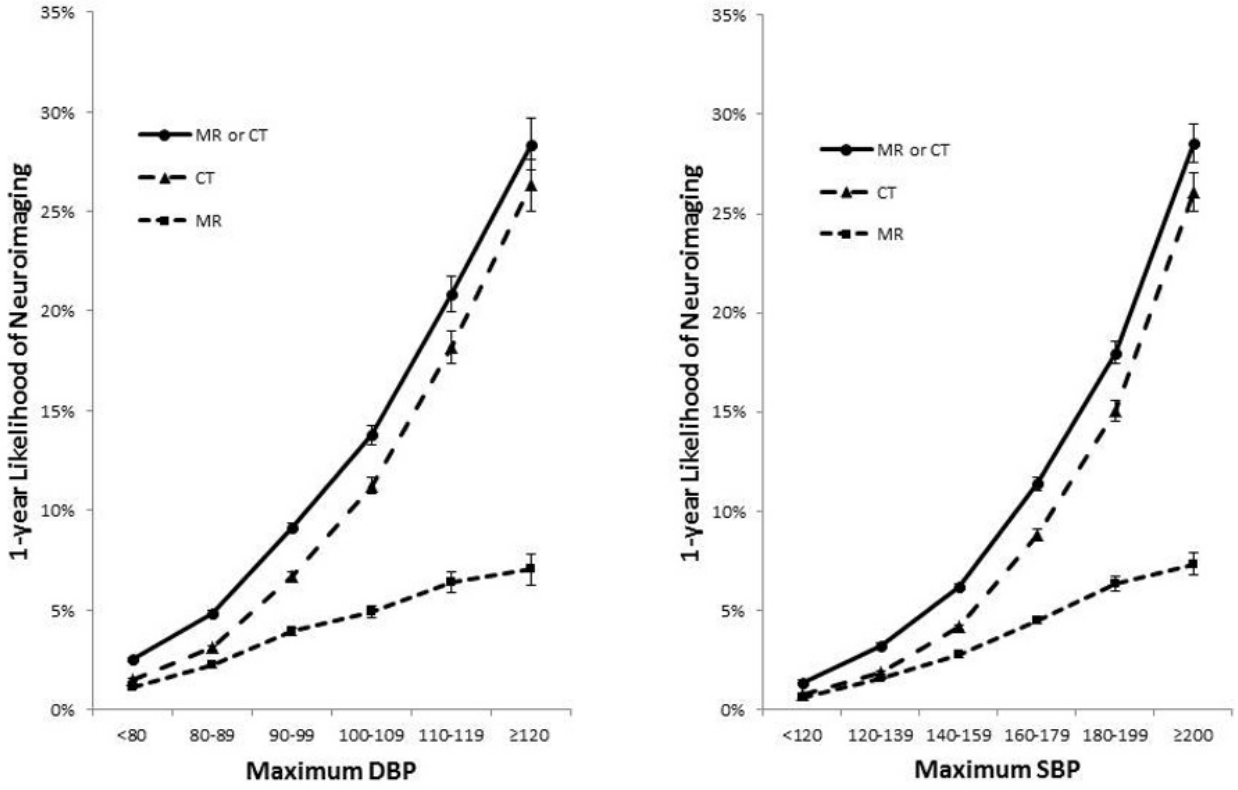
J Fritz[1], A Ajam[2], D Boulter[2], L Prevedello[3], M Luttrull[4], E Bourekas[5], X Nguyen[3]
[1]Wexner Medical Center at The Ohio State University, Columbus, OH, [2]The Ohio State University Wexner Medical Center, Columbus, OH, [3]Ohio State Wexner Medical Center, Columbus, OH, [4]The Ohio State University Wexner Medical, Columbus, OH, [5]The Ohio State University, Columbus, OH

Purpose
Hypertension is a well established risk factor for neurovascular disease, but the impact of hypertension on neuroimaging use within a healthcare population has not been quantified previously. This study examines the population impact of hypertension control on neuroimaging utilization.
Materials and Methods
Over 313000 patients with documented blood pressures in a university-based health system during the 2015 calendar year were analyzed retrospectively in this IRB-exempt study. Aggregate counts of patients with maximum documented diastolic blood pressures (DBP) and systolic blood pressures (SBP) within specified ranges were obtained, and percentages of those patients undergoing a brain neuroimaging exam, defined as an MRI, MRA, CT, or CTA study of the head, in 2015 were computed to quantify 1-year likelihood of neuroimaging as a function of maximum recorded blood pressure.
Results
Brain neuroimaging was performed in 2.5% of patients with DBP < 80 mmHg and in 1.4% of patients with SBP < 120 mmHg during the 1-year study period. Even modest elevations in DBP to 80-89 mmHg or SBP to 120-139 mmHg were associated with near doubling of neuroimaging usage to 4.8% and 3.2%, respectively, representing a statistically significant increase ($p<0.0001$ by the chi square test) (Fig.). At high extremes of DBP (≥120 mmHg) and SBP (≥200 mmHg), neuroimaging use increased 11-fold to 28.4% and 21-fold to 28.6%,

respectively. Increased neuroimaging use at higher blood pressures was due predominantly to CT, but MR use over the examined DBP and SBP ranges increased 6-fold and 11-fold, respectively.

Conclusions

The steep increase in neuroimaging usage with increasing blood pressure suggests that poorly controlled hypertension may represent a major driving force in neuroimaging utilization, presumably by contributing to cerebrovascular disease or by influencing providers' assessment of disease risk. Conversely, population-based efforts to treat hypertension could potentially have a substantial impact on reducing neuroimaging costs.



(Filename: TCT_O-352_HTNfig.jpg)

O-353

6:04PM - 6:12PM

Magnetic Resonance Imaging and Vagal Nerve Stimulators: Published Guidelines vs Clinical Practicality

J Ormsby[1], R Lee[2], S Fulton[3], A Choudhri[4]
[1]University of Tennessee Health Science Center/Methodist Healthcare, Memphis, TN, [2]University of Tennessee Health Science Center, Memphis, TN, [3]Le Bonheur Children's Hospital, Memphis, TN, [4]University of Tennessee Health Center, Memphis, TN

Purpose
To provide quality assurance for the use of receive-only coils in magnetic resonance imaging (MRI) of the brain for patients with vagal nerve stimulator (VNS).
Materials and Methods
Information on 50 consecutive patients who had an implanted VNS and received a brain MRI using a receiver-only head coil since 2010 was obtained. These scans were obtained at 1 institution with 3 scanners (1 1.5 T and 2 3.0 T). Any adverse outcomes including pain or burns while the patient was in the MRI scanner were reported by the MRI technician to the neuroradiologist. Additionally, each VNS was interrogated by a neurologist for any device malfunction after the scan.
Results
There was no patient-reported complications in any of the 50 patients scanned. There were no device complications reported. There were no device exchanges needed as result of scan.
Conclusions
While manufacturer and FDA have established successful testing parameters for the safety for use of transmit-and-receive coils while scanning patients with a VNS, our study helps to validate the use of receiver-only coils in patients receiving MRIs of the brain with implanted VNS.

O-354

6:12PM - 6:20PM

Clinical Usefulness of Brain Imaging for First Episode Psychosis

J Delorme[1], D Landry[2], M Belair[3]
[1]University of Montreal, Montreal, QC, [2]University of Montreal, Montreal, Quebec, [3]Université de Montréal, Montréal, Québec

Purpose
Many current guidelines recommend obtaining structural brain imaging for all patients presenting with first episode psychosis (FEP). However, recent research shows limited diagnostic yield of such practice. The objective of this study is to assess the clinical usefulness of brain CT and/or MRI in previously healthy patients presenting with FEP, without accompanying neurologic symptoms or signs.
Materials and Methods
We conducted a retrospective multicenter study in which brain CT and/or MRI were obtained for patients presenting with first episode psychosis from 2002 to 2016. Four

hundred twenty-one patients (yielding 409 CT and 19 MRI) aged between 18 and 65 years (146 females; mean age 34,6) were included. None had previously known medical conditions predisposing to neurologic disease, and all presented for a recent (<3 months) FEP without accompanying neurologic symptoms or signs. Results then were classified as clinically relevant, incidental or normal.
Results
One (0.2%) patient had a clinically relevant finding (acute frontal subdural hematoma). However, it was revealed after the examination that he showed longstanding psychotic symptoms (> 5 years) and had recently suffered from head trauma. Had this information been known at the time of imaging request, he would not have been included in the study. There were 93 (21.7%) examinations with incidental findings and 336 (78.0%) normal.
Conclusions
This study suggests that the diagnostic yield of structural brain imaging in previously healthy patients presenting with FEP without accompanying neurologic symptoms or signs is very low. We believe future guidelines should not recommend routine brain imaging in these patients.

O-355

6:20PM - 6:28PM

Comparison of Results Generated by Three Automated Segmentation Software Programs for Estimation of Brain Cortical and Subcortical Volumes

S Kosaraju[1], J Stevens[2], T Jovanovic[3], J Allen[3]
[1]Emory University School of Medicine, Atlanta, GA, [2]Emory University School of Medicine, Marietta, GA, [3]Emory University, Atlanta, GA

Purpose
A growing body of research is focused on investigating the impact of a variety of diseases ranging from trauma to psychiatric disease on regional brain volumes. Recently, there has been an increase in the number of available brain automated segmentation packages; however, limited studies have compared the results between methods. The purpose of this study was to determine the inter-method reliability of 3 commonly used segmentation packages to assess their interchangeability for research and clinical purposes.
Materials and Methods
A total of 39 subjects who underwent a research brain MRI that included a T1 MP-RAGE sequence as part of a study investigating structural variability in PTSD victims were used as the patient population. All MRIs were acquired on the same 3.0 T Siemens Prisma scanner. Images were processed and segmented using 3 separate software packages: FreeSurfer, NeuroQuant, and MRICloud. Comparable regions of interest (ROIs) from each package were saved and an intrasubject variability for these ROIs was calculated. A variance-to-mean ratio (VMR) was calculated for each structure within each subject.

Results

Regions of interest in small, commonly studied subcortical regions such as the amygdala, hippocampus, caudate, and putamen, showed significantly greater inter-method reliability than in larger regions of interest. A general trend also was observed that cortical segmentation showed less inter-method reliability than subcortical segmentation. When using a cut point of a VMR less than 0.10, only 13/73 regions had greater than 50% of subjects with the desired degree of variance. When using a more lenient cut point of 0.20 for the VMR, 33/73 regions had greater than 50% of subjects with the desired degree of variability.

Conclusions

While automated segmentation of MRI allows for rapid volumetric assessment of a variety of structures of interest, there was poor inter-method reliability in the structural volumes estimated by commonly used automated segmentation software packages, which is likely a function of the different atlases used for registration and segmentation of subjects. This limits the applicability of absolute volumes obtained using these methods.



a. FreeSurfer b. MRICloud c. NeuroQuant

Figure 1. Representative sagittal slices of segmentation for each of the 3 methods.

	FREESURFER		NEUROQUANT		MRICLOUD		VARIANCE-TO-MEAN RATIO	
	Left	Right	Left	Right	Left	Right	Left	Right
AMYGDALA	1603.2	1545.6	1660	1740	1496	1669	0.052	0.060
CAUDATE NUCLEUS	2513.6	2626.7	2170	2680	2622	2597	0.097	0.016
HIPPOCAMPUS	2939.2	2987.9	2760	2830	3077	3030	0.054	0.036
LATERAL ORBITOFRONTAL GYRUS	5690	5443	-	-	3516	3252	0.334	0.356
SUPERIOR TEMPORAL GYRUS	12604	12343	-	-	11277	14313	0.172	0.513
PREFRONTAL CORTEX	18262	16421	-	-	8864	7237	0.490	0.549

Figure 2. Structural volumes (mm^3) and variance-to-mean ratios for a representative selection of structures within one subject.

(Filename: TCT_O-355_KosarajuSegmentationASNR2017figures.jpg)

Wednesday
5:00PM - 6:30PM
Long Beach Convention Center, Room 203AB (Upper Level)

21G-Parallel Paper Session: More Aneurysm Management: Dealing with the Unruptured and Unknown

O-356

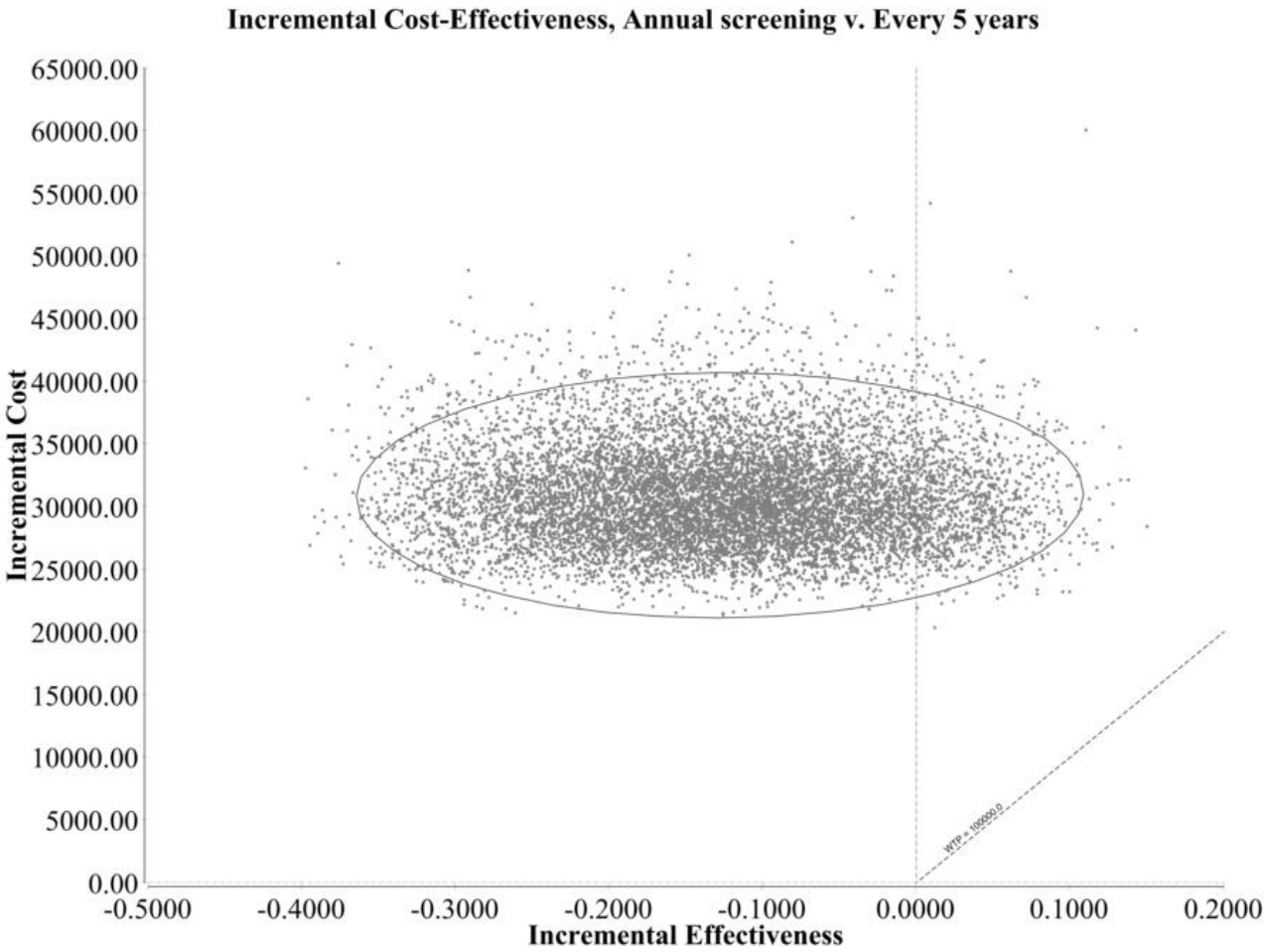
5:00PM - 5:08PM

Optimal Imaging Strategies and Follow-up in Patients with Unruptured Intracranial Aneurysms

X Wu[1], H Forman[1], P Sanelli[2], A Malhotra[1]

[1]*Yale University School of Medicine, New Haven, CT,* [2]*Northwell Health, Manhasset, NY*

Purpose
To determine the optimal follow-up strategy in patients with unruptured intracranial aneurysms (UIAs).
Materials and Methods
Unruptured intracranial aneurysms can be treated or followed by imaging to assess for growth or risk factors for rupture. One has to factor complications and costs associated with coiling, the risk of regrowth and rupture even after coiling and so on. No clear guidelines exist as to the frequency of follow-up imaging and its utility. A decision tree with Markov modeling was constructed with TreeAge Pro Suite from a payer's perspective. The horizon of the model is until the death of a patient. Three different screening frequencies, annual, biennial, and every 5 years are considered, as well as no follow up as the control strategy. All clinical parameters were derived from recently published large-cohort studies or meta-analyses. All costs parameters were derived from Medicare reimbursement rates whenever possible, and various cost studies otherwise, assigned with wide distributions.
Results
When using CTA as the imaging modality, annual and biennial screening strategies are shown to be not effective with higher costs and lower effectiveness than both no follow up and imaging every 5 years. No follow up is cheaper but also results in lower effectiveness. Overall, imaging every 5 years is the most cost-effective strategy. When using MRA as the imaging modality, the results are similar. One-way sensitivity analyses also are performed to test the robustness of the conclusion against the key variables. When the rupture rate of a UIA is lower than 0.9%, no follow up is better. otherwise, imaging every 5 years is better.
Conclusions
Multiple factors influence the decision to treat or follow up patients with unruptured intracranial aneurysms. We highlight their influence on the cost-effectiveness. The optimal imaging frequency for patients with UIAs may be every 5 years, when compared to annual, biennial and no follow up.



(Filename: TCT_O-356_IncrementalCEScatterPlot2.jpg)

O-357

5:08PM - 5:16PM

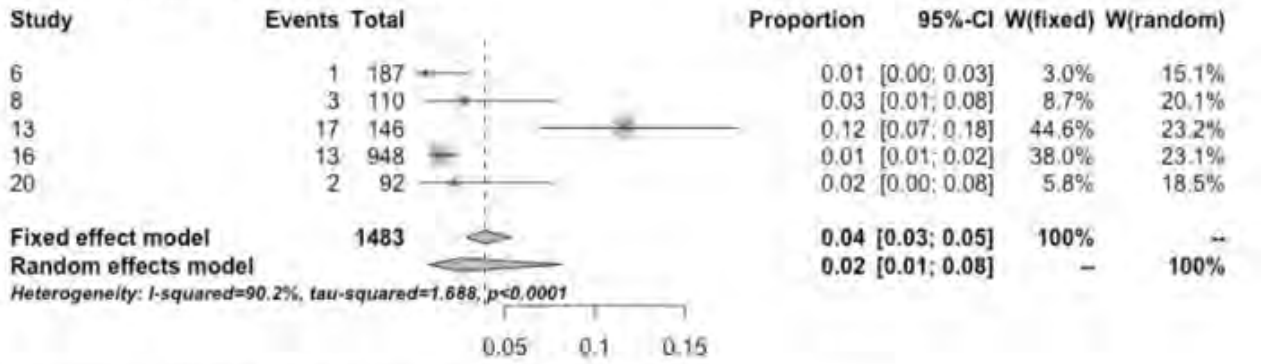
Growth and Rupture Risk of Small Unruptured Intracranial Aneurysms: A Systematic Review and Meta-Analysis

X Wu[1], H Grossetta Nardini[2], C Matouk[1], H Forman[1], D Gandhi[3], P Sanelli[4], A Malhotra[1]
[1]Yale University School of Medicine, New Haven, CT, [2]Yale University, New Haven, CT, [3]University of Maryland School of Medicine, Baltimore, MD, [4]Northwell Health, New York, NY

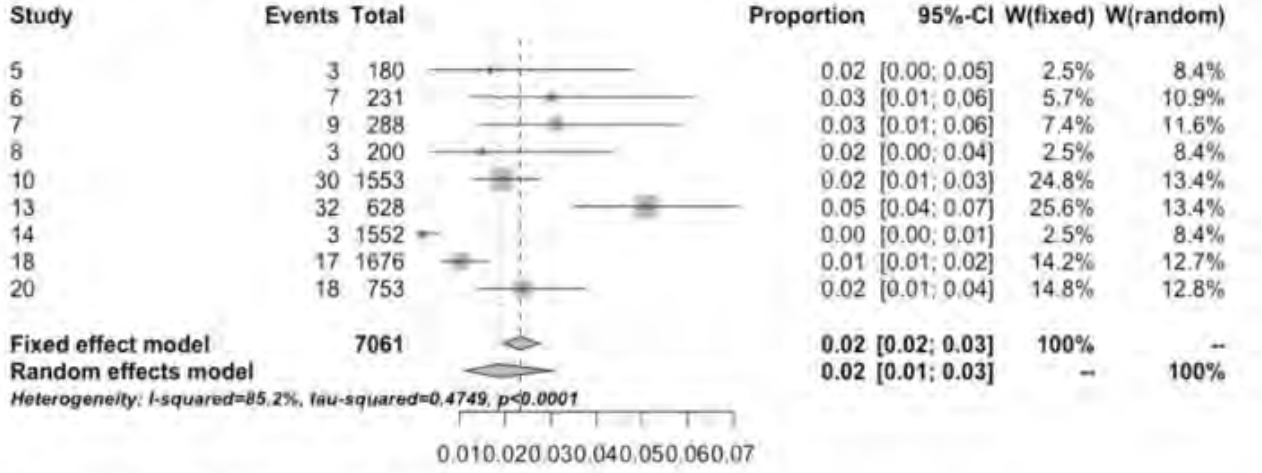
Purpose
Small, unruptured intracranial aneurysms (UIAs) are being increasingly diagnosed. Management depends on growth and rupture risks, which may be different for small aneurysms relative to aneurysms >7 mm.
Materials and Methods
A comprehensive literature search was performed. We calculated the growth and rupture

risks reported for small UIAs in 3 size groups (≤3 mm, ≤5 mm, and ≤7 mm). Incidence was pooled with both random and fixed-effects models. Subgroup analyses were performed for studies with low- and high-risks of bias.
Results
There were 1,846 studies returned from the initial literature search, and 25 studies were included in the final analysis. A total of 1,483, 7,061, and 4,787 aneurysm-years were available for follow up of aneurysms ≤3, 5, and 7 mm respectively to analyze annual growth rate. For annual rupture risk, 2,076, 15,739, and 24,448 aneurysm-years were available respectively. The pooled annual growth rates by fixed effect for aneurysms ≤3, 5, and 7 mm are 0.04 (CI: 0.03-0.05), 0.02 (CI: 0.02-0.03), and 0.03 (CI: 0.03-0.04) respectively. The rupture risk for aneurysms ≤7 mm is 0.02 under fixed effect model and 0.01 under random effects model. The pooled rupture risks of aneurysms ≤3 mm and ≤5 mm are 0.00 under both models.
Conclusions
Small UIAs (<7mm) have very low growth and rupture rates and there is relatively poor correlation between growth and rupture. Very small (<3 and <5 mm) UIAs have even lower risk of rupture. This should be considered for specific treatment or imaging follow-up recommendations. Standardization of definition of growth is needed.

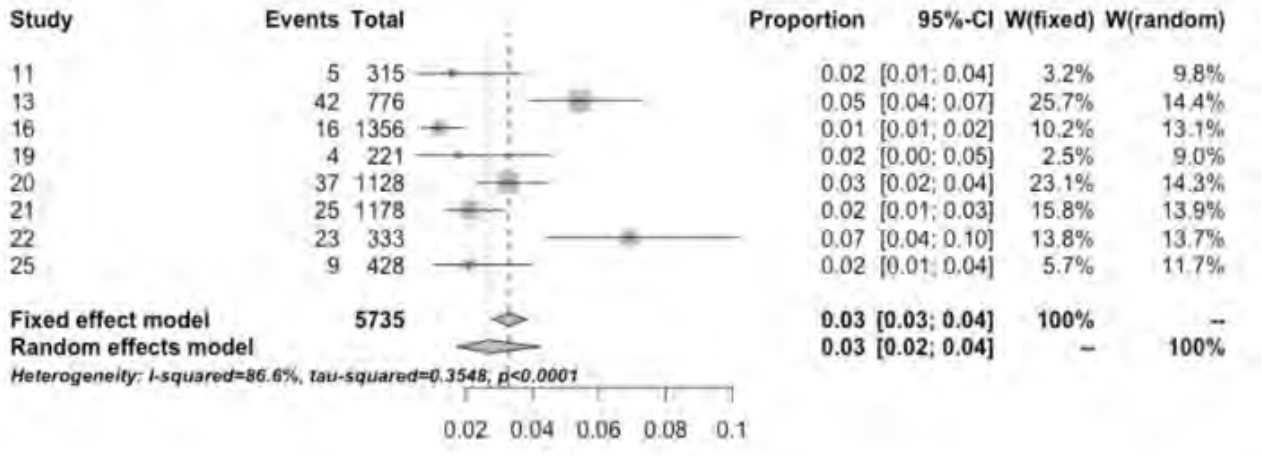
a) Growth Rate of UIA ≤3 mm



b) Growth Rate of UIA ≤5 mm



c) Growth Rate of UIA ≤7 mm



(Filename: TCT_O-357_Figure2_GrowthRate.jpg)

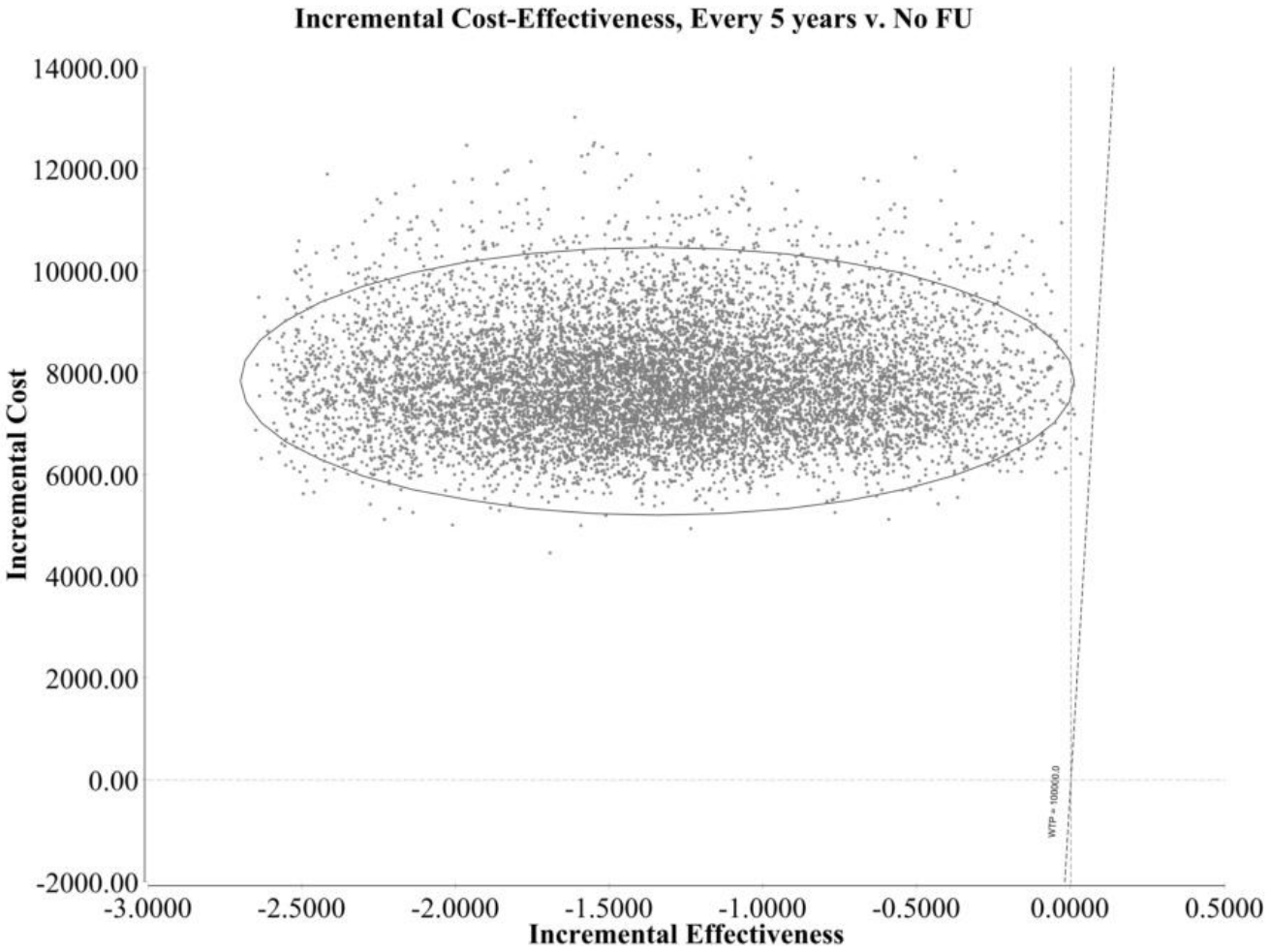
O-358

5:16PM - 5:24PM

Management of Tiny Unruptured Intracranial Aneurysms: A Cost-Effectiveness Analysis

X Wu[1], C Matouk[1], H Forman[2], D Gandhi[3], P Sanelli[4], A Malhotra[1]
[1]Yale University School of Medicine, New Haven, CT, [2]Yale University School of Medicine, new haven, CT, [3]University of Maryland School of Medicine, Baltimore, MD, [4]Northwell Health, New York, NY

Purpose
Unruptured intracranial aneurysms (UIAs) are relatively common, and a large number of incidental UIAs are tiny, measuring ≤ 3 mm. The natural history of tiny UIAs remains poorly understood. No clear guidelines exist regarding management specifically for tiny UIAs, including for aneurysm ablation or imaging follow- up to assess growth.
Materials and Methods
Cost-effectiveness analysis was performed for 5 different strategies for tiny UIAs - (a) annual MRA screening (b) biennial MRA screening (c) MRA screening every 5 years (d) coiling and follow-up and (e) no treatment or preventive follow-up. A decision tree with Markov modeling was constructed from a payer's perspective. Probabilistic, one-way, and two-way sensitivity analyses were performed.
Results
The base-case calculation shows no preventive follow-up to be the most cost-effective strategy. Among the imaging follow-ups, MRA every 5 years is the best strategy with the next highest effectiveness. The conclusion remains robust in probabilistic and 1-way sensitivity analyses. No routine follow-up remains the optimal strategy when the annual growth rate and rupture risk of growing aneurysms are varied. When the annual rupture risk of nongrowing UIAs is smaller than 2.7%, no follow-up is the optimal strategy. Otherwise, coiling should be performed directly.
Conclusions
Further studies are needed to understand the natural history of tiny UIAs in terms of growth and rupture rates. Given the current literature, our study reveals that no preventive treatment or imaging follow-up is the cost-effective strategy resulting in better health outcomes and lower healthcare spending.



(Filename: TCT_O-358_Figure2.jpg)

O-359

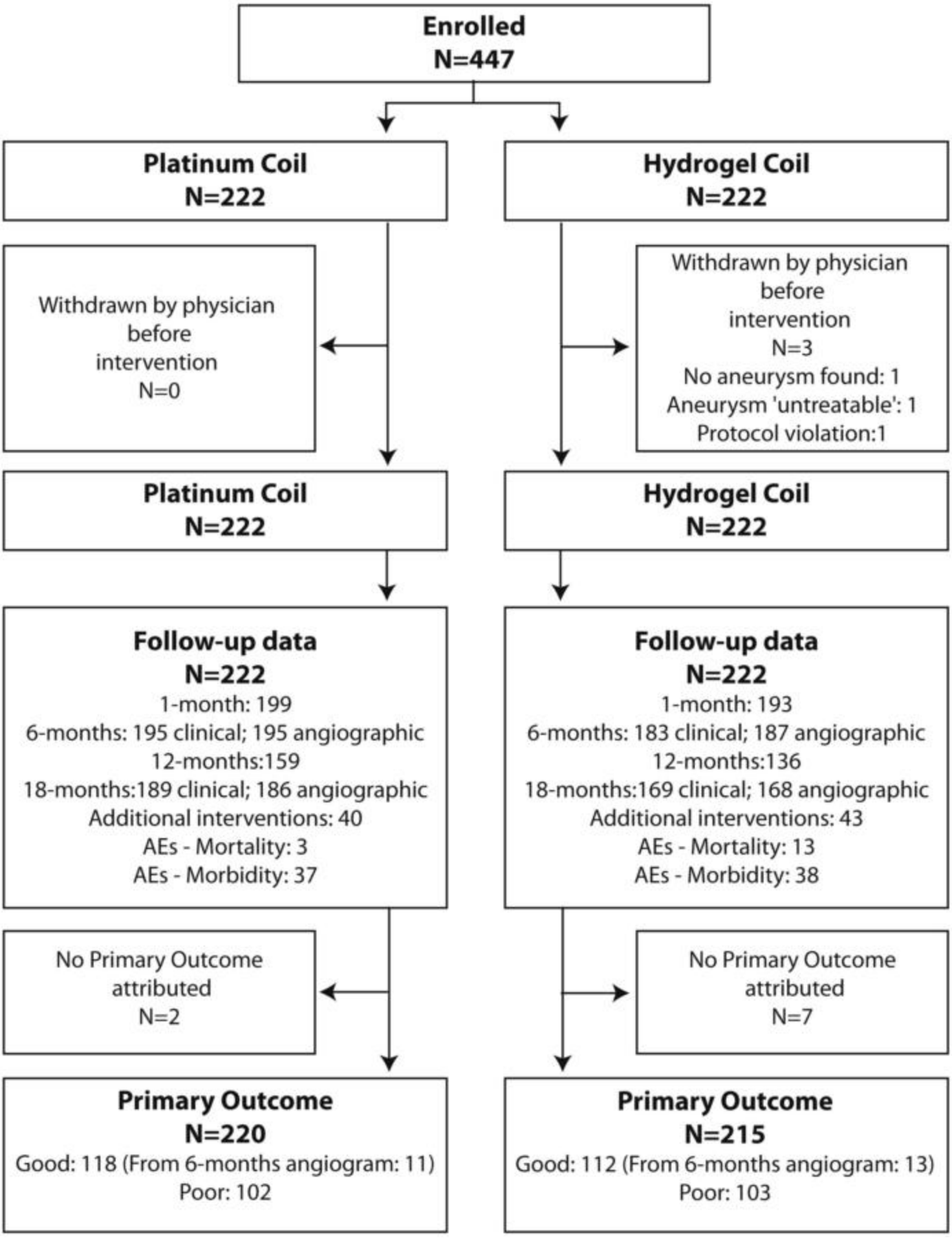
5:24PM - 5:32PM

Hydrogel versus Bare Platinum Coils in Patients with Large or Recurrent Aneurysms Prone to Recurrence after Endovascular Treatment (PRET): a Randomized Controlled Trial.

J Raymond[1]
[1]*CHUM Centre Hospitalier de l'Université de Montréal, Montréal, QC*

Purpose
* Presentation by Dr Roy on behalf of the PRET Collaborative Group. Purpose: Some patients are at high risk of aneurysm recurrence after endovascular treatment: patients with large aneurysms (PRET-1) or with aneurysms that have previously recurred after coiling (PRET-2). We aimed to establish whether the use of hydrogel coils improved efficacy outcomes as compared with bare platinum coils.

Materials and Methods
PRET was an investigator-led, pragmatic, multicenter, parallel, randomized (1:1) trial. Randomized allocation was performed separately for PRET-1 and PRET-2 patients, using a web-based platform ensuring concealed allocation. The primary outcome was a composite of a residual/recurrent aneurysm, adjudicated by a blinded core lab, or retreatment, intracranial bleeding, or mass effect during the 18-month follow-up period. Secondary outcomes included adverse events, mortality and morbidity (mRS>2). The hypothesis was that hydrogel would decrease the primary outcome from 50% to 30% at 18 months, necessitating 125 patients per group (500 for PRET-1 and PRET-2).
Results
The trial was stopped once 250 PRET-1 and 197 PRET-2 patients had been recruited, because of slow accrual. A poor outcome occurred in 55/124 [44.4% (35•5%-53•2%)] PRET-1 patients allocated to platinum, compared to 63/120 [52•5% (43•4%-61•6%)] patients allocated to hydrogel [OR: 1•387 (0•838-2•295); P=0•20] and in 47/96 [49•0% (38•8%-59•1%)] PRET-2 patients allocated to platinum, compared to 40/95 [42•1% (32•0%-52•2%)] allocated to hydrogel [OR: 0•959 (0•428-1•342); P=0•34]. Adverse events and morbidity were similar. There were 16 deaths (3•6%; 3 platinum; 13 hydrogel; P=0•011).
Conclusions
Coiling of large and recurrent aneurysms is safe but often poorly effective according to angiographic results. Hydrogel coiling was not shown to be better than platinum.


Enrolled
N=447
Platinum Coil
N=222
Hydrogel Coil
N=222
Withdrawn by physician before intervention
N=0
Withdrawn by physician before intervention
N=3
No aneurysm found: 1
Aneurysm 'untreatable': 1
Protocol violation:1
Platinum Coil
N=222
Hydrogel Coil
N=222
Follow-up data
N=222
1-month: 199
6-months: 195 clinical; 195 angiographic
12-months:159
18-months:189 clinical; 186 angiographic
Additional interventions: 40
AEs - Mortality: 3
AEs - Morbidity: 37
Follow-up data
N=222
1-month: 193
6-months: 183 clinical; 187 angiographic
12-months:136
18-months:169 clinical; 168 angiographic
Additional interventions: 43
AEs - Mortality: 13
AEs - Morbidity: 38
No Primary Outcome attributed
N=2
No Primary Outcome attributed
N=7
Primary Outcome
N=220
Good: 118 (From 6-months angiogram: 11)
Poor: 102
Primary Outcome
N=215
Good: 112 (From 6-months angiogram: 13)
Poor: 103

(Filename: TCT_O-359_flowchart.jpg)

O-360

5:32PM - 5:40PM

The Barrel Stent: New treatment option for stent assisted coiling of wide-neck bifurcation aneurysms: Results of a single center study

R Mühl-Benninghaus[1], A Simgen[1], w reith[2], U Yilmaz[3]
[1]Saarland University Hospital, Homburg, Saarland, [2]University clinic saarland, homburg, saarland, [3]Saarland University Hospital, Homburg, Germany

Purpose
The Barrel stent is a laser cut stent designed for stent-assisted coil embolization of wide-necked bifurcation or branch aneurysms with a single device, with the purpose of lowering the metal-to-artery ratio and its inherent risk of thromboembolic complications of multiple stents. We report our early experiences with this device in 17 patients in this retrospective single center analysis.
Materials and Methods
Seventeen consecutive patients who underwent stent-assisted coil embolization of wide-necked bifurcation aneurysms with the Barrel stent were identified retrospectively. We analyzed the feasibility of successful deployment and post-treatment angiographic results. Adverse events, clinical outcome, and angiographic follow-up results also were analyzed.
Results
Aneurysms were located in the internal carotid artery (n=3), the middle cerebral artery (n=9), the anterior communicating artery (n=3), and the basilar artery (n=2). In the immediate post-treatment angiography, adequate occlusion (neck remnant or total occlusion) was observed in 16/17 (94.1%) of aneurysms. One patient experienced a transient ischemic attack. No permanent neurologic deficits were observed. Thirteen of 17 (76.5%) patients underwent short-term follow-up angiography after 3 months, all of which showed adequate occlusion of the aneurysm.
Conclusions
In this small retrospective single center analysis we show that stent-assisted coiling with the Barrel stent is a safe and effective option for the endovascular treatment of intracranial wide-necked bifurcation aneurysms.

O-361

5:40PM - 5:48PM

Web treatment in acutely ruptured aneurysms

J Peluso[1], W van Rooij[2]
[1]Sint Elisabeth Ziekenhuis, Tilburg, Netherlanss, [2]Sint Elisabeth Ziekenhuis, Tilburg, AK

Purpose
The WEB device recently was introduced for intrasaccular treatment of wide-necked aneurysms without the need for adjunctive support. We present our first experience in using the WEB for small ruptured aneurysms.
Materials and Methods
From Feb 2015 to Nov 2016, 132 acutely ruptured aneurysms were treated endovascularly. Of those, 78 (59%) were treated with the WEB. There were 25 men and 53 women, mean age 59 years (range 23-82 years). Mean aneurysm size was 4.9 mm and 26 were ≤ 4mm. Two aneurysms were treated with WEB and coils and 1 with WEB and stent. Clinical follow up was assessed at 3 and 6 months according to mRS. Imaging follow up consisted of angiography at 3 months and MRA at 6 months.
Results
Of 78 aneurysms, 77 were adequately occluded after WEB placement. One aneurysm was deliberately partially occluded and was later clipped. There was 1 procedural rupture without clinical sequelae. In 5 patients, thromboembolic complications occurred followed by thrombectomy in 4. Three patients developed an infarction. Of those, 1 poor grade patient died, 1 patient had mild hemiparesis and 1 patient had no symptoms. One thromboembolic complication was caused by WEB protrusion in the parent artery. Procedural permanent morbimortality was 3% (2 of 77). Angiographic and clinical follow-up at 3 months was available in 54 patients: 11 poor grade patients died during hospital admission due to sequelae of SAH, 1 of a thromboembolic complication and 12 patients are scheduled for angiographic follow up. Of 54 aneurysms, 45 (83%) were completely occluded, 8 (15%) were adequately occluded with a small neck remnant and 1 (2%) had a deliberate aneurysm remnant. Clinical follow up at 3 months was mRs 0-2 in 53, mRs 3 in 2 and mRs 4-5 in 1. There were no rebleeds from the ruptured aneurysm during follow up. One aneurysm was additionally clipped.
Conclusions
WEB treatment of small ruptured aneurysms was safe and effective. Adjunctive stent support was needed only once. One patient required additional clipping after deliberate initial partial occlusion. No rebleeds occurred during follow up. Our preliminary experience indicates that the WEB may be a valuable alternative to coils in the treatment of acutely ruptured aneurysms.

O-362

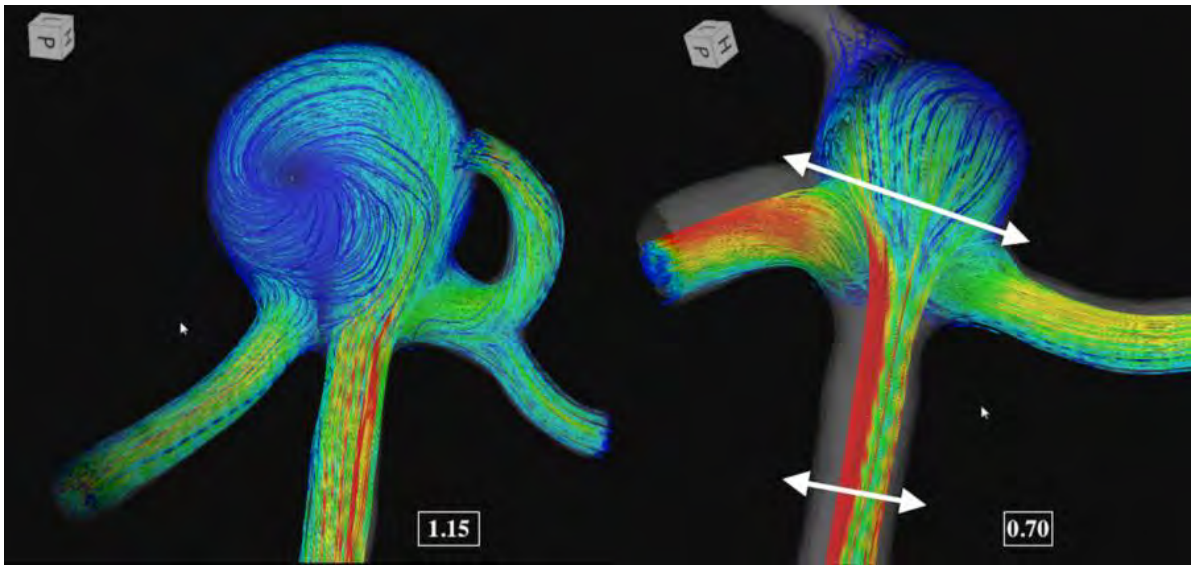
5:48PM - 5:56PM

A Computational Fluid Dynamics (CFD) study of WEB treated aneurysms: can CFD predict WEB "compression" during follow-up?

J Caroff[1], l spelle[2]

[1]Hôpital Bicêtre, Le Kremlin Bicêtre, France, [2]Hôpital Bicêtre, Le Kremlin-Bicêtre, Ile de France

Purpose
Recent reports have revealed a worsening of aneurysm occlusion between WEB treatment baseline and angiographic follow-up due to "compression" of the device. We utilized computational fluid dynamics (CFD) in order to determine whether the underlying mechanism of this worsening is flow related.
Materials and Methods
We included data from all consecutive patients treated in our institution with a WEB for unruptured aneurysms located either at the middle cerebral artery or basilar tip. The CFD study was performed using pre-operative 3D rotational angiography. Inflow ratio was analyzed as previously described (3). From digital subtraction follow-up angiographies patients were dichotomized into 2 groups: one with WEB "compression" and one without. We performed statistical analyses to determine a potential correlation between WEB compression and CFD inflow ratio.
Results
Between July 2012 and June 2015, a total of 22 patients with unruptured middle cerebral artery or basilar tip aneurysms were treated with a WEB device in our department. Three patients were excluded from the analysis and the mean follow-up period was 17 months. Eleven WEBs presented "compression" during follow-up. Interestingly, device "compression" was statistically correlated to the CFD inflow ratio ($p= 0.018$), although not to aneurysm volume, aspect ratio or neck size.
Conclusions
The mechanisms underlying the worsening of aneurysm occlusion in WEB treated patients due to device compression are most likely complex as well as multifactorial. However, it is apparent from our pilot study that a high arterial inflow is, at least, partially involved. Further theoretical and animal research studies are needed to increase our understanding of this phenomenon.



(Filename: TCT_O-362_Fig2-copie.jpg)

O-363

5:56PM - 6:04PM

Relationship between MR-DWI-Positive Lesions and Symptomatic Ischemic Complications after Coiling of Ruptured Intracranial Aneurysms

J Park[1]
[1]*Hallym University Dong-tan Sacred Heart Hospital, Gyunggi-do, Gyunggi-do*

Purpose
The aims of this study were to evaluate the risk factors for developing symptomatic ischemic complication (SIC, transient ischemic attack or stroke) and microembolism detected as magnetic resonance diffusion-weighted imaging positive (DWI positive) lesions in coiling of ruptured intracranial aneurysms. Plus, relationship between each factor and modified Rankin Scale (mRS) after 3 month was studied.
Materials and Methods
From March 2010 to March 2013, 42 subarachnoid hemorrhage patients with ruptured intracranial aneurysm underwent both coiling and postoperative magnetic resonance diffusion-weighted imaging (MR-DWI). The incidence and risk factors for SIC and DWI positive were analyzed retrospectively. The relationships between 3-mRS and DWI positive or SIC also were analyzed.
Results
The incidence of DWI positive was 50%. There is no big difference from incidence of unruptured aneurysm(54.5%). The incidence of SIC was 9.5% (4/42). Patients older than 65 years have a tendency for SIC (p=0.011). Patients with SIC appeared unfavorable 3 month mRS (mRS 3~6, p=0.032).

Conclusions
When endovascular surgeon tries coil embolization to ruptured intracranial aneurysm, the surgeon should try to reduce the occurrence of SIC, particularly in patients older than 65 years.

Table 1. Relationship between 3 month modified Rankin scale with DWI positive / symptomatic ischemic complication

Variable	Category	3-mRS+ (0~2)	3-mRS+ (3~6)	Puni**
SIC*	No	29 (76.3)	9 (23.6)	0.032
	Yes	1 (25.0)	3 (75.0)	
DWI positive	No	16 (76.2)	5 (23.8)	0.572
	Yes	14 (66.7)	7 (33.3)	

SIC* ; symptomatic ischemic complication, 3-mRS+ ; 3 month modified Rankin scale, Puni** ; P-value on univariate analysis

(Filename: TCT_O-363_table1001.jpg)

O-364

6:04PM - 6:12PM

Has Endovascular Treatment for Intracranial Aneurysm reached Technical Maturity?

C Yuan[1], T Karrison[1], S Lee[1]
[1]*University of Chicago, Chicago, IL*

Purpose
Standardized technique, reproducible success rate and comparable clinical outcome measures (COMs) to an established technique can be evidence of the technical maturity of a

new medical technology. We compared core COMs between coiling and clipping for both ruptured and unruptured intracranial aneurysms.
Materials and Methods
Nationwide Inpatient Sample (NIS) data for all hospitalizations between 2007 and 2013 were queried to extract both ruptured and unruptured cerebral aneurysms that were treated with either coiling or clipping. Clinical outcome measures included in-hospital mortality (IM), postoperative stroke (pS), combined mortality and stroke (cMS), all in-hospital complications (aIC) and home discharge rates (HD). Multivariable logistic regression and propensity score matching (PSM) adjusted for demographic, clinical, and disease severity measures were used to compare COMs. The volume-outcome relationships on COMs and annual trend of COMs also were assessed.
Results
In the ruptured aneurysm cohort, adjusting for case mix, coiling was associated with significantly lower rates of pS and cMS and a higher rate of HD ($p<0.05$). Clipping had significantly lower aIC unadjusted ($p<0.05$), but the difference was no longer significant after adjustment for covariates ($p=0.31$). Clipping had lower IM (10. 8%) than coiling (12.2%) without adjustment, however, the difference was reversed after PSM (estimated 1.2% higher rate of mortality for clipping), although not statistically significant ($p=0.20$). Increasing case volume correlated with decreasing IM, cMS and increasing HD in the clipping cohort ($p<0.05$) but no significant differences in the coiling cohort. Coiling showed improvement in IM and cMS during the observed time period ($p<0.05$) but clipping did not. Home discharge rates in the clipping group decreased and aIC rate increased over time in both cohorts ($p<0.05$). In unruptured aneurysms, mortality of both clipping (0.58%) and coiling (0.44%) were extremely low. Coiling was favored in PS, cMS, and HD ($p<0.05$). No statistically significant differences were found between clipping and coiling in IM or aIC after adjustment. Increasing case volume correlated with decreasing IM in coiling and with increasing HD in clipping and coiling ($p<0.05$). During the observed period, clipping demonstrated a significant decrease in IM but an increase in aIC ($p<0.05$).
Conclusions
Coiling demonstrated better or equivalent COMs comparing to clipping in both ruptured and unruptured cohorts in our study. Further analyses will include comparison of costs and more detailed study of the volume-outcome relationships. Limitations of the study include the observational nature of the data and the potential for unobserved confounders and selection bias.

O-365

6:12PM - 6:20PM

Anterior Communicating Artery Aneurysms post-treatment recurrence is associated with anatomic variations of the Anterior Cerebral artery and Aneurysm Configuration.

D Tampieri[1], V Onofrj[2], M Cortes[1]
[1]*Montreal Neurological Hospital and Institute, Montreal, Quebec,* [2]*Montreal neurological hospital and Institute, Montreal, Quebec*

Purpose
The purpose of this study is to assess an association between the presence of anatomical variants in patients receiving treatment for an anterior communicating artery (ACOA) aneurysm and post-treatment recurrence.
Materials and Methods
Two hundred twenty-four patients received treatment with coiling or clipping for an ACOA aneurysm between 2001 and 2016. Presence of A1 hypoplasia and/or ACOA trifurcation was assessed retrospectively and the geometry of the aneurysm was evaluated by assessing if the aneurysm axis direction was parallel to that of the parent vessel. One hundred twenty-three of the treated patients received follow up with MRA and/or angiography after 6,12 and 18 months respectively and were included. Aneurysm neck and sac recanalization were measured at each follow up. We analyzed the association between recanalization of the aneurysm, the presence of anatomic variations of the anterior cerebral artery and the aneurysm configuration.
Results
In 44% of patients hypoplasia of the A1 segment contralateral to the side of the aneurysm was identified. Eleven percent of patients had ACOA trifurcation. Forty-eight percent of the aneurysms were oriented parallel to the parent vessel. Aneurysm size and shape were similar between groups ($p>0.05$). Overall recurrence was significantly more frequent in patients with A1 hypoplasia ($P<0.01$), in patients with A1 hypoplasia with aneurysm axis orientation parallel to the parent artery axis ($p=0.015$) or both ($p=0.02$). No significant difference was found in patients with ACOA trifurcation.
Conclusions
Post-treatment recanalization of ACOA aneurysms is associated with the presence of A1 hypoplasia and with a specific conformation of the aneurysm with the main axis parallel to the parent vessel.

O-366

6:20PM - 6:28PM

Reproducibility of Microcatheter Tip Position in Patient-specific Aneurysm Models

A Frölich[1], M Nawka[1], J Sedlacik[1], J Fiehler[1], J Buhk[1]
[1]*University Medical Center Hamburg-Eppendorf, Hamburg, Hamburg*

Purpose
Microcatheters with differently shaped tips are available to facilitate aneurysm probing for endosaccular embolization, but evidence on how to select catheter shape is sparse. We

developed a method to define the location of the microcatheter tip inside a patient-specific aneurysm model as a 3-dimensional probability map. We hypothesized that microcatheter tip position and positional accuracy depend on the tip shape and the operator's experience.

Materials and Methods

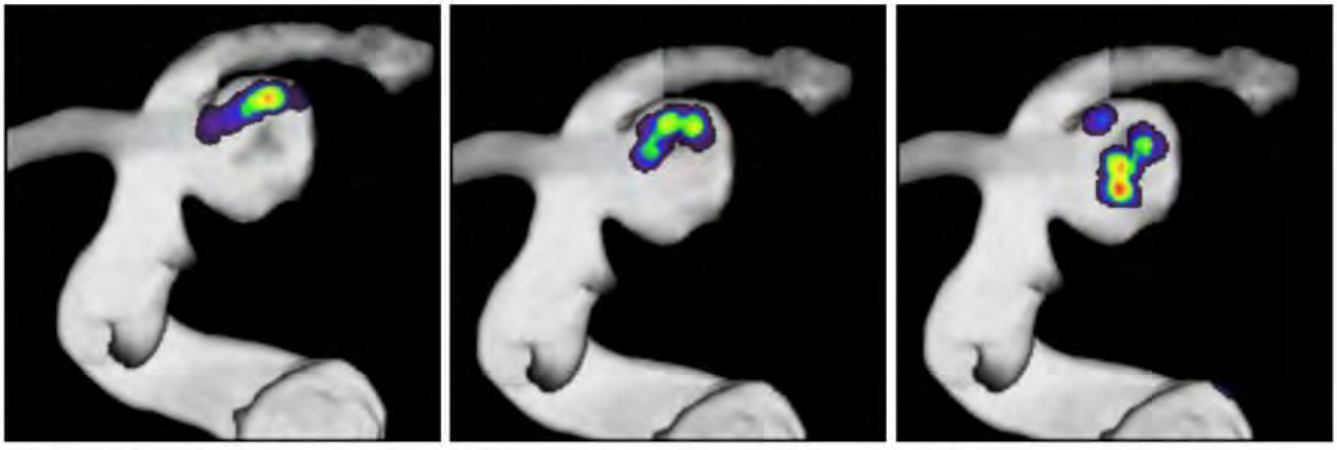
Two elastic, patient-specific aneurysm models were manufactured from 3D rotational angiography. Under fluoroscopic guidance, 3 operators (0, 3, 10 years of experience) independently and repeatedly introduced differently shaped microcatheters (straight, 45°, 90°) into the aneurysm. Each microcatheter position was recorded with flat-panel CT, which was processed to yield 3-dimensional probability maps of the microcatheter tip position. Maps were assessed with histogram analyses and compared between operators and tip shapes.

Results

Distinct, reproducible probability maps were generated for the different microcatheter tips. Among a total of 140 microcatheter insertions, the average distance between the microcatheter tip and the target position was 0.79±0.69mm, 1.23±0.62mm (p=0.01) and 1.21±0.94mm (p=0.07) with the straight, 45° and 90° tip, respectively. Positional accuracy was higher for the most experienced operator with the 90° tip (p=0.05), while operator experience was not significantly associated with accuracy for straight (p=0.91) and 45° tips (p=0.32).

Conclusions

Intra-aneurysmal microcatheter tip location and positional accuracy depend on tip shape and can, to a lesser degree, be influenced by operator experience. Our method can be used to statistically assess microcatheter behavior in patient-specific anatomy, which may improve the available evidence guiding microcatheter shape selection. Clinical validation is required.



(Filename: TCT_O-366_figure.jpg)

Wednesday
5:00PM - 6:30PM
Long Beach Convention Center, Room 102BC (Main Level)

21H-Parallel Paper Session: Dissection Collection and CTA Today

O-367

5:00PM - 5:08PM

Diagnostic Utility of CT Angiogram in Giant Cell Arteritis

R Conway[1], R Kavanagh[1], R O'Donohoe[1], E Heffernan[1], G McNeill[1], E Molloy[1], R Killeen[1], A Smyth[2]

[1]St. Vincent's University Hospital, Dublin, Ireland, [2]Saint Vincents University Hospital, Dublin, NY

Purpose

Giant cell arteritis (GCA) is the most common form of systemic vasculitis with a lifetime risk of 1% in populations of northern European origin. It is a devastating disease with 25% of patients suffering cranial ischemic complications such as vision loss and stroke. Temporal artery biopsy is positive in less than 50% of cases. There are no diagnostic criteria and the diagnosis is based on clinician gestalt. Imaging investigations potentially are useful in this setting; temporal artery ultrasound has a sensitivity of 54% and specificity of 81% for GCA diagnosis (1). Therefore almost half of GCA patients have normal imaging investigations; complementary imaging modalities are needed. The purpose of this study was to investigate the utility of intracranial CTA in GCA.

Materials and Methods

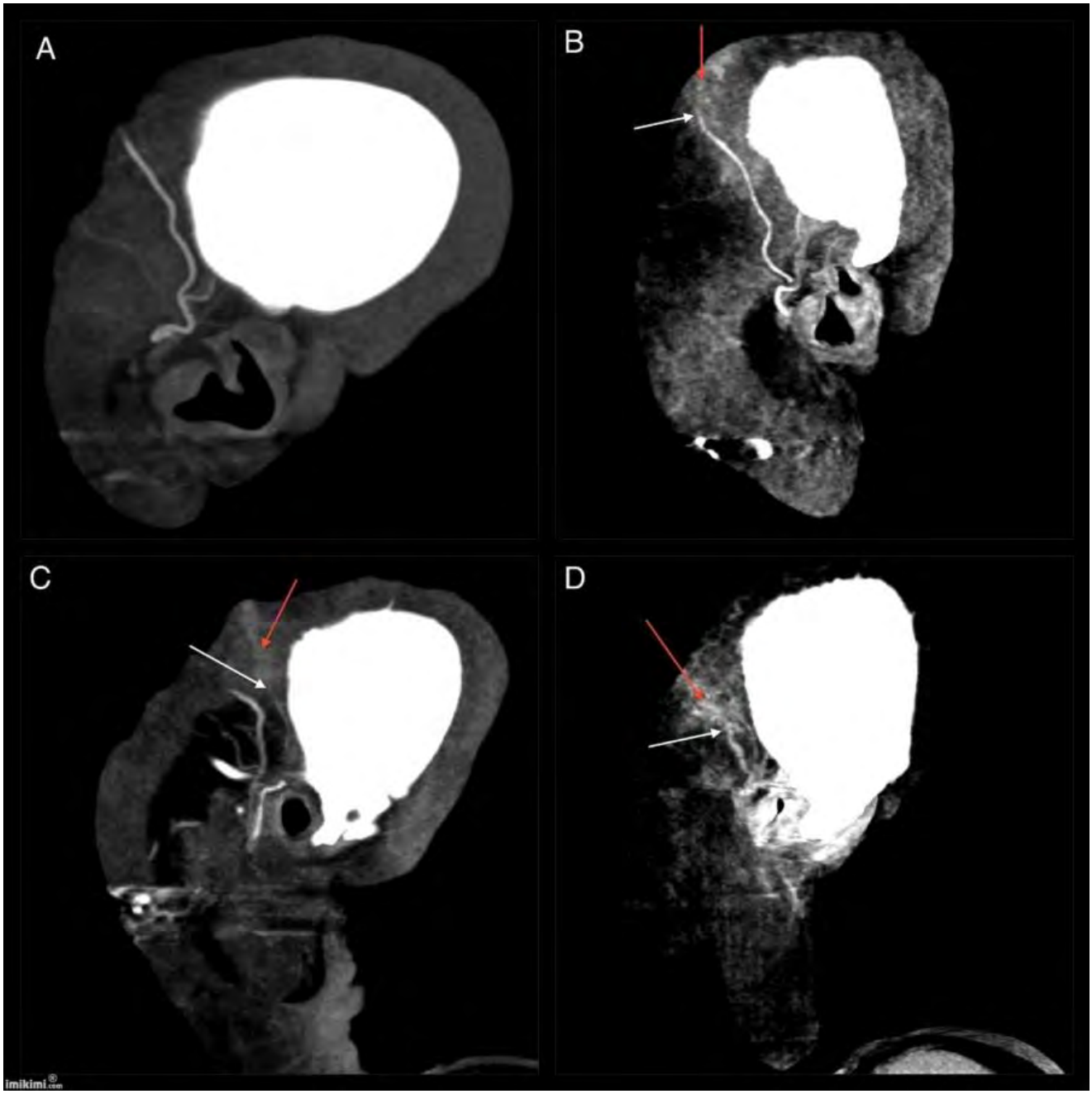
This study was performed in the setting of a prospective GCA registry which has recruited 290 patients since 2011. We included patients who presented to the emergency department from March 2013 to July 2015, who were ultimately diagnosed as the initial presentation of GCA and had an intracranial CTA performed for the assessment of suspected stroke. All patients met the American College of Rheumatology 1990 Criteria for GCA (2). Intracranial CTAs were evaluated for the presence of abnormalities indicative of vasculitis.

Results

Sixteen intracranial CTAs were performed in patients with stroke symptoms ultimately diagnosed as GCA. We noted characteristic abnormalities of the temporal and/or occipital arteries on CTA in this patient cohort. These are illustrated in Fig. 1(B-D), demonstrating abrupt discontinuation of the normal temporal artery (white arrows) with subsequent abnormal enhancement of the perivascular soft tissue distal to this cut-off point (red arrows) in patients with confirmed GCA. These findings were not seen in control subjects (Fig. 1A).

Conclusions

Computed tomography angiography (CTA) of the temporal arteries represents a potentially useful diagnostic adjunct in GCA and warrants further investigation in this population. Review of the temporal arteries is an important check area when interpreting CTA in patients with stroke symptoms.



(Filename: TCT_O-367_CTAfigure.jpg)

O-368

5:08PM - 5:16PM

Carotid Calcium Score Correlation with Internal Carotid Artery Stenosis Using Non-contrast CT and CT Angiography

S Dissanayake[1], C Liu[1], A Rajamohan[1], M Sondag[1], J Acharya[1]
[1]*University of Southern California, Los Angeles, CA*

Purpose

Coronary artery calcium scores predict hemodynamically significant coronary artery stenosis and are used in myocardial infarction risk stratification (1). Investigators have hypothesized that similarly carotid artery calcium scoring may predict carotid artery stenosis and prove useful in risk stratification for cerebrovascular accident (2). We provide the first study measuring the correlation between carotid calcium scores on noncontrast CT with carotid stenosis measured on CT angiography (CTA) of the neck using NASCET calculations and measuring calcium burden along the entire length of the cervical common and internal carotid arteries (3).

Materials and Methods

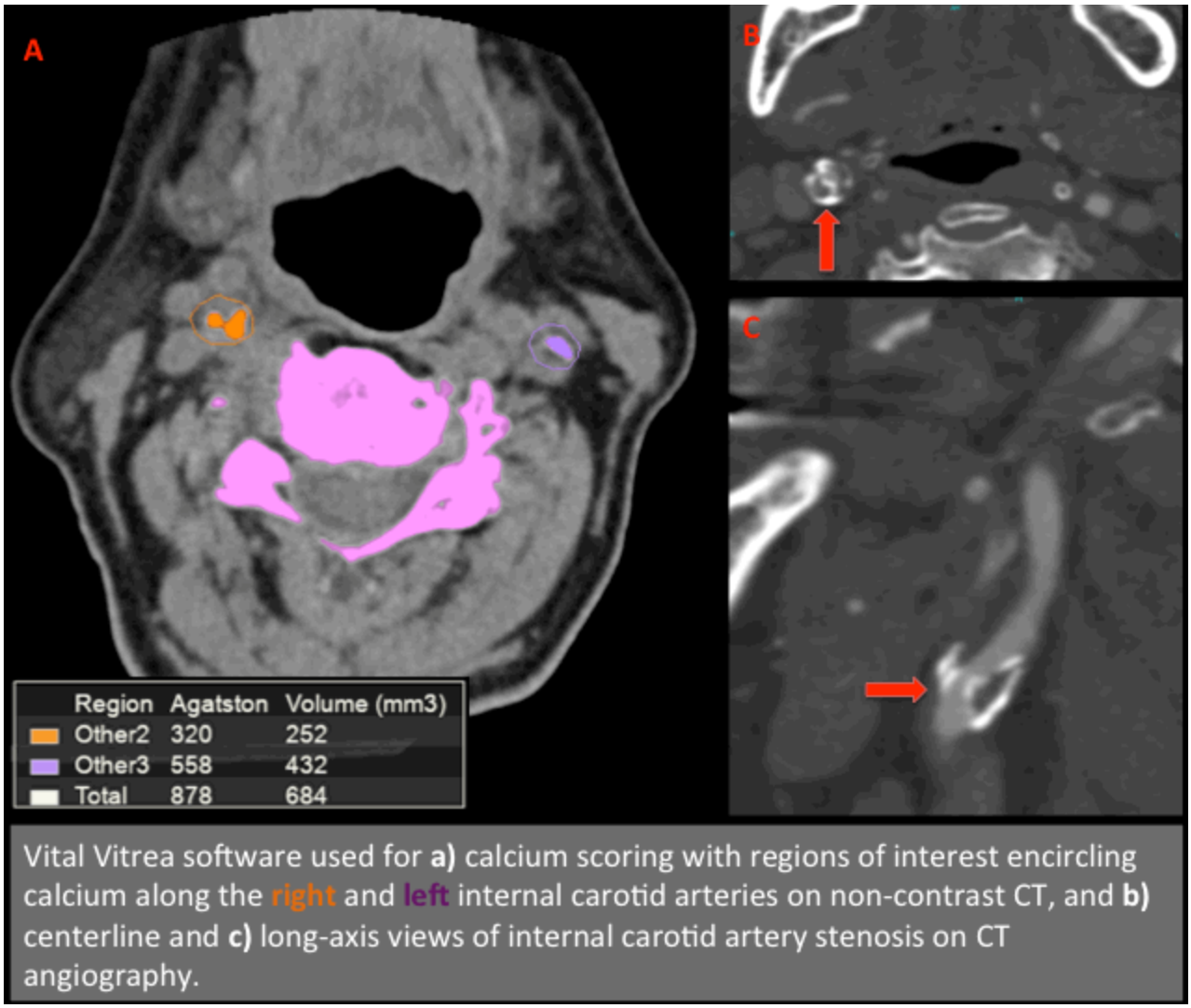
One hundred carotid systems from 50 consecutive trauma patients over age 65 (mean age 77.7 +/- 8.8 years, 26 female) who obtained CT noncontrast cervical spine and CTA neck studies within a 1 week interval between November 2014-2016 were evaluated retrospectively. All scans were performed on a 64-slice CT. Vital Vitrea software was used to semi-automatically measure calcium volume and Agatson scores on soft tissue windows with 3 mm slice thickness along the entire length of the cervical common and internal carotid arteries from above the thoracic inlet to the skull base using the standard calcium threshold of 130 HU. Measurements were made by a board certified radiologist with fellowship training in cardiothoracic imaging and neuroradiology. CTA neck studies for these patients were separately analyzed to determine the percentage of maximum internal carotid artery stenosis using NASCET calculations (percentage stenosis = 1 - (diameter at maximum ICA narrowing/normal diameter of distal ICA)) by a Neuroradiologist blinded to the calcium scores. Multiplanar reformatted images were created from the 0.5 mm CTA source images in order to optimally assess the greatest degree of carotid artery stenosis. The distal reference segment was always chosen such that the carotid walls were parallel and beyond the tapering after the internal carotid artery bulb. Spearman correlations were used to test relationships between carotid calcium volumes and Agatson scores and maximum percentage of internal carotid artery stenosis.

Results

Forty-five of 50 patients (90%) had a non-zero calcium score. Median calcium volume was 72.5 mm3, median Agatson score 86, and mean stenosis 9.2%. A significant correlation was found between both carotid calcium volume and Agatson score and percentage of internal carotid artery stenosis (both $r = 0.72$, $p < 0.0001$). A significant correlation also was found between patients' total calcium volume between both carotid systems and maximum carotid stenosis ($r = 0.8$, $p < 0.0001$). 5 out of 50 patients (10%) had a hemodynamically significant (>=50%) stenosis by NASCET criteria and 3 patients (6%) had a stenosis of over 60%.

Conclusions

Carotid calcium volume and Agatson scores on noncontrast CT are a significant predictor of carotid stenosis on CTA neck. Patients with a large carotid calcium burden on noncontrast CT may benefit from further imaging to screen for carotid stenosis.



Vital Vitrea software used for **a)** calcium scoring with regions of interest encircling calcium along the right and left internal carotid arteries on non-contrast CT, and **b)** centerline and **c)** long-axis views of internal carotid artery stenosis on CT angiography.

(Filename: TCT_O-368_Slide1.gif)

O-369

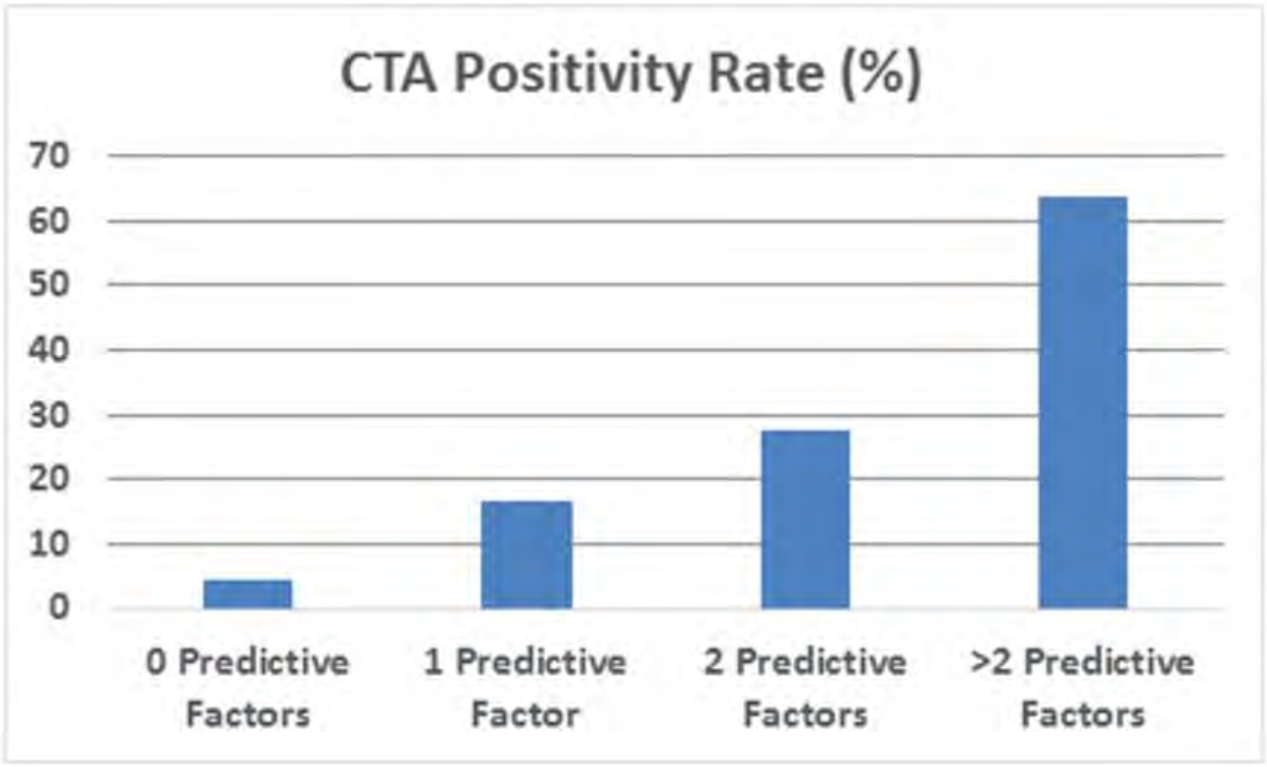
5:16PM - 5:24PM

The Effect of CT Angiography on Patient Management and Prognosis in the Setting of Trauma

H Orlowski[1], A Kansagra[2], A Sipe[3], M Miller-Thomas[4], K Vo[4], M Goyal[5]
[1]Washington University, St. Louis, MO, [2]Washington University School of Medicine, St. Louis, MO, [3]Washington University in St. Louis/Barnes Jewish Hospital (Mallinckrodt Institute of Radiology), Saint Louis, MO, [4]Mallinckrodt Institute of Radiology, St. Louis, MO, [5]Washington University in St. Louis, Saint Louis, MO

Purpose
Computed tomography angiography (CTA) is increasingly utilized to evaluate for traumatic

cerebrovascular injury. We aimed to determine the yield, management effect, and prognostic implications of a positive CTA in a large cohort of trauma patients.
Materials and Methods
A retrospective analysis was performed on 1290 blunt and penetrating trauma patients who underwent CTA of the head and/or neck at our level I trauma center from January 2006 – June 2015. Clinical variables were evaluated for each patient including mechanism of injury, justification and result of the CTA, subsequent findings including those that underwent catheter angiography, and patient management and outcome.
Results
Among 1290 patients who underwent CTA, 200 (15.5%) were positive or suspicious for traumatic cerebrovascular injury. Angiography was performed in 70 of these patients, among which 53 (75.7%) confirmed or extended the CTA findings, whereas 17 (24.3%) were normal. Several presenting factors predicted increased risk for a positive CTA in a general linear model ($p < 0.05$), including multiple cervical fractures and/or subluxation, fracture with foraminal or carotid canal involvement, gunshot injury, Glasgow Coma Scale (GCS) $\leq$ 13, and focal neurological deficit prior to CTA. Excluding these factors lowered the positive CTA rate to 4.3%. Of the 200 CTA positive patients, 99 were treated with antiplatelet therapy or anticoagulation, including 11 who also underwent endovascular management. Among the 200 patients, 9 (4.5%) had a subsequent stroke, as compared to 5 of the 1090 CTA negative patients (0.5%) (Fisher Exact Test, $p < 0.0001$).
Conclusions
Computed tomography angiography had a modest yield in identifying traumatic cerebrovascular injury in our cohort of patients. When positive it typically predicted angiography findings, influenced management, and predicted an increased risk of subsequent stroke. However, given the small number of subsequent strokes, a treatment-related benefit could not be determined.



(Filename: TCT_O-369_CTAfigurefinal.jpg)

O-370

5:24PM - 5:32PM

MR Vessel Wall Imaging of Blunt Cerebrovascular Injury identified on CT Angiography: a preliminary study

T Huynh[1], M Levitt[2], R Bonow[2], M Mossa-Basha[1]
[1]University of Washington, Seattle, WA, [2]University of Washington, Harborview Medical Center, Seattle, WA

Purpose
Recent studies have suggested that CT angiography (CTA) may overestimate mild blunt cerebrovascular injuries (Biffl grade 1 and 2) and have suggested that MRI may be more accurate in characterizing vessel injury (1). Our study aims to characterize MR vessel wall imaging (MR-VWI) findings in patient with blunt cerebrovascular injury identified on CTA.
Materials and Methods
Patients identified with BCVI on CTA underwent a dedicated MR-VWI of the neck including 3D-SPACE PD and T1-weighted sequences. Individual studies were interpreted independently and correlation between CTA and MRI findings was performed.
Results
In total, 9 patients with BCVI were identified with CTA (mean age 38 years, range 19-66

years; 7 male) with a total of 14 Biffl injuries. These included three Biffl grade 4, three Biffl grade 3, two Biffl grade 1, three Biffl grade 2, and five Biffl grade 1 injuries. Of the Biffl 1 and 2 injuries identified on CTA, only 1 (13%) demonstrated abnormality on MR-VWI. All Biffl 3 and 4 injuries were identified on MRI. Of the patients with Biffl 3 and 4 injury, 2 patients had associated cerebral infarcts while none of the Biffl 1 and 2 injury patients were associated with infarcts.
Conclusions
Low-grade BCVI identified on CTA is not commonly associated with abnormality on MR-VWI and may not be associated with true vascular injury. Given the potential overestimation of BCVI using CTA of the head and neck, MR-VWI may be a useful screening modality in further evaluating low-grade BCVI identified on CTA however further study is required.

O-371

5:32PM - 5:40PM

Stroke risk after blunt cerebrovascular injury with dissection

M Abdalkader[1], V Naragum[1], V Andreu[1], A Mian[1], T Nguyen[1]
[1]*Boston Medical Center, Boston, MA*

Purpose
Blunt cerebrovascular injuries (BCVI) are common in the setting of traumatic accidents. The natural history of stroke in patients with traumatic dissection has not been well investigated. The objective of this study was to evaluate the risk of stroke with BCVI, as it relates to the presence of dissection in the carotid or vertebral artery territory.
Materials and Methods
We instituted a protocol in 2007 for CTA imaging of the head and neck in patients with BCVI to look for dissection. Criteria for CTA were patients with skull base fractures, cervical spine fractures or neurological deficit. Patients with dissection seen on CTA were followed for development of stroke.
Results
We retrospectively reviewed all CTA imaging of patients presenting with BCVI from 2007-2016. We found 63 patients with either carotid or vertebral artery dissection. Exclusion criteria were dissection in the external carotid artery, vasospasm, <1 month clinical follow-up due to death. Injury mechanisms were motor vehicle accidents, falls and altercations. Location of injury was vertebral artery (VA, n=50), internal carotid artery (ICA, n=19), and posterior inferior cerebellar artery (PICA, n=1). Three patients had lesions in both the VA and ICA. Four patients had bilateral dissections (3 bilateral carotids and 1 vertebral). There were 7 pseudo-aneurysms (11%). Patients were treated with aspirin (n=48) and/or anticoagulants (n=12). Three patients had a carotid stent for progressive stenosis. Four patients received no treatment due to contraindications. Four patients were found to have an

intracranial stroke related directly to the dissection (6%), all of them were in the posterior circulation secondary to vertebral dissection and were treated conservatively.
Conclusions
Incidence of stroke after carotid or vertebral artery dissection related to blunt cerebrovascular injury is low with good prognosis. Larger prospective studies would be of interest to better define stroke risk in this patient population.

O-373

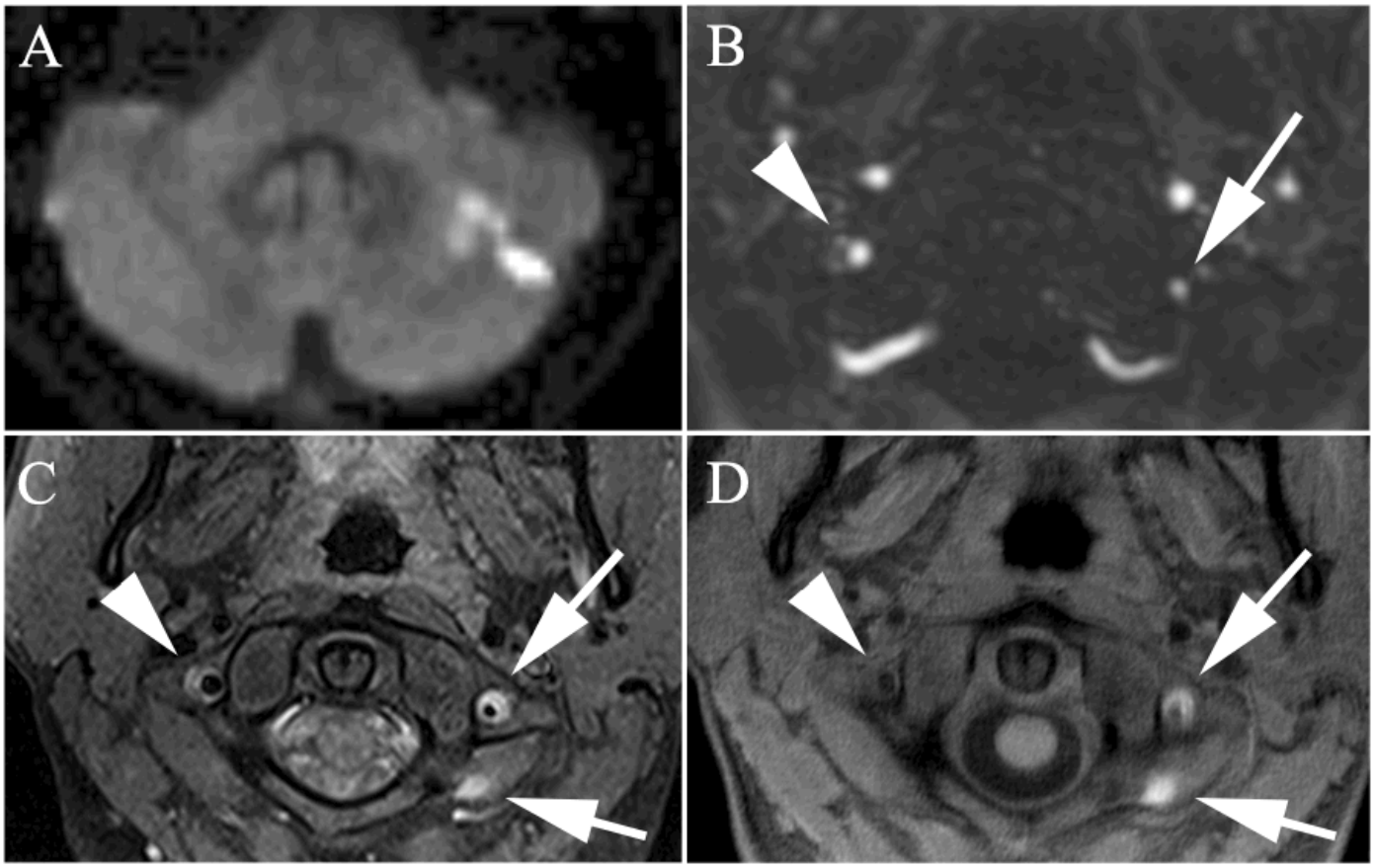
5:48PM - 5:56PM

MRI-detection of Intramural Hematoma in Carotid and Vertebral Artery Dissection: Head-to-Head Comparison of T1-weighted Sequences.

P Hinckley[1], L Eisenmenger[1], A Sakata[1], A DeHavenon[1], S Kim[1], D Parker[1], J McNally[1]
[1]*University of Utah, Salt Lake City, UT*

Purpose
The MPRAGE sequence has been validated in the detection of carotid intraplaque hemorrhage compared to histology (1, 2). Early studies suggest it also can detect intramural hematoma in dissections (3). Still, the clinical standard of care for dissection and intramural hematoma detection remains a conventional T1 fat saturation (T1FS) technique. Our purpose was to determine if MPRAGE could replace T1FS in the detection of intramural hematoma related to craniocervical dissection.
Materials and Methods
IRB approval was obtained for this retrospective analysis of 133 patients undergoing acute stroke and dissection workup with neck MRA including both the MPRAGE and T1FS techniques. Kappa analysis performed in 2 observers blinded to each other and separately determining T1-hyperintense signal using each technique, in each of the left and right carotid and vertebral arteries from each subject. A mixed effects Poisson regression model was used, accounting for 4 vessels per patient and prevalence ratios (PRs) were reported. Consensus MPRAGE signal and consensus T1FS signal were each reported as "positive" if both image raters agreed. The consensus signal for each technique was compared to the "true" diagnosis of dissection and vascular territorial stroke by an experienced third observer using all available images and clinical notes. For the comparison with vascular territorial stroke, patients with nondissection stroke sources were excluded, e.g. atrial fibrillation.
Results
Patients had a mean age of 45.9+/-16.2 years and were 55.6% female. A total of 66 "true" dissections, 25 strokes were detected by the third observer. Interrater reliability for T1-hyperintense signal was significantly higher for MPRAGE compared to T1FS (kappa = 0.89 versus 0.53, $p<0.001$). Consensus MPRAGE–positive signal had a high prevalence in true dissections (PR=12.1, $p<0.001$, 95%CI: 7.2, 20.2). Consensus T1FS–positive signal had a similar high prevalence in true dissections (PR=10.5, $p<0.001$, 95%CI: 6.2, 17.9). Stroke

prevalence with consensus MPRAGE-positive signal (PR=7.9, p<0.001, 95%CI: 3.3,18.9) was similar to that of consensus T1FS-positive signal (PR=8.4, p<0.001, 95%CI:3.5, 20.0).
Conclusions
A positive intramural hematoma detected by MPRAGE or T1FS has a similar high prevalence in dissections and strokes. The MPRAGE sequence, however, has the advantage of a higher interrater reliability compared to conventional T1FS. Together these results suggest that the MPRAGE sequence can replace the conventional T1FS technique for the detection of dissection. Fig. 1: 31-year-old female with a left vertebral artery dissection and intramural hematoma. A) Diffusion-weighted imaging demonstrating left cerebellar infarct. B) Contrast MRA demonstrates a normal caliber right vertebral artery (arrowhead) but asymmetric narrowing on the left (arrow). C) T1FS demonstrating moderate high signal along the right vertebral artery thought to represent intramural hematoma by both observers and dissection (arrowhead) as well as more evident high signal on the left (arrows). D) MPRAGE demonstrates no right vertebral artery intramural hematoma (arrowhead), and along with the normal caliber on MRA indicates that the T1FS signal was related to slow flow within the peri-arterial venous plexus and not a true dissection. On the left, clear intramural hematoma and associated narrowing on the MRA was consistent with a true dissection (arrows).



(Filename: TCT_O-373_Petervertdissectionfigure120916.gif)

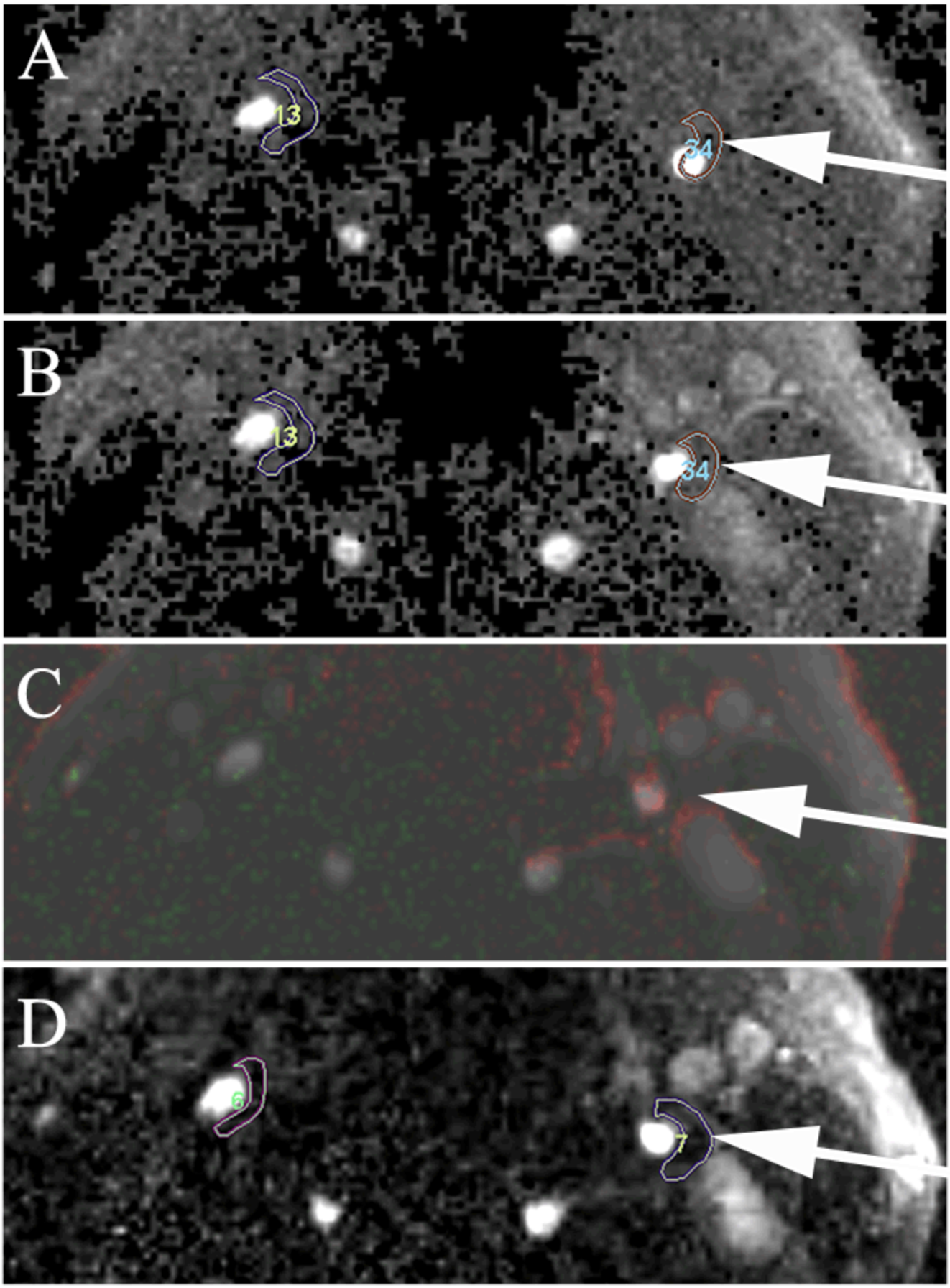
O-374

5:56PM - 6:04PM

Motion corrected dynamic contrast enhanced (DCE)-MRI of carotid plaque

J McNally[1], A Sakata[1], J Roberts[1], J Mendes[1], D Parker[1]
[1]*University of Utah, Salt Lake City, UT*

Purpose
The goal of this study was to determine if motion correction plays a role in dynamic contrast-enhanced (DCE) MRI of carotid plaque.
Materials and Methods
In this IRB-approved study, patients underwent carotid DCE-MRI after informed consent. In 40 selected vessel segments, image sets were selected for processing without or with motion correction. Dynamic contrast-enhanced MRI imaging consisted of a rapid, heavily T1-weighted multislice SPGR acquisition with injection of gadopentetate dimeglumine (Multihance ®) at 0.1 mmol/kg. Oleasphere was used for semi-automated processing of carotid plaque DCE-MRI data, with hand-drawn outlines of carotid plaque, extended Tofts processing and generation of Ktrans maps. Processing was performed without and with motion correction using the Advanced Normalization Tools (ANTs), version 2.1.0. Briefly, registration of spatial image volumes at different time points was performed in 3D mode with rigid, affine and deformable symmetric image normalization.
Results
Maximum Ktrans values obtained without motion correction were mean 0.32 +/- 0.20 min-1 and with motion correction were 0.32 +/- 0.26 min-1. The average difference between measurements in each carotid plaque was 0.09 +/- 0.10 min-1. Fig.: Cine images demonstrate motion of the carotid artery lumen through regions of interest drawn on carotid plaques. (A and B) DCE-MRI images of a patient with carotid artery motion during the scan with drift of the left carotid lumen into the region of interest (ROI) outlining the left carotid plaque (arrow). (C) Color scale representation of the motion (red) compared to ANTS correction (green), with more motion seen on the left carotid artery (arrow). (D) Final motion corrected dataset no longer has overlap of the carotid lumen with the ROI (arrow).
Conclusions
Motion correction can play a role in carotid plaque DCE-MRI by allowing more precise estimation of Ktrans values. Future studies will determine if this technique will give better Ktrans correlation with unstable carotid plaque and future stroke risk.


A
13
34
B
13
34
C
D
6
7

(Filename: TCT_O-374_dualcontrastDCE120916_2copy.gif)

O-375

6:04PM - 6:12PM

Head and Neck Angiographic Findings of Patients Presenting with Spontaneous Coronary Artery Dissection.

D Ferguson[1], J Shewchuk[1], M Mohammed[1], M Marangoni[2], A Starovoytov[1], P Teal[1], M Heran[2], J Saw[1]
[1]University of British Columbia, Vancouver, British Columbia, [2]Vancouver General Hospital, Vancouver, British Columbia

Purpose
Spontaneous coronary artery dissection (SCAD) has been associated with other extravascular abnormalities inclusive of fibromuscular dysplasia (FMD) and intracranial aneurysms (1, 2). In this study, we aim to assess for abnormalities involving the vascular structures of the head and neck in patients presenting with SCAD.
Materials and Methods
All patients presenting with SCAD to a tertiary referral had CT or MR angiography of their head and neck vessels performed for further assessment of potential vascular abnormalities. A retrospective review of this imaging was undertaken by 2 fellowship-trained neuroradiologists. Special attention was given to the presence of imaging characteristics of FMD, presence of vessel tortuousity and presence of intracranial aneurysms.
Results
One hundred fifty-four patients with SCAD were identified with a female preponderance, 93.5% v 6.5%, and a mean age of 54.4 years. Computed tomography (CT) or MR angiography from arch to vertex was performed in 139 and 12 patients respectively with 3 patients having both CTA and MRA performed. Forty-eight percent of patients had imaging findings of FMD present in 1 or more vessels, predominantly involving the C1 segment of the internal carotid artery or V3 segment of the vertebral artery. Fifteen patients (9.7%) had intracranial aneurysms with 3 aneurysms having been treated previously. Three intracranial aneurysms were ≥5mm with 2 of these being ≥8mm. Eighty-nine patients (57.8%) demonstrated tortuosity of 1 or both internal carotid arteries with 55 patients (35.7%) demonstrating a coil or kink between 0-90 degrees. Variant anatomy of the arch of the aorta was noted in 31 patients (20.1%) with an aberrant right subclavian artery present in 7 patients (4.5%). There was 87% concordance with the initial radiology report.
Conclusions
This study confirms the increased prevalence of fibromuscular dysplasia within the head and neck vessels in patients presenting with SCAD. The incidence of patients with SCAD with concurrent intracranial aneurysms in our study is 9.7%, and is greater than in the "normal" population (3.7%) (3). In our patient cohort, the overall variant anatomy of the aortic arch is

in keeping with "normal" (circa 20%). However, the presence of an aberrant right subclavian artery was seen in 4.5% and is markedly greater than in the "normal" population (0.4-2%) (4).

Thursday
9:00AM - 10:36AM
Long Beach Convention Center, Room 104B (Main Lobby)

23E-Parallel Paper Session: Imaging Issues, Quality and Safety: Making the Most of Dose, and More!

O-378

9:00AM - 9:08AM

Natural Language Processing for Classification of Acute, Communicable Findings on Head CT Reports: Comparison of Non-Neural and Neural Network Machine Learning Techniques.

F Chokshi[1], B Shin[2], T Lee[2], J Choi[2]
[1]Emory University School of Medicine, Atlanta, GA, [2]Emory University Department of Mathematics and Computer Science, Atlanta, GA

Purpose
Radiology reports are replete with unstructured, yet often important information that can be mined for many purposes including quality improvement, outcomes analysis, and cohort construction for epidemiological studies. Recent advances in deep learning present potentially impactful and scalable methods of using natural language processing (NLP) on radiology reports to classify whether acute and communicable findings are present anywhere in the document. We chose a common report type, the head CT, to evaluate the accuracy of several non-neural and neural network models using attention to classify 5 categories (classes) of acute and communicable findings and compared them to human (radiologist) performance.
Materials and Methods
1. Two neuroradiologists annotated 1,400 head CT reports for terms that indicated the presence or absence of acute communicable findings listed in Table 1. Each class was scored as 0 if normal, 1 if finding present but not new or worsening, or 2 if finding was new or worsening indicating an acute communicable finding that a typical radiologist would call the team about in clinical practice. After calculating inter-annotator agreement, the 1,400 head CT report set was adjudicated by the radiologists and served as the human reference to statistical machine learning. 2. Since our training data, although larger than most of the previous work, is yet small to develop robust statistical models, we used additional 80,000 unannotated head CT reports to best capture word semantics in the radiology domain by training word embeddings using the latest distributional semantics technique called

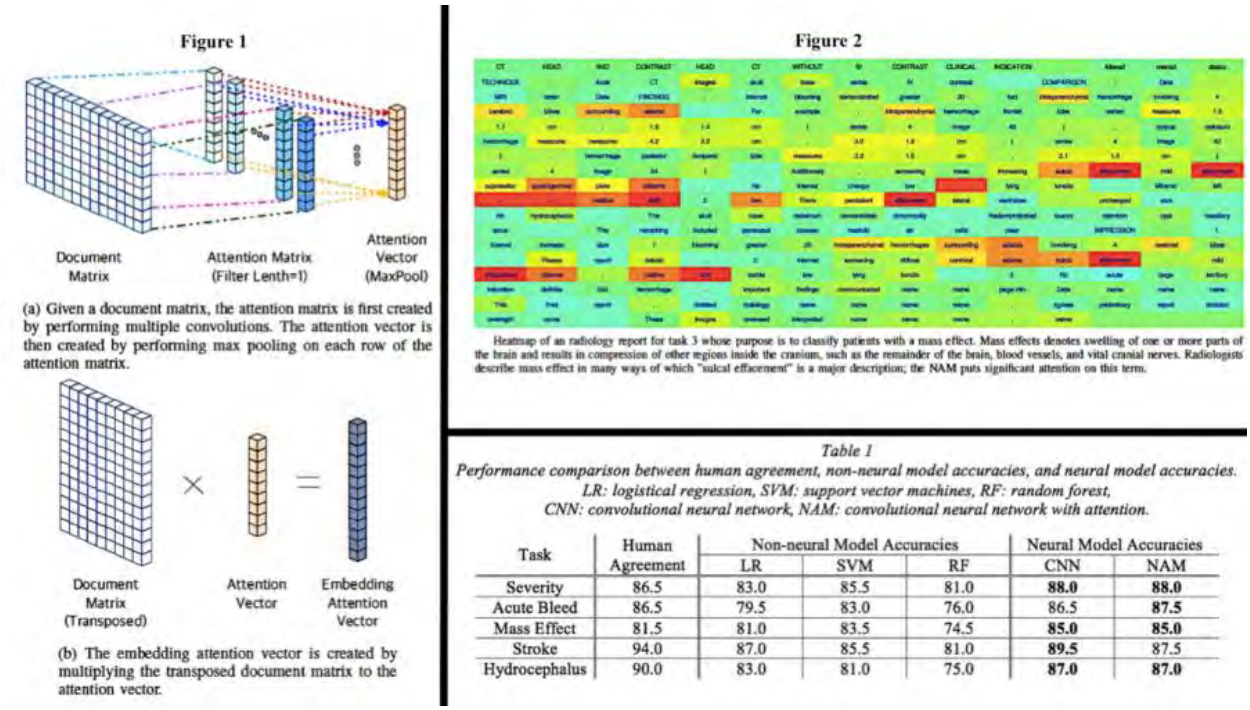
Word2Vec, which converts text into vectors in Cartesian space to establish proximity relationships between words. This word embedding training is completely unsupervised such that no manual annotation is required. Note that we did not calculate any machine learning technique accuracies at this point. 3. To establish strong baselines, we first experimented with 3 popular non-neural machine learning techniques, logistic regression (LR), support vector machines (SVM), and random forest (RF), using the 1,400 annotated head CT reports. Subsequently, we developed 2 neural network models: 1) a single-layer convolutional neural network (CNN) and 2) CNN with a neural attention mechanism (NAM) (Fig. 1). Convolutional neural network used several convolutions adapting word embeddings that are trained from the 80,000 unannotated head CT reports, whereas NAM adds the novelty of displaying a heatmap of the words that the machine found important during its decision making (Fig. 2). Accuracies were measured for all 3 methods and compared to the inter-annotator agreements of the 2 neuroradiologists.

Results

Table 1 shows the inter-annotator agreement between humans and accuracies of the machine learning systems. Radiologist agreement ranged from 81.5% for mass effect to 94.0% for acute stroke. This table also shows that the accuracies of the CNN and NAM systems were higher than the baseline approaches. For the first 3 classes, severity, acute bleed, and mass effect, CNN and NAM had higher accuracies than the agreement between 2 radiologists. For the last 2 classes, acute stroke and hydrocephalus, radiologist agreement was higher than the accuracies of any machine learning method; however, both neural network systems outperformed the baseline approaches. Between the neural network systems, NAM showed equal accuracy with CNN for 3 classes, severity, mass effect, and hydrocephalus, higher accuracy for the acute bleed class, and lower accuracy for the acute stroke class.

Conclusions

1. Convolutional neural network and CNN with NAM have higher accuracies for classification of all 5 classes compared to a baseline SVM method. These methods also can accommodate larger datasets. 2. Convolutional neural network exceed, equal, or are less than the inter-annotator agreement of 2 neuroradiologists. Further development of such neural network systems in the radiology domain may lead to increases in accuracy over all classes. 3. The CNN with NAM system adds the benefit of understanding why the machine made a particular classification system due to the development of heat maps of words that the machine "paid attention to" compared to other words.



(Filename: TCT_O-378_Graphic_ASNR.jpg)

O-377

9:08AM - 9:16AM

Machine Learning Enables Automated Identification of Severe Central Canal Stenosis on Lumbar Spine MRI with High Accuracy

N Swinburne[1], X Yang[1], J Schefflein[1], Y Sakai[1], K Nael[1], A Doshi[1]
[1]*Icahn School of Medicine at Mount Sinai, New York, NY*

Purpose
Recent advances in machine learning (ML) have demonstrated promise in identifying disease processes in the brain (1), however there exists a paucity of research establishing the performance of ML in evaluation of spinal imaging. We investigate whether ML analysis of sagittal T2W MRI of the lumbar spine can reliably identify severe central canal stenosis.
Materials and Methods
Patients with severe central canal stenosis diagnosed on lumbar spine MRI were reviewed retrospectively and matched with normal lumbar spine MRI controls. Sagittal unprocessed T2 and thresholded upper 50% signal intensity T2 images were utilized for supervised training of a ML classification kernel using the Pattern Recognition for Neuroimaging Toolbox (UCL, London, UK) v2.0 (2). Training entailed evaluation of labeled (i.e., severe stenosis vs. normal) MRI data for creation of a support vector machine (SVM) kernel, which was validated on unlabeled cases using the leave-one-subject-out method. Machine learning accuracy and receiver operating characteristic data were collected.

Results

Twenty consecutive patients with severe central canal stenosis on lumbar spine MRI (5 male, 15 female; age 74 ± 12 years) and 21 patients (5 male, 16 female; age 35 ± 11 years) with normal lumbar MRI were included. The trained ML kernel discriminated with 78.5% balanced accuracy (p=0.001) between severe central canal stenosis (class accuracy 95.0%; p=0.001) and normal (class accuracy 61.9%; p=0.34). The thresholded upper 50% signal intensity T2 data yielded an SVM with slightly lower accuracy (balanced accuracy 75.8%, p=0.001; severe stenosis class accuracy 66.7%, p=0.23; normal lumbar spine class accuracy 85.0%; p=0.004).

Conclusions

A trained SVM can identify severe central canal stenosis with high accuracy using unprocessed sagittal T2 MRI. Machine learning training using larger MRI data sets is required to validate these findings and improve SVM diagnostic accuracy.

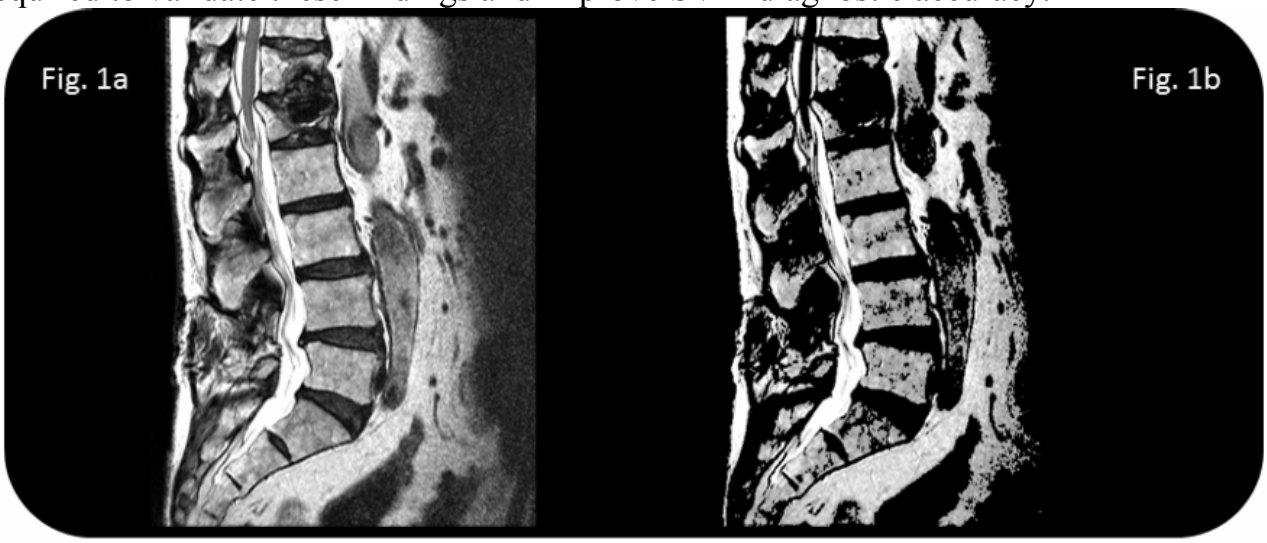
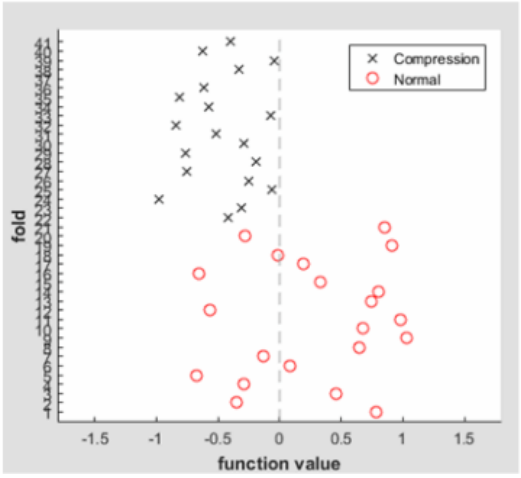


Fig. 2



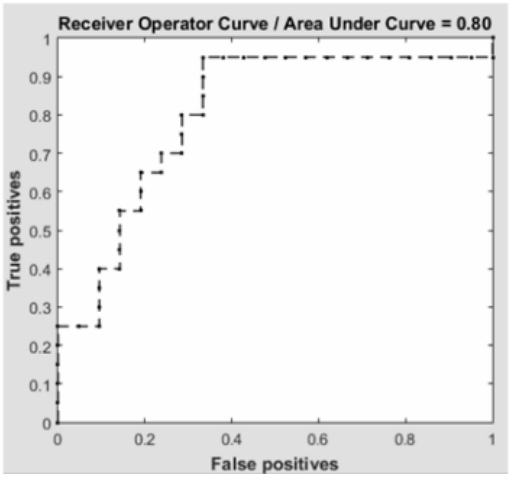


Fig. 3

(Filename: TCT_O-377_ASNRcordcompressionimages.gif)

O-376

9:16AM - 9:24AM

Semi-automated Evaluation of Lumbar Spine MRI for Differentiating Benign and Malignant Vertebral Body Compression Fractures: a Machine Learning Experiment

N Swinburne[1], J Schefflein[1], Y Sakai[1], P Pawha[1], K Nael[1], A Doshi[1]
[1]*Icahn School of Medicine at Mount Sinai, New York, NY*

Purpose
Differentiating benign osteoporotic and malignant vertebral compression fractures (VCFs) on spine MRI is a common diagnostic dilemma. Multiple quantitative markers have been described for discriminating VCF etiology, including the use of decreased ADC values as a marker of pathologic VCF (1). We investigate whether ML analysis of sagittal ADC MRI of the lumbar spine can reliably discriminate histopathologically-proven benign and malignant VCFs.
Materials and Methods
Patients with acute VCF identified on lumbar spine MRI including DWI who subsequently underwent histopathological sampling establishing either benign or pathologic etiology were reviewed retrospectively. Separate volumes of interest (VOIs) delineating the fractured vertebral body as well as an adjacent reference unfractured vertebral body were drawn manually on sagittal T2 images and subsequently applied to co-registered sagittal ADC images for each patient. The ADC voxels within each VCF VOI were divided by the mean ADC value for the reference level VOI using the fMRI Software Library (Analysis Group, Oxford, UK) v5.0 (2) in order to correct for potential variations in DWI calibration across scans. The corrected VCF ADC data were utilized for supervised training of a ML classification kernel using the Pattern Recognition for Neuroimaging Toolbox (UCL, London, UK) v2.0 (3). Training entailed evaluation of labeled (i.e., benign vs. malignant VCF) MRI data for creation of a support vector machine (SVM) kernel, which was validated on unlabeled cases using the leave-one-subject-out method. Volumes of interest imaging characteristics, ML accuracy and receiver operating characteristic data were collected.
Results
Twelve patients with benign VCF (10 female, 2 male; age 73 ± 15 years) and 11 patients with malignant VCF (6 female, 5 male; age 73 ± 11 years) were identified. The trained ML kernel discriminated with 41.7% balanced accuracy (p=0.61) between benign (class accuracy 83.3%; p=0.28) and malignant (class accuracy 0.00%; p=1.0) VCFs. Corrected ADC value means were 0.70 and 1.1 (p=0.16) for the 2 groups, respectively.
Conclusions
The trained SVM identified histopathologically proven benign and malignant VCFs using corrected ADC with an accuracy approaching random chance. Mean corrected ADC values were noncontributory for discriminating fracture etiology. Machine learning supervised training using additional VCF quantitative and qualitative markers is required.

O-379

9:24AM - 9:32AM

Simulating Low-Dose Head CT Imaging through Noise Algorithms

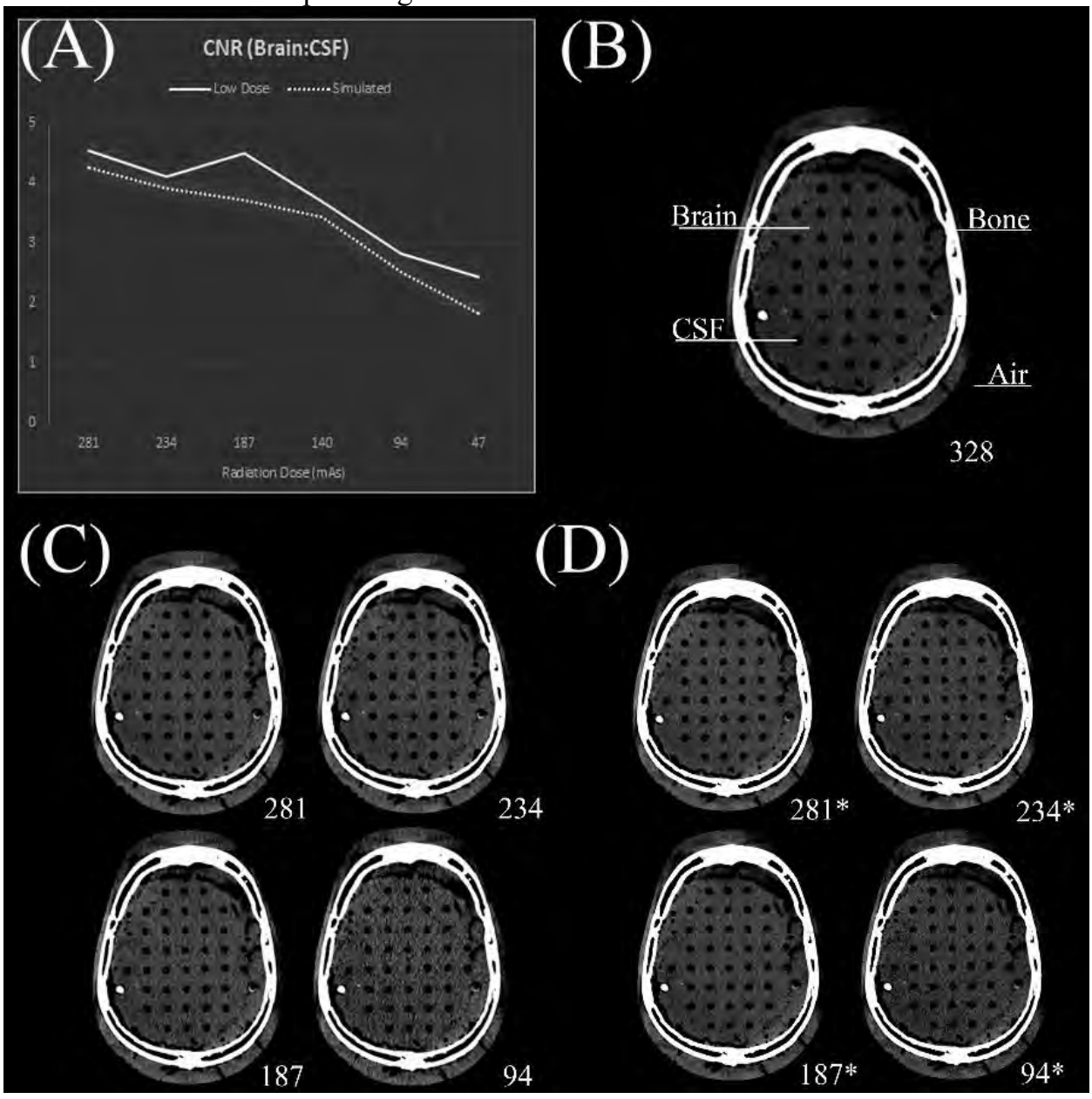
S Sadiq[1], V Sethi[2], Q Liang[2], P Shah[2]
[1]Temple University School of Medicine, Philadelphia, PA, [2]Temple University Hospital, Philadelphia, PA

Purpose
Currently, most radiology groups prescribe a single protocol for adult noncontrast head CT imaging whether it is for initial assessment or for follow-up imaging. Given the on-going interest in lowering patient radiation dose, neuroradiologists could advance their practice of as low as reasonably achievable (ALARA) and American College of Radiology (ACR) Image Wisely & Gently campaign missions if there was a safe and feasible method to quantitatively and qualitatively predict the effects of lower tube current on image quality. Given the lack of prospective data on low dose thresholds in neuroimaging as it pertains to specific CNS pathologies, we propose a novel method of image manipulation (noise simulation) that could assist imagers in predicting the effects of lower tube current setting. Using a Poisson noise distribution model on a phantom head we aim to demonstrate the feasiblity and reliablity of artifically introducing noise to simulate the qualitative and quantiative image degradation effects of low dose imaging on tissues such as brain, bone and cerebrospinal fluid (CSF). The Poisson distribution is a statistical model most commonly used to describe scenarios involving isolated events over time. Importantly, the likelihood of each event must be independent of the previous events, and the relative rate of events must remain constant over time. Previous studies have shown photon-detector noise in CT to adhere to this behavior.
Materials and Methods
Various phantom acquired low dose CT images were compared to those generated by Poisson-based algorithmic simulations using MATLAB software. To perform this comparison, regions of interest (ROIs) were placed in multiple locations to measure the amount of noise generated and determine its effects on contrast-to-noise values (CNR). Imaging was performed on a Rando male head phantom and 128 detector Phillips Brilliance iCT Scanner (Highland Heights, Ohio). Imaging parameters were 120 kvp, 47 to 320mAs range, pitch 0.3 and gantry speed of 0.5s. At least 3 equal sized ROIs were selected for brain, cerebrospinal fluid (CSF), bone and air. Region of interest coordinates were selected manually on the first image and propagated on subsequent images using MATLAB software.
Results
Results demonstrate an inverse relationship between radiation dose and image noise. The inverse relationship was on the order of $y \alpha x^{(-½)}$ with an R squared value of 0.99. Furthermore, standard deviations of brain ROIs in simulated vs real low dose images were correlated with a margin of error <1.0%. Computed CNR results for low dose and simulated images are summarized in Fig. A. The original image (at 328 mAs) is presented with ROI

measurements performed at brain, CSF, bone and air (Fig. B). The low dose images are presented in Fig. C and the simulated counterparts are presented in Fig. D.

Conclusions

Our results demonstrate that computer simulation with MATLAB can be performed to successfully generate images that are quantitavely and qualitatively comparable to acquired low dose scans. Additional refinement of our simulation model can be made by performing noise modeling on raw data (instead of processed images) and computing CNRs for specific CNS tissue types such as gray and white matter. More work will be done to refine the algorithm at very low doses (less than 140 mAs). Further validation of the low dose simulation model could be performed on previously acquired patient scans to determine its effects on various CNS pathologies.



(Filename: TCT_O-379_ASNR_Graphic_v2.jpg)

O-380

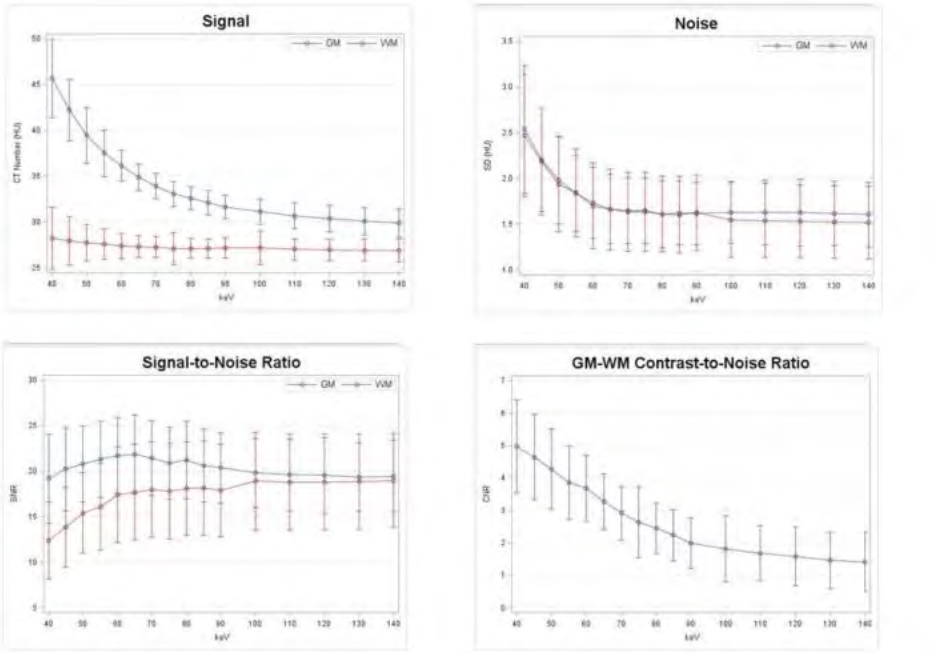
9:32AM - 9:40AM

Detection-based Spectral CT Scanner Yields Image Quality Improvement with Virtual Monoenergetic Reconstructions Compared to Conventional Unenhanced Head CT Utilizing Identical Radiation Dose

W Moore[1], M Pinho[1], A Jaster[1], Y Xi[1], S Abbara[1]
[1]*University of Texas Southwestern Medical Center, Dallas, TX*

Purpose
To analyze standard quality measures of virtual monoenergetic (VME) images of unenhanced head CT obtained using a preclinical detection-based spectral CT scanner (IQon, Philips Healthcare) with the following goals: (1) compare image quality metrics of VME to conventional polychromatic images, (2) determine energy levels that optimize gray white discrimination, and (3) evaluate the effect of VME images on posterior fossa beam hardening.
Materials and Methods
The study is IRB approved. Twenty consecutive unenhanced head CT scans were acquired with a preclinical detection-based spectral CT scanner (IQon, Philips Healthcare). Conventional polychromatic and VME reconstructions from 40-90 keV at 5 keV increments and from 90-140 keV at 10 keV increments were analyzed (360 CT datasets). Three gray matter (GM), 3 white matter (WM), and 1 posterior fossa regions of interest (ROI) were measured on VME and conventional images at identical locations. The data were analyzed using 4 quality measures: GM signal to noise ratio (SNR), WM SNR, GM-WM contrast to noise ratio (CNR), and posterior fossa noise. Conventional images were compared to VME images and optimal VME was identified. A multiple comparison analysis of variance with Dunnett adjustment was used to test for significant differences.
Results
There were 2520 ROIs evaluated. Maximum GM-WM CNR was observed at a VME of 40 keV. Maximum GM SNR and WM SNR were seen at a VME of 65 keV. Virtual monoenergetic images had significantly better GM-WM CNR relative to conventional images at energy levels of 40-70 keV ($p<0.001$). Virtual monoenergetic images had significantly better GM SNR relative to conventional images at all energy levels ($p<0.01$). Virtual monoenergetic images had significantly better WM SNR relative to conventional images at energy levels of 55-140 keV ($p<0.03$ - $p<0.0001$). The posterior fossa noise decreased as VME energy increased with statistically significant decrease in noise at VME levels 70-140 keV ($p<0.01$) relative to conventional images.
Conclusions
Virtual monoenergetic reconstructions of unenhanced head CT using detection-based

spectral CT outperformed conventional polychromatic images on the basis of CNR, GM SNR, and WM SNR at identical radiation doses. Virtual monoenergetic decreases posterior fossa streak artifact relative to conventional polychromatic CT.



(Filename: TCT_O-380_AJNRsubmissionfiguresjpg.jpg)

O-381

9:40AM - 9:48AM

Evaluation of the Temporomandibular Joint Degeneration by Ultra-Low-Dose Maxillofacial CT Using Spectral Shaping

F Sodagari[1], T Hijaz[1], M Lester[1], E McComb[1], V Yaghmai[1]
[1]*Northwestern University Feinberg School of Medicine, Chicago, IL*

Purpose
To assess the diagnostic confidence and image quality of maxillofacial CT scans using spectral shaping, in comparison to the conventional protocols, for assessment of temporomandibular joint (TMJ) degeneration in a phantom model.
Materials and Methods
An anthropomorphic head phantom with left TMJ degeneration was scanned on a third-generation dual-source CT scanner. The conventional protocols without spectral shaping included 7 levels of radiation settings by combinations of 120, 100, and 70 kV and tube currents ranging from 10 to 150 mAs. For spectral shaping, a 0.6 mm tin filter was used over the x-ray tubes to shape the output of Sn100 kV and Sn150 kV. Tube currents ranging from 25 to 500 mAs for Sn100, and 5 to 250 mAs for Sn150 were used (11 acquisitions). Images were reconstructed with advanced modeled iterative reconstruction (ADMIRE, strength 3).

A randomized set of 36 pairs of axial and coronal images of normal or abnormal TMJ were reviewed by 2 neuroradiologists who were blinded to the scanning protocols. Diagnostic confidence was assessed on a 5-point scale. Image quality was assessed on a 5-point scale (1: unacceptable, 5: excellent). Radiation dose parameters were recorded. Diagnostic accuracy of the conventional acquisitions was compared with the spectral shaping method.
Results
Mean diagnostic confidence scores did not show a significant difference between conventional and spectral shaped acquisitions (P = 0.642). The sensitivity of detecting TMJ degeneration was 100% for both protocols. Both reviewers incorrectly diagnosed a normal TMJ as abnormal in 70kV/10 mAs, resulting in a lower specificity (86%) for conventional method in comparison with spectral shaping (accuracy: 93% and 100%, respectively). The lowest radiation dose with good mean image quality (score 4) in conventional protocol was 70 kV/100 mAs (ED: 0.13 mSv). Spectral shaping had higher mean image quality scores (4.5 and 5) at lower radiation doses at Sn100/25 (0.01 mSv), Sn100/100 (0.04 mSv), Sn150/15 (0.05 mSv), Sn100/150 (0.06 mSv), and Sn150/25 (0.08 mSv).
Conclusions
Computed tomography (CT) with spectral shaping results in high image quality without affecting diagnostic confidence at substantially (> 10 fold) lower radiation doses in comparison with the conventional protocols. Thus use of spectral shaping in maxillofacial CT scanning can provide high image quality at significantly lower radiation doses that are similar to a single radiograph.

O-382

9:48AM - 9:56AM

Maxillofacial CT with Spectral Shaping for Assessing Different Anatomical Landmarks: Radiation Dose and Image Quality

F Sodagari[1], T Hijaz[1], M Lester[1], E McComb[1], V Yaghmai[1]
[1]*Northwestern University Feinberg School of Medicine, Chicago, IL*

Purpose
To determine the optimal CT settings for assessing different anatomical landmarks at maxillofacial CT using spectral shaping.
Materials and Methods
An anthropomorphic head phantom was scanned on a dual-source CT scanner with spectral shaping at Sn100kV and Sn150kV. Tube currents ranged from 25 to 500 mAs for Sn100, and 5 to 250 mAs for Sn150. Images were reconstructed with 2 strengths of advanced modeled iterative reconstruction (ADMIRE 3 and 5). In a randomized order, 22 sets of images were reviewed by 3 neuroradiologists who were blinded to the scanning protocols. Overall image quality (IQ) as well as diagnostic IQ for assessing teeth, peridental structures, bony septa of ethmoid cells, laminae papyracea, temporomandibular joints (TMJ), maxillary

sinus walls, mastoid air cells, and occipitomastoid sutures were graded on a 5-point scale (1: unacceptable, 5: excellent). Image noise was measured by an independent reviewer for all acquisitions. Inter-reviewer agreement was assessed by intra-class-correlation coefficients (ICC).
Results
Median overall IQ was 3.5 [Interquartile range (IQR): 1]. Image noise was significantly lower with ADMIRE 5 (87.9 ± 30.2) compared to ADMIRE 3 (152.5 ±41.8 HU) ($P<0.001$). At similar radiation levels, Sn100 with higher mAs had better IQ compared to Sn150 with lower mAs ($P < 0.05$).The anatomical structures with higher mean IQ scores were TMJ (3.8), teeth (3.8), sinus walls (3.8), peridental structures (3.8), and mastoid air cells (3.6). The ethmoid septa (2.6) and laminae papyracea (2.7) had lower IQ scores. All landmarks, except for the ethmoid septa and laminae papyracea had good IQ (score > 4) at Sn100/25 mAs, ADMIRE 3 (ED: 0.009 mSv; noise: 174 HU). The most dose efficient combination to achieve good IQ for all anatomical landmarks was Sn100/100, ADMIRE 5 (ED: 0.038 mSv; noise: 44 HU). The agreement of the reviewers on overall IQ was 0.76 (95% CI: 0.58 to 0.88). Inter-reviewer agreement on IQ for assessing all anatomical landmarks was good (ICCs > 0.75).
Conclusions
Maxillofacial CT using spectral shaping provides good image quality for assessing anatomical landmarks. Better image quality can be achieved by using higher strengths of iterative reconstruction. Maxillofacial CT scans can be performed with spectral shaping at doses below 0.04 msV, and dental CT scans can be performed with lower radiation dose levels compared to paranasal sinus CT scans.

O-383

9:56AM - 10:04AM

Reducing Radiation Dose for High-resolution Flat-panel CT Imaging of Superior Semicircular Canal Dehiscence.

M Pearl[1], M Martinez[1], A El Mekabaty[1], J Carey[1]
[1]*Johns Hopkins University School of Medicine, Baltimore, MD*

Purpose
High-resolution flat panel CT (FPCT) imaging is useful for the evaluation of temporal bone pathologies (1). While radiation exposure during neuroimaging procedures remains a concern, efforts have been devoted to reduce dose while maintaining image quality (2-4). We hypothesize that removing radiation scatter grids during FPCT results in decreased radiation exposure while maintaining diagnostic image quality for the evaluation of superior semicircular canal dehiscence (SSCD).
Materials and Methods
Ten patients with concern for SSCD participated in this IRB approved study and underwent

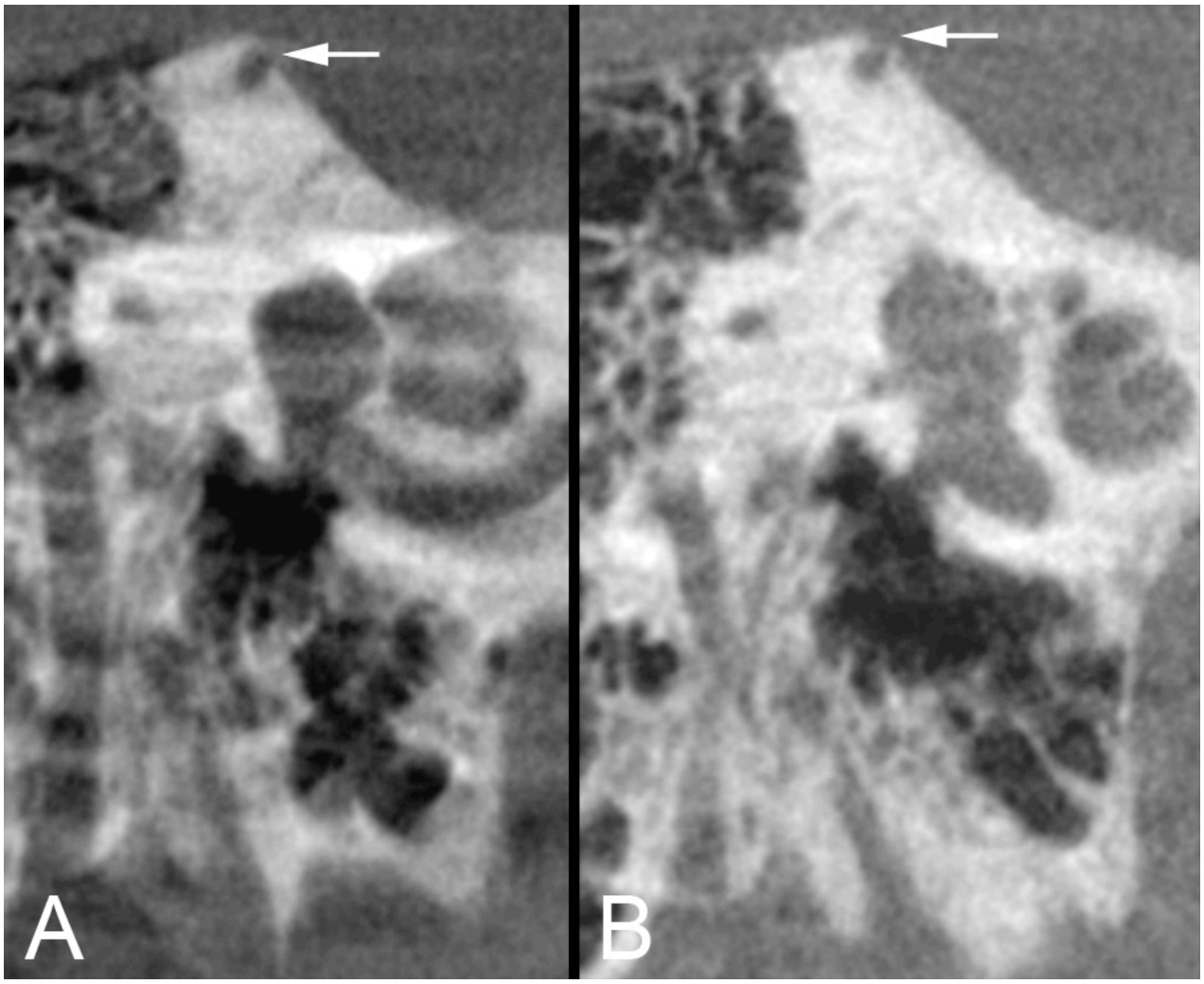
FPCT of the temporal bones. Radiopaque marking strips were placed on each patient to ensure the same field of view for each acquisition. Two collimated 20-second FPCTs were performed (first: grid in; second: grid removed): 109 kV, small focus, 200-degree rotation angle, and 0.4-degree/frame angulation step. Secondary reconstructions were created: manually generated VOI to include the middle ear, voxel size 0.10 mm, 512 x 512 matrix, Hounsfield units (HU) kernel type and "sharp" image characteristics. Three reviewers analyzed images for the ability to diagnose SSCD, to identify the stapes crura, and to determine if a radiation scatter grid was used. Radiation dose parameters (air kerma, mGy and PKA, uGym2) were recorded.

Results

Flat panel CT images with the radiation scatter grids removed were equivalent in diagnostic image quality to those with the grids in place. Both air kerma and PKA were reduced by greater than 30% when the grids were removed. Reviewers could not reliably differentiate when a radiation scatter grid was used or not. Fig. 1. Flat panel CT images with (A) and without (B) grid show the SSCD (arrow) and are equivalent in diagnostic image quality.

Conclusions

Removing radiation scatter grids during FPCT imaging of the temporal bones results in a greater than 30% reduction in radiation exposure while maintaining diagnostic image quality for the evaluation of superior semicircular canal dehiscence.



(Filename: TCT_O-383_Fig1.jpg)

O-384

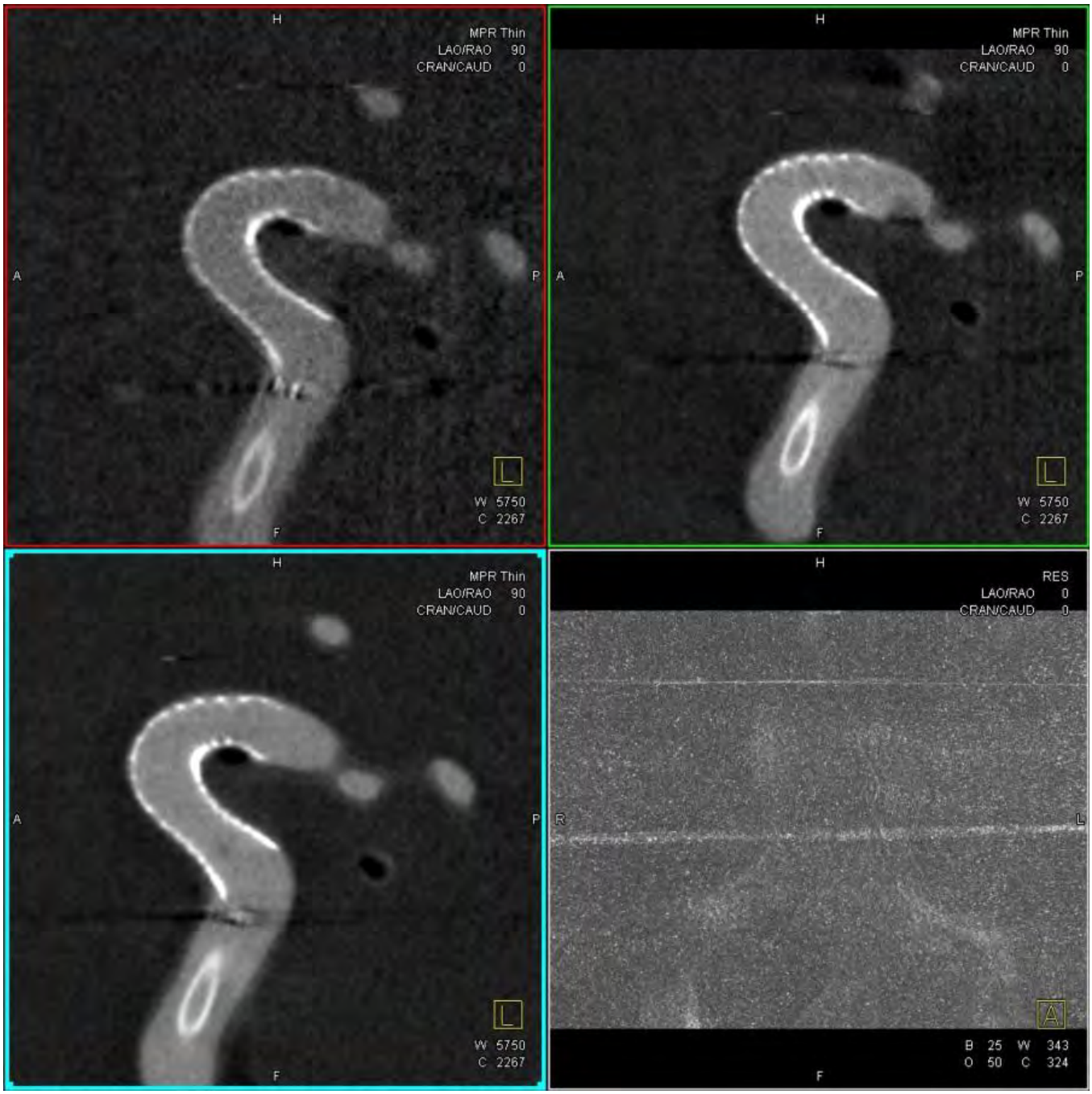
10:04AM - 10:12AM

Rapid Acquisition Cone-Beam Computerized Tomography (Dyna CT)

V Srinivasan[1], G Chintalapani[2], K Camstra[1], S Chen[1], P Kan[1]
[1]Baylor College of Medicine, Houston, TX, [2]Siemens Medical Solutions USA Inc., Hoffman Estates, IL

Purpose
Cone-beam computerized tomography (CBCT) allows the acquisition of cross-sectional imaging in angiography suites using a rotational arm and digital flat panel detectors. The applications are numerous, such as evaluation of implanted devices and localization of cerebrovascular lesions. However, it necessitates additional radiation exposure and the use of significant sedation, limiting use.

Materials and Methods
Five-second and 10-second CBCT (Dyna CT) protocols were developed and used in a phantom head model, swine model, and in patients. A blinded reviewer scored the quality of 5-second and 10-second CBCT images, compared to 20-second controls, on a 5-point scale. Radiation dose and quantitative scales also were determined.
Results
The 5-second protocol was applied in 1 phantom head and 1 swine. The 10-second protocol in 1 phantom head, 2 swines, and 10 patients. The 20-second control protocol was applied in the same phantom head and 2 swines as the experimental protocols. Several patient controls also were rated. The 5-second protocol received a mean rating of 3.7 on the 5-point scale, the 10-second protocol had a mean rating of 4.6, and the 20-second protocol had a mean rating of 4.7.
Conclusions
The 10-second CBCT protocol was rated similarly to the traditional 20-second CBCT protocol, with few subjective differences noticed across many different pathologies. The 5-second protocol, although beneficial in reducing the radiation dose by 75%, was insufficiently rated for routine application. Ten-second CBCT appears to be a useful protocol for routine application and can be used in mildly sedated patients.



(Filename: TCT_O-384_Figure1abstract.jpg)

O-385

10:12AM - 10:20AM

Comparison of radiation doses imparted during multislice and cone beam computed tomography for the postoperative cochlear implant assessment

N Guberina[1], U Dietrich[1], M Forsting[1], A Ringelstein[1]

[1]*Institute of Diagnostic and Interventional Radiology and Neuroradiology, University Hospital Essen, Essen, NRW*

Purpose
To assess and compare radiation doses imparted during multislice computed tomography (MSCT) and cone beam computed tomography (CBCT) for the postoperative examination of cochlear implant insertion.
Materials and Methods
Radiation doses were assessed during standardized petrous bone CT-protocols at different MSCT [(I) single-source CT-scanner Somatom Definition AS+, (II) 2nd generation of dual-source CT-scanner Somatom Definition Flash, (III) 3rd generation of dual-source CT-scanner Somatom Force (all Siemens Healthcare, Erlangen, Germany)] and at the CBCT Ziehm Vision RFD 3D (Ziehm Imaging GmbH, Nürnberg, Germany) [(IV) RFD-3D (Standard) and (V) RFD-3D (L-D)]. Image quality was examined independently by 2 experienced radiologists rating various important parameters like electrode array placement, quality control of cochlear implant surgery, the evaluation of the temporal bone in case of complications, etc. determined on real patients' examinations (n = 78). Wilcoxon signed rank test was used to determine statistically significant differences ($p < 0.05$). Inter-rater reliability was determined by calculating k values.
Results
In MSCT setting the following radiation doses were assessed (CTDIvol; DLP): (I) 21.5 mGy; 216 mGycm; (II) 19.7 mGy; 195 mGycm; (III) 12.7 mGy; 127 mGycm. In the CBCT setting radiation doses were distributed as follows: (IV) 1.9 mGy; 19.4 mGycm; (V) 1.24 mGy; 12.9 mGycm. Overall, the image quality of both settings was evaluated as "good" (Likert scale MSCT 1.4 and CBCT 1.9) with a good inter-rater reliability ($r = 0.81$).
Conclusions
Cone beam CT imaging bears considerable dose save potential for the postoperative examination of cochlear implant insertion. Radiation doses are markedly lower during CBCT compared to MSCT petrous bone examinations while maintaining sufficient image quality.

O-387

10:28AM - 10:36AM

Impact of Dose Reduction on CT Simulation Planning scans for Whole Brain Radiation Therapy

P Shah[1], Q Liang[2], C Miyamoto[2], S Li[3]
[1]*Temple University, Philadelphia, PA,* [2]*Temple University Hospital, Philadelphia, PA,* [3]*Temple University Hospital, philadelphia, PA*

Purpose
To investigate the feasibility of applying ALARA principles to radiation treatment planning

head CT scans. The aim of the study is to quantitatively verify lower dose scans do not alter prescribed radiation treatment plans.

Materials and Methods

A Gammex 467 tissue characterization phantom with inserts of 14 different materials was scanned at 7 different mA levels (30~300 mA)on a GE 16 slice scanner. CT Hounsfield (HU) numbers of different inserts were measured. An auto contouring treatment planning system (Pinnacle) for bone and lung (air) was used to evaluate the effect of CT number accuracy from a treatment planning aspect, on the 30 and 300 mA-scanned images. A routine head CT scan intended for a 3D whole brain radiation treatment was evaluated. Dose calculations were performed on routine scanned images using clinical protocol (120 kVP, Smart mA, maximum 291 mA) and the images obtained after adding noise to simulate a 'low dose' 70 mA scan. Plan parameters including isocenter, beam arrangements, block shapes, dose grid size and resolution, and prescription were kept the same for the 2 plans. The calculated monitor units (MUs) for these 2 plans then were compared to assess for differences in the prescribed treatment plans.

Results

No significant degradation of CT number (HU) accuracy was found at lower dose levels from either the phantom scans or the patient images with added noise. The CT numbers (HU) remained consistent when the prescribed tube current remained above 60 mA. The auto contoured volumes for air and cortical bone show 0.3% and 0.12% of differences between 30 mA and 300 mA respectively. The 2 forward plans created on regular and low dose images gave the same calculated MU, and 98.3% of points having <1% of dose difference.

Conclusions

Both phantom and generated patient low dose CT images provide similar accuracy for whole brain radiation treatment planning. Approximately 20-25% scan dose reduction can be performed safely when planning whole brain radiation. In conclusion, there is potential to optimize simulation head CT scan protocols to uphold ALARA principles and limit unnecessary radiation dose to nontarget tissues.

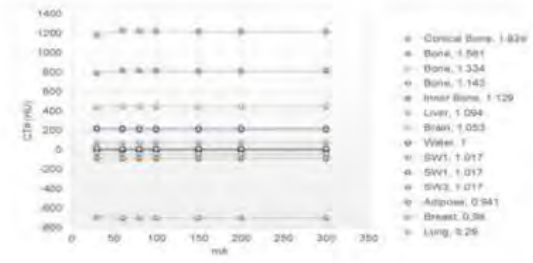


Figure 1

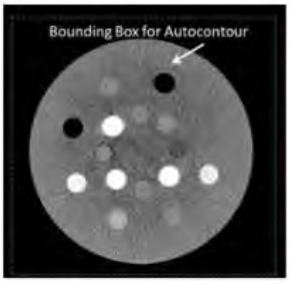


Figure 2

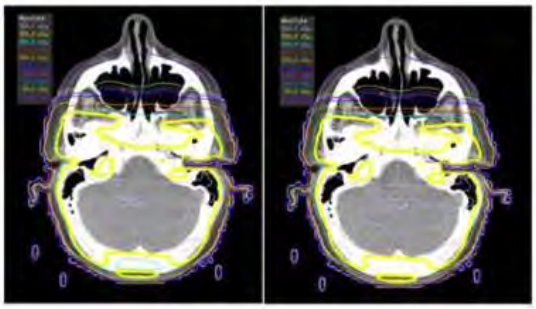


Figure 3

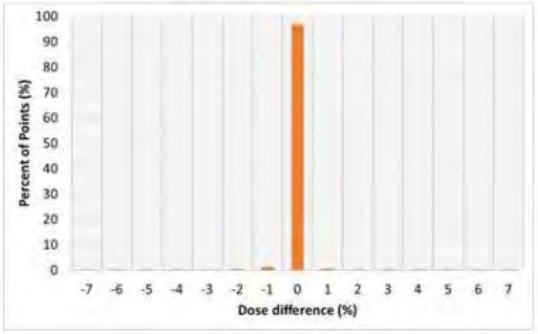


Figure 4

Figure 1: Measured CT # at different mA levels for different materials (density in unit of g/cm³).
Figure 2: Bounding box for autocontour
Figure 3: Isodose distributions planned on clinical images (left, 290 mA) and images with added noise (right, ~70 mA)
Figure 4: Percent of dose different for the two whole brain plans: 98.3% of points having <1% of dose difference

(Filename: TCT_O-387_ASNR2017abstractimages.jpg)

Thursday
9:00AM - 10:30AM
Long Beach Convention Center, Room 104C (Main Lobby)

23F-Parallel Paper Session: MR and CT Perfusion Imaging: Going with the Flow and What We Know

O-388

9:00AM - 9:08AM

Novel Automated MR Sequence for Acquisition of Combined Dynamic Susceptibility Contrast (DSC) and Dynamic Contrast Enhanced (DCE) MR Perfusion Using a Single Contrast Dose: Clinical Application in Brain Tumor Analysis

B Liu[1], Y Chen[2], T Parrish[2]
[1]Northwestern University Feinberg School of Medicine, Chicago, IL, [2]Northwestern University, Chicago, IL

Purpose

To describe the clinical application towards brain tumor analysis of a novel automated MR sequence for acquisition of combined dynamic susceptibility contrast (DSC) and dynamic contrast-enhanced (DCE) MR perfusion using a single contrast dose.

Materials and Methods

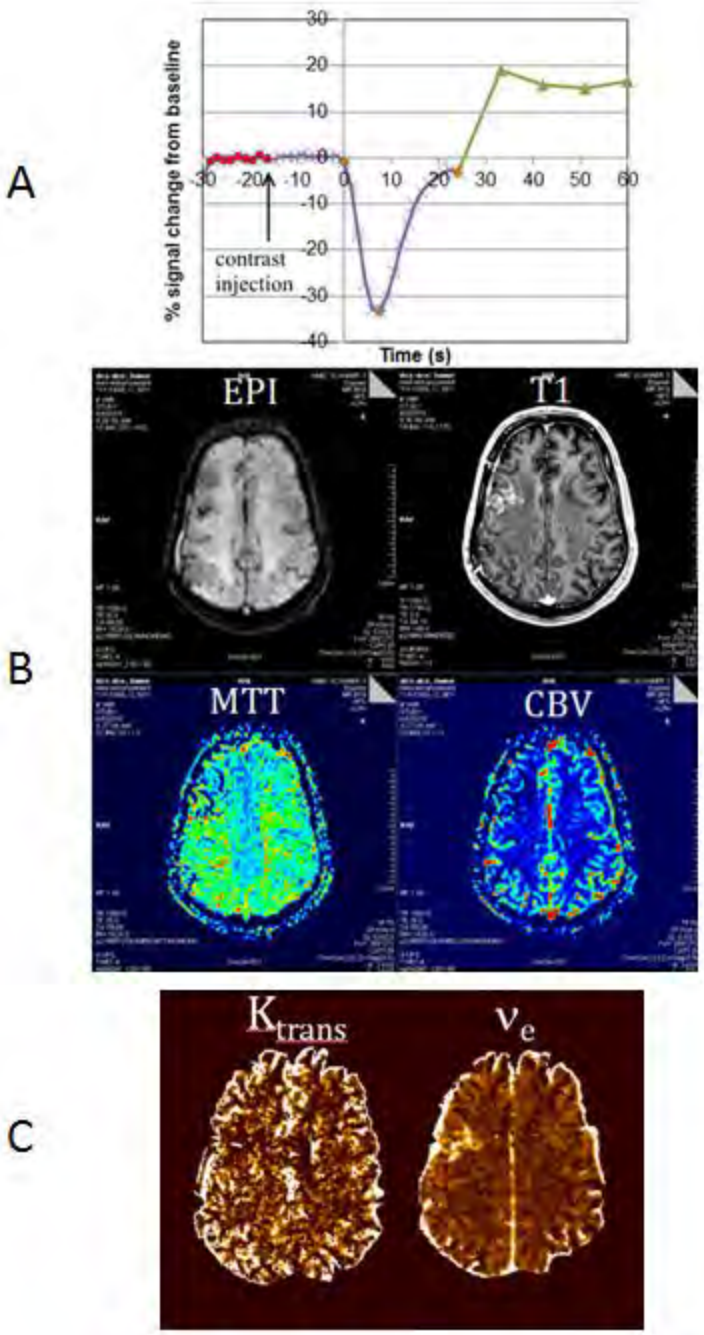
A combined DSC-DCE perfusion technique with automatic switching mechanism that requires only a single contrast dose injection was developed and tested in brain tumor patients. The studies were conducted on 1.5T and 3T Siemens MR scanners, obtaining precontrast MPRAGE images for T1 maps at flip angles 2, 7, 10, 15, 25, 14. First DSC perfusion was performed at 13x5mm thick slices, TE/TR=35/1500ms, 2.1x2.1mm2 in-plane resolution, 35 volumes with 0.1mmol/kg gadobutrol injected at volume 10. After automatic switching, DCE perfusion performed at flip angle 14, 26x3mm thick slices, TE/TR=1.52/3.85ms, 0.9x0.9mm2 in-plane resolution, 40 volumes.

Results

The clinical performance was evaluated in brain tumor patients by a neuroradiologist. The automatic algorithm successfully detected critical timepoints for switching between DSC and DCE perfusion (Fig. 1A). The resultant DSC and DCE perfusion maps and permeability parameters were robust and provided clinically relevant information in brain tumor imaging (Figs. 1B and 1C). In addition, the technique allowed measurement of patient-specific AIF during the DSC portion for improvement of DCE processing. Figure caption: 1A, Red time-points represent the baseline. Purple time-points represent the DSC signal curve. The 3 critical time-points: iStart, iMinimum and iStop are in orange. Green line time-points represent the subsequent DCE acquisition. 1B, DSC perfusion maps and 1C, DCE permeability maps in a glioblastoma multiforme (GBM) patient with stable imaging findings 8 months after surgery, radiation, temozolomide, and bevacizumab.

Conclusions

Advanced MRI techniques such as dynamic susceptibility contrast (DSC) and dynamic contrast-enhanced (DCE) perfusion imaging offer unique opportunities to query physiological information of brain tumors in situ noninvasively. Individually, DSC and DCE MR perfusion techniques have shown diagnostic, predictive, and prognostic value in brain tumor imaging. However, these techniques offer complementary perfusion and permeability information and are more powerful when considered in combination. A combined DSC-DCE MR perfusion technique was developed and clinically evaluated. This robust combined DSC-DCE perfusion technique only uses a single contrast dose injection, offers a clinically useful neuro-oncologic imaging method, and provides increased diagnostically relevant information in a single imaging session.



(Filename: TCT_O-388_DSC-DCEfig.JPG)

O-389

9:08AM - 9:16AM

Comparison of MRI perfusion hemodynamic models: Normal Saline transient hemodilution vs dynamic susceptibility weighted (Gd)

A Mian[1], C Farris[2], O Sakai[3], N Hua[2], M Horn[4], H Jara[1]

[1]Boston University/Boston Medical Center, Boston, MA, [2]Boston Medical Center/Boston University, Boston, MA, [3]Boston Medical Center, Boston University School of Medicine, Boston, MA, [4]Boston Medical Center, Boston, MA

Purpose

Normal saline (NS) recently has been shown to be a viable brain perfusion MRI technique. Our hypothesis is that the main hemodynamic difference between the NS perfusion technique and Gd DSC is a consequence of the blood-brain barrier (BBB) and the fact that water molecules are able to cross the BBB while Gd chelates in healthy brain tissue remains intravascular. This translates into a bolus tracking signal with rapid wash-in and rapid wash-out in DSC. The purpose of this work is to establish quantitative imaging processing methods to allow comparison of perfusion metrics between NS perfusion and the current gold standard, which is DSC perfusion.

Materials and Methods

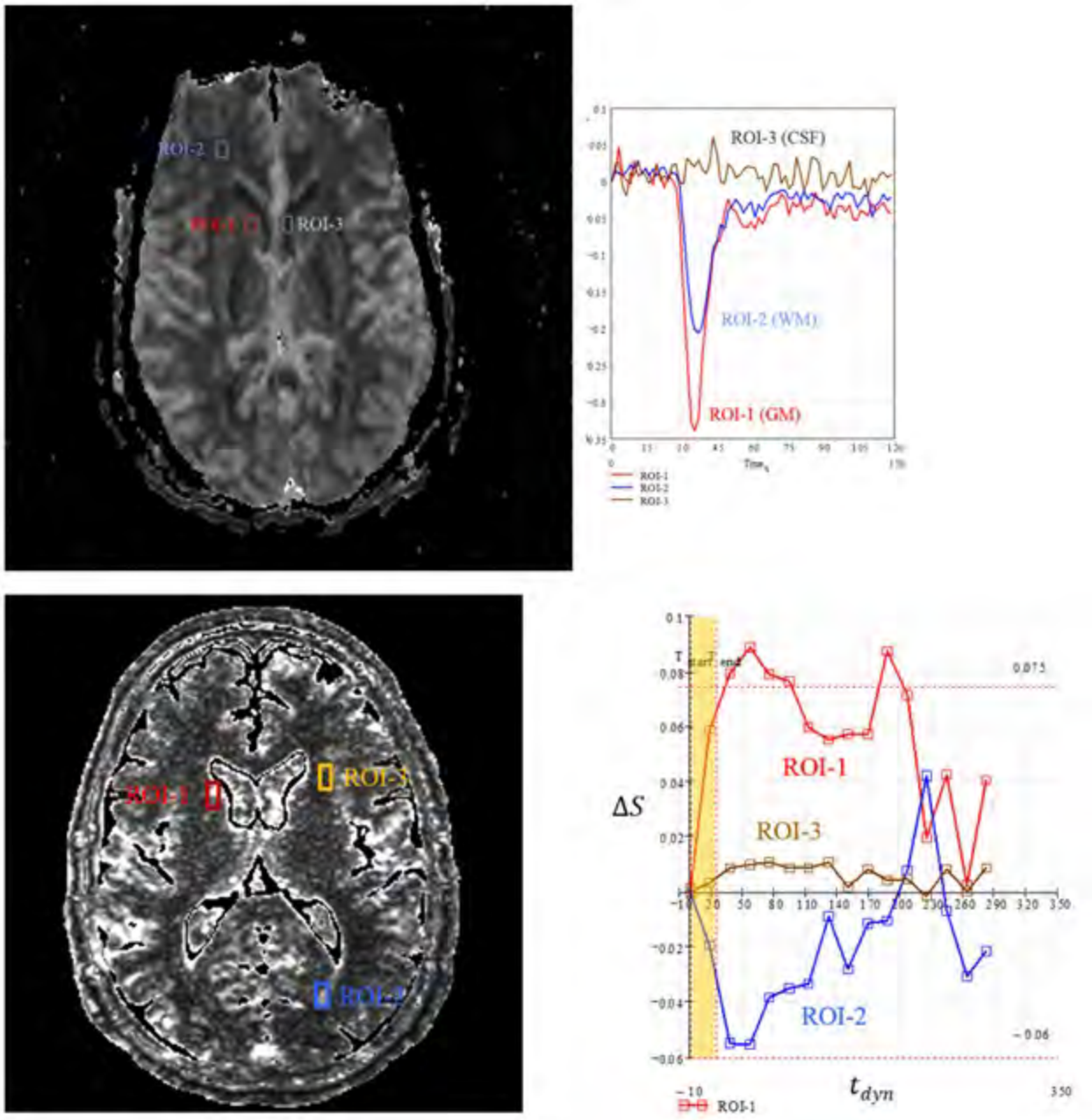
This study was approved by the IRB of our hospital. Magnetic resonance imaging (MRI) was performed at 1.5T (Achieva, Philips Healthcare): head array and body coil for RX/TX. Of the 29 patients scanned to date with the NS technique, 3 have been scanned concurrently with Gd DSC: 60 dynamics, 16 slices with weight-adjusted Gd dose. The IR pulse sequence was run during and after the NS injection for up to 5min: up to 150cc of NS were power injected via antecubital IV at 3-4cc/s. Images were processed with Mathcad (2001i, PTC, Needham, MA) algorithms to map maximum enhancement (maxENH), area under the curve (AUC), time-to-peak (TTP), and mean-transit-time (MTT). We further refined the software to quantify CBV, CBF and MTT.

Results

Figure 1 illustrates the different temporal signal responses in DSC (top) relative to NS-IR-TSE. The time curves from the DSC datasets are very rapid following closely the Gd bolus. In contradistinction, the NS time curves (Fig. 1, bottom) are slower and extend beyond the injection time, a phenomenon that is consistent with diffusion into the extravascular space.

Conclusions

Dynamic susceptibility contrast and NS perfusion-weighted MR exhibit fundamentally different temporal hemodynamics thus requiring separate mathematical models for the estimation of the chief perfusion parameters. This work could have implications for the establishment of 4-dimensional image processing techniques applicable across perfusion techniques.



(Filename: TCT_O-389_salinefigsASNR_2017.jpg)

O-390

9:16AM - 9:24AM

Robust Volumetric Non-Contrast Perfusion Imaging of the Whole Brain using a 3D TSE Acquisition

M Pinho[1], J Greer[1], X Wang[1], J Maldjian[1], A Madhuranthakam[1]
[1]*University of Texas Southwestern Medical Center, Dallas, TX*

Purpose

Arterial spin labeled (ASL) noncontrast perfusion images generally are acquired using multiple signal averages to account for the low signal to noise ratio (SNR) and the characteristic significant variations among the multiple dynamic acquisitions. To overcome these challenges, multi-slice 2D images with EPI readouts or 3D imaging using spiral acquisitions were recommended on a recent consensus paper (1). However, both these techniques are sensitive to B0 inhomogeneities that may affect image quality in challenging situations such as patients with intracranial hemorrhage, calcifications or metal such as craniotomies. In this study, we demonstrate a robust noncontrast perfusion imaging of the whole brain using a novel 3D TSE acquisition based on Cartesian Acquisition with SPiral Reordering (CASPR).

Materials and Methods

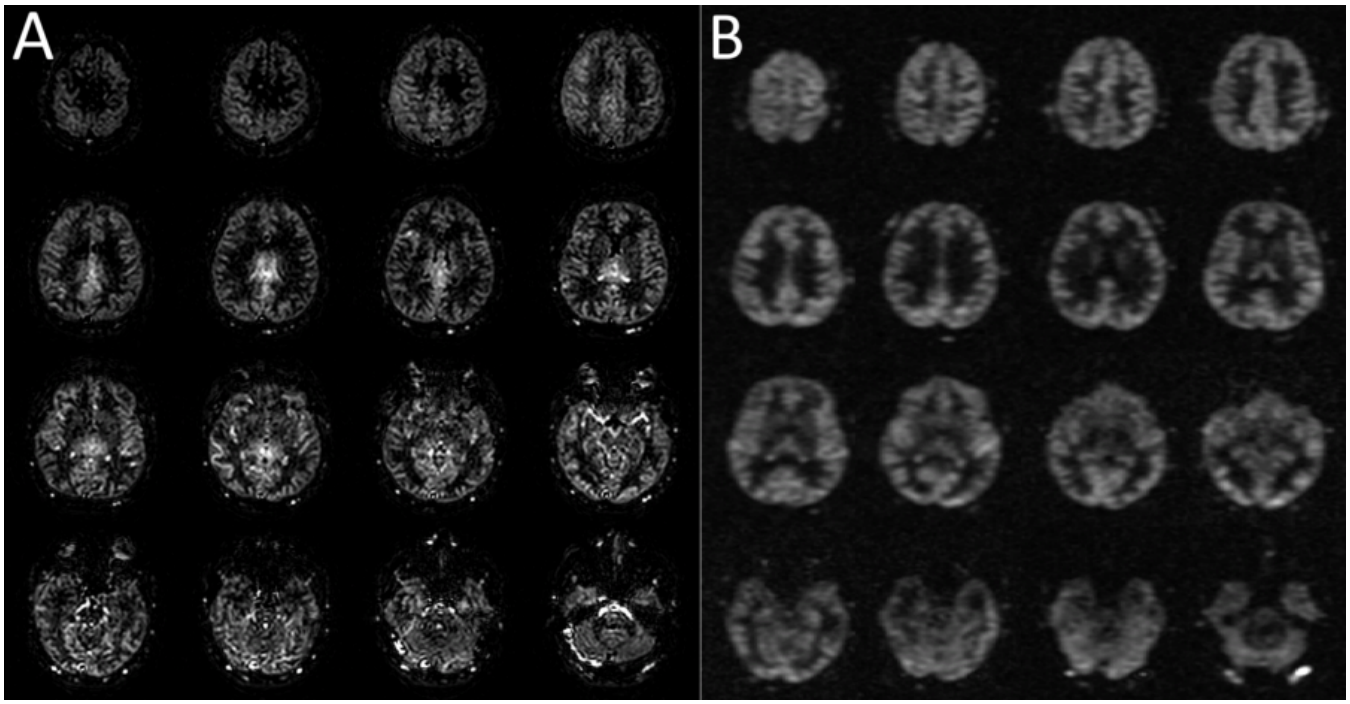
The 3D CASPR view ordering, which samples the k-space in a spiral-out trajectory while maintaining the sampling on a Cartesian ky-kz grid, was implemented for a pCASL acquisition with background suppression and inflow saturation on a 3T Ingenia scanner (Philips Healthcare, The Netherlands). Brain perfusion images were acquired using 3D CASPR and compared against 3D TSE using a linear sampling scheme, as well as multi-slice 2D gradient echo EPI in 3 volunteers with IRB approval and written informed consent. A label duration and post-label delay of 1.8s was used. The typical imaging parameters of the 3D pCASL with CASPR view ordering were: sagittal and/or axial orientation; FOV = 220×220×200 mm; Resolution = 3×3×3 mm; 52 slices; ETL = 100; total scan time = 5:30 minutes. Imaging parameters for with 2D pCASL with EPI were: Resolution = 3×3 mm; Slice thickness – 5 mm; 16 slices; 30 signal averages ETL = 100; total scan time = 4:20 minutes.

Results

Three-dimensional pCASL with CASPR view ordering (Fig. 1B) provided robust images of the whole brain compared to multi-slice 2D pCASL with EPI readout across all volunteers (Fig. 1A). Due to repeated sampling of the center of k-space in each shot, 3D CASPR trajectory provided robust images compared to 3D TSE with linear view ordering.

Conclusions

The proposed 3D CASPR trajectory provides robust volumetric noncontrast perfusion images of the whole brain by repeatedly sampling the center of k-space with increased robustness to ASL preparation. Compared to 2D EPI and/or 3D GraSE acquisitions, TSE-based acquisitions are more robust to B0 inhomogeneities and may provide robust image quality even in challenging situations such as imaging patients with cranial sources of magnetic susceptibility.



(Filename: TCT_O-390_figure.gif)

O-391

9:24AM - 9:32AM

COMPARISON of DELAY SENSITIVE and DELAY INSENSITIVE CT PERFUSION METHODS in ACUTE ISCHEMIC STROKE and THEIR VARIABILITY ACCORDING to LOCATION of CRITICAL STENOSIS

b Karaalioglu[1], A ARALASMAK[2], H Toprak[3], M Kolukısa[1], o uysal[1], S Yildiz[1], H Ozdemir[1], A Alkan[1]
[1]Bezmialem Vakif University, istanbul, istanbul, [2]Bezmialem Vakif University, Istanbul, Turkey, [3]Bezmialem Vakif University, istanbul, turkey

Purpose
To evaluate visual and quantitative differences of delay sensitive (SVD) and delay-insensitive (SVD+) CTP postprocessing methods in acute ischemic stroke patients and their variability according to location of critical stenosis.
Materials and Methods
The CTPs of 45 patients were processed retrospectively with 2 different methods. Comparing with the contralateral normal hemisphere, relative and difference of metrics were calculated (rCBV, rCBF, rMTT and dMTT). Patients were categorized into 5 groups according to superiority in visual assessment of penumbra between postprocessing methods. Locations of critical stenosis and their percentages in each group were identified and compared.

Results
Differences between 2 methods were formulated as (rCBF/1,5, rMTT x1.3, dMTT/3) SVD = (rCBF, rMTT, dMTT) SVD+. In group 1, penumbra was noted in SVD while pseudohyperperfusion in SVD+. In groups 2 and 3, penumbra was better distinguished in SVD than in SVD+ in decreasing easiness, respectively. In group 4, penumbra assessment was similar in both. In group 5, penumbra was better distinguished in SVD+. Groups 1 and 5 were the groups in which the frequency of critical distal stenosis was % 100. Groups 2, 3 and 4 were the groups having high rates of proximal critical stenosis in decreasing proportions, respectively (90%, 87%, and 77%).
Conclusions
In both CTP methods, the most prominent difference was found in dMTT. Visually, penumbra was better distinguished by SVD in proximal critical stenosis, whereas by SVD+ in distal critical stenosis. In cases having both ipsilateral critical proximal and distal stenosis, penumbra was noted in SVD but pseudohyperperfusion in SVD+. Variability of results of CTP methods in penumbra evaluation according to locations of critical vessel stenosis were not investigated so far in literature. This finding showed us that extraction of contrast delay in SVD+ method might cause false results in cases of ipsilateral critical proximal and distal stenosis.

O-392

9:32AM - 9:40AM

Validation of Cerebral Blood Flow in Moyamoya Disease by Arterial Spin Labeling MRI and [15O]-water PET with Simultaneous PET/MRI

A Fan[1], J Guo[1], M Khalighi[2], T Hjoernevik[3], P Gulaka[1], D Holley[1], H Gandhi[1], J Park[1], B Shen[1], T Haywood[1], F Chin[1], G Zaharchuk[1]
[1]Stanford University, Stanford, CA, [2]General Electric Healthcare, Stanford, CA, [3]Oslo University Hospital, Oslo, Norway

Purpose
Cerebral blood flow (CBF) measurements are critical to assessment of many cerebrovascular disorders including stroke. Arterial spin labeling (ASL) MRI is a promising, noninvasive technique to image CBF but suffers from quantification errors in the presence of long arterial transit delays. We aim to validate ASL MRI in patients with moyamoya disease that have challenging transit delays (1), against the [15O]-water PET reference standard on a hybrid PET/MRI scanner.
Materials and Methods
Time-of flight PET/MRI (Signa, GE Healthcare) scans of CBF were performed in 15 patients with moyamoya disease. Positron emission tomography (PET) imaging after injection of [15O]-water (550-925 MBq) was performed simultaneously with 2 ASL sequences: standard single delay of 2000ms (2) and sequential multi-delay (5 delays, 700-

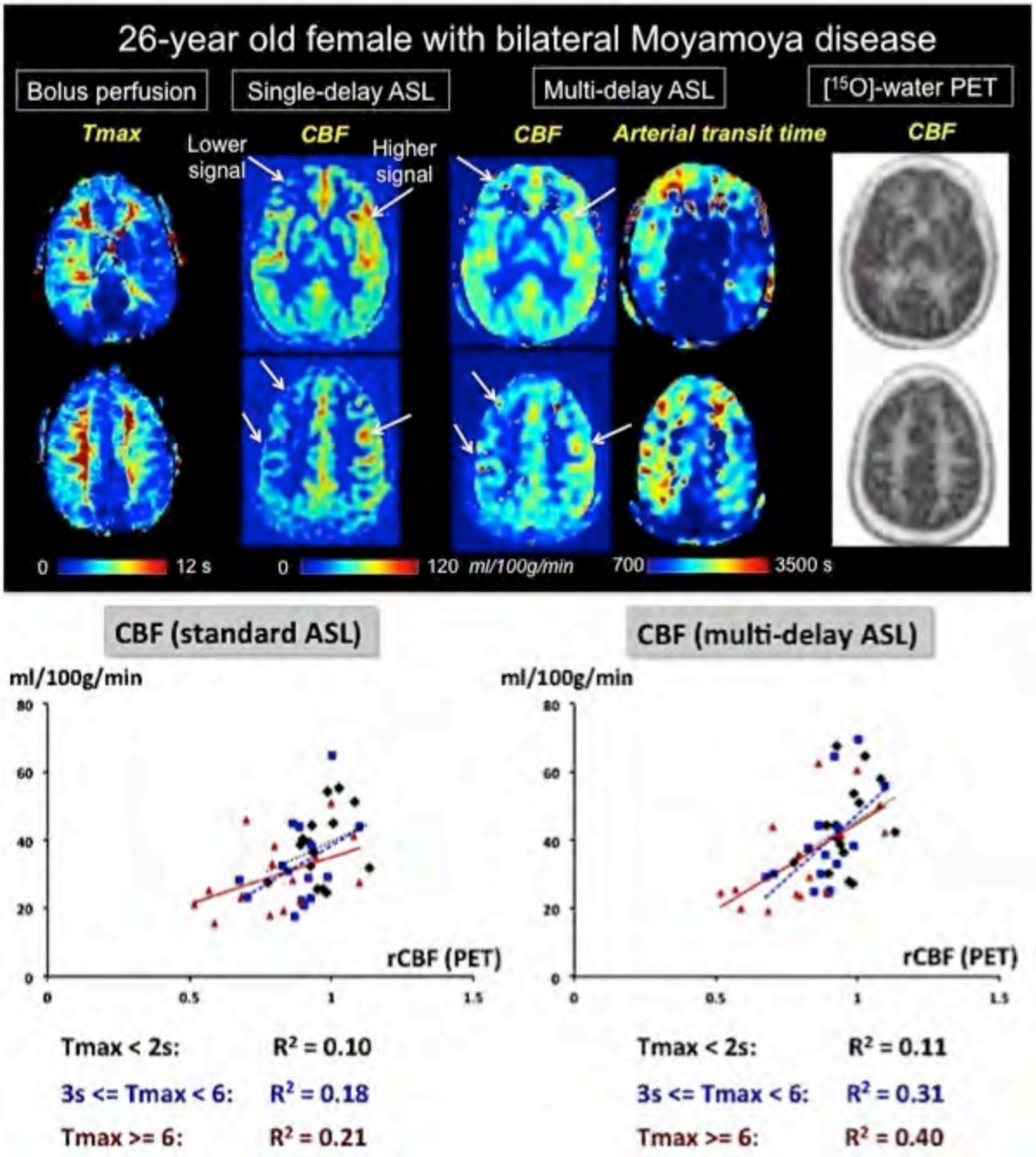
3000ms). Arterial spin labeling (ASL) scan parameters included pseudo-continuous labeling with label duration=1500ms; echo time=10.7ms; slice=4mm; bandwidth=62.5kHz; and spiral readout. At the end of the session, contrast perfusion-weighted imaging (PWI) also was performed to assess the time-to-max (Tmax) of different cortical regions in patients. All perfusion images were registered to the Montreal Neurological Institute template with Advanced Normalization Tools (ANTs) software.

Results

In areas of moderate Tmax (greater than 4s), standard single-delay ASL showed areas of underestimation (because the tagged spins did not arrive to the cortical tissue) and overestimation (where tagged spins were still in larger vasculature) relative to PET. Improvements were seen with multi-delay ASL, with patterns of arterial transit time that were similar to the contrast Tmax maps (Fig. 1). In 2 patients with severely long delays (average Tmax > 10s), both ASL sequences underestimated CBF in affected regions relative to PET. In each of the 15 patients, we categorized regions with normal Tmax (<2s), moderate Tmax (3s < Tmax < 6s), and severe Tmax (> 6s) for perfusion measurements (Fig. 2). Multi-delay ASL (right) showed stronger correlation with PET measurements, especially in regions of moderate and severe Tmax delays, compared to standard single-delay ASL (left).

Conclusions

Simultaneous PET/MRI is an ideal imaging approach to assess CBF as it reduces errors related to physiological changes. Multidelay ASL improved CBF measurements in areas of long Tmax over standard ASL for moyamoya patients, but the longer scantime necessitates reduced spatial resolution. In a few patients with severely delayed flow, longer-label long-delay or velocity-selective ASL (3) strategies may be required to accurately assess CBF.



(Filename: TCT_O-392_2017_ASNR_figure.jpg)

O-393

9:40AM - 9:48AM

A method for Quantitative Cerebrovascular Reserve: Animal Study

C Cantrell[1], G Christoforidis[2], Y Jeong[3], K Midlash[2], K Kawaji[2], T Carroll[2]
[1]northwestern university, Chicago, IL, [2]University of Chicago, Chicago, IL, [3]Northwestern, Chicago, IL

Purpose

In this study, we develop a method to accurately quantitate cerebrovascular reserve (CVR) using current MRI protocols. We show that the use of a WCF specific to the second injection allows for accurate quantification of CBF and CVR and validate this in canine models.

Materials and Methods

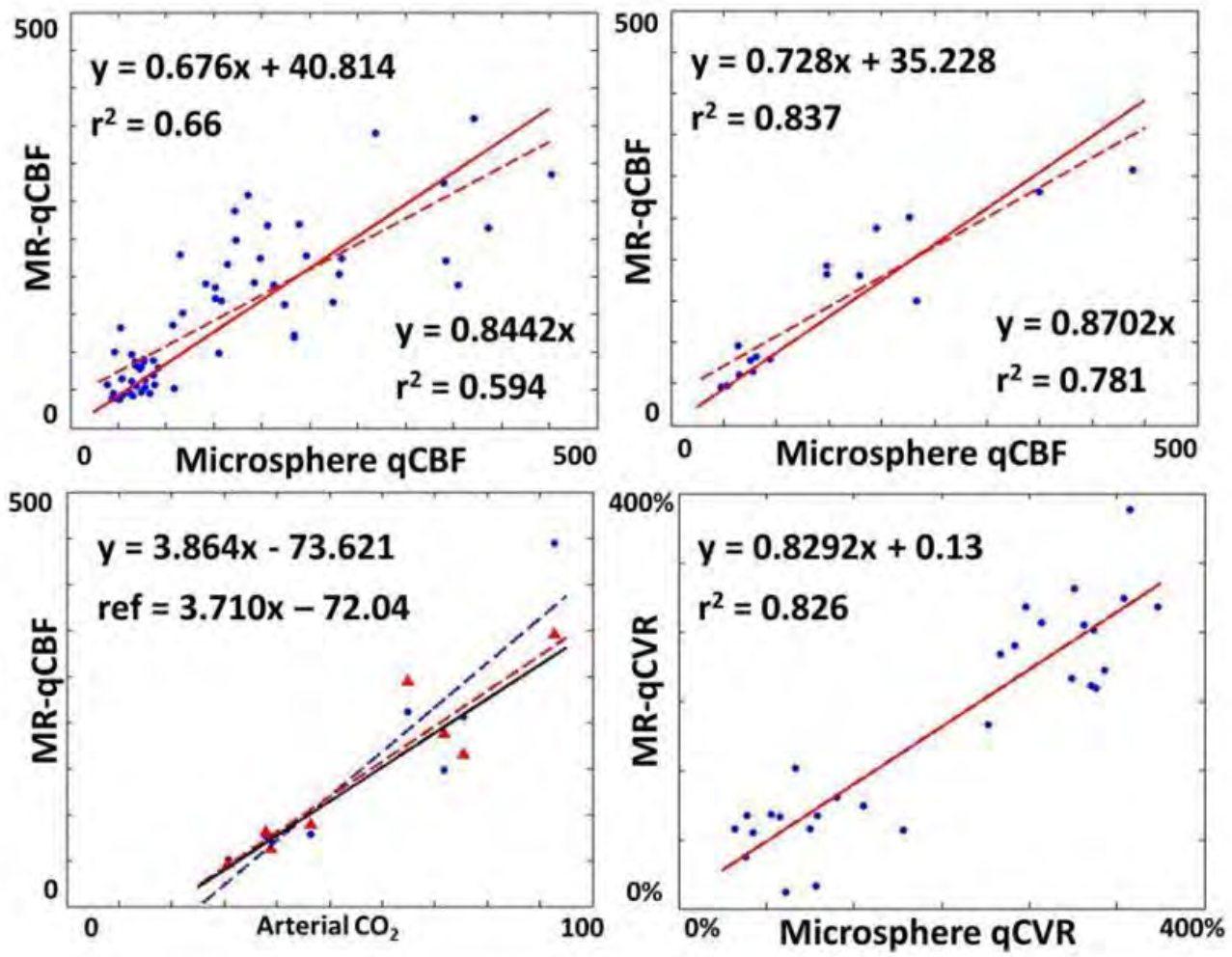
We investigate the accuracy of the bookend perfusion technique in quantifying cerebral blood flow (CBF) in back to back injections of contrast agent by implementing a second injection specific water correction factor in 5 mongrel dogs (20-30 kg) studied at baseline and under physiologic stress (vasodilation) induced by CO2 respiration. MR-qCBF and MR-qCVR values were compared against reference standard microspheres.

Results

Figure 1: Canine data show high agreement between microsphere and MR acquisitions. The upper left image compares qCBF between microsphere (x-axis) and MR (y-axis) where each dot represents a region of tissue. The upper right shows the same data but with each dot representing an average across the hemisphere. The lower left image shows agreement between measured qCBF and previously published data. And finally, the lower right shows high correlation of CVR measurements.

Conclusions

We present the first evidence of a method to accurately quantitate CVR using current MRI-protocols. We show that the use of a WCF specific to the second injection allows for accurate quantification of CBF and validate this in a canine model.



(Filename: TCT_O-393_CVRdog.jpg)

O-394

9:48AM - 9:56AM

A method for Quantitative Cerebrovascular Reserve: A Human Study

C Cantrell[1], G Christoforidis[2], Y Jeong[3], K Midlash[2], K Kawaji[2], T Carroll[2]
[1]northwestern university, Chicago, IL, [2]University of Chicago, Chicago, IL, [3]Northwestern, Chicago, IL

Purpose
We develop a method to accurately quantitate cerebrovascular reserve (CVR) using current MRI protocols. We show that the use of a WCF specific to the second injection allows for accurate quantification of CBF and examine this in a retrospective patient population.
Materials and Methods
Volunteer Study: To examine the effects of a second injection of gadolinium, 10 volunteers

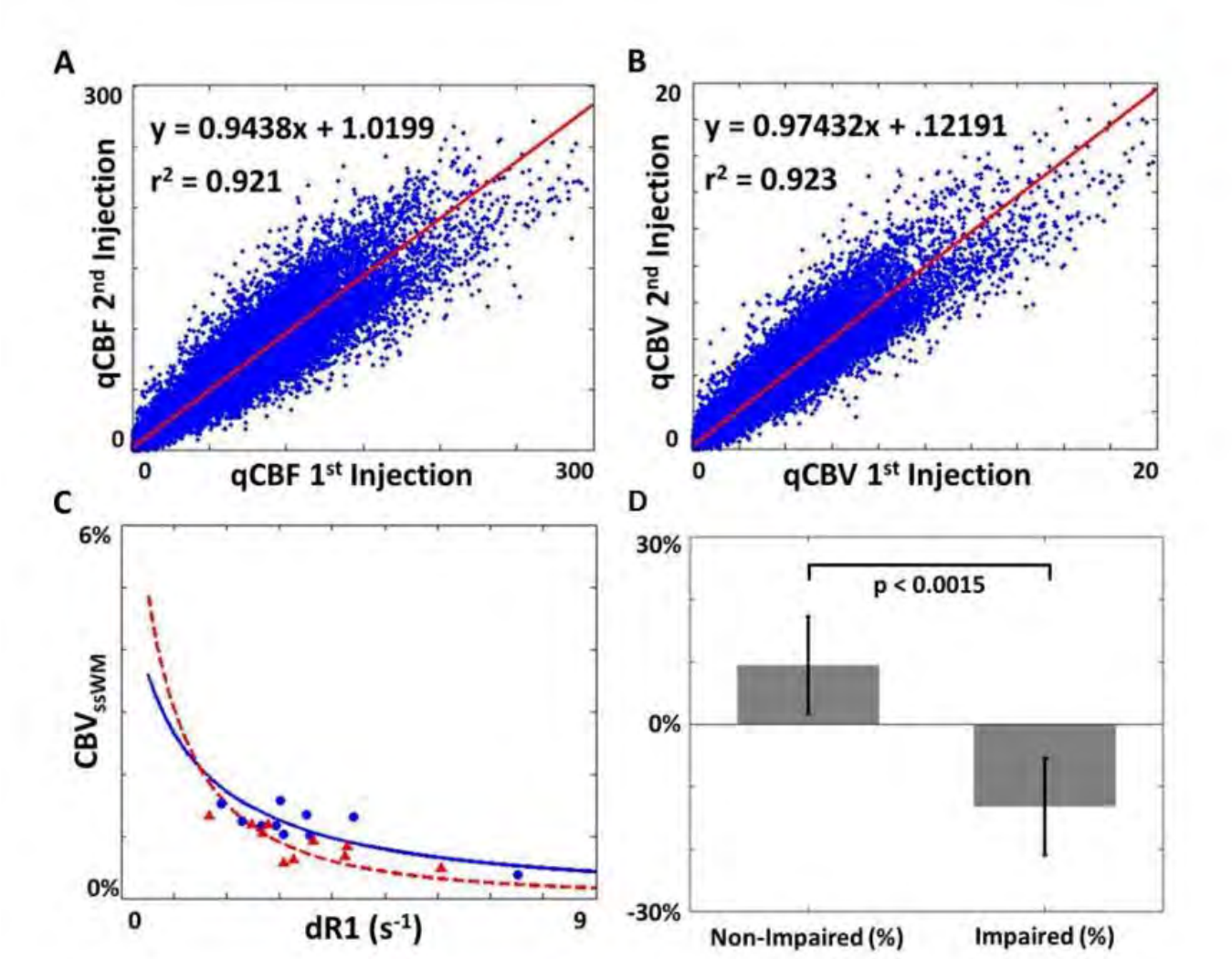
were imaged twice using a quantitative DSC perfusion MRI. The injection procedure was as follows: For each DSC scan a single dose injection (0.1 mmol/kg body weight) of Gd-DTPA followed by a 15 mL saline flush, at 4 mL/s. was used. The second DSC scan was taken 5 minutes after the completion of the first. A different water correction factor was fit using the ratio of T1s for the first and second injection. Patient Data: A series of consecutive patients with angiographically confirmed cerebral vascular disease who underwent an ACZ challenge MRI perfusion study were selected retrospectively. Cerebral perfusion was quantified using a previously reported DSC perfusion MRI pulse sequence. Patients then were given a 1000 mg injection of ACZ between scans. The final scan with the second Gd-DTPA injection measures perfusion changes in response to ACZ.

Results

Volunteer data show that injection specific WCF allows for high correlation of qCBF between first and second injections (A) and qCBV (B). WCF for the first (blue) and second (red) injections are show in (C). qCVR patient data shows ~25% diminished CVR in compromised regions when compared to unaffected tissue (D) in line with previous findings.

Conclusions

We present the first evidence of a method to accurately quantitate CVR using current MRI-protocols. We show that the use of a WCF specific to the second injection allows for accurate quantification of CBF and show that qCVR can clearly distinguish between stages of hemodynamic compromise.



(Filename: TCT_O-394_CVRhuman.jpg)

O-395

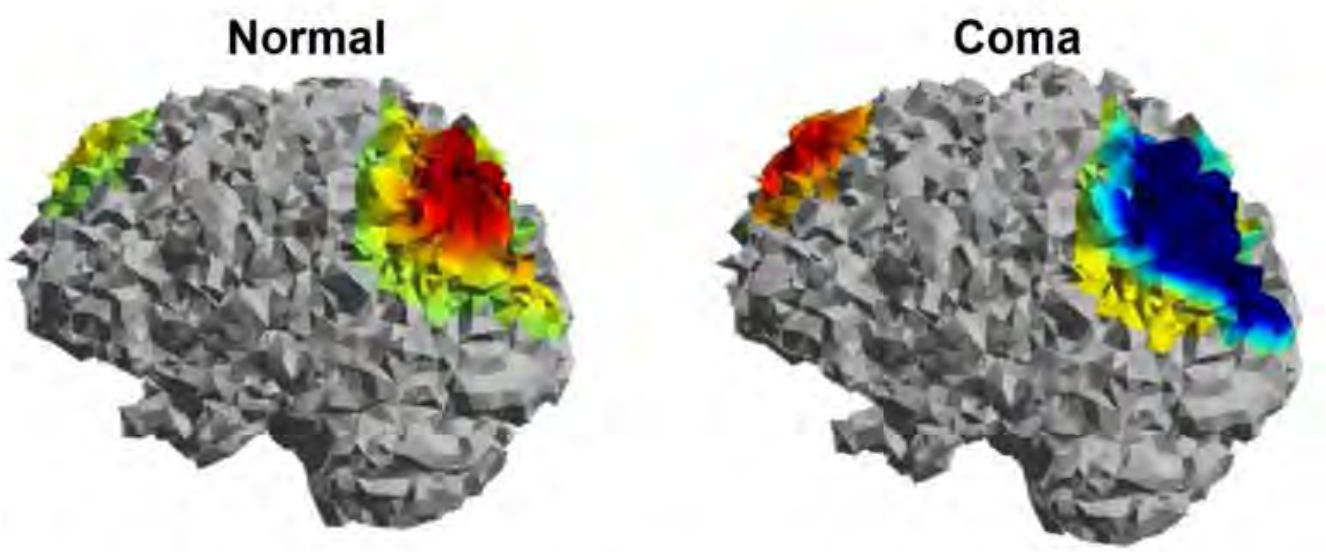
9:56AM - 10:04AM

Bedside Near-Infrared Spectroscopy for Detecting Coma-Related Disruption of Resting State Connectivity

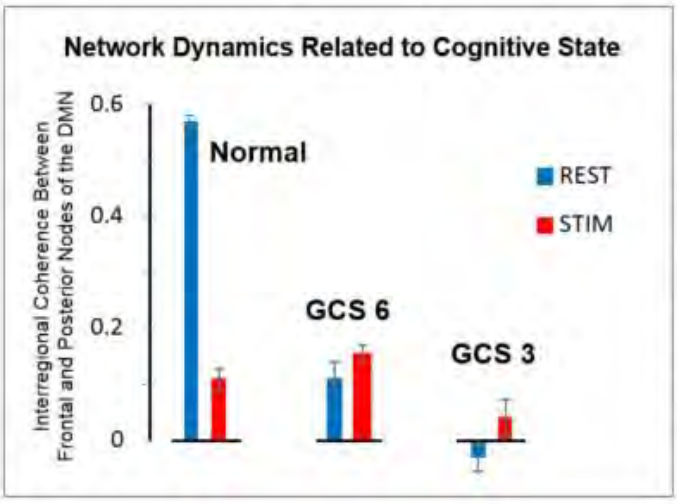
A Ardestani[1], F Moser[1]
[1]*Cedars Sinai Medical Center, Los Angeles, CA*

Purpose
Despite advances in critical care, no objective measure exists to assess preservation of cognitive activity in the unresponsive patient. Limited investigations have shown promise of functional MRI for predicting neurologic recovery in unconscious patients, however broader experimentation with this approach has been limited by significant logistical constraints of imaging comatose patients in the encumbered MRI environment. In this study, we propose a

noninvasive optical functional-imaging modality to measure network integrity in unconscious patients at the bedside.
Materials and Methods
Resting-state activity in 6 patients with loss of consciousness was compared to that of 6 healthy controls using near-infrared spectroscopy (NIRS). An array of 32 light emitting diodes and fiber optic detecting cables embedded in an elastic headcap was placed over the scalp to cover regions of the Default Mode Network (DMN), a network with a well established role in maintaining functional neural organization. Real-time measurements of optical absorption through the head were used to compute fluctuations in the cortical oxygenation profile across the DMN. Coherence maps of those hemodynamics were generated and correlated with the coma scale score for each subject.
Results
The pattern of resting DMN connectivity in the control group show spatial topography that matches that previously shown using fMRI. In addition, the connectivity maps generated using NIRS show the characteristic stimulation-induced desynchronization of the DMN. Unconscious subjects exhibit impairments in DMN connectivity, the degree of which is related to their coma score, as well as failure of the network to properly desynchronize upon external stimulation.
Conclusions
The novel application of NIRS for measuring DMN connectivity combines the advantages of a safe, inexpensive, and portable functional-imaging modality with an easily administrable resting-state paradigm to assess neural integrity in unresponsive patients. By substantiating a methodology with prognostic potential in such patients, these findings could significantly impact decision-making in neurointensive care.



Topographic activation maps in normal and comatose subjects. Still images from dynamic topographic activation maps recorded during the resting state show marked dyssynchrony between frontal and posterior nodes in the DMN of a comatose patient (right) when compared to that of a healthy control subject (left). Video clips of the activation profiles (unable to be shown here) allow real-time visualization of network activation and further underscore the relative loss of resting coherence seen in the unconscious subject. Red and blue colors denote relative activation above and below baseline, respectively.



DMN connectivity in three subjects with varying cognitive state. Bar graphs illustrate Pearson correlation values calculated between medial prefrontal cortex and the precuneus in both resting (in blue) and stimulated (in red) conditions. The normal coherence and task-induced desynchronization of the network is impaired in subjects in varying degrees of coma. Error bars denote standard error of the correlation, corrected for non-independence of consecutive acquisitions by a factor of 2s.

(Filename: TCT_O-395_ASNRData.JPG)

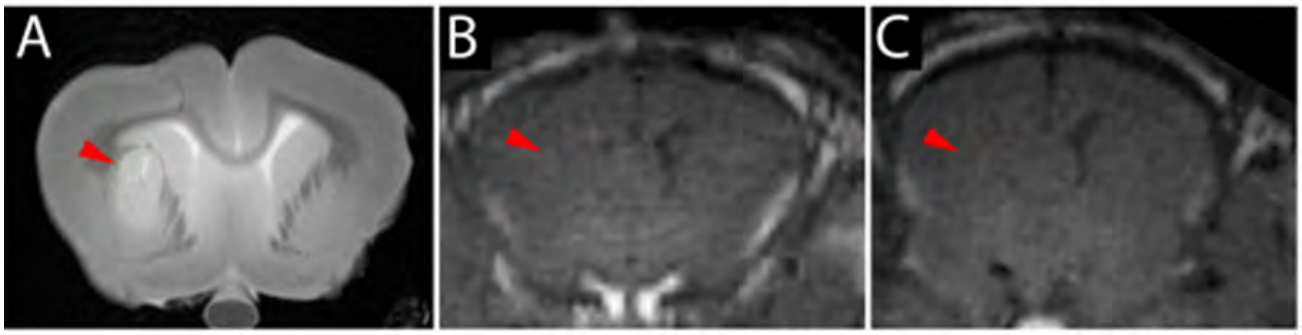
O-396

10:04AM - 10:12AM

Rabbit Model of Human Gliomas: Implications for Intra-arterial Drug Delivery

M Pearl[1], M Janowski[1]
[1]*Johns Hopkins University School of Medicine, Baltimore, MD*

Purpose
Animal models for intra-arterial drug delivery are promising for the future of interventional neuro-oncology. We have established a rabbit model for predictable intra-arterial osmotic blood-brain barrier opening (1); however, no glioma models are available in rabbits. We report on the xenotransplantation of a human glioblastoma (GBM-1) in adult New Zealand rabbits.
Materials and Methods
Xenotransplantation of a human glioblastoma (GBM-1) was performed in 3 adult New Zealand rabbits. Multi-drug immunosuppression (Mycophenolate Mofetil, Dexamethasone, Tacrolimus) was induced and GBM-1 tumor cells were implanted stereotactically into rabbit brains. The animals were followed for 42 days, monitored by MRI and body weight measurements, and underwent postmortem histopathological analysis.
Results
Brain tumors were identified on T2-weighted MRI scans of the brain. Tumors were detected on histopathology with hematoxylin/eosin and their human origin was confirmed with immunohistochemistry against human-specific antigens. Fig. 1. Tumors were visible on T2-weighted scans as oval-shaped regions near the thalamus that showed hyper-/isointensity (A). A moderate mass effect was evidenced by compression of the ipsilateral lateral ventricle. Gadolinium-enhanced T1 MRI did not show any enhancement within the tumor suggesting an intact BBB (B,C).
Conclusions
The GBM1 rabbit model of brain tumors is feasible as verified by MRI and pathologic findings, and may be a suitable platform for further studies, including intra-arterial targeted delivery of chemotherapeutics.



(Filename: TCT_O-396_ASNRGBM.jpg)

O-397

10:12AM - 10:20AM

T1 DCE MR PERFUSION in DIFFERENTIATION of BENIGN and MALIGN BRAIN LESIONS

E Cetinkaya[1], A ARALASMAK[2], B Atasoy[3], s tokdemir[3], H Toprak[4], a toprak[3], S Kurtcan[1], A Alkan[1]
[1]Bezmialem Vakif University, istanbul, istanbul, [2]Bezmialem Vakif University, Istanbul, Turkey, [3]bezmialem vakif university, istanbul, istanbul, [4]Bezmialem Vakif University, istanbul, turkey

Purpose
To compare the T1 DCE MRP between malign tumors and benign vascular lesions of the brain.
Materials and Methods
We retrospectively evaluated 11 patients; 6 with glioblastome-multiforme as malign group, 2 with cavernous malformations and 3 with developmental venous anomalies as benign lesions. K-trans, Kep, Ve and IAUC parameters were measured within the lesion, perilesional nonenhancing white matter (PLWM) and contralateral normal appearing white matter (CLWM).
Results
None of the DCE parameters showed difference between benign and malign groups. All benign and malign lesions showed significantly increased k-trans and IAUC values compared to those of PLWM and CLWM ($p < 0.001$). The ktrans and IAUC values of lesions were significantly different compared with PLWM ($p< 0.001$, $p=0.002$ respectively) and with CLWM ($p=0.008$, $p=0.001$ respectively). Upon differences between values of lesions and PLWM or CLWM, subtracted perfusion values were taken into consideration but found nonsignificant.
Conclusions
T1 DCE MRP cannot be used in differentiation of benign or malign lesions. Among the DCE parameters, only ktrans and IAUC values can be used to differentiate lesions from PLWM and CLWM.

O-398

10:20AM - 10:28AM

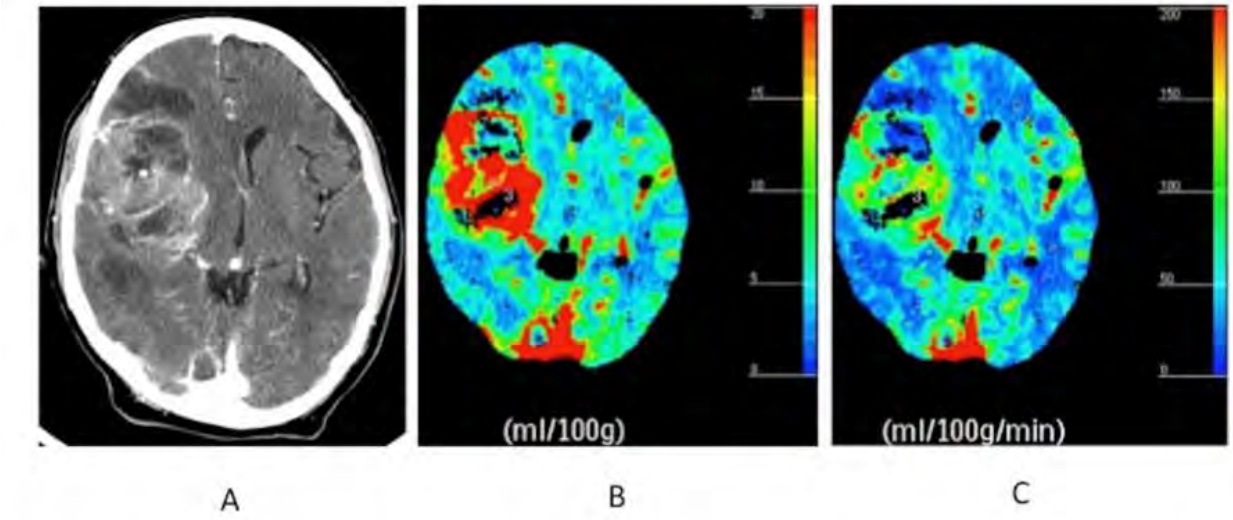
Correlation of Perfusion Computed Tomography (PCT) Parameters with Pathologic Grading of Intracranial Gliomas

N Bhatt[1], A Abdelbaki[2], J Jacob[1], P Kochar[3], Y Kumar[4]
[1]Bridgeport Hospital, Yale New Haven Health System, Bridgeport, CT, [2]Bridgeport Hopsital, Yale New Haven Health System, Bridgeport, CT, [3]Yale New Haven Health Bridgeport Hospital, Bridgeport, CT, [4]Yale New Haven Health at Bridgeport Hospital, Bridgeport, CT

Purpose
Gliomas are the most common primary brain tumors in adults. The World Health Organization (WHO) system of brain tumor classification describes 4 grades of gliomas. WHO Grade I and II are grouped under low-grade gliomas (LGG) and grade III and IV are grouped under high-grade gliomas (HGG). Gliomas typically demonstrate tumoral neoangiogenesis, which can be quantified using perfusion-based imaging including PCT. The first aim of this prospective study was to generate PCT parameters from the presumed intracranial gliomas from each patient by using 2 different software utilizing different algorithm. The first software utilized a deconvolution-based first pass bolus tracking technique. The second software utilized a singular value decomposition (SVD) algorithm. The PCT parameters generated were cerebral blood volume (CBV), cerebral blood flow (CBF) and mean transit time (MTT). PCT parameters obtained through both of these methods were correlated with pathologic grade of glioma in each case.
Materials and Methods
After obtaining institutional review board approval and informed consent, PCT was performed in 30 patients with presumed gliomas based on pre-operative neuroimaging. The maximal CBV, CBF and MTT were derived for each case using 2 different software-based algorithms. The values obtained through both of these 2 methods subsequently were normalized from the contralateral normal appearing white matter perfusion parameters. The normalized values were labeled as nCBV, nCBF and nMTT. Then patients underwent gross or subtotal resection of the tumor followed by histopathologic evaluation and graded as per the WHO classification. By using independent samples T test, LGG and HGG were compared for the difference in PCT parameters.
Results
Using the first of the 2 software, the nCBV in HGG ranged from 1.13 to 9.51 (mean 5.21; SD, 1.85) whereas in LGG, it ranged from 1.26 to 5.38 (mean, 2.90; SD, 1.29). The nCBF for HGG ranged from 0.57 to 9.08 (mean, 4.25; SD, 2.32) and in LGG it ranged from 0.99 to 2.66 (mean, 1.61; SD, 0.77). The nMTT for HGG ranged from 0.56 to 9.40 (mean, 1.95; SD, 2.00) and for LGG it ranged from 0.49 to 2.98 (mean, 1.26; SD, 0.77). A significant difference was found between HGG and LGG for nCBV and nCBF, which was suggested by P value of 0.001 and 0.000 respectively. No statistically significant difference was observed between the 2 groups for nMTT (P value=0.189). Using the second software, the nCBV in HGG ranged from 1.11 to 8.71 (mean, 4.94; SD, 2.48) whereas in LGG, it ranged from 1.48 to 2.20 (mean, 1.92; SD, 0.27). The nCBF for HGG ranged from 1.37 to 9.16 (mean, 5.12; SD, 2.40) and in LGG it ranged from 1.49 to 2.97 (mean, 2.11; SD, 0.50). The nMTT for HGG ranged from 0.66 to 1.37 (mean, 0.84; SD, 0.18) and for LGG it ranged from .77 to 1.03 (mean, 0.86; SD, 0.09). On using independent sample T test, the difference was highly significant for both nCBV (P value = 0.000) and nCBF (P value = 0.000) between these two groups. No statistically significant difference was observed between the two groups for nMTT (P value= 0.743).

Conclusions

The study showed good correlation between perfusion CT parameters and the histopathologic grade of the gliomas. The evidences were strong as results were validated using 2 different software based on slightly different algorithms. It was concluded that pre-operative PCT could help in pre-operative grading of gliomas. In addition, if a biopsy is being contemplated, it can help in reducing the sampling error by directing biopsy from the region of tumor with maximum CBV and CBF values. Another area where PCT might help is assessing response to antiangiogenesis-based treatments. The drawbacks of the PCT were increased radiation dose and use of intravenous iodinated contrast.



Glioblastoma multiforme. Fig. A.CT head with contrast showing large, infiltrative, enhancing and necrotic right frontotemporal mass with massive mass effect and edema. Fig. B. CBV perfusion map showing markedly elevated CBV in the region of tumor. Note that even the peritumoral region shows moderately increased CBV. Fig. C. CBF perfusion map shows increased CBF of the tumoral tissue with interspersed necrotic areas.

(Filename: TCT_O-398_Slide1.jpg)

Thursday
9:00AM - 10:30AM
Long Beach Convention Center, Room 203AB (Upper Level)

23G-Parallel Paper Session: Advanced Imaging for Best Assessment
O-399

9:00AM - 9:08AM

Increased Traumatic Brain Injury Lesion Visibility Using Total Field Inversion Quantitative Susceptibility Mapping (TFI QSM)

S Soman[1], Z Liu[2], U Nemec[3], S Holdsworth[4], B Lee[1], M Selim[1], K Main[5], J Yesavage[6], D Hackney[7], A Furst[6], M Adamson[8], Y Wang[9], P Spincemallie[10], M Moseley[11]
[1]Beth Israel Deaconess Medical Center, Harvard Medical School, Boston, MA, [2]Cornell University, New York, NY, [3]Medizinische Universität Wien, Boston, MA, [4]Stanford University, Stanford, CA, [5]Research Division, Defense and Veterans Brain Injury Center; General Dynamics Health Solutions, Silver Spring , MD, [6]Department of Psychiatry and Behavioral Sciences, Stanford University; VA Palo Alto Health Care Syst, Standford, CA, [7]Beth Israel Deaconess Medical Center, Boston, MA, [8]Defense and Veterans Brain Injury Center, VA Palo Alto Health Care System; Department of Psychiatry, Standford, CA, [9]Weill Cornell Medical College, New York, NY, [10]Department of Radiology, Weil Cornell Medical Center, New York , NY, [11]Stanford University Medical Center, Stanford, CA

Purpose

Traumatic brain injury often results in brain lesions which are subtle. Current conventional MRI techniques (GRE and SWI) are field strength and echo time dependent, causing lesions to possibly be missed. Quantitative susceptibility mapping (QSM) methods can overcome this, but with many artifacts and missed lesions due to masking artifacts (1, 2, 3) total field inversion (TFI) QSM can overcome this issue (4), as we demonstrate in this study of TBI patients.

Materials and Methods

Under an IRB approved protocol, outpatients with history of TBI and control subjects were recruited. Subjects underwent Imaging using a GE Discovery MR750 3.0 T MRI scanner (G.E., Waukesha, WI), using a 3D multi shot multi-echo EPI acquisition (3D MSME) [TR 98ms, Echoes=3 (TE=16, 39.5, 62.5), matrix 224x224, Resolution =1x1x1mm3], and a 3D FSPGR (TR/TE/TI 9.5/3.8/900 ms, Resolution =1x1x1mm3) using an 8-channel GE head coil. MEDI QSM images were created using the MEDI toolbox using the default mask (genmask.m) (3), and TFI QSM images were created using the method described by Liu et al (4). Both magnitude and QSM images were created from the 3DMSME data, and were reviewed with the T1-weighted FSPGR images by a board certified neuroradiologist and a radiology resident, evaluating for differences in depiction of normal anatomy and lesions.

Results

Eighty-five adult subjects were recruited, 63 subjects underwent 3DMSME imaging, and 56 subjects (44 tbi, 12 non tbi) had MEDI and TFI QSM images produced. Ten subjects demonstrated blood or blood products (all had TBI), in the occipital, temporal, parietal or frontal lobes, basal ganglia or cerebellum (Figs. 1A-C). All of these lesions were visible on TFI QSM, while 6 of these lesions were not visible or less conspicuous on MEDI QSM. Thirty subjects (53%) demonstrated brain parenchyma and/or lesions which were visible on TFI but were not included in the brain tissue on MEDI. One subject demonstrated less

frontal brain parenchyma on TFI than MEDI (Fig. 3). Five subjects demonstrated worse artifacts on TFI than MEDI, primarily in the region of the pons (Fig. 1D).

Conclusions

While QSM imaging can image subtle brain lesions independent of field strength and echo time, it often result in artifacts that distort normal brain tissues and can result in nonvisualization of lesions. Our work demonstrated TFI based QSM, which does not require brain masking, can preserve a greater amount of normal brain parenchyma and depict more lesions than non-TFI-based QSM methods. Furthermore, the greater preservation of anatomic landmarks, such as skull margins, has the potential to greatly aid clinical interpretation of QSM images.

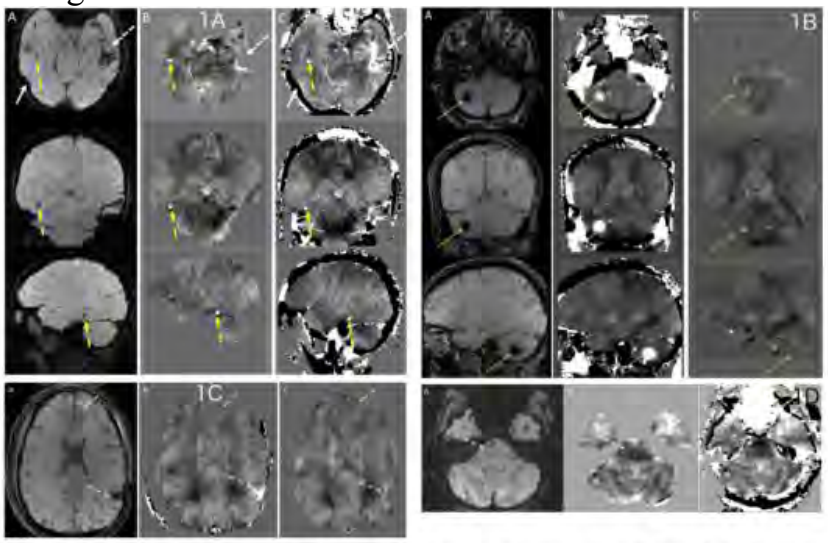


Figure 1A: (A) magnitude 3D GRE, (B) MEDI QSM and (C) TFI QSM images demonstrating right temporal hemorrhage, with magnitude images lesion is dark, and MEDI and TFI QSM images lesion is bright (yellow dashed arrows). This is in contrast to the mineralization heavy bone (white arrow), which is dark on TFI QSM images and dark on magnitude GRE images, and not present on MEDI QSM images secondary to masking. Left temporal brain parenchyma next to hemorrhage is not visualized on the MEDI QSM images, but can be seen on the magnitude and TFI QSM images (white dashed arrow).
Figure 1B: Right cerebellar hemorrhage on (A) magnitude 3D GRE, (B) TFI QSM and (C) MEDI QSM images . The magnitude and TFI QSM images demonstrate a right cerebellar hemorrhage, while the corresponding area on the MEDI QSM images has no brain parenchyma secondary to brain mask reconstruction artifact (orange arrows). Additionally, the MEDI QSM images demonstrate an absent section of right temporal brain parenchyma which is visible on the TFI QSM Images (white dashed arrows).
Figure 1C: (A) 3D GRE magnitude, (B) TFI QSM demonstrating left parietal hemorrhage, with absent brain parenchyma on (C) MEDI QSM images (white dashed arrow). Yellow dashed arrows highlight frontal brain parenchyma visible on magnitude GRE and MEDI QSM images, but not TFI QSM (yellow dashed arrows).
Figure 1D: (A) 3D GRE magnitude, (B) MEDI QSM and (C) TFI QSM images demonstrating pontine low signal on the QSM images with no corresponding abnormality on GRE image (white dashed arrows).

(Filename: TCT_O-399_ASNR_QSMTFI_Fig1V2.jpg)

O-400

9:08AM - 9:16AM

Quantitative Susceptibility Mapping of the “Swallow tail” and the Deep Gray Matter Nuclei in Parkinson disease

F Essbaiheen[1], S Chakraborty[2], G Melkus[3], T Mestre[3], D Grimes[3]
[1]University of Ottawa, King Saud University, Ottawa, Ontario, [2]University of Ottawa, The Ottawa Hospital, Ottawa, Ontario, [3]The Ottawa Hospital, Ottawa, Ontario

Purpose
The diagnosis of Parkinson disease (PD) has been mainly based on clinical findings (1). Although diagnostic criteria are well established, a large percentage of patients who initially are diagnosed with PD do not have the disease (2). The dorsolateral substantia nigra on axial susceptibility-weighted imaging (SWI) normally appears as a hypointense stripe that is split posteriorly by a hyperintense cleft, the nigrosome-1. This appearance resembles the tail of a swallow. Schwarz et.al. have described that the loss of this appearance in PD patients yielded high diagnostic accuracy (3). Quantitative susceptibility mapping (QSM) has been used recently in the evaluation of the substantia nigra and other brain structures in PD.
Materials and Methods
In this retrospective study we compared the QSM values in PD patients and sex/age matched controls. We excluded patients with degenerative, demyelinating disease or history of prior trauma in control group and studies that were degraded by artifact. Quantitative susceptibility was measured by drawing regions of interests (ROIs) in the following structures: caudate head, putamen, globus pallidus, thalamus, red nucleus and substantia nigra including the dorsolateral 'swallow tail' region. The QSM values then were compared between PD patients and controls. Gender, age, duration of symptoms (years), laterality and severity (UPDRS3 score) also were assessed.
Results
Twenty-one patients and 9 controls met the inclusion criteria. Susceptibility in the swallow tail area was higher in the PD group (0.021 ± 0.051 ppm vs -0.020 ± 0.037 ppm P=0.03). Higher susceptibility also was noted in the thalami (P=0.03) and red nuclei (P=0.01). No significant difference in susceptibility due to gender, age, duration of symptoms, laterality or severity was seen.
Conclusions
Increased susceptibility values in the dorsolateral 'swallow tail' substantia nigra is seen in patients with PD. This likely suggest increased iron deposition causing a masking effect that contributes to the disappearance of the 'swallow tail'.

O-401

9:16AM - 9:24AM

ZOOMED NODDI of the Adult Cervical Spinal Cord

C Conklin[1], M Alizadeh[2], S SAKSENA[1], D Middleton[2], T Johnston[1], S Faro[3], L Krisa[1], A Flanders[1], F Mohamed[1]
[1]Thomas Jefferson University, Philadelphia, PA, [2]Temple University, Philadelphia, PA, [3]Johns Hopkins University, Baltimore, MD

Purpose
Limitations of diffusion tensor imaging (DTI) have been partially overcome through neurite orientation dispersion and density imaging (NODDI) (1). Recent work has demonstrated

feasibility of NODDI in the adult cervical spinal cord (2) with use of cardiac gating. The purpose of this work is to gain greater understanding of typical NODDI values in the adult cervical spinal cord without cardiac gating in a larger normal population and demonstration in a single spinal cord injury (SCI) case.

Materials and Methods

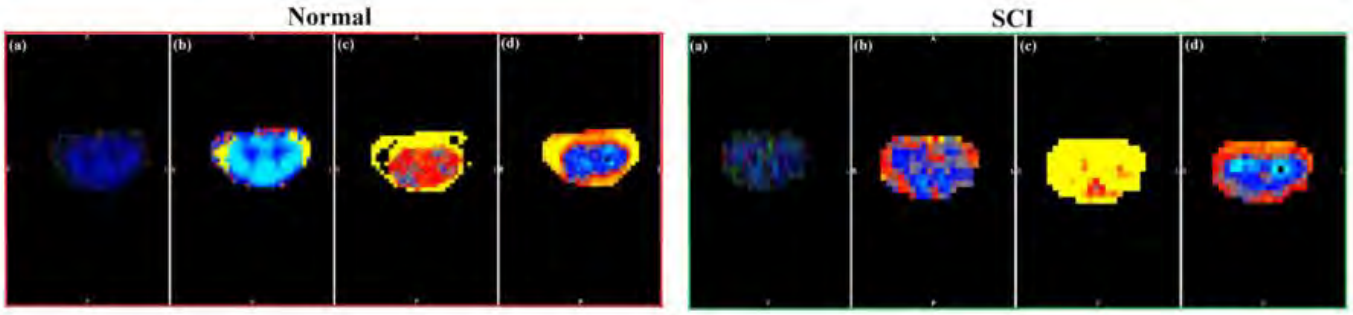
Multi-shell diffusion-weighted images of the cervical spinal cord were acquired using the Philips 3T Ingenia scanner on 10 healthy subjects and 1 patient with SCI (C5-C6 level injury). A ZOOM EPI sequence was used with parameters: TR=2200ms, TE=120ms, voxel size = 0.9mmx0.9mmx6mm, 90 total directions (30,60) at b=800 and 2800 s/mm2, respectively. Cardiac gating was not used. NODDI maps were calculated using the NODDI Toolbox in Matlab. Whole cord ROIs were drawn on NODDI and DTI maps at each vertebral level to extract quantitative information and averaged across all subjects.

Results

Figures 1 show NODDI maps [(a) FA, (b) ODI, (c) Vin, (d) Viso] in a representative normal subject at the C4-C5 level and in a patient with SCI at the same level. Results of the mean NODDI data of the cervical cord in the normal healthy subjects as well as the SCI case are shown in the table.

Conclusions

ODI offered the best qualitative gray/white contrast over DTI maps and may provide additional microstructural information compared to routine diffusion acquisitions. The increase in ODI for the SCI case potentially indicates wider dispersion of fibers, which is consistent with traumatic spinal cord injury. This work has demonstrated the feasibility of acquiring NODDI data on adult cervical spinal cords without cardiac gating and warrants investigation with a larger patient population. This technique could serve as a sensitive imaging biomarker.



	Healthy Mean	Std	CI(95%)⁻	CI(95%)⁺	SCI Mean
FA	0.47	0.083076	0.453537	0.48058	0.2487
MD(mm^2/s)	0.000492	9.97E-05	0.000476	0.000508	0.000311
AD(mm^2/s)	0.000774	0.000181	0.000745	0.000804	0.000407
RD(mm^2/s)	0.000351	6.98E-05	0.00034	0.000362	0.000263
V_{ic}	0.795109	0.147073	0.771171	0.819048	0.9851
ODI	0.157947	0.095161	0.142458	0.173436	0.39
V_{iso}	0.342204	0.120035	0.322667	0.361742	0.3462
KAPPA	0.962791	0.885527	0.818657	1.106925	0.1593
V_r	0.506482	0.138549	0.483963	0.529	0.6417

(Filename: TCT_O-401_noddi1.jpg)

O-402

9:24AM - 9:32AM

Pushing the limits of synthetic MRI in the Evaluation of Patients with Multiple Sclerosis: retrospective sequence parameter adjustments to increase image quality

f rueda lopes[1], T Doring[2], e figueiredo[2], E Gasparetto[3]
[1]Fluminense Federal University, Niteroi, AK, [2]GE, Niteroi, AK, [3]Instituto Estadual do Cerebro, rio de janeiro, Brazil

Purpose
The purpose of this study was to compare the standard MRI 3mm clinical acquisition protocol with a short 3mm postcontrast synthetic MRI protocol based on MDME sequence in patients with multiple sclerosis for lesion detection purpose and scan time reduction evaluation.
Materials and Methods
Sixteen relapsing-remitting multiple sclerosis patients following the Mc Donald criteria 1 with a wide range of disease duration and expanded disability status scale scores, underwent MRI at 1.5 T (Optima 450w, GE, USA). The acquisition protocol was divided into 2 steps: First: a clinical routine acquisition protocol, including individual sequences (precontrast: T1 FLAIR ax, postcontrast: FLAIR ax, T2 ax, PD ax, T1 FLAIR axial), Second: a single synthetic MRI (MDME FSE, MAGIC, GE, Milwaukee, USA) sequence included within the postcontrast protocol in the axial plane with same resolution and slice position as

conventional sequences (Table 1). The MDME raw images were postprocessed offline to synthetize equivalent image contrast weighting T1w FLAIR, T2w, PDw and FLAIR images with selected TR, TE and TI to fit the conventional equivalent imaging weightings. In the first step, an experienced neuroradiologist (10 years) evaluated the exams offline in a random order in 2 sessions 1 week apart (first session: evaluation of conventional images, second session evaluation of synthetic images). To evaluate overall perceived image quality a 4 level scale was used (1: poor - artifacts limiting the lesion detection, 2: sufficient - artifacts not limiting the lesion detection, 3: good - low artifacts, and 4: excellent - comparable with conventional images) within 2 regions (infratentorial and supratentorial brain segments). The number of MS T2/FLAIR lesions (disease burden), the number of T1 postcontrast enhancing lesions (active disease) were counted in the following locations: periventricular, juxta-cortical and cortical (including U fibers lesions), and infratentorial. In a second step, synthetic PD images of all subjects were generated with manually chosen sequence parameters TR=7500ms and TE=25ms, based on a visual optimization procedure previously done by the neuroradiologist. Perceived image quality and lesion count was done as described in step 1.

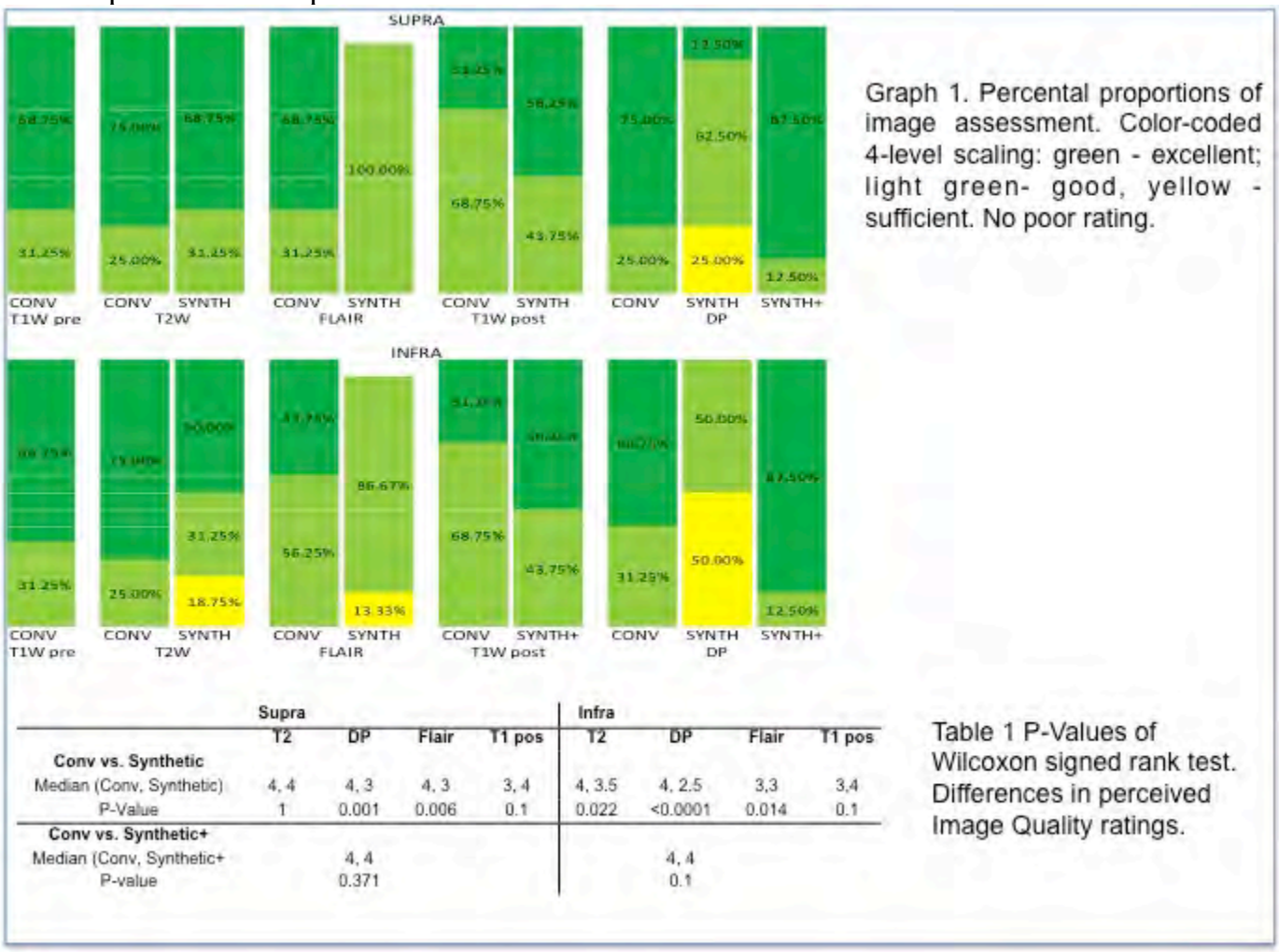
Results

Results of radiological image assessment are represented in Graph 1. No image was rated as poor within conventional or synthetic imaging techniques. Overall perceived image quality was rated higher in the supratentorial segment than in the infratentorial segment. Conventional FLAIR images all were rated as excellent or good. They had a lower proportion of excellent rating in the infratentorial segment, compared to the supratentorial (68.75%, 43.75%, respectively). Synthetic images were rated as excellent or good in the supratentorial segment, only the DPw had a proportion of sufficient perceived rating (25%). In the Infratentorial segment, synthetic T2w and FLAIR had an overall excellent and good rating, with a small proportion of sufficient ratings (18.75%, 13.33%), although pulsation artifacts were expected. Only the synthetic DP images had a proportion of 50% of sufficient ratings in the infratentorial region. Nevertheless, after TR and TE adjustment (synthetic+), the overall perceived image quality improved to good in the supra and infratentorial regions on PDw (Table 1). Lesion count was higher in conventional imaging compared to synthetic imaging (185/136), but there were no statistical significant differences detected in the juxta cortical (41/31), infratentorial (50/25), and black hole counts (44/44), unless for the periventricular region (94/80, p=0.02). After TR and TE PD synthetic adjustment, the absolute lesion number increased, becoming more similar to conventional sequences (185/144).

Conclusions

There was significant reduction in total exam time with synthetic MRI compared to conventional sequences with reduction in perceived image quality in synthetic images, which was smoothed after TR an TE adjustment on PD synthetic images, but without neglecting lesion detection capacity in most regions. The total scan time of the postcontrast conventional sequences were 8.15 min and synthetic MR sequence of 5.02 min,

corresponding to approximately 40% reduction in postcontrast exam time using synthetic MR. Considering the time intervals between the conventional sequences, like calibration time, this could further contribute to time reduction. Retrospective adjustment of the synthetic images parameters, such as TR and TE, can further improve overall image quality, with no penalties to acquisition time.



	Supra				Infra			
	T2	DP	Flair	T1 pos	T2	DP	Flair	T1 pos
Conv vs. Synthetic								
Median (Conv, Synthetic)	4, 4	4, 3	4, 3	3, 4	4, 3.5	4, 2.5	3,3	3,4
P-Value	1	0.001	0.006	0.1	0.022	<0.0001	0.014	0.1
Conv vs. Synthetic+								
Median (Conv, Synthetic+		4, 4				4, 4		
P-value		0.371				0.1		

Table 1 P-Values of Wilcoxon signed rank test. Differences in perceived Image Quality ratings.

(Filename: TCT_O-402_asnr.jpg)

O-403

9:32AM - 9:40AM

Evaluation of brain's viscoelasticity using MR-elastography

F Macruz[1], M Kurt[1], H Lv[2], L Wu[1], K Laksari[1], K Pauly[1], B Su[1], M Wintermark[1]
[1]Stanford University, Stanford, CA, [2]Stanford University, Stanford , CA

Purpose
Magnetic resonance elastography (MRE) is a technique that assesses noninvasively the mechanical properties of a tissue. By measuring an acoustic wave propagating through the

object, we can quantitatively image the elastic modulus of various normal and abnormal tissues. For the brain tissue, where palpation is not feasible, this technique may help understand its mechanical properties and how they relate to normal aging and pathologies. Magnetic resonance elastography results typically depend on the frequency of the acoustic wave selected. Because different published studies have used different frequencies, it is difficult to compare their results, and distinguish the impact of frequency versus age and other factors. In this study, we are proposing an original method to extract frequency-independent results from brain MRE.

Materials and Methods

Cerebral MRE was performed in 52 healthy volunteers, age range 18-70. Magnetic resonance elastography data were obtained for frequencies of 40, 60 and 80 Hz, and a simple spring-dashpot model (standard linear solid model, i.e., SLS) was fitted to the observed frequency-dependent data to extract frequency-independent MRE parameters: n that describes the solid-fluid behavior of the tissue, and E1 and E2 that describe the elastic solid behavior. Comparison between our results and the ones depicted for adult population in literature was conducted.

Results

The SLS fit to the observed frequency-dependent results yielded a correlation coefficient R2=0.85, which suggests that this mechanical model is a good representation of the average brain mechanical properties. We have found average E1, E2 and n values for the brain tissue to be 1085.9, 2096.5 and 4.49 Pa respectively. We have found that stiffness parameters (E1 and E2) increase with age however, the viscosity parameters (n), decrease with age.

Conclusions

Viscoelasticity of the brain tissue can be measured using MR, and frequency-independent parameters representing the brain elastic and viscous properties can be extracted from the MRE data collected at different frequencies. The viscous and elastic properties of the brain tissues evolve with age.

O-404

9:40AM - 9:48AM

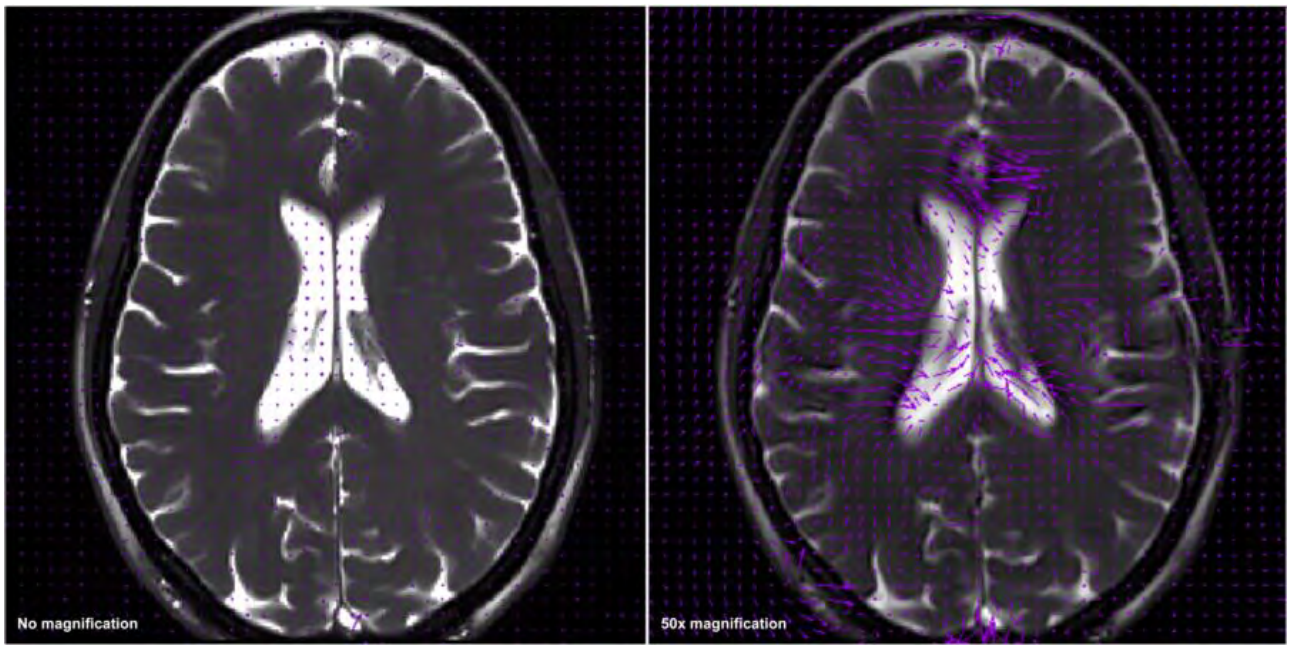
Seeing the Unseen, Revealing and Quantifying Brain Motion

T Stefani[1], D Heitz[2], M Bintner[3], J Bonny[4]
[1]University Hospital, Saint-Pierre, Reunion, [2]Univ Bretagne Loire, Rennes, [3]University Hospital, Saint Pierre, Reunion, [4]AgroResonance, Saint-Genès-Champanelle

Purpose

Brain pulsatile micro motion previously has been described indirectly but MR imaging techniques used failed at dynamically displaying and quantifying such imperceptible movement with high spatial and temporal resolution. Eulerian video magnification (EVM) is a novel postprocessing method based on spatial and temporal filtering suited to magnify

subtle motion. Optical flow is a broadly used method of postprocessing to quantify perceptible motion. The aim of this study was to investigate if phase-based EVM coupled with optical flow postprocessing on routine cinematic (CINE) TrueFISP sequence is capable of revealing and quantifying brain micro motion.
Materials and Methods
Five healthy volunteers were included in the study. 3T MRI brain imaging performed included 40-phases heart-triggered CINE TrueFISP sequences acquired in the lateral ventricles plane. Eulerian video magnification technique was used on postprocessing with a 50-fold magnification factor. Visual assessment was performed for qualitative analysis before and after motion magnification. Tissue displacement was quantified for every phase using optical-flow parametric mapping of regions of interest including scalp, ventricles, central and peripheral brain structures.
Results
On visual assessment, no perceptible brain motion was noticed on native CINE sequence. Oscillatory pattern of motion was revealed after 50-fold motion magnification postprocessing for every volunteer. Micro motion shown included ventricles dilation and contraction cycle. Also arteries and venous pulsatile motion and the resulting adjacent brain parenchyma motion were perceptible showing a peripheral to central gradient of motion. Optical flow displacement maps showed and quantified brain micro motion on magnified sequences but failed at showing neither quantifying micro motion on native sequences displacement maps. Difference of optical flow was significant (T Test $p<0.05$) after magnification, and mean quantified motion was 3,47 voxels (SD 0.91) for ventricles, 2.71 voxels (SD 0.77) for central structures, 2.26 voxels (SD 0.69) in peripheral structures and 1.7 voxels (SD 0.23) in scalp.
Conclusions
Brain pulsatile micro motion can be revealed dynamically and quantified using phase-based EVM postprocessing applied to routine CINE TrueFISP MRI sequences, giving access to tissue displacement visual assessment and quantification. Applications in hydrocephalus study, tumoral characterization and more generally brain stiffness assessement still need to be investigated.



(Filename: TCT_O-404_abstractimg.jpg)

O-406

9:56AM - 10:04AM

Diagnostic performance of reformatted isotropic thin-section helical CT images in the detection of superior semicircular canal dehiscence.

G Sparacia[1], f agnello[2], K Traylor[3], c speciale[4], f midiri[2], A Iaia[3]
[1]university of palermo, palermo, PA, [2]university of palermo, palermo, AZ, [3]Christiana Care Health System, Newark, DE, [4]university of palermo, palermo, AS

Purpose
To assess the diagnostic performance of highly collimated isotropic computed tomography (CT) reformatted images in the detection of superior semicircular canal (SSC) dehiscence.
Materials and Methods
Forty-two patients, with sound- and/or pressure-induced vestibular symptoms, and 42 control subject, underwent helical CT examination with highly collimated beam (0.5-mm). Reformatted images of the vestibular labyrinth structures were obtained from volumetric CT data in the standard axial, and coronal planes (group A images). Additionally, reformatted images in a plane oriented to be parallel (plane of Pöschl) and perpendicular (plane of Stenver) to the SSC were obtained (group B images). Group A and group B images were evaluated separately by 2 neuroradiologists in consensus to establish whether a dehiscence of the SSC was present at the arcuate eminence.Statistical analysis was performed to compare diagnostic performance obtained by evaluating the group A images alone and the group B images alone by using the area under the receiver operating characteristic (ROC) curve (AUC).

Results
The diagnostic performance of group A images measured by the area under the ROC curve (AUC) was 0.929 (sensitivity 85.7%, specificity 100%, TP 36, TN 42, FP 0, FN 6) with an overall accuracy of 92.9%. The diagnostic performance of group B images measured by the area under the ROC curve (AUC) was 0.988(sensitivity 97.6%, specificity 100%, TP 41, TN 42, FP 0, FN 1) with an overall accuracy of 98.8. Although the differences between the 2 AUCs were not statistically significant, group B images alone showed an improved diagnostic performance over the group A images alone.
Conclusions
Thin-section 0.5-mm collimation isotropic voxel CT with reformatted images oriented in the plane parallel (plane of Pöschl) and perpendicular (plane of Stenver) to the SSC improves diagnostic accuracy in assessing for SSC dehiscence in comparison to CT images with reconstructions limited to traditional axial and coronal planes.

O-408

10:12AM - 10:20AM

CT CoPilot improves sensitivity to changes in ventricular volume in shunted patients

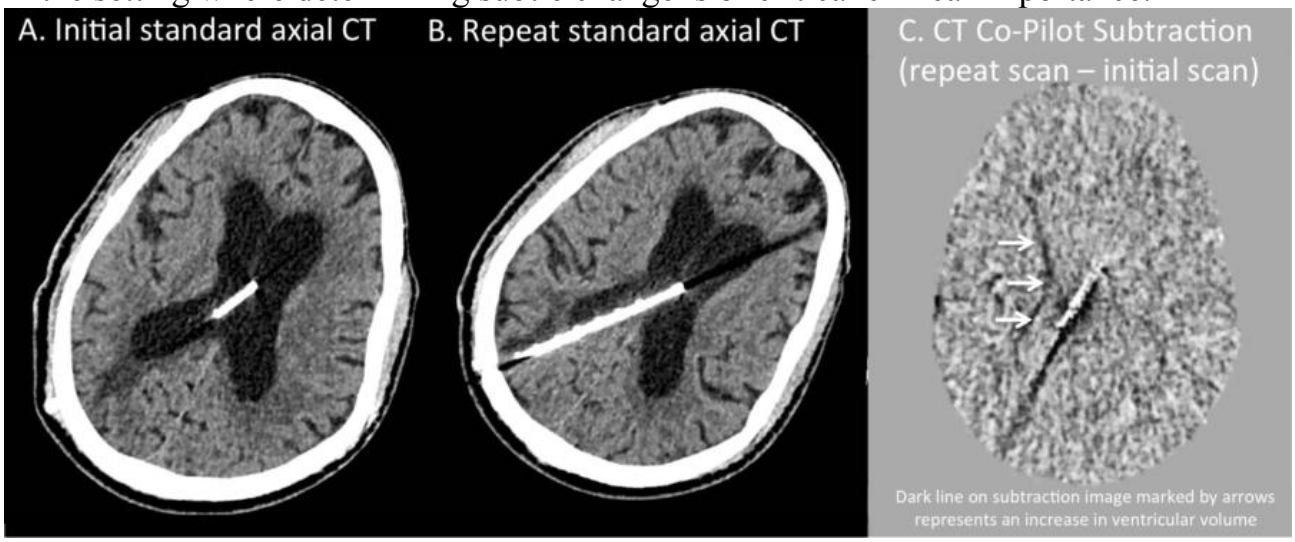
G Yamin[1], G Goel[1], A Sung[1], C Li[1], N Farid[1]
[1]*University of California, San Diego, San Diego, CA*

Purpose
Computerized tomography (CT) is the mainstay imaging modality for assessing changes in ventricular volume in patients with a ventricular shunt (1-2) or external ventricular drain (EVD) (3). Rapid and accurate assessment of ventricular volume is critical for determining stability or change and can be complicated by significant differences in head position between scans. We evaluated the performance of a novel fully automated CT registration and subtraction method, CoPilot, to improve reader accuracy and certainty compared with current standard-of-care CT.
Materials and Methods
In a retrospective evaluation of 49 ventricular shunt or EVD patients who underwent sequential head CT scans with CoPilot, reader performance (of 1 neurosurgery and 2 radiology residents) was assessed relative to a gold-standard read based on a board-certified neuroradiologist's interpretation. Reader ratings were assessed on ability to discern change versus stability in ventricular volume between scans using standard axial CT reformats versus CT CoPilot reformats and subtraction images.
Results
Of the 49 cases, ventricular volume was increased in 13, decreased in 17, and unchanged in 19. CT CoPilot showed significant improvement in detecting interval ventricular volume change (increase or decrease) ($p = 0.045$), but not unchanged volume. Furthermore, CT CoPilot improved reader certainty in determining increased (90 vs. 67%) or decreased

ventricular volume (92 vs. 78%) (p = 0.001). Inter-rater reliability (IRR) for interpretation of standard axial CT and CT CoPilot images were 86 and 93%, respectively.

Conclusions

Computed tomography CoPilot significantly improves the reader's ability to detect changes in ventricular volume between sequential scans in patients with ventricular shunts or EVD (i.e. improves agreement with the expert read), as well as the reader's degree of certainty. CoPilot may serve as an additional tool for rapid assessment of change in ventricular volume in the setting where determining subtle change is of critical clinical importance.



(Filename: TCT_O-408_ASNRGraphicver2.jpg)

O-409

10:20AM - 10:28AM

Theoretical and Empirical Evidence of Voltage Sensitivity of Macrocyclic Gadolinium-based Contrast Agents within Physiologic Ranges

R Bert[1], B Garabato[1], M Zhu[1], H Zheng[1], C Ng[2], P Kozlowski[1]
[1]University of Louisville, Louisville, KY, [2]University of Louisville, Louisivlle, KY

Purpose

Macrocyclic contrast agents are dota-based gadolinium-chelating molecules that have a cyclic structure related to iron-chelating porphyrins. The T1 shortening effects of the latter are known to vary in hemoglobin degradation, as the molecule changes conformation during chemical transition to methemoglobin, which results in shortening the Gd-H2O distance, r, and a significant change in observable contrast (1). The bond distance greatly affects contrast enhancement, as T1 relaxation (R = 1/T1) varies as 1/r6 (2). We hypothesized that an external electric field of neuronal physiologic strength might also alter the Gd-H2O distance in macrocyclic agents by both molecular conformation distortions and electron cloud shielding. We have tested this hypothesis by using computational modeling and phantom-based empirical measurements.

Materials and Methods

Molecular modeling was performed using the University of Louisville Cardinal Cluster (3) Gaussian 09 program suite for electronic structure calculations, at the density functional theory level. Structures were constructed manually, optimized using quadratic convergence (ignoring symmetry), in the presence a polarizable continuum solvent (H2O) with and without a general negative hexadecapole field in the range of 0.05-1.6 eV. Initial investigations included spin multiplicity and stability determination and used BP86 exchange-correlation functionality with Stuttgart Dresden (SDD) relativistic pseudo-potential basis sets. Final geometries were obtained at the SDD (4) level of theory. Results were compared to empirically observed contrast changes measured in a phantom using a 9.4 Tesla small animal MRI system (NSA=3/TR=1612/TE=7.672/Matrix=512x512/thickness=3mm/FOV= 873x723). The phantom was constructed by placing 5 mm-thick gadoterate impregnated agar between 2 copper plates held at 45 Volts potential (90V/cm).

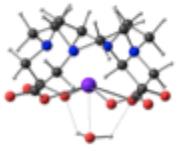
Results

Molecular structure and Gd-H2O bond lengths (Fig.) converged for field strengths of .05-1.05 eV. Gadoterate average bond length was 2.5042 Angstroms in absence of an electric field and 2.7026 in the presence of an electric field, yielding a 10% field-induced decrease in the Gd-H2O bond length. At 1/r6, this would predict Rv/Rnv=0.634 and T1v/T1nv=1.578 where v=voltage, nv=no voltage. While T1 was not measured directly, our preliminary phantom measurements produced measured S/N ratios (Fig.) varying from 1.33 - 2.0. We currently are conducting improved phantom experiments with actual T1 measurements and additional contrast agents, along with modeling of additional contrast agents.

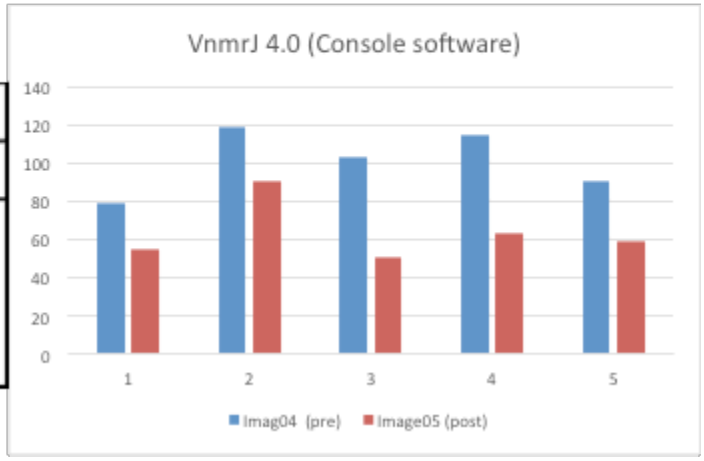
Conclusions

Gadoterate Gd-H2O bond lengths theoretically undergo a 10% lengthening in the presence physiologic electric fields and should lead to a detectable T1 signal drop. Phantom measurements demonstrated detectable signal drops in the expected range of predicted values, but more refined experiments are necessary.

Predicted Results

TPSSH/SDD, *H_2O implicit solvent (pcm)*	H_2O---Gd (Å) (0.0 – 1.633 eV hexadecapole field)
A 	2.5042-2.7026

Empirical Results



(Filename: TCT_O-409_Illustration2017.gif)

Thursday
9:00AM - 10:38AM
Long Beach Convention Center, Room 102BC (Main Level)

23H-Parallel Paper Session: Stroke: Core Concepts, Clots, and Collaterals

O-410

9:00AM - 9:08AM

Measurement of Infarct Core Volume Using Automated Computed Tomography Perfusion Processing Software (Rapid) and Comparison with DWI in Stroke Patients in a Daily Practice Population

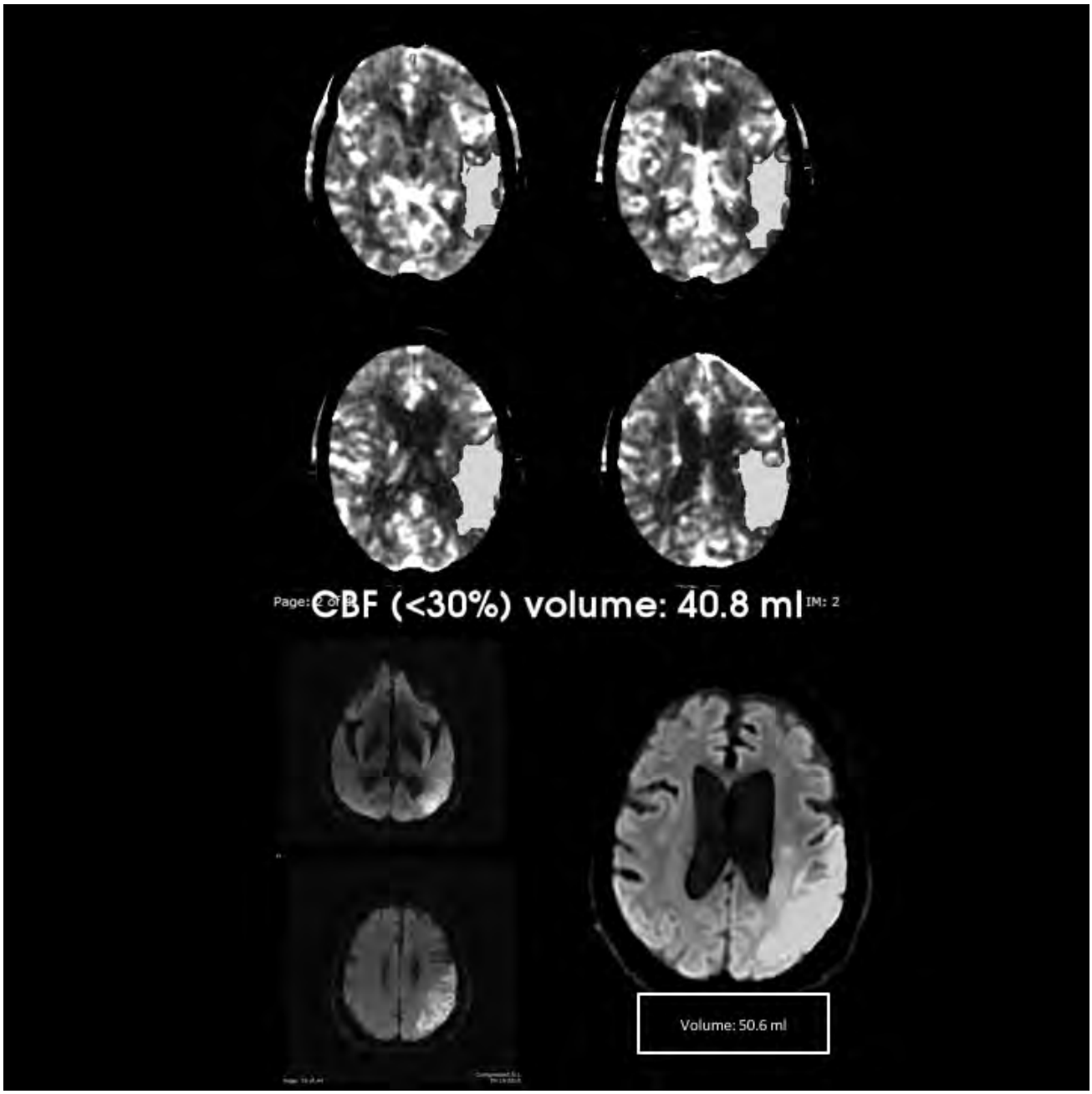
S Bergamaschi[1], M Law[1], R CORREIA[2], N Calixto[3], K Nayak[1], P Kim[1], A Amar[1], M Kim-Tenser[1], N Sanossian[1], S Cen[1]
[1]University of Southern California, Keck School of Medicine, Los Angeles, CA, [2]BRAIN STATE INSTITUTE PAULO NIEMEYER, RIO DE JANEIRO, CA, [3]Hospital das Clínicas da Faculdade de Medicina de Ribeirão Preto, Ribeirão Preto, SP

Purpose
Stroke is still a leading cause of death and disability worldwide. The optimal selection of patients for IV TPA or endovascular treatment is still a challenge. Computed tomography perfusion (CTP) is a technique that provides physiologic information about the perfusion of the tissue, and may demonstrate large penumbral areas, that would benefit from treatment. One of the challenges in clinical practice is the great variability of acquisition methods and postprocessing methods. Automated postprocessing approaches could overcome these issues of variability, and make CTP more reliable and reproducible in the clinical setting. The purpose is to investigate if the region of cerebral blood flow (CBF) abnormality (supposedly indicating infarct core), obtained by CT perfusion processed with RAPID, correlates with the infarct core determined by the DWI from MRI.
Materials and Methods
We selected patients with acute stroke, that underwent CT perfusion postprocessed with RAPID software that have a subsequent MRI scan within 24 hours. The area of CBF alteration was determined automatically by the software, using as threshold <30%. The area of mismatch was obtained subtracting the area of Tmax alteration (>6.0s) by the CBF alteration. The infarct core was obtained by measuring the volume of DWI restriction in the MRI scan using the b1000 images with Fuji Synapse 3D software. The correlation was calculated using Pearson correlation to obtain the r value.
Results
Fifty-six patients were included in the study. There were 28 females and 28 males, the mean age was 70 +-14.8 years, SD (Min 26 Max 93). The mean initial NIHSS was 16, and the

mean ASPECTS score was 7.4. Thirty-four patients received intravenous tPA, and 20 patients received endovascular therapy, 2 intra-arterial tPA and 18 mechanical thrombectomy. The mean core volume measured by the Rapid Software using the CBF was 15.3 (SD+- 27.2) the core volume measured by DWI was 66.1 (SD+- 67.5). The mean mismatch volume was 118.1 (SD +- 107.4). The Pearson correlation between the CBF and the DWI was 0.78 ($p < .0001$).

Conclusions

Our study shows that the CBF core obtained using the automatization software RAPID has a good correlation to the DWI volume measured. The lower volumes measured with CBF are not unexpected, since RAPID is likely thresholded underestimate CBF and overestimate Tmax, thereby over-estimating the mismatched area. This may allow more patients to receive endovascular therapy.



(Filename: TCT_O-410_ExempleStrokeCorrelation.jpg)

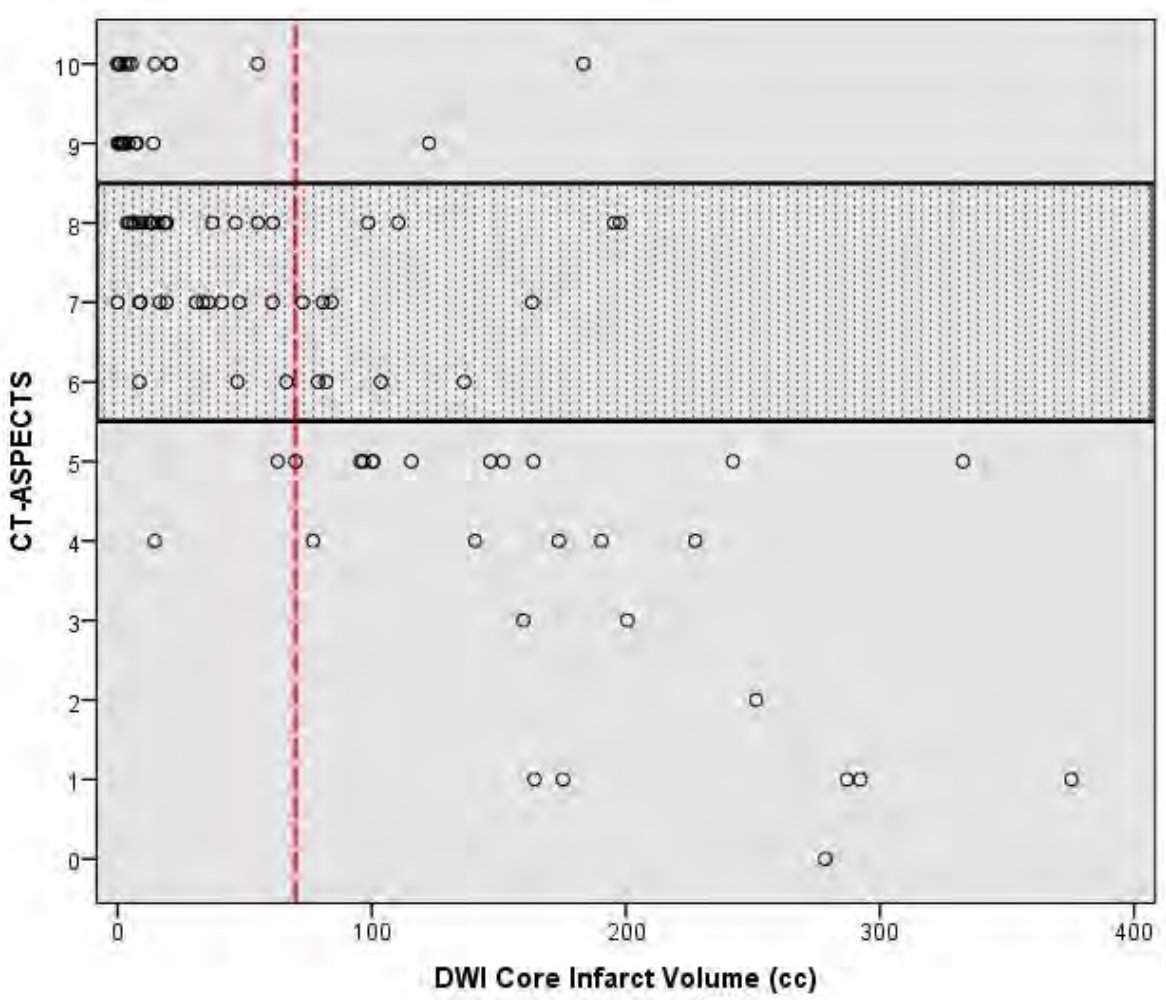
O-411

9:08AM - 9:16AM

Where is CT-ASPECTS Discrepant with Pretreatment DWI Core Infarct?

D Hoss[1], U Oyoyo[1], B Cristiano[1], S Harder[1], A Mesipam[1], J Jacobson[1]
[1]*Loma Linda University Medical Center, Loma Linda, CA*

Purpose
Thrombectomy has been shown effective in treatment of emergent large vessel occlusion (ELVO) stroke. Large presenting core infarct (> 70 cc) is strongly associated with poor patient outcomes. Internationally, varying imaging algorithms are used for excluding ELVO patients with large presenting core infarcts from futile mechanical thrombectomy, with some favoring CT alone due to its wide availability and speed of acquisition, and others favoring the additional utilization of MRI due to its accuracy in determining infarct core volume. Our aim was to assess the performance of CT-ASPECTS in predicting core infarct volume.
Materials and Methods
With local IRB approval, patients with anterior circulation ELVO evaluated for possible thrombectomy from February 2013 through August 2016 were included. Those without both CT and MRI, or who had greater than 120 minutes between CT and MRI were excluded. The resulting study group comprised 93 consecutive patients with anterior circulation ELVO and subsequent pretreatment MRI within 2 hours. For each patient, CT-ASPECTS and DWI-ASPECTS were recorded; presenting core volume was measured on DWI. The correlations between CT- and DWI-ASPECTS and presenting core volume were assessed with Spearman's rho. Receiver operating characteristic (ROC) curves were used to summarize the accuracy of using CT- or DWI-ASPECTS to predict core infarct volume > 70 cc. Sensitivity, specificity, positive predictive value, and negative predictive value for detecting core volume > 70 cc were calculated for dichotomized CT-ASPECTS of < 7 and DWI-ASPECTS of < 5.
Results
Diffusion-weighted imaging (DWI)-ASPECTS showed a very strong correlation with presenting core volume on DWI ($r = -0.93$, $p < 0.001$), whereas CT-ASPECTS showed a lesser correlation ($r = -0.72$, $p < 0.001$; figure). Computed tomography (CT)-ASPECTS and DWI-ASPECTS were moderately correlated with each other ($r = 0.75$, $p < 0.001$). The area under the ROC curve for predicting core volume > 70 cc was 0.88 for CT-ASPECTS and 0.98 for DWI-ASPECTS. For CT-ASPECTS over the range of 6-8, the area under the ROC curve decreased to 0.65, with 12/43 (28%) false negatives. When CT-ASPECTS < 7 was considered positive for detecting core volume > 70 cc, the sensitivity, specificity, positive predictive value, and negative predictive value were 0.74, 0.91, 0.85, and 0.83, and when DWI-ASPECTS < 5 was considered positive for the same, the parameters improved to 0.87, 0.94, 0.92, and 0.91, respectively. The difference between CT-ASPECTS and DWI-ASPECTS did not correlate with the time difference between CT and MRI exams ($r = 0.10$).
Conclusions
Computed tomography-ASPECTS shows poor accuracy in predicting threshold presenting core infarct volume over the mid-range of 6-8, but performs well when scores are low (< 6) or very high (> 8). Determination of thrombectomy candidacy using CT-ASPECTS over the midrange will fail to exclude a considerable proportion (25-30%) of futile interventions.



(Filename: TCT_O-411_ASNR300dpi.jpg)

O-412

9:16AM - 9:24AM

ASPECTS Derived from CTA Source Images Better Predicts CT Perfusion Lesion Core Volume, Target Mismatch Profile, and Good Clinical Outcome

A DeHavenon[1], A Linn[1], S O'Donnell[1], M Peckham[1], K Mickolio[1], M Park[1], J McNally[1]
[1]*University of Utah, Salt Lake City, UT*

Purpose
The Alberta Stroke Program Early CT Score (CT-ASPECTS) predicts early ischemic changes in stroke. Computed tomography (CT) angiogram source images (CTA-ASPECTS) also have been used (1), but few studies have compared the scoring techniques despite concern that CTA-ASPECTS is overly sensitive (2).
Materials and Methods
We reviewed acute ischemic stroke patients with proximal anterior circulation occlusion

from 2010-2014 that underwent CT, CTA, and CT perfusion (CTP) in the emergency department. ASPECTS was determined by 2 blinded raters using standard methodology (3). If there was disagreement, the senior rater's value trumped. We used Olea Sphere software's oscillating singular value decomposition to make CTP maps for volumetric measurements (Fig. 1) (4). Hypoperfused volume was defined as Tmax >6 seconds and lesion core as relative cerebral blood flow <40% and Tmax >2 seconds, which was correlated with ASPECTS (0-10) by linear regression. ASPECTS scores were dichotomized (bad=0-5 and good=6-10) to generate area under the curve (AUC) of a receiver operating curve (ROC) fitted to Target Mismatch profile (5) on CTP and good clinical outcome [modified Rankin Scale (mRS) of 0-1].

Results

We included 68 patients. Mean±SD age was 62±18 years, 60% were male, and NIH Stroke Scale was 14.5±7.9. Follow-up mRS was 3.0±2.3, obtained at 97±46 days from stroke onset. The mean CT-ASPECTS (6.5±3.6) was higher than CTA-ASPECTS (5.6±3.4). CTA-ASPECTS had better prediction of lesion core volume (coefficient=-8.9, adjusted R2=0.47, $p<0.001$) than CT-ASPECTS (coefficient=-5.5, adjusted R2=0.20, $p<0.001$). Good CTA-ASPECTS (6-10) had an AUC of 0.81 for Target Mismatch, which was significantly higher than CT-ASPECTS (AUC=0.66, $p=0.004$). Similarly, good CTA-ASPECTS was a better predictor of good clinical outcome (AUC=0.83 vs 0.70, $p=0.001$).

Conclusions

We found that although CTA-ASPECTS was lower on average than CT-ASPECTS, it was better at predicting ischemic lesion core on CTP, Target Mismatch, and good clinical outcome. Prior trials of endovascular therapy have used CT-ASPECTS, but future studies may benefit from using CTA-ASPECTS.

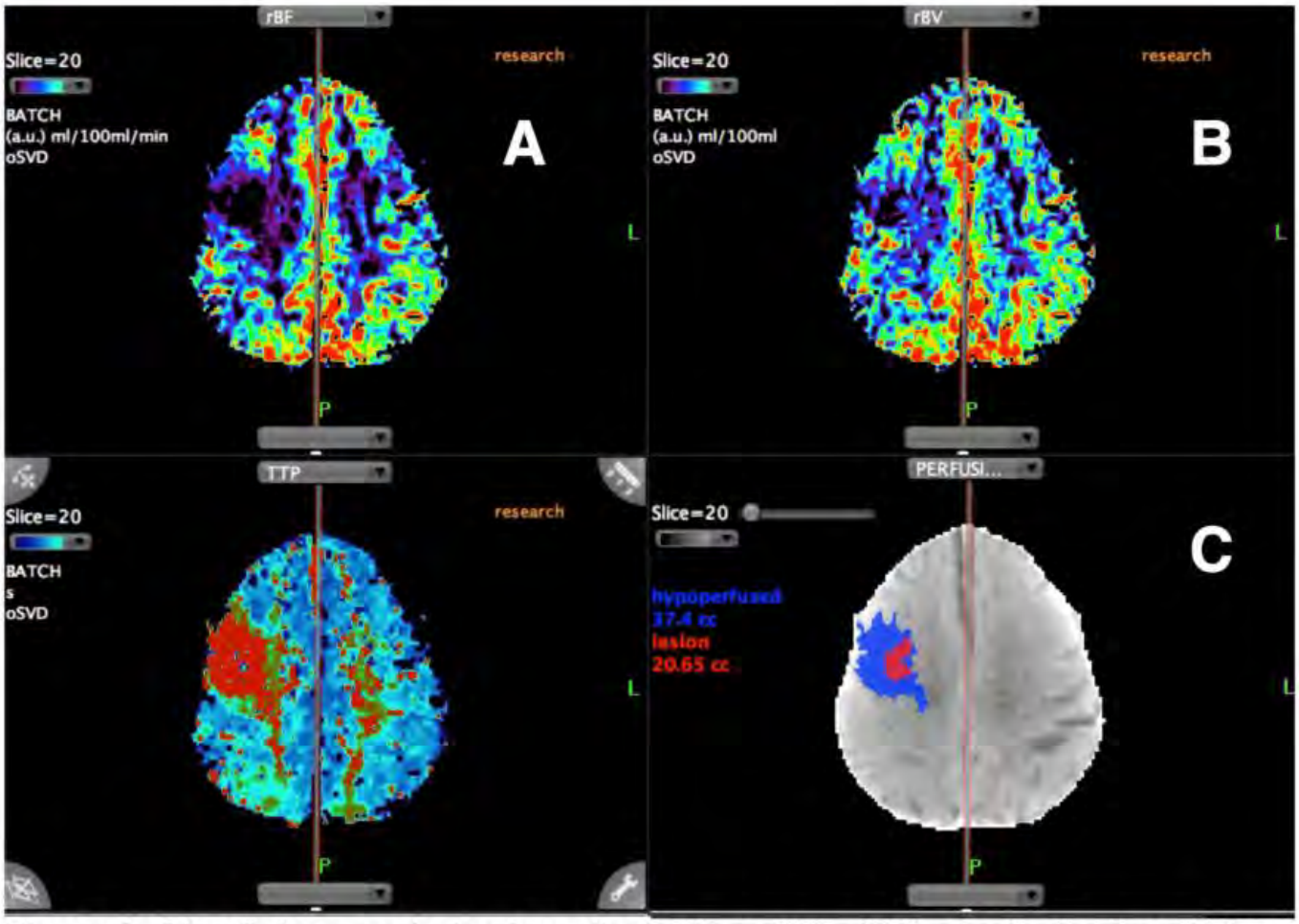


Figure 1: Olea Sphere analysis of a patient with a right middle cerebral artery stroke, showing cerebral blood flow (A), cerebral blood volume (B), and automated threshold-based volumetric data, with lesion core in red and hypoperfused area in blue (C).

(Filename: TCT_O-412_Fig1.jpg)

O-414

9:32AM - 9:40AM

Evaluating Late Acute to Subacute Infarcts Using Quantitative T1rho MR Imaging

J Soun[1], D Chow[2], C Esenwa[1], M Liu[1], T Lin[1], S Zhang[1], J Grinband[1], S Jambawalikar[1], C Filippi[3]
[1]Columbia University Medical Center, New York, NY, [2]University of California, San Francisco, San Francisco, CA, [3]Hofstra Northwell School of Medicine, New York, NY

Purpose
Timing of stroke onset is critical for time-sensitive thrombolytic treatments. Quantitative T1rho can evaluate physiologic processes with correlation times on the same order as the

reciprocal of the applied spin locking RF, including those that are disrupted in ischemia (1). The purpose of this study is to evaluate the utility of T1rho in characterizing late acute to subacute infarcts.

Materials and Methods

This IRB-approved, prospective study included 10 patients with late acute to subacute strokes. T1rho MR used a whole-brain, SNR efficient, 3D FSE-based volumetric technique with spin lock times (TSL) of 1, 10, 30, 50 and 70 ms and spin lock frequency of 300 Hz. T1rho maps were acquired by a weighted least squares regression assuming monoexponential decay. Diffusion-weighted imaging (DWI) and T1rho images were co-registered linearly (Fig. 1A). A region of interest (ROI) was drawn around the infarct volume and in the corresponding region in the contralateral hemisphere to serve as a within-subjects control. All ROIs then were applied to the registered T1rho images. Mean T1rho values (ms) of infarct and control ROIs were compared using a Student's two-tailed t-test. Simple linear regression was performed to assess the relationship between stroke onset time and T1rho values.

Results

Mean clinical onset of infarct was 56 hrs, and mean T1rho infarct volume was 19420 mm3. Mean T1rho values in the infarct ROI were significantly higher compared to contralateral control ROI (116.44 ms versus 89.53 ms respectively, $p < 0.002$). Linear regression analysis showed no significant correlation between stroke duration and T1rho values (Fig. 1B).

Conclusions

T1rho values in infarcts are higher than contralateral control regions, presumably because of the disruption of macromolecular interactions in ischemia. There was no significant relationship observed between stroke duration and T1rho values in the late acute/subacute period. Thus, T1rho can be quantified but does not necessarily provide further characterization of stroke duration in this time frame. Further studies are needed to determine if T1rho demonstrates predictable change in more acute infarcts and thus could serve as a surrogate marker of stroke onset.

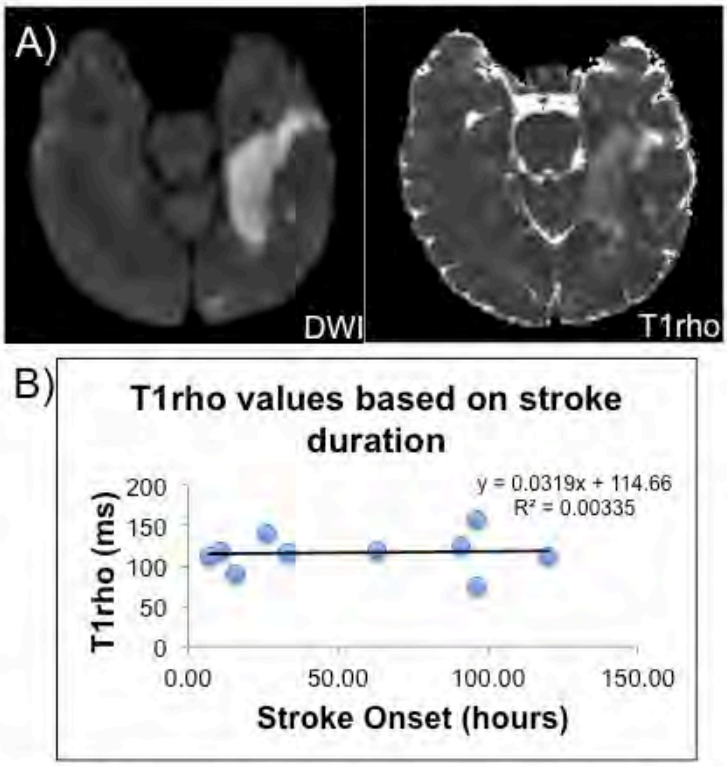


Figure 1. A) DWI (left) and T1rho (right) maps of a single subject demonstrating acute infarct in the left temporal lobe and B) Linear regression analysis showed no significant correlation between stroke

(Filename: TCT_O-414_Slide1.jpg)

O-415

9:40AM - 9:48AM

Estimation of Infarction Volume Using CT Perfusion: Comparison Between Bayesian and Singular-Value Deconvolution Postprocessing

K Nael[1], Y Sakai[1], J Marchione[1], N Swinburne[1], J Schefflein[1], J Puig[2], B Delman[1]
[1]Icahn School of Medicine at Mount Sinai, New York, NY, [2]Research Unit of Diagnostic Imaging Institute (IDI), IDIBGI, University Hospital Dr Josep Trueta, Girona, Girona

Purpose
Computed tomography perfusion (CTP)-based infarction estimation has been challenging mainly due to noise associated with CTP data. The Bayesian method is a robust probabilistic method that minimizes effects of oscillation, tracer delay and noise during residue function estimation compared with other deconvolution methods (1, 2). In this study we compared the CTP-estimated infarction volume between Bayesian method and commonly used block-circulant singular value deconvolution technique (cSVD).

Materials and Methods

Patients were included if they had 1) Anterior circulation ischemic stroke; 2) Baseline CTP; 3) Successful recanalization defined by TICI ≥ IIb; 4) Minimum infarction-volume of > 5mL on the follow-up MRI. Computed tomography perfusion data were processed with cSVD and Bayesian methods. Two established CTP threshold criteria for estimation of infarction volume were applied: Method-1 (rCBF < 30% within the region of delay more than 2 sec) (3) and Method-2 (CBV < 2 within the region of rMTT > 145%) (4). Statistical analysis was performed using repeated measure ANOVA, regression and Bland-Altman analysis.

Results

So far, 20 patients have met inclusion criteria. Infarct volume (Mean±SD, mL) was 23.7±28.6 on MRI; 30.4±28.4 (Bayesian) and 16.3±23.14 (cSVD) using Method-1; 20.6±24.3 (Bayesian) and 8.8±4.8 (cSVD) using Method-2. With MRI as the standard, there was no statistically significant ($p>0.05$) difference between CTP-estimated infarction volumes, except for cSVD-CBV ($p=0.006$). Bayesian-estimated infarction volume showed smaller mean differences when compared to MRI infarction volume. Mean-difference and correlation coefficient between MRI and CTP-estimated infarction are summarized in Table 1.

Conclusions

While cSVD provides acceptable estimation of infarction volume using rCBF<30%, volumetric accuracy for estimation of infarction from CTP is superior using Bayesian postprocessing regardless of the threshold methodology utilized.

CTP-estimated infarction volume compared to MRI				
		Mean difference volume with MRI	ANOVA, p	Correlation coefficient, p
Method-1 (rCBF<30% within the region of delay > 2sec)	Bayesian	6.7 mL	0.81	$r^2 = 0.64$, p<0.001
	cSVD	-9.0 mL	0.69	$r^2 = 0.54$, p<0.001
Method-2 (CBV<2 within the region of rMTT> 145%)	Bayesian	-3.1 mL	0.90	$r^2 = 0.50$, p=0.01
	cSVD	-22.6 mL	**0.006**	$r^2 = 0.1$, p=0.2

(Filename: TCT_O-415_Table-1.jpg)

O-416

9:48AM - 9:56AM

In acute stroke, clots visualized by thin slice NECT imaging do not match the contrast gap in CT angiography

F Gaertner[1], A Guerra[2], O Jansen[2], C Riedel[2]
[1]UKSH Kiel, Kiel, Germany, [2]UKSH Kiel, Kiel, -- SELECT --

Purpose
We aimed for comparing the anatomic relation between an intracranial thrombus as described using the hyper dense vessel sign on thin slice nonenhanced computed tomography (NECT) scans and the contrast gap displayed by CT angiography.
Materials and Methods
The NECT and CTA images of 164 patients with an acute ischemic stroke and proven vascular occlusion in the proximal middle cerebral artery were analyzed using Mevislab 2.8.2 (Mevis Medical Solutions). We first registered the NECT and CTA images. Next, we segmented the hyperdense voxels within the occluded artery using thin slice NECT reconstructions and displayed the segmented clot in an overlay mode on top of the CTA

images. Using these fused images we measured the shortest distances between the clot and the proximal and distal end of the contrast gap in the CTA images.
Results
In 92% (n=151) of our cases, the contrast medium reached the proximal end of the clot. The distal end of the clot was observed to attach to the distal end of the contrast gap in 25% (n=41) of cases. In the remaining 123 patients we found the distance between the hyperdense clot and the closest contrasted vessel to be larger than the clot length in 35% of cases (n=48). The average clot length was 11 mm.
Conclusions
The length of clots in the middle cerebral artery often is overestimated when it is measured based on the contrast gap in CT angiography images. Considering the fact that exact positioning of a stent retriever in relation to the clot increases efficiency of mechanical thrombectomy maneuvers, our simple postprocessing technique which superimposes hyperdense clots on the CTA images might be of value for the neurointerventionalist.

O-417

9:56AM - 10:04AM

Relatively Poorer Outcomes in Post-revascularization M2 Branch Occlusions. Secondary to an Antecedent, More Proximal Occlusion?

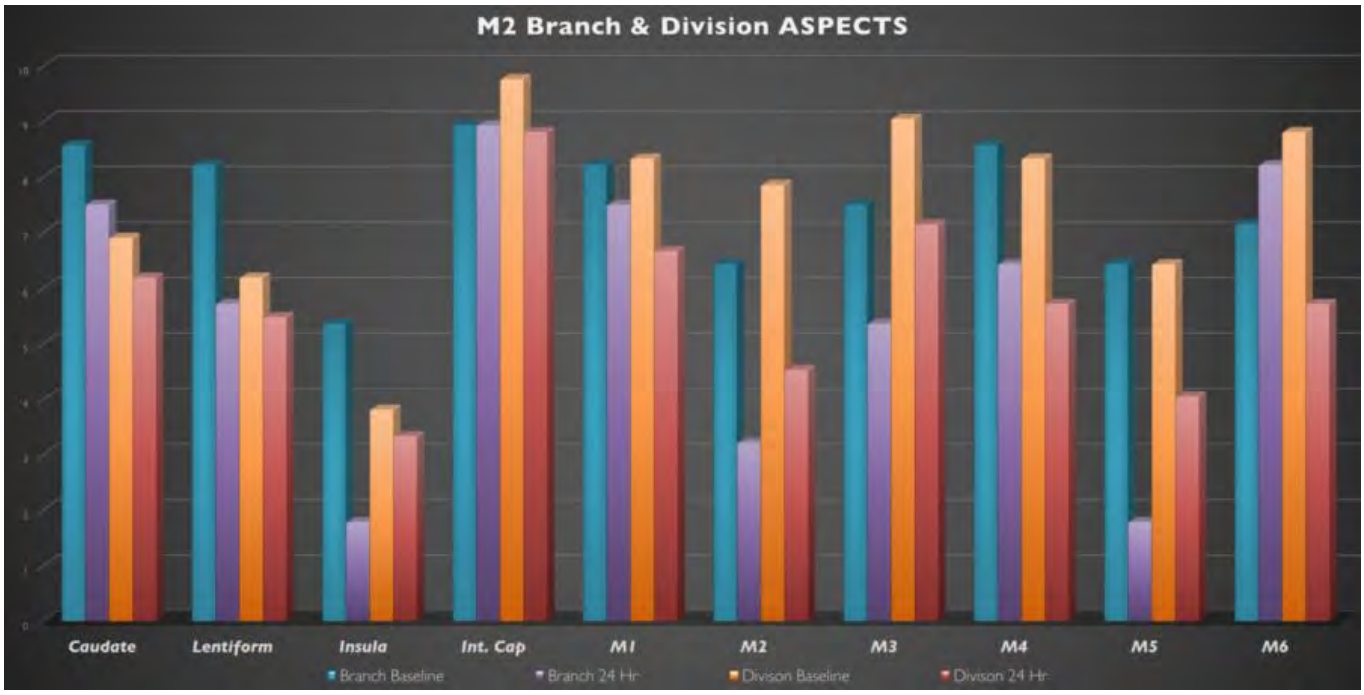
T Shujaat[1], T Tomsick[1]
[1]*University of Cincinnati Hospital, Cincinnati, OH*

Purpose
In the Interventional Management of Stroke III trial, relatively better modified Rankin Score (mRS) outcomes were seen in more proximal M2 division occlusions compared to more distal, smaller M2 branch occlusions postendovascular therapy (EVT) following IV tPA. This paradox raises the possibility that an antecedent, more proximal ICA or M1 occlusion had recanalized and passed distally, identified as an M2 branch occlusion on DSA prior to EVT.
Materials and Methods
A retrospective review of 85 M2 occlusions was performed, and 42 M2 division and 28 branch occlusions were identified. Baseline and 24-hour CT ASPECTS scores were stratified according to the specific areas affected by ischemic hypoattenuation in both groups. Baseline and 24-hour NIHSS in both groups were compared. Baseline CTAs were reviewed for identification of pre-IV tPA vascular occlusion. Modified Rankin Score (mRS) outcomes were assessed at 90 days.
Results
Average NIHSS were similar at baseline in M2 division (16.7) compared to M2 branch occlusion (17.9), and at 24-hours (11.0 vs. 13.9, p=0.10). Baseline CTA (n=30) demonstrated no differences in proximal occlusion prior to IV tPA in either group. Baseline

average ASPECTS were lower in division occlusions (7.7 vs. 8.1), but higher at 24-hours (6.3 vs. 5.7). A 67% decrease of insular ASPECTS (ASPECTS area 3, $p< 0.06$) and a 72% decrease of motor/premotor territory ASPECTS (ASPECTS area 5, $p < 0.0002$) was identified between baseline and 24-hours in M2 branch versus M2 division occlusions (decrease of 12.5% for ASPECTS area 3, and 37% for ASPECTS area 5, see Fig. 1). A smaller percentage of patients with M2 branch occlusions achieved a mRS 0-2 (32.1%) versus M2 division occlusions (45.2%) at 90 days. In patients with M2 branch occlusions and mRS >2 at 90 days, a 78% decrease was observed between the baseline and 24-hour CT insular ASPECTS, while no significant difference was seen in insular ASPECTS in patients with mRS 0-2 outcomes at 90 days.

Conclusions

There is no evidence that poorer outcomes in M2 branch occlusions are attributed to lower baseline ASPECTS or more frequent proximal vessel occlusion compared to division occlusion. This may relate to both more frequent and greater involvement of insular and motor-premotor cortices at 24 hours compared to baseline with branch occlusions. Involvement of the insular cortex greater than 50% despite small ischemic volumes has been shown to have poorer clinical outcomes. A deleterious treatment effect related to prolonged infusions into smaller caliber vessels leading to detrimental local blood-brain barrier effects and edema would be difficult to exclude.



(Filename: TCT_O-417_Untitled.jpg)

O-418

10:04AM - 10:12AM

M2 Trunk Occlusion: An M1-M2 Anatomic Variant with Greater Collateral Potential but Greater Lenticulostriate Risk

T Tomsick[1], D Liebeskind[2], T Shujaat[3]
[1]*University of Cincinnati Hospital, Cincinnati, OH,* [2]*Department of Neurology, Neurovascular Imaging Research Core, UCLA, Los Angeles, CA,* [3]*Ohio State Wexner Medical Center, Columbus, OH*

Purpose

The Interventional Management of Stroke Trials identified M2 trunk occlusion as occlusion beyond the anterior temporal artery (ATA) with only a patent posterior temporal artery (PT), or occlusion beyond a holotemporal artery (HT) which supplies the ATA and the remainder of the temporal lobe. M2 trunk occlusion simulates distal M1 trunk occlusion, but may enjoy better outcomes due to better collateral flow to the temporal lobe, or worse due to higher incidence of lenticulostriate arteries (LSA) arising from the M2 trunk that balance or offset any beneficial collateral effect.

Materials and Methods

We reviewed DSA of 9 M2 trunk occlusions for presence of L-S arteries arising from the occluded trunk, and 24-hr computed tomography or MR for evidence of infarction of areas supplied by the LSA (ASPECTS areas 1-4). Incidence of DSA LSA identification was compared to incidence of LSA arising from M2 in the setting of more distal division or branch occlusion. The incidence of infarction of deep structures was compared to incidence of involvement in M2 division and branch occlusions. Outcomes for M2 trunk, M2 division, M2 branch, proximal M1, and distal M1 occlusion are detailed.

Results

Nine M2 trunk occlusions. M2 occlusions in IMS III were associated with patent HT (n=7) or PT (n=2) branch origins, the latter simulating a large anterior temporal artery. Table 1 indicates average ASPECT scores for M2 trunk were lower for the 3 deep ASPECT areas compared to both division and branch occlusion, but greater for insular cortex. This suggests LSA originated from the occluded trunk leading to infarction. Six of 9 trunk occlusions achieved recanalization and mTICI 2b reperfusion. Lenticulostriate were identified arising from the trunk in 3 (33.3%) instances before or after revascularization, more frequent than in the setting of division or branch occlusion. mRS 0-2 outcomes were achieved in 3/9 trunk occlusions, compared to 46.5% division, and 34.5% branch occlusion, 38.2% distal M1 occlusion, and 26.9% proximal M1 occlusion.

Conclusions

Based on the functional IMS definition focusing on presence or absence of M2 branch filling, M2 trunk occlusions appear to represent hybrid M1 and M2 occlusions. Greater collateral flow from the PT or HT may contribute to reduced percent insular infarction compared to M2 division and branch occlusion. However, greater involvement of LSA with more frequent caudate, lenticular nucleus, and capsule/corona radiate infarction may balance or even outweigh collateral benefit. Further investigation is warranted.

	Trunk	Division	Branch
24-Hr ASPECT (Ave. score)			
Area 1 (Caudate)	0.25	0.69	0.75
Area 2 (Lentiform)	0.13	0.62	0.57
Area 3 (Insula)	0.5	0.33	0.17
Area 4 (Capsule)	0.13	0.88	0.89
Lenticulostriate origin	3/9 (33%)	8/42 (19.0%)	5/28 (17.9)

(Filename: TCT_O-418_Slide1.jpg)

O-419

10:12AM - 10:20AM

Hyperdense Middle Cerebral Artery Sign: A Revisit.

K Lam[1], E Spitzer[1], S Ifthikharuddin[1], A Desai[1]
[1]*Rochester General Hospital, Rochester, NY*

Purpose
The hyperdense middle cerebral artery sign (HMCAS) refers to the increased density of the occluded MCA branches from thrombus formation, often seen in hyperacute ischemic stroke on nonenhanced computed tomography (NECT). Studies have shown that the accuracy of reporting HMCAS can vary, depending on clinical experience. Few studies so far have published objective parameters that can help clinicians with diagnostic confidence in correct recognition and recommendation for further workup in a timely manner.
Materials and Methods
Brain nonenhanced computed tomographs obtained by standard protocol in our radiology department showing HMCAS between January 2013 and November 2016 with confirmation by CT or magnetic resonance angiograms (CTA/MRA) were analyzed. True positives are defined as subjective hyperdense MCA sign on NECT correlating with occlusion with that particular MCA segment on CTA/MRA. False positives are defined as hyperdense MCA on NECT without occlusion on CTA/MRA. Age-matched control cases also were analyzed for

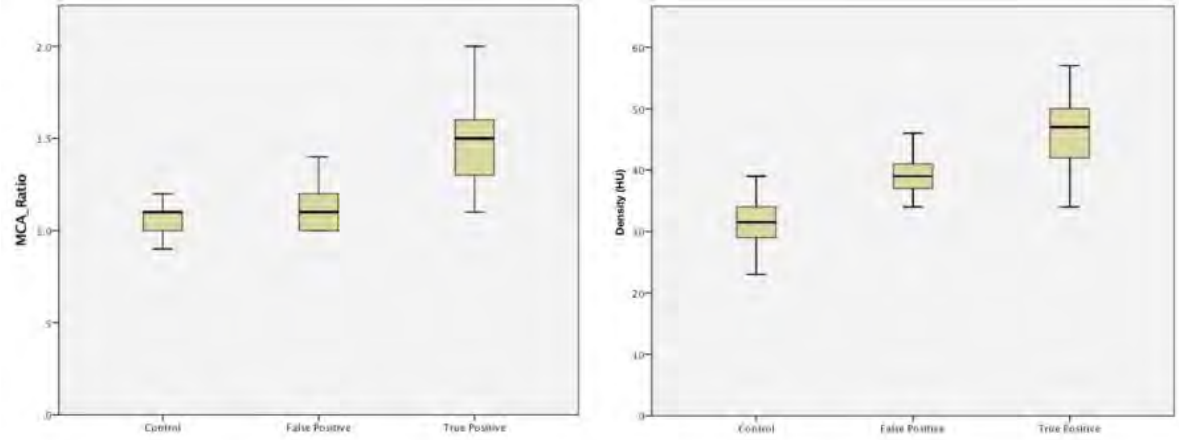
comparison. Freeform regions of interest were placed over the affected vessel and the contralateral unaffected vessel. The absolute attenuation in Hounsfield units (HU) was measured, and the ratio of the affected side to the other was calculated and compared.

Results

A total of 59 cases of hyperdense MCA sign was analyzed, including 46 true positives and 13 false positives. Sixty age-matched controls were included. The mean MCA attenuation was greater in the affected MCA of true positives compared to false positives [46.5 HU (95% confidence interval CI 45.0-48.0) vs. 39.2 HU (95% CI 37.3-41.2); $p < 0.0001$], and controls [31.8 HU (95% CI 30.8-32.7); $p < 0.0001$]. The MCA ratio between affected vessel and contralateral unaffected vessel was greater in true positives [1.49 (95% CI 1.42-1.55)] vs. false positives [1.12 (CI 1.04-1.21); $p < 0.0001$] vs. controls [1.07 (95% CI 1.05-1.09); $p < 0.0001$].

Conclusions

Hyperdense MCAs associated with early ischemic stroke can be distinguished objectively from normal vessels and false positives by measurement of absolute attenuation of affected and contralateral unaffected vessels. An absolute density of ≥ 45 and an MCA ratio of >1.21 are highly indicative of thrombosis. These objective thresholds are in accordance with prior studies and can help radiologists improve diagnostic confidence.



(Filename: TCT_O-419_Density_ratio_charts.jpg)

O-519

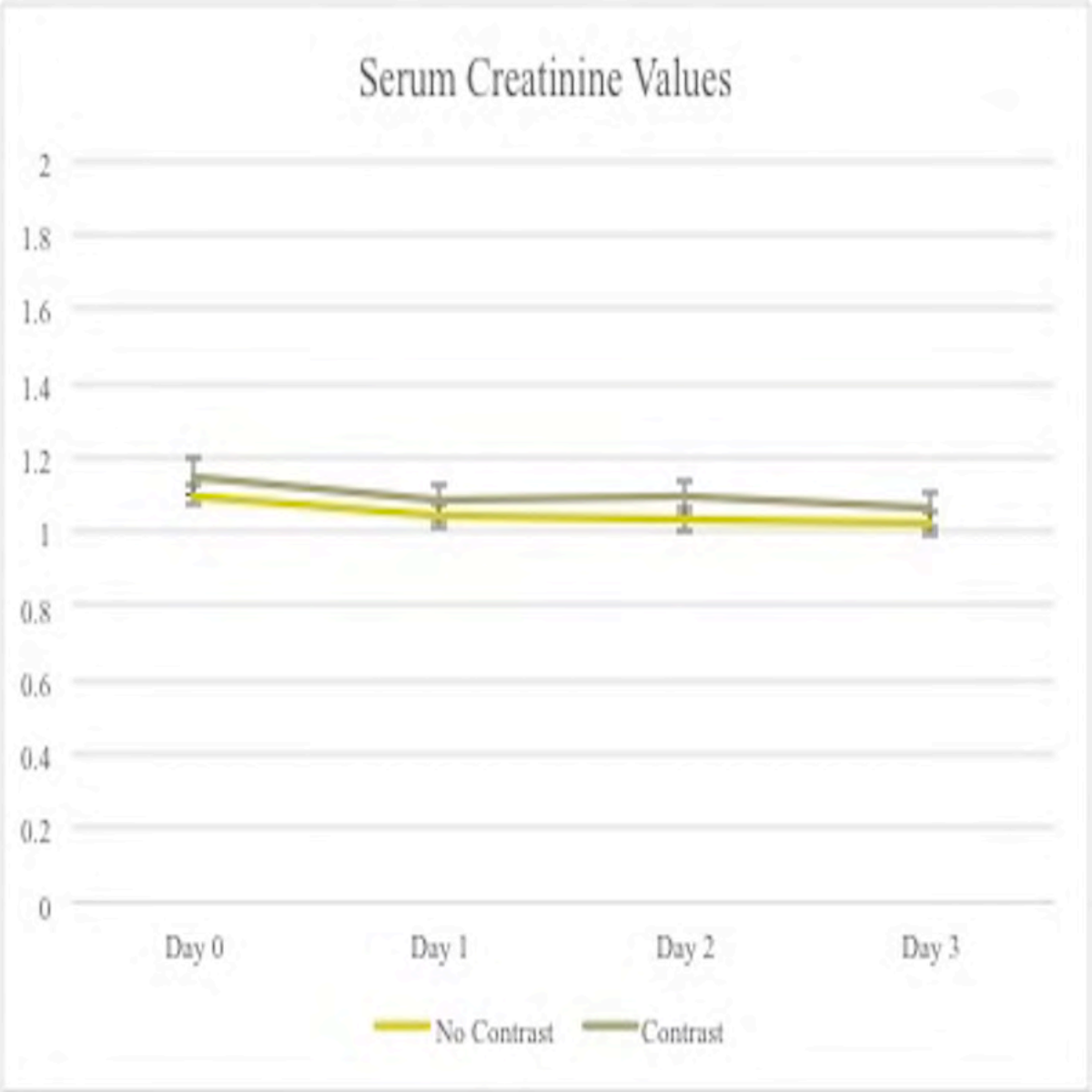
10:30AM - 10:38AM

Neurons Over Nephrons: Contrast Induced Nephropathy Following CT Perfusion for Evaluation of Acute Ischemic Stroke

A Copelan[1], R Tadros[2], W Brinjikji[3], O Copelan[4], J Wilseck[5]

[1]Beaumont Health System, Royal Oak, MI, [2]Oakland University William Beaumont School of Medicine, Rochester, MI, [3]Mayo Clinic, Rochester, MN, [4]Case Western Reserve University School of Medicine, Cleveland, OH, [5]Beaumont Hospital, Royal Oak, MI

Purpose
There remains apprehension in the utilization of intravenous iodinated contrast agents secondary to the risk of contrast induced nephropathy (CIN). This study evaluates whether there is a greater incidence of ≥ 25% increase in baseline creatinine levels within 48-72 hours for patients with acute ischemic stroke (AIS) who underwent CT perfusion imaging versus patients with AIS who did not undergo CT perfusion.
Materials and Methods
This single center study retrospectively reviewed 400 patients with AIS who underwent CT perfusion and 400 patients with AIS who did not undergo CT perfusion. Baseline data collected included age, gender, and comorbidities, including smoking history. Outcomes included the presence of ≥ 25% increase in baseline creatinine levels within 48-72 hours and serum creatinine levels at days 0, 1, 2 and 3. Continuous variables were compared using a Student's t test and categorical variables were compared using a chi-squared test. All statistical analysis was performed using JMP13.0.
Results
A total of 800 patients were included (400 in each group). Mean age of the control group was significantly larger than that of the CTP group (75.3 years versus 70.7 years, P<.0001). There was no difference in the proportion of patients with ≥ 25% increase in baseline creatinine levels within 48-72 hours in the control group (39 patients, 9.8%) when compared to the CT perfusion group (42 patients, 10.5%) (P=0.81). Mean creatinine levels at days 0, 1, 2 and 3 did not differ between groups (P=0.36, P=0.39, P=0.30, P=0.36 respectively).
Conclusions
In patients presenting with AIS, administration of iodinated contrast for CT perfusion imaging does not appear to increase the risk of acute kidney injury. Therefore, iodinated contrast media may not be the underlying etiology in stroke patients with acute kidney injury following CT perfusion imaging.



(Filename: TCT_O-519_ASNRFig1.jpg)

Thursday
11:00AM - 12:15PM
Long Beach Convention Center, Room 103 (Main Level)

24C-Parallel Paper Session: Head and Neck Topics: Take the Tour!

O-422

11:08AM - 11:16AM

Retinography as a model for studying chemotherapy-induced neuropathy: Proof of concept in an induced glaucoma model

L Le Roux[1], X Qui[1], D Ramos[1], D Piwnica-Worms[2], D Schellingerhout[1]
[1]UT MD Anderson Cancer Center, Houston, TX, [2]MD Anderson Cancer Center, Houston, TX

Purpose

There are 6.6 million blind or visually impaired people in the U.S. (National Foundation for Blindness 2012 estimates), 2.2 million people with glaucoma (Glaucoma Research Foundation, 2004), chemotherapy-induced neuropathy occurs in 4.6 million cancer survivors in the U.S. (Neuropathy Association, 2014) and thousands of new cases of cancer of the head, neck and brain will be treated with radiation therapy. Threats to vision and cancer treatment frequently intersect, and it is vital that we understand the threats to vision in cancer patients, particularly those threats that we ourselves cause iatrogenically. The immediate goal of this study is to use a fluorescent molecular nerve imaging probe based on a fast retrograde neural transport mechanism to visualize and quantitate retinal ganglion cell (RGC) neural uptake in an established glaucoma model. The long term goal is to extend this model to study the mechanism involved in the development of chemo-induced neuropathy as it pertains to neural transport.

Materials and Methods

Excitotoxic glaucoma was induced in rat (n=3) eyes by injecting NMDA (N-methyl-D-aspartic acid, 50 nmol/2.5 µL) into the vitreus of one eye. This model is known to induce apoptosis in RGCs. The contralateral control eye received no treatment. Twenty-four hours after the NMDA injection, a fluorescently labeled neural imaging probe consisting of the non-toxic, C-fragment of Tetanus Toxin (TTc790 and TTc546) was injected into the vitreus of both the glaucomatous and normal eye (8 µg TTc fluorescent probe/2µl PBS). In vivo imaging of the distribution of TTc790 was performed using a confocal-scanning laser ophthalmoscopy (cSLO) (Retinal Angiograph II, Heidelberg, Germany). Both eyes and associated neural tissues were harvested at 2-3 hours after TTc790 injection for ex vivo microscopic imaging using an epi-fluorescent microscope with NIR imaging capabilities (AxioZoom16, Zeiss Microscopy, Germany). Whole retinal mount fluorescent immuno-histology with antibodies against Gamma-Synuclein was performed. Permanently mounted retinas were imaged using laser scanning confocal microscopy (FV1000 Olympus). Whole eyes were embedded and cryo-sectioned to confirm optical imaging results.

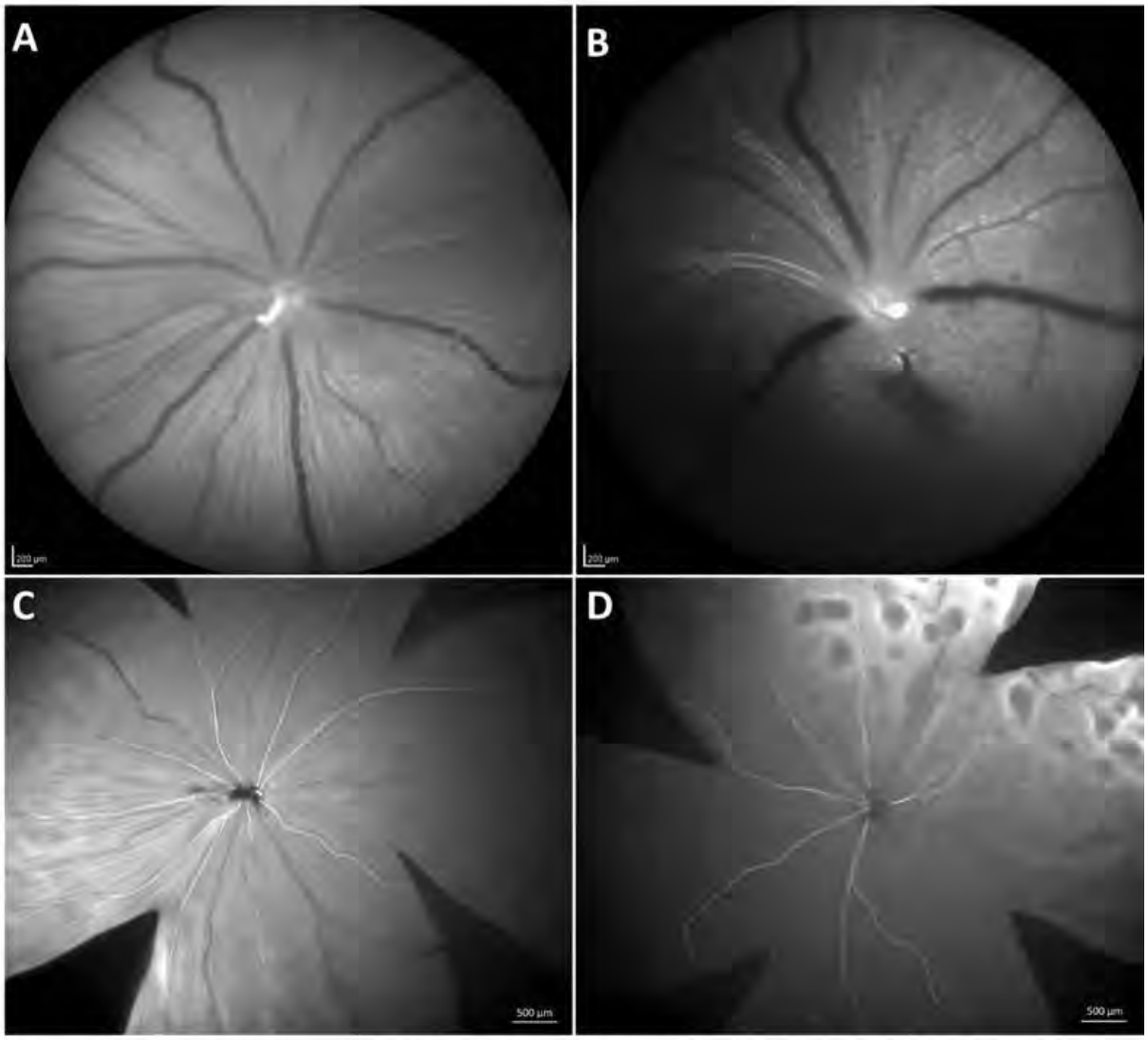
Results

Retinal ganglion cells showed extensive TTc790 and 546 uptake and demonstrated localization of TTc in both the projecting axons, the dendritic inputs and the neuronal cell bodies. This localization could be demonstrated by in vivo imaging in live animals, and was confirmed by ex vivo, fluorescent immuno-histology, illustrating the co-localization of TTc with Gamma-Synuclein, a marker for RGCs. The NMDA-induced model of glaucoma showed greatly reduced uptake and transport of TTc, demonstrated in both in living animals and excised tissues (See Fig.). Preliminary statistical data analysis of raw fluorescent output

from the retina showed 11,460 +/- 1,601 AU for normal and 9,255 +/- 224 NMDA-treated eyes ($p<0.05$, two-tailed paired t-test).

Conclusions

A novel, fluorescently labeled nerve imaging probe, TTc, allows the visualization and quantitation of retinal ganglion nerve cells in both the normal and diseased states. Glaucoma decreases neuronal uptake and transport of TTc in a glaucoma model, a condition in which the hallmark pathology is loss of RCGs. We have shown in previous work dealing with chemotherapy-induced neuropathy that failure of retrograde axonal transport is a key feature of this disease also in the peripheral nervous system. The retrograde transport mechanism is highly conserved and known to be present in all neurons, including both retinal neurons and peripheral nerve neurons. This suggests that the retina might be a suitable model system for the investigation of chemotherapy-induced neuropathy also.



In vivo NIR fluorescent photograph of the fundus of the eye (Heidelberg cSLO A,B) and flat mounted ex vivo micrographs of excised retinas (Zeiss AxioZoom16 epi-fluorescence microscope C,D) illustrating normal (A, C) versus NMDA/glaucoma induced (B,D) retinas 2-3 hours after intra-vitreal injection of a NIR labeled nerve transport probe (TTc790). Note the marked linear uptake in retinal ganglion cell axons radiating to the optic nerve head in normal eyes, but absent or markedly diminished in glaucoma eyes. Early retinal damage is visible as irregular areas of failed uptake in the glaucoma eyes. Note the close correspondence between in vivo and ex vivo findings, indicating the translational potential of this approach.

(Filename: TCT_O-422_RetinographyleRoux.jpg)

O-423

11:16AM - 11:24AM

Retrolaminar migration of inraocular silicone oill detected on CT: not uncommon phenomenon

M Abdalkader[1], M Chapman[2], G Barest[1], O Sakai[3]

[1]Boston Medical Center, Boston, MA, [2]Boston University Medical Center, Boston, MA, [3]Boston Medical Center, Boston University School of Medicine, Boston, MA

Purpose

Intraocular silicone oil injection has been used for the treatment of complicated retinal detachments. Recently, cases of intracranial migration of silicone oil, which may be associated with visual and neurologic symptoms, have been reported. However, the prevalence of retrolaminar migration of intra-ocular silicone is not well known. Our purpose is to review the prevalence and extent of retrolaminar migration of intra-ocular silicone on head CT.

Materials and Methods

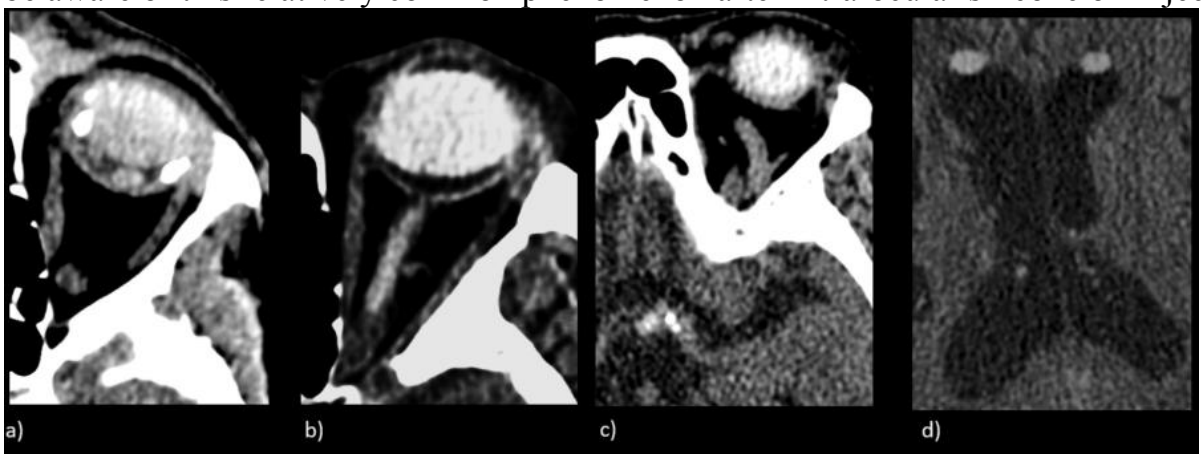
A retrospective review of patients with intra-ocular silicone injection who underwent head CT examinations in 2011-2016 was performed. All head CTs were performed with 1.25 mm thick (soft tissue and bone algorithm reconstructions) without intravenous contrast administration. All images were evaluated for retrolaminar migration of intra-ocular silicone.

Results

Sixty-eight patients with intra-ocular silicone injection who underwent unenhanced head CTs for various clinical indications were identified. Retrolaminar migration was seen in 8 out of the 68 patients (12%). Silicone was seen at the level of the subretinal space (1 case), optic head (2 cases), optic nerve (5 cases), optic chiasm (5 cases), optic tract (3 cases), and in the lateral ventricles (1 case). Two of the cases showed differences in density between the optic nerves. No significant symptoms or complications were documented in the chart of patients with retrolaminar migration of intra-ocular silicone.

Conclusions

Retrolaminar migration of intra-ocular silicone is not uncommon after intra-ocular silicone oil injection, and may be overlooked by radiologists. Although there were no apparent symptoms associated with silicone migration documented in the chart, the radiologist should be aware of this relatively common phenomenon after intra-ocular silicone oil injection.



(Filename: TCT_O-423_Siliconemigration.jpg)

O-424

11:24AM - 11:32AM

The “Black Turbinate Sign”: A Potential Diagnostic Pitfall. Evaluation of the Normal Enhancement Patterns of the Nasal Turbinates.

Q Han[1], E Escott[1]
[1]*University of Kentucky, Lexington, KY*

Purpose

Lack of enhancement of a nasal turbinate on MR scans has been reported to be a finding highly suggestive of invasive mucormycosis rhinosinusitis (aka, the "Black Turbinate Sign") in immunocompromised or diabetic patients (1, 2) (Fig. 1). Low or variable T2 signal and restricted diffusion also have been described. However, we have noticed nonenhancing turbinates in patients imaged for other indications who have essentially no possibility of having invasive mucormycosis rhinosinusitis. Therefore, we sought to determine the normal enhancement patterns of the nasal turbinates, to try to better understand what the positive predictive value of the "Black Turbinate Sign" might be. The purpose of this study therefore is to investigate the normal enhancement pattern of the nasal turbinates, and to determine whether there is statistically significant frequency of nonenhancing portions of the nasal turbinates on MR scans performed on immunocompetent patients who do not have a reasonable likelihood of having invasive fungal rhinosinusitis. We also sought to better characterize this incidental finding, evaluating whether it is transient, more frequently involves a specific turbinate or portion of a turbinate, or whether it has a predilection for a certain population.

Materials and Methods

This is a retrospective IRB-approved study involving the examination of patient medical records, such as medical history and MRI scans including the nasal turbinates. Patients were enrolled in the study via a reversed chronological order search of the PACS for MR scans with contrast and fat-saturation of the face/skull-base/orbit/neck from July 31, 2016 through June 1, 2016 (the fat-saturation group) and with contrast but no fat-saturation of the brain from July 10, 2016 through July 1, 2016 (the brain group). All patients' medical records were evaluated to confirm that there was not a reasonable likelihood for patient to have invasive fungal rhinosinusitis. Magnetic resonance scans were evaluated for the presence of areas of nonenhancement within the nasal turbinates (i.e., "Black Turbinate"). Each patient with a nonenhancing turbinate was further evaluated for the location of nonenhancement within the turbinate(s), the symmetry and size of the turbinates and their enhancement, and whether the nonenhancing areas persisted, improved or resolved over the course of the multiple postcontrast series within each scan. Additionally, signal intensity on the T2-weighted images of all nonenhancing turbinate(s) was compared with the vitreous (high), gray matter (intermediate), and extraocular muscles (low) for classification. A prior MR scan, if available, also was thoroughly reviewed to evaluate for any variability of nasal turbinate enhancement for each patient versus a different time point. Our exclusion criteria included

the following: • Scans from outside or satellite hospitals. • Internal auditory canal, pituitary, or research protocol scans. • Scans with significant artifact or postoperative changes involving the sinonasal region. • Scans with a significant portion of the inferior turbinate not imaged. • If more than 1 scan was obtained at the same session: only the first scan was counted and additional scans were used as further delayed series.

Results

Ninety-five MR scans of the fat-saturation group and 104 MR scans of the brain group were evaluated, among which 25 of the MR scans from the fat-saturation group and 34 of the MR scans from the brain group were excluded per the exclusion criteria. Therefore, 70 MR scans in each category were included. All scans were performed on 1.5 or 3 Tesla MR scanners. The demographic information of each group is shown in Table 1. Overall, the frequency of observed foci of turbinate nonenhancement (NE), i.e. black turbinates, was 36%, being seen in 29% of fat-saturation group scans and in 44% of brain group scans. The greatest frequency of nonenhancing areas was located in the concha of the inferior turbinates, sparing the anterior aspects (Fig. 2), with a similar distribution within the middle turbinates being the next most frequent site. Most cases of NE showed increased (improved) enhancement given time, with most NE resolved after 2 or 3 postcontrast sequences. Most initial NE cases also transitioned to scattered hypo-enhanced foci over time (Fig. 3). Furthermore, approximately 50% of patients showed scattered hypo-enhancing foci from the first postcontrast sequence, and this also improved, with the turbinates becoming more homogeneously enhancing over time. The nonenhancing areas were confined within the turbinate, with regular and noninvasive borders, contrasted with the more extensive findings seen in our case of invasive mucormycosis rhinosinusitis (Fig. 1). Another common observation was thin rim-enhancement around the nonenhancing areas (Figs. 2 and 3), which also was not seen in case reports (1, 2) or in our case of invasive mucormycosis rhinosinusitis. The signal intensity on the T2-weighted images of the nonenhancing turbinates was variable but was mostly intermediate to high.

Conclusions

Although a possible sign for invasive mucormycosis rhinosinusitis in the appropriate clinical setting, areas of nonenhancement within the nasal turbinates are not uncommon on both MR scans with or without fat-saturation in immunocompetent patients, who have little chance of having invasive fungal sinusitis. This knowledge of the normal patterns of nasal turbinate enhancement should help radiologists better distinguish findings suggestive of invasive mucormycosis rhinosinusitis from normal variations, and lead to a higher positive predictive value of the "Black Turbinate" sign.

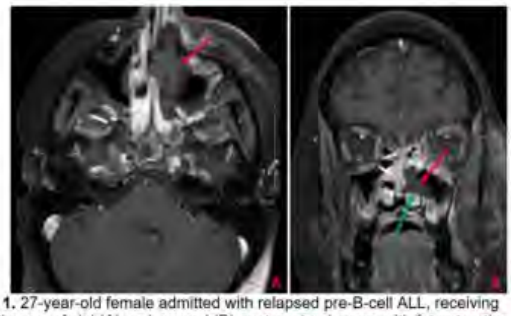


Figure 1. 27-year-old female admitted with relapsed pre-B-cell ALL, receiving chemotherapy. Axial (A) and coronal (B) post-contrast scans with fat-saturation show non-enhancement centered at the left middle turbinate (red arrows) with irregular and invasive borders into left inferior turbinate (green arrow). Patient had tissue proven invasive fungal rhinosinusitis, who went through series of 12 aggressive surgical debridement operations and eventually expired.



Figure 2. 24-year-old female, with history of gestational trophoblastic neoplasm, had MR brain scan for metastatic workup, who was immunocompetent at the time of the scan. Axial (A) and coronal (B) post-contrast T1 scans show non-enhancement of the left posterior inferior turbinate (red arrows) with faint rim enhancement (green arrows), which is a common location of observed "Black Turbinates" (BT) in immunocompetent patients.



Figure 3. 14-year-old female with right-sided blurred vision, had MR orbit scan followed MR brain scan for multiple sclerosis workup, who had no chance to have invasive fungal rhinosinusitis at the time of scan. Axial (A) and coronal (B) post-contrast T1 scans with fat saturation show non-enhancement of bilateral posterior inferior turbinate (red arrows) with rim-enhancement (green arrows) of bilateral inferior turbinates and scattered non-enhancing foci in the right middle turbinate (orange arrows). Again, the inferior turbinate, especially the posterior portion, is a common location of observed BT in immunocompetent patients. In the sagittal brain scan (C), which is the last post-contrast sequence available, the observed BT has almost completely resolved and transitioned into mildly scattered non-enhancing foci (blue arrow) in the right posterior inferior turbinate.

	Male	Female	Pediatric patients	Adult patients
Fat-Saturation Group	48%	52%	21% (11 months – 14 years)	79% (18 – 81 years)
Brain Group	56%	44%	23% (2 months – 17 years)	77% (23 – 86 years)

Table 1. Demographic summary of the recruited MR scans.

(Filename: TCT_O-424_ASNR2017_BT_figures_final.jpg)

O-425

11:32AM - 11:40AM

Rapid MR Evaluation of Rhinosinusitis - A Potential Paradigm Shift

Y Sun[1], K Golden[1], H Mehta[1], S Bobra[1]
[1]*New York Medical College - Westchester Medical Center, Valhalla, NY*

Purpose

Rhinosinusitis (RS) is inflammation of the nasal and paranasal sinus mucosa. Rhinosinusitis affects more than 16% of the U.S. population annually, accounting for over 26 million outpatient visits and greater than $4.3 billion in direct medical cost (1). Rhinosinusitis is typically a clinical diagnosis; however, in patients with an atypical presentation or when there is diagnostic uncertainty, imaging has a role. According to the American College of Radiology (ACR) Appropriateness Criteria, the initial study for uncomplicated RS is noncontrast CT of the sinus. Magnetic resonance imaging currently is viewed only as a complementary exam, with a rating of "usually not appropriate" or "may be appropriate" unless there is a suspected mass lesion. The purpose of our study is to examine the utility of Rapid MR (rMR) imaging in the evaluation of RS versus conventional CT.

Materials and Methods
This retrospective review was approved by Institutional Review Board (IRB). Fifty patients who underwent both CT of the sinus, head, or maxillofacial structures and rMR of the brain within 5 days of each other were included for a total of 100 exams. Both CT and rMR were reviewed independently by 2 board-certified neuroradiologists. Patients' demographics and radiology reports were blinded to the reviewers. Imaging findings were separately documented. Interobserver and intermodality agreement were analyzed.
Results
There were 50 patients (3 months - 69 years of age). Two CTs and one rMR were excluded due to artifact. There was a strong interobserver agreement between the 2 board-certified neuroradiologists (Table 1) and strong agreement across the 2 imaging modalities for assessment of mucosal thickening and degree of opacification (Table 2).
Conclusions
Rapid MRI of the brain is a potential alternative to CT in evaluation of RS, particularly as a radiation-sparing measure for pediatric and young adult patients.

Table 1. Interobserver agreement between two board-certified Neuroradiologists.

	Maxillary	Sphenoid	Frontal	Ethmoid
Mucosal Thickening	90%	90%	86%	92%
Degree of Opacification	88%	78%	72%	82%

Table 2. Intermodality agreement of two board-certified Neuroradiologists.

	Maxillary	Sphenoid	Frontal	Ethmoid
Mucosal Thickening	96%/94% *	88%/92%	90%/81%	86%/94%
Degree of Opacification	82%/89%	86%/80%	75%/84%	86%/88%

*Intermodality agreement for reviewer 1/reviewer 2.

(Filename: TCT_O-425_ASNRSinus.jpg)

O-426

11:40AM - 11:48AM

Identification of Hormone Secreting Pituitary Adenomas through Direction of Growth Analysis

D Pangal[1], M Shiroishi[2], G Zada[2], C Liu[2]

[1]University of Southern California, Los Angeles, CA, [2]University of Southern California Keck School of Medicine, Los Angeles, CA

Purpose

Pituitary adenomas of different histopathological subtypes have preferential growth patterns (1). Traditionally, suprasellar extension of pituitary tumors is characterized by extension superior to the diaphragma sellae, with infrasellar extension characterized by extension inferior to the floor of the sella. Because there is frequent obscuration of the diaphragma sellae or remodeling of the sellar floor by the tumor, using the easily identifiable planum sphenoidale to define suprasellar extension of tumor (2) and the imaginary plane inferior to the lacerum segment of the internal carotid arteries (C3) to define the infrasellar extension should allow for easier quantification of direction of tumor growth and help predict histology.

Materials and Methods

Eight patients with histologically confirmed hormone secreting tumors (5 growth hormone, 1 ACTH, 1 TSH/growth hormone, and 1 prolactin) and 11 patients with histologically confirmed nonfunctional adenomas were used for analysis. Magnetic resonance images were analyzed for maximum craniocaudal extent of the tumor. The extent of the tumor superior to the planum sphenoidale and inferior to C3 also were measured, with the values divided by the maximum craniocaudal extent of the tumor to generate suprasellar and infrasellar ratios, respectively. The ratios then were analyzed for statistically significant differences with Kruskal-Wallis test with post-test.

Results

Examples of the landmarks used for measurements are shown in Fig. 1. Hormone secreting adenomas demonstrate statistically significant propensity for infrasellar rather than suprasellar extension ($P < 0.001$), with nonfunctional adenomas demonstrating statistically significant propensity for suprasellar extension as compared to hormone secreting adenomas ($P < 0.01$) (Table 1).

Conclusions

Directionality of growth of pituitary adenomas can predict histology. The planum sphenoidale and inferior aspect of the lacerum segment of the ICA are useful landmarks for quantifying directionality of growth.

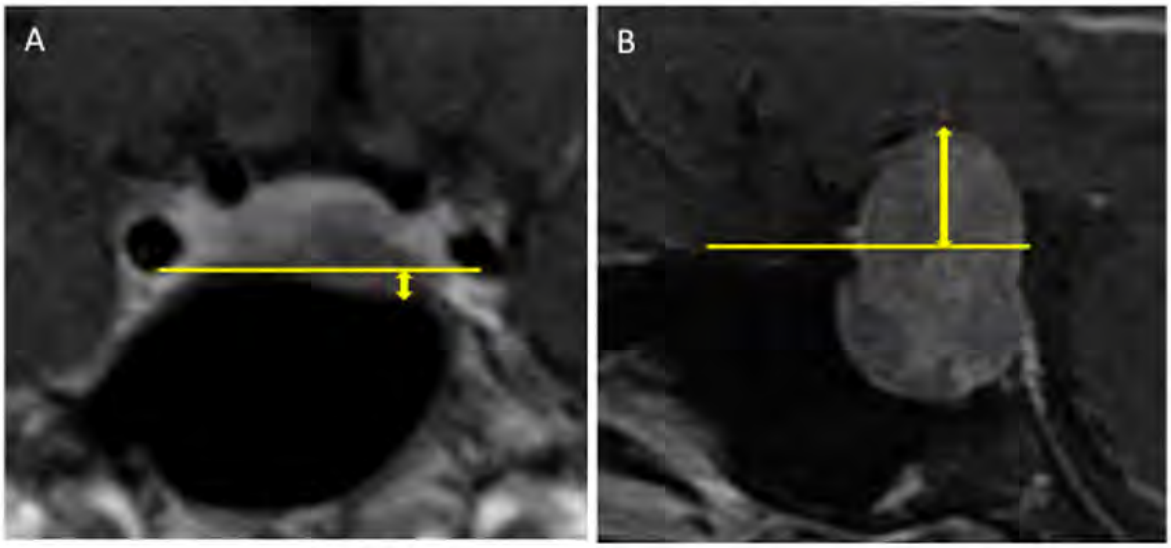


Figure 1: Landmarks used for adenoma directionality measurements. The extent of tumor inferior to the plane inferior to the lacerum segment of the ICA in a growth hormone adenoma (A) and extent of tumor superior to the planum sphenoidale in a nonfuncitonal adenoma (B) are shown.

Table 1: Summary of Pituitary Adenoma Measurements

Hormone Secreting Adenomas (n = 8)	
Mean craniocaudal size (mm):	15.5
Mean suprasellar ratio:	0.023
Mean infrasellar ratio:	0.44
Nonfunctional Adenomas (n = 11)	
Mean craniocaudal size (mm):	25.3
Mean suprasellar ratio:	0.37
Mean infrasellar ratio:	0.20

(Filename: TCT_O-426_asnr_figure1.jpg)

O-427

11:48AM - 11:56AM

MRI of Neonatal Brachial Plexus Birth Palsy

J Chang[1], P Shen[2], A Nidecker[3], E Neufeld[4]
[1]UC Davis medical center, Sacramento, CA, [2]Kaiser / UC Davis, Santa Clara, CA, [3]University of California, Sacramento, CA, [4]UC Davis Medical Center, Sacramento, CA

Purpose
Brachial plexus birth palsy is a condition in which the initial injury occurs secondary to downward traction of the shoulder girdle during birth. Postganglionic injuries include stretch injury, disruption of axons without perineurium disruption, complete nerve disruption, and neuroma. Preganglionic injuries include avulsion of the nerve roots within the neural

foramina. Currently, patients are referred for clinical evalution when detected and a scoring system is implemented to record initial deficits and track improvement, after which a serial clinical exam is performed every 3-6 months. Infants with decreasing or persistent scores are referred for surgical intervention, of which surgery entails extra-foraminal dissection of the entire brachial plexus and are repaired with nerve grafts. Intraforaminal exploration is not performed for preganglionic injuries and are repaired with distal nerve transfers. CT myelography was used previously; however required a lumbar puncture and ionizing radiation as well as the risks of intrathecal contrast. Recently, MRI has been used with highly weighted T2 sequences in the coronal plane of the cervical spine extended towards the shoulder. Imaging findings of preganglionic injuries include pseudomeningocele, or absent nerve roots whereas postganglionic injuries include thickening and/or hyperintensity of nerves or neuroma formation. We present indications and available options for imaging, optimal timing of imaging in the clinical course, MRI techniques in delineating anatomy and pathology, and surgical implications of findings.

Materials and Methods

IRB approval was obtained for a prospective study of which eligible infants included those less than 12 weeks old with brachial plexus birth palsy who presented at their first appointment with the orthopedic surgeon. Exclusion criteria were: infants greater than 12 weeks old, as they resist swaddling beyond this age; other birth injuries such as fractures; the presence of Horner syndrome or flail arm, as those patients would already proceed to surgery if present; or inability to complete the MRI. Enrolled infants underwent MRI on the same day as the clinical appointment and were followed with serial clinical exams and scoring per clinical standards every 4 weeks for 5-6 months. Patients then were grouped into positive or negative outcome groups of which those in the negative outcome group would be surgical candidates and those in the positive outcome groups demonstrated maintenance of mobility or serial improvement. Gold standard of clinical outcomes was compared with MRI findings at initial presentation. Magnetic resonance imaging findings then were compared to intra-operative findings. Scans on infants was performed using a 3T GE scanner with volumetric PD CUBE acquired coronally in the plane of the lower cervical spine and extended anterolaterally to include the brachial plexus. No sedation was required as infants were immobilized using a swaddling apparatus - the Med-Vac Infant Immobilizer. Images were reviewed independently by CAQ board certified neuroradiologists for levels of injury and preganglionic or postganglionic injury. A scoring system, the Shriners Radiologic Score was created and compared to the eventual need for surgery.

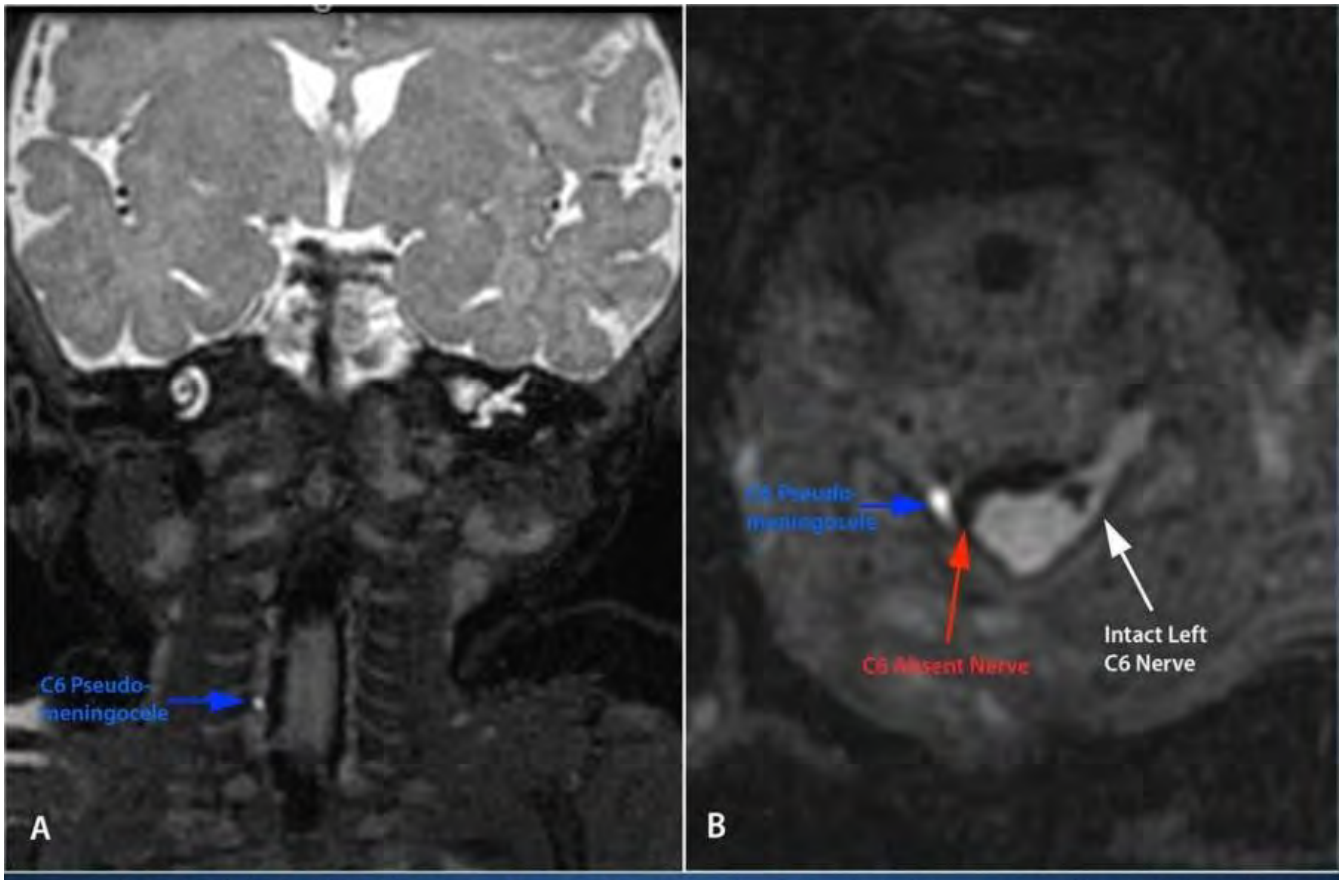
Results

Sixteen patients were considered initially of which 13 agreed to participate. Four patients were unable to complete the MRI due to motion and thus our study eventually had 9 subjects of which there were 4 boys and 5 girls with an average age of 5 weeks old. Four infants had negative functional clinical outcome and all went to surgery. Five infants had positive clinical outcome and were managed conservatively. Imaging findings included neuromas, nerve thickening, nerve thinning, and pseudomeningoceles. Using the Shriners Radiologic

Score, there was overall general correlation with eventual poor functional outcome and need for surgery with interclass correlation coefficient of 0.957 and statistically significant difference between the positive and clinical outcome groups with P=0.022.

Conclusions

It is important to distinguish between postganglionic and preganglionic injuries as outcomes and surgical management differs for both these conditions and MRI maybe a useful tool in their differentiation. We hope to demonstrate that MRI can reliably demonstrate the extent of injury as the clinical question is whether or not the patient would require surgery. Thus MRI could potentially avoid the need for multiple clinic visits, reduce stressful waiting for families, and perhaps surgery could be perfomed at an earlier age with probable better outcomes.



Coronal and axial PD CUBE images of one of our study patients with pre-ganglionic injury. Image A (Left) shows a pseudomeningocele at C6. Image B (Right) shows absence of the nerve roots. Findings are consistent with severe pre-ganglionic injury.

(Filename: TCT_O-427_brachialplexus1.jpg)

O-429

12:04PM - 12:12PM

Are 4D CT studies too sensitive?

J Reid[1], A Jay[1], F Berkowitz[2]
[1]MEDSTAR Georgetown University Hospital, Washington, DC, [2]MEDSTAR Georgetown University Hopspital, Washington , DC

Purpose
In the past few years, 4D CT has been well established in medical literature as a diagnostic tool for detecting parathyroid adenomas. The added benefits of 4D CT over traditional diagnostic studies (US and nuclear medicine sestimibi) are the exquisite spatial resolution the modality imparts and the ability to detect multiglandular disease. However, given the increase in spatial resolution, it is not always certain which of the parathyroid glands seen on 4D CT are contributing to the patient's hyperparathyroidism. At our institution, routine CT angiograms of the neck, such as for stroke evaluation, are very similar to the 4D CT protocol used for the evaluation of parathyroid adenomas. The purpose of this study is to determine how often normal parathyroid glands are visualized in euparathyroid patients.
Materials and Methods
Two fellowship-trained neuroradiologists retrospectively reviewed 30 neck CT angiograms each. The studies were performed for indications other than hyperparathyroidism, such as for the evaluation of acute stroke or hemorrhage. The electronic medical records (EMR) of patients were reviewed to ensure that patients did not have a history of hyperparathyroidism. The number, size, and location of visualized parathyroid glands were recorded. Discrepant glands were resolved by consensus.
Results
Of the possible 120 glands in 30 patients, 6 glands (5%) were visualized in 4 patients (13%). Three patients each had bilateral glands that were visualized. Five of 6 (83%) of the parathyroid glands were posterior to the superior pole of the thyroid gland. The axial sizes of the glands ranged from 2-6 mm, for a mean of 3.6 mm.
Conclusions
Using 4D CT, parathyroid adenomas have a characteristic enhancement curve which allows for increased sensitivity and specificity in detecting these lesions, particularly small (< 1 cm) lesions and in cases of multiglandular disease. As 4D CT allows for visualization of much smaller structures, we are finding that we are able to detect parathyroid glands at a higher rate than expected. Our assessment of a small group of patients shows that more than 10% of patients without a history of hyperparathyroidism had visible parathyroid glands. This raises the notion that we need to be more cautious in concluding that all visualized parathyroid glands on 4D CT studies represent adenomas.

Thursday
11:00AM - 12:15PM
Long Beach Convention Center, Room 104A (Main Lobby)

24D-Parallel Paper Session: Pediatric Neuroradiology: Exploring Beneath the Surface

O-430

11:00AM - 11:08AM

MRI Radiomic Features as Biomarkers to Predict Autism Spectrum Disorder

A Kotrotsou[1], D Giniebra[1], M Stosic[2], M Haque[2], M Proud[2], M Maletic-Savatic[2], R Colen[1]
[1]MD Anderson Cancer Center, Houston, TX, [2]Baylor College of Medicine, Houston, TX

Purpose

Autism spectrum disorder (ASD) is a heterogeneous group of neurodevelopmental disorders affecting 1 in 68 children in the USA. It is characterized by impairment in socio-communicative abilities, restricted and stereotyped behaviors. Significant advances have been made in the use of magnetic resonance imaging (MRI) to evaluate ASD. However, while current MRI analysis provides detailed knowledge on the macro-structure and function of the brain, it lacks to do so at the microscopic level (1). Texture analysis has emerged recently as a promising tool in medical imaging; MR texture analysis scrutinizes the data obtained during routine MRI and is able to evaluate tissue heterogeneity beyond the boundaries of the interpreting radiologist (2). The goal of this study was to identify MRI texture footprints in several brain regions of ASD children.

Materials and Methods

Twenty-eight children with ASD (mean age: 6.11 ± 3.53 years; 25 males) and 24 typically developing children (mean age: 8.96 ± 3.99; 15 males) were included in this study. High-resolution T1-weighted images were acquired on a 3T Philips scanner with a standard 8-channel head coil. Subcortical segmentation of the T1-weighted images was performed using FIRST (www.fsl.fmrib.ox.ac.uk/fsl/fslwiki/FIRST); 7 subcortical brain regions were segmented: thalamus, putamen, caudate, pallidum, amygdala, hippocampus, and nucleus accumbens. Following subcortical segmentation, texture analysis was performed using T1-weighted images on MatLab environment. A total of 310 rotation invariant texture features were obtained using: (i) the first-order histogram and (ii) the gray level co-occurrence matrix (3-5). The Maximum Relevance Minimum Redundancy technique was used to select the most relevant radiomic features. Receiver operating characteristic (ROC) analysis and leave-one-out cross-validation (LOOCV) were used to assess the performance of each support vector machine (SVM) classifier and AUC, sensitivity, specificity, PPV, NPV and p-values are reported.

Results

The best classification systems are reported for amygdala and nucleus accumbens with AUC above 80% and significant p-values, while the other regions reported AUC under 75% and nonsignificant p-values. For this 52 patient cohort we performed a LOOCV method to assess the performance of the SVM. In accumbens, we found 40 relevant features that significantly differentiate between patients with ASD and those in the control group (AUC 81.25%, 95% CI: 68.61%-93.89%, sensitivity 82.14%, specificity 83.33%, PPV 85.19%, NPV 80%, p= 0.00917016). Similarly, in amygdala, 100 features were significantly able to predict ASD

(AUC 83.33%, 95% CI: 70.95%-95.71%, sensitivity 96.43%, specificity 75%, PPV 81.82%, NPV 94.74%, p= 0.00341494). The predictive model did not show statistical significance in caudate region, where 110 features were selected (AUC 58.04%, 95% CI 41.82% - 74.25%, sensitivity 46.43%; specificity 83.33%, PPV 76.47%, NPV 57.14%, p=0.7283264); hippocampus, with 30 selected features (AUC 72.62%, 95% CI 58.76% - 86.48%, sensitivity 89.28%; specificity 50%, PPV 67.57%, NPV 80%, p=0.1769825); pallidum, with 80 selected features (AUC 70.09%, 95% CI 55.36% - 84.82%, sensitivity 85.71%; specificity 54.16%, PPV 68.57%, NPV 76.47%, p=0.3175248); putamen, with 10 selected features (AUC 74.4%, 95% CI 60.72% - 88.09%, sensitivity 50%; specificity 91.66%, PPV 87.50%, NPV 61.11%, p=0.1094463); thalamus, with 20 selected features (AUC 73.81%, 95% CI 59.62% - 88%, sensitivity 75%; specificity 75%, PPV 77.77%, NPV 72%, p=0.1292079). We used R software (version 3.3.1) for all the statistical analysis. Package mRMRe (version 2.0.5) for the feature selection task and the machine learning package mlr (version 2.8) to build the SVM classifier. Finally, ROC analysis was performed using pROC package (version 1.8).

Conclusions

In this study, we provide the first evidence that the micro structure of amygdala and nucleus accumbens in vivo predict ASD. These 2 brain regions are well known for their functional impairment in ASD, but the underlying cellular milieu that mediates this impairment could not be discerned in vivo. Thus, our study provides new knowledge related to the biology of ASD and points to novel postprocessing analyses that may become increasingly important for discerning important micro features of the tissue in brain diseases.

O-431

11:08AM - 11:16AM

Diffusion MR of the Auditory Pathway from Brainstem to Cortex and its Correlation with Conduction Velocity in Autism Spectrum Disorder

J Berman[1], T Roberts[1]
[1]*Children's Hospital of Philadelphia, Philadelphia, PA*

Purpose

Efficient conduction of auditory sensation to Heschl's gyrus requires mature white matter along the entire auditory pathway from the ear to the cortex. Autism spectrum disorder (ASD) is characterized by abnormal development of auditory radiation and superior temporal gyrus white matter. Correspondingly, the 100ms (M100) auditory response at the superior temporal gyrus, as measured with magnetoencephalography (MEG), is delayed in ASD, indicating abnormally slow conduction velocity and processing (1). Indeed, compromise of the structure-function relationship between auditory radiation white matter and conduction velocity has been observed in ASD (2, 3). These alterations to the auditory system and other whole-brain networks may comprise the biological basis for language

disorders prevalent in ASD. However, the structural (diffusion MR) and functional (M100 latency) measures used in these prior studies are inherently mismatched. The cerebral white matter of the auditory radiation only represents the final white matter portion of the auditory pathway. The M100 latency integrates conduction and processing speed along the entire length of the auditory system from the ear to auditory cortex. Indeed, auditory signaling is known to be proportionately delayed in ASD at early auditory brainstem nuclei (4). This study seeks to extend prior findings by combining brainstem and auditory radiation diffusion MR measures for correlation with M100 latency with the hypothesis that the structure-function relationship is altered in ASD.

Materials and Methods

This multimodal study included 29 children with ASD (mean age= 10.5±2.3 years) and 31 age-matched typically developing controls (mean age = 10.5±2.7 years) with diffusion MRI and MEG data. Diffusion tensor imaging (DTI) was acquired on a 3T Verio (Siemens) with 30 diffusion gradient directions at b=1000 s/mm2, one b=0 s/mm2 volume, TR/TE= 11s/76ms, voxel size 2x2x2mm, and 128x128 matrix. Probabilistic DTI tractography (FMRIB's Diffusion Toolbox) was used to define the left and right brainstem auditory pathway from the superior olivary complex to the medial geniculate nucleus (Fig. 1). Although difficult to obtain in children, high angular resolution diffusion imaging (HARDI) was acquired in a subset of participants. HARDI included 64 gradient directions at b=3000s/mm2 and 2mm isotropic resolution. The auditory radiation consists of complex crossing white matter was necessarily defined with probabilistic HARDI tractography. Fractional anisotropy (FA), mean diffusivity (MD) and radial diffusivity (RD) were measured voxelwise in left and right brainstem and auditory radiations.

Magnetoencephalography was performed with a whole head system (CTF). The M100 response for 4 frequencies and each hemisphere (8 total tone conditions) was source localized to the left and right superior temporal gyri and the M100 peak latency determined. For unimodal analysis, diffusion MR measures and M100 latency were separately modeled with effects of hemisphere, group, age, and their interaction terms. For the multimodal analysis, M100 was modeled with group, hemisphere, tone frequency, DTI measure, and their interactions as effects.

Results

Maturation of brainstem and auditory radiation FA ($p<0.05$, increases with age) and RD ($p<0.05$, decreases with age) was observed across all subjects. No significant effect of group was observed for DTI brainstem or auditory radiation measures. Similarly, M100 was observed to decrease with age at a rate of approximately 4.5ms per year ($p<0.0001$). M100 latencies were later in the left than the right hemisphere ($p<0.002$). No significant group effect on M100 or M100 developmental trajectory was observed. In the left (but not right) hemisphere auditory radiation, a significant group by age interaction indicated group differences in the scale of the developmental trajectory of FA and RD ($p<0.05$ each). No significant effect of hemisphere or group by age interaction was observed in the brainstem white matter. For the multimodal analysis, increased brainstem FA was predictive of faster

conduction (lower M100 latency, $p<0.01$) and increased brainstem MD and RD were correlated with slower conduction ($p<0.01$, each). The relationship of cortical M100 latency with brainstem diffusion properties showed a significant interaction with group ($p<0.05$ for FA and MD, $p=0.05$ for RD), indicating an altered structure-function relationship in ASD (Fig. 2). Similarly, increased auditory radiation RD was correlated with slower conduction ($p=0.04$). Examined separately by group, DTI brainstem and auditory radiation measures were each correlated with M100 latency in the typically developing controls but not the ASD group (Fig. 3).

Conclusions

This multimodal study of the auditory system examined associations between structural and functional neuroimaging to probe the possible neurobiological basis and mechanism of auditory and language dysfunction in ASD. Degree of auditory pathway myelination in both the brainstem and auditory radiation modulated the speed of auditory encoding in controls. A disassociation of this structure-function relationship was observed in both the brainstem and auditory radiation. These results indicate ASD pervasively impacts the structure-function relationship throughout the auditory system. Given that M100 latency has been observed previously to correlate with the severity of ASD symptoms, it is possible that the irregular relationship between microstructure and M100 contributes to the link between brain and behavior.

O-432

11:16AM - 11:24AM

Assessment of Rates of Reportable Language Mapping with Magnetoencephalography (MEG) in a Presurgical Pediatric Population

J Gadde[1], W Gaetz[1], T Roberts[1], E Schwartz[1]
[1]*Children's Hospital of Philadelphia, Philadelphia, PA*

Purpose

While it is known that hemispheric dominance for language increases with age, a paucity of literature exists on presurgical language mapping with MEG in children. A very small body of literature, focused on assessment of receptive language mapping in sedated or sleeping children, showed "successful" lateralization rates ≤ 78%.

Materials and Methods

Retrospective review of 94 patients (ages 4-19 years; 49 females; 80 right handed, 10 left handed, 2 ambidextrous, 2 unknown) referred for presurgical clinical language mapping from January 2012-August 2016 - 88 patients for intractable epilepsy, 3 for tumors, 3 for arteriovenous or cavernous malformations. Exclusion criteria included age > 21 years, prior surgical resection, excessive head motion, or poor task compliance. Each study was evaluated for the ability to localize and lateralize both receptive and expressive language areas using 1 to 3 language tasks (verbal word recall, verb generation, and/or picture

naming). Analysis for event-related desynchronization (ERD) of beta band (15-30Hz) oscillations was performed 200-700ms following stimulus presentation, and regions of significant ERD were depicted as color overlays on each patient's brain MRI. Visual assessment of hemispheric differences in ERD was made for Broca and Wernicke areas and their anatomic homologs. Language mapping was graded as: unsuccessful/0 (no language regions), bilateral/1 (but orthotopic), weak activity that lateralized/2 or strong activity that lateralized/3.
Results
Localization of receptive and/or expressive language cortex and subsequent determination of laterality was achieved in 90.4% (n=85) of patients. Mean age of patients in whom language mapping was unsuccessful (12 years) was not significantly different from group mean age (12.8 years), and there was no significant difference in grade with age (mean≤ 13 years 1.84;≥14 years 1.88), gender (females:199; males:1.73) or handedness (right:1.84; left:2.1).
Conclusions
Awake functional language mapping with clinical MEG across a range of pediatric ages has an equally high success rate and is useful for presurgical planning. Analysis of success rates and indeed the definition of success itself, especially as a function of development would extend the utility of both presurgical mapping with MEG as well as fMRI.

O-433

11:24AM - 11:32AM

Cognitive Phenotypes and Brain Network Architecture: Overcoming the Obstacle of Population Heterogeneity in Children with Focal Epilepsy.

M Paldino[1], L Vidal[1], W Zhang[1], Z Chu[1]
[1]*Texas Children's Hospital, Houston, TX*

Purpose
Architecture of the cerebral network has been shown to associate with IQ in children with epilepsy. Subject-level prediction on this basis, however, a crucial step toward harnessing such analyses for the benefit of epilepsy patients, has yet to be achieved; this is due in large part to heterogeneity across the population. We compared 2 methods that account for heterogeneity with regard to their capacity for patient-level IQ prediction.
Materials and Methods
Patients were identified retrospectively: 1. Focal epilepsy; 2. Resting state fMRI; 3. Full scale IQ. Brain network nodes were defined by anatomic parcellation, first in patient space (nodes defined for each patient) and again in template space (same nodes for all patients). Parcellation in both spaces was performed at 3 different network sizes: 350, 750, and 1500 nodes. Whole-brain, weighted graphs were constructed according to pair-wise correlation of BOLD-signal time courses between nodes. The following metrics were calculated: clustering coefficient, modularity, path length, and global efficiency. Metrics computed on graphs in

patient space were normalized to the same metric computed on a random network. A machine learning algorithm was trained on a subset of the cohort; we then assessed the ability of the algorithm to predict the IQ of the remaining individuals based on their network metrics. Accuracy for each condition was compared using Variation Explained.

Results

Twenty-six patients met criteria (4-18 years). Accounting for differences in network size inherent to a pediatric cohort was a dominant factor in accurate IQ prediction (Table 1). In this regard, network construction in patient space with normalization of metrics to a random network of identical size outperformed use of a standard template. Network size also was an important factor.

Conclusions

Our results provide guidelines for optimal construction of whole-brain networks based on resting state fMRI for patient-level predictions in children with epilepsy.

Network Size	Raw Time Series	Patient Space	Template Space
350 nodes	0.03 [0.01, 0.06]	0.17 [0.14, 0.20]	0.14 [0.12, 0.18]
750 nodes	0.07 [0.04, 0.11]	0.31 [0.28, 0.34]	0.17 [0.14, 0.20]
1500 nodes	0.13 [0.10, 0.16]	0.34 [0.31, 0.37]	0.20 [0.17, 0.23]

Table 1: Variation explained [95% confidence limits] of the machine learning algorithm for predicting IQ based on network metrics.

(Filename: TCT_O-433_table1.jpg)

O-434

11:32AM - 11:40AM

The Use of Hippocampal Volumetric Measurements to Improve Diagnostic Accuracy in Pediatric Patients with Mesial Temporal Sclerosis

G Guzman Perez-Carrillo[1], C Owen[2], K Schwetye[3], S Mar[2], A Vellimana[2], M Miller-Thomas[4], J Shimony[5], M Smyth[2], T Benzinger[6]

[1]University of Arizona- Banner Medical Center, Tucson, AZ, [2]Washington University in St. Louis, St. Louis, MO, [3]St. Louis University, St. Louis, MO, [4]Mallinckrodt Institute of

Radiology, St. Louis, MO, [5]Washington University School of Medicine, Saint Louis, MO, [6]Washington University in St. Louis, Saint Louis, MO

Purpose
Many patients with medically intractable epilepsy have mesial temporal sclerosis (MTS), which significantly affects their quality of life and life expectancy. The surgical excision of abnormal mesial temporal structures can result in marked improvement or complete resolution of the epileptic episodes. Reliable radiological diagnosis of MTS is a clinical challenge, confounding presurgical evaluations. The purpose of this study is to evaluate the utility of volumetric mapping of the hippocampi for the identification of MTS in a case-controlled series of pediatric patients who underwent surgical resection for medically refractory epilepsy using pathology as a gold standard.
Materials and Methods
A cohort of 57 pediatric patients who underwent surgical resection for medically intractable epilepsy between 2005 and 2015 was evaluated. This group included 24 patients with pathology-proven MTS and 33 patients with pathology-proven non-MTS. Retrospective quantitative volumetric measurements of the hippocampi were acquired for 37 of these 57 patients. Two neuroradiologists with more than 10 years of experience who were blinded to the patients' MTS statuses performed the retrospective review of magnetic resonance images. To produce the volumetric data, magnetic resonance scans were parcellated and segmented using the FreeSurfer software suite (Martinos, Massachusetts General Hospital, Boston, MA). Hippocampal regions of interest were compared against an age-weighted local regression curve generated with data from the pediatric normal cohort. Standard deviations and percentiles of specific subjects were calculated (See Fig. 1). The sensitivity, specificity, positive predictive value, and negative predictive value were determined for the original clinical read and the expert readers. Receiver operating characteristic curves were generated for the methods of classification to compare results from the readers with our results, and an optimal threshold was determined. From that threshold, sensitivity, specificity, positive predictive value, and negative predictive value were calculated for the volumetric analysis.
Results
With the use of quantitative volumetry, a sensitivity of 72%, a specificity of 95%, a positive predictive value of 93%, a negative predictive value of 78%, and an area under the curve of 0.84 were obtained using a percentage difference of normalized hippocampal volume. The resulting specificity (95%) and positive predictive value (93%) are superior to the original clinical read and Reader A and B (74 to 86% and 64-71% respectively). The sensitivity (72%) and negative predictive value (78%) are comparable to Reader A's (73% and 81% respectively) and better than those of the original clinical read and Reader B (45-63% and 70-71% respectively).
Conclusions
Volumetric measurement of the hippocampi outperforms expert readers in specificity and positive predictive value, and it demonstrates comparable to superior sensitivity and negative

predictive value. Volumetric measurements can complement anatomical imaging for the identification of MTS, much like a computer-aided detection tool would. The implementation of this approach in the daily clinical workflow could significantly improve diagnostic accuracy.

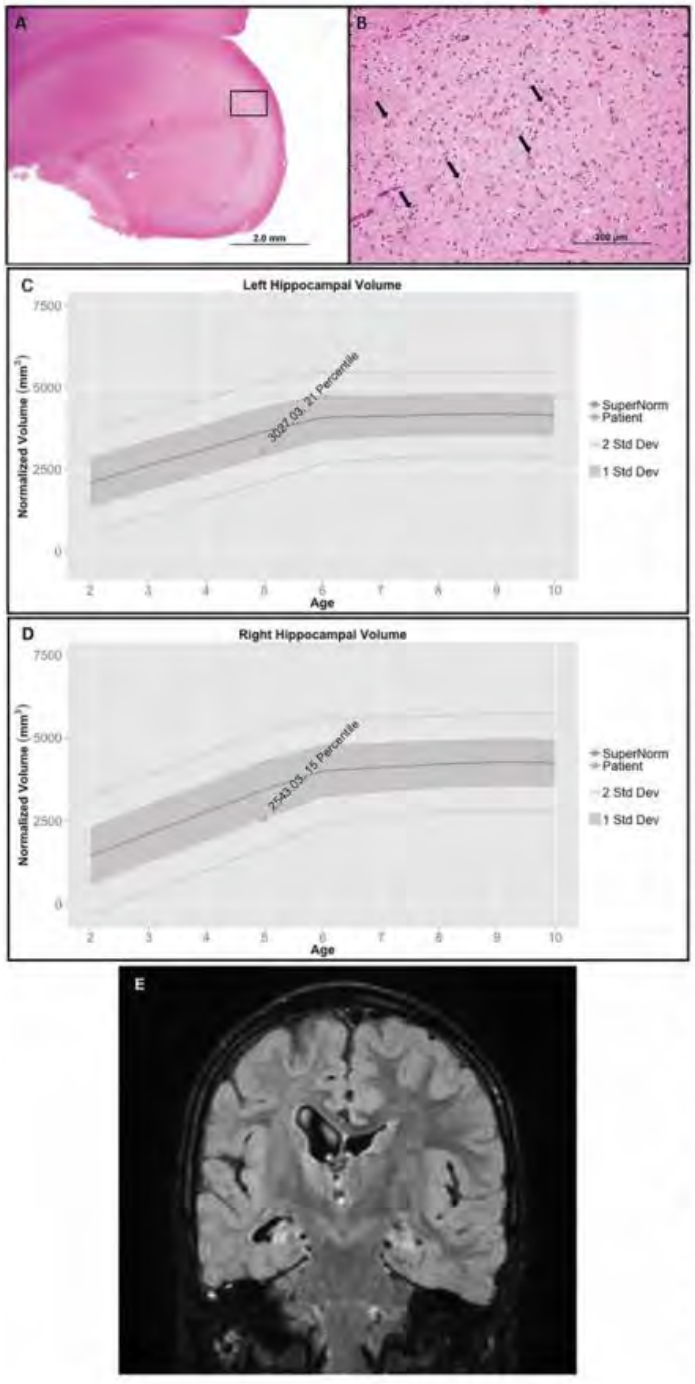


Figure 1: **A,** A low-power photomicrograph of the hippocampus in the region of the dentate gyrus (original magnification, ×20; hematoxylin-eosin [H-E] stain). **B,** A higher-power photomicrograph of the boxed region in A showing the CA1 region, with marked neuronal loss and gliosis; arrows indicate the few remaining neurons (original magnification, ×200; H-E stain). **C,** Corresponding left hippocampal volumetric quantitative graph. **D,** Corresponding right hippocampal volumetric quantitative graph. **E,** Corresponding coronal FLAIR showing right MTS. This patient's original magnetic resonance imaging clinical report and Reader A and B correctly identify the patient's pathology.

(Filename: TCT_O-434_FigureASNRMTSabstract.jpg)

O-435

11:40AM - 11:48AM

The structural connectome of the human brain in children with tuberous sclerosis complex

A Meoded[1], A Poretti[2], T Huisman[3]
[1]Johns Hopkins All Childrens' Hospital, St. Petersburg, FL, [2]The Johns Hopkins University School of Medicine, Baltimore, MD, [3]Johns Hopkins, Baltimore, MD

Purpose
Tuberous sclerosis complex (TSC) is a genetic neurocutaneous disorder with highly variable, unpredictable and potentially devastating neurological outcome. The development of cognitive impairment in TSC is not well understood. The structural connectome may help in elucidating the patho-etiology of cognitive impairment in children with TSC. We aim to determine if structural brain connectivity in children with TSC differs from age-matched controls.
Materials and Methods
Tuberous sclerosis complex patients younger than 18 years with high quality DTI data were included in the study. Age/gender matched controls were selected from our database. TORTOISE tool was used to preprocess DTI data. Subsequently data were aligned to MNI space using q-space diffeomorphic reconstruction implemented in DSI studio. AAL labels were applied for brain parcellation, and the connectivity matrix was calculated by interregional tractography. Network-based statistics (NBS) was used to evaluate differences in sub-network between groups.
Results
Twenty-eight patients and age/gender matched controls (mean age 8.75 years) were included. Structural connectivity was significantly different between patients and controls with decreased connectivity in patients. In children with TSC, we found subnetworks including the right posterior parietal, right thalamus, right superior temporal and middle occipital nodes ($p < 0.05$).
Conclusions
We observed abnormal right thalamo-cortical connectivity in children with TSC. Thalamo-cortical networks play an important role in consciousness and awareness modulation. In addition, it is postulated that cortical tubers may elicit aberrant connectivity of thalamo-cortical connections due to loss of normal cortical targets for thalamic fibers in the tuber during early brain development. These abnormal connections may cause seizures and cognitive dysfunction in children with TSC. A greater understanding of the patho-etiology underlying cognitive impairment in TSC could help in devising targeted and potentially more effective treatment strategies and hence decrease the long term neurological morbidity and health care-related financial burdens.

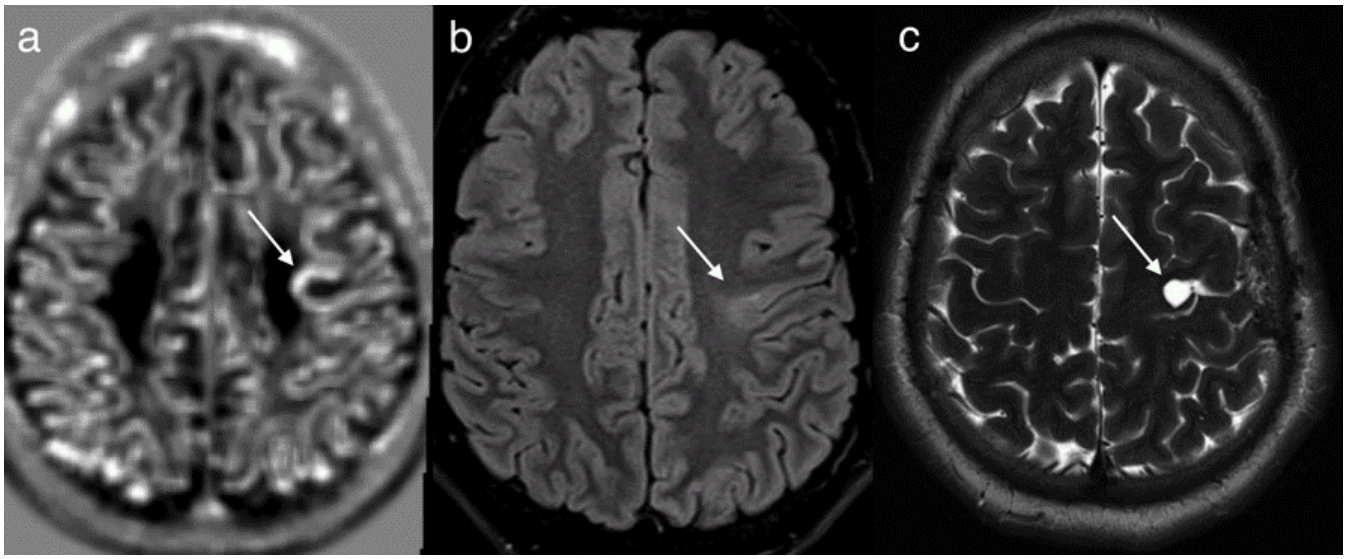
O-436

11:48AM - 11:56AM

Optimized Morphometric Analysis Program (MAP) in pediatric pharmacoresistant epilepsy: preliminary results from a prospective study.

M Rossi Espagnet[1], E Bassanelli[2], A Napolitano[2], L Pasquini[2], L De Palma[3], N Specchio[3], L Figà-Talamanca[2], D Longo[4]
[1]Bambino Gesù Children's Hospital, IRCCS, Rome, Italy, Rome, ROMA, [2]Bambino Gesù Children's Hospital, IRCCS, Rome, Italy, Rome, RM, [3]Bambino Gesù Children's Hospital, Rome, RM, [4]Bambino Gesù Children's Hospital, IRCCS, Rome, Italy, 00165, RM

Purpose
The morphometric analysis program (MAP) is a postprocessing whole-brain technique developed to improve identification of malformations of cortical development such as focal cortical dysplasias (FCD) in MRI-negative patients affected by pharmacoresistant epilepsy (PRE) (1, 2). The purpose of this prospective on-going study is to optimize the MAP technique for the presurgical evaluation of the pediatric brain in children with PRE.
Materials and Methods
In this prospective study a group of 9 patients with pharmacoresistant (PR) epilepsy (age range: 5-15 years) and a control group of 3 patients with treatable epilepsy (age range: 5-6 years) were included. All subjects underwent a MRI brain protocol acquisition (3T scanner, Siemens Skyra, Erlangen) including a volumetric T1-MPRAGE sequence that was used for MAP postprocessing. The MAP method was optimized for the pediatric brain analysis by calculating a specific template from 26 healthy controls (age range: 5-13 years) and applying a N4ITK correction (3). In order to avoid false positive cases, MAP junction images were considered + if the identified area with a z-score >4 overlapped with a signal alteration on MRI, and – if the area was not associated to MRI findings.
Results
Six of 9 patients from the PR epilepsy group were considered MAP + and the location of the imaging alteration correlated with EEG, PET or Stereo-EEG data. Surgical resection of the epileptic focus was performed in 3 of these patients and pathology confirmed the presence of a FCD (type 2a and b). Three of 9 patients from the PR epilepsy group were considered MAP –. None of these patients underwent to surgery, so far. All 3 patients with treatable epilepsy were considered MAP –.
Conclusions
From these preliminary results, optimized MAP postprocessing is a useful tool in the presurgical evaluation of pharmaco-resistant epilepsy in children. Further data are necessary to further optimize the template and validate these results.



(Filename: TCT_O-436_FigASNR.gif)

O-437

11:56AM - 12:04PM

Non-Homotopic Callosal Fibers: Depiction by DTI and Preliminary Gene Testing

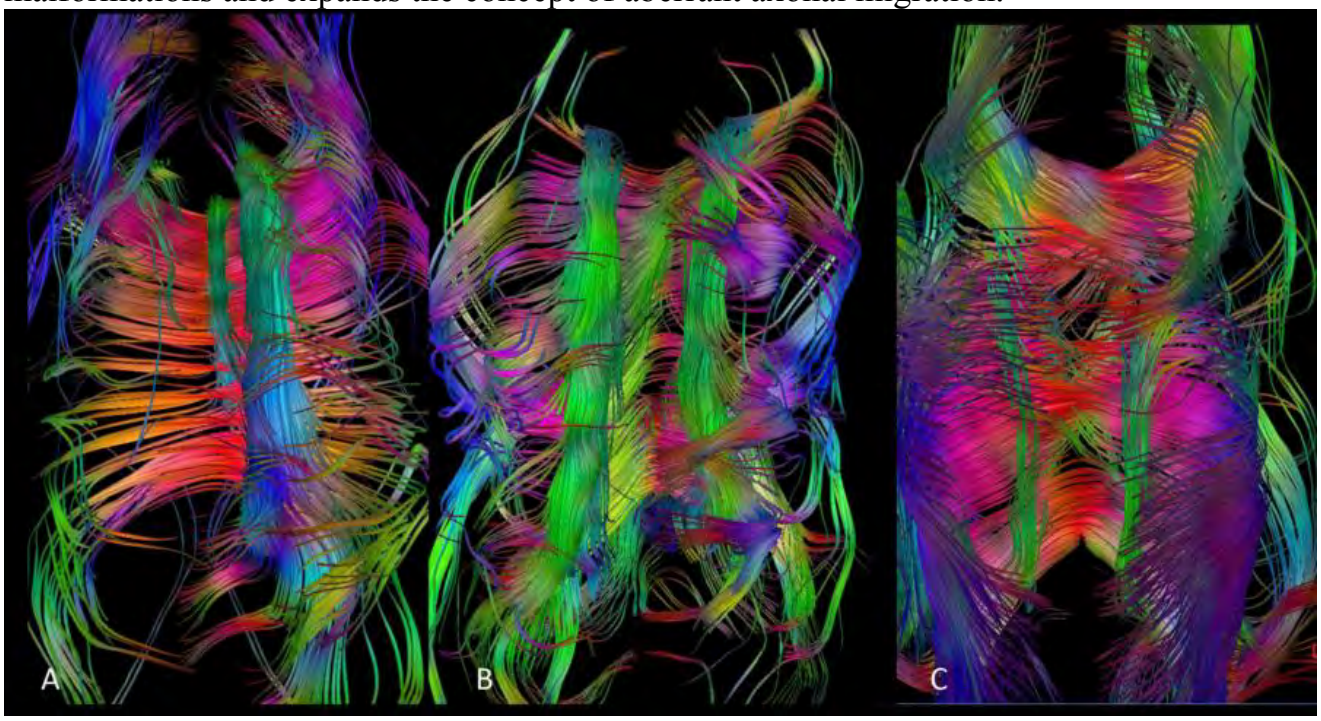
N Rollins[1], T Booth[2]
[1]UT Southwestern Medical Center, Children's Health Dallas, Dallas, TX, [2]Children's Health System Texas, UTSW, Dallas, TX

Purpose
The normal corpus callosum is composed of transversely oriented fibers the axons of which the contralateral hemisphere. We report nonhomotopic commissural fibers; e.g. fibers connecting disparate portions of 2 hemispheres seen by DTI and report associated brain anomalies and results of genetic testing.
Materials and Methods
We identified subjects in who DTI showed obliquely oriented intracallosal and/or longitudinal supracallosal fibers. Conventional MR images and DTI were evaluated by 2 experienced pediatric neuroradiologists who reached consensus. Medical records were reviewed for clinical indications for MR imaging and genetic testing. This study was IRB-approved and HIPAA compliant.
Results
There were 24 patients identified over 12 years; 14 males, 10 females, ages newborn-16 years. Clinical indications for MR imaging were seizures in 18/24 and development delay/static encephalopathy in 14 of the 20 patients old enough to assess developmental milestones. Nonhomotopic callosal fibers included longitudinal supracallosal fibers in 14 patients and diffusely nonhomotopic callosal fibers in 10. Callosal dysmorphology included variable AP shortening with splenial hypoplasia and focal rostral body thickening.

Associated malformations of cortical development were polymicrogyria in 5, posterior predominant LIS1 and diffusely simplified gyral pattern in 2 patients each, and hemimegencephaly in 1. Five patients had dysplastic basal ganglia; 4 had abnormalities on the inner limbic arches and 1 had unilateral absence of the cingulum. Mutations included partial 2p trisomy, del17p13.3, CNL EHMT1 gene, monoalleic TUBB3, and autosomal dominant missense variants of NMDA receptor and SNARE.

Conclusions

Diffusion tensor imaging (DTI) shows heterogeneity of callosal fibers in diverse brain malformations and expands the concept of aberrant axonal migration.



(Filename: TCT_O-437_ASNR2017.jpg)

O-438

12:04PM - 12:12PM

MR PERFUSION IN PEDIATRIC PRES

M Gencturk[1], A McKinney[1], S Khanipour Roshan[1], J Rykken[1]
[1]*University of Minnesota, Minneapolis, MN*

Purpose

Gadolinium-based contrast enhancement of parenchyma or meninges has been described in a higher percentage of pediatric (>50%) than adult patients (~30-40%) with posterior reversible encephalopathy syndrome (PRES) (1). While prior MR perfusion (MRP) studies in PRES have focused on adults, MRP has been applied rarely in children with PRES. Our

hypothesis was that the high rate of enhancement relates to blood-brain barrier (BBB) dysfunction in children, with perhaps greater vascular permeability.

Materials and Methods

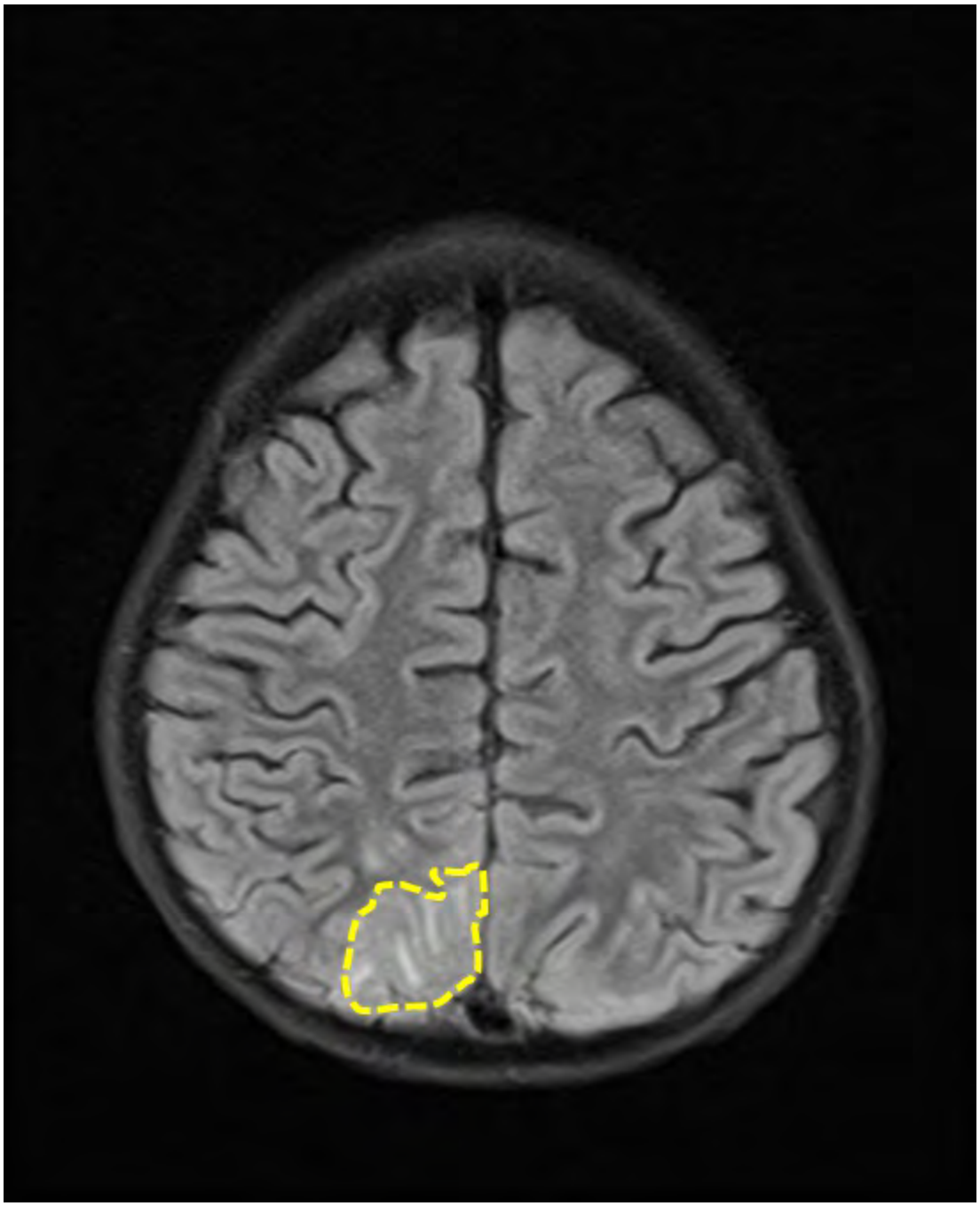
Five children with PRES and MRP imaging were evaluated retrospectively. Magnetic resonance perfusion parameter measurements were obtained in both affected posterior frontal-parietal cortical/subcortical regions in these 5 patients and in similar regions in 6 age-matched controls: relative CBV (rCBV), relative CBF (rCBF), MTT, TTP, relative peak height (rPH), and vascular permeability (K2, aka "dynamic leakage"). These were normalized to values obtained in nonaffected anterior frontal white matter.

Results

Comparing values from affected posterior cerebral regions in PRES patients with values obtained from the controls, the only statistically significant difference was between mean rPH (mean= 2.23 in PRES patients vs. 1.18 in controls, $p=0.030$). There was no statistically significant difference (each $p>0.05$) in mean rCBV (mean 3.28 in PRES vs. 1.76 in controls), rCBF (mean 2.1 in PRES vs. 1.91 in controls), MTT (mean 31.9 in PRES vs. 31.3 in controls), TTP (mean 31.9 in PRES vs. 31.0 in controls), or K2 (mean 0.0049 in PRES vs. 0.0024 in controls).

Conclusions

As pediatric PRES patients have a high rate of contrast enhancement, an elevated rPH may reflect a lack of BBB integrity. However, K2 ("dynamic leakage"), was higher in patients compared to controls, but this difference was not found to be statistically significant. Thus, these preliminary results suggest that children may have an immature BBB in response to PRES, which deserves evaluation by a larger study.



(Filename: TCT_O-438_Picture2.jpg)

Thursday
11:00AM - 12:15PM
Long Beach Convention Center, Room 104B (Main Lobby)

24E-Parallel Paper Session: Glial Tumors – A Deep Dive

O-439

11:00AM - 11:08AM

Differences in Patterns of Recurrence Between Patients with Mutant and Wild-type Isocitrate Dehydrogenase-1 Glioblastoma Multiforme

A Helmi[1], S Symons[2], P Maralani[2]
[1]*University of Toronto, Toronto, Ontario,* [2]*Sunnybrook Health Sciences Centre, Toronto, Ontario*

Purpose
With advances in personalized medicine, determination of mutation in isocitrate dehydrogenase-1 (IDH1) has become part of routine clinical care for glioblastoma. Patients with wtIDH1 exhibit more aggressive tumor behavior and poorer prognoses. The purpose of this study is to investigate whether there is a significant difference between the volume of tumor recurrence outside of high-dose radiation treatment area in patients with wtIDH1 GBM compared to those with the mutant form.
Materials and Methods
Inclusion criteria: 1. Adults (>18 year old) who had radiation for gliobastoma at Sunnybrook hospital in the last 4 years. Exclusion criteria: 1. Prior brain surgery or radiation 2. Other brain tumors. A 4-year retrospective search was performed to extract cases of GBM. For each case the radiation planning MRI and the MRI for recurrence were identified. The gross tumor volume (GTV), clinical target volume (CTV) and planning target volume (PTV) were acquired from radiation oncology. The percentage volume of recurrent tumor within and outside the GTV, CTV and PTV were calculated and compared using a two-tailed t-test.
Results
Preliminary data collected up to this point includes 2 cases and 3 controls. The average percent volume recurrence outside GTV was 62% lower in the mutant IDH-1 group than the wild-type group (81.5% vs. 19.8%, two-tailed t-test p-value = 0.0114). Outside-CTV and PTV comparisons exhibit the same trend, and are expected to show a statistically significant difference with additional data collection.
Conclusions
Preliminary results support the hypothesis that poorer clinical outcomes in patients with wt-IDH1 is at least in part, attributable to more infiltrative and invasive tumor behavior, allowing for a larger proportion of the tumor to go undetected on imaging and be left untreated by radiation oncology. This finding can have profound implications for the way radiation oncologists prescribe their treatment plans for wtIDH-1 GBM cases.

O-440

11:08AM - 11:16AM

Correlation between IDH mutation status, patient survival, and blood volume estimates in diffuse gliomas: a TCGA/TCIA project

I Littig[1], L Poisson[2], S Patel[3], L Nunes[4], A Chi[5], R Jain[5]
[1]New York University, New York, NY, [2]Henry Ford Health System, Detroit, MI, [3]University of Virginia Health System, Charlottesville, VA, [4]NYUMC, New York, NY, [5]NYU School of Medicine, New York, NY

Purpose

Prior studies have shown correlation between relative cerebral blood volume (rCBV) and patient survival as well as with tumor genomics(1-4). The purpose of this study was to determine whether rCBV values correlate with isocitrate dehydrogenase (IDH) mutation status and patient overall survival in diffuse gliomas.

Materials and Methods

Ninety-six treatment naive gliomas (62 patients from TCGA/TCIA dataset and 34 patients from our institute) with DSC T2* perfusion data were included (WHO grades II to IV). IDH mutation status (IDHmut-codel, IDHmut-non-codel, and IDHwt) and survival data were assayed by the TCGA, and presurgical imaging collected by the TCIA (The Cancer Imaging Archive). Relative cerebral blood volume was obtained from 4 regions of interests within the highest perfusion areas including enhancing and nonenhancing segments of each tumor, utilizing Olea Sphere software (Olea Medical, LaCiotat). Mean differences in rCBV are compared by ANOVA and t-test. Associations with overall survival, defined as the time from diagnosis to death or last follow-up, are estimated by Cox regression models and Kaplan-Meier methods.

Results

IDHwt gliomas (n=40) demonstrated higher rCBV (rCBV=6.36+3.05) values than IDHmut gliomas (n=46) (rCBV=2.07+1.83; t-test $p<0.0001$). A cox proportional hazards model of overall survival using rCBV alone shows that increasing rCBV is associated with increased risk of death (HR 1.15, $p<0.001$). Further, investigation suggests that the association displays a threshold. Gliomas with rCBV <2.0 showed better survival (n=14, median 117.3 months) than gliomas with rCBV >2.0 (n=48, median 15.4 months; log-rank $p<0.0001$). The estimated survival curves by IDHmut status are shown in Fig. 1. Among the IDH mutated tumors, the group with rCBV values >2.0 (n=8) showed poorer survival (36.5% surviving at 3 years) than IDHmut gliomas (n=11) with lower rCBV (87.5% surviving at 3 years; log-rank $p=0.0299$).

Conclusions

IDHwt gliomas have higher rCBV than IDHmut gliomas irrespective of the glioma grade. Higher BV measurements are associated with poor survival and especially also help IDHmut gliomas as IDHmut gliomas with rCBV higher than 2.0 also showed poor survival.

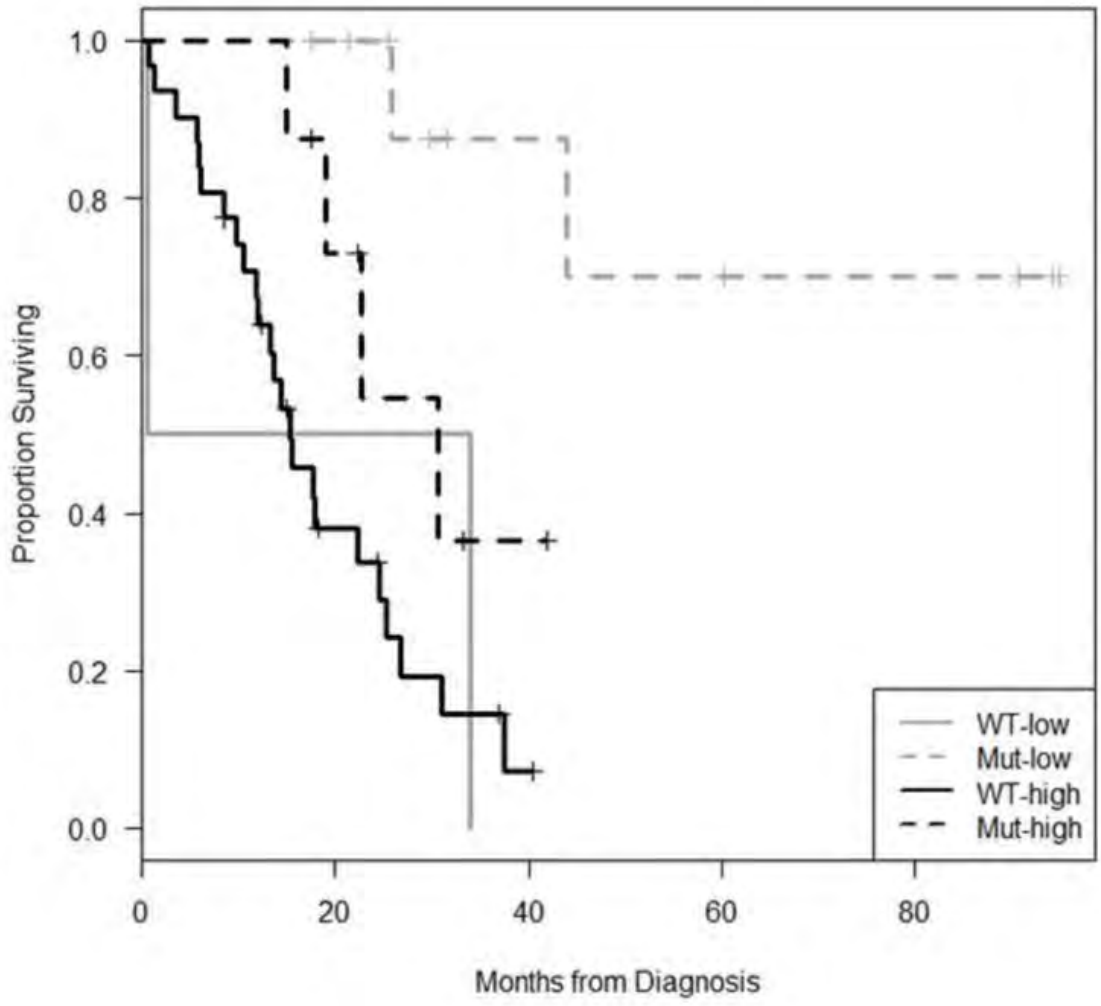


Figure 1. Kaplan-Meier estimates of overall survival for glioma, by IDH-mutation (Mut vs WT) and level of rCBV (<2, low; >2, high).

(Filename: TCT_O-440_ingrid300dpi.jpg)

O-441

11:16AM - 11:24AM

Gliosarcoma in the IDH Era.

M Peckham[1], C Palmer[1], K Salzman[2], A Osborn[1]
[1]University of Utah, Salt Lake City, UT, [2]University Of Utah, Salt Lake City, UT

Purpose

Treatment of high grade gliomas has changed as IDH status, obtained through immunostaining, has been used to predict tumor aggressiveness and changed the way these tumors are classified. While the IDH profile of glioblastoma (GBM) and other high grade glial tumors has been well established, the IDH profile gliosarcoma has not been fully elucidated. Current understanding of gliosarcoma is an intracranial lesion which often abuts a dural surface and is composed of glial and mesenchymal elements. These lesions can be primary or radiation-induced. While some gliosarcomas have indistinguishable imaging characteristics from glioblastoma, aggressive lesions can erode through the dura and skull and involve the extra-cranial soft tissues, features not seen in GBM. We present the largest known radiologic case series with immunohistochemical and histologic correlation.

Materials and Methods

Twenty-eight pathology proven gliosarcoma cases with MRI and IDH status were collected from our tertiary care center spanning the last 16 years. Twenty-two of these cases were de novo, and 6 were radiation-induced. Magnetic resonance imaging (MRI) characteristics were evaluated. When available, EGFR amplification, and MGMT methylation were recorded.

Results

All lesions contacted a dural or pial surface. One case initially showed a small lesion deep to the cortex without dural contact. The patient was lost to follow up for 12 years, but after presenting with headache, had imaging showing marked growth of the tumor which now contacted the dura (Fig. 1). All cases were negative for an IDH R132 mutation, including postradiation gliosarcoma which arose from a grade 2 diffuse fibrillary astrocytoma – a lesion usually found to be IDH-mutated. Seventeen of 17 cases showed nonamplification of EGFR/CEP7. MGMT methylation was present in 2/16. Imaging features included areas of nodular thickening in necrotic lesions which appeared to abut the site of pial or dural contact.

Conclusions

We present imaging of the largest reported collection of gliosarcoma cases with both molecular and histologic correlation.

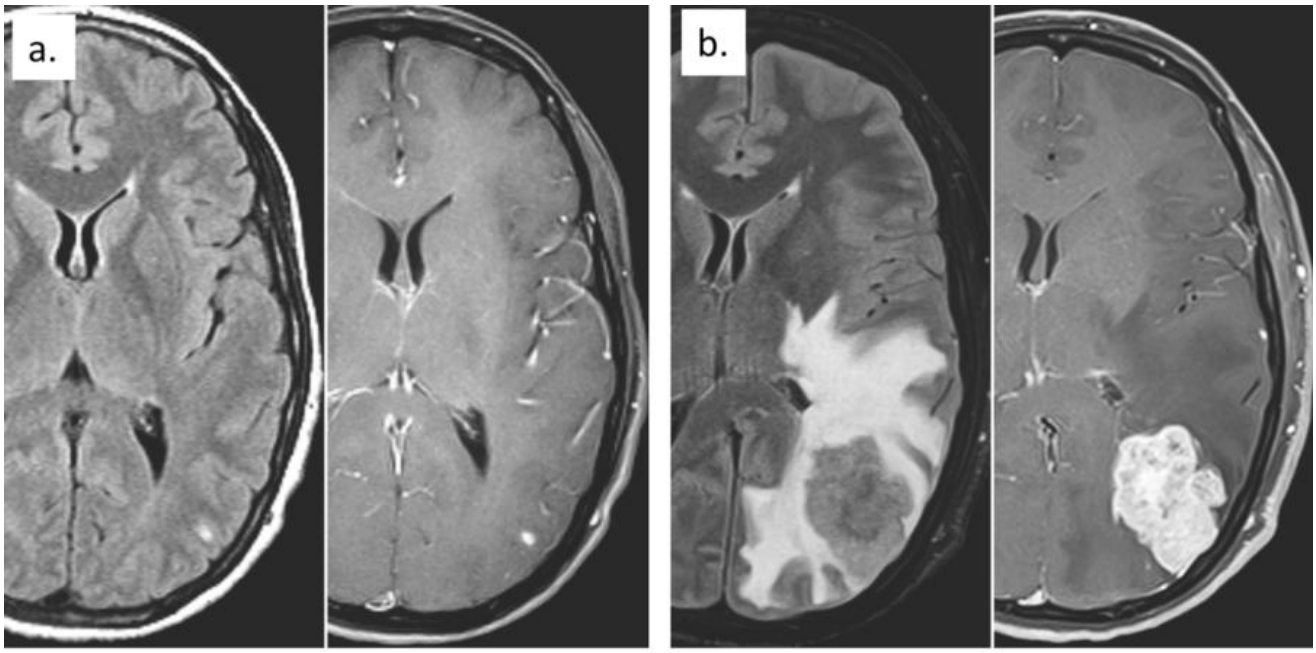


Figure 1: Composite FLAIR (left) and T1 post-contrast (right) images demonstrate a small subcortical enhancing lesion in the left parietal lobe (a) which subsequently grew in size and was found to contact the dura in a scan obtained 12 years later (b). This lesion was histologically confirmed to be gliosarcoma.

(Filename: TCT_O-441_GliosarcFigure12-5ccopy.jpg)

O-442

11:24AM - 11:32AM

Comparing Areas of Contrast Enhancement Between Wildtype Versus IDH-Mutated Glioblastoma

S Bergamaschi[1], M Law[1], J Acharya[1], W Gibbs[1], A Rajamohan[1], P Kim[1], G Zada[1], T Chen[1], J Go[1]

[1]*University of Southern California, Keck School of Medicine, Los Angeles, CA*

Purpose

The new 2016 WHO classification of brain tumors describes vastly different biology and outcomes for patients with glioblastoma (GBM) depending on whether these are primary GBMs (IDH wild type) versus secondary GBMs (IDH mutant). There is now considerable interest to determine if there are imaging differences which may help differentiate these 2 entities prior to surgery and tissue diagnosis.

Materials and Methods

We selected patients with pathologically proven GBM that had their molecular diagnosis (IDH mutant status) available. We used a commercially available software Synapse 3D to measure the volume of contrast enhancement, including the central areas of necrosis, and

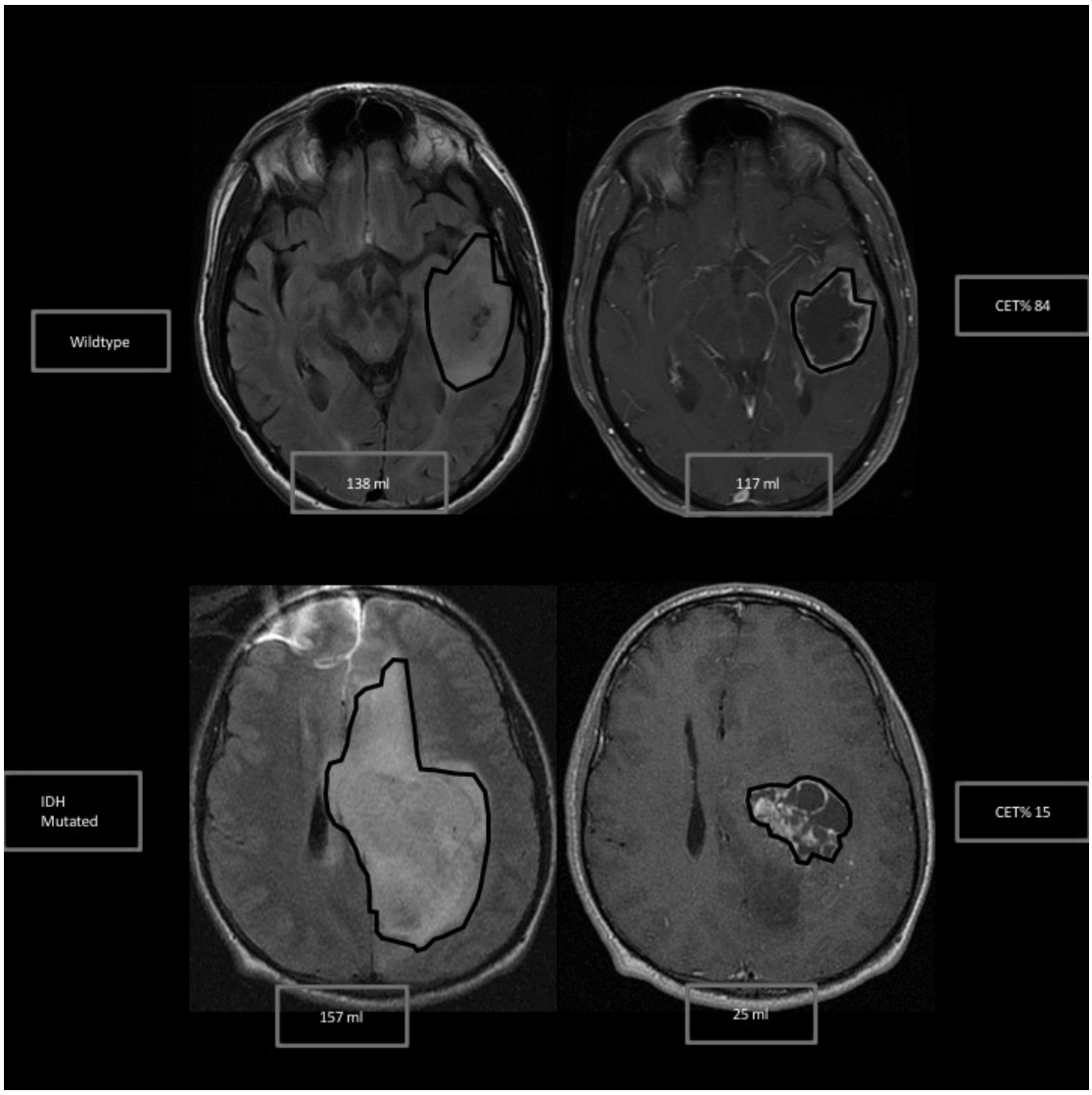
also measured the volume of signal abnormality on FLAIR. We then defined the percentage of T1 contrast enhancement compared to the FLAIR area, as contrast enhancing tumor fraction (CET%).

Results

Our study included 28 patients with wild-type GBM and 5 patients with IDH-mutated GBM. Patients with wild-type GBM showed a significantly higher percentage area of contrast enhancement (mean CET% of 48%), compared to the IDH mutated GBM (mean CET% of 9.8%). Patients with GBM wild-type also showed significantly higher Ki 67% compared to IDH mutated GBM (men 24% versus 8.2%) but the Pearson correlation between Ki67 and CET% was only weakly positive 0.37.

Conclusions

Our study demonstrates that there are conventional imaging differences in terms of the area of contrast enhancement to FLAIR signal (CET%) in IDH mutant vs IDH wild-type GBMs. This may allow us to presurgically predict the molecular signature of GBMs, thereby giving the neurosurgeon information to plan the size, location of the craniotomy, extent of safe resection and then the extent of radiation portal postsurgery for the radiation oncologist.



(Filename: TCT_O-442_ComparisonofthecontrastenhancingareaofGBM.jpg)

O-443

11:32AM - 11:40AM

MR Imaging Characterization of Multicentric Glioblastoma Multiforme and Correlation with Genetic Markers

Y Chen[1], T Tihan[1], S Cha[1]
[1]*University of California, San Francisco, San Francisco, CA*

Purpose
To characterize the MR imaging phenotypes and molecular genotypes of multicentric glioblastoma multiforme (MCGBM).
Materials and Methods
Institutional ethics approval was obtained for the study. MR imaging data of 168 consecutive

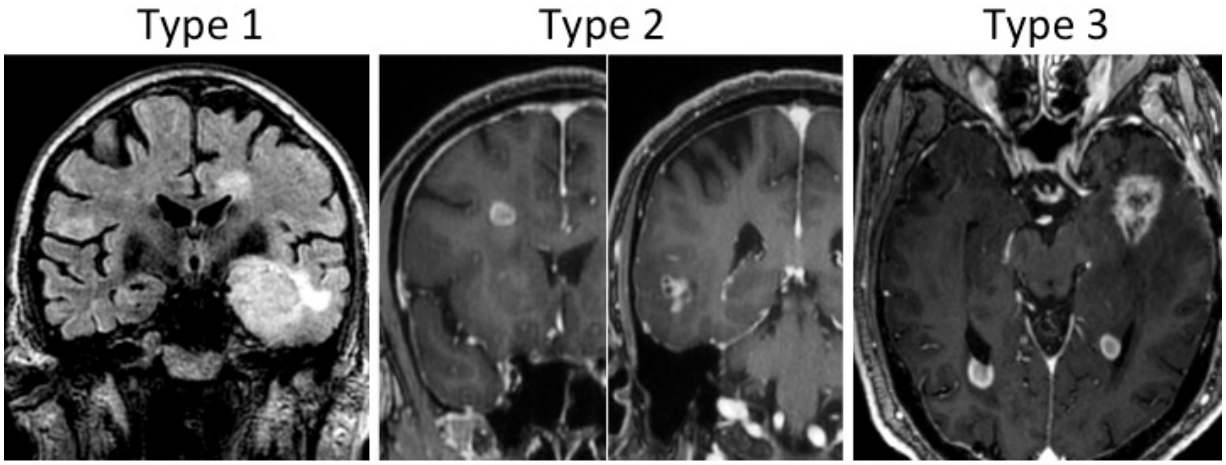
patients with pathology-proven GBM between June 2014 and September 2016 were reviewed. Molecular genetics and epigenetics data including IDH-1, MGMT promoter methylation, PTEN, and EGFR were collected. Multicentricity was defined as multiple discrete areas of enhancing or nonenhancing tumor without connecting T2/FLAIR signal abnormality. Molecular genotypes of multicentric glioblastoma multiforme were divided into 3 distinct imaging patterns based on author consensus: type 1 - single dominant lesion with small enhancing or nonenhancing parenchymal lesions (58.8%); type 2 - multiple codominant enhancing lesions (22.1%); and type 3 - single dominant lesion with small enhancing or nonenhancing ependymal lesions (19.1%). The dominant lesion was defined as the largest enhancing lesion by size. Chi-squared and ANOVA tests were used to determine statistically significant differences among the imaging subtypes.

Results

Sixty-eight out of 168 (40.4%) consecutively reviewed GBM patients had MCGBM (age 61.2 +/- 11.6 years), with 50 patients (29.8%) diagnosed with multicentricity at presentation. 37.3% had a single nondominant multicentric lesion, 40.2% had 2 lesions, and 22.4% had 3 or more lesions (average 2.1 lesions/patient). Based on the MCGBM imaging subtype groupings outlined above, no significant differences were found in the age and sex distributions among type 1-3 MCGBMs. All type 2 MCGBMs were diagnosed at presentation, compared to 68.8% of type 1 and 31.3% of type 3 MCGBMs ($p=0.037$). The location of the dominant lesion differs significantly among types 1-3 MCGBMs ($p=0.016$), with most occurring in the frontal lobe in type 1 MCGBMs (40%), but the temporal lobe in type 2 (60%) and type 3 (69.2%) MCGBMs. The nondominant lesions in type 2 MCGBM are more likely to occur in the same hemisphere as the dominant lesion ($p=0.003$), whereas type 3 MCGBMs are more likely to present with bilateral multicentric lesions than type 1 and 2 ($p=0.026$). Nondominant multicentric lesions in type 1 MCGBM are located most commonly in the gyral cortex (30.5%), white matter tracts (22%), corpus callosum (11.9%), limbic structures (11.9%), thalamus (8.5%), and brachium pontis (6.8%). IDH-1, PTEN, EGFR and methylation status were not found to predict for multicentric subtype.

Conclusions

We found a high incidence of MCGBM in our population. Categorization of MCGBM into 3 distinct imaging subtypes demonstrated significant intergroup differences in imaging patterns at presentation, location of dominant lesion, and laterality of multicentric lesions.



(Filename: TCT_O-443_ASNRMCGBMfigure.jpg)

O-444

11:40AM - 11:48AM

Non-Invasive, Contrast-Exempt Perfusion Assessment of High-Grade Gliomas

J Andre[1], S McKown[1], S Rane[1]
[1]*University of Washington, Seattle, WA*

Purpose

Assessment of cerebral and tumor perfusion often is advocated for initial prognostication, and evaluation for possible progression, of primary brain tumors, historically accomplished via intravenous injection of a gadolinium-based contrast agent (GBCA). The potential for intracranial and corporeal deposition of GBCA (1) invites the development and optimization of noninvasive, contrast-exempt (NICE) methods to assess cerebral perfusion. Inflow-vascular space occupancy (iVASO) is a GBCA-free method to evaluate cerebral blood volume (CBV) (2), generating CBV values that correlate well with dynamic susceptibility contrast (DSC) perfusion measures in neuronal disorders, and with reproducibility similar to that of arterial spin labeling (ASL) (2-4). While ASL and iVASO have been used separately for GBM evaluation in previous studies (5), our goal was to perform preliminary validation of a NICE protocol for concomitant CBF and CBV parametric map generation in patients with treated GBM using combined ASL and iVASO and compare it with gadolinium-based tumor evaluation.

Materials and Methods

Initial work: We performed multi-slice iVASO using a 3D-GRASE readout in 10 healthy young adults and measured cortical arterial CBV to be 0.7±0.2 ml/100g. Note that iVASO measures precapillary vascular components in healthy tissue and hence is lower than the total CBV, often measured with gadolinium-based CBV measurements. Experiment: Enlisted HGG patients underwent sequential multi-slice iVASO (3D GRASE) acquisition, pseudocontinuous ASL (pCASL), and 3D T1 (pre and post GBCA injection) acquisition

using a 12-channel SENSE head-coil on a Philips 3T Achieva scanner. The pCASL parameters were: matrix = 96x96x20, spatial resolution = 3x3x5 mm3, flip angle = 90°, TE=19 ms, TR=5000 ms, label duration = 1800 ms, post-labeling delay = 2000ms, 30 control/null pairs and a M0 image with TR = 10000 ms, SENSE factor =2.5. iVASO acquisitions were performed at TR of 5000 ms and TI of 1190 ms to capture the steady-state blood water signal nulled in null acquisitions even in the slow perfusion regions of the tumor, matrix = 96x96x12, spatial resolution = 3x3x5 mm3, flip angle = 90°, TE = 19 ms, 30 control/null pairs and a M0 image without iVASO preparation at TR = 10000 ms, R = 2.5. The multi-slice 3D GRASE imaging parameters were identical except TE = 22 ms and k-Space profile = low-high, turbo direction = Z, readout = 300 ms, SENSE factor = 2.5 (RL) and 2 (AP). Analysis: Both, iVASO and pCASL images were motion-corrected and registered to the respective M0 image. aCBV was calculated as outlined in previous studies (2, 3). Cerebral blood flow was calculated based on the International Society for Magnetic Resonance in Medicine (ISMRM) recommendations for quantification of pCASL data. Postcontrast T1 images were compared with CBF and aCBV maps to determine perfusion characteristics of HGG, i.e., degree of perfusion and blood volume as a measure of angiogenesis.

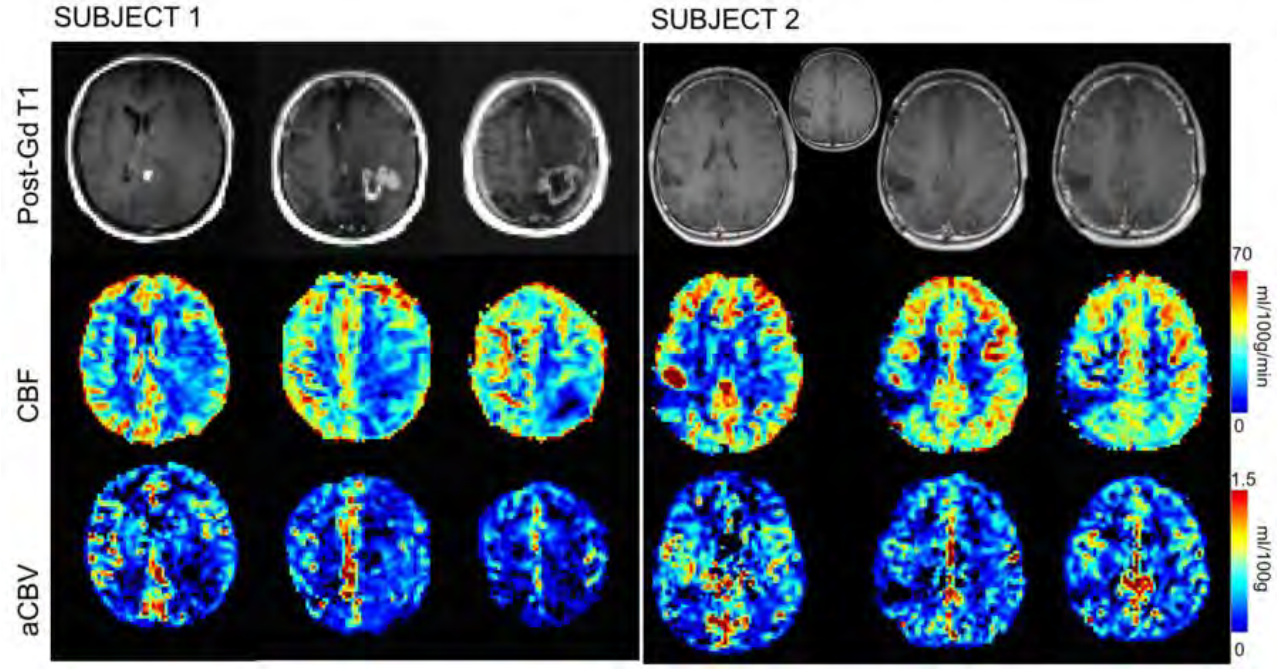
Results

Ten HGG subjects (mean age = 41±11.8 years; 3F/7M) with varying degrees of therapy provided informed consent in this prospective, preliminary pilot study. Subject 1 (left column in the attached figure, below) is a 35-year-old female with a large, peripherally enhancing biopsy-proven glioblastoma (unmethylated MGMT promoter) with central necrosis located in the right parietal lobe. Corresponding parametric NICE images demonstrate no compelling increase in CBF or CBV, suggesting a diagnosis of pseudoprogression rather than true progression, and commensurate with treatment effects from recent temozolomide chemoradiation. Subject 2 (right column in the attached figure, below) is a 24-year-old male with a path-proven anaplastic astrocytoma, status postresection and chemoradiation, currently undergoing cycle #10 of adjuvant temozolomide. No compelling enhancement is present about the resection cavity (small insert figure: corresponding pre-GBCA T1-weighted image for comparison). Unsuspected mass-like area of increased CBF is present anterior to the right frontoparietal resection cavity with less conspicuous, but elevated aCBV; findings concerning for recurrent tumor despite lack of convincing enhancement. The remaining 8 cases status postchemoradiation and surgery demonstrated expected minimal curvilinear enhancement about a resection cavity without significant compelling increased regional CBF and/or CBV to suggest tumor recurrence/progression. expected peritumoral and intratumoral results.

Conclusions

Implementation of a NICE CBF/CBV protocol, allowing for contrast-free evaluation of tumor and cerebral perfusion, is feasible in a clinical population of treated HGG patients and may aid in modulating therapy in this population. Future studies will compare the proposed NICE CBF/CBV protocol with the currently accepted GBCA-dependent methods of

dynamic susceptibility contrast (DSC) perfusion-weighted imaging in a treated HGG patient population.



(Filename: TCT_O-444_GBM_ASNR_Fig1_v2.jpg)

O-445

11:48AM - 11:56AM

Comparison of MR Imaging Phenotype and Molecular Genotype between Solitary and Multicentric Glioblastoma Multiforme

Y Chen[1], T Tihan[1], S Cha[1]
[1]*University of California, San Francisco, San Francisco, CA*

Purpose
To investigate the imaging phenotype and molecular genotype of multicentric vs. solitary glioblastoma multiforme (MCGBM vs. SGBM).
Materials and Methods
Institutional ethics approval was obtained for the study. Clinical and MR imaging data of 50 consecutive patients with MCGBM (age 62.1+/-12.2 years) and 68 consecutive patients with SGBM (age 58.6+/-14.4 years) at diagnosis between June 2014 and September 2016 were reviewed. Multicentricity was defined as multiple discrete areas of enhancing or nonenhancing tumour without connecting T2/FLAIR signal abnormality. Molecular genetics and epigenetics data including IDH-1, MGMT promoter methylation, PTEN, and EGFR were collected. Chi-squared test and student t-test were used to determine statistically significant differences between MCGBM and SGBM.

Results

No significant difference was found between MCGBM and SGBM in age of diagnosis and sex. The most common sites of occurrence of the dominant enhancing lesion (defined by size) in both SGBM and MCGBM are 1) the temporal lobe, 2) frontal lobe and 3) midline. There were more midline gliomas in the SGBM group (16.2% vs. 6%), however not statistically significant (p=0.09). In patients whose genetics data were available, we found no IDH-1 mutant tumors in the MCGBM cohort (0/50). The status of EGFR amplification, PTEN locus loss, p53 mutation, and MGMT promoter methylation were not significantly different between MCGBM and SGBM (Table).

Conclusions

IDH-1 mutant GBM presented only as SGBM in our cohort. Commonly tested genetic and epigenetic markers including p53, EFGR, PTEN and MGMT methylation status were not found to predict for multicentricity. Identification of other markers, including those related to neural stem cell dedifferentiation and migration, is needed to further understand the molecular differences between MCGBM and SGBM.

	Solitary GBM		Multicentric GBM		p-value
IDH-1					
Wildtype	63	94.0%	47	100.0%	
Mutant	4	6.0%	0	0.0%	0.97
MGMT Promoter					
Methylated	29	48.3%	20	52.6%	
Unmethylated	31	51.7%	18	47.4%	0.45
p53 mutation					
Positive	17	27.0%	8	18.2%	
Negative	38	60.3%	27	61.4%	
Equivocal	8	12.7%	9	20.5%	0.75
EGFR					
Amplified	26	41.3%	21	45.7%	
Not Amplified	37	58.7%	25	54.3%	0.62
PTEN					
Retained	18	29.5%	11	25.6%	
Loss	43	29.5%	32	25.6%	0.19

(Filename: TCT_O-445_ASNRGeneticsFigure.jpg)

O-446

11:56AM - 12:04PM

Radiogenomic Analysis of TERT Promoter Mutation Status and Blood-Brain-Barrier Permeability in Patients with Glioblastoma.

J Ivanidze[1], I Kovanlikaya[2], R Magge[3], R Ramakrishna[3], D Pisapia[3], H Fine[3], G Chiang[4]
[1]New York Pres. Hos. Cornell, New York, NY, [2]New York-Presbyterian Hospital, New York, NY, [3]NewYork-Presbyterian Hospital - Weill Cornell, New York, NY, [4]Weill Cornell Medical College, New York, NY

Purpose
Mutations in telomerase reverse transcriptase (TERT) are associated with worse prognosis in glioblastoma (GBM). Since TERT has been shown to regulate matrix metalloproteinase-9 (MMP9) expression, which regulates blood-brain barrier (BBB) permeability, we hypothesize that TERT-mutated GBM would show different permeability characteristics. As a result, BBB permeability metrics derived from dynamic contrast-enhanced (DCE) MR perfusion may serve as a correlate for TERT mutation status in vivo.
Materials and Methods
This IRB-approved retrospective pilot study included 17 patients with IDH1/2-negative GBM. Telomerase reverse transcriptase mutations were identified using the Foundation panel. Six patients were found to be TERT negative, and 11 patients were found to be TERT positive. All patients underwent a standard MR brain tumor imaging protocol, which included DCE-MR perfusion. Histogram analysis was performed on volumes-of-interest that included the entire enhancing tumor volume. Differences in plasma volume (Vp), the volume transfer constant (Ktrans), and the washout rate of contrast (Kep, inversely correlated with BBB permeability) were assessed using Mann-Whitney-U tests.
Results
The median Kep was significantly lower in the TERT-mutation-positive subgroup compared to the TERT-negative mutation subgroup (p-value: 0.048). There was a nonsignificant trend for a lower Kep at the 5th percentile in the TERT-positive subgroup (p-value: 0.18). There was no significant difference in Vp or Ktrans between the 2 subgroups.
Conclusions
Our pilot study demonstrated some evidence of altered permeability metrics associated with TERT mutations in GBM, particularly in the washout phase. Our findings highlight the need for further work evaluating TERT mutation status and the pathophysiology of BBB disruption in patients with GBM, as well as lower grade gliomas, opening up the possibility for targeted monitoring and therapy in the future.

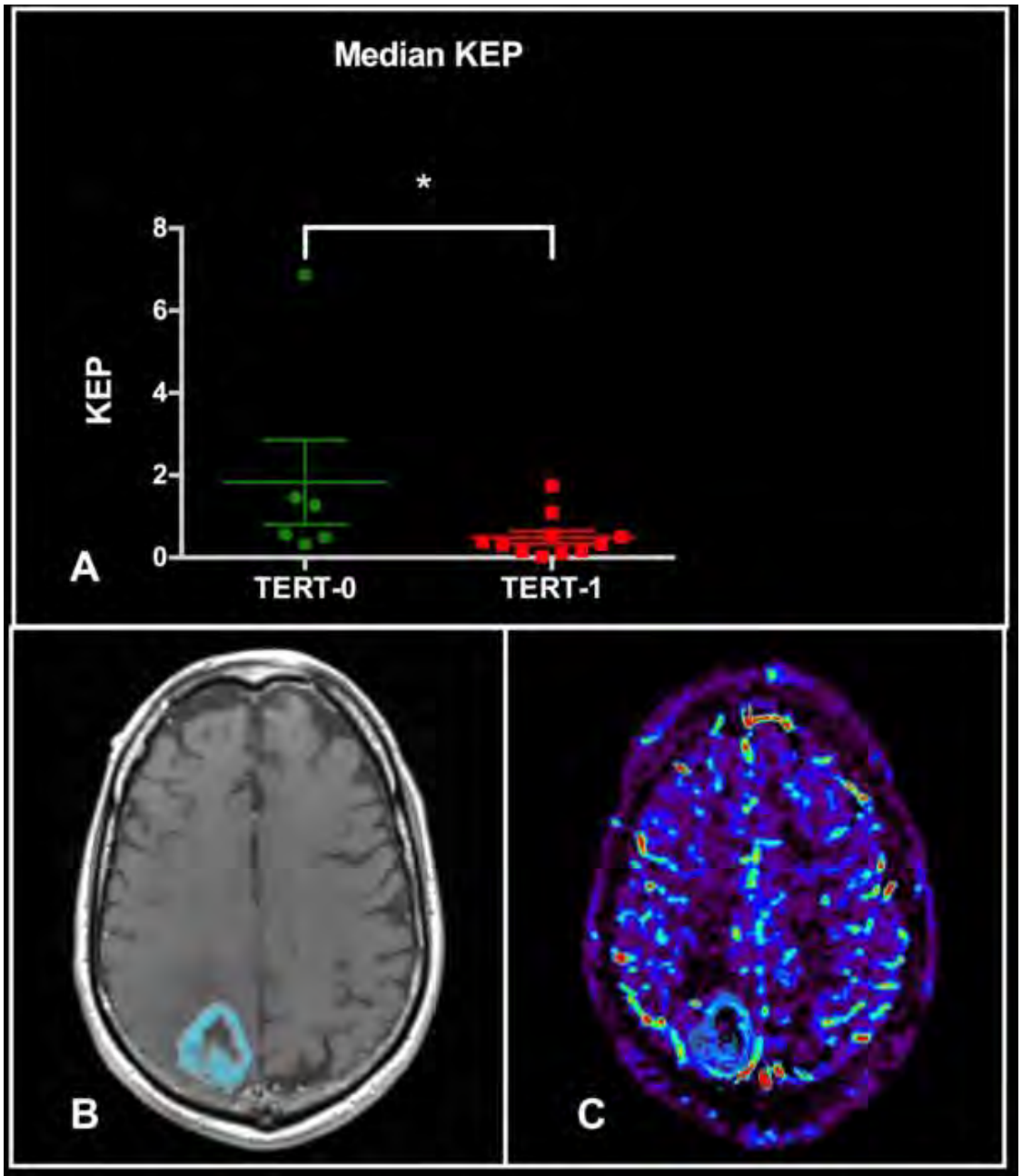


Figure 1A. Box-and-whiskers plots demonstrating the difference in median Kep values between the TERT-mutation-negative ("TERT-0") and TERT-mutation-positive ("TERT-1") subgroups. Mann-Whitney-U tests demonstrated that the difference between the two group median Kep values was statistically significant ($p = 0.048$).
Figure 1B. Postgadolinium T1-weighted axial image in a representative patient. The blue color highlights the volume-of-interest (enhancing tumor)
Figure 1C. Vp map of the same patient and image slice as Figure 1B. Permeability metrics were interrogated in the volume-of-interest (highlighted in blue) using histogram analysis.

(Filename: TCT_O-446_JIASNRDCETERTGBMFigure1.jpg)

Thursday
11:00AM - 12:20PM
Long Beach Convention Center, Room 104C (Main Lobby)

24F-Parallel Paper Session: Excerpta: Understanding the Adult Brain - Unexpected, Unusual and Unbelievable!

E-92

11:00AM - 11:04AM

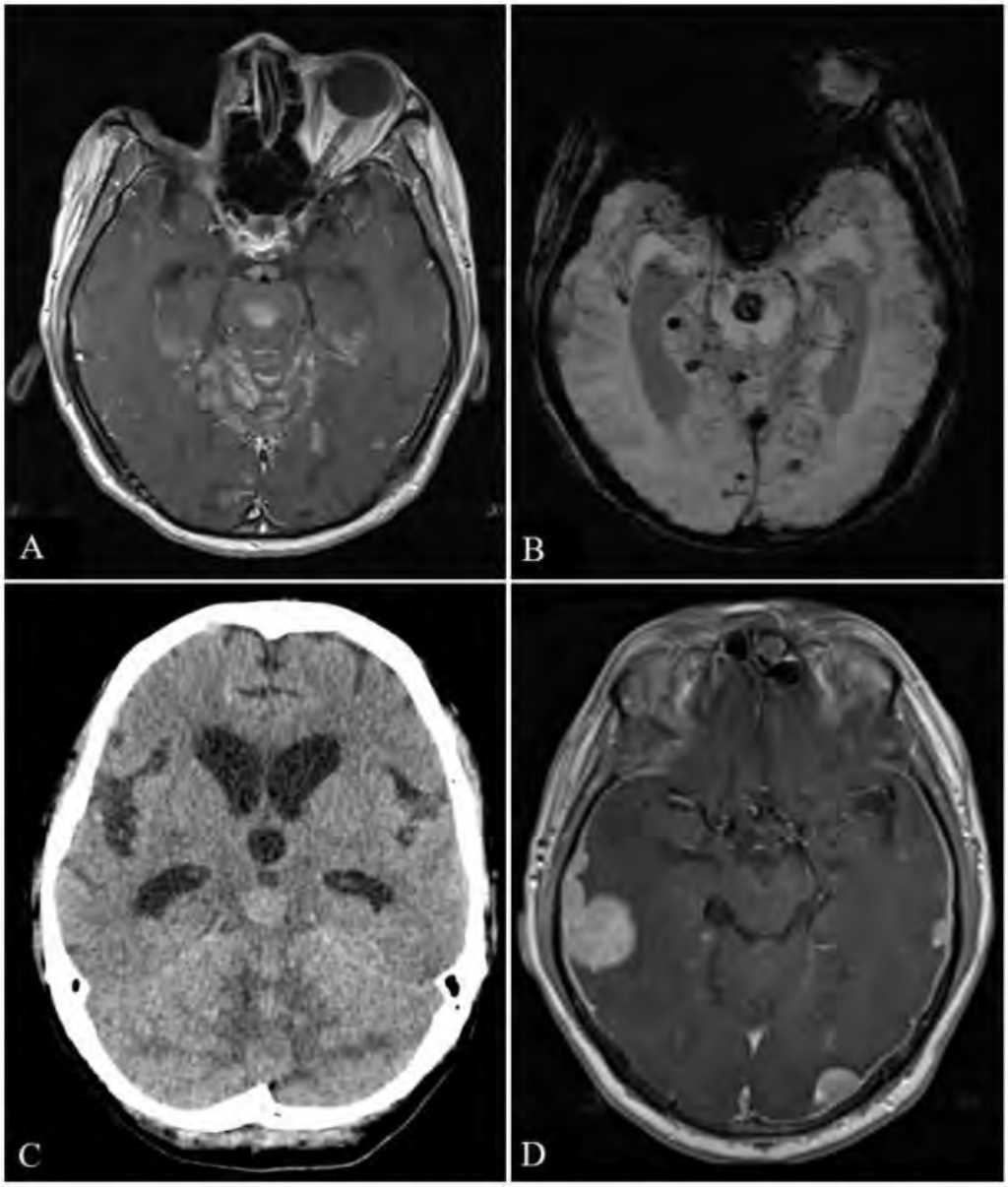
Imaging Features of Meningeal Myelomatosis: A Case Series

S Swaminathan[1], R Chen[2], C Ho[3]
[1]SingHealth, Singapore, Singapore, [2]Singapore General Hospital, Singapore, Not Applicable, [3]SengKang Health, Singapore, Singapore

Purpose
We describe the imaging characteristics, clinical features and outcome of 3 patients with meningeal myelomatosis.
Materials and Methods
Multiple myeloma is a hematological malignancy comprising of monoclonal cancerous plasma cells that usually affects the hematopoietic marrow, with extra-osseous infiltration being uncommon. Intracranial invasion of myeloma is a rare complication which is observed in only 1% of cases with reported survival of <6 months. It may manifest as dural myeloma, intraparenchymal infiltration or leptomeningeal involvement. In our series, 1 patient developed extensive leptomeningeal disease 2 years after right orbital exenteration for known intra-orbital myeloma metastasis. Another patient had leptomeningeal spread from intracranial invasion of an aggressive cavarial MM lesion. The third patient with underlying widespread osseous and extramedullary disease also developed multiple dural based masses. Treatment is aggressive, including intrathecal and systemic chemotherapy, bone marrow transplant and cranial irradiation. However, the outcome was invariably fatal with survival ranging from 10 of 60 days in our patients. This reflects the aggressiveness of this disease which often is associated with high-risk cytogenetic abnormalities, high myeloma burden and other extramedullary spread.
Results
These lesions were hyperdense on unenhanced CT and isointense to gray matter on T1- and T2-weighted sequences, with no evidence of restricted diffusion. All the lesions demonstrated avid but pleomorphic contrast enhancement, appearing as linear, diffuse thick or nodular areas of enhancement mimicking other intra-axial masses such as metastases and lymphoma. Some of them may demonstrate susceptibility on SWI sequence due to the presence of paramagnetic substance.

Conclusions

Prompt recognition of the imaging features of meningeal myelomatosis is imperative for early diagnosis and management of this aggressive disease.



Meningeal Myelomatosis: Image A – Post-contrast T1w image demonstrates multiple nodular areas of enhancement in the cerebellar sulci and surrounding the midbrain. The apparent intra-axial lesion within the midbrain is actually a leptomeningeal deposit along the surface of inter-peduncular fossa. Please note the right orbital exenteration for previous myeloma metastasis. **Image B** – MIP image of the SWI sequence demonstrates susceptibility artefacts in some of the meningeal lesions. **Image C** – Unenhanced CT brain demonstrates the meningeal lesion within the inter-peduncular fossa of midbrain appears hyperdense. **Image D** - Post-contrast T1w image in a different patient demonstrates several dural based metastases with avid contrast enhancement.

(Filename: TCT_E-92_MeningealMyelomatosis.JPG)

E-93

11:04AM - 11:08AM

Disseminated Leptomeningeal Hemangioblastomatosis Without a History of Von Hippel-Lindau.

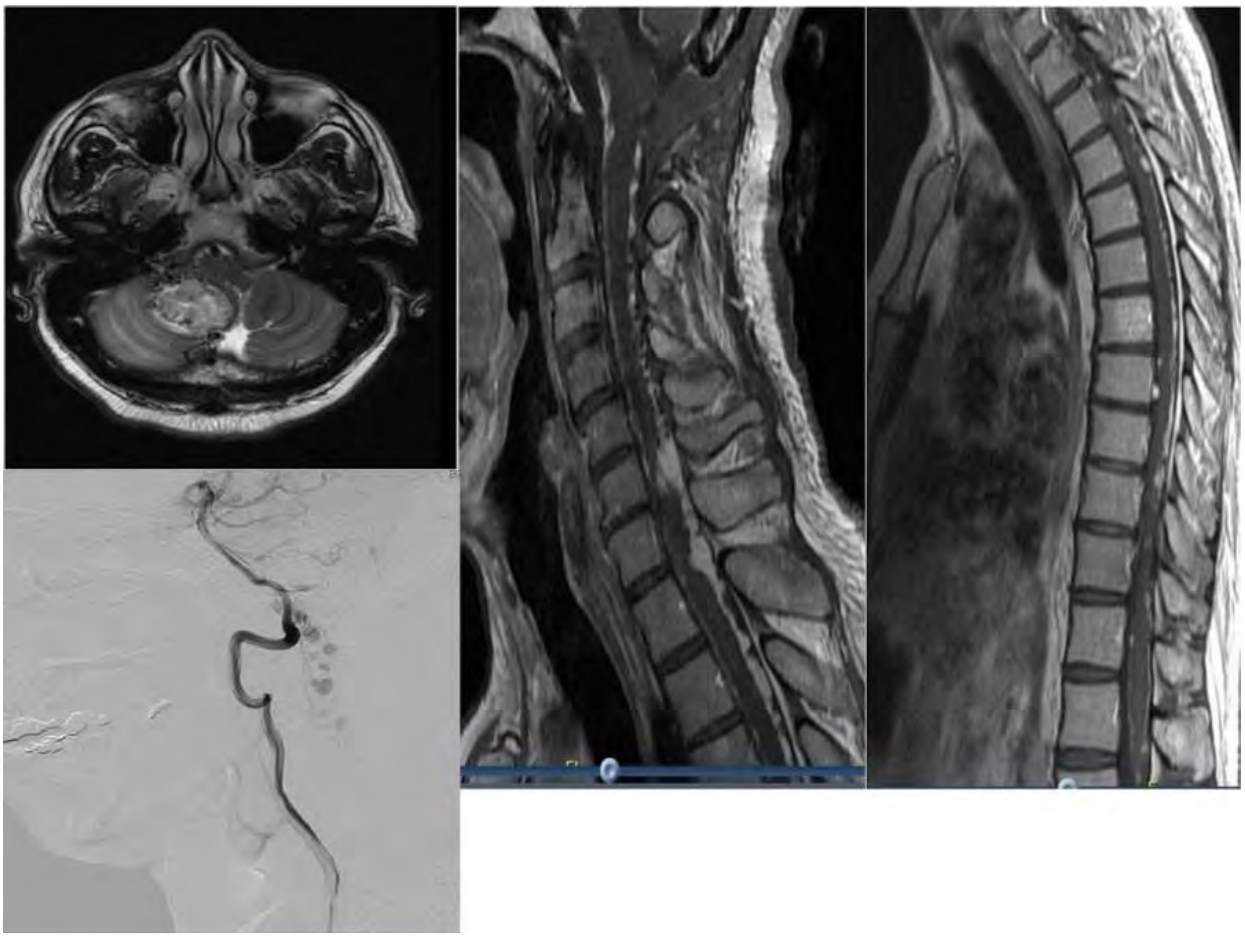
R Durel[1], T Sandow[1], J Milburn[1], A Steven[2]
[1]Ochsner Clinic Foundation, New Orleans, LA, [2]University of Maryland Medical Center, Baltimore, MD

Purpose
To demonstrate unusual presentation of disseminated hemangioblastomatosis of the leptomeninges in a patient with remote primary cerebellar hemangioblastoma resection and no history of Von Hippel-Lindau (VHL). Very few cases have been reported in the literature and treatment options are limited suggesting the need to further evaluate this disease entity.
Materials and Methods
A 63-year-old male that initially presented in August of 2011 with increasing headaches and gait abnormalities. The patient underwent suboccipital craniotomy and excision on 8/16/2011 for removal of a right cerebellar mass consistent with WHO grade I hemangioblastoma. Several follow up scans showed no evidence of recurrent or new disease. The patient did well until February of 2015 when he began to have neck and shoulder pain with associated weakness in the left upper and lower extremities. Magnetic resonance imaging (MRI) of the brain and cervical spine on 6/10/15, and subsequent thoracic and lumbar MRI on 6/19/15 demonstrated diffuse nodular leptomeningeal spread of disease. Computed tomography (CT) of the chest and abdomen were negative for other stigmata of VHL. Conventional angiography of the head and neck was performed to evaluate vascularity of the lesions for preoperative planning. The patient then underwent C5 - C7 laminectomy on 6/25/15. A large extra-axial cord tumor at the C6 level was removed en bloc. Pathology revealed hemangioblastoma similar to the cerebellar primary. The patient then underwent fractionated radiotherapy of the entire spine receiving 41.4 Gy from C1 - S4 which was completed on 10/9/15. As of the most recent documented physical exam on 10/1/16, the patient experiences only mild occasional headaches and mild residual left upper extremity weakness.
Results
Magnetic resonance imaging 8/2/11: Initial brain MRI shows avidly enhancing mass within the right cerebellum and several large flow voids. There is mass effect on the adjacent brainstem with effacement of the cerebral aqueduct resulting in hydrocephalus. Magnetic resonance imaging 6/10/15: Brain and cervical spine MRI show disseminated nodular extra-axial enhancement involving the right suprasellar cistern, in addition to leptomeningeal metastases throughout the cervical spine. There are associated large flow voids along the dorsal cord. There is mass effect with resultant cord edema, most prominent at the C6-T2 levels. Angiogram 6/18/15: Bilateral vertebral artery angiograms show numerous small

hypervascular nodules with early staining in the posterior fossa and cervical spinal canal. Magnetic resonance imaging 6/19/15: Thoracic and lumbar MRI shows extensive leptomeningeal metastases with involvement of the cauda equina. Pathology correlation: Pathology images of the resected cervical lesion show several clumped cells with clear cytoplasm and several vessels consistent with hemangioblastoma.

Conclusions

Primary cerebellar hemangioblastomas are WHO grade I lesions thought to be curative with surgical resection. Although leptomeningeal spread of disease is a relatively common entity seen in multiple disease processes, such as metastatic spread of primary gliomas and lymphoma, such extensive metastases with a low grade tumor is unexpected. A small number of cases, approximately 28, are described in the literature. Although the incidence of disseminated disease is higher with sporadic type hemangioblastomatosis, a more aggressive disease course typically is seen in the setting of VHL-related hemangioblastoma. The patient presented in this case was tested for major deletions or mutations in the VHL gene using fluorescent DNA sequence analysis and multiplex ligation dependent probe amplification (MLPA), all of which were negative. A case review series showed that somatic mutations in one copy of the VHL gene and NF1 gene may be the cause of more aggressive disseminated disease in sporadic cases, as opposed to germline mutations seen in the setting of a classical VHL presentation (Weil et al). Because no case of de novo development of disseminated hemangioblastomatosis without previous surgery has been reported, it is suggested that the spillage and spread of tumor cells through the CSF space can lead to hemangioblastomatosis in patients genetically predisposed to the condition (Kim et al). Tumor spillage during initial resection should be minimized and close follow up may allow for local control and better prognosis. Aggressive cases such as this portend a poor prognosis with high morbidity and mortality. The interval from surgery to dissemination ranges from 7 months to 22 years suggesting the need for long-term follow up (Koo et al). Treatment options are limited primarily to radiation therapy and debulking once dissemination has occurred. Additional research in medical and gene therapy options may provide added benefit to these rare cases.



(Filename: TCT_E-93_Slide1.JPG)

E-94

11:08AM - 11:12AM

Radiologic Presentation of Posterior Fossa Dermoid

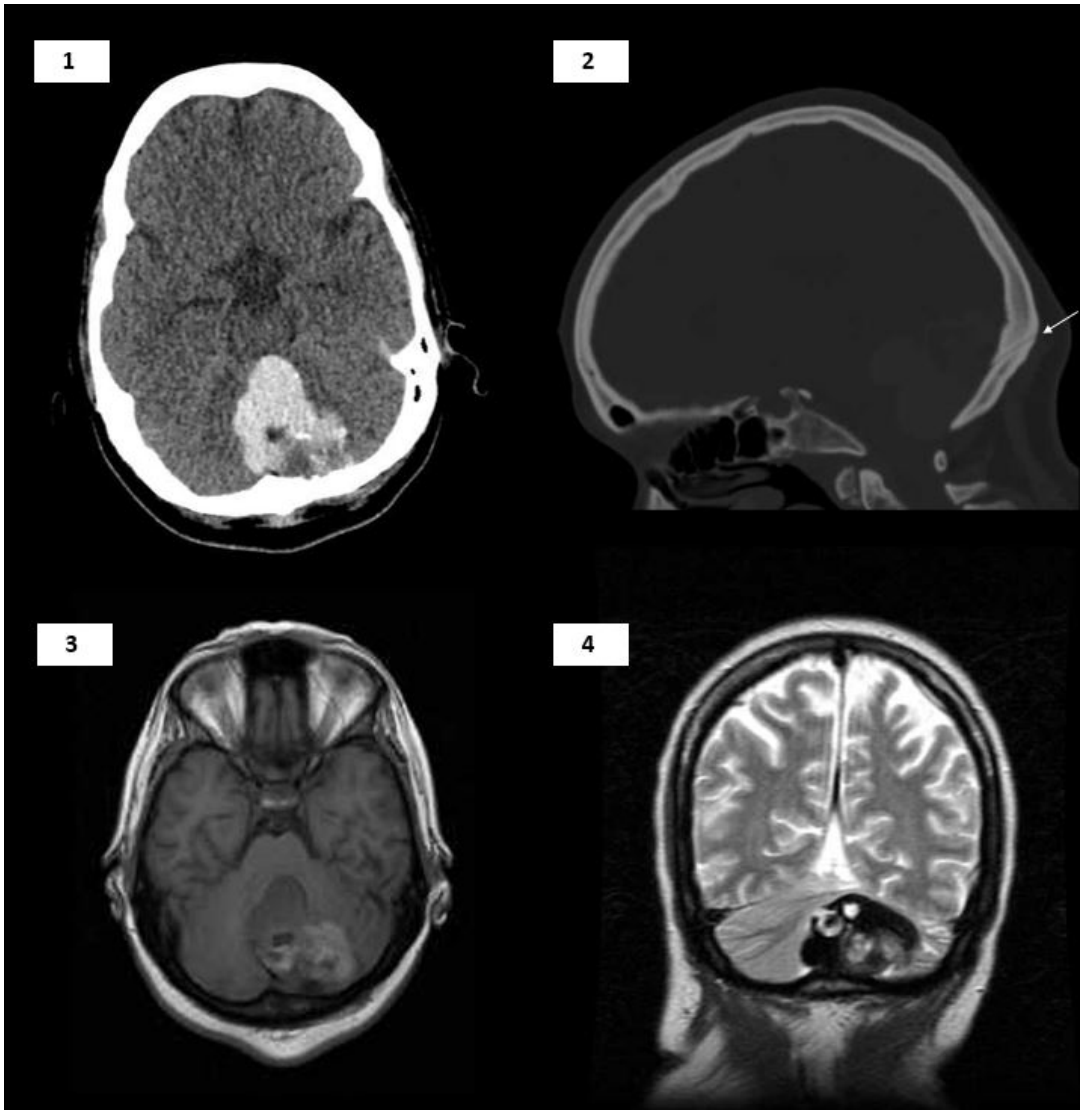
A Senaati[1], A Mlikotic[1]
[1]*Harbor UCLA, Torrance, CA*

Purpose
To present the radiologic characteristics of a rare dermoid cyst in the posterior fossa and illustrate the intra-operative and histopathological correlation.
Materials and Methods
A 29-year-old woman presented with intractable nausea and vomiting and without focal neurological deficit. Imaging revealed a complex posterior fossa mass with unexpected signal characteristics and a defect (sinus tract) in the adjacent calvarium. Surgical excision of the mass demonstrated a dermoid.
Results
Computed tomography (CT) imaging unveiled a 4.5 cm mass centered in the mid-line and

left posterior fossa, containing a mural solid component with calcifications and a large hyperatteunating component, initially concerning for acute hemorrhagic transformation (1). The mass compressed the fourth ventricle, causing mild hydrocephalus. There was a sinus tract within the occipital bone near mid-line that communicated between the lesion and the deep subcutaneous tissues of the scalp (2). MR imaging further demonstrated a frond-like mural nodule with areas of diffusion restriction, T1 hyperintensity, heterogeneous signal intensity on T2-weighted imaging, and minimal enhancement. The fluid component showed faint T1 hyperintensity although marked T2 and FLAIR hypointensity (3, 4). There was no magnetic susceptibility effect on gradient-recall echo (GRE) imaging to suggest recent hemorrhage. The lesion did not provoke surrounding vasogenic edema. Computed tomography and catheter angiography showed the mass to be avascular.

Conclusions

Based on the imaging findings, we considered a differential diagnosis of a hemorrhagic hemangioblastoma, atypical dermoid, and atypical craniopharyngioma. The lack of an intensely hypervascular mural nodule with prolonged staining excluded a hemangioblastoma. The density and signal intensity of the fluid component suggested either subacute hemorrhage, or the presence of emulsified fatty or cholesterol-rich material. The lack of susceptibility effect on GRE, however, disfavored the former. The finding of a posterior occipital sinus dermal sinus tract on CT favored a dermoid. The literature has identified a few cases of hyperatteunating intracranial dermoids on CT examination. A prior report also noted that all known dermoids with a hyperatteunating fluid component occurred in the posterior fossa, as was seen with our case. Surgical exploration yielded a yellowish mural nodule with a greasy consistency, and the fluid component contained dark, grumous material. On pathology, this hyperatteunating, T1 hyperintense fluid component correlated with keratin flakes suspended in cholesterol-rich fluid. This is produced by ductal and glandular structures in the hyalinized mass that correspond to skin adnexal structures, leading to the diagnosis.



(Filename: TCT_E-94_GraphicFile.JPG)

E-95

11:12AM - 11:16AM

Solitary Fibrous Tumor/Hemangiopericytoma: A Companion Case Discussion of a Spectrum of Rare CNS Mesenchymal Tumors and Their Evolving WHO Classification.

K Golden[1], Y Sun[2], A Arneja[3], T Li[3], C Salib[3], S Bobra[3], H Mehta[4]
[1]New York Medical College- Westchester Medical Center, Valhalla, NY, [2]New York Medical College - Westchester Medical Center, Valhalla, NY, [3]Westchester Medical Center, Valhalla, NY, [4]New York Medical College-Westchester Medical Center, Valhalla, NY

Purpose
Solitary fibrous tumor/hemangiopericytoma is an increasingly recognized, combined term describing a spectrum of rare mesenchymal tumors inclusive of the entity formerly known as

hemangiopericytoma. The term was first introduced in the 2016 WHO Classification of tumors of the central nervous system, have evolved following the discovery that solitary fibrous tumor and hemangiopericytoma share an inversion at 12q13. This inversion causes a NAB2/STAT6 gene fusion with resultant STAT6 nuclear expression, which can be detected by immunohistochemistry. STAT6 immunopositivity is now necessary for diagnosis. We present 2 cases of STAT6 immunopositive intracranial solitary fibrous tumor/hemangiopericytoma with histopathologic correlation and a brief discussion of imaging findings, pre-operative embolization, and surgical intervention.

Materials and Methods

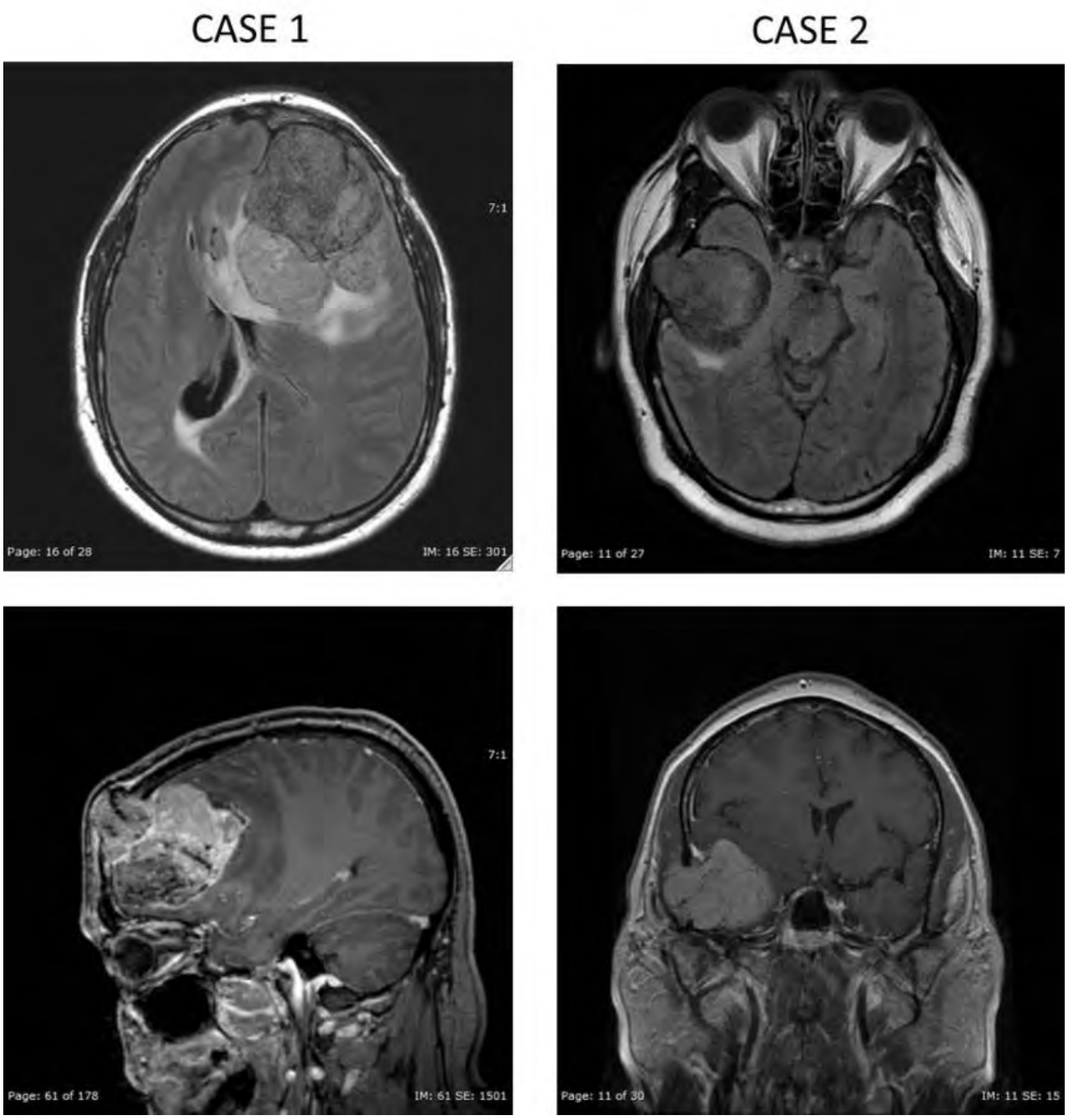
Case 1 is a 44-year-old previously healthy male who presented with 3 weeks of altered behavior, headache, and appetite loss. He described a slowly growing lump on his left forehead. Case 2 is a 50-year-old previously healthy male who presented to an outside hospital with headache, dizziness, and a right CN IV palsy.

Results

Case 1: Magnetic resonance imaging/magnetic resonance angiography (MRI/MRA) of the brain demonstrates a large left frontal lobe region, extra-axial mass eroding through the left frontal calvarium into the scalp soft tissues. The mass demonstrates heterogeneous signal characteristics, avid enhancement, and extensive tumor neovascularity. There is severe regional mass effect with associated vasogenic edema. Case 2: MRI of the orbits demonstrates a large, avidly enhancing, extra-axial mass within the right middle cranial fossa. There is erosion through the right temporal squamosa, marked mass effect on the adjacent temporal lobe, and moderate vasogenic edema. Numerous internal flow voids are noted.

Conclusions

Solitary fibrous tumor/hemangiopericytoma is a recently introduced, combined term describing a spectrum of rare mesenchymal tumors inclusive of the entity formerly known as hemangiopericytoma. The diagnosis is predicated on demonstration of STAT6 immunopositivity. We present 2 cases of STAT6 immunopositive intracranial solitary fibrous tumor/hemangiopericytoma.



(Filename: TCT_E-95_ImageFile-1.jpg)

E-96

11:16AM - 11:20AM

Epithelioid Glioblastoma with Osseous Metastases.

E Greif[1], G Cruciata[1], R Sharma[1], P Curl[1], E Stein[1], N Cornish[2]
[1]Maimonides Medical Center, Brooklyn, NY, [2]Maimonides Medical center, Brooklyn, NY

Purpose

The purpose of this abstract is to demonstrate a case of biopsy proven epithelioid glioblastoma with osseous metastases.

Materials and Methods

We are presenting a case of a 37-year-old male who presented with seizures and severe back pain. He went on to have a brain magnetic resonance imaging (MRI) which showed a left frontoparietal subcortical white matter calcification with minimal associated subacute hemorrhage with adjacent vasogenic edema. On follow-up MRI of the brain with and without intravenous contrast, there was interval increased size of the calcification, with a new associated peripherally ring-enhancing mass and increased associated vasogenic edema and mass effect. The patient had a biopsy, which demonstrated epithelioid glioblastoma. The patient went on to have an MRI of the spine, which showed multifocal bone marrow infiltration compatible with metastatic disease. This correlated with multiple osseous lytic lesions throughout the spine and pelvis, suspicious for metastatic disease on CT of the abdomen and pelvis. The patient had a bone biopsy of the lesions, which demonstrated metastatic epithelioid glioblastoma.

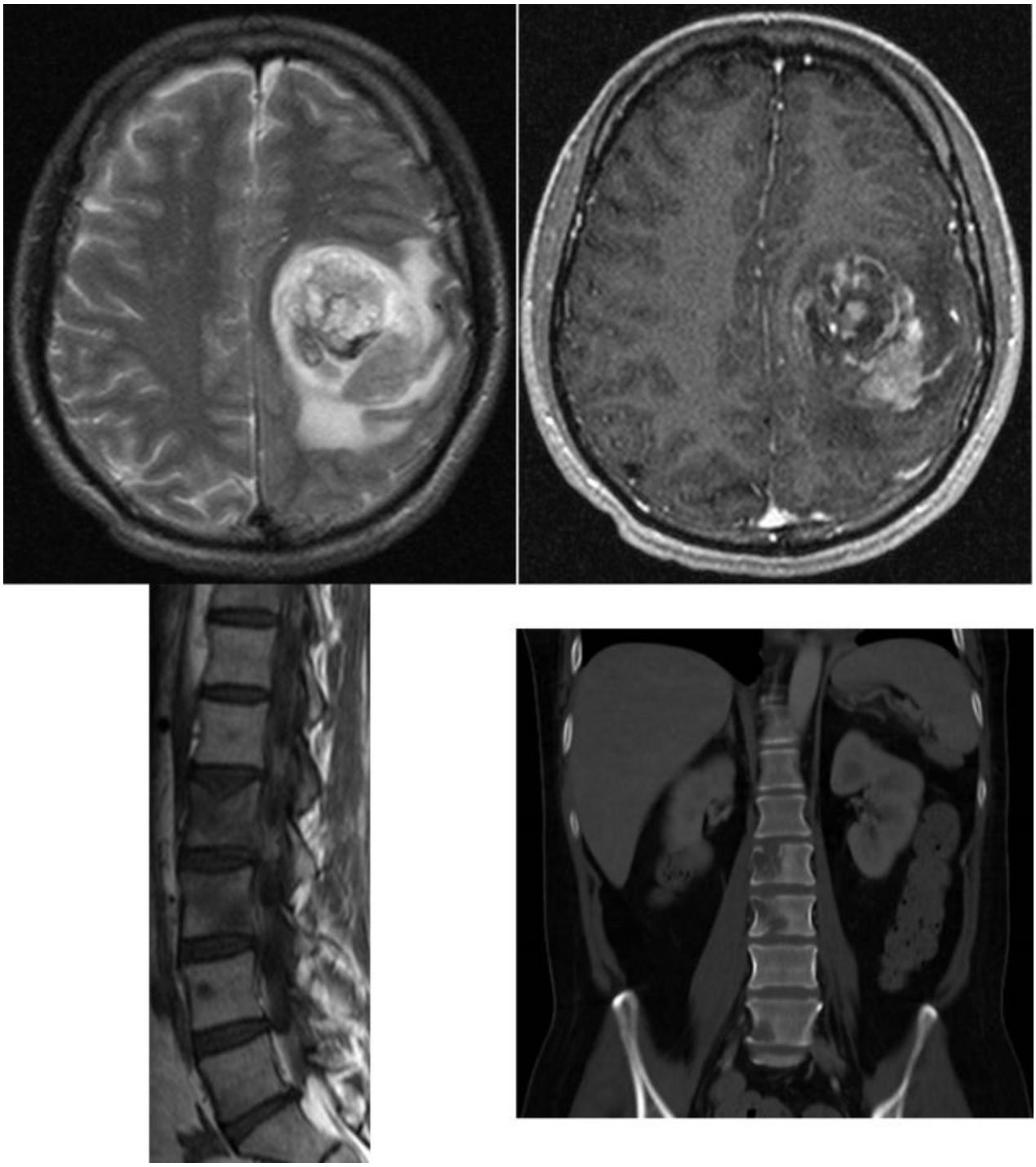
Results

On presentation, the patient had an MRI of the brain with and without intravenous contrast, which demonstrated a 1.4 x 1.6 cm calcification in the left frontoparietal centrum semiovale, with a small amount of peripheral T1 hyperintensity, compatible with subacute hemorrhage, and a small amount of surrounding edema or gliosis, thought to be a cavernous angioma or low grade glioma. Follow-up MRI of the brain with and without intravenous contrast demonstrated increased size of the calcification in the left frontoparietal centrum semiovale, measuring 1.8 x 2.1 cm, with increased surrounding vasogenic edema with effacement of the left lateral ventricle and 0.5 cm rightward bowing of the falx, not noted on prior study. There also was a newly developed 5.3 x 4.8 x 5.0 cm irregular thick walled peripherally enhancing mass, which extends superiorly to the cortex of the left frontoparietal lobe containing central necrosis and cystic change and areas of acute and subacute hemorrhage, consistent with a more aggressive tumor, such as glioblastoma multiforme. The patient also had an MRI of the thoracic and lumbar spine without intravenous contrast, which demonstrated multifocal bone marrow infiltration compatible with metastatic disease, predominating at T5-T6, with pathologic fracture at T5, and soft tissue extending posteriorly, impinging upon the right ventral lateral aspect of the spinal cord with mild central stenosis. This was correlated with multiple lytic lesions throughout the spine and pelvis, suspicious for metastatic disease on subsequent CT of the chest, abdomen, and pelvis with oral and intravenous contrast. Incidentally he also was noted to have pulmonary emboli in the bilateral lower lobe arteries.

Conclusions

One of the most common primary tumors of the central nervous system is astrocytomas, which are divided into grade I-IV, the most aggressive of which is grade IV, the glioblastoma. Glioblastoma is one of the most malignant central nervous system cancers in

children and adults. The World Health Organization divides glioblastoma into IDH-wildtype, which is primary, IDH-mutant, which is secondary with a history of prior lower grade diffuse glioma, and glioblastoma not otherwise specified, where full IDH evaluation cannot be performed. A new variant has emerged, the epithelioid glioblastoma , which joins the IDH-wildtype glioblastoma subtype. Epithelioid glioblastoma has a predilection for children and young adults, like our patient. It typically presents as superficial cerebral or diencephalic masses, similar to our patient. It is usually associated with areas of cystic necrosis with nodular enhancement. Epithelioid glioblastomas tend to have more significant adjacent vasogenic edema, mass effect, and midline shift. They also have been shown to occasionally have superficial attachment to the dura, appear well circumscribed, and have significant hemorrhage. Histologically it is characterized by large epithelioid cells with abundant eosinophilic cytoplasm, vesicular chromatin, and prominent nucleoli, and variably present rhabdoid cells. In addition, epithelioid glioblastoma tend to have more systemic metastases, such as osseous metastases observed in this patient. Treatment varies from local radiation therapy to chemotherapy, and surgical resection. Like glioblastoma multiforme, epithelioid glioblastoma has a poor prognosis, with a median survival of 169 days.



(Filename: TCT_E-96_Images.jpg)

E-97

11:20AM - 11:24AM

Central Neurocytoma of the Fourth Ventricle

Y Sun[1], H Mehta[1], K Golden[1], B Rigney[2], T Li[1], A Arneja[1], S Bobra[1], M Tenner[1]

[1]New York Medical College - Westchester Medical Center, Valhalla, NY, [2]Icahn School of Medicine at Mount Sinai, New York, NY

Purpose

Central neurocytomas (CN) are intraventricular brain tumors that commonly are found in the lateral ventricles and third ventricle. They are rare brain tumors, accounting for less than 1% of all primary brain malignancy (1). Central neurocytomas typically occur in young adults without gender predilection. Posterior fossa central neurocytoma, such as our patient with CN arising from the fourth ventricle, is exceedingly rare (2, 3). We present a novel case of a 61-year-old male with central neurocytoma of the fourth ventricle.

Materials and Methods

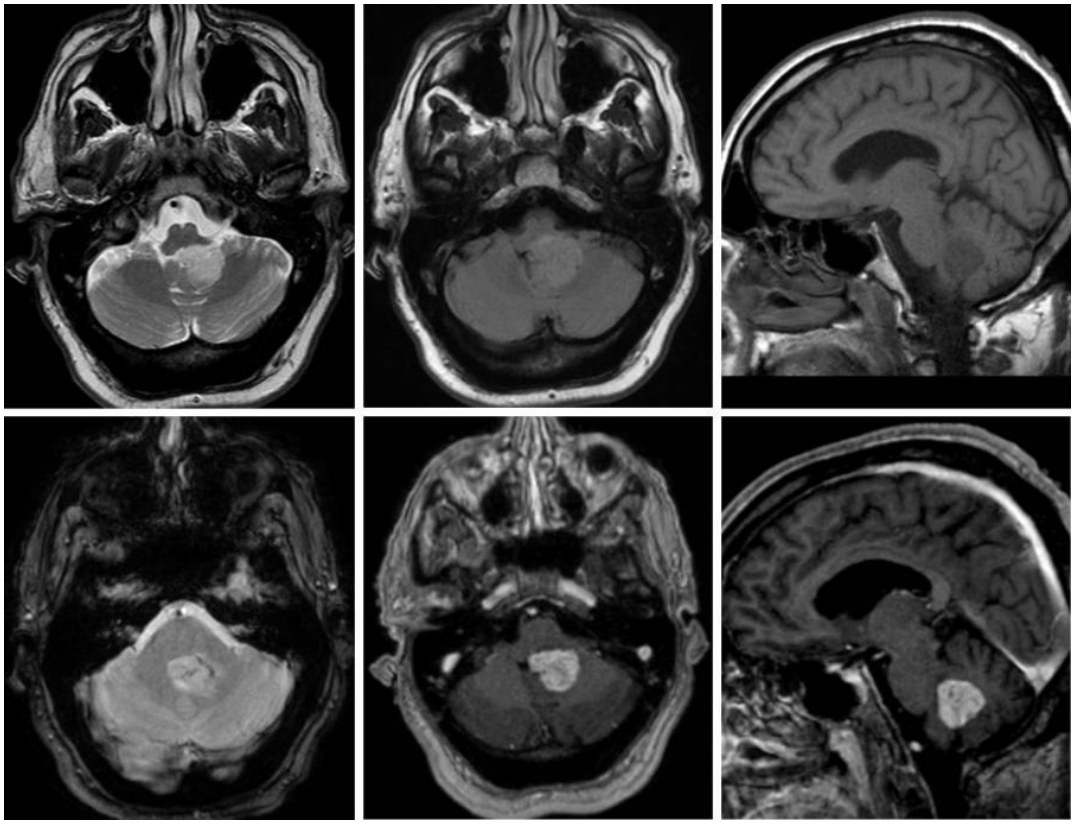
A 61-year-old male with past medical history of renal cell carcinoma status post nephrectomy presented with persistent headache, vomiting, and dizziness. The patient underwent craniotomy and surgical resection of the posterior fossa tumor. Pathology revealed central neurocytoma.

Results

Magnetic resonance imaging (MRI) of the brain demonstrates a heterogeneously enhancing intraventricular mass lesion in the fourth ventricle that measures approximately 2.1cm AP x 2.5cm TV x 2.2cm CC approaching the left foramen of Luschka. There is associated regional mass effect with partial effacement of the fourth ventricle and ventral displacement of the left dorsolateral medulla and pons. The mass demonstrates mild hyper-intensity on T2-weighted sequence and hypo-intensity on T1-weighted sequence. There also are small foci of peripheral T2-star signal loss, which may represent blood and/or calcifications.

Conclusions

Central neurocytoma of the fourth ventricle is exceedingly rare, which makes pre-operative imaging diagnosis difficult and was further confounded in our case by the patient's past medical history. Computed tomography and MRI are essential for characterization. Central neurocytomas have fairly characteristic imaging features on MRI. T1-weighted image may show iso- to hypo-intense signal to gray matter and T2-weighted sequence commonly reveal mildly increased signal intensity (1). Heterogeneous enhancement and punctate calcifications also are common. Surgical excision is the treatment of choice.


(Filename: TCT_E-97_ASNR2017.jpg)

E-98

11:24AM - 11:28AM

Third Ventricular Cavernoma: A Case Report

T Tragon[1], M Hughes[1]
[1]*University of Pittsburgh Medical Center, Pittsburgh, PA*

Purpose
Intraventricular cavernous malformations are rare, constituting 2.8-10% of intracranial cavernous malformations (1). Given their propensity to grow rapidly and hemorrhage these lesions can result in significant morbidity. We present a case of a third ventricular cavernoma with resultant hydrocephalus.
Materials and Methods
The patient is a 64-year-old female who presented with a 3-month history of progressive memory loss and anomic aphasia. An magnetic resonance imaging (MRI) of the skull base showed a third ventricular mass with inherent areas of increased T1 signal, and internal cystic foci with blood-fluid levels as well as an incomplete hemosiderin rim. She subsequently underwent bifrontal interhemispheric trans lamina terminalis approach and total excision. Histopathologic findings included numerous vessels with variable thick hyalinized walls surrounded by gliotic tissue with features of both acute and chronic

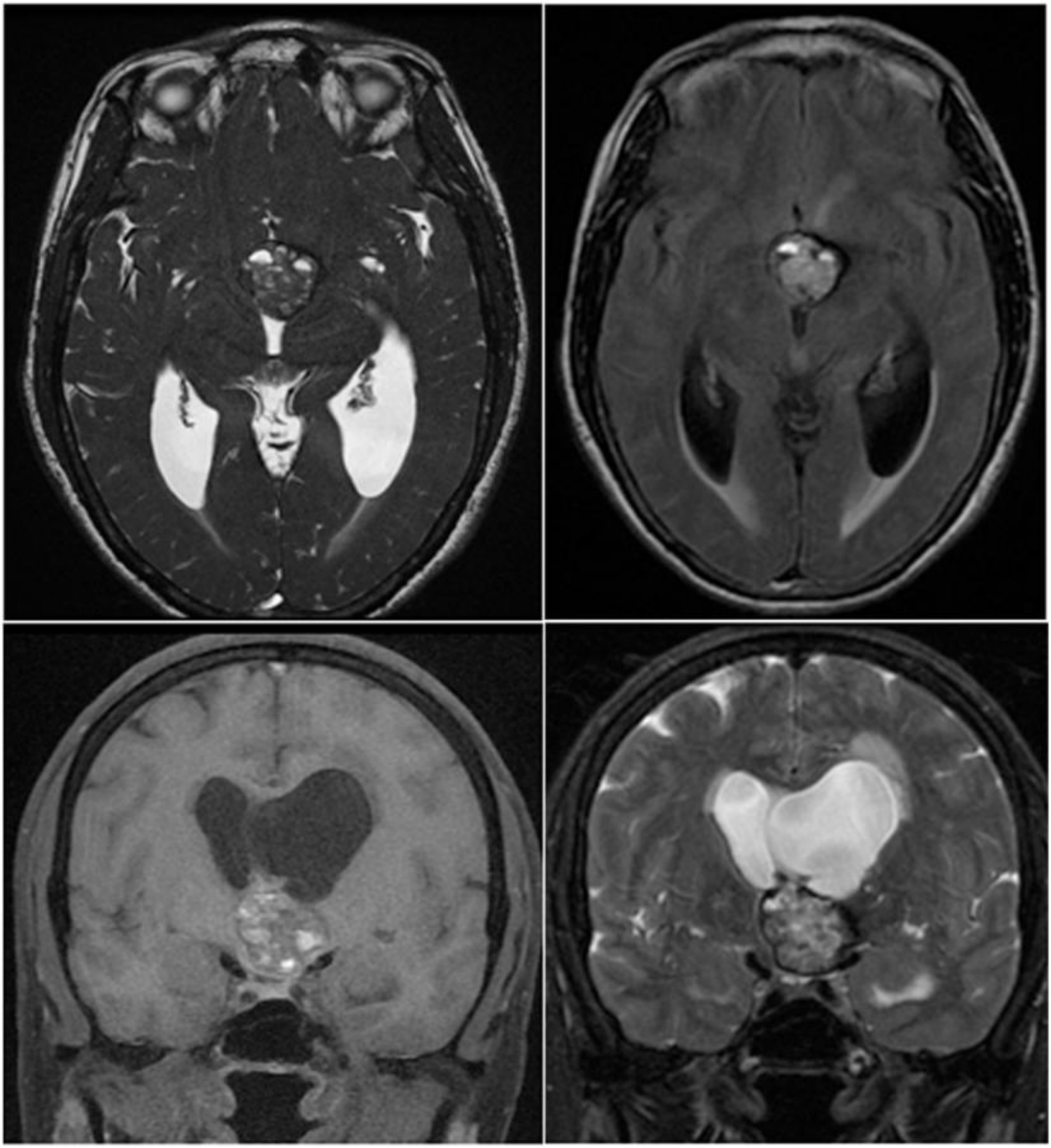
hemorrhage, sections of which are definitive for a vascular malformation, concordant with initial radiologic impression of cavernoma.

Results

1. Axial (top left) and Coronal FIESTA-C (bottom right): images at the level of the third ventricle demonstrate a complex, partially cystic mass with blood-fluid levels and an incomplete hemosiderin rim. 2. Axial FLAIR (top right): the third ventricular is mass causing obstructive hydrocephalus with transependymal flow of cerebrospinal fluid (CSF) appreciated. 3. Coronal T1- weighted image (bottom left): the mass demonstrates scattered areas of intrinsic increased T1 signal. Minimal enhancement was noted on the postcontrast T1- weighted images (not shown).

Conclusions

Third ventricular cavernous malformations represent a rare presentation of a common diagnosis. The imaging characteristics are similar to cavernomas found elsewhere in the brain. However, given their reported propensity for rapid growth and resultant acute hydrocephalus, radiologists should be aware of this entity.



(Filename: TCT_E-98_cavernomas.jpg)

E-99

11:28AM - 11:32AM

A Case of Lymphomatosis Cerebri: Radiology/Pathology Correlation

T Katsuura[1], J Taniguchi[1], K Ando[2], Y Wakata[1], R Ishikura[3], S Hirota[1]

[1]Hyogo College of Medicine, Nishinomiya, CA, [2]Hyogo College of Medicine, Nishinomiya, Japan, [3]Hyogo College of Medicien, Nishinomiya, CA

Purpose

Lymphomatosis cerebri (LC) is a rare manifestations of primary central nervous system lymphoma in which lymphoma cells diffusely infiltrate the brain parenchyma without evidence of a mass lesion. We report a case of LC with magnetic resonance imaging (MRI) and autopsy findings, and examine correlations between radiological and pathological findings in this case.

Materials and Methods

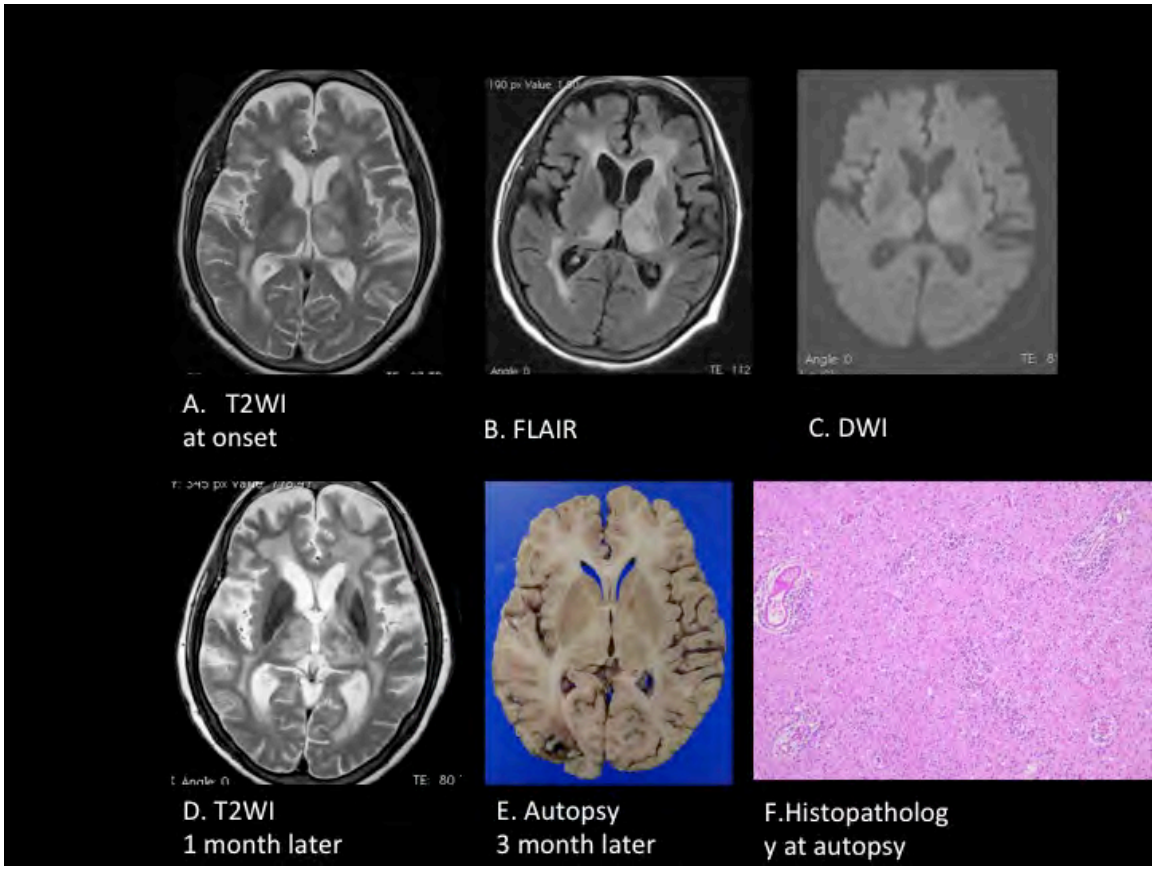
A 77-year-old woman presented with stagger and a 2-month history of disturbances of speech and memory. Neurological examination on admission revealed mild disturbance of consciousness, disorientation and lip dyskinesia. The patient died 3 months after admission. Autopsy was performed.

Results

T2-weighted/fluid-attenuated inversion recovery (FLAIR) images from MRI showed extensive hyperintense areas in bilateral thalami, the left globes pallidum, white matter of the left frontal lobe and mesencephalon. These lesions showed mild hyperintensity on diffusion-weighted imaging, without contrast enhancement from Gd-DTPA. Magnetic resonance imaging 1 month later showed exacerbation of lesions on T2-weighted/FLAIR images without contrast enhancement. The autopsy diagnosis was primary CNS malignant lymphoma (diffuse large B-cell lymphoma). No obvious macroscopic abnormalities were associated with any lesions.Histopathology showed diffuse lymphocytic infiltration into the brain parenchyma, but without lymphocytic infiltration into blood vessels. The diagnosis was consistent with LC. Hyperintensities on T2-weighted and FLAIR images correlated well with the pathological findings of white matter lesions with tumor cell infiltration.

Conclusions

In out case, signal alteration on T2-weighted and FLAIR images were most sensitive for detecting the pathological findings of white matter with microscopic tumor cell infiltration in lymphomatosis cerebri.



(Filename: TCT_E-99_2.jpg)

E-100

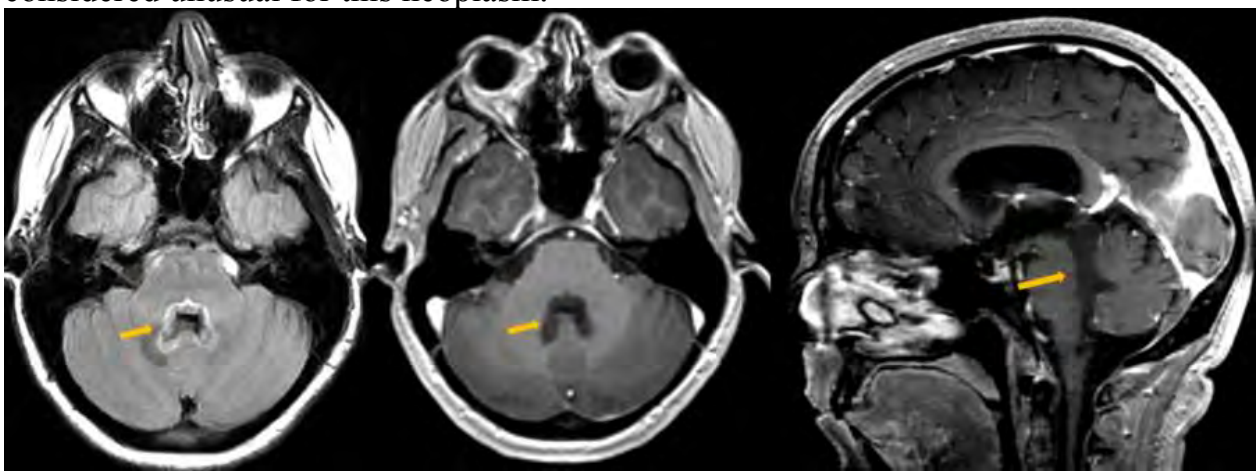
11:32AM - 11:36AM

Rosette-forming Glioneuronal Tumour (RGNT): A Case with Unusual Imaging Presentation

B Salehi[1], B Yoo[1]
[1]*UCLA, Los Angeles, CA*

Purpose
To show a rare case of rosette-forming glioneuronal tumor (RGNT) with unusual imaging presentation.
Materials and Methods
A 34-year-old woman presented with long-lasting headache. Imaging revealed hydrocephalus and nonenhancing, T2/FLAIR hyperintense mass surrounding the aqueduct and fourth ventricle. Patient underwent shunt placement and biopsy. Pathology review showed rosette-forming glioneuronal tumor without mitotic feature. Patient received proton radiation therapy due to progressive symptoms.
Results
Axial FLAIR (left), axial T1-weighted postcontrast (middle) and sagittal T1-weighted

postcontrast (right) images show nonenhancing expansile FLAIR hyperintensity involving the tissue around the aqueduct and fourth ventricle, resulting in partial effacement of the fourth ventricle and possible narrowing of the aqueduct. There were moderate hydrocephalus and transependymal edema which is not shown in these images. No cystic change or calcification was evident.
Conclusions
Rosette-forming glioneuronal tumor (RGNT) is a novel and distinctive type of primary central nervous system neoplasm. The same as this case, it usually presents with headache and symptoms associated with hydrocephalus. The imaging characteristics of this neoplasm are variable. Despite this case, RGNT usually produces contrast enhancement, which can be minimal, focal or homogenous. Based on the reported cases, nonenhancing appearance is considered unusual for this neoplasm.



(Filename: TCT_E-100_Figure-1.jpg)

E-101

11:36AM - 11:40AM

Pituitary Metastasis from Lung Carcinoma Presenting with Optic Tract Edema

D Lin[1], H Marin[1], S Patel[1], J Rock[1], B Griffith[1]
[1]*Henry Ford Health System, Detroit, MI*

Purpose
Pituitary metastasis is a rare entity, representing only 0.9% of intracranial malignancies. The clinical and radiologic findings of pituitary metastases often are nonspecific. Optic tract edema is known to occur in the setting of pituitary metastasis, although is associated more commonly with craniopharyngiomas. This excerpta describes a rare case of a pituitary metastasis from lung cancer presenting with edema in the bilateral optic tracts.
Materials and Methods
We present the case of a 59-year-old female with a 2-month history of progressive peripheral vision loss. Physical examination demonstrated bitemporal hemianopsia. Following imaging

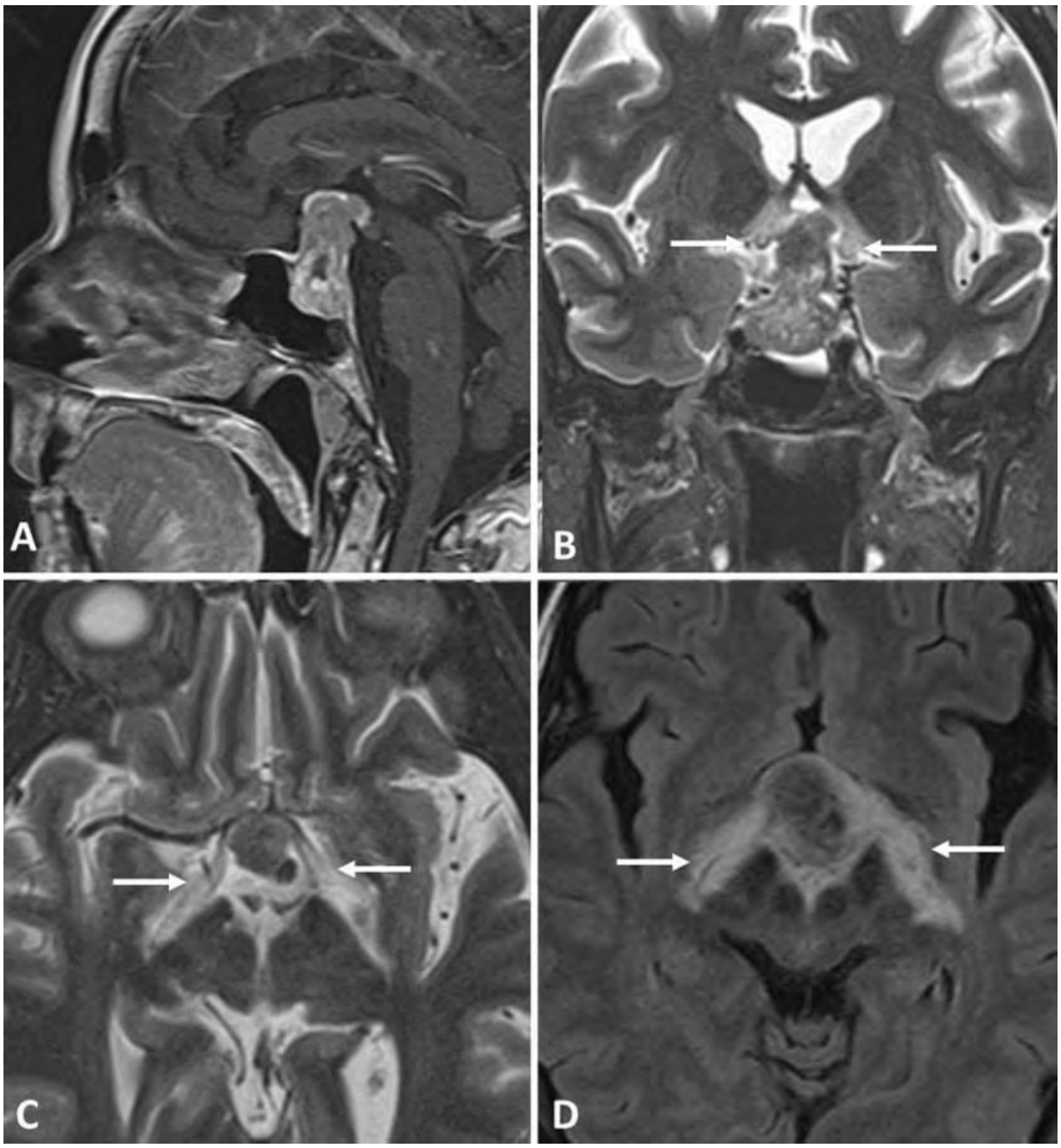
evaluation, the patient underwent partial resection of the pituitary tumor via a transsphenoidal approach. Pathology was positive for metastatic small cell carcinoma of the lung. The patient subsequently was treated with stereotactic radiation and chemotherapy with interval reduction in the size of the residual enhancing lesion, as well as near complete resolution of the optic tract edema.

Results

Computed tomography (CT) of the head demonstrated a large mixed-density sellar/suprasellar mass with expansion of the sella turcica and erosion of the dorsum sellae. Magnetic resonance imaging (MRI) of the brain and sella demonstrated a heterogeneously enhancing (Fig. 1A) T1 isointense and T2 mixed-intensity sellar mass with suprasellar extension measuring 3.8 x 2.3 x 2.2 cm. The mass compressed the optic chiasm, floor of the third ventricle, and hypothalamus with extensive T2/FLAIR hyperintensity extending into both optic tracts (Fig. 1B-D).

Conclusions

Pituitary metastasis is a rare entity with often nonspecific clinical and radiologic findings. Although optic tract edema is known to occur in the setting of pituitary metastasis, it is associated more commonly with craniopharyngiomas, which can influence the primary diagnostic considerations. This case of pituitary metastasis and subsequent discussion serves as a reminder that a number of etiologies must be considered when faced with a sellar/suprasellar mass and optic tract edema.



(Filename: TCT_E-101_FinalPituitaryMet.jpg)

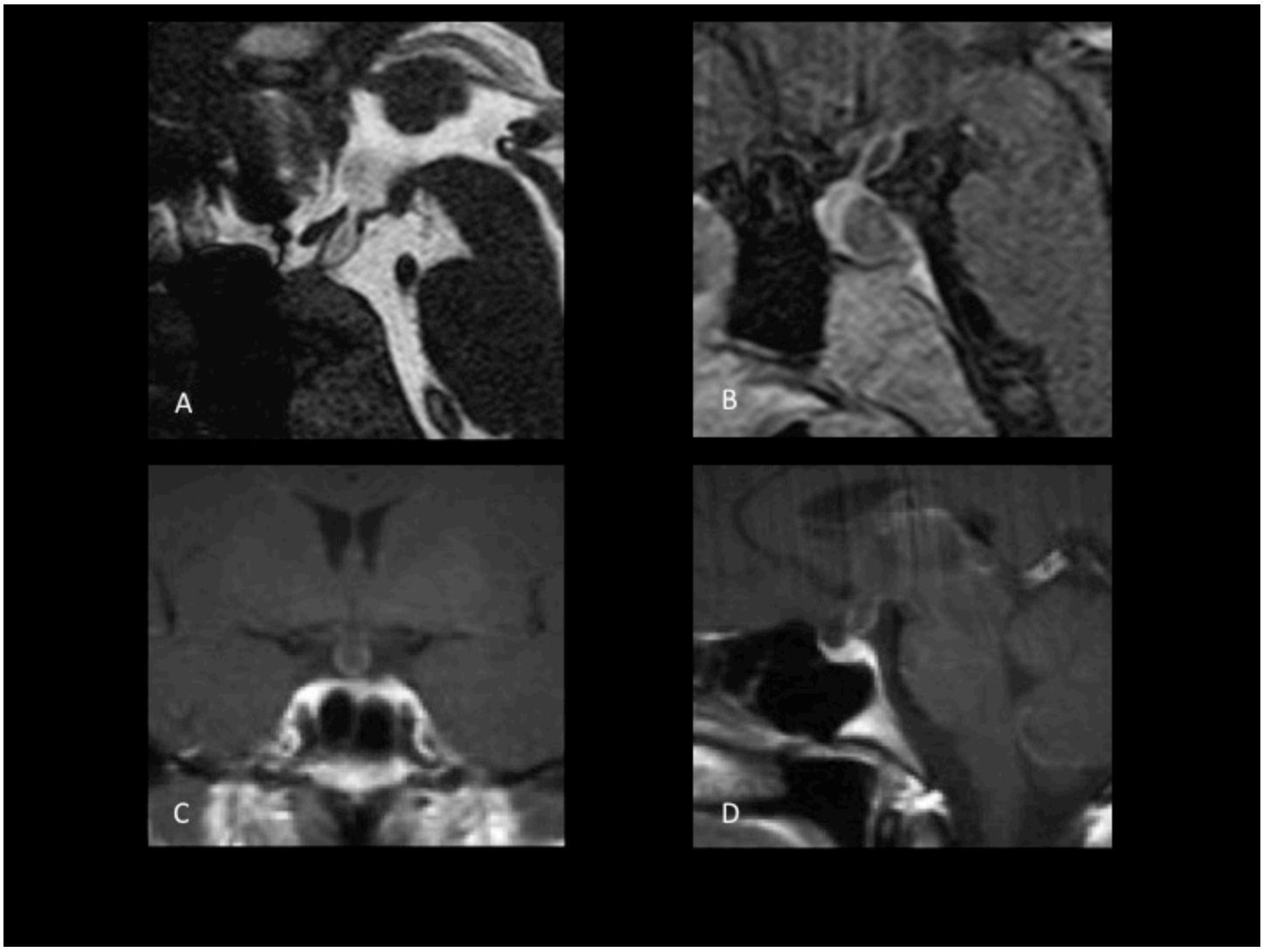
E-102

11:40AM - 11:44AM

Diverticulum of The Infundibulum: an Anatomic Variant

P Puac[1], P COIMBRA[2], R Camacaro[1], A Rodriguez[1], C Vallejo[1], M Castillo[1]
[1]University of North Carolina at Chapel Hill, Chapel Hill, NC, [2]CLINICA TRAJANO ALMEIDA, FORTALEZA, Brazil

Purpose
To show the magnetic resonance imaging (MRI) appearance of a diverticulum of the third-ventricle extending into infundibulum in 2 patients.
Materials and Methods
Two patients presenting with a clinical history of headache. In 1, MRI showed a posterior nonenhancing pituitary mass compatible with a macroadenoma. As an incidental finding, both patients presented an enlarged, fluid-filled, pituitary stalk communicating with the 3rd ventricle. Patients underwent an endocrine work up with no abnormalities detected.
Results
Magnetic resonance imaging showed diverticula of the 3rd ventricle into the infundibulum (patient 1, Fig. A and B) (patient 2, Fig. C and D). Both showed enlargement of the pituitary stalk in communication with the infundibular recess of the 3rd ventricles. The walls of the diverticula were thin and well defined, with homogenous enhancement in postcontrast imaging.
Conclusions
Diverticulum of the infundibulum is a normal variant when the infundibular recess of the anteroinferior portion of 3rd ventricle extends inferiorly and it may simulate a variety of diseases including cyst, epidermoid, infundibular fenestration, etc. However, its MRI features which include fluid intensity in all sequences and thin peripheral enhancement suggest the diagnosis.



(Filename: TCT_E-102_Diapositiva1.jpg)

E-103

11:44AM - 11:48AM

An Unexpected Presentation of Multiple Myeloma in a Young Man with a Large Intracranial Mass

T Phelps[1], M Opatowsky[1], C Gomez[1]
[1]*Baylor University Medical Center, Dallas, TX*

Purpose
Intracranial plasmacytomas are uncommon and they are rarely the initial presenting finding in the setting of newly diagnosed multiple myeloma. We present a case of an unusually large extra-axial mass in a young man subsequently proven to have multiple myeloma.

Materials and Methods

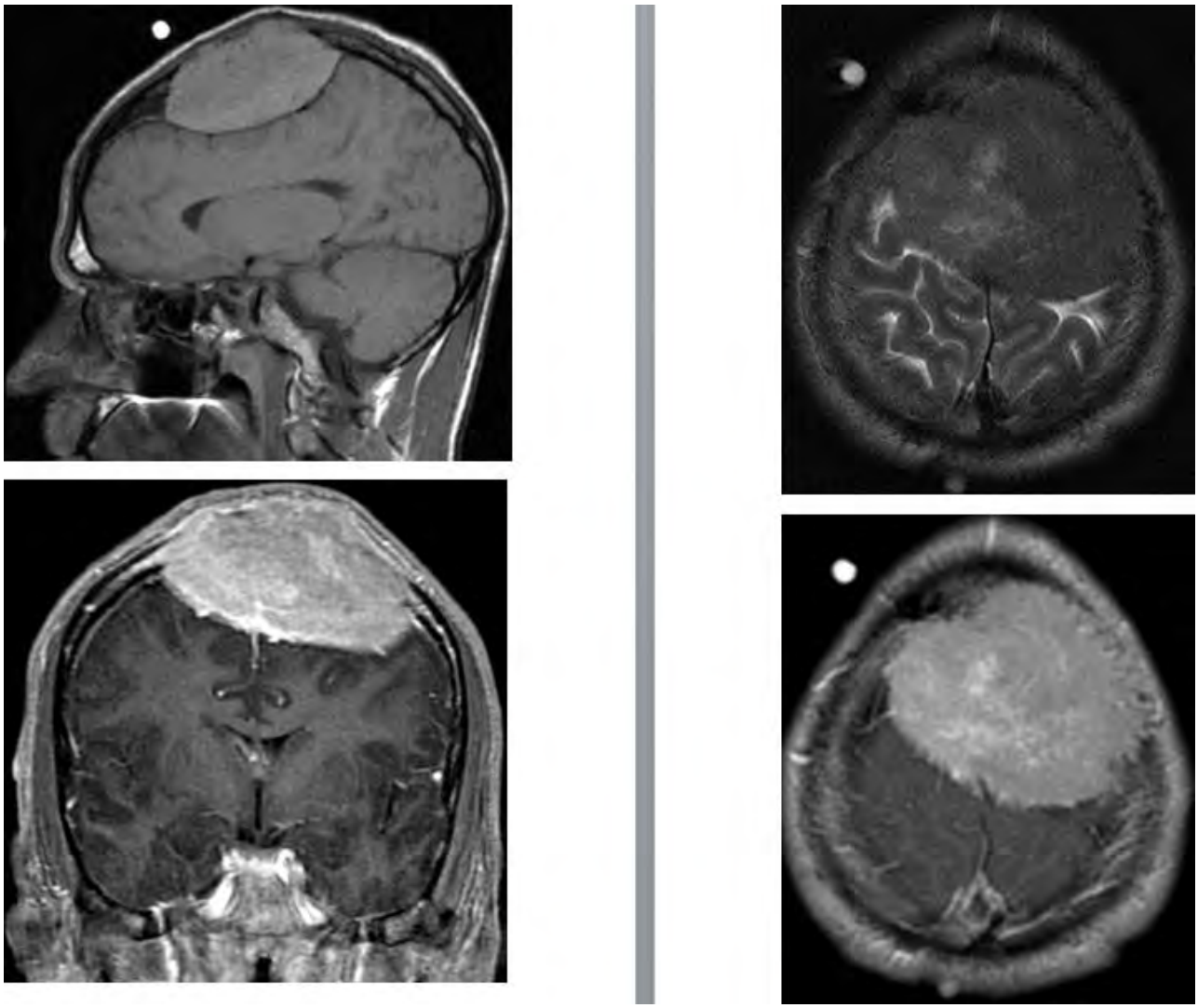
A 33-year-old male with no significant past medical history presented with 3 months of headaches and sought medical attention after noticing an enlarging "bump" on his scalp. MR imaging of the brain demonstrated a large extra-axial intracranial mass with findings interpreted as most compatible with an aggressive meningioma. No skeletal lesions were present on a traditional bone survey. Initial pathology findings intra-operatively revealed sheet-like infiltrates of plasma cells consistent with a plasmacytoma. A diagnosis of multiple myeloma then was made based on a bone marrow biopsy and urine protein electrophoresis (UPEP) results.

Results

A large enhancing extra-axial mass overlying the bifrontal convexities that measures in excess of 8 cm. The mass erodes through the calvaria without any evidence of involvement of the overlying scalp. A segment of the superior sagittal sinus deep to the mass was likely compromised. Moderate compression of the underlying bifrontal cerebral hemispheres. Foci of susceptibility are seen within the mass on the gradient-echo sequence. No evidence or perifocal vasogenic edema in the displaced frontal lobes. The extra-axial mass created slight left-to-right midline shift. No notable restricted diffusion or substantial intratumoral hemorrhage. No complicating hydrocephalus or notable herniation.

Conclusions

Only 3% of those diagnosed with multiple myeloma will present under 40 years old. A large solitary extra-axial mass as the initial presentation of this disease process is particularly rare. The case serves as a reminder that this diagnosis remains a consideration in such masses in this location, even in young patients.



(Filename: TCT_E-103_Plasmacytoma.JPG)

E-104

11:48AM - 11:52AM

Use of Ferumoxytol as a MRI Contrast Agent in a Case of Post-transplant Lymphoproliferative Disorder

E Miller[1], J Fritz[1], A Ajam[1], D Boulter[1], W Slone[1], C Fetko[1], P Giglio[1], E Bourekas[1]
[1]*The Ohio State University Wexner Medical Center, Columbus, OH*

Purpose
There has been off-label use of ultra-small iron-based particles as alternative contrast agents in patients with gadolinium contraindications, particularly Ferumoxytol (Feraheme, AMAG Pharmaceuticals, Cambridge, Massachusetts). An initial blood pool contrast agent, after 24-48 hours there is macrophage uptake and parenchymal enhancement. Studies have validated

Ferumoxytol in neuroimaging of glial neoplasms and lymphomas. We present a case of a Ferumoxytol contrasted magnetic resonance imaging (MRI) in a patient with multiple brain lesions and renal failure who could not receive gadolinium, which proved to be post-transplant lymphoproliferative disorder.

Materials and Methods

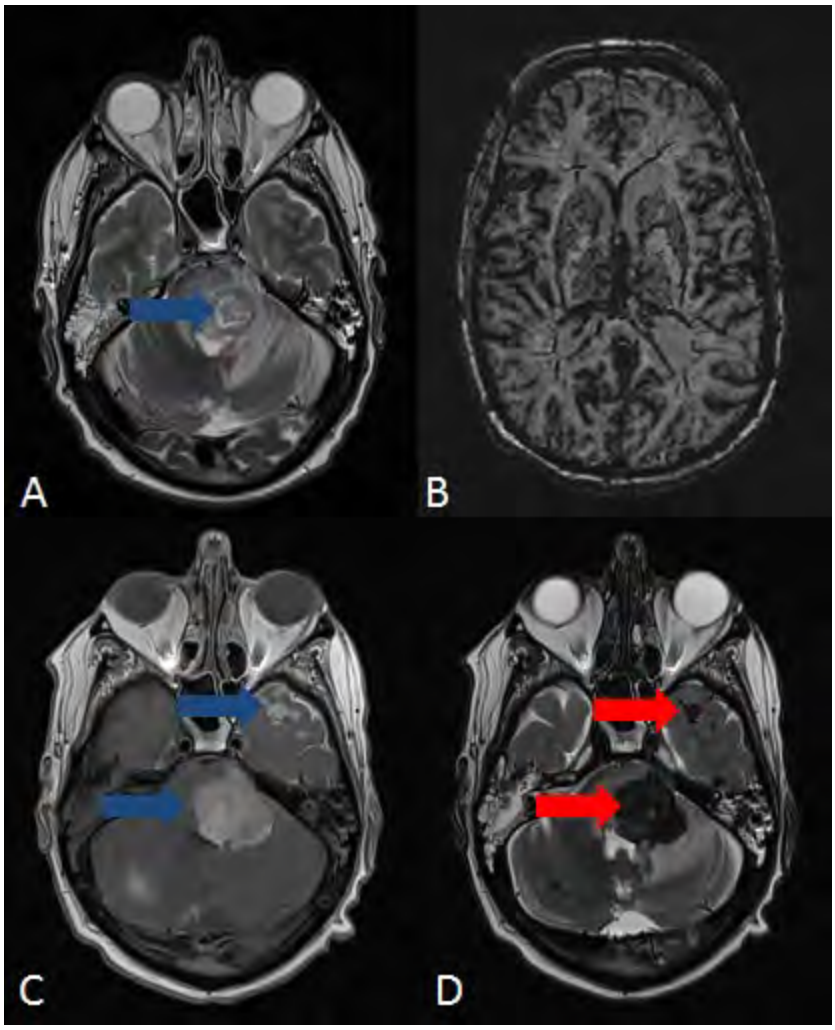
A 54-year-old male with chronic kidney disease on immune suppression presented with progressing balance deficits. Initial noncontrast MRI showed several lesions including a mass centered in the pons. Impediments to contrasted imaging included anaphylaxis to iodinated contrast and a GFR below threshold for gadolinium. Nephrology was hesitant to initiate dialysis to filter a gadolinium contrast load. We proceed with a contrasted MRI using intravenous Ferumoxytol in place of gadolinium with dynamic imaging and imaging 24 hours postinjection. On delay imaging there was avid enhancement in the lesions as well as diffuse leptomeningeal enhancement along the left temporal and occipital lobes. The contrasted study illustrated a less invasive biopsy tract and pathology from the biopsy revealed a B-cell post-transplant lymphoproliferative disorder of the central nervous system.

Results

A) T2-weighted images through the posterior fossa showing the mass within the pons (blue arrow). B) Axial susceptibility-weighted imaging demonstrates the intravascular ferumoxytol. C) Twenty-four-hour postaxial T1 VIBE images showing enhancement of the pontine and left temporal lobe mass with leptomeningeal and dural enhancement (blue arrows). D) Twenty-four-hour postinjection axial T2 images showing signal loss from iron accumulation (red arrows).

Conclusions

Ferumoxytol was used successfully as a MR contrast medium to evaluate a post-transplant lymphoproliferative disorder of the CNS when gadolinium could not be used.



(Filename: TCT_E-104_300dpiimages.jpg)

E-105

11:52AM - 11:56AM

Adult on Extracorporeal Membrane Oxygenation Therapy Being Evaluated for Acute Stroke.

M Peckham[1], C Kilburg[1], C Meyer[1], P Taussky[1], Y Anzai[1]
[1]*University of Utah, Salt Lake City, UT*

Purpose
To discuss pitfalls of performing computed tomography angiography (CTA) imaging in patients on extracorporeal membrane oxygenation (ECMO).
Materials and Methods
A 53-year-old woman with unstable angina had a complicated hospital course following coronary artery bypass graft with intra-operative graft occlusion necessitating ECMO. Postoperatively, she had sudden onset of decreased responsiveness and left upper extremity

weakness. Head and neck CTA and CT perfusion were performed for possible infarct. The patient went on to the angiography suite for possible mechanical thrombectomy.

Results

The brachiocephalic, right common carotid, right vertebral, and right subclavian arteries were nonopacified (Fig. 1a). There was partial nonopacification of the left common carotid artery, otherwise the left neck vessels opacified normally. Intracranial imaging demonstrated nonopacification of the right anterior circulation (Fig. 1b). The left anterior circulation and posterior circulation normally opacified. CT perfusion showed decreased CBV and CBF and increased MTT and TMax of the right MCA and ACA territories (Fig. 1c). Perfusion was preserved in the left anterior and bilateral posterior circulations. On DSA there was patency of all neck and intracranial vessels. Competing noncontrast flow was noted coming from the ECMO catheter within the right axillary artery. Subsequent noncontrast head CT showed areas of contrast staining in the right posterior MCA territory and cerebellum, likely reflecting blood-brain barrier breakdown from small infarcts.

Conclusions

Extracorporeal membrane oxygenation patients have increased risk of neurological complications including ischemic and hemorrhagic stroke. While ECMO is a common form of life-sustaining therapy in the pediatric population, it is increasingly used in adults. Computed tomography angiography brain, head, and neck imaging in the patient on axillary ECMO can be misleading because of competing high-pressure blood flow from the arterial ECMO catheter which can create the appearance of a large perfusion deficit, as well as multi-vessel occlusion. Neuroradiologists, specifically those in an adult practice not accustomed to ECMO, should be aware of these potential pitfalls.

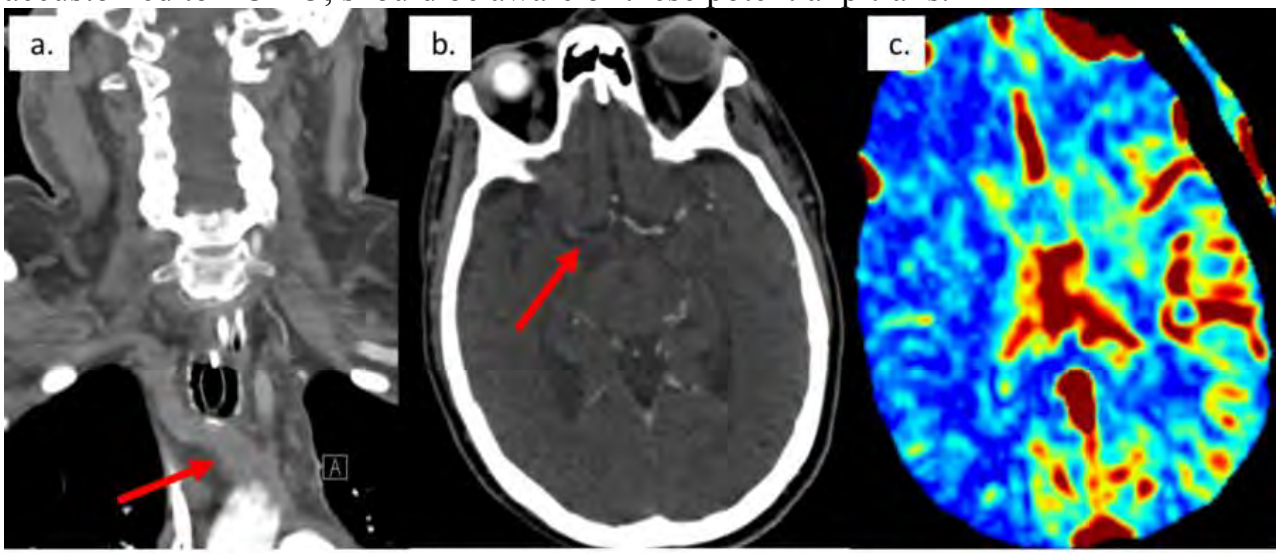


Figure 1: Coronal (a) and axial (b) CTA images demonstrating non-opacification of the brachiocephalic (a, red arrow) and right MCA (b, red arrow) arteries. Perfusion axial image (c) demonstrating decreased cerebral blood throughout the right hemisphere with some sparing in the right PCA territory. The left cerebral hemisphere is normally perfused. Subsequent DSA demonstrated patency of all cervical and intracranial vessels.

(Filename: TCT_E-105_ECMOfigureASNRcopy.jpg)

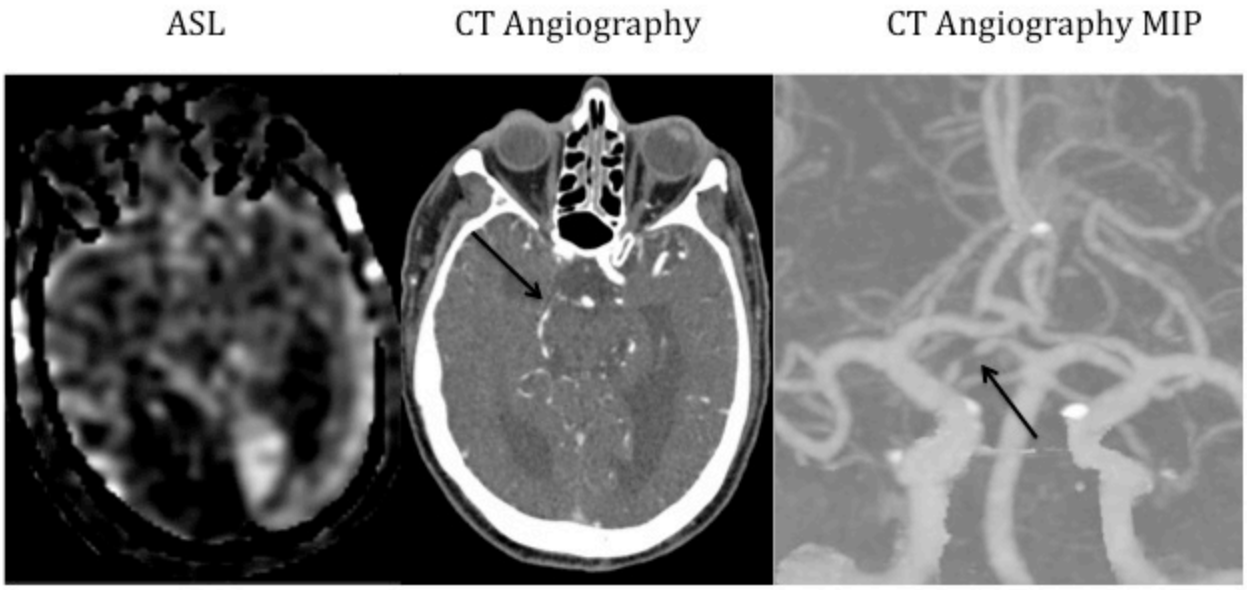
E-106

11:56AM - 12:00PM

Detection of Subclinical Cerebrovascular Stenosis with Arterial Spin Labeling (ASL)

R Delfanti[1], N Farid[1]
[1]*University of California, San Diego, San Diego, CA*

Purpose
Arterial spin labeling (ASL) is an magnetic resonance (MR) technique that quantifies perfusion using magnetically labeled blood as an endogenous contrast agent, and demonstrates promise in detecting subclinical cerebrovascular stenosis.
Materials and Methods
A 64-year-old man with history of an infarct 2 years prior without residual deficits who developed altered mental status and suffered a fall. The patient presented to the Emergency Room with persistent altered mental status as well as left gaze preference and right hemiparesis.
Results
Diffusion-weighted images from the brain MRI demonstrate restricted diffusion in the left corona radiata reflecting a small acute infarct corresponding to the patient's symptoms of right hemiparesis. A small acute left subdural hematoma also is noted, sequelae of the patient's fall. Arterial spin labeling images demonstrate asymmetrically decreased cerebral blood flow (CBF) in the right posterior cerebral artery (PCA) territory. Concurrent CT angiogram demonstrates a focal high-grade stenosis in the proximal P2 segment of the right PCA corresponding to the region of hypoperfusion demonstrated on ASL. There was no appreciable decrease in CBF on the ASL images in the region of the patient's acute infarct, likely due to the small size.
Conclusions
In patients undergoing work up for acute cerebrovascular ischemia, ASL may identify additional regions of hypoperfusion serving as a marker for subclinical yet hemodynamically significant cerebrovascular stenosis. These areas should be further evaluated with CTA, MRA, or conventional angiography possibly leading to earlier intervention and prevention of future morbidity and mortality.



Selected image from the ASL sequence demonstrates asymmetric decreased perfusion in the right posterior cerebral artery territory. The CT Angiogram and Maximum Intensity Projection (MIP) image demonstrate a focal high grade stenosis (arrows) in the proximal P2 segment of the right PCA corresponding to the region of decreased cerebral blood flow.

(Filename: TCT_E-106_ASLFigure_Final.jpg)

E-107

12:00PM - 12:04PM

Lateral Medullary Syndrome in a Young Adult: An Unusual Presentation of Fibromuscular Dysplasia

A Rich[1], J Newman[2]
[1]University Of Tennesse Health Science Center, Memphis, TN, [2]Memphis Radiological, PC, Memphis, TN

Purpose
Fibromuscular dysplasia (FMD) is a noninflammatory, nonatherosclerotic angiopathy typically involving small and medium arteries. Fibromuscular dysplasia usually is found in patients between ages 30-50 with a strong female predilection. Although the etiology has not

been well established, the pathologic changes involve fibromuscular thickening of any layer of the vessel wall with involvement of the media being the most common. Traditionally, FMD has been described most commonly in the renal and carotid arteries, but vertebral, mesenteric and coronary arterial involvement can be seen as well. Although many cases are asymptomatic, clinical findings such as secondary hypertension, stroke, arterial dissection, myocardial infarction, and mesenteric ischemia are among the many possible patient presentations. We present an unusual case of lateral medullary syndrome due to vertebral artery dissection and an asymptomatic internal carotid artery dissection in a patient with previously undiagnosed FMD.

Materials and Methods

A 38-year-old previously healthy female presented to the ER with sudden-onset vertigo and right-sided numbness with no history of trauma or chronic medical illness. Imaging at that time did not demonstrate an acute abnormality and patient was discharged to follow-up with Neurology in 1 week. The patient's symptoms did not resolve by the time of her Neurology appointment, and she also was found at that time to have left-sided ptosis, left-sided weakness, and hoarseness. Laryngoscopy then was performed by ENT, and the patient was found to have a left vocal cord paralysis, as well. These findings were highly suspicious for lateral medullary syndrome (Wallenberg syndrome), and magnetic resonance imaging (MRI) of the brain then was performed, which was followed by magnetic resonance angiography (MRA) and computed tomography angiography (CTA) evaluation of the head and neck.

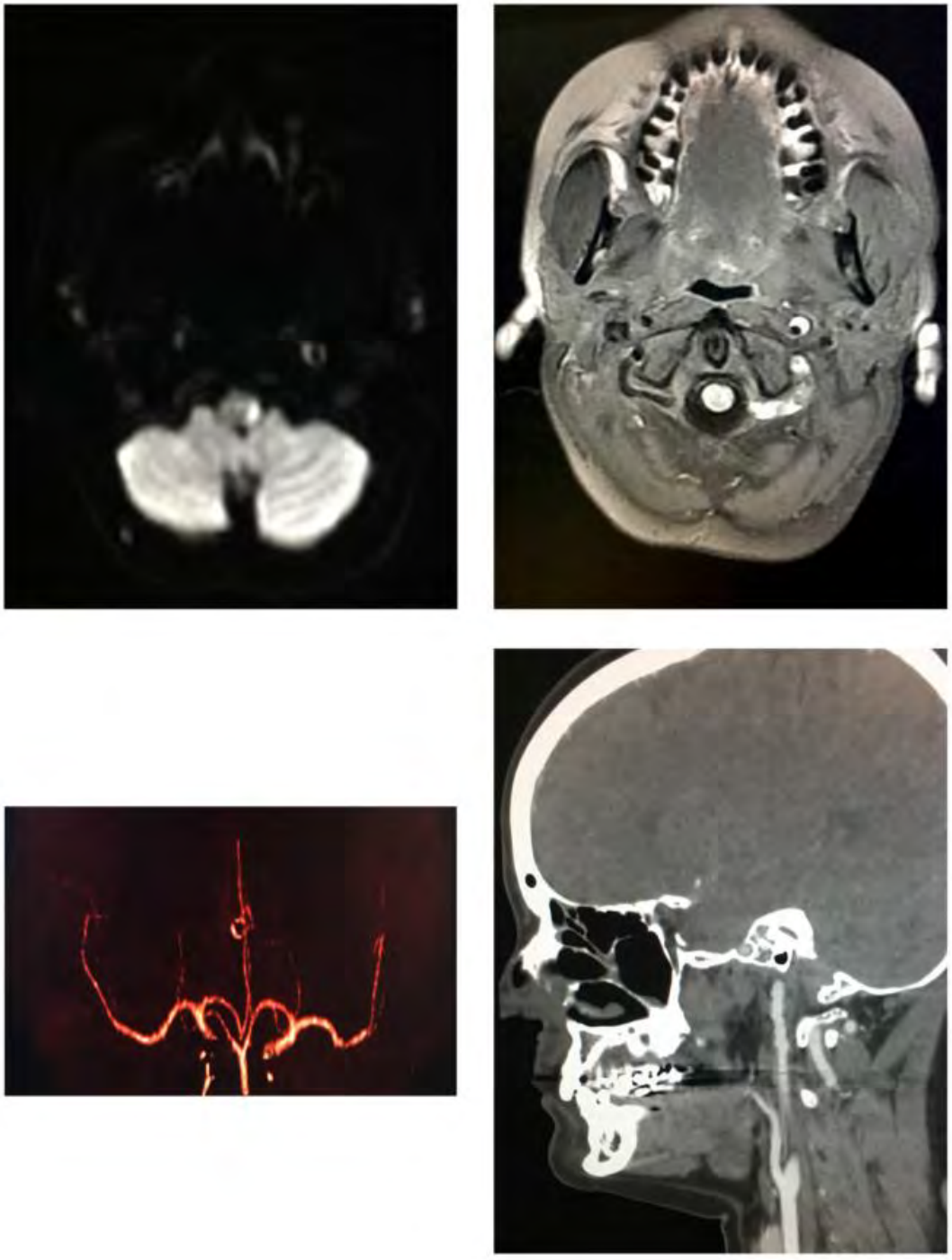
Results

Initial MRI imaging demonstrated a subtle focus of restricted diffusion in the left lateral medulla as well an absence of the normal flow void in the left vertebral artery. Further evaluation with CTA of the head and neck showed focal narrowing of the left vertebral artery at the C1-C2 level with occlusion of the left PICA, as well as an nonocclusive arterial dissection with mural hematoma of the distal cervical segment of the left ICA. Computed tomography angiography also demonstrated a classic "string of beads" contour irregularity involving the bilateral ICAs and cervical portions of both vertebral arteries. Magnetic resonance angiography imaging also showed similar vascular findings and a long segment dissection of the left vertebral artery with distal occlusion and redemonstration of the left ICA dissection. As the patient was outside of the therapeutic window for tPA administration, she was started on anticoagulation therapy and placed in observation. She gradually had partial resolution of her symptoms of weakness and numbness, and subsequent imaging demonstrated stability to the dissections and no additional infarcts. Of note, it also was discovered that the patient's sister had unusual CNS symptoms in the past as well, and eventually was diagnosed also with FMD after further work up.

Conclusions

Although FMD is a well known angiopathy of medium and small arteries with characteristic imaging findings, the disease often can be overlooked as a cause of unusual acute CNS pathology in young adults. As such, a radiologist can greatly aid in patient care by considering this disease in their differential in such cases. Additionally, given the propensity

of FMD for multi-vessel involvement it is important to evaluate all of the major arteries of the head and neck as well as the coronary and renal arteries for additional pathology, as was seen in the dissection of the left ICA in this case. By using appropriate clinical considerations and angiographic imaging, the diagnosis of FMD can be hastened and limit potential delays in treatment.



(Filename: TCT_E-107_FMDcasecollage.jpg)

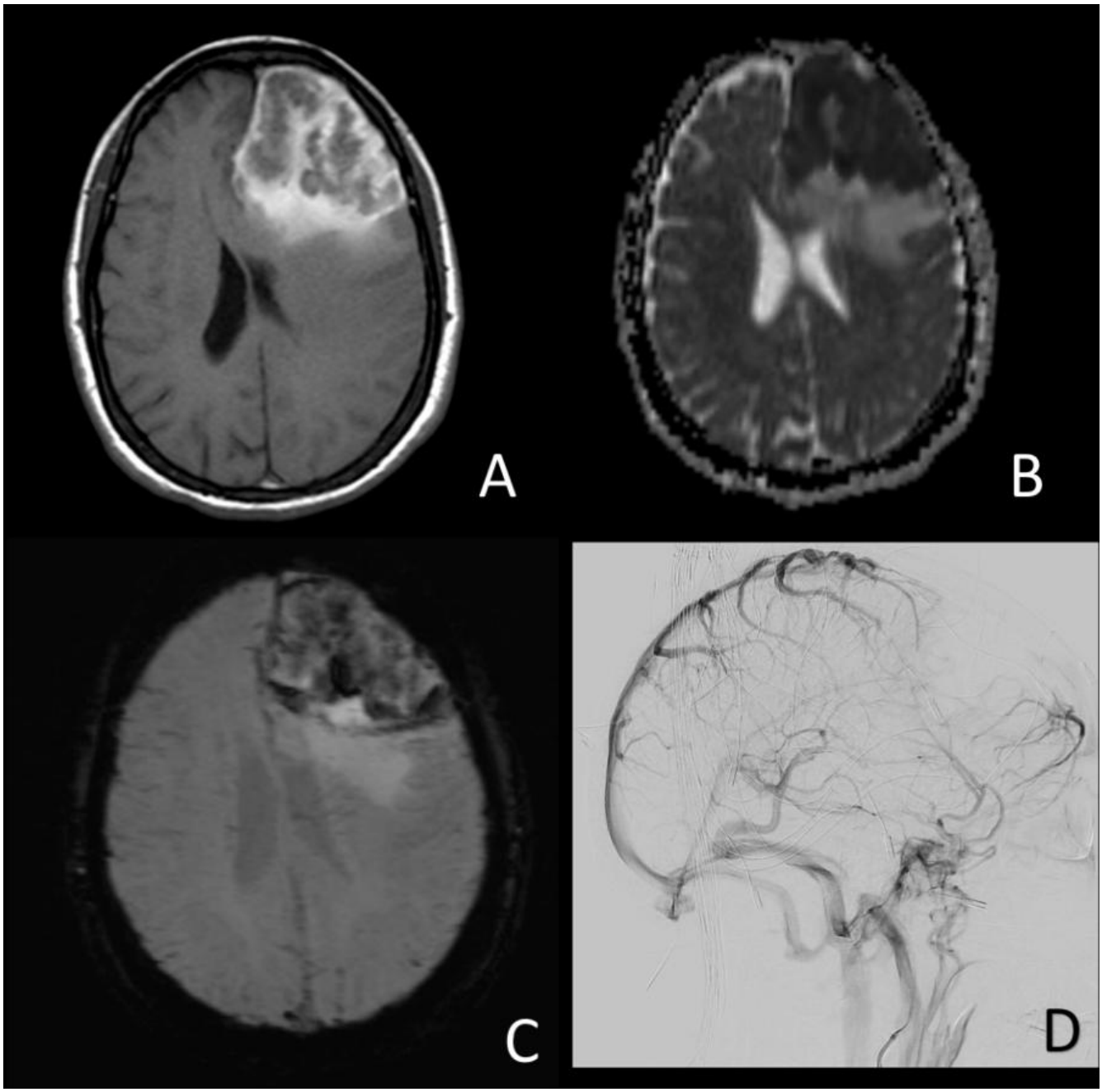
E-108

12:04PM - 12:08PM

Pitfalls in the Diagnosis of Anterior Superior Sagittal Sinus Thrombosis: A Case of a Large Unilateral Mass-like Venous Infarction

C Nguyen[1], E Kuoy[1], E Mendoza[2], R Venkatesh[1]
[1]University of California, Irvine, Orange, CA, [2]University of California, Irvine, ORANGE, CA

Purpose
Our purpose is to present a case of superior sagittal sinus thrombosis and venous infarction which presented as a large, unilateral frontal lobe mass. We will describe the clinical characteristics, radiologic appearances, and diagnostic pitfalls of venous infarctions.
Materials and Methods
A 47-year-old female, with no significant medical history, presents with worsening aphasia, right upper extremity weakness, and lethargy over a 1-week period. After initial presentation at a community hospital, the patient was transferred to a tertiary care center for evaluation and biopsy of a left frontal lobe lesion. Cerebrospinal fluid (CSF) studies were unremarkable. Work up for hereditary and acquired hypercoagulability was negative.
Results
A. T1-weighted, precontrast images demonstrate a large, heterogeneous, left frontal cortical gyriform mass-like lesion. The lesion demonstrates areas of intrinsic T1 hyperintensity and does not cross the midline. Postcontrast images demonstrate no enhancement. B. Diffusion-weighted imaging (DWI) demonstrates cortical and subcortical restricted diffusion. C. Susceptibility-weighted imaging (SWI) demonstrates internal areas of hypointensity, representing hemorrhagic blood products. There are curvilinear SWI hypointensities representing asymmetric irregularity of the left-sided cortical veins. D. Catheter directed angiogram demonstrates partial occlusion of the anterior third of the superior sagittal sinus, irregularity of the left-sided cortical veins, and asymmetric, decreased flow on the left side.
Conclusions
We present a case of a 47-year-old female with cerebral venous infarction secondary to superior sagittal sinus thrombosis. This case is atypical because the infarction was large, mass-like, and unilateral; and the patient had no identifiable risk factors. Although the initial plan of action was to biopsy the lesion, further review of imaging and work up led to an accurate diagnosis and obviated the need for biopsy. Venous infarctions can have a wide range of radiologic appearances and should be included on the differential for mass-like lesions with atypical characteristics.



(Filename: TCT_E-108_Venousinfarction.jpg)

E-109

12:08PM - 12:12PM

Third Ventricular Cyst-Like Herniation Dissecting through the Brainstem Resulting in Obstructive Hydrocephalus through Extrinsic Compression of the Aqueduct and Fourth Ventricle

J Houkal[1], S Imbesi[1], J Chen[2]

[1]University of California, San Diego, San Diego, CA, [2]San Diego VA / UCSD Med. Center, La Jolla, CA

Purpose

To present an uncommon case of cyst-like third ventricular herniation dissecting through the brainstem resulting in obstructive hydrocephalus by compression of the fourth ventricle and cerebral aqueduct.

Materials and Methods

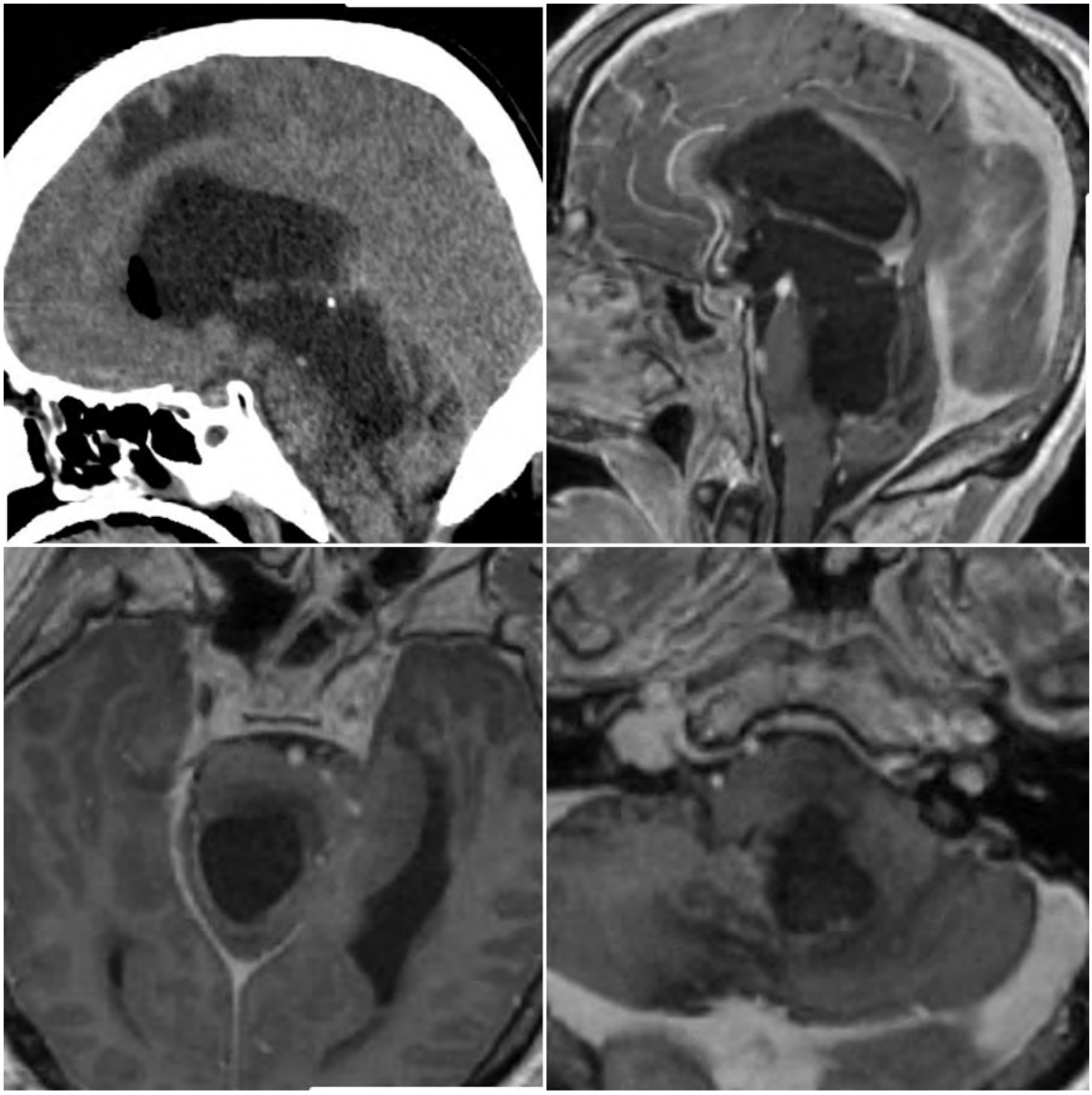
A 41-year-old male with previous traumatic brain injury requiring a ventriculoperitoneal shunt (VPS) for obstructive hydrocephalus presented with altered mental status and unresponsiveness. Despite multiple previous shunt revisions, shunt malfunction was clinically suspected and the patient was admitted for surgical management. The indwelling VPS was replaced by a lumbar drain. Despite cerebrospinal fluid (CSF) drainage from the lumbar drain, the patient worsened and hydrocephalus progressed until placement of a third ventricular drain.

Results

Consecutive CT exams show obstructive hydrocephalus varying with the size of fluid density lesion contiguous with the posterior aspect of the dilated third ventricle and dissecting inferiorly through the brainstem and compressing the fourth ventricle and cerebral aqueduct. Thin-section volumetric postcontrast T1-weighted magnetic resonance imaging (MRI) better demonstrates the thin brainstem parenchyma separating the lesion from the fourth ventricle and aqueduct. Head computed tomography (CT) after placement of lumbar drain demonstrates increasing lesion size and worsening fourth ventricular compression and hydrocephalus. Head CT after placement of a third ventricular drain and removal of the lumbar drain demonstrates improved hydrocephalus and decreased size of the fluid lesion.

Conclusions

This is an uncommon case of a third ventricular cyst-like herniation dissecting through the brainstem resulting in obstruction of the fourth ventricle and cerebral aqueduct. Literature review demonstrates scant case reports, last in 1975 by pneumoencephalography by Vencken and Sloof (1), without a case documented by cross-sectional imaging. A more recent case report by Jalessi et al (2) documents third ventricular herniation in transphendoidal fenestration although without resultant hydrocephalus. This case highlights the necessity of understanding ventricular anatomy in guiding the appropriate treatment approach from above the lesion.



(Filename: TCT_E-109_dissecting3rdventricle.jpg)

E-110

12:12PM - 12:16PM

Paradoxical Brain Herniation: A Potentially Life-Threatening Complication of Post-Craniectomy Cerebrospinal Fluid Removal

A Prabhuswamy[1], B Chow[1]
[1]*Santa Barbara Cottage Hospital, Santa Barbara, CA*

Purpose
Sinking skin flap syndrome, and its most severe radiologic co-manifestation, paradoxical

brain herniation, are rare potential complications of craniectomy. We report a case of paradoxical brain herniation following lumbar puncture to educate radiologists about the possible risks of cerebrospinal fluid (CSF) intervention in the postcraniectomy state.

Materials and Methods

A 24-year-old female with a history of polysubstance abuse was transferred to our institution after being found wandering the streets of her neighborhood confused. Admission computed tomography (CT) demonstrated a 7 cm intraparenchymal hematoma in the right frontal lobe with 1 cm of right to left subfalcine herniation. Cerebral angiography did not demonstrate a vascular lesion, therefore the patient underwent right pterional craniotomy for presumed substance-induced intracerebral hemorrhage. Intracranial pressure remained persistently elevated for 3 days postcraniotomy, and the patient required decompressive right craniectomy. Daily head CTs showed stable mild transcranial herniation of the brain through the craniectomy defect. Two weeks after craniectomy, she developed a fever of unknown origin. Diagnostic tests included lumbar puncture (LP), which was performed in the radiology department. Twenty milliliters of cerebrospinal fluid (CSF) was removed. Five days post-LP, head CT showed new concavity of the brain at the craniectomy site and new 1.2 cm of "paradoxical" right-to-left subfalcine herniation, away from the side of craniectomy. At this time the patient was complaining of mild to moderate headache, but was otherwise neurologically intact. Given the lack of significant clinical impairment, the neurosurgical team opted for conservative treatment rather than emergent epidural blood patch. She was discharged to a rehabilitation facility and eventually underwent cranioplasty.

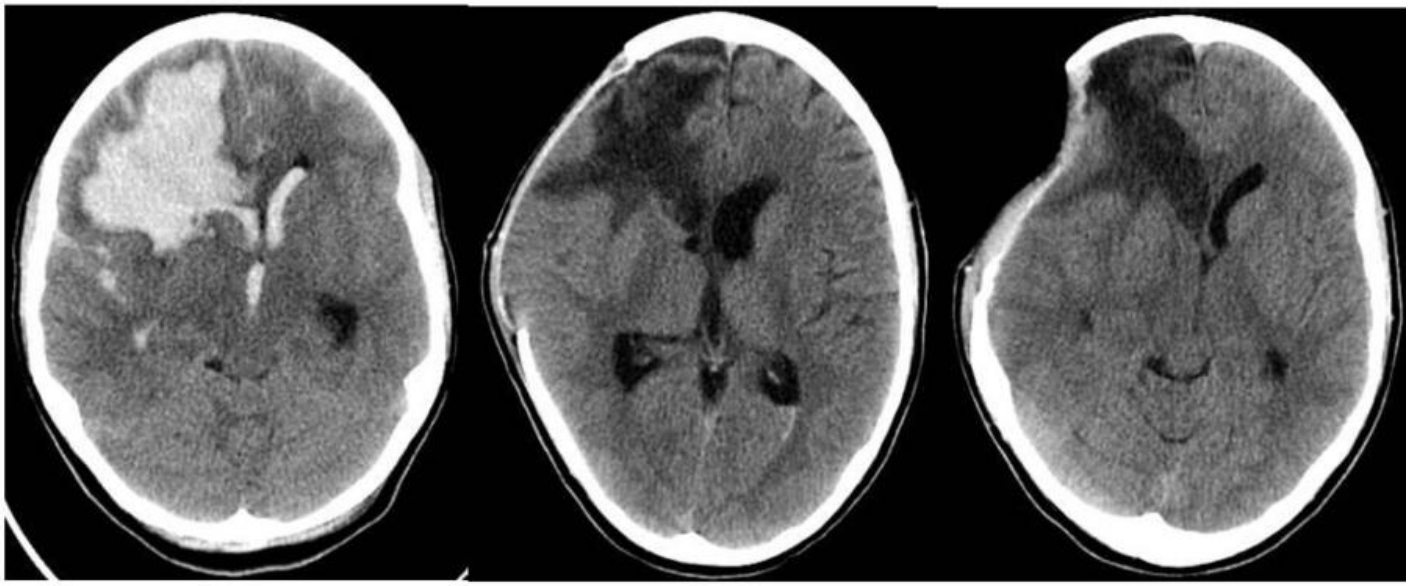
Results

Image 1 - Initial imaging. Axial noncontrast CT shows a large right frontal parenchymal hematoma. There is extensive subarachnoid and intraventricular hemorrhage. Moderate right-to-left subfalcine herniation is present. Image 2 - Post-right frontal craniectomy and hematoma evacuation. Axial noncontrast CT shows expected transcranial brain herniation across the calvarial defect. Subfalcine herniation has improved. Subarachnoid hemorrhage has resolved. There is trace residual intraventricular hemorrhage. Hypoattenuation of the right frontal lobe suggests developing encephalomalacia. Image 3 - Five days postlumbar puncture. There is a new concave appearance of the right frontal lobe contour and new "paradoxical" right-to-left subfalcine herniation, away from the site of craniectomy.

Conclusions

In the weeks following craniectomy, normal CSF circulation is deranged. Common manifestations include subdural hygroma and hydrocephalus. Sinking skin flap syndrome is a rare but important complication. It was described originally as neurological symptoms secondary to compression of the underlying brain by the skin flap, occurring as a result of atmospheric pressure exceeding intracranial pressure. Other authors have used the term Trephine syndrome interchangeably, or to specifically describe a scenario in which symptoms resolve following restoration of the normal convex cerebral contour and/or following cranioplasty. Symptoms include headache, seizure, undue fatigue, and in severe cases sequelae of brain herniation, termed "paradoxical" due to herniation away from the site

of decompressive craniectomy. CSF manipulation, including LP, is a known risk factor for the precipitation of sinking skin flap syndrome and paradoxical brain herniation because it further increases the gradient of atmospheric pressure to intracranial pressure. Nonsurgical restoration of intracranial pressure involves placing the patient in Trendelenburg position or decubitus position with the craniectomy side down, administration of IV fluids, clamping of extraventricular drain if present, and placement of an epidural blood patch if there is a history of LP. In more serious cases, emergent cranioplasty should be considered. We report a case of paradoxical brain herniation following LP to educate radiologists about this complication, and to encourage thorough consideration of the risks and benefits prior to CSF manipulation in the setting of cranial surgery.



1 2 3

(Filename: TCT_E-110_ALLIMAGES.jpg)

E-111

12:16PM - 12:20PM

Clandestine Charm Needles: A Radiologist's Challenge

M Jurkiewicz[1], T Lim[2], S Mohan[3]
[1]Hospital of the University of Pennsylvania, Philadelphia, PA, [2]National Neuroscience Institute, Singapore, Singapore, [3]University of Pennsylvania, Philadelphia, PA

Purpose

To review the imaging appearance of a bizzare case of these 'charm' needles so as to raise awareness of this potential diagnostic challenge and help the radiologist avoid confusion when interpreting images.

Materials and Methods

A 94-year-old Korean woman was seen in the Emergency Department after a fall. CT examination of the maxillofacial region found multiple small linear metallic densities in the subcutaneous soft tissues of the face. The appearance of these densities was unchanged when compared to a study performed 2 years prior, however the imaging interpretations of these densities were markedly different. Additional imaging during the course of her admission demonstrated numerous similar densities in the breasts, abdomen, hips, and legs. Although common practice in Southeast Asia (Loh and Yeo, 1989), with ever increasing globalization, these 'charm needles', or 'susuks', are being seen with greater frequency in North America.

Results

Fig. 1. A: 3D reconstructions of the face demonstrate the metallic densities over the bilateral maxillae with additional similar densities over the forehead and zygomatic arches and lateral orbital walls (not shown). B. Abdominal radiograph demonstrating approximately 100 small linear metallic densities projecting over the abdomen, pelvis, and hips. Abdomen/pelvis CT (not shown) demonstrated that the majority of these were in the posterior soft tissues over the back and over the gluteal muscles, with only a small few in the soft tissues anteriorly. C. Lateral chest radiograph demonstrating a single metallic density projecting over the breasts. D. Bilateral knee radiographs demonstrating numerous linear metallic densities projecting over the subcutaneous soft tissues of the thighs and knees. The patient had prior bilateral total knee arthroplasties.

Conclusions

The increasing ease with which people can now travel the world for holiday, business, medical tourism, or to live, makes awareness of the unique practice of charm needles important to all radiologists, helping to minimize any potential diagnostic challenge when these needles are found on imaging, thus avoiding mismanagement, and unnecessary or incorrect work up.



(Filename: TCT_E-111_Figure1.jpg)

Thursday
11:00AM - 12:15PM
Long Beach Convention Center, Room 203AB (Upper Level)

24G-Parallel Paper Session: Metastases – Imaging Makes a Difference

O-448

11:00AM - 11:08AM

Semi-Automated Assessment for Distinguishing Glioblastoma and Solitary Brain Metastasis on MRI: A Machine Learning Approach

N Swinburne[1], J Schefflein[1], Y Sakai[1], I Chen[1], S Tadayon[1], A Doshi[1], J Puig[2], K Nael[1]

[1]Icahn School of Medicine at Mount Sinai, New York, NY, [2]Research Unit of Diagnostic Imaging Institute (IDI), IDIBGI, University Hospital Dr Josep Trueta, Girona, Girona

Purpose
Differentiating glioblastoma and solitary brain metastasis on MRI can present a diagnostic dilemma. We investigate whether machine learning (ML) evaluation of multimodal MRI can reliably differentiate glioblastoma from brain metastasis.
Materials and Methods
Pre-operative MR imaging including FLAIR, DWI, dynamic contrast-enhanced (DCE), dynamic susceptibility contrast (DSC) perfusion and post-contrast T1 (T1C+) in patients with solitary enhancing lesions were reviewed retrospectively. Dynamic contrast-enhanced and DSC perfusion data sets were processed by an extended Toft model (1) and Bayesian probabilistic method (2), respectively, using Olea Sphere (Olea Medical SAS, La Ciotat, France). Conventional (T1C+, FLAIR), relative cerebral blood volume (rCBV) and relative cerebral blood flow (rCBF) from DSC, volume transfer constant from plasma to extravascular extracellular space (EES) (Ktrans), rate constant between EES to plasma (Kep), plasma volume per unit tissue volume (Vp) and EES-volume per unit tissue volume (Ve) from DCE in addition to apparent diffusion coefficient (ADC) maps from DWI then were analyzed using the fMRI Software Library (Analysis Group, Oxford, UK) Version 5.0 (3). Preprocessing steps included brain extraction, histogram normalization and coregistration. Two separate volumes of interest (VOIs) were drawn manually on enhancing tumor and nonenhancing T2 hyperintense (NET2) region using coregistered T1C+ and FLAIR images, respectively. These preprocessed data were utilized for supervised training of a ML classification kernel using the Pattern Recognition for Neuroimaging Toolbox (UCL, London, UK) v2.0 (4). Training entailed evaluation of labeled (i.e., glioblastoma vs. metastasis) MRI data for creation of a support vector machine (SVM) kernel, which was validated on unlabeled cases using the leave-one-subject-out method. Quantitative analysis from VOIs, ML accuracy, and receiver operating characteristic data were collected.
Results
Twelve patients (7 male, 5 female; age 52 ± 11 years) with glioblastoma (n=7) and metastasis (n=5; lung carcinoma=2, esophageal carcinoma=1, melanoma=1, neuroendocrine carcinoma=1) were identified. The trained ML kernel discriminated with 72.6% balanced accuracy (p=0.0001) between glioblastoma (class accuracy 64.3%; p=0.28) and metastasis (class accuracy 81.0%; p=0.004), with the highest accuracy achieved from combined evaluation of ADC, rCBV, ktrans and VP using enhancement-based VOIs.
Conclusions
Given a set of VOIs defined by lesional contrast enhancement, a trained SVM can accurately differentiate between glioblastoma and brain metastasis utilizing ADC, rCBV, ktrans and VP. A larger prospective study is required to validate these results.

O-449

11:08AM - 11:16AM

Does Multiphase Contrast-enhanced FLAIR MRI Enhance the Detectability of Small and Micro Brain Metastases in Non-Small Cell Lung Cancer Patients?

K Yi[1], J Kim[1], C Choi[1], S Cha[2], S Woo[3]
[1]Chungbuk National University Hospital, Cheongju, Chungbuk, [2]Chungbuk National University Hospital, College of Medicine and Medical Research Institute, Cheongju, Chungbuk, [3]Bayer Korea, Seoul, Kyunggi

Purpose
Contrast-enhanced (CE)-FLAIR MRI have advantages in detection of brain parenchymal and leptomeningeal metastases because CE-FLAIR images do not show enhancement in normal vascular structure and meninges. This is to validate our hypothesis that multiphase CE-FLAIR MRI may enhance the detectability of small or tiny brain metastasis prior to treatment in nonsmall cell lung cancer (NSCLC) patients.
Materials and Methods
Total 432 newly diagnosed small and micro metastatic nodules (size≤5 mm) of 125 NSCLC patients were enrolled. Diagnosis of brain metastasis was established by interpreting the initial and follow-up MRIs when the lesions showed changes in size or shape following treatment. Multiphase CE-FLAIR MRI was performed at 5 min 40s (first scan, n=57 nodules), 8 min (second scan, n=57 nodules), and 10 min (third scan, n=17 nodules) after contrast injection respectively. Enhancement ratio was calculated and compared each metastatic nodules on CE-T1WI and each CE-FLAIR MRI, respectively [(Ratio= PostCE(Nodule)/PreCE(Nodule))/(PostCE(Corpus callosum)]/PreCE(Corpus callosum). And single-phase CE-FLAIR (n=357 nodules) also was performed at the same time-interval as first scan of CE-FLAIR to validate the comparison results of multiphase CE-FLAIR/CE-T1WI. Visual assessment also was performed whether metastatic nodules were enhanced on CE-T1WI and CE-FLAIR MRIs, respectively. Paired t-test was used for the statistical analysis.
Results
Comparing with CE-T1WI and multiphase CE-FLAIRs, calculated enhancement ratios were significantly lower in all phases of CE-FLAIRs than CE-T1WI (RatioT1WI:Ratio1stFLAIR=1.42:1.15, RatioT1WI:Ratio2ndFLAIR=1.42:1.13, RatioT1WI:Ratio3rdFLAIR= 1.33:1.02, $p < 0.001$ respectively). Additional comparison between nodules of 1st scan CE-FLAIR + single-phase CE-FLAIR and CE-T1WI showed same result (RatioT1WI:RatioFLAIR =1.42:1.17, $p<0.001$). One hundred seventy-one among 432 nodules (39.6%) did not show contrast enhancement on CE-FLAIR, but only one nodule on CE-T1WI.
Conclusions
There may be many advantages of getting CE-FLAIR MRI images, but time consuming

multiphase CE-FLAIR MRI is not beneficial to detect small and micro brain metastasis in NSCLC patients.

O-450

11:16AM - 11:24AM

Detecting Additional Brain Metastases at Time of Steretactic Radiosurgery: Double-Dose Gadolinium Contrast Changes Management and Prognosticates Clinical Outcomes

B Liu[1], L Jaros[1], J Kalapurakal[1]
[1]*Northwestern University Feinberg School of Medicine, Chicago, IL*

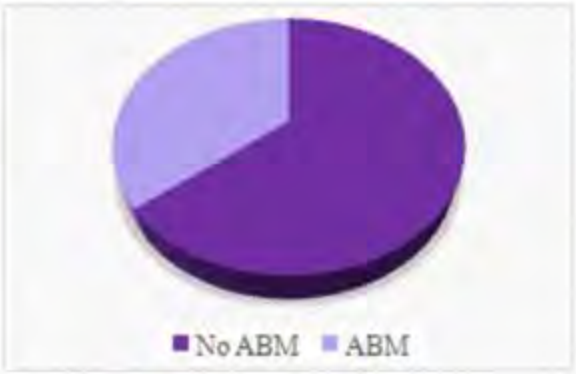
Purpose
The aims of this study were to assess the utility of double-dose gadolinium contrast in the detection of brain metastases at the time of stereotactic radiosurgery (SRS) and to determine the clinical prognostic value of detecting additional brain metastases.
Materials and Methods
In this single-center, retrospective cohort study, a series of 140 patients with a biopsy-proven non-neurological primary tumor underwent evaluation and SRS treatment for intracranial metastases. Each patient was screened first with standard institutional surveillance tumor protocol MRI using single-dose (0.1 mmol/kg) gadobutrol and then underwent a stereotactic planning brain MRI using double-dose (0.2 mmol/kg) gadobutrol. The number of intracranial metastases were counted based on radiology reports and confirmed visually on MRI to ensure accuracy. Additional demographic information including age, primary tumor type, weight, contrast dose and type, and renal function also were collected. Post-SRS follow-up MRI brain imaging was performed serially using single-dose gadobutrol to assess for recurrence of brain metastasis. Progression-free survival was recorded and analyzed using Kaplan-Meier analysis.
Results
Compared to single-dose, MR imaging with double-dose gadobutrol revealed additional metastases in 36% of patients on the day of stereotactic radiosurgery (SRS), with an average of 2.54 additional metastases in affected patients. The progression-free survival for patients with no additional brain metastases versus patients with additional brain metastases showed a statistically significant difference over the first 6 months but not over 4 years of follow up. Specifically, patients with newly discovered additional brain metastases at the time of SRS had an average time to recurrence of 2 months, compared to 4 months for patients without additional brain metastases found at time of SRS ($p=0.0021$). However, progression-free survival was not statistically significant between the 2 groups across a longer period of follow up over 4 years ($p=0.1965$).
Conclusions
Use of double-dose gadobutrol on pre-SRS MRI allowed for significantly improved

assessment of the number of intracranial metastases and changed management in 36% of patients by allowing their additionally detected brain metastases to be targeted and treated by radiosurgery. The discovery of additional brain metastases on pre-SRS MRI prognosticates poorer progression-free-survival, although the time-to-recurrence is only shorter during the first 6 months of follow up. Progression-free survival between patients with and without additional brain metastases detected at the time of SRS using double-dose gadolinium is not significantly different when patients are followed up over a longer period of 4 years. This finding supports the theory of micrometastases dominating the source of brain metastasis recurrence during the early post-SRS period (first 6 months) versus systemic cancer burden modulating the development of de novo brain metastases in long term follow up (after 6 months).

Discovering Brain Metastases: Single vs. Double Dose

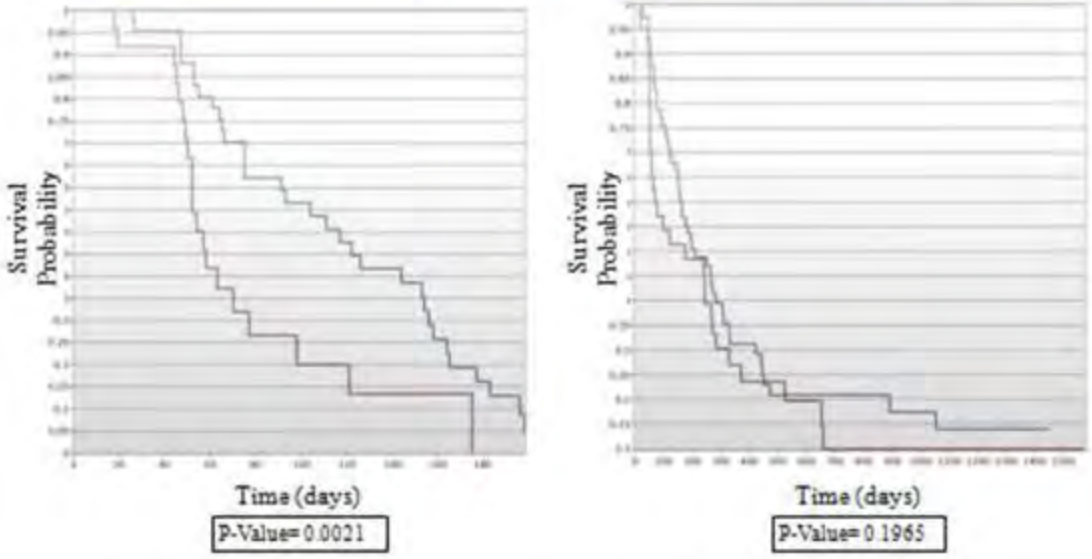
TABLE 1	
Patients	140
No ABM (%)	90 (64%)
ABM (%)	50 (36%)
Age Range (avg.)	26-85yrs (57)
Primary Neoplasm	*Number of patients (%)*
Lung	50 (35.7)
Breast	42 (30.0)
Melanoma	22 (15.7)
Other	26 (18.6)
Days Between Scans	
Average	17.3
Median	14
Range	2-125
Metastases	
Screening	432
Pre-GKRS	558
Percent increase	29.2%
Average ABM (range)	2.54 (1-9)

Table 1: A significant amount of additional metastases (29%) were discovered at the time of pre-SRS imaging with an average of 2.54 additional tumors in affected patients.



Graph 1: Additional brain metastases were found in 36% of patients at the time of pre-SRS MRI imaging.

Progression-Free Survival: aBM vs. No aBM



Graph 2: The progression free survival for patients with no additional brain metastases (blue line) vs. patients with additional brain metastases (red line) showed a statistically significant difference over the first 6 months (left) but not over 4 years (right).

(Filename: TCT_O-450_SRS-aBMfig2.jpg)

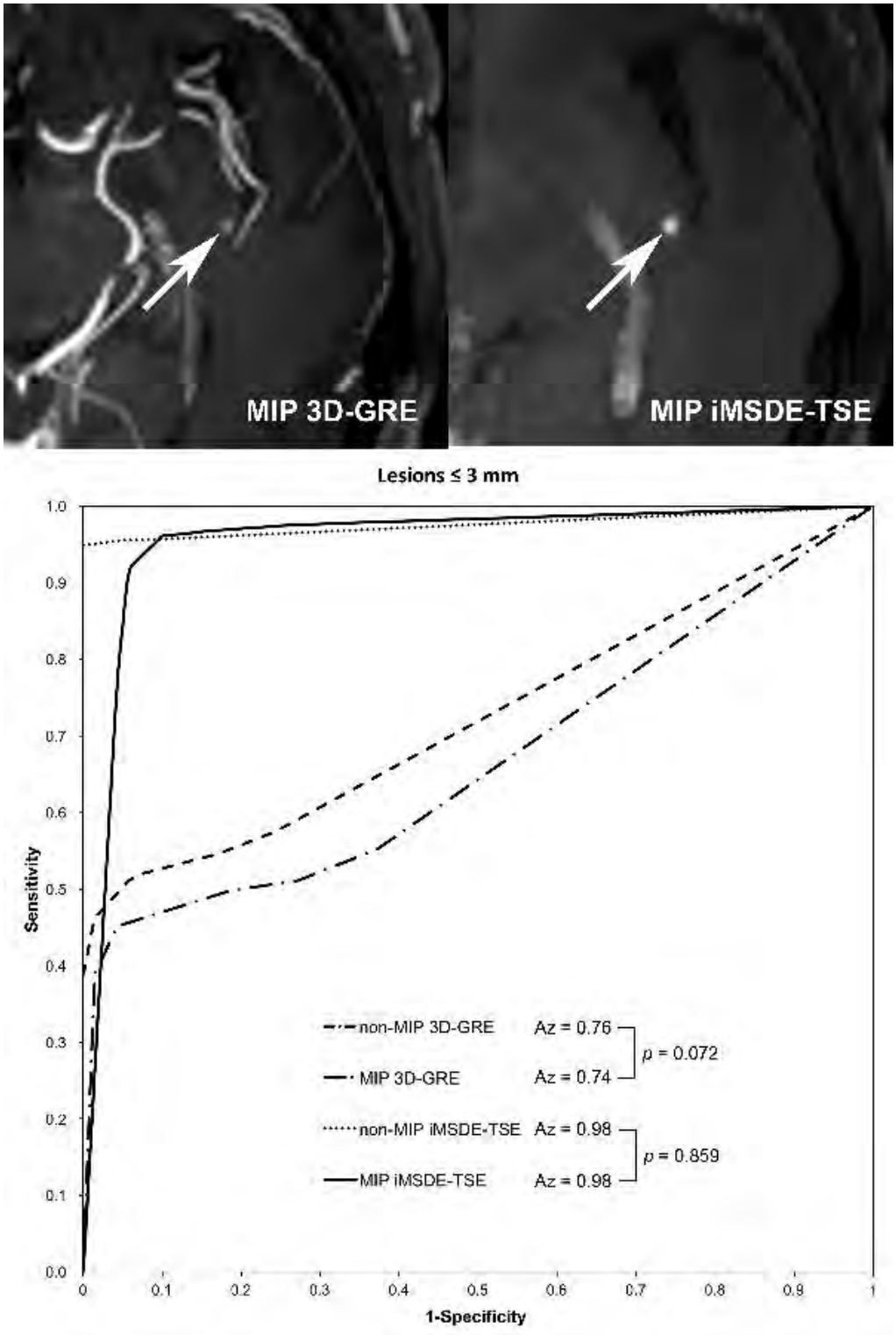
O-451

11:24AM - 11:32AM

Efficacy of Maximum Intensity Projection of Contrast-enhanced 3D Turbo-spin Echo Imaging with Improved Motion-sensitized Driven-equilibrium Preparation in the Detection of Brain Metastases

J Kim[1], B Choi[1], Y Bae[1], K Lee[2], L Sunwoo[1], C Jung[1], J Kim[1]
[1]Seoul National University Bundang Hospital, Seongnam, [2]Kyung Hee University Hospital, Seoul

Purpose
To evaluate diagnostic benefit of maximum intensity projection (MIP) of improved motion-sensitized driven-equilibrium prepared contrast-enhanced 3D T1-weighted turbo-spin echo imaging (MIP iMSDE-TSE) in the detection of brain metastases, compared with 1mm images of iMSDE-TSE (non-MIP iMSDE-TSE), those of contrast-enhanced 3D T1-weighted gradient-echo imaging (non-MIP 3D-GRE), and MIP 3D-GRE.
Materials and Methods
Institutional review board approved this retrospective study and waived informed consent. From October 2014 to July 2015, non-MIP 3D-GRE and non-MIP iMSDE-TSE were obtained from 30 patients with brain metastases, and 5-mm MIP reconstruction of these images was performed. Two independent neuroradiologists reviewed these 4 sequences. Their diagnostic performance in detecting brain metastases was compared by figure of merit (FOM) derived by JAFROC analysis, sensitivity, and reading time. Interobserver agreement also was tested.
Results
MIP iMSDE-TSE had mean FOM (all lesions; lesions≤3 mm, 0.984; 0.980) and the sensitivity (Reader 1, 97.3%; 96.2%, Reader 2, 97%; 95.8%) comparable to non-MIP iMSDE-TSE (0.985; 0.977, Reader 1, 96.7%; 99%, Reader 2, 97%; 95.3%), but superior to non-MIP and MIP 3D-GREs (all, $P<0.001$). The reading time was significantly shorter in MIP iMSDE-TSE (Reader 1, 47.7±35.9, Reader 2, 44.7±23.6) than in non-MIP iMSDE-TSE (78.8±43.7, $P=0.01$; 82.9±39.9, $P<0.001$). Interobserver agreement was excellent ($\kappa>0.7$) in both sequences.
Conclusions
MIP iMSDE-TSE had comparable detectability of brain metastases to non-MIP iMSDE-TSE, which was higher than non-MIP and MIP 3D-GREs. It also improved radiologists' performance by reducing reading time. Thus, MIP iMSDE-TSE can be used in combination with 1mm sequences for the evaluation of brain metastases.



(Filename: TCT_O-451_Fig.jpg)

O-452

11:32AM - 11:40AM

Melanoma Patients with Isolated Cerebral Susceptibility Artifacts: Are Rhey Metastases?

R Liu[1], X Wu[1], A Malhotra[1]
[1]*Yale University School of Medicine, New Haven, CT*

Purpose
Over 1/3 of patients with metastatic melanoma will develop clinically apparent brain metastases. The propensity of melanoma metastases to hemorrhage allows for the utilization of susceptibility-weighted imaging (SWI) in the assessment of metastases. However, it is unclear in the literature if the presence of abnormal signal solely on SWI signifies or predicts the presence of brain metastases.
Materials and Methods
A retrospective review of all patients with history of melanoma that underwent MRI of the brain from 1/1/2010 through 12/31/2014 was performed after IRB approval. Patients with metastatic disease on the initial examination were excluded from the study. Follow-up imaging was reviewed to assess changes over time and see if metastases developed at sites of susceptibility or at different sites.
Results
The initial search yielded 559 patients with melanoma and brain imaging over a 4-year period. After excluding patients with evidence of metastatic disease on the initial examination, 307 patients were included in the study. A total of 27 patients had isolated susceptibility artifact on SWI. All patients received follow-up MRI examinations according to the standard protocol. Of the 27 patients with evidence of isolated susceptibility artifact on SWI, no lesions subsequently developed into brain metastases.
Conclusions
In patients with a history of melanoma, the findings of isolated susceptibility artifact on SWI, with the absence of signal abnormality on additional sequences, do not signify or predict the presence of brain metastases in that location.

O-453

11:40AM - 11:48AM

Assessment of Intratumoral Vascularity obtained by Arterial Spin Labeling to Differentiate between Dural Metastases and Meningiomas

J Furtner[1], R Woitek[2], U Asenbaum[3], D Prayer[4]
[1]*Medical University of Vienna, Vienna, Vienna,* [2]*Department of Biomedical Imaging and Image-guided Therapy, Medical University of Vienna, 1090, Vienna,* [3]*Department of Biomedical Imaging and Image-guided Therapy, Medical University of Vienna, Vienna, Vienna,* [4]*Department of Biomedical Imaging and Image-guided Therapy, Medical University of Vienna, Vienna, Austria*

Purpose
Although dural metastases are rare, it is important to differentiate them from far more common meningiomas to take into account adjusted therapy options as well as different prognostic implications. This study evaluated the role of normalized vascular intratumoral signal (nVITS) obtained by pulsed arterial spin labeling imaging to differentiate between these 2 extra-axial tumor entities.
Materials and Methods
Fifteen consecutive patients with extra-axial tumorous lesions (meningiomas (n = 15; WHO I, n = 13; WHO II, n = 2) and dural metastases [n = 7; lung carcinoma metastasis, n = 4; colorectal carcinoma metastasis, n = 1; breast carcinoma metastasis, n = 2)] were prospectively included in this study. A pulsed arterial spin labeling sequence with a low inversion time (TI = 370 ms) was pre-operatively performed on a 3T MR scanner to depict intratumoral vascularization. Normalized vascular intratumoral signals were defined by signal intensity ratio between the tumor and the contralateral normal brain tissue as obtained by pulsed arterial spin labeling images. Potential differences in the nVITS between meningiomas and brain metastases were revealed using an unpaired T-test.
Results
Normalized vascular intratumoral signal obtained by pulsed arterial spin labeling sequences was significantly lower in brain metastases (mean nVITS =1.19; SD = 0.13) in comparison to meningiomas (mean nVITS = 2.57, SD = 0.98); p = 0.0016.
Conclusions
The findings of this study indicate that pulsed arterial spin labeling offers a fast and completely noninvasive assessment of tumorous vascularity, which may help to discriminate meningioma and dural metastasis in a routine clinical setting.

O-454

11:48AM - 11:56AM

Permeability imaging of metastatic brain lesions with Golden-Angle Radial Sparse Parallel MR imaging (GRASP) before and after stereotactic radiosurgery: Early Experience

I Littig[1], G Fatterpekar[2], D Kondziolka[3], T Shepherd[4]
[1]New York University, New York, NY, [2]NYU School of Medicine, New York, NY, [3]NYU Medical Center, New York , NY, [4]NYU Medical Center, New York, NY

Purpose
Improved systemic therapies improve cancer patient survival, but this has increased the number of patients with intracranial metastases. Gamma knife radiosurgery (GKRS) is highly effective for treating such metastases but relies almost solely on postcontrast MRI which provides limited tumor characterization. Unlike DSC-perfusion imaging, Golden-

Angle Radial Sparse Parallel (GRASP) MRI can provide higher temporal resolution and more complete coverage, including cortical lesions. This study used GRASP permeability imaging to characterize metastases before and after GKRS.

Materials and Methods

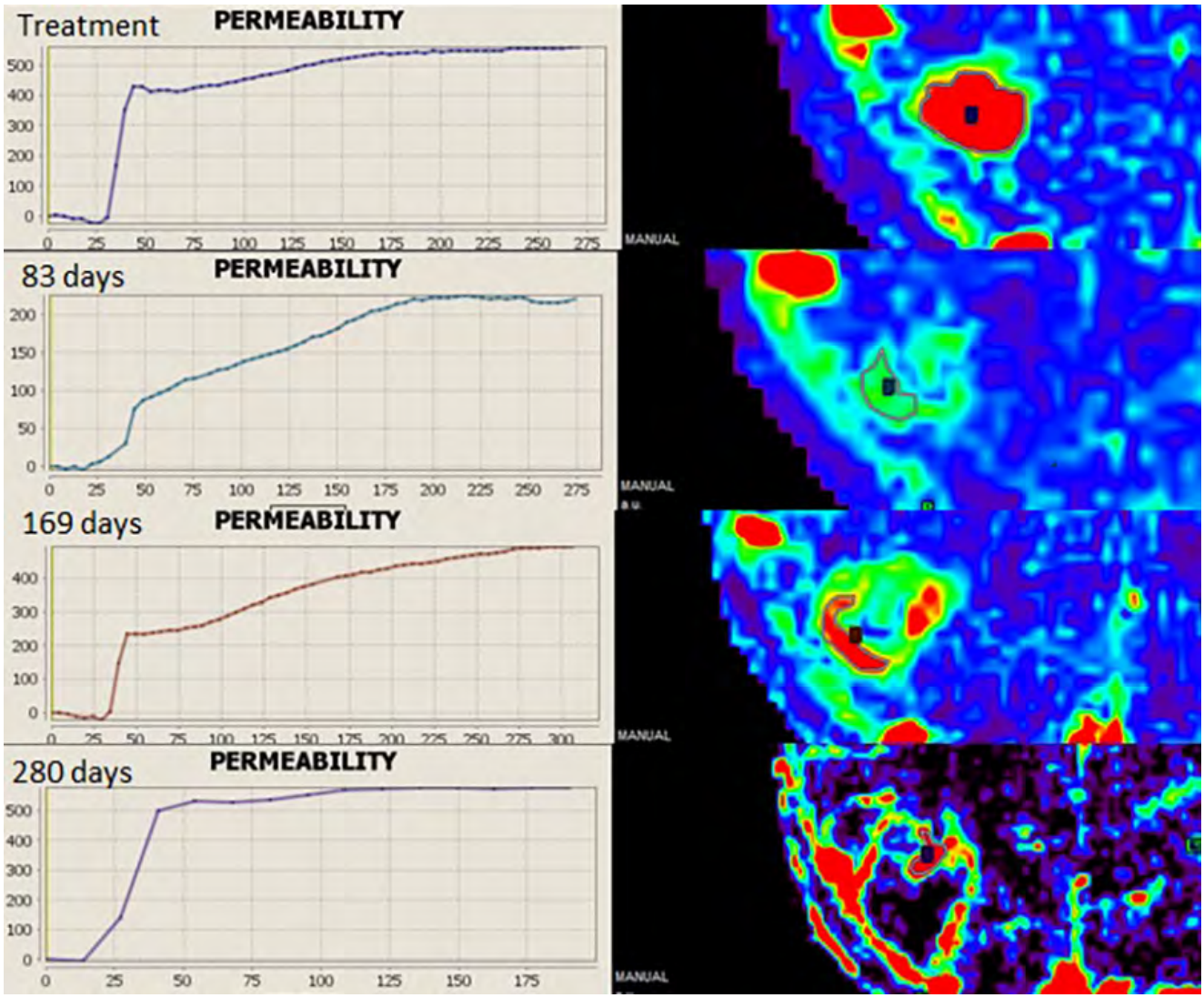
This HIPPA-compliant IRB-approved study characterized 32 patients with 56 metastases immediately prior to GKRS treatment using permeability parameters derived from GRASP MRI (Olea Medical, LaCiotat, France). Lesions <0.5 cm, with hemorrhage, prior surgical or radiotherapy were excluded. Follow-up data from 20 patients with 36 lesions were available 66±20 days following GKRS. Regions of interest were drawn in the solid enhancing tumor at both time-points with image co-registration. Permeability parameters including wash-in, wash-out, peak and area under the curve (AUC) for contrast enhancement were compared with unpaired t-tests.

Results

Metastatic lesions demonstrated a 41.3% reduction in AUC ($P=0.055$) and 51.1% reduction in wash-in kinetics ($P<0.0001$) following GKRS. Melanoma metastases had 84.5% greater AUC ($P=0.1248$) and 28.1% shorter wash-in kinetics ($P=0.2024$) compared to lung metastases at baseline. After GKRS, melanoma metastases demonstrated larger reductions in AUC (39.1% vs 20.1%, $P=0.1881$).

Conclusions

We observed significant reductions in AUC and wash-in for intracranial metastases ~60 days following GKRS attributed to frank destruction of tumor blood vessels and permeability. We observed trends for differences in baseline tumor capillary properties and response to GKRS that may be significant with greater subject enrollment. Early studies indicate return to baseline AUC and rapid wash-in kinetics may be specific for tumor recurrence over irradiation changes (see Fig.). Future studies will combine GRASP with other MRI parameters for better tumor characterization.



(Filename: TCT_O-454_FINALFIGURE.jpg)

O-455

11:56AM - 12:04PM

MRI Characteristics of EGFR-Positive Metastatic Non-Small Cell Lung Cancer

A Chaudhry[1], M Gul[2], A Chaudhry[3], H Sair[4], R Matthews[5]
[1]Johns Hopkins Medicine, Elkridge, MD, [2]National Institute of Health, Elkridge, MD, [3]Stony Brook University, Westbury, NY, [4]Johns Hopkins Medicine, Baltimore, MD, [5]Stony Brook University Medical Center, Stony Brook , NY

Purpose
Central nervous system metastases considerably outnumber primary brain neoplasms and carry a dismal prognosis. Lung cancer is the leading cause of cancer-related mortality worldwide and the propensity for lung cancer to metastasize to the central nervous system

(CNS) is one of the major causes of low survival rate in advanced stages of the disease. Recent studies have shown that patients with gene non-small cell lung cancer (NSCLC), mutations in the epidermal growth factor (EGFR) have increased propensity for brain metastasis and these patients carry worse prognosis. The aim of this study is to retrospectively evaluate imaging characteristics of lung cancer metastasis to the brain on computed tomography (CT) and MR imaging (MRI).

Materials and Methods

In this retrospective study, we identified 76 patients (46 females, 30 males; mean age, 70.1 years; age range, 48–91 years) who underwent pretreatment noncontrast CT and MRI at our institution from January 2009 to June 2014 with pathologically proven metastatic lung cancer to the brain. Patients' primary lung cancer histologic subtype (adenocarcinoma, squamous cell carcinoma and small cell lung cancer) and receptor mutations (EGFR, ALK, KRAS, etc.) were recorded. The exams were evaluated by 2 radiologists who were blinded to the pathology data.

Results

Fifty-two patients [29 females (56%) and 23 males (44%)] were identified with gain of function mutation in the EGFR gene. Most of these patients had adenocarcinoma (49/52; 94.2%) and most of these patients (43/52; 82.7%) had multiple CNS lesions. On noncontrast CT, only 11/52 (21.1%) of the patients had evidence of a lesion, which were relatively isodense to gray matter. On MRI, the lesions relative to gray matter were T1-hypointense (41/52, 78.8%) or isointense (11/52; 21.2%) on T1-weighted images and hyperintense (48/52; 92.3%) on T2 and FLAIR images and had heterogeneous postcontrast enhancement (51/52; 98%). The lesions varied in size ranging from 4.0 mm up to 37cm and average lesion size on postcontrast image was approximately 9.4mm. Thirty-three of 52 patients (63.5%) demonstrated susceptibility artifact on gradient sequences and none of these lesions demonstrated observable calcium on CT. On diffusion-weighted imaging (DWI), only 5.8% (3/52) demonstrated restricted diffusion.

Conclusions

Our study shows that in patients with metastatic lung cancer, EGFR mutation is seen more commonly in females and most of these patients have more than 1 CNS lesion. The rate of detection rate of metastasis on noncontrast CT exam is low. Magnetic resonance imaging characteristics of EGFR positive metastases include T1 hypointense, T2/FLAIR hyperintense mass without restricted diffusion, with evidence of susceptibility artifact and heterogeneous postcontrast enhancement.

O-456

12:04PM - 12:12PM

Correlation of MR image features with BRAF mutation status in patients with metastatic brain melanoma

B Yoon[1], D Das[1], P Rezaii[1], P Samghabadi[1], M Zhou[1], H Vogel[1], T Massoud[1], O Gevaert[1], K Yeom[2], M Iv[1]
[1]Stanford Hospital and Clinics, Stanford, CA, [2]Lucile Packard Children's Hospital, Palo Alto, CA

Purpose
Approximately 50% of melanomas harbor BRAF mutations, which are associated with features of more aggressive melanoma. The purpose of our study is to correlate MR image features with BRAF mutation status in patients with metastatic brain melanoma, in hopes to find a signature imaging profile of BRAF-mutated melanomas.
Materials and Methods
An IRB-approved retrospective study was performed of 37 adult patients (mean age +/- SD: 52.4 +/- 16.5 years, range 18-88 years) with surgically proven metastatic brain melanoma. BRAF mutation status was correlated with pre-operative MRI features including the presence of enhancement, restricted diffusion, T1 hyperintensity, hemorrhage, edema, necrosis, bony metastasis, dural or leptomeningeal involvement of the surgically resected or biopsied lesion. The number of additional brain metastases also were correlated. Demographic and functional status as measured by Karnofsky Performance Status (KPS) also were correlated with imaging findings. Fisher's exact and t-test were used for statistical analysis as appropriate.
Results
BRAF mutation was associated with a greater number of brain metastases; significantly more patients with BRAF mutation had greater than 10 brain metastases (n= 6 vs 0, p=0.020). There was no significant difference in the presence of enhancement, restricted diffusion, T1 hyperintensity, hemorrhage, edema, necrosis, bony metastasis, leptomeningeal or dural involvement (Table 1). There was a trend towards more male patients having BRAF mutations, although not statistically significant (77.8% vs 47.4%, p=0.091). No significant difference was found with KPS (70.8 in BRAF- vs 73.6 in BRAF+ patients, p=0.605).
Conclusions
A specific MR image feature (i.e. the presence of greater than 10 metastases) can be used to help predict BRAF-mutated melanomas metastatic to the brain.

Table 1. Correlation between BRAF mutation status and MR image features

	BRAF-	BRAF+	*p* value
Solitary brain metastasis	7/18 (38.9)	5/19 (26.3)	0.495
2-5 brain metastases	9/18 (50.0)	7/19 (36.8)	0.515
5-10 brain metastases	2/18 (11.1)	1/19 (5.3)	0.604
>10 brain metastases	0/18 (0)	6/19 (31.6)	0.020
Presence of bony metastasis	0/18 (0)	3/19 (15.8)	0.230
Dural involvement	7/18 (38.9)	7/19 (36.8)	1.000
Enhancement	14/15 (93.3)	18/19 (94.7)	1.000
Restricted diffusion	12/18 (66.7)	13/19 (68.4)	1.000
T1 hyperintensity	12/17 (70.6)	15/19 (78.9)	0.706
Hemorrhage	8/14 (57.1)	13/17 (76.5)	0.441
Edema	18/18 (100)	19/19 (100)	1.000
Necrosis	9/18 (50.0)	11/19 (57.9)	0.746
Leptomeningeal involvement	2/18 (11.1)	0/19 (0)	0.230

Data are in numbers/total numbers with percentages in parenthesis

(Filename: TCT_O-456_Melanomamets-Stats1-1.jpg)

Thursday
11:00AM - 12:15PM
Long Beach Convention Center, Room 102BC (Main Level)

24H-Parallel Paper Session: Keeping Track of Tracts

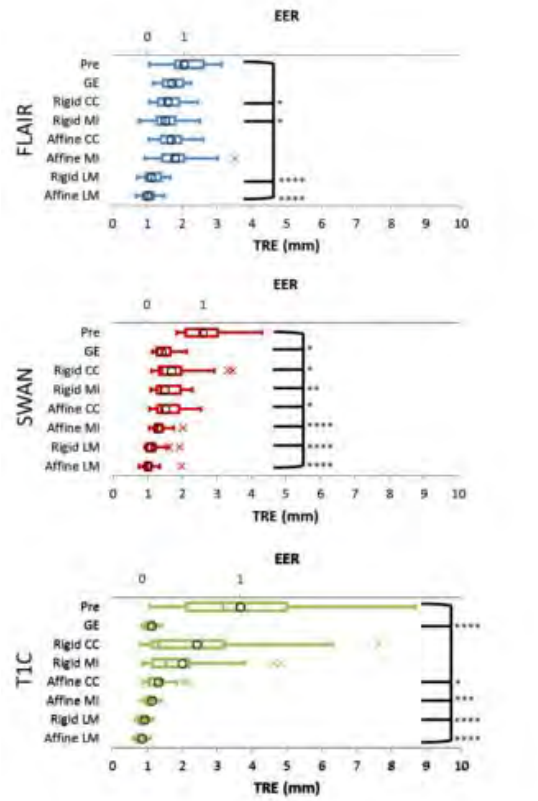
O-457

11:00AM - 11:08AM

Performance Assessment for Brain Magnetic Resonance Imaging Registration Methods

J Lin[1], D Fuentes[2], A Chandler[2], S Prabhu[3], J Weinberg[4], V Baladandayuthapani[2], J Hazle[2], D Schellingerhout[2]
[1]MD Anderson Cancer Center, Houston, TX, [2]UT MD Anderson Cancer Center, Houston, TX, [3]UT MD Anderson Cancer Center, Houston , TX, [4]MD Anderson Cancer Center, houston, TX

Purpose
Clinical brain MRI registration algorithms often are made available by commercial vendors without figures of merit. The purpose of this study was to suggest a rational performance comparison methodology for these products.
Materials and Methods
Twenty patients were imaged on clinical 3T scanners using 4 sequences: T2-weighted, FLAIR, susceptibility-weighted angiography (SWAN), and T1 postcontrast (T1C). Fiducial landmark sites (n=1175) were specified throughout these image volumes to define identical anatomic locations across sequences. Multiple registration algorithms were applied using the T2 sequence as fixed reference. Euclidean error was calculated before and after each registration and compared to a gold standard landmark registration. Euclidean Effectiveness Ratio is the fraction of Euclidean error remaining after registration, and the Statistical Effectiveness Ratio is similar, but accounts for dispersion and noise.
Results
Prior to registration, error values for FLAIR, SWAN, and T1C were 2.07±0.55 mm, 2.63±0.62 mm, and 3.65±2.00 mm, respectively. Postregistration, the best error values for FLAIR, SWAN, and T1C were 1.55±0.46 mm, 1.34±0.23 mm, and 1.06±0.16 mm, with Euclidean Effectiveness Ratio values of 0.493, 0.181, and 0.096 and Statistical Effectiveness Ratio values of 0.573, 0.352, and 0.929, for rigid mutual information, affine mutual information, and a commercial General Electric registration, respectively. These results are graphically compared in the figure.
Conclusions
We demonstrate a method for comparing the performance of registration algorithms, and suggest Euclidean Error, Euclidean Effectiveness Ratio, and Statistical Effectiveness Ratio as performance metrics for clinical registration algorithms. These figures of merit allow registration algorithms to be compared rationally.



(Filename: TCT_O-457_Figure4.jpg)

O-458

11:08AM - 11:16AM

Automated detection of volume-changing metastatic brain tumors on longitudinal brain MRI scans

O Shearkhani[1], S Symons[2], C Heyn[2], A Chan[1], A Khademi[3], P Maralani[2]
[1]University of Toronto, Toronto, Ontario, [2]Sunnybrook Health Sciences Centre, Toronto, Ontario, [3]University of Guelph, Guelph, Ontario

Purpose
Metastatic brain tumors (MBTs) occur in 24–45% of patients diagnosed with primary cancers outside the brain. Accurate detection and follow-up assessment of MBTs are critical factors for better prognosis, selecting the most appropriate treatment (e.g., chemotherapy, radiation, or surgery), and most importantly radiation planning. Contrast-enhanced (CE) 3-dimensional (3D) T1-weighted MRI is considered the modality of choice for detection, treatment planning, and follow up of MBTs. During follow up, serial volumetric imaging is obtained every 2–3 months but this results in a large amount of data to process and demanding workload for radiologists. Moreover, the inherent limitations associated with 2D image viewing and user subjectivity results in the potential for increased error rates in both

detection and volume assessment, especially in the detection of small MBTs and subtle volume changes. Computer-aided detection tools have been reported to increase radiologists' accuracy, especially in lung, prostate and breast cancers. Although several studies have investigated the efficiency of computer-aided detection techniques in the detection of MBTs on a single MR scan, the literature lacks studies that have evaluated the efficacy of computer algorithms in regards to follow up of MBTs and detection of volume-changing MBTs (vMBTs; i.e. growing or shrinking MBTs). Techniques based on deformation field, such as those centered around Jacobian operator, have been proposed as promising tools in detecting structural changes on serial brain MRI. These techniques attribute a vector to each voxel that describes its deformation from 1 longitudinal image to another, where a negative value corresponds to shrinkage and a positive value to expansion. In order to detect vMBTs on serial brain MRIs, a fully automated algorithm based on the Jacobian operator is proposed and evaluated here.

Materials and Methods

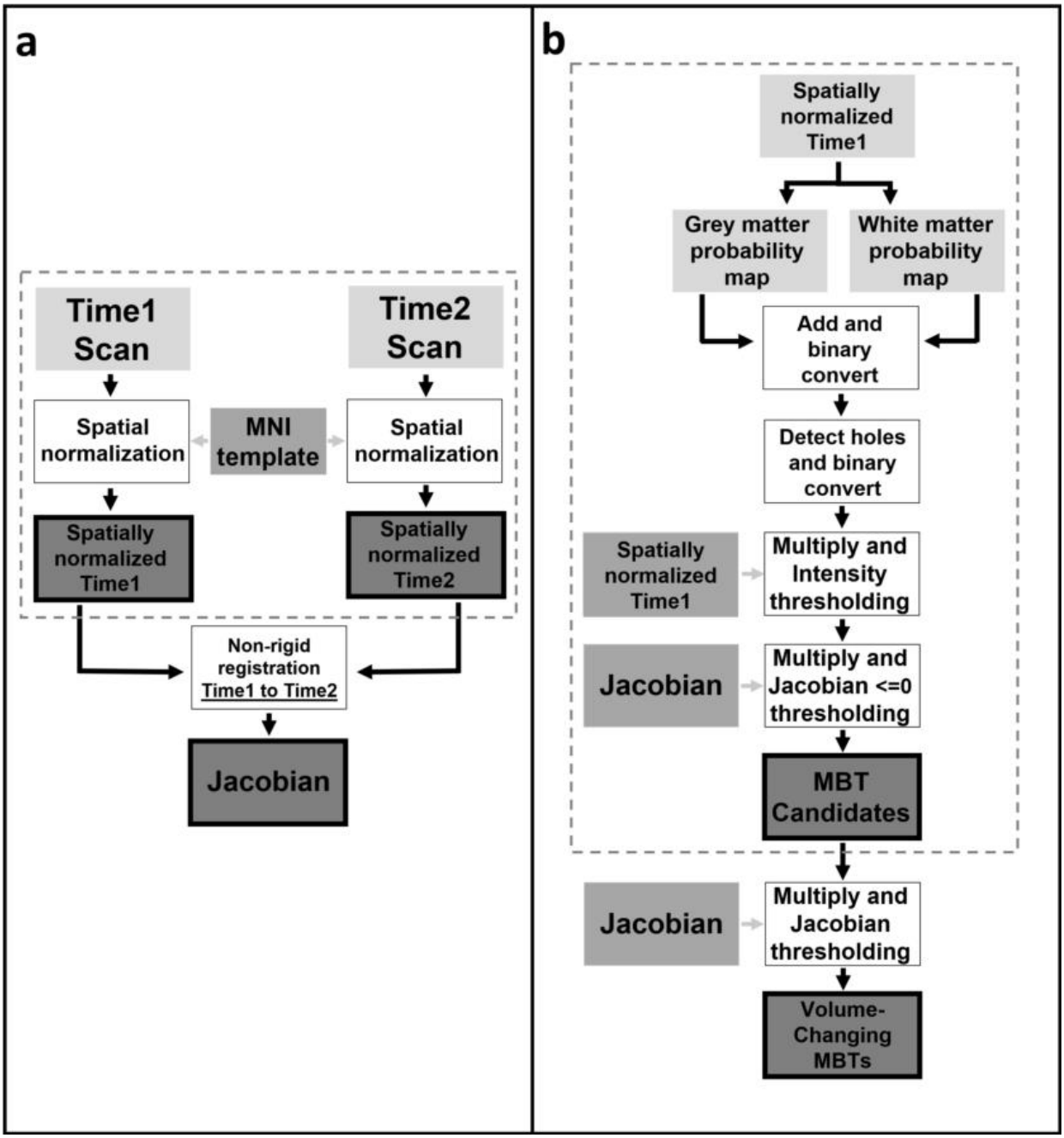
The image processing pipeline employed to detect vMBTs can be summarized as follows: 1) Spatial Normalization – registration of T1 MRI volumes to a standard atlas so that longitudinal scans can be compared to one another objectively; 2) Deformation Field – nonlinear registration of longitudinal scans and measurement of the 3D deformation field of voxels; 3) Jacobian – computation of the Jacobian operator field from the deformation field; 4) Tissue Segmentation – which detects MBT candidates on T1 volumetric MRI; and 5) Detection of vMBTs – which utilizes the Jacobian operator field to detect growing and shrinking MBTs on longitudinal scans, as well as to perform false-positive reduction. To validate the algorithm, we considered its accuracy in detecting vMBTs. Thirty patient MR datasets (each with 2 consecutive contrast-enhanced three-dimensional T1-weighted MR scans) were used, containing 132 vMBTs. All MR scans were performed on 2 identical 1.5T GE TwinSpeed Excite (GE Medical Systems, Milwaukee, WI) scanners using standard 8-channel head coil, as part of our institution's routine CE brain MRI protocol. The parameters for volumetric T1-weighted images included: repetition time/echo time/flip angle (TR/TE/FA) 8.6/4.2/20, field of view (FOV) 220×220 mm, and voxel size 0.43×0.43×1.5 mm. The presence and location of vMBTs were confirmed and extracted by a neuroradiologist, blinded to the technical details of our detection algorithm. This defined our reference standard. For statistical analysis of our algorithm's accuracy and to find the optimal threshold value of the Jacobian, we used receiver-operating characteristic (ROC) analysis. To ascertain the reproducibility of our results, we employed the bootstrapping approach.

Results

The area under the ROC curve (AUC) for detecting vMBTs was 0.925 (AUC > 0.9; statistically high accuracy). Furthermore, at its optimal performance, the algorithm achieved a sensitivity of 85.1%, specificity of 86.7%, and false positive rate of 0.208 per slice (25.1 per scan). Vessels were responsible for 79.0 ± 24.0% of false positives. Newly developed and resolved MBTs were a major source of false negatives.

Conclusions

Our fully automated algorithm presented here was able to detect growing and shrinking MBTs on longitudinal brain MRI with statistically high accuracy. Considering the lack of automated techniques for this purpose, high workload and ambiguity associated with manual reading, and the fact that longitudinal volume assessment of MBTs is crucial in their treatment, the results of this study demonstrated our technique's potential to be implemented as a computer-aided change detection tool to complement the performance of radiologists and radiation oncologists.



(Filename: TCT_O-458_jmriFig1.jpg)

O-459

11:16AM - 11:24AM

Relation of Brain Volumes and Structural Integrity to Treatment Response for PTSD

S Mukhi[1], E Wilde[2], B Taylor[3], J Tran[4], T Merkley[5], J Faber[6], B Biekman[7], G Vogt[7], R Yallampalli[7], S McCauley[7]

[1]Michael E. DeBakey VA Medical Center, Houston, TX, [2]Baylor College of Medicine/ MEDVAMC, Houston, TX, [3]Baylor College of Medicine/Micheal E. DeBakey VA Medical Center, Houston, TX, [4]Michael E. Debakey VA Medical Center, Houston, TX, [5]Barrow Neurological Institute, Phoenix, AZ, [6]University of Minnesota, Minneapolis, MN, [7]Baylor College of Medicine, Houston, TX

Purpose

Approximately 41% of U.S. veterans returning from conflicts in Afghanistan and Iraq have reported symptoms of PTSD and at least 20% have suffered 1 of more mild traumatic brain injuries (mTBI). More than 67% of veterans with PTSD also have a substance use disorder (SUD). PTSD, mTBI, and SUD result in characteristic patterns of neuropathology and comorbid presentation of these conditions complicates effective treatment. The objective of this study was to investigate how the neuropathology, as measured by imaging, of comorbid PTSD, mTBI, and SUD impacts treatment response magnitude for PTSD in veterans in an inpatient psychiatric setting.

Materials and Methods

Pretreatment 3T MRI was obtained from 31 combat-exposed veterans with varying severity of mTBI and SUD (all meeting criteria for PTSD) undergoing 5 weeks of closed-cohort, inpatient treatment for PTSD in a VA hospital. Using multiple regression analysis and maximum adjusted-R2 selection, volumetric and DTI data were interrogated in separate models to identify regions of interest (ROI) which were predictive of treatment response magnitude (post pretreatment difference score) for PTSD using the PTSD Checklist (PCL-C) as the continuous dependent variable.

Results

Volumetrics: Total intracranial volume-adjusted volumes of disorder-specific ROIs were included. The optimal model was significant [$F(7,23)=3.58, p<.01$; adjusted-$R2=0.38$] including the left amygdala, and bilateral orbitofrontal cortices, ventral striata, and hippocampi. Diffusion tensor imaging (DTI): The fractional anisotropy (FA) of disorder-specific ROIs was included. The optimal model was significant [$F(8,15)=2.6$, $p=.05$; adjusted-$R2=0.36$] including the corpus callosum, left cingulum bundle, and bilateral orbitofrontal cortices, ventral striata, and perforant pathways.

Conclusions

These results indicate that the volumes and structural integrity of disorder-specific ROIs are predictive of treatment response magnitude in veterans. These data could be used to identify

veterans at treatment admission who would most rapidly benefit from treatment versus those likely to require additional intensive treatment to maximize disorder remission.

O-460

11:24AM - 11:32AM

Diet-Microbiota Interactions Influence White Matter Structural Integrity

J Yu[1], J Guerrero[1], P Rowley[1], A Alexander[1]
[1]*University of Wisconsin-Madison, Madison, WI*

Purpose
The tremendous diversity and abundance of microbes comprising the gut microbiome and its impact in numerous aspects of human health, physiology, and disease has emerged as an area of intense interest. Already, many important associations have been made revealing the critical role the gut microbiome plays in inflammatory bowel disease, immunology, and host metabolism in both local and systemic disease. The central nervous system is no less susceptible with commensal bacteria able to shape complex behaviors including social, emotion, and anxiety-like behaviors in both mice and humans. Gut microbiota also have been shown to be integral to normal brain and behavioral development and in the regulation of the CNS and brain function with disruptions in the number, composition, and taxonomic diversity of the gut microbiome implicated in the development or exacerbation of mental disorders. Enigmatically, for all the evidence of the critical role that the gut microbiome serves during neurodevelopment and later in preserving and maintaining brain structure and function, intestinal microbial communities are surprisingly dynamic and responsive to environmental cues such as diet, exposure to antimicrobials, and disrupted sleep patterns. Diet-dependent microbiome populations also are strongly linked with psychopathological outcomes. Given the striking differences seen in brain function and behavior as a function of diet, we hypothesize that diet-dependent changes in brain function and behavior will manifest with corresponding changes in neural structure and organization.
Materials and Methods
Animals and Experimental Design: Forty male outbred SD rats (post natal day 22) were randomized to 1 of 4 experimental diets: a chemically purified control diet, a high-fat diet, a high-fiber low energy diet, or a high-protein low carbohydrate diet and fed for 21 days. Animals then were anesthetized and transcardiac perfused with 4% PFA. After perfusion, brain tissue was dissected en bloc, post-fixed in 4% PFA and subsequently rinsed in 0.9% saline for 48 hours prior to imaging. Brains then were placed in a custom-built holder and immersed in Fluorinert for image acquisition. For ex vivo DTI acquisition, brains are imaged simultaneously for 3 h using a 4.7-T Agilent MRI system and 3.5-cm diameter quadrature volume RF coil. Image Processing: FSL is employed for correcting eddy current. The FSL DTI output volumes then are converted to NIfTI tensor format for use with DTI-TK. Utilization of a group-wise template then was used for template estimation. The population-

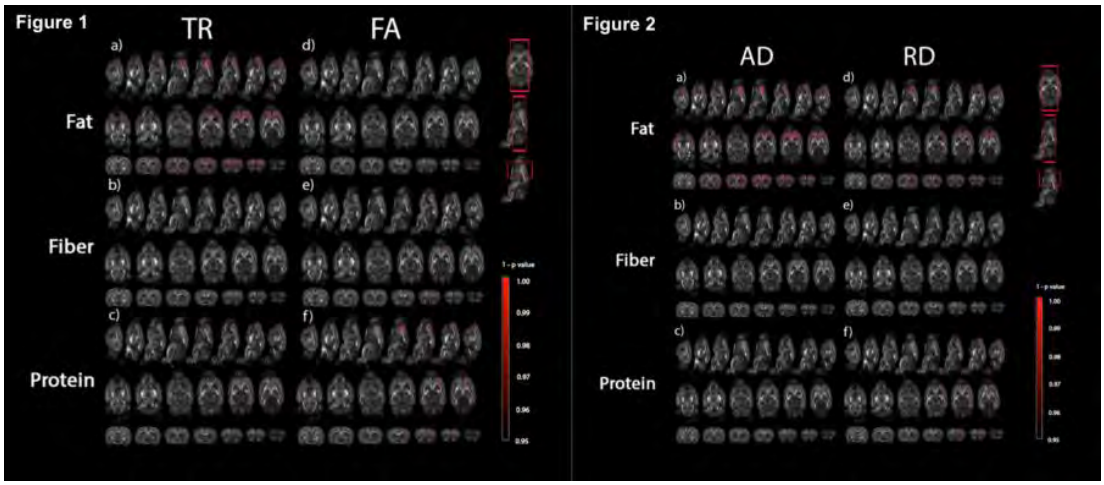
specific template is used as a target for spatially normalizing the individual tensor volumes using the DTI-TK tensor-based registration tools. The traditional TBBS formalism is implemented as recommended by replacing the standard TBSS registration with the DTI-TK registration routine that uses the full tensor information for the registration resulting in an improved alignment quality. A 0.2 FA threshold is used for creating the skeleton and a permutation test corrected for multiple comparisons and threshold-free cluster enhancement is implemented with FSL's Randomize for inter-group comparisons, with $p \leq 0.05$ as threshold for significance. Region of interest (ROI) analysis: A pre-existing atlas is nonlinearly aligned to the group-wise template. The registration includes elastic warping with a point-set based registration metric implemented in the ANTS platform. Mean values of the diffusion-tensor-derived indices then are computed within each ROI from each of the DTI volumes in the group-wise template.

Results

Tract-based spatial statistics (TBSS) revealed clusters of statistically significant differences in fractional anisotropy (FA) between the control diet group and both the fiber and protein diet groups. As compared to the control diet group, increased FA was found in 309 voxels for the fiber diet group (Fig. 1E) and in 512 voxels for the protein diet group (Fig. 1F). No significant FA differences were found between the control diet group and the fat diet group (Fig. 1D). To further explore these unexpected increases in fractional anisotropy, white matter axial diffusivity (AD), radial diffusivity (RD), and trace (TR) skeletons also were calculated for each diet group and again compared against the control diet group. Although no significant changes in AD were found in the high fiber diet group, 285 voxels demonstrated decreased RD (Fig. 2E) and 140 voxels showed decreased TR (Fig. 1B) with all mapping to voxels previously identified as demonstrating increased FA. As with the fiber diet group, the protein diet group comparison also demonstrated small group differences in AD but showed large clusters of significant changes with both decreased RD and TR (725 and 555 voxels, respectively; Fig. 2F; Fig. 1C). These regions of significantly decreased RD, AD, and TR are noted to map to the previously identified clusters demonstrating increased FA. The additional composite tensor information derived from TBSS analysis suggests that the regions with reduced RD in the fiber and protein diet groups might be driving the increases in FA observed in these regions. Additionally, our analysis demonstrates that despite the absence of FA differences between the fat and control diet group, there exist large clusters of decreased AD, RD, and MD between these groups and the concomitant reduction in both AD and RD largely explains the absence of FA differences in the high fat diet group.

Conclusions

Diffusion tensor imaging reveals that there exist diet-dependent alterations in neural structure, organization, and white matter integrity and with advanced modeling and predictive analytics, further demonstrate that these observed changes in neural structure, organization, and integrity can be associated with specific microbial populations.



(Filename: TCT_O-460_Figure.jpg)

O-461

11:32AM - 11:40AM

Diffusion Tensor Imaging in Hyperthyroidism: Tract-Based Spatial Statistics Assessment of Micro-structural White Matter Abnormalities

K Aslan[1], H Gunbey[1], S Cortcu[1], O Ozyurt[2], U Avcı[3], l incesu[1]
[1]Ondokuz Mayis University Faculty of Medicine, Department of Radiology, Samsun, Turkey, [2]Bogazici University, Institute of Biomedical Engineering, İstanbul, Turkey, [3]Ondokuz Mayis University Faculty of Medicine, Department of Endocrinology and Metabolism, Samsun, Turkey

Purpose
In patients with hyperthyroid, changes have been found in gray matter volume and cerebral metabolism related with neurological deficit. However, brain white matter (WM) abnormality, which could explain the pathophysiology underlying hyperthyroidism, has not been researched. The purpose of this study is to assess microstructural WM abnormality in patients with untreated hypothyroidism by using diffusion tensor imaging (DTI).
Materials and Methods
Eighteen patients with hyperthyroid and14 age-matched healthy control subjects were included in the study. Tract-based spatial statistics (TBSS) were used in the DTI study to investigate whole-brain WM abnormalities.
Results
Tract-based spatial statistics showed significant increase in radial diffusivity in corpus callosum, anterior and posterior corona radiata, posterior thalamic radiation, external capsule, cingulum, superior longitudinal fasciculus and retrolenticular part of the internal capsule of patients with hyperthyroid ($p < 0.05$).
Conclusions
This study showed increase in radial diffusivity in regions related with learning, intellectual

and executive function, memory, attention, emotion and vision in patients with hyperthyroid. It was suggested that these results can reflect the decrease in axonal membrane and myelin sheath integrity in regions related with neuropsychiatric symptoms in terms of hyperthyroidism.

O-462

11:40AM - 11:48AM

Diffusion Tensor Imaging Metrics and Cognitive Test Performance: African American–Diabetes Heart Study MIND

C Fountain[1], J Kim[1], C Whitlow[1]
[1]*Wake Forest School of Medicine, Winston-Salem, NC*

Purpose
Type 2 diabetes has been studied widely in European American cohorts, but African Americans with diabetes, particularly those with adequate access to care, remain understudied. In this study, we hypothesize that changes in diffusion tensor imaging (DTI) metrics will correlate with cognitive test performance. Determining the extent and location of white matter (WM) microstructural change, as evidenced by DTI, and its correlation with clinical tests of cognition will help to further characterize the effects of diabetes on the brain.
Materials and Methods
African Americans with type 2 diabetes enrolled in the study (n = 391) underwent cognitive testing and brain MR imaging. Cognitive tests included the modified Mini-Mental State Examination (3MS), Montreal Cognitive Assessment (MoCA), Rey Auditory Verbal Learning Test (RAVLT), Digit Symbol Coding Task (DSC), Verbal Fluency for Animals (VFA), and Stroop test. Diffusion tensor imaging metrics included fractional anisotropy (FA) and mean diffusivity (MD). For each subject, mean values of FA and MD were calculated for each region of the Johns Hopkins University WM atlas and globally defined as all atlas regions combined. Simple and multiple linear regression models were used to assess associations between DTI metrics and cognitive performance. Covariates included age, sex, BMI, hemoglobin A1c, duration of disease, presence of hypertension, education level, smoking, gray matter (GM) volume, and WM lesion volume.
Results
There was a positive correlation between global FA and DSC score ($R^2 = 0.0612$, $F = 26.3739$, $p = < 0.0001$) and a negative correlation between global MD and DSC score ($R^2 = 0.2319$, $F = 118.1547$, $p = < 0.0001$). Fractional anisotropy and MD were significantly correlated with additional tests, but with lower coefficients of determination. Digital symbol coding score was associated most strongly with FA in posterior thalamic radiations; and with MD in the fornix/stria terminalis, retrolenticular portions of the internal capsule, and body of the corpus callosum. Multiple regression showed DSC score was predicted by a model ($R^2 = 0.4150$, $F(10,361) = 26.6187$, $p < 0.0001$) with global FA as an insignificant predictor ($p =$

0.05086), and by a separate model (R^2 = 0.4383, F(9,388) = 34.6457, p < 0.0001) with global MD as a significant predictor (p < 0.0001).
Conclusions
It was found that lower cognitive test scores, particular DSC scores, are associated with decreased FA and increased MD, both globally and in specific WM bundles, in this population of African Americans with diabetes. This suggests that poorer cognitive performance is related to microstructural damage and diminished integrity in specific WM tracts. These findings mimic those seen in other disease processes, such as Alzheimer disease, which exemplifies the impact of type 2 diabetes on brain structure and function. After adjusting for the effects of GM volume and WM lesion volume, global MD remained as a significant predictor of cognitive performance, while global FA proved to be less strongly predictive.

O-463

11:48AM - 11:56AM

Central Serous Chorioretinopathy is Associated with Loss of White Matter Integrity in Visual Pathways

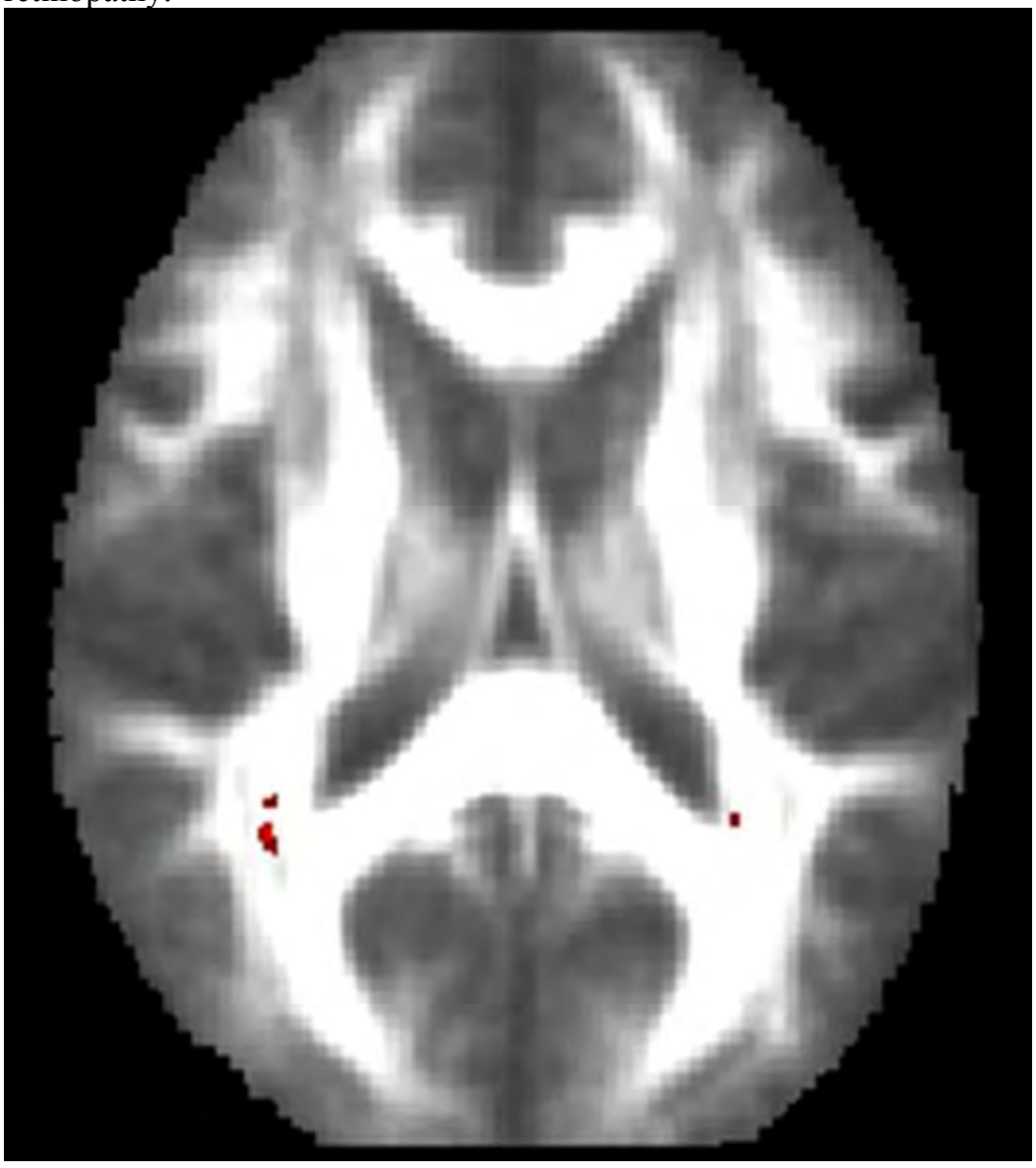
O Raslan[1], I Toslak[1], S Yildiz[2], M Erol[3], D Toslak[3], B Cekic[2], P Nucifora[1]
[1]Department of Radiology,Loyola University Medical Center, Maywood, IL, [2]Department of Radiology,Antalya Training and Research Hospital, Antalya, Turkey, ANTALYA, ANTALYA, [3]Department of Ophthalmology,Antalya Training and Research Hospital, Antalya, Turkey, ANTALYA, ANTALYA

Purpose
Central serous retinopathy (CSR) is associated with leakage of fluid into the subretinal space through the retinal pigment epithelium due to hyperpermeability of the choroid. Changes are confined most often to the macula and result in visual impairment (Nicholson, 2012). Recently several studies have changed the initial beliefs that CSR is a benign condition affecting young men with almost complete resolution (Ross, 2013), and suggested that the onset of disease occurred years before presentation. Our objective is to determine if the disease is associated with white matter damage.
Materials and Methods
Nineteen patients with central serous retinopathy and 11 healthy controls underwent diffusion tensor imaging at 1.5T using 15 motion probing gradient directions. Images were postprocessed offline to produce fractional anisotropy (FA) maps, which were aligned into a common space using a nonlinear registration tool (Smith, 2004). Voxelwise statistics were performed using cross-subject permutation analysis using threshold-free cluster enhancement to correct for multiple comparisons (corrected p<0.05).
Results
Decreased fractional anisotropy was found in the left posterior superior and bilateral

posterior periventricular partial regions at the expected location of the visual occipital fasciculus, optic radiation and superior longitudinal fasciculus (Fig.1). There were no areas of increased FA value in the brain.

Conclusions

We found decreased white matter integrity beyond the retina and along the visual pathways. These findings may reflect primary or secondary white matter degeneration in central serous retinopathy.



(Filename: TCT_O-463_Fig1.jpg)

O-464

11:56AM - 12:04PM

Brain Structural Changes Following HIV Infection: Meta-analysis

E O'Connor[1], T Zeffiro[2], T Zeffiro[3]
[1]University of Maryland Medical Center, Baltimore, MD, [2]Neurometrika, Potomac , MD, [3]Neurometrika, Potomac, MD

Purpose

Numerous studies have used structural neuroimaging to measure how HIV affects brain macroarchitecture and microarchitecture. While many have reported reduced total gray matter volume (GMv) and white matter volume (WMv); increased cerebrospinal fluid volume (CSFv) or reduced basal ganglia volume following HIV infection, quantitative inconsistencies observed across studies are large. In this project we evaluated the consistency of serostatus effects across a range of structural neuroimaging measures.

Materials and Methods

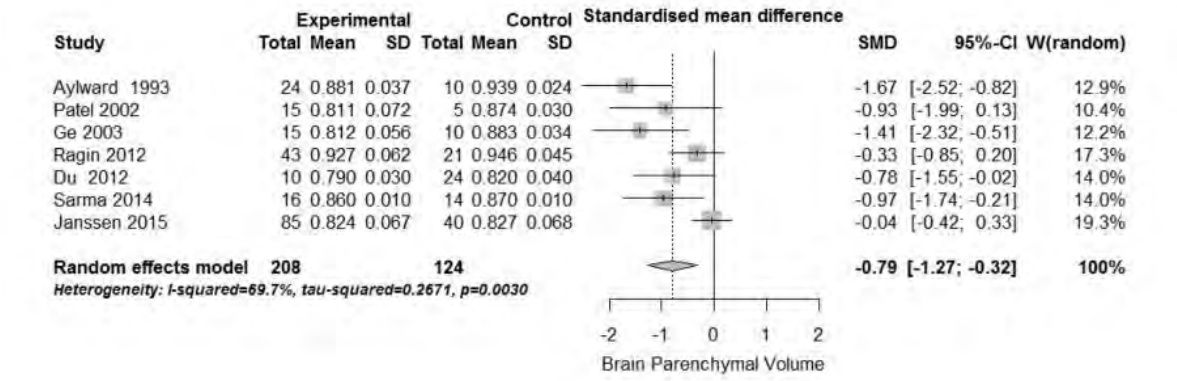
Sixteen cross-sectional studies reporting HIV effects on cortical and subcortical brain volume published between 1989 and 2016 were examined. Random effects meta-analysis was used to estimate individual study standardized mean differences (smd) and study heterogeneity.

Results

Meta-analysis comparing seropositive to seronegative groups revealed lower BPV (smd=-0.79; p=0.001), GMv (smd=-0.33; p=0.0013), WMv (smd=-0.28; p=0.09) and higher CSFv (smd=0.65; p=0.0006). Subcortical volume differences were smaller in the caudate (smd=-0.28, p=0.17), and putamen (smd=-0.30, p=0.22). Estimates of between study heterogeneity (I2) showed that >69% of the observed variance was between studies for all measures except GMv (I2=22%). Effect sizes related to serostatus tended to decrease with time for all measures (Fig. 1). Meta-regression did not reveal effects of MR system field strength or voxel size on serostatus effects.

Conclusions

Published studies of HIV effects on brain structure exhibit substantial variations that could result from acquisition, processing or cohort selection differences. Many studies pooled participants with varying treatment duration, disease duration and comorbidities, making identification of biological cohort effects impossible to determine in this study-level meta-analysis. During the years over which the studies were performed, different anti-retroviral agents were used, making isolation of treatment effects difficult.



(Filename: TCT_O-464_BPVfig1.jpg)

Thursday
1:30PM - 3:00PM
Long Beach Convention Center, Room 103 (Main Level)

25C-Parallel Paper Session: Head and Neck: Nodal Disease and Other Hot Topics

O-466

1:30PM - 1:38PM

Dual energy CT Iodine Quantification of Metastatic versus Non-metastatic Lymph Nodes in Squamous Cell Carcinoma of the Head and Neck.

A Foust[1], R Ali[2], X Nguyen[3], W Slone[4], j job[5], A Ajam[2], E Bourekas[6], D Boulter[2]
[1]The Ohio State University Wexner Medical, Columbus, OH, [2]The Ohio State University Wexner Medical Center, Columbus, OH, [3]Ohio State Wexner Medical Center, Columbus, OH, [4]he Ohio State University Wexner Medical, Columbus, OH, [5]University of Pittsburgh Medical Center, Pittsburgh, PA, [6]The Ohio State University, Columbus, OH

Purpose
In primary squamous cell carcinoma of the head and neck, the presence of even a single metastatic cervical lymph node may reduce 5-year survival by as much as 50%. Lymph node size on CT is a commonly used criterion for detecting lymph node metastases, but is neither sensitive nor specific. Dual energy CT (DECT) allows improved discrimination of materials such as iodinated contrast, which shows promise for improving upon the diagnostic performance in detection of lymph node metastases. We compared DECT derived quantitative iodine analysis data between metastatic and nonmetastatic lymph nodes in patients with newly diagnosed squamous cell carcinoma of the head and neck.
Materials and Methods
Nine patients with newly diagnosed primary squamous cell carcinoma of the head and neck

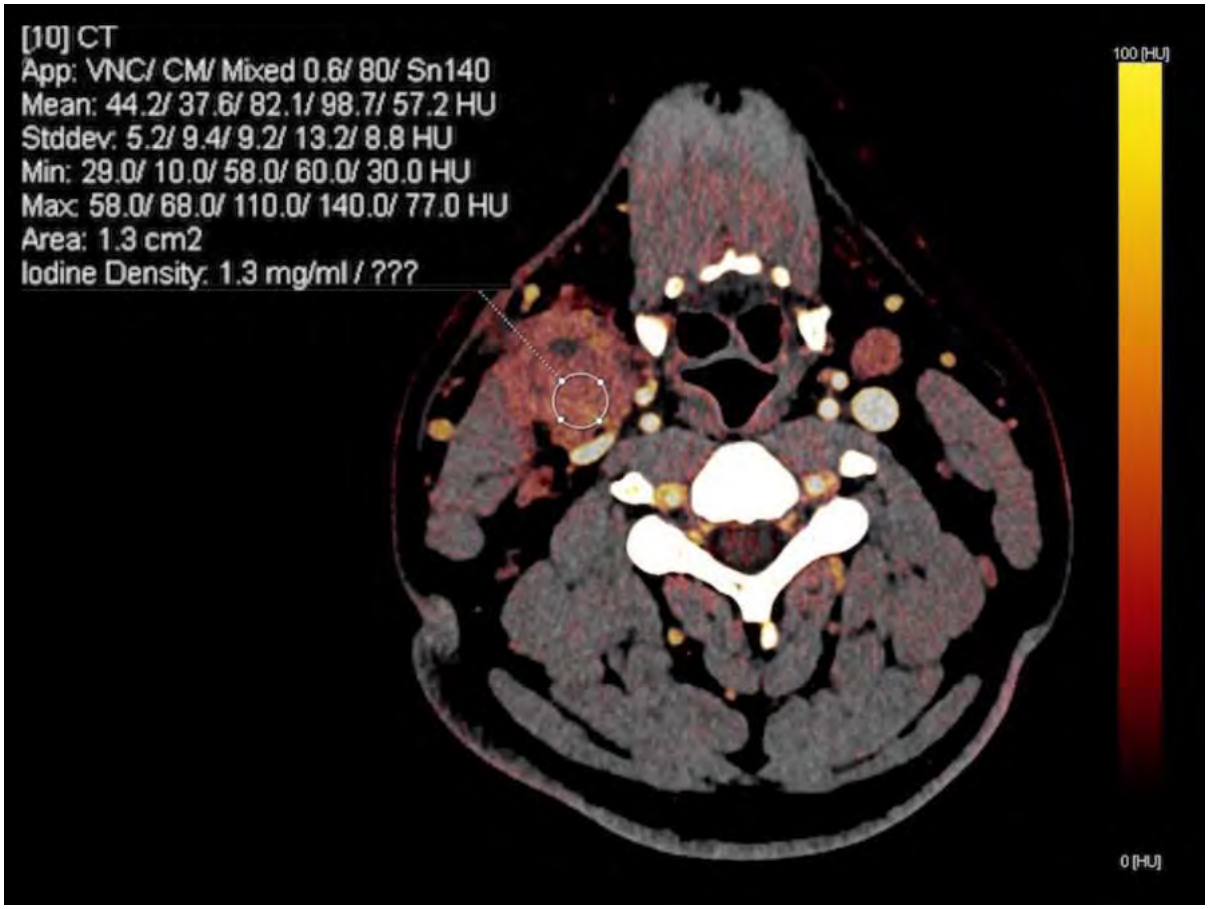
and at least 1 metastatic lymph node who underwent contrast-enhanced DECT of the neck were evaluated retrospectively. Thirteen metastatic nodes and 20 nonmetastatic nodes were identified. Dual energy CT derived iodine content (mg/mL), iodine overlay (HU), and virtual noncontrast (HU) data were obtained using circular regions of interest within metastatic nodes, nonmetastatic nodes, and the primary tumor if visible. Average values of metastatic nodes and control nodes in each patient were obtained and T-tests were used for data analysis.

Results

Iodine content was significantly lower in metastatic lymph nodes (1.06+0.63) compared with nonmetastatic lymph nodes (1.66+0.57), $p = 0.027$. The iodine overlay enhancement also was significantly lower in metastatic lymph nodes (27.86+18.01) compared to nonmetastatic lymph nodes (43.66+17.67), $p = 0.034$. There was no significant difference in between metastatic (47.98+6.87) and nonmetastatic (42.71+8.59) lymph nodes on virtual noncontrast images, $p = 0.112$.

Conclusions

Dual energy CT derived quantitative iodine analysis may improve the diagnostic accuracy of CT for lymph node metastases in patients with squamous cell carcinoma of the head and neck.



(Filename: TCT_O-466_ANSR2017Figure.jpg)

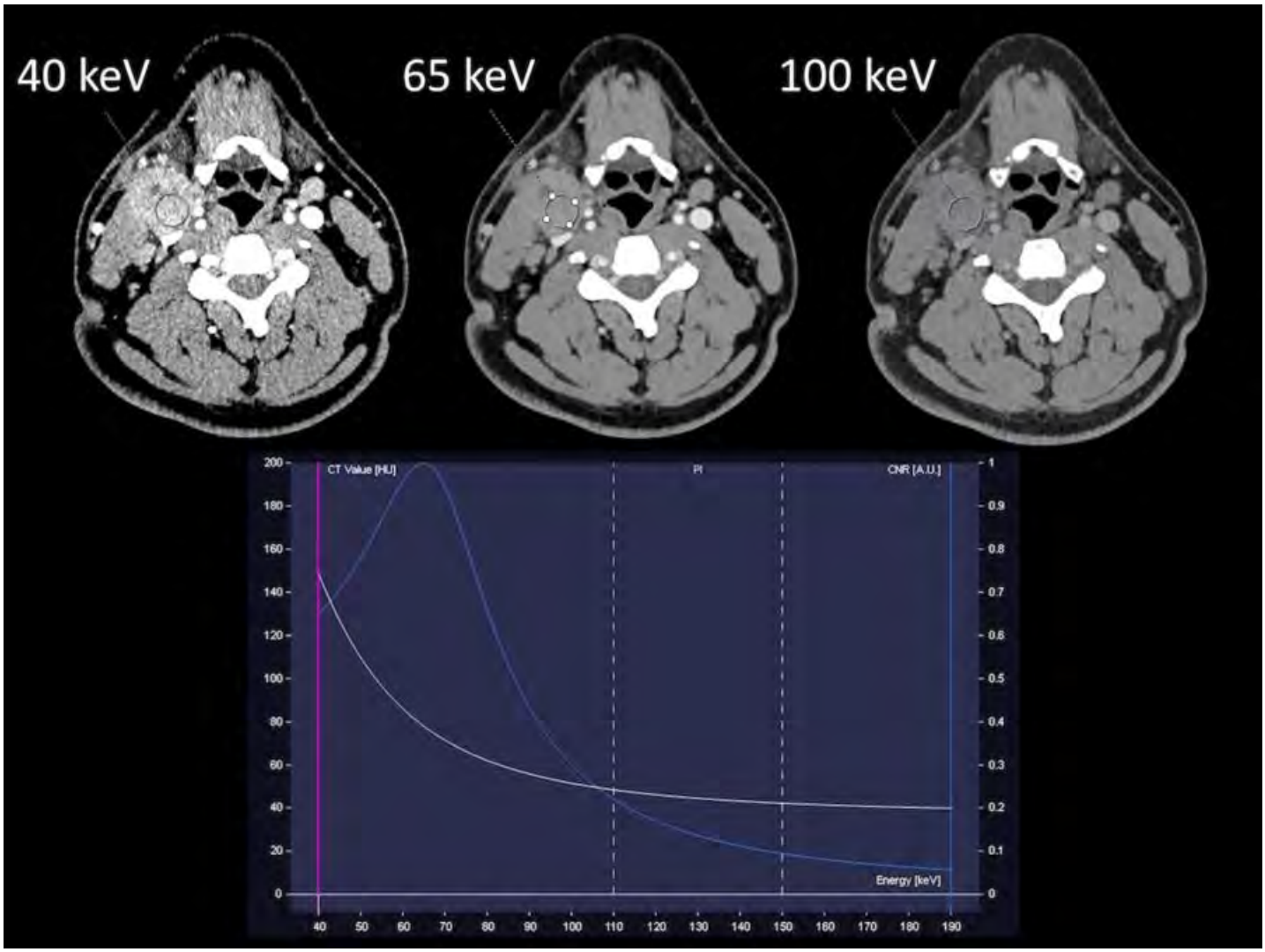
O-467

1:38PM - 1:46PM

Dual Energy CT Spectral Hounsfield Unit Curve Analysis of Metastases Lymph Nodes versus Non-metastatic Nodes in Squamous Cell Carcinoma of the Head and Neck

R Ali[1], A Foust[2], D Boulter[1], X Nguyen[3], A Ajam[1], W Slone[2], j job[4], E Bourekas[5]
[1]The Ohio State University Wexner Medical Center, Columbus, OH, [2]The Ohio State University Wexner Medical, Columbus, OH, [3]Ohio State Wexner Medical Center, Columbus, OH, [4]Ohio State University, columbus, OH, [5]The Ohio State University, Columbus, OH

Purpose
Studies have demonstrated that dual energy CT (DECT) of the neck may improve the detection and characterization of cervical lymph node metastases compared with single energy CT. Commonly used size criteria for cervical lymph node metastases are not reliable. Dual energy CT improves characterization of contrast material distribution within lymph nodes due to energy-dependent differences in the Hounsfield Units (HU) of iodine relative to soft tissues. The purpose of our study was to determine whether DECT spectral HU curve analysis can help differentiate between metastatic and nonmetastatic lymph nodes of patients with newly diagnosed squamous cell carcinoma (SCC).
Materials and Methods
We retrospectively analyzed 9 patients with newly diagnosed SCC of the head and neck and at least 1 metastatic lymph node who underwent contrast-enhanced dual energy neck CT. Thirteen metastatic nodes and 20 nonmetastatic lymph nodes were identified. Dual energy CT spectral HU data were obtained using circular regions of interest within enhancing portions of metastatic nodes, nonmetastatic nodes and the primary tumor if visible. Mean HU values of ROI were obtained at 40 keV and 100 keV mono-energetic levels. The slope of the spectral HU curve was calculated as the slope of a line between HU values at 40 kEV and 100 keV. Additionally, we analyzed the contrast-to-noise ratio (CNR) curves and determined the energy at which the CNR was the greatest for each lesion. Data analysis was performed using paired T-tests.
Results
Slope of the energy spectral HU curve was significantly lower in metastatic lymph nodes (1.33+0.89) compared with nonmetastatic nodes (2.10+0.80), $p = 0.011$. The monoenergetic level for optimal CNR ranged from 63-70 keV, with a mean value was 66.1 keV.
Conclusions
Dual energy CT spectral attenuation analysis may improve the diagnostic accuracy of metastatic lymph nodes in patients with SCC of the head and neck.



(Filename: TCT_O-467_VirtualMonoFigure.jpg)

O-468

1:46PM - 1:54PM

Texture analysis of cervical lymph nodes on CT to differentiate nodal metastases from reactive lymphadenopathy in HIV-positive head and neck cancer patients

H Kuno[1], N Garg[1], M Chapman[1], M Qureshi[1], B Li[1], S Meibom[1], O Sakai[1]
[1]*Boston Medical Center, Boston University School of Medicine, Boston, MA*

Purpose
Differentiating nodal metastases from reactive adenopathy in HIV-infected patients with 18F-FDG PET/CT can be challenging, since lymph nodes in HIV-positive patients often show increased 18F-FDG uptake(1-4). The purpose of this study was to assess the CT textural analysis characteristics of HIV-positive and HIV-negative lymph nodes on 18F-

FDG-PET/CT in order to differentiate nodal metastases from disease-specific nodal reactivity.

Materials and Methods

Nine HIV-positive head and neck cancer (HNC) patients (7 men, 2 women; 29–62 years; median age, 48 years) with 22 lymph nodes (≥10 mm) who underwent contrast-enhanced CT with 18F-FDG-PET for staging followed by pathological evaluation of cervical lymph nodes were reviewed retrospectively. Twenty-six HIV-negative HNC patients with 61 lymph nodes were evaluated as control group. Manual segmentation of each lymph node was performed, and an in-house developed MATLAB-based texture analysis program extracted 42 texture features from each segmented volume (5). An ANOVA analysis and mixed linear regression model (Proc MIXED) were used to compare the positive lymph nodes with negative nodes in the 2 enrolled groups.

Results

Thirteen (59%) lymph nodes in the HIV-positive group and 21 (34%) lymph nodes in the HIV-negative control group were confirmed as positive for metastases. There was no significant difference in the SUVmax (P=0.100), node size (P=0.264) and node volume (P=0.533) between positive and negative nodes for the HIV-positive group, while the SUVmax for the HIV-negative group showed a significant difference (P<0.007). For CT texture analysis, there were 5 histogram features (P=0.003-0.037), 3 gray-level co-occurrence features (P= 0.031-0.045) and 4 gray-level run-length features (P=0.011-0.026) that demonstrated a significant difference in HIV-positive patients with either negative or positive lymph nodes.

Conclusions

Computed tomography texture analysis may be useful as a noninvasive method to obtain additional quantitative information to differentiate nodal metastases from disease-specific nodal reactivity in HIV-positive HNC patients.

Table: Selected texture parameters differentiating between lymph node outcome in HIV-positive/HIV-negative HNC patients

Imaging and Texture parameters	HIV-positive (n=22)					HIV-negative control (n=61)				
	Negative nodes (n=9)		Positive nodes (n=13)		*P*-value	Negative nodes (n=39)		Positive nodes (n=22)		*P*-value
	mean	SE	mean	SE		mean	SE	mean	SE	
Imaging characteristics										
Nodal size (mm)	1.400	0.100	1.892	0.191	0.264	1.439	0.048	1.687	0.177	0.584
Nodal volume (cc)	0.547	0.121	2.535	0.615	0.533	1.122	0.147	3.468	1.006	**0.009**
SUVmax	5.111	0.537	8.562	1.078	0.100	3.388	0.682	6.457	0.835	**0.007**
Histogram features										
mean	627.4	32.6	733.3	28.4	**0.037**	670.6	11.0	720.5	23.2	0.190
2D std	92.69	9.76	61.94	8.47	**0.041**	81.23	3.20	70.87	5.42	0.586
range	270.7	27.9	180.0	24.3	**0.037**	236.8	9.2	206.2	15.5	0.523
std 5	80.7	9.3	51.9	8.0	**0.043**	70.3	2.9	61.7	4.9	0.823
std 9	97.9	14.2	50.8	12.4	**0.003**	76.0	4.2	61.7	5.7	0.457
4th moment	8.32E+10	1.88E+10	8.84E+10	1.74E+10	0.478	8.76E+10	1.38E+09	9.25E+10	1.70E+09	**0.032**
GLCM features										
contrast	112.6	7.7	86.4	6.7	**0.031**	102.5	2.9	88.2	5.0	0.063
energy	0.037	0.015	0.081	0.012	**0.045**	0.041	0.003	0.059	0.009	0.295
homogeneity	0.453	0.027	0.542	0.024	**0.036**	0.475	0.009	0.517	0.017	0.155
GLRL features										
SRE	0.177	0.004	0.160	0.003	**0.011**	0.164	0.002	0.159	0.003	0.698
LRE	0.197	0.006	0.176	0.005	**0.021**	0.182	0.002	0.176	0.004	0.975
GLN	0.183	0.005	0.164	0.004	**0.020**	0.169	0.002	0.164	0.003	1.000
RLN	0.195	0.005	0.176	0.005	**0.026**	0.183	0.002	0.176	0.004	0.478
SRHGE	233.7	17.66	309.8	30.75	0.797	254.3	19.4	342.8	26.0	**0.010**
LRLGE	295.2	21.05	396.0	33.66	0.638	324.5	22.4	445.8	31.1	**0.003**
LRHGE	224.6	17.27	299.1	24.4	0.649	258.7	6.8	346.6	20.6	**<0.001**

Note:—GLCM, gray-level co-occurrence matrix; GLRL, gray-level run length; SRE, short-run emphasis; LRE, long-run emphasis; GLN, gray-level nonuniformity; RLN, run-length nonuniformity; SRHGE, short-run high gray-level emphasis; SRHGE, short-run high gray-level emphasis; LRLGE, long-run low gray-level emphasis; LRHGE, long-run high gray-level emphasis.
Bold; Indicates a significant difference by ANOVA with bonferroni correction and mixed linear regression model (Proc MIXED) to adjust the variance-covariance matrix among multiple values recorded for each patient ($P<0.05$).

(Filename: TCT_O-468_Table1.jpg)

O-469

1:54PM - 2:02PM

Utility of Dual Energy CT Iodine Content and Spectral Hounsfield Unit Attenuation Curves for Distinction of Pathologic Nodes in the Neck

A Perez-Lara[1], J NAIR[2], A Srinivasan[3], R Forghani[4]
[1]Jewish General Hospital, Montreal, Quebec, [2]FootHills Medical Centre, Univesity of Calgary, Calgary, Alberta, [3]Univ. Of Michigan Health System, Ann Arbor, MI, [4]Jewish General Hospital & McGill University, Montreal, Quebec

Purpose
There is limited evidence suggesting advantages of dual energy CT (DECT) for the

evaluation of cervical lymphadenopathy. In this study, we compared normal, inflammatory, and different neoplastic cervical lymph nodes to evaluate the potential for distinguishing different pathologic nodes based on their DECT characteristics.

Materials and Methods

A total of 263 lymph nodes in 50 patients [10 patients each of normal, inflammatory, head and neck squamous cell carcinoma (HNSCC), papillary thyroid carcinoma (PTC), and lymphoma] were evaluated. All subjects were scanned with a 64-slice dual-energy scanner with fast kVp switching. All HNSCC and PTC lymph nodes were pathology proven based on biopsy or neck dissection. For lymphoma, lymph nodes > 2 cm were evaluated in patients with biopsy proven disease. Quantitative evaluation of each lymph node was performed using 3 nonoverlapping ROIs placed on the uniformly enhancing part of the node. Spectral Hounsfield unit attenuation curves (SHUAC) and iodine-water material decomposition maps were generated and compared.

Results

Spectral Hounsfield unit attenuation curves of normal and pathologic nodes demonstrated increasing density separation on low keV VMIs (Fig. 1a). There were statistically significant differences in node attenuation at some VMI energy levels depending on the nodes compared, with the most striking difference observed between metastatic PTC compared to the other nodes ($p<0.05$, Mann Whitney test). In addition, there were statistically significant differences in the iodine content ($p<0.05$, one-way ANOVA) of different nodes (Fig. 1b). Papillary thyroid carcinoma nodes had the highest iodine content (average 2.385 mg/cm3), 3.96x times higher than other malignant nodes ($p < 0.0001$, binary logistic regression). The area under the curve of PTC node iodine content was 0.7, with a sensitivity of 65% and specificity of 97% at a cutoff value of 2.1643 mg/cm3.

Conclusions

Dual energy CT may be useful for characterization and distinction of different pathologic lymph nodes, particularly metastatic PTC nodes.

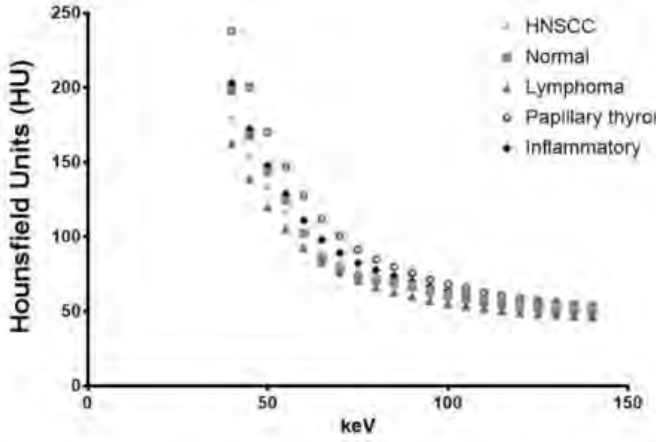


Fig 1a. SHUAC of the different subtypes of lymph nodes (average HU values)

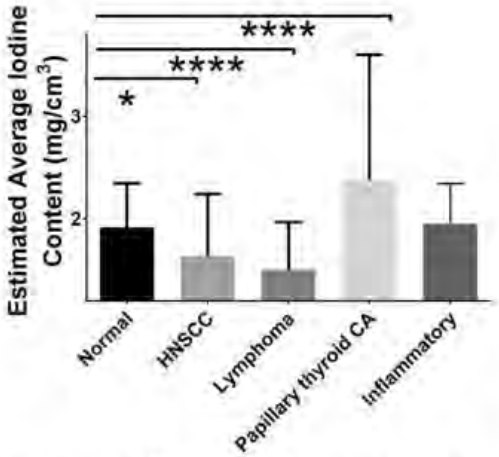


Fig 1b. Iodine content of the different subtypes of lymph nodes

(Filename: TCT_O-469_fig.jpg)

O-470

2:02PM - 2:10PM

The significance of punctate echogenic foci in cervical lymph nodes: When polka dots spell danger.

M Gule-Monroe[1], M Chen[2], T Vu[3], J Johnson[4], B Edeiken-Monroe[1]
[1]The University of Texas MD Anderson Cancer Center, Houston, TX, [2]Baylor College of Medicine, Houston, TX, [3]UT MD Anderson Cancer Center, Houston, TX, [4]University of Texas, MD Anderson, Houston, TX

Purpose
The accurate pre-operative detection of metastatic lymph nodes in differentiated thyroid cancer has become increasingly important with the increased incidence of thyroid cancer. High-frequency B-mode ultrasound (US) and power Doppler may demonstrate metastatic adenopathy that is occult both clinically and by alternate imaging modalities such as CT, MRI and PET/CT. This is dependent upon identification of even subtle intranodal changes. It has been our experience that intranodal punctate echogenic foci is a valuable subtle US finding that assists in the detection of metastatic adenopathy.
Materials and Methods
A retrospective case review was performed on 25 patients with punctate echogenic foci in a

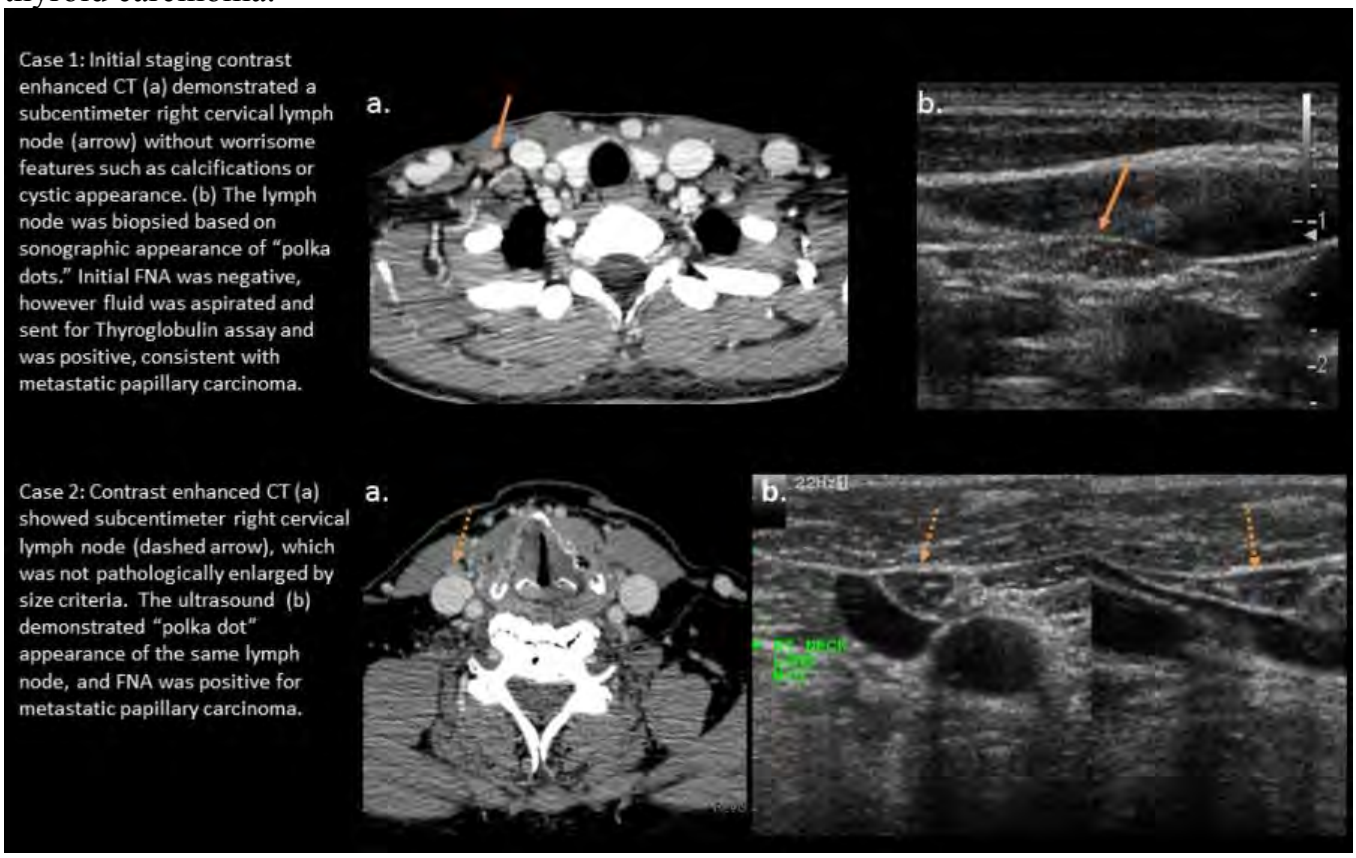
cervical lymph node imaged on US. Metastatic adenopathy was documented by US-guided FNA. Evaluation for traditional imaging characteristic of metastatic adenopathy included size, cystic change, disorganized vascularity and calcification were documented and correlated with CT.

Results

The accurate identification of the more aggressive phenotype of thyroid cancer with lymph node metastasis is paramount in allowing appropriate treatment and follow up. This review emphasized the importance of evaluation of lymph nodes for the presence of nonshadowing punctate echogenic foci, also termed micro-calcifications, or euphemistically as polka dots. In our case series, the presence of punctate echogenic foci on US was the only indication of nodal metastasis in 18 patients (72%).

Conclusions

The presence of subtle intranodal punctate echogenic foci is of particular importance as it may be the only US finding in metastatic adenopathy in patients with well differentiated thyroid carcinoma.



(Filename: TCT_O-470_Cervicalnodeabstractimages.jpg)

O-471

2:10PM - 2:18PM

MR Neurography as Part of Initial MRI Imaging of the Cervical Spine in ED Trauma Patients. Is it Worth it?

m kumar[1], R Samant[2], R Ramakrishnaiah[3], R Fitzgerald[3], E Angtuaco[2], R Van Hemert[2], T PANDEY[1], r ram[1]
[1]UAMS, little rock, AR, [2]UAMS, LITTLE ROCK, AR, [3]University of Arkansas for Medical Sciences, Little Rock, AR

Purpose
In patients with acute trauma to the cervical spine or multisystem trauma, injury to and stability of the cervical spine and early recognition of any injury to the spinal cord is of primary importance. Computed tomography study of the cervical spine generally is the first exam performed. In a large number of cases with suspected injury to the cord or ligamentous injury, MRI study of the cervical spine is performed. Imaging generally is performed with sequences covering 3 planes. In our institute, as in many other institutes, coronal and sagittal STIR sequences are performed in addition to other sequences. In addition to injuries to the bony spine, ligamentous structures and spinal cord, in a large majority of cases, injuries to the pre and paravertebral soft tissues of the cervical spine and the upper thoracic spine also are noted. The purpose of incorporating MR neurography by performing high resolution 3D STIR images with multiplane reconstructions, in the initial MRI evaluation of the cervical spine is manifold. 1. Increased sensitivity to subtle signal changes in the ligamentous, soft tissue, and bony structures of the cervical spine. Volumetric 3D acquistion gives the ability to perform reconstructions in any number of orthogonal and nonorthogonal planes. 2. Better visualization of soft tissue structures outside the cervical spine proper. This is particularly important in evaluation of brachial plexus, which are almost always in the field of view at the level of the roots, trunks, and divisions. The evaluation of brachial plexus generally is overlooked clinically and radiologically in the initial patient workup, leading to late discovery, increasing patient morbidity and cost.
Materials and Methods
Between January 2016 and November 2016, patients who presented with cervical spine trauma, and subsequently underwent MRI study of the cervical spine were selected for this study. A total of 90 consecutive patients were selected, with 57 males and 33 females. Age range was 18 to 86 years. Magnetic resonance imaging studies of the cervical spine in these patients were performed on a single 1.5 T Phillips magnet. T1, T2, STIR and gradient sagittal; T1 and T2 axial; and 3D STIR sequence in the coronal plane were acquired. For MR neurography, coronal and oblique coronal reconstructions using maximum intensity projection technique was performed, and images were reconstructed in regular and inverted formats.
Results
1. Out of the 90 patients, 41 patients had bony fractures and/or subluxation dislocation involving the cervical spine. 2. Eleven patients had spinal cord injury. 3. MR neurography exam was of diagnostic quality in 80 patients and of nondiagnostic quality in 10 patients. 4. In 20 patients there was definite evidence of abnormal signal involving the brachial plexus

components. In 46 patients, there was no radiological injury to the brachial plexus. In 24 patients, the findings were inconclusive.

Conclusions

1. Sensitivity to identify brachial plexus injury significantly improves with addition of MR neurography to the standard cervical spine MR protocol. 2. Evaluation of the brachial plexus is valuable in cases of MRI cervical spine using 3D STIR MR neurography technique, providing diagnostic information at initial evaluation decreasing potential subsequent patient morbidity.



Fig 1: Reconstructed inverted MIP 3D STIR coronal image shows thickening and increased signal of the left C5-T1 nerve roots.

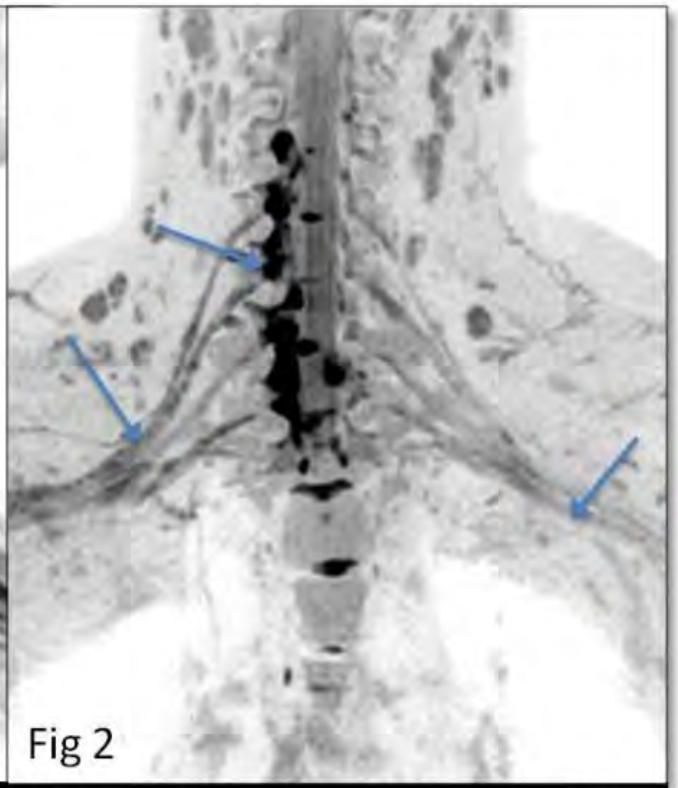


Fig 2: MIP inverted 3D STIR image shows thickened and hypointense right nerve roots from C4-T1 levels, cords and division with pseudomeningoceles from C3-T1 levels.

(Filename: TCT_O-471_ASNRfinalimage.jpg)

O-472

2:18PM - 2:26PM

Histogram Analysis of Globe Temperature using Diffusion-Based Thermometry

J Derakhshan[1], L Loevner[2], F Wehrli[1]

[1]University of Pennsylvania, Philadelphia, PA, [2]University of Pennsylvania, Philadelphia , PA

Purpose

Brain temperature determined using diffusion-based thermometry in the lateral ventricles has been found to vary in a variety of brain disorders (1-3). In a previous study this technique was extended to the globe using a single slice ROI-based method (4). In this study, a histogram-based method is used to increase robustness of temperature measurement.

Materials and Methods

Data from 10 patients scanned for purposes other than ocular disease were analyzed. DICOM images were imported into Matlab and each slice that the globe was visualized was segmented. The segmented ADC data were used to generate temperature and analyzed similar to Sakai et al. (5). Briefly, the histogram was fit to a polynomial. The polynomial was differentiated and the maximum and minimum of the derivative was used to determine the characteristic minimum and maximum values of the temperature distribution. The peak of the fit was used as the globe temperature. Paired t-tests were performed between the right and left eyes. Data from both eyes were combined and mean and standard deviation of each parameter was determined along with the difference between the eyes.

Results

Fig. 1a shows a representative globe temperature histogram. Note the Gaussian distribution of the temperature. Fig. 1b demonstrates the histogram fit as well as the derivative used to identify Tmin, Tmax and Tpeak. Fig. 1c shows the characteristic temperatures for 10 patients. Note that the temperatures are similar between the globes with small variations between patients. There was no significant difference between the right and left globes. Mean globe temperature is $37.2 \pm 2.0°C$. Average globe temperature difference is $0.6 \pm 0.5°C$.

Conclusions

Using a histogram method, globe temperatures and temperature differences have been determined noninvasively using diffusion-based thermometry for the first time. A temperature difference threshold of greater than 1.5°C is proposed as a biomarker for globe pathology.

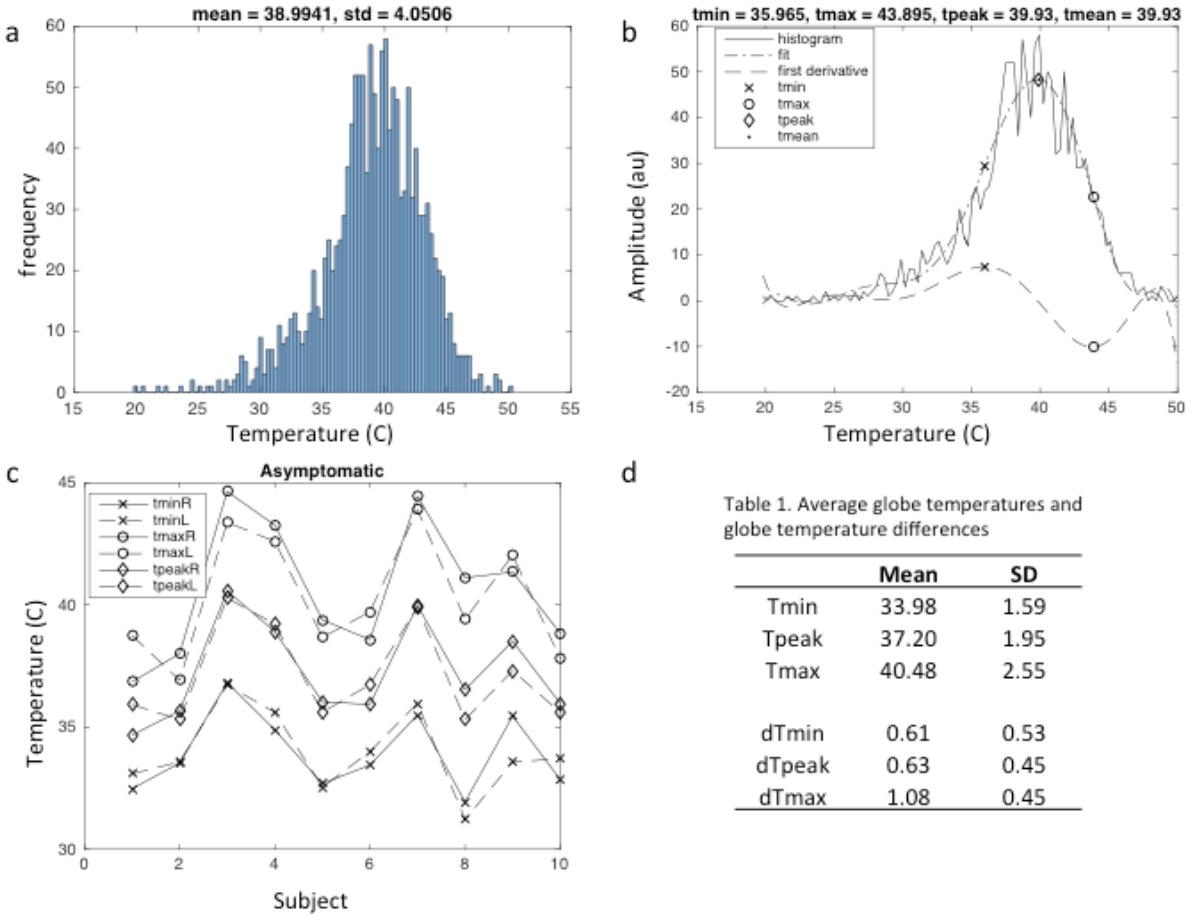


Table 1. Average globe temperatures and globe temperature differences

	Mean	SD
Tmin	33.98	1.59
Tpeak	37.20	1.95
Tmax	40.48	2.55
dTmin	0.61	0.53
dTpeak	0.63	0.45
dTmax	1.08	0.45

(Filename: TCT_O-472_ASNRfigure.gif)

O-473

2:26PM - 2:34PM

Semi-automated Middle Ear Volume Measurement as a Predictor of Postsurgical Outcomes for Congenital Aural Atresia

S Kabadi[1], D Ruhl[1], S Mukherjee[1], B Kesser[1]
[1]*University of Virginia Health System, Charlottesville, VA*

Purpose
The Jahrsdoerfer grading system (J-score) is currently the primary method used to determine surgical candidacy for congenital aural atresia (CAA). The purpose of this study is to introduce a semi-automated method for measuring 1 of its components, middle ear volume, and determine whether middle ear volume can be used, either independently or in combination with the Jahrsdoerfer score, to predict early postoperative audiometric outcomes.

Materials and Methods

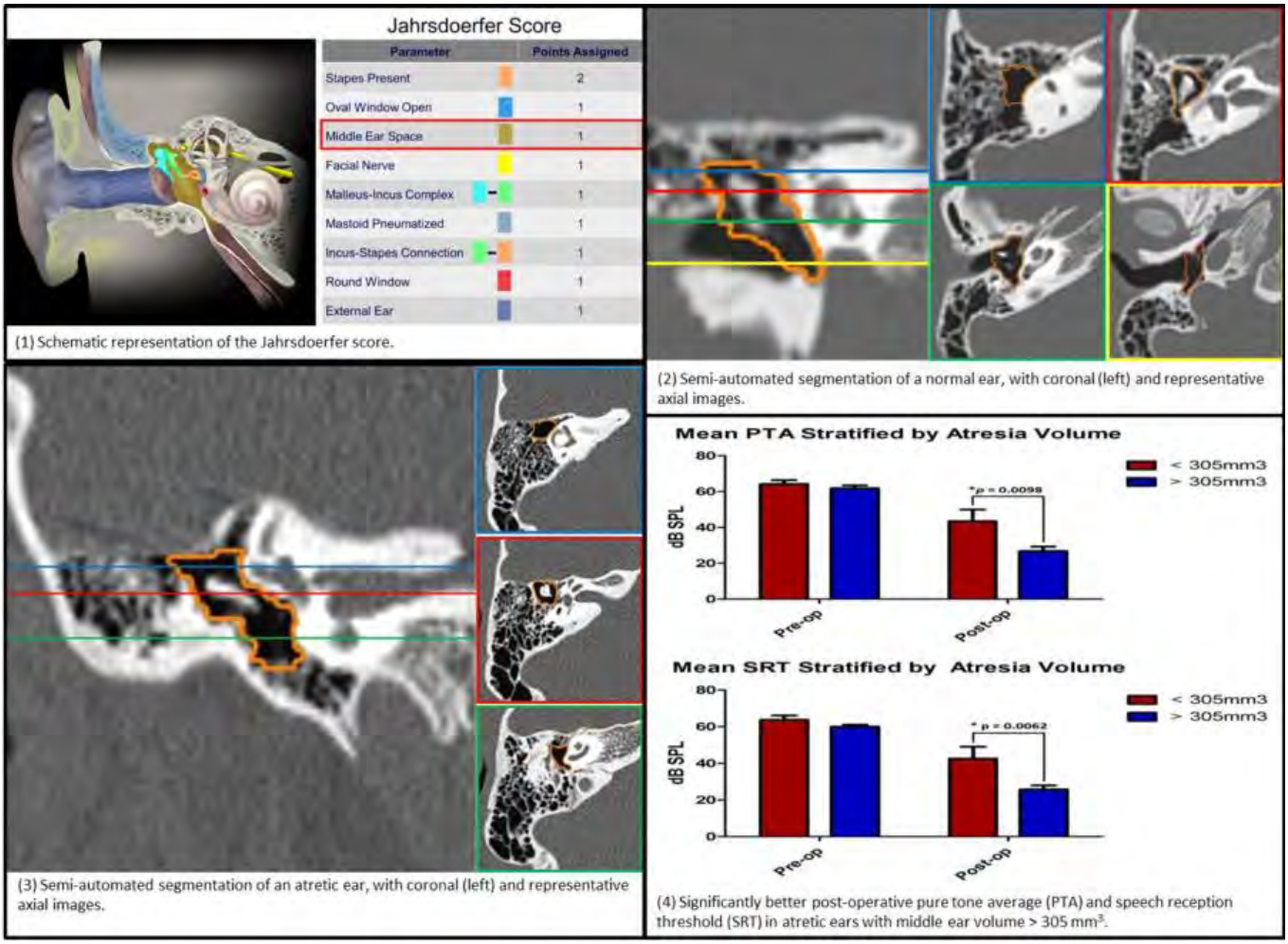
A retrospective analysis was conducted of 18 patients who underwent surgery for unilateral CAA at our institution, and who had high resolution CT imaging available. This resulted in 18 atretic ears and 18 normal ears available for analysis. Using the Livewire Segmentation tool in Carestream Vue PACS (Carestream Health, Rochester, NY), middle ear volumes were segmented using a semi-automated method for all atretic and normal ears. Specifically, manual segmentation was performed on every second axial slice through the volume of interest, and the remaining volume was interpolated in an automated fashion using the tool. Postsurgical audiometric outcome data then were analyzed in the context of these middle ear volumes.

Results

Atretic middle ear volumes were significantly smaller than contralateral normal ears (346 vs 627 mm^3, $p < 0.0001$). Patients with atretic middle ear volumes larger than 305 mm^3 had significantly better postoperative pure tone average (PTA) and speech reception threshold (SRT) than atretic ears below this threshold volume ($p = 0.0098$ and $p = 0.0062$ respectively). Atretic middle ear volume incorporated into the J-score (J+) offered the best predictor for normal postoperative hearing (SRT $\leq$ 30dB) (OR = 37.8, $p = 0.0123$).

Conclusions

Semi-automated measurement of middle ear volume, when quantitatively incorporated into the J-score (J+), has far more predictive value for postoperative hearing outcomes than either the classic J-score or middle ear volume alone, and may be used pre-operatively to better determine surgical candidacy.



(Filename: TCT_O-473_ImageFilev2.jpg)

O-474

2:34PM - 2:42PM

Methodology for Developing A Prototype CT Phantom of the Neck Utilizing Novel Multi-Material 3D Printing

R Javan[1], M Aulakh[1], C Liang[1], Z Anwarkhan[1]
[1]*George Washington University Hospital, Washington, DC*

Purpose
The aim of this project was to design a prototype semi-realistic multimaterial phantom of the neck compatible with computed tomography (CT).
Materials and Methods
Autodesk 3D Studio Max, MeshLab, OsiriX and Materialise Mimics software were used to 3-dimensionally reconstruct a multitude of virtual 3D models, including the cervical spine vertebral column, cervical spinal cord, trachea, thyroid gland, internal jugular vein and

carotid arteries. The latest multimaterial PolyJet 3D printer, i.e. the Connex J750 was used to 3D print the elements of the final phantom in different CT densities using commercially available services by Stratasys. The highest density was created using the rigid VeroWhitePlus material. The air column in the trachea was incorporated in the model. The soft tissues of the neck, i.e. fat and muscles were developed with flexible and translucent material. The spinal cord, vessels and trachea were developed with other materials with slightly different CT densities.
Results
A prototype multimaterial CT phantom of the neck was developed successfully without the requirement of assembly or molding techniques.
Conclusions
The phantom can serve as a quality control tool or a prototype for future models as the 3D printers become more advanced. The cervical spine is radiodense, which potentially can be used to practice cervical spine pain management interventions. Ideally, 3D printers may be developed that allow the user to fully adjust the CT density (Hounsfield Units) of all structures, and for that matter, each pixel to a desired amount. This neck model can serve as a guide for developing more complex 3D printed models.

O-475

2:42PM - 2:50PM

Augmented Reality Imaging as an Adjunct for Localization of Small Lesions Using Laryngoscopy on a 3D Printed Model of the Neck

J Gibby[1], A Gibby[2], S Cvetko[3], R Javan[2]
[1]George Washington University, School of Medicine and Health Sciences, Washington, DC, [2]George Washington University Hospital, Washington, DC, [3]Novarad, American Fork, UT

Purpose
Radiologic imaging has proven to be vital in diagnosing and treating pathologies within the larynx (1), including providing image-based parameters such as tumor volume, cartilaginous abnormalities, and post-therapeutic surveillance of patients with laryngeal cancers (2). Laryngoscopy has long been the gold standard for biopsy for mucosal lesions, but it is not as accurate in properly obtaining biopsies in deeper structures (3). The application of augmented reality by displaying computerized tomography (CT) images directly onto a patient when taking a biopsy could aid in accurately localizing and performing biopsies containing pathology in areas difficult to see on endoscopy.
Materials and Methods
A semi-realistic 3D printed model of the neck was created using a combination of 3D reconstructed components from CT data of a patient as well as graphically designed 3D meshes with a lesion placed in a location difficult to visualize on laryngoscopy. Novarad

software was used to translate the dataset into the proper format and upload to a Microsoft Hololens Augmented Reality headset. The computer-generated 3D images then were overlaid onto the phantom. Attempts then were made to perform the biopsy with assistance of the image overlays.
Results
The operator was able to perform a successful biopsy of the lesion incorporated in the model. However, at this time, the accuracy and stability of the technology does not appear to be ready for efficient use in actual patients where near-millimeter level of precision is necessary. Future advancement in augmented reality technologies may increase the feasibility of live patient biopsy. Our project serves to illustrate the practical potential of this technology in the setting of endoscopic biopsies.
Conclusions
Use of wearable augmented reality can provide benefit in localizing biopsies that are distinguished easily on imaging but are difficult to identify on laryngoscopy.

O-476

2:50PM - 2:58PM

An Advanced Color-Coded 3D Printed Educational Model of the Pterygopalatine Fossa

R Javan[1], P Heidari[2], M Aulakh[1], C Liang[1]
[1]George Washington University Hospital, Washington, DC, [2]University Hospital of Saarland University, Homberg, Germany

Purpose
To describe the methodology for designing an advanced educational physical 3D model of the pterygopalatine fossa from high-resolution computed tomography (CT) combined with custom graphic design, utilizing 3D printing technologies.
Materials and Methods
Images from a normal high-resolution CT of the facial bones was used to 3-dimensionally reconstruct the osseous structures that make up the pterygopalatine fossa. Materialise Mimics 17.0 was used for performing the initial 3D reconstruction, after manually perfecting the segmentation of bony anatomy on each thin slice of the scan. This 3D model was exported in STL format and then imported in Autodesk 3D Studio Max 9.0, where the intricate neurovascular anatomy of pterygopalatine fossa was added. This model then was enlarged and digitally split for easy visualization of its contents in color. Subsequently 3D printing was performed through commercially available services utilizing rapid prototyping technology on polyamide material with minimum detail of 0.3 mm. Magnets also were embedded in the model for assembly.
Results
An enlarged realistic multicolor physical model of the pterygopalatine fossa was created with intricate detail for the specific use of teaching complex anatomy. The new custom

educational possibilities that 3D printing has created for radiologists are discussed. The necessary software and the available options for acquiring 3D models as well as the possibly of obtaining low-price desktop 3D printers also are discussed.
Conclusions
Radiologists can take a leading role in taking advantage of the concept of 3D printing in creating numerous customizable tools for teaching complex anatomy (e.g. medical students and trainees in radiology, otolaryngology and neurosurgery) and for patient or parental education.

Thursday
1:30PM - 3:00PM
Long Beach Convention Center, Room 104A (Main Lobby)

25D-Parallel Paper Session: Good Techniques in Diagnosing Bad Tumors

O-477

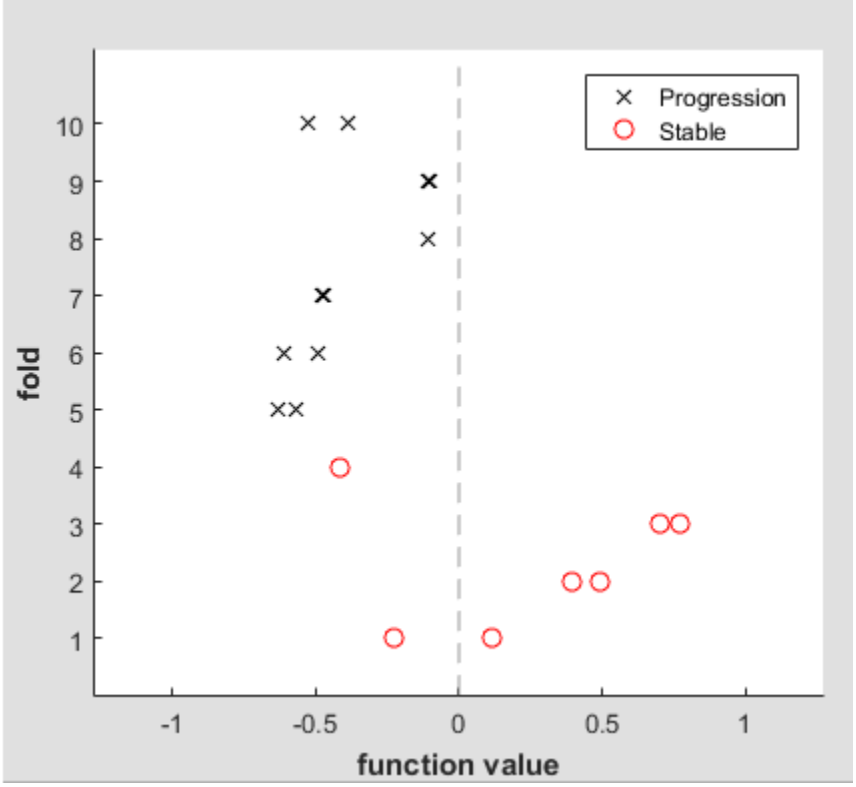
1:30PM - 1:38PM

Machine Learning Accurately Identifies Advancing Tumor Grade in Follow-up of Patients with Low Grade Glioma

N Swinburne[1], I Chen[1], S Tadayon[1], M Hefti[1], A Aggarwal[1], N Tsankova[1], K Nael[1]
[1]*Icahn School of Medicine at Mount Sinai, New York, NY*

Purpose
Patients with low grade glioma (LGG; WHO grade 1/2) often undergo tumor surveillance with serial brain MRIs to evaluate disease stability. Tumor advancement to high grade glioma (HGG; WHO grade 3/4) may be difficult to identify on conventional MRI. Advances in machine learning (ML) have demonstrated promise for semi-automated interpretation of multimodal radiologic imaging to differentiate brain neoplasms (1). We investigate whether ML evaluation of multimodal MRI can reliably identify tumor advancement to HGG.
Materials and Methods
Patients with histologically proven LGGs were included in this retrospective study if they had consecutive clinical and imaging follow-up from initial diagnosis until undergoing a second surgical biopsy. FLAIR, T1 post-contrast and ADC maps from baseline and a second MRI just before the second biopsy were preprocessed using the fMRI Software Library (Analysis Group, Oxford, UK) v5.0 (2), including histogram normalization and coregistration. Volumes of interest (VOIs) were drawn manually on FLAIR images and subsequently applied to other coregistered images for each patient. The preprocessed imaging data were utilized for supervised training of a ML classification kernel using the Pattern Recognition for Neuroimaging Toolbox (UCL, London, UK) v2.0 (3). Training entailed evaluation of labeled (i.e., stable LGG vs. advancement to HGG) MRI for creation of a support vector machine (SVM), which was validated on unlabeled cases using the leave-

one-subject-out method. Volumes of interest characteristics and ML accuracy and receiver operating characteristic data were collected.
Results
Ten patients (6 male, 4 female; age 43 ± 13 years; 4 stable LGG, 6 advancement to HGG) meeting the inclusion requirements were identified. Mean change in ADC 10th percentile for the 2 groups was 11.2% and -9.4% (p=0.30), respectively. The trained ML kernel discriminated with 81.3% balanced accuracy (p=0.004) between stable LGG (class accuracy 62.5%; p=0.001) and advancement to HGG (class accuracy 100%; p=0.001), with ADC most predictive of tumor grade.
Conclusions
A trained SVM can accurately differentiate LGG stability from advancement to HGG utilizing ADC. Larger studies are required to validate the observed association of declining ADC values with glioma grade advancement.



(Filename: TCT_O-477_LGG.gif)

O-478

1:38PM - 1:46PM

Recurrent glioblastoma pathologically proven in subtle hyperperfused regions otherwise appearing normal on conventional imaging

S Hurrell[1], E Cochran[1], J Connelly[1], P LaViolette[1]
[1]*Medical College of Wisconsin, Milwaukee, WI*

Purpose

Glioblastoma (GBM) is the most common central nervous system malignancy in adults, with a dismal 12-18 month median survival. Current clinical standards for imaging of GBM include standard T1-weighted imaging with (+C) and without contrast, diffusion-weighted imaging (DWI) and T2-weighted fluid attenuated inverse recovery (FLAIR) imaging. Perfusion imaging derived maps of relative cerebral blood volume (rCBV) are useful for predicting progression free survival, progression from low to high grade glioma, and distinguishing pseudoprogression from true tumor progression. This study looks at satellite hyper-perfused regions otherwise appearing normal to determine the underlying pathology at autopsy.

Materials and Methods

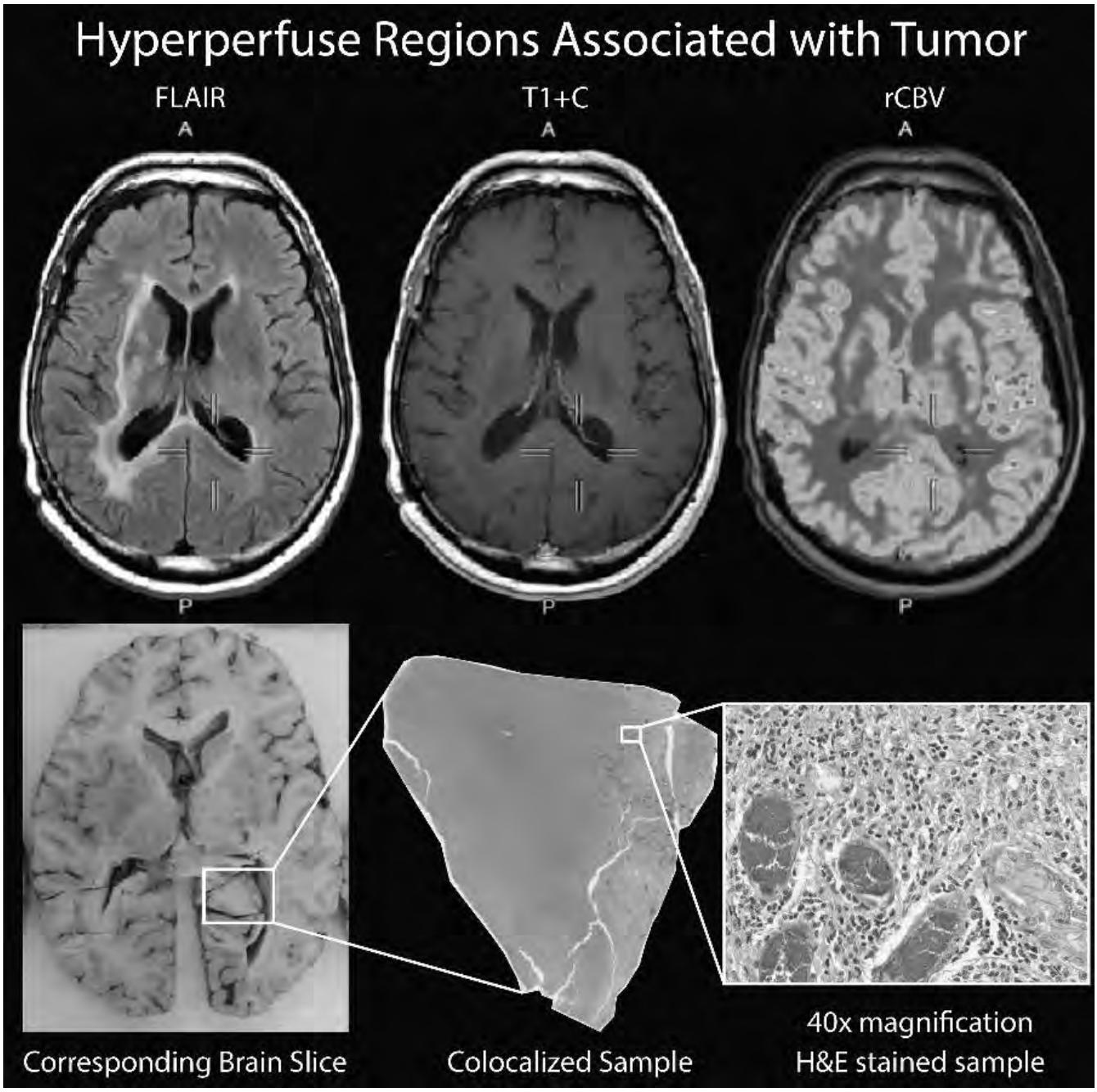
We retrospectively analyzed our pool brain donor patients, looking for suspicious regions of hyperperfusion outside of traditional tumor margins defined by T1+C enhancement and T2/FLAIR hyperintensity. Eight patients had lesions meeting these criteria. Tissue samples from these suspicious regions were obtained; hematoxylin and eosin (H&E) stained (Fig. 1), digitized and segmented using custom code on MatLab software (Mathworks Inc). A board-certified pathologist read each sample looking for viable recurrent tumor.

Results

Seven patients were found to have hypercellular tumor in regions of corresponding hyperperfusion on rCBV maps outside of T1+C and T2/FLAIR hyperintensity. Samples also included increased vasculature and necrosis. Radiologists mentioned the suspicious hyperperfused region in only 1 of the 7 subsequent reports.

Conclusions

Abnormal hyperperfusion outside of traditionally defined tumor margins proved to be a strong indicator for satellite tumor progression.



(Filename: TCT_O-478_rcbv.jpg)

O-479

1:46PM - 1:54PM

Multi-center Study finds Postoperative Residual Non-enhancing Component of Glioblastoma as a New Determinant of Patient Outcome

A Kotrotsou[1], A Elakkad[1], J Sun[1], G Thomas[1], S Abrol[1], W Wei[1], J Weinberg[1], A Shojaee Bakhtiari[1], M Luedi[1], M Kircher[2], R Sawaya[1], A Kumar[1], P Zinn[3], R Colen[1]

[1]MD Anderson Cancer Center, Houston, TX, [2]Memorial Sloan Kettering Cancer Center, New York, NY, [3]Baylor College of Medicine, Houston, TX

Purpose

Glioblastomas (GBMs) are the most common type of primary malignant brain tumor, with a mean survival rate of 12-15 months with standard treatment, which includes maximal safe surgical resection, followed by radiation therapy and concomitant and adjuvant chemotherapy (1). However, patient prognosis is unpredictable, suggesting that therapy planning must become more individualized. To this end, research has focused on identifying prognostic factors in GBM patients. However, there is insufficient knowledge about the independent contribution of postoperative residual volume of edema/invasion in patient outcome.The aim of the present study is to assess whether postoperative residual nonenhancing volume (PRNV) is correlated and predictive of overall survival (OS) in GBM patients.

Materials and Methods

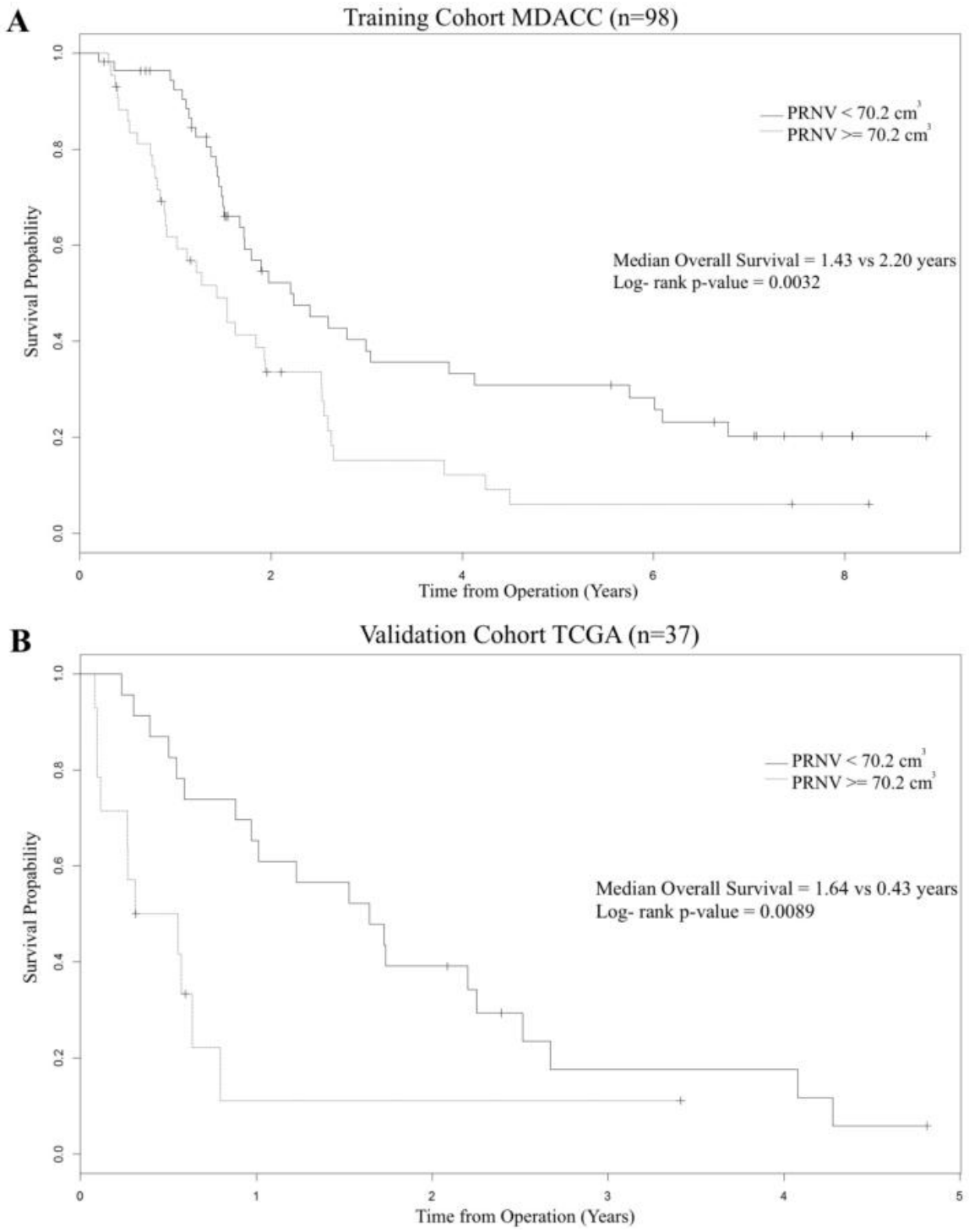
We retrospectively analyzed a total 135 GBM patients obtained from The University of Texas MD Anderson Cancer Center (training cohort, n=98) and The Cancer Genome Atlas (validation cohort, n=37). All patients had undergone postoperative magnetic resonance imaging (MRI) immediately after surgery (2). We evaluated the survival outcomes with regard to PRNV. The role of possible prognostic factors that may affect survival after resection, including age, sex, pre-operative Karnofsky performance status (KPS), postoperative nodular enhancement, surgically induced enhancement, and postoperative necrosis, was investigated using univariate and multivariate Cox proportional hazards regression analyses (3). Additionally, a recursive partitioning analysis (RPA) was used to identify prognostic groups.

Results

Our analyses revealed that a high PRNV (HR=1.294; p=0.0255) and old age (HR=1.031; p=0.0021) were independent predictors of overall survival. This trend also was observed in the validation cohort (higher PRNV: HR=2.142, p=0.0006; older age: HR=1.034, p=0.0148). Recursive partitioning analysis identified 2 prognostic risk groups: low-risk group (PRNV<70.2cm3; n=55) and high-risk group (PRNV>=70.2cm3; n=43). Glioblastoma patients with low PRNV had a significant survival benefit (9.3 months; p=0.0032) (Fig.).

Conclusions

In this study we showed that a high PRNV is predictive of poor OS. The PRNV, along with the well studied presence of residual tumor, can serve as prognostic biomarkers that are useable in clinical practice. These features may identify at-risk patients immediately after surgery, guide postoperative management and monitoring frequency, and suggest individualized therapy. Our results also suggest that a more aggressive surgical approach than the current practice will improve OS. Studies with larger sample sizes or multicenter trials, which are underway at our institution, are needed to further evaluate the relationship between PRNV and patient mortality, morbidity, and OS.



(Filename: TCT_O-479_Figure_2.jpg)

O-480

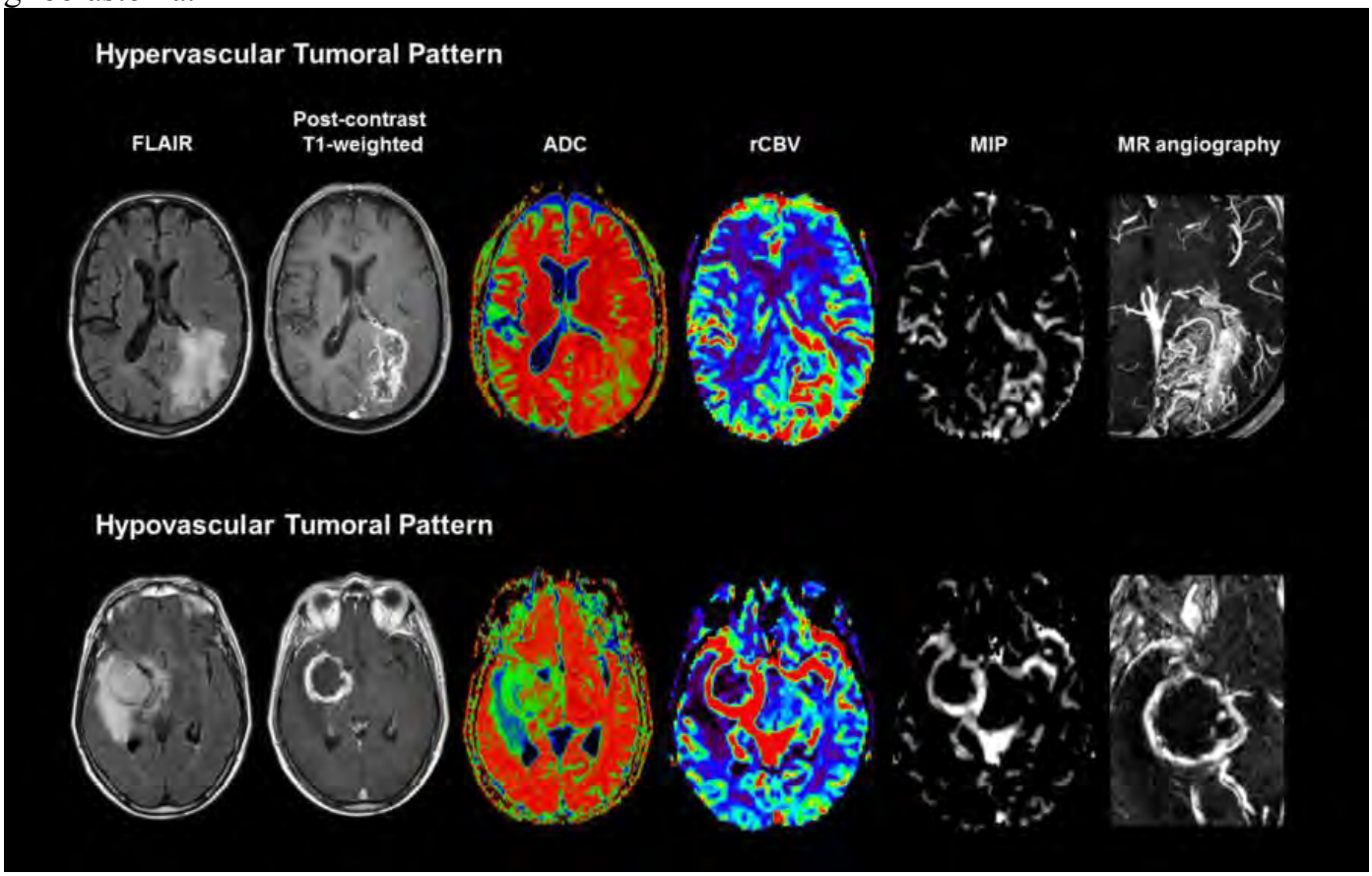
1:54PM - 2:02PM

Tumor vascular pattern on MRI as a biomarker for predicting survival in newly diagnosed glioblastoma

J Puig[1], G Blasco[2], P Daunis-i-Estadella[3], A Gimeno[4], C Biarnes-Duran[5], M Marti-Navas[6], S Thio-Henestrosa[3], J Sanchez-Gonzalez[7], A Alberich-Bayarri[8], M Puigdemont[9], M Wintermark[10], K Nael[11], R Jain[12], M Essig[13], P Salvador[2]
[1]Research Unit of Diagnostic Imaging Institute (IDI), IDIBGI, University Hospital Dr Josep Trueta, Girona, Spain, [2]Imaging Research Unit, IDI-IDIBGI, Hospital Dr Josep Trueta, Girona, None, [3]Department of Computer Science, Applied Mathematics and Statistics, University of Girona, Girona, Girona, [4]Department of Radiology (IDI), University Hospital Dr Josep Trueta, Girona, Girona, [5]Research Unit of Diagnostic Imaging Institute (IDI), Girona Biomedical Research Institute (IDIBGI), Girona, Girona, [6]Research Unit of Diagnostic Imaging Institute (IDI), IDIBGI, University Hospital Dr Josep Trueta, Girona, Girona, [7]Philips Healthcare Ibérica, Madrid, Madrid, [8]Hospital Universitario y Politecnico La Fe-QUIVIM, Valencia, None, [9]Catalan Institute of Oncology (ICO), Hospital Cancer Registry, University Hospital Dr Josep Trueta, Girona, Girona, [10]Stanford University, Stanford, CA, [11]Icahn School of Medicine at Mount Sinai, New York, NY, [12]NYU School of Medicine, New York, NY, [13]Department of Radiology, University of Manitoba, Winnipeg, Manitoba

Purpose
Vascularity is an important prognostic factor in malignant gliomas; increased vascularity correlates with shortened survival. Validated vascular biomarkers to monitor treatment with anti-angiogenic drugs are lacking. The usefulness of histological analysis is limited by its invasive nature, long processing time, and interobserver variability. We aimed to determine whether the tumor vascular pattern on MRI (MRI-TVP) is useful in predicting survival in patients with newly diagnosed glioblastomas, and to correlate MRI-TVP with dynamic susceptibility contrast (DSC) perfusion and diffusion parameters for contrast-enhancing lesion (CEL) and surrounding non-CEL.
Materials and Methods
Ninety-seven patients (59 men; mean age, 61 years) with histologically proven glioblastoma underwent 1.5T-MRI including anatomical sequences, first-pass DSC images, and postcontrast T1-weighted SE images after 0.1 mmol/kg gadobutrol (Gadovist; Bayer Schering Pharma, Berlin, Germany) with a 1 mm isometric voxel. We used Olea Sphere V.3.0 software (Olea Medical, La Ciotat, France) to analyze relative cerebral blood volume (rCBV), relative cerebral blood flow (rCBF), delay time (DT), mean temporal maximum intensity projection (tMIP), and apparent diffusion coefficient (ADC) in volumes of interest for CEL, non-CEL, and contralateral tissue. Tumors with >5 vessels on postcontrast T1-weighted SE images were classified as hypervascular (hyper-MRI-TVP). Prognostic factors were evaluated by Kaplan-Meier survival and Cox proportional hazards analyses.
Results
Fifty-five (56.7%) glioblastomas were hyper-MRI-TVP. Patients with hyper-MRI-TVP had higher mean age, volume-CEL, ADC-CEL, DT-CEL, rCBV-CEL, rCBV-nonCEL, and

tMIP-CEL and lower DT-non-CEL. Mean survival for hypo- and hyper-MRI-TVP glioblastomas treated with surgery, radiotherapy, andchemotherapy was 12.9±7.7 and 8.3±6.9 months, respectively. MRI-TVP was the best predictor of survival at 1 year (AUC 0.84, 88.5% sensitivity, 77.9% specificity, 82.3% positive predictive value, 87.8% negative predictive value).
Conclusions
MRI-TVP is a promising potential biomarker for predicting survival in newly diagnosed glioblastoma.



(Filename: TCT_O-480_TumoralVascularPatternGBM.jpg)

O-481

2:02PM - 2:10PM

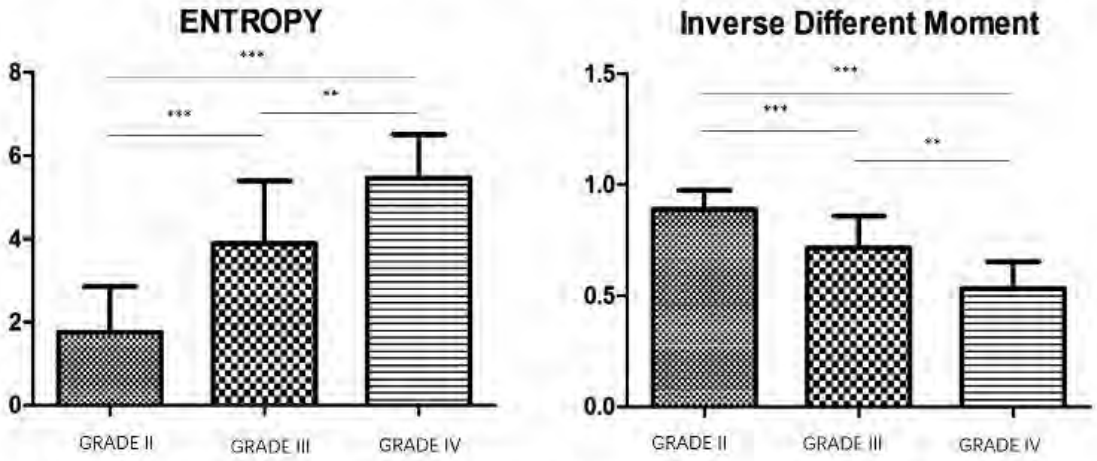
Model-Free Parameters of DCE-MRI with Texture Analysis Better Correlate with Malignancy of Glioma

T Xie[1]
[1]*Daping Hospital, Chongqing, China*

Purpose
To investigate the potency of DCE-MRI model-free parameters in grading intracranial

glioma with texture analysis, and evaluate the correlations between these parameters and histological prognostic features.
Materials and Methods
Forty-three pathologically confirmed supratentorial glioma patients, who underwent DCE-MRI pre-operatively were enrolled. Three most used pharmacokinetic models, Tofts, extended Tofts and Patlak were fitted to individual artery input function (AIF) to generate 2 to 4 model-based parameters (Ktrans, Kep, Ve ad vp). Three Mode-free parameters, initial area under curve (iAUC), maximum concentration (Max Conc), and Wash Slope, were derived from time-concentration curve in tumor region as well. Two experienced neuroradiologists independently drew region of interest (ROI) on cross-sectional images with the most heterogenous tumor lesion and texture feature were generated from a self-written software based on calculation of gray-level co-occurrence matrix (GLCM). One-way ANOVA test and receiver operating characteristic curve (ROC) were performed to grade glioma and testify the effectiveness of certain parameter in grading. The agreement between 2 observers was testified by interobserver agreement (kappa statistics). Correlations between DCE model-based or model-free parameters and histologic prognostic features were acquired by Pearson correlation coefficient.
Results
One-way ANOVA test revealed that most texture features of Ktrans, kep, ve and vp generated from pharmacokinetic models could effectively distinguish low-grade gliomas and high-grade ones ($p < 0.01$), However, none of them could significantly differentiate grade III from grade IV. In comparison, entropy and inverse difference moment, obtained from GLCM, of iAUC, Max Conc and Wash Slope could effectively differentiate grade III gliomas from grade IV gliomas ($p < 0.01$). Kappa statistics showed substantial interobservor agreement. Meanwhile, entropy and inverse difference moment of the 3 model-free parameters showed good correlation with vascular proliferation indices and vascular endothelial growth factor (VEGF) ($p < 0.01$).
Conclusions
Texture analysis of DCE-MRI model-free parameters displayed better potency and less time assuming efforts in assessing malignancy of glioma than that of model-based parameters. Moreover, these parameters showed better correlation with vascular proliferation and pro-angiogenic factors in glioma which linked with poor prognosis.

◆ Maximum Concentration of Contrast Agent (MAX Conc)



◆ Texture Analysis of Model-free and Model-Based DCE parameter in differentiating LGG and HGG

DCE-MRI parameters	Model-Free Parameters			Model-Based Parameters			
	AUC	Max Conc	Max Slope	Ktrans	Kep	Ve	Vp
Energy	*p<.001*	*p<.001*	*p<.001*	*p<.001*	*P=0.0019*	*ns*	*ns*
Entropy	*p<.001*	*p<.001*	*p<.001*	*p<.001*	*P=0.006*	*ns*	*p<.001*
Intreia	*p<.001*	*P=0.0013*	*p<.001*	*ns*	*p<.001*	*p<0.05*	*p<.001*
Correlation	*p<.001*	*p<.001*	*p<.001*	*ns*	*P=0.046*	*ns*	*ns*
Inverse Difference Moment	*p<.001*	*p<.001*	*p<.001*	*p<.001*	*p<.001*	*ns*	*p<.001*

◆ Texture Analysis of Model-free and Model-Based DCE parameter in differentiating Grade III and Grade IV

DCE-MRI parameters	Model-Free Parameters			Model-Based Parameters			
	AUC	Max Conc	Max Slope	Ktrans	Kep	Ve	Vp
Energy	*ns*	*ns*	*ns*	*ns*	*ns*	*ns*	*ns*
Entropy	*p<.001*	*p<0.05*	*p<0.05*	*ns*	*ns*	*ns*	*ns*
Inertia	*p<.001*	*ns*	*ns*	*ns*	*ns*	*ns*	*ns*
Correlation	*ns*	*ns*	*p<.001*	*ns*	*ns*	*ns*	*ns*
Inverse Difference Moment	*p<0.05*	*p<.005*	*p<.001*	*ns*	*ns*	*ns*	*ns*

(Filename: TCT_O-481_upload.jpg)

O-482

2:10PM - 2:18PM

Utility of arterial spin labeling as a noncontrast perfusion technique in the evaluation of high grade gliomas

A Sung[1], R Lee[2], S Imbesi[1], N Farid[1]

[1]University of California, San Diego, San Diego, CA, [2]UCSD/VA Medical Center, San Diego, CA

Purpose

This study compares arterial spin labeling (ASL) MR perfusion to dynamic susceptibility contrast (DSC) MR perfusion in the evaluation of high grade gliomas.

Materials and Methods

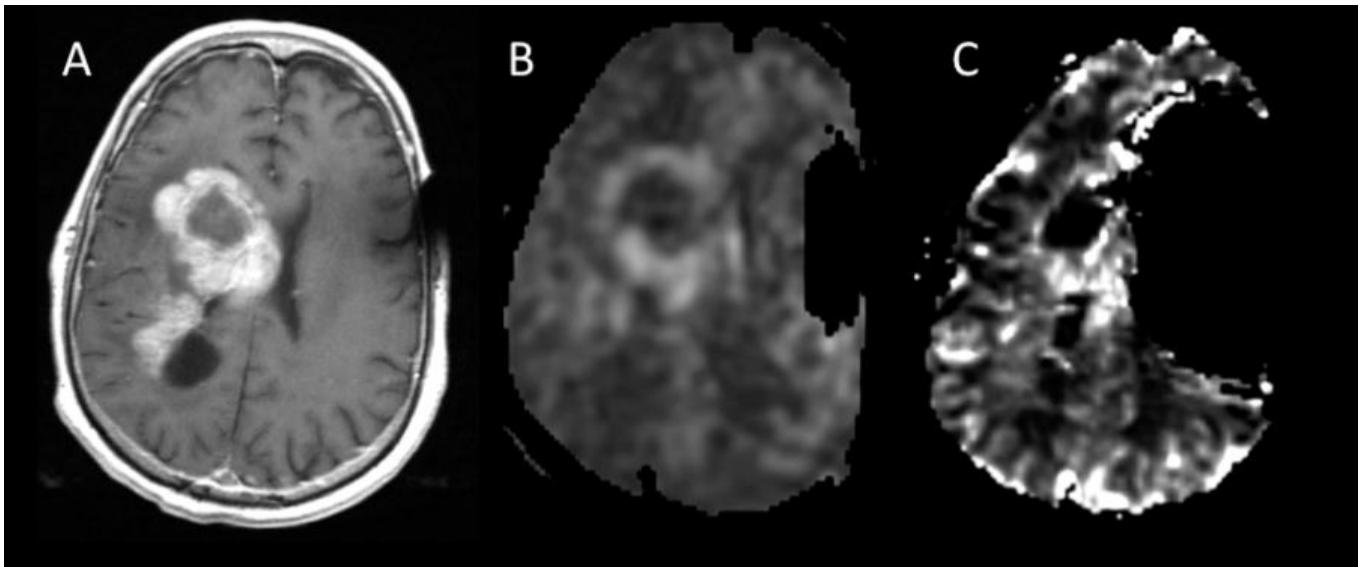
Retrospective review of all surgically proven cases of high grade glioma at a single institution for which concurrent ASL and DSC perfusion imaging was obtained. Arterial spin labeling was obtained using pseudo-continuous arterial spin labeling tagging with 3D fast spin-echo imaging. Dynamic susceptibility contrast perfusion was obtained using a T2* technique with a preloading dose to account for contrast leakage. Regions of interest (ROIs) were drawn within the region of contrast-enhancing tumor and normal-appearing contralateral white matter on the gray-scale ASL and DSC perfusion images, and relative cerebral blood flow and volume (rCBF and rCBV) were calculated.

Results

Seven cases identified: 6 glioblastoma, 1 grade III/IV glioma. Mean rCBF-DSC = 3.96, mean rCBF-ASL = 3.93 ($p = 0.49$). Mean rCBV-DSC = 4.81 (p-value rCBF-ASL vs. rCBV-DSC = 0.12, rCBF-DSC vs. rCBV-DSC = 0.14).

Conclusions

In our cohort, ASL and DSC demonstrated similar elevated rCBF in high grade gliomas. Relative CBV values were higher compared to both ASL- and DSC-derived measurements of rCBF, although not to statistical significance; however this may have been due to the small sample size. In 2 cases, ASL was able to detect elevated CBF in regions which were partially obscured by susceptibility artifact on the corresponding DSC images. This is likely due to the fast spin-echo acquisition for ASL compared to the gradient-echo acquisition for DSC, which is more sensitive to susceptibility artifact. In summary, ASL is a noncontrast perfusion technique which may be utilized as an alternative method of tumor surveillance in patients for whom contrast administration is contraindicated and in cases where DSC perfusion may be limited due to susceptibility.



Patient #3, Glioblastoma. A = T1-post contrast, B = Arterial spin labeling CBF, C = Dynamic susceptibility contrast CBF. Increased tumor conspicuity on ASL images due to decreased susceptibility artifact from the shunt reservoir.

Patient #	Tumor Type	Primary Dx/ Recurrent	CBF-ASL (mL/100g/min)	rCBF-ASL	rCBF-DSC	rCBV-DSC
1	Glioblastoma	Recurrent	72.2	3.47	4.14	5.24
2	Glioblastoma	Recurrent	95.4	3.04	3.84	3.95
3	Glioblastoma	Primary	78.5	5.45	5.38	5.38
4	Glioblastoma	Recurrent	76.1	2.50	2.44	2.58
5	Glioblastoma	Recurrent	97.6	4.88	5.98	6.30
6	Glioblastoma	Recurrent	138.0	5.90	4.59	4.62
7	Grade III/IV Glioma	Primary	50.3	2.26	1.31	5.60
	Mean		86.9	3.93	3.96	4.81

CBF = Cerebral Blood Flow, CBV = Cerebral Blood Volume, ASL = Arterial Spin Labeling, DSC = Dynamic Susceptibility Contrast, rCBF = CBF relative to normal-appearing white matter, rCBV = CBV relative to normal-appearing white matter.

(Filename: TCT_O-482_AbstractFigure.jpg)

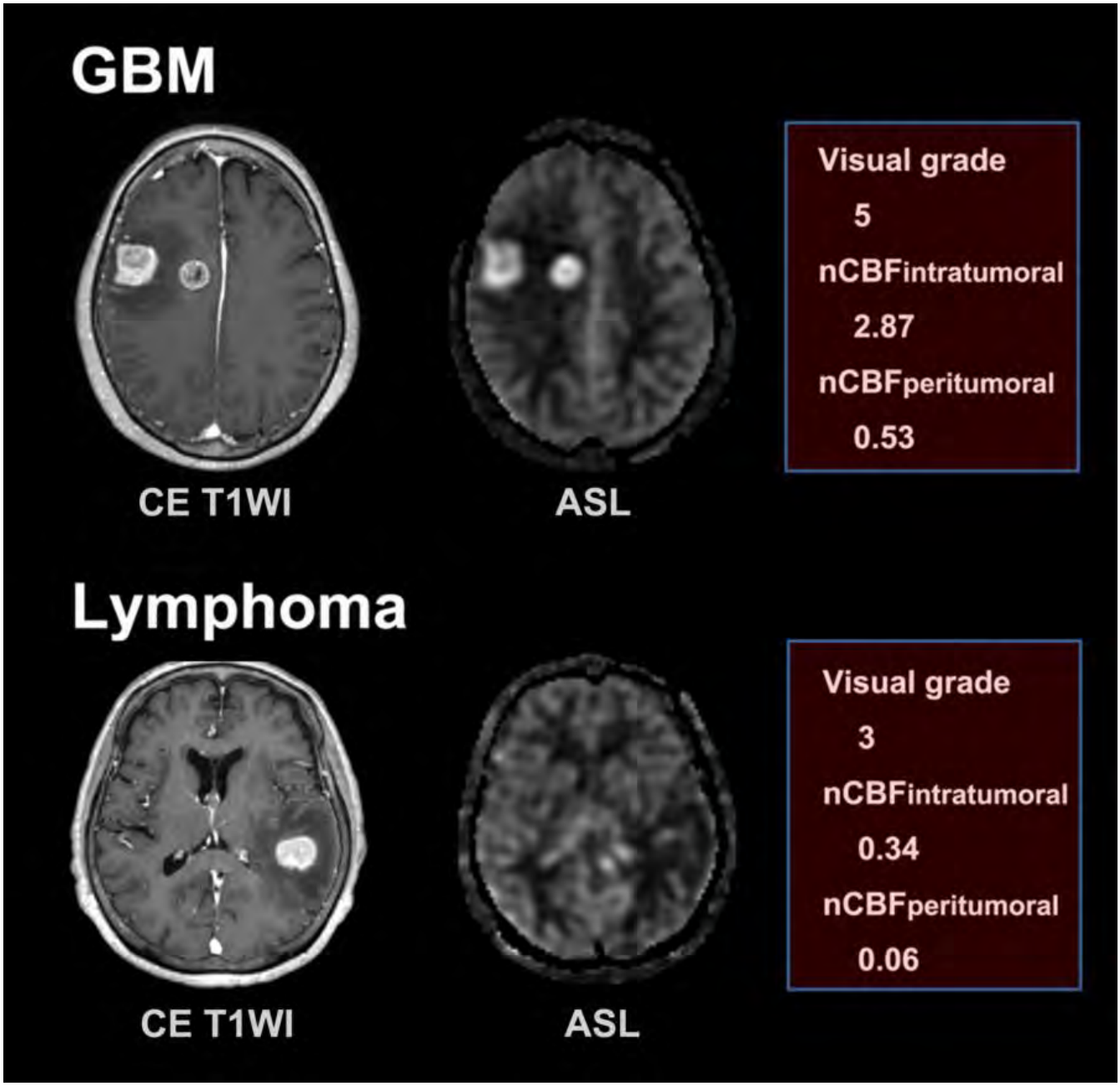
O-483

2:18PM - 2:26PM

Differentiation between Glioblastoma and Primary CNS Lymphoma: Qualitative and Quantitative Analysis Using Arterial Spin Labeling MR Imaging

S You[1], T Yun[2], R Yoo[3], H Choi[1], K Kang[3], S Choi[3], J Kim[3], C Sohn[3]
[1]Seoul National University Hospital, Seoul, Korea, Republic of, [2]Seoul National University Hospital, Seoul , Seoul , [3]Seoul National University Hospital, Seoul, Seoul

Purpose
To evaluate the diagnostic performance of CBF by using arterial spin labeling perfusion MR imaging (ASL-PWI) to differentiate between glioblastoma (GBM) and primary CNS lymphoma.
Materials and Methods
The institutional review board of our hospital approved this retrospective study. The study population consisted of 114 consecutive patients who histologically confirmed as either GBM (n = 93) or primary CNS lymphoma (n = 21). All participants underwent pre-operative MR imaging including ASL-PWI. For qualitative analysis, the tumors were graded visually into 5 categories based on ASL-CBF maps. For quantitative analysis, the reviewer drew regions of interest on ASL-CBF maps upon the most hyperintense portion within the tumor and peritumoral area upon peritumoral T2 hyperintensity. Signal intensities of intratumoral and peritumoral regions of interest for each subject were normalized by dividing the values by those of contralateral normal gray matter (nCBFintratumoral and nCBFperitumoral, respectively). Visual grading scales and quantitative parameters between GBM and primary CNS lymphoma were compared using Mann-Whitney test and unpaired t-test, respectively. In addition, the area under the receiver operating characteristic curve was used to evaluate the diagnostic performance of ASL-driven CBF to differentiate primary CNS lymphoma from GBM.
Results
For qualitative analysis, primary CNS lymphoma group showed significantly lower grade compared to GBM group ($P = .001$). For quantitative analysis, both nCBFintratumoral and nCBFperitumoral in primary CNS lymphoma were significantly lower than those in GBM (mean and SD for nCBFintratumoral, 0.9 ± 0.6 vs 2.7 ± 1.9, $P < .001$; mean and SD for nCBFperitumoral, 0.2 ± 0.1 vs 0.5 ± 0.3, $P < .001$, respectively). The areas under the curve for discriminating primary CNS lymphoma from by using visual grading, nCBFintratumoral, and nCBFperitumoral were 0.814, 0.849, and 0.908, respectively, $P < .001$ for all.
Conclusions
Arterial spin labeling-PWI has excellent performance in the differentiation between GBM and primary CNS lymphoma, and this technique has the potential to be used as a completely noninvasive imaging tool to evaluate the brain lesion in patients with suspected GBM or primary CNS lymphoma.



(Filename: TCT_O-483_ASNRREPRESENTATIVE92-iloveimg-converted.jpg)

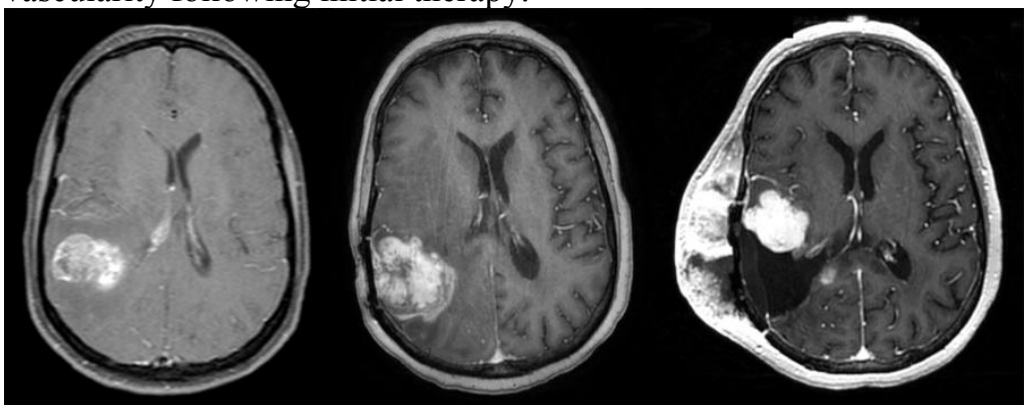
O-484

2:26PM - 2:34PM

Imaging Characteristics of Gliosarcoma with Special Emphasis On Dural Involvement At Initial Presentation and At Recurrence

B Merritt[1], T Tihan[1], S Cha[1]
[1]*University of California, San Francisco, San Francisco, CA*

Purpose
Gliosarcoma is a rare and distinct variant of glioblastoma comprised of both malignant glial and sarcomatous components. Few reports have suggested characteristic location of gliosarcoma associated with dura mater (1-2). The purpose of our study was to investigate MR imaging characteristics of gliosarcoma with particular attention to involvement of dura, recurrence pattern, and quantitative perfusion and diffusion-weighted imaging.
Materials and Methods
Forty patients with histopathologically confirmed gliosarcoma were selected retrospectively from the neuropathology database from 2010 to 2016 at our institution according to IRB-approved protocols. For each patient, detailed clinical history and MR imaging characteristics were analyzed including dural involvement at initial diagnosis or at recurrence. Apparent diffusion coefficient (ADC) and relative cerebral blood volume (rCBV) were measured prior to surgery.
Results
Of the 40 patients included in this study, 23 were primary gliosarcoma (PGS) and 17 were secondary gliosarcoma (SGS). Twenty of 23 (87%) PGS demonstrated dural involvement and 17 of 17 (100%) SGS showed dural or extradural involvement. Average ADC values for PGS and SGS were 0.608 +/- 0.194 (× 10-3 mm2/sec) and 0.513 +/- 0.234 (× 10-3 mm2/sec), respectively (p=0.19). Average rCBV values for PGS and SGS were 2.82 (+/- 1.25) and 1.97 (+/- 0.35), respectively (p=0.02).
Conclusions
Dural and extradural involvement were highly specific imaging features of gliosarcoma. There was no difference in ADC values between PGS and SGS; however, significantly lower rCBV values were found in SGS when compared to PGS suggesting altered tumor vascularity following initial therapy.



(Filename: TCT_O-484_ASNR.jpg)

O-485

2:34PM - 2:42PM

MR Features Associated with Glioma Mutation Count: Potential Biomarkers For Immunotherapy Response

M Bernieri[1], P Chang[2], J Steinman[2], F Iwamoto[3], A Lignelli[3]
[1]University of Rome, La Sapienza, Rome, RM, [2]Columbia University Medical Center, New York, NY, [3]Columbia University Medical Center, New York City, NY

Purpose

Anti-PD-1 immunotherapy represents a promising new approach in the treatment of low-grade (LGG) and high-grade gliomas (HGG). However given the targeted nature of immunotherapy agents, careful patient selection through molecular and radiographic biomarkers is key to treatment success. One proposed molecular marker for treatment response to immunotherapy agents is total mutation count, a proxy for the number of antigens available for targeting by host immune cells. Early studies have suggested that tumors with increased total mutation count have improved response to immunotherapy (1). We hypothesize that a deep learning algorithm can be used to identify gliomas with high total mutation count.

Materials and Methods

Patients with pathology proven LGG/HGG and complete pre-operative MR (FLAIR, T2, precontrast and postcontrast T1) were downloaded from The Cancer Imaging Archives. Corresponding mutation count information was obtained from Ceccarelli et al (2). A deep learning algorithm was trained for binary classification of tumors into above- or below-average number of total mutations (median of 34 mutations per tumor). The 8-layer neural network is comprised of 7 serial convolutional layers and a single fully connected layer, and classifies based on a single axial slice cropped to tumor margins. Final classification for each tumor is based on the mode of all slices per volume.

Results

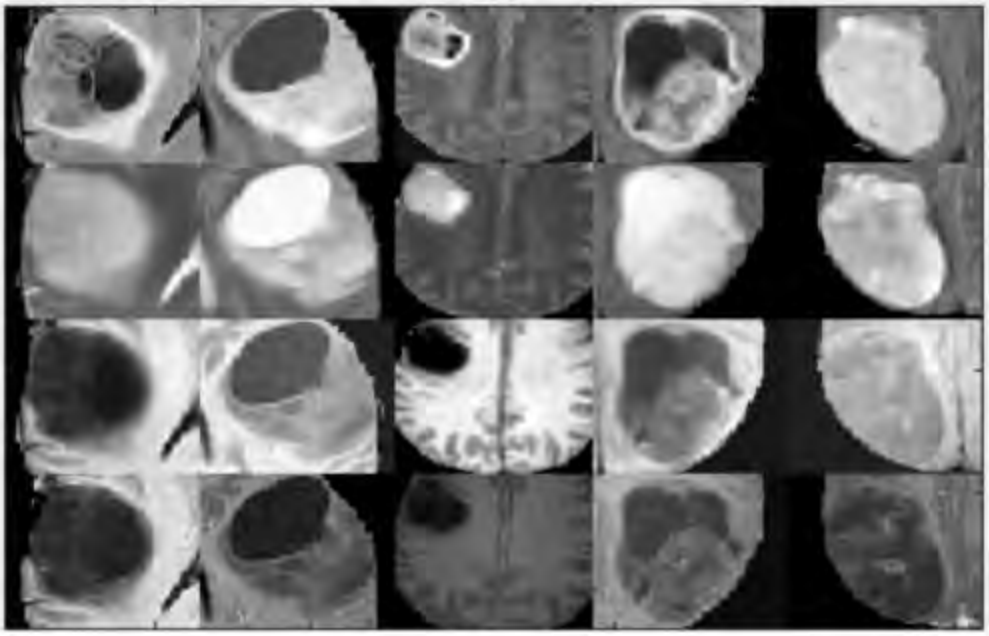
A total of 260 patients (145 HGG, 115 LGG) were included for analysis. Distinct MR features were learned by the algorithm for prediction of high or low total mutation count with 86% accuracy (Fig. 1). Upon visual inspection these features included: heterogeneity of T2 signal, pattern of FLAIR abnormality (well defined large regions of eccentric low signal with adjacent rim of high signal) and degree of enhancement.

Conclusions

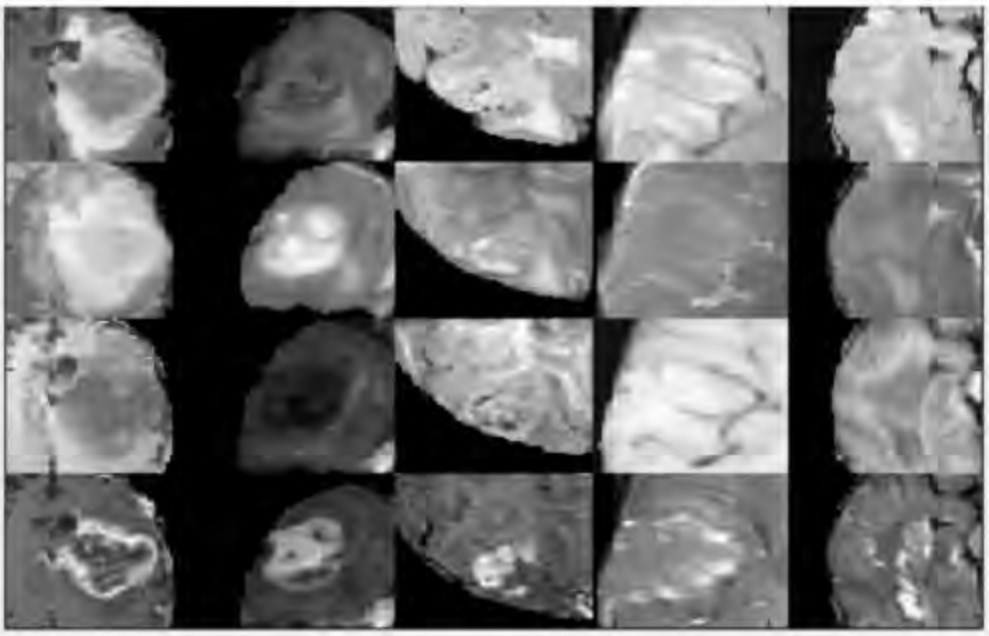
A deep learning algorithm can classify gliomas based on high or low total mutation count with 86% accuracy. The presence of distinct MR imaging features suggests that radiographic biomarkers for mutation count exist and may be useful in patient selection for immunotherapy.

Figure 1: Example prototypical tumors (each column represents one patient; modalities from top-bottom include FLAIR, T2, T1-precontrast and T1-postcontrast. (a) Cluster of imaging features associated with low total mutation count including well-defined margins along with areas of eccentric low signal centrally and peripheral rim of high signal on FLAIR images, as well as minimal enhancement. (b) Cluster of imaging feature associated with high total mutation count including poorly defined margins and regions of relative increased enhancement.

(a)



(b)



(Filename: TCT_O-485_Figure1.jpg)

O-486

2:42PM - 2:50PM

Diffusion Basis Spectrum Imaging with Extended Isotropic Spectrum (DBSI-EIS): Initial Experience in the Evaluation of Gliomas

G Guzman Perez-Carrillo[1], Q Wang[2], M Ponisio[2], P LaMontagne[2], S Song[2], S Dahiya[2], J McConathy[3], Y Wang[2], T Benzinger[4]
[1]University of Arizona- Banner Medical Center, Tucson, AZ, [2]Washington University in St. Louis, St. Louis, MO, [3]University of Alabama at Birmingham, Birmingham, AL, [4]Washington University in St. Louis, Saint Louis, MO

Purpose
Brain tumors typically are heterogeneous, and may contain different grades of tumor cells, different types of tumor cells, edema and/or abnormal vascular structures. Anatomical imaging alone can be limited in the evaluation of tumor heterogeneity, especially in those tumors that demonstrate little to no enhancement. While there are physiologic MR tools available in daily clinical practice such as perfusion or diffusion, we wanted to develop a more powerful, sensitive sequence for the characterization of tumor heterogeneity. We propose that diffusion basis spectrum imaging with extended isotropic spectrum (DBSI-EIS) (1) can provide quantitative distributions of different grades of tumor cells and capillary blood perfusion within the tumor in a single clinical imaging scan with more accuracy than previously reported with traditional diffusion techniques (2).
Materials and Methods
Ten of 11 enrolled adult patients with known or suspected brain gliomas that were nonenhancing or had substantial nonenhancing regions (>50%) underwent simultaneous 3,4-dihydroxy-6-[18F]fluoro-L- phenylalanine (18F-FDOPA) (3) PET/MRI prior to planned standard-of-care surgical resection and/or stereotactic biopsy. Of these, 7 patients also underwent DBSI-EIS, a new diffusion MRI protocol, microstructure modeling, and inverse computation technique. The DBSI-EIS maps then were compared to the 18F-DOPA and coordinate-guided biopsy or surgical resection results. Perfusion maps extracted from DBSI-EIS were calculated (4). Apparent diffusion coefficient (ADC) cut-offs for tumor grade based on the DBSI-EIS data then were determined and tumor grade maps created. (See Fig. 1).
Results
Grade 4 tumor ADC cutoff was 0.3-0.5 10−3 mm2/s. Grade 3 was 0.5-0.8 10−3 mm2/s. Grade 1 and 2 was 0.8-1.5 10−3 mm2/s. Table 1 summarizes the subject's demographic characteristics as well as the correlation between 18F-FDOPA and DBSI-EIS maps. We found that in 7/7 patients (100%) DBSI-EIS maps correlated with tumor grade on pathological evaluation. Interestingly, 18F-FDOPA was negative on subject S7, whereas

DBSI-EIS correctly identified not only the tumor, but the tumor grade at the region of stereotactic biopsy sample.

Conclusions

This preliminary study demonstrated the capability of a new diffusion MRI method, DBSI-EIS, to noninvasively characterize the structural heterogeneity in brain tumors, including various grades of tumor cells and capillary blood perfusion within the tumors, consistent with pathology assessment on biopsy tissues. Although our preliminary data suggest DBSI-EIS is a promising multi-parametric imaging technique to accurately measure cellularity and tumor grade, larger studies will be needed before definitive conclusions can be made about the role of this technique. This preliminary study also suggested the unmet need to develop a new generation of MRI technique that is capable to provide direct pathophysiological measures for tumor characterization.

Figure1. A 66-year-old women (S3) with recurrent oligodendroglioma, WHO grade II was imaged using FLAIR, FDOPA PET, perfusion and DBSI-EIS imaging. Region of interest was label in magenta.

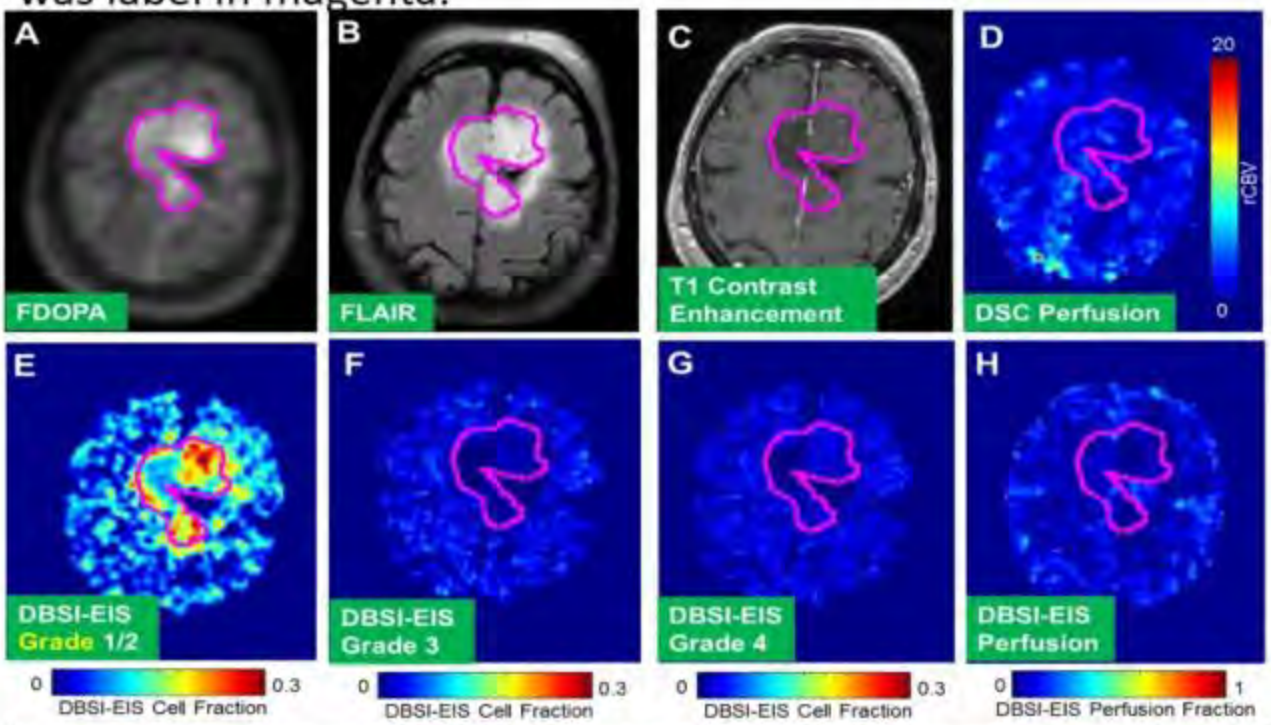


Table 1. Characteristics of patients and the tumor grades detected by biopsy and DBSI-EIS

Patient #	Age	Gender	FDOPA uptake	Tumor pathology	DBSI-EIS tumor grade
S3	66	Female	Yes	Oligoastrocytoma WHO grade II	Grade 1/2
S5	36	Female	Yes	Oligodendroglioma WHO grade II	Grade 1/2
S6	38	Male	Yes	Oligoastrocytoma WHO grade II	Grade 1/2
S7	30	Male	**No**	Diffuse astrocytoma WHO grade II	Grade 1/2
S8	33	Female	Yes	Oligodendroglioma WHO grade II	Grade 1/2
S9	48	Male	Yes	Oligodendroglioma WHO grade III	Grade 3
S11	62	Male	Yes	Glioblastoma WHO grade IV	Grade 4

(Filename: TCT_O-486_FinalFinalASNRAbstractFigure.jpg)

O-487

2:50PM - 2:58PM

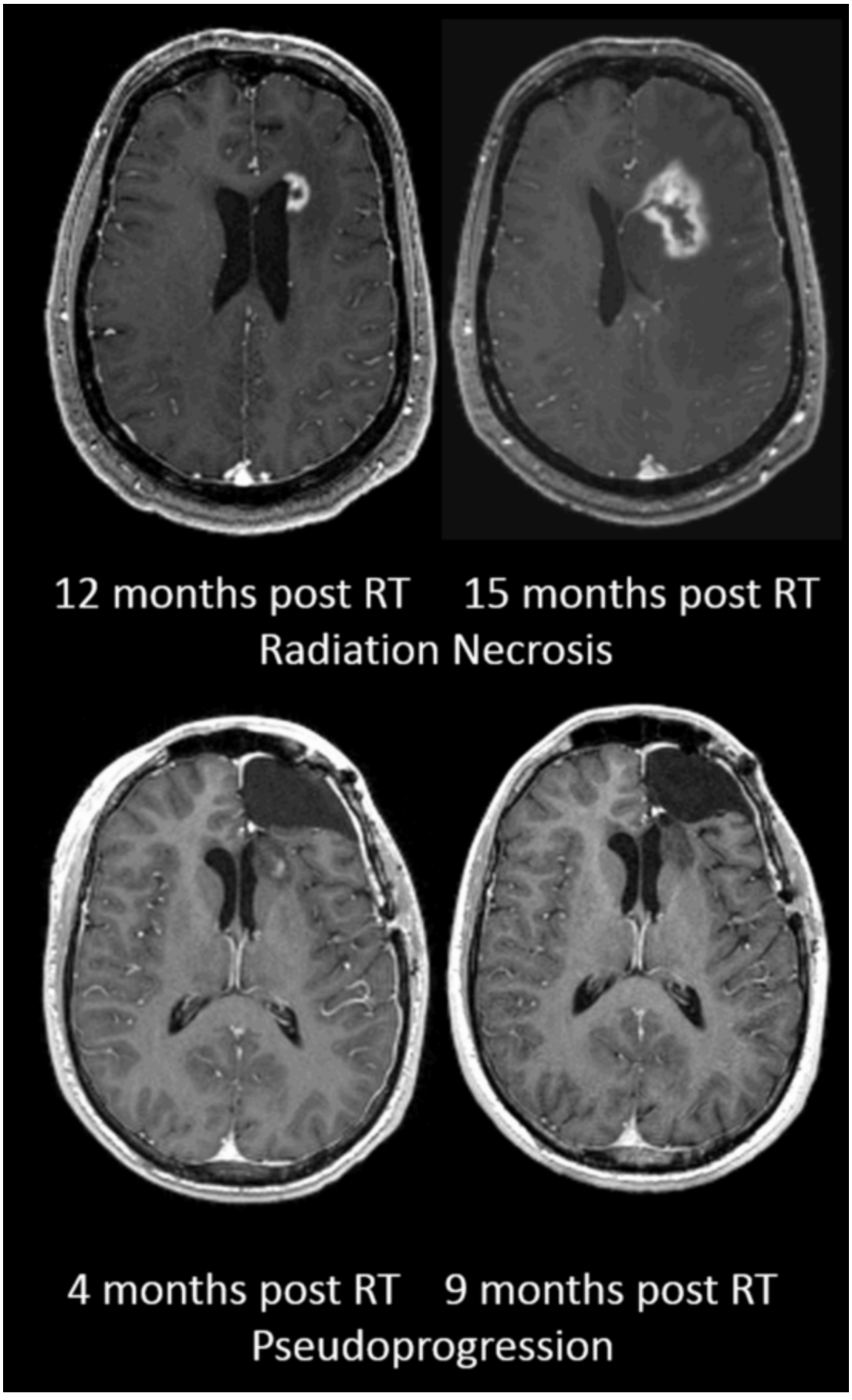
Radiation Necrosis and Pseudoprogression in Adults with Gliomas Treated with Proton Beam Radiotherapy

M Miller-Thomas[1], J Vu[1], C Tsien[1], T Benzinger[2], J Huang[1], C Robinson[1], K Sargar[1], A Salter[1]
[1]Washington University in St. Louis, St. Louis, MO, [2]Washington University in St. Louis, Saint Louis, MO

Purpose
Our aim is to evaluate the incidence, timing, and imaging patterns of radiation necrosis versus pseudoprogression in adults with gliomas treated with proton beam radiotherapy.
Materials and Methods
Twenty-seven consecutive adults with WHO Grade II or Grade III oligodendroglioma, oligoastrocytoma, or astrocytoma treated with proton beam radiotherapy were reviewed retrospectively by 2 neuroradiologists and a radiation oncologist. New contrast enhancement, change in size of treated lesion, and change in FLAIR signal intensity on follow-up brain MRI within the treatment field were categorized by group consensus as radiation necrosis, pseudoprogression, tumor progression, or uncertain taking into accounting supporting clinical follow up and biopsy data. Radiation necrosis was defined by progressive mass-like enhancement in treatment field with or without clinical symptoms, pseudoprogression by transient contrast enhancement in the treatment field that resolved during follow-up period in an asymptomatic patient, progression by growth of a mass with or without enhancement, and uncertain by contrast enhancement not fitting the other categories, or histological evidence of 1 of these processes on biopsy performed after radiotherapy.
Results
The follow-up periods ranged from 6 to 31 months after radiotherapy completion. Seven of 27 patients (26%, 95% CI 10% to 42%), including those with gross total and subtotal tumor resections, developed radiation necrosis with contrast enhancement localizing to the periventricular white matter, corpus callosum, or septum pellucidum remote from the unresected tumor or resection bed beginning at 7.6 months (range 1 to 13 months) following radiotherapy. Three of 27 patients (11%, 95% CI 3% to 29%), all with subtotal tumor resection, developed pseudoprogression with transient contrast enhancement localizing to unresected tumor developing at 5.7 months (range 4 to 8 months) and resolving at 8.7 months (range 7 to 11 months). Three of 27 patients (11%, 95% CI 3% to 29%) developed contrast enhancement within the treatment field of uncertain etiology. Fourteen of 27 patients (52%, 95% CI 34% to 69%) had stable or improving imaging and clinical findings that did not reflect radiation necrosis, pseudoprogression, or tumor progression.

Conclusions

Adults treated with proton beam radiotherapy for gliomas commonly develop contrast enhancement in the treatment field, with progressive contrast enhancement localizing to the periventricular white matter, corpus callosum, or septum pellucidum indicating radiation necrosis and transient contrast enhancement within unresected irradiated tumor following a subtotal surgical resection indicating pseudoprogression.


12 months post RT
15 months post RT
Radiation Necrosis
4 months post RT
9 months post RT
Pseudoprogression

(Filename: TCT_O-487_pspandrnimages300dpiresized.gif)

Thursday
1:30PM - 3:00PM
Long Beach Convention Center, Room 104B (Main Lobby)

25E-Parallel Paper Session: Finding the Fun in Functional Imaging

O-488

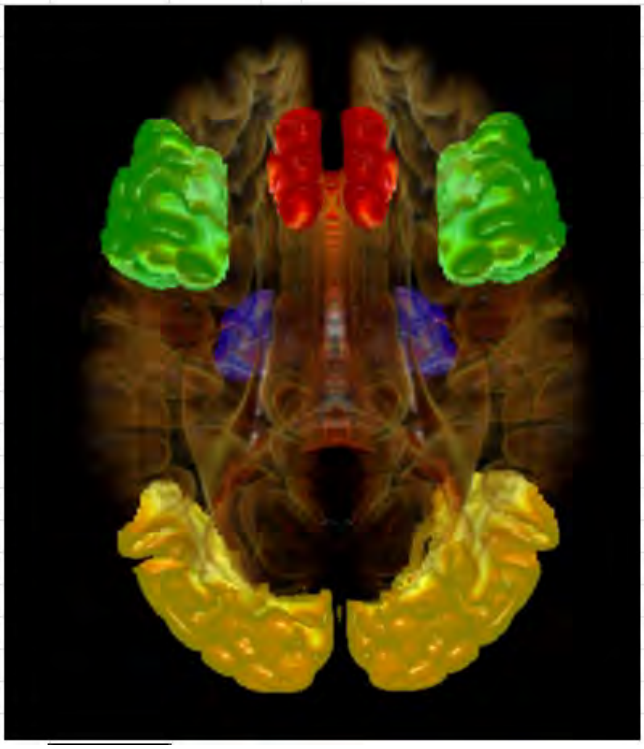
1:30PM - 1:38PM

FMRI Atlas for Control Comparison of 6 Neurofunctional Regions using Standardized Neuropsychological Tests

A Gibby[1], C Bartholomew[2], W Gibby[3], S Cvetko[4]
[1]George Washington University, Washington, DC, [2]Midwestern University, San Diego, CA, [3]University of California San Diego, San Diego, CA, [4]Novarad, American Fork, UT

Purpose
Historically we have segmented the brain for fMRI based upon a standard neuro anatomic atlas. Unfortunately, activation of the brain for a given test does not confine itself to a particular gyrus. In order to quantitate activation, the brain must be segmented into different areas to compare normative controls with specific patients. Using traditional atlases, this results in large regions of some gyri being measured where no or minimal activation is present. This results in more noise and potentially greater standard deviation of the data. We hypothesized that creating an atlas based on functional areas would result in more accurate comparisons. To that end, we have created an atlas of the functional circuits of the normal brain for 6 standardized neurofunctional tests in dicom format for use as control data.
Materials and Methods
Retrospective data from 47 patients who underwent fMRI during performance of a battery of 6 standardized neurofunctional tests were warped to fit a normalized brain from the MNI 152 template and areas of increased activity on BOLD imaging were segmented manually and averaged statistically for each area over 47 patients to achieve a normalized atlas of the functional map. Postprocessing was performed to subtract white matter and eliminate overlap.
Results
A robust fMRI atlas was created for 6 neurofunctional tests in dicom format which can be used as control data for future studies. In Table 1, as an example, long term facial memory recognition the following areas are compared with the standard Gibby-Cvetco Atlas versus the new neurofunctional atlas.
Conclusions
Utilizing a functional map of the brain as opposed to an anatomic map of the brain results in more accurate quantitation of fMRI activation with smaller errors in control data.

Gibby/Cvetko Atlas		±	Neurofunctional Atlas		±
Hippocampus	0.83	0.72	Memory Encoding Limbic System	1.1	0.9
Middle Frontal Gyrus	1.29	0.74	Frontal Language Areas	1.75	1.15
Medial Frontal Gyrus	0.96	0.66	Attentional Control Area/Medial Frontal	1.82	1.17
Visual Association Cortex	2.02	1.01	Visual Processing	3.2	1.6
Average	1.275	0.7825	Average	1.9675	1.205



(Filename: TCT_O-488_Untitled.jpg)

O-489

1:38PM - 1:46PM

Functional MRI and Handedness: The Need for Pre-Surgical fMRI Language Localization.

I Ikuta[1], W Zucconi[1], F Minja[1]
[1]*Yale University School of Medicine, New Haven, CT*

Purpose
Presurgical planning with functional MRI (fMRI) is used to localize eloquent regions such as those involved in language comprehension and speech production. While WADA testing has been well established for determining language dominance, there are inherent risks associated with angiography (stroke, hemorrhage, exposure to ionizing radiation, etc.). Functional MRI avoids these risks, can identify dominant language centers, and

simultaneously provide anatomic image registration for the neurosurgeons. While the majority of patients are left hemisphere dominant for language, a smaller but significant percentage of patients are right hemisphere dominant for language or even co-dominant. Handedness (left-handed, right-handed, or ambidextrous) is predominantly right-handed for the majority of the general population. While the correlation between handedness and speech dominance has been known for quite some time and tested in a research setting, findings have not been evaluated in a clinical fMRI setting. We explored the association between handedness and dominant language hemisphere (left, right, or co-dominant). We hypothesized that left-handed patients have an increased incidence of right-dominant or co-dominant language localization relative to right-handed patients. Such an increase would make presurgical fMRI very useful for all left-handed patients.

Materials and Methods

The PACS was queried for all patients undergoing fMRI at our academic, 1,541-bed, tertiary care referral center, with a date range of January 1, 2014 through December 7, 2016. The dictation was reviewed for dominant language lateralization and recorded in an Excel spreadsheet. Cases were excluded from statistical analysis if dominant language localization was indeterminate or if language paradigms were not performed as part of the fMRI. An electronic medical record (EMR) chart review was performed to identify the handedness (left-handed, right-handed, or ambidextrous). Statistical analysis was performed in the Excel spreadsheet, with a primary outcome measure of dominant language localization incidence for each kind of handedness. A secondary outcome of the prevalence of handedness in the EMR also was performed.

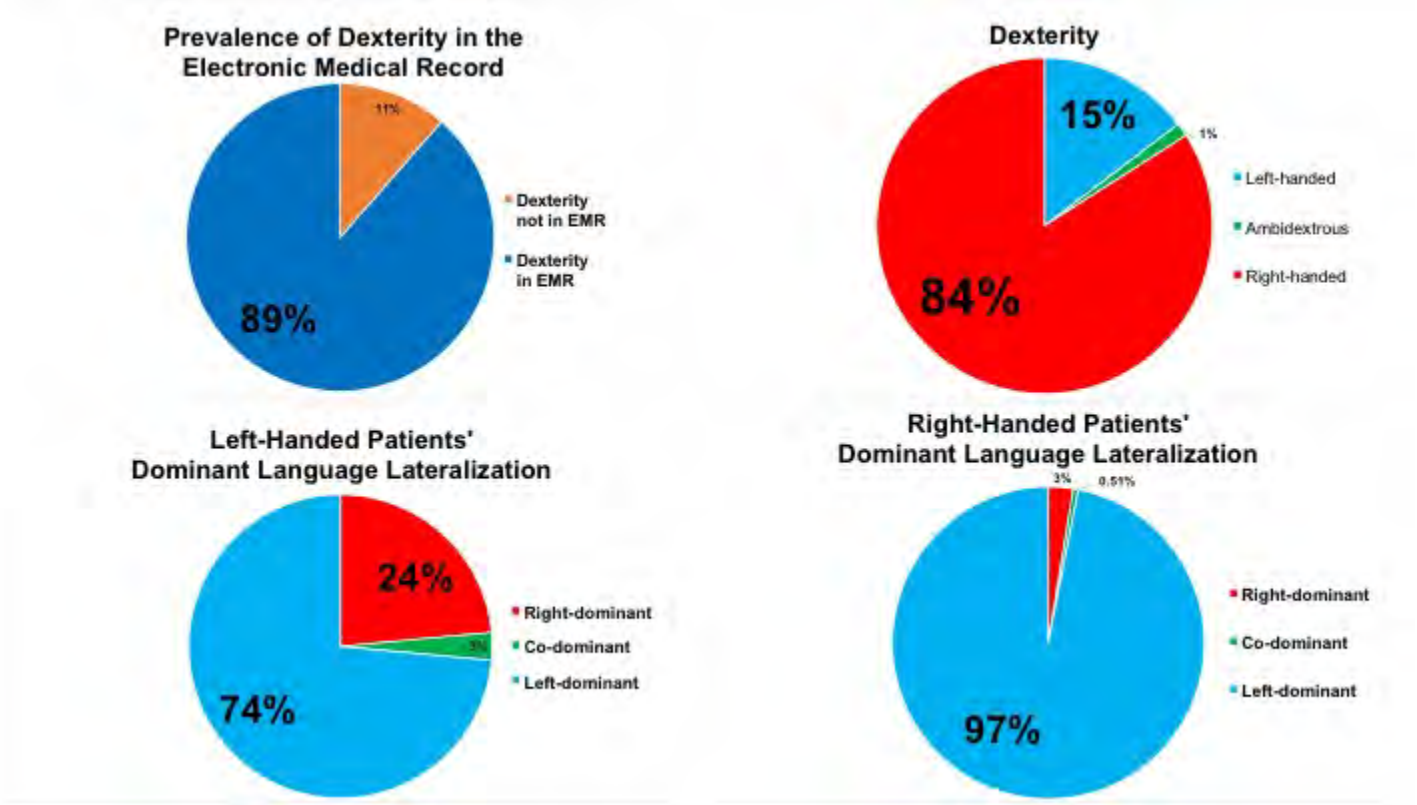
Results

A total of 262 fMRI were performed. Handedness could be determined in 232 (89.5%) of cases. For cases with handedness determined, 195 (84%) were right-handed, 34 (15%) were left-handed, and 2 (1%) were ambidextrous. Of those that were left-handed, 8 (24%) had right hemisphere language dominance, 1 (3%) were co-dominant, and 25 (73%) were left-dominant. Of those that were ambidextrous, none (0%) were right hemisphere dominant for language, none (0%) were co-dominant, and 2 (100%) were left-dominant. Of those that were right-handed, 5 (2.6%) had right hemisphere language dominance, 1 (0.5%) was co-dominant, and 189 (97%) were left-dominant.

Conclusions

Left-handed patients were nearly 10 times more likely to have language dominance lateralized to the right hemisphere relative to right-handed patients. Our fMRI results were concordant with estimates in the medical literature citing 95-99% of right handers and 70-80% of left handers were left hemisphere dominant for language lateralization. The medical literature cites an incidence of right hemisphere language dominance in right handers is 0-2%, which also is concordant with our fMRI results. With handedness alone, one cannot 100% determine the language dominance lateralization for patients, which supports the use of fMRI for presurgical planning. The handedness of patients was present in the EMR a high

percentage (89%) of these neurosurgical cases, providing both the neuroradiologist and the neurosurgeon with a valuable source for crucial clinical data.



(Filename: TCT_O-489_Abstract_ASNR17_fMRI_dexterity.jpg)

O-490

1:46PM - 1:54PM

Functional MRI (fMRI) and WADA Testing for Dominant Language Localization at an Academic Hospital: Evolving Utilization Trends

I Ikuta[1], W Zucconi[1], F Minja[1]
[1]*Yale University School of Medicine, New Haven, CT*

Purpose
The use of functional MRI (fMRI) for language localization has become much more widespread in clinical practice. In addition to dominant language localization, fMRI can provide anatomic image registration for the neurosurgeons, and avoids exposure to ionizing radiation. WADA has been used for language localization for years and is considered by many to be the "gold standard", but have risks of embolism/stroke, hemorrhage, and exposes the patient to ionizing radiation. We examine the utilization practices at our hospital for both fMRI and WADA. We hypothesize that fMRI usage has increased and WADA usage has decreased for presurgical localization of language dominance.

Materials and Methods

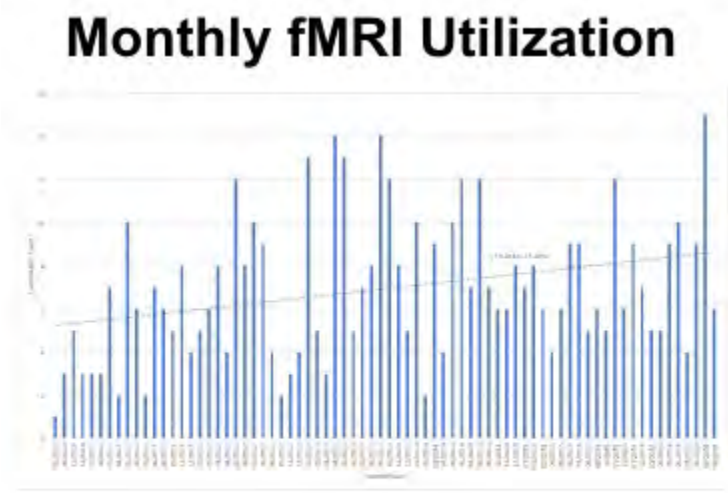
The radiology PACS was queried for all patients undergoing fMRI at our academic, 1,541-bed, tertiary care referral center, with a date range of January 1, 2010 through December 7, 2016. The dictation was reviewed for dominant language lateralization and recorded in a data spreadsheet. Cases were excluded from statistical analysis if dominant language localization was indeterminate or if language paradigms were not performed as part of the fMRI. Montage software was used to determine the number of WADA examinations performed. Statistical analysis was performed in the data spreadsheet, with a primary outcome measure of fMRI and WADA exam volume.

Results

The fMRI exam volume has increased steadily over recent years. Initially a monthly average of approximately 3 fMRI exams/month has increased to approximately 4 fMRI exams/month. Over the same time period, WADA exams have had variable utilization, with averages ranging from about 2-3 exams/month. While a maximum of 6 WADA exams were performed in 1 month, fMRI had several months during which more than 6 exams were performed. In fact, a maximum of 15 fMRI exams were performed in a single month, which is more than twice that of WADA.

Conclusions

The increased utilization of fMRI without a matching increase in WADA exams speaks to the solid clinical confidence in fMRI for language localization. While WADA will continue to have a place in the clinical realm, fMRI may become the workhorse for dominant language localization.





(Filename: TCT_O-490_ASNR17_abstract_fMRI_WADA.jpg)

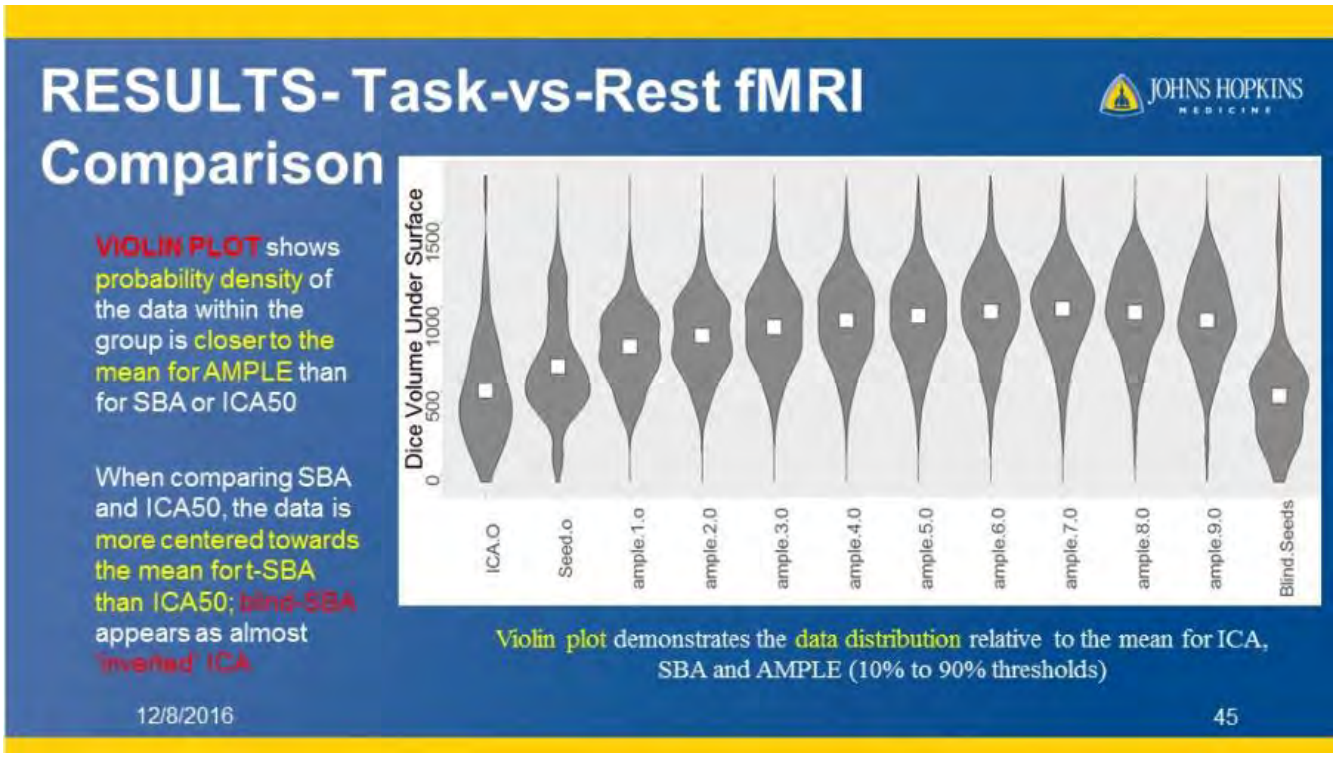
O-491

1:54PM - 2:02PM

Comparison of Task-vs-Blind Seed Based Analysis and Region-of-Interest Based Analysis in the Accuracy of Resting-State fMRI Language Networks in Brain Tumor Patients

A Chaudhry[1], H Sair[2]
[1]Johns Hopkins Medicine, Elkridge, MD, [2]Johns Hopkins Medicine, Baltimore, MD

Purpose
Compare concordance of language networks derived from task-fMRI with resting-state fMRI in patients with brain tumors using task-vs-blind seed-based analysis (SBA) and region of interest-based analysis (RBA).
Materials and Methods
Resting state fMRI was performed and language networks identified for patients presenting for presurgical task-fMRI mapping between 1/1/2009 and 7/1/2015. Seventy-nine patients were analyzed of which 49 met the inclusion criteria (presence of brain tumors without history of prior brain surgery, adequate task-fMRI performance). Language networks were obtained from rs-fMRI using ICA with 50 components, SBA maximal. Also, SBA using seeds generated from maximal task-fMRI activation in the inferior frontal gyrus (IFG), and RBA using bilateral IFG masks using AMPLE at thresholds ranging from 10% to 90%. Rs-vs-task-fMRI concordance for each resultant map was measured using Dice coefficients across varying fMRI thresholds. Multithreshold Dice coefficient volume under the surface (DiceVUS) and maximum Dice coefficient (MaxDice) were calculated. ANOVA was performed to determine significant differences in DiceVUS and MaxDice between the 3 methods of analysis.
Results
Group mean DiceVUS and MaxDice were highest for the AMPLE analyses. ANOVA with Tukey HSD demonstrated statistically significant differences for both DiceVUS and MaxDice between SBA and AMPLE thresholds from 20-90%. When comparing various AMPLE thresholds, optimal correlation was noted for AMPLE thresholds of 70%. Significant differences were found between AMPLE 10% and the range of AMPLE 50-80%.
Conclusions
Region of interest-based analysis is superior to both task-derived SBA and blind-SBA for assessment of language networks derived from rs-fMRI.



(Filename: TCT_O-491_violinplot.jpg)

O-492

2:02PM - 2:10PM

Resting-state fMRI in Presurgical Planning for Brain Tumors; Correlation with Task Based Motor and Language Paradigms.

C Gradinaru[1], S Peltier[1], J Kramer[1], G Shah[2]
[1]*University of Michigan Health System, Ann Arbor, MI,* [2]*University of Michigan, Ann Arbor, MI*

Purpose
Functional MRI (fMRI) is a promising way to map eloquent cortex in presurgical planning, offering a noninvasive alternative to electrophysiological or WADA testing. Task fMRI allows probing of a single neural system in compliant patients; while resting-state fMRI can evaluate multiple functional networks at once, with less burden on patients, and can be used to monitor physiological changes in the short, medium, and long term. The purpose of the presentation is to discuss the results at our institution.
Materials and Methods
Recent clinical work has demonstrated concordance between task activity and resting state maps in the motor network during tumor presurgical planning, with better correspondence at 3T as compared to 1.5T; while another study has shown discordance between the hand motor activity as determined by resting-state, task, and anatomical MR imaging. However, these

studies were relatively low-powered (n < 30), with less than optimal imaging parameters. In our study, a large number of surgical patients with brain tumors (62), were imaged using a 3T Philips scanner, acquiring anatomical, task, and resting-state images for each patient, along with concordant physiological recording.
Results
Task activation and resting-state correlation maps were generated for each subject, with coordinates of maximal activity compared to the anatomical identification of the hand-motor knob. Similarly agreements in the language area also were investigated. Results analysis is ongoing.
Conclusions
Functional MRI is a promising way for noninvasive mapping of eloquent cortex in presurgical planning for brain tumors. The results of our single institution study may help to establish the validity and utility of resting-state fMRI in presurgical planning of brain tumors; with possible application to prediction of patient outcomes.

O-493

2:10PM - 2:18PM

A Standardized Battery of Clinically Meaningful Tests for Use in fMRI

C Gibby[1], L Nguyen[2], W Gibby[3]
[1]Baylor College of Medicine, Houston, TX, [2]Novarad Corporation, American Fork, UT, [3]University of California San Diego, San Diego, CA

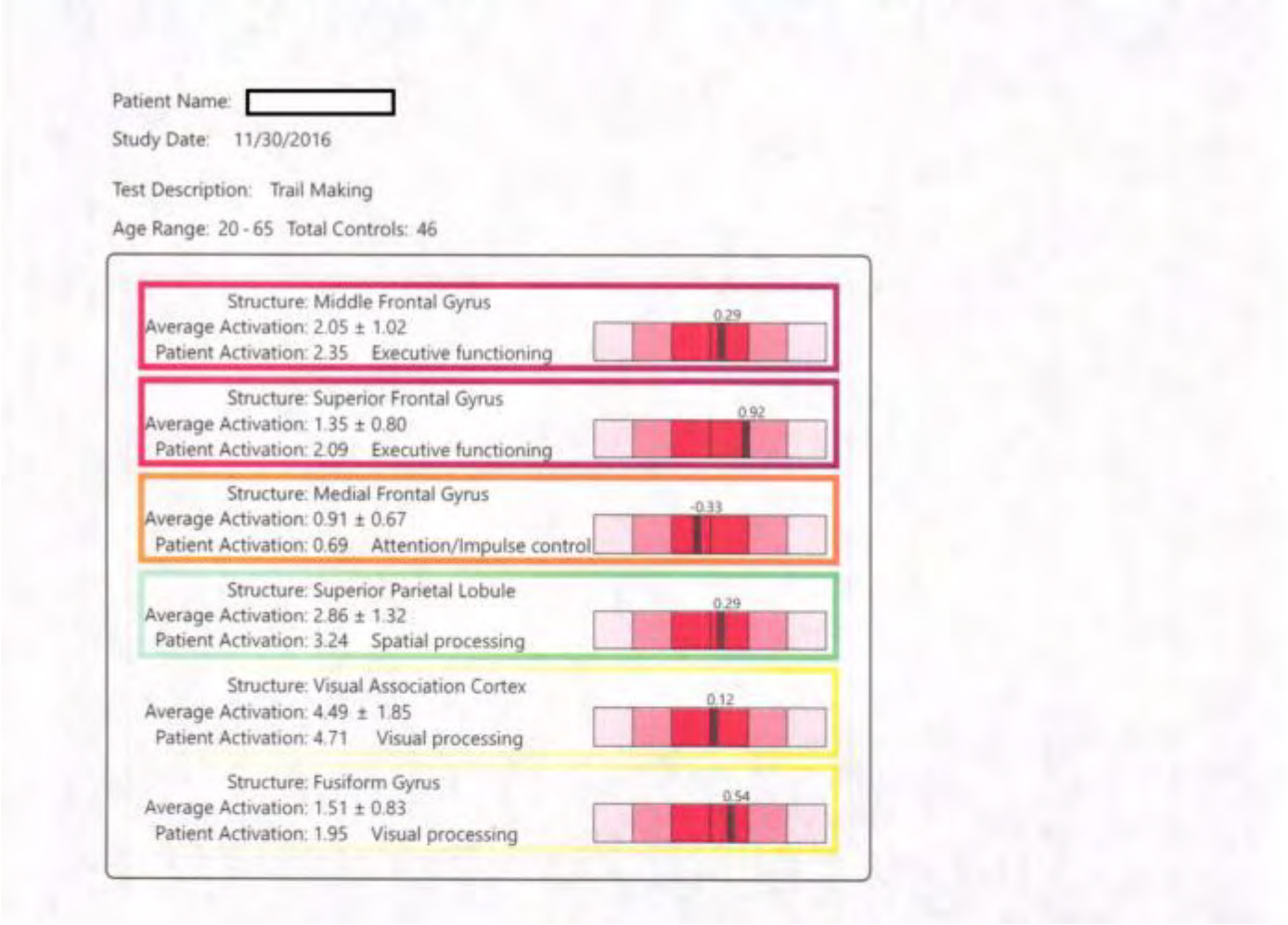
Purpose
Functional magnetic resonance imaging (fMRI) can detect and quantify dysfunction in brains that look anatomically normal. Clinical applications such as traumatic brain injury, depression, autism, attention deficit disorder, dementia, and their associated treatment courses can be assessed by fMRI, but clinically it currently is limited primarily to presurgical planning. One factor contributing to this is a lack of standardized tests beyond finger tapping. While some neuropsychological tests have been applied to fMRI in the research world, we bring fMRI into the clinical world with a well developed battery of functional tests to query well studied brain circuitry.
Materials and Methods
We adapted 6 well studied neurological and psychological tests for use in fMRI. These include the Boston Naming; Trail Making B; Matrix Reasoning (part of Weschler Adult Intelligence Scale); Facial and Verbal Memory; and Verbal Fluency tests. A single 1.5T MRI scanner, standard MRI audiovisual headset and a response button were used for all patients. Statistical analyses included up-to-date Statistical Parametric Mapping-based software with added enhancements of 3D motion correction and interpolation of the fMRI data sets. Each test was performed 4 times with 15 second rest interval in between.

Results

All 6 neuropsychological tests were administered during fMRI imaging for 46-48 patients with age ranging from 20-65 years old. After careful 3D segmentation of the brain, the quantified, average T-test activation of each primary index area (PIA) was obtained as follows. Standard deviation (SD) also was calculated. WAIS Matrix Reasoning (executive function): PIA of middle frontal 1.85 and inferior frontal 0.98 gyri with respective SD 0.86 and 0.76. Picture (Boston) Naming (complex object recognition): PIA of visual association cortex 2.32 with SD of 1.11. Trail Making B (problem solving): PIA of middle frontal 2.05 and superior frontal 1.35 gyri with respective SD of 1.02 and 0.80. Facial Memory (long term memory): PIA of hippocampus 0.83 with SD 0.72 and fusiform gyrus 1.15 with SD 0.72. Verbal Memory (phonological loop/working memory): posterior inferior frontal gyrus (Broca's) 1.70 with SD of 1.22. Verbal Fluency (word retrieval, working memory): left post superior temp lobe (Wernicke's) 0.56 with SD of 0.42.

Conclusions

A standardized battery of fMRI tests with control data now exists, which provides information of several key brain functions. Clinicians can use this to assess a variety of diseases, compare with age-matched normal patients, follow treatment responses, and query much more than that possible with finger tapping or lip-licking.



(Filename: TCT_O-493_StatsTrailMaking.jpg)

O-494

2:18PM - 2:26PM

Foreign Accent Syndrome (FAS) of Unknown Etiology Functional Magnetic Resonance Imaging (fMRI)

S Elias[1], T Yaltho[2], S Fung[3], C Karmonik[1]
[1]Houston Methodist Research Institute, MRI Core, Houston, TX, [2]Houston Methodist Sugar Land Neurology Associates, Sugar Land, TX, [3]Houston Methodist Hospital, Houston, TX

Purpose

Foreign accent syndrome (FAS) is a rare speech disorder, in which patients develop patterns of speech that are foreign to their native accent, it is associated with wide possible etiologies, some are caused by unknown reasons. The goal of this study is to analyze the neuroimaging foremost aspects of the FAS of unknown etiology using fMRI activation maps of the brain, and to investigate other findings that are unique to this type of FAS.

Materials and Methods

A 33-year-old woman was diagnosed with FAS, underwent an fMRI examination (EPI, TR/TE: 3000/35ms, 90 dynamic scans, 45 slices), with 3 types of tasks: word generation, word association and word rhyming. These tasks were performed twice in overt and covert versions. Utilizing the generalized linear model, fMRI blood oxygen level dependent (BOLD) activation maps were created using AFNI software.

Results

Functional MRI activation BOLD maps showed more activity for the overt tasks in the bilateral middle temporal gyri, thalamus, bilateral insula and bilateral Inferior frontal gyri. Higher activation was found for covert tasks in left posterior cingulate cortex (PCC), and left Inferior frontal gyrus.

Conclusions

Overt word creation tasks resulted in activating brain regions that were not detected with the covert tasks. The role of insula in detecting salient events explains a higher insular activation while trying to achieve a native-like accent during overt speech. The increased thalamic activity indicates efforts to process timing/rhythm in overt tasks. The middle temporal gyrus is known to be related accessing word meaning while reading showed higher activity during overt task as the patient trying to produce the words in her native accent (Fig. 1). In covert tasks the most highlighted activation is shown within the inferior frontal gyrus, which could be related to speech motor control issues. The decline in the PCC activity in overt speech may correlate to control network issues affecting her ability to process her native accent. The organized comparison of overt and covert versions of fMRI tasks is crucial, since the patient indicated her ability of processing native-like accent while asleep. Overt tasks were feasible with low motion artifact. Foreign accent syndrome could affect complex motor speech networks

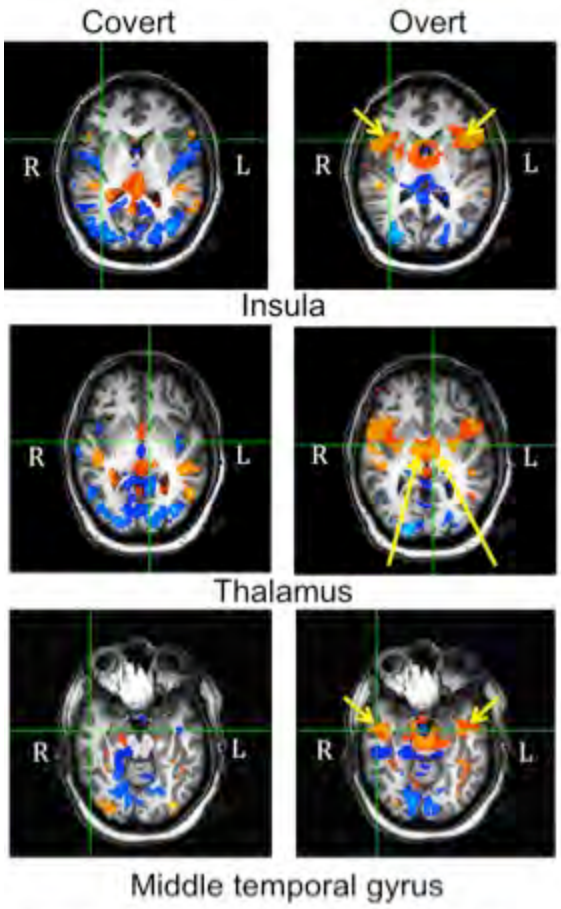


Figure 1: fMRI activation maps; covert vs. overt tasks. Yellow arrows represent the active brain regions.

(Filename: TCT_O-494_Figure1.jpg)

O-497

2:42PM - 2:50PM

Inhibiting the Insula in Smokers: Preliminary Results of an RCT using Transcranial Magnetic Stimulation and fMRI

M Regner[1], B Kluger[1], J Tregellas[1], B Mohl[1], D Yamamoto[1], J Tanabe[1]
[1]*University of Colorado, Aurora, CO*

Purpose
Most cigarette smokers are unable to quit despite multiple, repeated attempts. A major reason for persistent smoking is the urge or craving for cigarettes. Evidence that the insula plays a role in cigarette craving comes from both animal and human studies (1–3). Patients with stroke damage to the insula spontaneously or easily stop smoking without cravings (2). Animal studies involving stereotactic microinjections and deep brain stimulation also have shown that the insula is involved in drug-seeking behavior (4, 5). Repetitive transcranial

magnetic stimulation (rTMS) is a noninvasive neuromodulatory technique in which a pulsatile magnetic field is used to induce depolarization of cortical neurons and thought to affect synaptic activity; it can be excitatory or inhibitory based on pulse frequency. We hypothesized rTMS inhibiting the right anterior insula in smokers would (1) reduce nicotine craving, (2) reduce brain activity in response to cigarette cues, and (3) increase resting-state connectivity between the insula and networks implicated in craving and control of craving, including the salience, default mode, and executive control networks.

Materials and Methods

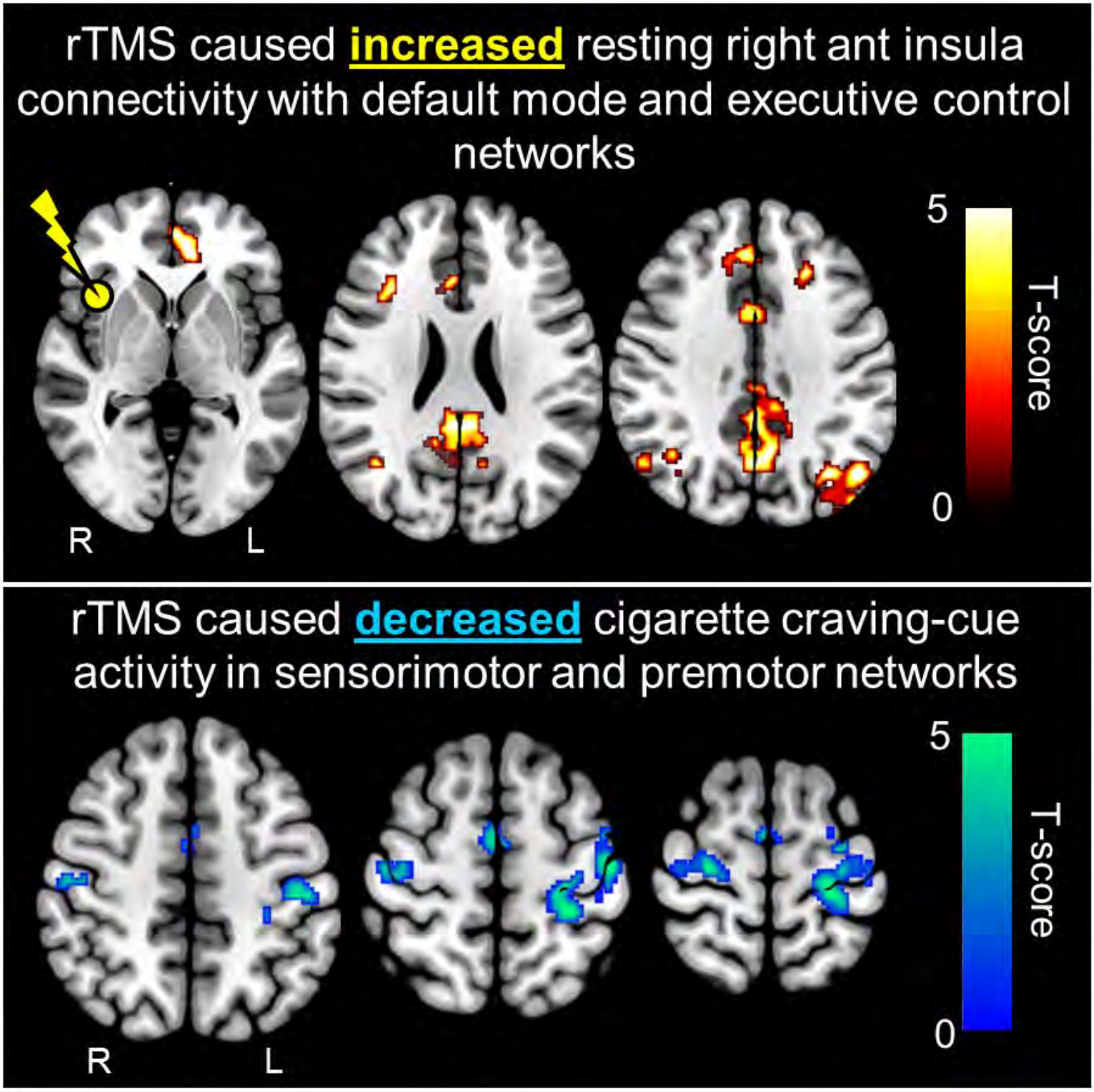
Eleven nontreatment seeking smokers moderately dependent on nicotine were recruited into a single-blinded 2-arm parallel group (n = 5 sham/placebo rTMS and n = 6 active inhibitory rTMS) randomized controlled trial. We collected craving measurements, task-based fMRI using a cigarette craving-cue paradigm, and resting state fMRI on a 3T MR system. Participants were studied before and after a single session of 20 minutes of 1 Hz rTMS targeting the right anterior insula to determine if inhibitory rTMS (1) reduces craving, (2) alters brain activity during smoking cues, and (3) alters resting state right anterior insula connectivity to default mode and executive control networks. Whole brain analyses were cluster corrected at familywise $p < 0.05$, voxelwise $p < 0.005$.

Results

Behavior: Compared to sham/placebo, active rTMS demonstrated a nonsignificant reduction in self-reported craving (–29% ± 26% versus –2% ± 24% sham, $p = 0.128$). Cigarette cue task-based fMRI: Compared to sham, real rTMS caused significantly decreased BOLD activity in bilateral premotor and sensorimotor cortex. Resting-state seed-based connectivity: Compared to sham, rTMS caused significantly increased right anterior insula connectivity with default mode and executive control network areas.

Conclusions

Noninvasive inhibitory rTMS of the insula in smokers is feasible and results in decreased cigarette craving-cue activity in premotor and sensorimotor cortices, which may reflect a decreased cognitive readiness to act upon a craving. Increased resting state connectivity between salience, default mode, and executive control networks after rTMS implicates these circuits in craving and craving mitigation. These findings suggest that the insula may play an important role in modulating the balance of craving or action selection.



(Filename: TCT_O-497_ASNRFigure2016-12-06.jpg)

O-498

2:50PM - 2:58PM

Mapping the amygdalo-diencephalic connections of the human limbic system.

A Kamali[1], R Patel[2], R Riascos[3], S Mirbagheri[4]

[1]University of Texas Houston, Houston, TX, [2]University of Texas Health Science Center, Houston, Houston, TX, [3]Univerisity of Texas at Houston, Houston, TX, [4]Mount Sinai Beth Israel, New York, NY

Purpose

The purpose of the current study is to demonstrate for the first time the feasibility of parcellation and tractography of fine limbic structures such as the fine neuronal connections the amygdala to the thalamic and hypothalamic nuclei of the human brain using high spatial resolution DTI data on 3T.

Materials and Methods

The amygdala is known to have a role in core processes regulated by the limbic system such as motivation, memory, emotion, social behavior, self-awareness as well as certain primitive instincts. Although the thalamus is not known primarily as a limbic structure, ample evidence points to the fundamental role of the thalamus as modulator of limbic functions indirectly through the amygdala. The underlying neuronal fiber connectivity of the amygdalo-diencephalon, as part of the limbic system, has not been delineated separately by prior diffusion-weighted imaging studies. Diffusion tensor tractography of white matter connections between the deep gray matter structures is challenged by the signal-to-noise ratio (SNR) due to overestimation of anisotropy at low SNR and partial volume averaging upon using large voxel volumes. To overcome these problems, recent DTI tractography studies have used 7T and 9T scanners for visualizing the neuronal fiber trajectories in primate and human central nervous system. This work aimed to demonstrate for the first time the feasibility of in vivo quantification and visualization of fine human brain amygdalo-diencephalic connections using high resolution DTI data on 3T. We also show the ability to separate and quantify the tract volume and corresponding diffusion tensor metrics of these small fiber tracts on fifteen subjects. Subjects: Fifteen healthy men (age range 24-37 years) were studied. Conventional and DT-MRI Acquisition: Data were acquired using a Philips 3.0 T. Diffusion tensor imaging data were acquired axially using single-shot multi-slice 2-D spin-echo diffusion with the balanced Icosa21 tensor encoding scheme. The b-factor = 500 sec mm-2, TR/TE = 14460/60 msec, FOV = 256 mm x 256 mm and slice thickness/gap/ #slices = 1 mm/0 mm/120. The EPI phase encoding used a SENSE k-space undersampling factor of 3, with an effective k-space matrix of 112x112 and an image matrix after zero-filling of 256x256.

Results

To our knowledge, the current study is the first to present the fine limbic trajectories of the amygdala to the hypothalamic and septal nuclei known as the amygdalofugal tract or direct projection of the amygdala to the mediodorsal nuclei of the thalamus known as the amygdalothalamic tract. We also demonstrate long limbic connections of the amygdala to the hypothalamic and septal nuclei through the fornix and stria terminalis using high spatial resolution DTI measurements on 3T. The fornix, stria terminalis, amygdalofugal tracts and amygdalothalamic tracts are clearly distinguishable in relation to the amygdala,

hypothalamus, thalamus and hippocampus nuclei. Using high spatial resolution specially reduced slice thickness (1mm) in this study reduced the partial volume effect as well as incoherency due to the fiber crossing within each voxel and we were able to reconstruct and show even the small limbic trajectories such as amygdalo-hypothalamic and amygdalothalamic connections using deterministic tractography approach. In our experiment the high resolution DTI method increased the detectable anisotropy within the gray matter structures and helped to trace the thin white matter fibers passing through the hippocampus and hypothalamus nuclei.

Conclusions

In this report we demonstrate for the first time, in vivo 3D reconstructions of the major neuronal connections of the amygdala to the diencephalic nuclei including the thalamic and hypothalamic nuclei using high resolution diffusion tensor tractography on 3T.

Fig. 1 amygdalofugal tract (pink) and anterior commissure (red)

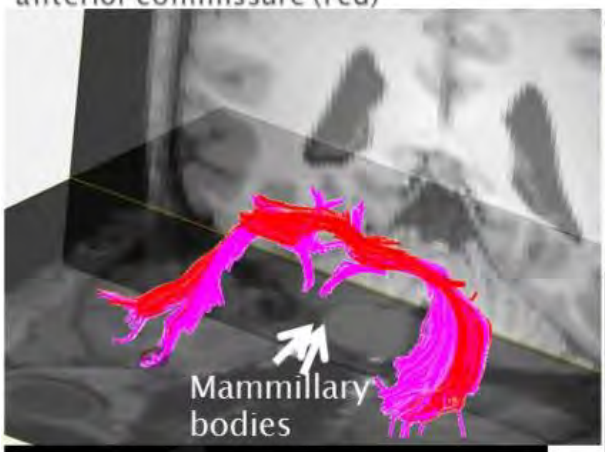
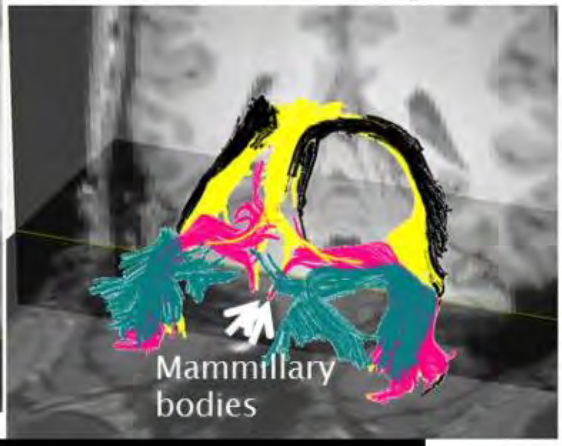


Fig. 2. amygdalofugal tract and relationship with the fornix (yellow) stria terminalis (black) and the uncinate fasciculus (green)



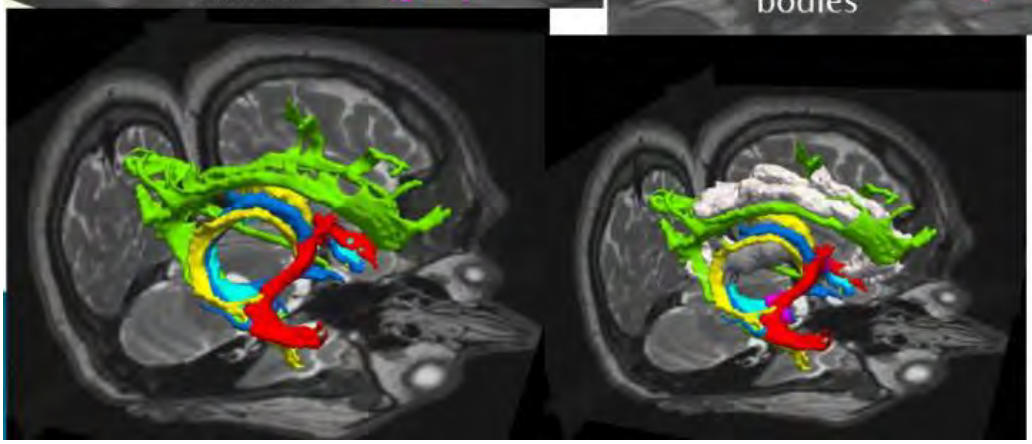


Fig. 3, 4. 3D reconstruction of the major white matter structures including the amygdalofugal tract (pink), fornix (blue), stria terminalis (yellow) and anterior commissure (red)

(Filename: TCT_O-498_amygdalo-diencephalicconnections.jpg)

Thursday
1:30PM - 3:00PM
Long Beach Convention Center, Room 104C (Main Lobby)

25F-Parallel Paper Session: Excerpta: Head and Neck Puzzles to Ponder

E-112

1:30PM - 1:34PM

Case Report of a Chylous Neck Collection Following Radical Neck Dissection

A Lee[1], A Ozturk[2], M Bobinski[3], r latchaw[4], J Chang[5]
[1]UC Davis Medical Center, Elk Grove, CA, [2]University of California, Davis Medical Center, Sacramento, CA, [3]UC Davis, sacramento, CA, [4]University of California Davis, sacramento, CA, [5]UC Davis medical center, Sacramento, CA

Purpose

Chylous leakage is a rare but serious complication of head and neck surgeries, with a reported incidence of approximately 1% to 2.5% following neck dissections and the majority (up to 92%) occurring on the left side. To our knowledge, there is limited data on the radiographic presentation of these cases in the literature. Here, we describe a case of chylous fluid collection from thoracic duct leakage following a neck dissection found on CT.

Materials and Methods

The patient is a 58-year-old woman with history of left salvage radical neck dissection with vagal nerve resection and carotid artery preservation and skin graft 2 months prior to presentation for squamous cell carcinoma of the hypopharynx. She was doing well until a week prior to her presentation to the ED, when she developed pain and swelling of her left neck with difficulty swallowing and breathing. A neck computed tomography angiography (CTA) was emergently performed, given the initial concern was for possible dissection.

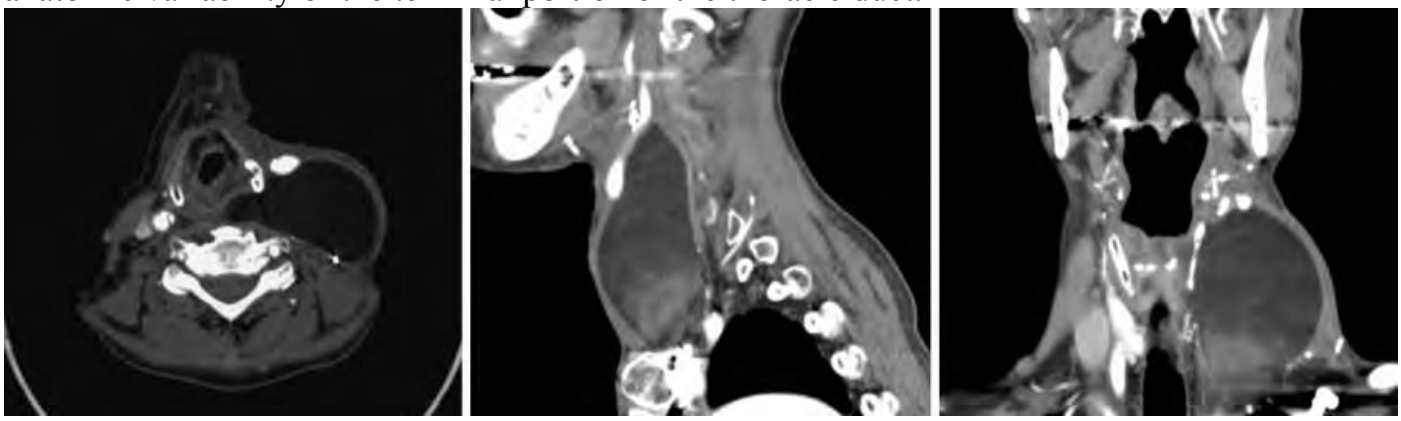
Results

On exam, a mixed attenuation left neck mass was found, with an overall attenuation of the majority of the mass demonstrating negative Hounsfield units consistent with that of fat. The mass was deep to the left sternocleidomastoid, abutting the left common carotid artery posteriorly and laterally, and extending minimally into the retropharyngeal space with mild mass effect on the midline structures of the neck. No communication with the left carotid arterial system was identified. The findings were suggestive of a mass of lymphatic or chylous origin. No evidence for chylothorax was seen.

Conclusions

The patient was taken to the OR for left neck exploration. A large chyle collection was identified in the left neck with active leakage from the thoracic duct. Surgical pathology showed no evidence of tumor recurrence. The thoracic duct originates in the cisterna chili, crosses from right to left in the posterior mediastinum, extending superiorly along the left posterolateral border of the esophagus. As the duct enters the neck, the duct then courses posterior to the carotid sheath structures. There is significant anatomic variation in the terminal portion of the thoracic duct, extending as high as up to 8 cm above the level of the clavicle, which is likely a contributing factor in surgical complications when it is higher than

expected. While chylous leaks are overall rare surgical complications in neck dissections, radiologists should consider these in the postoperative setting given the proximity and anatomic variability of the terminal portion of the thoracic duct.



(Filename: TCT_E-112_ASNR.jpg)

E-113

1:34PM - 1:38PM

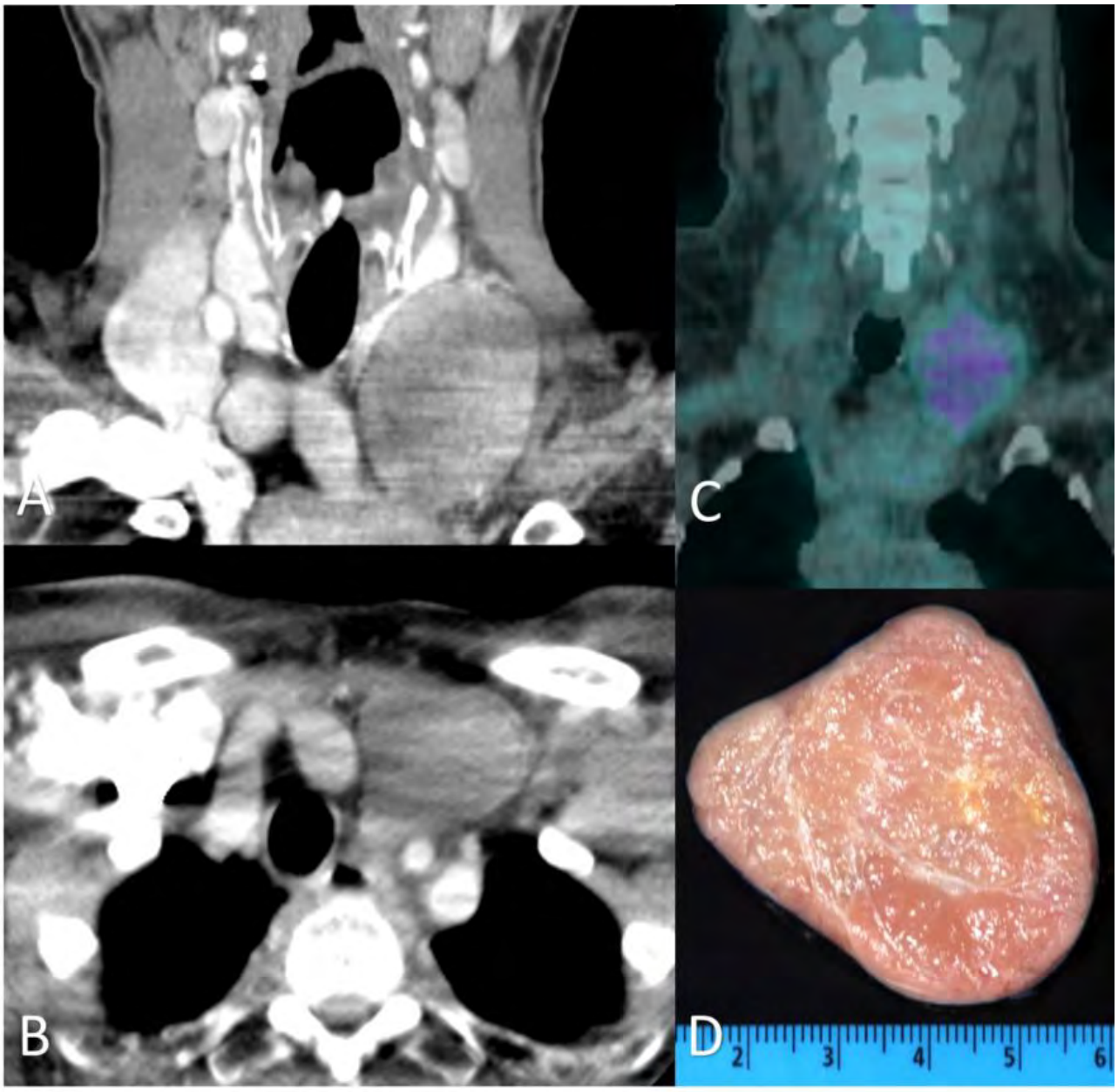
A Case of Cervical Thymoma: Ectopic or Arising from Residual Cervical Thymus?

R Yu[1], H Kale[2]
[1]University of Pittsburgh Medical Center, Pittsburgh, PA, [2]University of Pittsburgh Medical center, Pittsburgh, PA

Purpose
Residual cervical thymus is defined as tissue that is originally continuous with the mediastinal thymus during childhood but later becomes separated by atrophy. Detectable at any age, it is seen most commonly in the left paratracheal region. We present a case of a thymoma most likely arising from left paratracheal residual cervical thymic tissue, and describe its imaging features.
Materials and Methods
A previously healthy 57-year-old male presented with a slowly growing left neck mass which he first noticed 4 years ago. He reported hoarseness and occasional dysphagia with solid foods. He denies odynophagia and dyspnea. Biopsy of this left neck mass revealed a thymoma. Final pathology after excision reported a modified Masaoka Stage 2A thymoma.
Results
(A, B) Coronal and axial contrast-enhanced computed tomography (CT) of the lower neck reveals a well circumscribed mass which appears to arise from the left paratracheal region and extends superiorly along the lateral margin of the left thyroid lobe. (C) Coronal PET/CT image demonstrates hypermetabolic activity associated with the mass. (D) Gross specimen of the encapsulated mass with internal lobulated architecture separated by fibrous septa.

Conclusions

Residual cervical thymic tissue is a common variant of the normal thymus and can be seen at any age. It is defined as tissue that is originally continuous with the mediastinal thymus during childhood but later becomes separated by atrophy. Its frequency decreases with older age, and most commonly occurs in the left paratracheal region. Other locations include the pretracheal and right paratracheal regions, as well as in the left lower neck. In contrast, ectopic cervical thymus is the result of aberrant embryology, and can appear anywhere along the line from the angle of the mandible to the thyroid gland. Thymic pathology should be included in the differential diagnosis of lesions located where residual cervical thymus can be found.



(Filename: TCT_E-113_FiguresResidualCervicalThymoma.jpg)

E-114

1:38PM - 1:42PM

Uncommon Radiographic Features of Metastatic Nodal Disease in the Neck

W Fujioka[1], A Lignelli[2]
[1]Columbia University Medical Center, New York, NY, [2]Columbia University Medical Center, New York City, NY

Purpose
Diagnostic considerations of lipomatous masses in the soft tissues of the neck.
Materials and Methods
Male patient with pancreatic adenocarcinoma and known metastatic disease to the liver presents for computed tomography (CT) evaluation following discovery of a rubbery mass in the neck. Fatty mass with atypical features most consistent with lipoma was seen on CT. Due to increasing growth, mass was biopsied with histopathology revealing mostly acellular pancreatic adenocarcinoma.
Results
In the left posterior cervical space, there is a well circumscribed lesion composed predominantly of fat measuring 12 centimeters in maximum diameter. At its posterior margins, it contains mild thickened septae. There is no additional lymphadenopathy in the neck.
Conclusions
The posterior cervical space contains multiple structures including fat, spinal accessory lymph nodes, nerves (brachial plexus, accessory nerve XI), and remnants of the third branchial cleft. Deep cervical lymph nodes are a more common metastatic location for intra-abdominal neoplasms; which includes the deep cervical chain (including Virchow's node), spinal accessory chain, and transverse cervical chain. This patient has multiple risk factors including male sex and known primary malignancy. Given atypical radiographic features for lipoma and patient's risk factors, this lesion should be considered for biopsy. Atypical imaging features of lipomas include lesion size greater than 10 centimeters, thickened septa, and nodular/globular soft tissue components. Overall, in a lipomatous mass with atypical radiographic features or patient risk factors including known malignancy, further evaluation including biopsy may be considered.



(Filename: TCT_E-114_Fujioka.jpg)

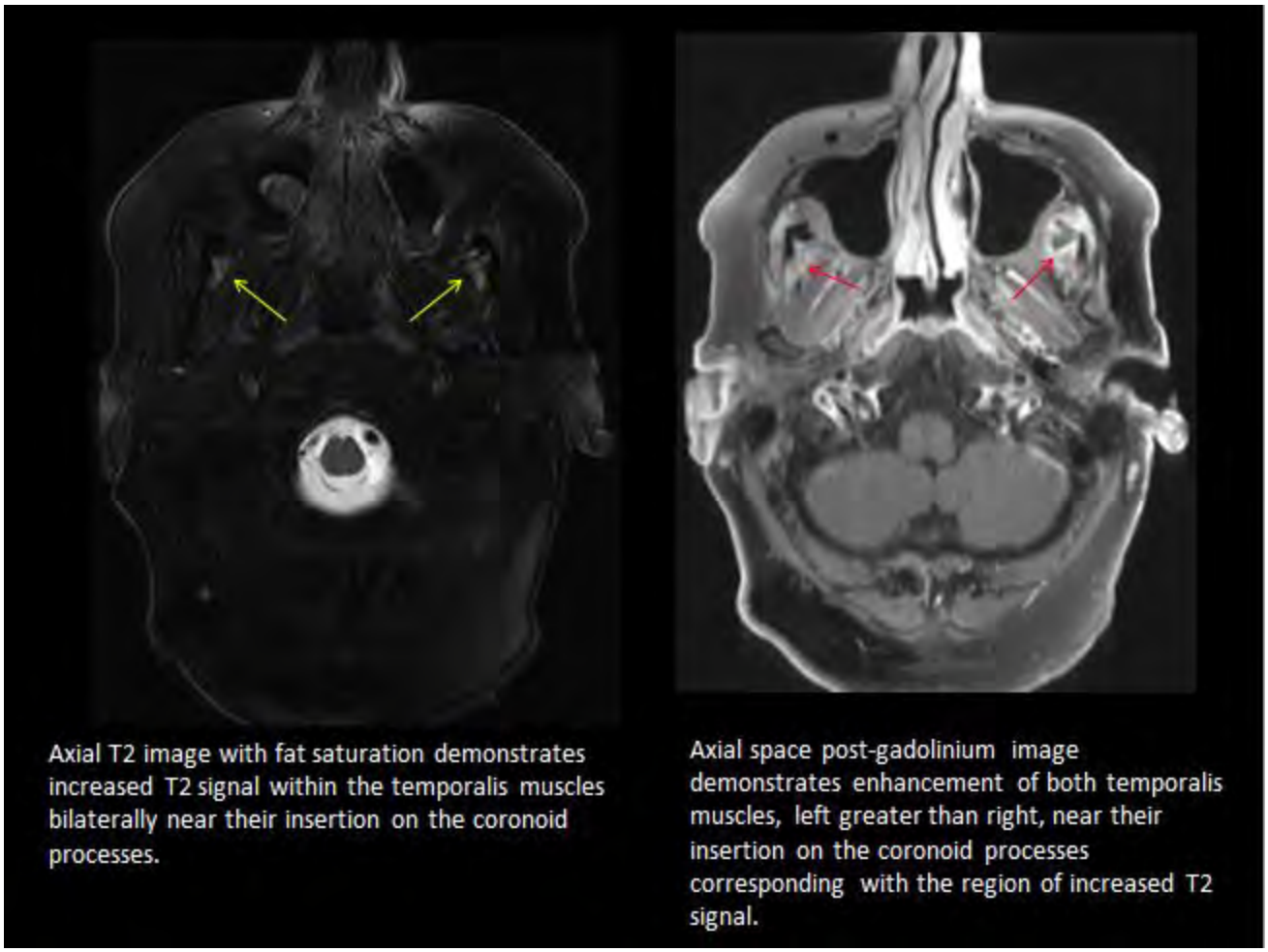
E-115

1:42PM - 1:46PM

Bilateral Temporalis Muscle Denervation in a Patient with Myasthenia Gravis

A Nagelschneider[1], K Krecke[2]
[1]*Mayo Clinic-Rochester, Rochester , MN,* [2]*Mayo Clinic-Rochester, Rochester, MN*

Purpose
Denervation atrophy in patients with myasthenia gravis is well documented in the histopathologic literature, however while we often see denervation changes well with magnetic resonance imaging (MRI) in other disease entities, little discussion is made in the radiology literature of denervation changes seen in this subset of patients. Our case provides an example of a patient with clinical symptoms of denervation involving the muscles of mastication with correlative imaging findings.
Materials and Methods
A 62-year-old male who originally presented to our institution with complaints of fluctuating diplopia and bilateral ptosis, as well as fatigue of his jaw with chewing. These findings were felt to be compatible with active denervation changes given his clinical history. An electromyography (EMG) was performed which showed significant decremental response in his facial nerve and borderline response in his spinal accessory, compatible with a moderate defect in neuromuscular transmission consistent with clinical diagnosis of myasthenia gravis. Subsequent lab testing demonstrated positive acetylcholine receptor binding antibodies, consistent with myasthenia gravis.
Results
Magnetic resonance imaging performed at time of his presentation demonstrated increased T2 signal and diffuse enhancement of the temporalis muscles bilaterally, greater on the left, most marked at their insertion on the coronoid processes. These findings were felt to be compatible with active denervation changes given his clinical history of fatigueable muscle weakness with chewing.
Conclusions
Our case provides an example of active muscle denervation changes on MRI attributable to myasthenia gravis. While the denervation changes in myasthenia gravis are well described in the neurology and histopathologic literature, few if any examples are seen in the radiologic literature aside from muscle atrophy secondary to chronic denervation. In patients with recent onset of symptomatology, the radiologist should be aware of the appearance of active denervation changes in this subset of patients.



(Filename: TCT_E-115_Abstract.JPG)

E-116

1:46PM - 1:50PM

Reproducible Monocular Blindness with Head Turning Secondary to a Vascular Eagle Syndrome.

S Moum[1], A Karagianis[1]
[1]*Northwestern University, Feinberg School of Medicine, Chicago, IL*

Purpose
We report a case of a patient who developed reversible, reproducible right monocular blindness upon turning his head to the right.
Materials and Methods
The patient was a 23-year-old male who presented with a 1-year history of progressive, reproducible right monocular blindness that occurred upon turning his head to the right. Medical history was noncontributory. On physical examination, the patient was

neurologically intact. Dilated fundoscopic exam was unremarkable. Of note, the ophthalmologic exam was performed with the patient in neutral position.

Results

An unenhanced CT of the brain was normal. A CT angiogram of the head was remarkable for a 3 mm wide neck, cephalad directed aneurysm involving the carotid-ophthalmic segment of the right internal carotid artery (ICA) that resulted in mild deformity of the adjacent right optic nerve. A concurrently performed CT angiogram of the neck performed in a neutral position demonstrated a mildly elongated and mildly thickened right styloid process associated with a mildly calcified proximal right stylohyoid ligament abutting and minimally deforming the right cervical ICA (Figs. 1A-B). However, the right cervical ICA was widely patent on this CTA. Because of a high index of suspicion, a conventional angiogram was obtained with the head in neutral positioning, and again with the head turned to the right and downward, the latter simulating the position that elicited the patient's symptoms. With the head in right inferolateral positioning, the right styloid process and mildly mineralized proximal stylohyoid ligament resulted in severe stenosis of the distal cervical right ICA (Fig. 1C), which resolved with neutral positioning.

Conclusions

Eagle syndrome is primarily known for an abnormally elongated (> 3 cm) styloid process and/or calcified stylohyoid ligament that results in odynophagia, neck pain, or globus sensation with head turning. However, Eagle syndrome also may result in carotid artery or internal jugular vein compression. In the above patient, intermittent right ICA occlusion presumably resulted in altered flow dynamics and the formation of the right carotid-ophthalmic aneurysm. In addition, it is hypothesized that the relative decreased ICA blood flow during head turning caused intermittent, reproducible right ophthalmic artery ischemia and right monocular blindness. These symptoms fully resolved following right styloid process resection, lending support for this hypothesis. Although Eagle syndrome is uncommon and has varying clinical presentations, it is crucial for clinicians and radiologists to maintain a high level of suspicion for this diagnosis when a patient presents with reproducible symptoms suggestive of ICA stenosis associated with head turning.

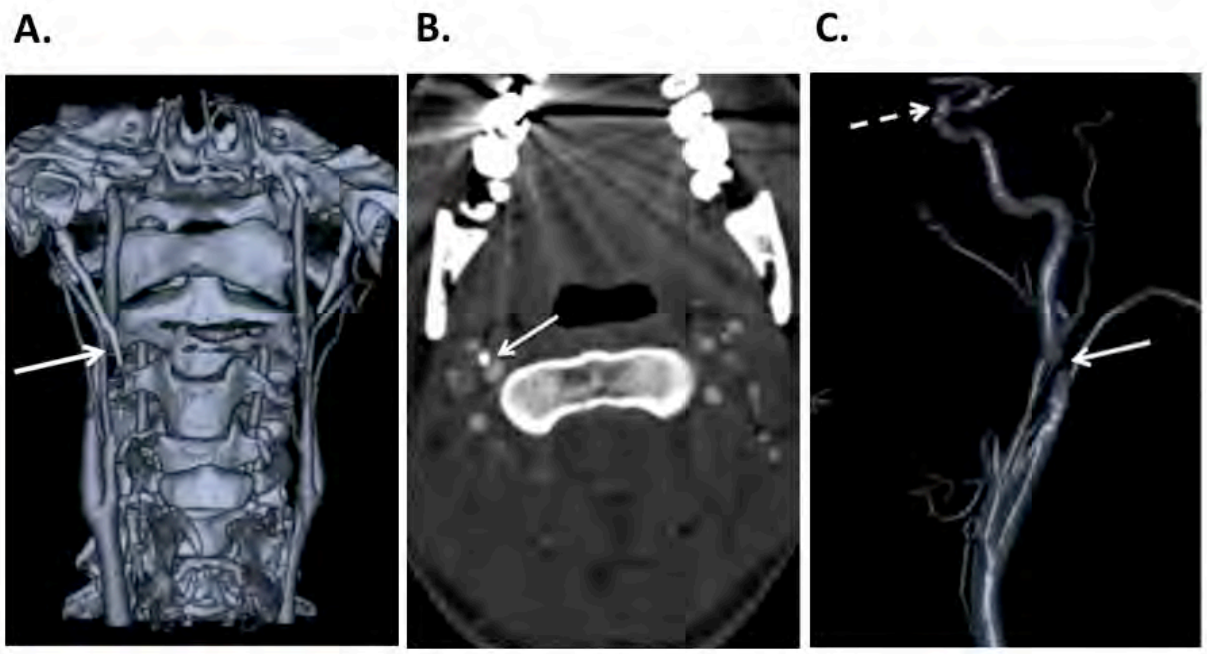


Figure 1. A. 3D reconstruction from CTA neck imaging demonstrating the elongated and mildly thickened right styloid process with a mildly calcified right stylohyoid ligament (white arrow). **B.** Mild deformity of the right cervical ICA (white arrow) secondary to the right styloid process and stylohyoid ligament on CTA neck imaging performed with the patient's head in neutral positioning. **C.** Severe stenosis of the right cervical ICA (white arrow) during conventional angiography with the patient's head turned to the right and downward. The aneurysm involving the right carotid-ophthalmic segment is also visualized (dotted white arrow).

(Filename: TCT_E-116_ASNR_Graphic.jpg)

E-117

1:50PM - 1:54PM

Panophthalmitis with corneal melt and herniation of the lens: A case report with clinical, imaging and pathologic correlation

B Addicott[1], M Nguyen[1], R Barajas[1]
[1]*Oregon Health & Science University, Portland, OR*

Purpose
We present a case of severe, rapidly progressive endophthalmitis resulting in complete

corneal melt with uveal prolapse and herniation of the ocular lens. The inciting event was direct injection of the globe with methamphetamine. To our knowledge this is the first such case described in the published literature and demonstrates critical imaging findings of orbital infection. Clinical, imaging and pathologic findings are discussed along with a imaging review of endophthalmitis and complications.

Materials and Methods

A 27-year-old pregnant female was transferred to our Emergency Department from an outside hospital (OSH) with concern for orbital cellulitis. Our patient reported to OSH earlier the same day with complaints of decreased vision and pain in her left eye 3-4 days after injecting methamphetamine directly into her globe. Contrast-enhanced CT of the orbits was performed demonstrating periorbital soft tissue stranding and thickening with enhancement of the sclera. Ophthalmology at OSH was concerned for pre-septal versus post-septal cellulitis with corneal infiltrate and possible retrobulbar abscess. She was given vancomycin and transferred to our hospital for definitive treatment. Upon arrival at our ED, ophthalmology evaluation was followed by repeat CECT of the orbits due to further decreased vision in left eye. Physical exam was notable for proptosis with ocular motility restriction and chemosis. Extensive overlying cellulitis and patient somnolence limited the exam; however, slit lamp exam demonstrated severe corneal ulceration without evidence of perforation. CECT performed within 2 hours of exam was remarkable for panophthalamitis with vitreous body hemorrhage, full thickness corneal ulcer and total herniation of the lens. Repeat ophthalmology evaluation noted 360 deg corneal melt with prolapse of uveal contents. Patient was taken urgently to operating room for left eye enucleation with lateral canthotomy and inferior catholysis. Intraoperative pathology demonstrated liquified vitreous body with perforation of the anterior chamber and herniation of the lens. Post operatively the patient was maintained on IV antibiotics with subsequent improvement of cellulitis and resolution of leukocytosis. On hospital day 8, patient returned to operating room for placement of left orbital implant.

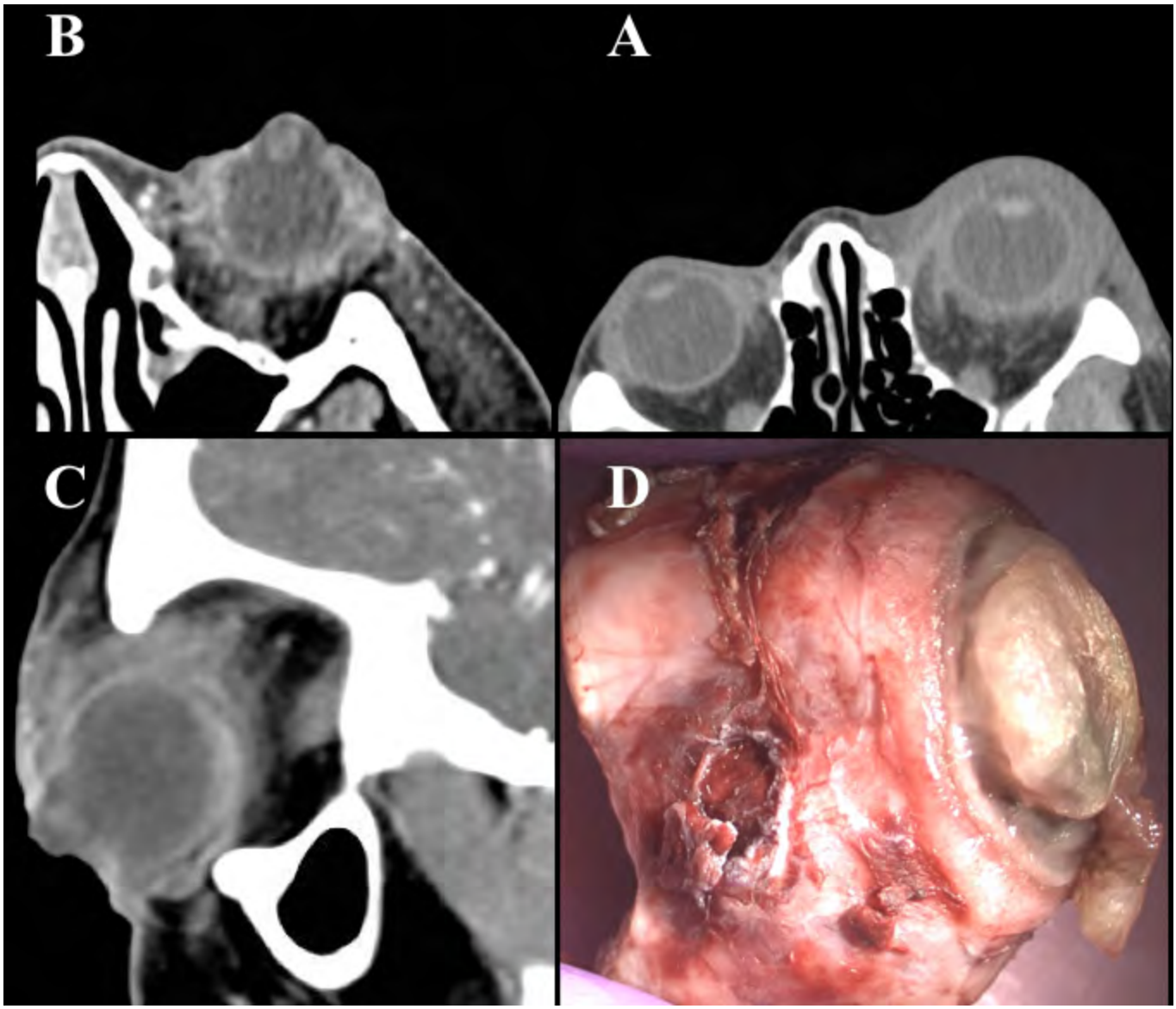
Results

Counter-clockwise from upper right hand corner, labeled as Fig 1: A-D, respectively: A) axial CECT taken at OSH, B) axial and C) sagital CECT taken several hours later at our institution and D) gross pathology post enucleation of left globe. Fig. 1 A: Coned in axial CECT taken from outside hospital shows thickening and stranding of the pre and postseptal soft tissues of the left orbit. The anterior, preseptal soft tissues are involved to a greater extent than the postseptal soft tissues. Note the moderate diffuse scleral thickening and enhancement when compared to contralateral globe. The lens and virtuous body are otherwise normal appearing. Figs. 1 B and C: Coned in axial and sagital CECT of the left orbit taken several hours after Fig. 1 A. There is increased soft tissues thicking and stranding about the left orbit with more pronounced involvement of the post septal structures. The globe is now slightly shrunken and deformed in contour compared with recent prior. Strikingly, there is a defect in the cornea with anterior herniation of the lens. Scleral thickening persists with new layering hyper density within the vitreous body. Fig. 1D:

Photograph of postsurgical gross pathology. A hazy cornea with ulceration yielding a herniated, deformed lens is seen. Patho-Histologic analysis revealed prominent inflammatory infiltrate within partially necrotic stroma with a predominance of neutrophils. The vitreous cavity contained inflammatory infiltrate composed nearly entirely of neutrophils that is admixed with erythrocytes, clumped pigmentation and retinal fragments. The choroid was noted to be diffusely infiltrated by neutrophils. The sclera also was infiltrated by acute inflammation and disrupted posteriorly.

Conclusions

Endophthalmitis is inflammation of the internal structures of the eye, including the uvea, retina, vitreous, and occasionally the lens. Panophthalmitis is purulent inflammation of all coats of the eye, and represents extension of endophthalmitis into the cornea and sclera. Most cases of endophthalmitis present acutely due to hematogenous bacterial seeding, either from underlying systemic infection, or from direct trauma. The incidence of endophthalmitis after surgical procedure/injection is estimated to be 0.25-1%. In 3-10% of cases, endophthalmitis occurs after penetrating trauma to the globe of the eye. Endophthalmitis is much more likely to occur following laceration with a metal object than after injury from glass or blunt trauma. Acute bacterial endophthalmitis is a vision-threatening condition in which clinical outcome depends on the virulence of the infecting organism as well as the timing of appropriate therapy. Risk of permanent vision loss from endophthalmitis is increased by the presence of retained intra-ocular foreign bodies, delay in repair of more than 24 hours, and disruption of the lens. We report a rare case of rapidly progressive endophthalmitis caused by direct, self-inflicted globe puncture. The patient's delay in seeking medical attention led to a remarkably severe presentation with progression to complete corneal melt and uveal herniation. To our knowledge, this is the first reported case of severe, rapidly progressive endophthalmitis in which acute pathology and complications are evidenced in stages on serial CECT, ultimately culminating in uveal prolapse. Clinical exam findings in addition to radio-pathological correlation demonstrate the sensitivity of CECT for detection of endophthalmitis and associated complications, thereby highlighting the high index of suspicion needed to initiate treatment and affect optimal clinical outcomes.



(Filename: TCT_E-117_ASNRFIG2.jpg)

E-118

1:54PM - 1:58PM

Common Tumor, Very Rare Location

J Masur[1], K Learned[2]
[1]Pennsylvania Hospital, Philadelphia, PA, [2]Univ. Pennsylvania Health System, Philadelphia, PA

Purpose
To describe a pathology-proven case of the exceedingly rare isolated laryngeal paraganglioma.

Materials and Methods

A 62-year-old female who initially presented to our institution upon referral to an otolaryngologist for multiple months of hoarseness/dysphonia and occasional dysphagia. The patient came with prior imaging including magnetic resonance imaging (MRI) of the neck performed at an outside institution approximately 1 month prior to presentation, as well as computed tomography angiography (CTA) of the neck performed 2 weeks prior (these images as well as further imaging are subsequently discussed). In-office laryngoscopy demonstrated left true vocal cord paralysis as well as a submucosal left laryngeal mass without mucosal component. The differential diagnosis at that time included hemangioma, venolymphatic malformation, low-grade chondroid tumor/chondrosarcoma, and the rare laryngeal paraganglioma. MIBG study was negative, though urine norepinephrine and dopamine were minimally elevated. Ultrasound-guided FNA yielded cytologic features consistent with paraganglioma. The patient is currently awaiting further surgical management.

Results

Review of the prior images by our neuroradiologists revealed an approximately 2.5 x 2.0 cm enhancing, T2 hyperintense submucosal left laryngeal mass centered about the lateral aspect of the cricoid cartilage and left paraglottic space, with destruction of the cartilage, medialization of the left true vocal fold, and extralaryngeal spread. Subsequent thyroid ultrasound demonstrated lack of thyroid involvement. Unenhanced CT of the neck demonstrated no calcification or chondroid matrix. MIBG scan was negative. US-guided FNA was performed.

Conclusions

Case report of the exceedingly rare isolated laryngeal paraganglioma.



(Filename: TCT_E-118_Images.jpg)

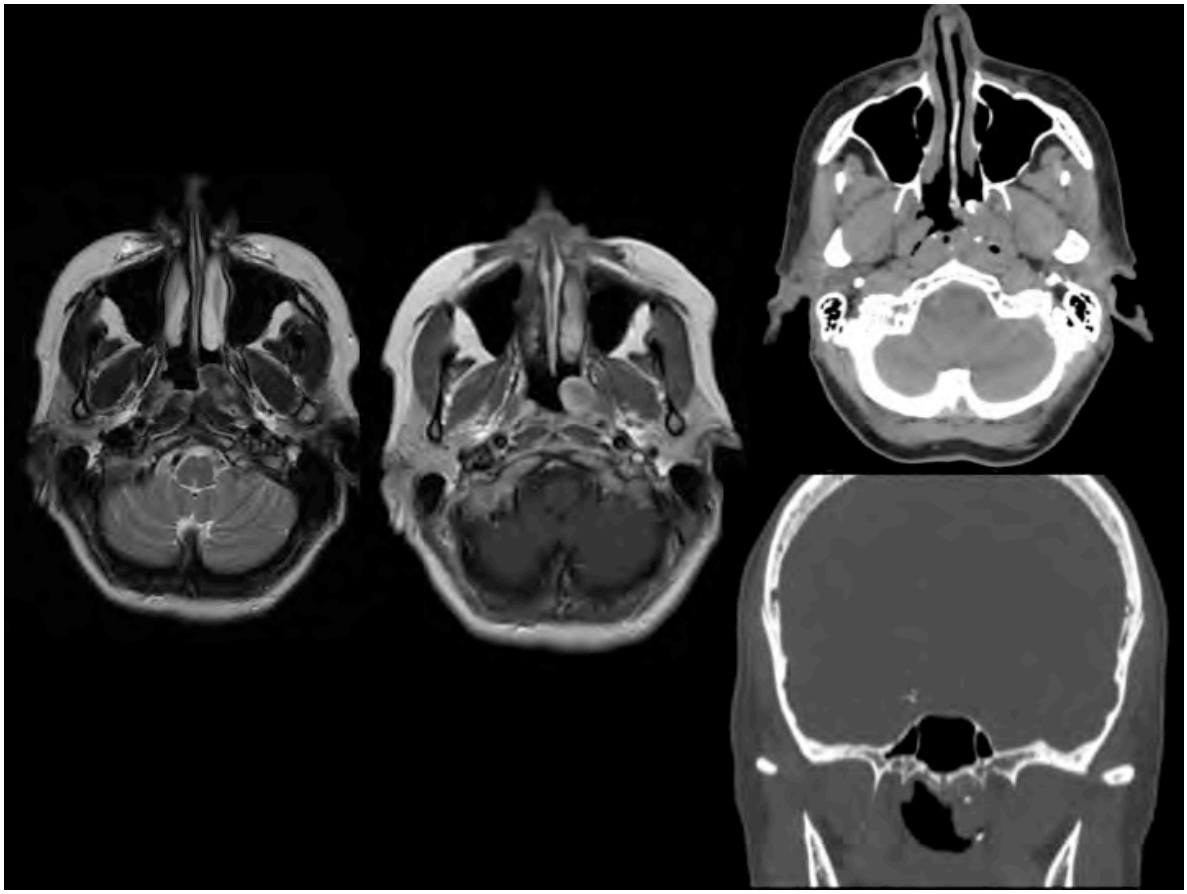
E-119

1:58PM - 2:02PM

Localized Nasopharyngeal Amyloidosis

M Achilleos[1], A Bhatki[1], M Gupta[1], M Opatowsky[1]
[1]*Baylor University Medical Center, Dallas, TX*

Purpose
Discuss the clinical and imaging presentation of localized nasopharyngeal amyloidosis (amyloidoma).
Materials and Methods
A 66-year-old female presented to the otolaryngology clinic with an asymptomatic left nasopharyngeal mass incidentally discovered on magnetic resonance imaging (MRI). She had a history of a mass in this region resected approximately 10 years prior to her current presentation. Pathology at that time revealed amyloid deposition without evidence of systemic amyloidosis. After this point in time the patient developed diagnosis of chronic lymphocytic leukemia (in remission) and melanoma. She is a nonsmoker. Audiometry and tympanography were unremarkable for the patient's age. Biopsy of the mass was obtained in the ENT clinic. Pathology again revealed findings consistent with amyloid.
Results
Magnetic resonance imaging prior to initial resection had shown a rounded T2 and FLAIR hypointense mass within the lateral aspect of the nasopharynx centered near the torus tubarius. The mass was submucosal in location and had shown faint enhancement on postcontrast imaging. Magnetic resonance imaging obtained 10 years after initial resection again revealed a submucosal mass with similar signal characteristics. Computed tomography (CT) showed an ill-defined, ovoid shaped, partially calcified, soft tissue attenuation mass without osseous destruction. Conspicuous plaque-like mucosal calcifications also were identified. Imaging findings regarding solitary amyloidomas described in the literature include their submucosal location, T2 signal hypointensity, soft tissue attenuation with possible scattered calcifications on CT, and enhancement. Osseous erosion of the skull base by an amyloidoma also has been reported (1, 2).
Conclusions
Localized amyloidosis of the head and neck is a rare clinical entity, particularly in the absence of systemic amyloidosis. This uncommonly involves the nasopharynx and can resemble a malignancy in its appearance. The clinical presentation can be protean, ranging from being entirely asymptomatic to dysfunction of multiple cranial nerves. Tissues involved by amyloid demonstrate distinct imaging characteristics, particularly on MRI, which may aid in differentiation from other pathologies such as malignancy.


(Filename: TCT_E-119_Slide1.jpg)

E-120

2:02PM - 2:06PM

Unique Case of Benign Metastasizing Pleomorphic Adenoma

L Lin[1], Q Shi[1], J Valentino[1], J Bumpous[2], E Escott[1]
[1]University of Kentucky, Lexington, KY, [2]University of Louisville, Lexington, KY

Purpose
Pleomorphic adenoma (PA) is a common benign neoplasm of the salivary glands that can undergo malignant transformation to carcinoma ex-pleomorphic adenoma (CXPA). Metastasizing PA is a controversial rare entity usually occurring years after initial diagnosis preceded by multiple local recurrences. Skin, other than of the head and neck, is a rare site for metastasis. A recent review of 81 cases of benign metastasizing PA cites 7 with cutaneous manifestations, all of which had other organ involvement. We present the unique case of benign right parotid PA with distant cutaneous metastasis without other organ involvement.
Materials and Methods
A 64-year-old man with right parotid PA complicated by local recurrence despite three

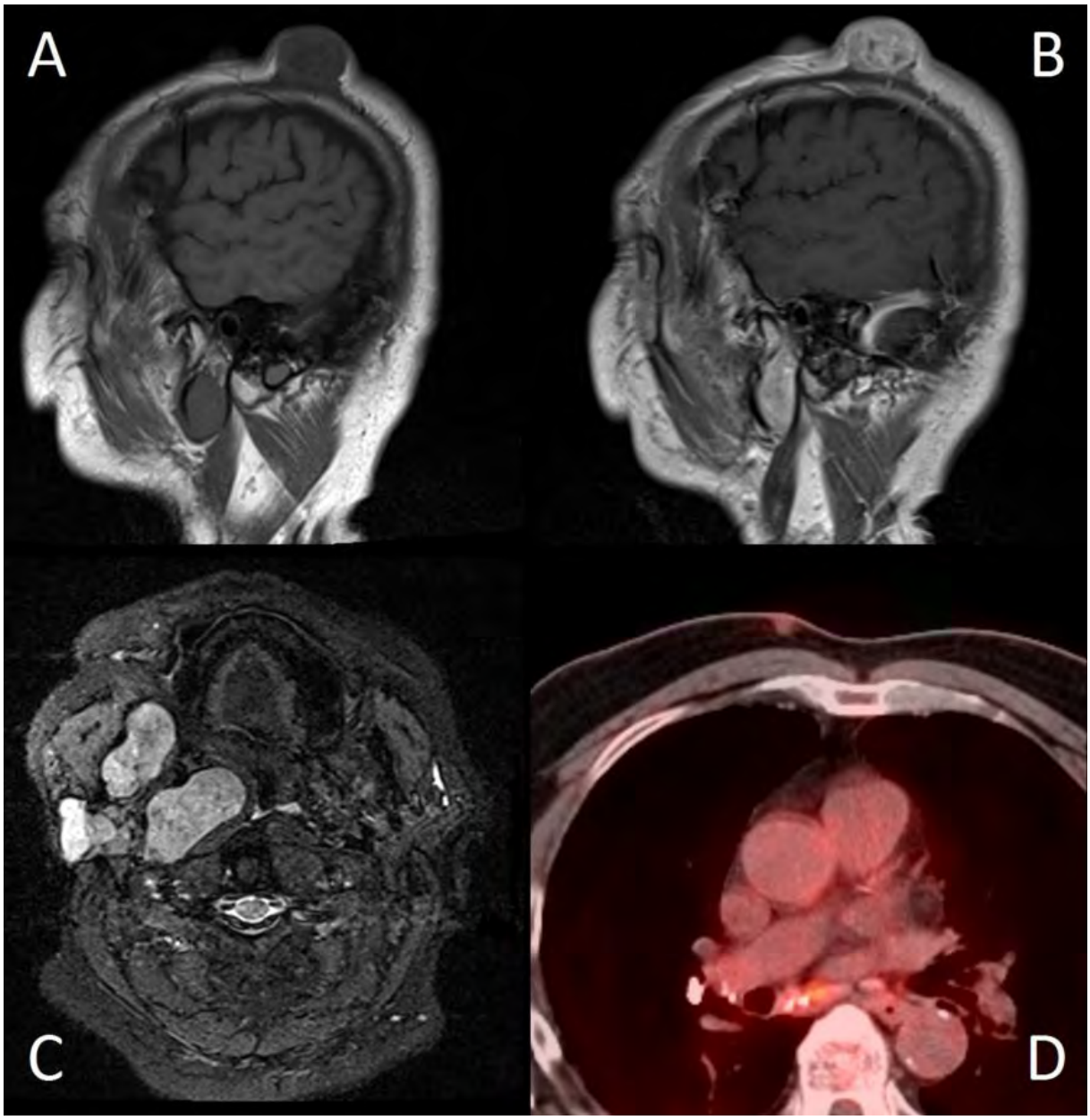
excisions, presented with multiple cutaneous nodules of the scalp and anterior chest over 20 years after initial presentation. He underwent excision of the subcutaneous lesions and pathology confirmed the diagnosis of benign pleomorphic adenoma for all lesions excised. Subsequent follow-up at an outside institution documented his scalp and chest subcutaneous lesions had not recurred and the nodules in and around his right parotid gland were stable.

Results

His head magnetic resonance imaging (MRI) showed multiple moderately T2 hyperintense nodules with heterogeneous enhancement along the right parotid tail extending into deep lobe, in the parapharyngeal and masticator spaces, and in the subcutaneous scalp. On whole body PET the local disease and subcutaneous scalp lesions were mildly hypermetabolic. Additionally, there was a slightly hypermetabolic right anterior chest subcutaneous nodule. There was no evidence of organ metastasis. Follow-up contrast-enhanced head CT 5 years later showed no recurrence of the excised subcutaneous lesions and the parotid region lesions were largely unchanged.

Conclusions

This is a rare case of benign PA with cutaneous metastasis which does not show any evidence of other organ involvement or malignant transformation.



(Filename: TCT_E-120_BMPAv3.jpg)

E-121

2:06PM - 2:10PM

Primary Mucosal Melanoma of the Lacrimal Sac and Nasolacrimal Duct: A Case Report

W Carson[1], C Glastonbury[2]
[1]University of California, San Francisco, San Francisco, CA, [2]University Of California, San Francisco, San Francisco, CA

Purpose

We report a case of primary mucosal melanoma of the lacrimal sac and nasolacrimal duct (NLD). Computed tomography (CT) and magnetic resonance imaging (MRI) findings will be discussed as well as a review of other primary tumors of the lacrimal drainage apparatus.

Materials and Methods

A 75-year-old female with a history of glaucoma presented to her primary care physician with increasing right periorbital pressure and epistaxis. She then was referred to an oculoplastic surgeon and a contrast-enhanced CT of the orbits was obtained. Based on suspicious findings on CT, she underwent an excisional biopsy. As the lacrimal sac was opened, the surgeon immediately encountered "black gelatinous material which was distending the lacrimal sac, NLD, and inferior meatus." Biopsies of all 3 areas yielded mucosal melanoma with lymphovascular invasion. She subsequently had an orbital MRI for more complete local staging as well as a PET/CT which was negative for distant metastases. Her case was discussed at our head and neck multidisciplinary tumor board, with the future plan being to resect the tumor via an endoscopic medial maxillectomy and combine this with adjuvant radiation.

Results

The orbital CT shows a rounded soft tissue mass centered in the right lacrimal fossa which extends inferiorly into an expanded NLD. Surrounding bony erosion of the right medial maxillary sinus wall is evident. Magnetic resonance imaging performed for local staging shows the soft tissue mass also extending into and expanding an accessory ostium of the right maxillary sinus. The mass is T1 hyperintense and T2 isointense relative to muscle. The inferior aspect of the right maxillary sinus is obstructed with trapped secretions, however the superior maxillary sinus and infundibulum remain patent.

Conclusions

Primary lacrimal drainage pathway tumors are exceedingly rare. Most are epithelial in origin and malignant, with squamous cell carcinoma being the most common tumor type (1). Other reported primary malignant tumors included lymphoma, transitional cell, adenoid cystic, and mucoepidermoid carcinoma. Even fewer cases of mucosal melanoma of the lacrimal drainage apparatus have been reported. Lacrimal sac melanoma constitutes only 5% of all lacrimal sac tumors [28 reported cases (2)], and only 6 cases of melanoma isolated to the NLD have ever been reported (1,3-4). The disease often masquerades as chronic dacryocystitis, and early detection is therefore difficult. Due to the paramagnetic properties of melanin, melanoma may show hyperintense signal on T1-weighted images, but other signal characteristics are possible due to amelanotic subtypes. Standard treatment at our institution is similar to other head and neck mucosal melanomas, which includes radical wide local excision combined with adjuvant radiotherapy. Chemotherapy has not been shown to have a positive effect, however newer immunotherapies are under investigation. It is important to remember that mucosal melanomas are far more aggressive and lethal as compared to skin melanomas, with the former having a 5-year survival of approximately

25% (5). Given the vascular nature of mucosal tissue, local recurrence and metastases are common.



(Filename: TCT_E-121_LacrimalCombinedImages.jpg)

E-122

2:10PM - 2:14PM

Primary Intranasal Esthesioneuroblastoma with Maxillary Sinus Metastatic Disease

K Capel[1], G Avey[2], T Kennedy[3], J Yu[4]
[1]University of Wisconsin Hospitals and Clinics, Madison, WI, [2]University of Wisconsin, Madison, WI, [3]University Of Wisconsin Hospital, Madison, WI, [4]University of Wisconsin-Madison, Madison, WI

Purpose

The purpose of the abstract is to (1) describe the salient imaging features and pathologic findings of a unique case of Kadish stage D esthesioneuroblastoma (olfactory neuroblastoma) with atypical focus of metastatic disease within the left maxillary sinus, (2) to detail the typical spread of esthesioneuroblastoma in comparison to our case, and (3) demonstrate a case example of how the increased soft tissue resolution of PET/MRI (as compared with conventional contrast-enhanced CT) ensured a more confident diagnosis of metastatic disease in the left maxillary sinus.

Materials and Methods

Esthesioneuroblastoma is a rare malignant neural crest tumor that arises from neurosensory receptor cells of the olfactory nerve and mucosa, which can originate anywhere from the cribriform plate to the turbinates. We present a unique case of a 63-year-old female who presented for evaluation prior to resection of a biopsy-proven right premalar basal cell carcinoma when a new left neck mass was palpated on exam. A contrast-enhanced neck CT revealed multiple enlarged left cervical lymph nodes and an unexpected left anterior nasal septal lesion. Fine needle aspiration of the submandibular lymph node and biopsy of the left intranasal lesion performed at the same time were consistent with Grade 3 esthesioneuroblastoma on pathology. The patient then elected to undergo left selective neck dissection (levels I-V) and septectomy with resection of the left nasoseptal tumor via a left alatomy approach, left endoscopic maxillary antrostomy with biopsy of the left maxillary sinus mass, left middle turbinectomy, and concurrent wide local excision of the right facial basal cell carcinoma with local flap closure. Subsequent pathologic analysis of the left maxillary sinus tumor revealed grade 3 esthesioneuroblastoma. Two level 1B nodes also were positive for esthesioneuroblastoma without extranodal extension while all other nodal stations were negative. The patient then underwent additional imaging evaluation with PET/MRI. Importantly, while the small left maxillary sinus lesion may not have been recognized as a metastatic focus by standard contrast enhanced CT imaging, the high soft tissue resolution of MR demonstrated imaging characteristics shared by the intranasal and intrasinus lesion, allowing for appropriate diagnosis. Following left endoscopic medial maxillectomy, pathology confirmed that the left maxillary sinus lesion exhibited identical pathologic markers as the primary intranasal lesion, consistent with Grade 3 esthesioneuroblastoma metastasis.

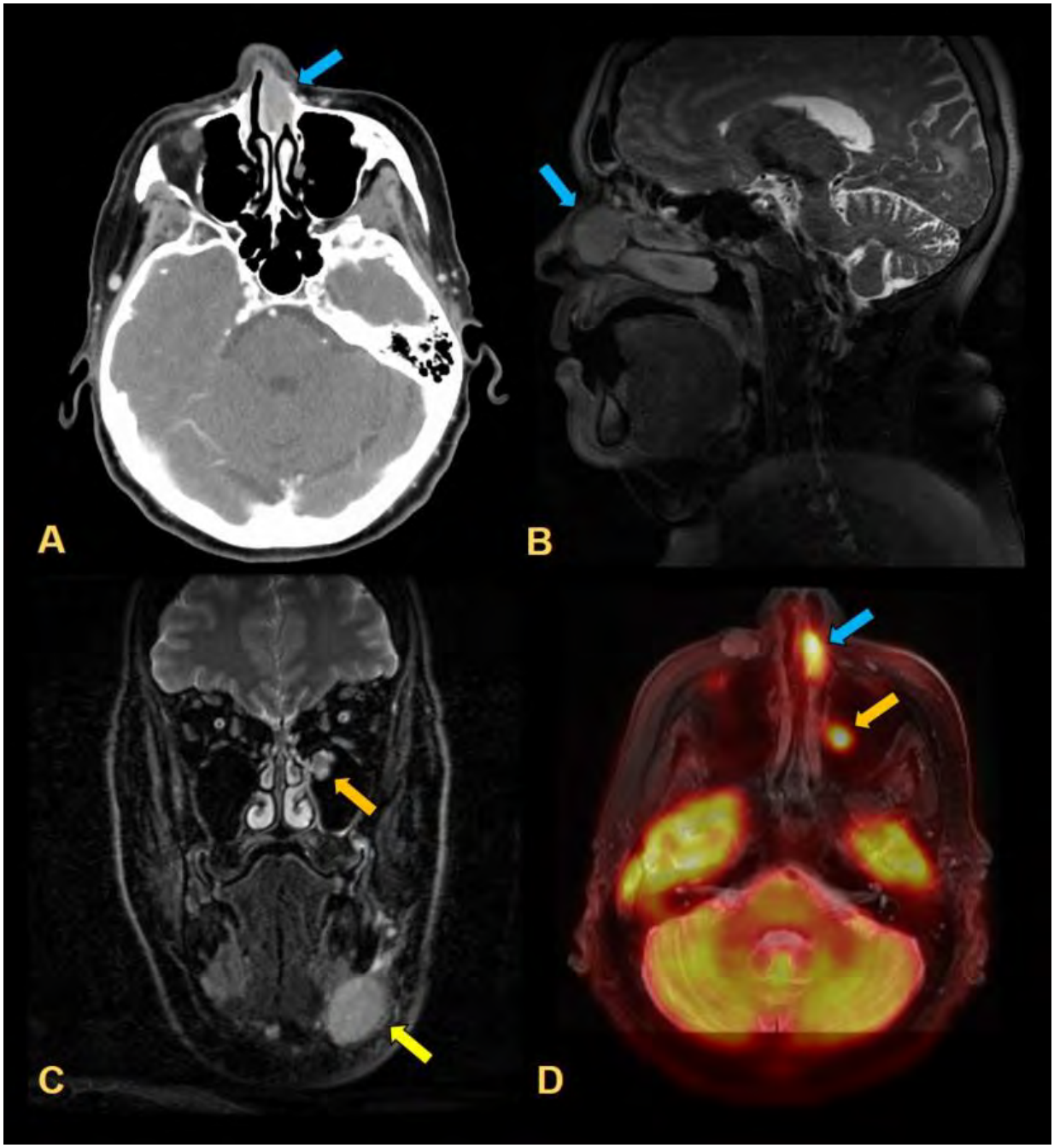
Results

A: Initial contrast-enhanced CT of the neck was obtained given new palpable left neck mass and history of biopsy-proven right premalar basal cell carcinoma. Enhanced axial CT image demonstrates a 2.1 x 0.9 cm enhancing soft tissue mass (blue arrow) within the anterior

aspect of the left nasal vestibule along the cartilaginous septum, concerning for second primary neoplasm. Biopsy revealed grade 3 esthesioneuroblastoma. B: Sagittal T2-weighted MR image obtained as a PET/MRI to evaluate extent of disease illustrates the 1.4 x 1.2 x 1.4 (AP x transverse x craniocaudal) highly cellular left intranasal lesion (blue arrow), with corresponding intermediate to low signal on T2-weighted images, typical for esthesioneuroblastoma. The intranasal lesion also showed avid enhancement and restricted diffusion (not shown), with findings similar to that of the left maxillary sinus lesion. C: Unexpectedly, the coronal postcontrast MR image as part of a PET/MR evaluation demonstrates a 1.2 X 0.9 X 1.0 cm (AP x transverse x CC) lobulated enhancing left maxillary sinus lesion (orange arrow). This sinus lesion demonstrated similar imaging characteristics as compared with the left intranasal lesion and later was found to represent a focus of metastatic esthesioneuroblastoma. Additionally, the large homogeneously enhancing left level 1B lymph node (yellow arrow) measuring 4.1 x 2.8 x 2.8 cm (AP x TR x CC) was found to represent another focus of metastatic disease without extranodal extension. D: Axial fused PET/MR image depicts the FDG avid left intranasal septal lesion (blue arrow) and metastatic focus within the left maxillary sinus (orange arrow), both confirmed to be grade 3 esthesioneuroblastoma on pathology. Enhancing lesion with minimal FDG activity consistent with known basal cell carcinoma within the right premalar soft tissues also is noted.

Conclusions

In this case of asymptomatic incidentally discovered Kadish stage D, Grade 3 esthesioneuroblastoma, the patient's primary left intranasal lesion initially metastasized to the left maxillary sinus and left submandibular gland. This case also highlights the clinical utility and sensitivity of PET/MRI in the evaluation of complex primary sinonasal tumors with widespread metastatic disease.



(Filename: TCT_E-122_ASNResthesioneuroblastomaARROWS.jpg)

E-123

2:14PM - 2:18PM

Multicentric Myofibromatosis Involving the Head and Neck

A Spiro[1], D Machleder[1], S Ali[1], J Burns[1], T Miller[2], J Bello[1], K Shifteh[1]
[1]Montefiore Medical Center, Bronx, NY, [2]Montefiore North Medical Centre, Bronx , NY

Purpose

To describe a case and review the clinical presentation, imaging, and treatment of multifocal fibromatosis of the head and neck, a rare entity.

Materials and Methods

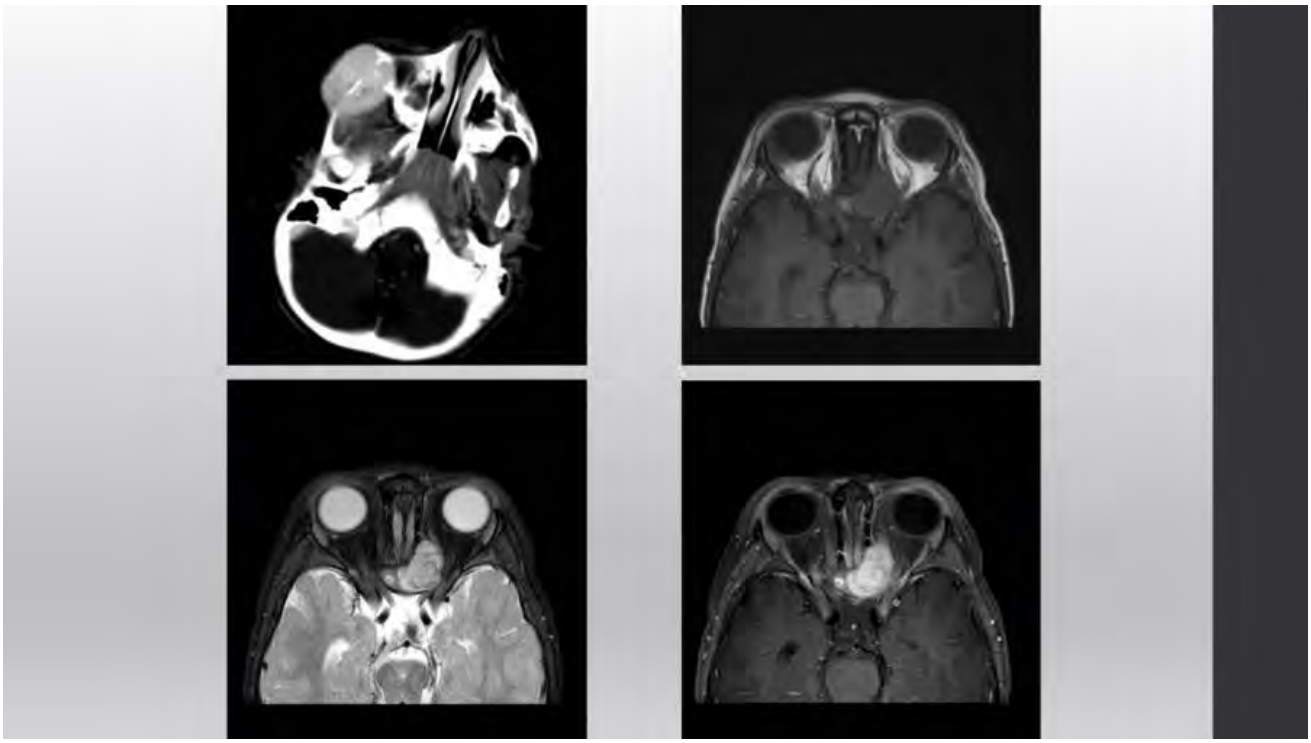
Patient is a 2-year-old male who presented with persistent right cheek swelling 2 weeks after facial trauma. Physical exam noted an approximately 2 cm firm, non-tender, subcutaneous mass of the right zygoma without overlying erythema or skin lesions. Core biopsy was performed and demonstrated a myofibroma of the zygomatic arch. The patient subsequently had tumor resection and right zygomatic arch reconstruction 6 weeks after pathologic diagnosis. Follow-up imaging over the course of the next 6 months demonstrated an enlarging mass along the roof of the left sphenoid sinus with extension into the left optic canal as well as the ethmoid sinus. Subsequent resection was performed which demonstrated a pathologic diagnosis of myofibroma.

Results

Initial CT demonstrates a 2.6 x 4.0 cm destructive mass centered in the right zygomatic arch. The mass demonstrates avid enhancement without calcifications. There is bony erosion. Postoperative follow-up magnetic resonance imaging (MRI) demonstrates a new lesion involving the roof left sphenoid sinus which is isointense to gray matter on T1- and T2-weighted images. There is homogenous enhancement.

Conclusions

Various types of myofibroblastic tumors can affect the head and neck area. They are rare and mostly benign, constituting less than 1% of all body tumors. Congenital myofibromatosis is characterized by solitary or multiple lesions involving the soft tissues and bone. The differential diagnosis of these lesions should include Langerhans cell histiocytosis and multiple metastases from neuroblastomas or sarcomas. Imaging features include: variable density of CT with bone erosion, remodeling or destruction. Hypointense T1-weighted and hypointense or hyperintense T2-weighted signal characteristics are common. Strong peripheral or target-like enhancement is expected, although occasional homogenous enhancement can be seen as well. Solitary lesions are amenable to conservative surgical resection. In the multicentric life-threatening forms, chemotherapy with vinblastine and methotrexate promotes tumor regression.


(Filename: TCT_E-123_asnrmyofibroma.jpg)

E-124

2:18PM - 2:22PM

Fungal Sinusitis in the Immunocompetent Patient: When Sphenoid "Disease" Matters

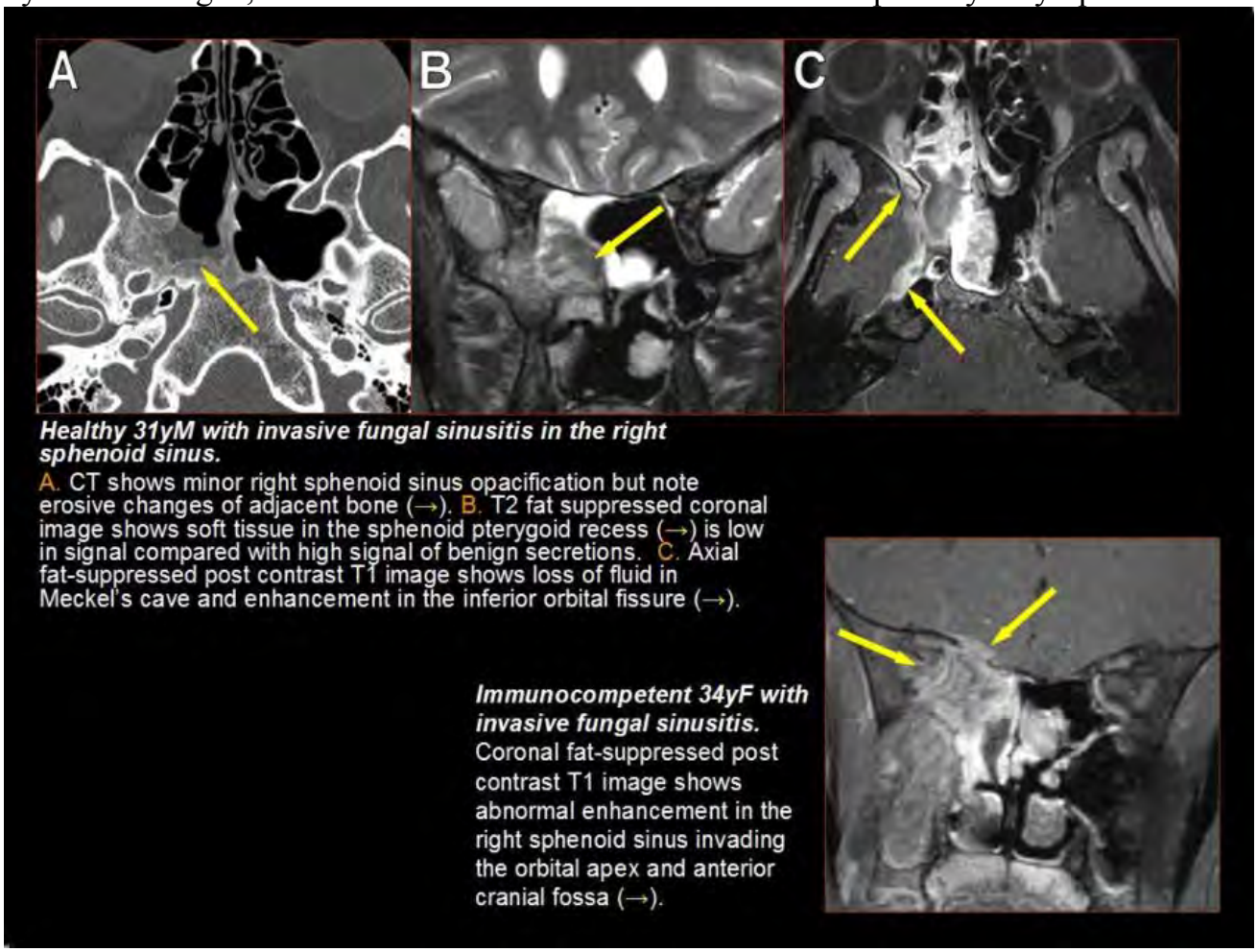
D Samardzic[1], A Aiken[2], K Baugnon[1], A Corey[3], P Hudgins[1]
[1]Emory University, Atlanta, GA, [2]Emory University Hospital, Atlanta, GA, [3]Emory, Fayetteville, GA

Purpose
Fungal sinusitis, particularly involving the sphenoid sinuses, can be invasive or noninvasive and typically afflicts the immunocompromised patient. In this retrospective review we provide examples of both invasive and noninvasive sphenoid sinus fungal infection in immunocompetent patients as a reminder that fungal sinusitis is not limited to the immunocompromised host.
Materials and Methods
Five immunocompetent patients (31-80 years) presenting with symptoms including retro-orbital pain, vision changes, and cranial nerve deficits referable to the cavernous sinuses are presented. Two patients with diabetes mellitus but with good glucose control were included.
Results
The spectrum of imaging findings on computed tomography (CT) and magnetic resonance (MR) in invasive fungal sinusitis ranged from mild mucosal thickening to complete opacification of the sinus. Erosive osseous changes or fatty stranding in adjacent fat were

subtle findings on CT. Trans-spatial, perineural and intracranial invasion were seen on MR particularly on pre and postcontrast T1 images. Characteristic low signal on T2 imaging added specificity for fungal infections.

Conclusions

Sphenoid sinus opacification, often seen in the hospitalized patient, typically represents reactive mucosal thickening. When seen as an isolated finding in an outpatient it should raise the suspicion of fungal infection. We review our experience with invasive and noninvasive sphenoid sinus fungal disease and summarize the imaging and clinical findings, stressing that not all sphenoid sinus opacification in an immunocompetent patient is incidental or reactive. Fungal sinusitis, although rare, can afflict immunocompetent hosts, can be missed by the radiologist, and should be a differential consideration especially if symptomatic.



(Filename: TCT_E-124_Abstractsample.JPG)

E-125

2:22PM - 2:26PM

Extramedullary CNS Acute Myeloid Leukemia: A Rare Cause of Antegrade Perineural Spread of Tumor

M Chen[1], J Teixeira[1], C Lewis[1], L Ginsberg[1]
[1]*UT MD Anderson Cancer Center, Houston, TX*

Purpose

We report 2 cases of antegrade perineural spread in the head and neck of extramedullary central nervous system (CNS) acute myeloid leukemia (AML), a finding that has not been reported previously in the literature. We also present a mimic of acute invasive fungal sinusitis, a sinonasal granulocytic (myeloid) sarcoma (GS), a separate finding in 1 of our patients.

Materials and Methods

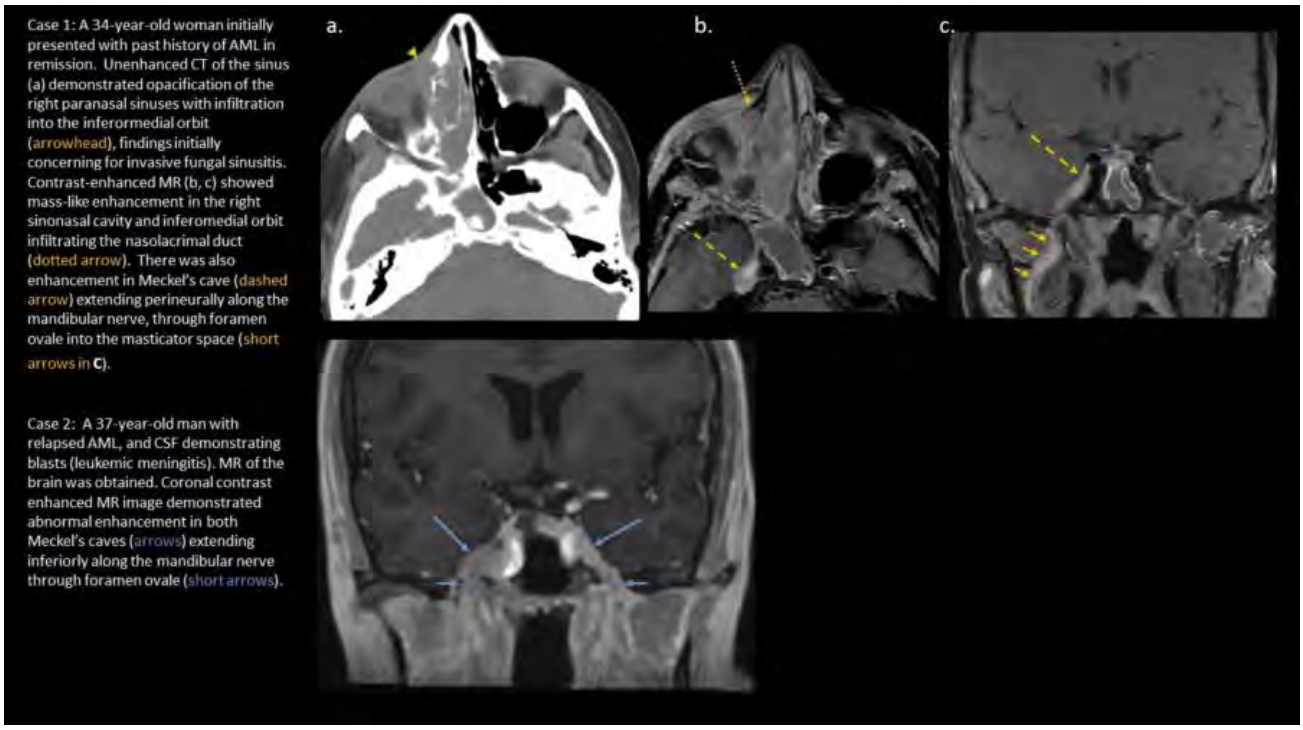
A 34-year-old woman with a history of acute myeloid leukemia in remission and diabetes presented with a 2-week history of progressive right facial swelling and numbness involving the face and tongue. Clinical history, MR imaging, a lumbar puncture and a biopsy of the sinonasal mass led to the final diagnosis. A 37-year-old man with acute myeloid leukemia initially presented with sciatic and worsening leg pain. An magnetic resonance imaging (MRI) of the spine demonstrated abnormal thickening of the sacral and lumbar nerve roots, and subtle leptomeningeal enhancement prompting work up for extramedullary CNS AML. Lumbar puncture confirmed CNS leukemia, and MR of the brain was obtained.

Results

Unenhanced CT of the sinus of the first case demonstrated opacification of the right sinonasal cavity and soft tissue density in the right inferior orbit. There was mild fat stranding in the retroantral fat, and excessive soft tissue in the right pterygopalatine fossa. Contrast-enhanced MR of the face showed mass like homogeneous enhancement in the sinonasal cavity, arguing against invasive fungal sinusitis (typically nonenhancing). In addition, there was abnormal enhancement of the cisternal segment of the trigeminal nerve, extending into Meckel's cave and inferiorly along the mandibular nerve through foramen ovale, into the masticator space to the level of the mandibular foramen. Magnetic resonance imaging of the brain in the second case showed abnormal enhancement in Meckel's cave bilaterally, with antegrade spread of tumor along the mandibular nerve through foramen ovale into the masticator space.

Conclusions

Central nervous system involvement of AML in adults is extremely rare, with 1.1% incidence reported in the literature (1). A few case reports in the literature show perineural spread of extramedullary AML from a sinonasal or orbital GS (2-4). Antegrade perineural spread of AML from CNS involvement has not been described previously. Separately we demonstrate that a sinonasal GS can be a mimic of invasive fungal sinusitis, a separate finding in one of our patients. Contrast-enhanced MR can help to differentiate the 2 pathologies.



(Filename: TCT_E-125_gspicture.JPG)

E-126

2:26PM - 2:30PM

A Rare Presentation of Extranodal Rosai-Dorfman Disease in the Head and Neck without Lymphadenopathy

B Brown[1], J Chang[1], M Bobinski[1], J Funamura[1], A Ozturk[1]
[1]*University of California, Davis Medical Center, Sacramento, CA*

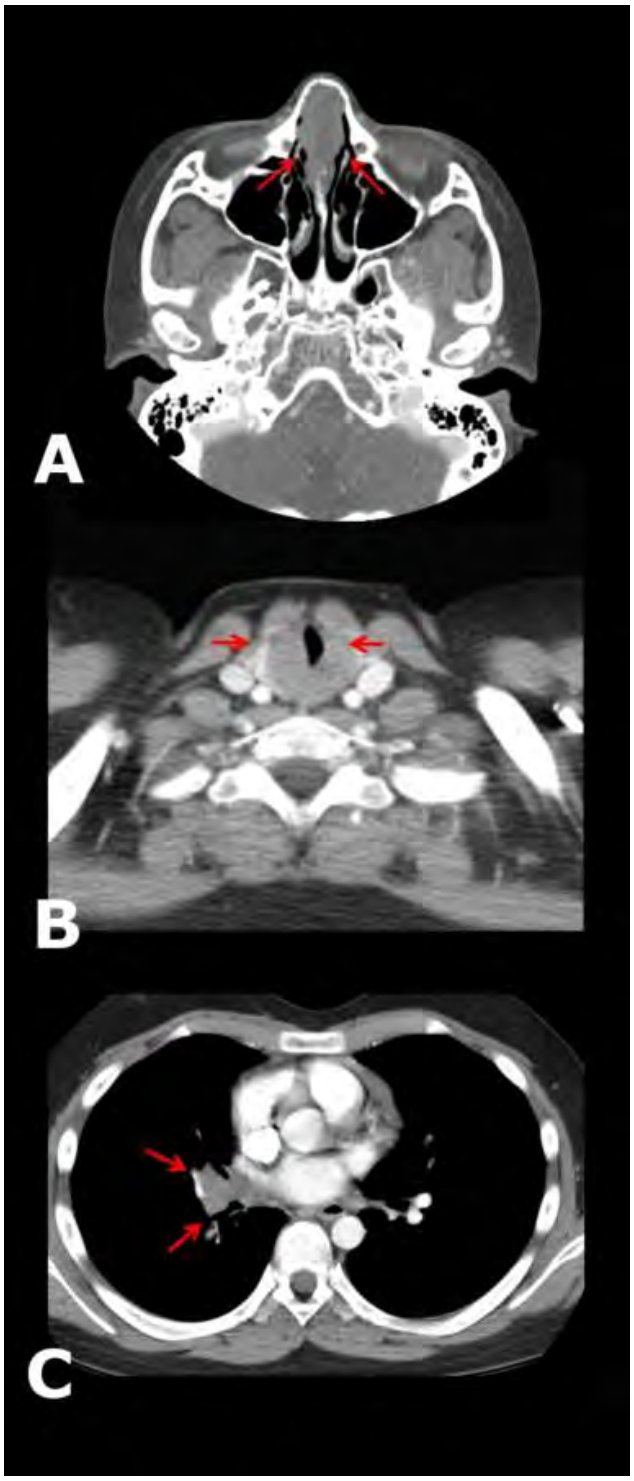
Purpose
Our purpose is to demonstrate imaging findings of a rare presentation of extranodal Rosai-Dorfman (RD) disease in the head and neck without lymphadenopathy (LAD).
Materials and Methods
A 14-year-old male presented with shortness of breath and a nasal mass. Computed tomography (CT) studies demonstrated a well circumscribed enhancing solid lesion arising from the midline nasal septal septum. There was submucosal soft tissue thickening and stenosis in the subglottic region with no evidence of LAD in the neck. Chest CT demonstrated infiltrative soft tissue thickening along the bronchus intermedius and middle and right lower lobe bronchi. Intranasal biopsy of the nasal mass showed dense lymphoplasmocytic and histiocytic infiltrates with large histiocytes engulfing inflammatory cells (emperipolesis). The large cells stained positive for S100, CD183, and CD88. No fungal elements or suspicious bacteria were identified at the culture.

Results

Fig. 1A: Axial CT image of face shows enhancing soft tissue mass originating from nasal septum (arrows). Fig. 1B: Axial CT image of neck shows enhancing soft tissue thickening in subglottic region with mild stenosis (arrows). Fig. 1C: Axial CT image of chest shows enhancing soft tissue thickening along the middle and lower lobe bronchi (arrows).

Conclusions

Rosai-Dorfman disease, or sinus histiocytosis with massive lymphadenopathy, is a rare disorder which usually presents with bilateral painless cervical lymphadenopathy. Fewer than half of patients have concurrent extranodal disease, usually within the paranasal sinuses, nasal cavity, neck soft tissues, and dural enhancing masses. Extranodal disease without lymphadenopathy is an unusual presentation with reported involvement of the orbit and the submucosal tissues of the nasal septum and trachea. Rosai-Dorfman disease is a benign entity with nonspecific imaging findings, requiring histologic and immunohistologic analysis for diagnosis. Consideration of this entity is useful to direct pathologic evaluation and facilitate proper symptom management.



(Filename: TCT_E-126_RD_Brown_et_al_figures.jpg)

E-127

2:30PM - 2:34PM

Sinonasal NUT Carcinoma: a Rare and Underdiagnosed Entity

B Chan[1], J Yu[1], T Kennedy[1], G Avey[1]
[1]*University of Wisconsin Hospitals and Clinics, Madison, WI*

Purpose

The purpose of this presentation is to discuss imaging findings, diagnostic considerations, and therapeutic options regarding sinonasal NUT carcinoma.

Materials and Methods

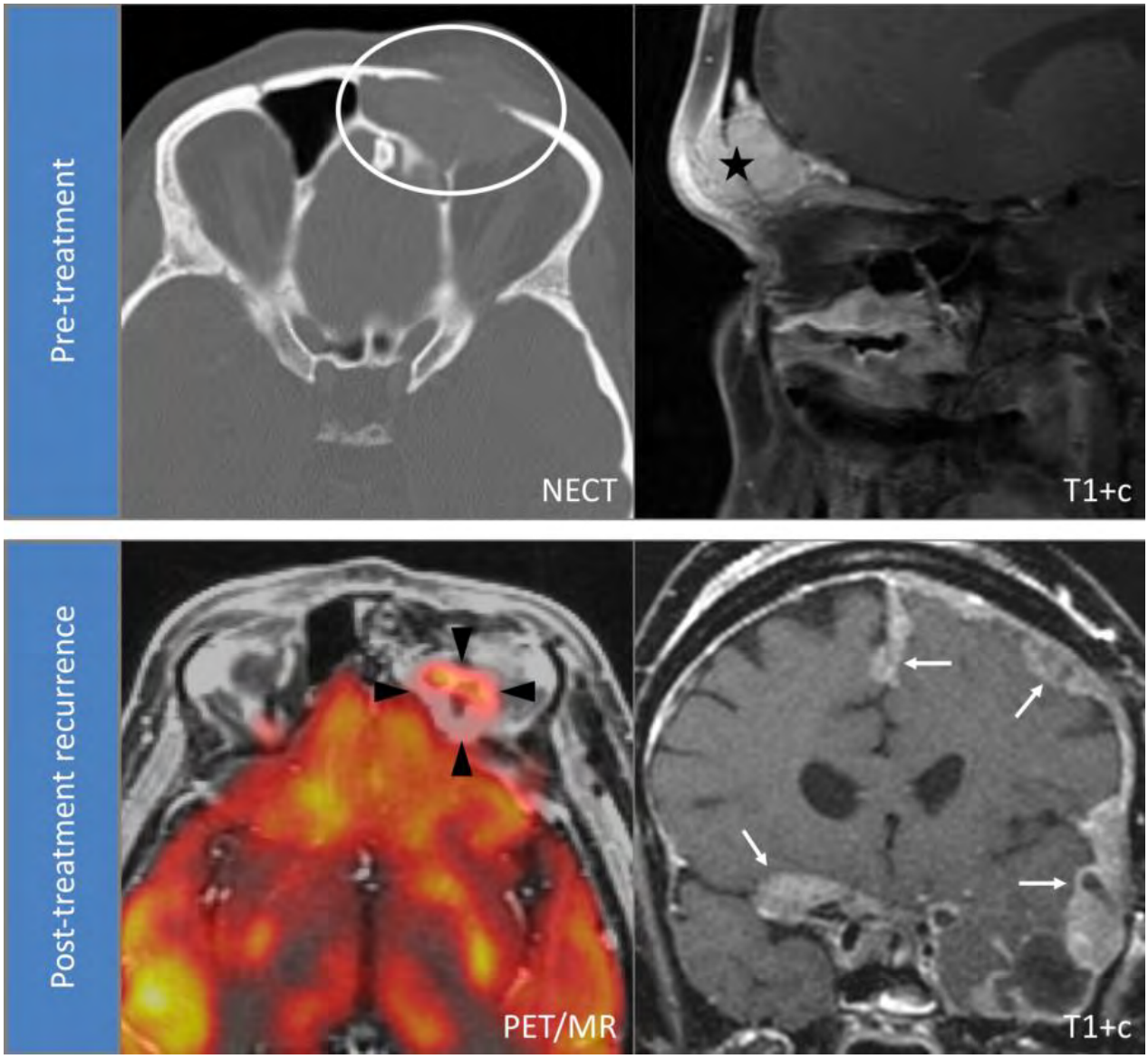
RV is a 44-year-old female with a 1-week history of left facial pain and blurry vision. She initially was treated for presumed sinusitis with functional endoscopic sinonasal surgery and antibiotics. However, 1 month postoperative imaging showed a left frontal sinus mass with extension into the left orbit. Fine needle aspiration yielded a poorly differentiated carcinoma. She was treated with induction chemotherapy, composite resection, and adjuvant radiotherapy. Immunohistochemical analysis of the operative specimen was positive for NUT. Three month follow-up imaging demonstrated local recurrence with transcranial extension. There was subsequent rapid progression of dural metastatic disease despite aggressive therapy, and the patient expired 16 months after initial presentation.

Results

The presenting head MR demonstrated T2 hypointense, non-enhancing material filling the left frontal sinus and frontal recess. The contemporaneous sinus CT demonstrated demineralization of the left frontal sinus walls without frank osseous destruction. One month follow-up demonstrated a progressive, diffusion restricting, and newly enhancing mass in the left frontal sinus with orbital invasion and encasement of the left superior oblique muscle. Positron emission tomography/magnetic resonance (PET/MR) 3 months after gross total resection demonstrated heterogeneously enhancing, hypermetabolic tumor in the resection bed extending into the superior extraconal orbit, involving the intraorbital V1 segment of the left trigeminal nerve, with extension posteriorly to involve the left frontal dura. The final head MR (obtained 16 months after initial presentation) demonstrated progressive intracranial spread of disease with thick, heterogeneous frond-like dural enhancement.

Conclusions

NUT carcinoma is a rare, highly aggressive, poorly differentiated squamous cell carcinoma that often arises in the head and neck. Incidence is underestimated due to frequent misdiagnosis. Treatment paradigms include chemotherapy, surgical resection, and/or radiotherapy but are not standardized. Prognosis is poor, with a median survival of 6.7 months.



(Filename: TCT_E-127_ASNR20201720images.jpg)

E-128

2:34PM - 2:38PM

Canalis Basilaris Medianus: An Anatomic Variant, Not a Skull Base Neoplasm

R Yu[1], M Hughes[1], C Snyderman[2]
[1]University of Pittsburgh Medical Center, Pittsburgh, PA, [2]University of Pittsburgh School of Medicine, Pittsburgh, PA

Purpose
Canalis basilaris medianus is a rare anatomic variant of the basiocciput occurring in 2-3% of adult dry skull specimens. It is typically asymptomatic and characterized by a well corticated

tubular channel located at the midline of the basiocciput. It is thought to represent an embryological remnant of the notochord. We present a case of canalis basilaris medianus initially described as a small chordoma.

Materials and Methods

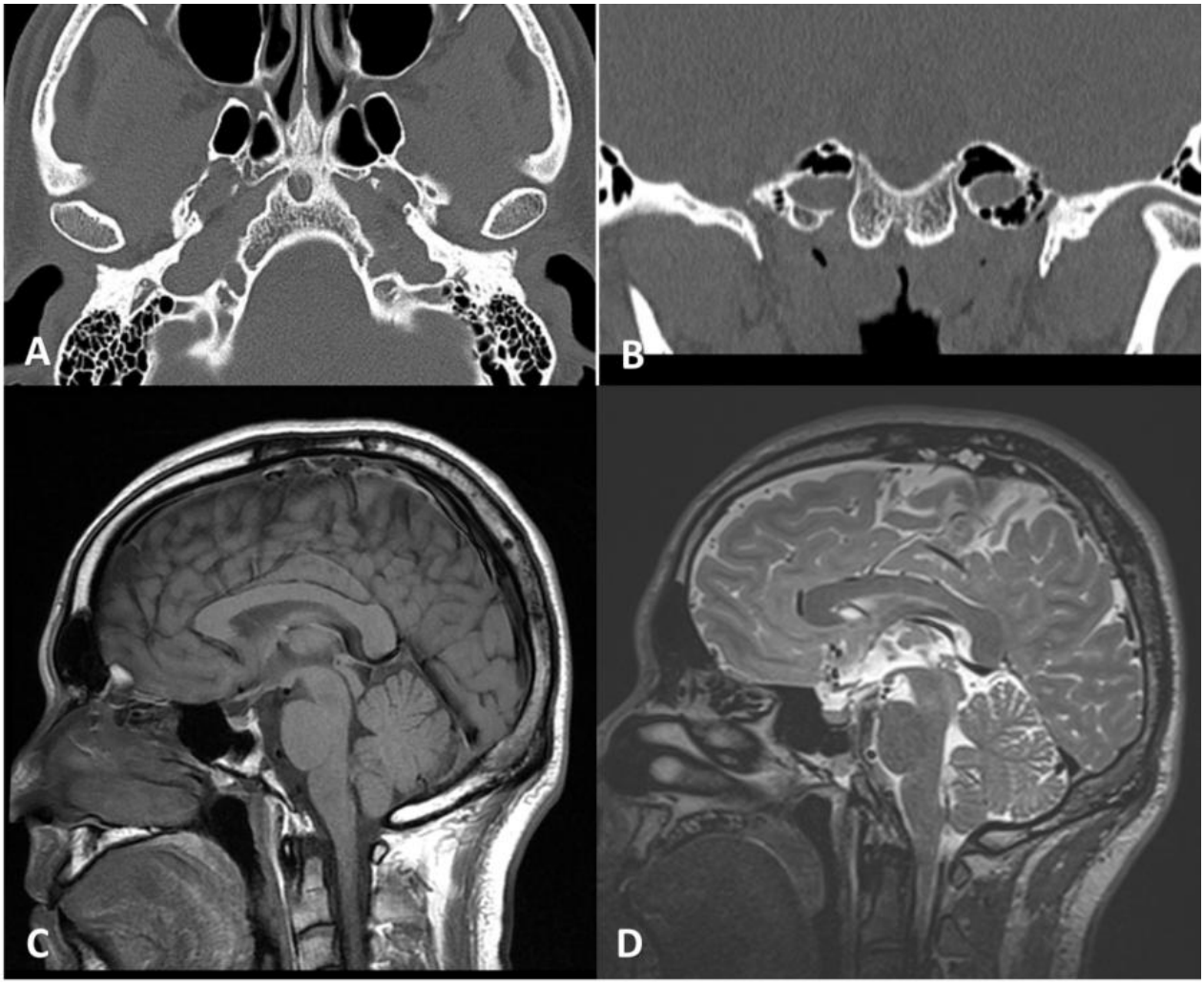
A 35-year-old male underwent an magnetic resonance imaging (MRI) for work up of his migraines. The MRI revealed a midline clival T2 bright lesion without enhancement along the ventral surface of the clivus. Initial interpretation at an outside facility suggested the presence of a small chordoma. Physical exam and nasal endoscopy were unremarkable. The patients had no nasal symptoms or cranial neuropathies.

Results

(A, B) Axial and coronal noncontrast-enhanced CT images show a well corticated channel at the midline of the basiocciput. (C) Sagittal T1, (D) sagittal T2 images demonstrate a low T1 signal high T2 signal lesion along the ventral surface of the clivus with a small channel extending to the dorsal margin of the clivus.

Conclusions

Canalis basilaris medianus is a rare anatomic variant of the central skull base and typically asymptomatic. It is a well corticated channel extending through the midline of the basiocciput. This differs from the craniopharyngeal canal, which is another rare, well corticated channel but extends through the midline of the basisphenoid. Knowledge of normal anatomic variants of the central skull base is important to avoid incorrect diagnoses and potential unnecessary intervention.



(Filename: TCT_E-128_Figure-CanalisBasilarisMedianus.jpg)

E-130

2:42PM - 2:46PM

Aneurysmal Bone Cyst of The Maxillary Sinus: A case report.

D Marcus[1], A Cano Duran[2], E Bonfante-Mejia[2], R Riascos[2]
[1]University of Texas Health Science Center at Houston, Houston, TX, [2]The University of Texas Health Science Center at Houston, Houston, TX

Purpose
Present a case of aneurysmal bone cyst (ABC) in an unusual presentation. This case increases our awareness of fibro-osseous lesions arising from the paranasal sinuses including ABC.
Materials and Methods
A 33-year-old female first presented with 4 months of progressive right maxillary pressure,

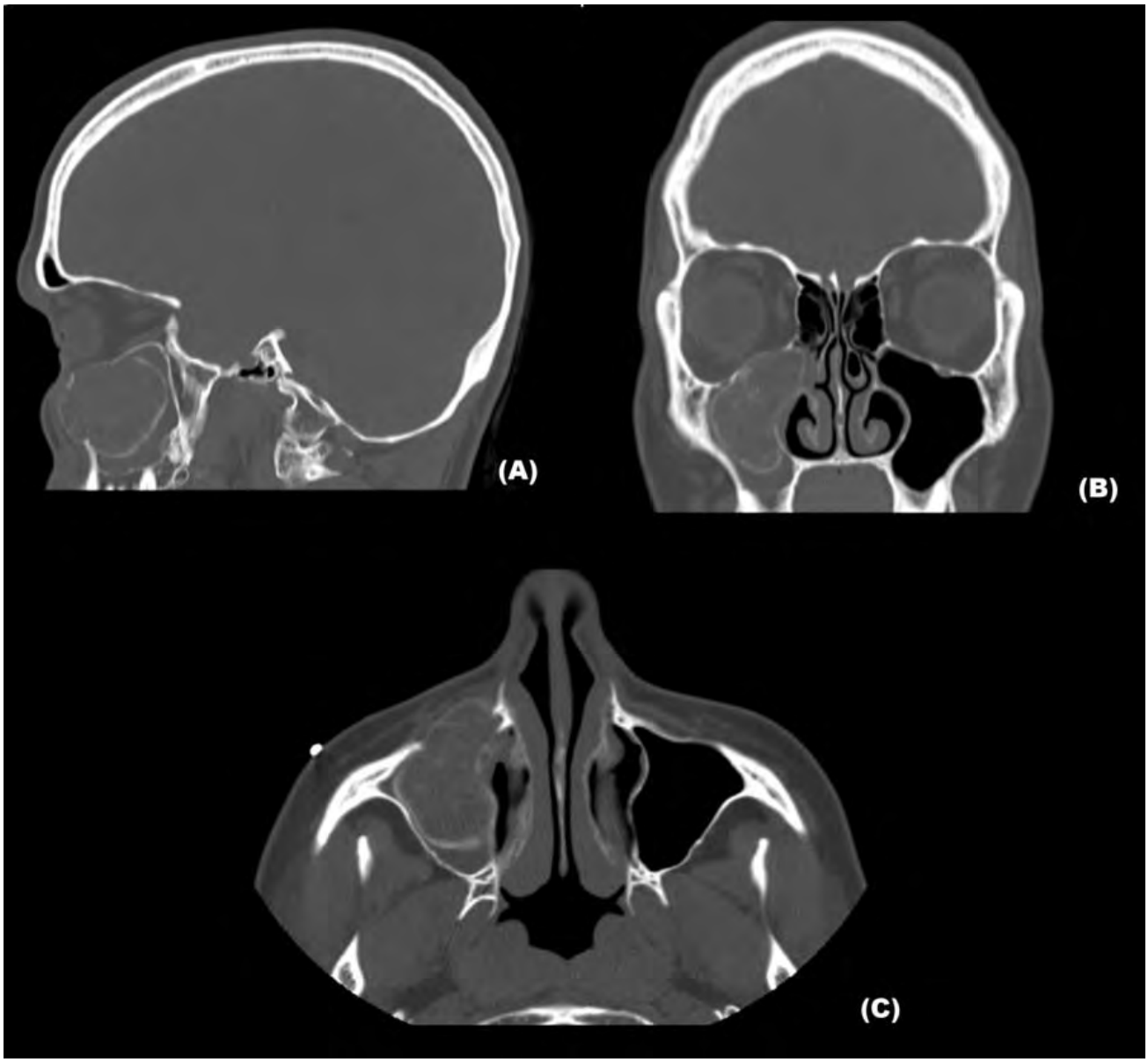
pain, and headache which were unresponsive to antibiotics, oral corticosteroids, and decongestants. A week prior to the evaluation, the patient developed periorbital swelling, headache, and worsening maxillary pain. Physical exam demonstrated a discrete fullness of the right maxillary sinus without tenderness. The physical exam was otherwise unremarkable. Past medical and surgical history were significant for surgery for tooth extraction. A noncontrast computed tomography (CT) was performed and showed a mass in the right maxillary sinus. The mass was removed at surgery. It was confirmed to be an ABC on microscopic analysis.

Results

Noncontrast CT of the sinuses demonstrates a right maxillary sinus mass eroding and remodeling the anterior, medial and superior walls of the right maxillary sinus. The mass is well circumscribed and exhibits a rim of calcification and a calcified matrix (Image 1).

Conclusions

Aneurysmal bone cysts are defined as a "blood-containing cysts (1)." It can be primary or secondary, arising from another lesion in up to one-third of the cases (1). Most ABCs originate in the long bones. Skull involvement occurs in less than 1% of cases (2). Aneurysmal blood cysts have been described on imaging as an expansile radiolucent "soap bubble" lesion that causes expansion of the bony cortex (3). It is proposed that ABC of paranasal sinuses is more likely to appear as an expansive, homogeneous soft tissue mass with focal areas of peripheral bone destruction (4). These features may mimic malignancy (4). Aneurysmal blood cyst identification on imaging alone is difficult and pathologic confirmation often is required.



(Filename: TCT_E-130_ASNRABCFINAL.jpg)

E-131

2:46PM - 2:50PM

A Rare Presentation of Metastatic Anaplastic Thyroid Cancer: Cardiac Metastases

S Ahmed[1], M Ghazarian[2]
[1]UT MD Anderson Cancer Center, Houston, TX, [2]UT Houston Medical School at Houston, Houston, TX

Purpose

Demonstrate a rare case of cardiac metastases from anaplastic thyroid cancer (ATC). Review the typical imaging findings in anaplastic thyroid cancer.

Materials and Methods

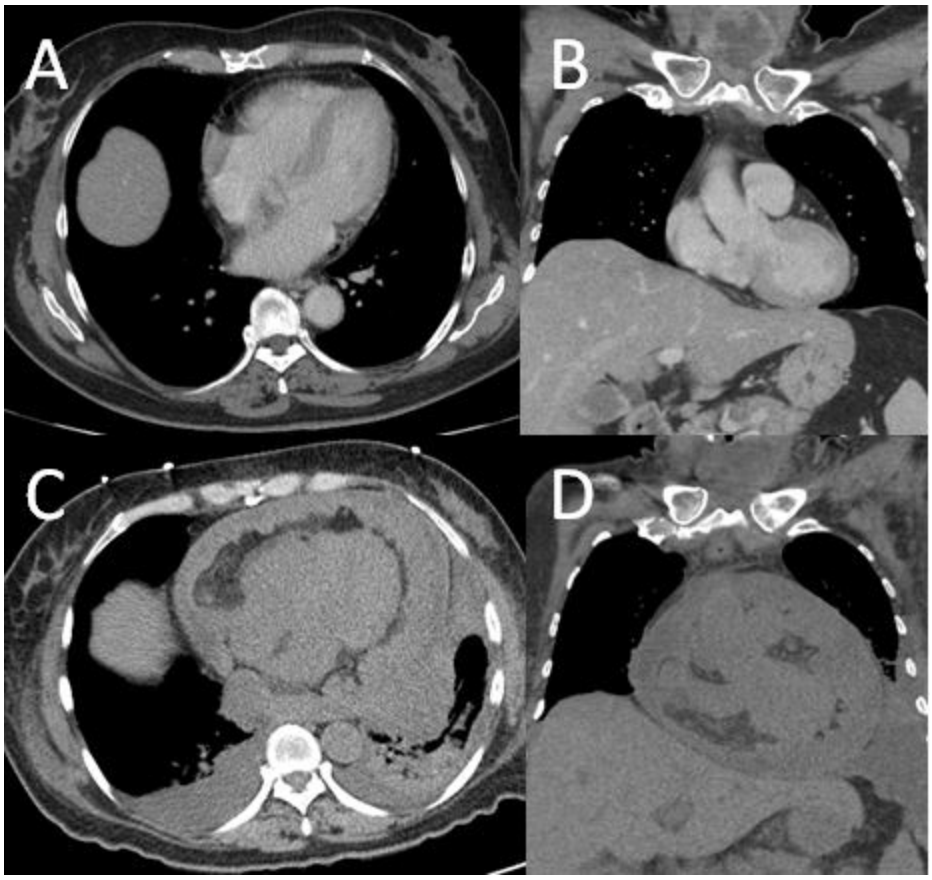
A 62-year-old female initially noticed a grape-sized midline neck mass 10 months ago. Four months later the patient noticed a larger left inferior neck mass, prompting a thyroid ultrasound. Ultrasound-guided biopsy revealed anaplastic thyroid cancer. She was referred to our institution and received concurrent chemoradiation. Two weeks after completing therapy, she presented to the ER with shortness of breath and was found to have diffuse pericardial metastases. The patient passed away 2 days later.

Results

Axial and coronal contrast-enhanced CT (CECT) (A, B) demonstrate normal appearance of the heart at initial presentation. Note the large, centrally necrotic thyroid mass on the coronal reconstruction. Nonenhanced CT images (NECT) (C, D) show a thick, irregular rind of soft tissue diffusely involving the pericardium consistent with metastasis. Mass effect results in constriction of cardiac wall motion.

Conclusions

Anaplastic thyroid cancer usually presents with a rapidly enlarging neck mass in an older patient. On CT, the primary tumor shows necrosis and size of at least 5 cm, typically. Necrotic lymphadenopathy and local organ invasion is common. Distant metastases are present in 50% of cases at presentation. However, cardiac metastases have rarely been reported, with only one case presented in the radiology literature, to our knowledge. Here we present a case of extensive diffuse pericardial metastases from ATC resulting in the death of the patient.



(Filename: TCT_E-131_ATCcardiacmetspic.JPG)

E-132

2:50PM - 2:54PM

Postpartum Thyroiditis Mimicking a Primary Thyroid Neoplasm

M Ghazarian[1], S Ahmed[2]
[1]UT Houston Medical School at Houston, Houston, TX, [2]UT MD Anderson Cancer Center, Houston, TX

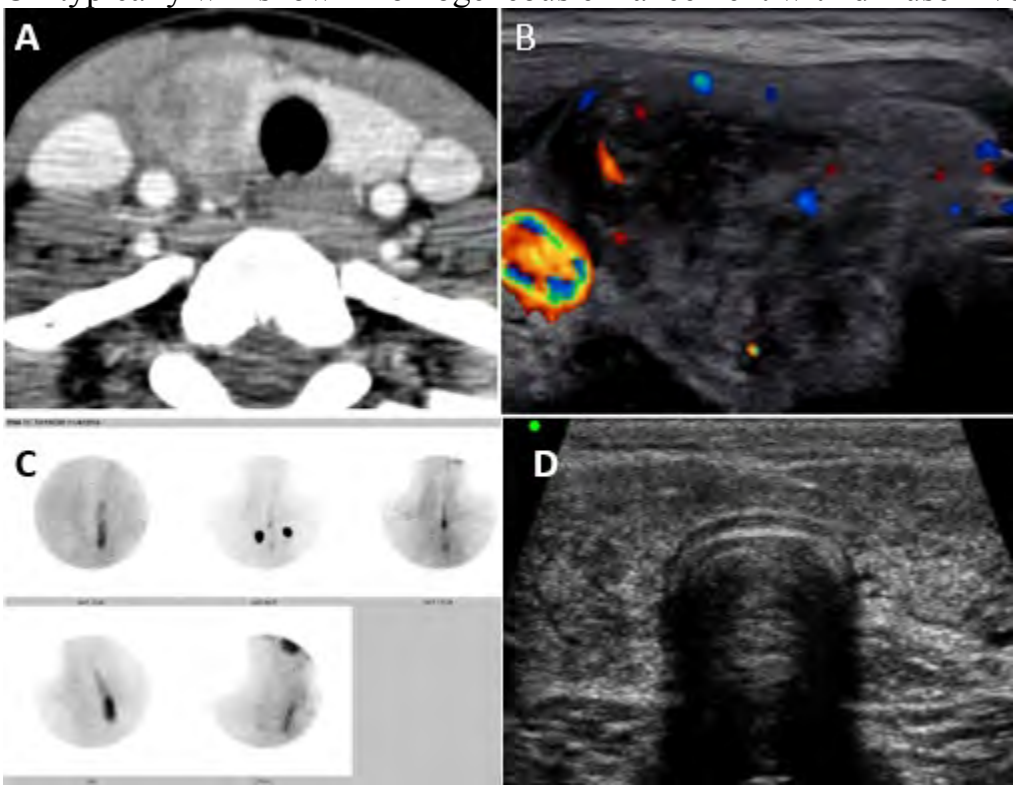
Purpose
Describe an atypical case of postpartum thyroiditis presenting as a unilobar thyroid mass mimicking a primary thyroid neoplasm. Understand the typical clinical presentation of postpartum thyroiditis that can assist in making the appropriate radiographic diagnosis.
Materials and Methods
Five months after giving birth to a stillborn, a 37-year-old female presented to the ED with high grade fever and right neck pain. Lab studies revealed TSH 0.02 and FT4 3.2. Thyroid ultrasound showed a right 3.3 cm complex thyroid nodule. She subsequently was seen in endocrine clinic and diagnosed with thyroiditis.

Results

Contrast-enhanced computed tomography (CECT) at initial presentation (A) demonstrates a heterogeneous hypodense mass involving the entire right lobe of the thyroid without extracapsular extension or other invasive features. There is a normal appearance of the isthmus and left lobe. Sonographic images (B) depict a heterogeneous, hypoechoic mass involving the right lobe without increased vascularity. Planar images from a technicium99M thyroid scan (C) 1 month later demonstrates no tracer activity within the thyroid. Ultrasound obtained (D) 6 weeks after initial presentation demonstrates resolution of mass effect within the right lobe, and persistent heterogenous hypoechoic echotexture, now involving both lobes.

Conclusions

This case of postpartum thyroiditis is unique in that it initially presented as a unilobar mass indistinguishable from neoplasm on CT and US. Postpartum thyroiditis is believed to be an autoimmune disorder with lymphocytic infiltration of the thyroid. Approximately 5-8% of women experience postpartum thyroiditis. Typical imaging features include gland hypoechogenicity on ultrasound which may be diffuse or multifocal. There is below normal radioiodine uptake and markedly reduced uptake on thyroid scintigraphy. Contrast-enhanced CT typically will show inhomogeneous enhancement with diffuse involvement of both lobes.



(Filename: TCT_E-132_1.jpg)

Thursday
1:30PM - 3:00PM
Long Beach Convention Center, Room 203AB (Upper Level)

25G-Parallel Paper Session: MS: Making a Fair Call – Flair for Flare? But That's Not All!

O-499

1:30PM - 1:38PM

Follow-up of Emergency Department MRI Scans Suggesting New Diagnosis of CNS Demyelination

J Pakpoor[1], D Saylor[2], I Izbudak[1], L Liu[3], E Mowry[4], J Probasco[1], D Yousem[5]
[1]Johns Hopkins University, Baltimore, MD, [2]Johns Hopkins Hospital, Baltimore, MD, [3]Hopkins Hospital, baltimore, MD, [4]The Johns Hopkins Hospital, Multiple Sclerosis Center, Baltimore, MD, [5]Johns Hopkins Medical Institution, Baltimore, MD

Purpose
Hospital emergency departments (EDs) represent one site for first clinical presentation by undiagnosed multiple sclerosis (MS) patients. However, the literature has shown that new MS often goes undiagnosed in the ED, causing unnecessary delays in patient treatment. In 2012, an MRI scanner was introduced into the ED at our institution. This study asked: 1) how concordant is the radiologist differential suggestion and the neurologist-determined subsequent diagnosis for undiagnosed MS patients in the ED, and 2) how does the order in which demyelinating disorders are mentioned in a differential diagnoses list vary with the final diagnosis.
Materials and Methods
In this retrospective study, electronic medical records were reviewed for patients without a prior diagnosis of a demyelinating disorder who had an ED MRI scan between 3/1/2014 and 3/1/2016, and for whom the radiologist reported a possible demyelinating disorder. Details surrounding patient disposition, imaging, final diagnosis and management were determined.
Results
Sixty-one females and 31 males (mean age: 41.2) met inclusion criteria. In 48/92 (52.2%) cases where the radiology report suggested a demyelinating diagnosis based on the ED MRI, the patient also was given such a diagnosis as the final outcome. Where a demyelinating disorder was placed as the only, first, second or third (or greater) differential, the final diagnosis was concordant with demyelination in 84.3% (43/51), 37.% (3/8) 18.2% (2/11) and 0% (0/22) of cases respectively ($p<0.01$).
Conclusions
When a radiologist suggests "demyelinating disease" as the top differential diagnosis on an ED-MRI there is a high concordance rate with that final diagnosis. The ED-MRI can be a useful guide toward an early MS diagnosis for clinicians and can enable an MS diagnosis to be made in the ED. Downstream effects may include reduced admission rates, avoidance of unnecessary use of other invasive MS-confirmatory procedures, and early commencement of disease-modifying therapy.

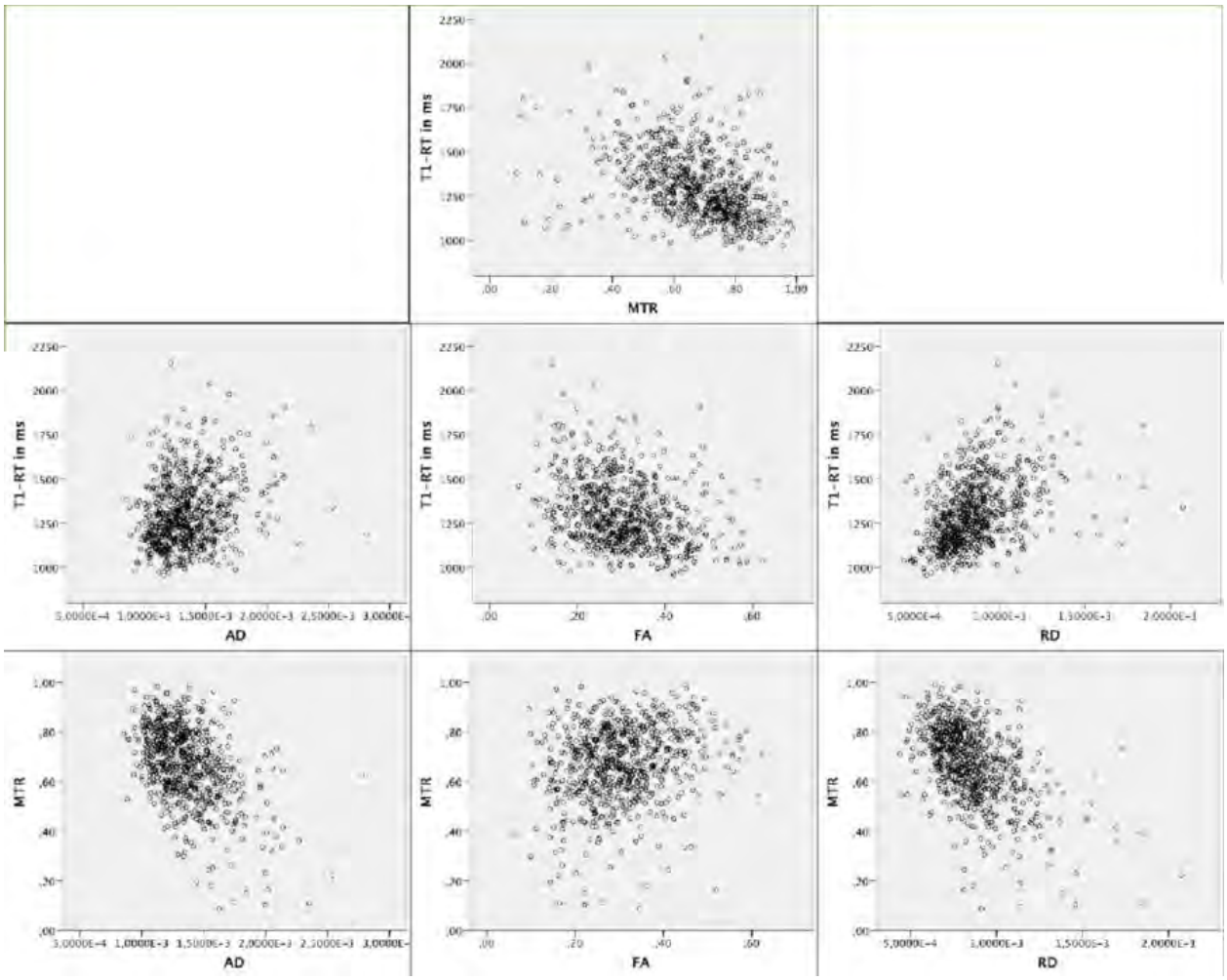
O-500

1:38PM - 1:46PM

Quantitative MRI in Multiple Sclerosis: Assessing Tissue Damage using T1, Magnetization Transfer and Diffusion Tensor Imaging.

C Thaler[1], T Faizy[1], G Broocks[2], J Sedlacik[1], C Heesen[1], J Fiehler[1], S Siemonsen[1]
[1]University Medical Center Hamburg-Eppendorf, Hamburg, Hamburg, [2]University Medical Center Hamburg-Eppendorf, Hamburg, Germany

Purpose
Quantitative magnetic resonance imaging (qMRI) allows deeper insight into histopathological processes in multiple sclerosis (MS) and helps to evaluate disease progression. To evaluate the degree of demyelination and axonal count, different techniques, such as diffusion tensor imaging (DTI), T1 relaxometry and magnetization transfer imaging (MTI), seem to correlate well with histopathological changes in MS lesions. The purpose of this study is to compare parameters generated from the above-mentioned qMRI techniques in different stages of MS lesions.
Materials and Methods
Magnetic resonance imaging (MRI) was performed in 28 MS patients and 12 healthy controls (HC), including double inversion-contrast magnetization-prepared rapid gradient echo (MP2RAGE) sequences, DTI and MTI. Lesion segmentation was performed for T2 hyperintense (FLAIR-L), T1 hypointense (Black Holes = BH), contrast enhancing (CE-L) and pure FLAIR lesions (pureFLAIR-L) and quantitative values [T1 relaxation time (T1-RT), magnetization transfer ratio (MTR), axonal diffusivity (AD), fractional anisotropy (FA), radial diffusivity (RD)] were determined for every single lesion.
Results
Significant differences were found for T1-RT, MTR, FA, MD and RD between the different MS lesion types ($p<0.05$). Highest deviations from HC were found in BH followed by FLAIR-/pureFLAIR-L and CE-L for all parameters except MTR. All lesions included, only low to moderate correlations were obtained for T1-RT and MTR vs. AD/FA/RD, ranging from $r = -0.52$ (MTR vs. RD) to $r = 0.2$ (MTR vs. FA) ($p<0.001$). Correlation coefficient for T1-RT and MTR was 0.4 ($p<0.001$) (see Fig. 1). Figure 1. Distributions of qMRI measures in FLAIR lesions.
Conclusions
Quantitative MRI is a useful tool to characterize MS lesions, as quantitative parameters showed significant differences between MS lesions types, indicating most pronounced tissue damage in Black Holes. However, only low to moderate correlations were obtained among the observed parameters. Though all parameters are thought to reflect tissue damage, axonal count or myelin breakdown, qMRI measures are altered to different degrees by the underlying histopathological processes in MS lesions and interpretation of these parameters needs to be considered carefully.



(Filename: TCT_O-500_qMRI_image_ASNR.jpg)

O-501

1:46PM - 1:54PM

Comparative Study of Linear and Volumetric Brain Atrophy Measures in MS Patients: Preliminary Results of a Cross-sectional and Longitudinal Analysis

S Cappelle[1], D Pareto[1], M Tintoré[2], R Alyafeai[2], M Alberich[1], J Sastre-Garriga[2], C Auger[2], X Montalban[2], À Rovira[1]
[1]Magnetic Resonance Unit, Radiology Department, Vall d'Hebron University Hospital, Barcelona, Spain, [2]Department of Neurology-Neuroimmunology and Cemcat, Vall d'Hebron University Hospital, Barcelona, Spain

Purpose
Linear measures such as corpus callosum index (CCI), corpus callosum area (CCA) and width of the third ventricle (W3V) are potentially robust biomarkers for brain atrophy and therefore could be a good alternative to global brain volumetric measures in clinical practice

for assessing the neurodegenerative component of multiple sclerosis (MS). Our objective is to test this hypothesis by comparing linear and volumetric measurements.
Materials and Methods
Seventy patients with a clinically isolated syndrome (CIS) (group 1), 57 MS patients treated with Interferon β (group 2) and 30 treated with Natalizumab (group 3) underwent a brain MRI (58 on 3T and 99 on 1.5T) at 2 time points (baseline and 1 year). Baseline and follow-up CCI, CCA and W3V were evaluated by 2 observers using Jim v.6.0. Volumetric tools (SIENA/x and FIRST) were used to calculate normalized brain volume (NBV), brain parenchymal fraction (BPF), ventricular volume (VV), percentage of brain volume change (PBVC) and thalamic volume (ThalV). Statistical analyses were performed with SPSS v.13.
Results
Intra-class correlation coefficient analyses showed very good intra-observer reliability for CCI (ICC=0.926) and W3V (ICC=0.947) and good reliability for CCA (ICC=0.898). Corpus callosum index correlations with NBV and BPF were weak in group 1 ($r=0.268$, $r=0.283$ respectively; $p<0.05$), moderate to weak in group 2 ($r=0.451$, $r=0.331$ respectively; $p<0.01$) and strong in group 3 ($r=0.774$ $r=0.768$ respectively; $p<0.01$). W3V showed a strong correlation with VV in group 2 ($r=0.627$, $p<0.05$) and group 3 ($r=0.695$, $p<0.5$) and a moderate correlation with ThalV in group 3 ($r=0.470$). No significant correlations were detected between changes in any of the 3 linear measures and PBVC.
Conclusions
Cross-sectional linear measures are highly reproducible and display differing associations with brain volumetric measures in CIS and MS patients. However, longitudinal changes in linear measurements do not seem to correlate with changes measured with SIENA.

O-502

1:54PM - 2:02PM

Impact of cortical lesion evolution and volume changes on the disease process in high-inflammatory relapsing-remitting multiple sclerosis patients – A 16 months follow-up study

T Faizy[1], G Broocks[2], C Thaler[1], T Ceyrowski[1], J Sedlacik[1], K Stürner[1], C Heesen[1], J Fiehler[1], S Siemonsen[1]
[1]University Medical Center Hamburg-Eppendorf, Hamburg, Hamburg, [2]University Medical Center Hamburg-Eppendorf, Hamburg, Germany

Purpose
In patients with multiple sclerosis (MS), double inversion recovery (DIR) magnetic resonance tomography (MRI) is used for the detection of cortical lesions (CL), which are thought to be partly responsible for disease progression and grade of clinical disability. The aim of this study was to evaluate the evolution of CL volumes over the follow-up period to

investigate an association to therapy effects, its relationship to other imaging and neurocognitive parameters and its relation to the extent of inflammatory activity.
Materials and Methods
Twenty-four relapsing-remitting MS patients (RRMS) were analyzed as part of a phase IIa clinical trial on boswellic acids in a baseline to treatment design. All 24 subjects received 12 MRI examinations during a 16-month longitudinal follow-up period divided into 3 study phases (T1-3). Therapy onset was after the 4th MRI follow up. The CL volume as well as the number of cortical and contrast-enhancing (CE) lesions was captured in each follow up. Moreover, at each time point a comprehensive clinical examination was performed including a battery of neurocognitive assessments.
Results
The median (range) baseline volume of cortical lesions was 134.8 mm3 (7.3-1490.9) and significantly decreased to 65.1 mm3 (0-995.7) after treatment. The number of contrast enhancing lesions was significantly lower after therapy compared to baseline ($p=0.02$). The other imaging parameters did not change significantly. The median number of T2 lesions was 31.5 (3-300) at baseline and increased to 39 (14-108) after therapy. A marginal improvement of clinical and neurocognitive parameters taken from the multiple sclerosis functional composite (MSFC) was detected.
Conclusions
The cortical lesion volume decreased significantly after therapy onset and was related to an improvement in neurocognitive assessments along with a decreased inflammatory activity. We conclude, that CL volume could be a potential imaging biomarker for therapy response and acute inflammation in RRMS.

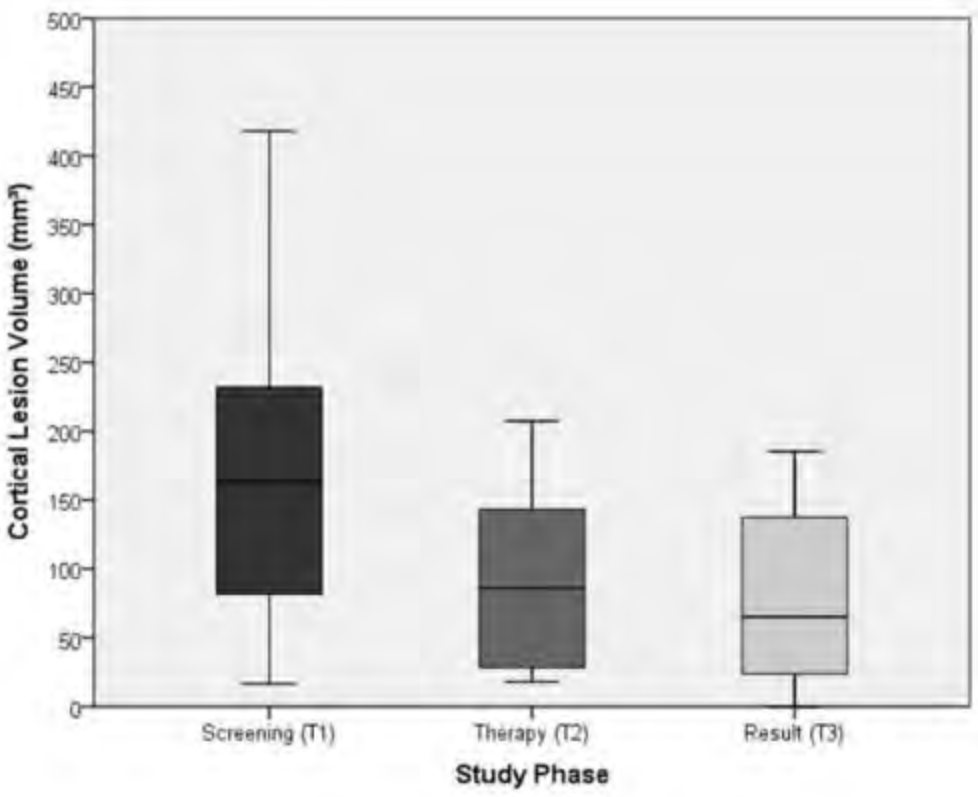
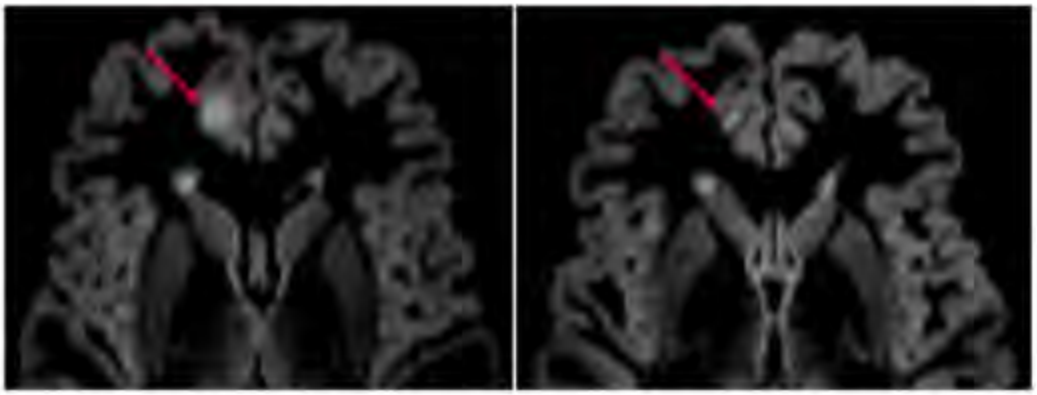


Figure 1: The volume of cortical lesions decreased significantly after therapy onset



pre therapy (T1)

post therapy (T2)

Figure 2:
Cortical lesion in the same patient pre and post therapy showing a significant volume decrease

(Filename: TCT_O-502_figure_abtract_new.jpg)

O-503

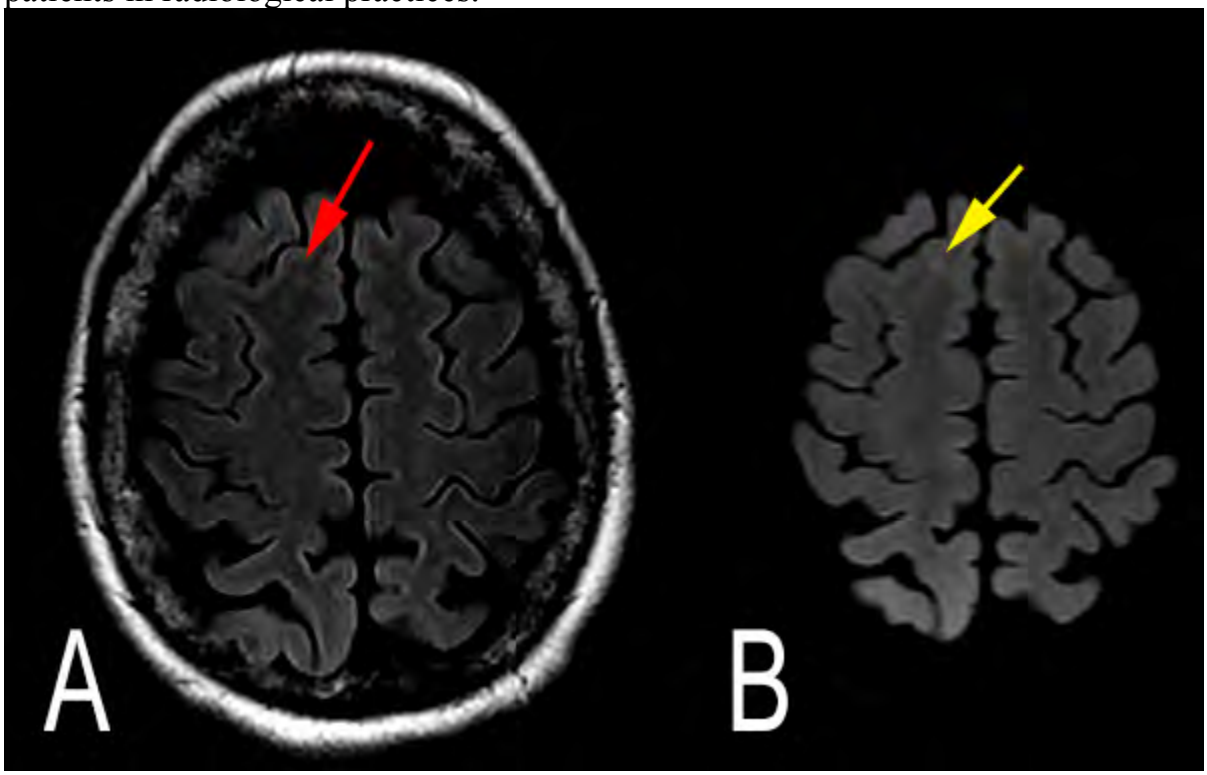
2:02PM - 2:10PM

Comparison of Lesions in Multiple Sclerosis by 2D and 3D FLAIR Sequences

K Wang[1], T Uribe[2], C Lincoln[1]
[1]Baylor College of Medicine, Houston, TX, [2]Baylor College of Medicine, Galveston, TX

Purpose
A substantial proportion of white matter lesions in multiple sclerosis (MS) is not detectable on 2D conventional spin-echo (1). 3D FLAIR has the advantage of increased spatial resolution, higher signal-to-noise ratio (SNR), near isotropic voxels, isotropic multiplanar reconstructions, improved detection of infratentorial lesions, and more accurate co-registration for spatiotemporal comparisons (2). Previous studies have demonstrated increased lesion volume, frequency, and contrast-to-noise ratio (CNR) in MS patients on 3D FLAIR (3-5), but are limited by small sample size. The aim of this study is to present our institutional experience with conventional 2D FLAIR and single-slab 3D FLAIR sequences in the detection of MS lesions in a retrospective study with a large sample size.
Materials and Methods
In response to the MAGNIMS (Magnetic Resonance Imaging in MS) consensus guidelines (2), an institutional protocol with 3D FLAIR was incorporated in November 2015 intended to replace the conventional 2D FLAIR. From November 2015 to April 2016, 333 MRIs of patients with an established diagnosis of MS with both 3D and 2D FLAIR sequences from the same scan were available for review. The images were performed on a 3T scanner with a slice thickness of 5 mm on 2D FLAIR and 3 mm on 3D FLAIR. Two board certified radiologists with certificate of added qualification in neuroradiology each with 7-8 years of experience evaluated and compared all white matter lesions between both sequences. Lesions were counted and classified according to anatomic location: periventricular, juxtacortical, or infratentorial. Contrast-to-noise and SNR were measured by randomly selecting 2 of the same corresponding lesions in both sequences. Statistical comparisons of the number of lesions, CNRs, and SNRs were performed using a paired Student's t test.
Results
A representative case demonstrating differences in conspicuity of a lesion in the same MS patient between 2D and 3D FLAIR sequences is shown in Panel A and B. The right superior frontal gyrus subcortical lesion seen on 2D FLAIR (Panel A) demonstrates better delineation on 3D FLAIR (Panel B). Statistical comparisons are pending upon completion of performing lesion counting, classification, CNR, and SNR measurements.
Conclusions
3D FLAIR is a promising technique with advantages for characterizing MS that are not accessible to 2D FLAIR. Such advantages and release of the MAGNIMS consensus

guidelines will likely lead to an increase in the adoption of 3D sequences imaging in MS patients in radiological practices.



(Filename: TCT_O-503_ASNR-Figure.jpg)

O-504

2:10PM - 2:18PM

Lesion Detection in Multiple Sclerosis- Comparison between Inverse Grayscale Magnetization Prepared Rapid Gradient Echo (MPRAGE), 2D T2 and 2D Fluid Attenuation Inversion Recovery (FLAIR) Sequences

T Eluvathingal Muttikkal[1], F Choudhry[1], S Mukherjee[1], D Ornan[1], T Druzgal[1]
[1]*University of Virginia, Charlottesville, VA*

Purpose
Sensitivity for enhancing lesions is higher for 3D T1 GRE than 2D spin echo T1 (1), but sensitivity for nonenhancing lesions is traditionally highest with 2D T2 and FLAIR, as bright lesions are better recognized than dark lesions. We performed a comparative analysis of T2 and FLAIR sequences versus MPRAGE with inverted grayscale to characterize the lesion conspicuity and explore potential benefit of this approach.
Materials and Methods
Retrospective study of 29 MS patients with lesion burden ≤10 as per institutional review board criteria. Axial T2, FLAIR, and Inverse Grayscale MPRAGE sequences were compared by 3 radiologists. For all lesions, Lesion Index was graded on a 5 point scale (range 0-4).

Combined average lesion index (CALI) for the 3 readers per sequence was calculated for brain stem, cerebellar, periventricular, and subcortical lesions.

Results

Brainstem and cerebellar CALI was highest with MPRAGE followed by T2 and FLAIR. Periventricular and subcortical CALI was highest with FLAIR, followed by T2 and MPRAGE.

Conclusions

Inverse Grayscale MPRAGE shows brain stem lesions better than T2/FLAIR. Although MPRAGE outperformed FLAIR and T2 in cerebellum, limited data points made it inconclusive. FLAIR demonstrated periventricular and subcortical lesions best. Given presence of MPRAGE in our institutional MS protocol, a simple reversal of grayscale improves detection of nonenhancing brain stem lesions. Given concern of gadolinium deposition and many young MS patients, there is potential for excellent noncontrast follow up of all lesions using FLAIR and MPRAGE. Study limitations include the exclusion criteria (>10 lesions), causing fewer posterior fossa lesions. This sets stage for a larger study with more posterior fossa lesions, to substantiate the findings. Postcontrast MPRAGE often is the last sequence performed, often with greater motion artifact than FLAIR/T2. This could have adversely affected the lesion detection by MPRAGE sequence in our study.

Lesion Detection Grading	0	Not seen
	1	Poorly seen
	2	Adequate
	3	Well seen
	4	Excellent

	Location	Lesion No:	FLAIR		T2		Inverse Grayscale MPRAGE	
			Total Score	Average Lesion Index	Total Score	Average Lesion Index	Total Score	Average Lesion Index
Observer 1	Brainstem	16	34	2.13	54	3.38	58	3.63
Observer 2	Brainstem	12	18	1.5	29	2.42	29	2.42
Observer 3	Brainstem	16	25	1.56	39	2.44	40	2.5
CALI				1.73		2.75		2.85
Observer 1	Cerebellum	5	15	3	13	2.6	16	3.2
Observer 2	Cerebellum	2	6	3	6	3	5	2.5
Observer 3	Cerebellum	6	10	1.67	15	2.5	15	2.5
CALI				2.56		2.7		2.73
Observer 1	Periventricular	59	187	3.17	182	3.08	173	2.93
Observer 2	Periventricular	70	196	2.8	192	2.74	191	2.73
Observer 3	Periventricular	79	232	2.94	221	2.8	201	2.54
CALI				2.97		2.87		2.73
Observer 1	Subcortical	40	141	3.53	131	3.28	124	3.1
Observer 2	Subcortical	49	145	2.96	140	2.86	124	2.53
Observer 3	Subcortical	45	142	3.16	111	2.47	88	1.96
CALI				3.22		2.87		2.53

(Filename: TCT_O-504_Results.jpg)

O-506

2:26PM - 2:34PM

Longitudinal Qualitative and Quantitative Evaluation of Pre-contrast MR Diffusion Weighted Imaging in Predicting Multiple Sclerosis Activity and Reducing Potential Risk of Gadolinium Deposition in Patients with Multiple Sclerosis

W Tian[1], X Liu[1], H Wang[2]
[1]University of Rochester Medical Center, Rochester, NY, [2]University of Rochester Medical Cente, Rochester, NY

Purpose
Postcontrast T1-weighted imaging (T1WI) is standard imaging protocol to monitor the activity status of multiple sclerosis (MS). However, recent studies raised the concern of gadolinium deposition in neuronal tissues induced by the repeated follow-up contrast-enhancing examinations in MS patients with normal renal function. Therefore, it is important to establish diagnostic screening algorithm with noninvasive techniques to clarify MS activity status so as to avoid unnecessary injection of MR contrast agents and subsequently reduce potential risk of gadolinium deposition in patients with stable MS lesions. The purpose of our retrospective study is to compare the screening performance between diffusion-weighted imaging (DWI) and apparent diffusion coefficient (ADC) to select optimal patients with possible active MS lesions for further postcontrast T1WI examination.
Materials and Methods
We reviewed sequential MR examinations, including postcontrast T1WI and DWI sequence of 250 MS patients from 2008 to 2014. Compared to the prior examination, the DWI and ADC imaging characteristics of these new MS lesions were evaluated. The sensitivity, specificity, positive predictive value (PPV), and negative predictive value (NPV) were calculated to assess the accuracy of DWI and ADC in predicting MS activity. Chi-Square test was performed to compare between DWI and ADC.
Results
Totally, 120 new MS lesions in 55 patients were enrolled in this study including 111 new enhancing lesions and 9 new nonenhancing lesions. Compared to the baseline, 116 new MS lesions presented as new hyperintensity on DWI image, and 4 new MS lesions presented enlarged hyperintensity. These new lesions showed hyperintensity (70), isointensity (44) and hypointensity (6) on ADC map. The new hyperintensity on DWI is significantly associated with lesion enhancement ($P<0.001$). The sensitivity, specificity, PPV and NPV of new and/or enlarged hyperintensity on DWI to predict MS enhancing status were 96%, and 84%, 93.9% and 89% respectively, which were better prognostic value than ADC. The sensitivity,specificity, PPV and NPV of hyper/hypo-intensity on ADC to predict MS enhancing status were 55%, and 43%, 32.5% and 46% respectively.

Conclusions
Our preliminary study suggests that lesions with new and/or enlarged hyperintensity on DWI indicate active MS lesions for further postcontrast T1WI sequences. This may lead to an updated imaging strategy, which could avoid repeated intravenous exposures to the patients with stable MS lesions.

O-508

2:42PM - 2:50PM

Overlapping Phenotypes between MS and Genetic Leukoencephalopathies: a Systematic MR Analysis

R La Piana[1], P Giacomini[1], B Brais[2], D Tampieri[3]
[1]Montreal Neurological Institute, Montreal, Quebec, [2]Montreal Neurological Institute and Hospital, Montreal, Quebec, [3]Montreal Neurological Hospital and Institute, Montreal, Quebec

Purpose
Multiple sclerosis (MS) is the most common white matter disease in the adult population, while genetic leukoencephalopathies rarely are considered in the differential diagnosis of MS. Advances in neuroimaging techniques have revealed a considerable variety of white matter abnormalities that do not meet the criteria for multiple sclerosis. As a result, undiagnosed leukoencephalopathies have become an emerging field in clinical neurosciences. The aim of this study is to describe new forms of adult-onset hereditary leukoencephalopathies and genetic MS mimickers by clustering overlapping clinical, MRI, and genetic data sets.
Materials and Methods
Patients with undiagnosed white matter disease that did not fit all the criteria for MS were recruited. MR data, clinical information, and DNA were collected. All MR images were reviewed following a systematic approach including qualitative assessment parameters, regional analysis, and quantitative data.
Results
Of the 19 recruited subjects, 16 initially assessed in MS clinics and 3 in a white matter neurogenetics clinic, we were able to cluster them in 3 distinct presentations: 1) Atypical primary progressive MS: Seven patients were interpreted initially as atypical primary progressive MS, but the review of MRI data documented a symmetric involvement of specific white matter structures, suggesting a genetic etiology currently under investigation. 2) MS genetic mimickers: 9 patients presented a suspected genetic condition with MS as part of the differential diagnosis. Seven patients belonging to 3 families had a strong family history supporting the hypothesis of a genetic etiology. A genetic diagnosis was established in 2 subjects; the remaining subjects currently are under investigation. 3) Co-occurrence of

MS and genetic disorders: Three patients presented white matter abnormalities and clinical symptoms compatible with MS in the context of a confirmed neurogenetic diagnosis.
Conclusions
Our study confirmed the overlapping between MS and genetic white matter diseases of various etiologies. The close collaboration between neuroradiologists, MS clinicians and neurogeneticists is critical to correctly refer and adequately diagnose these patients.

O-509

2:50PM - 2:58PM

A Pilot Study of PBR-111; A TSPO Agent in the Cuprizone Mouse Model of MS

V Jewells[1], Z Li[2], H Yuan[2], G Matsushima[2], N Nikolaishvili-Fienberg[2]
[1]University of North Carolina at Chapel Hill, Chapel Hill, NC, [2]University of North Carolina, Chapel Hill, NC

Purpose
PBR-111 is an 18-K translocator protein (TSPO). Increased PBR expression is found with brain injury or neuro-inflammation as microglia are activated in an inflammatory response (1). Microglial activation occurs in multiple sclerosis (MS) as well as the Cuprizone (a copper chelating agent) mouse model of MS. TSPO agents recently have shown potential as an imaging marker in MS (2). This pilot study assessed PRB-111 uptake in Cuprizone mice to ascertain its potential to assess disease expression and individual mouse therapy response.
Materials and Methods
Thirteen mice were fed a diet of Cuprizone with daily chow. They underwent same-day imaging with PET and 7T MRI at 3 and 5 weeks postfeeding to assess 50% and 100% demyelination. A subset of mice were imaged sequentially as well as 4 control mice. Postmortem autoradiography as well as snap frozen cryosectioned brain tissue (using bregma coordinates) pathologic evaluation of microglia/astrocytes using F4/80, CD11b and GFAP staining was performed.
Results
PET imaging revealed significant PRB-111 uptake in Cuprizone-treated mice compared to controls with increased uptake at 5 weeks compared to 3 weeks that correlated with autoradiography. T1 images revealed corpus callosal atrophy. Histologic analysis demonstrated correlative F4/80, CD11b and GFAP findings consistent with microglial and astrocyte upregulation.
Conclusions
PRB-111 can be used as a potential biomarker for study of disease progression and therapy response in the Cuprizone mouse model.

Thursday
1:30PM - 3:00PM

Long Beach Convention Center, Room 102BC (Main Level)

25H-Parallel Paper Session: Avoiding Strikes in Stroke . . . Can We Improve Our Batting Average?

O-510

1:30PM - 1:38PM

Multiparametric CT Perfusion to Determine the Collaterals Status in Patients With Acute Ischemic Stroke: A New Perfusion Index

A Awad[1], B Rigney[1], D Wei[1], T Oxley[2], J Puig[3], J Fifi[4], A Doshi[1], R Deleacy[1], J Bederson[1], J Mocco[1], K Nael[1]

[1]Icahn School of Medicine at Mount Sinai, New York, NY, [2]Mount Sinai Hospital, NY , NY, [3]Research Unit of Diagnostic Imaging Institute (IDI), IDIBGI, University Hospital Dr Josep Trueta, Girona, Girona, [4]Mount Sinai Hospital, New York, NY

Purpose

Good collateral flow is an independent predictor of reperfusion that can be used to extend the treatment window in the new era of endovascular therapies for patients with acute ischemic stroke (AIS). Perfusion time-maps depict delayed perfusion but often are inadequate for evaluation of blood flow dispersion beyond the point of occlusion if used alone. Using a multiparametric approach, we aimed to identify perfusion parameter/s that can represent the extent of collaterals in comparison to CTA.

Materials and Methods

Acute ischemic stroke patients with anterior circulation large vessel occlusion who had baseline CTA and CT perfusion were included. CT perfusion data were processed by Bayesian method to generate arterial tissue delay (ATD) maps at thresholds of 2 and 6 seconds. The volume of mild delayed perfusion (Vol-ATD>2sec), moderate delayed (Vol-ATD 2-6sec) and critical delayed perfusion (Vol-ATD>6sec) in addition to corresponding rCBV and rCBF were calculated. Baseline CTA collaterals were scored using an established scoring scale (1) and dichotomized to poor or good. The association of perfusion parameters and status of collaterals was assessed by repeated measure of analyses and receiver operating characteristic (ROC) to determine the optimal parameters for predicting the status of collaterals.

Results

In 28 patients included, 16 had good collaterals on CTA. After controlling for age, sex, baseline NIHSS and type of treatment, multivariate logistic regression analysis identified rCBV ($p<0.001$) and ATD 2-6sec ($p=0.003$), but not rCBF, Vol-ATD 2sec or Vol-ATD >6sec, as independent predictors of good collaterals. Receiver operating characteristic analysis showed AUC of 0.88 (sensitivity/specificity: 75%/100%) for rCBV and AUC of 0.84 (sensitivity/specificity: 93%/67%) for Vol-ATD 2-6sec. We defined a perfusion collateral index (PCI) calculated from Vol-ATD 2-6sec x its rCBV, that remained an

independent predictor of good collaterals with improved diagnostic accuracy over each measure alone resulting in nominal (not validated) AUC of 1 (sensitivity/specificity: 100%/100%).
Conclusions
Perfusion collateral index (PCI) defined as Vol-ATD 2-6sec x rCBV is a new perfusion index with a nominal diagnostic accuracy of 100% compared to baseline CTA to predict status of collaterals in our small cohort. Our results need to be validated in a larger prospective cohort.

O-512

1:46PM - 1:54PM

Time To Peak in the Evaluation of Patients with Minor Stroke and Distal Vessel Occlusion

G Romero-Sanchez[1], R La Piana[2], M Cortes[3], D Tampieri[4]
[1]Montreal Neurological Institute and Hospital, Montreal, QC, [2]Montreal Neurological Institute, Montreal, Quebec, [3]McGill University, montreal, Quebec, [4]Montreal Neurological Hospital and Institute, Montreal, Quebec

Purpose
Whole brain CT perfusion is the most accessible imaging technique in our Institution to assess acute stroke cases and determine optimal patient-management strategies. A consensus on the definition of minor stroke is lacking, therefore many patients with low National Institutes of Health Stroke Scale scores are treated based on arbitrary criteria. The aim of this study was to evaluate the time to peak maps characteristics in patients with minor stroke and distal vessel occlusion.
Materials and Methods
We included patients with ongoing symptoms of minor stroke (NIHSS equal or less than 6) who were evaluated with noncontrast CT, CT angiography, and whole brain CT perfusion within 4 hours of symptoms onset between May and November 2016. Patients with posterior circulation strokes, TIA, intracerebral hemorrhage and those who received TPA were excluded. The imaging characteristics and clinical data were analyzed.
Results
Ten patients with minor stroke met the criteria. Mean age at presentation was 71.7 years, and 70% were men. No early ischemic changes were found in the noncontrast CT. The CT angiography did not document major intracranial or extracranial vessel occlusion. All patients had whole brain CT perfusion abnormalities and all presented abnormal time to peak. Concomitant abnormal cerebral blood flow and cerebral blood volume were documented in 4 patients.
Conclusions
Our results suggest that the time to peak map is a very useful technique in the detection of

minor stroke. A prompt diagnosis in this group of patients is crucial in order to allow the best treatment decision and avoid poor outcomes.

O-513

1:54PM - 2:02PM

ASPECTS Reporting: Standardizing CT brain Stroke Protocol Evaluation to Better Patient Triage, Enhance Final Outcomes and Promote Research.

K Jobanputra[1], A Simonetta[1], R Riascos[1], C Sitton[1]
[1]*The University of Texas Health Science Center at Houston, Houston, TX*

Purpose
Noncontrast CT of the brain remains the mainstay of imaging in suspected stroke patients and sometimes is the only imaging option available. Early CT performance and evaluation with subsequent appropriate treatment has remained central philosophy geared to improved patient outcomes. The Alberta Stroke Program Early CT score described in the year 2000 is a robust reproducible semiquantitative grading system that has demonstrated predictive power in long term patient outcomes in the setting of medical therapy and intra-arterial thrombolysis. As a level I Stroke Center, we felt that including the score in the standard radiology report would facilitate acute stroke care by providing stroke neurologists with an important metric that they would otherwise generate on their own. A secondary benefit would be the prospective scoring of each exam, eliminating the need for retrospective scoring in multi-center trials and other research investigations. In this quality initiative project we discuss our departmental performance with regards to ASPECTS reporting before and after appropriate intervention.
Materials and Methods
A retrospective analysis of the CT brain exams including 'brain stroke without contrast CT' and 'brain/neck stroke perfusion CTA' for the month of June was performed. Utilization rates of ASPECTS scoring in resident preliminary and finalized reports were noted. A formal in-service lecture describing the scoring system, showing examples, and explaining the importance of the system in triage was delivered to the neuroradiology staff, and in a separate meeting, to the radiology residents. Use of the scoring system was made section policy. A second postintervention data set was obtained for the month of September.
Results
Of the 235 stroke protocol studies performed in July 2016,131 patients underwent CT brain at presentation as 'brain stroke without contrast CT'. ASPECTS score was reported in only 6 (4.58%) After the educational intervention, done in the month of August 2016, evaluation of the September data-set showed 211 stroke protocol studies performed on 143 patients, 47 of which had primary stroke. The ASPECTS reporting had significantly increased with 41 (41.8%) studies receiving ASPECTS scores. We noted significant differences in rates of

ASPECTS reporting between exams designated as "Brain stroke w/o contrast" and CTs performed for stroke without that designation.

Conclusions

The quality initiative project for ASPECTS reporting of the CT brain stroke protocol showed significant improvement in the number of studies including ASPECTS scores in the final report (tenfold increase): this in a limited time frame with basic educational intervention. Based on our initial data, the next level of planned interventions include adding the ASPECTS score to the standard CT voice dictation template of all users and better identification of acute strokes within the PACs system.

	No of stroke protocols	CT brain stroke	Stroke Perfusion/ CTA	No of patients	No of patients with stroke	ASPECTS reported
June	235	131	104	157	60	6 (4.58%)
September	211	98	113	143	47	41(41.8%)

Table 1. Results of evaluations of datasets of June and September months.

(Filename: TCT_O-513_Table1.jpg)

O-514

2:02PM - 2:10PM

Diffusion- and Perfusion-Weighted Imaging Alone May be Sufficient to Triage Acute Ischemic Stroke Patients for Endovascular Therapy

D Wolman[1], G Zaharchuk[1], M Wintermark[1], H Do[1], M Marks[1], J Heit[1]
[1]*Stanford University, Stanford, CA*

Purpose
Expeditious triage of acute ischemic stroke (AIS) patients to endovascular therapy requires rapid neuroimaging. Endovascular candidates optimally have: (i) a small core infarction, (ii) salvageable penumbra, (iii) large vessel occlusion (LVO), and (iv) absence of cerebral hemorrhage (1). Magnetic resonance imaging (MRI) is the gold standard in the assessment of cerebral ischemia, and rapid protocols typically include diffusion- (DWI) and perfusion-weighted imaging (PWI), MR angiography (MRA), and gradient-echo (GRE) sequences to assess these 4 characteristics (2). A detailed understanding of vascular anatomy may allow inference of the presence of a LVO from PWI data alone (3). We determined the accuracy of LVO identification and localization and endovascular candidacy using only DWI and PWI.
Materials and Methods
We performed a retrospective cohort study of 225 patients with suspected AIS who underwent MRI evaluation with DWI, GRE, MRA, and PWI; 74 of these patients underwent endovascular stroke therapy. Anonymized DWI and PWI images were blindly reviewed by 3 experienced neuroradiologists. Patients were scored for the presence of acute infarction, LVO and location (ICA/M1, M2, and vertebrobasilar), DWI-PWI mismatch, contraindications to treatment (cerebral hemorrhage, matched DWI-PWI, or core infarct volume >70 mL), and whether the patient should undergo endovascular treatment. Imaging scores were compared to final MRI and endovascular procedure reports. Comparisons were analyzed using a one-tailed chi-squared test ($\alpha = 0.05$). Inter-reader agreement was assessed using Fleiss' kappa test.
Results
Relative to the reference data and with high inter-reader agreement, readers accurately identified the presence of acute infarction ($\kappa = 0.938$; $P = 0.519$), LVO ($\kappa = 0.965$; $P = 0.744$), and a DWI-PWI mismatch ($\kappa = 0.907$; $P = 0.624$). Readers accurately localized vessel occlusions to the ICA/M1 (89%; $\kappa = 0.927$; $P = 0.182$) or M2 (85%; $\kappa = 0.735$; $P = 0.305$) segments. Localization to the posterior circulation was less accurate (75%; $\kappa = 0.907$; $P = 0.317$) but the number of patients was low ($n = 8$). Readers correctly and concordantly triaged 74/76 (97%) patients to endovascular stroke therapy ($\kappa = 0.931$; $P = 0.746$) and correctly excluded 147/149 patients (99%; $\kappa = 0.798$; $P = 0.768$). Thus, DWI and PWI have a sensitivity of 97.3% and a specificity of 98.7% for accurate endovascular triage. The 2 patients incorrectly excluded from endovascular treatment had cervical carotid stenoses and fluctuating neurologic symptoms, but readers were blinded to clinical data.
Conclusions
Patients with acute ischemic stroke due to a LVO are identified accurately on DWI and PWI alone, and the information provided by MRA may be inferred correctly from PWI. Omission of MRA may be considered to expedite AIS imaging and treatment.

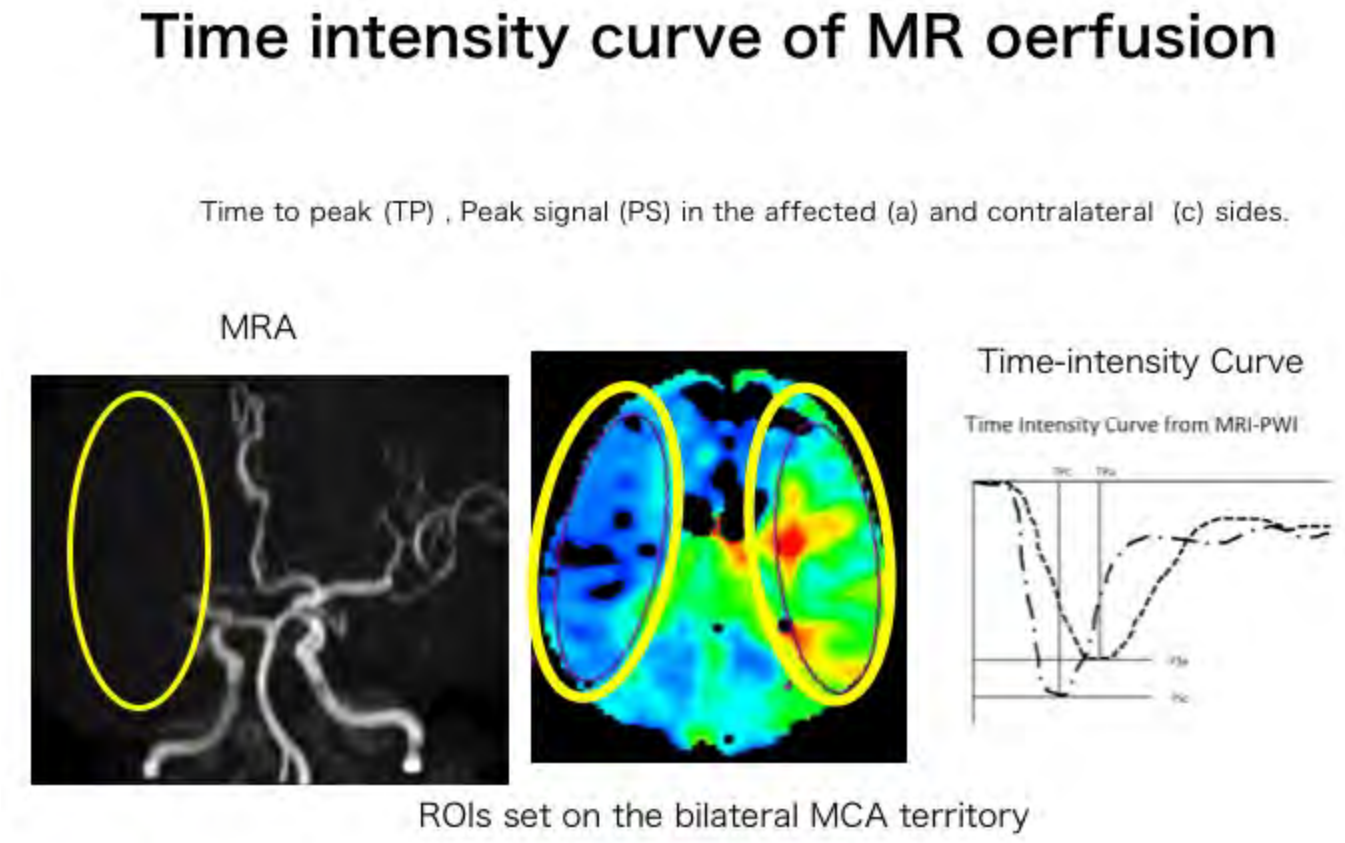
O-515

2:10PM - 2:18PM

MR Perfusion To Identify Candidates More Suitable To Endovascular Reperfusion Therapy Than Intravenous Thrombolysis in Middle Cerebral Artery Occlusion

T Mori[1]
[1]*Shonan Kamakura General Hospital Stroke Center, Kamakura, Japan*

Purpose
To investigate if standard application of MR perfusion (MRP) can identify candidates more suitable to endovascular therapy than tPA alone.
Materials and Methods
We included in our retrospective study patients: 1) who were admitted between 2005 and 2015 within 3.5 hours of onset, 2) who had MCA occlusion on MR angiograms (MRA) or MRP, 3) who had NIHSS score of 5 or more, 4) who had DWI-ASPECTS of 6 or more, 5) CBF grades of 2 or 3 and 6) who underwent intravenous tPA alone. We defined proximal M1 occlusion within less than 5 mm as MCA grade 1, distal M1 occlusion as grade 2, and M2 occlusion as grade 3 and no occlusion on MRA as grade 4. We generated time-intensity curves (TICs) by using standard MRP application at symmetrical positions of the bilateral MCA territories. According to time to peak (TTP) and peak signal (PS) comparing affected side (a) with contralateral side (c), we defined affected-sided PSa divided by TPa as CBFa, and contralateral-sided PSc divided by TPc as CBFc, and CBFa divided by CBFc (CBF%) less than 0.2 as CBF grade 1, CBF% of 0.2 or more and CBF% less than 0.7 as grade 2 and CBF% of 0.7 or more as grade 3. We excluded CBF grade 1 and evaluated relationship between MCA grades, CBF grades and favorable clinical outcome of mRS 0-2 at 3 months.
Results
Thirty-four patients matched our criteria. Their median ASPECTS was 9, NIHSS was 12. There were 9 patients in MCA grade 1, 9 in MCA grade 2, 15 in MCA grade 3 and 1 in MCA grade 4. There were 23 patients in CBF grade 2 and 11 in CBF grade 3. Only 2 patients (22%) obtained favorable clinical outcome in MCA grade 1. In MCA grade 2, 4 (57%) of 7 patients in CBF grade 2 obtained favorable clinical outcome and 2 (100%) of 2 in CBF grade 3 obtained favorable clinical outcome. In MCA grade 3, 6 (67%) of 9 in CBF grade 2 obtained favorable clinical outcome and 5 (83%) of 6 in CBF grade 3 obtained favorable clinical outcome. One patient in MCA grade 4 obtained favorable clinical outcome.
Conclusions
After tPA alone in patients with inclusive criteria, endovascular therapy is required in patients with MCA grade 1, probably with MCA grade 2 and CBF grade 2, possibly with MCA grade 3 and CBF grade 2.



(Filename: TCT_O-515_TIC.jpg)

O-516

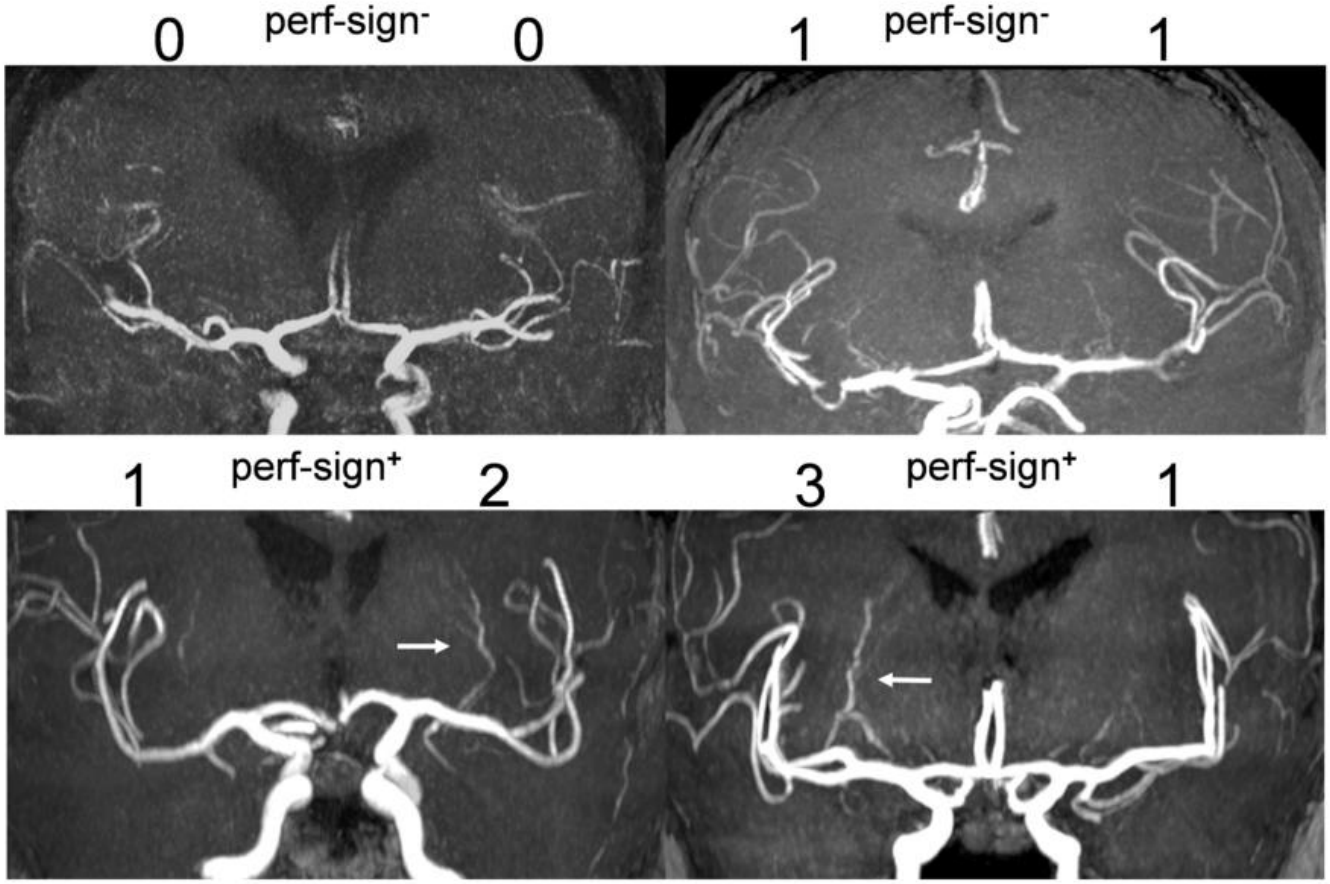
2:18PM - 2:26PM

Perforator Dilatation after Thrombectomy of Proximal MCA Occlusions: A Novel Sign to Improve Outcome Prediction

J Kaesmacher[1], K Kreiser[1], B Wiestler[1], T Boeckh-Behrens[1]
[1]*Klinikum rechts der Isar, Technical University Munich, Munich, Germany*

Purpose
Post-ischemic vasodynamic changes in infarcted brain parenchyma are common and range from hypo- to hyperperfusion (1-3). In the present study, an easy to assess imaging finding on post-interventional 3T TOF-MRA suggestive for post-stroke altered vasodynamics following thrombectomy was investigated.
Materials and Methods
Patients with ET of proximal MCA occlusions and available post-interventional 3T time-of-flight (TOF) MRA (range: 3 to 15 days postintervention) were included (n=98). Perforator

status was categorized into presence (perf-sign+) or absence (perf-sign-) of vasodilatation of the ischemic side with subsequent lenticulostriate artery asymmetry. Short- (discharge) and mid-term (day 90) functional outcome was determined using the modified Rankin scale (mRS). Early neurologic improvement was defined as either (I) difference between admission NIHSS and NIHSS at discharge ≥8 (ΔNIHSS ≥8), or (II) NIHSS at discharge ≤1.
Results
Perf-sign+ was observed in 77.5% of the patients (n=69). Atrial fibrillation tended to be associated with perf-sign- (adjusted OR 0.420, 95%-CI0.147-1.206, p=0.107). In multivariate logistic regression perf-sign+ was associated with early neurologic improvement (adjusted OR 10.189, 95%-CI: 2.691-38.571, p=0.001) and good functional short- and mid-term outcome (mRS ≤2, adjusted OR 14.198, 95%-CI: 2.978-67.999, p=0.001 and adjusted OR 10.817, 95%-CI 2.412-48.513, p=0.002, respectively) after correcting for age, admission NIHSS, reperfusion grade, symptom-onset to treatment time and infarct volume. For all endpoints, model fit improved when including the perf-sign term ($p<0.05$).
Conclusions
Occurrence of perf-sign+ suggests relatively long-lasting vasodilatative changes of the lenticulostriate arteries within the infarcted striatocapsular region, potentially suggestive of more active adaption and regeneration or enhanced vessel tone responsiveness to stress. Evaluation of the perf-sign may enhance patients' outcome prediction. Pathophysiological interpretation and clinical significance of this imaging sign should be determined in future prospective cohorts.



(Filename: TCT_O-516_Fig1.jpg)

O-517

2:26PM - 2:34PM

A Review of Recent Evidence in Thrombectomy for Ischemic Stroke

A Qureshi[1], G Fatania[2], T Booth[3]
[1]King's College Hospital NHS Foundation Trust, London, London, London, [2]Imperial College Healthcare NHS Trust, London, London, London, [3]King's College Hospital NHS Foundation Trust, London, London, London

Purpose
Immediate treatment of ischemic stroke aims to restore perfusion to the ischemic brain. Until recently, standard care was thrombolysis using tissue plasminogen activator. This results in approximately 44% recanalization of distal middle cerebral arteries (MCA), however the results for larger proximal vessels are poorer with approximately 10% for the internal carotid artery (ICA) and 29% for proximal middle cerebral arteries. This is a limiting factor of this treatment method as over a third of anterior circulation infarcts are due to proximal large vessel occlusions. Since 2015 there has been mounting class Ia evidence that thrombectomy

may yield superior outcomes, especially in large vessel occlusion. There is a need to review this evidence to better inform clinical practice.

Materials and Methods

All randomized control trials (RCTs) or meta-analyses of RCTs comparing thrombectomy to standard care in the acute management of ischemic stroke since 2015 were reviewed.

Results

The HERMES meta-analysis (1) of 2016 compared 5 RCTs (MR CLEAN, ESCAPE, EXTEND_IA, SWIFT PRIME and REVASCAT). In total 1287 patients were included (634 receiving thrombectomy and 653 receiving standard care alone). All of the trials included ICA/M1 occlusion and 2 included M2 occlusions. The mean time from symptom onset to groin puncture was 196 mins. There was an odds ratio of 2.49 (95% CI 1.76-3.53, $p<0.0001$) for reduction in MRS and a 20% difference in achieving functional independence (MRS 0-2). The THRACE trial (2) included 385 patients (190 receiving thrombectomy and 195 receiving standard care alone). ICA/M1 occlusions were included. The mean time from symptom onset to groin puncture was 250 mins. There was an odds ratio of 1.55 (95% CI 1.05-2.3) for reduction in MRS and an 11% difference in achieving functional independence (MRS 0-2). The PISTE trial (3) included 65. ICA/M1/M2 occlusions were included. The mean time from symptom onset to groin puncture was 202 mins. There was an odds ratio of 2.12 (95% CI 0.65-6.94) for reduction in MRS and whilst the difference in independence (MRS 0-2) did not reach statistical significance, there was a 20% difference in patients achieving an MRS of 0-1. The THERAPY trial (4) included 105 patients. ICA/M1/M2 occlusions were included. The mean time from symptom onset to groin puncture was 227 mins. There was an odds ratio of 2.2 (95% CI 1.0-5.0) for reduction in MRS in per-protocol analysis, but an insignificant difference in intention-to-treat analysis. There was a 12% difference in achieving functional independence in per-protocol analysis, which was not statistically significant. No significant difference was seen in the rates of adverse effects (including mortality and intracerebral hemorrhage) in any of the trials.

Conclusions

There is a growing body of class Ia evidence that thrombectomy is superior to standard care alone in large vessel occlusion. Clinical outcomes measured using the MRS show a clear benefit in these trials. The strongest evidence is for large vessel occlusions (ICA/M1) however there is insufficient data for smaller vessel occlusion (M2). The evidence provided by these trials should influence clinical practice and for those patients meeting similar criteria to the trial patients, thrombectomy should be used increasingly. It should be noted that in the majority of the trials, thrombectomy was used in addition to current standard care and therefore this should be continued, using thrombectomy as a therapeutic adjunct in those with large vessel occlusion. Further data are required to analyze whether these results are reproducible outside of a trial setting, especially in regards to time to treatment.

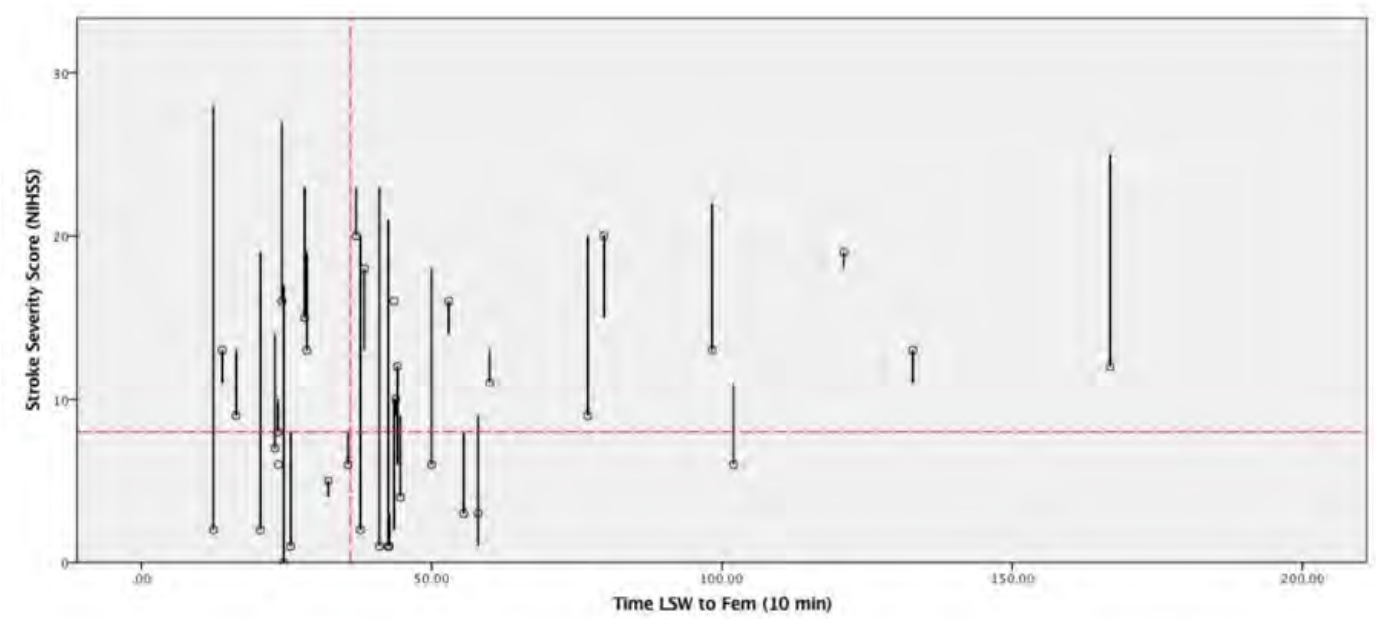
O-518

2:34PM - 2:42PM

Response to Mechanical Thrombectomy Among Late MR Selected LVO Candidates

B Cristiano[1], U Oyoyo[2], P Kim[3], M Pond[1], J Lee[1], K Cicilioni[1], J Jacobson[1]
[1]Loma Linda University Hospital, Loma Linda, CA, [2]Loma Linda University, Loma Linda, CA, [3]Loma Linda University Medical Center, Loma Linda, CA

Purpose
While the benefit of thrombectomy for acute large vessel occlusion (LVO) stroke in the first hours following symptom onset is certain there is a paucity of data regarding the treatment of patients with favorable brain imaging at extended timeponts. Here we present 90 day outcomes data for such a population in an effort to shed light on this important knowledge gap.
Materials and Methods
Logistic regression analysis of 50 LVO patients treated with thrombectomy after MRI selection with femoral access up to 28 hours from LSW and 90 day mRS≤2 the primary outcome. Covariates of age, time LSW to femoral access (tLSW), admission and 24 hour stroke severity scores were studied. Early response to therapy as determined by ≥ 5 point improvement in stroke severity score and symptomatic intracranial hemorrhage (SICH) were assessed as a secondary outcomes.
Results
The mean age and standard deviation was 65.7 (13.7), admission NIHSS 14.3 (6.38), time LSW to femoral access 503.6 min (358.6), ED arrival to femoral access 189.4 min (82.2), and presentation DWI volume 25.0 mL (31.2). Time LSW to femoral access ranged from 870 – 1669 min and admission NIHSS ranged from 3 – 28. TICI≥2B recanalization was achieved in 40/50 (80.0) of cases, and 5/50 (10.0) had SICH (defined as PH2, PH1, or HI2) on 24 hr NECT. 90d mRS was available for 39 patients with 11 achieving mRS≤2 (28.2), 6/13 with tLSW ≤ 6 hr and 5/21 with tLSW > 6 hr (p = 0.131). All patients with 90d mRS≤2 also had TICI≥2B recanalization (p = 0.040). Although the proportion of good outcomes was similar among patients presenting early and late, a weak correlation with time and 90d mRS≤2 was observed, (Spearman Rho = -0.322, p = 0.046). In a multivariate logistic regression model time accounted for a lesser proportion of the variance in outcome (b = -0.093 p =0.017) than age and admission NIHSS (b =-1.27, p = 0.024 and -0.15, 0.067 respectively), which were the dominant predictors of outcome. Time LSW did not correlate significantly with early response to therapy or SICH, and many late presenting patients demonstrated early response to therapy despite advanced tLSW (Fig.).
Conclusions
Among this cohort of MRI selected LVO patients, many treated at extended tLSW, time was a weak predictor of 90d mRS after thrombectomy, not as important as age or stroke severity. Many patients showed good response to thrombectomy despite advanced time suggesting that a late MRI selected population may benefit from intervention.



Figure, Early Response to Therapy. Response to therapy among patients with TICI≥2B recanalization (N=40) as determined by difference in admission and 24 hour NIHSSS is depicted. Bar indicates diference, open circle indicates 24 hour NIHSS. Vertical reference line indicates time LSW to femoral access = 6 hr, horizontal reference line indicates NIHSS = 8.

(Filename: TCT_O-518_Figure.jpg)

O-520

2:50PM - 2:58PM

Image Processing to Improve Conspicuity and Constrast-to-noise Ratio of Infracting Gray Matter

T Madaelil[1], A Sharma[2], M Goyal[3], M Miller-Thomas[4]
[1]Mallinckrodt Institute of Radiology, St Louis, MO, [2]Mallinckrodt Institue of Radiology, Saint Louis, MO, [3]Washington University in St. Louis, Saint Louis, MO, [4]Mallinckrodt Institute of Radiology, St. Louis, MO

Purpose
Using quantitative measures of conspicuity and contrast-to-noise ratio (CNR), we aimed to test whether an image-processing algorithm could facilitate recognition of acute cerebral infarction on head CT.
Materials and Methods
Thirty-five baseline head CT images across the level of cerebral infarction proven on subsequent reference standard imaging were processed using a custom algorithm (Correlative Image Enhancement, CIE) to generate corresponding enhanced images. Using reference standard images as a guide for placement of regions of interest, intensities of both abnormal and normal gray matter were measured and used to calculate infarct conspicuity

and CNR. In addition, 3 masked radiologists individually viewed these images to detect presence of infarction. Correlation was sought between baseline conspicuity/CNR measurements and frequency of infarct detection amongst 3 radiologists. We compared infarct conspicuity, CNR, and frequency of successful infarct detection on baseline and enhanced images.

Results

Baseline CNR and conspicuity of abnormal gray matter were 1.2 ± 1.1 and 12.3 ± 11.4 respectively. Spearman correlation test revealed that both baseline CNR (r = 0.40818; p=0.014) and baseline conspicuity (r=0.47276; p=0.004) correlated positively with the number of readers successfully detecting the infarction. All 3 readers failed to identify infarct in 21/35 (60%) baseline images. Numbers of infarcts detected by 1, 2, and all 3 readers were 6/35 (17.1%), 1(2.9%), and 7(20%) respectively. CIE resulted in a statistically significant increase in CNR to 1.84 ± 1.47 (p=0.04) and conspicuity to 23.5 ± 13.3 (p=0.001). There was corresponding shift towards successful infarct detection by higher number of readers. Infarction was successful detection on enhanced images by none, 1, 2 and all 3 readers in 16 (45.7%), 4 (11.4%), 7 (20%), and 8 (22.8%) cases.

Conclusions

CIE resulted in increased CNR and conspicuity of infracting gray matter, making the image more conducive for infarct detection.